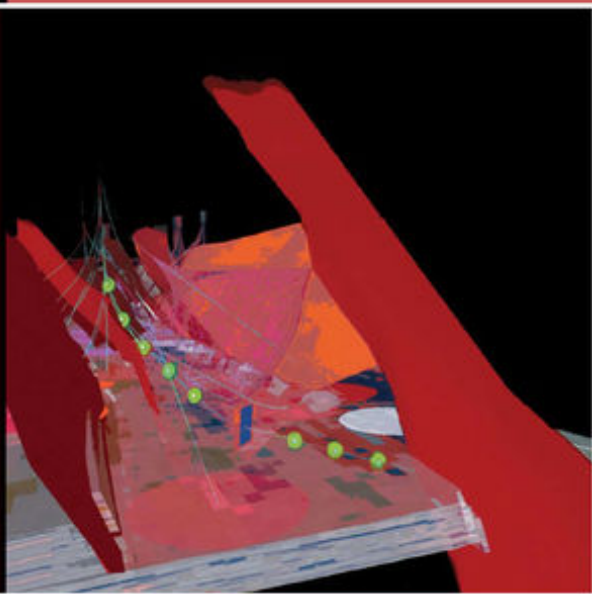


Volume **V**

RESERVOIR ENGINEERING and PETROPHYSICS

Edward D. Holstein, Editor

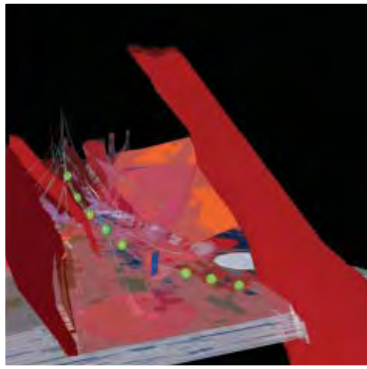


PETROLEUM ENGINEERING HANDBOOK

Larry W. Lake, Editor-in-Chief








SOCIETY OF PETROLEUM ENGINEERS





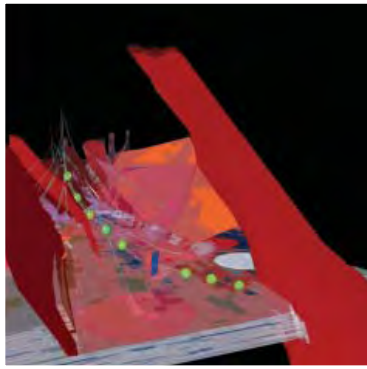
Welcome to the *Petroleum Engineering Handbook*

How to use the *Handbook*:

-  Use to navigate forward and backward through the *Handbook*.
-  Press at any point to be taken back to the Contents page.
-  Perform a word or phrase search of the entire *Handbook*.
-  Press to launch the print dialog box.
-  View an extended list of chapter and section bookmarks.
-  View the Adobe® Reader® help file.
-  Press to exit out of the *Handbook*.

Use the tool bar at the bottom of the screen to jump to a specific page.

Volume **V**
**RESERVOIR
ENGINEERING
and PETROPHYSICS**
Edward D. Holstein, Editor



**PETROLEUM
ENGINEERING
HANDBOOK**

Larry W. Lake, Editor-in-Chief

Petroleum Engineering Handbook

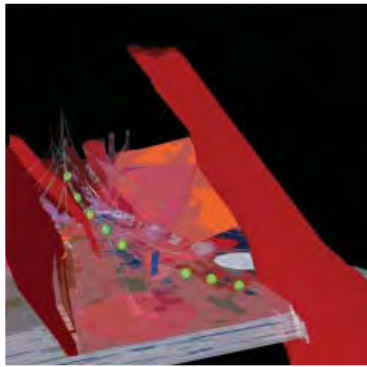
Larry W. Lake, Editor-in-Chief

- I General Engineering** *John R. Fanchi, Editor*
- II Drilling Engineering** *Robert F. Mitchell, Editor*
- III Facilities and Construction Engineering** *Kenneth E. Arnold, Editor*
- IV Production Operations Engineering** *Joe Dunn Clegg, Editor*
- V Reservoir Engineering and Petrophysics** *Edward D. Holstein, Editor*
- VI Emerging and Peripheral Technologies** *H.R. Warner Jr., Editor*
- VII Indexes and Standards**



SOCIETY OF PETROLEUM ENGINEERS

Volume **V**
**RESERVOIR
ENGINEERING
and PETROPHYSICS**
Edward D. Holstein, Editor



**PETROLEUM
ENGINEERING
HANDBOOK**

Larry W. Lake, Editor-in-Chief

Petroleum Engineering Handbook

Larry W. Lake, Editor-in-Chief
U. of Texas at Austin

Volume V

Reservoir Engineering and Petrophysics

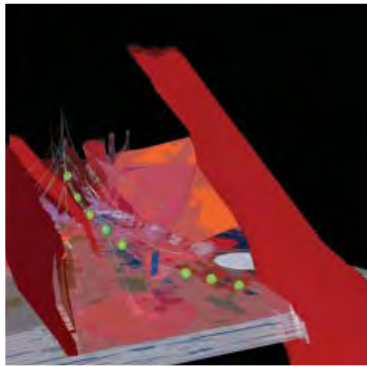
Edward D. Holstein, Editor
Consultant

Society of Petroleum Engineers



SOCIETY OF PETROLEUM ENGINEERS

Volume **V**
**RESERVOIR
ENGINEERING
and PETROPHYSICS**
Edward D. Holstein, Editor



**PETROLEUM
ENGINEERING
HANDBOOK**

Larry W. Lake, Editor-in-Chief

© Copyright 2007 Society of Petroleum Engineers

All rights reserved. No portion of this publication may be reproduced in any form or by any means, including electronic storage and retrieval systems, except by explicit, prior written permission of the publisher except for brief passages excerpted for review and critical purposes.

Manufactured in the United States of America.

ISBN 978-1-55563-120-8 (print)

ISBN 978-1-55563-121-5 (CD)

ISBN 978-1-55563-132-1 (print and CD)

ISBN 978-1-55563-126-0 (Complete 7-Vol. Set, print)

ISBN 978-1-55563-127-7 (Complete 7-Vol. Set, CD)

ISBN 978-1-55563-135-2 (Complete 7-Vol. Set, print and CD)

07 08 09 10 11 12 13 14 / 9 8 7 6 5 4 3 2 1

Society of Petroleum Engineers
222 Palisades Creek Drive
Richardson, TX 75080-2040 USA

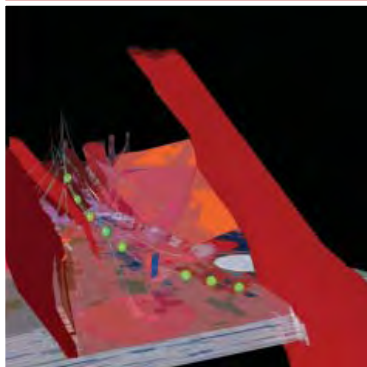
<http://store.spe.org/>
service@spe.org
1.972.952.9393



SOCIETY OF PETROLEUM ENGINEERS

Volume **V**
**RESERVOIR
ENGINEERING
and PETROPHYSICS**

Edward D. Holstein, Editor



**PETROLEUM
ENGINEERING
HANDBOOK**

Larry W. Lake, Editor-in-Chief

Foreword

This 2006 version of SPE's *Petroleum Engineering Handbook* is the result of several years of effort by technical editors, copy editors, and authors. It is designed as a handbook rather than a basic text. As such, it will be of most benefit to those with some experience in the industry who require additional information and guidance in areas outside their areas of expertise. Authors for each of the more than 100 chapters were chosen carefully for their experience and expertise. The resulting product of their efforts represents the best current thinking on the various technical subjects covered in the *Handbook*.

The rate of growth in hydrocarbon extraction technology is continuing at the high level experienced in the last decades of the 20th century. As a result, any static compilation, such as this *Handbook*, will contain certain information that is out of date at the time of publication. However, many of the concepts and approaches presented will continue to be applicable in your studies, and, by documenting the technology in this way, it provides new professionals an insight into the many factors to be considered in assessing various aspects of a vibrant and dynamic industry.

The *Handbook* is a continuation of SPE's primary mission of technology transfer. Its direct descendents are the "Frick" *Handbook*, published in 1952, and the "Bradley" *Handbook*, published in 1987. This version is different from the previous in the following ways:

- It has multiple volumes in six different technical areas with more than 100 chapters.
- There is expanded coverage in several areas such as health, safety, and environment.
- It contains entirely new coverage on Drilling Engineering and Emerging and Peripheral Technologies.
- Electronic versions are available in addition to the standard bound volumes.

This *Handbook* has been a monumental undertaking that is the result of many people's efforts. I am pleased to single out the contributions of the six volume editors:

General Engineering—John R. Fanchi, Colorado School of Mines

Drilling Engineering—Robert F. Mitchell, Landmark Graphics Corp.

Facilities and Construction Engineering—Kenneth E. Arnold, AMEC Paragon

Production Operations Engineering—Joe D. Clegg, Shell Oil Co., retired

Reservoir Engineering and Petrophysics—Ed Holstein, Exxon Production Co., retired

Emerging and Peripheral Technologies—Hal R. Warner, Arco Oil and Gas, retired

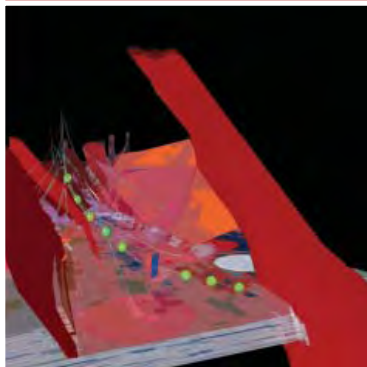
It is to these individuals, along with the authors, the copy editors, and the SPE staff, that accolades for this effort belong. It has been my pleasure to work with and learn from them.

—Larry W. Lake



Volume **V**
**RESERVOIR
ENGINEERING
and PETROPHYSICS**

Edward D. Holstein, Editor



**PETROLEUM
ENGINEERING
HANDBOOK**

Larry W. Lake, Editor-in-Chief

Preface

This volume consists of 27 chapters that deal with the many aspects of reservoir engineering. The chapters were assembled to provide information on acquiring and interpreting data that describe reservoir rock and fluid properties; acquiring, understanding, and predicting fluid flow in the reservoir; interpreting measurements of well performance; calculating the factors that impact both primary and improved recovery mechanisms from oil and gas reservoirs; estimating reserves and calculating project economics; simulating reservoir performance; and structuring and measuring the effectiveness of a reservoir management system.

These chapters have been written as a handbook and, as such, assume that the reader has a familiarity with fundamentals and some experience in the production of hydrocarbons and will use this publication as a refresher or to expand knowledge in certain areas of technology. Extensive references in each chapter indicate the amount of material that has been considered and distilled.

This updated version of SPE's *Petroleum Engineering Handbook* contains information on many of the subjects covered by the 1962 and 1987 versions. All chapters in this version are new and greatly expanded; chapters existing in the older versions have been revised extensively or rewritten completely, and new chapters have been added on geophysics; geology; petrophysics; production logs; chemical tracers; foam, polymer, and resin injection; miscible processes; valuation; and reservoir management.

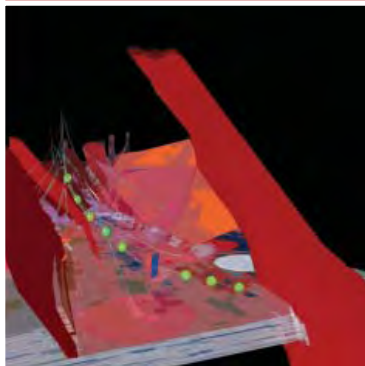
The high quality of this volume is a credit to the authors of each chapter; they were chosen for their extensive knowledge and experience. Special recognition and thanks go to E.C. Thomas, who is responsible for the quality and thoroughness of the chapters contained in the petrophysical section. The resulting product contains many good tips and guidelines that represent lessons learned in the practice of applying various technologies to a wide range of actual field conditions. Numerous field examples have been included to illustrate these applications.

—Edward D. Holstein



Volume **V**
**RESERVOIR
ENGINEERING
and PETROPHYSICS**

Edward D. Holstein, Editor



**PETROLEUM
ENGINEERING
HANDBOOK**

Larry W. Lake, Editor-in-Chief

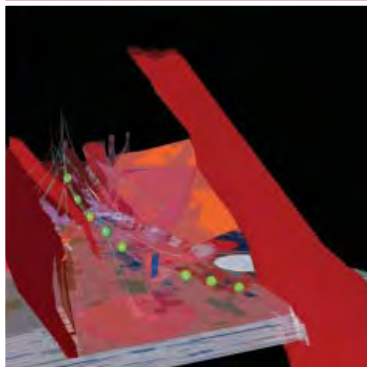
Contents

- 1 Reservoir Geology** - [click to view](#)
F. Jerry Lucia
- 2 Fundamentals of Geophysics** - [click to view](#)
Bob A. Hardage
- 3A Petrophysics** - [click to view](#)
E.C. Thomas
- 3B Resistivity and SP Logging** - [click to view](#)
T.D. Barber, A. Brie, and B.I. Anderson
- 3C Acoustic Logging** - [click to view](#)
Doug Patterson and Stephen Premsky
- 3D Nuclear Logging** - [click to view](#)
Gary D. Myers
- 3E Nuclear Magnetic Resonance Applications in Petrophysics and Formation Evaluation** - [click to view](#)
Stephen Premsky and Jack Howard
- 3F Mud Logging** - [click to view](#)
Dennis E. Dria
- 3G Specialized Well-Logging Topics** - [click to view](#)
Paul F. Worthington
- 3H Petrophysical Applications** - [click to view](#)
H.R. Warner Jr. and Richard Woodhouse
- 4 Production Logging** - [click to view](#)
R.M. McKinley and Norman Carlson
- 5 The Single-Well Chemical Tracer Test—A Method for Measuring Reservoir Fluid Saturations In Situ**
Harry Deans and Charles Carlisle - [click to view](#)
- 6 Well-To-Well Tracer Tests** - [click to view](#)
Øyvind Dugstad
- 7 Reservoir Pressure and Temperature** - [click to view](#)
David Harrison and Yves Chauvel
- 8 Fluid Flow Through Permeable Media** - [click to view](#)
John Lee
- 9 Oil Reservoir Primary Drive Mechanisms** - [click to view](#)
Mark P. Walsh
- 10 Gas Reservoirs** - [click to view](#)
Mark A. Miller and E.D. Holstein
- 11 Waterflooding** - [click to view](#)
H.R. Warner Jr.
- 12 Immiscible Gas Injection in Oil Reservoirs** - [click to view](#)
H.R. Warner Jr. and E.D. Holstein
- 13 Polymers, Gels, Foams, and Resins** - [click to view](#)
Robert D. Sydansk



Volume **V**
**RESERVOIR
ENGINEERING
and PETROPHYSICS**

Edward D. Holstein, Editor



**PETROLEUM
ENGINEERING
HANDBOOK**

Larry W. Lake, Editor-in-Chief

Contents

- 14 Miscible Processes** - [click to view](#)
E.D. Holstein and Fred I. Stalkup
- 15 Thermal Recovery by Steam Injection** - [click to view](#)
Jeff Jones
- 16 In-Situ Combustion** - [click to view](#)
William E. Brigham and Louis Castanier
- 17 Reservoir Simulation** - [click to view](#)
*Rod P. Batycky, Marco R. Thiele, K.H. Coats,
Alan Grindheim, Dave Ponting, John E. Killough,
Tony Settari, L. Kent Thomas, John Wallis,
J.W. Watts, and Curtis H. Whitson*
- 18 Estimation of Primary Reserves of Crude Oil,
Natural Gas, and Condensate** - [click to view](#)
Ron Harrell and Chap Cronquist
- 19 Valuation of Oil and Gas Reserves** - [click to view](#)
D.R. Long
- 20 Reservoir Management Programs** - [click to view](#)
E.D. Holstein and E.G. Woods
- Author Index** - [click to view](#)
- Subject Index** - [click to view](#)



Chapter 1

Reservoir Geology

F. Jerry Lucia, SPE, U. of Texas at Austin

1.1 Introduction

The efficient extraction of oil and gas requires that the reservoir be visualized in 3D space. Engineers need a conceptual model of reservoirs, an integral part of the decision-making process, whether it be selecting perforations or forecasting future production. However, most engineering measurements made on reservoirs have little or no spatial information. For example, a core measurement has no dimensional information, wireline logs and continuous core measurements are 1D, and production data and pressure information are volumetric but with unconstrained spatial information. Geologic information, on the other hand, contains valuable spatial information that can be used to visualize the reservoir in 3D space. Therefore, engineers should understand the geologic data that can improve their conceptual model of the reservoir and, thus, their engineering decisions.

The first and most important geologic information is the external geometry of the reservoir, which is defined by seals or flow barriers that inhibit the migration of hydrocarbons, forming a hydrocarbon trap. The buoyancy force produced by the difference in density between water and hydrocarbons drives migration. Migration will cease, and a hydrocarbon reservoir will form, only where hydrocarbons encounter a trap. Traps are composed of top, lateral, and bottom seals; the geometry of traps can have structural, sedimentary, or diagenetic origins.

The second most important geologic information is the internal reservoir architecture. A reservoir is composed of rock types of varying reservoir quality that are systematically stacked, according to stratigraphic and diagenetic principles. The lateral distribution of depositional textures is related to depositional environments, and the vertical stacking of textures is described by stratigraphy, which is the geological study of the form, arrangement, geographic distribution, chronologic succession, classification, and correlation of rock strata. Diagenesis, changes that happen to the sediment after deposition, can also control the lateral continuity and vertical stacking of reservoir rock types. This fact is most important in carbonate reservoirs, in which the conversion of limestone to dolostone and the dissolution of carbonate have a large effect on internal reservoir architecture.

The most basic concern for most engineers is the spatial distribution of petrophysical properties, such as porosity, permeability, water saturation, and relative permeability. To visualize the reservoir in petrophysical terms, the engineer must be able to equate measurements (log, core, or production) with geologic models because the measurements themselves do not contain

spatial information. Linking engineering measurements with geologic descriptions is best done at the rock-fabric level because rock fabric controls pore-size distribution, which, in turn, controls porosity, permeability, and capillary properties. Rock fabrics can be tied directly to stratigraphic models and, thus, to 3D space.

1.2 External Geometry—Reservoir Traps

1.2.1 Introduction. Hydrocarbons are formed by anaerobic decomposition of organic matter that accumulates from the deposition of plankton in deep ocean basins. Oil and gas are generated as the sediments are buried and the temperature rises. Oil is the first hydrocarbon to be generated, followed by wet gas, and lastly by dry gas. Once generated, oil and gas flow vertically and laterally through overlying sediments because of the density difference between hydrocarbons and formation water and they migrate through permeable formations until they encounter a reservoir trap in which oil and gas accumulate. Oil will fill the traps first because it is first to be generated. Higher temperatures resulting from continued burial cause gas to be generated. Migrating gas will displace oil from the traps because gas has a lower density. The displaced oil will migrate further updip and fill any trap encountered.¹

Traps filled with hydrocarbons are often referred to as pools. However, engineers normally use the term reservoir instead of pool for an oil and gas accumulation, and *reservoir* will be used throughout this chapter. A field is composed of one or more reservoirs in a single area. A trap is defined by the geometry of its seals, which are formations with very low permeability and very small pores that will impede or stop the flow of hydrocarbons. To trap migrating hydrocarbons, seals must contain flow in 3D: the seals must form a closure. In the simplest terms, a trap is similar to a box with its bottom removed. The box is the seal composed of top and lateral seals. A trap may also contain a bottom seal. Imagine a smaller box inserted into the base of the original box. The smaller box is also a seal and confines the reservoir to a layer within the larger box.

Seals may be in the form of impermeable lithologies or faults. The simplest traps are convex structures in which the sealing layer dips in all directions from a central structural high, forming domes or doubly dipping anticlines. More complex structural traps are formed when convex structures are truncated by faults or when faulting occurs around a piercement structure. Many traps are combinations of structural uplift, faulting, and stratigraphy, such as an updip pinchout of a sand body into an impermeable shale. A purely stratigraphic trap may form when deposition creates a topographic high that is encased by impermeable lithology, such as shale or salt.

The volume of oil and gas that can accumulate is defined partly by the height of the trap because any additional hydrocarbons will spill out the bottom. The base of the trap is therefore called the spill point (see [Fig. 1.1](#)). The trap may not be full because the height of the oil column will be controlled by the capacity of the seal to impede flow and the volume of oil that migrates to the trap. In addition, oil/water contacts need not be horizontal because subsurface fluids are rarely static, and the flow can cause the oil/water contact to tilt in the direction of flow.

1.2.2 Traps. Geologists commonly describe traps on the basis of their origin. Structural traps are closures formed by structural movements within the Earth, and stratigraphic traps are closures formed by sedimentation and diagenesis, without the need for structural movements. Structural/stratigraphic traps are closures formed by patterns of reservoir rock that impinge upon a structure. This organization will be used hereafter, even though new groupings based on sealing surfaces were suggested by Milton and Bertram.²

Structural traps are formed most commonly by structural uplift and differential compaction. Typical structural traps are structural domes and doubly plunging anticlines (see [Fig. 1.1](#)).

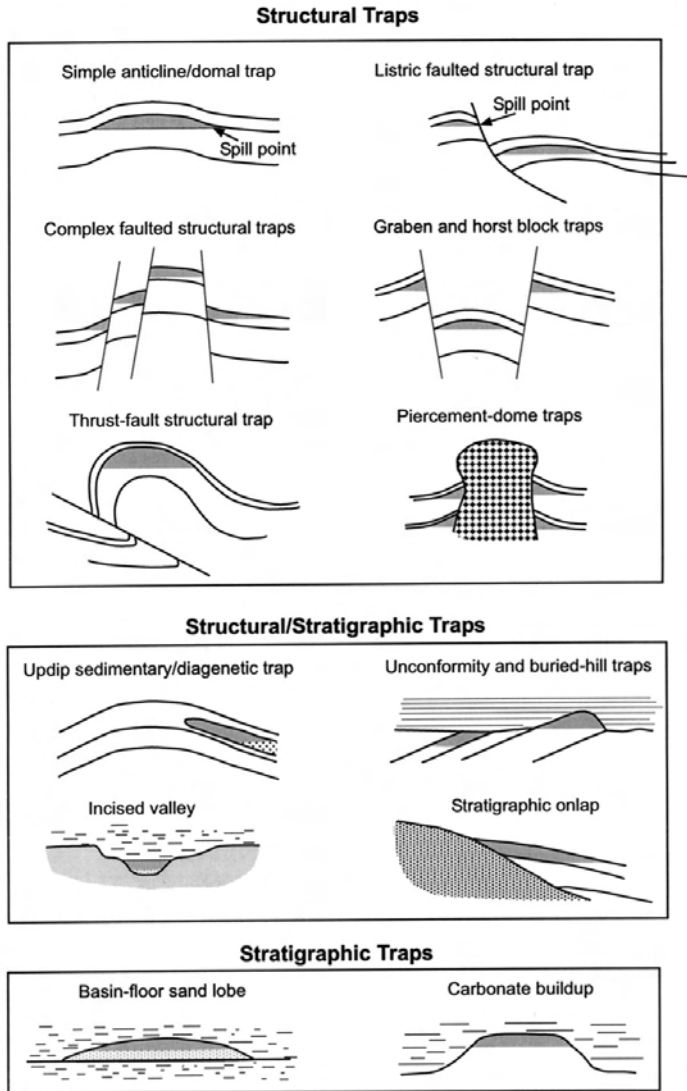


Fig. 1.1—Diagram description of hydrocarbon traps.

These traps have a structural high and quaquaversal dips (the seal dips away from a structural high in all directions). The bulk of the world’s oil is found in these four-way-closure traps,³ which were the first type to be exploited by surface mapping. Many major oil fields in the world were discovered by using surface mapping to locate domal structures.

A more complex method of forming a structural trap is by faulting and structural uplift (see Fig. 1.1). Faulted structures can vary from a simple faulted anticline to complex faulting around piercement structures and domal uplifts. Faulted structures are very common and form some of the most complex reservoirs known. Types of faults include normal, listric, reverse, and thrust, which are related to the stress fields generated during structural movement. Piercement traps (diapirs) are formed typically by salt moving up through a stack of sediment driven by the density difference between salt and quartz or carbonate. Closure is achieved by the uplift of sediments juxtaposed to the piercement dome, by the top seal being an overlying impervious bed and the lateral seals being formed by structural dip, by sealing faults, or by the

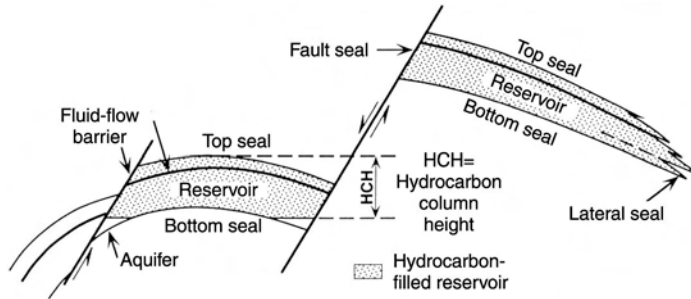


Fig. 1.2—Some typical seals; HCH is the hydrocarbon-column height that the weakest seal will hold. Figure courtesy of Sneider Exploration Inc.

piercement salt. Faulted reservoirs commonly have a bottom seal formed by the lower contact of sand with shale. The bottom seal, along with the oil/water contact within the sand body, forms the base of the reservoir.

Structural/stratigraphic traps are formed by a combination of structure, deposition, and diagenesis. The most common form, the updip pinchout of reservoir lithology into a sealing lithology (see Fig. 1.1), is found in the flanks of structures. The top and updip seal is normally an impervious rock type, and the lateral seals are formed by either structural dip or the lateral pinchout of reservoir rock into seal material. The base of the reservoir is defined by a bottom seal composed of impervious rock and by an oil/water contact. During relative sea-level fall, streams may erode deep valleys, thus forming lateral seals for fluvial sediments. Onlap of sand onto a paleotopographic high during relative sea-level rise can produce an updip seal for a sand body. Unconformity traps are formed by the truncation of dipping strata by overlying bedded sealing lithology. The reservoir rock may be found in the form of buried hills formed by erosion during the time of the unconformity. The oil/water contact forms the base of these reservoirs. A stratigraphic trap may be partly related to diagenetic processes; for example, the updip seal for the supergiant Coalinga field, California, is tar- and asphalt-filled sandstone and conglomerate. Many traps in the Permian reservoirs of west Texas, are formed by lateral changes related to stratigraphy from porous to dense dolomite in an updip direction.

Stratigraphic traps are formed by depositional processes that produce paleotopographic highs encased in impermeable material, such as evaporite or shale (Fig. 1.1). Closure occurs when there is contact between seal material and underlying sediment. The most common type is a carbonate buildup, usually erroneously called a “reef.” Piles of sand deposited on the seafloor by density currents often form broad topographic highs that, in turn, form stratigraphic traps. Structure may also play a part in the geometry of stratigraphic traps, although the defining characteristic is that structure is not required to form the trap.

1.2.3 Seals. A seal is a low-permeable to impermeable rock or immobile fluid, such as tar, with a capillary entry pressure large enough to dam up or trap hydrocarbons.⁴ Typical seals include top, bottom, lateral, and fault, as shown in Fig. 1.2. Faults may be sealing or nonsealing, depending on whether the sand offsets another sand (nonsealing) or shale (sealing).⁵ Any lithology can be a seal or flow barrier. The requirement is that the minimum capillary displacement pressure of the seal or flow-barrier material be greater than the buoyancy pressure of the hydrocarbons in the accumulation. The continuous, small, pore-throat sizes create a barrier to moving hydrocarbons, causing them to dam up or become trapped. Therefore, the size of the continuous pore throats and the density of the hydrocarbons and water are critical elements in evaluating a seal or flow barrier.

Porosity and permeability are not the best criteria for evaluating seal and flow-barrier behavior. The seal capacity of a rock can be best evaluated with a mercury porosimeter that can inject mercury into material using pressures as high as 60,000 psi. The key equation used in capillary pressure/saturation evaluation of reservoir rocks, seals, and flow barriers is:

$$h_c = \left(\frac{p_c}{\rho_w - \rho_{hc}} \right) 0.433 \text{ ft}, \dots\dots\dots (1.1)$$

in which h_c = the maximum hydrocarbon column held, p_c = the capillary entry pressure, ρ_w = the density of water, and ρ_{hc} = the density of the hydrocarbon. The capillary pressure used is usually not the capillary entry pressure but the capillary pressure at a mercury saturation of between 5 and 10% because of closure effects.

Effective hydrocarbon seals for exploration plays and reservoirs must be laterally continuous. Some typical seal lithologies, illustrated in **Fig. 1.3**, have entry pressures ranging from 14 to 20,000 psi. With data from more than 3,000 seals, we can group the data into Classes A through E to categorize the typical lithologies listed in **Fig. 1.3** from most to least ductile. **Fig. 1.3** also illustrates the hydrocarbon column that can be held, assuming that the fluid is 35°API oil and saline water. Evaporite and kerogen-rich shale can hold the greatest oil column—from 1,000 to more than 5,000 ft. Clay-mineral-rich shale, silty shales, and dense mudstones can hold between 500 and 1,000 ft of oil column. Sandy shales are ranked next, with a 100- to 500-ft capacity, whereas very shaly siltstone and sandstone, anhydrite-filled dolostones, and cemented sandstone each have between 50 and 100 ft of capacity. In addition, immobile fluids, such as tar, bitumen, and asphalt, can be effective seals and barriers. For example, the updip seal for the supergiant Coalinga field, California, is tar- and asphalt-filled sandstone and conglomerate.

1.3 Reservoir Base

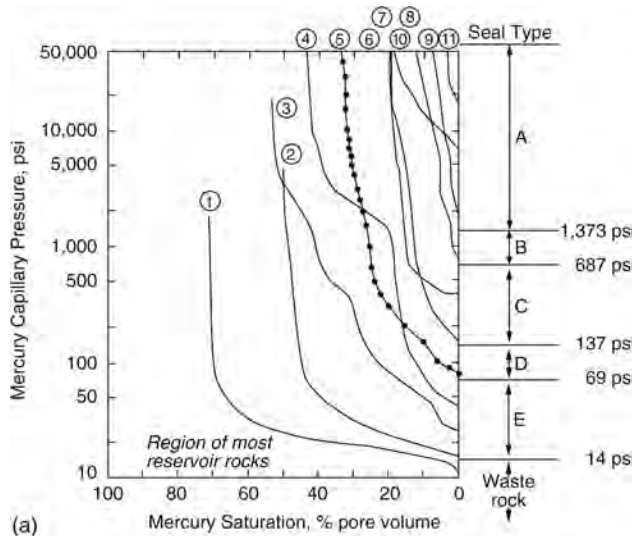
Whereas structure and stratigraphy most often define the reservoir trap or top of the reservoir, factors controlling the base of a petroleum reservoir include seal capacity, spill point, capillary forces, and hydrodynamics.^{6,7} The reservoir base is defined as the zero capillary pressure level, also referred to as the free-water level. Reservoir height is determined by the height from seal to spill point, if seal capacity is large enough. If the height is less than that from seal to spill point, seal capacity or hydrocarbon charge will determine the position of the reservoir base.

Subsurface groundwater is seldom static. Differences in water density, structural tilting, tectonic forces, and other factors combine to create a difference in hydrodynamic potentials that result in the movement of fluids in the subsurface. Fluid movement is controlled by the fluid potential as defined by Hubbert⁶ and illustrated by the following formula⁸:

$$H = Z + \frac{P}{\rho_w g}, \dots\dots\dots (1.2)$$

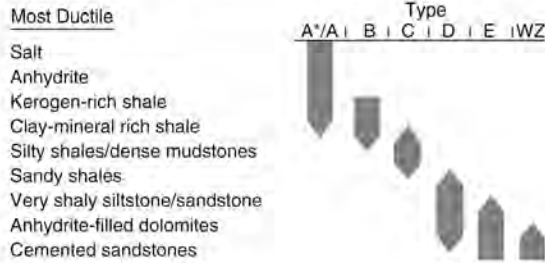
in which Z = elevation relative to a datum (sea level), P = measured static pressure, and ρ = density of the fluid (water).

A potentiometric map is a map that connects points of equal fluid potential within an aquifer. If the potentiometric surface is not horizontal, the aquifer will flow in the direction of lowest potential. Calculating fluid potential requires accurate subsurface pressure measurements in the aquifer. The flow of water under a reservoir will cause the zero-capillary-pressure level to tilt, referred to as a tilted water table. The degree of tilt can be estimated from the following equation.



(a)

Some Typical Seal/Flow Barrier Lithologies and Types



(b)

Seal - Flow Barrier Type	35° API Oil Column Held	
	Meters	Feet
A*	≥ 1500	≥ 5,000
A	≥ 300 to < 1,500	≥ 1,000 to < 5,000
B	≥ 150 to < 300	≥ 500 to < 1,000
C	≥ 30 to < 150	≥ 100 to < 500
D	≥ 15 to < 30	≥ 50 to < 100
E	< 15	< 50
F	Waste Zones Rocks	

(c)

Fig. 1.3—(a) Air/mercury capillary pressure curves of seal lithologies. The ordinate is a log scale. (b) Typical seal lithologies. (c) Sneider *et al.*³ classification of seals and flow barriers. The hydrocarbon column that can be held assumes that the fluids in the reservoirs are 35°API oil and saline water. Types are keyed to Figs. 3a and 3b. Figure courtesy of Sneider Exploration Inc.

$$\tan \theta = \frac{\Delta Z}{x} = \left(\frac{\rho_w}{\rho_w - \rho_o} \right) \frac{dh}{dx}, \dots\dots\dots (1.3)$$

in which $\frac{\Delta Z}{x}$ = change in reservoir height for distance x (tilt in water table), ρ_w = density of water in aquifer, ρ_o = density of hydrocarbon, and $\frac{dh}{dx}$ = change in potentiometric surface for distance x .

During primary development, the economic base of the reservoir is normally defined as the producing oil/water contact, or the level at which oil and water are first coproduced. This level is generally assumed to be at approximately 50% water saturation, according to relative permeability considerations. During tertiary development, the economic base of the reservoir may be defined as the level of zero oil saturation. However, because pore size can vary with stratigraphy, 50 or 100% water saturation may not occur at the same height throughout the reservoir. The economic base of the reservoir will not be horizontal.

Defining the base of a reservoir is often made difficult by the presence of residual-oil and tar zones below the producing oil/water contact. Residual-oil and tar zones can be as thick as 300 ft and are thought to form by a variety of processes, including biodegradation of hydrocarbons, flushing of part of the oil column as a result of hydrodynamic forces, and remigrating of hydrocarbons because of leaky seals and structural tilting. The presence of this material may indicate that the reservoir is in an imbibition rather than a drainage mode. Estimates of the original oil in place will depend on which capillary pressure model is assumed. An incorrect model can lead to large errors in estimates of the original oil in place.

1.4 Internal Geometry—Reservoir Architecture

1.4.1 Introduction. Information that defines the external reservoir geometry, including trap configuration, seal capacity, and the base of the reservoir, is of primary importance during exploration and initial development of a reservoir. As development continues, reservoir architecture becomes key to predicting the distribution of reservoir quality so that primary- and secondary-development programs can be planned. Reservoir architecture is important because it provides a basis for distributing petrophysical properties in 3D space. In most cases, this operation is done by relating lithofacies to petrophysical properties because lithofacies can be directly linked to depositional processes for prediction.

We commonly correlate lithofacies from one well to the next by assuming a degree of horizontality and continuity of similar facies. This approach leads to images with highly continuous lithofacies and porosity zones. Many depositional facies, however, are known to be highly discontinuous laterally and vertically, and correlating similar lithofacies from one well to the next can lead to unrealistic displays of reservoir architecture. Modern correlation methods rely more on the chronostratigraphic approach, one that uses time stratigraphy rather than lithostratigraphy to determine continuity between wells. This approach is referred to as sequence stratigraphy and provides a basis for correlating time surfaces between which lithofacies are distributed systematically in a predictable pattern.

1.4.2 Sequence Stratigraphy. Sequence stratigraphy is a chronostratigraphic method of correlation. It groups lithofacies into time-stratigraphic units between chronostratigraphic surfaces, which are sometimes defined by unconformities and facies shifts. A key premise is that the surfaces are formed in response to eustatic sea-level changes of various scales and periodicity (eustatic refers to worldwide sea-level changes affecting all oceans). It is thought that eustatic sea-level changes can be linked to climatic changes and to eccentricities in the Earth's orbit. The Russian astronomer Milanovitch defined cyclic variation in the shape of the Earth's orbit and in the tilt and wobble of the axis. These Earth cycles are precession (19,000 to 23,000 years), obliquity (41,000 years), and eccentricity (1,000,000 to 4,000,000 years) and are thought to cause changes in the Earth's climate, resulting in more or less water trapped as ice at the poles. The trapping or release of water from the ice caps is thought to result in sea-level rise and fall, referred to as eustasy.

Sequence stratigraphy is important for reservoir modeling because a chronostratigraphic surface is present in every well in the reservoir. This fact provides geologists with a powerful tool for correlating packages of lithofacies between wells. A more realistic image of reservoir archi-

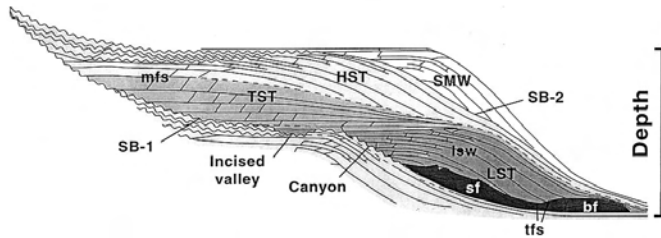


Fig. 1.4—Exxon idealized depositional-sequence cross-sectional model for siliciclastic sediments. Sequence boundary (SB), LST composed of basin-floor fan (bf), slope fan (sf), and lowstand prograding wedge (LSW), TST, HST, and shelf-margin wedge (SMW). Maximum flooding surface (mfs) separates the TST from the HST. Taken from Kerans and Tinker.¹⁰

ecture can, therefore, be constructed by distributing lithofacies and petrophysical properties within a detailed sequence-stratigraphic framework.

The terminology of sequence stratigraphy, like most geologic terminology, is complex and constantly evolves as concepts and ideas change.^{9,10} It is the intent here to present a basic overview of the terminology to provide the reader with sufficient understanding to communicate with reservoir geologists. The classic Exxon model (see [Fig. 1.4](#)) shows the terminology used in siliciclastic stratigraphy. The terms used in carbonate stratigraphy, although similar, have important differences because carbonates are organic in origin and clastics are terrigenous in origin. The terminology used in carbonate stratigraphy is illustrated in [Fig. 1.5](#).

The smallest time-stratigraphic unit is the high-frequency cycle (HFC), or parasequence, a unit composed of genetically related lithofacies deposited during one basic sea-level rise and fall. Assuming a constant rate of subsidence, each cycle begins with a flooding event as sea level rises. The flooding event is also referred to as transgression or retrogradation, the backward and landward movement or retreat of a shoreline or coastline. The sea transgresses the land, the shoreline retreats, and the space for sediment to accumulate increases. The space created by the transgression is referred to as accommodation space. Sea-level rise is followed by a stillstand, during which sediment completely or partly fills the accommodation space. The buildup of sediment by deposition is referred to as aggradation. The stillstand is followed by a relative sea-level fall during which accommodation space is reduced, forcing sediment to be transported into the basin and resulting in progradation of the sediment body. Progradation refers to the building forward and outward toward the sea of a shoreline or body of sediment. During sea-level fall, the most-landward sediment may become subaerially exposed, forming an unconformity. Farther basinward the water is deeper, and the shallowing event is identified by a facies shift in the vertical stacking of lithofacies. The next sea-level rise produces another flooding event, and the depositional cycle is repeated. Flooding events approximate chronostratigraphic surfaces and define the HFC as a time-stratigraphic unit.

Repeated eustatic sea-level cycles result in the vertical stacking of HFC. Cycles are stacked vertically into retrogradational cycles, aggradational cycles, and progradational cycles. Retrogradational cycles are formed when the eustatic sea-level rise for each cycle is much more than the fall. The shoreline will move farther landward with each successive cycle, a pattern described as back stepping or transgression. The sediments are said to be deposited in the transgressive system's track (TST). Aggradational cycles are formed when eustatic rise and fall are equal, and the resulting facies will stack vertically. These cycles are defined as part of the highstand system's tract (HST). Progradational cycles form when the eustatic fall for each cycle is greater than the rise. The shoreline for each successive cycle will move seaward, a pattern described as progradation or regression, and the sediments are said to be deposited in the HST. Sediments deposited when relative sea level is lowest are said to be deposited in the

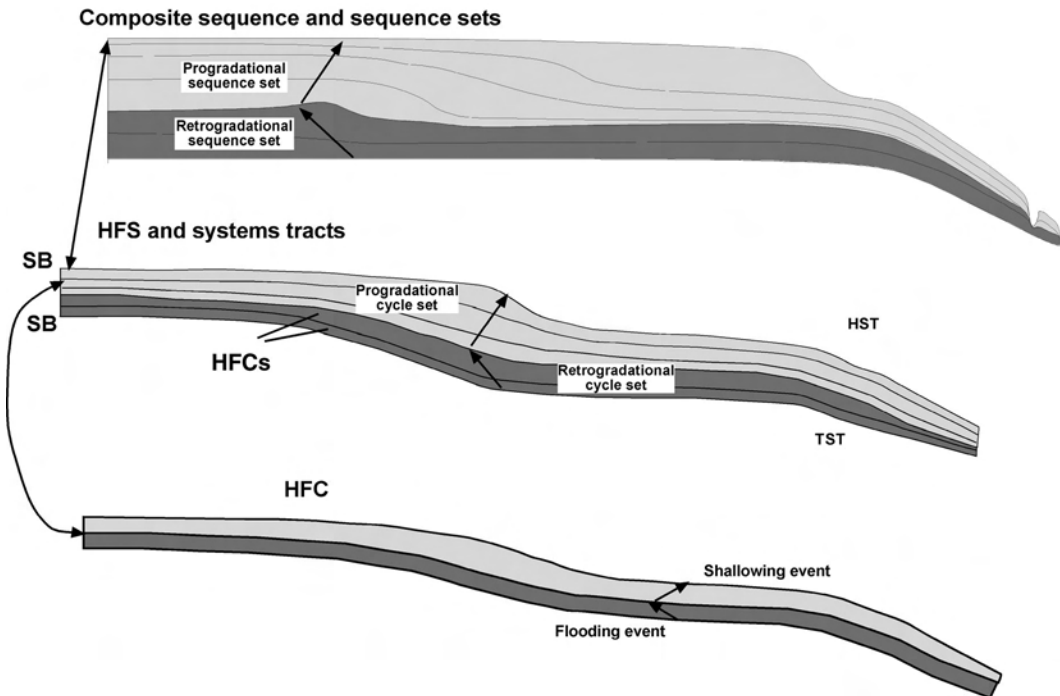


Fig. 1.5—Hierarchy of carbonate sequence-stratigraphic terminology in a cross-sectional view. An HFC is composed of a flooding event (transgression) and a shallowing event (prograding). HFSs are composed of a retrogradational cycle set that makes up the TST and a progradational cycle set that makes up the HST. Composite sequences are composed of a basal retrogradational set of HFSs and an upper set of progradational HFSs. The dark shading indicates transgressive units, and the light shading indicates progradational units. See Kerans and Tinker.¹⁰

lowstand system's track (LST). The sequence from TST to HST to LST defines a larger-scale sea-level signal referred to as a high-frequency sequence (HFS). The turnaround from transgression to aggradation and progradation is termed the maximum flooding surface (MFS). HFSs can be packaged into longer-term signals called composite sequences on the basis of the observation that they tend to stack vertically into transgressive, progradational, and lowstand sequences.

The terminology and duration of the cycle hierarchies estimated by Goldhammer¹¹ are shown in **Fig. 1.6**. HFC, HFS, and composite sequences are commonly referred to as fifth-, fourth-, and third-order cycles, respectively, with characteristic durations ranging from 0.01 to 10 million years (m.y.). First- and second-order cycles, or supersequences, have much longer durations, from 10 to more than 100 m.y., and are related more to structural movements than to eustasy. These major sequences are useful not only for regional but also for worldwide correlations. The durations of all these cycles and sequences are approximate and are based on radiogenic dates extrapolated to the numbers of cycles and sequences of various scales.

1.5 Carbonate Reservoirs

1.5.1 Introduction. A basic overview of carbonate-reservoir model construction was presented by Lucia,¹² and much of what is presented herein is taken from that book. Carbonate sediments are commonly formed in shallow, warm oceans either by direct precipitation out of seawater or by biological extraction of calcium carbonate from seawater to form skeletal material. The result is sediment composed of particles with a wide range of sizes and shapes mixed together to

Tectono-eustatic/eustatic cycle order	Sequence stratigraphic unit	Duration (m.y.)	Relative sea-level amplitude (m)	Relative sea-level rise/fall rate (cm/1,000 yr)
First		>100		<1
Second	Supersequence	10 to 100	50 to 100	1 to 3
Third	Depositional sequence composite sequence	1 to 10	50 to 100	1 to 10
Fourth	High-frequency sequence, parasequence and cycle set	0.1 to 1	1 to 150	40 to 500
Fifth	Parasequence, high-frequency cycle	0.01 to 0.1	1 to 150	60 to 700

(after Goldhammer and others, 1991)

Fig. 1.6—Terminology of cycle hierarchies and order of cyclicity from Goldhammer.¹¹

form a multitude of depositional textures. The sediment may be bound together by encrusting organisms or, more commonly, deposited as loose sediment subject to transport by ocean currents.

Depositional textures are described using a classification developed by Dunham.¹³ The Dunham classification divides carbonates into organically bound and loose sediments (see Fig. 1.7). The loose sediment cannot be described in simple terms of grain size and sorting because shapes of carbonate grains can vary from spheroid ooids to flat-concave and high-spiral shells having internal pore space. The grain content of a grain-supported sediment composed of shells can be as little as 30% of the bulk volume because the shells occupy less space than spheroids. Loose sediment is, therefore, described on the basis of the concept of mud vs. grain support. Mud refers to mud-size carbonate particles, not to mud composed of clay minerals. Grain-supported textures are grainstone, which lacks carbonate mud, and packstone, which contains mud. Mud-supported textures are referred to as wackestone, which contains more than 10% grains, and mudstone, which contains less than 10% grains. To complete the description, generic names are modified according to grain type such as “fusulinid wackestone” or “ooid grainstone.”

Dunham’s boundstone class was further divided by Embry and Klovan¹⁴ because carbonate reefs are commonly composed of large reef-building organisms, such as corals, sponges, and rudists, which form sediments composed of very large particles. They introduced the terms bafflestone, bindstone, and framestone to describe autochthonous (in-place) boundstone reef material. Floatstone and rudstone are used to describe allochthonous, (transported) reef sediment with particles larger than 2 mm in diameter. Rudstone is grain-supported, whereas floatstone is mud-supported sediment.

Enos and Sawatsky¹⁵ measured the porosity and permeability of modern carbonate sediments. The average porosity and permeability of grainstone are approximately 45% and 10 darcies, respectively, whereas the average porosity and permeability of a wackestone are approximately 65% and 200 md, respectively. The higher porosity in mud-supported sediments is caused by the needle shape of small aragonite crystals that make up the carbonate mud, and the decrease in permeability is caused by the small pore size found between mud-sized particles. An important observation based on this data is that all carbonate sediments have sufficient porosity and permeability to qualify as reservoir rocks.

Depositional texture					Depositional texture not recognizable (Subdivided according to classifications designed to bear on physical texture or diagenesis)
Original components not bound together during deposition				Original components were bound together during deposition as shown by intergrown skeletal matter, lamination, or sediment-floored cavities that are roofed over by organic or questionable organic matter and are too large to be interstices.	
Contains mud			Lacks mud and is grain supported		
Mud supported		Grain supported			
Less than 10% grains	More than 10% grains				
Mudstone	Wackestone	Packstone	Grainstone	Boundstone	Crystalline carbonate

Boundstone	Bafflestone	Bindstone	Framestone
Sediment Grains > 2 mm	Mud supported		Grain supported
	Floatstone		Rudstone

Fig. 1.7—Dunham¹³ and Embry and Klovan¹⁴ classification of carbonate sediments.

With modifications, the Dunham approach can be used to characterize the petrophysical properties of carbonate rocks. The classification must be modified, however, because diagenesis significantly alters the depositional texture, and a rock-fabric classification that incorporates diagenetic overprints and that can be linked to petrophysical properties is required. The classification proposed by Lucia¹⁶ is designed for this purpose (see Fig. 1.8). All pore space is divided into interparticle (intergrain and intercrystal) and vuggy (pore space within grains/crystals and much larger than grains/crystals). Interparticle pore space is classified with the Dunham classification approach. Instead of grain support vs. mud support, however, *grain-* and *mud-dominated* are used as a basic division. Grain-dominated fabrics include grainstone and grain-dominated packstone. Mud-dominated fabrics include mud-dominated packstone, wackestone, and mudstone. The packstone class is divided into grain- and mud-dominated packstone because the petrophysical properties of grain-dominated packstone are according to grain size, whereas mud size controls the properties of mud-dominated packstone. Diagenetic reductions in porosity by cementation and compaction are reflected in the amount of interparticle porosity.

Dolostones are classified similarly if the precursor limestone fabric can be determined. The principal petrophysical difference between limestones and dolostones occurs in mud-dominated fabrics. Limestone-mud-dominated fabrics have mud-sized particles (< 20 μm) and very small pores. Dolomitized mud-dominated fabrics have crystal sizes ranging from 10 μm or less to more than 200 μm, with corresponding pore sizes. Dolomitization must, therefore, improve reservoir quality by increasing particle and pore size.

The classification of vuggy pore space is an important aspect of rock-fabric classification that is not found in the classification of depositional textures. Vuggy pore space is divided into two groups on the basis of how the pore space is connected. Separate vugs are connected to each other through interparticle pore space, and touching vugs are connected directly to one another. Selective dissolution of grains, such as ooids or skeletal material, and intrafossil poros-

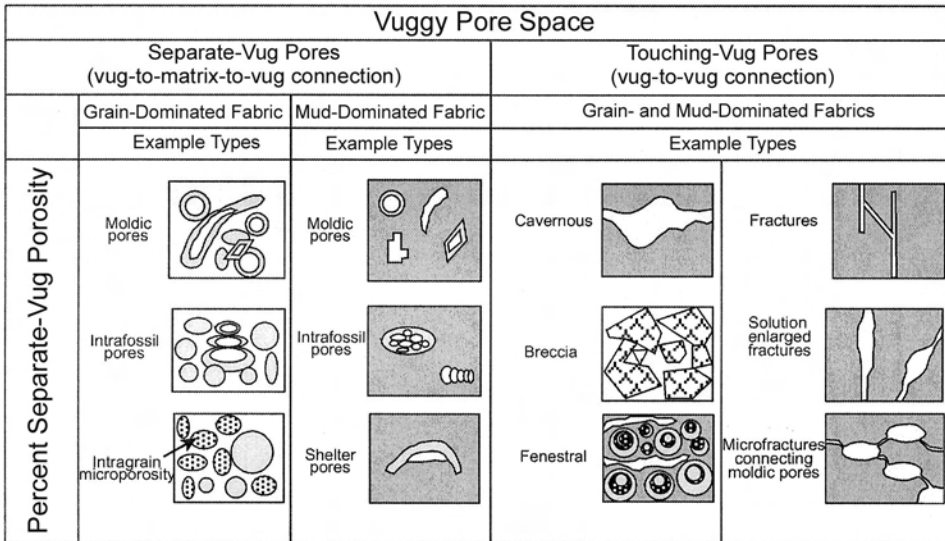
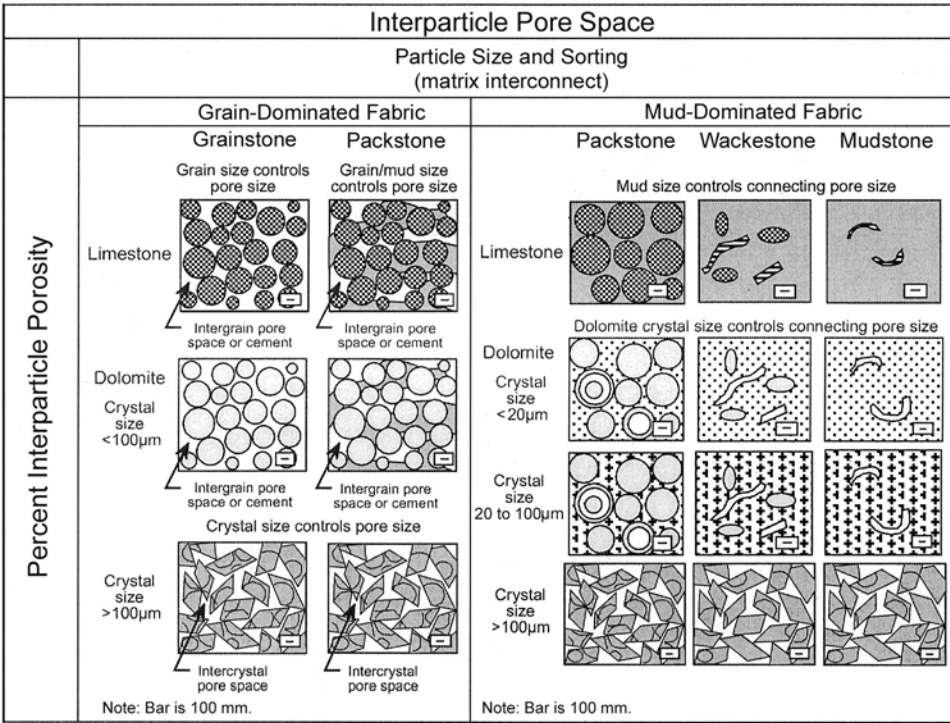


Fig. 1.8—Lucia¹⁶ classification of carbonate pore space.

ity are types of separate vugs. Because separate-vug porosity is poorly connected, it contributes less to permeability than would be expected if the porosity were located between the particles. Touching vugs are commonly formed by mass dissolution and fracturing. These processes can form reservoir-scale vuggy pore systems that dominate the performance of carbonate reservoirs.

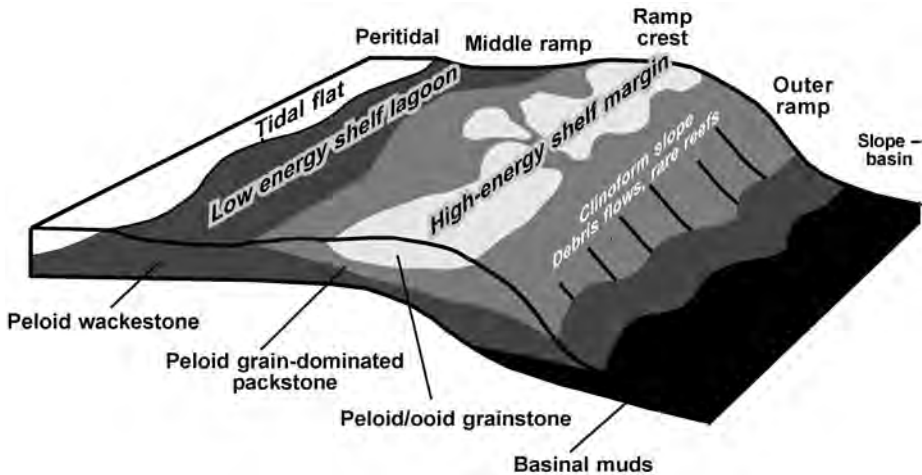


Fig. 1.9—Generalized block diagram illustrating carbonate-ramp facies patterns and topography.

1.5.2 Depositional Environments. Carbonate sediments accumulate in depositional environments that range from tidal flats to deepwater basins. Most carbonate sediments originate on a shallow-water platform, shelf, or ramp and are transported landward and basinward. “Platform” is a general term for the shallow-water environment, whereas “shelf” and “ramp” refer to topography—shelves with flat platform tops and steep foreslopes and ramps having gently dipping platform tops and slightly steeper foreslopes.

The lateral distribution of depositional environments reflects energy levels, topography, and organic activity. These changes can be related to the geometry of the carbonate platform. Ocean currents are produced by tides and waves and are concentrated at major topographic features, such as ramp and shelf margins, islands, and shorelines. Grainstones and boundstones are concentrated in the areas of highest energy, commonly at ramp and shelf margins. Sediment is transported from the shelf edge onto the shelf slope and into the basin environment. This transport occurs primarily during highstand and results in progradation of the shelf margin. Calcareous plankton is deposited in the basinal environment as well. Sediment is also transported landward onto the shoreline, creating tidal-flat deposits that prograde, primarily during regression. Transgressive sediments are generally wackestones and mudstones at all locations because rising sea level typically creates a low-energy depositional environment.

The combination of organic activity, ocean currents, topography, and eustasy produces a typical facies progression from land to basin during highstand: peritidal, middle ramp, ramp crest, ramp shelf or slope, and basin, as shown in Fig. 1.9. The peritidal facies, composed of tidal-flat-capped cycles, normally defines the most landward position of an HFC. The cycles are formed by filling accommodation space and depositing sediment above sea level by transporting carbonate sediment onto the mud flat with tidal and storm currents. Tidal-flat sediments are key indicator facies because they define sea level. The tidal-flat environment is divided into the intertidal zone overlain by the supratidal zone. Sediment in the intertidal zone is characterized by burrowed, pelleted, muddy sediment. Algal laminates are concentrated at the boundary between the intertidal and supratidal zones. The supratidal zone is easily identified by its characteristic irregular lamination, pisolites, mud cracks, intraclasts, and fenestral fabrics. The supratidal zone is sometimes called a “sabkha” environment, referring to the extensive evaporitic flats on the western shore of the Persian Gulf.

In arid climates, evaporite deposits may form by precipitation of gypsum ($\text{CaSO}_4 \cdot 2\text{H}_2\text{O}$) or anhydrite (CaSO_4) from evaporation of seawater trapped on or in the supratidal zone. Halite

(NaCl) is normally found in isolated basins similar to the Dead Sea. Sulfate minerals are found as deposits in hypersaline lakes and as beds and crystals within the peritidal sediments. Sulfates found within carbonate sediments are properly classified as diagenetic minerals and cannot be used to describe the depositional environment, but sulfate deposited out of a standing body of water, is properly classified as sediment and is characteristic of the depositional environment as well as the climate. For sulfate to precipitate from seawater, three conditions must be met:

1. The body of seawater must be highly restricted from the ocean.
2. The hypersaline water must be able to escape either by returning to the ocean or by seeping into the underlying sediment (*seepage reflux*), otherwise large volumes of Halite will precipitate forming a bed of salt.
3. The climate must be sufficiently arid to allow the seawater to evaporate to at least one-third its original volume.

The middle-ramp facies is characterized by quiet-water deposits typically composed of skeletal wackestones and mudstones. Burrowing organisms churn the muddy sediment and produce fecal pellets that, together with skeletal material, comprise the grain fraction of the sediment. During highstand, accommodation space may be reduced and water depth lessened to the point at which wave and storm energy increase, lime mud is winnowed out, and a packstone texture is produced. The increase in grain content, possibly capped by packstone, is used to define sea-level changes in this environment.

The ramp-crest facies is characterized by high-energy deposits, typically grainstones and packstones. The classic upward-shoaling succession of wackestone to packstone and grainstone typifies this environment. Typical high-energy deposits are as follows:

- Shelf-margin, tidal-bar, and marine-sand belts.
- Back-reef sands associated with landward transport of sediment for fringing reefs.
- Local middle-shelf deposits associated with gaps between islands or tidal inlets forming lobate tidal deltas.

Packstones are typically churned by burrowing organisms and show no evidence of current transport. Grainstones are commonly crossbedded, often in multiple directions, indicating deposition out of tidal currents. Reefs are also found in the ramp-crest facies. The term reef has been much misused in the petroleum industry. At one time, all carbonate reservoirs were referred to as reefs, and the term is commonly used today to describe any carbonate buildup. However, the term should be restricted to carbonate bodies composed of bindstone, bafflestone, and associated float- and rudstones.

The outer-ramp, or slope, facies is formed by transport of shelf-margin and inner-shelf sediment onto the shelf slope. Sediments are typically wackestones and mudstones, along with occasional packstones and grainstones, in channels associated with density flows into the basin. On steep slopes, sediments may be dominated by sedimentary breccias and debris flows produced by the collapse of a steep shelf margin. The basin facies is typically composed of thin-bedded, quiet-water lime muds that contain planktonic organisms. Wackestones are often punctuated by debris and grain flows. Classic turbidite textures and cycles are also found in basinal carbonate deposits.

1.5.3 Diagenetic Environments. Because all carbonate-reservoir rocks have undergone significant diagenesis, understanding their diagenetic history can be as important as understanding their depositional history. Modern carbonate sediments have sufficient porosity and permeability to qualify as reservoir rocks. Many ancient carbonates, however, lack the porosity and permeability needed to produce hydrocarbons economically. Loss of reservoir quality occurs when sediment changes after deposition. The processes that cause these changes are referred to as diagenetic processes, and the resulting fabric is often referred to as the diagenetic overprint.

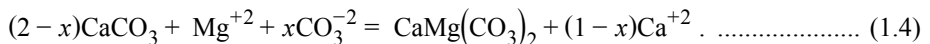
Carbonate diagenetic processes include calcium-carbonate cementation; mechanical and chemical compaction; selective dissolution; dolomitization; evaporite mineralization; and massive dissolution, cavern collapse, and fracturing. Whereas sedimentation is a one-time event, diagenesis is a continuing process, and diagenetic processes interact with one another in time and space. Thus, a sequence of diagenetic events may be extremely complicated and the pattern of diagenetic products difficult to predict if they are not related to depositional patterns.

The process of diagenetic overprinting of depositional textures must be understood to predict the distribution of petrophysical properties in a carbonate reservoir. To this end, diagenetic processes are grouped according to their conformance to depositional patterns. Calcium-carbonate cementation, compaction, and selective dissolution form the first group. These processes have the highest conformance to depositional patterns. Reflux dolomitization and evaporite mineralization form the second group. Although these processes depend greatly on geochemical and hydrological considerations, they are often predictable because they can be related to tidal-flat and evaporite depositional environments. Massive dissolution, collapse brecciation and fracturing, and late dolomitization form the third group. These processes have the lowest conformance to depositional patterns, and their products are quite unpredictable.

Calcium-carbonate cementation, compaction, and selective dissolution can often be linked to depositional textures. Because calcium-carbonate cementation begins soon after deposition, it is often connected to the depositional environment. It continues as the sediment is buried, so the distribution of late cements is often unpredictable. Cementation fills pore space from the pore walls inward, reducing both pore size and porosity in proportion to the amount of cement. Compaction and associated cementation are a function of depositional texture and the time-overburden history. Compaction is both a physical and a chemical process resulting from increased overburden pressure caused by burial. Textural effects include porosity loss; pore-size reduction; grain penetration, breaking, and deformation; and microstylolites. Compaction does not require the addition of material from an outside source and is often related to depositional textures. Experiments and observations have shown that mud-supported sediments compact more readily than those that are grain-supported.

Selective dissolution occurs when one fabric element is selectively dissolved in preference to others. Carbonate sediments are composed of three varieties of calcium carbonate—low-magnesium calcite, high-magnesium calcite (magnesium substituted for some calcium in the crystal lattice), and aragonite. Aragonite, in particular, is an unstable form and is rarely found in carbonate rocks. Grains composed of aragonite tend to be dissolved, and the carbonate is deposited as calcite cement. This distribution of aragonite grains can be predicted on the basis of depositional models.

Dolostone (a rock composed of dolomite) is an important reservoir rock. The composition of dolomite is $\text{CaMg}(\text{CO}_3)_2$, and it is formed by replacement of calcite and by occlusion of pore space. In the following dolomitization equation, x = the amount of carbonate added to the rock in excess of the amount in the sediment.



A main source of magnesium is thought to be modified seawater circulating through the sediment in response to various hydrodynamic forces, including density, elevation, and temperature differences. Many pore volumes of dolomitizing fluid are needed to convert a limestone to a dolostone. Therefore, the hydrologic system must be understood for the distribution of dolostone to be predicted. The hypersaline reflux model can be used to predict dolomite patterns because it can be linked to an evaporitic environment. In an arid climate, seawater is trapped in tidal-flat sediment and hypersaline lakes and is concentrated through evaporation, producing a dolomitizing fluid. A hydrodynamic potential is created because the evaporated fluid is

denser than seawater or groundwater and the tidal flats are at a slightly higher elevation than sea level. As a result, the hypersaline fluid will reflux down through the underlying sediment, converting it to dolomite. The geometries of dolostone bodies formed by this mechanism can be predicted if the distribution of evaporitic tidal-flat facies is known.

The hypersaline reflux model also accounts for the addition of CaSO_4 , commonly an evaporite mineral in carbonate reservoirs. CaSO_4 is most commonly formed near the Earth's surface in its hydrous form, gypsum ($\text{CaSO}_4 \cdot 2\text{H}_2\text{O}$). However, at higher temperatures, the stable form is anhydrite CaSO_4 , which is the form most commonly found in carbonate reservoirs. In some locations, tectonics has uplifted carbonate strata into a cooler temperature, and anhydrite has hydrated, forming gypsum.

Four types of anhydrite are commonly found in dolostone reservoirs. Pore-filling anhydrite is typically composed of large crystals filling interparticle and vuggy pore space. Poikilotopic anhydrite is found as large crystals with inclusions of dolomite scattered throughout the dolostone. They are both replacive and pore filling. Nodules of anhydrite are composed of microcrystalline anhydrite, often showing evidence of displacing sediment. They make up a small percentage of the bulk volume and have little effect on reservoir quality. Bedded anhydrite is found as beds composed of both coalesced nodules and laminations. Anhydrite beds are flow barriers and seals in reservoirs.

Massive dissolution, collapse brecciation and fracturing, and late dolomitization are the most unpredictable diagenetic processes. Massive dissolution refers to nonfabric selective dissolution, including cavern formation at any scale, collapse brecciation and fracturing, solution enlargement of fractures, and dissolution of bedded evaporites. This process is thought to be most commonly related to the flow of near-surface groundwater, referred to as meteoric diagenesis but often included under the general heading of karst. The products of this diagenetic environment are controlled by precursor diagenetic events, tectonic fracturing, and groundwater flow and show little relationship to depositional environments. Reservoirs of this type are, therefore, difficult to model.

1.6 Siliciclastic Reservoirs

1.6.1 Introduction. Siliciclastic rocks are composed of terrigenous material formed by the weathering of pre-existing rocks, whereas carbonate rocks are composed principally of sediment formed from seawater by organic activity. Clastic sediments are composed of grains and clay minerals, and siliciclastic sediments are first classified according to grain type. The three basic grain types are quartz, feldspar, and rock fragments, and the end members are quartz sandstone, arkosic sandstone, and lithic sandstone, as shown in [Fig. 1.10a](#). Second, siliciclastics are described in terms of grain size ([Fig. 1.10b](#)). Grain-size classes include gravels (boulder size to 2 mm in diameter), sands (2 to 0.0625 mm), and mud, which includes silts (0.0625 to 0.004 mm) and clay (< 0.004 mm). Mixtures are described with a modifying term for a less-abundant size, such as clayey sandstone, sandy siltstone, or muddy sandstone ([Fig. 1.10c](#)). Mudstone, composed of clay and silt, is not to be confused with carbonate mudstone. In this classification, mud and clay are terms used to indicate size, not mineralogy.

The porosity and permeability of unconsolidated siliciclastic sediments were measured by Beard and Weyl.¹⁷ Porosity varies from 45% for well-sorted sands to 25% for very poorly sorted sands and does not vary with changes in grain size for well-sorted media. Permeability ranges from 400 darcies in well-sorted, coarse-grained sands to 0.1 darcies (100 md) in very poorly sorted, fine-grained sands. Permeability varies with grain size and sorting because it is controlled by pore-size distribution. Most modern sands are reservoir-quality rock. Modern claystones and mudstones, which are composed primarily of clay minerals, have little permeability and are not reservoir quality.

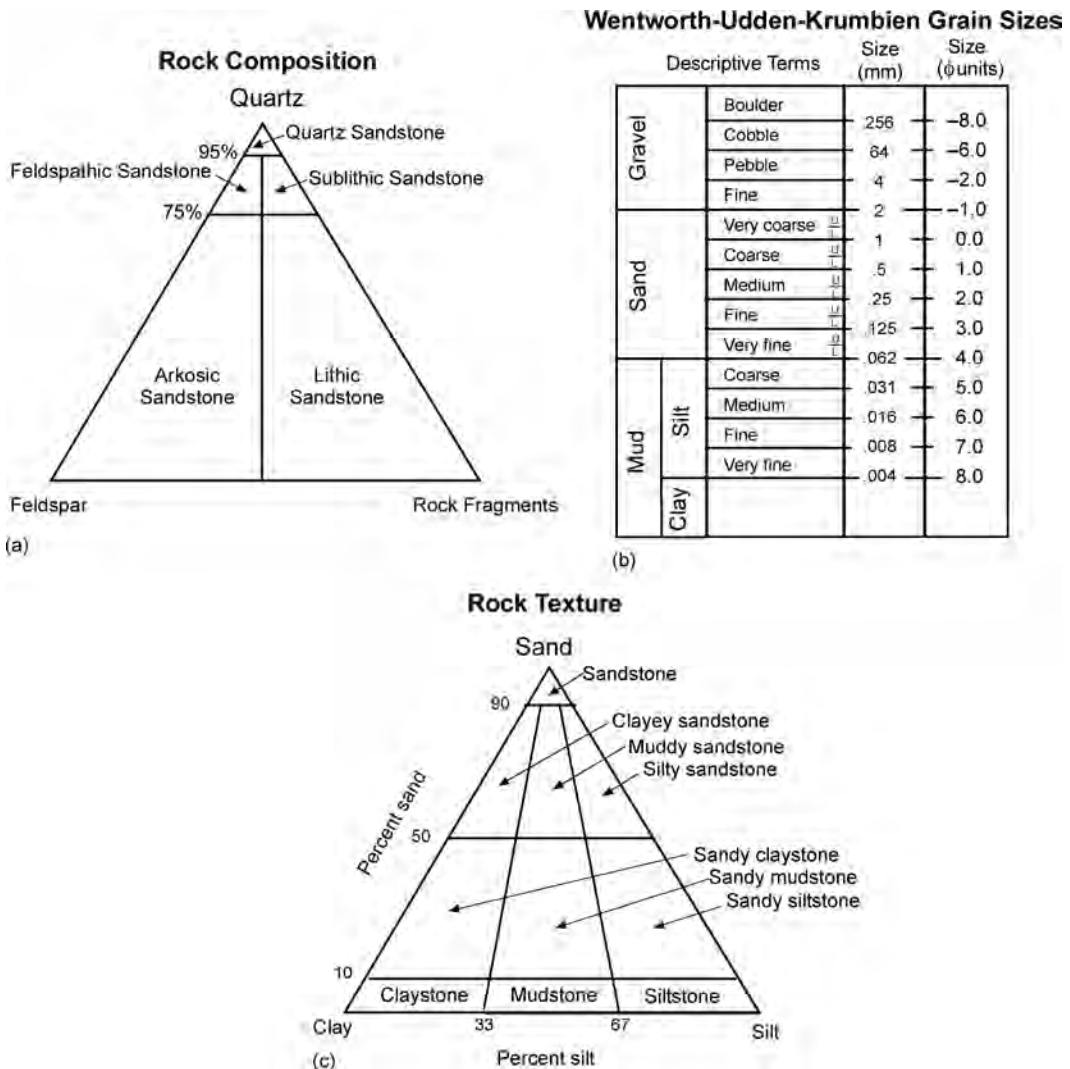
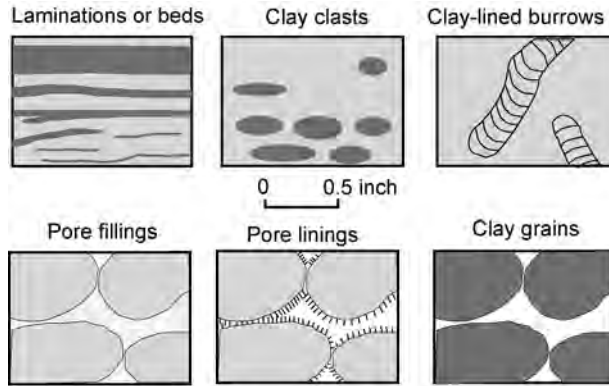


Fig. 1.10—Classification of siliciclastic rocks by (a) composition, (b) grain size, and (c) texture. The ϕ scale is defined as $\phi = -\log_2(\text{size})$.

The type, amount, and habit of clay minerals in siliciclastic rocks are important characteristics (see Fig. 1.11). Clay minerals are sheet-structure silicates that have a profound impact on the petrophysical and production properties of sandstones. They can be deposited as muddy sediment or formed during burial by diagenetic processes (sometimes referred to as authigenic clay). Common clay minerals are kaolinite $[Al_2Si_2O_5(OH)_4]$, illite $[KA_3Si_3O_{10}(OH)_2]$, chlorite $[(Al, Mg, Fe)Si_4O_{10}(OH)_2]$, and smectite or montmorillonite $[(Al, Mg)Si_4O_{10}(OH)_2]$.

The mineralogy of the clay minerals has a great effect on pore size and petrophysical properties.¹⁸ For example, kaolinite-cemented sandstones are more permeable than are illite-cemented sandstones because kaolinite tends to form boolets that reduce pore size and porosity, whereas illite tends to form thin threads that reduce pore size with little effect on porosity. Clay minerals are also known to hinder inflow into the wellbore. Smectite, for example, tends to swell, reducing permeability when in contact with fresh water. Kaolinite is known to get



Courtesy of R.E. Sneider Exploration (2001)

Fig. 1.11—Diagrammatic illustration of the basic, different types of clay habit in siliciclastic rocks. Figure courtesy of Sneider Exploration Inc.

dislodged by high-velocity flow and plug pore throats near the wellbore, reducing permeability. The iron in chlorite is commonly released during acid treatments, plugging perforations.

1.6.2 Depositional Environments. The following discussion is taken primarily from Galloway and Hobday.¹⁹ Grain type, size, and sorting, as well as other characteristics of siliciclastic reservoirs are most commonly controlled by the depositional environment. Many siliciclastic reservoirs are geologically young, and the sediment has undergone only moderate compaction and cementation. Therefore, diagenesis is not a major factor, and petrophysical properties can be predicted on the basis of sedimentology.

Siliciclastic sediments are transported and deposited by wind and flowing water. On land, clastics are deposited by wind and stream flow. In the marine environment, they are transported by tidal, wave, ocean, and density currents. Land-based environments are grouped into alluvial-fan, fluvial, and eolian systems. Ocean-center environments include delta systems and barrier bars, which are transitional between land and marine environments, and shelf, slope, and basinal systems, which are marine (see Fig. 1.12).²⁰

Alluvial fans are conical, lobate, or arcuate accumulations of predominately coarse-grained clastics extending from a mountain front or escarpment across an adjacent lowland. Some fans terminate directly in lakes or ocean basins as fan deltas, which generally show some degree of distal modification by currents or waves. Most sediment is deposited by stream and debris flow. Stream flow is commonly confined to one or two channels but may spread across the fan as sheet-flow. Debris flows result when clay and water provide a low-viscosity medium of high yield strength capable of transporting larger particles under gravity. Wave and tidal currents modify the distal terminations of fans that build into lakes or the ocean, improving sorting and reservoir quality.

Eolian deposits are typically fine- to medium-grained, well-sorted, quartzose sand with pronounced crossbedding. The sand is transported and deposited by wind currents, which are the most effective agents for sorting clastic particles. Hot, arid regions are the most favored locales for eolian accumulation. Eolian environments can be divided into dune and interdune facies. Dunes are large bed forms that come in an array of forms. Barchans, barchanoid ridges, and transverse dunes form in response to essentially unidirectional winds. Longitudinal dunes arise from varying wind directions. Draas comprise large stellate rosettes with a high central peak and radiating arms and form in response to intense, multidirectional wind systems. The interdune environment is generally a broad, featureless plain covered by lag gravels resulting from

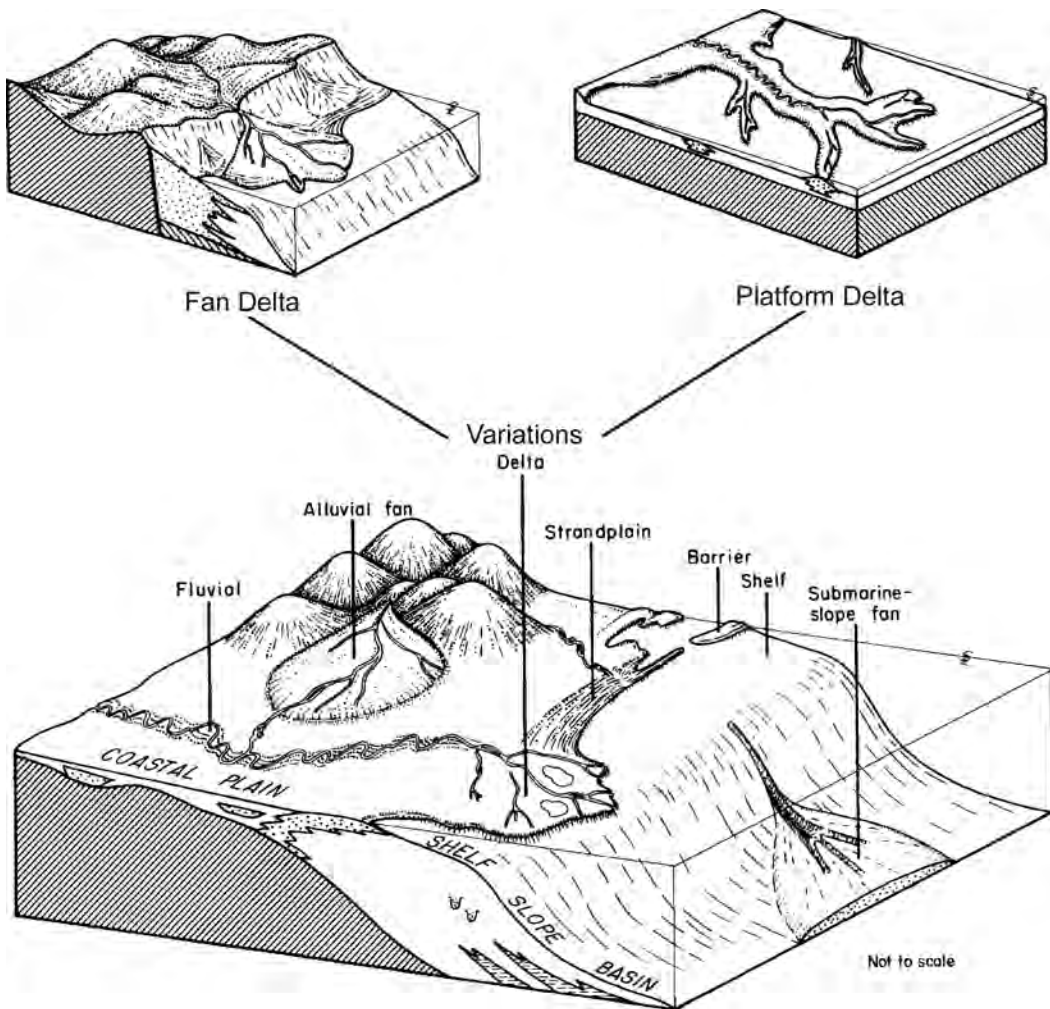


Fig. 1.12—Range of sandstone depositional systems that typically host hydrocarbon resources.²⁰

deflation (erosion). Deposition in the interdune area results from rainfall in desert highlands, promoting ephemeral streams that deposit sediment in streambeds and small alluvial fans. Flooding may produce interdune braided-stream deposits. Ponding of water between dunes can create lakes that can precipitate evaporite minerals if the groundwater is sufficiently saline.

Fluvial systems are a collection of stream channels and their floodplains. The channels are sinuous (meandering), with the degree of sinuosity increasing seaward. Braided streams are the result of sand-rich channels. Channel deposits are composed of sand bars and lag deposits. The point bar, a major feature of a high-sinuosity channel, forms by lateral accretion of sediment in the lower-energy, leeward side of a meander. Deposition normally occurs during the ebbing phase of a flood. The highest energy, found in the channel proper, erodes the channel bank, causing the channel to shift constantly; lag deposits are characteristic of the channel. Abandoned channels are commonly clay filled.

Floodplain deposits are deposited as levees, crevasse splays, and flood-basin sediments. Levee deposits are fine sand, silt, and clay deposited along the margins of the channels, when decelerating water rich in suspended sediment spills over the banks during flood stage. Crevasse splays are formed when local breaches in the levees funnel floodwater into near-chan-

nel parts of the flood plain. These sediments tend to be highly heterogeneous, composed of sand of variable size, plant debris, and mud clasts. Flood-basin deposits are broad, clay-rich sediments that have been reworked by burrowing animals, plant growth, and pedogenic (soil-forming) processes.

Delta systems form when a river transporting sediment enters a standing body of water, commonly an ocean or a lake, and consist of both fluvial and marine sediments. The depositional architecture of a delta system is characteristically progradational and may fill a small basin. The combination of fluvial and marine processes creates a unique facies assemblage and reservoir architecture. Deltaic sediments are deposited as channel fills, channel-mouth sands, crevasse splays, and delta-margin sand sheets. Together, these facies compose a delta lobe, which is a fundamental building block of a delta system. Delta systems are divided into fluvial-, wave-, and tidal-dominated deltas according to major energy type. Each system has a unique depositional architecture.

Shore-zone systems, excluding deltas, compose a narrow transitional environment that extends from wave base (≈ 50 ft of water) to the seaward edge of the alluvial coastal plain. They include shoreface, beach, barrier, lagoon, and tidal-flat facies. These systems are supplied principally by onshore transport of river-derived and shelf sediments. Sands are concentrated in barrier-island complexes and tidal sand bodies, with finer sediment landward. Accretion of beach ridges seaward can form a sheetlike sand body referred to as a strandplain sand. The “shoreface facies” refers to that part of the shore zone that is below the zone of wave swash. It is commonly divided into lower-, middle-, and upper-shoreface deposits partly on the basis of water depth and associated energy levels, the highest energy level being the surf zone (upper shoreface). Beach facies includes wave swash and dune zone, all deposited above mean tide. The barrier is formed by aggradation or by progradation of shoreface sands seaward. The lagoon facies, located behind the barrier, is generally composed of clay and fine sand. The barrier may be breached during storms, allowing tidal currents to transport coarser sediment from the ocean into the lagoon, forming tidal deltas.

Shelf systems are broad, deepwater platforms covered by terrigenous sediment. Sediment distribution is controlled by ocean currents, including tidal, wave, storm surge, and density. Facies are defined by bed form and include sand ribbon, wave, ridge, storm, and mud.

Slope and basin systems are found in the relatively deep water beyond the shelf break. Deposition is characterized by the dominance of sediment transport by gravity and density flow, although pelagic settling also occurs. The upper slope is typically a zone of sand remobilization and bypass, with characteristic erosion and channel cutting; the lower slope and basin floor are sites of deposition. Regionally, grain size is the coarsest in the upper slope and decreases in the basin-floor direction. Slope and basin systems are typically distinguished from other systems by their fining-upward-graded bedding, which results from grain settling from a suspended sediment load. Submarine fans are typical slope and basin-floor deposits. Fed from point sources, such as river mouths or submarine canyons, they receive the bulk of their sediments from turbidity currents, a density current produced by sediment-rich water. The upper-fan environment is characterized by feeder channels or canyons that serve as sediment conduits, and sediments are typically coarse gravels. The midfan is characterized by a series of bifurcating, distributary, or braided channels that accumulate massive and pebbly sands showing lenticular bedding, and the lower fan is a smooth, gently sloping surface that received slowly deposited, suspended sediment punctuated by pulses of fine-grained to silt-sized sand. The resulting graded beds are thin, laterally persistent, and monotonously repetitive, commonly through a considerable thickness.

1.6.3 Diagenetic Environments. Sandstones are less susceptible to diagenetic change than carbonates. Common diagenetic processes in sandstones are quartz overgrowth cement, carbonate (calcite and dolomite) cement, compaction, grain dissolution and associated formation of clay

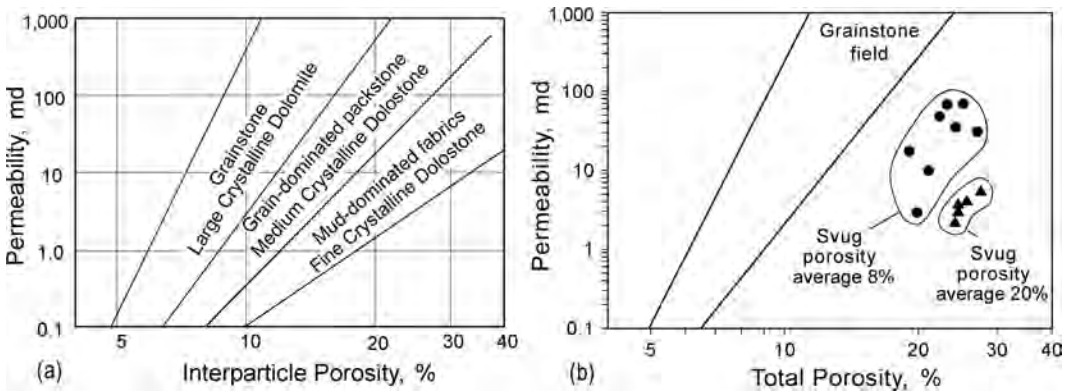


Fig. 1.13—Relationship between carbonate rock-fabric facies, porosity, and permeability.¹² (a) Crossplot of interparticle porosity and permeability showing rock-fabric fields. (b) Crossplot of total porosity and permeability showing effect of separate-vug (Svug) porosity on permeability of grainstone.

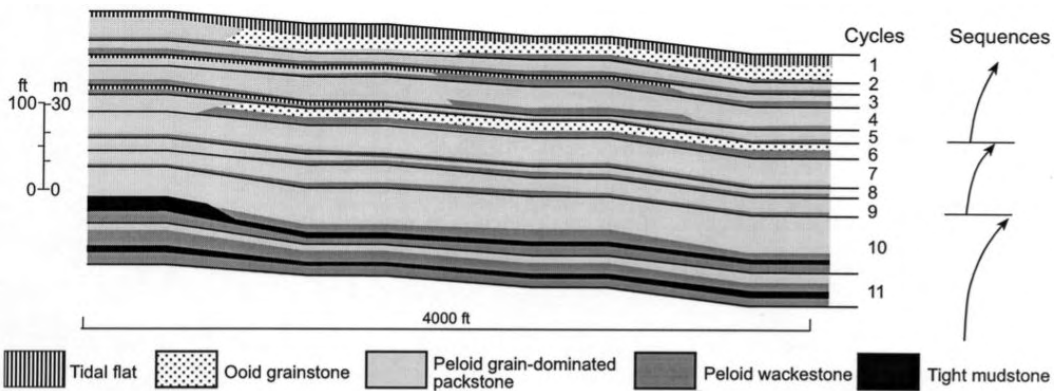


Fig. 1.14—Rock-fabric, sequence-stratigraphic carbonate reservoir suitable for petrophysical quantification.

minerals, and alteration of sedimentary clay minerals. Many of these products can be related to the burial history. Pore space is reduced by mechanical and chemical compaction, resulting in more closely spaced grains and smaller pores, and by quartz overgrowths, which are commonly sourced from chemical dissolution of quartz grains during burial. Carbonate cements are formed by dissolution and precipitation of indigenous carbonate shell material and by importation of carbonate from a more distant source. Iron-rich, pore-filling dolomite is not uncommon.

Feldspar minerals found in rock fragments are commonly unstable in the burial environment and are susceptible to dissolution, forming grain molds similar to those in carbonate rocks. Clay minerals (commonly chlorite) are deposited in the intergrain spaces associated with this dissolution process. Chlorite linings of pore space are thought to inhibit burial cementation and compaction and preserve porosity at depth. Clay minerals are altered during burial diagenesis, and authigenic (diagenetic) clay minerals are formed. Clay-mineral diagenesis causes large increases in surface area and microporosity that, in turn, have large effects on reservoir performance and log analysis.

1.6.4 Reservoir Models. Reservoir models are constructed by distributing petrophysical properties in 3D space with geologic models as a template. Geologic models are constructed by

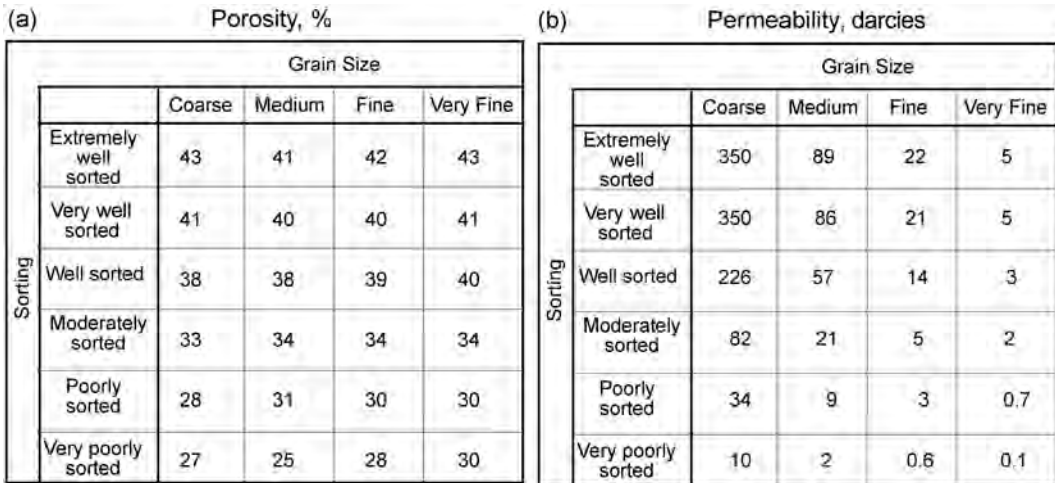


Fig. 1.15—Relationship between siliciclastic texture, porosity, and permeability in unconsolidated sediments.¹⁷ (a) Porosity varies with sorting and not with grain size. (b) Permeability varies with grain size and sorting.

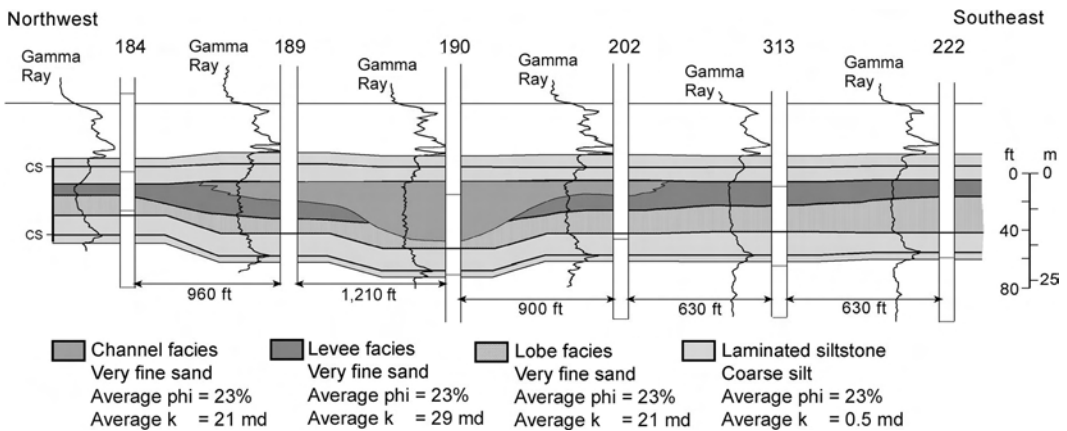


Fig. 1.16—Depositional facies model in a basin-floor fan showing grain size, average porosity, and average-permeability data.²¹

distributing facies within a sequence stratigraphic framework using the systematic distribution of facies within a depositional model as a guide. There are many types of facies, and facies selection is normally based on the question asked. Water depth and changes in sea level are key questions when building a sequence stratigraphic model, and fossil and other grain types together with depositional textures are keys to estimating water depth. Thus, numerous “depositional” facies are commonly described from core material. Once a sequence model is built, however, the problem is to convert the geologic model into a reservoir model by populating the geologic model with petrophysical data. This problem is best resolved by linking petrophysical measurements to rock fabric or texture, and the number of “rock-fabric” facies needed to quantify the geologic model is generally much lower than depositional facies.

Examples of carbonate rock-fabric facies include grain-dominated packstone, medium crystalline dolowackestone, and moldic grainstone. In carbonate reservoirs, rock fabrics include diagenetic overprints as well as depositional textures because diagenesis plays an important

role in forming most carbonate pore space. An example of how rock-fabric facies relate to porosity and permeability is illustrated in [Fig. 1.13](#).¹² Particle size, sorting, interparticle porosity, and vuggy porosity are used to characterize pore-size distribution. Petrophysical quantification of a carbonate stratigraphic model is accomplished by mapping rock-fabric facies and interparticle porosity and calculating permeability and initial water saturation from rock-fabric-specific relationships to porosity. An example of a rock-fabric reservoir model is illustrated in [Fig. 1.14](#).

Petrophysical properties of siliciclastic rocks are often directly related to facies characterized by grain size and sorting because pore space is generally located between grains and the variability of porosity within a facies is small. Porosity generally decreases with decreasing sorting and remains constant with changes in average grain size (see [Fig. 1.15](#)). However, porosity will vary with cementation and compaction. Permeability decreases with decreasing sorting and grain size ([Fig. 1.15](#)), and as porosity decreases even though grain size and sorting remain constant. The finest grain size is found in shales (mudstones) that typically have little permeability. Once the depositional facies are distributed in 3D space, the model can be quantified with petrophysical properties by using grain size, sorting, and porosity characteristics of the depositional facies. As illustrated in [Fig. 1.16](#)²¹ (a geologic model from a deepwater sediment fan), depositional facies commonly have similar petrophysical properties that reduce the number of textural facies needed to quantify the geologic model. The distribution of shales (mudstone) is important for reservoir modeling because they typically have little permeability and act as flow barriers in the reservoir.

Fracture porosity can have a large influence on performance of a carbonate or siliciclastic reservoir. Characterizing and modeling fracture porosity is difficult and is beyond the scope of this discussion. The book on fractured reservoirs by Aguilera²² is suggested as a good general overview of the problem.

Nomenclature

g	= acceleration of gravity, ft/sec ²
h_c	= maximum hydrocarbon column, ft
H	= fluid potential, ft
P	= measured static pressure, psia
p_c	= capillary entry pressure, psia
x	= horizontal distance, ft
Z	= elevation relative to a datum, sea level, ft
θ	= angle between horizontal and dip of water table, degrees
ρ_w	= density of water, g/cm ³
ρ_{hc}	= density of the hydrocarbon, g/cm ³
ρ_o	= density of oil, g/cm ³
ϕ	= porosity, fraction
k	= permeability, md

References

1. Hunt, J.M.: *Petroleum Geochemistry and Geology*, W.H. Freeman and Co., San Francisco (1979) 617.
2. Milton, N.J. and Bertram, G.T.: "Trap Styles—A New Classification Based on Sealing Surfaces," *AAPG Bull.* (1992) **76**, No. 7, 983.
3. Demaison, G. and Huizinga, B.J.: "Genetic Classification of Petroleum Systems," *AAPG Bull.* (1991) **75**, No. 10, 1626.

4. Sneider, R.M. *et al.*: “Comparison of Seal Capacity Determinations: Conventional Cores Versus Cuttings,” *Seals, Traps, and the Petroleum System*, R.C. Surdam (ed.), *AAPG Memoir 67* (1997) 12.
5. Smith, D.A.: “Theoretical Considerations of Sealing and Non-Sealing Faults,” *AAPG Bull.* (1966) **50**, No. 2, 363.
6. Hubbert, M.K.L.: “Entrapment of Petroleum under Hydrodynamic Conditions,” *AAPG Bull.* (1953) **37**, No. 8, 1954.
7. Schowater, T.T.: “Mechanics of Secondary Hydrocarbon Migration and Entrapment,” *AAPG Bull.* (1979) **63**, No. 5, 723.
8. North, F.K.: *Petroleum Geology*, Unwin Hyman Inc., Boston, Massachusetts (1985) 631.
9. Von Wagoner, J.C.: “Overview of Sequence Stratigraphy of Foreland Basin Deposits: Terminology, Summary of Papers, and Glossary of Sequence Stratigraphy,” *Sequence Stratigraphy of Foreland Basin Deposits; Outcrop and Subsurface Examples from the Cretaceous of North America*: J.C. Van Wagoner and G.T. Bertram (eds.), *AAPG Memoir 64* (1995) 4.
10. Kerans, C. and Tinker, S.W.: “Sequence Stratigraphy and Characterization of Carbonate Reservoirs,” *SEPM Short Course Notes No. 40* (1997) 130.
11. Goldhammer, R.K.: “Hierarchy of Stratigraphic Forcing: Example from Middle Pennsylvanian Shelf Carbonates of the Paradox Basin,” *Sedimentary Modeling: Computer Simulations and Methods for Improved Parameter Definition*, E.K. Franseen, *et al.* (eds.) *Kansas Geological Survey Bull.* 233 (1991) 361.
12. Lucia, F.J.: *Carbonate Reservoir Characterization*, Springer, New York (1999) 226.
13. Dunham, R.J.: “Classification of Carbonate Rocks According to Depositional Texture,” *Classification of Carbonate Rocks—A Symposium*, W.E. Ham (ed.), *AAPG Memoir No. 1* (1962) 108.
14. Embry, A.J. and Klovan, R.E.: “A Late Devonian Reef Tract of Northeastern Banks Island, N.W.T.,” *Bulletin of Canadian Petroleum Geology* (1971) **19**, No. 4, 730.
15. Enos, P. and Sawatsky, L.H.: “Pore networks in Holocene carbonate sediments,” *J. of Sedimentary Petrology* (1981) **51**, No. 3, 961.
16. Lucia, F.J.: “Rock-Fabric/Petrophysical Classification of Carbonate Pore Space for Reservoir Characterization,” *AAPG Bull.* (1995) **79**, No. 9, 1275.
17. Beard, D.C. and Weyl, P.K.: “Influence of Texture on Porosity and Permeability of Unconsolidated Sand,” *AAPG Bull.* (1973) **57**, No. 2, 349.
18. Neasham, J.W.: “The Morphology of Dispersed Clay in Sandstone Reservoirs and Its Effect on Sandstone Shaliness, Pore Space and Fluid Flow Properties,” paper SPE 6858 presented at the 1977 SPE Annual Technical Conference and Exhibition, Denver, 9–12 October.
19. Galloway, W.E. and Hobday, D.K.: *Terrigenous Clastic Depositional Systems; Applications to Petroleum, Coal, and Uranium Exploration*, Springer-Verlag, New York (1983) 423.
20. Galloway, W.E. *et al.*: *Atlas of Major Texas Oil Reservoirs*, U. of Texas at Austin, Bureau of Economic Geology (1983) 139.
21. Dutton, S.P., Barton, M.D., Asquith, G.B., Malik, M.A., Cole, A.G., Gogas, J., Guzman, J.I., and Clift, S.J.: *Geologic and Engineering Characterization of Turbidite Reservoirs, Ford Geraldine Unit, Bell Canyon Formation, West Texas*, The U. of Texas at Austin, Bureau of Economic Geology Report of Investigations No. 255 (1999) 88.
22. Aguilera, R.: *Naturally Fractured Reservoirs*, PennWell Publishing Co., Tulsa (1995).

SI Metric Conversion Factors

°API	141.5/(131.5 + °API)	= g/cm ³
ft ×	3.048*	E - 01 = m
g/cm ³ ×	1.0*	E + 03 = kg/m ³
mm ×	2.54*	E + 01 = in.
psi ×	6.894 757	E + 00 = kPa

*Conversion factor is exact.

Chapter 2

Fundamentals of Geophysics

Bob A. Hardage, U. of Texas at Austin

2.1 Introduction

Geophysics is a broad subject that encompasses potential field theory (gravity and electromagnetic fields) and seismic technology. Potential field data are valuable in many studies, but seismic data are used in more reservoir characterization and reservoir management applications. This chapter focuses on seismic fundamentals and does not consider gravity, magnetic, or electrical concepts.

Seismic data have been used for many years to guide exploration. More recently, seismic data have been used to support reservoir characterization in field development planning and subsequent reservoir management. As the technology in equipment and interpretation techniques has advanced, so has the ability to define the size, shape, fluid content, and variation of some petrophysical properties of reservoirs. This chapter provides insight into the fundamentals of seismic data acquisition, interpretation techniques, and the types of information that can be derived. See the chapter on reservoir geophysics in the Emerging and Peripheral Technologies section of this *Handbook* for information on emerging technologies that apply geophysical data.

Most seismic data are acquired with surface-positioned sources and receivers. For the first 4 or 5 decades that seismic-reflection data were acquired, sources and receivers were deployed along the same straight line to create 2D seismic profiles. Two-dimensional seismic data do not yield a correct image of subsurface stratigraphy when a 2D seismic line crosses a complex subsurface structure because the acquisition geometry cannot distinguish reflections that originate from outside the profile plane from reflections that occur within the 2D vertical image plane.

This imaging deficiency of 2D seismic profiling has been remedied by the implementation of 3D seismic data acquisition, which allows data processing to migrate reflections to their correct image coordinates in 3D space. Industry largely abandoned 2D seismic profiling in the 1990s and now relies almost entirely on 3D seismic data acquisition. This chapter covers the basics of 3D seismic technology, but does not consider 2D seismic technology involving surface-positioned equipment.

In some reservoir applications, seismic data are acquired with downhole sources and receivers. If the receiver is stationed at various depth levels in a well and the source remains on the surface, the measurement is called vertical seismic profiling (VSP). This technique produces a high-resolution, 2D image that begins at the receiver well and extends a short distance (a few tens of meters or a few hundred meters, depending on the source offset distance) to-

ward the source station. This image, a 2D profile restricted to the vertical plane passing through the source and receiver coordinates, is useful in tying seismic responses to subsurface geologic and engineering control.

If the source is deployed at various depth levels in one well and the receiver is placed at several depth stations in a second well, the measurement is called crosswell seismic profiling (CSP). Images made from CSP data have the best spatial resolution of any seismic measurement used in reservoir characterization because a wide range of frequencies is recorded. CSP data are useful for creating high-resolution images of interwell spaces and for monitoring fluid movements between wells. However, a CSP image is also a 2D profile with the image limited to the vertical plane that passes through the source and receiver coordinates. This chapter includes brief descriptions of the fundamentals of subsurface VSP and CSP technologies to complement the descriptions of surface-positioned seismic technology.

2.2 Impulsive Sources

A variety of seismic sources exist that can apply vertical impulse forces to the surface of the ground. These devices are viable energy sources for onshore seismic work. Included in this source category are gravity-driven weight droppers and other devices that use explosive gases or compressed air to drive a heavy pad vertically downward. Refs. 1 through 3 describe these types of sources.

Chemical-explosive energy sources are popular for onshore seismic surveys but are prohibited at some sites because of environmental conditions, cultural restrictions, or federal and state regulations. Chemical explosives are no longer used as marine energy sources for environmental and ecological reasons.

Field tests should always be made before an extensive seismic program is implemented. First, it should be determined whether the selected impulsive source creates adequate energy input to provide data with an appropriate signal-to-noise ratio and a satisfactory signal bandwidth at appropriate offset distances. Second, it is important to determine whether an impulsive source causes unwanted reverberations in shallow strata.

2.3 Vibrators

Vibroseis™ energy sources are some of the more popular seismic source options for onshore hydrocarbon exploration. The generic term vibrator refers to these types of seismic sources. Vibrators have several features that make them attractive for seismic data acquisition. They are quite mobile and allow efficient and expeditious illumination of subsurface targets from many different shotpoint locations. Also, the frequency content of a vibrator signal often can be adjusted to better meet resolution requirements needed for a particular target. In addition, the magnitude of the energy input into the Earth can be tailored for optimal signal-to-noise conditions by varying the size and number of vibrators or by altering the output drive of individual vibrators. For these reasons, vibrators are one of the most versatile onshore seismic energy sources.

Vibrators work on the principle of introducing a user-specified band of frequencies, known as the sweep, into the Earth and then crosscorrelating that sweep function with the recorded data to define reflection events. The parameters of a vibrator sweep are start frequency, stop frequency, sweep rate, and sweep length. A vibrator can do an upsweep that starts with a frequency as low as 8 to 10 Hz and stops at a high value of 80, 100, or 120 Hz. Alternatively, vibrators can do a downsweep that starts with a high frequency and finishes with a low frequency. Most Vibroseis data are generated with upsweeps.

Sweep rate can be linear or nonlinear. A linear rate causes the vibrator to dwell for the same length of time at each frequency component. Nonlinear sweeps are used to emphasize higher frequencies because the vibrator dwells longer at higher frequencies than it does at lower frequencies.

Sweep length defines the amount of time required for the vibrator to transverse the frequency range between the start and stop frequencies. As sweep length is increased, more energy is put into the Earth because the vibrator dwells longer at each frequency component. Sweep length is usually in the range of 8 to 14 seconds.

If a vibrator sweep is 12 seconds long, then each reflection event also spans 12 seconds in the raw, uncorrelated data. It is not possible to interpret uncorrelated Vibroseis data because all reflection events overlay each other and individual reflections cannot be recognized. The data are reduced to an interpretable form by a crosscorrelation of the known input sweep with the raw data recorded at the receiver stations. Each time the correlation process finds a replication of the input sweep, it produces a compact symmetrical correlation wavelet centered on the long reflection event. In this correlated form, Vibroseis data exhibit a high signal-to-noise ratio, and reflection events are robust wavelets spanning only a few tens of milliseconds.

As a general observation, if an area is plagued by random noise, vibrators are an excellent energy source because the correlation process used to reduce the vibrator sweep to an interpretable form discriminates against noise frequencies that are outside the source sweep range. If several sweeps are summed, unorganized noise within the sweep range is attenuated. However, if coherent noise with frequencies within the vibrator sweep frequency range is present, then the correlation process may accentuate these noise modes. Refs. 4 through 13 are a portion of the available literature that describes the operating characteristics of vibrators and their ability to optimize signal-to-noise ratios.

Probably the most important improvement in vibrator operations has been the development of ground-force phase-locking technology.¹³ Application of this technology results in the same ground-force function (i.e., the same basic seismic wavelet) being generated during hundreds of successive sweeps by vibrators positioned over a wide range of ground-surface and soil conditions and by all vibrators in a multivibrator array. All aspects of seismic data processing benefit when a source generates consistent output wavelets throughout a seismic survey, hence the appeal of vibrators as the source of choice for most onshore surveys.

2.4 Shear Wave Sources

All seismic energy sources generate compressional (P) and shear (S) body waves. To study the physics and exploration applications of S-waves, it is often necessary to increase the amount of S-wave energy in the downgoing wavefield and to produce a shear wavefield that has a known vector polarization. These objectives can be accomplished with sources that apply horizontally directed impulses to the Earth or by vibrators that oscillate their baseplates horizontally rather than vertically. In either case, a heavy metal pad is used to impart horizontal movement to the Earth by means of cleats on the bottom side of the pad that project into the Earth. A specific design for a horizontal shear-wave vibrator can be found in a patent issued to Fair.¹⁴

Horizontal vibrators have also been improved with the introduction of ground-force phase-locking technology that results in more consistent shear wavelets from sweep to sweep as horizontal vibrators move across a prospect. Surface damage has been minimized by reducing the size of the cleats underneath the baseplate so that they make only shallow ground depressions.

2.5 Marine Air Guns

Air guns are now the primary energy sources used in offshore seismic profiling. Chemical explosives are no longer used for safety reasons and because of their adverse effects on marine biology. Modern seismic vessels tow multiple arrays of air guns, and each array sometimes has 10 or more air guns. The size and position of each air gun in the array are engineered so that the output wavelet has minimal bubble oscillations and optimal peak-to-peak amplitude. Fig. 2.1 shows map and section views of the deployment of air guns from a seismic vessel. The air guns and hydrophone cable are positioned at proper lateral offsets from each other by steering

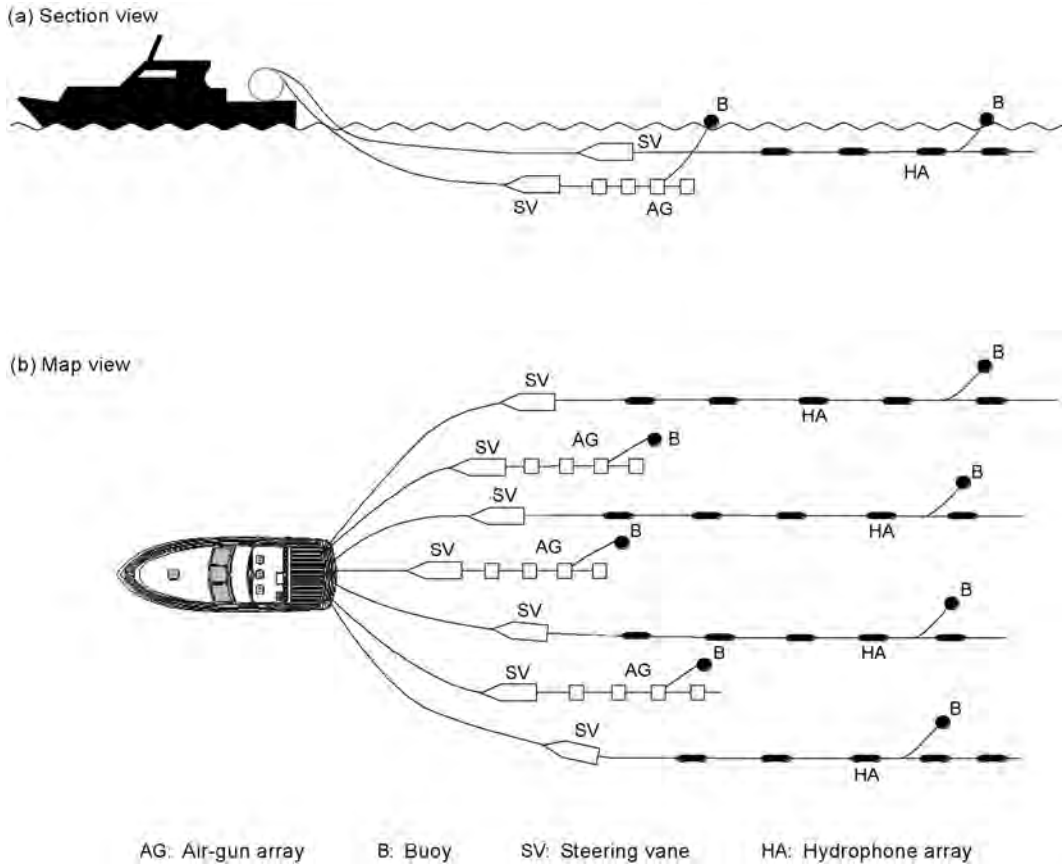


Fig. 2.1—Equipment deployed by marine seismic vessel with towed-cable technology.

vanes. Combinations of depth-control vanes and surface buoys keep the air guns and hydrophones at a constant depth as they are towed across a survey area.

The air-gun arrays are powered by large onboard compressors that allow the guns to fire and repressure (to approximately 2,000 psi) at intervals of 8 to 10 seconds as the vessel steams along a prescribed course at constant speed. These high-repetition firing rates create shotpoints at regular spacings of 20 to 100 m, depending on boat speed, along the length of the source line. In wide-line profiling, a vessel tows several air-gun arrays spaced 50 to 100 m apart laterally to create parallel source lines in one traverse of the vessel across a prospect area (Fig. 2.1).

Fig. 2.2 shows the raypaths involved in air-gun illumination of a geologic target. The seismic energy produced by an air-gun shot propagates up and down from the source array. The downgoing raypath creates the primary arrival. The upgoing raypath reflects from the water surface (where the reflection coefficient is -1 for an upgoing pressure wave) and travels downward as a time-delayed ghost event. Reduced-amplitude versions of the primary and ghost events follow at later times as the air bubble created by the shot oscillates and decays. These three components—primary arrival, ghost arrival, and bubble oscillations—combine to form the air-gun source wavelet.

The effectiveness of air-gun array parameters is tested in deepwater environments in which a hydrophone can be positioned at a deep, far-field station to record the source output wavelet, as shown in Fig. 2.2. The term far field refers to that part of wavefield propagation space that

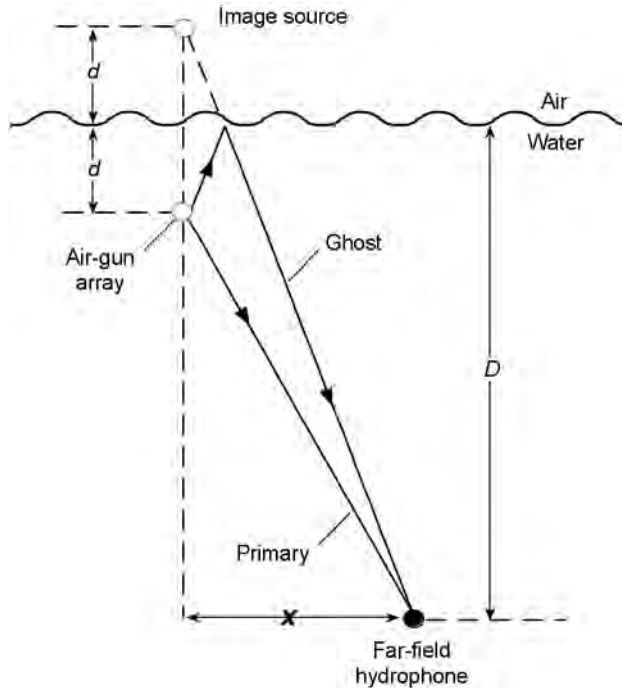


Fig. 2.2—Seismic raypaths involved in air-gun illumination of geologic targets.¹⁵

is several seismic wavelengths away from the source. This far-field requirement means that the hydrophone depth, D , shown in Fig. 2.2 is several hundreds of meters.

Air-gun arrays are designed to create source wavelets that are as compact in time as possible and that have minimal bubble oscillations. Compact wavelets are desired because such wavelets have wide signal-frequency spectra; minimal bubble oscillations are desired so that the signal spectrum will be as smooth as possible.

Fig. 2.3 shows an ideal source wavelet. The vertical dash line marks the arrival time of the bulk of the energy that travels the primary raypath (Fig. 2.2). The energy that travels the ghost raypath (Fig. 2.2) arrives at a time delay, $2d/v$, where v is the velocity of the pressure pulse in seawater and d is the depth of the air-gun array. The ghost event has a polarity opposite that of the primary arrival because the reflection coefficient for an upgoing pressure wave at the air/water interface is -1 . The primary and ghost arrivals define the peak-to-peak amplitude of the source wavelet. Small-amplitude events occur at later times in the source wavelet because the air bubble produced by the air-gun discharge oscillates as it decays (Fig. 2.3). The number, sizes, and relative separations of the guns in the array control the amplitude of these residual bubble oscillations.

The two wavelet properties of greatest interest are its peak-to-peak strength (PTP) and its primary-to-bubble ratio (PBR). The objectives of air-gun array design are to maximize the PTP property of an air-gun wavelet, which is the difference, $A-B$, in Fig. 2.4, and to minimize the PBR parameter, which is the ratio $(A-B)/(C-D)$.

Many factors, such as the number of guns in the array, the volume of the guns, and the depth of the guns, affect the amplitude, phase, and frequency character of an air-gun array wavelet. Table 2.1 summarizes Dragoset's¹⁵ analysis of air-gun array parameters and their effects on the fundamental PTP and PBR properties of air-gun wavelets. A key point in this

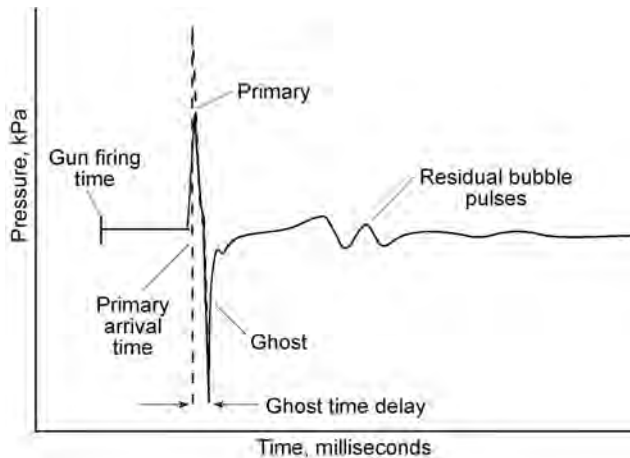


Fig. 2.3—Key features of an air-gun wavelet.¹⁵

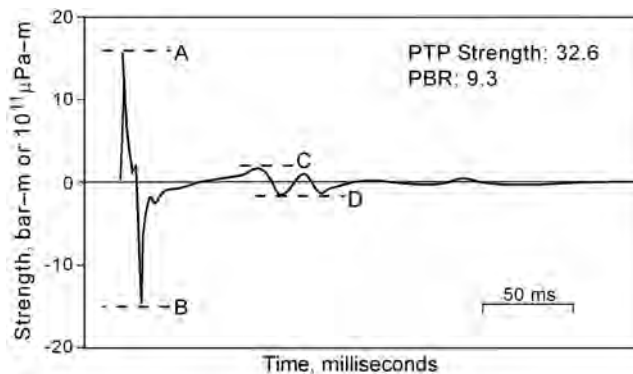


Fig. 2.4—Two important properties of an air-gun wavelet: peak-to-peak strength (A to B) and primary-to-bubble ratio [(A-B)/(C-D)].¹⁵

table is that the number of guns in an array has a greater impact on the peak-to-peak amplitude (or wavelet energy) than does the volume of the guns.

2.6 Seismic Sensors

Two classes of seismic sensors are used to acquire seismic data: scalar sensors and vector sensors. A scalar sensor measures the magnitude of Earth motion created by a seismic disturbance but does not indicate the direction of that motion. A hydrophone is an example of a popular scalar sensor used throughout the seismic industry. Hydrophones measure pressure variations (scalar quantities) associated with a seismic disturbance. A hydrophone cannot distinguish a pressure variation caused by a downgoing wavefield from a pressure change created by an upgoing wavefield. Hydrophones provide no directional (vector) information about a propagating seismic event.

A vector sensor indicates the direction that a seismic event causes the Earth to move. The classic example of a vector sensor is the moving-coil geophone that has been used for decades to record onshore seismic data. The principal of a moving-coil geophone is that a lightweight coil, with several hundred turns of thin copper wire, is suspended by springs that are, in turn,

TABLE 2.1—AIR-GUN SPECIFICATIONS AND ARRAY PARAMETERS (after Dragoset ¹⁵)		
	PTP Strength	Primary-to-Bubble Ratio
Number of guns	Proportional to number of guns	No direct relation
Gun volume	Proportional to cube root of gun volume	Increases as volume increases
Gun depth	Increases at first, then decreases as depth increases	Decreases as gun depth increases
Initial firing pressure	Increases as firing pressure increases	Increases as firing pressure increases
Port area	Proportional to square root of port area	Increases as port area increases
Port-closure pressure	No effect if closure pressure < 0.5 of firing pressure	Decreases as port-closure pressure increases
Gun synchronization	Decreases as spread in firing time increases	Decreases as spread in firing times increases
Horizontal separation of gun	Decreases as guns move closer together	Increases dramatically when gun bubbles coalesce

attached to the case of the geophone. The springs are designed to allow the geophone case and the lightweight coil to move independently of each other over a frequency band of interest. Permanent magnets are attached to the geophone case to create a strong internal magnetic field. When the case is moved by a seismic disturbance, an electrical voltage is created as the coils cut the magnetic lines of force. The magnitude of the voltage output is proportional to the number of magnetic lines of force cut per unit time; thus, geophone response indicates the velocity of the geophone case, which, in turn, is proportional to Earth particle velocity at the geophone station.

The polarity of the geophone output voltage depends on the direction that the electrical conductors are moving as they cut across the magnetic lines of force. If an upward movement creates a positive voltage, a downward movement produces a negative voltage. Thus, a geophone is a vector sensor that defines not only the magnitude of Earth motion, but also the direction of that motion.

Because geophones are directional sensors and can distinguish between vertical and horizontal Earth motions, they are used to record multicomponent seismic data. Three-component (3C) geophones are used to record compressional and shear seismic data onshore. Shear waves do not propagate in fluids. In marine environments, geophones have to be placed in direct contact with the Earth sediment on the seafloor, with data-recording cables connected to surface-positioned ships or telemetry buoys. Four-component (4C) sensors used for this service are encased in large, robust, watertight enclosures that include a hydrophone and a 3C geophone. **Fig. 2.5** illustrates a segment of an ocean-bottom cable (OBC) used for deploying 4C marine seismic sensors. In this cable design, a 4C sensor station is positioned at intervals of 50 m along the 150-m cable segment. A large number of these segments, each containing three receiver stations, are connected end to end to make a continuous OBC receiver line several kilometers long. The exact length of the receiver line is determined by the depth of the target that is to be imaged.

Fig. 2.6 shows an OBC line deployed on the seafloor and connected to a stationary data-recording vessel. A second boat towing an air-gun array traverses predesigned source lines either parallel to, or orthogonal to, the OBC cable. The 4C sensors remain motionless on the seafloor as data are recorded, just as onshore geophones do when onshore seismic data are acquired. Seafloor sensors are not towed as are the conventional marine hydrophone cables shown in **Fig. 2.1**.

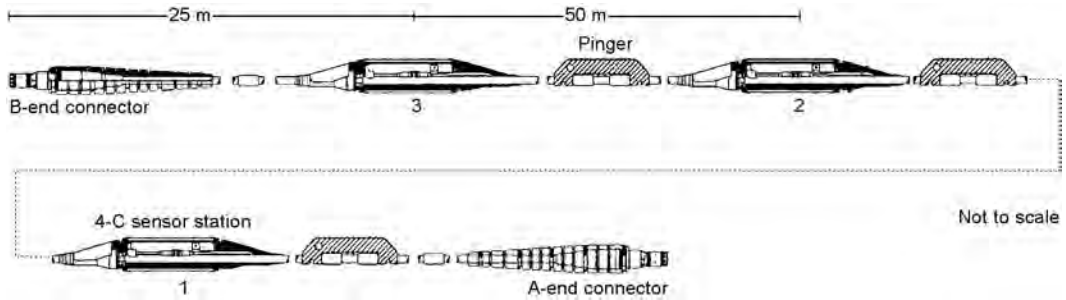


Fig. 2.5—Segment of ocean-bottom cable with three 4C sensor stations spaced 50 m apart.

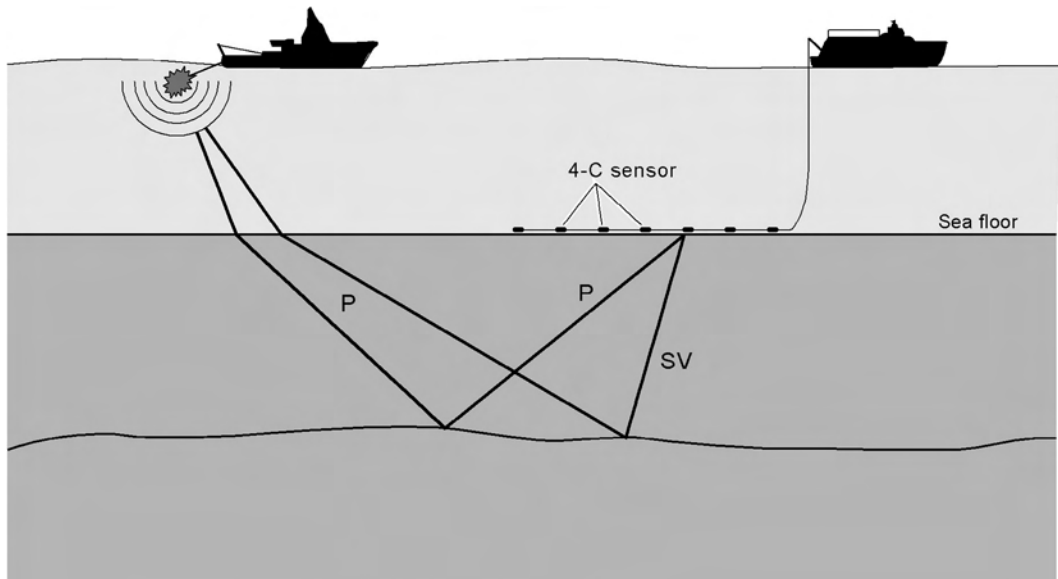


Fig. 2.6—Basic elements of ocean-bottom cable data acquisition. P denotes a seismic compressional wave; SV is a converted shear mode.

2.7 Seismic Wave Propagation

The full elastic seismic wavefield that propagates through an isotropic Earth consists of a P-wave component and two shear (SV and SH) wave components. Marine air guns and vertical onshore sources produce reflected wavefields that are dominated by P and SV modes. Much of the SV energy in these wavefields is created by P-to-SV-mode conversions when the downgoing P wavefield arrives at stratal interfaces at nonnormal angles of incidence (Fig. 2.6). Horizontal-dipole sources can create strong SH modes in onshore programs. No effective seismic horizontal-dipole sources exist for marine applications.

A principal difference among P, SV, and SH wavefields is the manner in which they cause rock particles to oscillate. Fig. 2.7 illustrates the relationships between propagation direction and particle-displacement direction for these three wave modes. A compressional wave causes rock particles to oscillate in the direction that the wavefront is propagating. In other words, a P-wave particle displacement vector is perpendicular to its associated P-wave wavefront. In contrast, SV and SH waves cause rock particles to oscillate perpendicular to the direction that the wavefront is moving, with the SH and SV displacement vectors orthogonal to each other.

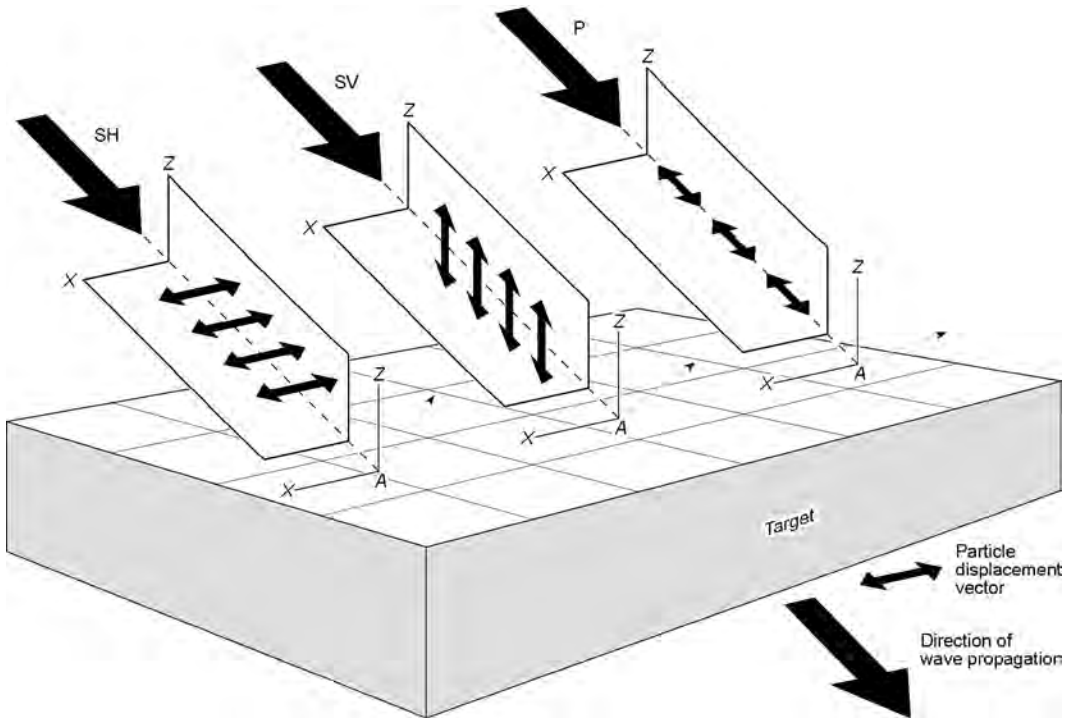


Fig. 2.7—Distinction between the three components of an elastic wavefield.

A shear-wave particle-displacement vector is thus tangent to its associated wavefront. In a flat-layered isotropic Earth, the SH displacement vector is parallel to stratal bedding, and SV displacement is in the plane that is perpendicular to bedding.

To create optimal images of subsurface targets, a seismic wavefield must be segregated into its P, SV, and SH component parts so that a P-wave image can be made that has minimal contamination from interfering SV and SH modes. Likewise, an SV image must have no interfering P and SH modes, and an SH image must be devoid of P and SV contamination.

A P wave travels at velocity V_p in consolidated rocks, which is approximately two times faster than velocity V_s of either the SH or SV wave. In carbonates, the velocity ratio (V_p/V_s) tends to be approximately 1.7 or 1.8. In siliciclastics, V_p/V_s varies from approximately 1.6 in hard sandstones to approximately 3 in some shales. This velocity difference aids in separating interfering P and S wave modes during data processing. An equally powerful technique for separating a seismic wavefield into its component parts is to use data-processing techniques that concentrate on the distinctions in the particle displacements associated with the P, SH, and SV modes (Fig. 2.7).

The P, SH, and SV particle displacements shown in Fig. 2.7 form an orthogonal coordinate system. The fundamental requirement of multicomponent seismic imaging is that reflection wavefields must be recorded with orthogonal 3C sensors that allow these P, SH, and SV particle motions to be recognized. To date, most exploration seismic data have been recorded with single-component sensors that emphasize P-wave modes and do not capture SH or SV wave modes.

2.8 Body Waves and Surface Waves

Seismic wavefields propagate through the Earth in two ways: body waves and surface waves. Body waves propagate in the interior (body) of the Earth and illuminate deep geologic targets.

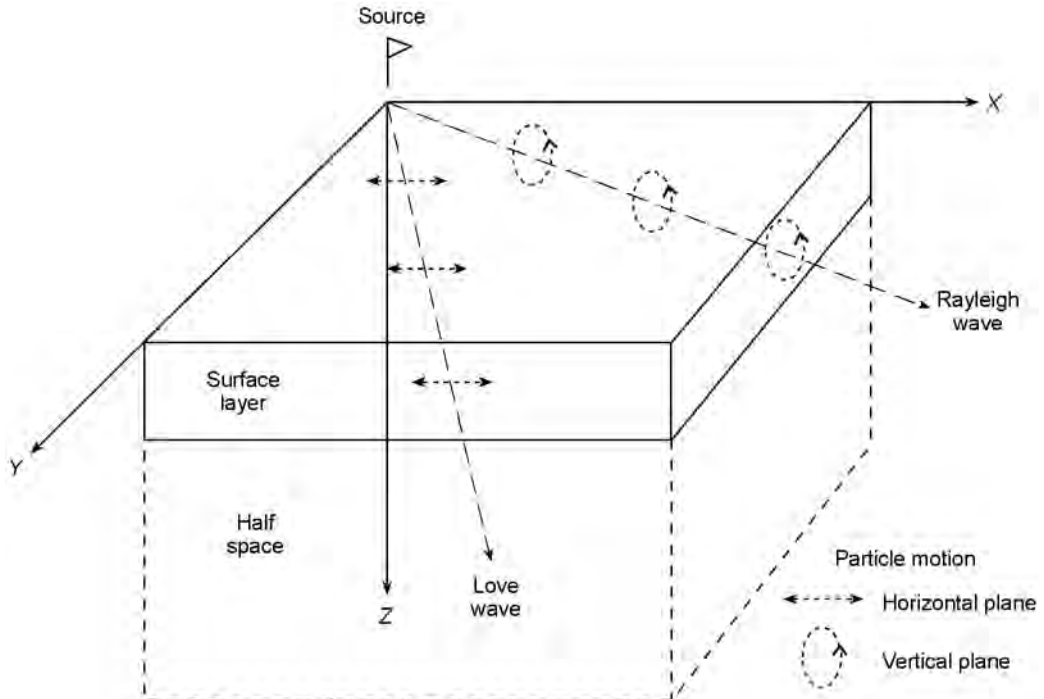


Fig. 2.8—Particle motions produced by the two principal seismic surface-wave noise modes: the Love wave and the Rayleigh wave.

These waves generate the reflected P, SH, and SV signals that are needed to evaluate prospects and to characterize reservoirs. Reflected (or scattered) body waves are the fundamental signals sought in seismic data-acquisition programs.

Surface waves travel along the Earth/air interface and do not illuminate geologic targets in the interior of the Earth. Surface waves are noise modes that overlay the desired body-wave reflections. Surface waves can be a serious problem in onshore seismic surveys. Surface waves do not affect towed-cable marine data because they require some shear-wave component to propagate, and shear waves cannot propagate along the air/water interface. An exception in the marine case is sometimes encountered when data are recorded with ocean-bottom sensors (OBS) because interface waves can propagate along the water/sediment boundary and become a type of surface-wave noise that degrades OBS marine seismic data.

There are two principal surface waves: Love waves and Rayleigh waves (**Fig. 2.8**). Love waves are an SH-mode surface wave and do not affect conventional P-wave seismic data. Love waves are a serious noise mode only when the objective is to record reflected SH wavefields. The more common surface wave is the Rayleigh wave, which combines P and SV motions and is referred to as ground roll on P-wave seismic field records. Love waves create particle displacements in the horizontal plane; Rayleigh wave displacements are in the vertical plane (**Fig. 2.8**).

Much of the field effort in onshore seismic programs concentrates on designing and deploying receiver arrays that can attenuate horizontally traveling surface waves (ground-roll noise) and, at the same time, amplify upward-traveling reflection signals. The most effective field technique is to deploy 10, 12, 16, or more geophones at a uniform spacing at each receiver station so that the distance from the first geophone to the last geophone is the same as the dominant wavelength of the ground-roll event. All geophone responses are then summed to create a single output response at that receiver station. The idea is to create a sensor array length such that

half of the geophones are moving up and half are moving down as the horizontally traveling ground roll passes the receiver station. The summed output of the geophone array is essentially zero because of the passage of the ground-roll event. In contrast, upward-traveling reflections arriving at this same receiver array are not attenuated because such events cause all geophones to move up and down in unison. The summed output of the array for an upward-traveling reflection wavefield is thus a strong voltage signal.

2.9 Seismic Impedance

The concept of acoustic (or seismic) impedance is critical to understanding seismic reflectivity. Seismic impedance controls the seismic reflection process in the sense that seismic energy is reflected only at rock interfaces in which there are changes in impedance across the interface. Seismic impedance is defined as

$$I = \rho V, \dots\dots\dots (2.1)$$

where I = impedance, ρ = the bulk density of the rock, and V = the velocity of seismic wave propagation through the rock. V is set to V_p if the wave mode of interest is a P wave; it is set to V_s if S-wave reflectivity is being considered. Any alteration in rock properties that causes ρ and/or V to change can be the genesis of a seismic reflection event; therefore, areal and vertical variations in seismic reflectivity can be used to infer spatial distributions of rock types and porosity trends.

2.10 Reflection Coefficients

Seismic reflectivity is best explained with a simple two-layer Earth model in which Layer 1 is above Layer 2 (Fig. 2.9). The seismic reflection coefficient, R , for a downgoing particle-velocity wave mode that arrives perpendicular to the interface between the two layers is

$$R = \frac{I_1 - I_2}{I_1 + I_2} = \frac{\rho_1 V_1 - \rho_2 V_2}{\rho_1 V_1 + \rho_2 V_2} \dots\dots\dots (2.2)$$

A negative algebraic sign has to be inserted on the right side of Eq. 2.2 if the downgoing wavefield is a pressure wavefield (hydrophone measurement) rather than a particle-velocity wavefield (geophone measurement). The velocity parameters, V_1 and V_2 , are P-wave velocities if P-wave reflectivity is being calculated; they are S-wave velocities if S-wave reflectivity is to be determined. At any interface, R can be positive, negative, or zero, depending on the impedance contrast ($\rho_1 V_1 - \rho_2 V_2$) across the interface.

A seismic reflection/transmission process is indicated in Fig. 2.9 by the raypaths labeled A_o , A_r , and A_t . For nonnormal incidence angles, the expression for reflection coefficient involves trigonometric functions that ensure that horizontal slowness (the inverse of horizontal velocity) is conserved and is a more complex expression than that given in Eq. 2.2. Ref. 16 gives a detailed mathematical treatment. The seismic reflection, A_r , is given by

$$A_r = R A_o, \dots\dots\dots (2.3)$$

and the transmitted seismic event, A_t , is given by

$$A_t = (1 + R) A_o \dots\dots\dots (2.4)$$

The magnitude and algebraic sign of A_r depends on R and, in turn, the basic control on R is the variation of impedance ρV across the interface (Eq. 2.2). Table 2.2 lists the common geo-

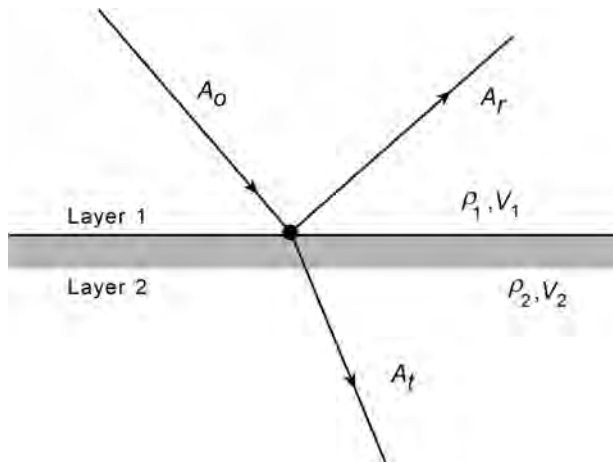


Fig. 2.9—Two-layer Earth model describing seismic reflectivity parameters.

TABLE 2.2—GEOLOGICAL INFLUENCES ON ACOUSTIC IMPEDANCE

Geologic Condition	Impedance Effect
Lithological interfaces	A common cause of impedance contrasts. Generally ρ and V change whenever there is a change in lithology.
Porosity variations	ρ and V are porosity dependent. Gradual changes in porosity generate modest impedance contrasts. Abrupt changes in porosity can create large reflection coefficients.
Changes in pore fluid	Pore-fluid density affects bulk density ρ and velocity V . A change of pore fluid from water to oil creates a small impedance contrast that can be detected seismically only in ideal signal-to-noise conditions. A change from liquid (either water or oil) to gas can produce large impedance contrasts and robust seismic reflections.
Overpressure	ρ and V decrease in overpressure zones. If the onset of overpressure is gradual, the impedance contrasts may be too small to create detectable seismic reflections. Abrupt onsets of overpressure can produce strong reflections.
Cementation	Cementation affects the mechanical strength of rocks. V generally increases as mechanical strength increases (assuming a constant rock type). In some instances, variations in cementation can create impedance contrasts sufficient to result in seismic reflections.

logic conditions that often create impedance contrasts that result in nonzero reflection coefficients at rock interfaces.

Two types of petrophysical properties control the value of acoustic impedance in individual rock layers: elastic properties of the rock matrix and properties of the fluid in the pore spaces of the rock. P-waves travel through elastic materials and fluids; thus, any change in either the rock matrix (such as a change in mineralogy or porosity) or in the type of fluid occupying the pore spaces will create a discontinuity in the P-wave seismic impedance of the rock system.

Fig. 2.10 illustrates the relationships between petrophysical conditions that occur at an impedance boundary and the existence of P and S reflections at that boundary. A P-wave reflection will occur at boundaries at which there is a change in either the rock matrix or the pore fluid, or both. In contrast, S-waves are not affected by changes in pore fluid or are only weakly affected. Consequently, a change in the properties of the rock matrix can create a re-

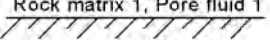
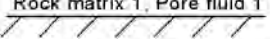
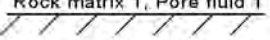
Boundary conditions	P-reflection	S-reflection
Rock matrix 1, Pore fluid 1  Rock matrix 1, Pore fluid 2	Yes	No (may be weak)
Rock matrix 1, Pore fluid 1  Rock matrix 2, Pore fluid 1	Yes	Yes
Rock matrix 1, Pore fluid 1  Rock matrix 2, Pore fluid 2	Yes	Yes

Fig. 2.10—Relationships between petrophysical conditions that occur at an impedance boundary and the existence of P and S reflections at that boundary.¹⁷

fecting boundary for S-waves, but a change in pore fluid will create only a small (usually negligible) S-wave reflection boundary (Fig. 2.10). If a small, nonzero S-wave reflection coefficient occurs at a fluid boundary, that reflection coefficient usually exists because the bulk density of the rock system varies across the fluid boundary.

These wave physics provide valuable geologic insights when both P and S reflection data are acquired across a prospect area. When P and S reflections occur at the same depth coordinate, the reflecting boundary at that depth is associated with a change in the rock matrix (that is, with a lithological change). There may or may not be a change in pore fluid at that boundary. When a P reflection occurs at a boundary but there is no S reflection, that boundary quite likely marks a change in pore fluid and not a change in rock matrix. (That is, the lithology probably does not change at that depth, but the type of pore fluid does.)

2.11 Seismic Attributes

The fundamental properties of processed seismic data that are used in interpretation are temporal and spatial variations of reflection amplitude, reflection phase, and wavelet frequency. Structural and stratigraphic interpretations of 3D seismic data are inferences of geologic conditions made by analyzing areal patterns of these three seismic attributes—amplitude, phase, and frequency—across selected seismic time surfaces. Any procedure that extracts and displays these seismic parameters in a convenient, understandable format is an invaluable interpretation tool.

Taner and Sheriff¹⁸ and Taner *et al.*¹⁹ began using the Hilbert transform to calculate seismic amplitude, phase, and frequency instantaneously, meaning that a value of amplitude, phase, and frequency is calculated for each time sample of a seismic trace. Since that introduction, numerous Hilbert transform algorithms have been implemented to calculate these useful seismic attributes (e.g., Hardage²⁰).

2.12 Complex Seismic Trace

Fig. 2.11 illustrates the concept of a complex seismic trace in which $x(t)$ represents the real seismic trace and $y(t)$ is the Hilbert transform of $x(t)$. In this discussion, we ignore what a Hilbert transform is and how the function $y(t)$ is calculated. Most modern seismic data-process-

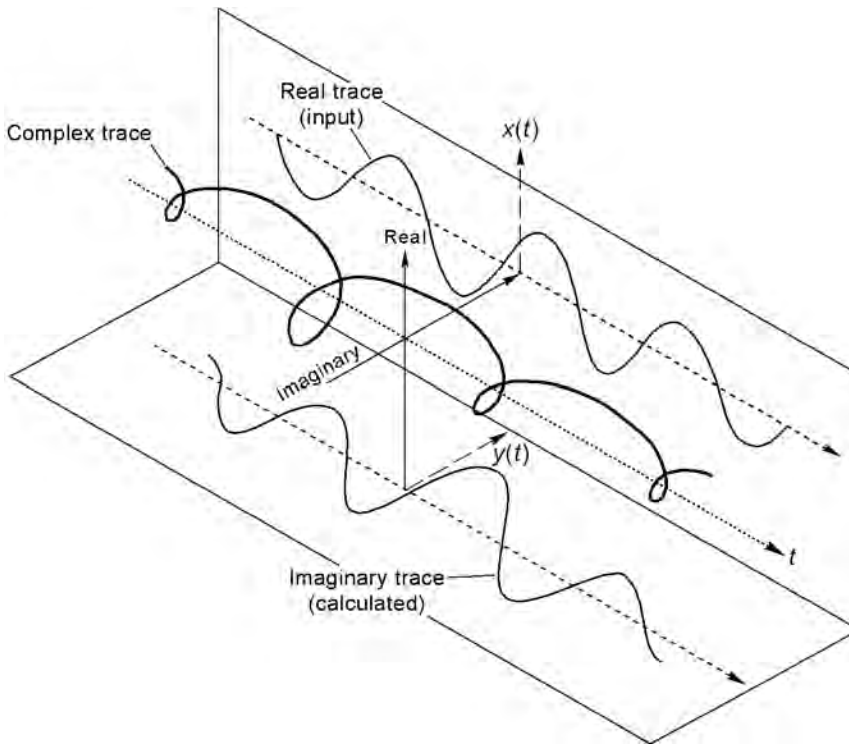


Fig. 2.11—A complex seismic trace.²¹

ing software packages provide Hilbert transform algorithms and allow processors to create the function $y(t)$ shown in Fig. 2.11 easily. These two data vectors are displayed in a 3D (x, y, t) space in which t is seismic travelt ime, x is the real data plane, and y is the imaginary plane. In this complex trace format, the actual seismic trace, $x(t)$, is confined to the real x plane, and $y(t)$, the Hilbert transform of $x(t)$, is confined to the imaginary y plane. When $x(t)$ and $y(t)$ are added vectorally, the result is a complex seismic trace, $z(t)$, in the shape of a helical spiral extending along, and centered about, the time axis t . The projection of this complex function $z(t)$ onto the real plane is the real seismic trace, $x(t)$, and the projection of $z(t)$ onto the imaginary plane is $y(t)$, the calculated Hilbert transform of $x(t)$.

Fig. 2.12 illustrates the reason for converting the real seismic trace, $x(t)$, into what first appears to be a more mysterious complex seismic trace, $z(t)$, in which the attributes known as instantaneous seismic amplitude, instantaneous phase, and instantaneous frequency are introduced. At any point on the time axis of this complex seismic trace, a vector $a(t)$ can be calculated that extends away from the t axis in a perpendicular plane to intersect the helically shaped complex seismic trace, $z(t)$. The length of this vector is the amplitude of the complex trace at that particular instant, hence the term instantaneous amplitude. This amplitude value is calculated with the equation for $a(t)$ shown in Fig. 2.12.

The orientation angle, $\phi(t)$, of the amplitude vector, $a(t)$, at time t , which is generally measured relative to the positive axis of the real x -plane, is defined as the phase of $z(t)$ at that moment in time. Numerically, the phase angle is calculated from the equation for $\phi(t)$ defined in Fig. 2.12. As seismic time progresses, vector $a(t)$ moves along the time axis and rotates continually about the time axis to maintain contact with the spiraling complex trace, $z(t)$. Each full rotation of the vector around the time axis increases the phase value by 360° .

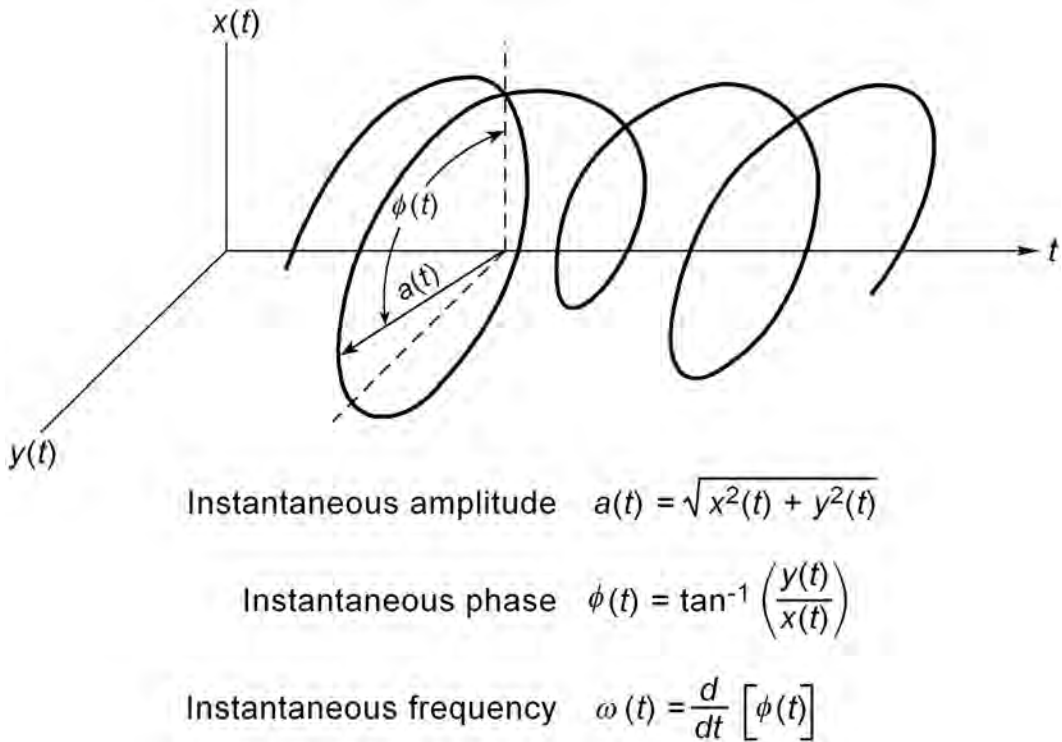


Fig. 2.12—Key seismic attributes (instantaneous amplitude, instantaneous phase, and instantaneous frequency) that can be calculated once a complex seismic trace is created.²¹

In any oscillating system, and specifically for a seismic trace, frequency can be defined as the time rate of change of the phase angle. This fundamental definition describes the frequency of the complex seismic trace so that the instantaneous frequency, $\omega(t)$, at any seismic time sample is given by the time derivative of the phase function specified by the equation in Fig. 2.12.

2.13 Instantaneous Phase and Instantaneous Frequency Calculations

Fig. 2.13 illustrates calculations of the instantaneous phase associated with a typical seismic trace. The figure's bottom panel shows the actual seismic trace, and the center panel shows the real and imaginary components of the associated complex trace. Applying the second equation of Fig. 2.12 to the real and imaginary components of the complex seismic trace (center panel) produces the instantaneous phase function at the top of Fig. 2.13. The phase behavior at times t_1 , t_2 , t_3 is critical to understanding the geologic significance of anomalous frequencies. Although phase is a positive function that monotonically increases in magnitude with seismic time, it is customarily plotted as a repetitive, wraparound function with plot limits of 0 to 360° (or -180° to +180°). Each wraparound of 360° corresponds to a full rotation of vector $a(t)$ around the seismic time axis while the vector stays in contact with the spiraling complex seismic trace $z(t)$ (see Fig. 2.12).

The top panel of Fig. 2.14 shows the instantaneous frequencies calculated for the seismic trace presented in Fig. 2.13. Although the calculated frequency values at times t_1 and t_2 shown by the solid-line curve are physically impossible because they are negative, these anomalous frequency behaviors are some of the most useful seismic attributes that an interpreter can use. They should be preserved because, when displayed in an eye-catching, contrasting color, they

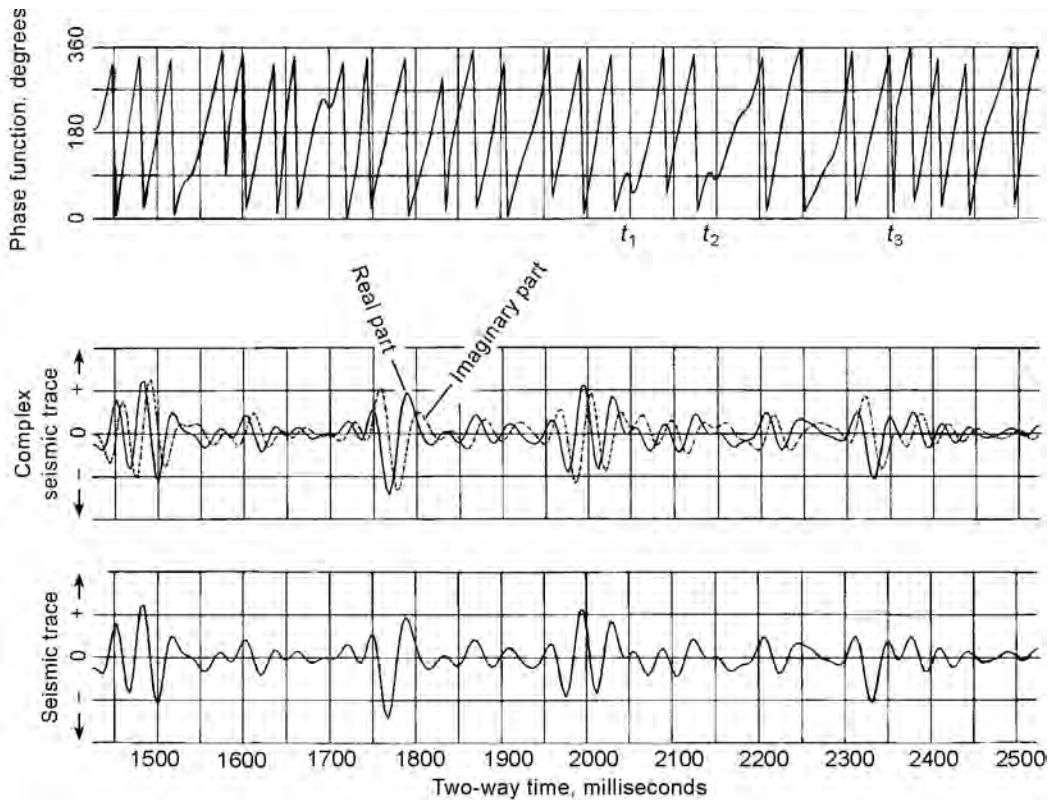


Fig. 2.13—Instantaneous phase seismic attribute function.²¹

serve to shift an interpreter's attention quickly to subtle structural and stratigraphic discontinuities in a seismic image.

Comparing the time coordinates of these anomalous frequency values with the time coordinates of the instantaneous phase function in Fig. 2.13 shows that rather than exhibiting its typical, monotonically increasing behavior in these time intervals, the phase momentarily decreases in magnitude. This causes the time rate of change of phase (or the slope of the phase function), which is the instantaneous frequency, to be negative at time samples t_1 and t_2 . Numerical algorithms should not camouflage these unrealistic frequency values, which some algorithms do by arbitrarily reversing the algebraic sign of any negative frequency. The dashed-curve segments in the enlargement show how some software algorithms change the algebraic sign of negative frequency values to positive values. Although this seems like a logical correction, it should be avoided because it reduces the interpretive value of a 3D volume of instantaneous frequencies.

At times t_1 , t_2 , and t_3 , some type of wavelet interference (that is, a wavelet distortion) occurs in the seismic trace (bottom panel). As a result, the reflection waveform at times t_1 , t_2 , and t_3 is slightly distorted (bottom panel) because of the destructive interference of two or more overlapping wavelets, demonstrating that anomalous frequencies tend to coincide with, and emphasize, distorted wavelets such as are produced at structural and stratigraphic discontinuities. High positive frequency values also occur at 1580, 1650, 1740, and 1840 milliseconds, but these values are not anomalous in the sense that they do not exceed the Nyquist limit (125 Hz). However, they too coincide with distorted wavelets (bottom panel).²¹

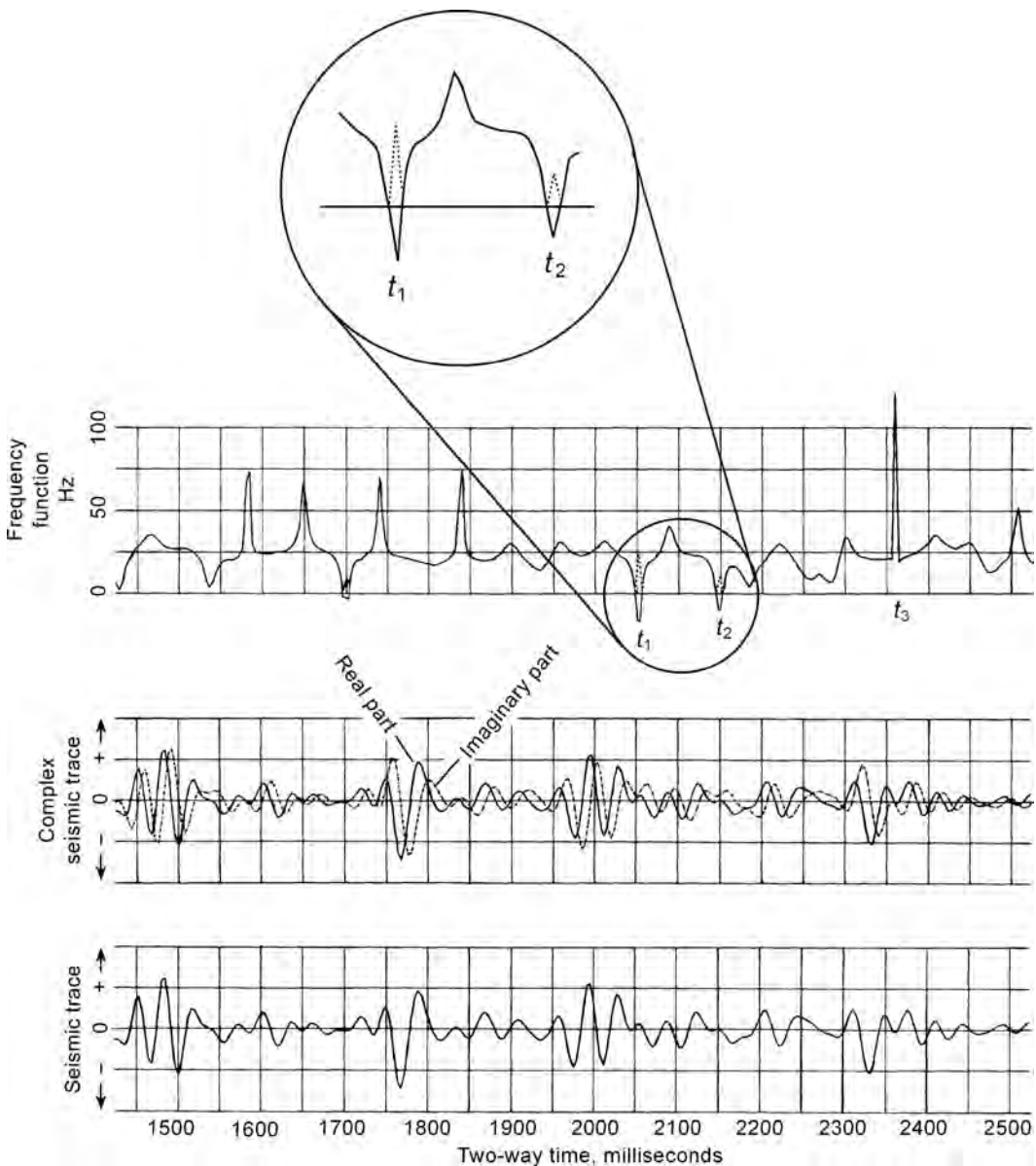


Fig. 2.14—Instantaneous frequency seismic attribute function calculated for the same seismic trace discussed in Fig. 2.13.

2.14 Applications of Seismic Attributes

All instantaneous seismic attributes (amplitude, phase, frequency) can be used in interpretation. In practice, most interpreters use instantaneous amplitude, or some variation of an amplitude attribute, as their primary diagnostic tool. Amplitude is related to reflectivity, which in turn is related to subsurface impedance contrasts. Thus, amplitude attributes provide information about all the rock, fluid, and formation-pressure conditions listed in Table 2.2.

Instantaneous phase is useful for tracking reflection continuity and stratal surfaces across low-amplitude areas where it is difficult to see details of reflection waveform character. In general, instantaneous phase is the least used of the seismic attributes.

Instantaneous frequency sometimes aids in recognizing changes in bed thickness and bed spacing. Anomalous values of instantaneous frequency (negative values or unbelievably high positive values) are particularly useful for recognizing edges of reservoir compartments, subtle faults, and stratigraphic pinchouts. Hardage²² demonstrated these applications of instantaneous frequency.

2.15 Seismic Interpretation

A stratal surface is a depositional bedding plane: a depositional surface that defines a fixed geologic time. A siliciclastic rock deposited in a high-accommodation environment contains numerous vertically stacked stratal surfaces. A fundamental thesis of seismic stratigraphy is that a seismic reflection event follows an impedance contrast associated with a stratal surface; that is, a seismic reflection is a surface that represents a fixed point in geologic time.^{23,24} The term chronostratigraphic defines this type of seismic reflection event. Because lithology varies across the area spanned by a large depositional surface, the implication of this interpretation principle is that an areally pervasive seismic reflection event does not necessarily mark an impedance contrast boundary between two fixed rock types as that reflection traverses an area of interest. The application of this fundamental concept about the genetic origin of seismic reflections to seismic interpretation is referred to as stratal-surface seismic interpretation.

Tipper²⁵ illustrated and discussed situations in which a seismic reflection can be either chronostratigraphic or diachronous (meaning that the event moves across depositional time surfaces), depending on the vertical spacings between beds, the lateral discontinuity between diachronous beds, and bed thickness. The conclusion that a seismic reflection is chronostratigraphic or diachronous needs to be made with caution because the answer depends on the local stratigraphy, the seismic bandwidth, and the horizontal and vertical resolution of the seismic data.

If two seismic reflection events, A and B, are separated by an appreciable seismic time interval (a few hundred milliseconds) yet are conformable to each other (that is, they parallel each other), then the uniform seismic time thickness between these two events represents a constant and fixed period of geologic time throughout the seismic image space spanned by reflectors A and B. An implication of seismic stratigraphy that can be invoked in such an instance is that any seismic surface intermediate to A and B, which is also conformable to A and B, is also a stratal surface.

A key first step in seismic interpretation is to use well logs and cores to identify the three types of stratal interfaces that exist in geologic intervals of interest: flooding surfaces, maximum flooding surfaces, and erosion surfaces. Flooding surfaces are widespread interfaces that contain evidence of an upward, water-deepening facies dislocation, such as contact between rooted, unfossiliferous floodplain mudstones and overlying fossiliferous marine shale. A ravine-ment surface is a specific type of flooding surface that suggests that transgressive passage of a surf zone has eroded underlying shallower-water facies.

Maximum flooding surfaces are interfaces that contain evidence of a widespread, upward, water-deepening facies dislocation that is associated with the inferred, deepest water facies encountered in a succession of strata. A maximum flooding surface is commonly represented by a thin condensed section, typically a black, organic-rich shale with a low-diversity fossil assemblage representing deepwater, sediment-starved conditions.

Maximum flooding surfaces bound and define upward-coarsening facies successions that are called genetic sequences by Galloway.²⁶ These genetic sequences are similar to cycles or cyclothems in other terminology.^{27,28}

An erosion surface is an interface in which there is evidence of a facies offset that indicates that an abrupt decrease in water depth occurred. If an erosion surface is widespread, truncation of older strata can be documented on well log cross sections. Some of these surfaces may be disconformities representing downcutting during periods of subaerial exposure caused by allocyclic (extrabasinal) mechanisms, such as eustatic sea-level changes. These major

chronostratigraphic surfaces are often manifested as mappable seismic reflections. All 3D seismic data volumes should be calibrated with mappable, key surfaces recognized from cores and well logs, with priority given to flooding surfaces, maximum flooding surfaces, and erosion surfaces. See the chapter on reservoir geology in this volume for more discussion on sequence stratigraphy and depositional environments.

2.16 Structural Interpretation

The original use of seismic reflection data (circa 1930 through 1960) was to create maps depicting the geometry of a subsurface structure. Because many of the world's largest oil and gas fields are positioned on structural highs, structural mapping has been, in a historical sense, the most important application of exploration seismic data. When the seismic industry converted from analog to digital data recording in the mid-1960s, digital technology increased the dynamic range of reflected seismic signals and allowed seismic data to be used for applications other than structural mapping, such as stratigraphic imaging, pore-fluid estimation, and lithofacies mapping. These expanded seismic applications have led to the discovery of huge oil and gas reserves confined in subtle stratigraphic traps, and seismic exploration is now no longer limited to just "mapping the structural highs." However, even with the advances in seismic technology, structural mapping is still the first and most fundamental step in interpretation. When 3D seismic data are interpreted with modern computer workstations and interpretation software, structural mapping can be done quickly and accurately.

Different seismic interpreters use different approaches and philosophies in their structural interpretations. The technique described here is particularly robust and well documented.²⁹ The first step of the procedure is to convert the 3D seismic data volume that has to be interpreted to a 3D coherency volume. Coherency is a numerical measure of the lateral uniformity of seismic reflection character in a selected data window. As the waveform character of side-by-side seismic traces becomes more similar, the coherency value for the traces approaches a value of +1.0; as the traces become more dissimilar, the coherency of the traces approaches zero. All modern seismic interpretation software can perform the numerical transform that converts 3D seismic wiggle-trace data into a 3D coherency volume.

Fig. 2.15 shows an example of a horizontal time slice through a 3D coherency volume from the Gulf of Mexico. This figure is also discussed in the chapter on reservoir geophysics in the *Emerging Technologies* volume of this *Handbook*. The narrow bands of low coherency values that extend across this time slice are created by faults that disrupt the lateral continuity of reflection events. Fault mapping is a major component of structural mapping, and this type of coherency display can be used to create fast, accurate fault maps. Coherency technology has evolved into the optimal methodology for detecting and mapping structural faults in 3D seismic image space.

The second step of the structural interpretation procedure is to transfer the fault pattern defined by coherency data to the associated 3D seismic wiggle-trace data volume. **Fig. 2.16** illustrates the projection of the faults in **Fig. 2.15** onto a vertical profile through 3D seismic image space. The coherency time slice in **Fig. 2.15** defines the X, Y coordinates of each intersected fault at one constant, image-time coordinate across the image space. Additional coherency time slices are made at image-time intervals of 100 or 200 milliseconds to define the X, Y coordinates of each fault as a function of imaging depth. This procedure causes the orientations and vertical extents of faults transferred to a 3D seismic wiggle-trace volume to be quite accurate.

The first-order fault labeled in **Fig. 2.16** extends through the entire stratigraphic column and create large vertical displacements of strata. The second-order faults have less vertical extent and cause less vertical displacement than the first-order faults. Other structural and stratigraphic features that are common in Gulf of Mexico geology are labeled. These features are identified to indicate the imaging capabilities of seismic data. Rollover indicates fault-related flexing of bedding, which results in structural trapping of hydrocarbons. The bright spot is an

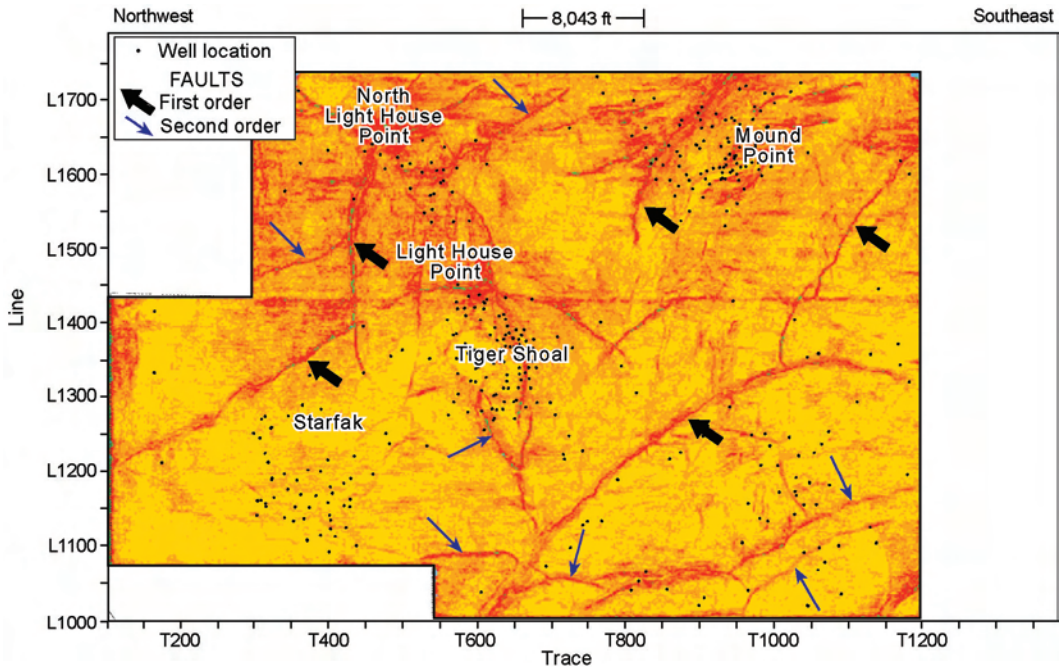


Fig. 2.15—Horizontal slice through a 3D coherency volume imaging a producing area in the Gulf of Mexico.²⁹

example of reflection amplitude reacting as a direct hydrocarbon indicator (see changes in pore fluid in Table 2.2). The velocity sag feature is a false structural effect caused by anomalously low seismic propagation velocity that delays reflection arrival times, leaving the misleading appearance of a structural sag.

The third step of this approach to structural mapping is to interpret a series of chronostratigraphic surfaces across the seismic image space. These surfaces can be any of the chronostratigraphic surfaces (flooding surfaces, maximum flooding surfaces, and erosion surfaces) described in Sec. 2.15, depending on the amount and quality of subsurface well control available to the interpreter. If there is no well control, interpreters must use their best judgment as to how to correlate equivalent strata across a seismic image space and then adjust their interpretation, if necessary, as wells are drilled.

When a selected stratal surface is extended across the complete seismic image space, the geometrical configuration of that chronostratigraphic surface can be displayed as a structure map. The structure map in Fig. 2.17 is one of the chronostratigraphic surfaces interpreted across this Gulf of Mexico prospect with the fault geometry information defined by coherency slices (Fig. 2.15) and vertical slices (Fig. 2.16). The producing fields shown in the map are positioned on local structural highs associated with one or more first-order faults.

In the lower left of the map in Fig. 2.17, an arbitrary profile XX' is shown crossing the fault swarm. Fig. 2.18 displays a vertical section along this profile to demonstrate the degree to which faults compartmentalize producing strata. This expanded view of the seismic reflection character also reveals critical stratigraphic features, such as lowstand wedges, that are embedded in the faulted structure. (A lowstand wedge is a sedimentary wedge deposited during a period of low sea level.) This type of seismic interpretation allows stratigraphers to construct detailed models of the internal architecture of targeted reservoir systems.

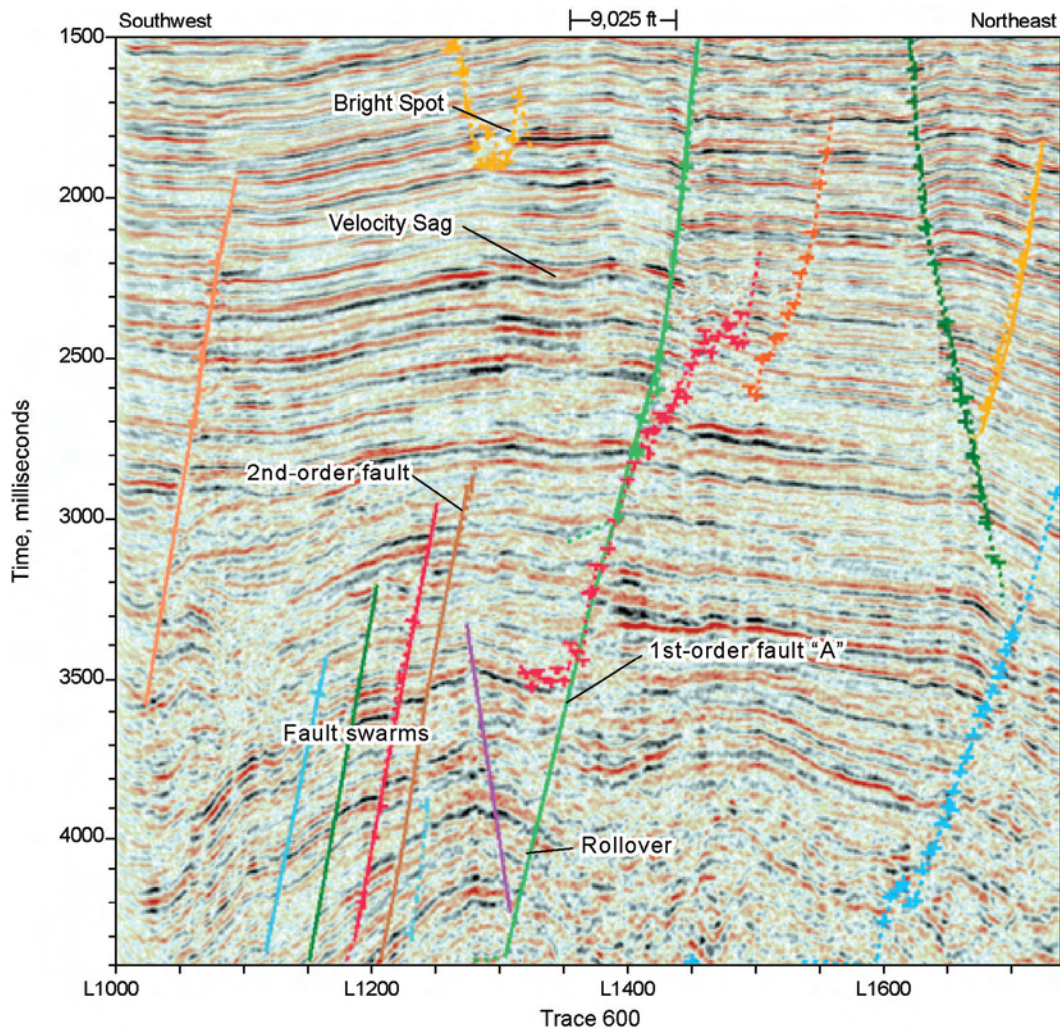


Fig. 2.16—Vertical seismic slice along crossline T600 of Fig. 2.15.²⁹

Fig. 2.19 shows a second structural map constructed from a shallower chronostratigraphic surface to illustrate that less fault compartmentalization is in shallow reservoirs than in the deeper reservoirs associated with the structure shown in Fig. 2.17. The first-order faults still displace strata at this shallow level, but most second-order faults have terminated at deeper depths and no longer cause reservoir compartmentalization.

The structure maps shown in Figs. 2.17 and 2.19 are time-structure maps. These maps can be converted to depth maps once seismic propagation velocities are determined through the stratigraphic column.

2.17 Imaging Reservoir Targets

Fig. 2.20 shows a data window from a vertical slice of a 3D seismic data volume that is centered on a targeted channel system. These data include a good-quality reflection peak labeled “reference surface.” The reference surface is a reference seismic stratal surface used to construct additional stratal surfaces that pass through the targeted thin-bed interval.³⁰ The fluvial system is embedded in the reflection peak that occurs at 0.73 seconds at inline coordinate 120.

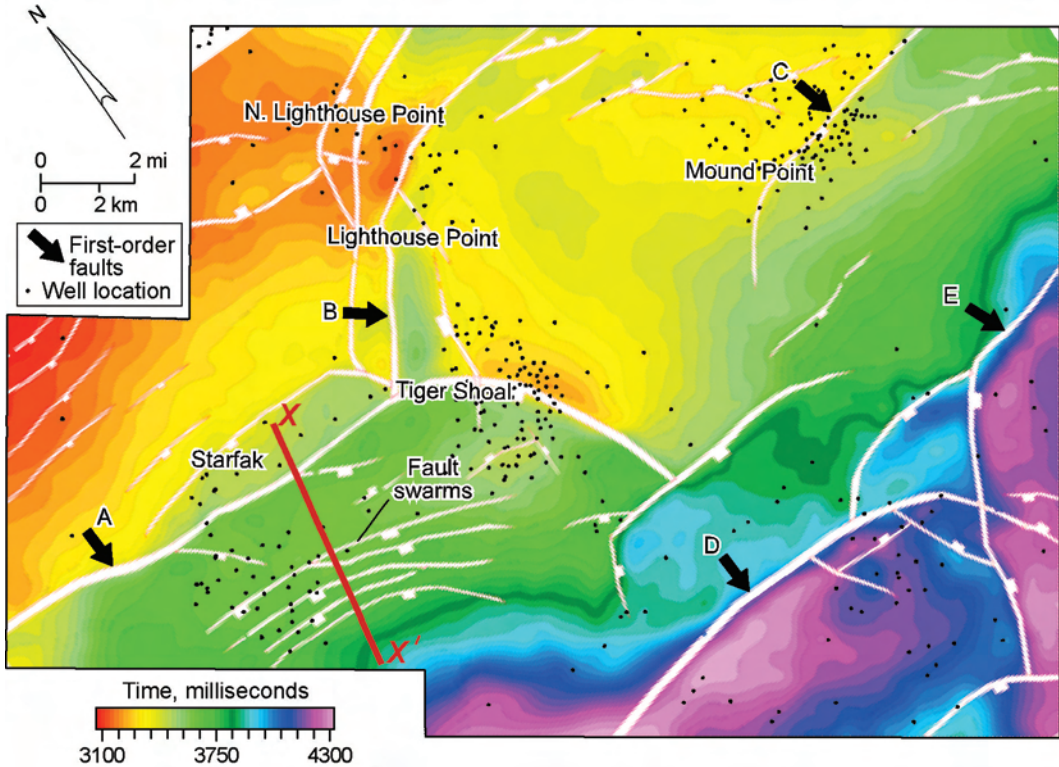


Fig. 2.17—Time-structure map of a deep reservoir system exhibiting considerable fault-induced compartmentalization.²⁹

This particular reflection peak satisfies the fundamental criteria required of a reference stratal surface used to study thin-bed sequences: the event extends over the total 3D image space and has a high signal-to-noise character; the event is reasonably close to the targeted thin-bed sequences that need to be studied (i.e., the strata related to the anomalous reflection waveforms labeled “Channel 1” approximately 90 milliseconds above the reference surface); and the event is conformable to (i.e., parallel to) this targeted thin-bed sequence. The third criterion is the most important requirement for any seismic stratal surface that is to be used as a reference surface. Because this reference surface follows the apex of an areally continuous reflection peak, the basic premise of seismic stratigraphy is that this reference surface follows an impedance contrast that coincides with a stratal surface.

Fig. 2.21 displays this crossline section view with four conformable surfaces (A, B, C, and D) that pass through the targeted thin-bed interval added to the profile. These four surfaces are, respectively, 92, 90, 88, and 86 milliseconds above—and conformable to—the reference surface. Visual inspection of the reflection events above and below surfaces A, B, C, and D shows that all these reflection peaks and/or troughs are reasonably conformable to the reference surface event. Surfaces A, B, C, and D can thus be assumed to be stratal surfaces, or constant-depositional-time surfaces, because they are conformable to a known stratal surface (the reference surface) and are embedded in a 200-millisecond seismic window in which all reflection events are approximately conformable to the selected reference surface. The highlighted data window encircles subtle changes in reflection waveform that identify the seismic channel facies.³⁰

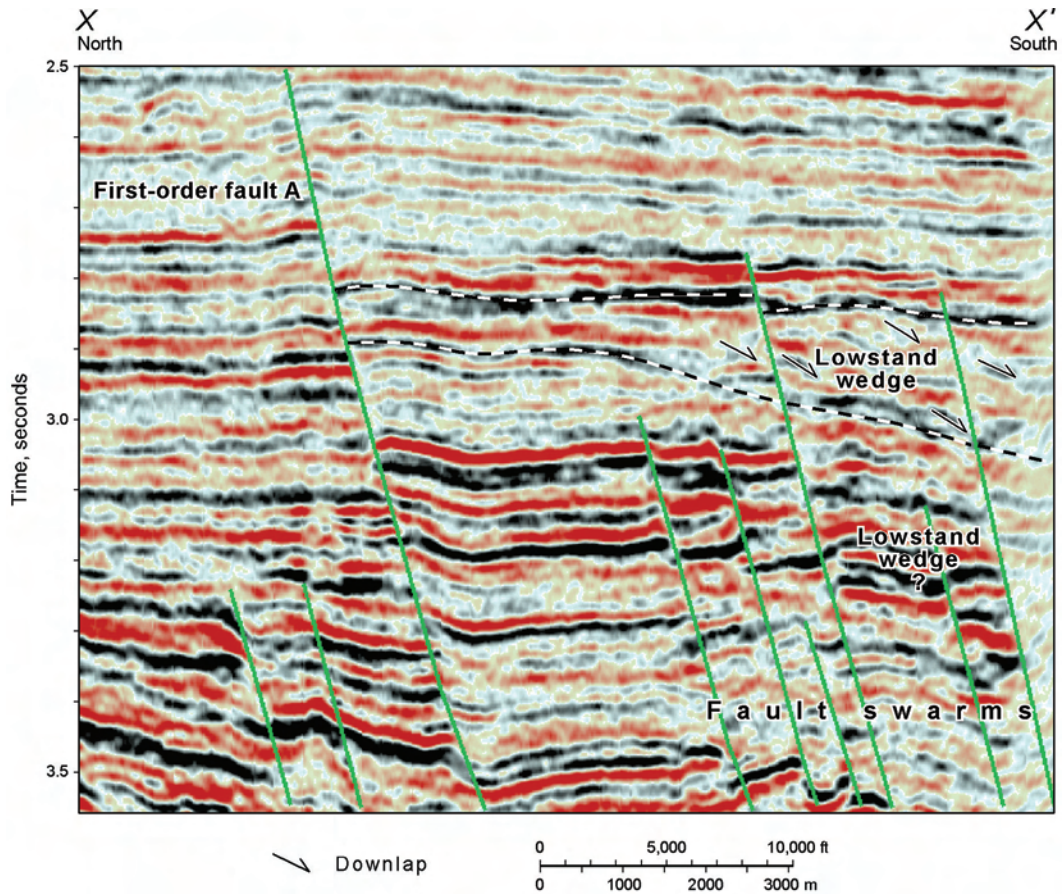


Fig. 2.18—Vertical seismic slice along profile XX' (Fig. 2.17) showing faulted stratigraphic features.²⁹

The circled features in Fig. 2.21 identify locations where stratal surfaces A, B, C, and D intersect obvious variations in reflection waveform. These waveshape changes are the critical seismic reflection character that distinguishes channel facies from nonchannel facies, as can be verified by comparing the inline coordinates spanned by the circled features (coordinates 60 to 70) with these same inline coordinates where this crossline (number 174) intersects the channel features labeled “Channel 1” in Fig. 2.22.

Fig. 2.22 shows reflection-amplitude behavior on stratal surface B, which is 90 milliseconds above, and conformable to, the selected seismic reference surface. This surface shows portions of the Channel 1 system in the lower right quadrant of the image. A second channel system (Channel 2) is located in the upper right quadrant.³⁰ The channel-system image shown in Fig. 2.22 is a surface-based image; that is, the seismic attribute that is displayed (which is reflection amplitude in this instance) is limited to a data window that vertically spans only one data sample. When a 1-point-thick data window is a good approximation of a stratal surface that passes through the interior of a targeted thin-bed sequence, then the seismic attributes defined on that surface can be important depictions of facies distributions within the sequence, as the image in this figure demonstrates.

An alternate, and usually more rigorous, way of determining facies distributions within a thin-bed sequence is to calculate seismic attributes in a data window that spans several data points vertically, yet is still confined (approximately) to only the thin-bed interval that needs to be

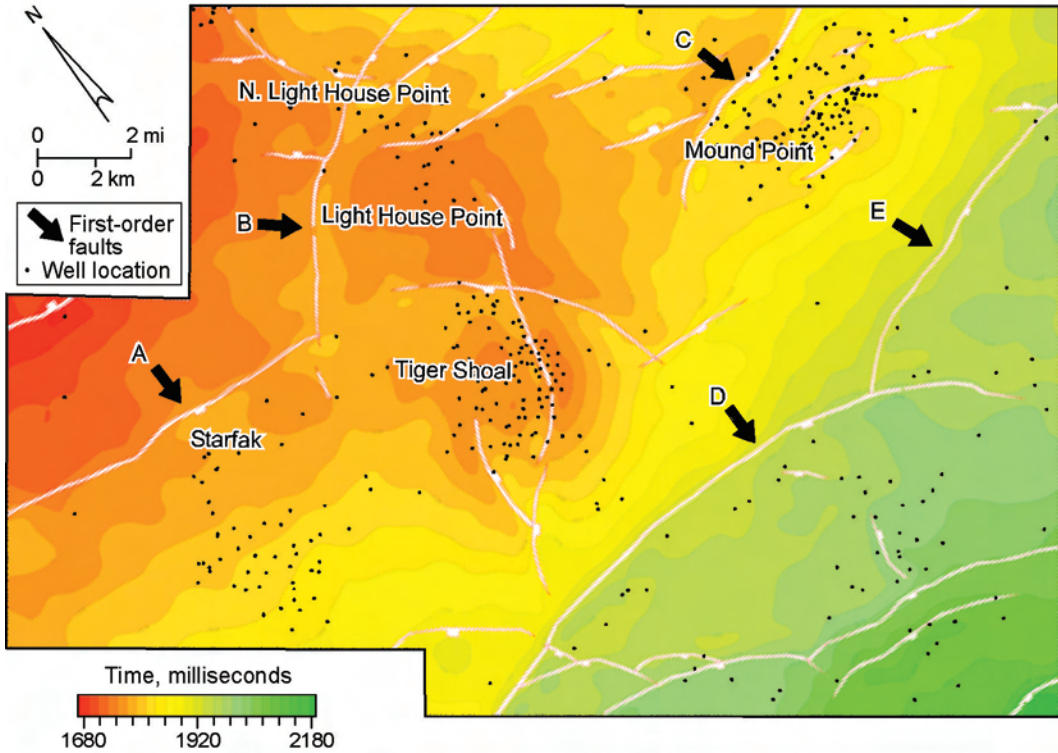


Fig. 2.19—Shallow time-structure map showing reduced influence of second-order faults compared with the deeper structure of Fig. 2.17.²⁹

studied. The bottom stratal surface of this data window must reasonably coincide with the onset depositional time of the sequence, and the top stratal surface must be a good approximation of the shutoff depositional time of the sequence. Such a data window is called a stratal-bounded seismic analysis window.

Stratal surfaces A and D shown in the section view in Fig. 2.21 are examples of surfaces that define a stratal-bounded data analysis window that spans a targeted thin-bed sequence, specifically a thin-bed fluvial channel system that was the interpretation objective of this 3D seismic program. In this instance, the analysis window is 4 data points (8 milliseconds) thick. As stated in the discussion of Fig. 2.21, surfaces A, B, C, and D are good-quality stratal surfaces because each horizon images a significant part of the thin-bed fluvial system that was deposited over a “short” geological time period. Because each of these four seismic horizons is a good approximation of a constant-depositional-time surface, the four surfaces collectively are a good representation of the facies distribution within the total thin-bed sequence that they span.

One way to evaluate facies-sensitive seismic information spanned by surfaces A and D is to calculate some type of an averaged seismic attribute in each stacking bin (the concept of a stacking bin is described in Sec. 2.18.1) of the 4-point-thick data analysis window bounded by horizons A and D. For example, the average peak amplitude between A and D could be used to show an alternate image of the total channel system.

In thin-bed interpretations such as the fluvial channel system considered here, it is important to try to define two seismic reference surfaces that bracket the thin-bed system to be interpreted: one reference surface below the interpretation target and the second reference surface above the target. By creating conformable reference stratal surfaces above and below a thin-

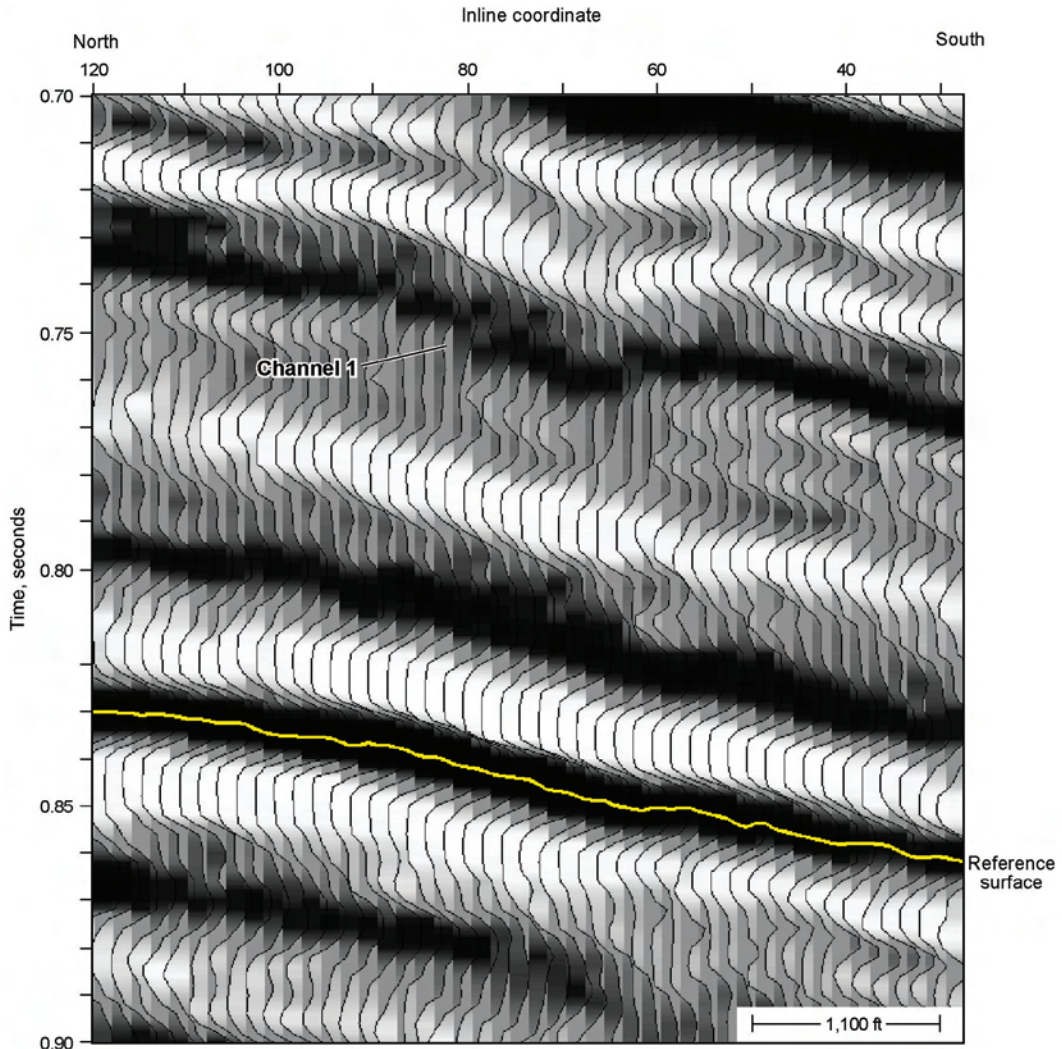


Fig. 2.20—Data window from a vertical slice of a 3D seismic data volume that is centered on a targeted channel system (Channel 1).

bed system, an interpreter can extend a series of conformable seismic stratal surfaces from two directions to sweep across a thin-bed target. A set of seismic stratal surfaces extended across an interval from above the interval is often a better approximation of constant-depositional-time surfaces within a targeted thin-bed sequence than is a set of stratal surfaces extended across the interval from below the interval (or vice versa). The more accurate set of surfaces will produce more reliable images of facies patterns within the thin-bed unit.

To illustrate the advantage of this opposite-direction convergence of seismic stratal surfaces onto a thin-bed target, a second reference surface was interpreted above (and, in this case, closer to) the targeted fluvial system studied in Figs. 2.20 through 2.22. Specifically, this second stratal reference surface followed the apex of the reflection troughs immediately above the thin-bed channels. Fig. 2.23 shows the location of reference surface 2 on a second vertical slice (crossline 200) through the 3D seismic data volume. Reference surface 1 is the horizon labeled “reference surface” in Fig. 2.20. Reference surface 2 is an alternate seismic stratal surface posi-

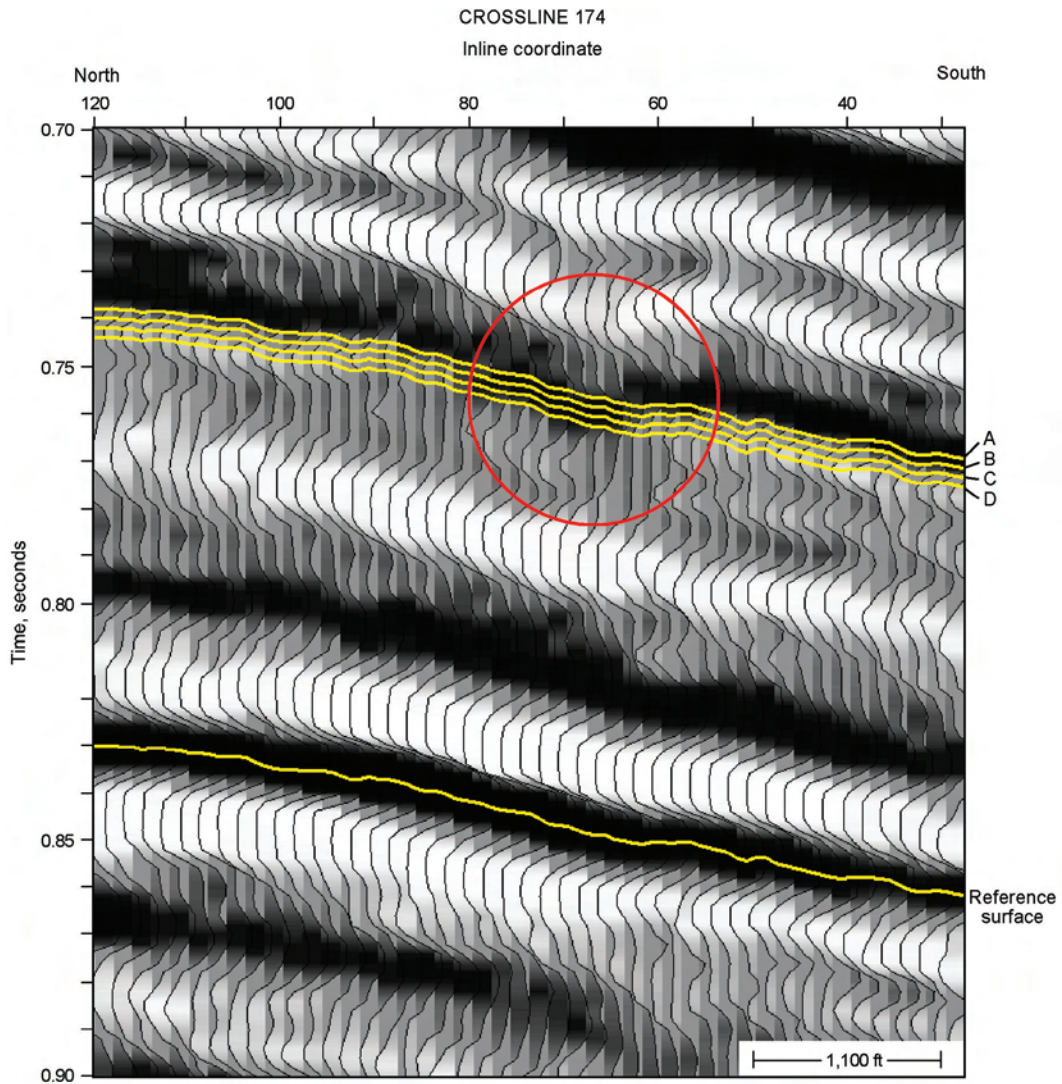


Fig. 2.21—Data window from the selected vertical slice showing stratal surfaces that traverse the channel system.³⁰

tioned above the Channel 1 thin-bed target.³⁰ The targeted fluvial system referred to as Channel 1 is approximately 24 to 30 milliseconds below this second reference surface.

Fig. 2.24 displays the reflection-amplitude response across the channel systems observed on a stratal surface 26 milliseconds below and conformable to reference surface 2, as defined in Fig. 2.23. An improved channel image occurs, when compared with the image in Fig. 2.22, because in this case stratal surfaces that are conformable to the overlying seismic stratal surface happen to be better approximations of constant-depositional-time surfaces for this channel system than are stratal surfaces that are conformable to the deeper reference surface. This result illustrates that the combination of upward and downward extrapolations of conformable stratal surfaces across a thin-bed target is a good interpretation procedure, especially in those instances in which valid stratal reference surfaces can be interpreted both above and below the targeted thin bed.

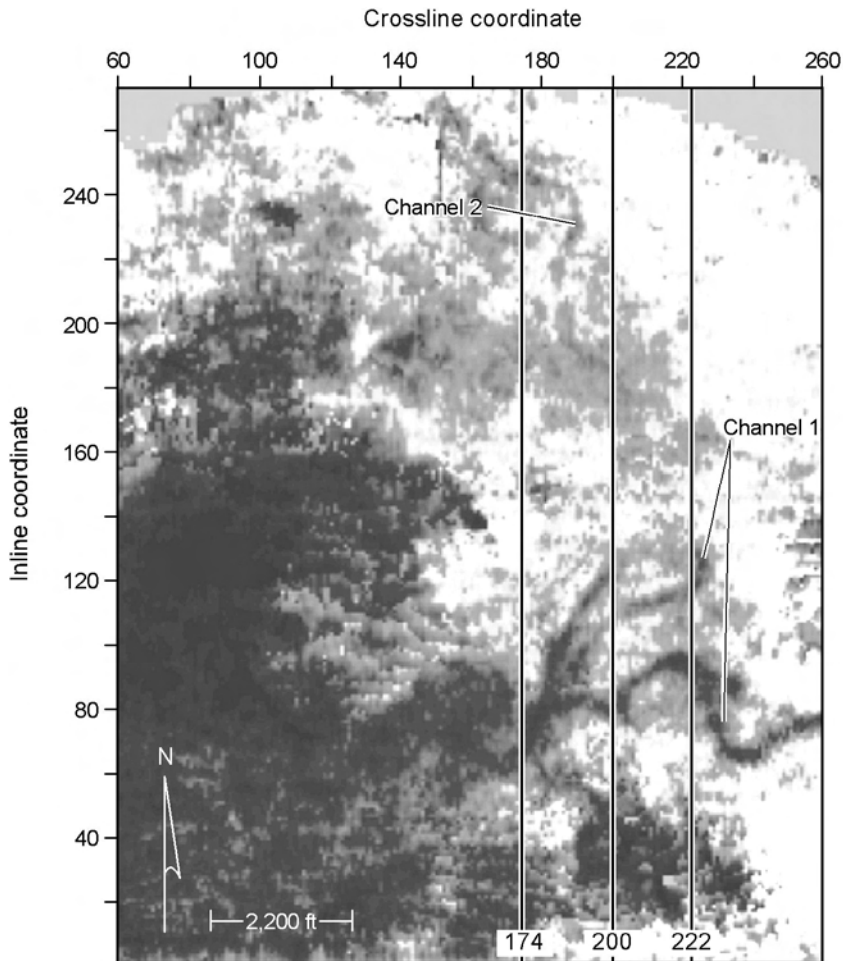


Fig. 2.22—Reflection-amplitude behavior on stratal surface B, which is 90 milliseconds above, and conformable to, the selected seismic reference surface.³⁰

In summary, a good technique for interpreting thin-bed targets in 3D seismic data volumes is to interpret a reference surface that is conformable to the areal geometry of the thin-bed sequence and then to create seismic stratal surfaces conformable to this reference surface that pass through the thin-bed target. If the seismic stratal surfaces constructed according to this logic are satisfactory approximations of constant-depositional-time surfaces that existed during the deposition of the thin-bed sequence, the seismic attributes across these stratal surfaces are usually valuable indicators of facies distributions within the sequence.

A second technique is to expand the application of this stratal-surface concept by calculating seismic attributes inside a thin, stratal-bounded analysis window that is centered vertically on the thin-bed target. Facies-sensitive attributes extracted from carefully constructed stratal-bounded windows are often better indicators of facies distributions within a thin-bed target than are attributes that are restricted to a 1-point-thick stratal surface that passes through the target. This fact implies that the geologic time interval during which a thin-bed sequence is deposited can sometimes be portrayed satisfactorily by a stratal-bounded data window, whereas a fixed geologic time during the thin-bed deposition is not well approximated by a 1-point-thick seismic stratal surface. Interpreters have to try both approaches to determine an optimal procedure.

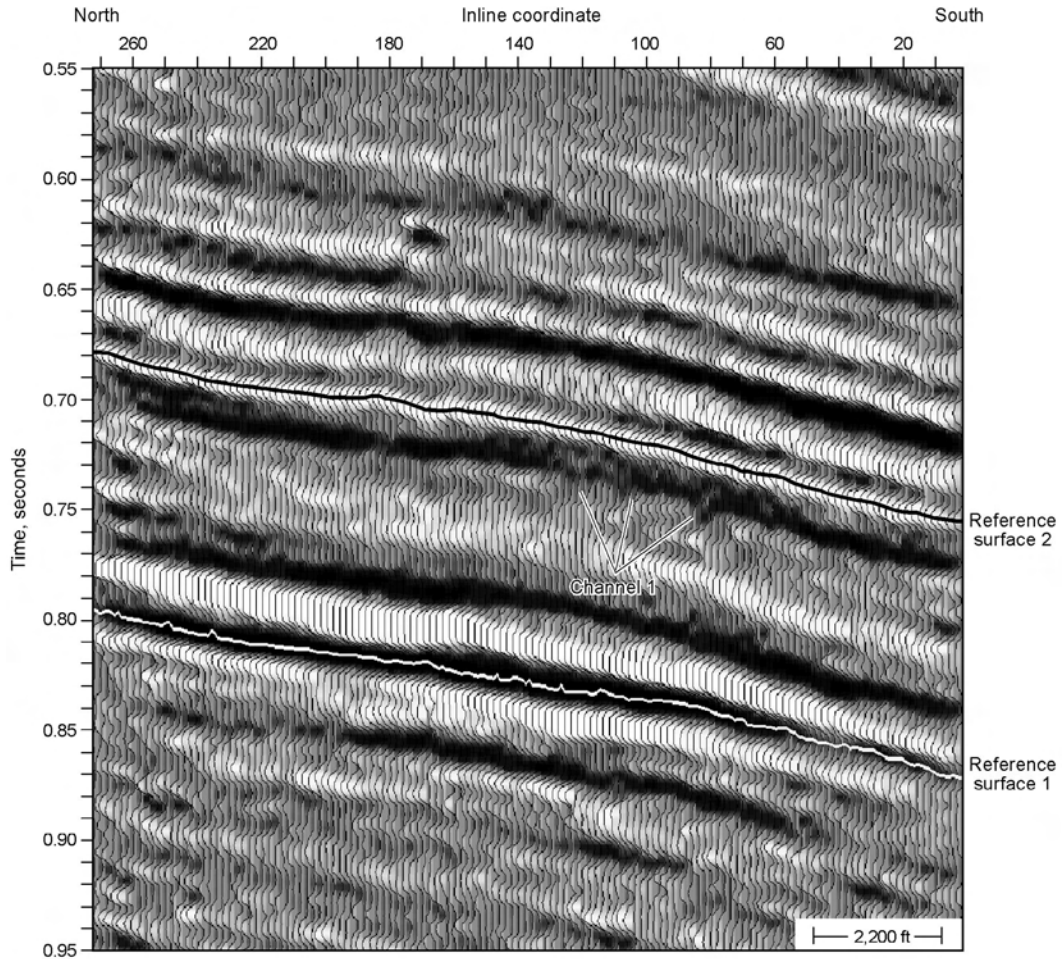


Fig. 2.23—Location of reference surface 2 on a second vertical slice (crossline 200) through the 3D seismic data volume.³⁰

A third technique is to extend a series of conformable seismic stratal surfaces and stratal-bounded windows onto the thin-bed target from opposite directions, that is, from both below and above the thin-bed target. The logic in this dual-direction approach is that one of the seismic reference surfaces may be more conformable to the thin-bed sequence than the other reference surface and that this improved conformability will lead to improved attribute imaging of facies distributions within the thin bed.

2.18 Three-Dimensional Seismic Survey Design

2.18.1 Stacking Bins. The horizontal resolution a 3D seismic image provides is a function of the trace spacing within the 3D data volume. As the separation between adjacent traces decreases, horizontal resolution increases. At the conclusion of 3D data processing, the area spanned by a 3D seismic image is divided into a grid of small, abutted subareas called stacking bins. Each trace in a 3D seismic data volume is positioned so that it passes vertically through the midpoint of a stacking bin.

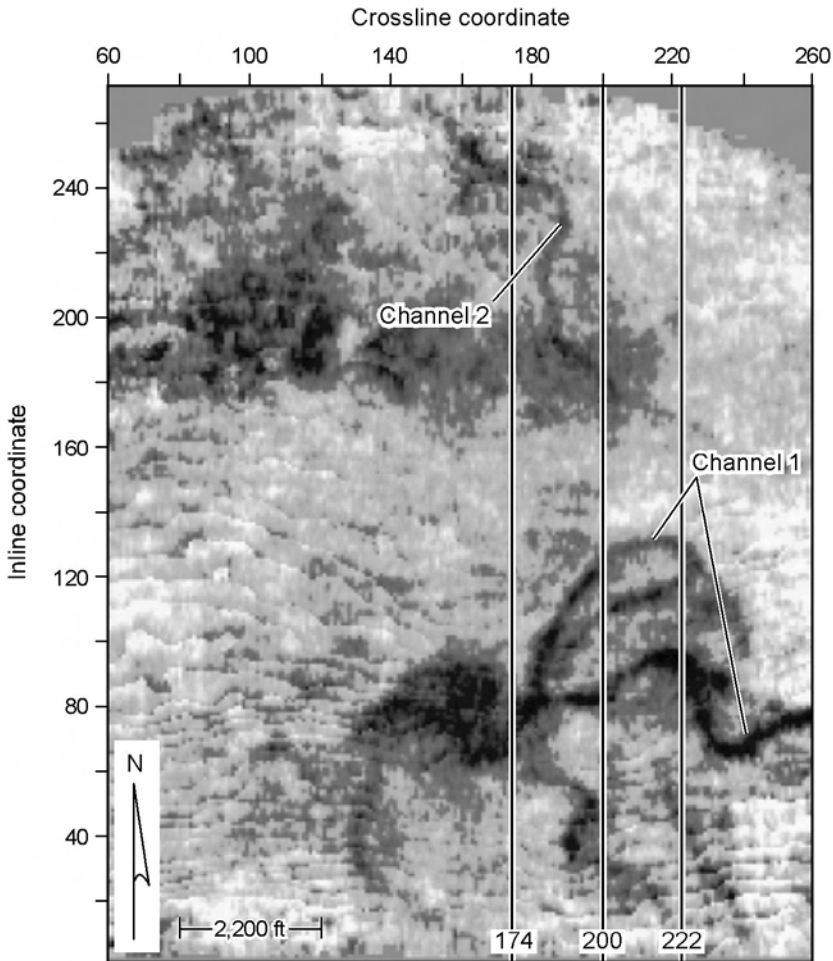


Fig. 2.24—Three-dimensional seismic image of the targeted thin-bed fluvial channel system.³⁰

In Fig. 2.25, each stacking bin has lateral dimensions of Δx and Δy . The horizontal separations between adjacent processed traces in the 3D data volume are also Δx and Δy . The term inline is defined as the direction in which receiver cables are deployed, which is north/south in this example. Inline coordinates increase from west to east as shown. Crossline refers to the direction that is perpendicular to the orientation of receiver cables; thus, the crossline coordinates increase from south to north.³¹ These stacking bins can be square or rectangular, depending on an interpreter's preferences. The dimension of the trace spacing in a given direction across a 3D image is the same as the horizontal dimension of the stacking bin in that direction. As a result, horizontal resolution is controlled by the areal size of the stacking bin.³²

The imaging objective dictates how small a stacking bin should be. Smaller stacking bins are required if the resolution of small stratigraphic features is the primary imaging requirement. As a general rule, there should be a minimum of three stacking bins, and preferably at least four bins, across the narrowest stratigraphic feature that needs to be resolved in the 3D data volume. This imaging principle causes the targeted stratigraphic anomaly to be expressed on three or four adjacent seismic traces.

As Fig. 2.26 illustrates, the critical parameter to be defined in 3D seismic design is the smallest (narrowest) horizontal dimension of a stratigraphic feature that must be seen in the 3D

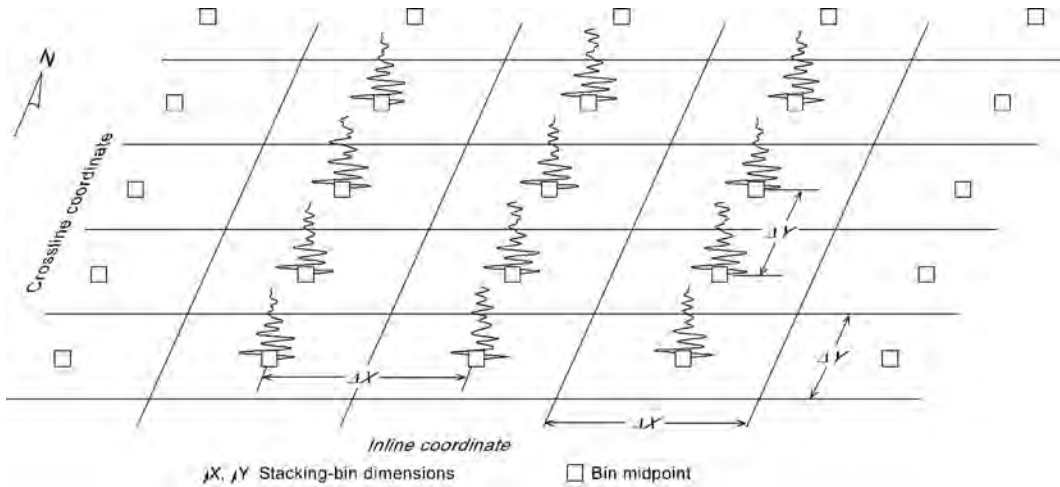


Fig. 2.25—Oblique view of 3D stacking bins.

data volume. For purposes of illustration, it is assumed that the narrowest feature to be interpreted is a meander channel. At least three, and ideally four, stacking bins (that is, seismic traces) must lie within the narrowest dimension, W , of this channel if the channel is to be reliably seen in the seismic image during workstation interpretation. Once W is defined, the dimensions of the stacking bins are also defined. The bin dimensions should be no wider than $W/3$. Ideally, they should be approximately $W/4$.³¹ A variation in seismic reflection character on three to four adjacent traces is usually noticed by most interpreters, whereas anomalous behavior on fewer traces tends to be ignored or may not even be seen when a 3D data volume is viewed.

For example, if the interpretation objective is to image meandering channels that are as narrow as 200 ft, then the stacking bins should have lateral dimensions of approximately 50 ft (Fig. 2.26). This would cause a 200-ft channel to affect four adjacent traces. One of the first 3D design parameters to define, therefore, is the physical size of the stacking bin to be created. The bin size, in turn, can be determined by developing a stratigraphic model of the target that is to be imaged and then using that model to define the narrowest feature that needs to be seen. Once this minimum target dimension is defined, stacking bins with lengths and widths that are approximately one-fourth the minimum target width must be created if the target is to be recognized in a 3D data volume. Conversely, once a stacking-bin size is established, the narrowest stratigraphic feature that most interpreters can recognize will be a facies condition that spans at least three or four adjacent stacking bins.

2.18.2 Station Spacings. The distance between adjacent source points along a seismic line is the source-station spacing; the distance between adjacent receiver arrays along that same line is the receiver-station spacing. Previous publications on the topic of seismic acquisition^{33,34} show that the trace spacing (i.e., the stacking-bin dimension) along a 2D seismic profile is one-half the receiver-station spacing (assuming the usual condition that the source-station spacing along the line is equal to or greater than the receiver-station spacing). Applying this principle to 3D seismic design leads to the following: the dimension of a 3D stacking bin in the direction in which receiver lines are deployed in a 3D grid is one-half the receiver-station spacing along these receiver lines, and the dimension of the stacking bin in the direction in which source lines are oriented is one-half the source-station spacing along the source lines.

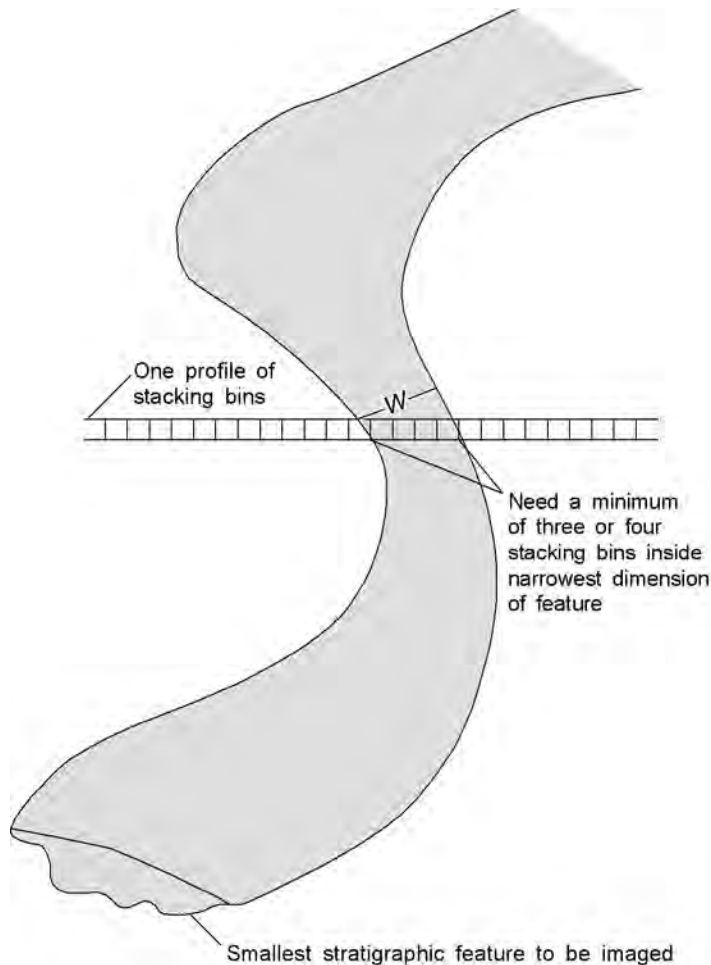


Fig. 2.26—Example of the narrowest feature that must be seen in a 3D image.³¹

As stated previously, once a decision has been made about the narrowest target that must be imaged, the required size of a stacking bin is automatically set at one-third or one-fourth that target dimension (Fig. 2.26). As a result, the source-station and receiver-station spacings are also defined because source-station spacing is twice the horizontal dimension of the chosen stacking bin in the source-line direction, and receiver-station spacing is twice the dimension of the stacking bin in the receiver-line direction. Stated another way, the source-station and receiver-station spacings should be one-half the narrowest horizontal dimension that needs to be interpreted from the 3D data.

When the geology involves steep dips or large changes in rock velocity across a fixed horizontal plane, rigorous calculations of station spacing (or bin size) should be made with commercial 3D seismic design software rather than by following the simple relationships described here.

2.18.3 Stacking Fold. The stacking fold associated with a particular 3D stacking bin is the number of field traces that are summed during data processing to create the single image trace positioned at the center of that bin (Fig. 2.25). In other words, the stacking fold is the number

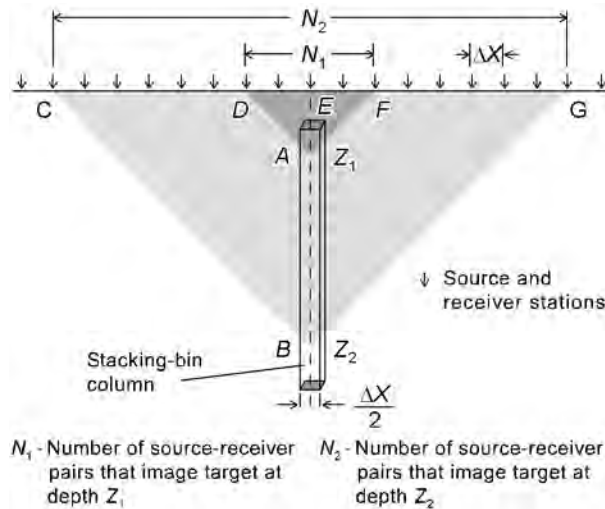


Fig. 2.27—Vertical variation in stacking fold.³¹

of distinct reflection points that are positioned inside a bin because of the particular source-receiver grid that is used.

At any given stacking-bin coordinate, the stacking fold inside that bin varies with depth. **Fig. 2.27** illustrates vertical variation in stacking fold. The source-station and receiver-station spacings along this 2D profile both have the same value for Δx , which results in a stacking bin width of $\Delta x/2$. The vertical column shows the coordinate position of one particular stacking bin. For a deep target at depth Z_2 , the stacking fold in this bin is a high number because there is a large number, N_2 , of source-receiver pairs that each produce a raypath that reflects from subsurface point B. Only one of these raypaths, CBG, is shown. For a shallow target depth, Z_1 , the stacking fold is low because there is only a small number, N_1 , of source-receiver pairs that can produce individual raypaths that reflect from point A. One of these shallow raypaths, DAF, is shown. When a 3D seismic data volume is described as a 20-fold or 30-fold volume, the designers are usually referring to the maximum stacking fold created by the 3D geometry, which is the stacking fold at the deepest target.³¹

In **Fig. 2.27**, when the stacking bin is centered around deep reflection point B, the stacking fold is at its maximum because the largest number of source and receiver pairs can be used to produce individual reflection field traces that pass through the bin. The number of source-receiver pairs that can contribute to the image at B is typically confined to those source and receiver stations that are offset horizontally from B by a distance that is no larger than depth Z_2 to reflection point B. Thus, the distances CE and EG are each equal to Z_2 .

With this offset criterion to determine the number of source-receiver pairs that can contribute to the seismic image at any subsurface point, we see that the stacking fold at depth Z_2 would be N_2 , as **Fig. 2.27** shows, because N_2 unique source-receiver pairs can be found that produce N_2 distinct field traces that reflect from point B. When the stacking bin is kept at the same x and y coordinates but moved to shallower depth, Z_1 , the stacking fold decreases to the smaller number, N_1 . Only N_1 source-receiver pairs generate field traces that reflect from A and still satisfy the geometrical constraint that these pairs are offset by distance DE (or EF) that does not result in critical wavefield refractions at interfaces above A. When critical refraction occurs, the transmitted raypath, bent at an angle of 90° , follows a horizontal interface rather than continuing to propagate downward and illuminating deeper targets.

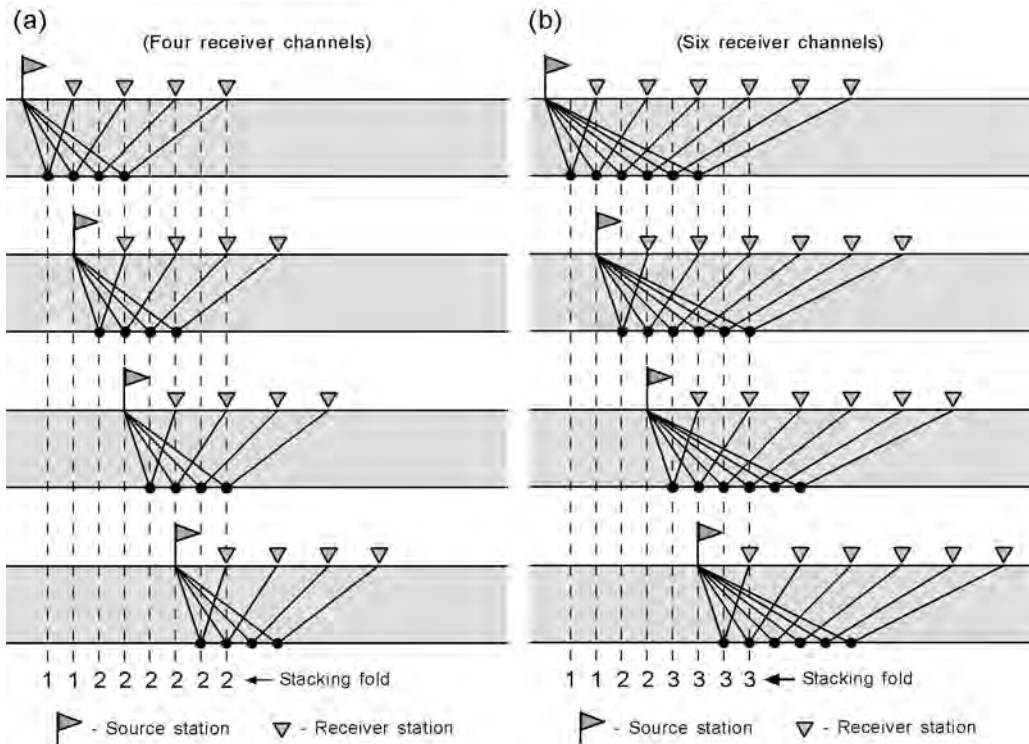


Fig. 2.28—Effect of number of active receivers on inline stacking fold.³¹

In 2D acquisition geometry, the inline stacking fold, F_{IL} , is a function of two geometrical properties: the number of active receiver channels and the ratio between the source-station interval and the receiver-station interval. The raypath diagrams in **Figs. 2.28 and 2.29** illustrate the manner in which each of these geometrical parameters affects inline stacking fold. **Fig. 2.28** establishes the principle that inline stacking fold is one-half of the active receiver stations when the source-station interval equals the receiver-station interval.

$$F_{IL} = \frac{n_c}{2} \dots\dots\dots (2.5)$$

The raypaths in **Fig. 2.28a** show the distribution of reflection points (the solid circles on the subsurface interface) when there are four active receiver channels and the source-station interval is the same as the receiver-station interval. The vertical dashed lines pass through successive reflection points. The stacking-fold numbers at the bottom of the diagram define the number of distinct source-receiver pairs that create a reflection image at each subsurface point, that is, the number of reflection points that each vertical dashed line intersects.

The maximum stacking-fold for this four-receiver situation is 2. The raypaths in **Fig. 2.28b** show the distribution of reflection points and the stacking fold that results when there are six-receiver channels. The maximum stacking fold for this six-receiver geometry is 3.³¹

Fig. 2.29 expands the inline stacking-fold analysis to show that for geometries in which the source-station interval does not equal the receiver-station interval, then

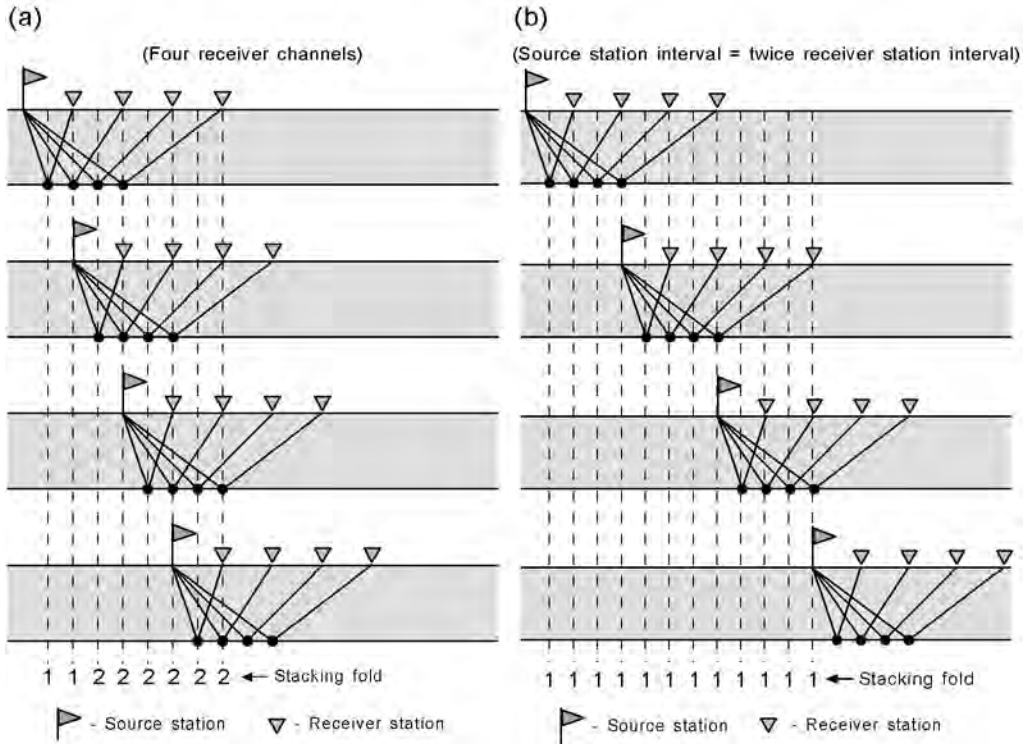


Fig. 2.29—Effect of source-station spacing on inline stacking fold.³¹

$$F_{IL} \sim \frac{i_r}{i_s}, \dots \dots \dots (2.6)$$

where ~ means “is proportional to.”

The raypath diagram in Fig. 2.29a shows the distribution of subsurface reflection points (the solid circles on the subsurface interface) when there are four active receiver channels and the source-station spacing equals the receiver-station spacing. The inline stacking fold is the number of independent reflection points that occur at the same subsurface coordinates, which is the same as the number of reflection points intersected by each vertical dashed line. The stacking fold is shown by the sequence of numbers at the base of the diagram and, in this geometry, the maximum fold is 2.

The raypath picture in Fig. 2.29b shows the distribution of reflection points when the number of active receiver channels is the same as in Fig. 2.29a; that is, there are four receiver groups, but the source-station spacing is now twice the receiver-station spacing. (Note that the incremental movement of the source-station flag in Fig. 2.29b is two times greater than the flag movement in Fig. 2.29a.) The resulting stacking fold is shown by the number written below each vertical dashed line, which is the number of reflection points intersected by each of those lines. The maximum stacking fold in this geometry is only 1. These two diagrams establish the principle that inline stacking fold is proportional to the ratio of the receiver-station interval to the source-station interval.

Combining Eqs. 2.5 and 2.6 leads to the design equation for inline stacking fold:

$$F_{IL} = \frac{1}{2}(n_c) \times \left[\frac{i_r}{i_s} \right] \dots\dots\dots (2.7)$$

In 2D seismic profiling, the source-station interval is usually the same as the receiver-station interval, making the ratio term in the brackets in Eq. 2.7 equal to 1. However, in 3D profiling, the source-station spacing along a receiver line is the same as the source-line spacing, which is several times larger than the receiver-station spacing. Crossline fold, F_{XL} , is given by

$$F_{XL} = \frac{1}{2}n_l \dots\dots\dots (2.8)$$

In a 3D context, the stacking fold is the product of the inline stacking fold (the fold in the direction in which the receiver cables are deployed) and the crossline stacking fold (the fold perpendicular to the direction in which the receiver cables are positioned). This principle leads to the important design equation:

$$F = F_{IL} \times F_{XL} \dots\dots\dots (2.9)$$

To build a high-quality 3D image, it is critical not only to create the proper stacking fold across the image space but also to ensure that the traces involved in that fold have a wide range of offset distances and azimuths. Eq. 2.9 provides no information about the distribution of either the source-to-receiver offset distances or azimuths that are involved in the stacking fold. When it is critical to know the magnitudes and azimuth orientations of these offsets, commercial 3D seismic design software must be used. Offset analysis is a technical topic that goes beyond the scope of this discussion. Ref. 35 describes the parameters involved in onshore 3D seismic survey design.

2.19 Vertical Seismic Profiling

In vertical seismic profiling (VSP), a seismic sensor is lowered to a sequence of selected depths in a well by wireline. Fig. 2.30 shows the source-receiver geometry involved in VSP. A wall-locked seismic sensor is manipulated downhole by wireline so that the receiver occupies a succession of closely spaced vertical stations. This receiver records the total seismic wavefield, both downgoing and upgoing events, produced by a surface-positioned energy source. Only 6 receiver stations are indicated here for simplicity, but a typical VSP consists of 75 to 100 receiver stations. The vertical spacing between successive stations is a few tens of feet. A common receiver spacing is 50 ft (15 m). The horizontal distance, X , between the surface source and the downhole receiver is the offset and can assume different magnitudes, depending on the specific VSP imaging application. Fig. 2.30 depicts a VSP measurement made in a vertical wellbore, but the VSP technique can also be implemented in deviated wells.³⁷

Because the receiver stations are aligned vertically, the data-recording procedure is called VSP to distinguish the technique from conventional horizontal seismic profiling, in which seismic receivers are deployed across the surface of the Earth. In horizontal seismic profiling along the Earth surface, only upgoing seismic wavefields are recorded. The crucial information of the downgoing wavefields is not available to assist seismic data processors and interpreters. Seismic data recorded with a vertical receiver array have many valuable applications,^{36,37} but the only uses stressed here are the abilities of such data to calibrate stratigraphic depth to specific waveform features of surface-recorded seismic reflection data and to provide an independent, high-resolution image of the subsurface in close proximity to the VSP receiver well.

Velocity check-shot data are recorded with the same source-receiver geometry used for VSP data recording (Fig. 2.30). However, the vertical distance between successive receiver sta-

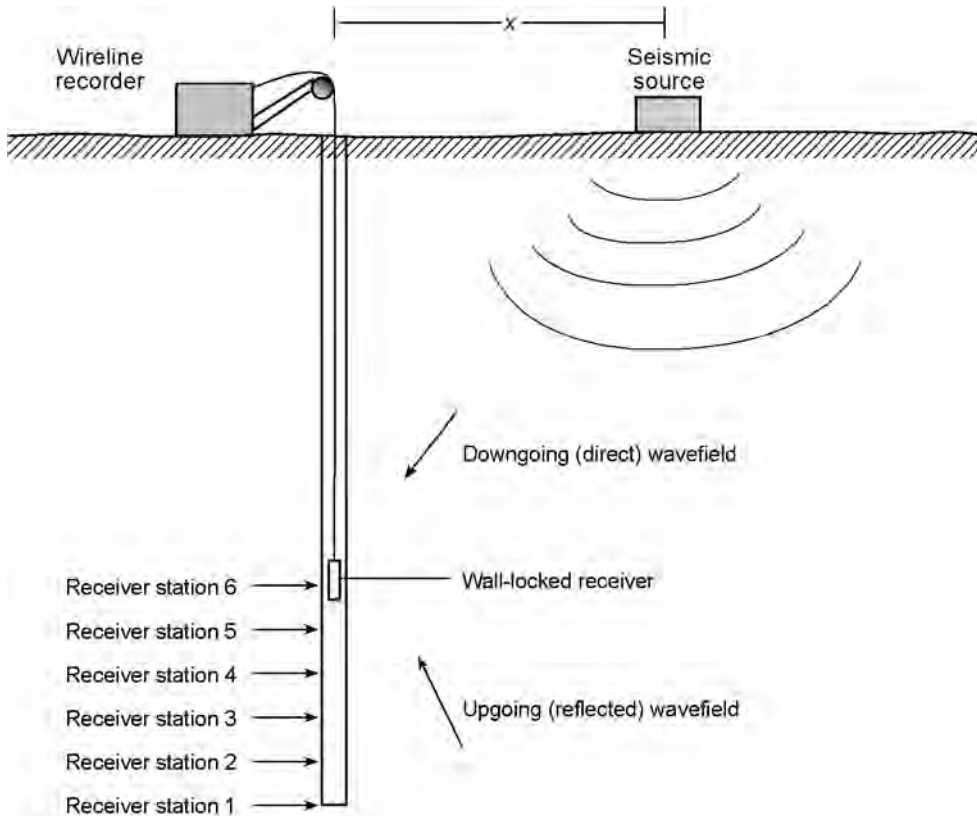


Fig. 2.30—Source-receiver geometry used in vertical seismic profiling.³⁸

tions is on the order of 500 ft (150 m) or more, compared with a smaller station spacing of approximately 50 ft (15 m) used to record VSP data. This order-of-magnitude difference in the spatial sampling of subsurface seismic wavefields is the principal difference between VSP and velocity check-shot data. The primary use of velocity check-shot data is to create a rigorous relationship between stratigraphic depth coordinates and seismic image-time coordinates. These depth-to-time relationships are critical for transforming log data and engineering data from the depth domain to the seismic image-time domain. This coordinate transformation allows critical geologic and engineering information to be associated with proper data windows in the seismic image.

Because equivalent source-receiver recording geometries are used, velocity check-shot data can provide a rigorous relationship between stratigraphic depth and seismic travel-time, just as VSP data do. One shortcoming of check-shot data, however, is that they do not provide an independent seismic image that can be correlated with surface-recorded seismic reflection images. Such a correlation can verify the precise amount of time shift that should be imposed to bring subsurface stratigraphy into exact phase agreement with a surface-recorded 3D seismic image. To a seismic interpreter, two images are in phase agreement when the peaks and troughs of the two sets of wiggle-trace data occur at the same time coordinates over a window of interest and the waveshapes of key events in the two images are similar over that window. In contrast to check-shot data, VSP data provide an independent seismic image, and this VSP image is the unique feature of the VSP technique that allows subsurface stratigraphy to be inserted into 3D seismic image volumes at precise seismic travel-time coordinates.³⁸

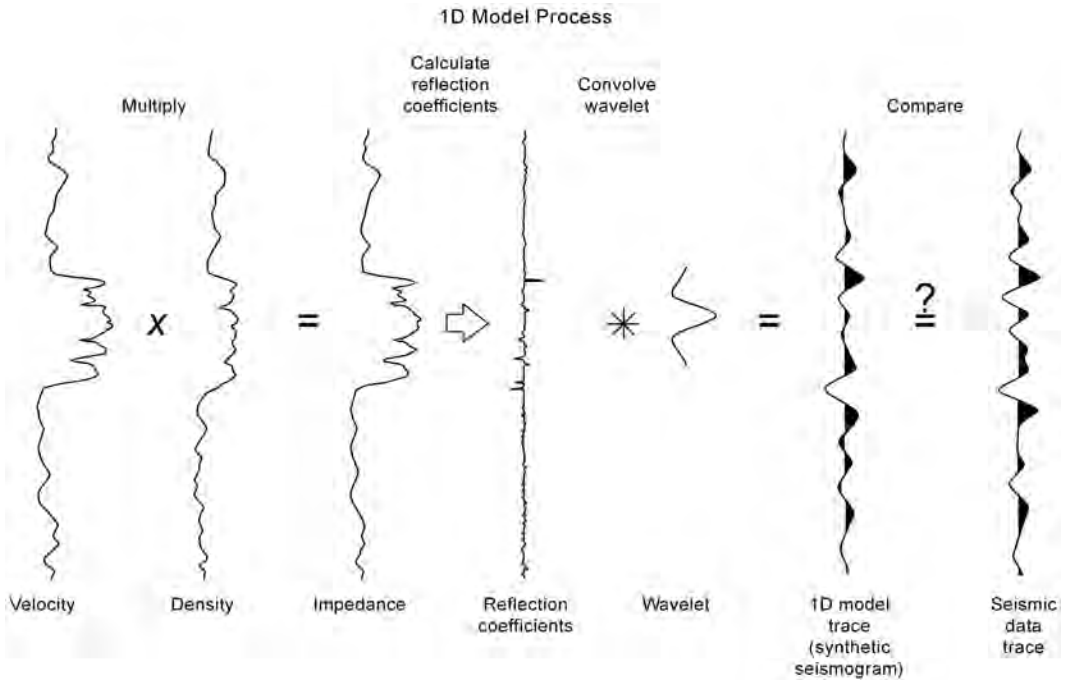


Fig. 2.31—Computational steps involved in calculating a synthetic seismogram.

2.19.1 Synthetic Seismograms. Some seismic interpreters argue that a synthetic seismogram made from sonic and density log data can provide an independent image that can be used to determine the proper time shift between surface-recorded seismic data and check-shot-positioned stratigraphy encountered in the check-shot well. **Fig. 2.31** illustrates the steps taken to create a synthetic seismogram and to use that synthetic model in interpretation.

First, sonic log data and density log data recorded in a chosen calibration well are multiplied to create a log of the layer impedances penetrated by the well (left three curves of **Fig. 2.31**). **Eq. 2.1** describes this calculation. Either before or after this multiplication, these log data have to be converted from functions of depth to functions of vertical seismic travel time. Such a transformation is done with a simple equation:

$$D = v \times t \dots\dots\dots (2.10)$$

The velocity function in this equation is provided by the sonic log used in the calculation. Sonic log data usually have to be adjusted by small percentage amounts so that the integrated sonic log time agrees with seismic check-shot time. With **Eq. 2.2**, the time-based layer impedance wave is converted to a time series of reflection coefficients, and an estimated seismic wavelet is convolved with this reflectivity series. The result is the synthetic seismogram trace shown in **Fig. 2.31**. The interpretation step is done by comparing the synthetic seismogram with real seismic traces near the calibration well (last step of **Fig. 2.31**). During this comparison, the synthetic trace is shifted up and down in time to determine what time shift, if any, is required to create an optimal alignment of reflection peaks and troughs between the synthetic and real traces. Most geophysicists would describe the wiggle-trace alignment shown in **Fig. 2.31** as a good phase tie.

There are instances in which synthetic seismograms are a poor match to seismic data. When there are only a few well penetrations, this can be a problem best addressed with VSP

data. As the number of wells increase and greater areal coverage is provided, poor synthetic data can be eliminated and reliable synthetic seismograms can be used to leverage a limited number of VSP surveys. There are several reasons that synthetic seismograms sometimes fail to provide the reliability needed for calibrating thin-bed stratigraphy with seismic reflection character.³⁹ The more common failures are usually related to one or more of the following factors:

- The log-determined velocity and density values used in a synthetic seismogram calculation represent petrophysical properties of rocks that have been mechanically damaged by drilling and altered by the invasion of drilling fluids. In addition, irregular changes in borehole diameter sometimes induce false log responses. As a result, well log determinations of rock velocity and density, which are the fundamental data used to produce the reflection coefficients needed for a synthetic seismogram calculation, may not represent the velocity and density values in undrilled rocks near the logged well, which are the fundamental rock properties that determine the reflection waveshape character of seismic data recorded at the wellsite.

- A synthetic seismogram represents an estimate of the seismic image that would result if the imaging raypath traveled vertically downward from a source and then reflected vertically upward along that same travel path to a receiver located exactly at the source position. In contrast, each trace of an actual seismic profile is a composite of many field traces that represent wavefield propagation along a series of oblique raypaths between sources and receivers that are laterally displaced from each other, with each of these raypaths reflecting from the same subsurface point. These two images (synthetic seismogram and actual seismic trace) thus involve raypaths that travel through different portions of the Earth.

- Even when log-determined velocity and density values (and any synthetically calculated seismic reflectivity derived from these log data) represent the correct acoustic impedances of a stratigraphic succession, that stratigraphy may be localized around the logged well and not be areally large enough to be a reflection boundary for a surface-generated seismic wavefield. This situation may be more common in heterogeneous rock systems than many interpreters may appreciate.

- The effects of the near surface are not included in a synthetic seismogram calculation because logs are not recorded over shallow depths. At some wellsites, the near surface can induce significant effects into the waveform character of surface-recorded seismic data. In contrast, near-surface effects, such as peg-leg multiples, frequency absorption, and phase shifting, are included in VSP data because VSP wavefields propagate through the total stratigraphic section, including the near surface, just as surface-recorded seismic wavefields do.

2.20 Calibrating Seismic Image Time to Depth

VSP recording geometry causes the stratigraphy at the VSP well, where sequence boundaries are known as a function of depth from well log and core control, to be locked to the VSP image. This stratigraphy, in turn, is also known as a function of VSP reflection time. This fixed relationship between stratigraphy and the VSP image results because VSP receivers are distributed vertically through the seismic image space. This data-recording geometry allows both stratigraphic depth and seismic traveltime to be known at each receiver station. The dual-coordinate domain (depth and time) involved in a VSP measurement means that any geologic property known as a function of depth at the VSP well can be accurately positioned on, and rigidly welded to, the time-coordinate axis of the VSP image.

Fig. 2.32 illustrates the VSP depth-to-time calibration. VSP data are unique in that they are the only seismic data that are recorded simultaneously in the two domains critical to geologic interpretation: stratigraphic depth and seismic reflection time (**Fig. 2.32a**). As a result, specific stratigraphic units, known as a function of depth from well log data, can be positioned precisely in their correct VSP-image time windows (**Fig. 2.32b**). Each numbered stratigraphic unit shown in **Fig. 2.32b** is a thin-bed reservoir penetrated by the VSP well. When the VSP image is shifted up or down to correlate better with a surface-recorded seismic reflection image that

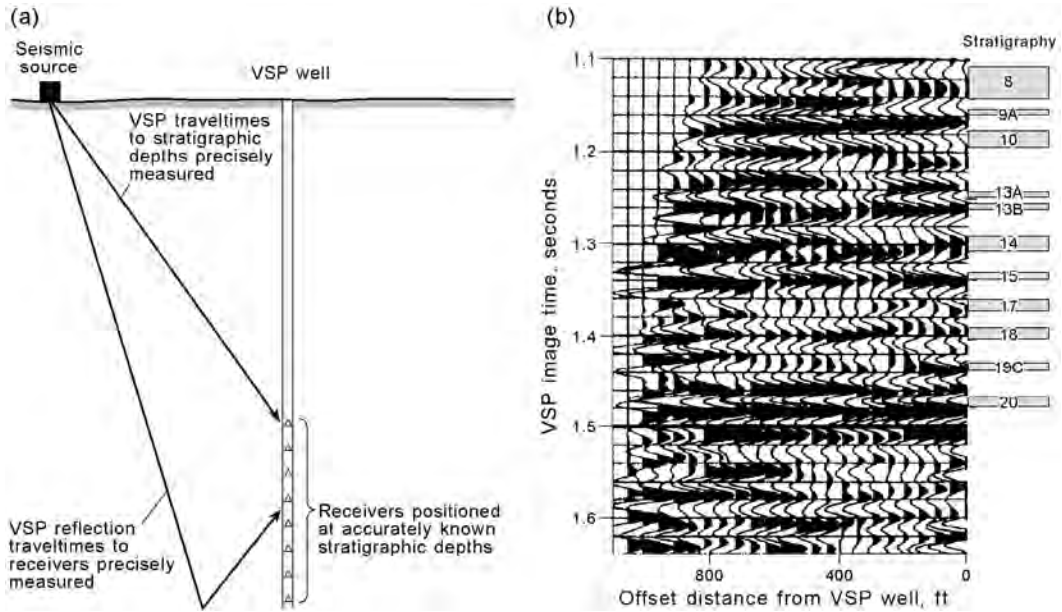


Fig. 2.32—Concept of VSP depth-to-time calibration.³⁸

crosses the VSP well, the VSP-defined time window that spans each stratigraphic unit should be considered to be welded to the VSP data. This causes the stratigraphy to move up and down in concert with the VSP image during the VSP-to-surface seismic correlation process. The seismic time scale involved in the depth-to-time calibration illustrated here is VSP image time, which may be different from the image time for surface-recorded reflection data. Fig. 2.33 illustrates the transformation of stratigraphy from VSP image time to 3D seismic image time.

The reverse situation is also true; that is, the VSP image could be positioned on, and welded to, the depth-coordinate axis of the stratigraphic column at the VSP wellsite. This option of transforming a VSP image to the stratigraphic depth domain is not often done because the common objective of seismic interpretation is to insert stratigraphy into 3D seismic data volumes that are defined as functions of seismic traveltime, not as functions of stratigraphic depth.

The concept of a welded bond between a VSP image and the stratigraphy at the VSP wellsite means that whenever a VSP image is moved up to better correlate with a 3D seismic image, the stratigraphy moves up by that same amount of time in the 3D image. If the VSP image has to be moved down to create a better waveform character match with the 3D data, then the stratigraphy shifts down by the same amount in the 3D data volume. The fact that VSP data provide an independent image that can be moved up and down to find an optimal match between VSP and 3D reflection character is the fundamental property of the VSP-to-seismic calibration technique, which establishes the correct time shift between 3D seismic reflection time and VSP reflection time.

When the time shift between these two images is determined, the correct time shift between the 3D seismic image and the stratigraphy at the VSP-calibration well is also defined because that stratigraphy is welded to the VSP travelttime scale and moves up and down in concert with the VSP image time coordinate. Fig. 2.33 shows a specific example of a VSP-based stratigraphic calibration of a 3D data volume. The rigid welding of stratigraphic depth to VSP travelttime as described in Fig. 2.32 is repeated here as Fig. 2.33a. In this example, the VSP image must be advanced (moved up) by 18 milliseconds to optimally align with the 3D seismic image at

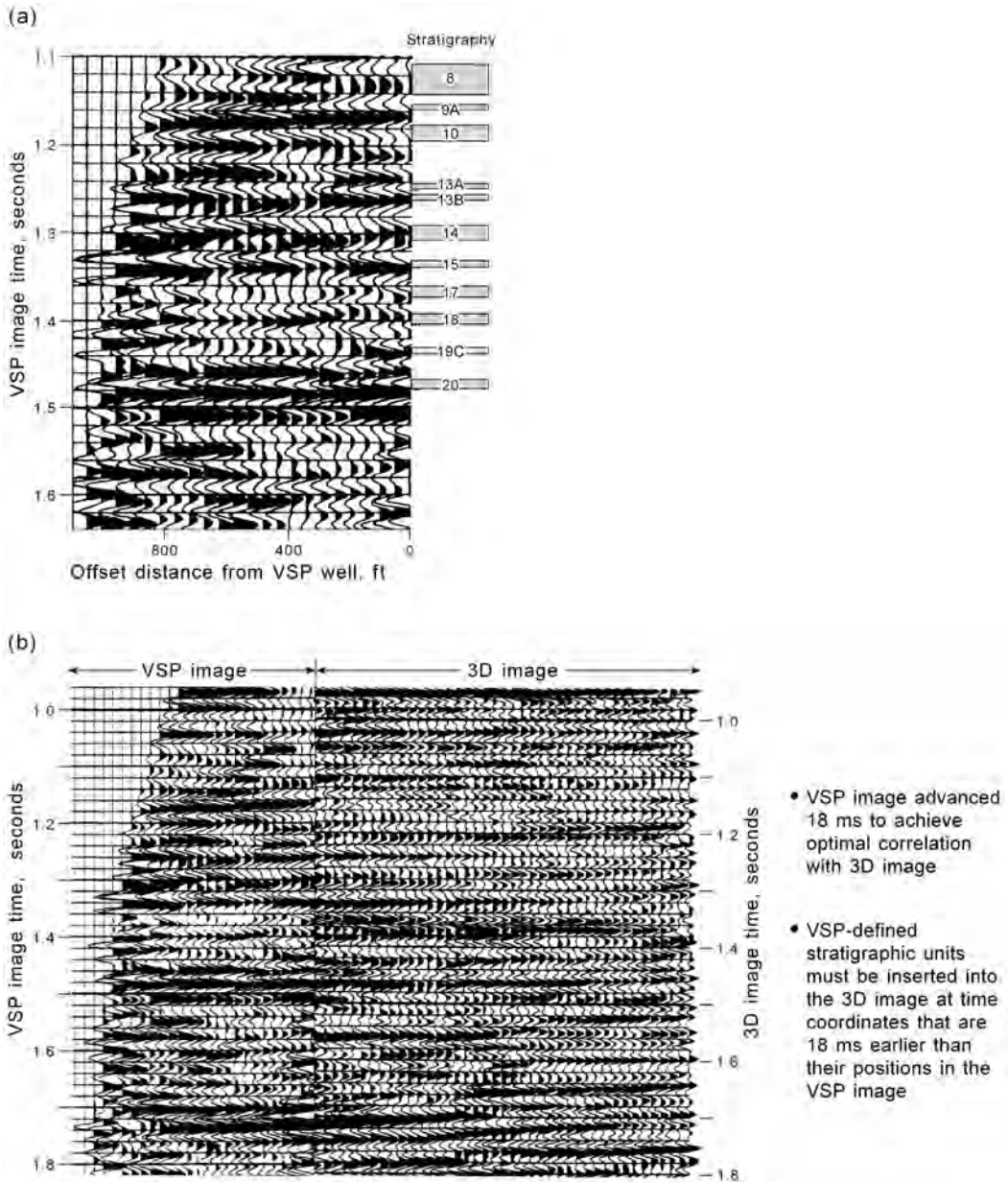


Fig. 2.33—VSP-based calibration of thin-bed stratigraphy in 3D seismic images.³⁸

the VSP well (Fig. 2.33b). Because the stratigraphy penetrated by the VSP well is welded to the VSP image, the positions of the targeted thin-bed time windows in the 3D image also move up by 18 milliseconds to align with their positions in the VSP image. The VSP technique provides not only a time-vs.-depth calibration function but also an independent reflection image that can be time shifted to correlate with a surface-recorded image in the manner shown here. This is the unique feature that makes a VSP calibration of stratigraphy to 3D seismic image time more reliable than a check-shot-based stratigraphic calibration.³⁸

This VSP image was produced from a large-offset VSP survey in which the offset distance, X (Fig. 2.30), was a little more than 2,000 ft (600 m). In Fig. 2.33, the VSP-based interpreta-

tion procedure leads to the conclusion that although the tops of thin-bed reservoirs 19C and 15 are positioned at VSP travel times of 1.432 and 1.333 seconds, they have to be inserted into the 3D data volume at 3D seismic travel times of 1.414 and 1.315 seconds.

Three-dimensional VSP data can be acquired when many source stations encircle a receiver well. Technically, there is no barrier to 3D VSP imaging. The major industry objection to 3D VSP technology is the relatively high cost of data acquisition and processing compared with the cost of conventional 3D surface-based seismic imaging. In special cases that have justified the cost, 3D VSP imaging has been done to create high-resolution images around a receiver well. To date, only a few such surveys have been done worldwide.

2.21 Crosswell Seismic Profiling

Fig. 2.34 shows distinctions among the source-receiver geometries involved in vertical seismic profiling (VSP), reverse vertical seismic profiling (RVSP), and crosswell seismic profiling (CSP). **Fig. 2.34a** shows the field geometry used in conventional VSP. Source S is positioned on the surface of the Earth, and seismic receiver R is lowered into the well where the data are to be recorded. The direct arrival path is SR, and the reflected travel path is SPR. The position of reflection point P can be varied by moving either source S or receiver R. If the source is directly above the receiver, the measurement is called a zero-offset VSP. If the source is not directly above the receiver, the measurement is called an offset VSP.

In RVSP, the positions of the source and receiver are exchanged. As **Fig. 2.34b** shows, receiver R is on the surface for an RVSP, and source S is located in the well. The offset in this diagram has the same meaning as it does for a conventional VSP. (Offset is the lateral distance between a vertical line passing through the source position and a vertical line passing through the receiver position.) In a vertical well, offset can be measured relative to the well-head, if desired. In nonvertical wells, offset must be measured strictly between the coordinates of the source and the receiver. Three-dimensional RVSP data can be acquired at rather low cost because it is not difficult to distribute a large number of receiver stations on the Earth's surface in an areal pattern around a source well.

In a CSP measurement, both the source and the receiver are below the surface and in separate wells, as **Fig. 2.34c** shows. The direct travel path is again SR, and the reflected path is SPR. One of the attractions of CSP data is that no part of either path SR or path SPR passes through the near-surface weathered layer, as occurs when VSP and RVSP data are recorded. As a result, crosswell data do not suffer a significant loss of the higher-frequency components of the source wavefield. These components are usually attenuated as they pass through the surface weathered layer to complete any of the VSP-type travel paths. Because spatial resolution improves as the frequency content of the signal is increased, crosswell data reveal greater reservoir detail than do either type of VSP measurement.

In crosswell data acquisition, two types of source-receiver offsets can be considered, depending on whether the direct or the reflected wavefield is being analyzed. These two offsets are transmission offset and reflection offset, respectively. Transmission offset in a crosswell geometry (**Fig. 2.34c**) is measured orthogonal to the direction in which reflection offset (**Figs. 2.34a and 2.34b**) is measured and can be defined as the vertical distance between a horizontal line passing through the source position and a horizontal line passing through the receiver position.

There are three techniques by which the interwell space of a reservoir system can be investigated using CSP data: attenuation tomography, for which the basic measurement is the amplitude of the direct seismic arrival wavelet; velocity tomography, for which the principal measurement is the traveltimes required for the direct seismic arrival to propagate across the interwell space; and elastic wavefield imaging.

In velocity and attenuation tomography, the only information in the crosswell wavefield that is used are the travel times and amplitudes of the seismic direct arrival. In elastic wave-

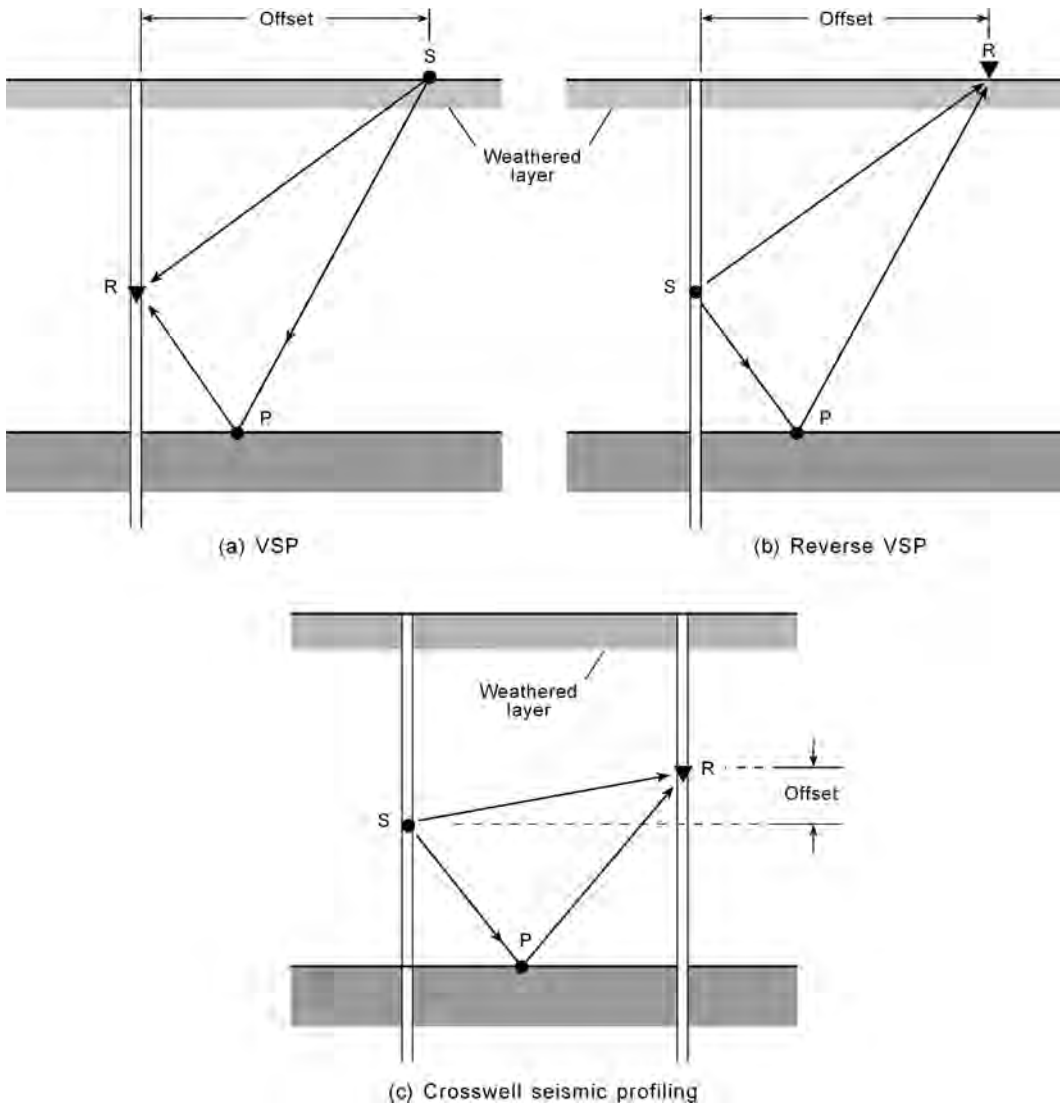


Fig. 2.34—Source-receiver geometries involved in VSP, RVSP, and CSP data acquisition.⁴⁰

field imaging, the complete seismic wavefield is used. The major imaging contributions come from the scattered wavefield that occurs after the direct arrival.

Tomographic data are used to infer spatial distributions of rock and fluid properties in interwell spaces. Velocity tomograms are more widely used than are attenuation tomograms. Table 2.2 lists several reservoir properties (lithological variations, porosity, pore fluid) that affect seismic wave velocity. In concept, crosswell velocity tomograms can define the spatial patterns of these properties in the 2D vertical plane passing through the source and receiver wells.

Elastic wavefield imaging of CSP data provides more information about interwell conditions than do velocity tomograms because the images are presented in wiggle-trace format similar to surface-recorded seismic data. Interpreters can use standard seismic interpretation software to analyze these images, calculate amplitude and frequency attributes, and map stratal surfaces.

Because CSP technology provides data with signal frequencies as high as 1000 to 2000 Hz, some CSP data have dominant wavelengths as short as 3 m [10 ft]. Thus, CSP technology provides a better spatial resolution of reservoir properties than does surface-based seismic technology. By acquiring CSP data in a time-lapse sequence (usually 12 to 15 months between surveys), engineers can often track fluid movements in interwell spaces to determine if secondary recovery processes are performing as planned.

Fig. 2.35 gives a visualization of the portions of a crosswell wavefield that are involved in these approaches to CSP imaging. In this measurement, a source was kept at the depth labeled “Source” in a well that was 1,800 ft [550 m] away from the receiver well in which the data were recorded. A wall-clamped 3C geophone was then positioned in the receiver well at depth stations 25 ft apart, starting at a depth of 6,100 ft and extending up to a depth of 500 ft. **Fig. 2.35** displays the response of the vertical geophone in the top wavefield, and the bottom wavefield shows the summed response of both horizontal geophones. It is probably not wise to sum the responses of the two horizontal geophones into a single wavefield because then the SV and SH shear modes (see **Fig. 2.7**) cannot be distinguished. As a result of this summation, all shear events in **Fig. 2.35** are labeled as S, not as SH or SV.

The compressional (P) wavefield arrives first and is followed by the shear (S) wavefield. The arrival times of these wavefields are labeled on the shallow geophone trace. The S wavefront has more curvature than the P wavefront because S velocity is less than P velocity. CSP data record both downgoing reflection events (when the reflecting interface is above the receiver depth) and upgoing reflection events (when the reflecting interface is below the receiver depth). The opposite traveling reflection events create a crisscross pattern in the data, an effect that is pronounced in the S wavefield. The depth at which each S reflection occurs can be determined by extending each of these crisscrossing events back to its point of origin on the S first-arrival wavefront. Many P reflection events exist in the data at times later than the P first-arrival wavefront, but they are difficult to see in these unprocessed data. The labeled linear events sloping up and down behind the P first-arrival wavefront are SV events created by P-to-SV mode conversions at stratal interfaces. These events are better seen on the display of the horizontal-geophone data. The depth at which a reflection occurs can be determined by extrapolating a linear event to intersect the P-wave first arrival. The interpreted reflector depths can then be compared with the depths of rock and fluid interfaces defined by logs recorded in the receiver well and with the formation depths calculated from surface-recorded seismic data.

For a velocity tomography analysis of the interwell space illuminated by the wavefields in **Fig. 2.35**, the P and S first-arrival times can be picked at each depth station. These travel times then can be used to synthesize the interwell velocity structure by some type of iterative travel-path reconstruction technique. The particular downhole source used in this instance was a vibrator that produced a symmetrical wavelet. In this example, the data are not deconvolved to reduce the wavelet side lobes; thus, the arrival times would be the center point of the long, ringing, symmetrical direct arrivals.

To produce an estimate of the spatial distribution of seismic attenuation properties of the interwell space, amplitudes of the P and S direct arrivals have to be analyzed with other factors such as the consistency of the receiver couplings, the shot-to-shot energy levels, and the geometric shapes of the source radiation and receiver antenna patterns.

To produce P and S seismic images of the interwell space, the reflection portions of the wavefields that are noted need to be processed with interwell velocities determined by the velocity tomography analysis to position each reflection wavelet at its subsurface point of origin. The vertical axis of images created from CSP data is true stratigraphic depth, not image time, because the source and receiver stations are distributed over known depth coordinates. CSP images can be correlated to surface-based seismic images only if the surface data are transformed from the image-time domain to the depth domain.

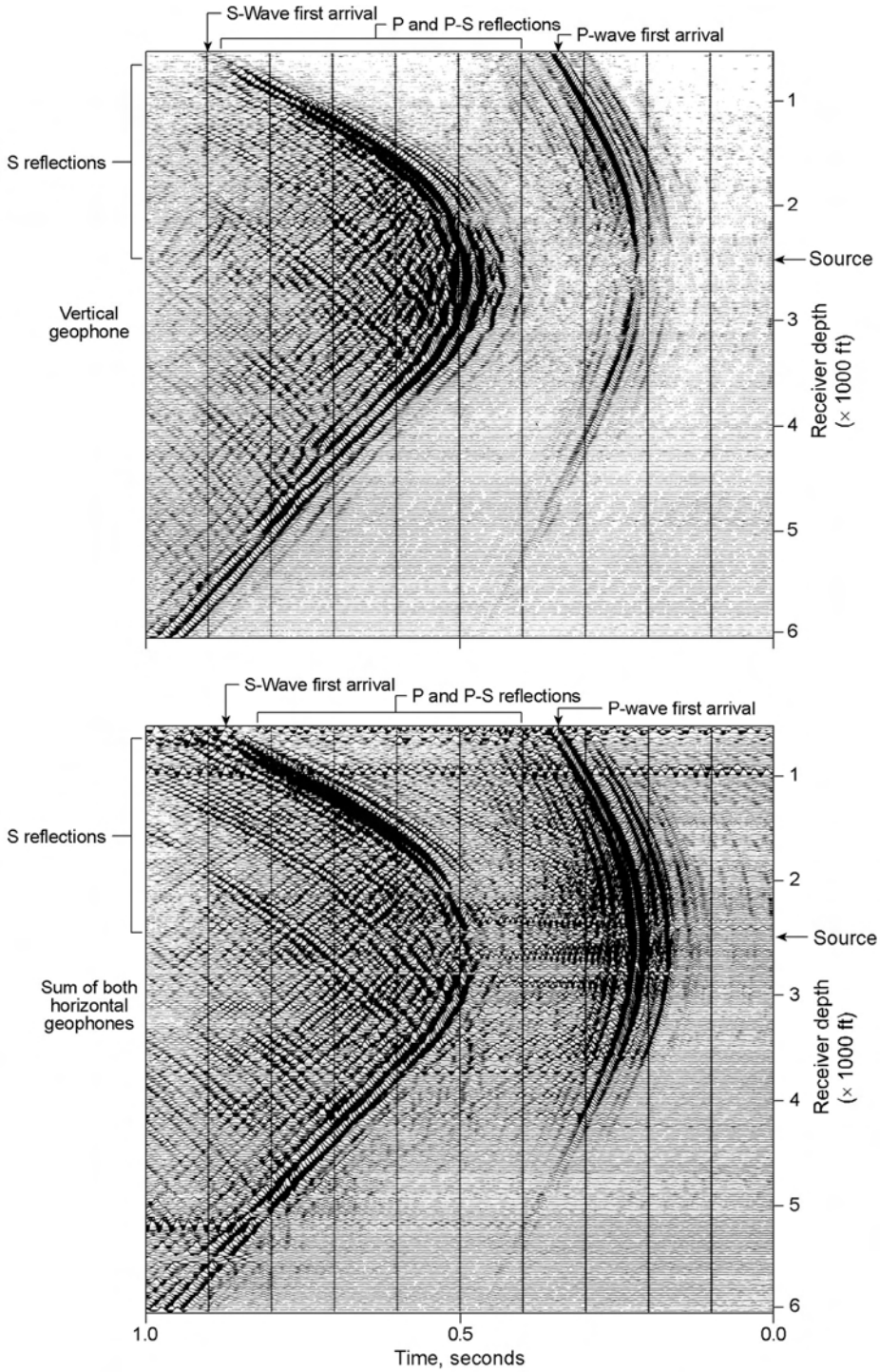


Fig. 2.35—Crosswell seismic wavefield that allows velocity tomograms, amplitude attenuation tomograms, and elastic wavefield (P and S) images of the interwell space between a source well and a receiver well to be constructed.⁴⁰

Nomenclature

- $a(t)$ = seismic trace amplitude value
 A_o = incident seismic amplitude
 A_r = seismic reflection amplitude
 A_t = transmitted seismic amplitude
 d = depth of air-gun array, L, ft or m
 D = depth, L, ft or m
 F = 3D stacking fold
 F_{IL} = inline stacking fold
 F_{XL} = crossline stacking fold
 i_r = receiver-station interval, L, ft or m
 i_s = source-station interval, L, ft or m
 I = seismic impedance, (g·m)/(cm³·sec)
 n_c = number of receiving channels
 n_l = number of receiver lines in the recording patch
 N_1 = number of source-receiver pairs that image target at depth Z_1
 N_2 = number of source-receiver pairs that image target at depth Z_2
 R = seismic reflection coefficient or seismic receiver
 t = seismic travelttime, t, second
 v = velocity, L/t
 V = velocity of seismic wave propagation, L/t
 V_p = propagation velocity of a compressional (P) wave, L/t
 V_s = propagation velocity of a shear (S) wave, L/t
 W = minimum target width, L, ft or m
 x = real data plane
 $x(t)$ = real seismic trace
 X = offset distance, L, ft or m
 y = imaginary plane
 $y(t)$ = Hilbert transform of $x(t)$
 $z(t)$ = complex seismic trace
 Z_1 = shallow target depth, L, ft or m
 Z_2 = deep target depth, L, ft or m
 Δx = inline dimension of stacking bin, L, ft or m
 Δy = crossline dimension of stacking bin, L, ft or m
 ρ = bulk density of the rock, m/L³, g/cm³
 $\phi(t)$ = phase angle
 $\omega(t)$ = instantaneous frequency, cycles/sec

References

1. Dobrin, M.B.: *Introduction to Geophysical Prospecting*, McGraw-Hill Book Co., New York City (1976) 630.
2. Telford, W.M. *et al.*: *Applied Geophysics*, Cambridge U. Press, Cambridge, U.K. (1976) 860.
3. Cholet, J. and Pauc, A.: "Device for Generating Seismic Waves by Striking a Mass Against a Target Member," U.S. Patent No. 4,205,731 (1980).
4. Crawford, J.M., Doty, W.E.N., and Lee, M.R.: "Continuous Signal Seismograph," *Geophysics* (1960) **25**, 95.
5. Geyer, R.L.: "Vibroseis Parameter Optimization," *Oil & Gas J.* (1971) **68**, No. 15, 116, and (1971) **68**, No. 17, 114.

6. Geyer, R.L.: "The Vibroseis System of Seismic Mapping," *Canadian J. of Exploration Geophysics* (1970) **6**, No.1, 39.
7. Seriff, A.J. and Kim, W.H.: "The Effect of Harmonic Distortion in the Use of Vibratory Surface Sources," *Geophysics* (1970) **35**, 234.
8. Goupillaud, P.L.: "Signal Design in the Vibroseis Technique," *Geophysics* (1976) **41**, 1291.
9. Bernhardt, T. and Peacock, J.H.: "Encoding Techniques for the Vibroseis System," *Geophysical Prospecting* (1978) **26**, 184.
10. Waters, K.H.: *Reflection Seismology—A Tool for Energy Resource Exploration*, John Wiley & Sons, New York City (1978).
11. Cunningham, A.B.: "Some Alternate Vibrator Signals," *Geophysics* (1979) **44**, 1901.
12. Edelmann, H.A.K., and Werner, H.: "The Encoded Sweep Technique for Vibroseis," *Geophysics* (1982) **47**, 809.
13. Sallas, J.J.: "Seismic Vibrator Control and the Downgoing P-Wave," *Geophysics* (1984) **49**, 732.
14. Fair, D.W.: "Shear Wave Transducer," U.S. Patent No. 3,159,232 (1964).
15. Dragoset, W.H.: "Air-Gun Array Specs—A Tutorial," *The Leading Edge* (1990) **9**, No. 1, 24.
16. Aki, K. and Richards, P.G.: *Quantitative Seismology—Theory and Methods*, W.H. Freeman and Co., New York City (1980).
17. Hardage, B.A.: "Combining P-Wave and S-Wave Seismic Data To Improve Prospect Evaluation," Bureau of Economic Geology Report of Investigations, No. 237, U. of Texas, Austin, Texas (1996).
18. Taner, M.T. and Sheriff, R.E.: "Application of Amplitude, Frequency, and Other Attributes to Stratigraphic and Hydrocarbon Determination," *American Assn. of Petroleum Geologists Memoir* (1977) **26**, 301.
19. Taner, M.T., Koehler, F., and Sheriff, R.E.: "Complex Seismic Trace Analysis," *Geophysics* (1979) **44**, 1041.
20. Hardage, B.A.: *Seismic Stratigraph*, Geophysical Press, London (1987).
21. Hardage, B.A.: "Instantaneous Frequency—A Seismic Attribute Useful in Structural and Stratigraphic Interpretation," technical summary, GRI-96/0019, Bureau of Economic Geology (1996).
22. Hardage, B.A. *et al.*: "3-D Instantaneous Frequency Used as a Coherency/Continuity Parameter To Interpret Reservoir Compartment Boundaries Across an Area of Complex Turbidite Deposition," *Geophysics* (1998) **63**, 1520.
23. Mitchum, R.M. Jr., Vail, P.R., and Thompson, S. III: "Seismic Stratigraphy and Global Changes in Sea Level, Part 2, The Depositional Sequence as a Basic Unit for Stratigraphic Analysis," *Seismic Stratigraphy—Applications to Hydrocarbon Exploration*, C.E. Payton (ed.), American Assn. of Petroleum Geologists, Memoir 26 (1977) 53.
24. Vail, P.R. and Mitchum, R.M. Jr.: "Seismic Stratigraphy and Global Changes of Sea Level, Part 1, Overview," *Seismic Stratigraphy—Applications to Hydrocarbon Exploration*, C.E. Payton (ed.), American Assn. of Petroleum Geologists, Memoir 26 (1977) 51–52.
25. Tipper, J.C.: "Do Seismic Reflections Necessarily Have Chronostratigraphic Significance?" *Geology* (1993) **130**, 47.
26. Galloway, E.W.: "Genetic Stratigraphic Sequences in Basin Analysis I: Architecture and Genesis of Flooding-Surface Bounded Depositional Units," *American Assn. of Petroleum Geologists Bull.* (1989) **73**, No. 2, 125.
27. Wanless, H.R. and Weller, J.M.: "Correlation and Extent of Pennsylvanian Cyclothems," *Geol. Soc. Am. Bull.* (1932) **43**, 1003.
28. Moore, R.C. *et al.*: "Correlation of Pennsylvanian Formations in North America," *Geol. Soc. Am. Bull.* (1944) **55**, No.6, 657.
29. De Angelo, M.V. and Wood, L.J.: "3-D Seismic Detection of Undrilled Prospective Areas in a Mature Province, South Marsh Island, Gulf of Mexico," *The Leading Edge* (2001) **20**, 1282.
30. Hardage, B.A. and Remington, R.L.: "3-D Seismic Stratal Surface Concepts Applied to the Interpretation of a Fluvial Channel System Deposited in a High-Accommodation Environment," *Geophysics* (1999) **64**, 609.
31. Hardage, B.A.: "Principles of Onshore 3-D Seismic Design," *Geological Circular 97–5*, Bureau of Economic Geology, U. of Texas, Austin, Texas (1997).

32. Ebrom, D., Li, X., and McDonald, J.: “Bin Spacing in Land 3-D Seismic Surveys and Horizontal Resolution in Time Slices,” *The Leading Edge* (1995) **14**, No. 1, 37.
33. Stone, D.G.: *Designing Seismic Surveys in Two and Three Dimensions*, Soc. of Exploration Geophysicists, Geophysical References Series (1994).
34. Cordsen, A., Galbraith, M., and Peirce, J.: *Planning Land 3-D Seismic Surveys*, Geophysical Developments, Soc. of Exploration Geophysicists, Tulsa (2000) **9**.
35. Galbraith, M.: *Land 3-D Survey Design by Computer*, Exploration Geophysics, Australian Soc. of Exploration Geophysicists (1994) **25**, 71–77.
36. Balch, A.H. and Lee, M.W.: *Vertical Seismic Profiling—Technique, Applications, and Case Histories*, Intl. Human Resources Development Corp., Boston, Massachusetts (1984).
37. Hardage, B.A.: *Vertical Seismic Profiling—Principles*, third edition, Amsterdam, Elsevier (2000).
38. Hardage, B.A.: “A Practical Use of Vertical Seismic Profiles—Stratigraphic Calibration of 3-D Seismic Data,” Geological Circular 97–4, Bureau of Economic Geology, U. of Texas, Austin, Texas (1997).
39. Geotz, J.F., Dupal, L., and Bowler, J.: “An Investigation Into Discrepancies Between Sonic Log and Seismic Check-Shot Velocities,” *Australian Petroleum Exploration Assoc. J.* (1979) **19**, part 1, 131–141.
40. Hardage, B.A.: *Crosswell Seismology and Reverse VSP*, Geophysical Press, London (1992).

Glossary

2D (two-dimensional) is an adjective used to describe seismic data acquisition when a single vertical plane can pass through all source and receiver stations. The resulting image is restricted to the vertical plane passing through the source and receiver stations.

3D (three-dimensional) is an adjective used when seismic receivers are distributed across an expansive area surrounding a seismic source station. The point of origin of a reflection event recorded by this areal receiver patch can then be positioned correctly in x , y , z space.

3C (three-component) is an adjective used to describe seismic data acquired with three orthogonal sensors at each receiver station. These sensors measure Earth movement as a vector quantity in x , y , z coordinate space.

4C (four-component) is an adjective used to describe seismic data acquired on the seafloor. These seafloor receivers consist of a 3C geophone that measures vector movement of the seafloor in x , y , z space plus a hydrophone that measures scalar pressure variations at the seafloor.

Air gun is a marine seismic energy source that releases a high-pressure (~2,000 psi) pulse of compressed air to produce a robust, high-resolution seismic wavelet.

Body wave is a seismic wave that propagates in the interior (body) of the Earth. See surface wave.

Bright spot is a dramatic increase in seismic reflection amplitude that makes a subsurface object the dominant feature on any amplitude-based data display. A “true” bright spot is caused by gas replacing liquid in the pore spaces of a reservoir rock. A “false” bright spot is caused by a change in the rock matrix, such as a lateral transition from sand to coal.

Check-shot survey is a seismic measurement involving a seismic source on the Earth surface and a seismic sensor suspended by wireline in a well. The objective is to measure the travel time required for a seismic wavelet to travel from the Earth’s surface to the downhole receiver. Check-shot data allow interpreters to convert seismic image times to stratigraphic depth (or vice versa).

Chronostratigraphic is an adjective meaning “time layer” (chrono=time, strata=layer). Interpreters must define the context in which they are using the term “time” (i.e., geologic time or seismic image time).

Coherency is a numerical measure of the similarity of reflection wave shapes in a user-specified data window. Coherency values are scaled to the numerical range +1 to -1. A value near +1 means the comparison wave shapes are identical; a value near -1 means the wave shapes are identical but have opposite polarities. A value near zero means the comparison wave shapes have little similarity.

Complex seismic trace is the result of applying a Hilbert transform to a seismic trace. A complex seismic trace consists of a real part (the input seismic trace) and an imaginary part produced by the Hilbert transform. The reason for transforming seismic data from the “real” domain to the “complex” domain is that reflection amplitude, phase, and frequency can then be calculated at each time sample point of the seismic wiggle trace.

Crossline is the direction that is perpendicular to seismic receiver lines. See inline.

Crosswell seismic profiling (CSP) data are acquired with a downhole seismic source in one well and downhole seismic sensors in a second well. CSP data provide high-resolution 2D images of geologic conditions across interwell spaces.

Depth-structure map is a seismic-derived map showing the geometry of subsurface structure in terms of depth coordinates. See time-structure map.

Diachronous is a term used to describe a surface or a seismic reflection that cuts across geologic time (dia=across, chrono=time). See chronostratigraphic and stratal surface.

Erosion surface (ES) is a subsurface interface marking an ancient erosional event that has removed portions of one or more stratigraphic units.

Far field is that portion of a seismic propagation medium that is a distance of at least 3 or 4 wavelengths away from a source station.

Flooding surface is a depositional surface marking the transgression of a flooding event across an area. Deeper-water fauna occur above a flooding surface; shallower-water fauna exist below that surface.

Genetic sequence is a package of stratigraphic units that are genetically related. Genetic sequences are bounded by erosional surfaces, flooding surfaces, or maximum flooding surfaces.

Ground force phase locking is a technology that ensures each vibrator in an array of vibrators generates the same source wavelet regardless of variations in soil conditions beneath the vibrator base plates.

Ground roll is a robust, high-amplitude wave produced by onshore seismic sources that travels along the Earth/air interface. A ground-roll wave does not propagate in the interior (body) of the Earth. See Rayleigh wave.

Impedance is the product of bulk density and seismic propagation velocity in the medium in which the wavefield propagates.

Inline is the direction in which receiver lines are deployed. See crossline.

Instantaneous amplitude is the amplitude of a complex seismic trace at a specified time coordinate along that trace. Instantaneous amplitude is not the same as trace amplitude. See complex seismic trace.

Instantaneous frequency is the frequency of a complex seismic trace at a specified time coordinate along that trace. Instantaneous frequency is the time derivative of instantaneous phase. See complex seismic trace.

Instantaneous phase is the phase of a complex seismic trace at a specified time coordinate along that trace. Instantaneous phase is the inverse tangent of the ratio: real part of the complex trace divided by imaginary part of the complex trace. See complex seismic trace.

Love wave is a surface wave that propagates along the Earth/air interface and creates a particle displacement that is tangent to the Earth surface and also perpendicular to the direction of wave propagation. A Love wave does not propagate in the interior of the Earth. See body wave, ground roll, Rayleigh wave, and surface wave.

Low-stand wedge is an asymmetrical accumulation of sediment and strata occurring during a period of lower sea level.

Maximum flooding surface (MFS) is a depositional surface that marks conditions associated with the deepest water depth occurring in a geologic time period of interest.

Ocean-bottom cable (OBC) is a cable-based seismic receiver system that is positioned on the seafloor so shear-wave data can be acquired in addition to compressional wave data. OBC technology usually involves 4C sensors. See 4C.

P wave is a compressional wave. It is sometimes called a primary (P) wave because it is the portion of a seismic wavefield that arrives first at an observation point. A P wave causes rock particles to oscillate in a direction that is perpendicular to its wavefront.

Peak-to-peak (PTP) is a parameter used to describe air-gun performance. An air-gun wavelet consists of a high-amplitude peak followed by a high-amplitude trough. The parameter PTP defines the magnitude of the source wavelet amplitude measured from the apex of the leading peak of the wavelet to the apex of the following trough. A high PTP value indicates a high energy output.

Primary-to-bubble ratio (PBR) is a parameter used to define the performance of a marine airgun array. “Primary” refers to the amplitude of the wavelet created by the output pulse of high-pressure air. “Bubble” refers to the amplitude of the wavelet created by the subsequent collapse of the air bubble in the water column. A high PBR value (~30) is desired.

Rayleigh wave is the correct name for a ground-roll wave. A Rayleigh wave is a surface wave that propagates along the Earth/air interface, not in the body of the Earth. A Rayleigh wave creates an elliptical motion of Earth particles along its propagation path. The horizontal particle displacement associated with this ellipse is oriented in the direction of wave propagation. The horizontal displacements associated with Love waves and Rayleigh waves are orthogonal to each other.

Reflection coefficient is a parameter that defines the amplitude of the wave that reflects from an interface. The magnitude of a reflection coefficient at an interface is linearly propor-

tional to the difference in seismic impedance across that interface. The algebraic sign of a reflection coefficient defines the polarity of the reflection event.

Rollover is a downward bending of strata that often forms a structural trap for oil and gas. The bending movement is initiated by tectonic forces.

S wave is a shear wave. It is sometimes called a secondary (S) wave because it arrives later than the primary wave (see P wave). The term S wave needs to be used carefully because there are several types of shear waves. S waves include SH and SV modes and, in a complex anisotropic Earth, each of these modes (SH and SV) divides into a fast and slow component. Converted SV waves (called C waves) that result when P waves arrive at interfaces at nonnormal angles of incidence are another type of S wave. The term “S wave” spans a large family of distinct wave types.

SH is a shear wave mode that has its particle-displacement vector oriented perpendicular to the vertical plane passing through the source and receiver stations. In a flat-layered isotropic Earth, an SH mode has its particle-displacement vector oriented parallel to horizontal interfaces. See SV.

Stacking bin is the smallest definable area within a 3D seismic image space. The number of stacking bins in a 3D seismic volume is the same as the number of seismic traces in that volume. At the conclusion of 3D data processing, one image trace passes vertically through the center of each stacking bin. The lateral dimension of a stacking bin is the same as the spacing between adjacent traces in the 3D volume.

Stacking fold is a number that specifies how many seismic field traces are summed to create a final image trace in a 3D seismic volume. A stacking fold of 20 means that 20 field traces were summed to create one stacked trace.

Stratal surface is a depositional surface associated with a fixed geologic time. Geologic time is constant along a stratal surface, but the rock types above and below the surface can vary.

Surface wave is a seismic wave that trends along an interface, particularly along the Earth/air interface. Surface waves do not enter the body of the Earth and image deep targets. See ground roll, Love wave, and Rayleigh wave.

SV is a shear-wave mode that has its particle-displacement vector oriented in the vertical plane passing through the source and receiver stations. An SV displacement vector is orthogonal to an SH displacement vector. See SH.

Synthetic seismogram is a mathematical construction of a seismic wavefield. Synthetic seismograms can be calculated in 1D, 2D, or 3D data space. Either downgoing wavefields, upgoing wavefields, or both can be included in the calculation.

Thin bed is a sedimentary layer with a thickness less than one-fourth of the length of the dominant wavelength in the illuminating seismic wavefield. Typical dominant wavelengths can be 200 to 300 ft (~65 to 100 m); therefore, many thin beds have thicknesses of 50 to 75 ft (~15 to 22 m). The top and base of a thin bed cannot be resolved in a seismic image.

Time slice is a horizontal slice through a 3D seismic data volume. Seismic image time is constant across a time slice, but geologic time is not, unless the stratigraphy is perfectly flat.

Time-structure map is a map identifying the seismic image times at which subsurface structure is located. Time-structure maps can be converted into depth-structure maps if seismic propagation velocity can be defined throughout 3D seismic image space. See depth-structure maps.

Tomograms are popular products produced by crosswell seismic profiling. A CSP velocity tomogram shows the spatial distribution of seismic propagation velocities in the interwell space between a source well and a receiver well.

Vibrator is a popular onshore seismic energy source. Vibrators are large vehicles weighing 60,000 lbs or more. They transmit seismic energy into the Earth through a heavy baseplate that is pressed to the ground and then vibrated over a prescribed frequency range.

Vertical seismic profile (VSP) data are acquired with an energy source on the Earth's surface and a vertical array of closely spaced receiver stations in a well. VSP receiver stations are positioned vertically at increments of approximately 50 ft (15 m). This small spatial sampling allows all wave modes (downgoing, upgoing, shear, compressional) to be separated from the raw data.

SI Metric Conversion Factors

ft × 3.048*	E - 01 = m
mile × 1.609 344*	E + 00 = km
psi × 6.894 757	E + 00 = kPa

*Conversion factor is exact.

Chapter 3A

Petrophysics

E.C. Thomas, Bayou Petrophysics

3A.1 Introduction

3A.1.1 Definitions. The term “petrophysics” was coined by G.E. Archie and J.H.M.A. Thomeer in a quiet bistro in The Hague.¹ By their definition, petrophysics is the study of the physical and chemical properties of rocks and their contained fluids. It emphasizes those properties relating to the pore system and its fluid distribution and flow characteristics. These properties and their relationships are used to identify and evaluate hydrocarbon reservoirs, hydrocarbon sources, seals, and aquifers.

The petrophysicist or petrophysical engineer practices the science of petrophysics as a member of the reservoir management team (RMT). (See the chapter on reservoir management in this section of the *Handbook*.) The petrophysicist provides answer products needed and used by team members, as well as physical and chemical insights needed by other teammates. The reservoir and fluid characteristics to be determined are thickness (bed boundaries), lithology (rock type), porosity, fluid saturations and pressures, fluid identification and characterization, permeability (absolute), and fractional flow (oil, gas, water).

It is easy to define these characteristics and to appreciate their part in the assessment of reserves. The difficult part comes in determining their actual value at a level of certainty needed to make economic decisions leading to development and production. The seven characteristics listed are interdependent (i.e., to properly determine porosity from a wireline log, one must know the lithology, fluid saturations, and fluid types). The science of petrophysics is then used to unscramble the hidden world of rock and fluid properties in reservoirs from just below the Earth’s surface to ones more than four miles deep. The petrophysicist then takes on many characteristics of the fictional sleuth Sherlock Holmes to extrapolate, from the most meager of clues, the true picture of the subsurface reservoir using dogged determination to wrest all possible information from the available data, all the while enjoying the thrill of the hunt.

How does the petrophysicist solve this difficult problem? Archie’s general method is to subdivide the problem into smaller segments and iterate using all data until all data agree. One starting point is to determine rock types (petrofacies) wherein we identify pore type, pore size distribution, pore throat type, and pore throat distribution. When coupled with fluid type, one can establish a capillary pressure model that will lead to understanding in-situ fluid saturations and fluid flow. The discussion of the process is lengthy and is covered here and throughout the

TABLE 3A.1—TOOL CHOICES FOR A PARTICULAR RESERVOIR PROPERTY*

Reservoir Property	Primary Tool	Secondary Tool	Backup
Thickness (bed boundaries)	Gamma ray log (borehole image log when available)	Electric log with SP log	Density/neutron log
Lithology/rock type	Core and core analysis	Mud log	Gamma ray spectroscopy log
Porosity	Density log (given rock type and fluid identification)	Neutron log (given rock type and fluid ID)	Core and core analysis
Saturations (oil, gas, water)	Electric log (given porosity, rock type, and fluid ID) calibrated with a capillary pressure model	Carbon-oxygen log (given favorable borehole/formation environment)	Core and core analysis (given appropriate drilling environment and reservoir position)
Fluid ID/characterization	Wireline formation tester	Mud log	Core and core analysis
Permeability (absolute)	Core and core analysis	Wireline formation tester	Drillstem test
Fractional flow (oil, gas, water)	Core and core analysis	Wireline formation tester	Drillstem test

*The choices in this table are subjective and can change depending on the investment risk a particular client company can tolerate and the geographical circumstances involved.

Handbook. However, the tools available to the petrophysicist are mud logging (solids, liquids, gasses, volumes, rates, concentrations, and temperature); measurements while drilling (MWD) and logging while drilling (LWD); wireline logging (open- and cased-hole); core sampling [(wireline (percussion and drilled) and whole] and core analysis; and fluid sampling (wireline and/or drillstem tests). This list is arranged in order of the usual acquisition sequence. The economics of a given evaluation may restrict the application of any of these tools.

These topics are discussed in further detail in this and other sections of the *Handbook*. These chapters explain how to make the necessary measurements and how to ensure that the resulting data are accurate enough. We will now demonstrate how to choose the appropriate tools to determine the required reservoir and fluid characteristics.

3A.1.2 Choosing Tools. The choices of tools for the evaluation program are usually made by the RMT with recommendations from the petrophysicist. Cost and accuracy are usually highly correlated; thus, the team's choices quickly become one of finding the maximum allowable risk for the minimum cost (time and money) of the evaluation. **Table 3A.1** summarizes the typical evaluation program choices and can be used as a reference during subsequent discussions on determination of various reservoir properties.

3A.1.3 Determining Layer Thickness. Bed boundaries are usually the easiest of all reservoir properties to measure; however, there are some fatal traps that await the unwary. The geologist's knowledge of the rock types in the play, in general (and in the well of interest, in particular) can be used. By convention, reservoir thickness is expressed in feet and is rounded to the nearest foot, even though most modern wireline logs are recorded digitally every 6 in. Many of the world's reservoirs are logged in metric units, and thickness is expressed in meters. In this regime, thickness is rounded to the nearest 0.1 m.

Sands and Shales. The term sand is used generically and can also refer to sandstone or other siliciclastic formations. The term shale is used generically and can also refer to mudrock or claystone. When the reservoir beds are mostly sand [typically low gamma ray (GR)] and shale (typically high GR), then the GR log can usually be used to select bed boundaries. The inflection point of the GR count rate expressed in American Petroleum Institute (API) units is

selected as the bed boundary. (See examples in the chapter on nuclear logging in this section of the *Handbook*.) The choice of which bed thickness is to be determined is usually made by the geologist largely on the basis of pattern recognition skills developed during the play definition. Not all sand beds have low GR levels. If the sand bed contains sizable amounts of potassium feldspar, mica, or volcanic debris, the sands may be as radioactive as the shales and difficult to tell apart. In this case, the spontaneous potentials (SP) log is often used if the well is drilled in water-based mud. Again, the inflection point of the log is used to denote the bed boundary. (See examples in the chapter on resistivity and SP logging in this section of the *Handbook*.) However, in low-porosity and high-resistivity environments, the SP is suppressed and cannot be relied on as a bed boundary indicator.

Another tool that can be used to mark bed boundaries is the electric (resistivity or conductivity) log. This log is most useful when the shales are water-bearing and the sands are shale-free and hydrocarbon bearing. However, the bed boundary is no longer at the inflection point on the log, but is offset by one-half of the electrode spacing of the tool used to measure resistivity. Each service company has charts to aid the petrophysicist in determining the correct offset, while many wellsite computer products take this offset into account automatically. The finest resolution of all is afforded by electric or acoustic borehole image logs, but these logs are not routinely run because of their expensive acquisition and processing costs. The chapter on specialized logging topics in this section of the *Handbook* shows examples of borehole image logs. If the well is drilled in oil-based mud, then the SP log is not available and the density/neutron log can be used to define sand from shale. If the density/neutron log is a modern digitally sampled tool, then the inflection point can be used as the bed boundary. If, however, the density/neutron log is an older analog tool, the bed boundary can be offset because of drag settings. Vendor publications are available to aid the user in determining the offset. Acoustic borehole image logs are an option in small boreholes and lightweight oil-based muds. Nuclear magnetic resonance (NMR) logs are also useful in distinguishing zones that have movable fluids from those containing bound fluids (examples are shown in the chapter on NMR logging in this section of the *Handbook*).

Carbonates. When the reservoir beds are generally composed of carbonates (i.e., limestones and/or dolomites), bed definition becomes more complex. In this case, the presence and absence of porosity defines the reservoir from the seal; thus, the GR log may not be useful in demarking bed boundaries. Likewise, carbonates are generally in a higher resistivity regime, and the SP log is of little use. Thus, in this environment, one relies on a tool sensitive to porosity to delineate the bed boundaries, such as the density, neutron, or acoustic log. Borehole image logs are also useful when the borehole is relatively smooth. Large vugs and washouts invalidate readings from these tools. (The chapter on specialized logging topics in this section of the *Handbook* includes an example of a borehole image log in a carbonate formation.)

What To Count. Determining gross bed thickness is straightforward; however, determining what part of a given bed contains producible hydrocarbons is tricky. At present, there is no single standard sanctioned by SPE or API as to the definition of, or the method for determining, net pay. One of the more common complications is a result of the small thickness of layers containing hydrocarbons. Some common depositional environments can result in sands and shales being laid down into zones thinner than the resolving power of almost all wireline logs. One cannot count directly what one cannot see. In this case, we settle for thicker averages that mathematically equate to correct fluid volumes (i.e., calculate that from depth X to depth $X+30$ ft, the ratio of sand to shale is 0.5; thus, it contains 15 ft of reservoir-quality rock in layers too thin to individually resolve). Finally, one can cut a continuous core from the top through the bottom of the reservoir in question and, given the good fortune to recover 100% of the core at the surface, one can use sophisticated core-analysis techniques to determine the thickness of the layers with a precision and accuracy better than any other part of the reservoir

remaining in the Earth. Because of the high cost of cutting and analyzing whole core, this method is seldom used, unless no other method can be proven to work.

3A.1.4 Determining Lithology and Rock Type. The identification of a bed's lithology is fundamental to all reservoir characterization because the physical and chemical properties of the rock that holds hydrocarbons and/or water affect the response of every tool used to measure formation properties.

Definitions. The term lithology is used as a gross identification for a rock layer in the subsurface and uses familiar names such as sandstone (or sand), limestone, dolostone (or dolomite), claystone (or clay), chert, coal, shale (or mudrock), diatomite, halite, anhydrite, gypsum, and tuff. (The preceding list is not exhaustive. For detailed lists, see [Ref. 2](#).) The term rock type is a more detailed description than lithology because it reflects the natural groupings of pore systems that produce recognizable properties used to predict flow properties, volumes, and fluid saturations. Lithology focuses on grains, while rock type focuses on pores. The list of rock types contains more than 250 classifications.* (See the chapter on petroleum geology in this section of the *Handbook*.) Another term used in the literature is the Greek equivalent "petrofacies." (Another term that is finally dropping from use is the incorrectly named "electrofacies.")

Direct Determination. Obtaining a physical sample of the reservoir is the surest way to unambiguously determine lithology and rock type, but obtaining this physical sample is not always easy. Mud logs are the first choice in wildcat wells, but exact assignment of a rock fragment to a particular depth is not without error. The size of the individual rock sample examined at the surface is rather small because it is limited by the size of drill cuttings and rock strength. Weak rocks, ones without cement, are often reduced to original detrital grain size by the drilling process, making it difficult to determine rock type, but still possible to determine lithology. Once the well is drilled and logged and rock layers are marked for further study, rock samples can be obtained through the use of wireline core takers or sidewall core drills.

Recovery of sidewall samples is not always a sure thing, and we often fail to get rock samples from zones of interest. In a wildcat well with a zone of high interest identified with logs, rock samples, and fluid samples, we can plug back the well several hundred feet, set a whipstock, perform a parallel sidetrack (called a bypass hole), and then take a whole core across the zone of interest. Because the two holes are parallel, we know exactly at which depth to swap out the drill bit with a core barrel. The resulting whole core can be sampled, and sophisticated core analysis can be used to identify the rock type of each zone and determine petrophysical parameters, which are used to refine the formation evaluation from the log data.

Indirect Determination. If no direct rock sample is available in a given zone, log responses must be used alone to simultaneously determine lithology, porosity, and fluid saturations. Rock typing is much more involved and requires the use of commercially available catalogs of analog data^{3,4} or locally collected data to pinpoint petrophysical properties that can be used to refine porosity and fluid-saturation calculations. If, in a given wellbore, one is lucky enough to encounter parts of the desired reservoir below the free-water level, then fluid saturation is known and gross lithology can be determined from routine wireline logs such as density, neutron, and acoustic tools. All wireline service companies provide charts and answer products that convert wireline logging data into lithology; however, few beds are simple homogeneous layers. (See the chapter on Reservoir Geology in this section of the *Handbook*.) If some of the layers are beneath the resolving thickness of the tool, some average response of the layers, depending on bed and borehole geometry, can be observed. Single layers of salt (NaCl), anhydrite, gypsum, coal, or tuff are easily identified when several feet thick or thicker; however, salt-

* Personal communication with R.M. Sneider, R.M. Sneider Exploration Inc., Houston (1990).

plugged sandstone can mimic gas-filled clean sandstone, or a very shaly rock type can hide the presence of gas.

Mica or potassium feldspar, when abundant in sandstones, can confuse lithology determination on the basis of the GR response. The more sophisticated GR spectroscopy tools can help to identify the chemical species in a given rock and often can lead to deducing its lithology. (See the chapter on nuclear logging in this section of the *Handbook*.) However, no single wireline log or set of logs can determine pore size distribution and pore throat size distribution. These data are used to establish rock type, resulting fluid flow characteristics, and other petrophysical parameters needed to determine fluid saturation. If every reservoir in our wildcat well is hydrocarbon filled, the problem of quantification becomes more difficult, particularly when formation water resistivity, R_w , is unknown. In difficult areas, a follow-up well and a whole core, drilled with oil-based mud that is taken high in the hydrocarbon column, must be drilled to guarantee no in-situ water displacement. Subsequent sophisticated core analysis can determine the value of in-situ water salinity. (See the chapter on petrophysical applications in this section of the *Handbook*.) If coring is not an option, a well will have to make a significant amount of water to test. In pressure-depletion reservoirs that never produce much water, the accurate determination of water salinity may never happen if the reservoir is drilled with oil-based mud, negating the use of the SP log.

3A.1.5 Determination of Porosity. The determination of porosity is paramount because it determines the ultimate volume of a rock type that can contain hydrocarbons. The value and distribution of porosity, along with permeability and saturation, are the parameters that dictate reservoir development and production plans. Determination of porosity from a wireline log is only part of the problem, because the values determined in one well must be upscaled into the space between wells. To extrapolate correctly, the team must identify depositional environments and rock types and then have access to analog data sets. Only then can the correct statistical distributions be extrapolated across the reservoir. (See the chapter on geostatistics in the Emerging and Peripheral Technology section of the *Handbook*.)

Direct Determination. If one has access to an undamaged whole core from the reservoir in question, direct measurement of the porosity is possible, if care is taken. Some profess that all cores are damaged by the coring process, thus no accurate assessment of porosity is possible by coring. This author does not agree with that premise. X-ray computerized tomography scans, thin sections, and scanning electron microscope examination can verify that grain contacts are unmoved, authigenic pore linings are undamaged, and heavy-weight drilling fluids and/or particles are absent. Thus, given a satisfactory core, porosity can be determined accurately by several different methods specified in API RP 40.⁵

There are a number of pitfalls to avoid. One pitfall is that cleaning the core of crude and brine must be both thorough and gentle. One must remove all the heavy ends of the crude (typically asphaltenes) but not damage the authigenic minerals. NaCl crystals left from the in-situ brine when the water is removed must also be removed, but the authigenic clay minerals must not be removed or disturbed. Tar must not be removed if it occurs naturally in situ, and NaCl pore linings must not be removed if it occurs naturally in situ. Gypsum, when present, must not be dehydrated during the determination of porosity, and hydroxyl water of clay minerals must not be removed and counted as part of the pore space. Pore space must not be created during the cleaning process by flowing large volumes of fluid through rocks with soluble grains, such as gypsum, anhydrite, limestone, or salt.

Another pitfall to avoid is that some rock samples are mechanically weak and uncompact when brought to the surface and freed from the overburden load. These rock samples must be returned to in-situ conditions of effective stress to return the rock sample to its in-situ value of porosity. Correct procedures to make these measurements have been published by several

authors.^{6,7} Typically, stressed porosity measurements are more time consuming and more costly. If the core is subdivided into rock types, empirical correlations between stressed and unstressed measurements on a given rock type can be used to extrapolate to a larger data set.

An additional pitfall is that some sandstones contain fibrous pore-bridging clay minerals. These clay types are fragile and are damaged by most routine methods used to clean the core before porosity determination. When this type of clay is determined to be present, all subsequent core cleaning must be done using critical point drying methods.⁸ In addition to the methods defined in API *RP 40*, NMR spectroscopy methods can be used to determine porosity on small core samples. When care is taken to ensure that the core sample is 100% saturated with water and or liquid hydrocarbon, the NMR method yields an accurate value of porosity. The NMR method for porosity determination can also be used in the borehole using wireline NMR tools with excellent results. The chapter on NMR logging in this section of the *Handbook* shows examples.

Indirect Determination. Direct determination of porosity by core analysis is the “gold standard” and is used where available to calibrate all indirect measurements. Indirect methods allow leveraging of limited core data to provide more information on areal and vertical variations in porosity when coring is too expensive and/or only partial cores are recovered.

Sands. Patchett and Coalson⁹ determined that the density log is the most accurate method to determine porosity when one has knowledge of grain density and fluid density. While this method is standard in production wells, these parameters are often unknown for wildcats. Grain density can change rapidly along the borehole as lithology changes. Fluid types and saturations change more slowly, except at fluid contacts. Thus, we have four unknowns: porosity, grain density, hydrocarbon saturation, and water saturation, and one measurement: bulk density. A statistical method would be used to combine the environmentally corrected log readings from the density, neutron, acoustic, and GR to solve for the four unknowns. Often, a shallow resistivity log is included in the mix, and the acoustic log is dropped. Every logging vendor provides an answer product that uses this type of method, and most larger oil companies have published their own method.¹⁰ If we are certain that we are below the free water level and if we assume that we know the rock type is sand with a grain density of 2.65 g/cm^3 , the measured density log reading of bulk density can be converted into porosity, as the chapter on nuclear logging in this section of the *Handbook* shows.

Another simplified method is to use the density-neutron crossplot provided by each of the logging vendors. Patchett and Coalson⁹ found no benefit to using the density-neutron crossplot over a density log if one used known and variable grain density. The novice often uses a simple method with little regard for changes in rock type, fluid type, or borehole conditions, and the result is considerable error in the determination of porosity. The density log can be quite accurate when logged in ideal to semi-ideal borehole conditions. However, in rugose boreholes, extremely thick mudcakes, or unusual weighting materials in the mudcake (e.g., hematite), the bulk density readings seen on the log will no longer reflect those of the borehole wall, and these readings must be discarded and the value of porosity determined by other methods. The borehole caliper and density correction curves are used to validate the quality of the bulk density readings.

Heterogeneity. The foregoing discussion on sands provides an answer for porosity that is correct, but it reflects the average porosity over the depth of resolution of the tools (i.e., approximately 3 ft). Sophisticated digital processing can increase the resolution to approximately 1 ft. Thus, when the reservoir is heterogeneous on a scale smaller than 1 ft, one must use other methods to deconvolve the resulting averages into values that reflect the true porosity of the individual rock types. One of the most common heterogeneous reservoirs is the laminated sand-shale sequence, in which the shale layers are often less than 1 in. thick. One published method used to determine the porosity of the sand layers free of the unresolved shale layers is the Thomas-

Stieber method.¹¹ In a sand-shale reservoir in which the shale laminations have a porosity lower than the sand layers, one will consistently understate the value of reservoir porosity if the unresolved shale laminations are not properly accounted for. Furthermore, if one is using porosity-to-permeability transforms, the value of permeability will be underpredicted.

Carbonates. Determination of porosity in carbonates is generally straightforward unless the rock type is one with large vugs (i.e., fist-sized or larger) or fractures. Density-neutron and neutron-acoustic crossplot have been historically useful and accurate when calibrated to core measurements. When the rock types become complex and numerous, then statistical, multiple-log methods that match the number of unknowns to independent log measurements are required. Every logging vendor provides an answer product to produce a reasonable value of porosity when all logs are environmentally corrected and validated. Large vugs can be spotted with borehole image logs (see the chapter on specialized logging topics in this section of the *Handbook*) and with large diameter cores (see the chapter on relative permeability and capillary pressure in the General Engineering section of the *Handbook*). With appropriate sampling, the borehole readings can be corrected for the effects of large vugs. Logging tools that investigate larger volumes are given higher weights in the analysis.

Fractured Reservoirs. The dual-porosity system that exists in a fractured matrix reservoir provides a challenge in the opposite direction in that often the overall value of porosity is quite low (2 to 3%). Because most wireline porosity logs have random statistical error of 1 to 2%, the error is as big as the value being measured. Under these conditions, reservoir simulation and history match is the most reliable method to determine storage capacity and reserves, and porosity becomes moot. Borehole image logs are used to locate the fractures and provide probable production intervals.

3A.1.6 Oil, Gas, and Water Saturation. The determination of in-situ saturations relies on interpretations of logging devices that read far from the borehole and away from any fluid alterations caused by invasion during drilling.

The workhorse tools are the deep induction and deep laterolog. All other tools such as density, neutron, acoustic, NMR, shallow laterologs, and GR provide readings from the flushed zone that has altered saturations. The most important transform that converts resistivity readings into water saturation is the well-known Archie relationship, which is discussed in the chapter on resistivity and SP logging in this section of the *Handbook*. The Archie relationship has many unknowns [i.e., porosity (which may have three or four unknowns itself), R_w (resistivity of the in-situ water), m (an empirical fitting parameter between porosity and resistivity, often called Archie's cementation exponent), and n (an empirical fitting parameter between water saturation and resistivity often called Archie's saturation exponent)], and one measured parameter, the formation resistivity, often called the true resistivity. Thus, we have six or seven unknowns and one measurement, which is why a standard is needed (but a standard is rarely available).

In most cases, the saturations in a core have been flushed by the mud filtrate and are not representative of the in-situ reservoir value. Only when we drill with oil-based mud and core high in the oil column where the relative permeability to water is quite low (practically zero) do we recover a core with a value of water saturation at in-situ conditions, after we correct for blowdown from dissolved gas and stress effects on the pore volume of the core sample. The result is an accurate value of in-situ water saturation for zones with less than $S_w=50\%$.^{12,13} Even under these ideal conditions, we have to make empirical corrections to our gold standard. The other case that can be used to calibrate Archie's relationship is when heavy crude or tar does not move when we core. These cores usually have little or no blowdown because there is little or no dissolved gas. The only correction that is needed is for a stress correction to the pore volume; the result is an accurate value of in-situ oil saturation.

Calibration. Because the Archie method relies on so many adjustable and often unknown parameters, a calibration step is required to ensure that saturation values are accurate. The method of choice is calibration to a capillary model, which uses multiple core samples for each rock type to provide statistical precision. For a given rock type, several capillary pressure curves are averaged to provide a capillary pressure vs. saturation relation. With some information about the type of hydrocarbon in the reservoir, this relation can be converted into saturation vs. height above the free water level relation. With this model, we can predict, for a given rock type, the hydrocarbon saturation at any elevation in the reservoir and compare it with that computed from the Archie method. Discrepancies between the methods must be resolved by further study, but typically they result in adjustment to one of the many parameters in the Archie method.

Invaded Zone Saturations. The near-wellbore environment is usually altered by the drilling process in several ways, one of which is mud filtrate invasion as a result of overbalance and/or imbibition. The size of the invaded zone depends on many parameters. Some are overbalance magnitude, mud-fluid-loss parameters, mudcake permeability, formation porosity, formation permeability, and in-situ fluid viscosity. The exact shape of the invaded zone is unknown but is assumed to be cylindrical. (This cylindrical assumption is not as robust when the borehole encounters dipping beds or is drilled as a deviated hole.)

The radial extent of this invaded zone can be determined with multiple-spaced resistivity tools if the invasion process has altered resistivity, unless the depth of invasion is beyond the zone of investigation of the resistivity tool. If one is comfortable that the shallow-reading resistivity device responds solely from the invaded zone, then one can use the Archie relationship to compute water saturation, as discussed previously. One must take care to determine if the n parameter has changed because the invaded zone is on the imbibition cycle, rather than the drainage cycle usually observed deep within the reservoir. NMR is another method that can be used to determine the invaded zone saturation. Wireline NMR tools do not see deeply into the formation and usually read invaded zone values. The chapter on NMR logging in this section of the *Handbook* shows examples of these responses. Generally, filtrate invasion results from the use of either water-based or oil-based mud. Filtrate invasion from water-based mud into the water leg of a reservoir makes no change in S_w . It remains at 100%.

Water-based mud filtrate invasion into the hydrocarbon leg of the reservoir can dramatically decrease the hydrocarbon saturation caused by imbibition, viscous stripping, and gas dissolution. The measured value of fluid saturations in the invaded zone should not be used to predict the residual hydrocarbon saturation by water displacement within the body of the reservoir because the dynamics of displacement are too different.

In the case of oil-based mud filtrate invasion, water saturation will remain immobile if S_w is less than 50% and mild surfactants are used in the mud. There will be no change in oil saturation in the invaded zone when compared with that deeper in the reservoir, unless extreme overbalance is being used. Shallow resistivity logs and NMR logs can be used to determine oil saturation in the invaded zone. These values can then be extrapolated to similar rock types throughout the reservoir.

3A.1.7 Fluid Identification and Characterization. Detection of a change in fluid type in the rocks while drilling is usually straightforward with the use of gas and chromatographic measurements. The chapter on mud logging in this section of the *Handbook* discusses these methods. Gas shows and oil shows while drilling are time-honored indicators of zones that need further investigation through logs, testers, and cores. In the rare case of gas-bearing, high-permeability rock drilled with high overbalance, gas will be flushed from the rock ahead of the bit, will not be circulated to the surface in the mud, and will not produce a gas show.

Water-Based Drilling Mud. Because hydrocarbons are not always part of a water-based-mud formulation, sophisticated analytical chemical techniques can be used on the oil and gas

samples circulated to the surface and captured to determine the properties of hydrocarbons in a given zone penetrated by the drill bit. Occasionally, small amounts of hydrocarbons are added to water-based mud to reduce friction on the drillpipe. This hydrocarbon response must be accounted for in any analysis. Sidewall samples will contain some remaining hydrocarbons when brought to the surface. If promptly wrapped, frozen, and analyzed, the crude remaining in the core can be used to characterize density, gas/oil ratio, viscosity, and other fluid properties. Companion sidewall samples can be analyzed at the wellsite for odor, color, fluorescence, and cut-fluorescence, which can be used to distinguish oil/water and gas/oil contacts. If one is uncomfortable predicting reservoir fluid properties from such a small sample, the zone in question can be sampled with a wireline formation tester or ultimately subjected to a drillstem test. Wireline formation testers are often unsuccessful in obtaining a hydrocarbon sample because of the extent of the invaded zone. The low oil saturation in the invaded zone has a low relative permeability resulting in little oil production and little, if any, movement while being sampled by a wireline tester tool until all of the invaded, water-based fluid has been removed.

The other fluid in the rock of interest is water. The value of the water resistivity in the virgin reservoir is needed to interpret the deep-reading resistivity tools. However, the water-based mud filtrate dilutes the in-situ water, making its characterization problematic. Some authors have proposed a method to tag the mud filtrate with radioactive tritium while coring the reservoir. The resulting core is sampled, its water extracted and analyzed for tritium. The measured concentration of tritium is used with the measured porosity to compensate the fluid properties for the effect of dilution from mud filtrate. Other methods use an uncommon anion as the tagged material to avoid radiation-based methods. The formation tester tool can also be used to obtain a water sample in the water leg of the reservoir. Although the zone is invaded with mud filtrate, we can use the pump-out feature available on all vendors' tools to pump fluid from the invaded zone into the wellbore until the entire invasion has been removed. At this point, a water sample can be taken. The tester tool has an onboard water resistivity cell that is used to monitor the change in resistivity as the invasion fluid is pumped. When this value no longer changes, we switch over and take a water sample for analysis.

Oil-Based Drilling Mud. The overwhelming presence of oil in this type of mud dilutes the hydrocarbon in the invaded zone to such a point that analysis of the hydrocarbon in sidewall samples can no longer be used to predict hydrocarbon fluid properties. On the other hand, the water phase is now intact and can be sampled and analyzed with usual methods.

To determine hydrocarbon properties, wireline formation testers must be used. Two methods are useful. One method requires that many judiciously placed pressure tests be taken in the wellbore. This will permit the determination of the fluid-pressure gradient and density, which can be used to identify gas, oil, or water. Another method requires the use of the pump-out feature available on all wireline vendor tester tools to pump invaded zone fluid into the wellbore until the invading fluid has been reduced to a sufficiently low value, and then switches the pump to capture fluids in a removable, transportable fluid chamber. The feature of these tester tools that makes this possible is onboard spectrometers that have the ability to discern oil-based mud filtrate from in-situ hydrocarbons that guide the changeover from pumping into the wellbore to the sample chamber. Pressure/volume/temperature laboratories for the required fluid properties can then analyze these fluids. The operation of wireline formation testers is neither cheap nor without risk of tool sticking; thus, some operators choose not to run these wireline tools and opt instead for a drillstem test. All wireline tester tools can be used to take a water sample in the water leg, and this practice is encouraged. Not only are errors in water resistivity reduced, but possible incompatibilities between in-situ water and completion fluids are discovered before completion attempts.

3A.1.8 Determination of Absolute Permeability. The “gold” standard for permeability is to make measurements on core samples and to determine permeability with the methods outlined

in API *RP 40*.⁵ All other techniques are calibrated back to core measurements. However, because core measurements sample such a minute part of the reservoir, we must rely on techniques that can be applied in a widespread fashion across the reservoir. These methods rely on measurements on sidewall samples, correlation to wireline logging responses, interpretation of NMR logs, wireline formation tester pressure responses, and drillstem tests.

Sidewall Samples. This technique is valid for slightly to unconsolidated sandstone rock types. Carbonate rock types are generally too heterogeneous for small samples to provide any meaningful reservoir-wide value for permeability. Sidewall samples of sandstone rock types are inherently contaminated with drilling mud particles and are of little use for direct measurement of permeability. However, we can inspect the rock sample with a binocular microscope to estimate median grain size, sorting, and degree of consolidation, and to characterize pore fills. With these data, we can develop correlations to permeability on the basis of whole core measurements. An alternative is to disaggregate the sample and determine a grain size analysis with laser light scattering, which can then be correlated to permeability on the basis of whole core analysis.

Wireline Logging Correlations. Permeabilities measured in cores can be correlated to wireline measurements taken in the cored borehole. At various times and places, almost every wireline log has been used to correlate to permeability. The porosity-permeability crossplot is, perhaps, the most used; however, it is subject to considerable error. In select basins, the GR log response can be used to correlate to permeability while, in other basins, the neutron log or acoustic log seems to provide the correlation with least statistical scatter.

NMR Logs. Interpretation of NMR logging responses provides a volumetric distribution of pore sizes. If the pores are assumed to be spherical in shape, a value for permeability can be computed. These size-dependent data have been coupled with NMR pore volumes and NMR fluid saturations to produce an NMR permeability log. The chapter on NMR logging in this section of the *Handbook* shows examples of these techniques.

Wireline Formation Testers. All wireline tester vendors provide answer products that take the drawdown and buildup pressure vs. time responses and compute mobility. Mobility can be converted into permeability if a value of fluid viscosity is assumed. This permeability must be used with some caution. First, the pressure measurements are made on the borehole wall that has suffered possible drilling damage and pore throat plugging from mud solids. Second, one must take note if the measurement is in an invaded zone with two phases and, hence, the permeability determined is an effective permeability, not an absolute permeability. Depending on rock type and fluid saturations, the effective permeability may be an order of magnitude too small. The chapter on fluid sampling in the General Engineering section of this *Handbook* presents examples of wireline formation tester responses and derived permeability and the use of these pressure measurements to determine fluid gradients.

Drillstem Tests. These measurements are covered in the chapter on data acquisition and interpretation in the Drilling section of this *Handbook*.

3A.1.9 Fractional Flow. To predict the fractional flow from a given zone in a wellbore, the absolute and relative permeability of the rock types open to flow in the wellbore must be characterized. Determining the complete relative permeability function vs. fluid saturations measured on cores maintained at reservoir conditions of temperature, pressure, and the use of live reservoir crude is a daunting task. Most reservoirs never have these measurements performed on them. Usually, we take small snippets of these curves and attempt to characterize their entire response with various models. Proof of success is often taken to be a successful history match; others prefer to look for agreement between future predictions and future performance.

Regardless of our ability to measure these parameters in the laboratory, the scaleup to a heterogeneous, faulted reservoir is a challenge of immense proportions. These subjects are cov-

ered in the chapter on reservoir simulation in this section and the chapter on relative permeability and capillary pressure in the General Engineering section of this *Handbook*.

3A.1.10 How To Put It Into Use. This chapter is designed to show the reader how to use petrophysics in a general sense—how the many facets of petrophysics are tied together and how they relate to other elements of petroleum engineering. However, there is nothing like examples to show new practitioners how petrophysics really works and how they may put it to use themselves. The chapter on petrophysical applications provides these examples.

Nomenclature

- m = Archie's cementation exponent
- n = Archie's saturation exponent
- R_w = resistivity of the in-situ water, ohm m²/m
- S_w = water saturation, fraction of pore volume
- X = a specific depth

References

1. Thomas, E.C.: "50th Anniversary of the Archie Equation: Archie Left More Than Just an Equation," *The Log Analyst* (May–June 1992) 199.
2. Deeson, A.F.L.: *The Collector's Encyclopedia of Rocks & Minerals*, Clarkson N. Potter Inc., New York City (1973).
3. *A Catalog of Petrophysical and Geological Properties of Typical Reservoir Rocks*, Shell Oil Co., Houston (1995).
4. *The World Wide Rock Catalog*, Reservoirs Inc., Houston (1990).
5. *RP 40, Recommended Practices for Core Analysis*, second edition, API, Washington, DC (1998).
6. Swanson, B.F. and Thomas, E.C.: "The Measurement of Petrophysical Properties of Unconsolidated Sand Cores," *The Log Analyst* (September–October 1980) 22.
7. Wei, K.K., Morrow, N.R., and Brower, K.R.: "The Effect of Fluid, Confining Pressure, and Temperature on Absolute Permeabilities of Low-Permeability Sandstones," *SPEFE* (August 1986) 413.
8. Wawak, B.E. and Campbell, W.L.: "Characterization of Clay Fabric Using Critical Point Drying to Preserve Clay Texture and Morphology," *Scanning Electron Microscopy* (1986) **4**, 1323.
9. Patchett, J.G. and Coalson, E.B.: "The Determination of Porosity in Sandstone: Part Two, Effects of Complex Mineralogy and Hydrocarbons," paper T presented at the 1982 Annual Soc. of Professional Well Log Analysts Symposium, Corpus Christi, Texas, 6–9 July.
10. Peeters, M. and Visser, R.: "A Comparison of Petrophysical Evaluation Packages: LOGIC, FLAME, ELAN, OPTIMA and ULTRA," *The Log Analyst* (1991) **32**, No. 4, 350.
11. Thomas, E.C. and Stieber, S.J.: "The Distribution of Shale in Sandstones and Its Effect on Porosity," paper presented at the 1975 Annual Soc. of Professional Well Log Analysts Symposium, New Orleans, 4–7 June.
12. Richardson, J.G. *et al.*: "Investigation of As-Received Oil-Base-Core Water Saturation From the Ivishak Reservoir, Prudhoe Bay Field," paper SPE 28592 presented at the 1994 SPE Annual Technical Conference and Exhibition, New Orleans, 25–28 September.
13. Holstein, E.D. and Warner, H.R. Jr.: "Overview of Water Saturation Determination for the Ivishak (Sadlerochit) Reservoir, Prudhoe Bay Field," paper SPE 28573 presented at the 1994 SPE Annual Technical Conference and Exhibition, New Orleans, 25–28 September.

SI Metric Conversion Factors

$$\begin{array}{ll} \text{bbl} \times 1.589873 & \text{E} - 01 = \text{m}^3 \\ \text{ft} \times 3.048^* & \text{E} - 01 = \text{m} \end{array}$$

*Conversion factor is exact.

Chapter 3B

Resistivity and SP Logging

T.D. Barber, A. Brie, and B.I. Anderson, Schlumberger

3B.1 Fundamentals

Resistivity logging is an important branch of well logging. Essentially, it is the recording, in uncased (or, recently, even cased) sections of a borehole, of the resistivities (or their reciprocals, the conductivities) of the subsurface formations, generally along with the spontaneous potentials (SPs) generated in the borehole. This recording is of immediate value for geological correlation of the strata and detection and quantitative evaluation of possibly productive horizons. The information derived from the logs may be supplemented by cores (whole core or sidewall samples of the formations taken from the wall of the hole).

As will be explained later, several types of resistivity measuring systems are used that have been designed to obtain the greatest possible information under diverse conditions (e.g., induction devices, laterolog, microresistivity devices, and borehole-imaging devices). Many service companies offer resistivity-logging services, and most offer a Web-based catalog that describes each service.

3B.1.1 Earth Resistivity. Formation resistivity is a key parameter in determining hydrocarbon saturation. An electric current can pass through a formation because it contains water with enough dissolved ions to be conductive. With a few rare exceptions, such as metallic sulfides and graphite, dry rock matrix is a good electrical insulator. However, perfectly dry rocks seldom occur below ground level, so nearly all subsurface formations have finite, measurable resistivities because of the water in their pores, adsorbed onto their grain surfaces, or absorbed into a clay structure.

The resistivity of a formation depends on the resistivity of the formation water, the amount of water present, and the structure and geometry of the pores. The resistivity (specific resistance) of a substance is the electrical resistance measured between opposite faces of a unit cube of the substance at a specified temperature or, generally,

$$R = r \frac{A}{L}, \dots\dots\dots (3B.1)$$

where R = resistivity in ohm·m, r = resistance in ohm, A = area in m², and L = length in m.

Conductivity, σ , is the reciprocal of resistivity, expressed in Siemens/m. To avoid the excessive use of small decimal numbers in well logging, conductivity is expressed in milliSiemens/m (mS/m), where 1000 mS/m = 1 Siemens/m, so

$$\sigma = \frac{1000}{R} \dots\dots\dots (3B.2)$$

Formation resistivities are usually in the range of 0.2 to 1000 ohm-m. Resistivities higher than 1000 ohm-m are uncommon in most permeable formations but are observed in impervious, low-porosity formations such as evaporites. A few low-porosity hydrocarbon-bearing formations with almost no formation water can have resistivities as high as 20 000 ohm-m.

Formation resistivities are measured either by passing a known current through the formation and measuring the electrical potential (electrode or galvanic devices) or by inducing a current distribution in the formation and measuring its magnitude (induction devices).

Because resistivities cannot be read accurately over the entire measurement range when displayed on a linear scale, all resistivity logs are now presented on logarithmic grids, usually in 4 decades across two log tracks. This allows the display of readings from 0.2 to 2000 ohm-m, with a single curve covering the useful range of nearly all logs. A backup curve is used in the exceptional cases of readings outside that range. As resistivity data are used more and more digitally, and the log plots are mostly for reference, other formats are in wide use.

Most wireline resistivity-logging tools also have the ability to measure and record small differences in electrical potential that occur spontaneously in conductive muds as a continuous SP curve. The SP curve records the electrical potential differences generated by the interaction of formation water, conductive drilling fluid, and ion-selective shales. It has a wide range of formation-evaluation applications, including differentiating potentially porous and permeable reservoir rocks from impermeable clays and shales, defining bed boundaries, correlating nearby wells, indicating the shaliness of shaly formations, and estimating formation-water resistivity, R_w .

3B.2 The Logging Environment

Measuring the resistivity of formations of interest is complicated by the invasion of drilling fluids into permeable rocks. The invaded fluid can displace some or all of the connate water or hydrocarbon present. The resistivity of the borehole is often much less than the formations of interest, sometimes by orders of magnitude. In addition, the formation often consists of rock layers with widely varying resistivity. **Fig. 3B.1** shows these factors.

To measure the uninvaded portion of the rock from the borehole, a resistivity device must include a large volume of formation—there must be adequate sensitivity to the region of interest. Over the years, the main developments in resistivity-logging tools have been targeted at eliminating response from unwanted parts of the formation and recovering the resistivity of the uninvaded portion of a single layer. The response from unwanted parts of the formation is lumped under the term “environmental effects.”

The main objectives of resistivity logs are the determination of R_t and R_{xo} and, for the newer imaging devices, the mapping of resistivity profiles into and around the borehole. This is accomplished by incorporating devices with at least three, and preferably more, depths of investigation. The deep-reading focused devices include the deep laterolog device (LLd) and the deep induction (ILd) device. Medium-depth devices include the shallow laterolog (LLs) and the medium induction (ILm). The shallow devices include the microresistivity device or the spherically focused log (SFL). The latest laterolog and induction tools include arrays focused at many depths of investigation—from five to eight depths—measured simultaneously. These al-

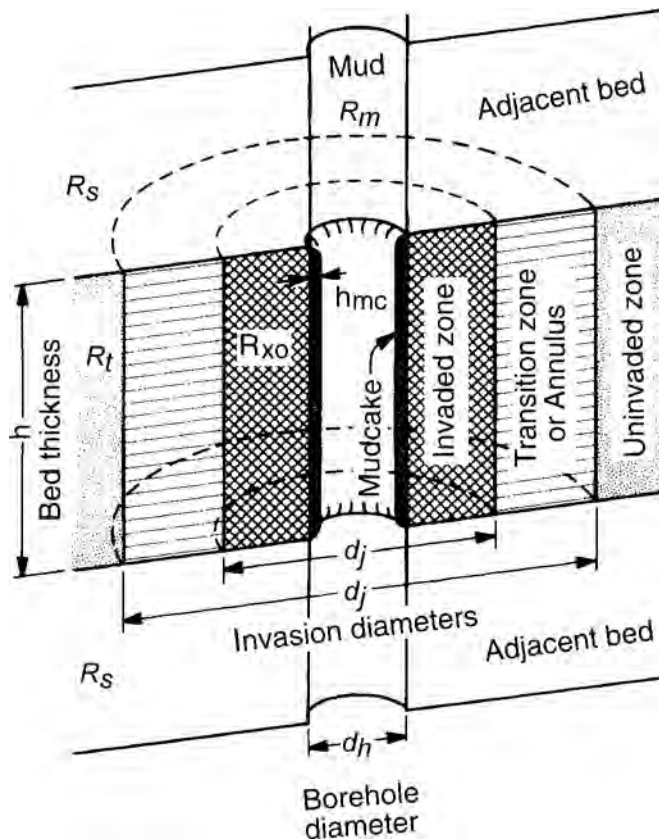


Fig. 3B.1—The borehole/formation environment for well logging.

low a better description of the invaded zone and allow for interpretation of complex invasion profiles.

3B.3 Electrode Resistivity Devices

3B.3.1 Normal and Lateral Devices. During the first quarter century of well logging, the only electrical surveys (ES) available were the resistivity logs made with so-called lateral and normal devices plus the SP. Thousands of them were run each year all over the world. Since then, new logging methods have been developed to measure values much closer to R_{xo} and R_t . Nevertheless, the conventional ES logs (consisting of SP; 16-in. normal; 64-in. normal; and 18-ft, 8-in. lateral) are stored in log archives all over the world. Because new information can often be obtained by reinterpreting old ES logs, this chapter includes discussion of the principles and responses of the ES measurements.

The first resistivity devices were the normals and laterals.¹⁻³ These were, in concept, extensions to laboratory four-terminal resistivity-measuring cells. Current is injected in the formation from a single electrode and returned to a point remote from the well. The current near the injection electrode spread out radially from the electrode. Two voltage-measuring electrodes (M and N) on the sonde approximated the measurement of a constant-voltage spherical shell around the injection electrode. The measurements of voltage and current are converted to a resistivity measurement.

For normal devices (Fig. 3B.2), the distance AM is small: 1 to 6 ft as compared with MN, MB, and BN. In practice, N or B may be placed in the hole at a large distance above A and M

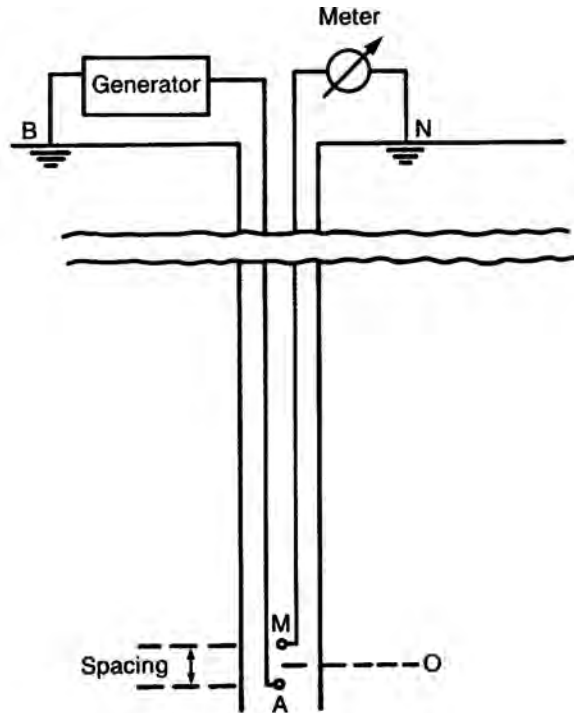


Fig. 3B.2—Schematic representation of the normal device.

[the voltage measured is practically the potential of M (because of current from A), referred to an infinitely distant point]. The distance AM of a normal device is its spacing. The point of measurement is midway between A and M. The most common normal spacings were 16 and 64 in.

The lateral device was designed to provide a deeper resistivity measurement than the normal tools, while at the same time improving the detection of thin beds. For lateral devices (**Fig. 3B.3**), measuring electrodes M and N are close to each other and located several feet below current electrode A. Current-return electrode B is at a great distance above A or at the surface. The voltage measured is approximately equal to the potential gradient at the point of measurement O, midway between M and N. The distance AO is the spacing of the lateral device.

In an alternate version of the lateral, the positions of the current and voltage electrodes are interchanged. A and B are moved to M and N, and N and M are moved to B and A. This tool is called the “inverse,” and it records the same resistivity values as the lateral by reciprocity. The inverse arrangement made it more practical to record measurements by the two normals and the lateral simultaneously.

Interpretation of laterals and normals is very complicated because the response is a complicated function of the formation being measured.⁴ **Fig. 3B.4** shows a computed response of the 16- and 64-in. normals for a series of beds with and without invasion. The separation is not a clear function of invasion, but is also a function of bed thickness. **Fig. 3B.5** shows the 18-ft, 8-in. lateral tool in the same series of beds. The relation of the curve to the bed is not clear at all. Many charts (called departure curves) were published to aid in interpretation of the ES logs. Modern interpretation methods include 2D inversion (after the curves are digitized) and iterative forward modeling for when they are not digitized.⁵

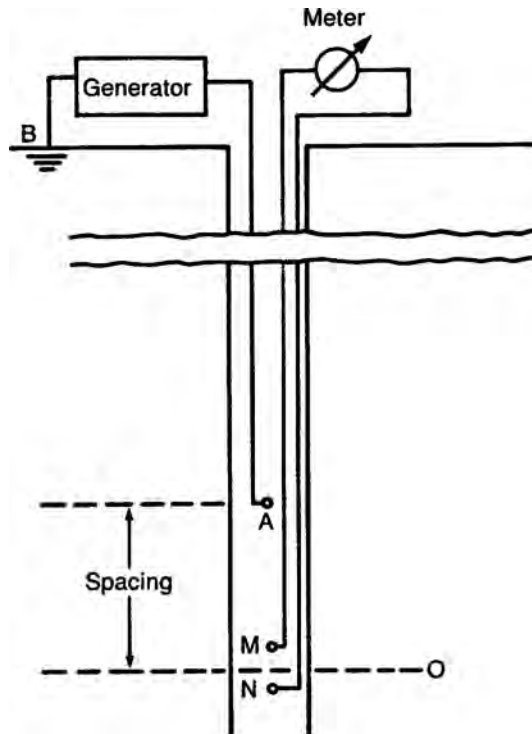


Fig. 3B.3—Schematic representation of the lateral device.

3B.3.2 Laterologs. Laterolog devices are designed to minimize the influence of near-tool effects (i.e., the borehole and the invaded zone) for a deep laterolog measurement, as well as to reduce the response from adjacent beds.⁶

To estimate R_t under a variety of different logging conditions and in different formations, a simple three-parameter, step-profile invasion model is often used. This model consists of a flushed zone of resistivity R_{xo} and a sharp boundary at diameter d_i , with the uninvaded zone of resistivity R_t . Three independent, borehole-corrected resistivity measurements with appropriately chosen depths of investigation contain enough information from the formation to reliably solve for R_t using this model. Measurements with the following features should be chosen: small, correctable borehole effects; similar vertical resolutions; and well-distributed radial depths of investigation—one reading as deep as practical, one very shallow reading, and one intermediate reading.

In conductive muds, the Dual Laterolog (DLL) Resistivity- R_{xo} combination tool provides simultaneous measurements suitable for evaluating R_t , R_{xo} , and d_i .⁷ It should be said that the value of R_t in a given bed is an interpreted parameter, and is almost never measured. As long as the formation is invaded, assumptions about the invasion profile must be made to estimate R_t .

Dual Laterolog Resistivity Measurements. Fig. 3B.6 shows the electrode array used for deep and shallow laterolog measurements (LLd and LLs, respectively). Both logs share the same electrodes and have the same current-beam thickness, but different focusing currents give them different depths of investigation. The measure current (I_0) is emitted from the central A0 electrode, returning to an “infinitely distant” electrode, usually at the surface. The focusing current (I_a) flows from the A1 and A2 (and A1' and A2') electrodes to a distant electrode for the

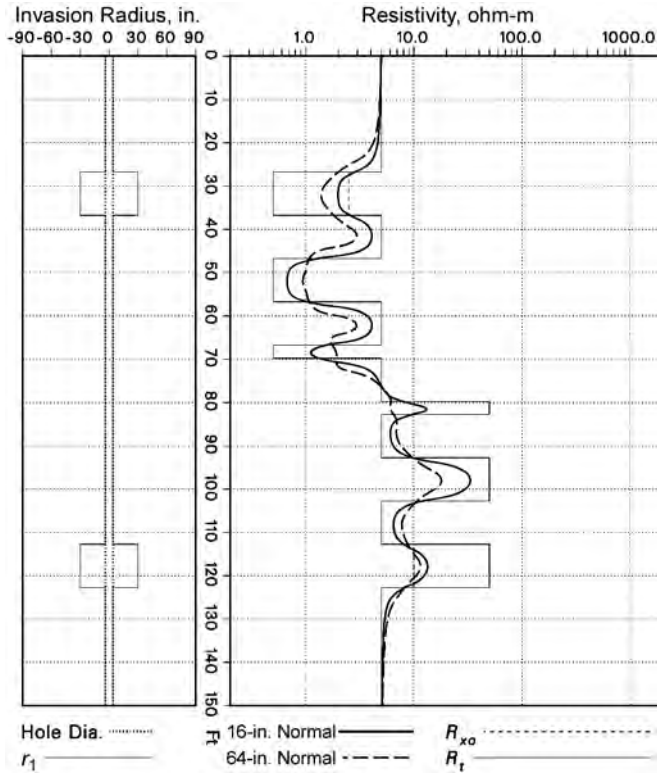


Fig. 3B.4—Computed response of 16- and 64-in. normals in beds of varying thickness.

LLd measurement and from A1 to A2 (and A1' to A2') for the LLs measurement. The focusing current is adjusted so that electrodes M1 and M2 (and M1' and M2') remain at the same potential.

A constant-power measuring system ensures measurement accuracy over a wide range of resistivities (from 0.2 to 40,000 ohm·m). Both the measure current and measure voltage (V_0) are varied and measured, but their product power $I_0 V_0$ is kept constant.

Long guard electrodes are required to achieve the desired depth of investigation and measurement range. For electrode tools focused using guard electrodes, the depth of investigation increases only as the square root of the length of the guard electrodes. This requirement results in the 28-ft [8.5-m] total length of the LLd electrode array. A beam thickness of only 28 in. [0.7 m], however, ensures good vertical resolution.

The LLs measurement shares most of the electrodes with the deeper measurement. This is achieved by operating LLs and LLd at different frequencies. The LLs and LLd measurements have the same vertical resolution, but the LLs device uses a less constrained focusing condition in which the focusing current returns to electrodes on the array instead of to a remote electrode. The LLs measurement therefore has a shallower depth of investigation and responds more strongly to the region around the borehole that is usually affected by invasion.

Laterolog Anomalies. The Groningen effect was named after the large Dutch gas field where the anomaly was first identified. The effect⁸ is an anomalously high resistivity reading that occurs for approximately 100 ft [30 m] below a thick, highly resistive bed such as the thick evaporitic Zechstein caprock at the Groningen field. The effect is maximum around 1 ohm·m. Because the DLL measure current is AC (albeit very low frequency), skin effect re-

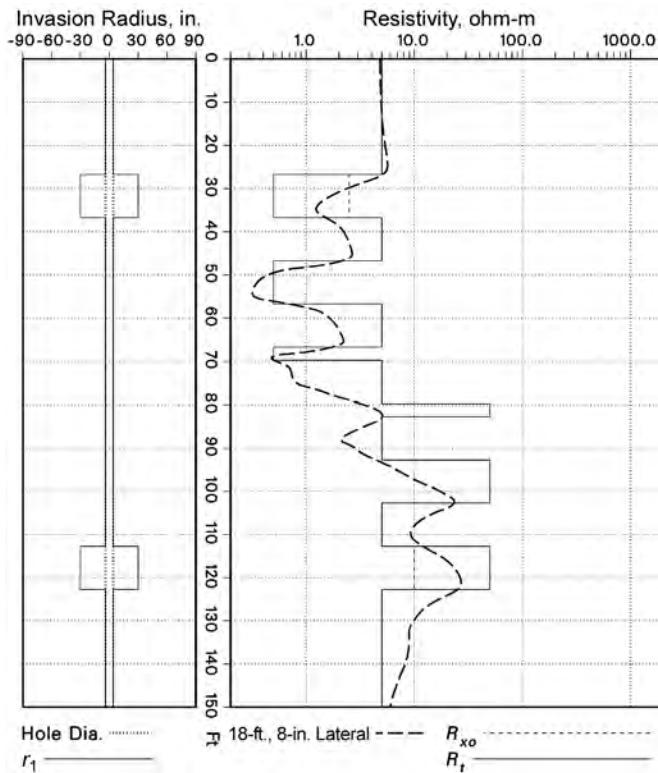


Fig. 3B.5—The 18-ft, 8-in. lateral in the same series of beds as in Fig. 3B.4.

duces the volume around the well where the measure and focusing current can flow. Little of the current is able to return to the remote electrodes through the highly resistive formation, with the majority flowing in the conductive mud in the borehole. This creates a negative potential at the far reference electrode used as the potential reference for the laterolog measurement. If casing has been set in or below the resistive zone, it accentuates the “short circuit” effect of the borehole, and the Groningen effect is more pronounced. Drillpipe conveyance produces the same effect, with the drillpipe becoming the “short circuit.” This problem severely limits the use of drillpipe conveyance of the DLL in high-angle or horizontal wells in many reservoirs.

A mild Groningen effect may be difficult to identify from the LLd curve alone. The Schlumberger DLL has a modified-geometry measurement that can also be recorded. This provides an LLg curve that separates from the LLd curve when Groningen effect is present. If the Groningen effect is positively identified, an estimate of its magnitude can be made by analyzing the signal phases in the tool, and an approximate correction can be applied to the log. The LLs measurement uses different current paths and does not suffer from the Groningen effect. The array laterolog (see the following) is not affected by Groningen effect.

Azimuthal Dual Laterologs. In the early 1990s, a new dual laterolog that had an additional azimuthally segmented current electrode was introduced.⁹ The Schlumberger ARI* Azimuthal Resistivity Imager has a set of segmented azimuthal electrodes incorporated in a conventional dual laterolog array. The tool records azimuthal resistivity variations around the borehole and

* Throughout this chapter, tool names are service marks of the referenced companies.

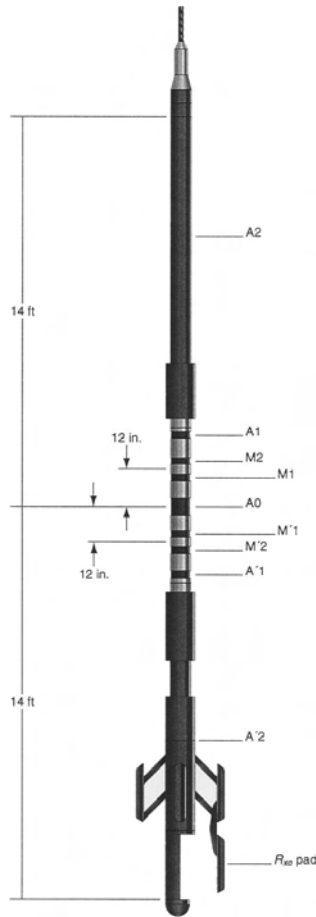


Fig. 3B.6—The dual laterolog array layout.

produces an image of the variations. The azimuthal electrodes are placed at the center of the A2 electrode of the DLL tool and do not interfere with the standard LLd and LLs measurements.

The deep azimuthal measurement operates at the same frequency as the deep laterolog measurement, and the currents flow from 12 azimuthal current electrodes to the surface. They are focused by the current from the A2 electrode's upper and lower portions and by currents from the other current electrodes. In addition, the current from each azimuthal electrode is focused passively by the currents from its neighbors. The resulting operation of the azimuthal array has no effect on the LLd and LLs measurements.

Twelve azimuthal resistivities are computed, and from their sum, a high-resolution resistivity measurement, LLhr, is derived. This is equivalent to replacing the azimuthal electrodes with a single cylindrical electrode of the same height.

The high-resolution LLhr curve reads almost as deeply into the formation as a deep laterolog LLd curve, particularly when R_{yo} is less than R_t . An LLhr log can therefore replace an LLd log for interpretation, especially where its vertical resolution is an advantage. Individually selected azimuthal resistivities can be used in the same manner where the logged interval is azimuthally anisotropic or includes highly dipping thin beds.

The azimuthal resistivity measurements are sensitive to tool eccentricity in the borehole and to irregular borehole shape. Auxiliary measurements are made that are very shallow, with current paths close to the tool. Most of the current returns to the A2 electrode near the azimuthal

array. Because the borehole is generally more conductive than the formation, the current tends to stay in the mud, and the measurement responds primarily to the volume of mud in front of each azimuthal electrode. The measurement is therefore sensitive to borehole size and shape and to eccentricity of the tool in the borehole. However, for best use of the azimuthal measurements, the tool should be well centralized in the borehole.

A High-Resolution Azimuthal Laterolog Sonde (HALS) resembles an ARI or a dual laterolog array.¹⁰ Although it is shorter than either of these tools, the HALS is not just a scaled-down version. Its dimensions are optimized to achieve similar performance as an ARI sonde with a tool that is only approximately one-half its overall length.

Like the ARI tool, the azimuthal array of the HALS makes deep and shallow resistivity measurements around the borehole with a 1- or 2-ft [0.3- or 0.6-m] vertical resolution. (In this chapter, vertical resolution is defined as the 90% width of the vertical response function.) Formation resistivity images can be derived from either the deep or the shallow measurements. Mud resistivity and tool standoff are also measured. In addition to providing a visual image of formation lamination and anisotropy, the azimuthal images can be used to estimate the gross formation dip and to correct deep resistivity measurements in dipping beds.

Because the HALS is shorter than ARI and DLL sondes, the borehole effect of the shallow measurement is larger. Combined with the slightly reduced depth of investigation of the deep array, this reduces the precision of the invasion correction in cases of invasion where $d_i > 50$ in. [1.3 m]. The inherent vertical resolution is sharper—24 in. [0.6 m] for the HALS deep and shallow resistivity curves (HLLD and HLLS, respectively) compared with 40 in. [1 m] for the LLD and LLs curves of the DLL log. The HALS provides high-resolution deep and shallow curves (HRLd and HRLs, respectively) with the same 12-in. vertical resolution as the LLhr curve of an ARI log.

Real-time corrections can be made for Groningen effect, electrical path changes imposed by tough logging conditions (TLC) logging in which the logging tool is transported on drillpipe, and borehole effects. A two-parameter inversion model can also be used in real time to solve for R_t and d_i , with R_{xo} provided by the microcylindrically focused log (MCFL) measurements of the Platform Express tool.

3B.3.3 Array Electrode Tools. The most recent development in electrode tools is the array laterolog or array lateral tools. These combine multiple depths of investigation with 2D inversion of the data to give much improved response in invaded thin beds with conductive mud.

The Schlumberger high-resolution laterolog array (HRLA) tool consists of five laterolog arrays with different depths of investigation.¹¹ All current is returned to electrodes above and below the array, so no bridle is used. Because it has no bridle, it does not suffer from Groningen effect.

Borehole and shoulder effects are minimized by the use of laterolog-style focusing. Focusing involves injecting current from guard or bucking electrodes to ensure that the current from the central measure electrode flows into the formation rather than along the borehole. By having all currents return to the tool body rather than surface, Groningen effect is eliminated and shoulder-bed effect reduced. More importantly, the surface current return and insulating bridle are no longer needed. All signals are measured at the same time and logging position. This avoids horns or oscillations caused by irregular tool motion and ensures that the measurements are always exactly depth-aligned.

The HRLA tool uses segmented bucking electrodes and multifrequency operation (ranging from 75 to 270 Hz) to acquire six simultaneous measurements. The six modes are focused by a combination of hardware and software focusing. The hardware injects the currents in a way that is as close to focused as possible. The shallowest mode, RLA0, is mostly sensitive to the borehole and is used to estimate the mud resistivity. The apparent resistivities RLA1 through RLA5 are all sensitive to the formation, becoming progressively deeper in investigation.

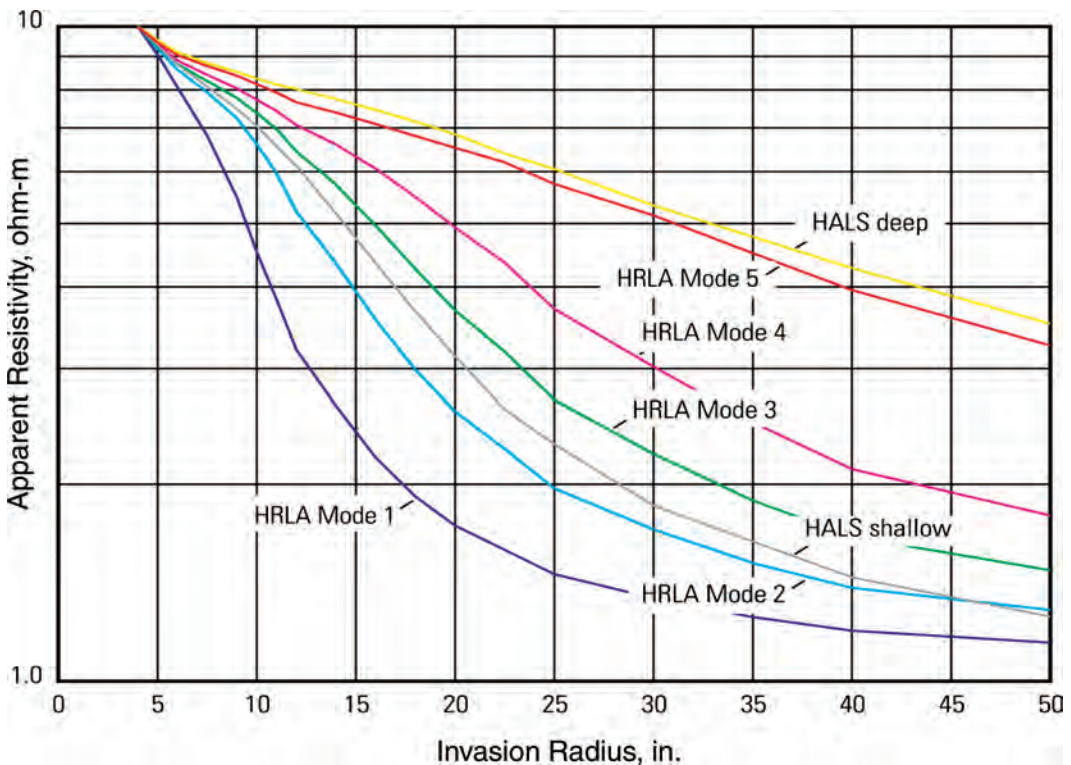


Fig. 3B.7—Computed radial response of the HRLA logs compared to the HALS, HLLD, and HLLS.

Fig. 3B.7 shows the radial response of the optimized HRLA tool compared to the HLLD and HLLS measurements from the HALS tool. Fig. 3B.8 shows the HRLA logs compared to the DLL, LLd, and LLs logs.

The shoulder-bed and invasion responses of laterolog tools are combined in the tool response in ways that are difficult to separate. For this reason, some sort of 2D inversion is necessary to determine the formation parameters accurately in the case of invaded thin beds. An automatic 2D inversion is available that yields the best results from the data in invaded thin beds. Fig. 3B.9 shows the field logs, 1D inversion results, and 2D inversion results in the same well.

The Baker Atlas high-definition lateral log (HDLL) tool¹² acquires 8 potential and 16 first differences, and computes 14 second differences. These are used as inputs to a 2D inversion to solve for formation resistivities. The inversion process begins with the raw data input and an initial estimate of a parametric model describing the formation resistivity distribution. Simulated logs or synthetic tool responses for each of the array sensors are derived for the selected initial formation parameters as a solution to Maxwell's equations.

The inversion process is initiated by using the shallow measurements (associated with short-spacing sensors) to identify and evaluate the shallow-formation resistivity structure. Deep measurements (associated with the longest sensor spacings) are used in evaluating the uncontaminated formation resistivity structure. The intermediate measurements are used to derive the radial-invasion profile. Using inversion processing, measurements of different vertical resolution and depths of investigation are combined in a single interpretation process to provide an accurate resistivity distribution image.

Final inversion results consist of the estimated resistivity structure satisfying all HDLL data and the statistical quality indicators represented in terms of the importance of the formation

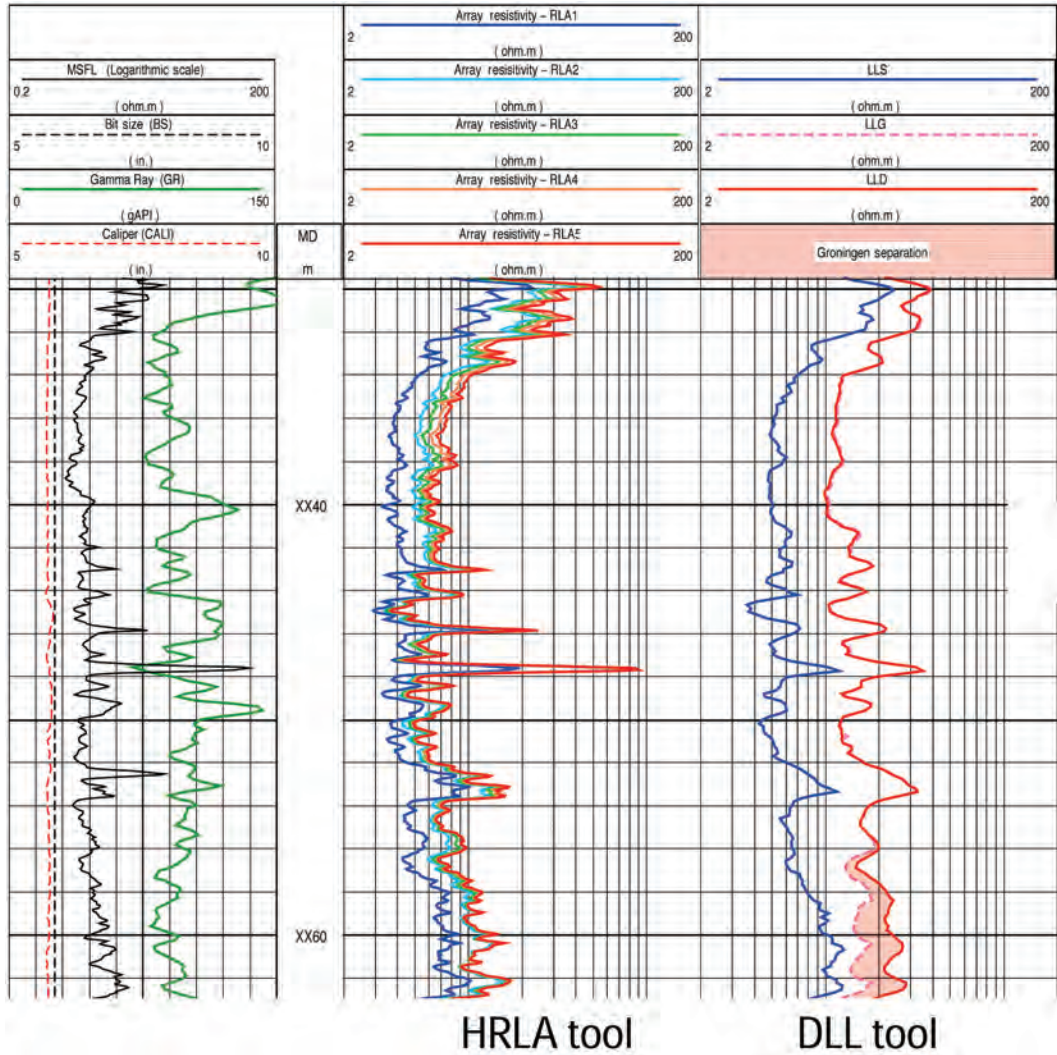


Fig. 3B.8—A log showing the high resolution of the HRLA vs. DLL.

parameter along with its corresponding error bounds. Fig. 3B.10 shows a comparison of HDLL R_t and R_{xo} inversion results with conventional Dual Laterolog (RS is DLL shallow and RD is DLL deep) and Micro Laterolog (MLL) measurements.

3B.3.4 SFLs. The SFL device measures the conductivity of the formation near the borehole. It uses small electrodes that can be combined with the dual-induction tool to provide shallow-investigation data for invasion evaluation.

The SFL device uses two independent current systems. A focusing current system establishes constant-potential spherical “shells” around the current electrode, even in the presence of a conductive borehole, and the I_0 survey current flows through the volume of investigation.

The SFL electrode array consists of current-emitting, current-return, and measure electrodes. Two equipotential spheres are established around the I_0 survey current electrode; the first sphere is approximately 9 in. [0.2 m] from the electrode, and the other is approximately 50 in. [1.3 m] from it. The volume of formation between these two surfaces is constant, and

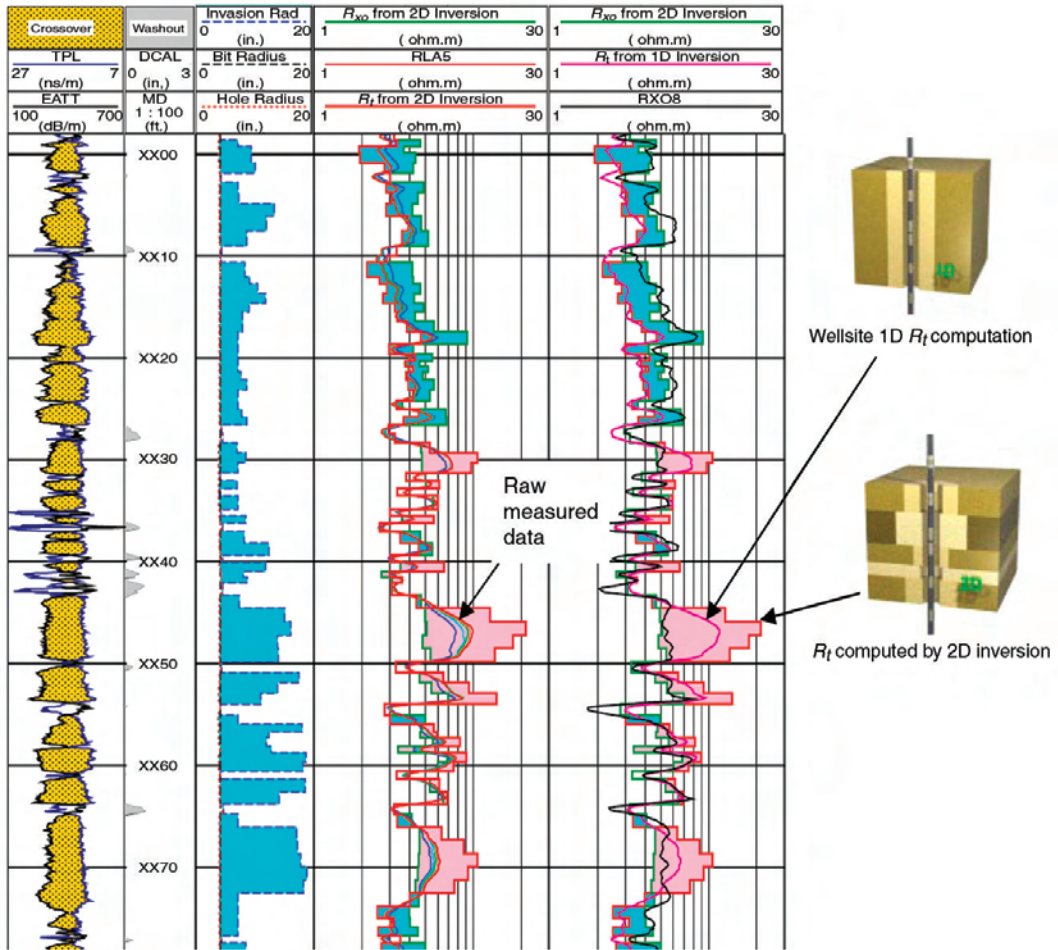


Fig. 3B.9—HRLA field logs, 1D real-time inversion results, and 2D inversion results.

because a potential difference of 2.5 mV is maintained between the spheres, the conductivity of this volume of formation is proportional to the I_0 survey current intensity.

3B.3.5 Cased-Hole Resistivity Tools. Despite the apparent paradox of measuring formation resistivity through the highly-conductive steel casing, tools are now available that can measure the formation resistivity to considerable accuracy. The idea originated in the 1930s¹³ and was revisited by Kaufman¹⁴ and Vail¹⁵ in the late 1980s. Commercial tools were introduced in 2000 by Schlumberger¹⁶ and Baker Atlas.¹⁷ Both of these tools operate on the Kaufman-Vail principles.

The Schlumberger cased-hole formation resistivity (CHFR) tool has three sets of four arms that contain electrodes that are forced into contact with the inside of the casing. A current generator on the surface is connected to an electrode at the top of the tool. The current is injected into the casing and returns to an electrode in the earth some distance from the casing. Although most of the current returns through the casing, some small fraction of it will leak off from the outside of the casing and will return through the earth. This leakoff current forms the basis for the CHFR measurement.

The leakoff current is determined by measuring the voltage drop along a section of the casing. The double-differenced voltage Δ contains both the leakoff term and the voltage drop

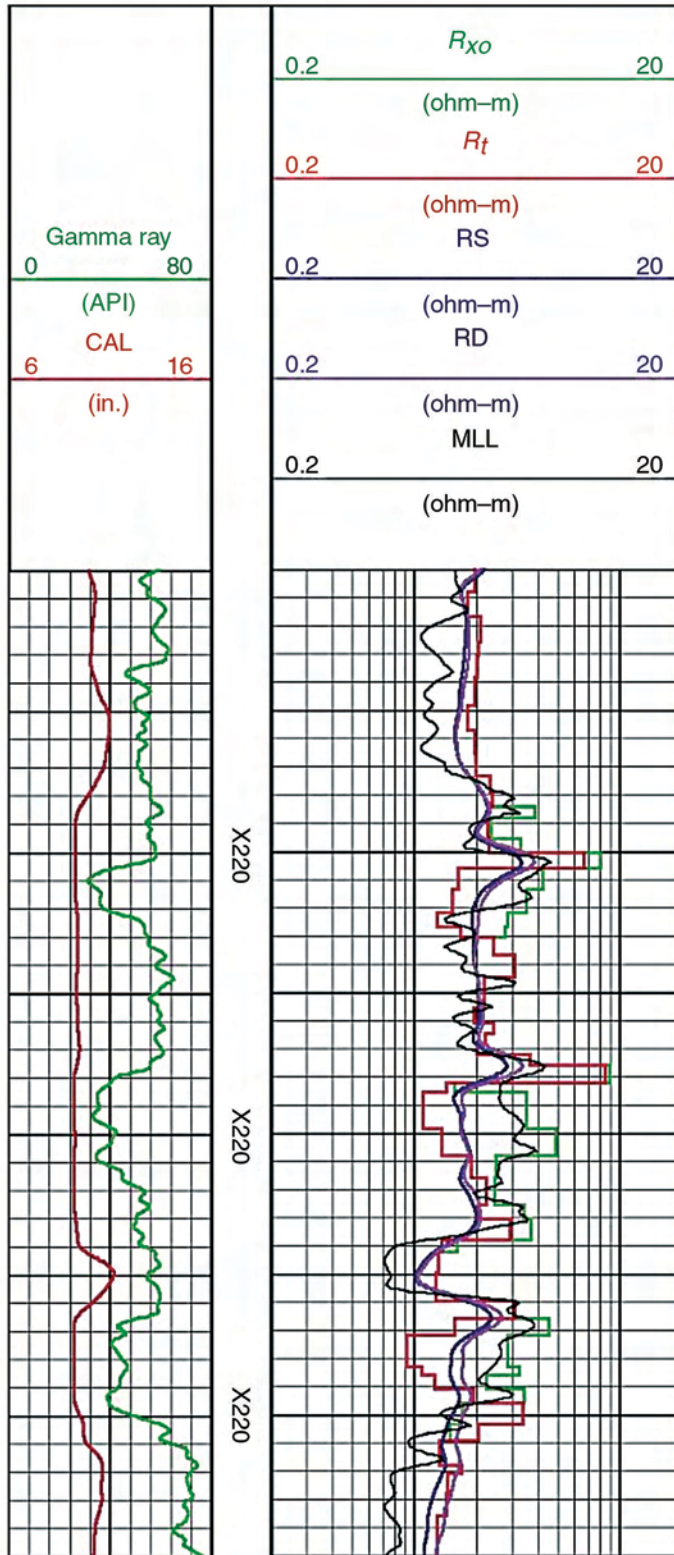


Fig. 3B.10—HDLL 2D inversion results compared with DLL logs.

produced by the current flowing through the casing and the resistance, R , of the casing. The current switch is changed to position 2. Now a current from inside the tool is sent from the upper electrode to a lower electrode. The voltage difference is now measuring the resistance of the casing, R_1 . All of the measurements are combined in the equation

$$I_f = \left(\frac{1}{R_1}\right) \left[\Delta - E \left(\frac{I_2}{I_0}\right) \right] \dots\dots\dots (3B.3)$$

to produce a formation resistivity measurement. The measurements are taken while the tool is stationary and take approximately a minute per station.

Fig. 3B.11 shows a log of the CHFR in a newly cased well compared with open-hole HALS and AIT logs. The comparison is very good, and in the zone from 865 to 900 ft, with $R_{xo} > R_s$, the CHFR agrees well with the AIT 90-in. log, showing the great depth of investigation of the CHFR log.

Cased-hole resistivity is becoming accepted for applications including contingency logging, reservoir monitoring, and evaluation of old producing wells. One application combines CHFR with pulsed-neutron logs to do cased-hole formation evaluation.

The Baker Atlas Through-Casing Resistivity (TCR) tool operates on a similar measurement principle as the CHFR. It is smaller in diameter (2 $\frac{1}{8}$ vs. 3 $\frac{3}{8}$ in. for the CHFR).

GVR Resistivity-at-the-Bit Tool. The Schlumberger Geovision Resistivity (GVR) tool¹⁸ is an electrode resistivity tool that measures five resistivity values—bit, ring, and three button resistivities—as well as gamma-ray and shock measurements.

A 1500-Hz alternating current passes through the toroidal-coil lower transmitter that is 1 ft from the bottom of the tool, inducing a voltage in the collar below. Current flows through the collar and bit and into the formation in front of the bit, returning to the collar farther up the drillstring. The resistivity at the bit is derived from the axial current, which is measured by a ring monitor toroid, and the induced voltage, which is a function of the transmitter current.

When the GVR tool is positioned directly above the bit, the resistivity measurement has a resolution of approximately 2 ft [61 cm], which is usually adequate for “geostopping”—stopping drilling precisely at casing or coring depths.

Focused Multidepth Resistivity. There are four focused-resistivity measurements incorporated in the RAB tool. These include the ring electrode measurement, with a depth of investigation of approximately 9 in. [0.23 m], and three button electrode measurements, with depths of approximately 1, 3, and 5 in. [2.5, 8, and 13 cm, respectively] into the formation.

The button measurements are radial, acquiring azimuthal resistivity profiles as the tool rotates in the borehole. A rotational speed of at least 30 rpm is required for full profile recording, with each button recording 56 resistivity measurements per rotation. The data are usually stored downhole for later retrieval, although a compressed image and selected button data may be transmitted to the surface in real time together with the ring and bit resistivities and gamma-ray measurements. **Fig. 3B.12** shows a recorded GVR image compared with an image from the wireline FMI borehole resistivity image tool (see the following for a description of this tool).

All four focused resistivities use the same measurement principle: Current from the upper transmitter flows down the collar and out into the formation, leaving the collar perpendicular to its surface and returning to the collar above the transmitter. Low-impedance circuits measure the current at each button electrode, and the axial current flowing down the collar is measured at the ring electrode by the ring monitor toroid and at the lower transmitter by the lower monitor toroid. These resistivity measurements are repeated using current from the lower transmitter.

In a homogeneous formation, the equipotential surfaces near the button and ring electrodes on the RAB tool are cylindrical. However, in layered formations, there is a tendency for cur-

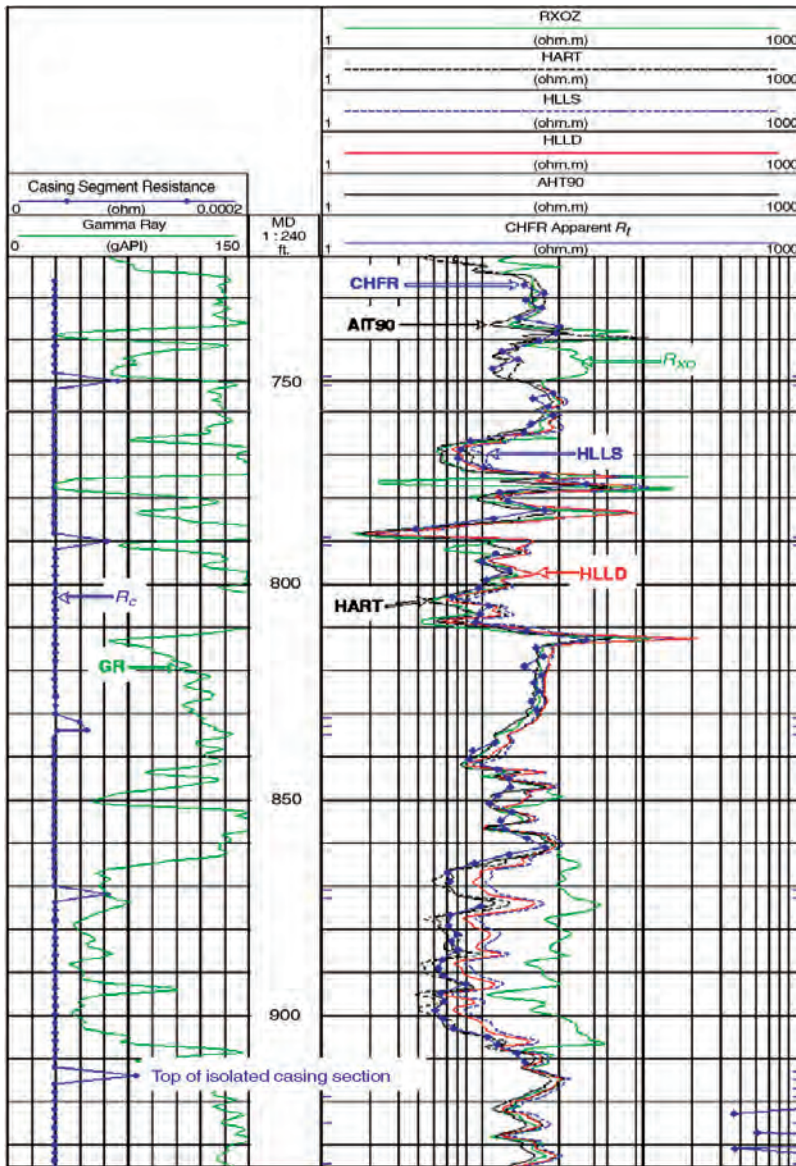


Fig. 3B.11—CHFR log vs. HALLS laterolog and array induction openhole logs.

rent to flow preferentially in the more conductive beds and avoid the more resistive beds. This effect is known as “squeeze” for conductive beds and “antisqueeze” for resistive beds, and it leads to horn-like distortion of resistivity readings at bed boundaries.

A cylindrical focusing technique (CFT) is used to measure and compensate for this distortion by restoring the cylindrical geometry of the equipotential surfaces in front of the measurement electrodes. This is achieved by regulating the currents generated by the upper and lower transmitters for zero axial current flow at the ring monitor electrode, which avoids current flow along the borehole and focuses the ring current into the formation. This focusing technique produces a response very similar to that of a wireline laterolog.

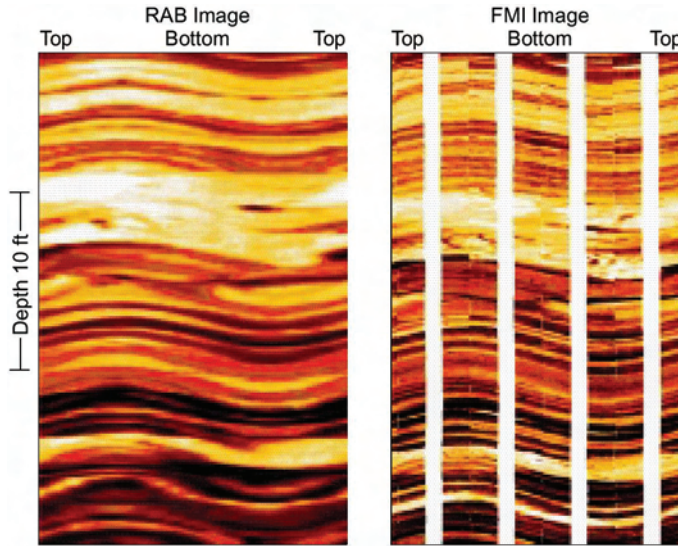


Fig. 3B.12—GVR button measurements image compared with wireline FMI tool images.

3B.4 Environmental Effects on Laterolog Tools. Laterolog and SFL log readings are influenced by the borehole mud, adjacent shoulder beds, and the invaded zone as well as the uninvaded formation. If automatic corrections are not available, log-interpretation charts provided by the service company are used to manually correct the log readings for these influences. The borehole corrections must always be made first, followed by bed-thickness corrections and finally invasion corrections of the determination of R_t , R_{xo} , and d_i .

Invasion Corrections. The “geometric factor” relates the effect of a portion of formation on the logging tool reading to its position relative to the tool in an infinite homogeneous medium. It has a particular application to induction logging tools, but pseudogeometrical factors are a useful comparative tool for other resistivity devices.

Fig. 3B.13 is a plot of integrated pseudogeometrical factors for several focused resistivity logs. It graphically compares the relative contributions of the invaded zone to the tool responses and their relative depths of investigation. The good spread in radial characteristics of the LLd and LLs measurements enables accurate resistivity analysis over a wide range of invasion conditions.

To evaluate the three unknowns of the simple step-profile invasion model (R_{xo} , R_t , and d_i), a combination of at least three carefully chosen resistivity measurements is required. LLd and LLs curves, with a very shallow resistivity measurement that reads R_{xo} directly, may be sufficient. See the section on invasion interpretation for more details on the determination of R_t , R_{xo} , and d_i .

3B.4 Induction Logging

Induction logging¹⁹ was originally developed to measure formation resistivities in boreholes containing oil-based muds and in air-drilled boreholes because electrode devices could not work in these nonconductive boreholes. However, because the tools were easy to run and required much less in the way of chart corrections than laterals or normals, induction tools were used in a wide range of borehole salinity soon after their introduction.

3B.4.1 Principles. Commercial induction tools consist of multiple coil arrays designed to optimize vertical resolution and depth of investigation. However, to illustrate induction-tool funda-

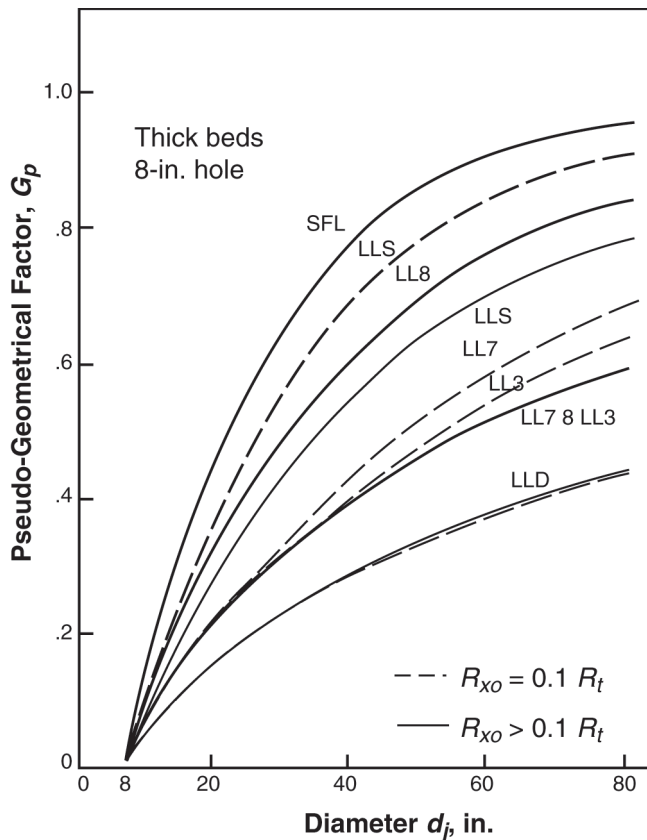


Fig. 3B.13—Pseudogeometrical factors, or radial response functions, for several laterolog tools.

mentals, it is instructive to first examine the basic building block of multiple-coil arrays, the two-coil sonde.

Fig. 3B.14 shows that a two-coil sonde consists of a transmitter and receiver mounted coaxially on a mandrel. Typical coil separations range from 1 to 10 ft apart. In practice, each coil can consist of from several to 100 or more turns, with the exact number of turns determined by engineering considerations. The operating frequency of commercial induction tools is in the tens to hundreds of kilohertz range, with 20 kHz being the most commonly used frequency before 1990.

The induction transmitter coil is driven by an alternating current that creates a primary magnetic field around the transmitter coil. The primary magnetic field causes eddy currents to flow in a continuous circular distribution (often mistakenly called “ground loops”) centered around the borehole axis. The color contours in Fig. 3B.14 show the current distribution. These eddy currents are proportional to the formation conductivity, and they in turn generate a secondary magnetic field, which induces an alternating voltage in the receiver coil. This receiver voltage is first-order proportional to the conductivity of the formation.²⁰

Because the transmitter current is alternating, there is a phase shift between the transmitter current and the current density in the formation. This phase shift is not the same in all parts of the formation—it increases with distance into the formation (Fig. 3B.14). Similarly, the phase in the receiver is even further shifted. At very low conductivities, the total phase shift is approximately 180° and increases with increasing formation conductivity. Induction tools have always

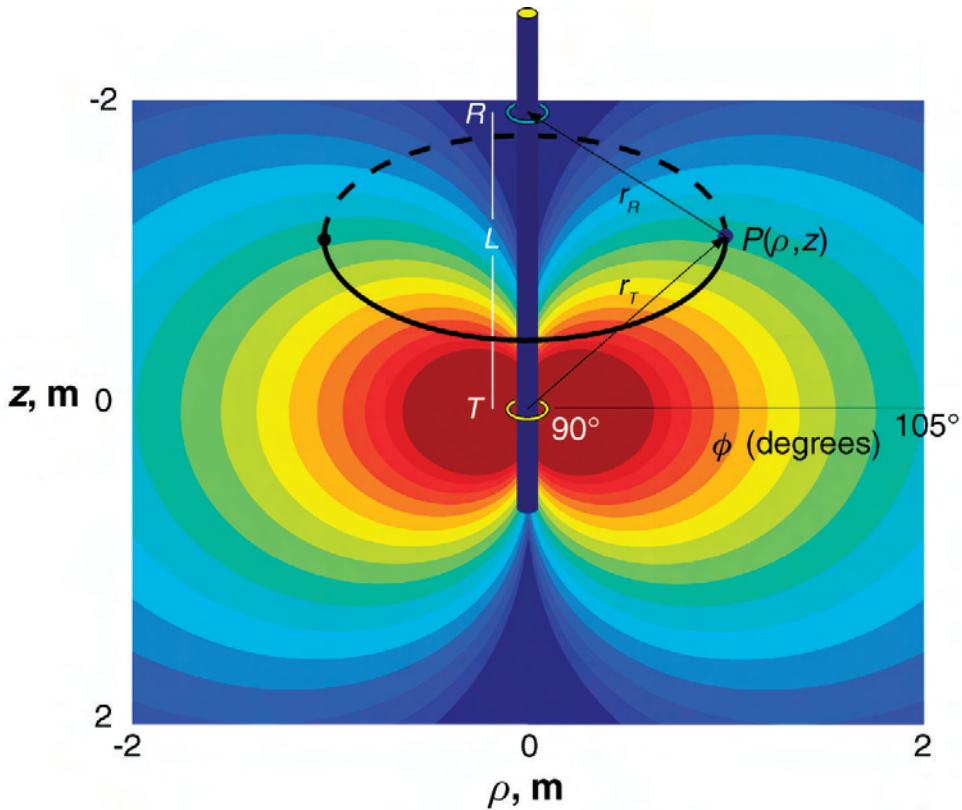


Fig. 3B.14—Schematic representation of a two-coil induction array showing the distribution of the currents induced in the formation by the transmitter coil.

measured the part of the voltage that is exactly 180° phase-shifted from the transmitter current (called the R-signal). As the conductivity increased, and the phase shifted, the voltage was a bit less than expected from a linear relationship. This difference is called skin effect. Modern induction tools make an additional measurement at a phase shift of 270° from the transmitter current (called the X-signal). These two measurements, being in quadrature, allow precise phase and amplitude measurement of the receiver voltage.

3B.4.2 Induction Response. To produce adequate sensitivity to the uninvaded zone, induction tools perform include signals from a large volume of formation. The challenge is to determine exactly where the measurement is coming from in the formation. Doll defined the geometrical factor as a 2D function $g(\rho, z)$, which defines the part of the total signal that comes from an infinitesimally thin loop around the borehole. This definition is valid only at very low conductivities. Moran defined a modification of the geometrical factor that is valid in low contrast formations at any conductivity. This response is known as the Born response.²¹

The response to formation layers is given by the vertical response function $g_v(z)$, which is defined as the integral of the 2D response function $g(\rho, z)$ over radius ρ . The response to radial variations in a thick bed is given by the radial response function $g_R(\rho)$, which is defined as the integral of $g(\rho, z)$ over z . The response of the array to invasion in a thick bed is characterized by the integrated radial response G_R , which is the cumulative integral of $g_R(\rho)$ over radius.

3B.4.3 Multicoil Arrays. Because the direct transmitter-receiver mutual coupling of a two-coil array can produce a voltage several thousand times that from a formation, two-coil arrays are

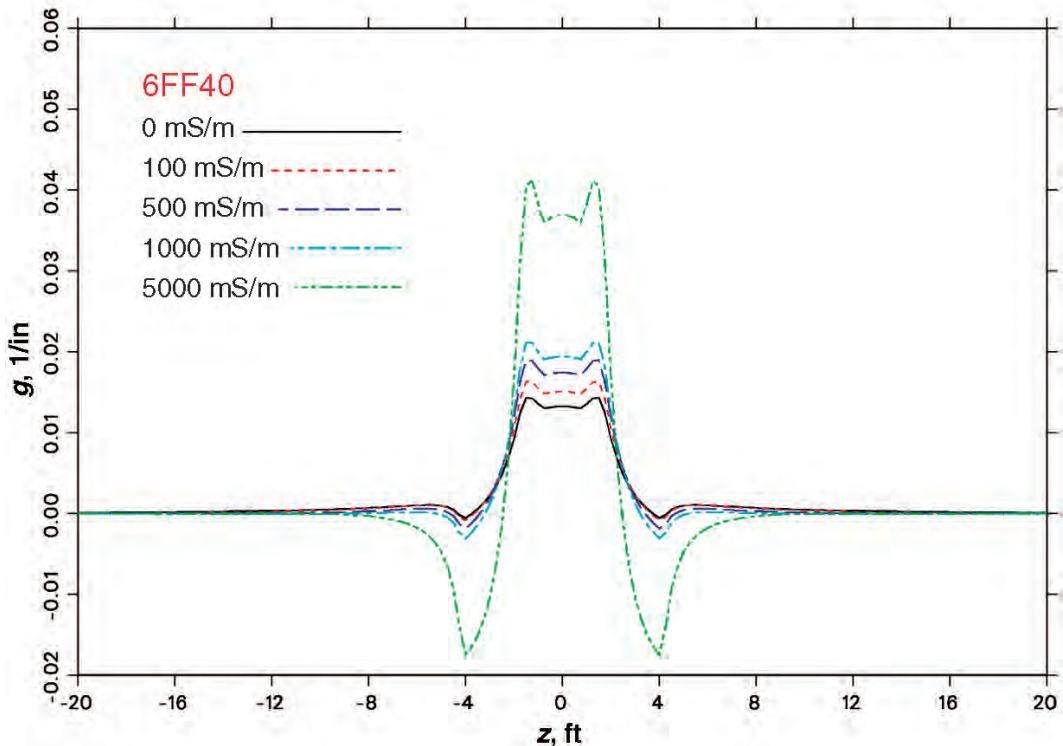


Fig. 3B.15—Vertical response function $G(R)$ for the 6FF40 array at several formation conductivities.

not practical. The simplest practical array is a three-coil array with a transmitter and two receivers. The second receiver is placed between the transmitter and main receiver, and is wound oppositely so that the voltages in the two receivers exactly cancel when the array is in free space. The response is the sum of the coil-pair responses.

One of the most successful induction arrays was the 6FF40 array introduced in 1960.²² It had three transmitters and three receivers, with a symmetric Born response g . Figs. 3B.15 and 3B.16 show its vertical and radial responses. The array was designed to achieve deep investigation, reasonable vertical resolution, and a low borehole effect. However, the large peaks in the 2D response along the tool resulted in sensitivity to borehole washouts, called cave effect.

3B.4.4 Dual-Induction Tools. One of the challenges of measuring formation resistivity is to sort out the resistivity of the invaded zone from that of the virgin zone. The earliest concept to successfully solve the problem (at least in thick beds with uncomplicated invasion profiles) was the dual-induction tool. This tool combined a 6FF40 array as a deep-induction measurement (ID or ILD) with a set of receivers that worked with the 6FF40 transmitters to produce a shallower measurement. This was referred to as the medium-depth induction (IM or ILM).^{23,24}

Because there are three parameters in the simplest step-profile invasion model, at least three measurements are required to solve for these parameters. The shallow measurement was a shallow laterolog (LL8 or SFL) collocated with the induction arrays. The radial response function involves very complicated mathematics, and the solution offered to users of the dual induction logs was a graphical solver called the tornado chart.

The ILD-ILM-SFL logs separate when there is invasion, and this separation is what allows interpretation for invasion parameters. Fig 3B.17 shows the modeled response of the dual induction-SFL tool (DIT) in a typical Gulf of Mexico pay zone with a transition over a water zone.

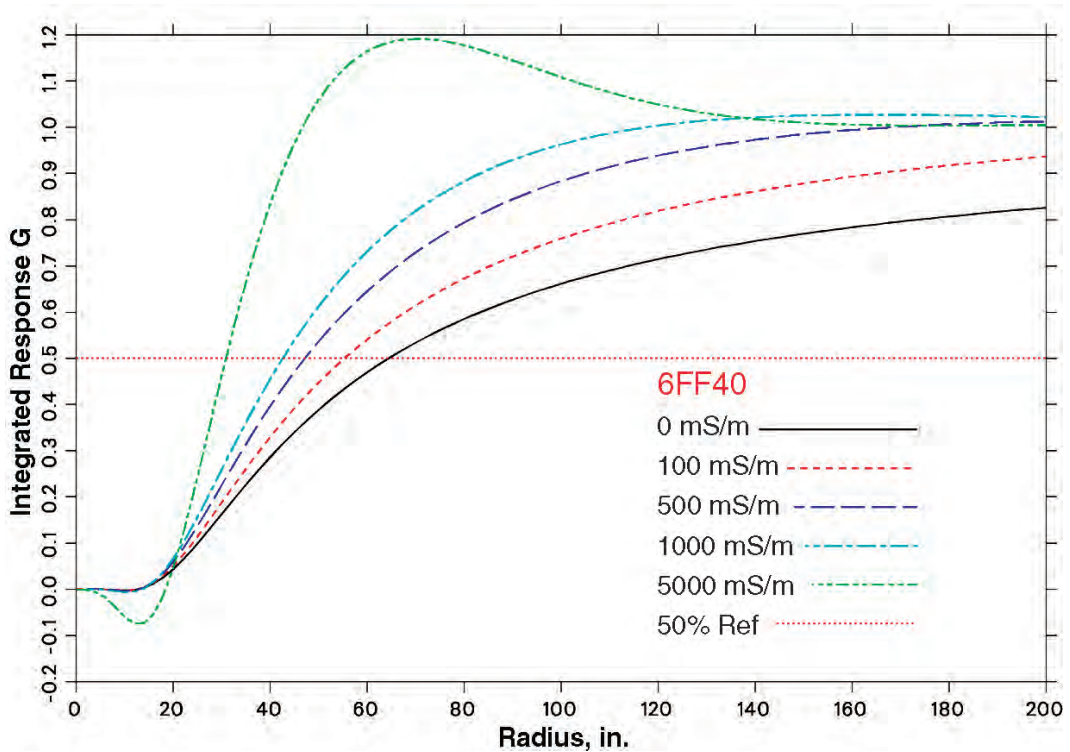


Fig. 3B.16—Integrated radial response function $G(R)$ for the 6FF40 at several conductivities.

The ILM and ILd measurements do not respond linearly to the formation conductivity. This nonlinearity is closely related to the changes in the response shape and depth of investigation with increasing conductivity. This nonlinear response of an induction array is called skin effect because it is related to the “skin depth” effect of AC current flowing in conductors.

Some sort of function must be applied to the tool voltages to correct for this nonlinearity. The processing applied to the Schlumberger DIT²⁵ consisted of a skin-effect function (“boost”) applied to the measured R-signals from the induction arrays. This was based on computations of the response in an infinite homogeneous medium. The ILd was further processed using a three-station deconvolution filter to slightly sharpen the bed-boundary transition and to correct for shoulder effect over a limited resistivity range (1 to 10 ohm·m). At other formation-resistivity ranges, the response either produced horns or large shoulder effects. Fig. 3B.18 shows the DIT logs in a set of formation layers with the same shoulder-bed contrasts, but centered on 1, 10, and 100 ohm·m.

Borehole correction was also hand-applied to the induction and SFL logs. The borehole correction chart was derived from measurements made with a DIT in plastic pipes full of salt water. The 6FF40-based dual induction-shallow electrode tool was offered by most service companies.

3B.4.5 Phasor Induction. The DIT tool became the standard resistivity tool and remained virtually unchanged for more than 20 years. However, as its application moved from the original Gulf of Mexico formation contrasts to higher-resistivity formations, the shoulder-effect problem became much worse. Although shoulder-correction charts were provided for high resis-

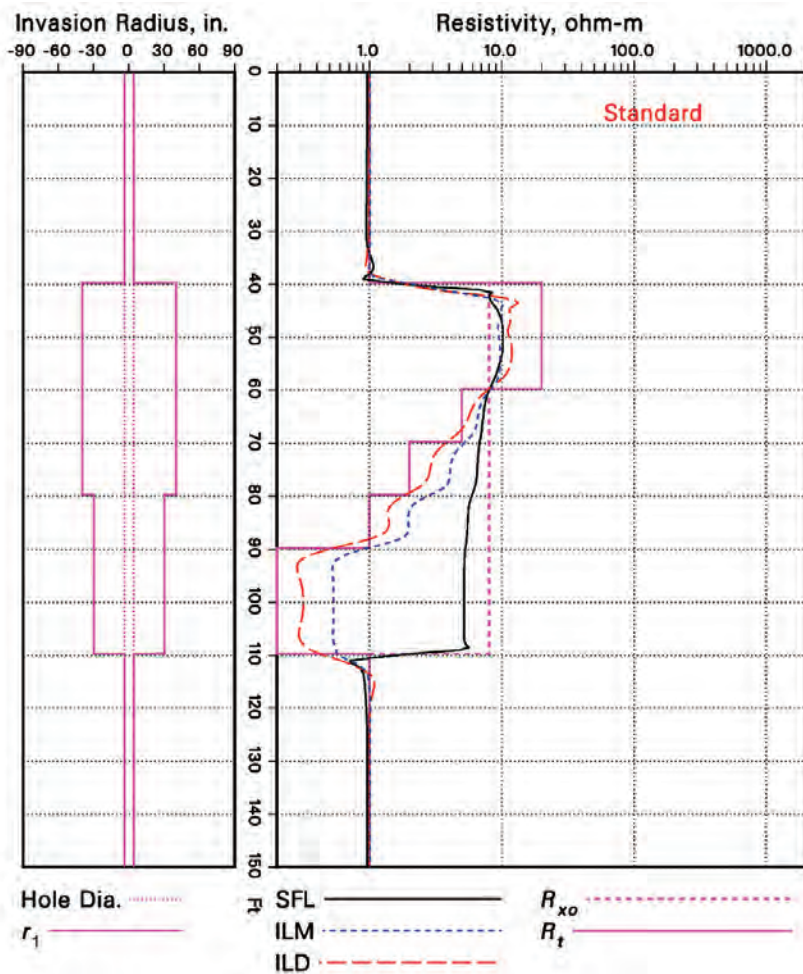


Fig. 3B.17—Modeled DIL logs in a typical Gulf of Mexico formation in a pay zone, a transition zone, and a water zone.

tivity, they mainly indicated that the problem was bad rather than serving as a usable correction mechanism.

The fundamental problem in induction log interpretation is to isolate the response of a thin bed and the virgin zone from the shoulders and the invaded zone after the measurement process has thoroughly mixed them. The Phasor induction tool was introduced in the mid-1980s and was the first tool to automate the environmental corrections. It uses a linear deconvolution function to correct for shoulder effect and uses the X-signal measurement to correct for skin effect. This algorithm was the basis for Phasor Processing.²⁶ It can be shown that a filter fitted at low conductivity works well at low conductivity but produces large errors at high conductivity. The error is, however, a slowly varying function closely related to the X-signal. An algorithm applied to the X-signal to match it to the skin-effect error allows a single FIR filter to correct for shoulder effect over a wide range of conductivities.

Fig. 3B.19 shows the results of Phasor processing in the formation models of Fig. 3B.18. The induction logs are fully shoulder-effect-corrected at all conductivity levels. Phasor logs in the Gulf of Mexico simulation of Fig. 3B.17 are not very different from the DIT logs. This is

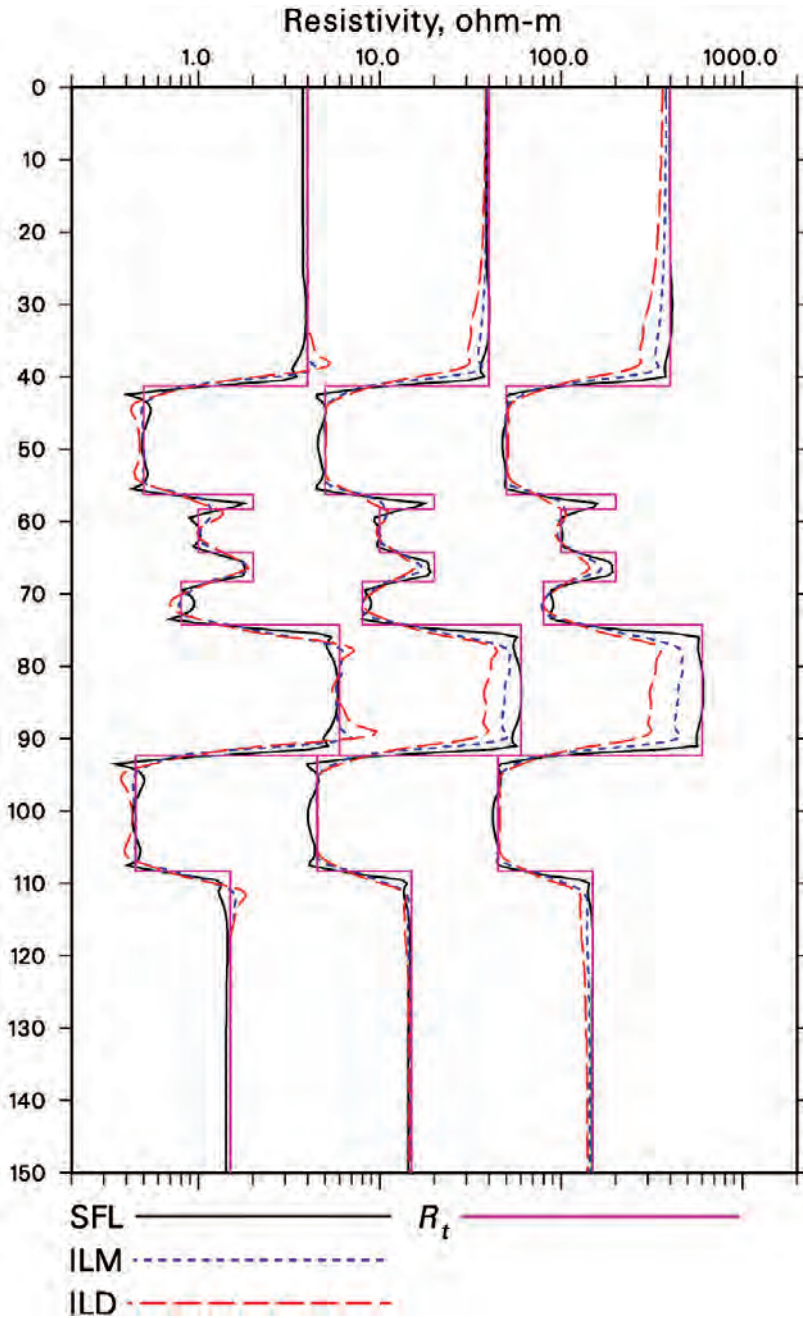


Fig. 3B.18—Modeled DIT logs in a set of formation layers with the same shoulder-bed contrasts, but centered on 1, 10, and 100 ohm-m.

in part because this formation is where the DIT logs were designed to work well. Although tornado charts were published for the Phasor induction logs, the invasion parameters are computed in real time at the wellsite. Borehole corrections are based on computer models of an eccentric tool in a wide range of borehole salinities and formation conductivities.²⁷ Borehole corrections are applied in real time at the wellsite. The Phasor induction tool was the first in-

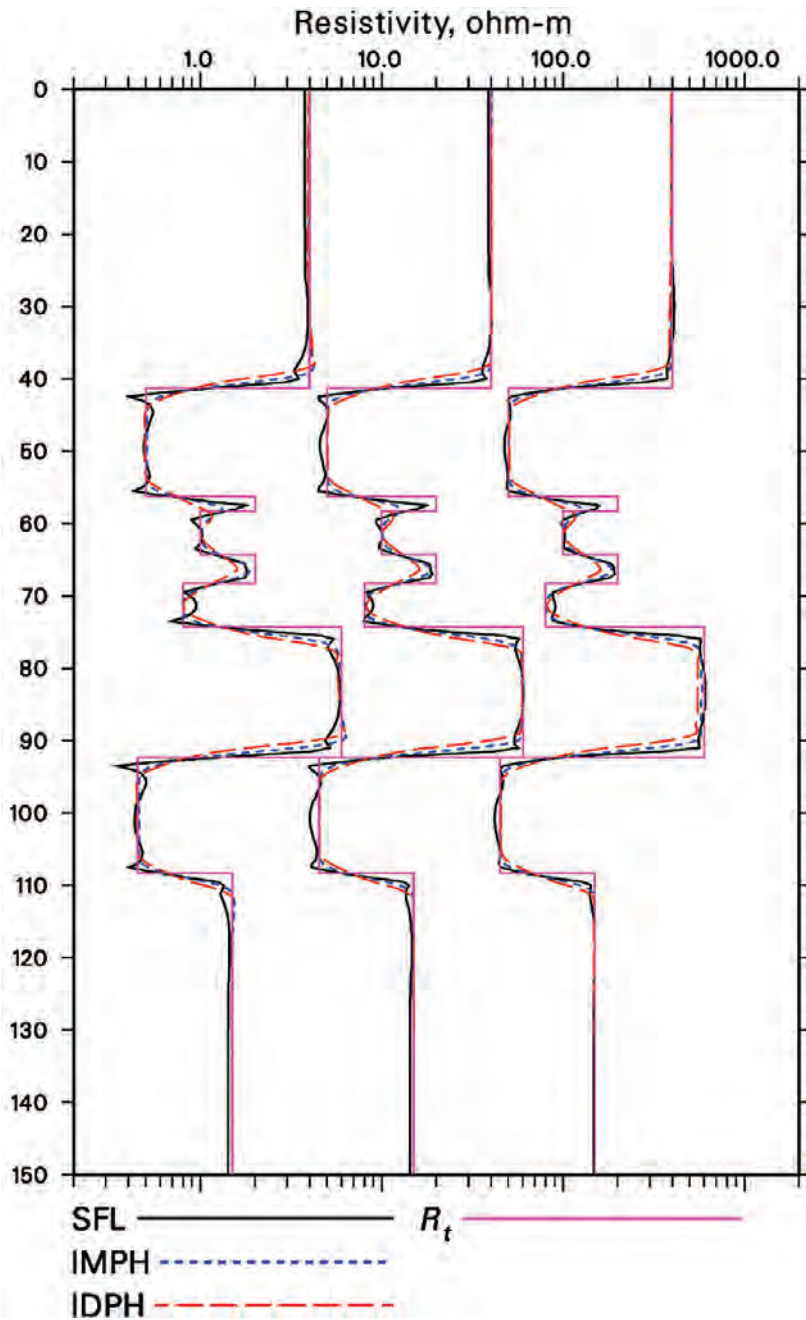


Fig. 3B.19—Phasor logs in the cases of Fig. 3B.18.

duction tool that could provide full environmental correction and invasion parameter determination at the wellsite. In 1987, changes to the deconvolution filters allowed induction logs with a 2-ft vertical resolution (compared with 5 ft for ILM and 8 ft for ILd).

Dual-induction tools that measured both R and X signals and applied automatic shoulder-effect corrections were introduced by Atlas (the Dual-Phase Induction Tool, or DPIL) and Gearhart (the High-Resolution Induction Tool, or HRI tool). The HRI tool also achieved a ver-

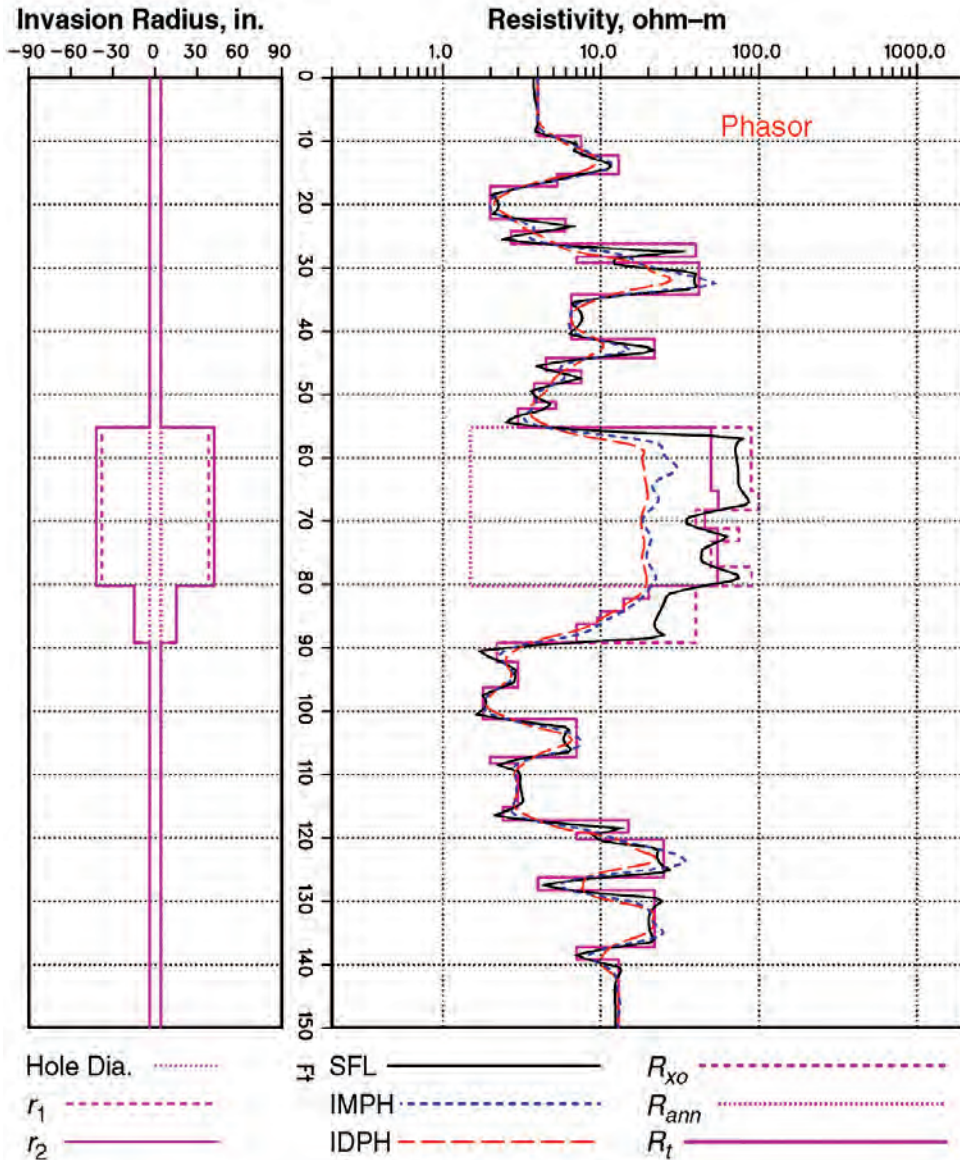


Fig. 3B.20—Phasor logs in a simulation of a gas-bearing formation where an annulus has formed.

tical resolution of 2 ft. It was also the first dual-induction tool to be based on a different array from the 6FF40. Its deep array had a median depth of investigation of approximately 90 in. After the breakup of Gearhart, Halliburton acquired the HRI tool and commercialized it.

However, all of these tools are based on two induction arrays—a shallow array and a deep array. Performance in complex invasion profiles is limited by the small number of measurements. Fig. 3B.20 shows the Phasor logs in a simulation taken from a field log in a gas reservoir. Here an annulus has developed, and the deep log reads much less than R_t . In this well, the three-parameter invasion model will not return the correct value of R_t .

In the case of oil-based mud (OBM), the SFL is not usable. Separation between the medium and deep logs is only a qualitative indication of invasion and is not quantitatively interpretable.

3B.4.6 Array-Induction Tools. With the Phasor Induction tool, the dual-induction concept had reached its limits. In particular, improvements were needed in better estimates of R_t in the presence of deep-invasion or complex transition zones. As the grosser environmental distortions were corrected by Phasor Processing or similar processing, annulus profiles and other transitions were encountered more often.

These response problems, coupled with an increasing use of OBM, led to the concept of using several induction arrays with different depths of investigation. With the problems of applying linear deconvolution filters solved, then Doll’s approach of using a simple array was applicable. The Schlumberger AIT was designed with eight simple three-coil arrays ranging in length from 6 in. to 6 ft.²⁸

Array-Induction Principles. The first step in log formation in the AIT family of tools is to correct all raw array signals for borehole effects. This process is based on a forward model of the arrays in a circular borehole, and it includes an exact description of the tool in the model.²⁹

The signal measured by an induction sonde eccentered in a borehole can be described mathematically as a function of four parameters. These are the borehole radius r , the mud conductivity σ_m , the formation conductivity σ_f , and the tool position x with respect to the borehole wall (commonly referred to as the “standoff”).

The correction algorithm is designed to solve for some of these parameters by minimizing the difference between the modeled and actual logs from the four shortest arrays. The information content of these measurements is not sufficient to solve for all the borehole parameters at the same time. In practice, two of the four parameters can be reliably determined by this method. The other two parameters have to be either measured or fixed. The equivalent homogeneous formation conductivity σ_f must always be solved for because no measurement is closely enough related to it. This leaves one of the other parameters to be determined, and the remaining two parameters must be entered as measurements. This leads to the three borehole correction methods to compute mud resistivity, hole diameter, and standoff. All of the AITs except the original AIT-B have integral mud resistivity sensors,³⁰ and “compute standoff” is the default borehole-correction method in water-based mud (WBM).

A method was developed³¹ to combine these array measurements to focus the resulting log to the desired depth of investigation, while at the same time doing so with a high vertical resolution and minimizing cave effect. The log-formation process is described by the equation

$$\sigma_{\log}(z) = \sum_{n=1}^N \sum_{Z=Z_{\min}}^{Z_{\max}} w_n(z') \sigma_a^{(n)}(z-z') \dots\dots\dots (3B.4)$$

In this equation, σ_{\log} is the recorded AIT log, $\sigma_a^{(n)}$ is the measured log from the n th channel, and N is the total number of measure channels. This process produces a log that is different from that produced by any of the individual arrays. It is still characterized by a response function. This response function is a weighted sum of the response functions of each of the individual channels n . Skin effect is handled in a manner similar to the Phasor tool.

The result of this equation is a combination of the logs from the eight array that “distills” the radial information from the eight arrays into five independent logs with depths of investigation of 10, 20, 30, 60, and 90 in. Each of these five logs is available at a resolution of 1, 2, and 4 ft. The radial profile is identical at all resolutions, and the vertical resolution is identical for all radial depths. The set of weights w in Eq. 3B.1 determines which log is produced.

If the mud is very salty, or if the borehole is very large, the signal in the AIT arrays from the borehole will be very large. With salty mud, even normal variations in the borehole surface from the drilling operation can cause “wiggles” on the short array data. Several years of practice have shown that these can affect the final logs, especially the 1-ft logs. This experience

has shown that in an 8-in. borehole with 1½-in. standoffs, the 1-ft logs are normally usable at R_t / R_m contrasts up to 100; the 2-ft logs are usable up to a contrast of 450, and the 4-ft logs are usable up to contrasts of 1000. Algorithms based on the real-time use of a chart and “road-noise” analysis of the 6-in. array allow real-time selection of the appropriate resolution based on actual logging conditions.

AIT logs separate in invaded zones and give a good visual indication of invasion, even with OBM. Fig. 3B.21 shows the AIT logs in the same formation as Fig. 3B.17 (left). In the annulus case, Fig. 3B.21 (right), the AIT logs are “out of order,” clearly indicating the nonstep nature of the invasion profile.

With the additional curves, the invasion profile parameters can be solved for using inverse methods. AIT invasion processing has three models that can be selected: step, ramp, and annulus. All are available at the computing center, while the ramp profile is used for real-time logs.

Interpretation of logs in deviated wells or where the apparent dip is high is considerably complicated. First, one has to recognize that the logs are at high apparent dip. Fig. 3B.22 shows AIT logs in a formation with an apparent dip of 85°. Although this is high, the characteristics that appear here—horns and strange log order—appear in logs with dips as low as 40°. In many fields, faults and slumping of young sediments can produce high apparent dips that are not detectable on seismic profiles. Merlin processing has been developed to produce logs fully corrected for dip effect.³² Recently, real-time high-angle processing was made available.³³ This processing produces logs that are independent of dip angle. However, the resulting logs are also shallow. Fig. 3B.23 shows dip-invariant processing (Grimaldi) on the right.

Users of induction logs should be very careful making quantitative analyses in wells that are deviated, or if the formation is dipping. If the shoulder-bed contrast is 20 or less, then the minimum angle where dip correction is needed is approximately 30°. At shoulder-bed contrast of over 100, the logs will need correction at dips as low as 10°.

3B.4.7 Field-Log Examples. A few field-log examples will illustrate the richness of information available in array-induction logs. The first example, Fig. 3B.24, is a comparison of AIT and Phasor induction logs in a gas zone from Canada. The AIT shows a nonmonotonic curve order, indicating an annulus profile. If the data from this zone is inverted into an annulus profile using material-balance constraints to determine the thickness of the annulus, then the complete annulus parameters can be recovered (Fig. 3B.25).

The next example is from south Texas, and is in a well drilled with oil-based mud. Fig. 3B.26 shows the AIT logs compared to the Phasor logs in this well. Because of the OBM, only the induction logs from the DIT are available. In the lower zone, the AIT logs show a conductive invasion profile, suggesting that the OBM has broken down as it has invaded into the formation.³⁴ The invasion profile is much clearer with the AIT logs.

The final example is from a deviated well in Canada in a 4¾-in. borehole drilled with OBM (Fig. 3B.27). The well was air-drilled and turned horizontal. This part was at a deviation of approximately 60°—going “round the bend.” The 2-ft field logs in the left track have a scrambled curve order—shallow logs are higher than deep in the resistive beds and then reversed in the conductive beds. This is a signature of high-dip response. The dip-invariant logs in the center track do not exhibit the curve scrambling. The Merlin logs also show no scrambling and high resolution as well.

3B.4.8 Other Array Induction Tools. Baker Atlas introduced its High-Definition Induction Log (HDIL) array induction tool in 1996.³⁵ It is a seven-array tool that operates at eight frequencies. This information can be processed in a variety of ways, depending on the environment. The multiple frequencies are used for skin-effect correction. This algorithm is developed by computing the R signal measured by a given array at each frequency at a wide range of

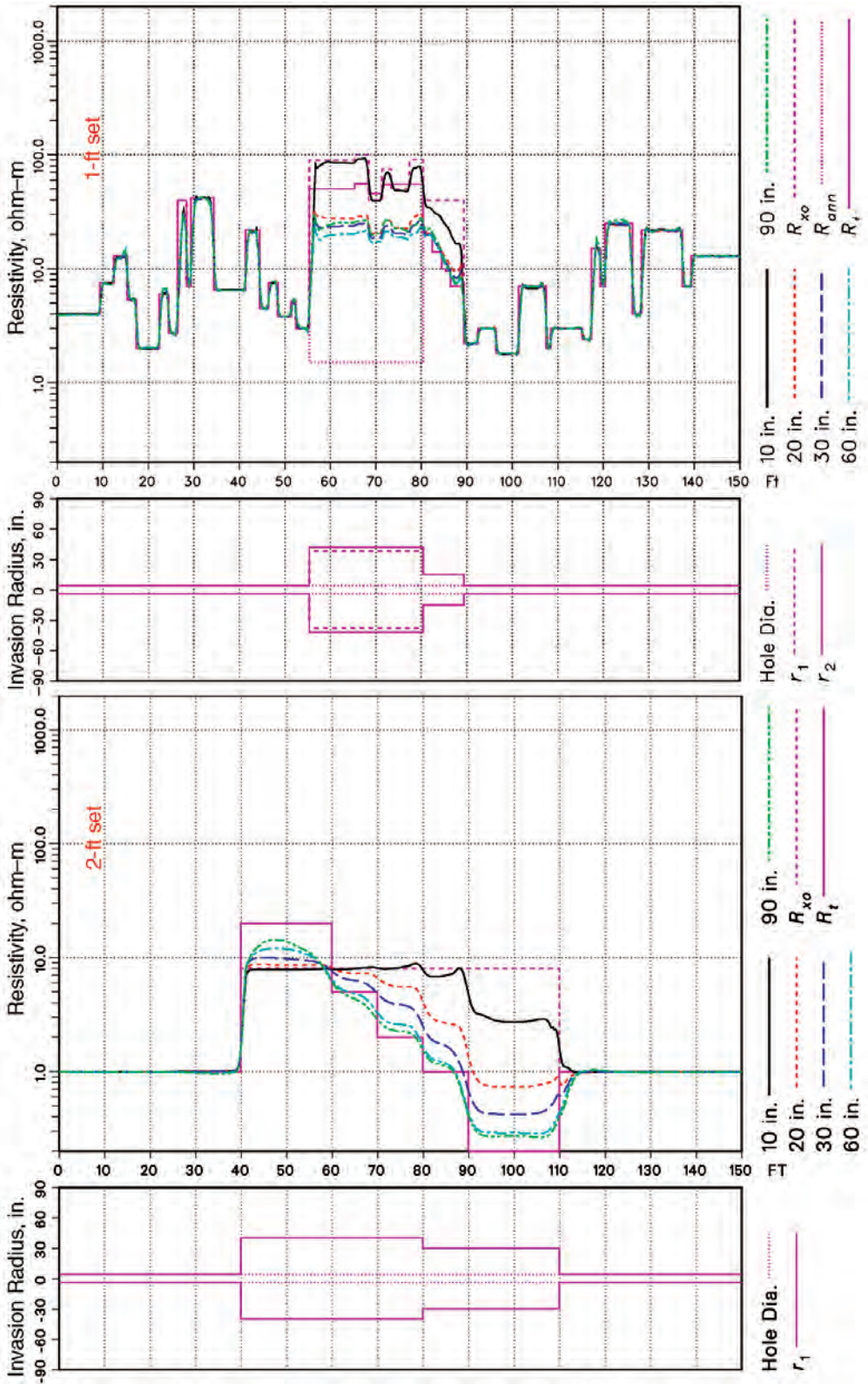


Fig. 3B.21—Phasor logs in the cases of Fig. 3B.18.

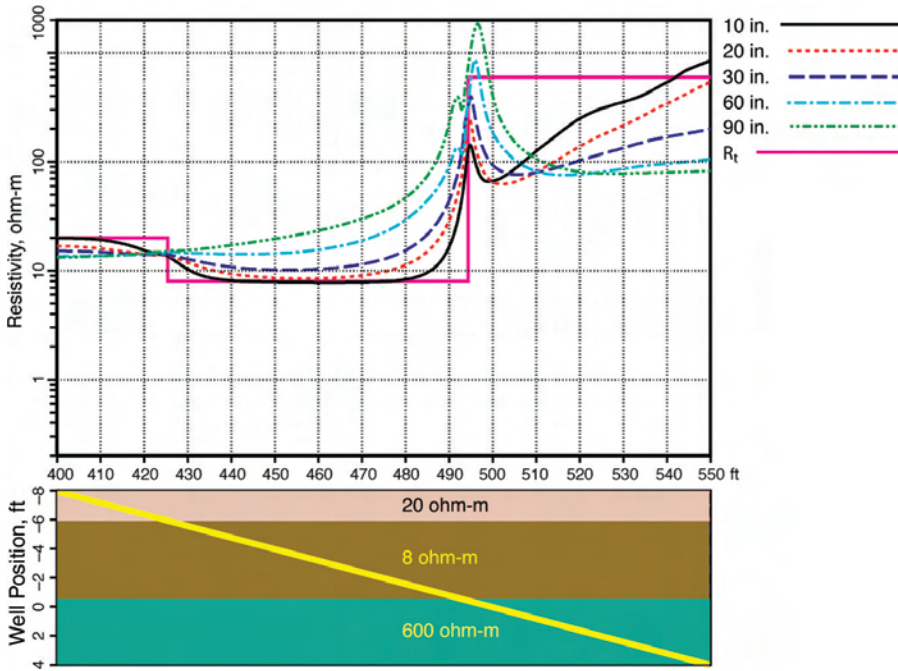


Fig. 3B.22—Modeled AIT logs in a formation with a relative dip of 85°.

formation conductivities. The data at each frequency are fitted to the true formation conductivity. The resulting function is used for the skin-effect correction.

The skin-effect-corrected conductivities are then deconvolved with filters to form six logs at depths of 10, 20, 30, 60, 90, and 120 in., and at three matched resolutions of 1, 2, and 4 ft. An additional presentation is the “true resolution” log set. This has the same six depths, but the resolution of each depends on the depth of investigation. This presents the resolution information content that actually comes from the formation region near the midpoint of the integrated radial response function. Dip correction is provided at the computing center. Fig. 3B.28 shows an example. Fig. 3B.29 shows a 2D inversion available at the computing center.

Halliburton introduced its High-Resolution Array Induction (HRAI) tool in 2000.³⁶ It is a six-array tool based on the array layout of the HRI. Standard HRAI tool logs present resistivities at vertical resolutions of 4, 2, and 1 ft, each with six depths of investigation (10, 20, 30, 60, 90, and 120 in.). The log resistivities are inverted to yield true resistivities of the formation in the virgin zone, R_t , and in the invaded zone, R_{xo} , near the borehole. Invasion diameters (D_i) corresponding with R_t and R_{xo} are also presented. HRAI tool answer products are available in real time while logging.

A variant on the array induction principle was introduced by Weatherlord (previously Reeves Wireline).³⁷ The array induction donde (AIS) combines four simple induction arrays with a shallow focused-electrode array. The induction data have been presented in two ways. Originally, the four arrays were combined in software to match the response of the ILd and ILM arrays. Later, the Vectar processing was introduced to produce a higher-resolution log.³⁸ Data from each array is skin-effect-corrected and then resolution-matched to the shortest array. Up to six curves are presented from the four arrays.

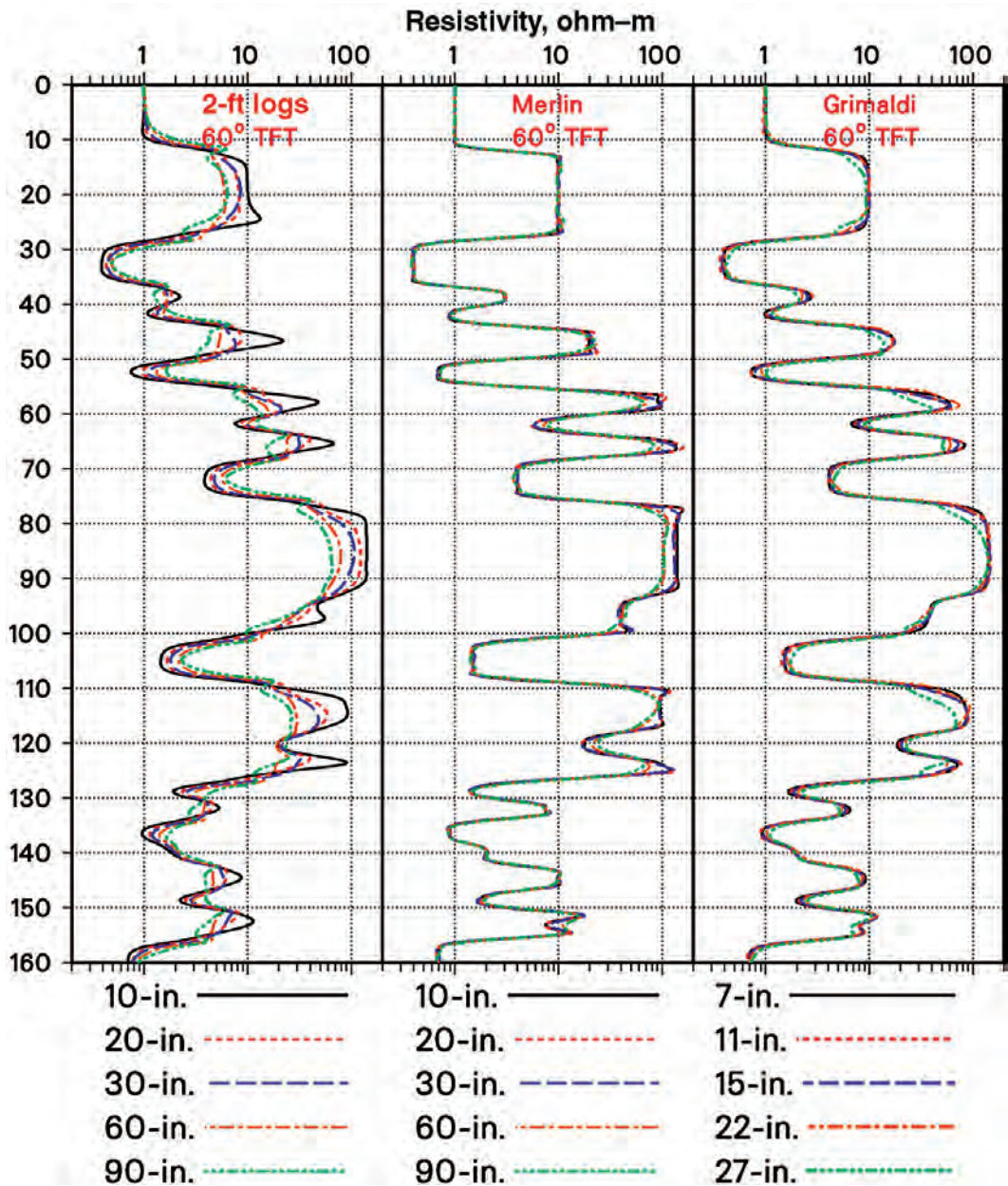


Fig. 3B.23—AIT dip-invariant logs.

3B.5 LWD Induction Tools

3B.5.1 Induction Tools on the Drillpipe. Commercial resistivity measurements made while drilling first became available in the late 1970s. Because the drilling environment is much more adverse than the wireline logging environment, a simple short normal tool mounted behind the drill bit was used as the first LWD resistivity tool.³⁹ However, short normal tools were only able to provide information for basic interpretation, such as correlation of geological markers and estimation of gross water saturation,⁴⁰ because of their shallow depth of investiga-

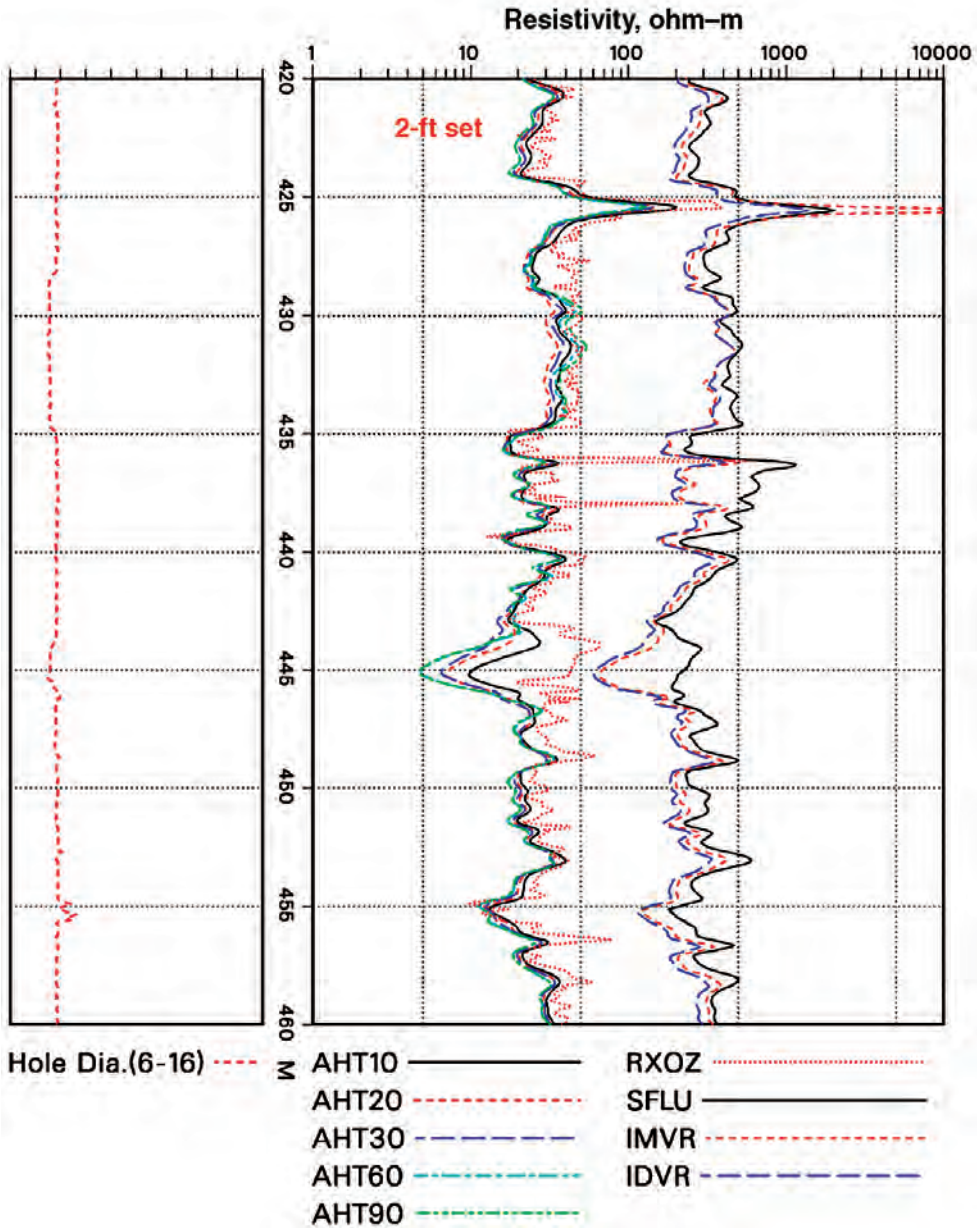


Fig. 3B.24—Comparison of AIT and Phasor logs in a gas zone in Canada.

tion and relatively poor vertical resolution. Being DC electrode devices, normal tools are also limited to conductive mud environments.

To expand the LWD resistivity market to OBM environments, induction-type propagation measurements were introduced in the early 1980s. The first commercial device was the electromagnetic wave resistivity (EWR)^{41,42} tool from NL Information Services (later merged with Sperry-Sun). Shortly after this, Schlumberger introduced the compensated dual resistivity (CDR)^{43,44} tool. All LWD propagation tools are run with a gamma ray tool for lithology estima-

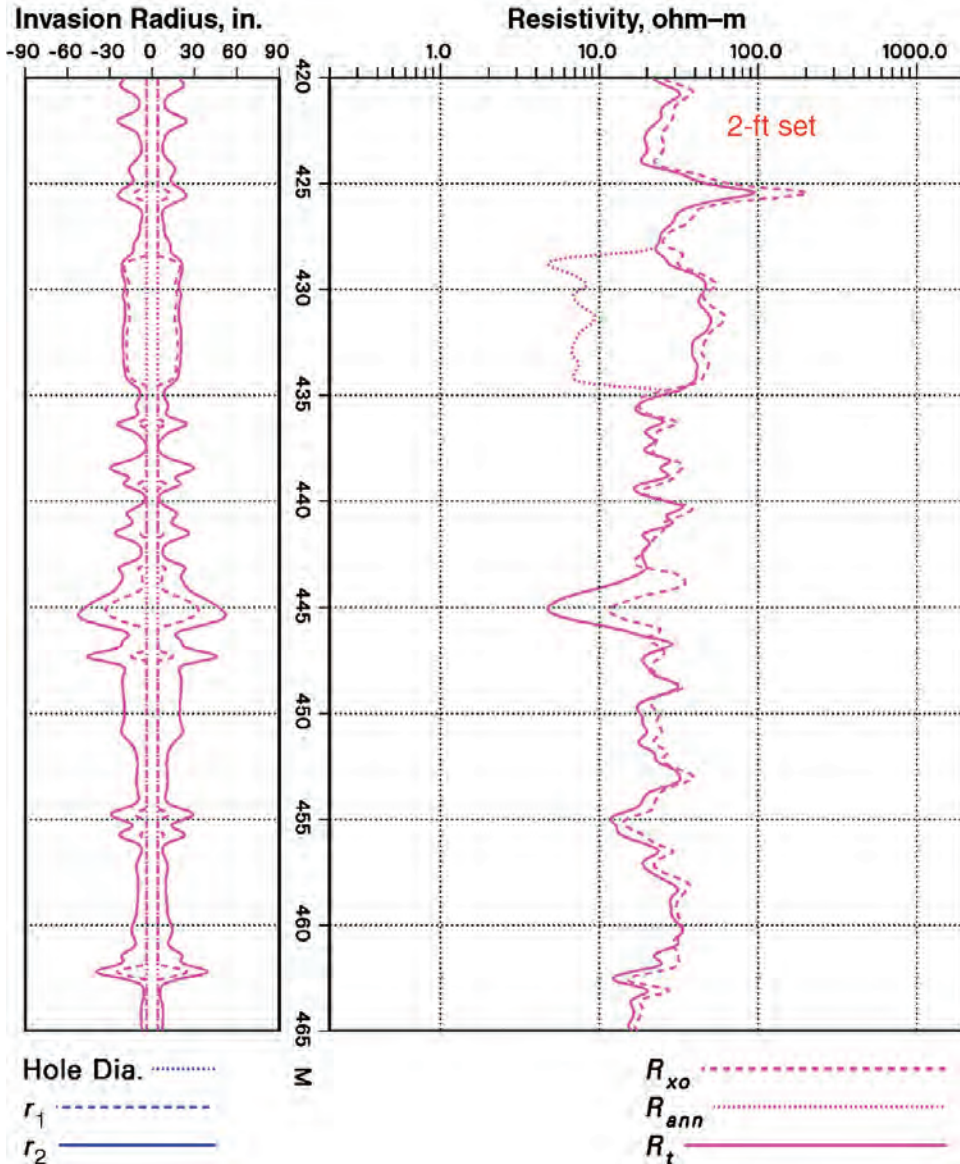


Fig. 3B.25—Radial inversion of the AIT logs in Fig. 3B.24 for invasion parameters using the annulus model.

tion and correlation. Log data are transmitted uphole in real time using mud-pulse telemetry. Downhole memory and batteries allow raw and processed data to be stored for later retrieval.

3B.5.2 Principles of the Propagation Measurement. Because the CDR is a simple tool that measures both attenuation and phase shift, it is used to demonstrate the basic concepts of propagation measurements. Conventional induction measurements are made with mutually balanced arrays of transmitter and receiver coils operating in the kilohertz frequency range and that phase-lock measurement electronics. Because it was difficult to engineer this type of measurement on a steel drill collar using the technology of the early 1980s, a higher-frequency propagation measurement was considered to be more practical for LWD. A frequency of 2 MHz was chosen

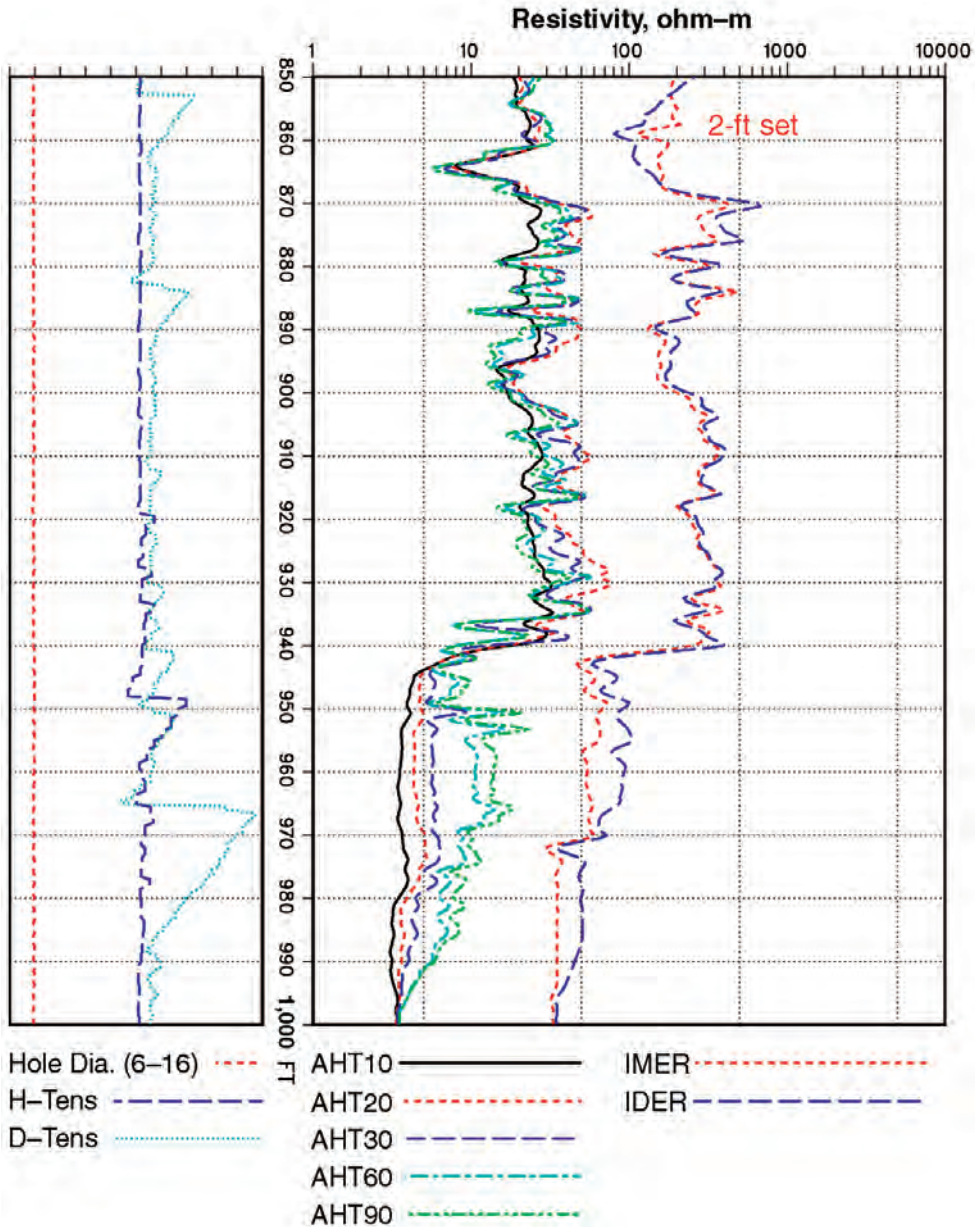


Fig. 3B.26—AIT and Phasor logs in a south Texas well drilled with OBM. Note the conductive invasion profile despite the OBM.

because it was the lowest frequency at which accurate propagation measurements could be made on a drill collar at that time.

The CDR tool broadcasts a 2-MHz electromagnetic wave. A propagation measurement is made by taking the difference between the phases (phase shift) and amplitudes (attenuation) of the voltages recorded at the two receivers. Attenuation increases as a function of increasing conductivity, while the wavelength decreases as conductivity increases. Thus, the two measurements are proportional to formation conductivity and can be used to generate resistivity logs.

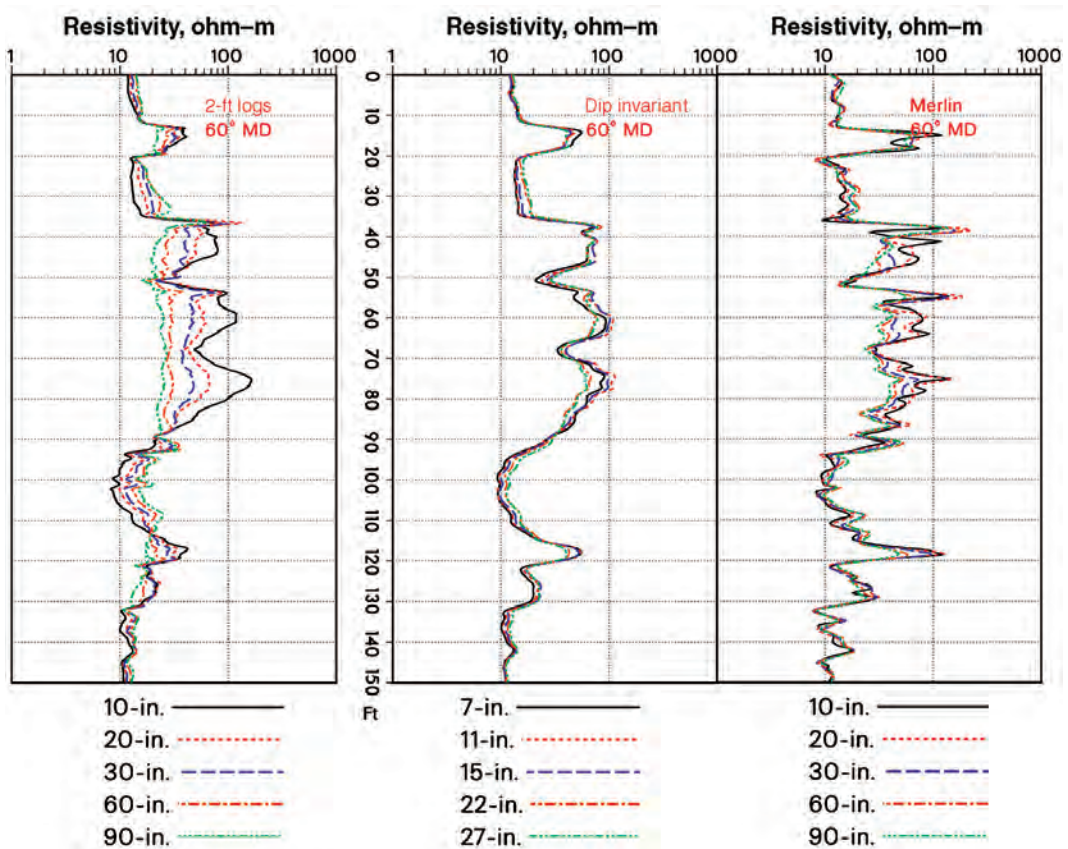


Fig. 3B.27—Slim-access AIT logs from a well in Canada. Relative dip is approximately 60°. Field processing, dip-invariant processing, and Merlin logs are shown.

Note that the CDR tool has two transmitters. The phase-shift and attenuation measurements generated by the upper transmitter between the two receivers, and by the lower transmitter between the two receivers, are averaged to symmetrize the tool response. This averaging is known as borehole compensation because it also reduces the effect of borehole rugosity. The transmitter-to-receiver spacings for the CDR tool are 25 and 31 in.

The phase-shift and attenuation measurements are transformed to two independent resistivities, which for the CDR tool are known as RPS (phase shift, shallow) and RAD (attenuation, deep). Because at 2 MHz dielectric effect can be significant at high resistivity levels, a dielectric correction is performed before the raw data are converted to apparent resistivity. Most service companies have developed their own proprietary algorithms to perform dielectric correction. Joint inversion for both resistivity and dielectric constant is also possible with today's multiarray propagation tools. The dielectric-corrected phase shift and attenuation are converted to resistivity using a table look-up algorithm based on computed tool response in homogeneous isotropic media of known resistivity, R_t .

The phase-shift and attenuation measurements are both relatively insensitive to borehole size and mud resistivity. Borehole correction is only necessary in conductive holes with large washouts when the R_t/R_m contrast is greater than 100 to 1.

Invasion is usually quite shallow at the time of drilling when most LWD logs are run. However, LWD logs may also be recorded each time that the drillstring is pulled to replace the

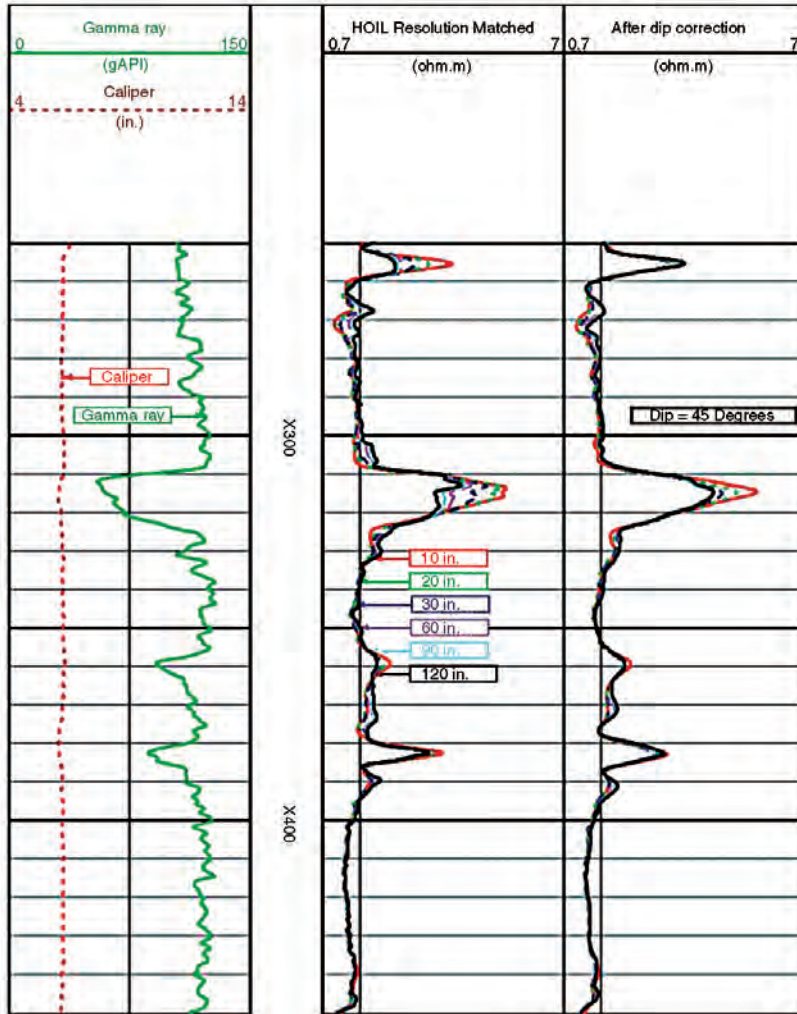


Fig. 3B.28—HDIL logs in a formation with 45° relative dip before and after dip correction.

drill bit. At these later times, invasion can be much deeper. The two resistivity values, RPS and RAD, provide two independent depths of investigation as an indication of invasion.

The reason that two depths of investigation can be obtained from a single measurement is made clearer by examining the behavior of the electromagnetic field. The surfaces of constant phase are spheres because the wave travels with the same speed in all directions. The surfaces of constant amplitude are toroids because the wave is stronger in the radial direction than in the vertical direction, which is a normal characteristic of vertical magnetic dipole antennas. If we compare the phase and amplitude contour lines passing through the receivers, the amplitude extends to a significantly deeper region of the formation than the phase.

Depth of investigation can also be studied by modeling tool response in invaded formations. Fig. 3B.30 shows CDR radial response for a case with $R_{xo} > R_t$, and Fig. 3B.31 shows the radial response for $R_{xo} < R_t$. In both figures, RPS and RAD are plotted as a function of increasing invasion radius. In Fig. 3B.30, RPS reads consistently closer to R_{xo} , indicating that RPS is the shallower of the two measurements. In Fig. 3B.31, RPS is again consistently shallower than RAD. In this case, the RPS curve extends below the value of R_{xo} between radii of

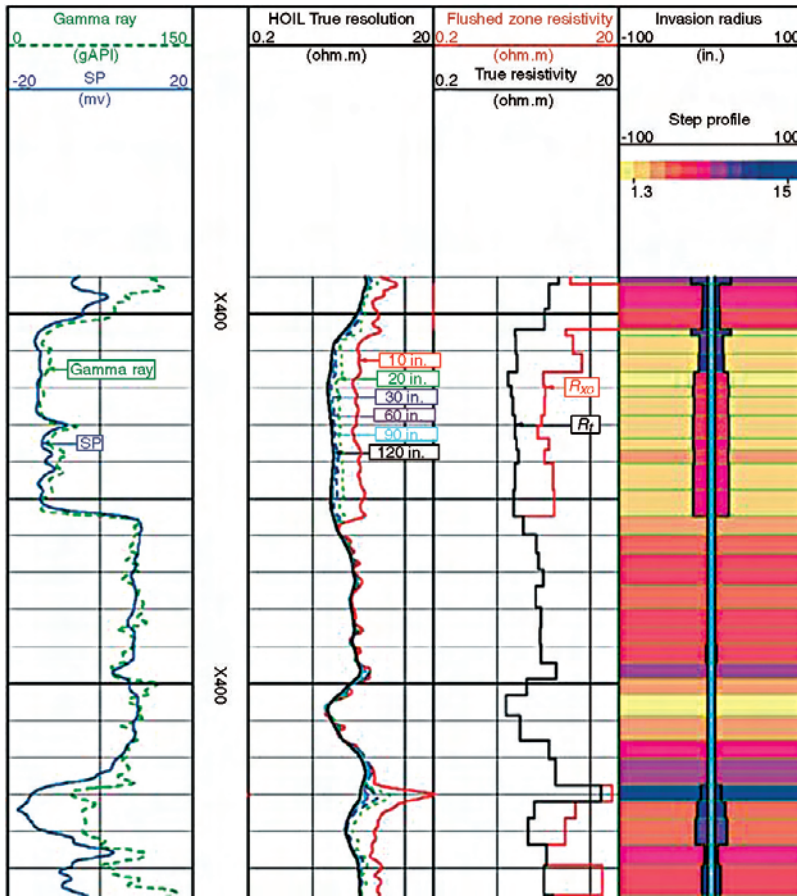


Fig. 3B.29—HDIL logs with 2D inversion for invasion parameters.

30 and 50 in. because of wave reflection at the invasion front. In general, the depth of investigation of RPS is 10 to 20 in. shallower than that of RAD.

The depth of investigation and vertical resolution of 2-MHz tools is influenced to a significant degree by skin effect. 2D tool response can be characterized using Born response functions,⁴⁵ which are geometrical factors that take skin effect into account. They show the amount of tool signal coming from a specific volume of the formation. The depths of investigation of both the phase-shift and attenuation measurements are shallower at lower formation-resistivity levels (higher conductivities) because the electromagnetic signal is more attenuated because of skin effect. In general, 2-MHz tools have a shallower depth of investigation and higher vertical resolution in low-resistivity formations, and a deeper depth of investigation and lower vertical resolution in high-resistivity formations.

Vertical resolution is characterized in more detail in Fig. 3B.32, which compares CDR and Phasor induction logs. In this low-resistivity formation, the vertical resolution of CDR log is slightly sharper than that of the Phasor log. (The SFL log indicates that shallow invasion has taken place at wireline time.) However, the vertical resolution of 2-MHz logs deteriorates as the formation resistivity level increases. Because conventional induction logs always undergo vertical processing, while 2-MHz logs are seldom processed because their depth sampling is irregular, care must be taken when comparing wireline induction and 2-MHz logs in resistive

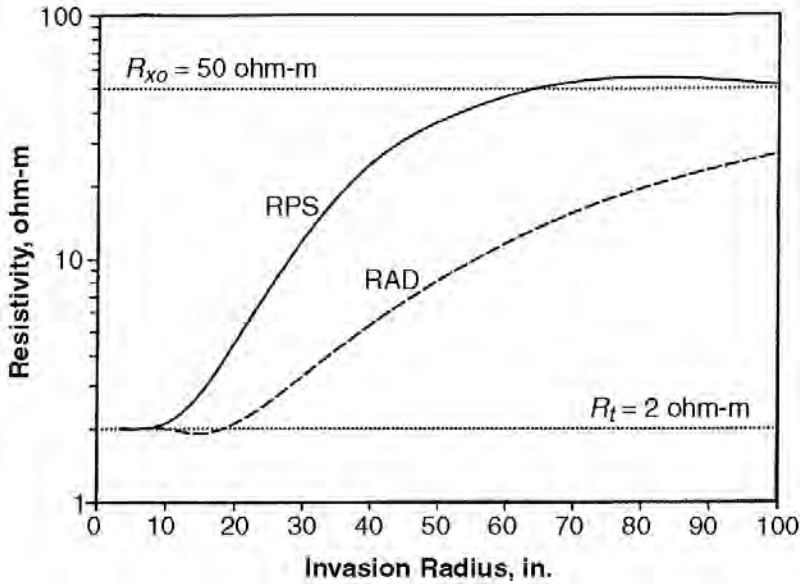


Fig. 3B.30—CDR radial response for $R_{xo} < R_t$.

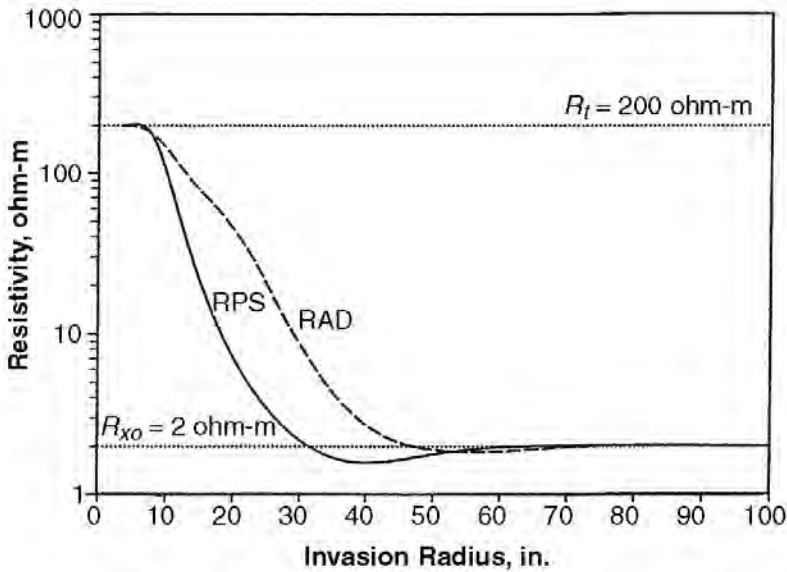


Fig. 3B.31—CDR radial response for $R_{xo} > R_t$.

formations. Fig. 3B.33 shows the variation in CDR vertical resolution as a function of resistivity level.

3B.5.3 Multiarray Propagation Tools. During the 1990s, all major service companies developed multiarray versions of 2-MHz tools. Schlumberger introduced the array resistivity compensated tool (ARC5)⁴⁶ as a replacement for the CDR tool and to accommodate the increasing

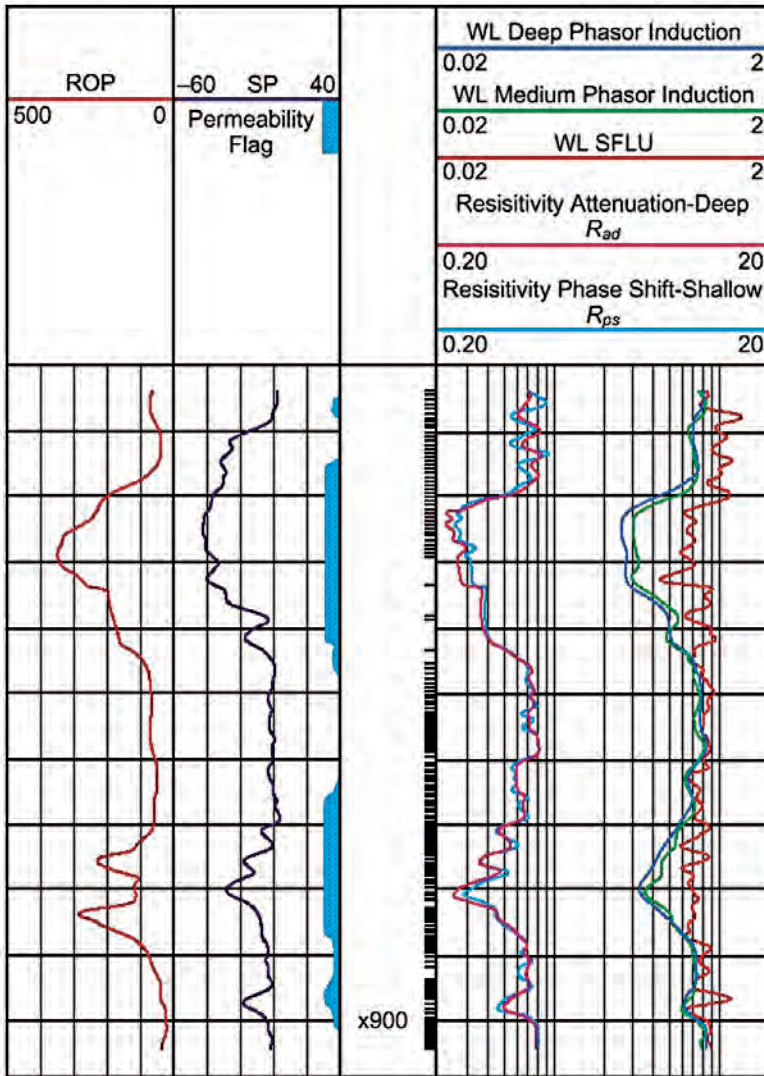


Fig. 3B.32—Comparison of CDR and Phasor induction wireline logs in a Gulf of Mexico well at low resistivity. The “permeability flag” is a function of separation between the phase and attenuation resistivities.

number of slimholes being drilled. The ARC5 tool makes five independent phase-shift and attenuation measurements. The number of measurements was deliberately chosen to be the same as that of wireline array-induction tools to allow the sharing of interpretation methods for analyzing complex invasion profiles and estimating R_T .

The ARC5 antenna configuration has five transmitters and two receivers. The phase shift and attenuation of the signal broadcast by each transmitter is measured between the two receivers for a total of five raw phase shifts and five raw attenuations. Because the transmitters are not arranged symmetrically above and below the receivers, conventional borehole compensation cannot be performed. Instead, the ARC5 relies on linear combinations of three transmitters to provide “mixed borehole compensation.”⁴⁶ This process results in five calibrated phase-shift and attenuation-resistivity logs which are characterized by the antenna spacings: 10, 16, 22, 28, and 34 in. The 28-in. spacing yields a log identical to a CDR tool.

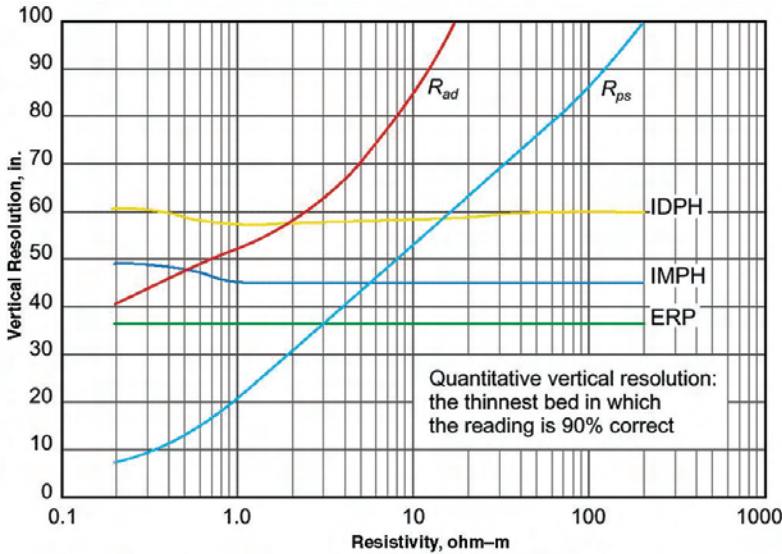


Fig. 3B.33—Vertical resolution of CDR measurements as a function of formation resistivity compared with Phasor and enhanced Phasor induction. The highly nonlinear response of propagation measurements makes resolution-matching and shoulder-effect correction difficult.

Vertical resolution is related to the 6-in. receiver spacing that is common to all the measurements, but the depth of investigation increases as the transmitter spacing increases. The result is five phase-shift resistivity logs with different depths of investigation, and five deeper attenuation-resistivity logs, also with different depths of investigation. The phase-shift logs are matched in vertical resolution in conductive beds, but not in resistive beds. Similarly, the attenuation logs are better matched in conductive beds than resistivity beds. This difference in apparent vertical resolution is shown in Fig. 3B.32.

The ARC5 makes a set of measurements at 2 MHz. Larger versions of the tool (6¾ and 8¾ in.) make measurements at both 2 MHz and 400 kHz. The 400-kHz measurement provides higher signal level in conductive formations (less than 1 ohm·m) and is less sensitive to borehole conditions, particularly in formations where $R_t < 1$ ohm·m and with OBM. It also has a deeper depth of investigation than the 2-MHz measurement in conductive formations. However, 400-kHz measurements have less sensitivity to R_t in resistive formations than 2-MHz measurements.

Fig. 3B.34 compares ARC5 phase shift and wireline AIT logs. The vertical resolution of both sets of logs is similar, with the deeper AIT 90-in. curve giving a slightly higher value for R_t in the resistive beds. Fig. 3B.35 shows a comparison with the ARC and the ARI dual laterolog in very nonconductive mud. In the bottom track, the ARC logs are inverted for invasion parameters.

In addition to the tools described here, the following LWD resistivity services are also available. References describing early versions of current tools are listed because old logs are sometimes used to interpret existing reservoirs. In 1991, Sperry-Sun introduced a version of the EWR tool with three phase-shift measurements and three attenuation measurements.⁴⁷ In 1993, it introduced the EWR-Phase 4⁴⁸ tool with four phase-shift measurements and four attenuation measurements, giving a total of eight apparent-resistivity curves. The three shortest measurements are made at 2 MHz, while the longest measurement is made at 1 MHz. Both versions of the EWR are run without borehole compensation.

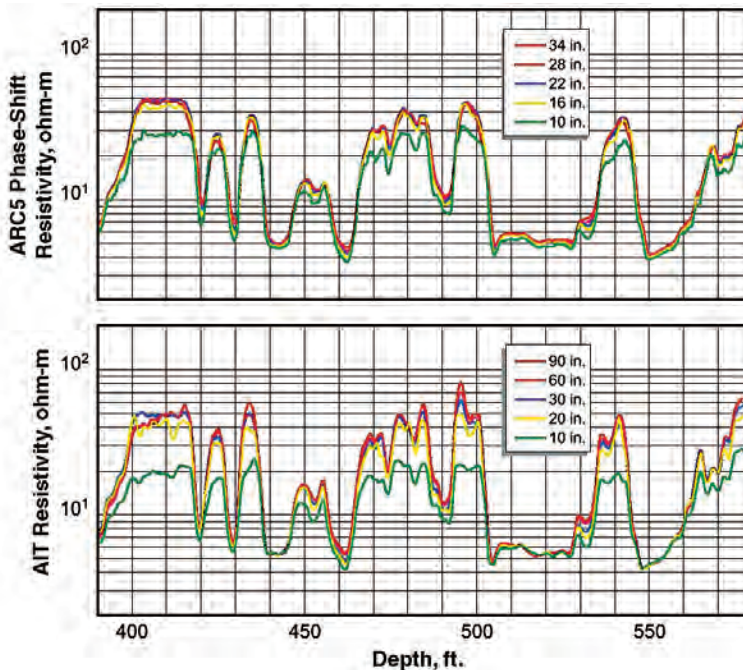


Fig. 3B.34—Comparison of ARC5 phase shift and wireline AIT logs at 2-ft vertical resolution.

In 1989, Teleco introduced the 2-MHz Dual Propagation Resistivity (DPR)⁴⁹ tool. This tool measured the phase shift and attenuation at receivers located 27 and 35 in. from a single transmitter (borehole compensation was not used). Teleco was taken over by Baker Hughes, and in 1993 the DPR tool was replaced by the multiple propagation-resistivity (MPR)⁵⁰ tool. The MPR configuration consists of upper and lower long- and short-spaced transmitters surrounding a central receiver pair. Antenna spacings range from 23 to 35 in. The two receivers measure the phase shift and attenuation of 2-MHz and 400-kHz signals broadcast by each transmitter. Borehole compensation is performed by averaging the measurements from the symmetrically opposed long and short transmitter pairs. This yields a total of eight logs (long-spaced and short-spaced phase shift and attenuation at 2 MHz and 400 kHz). Resistivity is calculated and displayed either as “apparent” or “borehole-corrected” (hole size and mud-resistivity corrected). Further processing of the logs is available in the MPRteq processing. This processing corrects for a variety of environmental effects. Fig. 3B.36 compares the processed logs with unprocessed logs.

In 1993, Halliburton introduced the 2-MHz compensated wave-resistivity (CWR)⁵¹ tool. After Halliburton’s acquisition of Sperry-Sun, the existing Halliburton business was spun off as PathFinder. The CWR tool makes a set of shallow and deep phase-shift and attenuation measurements with borehole compensation. The transmitter to receiver spacing is approximately 40 in. for the deep mode and 20 in. for the shallow mode.

Geosteering With LWD Propagation Tools. Because 2-MHz resistivity measurements are made behind the bit and can be sent uphole in real time, they are often used to steer the drilling of horizontal wells. Before drilling a horizontal well, potential hydrocarbon-bearing zones are first identified using vertical exploration wells. Then the horizontal well is drilled toward a target bed, with marker beds used to maintain the wellbore trajectory. 2-MHz resistivity logs recorded behind the bit are compared to logs from the exploration wells to identify the

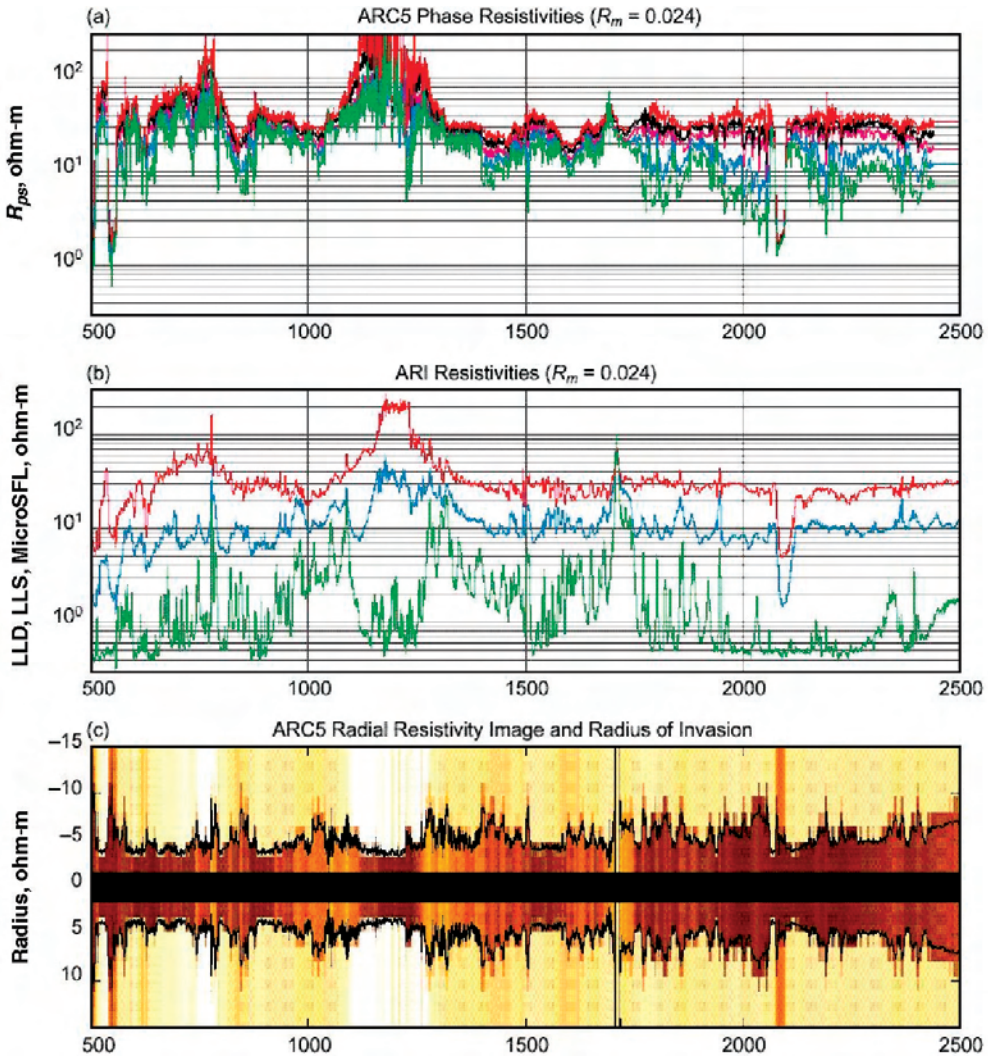


Fig. 3B.35—ARC logs compared with wireline ARI dual laterolog logs. In the bottom track, the ARC logs are inverted for invasion parameters.

marker beds. Computer modeling of predicted resistivity-tool response at different well deviation angles is used to modify the well path. This process is called geosteering.

When comparing resistivity logs in a horizontal well to logs from a vertical exploration well in the same zone, the resistivity value often differs in shales and in laminated formations. This difference is caused by anisotropy (the variation of resistivity with direction). In addition to particle-size anisotropy, formations consisting of a series of thin beds of different lithology (such as sequences of sand and shales) also behave anisotropically if a logging tool is significantly longer than the bed thickness. In vertical wells, resistivity tools (conventional induction, 2-MHz and laterologs) read the effective horizontal resistivity, R_h , which can be calculated from the volume average of the layer conductivities (inverse resistivities),

$$\sigma_h = V_{\text{sand}}\sigma_{\text{sand}} + V_{\text{shale}}\sigma_{\text{shale}}, \dots\dots\dots (3B.5)$$

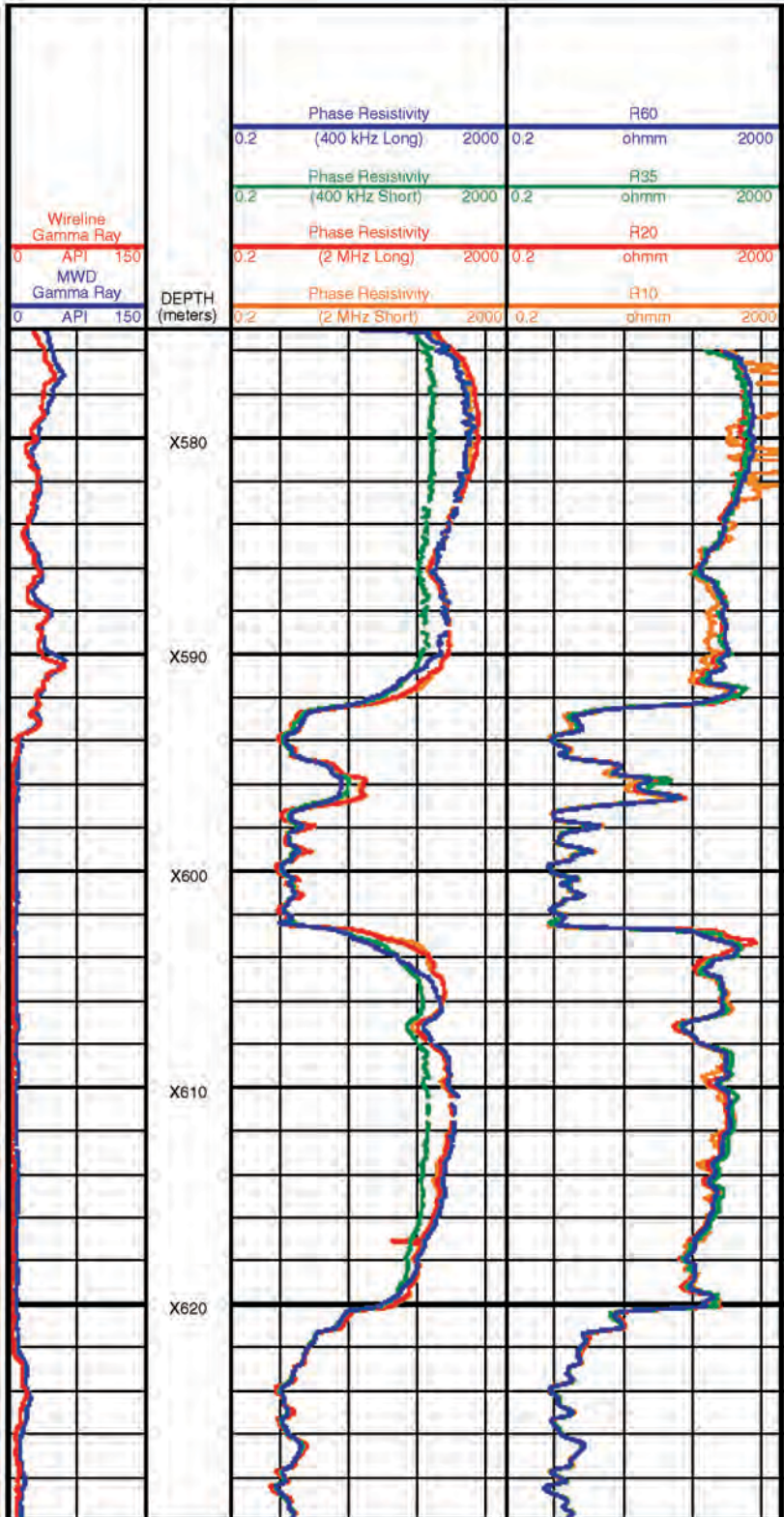


Fig. 3B.36—Comparison of unprocessed MPR logs and MPRteq processed logs (courtesy of Baker Inteq).

where conductivities are expressed in mS/m. V_{sand} and V_{shale} are the bulk volume fractions (percentages) distributed throughout the layered region (layers are all assumed to be approximately uniform in thickness). The effective vertical resistivity, R_v , can be calculated in a similar manner from the volume average of the layer resistivities,

$$R_v = V_{\text{sand}}R_{\text{sand}} + V_{\text{shale}}R_{\text{shale}} \dots\dots\dots (3B.6)$$

In deviated wells, the apparent resistivity R_a in anisotropic media can be calculated using the approximation

$$R_a = \frac{R}{\sqrt{\sin^2\alpha + \lambda^2\cos^2\alpha}}, \dots\dots\dots (3B.7)$$

where α is the angle between the tool axis and vertical,

$$\lambda = \sqrt{\frac{R_v}{R_h}}, \dots\dots\dots (3B.8)$$

and

$$R = \sqrt{R_v R_h} \dots\dots\dots (3B.9)$$

For $\alpha = 90^\circ$ (horizontal wells), $R_a = R$. For $\alpha = 0^\circ$ (vertical wells), $R_a = R_h$. Thus, the vertical resistivity cannot be detected at all by conventional resistivity logging tools in vertical wells.

Fig. 3B.37 shows a modeled tool response illustrating differences caused by anisotropy between CDR logs in a vertical well (0° dip) and in a highly deviated well (80° dip). At 0° dip, the CDR log reads R_h . At 80° , the two CDR curves increase in the direction of R_v in the anisotropic bed, with the phase-shift resistivity reading higher than the attenuation resistivity.

Induction and 2-MHz tools both generate azimuthally polarized electric fields that induce current loops that are tilted with respect to the bedding anisotropy. These tilted current loops sense a weighted average of R_v and R_h that depends on dip angle. Extensive modeling and analysis of 2-MHz tool response has demonstrated that radiation effects control the phase-shift measurement more strongly than the attenuation measurement. Thus, separation between 2-MHz phase-shift and attenuation logs provides a good indication of anisotropy (in the absence of invasion and shoulder-bed effect). There is sufficient sensitivity to invert for R_h and R_v only at considerable distances from bed boundaries. Also, note the polarization horn that occurs near the bed boundary at 80° . Polarization horns are a common occurrence at high dip angles, and are an indication in geosteering that the well has crossed into a target bed.

3B.6 Induction vs. Laterolog Measurements

Laterolog and induction logging tools each have unique characteristics that favor their use in specific situations and applications.

The induction log is generally recommended for holes drilled with only moderately conductive drilling muds or nonconductive muds (e.g., OBM) and for empty or air-drilled holes. The laterolog is generally recommended for holes drilled with very conductive drilling muds (i.e., salt muds).

Induction tools are conductivity-sensitive devices, which are most accurate in low- to medium-resistivity formations. Laterolog tools are resistivity devices, which are most accurate in

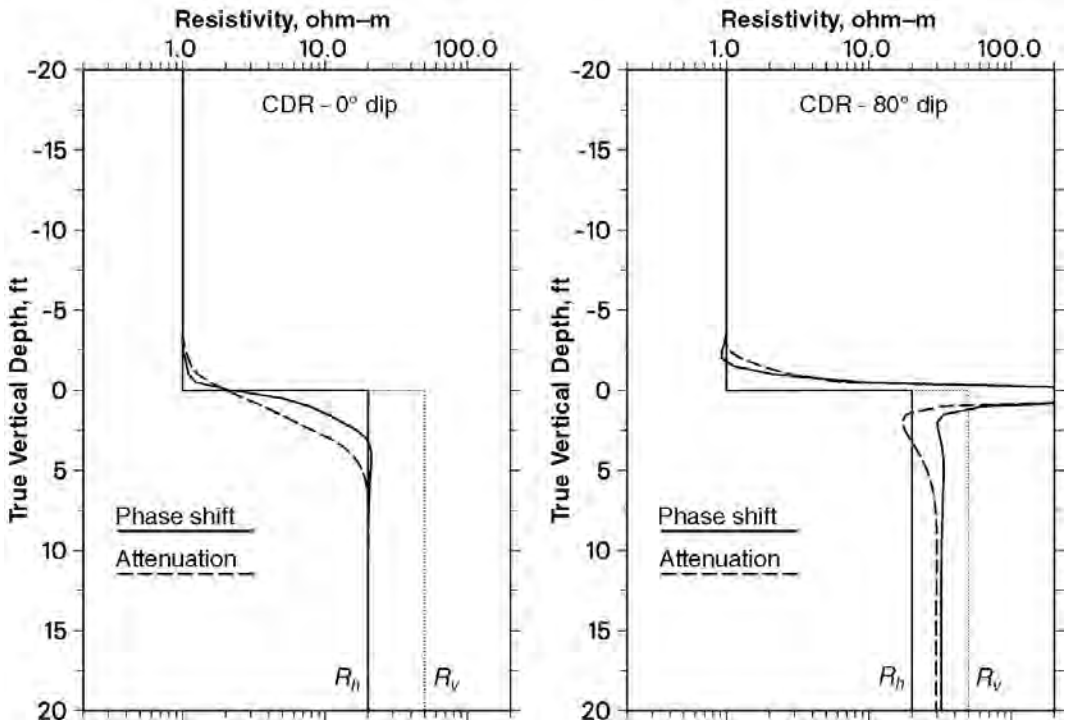


Fig. 3B.37—CDR response at different dips as the tool logs an isotropic bed above an anisotropic bed.

medium- to high-resistivity formations. In practice, both modern laterolog and induction-logging tools are suitable for most logging conditions, and it is no longer practical to make a specific recommendation for one type in preference to the other, except in extreme conditions.

Laterolog devices see the more resistive zones, and induction tools see the more conductive zones. Therefore, when R_{xo} is greater than R_t , an induction tool is preferred for R_t determination because laterolog tools will be affected mostly by R_{xo} . Conversely, a laterolog tool is preferred when R_{xo} is less than R_t . Conductivity in the borehole has a strong influence on an induction measurement, but little influence on a laterolog measurement.

Starting with the Phasor Induction tool, borehole-corrected logs for induction tools have been available at the wellsite. A caliper and estimate of mud resistivity is essential for induction-borehole correction, either by hand using a chart or automatically.

The AITs have only automatic borehole correction—no charts exist. An analytic forward model was used to compute thousands of cases for the AIT covering the range of each of these parameters. At the wellsite, a caliper and accurate measurement of R_m are used as inputs, and the other two parameters are solved for in a least-squares inversion through the computed table. This method is essential to produce an accurate 10-in. log over a wide range of borehole sizes and mud resistivities.

The following are guidelines for running induction logs, especially array-induction tools:

1. A caliper is required *in the same toolstring* as the induction tool.
2. R_m must be measured adequately, preferably downhole, using an accurate sensor. There can be large errors in values of mud resistivity based on surface measurements.
3. Adequate standoff is essential. Never run slick.

If these guidelines are followed, modern AITs can give accurate estimates of R_t even when R_{xo}/R_t is as low as 0.2.

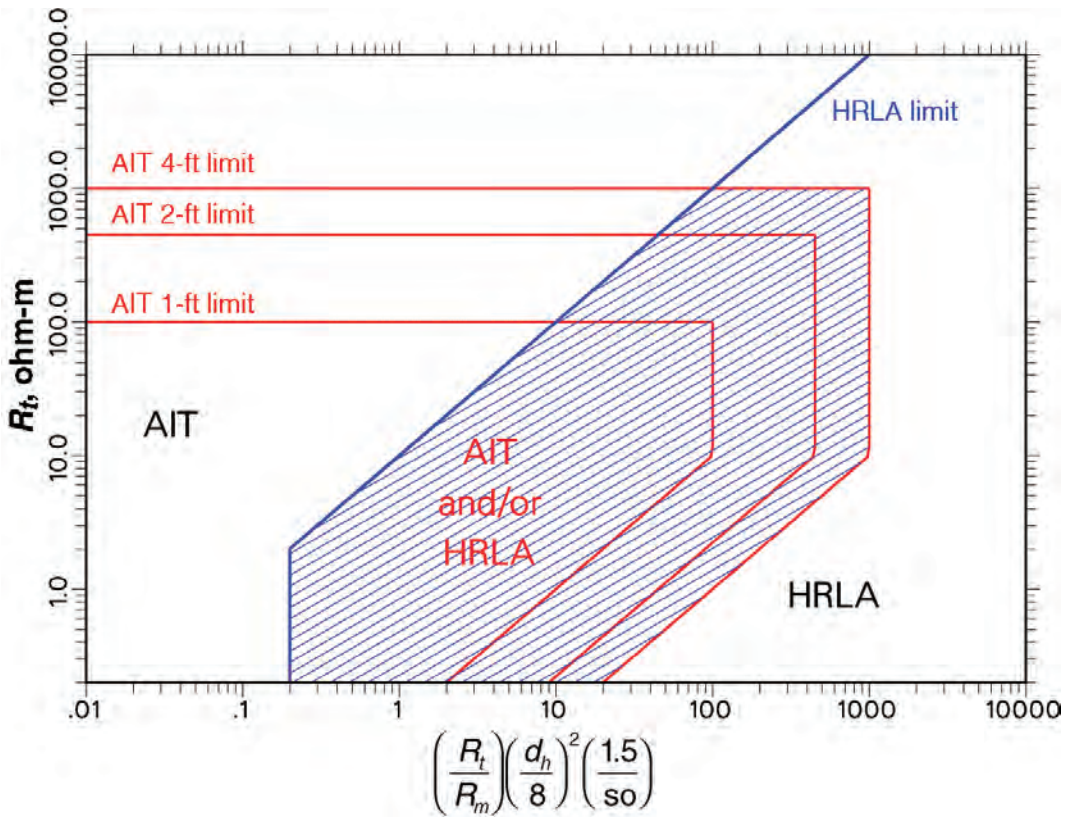


Fig. 3B.38—Chart showing the usable range of the AIT and HRLA logs.

The HRLA array laterolog tool with its inversion of the five array logs has extended the usability of laterolog tools further into the $R_{xo} > R_t$ region. The AITs, again with inversion of the logs, have extended the induction range in the $R_{xo} < R_t$ region. Fig. 3B.38 shows the range of usability of the AIT and HRLA tools. In the broad overlap region, both tools can be used. In this region, the HRLA array laterolog tool can be combined with the AIT to determine anisotropic resistivity— R_v and R_h in vertical wells.⁵²

When looking at both induction and laterolog logs from the same well or the same field, do not expect the logs to overlay. The R_t values for both tools should be close, but the logs themselves, uncorrected for environmental effects, can be quite different.⁵³

When working with older logs, one must keep in mind that both laterolog and induction measurements are influenced by the borehole and by surrounding beds. Surprisingly, thick beds may have some effect on their measurements, depending on shoulder-bed contrast. The measurements of both devices should always be corrected for borehole and surrounding bed effects. Although these corrections are in many cases small, it is good practice to make them routinely. This will ensure that they are not overlooked in the larger number of cases where they are significant.

With either laterolog or induction deep-resistivity measurements, it is essential to record at least three resistivity-log curves with different depths of investigation. With fewer than three competent measurements, it is not possible to make an estimate of the invasion parameters, and R_t and R_{xo} become guesses. Array-induction and array-laterolog tools make a sufficient number of measurements to use the more rigorous inversion solutions, deriving even more reliable values of R_t and R_{xo} .

3B.7 Microresistivity Logs

Microresistivity devices measure the resistivity of the flushed zone and delineate permeable beds by detecting the presence of mudcake.

When invasion is moderate to deep, knowledge of R_{xo} is required to derive R_t from the deep-resistivity measurement. To evaluate a formation with logs, the R_{xo}/R_t ratio is required for some saturation-estimation methods. In clean formations, a value of the formation resistivity factor F can be computed from R_{xo} and R_{mf} if S_{xo} is known or can be estimated.

Tools designed to measure R_{xo} have a very shallow depth of investigation, because the flushed zone may extend only a few inches beyond the borehole wall. To avoid the effect of the borehole, a sidewall-pad tool is used. The pad, carrying an array of closely spaced electrodes, is pressed against the formation to minimize the short-circuiting effect of the mud. Currents from the electrodes on the pad must pass through any mudcake to reach the flushed zone.

Microresistivity readings are affected by mudcake; the effect depends on the mudcake resistivity and thickness (h_{mc}). Mudcakes are usually anisotropic, with the resistivity parallel to the borehole wall lower than the resistivity across the mudcake. This increases the mudcake effect on microresistivity readings to make the effective, or electrical, mudcake thickness greater than the physical thickness indicated by the caliper.

Microresistivity measurements have evolved from the first microlog, through the obsolete microlaterolog⁵⁴ and proximity-log devices, to the current MicroSFL and Platform Express MCFL microresistivity measurements.

3B.7.1 Microlog. The microlog⁵⁵ is still used qualitatively for its ability to detect permeable intervals with a fine vertical resolution, but not for the evaluation of R_{xo} . The measurement comprises two short-spaced devices with different depths of investigation, providing resistivity measurements of small volumes of mudcake and formation adjacent to the borehole. The presence of a mudcake, identified by a “positive” separation of the two curves, indicates an invaded and, therefore, permeable formation. As a qualitative log, the microlog is usually presented on a linear grid.

Principles. The flexible oil-filled microlog pad is pressed against the borehole wall by arms and springs. The face of the pad has three small in-line electrodes spaced 1 in. [2.5 cm] apart. The electrodes record a 1×1-in. “microinverse” log and a 2-in. “micronormal” log simultaneously.

In an invaded permeable zone, R_{mc} is usually significantly lower than R_{xo} . The 2-in. micronormal device has a greater depth of investigation than the microinverse. It is, therefore, less influenced by the mudcake and reads a higher resistivity when mudcake is present. In impermeable formations, the two curves read approximately the same resistivity or have a small negative separation, and the resistivities are usually much greater than in permeable formations.

Positive separation occurs in a permeable zone. Although the microlog curves identify permeable formations, quantitative inferences of permeability are not possible.

Under favorable circumstances, R_{xo} values can be derived from microlog measurements using charts provided by the service companies. R_{mc} values for this purpose can be measured directly or estimated from other charts, and h_{mc} is obtained from comparing the caliper curve to bit size. The limitations of the method are as follows:

1. The ratio R_{xo}/R_{mc} must be less than approximately 15 (porosity more than 15%).
2. The value of h_{mc} must be no greater than 0.5 in. [1.3 cm].
3. Depth of invasion must be greater than 4 in. [10 cm]; otherwise, the microlog readings are affected by R_t .

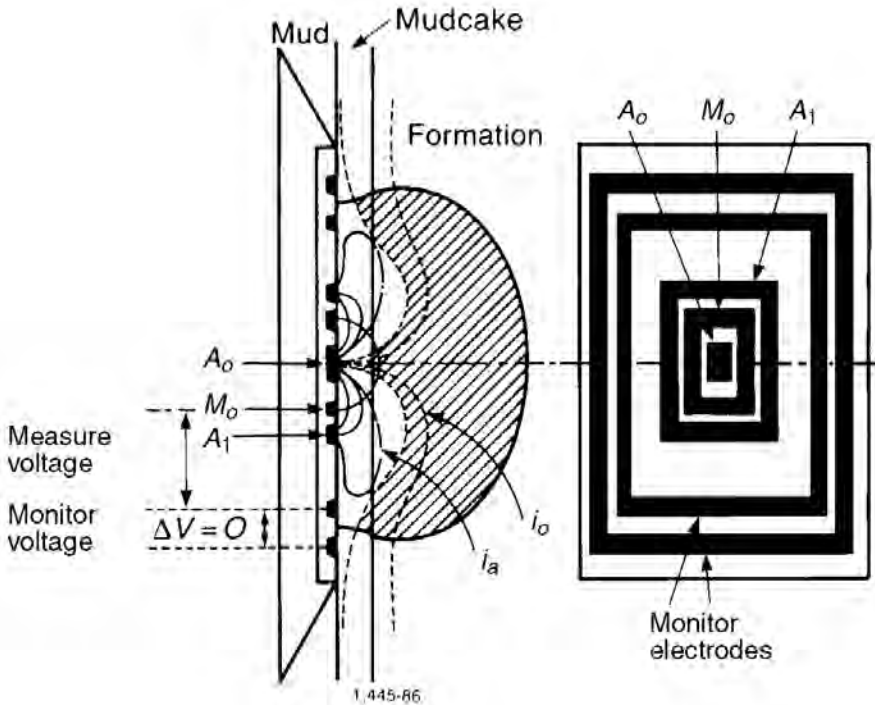


Fig. 3B.39—Pad layout of the MicroSFL tool.

3B.7.2 MicroSFL Log. The MicroSFL (MSFL) device⁵⁶ is a pad-mounted spherically focused logging sensor with two distinct advantages over the microlaterolog and proximity tools it replaced. Unlike these earlier R_{xo} devices, the MSFL tool is combinable with other logging tools, which eliminates the necessity of a separate logging run to obtain R_{xo} information. The MSFL log also performs better in shallow invaded zones in the presence of mudcake.

Fig. 3B.39 shows the electrode arrangement (right) and current patterns (left) of the MSFL tool. The surveying current flows outward from a central electrode, A₀. Bucking currents, passing between electrodes A₀ and A₁, flow in the mudcake and the formation. The measuring current, I_0 , is confined to a path directly into the formation, where it quickly spreads and returns to a remote electrode. By forcing the measure current to flow initially directly into the formation, the effect of mudcake resistivity on the tool response is minimized, yet the tool still has a very shallow depth of investigation.

Synthetic microlog curves (microinverse and micronormal) can be computed from MSFL parameters, because the measure current sees mostly flushed zone and the bucking current sees primarily mudcake.

Environmental Corrections. Although the influence of mudcake on the readings is relatively small, MSFL measurements must be corrected for thickness. Mudcake thickness is normally deduced from a comparison of the actual borehole size, as measured with the caliper, to the known bit size.

3B.7.3 MCFL Log. The Schlumberger MCFL microresistivity measurements⁵⁷ made with Platform Express tool strings are different from previous measurements in several respects:

1. Electrodes are mounted on a rigid, mostly metal pad that is not deformed by the borehole wall, allowing a more consistent standoff measurement.

2. Survey currents are independently focused in planes parallel and perpendicular to the tool axis, reducing the sensitivity to borehole geometry.

3. Three measurements are made with different depths of investigation, which allows a more reliable resolution of mudcake and formation properties with independent response equations.

4. The microresistivity sensors are interlaced with the density sensors, so both measurements sample the same volume of formation at the same time.

A vertical resolution of the raw measurements better than 1 in. [2.5 cm] is achieved, and R_{xo} , R_{mc} , and h_{mc} are solved simultaneously. Two curves can be displayed in a microlog-like presentation. When the two curves are superimposed, they both read R_{xo} . Any separation indicates pad standoff from the formation, which is usually caused by mudcake and indicates a permeable formation.

Because R_{xo} , R_{mc} , and h_{mc} are obtained directly from the Platform Express microresistivity measurements by inversion processing, no mudcake thickness corrections are required. The values of R_{xo} can be used directly with medium and deep-resistivity measurements (or array-resistivity measurements) to derive R_t .

3B.8 Formation-Resistivity Determination

Resistivity is the one of the most difficult formation parameters to measure accurately because of the complex changes that occur during and after drilling a well and that may still be occurring during logging. The various components of the downhole environment may have strongly contrasting resistivities, some of which cannot be measured directly, and their physical dimensions may not be readily available. Fig. 3B.1 shows an idealized relationship of the main environmental components. The resistivities and dimensions of all these “layers” (mud, mudcake, flushed zone, and zone of transition) influence all deep-reading resistivity measurements. There is no direct measurement of R_t . It must be inferred from the multiple-depth resistivity measurements.

In a permeable formation, mud resistivity is commonly 1 to 3 orders of magnitude lower than the formation resistivity, or, in the case of OBM, it can be much higher. The downhole mud resistivity can be estimated approximately by measuring the resistivity of a surface sample taken just before mud circulation was stopped before logging and adjusting it for the difference in temperature using an appropriate chart or equation. The shape and size of the borehole and the position of the logging tool in the hole have an influence on resistivity measurements that will not be apparent from a single hole-size measurement.

Attempts to measure the resistivity of an artificially formed sample of mudcake is unlikely to represent in-situ mudcake resistivity accurately. Mudcake thickness cannot be directly measured with current logging tools; it can only be estimated with some uncertainty.

The resistivity of the flushed zone can be measured with reasonable precision if the depth of invasion is greater than the depth of investigation of the R_{xo} logging tool, but the depth of invasion and the resistivity profile and geometry of the zone of transition are difficult to estimate.

3B.9 Traditional R_t Methods

Evaluation of the uninvaded formation resistivity R_t is sometimes referred to as invasion correction. It is usually performed assuming a simple three-parameter, step-profile invasion model consisting of a flushed zone of uniform resistivity R_{xo} with a sharp boundary at the diameter of invasion d_i to resistivity R_t . This is clearly not realistic, but it allows a complex problem to be solved relatively simply, usually with acceptable accuracy, by using a minimum of three resistivity measurements with different depths of investigation.⁵

A shallow microresistivity measurement, such as the MicroSFL log, is corrected for the influence of the mudcake by using the best available estimates of mudcake thickness and resistivity. It is assumed that d_i is greater than the depth of investigation of the MicroSFL, so that

the MicroSFL log reads only the flushed zone and the mudcake-corrected MicroSFL reading is R_{xo} .

Next, the deep- and medium-resistivity measurements are corrected for environmental effects using the charts for the tool used. These effects are always corrected in the following order: borehole effect, bed thickness, and shoulder effect. Then the invasion parameters (R_{xo} , R_i , d_i) can be found for induction tools using tornado charts. For laterolog tools, butterfly charts are used. Some service companies offer charts for R_i and d_i when R_{xo} is known from a microresistivity device.

3B.9.1 Inversion for Invasion Parameters. The latest array-induction and array-electrode tools all use some form of inversion (rather than charts) to estimate the invasion parameters— invasion radius or diameter, d_i , R_{xo} , and R_i . There are two types of inversion used: 1D and 2D. The formation geometry of each is shown in Fig. 3B.9.

Inversion means first building a parametric model of the formation, then estimating from the log values a “first guess” of the parameter values. Then, a modeling code is used to compute the log response to the model. This is compared with the actual logs. The difference between modeled and measured is used to pick a new set of model parameters, and the log response computed. Again, the modeled logs are compared to the actual logs. This continues until the difference reaches some preset minimum, and then the model parameters are output as the invasion parameters.

Induction response is mostly a function only of coil spacings, with a weak response to the large-scale average formation conductivity. If we can assume that each formation layer is more or less uniformly invaded, then an inversion through a 1D radial forward model⁵⁸ will give a close estimate of invasion parameters R_{xo} and R_i . This is most often true when $R_{xo} > R_i$.

Laterolog tools are much more affected at the same time by both bed thickness and invasion parameters in that bed. For this reason, when the formation of interest consists of thin (< 30 ft [10 m]) beds, 2D inversion is necessary for accurate estimation of R_{xo} , R_i , and d_i . 1D inversion tends to be used in real-time processing, and 2D inversion is used at the computing center. Some commercial 2D-inversion applications allow very sophisticated choices of parametric models, including transition zones and annulus models.

Inversion methods also return “goodness-of-fit” criteria. At the same time, the modeled logs can be compared with the actual logs as a quality control. Inversion methods also allow the parametric model to be selected to better fit the situation at hand. A four-parameter inversion model, with a zone of transition defined from d_i to the diameter of the limit of invasion at d_j , gives reliable answers in a much wider range of conditions than the traditional three-parameter model. It also generates “quality-of-fit” parameters that indicate when the log readings are not consistent with the model.

Annulus formation is a common phenomenon, caused by the sweeping of conductive ions from the formation by the invading borehole fluid. Fluid-flow models predict annulus formation in a wide range of formation/borehole fluid conditions. Annulus formation has been observed with both WBM and OBM. Even with five or six depths of investigation, the information content is not sufficient to solve for the five annulus parameters (R_{xo} , R_{ann} , R_i , r_1 , and r_2) independently. However, by invoking the constraint of material balance⁵⁹ and supplying an estimate of R_w , the annulus problem can be reduced to three parameters: R_{xo} , r_1 , and R_i . r_2 is tied to r_1 through the material-balance constraint, and R_{ann} can be estimated from R_{mf} , R_{xo} , and R_w .

Invasion also changes with time, sometimes rapidly. For this reason, the combination of data taken at different times (e.g., wireline and LWD, or LWD time-lapse), must be done with care. One method that has shown promise is to use a consistent parametric model (step or annulus) and assume R_{xo} and R_i are constant, allowing only for the invasion radius to change.

Before performing an inversion for invasion parameters, be sure the cause of curve separation is actually invasion. Causes of curve separation include tool-response effects such as shoulder effect, not matching the resolution of the curves, and improper borehole correction. Other formation effects that can cause curve separation include dipping beds and drilling-induced fractures.

The introduction of array-resistivity tools has clearly delineated invasion profiles that were not as expected, even after years of logging in a region. In some regions, it was assumed that the formation was uninvaded because the ILd, ILM, and SFL logs all were very close in pay zones. Logs made by an array-induction tool showed an $R_{xo} < R_t$ profile. The discrepancy exists because the SFL, being a laterolog, can have a depth of investigation as deep as ILd under $R_{xo} < R_t$ conditions. The ILM was long considered an inferior measurement to ILd because it would lie lower in resistivity than either SFL or ILd. Modeling shows that either an annulus or $R_{xo} < R_t$ will produce this curve order.

A powerful method for handling the fundamentally underdetermined problem of invasion correction of resistivity logs is iterative forward modeling.⁵ Complex formation geometries and invasion profiles can be worked out by building a model of the best estimate of formation parameters from logs, field knowledge, and petrophysical constraints; modeling the resistivity logs; and varying the parameters until a fit is obtained.

Finally, keep in mind that R_t cannot be measured directly, but must be inferred from multiple-depth resistivity measurements.

3B.9.2 Resistivity Imaging. Many modern resistivity- and microresistivity-logging tools have arrays of sensors that make multiple measurements, enabling the creation of 2D images of formation resistivity. The images represent resistivity variations with the azimuth around the borehole or with distance away from the borehole.

Inspired by the images produced by early acoustic borehole televiewer tools, borehole resistivity imaging was developed to see actual formation variations, rather than the surface effects that the acoustic images depicted. The first practical resistivity images were produced by an array of closely spaced, shallow-reading button electrodes applied to the borehole wall.

The borehole coverage of this high-resolution microresistivity image was increased on later tools, and deeper reading tools with imaging capabilities have been subsequently developed.

Microresistivity Images. The first microelectrical imaging tool had an array of button electrodes mounted on an enlarged section of the tool mandrel. Electrodes were then placed on two of the four pads of the Dual Dipmeter tool. The Fullbore Formation MicroImager (FMI) tool⁶² has button electrodes on all four pads, with extension flaps on each pad to increase the borehole coverage.

FMI image data have sufficient resolution and character to allow using selected electrode signals for conventional dipmeter computations, and the tool's borehole coverage provides a detailed visual appreciation of geologic features, **Fig. 3B.40**. Formation dips and fracture orientations can also be derived directly from the images.

Seeing the shape of formation-resistivity variations often provides understanding of the lack of coherent dip found by a dipmeter computation program.

Halliburton's Electromagnetic MicroImager (EMI) tool is a six-arm resistivity borehole imager tool. Its principle of operation is similar to the FMI tool. Baker Atlas' Simultaneous Acoustic and Resistivity (STAR) Imager tool integrates resistivity and acoustic borehole imaging sensors into one instrument. The resistivity imager is a six-arm device with powered centralization to keep the acoustic transducer centered. The acoustic sensor also works in OBM where the resistivity imager performance is poor.

ARI Images. The formation resistivity around the borehole is displayed in ARI images as a 2D azimuthal image, with the same dimensions of well depth and azimuthal angle around the

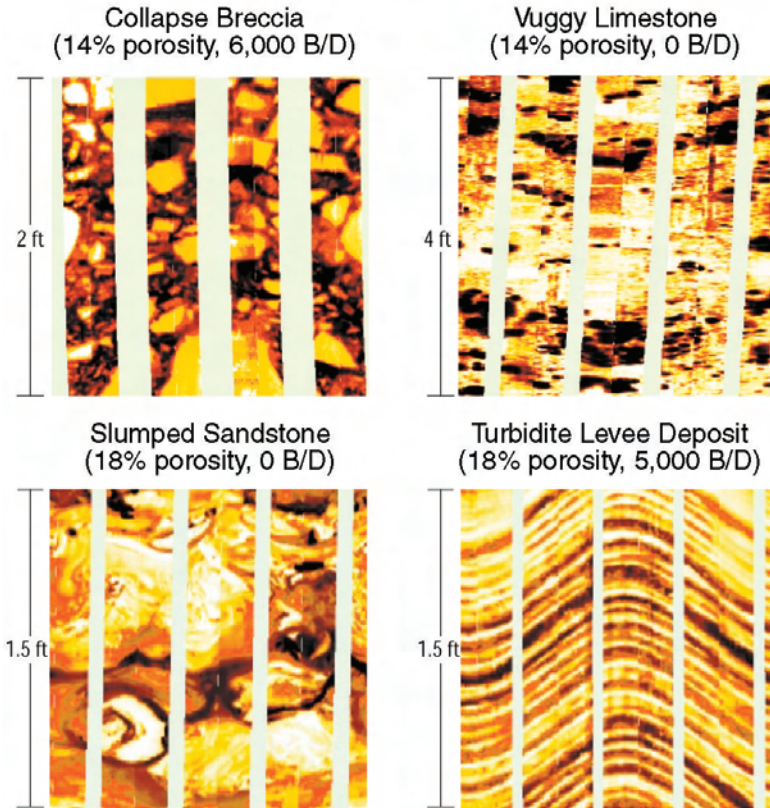


Fig. 3B.40—FMI images in four different geological settings.

well as FMI images. This image has much lower spatial resolution than acoustic or microelectrical images from the UBI and FMI tools, but it complements them well because of its sensitivity to features beyond the borehole wall and its lower sensitivity to shallow features.

AIT Images. The AIT provides images of variations in formation resistivity or conductivity with distance away from the borehole. This capability brings a new dimension to formation image data, because the image contains invasion information useful for understanding how deeply the formation can be invaded.

Radial response functions are used to invert the set of matched vertical resolution logs in the four-parameter invasion model, producing a detailed description of the radial resistivity. Introducing other petrophysical parameters, such as F , R_w , and R_b , and a suitable saturation equation (see Saturation Determination section) allows imaging-computed virgin and invaded-zone saturations.

3B.9.3 LWD Resistivity Images. The GVR tool incorporates three 1-in.-diameter azimuthal button electrodes that produce borehole resistivity images during rotary drilling by recording 56 resistivity measurements per rotation with each electrode. The data are processed and recorded downhole for later retrieval.

Because the GVR button electrodes are larger than FMI electrodes and are not in contact with the formation, GVR images are less sharp than FMI images, as seen in Fig. 3B.12. However, often the timeliness of the images more than makes up for the resolution. A compression algorithm allows the images to be sent up in real time for geosteering.

Formation Dip From LWD Images. Dip computation by conventional dipmeter data processing is most effective when the apparent dips (i.e., dips relative to tool inclination) are less than approximately 70° , which is suitable for most vertical and normally deviated wells. LWD has major applications (e.g., geosteering) in highly deviated and horizontal wells, where apparent dips are commonly greater than 70° . A dip-computation process that returns dip from the GVR in real time was developed for high-angle wells.⁶¹ The dip-azimuth and magnitude computations are performed by a robust algorithm in the downhole tool, allowing real-time transmission of the dip data. Although the well deviation is accurately measured by instruments in the drill collar, the relative dip with respect to the bedding is important for geosteering wells along the bedding planes. This method allows improved well placement.

The confidence in computed GVR dips is increased by using data from all three electrodes. Because the electrodes are at fixed distances from each other, irregular tool movement in the hole is unimportant.

3B.10 SP Log

The SP curve is a continuous recording vs. depth of the electrical potential difference between a movable electrode in the borehole and a surface electrode.¹ Adjacent to shales, SP readings usually define a straight line known as the shale baseline. Next to permeable formations, the curve departs from the shale baseline; in thick permeable beds, these excursions reach a constant departure from the shale baseline, defining the “sand line.” The deflection may be either to the left (negative) or to the right (positive), depending on the relative salinities of the formation water and the mud filtrate. If the formation-water salinity is greater than the mud-filtrate salinity (the more common case), the deflection is to the left.

The relevant features of the SP curve are its shape and the size of its departure from the shale baseline. Because the absolute reading and position of the shale baseline on the log are irrelevant, the SP sensitivity scale and shale-baseline position are selected by the logging engineer for convenience. The SP log is typically scaled at 100 mV per log track. If the resistivities of the mud filtrate and formation water are similar, the SP deflections are small and the curve is rather featureless. An SP curve cannot be recorded in holes filled with nonconductive muds, such as OBMs.

3B.10.1 Origin of the SP. Deflections of the SP curve are the result of electrochemical and electrokinetic potentials in the formations that cause electric currents to flow in the mud in the borehole.

Electrochemical Component. Membrane Potential. The structure of clay minerals in shales and the concentration of negative electric charges on the clay particle surfaces give shales a selective permeability to electrically charged ions. Most shales act as “cationic membranes” that are permeable to positively charged ions (cations) and impermeable to negative ions (anions).⁶²

The upper part of [Fig. 3B.41](#) shows saline formation water in a sandstone formation and mud in the borehole separated by a shale. Sodium chloride, which is usually present in both the formation water and the drilling mud, separates into charged ions (Na^+ and Cl^-) in solution in water. The Na^+ and Cl^- ions tend to migrate from a more-concentrated to a less-concentrated solution, but because the intervening shale is a cationic membrane, impervious to Cl^- ions, only the Na^+ ions can migrate. If, as usual, the formation water is a more concentrated NaCl solution than the mud, there is a net flow of positive ions through the shale from the sandstone to the borehole. This corresponds to a positive electric current in the same direction (indicated by the curved arrow) driven by an electric potential, or electromotive force (EMF), across the shale. Because the shale acts as an ion-selective membrane, the electric potential is known as the membrane potential.

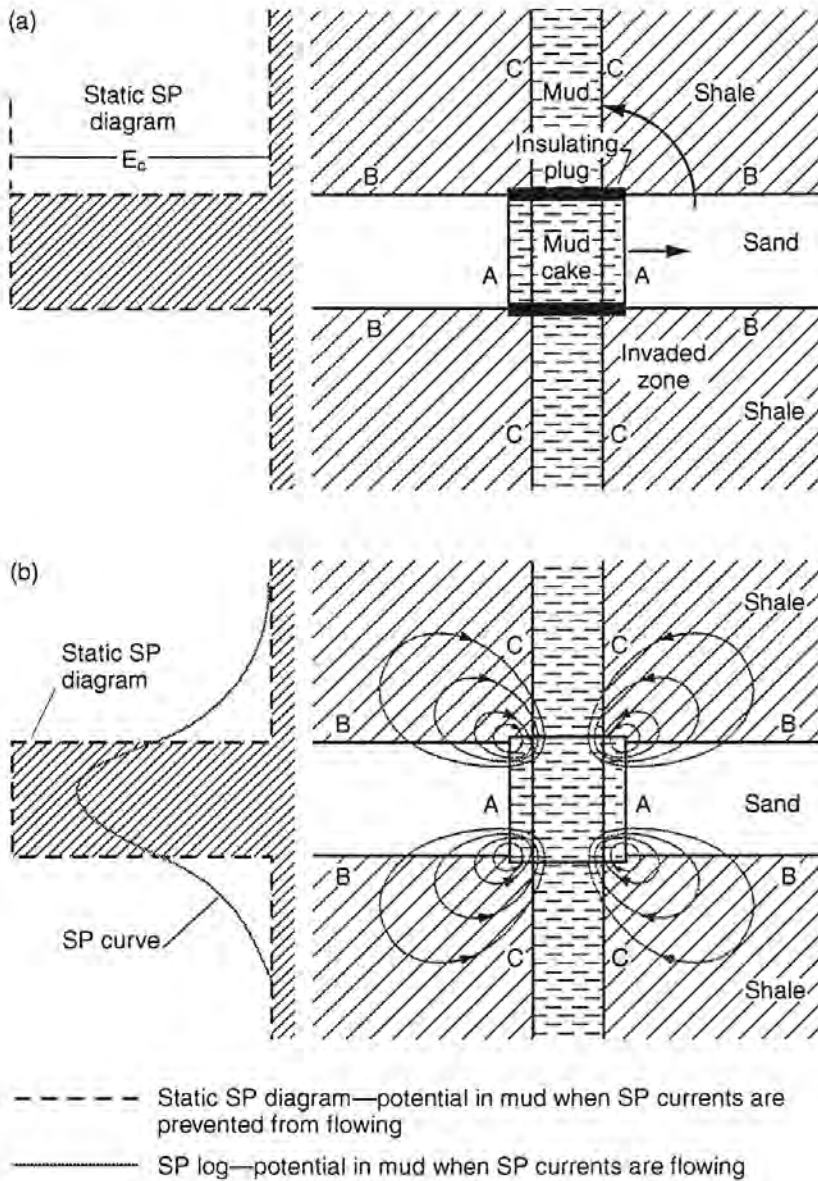


Fig. 3B.41—Schematic representation of potential and current distribution in and around a permeable bed.

Liquid-Junction Potential. At the edge of the invaded zone, where the mud filtrate and formation water are in direct contact, Na^+ and Cl^- ions can move freely from one solution to the other. But Cl^- ions are smaller and have greater mobility than Na^+ ions, so the net diffusion of ions from the more-concentrated formation water to the less-concentrated mud filtrate includes a greater number of Cl^- ions than Na^+ ions. This is equivalent to a positive current flow in the opposite direction (indicated by the straight arrow at A in Fig. 3B.41.)

The current flowing across the junction between solutions of different salinity is driven by an EMF called the liquid-junction potential. The magnitude of the liquid-junction potential is only approximately one-fifth of the membrane potential.

If the solutions contain substantial amounts of salts other than NaCl, the value of K at 77°F may not be 71. If the permeable formation contains some shale or dispersed clay, the total electrochemical potential, and therefore the SP deflections, is reduced.

Electrokinetic Component. An electrokinetic potential (E_k , also called the streaming potential or electrofiltration potential) is produced when an electrolyte flows through a permeable medium.^{63,64} The size of the electrokinetic potential is determined mainly by the differential pressure producing the flow and the resistivity of the electrolyte.

In the borehole, the electrokinetic potential E_{kmc} is produced by the flow of mud filtrate through the mudcake deposited on the borehole wall opposite permeable formations. Little or no electrokinetic potential is generated across the permeable formation itself because the differential pressure is usually low. The electrokinetic potential E_{ksh} may, however, be produced across a shale if it has any permeability.

Typically, E_{kmc} and E_{ksh} are similar in magnitude, and the net electrokinetic contribution to the SP deflection is negligible. If the formation water is fairly saline (resistivity less than 0.1 ohm·m) and the differential pressure is in the normal range of only a few hundred psi, the contribution of the electrokinetic potential can usually be ignored.

Electrokinetic effects may be significant in highly depleted formations or when heavy drilling muds are used because of unusually large differential pressures. Significant electrokinetic effects may also occur in very-low-permeability formations, where an appreciable part of the pressure differential occurs in the formation itself, especially if little or no mudcake is formed. If the formation water is brackish, the mud is resistive, and the low-permeability formation is clean and has some porosity, the electrokinetic effect could be as large as –200 mV.

3B.10.2 SP and Permeability. The movement of ions, essential to develop an SP, is possible only in formations with some permeability, however small—a small fraction of a millidarcy is sufficient. There is no direct relationship between the magnitude of the SP deflection and the value of either the formation's permeability or its porosity.

3B.10.3 Static SP. The lower part of Fig. 3B.41 shows SP currents in the borehole and formations. The current directions indicated correspond to the more usual case of formation-water salinity greater than mud-filtrate salinity, producing a potential by the permeable bed lower than the potential by the shale. This corresponds to a deflection to the left on the SP log by the permeable bed.

If the mud-filtrate salinity is greater than the formation-water salinity, the currents flow in the opposite direction, producing positive SP deflections. If the salinities of the mud filtrate and formation water are similar, no SP is generated.

The SP currents flow through four different media: borehole fluid, the invaded zone, the uninvaded part of the permeable formation, and surrounding shales. The SP log measures only the potential drop from the SP currents in the borehole fluid, which may not represent the total SP because there are also potential drops in the formation. If the currents could be interrupted by hypothetical insulating plugs (see the upper part of Fig. 3B.41), the potential observed in the mud would be the total spontaneous potential. This idealized SP deflection is called the static SP (or SSP). The SP deflection practically reaches the SSP in a thick, clean formation.

The borehole presents a much smaller cross-sectional area to current flow than the formations around it, so the resistance of the borehole part of the SP current loop is much higher than the formation part. Nearly all the SP potential drop, therefore, occurs in the borehole if formation resistivities are low-to-moderate and formation beds are thick, so, in practice, the recorded SP deflection approaches the static SP value in thick, permeable beds.

Determination of SSP. To determine the SSP, a sand line is drawn through the maximum (usually negative) excursions of the SP curve adjacent to the thickest permeable beds. A shale

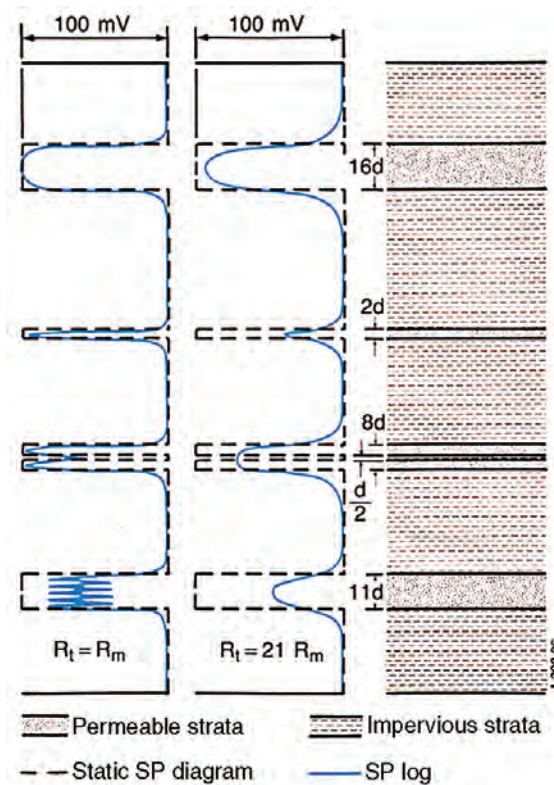


Fig. 3B.42—SP curve in beds of different thickness for $R_t = R_m$ (left) and $R_t = 21 R_m$ (center).

baseline is drawn through the SP through the intervening shale beds. The separation of the sand line from the shale baseline, measured in mV, is the SSP. Any SP anomalies are discounted.

If there are no thick, clean, permeable invaded beds in the zone under study, the SP reading can be corrected for the effects of bed thickness and invasion to estimate the SSP by using charts available from service companies.

Shape of the SP Curve. The slope of the SP curve is proportional to the intensity of the SP currents in the borehole at that depth. Because the current intensity is highest at the boundaries of the permeable formation, the slope of the SP curve is at a maximum, and an inflection point occurs at these bed boundaries.

The shape of the SP curve and the amplitude of its deflection in permeable beds depend on the following factors: thickness and true formation resistivity of the permeable bed, resistivity of the flushed zone (R_{xo}) and diameter d_i , resistivity of the adjacent shale bed (R_s), and resistivity of the mud and the diameter of the borehole (d_b).

Fig 3B.42 shows examples of SP curves computed for $R_t = R_s = R_m$ (on the left) and $R_t = R_s = 21R_m$ (in the center). In the first case ($R_t = R_s = R_m$), the SP curve gives a much sharper definition of the boundaries of the permeable beds, and the SP deflections approach the SSP value more closely than in the case where the formation-to-mud resistivity ratio is 21.

SP Anomalies. The SP curve may be difficult to interpret and use for R_w determination because it does not always behave ideally. The following are a few cases of apparently anomalous SP responses.

Highly Resistive Formations. Highly resistive formations between some shales and permeable beds can significantly alter the distribution of the SP currents and change the expected

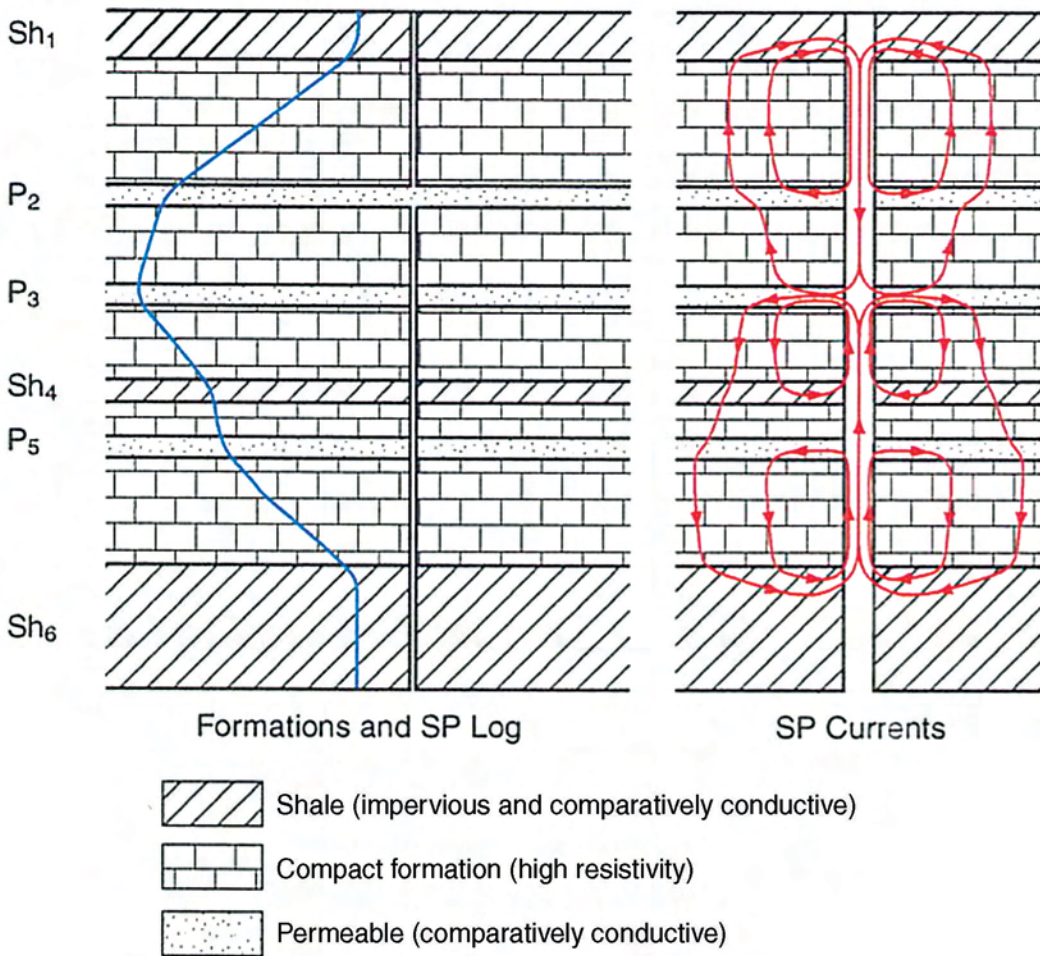


Fig. 3B.43—Schematic representations of SP phenomena in highly resistive formations.

shape of the SP curve. The currents shown flowing from shale bed Sh_1 toward permeable bed P_2 in Fig. 3B.43 are largely confined to the borehole by the high resistivity of the formation separating Sh_1 and P_2 . The current in the borehole over this interval is constant, so for a constant borehole diameter, the SP curve is a straight line inclined to the shale baseline.

The SP curve consists of straight portions adjacent to the high-resistivity zones with a change of slope at each more conductive permeable interval (the SP curve is concave toward the shale line) and opposite every shale bed (the SP curve is convex toward the shale line). Defining permeable bed boundaries from the SP log is difficult in the vicinity of highly resistive formations.

Shale-Baseline Shifts. A shift of the shale baseline can occur when formation waters of different salinities are separated by a shale bed that is not a perfect cationic membrane.⁶⁵ Fig. 3B.44 shows an SP log recorded in a series of sandstones (B, D, F, and H) separated by thin shales or shaly sandstones (C, E, and G). The SSP of Sandstone B is -42 mV. Shale C is not a perfect cationic membrane, and the SP curve does not return to the shale baseline defined by Shale A. A new shale baseline defined by Shale E gives SP deflections of $+44$ mV in Sandstone D and -23 mV in Sandstone F.

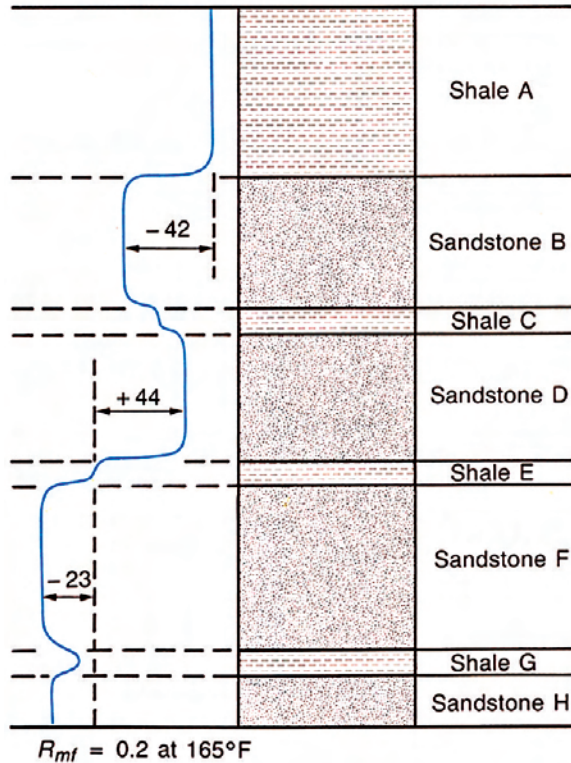


Fig. 3B.44—SP baseline shift.

Baseline shifts also occur when formation waters of different salinities are separated by an impermeable layer that is not a shale. In this case, the SP curve shows little or no variation at the level of the change in salinity, but the deflections at the upper and lower shale boundaries are different and may even have different polarities.

Invasion-Related Anomalies. If the mud filtrate and the formation water have significantly different salinities, and therefore different densities, gravity-induced fluid migration can cause SP anomalies in highly permeable formations, as shown in Fig. 3B.44. Invasion is very shallow near the lower boundary of each permeable interval and deeper near the upper boundary.

The SP curve is rounded at the upper boundary because of the deep invasion, and it may have a sawtooth profile at thin, impervious shale streaks in which the SP deflection exceeds the SSP above the shale streak. A reading greater than the SSP is caused by the accumulation of filtrate below the shale streak. Encircling the hole is a horizontal disk of shale sandwiched between salt water and fresher mud filtrate that acts like a battery cell. The EMF of this cell is superimposed on the normal SSP, producing the sawtooth profile.

Noisy SP Logs. SP measuring circuits are sensitive and therefore prone to recording spurious electrical noise superimposed on the SP curve. Occasionally, the source of noise cannot be eliminated during logging, and a noisy log is recorded. However, this does not always render the log unusable.

A regular sine-wave signal may be superimposed on the SP curve when some part of the logging winch is magnetized. An intermittent contact between the casing and cable armor may also cause spurious spikes on the SP curve. In these situations, the SP curve can usually be read so that the sine-wave amplitude or noise spikes are not added to or subtracted from the authentic SP deflection.

Direct currents flowing through formations near the SP electrode can cause erroneous SP readings, particularly where formation resistivities are high. These currents may be caused by “bimetallism,” when the logging tool has exposed metal housings. The currents are small and have a significant effect on the SP only in highly resistive formations. If an SP curve looks questionable in highly resistive formations, it should be relied on only in lower-resistivity intervals.

The offshore logging environment is notorious for its ample supply of sources of electrical noise, such as wave motion, cathodic protection systems, rig welding, onboard generators, and leaky power sources. On land, proximity to power lines and pumping wells may have a similar effect on the SP curve, but the effects can usually be minimized by carefully choosing the ground-electrode location.

3B.11 Uses and Interpretation of Well Logs

3B.11.1 Determination of Saturation. Water saturation is the fraction of the pore volume of the reservoir rock that is filled with water. It is generally assumed, unless otherwise known, that the pore volume not filled with water is filled with hydrocarbons. Determining water and hydrocarbon saturation is one of the basic objectives of well logging.

Clean Formations. All water saturation determinations from resistivity logs in clean (non-shaly) formations with homogeneous intergranular porosity are based on Archie’s water saturation equation, or variations thereof.^{66,67} The equation is

$$S_w^n = \frac{FR_w}{R_t} \dots\dots\dots (3B.10)$$

R_w is the formation water resistivity, R_t is the true formation resistivity, and F is the formation resistivity factor. F is usually obtained from the measured porosity of the formation through the relationship

$$F = a / \phi^m \dots\dots\dots (3B.11)$$

For S_{xo} , the water saturation in the flushed zone, a similar expression exists:

$$S_{xo}^n = \frac{FR_{mf}}{R_{xo}} \dots\dots\dots (3B.12)$$

where R_{mf} is the mud filtrate resistivity and R_{xo} is the flushed zone resistivity.

For simplicity, the saturation exponent n is usually taken as 2. Laboratory experiments have shown that this is a reasonable value for average cases. For more exacting work, electrical measurements on cores will produce better numbers for n , a , and m . When core measured values are unavailable, the values of a and m in Eq. 3B.7 can be estimated as follows: in carbonates, $F = 1 / \phi^2$ is usually used; in sands, $F = 0.62 / \phi^{2.15}$ (Humble formula), or $F = 0.81 / \phi^2$ (a simpler form practically equivalent to the Humble formula). These equations are easily programmed into spreadsheets and are available in most log interpretation software.

The accuracy of the Archie equation, Eq. 3B.10 and its derivatives, depends in large measure, of course, on the accuracy of the fundamental input parameters: R_w , F , and R_t . The deep resistivity measurement (induction or laterolog) must be corrected, therefore, for borehole, bed thickness, and invasion (see Sections 3B.8 and 3B.9). It is almost never safe to make the assumption “deep = R_t .” The most appropriate porosity log (sonic, neutron, density, magnetic

resonance, or other) or combination of porosity and lithology measurements must be used to obtain porosity, and the proper porosity-to-formation factor relationship must be used. Finally, the R_w value should be verified in as many ways as possible: calculation from the SP curve, water catalog, calculation from nearby water-bearing formation, and/or water sample measurement.

Alternate methods for determining water saturation include analysis of cores cut with low-invasion OBMs and single-well chemical-tracer tests (described in the chapter on single-well chemical-tracer testing in this section of the *Handbook*). These independent methods can be used to calibrate log analyses.

Resistivity-vs.-Porosity Crossplots. Combining Eqs. 3B.10 and 3B.11, the Archie saturation equation may be written

$$S_w^n = \frac{aR_w}{\phi^m R_t} \dots\dots\dots (3B.13)$$

If n and m are equal to 2, and $a = 1$, then

$$\phi S_w = \sqrt{R_w / R_t} \dots\dots\dots (3B.14)$$

Eq. 3B.14 shows that for R_w constant, ϕS_w is proportional to $1/\sqrt{R_t}$; ϕS_w is the quantity of water per unit volume of formation. To emphasize the proportionality between ϕ and $1/\sqrt{R_t}$, Eq. 3B.14 may be rewritten:

$$\phi = \frac{\sqrt{R_w}}{S_w} \frac{1}{\sqrt{R_t}} \dots\dots\dots (3B.15)$$

For a 100% water-saturated formation, $S_w = 1$ and $R_t = R_0$. If R_0 for water-saturated formations is plotted on an inverse square-root scale vs. ϕ , all points should fall on a straight line given by $\phi = \sqrt{R_w / R_0}$.

Furthermore, the points corresponding to any other constant value of S_w will also fall on a straight line, because in Eq. 3B.14 the coefficient is constant for constant values of R_w and S_w .

Fig. 3B.45 shows several points plotted over an interval in which formation-water resistivity is constant (as indicated by constant SP deflections opposite the thick, clean permeable beds). Assuming that at least some of the points are from 100% water-bearing formations, the line for $S_w = 1$ is drawn from the pivot point ($\phi = 0, R_t = \infty$) through the most northwesterly plotted points. The slope of this line defines the value of R_w as shown on Fig. 3B.45, for $\phi = 10\%$, $R_0 = 6.5$ ohm-m. For this formation, the most appropriate F - ϕ relation is $F = 1/\phi^2$. Thus, for $\phi = 10\%$, $F = 100$. Because $R_w = R_0/F$, $R_w = 0.065$ ohm-m, as shown.

For other S_w values, R_t and R_0 are related by the equation $R_t = R_0 / S_w^2$. For $S_w = 50\%$, and $1/S_w^2 = 4$, and $R_t = 4 R_0$. This relation establishes the line for $S_w = 50\%$. Other S_w lines may be defined in a similar manner.

If the matrix composition remains constant over the formations under investigation, the basic measurement from the sonic, density, or neutron logs can be plotted directly vs. R_t with similar results.⁶⁸ This is possible because of the linear relationship between porosity and bulk density, sonic transit time, or neutron-hydrogen index response. An example of a sonic-induction crossplot is shown in Fig. 3B.46. The transit time has been plotted against the induction resistivity for several levels. The northwesterly points define the 100% water saturation line.

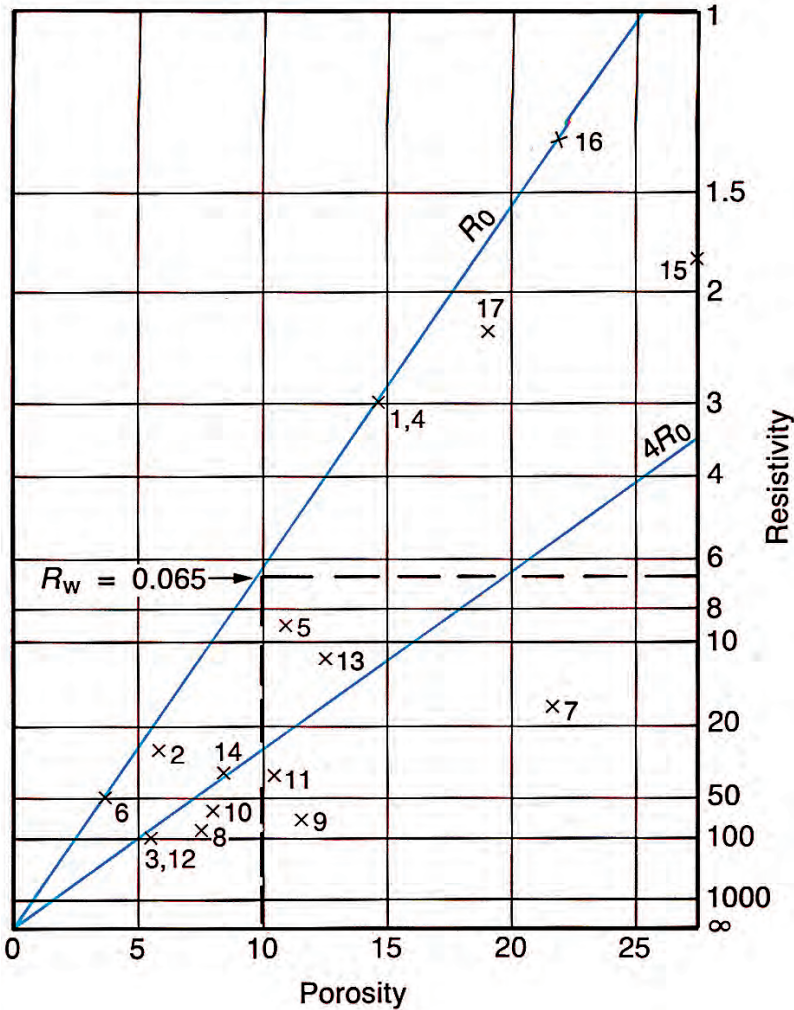


Fig. 3B.45—Resistivity-porosity crossplot for determining R_w and S_w .

The transit-time value at the point where this line intersects the horizontal line of infinite resistivity is the matrix-transit time, t_{ma} . In Fig. 3B.46, t_{ma} is found to be approximately 47.5 $\mu\text{s}/\text{ft}$ (156 $\mu\text{s}/\text{m}$). This corresponds to a matrix velocity of 21,000 ft/sec (6,400 m/s).

By knowing t_{ma} , a porosity scale, a scale of formation factor (e.g., from $F = 1/\phi^2$) can be easily derived. A vertical line drawn through $F = 100$ (or $\phi = 10$) intersects the water line at $R_0 = 5$ ohm·m; accordingly, $R_w (= R_0/F)$ is 0.05 ohm·m.

The lines for other S_w values are straight lines, determined as previously described, radiating out from the $R_t = \infty, t_{ma} = 47.5$ pivot point.

Density and neutron logs can be crossplotted against resistivity in a manner identical to the sonic logs. For density logs, the intersection of the 100% water line with the infinite-resistivity line yields the matrix-density value, ρ_{ma} . For neutron logs, the intersection defines the matrix-hydrogen index, or apparent matrix porosity. Knowledge of matrix density or hydrogen index permits the ρ_B or ϕ_N scale to be rescaled in ϕ and F units. With the F scale defined, R_w can

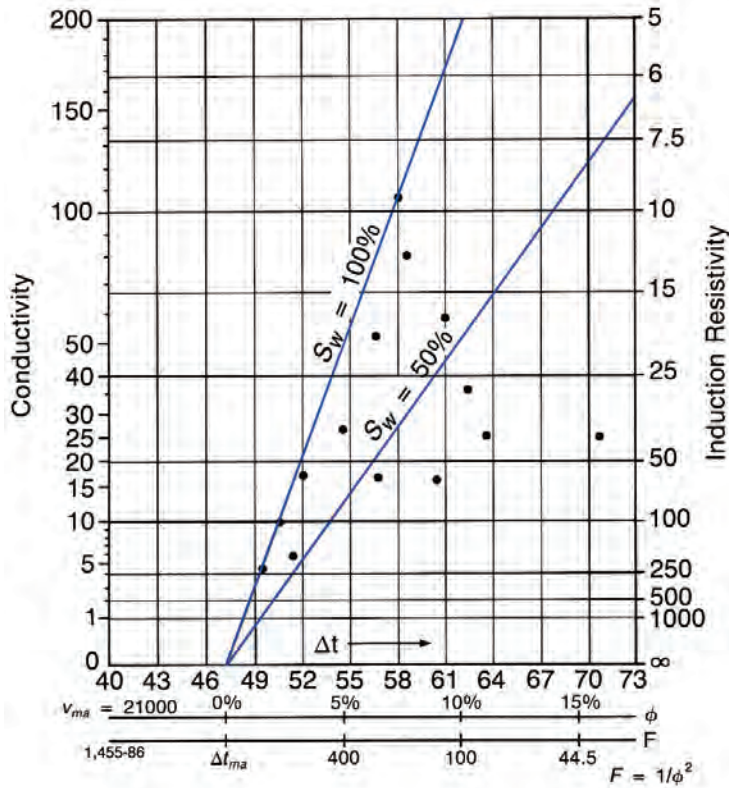


Fig. 3B.46—Acoustic-induction crossplot.

be calculated as for the sonic-resistivity crossplot, and lines of constant water saturation can be constructed in a similar manner.

These resistivity-vs.-porosity crossplots require that formation water resistivity be constant over the interval plotted, that lithology be constant, that invasion not be deep, and that the measured-porosity log parameter (i.e., t , ρ_B , or ϕ_N) can be linearly related to porosity. This last condition implies that the time-average transform for the conversion of t into porosity is appropriate.

The neutron-resistivity crossplot is not as satisfactory in gas-bearing formations as are the sonic- or density-resistivity crossplots. The apparent porosity measured by the neutron log in gas zones is often much too low. This results in overstated S_w values in gas zones. Indeed, in a gas zone, the neutron resistivity may indicate a porous gas-bearing zone to be near zero porosity and 100% water bearing. In contrast, the sonic- or density-resistivity tends to be slightly optimistic in gas zones (i.e., porosities may be slightly high and water saturations slightly low).

Microresistivity-vs.-Porosity Crossplots. This method is particularly useful for older logs or cases in which the analyst has only a paper copy of the log. A resistivity-porosity plot can also be made using the values from a shallow-investigation resistivity log such as the micro-laterolog, MSFL, or MCFL log. If the microresistivity log reads approximately R_{xo} , then a line through points of mud-filtrate-saturated formations ($S_{xo} = 1$) should have a slope related to R_{mf} . R_{mf} is an important parameter, and this check of its value by means of a sonic-microresistivity or density-microresistivity crossplot is often useful.

These plots are also valuable for improved determinations of matrix parameters (either t_{ma} or ρ_{ma}), particularly in cases where the sonic-resistivity or density-resistivity plot does not give

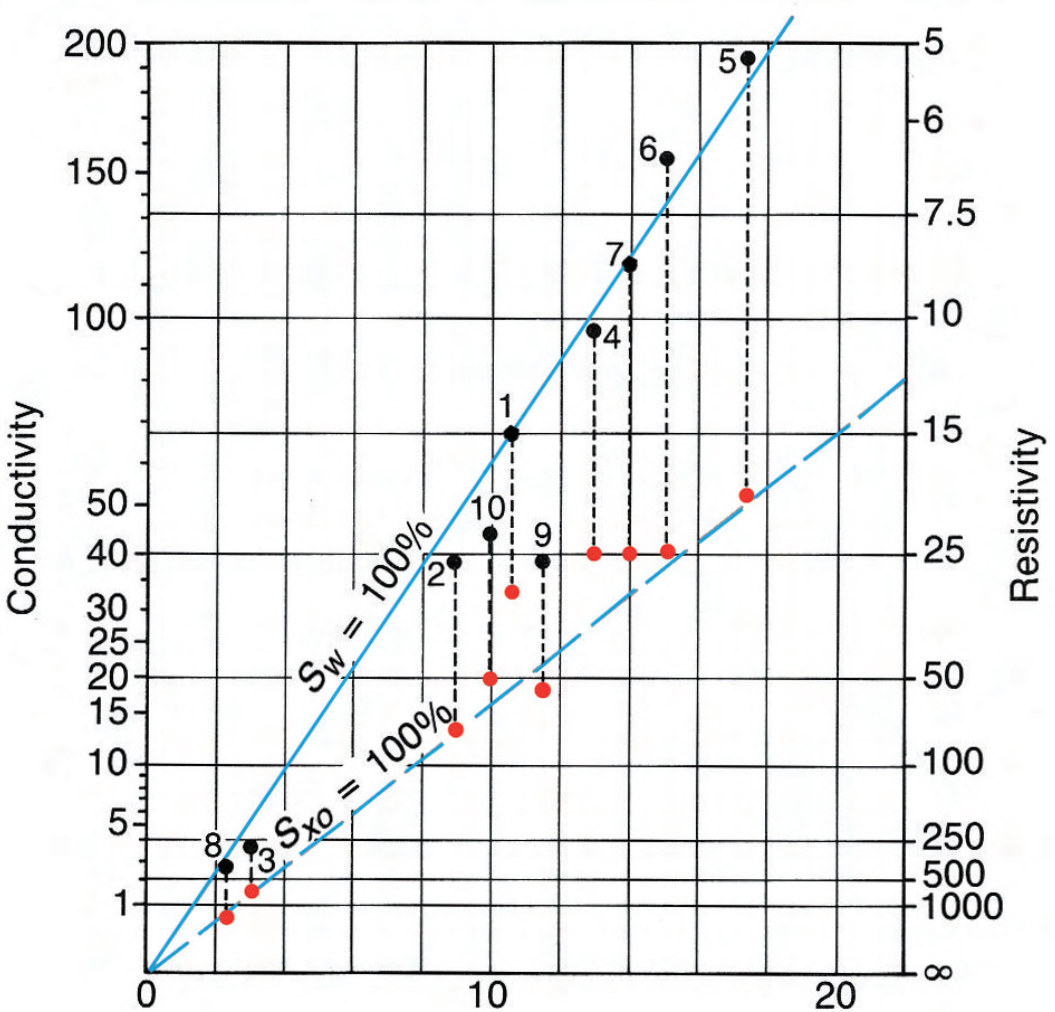


Fig. 3B.47—Resistivity-porosity crossplot showing points from deep-induction and microlaterolog. $S_w = 1$ and $S_{xo} = 1$ lines are shown.

a clear answer because of hydrocarbon saturation. The $F R_{mf}$ line should be easier to determine because S_{xo} is usually fairly high even in hydrocarbon-bearing formations.

Fig. 3B.47 shows a resistivity-porosity plot in which both the deep induction reading and the microlaterolog at the same levels are plotted in a series of water-bearing formations. The porosity values were derived in this case from a neutron-density crossplot. The plots from the two logs define two trends corresponding respectively to $S_w = 1$ (using deep induction) and $S_{xo} = 1$ (using microlaterolog data). The points not in these trends can be divided into two groups:

1. Points whose microlaterolog readings fall on the $S_{xo} = 1$ line but whose deep induction log readings fall below the $S_w = 1$ line (Points 2, 9, and 10) are probably the result of either deep invasion or adjacent-bed effect in which deep resistivity is greater than R_t .

2. Points whose induction log readings fall on the $S_w = 1$ line but whose microlaterolog points fall above the $S_{xo} = 1$ line are possibly a result of shallow invasion in which RMLL is lower than R_{xo} .

Resistivity-porosity plots are thus often more informative if the short-spaced resistivity or medium-induction values are also plotted. Not only does this permit an appreciation of invasion effects, but it may also indicate moved oil.

3B.11.2 R_{wa} Comparison. If water saturation is assumed to be 100%, the Archie water saturation equation (Eq. 3B.10) reduces to

$$R_{wa} = \frac{R_t}{F} \approx \frac{R_{ID}}{F} \dots\dots\dots (3B.16)$$

The term R_{wa} is used in Eq. 3B.16 rather than R_w to indicate that this is an apparent formation water resistivity. It is only equal to R_w in 100% water-bearing formations. In hydrocarbon-bearing formations, R_{wa} computed from Eq. 3B.12 will be greater than R_w . Indeed, by combining Eqs. 3B.16 and 3B.10, the relationship between S_w , R_{wa} , and, R_w can be shown to be

$$S_w = \sqrt{R_w / R_{wa}} \dots\dots\dots (3B.17)$$

The R_{wa} technique can, therefore, be useful for identifying potential hydrocarbon-bearing zones and for obtaining R_w values.

In practice, R_{wa} is obtained by simply dividing the deep induction resistivity (or deep laterolog resistivity) by the formation factor obtained from a porosity log or a combination of porosity logs. Today, a continuous R_{wa} computation is made over a long interval of the borehole in real time. If one has only paper logs, many individual manual computations are made so as to approximate a continuous computation.

Resistivity-Ratio Methods. In resistivity-ratio methods, it is assumed that a formation is divided into two distinct regions—a flushed zone and a noninvaded zone. Both zones have the same F , but each contains water of a distinct resistivity (R_{mf} in the invaded zone and R_w in the noninvaded zone). The resistivities of the two zones must be measurable or derivable from logs, and methods for determining the resistivity of the water in each zone must be available.

Because of the necessary assumptions, the resistivity-ratio methods have limitations, but when no porosity or formation factor data are available, they are sometimes the only choice. The principal limitation arises from the inability of any resistivity device to measure either R_x or R , totally independent of the other. Simply put, invasion must be deep enough to allow a shallow investigating resistivity device to measure R_{xo} but not so deep that a deep-resistivity device cannot measure R_t .

Another difficulty appears when hydrocarbons are present. In this case, some knowledge or assumption of the value of the flushed or invaded zone saturation is necessary.

Flushed-Zone Method. If $n = 2$ is assumed and Eq. 3B.10 is divided by Eq. 3B.12,

$$\left(\frac{S_w}{S_{xo}} \right)^2 = \frac{R_{xo} / R_t}{R_{mf} / R_w} \dots\dots\dots (3B.18)$$

This equation gives the ratio of S_w to S_{xo} , and no knowledge of formation factor or porosity is needed. R_{xo} may be found from a microresistivity log, R_t from an induction or laterolog, and R_{mf}/R_w from measured values or from the SP curve.

The ratio is valuable in itself as an index of oil movability. If $S_w / S_{xo} = 1$, then no hydrocarbons have been moved by invasion, whether or not the formation contains hydrocarbons. If $S_w /$

S_{xo} is approximately 0.7 or less, movable hydrocarbons are indicated. The value of S_w / S_{xo} , along with ϕ and S_{wo} , is useful in evaluating reservoirs.

To determine S_w from Eq. 3B.18, S_{xo} must be known. For moderate invasion and average residual oil saturation, an empirical relation between S_w and S_{xo} has been found useful: $S_{xo} = S_w^{1/5}$. Inserting this into Eq. 3B.18 gives:

$$S_w = \left(\frac{R_{xo} / R_t}{R_{mf} / R_w} \right)^{0.625} \dots \dots \dots (3B.19)$$

Service companies provide charts for graphical solution of this equation, or it can be easily programmed into a spreadsheet.

Invaded-Zone Method. The invaded-zone method is useful for water saturation determination when only an ES, IES, or other early-resistivity log is available and no porosity-log or formation-factor data exist. (This section also uses some early nomenclature.) For application of the method, R_i / R_m must be at least 10.

Archie’s equation for the invaded zone is

$$S_i^2 = \frac{F R_z}{R_t}, \dots \dots \dots (3B.20)$$

where R_z is the resistivity of the water in the invaded zone. Because of incomplete flushing, R_z is a mixture of mud filtrate, R_{mf} , and formation water, R_w .

Studies of many logs suggest that S_i and S_w are related by

$$S_i = \sqrt{S_w} \dots \dots \dots (3B.21)$$

Dividing the noninvaded-zone water saturation equation (Eq. 3B.10) by Eq. 3B.20 and using the relationship presented in Eq. 3B.21 yields an expression for S_w :

$$S_w = \frac{R_i / R_t}{R_z / R_w} \dots \dots \dots (3B.22)$$

To use Eq. 3B.22, R_t is taken from a deep resistivity device such as a deep induction or deep laterolog (corrected for borehole effect and bed thickness). R_i is taken from a shallow resistivity device such as a Laterolog 8, 16-in. normal, or SFL (corrected for borehole effect and bed thickness).

R_z is given by the relationship

$$\frac{1}{R_z} = \frac{z}{R_w} + \frac{(1 - z)}{R_{mf}}, \dots \dots \dots (3B.23)$$

where z is the fraction of the invaded zone pore water, which is formation water, and $1 - z$ is the fraction that is mud filtrate. Experience has indicated that z varies from 0.075 in cases of normal invasion to 0.035 in cases of deep invasion or vuggy formations.

Fig. 3B.48 solves Eq. 3B.22. It is entered with R_{mf} / R_w on the appropriate z scale and R_i / R_t (oblique lines) to determine S_w . When R_i / R_t is close to unity, some caution is required. The formation may be extremely invaded or there may be little invasion, or it may be dense and

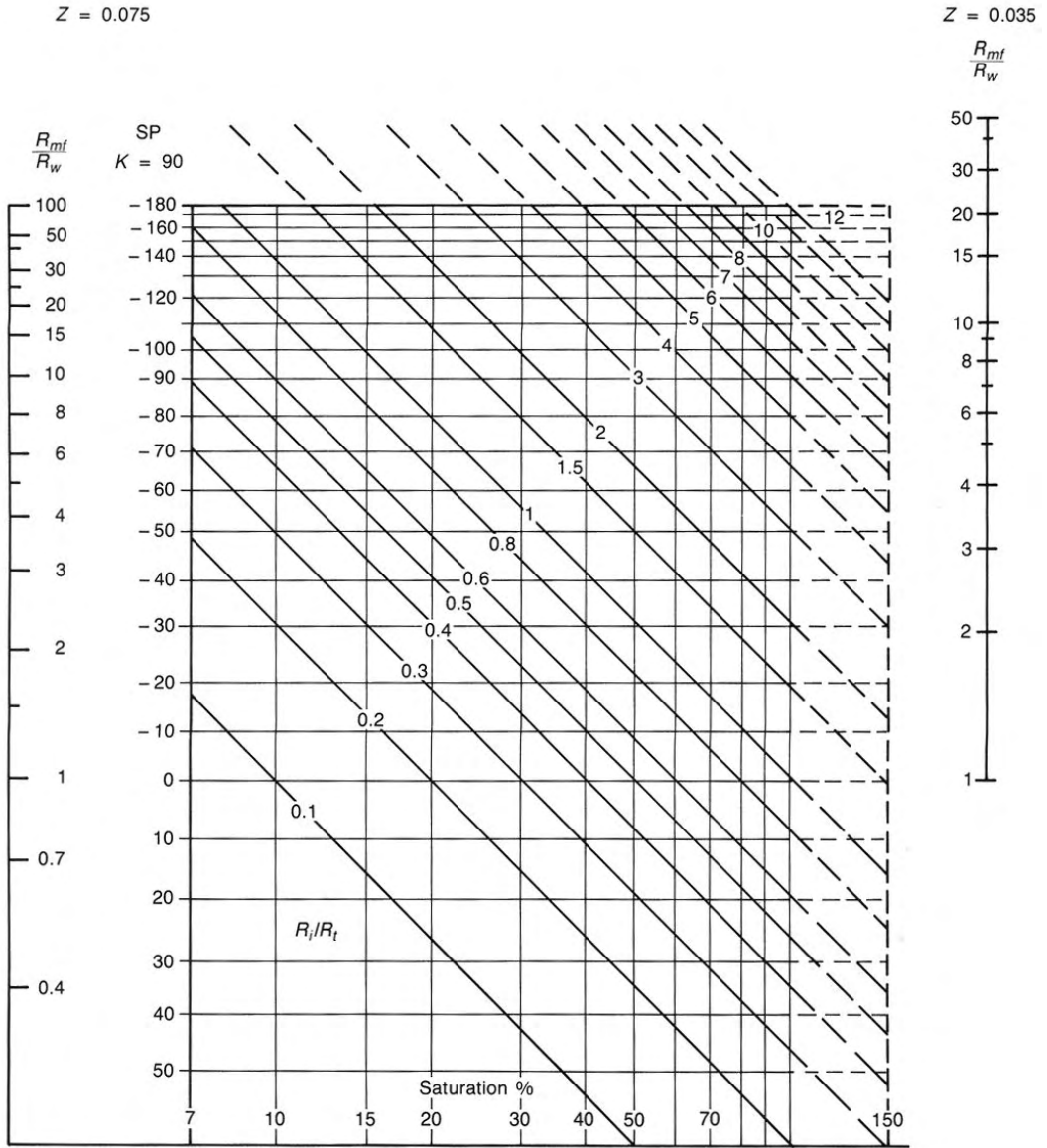


Fig. 3B.48—Empirical resistivity-ratio method.

impermeable. On the other hand, many good hydrocarbon-bearing reservoirs will have $R_i/R_t \approx 1$.

3B.11.3 R_{xo}/R_t Quicklook. The R_{xo}/R_t quicklook method can be used to identify hydrocarbon-bearing formations and to indicate hydrocarbon movability (producibility). When S_w/S_{xo} is 1 in a permeable zone, the zone will produce water or be nonproductive regardless of water saturation. A value S_w/S_{xo} significantly less than 1 indicates that the zone is permeable and contains some hydrocarbons, and that the hydrocarbons have been flushed (moved) by invasion. Thus, the zone contains producible hydrocarbon.

Eq. 3B.18 can be written as

$$\frac{S_w}{S_{xo}} = \left[\frac{R_{xo}/R_t}{(R_{mf}/R)_{SP}} \right]^{1/2}, \dots\dots\dots (3B.24)$$

which shows that an indication of S_w/S_{xo} can be obtained by comparing R_{xo}/R_t with R_{mf}/R_w , where the subscript SP emphasizes that R_{mf}/R_w is derivable from the SP. Equivalently, the comparison can be between $\log R_{xo}/R_t$ and the SP curve for an indication of $\log S_w/S_{xo}$.

The value of $\log R_{xo}/R_t$ is computed from solving the three or more resistivity logs for invasion parameters. It is used as an overlay comparison curve with the SP. Separations between the $\log R_{xo}/R_t$ curve, properly scaled to match the SP, and the SP curve provide a quick-look location of producible hydrocarbons.

Originally, $\log R_{xo}/R_t$ was computed from R_{LL8}/R_{ID} or R_{SFL}/R_{ID} . Use was made of the observation that over a wide range of invasion diameters (from approximately 20 to 100 in.), R_{xo}/R_t depends primarily on the value of R_{LL8}/R_{ID} or R_{SFL}/R_{ID} . The relationship used for the LL8 device was

$$R_{xo}/R_t = 1.85(R_{LL8}/R_{ID}) - 0.85. \dots\dots\dots (3B.25)$$

For the SFL device, it was

$$R_{xo}/R_t = 1.45(R_{SFL}/R_{ID}) - 0.45. \dots\dots\dots (3B.26)$$

Much more sophisticated algorithms are now used to obtain R_{xo}/R_t . These values are output in real time as separate logs.

To interpret the R_{xo}/R_t quick-look curve, the impermeable zones must be eliminated by reference to the SP, GR, or microlog curves or by resistivity ratios. Then, if the SP and R_{xo}/R_t (actually $-\log R_{xo}/R_t$) curves coincide in a permeable zone, the zone will most probably produce water. If, however, the R_{xo}/R_t curve reads appreciably lower (i.e., to the right) than the SP, the zone should produce hydrocarbons. An R_{xo}/R_t value less than the SP amplitude indicates movable hydrocarbons are present.

The R_{xo}/R_t quick-look technique is applicable to fresh mud conditions ($R_{xo} > R_t$) in formations where invasion falls within the limits demanded by the R_{xo}/R_t computation. For the simpler computation technique using Eq. 3B.25 and -25 , that is for d_i 30 to 70 in.; for the more sophisticated techniques, that is, between 20 and 120 in. Even in the more restrictive case, however, any errors are optimistic. In other words, water zones may appear to be hydrocarbon-productive. This constitutes a safeguard against overlooking pay zones, and it is considered a desirable feature in any quick-look approach.

The R_{xo}/R_t technique efficiently handles variations in formation water resistivity, R_w , and in shaliness. Any change in R_w is reflected similarly into both the computed R_{xo}/R_t and the SP amplitude. Thus, comparing the two curves still permits formation-fluid identification. Shaliness also affects the two curves in a similar manner. All other things remaining constant, shaliness reduces the R_{xo}/R_t value and the SP amplitude. Finally, the R_{xo}/R_t quick-look technique does not require porosity data, nor use of any $F-\phi$ relationships.

Fig. 3B.49 is an example of a shaly gas sand at 3,760 through 3,788 ft and several water-productive sands with varying amounts of shaliness. The productive-gas sand is identified by the separation between the R_{xo}/R_t and SP curves. Water-productive zones are shown by lack of separation. In shaly water zones, the variation in the SP curve is essentially the same as the variation in the R_{xo}/R_t ratio—a result of the same shale. Therefore, the comparison is not significantly disturbed by shaliness. Neither is it disturbed by variations in R_w .

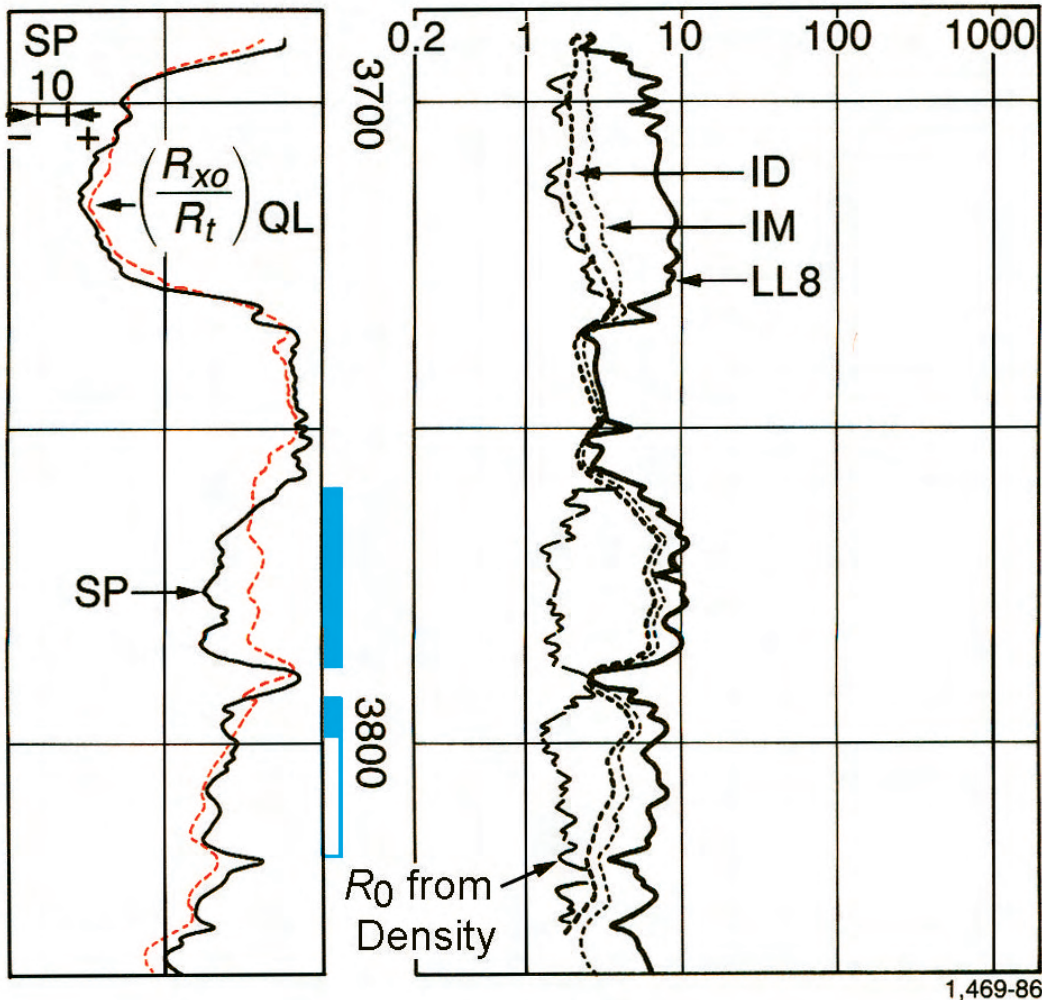


Fig. 3B.49—Examples of R_{xo}/R_t quick-look curve used for comparison with SP to identify zones with movable hydrocarbons.

Estimates of water saturation and saturation ratio in clean formations can be made by comparing the R_{xo}/R_t and SP curves. Eq. 3B.24 permits S_w/S_{xo} to be estimated, and then Eq. 3B.19 allows S_w to be estimated.

3B.12 Shaly Formations

Shaly-sand analysis has been the subject of much continuing work over the past 20 years, and a detailed coverage of that work is far beyond the scope of this *Handbook*. We will present the problem to be solved and a couple of methods that can be applied to older logs where detailed information is not available.

Shales are one of the more important common constituents of rocks in log analysis. Aside from their effects on porosity and permeability, this importance stems from their electrical properties, which have a great influence on the determination of fluid saturations.

Shales are loose, plastic, fine-grained mixtures of clay-sized particles or colloidal-sized particles and often contain a high proportion of clay minerals. Most clay minerals are structured in sheets of alumina-octahedron and silica-tetrahedron lattices. There is usually an excess of nega-

tive electrical charges within the clay sheets. The substitution of Al^{+++} by ions of lower valence is the most common cause of this excess; the structure of the crystal remains the same. This local electrical imbalance must be compensated to maintain the electrical neutrality of the clay particle. The compensating agents are positive ions—cations or counterions—which cling to the surface of the clay sheets in a hypothetical dry state. The positive surface charge is usually measured in terms of milli-ions equivalents per 100 grams of dry clay minerals and is called the cation exchange capacity (CEC). When the clay particles are immersed in water, the Coulomb forces holding the positive surface ions are reduced by the dielectric properties of water. The counterions leave the clay surface and move relatively freely in a layer of water close to the surface (the electrical balance must be maintained so that the counterions remain close to the clay water interface) and contribute to the conductivity of the rock.

The Archie water saturation equation, which relates rock resistivity to water saturation, assumes that the formation water is the only electrically conductive material in the formation. The presence of another conductive material (i.e., shale) requires either that the Archie equation be modified to accommodate the existence of another conductive material, or that a new model be developed to relate rock resistivity to water saturation in shaly formations. The presence of clay also complicates the definition or concept of rock porosity. The layer of closely bound surface water on the clay particle can represent a very significant amount of porosity. However, this porosity is not available as a potential reservoir for hydrocarbons. Thus, a shale or shaly formation may exhibit a high total porosity, yet a low effective porosity as a potential hydrocarbon reservoir.

The way shaliness affects a log reading depends on the amount of shale and its physical properties. It may also depend on the way the shale is distributed in the formation. Shaly material can be distributed in the formation in three ways:

- Shale can exist in the form of laminae between which are layers of sand. The laminar shale does not affect the porosity or permeability of the sand streaks themselves. However, when the amount of laminar shale is increased and the amount of porous medium is correspondingly decreased, overall average effective porosity is reduced in proportion.
- Shale can exist as grains or nodules in the formation matrix. This matrix shale is termed structural shale; it is usually considered to have properties similar to those of laminar shale and nearby massive shales.
- The shaly material can be dispersed throughout the sand, partially filling the intergranular interstices. The dispersed shale may be in accumulations adhering to or coating the sand grains, or it may partially fill the smaller pore channels. Dispersed shale in the pores markedly reduces the permeability of the formation.

All these forms of shale can, of course, occur simultaneously in the same formation.

Over the years, a large number of models relating resistivity and fluid saturations have been proposed. Many have been developed assuming the shale exists in one of the three specific geometric forms. All these models are composed of a clean sand term, described by the Archie water saturation equation, plus a shale term. The shale term may be fairly simple or quite complex; the shale term may be relatively independent of, or it may interact with, the clean sand term. All the models reduce to the Archie water saturation equation when the fraction of shale is zero; for relatively small amounts of shaliness, most models and methods yield quite similar results.

Only a very few of these models will be reviewed here to provide some flavor and understanding for the evolution of shaly-sand interpretation logic.

3B.12.1 Laminated Sand/Shale—Simplified Model. In this laminar shale model, R_t , the resistivity in the direction of the bedding planes, is related to R_{sh} (the resistivity of the shale laminae) and to R_{sd} (the resistivity of the clean sand laminae) by a parallel resistivity relationship,

$$\frac{1}{R_t} = \frac{1 - V_{lam}}{R_{sd}} + \frac{V_{lam}}{R_{sh}}, \dots\dots\dots (3B.27)$$

where V_{lam} is the bulk-volume fraction of the shale, distributed in laminae, each of more-or-less uniform thickness.

For clean-sand laminae, $R_{sd} = F_{sd}R_w/S_w^2$, where F_{sd} is the formation resistivity factor of the clean sand. Because $F_{sd} = a/\phi_{sd}^2$ (where ϕ_{sd} is the sand-streak porosity) and $f = (1 - V_{lam})\phi_{sd}$ (where ϕ is the bulk-formation porosity), then

$$\frac{1}{R_t} = \frac{\phi^2 S_w^2}{(1 - V_{lam})aR_w} + \frac{V_{lam}}{R_{sh}} \dots\dots\dots (3B.28)$$

To evaluate S_w by the laminated model, R_t , R_w , ϕ , V_{lam} , and R_{sh} must be determined.

For the determination of R_t , the problem is the same as for clean formations. If R_w is not known, its determination usually involves looking at a nearby clean sand and solving for R_w using the SP measurement. If the formation is water-bearing, the resistivity and porosity measurements can be used.

For the determination of ϕ and V_{lam} , a combination of porosity logs can be used. For example, as illustrated in **Fig. 3B.50**, a crossplot of ϕ_N and ϕ_B from a density log is effective. The triangle of the figure is defined by the matrix point, water point, and shale point. In this example, the matrix point is at $\phi_N = 0$ (the neutron log was scaled in apparent sandstone porosity) and $\phi_{ma} = 2.65 \text{ g/cm}^3$ (quartz matrix). The shale point is at $\phi_N = 50 \text{ p.u.}$ and $\phi_{sh} = 2.45 \text{ g/cm}^3$. These values were taken in a nearby thick shale bed; it is assumed that shale laminae in the shaly sand under investigation are similar to the nearby massive shale beds. The water point is, of course, located at $\phi_N = 100 \text{ p.u.}$ and $\phi_B = 1 \text{ g/cm}^3$. The matrix-water line and shale-water line are linearly divided into porosity; the matrix-shale line and water-shale line are linearly divided into shale percentages.

Point A, plotted as an example, corresponds to log readings of $\phi_B = 2.2 \text{ g/cm}^3$ and $\phi_N = 33 \text{ p.u.}$ Interpretation by the lines on the plot yields 23% and V_{sh} (or V_{lam}) = 16 %.

Direct use of this crossplot assumes 100% water saturation in the zone investigated by the tools. Because oil has a density and hydrogen content normally not greatly different from water, this crossplot technique can be used with acceptable accuracy in oil-bearing formations. The presence of gas or light hydrocarbon, however, decreases ϕ_N and decreases ϕ_B . This would cause the point to shift in a northwesterly direction. When gas or light hydrocarbons are present, an additional shaliness indicator, such as GR or SP data, is needed to evaluate the amount of the shift.

Using the laminated model, an equation for R_{xo} analogous to **Eq. 3B.28** could be written. S_{xo} would replace S_w , and R_{mf} would replace R_w . The other terms (ϕ , V_{lam} , and R_{sh}) remain the same in the two equations. Assuming $S_{xo} = S_w^{1/5}$ (as in the flushed-zone ratio method) and the ratio of the PSP (SP deflection in the shaly sand) to the SSP (SP deflection in a nearby clean sand of similar formation water) is a measure of shaliness, V_{lam} , water saturation could be calculated from R_{xo}/R_t and PSP in the shaly sand and SSP (or R_{mf}/R_w) in a nearby clean sand.

3B.12.2 Dispersed Clay. In this model, the formation conducts electrical current through a network composed of the pore water and dispersed clay. As suggested by de Witte,⁶⁷ it seems acceptable to consider that the water and the dispersed shale conduct an electrical current like a mixture of electrolytes. Development of this assumption yields

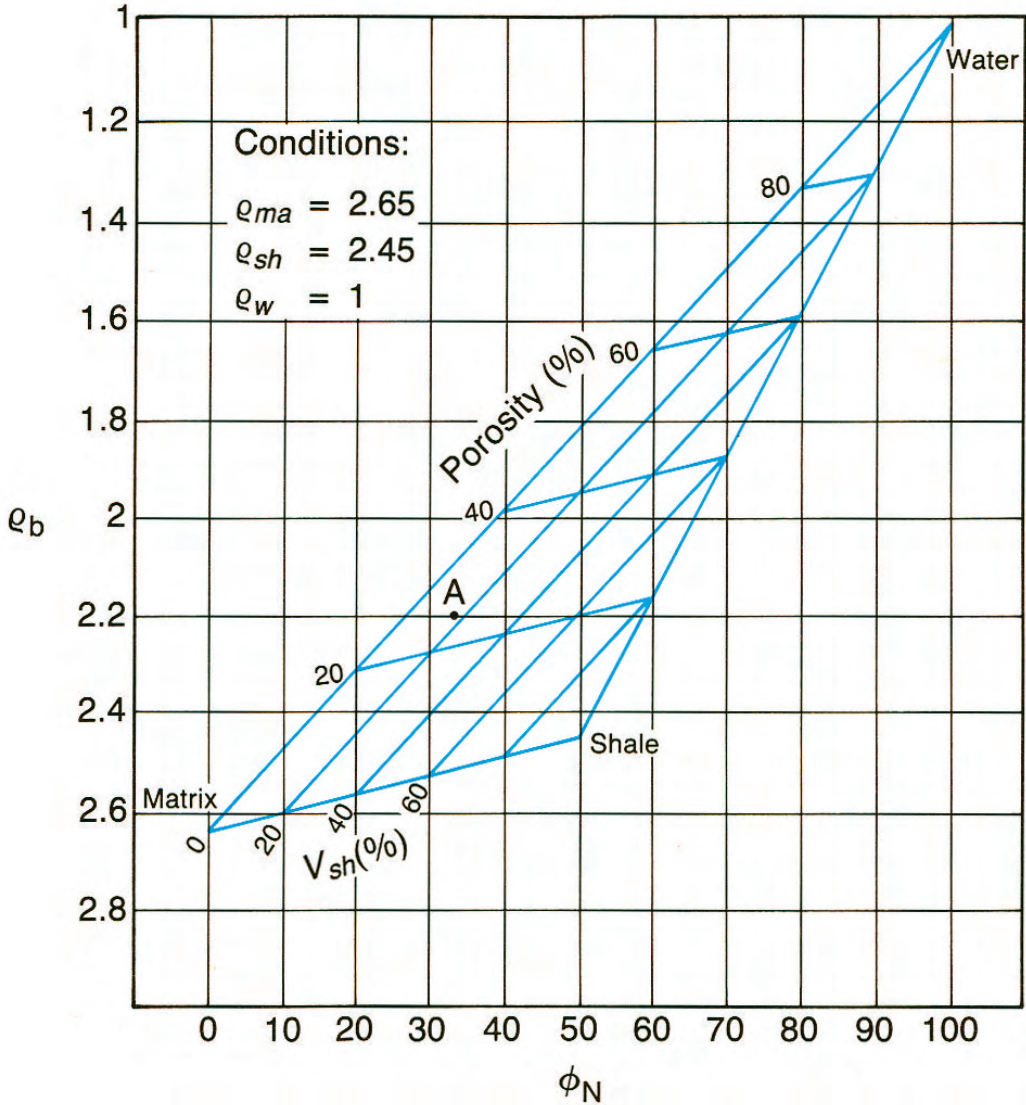


Fig. 3B.50—Neutron-density crossplot showing matrix, water, and shale points, scaled for determination of V_{shale} and porosity.

$$\frac{1}{R_t} = \frac{\phi_{im} S_{im}}{a} \left(\frac{q}{R_{shd}} + \frac{S_{im}}{R_w} \right), \dots\dots\dots (3B.29)$$

where ϕ_{im} = intermatrix porosity, which includes all the space occupied by fluids and dispersed shale; S_{im} = the fraction of the intermatrix porosity occupied by the formation-water, dispersed-shale mixture; q = the fraction of the intermatrix porosity occupied by the dispersed shale; and R_{shd} = the resistivity of the dispersed shale. Also, it can be shown that $S_w = (S_{im} - q)/(1 - q)$, where S_w is the water saturation in the fraction of true effective formation porosity.

Combining these relations and solving for S_w yields

$$S_w = \frac{\sqrt{\frac{aR_w}{\phi_{im}^2 R_t} + \left[\frac{q(R_{shd} - R_w)}{2R_{shd}} \right]^2} - \frac{q(R_{shd} + R_w)}{2R_{shd}}}{1 - q} \dots\dots\dots (3B.30)$$

Usually, ϕ_{im} can be obtained directly from a sonic log because dispersed clay in the rock pores is seen as water by the sonic measurement. The value of q can be obtained from a comparison of a sonic and density log. Indeed, if $\rho_{shd} \cong \rho_{ma}$, then $qsv \phi (\phi_{SV} - \phi_D)/\phi_{SV}$, where ϕ_{SV} and ϕ_D are the sonic and density derived porosities, respectively. In this case, ϕ_D approximates ϕ , the effective porosity available for fluid saturation.

The value of R_{sh} is more difficult to evaluate. It is usually taken as equal to R_{sh} in nearby shale beds. Fortunately, its value is not too critical if it is at least several times greater than R_w . In fact, when R_w is small compared to R_{sh} and the sand is not too shaly, Eq. 3B.30 can be simplified to a form independent of R_{sh} :

$$S_w = \frac{\sqrt{\frac{aR_w}{\phi_{im}^2} + \frac{q^2}{4}} - \frac{q}{2}}{1 - q} \dots\dots\dots (3B.31)$$

3B.12.3 Total Shale Relationship. Based upon the previously described ideas, laboratory investigations, and field experience, it has been found that a simple relationship of the following form works well for many shaly formations independent of the distribution of the shale and over the range of S_w values encountered in practice:

$$\frac{1}{R_t} = \frac{\phi^2 S_w^2}{(1 - V_{sh})aR_w} + \frac{V_{sh}S_w}{R_{sh}} \dots\dots\dots (3B.32)$$

In using this equation, R_{sh} is taken equal to the resistivity of the adjacent shale beds, and V_{sh} is the shale fraction as determined from a total shale indicator.

Before the Waxman-Smits formulation, equations of the form of Eq. 3B.29 and 3B.32 gained wide acceptance in the evaluation of shaly sands. These equations have a general form of

$$\frac{1}{R_t} = \alpha S_w^2 + \gamma S_w, \dots\dots\dots (3B.33)$$

where α denotes a predominant sand term that is dependent on the amount of sand, its porosity, and the resistivity of the saturating water. The sand term always reduces to Archie’s water saturation equation when the shale fraction is zero. γ denotes a predominant shale term that depends on the amount and resistivity of the shale.

3B.13 Dual Water Models

In 1968, Waxman and Smits proposed, based on extensive laboratory work and theoretical study, a saturation-resistivity relationship for shaly formations that related the resistivity contribution of the shale (to the overall resistivity of the formation) to the CEC of the shale.⁶⁹ The Waxman-Smits relationship is

TABLE 3B.1—DUAL-WATER MODEL					
Solids			Fluids		
Matrix	Silt	Dry clay	Bound water	Free water	Hydrocarbons
Matrix		Shale		Effective porosity	
				Total porosity	

$$\frac{1}{R_t} = \frac{S_w^2}{F^* R_w} + \frac{B Q_v S_w}{F^*}, \dots\dots\dots (3B.34)$$

where F^* is the formation factor of the interconnected porosity, S_w also relates to the interconnected pores, B is the equivalent conductance of the sodium clay-exchange cations as a function of the formation water conductivity, and Q_v is the CEC of the rock per unit pore volume.

Unfortunately, a continuous in-situ measurement of rock CEC was not available when this study was presented. As a result, the dual water model was developed as a practical solution.⁷⁰ The dual water method is based on three premises:

- The conductivity of clay is because of its CEC.
- The CEC of pure clays is proportional to the specific surface area of the clay.
- In saline solutions, the anions are excluded from a layer of water around the surface of the grain. The thickness of this layer expands as the salinity of the solution (below a certain limit) decreases, and the thickness is a function of salinity and temperature.

Therefore, because CEC is proportional to specific area (area per unit weight) and to the volume of water in the counter-ion exclusion layer per unit weight of clay. Consequently, the conductivity of clay is proportional to the volume of the counter-ion exclusion layer, this layer being “bound” to the surface of the clay grains. For clays, this very thin sheet of bound water is important because of the large surface areas of clays relative to sand grains (several magnitudes greater). Therefore, in the dual water model, a clay is modeled as consisting of two components: bound water and clay minerals.

The clay minerals are modeled as being electrically inert; the clay electrical conductivity is modeled as being derived from the conductivity of the bound water, C_{wb} . C_{wb} is assumed to be independent of clay type (from the second postulate described previously). The amount of bound water varies according to clay type, being higher for the finer clays (with higher surface areas), such as montmorillonite, and lower for coarser clays, such as kaolinite. Salinity also has an effect; in low-salinity waters (roughly < 20,000 ppm NaCl), the diffuse layer expands.

The bound water is immovable under normal conditions; therefore, the volume it occupies cannot be displaced by hydrocarbons. Because the clay minerals (dry colloids) are considered electrically inert, they may be treated just as other minerals. Schematically, shaly formations are modeled with the dual water model, as illustrated in **Table 3B.1**.

For most rocks (except for conductive minerals such as pyrite, which cannot be treated in this way) only the porous part needs to be considered when discussing electrical properties, and it is treated according to the Archie water-saturation equation. The equation becomes

$$\sigma_t = \frac{\phi_t^m S_{wt}^n}{a} \sigma_{we}, \dots\dots\dots (3B.35)$$

where a , m , and n have the usual Archie connotations. σ_t is the conductivity of the noninvaded, virgin formation ($1/R_t$), and σ_{we} is the equivalent conductivity of the waters in the pore space.

Note that ϕ_t and S_{wt} refer to total pore volume; this includes the pore volumes saturated with the bound water and the formation connate water (sometimes called the “free” water). The equivalent water conductivity, σ_{we} , is

$$\sigma_{we} = \frac{V_w\sigma_w + V_{wb}\sigma_{wb}}{V_w + V_{wb}}, \dots\dots\dots (3B.36)$$

where V_w and V_{wb} are the bulk volumes of formation water and bound water, respectively, and σ_w and σ_{wb} are their conductivities.

In terms of saturation, Eq. 3B.36 becomes

$$\sigma_{we} = \frac{\phi_t\sigma_w(S_{wt} - S_{wb}) + \phi_t\sigma_{wb}S_{wb}}{\phi_t(S_{wt} - S_{wb}) + \phi_tS_{wb}}, \dots\dots\dots (3B.37)$$

or

$$\sigma_{we} = \sigma_w \frac{S_{wt} - S_{wb}}{S_{wt}} + \sigma_{wb} \frac{S_{wb}}{S_{wt}}, \dots\dots\dots (3B.38)$$

or

$$\sigma_{we} = \sigma_w + (\sigma_{wb} - \sigma_w) \frac{S_{wb}}{S_{wt}}, \dots\dots\dots (3B.39)$$

where S_{wb} is the bound water saturation (i.e., the fraction of the total pore volume occupied by the bound water).

Eq. 3B.39 describes the equivalent-water conductivity as a function of the formation water conductivity plus the bound-water conductivity. The saturation equation (Eq. 3B.35) becomes

$$\sigma_t = \frac{\phi_t^m S_{wt}^n}{a} \left[\sigma_w + \frac{S_{wb}}{S_{wt}} (\sigma_{wb} - \sigma_w) \right]. \dots\dots\dots (3B.40)$$

The porosity and water saturation of the sand (clean formation) phase (that is, the nonclay phase) of the formation is obtained by subtracting the bulk-volume fraction of bound water ($\phi_t S_{wb}$). Therefore, the effective porosity is

$$\phi = \sigma_t (1 - S_{wb}), \dots\dots\dots (3B.41)$$

and the water saturation is

$$S_w = \frac{S_{wt} - S_{wb}}{1 - S_{wb}}. \dots\dots\dots (3B.42)$$

To evaluate a shaly formation using the dual water model, four parameters must be determined. They are σ_w (or R_w), σ_{wb} (or R_{wb}), ϕ_t , and S_{wb} . A neutron-density crossplot provides a good value of ϕ_t . S_{wb} is obtainable from a variety of shale-sensitive measurements (SP, GR,

ϕ_N , R_t , $\phi_N - \rho_B$, $t - \rho_B$, etc.). R_{wb} and R_w are usually determined by the log analyst and entered as input parameters.

3B.14 Summary

This chapter presents the fundamentals of the various logging tools used to measure formation resistivities, conductivities, and naturally occurring currents that normally exists in wellbores containing conductive fluids. The borehole and formation environments are described, along with their effect on log response and what can be done to determine true formation resistivity. Simplified manual methods for interpreting log responses are presented, along with a description of the expanded amount of information that can now be generated with sophisticated computer programs. It has been the objective to provide sufficient insight to use existing log data and to indicate what tools are available to capture data in new wells. Other sections in this petrophysics chapter contain information on other types of logs that are needed in conjunction with resistivity logs to obtain an understanding of reservoir rock and fluid properties.

Service companies, oil companies, and many third parties have developed software to calculate S_w in most situations. Planning logging jobs will always be a balance of the types of tools available, the data needed, and the costs of acquisition. In the long run, it is best to include all tools that provide sufficient data for the formation at hand.

Nomenclature

a_{mf}	=	mud filtrate chemical activity
a_w	=	formation water chemical activity
A	=	area, m ²
d_i	=	diameter of invasion (in., m)
E_k	=	electrokinetic potential
E_{kmc}	=	electrokinetic potential of the mudcake
E_{ksh}	=	electrokinetic potential of shale
F	=	formation factor relating resistivity to porosity
g	=	induction-response function
G	=	induction integrated radial-response function
h_{mc}	=	mudcake thickness
I	=	electrical current, Amperes
L	=	length, m
r	=	resistance, ohm
R	=	resistivity (ohm·m)
R_{ann}	=	resistivity of the annulus
R_h	=	resistivity in the horizontal direction (ohm·m)
R_m	=	resistivity of the mud column (ohm·m)
R_{mc}	=	resistivity of the mudcake
R_{mf}	=	resistivity of the mud filtrate
R_{xo}	=	resistivity of the invaded zone
R_t	=	resistivity of the uninvaded formation
R_v	=	resistivity in the vertical direction (ohm·m)
R_w	=	resistivity of the formation connate water (ohm·m)
R_{wa}	=	apparent water resistivity from deep resistivity and porosity
S_{xo}	=	water saturation of the invaded zone
S_w	=	water saturation in the uninvaded zone
t	=	acoustic travel time (μs/ft)
t_{ma}	=	acoustic travel time of the rock matrix(μs/ft)

- V = electrical voltage, volts
 V_{sd} = fraction of the total formation volume that is sand
 V_{sh} = fraction of the total formation volume that is shale
 ρ = density
 ρ_{ma} = density of the rock matrix
 σ = conductivity, mS/m
 σ_m = conductivity of the mud column, mS/m
 ϕ = porosity

References

- Schlumberger, C., Schlumberger, M., and Leonardon, E.G.: "A New Contribution to Subsurface Studies by Means of Electrical Measurements in Drill Holes," *Trans.*, AIME (1933) **103**.
- Schlumberger, C., Schlumberger, M., and Leonardon, E.G.: "Electrical Coring; A Method of Determining Bottom-Hole Data by Electrical Measurements," *Trans.*, AIME (1932).
- Schlumberger, C., Schlumberger, M., and Leonardon, E.G.: "Some Observations Concerning Electrical Measurements in Anisotropic Media and Their Interpretation," *Trans.*, AIME (1934).
- Lynch, E.J.: "Formation Evaluation," *Harper's Geoscience Series*, Harper and Row, New York City (1962).
- Anderson, B.I.: *Modeling and Inversion Methods for the Interpretation of Resistivity Logging Tool Response*, Delft U. Press, Delft, The Netherlands (2001).
- Doll, H.G.: "The Laterolog: A New Resistivity Logging Method With Electrodes Using an Automatic Focusing System," *Trans.*, AIME (1951) **192**, 305.
- The Dual Laterolog*, Schlumberger, Houston (1970).
- Woodhouse, R.: "The Laterolog Groningen Phantom Can Cost You Money," paper R presented at the 1978 SPWLA Annual Logging Symposium.
- Davies, D.H. *et al.*: "Azimuthal Resistivity Imaging: A New Generation Laterolog," paper SPE 24676 presented at the 1992 SPE Annual Technical Conference and Exhibition, Washington, DC, 4–7 October.
- Smits, J.W. *et al.*: "High Resolution From a new Laterolog With Azimuthal Imaging," paper SPE 30584 presented at the 1995 SPE Annual Technical Conference and Exhibition, Dallas, 22–25 October.
- Smits, J.W. *et al.*: "Improved Resistivity Interpretation Utilizing a New Array Laterolog Tool and Associated Inversion Processing," paper SPE 49328 prepared for presentation at the 1998 SPE Annual Technical Conference and Exhibition, New Orleans, 27–30 September.
- Iskovick, G.B. *et al.*: "High Definition Lateral Log," paper PP presented at the 1998 SPWLA Annual Logging Symposium, Keystone, Colorado, 6–9 June.
- Alpin, L.: "The Method of Electric Logging in the Borehole With Casing," U.S. Patent 56,026 (1939).
- Kaufman, A.A.: "Conductivity Determination in a Formation Having a Cased Well," U.S. Patent 4,796,186 (1989).
- Vail, W.B.: "Method and Apparatus for Measurement of Resistivity of Geological Formations From Within Cased Boreholes," U.S. Patent 4,820,989 (1989).
- Béguin, P. *et al.*: "Recent Progress on Formation Resistivity Through Casing," paper CC presented at the 2000 SPWLA Annual Logging Symposium, Dallas, 4–7 June.
- Maurer, H.M. and Hunziker, J.: "Early Results of Through-Casing Field Tests," paper DD presented at the 2000 SPWLA Annual Logging Symposium, Dallas, 4–7 June.
- Rosthal, R.A. *et al.*: "Formation Evaluation and Geological Interpretation From the Resistivity-at-the-Bit Tool," paper SPE 30550 presented at the 1995 SPE Annual Technical Conference and Exhibition, Dallas, 22–25 October.
- Doll, H.G.: "Introduction to Induction Logging and Application to Wells Drilled With Oil Base Mud," *JPT* (June 1949) 148; *Trans.*, AIME, **186**.

20. Moran, J.H. and Kunz, K.S.: "Basic Theory of Induction Logging and Application to Study of Two-Coil Sondes," *Geophysics* (December 1962) **44**, No. 7, 829.
21. Anderson, B. and Barber, T.: *Induction Logging*, Schlumberger, Houston (1995).
22. Tanguy, D.R.: "Induction Well Logging," U.S. No. Patent 3,067,383 (1962).
23. Tanguy, D.R.: "Methods and Apparatus for Investigating Earth Formations Featuring Simultaneous Focused Coil and Electrode System Measurements," U.S. Patent No. 3,329,889 (1967).
24. Attali, G.: "Methods and Apparatus for Investigating Earth Formations Including Measuring the Resistivity of Radially Different Formation Zones," U.S. Patent No. 3,453,530 (1969).
25. Anderson, B.I. and Barber, T.D.: "Deconvolution and Boosting Parameters for Obsolete Schlumberger Induction Tools," *The Log Analyst* (1999) **40**, No. 1, 133.
26. Barber, T.: "Introduction to the Phasor Dual Induction Tool," *JPT* (September 1985) 1699.
27. Kienitz, C. *et al.*: "Accurate Logging in Large Boreholes," paper III presented at the 1986 SPWLA Annual Logging Symposium, Houston, 9–13 June.
28. Hunka, J.F. *et al.*: "A New Resistivity Measurement System for Deep Formation Imaging and High-Resolution Formation Evaluation," paper SPE 20559 presented at the 1990 SPE Annual Technical Conference and Exhibition, New Orleans, 23–26 September.
29. Grove, G.P. and Minerbo, G.N.: "An Adaptive Borehole Correction Scheme For Array Induction Tools," paper P presented at the 1991 SPWLA Annual Logging Symposium, Midland, Texas, 16–19 June.
30. Barber, T.D. *et al.*: "A Multiarray Induction Tool Optimized for Efficient Wellsite Operation," paper SPE 30583 presented at the 1995 SPE Annual Technical Conference and Exhibition, Dallas, 22–25 October.
31. Barber, T.D. and Rosthal, R.A.: "Using a Multiarray Induction Tool To Achieve Logs With Minimum Environmental Effects," paper SPE 22725 presented at the 1991 SPE Annual Technical Conference and Exhibition, Dallas, 6–9 October.
32. Barber, T.D.: "Interpretation of AIT-Family Logs in Invaded Formations at High Relative Dip Angles," paper A presented at the 1998 SPWLA Annual Logging Symposium, Keystone, Colorado, 26–29 May.
33. Barber, T.D. and Minerbo, G.N.: "An Analytic Method of Producing Multiarray Induction Logs That Are Free of Dip Effect," paper SPE 77718 presented at the 2002 SPE Annual Technical Conference and Exhibition, San Antonio, Texas, 29 September–2 October.
34. La Vigne, J., Barber, T., and Bratton, T.: "Strange Invasion Profiles: What Multiarray Induction Logs Can Tell Us About How Oil-based Mud Affects the Invasion Process and Wellbore Stability," paper B presented at the 1997 SPWLA Annual Logging Symposium, Houston, 15–18 June.
35. Beard D.R., Zhou, Q., and Bigelow, E.L.: "Practical Application of a New Multichannel and Fully Digital Spectrum Induction System," paper SPE 36504 presented at the 1996 SPE Annual Technical Conference and Exhibition, Denver, 6–9 October.
36. Beste, T. *et al.*: "A New High Resolution Array Induction Tool," paper C presented at the 2000 SPWLA Annual Logging Symposium, Dallas, 4–7 June.
37. Martin, D.W., Spencer, M.C., and Patel, H.K.: "The Digital Induction—A New Approach To Improving the Response of the Induction Measurement," paper M presented at the 1984 SPWLA Annual Logging Symposium, New Orleans, 10–13 June.
38. Samworth, J.R. *et al.*: "The Array Induction Tool Advances Slim-hole Logging Technology," paper Y presented at the 1994 SPWLA European Formation Evaluation Symposium, Aberdeen, 11–13 October.
39. Tanguy, D.R. and Zoeller, W.A.: "Applications of Measurements While Drilling," paper SPE 10324 presented at the 1981 SPE Annual Technical Conference and Exhibition, San Antonio, Texas, 5–7 October.
40. Jan, Y.M. and Campbell, R.L.: "Borehole Correction of MWD Gamma Ray and Short Normal Resistivity Logs," paper PP presented at the 1984 SPWLA Annual Logging Symposium, New Orleans, 10–13 June.
41. Rodney, P.F. *et al.*: "The Electromagnetic Wave Resistivity MWD Tool," *SPEDE* (October 1986) 337.

42. Coope, D., Shen, L.C., and Huang, F.S.: "The Theory of 2 MHz Resistivity Tool and Its Application to Measurement While Drilling," *The Log Analyst* (May/June 1984) 35.
43. Clark, B. *et al.*: "Electromagnetic Propagation Logging While Drilling: Theory and Experiment," *SPEFE* (September 1990) 263.
44. Clark, B. *et al.*: "A Dual Depth Resistivity Measurement for Formation Evaluation While Drilling," paper A presented at the 1988 SPWLA Annual Logging Symposium, San Antonio, 5–8 June.
45. Habashy, T. and Anderson, B.: "Reconciling Differences in Depth of Investigation between 2-MHz Phase Shift and Attenuation Resistivity Measurements," paper E presented at the 1991 SPWLA Annual Logging Symposium, Midland, Texas, 16–19 June.
46. Bonner, S.D. *et al.*: "New 2-MHz Multiarray Borehole-Compensated Resistivity Tool Developed for MWD in Slimholes," paper SPE 30547 presented at the 1995 SPE Annual Technical Conference and Exhibition, Dallas, 22–25 October.
47. Rodney, P.F. *et al.*: "An MWD Multiple Depth of Investigation Electromagnetic Wave Resistivity Sensor," paper D presented at the 1991 SPWLA Annual Logging Symposium, Midland, Texas, 16–19 June.
48. Oberkircher, J., Steinberger, G., and Robbins, B.: "Applications for a Multiple Depth of Investigation MWD Resistivity Measurement Device," paper OO presented at the 1993 SPWLA Annual Logging Symposium, Calgary, 13–16 June.
49. Fredericks, P.D., Hearn, F.D., and Wisler, M.M.: "Formation Evaluation While Drilling With a Dual Propagation Resistivity Tool," paper SPE 19622 presented at the 1989 SPE Annual Technical Conference and Exhibition, San Antonio, Texas, 8–11 October.
50. Meyer, W.H. *et al.*: "A New Slimhole Multiple Propagation Resistivity Tool," paper NN presented at the 1994 SPWLA Annual Logging Symposium, Tulsa, 19–22 June.
51. Gianzero, S. *et al.*: "New Developments in 2 MHz Electromagnetic Wave Resistivity Measurements," paper MM presented at the 1994 SPWLA Annual Logging Symposium, Tulsa, 19–22 June.
52. Griffiths, R., Barber, T., and Faivre, O.: "Optimal Evaluation of Formation Resistivities Using Array Induction and Array Laterolog Tools," paper BBB presented at the 2000 SPWLA Annual Logging Symposium, Dallas, 4–7 June.
53. Cray, S. *et al.*: "Effect of Resistive Invasion on Resistivity Logs," paper SPE 71708 presented at the 2001 SPE Annual Technical Conference and Exhibition, New Orleans, 30 September–3 October.
54. Doll, H.G.: "The Microlaterolog," *JPT* (January 1953) 17; *Trans.*, AIME, **198**.
55. Doll, H.G.: "The MicroLog: A New Electrical Logging Method for Detailed Determination of Permeable Beds," *Trans.*, AIME (1950) **189**, 155.
56. Suau, J. *et al.*: "The Dual Laterolog-Rxo Tool," paper SPE 4018 presented at the 1972 SPE Annual Meeting, Dallas, 8–11 October.
57. Eisenmann, P. *et al.*: "Improved R_{xo} Measurements Through Semi-Active Focusing," paper SPE 28437 presented at the 1994 SPE Annual Technical Conference and Exhibition, New Orleans, 25–28 September.
58. Howard, A.Q.: "A New Invasion Model for Resistivity Log Interpretation," *The Log Analyst* (March–April 1992) **33**, No. 2, 96.
59. Singer, J. and Barber, T.: "The Effect of Transition Zones on the Response of Induction Logs," paper L presented at the 1988 SPWLA Annual Logging Symposium, San Antonio, Texas, 5–8 June.
60. Ekstrom, M. *et al.*: "Formation Imaging With Microelectrical Scanning Arrays," *The Log Analyst* (March 1987) 294.
61. Rosthal, R. *et al.*: "Real-Time Formation Dip From a Logging-While-Drilling Tool," paper SPE 38647 presented at the 1997 SPE Annual Technical Conference and Exhibition, San Antonio, Texas, 5–8 October.
62. Gondouin, M., Hill, H.J., and Waxman, M.H.: "A Tri-Chemical Component of the SP Curve," *JPT* (March 1962) 301.
63. Gondouin, M. and Scala, C.: "Streaming Potential and the SP Log," *JPT* (August 1958) 170; *Trans.*, AIME, **213**.

64. Wyllie, M.R.J.: "A Quantitative Analysis of the Electro-Chemical Component of the SP Curve," *JPT* (1949) 17; *Trans.*, AIME, **186**.
65. Pied, B. and Poupon, A.: "SP Base Line Shifts in Algeria," presented at the 1966 SPWLA Annual Logging Symposium, Tulsa, 9–11 May.
66. Archie, G.E.: "Electrical Resistivity Log as an Aid in Determining Some Reservoir Characteristics," *Trans.*, AIME (1942) **146**.
67. de Witte, L.: "Relations Between Resistivities and Fluid Contents of Porous Rocks," *Oil & Gas J.* (24 August 1950).
68. Lindley, R.H.: "Use of Differential Sonic-Resistivity Plots to Find Movable Oil in Permian Formations," *JPT* (August 1961) 749.
69. Waxman, W.H. and Smits, L.J.M.: "Electrical Conductivities in Oil-Bearing Sands," *SPEJ* (June 1968) 107.
70. Clavier, C., Coates, G., and Dumanoir, J.: "Theoretical and Experimental Bases for the Dual-Water Model for Interpretation of Shaly Sands," *JPT* (April 1984) 153.

SI Metric Conversion Factors

cycles/sec	× 1.0*	E + 00 = Hz
ft	× 3.048*	E - 01 = m
ft ²	× 9.290 304*	E - 02 = m ²
in.	× 2.54*	E + 00 = cm
in. ³	× 1.638 706	E + 01 = cm ³

*Conversion factor is exact.

Chapter 3C

Acoustic Logging

Doug Patterson, Baker Hughes and Stephen Prenskey, SPE, Consultant

3C.1 Introduction

Petroleum applications of acoustic-wave-propagation theory and physics include both surface- and borehole-geophysical methods. These data-acquisition methods cover a broad range of scales from millimeters to hundreds of meters (**Fig. 3C.1**). Acoustic logging is a subset of borehole-geophysical acoustic techniques. This chapter provides an overview of borehole acoustic-logging theory, modern tool design, data processing methods, and data applications. **Table 3C.1** lists other common surface- and borehole-geophysical methods. The chapter on the Fundamentals of Geophysics, in this volume, and the chapter on Reservoir Geophysics, in the Emerging and Peripheral Technologies volume of this *Handbook*, also discuss these methods.

A virtual explosion in the volume of acoustic research conducted over the past 20 years has resulted in significant advances in the fundamental understanding of downhole acoustic measurements. These advances, in turn, have greatly influenced practical logging technology by allowing logging-tool designs to be optimized for specific applications.¹

Borehole acoustic-logging measurements are used in a wide variety of geophysical, geological, and engineering applications and play an important role in evaluating reservoirs, reducing exploration and production risks, selecting well locations, designing completions, and increasing hydrocarbon recovery (**Table 3C.2**).

Modern logging tools include conventional borehole-compensated (BHC) monopole devices as well as the newer array devices—both monopole and multipole (monopole/dipole)—and logging-while-drilling (LWD) acoustic services. These logging tools provide acoustic measurements in all borehole mud types (but not in air- or foam-filled boreholes) in vertical, deviated, and horizontal wells, in both open and cased hole. They are combinable with other logging devices and are available in a variety of sizes to accommodate a range of borehole and casing diameters. Specialized tool designs are used for cement and casing evaluation and borehole imaging.

Historically, the primary and the most routine uses of acoustic logs in reservoir engineering have been porosity determination, identification of gas-bearing intervals, and cement evaluation. Continuing developments in tool hardware and in interpretation techniques have expanded the utility of these logs in formation evaluation and completion (fracture) design and evaluation. This chapter discusses the potential applications of these logs to allow the reader to evaluate the appropriate applications for a particular well or field. However, site-specific assess-

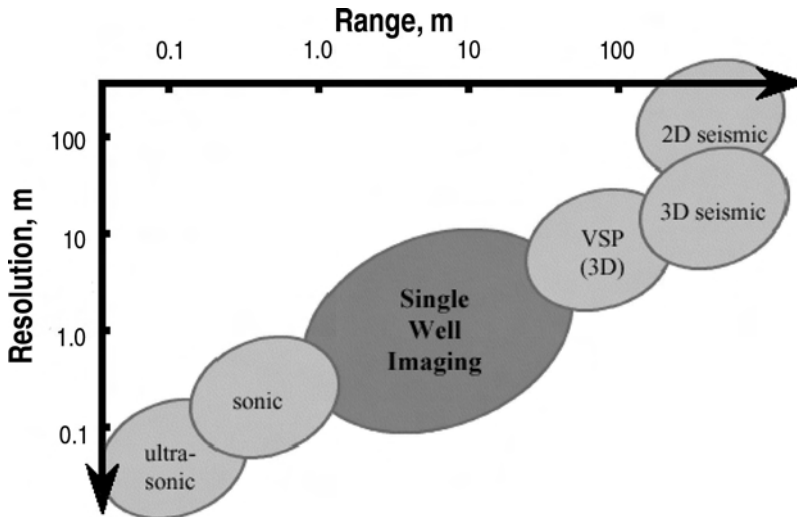


Fig. 3C.1—Diagram showing the maximum and minimum ranges vs. the resolution for various acoustic methods.²¹¹ Acoustic logging includes the sonic and ultrasonic ranges (courtesy of SPE).

ments are required to determine whether acoustic logs, with the proper planning, can provide the desired results in a cost-effective manner.

3C.2 Acoustic Theory and Wave Propagation

The principles of borehole acoustic logging (and surface seismic methods) are based on the theory of wave propagation in an elastic medium, as detailed in Refs. 2 through 5. The oscillating motion generated by a sound source (transducer) in an elastic medium (rock formation) is called an elastic wave or acoustic wave (also called head or body waves). Wave theory predicts how an acoustic signal propagates through the borehole and formation. Snell's law explains how the acoustic signal behaves at the velocity boundary separating the borehole and the formation, that is, how it is transmitted into the formation and back to the receivers. Elasticity is the property of matter that causes it to resist deformation in volume or shape. It is the elastic nature of rock formations that permits wave propagation. Acoustic waves have four measurable properties: velocity, amplitude, amplitude attenuation, and frequency. Acoustic logging tools are designed to measure one or more of these properties, with velocity (slowness) being the most common.

The waveform recorded at the logging tool's receivers is a composite signal containing different energy modes, each with a different frequency, velocity, and amplitude. For borehole logging, the modes of primary interest are (in order of arrival) compressional, shear, and Stoneley (tube) waves (Fig. 3C.2). The waveform is recorded as acoustic amplitude as a function of time.

These waves are transmitted through the medium some distance from the origin of displacement. The particles of the medium do not travel with the wave, but only vibrate around their mean central position. Acoustic waves are classified according to the direction of particle displacement with respect to the direction of wave propagation as either longitudinal (i.e., particle displacement is parallel to the direction of propagation) or transverse (i.e., direction of particle displacement is perpendicular to the direction of propagation). In acoustic logging, the longitudinal wave is known as the compressional wave and the transverse wave is known as the shear wave. The presence of the borehole excites two additional acoustic energy modes, called guided waves: normal (pseudo-Rayleigh) and tube (Stoneley) waves.

Acquisition Mode	Geophysical Method
Surface	2D and 3D
Reflection seismic	Time-lapse reservoir monitoring (4D) Amplitude variation with offset (AVO)
Borehole	Acoustic logging
Wireline	Vertical seismic profiling (VSP) Amplitude variation with offset (AVO) Continuity logging Crosswell surveys
Wireline/LWD	Fracture surveys (microseismicity) Seismic while drilling (Reverse VSP)
Permanent sensors	Reservoir monitoring

Discipline Application	Geophysics	Geology	Formation Evaluation	Production Engineering	Reservoir Engineering	Well Completion	Enhanced Drilling	Enhanced Recovery
Synthetic seismogram	X	X	X					
VSP analysis	X	X	X					
AVO calibration	X	X	X		X			X
Porosity evaluation	X	X	X		X	X		X
Lithology estimate	X	X	X		X	X		X
Saturation evaluation		X	X	X	X			X
Gas detection	X	X	X	X	X	X	X	X
Hydrocarbon typing	X	X	X		X		X	X
Fracture analysis	X	X	X		X	X	X	X
Permeability index		X	X		X	X		X
Abnormal pressure		X	X	X	X	X	X	
Wellbore stability		X	X	X		X	X	
Perforation stability			X	X	X	X		X
Anisotropy	X	X	X	X	X	X	X	X
Cement evaluation			X	X	X	X		X

Acoustic-wave velocity is controlled by a number of factors: lithology (mineralogy), cementation, clay content, texture, porosity, pore-fluid composition and saturation, overburden and pore-fluid pressure (stress), and temperature. The rock's mechanical properties, elastic dynamics, and density are a constant for a particular homogeneous and isotropic material. Acoustic-wave velocity can be related to rock elastic properties through three constants of proportionality, elastic moduli (e.g., Young's, shear, and bulk), and Poisson's ratio. This serves as the basis for mechanical-property evaluation by acoustic logs (see the additional discussion under Geomechanical Applications—Rock Mechanical Properties). In reality, most petroleum reservoirs contain varying pore sizes, pore fill (e.g., clays), fractures, etc. and consequently, are neither truly isotropic nor homogeneous. Furthermore, in fluid-saturated rocks, these acoustic properties also depend on the type and volume of fluids present.

3C.2.1 Compressional Waves. Compressional (P, primary, or pressure) waves are longitudinal waves that are transmitted through an elastic formation by compression or pressure. Particle motion is parallel to the direction of wave propagation (**Fig. 3C.3**). They can travel through solids, liquids, and gases and are the fastest wave type—they represent the acoustic first arrival. Of all acoustic wave types, they are least affected by faults, unconsolidated formations, and borehole fluids, and are, therefore, the most reliable. The wave is transmitted by both the

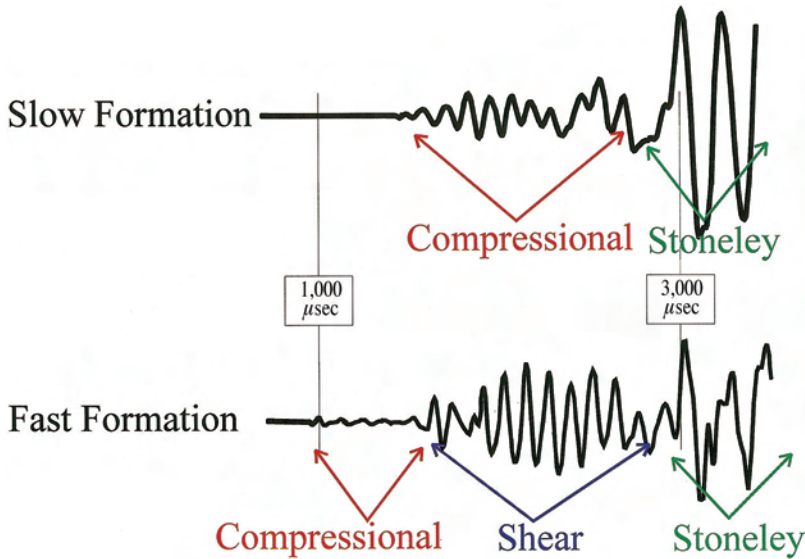


Fig. 3C.2—Generalized acoustic waveform showing the wave signature of different energy modes (courtesy of Baker Atlas).

rock matrix (i.e., the framework) and the fluid present in the pore throats. A compression, together with an adjacent rarefaction preceding or following it, constitutes a complete cycle. The distance between complete cycles is called the wave length and the number of cycles propagating through a point in the medium per unit time is the frequency. The velocity of elastic-wave propagation in an isotropic homogeneous medium can be derived from a combination of the theory of elasticity with Newton's law of motion. Compressional-wave velocity (or travel time) is a function of the density and elasticity of the medium and is a constant for a given material.

3C.2.2 Shear and Borehole Flexural Waves. Shear (S, secondary) waves are transverse waves that are transmitted by lateral displacement of particles in a rigid elastic formation. Particle motion is perpendicular to the direction of motion (Fig. 3C.3). Normally, shear waves are the second arrival in an acoustic wave train. In most reservoir rocks, shear waves generally have higher amplitudes than compressional waves but lower velocities, by as much 40 to 50%. There are two types of borehole shear waves—direct and indirect, also known as refracted or induced. Indirect shear waves are induced in a formation through a process known as mode conversion in which some of the compressional energy is transferred from the borehole fluid into the rock formation. Monopole transmitters generate these indirect shear waves while dipole transmitters generate direct shear waves by inducing a flexural (asymmetric mode) in the borehole. Shear-wave propagation requires a medium that has shear strength (rigidity). Consequently, shear waves can only travel in solids, not in liquids or gas. In liquids and gas, the shear head-wave generated within the formation is converted into a compressional wave and propagated back across the borehole fluid to the acoustic receivers as a later-arriving compressional wave.

Unconsolidated or poorly consolidated sandstones ("soft" or "slow" rocks) are less rigid and more compressible than well-consolidated ("hard" or "fast") rocks. When the formation shear-wave velocity is less than the acoustic velocity of the borehole fluid ($V_s < V_f$), a rock formation is called "slow." There is no refracted shear-wave from monopole devices in slow formations and low-frequency dipole transmission and reception is required to adequately de-

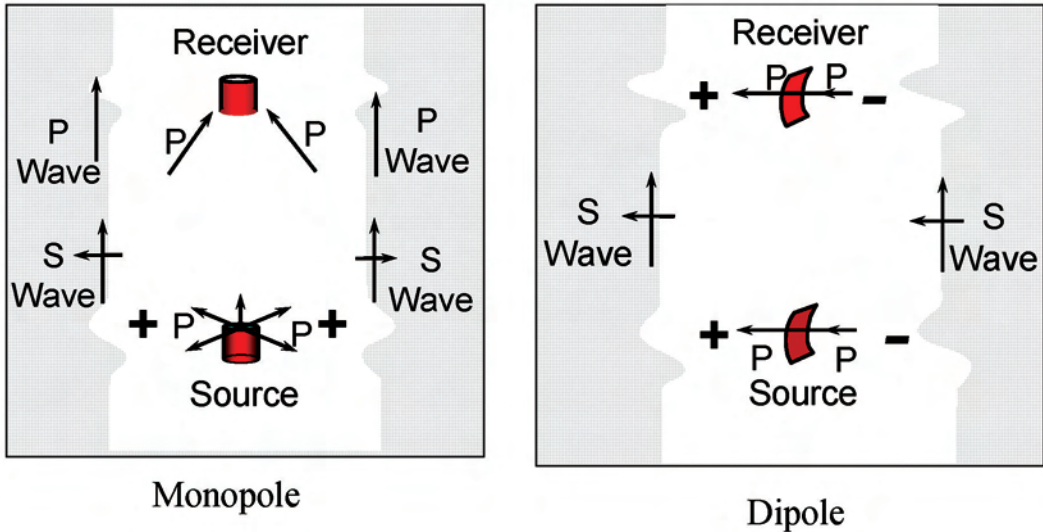


Fig. 3C.3—Direction of particle motion in compressional and shear waves and wave motion generated by monopole and dipole transmitters (courtesy of Baker Atlas).

tect low-frequency flexural arrivals for the shear-wave slowness determination. However, if a monopole-array tool is used in these conditions, a shear-wave slowness can be estimated from Stoneley-wave velocity dispersion.⁶ In very slow formations, where $V_c < V_f$, special processing may be required to extract the formation compressional signal.⁷

Flexural-wave velocity varies with frequency—a phenomenon called dispersion. In contrast, the compressional and shear headwaves generated by monopole sources are generally not dispersive. At very low frequencies, the flexural wave travels at the formation shear velocity. This dispersion effect diminishes as the wavelength of the flexural-wave increases and is generally minimal when the wavelength is at least three times the borehole diameter. Fast formations exhibit a center frequency slightly greater than 3 kHz, while slow formations exhibit a center frequency of ≈ 1 kHz, or less. The received frequency spectrum of a dipole array is a function of transmitter frequency, rock properties, and borehole size. Modern dipole transmitters are broadband transmitters, i.e., they operate over a range of frequencies, to account for dispersion and to accommodate different formation types.

3C.2.3 Stoneley Waves. Stoneley (tube) waves are high-amplitude guided waves that are generated by a radial (symmetric) flexing of the borehole as the acoustic energy passes from the borehole fluid into the rock formation. They propagate at low frequencies along the fluid-rock interface at the borehole wall; hence, they are sensitive to the rock properties adjacent to the borehole wall. They are the slowest acoustic mode. They can be measured in both open and cased boreholes, but in cased holes Stoneley-wave features are primarily controlled by the casing rigidity. Similarly to shear waves, Stoneley waves are also dispersive; i.e., wave velocity varies with frequency—the amount of dispersion is related to formation rock properties. However, Stoneley waves are notable for several special properties: there is no cut-off frequency; dispersion is very mild; for all frequencies, Stoneley-wave velocity is less than fluid velocity; and group velocity nearly equals phase velocity over the frequency range.

All acoustic waves undergo attenuation, a reduction in signal amplitude away from the source. For logging devices this means radially away from the borehole wall. Signal attenuation results from the geometric spread of energy through reflection, refraction, and scattering, and through absorption by the medium through which the acoustic energy travels. Attenuation,

usually expressed in dB/ft, is characteristic of different materials and increases with frequency of the acoustic wave. Generally, attenuation is large in slow formations and very small to negligible in fast formations. Because of these features, Stoneley waves are used to identify acoustic leakage away from the borehole that may be caused by formation permeability or the presence of fractures.

3C.3 Acoustic-Logging Tools

Acoustic-logging devices are comprised of transmitters (sources), receiver arrays, and accompanying electronics. They have been designed to measure one or more acoustic-wave properties. Acoustic sources (transmitters) generally consist of piezoelectric transducers that generate the acoustic signal by converting electrical signals into a sonic vibration that travels through the borehole and adjacent rock formations. Monopole (axisymmetric) transducers generate omnidirectional acoustic waves around the tool circumference, while dipole (nonaxisymmetric) transducers generate azimuthally oriented acoustic waves (Fig. 3C.3).

Modern receivers are piezoelectric crystals that transform the received (measured) acoustic signal back into electrical signals. Different logging tools use different piezoelectric materials and operate at different frequencies to measure different energy modes (wave types). The pressure variation produced by an acoustic wave displaces the piezoelectric material causing it to ring or oscillate. When the receiver oscillates, it develops a small voltage. This voltage is amplified and the raw data are processed downhole and sent to the surface-acquisition system in the form of a waveform signal (wireline) or acoustic slowness (wireline and LWD). Digital data are stored, either at the surface (wireline) or downhole (LWD), for wellsite log presentations and post-acquisition processing and playback.

The energy (amplitude) of acoustic waves is lost (attenuated or dispersed) primarily by travel through the borehole fluid and rock matrix. Additional attenuation may result from a number of other factors that include internal particle friction within the propagation medium, changes in acoustic impedance [the product of density (ρ) and acoustic velocity (V)] at interfaces (boundaries) between different mediums, borehole rugosity, and signal cancellation resulting from tool eccentricity. In general, the largest signal possible occurs when the instrument is in the center of the hole; a dipole tool in an extremely large borehole may be exception to this rule. For high frequencies, the monopole signal is reduced by as much 50% of the centralized value by displacing the instrument only inches from the center of the hole. Consequently, whenever possible, centralizers should be used with acoustic-logging tools.

3C.3.1 Critical Spacing. The acoustic wave travels through the formation much faster than it does through the borehole fluid and reaches the receiver by the longer formation route first. This is true as long as the critical spacing is less than actual spacing. Critical spacing is the transmitter-to-receiver spacing at which the fluid-signal and formation-signal arrive at the receiver at the same time. The critical-spacing value depends on the diameter of the logging sonde, the diameter of the borehole, the time of travel through the fluid, and the time of travel through the rock.

In soft formations, and under certain conditions, the critical spacing can exceed actual spacing and the fluid arrival, which exists for a noncentralized tool, can interfere with the acoustic signal. When this occurs, data-processing methods can exclude this fluid arrival, thereby reducing or possibly eliminating interference from the fluid arrival. Longer transmitter-receiver spacings are used to minimize this occurrence.

The transmitter-to-receiver spacing in modern monopole tools is set to enable separation of the compressional- and shear-energy packets to allow for accurate measurement of both in fast formations. When logging with an array-acoustic device, the receivers nearest the transmitter see stronger acoustic waves than the more distant receivers.

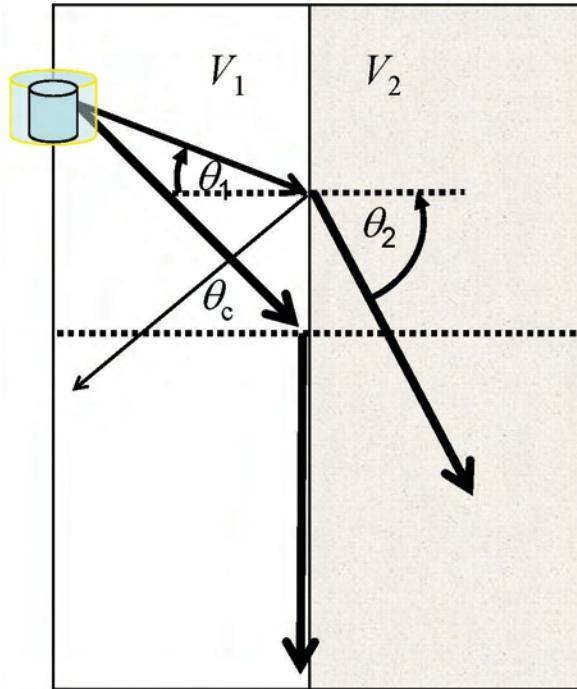


Fig. 3C.4—Illustration of Snell's law showing how acoustic waves are refracted (wave A), reflected (wave C), or converted (wave B) as they encounter a boundary separating media having different velocities (indices of refraction) (courtesy of Baker Atlas).

3C.3.2 Monopole Excitation. The transmitter emits acoustic energy uniformly around the tool. In fast formations, this energy excites three waves that travel down the borehole wall: compressional, shear, and Stoneley. The compressional wave travels away from the transmitter with a velocity, V_f , in the mud. When these waves reach the borehole face, they are reflected, refracted, and converted according to Snell's law (Fig. 3C.4).

For angles of incidence less than the compressional-wave critical angle (θ_c , Fig. 3C.4), part of the energy is transmitted into the formation in the form of compressional wave (Wave A, Fig. 3C.4), another part is converted as a (refracted) shear wave (Wave B, Fig. 3C.4), and the remainder is reflected back into the mud as a compressional wave (Wave C, Fig. 3C.4). The transmitted waves travel at velocity V_p and V_s in the formation, close and parallel to the borehole wall, while continuously radiating energy back into the mud as converted compressional-waves, at the same compressional-wave critical angle at which it entered. It is this radiated energy that is detected by the receivers.

If the formation shear-wave velocity is slower than borehole-fluid compressional velocity ($V_s < V_f$), shear waves cannot be refracted along the borehole wall, and no shear wave is measured. Beyond the shear-wave critical angle, all the incident energy is reflected back into the mud to form the guided waves. The Stoneley wave travels at approximately the velocity of compressional waves in the borehole fluid. Compressional and Stoneley arrivals are always present. In the absence of a refracted shear-wave arrival (i.e., in formations in which $V_p < V_f$), the Stoneley wave can be used to estimate formation shear-wave velocity when a formation bulk-density measurement is available, using certain assumptions. However, because of the uncertainty associated with these assumptions, dipole shear-wave measurements are recommended in slow formations. Stoneley-wave amplitude decreases (attenuates) significantly at high frequen-

TABLE 3C.3—VELOCITY AND ACOUSTIC SLOWNESS (TRANSIT TIME) VALUES FOR COMMON RESERVOIR FLUIDS AND LITHOLOGIES (after Carmichael ⁸)			
Fluid	V_f (ft/sec)	Δt_f (μ sec/ft)	
Water with 20% NaCl	5,300	189	
Water with 15% NaCl	5,000	200	
Water with 10% NaCl	4,800	208	
Water (pure)	4,600	218	
Oil	4,200	238	
Methane	1,600	626	
Air	1,100	910	
Lithology (matrix)	V_{mn} (ft/sec)	Compressional Δt_{mn} (μ sec/ft)	Shear Δt_{ms} (μ sec/ft)
Sandstone			
Unconsolidated	17,000 or less	58.8 or more	93
Semiconsolidated	18,000	55.6	92.9
Consolidated	19,000	52.6	92.9
Limestone	21,000	47.6	
Dolomite	23,000	43.5	72
Shale	6,000 to 16,000	167 to 62.5	
Salt (halite)	15,000	67	116
Coal			
Lignite	7,150	140	
Bituminous	8,300	120	
Anthracite	9,500	105	
Granite	20,000	50	
Minerals			
Calcite	22,000	46	89
Quartz	18,000	51	74
Evaporites			
Anhydrite	20,000	54	98
Gypsum	19,000	53	
Trona		65	
Iron Minerals			
Limonite		57	103
Pyrite		38	59
Siderite		44	85
Hematite		46	72
Micas			
Biotite		51	224
Muscovite		47	79

cies and modern tools use low-frequency transmitters (< 1 to 12 kHz) to ensure acquisition of the Stoneley arrival in slow formations.⁸

3C.3.3 Dipole Excitation. The dipole transmitter exerts a differential pressure on one side of the transmitter element that creates a flexural wave in the borehole, much like the wave produced when a vertical rope is shaken from side to side. The flexural wave is dispersive, but at low frequencies this wave travels down the borehole at the formation shear velocity. Receivers, sensitive only to differential pressures, are used to detect this flexural wave. Because the receivers are not sensitive to axially symmetric pressure fields, both the compressional head wave and the Stoneley waves are suppressed. This is desirable because it simplifies data processing. The desired output is the velocity of the formation shear wave. If the wavelength of the flexural wave is at least three times the diameter of the borehole, the flexural wave travels at very nearly the formation bulk-shear velocity. However, because this is a dispersive mode, if

<u>Application</u>	<u>Date</u>	<u>Device</u>
Velocity Wireline	1950s	Single receiver
		Dual receiver
	1960s	Borehole-compensated log
		Long-spaced sonic
	1970s	Monopole array Circumferential sonic
1980s	Digital array	
LWD	1990s	Dipole array Multipole array Crossed-dipole array
	Early 1990s	Monopole array
	Late 1990s–early 2000s	Multipole array
Openhole Borehole Imaging	1960s	Borehole televiewer (BHTV)
	1980s–1990s	Improved designs
Cement Evaluation	1960s	Amplitude (CBL)
	1980s	Attenuation rate (e.g., CBT, RBT)
	1980s	Radial (pad, ultrasonic) (e.g., SBT, PET, CET)
	1990s	Reflection (pulse/echo) (e.g., USI)
Casing Evaluation	1980s	Ultrasonic (e.g., CET, PET)
	1990s	Reflection (pulse/echo) (e.g., USI)

the wavelength is shorter (because of higher frequency), this flexural mode will travel slower than the shear velocity and dispersion corrections are needed.

3C.3.4 Logging Documentation. All types of well logs, both open- and cased-hole, should be accompanied by complete documentation to ensure good-quality logs and sound interpretation. It is important to remember that any acoustic analysis represents an interpretation of measured acoustic waves. The wellsite engineer or geologist must ensure that all data pertaining to a particular log run, including borehole information (bit and casing sizes and depths), tool configuration, borehole fluid, formation parameters, and tool centralization are recorded in the well-log header for future reference. Cased-hole logs should also contain information on cement composition, casing weight and thickness, if the log was run with pressure, and the amount of that pressure.

3C.4 Evolution of Acoustic-Logging Tools

The most commonly used acoustic-wave property acquired in borehole logging is the compressional-wave velocity. Modern velocity-logging tools measure the time, Δt , required for a compressional or shear wave to travel through a fixed distance of formation; it is recorded as a function of depth. This parameter, Δt , referred to as the interval transit time, transit time, travel time, or slowness, is the reciprocal of the velocity of the compressional waves, $\Delta t = 1/V_p$. For

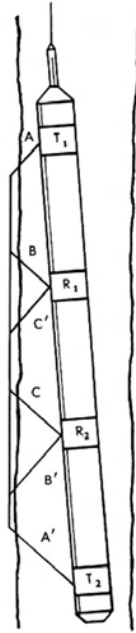


Fig. 3C.5—Two-transmitter, two-receiver scheme used for borehole compensation (courtesy of Baker Atlas).

the formations typically encountered in acoustic logging, travel times range from 40 to 250 $\mu\text{sec}/\text{ft}$, corresponding to velocities ranging from 25,000 to 4,000 ft/sec (**Table 3C.3**).

The resolution of any acoustic method is a function of the signal wavelength; the lower limit is one-quarter of the propagating wavelength. Seismic-reflection exploration methods typically operate in the frequency range of 10 to 50 Hz. In typical petroleum reservoir rocks, the resolution of these methods is approximately 30 to 160 ft (10 to 50 m), depending on depth (signal strength). In contrast, conventional BHC logging tools operate within the frequency range of 10 to 40 kHz, while newer array devices operate at even lower frequencies, 1 to 12 kHz. Logging-tool resolution is also a function of both the array aperture and the methodology employed for the array processing. Consequently, acoustic-logging tools typically have resolutions on the order of 1.0 to 4.0 ft (0.3 to 1.2 m) (see the section on Resolution Enhancement in this chapter).

3C.4.1 Velocity/Porosity Logging. Acoustic well logging developed out of the need for downhole velocity (time-depth) measurements to improve the accuracy (calibrate) of surface seismic measurements. Surface seismic maps out sub-surface structures referenced to time and borehole acoustic tools provide a bridge to understand how time is related to depth. Downhole geophones were introduced in the 1930s to provide acoustic travel times to the surface, and continuous-velocity-logging tools were introduced in the 1950s (**Table 3C.4**). Soon after the introduction of the continuous-velocity log, it was recognized that these data also provided an excellent means for stratigraphic correlation, lithologic identification, and for evaluation of formation porosity.

The first acoustic-logging tools used a single monopole transmitter and a single receiver. Tool designs rapidly evolved to improve the accuracy of the velocity measurement by minimizing or eliminating influences related to borehole effects, i.e., fluid, geometry, and tool position

TABLE 3C.5—FACTORS AFFECTING BHC SLOWNESS

Factor	Cause	Effect on Slowness
Borehole diameter	Signal attenuation dependent on TR spacing	Reads mud Δt if TR > critical spacing
Noise	Intermittent; far receiver more susceptible	Underestimated or erratic
Cycle skip	Near receiver not triggered because of signal attenuation. Possible causes: unconsolidated formations, fractures, gas-cut mud, excessively large, rugose, or washed-out borehole.	Overestimated
Δt stretch	Signal attenuation; can produce serious errors in integrated travel time.	Overestimated
Velocity inversion	Increase in slowness near borehole because of invasion or formation alteration	Underestimated
Gas effect	Gas present in flushed (measurement) zone	Overestimated
High apparent dip	Acoustic signal may travel along dip planes rather than along borehole. May result in false thickness in fast formations	Underestimated
Signal splitting	Signal cancellation because of tool eccentricity (reduces signal-to-noise ratio)	Same as noise

(tilt) within the borehole (see the next section of this chapter); and to measure additional acoustic-wave properties.

These simple devices were soon replaced by two receiver designs that had the advantage of eliminating the need to correct for travel time in the drilling mud (for more on the historical development of acoustic logging, consult Refs. 10 through 13). Modern borehole-compensated designs, introduced in the 1960s, use two transmitters and two receivers to compensate for variations in borehole diameter and tool position within the borehole (Fig. 3C.5). Two separate values of two receiver (R_1 and R_2) and two transmitters (T_1 and T_2) interval-transit times are provided, and an average of the two effectively compensates for any problems (Eq. 3C.1).

$$\Delta t = \frac{(t_1 - t_2) + (t_4 - t_3)}{2X_{12}}, \dots\dots\dots (3C.1)$$

where t_1 = travel time between T_2 and R_1 ; t_2 = travel time between T_2 and R_2 ; t_3 = travel time between T_1 and R_1 ; t_4 = travel time between T_1 and R_2 ; and X_{12} = distance between R_1 and R_2 . Fig. 3C.5 illustrates travel paths that show that the averages of AA', BB', and CC' are essentially equal.

The BHC tools' velocity measurements may be affected by a variety of factors including borehole diameter, signal noise, cycle skipping, Δt stretch, velocity inversion, gas effect, and dip angle, with respect to the borehole (Table 3C.5). Modern digital-circuitry and array-tool designs reduce or eliminate many of these problems, but they may still be present on older logs.

Conventional BHC monopole-acoustic logs, with their short transmitter-to-receiver spacing, have shallow depths of investigation and they largely measure mud filtrate that fills the pore space in the invaded (flushed) zone around the borehole. Long-spaced and array devices can acquire measurements beyond the filtrate and altered zone.

3C.4.2 Long-Spaced Acoustic Tools. Typical BHC devices have a transmitter-to-receiver spacing (TR) of 3 to 5 ft. These work well in many circumstances; however, in cases which borehole enlargement prevents acquisition of reliable data, due to the increase of the critical spacing, or in which the drilling process damages or alters the shales surrounding the borehole, long-spacing tools (TR = 8 to 15 ft) may be necessary, or advised, to obtain accurate measurements. In contrast to conventional BHC devices, in which the transmitters and receivers are

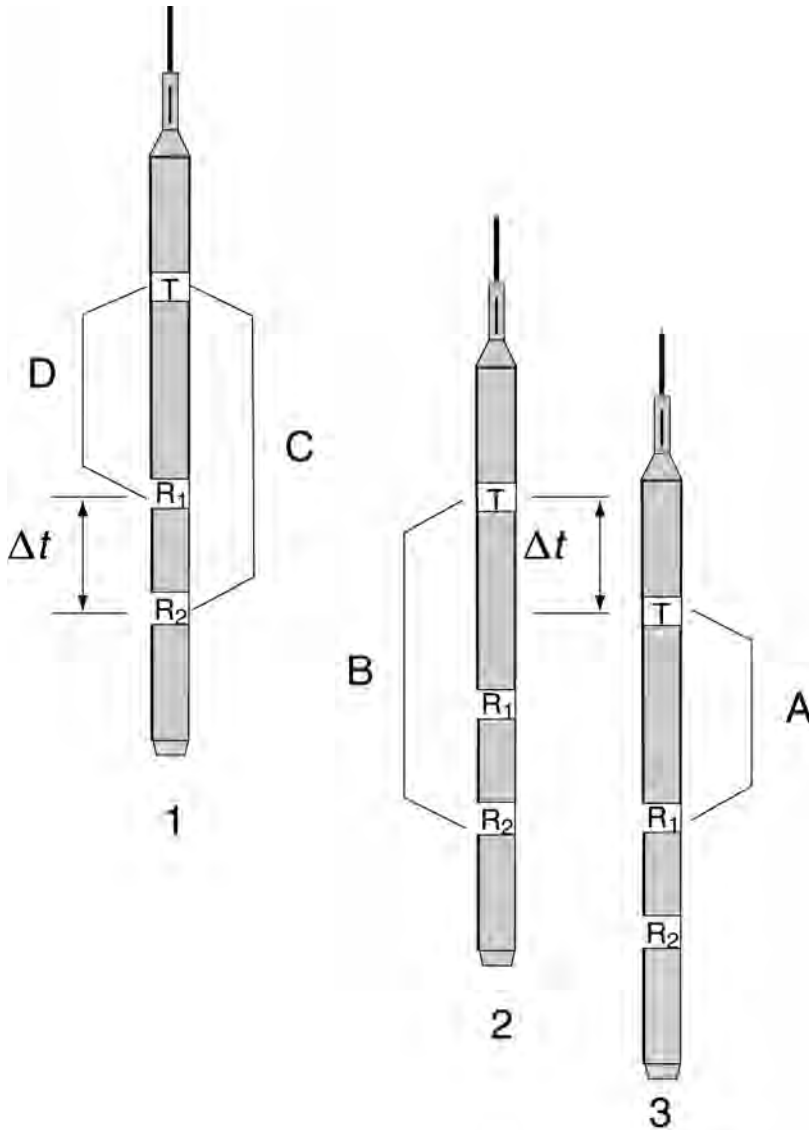


Fig. 3C.6—Schematic illustration of the asymmetric TR arrangement used by long-spaced acoustic and array acoustic tools and the depth-derived borehole-compensation (DDBHC) method (courtesy of Baker Atlas).

arranged symmetrically, long-spacing tools use an asymmetric arrangement with the receivers at varying distances from the monopole transmitter (Fig. 3C.6). Consequently, these devices have deeper depths of investigation that make them less susceptible to borehole conditions such as enlargement and shale alteration. These tools operate in both open and cased holes.

Because long-spaced and array tools use an asymmetric configuration of transmitters and receivers, borehole compensation is achieved through a process called depth-derived borehole compensation (DDBHC)¹⁴ (Fig. 3C.6). The processing is accomplished downhole by either the tool's electronics or in the surface recording system and uses a depth-based delay to create synthetic transmitter arrays from multiple tool positions. The compensated travel-time measurement, Δt , is determined through the following procedure. At position three (Fig. 3C.6), the

transmitter (T) is at the depth where the far receiver (R_2) will be when the tool is moved to position one. The interval-transit time (A) between the transmitter (T) and near receiver (R_1), which includes mud and formation signals, is recorded and delayed (memorized). At position two (Fig. 3C.6), the transmitter (T) is at the same depth the near receiver (R_1) will be when the tool moves to position one. The interval transit time or waveform (B) between T and R_2 is recorded and delayed. When the tool reaches position one, the two interval transit times (A and B) are equal to the interval transit time that would result if a second transmitter were below the receivers. The correct compensated value of Δt is obtained by combining the two delayed values of transit time (recorded at positions two and three) with transit times C and D , recorded at position one. Compensated transit time (Δt) is then correctly represented by

$$\Delta t = \frac{(B - A) + (C - D)}{2x}, \dots\dots\dots (3C.2)$$

where x = the distance between R_1 and R_2 .

Analog recording of full acoustic waveforms, called “amplitude” logging, was developed in the 1960s. However, it was not until digital technology, instrumentation, and signal-processing methods were introduced in the late 1970s that the recording of full-waveform data became routine. While these techniques enabled the extraction of shear-wave data from conventional BHC acoustic data, determination of shear arrivals using conventionally spaced BHC tools (TR = 3 to 5 ft) suffers from interference between late-arriving compressional waves and shear-wave arrivals. The use of long-spaced tools reduced this problem by allowing greater temporal separation between the different wave packets and provided accurate estimates of shear-wave slowness.¹⁵⁻¹⁸

3C.4.3 Monopole Array Devices. Modern array tools are a natural outgrowth of the long-spaced tool design. Additional receivers (4 to 13) were added to provide the statistical redundancy needed to enhance extraction of wave arrival times; some designs also include multiple transmitters. The monopole transmitters in these tools use lower frequencies (e.g., 1 to 12 kHz vs. 20 to 40 kHz) and have broader frequency ranges than earlier tools to permit acquisition of high-quality acoustic waveforms. These devices are typically comprised of several sections or subs that house the tool components: electronics, receiver array, acoustic isolator, and transmitters. The acoustic isolator, placed between the transmitter and receiver sections, prevents or minimizes and delays direct sound transmission between transmitters and receivers. The electronics section provides timing and control for the transmitter and receiver sections, digitizes the received acoustic waves, analyzes the acquired waveforms, and transmits the data to the surface-data-acquisition system, all in real time.

Array tools can record full waveforms: compressional, shear, and Stoneley arrivals. These tools operate in either a single or a variety of combination-acquisition modes that include full waveform, compression Δt , and cement-bond logging. The number of modes that can be activated during a single log run is a function of the logging speed. Acquisition of full waveforms permits the use of waveform-correlation techniques for waveform amplitude, coherent slowness from the coherent-wave moveout, arrival-time processing, and most importantly, allows for detailed post-acquisition processing that improves the interpreted results. Because these techniques are insensitive to cycle skipping, they are particularly effective in gas-saturated, rugose, and washed-out boreholes.

3C.4.4 Through-Casing Acoustic Measurements. The extended transmitter-to-receiver offset (6 to 19 ft) provided by array instruments allows them to quantify formation-compressional and shear-wave energy through casing. Successful cased-hole operation requires a good cement bond to provide the necessary acoustic coupling to the formation and to minimize or eliminate

the casing arrival.^{19–21} New processing techniques may allow valid acoustic evaluation even in cases of poor bonding.²²

3C.4.5 Dipole and Multipole Array Devices. In hard (fast) formations, monopole array tools can acquire a refracted shear wave but not in soft and unconsolidated (slow) formations. Before the introduction of dipole transmitters, processing techniques were developed to derive shear-wave transit time from Stoneley-wave data.^{1,23,24}

Tools using dipole transmitters were conceived as early as the 1960s,²⁵ but were not actually developed until the 1980s.²⁶ In contrast to monopole logging tools, dipole acoustic devices can excite a low-frequency flexural wave in the borehole at shear velocity. Low-frequency (< 1 kHz) dipole sources allow for shear-velocity determination that is much closer to seismic shear waves and permits acquisition of direct-shear velocities in slow and fast formations. However, increased noise (i.e., a lower signal-to-noise ratio) is one limitation of low-frequency operation. Noise has been reduced through improved acquisition electronics, the use of semi-rigid tool designs, and by choosing the operational mode of the dipole source. A semi-rigid tool body not only reduces the influence of the tool body on the measurement but also permits operation in deviated wells.

At high frequencies, or when the borehole diameter is large, flexural-mode propagation is slower and a dispersion correction is needed to obtain the shear velocity from the measured flexural velocity. This dispersion correction is a function of mud compressional velocity, formation compressional and shear velocities, the ratio of formation and mud densities, and the product of borehole diameter and processing frequency. Few, if any corrections are required if the flexural wavelength (velocity/frequency) is at least three times the borehole diameter, which is why low frequencies (< 1 kHz) are used. Where a correction is necessary, it is typically only a few percent, but can be higher under certain conditions.

The latest commercial tool designs are multipole array devices that operate in open and cased hole. These tools typically integrate multiple transmitters (monopole and dipole) and one or more arrays of monopole and dipole receivers. Multiple monopole transmitters, or a single “programmable” transmitter,^{19,27,28} provide the preferred frequency-range for optimal acquisition of conventional BHC and long-spaced compressional, shear, low-frequency Stoneley modes along with cement-bond logs. The dipole transmitter, more recently a variable-frequency (wide bandwidth) transmitter, provides the crossed-dipole mode.^{28–32} The receivers are positioned axially along the length of the tool, for short- and long-spaced measurements, and may be interlaced or independent. At each axial position a group of receivers (e.g., 4 or 8) is positioned azimuthally around the circumference of the sonde. The receivers are oriented with the transmitter to allow for alignment of directional (multimode) source excitation and data acquisition. This allows radial imaging of acoustic parameters and measured properties.^{33,34} The dipole receivers may be aligned inline with the dipole transmitters or orthogonal (crossed) to them for crossed-dipole analysis.

Multipole tools provide enhanced Stoneley-wave and crossed-dipole shear-wave data for analysis of formation permeability and anisotropy (e.g., stress and fractures) (see later discussion).

3C.4.6 Logging While Drilling. Acoustic slowness measurements are a relatively recent addition to the suite of LWD measurements.^{35,36} Similar to wireline devices, LWD tools consist of transmitter, isolator, and receiver-array sections contained in either a single or separate drill-collars and use monopole-type (axisymmetric) transmitters. However, unlike wireline devices, which are small relative to the borehole size, the rigid collar, structural design, and large diameter of acoustic LWD drill collars may actually interfere with the physics of acoustic-energy propagation, making it more difficult to decouple the transmitter-to-receiver signal traveling along the tool body and complicating generation of borehole guided modes, such as Stoneley and flexural.

TABLE 3C.6—ADVANTAGES AND DISADVANTAGES OF LWD ACOUSTIC ACQUISITION	
Advantages	Disadvantages
Real-time Δt	Relies on downhole processing; waveforms stored in memory
Preinvasion	Increased noise from drilling
Compressional and shear measurement in fast formations.	Time based, depths can be irregular
Time-lapse studies	Tool centralization may be poor
	Pure dipole-shear measurement not possible

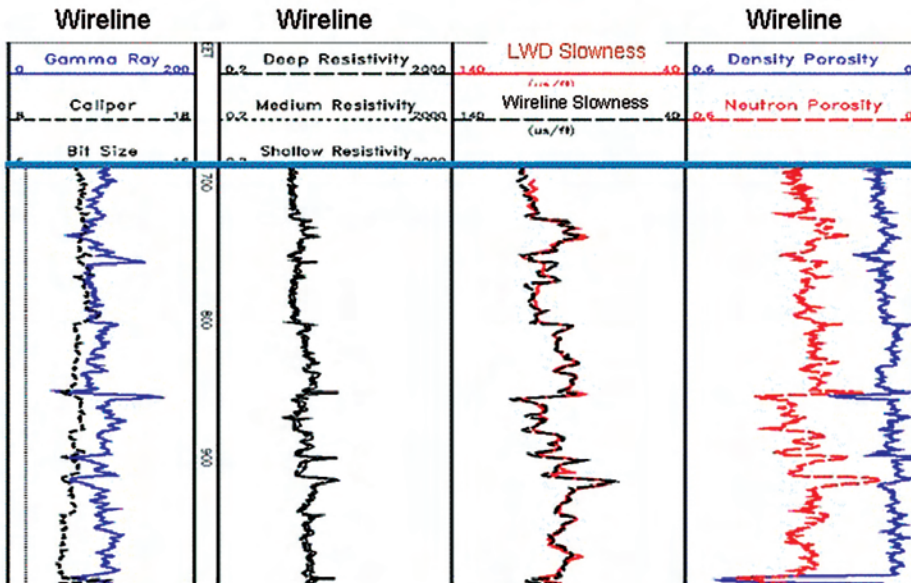


Fig. 3C.7—Comparison of LWD (red, Track 3) and wireline (blue, Track 3) acoustic slowness in a fast formation (courtesy of Baker Atlas).

Downhole processing provides acoustic slowness data in real time and also allows for storage of raw waveform data in downhole memory that can be downloaded during bit trips. The receiver array provides data redundancy and is coupled with a much narrower recording bandwidth to enhance the signal-to-noise ratio in the presence of the drilling-related noise. This results in more accurate measurements of acoustic slowness. As with all types of LWD tools, the primary advantage of LWD acoustic measurements is the acquisition of data before significant fluid invasion or alteration of the formation can occur, and providing the data in sufficient time to influence drilling decisions for improved safety, well placement, and well productivity.^{37,38} Table 3C.6 summarizes the advantages and disadvantages of LWD acoustic measurements. LWD acoustic data recorded in casing during bit trips offers the potential for cased-hole evaluation, e.g. formation velocity and cement-evaluation, during bit trips.³⁹

Multipole tools (monopole and pseudo-dipole or quadrupole) have recently been introduced and continue to be developed.^{40–43} These devices use the monopole transmitter for compressional-slowness and shear-slowness in fast formations. Similar to wireline tools, these tools may include an azimuthal receiver array.^{42,43} With these tools, the compressional-slowness measurement is obtained in fast and slow formations by summing the azimuthal measurements at each receiver level. Fig. 3C.7 illustrates the excellent agreement between LWD data and wireline

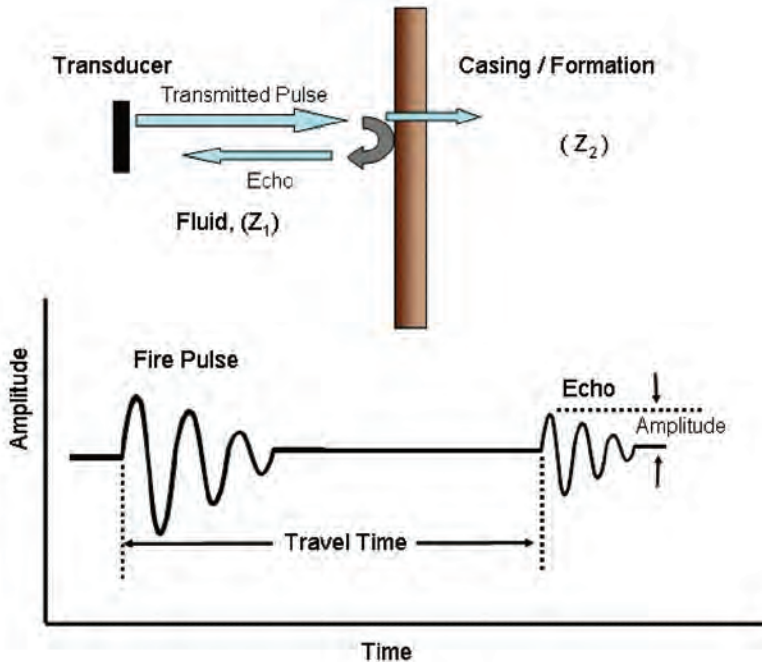


Fig. 3C.8—A simplified representation of the path of the televiwer pulse-echo signal (upper) and the measurements made (lower) (courtesy of Baker Atlas).

data. Measurement of compressional and shear slowness in slow formations is especially impacted as the diameter of the LWD drill collar approaches the borehole diameter. Because the drilling environment precludes propagation of a true dipole flexural mode, different methodologies are being used to obtain a pseudo-shear measurement using other borehole-guided modes, either through tool design, data processing, or both.^{41,44-51} Current solutions include multiple-frequency and higher-frequency dipole-type transmitters, and quadrupole transmitters. These measurements require corrections for frequency dispersion and eccentricity.⁵²⁻⁵⁵

Acoustic LWD can provide a limited real-time seismic-while-drilling capability in combination with a surface source.⁵⁶⁻⁵⁸ There is also great interest among drillers and geophysicists to develop a viable drilling-based system in which the drillbit acts as the acoustic source and the sensors (ruggedized geophones) are located in the borehole, as part of an LWD bottomhole assembly. Both types of systems provide checkshot surveys for time-depth correlation with pre-drill surveys and look-ahead seismic capability.⁵⁹

3C.4.7 Ultrasonic Reflection (Pulse/Echo) Acoustic Devices. Reflection (pulse/echo) acoustic devices were introduced in 1967 with the borehole televiwer (BHTV).⁶⁰ In contrast to conventional acoustic-logging devices, which record the transmission of acoustic waves through the formation, pulse/echo devices record the travel time, amplitude, and azimuth of ultrasonic acoustic pulses (echoes) that are reflected off the formation wall in openhole or off the casing or cement in cased hole (Fig. 3C.8). The difference between the acoustic impedance of the borehole fluid and formation determines the magnitude (amplitude) of the transmitted ultrasound pulse that is reflected off the formation and back to the transducer. A portion of the transmitted signal is not reflected and continues to travel into the formation (openhole) or casing (cased hole) (Fig. 3C.8).

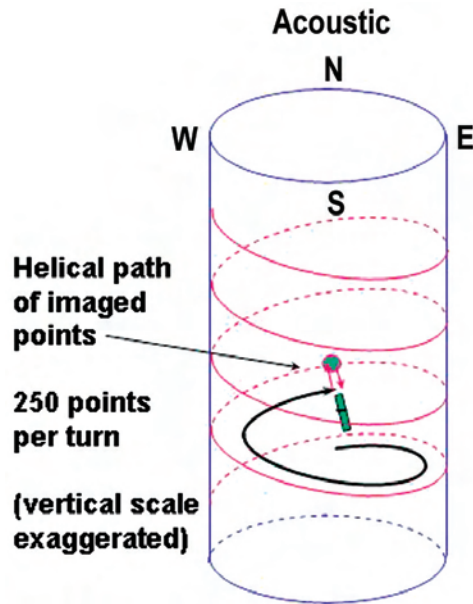


Fig. 3C.9—Figure illustrating the helical-scan data-acquisition path used by pulse/echo tools (courtesy of Baker Atlas).

Televiwer-type devices use a rotating transducer that acts as both transmitter and receiver, to acquire as many as 250 samples per revolution. Because the tool is moving uphole continuously, data are acquired as a helical scan along the borehole (Fig. 3C.9). Magnetometers provide azimuthal information for each scan. Acoustic devices operate in both conductive (water-based) and nonconductive (oil-based) muds. Televiwer-type tools cannot operate in air- or gas-filled boreholes.

The ultrasonic pressure pulses transmitted from the front face of the transducer form a beam pattern that defines the resolution and detection capabilities of the tool. While image resolution is directly proportional to signal frequency, the operating frequency (200 to 650 kHz) is a compromise between the desire for high image resolution and the need to operate in high-density muds in which signal attenuation is directly related to the frequency. In openhole, in which high-resolution, focused transducers are used, resolution may be as fine as 0.2 in. Image resolution in cased hole, in which unfocused transducers may be used, is generally lower.

The peak amplitude of the reflected signal is used to generate a 360° image of the borehole wall and the travel-time measurements are used as a caliper to provide a measurement of borehole geometry or casing corrosion. The primary factors that contribute to the measured pulse/echo amplitude are borehole-fluid ultrasonic attenuation, borehole-fluid/formation reflection coefficient, physical features of the formation, and transducer-beam angle of incidence on the formation. Loss in signal amplitude (image quality) results from conditions that either scatter, absorb, or spread the acoustic energy, such as tool eccentricity, irregularities in the borehole shape and surface, high-density and some oil-based drilling muds, and contrasts in acoustic impedance between the borehole fluid and borehole wall or casing (Table 3C.7). A separate transducer, commonly in the “mud-sub,” continually measures the borehole-fluid velocity for the caliper measurement.

In openhole, amplitude images of the borehole wall are used for fracture analysis, stress analysis (borehole breakouts), and formation evaluation. Cased-hole applications include cement evaluation (distribution and quality), casing evaluation (wear and damage), and perfora-

TABLE 3C.7—FACTORS AFFECTING PULSE/ECHO AMPLITUDE	
Factor	Effect
Fluid attenuation	Primary factor. High-fluid attenuation or large-diameter boreholes can result in a complete loss of useful information. OBMs (synthetic or otherwise) generally produced more signal loss than water-based mud of the same weight. For any particular fluid, attenuation usually increases with increasing fluid density, temperature, oil/water ratio, and any increase in particle size or gas content. Fluid attenuation generally decreases with greater concentrations of CaCl. High ultrasound attenuation in large boreholes will produce speckles (similar to snow on a weak television signal), fuzziness, and streaks.
Eccentering	Tool decentralization and/or borehole ellipticity can cause vertical dark streaks or bands.
Reflection coefficient	The difference between the acoustic impedance of the fluid and formation
Physical features	e.g., rugosity, fractures, or pitting
Beam angle of incidence (non-normal)	e.g., tool tilting and angular deformations on surface

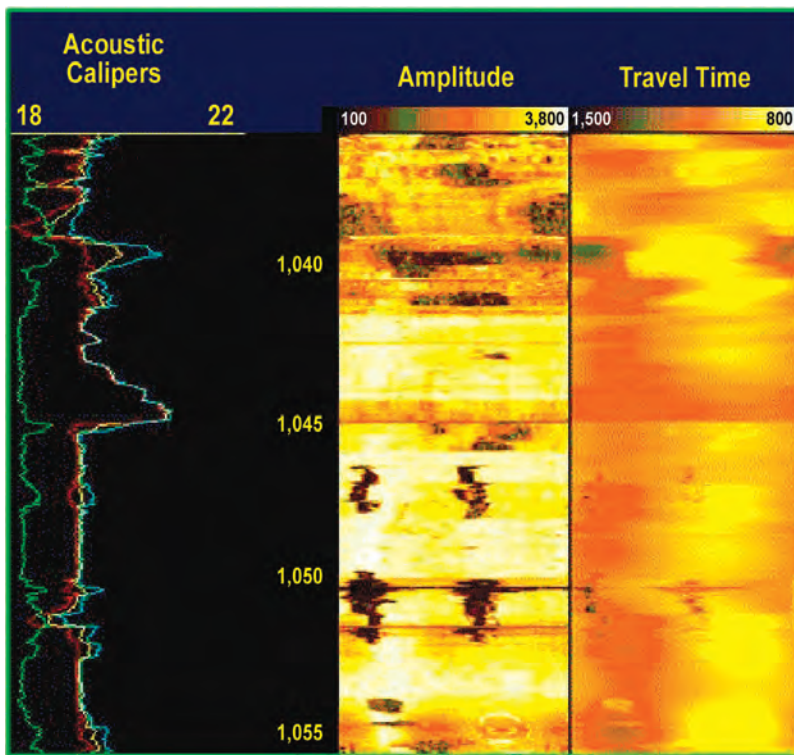


Fig. 3C.10—Typical televiewer “open-cylinder” image presentation; Track 1 contains the gamma ray curve and acoustic caliper; Track 2 is the reflected acoustic amplitude; and Track 3 is acoustic travel time (courtesy of Baker Atlas).

tion control.⁶¹ Smooth casing or borehole walls produce high-amplitude reflections (light), whereas openings (e.g., fractures or vugs) or imperfections (e.g., rugosity or pitting) in the borehole wall or casing result in low-amplitude reflections (dark). These images are displayed in the typical open-cylinder image presentation (Fig. 3C.10).

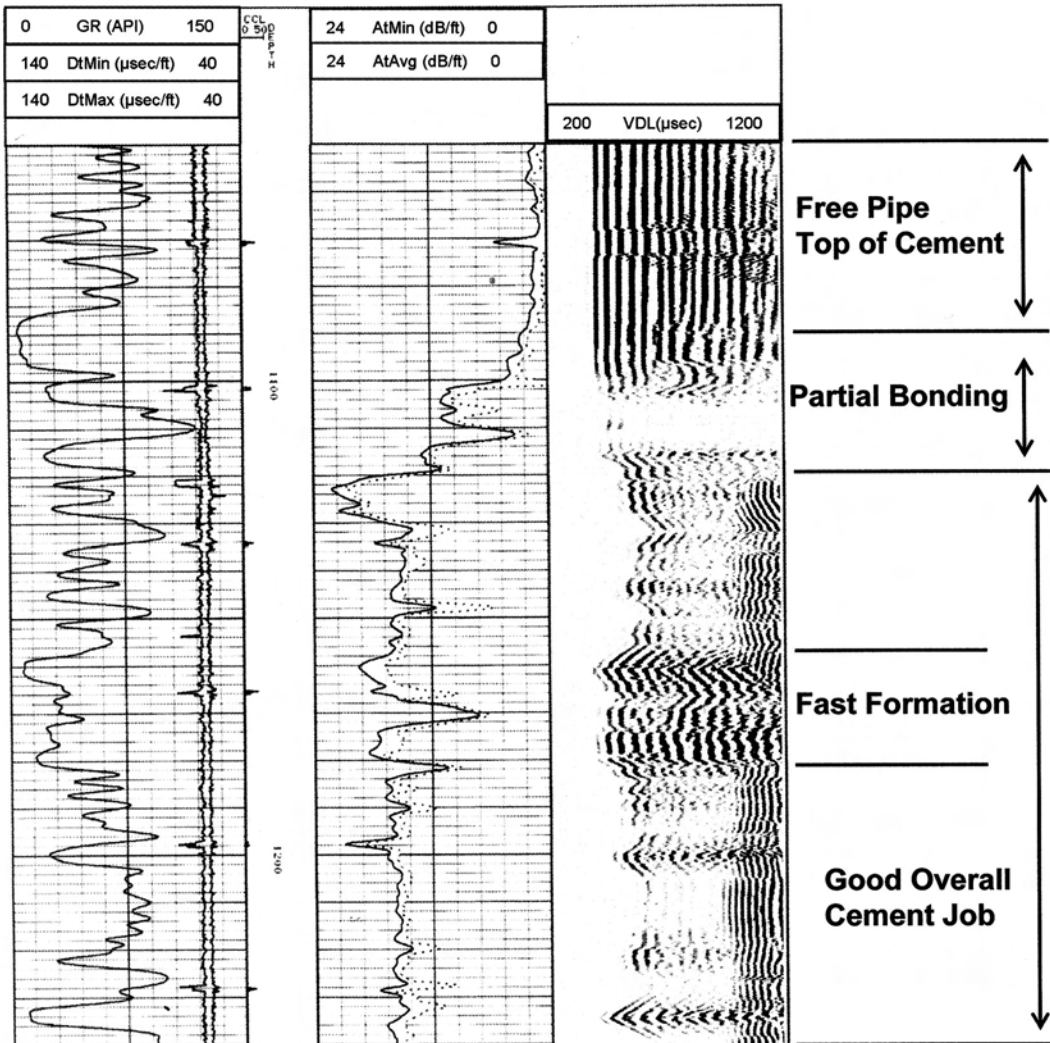


Fig. 3C.11—Typical cement-bond log presentation (courtesy of Baker Atlas).

3C.4.8 Cement-Bond Logging. Proper cement placement between the well casing and the formation is essential to support the casing (shear bond), to prevent fluid from leaking to the surface, and for isolating producing zones from water-bearing zones (hydraulic bond). Acoustic logs provide the primary means for evaluating the mechanical integrity and quality of the cement bond.⁶²⁻⁶⁶ Acoustic logs do not measure cement quality directly, rather, this value is inferred from the degree of acoustic coupling of the cement to the casing and to the formation. Properly run and interpreted, cement-bond logs (CBL) provide highly reliable estimates of well integrity and zone isolation. Just as filtrate invasion and formation alteration may produce changes in formation acoustic properties, and thus variation in acoustic logs over time,⁶⁷⁻⁶⁹ so too, cement-bond logs may vary over time as the cement cures and its properties change.

Modern acoustic cement-evaluation (bond) devices are comprised of monopole (axisymmetric) transmitters (one or more) and receivers (two or more). They operate on the principle that acoustic amplitude is rapidly attenuated in good cement bond but not in partial bond or free pipe. These cased-hole wireline tools measure compressional-wave travel time (transit time),

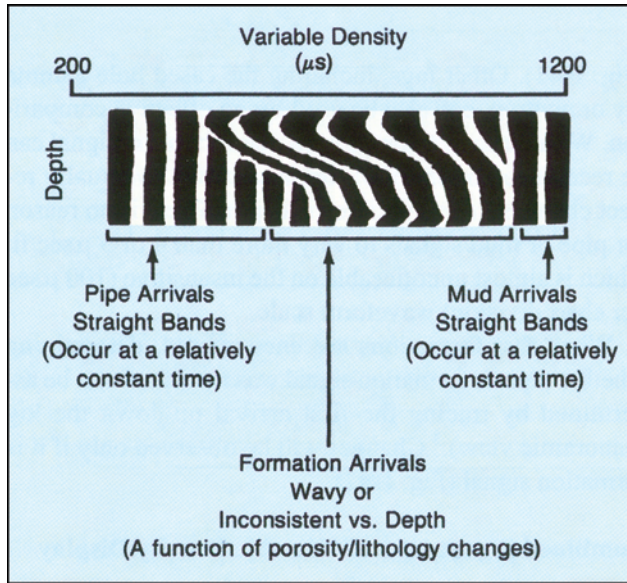


Fig. 3C.12—Identification of important features on a variable-density log (courtesy of Baker Atlas).

amplitude (first pipe arrival), and attenuation per unit distance. Conventional CBL tools provide omnidirectional measurements, while the newer radial cement-evaluation tools provide azimuthally sensitive measurements for channel evaluation.

When the acoustic wave generated by the transmitter reaches the casing, part is refracted down the casing (amplitude and travel-time measurement), part travels through the mud (fluid arrival), and other parts are refracted into the annulus and the formation and received back (formation arrival). Amplitude, measured directly or as an attenuation ratio, is the primary bond measurement and is used to provide quantitative estimations of cement compressive strength, bond index, and qualitative interpretation of the cement-to-formation interface. Tool response depends on the acoustic impedance of the cement, which, in turn is function of density and velocity. On the basis of empirical data, the log can be calibrated directly in terms of cement compressive strength. However, in foamed cements or when exotic additives are used, these calibrations can be inaccurate. In these situations, users are advised to consult with the logging service company regarding the appropriate calibrations.

A typical cement-log presentation includes a correlation curve (gamma ray), travel time (μsec), amplitude (mV), and attenuation (dB/ft) curves, and a full-waveform display (μsec). Presentation of the full acoustic waveform assists in resolving bond ambiguities arising from use of an amplitude measurement alone and provides qualitative information about the cement-to-formation bond. Waveform displays may be in variable density (VDL) or intensity (also called microseismograms) formats, oscilloscope waves (also known as x-y or “signature”), or both (Fig. 3C.11).

Variable density is a continuous-depth time display of full-waveform amplitude presented as shades of black and white. Positive waveform amplitudes are shown as dark bands and negative amplitudes as gray or white bands; contrast is proportional to amplitude. On a variable-density log, free pipe and fluid arrivals (if present) are easily identified as straight dark and light lines (indicating homogenous acoustic properties) at either side of the display (Fig. 3C.12). The zigzag, wavy, or chevron pattern between these two arrivals is the formation signal (indicating varying acoustic transit time). In cases of poor bonding, casing-collar signals may also be identified as “w” patterns (anomalies) (Fig. 3C.13).⁷⁰

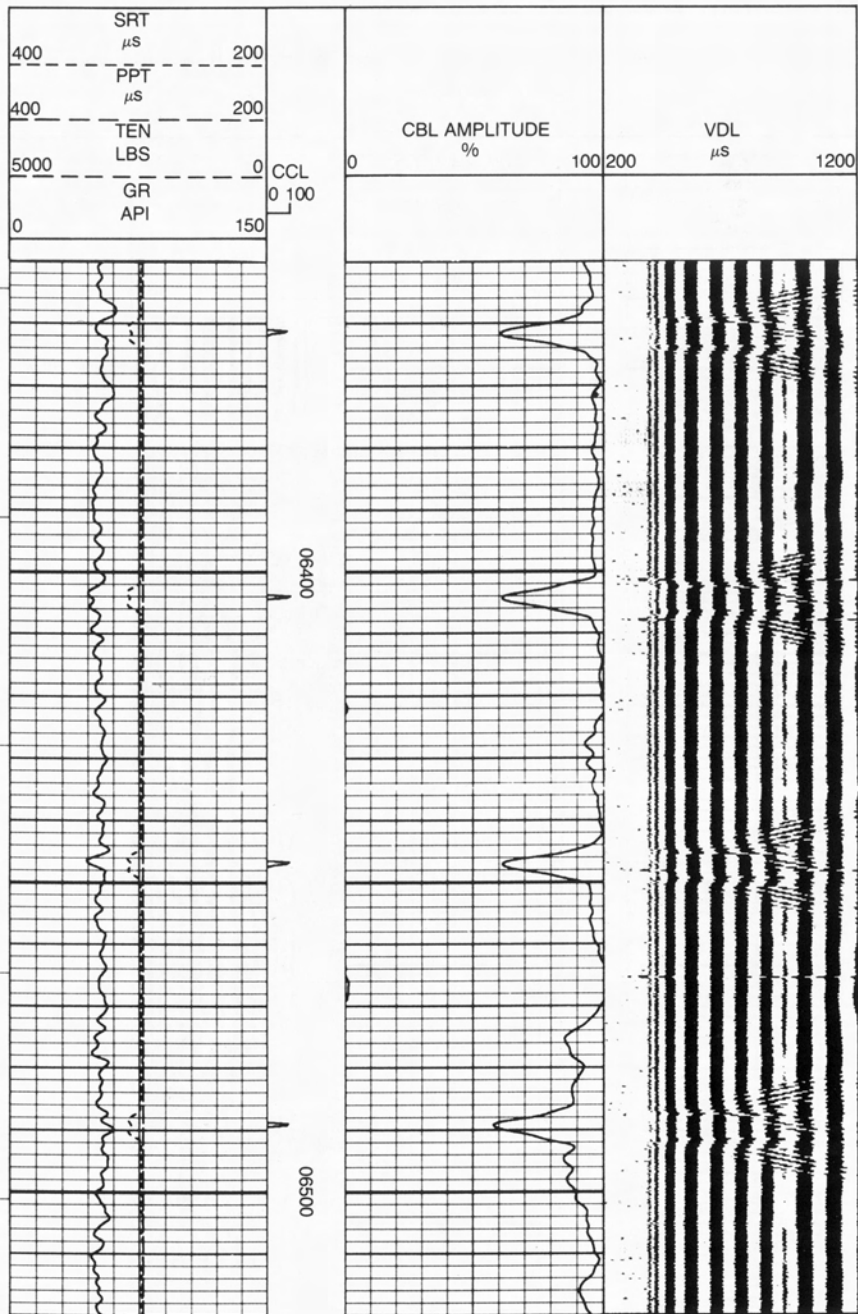


Fig. 3C.13—Casing-collar arrivals indicated on peak amplitude curve (Track 2) and variable density (Track 3). The height of the collar disturbance is a function of measurement TR spacing (amplitude, 3-ft interval; variable density, 5-ft interval) (courtesy of Baker Atlas).

Conventional Cement-Bond Devices. Early CBL designs (1960s) used a single transmitter and single receiver for an amplitude measurement. In an evolution similar to that of openhole acoustic logs (Table 3C.4), new designs were subsequently introduced that measured signal am-

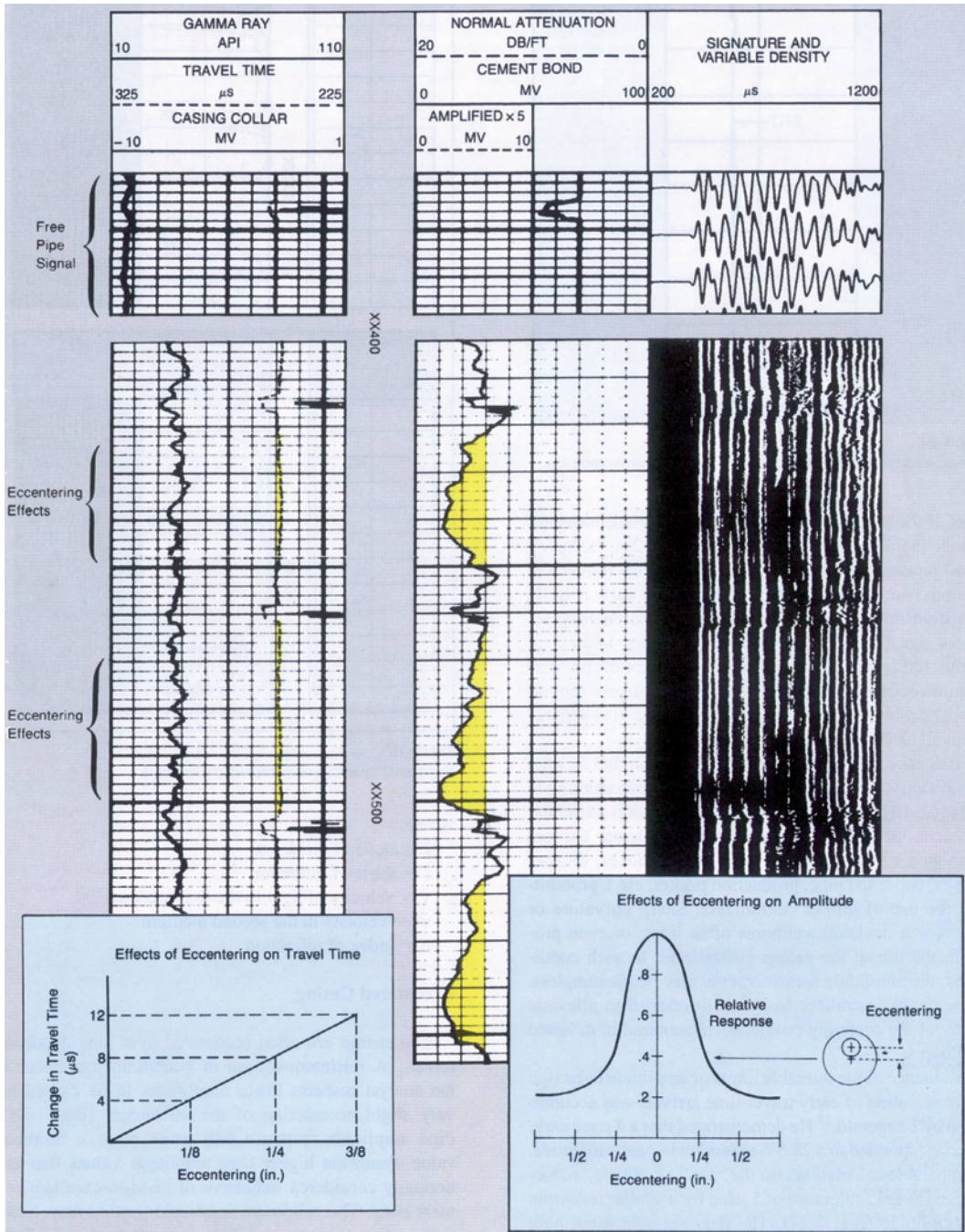


Fig. 3C.14—Effects of tool eccentricity (courtesy of Baker Atlas).

plitude at a near receiver and a full waveform from a far receiver. Eventually, borehole-compensated devices using dual transmitters and dual receivers were introduced in the 1980s, and today most commercial devices use multiple transmitters and receivers in a variety of arrangements to provide compensated measurements. These devices measure the attenuation between two transmitters and receivers as a way of eliminating, or at least minimizing, the

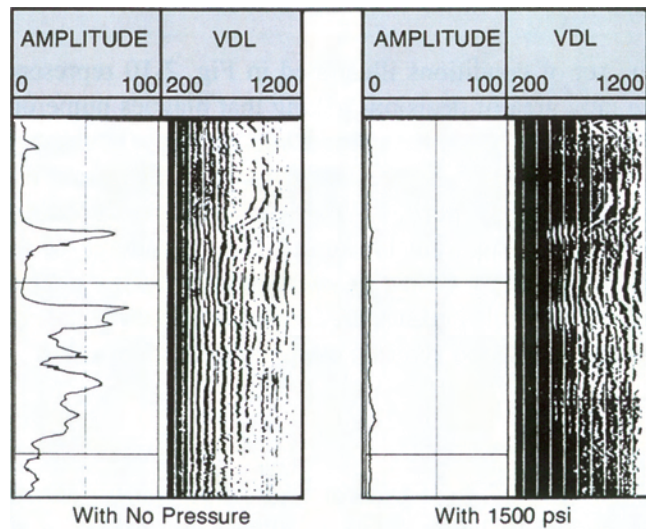


Fig. 3C.15—Field example showing microannulus effect on amplitude and VDL log displays (courtesy of Baker Atlas).

effects of tool eccentricity, fluid attenuation, receiver sensitivity, temperature drift, and calibration. In addition to specialized cement-bond devices, modern openhole array tools are designed to also provide conventional cement-evaluation measurements in cased hole. The cement-bond instrument sleeve is typically slotted to suppress and delay the tool signal that might otherwise be confused with the important casing signals.

TR spacing typically ranges from 3 to 5 ft. The shorter spacing (e.g., 3 ft) provides optimum signal level and resolution at high attenuation rates and is normally used for amplitude and travel-time (TT) measurements. A longer spacing, commonly ≥ 5 ft, is used for the full-waveform recording because longer TR spacing provides greater separation of the casing and formation-signal arrival times. This separation allows for easier analysis of the formation-signal strength and is used to monitor cement-to-formation bonding.

These tools typically operate at higher frequencies than conventional openhole tools—between 20 and 30 kHz. As with openhole tools, cement-bond tools require centralization to ensure accurate measurements. Centering in the cased hole is more critical because the higher-operating frequencies (i.e., shorter wavelengths) and the tool measurement are based on signal amplitude. Tool eccentricity reduces signal amplitude and travel time ([Fig. 3C.14](#)).

Cement-bond logging tools use gated systems to measure the specific parts of the acoustic waveform needed for the primary bond-amplitude measurement. Gates are time periods during which measurements are made—they can be either fixed or sliding (floating). Fixed-gate systems are commonly used for amplitude measurements and floating gates for travel-time measurements. Fixed gates are set (generally at the wellsite) to open, remain open, and close at designated times; opening time for the gate is a function of the casing size and the borehole-fluid velocity. If the gate opening is too large, there may be interference between early and late-arriving signals. Floating gates remain open, but recording is only triggered by an amplitude value greater than a designated threshold value.

A casing cement job can result in one or more of the following situations: free pipe, good bond, bond to casing only, and partial bond. In the first scenario, free pipe, there is no cement bond between the casing and cement. Consequently, there is no acoustic coupling with the formation and most of the transmitted acoustic energy is confined to the casing and the borehole

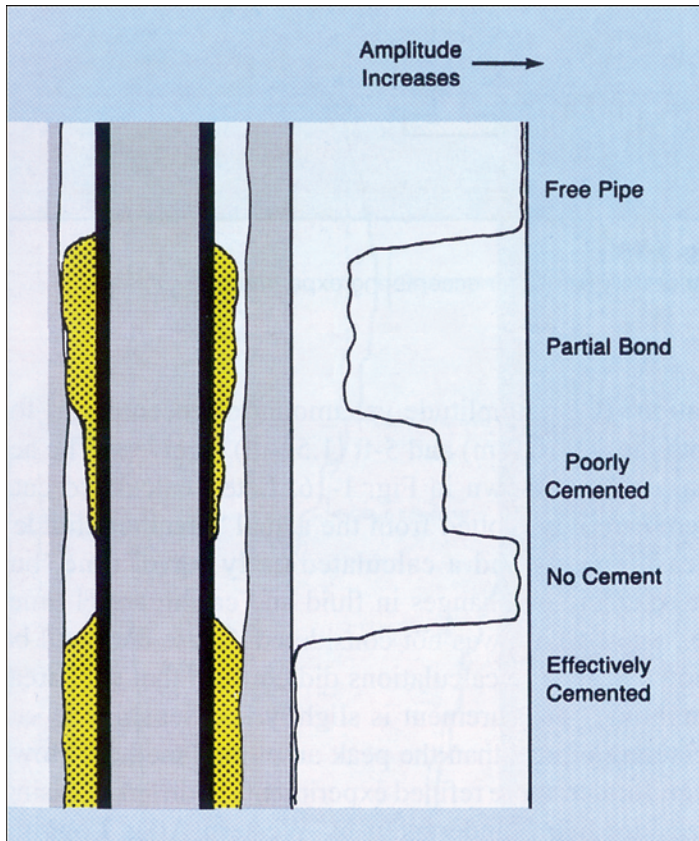


Fig. 3C.16—Summary of qualitative interpretation based on the amplitude curve (courtesy of Baker Atlas).

TABLE 3C.8—FACTORS AFFECTING BOND INTERPRETATION FROM AMPLITUDE RESPONSE ^{62,71}	
Factor	Description
Detection method	Fixed or floating gates
Gate width	Wide or narrow (multiple casing strings)
Measurement threshold	Cycle skipping
Eccentering	Tool or casing
Presence of gas	In borehole fluid or the cement
Casing variability	Size and weight (thickness)
Cement variability	Thickness [< 0.75 in. (2 cm)], voids (foam)
Formation type	In fast formations (e.g., low-porosity carbonates and evaporites) the formation signal may arrive at the same time or before the casing signal
Borehole-fluid variability	Density and viscosity; gas cut

fluid. As a result, a free-pipe acoustic signal is long-lived, high-amplitude, and of uniform frequency.

In the second scenario, good bond, cement is properly bonded to casing and to the formation. This provides good acoustic coupling and most of the acoustic energy is transmitted to the formation, resulting in little (weak) to no casing signals and little amplitude until the arrival of the strong formation signal.

<u>Operating Factor</u>	<u>Limitation</u>
Centralization	Required
Detecting small channels	Difficult to distinguish between the case of high-strength cement with a channel vs. an even distribution of low-strength (foam) cement (similar amplitude response)
Shear coupling	Required (microannulus may have a free-pipe signal)
Tool calibration	May not apply in fast formations in which the formation arrival precedes the casing arrival
Pressurization of casing	Recommended to eliminate microannulus effect

The third scenario, bond to casing only, is a common condition in which cement is bonded to the casing but not to the formation. This can occur because the mudcake dries and shrinks away from cement, or because the cement did not bond with mudcake in poorly consolidated formations. In this situation, energy traveling through the casing is attenuated drastically because of the highly attenuating cement sheath. At the same time, the annulus outside the cement sheath provides poor acoustic coupling. The result is that little energy is transferred to the annular fluid and virtually none is transferred to the formation. This condition is indicated by the lack of later-arriving formation energy. A similar response can be caused by the presence of formation gas in shallow, high-porosity zones.

In the last scenario, partial bond, a space exists within an otherwise well-bonded casing. This may occur with the presence of a microannulus or channels within the cement. The resulting waveform is comprised of a casing signal and a formation signal; the casing signal arrives first, followed by the formation signal.

When channeling occurs, it is generally localized and nonuniform; that is, it occurs over relatively short intervals and can frequently be identified by variations in the amplitude response. Channeling is significant because it prevents a hydraulic seal. In contrast, a microannulus (a small gap between the casing and cement sheath) may extend over long sections of casing but may not prevent a hydraulic seal. Microannulus may result from thermal expansion or contraction of the pipe during cementing or to the presence of contaminants, such as grease or mill varnish, on the casing's exterior surface. A common practice is to run cement-bond logs with the casing under pressure to expand the casing against the cement, thereby decreasing any microannulus that might exist. If the initial log was not under pressure and the log indicates poor bond, the presence of a microannulus can be evaluated by running a second bond log under pressure to see if there is a difference. Pressuring the casing improves the acoustic coupling to the formation and the casing signal will decrease and the formation signal will become more obvious (**Fig. 3C.15**). However, if only channeling exists, pressuring the casing will not significantly change the log. When conducting a cement evaluation, information on the type of cement used is essential. For example, foam cements, which intentionally create void spaces in the cured cement, can be misinterpreted as partial bond if normal cement is assumed. **Fig. 3C.16** summarizes this discussion, and **Table 3C.8** lists additional factors that may affect interpretation of bond quality from the amplitude response.

One caveat regarding the use of the amplitude curve for bond evaluation: pipe amplitude represents the quality of the bond of pipe to cement but provides no indication of the quality of the bond between the cement and the formation. Whenever possible, amplitude data should be used in conjunction with the other measurements presented on the log (e.g., travel time or full waveform) for a more-reliable bond evaluation. For example, the presence of shear-wave amplitudes on the full-waveform display is an indication of good acoustic coupling to the formation. **Table 3C.9** lists the limitations of conventional cement-bond logs.

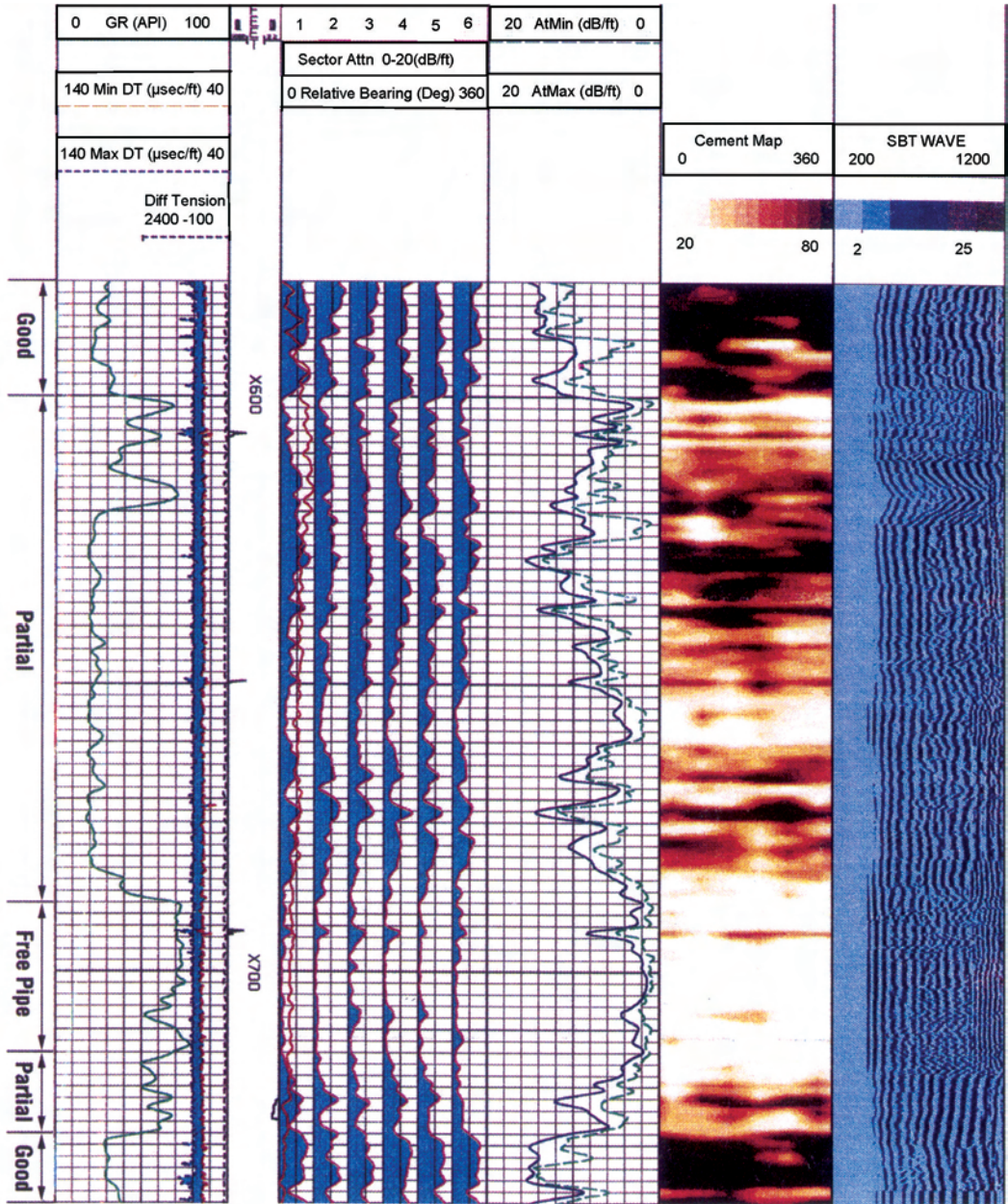


Fig. 3C.17—Log presentation for the Baker Atlas SBT tool containing individual log curves, cement map, and VDL display (courtesy of Baker Atlas).

Formations with transit times less than casing (57 μsec/ft) can cause problems when interpreting the amplitude curves because the formation signal can arrive in the amplitude gate. The VDL should be examined to ensure that the formation arrival is impacting the amplitude curve.

The bond index (BI) is a qualitative measure of cement bond based on signal amplitude. This dimensionless quantity is the ratio of measured attenuation to maximum attenuation:

$$\text{Attenuation} = 20 / \text{TR} \log (\text{measured amplitude} / \text{free-pipe amplitude}) \dots\dots\dots (3C.3)$$

	Conventional CBL	Radial Ultrasonic	Radial Pad
Amplitude/attenuation	Yes	Yes (different)	Yes
Travel time (transit time)	Yes	Yes (different)	Yes
Full waveform	Yes	No	Yes
Good bond identification	Yes	Yes	Yes
	(if shear arrival)		
Partial bond identification	Yes	Yes	Yes
Channel identification	No	Yes	Yes
Microannulus effect	Strongly affected (repeat log under pressure)	Moderately affected	Yes
Repeat (calibration) runs	Yes	Yes	Yes
Centralization	Essential (Use attenuation-ratio log where centralization is difficult)	Less critical	Not a factor
Free-pipe calibration (above top of cement)	Desirable	Not necessary	Not a factor
Heavy mud	Moderately affected	Strongly affected	Not a factor
Gas in microannulus	Strongly affected	Strongly affected	Strongly affected
Casing geometry	No	Yes	No
Casing thickness	No	Yes	No
Casing corrosion	No	Yes	No

A BI value of 1.0 represents a perfect cement bond. A value of less than 1.0 indicates an incomplete bond. This technique requires attenuation measurements in zones with 100% bond and in free pipe.

Radial-Cement Evaluation. Radial-cement-evaluation devices were developed to overcome some limitations of conventional cement-bond tools and to permit more accurate evaluation of cement distribution behind casing by providing the precise location of partial bond and channeling. These tools use one or more azimuthally sensitive transducers to evaluate cement quality around the circumference of the casing. Data from these tools are presented as individual log curves or as azimuthal images (“maps”) of cement quality generated by interpolating between the individual azimuthal measurements (Fig. 3C.17). In addition, each tool design also provides a conventional 5-ft VDL waveform measurement to provide information about the cement-to-formation bond.

There are four radial-evaluation-tool designs in current use: televiewer-types that use a single rotating ultrasonic transducer,^{72,73} circular ultrasonic pulse/echo transducers arranged in a fixed helical pattern around the sonde,^{74,75} a multipad device that provides six compensated attenuation measurements,⁷⁶ and an array of eight TR pairs, arranged azimuthally around the sonde, that provide compensated CBL amplitude.^{77,78}

The ultrasonic tools compute the acoustic impedance of the material beyond the casing. To do this, repeated acoustic pulses are directed at the casing to make it resonate in its thickness mode and the energy level (attenuation) of the decaying reflected wave is measured. Good cement bond to casing produces a rapid damping (higher impedance) of this resonance; poor cement bond results in longer resonance decay (lower impedance). Measurements from these devices are influenced by the same factors as openhole televiewer devices.

The pad device makes multiple short-spaced, compensated, azimuthal-attenuation measurements. Because the pads are in direct contact with the casing—in contrast to ultrasonic measurements—measurements are unaffected by gas in the borehole, fast formations, heavy-mud conditions, or minor tool eccentricity. The attenuation in each segment is measured in two directions using a pair of acoustic receivers and two transmitters. The two measurements are

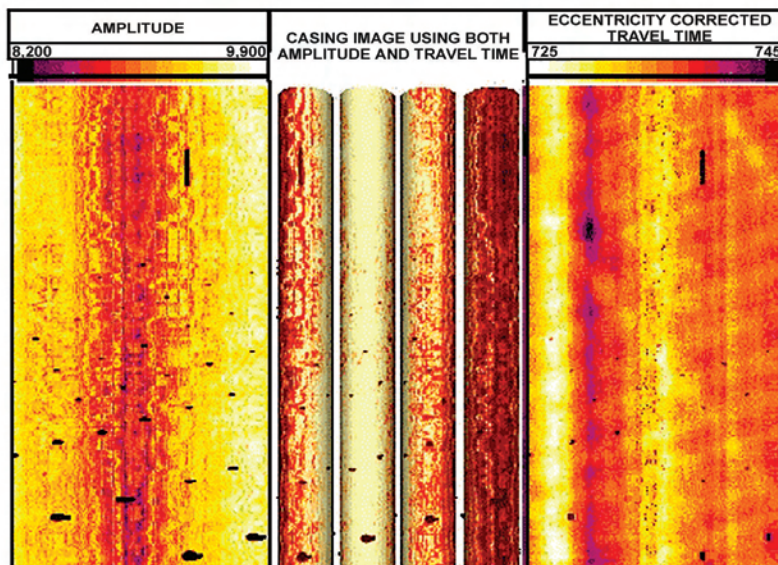


Fig. 3C.18—Casing-evaluation log display. Holes in the casing are visible in the series of ultrasonic images that are based on amplitude (left) and corrected travel time (right). The center 3D images show the pipe in 90° quadrants. The image shading is generated from the amplitude data⁸⁶ (courtesy of SPE).

combined to form a result that compensates for surface roughness and the effects of minor residual cement on the inside of the casing. Transmitting elements and the firing sequence are controlled to direct (steer) and enhance the acoustic-energy output of both the pad transmitters and the VDL transmitter. This has the effect of improving the signal strength of both the casing and cement-to-formation arrivals, respectively. This technique improves VDL interpretation, particularly in soft formations in which the standard VDL may wash out.

The use of new high-performance low-density, foam, and complex cements is increasing. However, the presence of gas in cement slurries, as an inert component or as contamination, may seriously affect ultrasonic-tool interpretation. New interpretation methods integrate ultrasonic and attenuation measurements from conventional tools to provide improved cement evaluation in these conditions.^{79–82} The latest ultrasonic tool has a conventional pulse-echo transducer plus a flexural transmitter and two flexural receivers that provide greater depth of investigation. Interpretation techniques combining these different measurements provide improved evaluation in lightweight cements, especially in the annulus, beyond the casing-cement bond.⁸³ **Table 3C.10** summarizes the capabilities and guidelines for running the different types of cement-bond evaluation tools.

Casing Evaluation. Preventing casing failure caused by deformation, physical wear, or corrosion is critical to maintaining well production. Ultrasonic radial-cement-evaluation devices and modified openhole-imaging devices are also used to evaluate casing for indications of potential collapse, thinning, and internal or external metal loss.^{73,84–86} Echo amplitude and travel time provide images of the condition of the inside casing surface (e.g., buildup, defects, and roughness such as pitting and gouges) (**Fig. 3C.18**), and travel-time and resonant-frequency analysis provide casing thickness (**Fig. 3C.19**).

The acoustic caliper generated from the pulse/echo travel time provides the casing inside diameter (an average of all transducers or a single circumferential scan). An estimate of casing ovality is obtained using only the maximum and minimum measurements. Then, if the nominal value of the outside casing diameter is assumed, changes in thickness can be calculated and internal defects identified. Frequency analysis determines the casing resonant frequency from

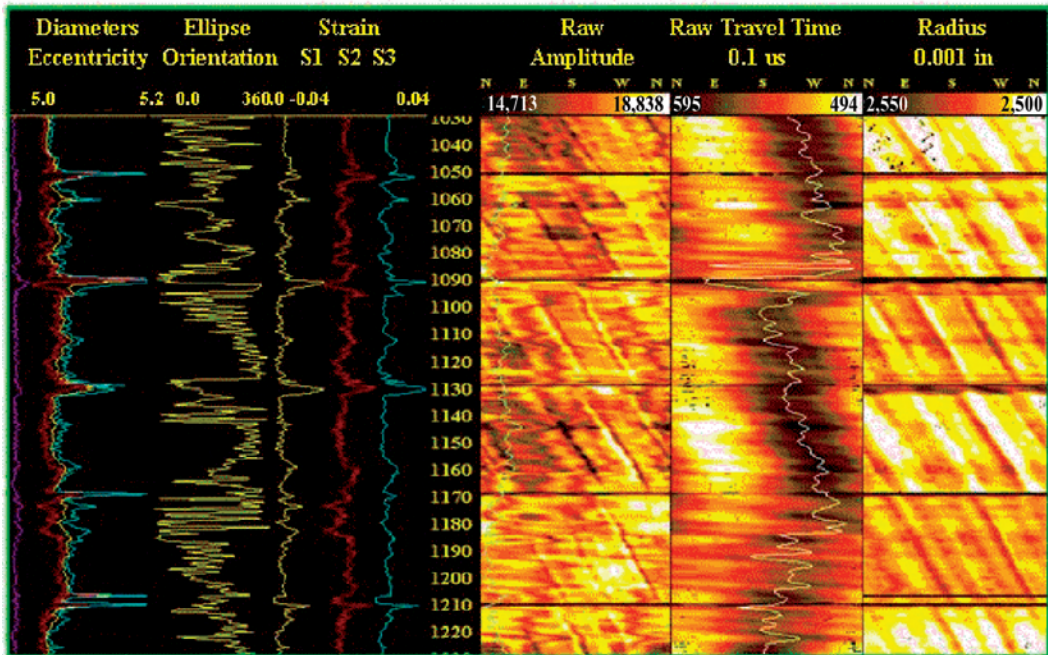


Fig. 3C.19—Ultrasonic casing-evaluation display. In this example, casing radius and shape are presented as log curves and image maps and deformed casing is easily identified (courtesy of Baker Atlas).

the acoustic waveform; casing thickness is inversely related to the resonant frequency. By combining travel time and resonant-frequency measurements and using data from all available transducers (or a single scan), presentations showing casing cross sections are used to highlight casing damage such as thinning, corrosion metal loss, and collapse (Fig. 3C.19).

3C.5 Conventional Applications

Interpretation of acoustic-log data begins with the slowness values obtained from processing the recorded waveforms. Slowness, or porosity derived from slowness, may be corrected for additional factors (discussed below) before use in applications. Today, log analysis and interpretation is routinely performed by computers during data acquisition (in real time) or in post-acquisition processing in offices and computing centers. Modern interpretation software is built on algorithms derived from the empirical relationships originally used to create a variety of graphical solutions contained in crossplots and nomograms.⁸⁷ Because porosity tools vary in their sensitivity to lithology, porosity, and fluid properties, the combination of different measurements allows more-accurate determination of porosity, petrophysical, and geological characteristics. The logging service companies issue chartbooks with tool-specific charts to facilitate rapid manual determination of porosity, lithology, shaly-sand analysis, saturation, mechanical properties, and cement-bond evaluation. These charts, which are accompanied by instructions for their use, form the basis for quick-look interpretations and for quality control of computer interpretations.^{88,89}

The earliest applications of acoustic-logging measurements made use of compressional slowness, used alone or in combination with resistivity logs and other porosity logs. This group of applications, which includes velocity, porosity, gas identification, lithology, fluid saturation, and rock strength, still comprises the basic set of applications for acoustic-log data. In the 1960s, laboratory studies indicated that shear-wave data could also prove useful in formation evaluation.⁹⁰ The development and introduction of reliable shear-wave acquisition and full-wave-

TABLE 3C.11—ACOUSTIC-LOG APPLICATIONS BY WAVE TYPE		
Wave Type (Energy Mode)	Acoustic Property	Application
Transmission Compressional	Velocity	Porosity evaluation
	Velocity	Lithology identification
	Velocity	Gas identification
	Velocity	Fluid saturation
	Velocity	Rock-strength determination
	Velocity	Seismic time/depth correlation
	Velocity	Synthetic seismic
	Velocity	Geopressure prediction
	Attenuation	Cement evaluation
	Shear	Velocity
Velocity		Lithology evaluation
Velocity		Hydrocarbon typing (combined with compressional)
Velocity, amplitude		Azimuthal anisotropy analysis
Velocity		Rock-strength determination
Amplitude, attenuation		Fracture identification and evaluation
Velocity		Seismic correlation and calibration, AVO, VSP
Velocity		Geopressure prediction
Velocity		Completion design (hydrofracture evaluation)
Velocity		Sand control
Attenuation	Permeability	
Stoneley (tube)	Velocity, attenuation	Permeability analysis
	Amplitude	Fracture evaluation
Reflection Ultrasonic	Velocity/amplitude	Borehole imaging
	Velocity/amplitude	Cement evaluation
	Velocity/amplitude	Casing evaluation

form logging in the late 1970s and 1980s resulted in improved accuracy in these conventional applications.⁹¹ Further advances throughout the 1980s and 1990s, in both basic and applied research as well as in tool technology, led to new and advanced applications, e.g., permeability estimation, anisotropy determination, and direct hydrocarbon indicators, that use shear- and Stoneley-wave amplitude and attenuation ([Table 3C.11](#)).

3C.5.1 Petrophysical Applications. Porosity Evaluation. The compressional velocity of sound in fluid is less than the velocity in rock. If there is pore space in the rock, and it is fluid-filled, the acoustic energy will take longer to get from the transmitter to the receiver (i.e., low velocity indicates high porosity). The recorded velocity or travel time represents the sum of the velocity of the solid part or framework of the rock (i.e., the rock matrix), the rock lining the pores, and the fluid filling the pore space. In turn, travel time in the rock matrix, Δt_{ma} , is influenced by variations in lithology (i.e., the chemical composition) and confining pore pressure (i.e., compaction).⁹² These factors are related through an empirical relationship known as the Wyllie time-average equation.⁹³ When the velocity (transit time, Δt , or travel time, t) of the rock matrix and borehole fluids are known, porosity can be computed the following ways ([Eq. 3C.4](#) to [Eq. 3C.7](#)).

- In terms of velocity, v :

TABLE 3C.12—GUIDELINES FOR SELECTING MATRIX TRANSIT TIME		
Δt_{stn} ($\mu\text{sec}/\text{ft}$)	V_{ma} (ft/sec)	Δt_{ma} ($\mu\text{sec}/\text{ft}$)
70 to 80	20,000	50
80 to 90	19,000	52.5
90 to 100	18,000	55.5
> 100	Use compaction correction (C_p) adjustments	

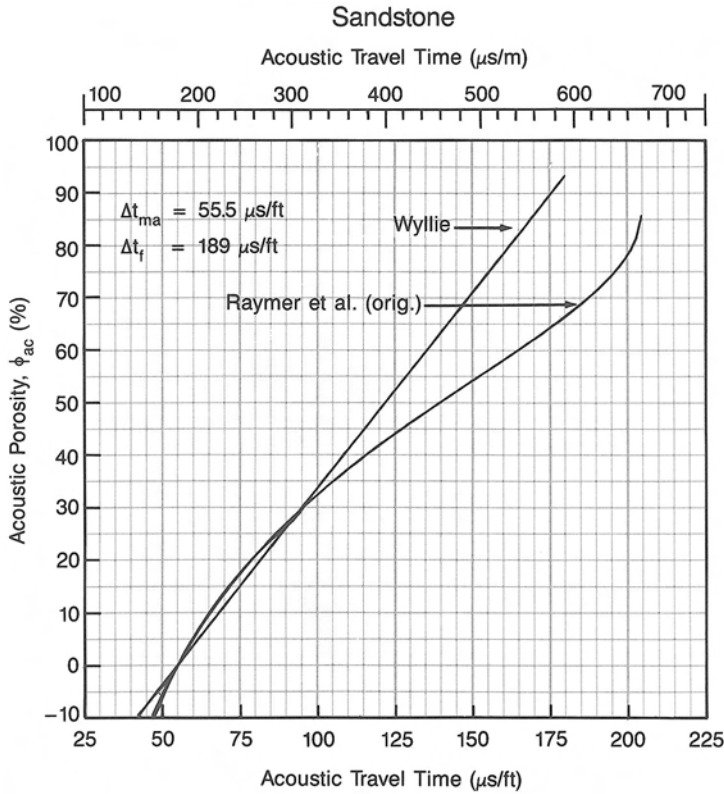


Fig. 3C.20—Graphical solutions of the Wyllie and Raymer velocity-porosity relationships (sandstone matrix) (courtesy of Baker Atlas).

$$\frac{1}{v} = \frac{\phi}{v_f} + \frac{(1 - \phi)}{v_{ma}}, \dots\dots\dots (3C.4)$$

where ϕ = fractional porosity of the rock, v = velocity of the formation (ft/sec), v_f = velocity of interstitial fluids (ft/sec) and, v_{ma} = velocity of the rock matrix (ft/sec).

• In terms of transit time (Δt):

$$\Delta t = \phi \Delta t_f + (1 - \phi) \Delta t_{ma}, \dots\dots\dots (3C.5)$$

or

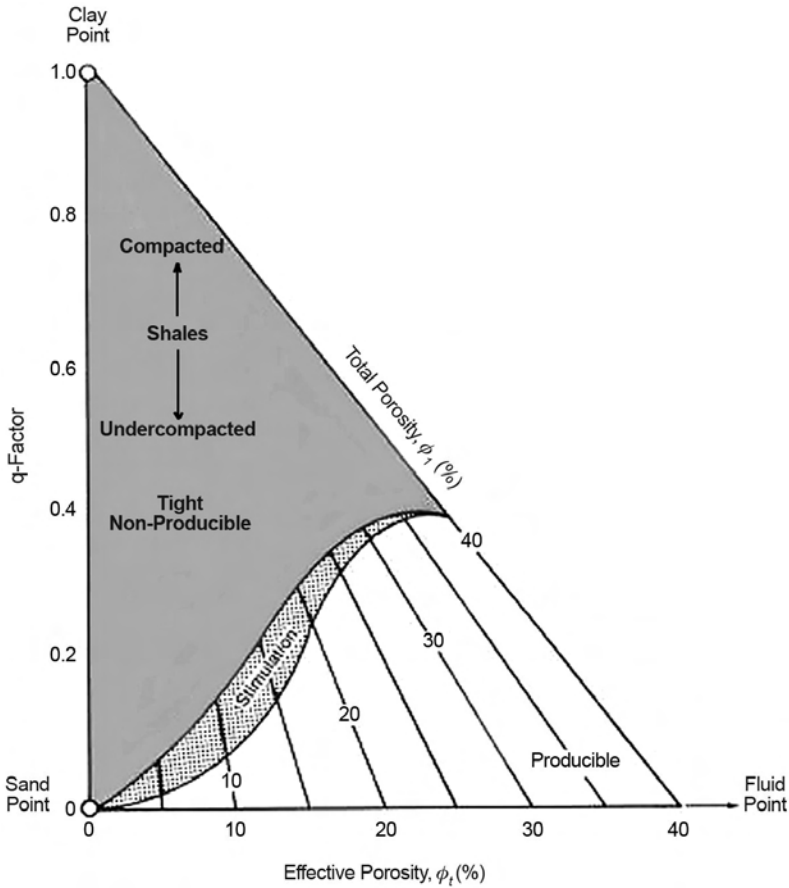


Fig. 3C.21—Chart used to predict productivity in shaly-sand reservoirs (courtesy of Baker Atlas).

$$\phi = \frac{\Delta t - \Delta t_{ma}}{\Delta t_f - \Delta t_{ma}}, \dots\dots\dots (3C.6)$$

where Δt = acoustic transit time ($\mu\text{sec}/\text{ft}$), Δt_f = acoustic transit time of interstitial fluids ($\mu\text{sec}/\text{ft}$), and Δt_{ma} = acoustic transit time of the rock matrix ($\mu\text{sec}/\text{ft}$). (See Table 3C.3 for typical values of Δt_{ma} and Δt_f .)

- In terms of travel time:

$$\begin{aligned} t_{\log} &= t_f \phi + t_{ma}(1 - \phi) \\ t_{\log} &= t_f \phi + t_{ma} - t_{ma}\phi \\ t_{\log} - t_{ma} &= t_f \phi - t_{ma}\phi \\ t_{\log} - t_{ma} &= (t_f - t_{ma})\phi \\ &\vdots \\ \phi &= \frac{t_{\log} - t_{ma}}{t_f - t_{ma}} \dots\dots\dots (3C.7) \end{aligned}$$

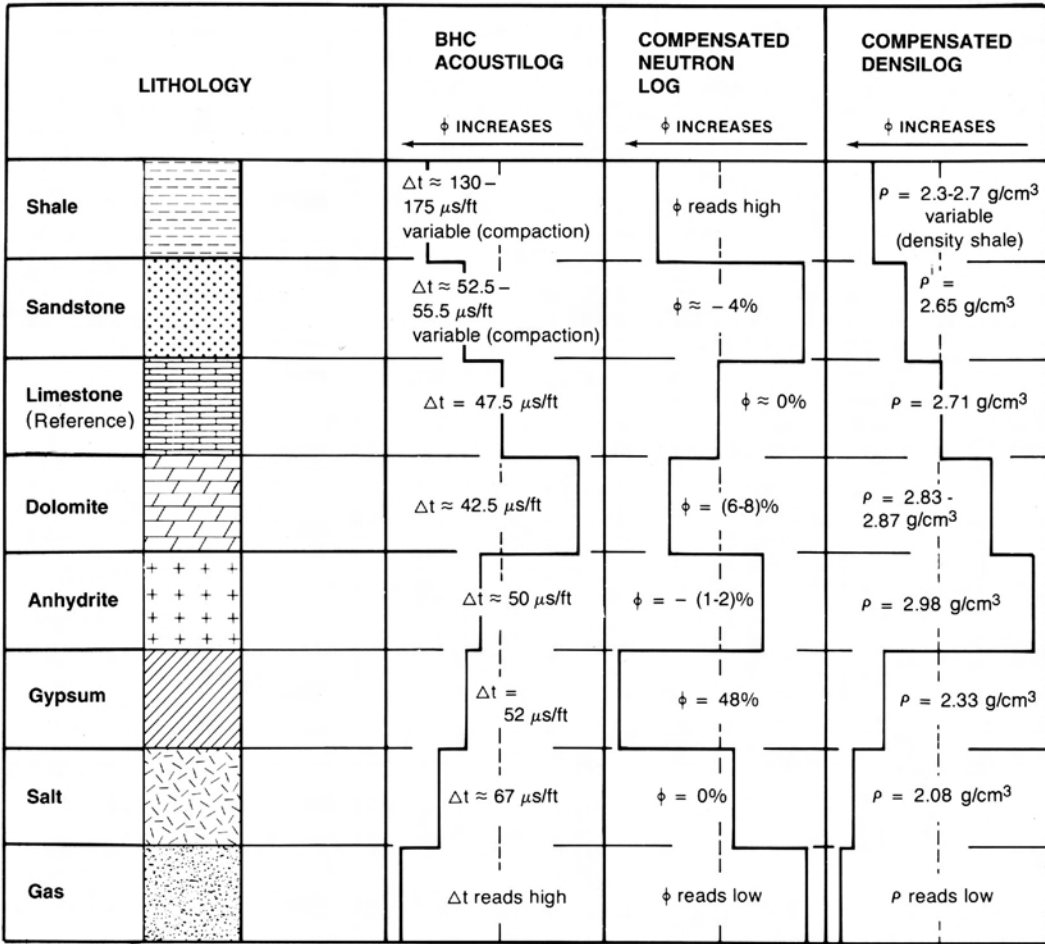


Fig. 3C.22—Generalized comparison of acoustic-, neutron-, and density-log responses in common reservoir lithologies and to gas (courtesy of Baker Atlas).

The velocity of most borehole and reservoir fluids (except gas) does not vary greatly and a fluid velocity (Δt_f) of 189 $\mu\text{sec/ft}$ (5,300 ft/sec) is generally assumed for fresh drilling fluids; a slightly lower value, 185 $\mu\text{sec/ft}$, is used for salt muds. Fluid type becomes more of a concern when oil-based mud (OBM) is used if the formation of interest is not invaded or if invasion is very shallow. The lithology must be known or estimated in order to select the appropriate matrix velocity.

The Wyllie equation represents consolidated and compacted formations. In poorly consolidated or unconsolidated rocks, a correction factor is necessary (Eq. 3C.8). Also, the presence of shale or clay within the sand matrix will increase Δt by an amount proportional to the bulk-volume fraction of the clay. An empirical equation is used for calculating porosity in sandstones in which adjacent shale values (Δt_{sh}) exceed 100 $\mu\text{sec/ft}$ (Eq. 3C.9):

$$\phi = \frac{\Delta t - \Delta t_{ma}}{\Delta t_f - \Delta t_{ma}} \times \frac{1}{C_p}, \dots\dots\dots (3C.8)$$

where the compaction correction factor C_p is

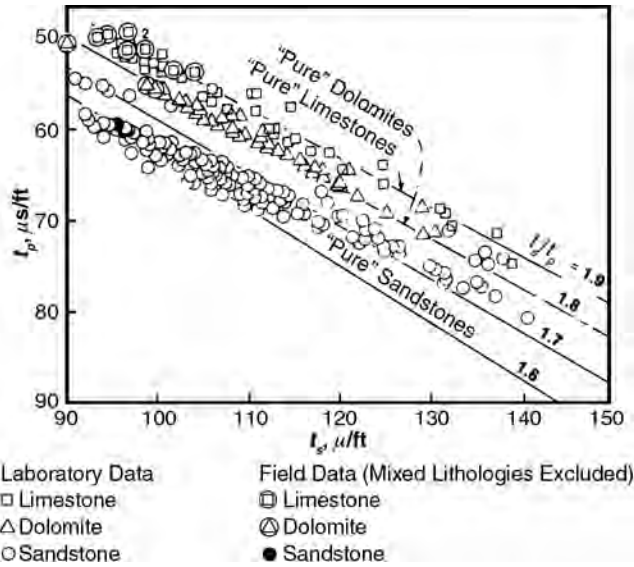


Fig. 3C.23— Δt_p vs. Δt_s crossplot demonstrates sensitivity to variations in lithology⁹⁰ (courtesy of SPE).

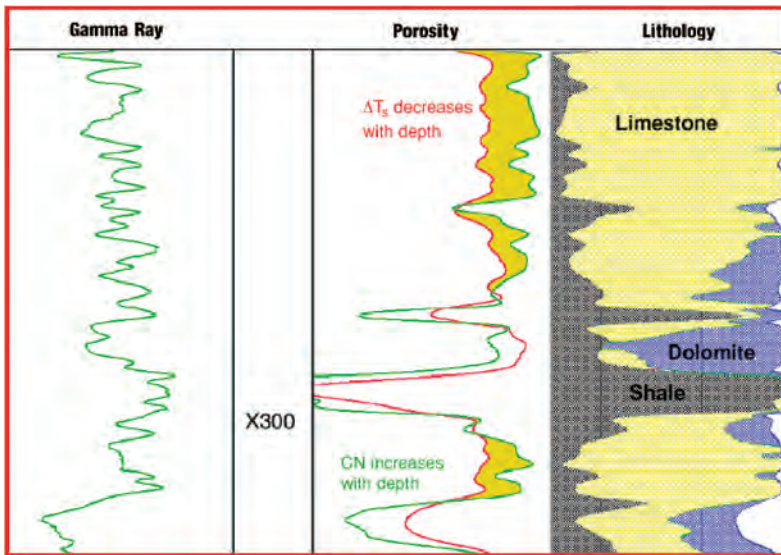


Fig. 3C.24—Shear slowness as a lithology indicator. The cased-hole apparent compensated-neutron porosity (Track 2) appears to increase with depth, while the dipole tool shear-velocity data decrease with depth. This indicates a lithology change rather than a porosity change, which is confirmed in the lithology track (courtesy of Baker Atlas).

$$C_p = \frac{\Delta t_{sh}(C)}{100}, \dots\dots\dots (3C.9)$$

where Δt_{sh} = specific acoustic transit time in adjacent shales ($\mu\text{sec}/\text{ft}$), and 100 = acoustic transit time in compacted shales ($\mu\text{sec}/\text{ft}$). The shale compaction coefficient (C) generally ranges from 1.0 to 1.3, depending on the regional geology.

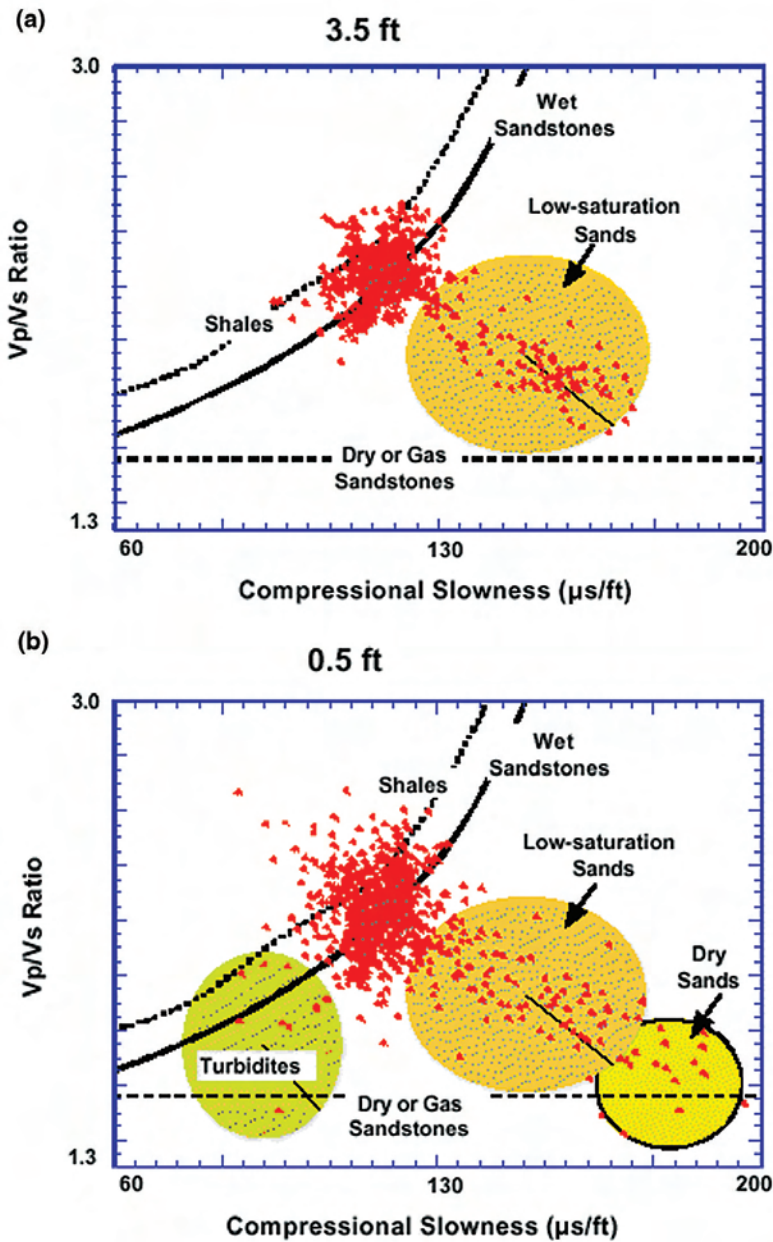


Fig. 3C.25— V_p/V_s vs. Δt_p crossplot. In addition to the low-saturation sands identified in (a), the high-resolution result (b) also resolves turbidite and dry sand intervals²²⁴ (courtesy of SPWLA).

The highest velocities observed in sandstones approach 20,000 ft/sec (50 $\mu\text{sec}/\text{ft}$), but most sandstones have a lower matrix velocity. Velocities in adjacent shales are used to adjust the matrix velocity for sands with velocities lower than 18,000 ft/sec. **Table 3C.12** provides guidelines for selecting the appropriate value of Δt_{ma} . If the lithology of carbonate rocks can be reasonably estimated and if the porosity distribution is fairly uniform, the Wyllie time-average formula can provide reliable determination of porosity for this group.

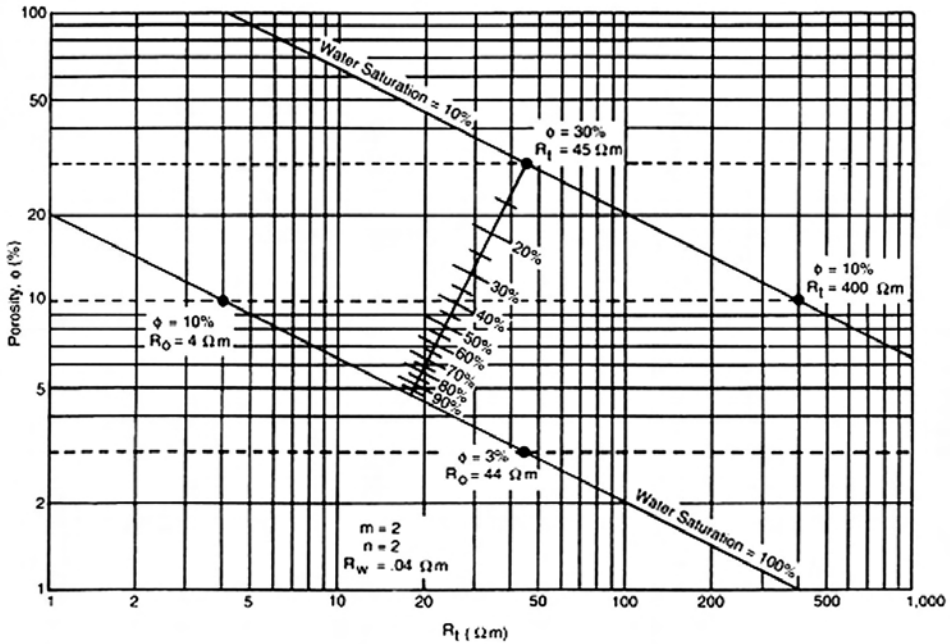


Fig. 3C.26—Example of a Pickett plot, including a saturation scaler (courtesy of Baker Atlas).

A second empirical velocity/porosity relationship, the Raymer-Hunt-Gardner equation,⁹⁴ was introduced to correct for observed anomalies and shortcomings of the Wyllie time-average formula (Eq. 3C.10). It provides improved porosity correlation over the entire porosity range and is applicable to both consolidated and some unconsolidated formations, thus eliminating the need for a compaction correction. However, in high-porosity, unconsolidated, and uncemented (slow) rocks, neither of the empirical velocity/porosity transforms may be adequate⁹⁵

$$\phi_{\log} = -\alpha - [\alpha^2 + (\Delta t_{ma} / \Delta t_{\log}) - 1]^{0.5}, \dots\dots\dots (3C.10)$$

where $\alpha = (\Delta t_{ma} / 2\Delta t_f) - 1$.

Graphical solutions for both algorithms for a sandstone matrix are compared in Fig. 3C.20. One caveat regarding the use of empirically derived porosity transforms: they do not account for all the factors influencing acoustic velocity. Consequently, these relationships may not be valid for all reservoirs.

In fast formations, the shear velocity can also be used for porosity evaluation in a manner similar to that described above for compressional velocity.⁹¹ Further, the combination of compressional and shear slowness can provide an enhanced porosity determination.⁹⁶ Using shear velocity for porosity determination offers several distinct advantages because shear velocity is: generally more sensitive to porosity than compressional velocity, insensitive to gas effects, less affected by borehole washout, can be used to replace nuclear porosity in some situations,⁹⁷ and porosity evaluation can be conducted in cased hole using dipole tools (or in some cases, monopole-array tools using special processing).^{98,99}

These velocity/porosity methods are for clean (shale free), water-filled formations. The calculated apparent porosity must still be corrected for the volume of pore-filling material (shale). If the formation contains shale or dispersed-clay particles, or is hydrocarbon bearing and invaded to only a very shallow depth, corrections to the basic log data are necessary before reasonable porosity values can be calculated.

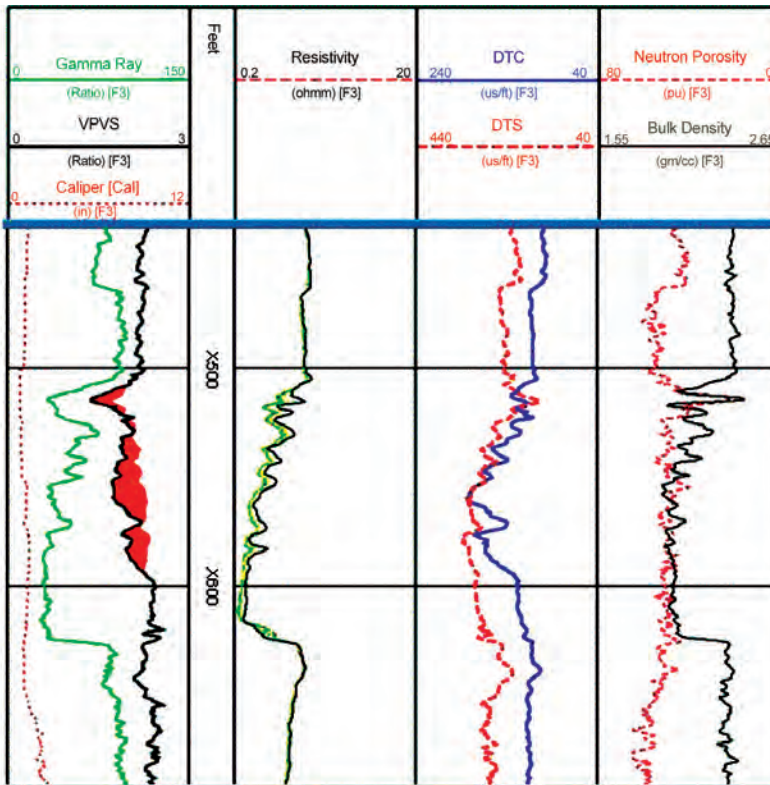


Fig. 3C.27—Log presentation illustrating the use of Δt_c and Δt_s curves as a quick-look gas indicator (courtesy of Baker Atlas).

Because shale transit times range from 62 to 167 $\mu\text{sec}/\text{ft}$, failure to correct for the presence of shale may result in overly optimistic porosity calculations. The acoustic measurement is also influenced by the way the shale is distributed within the sandstone reservoirs. The fraction of shale, or shale volume, can be estimated using a combination of log measurements that are influenced by shale, such as neutron porosity, density, gamma ray, or spontaneous potential (SP). Chartbook nomograms developed for porosity determination include graphical solutions for both undercompaction and shale volume.

In some producing regions, producibility indexes based on the volume of shale in producing sandstone reservoirs have been developed. The fraction of total porosity occupied by dispersed clay (q factor) is empirically related to effective and total porosity and production characteristics. Local experience is used to create permeability cutoffs using the q factor (Fig. 3C.21).⁸⁷

Acoustic travel time in gas and oil is higher than in water. The presence of unflushed hydrocarbons in an interval can result in high values of apparent formation porosity. Commonly used correction factors are 0.9 in oil zones and 0.7 in gas zones.⁹² More recently, a gas-zone porosity-correction technique using shear slowness has been developed.¹⁰⁰

An additional empirical velocity-porosity predictive model has recently been proposed and is still in the experimental phase.^{101,102}

Carbonate and complex lithology reservoirs are generally comprised of varying proportions of limestone, dolomite, chert, quartzite, and occasionally, evaporites. The primary influences on porosity in these rocks are lithology and pore type. Generally, any shale present is in dispersed form and in small amounts that do not significantly impact porosity calculations. Acoustic poros-

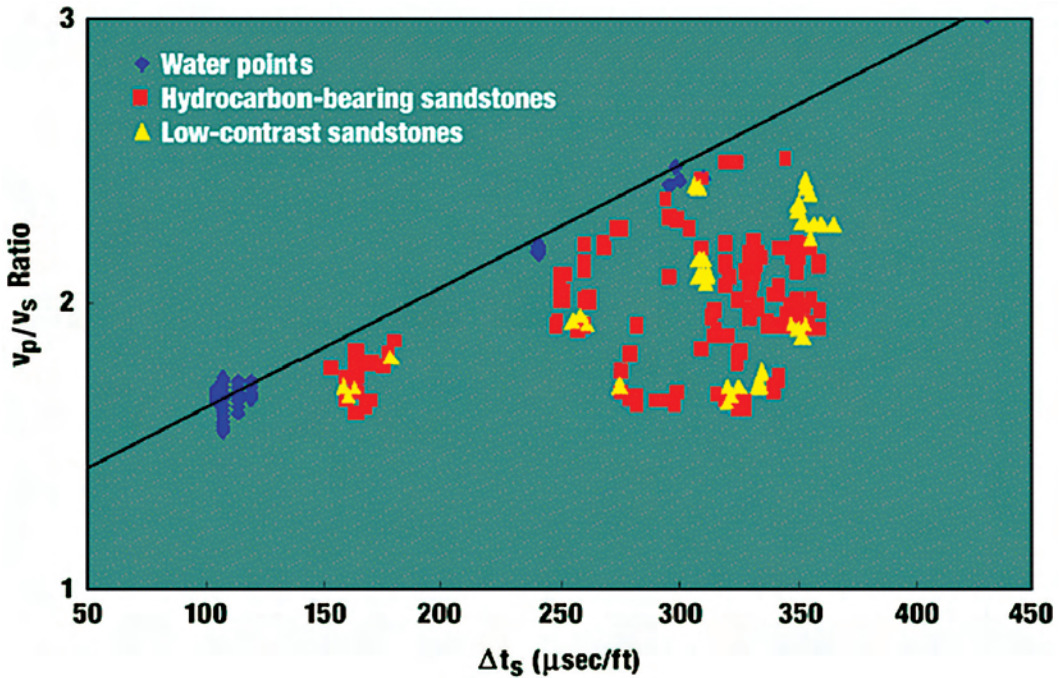


Fig. 3C.28—Crossplot of shear slowness vs. V_p/V_s serves as a quick-look hydrocarbon indicator. Compressional-slowness travel times increase where the rock pore space is occupied by more compressible fluid⁸¹ (modified from original, courtesy of Baker Atlas).

ity is a measure of the primary or intergranular (matrix) porosity. In dual-porosity reservoirs, the secondary porosity (e.g., isolated pores, vugs, and fractures) may significantly influence the rock-pore distribution, but may be overlooked by acoustic-log measurements. This topic is the subject of ongoing research.¹⁰³ In contrast, nuclear-porosity devices, such as density and neutrons, measure total porosity. The difference between the nuclear-porosity and acoustic-porosity measurements is an approximation of the secondary porosity.

Lithology Identification. Acoustic velocity is primarily a function of the rock matrix and can be used to identify different lithologies and for stratigraphic correlations. A variety of crossplot techniques, using acoustic measurements alone, or in combination with other porosity logs (neutron and density), have been devised to assist in lithologic identification (Fig. 3C.22). In particular, the M-N and mineral-identification-plot (MID) techniques use all three porosity logs in different combinations.^{104,105} Before lithology determination, the individual log measurements must be corrected for influences of gas effect, secondary porosity, bad hole conditions, and shaliness. In general, the MID plot is more sensitivity to lithology, gas, and secondary porosity and provides superior results to M-N plots. Crossplots, using a variety of log measurements or combinations of measurements can be used to resolve specific lithologic problems related to local or regional geology.^{87,106}

The ratio of compressional to shear velocity, V_p/V_s , is an effective lithology indicator because each lithology exhibits a defined trend that is independent of porosity and depth (Fig. 3C.23).^{90,107,108} However, because the V_p/V_s ratio is affected by formation anisotropy, the ratio values may not be absolute indicators of a particular lithology.¹⁰⁹

The addition of shear slowness to lithology identification provides a more robust result that can be particularly useful in cased-hole evaluations where density logs are not available. In Fig. 3C.24, the combined use of shear slowness and cased-hole neutron porosity results in en-

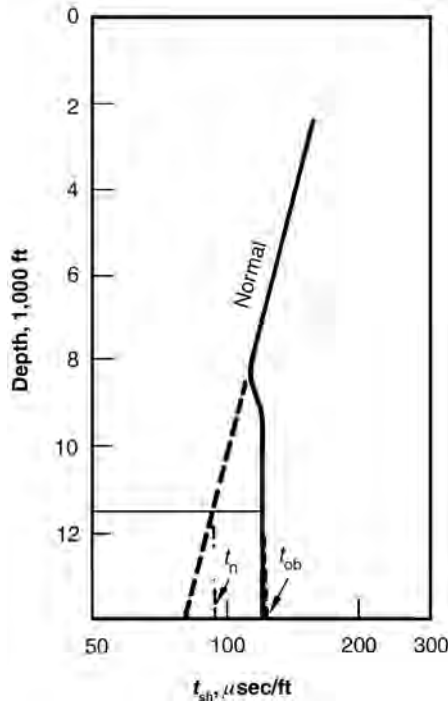


Fig. 3C.29—Semi-log plot illustrating acoustic detection of geopressure by use of shale slowness¹⁴⁸ (courtesy of SPE).

hanced-porosity determination in a complex lithology. Crossplots of V_p/V_s ratio vs. compressional travel time, Δt_c , facilitate identification of lithology trends with respect to porosity and lithology (Fig. 3C.25). Recent studies of complex carbonate reservoirs indicate that the V_p/V_s ratio is a function of porosity and in some cases, can differentiate higher-permeability facies.^{110,111}

Saturation Determination. The potential of acoustic velocity for determination of fluid saturation was recognized soon after development of the first logging devices and quickly became a staple input for log-interpretation methods and software. Acoustic-derived porosity serves as one variable, together with resistivity, in a variety of graphical and empirical methods used for solving the Archie saturation equation. Hingle and Pickett plots are the two most commonly used resistivity-porosity plots. Depending on the data available, the Hingle plot^{112,113} can solve for R_w , Δt_{ma} , and water saturation (S_w). Pickett plots^{114,115} (Fig. 3C.26) solve for Archie parameters a and m , formation factor, resistivity index, and S_w . A new technique using an empirical equation based on acoustic- and resistivity-log parameters is reported to successfully estimate water saturation in clean and shaly sandstones.¹¹⁶

Hydrocarbon Identification. *Gas.* Acoustic coupling between solid and gas or fluid and gas is poor, resulting in a high loss of energy. A sudden loss of energy (amplitude) in the measured acoustic signal, primarily in the compressional wave and only secondarily in the shear wave: (e.g., the cycle skipping or high slowness values) may indicate gas-filled pore space (gas effect). In the case of gas-filled porosity, the acoustic-neutron crossplot can be useful for this purpose because neutron porosity is lower than acoustic porosity in gas zones.

Compressional velocities are affected (slowed) by the compressive fluids in the pore space, while shear velocity is affected only by the rock matrix. Consequently, the presence of gas is especially noticeable in compressional-wave slowness. The combination of compressional and

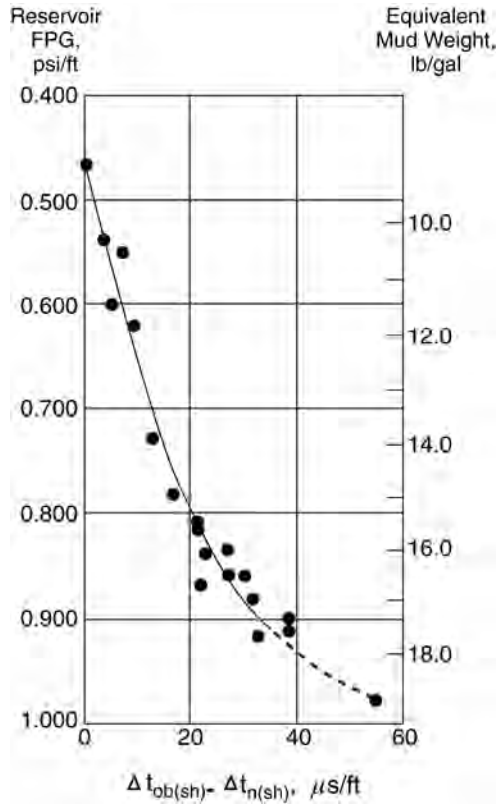


Fig. 3C.30—Relationship between fluid-pressure gradient (FPG) and the acoustic slowness difference for U.S. Gulf Coast¹⁴⁸ (courtesy of SPE).

shear slowness, either as a ratio or as a log overlay, provides a quick-look gas indicator (Fig. 3C.27).

The ratio of V_p/V_s offers a quicklook technique to distinguish between reservoir fluids^{117–120} and is especially effective in identifying light hydrocarbons (gas).^{121,122} When Δt_s is plotted against the V_p/V_s ratio, water-bearing sands and shales show a linear relationship and points falling below matrix lines result from the slowing effect of Δt_p in light hydrocarbons (Fig. 3C.28). These relationships are used for correcting porosity in gas-bearing intervals.¹⁰⁰ Further, laboratory investigations suggest that the V_p/V_s ratio can be used for saturation determination in some situations¹²³ as well as time-lapse changes accompanying steam flood of heavy-oil reservoirs.¹²⁴

Oil. Recent work suggests that the V_p/V_s ratio may also serve as an indicator of bypassed oil in cased wells.^{125,126} Research on the acoustic properties of heavy oils indicates that under the proper conditions of temperature and viscosity, these oils may behave as solids and generate shear waves that may be detectable at logging-tool frequencies.¹²⁷

3C.5.2 Geophysical Applications. The higher operating frequency of acoustic-logging tools and the smaller TR distances allows for higher-quality velocity data and finer vertical resolution than surface reflection techniques. Acoustic-velocity logs were originally developed for calibrating surface seismic velocities and reflectors. Acoustic-log interval travel time or transit time, Δt , can be summed, i.e., integrated, over the entire logged interval to provide the equiva-

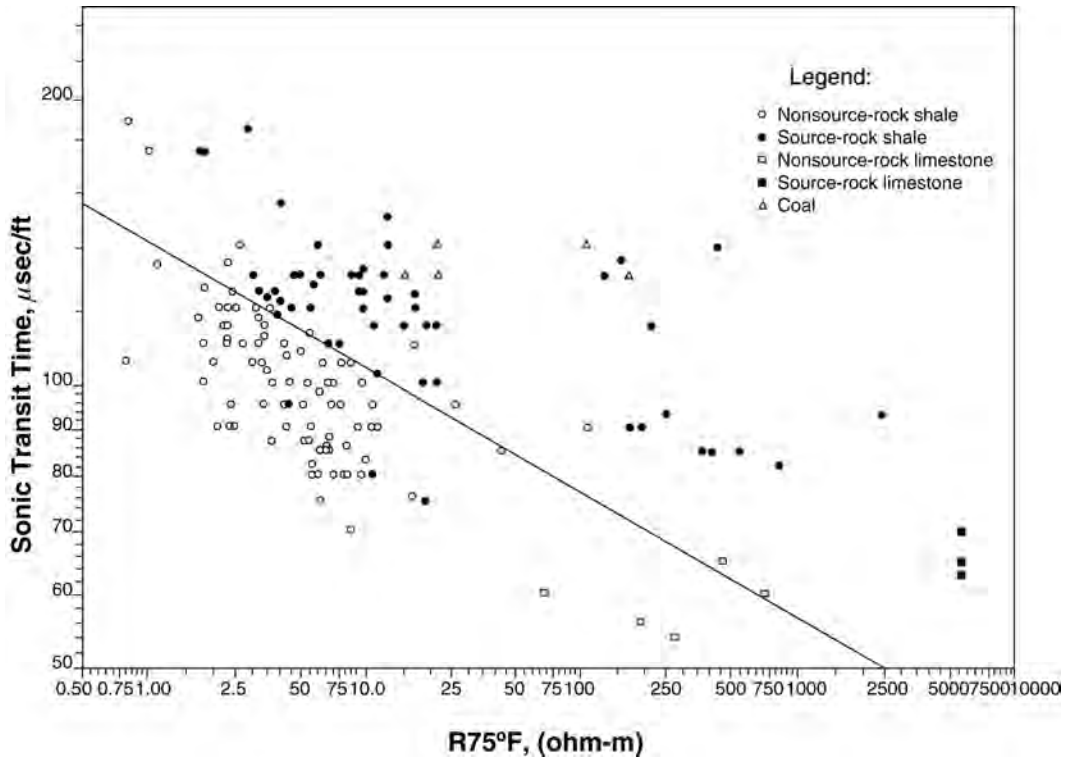


Fig. 3C.31—Identification of source-rock potential using a sonic transit-time-resistivity crossplot—points plotted above the line are source rocks, while those below are not.¹⁸¹ R75°F is well-log resistivity corrected to 75°F (courtesy of AAPG).

lent of seismic one-way time which is compared to borehole seismic surveys and reflection seismic two-way time.

Acoustic-log data are commonly calibrated using checkshot (velocity) or vertical seismic profile (VSP) surveys prior to use in geophysical applications. Data from these surveys, which use downhole receivers and surface acoustic sources, are used to adjust the log data for drift and borehole conditions and result in improved time-depth correlation. Acoustic-log data are combined with density-log data, to generate an impedance log that in turn is used to produce a synthetic seismogram. Synthetic seismograms are artificial seismic records that tie seismic time to log depth and are also used to match well-log quantities to seismic attributes for distinguishing primary seismic events (geologic structure and stratigraphy). It is possible, however, that a synthetic seismogram may not provide a very good match to the seismic field data. Disagreements commonly result from the differences scale and acquisition physics used in seismic and well-log measurement; for example, operational frequency (wavelength), borehole condition, and angle of measurement (particularly in the presence of anisotropy).^{128–132} Acoustic-log data provide a fundamental and essential element of modern seismic reservoir characterization.¹³³ The chapter on Fundamentals of Geophysics in this volume of the *Handbook* contains more information on the determination and use of these types of analyses.

3C.5.3 Drilling and Reservoir Engineering Applications. Pore Pressure and Overpressure Detection and Evaluation. Abnormal pressure is defined as any departure from normal hydrostatic pressure at a given depth.¹³⁴ Abnormal subsurface pressures, either overpressure (geopressure) or underpressure, are encountered in hydrocarbon basins throughout the world in

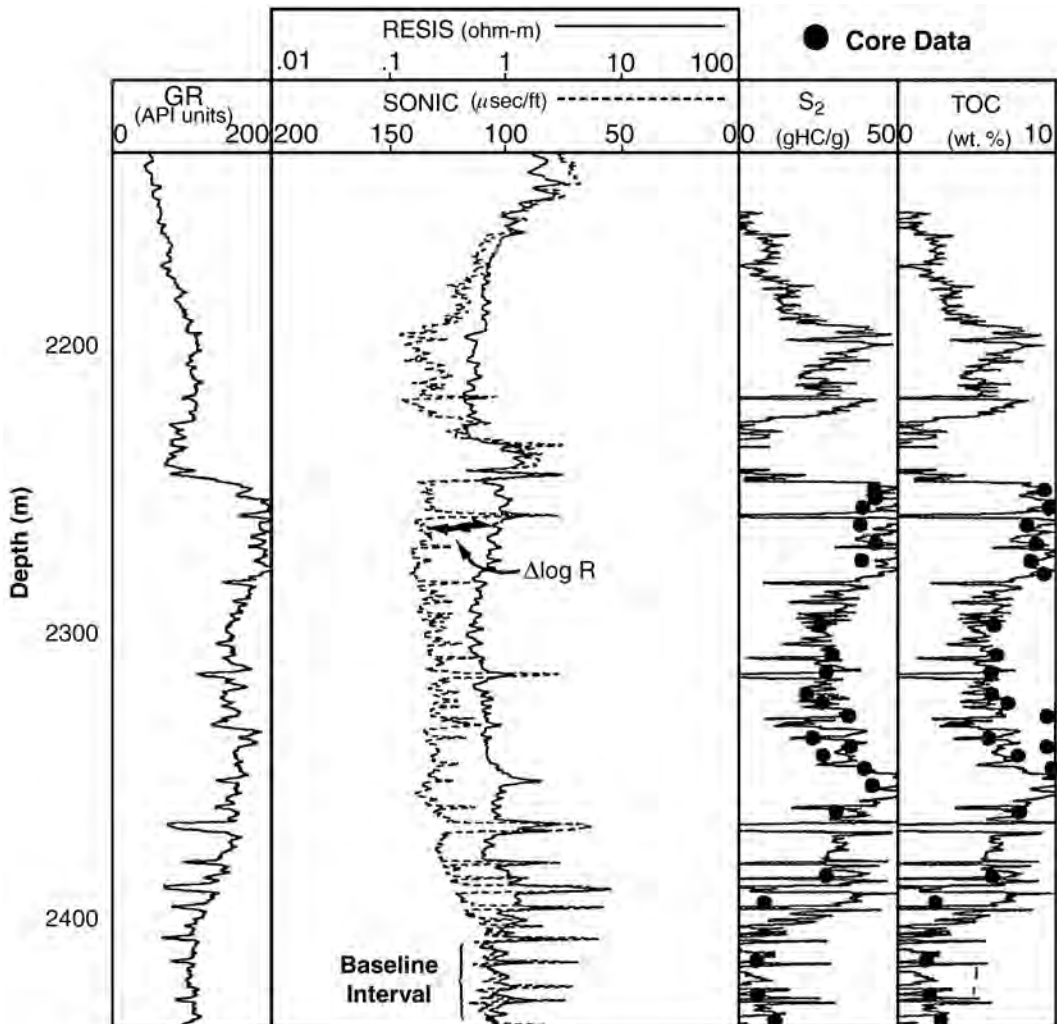


Fig. 3C.32—Source-rock identification and assessment using an acoustic/resistivity overlay technique. Separation of the acoustic and resistivity curves (Track 2), labeled $\Delta \log R$, indicates organic-rich intervals as shown by the core analyses in Tracks 3 and 4. The amount of separation is directly related to the amount of total organic carbon and is a function of thermal maturity¹⁸² (courtesy of AAPG).

all lithologies, all geologic ages, and at all depths.¹³⁵ Early and reliable detection of geopressure is vital to avoid or mitigate potential drilling and safety hazards, e.g., shallow water flow, blowouts, and shale instability. During drilling, advanced warning of approaching geopressuring enables the mud weight to be adjusted to avoid well and reservoir damage and to determine casing points. This is a particular concern in deepwater wells in which the pressure difference; i.e., the operating window, between the hydrostatic gradient and the fracture gradient can be very narrow.

Geopressuring in hydrocarbon reservoirs may result from a variety of geologic and tectonic processes.^{135–137} Borehole-acoustic detection methods using compressional and shear slowness can identify abnormally pressured zones before they are drilled and can quantify pressure gradients. These methods, discussed below, are used in conventional borehole logging (wireline and LWD), new seismic-while-drilling techniques, and more recently, surface seismic data.^{37,56,136,138–147}

TABLE 3C.13—DEFINITIONS OF THE ELASTIC MODULI AND POISSON'S RATIO			
Elastic Constants	Basic Equations	Interrelation of Equations	Equations in Well Logging Terms
Young's modulus	$E = \frac{9Kpv_s^2}{3K + pv_s^2}$	$E = \frac{3K\mu}{3K + \mu} = 2\mu(1 - \sigma) = 3K(1 - 2\sigma)$	$E = \left(\frac{p}{\Delta t_s^2}\right) \left(\frac{3\Delta t_s^2 - 4\Delta t_c^2}{\Delta t_s^2 - \Delta t_c^2}\right) \times 1.34 \times 10^{30}$
Bulk modulus	$K = pv_p^2 - \frac{4}{3}v_s^2$	$K = \frac{E\mu}{3(3\mu) - E} = \mu \frac{2(1 + \sigma)}{3(1 - 2\sigma)} = \frac{E}{3(1 - 2\sigma)}$	$K = p \left(\frac{3\Delta t_s^2 - 4\Delta t_c^2}{3\Delta t_s^2 \Delta t_c^2}\right) \times 1.34 \times 10^{30}$
Shear modulus	$\mu = pv_s^2$	$\mu = \frac{3KE}{9K + E} = 3K \frac{1 - 2\sigma}{2 + 2\sigma} = \frac{E}{2 + 2\sigma}$	$\mu = \frac{p}{\Delta t_s^2} \times 1.34 \times 10^{30}$
Poisson's ratio	$\sigma = \frac{1}{2} \left(\frac{v_p^2}{v_s^2} - 2 \right) = \frac{1}{2} \left(\frac{v_p^2}{v_s^2} - 1 \right)$	$\sigma = \frac{3K - 2\mu}{2(3K + \mu)} = \left(\frac{E}{2\mu} - 1 \right) = \frac{3K - E}{6K}$	$\sigma = \frac{1}{2} \left(\frac{\Delta t_s^2 - 2\Delta t_c^2}{\Delta t_s^2 - \Delta t_c^2} \right)$

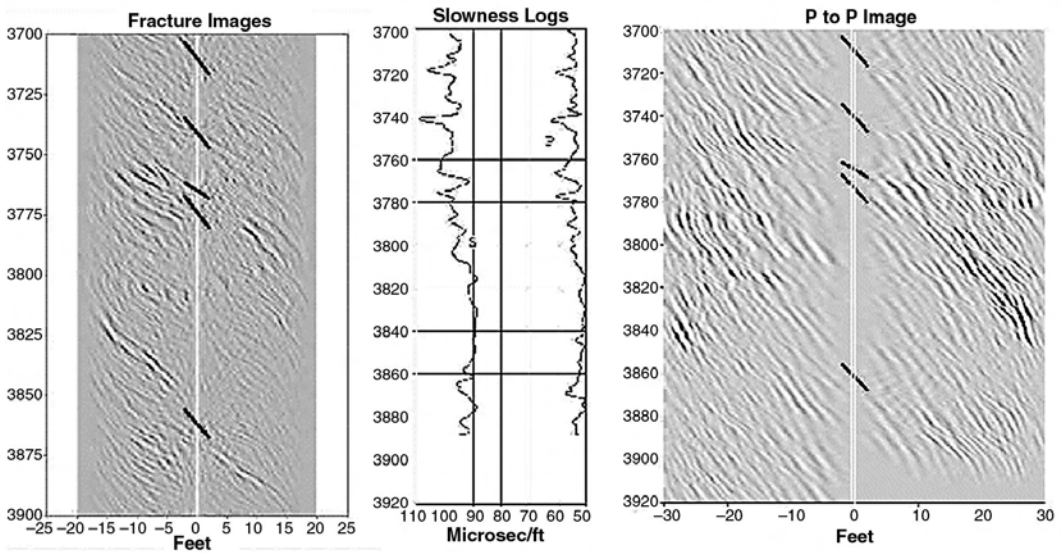


Fig. 3C.33—Near-well acoustic image of a fractured reservoir using direct (compressional) (right panel) and converted (shear) (left panel) acoustic modes. The fractures indicated in the converted mode data are more apparent than in the direct data and also correlate better with fractures seen on the televiewer image²¹¹ (not shown) (courtesy of SPE).

Undercompaction is the primary mechanism for creating overpressure, particularly in deltaic basins in which high rates of deposition commonly prevent the escape of pore water trapped in shales. Undercompacted shales have higher acoustic transit times (i.e., higher apparent porosity) than normally pressured shales at the same depth.^{148–151} With the onset of overpressuring, a semi-logarithmic plot of acoustic slowness with depth will diverge from a normal (hydrostatic) straight-line trend of decreasing slowness (increasing velocity) with depth (Fig. 3C.29).

The “normal,” or hydrostatic, trend for the well, which may vary with different geologic provinces, is defined by plotting slowness values for shale beds (> 10-ft thickness) in the well. A constant overburden gradient of 1.0 psi/ft is generally assumed. The difference in acoustic slowness between the normal and abnormal trends can be converted to an equivalent fluid-pres-

TABLE 3C.14—TECHNIQUES USED IN ACOUSTIC SLOWNESS PROCESSING

Method	Output	Comments
Data stacking		Improves signal-to-noise ratio
Single-mode analysis	First break; wave slowness, filtered wave signatures	Slowness of individual energy mode (e.g., compressional or shear)
Multimode analysis	First break; wave slowness, filtered wave signatures	Two or more energy modes in an acoustic array; recommended for openhole shear and cased-hole compressional slowness
First-motion analysis	DDBHC acoustic slowness	Travel time of first coherent amplitude change on each array signature. Quick-look technique; affected by tool noise, signal amplitude, and cycle skipping; openhole only
Cross correlation	DDBHC acoustic slowness	Statistical correlation method based on first motion over a fixed range of slowness; rapid with 6-in. resolution; not affected by cycle skipping or signal amplitude; openhole only
Semblance	Slowness, quality curves	Statistical correlation; high confidence; openhole and cased hole; resolution limited to 3.5 ft
N th-root stacking	Slowness, quality curves	Statistical correlation; high confidence; openhole and cased hole; resolution limited to 3.5 ft
Waveform matching	Slowness, quality curves	Subarray processing, resolution < 3.5 ft (to 1 ft)

sure gradient and formation pressure for a given depth (Fig. 3C.30). This method may not be applicable or effective in all areas or where undercompaction is not the mechanism for overpressuring.^{152,153} More-general approaches to determination of pore pressure and fracture gradient use an effective-stress, rock-mechanics approach.^{152,154,155}

Recent investigations into the effects of pressure on shale porosity suggest that the relationship is more complex than previously thought. While additional study is necessary, the results to-date suggest that it may be necessary to reconsider or revise the well-log methods currently used in pore pressure and exhumation analysis (see section on Geological Applications below).^{147,156–158}

Fracture Identification. Locating fractures, recognizing fracture morphology, and identifying fluid-flow properties in the fracture system are important criteria in characterizing reservoirs that produce predominantly from fracture systems. However, fracture identification and evaluation using conventional resistivity and compressional-wave acoustic logs is difficult, in part because fracture recognition is very dependent on the dip angle of fractures with respect to the borehole.

Fractures are physical discontinuities that generate acoustic reflection, refraction, and mode conversion—all of which contribute to a loss of transmitted acoustic energy. In particular, compressional- and shear-wave amplitude and attenuation and Stoneley-wave attenuation are significantly affected by the presence of fractures. Compressional waves are primarily affected by oblique fractures—those with dip angles between 15° and 85°—while shear waves are primarily affected by horizontal or near-horizontal fractures.¹⁵⁹ On conventional-velocity logs, fracture-induced attenuation may be evidenced as cycle skipping, variations in the V_p/V_s ratio and on VDL presentations, or as chevron (crisscross) patterns caused by mode-conversion interference.^{160,161} Borehole-televuewer-type imaging devices provide a higher degree of success in identifying fractures and determining whether or not they are open (producing) or closed.

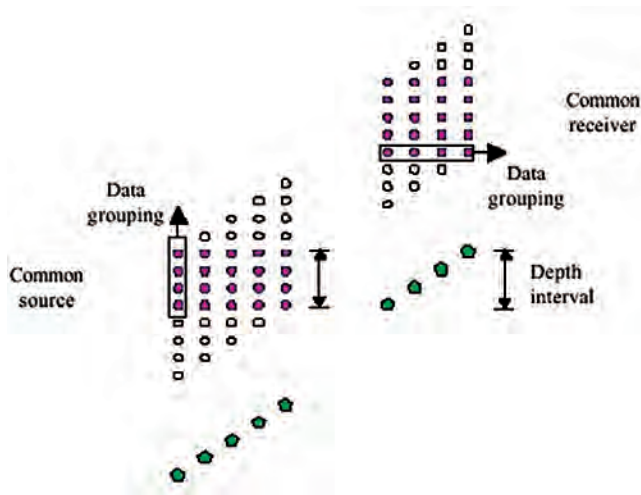


Fig. 3C.34—Diagram showing the gather of array acoustic data into either common-source subarrays or common-receiver subarrays. These subarrays cover the same depth interval. Data grouping is in the vertical direction for the source gather, and in the horizontal direction for the receiver gather²²⁴ (courtesy of SPWLA).

The development of reliable full-waveform shear- and borehole-imaging devices enabled enhanced fracture identification and evaluation.^{61,162} Aguilera¹⁶³ summarizes the use of conventional acoustic-log methods for fracture identification.

Recently developed anisotropy-analysis methods use crossed-dipole shear, Stoneley-wave, and acoustic-imaging data—individually or in combination—to provide reliable identification and evaluation of in-situ and induced fractures (see the Crossed-Dipole Anisotropy Analysis section of this chapter).

3C.5.4 Geological Applications. *Estimates of Erosion and Uplift (Exhumation).* The amount of erosion that has occurred in a region that has been uplifted can be estimated from the degree of shale compaction measured by acoustic travel time.^{164–166} This technique assumes that shale compaction is irreversible and that the shale retains the degree of compaction it gained at its maximum burial depth. Uplift and erosion will result in lower porosities than expected for the current burial depth (i.e., a shale will appear to be overcompacted).^{147,167–177}

Determination of Organic Richness and Source-Rock Potential. Acoustic slowness, used alone or in conjunction with formation resistivity, can provide qualitative indications and quantitative determination of source-rock potential (when calibrated to laboratory data). The identification of potential petroleum-source rocks and characterizing the thermal maturity of these rocks is important for assessing petroleum potential (risking) and for basin modeling.

Studies of coals and organic-rich shales have demonstrated that acoustic velocity is reduced by the presence of organic material, that changes in velocity are proportional to the volume of organic material present, and that increases in thermal maturity (largely a function of burial depth and temperature) are accompanied by increases in acoustic velocity (decreases in transit time, Δt). Total organic carbon and the level of organic thermal maturation, expressed in terms of vitrinite reflectance, are two key parameters used for determining the potential of a formation to source hydrocarbons, and each can be mathematically related to Δt .^{178–180} Because acoustic velocity is influenced by a number of factors in addition to organic carbon content, a combination of log measurements can provide improved results when other factors do not mask responses. In particular, acoustic-resistivity crossplot techniques (Fig. 3C.31) and log overlays (Fig. 3C.32) have proved successful.^{181–183}

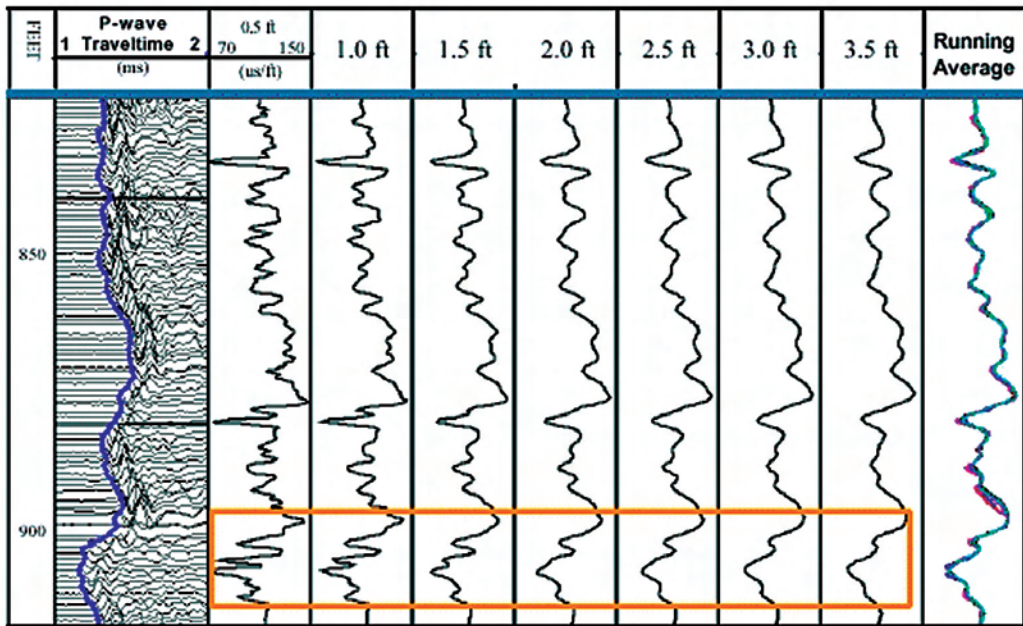


Fig. 3C.35—Compressional-wave-slowness curves obtained for various configurations (apertures) of possible overlapping subarrays based on an array tool having four transmitters and eight receivers. Note the increasing resolution of the curves with decreasing subarray aperture. Track 9 is a consistency check obtained by averaging the curves to 3.5-ft aperture and overlaying the results²²⁴ (courtesy of SPWLA).

3C.5.5 Geomechanical Applications. Rock Mechanical Properties. The determination of a reservoir's mechanical properties is critical to reducing drilling risk and maximizing well and reservoir productivity. Estimates of rock mechanical properties are central to drilling programs, well placement, and well-completion design.¹⁸⁴ Mechanical properties include the elastic properties (Young's modulus, shear modulus, bulk modulus, and Poisson's ratio) and the inelastic properties (fracture gradient and formation strength).

Elasticity is the property of matter that causes it to resist deformation in volume or shape. Hooke's law describes the behavior of elastic materials and states that for small deformations, the resulting strain is proportional to the applied stress. Stress is the force applied per unit area, and strain is the fractional distortion that results because of the acting force. The modulus of elasticity is the ratio of stress to strain. Depending on the mode of the acting geological force and type of geological media the force is acting upon, three types of deformation can result as well as three elastic moduli that correspond to each type of deformation. Young's modulus, E , is the ratio of uniaxial compressive (tensile) stress to the resultant strain. Bulk modulus, K , is the change in volume under hydrostatic pressure (i.e., the ratio of stress to strain). (K is the reciprocal of compressibility.) Shear modulus, μ , is the ratio of shearing (torsional) stress to shearing strain. An additional parameter, Poisson's ratio, σ , is a measure of the geometric change of shape under uniaxial stress. These four elastic parameters are interrelated such that any one can be expressed in terms of two others and can also be expressed in terms of acoustic-wave velocity and density (Table 3C.13).

The data needed to compute mechanical rock properties are compressional and shear velocities (slowness) and density. Shear and compressional velocities are a function of the bulk modulus, shear modulus, and density of the formation being measured. The V_p/V_s ratio, combined with formation density, ρ , is used to calculate Poisson's ratio, Young's modulus, the bulk modulus, and the shear modulus. Whenever possible, log-derived, dynamic rock properties

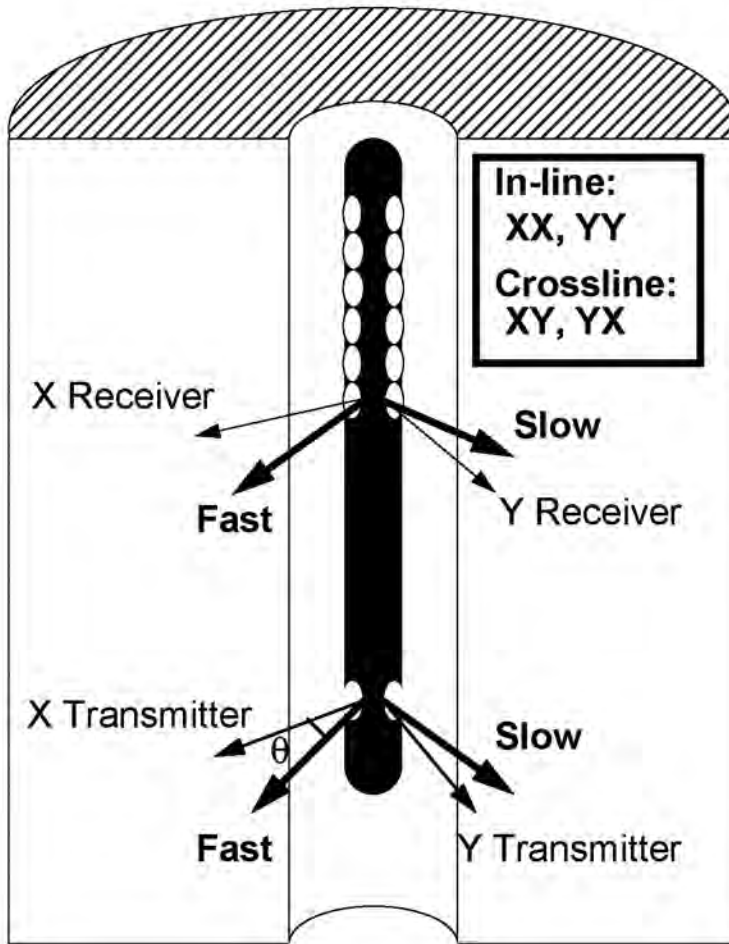


Fig. 3C.36—Diagram illustrating the principle and configuration of crossed-dipole logging: two orthogonal dipole transmitter and receiver array systems. The tool acquires four array data sets, two in-line, XX and YY; two crossed-line, XY and YX, and uses the physics of shear-wave splitting in azimuthally anisotropic rocks to determine the fast-shear polarization azimuth (courtesy of Baker Atlas).

should be calibrated to core-derived static (laboratory) properties, because the static measurements more accurately represent the in-situ reservoir mechanical properties.^{185–189} Rock mechanical properties can be determined using conventional empirical charts¹⁹⁰ or computer programs. The elastic moduli and Poisson's ratio are used in a variety of applications.¹⁹¹ These applications include predictions of formation strength,^{192–196} well stimulation (fracture pressure and fracture height),^{197–200} borehole and perforation stability,²⁰¹ sand production and drawdown limits in unconsolidated formations,^{202–204} coal evaluation,²⁰⁵ and determining the roof-rock-strength index for underground mining operations.^{206,207} Rock-mechanics applications of modern multiple tools are discussed in the Anisotropy Analysis section following.

3C.5.6 Near-Well Imaging. Acoustic data acquired using modern array tools can provide high-resolution (0.5 m), microscale “seismic” 2D and 3D images of structural features in the near-borehole region (10 to 15 m). Conventional seismic-processing techniques, including filtering and migration, are used to extract compressional and shear reflections from the acoustic data. The reflections are then used to image geological features near the borehole. This technique

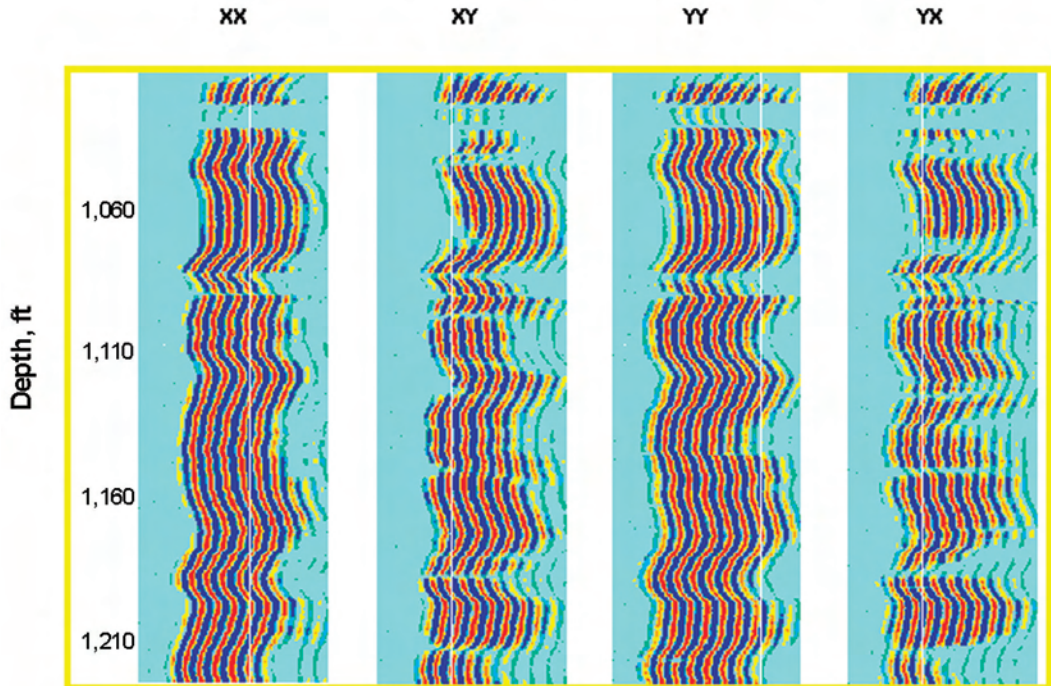


Fig. 3C.37—Example of four-component, crossed-dipole waveform log data showing shear-wave splitting caused by formation anisotropy (courtesy of Baker Atlas).

allows the imaging of bed boundaries, thin beds (stringers), fractures, and faults in openhole and cased wells (Fig. 3C.33).^{32,208–215}

3C.6 Advanced Data Analysis and Applications

Processing acoustic data downhole as well as at the surface is necessary to transform the raw acoustic signals recorded by modern logging instruments into data suitable for interpretation and analysis. Data processing takes place during acquisition, in the logging tool itself and in the surface acquisition unit, and also in post-acquisition processing at computing centers. There are a variety of sources of noise in the downhole environment that contaminate the recorded acoustic signal: tool (“road”) noise, measurement error, reflection and scattering from rough borehole or bed boundaries, mode conversion, and interferences that occur in the downhole environment. The goal of acoustic-data processing is to minimize the data noise while maximizing the petrophysical information.²¹⁶ Data preprocessing reduces the influences of these sources, thus allowing extraction of the true formation signal.

Following the rapid theoretical advances in acoustic-wave propagation made during the 1980s and 1990s, significant advances in data processing provided improved quality in slowness measurements and enabled a number of new applications using Stoneley and dipole-shear wave in open and cased holes. The combined interpretation of Stoneley and dipole-shear acoustic measurements with NMR and borehole imaging enhances formation evaluation.

3C.6.1 Slowness Analysis. One of the primary goals in borehole acoustic logging is to obtain formation slowness from array measurements. Accurate slowness analysis is vital to most petrophysical, geophysical, and seismic applications. A variety of techniques are used for computing slowness from array tools (Table 3C.14).

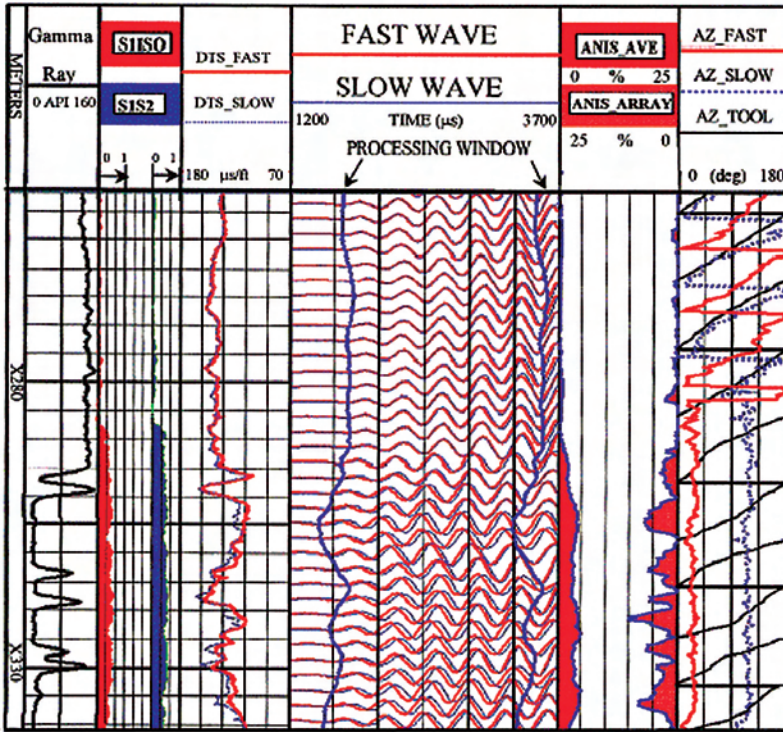


Fig. 3C.38—Post-processing results from crossed-dipole analysis indicating the magnitude and azimuth of anisotropy (courtesy of Baker Atlas).

Semblance and Nth-Root Stacking. The two most commonly used techniques to determine slowness from borehole acoustic array are semblance²¹⁷⁻²¹⁹ and Nth-root stacking^{220,221}; both are cross-correlation, coherency techniques that compare signatures in an acoustic array and find the similarities that correspond to coherent wave types. Semblance has a direct physical interpretation, whereas Nth-root stacking is a purely mathematical solution. Although the semblance method is faster, the Nth-root stacking method is more tolerable to noise and ignores amplitude variations across the array and, in general, provides better results. Collecting the array data, either as receiver or transmitter (source) arrays (Fig. 3C.34), enhances the slowness output from both of these techniques.

The primary application of the receiver- and transmitter-array-derived slowness curves is to provide compensation (DDBHC) to the monopole compressional and shear slowness for borehole irregularities such as washouts or cave-ins. Borehole compensation is achieved by averaging the slowness estimates from the receiver and transmitter arrays. The dipole-shear wave does not require borehole compensation because the flexural-shear wave is not as sensitive to the borehole geometry although it is often used to improve results in rough boreholes.

The objective of the semblance technique is to find the slowness that maximizes the coherence (time domain) among the wave power spectra over the receiver array. The Nth-root stacking technique is very similar to the semblance technique, except that the waveform amplitudes are modified in a different way to produce a so-called “pseudo” power spectrum instead of the true power spectrum.

Although the algorithms used in semblance and Nth-root stacking differ, the processing procedure is similar. A time window of fixed length is set up on each signature in the array. The windows are offset by a specified time interval on the successive signatures and a correlation

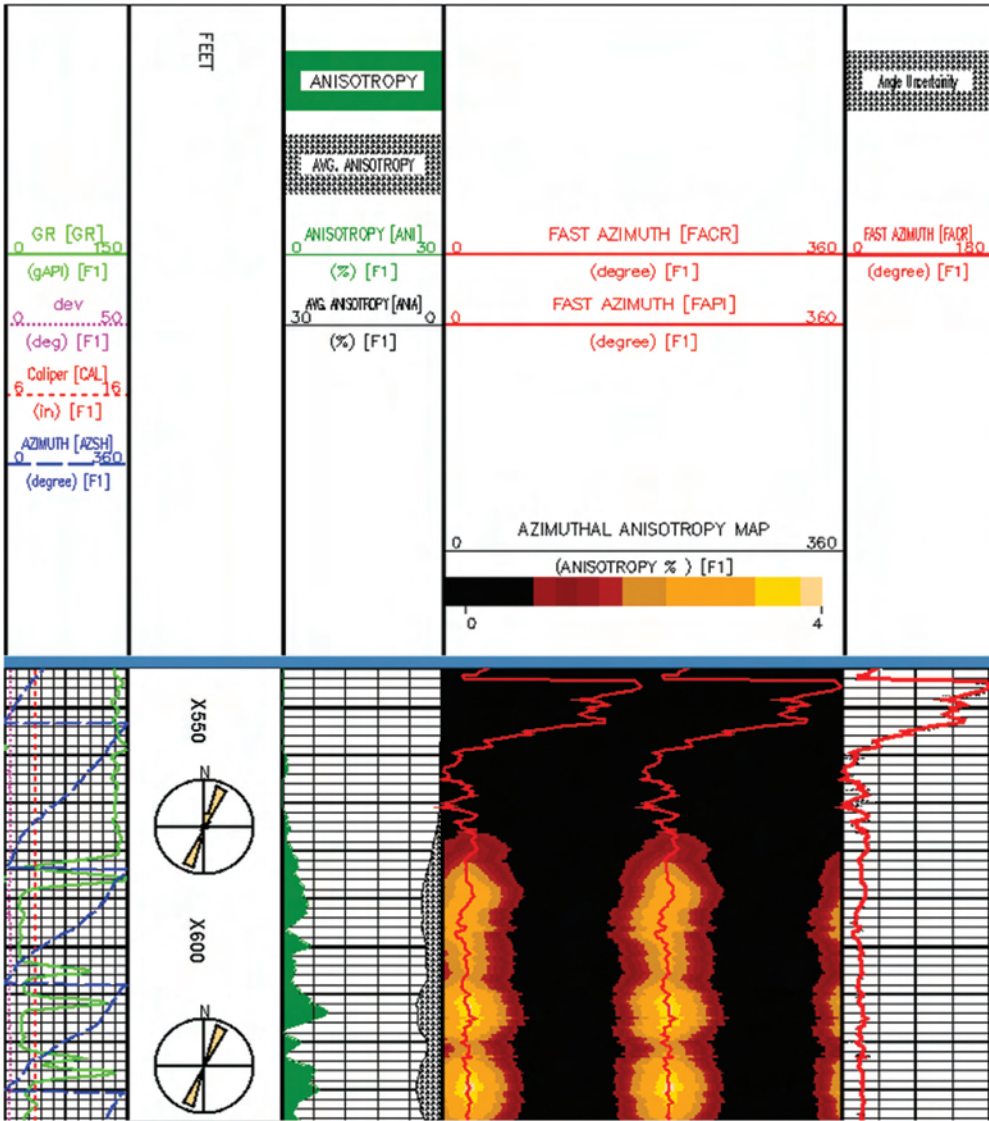


Fig. 3C.39—The results of anisotropy analysis displayed as an anisotropy map (courtesy of Baker Atlas).

is computed over these windows. The windows on all but the first signature are then stepped a certain distance out in time and another correlation value is computed. The process continues for the range of anticipated slowness in the well. This process is repeated as the window is progressively stepped on the first signature.

The group of correlation values obtained is known as a correlogram, in which the waveform coherence or correlation values either from semblance or *N*th root method are displayed as a function of slowness and arrival time creating a 3-D surface. The correlation values in a range of arrival times are further combined to form a “combined correlogram,” which is a projection of the 3-D surface on the slowness axis. The correlogram peak at each measured-depth level is used to obtain the Δt slowness for the wave type. These individual slowness values are then displayed as a continuous log curve. Filtering for the compressional wave or for the dispersive shear wave is normally required before using either method. As a quality check, the

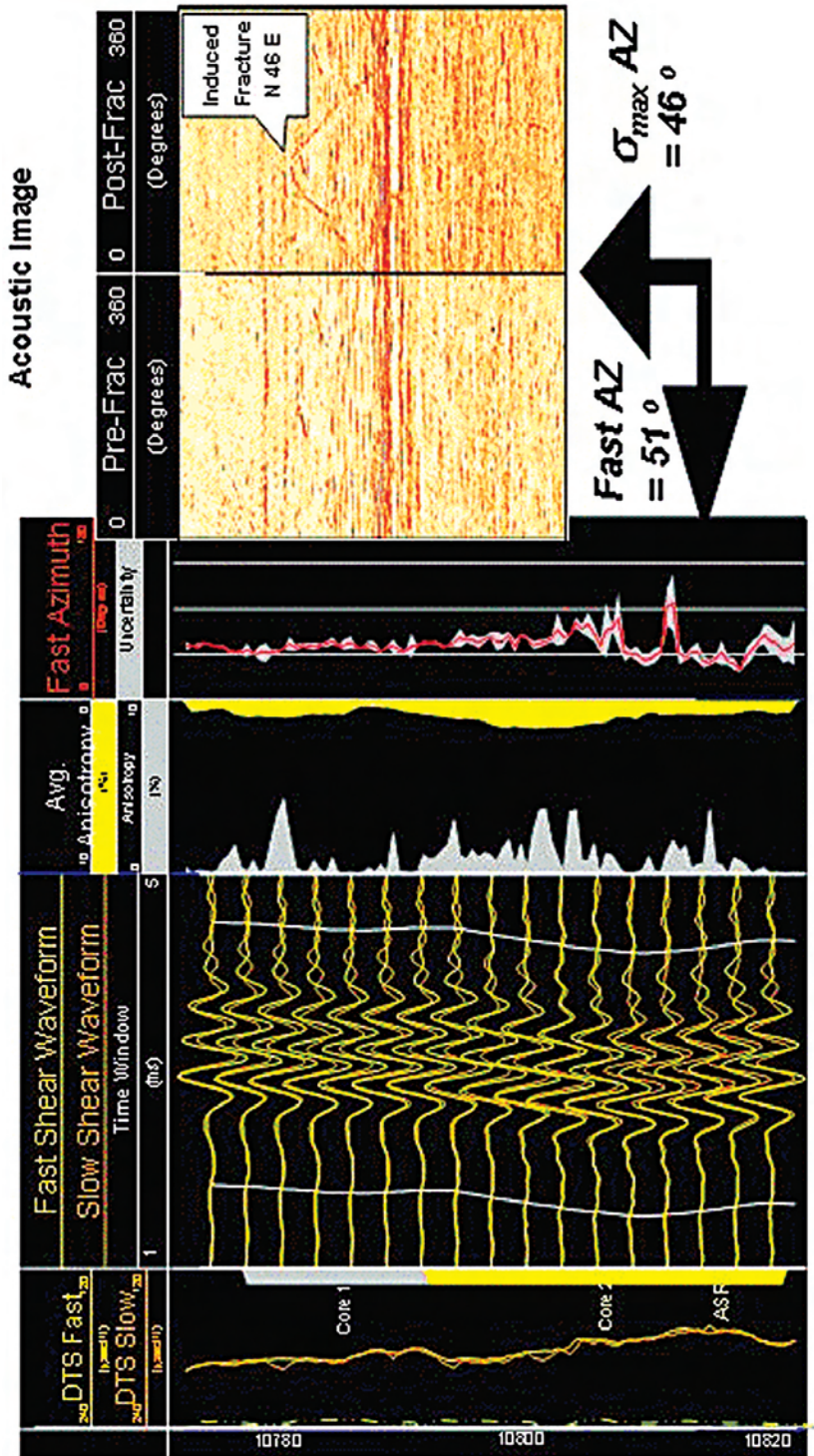


Fig. 3C.40—Crossed-dipole logging determines a fast shear azimuth of 51° before fracture treatment. The maximum stress direction of 46°, determined after the fracture job, is in good agreement with the stress direction from the crossed-dipole log results (courtesy of Baker Atlas).

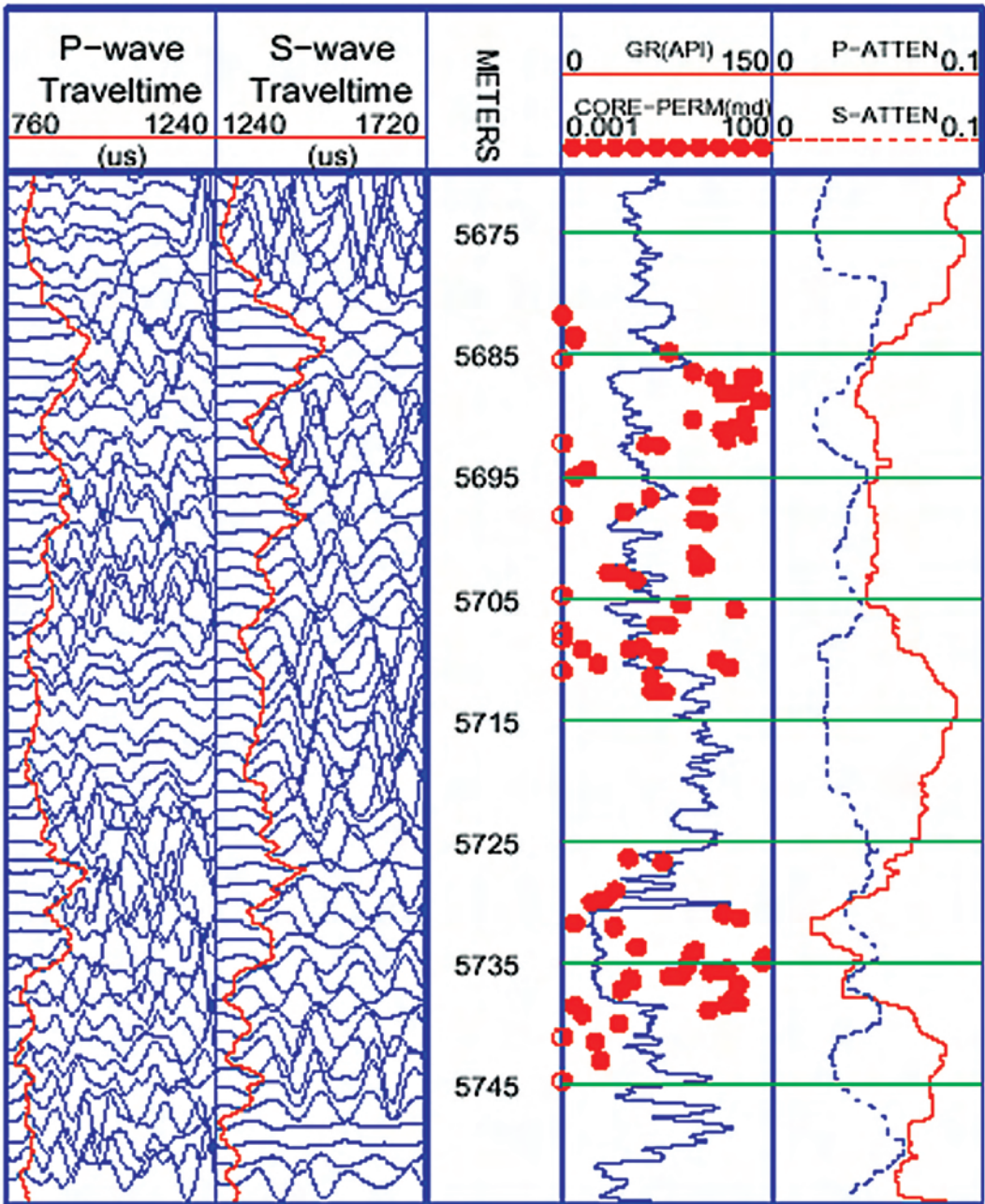


Fig. 3C.41—Comparison between shear-wave attenuation logs and core permeability in a permeable oil zone. The two attenuation curves agree in high-permeability zones²⁷⁸ (courtesy of SEG).

slowness results of semblance or N th-root stack processing can also be plotted in the combined correlogram together with a “computed travel time” which is plotted against the waveform. The computed travel time represents the sum of the transit-time measurements from the transmitter to the receiver along with the mud travel time. Dipole shear-slowness processing must

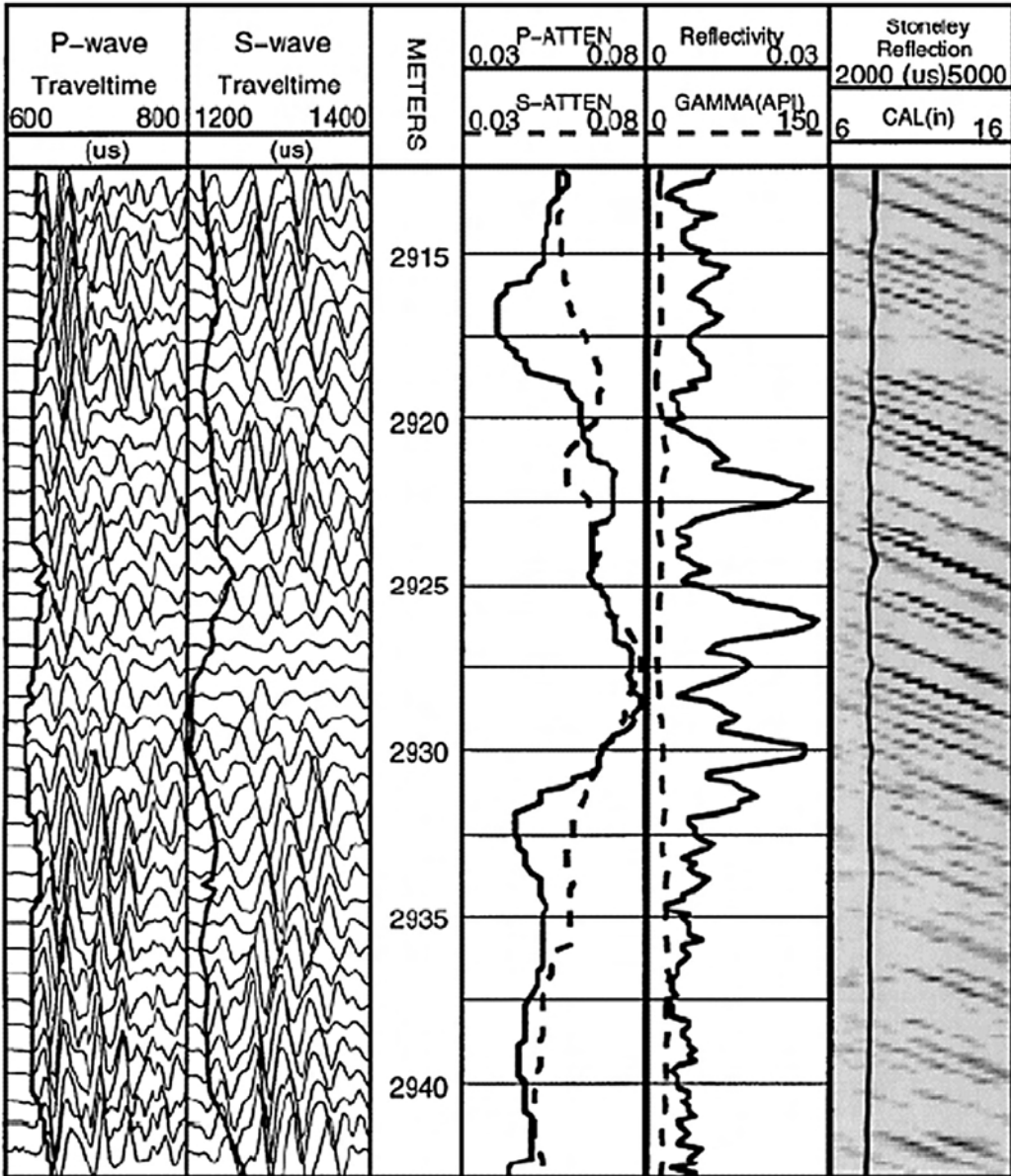


Fig. 3C.42—Correlation between compressional- and shear-wave attenuation and fracture location. The interval of 2920 to 2930 m in which P- and S-wave attenuation curves overlay corresponds to the interval of high acoustic reflectivity (Track 4) and fractures identified by the down-going Stoneley-wave reflectivity (Track 5)²⁷⁸ (courtesy of SEG).

also take into account dispersion of the flexural wave.²²² Depending on the frequency of the flexural mode, a correction may be required to obtain shear-wave slowness.

Resolution Enhancement. The aperture (vertical resolution) of array tools is typically 3.5 ft. This means that a bed must be at least that thickness to measure true acoustic slowness, although such tools can detect (resolve) beds down to 2-ft thickness. To meet the need for the higher resolution necessary for thin-bed evaluation, waveform-matching (multishot) processing techniques use the redundant information contained in overlapping receiver subarrays to im-

prove vertical resolution (Fig. 3C.34).²²³ Recently introduced processing techniques reduce the aperture to 0.5 ft and thus achieve a true vertical resolution of 1.0 ft (Fig. 3C.35).²²⁴ However, reducing the aperture makes the measurements more susceptible to noise.

3C.6.2 Anisotropy Analysis. Formation anisotropy—the directional variation of physical properties—can be the result of depositional processes (intrinsic) or tectonic processes (stress-induced). Formation anisotropy is evidenced through variations in permeability, rock strength, fractures, and borehole failure. In acoustic/seismic terms, intrinsic anisotropy is structural in nature and is commonly seen as transverse isotropy (TI or vertical transverse isotropy, VTI), in which properties differ in the vertical or horizontal planes, such as in shales or thinly bedded intervals.²²⁵ Stress-induced anisotropy is known as azimuthal anisotropy (or horizontal transverse isotropy, HTI), in which acoustic parameters in a vertical borehole vary with azimuthal orientation, such as the case of fractures parallel to the borehole.

Analyses of in-situ anisotropy (primarily stress induced) are made using direct or derived shear-wave velocity and provide the magnitude and azimuth of anisotropy (i.e., direction of the maximum and minimum horizontal stresses as well as an indication of their difference). Anisotropy analysis has been widely used in solid-earth seismology, geothermal studies, and more recently, in exploration geophysics (see summaries in Crampin and Chastin²²⁶ and Helbig and Thomsen²²⁷). In the petroleum industry, these results are used in well design and well placement for optimum reservoir drainage,²²⁸ to detect and characterize faults and fractures in openhole and cased hole,²²⁹ to predict borehole instability and sand production,²³⁰ and for optimizing the design and evaluation of well completions (perforations and hydraulic fracturing) (see following section on Crossed-Dipole Anisotropy Analysis).

Compressional-, shear- and Stoneley-wave properties are each affected, to some degree, by the presence and type of formation anisotropy. While the shear-wave response to azimuthal anisotropy (see the following section on Crossed-Dipole Anisotropy Analysis) and Stoneley waves to VTI anisotropy is well known, the effect on compressional-wave energy is less well characterized.^{231–234} In some situations, information from additional measurements, such as borehole images, dip logs, or both, may be necessary for relating the measured anisotropy to geological features.

Borehole acoustic azimuthal and VTI anisotropy analysis is an advance made possible by the recent introduction of new inversion methods.^{235–242} These methods use the crossed-dipole shear to derive azimuthal anisotropy and the Stoneley wave to derive TI anisotropy in slow formations, or a combination of these modes in deviated wells. A reasonable shear velocity can be derived using inversion techniques with low-frequency Stoneley-wave dispersion which is sensitive to the horizontal shear (in contrast to the dipole's sensitivity to the vertical shear).^{6,23,243}

Several new applications have been made possible by anisotropy analysis: identification of formation alteration using dipole-shear dispersion,^{33,237,244,245} stress estimation,²³⁹ and distinguishing between intrinsic and stress-induced anisotropy using dispersion crossover.^{246–249} Anisotropy analysis can also be conducted using shear-wave parameters derived from Stoneley-wave dispersion.^{242,250}

Crossed-Dipole Anisotropy Analysis. In anisotropic media, shear waves (both monopole refracted and dipole flexural) split into orthogonally polarized components having different velocities. This is known as shear-wave splitting, shear-wave birefringence, or shear-wave velocity anisotropy.^{251–254} The difference in fast and slow shear-wave slowness provides a measure of the magnitude of anisotropy. Shear-wave splitting is useful for evaluating fractures, faults, bedding planes that intersect the borehole at an angle, and unbalanced tectonic stresses perpendicular to the borehole.

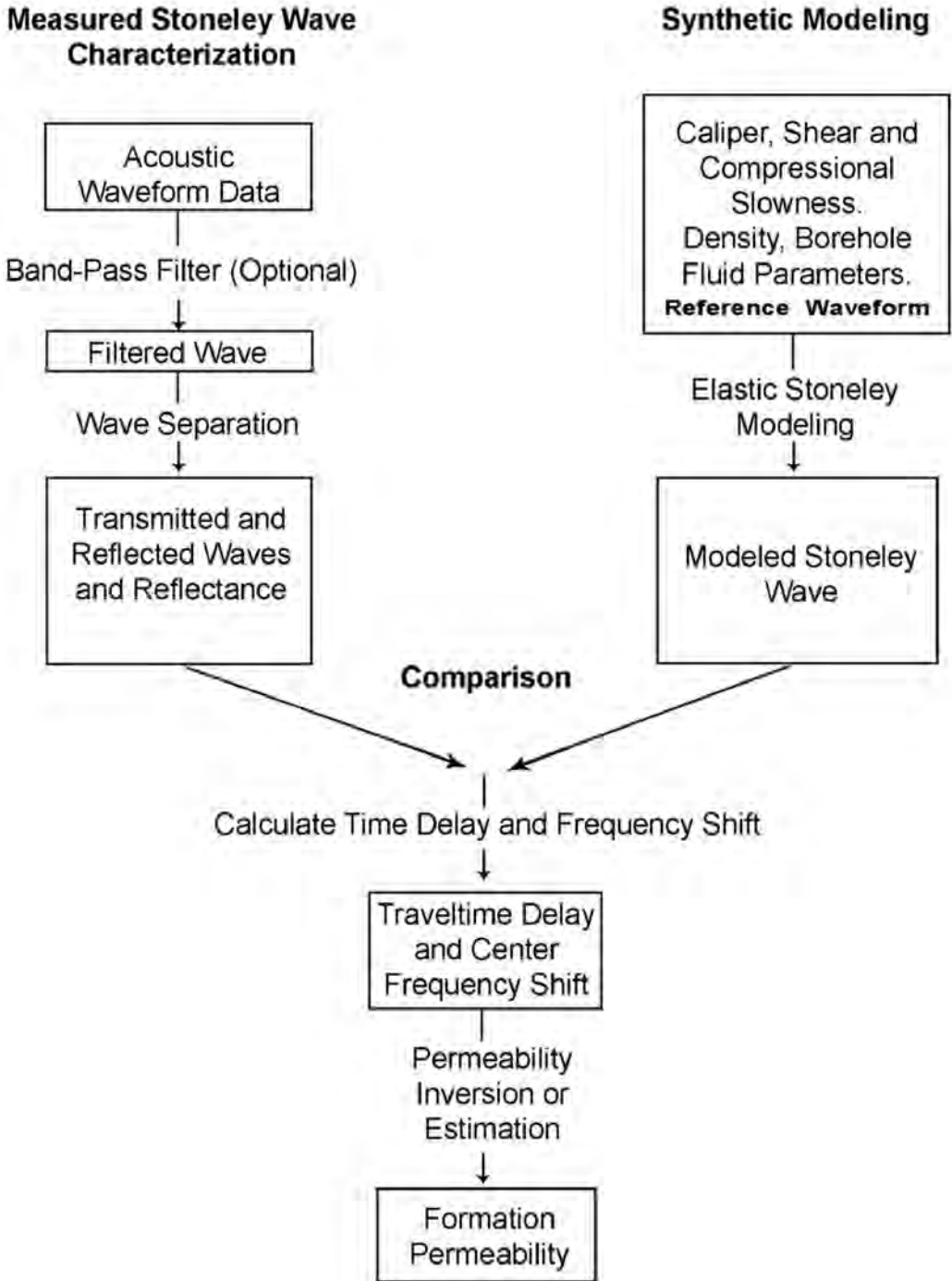


Fig. 3C.43—Stoneley-derived-permeability processing flow (courtesy of Baker Atlas).

Because the flexural waves induced by dipole-acoustic sources have a directional component, the use of mutually perpendicular (crossed) pairs of dipole transmitters and receivers can detect and measure dipole shear-wave splitting.²⁵⁵⁻²⁵⁸ In isotropic formations, both receiver com-

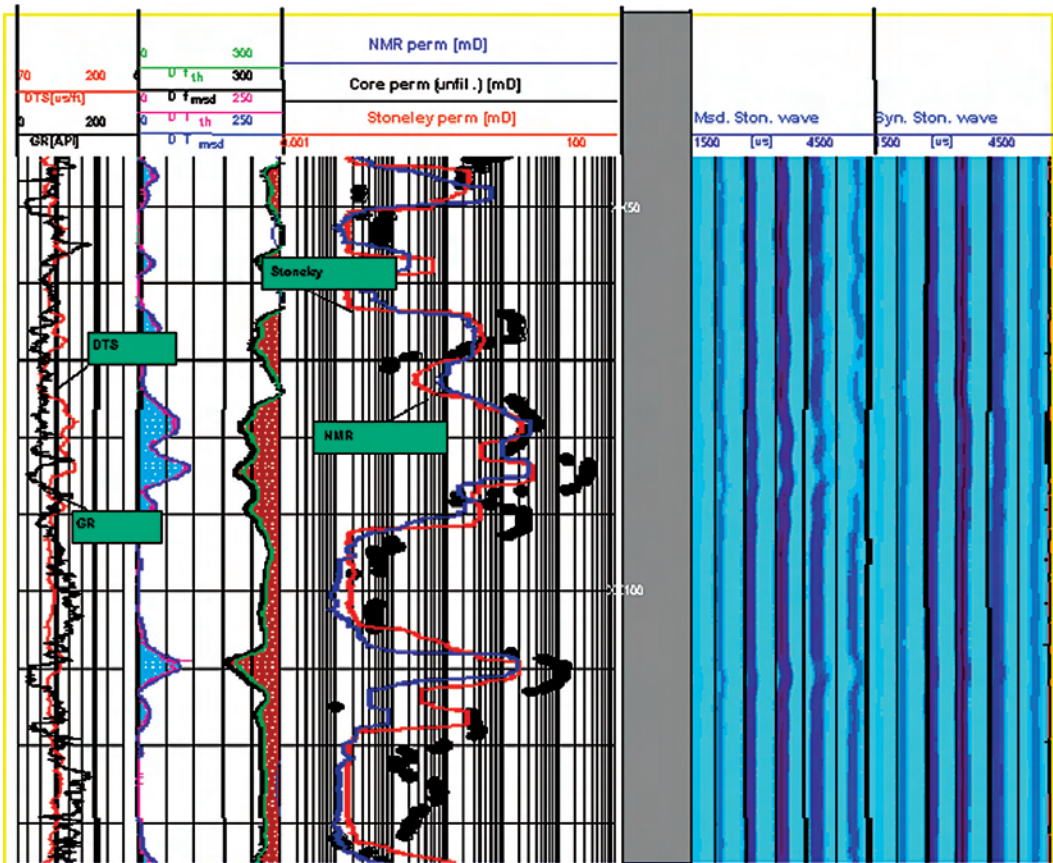


Fig. 3C.44—Comparison of Stoneley-, NMR- and core-permeability profiles. The agreement of these fundamentally different measurements confirms the validity of each (courtesy of Baker Atlas).

ponents (X and Y) will measure the same shear-wave arrival time. However, in an azimuthally anisotropic formation, the shear wave measured at the X-component of the receiver pair will be different from the one measured at the Y-component; one is called the fast shear component, the other, the slow shear component (Fig. 3C.36). To measure the fast and slow shear-wave slowness, four components are measured: two inline components, X-X and Y-Y, and two crossline components, XY and YX (Fig. 3C.37).

The dipole flexural shear mode is affected by a variety of factors including formation anisotropy. Significant borehole ellipticity (the result of borehole failure or breakouts)²⁵⁹ and high relative inclination between the borehole and formation^{260,261} may result in erroneous interpretation of dipole-derived anisotropy and must be accounted for during data processing.²⁶² Additionally, the presence of shale anisotropy in high-angle and horizontal wells, can significantly influence compressional velocity, which must be corrected for this effect.²⁶³

Initially, mathematical rotation methods originally developed for use in processing surface seismic data²⁶⁴ were used to determine the fast-wave direction together with the slowness values for the fast and slow shear wave. More recently, inversion methods²⁶⁵ are being applied to the four data sets to simultaneously determine the azimuth and magnitude of the anisotropy (Fig. 3C.38).

An anisotropy map (Fig. 3C.39) combines the derived average anisotropy and its azimuth to generate an azimuthal image. This display facilitates interpretation by allowing the analyst to

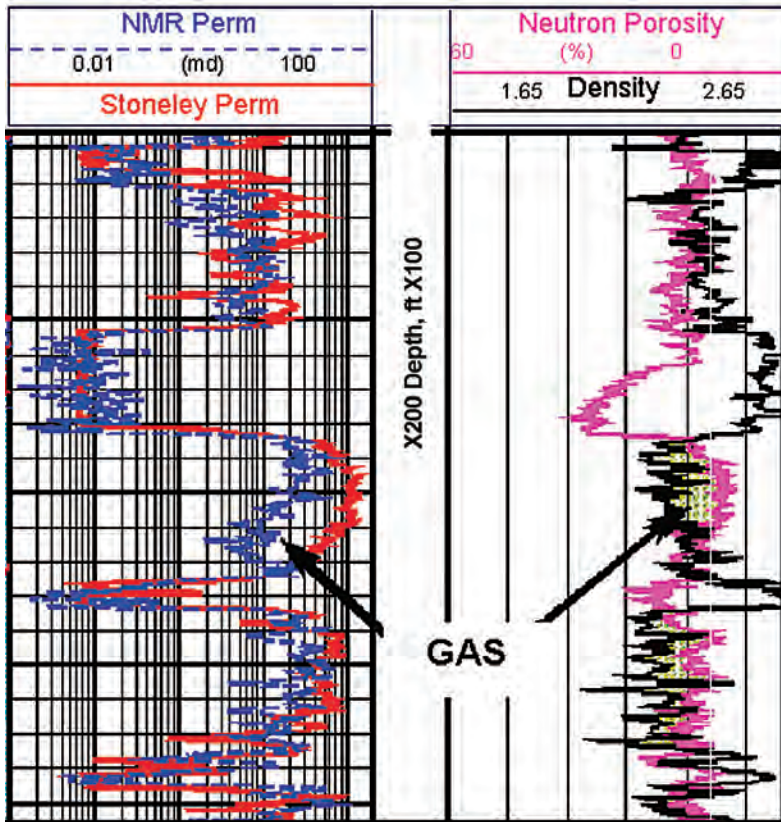


Fig. 3C.45—Stoneley-NMR-permeability gas indicator (courtesy of Baker Atlas).

quickly assess depth intervals of interest by looking at the brightness, direction, and continuation of the features on the map. The map also facilitates comparison with borehole-image logs. Rose diagrams (Track 3) provide an accurate indication of the fast shear azimuth over each labeled depth interval. The integration of monopole and dipole measurements yields improved estimates of anisotropy, magnitude of anisotropy, and permeability.^{243,266}

Horizontal Stress and Hydraulic Fracturing. Fractures, both natural and hydraulically induced, develop in relation to regional or localized stress patterns and play a major role in optimizing production and reservoir drainage. An estimate of the magnitude and azimuth of the horizontal stresses surrounding a borehole is needed for accurately placing wells to take advantage of existing fracture patterns and for artificially inducing fracture patterns during well completion through hydraulic stimulation.^{228,267}

The stresses operating on a rock formation are described by a triaxial coordinate system that consists of two principal horizontal stresses, σ_x and σ_y , and a vertical stress component, σ_z , which is the overburden. In a borehole, these downhole stresses are expressed as radial components at the borehole wall: the vertical component, σ_z , the radial component, σ_r , and the tangential component, σ_θ , and the (azimuthal) shear component, $\sigma_{r\theta}$.

Unbalanced-formation-stress components produce distortion around the borehole (stress-induced anisotropy) that results in shear-wave splitting. The azimuth of the fast-shear wave parallels the direction of maximum horizontal stress and the azimuth of the slow-shear wave parallels the direction of the minimum horizontal stress. Hydraulic-fracture azimuth is parallel to the direction of maximum horizontal stress.²⁶⁸

Hydraulic well stimulation consists of perforating an interval, then packing and pressuring these perforations to create fractures behind casing to allow increased production. Crossed-dipole anisotropy logging can estimate the vertical extent of the formation-stress fracture along the borehole and its azimuth in the formation (**Fig. 3C.40**).^{34,239–241,258,269–274}

3C.6.3 Attenuation Analysis. Acoustic-wave attenuation correlates with a variety of petrophysical parameters, including formation lithology and pore-fluid permeability, the degree of fluid saturation, and fractures type.^{275–278} A recent study suggests that the combination of compressional- and shear-wave attenuation logs may provide a potential formation-evaluation tool (**Figs. 3C.41 and 3C.42**).²⁷⁸

3C.6.4 Stoneley-Wave Analysis. Permeability. Stoneley-wave velocity and attenuation are sensitive to formation and fracture permeability, particularly at low frequencies.^{2,279–281} Stoneley-wave velocity decreases, and its attenuation increases, as permeability increases. Initial efforts (begun in the 1970s) to derive permeability information from Stoneley data were unsuccessful because neither the necessary low-frequency tools nor the appropriate processing methods had been developed. The parallel development of modern multipole array tools and sophisticated semblance- and inversion-processing methods enable computation of continuous profiles of formation permeability from monopole Stoneley-wave data.^{282–284} Typically, these methods first model the nonpermeability effects using the elastic-wave theory and then relate differences between the modeled and the measured data to formation permeability. One approach to Stoneley-wave processing is comprised of three parts^{284,285}: slowness analysis, reflectance mapping, and permeability estimation (**Fig. 3C.43**).

Stoneley-wave data are typically presented as an interval transit time, Δt_i and as a ratio of the amplitudes for the two receivers used. Both traces have been shown to correlate well with permeability changes and compare well with core data, when it is available. Stoneley-wave amplitude can be computed and used in conjunction with the slowness and the signatures to analyze dispersion and attenuation characteristics. Use of the attenuation (center-frequency shift) and dispersion (travel-time delay) provide good permeability indication and better quality control for permeability estimation.

Wave-separation processing minimizes the effects of nonpermeability-related influences (e.g., road noise and borehole scattering) and yields reflectance logs for the direct and reflected Stoneley-wave data. The center-frequency log for the reflected wave data characterizes the Stoneley-wave attenuation and can be used to indicate fractures, vugs, and bed boundaries. The center-frequency log for the direct (transmitted) data is used to estimate formation permeability. Knowledge of the formation-fluid properties (viscosity and compressibility from core or NMR) enables quantitative estimates. Without this information log-derived permeability estimates are only qualitative.

These models require sophisticated computer processing. A simplified, field-oriented technique based on Stoneley amplitude²⁸⁶ has so far provided good results in ideal conditions and when calibrated to core or NMR data.

Stoneley-derived formation permeability compares well with estimates obtained by nonacoustic methods, including core analysis and NMR logs (**Fig. 3C.44**).^{287,288} Additional improvement in permeability estimation is possible when anisotropy information is incorporated in the process.²⁸⁹ Formation evaluation is further enhanced when these diverse measurements are integrated through joint interpretation.²⁹⁰ As indicated by the plots in **Fig. 3C.44**, calibration of log responses to core data would improve log-predicted values in noncored intervals.

The Stoneley wave measures total permeability and NMR measures vuggy permeability. A comparison of these two measurements in carbonate formations makes it possible to evaluate the permeability contributions arising from fractures and vugs.²⁹⁰ A combination of these two

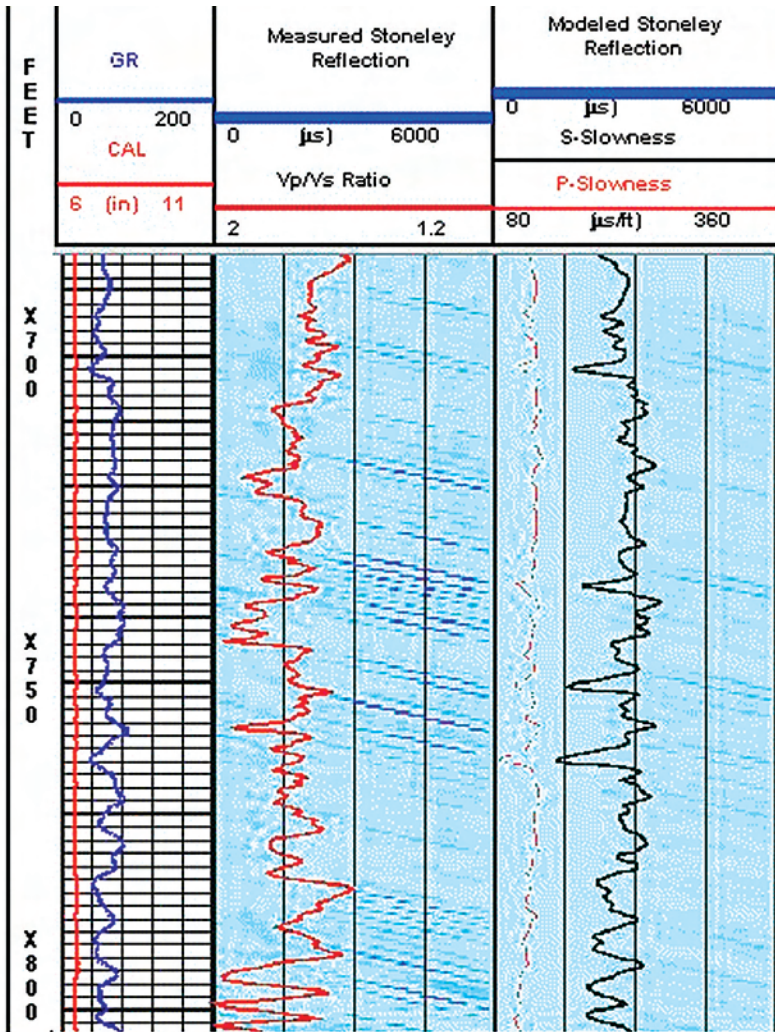


Fig. 3C.46—Gas detection in a high-porosity, laminated formation using thin-bed slowness and Stoneley reflection. The increase in P-wave slowness (Track 2) across the interval of thin gas sands, X740 to X800 m, is accompanied by low density values (Track 2) and numerous Stoneley-wave reflections (Track 3) (courtesy of Baker Atlas).

measurements calibrated using wireline formation-tester data enables improved permeability estimation in these reservoirs.²⁹¹

Gas Detection. Stoneley-wave properties, used in combination with other data, facilitate identification of gas-bearing intervals. A gas-saturated formation interval has drastically different fluid mobility and compressibility compared to those of the surrounding formations. In the presence of gas, Stoneley-derived permeability is overestimated because of increased pore-fluid mobility (decreased viscosity) and compressibility, and NMR permeability may be underestimated because of a decreased hydrogen index. If first calibrated in a nongas-bearing interval, separation of the two permeability curves indicates the presence of gas (Fig. 3C.45).²⁹⁰ The plot also shows the neutron-density crossplot is effective in detecting the gas zone and may be more sensitive in some intervals.

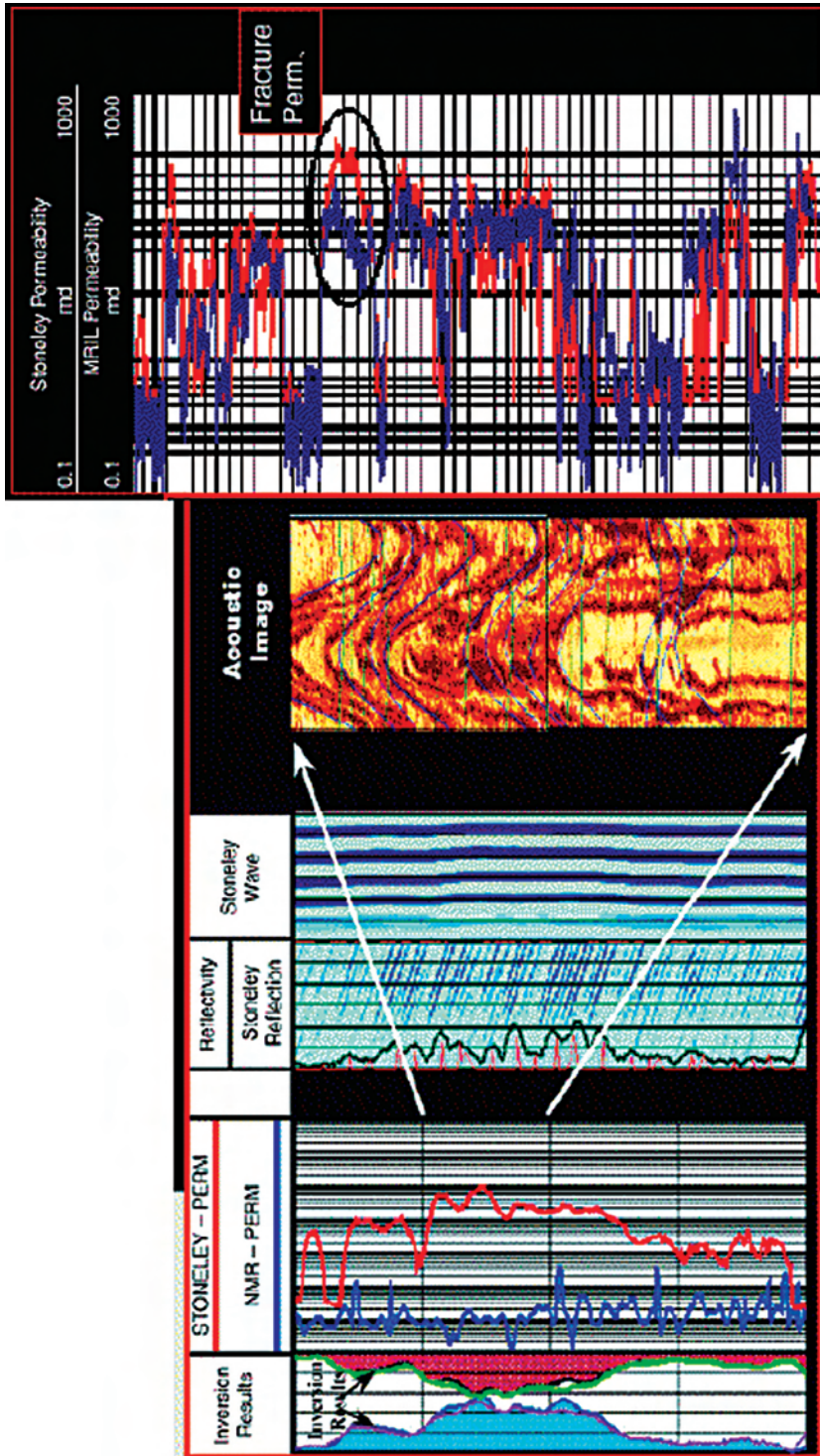


Fig. 3C.47—Stoneley-wave and NMR permeability profiles in the presence of borehole fractures. Stoneley-wave results are dominated by the fracture-system contribution, while the NMR results are dominated by the matrix-based permeability. The fractured sandstone interval, indicated by separation of the two permeability curves (Tracks 2 and 6), is confirmed by Stoneley-wave reflection data (Track 3) and the acoustic image log (Track 5) (courtesy of Baker Atlas).

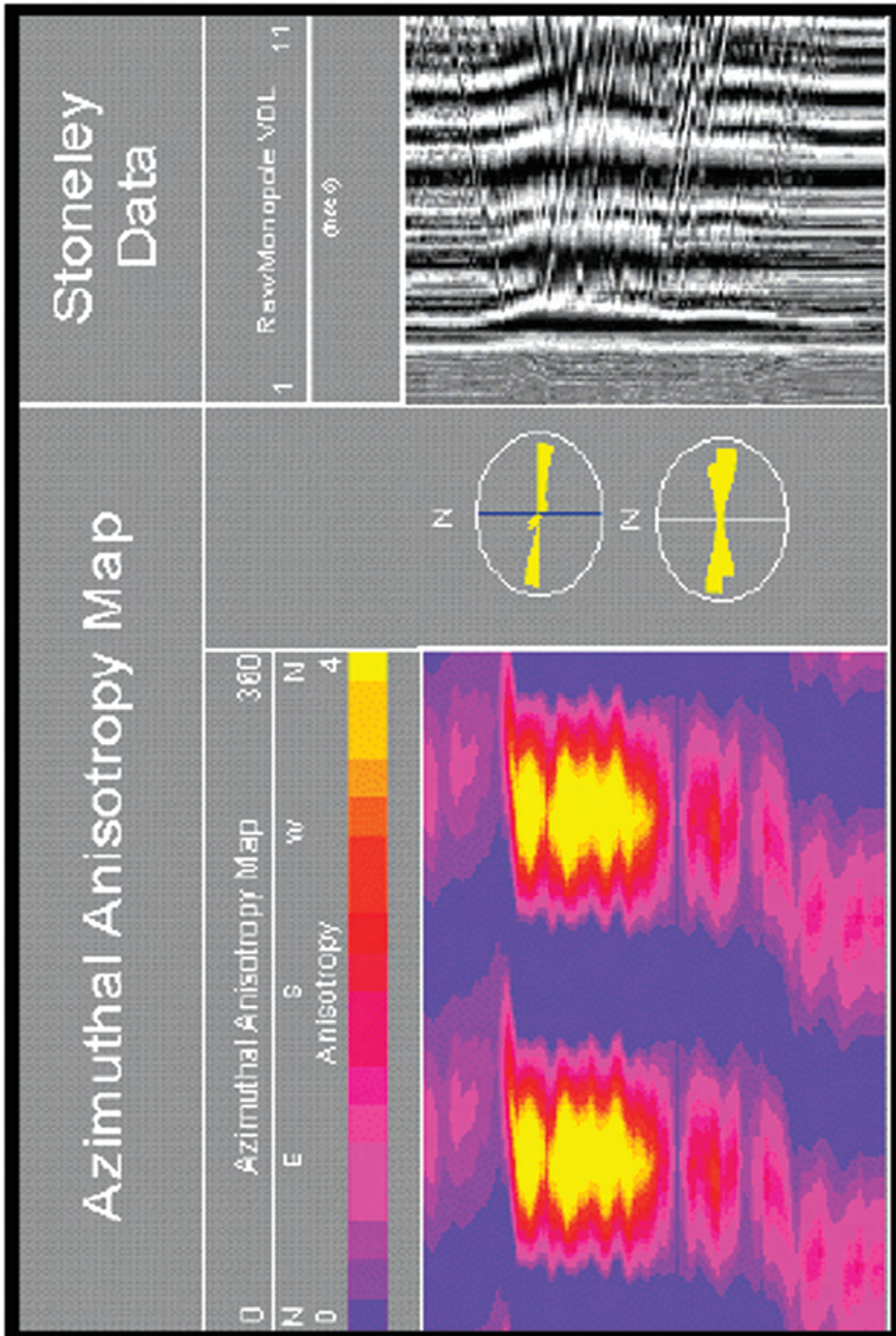


Fig. 3C.48—Correlation between azimuthal anisotropy and Stoneley reflections. A fracture zone in a U.S. mid-continent well causes both shear-wave splitting and Stoneley-wave reflections—in the anisotropy map (left), brighter colors represent higher anisotropy. The azimuth of the fast shear arrival is east/west (center). The fractures intersecting the borehole cause significant up- and down-going Stoneley-wave reflections seen in Stoneley-waveform amplitudes (right) (courtesy of Baker Atlas).

The significant contrast in fluid mobility and compressibility in a gas zone also generates a measurable Stoneley-wave reflection. The presence of these reflections, together with an increase in compressional slowness or a decrease in the V_p/V_s ratio, identifies a gas-bearing zone (Fig. 3C.46).²⁹² This type of joint interpretation is particularly effective in thin-bed evaluation.

Fracture Evaluation. The pressure-driven, fluid-borne nature of Stoneley waves makes them sensitive to fluid movement, and thus, to open fractures. The effects of open fractures on Stoneley waves are amplitude reduction, an increase in Stoneley slowness, the occurrence of mode conversion, and the occurrence of Stoneley reflections.^{162,293,294}

The Stoneley wave responds to fracture permeability while NMR does not, thus, the Stoneley-wave permeability is greater in the presence of fractures than NMR permeability. The combined use of Stoneley- and NMR-derived permeability provides a fracture indicator in both sandstones (Fig. 3C.47) and carbonates (Fig. 3C.48).²⁹⁰

3C.7 Summary

This chapter has summarized the characteristics and capabilities of acoustic-logging tools. Although determination of geophysical (seismic) and petrophysical (porosity) properties have traditionally been the most widely used applications for acoustic-log data, new and advanced applications in geomechanics (anisotropy, fracture, and stress evaluation) and petrophysics (permeability) have been made possible by the multiarray tools and inversion processing methods now available. Interpretation methods that combine acoustic data with core and other log data, such as resistivity, nuclear, NMR, and borehole images, facilitate determination of fluid saturation and typing when logging conditions provide reliable data. For all applications of acoustic logging careful planning is critical to ensure successful acquisition of the desired data.

Nomenclature

a	= Archie parameter
C	= shale compaction coefficient
C_p	= compaction correction factor
E	= Young's modulus
K	= bulk modulus
m	= Archie parameter
R	= resistivity, ohm-m
R_1	= receiver one in a two-receiver tool configuration
R_2	= receiver two in a two-receiver tool configuration
S_w	= water saturation, fraction
t	= travel time
t_1	= travel time between T_2 and R_1
t_2	= travel time between T_2 and R_2
t_3	= travel time between T_1 and R_1
t_4	= travel time between T_1 and R_2
T	= transmitter
TR	= transmitter-to-receiver spacing (ft)
T_1	= transmitter one in a two-transmitter tool (BHC) configuration
T_2	= transmitter two in a two-transmitter tool (BHC) configuration
v	= velocity of the formation
V	= velocity, ft/sec
x	= distance between R_1 and R_2
X_{12}	= distance between R_1 and R_2
α	= porosity correction factor
Δt	= transit time, sec

Δt_c	=	compressional travel time
ϕ	=	fractional porosity of rock
θ	=	angle, degrees
ρ	=	formation density, lbm/ft ³
μ	=	shear modulus
σ	=	Poisson's ratio
σ_r	=	borehole radial stress
σ_x	=	principal horizontal stress x-direction
σ_y	=	principal horizontal stress y-direction
σ_z	=	principal vertical stress z-direction
σ_θ	=	borehole tangential stress

Subscripts

c	=	compressional wave
c'	=	critical
f	=	fluid
ma	=	rock matrix
p	=	compressional wave
s	=	shear wave
sh	=	shale
w	=	water

References

1. Paillet, F.L., Cheng, C.H., and Pennington, W.D.: "Acoustic-Waveform Logging—Advances in Theory and Application," *The Log Analyst* (1992) **33**, No. 3, 239.
2. Paillet, F.L. and Cheng, C.H.: *Acoustic Waves in Boreholes*, CRC Press, Boca Raton, Florida (1991) 1–264.
3. Mavko, G., Mukerji, T., and Dvorkin, J.: *The Rock Physics Handbook—Tools for Seismic Analysis in Porous Media*, Cambridge U. Press, Cambridge, England (1998) 1–329.
4. Hearst, J.R., Nelson, P.H., and Paillet, F.L.: "Acoustic Logging," *Well Logging for Physical Properties*, second edition, Wiley and Sons Inc., New York City (2000) Chap. 8, 257–303.
5. Tang, X.-M. and Cheng, A.: "Quantitative Borehole Acoustic Methods," *Handbook of Geophysical Exploration*, Seismic Exploration **24**, Pergamon Press (Elsevier) (2004).
6. Cheng, C.H. and Toksoz, M.N.: "Determination of Shear Wave Velocities in 'Slow' Formation," paper V, *Trans.*, 1983 Annual Logging Symposium, Soc. of Professional Well Log Analysts (SPWLA) 1–18.
7. Valero, H.P. *et al.*: "Processing of Monopole Compressional in Slow Formation," paper BG 2.5, in *Expanded Abstracts*, 2004 Annual Meeting Technical Program, Soc. of Exploration Geophysicists (SEG) 318–321.
8. Wu, P.T., Darling, H.L., and Scheibner, D.: "Low-Frequency P-Wave Logging for Improved Compressional Velocity in Slow Formation Gas Zones," paper BG1.3, *Expanded Abstracts*, 1995 Annual Meeting Technical Program, SEG, 9–12.
9. *Handbook of Physical Properties of Rocks*, R.S. Carmichael (ed.) CRC Press Inc., Boca Raton, Florida (1982) **2**, 1–228.
10. Leonardon, E.G.: "Logging, Sampling, and Testing," *History of Petroleum Engineering*, American Petroleum Inst., Div. of Production, Dallas (1961) Chap. 8, 493–578.
11. Snyder, D.D. and Fleming, D.B.: "Well-Logging—A Twenty-Five-Year Perspective," *Geophysics* (1985) **50**, No. 12, 2,504–2,529.
12. Jordan, J.R. and Campbell, F.L.: *Well Logging II—Electric and Acoustic Logging*, Monograph Series, SPE, Richardson, Texas (1986) **10**, 95–151.

13. Timur, A.: "Acoustic Logging," *Petroleum Engineering Handbook*, H.B. Bradley (ed.), SPE, Richardson, Texas (1987) Chap. 7, 51-1-51-52.
14. Liu, O.Y.: "The Sources of Errors in Slowness Measurements and an Evaluation of Full Waveform Compensation Techniques," paper SPE 16772 presented at the 1987 SPE Annual Technical Conference and Exhibition, Dallas, 27-30 September.
15. Aron, J., Murray, J., and Seeman, B.: "Formation Compressional and Shear Interval Transit Time Logging by Means of Long Spacings and Digital Techniques," paper SPE 7446 presented at the 1978 SPE Annual Technical Conference and Exhibition, Houston, 1-3 October.
16. Koerperich, E.A.: "Shear Wave Velocities Determined from Long- and Short-Spaced Borehole Acoustic Device," *SPEJ* (October 1980) 317.
17. Morris, C.F., Little, T.M., and Letton, W. III: "A New Sonic Array Tool for Full Waveform Logging," paper SPE 13285 presented at the 1984 SPE Annual Technical Conference and Exhibition, Houston, 16-19 September.
18. Williams, D.M. *et al.*: "The Long Spaced Acoustic Logging Tool," paper T, *Trans.*, 1984 Annual Logging Symposium, SPWLA, 1-15.
19. Chen, S.T. and Eriksen, E.A.: "Compressional- and Shear-Wave Logging in Open and Cased Holes Using a Multipole Tool," *Geophysics* (1991) **56**, No. 4, 550-557.
20. Georgi, D.T. *et al.*: "Application of Shear and Compressional Transit-Time Data to Cased-Hole Carbonate Reservoir Evaluation," *The Log Analyst* (1991) **32**, No. 3, 129.
21. Valero, H.P., Skelton, O., and Cao, H.: "An Overview of Sonic Slowness Evaluation Behind Casing," paper I, *Trans.*, 2000 Well Logging Symposium Japan, SPWLA, Japan Chapter, 1-8.
22. Tang, X., and Patterson, D.: "Analyzing and Processing Acoustic Logging Data for Poorly Bonded Cased Boreholes," paper OO, *Trans.*, 2005 Annual Logging Symposium, SPWLA, 1-11.
23. Stevens, J.L. and Day, S.M.: "Shear Velocity Logging in Slow Formations Using the Stoneley Wave," *Geophysics* (1986) **51**, No. 1, 137-147.
24. Liu, O.Y.: "Stoneley Wave-Derived Delta-T Shear Log," paper ZZ, *Trans.*, 1984 Annual Logging Symposium, SPWLA, 1-14.
25. White, J.E.: "The HULA Log—A Proposed Acoustic Tool," paper I, *Trans.*, 1967 Annual Logging Symposium, SPWLA, 1-30.
26. Zemanek, J. *et al.*: "Continuous Acoustic Shear Wave Logging," paper U, *Trans.*, 1984 Annual Logging Symposium, SPWLA, 1-14.
27. Kessler, C. *et al.*: "New Development in Monopole Acoustic Logging," paper Z, *Trans.*, 2004 Annual Logging Symposium, SPWLA, 1-12.
28. Harrison, A.R. *et al.*: "Acquisition and Analysis of Sonic Waveforms from a Borehole Monopole and Dipole Source for the Determination of Compressional and Shear Speeds and Their Relation to Rock Mechanical Properties and Surface Seismic Data," paper SPE 20557 presented at the 1990 SPE Annual Technical Conference and Exhibition, New Orleans, 23-26 September.
29. Tello, L.N. *et al.*: "A Dipole Array Sonic Tool for Vertical and Deviated Wells," paper SPE 56790 presented at the 1999 SPE Annual Technical Conference and Exhibition, Houston, 3-6 October.
30. Oden, C.P., Stowell, J.R., and LoCoco, J.J.: "Variable Frequency Monopole-Dipole Sonic Logging for Shear Velocity—Applications and Test Results," *Proc.*, 2000 Intl. Symposium on Borehole Geophysics for Minerals, Geotechnical, and Groundwater Applications, Minerals, and Geotechnical Logging Soc., SPWLA, 71-76.
31. Kessler, C. *et al.*: "A New Generation Crossed Dipole Logging Tool: Design and Case Histories," paper SPE 71740 presented at the 2001 SPE Annual Technical Conference and Exhibition, New Orleans, 30 September-3 October.
32. Pistre, V. *et al.*: "A Modular Wireline Sonic Tool for Measurements of 3D (Azimuthal, Radial, and Axial) Formation Acoustic Properties," paper P, *Trans.*, 2005 Annual Logging Symposium, SPWLA, 1-13.
33. Plona, T. *et al.*: "Mechanical Damage Detection and Anisotropy Evaluation Using Dipole Sonic," paper F, *Trans.*, 2002 Annual Logging Symposium, SPWLA, 1-14.
34. Sinha, B. *et al.*: "Optimal Well Completions Using Radial Profiling of Formation Shear Slownesses," paper SPE 95837 presented at the 2005 SPE Annual Technical Conference and Exhibition, Dallas, 9-12 October.
35. Aron, J. *et al.*: "Sonic Compressional Measurements While Drilling," paper SS, *Trans.*, 1994 Annual Logging Symposium, SPWLA, 1-17.

36. Minear, J. *et al.*: “Compressional Slowness Measurements While Drilling,” paper VV, *Trans.*, 1995 Annual Logging Symposium, SPWLA, 1–12.
37. Hsu, K. *et al.*: “Interpretation and Analysis of Sonic While Drilling Data in Overpressured Formations,” paper FF, *Trans.*, 1997 Annual Logging Symposium, SPWLA, 1–14.
38. Hashem, M. *et al.*: “Seismic Tie Using Sonic-While-Drilling Measurements,” paper I, *Trans.*, 1999 Annual Logging Symposium, SPWLA, 1–13.
39. Market, J., Schmitt, D., and Deady, R.: “LWD Sonic Logging in Cased Holes,” paper U, *Trans.*, 2004 Annual Logging Symposium, SPWLA, 1–14.
40. Varsamis, G. *et al.*: “A New MWD Full Wave Dual Mode Sonic Tool Design and Case Histories,” paper F, *Trans.*, 1999 Annual Logging Symposium, SPWLA, 1–12.
41. Varsamis, G.L. *et al.*: “LWD Shear Velocity Logging in Slow Formations—Design Decisions and Case Histories,” paper O, *Trans.*, 2000 Annual Logging Symposium, SPWLA, 1–13.
42. Joyce, B. *et al.*: “Introduction to a New Omni-Directional Acoustic System for Improved Real Time LWD Sonic Logging—Tool Design and Field Test Results,” paper SS, *Trans.*, 2001 Annual Logging Symposium, SPWLA, 1–14.
43. Leggett, J.V. III *et al.*: “Field Test Results Demonstrating Improved Real-Time Data Quality in an Advanced LWD Acoustic System,” paper SPE 71732 presented at the 2001 SPE Annual Technical Conference and Exhibition, New Orleans, 30 September–3 October.
44. Tang, X. *et al.*: “Shear-Velocity Measurement in the Logging-While-Drilling Environment—Modeling and Field Evaluations,” *Petrophysics* (2003) **44**, No. 2, 79–90.
45. Market, J. *et al.*: “Processing and Quality Control of LWD Dipole Sonic Measurements,” paper PP, *Trans.*, 2002 Annual Logging Symposium, SPWLA, 1–14.
46. Dubinsky, V. *et al.*: “Engineering Aspects of LWD Quadrupole Measurements and Field Test Results,” paper SPE 84248 presented at the 2003 SPE Annual Technical Conference and Exhibition, Denver, 5–8 October.
47. Goldberg, D. *et al.*: “Analysis of LWD Sonic Data in Low-Velocity Formations,” paper BH 1.5, *Expanded Abstracts*, 2003 Annual Meeting Technical Program, SEG, 301–304.
48. Boonen, P. and Yogeswaren, E.: “A Dual-Frequency LWD Sonic Tool Expands Existing Unipolar Transmitter Technology to Supply Shear Wave Data in Soft Formations,” paper X, *Trans.*, 2004 Annual Logging Symposium, SPWLA, 1–11.
49. Endo, T., Yoneshima, S., and Valero, H.-P.: “Analysis of LWD Sonic Data in Very Slow Formation—Compressional Processing and Indirect V_p/V_s Estimation,” paper G, *Proc.*, 2004 Formation Evaluation Symposium of Japan, SPWLA Japan Chapter, 1–8.
50. Tang, X., Zheng, Y., and Dubinsky, V.: “Logging While Drilling Acoustic Measurement in Unconsolidated Slow Formations,” paper R, *Trans.*, 2005 Annual Logging Symposium, 1–13.
51. Zhu, Z. *et al.*: “Experimental Studies of Multipole Acoustic Logging with Scaled Borehole,” paper BG 2.6, *Expanded Abstracts*, 2005 Annual Meeting Technical Program, SEG, 376–379.
52. Tang, X. *et al.*: “Logging-While-Drilling Shear and Compressional Measurements in Varying Environments,” paper II, *Trans.*, 2003 Annual Logging Symposium, SPWLA, 1–13.
53. Wang, T., and Tang, X.: “Investigation of LWD Quadrupole Shear Measurement in Real Environments,” paper KK, *Trans.*, 2003 Annual Logging Symposium, SPWLA, 1–12.
54. Haugland, S.: “Frequency Dispersion Effects on LWD Shear Sonic Measurements in Acoustically Slow Environments,” paper SPE 90505 presented at the 2004 SPE Annual Technical Conference and Exhibition, Houston, 26–29 September.
55. Huang, X., Zheng, Y., and Toksoz, N.M.: “Effects of Tool Eccentricity on Acoustic Logging While Drilling (LWD) Measurements,” paper BG 1.4, *Expanded Abstracts*, 2004 Annual Meeting Technical Program, SEG, 290–293.
56. Underhill, W. *et al.*: “Demonstrations of Real-Time Borehole Seismic from an LWD Tool,” paper SPE 71365 presented at the 2001 SPE Annual Technical Conference and Exhibition, New Orleans, 30 September–3 October.
57. Haldorsen, J.B.U. *et al.*: “Optimizing the Well Construction Process: Full-Waveform Data from While-Drilling Seismic Measurements in the South Caspian Sea,” paper SPE 79844 presented at the 2003 SPE/IADC Drilling Conference, Amsterdam, 19–21 February.
58. Esmersoy, C. *et al.*: “Seismic MWD: Drilling in Time, on Time, It’s About Time,” *The Leading Edge* (2005) **24**, No. 1, 56–62.

59. Althoff, G. *et al.*: “New Concepts for Seismic Surveys While Drilling,” paper SPE 90751 presented at the 2004 SPE Annual Technical Conference and Exhibition, Houston, 26–29 September.
60. Zemanek, J. *et al.*: “The Borehole Televier: A New Logging Concept for Fracture Location and Other Types of Borehole Inspection,” *JPT* (June 1969) 762.
61. Prensky, S.: “Advances in Borehole Imaging Technology and Applications,” *Borehole Imaging—Applications and Case Histories*, M.A. Lovell, G. Williamson, and P.K. Harvey (eds.), Geological Soc., London, Special Publication No. 159 (1999) 1–44.
62. Bigelow, E.L.: *Cement Evaluation*, Atlas Wireline Services, Houston (1990) 1–142.
63. Hill, A.D.: “Cement-Quality Logging,” *Production Logging—Theoretical and Interpretative Elements*, Monograph Series, SPE, Richardson, Texas (1990) **14**, 123–140.
64. Jutten, J. and Morriss, S.L.: “Cement Job Evaluation,” *Well Cementing*, E.B. Nelson (ed.), Elsevier, Amsterdam, Developments in Petroleum Science No. 28 (1990) Chap. 16, 16-1–16-44.
65. Rouillac, D.: *Cement Evaluation Logging Handbook*, Editions Technip, Paris (1994) 1–176.
66. Smolen, J.J.: *Cased Hole and Production Log Evaluation*, PennWell Publishing Co., Tulsa (1996) Chaps. 10 and 11, 161–213.
67. Baker, L.J.: “The Effect of the Invaded Zone on Full Wavetrain Acoustic Logging,” *Geophysics* (1984) **49**, No. 6, 796–809.
68. Alberty, M.: “The Influence of the Borehole Environment upon Compressional Sonic Logs,” *The Log Analyst* (1996) **37**, No. 4, 30–44.
69. Chi, S. *et al.*: “Assessment of Mud-Filtrate Invasion Effects on Borehole Acoustic Logs and Radial Profiling of Formation Elastic Parameters,” paper SPE 90159 presented at the 2004 SPE Annual Technical Conference and Exhibition, Houston, 26–29 September.
70. Walker, T.: “Origin of the ‘W’ Pattern on Cased Hole Micro-Seismogram Logs,” *The Log Analyst* (1968) **9**, No. 2, 30–32.
71. Pilkington, P.E.: “Cement Evaluation—Past, Present, and Future,” *JPT* (February 1992) 132.
72. Hayman, A.J., Hutin, R., and Wright, P.V.: “High-Resolution Cementation and Corrosion Imaging by Ultrasound,” paper KK, *Trans.*, 1991 Annual Logging Symposium, SPWLA, 1–25.
73. Graham, W.L. *et al.*: “Cement Evaluation and Casing Inspection with Advanced Ultrasonic Scanning Methods,” paper SPE 38651 presented at the 1997 SPE Annual Technical Conference and Exhibition, San Antonio, Texas, 5–8 October.
74. Froelich, B. *et al.*: “Cement Evaluation Tool: A New Approach to Cement Evaluation,” *JPT* (August 1982) 1835.
75. Sheives, T.C. *et al.*: “A Comparison of New Ultrasonic Cement and Casing Evaluation Logs with Standard Cement Bond Logs,” paper SPE 15436 presented at the 1986 SPE Annual Technical Conference and Exhibition, New Orleans, 5–8 October.
76. Bigelow, E.L., Domangue, E.J., and Lester, R.A.: “A New Innovative Technology for Cement Evaluation,” paper SPE 20585 presented at the 1990 SPE Annual Technical Conference and Exhibition, New Orleans, 23–26 September.
77. Schmidt, M.G.: “The Micro CBL—A Second Generation Radial Cement Evaluation Instrument,” paper Z, *Trans.*, 1989 Annual Logging Symposium, SPWLA, 1–16.
78. Tello, L.N. *et al.*: “New Efficient Method for Radial Cement Bond Evaluation,” *Canadian Well Logging Soc. J.* (1995) **20**, 60–69.
79. Butsch, R.J.: “Overcoming Interpretation Problems of Gas-Contaminated Cement Using Ultrasonic Cement Logs,” paper SPE 30509 presented at the 1995 SPE Annual Technical Conference and Exhibition, Dallas, 22–25 October.
80. Frisch, G.J., Graham, W.L., and Griffith, J.: “Assessment of Foamed-Cement Slurries Using Conventional Cement Evaluation Logs and Improved Interpretation Methods,” paper SPE 55649 presented at the 1999 SPE Rocky Mountain Regional Meeting, Gillette, Wyoming, 15–18 May.
81. Frisch, G., Graham, L., and Griffith, J.: “A Novel and Economical Processing Technique Using Conventional Bond Logs and Ultrasonic Tools for Enhanced Cement Evaluation,” paper EE, *Trans.*, 2000 Annual Logging Symposium, SPWLA, 1–14.
82. Frisch, G. *et al.*: “Advances in Cement Evaluation Tools and Processing Methods Allow Improved Interpretation of Complex Cements,” paper SPE 97186 presented at the 2005 SPE Annual Technical Conference and Exhibition, Dallas, 9–12 October.

83. Van Kuijk, R. *et al.*: “A Novel Ultrasonic Cased-Hole Imager for Enhanced Cement Evaluation,” paper IPTC 10546 presented at the 2005 International Petroleum Technology Conference, Doha, Qatar, 21–23 November.
84. Dumont, A., Patin, J.-B., and Le Floch, G.: “A Single Tool for Corrosion and Cement Evaluation,” paper SPE 13140 presented at the 1984 SPE Annual Technical Conference and Exhibition, Houston, 16–19 September.
85. Roberts, D.L. and Richards, J.W.: “Casing Corrosion Evaluation Using Ultrasonic Techniques: A Unique Approach for West Texas Wells,” *Proc.*, 1987 Annual Short Course, Southwestern Petroleum Short Course Association, Lubbock, Texas, 20–33.
86. Frisch, G. and Mandal, B.: “Advanced Ultrasonic Scanning Tool and Evaluation Methods Improve and Standardize Casing Inspection,” paper SPE 71399 presented at the 2001 SPE Annual Technical Conference and Exhibition, New Orleans, 30 September–3 October.
87. Fertl, W.H.: “Openhole Crossplot Concepts: A Powerful Technique in Well Log Analysis,” *JPT* (March 1981) 535.
88. Bigelow, E.L.: *Introduction to Wireline Log Analysis*, Baker Atlas, Houston (1995) 1–312.
89. Boyer, S. and Mari, J.-L.: *Seismic Surveying and Well Logging Oil and Gas Exploration Techniques*, Editions Technip, Paris (1997) 1–192.
90. Pickett, G.R.: “Acoustic Character Logs and Their Applications in Formation Evaluation,” *JPT* (June 1963) 659.
91. Medlin, W.L. and Alhilali, K.A.: “Shear-Wave Porosity Logging in Sands,” *SPEFE* (March 1992) 106.
92. Tixier, M.P., Alger, R.P., and Doh, C.A.: “Sonic Logging,” *JPT* (1959) 106; *Trans.*, AIME, **216**.
93. Wyllie, M.R.J., Gregory, A.R., and Gardner, L.W.: “Elastic Wave Velocities in Heterogeneous and Porous Media,” *Geophysics* (1956) **21**, No. 1, 41–70.
94. Raymer, L.L., Hunt, E.R., and Gardner, J.S.: “An Improved Sonic Transit Time-to-Porosity Transform,” paper P, *Trans.*, 1980 Annual Logging Symposium, SPWLA, 1–12.
95. Dvorkin, J. and Nur, A.: “Time-Average Equation Revisited,” *Geophysics* (1998) **63**, No. 2, 460–464.
96. Krief, M. *et al.*: “A New Petrophysical Interpretation Using the Velocities of P and S Waves (Full Waveform Sonic),” *The Log Analyst* (1990) **31**, No. 6, 355–369.
97. Spears, R., and Nicosia, W.: “Porosity Estimation from Shear Wave Interval Transit Time in the Norphlet Aeolian Jurassic Sandstone of Southern and Offshore Alabama,” paper N, *Trans.*, 2003 Annual Logging Symposium, SPWLA, 1–12.
98. Valero, H.-P., Skelton, O., and Almeida, C.M.: “Processing of Monopole Sonic Waveforms Through Cased Hole,” paper BH 1.1, *Expanded Abstracts*, 2003 Annual Meeting Technical Program, SEG, 285–288.
99. Tello, L.N. *et al.*: “Through-Tubing Hostile-Environment Acoustic Logging Tool,” paper Y, *Trans.*, 2004 Annual Logging Symposium, SPWLA, 1–11.
100. Smith, J., Fisburn, T., and Bigelow, E.: “Acoustic Porosity Corrections for Gas and Light Hydrocarbon-Bearing Sandstones,” paper AAA, *Trans.*, 1996 Annual Logging Symposium, SPWLA, 1–9.
101. Knackstedt, M.A., Arns, C.H., and Pinczewski, W.V.: “Velocity-Porosity Relationships, Part 1: Accurate Velocity Model for Clean Consolidated Sandstones,” *Geophysics* (2003) **68**, No. 6, 1822–1834.
102. Knackstedt, M.A., Arns, C.H., and Pinczewski, W.V.: “Velocity-Porosity Relationship: Predictive Velocity Model for Cemented Sands Composed of Multiplemineral Phases,” *Geophysical Prospecting* (2005) **53**, No. 3, 349–372.
103. Kazatchenko, E., Markov, M., and Mousatov, A.: “Determination of Primary and Secondary Porosity in Carbonate Formations Using Acoustic Data,” paper SPE 84209 presented at the 2003 SPE Annual Technical Conference and Exhibition, Denver, 5–8 October.
104. Burke, J.A., Campbell, R.L. Jr., and Schmidt, A.W.: “The Litho-Porosity Cross Plot—A Method of Determining Rock Characteristics for Computation of Log Data,” paper SPE 2771 presented at the 1969 SPE Illinois Basin Regional Meeting, Evansville, Indiana, 30–31 October.
105. Clavier, C. and Rust, D.H.: “MID Plot: A New Lithology Technique,” *The Log Analyst* (1976) **17**, No. 6, 16–24.

106. Robert, H.V. and Campbell, R.L. Jr.: "Applications of CORIBAND to the Evaluation of Sandstones Containing Mica," *The Log Analyst* (1976) **17**, No.1, 33–40.
107. Nations, J.F.: "Lithology and Porosity from Acoustic Shear and Compressional Wave Transit Time Relationships," *The Log Analyst* (1974) **15**, No. 6, 3–8.
108. Eastwood, R.L. and Castagna, J.P.: "Interpretation of V_p/V_s Ratios from Sonic Logs," *Shear-Wave Exploration*, S.H. Danbom and S.N. Domenico (eds.), SEG, Geophysical Development Series No. 1 (1987) 139–153.
109. Johnston, J.E. and Christensen, N.I.: "Compressional to Shear Velocity Ratios in Sedimentary Rocks," *Intl. J. of Rock Mechanics and Mining Sciences and Geomechanical Abstracts* (1993) **30**, No. 7, 751–754.
110. Assefa, S., McCann, C., and Sothcott, J.: "Velocities of Compressional and Shear Waves in Limestone," *Geophysical Prospecting* (2003) **51**, No. 1, 1–13.
111. Tsuneyama, F. *et al.*: " V_p/V_s Ratio as a Rock Frame Indicator for a Carbonate Reservoir," *First Break* (2003) **21**, No. 7, 53–58.
112. Hingle, A.T. Jr.: "The Use of Logs in Exploration Problems," *Technical Program*, 1959 Annual Meeting, SEG, 38.
113. Berry, J.E.: "Acoustic Velocity in Porous Media," *JPT* (1959) 262; *Trans.*, AIME, **216**.
114. Pickett, G.R.: "A Review of Current Techniques for Determination of Water Saturation from Logs," *JPT* (November 1966) 1425.
115. Pickett, G.R.: "Pattern Recognition as a Means of Formation Evaluation," *The Log Analyst* (1973) **14**, No. 4, 3–11.
116. Kamel, M.H., and Mabrouk, W.M.: "An Equation for Estimating Water Saturation in Clean Formations Utilizing Resistivity and Sonic Logs: Theory and Application," *J. of Petroleum Science and Engineering* (2002) **36**, No. 3–4, 59–168.
117. Souder, W.W.: "Using Sonic Logs to Predict Fluid Type," *Petrophysics* (2002) **43**, No. 5, 412–419.
118. Chardac, O., Brie, A., and Chouker, A.C.: "Correlations of Shear vs. Compressional in Shaly Sands and Application to Quicklook Hydrocarbon Detection," paper SPE 84205 presented at the 2003 SPE Annual Technical Conference and Exhibition, Denver, 5–8 October.
119. Hamada, G.M.: " V_p/V_s Crossplots Identify Reservoir Fluids," *Oil & Gas J.* (28 June 2004) **102**, No. 24, 41–44.
120. Khazanehdari, J., and McCann, C.: "Acoustic and Petrophysical Relationships in Low-Shale Sandstone," *Geophysical Prospecting* (2005) **53**, No. 4, 447–462.
121. Williams, D.M.: "The Acoustic Log Hydrocarbon Indicator," paper W, *Trans.*, 1990 Annual Logging Symposium, SPWLA, 1–22.
122. Brie, A. *et al.*: "Shear Sonic Interpretation in Gas-Bearing Sands," paper SPE 30595 presented at the 1995 SPE Annual Technical Conference and Exhibition, Dallas, 22–25 October.
123. Rogen, B. *et al.*: "Ultrasonic Velocities of North Sea Chalk Samples: Influence of Porosity," *Geophysical Prospecting* (2005) **53**, No. 4, 481–496.
124. Watson, I.A., Lines, L.R., and Brittle, K.F.: "Heavy-Oil Reservoir Characterization Using Elastic Wave Properties," *The Leading Edge* (2002) **21**, No. 8, 736–739.
125. Gutierrez, M., Dvorkin, J., and Nur, A.: "In-Situ Hydrocarbon Identification and Reservoir Monitoring Using Sonic Logs, La Cira-Infantas Oil Field (Colombia)," paper RPB 2.6, *Expanded Abstracts*, 2000 Annual Meeting Technical Program, SEG, 1727–1730.
126. Gutierrez, M.A., Dvorkin, J., and Nur, A., "Theoretical Rock Physics for Bypassed Oil Detection Behind the Casing—La Cira-Infantas Oil Field," *The Leading Edge* (2001) **20**, No. 2, 192–198.
127. Batzle, M. *et al.*: "Heavy Oils: Seismic Properties," paper RP P2.2, *Expanded Abstracts*, 2004 Annual Meeting Technical Program, SEG, 1762–1765.
128. Thomas, D.H.: "Seismic Applications of Sonic Logs," *The Log Analyst* (1978) **19**, No. 1, 23–32.
129. Liner, C.L.: "Interpreting Seismic Data," *Exploring for Oil and Gas Traps, Treatise of Petroleum Geology, Handbook of Petroleum Geology* E.A. Beaumont, and N.H. Foster (eds.), AAPG (1999) Chap. 12, 12-13–12–17.
130. Bork, J. and Wood, L.C.: "Seismic Interpretation of Sonic Logs," paper INT 1.4, *Expanded Abstracts*, 2001 Annual Meeting Technical Program, SEG, 510–513.
131. Box, R., and Lowrey, P.: "Reconciling Sonic Logs with Check-Shot Surveys; Stretching Synthetic Seismograms," *The Leading Edge* (2003) **22**, No. 6, 510–517.

132. White, R.E.: “Tying Well-Log Synthetic Seismograms to Seismic Data: The Key Factors,” paper W-3.7, *Expanded Abstracts*, 2003 Annual Meeting Technical Program, SEG, 2449–2452.
133. Walls, J., Dvorkin, J., and Carr, M.: “Well Logs and Rock Physics in Seismic Reservoir Characterization,” paper OTC 16921 presented at the 2004 Offshore Technology Conference, Houston, 3–6 May.
134. Bruce, B. and Bowers, G.: “Pore Pressure Terminology,” *The Leading Edge* (2002) **21**, No. 2, 170–173.
135. Fertl, W.H., Chapman, R.E., and Holz, R.F. (eds.): *Studies in Abnormal Pressure*, Developments in Petroleum Science No. 38, Elsevier, Amsterdam (1994) 1–454.
136. Bowers, G.L.: “Detecting High Pressure,” *The Leading Edge* (2002) **21**, No. 2, 174–177.
137. Chilingar, G.V., Serebryakov, V.A. and Robertson, J.O. Jr. (eds.): *Origin and Prediction of Abnormal Formation Pressures*, Developments in Petroleum Science No. 50, Elsevier, Amsterdam (2002) 1–390.
138. Evans, B.J.: “Developments in Pore Pressure Prediction Using Seismic-While-Drilling Technology,” *Australian Petroleum Production and Exploration Assn. J.* (1999) **39**, Part 1, 461–474.
139. Walls, J. *et al.*: “Use of Compressional and Shear Wave Velocity for Overpressure Detection,” paper OTC 11912 presented at the 2000 Offshore Technology Conference, Houston, 1–4 May.
140. Badri, M.A. *et al.*: “Pore Pressure Prediction Data Using Seismic Velocities and Log Data in the Offshore Nile Delta, Egypt,” paper SPE 68195 presented at the 2001 SPE Middle East Oil Show, Bahrain, 17–20 March.
141. Carcione, J.M. and Tinivella, U.: “The Seismic Response to Overpressure—A Modelling Study Based on Laboratory, Well and Seismic Data,” *Geophysical Prospecting* (2001) **49**, No. 5, 523–539.
142. Huffman, A.R.: “The Future of Pore-Pressure Prediction Using Geophysical Methods,” paper OTC 13041 presented at the 2001 Offshore Technology Conference, Houston, 30 April–3 May.
143. Sayers, C.M. and Woodward, M.J.: “Seismic Pore-Pressure Prediction Using Reflection Tomography and 4-C Seismic Data,” *The Leading Edge* (2002) **21**, No. 2, 188–192.
144. Citta, F. *et al.*: “Deepwater Hazard Avoidance in a Large Top-Hole Section Using LWD Acoustic Data,” *The Leading Edge* (2004) **23**, No. 6, 566–573.
145. Althoff, G. *et al.*: “New Concepts for Seismic Surveys While Drilling,” paper SPE 90751 presented at the 2004 SPE Annual Technical Conference and Exhibition, Houston, 26–29 September.
146. Mancilla-Castillo, J., Mendez-Hernandez, E., and Santana-Fernandez, J.: “Geopressure Evaluation from Seismic Data and Its Application for Exploratory Wells in Mexico,” paper OTC 15250 presented at the 2003 Offshore Technology Conference, Houston, 5–8 May.
147. Storvoll, V., Bjorlykke, K., and Mondol, N.M.: “Velocity-Depth Trends in Mesozoic and Cenozoic Sediments from the Norwegian Shelf,” *AAPG Bulletin* (2005) **89**, No. 3, 359–381.
148. Hottman, C.E. and Johnson, R.K.: “Estimation of Formation Pressures from Log-Derived Shale Properties,” *JPT* (June 1965) 717; *Trans.*, AIME, **234**.
149. Ham, H.H.: “A Method of Estimating Formation Pressures from Gulf Coast Well Logs,” *Trans., Gulf Coast Assn. of Geological Soc.* (1966) **16**, 185–197.
150. Japsen, P.: “Overpressured Cenozoic Shale Mapped from Velocity Anomalies Relative to a Baseline for Marine Shale, North Sea,” *Petroleum Geoscience* (1999) **5**, 321–336.
151. Draou, A. and Osisanya, S.O.: “New Methods for Estimating Formation Pressures and Fracture Gradients from Well Logs,” paper SPE 63263 presented at the 2000 SPE Annual Technical Conference and Exhibition, Dallas, 1–4 October.
152. Bowers, G.L.: “Pore Pressure Estimation from Velocity Data: Accounting for Overpressure Mechanisms Besides Undercompaction,” *SPEDC* (June 1995) 89.
153. Swarbrick, R.E.: “Pore-Pressure Prediction—Pitfalls in Using Porosity,” paper OTC 13045 presented at the 2001 Offshore Technology Conference, Houston, 30 April–3 May.
154. Eaton, B.A.: “The Equation for Geopressure Prediction from Well Logs,” paper SPE 5544 presented at the 1975 SPE Annual Technical Conference and Exhibition, Dallas, 28 September–1 October.
155. Eaton, B.A. and Eaton, T.L.: “Fracture Gradient Prediction for the New Generation,” *World Oil* (1997) **218**, No. 10, 93–94 and 96–100.

156. Lahann, R.W., McCarty, D.K., and Hsieh, J.C.C.: "Influence of Clay Diagenesis on Shale Velocities and Fluid-Pressure," paper OTC 13046 presented at the 2001 Offshore Technology Conference, Houston, 30 April–3 May.
157. Domesteanu, P., McCann, C., and Sothcott, J.: "Velocity Anisotropy and Attenuation of Shale in Under- and Overpressured Conditions," *Geophysical Prospecting* (2002) **50**, No. 5, 487–503.
158. Dewhurst, D.N., Siggins, A.F., and Raven, M.D.: "Influence of Pore Pressure, Composition, and Microstructure on the Acoustic Properties of Shales," paper SPE 78197 presented at the 2002 SPE/ISRM Rock Mechanics Conference, Irving, Texas, 20–23 October.
159. Morris, R.L., Grine, D.R., and Arkfeld, T.E.: "Using Compressional and Shear Acoustic Amplitudes for the Location of Fractures," *JPT* (June 1964) 623.
160. Minne, J.-C. and Gartner, J.: "Fracture Detection in the Middle East," paper SPE 7773 presented at the 1979 SPE Middle East Technical Conference and Exhibition, Bahrain, 25–28 February.
161. Cheung, P.S.V.: "Fracture Detection Using the Sonic Tool," paper 42, *Trans.*, 1984 Intl. Formation Evaluation Symposium, SPWLA, Paris Chapter (SAID) 1–8.
162. Paillet, F.L.: "Qualitative and Quantitative Interpretations of Fracture Permeability by Means of Acoustic Full-Waveform Logs," *The Log Analyst* (1991) **32**, No. 3, 256–270.
163. Aguilera, R.: "Formation Evaluation by Well Log Analysis," *Naturally Fractured Reservoirs*, second edition, PennWell Publishing Co., Tulsa (1995) Chap. 3, 181–315.
164. Magara, K.: "Thickness of Removed Sedimentary Rocks, Paleopore Pressure, and Paleotemperature, Southwestern Part of Western Canada Basin," *AAPG Bulletin* (1976) **60**, No. 4, 554–565.
165. Magara, K.: "Thickness of Erosion," *Geological Models of Petroleum Entrapment*, Elsevier Applied Science Publishers, London (1986) Chap. 7, 129–151.
166. Bulat, J., and Stoker, J.S.: "Uplift Determination from Interval Velocity Studies, UK Southern North Sea," *Petroleum Geology of North West Europe*, Brooks, J. and Glennie, K. (eds.), Graham and Trotman, London (1987) **1**, 293–305.
167. Hillis, R.R.: "Quantifying Erosion in Sedimentary Basins from Sonic Velocities in Shales and Sandstones," *Exploration Geophysics* (1993) **24**, 561–566.
168. Hillis, R.R., Thomson, K., and Underhill, J.R.: "Quantification of Tertiary Erosion in the Inner Moray Firth Using Velocity Data from the Chalk and the Kimmeridge Clay," *Marine and Petroleum Geology* (1994) **11**, No. 3, 283–293.
169. Hansen, S.: "A Compaction Trend for Cretaceous and Tertiary Shales on the Norwegian Shelf Based on Sonic-Transit Times," *Petroleum Geoscience* (1996) **2**, No. 1, 59–68.
170. Heasler, H.P. and Kharitonova, N.A.: "Analysis of Sonic Well Logs Applied to Erosion Estimates in the Bighorn Basin, Wyoming," *AAPG Bulletin* (1996) **80**, No. 5, 630–646.
171. Evans, D.J.: "Estimates of the Eroded Overburden and the Permian-Quaternary Subsidence History of the Area West of Orkney," *Scottish J. of Geology* (1997) **33**, Part 2, 169–181.
172. Japsen, P.: "Regional Velocity-Depth Anomalies, North Sea Chalk—A Record of Overpressure and Neogene Uplift and Erosion," *AAPG Bulletin* (1998) **82**, No. 11, 2,031–2,074.
173. Densley, M.R., Hillis, R.R., and Redfearn, J.E.P.: "Quantification of Uplift in the Carnarvon Basin Based on Interval Velocities," *Australian J. of Earth Sciences* (2000) **47**, No. 1, 111–122.
174. Fuh, S.-C.: "Magnitude of Cenozoic Erosion from Mean Sonic Transit Time, Offshore, Taiwan," *Marine and Petroleum Geology* (2000) **17**, No. 9, 1,011–1,028.
175. Al-Chalabi, M.: "The Use of Instantaneous Velocity in Uplift Investigation," *Geophysical Prospecting* (2001) **49**, 645–655.
176. Ware, P.D. and Turner, J.P.: "Sonic Velocity Analysis of the Tertiary Denudation of the Irish Sea Basin," *Exhumation of The North Atlantic Margin; Timing, Mechanisms and Implications for Petroleum Exploration*, Dore, A.G., Cartwright, J.A., Stoker, M.S., Turner, J.P., and White, N.J. (eds.), Special Publication 196, Geological Society, London (2002) 355–370.
177. Mavromatidis, A., and Hillis, R.: "Quantification of Exhumation in the Eromanga Basin and Its Implications for Hydrocarbon Exploration," *Petroleum Geoscience* (2005) **11**, No. 1, 79–92.
178. Stocks, A.E. and Lawrence, S.R.: "Identification of Source Rocks from Wireline Logs," *Geological Applications of Wireline Logs*, A. Hurst, M.A. Lovell, and A.C. Morton (eds.), Geological Soc. of London Special Publication No. 48 (1990) 241–252.

179. Herron, S.L.: "In Situ Evaluation of Potential Source Rocks by Wireline Logs," *Source and Migration Processes and Evaluation Techniques*, Treatise of Petroleum Geology, R.K. Merrill (ed.), *Handbook of Petroleum Geology*, AAPG (1991) Chap. 13, 127–134.
180. Lang, W.H.: "The Determination of Thermal Maturity in Potential Source Rocks Using Interval Transit Time/Interval Velocity," *The Log Analyst* (1994) **35**, No. 6, 47–59.
181. Meyer, B.L., and Nederlof, M.H.: "Identification of Source Rocks on Wireline Logs by Density/Resistivity and Sonic Transit Time/Resistivity Crossplots," *AAPG Bulletin* (1984) **68**, No. 2, 121–129.
182. Passey, Q.R. *et al.*: "A Practical Model for Organic Richness from Porosity and Resistivity Logs," *AAPG Bulletin* (1990) **74**, No. 12, 1,777–1,794.
183. Huang, Z. *et al.*: "Cyclicality in the Egret Member (Kimmeridgian) Oil Source Rock, Jeanne d'Arc Basin, Offshore Eastern Canada," *Marine and Petroleum Geology* (1996) **13**, No. 1, 91–105.
184. Fjaer, E. *et al.*: *Petroleum Related Rock Mechanics*, Developments in Petroleum Science No. 33, Elsevier, Amsterdam (1992) 1–338.
185. Montmayeur, H. and Graves, R.M.: "Prediction of Static Elastic/Mechanical Properties of Consolidated and Unconsolidated Sands from Acoustic Measurements: Basic Measurements," paper SPE 14159 presented at the 1985 SPE Annual Technical Conference and Exhibition, Las Vegas, Nevada, 22–26 September.
186. Montmayeur, H. and Graves, R.M.: "Prediction of Static Elastic/Mechanical Properties of Consolidated and Unconsolidated Sands from Acoustic Measurements: Correlations," paper SPE 15644 presented at the 1986 SPE Annual Technical Conference and Exhibition, New Orleans, 5–8 October.
187. Holt, R.M., Ingsoy, P., and Mikkelsen, M.: "Rock Mechanical Analysis of North Sea Reservoir Formations," *SPEFE* (March 1989) 33.
188. Gatens, J.M. III *et al.*: "In-Situ Stress Tests and Acoustic Logs Determine Mechanical Properties and Stress Profiles in the Devonian Shales," *SPEFE* (September 1990) 248.
189. Yale, D.P. and Jamieson, W.H. Jr.: "Static and Dynamic Rock Mechanical Properties in the Hugoton and Panoma Fields, Kansas," paper SPE 27939 presented at the 1994 SPE Mid-Continent Gas Symposium, Amarillo, Texas, 22–24 May.
190. Kowalski, J.J.: "Formation Strength Parameters from Well Logs," paper N, *Trans.*, 1978 Annual Logging Symposium, SPWLA, 1–19.
191. Sethi, D.K.: "Well Log Applications in Rock Mechanics," paper SPE 9833 presented at the 1981 SPE/DOE Low Permeability Gas Reservoirs Symposium, Denver, 27–29 May.
192. Tixier, M.P., Loveless, G.W., and Anderson, R.A.: "Estimation of Formation Strength from the Mechanical Properties Log," *JPT* (March 1975) 283.
193. Stein, N.: "Mechanical Properties of Friable Sands from Conventional Log Data," *JPT* (July 1976) 757.
194. Onyia, E.C.: "Relationships Between Formation Strength, Drilling Strength, and Electric Log Properties," paper SPE 18166 presented at the 1988 SPE Annual Technical Conference and Exhibition, Houston, 2–5 October.
195. Stein, N.: "Sonic Log Data Help Determine Formation Strength," *Oil & Gas J.* (28 December 1992) 96.
196. Raaen, A.M. *et al.*: "FORMEL—A Step Forward in Strength Logging," paper SPE 36533 presented at the 1996 SPE Annual Technical Conference and Exhibition, Denver, 6–9 October.
197. Anderson, T. and Walker, T.: "Log-Derived Rock Properties for Use in Well Stimulation Design," paper SPE 4095 presented at the 1972 SPE Annual Meeting, San Antonio, Texas, 8–11 October.
198. Anderson, R.A., Ingram, D.S., and Zanier, A.M.: "Determining Fracture Pressure Gradients from Wells Logs," *JPT* (November 1973) 1259.
199. Newberry, B.M., Nelson, R.F., and Ahmed, U.: "Prediction of Vertical Hydraulic Fracture Migration Using Compressional and Shear Wave Slowness," paper SPE 13895 presented at the 1985 SPE/DOE Low Permeability Gas Reservoirs Symposium, Denver, 19–22 May.
200. Stein, N.: "How to Calculate Fracture Pressures from Well Logs," *Petroleum Engineer Intl.* (1988) **60**, No. 8, 36–38.
201. Bruce, S.: "A Mechanical Stability Log," paper IADC/SPE 19942 presented at the 1990 IADC/SPE Drilling Conference, Houston, 27 February–2 March.

202. Stein, N. and Hilchie, D.W.: "Estimating the Maximum Production Rate Possible from Friable Sandstones Without Using Sand Control," *JPT* (September 1972) 1157.
203. Edwards, D.P., Sharma, Y., and Charron, A.: "Zones of Sand Production Identified by Log-Derived Mechanical Properties—A Case Study," paper S, *Trans.*, 1983 European Formation Evaluation Symposium, SPWLA, London Chapter, 1–23.
204. Ong, S. *et al.*: "An Accurate Characterization of Sand Strength in Weak and Unconsolidated Formations Aids Offshore Production Test Designs—A Bohai Bay Case Study," paper SPE 64738 presented at the 2000 SPE International Oil and Gas Conference and Exhibition in China, Beijing, 7–10 November.
205. Fertl, W.H. and DeVries, M.R.: "Coal Evaluation Using Geophysical Well Logs," paper F, *Trans.*, 1997 Formation Evaluation Symposium, Canadian Well Logging Society, 1–17.
206. Bond, L.O., Alger, R.P., and Schmidt, A.W.: "Well Log Applications in Coal Mining and Rock Mechanics," *Trans.*, AIME (1971) **250**, 355–362.
207. Kowalski, J. and Fertl, W.H.: "Application of Geophysical Well Logging to Coal Mining Operations," *Energy Sources* (1977) **3**, No. 2, 133–147.
208. Hornby, B.E.: "Imaging of Near-Borehole Structure Using Full-Waveform Sonic Data," paper SPE 19872 presented at the 1989 SPE Annual Technical Conference and Exhibition, San Antonio, Texas, 8–11 October.
209. Hornby, B.E.: "Use of Full-Wave Sonic Data to Image Near-Borehole Structural Features," *Petroleum Geoscience* (1995) **1**, No. 2, 109–114.
210. Esmeroy, C. *et al.*: "Sonic Imaging—A Tool for High-Resolution Reservoir Description," paper BH 2.7, *Expanded Abstracts*, 1997 Annual Meeting Technical Program, SEG, **1**, 278–281.
211. Coates, R. *et al.*: "Single-Well Sonic Imaging: High-Definition Reservoir Cross-Sections from Horizontal Wells," paper SPE 65457 presented at the 2000 SPE/PS-CIM International Conference and Exhibition on Horizontal Well Technology, Calgary, 6–8 November.
212. Chabot, L. *et al.*: "Single-Well Imaging Using the Full Waveform of an Acoustic Sonic," paper BH 3.7, *Expanded Abstracts*, 2001 Annual Meeting Technical Program, SEG, 420–423.
213. Yamamoto, H. *et al.*: "Borehole Acoustic Reflection Survey Experiments in Horizontal Wells for Accurate Well Positioning," paper SPE 65538 presented at the 2000 SPE/CIM International Conference on Horizontal Well Technology, Calgary, 6–8 November.
214. Tang, X.M.: "Imaging Near-Borehole Structure Using Directional Acoustic-Wave Measurement," *Geophysics* (2004) **69**, No. 6, 1378–1386.
215. Zheng, Y., and Tang, X.: "Imaging Near-Borehole Structure Using Acoustic Logging Data with Prestack F-K Migration," paper BG 2, *Expanded Abstracts*, 2005 Annual Meeting Technical Program, SEG, 360–363.
216. Mari, J.-L., Glangeaud, F., and Coppens, F.: *Signal Processing for Geologists and Geophysicists*, Editions Technip, Paris (1999) 1–458.
217. Neidell, N.S. and Taner, M.T.: "Semblance and Other Coherency Measures for Multichannel Data," *Geophysics* (1971) **36**, No. 3, 482–497.
218. Kimball, C.B. and Marzetta, T.M.: "Semblance Processing of Borehole Acoustic Array Data," *Geophysics* (1984) **49**, No. 3, 274–281.
219. Kimball, C.V.: "Shear Slowness Measurements by Dispersive Processing of the Borehole Flexural Mode," *Geophysics* (1998) **63**, No. 2, 337–344.
220. McFadden, P.L., Drummond, B.J., and Kravis, S.: "The Nth-Root Stack—Theory, Applications, and Examples," *Geophysics* (1986) **51**, No. 10, 1,879–1,892.
221. Kravis, S.: "The Nth Root Slant Stack—A New Method of Coherency Enhancement," *First Break* (1990) **8**, No. 9, 339–344.
222. Brie, A. *et al.*: "Shear Slowness Determination from Dipole Measurements," paper F, *Trans.*, 1997 Annual Logging Symposium, SPWLA, 1–14.
223. Hsu, K. and Chang, S.K.: "Multiple-Shot Processing of Array Sonic Waveforms for High Resolution Sonic Logs," *Geophysics* (1987) **52**, No. 10, 1,376–1,390.
224. Zhang, T., Tang, X.M., and Patterson, D.: "Evaluation of Laminated Thin Beds in Formations Using High-Resolution Acoustic Slowness Logs," paper XX, *Trans.*, 2000 Annual Logging Symposium, SPWLA, 1–14.
225. Wang, Z.: "Seismic Anisotropy in Sedimentary Rocks, Part 1—A Single-Plug Laboratory Method; Part 2—Laboratory Data," *Geophysics* (2002) **67**, No. 5, 1415–1440.

226. Crampin, S. and Chastin, S.: "A Review of Shear Wave Splitting in the Crack-Critical Crust," *Geophysical J. Intl.* (2003) **155**, 221–240.
227. Helbig, K. and Thomsen, L.: "75-plus Years of Anisotropy in Exploration and Reservoir Seismics: A Historical Review of Concepts and Methods," *Geophysics* (2005) **70**, No. 6, 9ND–23ND.
228. Franco, J.L.A.: "Using Shear-Wave Anisotropy to Optimize Reservoir Drainage and Improve Production in Low-Permeability Formations in the North of Mexico," paper SPE 96808 presented at the 2005 SPE Annual Technical Conference and Exhibition, Dallas, 9–12 October.
229. Klimentos, T.: "Shear-Wave Anisotropy Applications for Perforation Strategy and Production Optimization in Oil Bearing Porous Sands," paper LL, *Trans.*, 2003 Annual Logging Symposium, SPWLA, 1–12.
230. Klimentos, T., Farghaly, A., and Qleibo, M.: "Finding Faults with Shear-Wave Anisotropy," paper F, *Trans.*, 2003 Annual Logging Symposium, SPWLA, 1–12.
231. Furre, A.-K. and Brevik, I.: "Characterization of Angle Dependency in Sonic Logs," paper BH 2.1, *Expanded Abstracts*, 1998 Annual Meeting Technical Program, SEG, 292–295.
232. Hornby, B., Howie, J., and Ince, D.: "Anisotropy Correction for Deviated Well Sonic Logs—Application to Seismic Well Tie," paper BH/RP 4.7, *Expanded Abstracts*, 1999 Annual Meeting Technical Program, SEG, 112–115.
233. Wang, Z.: "Seismic Anisotropy in Sedimentary Rocks," paper RP 2.4, *Expanded Abstracts*, 2001 Annual Meeting Technical Program, SEG, 1740–1743.
234. Sun, Y. *et al.*: "Effects of Stress-Induced Anisotropy on Monopole and Dipole Logging," paper RBG P1.2, *Expanded Abstracts*, 2003 Annual Meeting Technical Program, SEG, 1282–1285.
235. Koster, K. *et al.*: "Applied Production Geophysics Using Shear-Wave Anisotropy—Production Applications for the Dipole Shear Imager and the Multicomponent VSP," paper DP1.1, *Expanded Abstracts*, 1994 Annual Meeting Technical Program, SEG, 233–235.
236. Esmersoy, C. *et al.*: "Fracture and Stress Evaluation Using Dipole-Shear Anisotropy Logs," paper J, *Trans.*, 1995 Annual Logging Symposium, SPWLA, 1–12.
237. Tang, X.: "Processing Dipole Waveform Logs for Formation Alteration Identification," paper BG 3.4, *Expanded Abstracts*, 1996 Annual Meeting Technical Program, SEG, **1**, 162–165.
238. Huang, X. *et al.*: "Formation Stress Estimation Using Standard Acoustic Logging," paper BH/RP 2.6, *Expanded Abstracts*, 1999 Annual Meeting Technical Program, SEG, 53–56.
239. Tang, X., Cheng, N., and Cheng, A.: "Identifying and Estimating Formation Stress from Borehole Monopole and Cross-Dipole Acoustic Measurements," paper QQ, *Trans.*, 1999 Annual Logging Symposium, SPWLA, 1–14.
240. Badri, M., Sousa, S., and Klimentos, T.: "Shear Anisotropy Applications in Production Optimization, Western Desert, Egypt," paper RPB 1.5, *Expanded Abstracts*, 2000 Annual Meeting Technical Program, SEG, 1695–1698.
241. Tang, X., Patterson, D., and Markovic, M.: "Fracture Measurements in Open/Cased Holes Using Cross-Dipole Logging—Theory and Field Results," paper RPB 1.6, *Expanded Abstracts*, 2000 Annual Meeting Technical Program, SEG, 1699–1702.
242. Tang, X.M.: "Determining Shear-Wave Transverse Isotropy from Borehole Stoneley Waves," *Geophysics* (2003) **68**, No. 1, 118–126.
243. Cheng, N. and Cheng, C.H.: "Estimations of Formation Velocity, Permeability, and Shear-Wave Velocity Using Acoustic Logs," *Geophysics* (1996) **61**, No. 2, 437–443.
244. Murray, D., Plona, T., and Valero, H.P.: "Case Study of Borehole Sonic Dispersion Curve Analysis," paper BB, *Trans.*, 2004 Annual Logging Symposium, SPWLA, 1–14.
245. Sinha, B. *et al.*: "Near-Wellbore Alteration and Formation Stress Parameters Using Borehole Sonic Data," paper SPE 95841 presented at the 2005 SPE Annual Technical Conference and Exhibition, Dallas, 9–12 October.
246. Plona, T.J. *et al.*: "Measurement of Stress Direction and Mechanical Damage Around Stressed Boreholes Using Dipole and Microsonic Techniques," paper SPE 47234 presented at the 1998 SPE/ISRM Rock Mechanics in Petroleum Engineering Conference, Trondheim, Norway, 8–10 July.
247. Plona, T. *et al.*: "Stress-Induced Dipole Anisotropy—Theory, Experiment and Field Data," paper RR, *Trans.*, presented at the 1999 Annual Logging Symposium, SPWLA, 1–14.
248. Plona, T.J. *et al.*: "Using Acoustic Anisotropy," paper H, *Trans.*, 2000 Annual Logging Symposium, SPWLA, 1–12.

249. Sinha, B.K., Kane, M.R., and Frignet, B.: "Dipole Dispersion Crossover and Sonic Logs in Limestone Reservoir," *Geophysics* (2000) **65**, No. 2, 390–407.
250. Xu, S., Wu, X., Huang, X., and Yin, H.: "Evaluation of Anisotropic Rock Properties in Sedimentary Rocks from Well Logs," paper OTC 17251 presented at the 2005 Offshore Technology Conference, Houston, 2–5 May.
251. Crampin, S.: "Evaluation of Anisotropy by Shear-Wave Splitting," *Geophysics* (1985) **50**, No 1, 142–152.
252. Rai, C.S. and Hanson, K.E.: "Shear-Wave Velocity Anisotropy in Sedimentary Rocks—A Laboratory Study," *Geophysics* (1988) **53**, 800–806.
253. Yale, D.P. and Sprunt, E.S.: "Prediction of Fracture Direction Using Shear Acoustic Anisotropy," *The Log Analyst* (1989) **30**, No. 2, 65–70.
254. Winkler, K.W.: "Azimuthal Velocity Variations Caused by Borehole Stress Concentrations," *J. of Geophysical Research* (1996) **101**, No. B4, 8,615–8,621.
255. Esmersoy, C. *et al.*: "Dipole Shear Anisotropy Logging," paper SL 3.7, *Expanded Abstracts*, 1994 Annual Meeting Technical Program, SEG, 1,139–1,142.
256. Hatchell, P.J. *et al.*: "Quantitative Comparison Between a Dipole Log and VSP in Anisotropic Rocks from Cymric Oil Field, California," paper BG1.4, *Expanded Abstracts*, 1995 Annual Meeting Technical Program, SEG, 13–16.
257. Beckham, W.E.: "Seismic Anisotropy and Natural Fractures from VSP and Borehole Sonic Tools—A Field Study," *Geophysics* (1996) **61**, No. 2, 456–466.
258. Walls, J.D., Dvorkin, J., and Mavko, G.: "In-Situ Stress Magnitude and Azimuth from Well Log Measurements, Final Report," Report GRI-95/0356, Gas Research Inst., Chicago (1996) 1–147.
259. Grandi, S.K. *et al.*: "In Situ Stress Modeling at a Borehole—A Case Study," paper BH 1.4, *Expanded Abstracts*, 2003 Annual Meeting Technical Program, SEG, 297–300.
260. De, G.S. and Schmitt, D.P.: "Issues with Shear-Wave Azimuthal Anisotropy in Highly Deviated Wells," paper OTC 17647 presented at the 2005 Offshore Technology Conference, Houston, 2–5 May.
261. Tang, X.M. and Patterson, D.: "Characterizing Seismic Anisotropy Using Cross-Dipole Measurement in Deviated Wells," paper BG 2.5, *Expanded Abstracts*, 2005 Annual Meeting Technical Program, SEG, 372–375.
262. Patterson, D.J. and Tang, X.: "Pit Falls in Dipole Logging—Anisotropy: Cause of Discrepancy in Borehole Acoustic Measurements," paper OTC 17644 presented at the 2005 Offshore Technology Conference, Houston, 2–5 May.
263. Hornby, B.E., Howie, J.M., and Ince, D.W.: "Anisotropy Correction for Deviated-Well Sonic Logs—Application to Seismic Well Tie," *Geophysics* (2003) **68**, No. 2, 464–471.
264. Alford, R.M.: "Shear Data in the Presence of Azimuthal Anisotropy—Dilley, Texas," paper S9.6, *Expanded Abstracts*, 1986 Annual Technical Meeting Program, SEG.
265. Tang, X.M. and Chunduru, R.K.: "Simultaneous Inversion of Formation Shear-Wave Anisotropy Parameters from Cross-Dipole Acoustic Array Waveform Data," *Geophysics* (1999) **64**, No. 5, 1,502–1,511.
266. Gelinsky, S. *et al.*: "Anisotropic Permeability in Fractured Reservoirs from Integrated Acoustic Measurements," paper RC 3.5, *Expanded Abstracts*, 1998 Annual Meeting Technical Program, SEG, 956–959.
267. Smith, M.B.: "Effect of Fracture Azimuth on Production with Application to the Wattenburg Gas Field," paper SPE 8298 presented at the 1979 SPE Annual Technical Conference and Exhibition, Las Vegas, Nevada, 23–26 September.
268. Hubbert, M.K. and Willis, D.G.: "Mechanics of Hydraulic Fracturing," *Trans., AIME* (1957) **210**, 153–166.
269. Cipolla, C.L., Liu, D., and Kyte, D.G.: "Practical Application of In-Situ Stress Profiles," paper SPE 28607 presented at the 1994 SPE Annual Technical Conference and Exhibition, New Orleans, 25–28 September.
270. Cipolla, C.L.: "Hydraulic Fracture Technology in the Ozona Canyon and Penn Sands," SPE 35196 presented at the 1996 SPE Permian Basin Oil and Gas Recovery Conference, Midland, Texas, 27–29 March.
271. De, G.S. *et al.*: "Predicting Natural or Induced Fracture Azimuths from Shear-Wave Anisotropy," *SPEEE* (August 1998) 311.

272. Garg, A., Desai, A.M., and Towler, B.F.: "Horizontal Stresses in Anisotropic Formation and Prediction of Hydraulic Fracture Direction," paper SPE 38342 presented at the 1997 SPE Western Regional Meeting, Long Beach, California, 25–27 June.
273. Aguila, F.J.: "Using Cross-Dipole Sonic-Anisotropy Data to Improve Reservoir Understanding in the Southern/Marine Areas of Mexico," paper SPE 84204 presented at the 2004 SPE International Symposium and Exhibition on Formation Damage Control, Lafayette, Louisiana, 18–20 February.
274. Barajas, J.: "Case History—Cased Hole Dipole Sonic Applications in Mexico," paper SPE 90703 presented at the 2004 SPE Annual Technical Conference and Exhibition, Houston, 26–29 September.
275. Klimentos, T. and McCann, C.: "Relationships Between Compressional Wave Attenuation, Porosity, Clay Content, and Permeability in Sandstones," *Geophysics* (1990) **55**, 998–1,014.
276. Klimentos, T.: "Attenuation of P- and S-Waves as a Method of Distinguishing Gas from Oil and Water," *Geophysics* (1995) **60**, No. 2, 447–458.
277. Akbar, N., Dvorkin, J., and Nur, A.: "Relating P-Wave Attenuation to Permeability," *Geophysics* (1993) **58**, No. 1, 20–29.
278. Sun, X. *et al.*: "P- and S-Wave Attenuation Logs from Monopole Sonic Data," *Geophysics* (2000) **65**, No. 3, 755–765.
279. Burns, D.R.: "Predicting Relative and Absolute Variations of In-Situ Permeability from Full-Waveform Acoustic Logs," *The Log Analyst* (1991) **32**, No. 3, 246–255.
280. Tang, X.M., Cheng, C.H., and Toksoz, M.N.: "Dynamic Permeability and Borehole Stoneley Waves—A Simplified Biot-Rosenbaum Model," *J. of the Acoustical Soc. of America* (1991) **90**, No. 3, 1,632–1646.
281. Tang, X., Cheng, C.H., and Toksoz, M.N.: "Stoneley-Wave Propagation in a Fluid Filled Borehole with a Vertical Fracture," *Geophysics* (1991) **56**, 447–460.
282. Saxena, V.: "Permeability Quantification from Borehole Stoneley Waves," paper T, *Trans.*, 1994 Annual Logging Symposium, SPWLA, 1–22.
283. Kimball, C.V. and Endo, T.: "Quantitative Stoneley Mobility Inversion," paper BH 1.1, *Expanded Abstracts*, 1998 Annual Meeting Technical Program, SEG, 252–255.
284. Tang, X.M. *et al.*: "Permeability from Borehole Acoustic Logs—An Overview with Recent Advances," paper BH 2.6, *Expanded Abstracts*, 1997 Annual Meeting Technical Program, SEG, 274–277.
285. Sinha, A. *et al.*: "A New Method for Deriving Permeability from Borehole Stoneley Waves and Its Application in the North Mongas Field of Eastern Venezuela," paper P, *Trans.*, 1998 Annual Logging Symposium, SPWLA, 1–12.
286. Canaday, W., Spooner, P., and Vasquez, R.: "Permeability Estimation from Stoneley Amplitude, Corrected for Borehole Geometry and Rugosity," paper SPE 96598 presented at the 2005 SPE Annual Technical Conference and Exhibition, Dallas, 9–12 October.
287. Geerits, T. *et al.*: "Comparison Between Stoneley, NMR, and Core-Derived Permeabilities," paper TT, *Trans.*, 1999 Annual Logging Symposium, SPWLA, 1–14.
288. Qobi, L. *et al.*: "Permeability Determination from Stoneley Waves in the Ara Group," paper SPE 63140 presented at the 2000 SPE Annual Technical Conference and Exhibition, Dallas, 1–4 October.
289. Tang, X.M., and Patterson, D.: "Estimating Formation Permeability and Anisotropy from Borehole Stoneley Waves," paper W, *Trans.*, 2004 Annual Logging Symposium, SPWLA, 1–14.
290. Tang, X.M., Altunbay, M., and Shorey, D.: "Joint Interpretation of Formation Permeability from Wireline Acoustic NMR, and Image Log Data," paper KK, *Trans.*, 1998 Annual Logging Symposium, SPWLA, 1–13.
291. Aladeddin, E., Tchambaz, M., and Al-Adani, N.: "Combining NMR and Stoneley Analysis for a Better Estimation of Permeability in Carbonate Reservoirs," paper E, *Proceedings*, 2004 Formation Evaluation Symposium of Japan, Society of Petrophysicists and Well Log Analysts, Japan Chapter, 7 p.
292. Tang, X.M. and Patterson, D.: "Detecting Thin Gas Beds in Formations Using Stoneley Wave Reflection and High-Resolution Slowness Measurements," paper OO, *Trans.*, 2001 Annual Logging Symposium, SPWLA, 1–14.

293. Hornby, B.E. *et al.*: "Fracture Evaluation Using Reflected Stoneley-Wave Arrivals," *Geophysics* (1989) **54**, No. 10, 1,274–1,288.
294. Medlin, W.L.: "Fracture Diagnostics with Tube-Wave Reflection Logs," *JPT* (March 1994) 239.

SI Metric Conversion Factors

dB/ft × 3.048*	E - 01 = dB/m
ft × 3.048*	E - 01 = m
ft/sec × 3.048*	E - 01 = m/sec
in. × 2.54*	E + 00 = cm
psi/ft × 2.262 059	E + 01 = kPa/m
μsec/ft × 3.280 840	E + 00 = μsec/m

*Conversion factor is exact.

Chapter 3D

Nuclear Logging

Gary D. Myers, ConocoPhillips Inc.

3D.1 Introduction

Nuclear logging has been used in some form since the late 1920s to provide information on lithology and rock characteristics. Continued technological advances have provided improved methods for analyzing the measurements of natural and induced nuclear readings. Even with better tool designs, the long-standing problem remains that logging tools do not directly measure the formation properties that engineers, geologists, and petrophysicists need to describe a reservoir. The goal of log analysis is to map out the downhole values of reservoir characteristics chiefly as porosity, fluid saturations, and permeability. Unfortunately, nuclear-logging tools only measure gamma ray or neutron count rates at cleverly positioned detectors. Inference, empiricism, experience, and alibis bridge these count rates to the rocks and fluids in the reservoir. Nuclear-log interpretation rests on smarter processing of these tool readings. Understanding what the tools really measure is the key to better log analysis.

Consider some of the limitations of the current technology. Grouping nuclear logs according to their underlying nuclear physics highlights the blurry relationship between what they measure and what we expect from them. **Table 3D.1** summarizes such a classification scheme. Two types of problems skew tool measurements away from their targets. First, because a nuclear tool averages over a shallow bulk volume, the borehole often represents a major part of the tool's response. Second, even if all borehole effects can be removed, the fact remains that nuclear tools do not respond directly to reservoir properties. Sometimes, the reservoir parameter of interest does not even dominate the underlying physics of the tool. Historically, such problems have been addressed with calibrations at a few points accessible in the laboratory; these are then generalized into correction charts. Two books^{1,2} serve as excellent general introductions to the convoluted physics of logging tools.

Nuclear logs work because gamma rays and neutrons are penetrating radiation. Unlike visible light, they can traverse tool housings and boreholes and still sample a significant volume of the formation. They can even penetrate casing, giving them a near monopoly in cased-hole formation evaluation. They also respond to different properties than resistivity logs, which merely measure the conductivity of a formation.

To exploit a reservoir, the engineer must characterize it. That basically means building an understanding of two things: the amount and distribution of hydrocarbons and the recoverabili-

TABLE 3D.1—SELECTION OF COMMON NUCLEAR-LOGGING TOOLS: HOW THEY WORK AND WHAT LOG ANALYSTS REALLY WANT FROM THEM TO DESCRIBE HYDROCARBON RESERVOIRS

Tool	Physics Exploited	Reads	Desired Information
Gamma ray	Natural gamma rays	Gamma ray counts, K-U-Th counts	Clay type and bedding
Gamma density	Gamma ray scattering	Bulk Compton cross section	Formation density, porosity
Neutron porosity	Neutron slowing	Migration length	Porosity, lithology
Pulsed neutron	Neutron lifetime	Bulk capture cross section	S_w , porosity
Carbon/oxygen, geochemical	Neutron-induced gamma ray	Elemental count rates	S_0 , lithology

ty of those hydrocarbons. Amount and distribution starts with a description of hydrocarbon volume in place. To the first order, this means bulk volume hydrocarbon:

$$V_{bh} = \phi(1 - S_w)h_V A . \dots\dots\dots (3D.1)$$

Estimating porosity requires detailed knowledge of rock fabric, one of the primary uses of nuclear logs. Rock-fabric information runs the gamut from primary lithology (e.g., sandstone vs. limestone) to diagenesis to clay volume and distribution. Nuclear logs can provide estimates of bulk formation properties such as density and hydrogen content. With some geologic insight and simplifications, these bulk properties can be related to reservoir fabric through simple bulk mixing laws. One of the virtues of nuclear tools is that they are bulk-averaging devices. They average formation properties over a volume on the order of 1 ft³. While nuclear logs are much less sensitive to the difference between water and liquid hydrocarbons than resistivity logs, they are very sensitive to the difference between liquid- and gas-phase fluids.

The second class of reservoir properties, the actual production of hydrocarbons, is less directly accessible to nuclear measurements. Producibility depends on two broad factors: heterogeneity and permeability. At some level, log measurements can give insight into heterogeneity. Laterally, multiple wells can be correlated and overlaid on seismic cross sections to track the continuity of layers of similar properties. Logs certainly can speak to vertical continuity, at least within the limitations of their vertical resolutions. Nuclear logs do provide the best vertical resolution of any of the standard suite of log measurements (as fine as 6 in. for gamma ray-based measurements). Bedding thinner than that can be assessed only with some sort of special borehole-imaging log. In electrical logs, thin bedding may manifest itself as anisotropy, but nuclear logs' bulk-averaging nature removes most sensitivity to the detailed internal structure of the volume they investigate. This also means that nuclear logs cannot speak directly to permeability because that does depend on the microscopic details of grain shape and size, the arrangement of the grains, clay minerals, and their distributions, nor can nuclear logs discriminate secondary porosity in vugs or fractures from primary intergranular porosity. In the end, nuclear-log interpretation is a matter of model choice as much as tool reading.

3D.2 The Physics of Nuclear Logs

3D.2.1 Nuclear Measurements and Statistics. For logging purposes, all nuclear radiation behaves as particles, and all nuclear-log measurements are particle-counting experiments. There is randomness to the arrival of the particles, so accurate count-rate measurements need to be very long-term averages. As a result, fluctuations in radioactive logs may be statistical rather than

the result of a real change in formation properties. This accounts for the apparent chatter in most nuclear logs. Because of this, nuclear logs almost always set the maximum logging speed of a simple quad-combo logging suite [i.e., a tool string with no specialty logs like borehole images, nuclear magnetic resonance (NMR), or waveform sonic].

Counting experiments obey Poisson statistics. A Poisson distribution, as Fig. 3D.1 shows, characterizes such experiments. If the expected value of the number of counts received in a given period of time is μ , then the probability of obtaining a particular number of counts, x , on a given repetition of the experiment is given by

$$P_x = \mu^x \frac{e^{-\mu}}{x!} \dots\dots\dots (3D.2)$$

This is the familiar bell-shaped curve, with its width or standard deviation, σ , given by

$$\sigma = \sqrt{\mu} \dots\dots\dots (3D.3)$$

(Generally, a Poisson distribution applies to discrete events like nuclear counting experiments, while a Gaussian or normal distribution applies to continuous properties like the length of a rod; shapes and moments are nearly identical.) This means that unlike sonic- or resistivity-log measurements, nuclear-log measurements do not have a fixed precision. The precision of a nuclear measurement depends on the number of counts received. If the expected value of the nuclear counts is N , then approximately 32% of all attempts to measure N will fall outside the range $N \pm \sqrt{N}$. Realizing that the number of counts is simply the count rate times the integration time, to improve the precision of a nuclear-log measurement by a factor of two, one must count four times longer. Log measurements are depth-based (i.e., measurements are made approximately twice per foot). To count four times longer, one needs to log four times slower (e.g., 5 ft/min instead of 20).

3D.3 Nuclear Radiation Transport

Nuclear logs are based on the interaction of nuclear radiation with matter—materials like sand, clay, water, and hydrocarbons that together make up a reservoir. For logging, the interactions are primarily particle-scattering interactions. Even though gamma rays are usually discussed as electromagnetic radiation, for nuclear logging they are treated as photons—classical particles. Even in well logging, quantum mechanics rears its head.

Well logs exploit two types of nuclear radiation: gamma rays and neutrons. Depending on the type and energy of the particle, different scattering processes predominate. Fig. 3D.2 shows a beam of particles impinging on a slab of formation from the left. Particle beams are characterized in terms of their flux, which has units of particles per unit area per unit time. The incoming flux is labeled ϕ_i . For scattering, the slab is characterized by the number density of potential scattering particles within it (in other words, the number of atoms per cm^3). Suppose the slab in the figure has an average of N_p atoms/ cm^3 . If the slab is h cm thick, a beam of unit area will encounter and have a chance to interact with $N_p \times h$ atoms as it passes through the slab. The actual probability of a given radiation particle interacting with a given atom in the slab of formation depends on a number of factors, including the nature and energy of the radiation and the characteristics of the target atom. Physicists lump these probabilities as cross sections, typically labeled $\sigma(E)$, where E refers to the energy dependence of the cross section. A cross section has the units of area because it corresponds to the apparent size of the scattering target as seen by the incoming particle. Because these are atomic-scale interactions, the apparent target sizes are on the order of 10^{-29} cm^2 . Because humans relate best to numbers

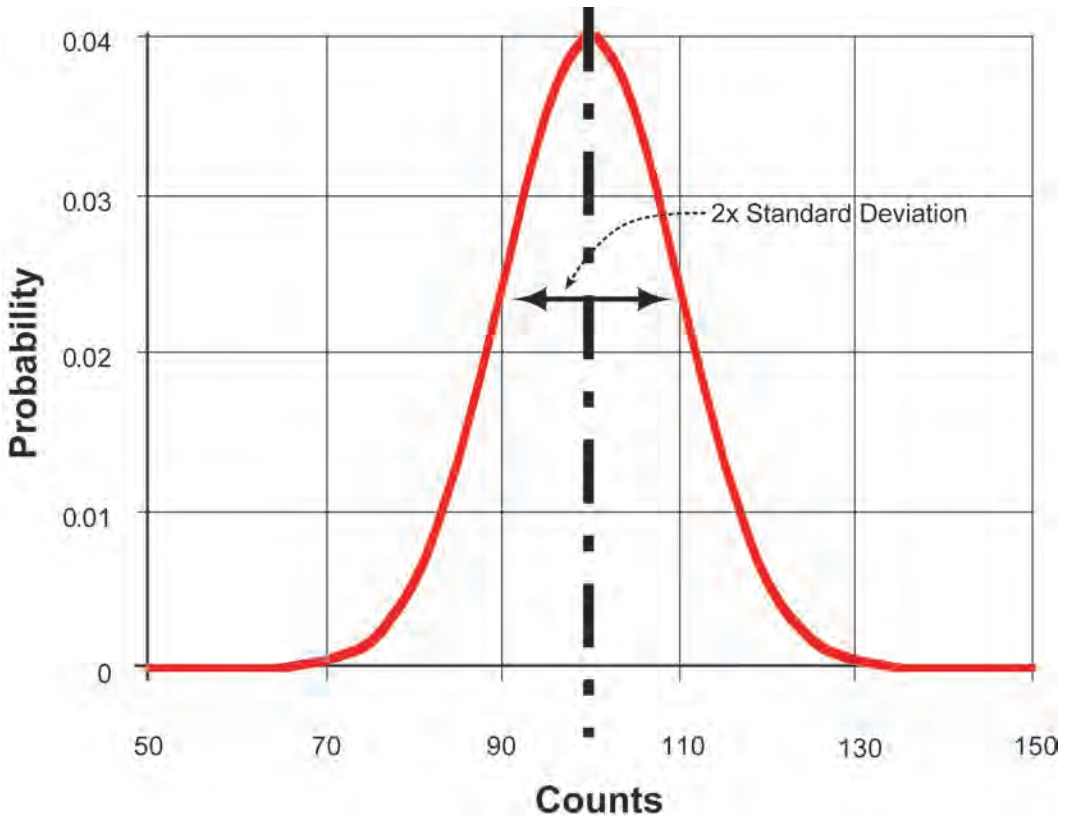


Fig. 3D.1—The Poisson distributions capture how the statistical nature of nuclear counting measurements influences the precision of such measurements.

they can count on their fingers, a special unit of cross section, the barn, equal to 10^{-24} cm^2 , was created.

The number of particles that will be scattered out of the original beam of radiation as it passes through the slab of formation can be written as

$$\delta\phi = \phi_i N_p \sigma(E) h \dots\dots\dots (3D.4)$$

$\phi_i N_p \sigma$ is interpreted as a reaction rate per unit volume of formation resulting from the incident beam of radiation. Number density can be calculated from bulk density, ρ_b , average atomic weight, A , and Avogadro’s number, N_A , according to the formula

$$N_p = \frac{N_A}{A} \rho_b \dots\dots\dots (3D.5)$$

In practice, cross sections are measured experimentally and tabulated as a function of energy for various reaction types and target nuclei. The discussion above is simplified to a slab of formation made up of a single type of atom. For real formations with a variety of atoms, the actual amount of scattering is just a volume-weighted sum of the various atoms in the formation. Many times, as **Tables 3D.2 through 3D.4** show, only one type of atom will account for the vast majority of the scattering. This is in fact the basis of nuclear logging.

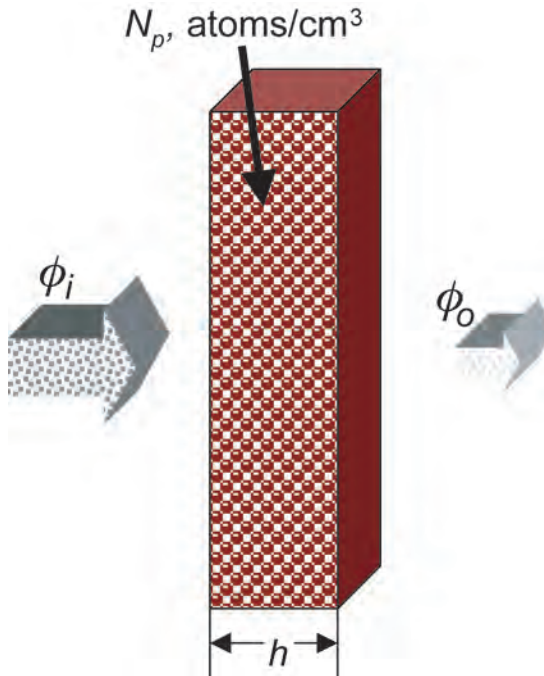


Fig. 3D.2—A schematic of a beam of radiation passing through a uniform slab of material.

TABLE 3D.2 —NEUTRON SLOWING-DOWN POWER OF COMMON RESERVOIR ELEMENTS, EXPRESSED AS THE NUMBER OF COLLISIONS REQUIRED TO THERMALIZE A NEUTRON (i.e., TO SLOW IT DOWN FROM 4 MeV TO LESS THAN 0.1 MeV)	
Element	Number of Collisions to Thermalize
Hydrogen	18
Carbon	114
Oxygen	150
Silicon	257
Chlorine	329
Calcium	368

Integrating the differential flux equation, Eq. 3D.4, produces the unscattered flux that emerges through a thickness of formation, h , as Fig. 3D.2 shows.

$$\phi_o = \phi_i e^{-N_p \sigma h} \dots\dots\dots (3D.6)$$

This leads naturally to the concept of mean free path. The mean free path, λ , is the thickness of formation that will reduce a beam of radiation to $1/e$ (approximately 37%) of its original value.

TABLE 3D.3—CAPTURE CROSS SECTION FOR SLOW (THERMAL-ENERGY) NEUTRONS BY SOME COMMON FORMATION ELEMENTS

Element	Capture Cross Section (barns)
Gadolinium	40,000
Boron	771
Lithium	71
Chlorine	33.4
Manganese	13.3
Titanium	6.4
Copper	3.8
Potassium	2.2
Iron	2.56
Calcium	0.44
Hydrogen	0.332
Aluminum	0.232
Silicon	0.16
Magnesium	0.064
Carbon	0.0034
Oxygen	0.0002

TABLE 3D.4—HYDROGEN CONTENT OF SOME COMMON EARTH ELEMENTS

Material	Hydrogen Density (atm/cm ³ × 10 ²³)	Hydrogen Index
Water (60°F, 14.7 psi)	0.669	1.000
Water (200°F, 2,000 psi)	0.667	1.000
Brine (200 kppm NaCl)	0.614	0.920
Methane (60°F, 14.7 psi)	0.001	0.002
Methane (200°F, 2,000 psi)	0.329	0.490
<i>n</i> -octane (60°F, 14.7 psi)	0.667	1.000
<i>n</i> -octane (200°F, 2,000 psi)	0.639	0.960
Gypsum	0.325	0.490
Anthracite	0.268	0.400
Kaolinite	0.250	0.370
Chlorite	0.213	0.320
Illite	0.059	0.090

$$\lambda = \frac{1}{N_p \sigma} \dots \dots \dots (3D.7)$$

It depends on the amount of material in the formation and its cross section. The mean free path of radiation in a formation determines its depth of investigation and its vertical resolution.

Density tools and neutron-porosity tools simply measure the drop-off in radiation with distance from the source of radiation. While this can be done with a single detector at an appropriate distance from a source of known strength, all modern tools use at least two detectors at different distances from the source. These designs are referred to as compensated. With a near and a far detector, it is possible for the tool designer to compensate for the borehole effects and variations in source strength.

Nuclear-logging tools exploit only two types of radiation: gamma rays and neutrons. Both follow the basic scattering principles defined above but have unique reaction types and cross sections.

3D.4 Single-Log Interpretation

Nuclear log interpretation is simply the practice of solving tool-response mixing-law equations with the judicious application of some assumptions and constraints.

3D.4.1 The Generalized Interpretation Process. All interpretation is an approximate model. As more factors are taken into account, the interpretation usually improves, but the model becomes more complicated.

For the neutron-porosity log, the simplest interpretation model is to naively accept the raw log reading. This is acceptable in a clean, water-filled reservoir, with a single known matrix lithology:

$$\phi_o = \phi_{CNL} \dots\dots\dots (3D.8)$$

If the reservoir is shaly, or if the fluid density is not the same as water, a hydrogen-index linear-mixing law will generally do.

$$\begin{aligned} \phi_{CNL} = & \phi_{CNLma} \times (1 - V_{sh} - \phi_e) + \phi_{CNLsh} \times V_{sh} \\ & + \phi_e \times [I_{H_{hc}} \times (1 - S_w) + I_{H_w} \times S_w] \dots\dots\dots (3D.9) \end{aligned}$$

This equation can be solved for ϕ_e given the neutron-tool response to each of the various formation components. If S_w is not known and the hydrogen index of the hydrocarbon and connate water phases differ appreciably, it may be necessary to solve for porosity and fluid content simultaneously or at least iteratively.

Invasion adds the next level of complexity. Depending on the degree of invasion, the analyst may need to generate an average fluid hydrogen index, weighted by the invasion diameter and the corresponding radial geometric function for the logging tool. If the porosity is gas-filled, the simple bulk mixing law fails because the neutron response becomes nonlinear. In that case, the next level of interpretation sophistication accounts for this nonlinearity through an “excavation effect,” another term added to Eq. 3D.9.

As the lithology becomes more complex, the analyst can move to a macroparameter approach characterized by a neutron migration length. Finally, if the standard environmental correction charts do not cover borehole effects, a full-blown Monte Carlo model may be needed. Fortunately, this is a very rare circumstance.

3D.4.2 Single-Log Interpretation—More Details. Even though log analysts’ primary interest is only in virgin formation properties, there are at least three regions that contribute to a nuclear log measurement: the borehole (including borehole size, composition, temperature, and even the tool body), the invaded zone, and the real target, the virgin formation. The tool will respond to a weighted average of all three. For nuclear tools, the weights given to the borehole and invaded zone may be large because they are closer to the sources and detectors.

Log analysts typically divide the problem into three corresponding parts and attempt to handle them sequentially. First, one compensates for borehole effects by applying semiempirical environmental corrections, either from chart books or equivalent computerized correction formulas. Second, one finesses the invaded-zone problem if possible. For liquids, the density and hydrogen index of the mud filtrate may be similar enough to those of the formation fluids that the effect of invasion can be ignored, and average fluid properties can be assigned with little damage to the accuracy of the calculated porosity. If all of the potential fluid properties are not similar enough, analysts frequently assume that a log responds primarily to either the invaded zone or the deeper, uninvaded zone. The gamma-gamma scattering density log's depth of invasion may be less than 6 in. Because of this very shallow penetration, it is usually safe to assume that the density tool responds only to the invaded zone. The neutron log is often problematic. With shallow invasion, it may primarily see the virgin formation. With deep invasion, even the neutron log may be responding only to the invaded zone. If the formation fluid is gas, the fluid density and hydrogen index differ wildly from those of a typical drilling mud. This is especially the case at shallow depths, where gas density is low. In this case, partial saturation may also feed into the solution of the log's response. While iterative solutions for light hydrocarbons frequently work well enough, the simultaneous solution of all the log responses (including resistivity logs and saturation equations) gives the best result in these cases. While there are numerous commercial simultaneous-solver computer programs, an interesting treatment, including the effects of invasion, was given by Patchett and Wiley.³

To put depths of investigation for nuclear tools in perspective, it is useful to introduce the concept of integrated radial geometric factors, or J -factors.⁴ This is a method of standardizing the data from tools with different depths of investigation. The function is a measure of what fraction of a tool's response comes from inside a certain radius, x , defined by

$$J(x) = \frac{(U_x - U_T)}{(U_i - U_T)} \cdot \dots\dots\dots (3D.10)$$

Here, U_x refers to the tool response integrated out to some distance x into the formation, U_T is the tool's full response out to infinity in the absence of invasion, and U_i is the tool response to a fully invaded formation. Depth of investigation is commonly defined as the radial distance into the borehole wall at which the tool response reaches 90% of the final value.

Fig. 3D.3 compares the radial geometric response functions for the three basic nuclear logs. The radial geometric function is a quick, approximate contrivance for determining whether tool response is predominantly coming from the invaded zone or the virgin formation. The curve labeled "gr-reservoir" corresponds to a bulk density of 2.35 g/cm³. For comparison, a deep induction log does not reach its 50% response point until approximately 150 radial in. The base case shown is for a 20% porosity limestone. Obviously, the depth of investigation varies with formation composition, which is, after all, the principle on which density and neutron tools are based. The depth of investigation of a density log ranges from 4.4 in. at 5% porosity to 5.0 in. at 40%. For compensated neutron logs, depth of investigation ranges from 9.5 in. at 40% porosity limestone to 16 in. at 2.5 p.u. (porosity unit or % porosity). Note that increasing porosity increases the depth of investigation of the density log but decreases the depth of investigation of the neutron log. This makes sense in light of the different dominant scattering processes for neutrons (as opposed to gamma rays). A passive gamma ray response function for 100% water is shown for comparison. Even though it is stretched somewhat, as expected, the difference is not nearly as large as between nuclear measurements, and a deep induction log with a 90% response point may be deeper than 20 ft.

No matter what the approach, the trick is estimating the invasion diameter so that it can be compared to the tool's depth of investigation. Invasion is a complicated function of mud

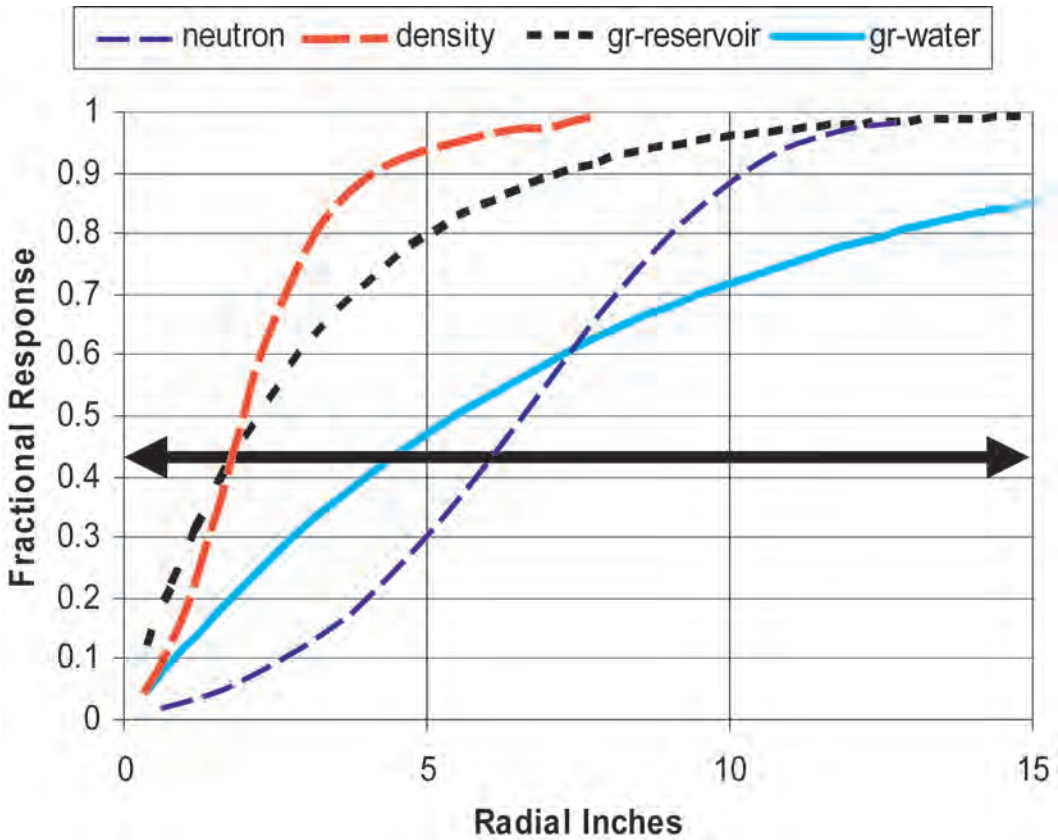


Fig. 3D.3—Nuclear radial geometric functions: comparison of radial geometric functions for various nuclear logs in a 20-p.u. limestone.

weight, mud composition, formation pressure, porosity, and permeability, so a quick and dirty estimate of its extent is rarely possible. If the standard three resistivity logs with three different depths of investigation have been run, a rough estimate of the diameter of invasion can be made from so-called tornado-chart calculations. In addition to refined estimates of the true formation resistivity and the invaded-zone resistivity, a diameter of invasion also will be derived. This is based on the assumption of piston displacement of formation fluids by drilling mud, as suggested schematically in Fig. 3D.4. This step-function invasion model is far from physically correct, but at least it is a step in the right direction. As a first hurdle, this diameter of invasion can be compared to the appropriate integrated radial geometric function to confirm (or contradict) the validity of assumptions that a log’s response is predominantly from the invaded zone or the unadulterated formation. While modern array resistivity tools can produce much more detailed descriptions of the invaded zone, the response to an equivalent step-invasion profile is much more tractable. If a log’s response includes significant elements of both zones (i.e., the diameter of invasion lies somewhere between the 10 and 90% points on the J -function), then its response can be weighted to the two regions. For step invasion, this is simply

$$R = J(x)I + [1 - J(x)]T, \dots\dots\dots (3D.11)$$

where R = the tool reading, I = the tool’s bulk response in the case of complete invasion, and T = the likely bulk response to no invasion.

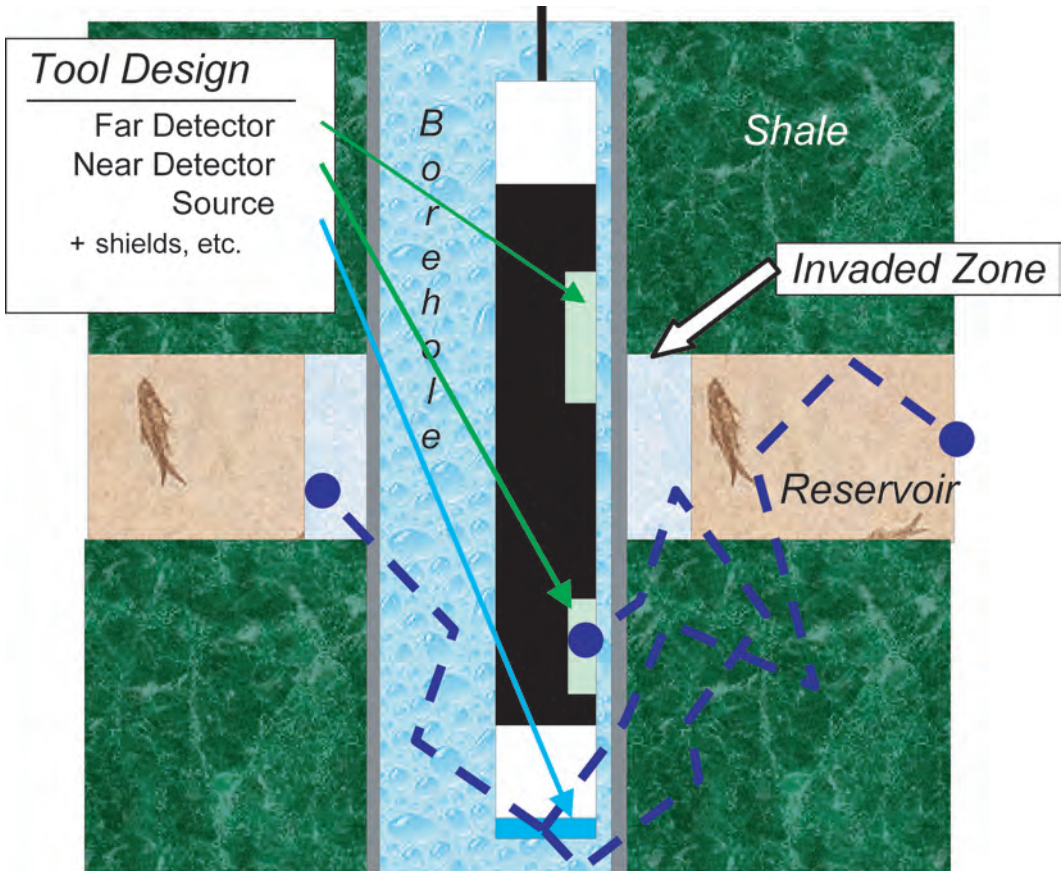


Fig. 3D.4—Monte Carlo modeling predicts tool response from a detailed description of geometry and composition.

The third and final step, and the one on which the log analyst spends the most time, is the understanding of the tool’s bulk response to a formation, the T in Eq. 3D.11. Consider a small cube of formation. While the cube is heterogeneous on the microscopic scale, it can be treated as uniform on the scale of nuclear scattering. At the scale of 10 cm, the exact arrangement of crystalline rock and fluids does not matter, only the bulk average number of scattering centers of a given type. Tool response is determined by these bulk averages. Fortunately, these can be related to bulk average formation properties. Fig. 3D.5 summarizes the process. Mathematically, this bulk averaging corresponds to a linear mixing law:

$$R = \sum_{i=1}^n V_i R_i, \dots\dots\dots (3D.12)$$

where R is the bulk tool response, V_i is the fractional volume of the i th material, R_i is the response to that material only, and n is the total number of materials present. For example, if water occupies 10% of the pore space and the porosity is 20%, the fractional volume of water (also known as bulk volume water) is $0.1 \times 0.2 = 0.02$. For a density, $\log R_i$ is the density of the i th component. Pure water has a density of 1.0 g/cm^3 , so R of water is 1.0 g/cm^3 . The

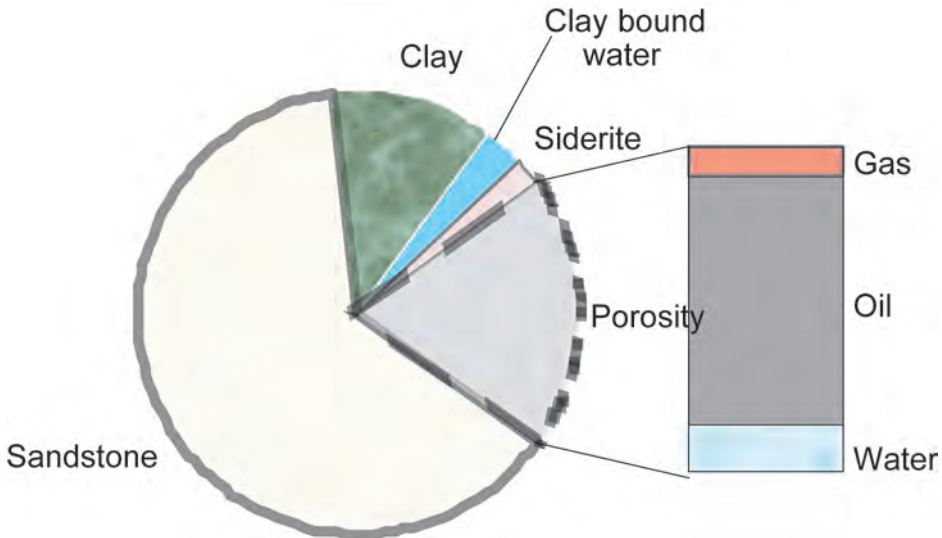


Fig. 3D.5—Bulk formation volumes and their properties are the key to the interpretation of nuclear logs.

contribution of that water to the tool response is $V_i \times R_i = 0.02 \times 1.0 = 0.02 \text{ g/cm}^3$. Similarly, for a neutron-porosity log, R_i is the hydrogen index of material i .

More generally, the responses may not be linear, but there is still an equation or mixing law:

$$R = R(V_i, R_i) \dots\dots\dots (3D.13)$$

An example of this would be the nonlinear response of a neutron-porosity log to gas, referred to as the excavation effect or any of the numerous *ad hoc*, nonlinear gamma ray models.

Single-log interpretation amounts to the assumption that considering just two components (or at least only two at a time) can capture the log’s response to a formation. Examples include the determination of shale volume or total porosity from a single log curve. As an example, consider calculating shale volume from a gamma ray curve. According to the linear mixing-law equation, the gamma ray tool’s response can be written as

$$\gamma = \gamma_{sh}V_{sh} + \gamma_{ns}V_{ns} \dots\dots\dots (3D.14)$$

This seems to be one equation in two unknowns, but there is another, implicit equation, namely that the formation is composed entirely of shale and nonshale (or reservoir or clean sand); that is,

$$V_{sh} + V_{ns} = 1 \dots\dots\dots (3D.15)$$

This really amounts to an assumption. Most importantly, it assumes that there is such a thing as “reservoir rock” characterized by a single bulk gamma ray response. Even in the simplest case, reservoir rock consists of matrix- and water-filled porosity.

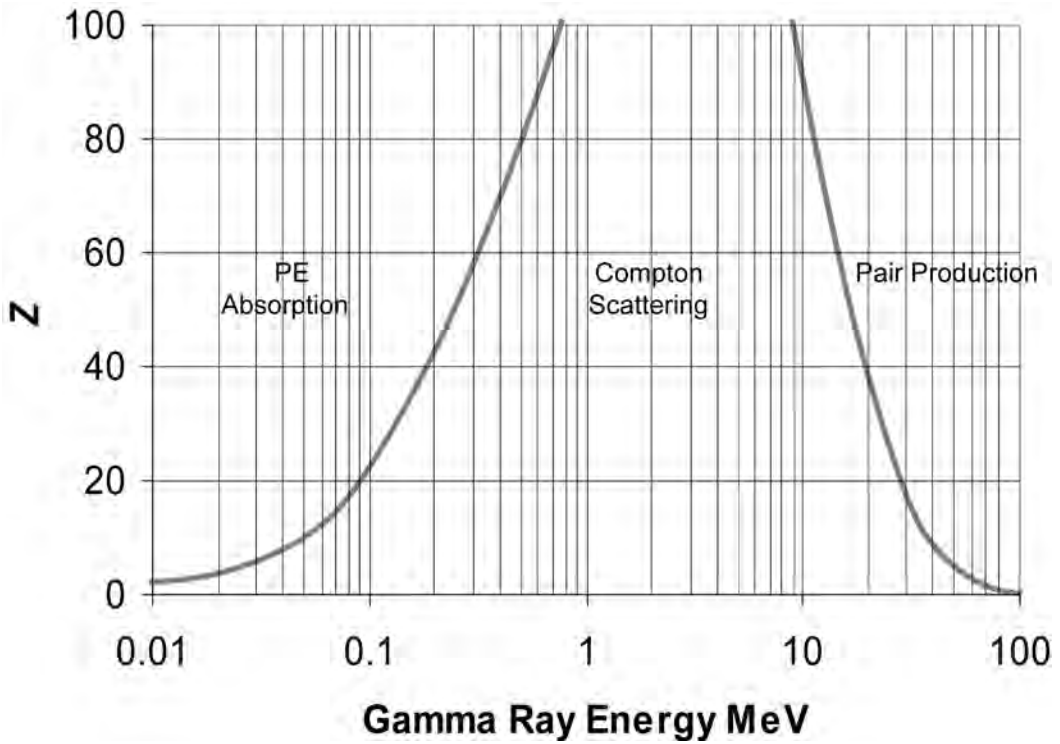


Fig. 3D.6—Illustration of dominant gamma-ray interactions with a formation as a function of gamma-ray energy.

3D.5 Logs Exploiting Gamma Rays and Gamma Ray Transport

3D.5.1 Gamma Ray Interactions With Formations. Gamma rays interact with formations in three different ways: photoelectric absorption, Compton scattering, and, to a limited extent, pair production. One of these will dominate depending on the energy of the gamma ray, as Fig. 3D.6 shows.

Compton Scattering. The most important interaction for logging measurements involving gamma rays is Compton scattering, which dominates in the middle energy range. The density log itself is designed to exploit Compton scattering. Compton scattering also controls the transport of natural gamma rays through a formation to the standard gamma ray tool. Compton scattering is scattering off an atomic electron. In the process, the gamma ray loses some of its energy to the electron. Compton scattering is the dominant form of gamma ray interaction with a formation, from several hundred keV (kilo electron volts, a unit of energy) all the way to 10 MeV (mega electron volts). The cross section for Compton scattering changes very little with energy. The loss of gamma rays is proportional to

$$\sigma_{co} \frac{N_A}{A} \rho_b Z, \dots\dots\dots (3D.16)$$

where Z is the average atomic number of the formation. The attenuation law for gamma ray intensity falloff is then

TABLE 3D.5—VALUES OF BULK DENSITY, ELECTRON DENSITY, AND APPARENT DENSITY (AS READ BY A LOGGING TOOL) FOR SOME COMMON MINERALS AND FLUIDS

Material	Formula	Bulk Density (ρ_b), g/cm ³	Electron Density (ρ_e), g/cm ³	Apparent Density(ρ_a), g/cm ³
Quartz	SiO ₂	2.654	2.650	2.648
Calcite	CaCO ₃	2.710	2.708	2.710
Dolomite	CaCO ₃ *Mg	2.870	2.863	2.876
Fresh water	H ₂ O	1.000	1.110	1.000
Salt water	200 kppm	1.146	1.237	1.135
Oil	n(CH ₂)	0.850	0.970	0.850
Gas	C _{1.1} H _{4.2}	ρ_g	1.238 ρ_g	1.325 ρ_g -0.188

$$\phi_o = \phi_i e^{\rho_b \frac{Z}{A} N_A \sigma_{co} h} \dots\dots\dots (3D.17)$$

For Compton scattering to be a true measure of bulk density, ρ_b , Z/A must be a constant. For almost all formation elements, $Z/A = 1/2$, and a measurement of gamma ray attenuation in the 1- to 10-MeV range can indeed be calibrated to bulk density. The notable exception is hydrogen, for which $Z/A=1$. **Table 3D.5** lists some density values for comparison.

Photoelectric (PE) Absorption. Not surprisingly, the PE log is based on the photoelectric absorption of gamma rays, the scattering process that dominates at low energy. In this process, the incoming gamma ray is absorbed by an atomic electron, giving up all its energy to the electron in the process. If the gamma ray is energetic enough, the added energy causes the electron to break free from its atom. As another electron falls into the vacancy, a characteristic X-ray, generally less than 100 keV, is emitted. These X-rays are too low in energy to contribute to logging measurements.

The PE cross section falls off very strongly as the energy of the incoming gamma ray increases. The cross section is proportional to

$$\frac{Z^{4.6}}{E_{GR}^{3.15}} \dots\dots\dots (3D.18)$$

It is a significant factor in gamma ray scattering only for energies less than 100 keV. This means that it is easy to separate the effects of PE absorption from those of Compton scattering by simply windowing the energies of the gamma rays detected. The same tool can make both measurements simultaneously. By examining the falloff of low-energy gamma ray flux, a logging tool can be calibrated to measure the PE factor (PEF). The PEF, in turn, is primarily sensitive to the average atomic number, Z , of the formation. Because hydrocarbons and water have very low Z values, they contribute very little to the average PE of a formation. Conversely, because the major rock matrices have very different Z s, the PE factor is a nearly porosity-independent lithology indicator.

Pair Production. The final process by which gamma rays interact with a formation needs only a passing comment because its impact on logging measurements is minimal. This process, pair production, occurs only at very high gamma ray energies. It is another absorption process, with a threshold of 1.022 MeV. The incoming gamma ray interacts with the electric field of the nucleus and is absorbed if it has enough energy. This generates an electron-positron pair. The positron (actually just an antimatter electron) is quickly annihilated, yielding two 511-keV

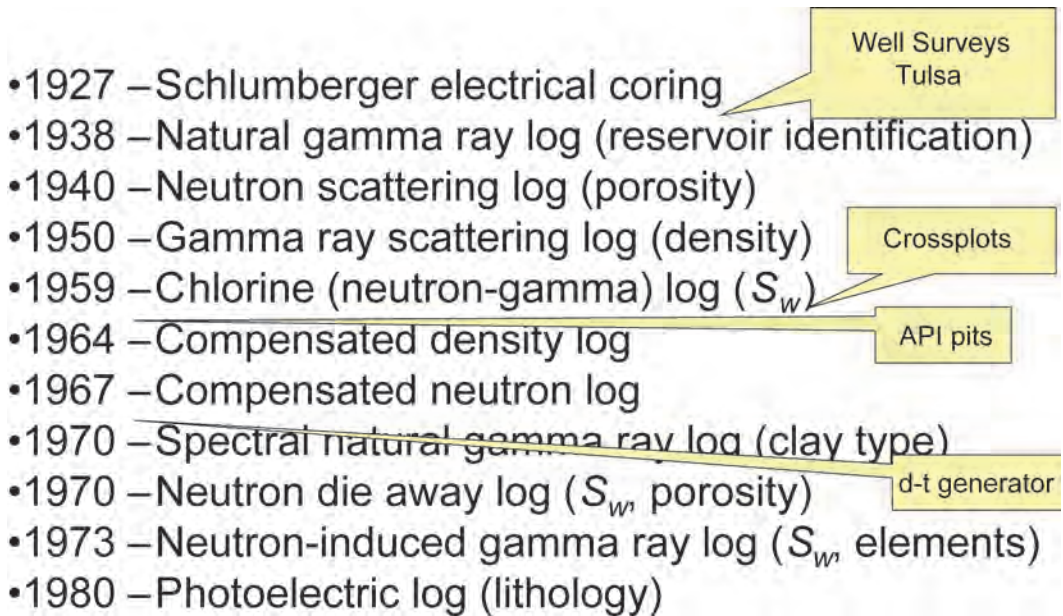


Fig. 3D.7—A timeline of nuclear logging highlights the introduction and evolution of commercial nuclear-logging measurements.

gamma rays. This has little impact on passive gamma ray or gamma-scattering density measurements but does play a role in the appearance and analysis of gamma ray spectra from neutron-induced gamma ray logs.

3D.6 Passive Gamma Ray Tools

Conceptually, the simplest tools are the passive gamma ray devices. There is no source to deal with and generally only one detector. They range from simple gross gamma ray counters used for shale and bed-boundary delineation to spectral devices used in clay typing and geochemical logging. Despite their apparent simplicity, borehole and environmental effects, such as naturally radioactive potassium in drilling mud, can easily confound them.

The gamma ray tool was the first nuclear log to come into service, around 1930 (see [Fig. 3D.7](#)). Gamma ray logs are used primarily to distinguish clean, potentially productive intervals from probable unproductive shale intervals. The measurement is used to locate shale beds and quantify shale volume. Clay minerals are formed from the decomposition of igneous rock. Because clay minerals have large cation exchange capacities, they permanently retain a portion of the radioactive minerals present in trace amounts in their parent igneous micas and feldspars. Thus, shales are usually more radioactive than sedimentary rocks. The movement of water through formations can complicate this simple model. Radioactive salts (particularly uranium salts) dissolved in the water can precipitate out in a porous formation, making otherwise clean sands appear radioactive.

There are only three radioactive elements that occur naturally: potassium, uranium, and thorium. Thorium and uranium both decay to daughters that are also radioactive, and those daughter elements in turn decay to other radioactive daughters, and so on for several generations. Most of these decays result in gamma rays. The energies of the gamma rays are characteristic of the element decaying. This leads to a characteristic pattern or spectrum of gamma ray energies for thorium and uranium, as shown in [Fig. 3D.8](#). Potassium, for example, decays directly to a stable daughter, argon, emitting a single gamma ray with energy 1.46 MeV.

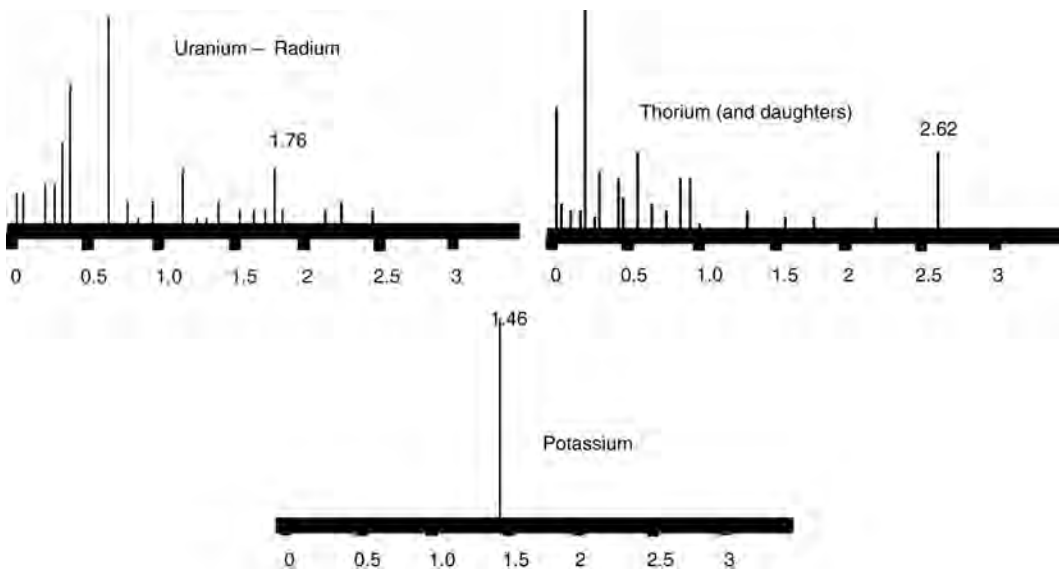


Fig. 3D.8—The spectra of gamma rays emitted by the three naturally occurring radioactive measurements (MeV) and, in the case of uranium and thorium, their daughters.

Before getting into how to use the log readings, let us consider the workings of the tool. Unlike all other nuclear tools (and, in fact, all other logging measurements), it is completely passive. It emits no radiation. Instead, it simply detects incoming gamma rays from the formation and (unfortunately) the borehole. Gamma rays are electromagnetic radiation, generally in the energy range 0.1 to 100 MeV. As light, this would correspond to very short wavelengths indeed. The difference between gamma rays and X-rays is largely semantic because they overlap in energy.

Originally, the detector was a Geiger-Müller tube, just as in the Geiger counter. More recently, the detectors have been switched to solid-state scintillation crystals such as NaI. When a gamma ray strikes such a crystal, it may be absorbed. If it is, the crystal produces a flash of light. This light is “seen” by a photomultiplier staring into the end of the crystal. The photomultiplier shapes the light into an electrical pulse that is counted by the tool. Hence, like all nuclear tools, the raw measured quantity in a gamma ray log is counts. As discussed above, this means that the precision of gamma ray log measurements is determined by Poisson statistics. The precision is the square root of the total number of counts recorded at a given depth. Counts recorded are basically proportional to the volume of the detector crystal times its density (which determine the probability that a gamma ray will be captured within the crystal) times the length of time counted. As with all nuclear-logging measurements, the only part of this that the logger controls is the counting time. Because log measurements are depth driven, the length of time the logger counts is inversely proportional to the logging speed.

Historically, gamma ray sondes have recorded the total flux of gamma radiation integrated over all energies emanating from a formation as a single count rate, the gamma ray curve. Logging tools are not uniform in their energy sensitivity. No detector responds to all the gamma rays that impinge on it. Many pass through with no effect. The sizes of a detector, the solid angle it subtends, and its thickness, as well as its composition (particularly its density), all affect its efficiency for detecting gamma rays. The tool housing around the detector, the casing, and even the density of the borehole fluid can all filter the gamma rays coming from the formation. All these factors not only lower the overall tool efficiency, they also lead to variations in efficiency for gamma rays of different energies. In short, the count rate recorded

in a particular radioactive shale bed is not a unique property of the shale. It is a complex function of tool design and borehole conditions as well as the actual formation's radioactivity. Even though gamma ray readings are generally used only in a relative sense, with reservoir (clean) and shale values determined in situ, there are advantages to a common scale. In the U.S. and most places outside the former Soviet Union, gamma ray logs are scaled in American Petroleum Inst. (API) units. This harkens back to a desire to compare logs from tools of different designs. Tools with different detector sizes and compositions will not have the same efficiency and thus will not give the same count rate even in the same hole over the same interval. To provide a common scale, API built a calibration facility at the U. of Houston. It consists of a concrete-filled pit, 4 ft in diameter, with three 8-ft beds penetrated by a 5½-in. hole cased with 17-lbm casing. The top and bottom beds are composed of extremely-low-radioactivity concrete. The middle bed was made approximately twice as radioactive as a typical midcontinent U.S. shale, resulting in the zone containing 13 ppm uranium, 24 ppm thorium, and 4% potassium. The gamma ray API unit is defined as 1/200 of the difference between the count rate recorded by a logging tool in the middle of the radioactive bed and that recorded in the middle of the nonradioactive bed.

While it has served fairly well for more than 40 years, this is a poor way to define a fundamental unit. Different combinations of isotopes, tool designs, and hole conditions may give the same count rate, so the calibration does not transfer very far from the calibration-pit conditions. In contrast, Russian gamma ray logs are typically scaled in microrentgens ($\mu\text{R}/\text{hr}$), which does correspond to a specific amount of radiation. Converting this to API units is a bit vaguely defined, but it is often suggested that the conversion factor is $1 \mu\text{R}/\text{hr} = 10 \text{ API units}$ for Geiger tube detectors, but $15 \mu\text{R}/\text{hr} = 10 \text{ API}$ for scintillation detectors. This falls in with the previous discussion of the many factors that can affect gamma ray readings. As will be seen later, the problem is further aggravated in logging-while-drilling (LWD) measurements. The API unit provides a degree of standardization, but despite the best efforts of tool designers, one cannot expect tools of different designs to read exactly the same under all conditions. Fortunately, none of this is very important because gamma ray measurements are generally used only in a relative way.

Because we use gamma ray logs as relative measures, precise calibration is not very important except as a visual log display feature. Environmental effects are much more important. Consider a radioactive volume of rock traversed by a borehole. Referring back to the bit of nuclear physics above, gamma rays are absorbed as they pass through the formation. For typical formations, this limits the depth of investigation to approximately 18 in. Considering only the geometry, the count rate opposite a given rock type will be much lower in a larger borehole in which the detector is effectively farther from the source of gamma rays. In an open hole, borehole size almost always has the greatest effect on the count-rate calibration. This problem can go well beyond changes in bit size. Especially if shales or sands are selectively washed out, borehole size can imprint itself of the expected gamma ray contrast between shales and sands. If the borehole is large enough, the density of the fluid filling the borehole can also impact the calibration by absorbing some of the gamma rays before they get to the tool.

Barite in the mud is another complication, filtering the incoming gamma rays. Thus, the gamma ray borehole size and fluid corrections are often very important and should be made if at all possible. Obviously, casing absorbs a large fraction of the gamma rays traversing it on their way to the borehole, so if the tool is run in a cased hole, casing corrections are very important. Tool design has a large impact on environmental corrections. The housing and location of the detectors all filter the incoming gamma rays. It is important to use the right environmental corrections for the tool being run. This is especially true for LWD tools that may consist of multiple detectors embedded in large, heavy drill collars that filter the incoming gamma rays in unique ways.

Now that we know how the tools work, we are ready to discuss how gamma ray logs are used in log analysis. While the gamma ray log traditionally has been used primarily for well-to-well correlation, it also plays a role in quantitative log analysis. As mentioned at the outset, gamma ray logs are used primarily to define and quantify productive intervals. As discussed above, there are only three naturally occurring radioactive elements—potassium, uranium, and thorium (or K, U, and Th by their elemental symbols)—and all of these tend to be associated with shales, not clean matrix minerals (e.g., quartz sand, SiO₂, limestone CaCO₃).

The most common interpretation method is the simple bulk linear mixing law presented previously.

$$\gamma = \sum_i V_i \gamma_i \dots\dots\dots (3D.19)$$

Even though we know that the distribution of clays in shales and reservoir rocks is quite complex, to first order, log analysts frequently simplify the linear bulk mixing law to the determination of shale volume:

$$\gamma = \gamma_{sh} V_{sh} + \gamma_{ma} V_{ma} + \gamma_f V_f \dots\dots\dots (3D.20)$$

Standard log analysis separates the log-analysis problem into a series of sequential, independent steps. Because shale-volume determination is usually the first step in the sequential process of formation evaluation from logs, porosity and fluid volumes are not yet known. As a result, the equation is further simplified to

$$\gamma = \gamma_{sh} V_{sh} + \gamma_{cn} V_{cn} \dots\dots\dots (3D.21)$$

Adding closure,

$$V_{sh} + V_{ma} = 1 \dots\dots\dots (3D.22)$$

leads to the familiar formula for calculating shale volume from a borehole-corrected gamma ray log:

$$V_{sh} = \frac{\gamma_{log} - \gamma_{cn}}{\gamma_{sh} - \gamma_{cn}} \dots\dots\dots (3D.23)$$

where the “clean” terms represent the lumped response to the matrix grains and the fluids in the porosity. Further complications arise because the shale values are taken from overlying shale beds. The clays distributed in the reservoir rock are almost certainly not simply dispersed versions of the shales, unless they occur as thin laminations. At the very least, there will be differences between shale, made up of clay minerals, clay bound water, and silt-size particles, and the clay minerals alone distributed in the matrix. Worse, because of differences in the processes at work when the shales were laid down vs. the shaly sands, the clay minerals in the sands may not be the same as those in the matrix. To compensate for this, numerous nonlinear relationships have been proposed. These have geologically significant-sounding names like Larinov older rocks but are simply empirical and have no physical basis.⁵ They are used to improve the correlation between gamma ray-derived shale volumes and other estimates of the shale volume, especially from core. The equations all start with the linear gamma ray index discussed above and reduce the intermediate values from there. **Fig. 3D.9** lists a few of the

$$\text{Linear: } I_{GR} = \frac{GR_{log} - GR_{clean}}{GR_{sh} - GR_{clean}}$$

$$\text{Larinov_older: } V_{sh} = 0.33 \times (2^{2 \times I_{GR}} - 1)$$

$$\text{Larinov_tertiary: } V_{sh} = 0.083 \times (2^{3.7 \times I_{GR}} - 1)$$

$$\text{Clavier: } V_{sh} = 1.7 - [3.38 - (I_{GR} + 0.7)^2]^{0.5} \quad V_{sh} = 1.7 - [3.38 - (I_{GR} + 0.7)^2]^{0.5}$$

$$\text{Stieber: } V_{sh} = \frac{I_{GR}}{3 - 2 \times I_{GR}}, \quad V_{sh} = \frac{I_{GR}}{2 - I_{GR}}, \text{ etc.}$$

Fig. 3D.9—A summary of various nonlinear shale-volume models used to reduce the amount of shale below the linear, bulk mixing-law prediction.

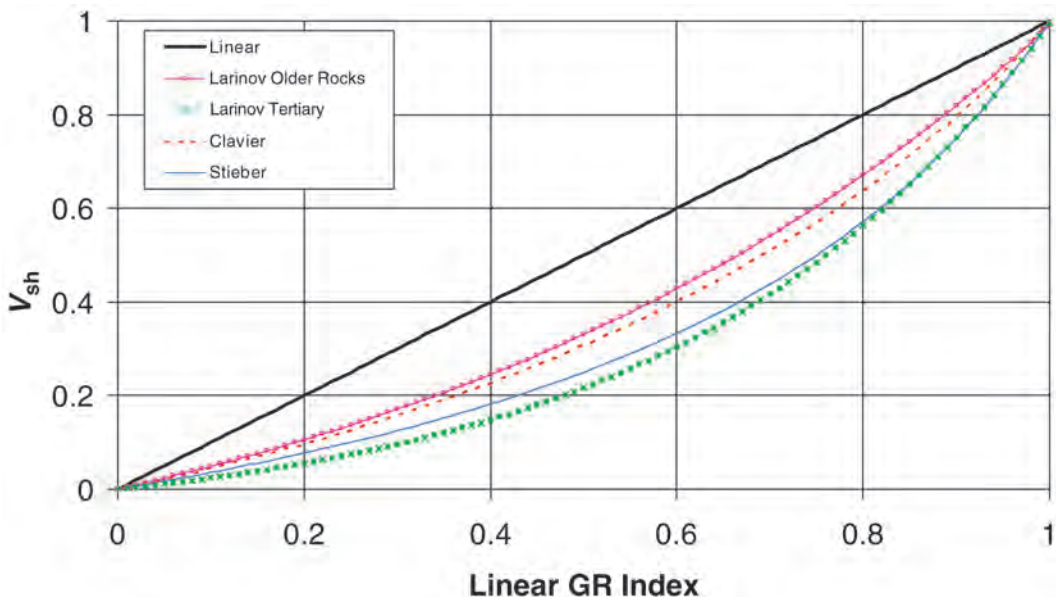


Fig. 3D.10—Illustration of the amount of shale reduction predicted by various nonlinear shale-volume models listed in Fig. 3D.9.

more common equations. Fig. 3D.10 illustrates the degree of shale reduction that the various models afford. If one of these models must be used, select the one that best fits other available estimates of clay volume.

One disadvantage of the various empirical, nonlinear models is that they generally require core data for calibration or at least justification. This is a generic problem with more complex models; they require more parameters to characterize them. To set or calibrate those parameters in turn requires more independent log or core measurements.

It is also assumed that the clean reservoir material (the sum of the pore fluids and matrix minerals) has a fixed amount of radiation associated with it. As long as the gamma ray reading associated with the clean reservoir material is small compared to the shales, this assumption is safe. As the sands become hotter (more radioactive), lumping the fluids and matrix together becomes problematic, particularly if the porosity is large.

The latest variant on the gamma ray log is the spectral gamma ray log. This starts out exactly the same as the standard gross gamma ray count log discussed above. Gamma rays from the formation are counted in a detector system. However, there is an added level of sophistication. The energy of the gamma ray captured by the detector is proportional to the brightness of the light pulse it produces, and this brightness, in turn, determines the size of the electrical pulse produced by the photomultiplier. By sorting the pulses from the photomultiplier into bins by their size, a spectrum equivalent to the energy spectrum of the incoming gamma rays is produced. As noted above, the energy of the gamma rays is determined by which element emitted them.

Spectral gamma ray measurements offer several advantages. They can help with clay typing. Variations of the relative amounts of potassium, thorium, and uranium are associated with specific shale minerals. As is so often the case in log analysis, crossplots are used to highlight these differences. Different clay minerals may (sometimes) array themselves in the pie slices of a thorium/potassium crossplot. Clays of different types also may plot in different regions on a crossplot of potassium or the thorium/potassium ratio against P_e , the PE factor. For the mathematically inclined, the same relationships may be captured in an equation of the form

$$\gamma_{API} = A[\text{Th}] + B[\text{U}_{(\text{ppm})}] + C[\text{K}_{(\text{wt} \%)}] \dots \dots \dots (3D.24)$$

For a typical shale, the coefficients are in the ratio of A:B:C=1:2:4. Uranium is more often associated with fluid movement in porous rocks than shale minerals. At the very least, the effects of uranium can be removed. In other cases, potassium may be associated with feldspar rather than shale. Differences in the ratios between the overlying reference shale and the shaly sands may highlight the problems with carrying clay properties from the overlying shale into the shaly-sand interval.

3D.6.1 Precision. Consider briefly some details of how a standard, gross-count-rate gamma ray tool works. Most modern tools (in nuclear logging, “modern” means within the past 25 years) use a solid-state scintillator crystal (most often sodium iodide, NaI) to detect gamma rays. When a gamma ray strikes the crystal, there is some probability that it will be captured. That probability is mostly proportional to the size and density of the crystal. If it is captured, it gives off a flash of light. A photomultiplier mounted on one end of the crystal converts that light to an electrical pulse, which is then fed to an electronic pulse counter. To measure a count rate with a given precision in the laboratory, one counts until enough counts are registered to give the desired level of precision (see the discussion of counting statistics above). Then, one divides that number of counts by the time it took to get that many to obtain a count rate. Unfortunately, in a logging tool, all measurements are depth-based. To measure a count rate, the tool counts for the length of time it takes the tool to move ½ ft (or whatever the depth increment is), then divides by the length of time it took the tool to move that distance. This means that the precision of a nuclear-logging measurement in a given lithology is proportional to one over the square root of the logging speed. Remember that the number of counts received crossing a clean ½ ft will be much less than the number when crossing a shaly ½ ft.

3D.6.2 Environmental Effects. The simple consideration of the discussion of radiation transport above helps clarify which environmental effects most seriously distort the gamma ray log. Imagine what happens as borehole size increases. There is less of the radiating radioactive material near the detector, and the measured count rate goes down, even though the actual level of radioactivity in the formation remains the same. Further imagine the rather typical case in which the shales are eroded and broken out while the sands remain in gauge. This would sup-

press the apparent gamma ray count rate in the eroded shales much more than in the sands, suppressing the gamma ray contrast between eroded shales and sands. This is typically one of the largest environmental effects on the gamma ray count rate. Again from the discussion of radiation transport, heavier materials in the path that the gamma rays must follow from the formation through the detector will absorb more gamma rays than lighter materials (as will be seen in a later section, this is the basis for the bulk density log, but that is another story and a different log). Worse yet, barite is a big absorber of gamma rays. The lesson to carry away is that borehole size and fluid corrections are almost always important when running the gamma ray log.

3D.6.3 Spectral Gamma Ray Logs. As we saw earlier, the energy of a gamma ray depends on its source. Each of the standard naturally occurring radioactive elements (K, U, and Th) gives off a gamma ray of a unique energy when it decays. Potassium gives off only a gamma ray. The other elements give off a gamma ray, then decay to other elements called daughters, which, because they are still radioactive, give off other gamma rays, and so on. This gives rise to the pattern of gamma ray energies in Fig. 3D.8. These are called spectra of the elements and are as unique as fingerprints. It is not surprising that the brightness of a light pulse produced in a scintillator crystal is proportional to the energy of the gamma ray. The amount of current in the electrical pulse from the photomultiplier is in turn proportional to the brightness of the pulse of light. It is a simple matter to sort the pulses coming out of the photomultiplier into bins according to their pulse size before counting them. This is called pulse-height spectrum analysis and gives rise to a histogram of count rates such as those in Fig. 3D.8 instead of a single count rate. Common scintillators lack the resolution to break the gamma rays into fine enough bins to reproduce the spectra in Fig. 3D.8, so some sophisticated mathematical deconvolution is needed to infer proportions of uranium, potassium, and thorium from broadly windowed pulse-height spectra.

There are several new things that can be done once we have K, U, and Th count rates rather than just total gamma ray. The most important is that we can produce a count rate only because of potassium and thorium. This is very useful because these elements most often tag only clays, while uranium salts can be associated with moved water. These uranium salts can be precipitated out in porous reservoir rock, especially at the wellbore, where pressure changes may occur. This uranium can produce what appear to be hot sands on a gross gamma ray log. Using the uranium-free gamma ray curve from a spectral tool (CGR, in Schlumberger's mnemonics) can circumvent this problem and improve sand/shale discrimination in such environments. Occasionally, the ratio of thorium to potassium can be exploited in clay typing. The downside of spectral gamma ray curves is reduced count rate and the accompanying reduced precision. By dividing the spectra into three components, the count rate for any one component may be less than one-third that of the total gamma ray measurement. Further errors occur in the math of deconvolution. If high-precision spectral gamma ray measurements are needed, reduced logging speed is required. The service companies have charts and computer programs that can help in the selection of logging speeds to achieve specific precisions.

3D.6.4 LWD. LWD gamma ray tools typically embed the detector inside of a drill collar. Two to three inches of steel are interposed between the detectors and the formation. That steel acts as an energy-cutoff filter, passing high-energy gamma rays better than lower-energy ones. As a result, these tools are more sensitive to the high-energy potassium gamma rays than the lower-energy uranium and thorium. The API gamma ray unit defined in the U. of Houston facility fails to recognize that different gamma ray energy distributions (arising from different relative concentrations of potassium, uranium, and thorium in the formation, as well as different borehole conditions and detector response functions) can cause the same counting rate at the detector in the borehole. In addition, the borehole diameter of the calibration pit is too

small to accommodate most measurement-while-drilling (MWD) tools. To allow direct comparison with familiar wireline gamma ray logs, MWD contractors have attempted to transfer the API unit to the new (and larger-diameter) spectral gamma ray calibration pits, also at the U. of Houston. Because of the differences in spectral response between wireline and MWD tools, there is no unambiguous way to transfer the API unit to MWD tools. This problem is not unique to MWD tools, but because of their suppressed low-energy sensitivity, it is particularly severe for them.

To offset these effects, most MWD gamma ray tools are spectral gamma ray tools that divide the spectrum into 256 channels downhole. The precise use of these windows is still evolving, but they clearly can be used for K-U-Th determination. In one case, the shielding provided by the drill collar is turned to an advantage to produce a directional gamma ray log. As the tool rotates in the hole, it looks in different directions. At a dipping bed boundary with gamma ray contrast, such as when entering or leaving a shale bed, the gamma ray reading oscillates as the tool first sees the bed on the top of the hole and then the bottom. This fact can be used to estimate the angle at which the drillstring is striking the bed and to keep drilling within a bed.

3D.6.5 Other Applications. Gamma ray logs have a number of other niche applications. For example, injected fluids can be tagged with radioactive tracers and their progress through a field monitored with gamma ray logs in wells adjacent to the injection site.

Spectral natural gamma ray systems designed for K-U-Th logging have been applied to evaluate stimulations and completions.⁶ One or more radioactive isotopes tag the various materials sent downhole. From a spectral log that separates the different isotopes, engineers establish the vertical zones of each of the different phases of the treatment. By examining peak-to-Compton-background ratios from the spectra, it is also possible to discriminate material inside the borehole from that outside the borehole. The same data yield a feeling for how far into the formation (remembering that gamma rays penetrate reservoir rocks only approximately 6 in.) the materials extend. By applying directional gamma ray detection schemes, it is also possible to infer fracture direction.

3D.6.6 Gamma-Gamma Scattering Density Tools. A density-logging tool sends gamma rays into a formation and detects those that are scattered back. Typical logging sondes use a Cesium-137 source, which emits gamma rays of 0.66MeV. At this high energy level, Compton scattering dominates. The average electron density in the volume of formation probed by the tool controls the scattered gamma ray count rates at the detectors. As we saw above, average electron density, in turn, correlates strongly (but not perfectly) with bulk density. Because the gamma rays cannot penetrate far into the formation, the volume of investigation is small. Mud-cake and tool standoff have particularly strong effects on this measurement. For less energetic gamma rays, PE absorption controls the observed count rates. Here, the average atomic number (which correlates with rock type) sets the amount of PE absorption that a formation exhibits. Again, all the bulk average effects accrue, with special problems posed by barium-weighted mud.

The depth of investigation of a density tool decreases with increasing density and never exceeds 6 in., as the pseudogeometric factor in Fig. 3D.3 shows. The log almost always measures the invaded zone, at least in porous, permeable formations. As is typical of the nuclear scattering family of measurements, the density tool uses two detectors at progressively longer distances from the source. The distance between the near and far detectors sets the vertical resolution, approximately 10 in. typically. Correction is by the spine-and-ribs technique. The spine is the normal calibrated relationship between the density measured by the near-spaced and far-spaced detectors in the absence of any gap between the tool and the borehole wall. Gaps cause departures from this spine and lead to density corrections that are applied to the density from the long-space detector. This correction is presented as a curve with the density

log. Above an inch or so of standoff, the compensation fails. There is no universal correction threshold, but corrections greater than 0.05 to 0.1 g/cm³ are suspicious. Unfortunately, a low correction does not guarantee a good measurement. Connecting a particular rib back to the correct location on the spine (and, hence, to the correct bulk density) requires that the density pad be parallel to the borehole wall. Likewise, very small water-filled gaps can give rise to large corrections that are perfectly correct.

3D.6.7 LWD. This is the one case in which the difference in design between wireline and LWD tools is significant. Wireline tools use a skid-mounted pad that is pressed directly against the borehole wall. The pad follows hole rugosity, at least at the 1- to 2-ft vertical frequency level, minimizing the tool standoff. Because this is a very shallow measurement, minimizing the thickness of the layer of mud and borehole fluid between the tool and the formation is very important. The location of the sensor in the rotating drill collar precludes pad mounting of the LWD gamma ray density sensor. Thus, direct contact with the formation is eliminated, and a large and variable mud layer is introduced into the volume of investigation. Two different approaches are used to compensate for this mud effect. One design places the source and detector in stabilizer blades. These blades displace the drilling mud, providing a nearly direct path to the formation for the probing gamma rays. Because a stabilizer can steer the bit, tool subs using them must be run several joints behind the bit to maintain directional control. The blades are also subject to wear that can affect the tool calibration. A focused source and careful detector-window design further minimize borehole effects. Measurements generally use tool rotation to correct for hole-size variations. Spectral detection of scattered gamma rays is exploited in combination with low-density windows to produce a PE measurement. In an alternate approach to solving the mud problem, multiple detectors are placed radially around the collar, and the results are averaged to remove mud effects when the mud density is known. Of course, the tool may undergo complex motion, requiring a more sophisticated algorithm. This procedure can be misled by tool precession in nearly vertical holes.

3D.6.8 Density-Porosity Interpretation. In the standard sequential interpretation process, the analyst determines porosity directly from the density log. It is conceptually the easiest of the porosity logs to interpret because, if ever a tool obeyed a linear bulk mixing law, it is the density logs.

In a simple clean reservoir, the interpretation model is:

$$\rho_b = \phi \rho_{fl} + (1 - \phi) \rho_{ma} \dots\dots\dots (3D.25)$$

Solved for porosity, this yields

$$\phi_T = \frac{\rho_{ma} - \rho_b}{\rho_{ma} - \rho_{fl}} \dots\dots\dots (3D.26)$$

This porosity is subscripted with a *T* for total porosity because it draws no distinction between pore fluid and fluid possibly bound in shales. As mentioned in the general interpretation discussion, the density log rarely sees past the invaded zone, so $\rho_{fl} = \rho_{mf}$, the mud-filtrate density. Even if shale is present, the interpretation merely requires an additional term:

$$\rho_b = \phi_e \rho_{fl} + (1 - \phi_e - V_{sh}) \rho_{ma} + V_{sh} \rho_{sh} \dots\dots\dots (3D.27)$$

and the corresponding shale correction to turn total porosity into effective porosity is straightforward. Again, more sophisticated formation descriptions require more parameters, which in turn require more measured data for calibration.

In known lithology, the grain density, ρ_{ma} , can be chosen from a table like [Table 3D.5](#). Sensitivity can be analyzed directly by taking the partial derivative of the response equation with respect to grain density. For a 30-p.u., water-filled sandstone, an error of 0.05 g/cm³ in the supposed grain density will only alter the calculated porosity by 2 p.u. A similar analysis of the sensitivity to fluid density shows that a variation of more than 0.1 g/cm³ in the fluid density corresponds to a similar 2-p.u. error in the calculated porosity.

This is fortunate because fluid density within the density tool’s volume of investigation may be very difficult to estimate. As already discussed, because of its shallow depth of investigation, the density log is commonly a flushed-zone device, and the fluid density that it sees may be taken to be that of the mud filtrate. The effect of a small amount of immovable hydrocarbon or connate water can, more often than not, be ignored. If gas is present, its low density will produce an apparent increase in porosity. Here, we could have a case in which, to calculate density porosity, we must first know the average flushed-zone fluid saturation.

As discussed in the section about radiation transport, the biggest hitch in gamma-gamma scattering density evaluation is the difference between bulk density and electron density. The device measures electron density. As [Table 3D.5](#) shows, this matters only for fluids. Knowing that the tool will be used in fluid-filled rocks, the service companies transform the electron density to a water-filled, porous limestone, calibrated bulk density. The apparent density as read by the tool is thus altered to read:

$$\rho_{b_log} = 1.0704\rho_e - 0.188 \dots \dots \dots (3D.28)$$

In the principal lithologies of interest, this transformed density departs less than 0.004 g/cm³ from the true bulk density. The case of a high-porosity reservoir filled with gas (and with minimal invasion) may require additional correction beginning with the removal of this “calibration.” In those cases, the analyst should use the apparent density rather than the true bulk density in any mixing-law equation.

3D.6.9 PE. In addition to gamma ray scattering, modern density tools also analyze the low-energy region of the scattered gamma ray spectrum separately. These low-energy gamma rays are subject to photoelectric absorption, which is controlled by the atomic number, Z . Z , in turn, strongly correlates with lithology (see [Fig. 3D.11](#)). The length of the lines represents a variation from 0 (top) to 40 p.u. Note how effectively the lithologies are discriminated independent of porosity.

The PE absorption cross section, in barns (10⁻²⁴ cm²), is strongly dependent on the energy of the gamma rays, E , as well as the average atomic number, Z .

$$\sigma = 12.1E^{-3.15}Z^{-4.6} \dots \dots \dots (3D.29)$$

This means that low-energy gamma ray flux is attenuated according to

$$\Phi = \Phi_o e^{-n\tau x} \dots \dots \dots (3D.30)$$

To suppress this energy dependence, the PE log is scaled as a PE index or factor:

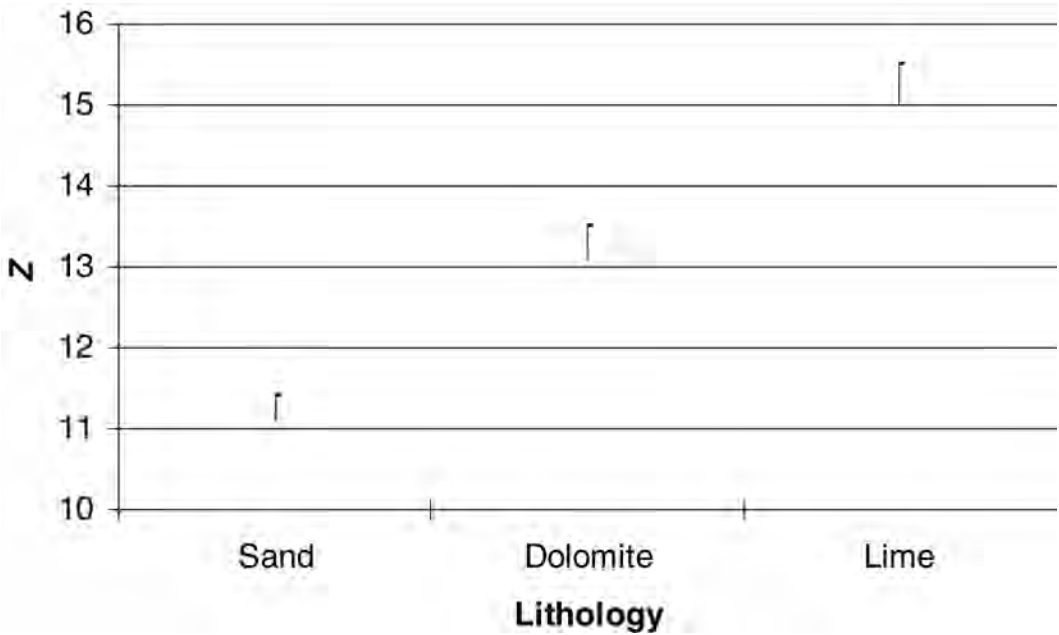


Fig. 3D.11—Z and, hence, the PEF measurement, discriminates lithologies, largely independent of porosity. The line lengths represent ranges of porosity from 0 to 40% in the respective lithologies. (There are three vertical lines corresponding to the porosity, ranging from 0 p.u. at the top to 40 p.u. at the bottom for each of the three common reservoir matrix lithologies. This illustrates that Z and, hence, PE is nearly porosity independent while strongly discriminating lithology. The x-axis takes on only three discrete values for each of the three lithologies.)

$$P_e \equiv F_{pe} \equiv \left[\frac{Z}{10} \right]^{3.6} \dots\dots\dots (3D.31)$$

So, in terms of P_e , the attenuation (which is what the tool actually measures) of low-energy gamma rays is simply

$$\Phi \propto \Phi_0 e^{-n_e P_e x}, \dots\dots\dots (3D.32)$$

where n_e is the electron-number density.

3D.6.10 U. Unfortunately, P_e does not obey a linear, volumetric mixing law on which log analysis thrives. To get around this, a new parameter, U , was developed.

$$U = F_{pe} \rho_e = \frac{F_{pe}(\rho_b + 0.1883)}{1.0704}, \dots\dots\dots (3D.33)$$

where ρ_b is the formation density in g/cm³. In terms of multiple components,

$$U_T = \sum_i P_{e,i} \rho_{e,i} V_i = \sum_i U_i V_i, \dots\dots\dots (3D.34)$$

Material	PEF (barns/electron)	U (barns/cm ²)
Quartz	1.80	4.80
Calcite	5.10	13.80
Dolomite	3.10	9.00
Kaolinite	1.80	4.40
Illite	3.50	8.70
Chlorite	6.30	17.00
Fresh water	0.36	0.40
Brine (120 kppm NaCl)	0.81	0.96
Oil	0.12	0.12

which is a linear bulk mixing equation. [Table 3D.6](#) shows typical values of PEF and U for some common formation constituents.

3D.7 Neutron Logs

3D.7.1 Neutron-Scattering Porosity Tools. By far, the most difficult nuclear logs to interpret are those that exploit neutron scattering to estimate porosity. The log targets the average hydrogen density of the volume investigation. If all the hydrogen in the formation is in the form of porosity-filling liquid, in particular water or oil, the hydrogen index will track the porosity. A modern, compensated tool actually estimates the size of a cloud of neutrons around a source by measuring the ratio of count rates at two different distances from the source. The straight-line distance that the average neutron travels away from the source before collisions with formation atoms slow it down to thermal energy sets the size of the neutron cloud. Once a neutron slows to thermal energy and is thus in equilibrium with the rock matrix, it diffuses only very slowly away from the source. This forms the static cloud of neutrons whose size the tool measures. This characteristic distance is called the slowing-down length. Neutrons slow down through elastic, billiard-ball-type collisions. Conservation of momentum requires that they lose the most speed in collisions with nuclei of nearly their own mass (e.g., hydrogen). Obviously, collisions with other nuclei also slow neutrons, but less effectively than those with hydrogen. [Table 3D.2](#) summarizes just how dominant hydrogen is at slowing down neutrons compared to the other common formation elements. Ideally, a porosity tool would count only epithermal neutrons because the slower thermal neutron population depends as much on the absorption cross section of the formation as it does on the slowing-down length. To get count rates high enough for statistical accuracy, logging tools typically count all neutrons, epithermal and thermal. Thus, the tool reading must be corrected for the effects of neutron capture in the formation. [Fig. 3D.12](#) outlines the conversion from tool reading to porosity.

The neutron-porosity log first appeared in 1940. It consisted of an isotopic source, most often plutonium-beryllium, and a single detector. Many variations were produced exploiting both thermal and epithermal neutrons. In most of the early tools, neutrons were not detected directly. Instead, the tools counted gamma rays emitted when hydrogen and chlorine capture thermal neutrons. Because hydrogen has by far the greatest effect on neutron transport, the borehole effects on such a tool are large. Until recently, this type of tool was still in common use in the former Soviet Union. The now-standard compensated neutron-porosity logging (CNL) tool, in common use since the 1970s, is still a very simple tool. Like a density tool, it

Chain of Inference

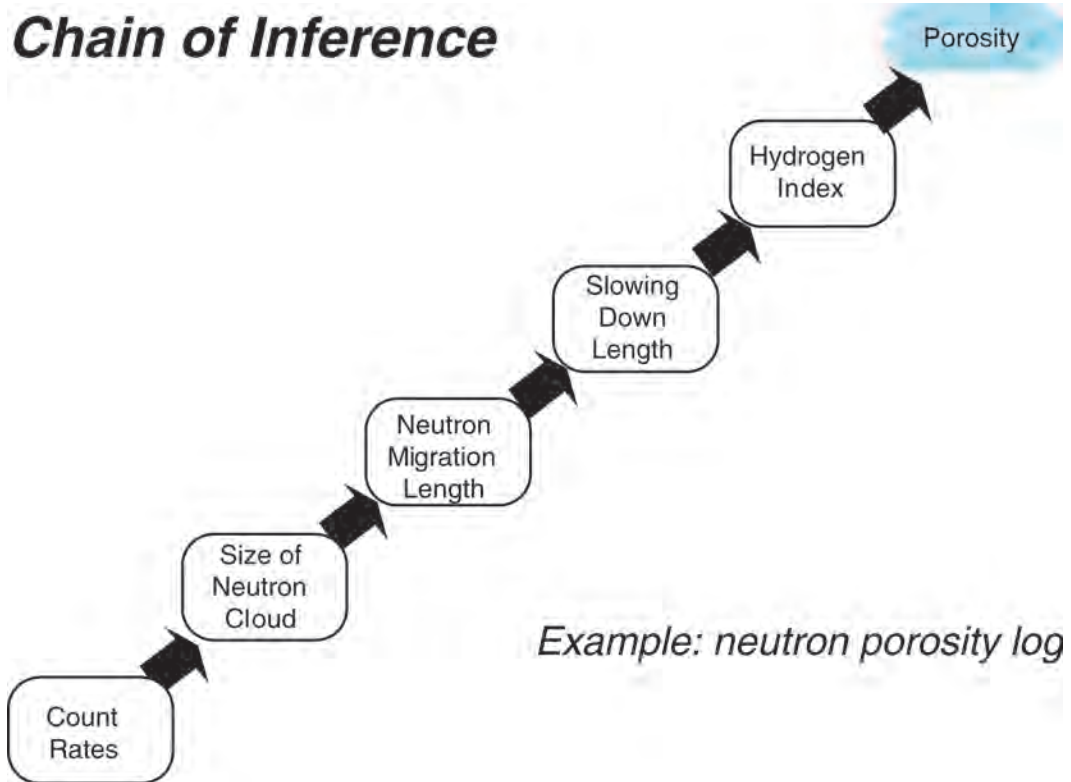


Fig. 3D.12—The nuclear-log-interpretation process can be seen as a chain of inferences, as illustrated by the neutron-porosity log.

consists of an isotopic source (now most often americium-beryllium, although at least one tool uses an accelerator source) and two neutron detectors. The tool measures the size of the neutron cloud by characterizing the falloff of neutrons between the two detectors. Because neutrons penetrate considerably further than gamma rays, the design is much simpler than that of a density tool. It requires little collimation and does not need to be pressed against the borehole wall. The size of the fluid-filled borehole is obviously an important environmental effect that must be taken into account. As a result, even “raw” CNL porosities are reported with a borehole-size correction already applied.

3D.7.2 LWD. As expected, some of the most interesting variations in design occur for the most troublesome measurement, the LWD tools. Although all MWD devices share the basic wireline configuration of a neutron source and two differently spaced detectors, the drillstring environment forces changes. Again, a pad-mounted tool is not possible, increasing potential borehole effects. He-3 detectors with long central wires, the standards in wireline tools, are sensitive to the effects of vibration that can cause false counts. One service company uses a new neutron detector, an Li-6 scintillator. Because this detector can respond to gamma rays as well as neutrons, spectral processing is required to strip out the gamma ray counts that show up as low-height pulses. The detector absorbs essentially all incident thermal neutrons, resulting in a high counting efficiency, but the metal hatch over the detector acts as a filter, giving a substantial epithermal character to the response, which lies somewhere between the thermal and epithermal responses of a wireline tool. In another novel approach, multiple Geiger Marsden tubes arrayed around the circumference of the collar detect capture gamma rays. In

principle, most detected gamma rays come not from neutron capture in the formation, but from capture in the iron of the collar. They thus reflect the neutron population near the detector as if they were neutron detectors. In practice, this tool can exhibit lithology and salinity effects. In formations containing siderite, some correlation between porosity and grain density has been observed from this design. This indicates that some of the gamma rays recorded by the detector do indeed come from the formation. A third design takes a wireline-like approach. The primary measurement uses banks of He-3 detectors at two different spacings from an americium-beryllium source. The source is centered in the drill collar rather than near the formation. Although this makes the source separately retrievable, it also filters and lowers the neutron flux at the formation. Source-to-detector spacings are similar to wireline tools. Porosity is calculated much as it is for wireline logs. A near-to-far count-rate ratio is taken. Shop calibration factors, borehole diameter, mud weight, salinity, temperature, pressure, and matrix corrections are applied to the ratio before finally calculating porosity. This procedure is superior to correcting porosities for these effects in that it reflects perturbations on what the tool measures: neutron slowing-down length, not porosity. Because of absorption of thermal neutrons by the drill collar, the measurement has an epithermal flavor. Each bank of detectors consists of three detectors distributed radially around the circumference of the drill collar. Examining the count rates from the three detectors allows for correction for tool position in the borehole.

Like the gamma ray API unit, some historical baggage accompanies the presentation and scaling of neutron-porosity logs. The curve is presented as porosity, frequently without reference to the matrix, even though the matrix does matter. Although the curve is most often scaled as apparent limestone porosity, as we have seen earlier, it is actually a measurement of the distance required for a neutron to slow down, referred to by physicists as the slowing-down length, L_s . Neutrons produced by an americium-beryllium ($\text{Am}^{241}\text{Be}^9$) isotopic source have an energy of approximately 4.3 MeV, corresponding to a speed of more than 2000 cm/ μs (44 million mph). Above approximately 0.1 eV (a mere 6,000 mph), neutrons slow down primarily through elastic collisions with the nuclei of atoms in the formation. Elastic collisions are like billiard-ball collisions: the nearer the nucleus struck is to the mass of the neutron, the more energy the neutron loses in the collision. This means that hydrogen, the nucleus of which has only a single proton (and which has altogether the same mass as the incoming neutron), is by far the most effective atom at slowing down a neutron (see [Table 3D.2](#)). Neutron slowing down by elastic collisions (thermalization) may be visualized as a random walk (see [Fig. 3D.13](#)). The average straight-line distance that a neutron manages to get from the source before it comes to thermal equilibrium with the reservoir is the slowing-down length, L_s . Note how much longer the slowing-down length for limestone is than for water, as shown in the figure.

Logging tools measure the size of the neutron cloud by looking at the falloff in neutron flux between two detectors. The falloff is inferred from a ratio of near-to-far neutron counting rates. As shown in the top half of [Fig. 3D.14](#), this ratio can be uniquely related to slowing-down length. The data points in the plot represent a variety of lithologies and porosities, but all fall along the same trend line. Although it depends on details of lithology and fluid composition, conversion of slowing-down length to porosity is straightforward, as will be seen in the discussion of macroparameters later.

The standard neutron-porosity measurement counts all neutrons, not just the unthermalized or epithermal ones. They are designed this way because the epithermal count rate represents only a small fraction of the neutrons at a distance from the source. To get the count rate (and the precision) up, all available neutrons are counted. This is a textbook example of trading accuracy for precision. While elastic scattering and, thus, the hydrogen content of the formation control epithermal neutron flux, thermal neutrons can interact with the formation in other ways. In particular, they can be captured by other elements in the formation. Neutron capture is not dominated by hydrogen, as [Table 3D.3](#) shows. This means that the standard thermal

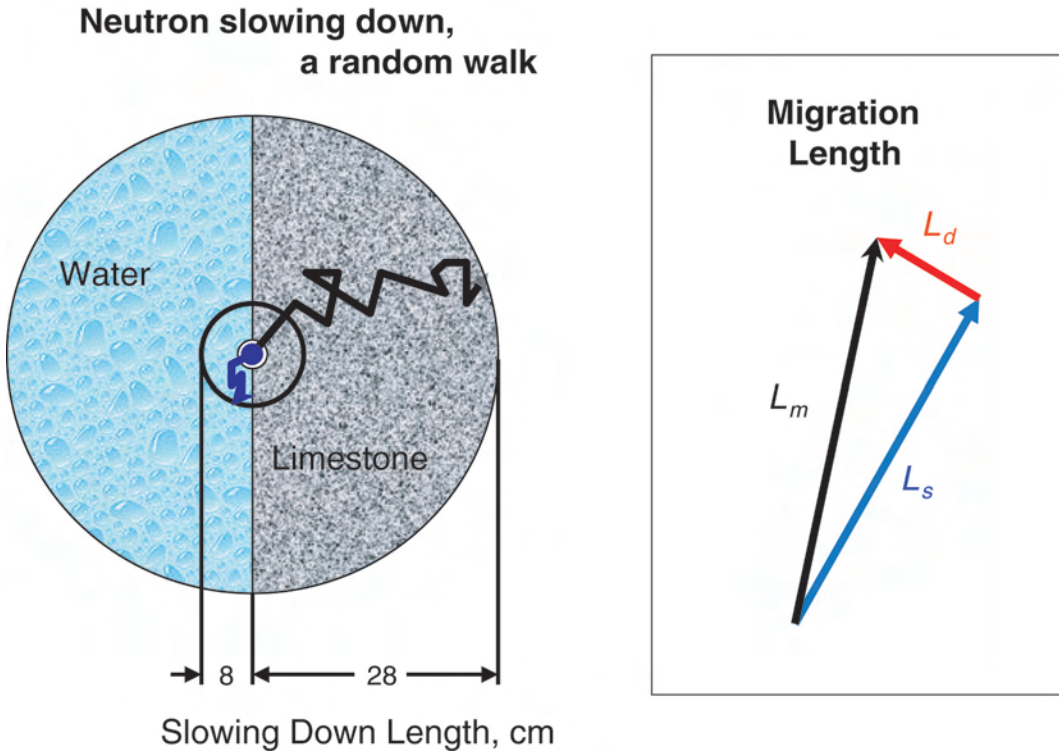


Fig. 3D.13—Neutron scattering determines the size of a cloud of neutrons surrounding a source embedded in a formation.

neutron porosity is contaminated by the subsequent diffusion distance, L_d , that the thermalized neutrons travel before they are finally captured. This is illustrated by the vector sum in Fig. 3D.13. This total distance the neutron travels, slowing down plus diffusion, is called the migration length, L_m . Because of the enduring confusion around the matrix assumed for a particular display of neutron porosity and the tenuous relationship between what the tool measures and porosity, values would be better reported in migration length than apparent porosity. It is as if density logs were always displayed as density porosity without always reporting the assumed matrix and fluid densities.

These problems with the interpretation of the standard compensated thermal neutron log have started a search for a new neutron-porosity tool with a more epithermal character. Accelerator neutron sources have begun to appear in commercial porosity tools. These tools take a more sophisticated approach than the simple CNL-like count-rate ratios used by current pulsed-neutron lifetime tools to obtain porosity. For example, Schlumberger has fielded a neutron generator-based porosity sonde that measures several different “neutron porosities” with both thermal and epithermal characters. These different measurements of porosity can be compared and combined to improve the final porosity estimate. While the measurement may be a better hydrogen-index porosity measurement, it is not the same as a standard compensated thermal neutron-porosity log.

3D.7.3 Log Interpretation. Because we are stuck with values reported in apparent neutron porosity, that is how we typically interpret them. Most interpretation schemes assume that the neutron porosity is scaled in apparent limestone units; that means a limestone matrix and water-filled porosity. If the neutron matrix is not known for certain, but the actual formation matrix

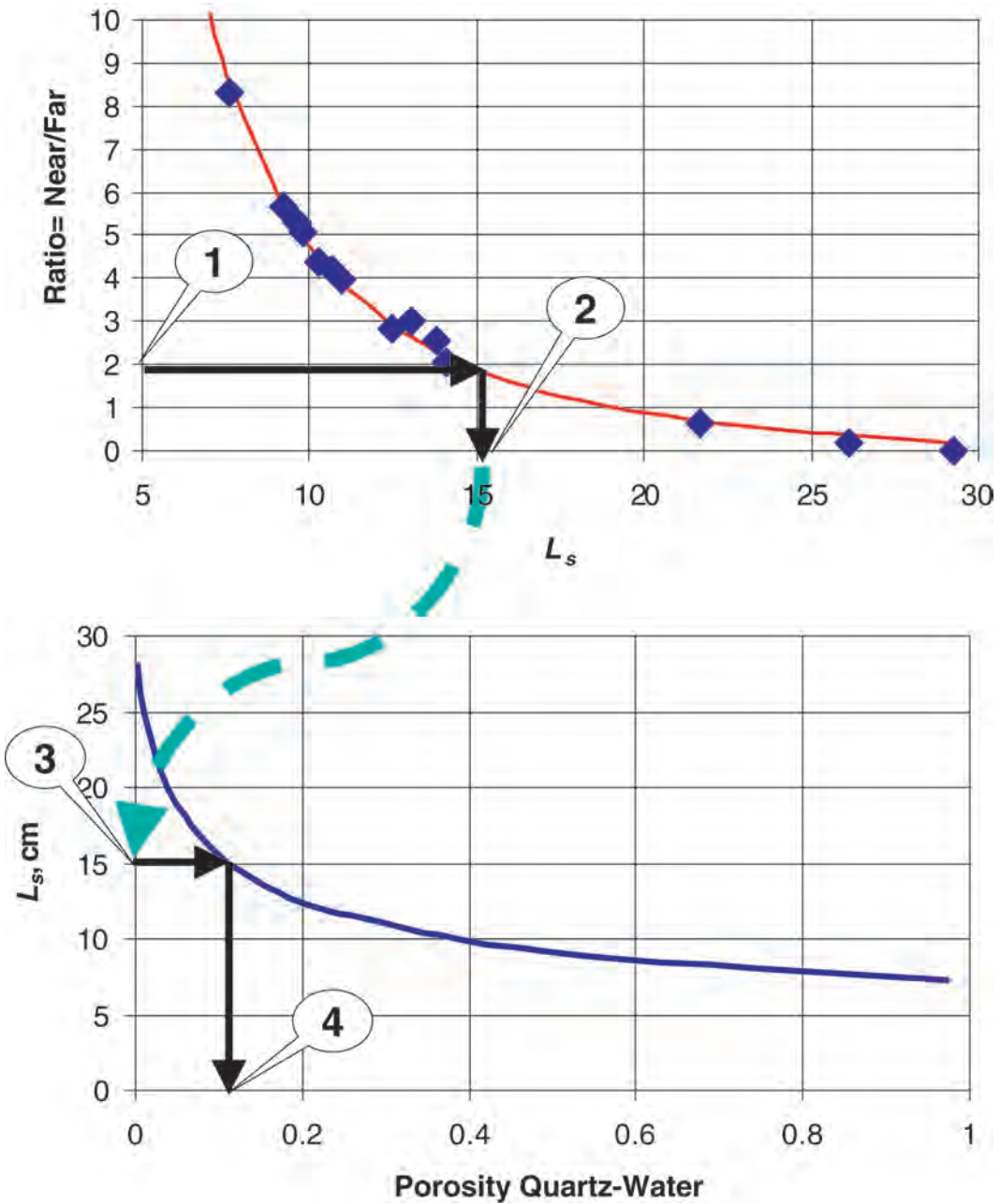


Fig. 3D.14—In an alternate neutron-porosity log-interpretation process, the intermediate response parameter, slowing-down length, relates better to basic tool response. The data points in the top plot represent a variety of lithologies and porosities, but all fall on a single trend.

is, the matrix on which the neutron-porosity log was recorded can be verified by making a density-neutron crossplot. Fig. 3D.15 shows a schematic example. If the points fall along the overlay line for the actual formation matrix, the neutron log is most likely in limestone (calcite) units. If the points fall along the calcite overlay line, the log matrix is the same as the formation matrix. In particular, if the points fall along the limestone line and the reservoir is known to be

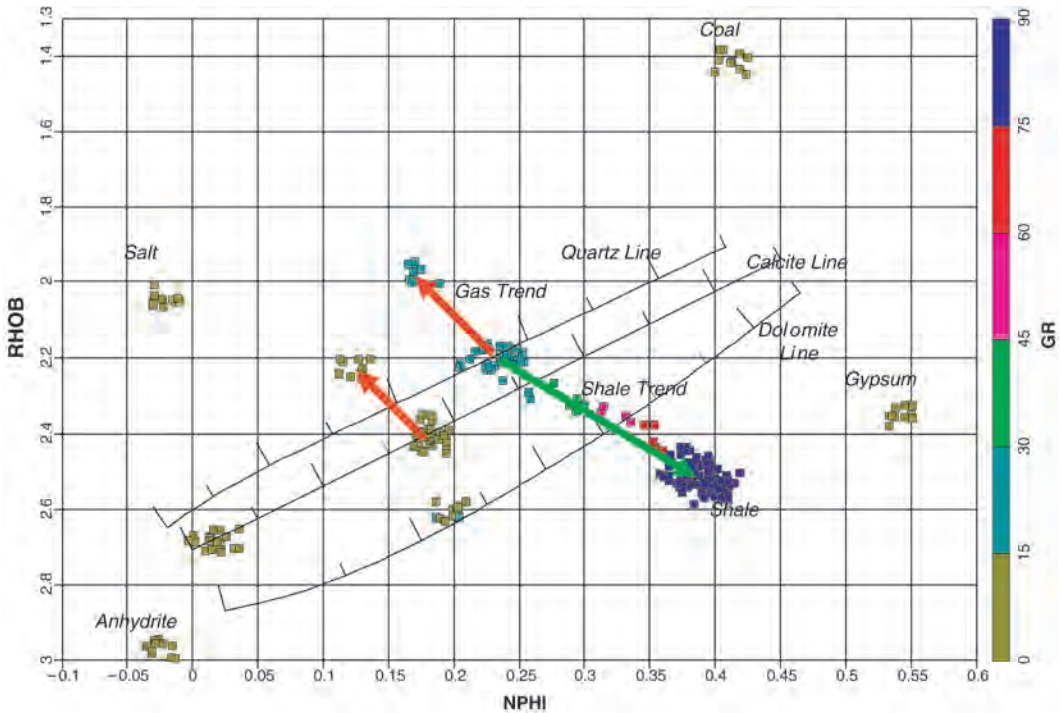


Fig. 3D.15—Neutron-density crossplot showing where the common lithologies in Fig. 3D.16 fall.

sandstone, the neutron log is in sandstone units and should be transformed to limestone units before proceeding with interpretation. As the schematic shows, gas and shale can obscure these trends.

To first order, once the log has been environmentally corrected, its reading can be characterized by a linear mixing law

$$\phi_{CNL} = \sum_i V_i \phi_{appi} \approx \sum_i V_i I_{H-i} \dots \dots \dots (3D.35)$$

In the case of a purely epithermal neutron log, the approximately equal sign can be replaced by an equal sign. Because most logs encountered are thermal neutron logs, the rest of the discussion will center on thermal neutron interpretation.

The linear mixing law implies that matrix and shale effects can be handled by a simple apparent porosity of a 0-p.u. mineral. Some examples of apparent neutron porosity (on a limestone matrix) for a number of materials are given in Table 3D.7. As can be seen from the matrix overlays on the density-neutron crossplot (Fig. 3D.15), this mixing law is not quite linear, and these apparent porosities vary with true porosity. While they are correct at 0 p.u., by the time true porosity reaches 10 p.u., quartz’s apparent porosity has climbed to -4 p.u. and dolomite’s to +6 p.u. These values also can vary somewhat with tool design. In a known, single clean lithology, it is best to use the contractor’s more elaborate transforms. However, in shaly sands or dolomitized limestone, canned transforms will not exist, and the analyst falls back on the linear mixing law. In the shaly sand case, the mixing law is of the form

$$\phi_{CNL} = (1 - V_{sh} - \phi_e) \phi_{ma,app} + V_{sh} \phi_{sh,app} + \phi_e I_{H-pf}, \dots \dots \dots (3D.36)$$

TABLE 3D.7—APPARENT THERMAL NEUTRON POROSITIES OF SOME COMMON RESERVOIR MATERIALS

Material	Apparent ϕ_{CNL}
Quartz	-0.020
Calcite	0.000
Dolomite	0.020
Siderite	0.120
Glauconite	0.380
Coal	>0.40
Kaolinite	-0.370
Illite	-0.300
Anhydrite	-0.020
Water	1.000
Brine (200 kppm)	0.920
Gas (STP)	0.002
Gas (reservoir)	0.540
Oil	-0.900

Note: "Gas (STP)" refers to gas at standard temperature and pressure (20°F, 14.7 psia), and "Gas (reservoir)" refers to gas at the nominal reservoir conditions of 200°F and 7,000 psia.

where ϕ_{app} and I_H are used interchangeably because both are calibrated to the apparent neutron porosity of pure water.

Fluid Effects. The hydrogen index of the pore fluid (see Table 3D.4) and its equivalent apparent neutron porosity (Table 3D.7) can have a much bigger effect. The difference between pure water, most brines, and typical oils is small, but as the table shows, gas can have much different neutron-response properties. While the presence of gas increases the apparent porosity seen by a density log, it decreases the apparent porosity seen by the neutron log. This is the source of "gas crossover" on neutron density-log displays (see Fig. 3D.16). Moreover, the shallow-reading density log frequently is an invaded-zone measurement, completely masking the gas effect on it. Because the neutron porosity is deeper reading, it is often the only log that can be used for gas detection. Even when not completely reading the invaded zone, the neutron-porosity log probably reads a mixture of invaded and virgin formation. This leads to a very complex response equation, even in a clean reservoir:

$$\phi_{CNL} = (1 - \phi_e)\phi_{ma,app} + f(r_i)[\phi_e S_{xo} I_{H_mf} + (1 - S_{xo})\phi_e I_{H_hc}] + [1 - f(r_i)][\phi_e S_w I_{H_w} + (1 - S_w)\phi_e I_{H_hc}], \dots \dots \dots (3D.37)$$

where $f(r_i)$ is the radial geometric function discussed above, r_i is the step-invasion profile approximation for the radius of invasion, mf refers to mud filtrate, hc refers to hydrocarbon, and w refers to formation water. Of course, shaly or multimineral interpretations add additional terms.

Furthermore, the response equation becomes decidedly nonlinear when gas is introduced. To compensate for this, an additional term was introduced to the response equation. This artifact of the gas is labeled the excavation effect.

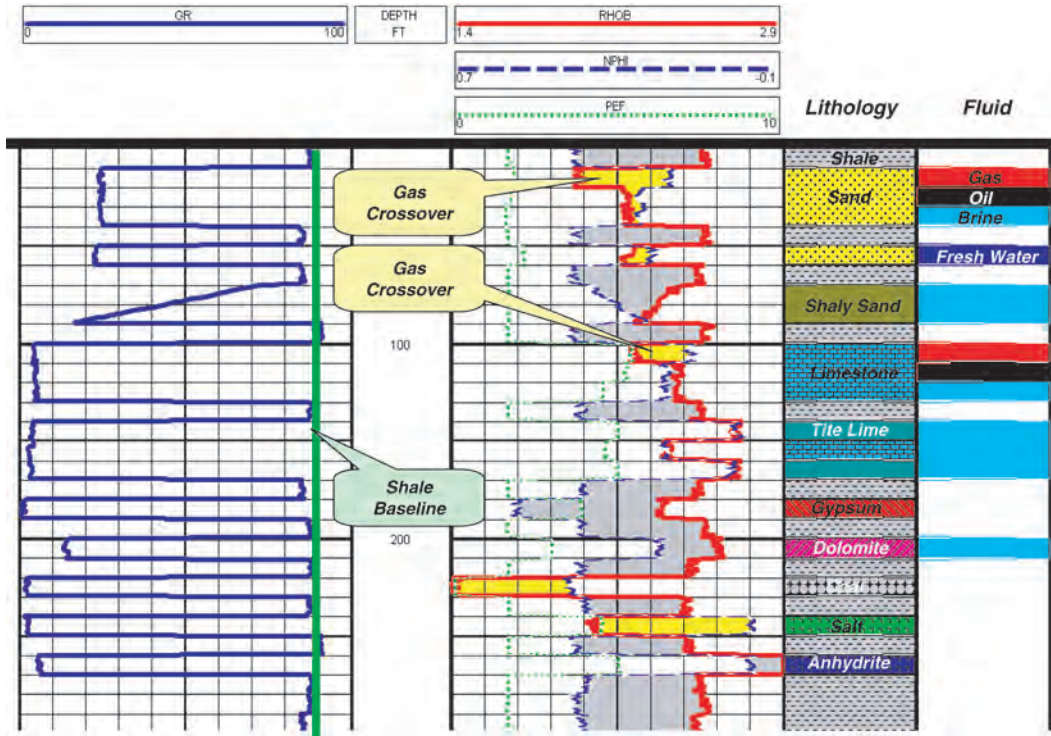


Fig. 3D.16—Schematic nuclear-log responses for some common lithologies.

Advanced Processing. The effect of formation absorption has long been recognized. Chart-book corrections for environmental effects on the thermal neutron log are extensive but confusing. This situation reflects more on the futility of attempts to handle every downhole situation with a handful of correction charts rather than any real error by service companies or log analysts. Clearly, a new approach is needed.

New log-processing methods that extend laboratory benchmark data with a more detailed mathematical description of the tool's response have been developed. Such methods replace one-size-fits-all correction charts. Effectively, log analysts using such techniques generate custom correction charts that exactly match their downhole situations. In lithologies that depart significantly from the standard limestone/sandstone/dolomite triplet, most particularly those with high capture cross-sectional minerals or fluids, the results can be dramatically different from chart-book values. With such model-based processing, corrections need not be made serially, nor are they limited to a few cases. Using laboratory benchmarked forward modeling, analysts can generate a broader range of corrections for complex lithologies and fluids. These procedures permit access to temperature and pressure regimes unattainable in laboratory formation models. This is especially important for neutron-porosity tools, whose response to porosity is both complex and tenuous (Fig. 3D.12).

Unfortunately, this approach requires iterative, forward modeling. Logging-tool response is rarely unique; many different lithology/fluid/borehole combinations can produce the same log reading. The availability of other well information and the judgment of the analyst becomes important. Such other reservoir knowledge limits the inputs to the forward model and reduces the number of trial-and-error cycles required to interpret logs with this method.

For neutron tools, there is a need to rethink what the tools measure and how we parameterize the measurement. The tools measure the size of a neutron cloud, expressed as a function of

a neutron macroparameter, migration length. In the past, several analysts have formulated the use of forward tool-response modeling to improve neutron-log interpretation in greater detail and include field examples. They range from mixing-law treatments⁷ to more elaborate use of neutron transport properties.⁸

There are two broad approaches to forward modeling of nuclear-tool response: macroparameters such as neutron migration length and Monte Carlo modeling. Macroparameters characterize tool response to bulk average formation composition (Fig. 3D.5), while Monte Carlo models treat geometry as well as composition (Fig. 3D.4).

Macroparameters. For porosity tools, macroparameters include such things as slowing-down length (when only epithermal neutrons are considered) and migration length (when thermal neutrons are considered as well). They are averaged over composition, geometry, and energy. This approach uses simplified but physically realistic theory to calculate bulk tool response. It is important to recognize that porosity tools measure neutron migration length, not porosity. A macroparameter model calculates migration length from average porosity, matrix, and fluid types. Macroparameter methods are fast, particularly compared to Monte Carlo methods, and are tractable as part of the routine interpretation process.⁹ Schlumberger published the SNUPAR program,¹⁰ which generates macroparameters for a variety of neutron and gamma ray transport tools. Once the macroparameters are understood, it is necessary to map them into the count-rate-ratio response of a particular tool design to complete the analysis. This mapping can be accomplished by regression analysis of laboratory data taken with the particular tool.⁹

Monte Carlo Modeling. When the detailed effects of geometry cannot be ignored, service companies (and, occasionally, even log analysts) resort to Monte Carlo modeling. It can account for borehole effects, standoff, invasion, thin beds, and tool design. All effects are calculated simultaneously as they occur physically and account for interactions and interdependencies that are ignored in the serial chart-book approach. The problem is not artificially divided into independent, noninteracting regimes, and no effects need be ignored.

In its most straightforward form, analog Monte Carlo modeling simulates millions of particle trajectories, tracing the progress of every particle emitted by the source. It begins with their emission at the source and follows their movement in straight-line segments. Probability distributions for interactions are accessed with random numbers generated by the computer (hence the name Monte Carlo, like a roll of the dice). These simulate particle collisions (i.e., mean distance between collisions, what the particle collides with, and its direction and speed after the collision). It is a brute-force, but fairly intuitive, approach. The models are limited primarily by the quality of the input data, particularly the nuclear cross sections of the materials involved. For real-world tools, the considerable amount of information about tool design that must be included in the model may also limit the accuracy of the Monte Carlo method.

The problem with analog Monte Carlo is that very few of the particles traced end up at the detector. Therefore, enormous numbers of particle histories must be followed to score enough counts at the detector to be statistically significant; even on fast computers, days of computations may be required. The answer is a mixed bag of tricks for ignoring some particles, steering others toward the detectors, and counting still others more than once. This approach can be mathematically valid but is quite tricky, especially with general-purpose codes like Los Alamos' Monte Carlo Nuclear Parameters (MCNP).

The biggest problem is that the models run very slowly, far too slowly to be used as the foot-by-foot forward model in an iterative interpretation process. Geometric effects are still separated from the interpretation process into the environmental-correction process. Monte Carlo modeling is generally confined to creating special-purpose correction charts. Indeed, most current service-company correction charts are generated by Monte Carlo modeling benchmarked to a few lab measurements.

3D.7.4 Pulsed-Neutron-Lifetime (PNL) Devices. PNL logs measure the die-away time of a short-lived neutron pulse. They probe the formation with neutrons but detect gamma rays. Chlorine has a particularly large capture cross section for thermal neutrons. If the chlorine in the formation brine dominates the total neutron capture losses, a neutron-lifetime log will track chlorine concentration and, thus, the bulk volume of water in the formation. For constant porosity, the log will track water saturation, S_w . The neutrons are little affected by steel casing, so this is the standard cased-hole saturation tool. Like other nuclear tools, modern PNL tools incorporate two detectors for borehole compensation. These detectors also permit the calculation of a ratio porosity. This ratio porosity is similar, but not identical, to that of a compensated neutron-porosity tool. They differ because the energy of the neutrons from the pulsed accelerator source is higher than the energy from the isotopic source used in compensated neutron logging. Also, the neutron-lifetime tools detect capture gamma rays rather than direct neutrons.

The basis of operation is similar to the other nuclear radiation transport tools in that the tool infers a cross section. In this case, the tool measures the time required for a pulse of neutrons to be absorbed by a formation. The mechanism by which the neutrons disappear is primarily thermal neutron capture. The time evolution of a pulse of neutrons follows the usual exponential decay law:

$$N_t = N_0 e^{-\frac{\Sigma_{\text{abs}}}{4550} t}, \dots\dots\dots (3D.38)$$

where Σ_{abs} is the total neutron capture cross section of the formation expressed in capture units (c.u. = $1000 \times \text{cm}^2/\text{cm}^3$, which has units of cross-sectional area per unit volume). The total capture cross section for a formation follows the standard linear volumetric mixing law discussed above:

$$\Sigma_{\text{abs}} = \sum_{i=1}^n V_i \Sigma_i, \dots\dots\dots (3D.39)$$

where V_i is the volume of a particular constituent (mineral or fluid) of a formation and Σ_i is the capture cross section of that constituent. Because the corrected tool reads the total capture cross of the formation, this equation forms the basis of interpretation. For example, in the case of a clean sand with a porosity that is filled with oil and water, the tool reading will be

$$\Sigma_{\text{abs}} = (1 - \phi) \Sigma_{\text{quartz}} + \phi S_w \Sigma_w + \phi (1 - S_w) \Sigma_o \dots\dots\dots (3D.40)$$

If porosity is known either from openhole logging or the ratio porosity measured by the pulsed neutron tool itself, the various cross sections can be looked up in a table, and it is a simple matter to solve for S_w . **Table 3D.8** lists the capture cross sections for several materials that commonly make up reservoirs. Several things can be observed on the basis of this table and the response equation above. First and foremost, for this measurement to be very sensitive to replacing oil by water in the pore space, the water salinity needs to be higher than 50,000 ppm NaCl. Otherwise, the oil and water capture cross sections are so similar that the measured formation cross section will not change perceptibly when one is substituted for the other. These sensitivities can be evaluated easily by setting up a simple spreadsheet and varying the values in the equation above. **Eq. 3D.40** also suggests the value of running this log in a baseline monitor mode or time-lapse mode. Differences between successive logging runs will depend only on differences in fluid volumes because the terms involving the unchanging rock matrix will

TABLE 3D.8—THEORETICAL MACROSCOPIC CAPTURE CROSS SECTIONS OF A FEW MATERIALS OF RESERVOIR INTEREST	
Mineral	Capture Cross Section (c.u.)
Quartz	4.3
Calcite	7.3
Dolomite	4.8
Glauconite	25
Chlorite	25
Shale	35–55
Fresh water	22
Gas	0–12
Oil	18–22
Brine (50 kppm NaCl)	35–40
Brine (200 kppm NaCl)	95–100

subtract out. In this way, no explicit knowledge of the capture cross sections of the minerals and clays is required to interpret saturation changes.

$$S_{w1} - S_{w2} = \frac{\Sigma_1 - \Sigma_2}{\phi(\Sigma_w - \Sigma_o)} \dots\dots\dots (3D.41)$$

While it is rarely done, this method is particularly valuable if a baseline run is made early in the production history of the well before S_w has had a chance to change significantly.

Other Applications. Pulsed-neutron logging tools have been applied in nonconventional ways to solve several production-logging problems. Not all of these applications make use of neutron die-away time. Instead, they monitor gamma rays from neutron activation of specific elements that can be thought of as tracers. In other applications, the pulsed-neutron ratio porosity can be used for excavation-effect-style gas interpretations.

3D.7.5 Log-Inject-Log Measurements for Residual Oil Saturation. In a variation on the baseline monitor mode of operation suggested above, residual oil saturation can be determined by a log-inject-log procedure. In this procedure, a pulsed neutron log is run over a zone of interest to get a baseline reading. Then, a brine of contrasting salinity is injected into the formation while logging pass after pass with the pulsed neutron tool. Over time, all of the movable, original formation fluids are displaced by the new brine until S_{orw} (residual oil saturation to waterflood) is achieved. Differences between the preinjection-pass and the final-pass formation capture cross sections give direct access to S_{orw} . As a bonus, changes in the capture cross-section profile over time during injection highlight permeability variations in the formation.

3D.7.6 Mechanical Integrity. Oxygen-activation flow logging may be used as a test of well integrity and zonal isolation. This is a stopwatch measurement. The neutron generator activates the oxygen in a slug of water. The time it takes the slug to move from its birthplace at the generator until it is opposite one of several remote detectors is measured. The flow velocity is just the distance from source to detector divided by the transit time. Because of the short half-life of oxygen, a particular source-to-detector spacing will be optimal only for a narrow range

of flow rates. This procedure works equally well for flow inside and behind pipe. In principle, similar measurements can discern distance to the flow.

Boron has a very high neutron-absorption cross section that greatly reduces the neutron lifetime measured by a pulsed-neutron tool. This makes it a useful tracer when used in conjunction with pulsed-neutron logging. It has been exploited in mechanical-integrity testing by injecting borated water into a well. Any place to which the boron-tagged water finds its way will stand out on the pulsed-neutron log.

Gravel-Pack Logs. In another example, silicon activation is used to evaluate gravel-pack quality.¹¹ Gravel packs are placed in oil and gas wells to prevent the accumulation of formation material that otherwise would clog wellbores and production facilities. In the conventional logging method for gravel-pack evaluation, a nonfocused density tool detects the density contrast between packing material and completion fluid. When a pulsed-neutron log is used, it detects activation gamma rays from silicon and aluminum in the packing material that have a half-life of approximately 2.24 minutes. Of the other common downhole elements, oxygen has a much shorter half-life (7.2 seconds), and chlorine, sodium, and iron have half-lives of 30 minutes or longer. Thus, a judicious choice of logging speed can maximize sensitivity to silicon and aluminum. Because the threshold for silicon activation is high (4 to 5 MeV), the measurement is very shallow, maximizing sensitivity to the gravel-pack region.

3D.7.7 Induced Gamma Ray Spectroscopy Tools. A final class of neutron logs, neutron-induced gamma ray logging, records the energy spectra of the induced gamma rays. Because elements excited by neutrons emit characteristic gamma rays, such spectra can be analyzed for elemental concentrations. Most commonly, carbon and oxygen concentrations are used to determine oil saturation, although more detailed geochemical information lies buried in the spectra.

3D.7.8 Carbon/Oxygen (C/O) Logs. Recompletion of existing wells and the search for bypassed oil in established fields require knowledge of the current oil saturation behind pipe. In fields with connate water salinity > 20,000 ppm chlorides, PNL logs provide a convenient measurement of water saturation through tubing and casing. If the salinity is low, the neutron lifetime is not determined by the chlorine concentration in the formation. If the salinity is variable, the chlorine concentration does not track the water saturation. In both cases, a PNL log fails to give useful fluid saturations. C/O logging was developed for these situations. The tools exploit inelastic scattering of high-energy neutrons off carbon and oxygen to induce gamma rays. Spectral analysis of the resulting gamma rays yields the amounts of oxygen and carbon in the volume of investigation. Unfortunately, the carbon sensitivity of the measurement is low. The depth of investigation is extremely shallow (only a few inches into the formation). Such a small volume necessarily includes a large percentage of borehole compared to the amount of formation. It is also true that although carbon is present in oil but not in water, and oxygen is present in water but not in oil, the rock matrix (particularly carbonates) may contain significant amounts of both. Together, these result in substantial borehole and formation effects that must be accounted for in the C/O log-interpretation process. To obtain a lithology compensation, most C/O tools also record neutron capture spectra in which elements such as calcium, silicon, and iron reveal themselves. Neutron capture only occurs shortly after the neutrons have slowed down to thermal energies. Buffer timing separates inelastic C/O spectra (during the neutron burst) from capture spectra (slightly after the burst). Experience with C/O logging has been uneven at best.

3D.7.9 Geochemical Logs. Geochemical logging is still struggling to find applications. Schlumberger's latest incarnation is called the environmental capture sonde (ECS).¹² Applications lie primarily in rock and clay typing for reservoir description. The goal is to add additional elemental concentrations to the formation model. Natural gamma ray spectroscopy

measurements provide potassium, uranium, and thorium data. The capture spectroscopy tool detects silicon, calcium, iron, sulfur, gadolinium, titanium, chlorine, and hydrogen.

In analyzing the data, elemental concentrations are derived and processed to obtain a complete mineralogical description. There are several sources of ambiguity. Most importantly, uncertainties in the measurements of the elemental concentrations are not explicitly accounted for. Because elemental concentrations derive from least-squares deconvolution of unresolved gamma ray spectra, they are not determined independently. Furthermore, sensitivities to different elements vary by orders of magnitude and often are very small, requiring large integration times. Finally, element-to-mineral mapping is not sufficiently unique. For best results, a limited suite of minerals must be selected before analyzing the data. The correct choice of a mineral suite depends on knowledge of local mineralogy from other experiences, such as core in an offset well. This arises in part from incomplete and inaccurate elemental analysis and partly from the nearly infinite variety of minerals and the small number of elements. As an example, quartz and opal contain the same elements but are quite different in their impact on a reservoir.

Mineralogy can in turn be related to such properties as permeability, porosity, and cation/ion-exchange capacity. Unfortunately, the minerals-to-petrophysical-properties inversion is not unique either, partly because the tool has no information about the physical configuration of the minerals (for example, grain size or fractures). Even when geochemical logging can give accurate elemental abundances, conversion of those numbers to mineralogy and petrophysical parameters such as permeability still requires a locally calibrated interpretation model. With limited goals and careful local calibration, geochemical logs do provide useful information. The logs remain tied to a local database and *ad hoc* knowledge to relate mineralogy to petrophysical properties.

3D.8 Multiple-Log Interpretation

3D.8.1 Visualization—The Multitrack Log Display. Multiple-log interpretation began with, and still revolves around, simple, quick-look visual displays. The familiar third track on a standard log display is the best example. At first glance, it may seem strange and the product of hidebound tradition. The familiar and seemingly arcane display and scales provide a great deal of information at a glance. The three principal porosity logs (density, neutron, and sonic) are scaled and placed so that they overlay and track one another in a particular clean matrix. Violated assumptions as to matrix and fluids stand out when the logs do not overlay. A particular matrix must, of course, be chosen. Most often, all logs are displayed on a limestone matrix. The standard scales are 1.95 to 2.95 g/cm³ for the density log and 0.45 to -0.15 for the neutron log. Running the density/porosity response equation presented above for water-filled limestone confirms that 1.95 g/cm³ does indeed correspond to 0.45 porosity, and 2.95 corresponds to the curious number -0.15; 140 and 40 μs/ft also correspond, but that is the subject of another chapter.

Fig. 3D.16 shows how the various nuclear-log curves would overlay on these scales for a variety of common lithologies. Note the several porosity units (1 p.u. = 1% = 0.01 fractional) of mismatch between the density and neutron logs when the matrix is sandstone instead of limestone, as is implicit in this choice of scales. This positive crossover corresponds to the apparent density porosity being larger than the apparent neutron porosity. The word “apparent” is belabored on purpose. As discussed above, logs do not read porosity until they have been passed through an interpretation model, and that interpretation model requires assumptions about rock and fluid type. In these examples, the logs are plotted as if they were water-filled limestone. If they are not, assumptions have been violated, and logs will not overlay. The 5 to 7 p.u. of matrix crossover in sandstones plotted as if they were limestones is often mistaken for a gas effect. As the simulated logs show, gas effect is in the same direction but should result in even more crossover depending on the gas properties. In gas crossover, the violated

assumptions are fluid properties. The pore space is filled with gas, not water. Gas has a lower density than water, so apparent density porosity will calculate higher than the true porosity. Neutron porosity calculates lower because gas also has a lower hydrogen index than water. Thus, apparent density and neutron porosity are “off” in opposite directions in a gas zone, resulting in large crossover in the conventional log display. As in the discussion of gas response with the individual logs, invasion often confuses the matter. The shallow penetrating density log may be reading entirely from the invaded zone, where mud filtrate (not gas) fills the porosity. With luck, the neutron log may be seeing at least some distance beyond the invasion front, so at least part of its response includes gas-filled porosity. In any case, gas crossover may be largely a neutron-log artifact, and the amount often will be less than expected. Depth (or, more precisely, pressure) also suppresses the gas crossover because gas fluid properties depend strongly on pressure.

In a known sandstone reservoir, the third track is sometimes displayed on a sandstone matrix. In this case, the density log is scaled from 1.65 to 2.65 g/cm³, and the neutron log is scaled from 60 to 0% porosity, in sandstone units. As above, 1.65 g/cm³ does indeed correspond to 60% porosity, assuming a quartz matrix density (2.65 g/cm³) and freshwater-filled porosity (fluid density equal to 1.0 g/cm³). In similar fashion to the limestone display, the curves will overlay each other exactly in clean sandstone. Generally, the neutron porosity will read to the left of the density in shales and to the right in gas-affected intervals.

3D.8.2 Visualization—Crossplots. The crossplot is another method for visualizing petrophysical data. A clever crossplot can reveal even more about a formation than a standard log-depth display. In a crossplot, the analyst plots one log value on the *x*-axis against a different log value, at the same depth, on the *y*-axis. This is repeated for all depths of interest, creating a scatterplot such as that shown in Fig. 3D.15. With luck, the location of points on such a plot can discriminate underlying mineralogy and reveal trends such as shaliness or porosity. Each pure mineral will plot as a single point. The power to discriminate depends on the independence and uniqueness of log responses to the lithologies of interest. Crossplots frequently include calculated overlay points and lines. The points locate various lithologic endpoints of interest, while the lines track the simultaneous solution of the response equations for the two logs over a range variable such as porosity, or percentage of one mineral vs. another. These response equations are simply the linear mixing-law response equations discussed in the sections above on the individual logs. With only two variables—the two logs—only two unknowns can be extracted. For example, one could determine matrix type (and its associated endpoint-log readings) and the amount of water-filled porosity.

In crossplots, nuclear logs have a clear advantage over sonic or resistivity laws. As we have seen, nuclear logs generally obey simple, linear, bulk mixing laws that have a firm basis in physics. The mixing laws for sonic and resistivity measurements are not only nonlinear but also largely empirical, with only weak connections to theory. Nonlinear terms in a mixing law show up on crossplots as curved lines (the simultaneous solution for a given set of conditions corresponds to a line). In this section, the discussion will be confined to crossplots involving only nuclear logs, although many other useful combinations are possible.

A third variable is sometimes displayed as a *z*-axis in the form of a color scale. In the example, the color of each point represents its gamma ray log reading according to the key along the right side. This highlights the location of shales and facilitates the selection of shale properties. This highlights the location of shales and facilitates the selection of shale properties needed in further log analysis. For example, the shale density and apparent neutron porosity of the shale can be read off the plot as the values corresponding to the cluster of shale points (in this case, approximately 2.5 g/cm³ and 40 p.u.).

Perhaps the most useful crossplot in log analysis is an old standard, the neutron-density crossplot. An example based on the synthetic-type logs in Fig. 3D.16 is shown in Fig. 3D.15.

By convention (and convention is very important to quick-look, visual techniques), the neutron log, expressed in limestone porosity units, is plotted on the x -axis against the density log in g/cm^3 on the y -axis, with the scales reversed (i.e., from highest to lowest density). Ideally, because both are porosity logs, points of a given porosity in a pure lithology will fall along a diagonal line. Such a line represents the simultaneous solution of the density and neutron mixing laws as a function of varying porosity. Three such lines are generally plotted as overlays on this crossplot. They correspond to a calcite, dolomite, or quartz matrix with water-filled porosity. If the neutron log were a true hydrogen index log, the lines would extend from a y -intercept corresponding to the grain density of the particular lithology (the zero-porosity limit) to a common upper-right point corresponding to 100% water (i.e., 1.0 g/cm^3 density and 100% neutron porosity). While this is largely true, neutron logs are not perfect hydrogen index measures.

As discussed above, the most commonly run compensated neutron log actually measures neutron migration length, which is a mixture of a large hydrogen index-controlled term and a smaller term controlled by neutron capture that is matrix- and fluid-type dependent. The mix of the two terms in a given tool is design dependent. For example, epithermal neutron porosity is a nearly perfect hydrogen index log. The more commonly used thermal neutron porosity includes some capture effect. This superimposes a linear, matrix-dependent term on the neutron response and a small amount of nonlinearity when hydrogen index is low, such as in gas. Because tool design affects the relative contribution of these terms, each service company generates its own, slightly different overlays for the neutron-density crossplot. This also explains apparent differences between wireline and LWD neutron-porosity measurements.

Returning to the example in [Fig. 3D.15](#), the location of points on the neutron-density crossplot can be mapped to specific lithologies, a number of which are shown on the figure. Other lithology points can be plotted from their neutron- and density-log readings taken from [Tables 3D.7](#) and [3D.5](#), respectively. Edmundson and Raymer¹³ present a more complete tabulation of pure mineral-log readings, as do most service-company chart books. Lines connecting two points on a crossplot represent the mixing of the two lithologies. Remember that water can be used as a lithology endpoint on a crossplot. This creates a porosity trend line from the pure, 0% porosity point for a given matrix to the 100% water point. Lines and points on the crossplot represent specific, simultaneous solutions of the neutron and density mixing for specific supposed lithologies. Cross-cutting lines may represent lithology trends—changes from one lithology to another or simultaneous changes in lithology and porosity. Violated assumptions can be especially revealing. A given formation thought to be a limestone may actually lie along the dolomite line, indicating that it is a dolomite or a sand plot to the lower right of the sand line and, thus, may not be as clean as hoped. The most commonly violated assumption is that the pore space is filled with a liquid (specifically water, although liquid hydrocarbons do not fall very far from the water-filled porosity line). If it were filled with gas instead, the points on the crossplot would move to the upper left, away from the water-filled porosity line. This is the same effect demonstrated by neutron-density crossover on a standard log display. More subtly, a neutron-density crossplot can flag diagenesis. For instance, dolomitization of a limestone might reveal itself as a trail of points scattering from the tight end of the limestone line to the moderate-porosity region of the dolomite one. This can be a very beneficial process, increasing the porosity of the formation. If this process were missed and the formation treated as a pure limestone, much lower porosity would be calculated, and the reservoir might be bypassed. Examination of the neutron-density crossplot should often be one of the first steps in reconnaissance log analysis. A crossplot can help the analyst identify rock types and porosity ranges and guide the selection of facies and zones.

By exploiting the principal of closure (the fact that the volume percentages of all the constituents of a formation must add up to exactly 1), three components can be extracted from a 2D crossplot. Consider a three-component system composed of sand, shale, and water-filled

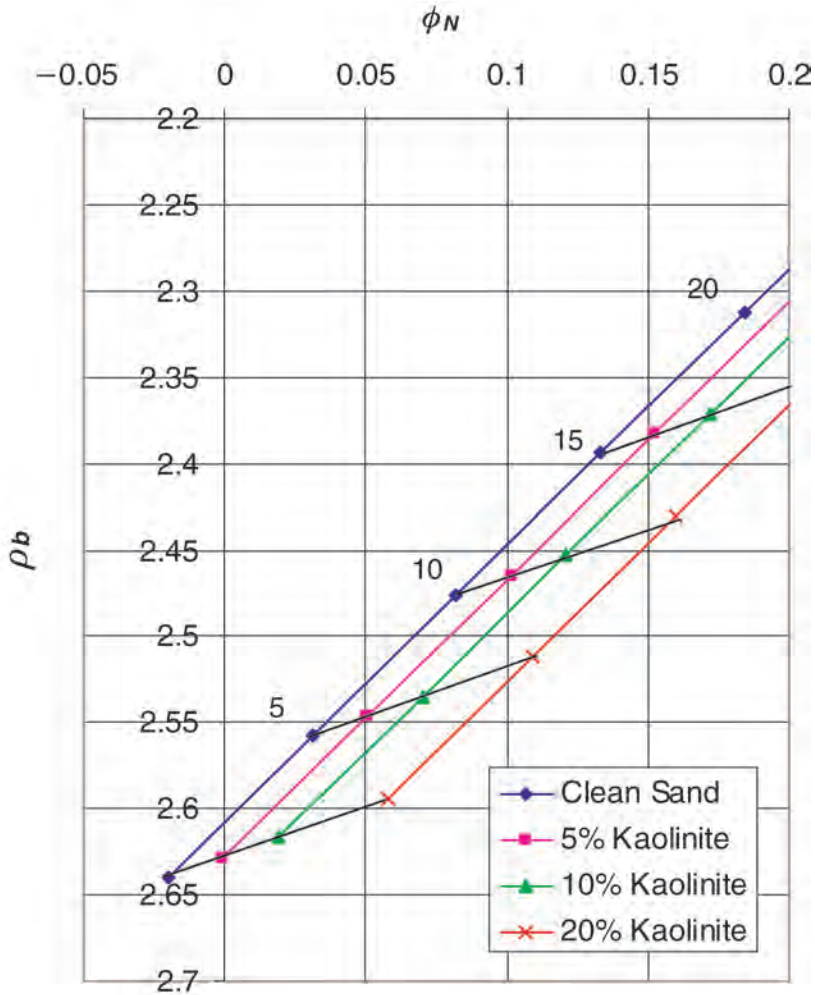


Fig. 3D.17—The neutron-density crossplot can be used to quantify clay volume and porosity in sand/shale mixtures using simple linear mixing laws to plot lines for given bulk properties (e.g., shale volumes).

porosity. Qualitatively, the shaly sand progression beginning at a single clean-sand porosity is sketched in Fig. 3D.15 as a trend line. Even if not done quantitatively, this process can indicate the direction that points would move in the presence of a change in composition. As this suggests, the neutron-density crossplot can be a useful alternative to simple gamma ray interpretation for the determination of shale volume. Fig. 3D.17 is a neutron-density crossplot overlaid with a grid of lines. The grid is calculated from the density and neutron response equations, varying relative amounts of sand, water-filled porosity, and clay.

An example of a different, less commonly used nuclear-log crossplot is shown in Fig. 3D.18. As in the neutron-density example, the sample data from the logs in Fig. 3D.16 are plotted as small squares. This display crossplots synthetic variables, not raw logs. On the x -axis is the U matrix apparent. As discussed above, this transformation converts the nonlinear P_e log to U_{mas} , a characteristic that obeys linear volumetric mixing. On the y -axis is apparent grain density from the neutron and density logs. Somewhat simplified, this is the grain density needed to produce the neutron-log porosity from the density-log reading, assuming water-filled porosity. The blue, ternary grid shows the generic endpoints for sandstone, calcite, and

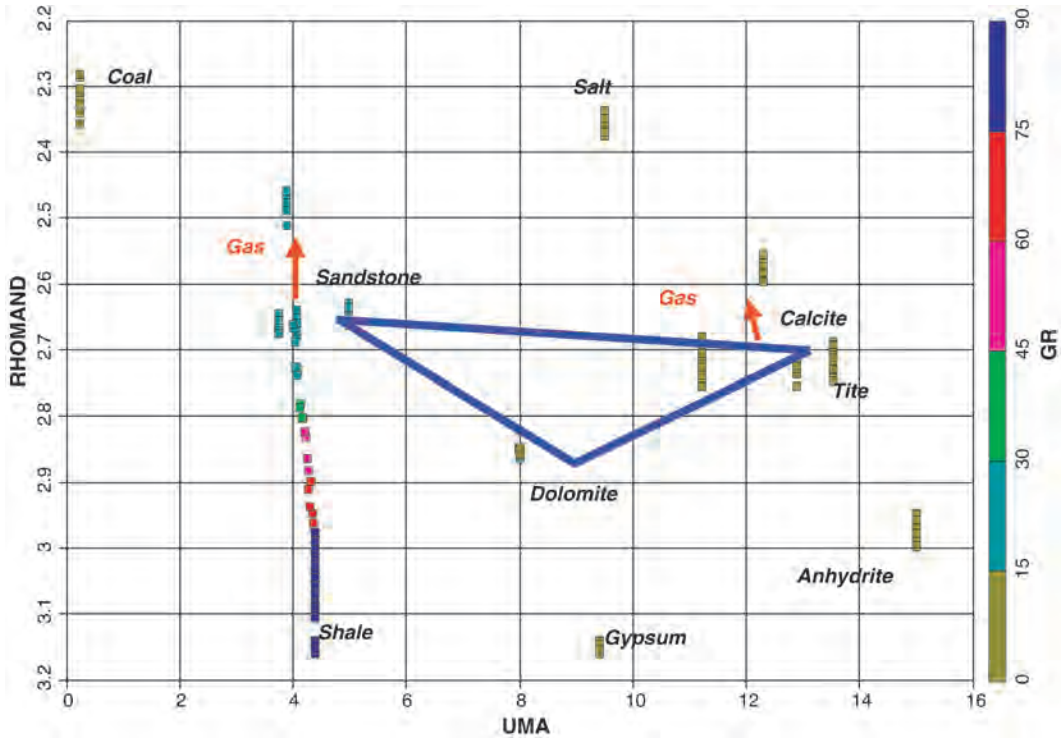


Fig. 3D.18—Example MID plot for the logs in Fig. 3D.16.

dolomite. The various labels (e.g., coal and anhydrite) mark the locations at which those minerals should ideally fall on the plot. This technique, sometimes called the matrix-identification (MID) plot, is especially useful in unwinding multicomponent lithologies, as the widely separated overlay points suggest. It gets much of its power from the fact that P_e is largely porosity independent. This accounts for the near-vertical trends in much of the overlaid data from Fig. 3D.16. As in all crossplots, uncorrected environmental effects may show up as misplaced points, the hallmark of a violated assumption. For instance, because the P_e is a very shallow measurement, barite (with its high iron content) in the mud can cause a wholesale shift of the data cloud to the right.

These are but two examples of the visualizations possible with petrophysical crossplots. Other derived parameters useful in crossplotting incorporate sonic logs. These include the n lith and m lith crossplot (where m lith and n lith are derived from combining density, neutron, sonic, and PE logs) and the crossplot of apparent matrix density (from the neutron-density crossplot) vs. apparent matrix travel time (from the neutron-sonic crossplot). These procedures can reduce the simultaneous solution of more than two log responses to an x - y plot visualization. Much of this can, of course, be done mathematically by solving multiple-log response equations simultaneously. Crossplot visualizations, however, may set limits on the possible formation constituents and define the input parameters to the formation model before attempting a mathematical solution.

3D.9 Conclusions

Despite the absence of any fundamentally new nuclear-logging measurements on the horizon, the future holds significant promise. LWD continues to mature. By getting the measurements made before significant invasion occurs, LWD mitigates one of the most serious problems of

nuclear logs: their limited depths of investigation. New array resistivity measurements better map the invaded zone. This better understanding of the invaded zone should benefit nuclear-log interpretation by letting the analyst better deconvolve the invaded-zone and virgin-zone portions of the tool response. More generally, the evolution and application of simultaneous solver techniques is accelerating. It may soon be common to solve the invasion problem explicitly, simultaneously getting all the invaded and virgin formation fluids correct while interpreting porosity and ensuring consistent solution of all of the log-response equations. This is, after all, where environmental corrections, multiple-log overlays, and crossplots have been heading all along. Nuclear logging is about tools and response models, and for the foreseeable future, progress may come more from more sophisticated handling of the response models than from better measurements. Several once-promising nuclear-log measurements failed to gain traction over the last decade. The passive spectral gamma ray measurement remains a niche tool. Geochemical logging (neutron-induced gamma ray spectroscopy) failed to mature.

Nomenclature

A	= area, L^2
A	= atomic weight
e	= natural logarithm base
E	= energy dependence of the cross section
E_{GR}	= gamma ray energy
F_{pe}	= photoelectric factor
h	= thickness traversed
h_v	= vertical thickness, L^2
I_H	= hydrogen index
$I_{H_{hc}}$	= hydrogen index hydrocarbon
$I_{H_{pf}}$	= hydrogen index pore fluid
I_{H_w}	= hydrogen index water
J	= radial geometric function
L_d	= neutron diffusion length
L_m	= neutron migration length
L_s	= neutron slowing-down length
n_e	= electron-number density
N	= a counting number
N_A	= Avogadro's number = 6.02×10^{23} molecules/gram molecular weight
N_p	= particle number density
P_e	= the photoelectric factor
P_x	= Poisson probability distribution
R	= tool reading
R_i	= tool reading for pure material
S_o	= oil saturation
S_{orw}	= residual oil saturation to waterflood
S_w	= water saturation
S_{xo}	= flush zone water saturation
U	= density-weighted F_{pe}
U_i	= tool response to flushed zone
U_{maa}	= U matrix apparent
U_T	= tool response integrated to infinity
U_x	= tool response integrated out to a radial distance x

V_{bh}	= bulk volume of hydrocarbon
V_{cn}	= volume of clean formation
V_f	= volume of fluid
V_i	= volume of a particular constituent (mineral or fluid) of a formation
V_{ma}	= volume fraction of matrix mineral
V_{ns}	= nonshale volume
V_{sh}	= volume of shale
x	= particular number of counts
Z	= average atomic number
γ	= gamma ray tool reading in API units
γ_{cn}	= gamma ray flux from 100% clean formation component
γ_f	= gamma ray flux from 100% fluid
γ_{ma}	= gamma ray flux from 100% matrix
γ_{ns}	= gamma ray tool reading in nonshale
γ_{sh}	= gamma ray tool reading in 100% shale
$\delta\phi$	= a change in flux
λ	= mean free path
μ	= mean or expected value of a quantity
ρ_b	= bulk density
ρ_e	= electron number density
ρ_{fl}	= bulk density of fluid
ρ_g	= gas density
ρ_{ma}	= bulk density of matrix mineral
ρ_{mf}	= bulk density of mud filtrate
ρ_{sh}	= shale density
σ	= standard deviation of a Poisson distribution
$\sigma(E)$	= energy-(E) dependent scattering cross section
σ_{co}	= Compton scattering cross section
Σ_{abs}	= total neutron capture cross section
Σ_i	= capture cross section of i th formation component
Σ_w	= capture cross section of water
τ	= decay time
ϕ	= porosity
ϕ_{appi}	= apparent porosity measured by a CNL in lithology i
ϕ_{CNL}	= porosity measured by a compensated neutron-logging tool
ϕ_{CNLx}	= apparent porosity measured by a CNL in lithology x (e.g., shale)
ϕ_e	= effective porosity
ϕ_i	= initial particle flux
ϕ_{ma}	= apparent matrix porosity
ϕ_N	= neutron porosity
ϕ_o	= unscattered particle flux
ϕ_{sh}	= shale porosity
ϕ_T	= total porosity

Subscripts

GR = gamma ray

hc = hydrocarbon
 i = item count or index
 t = time

References

1. Hearst, J.R., Nelson, P.H., and Paillet, F.L.: *Well Logging for Physical Properties*, second edition, John Wiley & Sons, New York City (2000).
2. Ellis, D.V.: *Well Logging for Earth Scientists*, Elsevier Science Publishing, New York City (1987).
3. Patchett, J.G. and Wiley, R.: "Inverse Modeling Using Full Nuclear Response Functions Including Invasion Effects Plus Resistivity," paper H presented at the 1994 SPWLA Annual Logging Symposium, Tulsa, 19–22 June.
4. Sherman, H. and Locke, S.: "Effect of Porosity on Depth of Investigation of Neutron and Density Sondes," paper SPE 5510 presented at the 1975 SPE Annual Technical Conference and Exhibition, Dallas, 28 September–1 October.
5. Katahara, K.: "Gamma Ray Log Response in Shaly Sands," *The Log Analyst* (1995) **36**, No. 4, 50.
6. Gadeken, L.L. *et al.*: "The Interpretation of Radioactive Tracer Logs Using Gamma ray Spectroscopy Measurements," *The Log Analyst* (1991) **32**, No. 1, 24.
7. Dahlberg, K.E.: "A Practical Model for Analysis of Compensated Neutron Logs in Complex Formations," paper PP presented at the 1989 SPWLA Annual Logging Symposium, Denver, June 1989.
8. Wiley, R. and Pachett, J.G.: "CNL (Compensated Neutron Log) Neutron Porosity Modeling, A Step Forward," *The Log Analyst* (1990) **31**, No. 3, 133.
9. Tittle, C.W.: "Prediction of Compensated Neutron Response Using Neutron Macroparameters," *Nuclear Geophysics* (1988) **2**, No. 2, 95.
10. McKeon, D.C. and Scott, H.D.: "SNUPAR (Schlumberger nuclear parameters)—A nuclear parameter code for nuclear geophysics applications," *Nuclear Geophysics* (1988) **2**, No. 4, 215.
11. Olesen, J.R., Hudson, T.E., and Carpenter, W.W.: "Gravel Pack Quality Control by Neutron Activation Logging," paper SPE 19739 presented at the 1989 SPE Annual Technical Conference and Exhibition, San Antonio, Texas, 8–11 October.
12. Herron, S.L. and Herron, M.M.: "Quantitative Lithology—An Application for Open and Cased Hole Spectroscopy," paper E presented at the 1996 SPWLA Annual Logging Symposium.
13. Edmundson, H.N. and Raymer, L.L.: "Radioactive Logging Parameters for Common Minerals," *The Log Analyst* (1979) **19**, No. 1, 38.

General References

This is a small bibliography of papers and books that compose a basic library in nuclear well logging.

Bibliographies

Mills, W.R., Stromswold, D.C., and Allen, L.S.: "Advances in Nuclear Oil Well Logging," *Nuclear Geophysics* (1991) **5**, No. 3, 209.

Myers, G.D.: "A Review of Nuclear Logging," *The Log Analyst* (1992) **33**, No. 3, 228.

Density Logs

Bertozzi, W., Ellis, D.V., and Wahl, J.S.: "The Physical Foundations of Formation Lithology Logging with Gamma Rays," *Geophysics* (October 1981) **46**, No. 10, 1439.

Tittman, J. and Wall, J.S.: "Formation Density Logging (Gamma-Gamma) Principles and Practice," *Society of Professional Well Log Analysts; Gamma Ray, Neutron and Density Logging Reprint Volume*, SPWLA (1978) paper D.

Gamma Ray Logs

Wahl, J.S.: "Gamma ray Logging," *Geophysics* (1983) **48**, No. 11, 1536.

General

Ellis, D.V.: "Neutron and Gamma Ray Scattering Measurements for Subsurface Geochemistry," *Science* (5 October 1990) **250**, 82.

Patchett, J.G. and Wiley, R.: "The Effects of Invasion on Density/Thermal Neutron Porosity Interpretation," paper G presented at the 1994 SPWLA Annual Logging Symposium, Tulsa, 19–22 June.

Tingey, J.C., Nelson, R.J., and Newsham, K.E.: "Comprehensive Analysis of Russian Petrophysical Measurements," paper S presented at the 1995 SPWLA Annual Logging Symposium, Paris, June 1995.

Tittle, C.W.: "A History of Nuclear Well Logging in the Oil Industry," *Nuclear Geophysics* (1989) **32**, No. 2, 75.

Neutron-Induced Gamma Ray Logs

Oliver, D.W., Frost, E., and Fertl, W.H.: "Continuous Carbon/Oxygen (C/O) Logging—Instrumentation, Interpretive Concepts and Field Applications," paper TT presented at the 1981 SPWLA Annual Logging Symposium, Mexico City, June 1981.

Woodhouse, R. and Kerr, S.A.: "The Evaluation of Oil Saturation Through Casing Using Carbon/Oxygen Logs," *The Log Analyst* (1992) **33**, No. 1, 1.

Youmans, A.H. *et al.*: "Neutron Lifetime, A New Nuclear Log," *Society of Professional Well Log Analysts; Pulsed Neutron Logging Reprint Volume, revised edition*, SPWLA (1979) 3.

Neutron-Porosity Logs

Ellis, D.V.: "Some Insights on Neutron Measurements," *IEEE Trans. on Nuclear Science* (1990) **37**, No. 2, 959.

Tittle, C.W.: "Porosity—An Improved Porosity Code for Processing CNL Data on Desktop Computers," *The Log Analyst* (1994) **35**, No. 1, 27.

Textbooks

Doveton, J.H.: *Geologic Log Analysis Using Computer Methods*, AAPG, Tulsa (1994).

Tittman, J.: *Geophysical Well Logging*, Academic Press, New York City (1986).

SI Metric Conversion Factors

barns	× 1.0	E - 24 = cm ²
ft	× 3.048*	E - 01 = m
in.	× 2.54*	E + 00 = cm
in. ²	× 6.451 6*	E + 00 = cm ²
in. ³	× 1.638 706	E + 01 = cm ³
psi	× 6.894 757	E + 00 = kPa

*Conversion factor is exact.

Chapter 3E

Nuclear Magnetic Resonance Applications in Petrophysics and Formation Evaluation

Stephen Prensky, SPE, Consultant and Jack Howard, SPE, Halliburton

3E.1 Introduction

Nuclear magnetic resonance (NMR) has been, and continues to be, widely used in chemistry, physics, and biomedicine and, more recently, in clinical diagnosis for imaging the internal structure of the human body. The same physical principles involved in clinical imaging also apply to imaging any fluid-saturated porous media, including reservoir rocks. The petroleum industry quickly adapted this technology to petrophysical laboratory research and subsequently developed downhole logging tools for in-situ reservoir evaluation (see the next section of this chapter).

NMR logging, a subcategory of electromagnetic logging, measures the induced magnet moment of hydrogen nuclei (protons) contained within the fluid-filled pore space of porous media (reservoir rocks). Unlike conventional logging measurements (e.g., acoustic, density, neutron, and resistivity), which respond to both the rock matrix and fluid properties and are strongly dependent on mineralogy, NMR-logging measurements respond to the presence of hydrogen protons. Because these protons primarily occur in pore fluids, NMR effectively responds to the volume, composition, viscosity, and distribution of these fluids (i.e., oil, gas, and water). NMR logs provide information about the quantities of fluids present, the properties of these fluids, and the sizes of the pores containing these fluids. From this information, it is possible to infer or estimate the volume (porosity) and distribution (permeability) of the rock pore space, rock composition, type and quantity of fluid hydrocarbons, and hydrocarbon producibility (**Fig. 3E.1**).

NMR logging provides measurements of a variety of critical rock and fluid properties in varying reservoir conditions (e.g., salinity, lithology, and texture), some of which are unavailable using conventional logging methods (**Fig. 3E.1**) and without requiring radioactive sources (**Table 3E.1**). Whether run independently as a standalone service or integrated with conventional log and core data for advanced formation and fluid analyses, NMR logging has significantly contributed to the accuracy of hydrocarbon-reservoir evaluation. During the past decade, a new generation of wireline-logging devices has been introduced into commercial service. In the past few years, logging-while-drilling (LWD) devices and downhole NMR spectrometers have also been introduced.

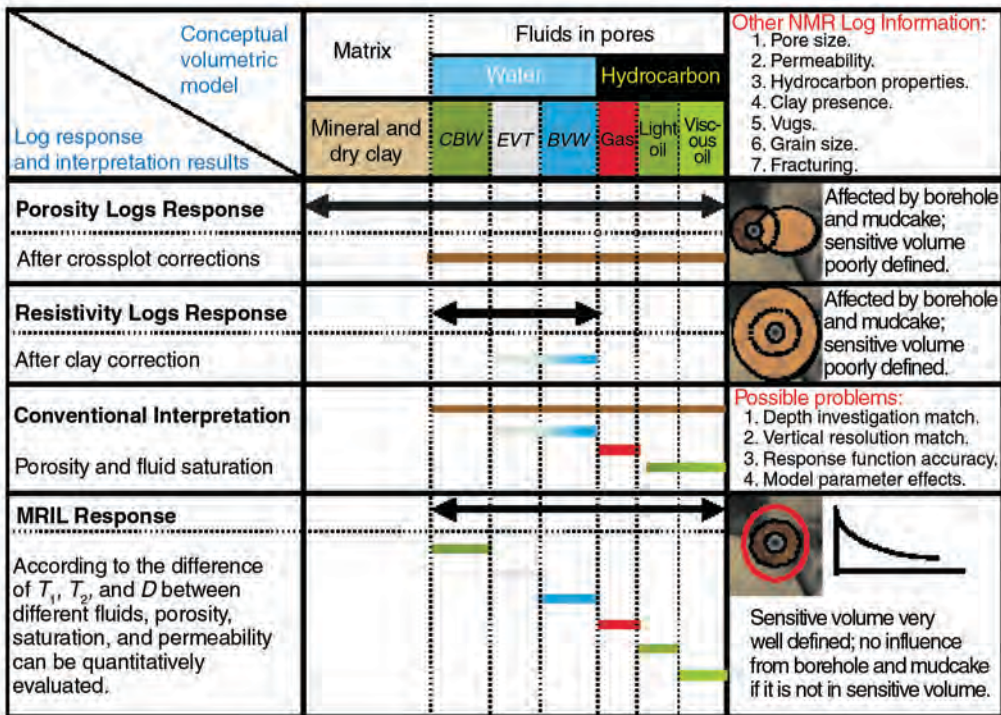


Fig. 3E.1—NMR logging-tool response compared to conventional logging tools. NMR porosity is independent of matrix minerals, and the total response is very sensitive to fluid properties. Differences in relaxation times and/or fluid diffusivity allow NMR data to be used to differentiate clay-bound water, capillary-bound water, movable water, gas, light oil, and viscous oils. NMR-log data also provide information concerning pore size, permeability, hydrocarbon properties, vugs, fractures, and grain size.

3E.2 Historical Development

Within a few years after the first successful observations of NMR in 1946, and the demonstration of free-precession NMR in the earth’s magnetic field in 1948, the petroleum industry recognized the potential of NMR measurements for evaluating reservoir rocks, pore fluids, and fluid displacement (flow).

In the early 1950s, several companies—particularly California Research (Chevron), Magnolia (Mobil), Texaco, Schlumberger, and Shell—began extensive investigations to understand the NMR properties of fluids in porous media for the purpose of characterizing reservoir rocks (porosity, permeability, and fluid content).¹⁻³ In addition to laboratory research, these investigations included proposals for logging devices and the development of well-logging methods to permit formation evaluation in situ.^{1,4} Although a number of patents for logging tools were issued in the 1950s, it was not until Chevron completed an experimental Earth’s field nuclear-magnetic-log (NML) logging device in 1958 that a functioning device was actually developed.^{1,5} Limited commercial service of these devices was introduced in 1962 by Atlas, using the Chevron centralized design, and followed in 1965 by Schlumberger, using a pad-type tool of its own design. An improved version of the Schlumberger tool was introduced in 1978. Although the potential applications for this measurement were significant, particularly in the shallow, heavy-oil fields of the San Joaquin Valley,⁶ in general, they did not live up to expectations and were not commercially successful.⁷ Tool reliability and operational limitations proved to be major obstacles: the tool was not combinable, it required high (surface) power; the signal

**TABLE 3E.1—APPLICATIONS OF NMR-LOGGING
DATA FOR RESERVOIR CHARACTERIZATION**

Petrophysical Analyses
Porosity and porosity distribution
Determination of effective porosity, ϕ_e
Determination of total porosity, ϕ_t
Evaluation for clay-bound water (CBW) and bulk-volume irreducible (BVI) water in shaly sands
Evaluation of permeability (k)
Hydrocarbon Identification, Characterization, and Typing
for hydrocarbon vs. water
for gas vs. oil
for heavy vs. light oil
Estimating viscosity
Reserves Estimates
Evaluation of low-resistivity/low-contrast pay
Evaluation of low porosity/low permeability, "tight" formations
Determinations of residual-oil saturations
Evaluation of producible (movable) fluids by means of the free-fluid index (FFI)
Characterization of Lithologies in Formations
Determinations of grain size and sorting
Mineralogy
Other Applications
Enhancing stimulation design by selection of "best sites" for well paths and perforations

level varied geographically and was generally very low as a result of the low-operational frequency (2 kHz); and the borehole had to be doped with powdered magnetite to suppress the proton signal from the mud.^{1,2,8} The final version of the Schlumberger NML tool—a centralized tool introduced in 1984—proved reliable and commercially successful and was in service until the advent of modern pulse-echo tools in 1994.

In 1978, the Los Alamos Natl. Laboratory developed a logging tool that employed permanent magnets and used a pulsed radio frequency (RF) (pulse-echo) NMR method. Although this particular design had serious limitations—such as a low signal-to-noise ratio (S/N) that prohibited continuous, nonstationary logging—the concept set the stage for the development of modern commercial NMR tools. This advance was soon followed by improvements in magnet and coil design that enabled continuous logging. During the 1980s, while developing a commercial logging tool, industry also carried out laboratory experiments to further understand NMR behavior in fluid-filled porous media and to develop petrophysical interpretations from these data. Ultimately, two wireline tools using different magnet and coil configurations emerged from these efforts: Numar's mandrel device (MRIL) and Schlumberger's skid (sometimes called "pad") design [Combinable Magnetic Resonance (CMR) tool]. Commercial logging began with these tools in 1991 and 1995, respectively. These wireline-tool designs continue to evolve (see section on Tool Design in this chapter). Recent improvements allow simultaneous acquisition of more measurements, operation in a wider range of borehole conditions, and faster logging speeds. Detailed accounts of the historical development of NMR and NMR logging are available in several published references.^{4,9–11}

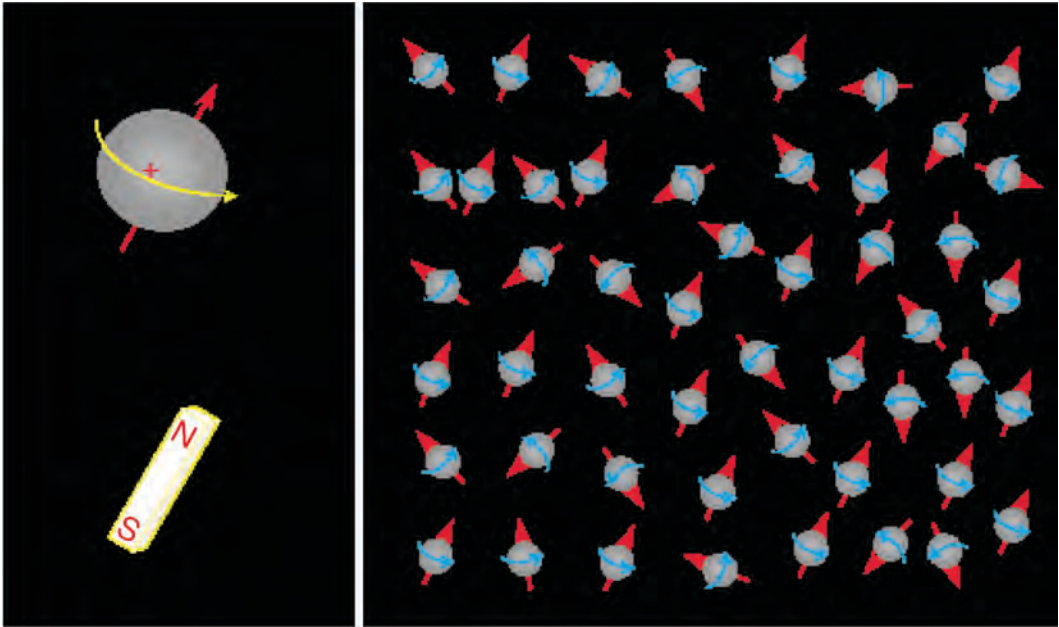


Fig. 3E.2—Because of their inherent nuclear magnetism, hydrogen nuclei (left) behave as though they are tiny bar magnets aligned with the spin axes of the nuclei. In the absence of an external magnetic field, the nuclear-magnetic axes (right) are randomly aligned.

In addition to improvements in wireline tools, new acquisition schemes and processing methods have improved the resolution, quality, and utility of the acquired data and enabled enhanced interpretation methods and data analysis. Concurrent with wireline improvements, LWD NMR logging services were being developed and have been introduced in the past few years. In a related development, a downhole NMR spectrometer is now available for use with a formation-testing tool for in-situ fluid analysis.

3E.3 NMR Physics

Atomic nuclei spin, and this angular momentum produces a magnetic moment (i.e., a weak magnetic field). The NMR technique measures the magnetic signal emitted by spinning protons (hydrogen nuclei are the protons of interest in NMR logging) as they return to their original state following stimulation by an applied magnetic field and pulsed RF energy. These signals, which are observed (measured) as parallel or perpendicular to the direction of the applied magnetic field, are expressed as time constants that are related to the decay of magnetization of the total system.

NMR devices—both laboratory spectrometers and logging tools—use strong magnets to create a static magnetic field, B_0 , that aligns (polarizes) the protons in the pore fluid from their resting (random) state to the direction of the imposed magnetic field (Fig. 3E.2).

Polarization is not instantaneous—it grows with a time constant, which is called the longitudinal relaxation time, denoted as T_1 . Once full polarization (magnetic equilibrium) has been achieved, the applied static magnetic field, B_0 , is turned off.

The protons begin to lose energy as the imposed magnetization, M_0 , decays and the protons fall out of alignment, back to their original orientation and low-energy state. The protons' angular momentum causes them to behave like tiny gyroscopes, and the loss of energy occurs during a wobbling or axial rotation (called precession) in the direction of the applied magnetic field. M_0 , also known as the bulk magnetization, provides the signals measured by NMR de-

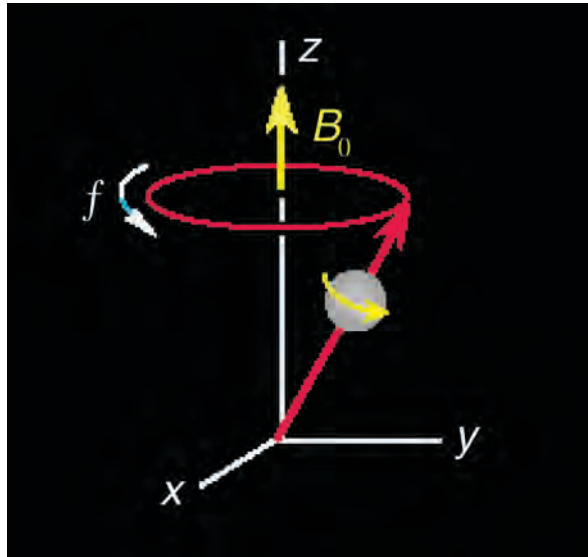


Fig. 3E.3—In an external magnetic field, the precessional frequency (f) of a nucleus depends on the gyromagnetic ratio (γ) of the nucleus and the strength of the external field (B_0).

ances. The frequency at which the energy is emitted or is initially absorbed, f , called the Larmor or resonance frequency, is proportional to the strength of the external magnetic field, B_0 , (**Fig. 3E.3**). The Larmor frequency is used to tune a NMR probe, permitting it to image very thin slices of a sample at different distances from the tool.

An antenna detects and records the decaying magnetic field generated by the precessing nuclei. At any given time, t , the strength of this magnetic field, M_z , is proportional to the number of protons, the magnitude of B_0 , and the inverse of the absolute temperature (**Eq. 3E.1**):

$$M_z(t) = M_0 \left(1 - e^{-\frac{t}{T_1}} \right), \dots\dots\dots (3E.1)$$

where $M_z(t)$ = the magnitude of magnetization at t , M_0 = the final and maximum magnetization at a given magnetic field, and t = the time that the protons are exposed to the B_0 field.

The signal recorded parallel to the direction of the applied magnetic field (z plane) is called T_1 , or longitudinal (spin-lattice) relaxation. T_1 describes how quickly the protons align within the static magnetic field. The T_1 curve is an exponential curve that characterizes the rate of change of the proton magnetization (**Fig. 3E.4**).

T_1 is the time at which the magnetization reaches 63% of its final value, and three times T_1 is the time at which 95% polarization is achieved. Full polarization of typical reservoir-pore fluids may take several seconds. Large values of T_1 (measured in milliseconds) correspond to weak coupling between the fluid and its surrounding environment and a slow approach to magnetic equilibrium, whereas, small T_1 values represent strong coupling and a rapid approach to equilibrium.¹ Different fluids, such as water, oil, and gas, have very different T_1 values. T_1 is directly related to pore size and viscosity.

Pulse NMR devices use precisely timed bursts (pulse sequences) of RF energy that generate an oscillating magnetic field (B_1) that tilts or “tips” the aligned protons perpendicular (x - y plane) to the direction of the applied magnetic field. The application of B_1 results in a change

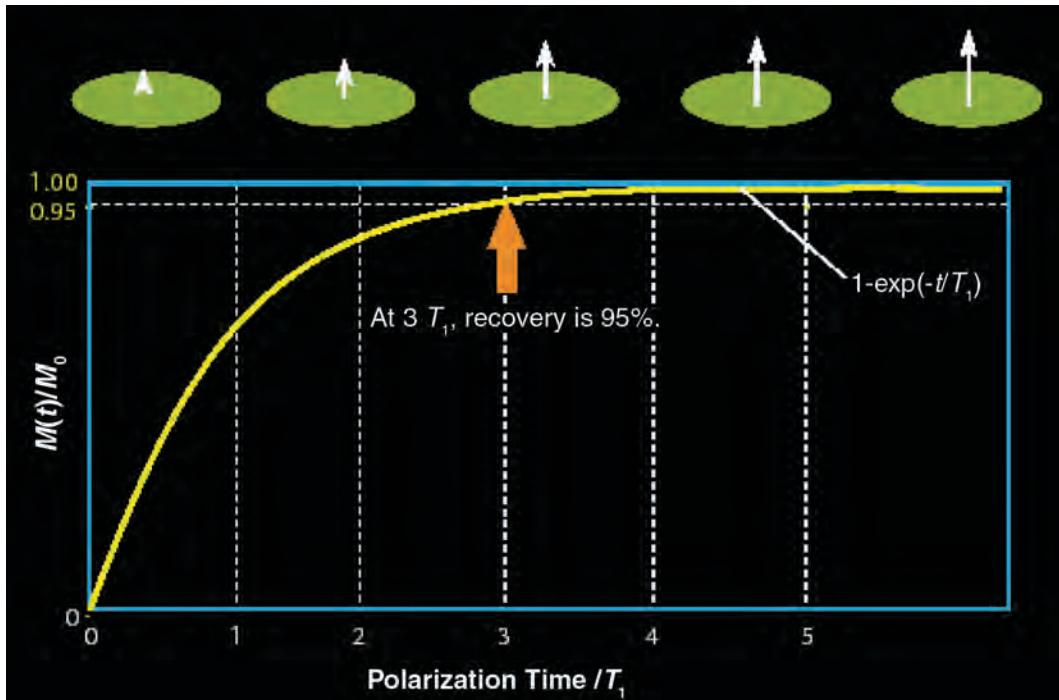


Fig. 3E.4— T_1 -relaxation (polarization) curves indicate the degree of proton alignment, or magnetization, as a function of the time that a proton population is exposed to an external magnetic field.

in energy state that causes the protons to precess in phase to one another. These changes are known as NMR.

When the B_1 field is turned off, the precessions of the protons are no longer in phase with one another, and the net magnetization decreases. In this situation, a receiver coil (antenna) that measures magnetization in the transverse direction will detect an exponential decaying signal called free-induction decay (FID); see Fig. 3E.5. NMR-logging tools use the same antenna to transmit the RF pulse (kilowatt scale) and receive the decay signal (nanovolt scale).

The FID signal measured in the x - y plane is called T_2 —the transverse or spin-spin relaxation. In contrast to T_1 , T_2 of hydrocarbons is much shorter (see Table 3E.2).

The primary objectives in NMR logging are measuring T_1 signal amplitude (as a function of polarization), T_2 signal amplitude and decay, and their distributions. The total signal amplitude is proportional to the total hydrogen content and is calibrated to give formation porosity independent of lithology effects. Both relaxation times can be interpreted for pore-size information and pore-fluid properties, especially viscosity.

In the laboratory, T_1 is generally measured by either of two pulse sequences: inversion recovery or saturation recovery. Inversion recovery consists of a 180° spin inversion followed by a variable recovery time and then a 90° read pulse. The magnetization vector is entirely in the longitudinal range and, thus, has a higher dynamic range than the other method. Saturation recovery uses a 90° pulse, followed by a 90° read pulse. Saturation recovery is generally considered the more robust and efficient method. Although the actual T_1 sampling sequence is very short—involving several short echoes trains, each of which requires only a few milliseconds—the total amount of time required to obtain the number of samples sufficient to define the T_1 spectrum is significantly greater.

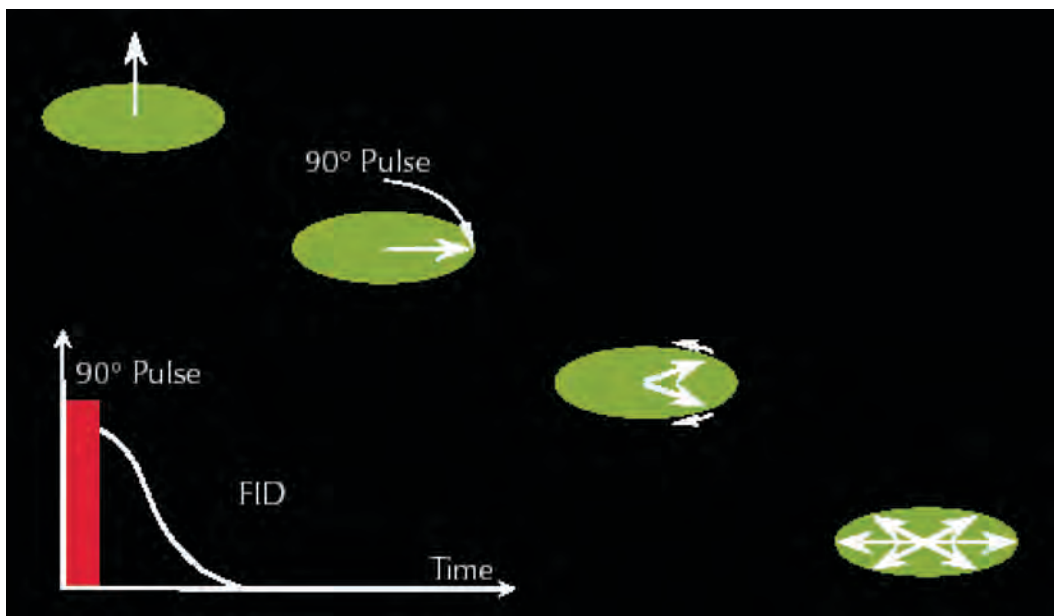


Fig. 3E.5—After application of a 90° pulse, the proton population dephases and an FID signal can be detected.

Pore Fluid	T_1 (ms)	T_2 (ms)	$\xi(T_1/T_2)$	HI	η (cp)	$D_0 \times 10^{-5}$ (cm ² /s)
Brine	1–500	1–500	2	1	0.2–0.6	4–14
Oil	3,000–4,000	300–1,000	4	1	1–1,000	3–9
Gas	4,000–5,000	30–60	80	0.2–0.4	0.011–0.014	80–100

Depending on the activation used, the computation of a T_1 spectrum requires at least 25% more, and sometimes double, the time needed for the computation of a T_2 spectrum. In NMR logging, T_1 measurement initially required either a stationary mode or very slow logging speeds. With the latest multifrequency tools, a technique used for speeding up T_1 measurements is to make simultaneous measurements of the individual steps observed during a T_1 recovery experiment in adjacent volumes; at least two such volumes are required. This technique enables T_1 acquisition in less time, thereby permitting faster logging speeds.

T_2 measurement uses the spin-echo technique,¹² in which the protons are first tipped into the transverse (x - y) plane by a 90° RF pulse and then inverted (flipped) by a subsequent 180° RF pulse at a fixed-time interval to rephase the dephasing protons. Rephasing the protons creates a detectable signal called a spin echo (Fig. 3E.6).

In practice, a sequence of pulses is used to generate a series of spin echoes (echo train) in which echo amplitude decreases exponentially with the time constant, T_2 . A variety of multiple-pulse sequences have been developed for different purposes.¹¹ In well logging and petrophysical studies, the most widely used is the Carr-Meiboom-Purcell-Gill (CPMG) sequence.^{13,14} A polarization period is followed by a 90° tip pulse, which in turn is followed by

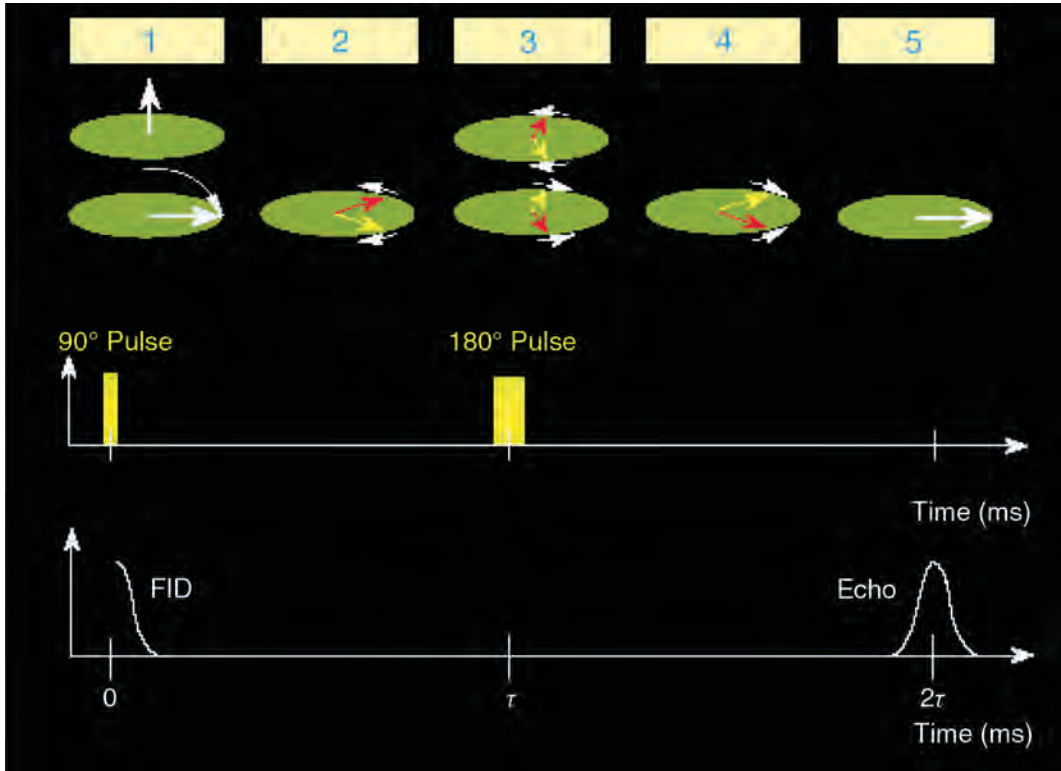


Fig. 3E.6—NMR spin echo: (1) to generate a spin echo, a 90° B₁ pulse is first applied; (2) after cessation of the 90° pulse, dephasing starts; (3) at τ, a 180° B₁ pulse is applied to reverse the phase angles and, thus, initiate rephasing; (4) rephasing proceeds; and (5) rephasing is complete, and a measurable signal (a spin echo) is generated at 2τ.

a series of alternating RF pulses and measurements of echo amplitudes detected by the logging-tool antenna. Successive 180° pulses are applied at a fixed-time interval (echo spacing, *T_E*), and the echoes are recorded between the pulses (Fig. 3E.7). By recording an echo train, *T₂* can be calculated from the decay in the height (amplitude) of successive echoes¹¹ using Eq. 3E.2:

$$M_x(t) = M_{0x} e^{-\frac{t}{T_2}}, \dots\dots\dots (3E.2)$$

where *M_x(t)* = the amplitude of the transverse magnetization (i.e., the amplitude of the spin-echo train) at time *t*, and *M_{0x}* = the magnitude of the transverse magnetization when *t* = 0 (i.e., the time at which the 90° pulse stops).

A single *T₂*-pulse sequence may involve several hundred or thousand echoes. Only the amplitude (peak) of each spin echo is measured and stored. A series of echo trains is recorded and the signals stacked to improve S/N, especially at shorter relaxation times.

When recording multiple CMPG sequences, the time period between spin-echo recovery and the next 90° CMPG excitation—during which the protons are repolarized by the static magnetic field—is called the wait time, *T_w* (Fig. 3E.8). Each CMPG sequence may use a different wait time, echo spacing, and number of echoes. An additional advantage of the CMPG sequence is that a small echo spacing, *T_E*, in the CMPG sequence can minimize the diffusion

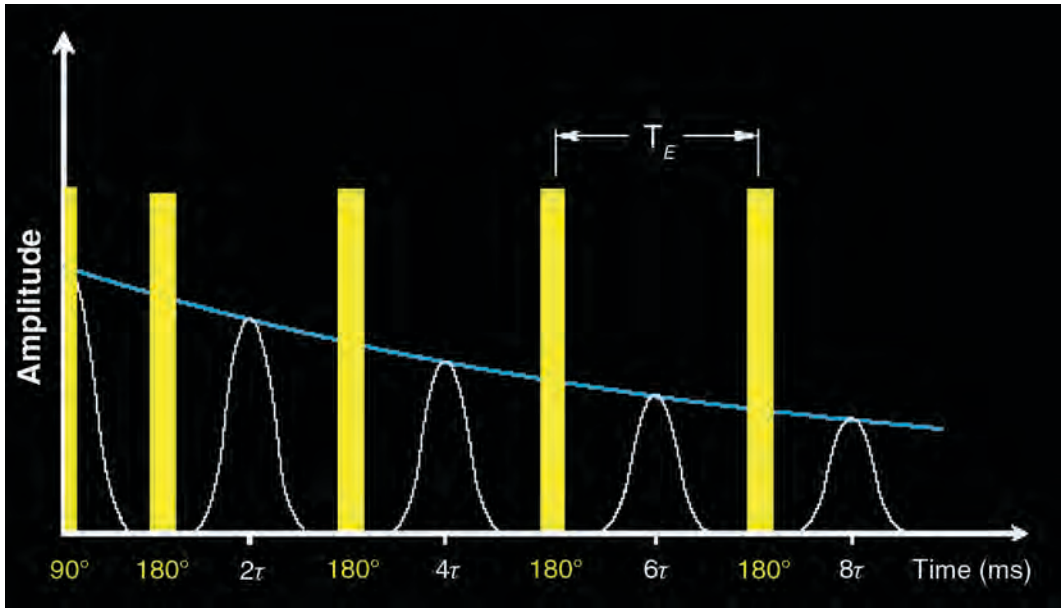


Fig. 3E.7—The CPMG pulse sequence is used in NMR logging to generate a spin-echo train; a $90^\circ B_1$ pulse is followed by a sequence of $180^\circ B_1$ pulses. Spin echoes of decreasing amplitude follow the $180^\circ B_1$ pulses.

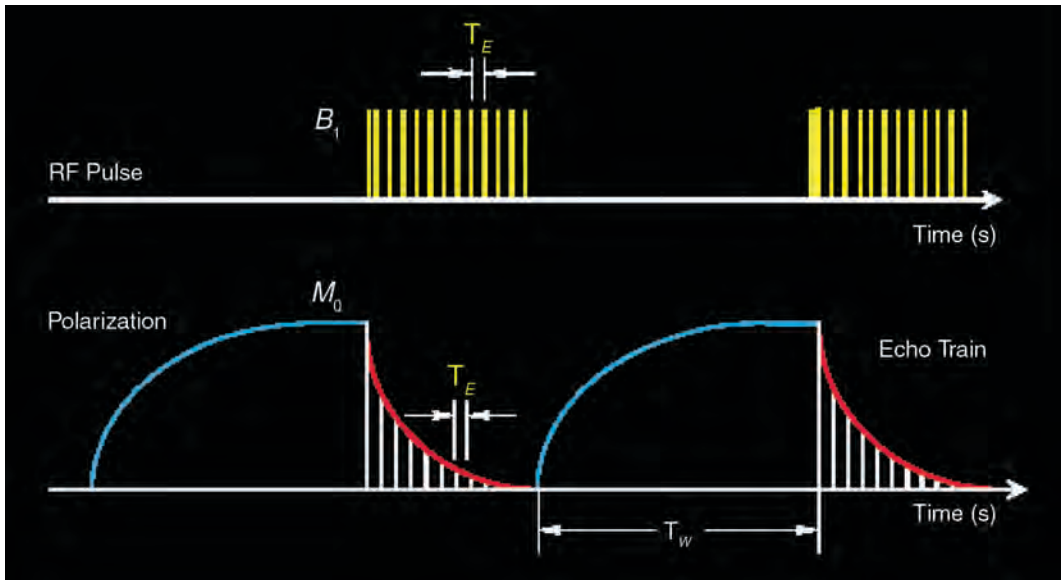


Fig. 3E.8—CPMG pulse sequences (top) and alternating polarization (T_1 -relaxation) curves and spin-echo train acquisition (bottom).

effect on T_2 . CPMG measurement sets are always collected in phase-alternate pairs (PAP) to preserve the signal and to eliminate low-frequency electronic offsets. In general, pulse NMR offers better methods to measure relaxation times and quantify liquid displacement in rock.¹⁵

3E.3.1 In-Gradient Diffusion. FID is caused by inhomogeneities in the magnetic field that are primarily caused by the existence of magnetic-field gradients. Gradients in the magnetic field occur, in part, because of the distance from the magnet to the sensitive (measurement) volume. For a given geometry, the gradient is inversely related to magnetic-field strength. Compared to laboratory and clinical NMR devices, NMR-logging tools produce a relatively weak and inhomogeneous static magnetic field. In the case of reservoir rocks, differences between the magnetic properties of the rock matrix and pore fluids may also contribute to a magnetic-field gradient. T_2 , but not T_1 , is affected by this phenomenon, which is called diffusion. In the presence of high magnetic-field gradients, diffusion effects make T_2 interpretation difficult. However, because the gradients produced by NMR-logging tools are relatively constant, they can be accounted for in T_2 interpretation. In fact, the existence of these field gradients has actually proved beneficial in NMR logging. Magnetic resonance imaging (MRI) is the process by which NMR measurements are obtained in a gradient magnetic field.

3E.4 NMR Petrophysics

3E.4.1 Laboratory Studies. Extensive laboratory studies on NMR behavior and on the properties of fluid-saturated porous media have been conducted since the inception of NMR and throughout the development of NMR-logging tools. The results from these investigations have provided the petrophysical foundation for understanding the logging measurements and for developing interpretation models and applications.

Low-field, bench-top pulse-NMR spectrometers were developed concurrently with logging tools so that wellbore measurements could be duplicated on core samples in the laboratory.^{16,17} These instruments operate and record data in the same manner as NMR-logging tools.¹⁸ Because NMR analysis is nondestructive, NMR and conventional capillary-pressure measurements can be performed on the same samples, in both the saturated and partially saturated states. Low-field spectrometers provide the ability to make repeatable measurements of rock- and fluid-NMR properties. This ability, in turn, permitted correlation and calibration of laboratory and field measurements and also permitted direct transfer of interpretation models developed in the laboratory to logging data. Where core is unavailable for NMR-log calibration, new technology and methods now allow NMR petrophysical measurements on drill cuttings.¹⁹

Laboratory NMR studies are routinely conducted for the following purposes:

- Verifying formation porosity.
- Evaluating textural effects, such as microporosity, on NMR-log response.
- Determining formation-specific models that enhance the accuracy of determining bulk-volume-irreducible (BVI) water, free-fluid index (FFI), and, ultimately, permeability.
- Developing models to identify and quantify hydrocarbons, including residual oil.
- Developing models to predict changes in pore size (facies).

Much of this work is summarized in Kenyon,²⁰ Murphy,²¹ Woessner,³ and Dunn *et al.*¹¹ The most recent laboratory studies have suggested that some established NMR core-log relationships should be further investigated to better account for data scatter.²² A related area of study not dealt with here is NMR imaging of fluid flow in core.²³

As in NMR logging, data quality is critical. To achieve the desired objectives, laboratory NMR studies should include a preplanning phase similar to that used in logging. (See the Job Planning section of this chapter).

3E.4.2 Petrophysical Properties. The basic petrophysical parameters of porosity, permeability, and producibility can be determined from either T_1 or T_2 echo-decay data. Until low-field spectrometers were developed, T_1 was the preferred acquisition method in the laboratory, where time is not a concern.^{18,20} Because T_1 measurement requires more time than T_2 , T_2 became the

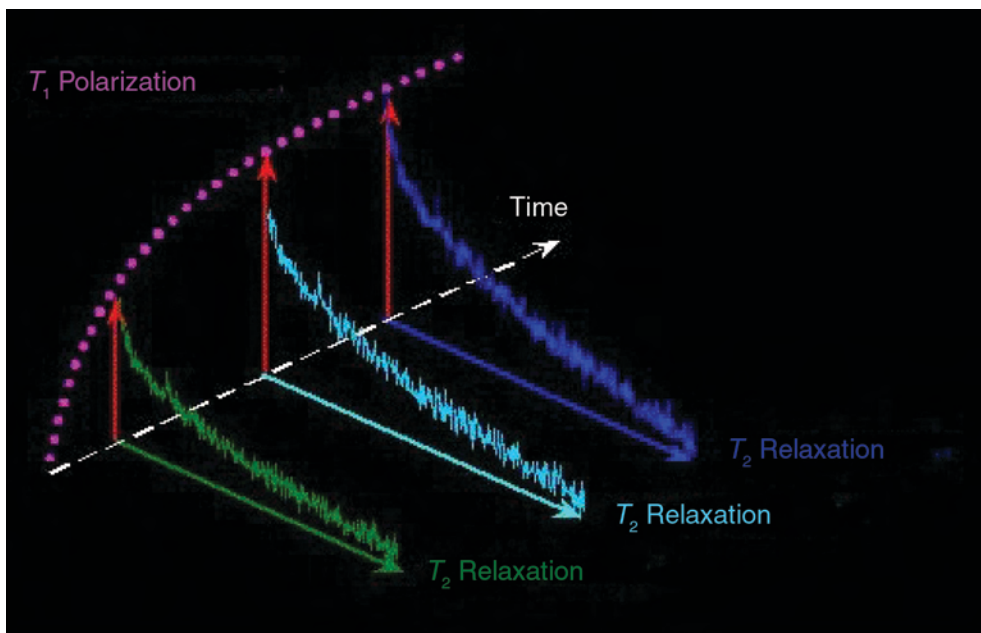


Fig. 3E.9— T_1 can be determined from a series of multiple wait-time T_2 measurements. The peak amplitudes from the T_2 measurements trace the outline of the T_1 curve (dotted).

primary acquisition mode in pulse-NMR logging because it allowed logging at speeds that were commercially viable. Fortunately, there is a correlation between T_1 and T_2 ²⁴, and T_1 can be estimated from T_2 data by extrapolating the T_2 decay-obtained-polarization pulses of different lengths (i.e., using different values of T_w ; see Fig. 3E.9).

Modern logging tools are capable of operating in either T_1 - or T_2 -acquisition modes. The logging mode is dictated by operational factors and job objectives and may, in fact, switch back and forth, as needed. (See further discussion in the LWD Tool section of this chapter.)

3E.4.3 NMR Properties of Fluids. T_1 relaxation occurs when the precessing proton system transfers energy to its surroundings. T_2 relaxation occurs through a similar transfer in energy and also through dephasing. Consequently, transverse relaxation, T_2 , is always faster than longitudinal relaxation, T_1 . The emphasis of the proton NMR techniques used in formation evaluation is on the NMR fluid response from the pore fluids where $T_2 \leq T_1$. The NMR response in solids (i.e., the non-shale/clay component of the rock matrix) is very short compared to the pore-fluid signal, and is generally not measured by laboratory or logging devices.

NMR relaxation of fluids depends on whether the fluid is measured in bulk form as a wetting-pore fluid within a rock matrix or in a gradient magnetic field. Bulk relaxation is the intrinsic relaxation property of a fluid that is controlled by viscosity, chemical composition, temperature, and pressure: $T_{2\text{bulk}} \cong T_{1\text{bulk}}$. Fluids contained within pores have different relaxation characteristics, namely those of surface relaxation.

Surface relaxation occurs at the fluid-solid interface between a wetting-pore fluid and the rock-pore walls (Fig. 3E.10) and is different from the relaxation in either the solid or the fluid, individually. Surface relaxation dramatically decreases both T_2 and T_1 and is the dominant component contributing to T_2 . When a nonwetting fluid (e.g., oil) is also present in rock pores, the nonwetting fluid may continue to relax at its bulk-relaxation rate.

Surface relaxation is expressed by the following equations (Eqs. 3E.3 and 3E.4):

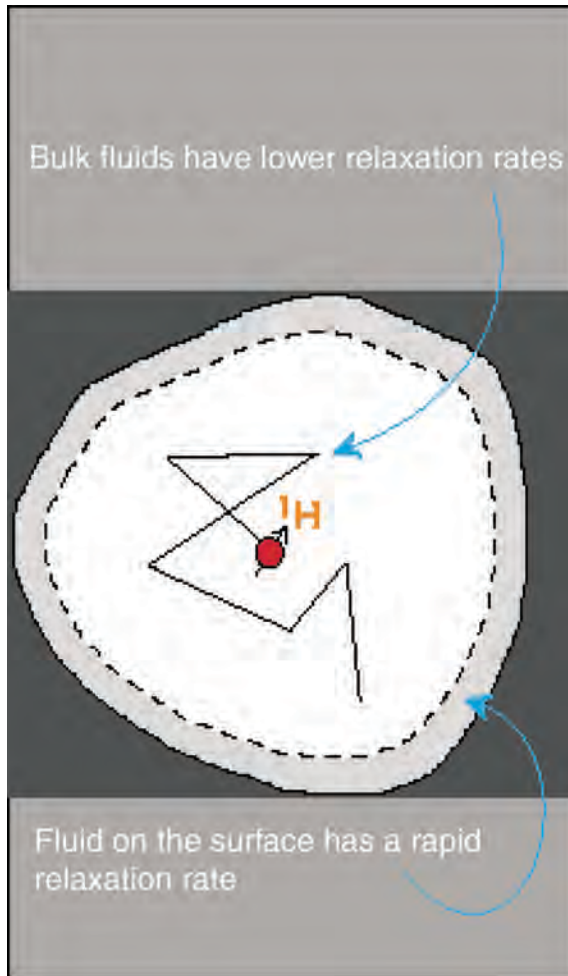


Fig. 3E.10—Schematic illustrating surface relaxation.

$$\frac{1}{T_{2\text{surface}}} = \rho_2 \times \left(\frac{S}{V}\right)_{\text{pore}} \dots\dots\dots (3E.3)$$

and

$$\frac{1}{T_{1\text{surface}}} = \rho_1 \times \left(\frac{S}{V}\right)_{\text{pore}}, \dots\dots\dots (3E.4)$$

where $\rho_2 = T_2$ surface relaxivity (i.e., T_2 relaxing strength of the grain surfaces); $\rho_1 = T_1$ surface relaxivity (i.e., T_1 relaxing strength of the grain surfaces); and $(S/V)_{\text{pore}} =$ ratio of pore surface to fluid volume.

Surface relaxivity varies with mineralogy; and, for simple pore shapes (S is the surface area of a pore and V is the volume of the same pore), S/V is a measure of pore size. In a brine-wet rock, T_2 in smaller pores will be less than T_2 in large pores; consequently, identical pore water in different rocks can have a wide range of relaxation times because of variations in surface

TABLE 3E.3—PRIMARY T_2 RELAXATION MECHANISM IN WATER-WET ROCKS		
Fluid in Pores of Water-Wet Rock	Dominant T_2 Relaxation Mechanism	Application of Capability
Brine	$T_{2\text{surface}}$	Evaluate clay- and capillary-bound water
Heavy oil	$T_{2\text{bulk}}$	Identify heavy oil as T_2 is notably less than light oil and water
Intermediate viscosity and light oil	$T_{2\text{bulk}}$ and $T_{2\text{diffusion}}$ (viscosity dependent)	Fluid typing
Gas	$T_{2\text{diffusion}}$	Fluid typing

relativity. Laboratory studies have demonstrated that in water-wet rocks, the surface and volume ratio (S/V) is also a measure of permeability.

Fluids controlled by surface relaxation exhibit T_2 values that are not dependent on temperature and pressure. For this reason, laboratory NMR measurements made at room conditions are commonly used to calibrate formulas used to estimate petrophysical parameters such as permeability and bound water.^{25,26}

Diffusion-induced relaxation occurs when a significant gradient exists in the static magnetic field. Molecular diffusion in this gradient causes additional dephasing that contributes to increased T_2 relaxation. In addition to the magnetic-field gradient, diffusion is also controlled by inter-echo spacing and fluid diffusivity, viscosity, molecular composition, temperature, and pressure.

Bulk-fluid processes and surface relaxation affect both T_1 and T_2 , while diffusion only affects T_2 relaxation. All three processes are independent and act in parallel according to the following equations (Eqs. 3E.5 and 3E.6):

$$\frac{1}{T_2} = \frac{1}{T_{2\text{bulk}}} + \frac{1}{T_{2\text{surface}}} + \frac{1}{T_{2\text{diffusion}}} \dots\dots\dots (3E.5)$$

and

$$\frac{1}{T_1} = \frac{1}{T_{1\text{bulk}}} + \frac{1}{T_{1\text{surface}}} \dots\dots\dots (3E.6)$$

The relative importance of the three diffusion-relaxation mechanisms depends on the fluid type in the pores (e.g., water, oil, or gas), the sizes of the pores, the strength of the surface relaxation, and the wettability of the rock surface (see Table 3E.3).

3E.4.4 T_2 Decay. Eq. 3E.2 states that the T_2 decay associated with a single pore size in water-saturated rocks is proportional to the pore size.²⁰ In fact, because reservoir rocks typically comprise a distribution of pore sizes and frequently contain more than one fluid type, a CPMG T_2 spin-echo train actually consists of a distribution of T_2 decays, rather than a single T_2 decay. In these cases, the exponential decay is described by Kenyon *et al.*²⁷ as follows:

$$M(t) = \sum M_i(0) e^{-\frac{t}{T_{2i}}} \dots\dots\dots (3E.7)$$

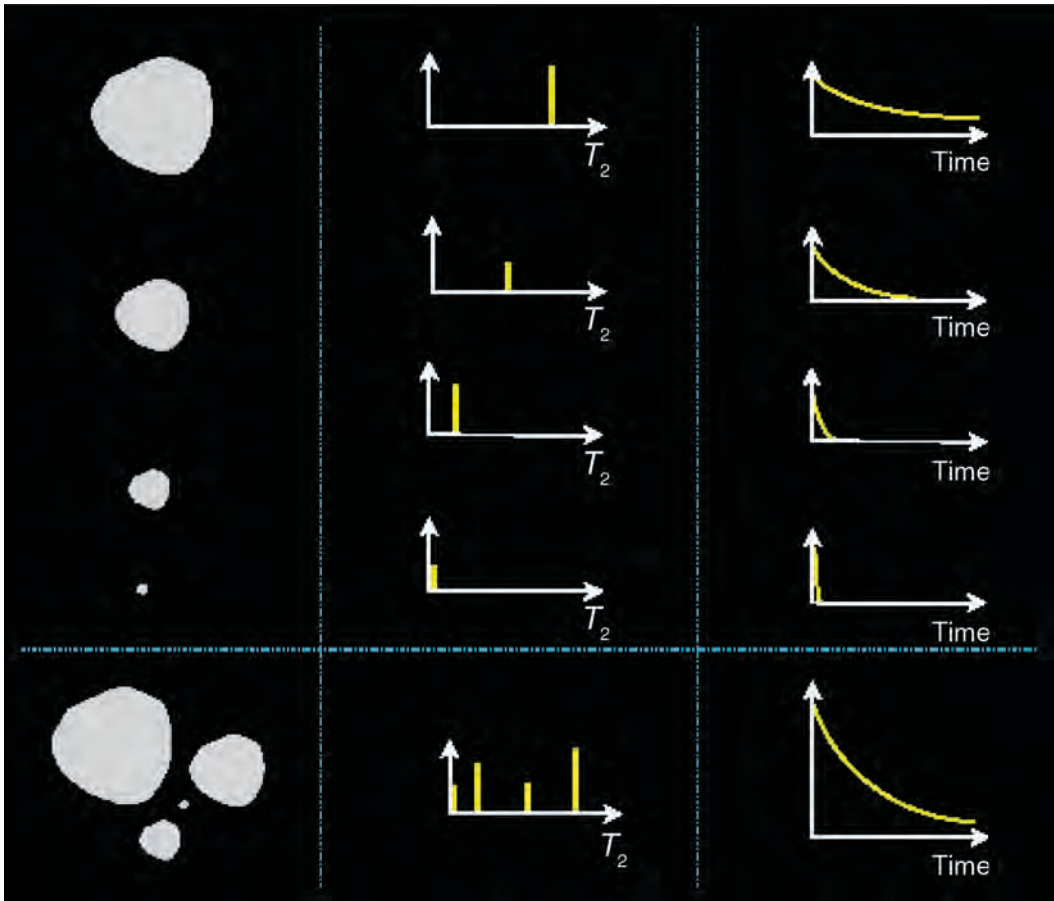


Fig. 3E.11—A 100% water-saturated pore (upper left) has a single T_2 value (upper center) that depends on pore size and, thus, its spin-echo train exhibits a single exponential decay (upper right) that also depends on pore size. Multiple pores at 100% water saturation (bottom left) have multiple T_2 values (bottom center) that depend on the pore sizes and, thus, their composite spin-echo train exhibits multiexponential decay (bottom right) that also depends on the pore sizes.

where $M(t)$ = measured magnetization at t ; $M_i(0)$ = initial magnetization from the i th component of relaxation; and T_{2i} = decay constant of the i th component of transverse relaxation. The summation is over the entire sample (i.e., all pores and all different types of fluid).

Fig. 3E.11 illustrates the multiexponential decay character of a porous medium containing pores of different sizes and a single wetting phase. Surface relaxation dominates when a short inter-echo spacing is used and the formation is only brine saturated. Under this condition, T_2 is directly proportional to pore size. When all pores are assumed to have similar geometric shape, the largest pores (see Fig. 3E.11, left column) have the lowest S/V and, thus, the longest T_2 . Medium-size pores have smaller S/V, yielding shorter T_2 values. The smallest pores have the highest S/V and the shortest T_2 values.

Eq. 3E.7 can also be expressed as follows:²⁸

$$M(t) = \sum M_{0i} e^{-\rho_2 \left(\frac{S}{V}\right)_i t}, \dots \dots \dots (3E.8)$$

where $(S/V)_i$ is the surface-to-volume ratio of the i th pore. When $t = 0$, the following is true:

$$M(0) = \sum M_{0i} \quad \dots\dots\dots (3E.9)$$

If the measured magnetization for 100% bulk water, $M_{100\%}(0)$, is known, then $M(0)$ and M_{0i} can be calibrated to porosity by the following equation:

$$\phi = \frac{M(0)}{M_{100\%}(0)} = \frac{\sum M_{0i}}{M_{100\%}(0)} = \sum \frac{M_{0i}}{M_{100\%}(0)} = \sum \phi_i, \quad \dots\dots\dots (3E.10)$$

where ϕ = calibrated porosity of the formation, ϕ_i = calibrated porosity associated with all pores of the i th pore size (also known as the incremental porosity). Therefore, the T_2 distribution (in the form of the amplitudes, M_{0i} , associated with the time constants, T_{2i} , is calibrated to the porosity distribution (i.e., the individual pores ϕ_i with the associated time constants T_{2i}).

If the rock is water-wet and the pores are partially saturated (i.e., the pores contain oil and/or gas in addition to water), then the total signal comprises contributions from each component in the following equation:

$$M(t) = \sum M_{0i} e^{-\rho_2 \left(\frac{S}{V}\right)_i t} + M_{\text{oil}} e^{-\frac{t}{T_{2\text{oil}}}} + M_{\text{gas}} e^{-\frac{t}{T_{2\text{gas}}}}, \quad \dots\dots\dots (3E.11)$$

where M_{oil} = magnetization produced by oil protons in the pores, M_{gas} = magnetization produced by gas protons in the pores, $T_{2\text{oil}} = T_2$ of oil measured with a CPMG sequence, and $T_{2\text{gas}} = T_2$ of gas measured with a CPMG sequence.

In a brine-saturated rock, the T_2 decay spectrum represents a pore-size distribution. However, when nonwetting fluids (e.g., oil or gas) are present, the T_2 spectrum includes a bulk response from the nonwetting fluid, in addition to the pore-size response. Pores containing the nonwetting fluid either appear in the spectrum at a decay time that is faster than is normally associated with the pores, or do not appear at all if the surface layer is too thin. This behavior affects the appearance of the T_2 spectrum and associated T_2 distribution but not the total signal amplitude (i.e., porosity).

3E.4.5 Data Fit—Inversion. The raw data recorded by an NMR device are a series of spin-echo amplitudes (echo train) as a function of time, usually at fixed time increments (bins). These NMR measurements are statistical, and stacking is required to improve the precision of the log outputs. The precision depends on formation-fluid properties, activation (acquisition) type, and the number of pulses stacked.²⁹ The data are mathematically inverted (mapped) by use of a best-fit curve to produce a distribution of T_2 values as a function of relaxation time (Figs. 3E.12 and 3E.13). Initially, biexponential-fitting algorithms were used³⁰; however, T_2 decay in fluid-saturated rocks is multiexponential, because of this, multiexponential models were developed and are commonly used for inverting the data.¹¹ The inverse solution (T_2 distribution) is a function of both the measured echo data and the chosen smoothness (regularization) for the inversion. However, because regularization is controlled in part by the S/N, the fit that is actually used is not unique; that is, there can be a number of differently shaped T_2 distributions that fit the original echo-decay curve. In general, the area under the T_2 -distribution curve (porosity) and the general location in time of the high-porosity bins are robust; however, caution is advised when interpreting the fine details of the distribution.³¹ Because the spin echoes are measured over a very short time, an NMR tool travels no more than a few inches

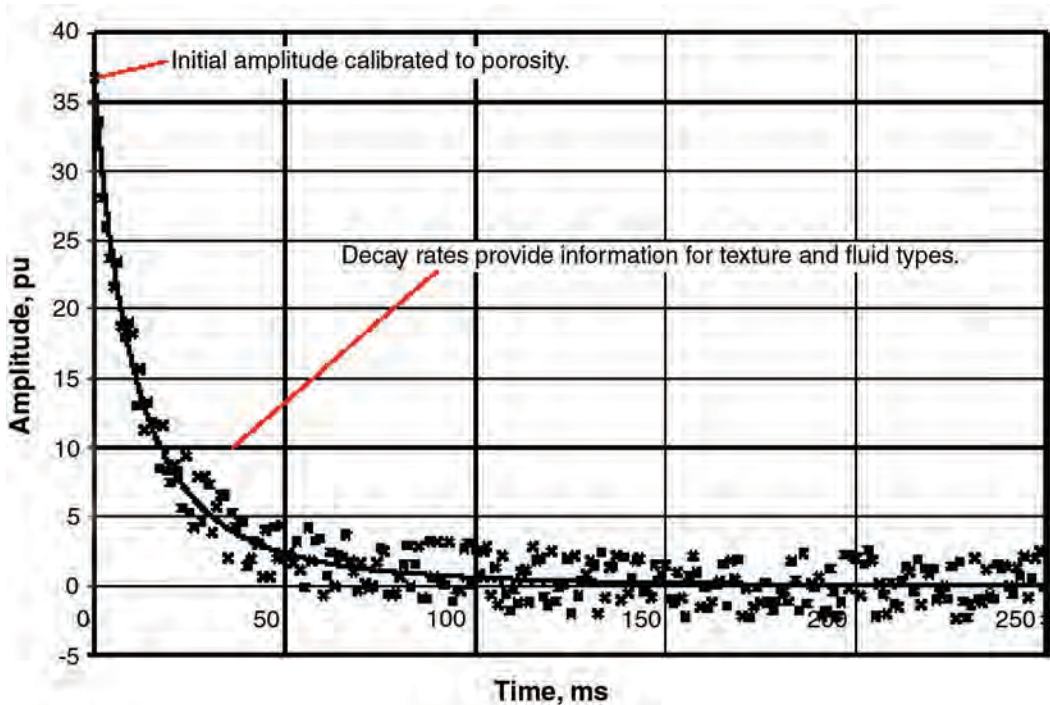


Fig. 3E.12—Spin-echo-decay train. The amplitudes of the spin echoes are recorded over time. A best fit line is applied to the data before inversion. In this example, the raw spin-echo measurements recorded at $T_E = 1$ ms are shown together with a data-fitting curve (solid).

along the wellbore while recording the spin-echo train; thus, the recorded spin-echo data can be displayed on a log as a function of depth.

3E.4.6 T_2 Distribution. The mathematical statement (Eq. 3E.10 and Eq. 3E.11) that T_2 distribution observed in water-saturated rock represents the pore-size distribution and porosity of the rock has been confirmed using mercury-injection capillary pressure (MICP) methods (see Figs. 3E.14 and 3E.15).^{32,33}

NMR responds to pore-body size, and MICP responds to pore-throat size.^{32,34–36} In elastic rocks in which there is a good correlation between pore-body and pore-throat size, there is often good qualitative agreement between NMR and MICP data, as Figs. 3E.14 and 3E.15 illustrate. The NMR porosity, reflected in the T_2 distribution, is a spectrum comprising rock matrix and fluid components (see Fig. 3E.16).

Although matrix minerals and dry clay may contain hydrogen atoms in the form of hydroxyl groups, the T_1 relaxation times of these nuclei are too long to be polarized by a moving NMR-logging tool, and their T_2 relaxation times are too short to be recorded.³⁷ The fluid component is subdivided into bound and free subcomponents. The hydrogen nuclei of clay-bound water are adsorbed on the surfaces of clay grains. These hydrogen protons can be polarized by NMR-logging tools and recorded when a sufficiently short T_E is used.³⁸ Similarly, hydrogen protons in capillary-bound water and movable fluids (e.g., free water, mud filtrates, oil, and gas), are polarized and recorded by NMR-logging tools with appropriate values for T_E and T_W .

The porosity and pore-size information from NMR measurements can be used to estimate producible porosity (i.e., the movable fluids) and permeability and for hydrocarbon identification (see the Applications section of this chapter).

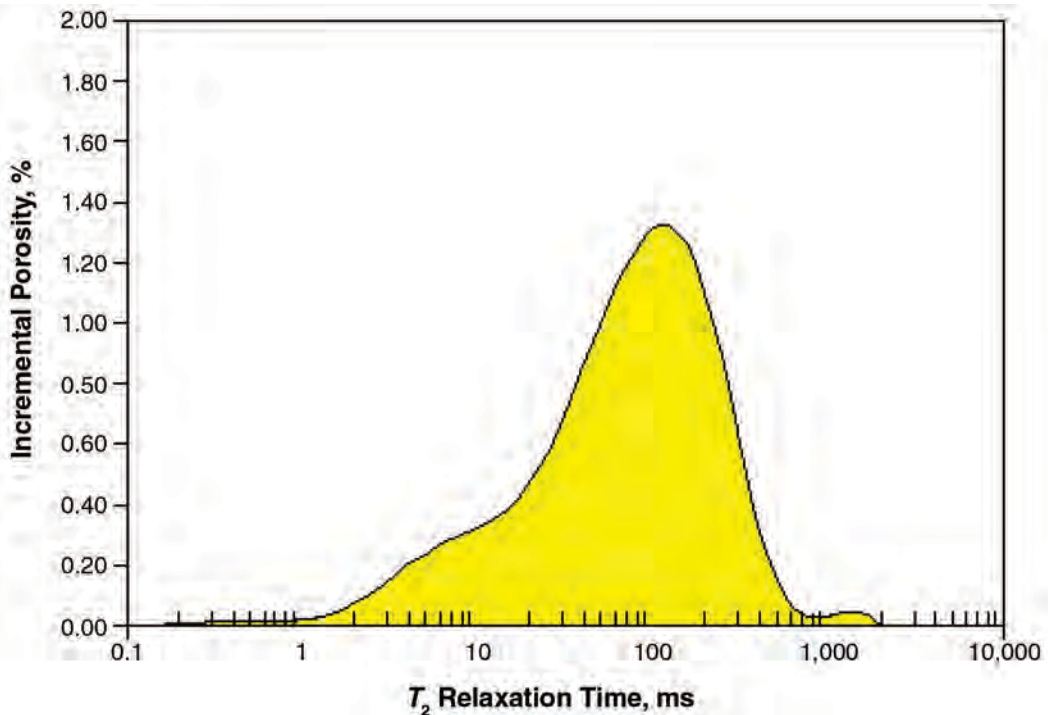


Fig. 3E.13— T_2 distribution. Mathematical inversion is used to convert the spin-echo-decay data to a T_2 distribution. This distribution is the most likely distribution of T_2 values that produce the echo train. With proper calibration, the area under the T_2 -distribution curve is equal to the porosity. When the rock is water-saturated, this distribution will correlate with pore-size distribution. The presence of hydrocarbons will affect the T_2 distribution depending on the hydrocarbon type, viscosity, and saturation.

3E.5 Logging Tools

Compared to laboratory or clinical NMR, the dimensions of a typical borehole and the nature of continuous logging impose severe constraints on the physics, equipment, and operation of NMR-logging tools. Unlike laboratory devices, logging measures an external sample by use of a weaker magnetic field while in motion relative to the sample.

3E.5.1 NML Tool. The NML tool—the first generation of NMR logging (1960–1994)—was an Earth’s field device that measured the free-induction decay in the Earth’s magnetic field. Proton polarization (alignment) was achieved using a magnetic field produced by a coil energized with a strong direct current. Each experiment required several seconds to allow complete polarization. The power was turned off, and the same coil was used to receive the free-induction signal.

There were a number of problems inherent in this technology. NML devices measured the proton signal in the borehole fluid as well as in the surrounding formation. Magnetite powder was circulated into the mud system to cancel the borehole hydrogen signal thereby preventing it from overwhelming the formation signal. This was a time-consuming process. The low intensity of the Earth’s magnetic field (0.5 gauss) resulted in a low S/N. The NML had a large dead time (i.e., time between the cessation of the static magnetic field and the first measurement), approximately 20 ms; pore fluids with relaxation times less than the dead time were not measurable. The initial signal amplitude had to be extrapolated backwards from the subsequent free-induction decay data. The NML could not distinguish between oil and water or measure total

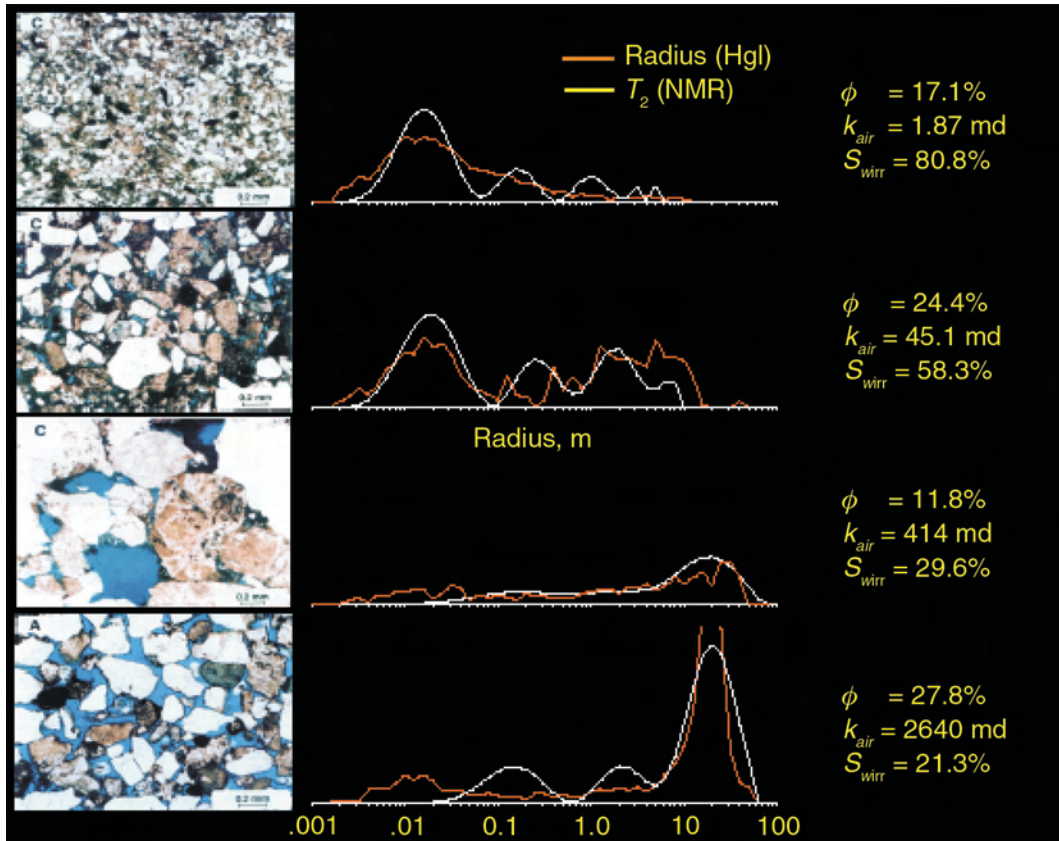


Fig. 3E.14—The correlation between MICP and T_2 distribution in water-saturated sandstones.

porosity; however, the dead time was close to the T_2 cutoff established for irreducible water saturation. The NML could detect movable fluids and provided a measurement called the Free Fluid Index (FFI).¹¹ An expanded discussion of the NML technology can be found in Brown and Neuman³⁹ and Brown.¹

3E.5.2 Pulse NMR. Unlike conventional magnetic resonance imaging (MRI) devices in which the sample is placed inside the stationary coil, a borehole-logging device investigates a sample (rock volume) that is outside the device itself while moving along the borehole. This setup has been called the “inside-out” NMR problem because the geometry of the magnets and coils is inverse to that used in laboratory-NMR spectrometers.^{40–44} To obtain useful measurements, a logging tool must generate a large, radially symmetric static magnetic field and also a high-frequency oscillating magnetic field. Each must be capable of penetrating one or more inches into the formation surrounding the borehole. The diameter of a typical well limits the size of the permanent magnets that can be used and, therefore, the strength of the magnetic field that can be generated by a logging device. In comparison with laboratory-NMR and clinical-NMR devices, which may operate at 10 MHz and the static magnetic fields of which are commonly in the range 1 to 2 Tesla (high field), modern logging tools and laboratory spectrometers designed for petroleum investigations are considered low-field devices. They operate at or below 2 MHz and generate relatively weak (< 200 gauss) and inhomogeneous magnetic fields (i.e., gradients up to 20 gauss/cm). By comparison, the NML operating frequency was only 2 kHz,

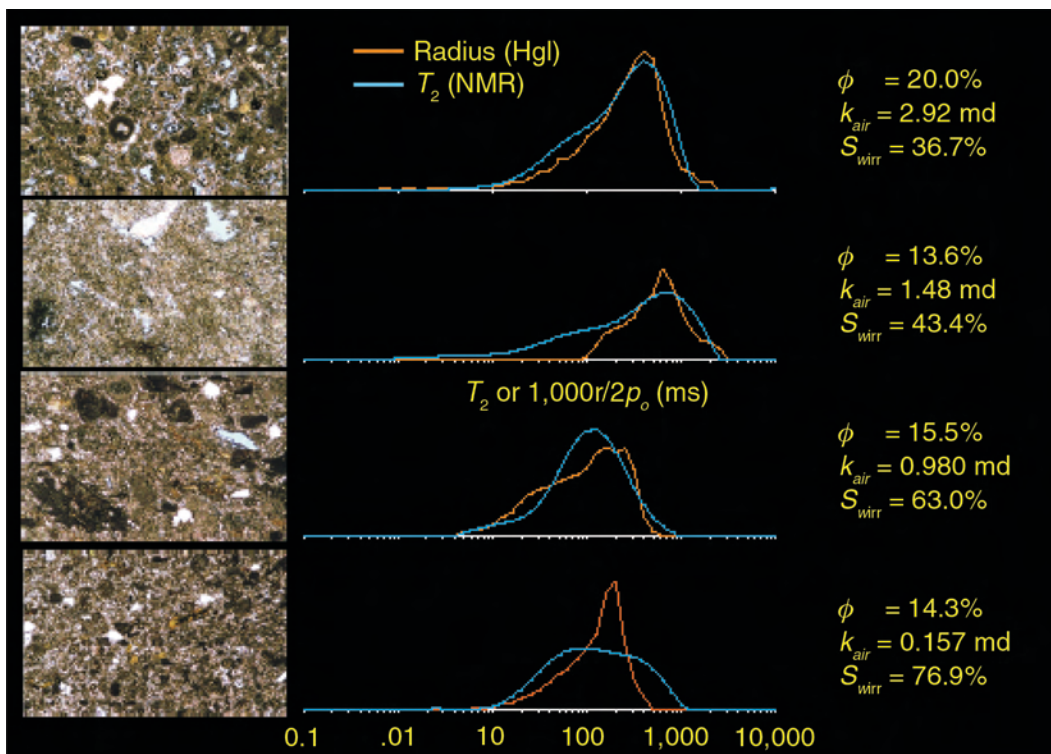


Fig. 3E.15—The correlation between MICP and T_2 distribution in water-saturated carbonates.

and the Earth's magnetic field is only 0.5 gauss. These factors limit borehole investigation to protons (hydrogen) and the use of relaxation data only. Chemical shifts (widely used in the biological field) are not observable.⁷ Furthermore, to compensate for the lower S/N that results from low-field intensity, logging tools must acquire more echoes and/or stack data to improve S/N. As mentioned previously, with the introduction of pulse-echo tools, T_2 became the primary acquisition mode because it permitted faster logging—a major factor in high-cost wells.

This new design provides a number of operational advantages over the NML:

- Using permanent magnets rather than electromagnets reduces the surface-power requirement.
- Focusing the sensitive region of the magnetic field at some distance into the formation eliminates the requirement for suppressing the mud signal.
- Using an RF pulse from a coil tuned to the Larmor frequency ensures that only nuclei in the sensitive region are in resonance.
- Controlling the pulse duration means shorter dead times that, in turn, allow a better estimate of initial decay amplitude (porosity) measurement for short T_2 components (bound-fluid evaluation).
- Enabling more sophisticated pulse sequences allows for measurement of additional rock and fluid properties.⁴⁴

One initially unwanted product of this design is the creation of gradients in the static magnetic field that causes molecular diffusion. The strength of the magnetic field gradient, G , is controlled by tool design and configuration (i.e., tool size and tool frequency); by environmental conditions such as formation temperature; and by internal gradients induced by the applied field, B_0 . Subsequent characterization of these gradients has enabled the in-gradient diffusion to be used for hydrocarbon typing.

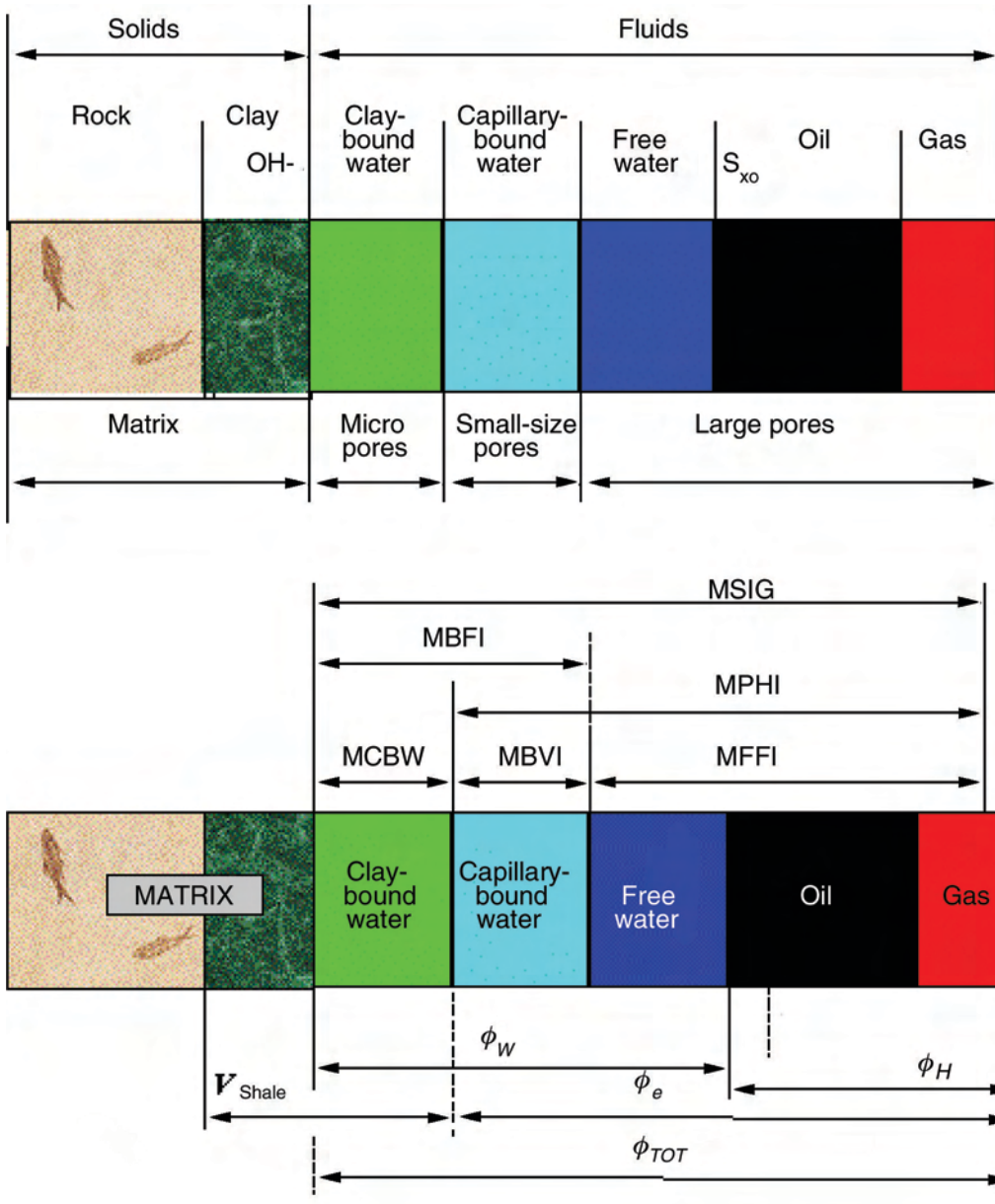


Fig. 3E.16—NMR-porosity model. These figures illustrate the distribution of pore size and pore fluids used in NMR logging. The suggested NMR mnemonics are Halliburton's. Because NMR tools respond to the invaded zone, a mud-filtrate component is added between movable water and oil. NMR-logging tools are sensitive to fluids but not to matrix materials and dry clay. NMR porosity is affected by HI, T_w , and T_E .

3E.5.3 Wireline-Tool Designs. From the beginning, a debate in NMR logging has been whether to use a centralized or ecentered tool design. There are two different wireline designs in current commercial service: (1) the Numar (now a part of Halliburton) magnetic resonance imaging tool (MRIL), a centralized mandrel device^{30,45-48}; and (2) the Schlumberger CMR tool⁴⁹⁻⁵⁵ and the Baker Atlas MREX⁵⁶ ecentered devices, both of which require contact with the borehole wall. The general designs of both the MRIL (mandrel-type) and CMR (pad-type) have evolved over the past decade with the addition of new capabilities and faster logging

Measurement Capability			Relative Influence on Measurement		
Quantity	T_1	T_2	Parameter	T_1	T_2
Porosity	Yes	Yes	Field sensitivity	Low	High
Permeability	Yes	Yes	Signal decay	No	Yes
Producibility	Yes	Yes	Experiment time	Long	Short
Viscosity	No	Yes	S/N (at logging frequency)	High	Low
Diffusion effect	No	Yes*	Motion sensitivity		
Signal amplitude	Yes	Yes	Vertical	High	Low
			Lateral	Low	High**
			Bed-boundary effects	High	Low

* constrained by echo spacing
** constrained by tool design

speeds, made possible by improved electronics and improved data acquisition and processing. Computalog is field testing a prototype mandrel device: the Nuclear Magnetic Resonance Tool (NMRT) developed by NPF Karotazh.⁵⁷

A centralized NMR-logging tool like the MRIL must be longer than a pad device, simply to contain magnets of sufficient strength to project the required magnetic field, through the borehole and into the formation. This factor results in a greater sensitivity to borehole salinity than a pad device, which can exclude the mud from its measurement. The MRIL design generates relatively thin (1 to 2 mm) sensitive volumes, but the reduced S/N that accompanies these volumes is compensated by the vertical size of the sensitive area. It also generates a relatively high magnetic gradient. In contrast, a contact device, such as the CMR, can use smaller magnets and electronics, which provide higher vertical resolution but a shallower depth of investigation (DOI) and greater sensitivity to borehole rugosity. In addition to the standard permanent magnets, some designs now include “prepolarization” magnets, which are added to ensure full polarization at typical logging speeds.

The latest wireline NMR-logging tools operate simultaneously in several RF frequencies to measure (image) multiple sample volumes. In the presence of a gradient magnetic field, pulses with different frequencies will cause protons in different (and parallel) regions of space (i.e., measurement or sensitive volumes) to resonate.³¹ Cycling through several frequencies excites protons in different cylindrical volumes, allowing measurements to be made more quickly. If the frequencies of multifrequency measurements are very close together, then the sensitive volumes are very close together; and, for practical purposes, the rocks sampled can be considered to be the same. This principle is the same as that used for slice selection in medical MRI imaging. These tools acquire multiple echo trains using different values of T_W , T_E , and variable magnetic gradients (G) in a single logging pass. The time between measurements made at multiple frequencies can be as little as the time of an echo train, and the time between measurements made at a single frequency is essentially the time needed to repolarize (T_W). The thickness of these sensitive volumes may be as small as 1 mm. Furthermore, recent advances in tool design now permit cost-effective T_1 acquisition.⁵⁸ **Table 3E.4** summarizes the capabilities, advantages, and disadvantages of T_1 and T_2 acquisition. These differences influenced the designs of the LWD tools discussed in the next section. Multifrequency operation provides measurements at multiple DOIs (typically 1 to 4 in.). This allows invasion effects to be accounted for in the data interpretation, thus enabling determination of near-wellbore fluid saturation and oil properties at high resolution.^{54,58–60}

3E.5.4 LWD Tools. The latest entries into NMR logging are LWD tools. The development of LWD-NMR is ongoing and significant changes in hardware design, as well as significant changes and improvements in data acquisition and processing, can be expected in the next few years. The general benefits of LWD have been discussed elsewhere—in particular, NMR-LWD offers a nonradioactive alternative for porosity measurement, an NMR alternative to wireline in high-risk and high-cost wells, and enables high-resolution fluid analysis in thin beds and laminated reservoirs.⁶¹

By definition, logging tools operating in the drilling environment are built into drill collars and are, therefore, mandrel devices. In contrast to wireline tools, they must be capable of making measurements when the drillstring is stationary, sliding or rotating, centered or eccentric.

LWD-tool measurements are either omnidirectional or azimuthal, depending on tool design. The incorporation of magnetometers allows binning of the data into azimuthal sectors. Omnidirectional measurements can be generated from azimuthal data, but not the reverse. Although current LWD-NMR services provide only omnidirectional data, patents have been issued for tools with azimuthal capability.⁶²

A major concern introduced with the advent of LWD-NMR is the effect of drillstring lateral motion on the basic NMR measurement.⁶³ NMR measurements are not instantaneous, they involve both polarization and decay, time-dependent components. Lateral movement of a wireline tool or LWD drillstring shifts the polarization volume and the sensitive-measurement area, relative to one another, and these shifts may result in incomplete polarization or incomplete measurement of the decay. Low-velocity motion affects only the decay, but high-speed motion can also affect the initial decay amplitude.

The currently available LWD tools offer different solutions to this concern. While both tool designs can operate in either T_1 or T_2 acquisition mode and both incorporate accelerometers and magnetometers for detecting lateral motion for quality control of the NMR measurements, they differ in their choice of primary measurement mode. Operational factors, such as the slower logging speed (i.e., rate of penetration in drilling), compared with typical wireline logging, also affect the choice of measurement mode.

The NMR acquisition sequences are programmable and interchangeable with those used in wireline tools. Switching between these acquisition modes is accomplished by a variety of methods, including elapsed time, counting measurements, and differentiating between drilling and nondrilling conditions. T_1 -mode records echo amplitudes as a function of time. Data output consists of porosity, free-fluid, and bound-water volumes, and can provide a quick-look permeability estimate. T_2 -mode is a multifrequency mode that records multiple wait-time CMPG spin-echo amplitudes and is capable of using all wireline-pulse sequences. T_2 -mode output includes porosity, free fluid, clay- and capillary-bound water, and differences in the multiple wait-time data are used for hydrocarbon indication.

The Halliburton tool (MRI-LWD)⁶⁴⁻⁶⁸ uses T_1 as its preferred acquisition mode. Halliburton considers T_1 more robust for determining porosity and free-fluid volume. The anticipated maximum rates of penetration for LWD—1 to 3 ft/min—allow T_1 acquisition. T_1 is motion tolerant compared with T_2 . A sequence of interleaved measurements made at different recovery times is used to construct the T_1 relaxation decay (buildup). As long as the sensitive volume (shell) is contained within the much larger volume reached by the saturation pulse, the measurement is valid. During post-processing, drilling and nondrilling periods are identified, and the invalid T_1 data recorded during drilling are discarded.

Schlumberger's tool (ProVision LWD-NMR)⁶⁹⁻⁷¹ uses T_2 for its primary measurement. While both companies agree that T_1 is motion tolerant, Schlumberger considers T_1 to be less robust for estimating porosity, bound-fluid, and free-fluid volumes because of the poor S/N resulting from the longer time require for equivalent-quality T_1 measurements. A reduced S/N impacts data quality (e.g., statistical repeatability and vertical resolution), logging speed, and,

ultimately, the results. T_2 measurement also enables rapid calibration and correlation with the large body of wireline-NMR data. The multiple wait-time acquisition includes a fully polarizing (3 to 12 seconds), a partially polarizing (normally 0.6 to 1 seconds), and a very fast wait time (typically 0.08 seconds). Porosity and bound-fluid volume are calculated for both the long- and the medium-wait-time measurements, and significant differences between the long-wait-time and medium-wait-time porosity provide real-time hydrocarbon indication. When necessary, logs are corrected for incomplete polarization of the hydrogen nuclei, and T_1 distributions are estimated from the measured T_2 relaxation.

Baker Atlas is presently field testing a new LWD device (MagTrak) that operates in T_2 acquisition mode and has a vertical resolution of less than 3 in.⁷² This tool design achieves a motion-tolerant T_2 measurement through a combination of a very-low gradient magnetic field, circuitry that permits a T_E as low as 0.6 ms, and the use of special stabilizers.

3E.5.5 Downhole NMR Spectrometer. Contamination of hydrocarbon reservoirs by oil-based mud (OBM) and synthetic oil-base mud (SOBM) is a significant problem for accurate reservoir and fluid analysis in wells in which OBMs are used, especially offshore. Direct knowledge or an estimate of the OBM's NMR characteristics is required to distinguish it from connate oil in fluid samples obtained by formation testers. Acquisition of T_1 , T_2 , and D_0 (the self-diffusion coefficient) permits evaluation of connate oil, oil viscosity, and gas/oil ratio.^{31,73} Furthermore, in costly drilling environments, real-time acquisition of NMR properties permits immediate, rather than delayed, fluid evaluation. Information on NMR fluid properties is also valuable for the interpretation of NMR wireline and LWD logs.

The recently introduced downhole NMR spectrometer, incorporated into a formation-testing tool, can obtain NMR measurements of OBM contamination directly, on live samples at in-situ conditions.⁷⁴⁻⁷⁷ As the testing tool pumps fluid from the reservoir into the borehole or sample chamber, the spectrometer—using a measurement time of 30 seconds—measures the hydrogen index (HI), T_1 , T_2 , and diffusion. The T_1 measurement is made while flowing; T_2 and diffusion are static measurements. The T_1 distribution is important in differentiating between highly refined OBM filtrates and native oil. The T_1 characteristics of these common filtrates are measured and cataloged so that the data from oil-based filtrates can be distinguished from native hydrocarbons.

3E.6 Log Presentation

NMR-log data are presented in a variety of formats designed to emphasize specific aspects of the data and thus enable rapid visual interpretation of movable and immovable fluids, porosity, and permeability. Data interpretation is further enhanced when additional log and core information are also included in the log presentation.

The T_2 distribution is typically displayed in waveform presentation, image (variable-density log, VDL) format, and bin-distribution plot. Each T_2 format represents the distribution of the porosity over T_2 values, and hence, over the pore sizes (Figs. 3E.17 and 3E.18).

3E.7 NMR Applications

NMR-log data can be analyzed independently or in combination with conventional-log and core data. As an independent logging service, NMR can provide porosity, permeability index, and complete information on fluid type and saturation of the flushed zone. Some data-interpretation methods operate in the echo-decay time domain, while others operate in the T_2 -relaxation domain.

3E.7.1 Porosity Determination with NMR. The initial amplitude of the spin-echo train is proportional to the number of hydrogen nuclei associated with the fluids in the pores within the sensitive volume. This amplitude is calibrated in porosity units (see Eq. 3E.10). The accuracy

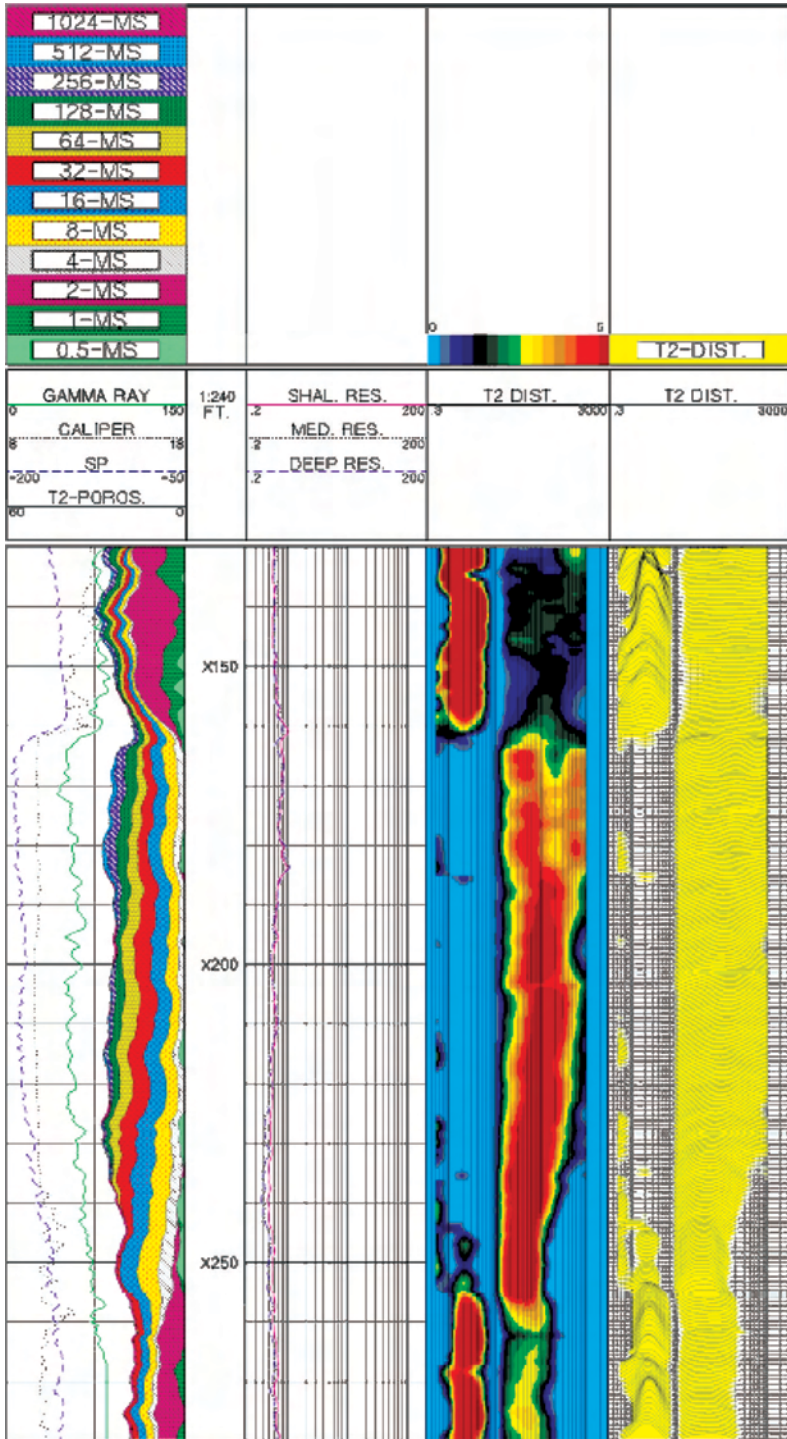


Fig. 3E.17—Log presentation illustrating some of the formats used to present T_2 distributions: Track 1, a plot of the cumulative amplitudes from the binned T_2 -distribution; Track 2, shallow, medium, and deep resistivity log curves; Track 3, a color VDL image of the binned T_2 distribution; Track 4, a waveform presentation of the same information. The displayed T_2 distribution typically corresponds to binned amplitudes for exponential decays that may range from 0.5 to 1,024 ms. Logging data are much noisier than laboratory data, and the T_2 distribution shown on well logs is comparatively coarse.

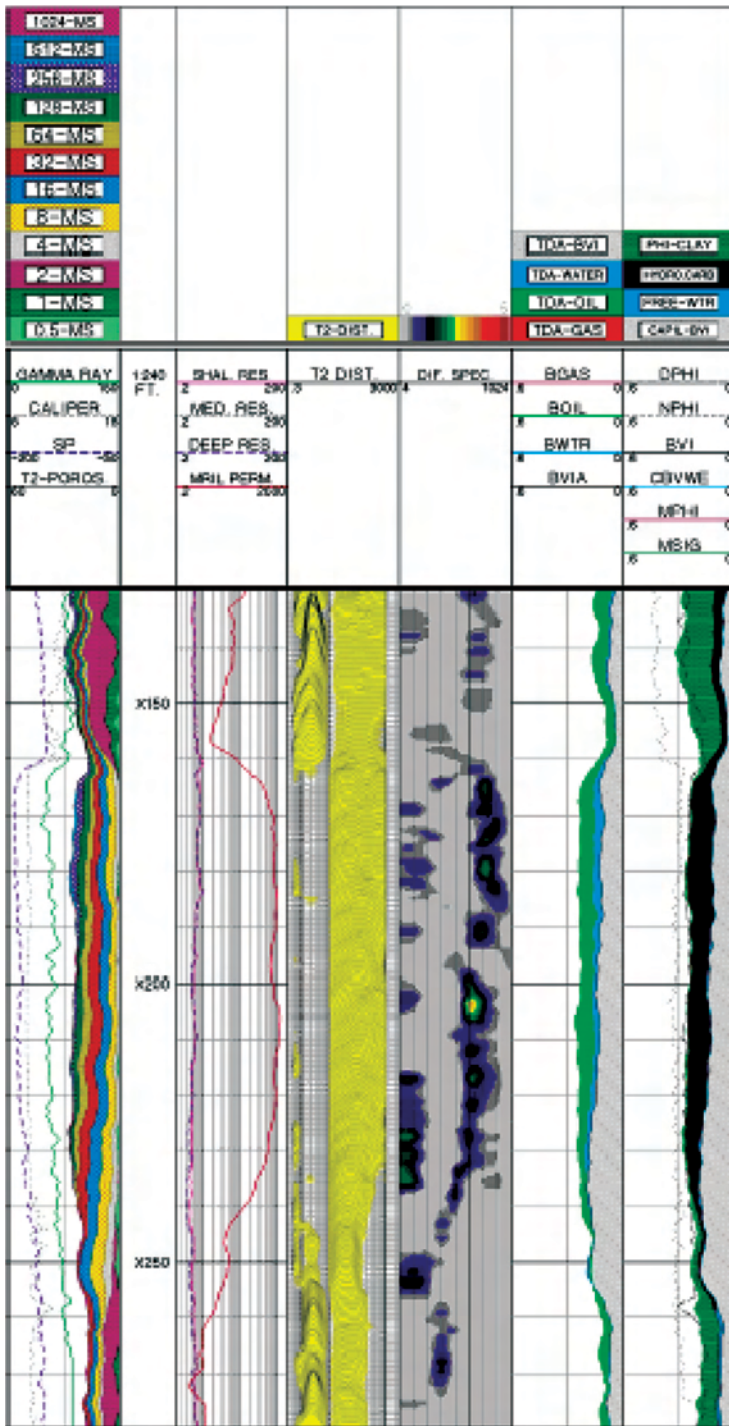


Fig. 3E.18—Integrated NMR-log evaluation. This log presentation includes GR, caliper, and SP (Track 1), resistivity data (Track 2), NMR T_2 distribution (Track 3), DSM-analysis results (Track 4), TDA-analysis results (Track 5), and NMR-resistivity integrated analysis results (MRIAN, Track 6).

of this amplitude measurement depends on three factors: first, a sufficiently long polarization time, T_w , is needed to achieve complete polarization of the hydrogen nuclei in the fluids; sec-

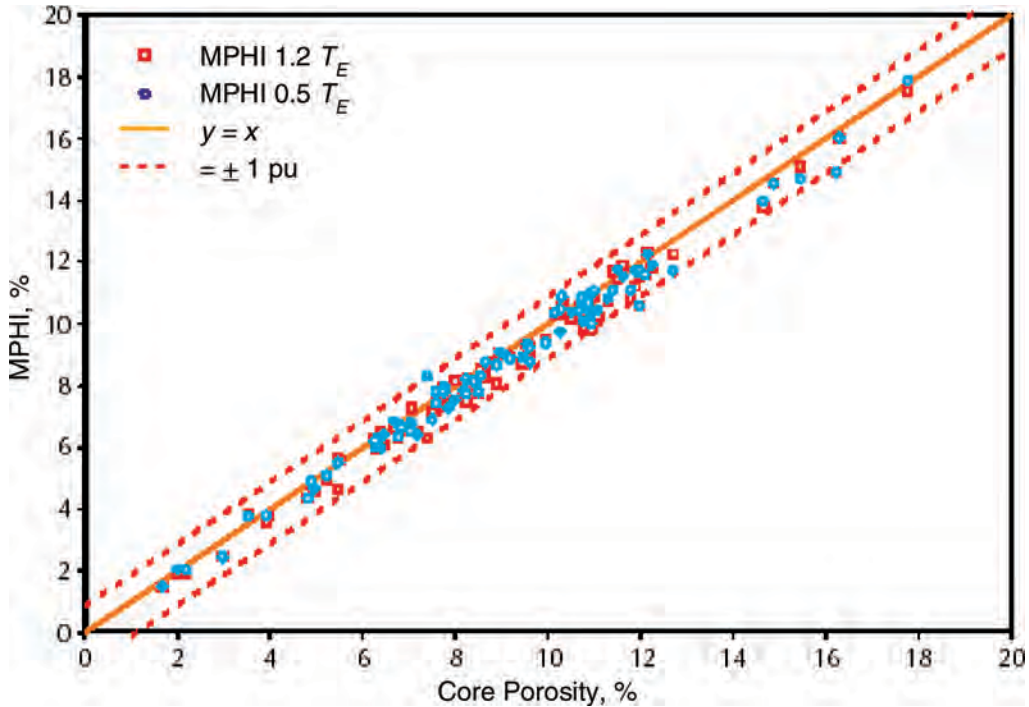


Fig. 3E.19—Comparison of core- and log-NMR porosity. In this clean sandstone example, there is good agreement between porosity derived from laboratory-NMR measurements and porosity derived from conventional core analysis. NMR-porosity values typically fall within ± 1 p.u. of the measured core-porosity values. Here, NMR-laboratory data were measured at $T_E = 0.5$ ms and $T_E = 1.2$ ms.

ond, a sufficiently short inter-echo spacing, T_E , is needed to record the decays for fluids associated with clay pores and other pores of similar size—if either T_W is too short or T_E too long, NMR porosity will be underestimated; third, the number of hydrogen nuclei in the fluid should equal the number in an equivalent volume of water (i.e., $HI = 1$); if the HI of any of the pore fluids is significantly less than 1, a correction to porosity is necessary.

Porosity was one of the earliest NMR measurements and is still an important one. Assuming that the logging tool is properly calibrated and functioning normally (see discussion of Quality Control in this chapter), interpretation of the porosity measurement depends on several other factors, including vintage of the logging tool, whether hydrocarbons are present, and fluid type.

There are two major contrasts between NMR porosity and conventional density and neutron-nuclear-porosity logs. First, NMR porosity does not depend on the mineralogy of the matrix, except in cases in which the formation contains significant amounts of ferromagnetic or paramagnetic materials, and in most cases, it is considered a lithology-independent measurement. Second, NMR porosity is not sensitive to either borehole or mudcake and does not require corrections because the measurement zone (i.e., sensitive volume) is focused within the formation, beyond the borehole wall and these influences. The accuracy and precision of NMR-derived porosity has been confirmed through comparisons with core porosity obtained using conventional laboratory measurement methods (Fig. 3E.19).

Influence of Tool Version on the Porosity Measurement. The original NML tool had such a large dead time (e.g., minimum echo spacing, T_E) that it could not measure clay- and capillary-bound fluids; thus, it was only capable of measuring free-fluid porosity, which is now called

NMR effective porosity (MPHI). The minimum T_E used in the early versions of pulse-NMR tools was still relatively large, and those tools still could not see all the clay-bound fluids. With improvements in logging technology, most NMR logs recorded after 1997 are considered “total-porosity” logs. Current logging tools use a minimum T_E of 0.3 ms in continuous mode and a T_E as small as 0.1 ms in stationary mode.

In clean, water-filled formations, MPHI should approximately equal neutron-density cross-plot porosity. In shaly sands, MPHI should approximately equal density porosity, calculated with the correct grain density; however, the MPHI may not equal effective porosity because of the effects of HI and long T_1 components (Eq. 3E.12):

$$\text{MPHI} = \phi_e \cdot \text{HI} \cdot \left[1 - e^{-\left(\frac{T_W}{T_1}\right)} \right], \dots\dots\dots (3E.12)$$

where MPHI is measured by the NMR tool; ϕ_e is effective porosity of the formation; HI is related to the amount of fluid in the effective porosity system; T_W is polarization time used during logging; and T_1 is longitudinal relaxation time of the fluid in the effective porosity system. Older NMR logs may indicate very low porosity in shales.

MPHI is almost always less than NMR total porosity (MSIG):

$$\text{MSIG} = \text{MPHI} + \text{MCBW}, \dots\dots\dots (3E.13)$$

where MSIG is measured by NMR total-porosity logging, and clay-bound-water porosity (MCBW) is measured by the NMR tool with partial-polarization acquisition. In very clean formations, however, NMR MCBW is virtually zero, and then MPHI equals MSIG (see Fig. 3E.16).

NMR total porosity may approximate density or neutron-density porosity. The reported clay-bound volume should not be considered absolute because the boundary between clay- and capillary-bound porosity components can vary with clay type and distribution. Whenever possible, the relationship of clay type and volume should be confirmed through core analysis and comparison with other log data.

Porosity-Logging Modes. Several modes of porosity logging are currently in use: standard T_2 mode, short T_W (e.g., bound-fluid logging), intermediate T_W (e.g., polarization correction and the “clean, wet formation” method), and long T_W , or multiple-wait-time acquisition (e.g., total-porosity logging).

Total-porosity-logging mode provides data to determine porosity, permeability, and productivity (mobile fluids). Total-porosity acquisition is a multiple-wait-time acquisition that acquires two echo trains to obtain the total porosity. One echo-train acquisition uses a long T_E (e.g., 0.9 or 1.2 ms) and a long T_W (3 to 8 seconds) to achieve complete polarization. This echo train provides the effective porosity. The second echo-train acquisition uses a short T_E (0.2 to 0.6 ms) and a short T_W (20 ms) that is only long enough to achieve complete polarization of the fluids in the small pores (i.e., clay-bound porosity).⁴⁶ Although the long T_W acquisition may achieve full polarization in gas zones, the porosity may still require HI correction. The short T_W echo trains are stacked to improve S/N. Total porosity is obtained by combining the two separate T_2 distributions, usually at 4 ms. The standard T_2 acquisition is used in situations in which there is little to no diffusion or T_1 contrast. The benefits of standard T_2 acquisition are increased logging speed without degradation of data quality; or superior data quality at normal logging speeds.

In bound-fluid logging mode, T_W is kept relatively short, ranging from 0.3 to 1.0 seconds. The benefit of using a short T_W is faster logging speeds while determining the clay- and capillary-bound fluid volumes. The drawback is underpolarization of the free-fluid volume.

When this logging mode is used, the free-fluid volume is computed from other log data (e.g., density, neutron-density crossplot, or acoustic). In polarization mode (CMR tool), a correction to the free-fluid volume is made using the observed relationship of T_1 to T_2 , on the basis of the T_2 acquired while logging. The magnitude of the polarization correction must be monitored because, in addition to porosity, the T_1/T_2 ratio is also influenced by changes in the types of formation and pore fluid. This method generally works well in clastics, but in conditions of high T_1 and T_2 , such as in carbonates or light oil, the correction may actually introduce additional error.⁷⁸

Another mode of operation is to find a clean, wet formation and perform a sweep of different wait times (T_W) ranging from 2 to 5 seconds to determine the one needed for full polarization. Because oil and gas may have very long T_1 values or require an HI correction, the use of intermediate T_W methods does not guarantee that the NMR porosity will be fully reported.

Optimization of the acquisition is critical to accurate NMR measurements and interpretation (see the Job Planning section of this chapter). The effect of incorrect acquisition parameters on the T_2 distribution is illustrated in **Fig. 3E.20**. In this figure, the sequence of graphs shows the effects of T_E , T_W , pulsing time (T_P), and S/N on the measured NMR characteristics of a core sample:

- A: Initial acquisition results show an apparent unimodal distribution.
- B: Increasing the T_P shows that this sample is, in fact, bimodal. There is a significant change in the T_2 distribution, but little to no change in the cumulative porosity.
- C: Decreasing the echo spacing (T_E) reveals fast components in this sample that were previously masked by a T_E that is too long. There is a significant change in the cumulative porosity with a characteristic shift of the fastest components in the distribution to shorter T_2 values.
- D: Increasing the wait time (T_W) has significantly increased cumulative porosity. After correction for a T_W that is too short, there is a characteristic shift in the slow T_2 components to longer T_2 values.
- E: Increasing the S/N results in sharper resolution of the two major components. Although the definition of each component in the T_2 distribution improves, little change is noted in the cumulative porosity.
- F: The final result, in which all acquisition parameters have been optimized (red), is compared with the initial result (blue).

BVI Determination. Determining the BVI of water in a formation is one of the earliest and most widely used applications of NMR logging. BVI refers to the immovable or bound water in a formation. BVI is a function of both the capillary-pressure curve for the rock and the height above free water (**Fig. 3E.21**).

In practice, BVI serves as an indicator of, and is used for, estimating producibility and permeability. There are two methods currently used for BVI determination. One is the cutoff-BVI (CBVI) model, which is based on a fixed- T_2 value ($T_{2\text{cutoff}}$) that divides BVI and FFI. The second is the spectral BVI (SBVI) model, which assumes the coexistence of free and bound fluids in any pore described by the T_2 distribution at water saturation (S_w) = 100%. This coexistence is expressed through a weighting factor that defines the fraction of bound water associated with each pore size.⁷⁹ The SBVI method is used primarily for quantifying movable water and, secondarily, for estimating permeability.

CBVI (Cutoff) Model. The T_2 signal from the rock matrix is actually so rapid that even modern logging tools cannot detect it. Consequently, the recorded T_2 distribution represents only the porosity occupied by movable (FFI) water and immovable BVI and clay-bound-water

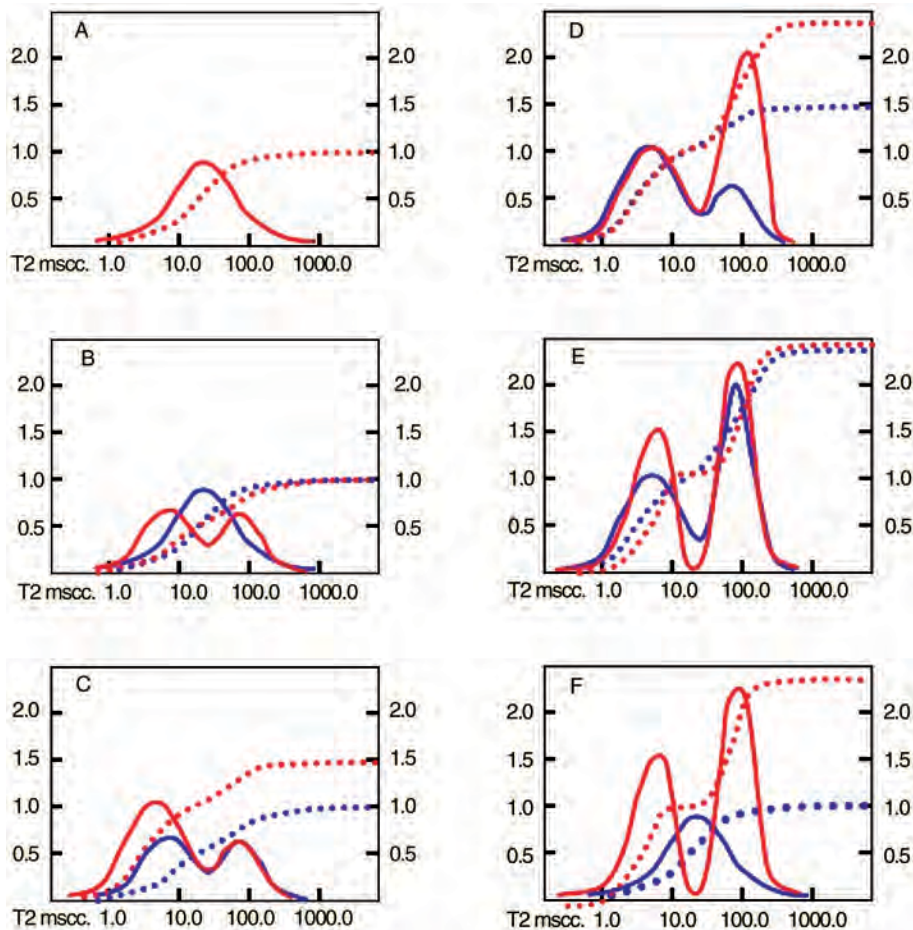


Fig. 3E.20—Dependence of T_2 distribution on NMR-acquisition parameters. In all figures, blue represents previous results, red represents new results, solid lines represent incremental T_2 (read on the left axis), and dashed lines represent cumulative T_2 vs. T_2 relaxation time (read on the right axis).

(CBW) components. Assuming that the mobility of reservoir fluids is primarily controlled by pore size (i.e., the producible fluids reside in large pores and the immobile, or bound, fluids reside in small pores), a fixed- T_2 value can relate directly to a pore size at or below which fluids will not move. This value ($T_{2\text{cutoff}}$) is used to divide the T_2 distribution into movable (i.e., producible or free fluids and FFI) and immovable (i.e., bound-fluid, BVI, and CBVI) components (Fig. 3E.22).⁸⁰ $T_{2\text{cutoff}}$ is a variable that differs from one formation to another and is influenced by a variety of factors including capillary pressure, lithology, grain size, compaction, and pore characteristics.

In practical use, $T_{2\text{cutoff}}$ is either determined in the laboratory or a default value is assumed. If time and expense permit, accurate $T_{2\text{cutoff}}$ values can be defined by comparing the T_2 distributions obtained on fully and partially water-saturated core samples taken from the logged interval^{81,82} (Fig. 3E.23).

In the absence of laboratory data, lithology-dependent default values are used for $T_{2\text{cutoff}}$. Default $T_{2\text{cutoff}}$ values are based on local field experience or common practice; for example, typical values used in the Gulf of Mexico are 33 ms for clastics (sandstones) and 92 or 100 ms

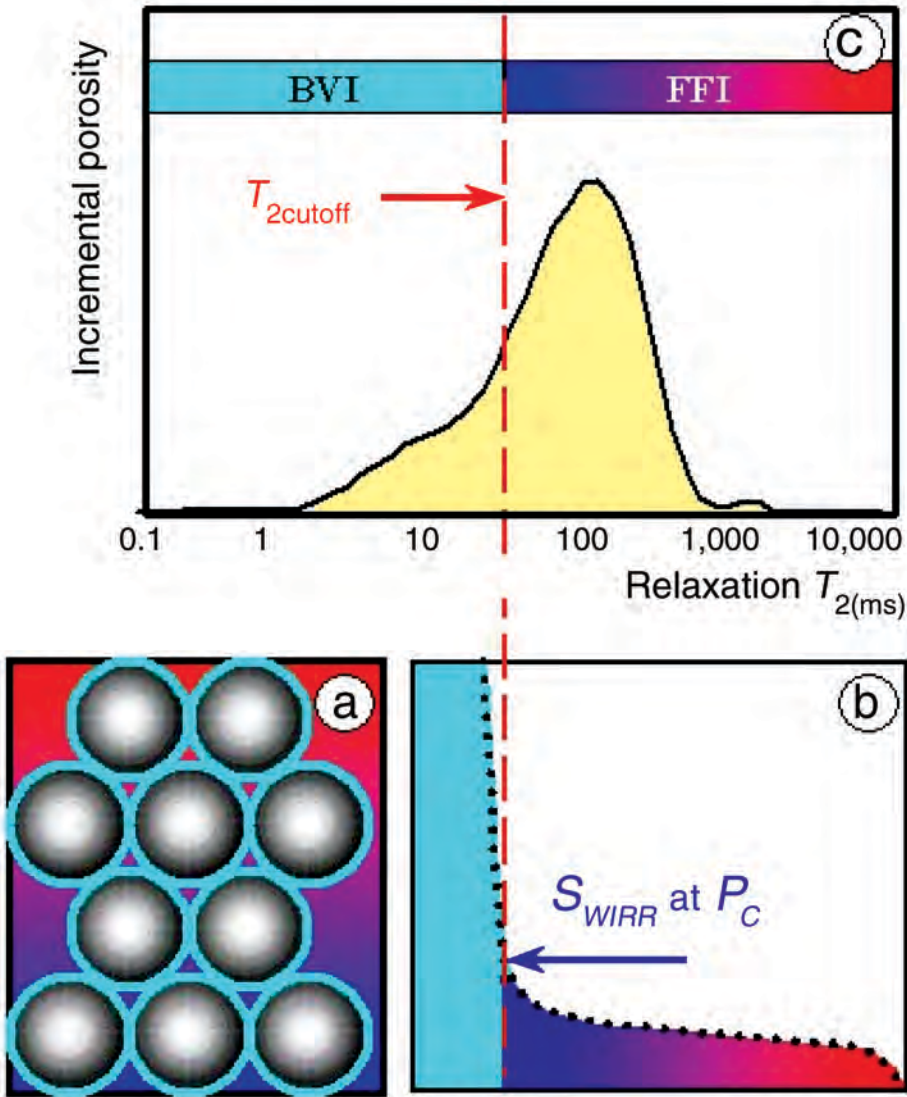


Fig. 3E.21—Correlating NMR $T_{2cutoff}$ to capillary pressure: (a) grains are shown in gray, capillary-bound water (BVI) in light blue, and free fluids in a gradient tone blue/red; (b) capillary pressure curve (black dots) defines capillary pressure (P_c) in which water saturation becomes irreducible (S_{wirr}); (c) a single-porosity cutoff value on the T_2 distribution, corresponding to this pressure.⁷⁹

for carbonates.^{83–85} When using a default value, remember that, in fact, the $T_{2cutoff}$ can actually vary within a single lithology because the capillary pressure at which irreducible water saturation (S_{wirr}) is achieved varies between the actual rocks. In addition, $T_{2cutoff}$ is also influenced by pore-wall chemistry, the presence of minor paramagnetic or ferromagnetic components, texture, and pore-throat to pore-body ratios. The use of an incorrect value for $T_{2cutoff}$ may result in underestimation of recoverable reserves or in bypassing a pay zone.

SBVI (Spectral) Model. The SBVI model was developed to address the limitations of the CBVI model in some rocks, particularly in very-well-sorted rocks in which there is a very narrow range of grain and pore sizes. In these rocks, the NMR echo-decay can typically be fit by

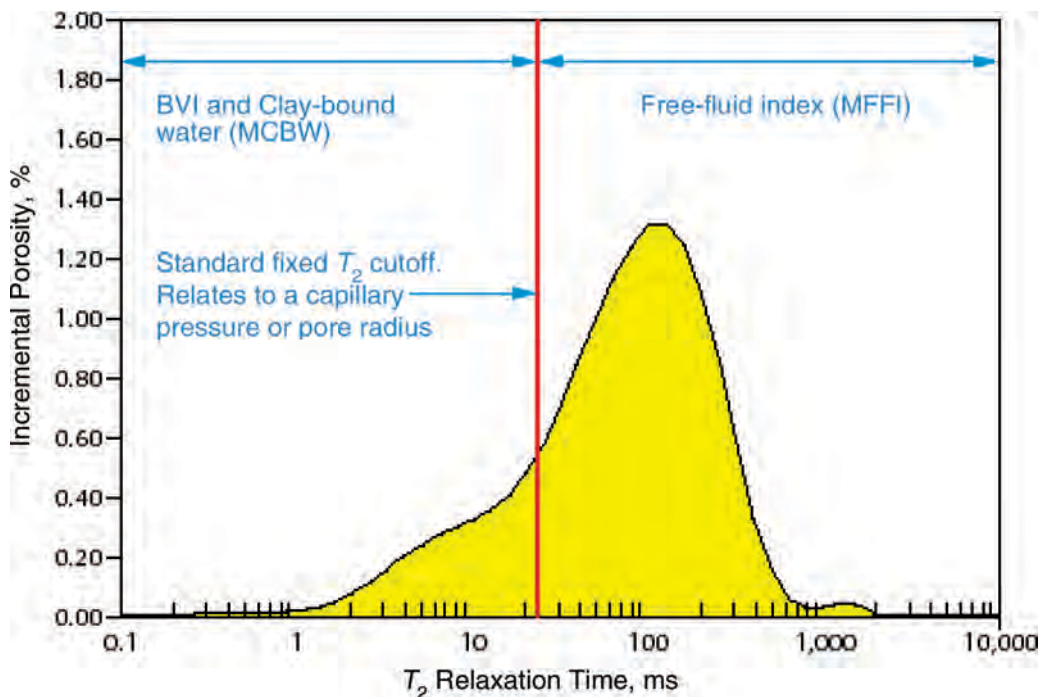


Fig. 3E.22—Illustration of the $T_{2\text{cutoff}}$ used in the CBVI model to divide NMR porosity into movable and immovable components.

a single-exponential decay that produces a sharp peak in the T_2 distribution. When a fixed cut-off is used for determining BVI, it may result in significant error because of the presence of immovable water contained in microporosity associated with pore irregularities.⁸⁴ This microporosity component is apparent at $S_{w\text{irr}}$, but not at $S_w = 100\%$ (Fig. 3E.24).

A weighting function defines the fraction of bound water in each pore size that is present in the T_2 distribution at $S_w = 100\%$ (Fig. 3E.25). Several methods have been proposed for obtaining the weighting function.^{31,85,86}

In general, the SBVI method is superior to the CBVI method for determining BVI in rocks in which $S_w = 100\%$. The presence of hydrocarbons (i.e., $S_w < 100\%$), however, introduces complications to the SBVI method. To overcome the limitations of both methods for determining BVI, the recommended practice is to compute two bound-water values—one from the cutoff (CBVI) and one from the spectral (SBVI) method—and take the larger of the two.

3E.7.2 Permeability Estimation. The ability to estimate formation permeability is one of the earliest benefits of NMR logging and remains the most important application. Laboratory studies demonstrate that pore-water relaxation time is inversely related to the S/V ratio of the pore space (Fig. 3E.26). The NMR estimate of permeability is based on theoretical and core-based models that show that permeability increases with increasing porosity and pore size (S/V).^{80,87–90}

The measurement of formation permeability, in general, is greatly influenced by the method used, the limitations of each, and the scale at which the measurements are made.⁹¹ As stated previously, MICP curves obtained on core samples correlate to pore-throat size, while NMR measures pore-body size.

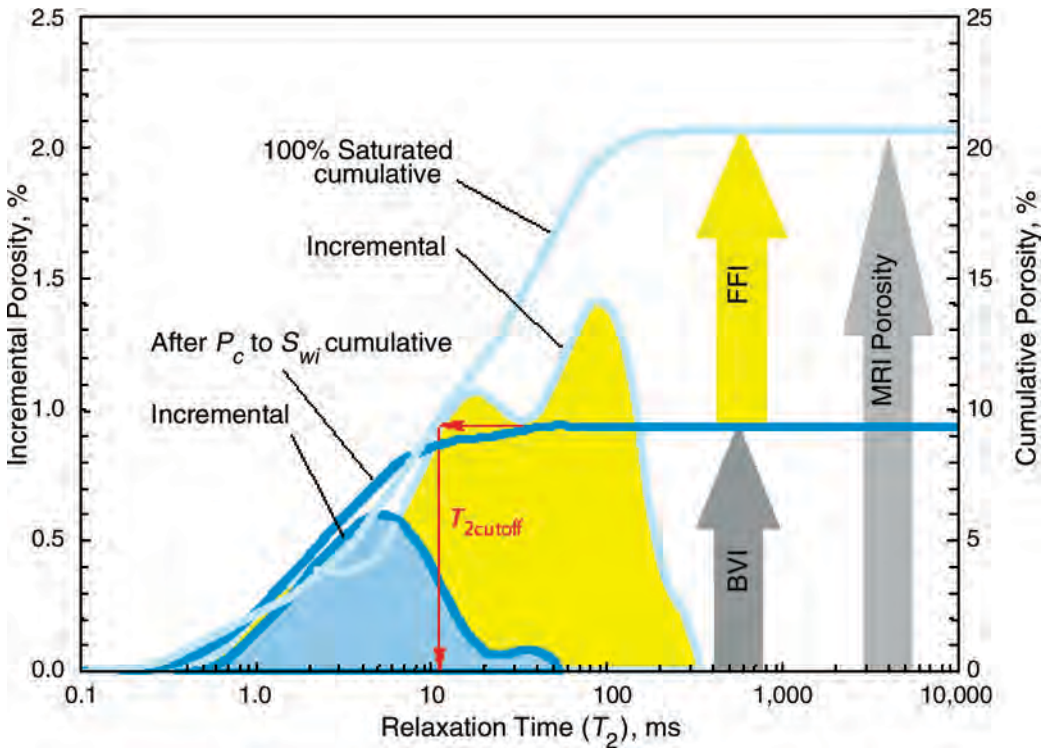


Fig. 3E.23—Determination of $T_{2\text{cutoff}}$ from core measurements. NMR measurements on fully saturated ($S_w = 100\%$) core samples and on samples at irreducible saturation ($S_{w\text{irr}}$) can be used to establish a $T_{2\text{cutoff}}$ for use in a CBVI model. The T_2 distributions are displayed as incremental porosity and cumulative porosity. The cumulative curves are used to determine $T_{2\text{cutoff}}$.

NMR logging does not provide direct and continuous measurement of permeability; rather, a formation-permeability estimate, or index, is calculated from the spectral-porosity measurements using permeability models that are based on a combination of empirical and theoretical relationships. Several permeability models have been developed, and two are in common use: the free-fluid (Timur-Coates or Coates) model and the mean- T_2 [the Schlumberger-Doll-Research (SDR)] model.^{27,92–94} The free-fluid model can be applied to water-saturated and hydrocarbon-saturated reservoirs, and the mean- T_2 model can be applied to water-saturated reservoirs.⁹⁵ These permeability models assume that a good correlation exists between porosity, pore-body and pore-throat size, and pore connectivity. This assumption is generally valid in clastic (e.g., sand/shale) sequences, but in carbonates or other lithologies, model-derived permeabilities may not be reliable.

Typically, a permeability model is calibrated over a particular zone of interest and verified, wherever possible, by core or well/formation test data. Once this is done, the NMR log can provide a robust continuous-permeability estimate within the zone of interest.

Both models treat permeability as an exponential function of porosity, ϕ^4 , and include a parameter to account for the fact that NMR measures pore-body size, not pore-throat size²⁰ (Fig. 3E.27). In the Coates model, the pore-size parameter enters implicitly through $T_{2\text{cutoff}}$, which determines the ratio of FFI to BVI. In the SDR model, the size parameter enters through the geometrical mean of the relaxation spectra, T_{2gm} . In water-saturated rocks, both models provide similar and good results; however, when hydrocarbons are present, the SDR model fails because T_{2gm} is no longer controlled exclusively by pore size.⁹⁶

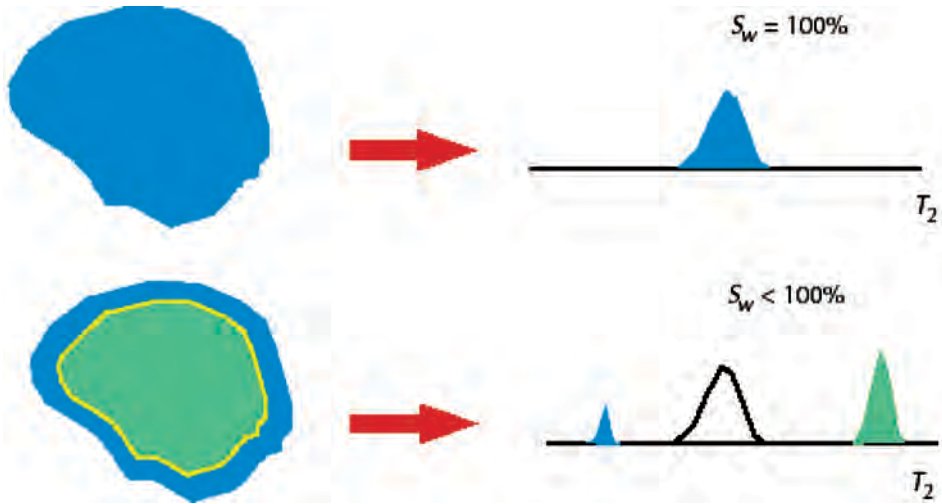


Fig. 3E.24—BVI associated with microporosity in a coarse-grained rock having a narrow range in pore sizes. The T_2 distribution at $S_w=100\%$ exhibits a single sharp peak (upper). The T_2 distribution at $S_w<100\%$ exhibits two peaks (lower). One appears below the $T_{2cutoff}$ value, the result of irreducible water on the pore surfaces. The other appears above the $T_{2cutoff}$ and represents the oil in the pore fluid. The T_2 value of the second peak is close to the T_2 of bulk oil. This same effect is seen in a North Sea chalk.

Free-Fluid (Timur-Coates or Coates) Model. In the simplest form of the free-fluid model, permeability, k_{Coates} , is expressed as follows (Eq. 3E.14):

$$k_{Coates} = \left[\left(\frac{\phi}{C} \right)^2 \frac{MFFI}{MBVI} \right]^2, \dots\dots\dots (3E.14)$$

where ϕ is MSIG, MBVI is obtained through the CBVI or SBVI method, MFFI is the difference between MSIG and MBVI (assuming that there is no clay-bound water, see Fig. 3E.16), and C is a formation-dependent variable. The free-fluid model is very flexible and has been calibrated using core data for successful use in different formations.

To calibrate the model to core, Eq. 3E.14 is solved in the form of a straight line, $y = mx + b$:

$$\sqrt{\frac{MFFI}{MBFV}} = m \left(\frac{\sqrt[4]{k}}{MSIG} \right) + b \dots\dots\dots (3E.15)$$

Assuming $b = 0$ in the equation (3E.15), core permeability is substituted for k . The slope of the line, m (i.e., C value in Eq. 3E.15), is determined using a least-squares regression (Fig. 3E.28).

Despite the flexibility of this model there are formation conditions that limit the effectiveness of the model and may require a correction (Table 3E.5). The presence of hydrocarbons (i.e., oil, oil filtrate, or gas) in the BVI component may result in an overestimate of BVI by either the CBVI or SBVI methods, leading to an underestimate of permeability. An HI correction can be applied when gas is present. The very short T_2 values associated with heavy oil may be counted in the BVI component and result in an underestimate of permeability.

Mean- T_2 [Schlumberger-Doll-Research (SDR)] Model. Using the SDR model, permeability is expressed as

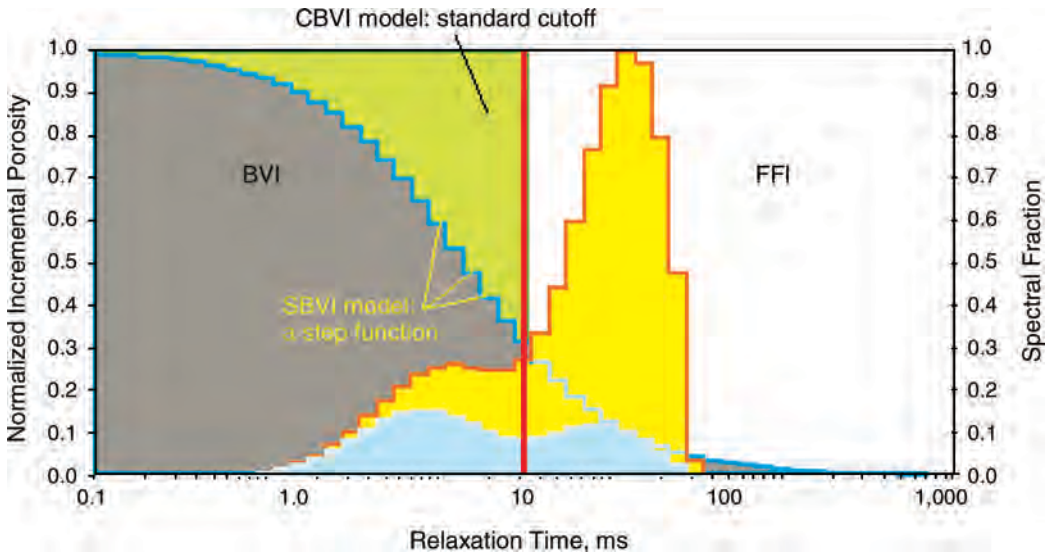


Fig. 3E.25—SBVI model. For a given T_2 , the SBVI-weighting factor provides the fractional volume of irreducible fluids in the pores whose size is associated with that T_2 . The model shown is a step function and is commonly used to describe the weighting factors.

$$k_{SDR} = C \times T_{2gm}^2 \times \phi^4, \dots\dots\dots (3E.16)$$

where ϕ is NMR effective porosity (MPHI), T_{2gm} is the geometric mean of the T_2 distribution, and C is a formation-dependent variable. The SDR model works very well in water-saturated zones. In the presence of oil or oil filtrates, the mean T_2 is skewed toward the T_{2bulk} , because of the effects of partial polarization, leading to an overestimate of permeability. In unflushed gas zones, mean- T_2 values are too low relative to the flushed-gas zone; and permeability is underestimated. Because hydrocarbon effects on T_{2gm} are not correctable, the SDR model fails in hydrocarbon-bearing formations. The Coates and SDR models represent matrix permeability and, therefore, are not applicable to estimation of permeability in fractured formations.

Other Comments on NMR-Based Permeability Estimation. Table 3E.5 compares the Coates and SDR models under different reservoir conditions, and it may be advisable to use both methods in an effort to constrain values for permeability.

There are a number of benefits in having available NMR-derived permeability and BVI. This information enables more-accurate quantification of reservoir heterogeneity and improves estimation of reserves and ultimate recovery. Other applications include optimizing the locations of perforations, well spacing, tailoring completions to maximize recovery rates and efficiencies, and improving primary and secondary recovery design schemes.

3E.7.3 Hydrocarbon (Fluid) Typing. The NMR T_2 -porosity relationship in which T_2 is a function of pore size (i.e., S/V ratio, see Eq. 3E.8) holds for water-saturated rocks. The presence of hydrocarbons in water-wet rocks alters the T_2 distribution, thus affecting the porosity interpretation. Despite the variability in the NMR properties of fluids, the locations of signals from different types of fluids in the T_2 distribution can often be predicted or, if measured data are available, identified (Fig. 3E.29).

Hydrocarbon typing and prediction of fluid properties by NMR logs is predicated on reliable laboratory correlations between NMR measurements (i.e., relaxation times and diffusion)

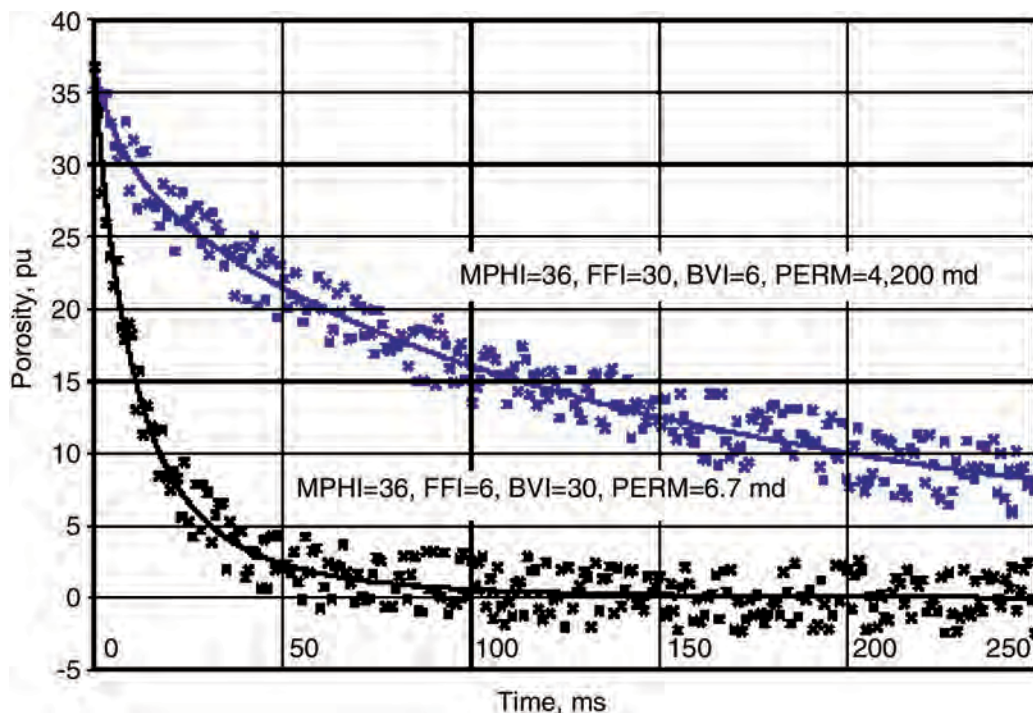


Fig. 3E.26—Variation in T_2 decay with permeability. This plot illustrates the difference between echo trains obtained from formations with similar porosity but different pore sizes. In terms of T_2 distribution, this difference is expressed in different FFI/BVI ratios. The permeabilities were computed using the Timur-Coates model.

and fluid properties [e.g., specific gravity, viscosity, and gas/oil ratio (GOR)]. Early studies were limited to investigations at ambient conditions;⁹⁷ however, using the standard correlations derived from these studies may result in seriously underestimating viscosity. More-recent studies have expanded these correlations to oils and mud filtrates at reservoir conditions.^{97–99}

NMR logging uses specialized CMPG pulse-acquisition sequences to exploit these differences in pore-fluid NMR properties to achieve specific objectives. The CMPG parameters—wait time (T_W), echo spacing (T_E), the number of echoes (N_E), and the number of sequence repetitions—are selected to take advantage of the wide variation in NMR fluid properties (Fig. 3E.30) for estimating total porosity and for hydrocarbon typing. Table 3E.2 illustrates the range of NMR-related properties of fluids for Gulf of Mexico sandstones, for example. Table 3E.6 lists variations in CMPG pulse sequences for different objectives using time-domain analysis (TDA) and Enhanced Diffusion Method (EDM). The multifrequency tools now in service permit the simultaneous acquisition of multiple measurements on the same rock volume using different acquisition sequences during the same logging run. The general approach is to log in a mode that allows gathering the full spectrum of data. Specialized applications, including some direct fluid-identification methods, involve customized-acquisition sequences that require slower logging and acquisition of more echoes.

Determination of the appropriate interpretation method is largely based on the estimated viscosity of the anticipated hydrocarbons (see Fig. 3E.31). These methods will be explained in the following paragraphs.

Selection of the appropriate acquisition sequence and the choice of acquisition parameters depend on the logging objectives and are part of prejob planning. This process considers sever-

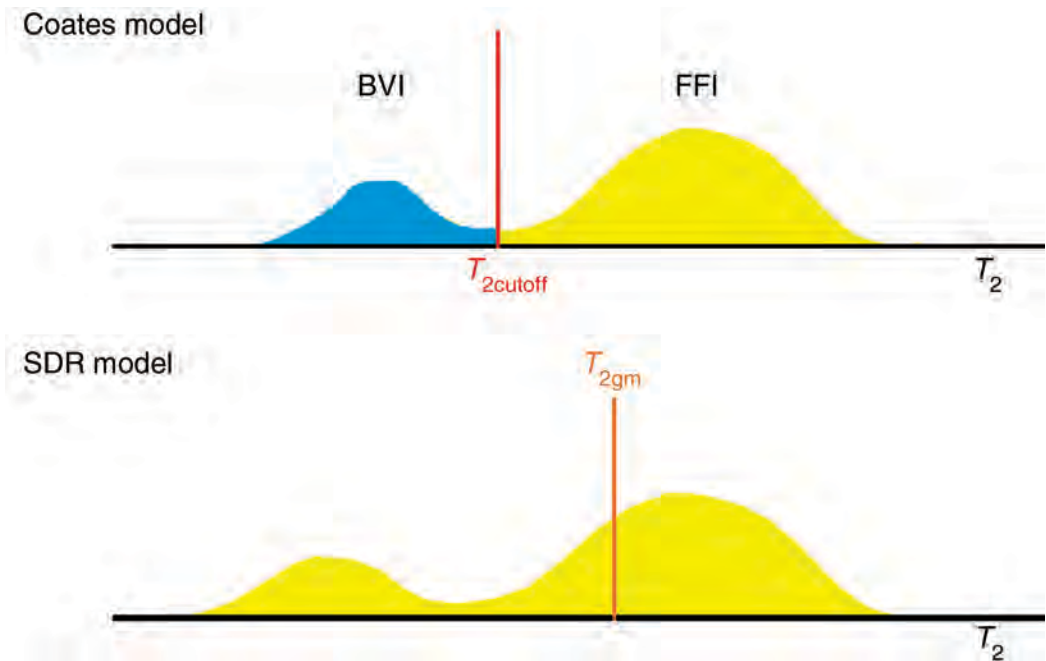


Fig. 3E.27—NMR-permeability models. The free-fluid permeability, Coates, model (top) uses the MFFI/MBVI ratio to describe changes in S/V ratio. The SDR permeability model (bottom) uses an average T_2 value to describe changes in S/V.

al factors regarding the anticipated rock and pore-fluid properties. For example, for characterizing large pores (clastics), clean formations, carbonates, and light oil—all of which are associated with long- T_2 values¹⁰³—a large number of echoes should be acquired, and a long T_W should be used. However, more echoes and longer T_W may require reduced logging speeds. In contrast, characterization of small pores (i.e., low permeability), shaly formations, low porosity, and BVI determination involves the short T_2 component of the NMR-porosity spectrum and often it can be accomplished using fewer echoes and shorter T_W , which may allow normal logging speeds.

Fluid-typing methods fall into two broad categories depending on the NMR properties that are being exploited: (1) T_1 -weighting mechanisms take advantage of differences in fluid T_1 values, and (2) diffusion-weighted mechanisms make use of the diffusion-constant differences between oil and water. There are two general types, or sets, of CPMG acquisitions that are associated with each mechanism: dual T_W and dual T_E . These two sets cover the range of major fluid-typing objectives; some interpretation techniques can use one or the other, or both. Each serves specific purposes and is optimized to provide data for specialized analysis programs. In general terms, each consists of at least two echo-train acquisitions in which one or more parameters are varied. The total, or the difference between the echo-train signals, provides an estimate or indicator of porosity, light hydrocarbons, or oil (Fig. 3E.32).

Advanced hydrocarbon-typing objectives can involve customized-acquisition sequences¹⁰⁴ that are run at reduced logging speeds or even in stationary mode.

T_1 -Weighted Mechanism (Dual- T_W Acquisition). The dual- T_W acquisition method is used primarily to identify and quantify light hydrocarbons (gas and light oil) by separating them from the water signal through T_1 weighting. The dual- T_W acquisition can also provide the standard- T_2 acquisition dataset for determination of spectral NMR porosity, permeability, and

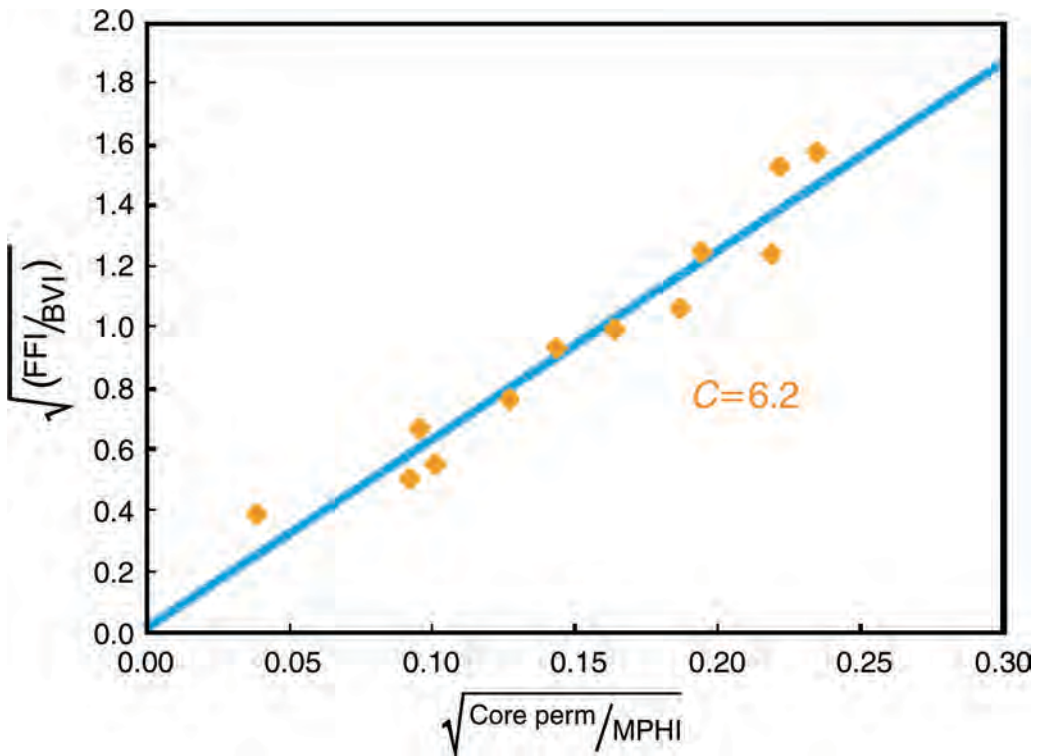


Fig. 3E.28—Crossplot of core and NMR data used for determining the Coates permeability constant, *C*. Assuming *b* = 0 in Eq. 3E.15, core permeability is substituted for *k*, and the slope of the line, *m*, is the *C* value in Eq. 3E.14.

TABLE 3E.5—COMPARISON OF COATES AND SDR MODELS FOR ESTIMATING PERMEABILITY UNDER DIFFERENT FORMATION CONDITIONS		
Formation Condition	Free-Fluid (Coates) Model	Mean <i>T</i> ₂ (SDR) Model
Water saturated	Accurate	Accurate
Oil and oil filtrates	Affected by filtrates	Underestimates
Unflushed gas	Underestimates	Underestimates
Heavy oil	Underestimates	Underestimates
Fractures	Underestimates	Underestimates

Note: The free-fluid model can be corrected for HI in hydrocarbon-bearing intervals, but the SDR cannot be corrected. Both models represent matrix permeability and underestimate fracture permeability.

productivity (mobile fluids). The *T_E* is kept the same in both echo-train acquisitions (0.9 or 1.2 ms), and a short *T_w* (1 second) and long *T_w* (8 seconds) are used. The water signal is contained in both acquisitions, but because of the light hydrocarbons (which have long *T₁* values), the signal is suppressed in the acquisition using the short *T_w*. Thus, the presence of a signal in the difference of the measurements (differential spectrum) is considered a strong indicator of gas or light oils¹⁰⁵ (Fig. 3E.33).

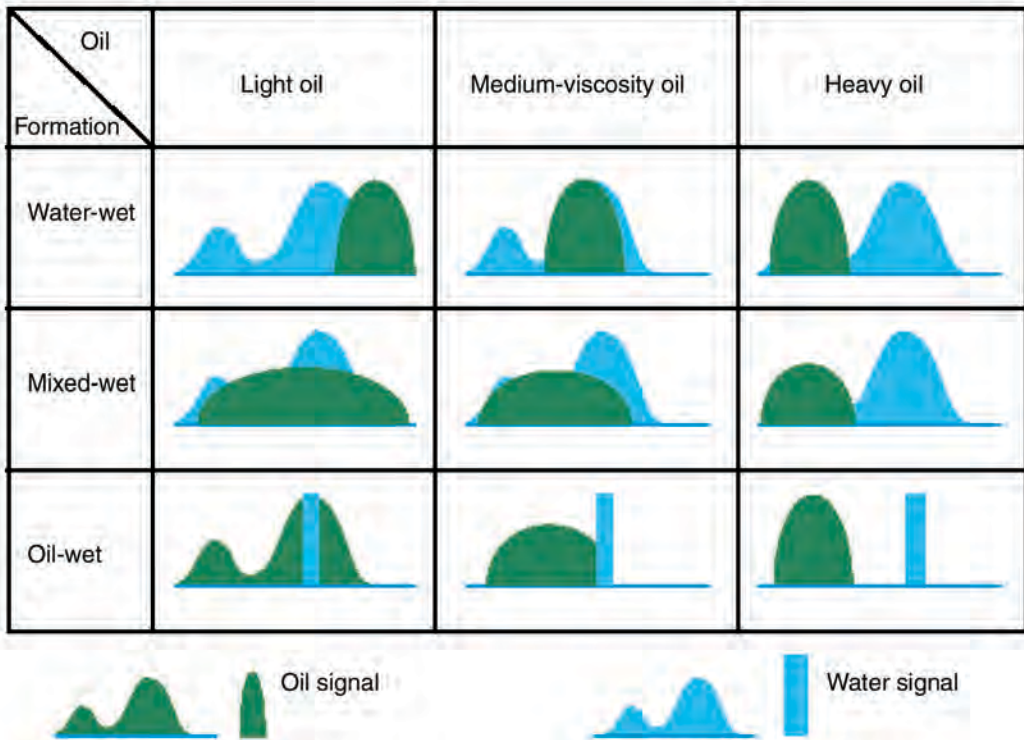


Fig. 3E.29—NMR-oil typing. The position and spread of the oil component in the T_2 distribution depends on oil viscosity and formation wettability. Oil typing is easiest in water-wet formations because of the moderate breadth and distinct positions of the different oil components in the T_2 distribution. Oil typing is most difficult in mixed-wet formations because the oil and water components are broad and overlap one another.

CMPG Sequence Variation	Effect	Objective	Method
Short T_E	Emphasize short T_2 species	Distinguish oil from gas	EDA
Long T_E	Increase diffusion-in-gradient effects	Distinguish gas from oil	EDA
Long T_W	Obtain full-porosity response of long T_1 components	Distinguish gas from oil	TDA
Short T_W	Discriminate against long-polarizing components by incomplete polarization	Distinguish gas from oil	TDA

Fluid volumes can be quantified by integrating the difference into T_2 spectra and correcting for the polarization difference between long and short wait times. Fluid typing and quantification are performed through the differential-spectrum (DSM) method and the TDA method. Two conditions must be met to ensure successful DSM interpretation: T_1 contrast between the hydrocarbon and brine phases (i.e., a water-wet formation containing light hydrocarbons), and T_2 contrast between the gas and oil phases. DSM assumes that the hydrocarbon phases relax unisex-

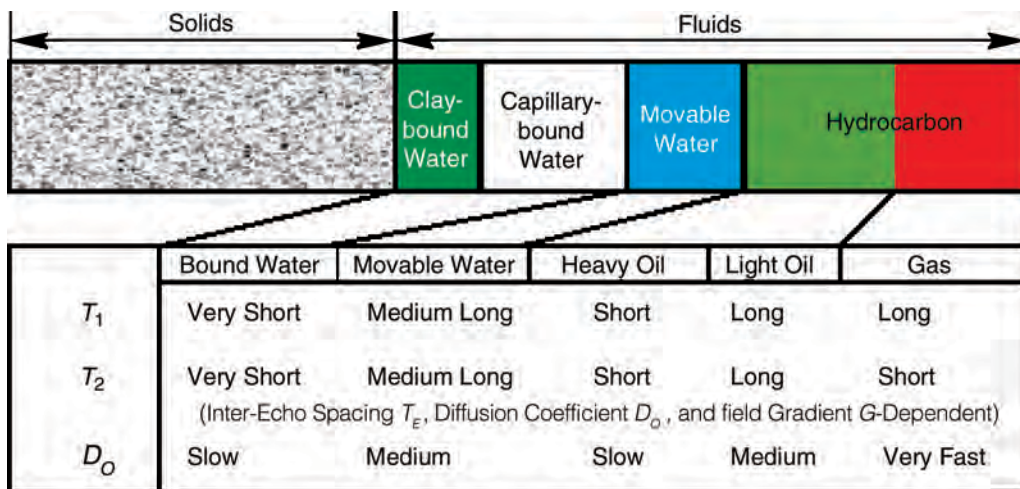


Fig. 3E.30—Typical NMR properties for pore fluids. Differences in these properties between fluids are exploited by methods that use specific acquisition sequences for hydrocarbon typing by use of T_1 or diffusion-weighting mechanisms.

ponentially. DSM is commonly used for: (1) hydrocarbon typing in shaly sands, where the the neutron-density crossover may be suppressed because of the high amount of clay minerals in the rock^{106,107} to confirm the presence of light oil in fine-grained rock, and (2) for gas detection in the presence of OBM invasion.¹⁰⁸ Ideally, DSM can be used to compensate for the hydrocarbon effects on NMR measurements and thereby enable correction of NMR total porosity and NMR effective porosity; however, because of S/N requirements, TDA is the preferred technique for correcting NMR logs.

In contrast to the DSM approach, the TDA technique works directly with the echo-decay data (i.e., in the time domain rather than the T_2 domain; see Fig. 3E.34). The measured long- and short-wait-time decay trains are subtracted into an echo difference that indicates the presence of a long- T_2 component (usually a hydrocarbon). By working in the time domain, when the T_2 inversion is performed, only the hydrocarbon T_2 component will be present.

TDA—an outgrowth of the DSM technique—is based on the fact that different fluids have different rates of polarization (i.e., different T_1 relaxation times).¹⁰⁹ TDA provides the following results:

- Fluid types in the flushed zone.
- Corrected NMR porosity in gas reservoirs.
- Corrected NMR porosity in light oils.
- Complete fluid-saturation analysis in the flushed zone, using only NMR data.

The TDA technique is a more robust method than DSM, in part because it provides better corrections for underpolarized hydrogen and HI effects¹⁰¹ (Figs. 3E.34 and 3E.35).

Several factors inherent in the dual- T_w acquisition require reduced logging speeds: to achieve full polarization (long T_w) in one acquisition channel, to acquire the small signal amplitudes associated with the short T_w values in another other channel, and to meet the requirement for acceptable S/N levels. A new triple-wait-time method addresses these issues and also allows T_1 acquisition.¹¹⁰

Diffusion-Weighted Mechanism (Dual- T_E Acquisition). NMR-logging tools generate relatively large field gradients, which are a function of the operating frequency and tool type. If the pore fluids have high diffusivity constants (D_0), these large gradients may cause diffusion

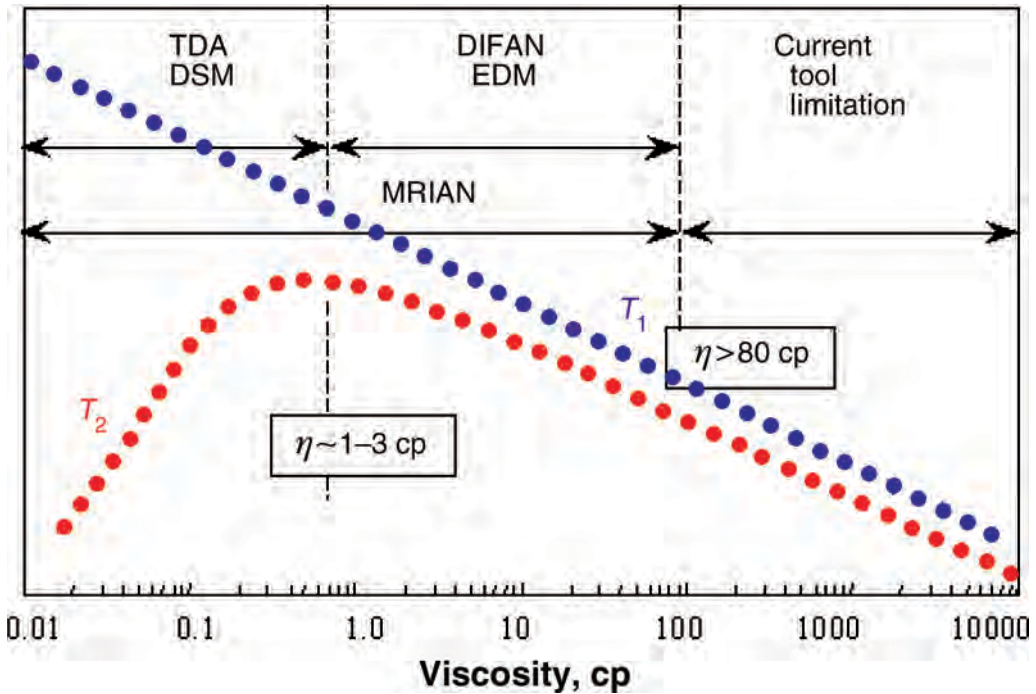


Fig. 3E.31—Graph indicating the current viscosity limits for NMR-interpretation techniques. The resistivity-density technique is limited to gas reservoirs, and the SSM method has been effectively replaced by the newer DSM method. The y-axis is the relaxation time.

to become the dominant T_2 -relaxation mechanism, even at a reasonably short interecho time. The T_2 contrast between the liquid and gas phases can then be exploited for hydrocarbon typing.

The identification of viscous oil in water-wet rock using T_1 -weighting mechanisms (dual- T_W acquisition) is very difficult because there is little T_1 contrast between water and viscous oil. However, a significant difference in the diffusion characteristics of water and viscous oil is used to create a T_2 contrast that separates the two NMR signals, thereby permitting identification.¹⁰² The inter-echo spacing, T_E , is chosen long enough that the water and oil signals are fully separated in the T_2 -domain (i.e., water is at lower T_2 than oil; see Fig. 3E.36).

Diffusion-weighting techniques, such as shifted-spectrum method (SSM), enhanced-diffusion method (EDM), and diffusion analysis (DIFAN), use the dual- T_E acquisition to create this T_2 contrast. T_E is chosen such that diffusion, rather than surface relaxation, is the dominant relaxation mechanism, and thus, the upper limit of T_2 for pore water is T_2 diffusion, designated T_{DW} . The dual- T_E acquisition set uses long T_W and T_E values, typically 0.9 or 1.2 ms and 3.6 or 4.8 ms, respectively. In this acquisition, the fluid with the larger diffusion constant (water) has a spectrum shifted more to earlier times than the fluid with the smaller diffusion constant (viscous oil). The presence in the spectra of a minimally shifted portion identifies high-viscosity oil in the formation (see the lower portion of Fig. 3E.37).^{102,111} These techniques are primarily used for identifying the presence of viscous oil. They are also used in carbonates in which a reduced surface relaxation (compared to clastics) may also result in a reduced T_1 contrast.^{112,113}

SSM. This method was the first developed using the diffusion-weighted mechanism and was originally developed for use in gas reservoirs as a qualitative technique (see the upper portion of Fig. 3E.37). However, because of signal-processing difficulties and slower logging speeds, this method was effectively replaced by the EDM.¹⁰⁵

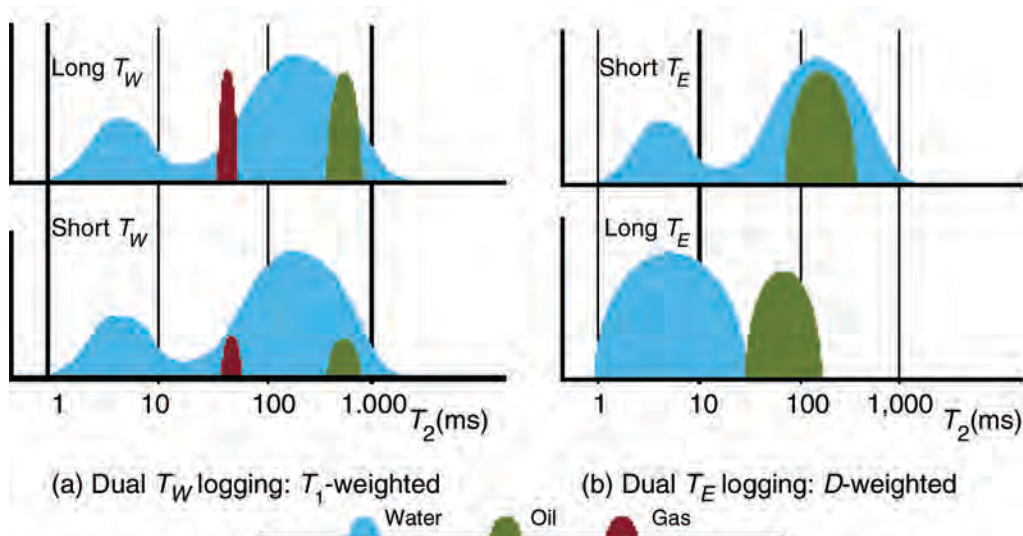


Fig. 3E.32—CPMG acquisition types used for hydrocarbon typing: (a) a T_1 -weighted method is used to differentiate hydrocarbons from water, and (b) a diffusivity-weighted method is used to differentiate viscous oil from water or to differentiate gas from liquids.

EDM. This method is the later variation of SSM. Depending on oil-NMR properties and the job objective, EDM data processing can be done in either the T_2 domain or time domain.¹⁰² If the EDM objective is to discriminate pay from nonpay, then a single CPMG measurement with long T_W (for full polarization) and long T_E (for diffusion enhancement) is sufficient; thus, standard- T_2 logging with a long T_E can be used. If the EDM objective is to quantify fluids in a pay zone, then dual- T_E logging will be required. The short- T_E measurements will provide correct MPHI and BVI. If the T_2 contrast over the zone of interest is not expected to be large enough to separate the T_2 values of water and oil, then dual- T_W logging with a single, long T_E may be required to obtain data for TDA processing.

One caveat for users of the EDM: the flushed-zone saturation (S_{xo}) obtained from EDM may not reflect the true volume of residual hydrocarbons in the flushed zone if the faster portion of the hydrocarbon's T_2 spectrum gets fully polarized by both wait-time measurements. A correction to S_{xo} can be applied if the full-hydrocarbon T_1 spectrum can be determined by other means, such as laboratory measurements.

DIFAN. DIFAN is an empirical model used for quantitative-diffusion analysis. This method uses a dual- T_E acquisition and is useful for typing and quantifying oils with viscosities ranging between 0.5 to 35 cp at reservoir conditions (i.e., temperature $\geq 200^\circ\text{F}$ and pressure $\geq 2,000$ psi). It is not recommended for light oils and condensates because the D_0 contrast between hydrocarbons and water is too small.

Neither EDM nor DIFAN is recommended for use in high-viscosity oil (heavy oil) because the difference between the T_2 values of dead oil and irreducible water is too small. The DIFAN model generates two T_2 distributions using the two echo trains generated from dual- T_E logging.

Echo Ratio Method. An apparent diffusion coefficient, calculated from the ratio of long and short T_E echo-train data (time domain), serves as a qualitative gas indicator.¹¹⁴ This method is accurate and provides a direct measurement of gas volume, but requires high HI values for good results.

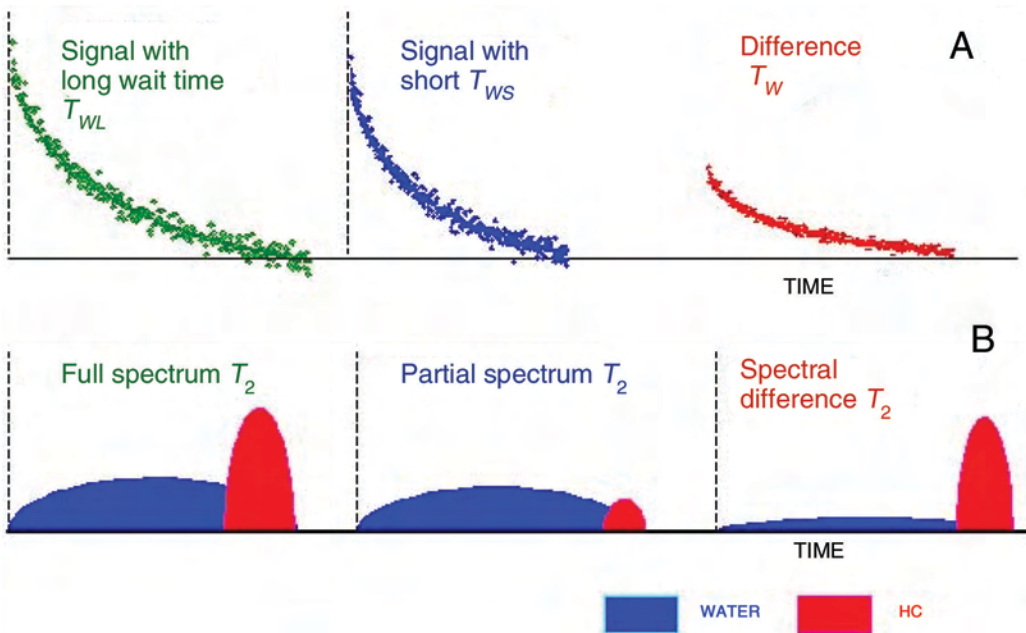


Fig. 3E.33—Methods using T_1 -weighting for hydrocarbon typing: (a) in TDA, T_2 echo-train subtraction takes place in the time domain, and (b) in the differential-spectrum method (DSM), T_2 echo-train subtraction takes place in the T_2 domain.

Multifluid (Forward Modeling) Methods. The dual- T_W and dual- T_E techniques described above only provide T_2 distributions and are considered one-dimensional methods.¹¹⁵ Oil-saturation determination using these methods may be difficult or even impossible because differential diffusion-weighted methods assume that NMR water and hydrocarbon signals can be cleanly separated by subtracting the acquisitions made at different T_E values. In practice, however, partial—or even total—overlap is common.

To avoid these problems, new multifluid-forward models were developed to take advantage of the full suite of data obtained using the latest multifrequency logging tools. These models perform a simultaneous inversion of the NMR fluid properties obtained in multiple parameter-domain dimensions (e.g., T_1 , T_2 , and D_0).^{59,116–120} These methods make use of the enhanced T_2 relaxation in a magnetic-field gradient (i.e., incorporate measurement of the diffusion coefficient, D_0) and the large contrast between diffusion coefficients of oil and water. In effect, they are simultaneously combining both T_1 - and diffusion-weighted processing techniques, and thus, provide more accurate and robust results. In addition to porosity and permeability information, the output data from these inversion models are plotted as two-dimensional plots (e.g., D - T_2 plot) in which the oil and water signals are clearly separated.¹²¹ Recent two-dimensional NMR techniques include diffusion editing, diffusion mapping, and relaxation-diffusion 2D.^{26,118,122–125}

Multidimensional (2D and 3D) NMR analysis greatly increases the accuracy of fluid typing and saturation determination.¹¹⁵ These methods are particularly useful for identifying highly diffusive fluids (e.g., gas, condensate, and light oil)^{59,125–128} and for identifying wettability alteration caused by OBM-filtrate invasion or chemical surfactants used in enhanced recovery operations.^{118,127,129} This information is essential for reservoir simulation, development, and production.¹³⁰

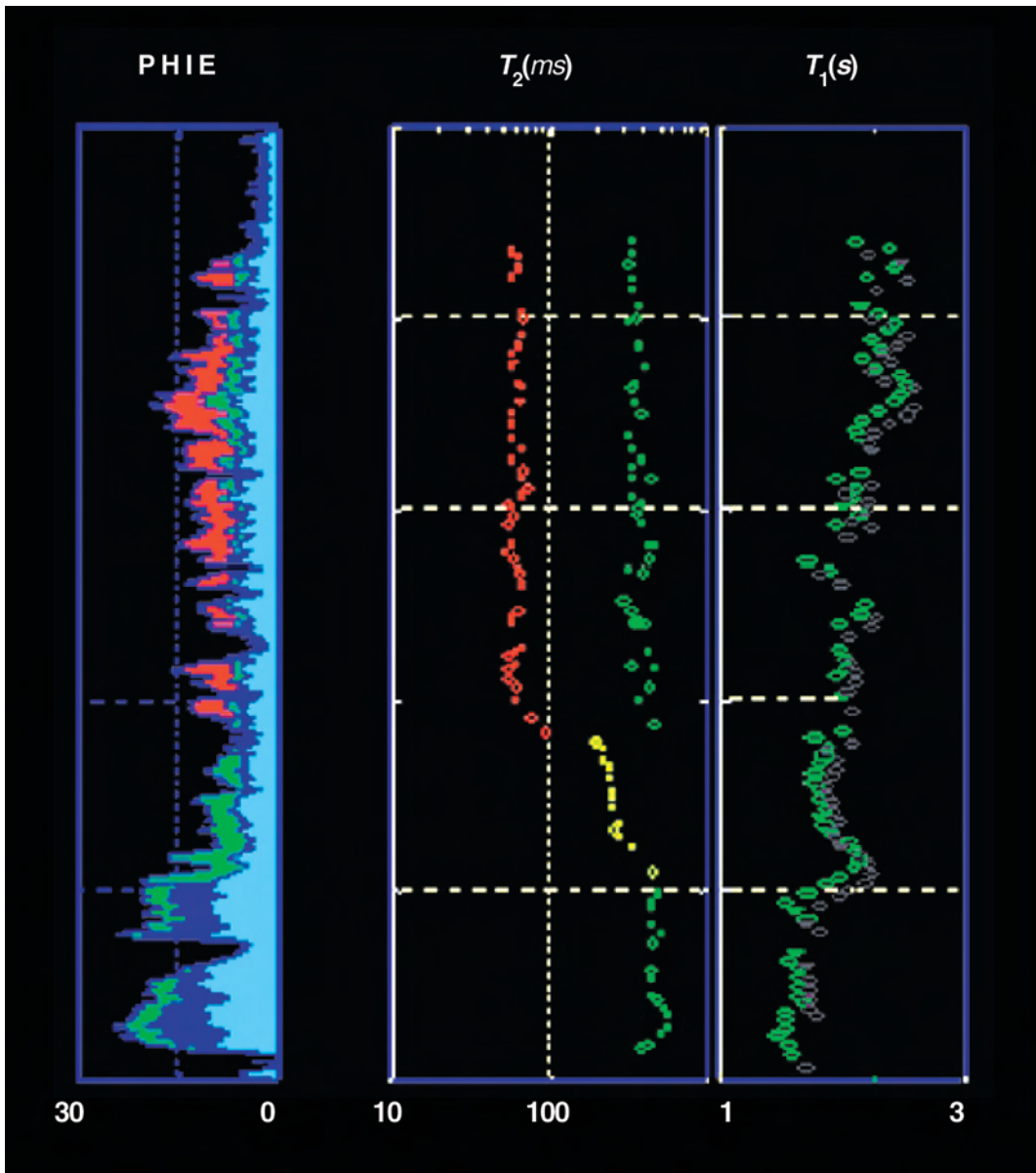


Fig. 3E.34—Example of TDA. Track 1 shows the pore volumes for gas (red), OBM filtrate and/or native oil (green), movable water (dark blue), and capillary-bound water (light blue) obtained from TDA quantitative analysis using an MRIL data set. Tracks 2 and 3 show the T_2 and T_1 values, respectively, of gas and light oil calculated through TDA. The lower part of Track 2 shows the oil/water and gas/oil contacts, while the upper part of the track indicates the presence of gas and oil.

3E.7.4 Residual Oil (S_{xo}) Calculation. Estimation of residual-oil saturation is one of the oldest applications of NMR logging. Unlike resistivity-log analysis, NMR analysis does not rely on formation-water salinity to obtain water saturation. This feature provides NMR logging with a distinct advantage over conventional resistivity analysis in mixed or unknown salinity conditions—an advantage that can be extremely useful in waterflood or steamflood projects for evaluating residual-oil saturation after the flood or to look for bypassed oil. Initially, NMR evaluation

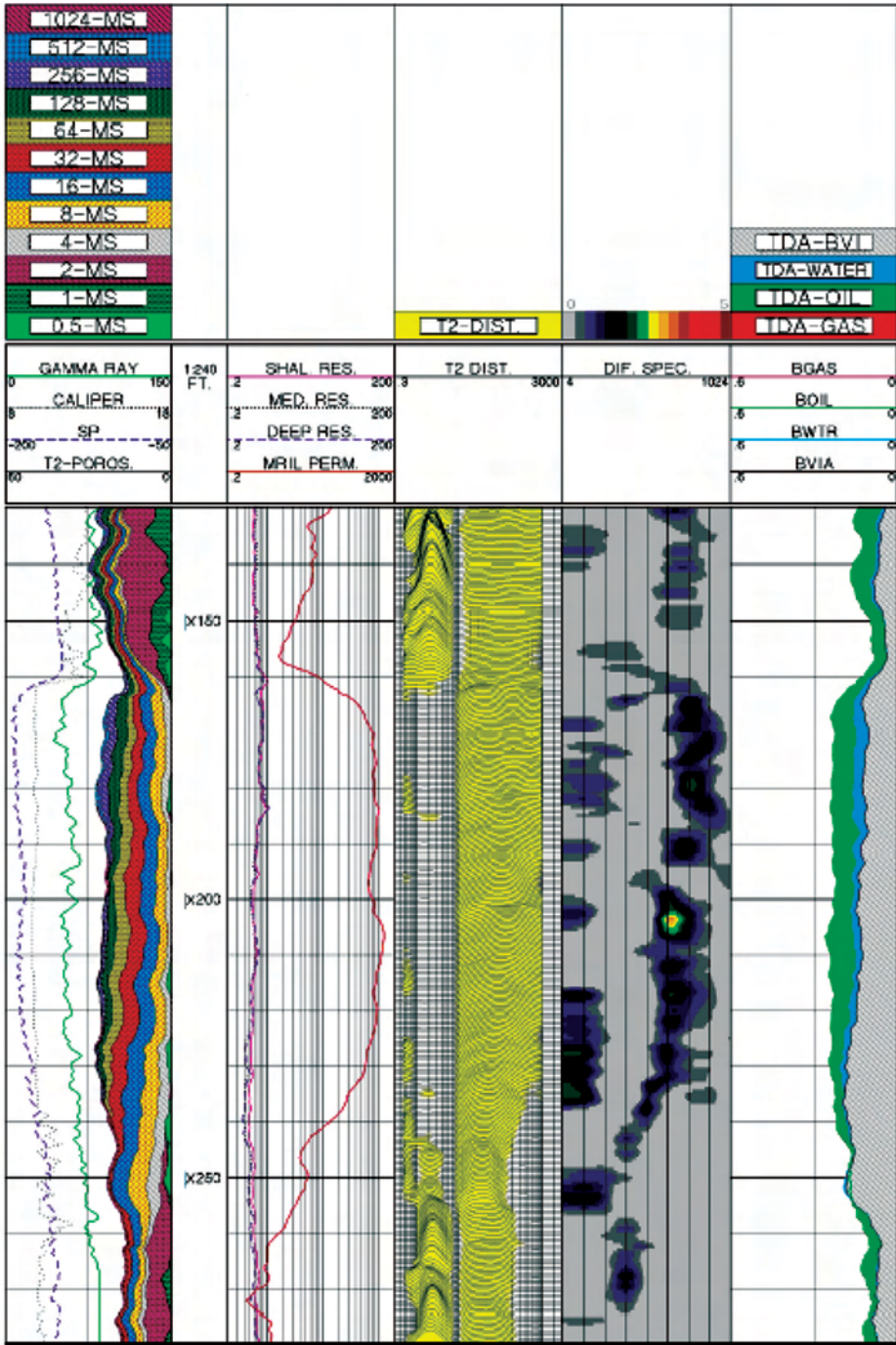


Fig. 3E.35—Log example showing the results of DSM and TDA analysis. Light hydrocarbons can be identified through the subtraction of echo trains obtained at two polarization times. Track 4 displays the differential spectrum obtained from the subtraction of the two separate T_2 distributions derived from echo trains acquired with short- (T_{WL}) times, $T_{WS} = 1$ second and $T_{WL} = 8$ seconds. The water signals in each completely cancel, while hydrocarbon signals only partially cancel and remain when the two T_2 distributions are subtracted from one another. Track 5 displays the TDA results. TDA is performed in time domain (as opposed to T_2 domain), and can quantify up to three phases (gas, light oil, and water; gas and water; or light oil and water).

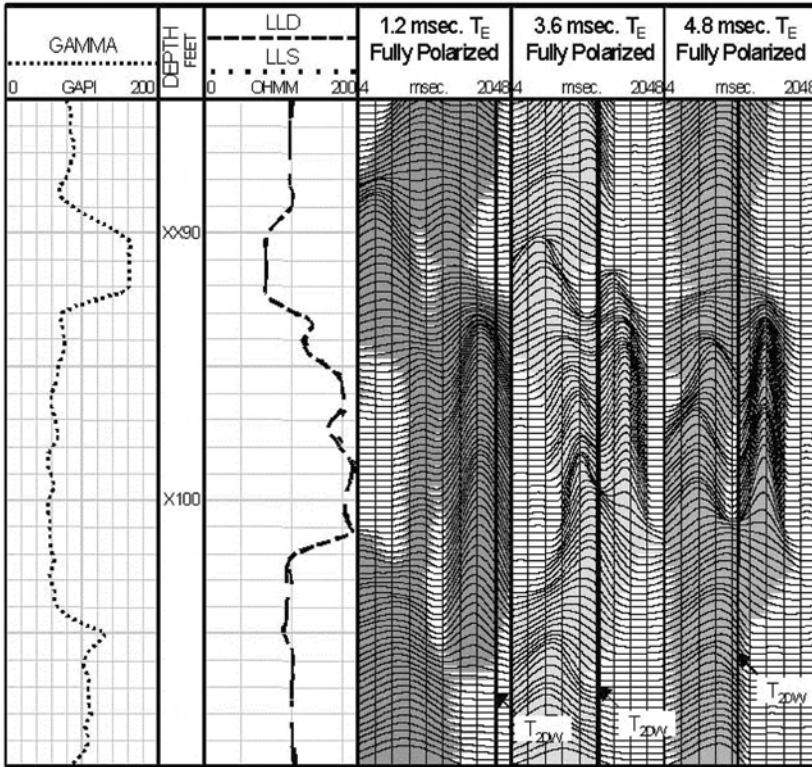


Fig. 3E.36—EDM example. The existence of a signal on the T_2 distribution longer than T_{2Dw} indicates the presence of oil in the formation. In this log display, the T_2 distributions from $T_E = 1.2, 3.6,$ and 4.8 ms are shown in Tracks 3, 4, and 5, respectively. In the EDM results, in Track 4 and 5, a significant signal to the right of the T_{2Dw} line indicates obvious oil zones. Also note the increased definition and separation in the fluid signal that occurs in Track 5 because of the increased T_E . This observation is used to recognize pay in EDM-log displays.

of residual-oil saturation required use of a dopant (e.g., Mn-EDTA and MnCl₂) to flush the invaded zone with paramagnetic ions to shorten the bulk relaxation time of the brine. This process enabled separation of the oil and water signals, leading to direct measurement of S_{xo} . With the combination of modern multifrequency NMR tools and new methods of analysis, such as EDM and TDA, the use of borehole dopant is no longer necessary.^{25,111} Standalone NMR interpretation is possible in OBM, but in water-base-mud (WBM), it is possible only when S_{wirr} is known.

3E.7.5 Viscosity Evaluation. In water-wet rocks, the NMR-relaxation spectrum is controlled by viscosity^{118,131}; relaxation is directly related to viscosity, η , by Eq. 3E.17:

$$T_1 = 1.2 \times T_K / 298\eta . \dots\dots\dots (3E.17)$$

For oil and water, the diffusion constant, D_0 , can be approximated by Eq. 3E.18:

$$D_0 = A \times T_K / 298\eta, \dots\dots\dots (3E.18)$$

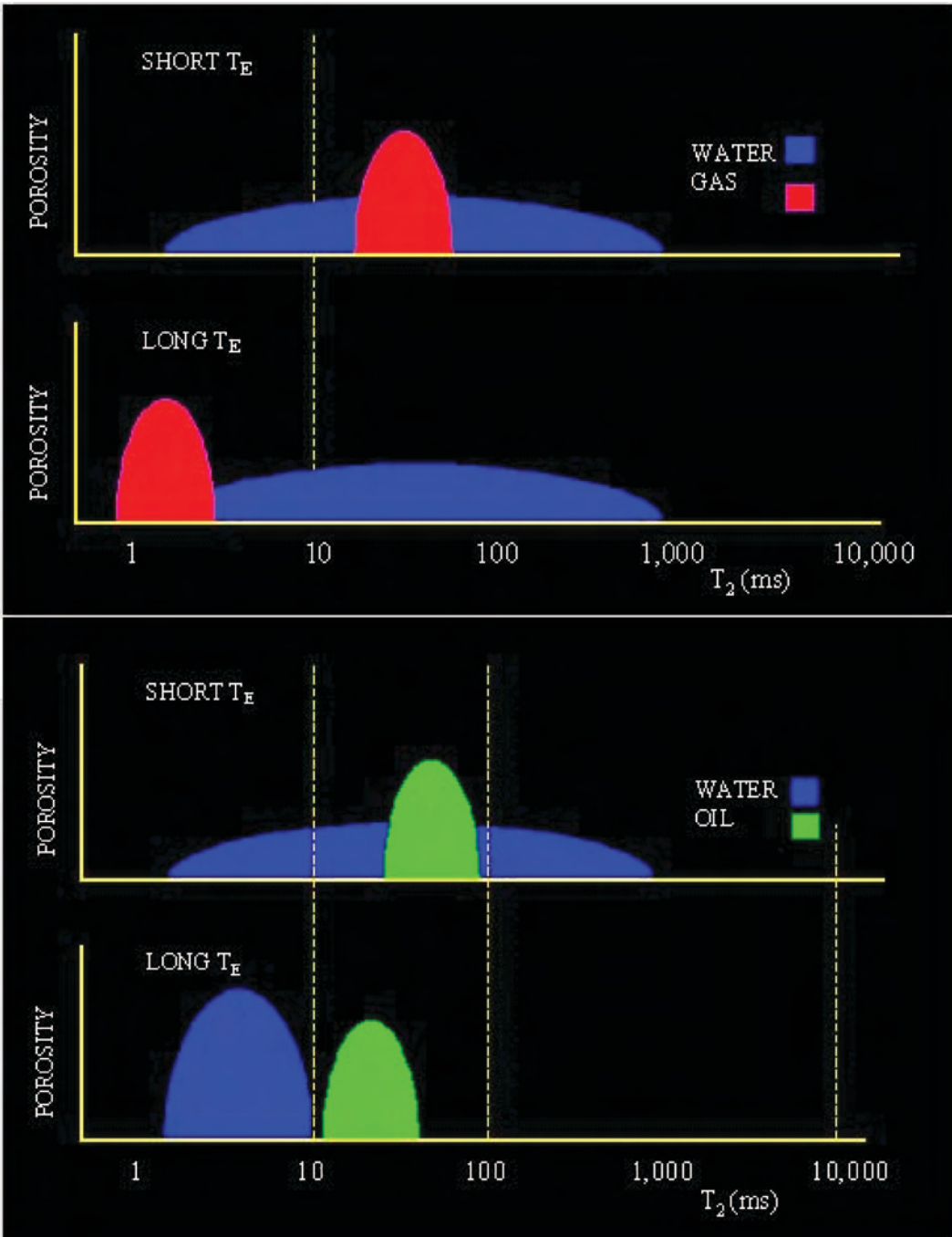


Fig. 3E.37—SSM application in gas (upper) and oil (lower) reservoirs.

where $A = 2.5$ for water, $A = 1.3$ for oil, and T_K is temperature in K.

NMR properties of gas can be obtained from published charts that relate viscosity to (1) the center of the relaxation curve, (2) to an American Petroleum Inst. (API) standard value,¹⁰⁵ or (3) from published formulas.¹⁰¹ These published sources assume that methane is the dominant component of the gas. In the absence of laboratory data at in-situ conditions, reservoir

NMR properties can be estimated by use of Eq. 3E.17. One note of caution: Eqs. 3E.17 and 3E.18 are based on “dead oil” measurements. As mentioned earlier, the relaxation-time dependence on viscosity/temperature of live crude oil may differ significantly from correlations based on hydrocarbon liquids at ambient conditions.^{97–99}

3E.7.6 Anisotropy and Geomechanics. NMR T_1 and T_2 relaxometry and derived permeability can be used to determine the Biot elastic constant, which is used for estimating pressures that are critical to sand control, hydraulic fracturing, wellbore stability, and determination of formation stress.^{132,133}

3E.7.7 Low-Permeability (Tight) Sandstones. Field experience indicates that invasion or imbibition in tight sands is very shallow. Depending on borehole size, the diameter of invasion, and fluid properties, a mandrel tool may have sufficient DOI to measure beyond the flushed zone. A combined interpretation using both T_1 and T_2 can provide positive identification of fluids in these reservoirs.¹³⁴ In addition, in these tight formations, in which formation testers typically may not obtain a fluid sample within a reasonable time period, NMR fluid characterization can separate hydrocarbon from oil filtrate and other pore fluids.¹³⁵

3E.7.8 Heavy Oil, Tar Sands, and Tar Mats. The early acquisition of reliable viscosity information is essential to efficient development of heavy-oil reservoirs. NMR logs offer a viable alternative to downhole fluid sampling for determining viscosity information in heavy-oil reservoirs.^{136–138} The presence of tar mats in a reservoir, commonly near the bottom of the oil column, may form vertical permeability barriers and, thereby, isolate the oil leg from the water-drive aquifer. NMR logs, in conjunction with conventional logs, can provide accurate identification of tar-mat levels and viscosity estimation, from empirical relationships.¹³⁹ (See the Job Planning section of this chapter.)

3E.7.9 Carbonates and Complex Lithologies. NMR-log evaluation is relatively routine in what might be termed “conventional reservoirs,” namely those of homogenous lithology and uniform pore sizes, typically sandstone and chalk reservoirs.^{62,140} In contrast, log evaluation of complex and heterogeneous reservoirs, with complex pore geometries, is not straightforward. These reservoirs include, in particular, the highly important Middle East carbonates, as well as other reservoirs comprised of mixed lithologies and mineralogies, or both, in which wettability may also vary. In these reservoirs, there is likely no simple relationship between petrophysical properties and porosity. Instead of a dependence on the volume of pore space, they are dependent on the typically heterogeneous pore distribution, pore types, pore connectivity, and grain sizes. This fundamental difference between siliciclastic and carbonate rocks (primarily the result of diagenetic processes) limits the applicability of routine NMR methods, especially permeability evaluation.¹⁴¹ Improving NMR evaluation of carbonates has proved challenging and is the subject of a number of recent studies and proposed techniques.^{120,141–144} (See the Job Planning section of this chapter.)

3E.7.10 Pseudocapillary-Pressure Curves. As discussed in the Petrophysics section, establishing a correlation between NMR T_2 distribution and MICP is fundamental to NMR interpretation and the computation of S_w . Once such correlations are established for a particular reservoir or field, pseudocapillary-pressure curves can be generated directly from the NMR-log relaxation-time distributions.^{145–148}

3E.7.11 Producibility. Accurate determination of BVI enables evaluation of reservoir-fluid (e.g., gas, oil, and water) contacts, production characteristics (producibility), and the determination of net and recoverable reserves.^{149,150} Furthermore, NMR-derived permeability can be used

to generate idealized flow profiles across a completion interval. These profiles provide a diagnostic tool for identifying nonflowing portions of the zone and the need for remedial work.^{151,152}

3E.8 Combined NMR Applications

NMR tools have shallow depths of investigation and provide results only for the invaded zone. NMR-log data can be integrated with core data and conventional log data (i.e., neutron, density, acoustic, and resistivity) in post-acquisition processing to provide improved determinations of reservoir rock properties, hydrocarbon storage capacity, and reservoir productivity in a variety of environments including gas-bearing and low-resistivity reservoirs. Interpretation models that include NMR data can provide more reliable results than those using only conventional logs.

3E.8.1 NMR-Resistivity Combination. The combination of NMR and deep-resistivity data provides a complete analysis of the fluids in the uninvaded zone. Resistivity measurements alone cannot distinguish between capillary-bound and movable water, but they do represent deep investigations of fluid saturation. Furthermore, resistivity-based methods are often inadequate or unreliable in reservoirs in which salinity and lithology vary. The addition of NMR-derived BVI and CBW from the flushed or invaded zone can significantly enhance the estimation of resistivity-based fluid saturation, both in clastics and carbonates. The addition of NMR data allows the identification and evaluation of water-free production in low-resistivity formations (**Fig. 3E.38**).^{107,153,154}

The combination of conventional deep-resistivity data with NMR-derived CBW, BVI, FFI, and MPHI can greatly enhance petrophysical estimations of effective pore volume, water cut, and permeability. It is the preferred technique for identifying low-resistivity pay zones. **Fig. 3E.38** presents the results of Halliburton's MRI analysis (MRIAN) service in a turbidite sequence. The sand below XX200 depth has an average resistivity of approximately 0.5 ohm-m (Track 2) and average neutron-density porosity of approximately 38% (Track 4). A quick look, or preliminary analysis, using only the conventional data presented in Tracks 1, 2, and 4, would label this a wet zone. MRIL-NMR data are also presented in Track 1 (T_2 -distribution bin data), Track 2 [NMR-derived permeability (Coates)], and Track 3 (VDL presentation of T_2 distribution). The MRIAN results, BVI, and FFI are presented in Track 4. BVI gradually increases with depth, suggesting that the sand is fining downward (i.e., as sand grains become finer, the volume of capillary-bound water that they hold increases). Comparison of the BVI with the resistivity profile (Track 2) shows that the resistivity decreases where the bound water increases. The MRIAN analysis clearly shows that the zone does not contain any movable water and will produce only oil. The interval below XX200 was tested and produced oil with no water.³²

The combination of NMR fluid identification with resistivity-derived saturation provides a better understanding of hydrocarbon movement in gas monitoring, as seen in the following field example (**Fig. 3E.39**).

NMR and LWD logs were run in a deviated Middle East light-oil carbonate reservoir to monitor gas injection. NMR logs were well suited for gas monitoring by use of the TDA technique and were not affected by formation-water salinity.³¹ NMR gas-corrected porosity was in close agreement with core porosity; conventional log-porosity was low because of salinity effects. Combined interpretation of water-saturation analyses from tools with different depths of investigation identified the movable fluid present in the reservoir as WBM filtrate. Track 1 contains T_2 bin data and conventional SP and gamma ray curves; Track 2 shows NMR-permeability derived from the standard Coates model and LWD resistivity; Track 3 contains a T_2 distribution in a variable-density format; Track 4 contains T_2 distributions of data acquired with long T_W and short T_W ; Track 5 is the differential spectrum; Track 6 contains TDA results; and Track 7 contains MRIAN results.

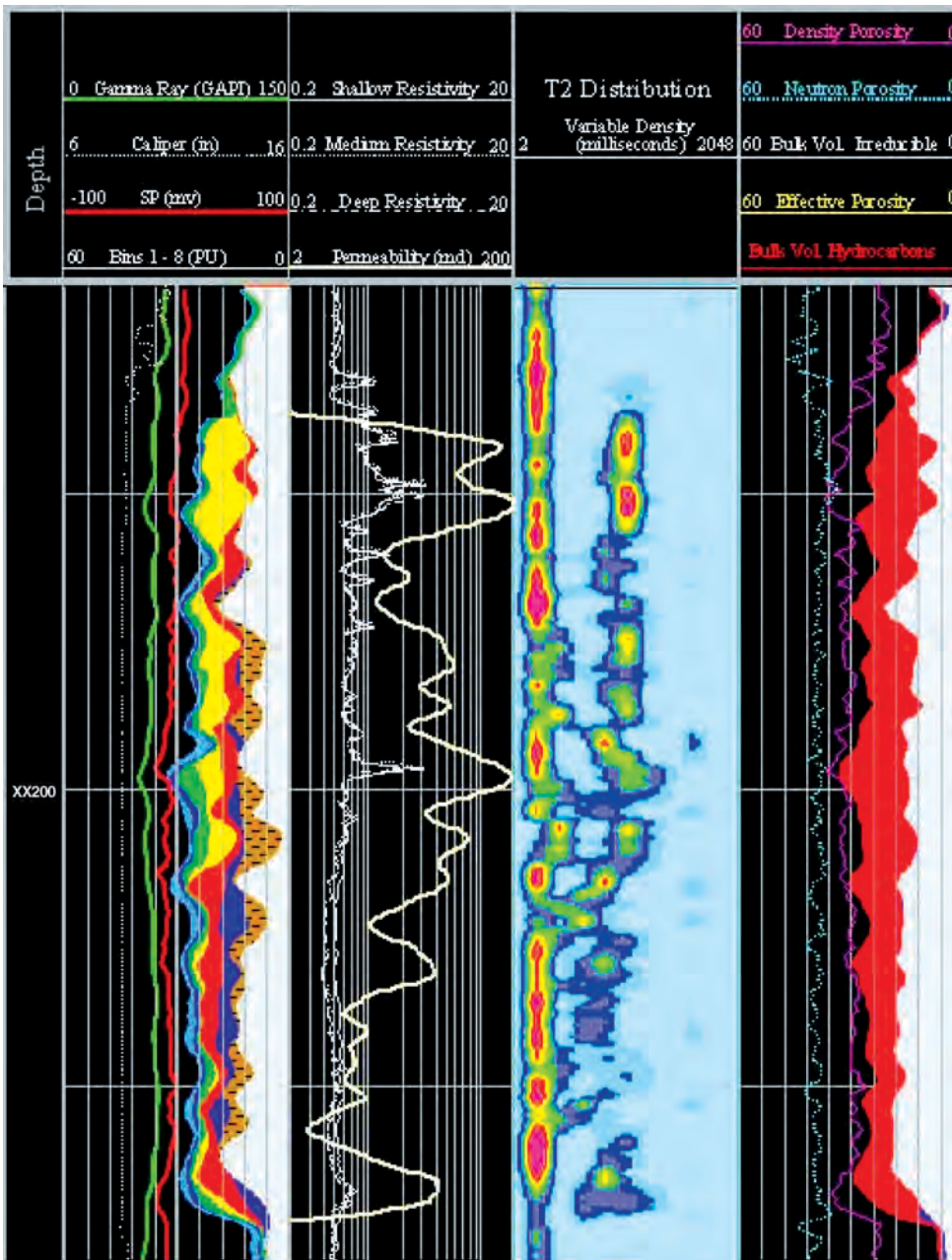


Fig. 3E.38—Integrated-NMR-resistivity shaly sand analysis. Whereas resistivity logs (Track 2) read very low values and indicate that the zone below XX200 is water wet, NMR measurements show that BVI (Track 4, gray) increases with depth. However, T_2 measurements (Tracks 3 and 4) suggested the presence of hydrocarbon, which testing confirmed in what turned out to be a water-free zone.

3E.8.2 NMR Acoustic/Density Combination. Because NMR tools are affected by the lower HI in gas-bearing reservoirs, a moving tool may not fully polarize the gas, which has a long T_1 . Conventional acoustic and density logs are not influenced by these factors and, when used jointly with NMR logs, they can provide robust porosity evaluation.^{155,156} The basic assump-

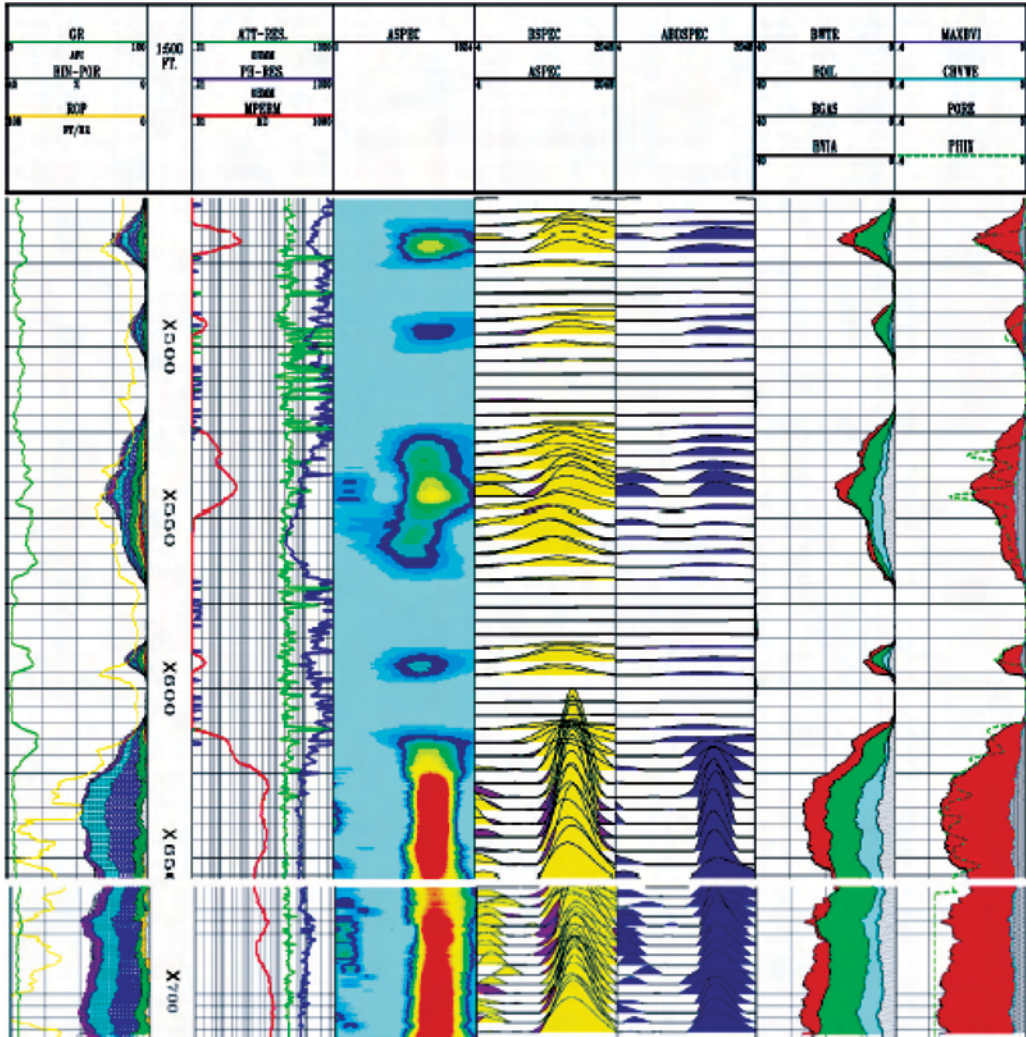


Fig. 3E.39—Integrated-NMR and resistivity analysis.

tions of these techniques are that the reference porosity is measured correctly (e.g., appropriate matrix density is used) and that the NMR T_w is long enough to recover the water but not all of the gas. If the T_w is too short, a false gas signal may be seen. One way to check whether the T_w is appropriate is to log with a longer wait time (e.g., $T_w = 2$ seconds rather than 1 second) and look for a significant difference in porosity (i.e., the porosity may be slightly higher because of increased polarization of the gas).

3E.9 NMR-Log Quality Control

Quality control (QC) procedures are especially important during the creation of integrated computed products^{31,78,157} and to ensure optimal NMR data acquisition. NMR tools have calibration standards and real-time QC indicators. Standard techniques include examination and verification of service company calibrations and QC curves, and calibrations and examination of the repeatability of the computed porosities. Processed results should agree with other data from

logs, core, and/or formation test results. NMR QC includes a series of prejob and post-job checks and calibrations.

3E.9.1 Prejob Calibration and Quality Checks During Logging. Several prejob QC steps are necessary to ensure reliable results. These steps are described in this section.

Frequency Check. The amplitude of the NMR measurement is proportional to the square of the magnetic field strength in the measurement region. To attain maximum signal strength, the tool must operate at the correct frequency. Because temperature affects magnetic field strength, a frequency sweep is recorded before the calibration and logging run and is repeated downhole to account for changes in temperature. The CMR tool includes sensors that monitor temperature and changes in the magnetic field strength and adjusts frequency automatically to changes in sonde temperature. The accumulation of metal drilling debris on the magnets can adversely affect the NMR measurements, and the tool may require occasional retuning. The MRIL-gradient field creates a self-correcting effect, and the tool rarely requires retuning after the initial downhole tuning. Drifting off frequency may present itself as a loss of porosity (CMR) or loss of precision (MRIL). Field calibration should be included on the log.

Statistical Calibration. A statistical calibration to 100% porosity (water) should be made at the shop and/or wellsite before and after every logging job for all combinations of T_E frequency and for expected quality factor (Q level); calibration should be done at the shop at least monthly. Primary calibration involves either a flask of fluid (for the CMR tool) or a water tank (for the MRIL tool).

HI. NMR-tool calibration uses water where $HI = 1$. However, when the HI of the formation pore fluids is expected to be less than one, the NMR-porosity readings will be proportionally lower, and correction is necessary. An NMR tool's processing software will, therefore, compute a correction based on the salinity of the mud filtrate and on the maximum formation pressure and temperature. In general, a mud-filtrate relaxation time of < 200 ms may suppress the long T_2 components in a T_2 distribution. A specific HI value may be used when residual hydrocarbons or OBM filtrates are present.

System Gain. CMR and MRIL tools monitor and calibrate in real time for downhole changes in system gain. A gain measurement is made as a part of each pulse sequence. Gain indicates the amount of loading applied to the NMR tool's transmitter circuit by borehole fluid and formation resistivity. Gain is affected by changes in temperature, mud conductivity, and borehole size. Because gain is frequency dependent, the operating frequency of a tool should be set to achieve maximum gain. Abrupt changes or spikes in gain should not be present. For a particular MRIL tool, the gain value determines the appropriate acquisition power (Q) level.

System Noise (Ringing). Noise contamination of the spin-echo signal, known as ringing, may be a remnant of the RF pulsing process. Noise can interfere with the echo trains and, when present, is usually evident in the NMR porosity readings, either as poor repeatability or lack of agreement with other tools. Both tools (CMR tool and MRIL tool) monitor ringing.

χ . χ is a measure of the quality of fit between the calculated decay curve and the recorded echo amplitudes. Problems with the echo data are likely to be reflected in the χ curve. In general, the value of χ should be less than two but may average slightly higher in certain situations. Spikes in χ may correlate with spikes in porosity⁷⁸ and usually indicate tool problems, even if χ remains lower than two. χ serves as a primary MRIL log-quality indicator and is monitored while logging.

Correction for RF-Tipping Pulse. The strength of the CMPG RF pulse (B_1) that produces proton tipping and rephasing is measured as part of every pulse sequence and requires correction for changes in borehole temperature. If the pulse angles are either $< 90^\circ$ or $> 90^\circ$, the magnetization will be undertipped or overtipped, respectively. The measured amplitude will, thus, be too small, and porosity will be underestimated. The B_1 curve should be relatively con-

stant but should show some variation with changes in borehole and formation conductivity. B_1 will decrease across conductive washouts and conductive formations. Changes in the B_1 values should track changes in total conductivity and vary together in the same direction as gain. The need for excessive correction (i.e., $> 5\%$ of the optimum shop-peak value) may indicate a tool problem and can result in undertipping or overtipping of the protons, a reduced S/N ratio, and a loss of precision in determining porosity. Sudden changes in the B_1 correction curve may also indicate a tool problem.

γ . Regularization methods are used to select a smooth T_2 distribution that is consistent with the spin-echo sequence. These methods require a parameter γ that is automatically computed from the raw echo data. Values of γ are dependent on the S/N ratio and the shape of the underlying T_2 distribution. In high-S/N environments (i.e., medium-to-high-porosity formations), typically $\gamma < 5$; in low-S/N environments (i.e., tight sands and shales), $\gamma > 10$.

Repeatability. Whenever possible, a repeat pass should be recorded with parameters identical to those used in the main pass. These parameters include T_W , N_E , and T_E , as well as computation parameters such as the echoes selected for processing, and for $T_{2\text{cutoff}}$. The generally accepted goal for porosity is a standard deviation of 1 porosity unit (p.u.). Repeatability of BVI is usually > 1 p.u., and repeatability of FFI is usually $\gg 1$ p.u.

If repeatability is a concern, decreasing logging speed or increasing the degree of echo data stacking during logging in post-job processing can improve S/N ratio and repeatability. Typically, fluid-typing applications using dual- T_W or dual- T_E methods are more sensitive to data repeatability than a standard NMR log acquired for porosity, bound fluid, and permeability.

A given data set should agree with similar data acquired by other logs, formation tests, and/or core analysis.

Environmental Corrections. NMR logs are similar to neutron logs in that they respond to the hydrogen volume present in a sample. Because the hydrogen volume changes with temperature and pressure, NMR logs require environmental corrections for temperature and pressure similar to those applied to neutron logs. Also, the magnitude of NMR resonance (and S/N ratio) varies inversely with temperature. NMR-logging tools include a temperature sensor to acquire the data needed for this correction. At high temperatures, data stacking can be increased or logging speeds reduced to compensate for a lower S/N ratio.

Porosity Check. NMR porosity can serve as an important diagnostic of data quality. High porosity readings may result from washouts (e.g., borehole fluid in the sensed volume), tool problems, improper environmental corrections or calibration issues, loss of pad contact (for the CMR tool), tool eccentricity, or borehole ellipticity (for the MRIL tool). Low porosity readings may result from insufficient wait time, light-hydrocarbon effects, the presence of heavy oil, improper frequency tuning, and/or calibration error.

3E.9.2 Post-Logging Quality Check. NMR-log responses should be checked against conventional logs when they are available (see the Applications section of this chapter).

3E.10 NMR-Log Job Planning

In some complex reservoirs, low-resistivity/low-contrast pay, low-porosity/low-permeability, and medium-to-heavy oil, NMR-log data—independently or in combination with other log data—provide the best and/or only means of accurate formation and fluid evaluation. Because NMR-log data acquisition is complex, job preplanning is essential to ensure optimal selection of acquisition parameters that will result in reliable and accurate data and in the maximum information possible in any given reservoir and logging environment. A clear understanding of the logging job objectives is necessary for optimizing the NMR acquisition parameters to best achieve these objectives.^{31,122,157,158} This process must take place before the actual logging.

Typical preplanning consists of three steps:

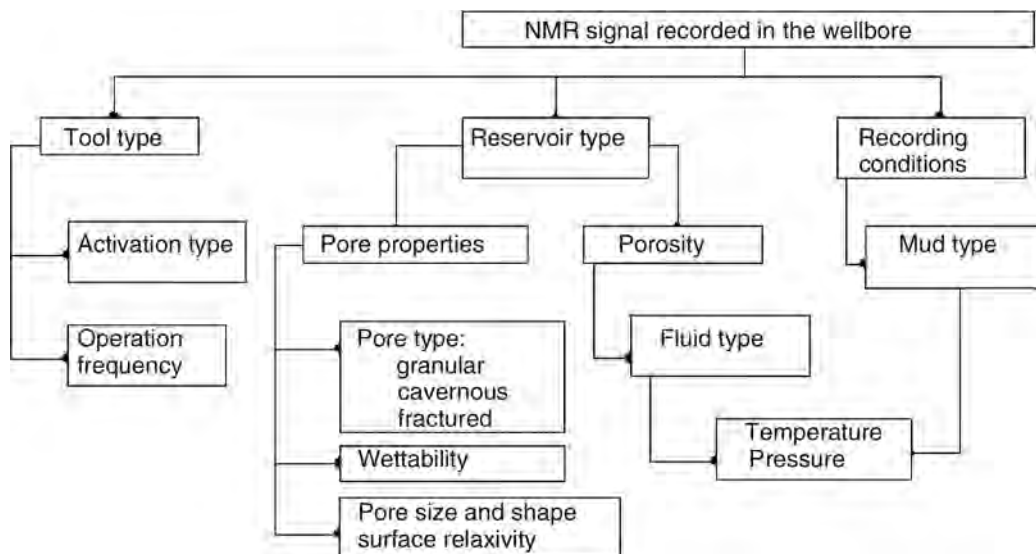


Fig. 3E.40—Reservoir and operational factors influencing the choice of CPMG acquisition.

1. Define the need for NMR measurements.
2. Collect all available borehole (e.g., diameter, mud, salinity, and temperature) and reservoir (e.g., formation and fluid properties) information needed to assess the expected NMR responses in the zone of interest, and understand what can and cannot be resolved with NMR.
3. Select the appropriate tool (on the basis of operational considerations, borehole size, and condition) and acquisition type (i.e., determining the appropriate acquisition parameters, data resolution, and logging speed) that will provide maximum answers for a given job.³¹

Although the actual in-situ reservoir characteristics may be unknown, estimates of the anticipated fluid properties, based on available information such as reports for nearby wells or fields, are used to define and optimize an acquisition sequence that will provide the data needed to meet the job objectives.

In addition to job objectives, determination of the appropriate NMR-acquisition parameters is also influenced by operational considerations and the anticipated in-situ reservoir properties (Fig. 3E.40). The most critical factors follow.

3E.10.1 Lithology. Although reservoir lithology generally plays a minor role in NMR-data acquisition, it does play a significant role in data analysis and interpretation. Aspects of reservoir lithology that influence reservoir T_2 values include the following.

Carbonates. Different $T_{2\text{cutoff}}$ values are required because surface relaxivity in carbonates is weaker than in sandstones, resulting in slower relaxation rates (longer T_2). Longer T_1 in carbonates than in sandstones may require longer T_W during acquisition.¹⁰³ (See the Application section of this chapter.)

Isolated Pores. The presence of relatively isolated pores (e.g., vugs) will not affect NMR porosity, but it will cause the standard permeability equations (Coates and SDR) to overestimate permeability. (See the Permeability section of this chapter.)

Ferromagnetic and Paramagnetic Minerals. The presence of these minerals may enhance surface relaxation significantly, shifting the T_2 spectrum to very short relaxation times. Depending on the amount of paramagnetic material, relaxation may become too fast to be detected, and the NMR measurement will underestimate porosity. In these cases, standard cutoff values do not apply.¹⁵⁹

Heavy Oil and Tar Sands. Intervals containing these types of hydrocarbons have very fast relaxation components and may not be detected using conventional acquisition methods. Special methods have been developed for detection and accurate evaluation of these reservoirs.^{136,137,160–167} (See the Applications section of this chapter.)

3E.10.2 Wettability. Wettability can have a significant impact on NMR-log response.¹⁶⁸ The use of NMR for determination of wettability has been extensively studied both in laboratory^{129,169} and in the field. In general, petrophysical-NMR studies and NMR-logging applications assume reservoir rocks are water wet; however, because mixed-wettability reservoirs do exist (e.g., some carbonates, black shales, and heavy-oil reservoirs),¹¹² this assumption may lead to incorrect reserve estimates and to unexpected dynamic behavior during waterflood. When a pore is water wet, oil relaxes at its bulk rate. In mixed-wettability reservoirs, the oil and water each relax through a combination of bulk relaxation and surface interaction and depend on the ratio of water-wet surface area to water volume and oil-wet surface area to oil volume. The oil relaxation spectra will be shifted from bulk relaxation into the irreducible-water part, resulting in complex spectra that are difficult to interpret.^{170,171} Nevertheless, these shifts provide qualitative wettability indicators that allow NMR logs to provide an early indication of reservoir wetting behavior.^{113,118,172–174}

The invasion of OBM or SOBM can alter formation wettability and is a significant concern in NMR logging,^{113,131,175} which typically measures fluid and formation properties in the flushed zone. Invasion by these muds can alter strongly water-wet sandstones and carbonates to intermediate-wet or oil-wet rocks. In water-wet reservoirs that have undergone OBM or SOBM invasion, the $T_{2\text{cutoff}}$ model may significantly underestimate S_{wirr} because wettability alteration changes the water and oil relaxation-time distributions. The magnitude of underestimation depends on the type of OBM surfactants, their concentration in the flushing fluid, and the flushing volume. Controlling the volume of OBM invasion and the concentration of OBM surfactants should minimize the effects of OBM invasion on estimation of S_{wirr} .^{176,177}

3E.10.3 Borehole Rugosity. NMR-logging tools have relatively shallow DOIs. Pad-type tools (e.g., the CMR tool) are run eccentric and require good contact with the borehole wall for accurate measurements. Measurements made by pad-type tools can be significantly affected by severe borehole rugosity and washouts, resulting in overestimation of porosity.

Mandrel devices are run centered, and DOI can range from 1 to 4 in., depending on borehole size. The sensitive area is normally beyond minor borehole rugosity. When borehole conditions result in an elliptical borehole (e.g., breakouts or erosion) or otherwise inhibit or prevent centralization (e.g., in highly deviated or horizontal boreholes), contact tools may be a better choice if pad alignment and contact with the borehole wall can be maintained.

3E.10.4 Mud Type. The quality of NMR data acquired in OBM is generally superior to that acquired in WBM. The conductivity of OBM is lower; lower conductivity reduces loading effects on the transmitter/receiver system, resulting in higher S/N ratio. This issue is of greater concern for mandrel tools (e.g., MRIL tool) because, in conductive muds, the power of the RF pulse is reduced as the pulse is transmitted across the borehole. The use of fluid-excluding sleeves can minimize this problem.

Signal dissipation in conductive mud is not a serious concern for pad-type tools (CMR) that maintain contact with the borehole wall. Because NMR tools read the flushed zone, OBM filtrate invasion produces an additional hydrocarbon signal that may significantly complicate log interpretation.¹⁷⁸ Careful prejob planning can reduce interference of the OBM-filtrate signal and the response from the native fluids. The relatively long T_1 relaxation times and diffusivity of OBM make it difficult to differentiate its signal using the shifted-spectrum or differential-spectrum approaches.

3E.10.5 Metal Debris. Metal drilling debris in the borehole fluid may affect NMR-measurement quality by distorting and altering the logging tool's magnetic field. The pad-type tool is more susceptible to field distortion. Metal debris should be removed from the mud, either through the use of the prepolarizing magnets (included in the latest tool designs) or by using magnets at the shale shaker. A new wireline tool uses an autotuning feature to correct the operating frequency for changes in the static magnetic field caused by metallic debris in the borehole.⁵⁵

3E.10.6 Logging Speed and Running Average. The logging speed of an NMR tool is influenced by a number of factors, primarily by tool type (e.g., centered or eccentered, number of operating frequencies, or length of antenna), logging objectives (e.g., acquisition type— T_W , T_E , or N_E —sequence repetitions and vertical resolution), and borehole properties (e.g., diameter and mud resistivity). S/N ratio is primarily controlled by borehole size and mud resistivity. As S/N ratio decreases, the running average (RA) needed to maintain a specified error in porosity increases. The general practice is to require a porosity standard deviation of ≤ 1 p.u. The value of RA and the antenna aperture (i.e., length), combined with the logging speed, determines the vertical resolution. Even so, there is always a complex tradeoff in logging speed, accuracy (e.g., S/N ratio or N_E), and job objectives. High accuracy and precision require reduced logging speeds. A method for increasing the overall logging speed is to reduce the vertical resolution in zones of secondary or no interest and also to reduce the vertical resolution in homogeneous intervals.

3E.10.7 Vertical Resolution. The vertical resolution of NMR-logging tools is primarily a function of antenna length (i.e., tool design) and logging speed. The maximum vertical resolution, usually obtained when the tool is at rest (e.g., in stationary mode), is the length of the antenna. During continuous logging, vertical resolution decreases at a rate proportional to logging speed. Contact-logging tools, in general, use smaller sensors and antennae and, thus, have better vertical resolution than centered tools. The contact-NMR tool (i.e., the CMR tool) has a resolution advantage when bed thickness is in the range between 0.5 and 5 ft. Outside of this range, both designs deliver similar results. Prejob planning includes selecting a logging speed to obtain the optimum resolution.

Post-job data reprocessing to enhance bed resolution may result in a loss of repeatability. Vertical resolution can also be improved by optimizing the NMR signal through the removal of signal noise during data processing.^{179,180}

3E.11 Summary

This chapter has outlined the fundamental properties that are measured by NMR tools and has reviewed the use of these measurements to discern various characteristics of the reservoir rock including its fluid contents. Whether used as a standalone service or in combination with other logs and core data, NMR logs can provide an improved understanding of reservoir petrophysics and producibility. However, NMR logs are the most complex logging service introduced to date and require extensive prejob planning to ensure optimal acquisition of the appropriate data needed to achieve the desired objectives. Review of the references cited in this chapter indicates the rapid pace of advancement in NMR logging research, development, and applications. Users of NMR logging, including engineers, log analysts, petrophysicists, and geologists, should anticipate new developments in this discipline, as reported by SPE, the Soc. of Petrophysicists and Well Log Analysts (SPWLA), and other publications noted in the references.

3E.12 NMR-Tool Mnemonics

Table 3E.7 presents a cross reference of logging-tool output-data mnemonics for the different service companies currently offering NMR-logging services.

**TABLE 3E.7—CROSS REFERENCE OF OUTPUT-CURVE MNEMONICS FROM
NMR-LOGGING SERVICE PROVIDERS**

Measurement	Baker Atlas	Computalog	Halliburton	Schlumberger
Generic porosity	MPHI	MPHI	MPHI	CMPR
Total porosity	MPHS	MSIG	MSIG	TCMR
Effective porosity	MPHE	MPHI	MPHI	CMPR
Free-fluid volume	MBVM	FFI	MFFI	CMFF
Capillary-bound fluid volume	MBVI	MBVI	MBVI	BFV
Clay-bound water	MCBW	MCBW	MCBW	—
Permeability	MPRM	MPERM	MPERM	KTIM/KSDR
Binary/spectral porosities	P01-P0x	BIN1-BIN8	BIN1-BINx or P ₁ -P _x (PR-total)	CBP1-CBP8
Spectral/cutoff bound fluid volume			SBVI/CBVI	
Total bound fluid volume			MBFV	

Nomenclature

- A = pore-fluid-specific value used to approximate the diffusion constant
 a = constant in the mean- T_2 and viscosity relationship
 B_0 = static magnetic field, gauss
 B_1 = amplitude of the oscillating magnetic field perpendicular to B_0 , gauss
 C = coefficient in the Coates permeability model
 D_0 = molecular diffusion coefficient, gauss/cm
 f = Larmor (precessional) frequency, Hz
 G = field-strength gradient, gauss/cm
 k = permeability, darcy
 k_{Coates} = permeability derived using the Timur-Coates model, darcy
 k_{SDR} = permeability derived using the mean- T_2 model, darcy
 M = magnetization, gauss/cm³
 M_0 = macroscopic magnetization, gauss/cm³
 M_{0i} = magnitude of the initial magnetization from the i th component, gauss/cm³
 M_{0x} = magnitude of the transverse magnetization at $t = 0$, gauss/cm³
 $M_{100\%}$ = magnitude of the magnetization for 100% bulk water, gauss/cm³
 $M_i(0)$ = magnitude of the initial magnetization from the i th component of relaxation
 gauss/cm³
 $M(0)$ = magnitude of the initial magnetization, gauss/cm³
 $M(t)$ = measured magnetization at time t , gauss/cm³
 $M_x(t)$ = transverse magnetization at time t , gauss/cm³
 M_z = strength of magnetic field, gauss/cm³
 $M_z(t)$ = longitudinal magnetization at time t , gauss/cm³
 N_E = number of echoes
 P_c = capillary pressure, dynes/cm²
 Q = quality factor of a resonant circuit
 R_f = true formation resistivity, ohm-m
 $(S/V)_i$ = ratio of pore surface (S) to fluid volume (V), of the i th pore, 1/cm
 $(S/V)_{\text{pore}}$ = ratio of pore surface (S) to fluid volume (V), 1/cm

- S_w = water saturation, %
 S_{wirr} = irreducible water saturation, %
 S_{wb} = clay-bound water saturation, %
 S_{xo} = flushed-zone saturation, %
 t = time, seconds
 T = temperature, °C
 T_1 = longitudinal relaxation time, seconds
 T_{1bulk} = pore-fluid bulk- T_1 relaxation time, seconds
 $T_{1surface}$ = pore-surface T_1 relaxation time, seconds
 T_2 = transverse relaxation time, seconds
 T_{2bulk} = pore-fluid bulk- T_2 relaxation time, seconds
 $T_{2cutoff}$ = T_2 cutoff value, seconds
 $T_{2diffusion}$ = pore-fluid T_2 relaxation time in a magnetic field gradient, seconds
 T_{2DW} = upper limit of the measured T_2 for water, seconds
 T_{2gm} = T_2 geometric mean value, seconds
 T_{2i} = pore-fluid surface T_2 relaxation time of the i th component, seconds
 $T_{2surface}$ = pore-fluid surface T_2 relaxation time, seconds
 T_{DW} = dual wait time—the value of T_E such that diffusion, rather than surface relaxation, is the dominant relaxation mechanism, seconds
 T_E = CPMG interecho spacing, seconds
 T_K = absolute temperature, K
 T_p = pulsing time, seconds
 T_W = polarization (wait) time, seconds
 T_{WL} = polarization time, long, seconds
 T_{WS} = polarization time, short, seconds
 V_{shale} = shale volume, %
 x, y, z = cartesian space coordinates
 γ = gyromagnetic ratio—the ratio of the magnetic dipole moment to the mechanical angular momentum, Hz/gauss
 Δ_{TE} = incremental change in echo spacing, seconds
 Δ_{TW} = incremental change in wait time, seconds
 η = fluid viscosity, cp
 ζ = apparent T_1/T_2 ratio of fluid
 ρ_1 = T_1 surface relaxivity, cm/sec
 ρ_2 = T_2 surface relaxivity, cm/sec
 τ = time over which an oscillating field is applied
 ϕ = porosity, %
 ϕ_e = effective porosity, %
 ϕ_{eff} = effective porosity, %
 ϕ_H = hydrocarbon porosity, %
 ϕ_i = calibrated porosity associated with all pores of the i th pore size
 ϕ_t = total porosity, %
 ϕ_w = water porosity, %
 χ = goodness of fit

Acknowledgments

The authors of this chapter wish to acknowledge the help provided by the many former and current staff of Halliburton Energy Services who have been involved with the development of NMR logging. All figures except Fig. 3E.21 were provided courtesy of Halliburton Energy Services.

References

1. Brown, R.J.S.: "Earth's Field Nuclear Magnetic Resonance," *Concepts in Magnetic Resonance* (2001) **13**, No. 6, 344.
2. Chandler, R.: "Proton Free Precession (Earth's Field) Logging at Schlumberger (1956–1988)," *Concepts in Magnetic Resonance* (2001) **13**, No. 6, 366.
3. Woessner, D.E.: "The Early Days of NMR in the Southwest," *Concepts in Magnetic Resonance* (2001) **13**, No. 2, 77–102.
4. Brown, R.J.S. *et al.*: "History of NMR Well Logging," *Concepts in Magnetic Resonance* (2001) **13**, No. 6, 340.
5. Brown, R.J.S. and Gamson, B.W.: "Nuclear Magnetism Logging," *JPT* (August 1960) 199; *Trans.*, AIME, **219**.
6. Nikias, P.A. Jr. and Eyraud, L.E.: "Field Examples Of Nuclear Magnetism Logging in the Poso Creek, Kern Front and Kern River Fields of the San Joaquin Valley," *JPT* (January 1963) 23.
7. Kleinberg, R.L. and Jackson, J.A.: "An Introduction to the History of NMR Well Logging," *Concepts in Magnetic Resonance* (2001) **13**, No. 6, 340.
8. Kleinberg, R.L.: "NMR Well Logging at Schlumberger," *Concepts in Magnetic Resonance*, (2001) **13**, No. 6, 396.
9. Becker, E.D., Fisk, C.L., and Khetrpal, C.L.: "The Development of NMR," *Encyclopedia of Nuclear Magnetic Resonance*, D.M. Grant and R.K. Harris (eds.), John Wiley and Sons, New York City (1996) **1**, 1.
10. Kleinberg, R.L.: "Nuclear Magnetic Resonance," *Methods in the Physics of Porous Media, Experimental Methods in the Physical Sciences Series 35*, P. Wong (ed.), Academic Press, San Diego (1999) Chap. 9, 337–385.
11. Dunn, K.-J., Bergman, D.J., and LaTorraca, G.A.: *Nuclear Magnetic Resonance—Petrophysical and Logging Applications, Seismic Exploration, Series 32*, Pergamon Press (2002).
12. Hahn, E.L.: "Spin Echoes," *Physical Review* (1950) **80**, 580.
13. Carr, H.Y. and Purcell, E.M.: "Effects of Diffusion on Free Precession in Nuclear Magnetic Resonance Experiments," *Physical Review* (1954) **94**, 630.
14. Meiboom, S. and Gill, D.: "Modified Spin-Echo Methods for Measuring Nuclear Relaxation Times," *Review of Scientific Instruments* (1958) **29**, No. 8, 699.
15. Woessner, D.E.: "In a Maze in NMR," *Encyclopedia of Nuclear Magnetic Resonance*, D.M. Grant and R.K. Harris (eds.), John Wiley and Sons, New York City (1996) **1**, 700.
16. Griffith *et al.*: "Low Frequency NMR Spectrometer," *Measurement Science and Technology* (1993) **4**, 968.
17. Taicher, Z. *et al.*: "A Comprehensive Approach to Studies of Porous Media (Rocks) Using a Laboratory Spectrometer and Logging Tool With Similar Operating Characteristics," *Magnetic Resonance Imaging* (1994) **12**, No. 2, 285.
18. Straley, C. *et al.*: "Core Analysis by Low Field NMR," *The Log Analyst* (1997) **38**, No. 2, 84.
19. Mirotnich, K., Kryuchkov, S., and Strack, K.: "A Novel Method to Determine NMR Petrophysical Parameters from Drill Cuttings," paper MM presented at the 2004 Soc. of Petrophysicists and Log Analysts Annual Logging Symposium, Noordwijk, The Netherlands, 6–9 June.
20. Kenyon, W.E.: "Petrophysical Principles of Applications of NMR Logging," *The Log Analyst* (1997) **38**, No. 2, 21.
21. Murphy, D.P.: "NMR Logging and Core Analysis—Simplified," *World Oil* (1995) **216**, No. 4, 65.

22. Lonnes, S., Guzman-Garcia, A., and Holland, R.: "NMR Petrophysical Predictions on Cores," paper DDD presented at the 2003 Soc. of Professional Well Log Analysts Annual Logging Symposium, Galveston, Texas, 22–25 June.
23. Chang, C.T.P., Watson, A.T., and Edwards, C.M.: "NMR Imaging of Fluids and Flow in Porous Media," *Methods in the Physics of Porous Media, Experimental Methods in the Physical Sciences*, P. Wong (ed.), Academic Press, San Diego, California (1999) 387–423.
24. Kleinberg *et al.*: " T_1/T_2 Ratio and Frequency Dependence of NMR Relaxation in Porous Sedimentary Rocks," *J. of Colloid Interface Science* (1993) **158**, No. 1, 195.
25. Flaum, C., Kleinberg, R., and Bedford, J.: "Bound Water Volume, Permeability and Residual Oil Saturation From Incomplete Magnetic Resonance Logging Data," paper UU presented at the 1998 Soc. of Professional Well Log Analysts Annual Logging Symposium, Keystone, Colorado, 26–29 May.
26. Freedman, R. *et al.*: "A New NMR Method of Fluid Characterization in Reservoir Rocks: Experimental Confirmation and Simulation Results," *SPEJ* (December 2001) 452.
27. Kenyon, W.E. *et al.*: "A Three-Part Study of NMR Longitudinal Relaxation Properties of Water-Saturated Sandstones," *SPEFE* (September 1988) 622.
28. Kenyon, W.E. *et al.*: "Pore-Size Distribution and NMR in Microporous Cherty Sandstones," paper LL presented at the 1989 Soc. of Professional Well Log Analysts Annual Logging Symposium, Denver, 11–14 June.
29. Freedman, R. and Morriss, C.E.: "Processing of Data From an NMR Logging Tool," paper SPE 30560 presented at the 1995 SPE Annual Technical Conference and Exhibition, Dallas, 22–25 October.
30. Miller, M.N. *et al.*: "Spin Echo Magnetic Resonance Logging: Porosity and Free Fluid Index Determination," paper SPE 20561 presented at the 1990 SPE Annual Technical Conference and Exhibition, New Orleans, 23–26 September.
31. Coates, G.R., Xiao, L.Z., and Prammer, M.G.: *NMR Logging: Principles and Applications*, Halliburton Energy Services, Houston (1999) 234.
32. Marschall, D. *et al.*: "Method for Correlating NMR Relaxometry and Mercury Injection Data," paper SCA-9511 presented at the 1995 Soc. of Core Analysts Intl. Symposium, San Francisco, 12–14 September.
33. Ausbrooks, R. *et al.*: "Pore-Size Distributions in Vuggy Carbonates From Core Images, NMR, and Capillary Pressure," paper SPE 56506 presented at the 1999 SPE Annual Technical Conference and Exhibition, Houston, 3–6 October.
34. Pittman, E.D.: "Relationship of Porosity and Permeability to Various Parameters Derived From Mercury Injection-Capillary Pressure Curves for Sandstones," *AAPG Bull.* (1992) **76**, No. 2, 191.
35. Nelson, P.H.: "Permeability-Porosity Relationships in Sedimentary Rocks," *The Log Analyst* (1994) **35**, No. 3, 38.
36. Mirotnich, K., Allsopp, K., and Kantzas, A.: "Combination of NMR and Ultracentrifuge Techniques for Effective Carbonate Reservoir Characterization," paper SCA-9703 presented at the Soc. of Core Analysts 1997 Intl. Symposium, Calgary, 8–10 September.
37. Prammer, M.G. *et al.*: "Measurements of Clay-Bound Water and Total Porosity by Magnetic Resonance Logging," paper SPE 36522 presented at the 1996 Annual Technical Conference and Exhibition, Denver, 6–9 October.
38. Chitale, D.V., Day, P.I., and Coates, G.R.: "Petrophysical Implications of Laboratory NMR and Petrographical Investigation on a Shaly Sand Core," paper SPE 56765 presented at the 1999 SPE Annual Technical Conference and Exhibition, Houston, 3–6 October.
39. Brown, R.J.S. and Neuman, C.H.: "The Nuclear Magnetism Log—A Guide for Field Use," *The Log Analyst* (1982) **23**, No. 5, 4.
40. Cooper, R.K. and Jackson, J.A.: "Remote (Inside-Out) NMR: Part 1, Remote Production of a Region of Homogeneous Magnetic Field," *J. of Magnetic Resonance* (1980) **41**, 400.
41. Burnett, L.J. and Jackson, J.A.: "Remote (Inside-Out) NMR: Part 2, Sensitivity of Detection for External Samples," *J. of Magnetic Resonance* (1980) **41**, 406.
42. Jackson, J.A., Burnett, L.J., and Harmon, J.F.: "Remote (Inside-Out) NMR: Part 3, Detection of Nuclear Magnetic Resonance in a Remotely Produced Region of Homogeneous Magnetic Field," *J. of Magnetic Resonance* (1980) **41**, 411.

43. Jackson, J.A.: “Nuclear Magnetic Resonance Well Logging,” *The Log Analyst* (1984) **25**, No. 5, 16.
44. Jackson, J.A.: “Los Alamos NMR Well Logging Project,” *Concepts in Magnetic Resonance* (2001) **13**, No. 6, 368.
45. Chandler, R.N. *et al.*: “Improved Log Quality with a Dual-Frequency Pulsed NMR Tool,” paper SPE 28365 presented at the 1994 SPE Annual Technical Conference and Exhibition, New Orleans, 25–28 September.
46. Prammer, M.G. *et al.*: “Measurements of Clay-Bound Water and Total Porosity by Magnetic Resonance Logging,” *The Log Analyst* (1996) **37**, No. 6, 61.
47. Prammer, M. *et al.*: “Theory and Operation of a New, Multi-Volume NMR Logging System,” paper DD presented at the 1999 Soc. of Professional Well Log Analysts Annual Logging Symposium, Oslo, Norway, 30 May–3 June.
48. Prammer, M.G. *et al.*: “A New Multiband Generation of NMR Logging Tools,” *SPEREE* (February 2001) 59.
49. Kleinberg, R.L. *et al.*: “Novel NMR Apparatus for Investigating an External Sample,” *J. of Magnetic Resonance* (1992) **97**, 466.
50. Morris, C.E. *et al.*: “Field Test of an Experimental Pulsed Nuclear Magnetism Tool,” paper GGG presented at the 1993 Soc. of Professional Well Log Analysts Annual Logging Symposium, Calgary, 13–16 June.
51. Freedman, R. *et al.*: “Measurement of Total NMR Porosity Adds New Value to NMR Logging,” paper OO presented at the 1997 Soc. of Professional Well Log Analysts Annual Logging Symposium, Houston, 15–18 June.
52. McKeon, D. *et al.*: “An Improved NMR Tool for Faster Logging,” paper CC presented at the 1999 Soc. of Professional Well Log Analysts Annual Logging Symposium, Oslo, Norway, 30 May–3 June.
53. Heaton, N.J. *et al.*: “Applications of a New-Generation NMR Wireline Logging Tool,” paper SPE 77400 presented at the 2002 Annual Technical Conference and Exhibition, San Antonio, Texas, 29 September–2 October.
54. DePavia, L. *et al.*: “A New Generation Wireline NMR Logging Tool,” paper SPE 84482 presented at the 2003 SPE Annual Technical Conference and Exhibition, Denver, 5–8 October.
55. Minh, C.C. *et al.*: “Field Test Results of the New Combinable Magnetic Resonance Autotune Logging Tool,” paper SPE 96759 presented at the 2005 SPE Annual Technical Conference and Exhibition, Dallas, 9–12 October.
56. Chen, S. *et al.*: “MR Explorer Log Acquisition Methods—Petrophysical-Objective-Oriented Approaches,” paper ZZ presented at the 2003 Soc. of Professional Well Log Analysts Annual Logging Symposium, Galveston, Texas, 22–25 June.
57. Khamatdinov, R. *et al.*: “Field Test of a New Nuclear Magnetic Resonance Tool,” paper AAA presented at the 2003 Soc. of Professional Well Log Analysts Annual Logging Symposium, Galveston, Texas, 22–25 June.
58. Bonnie, R.J.M. *et al.*: “Wireline T_1 logging,” paper SPE 84483 presented at the 2003 SPE Annual Technical Conference and Exhibition, Denver, 5–8 October.
59. Heaton, N. *et al.*: “Saturation and Viscosity From Multidimensional Nuclear Magnetic Resonance Logging,” paper SPE 90564 presented at the 2004 SPE Annual Technical Conference and Exhibition, Houston, 26–29 September.
60. Lippincott, B. *et al.*: “Advanced NMR Acquisition Has Improved the Assessment of Hydrocarbons in Place in the Gulf of Mexico,” paper II presented at the 2004 Soc. of Petrophysicists and Well Log Analysts Annual Logging Symposium, Noordwijk, The Netherlands, 6–9 June.
61. Reppert, M. *et al.*: “Porosity and Water Saturation from LWD NMR in a North Sea Chalk Formation,” paper D presented at the 2005 Soc. of Petrophysicists and Well Log Analysts Annual Logging Symposium, New Orleans, 26–29 June.
62. Prammer, M. *et al.*: “Directional Resonance: New Applications for MRIL,” paper SPE 84479 presented at the 2003 SPE Annual Technical Conference and Exhibition, Denver, 5–8 October.
63. Speier, P. *et al.*: “Reducing Motion Effects on Magnetic Resonance Bound Fluid Estimates,” paper II presented at the 1999 Soc. of Professional Well Log Analysts Annual Logging Symposium Oslo, Norway, 30 May–3 June.

64. Drack, E.D. *et al.*: “Advances in LWD Nuclear Magnetic Resonance,” paper SPE 71730 presented at the 2001 SPE Annual Technical Conference and Exhibition, New Orleans, 30 September–3 October.
65. Prammer, M.G.: “NMR Logging-While-Drilling (1995–2000),” *Concepts in Magnetic Resonance* (2001) **13**, No. 6, 409.
66. Prammer, M.G. *et al.*: “A New Direction in Wireline and LWD NMR,” paper DDD presented at the 2002 Soc. of Professional Well Log Analysts Annual Logging Symposium, Oiso, Japan, 2–5 June.
67. Prammer, M.G. *et al.*: “The Magnetic-Resonance-While-Drilling Tool: Theory and Operation,” *SPEREE* (August 2001) 270.
68. Appel, M. *et al.*: “Nuclear Magnetic Resonance While Drilling in the Southern North Sea,” *SPEREE* (October 2003) 351.
69. Morley, J. *et al.*: “Field Testing of a New Nuclear Magnetic Resonance Logging-While-Drilling Tool,” paper SPE 77477 presented at the 2002 SPE Annual Technical Conference and Exhibition, San Antonio, Texas, 29 September–2 October.
70. Horkowitz, J. *et al.*: “Applications of a New Magnetic Resonance Logging-While-Drilling Tool in a Gulf of Mexico Deepwater Development Project,” paper EEE presented at the 2002 Soc. of Professional Well Log Analysts Annual Logging Symposium, Oiso, Japan, 2–5 June.
71. Heidler, R., Morriss, C., and Hoshun, R.: “Design and Implementation of a New Magnetic Resonance Tool for the While Drilling Environment,” paper BBB presented at the 2003 Soc. of Professional Well Log Analysts Annual Logging Symposium, Galveston, Texas, 22–25 June.
72. Borghi, M. *et al.*: “Magnetic Resonance While Drilling Streamlines Reservoir Evaluation,” paper HHH presented at the 2005 Soc. of Professional Well Log Analysts Annual Logging Symposium, New Orleans, 26–29 June.
73. Kleinberg, R.L. and Vinegar, H.J.: “NMR Properties of Reservoir Fluids,” *The Log Analyst* (1996) **37**, No. 6, 20.
74. Prammer, M.G., Bouton, J., and Masak, P.: “The Downhole NMR Fluid Analyzer,” paper N presented at the 2001 Soc. of Professional Well Log Analysts Annual Logging Symposium, Houston, 16–20 June.
75. Bouton, J. *et al.*: “Assessment of Sample Contamination by Downhole NMR Fluid Analysis,” paper SPE 71714 presented at the 2001 SPE Annual Technical Conference and Exhibition, New Orleans, 30 September–3 October.
76. Masak, P. *et al.*: “Field Test Results and Applications of the Downhole Magnetic Resonance Fluid Analyzer,” paper GGG presented at the 2002 Soc. of Professional Well Log Analysts Annual Logging Symposium.
77. Akkurt, R. *et al.*: “Fluid Sampling and Interpretation with the Downhole NMR Fluid Analyzer,” paper SPE 90971 presented at the 2004 SPE Annual Technical Conference and Exhibition, Houston, 26–29 September.
78. Stambaugh, B., Svor, R., and Globe, M.: “Quality Control of NMR Logs,” paper SPE 63212 presented at the 2000 SPE Annual Technical Conference and Exhibition, Dallas, 1–4 October.
79. Marschall, D.M.: “HBVI—An NMR Method To Determine BVI as a Function of Reservoir Capillarity,” paper KK presented at the 2000 Soc. of Professional Well Log Analysts Annual Logging Symposium, Dallas, 4–7 June.
80. Timur, A.: “Effective Porosity and Permeability of Sandstones Investigated Through Nuclear Magnetic Principles,” *The Log Analyst* (1969) **10**, No. 1, 3.
81. Chen, S., Ostroff, G., and Georgi, D.T.: “Improving Estimation of NMR Log T_2 Cutoff Value With Core NMR and Capillary Pressure Measurements,” paper SCA-9822 presented at the 1998 Soc. of Core Analysts Intl. Symposium, The Hague, 14–16 September.
82. Agut, R., Levallois, B., and Klopff, W.: “Integrating Core Measurements and NMR Logs in Complex Lithology,” paper SPE 63211 presented at the 2000 SPE Annual Technical Conference and Exhibition, Dallas, 1–4 October.
83. Zhang, Q. *et al.*: “Some Exceptions to Default NMR Rock and Fluid Properties,” paper FF presented at the 1998 Soc. of Professional Well Log Analysts Annual Logging Symposium, Keystone, Colorado, 26–29 May.
84. Coates, G.R. *et al.*: “A New Characterization of Bulk-Volume Irreducible Using Magnetic Resonance,” *The Log Analyst* (1998) **39**, No. 1, 51.

85. Chen, S. *et al.*: “Methods for Computing SWI and BVI From NMR Logs,” paper HH presented at the 1998 Soc. of Professional Well Log Analysts Annual Logging Symposium, Keystone, Colorado, 26–29 May.
86. Kleinberg, R.L. and Boyd, A.: “Tapered Cutoffs for Magnetic Resonance Bound Water Volume,” paper SPE 38737 presented at the 1997 SPE Annual Technical Conference and Exhibition, San Antonio, Texas, 5–8 October.
87. Seevers, D.: “A Nuclear Magnetic Method for Determining the Permeability of Sandstone,” paper L presented at the 1966 SPWLA Annual Logging Symposium, Tulsa, 8–11 May.
88. Timur, A.: “Pulsed Nuclear Magnetic Resonance Studies of Porosity, Movable Fluid, and Permeability of Sandstones,” *JPT* (June 1969) 775.
89. Timur, A.: “An Investigation of Permeability, Porosity, and Residual Water Saturation Relationships for Sandstone Reservoirs,” *The Log Analyst* (1968) **9**, No. 4, 8.
90. Ahmed, U., Crary, S.F., and Coates, G.R.: “Permeability Estimation: The Various Sources and Their Interrelationships,” *JPT* (May 1991) 578.
91. Worthington, P.F.: “The Effect of Scale on the Petrophysical Estimation of Intergranular Permeability,” paper A presented at the 2003 Soc. of Professional Well Log Analysts Annual Logging Symposium, Galveston, Texas, 22–25 June.
92. Bryant, S., Cade, C., and Mellor, D.: “*Permeability Prediction from Geologic Models*,” AAPG Bulletin (1993) **77**, No. 8, 1338.
93. Chang, D. *et al.*: “Effective Porosity, Producing Fluid and Permeability in Carbonates From NMR Logging,” *The Log Analyst* (1997) **38**, No. 2, 60.
94. Babadagli, T. and Al-Salmi, S.: “Improvement of Permeability Prediction for Carbonate Reservoir Using Well Log Data,” paper SPE 77889 presented at the 2002 SPE Asia Pacific Oil and Gas Conference and Exhibition, Melbourne, Australia, 8–10 October.
95. Marschall, D., Gardner, J., and Curby, F.M.: “MR Laboratory Measurements—Requirements to Assure Successful Measurements that Will Enhance MRI Log Interpretation,” paper SCA-9704 presented at the 1997 Society of Core Analysts International Symposium, Calgary, 8–10 September.
96. Prammer, M.G.: “NMR Pore Size Distributions and Permeability at the Well Site,” paper SPE 28368 presented at the 1994 SPE Annual Technical Conference and Exhibition, New Orleans, 25–28 September.
97. Winkler, M., Freeman, J., and Appel, M.: “The Limits Of Fluid Property Correlations Used in NMR Well Logging: an Experimental Study of Reservoir Fluids at Reservoir Conditions,” paper DD presented at the 2004 Soc. of Petrophysicists and Log Analysts Annual Logging Symposium, Noordwijk, The Netherlands, 6–9 June.
98. Hirasaki, G.J., Lo, S.-W., and Zhang, Y.: “NMR Properties of Petroleum Reservoir Fluids,” *Magnetic Resonance Imaging* (2003) **21**, No. 3–4, 269.
99. Chen, S. *et al.*: “Laboratory Investigation of NMR Crude Oils and Mud Filtrates Properties in Ambient and Reservoir Conditions,” paper SPE 90553 presented at the 2004 SPE Annual Technical Conference and Exhibition, Houston, 26–29 September.
100. Prammer, M.G.: “Hydrocarbon Saturation Measurements by NMR,” *Concepts in Magnetic Resonance* (2001) **13**, No. 6, 406.
101. Prammer, M.G. *et al.*: “Lithology-Independent Gas Detection by Gradient-NMR Logging,” paper SPE 30562 presented at the 1995 SPE Annual Technical Conference and Exhibition, Dallas, 22–25 October.
102. Akkurt, R. *et al.*: “Enhanced Diffusion—Expanding the Range of NMR Direct Hydrocarbon-Typing Applications,” paper GG presented at the 1998 Soc. of Professional Well Log Analysts Annual Logging Symposium, Keystone, Colorado, 26–27 May.
103. Timur, A.: “Nuclear Magnetic Resonance Study of Carbonate Rocks,” *The Log Analyst* (1972) **13**, No. 5, 3.
104. Hurlimann, M.D.: “Diffusion and Relaxation Effects in General Stray Field NMR Experiments,” *J. of Magnetic Resonance* (2001) **148**, 367.
105. Akkurt, R. *et al.*: “NMR Logging of Natural Gas Reservoirs,” *The Log Analyst* (1996) **37**, No. 5, 33.

106. Coates, G.R., Gardner, J.S., and Miller, D.L.: "Applying Pulse-Echo NMR to Shaly Sand Formation Evaluation," paper B presented at the 1994 Soc. of Professional Well Log Analysts Annual Logging Symposium, Tulsa, 19–22 June.
107. Chitale, D.V., Day, P.I., and Coates, G.R.: "Petrophysical Implications of Laboratory NMR and Petrographical Investigation on a Shaly Sand Core," paper SPE 56765 presented at the 1999 SPE Annual Technical Conference and Exhibition, Houston, 3–6 October.
108. Moore, M.A. and Akkurt, R.: "Nuclear Magnetic Resonance Applied to Gas Detection in a Highly Laminated Gulf of Mexico Turbidite Invaded With Synthetic Oil Filtrate," paper SPE 36521 presented at the 1996 SPE Annual Technical Conference and Exhibition, Denver, 6–9 October.
109. Buller, D.: "Carbonate Evaluation Using NMR Time Domain Analysis," paper GGG presented at the 2000 Soc. of Professional Well Log Analysts Annual Logging Symposium, Dallas, 4–7 June.
110. Hou, B.L. and Miller, D.: "Determining Fluid Volume in Gas and/or Light Oil Reservoirs—Using a New Triple-Wait-Time NMR Logging Method," paper U presented at the 2000 Soc. of Professional Well Log Analysts Annual Logging Symposium, Dallas, 4–7 June.
111. Akkurt, R. *et al.*: "Determination of Residual Oil Saturation by Use of Enhanced Diffusion," *SPEEE* (June 1999) 303.
112. Horkowitz, J.P. *et al.*: "Residual Oil Saturation Measurements in Carbonates With Pulsed NMR Logs," *The Log Analyst* (1997) **38**, No. 2, 73.
113. Howard, J.J.: "Wettability and Fluid Saturations Determined From NMR T_1 Distributions," *Magnetic Resonance Imaging* (1994) **12**, No. 2, 197.
114. Flaum, C., Kleinberg, R., and Hurlimann, M.: "Identification of Gas With the Combinable Magnetic Resonance Tool (CMR)," paper L presented at the 1996 Soc. of Professional Well Log Analysts Annual Logging Symposium, New Orleans, 16–19 June.
115. Sun, B. *et al.*: "Two-Dimensional NMR Logging and Field Test Results," paper KK presented at the 2004 Soc. of Petrophysicists and Log Analysts Annual Logging Symposium, Noordwijk, The Netherlands, 6–9 June.
116. Slijkerman, W.F.J. *et al.*: "Processing of Multi-Acquisition NMR Data," *SPEEE* (2000) 492.
117. Chen, S. *et al.*: "G-Te Correction for Processing Multigradient, Multiple-Te NMR Log Data," paper SPE 84481 presented at the 2003 SPE Annual Technical Conference and Exhibition, Denver, 5–8 October.
118. Freedman, R. *et al.*: "Wettability, Saturation, and Viscosity Using the Magnetic Resonance Fluid Characterization Method and New Diffusion-Editing Pulse Sequences," *SPEJ* (2003) 317.
119. Fang, S. *et al.*: "Quantification of Hydrocarbon Saturation in Carbonate Formations Using Simultaneous Inversion of Multiple NMR Echo Trains," paper SPE 90569 presented at the 2004 SPE Annual Technical Conference and Exhibition, Houston, 26–29 September.
120. Sun, B. and Dunn, K.J.: "A Global Inversion Method for Multi-Dimensional NMR Logging," *J. of Magnetic Resonance* (2005) **172**, 152.
121. Sun, B. and Dunn, K.J.: "Two-Dimensional Nuclear Magnetic Resonance Petrophysics," *Magnetic Resonance Imaging* (2005) **23**, No. 2, 259.
122. Bonnie, R.J.M. *et al.*: "Advanced Forward Modeling Helps Planning and Interpreting NMR Logs," paper SPE 71735 presented at the 2001 SPE Annual Technical Conference and Exhibition, New Orleans, 30 September–3 October.
123. Hurlimann, M.D. and Venkataraman, L.: "Quantitative Measurement of Two-Dimensional Distribution Functions of Diffusion and Relaxation in Grossly Inhomogeneous Fields," *J. of Magnetic Resonance* (2002) **157**, 31.
124. Hurlimann, M.D. *et al.*: "Diffusion Editing: New NMR Measurement of Saturation and Pore Geometry," paper FFF presented at the 2002 Soc. of Professional Well Log Analysts Annual Logging Symposium, Oiso, Japan, 2–5 June.
125. Sun, B., and Dunn, K.: "Core Analysis With Two Dimensional NMR," paper SCA 2002-38 presented at the 2002 Soc. of Core Analysts Annual International Symposium, Monterey, California, 23–25 September.
126. Hurlimann, M.D. *et al.*: "Diffusion-Relaxation Distribution Functions of Sedimentary Rocks in Different Saturation States," *Magnetic Resonance Imaging* (2003) **21**, No. 3–4, 305.

127. Toumelin, E. *et al.*: “A Numerical Assessment of Modern Borehole NMR Interpretation Techniques,” paper SPE 90539 presented at the 2004 SPE Annual Technical Conference and Exhibition, Houston, 26–29 September.
128. Hursan, G., Chen, S., and Murphy, E.: “New NMR Two-Dimensional Inversion of T_1/T_{2app} vs. T_{2app} Method for Gas Well Petrophysical Interpretation,” paper GGG presented at the 2005 Soc. of Petrophysicists and Well Log Analysts Annual Logging Symposium, New Orleans, 26–29 June.
129. Flaum, M., Chen, C., and Hirasaki, G.: “NMR Diffusion Editing for D- T_2 Maps—Application to Recognition of Wettability Change,” paper JJ presented at the 2004 Soc. of Petrophysicists and Log Analysts Annual Logging Symposium, Noordwijk, The Netherlands, 6–9 June.
130. Sun, B. *et al.*: “NMR Imaging with Diffusion and Relaxation,” paper SCA2003-24 presented at the 2003 Soc. of Core Analysts Annual International Symposium, Pau, France, 21–24 September.
131. Leu, G. *et al.*: “NMR Identification of Fluids and Wettability In Situ in Preserved Cores,” *Petrophysics* (2002) **43**, No. 1, 13.
132. Klimentos, T.: “NMR Applications in Petroleum Related Rock-Mechanics: Sand Control, Hydraulic Fracturing, Wellbore Stability,” paper HHH presented at the 2003 Soc. of Petrophysicists and Well Log Analysts Annual Logging Symposium, Galveston, Texas, 22–25 June.
133. Van der Zwaag *et al.*: “Deformation and Failure of Rock Samples Probed by T_1 and T_2 Relaxation,” *Magnetic Resonance Imaging* (2003) **21**, No. 3–4, 405.
134. Mullen, M. *et al.*: “Fluid Typing With T_1 NMR: Incorporating T_1 and T_2 Measurements for Improved Interpretation in Tight Gas Sands and Unconventional Reservoirs,” paper III presented at the 2005 Soc. of Petrophysicists and Well Log Analysts Annual Logging Symposium, New Orleans, 26–29 June.
135. Longis, C., Vignau, S., and White, S.: “NMR and Capture Spectroscopy Help Resolve Producibility and Fluid Distribution in the North Alwyn Triassic,” paper SPE 96609 presented at the 2005 SPE Annual Technical Conference and Exhibition, Dallas, 9–12 October.
136. LaTorraca, G. *et al.*: “Heavy Oil Viscosity Determination Using NMR Logs,” paper PPP presented at the 1999 Soc. of Professional Well Log Analysts Annual Logging Symposium, Oslo, Norway, 30 May–3 June.
137. Galford, J.E. and Marschall, D.M.: “Combining NMR and Conventional Logs to Determine Fluid Volumes and Oil Viscosity in Heavy-Oil Reservoirs,” paper SPE 63257 presented at the 2000 SPE Annual Technical Conference and Exhibition, Dallas, 1–4 October.
138. Secombe, J. *et al.*: “Ranking Oil Viscosity in Heavy Oil Reservoirs,” paper EE presented at the 2005 Soc. of Petrophysicists and Well Log Analysts Annual Logging Symposium, New Orleans, 26–29 June.
139. Nascimento, J. de D.S., and Gomes, R.M.R.: “Tar Mats Characterization from NMR and Conventional Logs, Case Studies in Deepwater Reservoirs, Offshore Brazil,” paper FF presented at the 2004 Soc. of Petrophysicists and Log Analysts Annual Logging Symposium, Noordwijk, The Netherlands, 6–9 June.
140. Breda, E. *et al.*: “Detecting Restricted Diffusion Effect When Identifying Hydrocarbons with NMR Logs,” paper SPE 90089 presented at the 2004 SPE Annual Technical Conference and Exhibition, Houston, 26–29 September.
141. Westphal, H. *et al.*: “NMR measurements in Carbonate Rocks: Problems and an Approach to a Solution,” *Pure and Applied Geophysics* (2005) **162**, No. 3, 549.
142. Rose, D. *et al.*: “A Novel Approach to Real Time Detection of Facies Changes in Horizontal Carbonate Wells Using LWD NMR,” paper CCC presented at the 2003 Soc. of Petrophysicists and Well Log Analysts Annual Logging Symposium, Galveston, Texas, 22–25 June.
143. Chen, S. *et al.*: “Simple, Robust NMR-Based Indicators for Detection of Hydrocarbon Gas or Oil, Borehole Contamination, and Vugs,” paper SPE 96409 presented at the 2005 SPE Annual Technical Conference and Exhibition, Dallas, 9–12 October.
144. Fleury, M., Al-Nayadi, K., and Boyd, D.: “Water Saturation from NMR, Resistivity and Oil Base Core in a Heterogeneous Middle East Carbonate Reservoir,” paper JJJ presented at the 2005 Soc. of Petrophysicists and Well Log Analysts Annual Logging Symposium, New Orleans, 26–29 June.
145. Volotikin, Y. *et al.*: “Constructing Capillary Pressure Curves from NMR Log Data in the Presence of Hydrocarbons,” *Petrophysics* (2001) **42**, No. 4, 334.

146. Glorioso, J.C. *et al.*: “Deriving Capillary Pressure and Water Saturation from NMR Transversal Relaxation Times,” paper SPE 81057 presented at the 2003 Latin American and Caribbean Petroleum Engineering Conference, Port-of-Spain, Trinidad, 27–30 April.
147. Grattoni, C.A. *et al.*: “An Improved Technique for Deriving Drainage Capillary Pressure from NMR T_2 Distributions,” paper SCA2003-25 presented at the 2003 Soc. of Core Analysts Annual International Symposium, Pau, France, 21–24 September.
148. Dastidar, R., Rai, C., and Sondergeld, C.: “Integrating NMR with Other Petrophysical Information to Characterize a Turbidite Reservoir,” paper SPE 89948 presented at the 2004 SPE Annual Technical Conference and Exhibition, Houston, 26–29 September.
149. Corbelleri, A. *et al.*: “Application of the Magnetic Resonance Logging in San Jorge Basin (Argentina),” paper VV presented at the 1996 Soc. of Professional Well Log Analysts Annual Logging Symposium, New Orleans, 16–19 June.
150. Davis, B., McDonald, T., and Aly, M.: “Practical Applications of NMR Technology Enhance Formation Evaluation, Testing and Completion Decisions,” paper SPE 76717 presented at the 2002 SPE Western Regional/AAPG Pacific Section Joint Meeting, Anchorage, 20–22 May.
151. Soliman, M.Y. *et al.*: “Technology Integration of Conformance and Magnetic Resonance Imaging Enhances Stimulation Treatment,” paper SPE 59530 presented at the 2000 SPE Permian Basin Petroleum Engineering Conference, Midland, Texas, 21–23 March.
152. Weiland, J., Teff, C., and Donovan, G.: “Integrating NMR, Rock Mechanics, and Production Evaluation to Optimize Hydrocarbon Production in Deepwater GOM,” paper VVV presented at the 2004 Soc. of Petrophysicists and Log Analysts Annual Logging Symposium, Noordwijk, The Netherlands, 6–9 June.
153. Hodgkins, M.A. and Howard, J.J.: “Application of NMR Logging to Reservoir Characterization of Low-Resistivity Sands in the Gulf of Mexico,” AAPG *Bulletin* (1999) **83**, No. 1, 114.
154. Ostroff, G.M. and Shorey, D.S.: “Integration of NMR and Conventional Log Data For Improved Petrophysical Evaluation of Shaly Sands,” paper OOO presented at the 1999 Soc. of Professional Well Log Analysts Annual Logging Symposium, Oslo, Norway, 30 May–3 June.
155. Freedman, R. *et al.*: “Combining NMR and Density Logs for Petrophysical Analysis in Gas-Bearing Formations,” paper II presented at the 1998 Soc. of Professional Well Log Analysts Annual Logging Symposium, Keystone, Colorado, 26–29 May.
156. Minh, C.C. *et al.*: “Sonic-Magnetic Resonance Method: A Sourceless Porosity Evaluation in Gas-Bearing Reservoirs,” paper SPE 56767 presented at the 1999 SPE Annual Technical Conference and Exhibition, Houston, 3–6 October.
157. Chen, S. *et al.*: “Optimization of NMR Logging Acquisition and Processing,” paper SPE 56766 presented at the 1999 SPE Annual Technical Conference and Exhibition, Houston, 3–6 October.
158. Akkurt, R., Prammer, M., and Moore, A.: “Selection of Optimal Acquisition Parameters for MRIL Logs,” *The Log Analyst* (1996) **37**, No. 6, 43.
159. Tourmelin, E., Torres-Verdin, C., and Chen, S.: “Quantification of Multiphase Fluid Saturations in Complex Pore Geometries From Simulations of Nuclear Magnetic Resonance Measurements,” paper SPE 77399 presented at the 2002 SPE Annual Technical Conference and Exhibition, San Antonio, Texas, 29 September–2 October.
160. Appel, M. *et al.*: “Fluid Identification in Heavy Oil Reservoirs by Nuclear Magnetic Resonance at Elevated Temperature,” paper SCA-9917 presented at the 1999 Soc. of Core Analysts International Symposium, Golden, Colorado, 1–4 August.
161. Mirotnich, K.D. *et al.*: “Low Field NMR Tool for Bitumen Sands Characterization: A New Approach,” *SPEE* (April 2001) 88.
162. Wyatt, D.F.: “Nuclear Magnetic Resonance Logging Aids in Defining Heavy Oil Types,” paper SPE 54121 presented at the 1999 SPE International Thermal Operations and Heavy Oil Symposium, Bakersfield, California, 17–19 March.
163. Carmona, R. and Decoster, E.: “Assessing Production Potential of Heavy Oil Reservoirs From the Orinoco Belt with NMR Logs,” paper ZZ presented at the 2001 Soc. of Professional Well Log Analysts Annual Logging Symposium, Houston, 17–20 June.
164. Padilha, S. and Baudot, P.: “Application of NMR Logging for Heavy Oil Identification and Quantification in OBM Environment,” paper FF presented at the 2001 Soc. of Professional Well Log Analysts Annual Logging Symposium, Houston, 17–20 June.

165. Manalo, F.P., Bryan, J.L., and Kantzas, A.: "Addressing the Clay/Heavy Oil Interactions When Interpreting Low Field Nuclear Magnetic Resonance Logs," paper SPE/PS-CIM/CHOA 78971 presented at the 2002 SPE International Thermal Operations and Heavy Oil Symposium and International Horizontal Well Technology Conference, Calgary, 4–7 November.
166. Najia, W. *et al.*: "Nuclear Magnetic Resonance (NMR), A Valuable Tool for Tar Detection in a Carbonate Formation of Abu Dhabi," paper SPE 78485 presented at the 2002 SPE Abu Dhabi International Petroleum Exhibition and Conference, Abu Dhabi, UAE, 13–16 October.
167. Manalo, F. *et al.*: "Separating the Signals from Clay Bound Water and Heavy Oil in NMR Spectra of Unconsolidated Samples," paper SPE 84480 presented at the 2003 SPE Annual Technical Conference and Exhibition, Denver, 5–8 October.
168. Zhang, Q., Huang, C., and Hirasaki, G.: "Interpretation of Wettability in Sandstones with NMR Analysis," *Petrophysics* (2000) **41**, No. 3, 223.
169. Guan, H. *et al.*: "Wettability Effects in a Sandstone Reservoir and Outcrop Cores from NMR Relaxation Time Distributions," *J. of Petroleum Science and Engineering* (2002) **34**, No. 1–4, 35.
170. Eidesmo, T., Relling, O., and Rueslatten, H.: "NMR Logging of Mixed-Wet North Sea Sandstone Reservoirs," paper PP presented at the 1996 Soc. of Professional Well Log Analysts Annual Logging Symposium, New Orleans, 16–19 June.
171. Akkurt, R. *et al.*: "Remaining Oil Saturation From NMR in a Mixed-Wet, Three-Phase Carbonate Reservoir," paper SPE 63216 presented at the 2000 SPE Annual Technical Conference and Exhibition, Dallas, 1–4 October.
172. Al-Mahrooqi, S.H. *et al.*: "An Investigation of the Effect of Wettability on NMR Characteristics of Sandstone Rock and Fluid Systems," *J. of Petroleum Science and Engineering* (2003) **39**, 389.
173. Fleury, M., Al-Nayadi, K., and Boyd, D.: "Water Saturation from NMR, Resistivity and Oil Base Core in a Heterogeneous Middle East Carbonate Reservoir," paper JJJ presented at the 2005 Soc. of Petrophysicists and Well Log Analysts Annual Logging Symposium, New Orleans, 26–29 June.
174. Looyestijn, W. and Hofman, J.: "Wettability Index Determination by Nuclear Magnetic Resonance," paper SPE 93624 presented at the 2005 SPE Middle East Oil and Gas Show and Conference, Bahrain, 12–15 March.
175. Howard, J.J.: "Quantitative Estimates of Porous Media Wettability From Proton NMR Measurements," *Magnetic Resonance Imaging* (1998) **16**, Nos. 5 and 6, 529.
176. Chen, J., Hirasaki, G., and Flaum, M.: "Effects of OBM Invasion on Irreducible Water Saturation—Mechanisms and Modifications of NMR Interpretation," paper SPE 90141 presented at the 2004 SPE Annual Technical Conference and Exhibition, Houston, 26–29 September.
177. Shafer, J. *et al.*: "Core and Log NMR Measurements Indicate Reservoir Rock is Altered by OBM Filtrate," paper CC presented at the 2004 Soc. of Petrophysicists and Log Analysts Annual Logging Symposium, Noordwijk, The Netherlands, 6–9 June.
178. Rodrigues, P., Alcocer, Y., and Matheus, J.: "NMR Signal Pattern Classification for Estimation of Petrophysical Properties," paper SPE 63258 presented at the 2000 SPE Annual Technical Conference and Exhibition, Dallas, 1–4 October.
179. Sigal, R.F. *et al.*: "A Method for Enhancing the Vertical Resolution of NMR Logs," paper SPE 63215 presented at the 2000 SPE Annual Technical Conference and Exhibition, Dallas, 1–4 October.
180. Akkurt, R. and Cherry, R.: "The Key to Improving the Vertical Resolution of Multi-Frequency Logging Tools," paper YY presented at the 2001 Soc. of Professional Well Log Analysts Annual Logging Symposium, Houston, 17–20 June.

SI Metric Conversion Factors

cm ² /sec	× 1.0*	E + 02	= mm ² /sec
cp	× 1.0*	E - 03	= Pa·s
°C	+ 273.15		= K
dynes/cm ²	× 1.0*	E - 01	= Pa
ft	× 3.048*	E - 01	= m
ft/min	× 5.080*	E - 03	= m/sec
°F	(°F + 459.67)/1.8		= K
gauss	× 1.0*	E - 04	= Tesla

$$\text{in.} \times 2.54^*$$

$$\text{ohm-m} \times 1.0^*$$

$$\text{psi} \times 6.894\,757$$

$$\text{E} - 02 = \text{m}$$

$$\text{E} - 02 = \text{ohm-cm}$$

$$\text{E} + 00 = \text{kPa}$$

*Conversion factor is exact.

Chapter 3F

Mud Logging

Dennis E. Dria, Shell Intl. Exploration and Production Inc.

3F.1 Introduction

Mud logging, in its conventional implementation, involves the rig-site monitoring and assessment of information that comes to the surface while drilling, with the exclusion of data from downhole sensors. The term mud logging is thought, by some, to be outdated and not sufficiently descriptive. Because of the relatively broad range of services performed by the geologists, engineers, and technicians traditionally called mud loggers, the term “surface logging” is sometimes used, and the personnel performing the services may be called surface-logging specialists. Additional specialist designations may include pore pressure engineer, formation evaluation engineer, logging geologist, or logging engineer. For the sake of generality, the terms mud logging and mud logger are used here with the understanding that the hybrid discipline encompasses much more than monitoring the mud returns and that the trained specialists perform engineering and geological tasks that span several traditional disciplines.

There are several broad objectives targeted by mud logging: identify potentially productive hydrocarbon-bearing formations, identify marker or correlatable geological formations, and provide data to the driller that enables safe and economically optimized operations. The actions performed to accomplish these objectives include the following:

- Collecting drill cuttings.
- Describing the cuttings (type of minerals present).
- Interpreting the described cuttings (lithology).
- Estimating properties such as porosity and permeability of the drilled formation.
- Maintaining and monitoring drilling-related and safety-related sensing equipment.
- Estimating the pore pressure of the drilled formation.
- Collecting, monitoring, and evaluating hydrocarbons released from the drilled formations.
- Assessing the producibility of hydrocarbon-bearing formations.
- Maintaining a record of drilling parameters.

Mud logging service first focused on monitoring the drilling mud returns qualitatively for oil and gas content.^{1,2} This included watching the mud returns for oil sheen, monitoring the gas evolving from the mud as it depressured at the surface, and examining the drill cuttings to determine the rock type that had been drilled, as well as looking for indication of oil on the cuttings. Detection of the onset of abnormal formation pressures using drilling parameters was proposed with the introduction of the d exponent.³ Gas chromatography, which was developed

early in the 20th century, saw its introduction in mud logging in the 1970s when electronics became sufficiently compact, rugged, and robust to be used at rig sites. The literature provides excellent reviews of the early history.^{4,5}

Computerized data acquisition and the ability to routinely transfer continuously acquired data to the office data center enabled the broader application of more sophisticated interpretive techniques and the integration of data from different sources into the geological and reservoir model, in near real time. This, coupled with the blossoming of measurement-while-drilling (MWD) and logging-while-drilling (LWD) tools, moved the mud-logging unit into a new role as a hub for rig-site data gathering and transmission.⁵ Starting in the 1980s, significant improvements to existing technologies, as well as major technical breakthroughs, have given the geologist and petroleum engineer a great number of powerful mud-logging tools to interpret and integrate geological, drilling, and geochemical data. These tools are discussed in subsequent sections of this chapter.

The traditional products delivered by a mud-logging vendor include geological evaluation, petrophysical/reservoir formation evaluation, and drilling engineering support services. In this overview, we consider that these products support three basic processes associated with drilling and evaluation of wells: formation evaluation (building or refining the geological and reservoir models), drilling engineering and operations (the planning and execution of the well construction process), and maintaining drilling and evaluation operations with appropriate health, safety, and environmental (HSE) consideration. The following section describes the path that drilling fluid follows during the drilling operation to explain where the logger obtains data.

3F.2 Mud Logging Data Acquisition

Fig. 3F.1 schematically shows the components of a drilling operation that have a part in mud logging. The most critical component is the drilling fluid (drilling mud), which, in addition to its role in drilling mechanics, carries most of the information from the formation up to the surface where it is acquired, decoded, or extracted from the mud stream by various techniques. Drilling liberates gas and liquid formation fluids, and circulation of the drilling fluid carries these to the surface (except during riserless drilling in a deepwater offshore environment, in which the drilling returns circulate only up to the sea floor). Cuttings, pieces of formation rock, are also carried in the circulated drilling fluid. MWD and LWD data are frequently encoded as pressure pulses and transmitted to the surface. Mud temperature is not a direct indicator of subsurface formation temperature, but monitoring the trend is important to understanding gas extraction efficiency and recycling. In deepwater drilling environments, the mud can be cooled significantly on the trip from the sea floor to the surface.

Drilling fluid is stored in the mud pit, drawn into the mud pumps, and pumped into the drillpipe via the kelly. Mud travels down the drillpipe, through any MWD tools and drill motors, and through the bit nozzles where its discharge aids drilling mechanics. At this point, the drilling fluid carries away rock fragments from drilled formation, along with any liberated reservoir fluids (water, oil, or gas). Cuttings and reservoir fluids are transported to the surface. Any gaseous components are dissolved in the base fluid of the drilling mud under most overbalanced drilling conditions. Drilling mud continues its flow up the wellbore drillstring annulus, through the casing-drillpipe annulus and the BOP stack, and, in the case of an offshore well, up the riser. At the bell nipple, the returning drill fluid is exposed to atmospheric pressure and flows down the mud return line. If an underbalanced drilling operation is being used, there is a rotating seal around the drillpipe, and the pressurized drilling returns stream moves through the “blooey line” to a separator and flair.

The return mud stream continues down the return line to the shaker box or “possum belly.” This is the standard location for the “gas trap” gas extractor. Mud pours over the shaker screens, with cuttings getting discharged off the top of the screen, while the drilling fluid that

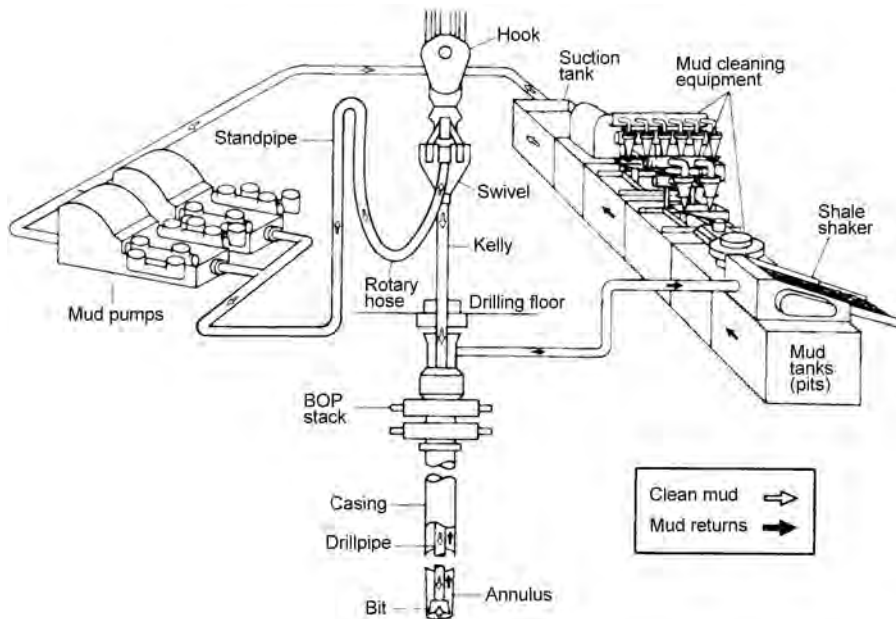


Fig. 3F.1—Drilling fluid flow path during drilling operations.

falls through the screens travels on through the degasser, desander, and desilter to the mud pits. The mud logger takes samples or acquires data at the following points in the process.

- Whole mud samples are taken at the mud suction pit and at the possum belly and are used to do whole-mud extraction using a steam still. They may be taken on an occasional basis during coring and wireline logging to assess the effects of mud filtrate and solids.

- Drill cuttings samples are taken off the shaker screen and off a “catch board” where cuttings fall from the screen to disposal. These are used for lithological and mineralogical description, paleo description, and sometimes “canned” for laboratory-based carbon-isotope analysis, detailed geological examinations such as thin-section preparation and analysis, chemostratigraphy, and source rock evaluation.

- Gas sampling is done through an extractor at the possum belly, in some cases at the bell nipple or off the mud return line to minimize losses to the atmosphere, and at the mud suction line or mud pit to monitor recycle gas content of the mud. After extraction, gas analysis may be performed at the sampling location,⁶ or, more routinely, the gas is continuously transferred via a vacuum line to the logging unit where it passes through the manifold of analytical instruments (total HC, GC, MS, H₂S, etc) and may be captured for laboratory-based analysis (carbon isotope, molecular composition).⁷

- Mud temperatures are monitored at the mud suction pit and mud return line.

The mud engineer collects mud samples for analyses that are used to determine any adjustments to mud properties needed for drilling.

Contamination is defined here as any material that does not come from the formation that has been drilled at the time that a specific volume element of mud exits the bit. Mud contamination has several potential sources:

- Air, which can enter the top of the drillpipe when the Kelly-drillpipe joint is broken during a connection.

- Pipe scale and pipe dope from inside the drillpipe (pipe dope fluoresces and may interfere with show identification or description).

- Rock sloughing or rubbing off formations further up hole.

- Cuttings that have bedded or built up because of improper hole cleaning dynamics that are mobilized by changes in mud viscosity, pumping rate, or drillpipe or collar rotation.
- Uphole fluids that flow or are swabbed into the annulus.
- Cuttings that have built up on the shaker screen or in the possum belly.

The logger should be watching for any change in cuttings or mud-conveyed hydrocarbon fluids that indicate contamination. Mud additives such as weighting agents and lost-circulation material are not considered contaminants, but must be monitored because some of these interfere with analytical observations and descriptions or give interfering instrument responses. Some base mud fluids, particularly some of the synthetic fluids, create challenges for the mud logger, as do some chemical additives (e.g., some sulfate or sulfonate wetting agents may give a false positive H₂S indication).

Samples of the drill cuttings are taken at the shale shaker. Wellsite geologists or engineers should specify the appropriate procedure for collecting samples, which may be done by the mud logger or the mud logger's sample catcher. Cuttings have a relatively short residence time on the shaker screen. Sampling protocol should include taking a composite sample with portions from different areas of the screen, combined with cuttings that have been retained on a "cuttings board." A cuttings board is a wooden board, steel angle iron, or other such device that is hung just below the base of the shaker screens to catch cuttings as they fall off the edge of the screen. Immediately after samples are collected, the screen and catch board should be washed down with clean drilling mud base fluid. The logger should mix this composite sample and take divided portions for cleaning, interpretation, and bagging. The wellsite planner should specify the sampling frequency (typically a composite over 10-, 30-, or 90-ft intervals or on a timed basis).

Gas sampling is traditionally done with a mechanical degasser, generically called a "gas trap." Fig. 3F.2 shows an example.⁸ Typically placed in the shaker box, the trap pulls in drilling mud through the centrifugal action of the stirrer. The mechanical action of the stirrer, combined with a slight vacuum pulled in the trap head space, allows the gas to partition between the liquid and gas phase. The head-space gas is pulled by vacuum through tubing, into the logging unit, and on through the gas analysis manifold.

Alternative methods for sampling gas may be accomplished by continuously operating controlled-volume mechanical or thermomechanical slip-stream gas extractors^{9,10} and membrane-type extractors.⁶ The mud logger may place the sampling point for these gas extraction devices at the bell nipple, the mud return line, or in the shaker box. Other methods require taking discrete samples, followed by thermal extraction techniques [such as the steam still, where samples of the whole mud are collected and portions heated in a steam-distillation apparatus (Fig. 3F.3)] and microwave heating methods.⁸

The gas manifold may include provisions for a portion of the gas stream to be pumped into sample containers, either laminated gas bags or stainless steel tubes* (see Fig. 3F.4). These gas samples are then shipped from the rig for laboratory analyses. There are new mass-spectrometer-based techniques that may not require a bulk extraction of the gas from the mud for analysis.¹¹

Once gas is extracted from the drilling fluid, various analytical techniques determine properties of the gas at the rig site. The basic measurements include a determination of the "total" gas concentration and the composition and concentrations of the constituent components.

3F.3 Total Gas Analysis

The total gas analyzer (TGA), also referred to as the total hydrocarbon analyzer (THA), measures the total amount of gas, typically the total amount of combustible gas. The usual unit of TGA measurement is total methane equivalents (TME), which is essentially the BTU content

* Personal communication with D. Coleman, IsoTech Laboratories, Champaign, Illinois (2002).

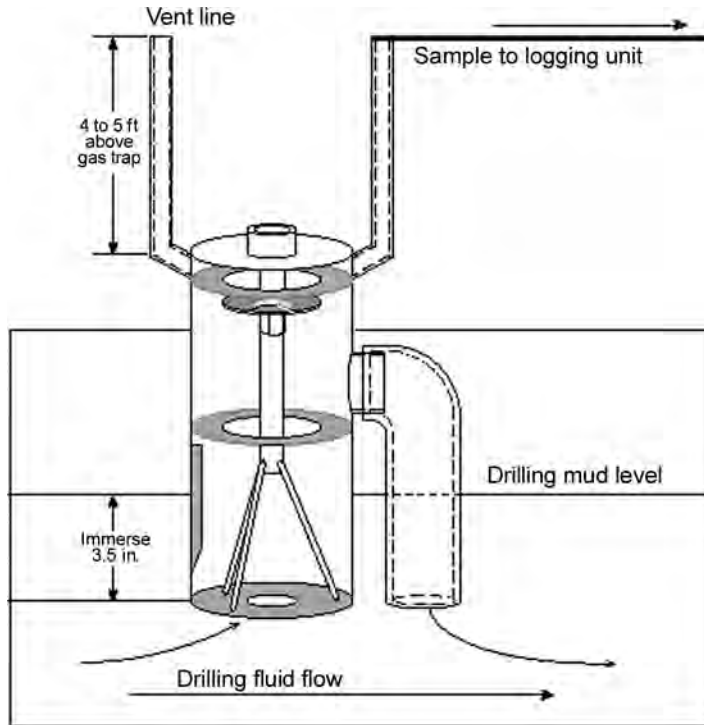


Fig. 3F.2—Schematic of a gas-trap type gas extractor.

of the gas extracted from the drilling fluid, expressed as that which would be obtained from an equivalent concentration of pure methane in air. The TGA, while giving an undifferentiated indication of gas entrained in the drilling fluid, has the advantage of operating in a continuous mode. Today, most TGAs use either a thermal conductivity detector (TCD) or a flame ionization detector (FID).

3F.4 Component Analysis

There are several analytical techniques used at the rig site to measure the molecular composition and component concentrations of the reservoir fluids entrained to the surface in the drilling fluid. These techniques are the gas chromatograph (GC), the mass spectrometer (MS), and the infrared spectrometer.

3F.4.1 Gas Chromatograph. The most widely used technique, and among the more accurate, is the GC (Fig. 3F.5). This instrument separates components from a mixture by selectively adsorbing and desorbing each compound at different rates, either on the surface of a granular packing contained in a column made of small-diameter tubing or on the internal surface of the tubing itself. A small, usually submilliliter, volume of the mixture (i.e., the gas extracted from the drilling fluid) is injected into a carrier gas stream, which carries the sample into the GC column. Components start to separate, depending on their affinity for the active surface of the packing or the column tubing. At the end of the column, components elute, each with a unique retention time, and pass into a detector. The different detectors used to analyze the compounds eluting from the GC column include the FID, the TCD, the catalytic combustion detector (CCD), the MS detector, and the infrared (IR) absorption spectrometer.

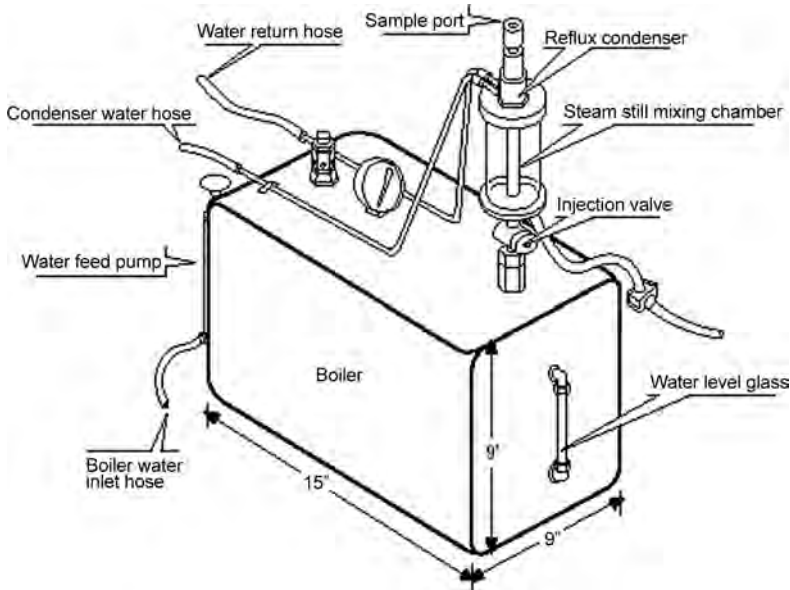


Fig. 3F.3—Schematic of a steam still-gas extractor.

Flame Ionization Detector. The FID uses a flame of burning hydrogen to combust the eluting compound. As the compounds undergo combustion, ionized single-carbon intermediates are captured by the collector electrode. Very sensitive circuitry (the electrometer) measures the extremely small, microamp-level current generated by this flow of ions, which is proportional to the total number of carbon atoms in the combusting gas mixture. Fig. 3F.6 shows the FID device schematically. The hydrocarbon species present are known because the operator, by design, knows which hydrocarbon component is eluting; therefore, concentration of that component may be calculated.

Thermal Conductivity Detector. The TCD (or hot wire detector) measures the thermal conductivity of the gas mixture passing over a filament. The typical TCD uses a Wheatstone Bridge circuit to measure the resistance of a platinum filament. The filament is heated to a constant temperature. As a gas passes over the filament, the temperature is reduced by an amount that is related to the thermal conductivity of the gas and the gas-flow rate. The resistance of the filament changes with temperature. At a constant flow rate through the sensing cell, gases of different composition and, hence, different thermal conductivity cool the filament by different amounts. In most TCD devices, there are two cells: a reference cell through which the pure carrier gas (in these cases, usually air) flows and a sample cell through which the gas mixture extracted from the drilling fluid flows. The filaments from the cells form two of the four arms of the Wheatstone Bridge (Fig. 3F.7).

Catalytic Combustion Detector. The CCD measures the temperature change in a platinum filament when the gas mixture is combusted. Rather than using a flame, the CCD device has the filament imbedded in a catalytic bead, which catalyzes the combustion chemical reaction, allowing it to occur at temperatures lower than normal flames. Heat is released according to the “heat of combustion,” and this released heat increases the filament temperature and, hence, its resistance. The resistance of the sample filament is compared with the resistance of a reference filament, in a fashion similar to the TCD, and provides an output that is a function of the composition of the gas mixture. This device provides an output signal that is more or less related to the BTU content of the gas mixture it is measuring.

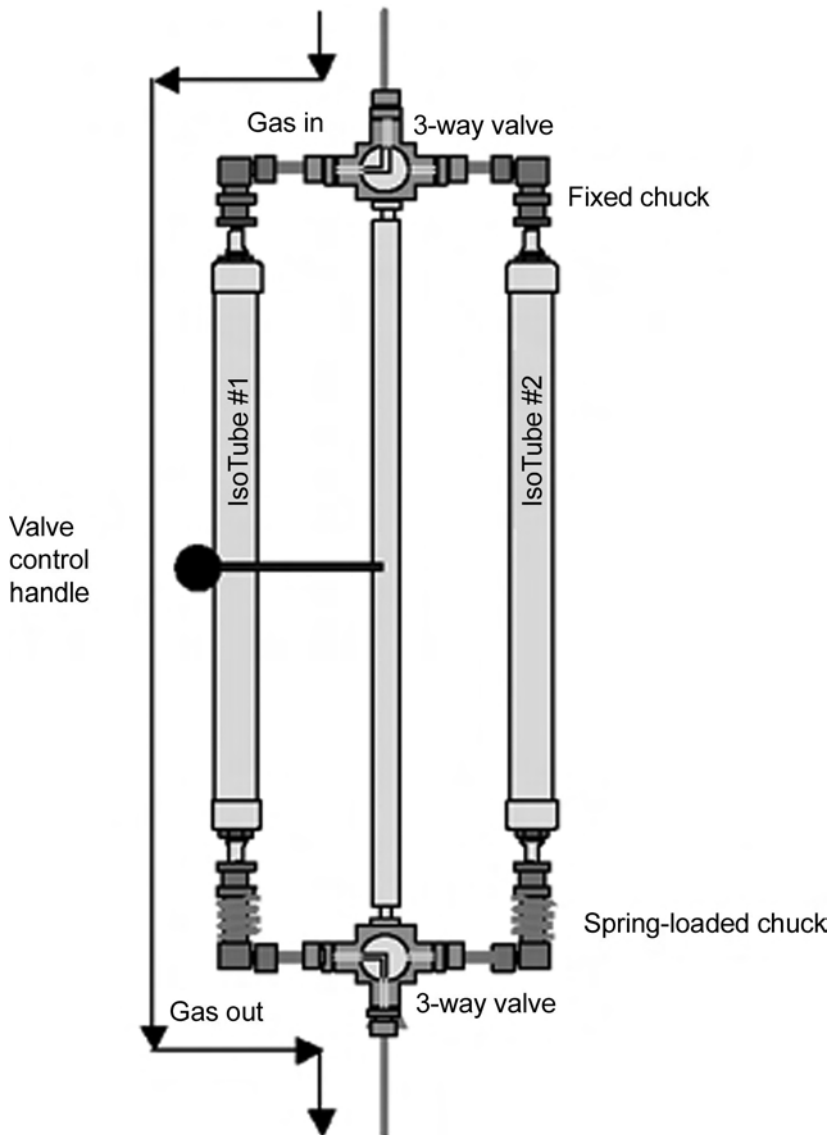


Fig. 3F.4—Low-pressure gas sampling tubes mounted two to a rack for continuous, sequential gas collection.

Mass Spectrometer Detector. The MS detector measures the quantity of a particular compound by determining the amount of material with a specific molecular weight. (Fig. 3F.8 shows the magnetic-sector MS.) This is done by ionizing a small quantity of material, during which multiple fragments of the molecule may be produced. Each fragment has a specific mass-to-charge ratio. Ionized fragments are separated in space or time, on the basis of their respective mass-to-charge ratio, and are then quantified by an ion detector. These devices have been used only in laboratory-based analyses until recently, when compact, robust MS detectors have been introduced for rig-site use.¹⁰ The MS has commonly been used to quantify components eluting from a GS (the GC-MS system) and has the advantage of being able to differentiate mixes of several components that may coelute, as long as the individual molecular species dif-

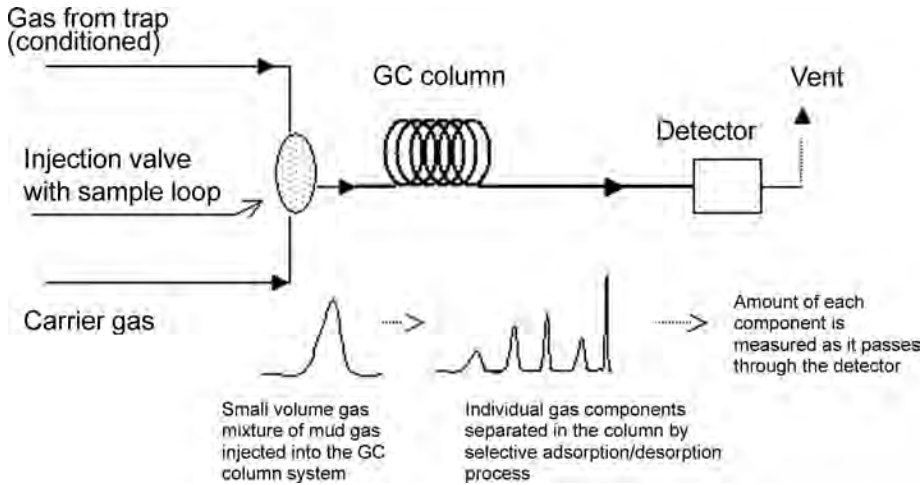


Fig. 3F.5—Schematic of a single-column gas chromatograph with generic detector.

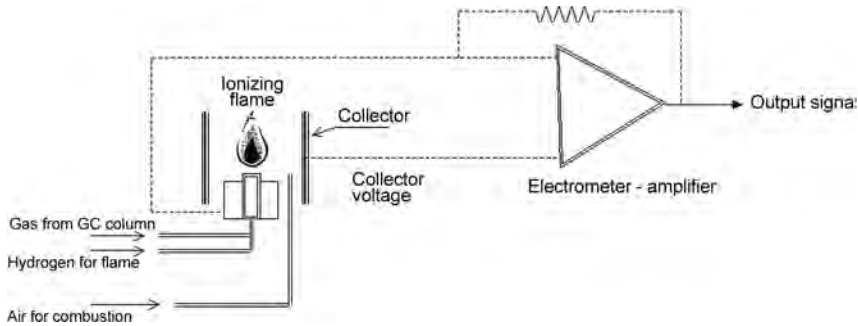


Fig. 3F.6—Flame ionization gas detector.

fer sufficiently in molecular weight. By principle of detection, this advantage allows simultaneous analysis of saturated and aromatic hydrocarbons, as well as the acid gases CO_2 and H_2S and inert gases such as nitrogen.

Recent advances in MS instrumentation and methods may allow its use at the rig site to measure directly the amounts of specific paraffinic and aromatic hydrocarbon compounds, CO_2 , and H_2S without the need for chromatographically separating the components. This would replace the function of the GC for HC component analysis, along with in-mud hydrogen sulfide detectors. These specific methods¹¹ are in relatively early stages of development and are not described here in detail.

Infrared Absorption Spectrometer. On input of IR energy to a molecule, its bonds will vibrate in any of a variety of modes, such as stretching, bending, rotating, and twisting. The mode of vibration will vary depending on the specific bond and the wavelength of the exciting radiation. IR radiation passes through a cell filled with the gas mixture. Portions of the incident IR spectrum are absorbed by the molecules in the gas, according to the characteristic absorption wavelengths of the specific molecules comprising the gas. The amount of IR radiation absorbed is a function of the path length and the concentration.

For a variety of physical reasons, the absorption spectrum is not manifested as a series of discrete wavelengths, but rather as a series of broader bands that, particularly in hydrocarbon

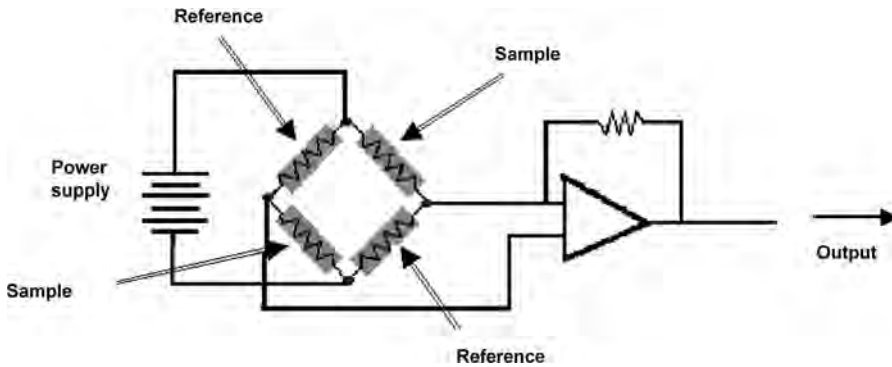


Fig. 3F.7—Thermal conductivity gas detector.

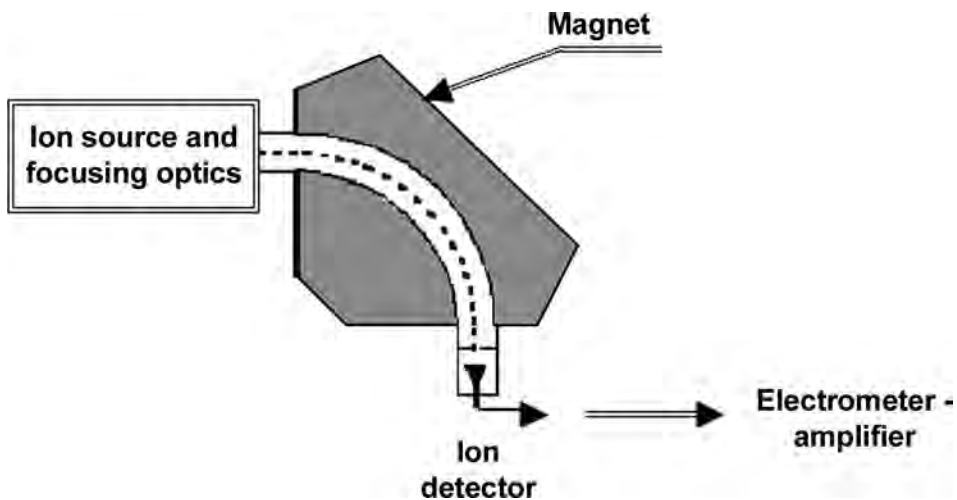


Fig. 3F.8—Magnetic sector mass spectrometer.

systems, overlap to the point of being difficult to explicitly deconvolve. Because IR sensors also tend to have poor resolution compared with band. When comparing differences in principles of operation, relative accuracy over a wide dynamic range of gas concentrations and operational robustness under rig site, for most applications the FID is the preferred detector system for both the GC and the THA.

3F.5 Cuttings Analysis

Cuttings provide the first opportunity and, in some wells, the only opportunity to actually look at the rock that has been drilled. Cuttings give the geologist information about the formation lithology needed for geologic correlation, the mineral composition for marker beds, input for the petrophysicist or log analyst, and, in some cases, enough hydrocarbon to allow some oil-quality measurements to be performed. Cuttings are also a source for microfossils used in biostratigraphy.

3F.5.1 Sample Lagging. Proper sample collection and preparation is of paramount importance. The first step is to know where the cuttings are from, which is done by performing a lag calculation. “Lagging” is performed by any of several methods. The most accurate method is to inject a tracer of some sort into the drilling fluid stream at the surface and time its exit as it

is circulated out. The volume of the mudlines and drillpipe, from the point of injection to the bit, can be calculated from the pipe measurements (inside diameter and length). The total tracer residence time in the drill fluid is

$$t_t = t_s + t_{dp} + t_{an}, \dots\dots\dots (3F.1)$$

$$\text{and } t_s + t_{dp} = q \cdot (V_s + V_{dp}), \dots\dots\dots (3F.2)$$

so that

$$t_{an} = t_t - q \cdot (V_s + V_{dp}), \dots\dots\dots (3F.3)$$

where t_{an} = the lag time from the bit to the point at the surface where the tracer is measured (usually the shaker box), t_t = the total elapsed pumping time from injection to measurement, q = the mud pump flow rate, V_{dp} = the internal volume of the drillpipe and drill collars, and V_s = the internal volume of any surface lines from the point of tracer injection to the kelly. Commonly used tracers include calcium carbide, air, and injected reference gas.

Solid carbide is put into the drillpipe when making a connection and pumped down with the circulating mud. Calcium carbide chemically reacts with water in the drilling fluid to form acetylene, which is then detected with the THA as it circulates out. Ease of handling and injection into the circulating mud system makes carbide lagging a popular choice. Disadvantages include the need for a manual operation, particularly the need for an additional person on the drill floor during the busy operation of making a connection, and the requirement that there be ample free water in the drilling fluid, which is not always the case with oil-based and synthetic mud systems.

Other materials may be injected into the drillpipe while making a connection. Virtually any benign pulverized solid that can be seen in the mud returns, such as ground-up bricks. If a high-viscosity sweep is being pumped, that can also be used to measure lag. These methods do require that logging personnel carefully watch the shaker screens to catch the appearance of the lag tracer.

When the kelly reaches the rotary table, the drillpipe is raised slightly so that the current connection between the kelly and the top pipe can be broken. This action reduces the mud pressure at the bit and can “swab” some formation fluids into the wellbore. The gas dissolved in this fluid is carried to the surface with circulation, appearing as “connection gas,” and may be used as a lag indicator. Swabbing at connections may also bring gas in from locations above the bit, depending on pore pressure gradient, drilling fluid rheology, and annular geometry. If this occurs, an erroneous lag results.

A less frequently used method for lag determination involves the injection of a reference gas into the mud pump intake.¹² Reference gas injection, by its original design, serves primarily as an internal standard for quantifying mud gas concentration. A noninteracting gas is injected at low rates into the mud pump intake line, which is controlled to maintain a constant concentration of the referencing gas in the drilling fluid. Momentarily increasing or decreasing the injection rate results in a subsequent increase or decrease in gas concentration in the drilling fluid. This concentration perturbation is noted while monitoring the mud gas using the logger’s gas analyzer, and its residence time in the system is used in the lag calculation. Advantages of this measurement include that it can be done on demand without waiting for a connection, it is independent of drilling fluid composition (no need for water in the case of nonaqueous drilling fluids), and that it can easily be automated.

3F.5.2 Cuttings Collection. Samples of drilled cuttings are normally taken at the shaker screens, although some have proposed and tested devices for diverting a small stream of cuttings-laden mud from the return line.¹³ At predetermined depth or time intervals, the logger or sample catcher collects a composite sample that contains cuttings representative of the entire interval drilled since the previous collection. Very typically, cuttings samples will be taken every 30 ft (10 m), until target bed boundaries are approached, such as thin marker beds, anticipated reservoir sections, casing points, or coring points.

By placing a board at the base of the shaker screen in line to catch cuttings as they fall off the end of the screens, the sample catcher assures that a composite sample accumulates. At the desired sampling time, the sampler scrapes cuttings off the board into a sampling bucket and adds additional cuttings from several locations across the screen (the latter, to catch the very latest drilled material circulated up). This collection yields a composite sample that is fairly representative of the formations drilled since the last collection. Immediately after sampling, the sampler should hose down the screen and catching board with water for aqueous drilling fluids or with the appropriate base fluid for nonaqueous drilling fluids. Proper cleaning of the composited cuttings calls for placing the cuttings on a fine mesh screen and flushing with the base drilling fluid.

3F.5.3 Cuttings Sample Examination and Description. Proper handling, examination, and description guidelines should be specified when contracting mud-logging services. This section is not meant to replace an experienced professional geologist's interpretation of cuttings, but serves as a guide to the important "high points" that the logger should remember in applying procedures presented in appropriate geological guidelines and manuals. Several excellent references are available.¹⁴⁻¹⁶ Swanson's thorough summary¹⁷ is presented as a detailed manual.

Scanning a series of samples laid out on the counter allows the logger to get a good overview of trends, to highlight sample differences that may be the result of quality variation or contamination, and to help identify bed boundaries. Individual samples are then examined under a low-power stereomicroscope (10 to 50X) with either ample natural light or a lamp with a "blue" light or blue filter. Proper illumination is required so that the true colors of the sample constituent minerals are not distorted. Digital image capture of select samples adds significantly to the end-of-well documentation. A quick examination should identify all material present in significant quantity, including contaminants, metal, drilling additives, lost-circulation material, and suspected caved material, in addition to the drilled-formation rock cuttings. This examination should include an assessment of sample quality.

The well databases containing the cuttings log should include an estimate of the percentage of each rock type, which is an assessment of what is actually seen in each individual sample, as well as an interpretation of the lithology, which is based on all the data available to the logger. The logger's manual should call for a standardized description protocol containing rock type (with classification), color, texture (grain size, roundness, sorting), cement and/or matrix material, fossils, sedimentary structures, and porosity and oil shows. Standard abbreviations should be used in the description, as well as standard symbols as the log is being drawn.¹⁷

Many special tests are run on rock samples to make on-the-spot determination of specific minerals. These tests vary from such standard chemicals as alzarin red for calcite detection to calcimetry for quantitative determination of carbonate content. A qualified logging geologist will have experience in suggesting and implementing them.

The sample should be viewed under ultraviolet (UV) light, and any fluorescence noted (mineral or hydrocarbon). Certain types of hydrocarbons, in the rock pores or "stained" on the grain surface, may not fluoresce. To test for these, the rock samples may then be treated with an appropriate organic solvent while being viewed under UV light. "Streaming" fluorescence may be noted (streamers or wisps of hydrocarbon) as it moves from the rock cutting into the

solvent surrounding the cutting. As the solvent dries, “residual cut” may be observed as a fluorescing ring or residue in the examination dish. These are examples of “cut fluorescence.”

Sometimes there will be more extraneous material present in the cuttings sample than actual drilled formation fragments. Commonly seen nonformation solids include the following:

- Cavings from uphole, previously penetrated beds. These will be recognized as formation material logged earlier and individual cuttings may have shapes that distinguish them from bit cuttings.
- Recirculated cuttings. These are usually smaller, individual grains or microfossils.
- Lost circulation material. Extraneous solids, which have a size to plug up lost circulation zones, are added to the drilling fluid. These may be as unusual as cotton seed hulls, ground-up pecan shells, and shredded rubber.
- Cement fragments. Close attention should be paid to the drilling record.
- Drilling mud. Washing samples using procedures and solvents that are appropriate for the specific mud system. Consideration for the health of the logger and the environment is critical.
- Pipe dope. This contaminant may fluoresce, giving a false show indication.

This list of contaminant examples is not all inclusive, and judgment, combined with close attention to the drilling and mud engineers’ records, is critical.

3F.6 Maintaining Data Quality

Many different data are available, obtained through technologies that range from tried-and-true classical “wet chemistry” techniques through high-tech sensors that use procedures established after countless years of thoughtful research, development, and field testing. Even the best planned operations may, from time to time, provide data of poor quality or even totally miss data from important geologic intervals. Proper planning of surface data logging operations should include provisions for “whole-system” qualification before starting the operation, as well as a plan for the occasional quality audit. Details will vary widely depending on the location of the operations, availability of staff, project magnitude, and economics. An appropriate quality assurance program may be as simple as receiving a weekly e-mail or fax with GC calibration information or as intensive as scheduling rig-site audits, depending on the exact circumstances and well logging objectives.

3F.7 Formation Evaluation

Formation evaluation, for this discussion, is the process of describing a geologic formation, and any fluids contained within, in terms of their constituent properties and determining the properties of the rock to assess the total and recoverable volume, value, and producibility of the fluids and the placement, and the engineering design and economics of drilling and completing the wells that are needed to produce the fluids. Many data are interpreted to evaluate a petroleum-bearing formation, and we discuss the interpretations of data acquired through surface data logging in terms of the rock formation and fluid properties they help determine.

3F.7.1 Fluid Type. The logging engineer or geologist gets information about the formation fluids directly from fluids that are released into the wellbore while drilling and circulating out suspended immiscibly in the drill fluid or remaining in the pores of larger cuttings that may not have been flushed. They receive information indirectly from remnants of the fluid that remain in pores of rock cuttings, as stains on the grain surface, or in solution in the drilling fluid.

Oil may be identified as a sheen on the surface of water-based drilling fluid. If the circulating fluid density is sufficiently low as to render an underbalanced drilling condition, oil may be produced in large enough quantities that a sample may be skimmed off a whole mud sample. Similarly, the underbalanced penetration of a gas-bearing formation yielding only a small quantity of free gas in the mud system at the bit will expand according to the real gas law as it is circulated to the surface, where it may be detected and possibly sampled (although, in an

uncontrolled situation, this results in hazardous safety and environmental conditions). These are all fairly obvious, direct indicators.

The ratio of various mud-gas components (e.g., the molar or volumetric ratio of methane to ethane) may be crossplotted or correlated with fluid type.¹⁸⁻²¹ The modified Pixler method,¹⁹ for example, plots ratios of methane (C_1) to, respectively, ethane (C_2), propane (C_3), butanes and heavier (C_{4+}), and pentanes and heavier (C_{5+}):

$$C_1 / C_2, \dots \dots \dots (3F.4)$$

$$C_1 / C_3, \dots \dots \dots (3F.5)$$

$$C_1 / C_{4+}, \dots \dots \dots (3F.6)$$

$$\text{and } C_1 / C_{5+} \cdot \dots \dots \dots (3F.7)$$

Through a correlated analysis, ranges of these ratio values had been determined that were representative of productive and nonproductive gas and oil (see Fig. 3F.9).

The Haworth *et al.* “wetness” method²⁰ defines several correlatable ratios: wetness, W_h ; balance, B_h ; and character, C_h .

$$W_h = \frac{C_2 + C_3 + iC_4 + nC_4 + C_5}{C_1 + C_2 + \dots + C_5} \cdot \dots \dots \dots (3F.8)$$

$$B_h = \frac{C_1 + C_2}{C_3 + iC_4 + nC_4 + C_5} \cdot \dots \dots \dots (3F.9)$$

$$C_h = \frac{iC_4 + nC_4 + C_5}{C_3} \cdot \dots \dots \dots (3F.10)$$

The values of these ratios determine, through the interpretation shown in Fig. 3F.10, whether the hydrocarbon is gas or oil, very dry gas, and, with enough data, whether the oil is tending towards being a light oil, heavy oil, or residual oil.

These ratio methods tend to work robustly only within the basins in which they are calibrated, the number and quality of data from the basin within which they are calibrated, and the errors inherent in obtaining the calibration set as well as the unknown data set. Examples of these inherent errors include the unknown or varying extraction efficiency at the gas trap and the accuracy of the gas-measurement system. Normalization techniques,^{22,23} either against an internal standard or other parameters, can improve the consistency and robustness of the ratios.

3F.7.2 Fluid Properties. If determining fluid type is difficult because of errors and unknowns in measuring the composition of formation hydrocarbons entrained in the drilling fluid, even more difficulty can be anticipated in estimating the fluid properties, such as viscosity or API gravity. The more robust methods involve either quantitatively measuring the methane-through-pentane composition of the drilling fluid returns and correlating these with the HC fluid properties²⁴ or involve spectroscopy techniques to get particular spectra and correlating these to oil properties or type.^{25,26}

The QGM™ process⁸ involves the use of a gas-trap extractor that was characterized and field tested extensively. This trap, when used in a controlled fashion, can give a quantitative

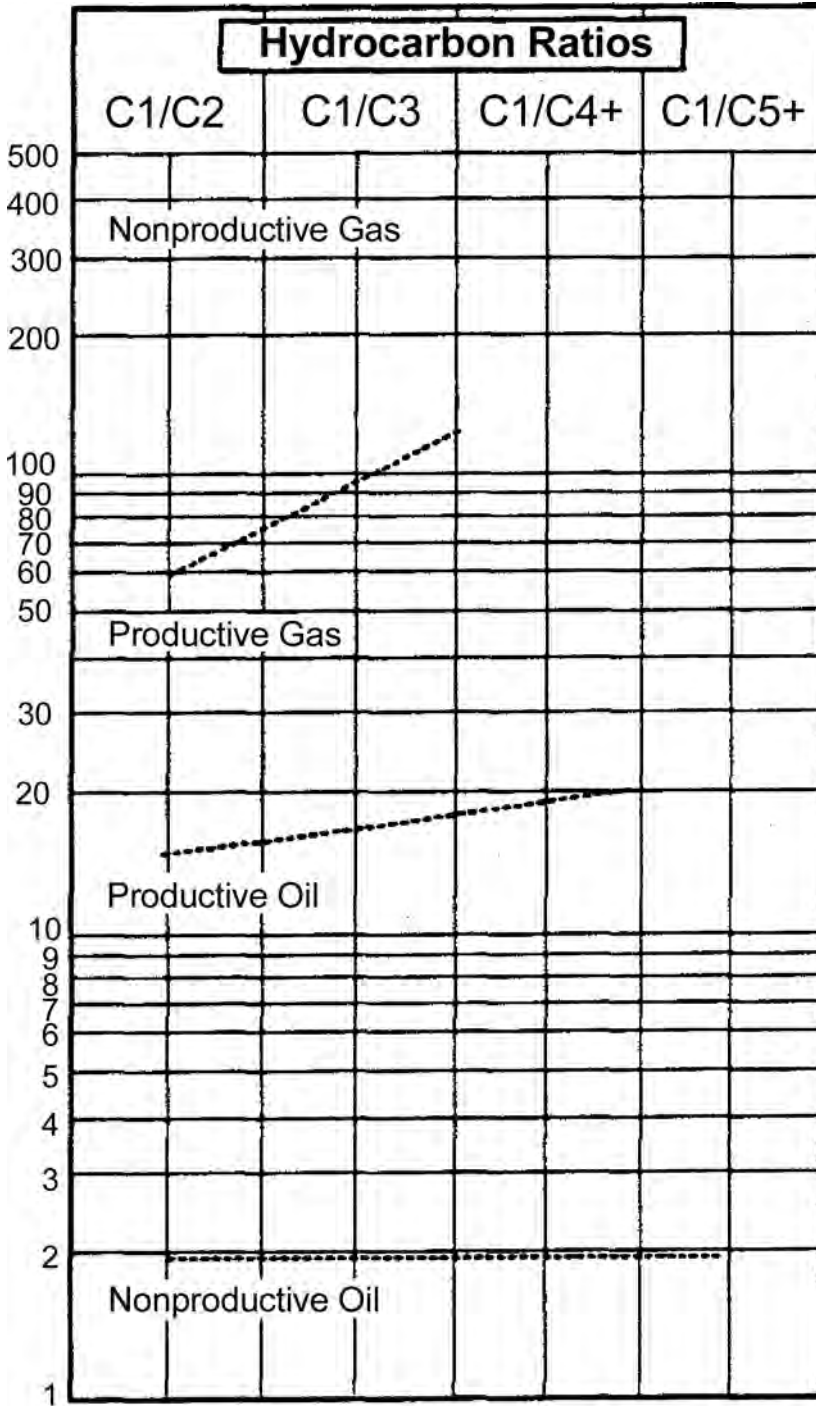


Fig. 3F.9—Template for plotting gas ratios with the modified Pixler method.

measurement of gas-trap extraction efficiency when calibrated with a measurement of thermally extracted mud-gas composition. With proper control and calibration, this process gives highly

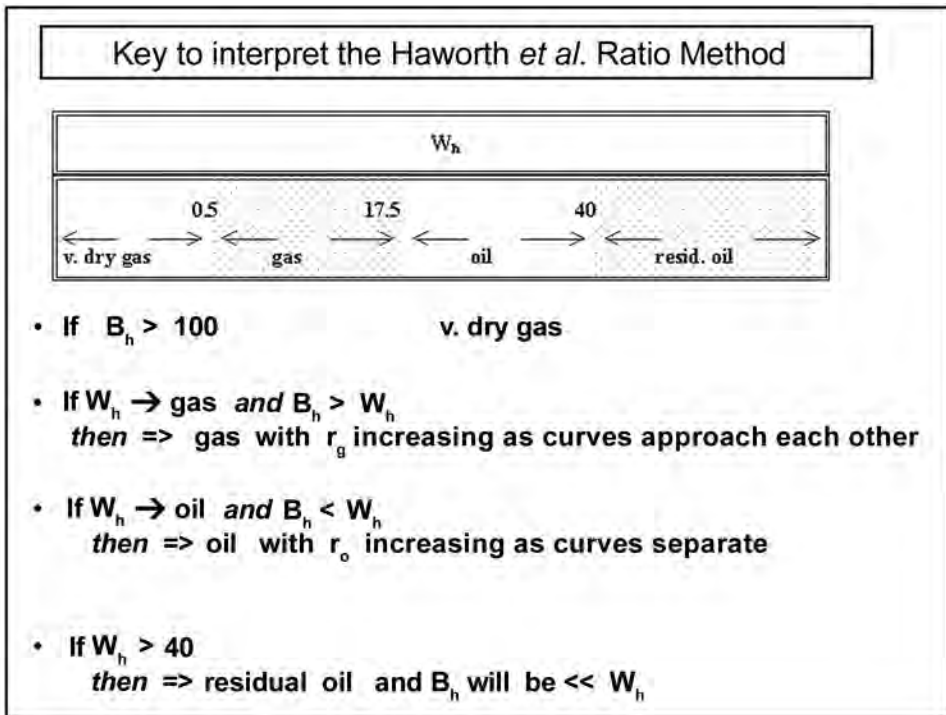


Fig. 3F.10—Interpretation legend for the Haworth *et al.* “wetness method.”

accurate gas-in-mud compositions. With these, correlations have been developed that relate composition parameters to oil properties.

An enhanced quantitative UV-fluorescence technique²⁶ monitors the intensity of two emission wavelengths resulting from exciting an oil sample with UV radiation. The ratio of the intensities varies according to the oil composition or, more exactly, according to the concentrations of certain aromatic compounds in the oil sample.

3F.7.3 Formation Porosity. Formation porosity is estimated by visually inspecting rock cuttings, which requires a sufficient description and classification of the rocks. Several references supply discussion.¹⁴⁻¹⁷ The requirement of rock fragments with intact pore systems eliminates the use of this method when drilling poorly consolidated or unconsolidated sands and when bit types, such as the PDC, reduce most of the potential reservoir cuttings to grain-sized fragments.

The method described by Boone²⁷ calculates the rock porosity that would be required to liberate the specific amount of gas measured when a set volume of formation is drilled. This assumes low fluid spurt loss while drilling (near-zero flushing of the rock ahead of the bit), which is frequently violated except in near-balance drilling and low-permeability formations.

3F.7.4 Formation Permeability. The formation permeability may be estimated visually by the logger from the grain size and sorting. At best, this may give order of magnitude estimates, but, frequently, the smaller, clay-sized particles, which may control the permeability if present in appreciable amounts, cannot be quantified with any confidence. Another limitation occurs because the cutting sample is acquired over a relatively large depth interval, and “smearing” of the data occurs in zones where grain size, sorting, and clay content vary significantly.

3F.7.5 Pore Pressure. Pore-pressure variations, particularly transitions from normal to geopressures, trend with several measurable parameters. These parameters are discussed more in the Drilling section.

3F.7.6 Geological or Petrophysical Information for Evaluation Away From the Wellbore.

The correlation of geologic strata relies on determining certain characteristic properties or constituents of a particular geologic formation. Geologists use these properties in one of several techniques to correlate formations from well to well within a field as well as in broader, basin-wide studies. Particular formations may serve as “markers” by having one or a set of distinguishing characteristics. Mud-logging services provide rock-cutting samples for the determination of these characteristics and, in some cases, may acquire the data on site. The acquisition of cuttings samples for these tests may impact the cuttings sampling or preparation techniques and should be considered when specifying a mud-logging service.

Microscopic fossils identified and correlated by paleontologists yield “biomarkers,” which become the working data for biostratigraphy. These biomarkers frequently appear in the cuttings in very low quantities because of the grinding and abrasion the cuttings see under the action of the drill bit and transport uphole in the returning mud stream. Their preparation calls for consistently applied cleaning with the use of a screen or sieve with openings small enough to retain the microfossils.

Specific mineral assemblages may be present in a particular geologic formation with compositions nearly constant or in relative abundances that are nearly constant over an extensive areal. The use of such mineral compositions as stratigraphically correlatable parameters is called chemostratigraphy. The ratio of concentrations of these certain minerals, as well as of other compounds associated with the deposition and diagenesis of the particular formation, must then be determined relatively quickly and cheaply. It has been shown that the ratios Ca/Al, Na/Al, and K/Al are related to clay mineral concentration ratios, and that relative amounts of such elements as Ti, Cr, and Zr are frequently associated with the clay minerals.^{28–30} Chemostratigraphers determine the amounts of these elements using laboratory or rig-based instruments such as inductively coupled plasma spectrometry and laser-induced breakdown spectroscopy.

Pore fluids present during diagenetic processes become crystallographically trapped in small volumes called fluid inclusions. These tiny drops of fluids, sealed in cavities typically 2 to 20 μm in size, are thought to be representative of the pore fluid composition that existed at the time of their formation.³¹ After appropriately cleaning portions of the drill cuttings, geologists chose grain samples containing fluid inclusions for analysis, which includes heating to volatilize the fluids and rupture the inclusion walls. Liberated vapor passes to an MS, which measures fluid composition for hydrocarbons, and other geochemical species such as H_2S , CO_2 acetic acid, and aromatics. Occasionally, a crude-oil fluid inclusion volume may be large enough to characterize the crude sufficiently to assess physical properties and the degree of biodegradation and thermal alteration.³² Fluid inclusion stratigraphy, which uses included-fluid composition as the correlating parameter, has been proposed to assess the location of fluid contacts, identify migration pathways, characterize compartmentalization, and determine distance to pay zones.^{31–33}

3F.8 Drilling Engineering and Operations

There is significant overlap between data gathered for geological, petrophysical, and reservoir engineering needs vs. data gathered for the driller. Information about pore pressure, formation gas, and rock type and strength are an integral part of well planning. Continuously tracking these parameters as a well is drilled and comparing the actual data with what was used in the well plan allows for quick response by the driller when trouble occurs. It also allows the driller to “fine tune” his operations to optimize drilling performance, which is measured by drill rate,

trouble time and cost, and delivery of well specifications (e.g., in terms of being a producing asset, an exploration well, or an appraisal well). We will leave these items in the “evaluation” bin, with the acknowledgement that they could just as easily be lumped into the drilling engineering category. This section discusses the data types and processes that are used to a large extent, and in some cases exclusively, by the driller.

Any measurable parameter that gives an indication of pore pressure provides the driller with an estimate of the degree of overbalance, which directly affects the rate of penetration (ROP). Mud weight will be adjusted to be within the desired window for a well’s particular set of drilling dynamics and rock strengths on the basis of modeled drill rate. The various measurements described in other sections of this chapter become important, to some degree, to the driller. These services may be provided by the mud logging contractor.

3F.8.1 Weight on Bit And Rate of Penetration. These data are collected to indicate drilling performance. The driller would like to know how to predict his drilling or penetration rate. Bourgoyne *et al.*³⁴ describes several models that have been developed and used. Jordan³ proposed modifying the Bingham model and defined a normalized parameter called the drilling exponent (the *d*-exponent):

$$d_{\text{exp}} = \frac{\log \left(\frac{R}{60N} \right)}{\log \left(\frac{12W}{1,000d_b} \right)}, \dots\dots\dots (3F.11)$$

where *R* = the penetration rate in ft/hr, *N* = the rotary speed in rpm, *W* = the weight on bit in Mlb, and *d_b* = the bit diameter in inches. The *d*-exponent is sometimes corrected for mud density changes³⁵ by considering the effects of *ρ_n*, the mud density equivalent to a normal formation pore pressure, and *ρ_e*, the equivalent mud density at the bit while circulating:

$$d_c = d_{\text{exp}} \frac{\rho_n}{\rho_e} \dots\dots\dots (3F.12)$$

3F.8.2 Mud Pit Level. Indicators specify changes in the volume of mud in the pit. The total volume of mud changes continuously with depth as the hole volume increases. Rapid increases in pit volume may mean an influx of reservoir fluids, and well control measures may need to be implemented. A rapid decrease in volume indicates a downhole loss of mud, and lost-circulation material will probably be added to the drilling fluid.

3F.8.3 Mud Chloride Content. Mud chloride content is monitored in all systems, along with the water content in nonaqueous drilling fluid systems. Significant changes in content may indicate influx of formation water, which means that an underbalance condition may be close, and mud weight may need to be increased.

3F.8.4 Lithology and Mineralogy. Lithology and mineralogy may change as a fault is approached. Warmer water, with higher concentrations of dissolved salts, can flow along faults during some phases of their development. As the water moves into cooler zones, salts will precipitate, plugging pores and showing up in the cuttings. Indication of an approaching fault may warn of a potential jump across the fault, which, in some areas, is accompanied by a significant change in pore pressure. Advance knowledge of this allows the driller to adjust the mud weight before he encounters problems.

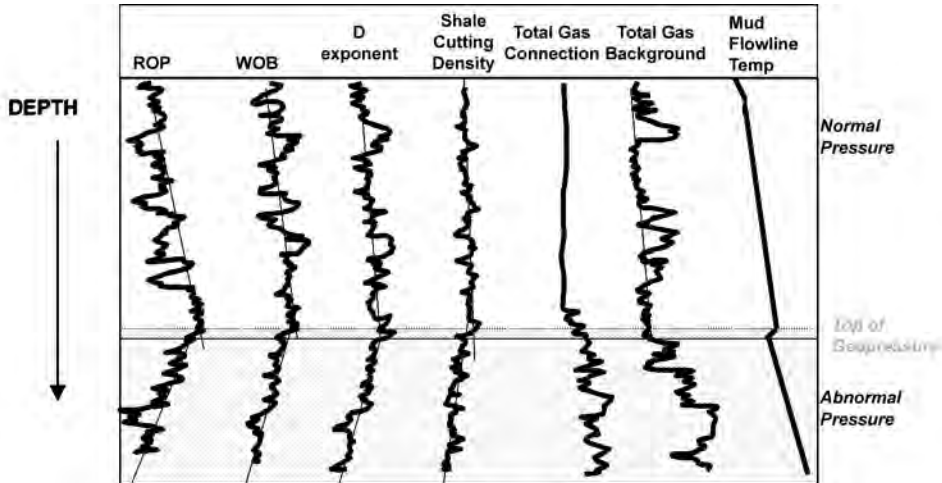


Fig. 3F.11—Schematic description of drilling and mud logging parameter changes with depth, normal pressure trends, and geopressure trends.

3F.8.5 Total Gas. Concentrations in the drilling fluid returns indicate the degree of overbalance or underbalance between the equivalent mud density and the formation pore pressure. The total gas concentration measured while drilling shales establishes a baseline or background level that is useful in tracking pore pressure, with the assumption that the shale pore fluids are in equilibrium with any neighboring permeable sands.

Fig. 3F.11 indicates how trends of several parameters vary with pore pressure and depth. Monitoring and plotting these can give indications of the transition from normally pressured zones to geopressures. The ROP, drilling exponent, shale cutting density, and background total gas all follow a normal trend with depth. Attempts to calibrate these measurements directly to pore pressure have been somewhat successful and usually are on the basis of establishing the trend for normally pressured formations. When a deviation from the normal trend occurs, correlations specific to the basin or geographic region are used to estimate the formation pore pressure. Most logging companies offer pore pressure service, which requires experienced pore pressure engineers who, frequently through experience, add subjective input to the model as well as the objective parametric inputs.

While the accuracy of these particular methods will vary from site to site, such plots are extremely useful in identifying the transition into geopressures (i.e., when passing from normally pressured to abnormally pressured zones). At the transition to geopressures, the trend lines change slope. Because some of the changes may be subtle, looking at all the available data helps pinpoint the transition.

3F.8.6 Connection Gas. As Sec. 3F.5.1 describes, connection gas is a good indicator of swabbing the wellbore at the bit (i.e., reducing the mud pressure at the bottom of the hole to below the pore pressure). If the pore pressure is less than the swabbed bottomhole pressure, little or no connection gas is seen. Some knowledge of the dynamic rheology of the drilling fluid is needed to perform input into a “swab model.”

3F.8.7 Normal Geothermal Gradient. The normal geothermal gradient may shift on transition into geopressures. Other thermal anomalies, such as proximity to subsurface salt bodies, may interfere with this phenomenon. A more thorough discussion of these techniques and their application to detect overpressure may be found in several references.^{3,4,34,35}

3F.8.8 Monitoring the Rate of Cuttings Return. As a formation is drilled, the cuttings should be circulated to the surface. Improper hole cleaning results in the downhole retention of cuttings, frequently as a cuttings bed on the low side of the hole in inclined wells. This causes an increased drag on the drillpipe and, if buildup is severe, may pack off the drillpipe, causing it to stick. Monitoring the rate of cuttings production from the drilling fluid returns indicates an approaching problem and warns the driller, which allows for remedial action before the pipe sticks. Watching for an increase in cuttings return rate can flag sloughing or extruding shale conditions, which call for an adjustment of mud density, as well as extreme washout conditions. Naegel *et al.*³⁶ describe a device for continuously weighing the cuttings as they come off the shaker screens and comparing this with what would be expected for a given ROP and mud pump rate.

3F.9 Health, Safety, and Environmental Considerations

Various parameters measured for formation evaluation and to monitor drilling operations and equipment are also indicators of conditions that could pose health, safety, and environmental concerns. Pore pressure changes that result in loss of well control pose obvious safety concerns. Any loss of control that results in a hydrocarbon release also poses serious environmental issues. Ambient monitoring for natural gas is done for health and fire safety. Monitoring hydrogen sulfide (H_2S) is essential in areas in which the potential has been shown historically to exist, as well as in rank wildcat wells in which the characteristics of the geological basin are poorly known.

Hydrogen sulfide is detectable by GC but can not be measured with an FID. Thermal conductivity, MS, and solid state sensors detect H_2S . The Delphian Mud Duck, which uses an electrochemical sensor, monitors dissolved H_2S , HS^- , and S^{2-} ionic concentrations to give total sulfide content of the drilling fluid. This tool continuously follows sulfide trends before its concentration increases to the point that gaseous H_2S is released from the mud. Draeger tubes are used for spot measurement of hydrogen sulfide, as a backup or as a check on other sensing equipment.

Nomenclature

B_h	=	balance ratio
C_1	=	methane
C_2	=	ethane
C_3	=	propane
C_{4+}	=	butanes and heavier
C_{5+}	=	pentanes and heavier
C_h	=	character ratio
d_b	=	bit diameter, L, in.
d_c	=	corrected drilling exponent, dimensionless
d_{exp}	=	drilling exponent, dimensionless
N	=	rotary speed, rpm
q	=	mud pump flow rate, B/D
r_g	=	residual gas
r_o	=	residual oil
R	=	penetration rate, ft/hr
t_{an}	=	lag time from the bit to surface, min
t_{dp}	=	lag time in the drill pipe, min
t_s	=	lag time in surface lines, min
t_t	=	total elapsed pumping time from injection to measurement, min

- V_{dp} = internal volume of the drillpipe and drill collars, bbl
 V_s = internal volume of any surface lines tracer injection point to kelly, bbl
 W = weight on bit, k-lbf
 W_h = wetness ratio
 ρ_e = equivalent mud density at the bit while circulating, m/L^3 , g/cm^3
 ρ_n = mud density equivalent to a normal formation pore pressure, m/L^3 , g/cm^3

Acknowledgments

The author thanks Shell Intl. E&P Inc. for permission to publish this chapter and is very grateful to Geoservices, Datalog, and Halliburton for the help and advice he has had in gathering gas-sensing information. The reference list provides excellent sources for general information.³⁷⁻⁴²

References

- Haywood, J.T.: "Continuous Logging at Rotary Drilling Wells," presented at the 1940 Drilling Practices Annual Meeting, Chicago, November.
- Wilson, R.W.: "Mud Analysis Logging and Its Use in Formation Evaluation," AIME technical paper 587-G presented at the U. of Houston, October 1955.
- Jorden, J.R.: "Application of Drilling Performance Data to Over Pressure Detection," *JPT* (November 1966) 1387.
- Jorden, J.R. and Campell, F.L.: *Well Logging I—Rock Properties, Borehole Environment, Mud and Temperature Logging*, Monograph Series, SPE, Richardson, Texas (1984) 9.
- Whittaker, A.H.: "Mud Logging," *Petroleum Engineering Handbook*, SPE, Richardson, Texas (1992) Chap. 52.
- Brumboiu, A.O. *et al.*: "Application of Semipermeable Membrane Technology in the Measurement of Hydrocarbon Gases in Drilling Fluids," paper SPE 62525 presented at the 2000 SPE/AAPG Western Regional Meeting, Long Beach, California, 19–23 June.
- Ellis, L, Brown, A., Schoell, M., and Haught, M.: "Mudgas Isotope Logging While Drilling: A New Field Technique for Exploration and Production," presented at the 19th International Meeting on Organic Geochemistry, 6–10 September, 1999, Istanbul, Turkey, *Abstracts Part 1*, 67–68.
- Wright, A.C., Hanson, S.A., and Delaune, P.L.: "A New Quantitative Technique for Surface Gas Measurements," paper A presented at the 1993 SPWLA Annual Logging Symposium, 13–16 June.
- De Pazzis, L.L. *et al.*: "New Gas Logging System Improves Gas Shows Analysis and Interpretation," paper SPE 19605 presented at the 1989 SPE Annual Technical Conference and Exhibition, San Antonio, Texas, 8–11 October.
- Brevier, J., Herzhaft, B. and Mueller, N.: "Gas Chromatography—Mass Spectrometry (GCMS)—A New Wellsite Tool for Continuous C1-C8 Gas Measurement in Drilling Mud—Including First Original Gas Extrator and Gas Line Concepts. First Results and Potential," paper J presented at the 2002 SPWLA Annual Logging Symposium, Oiso, Japan, 2–5 June.
- Sterner, M.: "Internal Marketing Literature," Fluid Inclusion Technology Inc., Tulsa (2002).
- Amen, R.: "Quantifying Hydrocarbon Shows Using On-Line Gas Referencing," paper HH presented at the 1994 SPWLA Annual Logging Symposium, 19–22 June.
- Williams, R.D. and Ewing, S.P. Jr.: "Improved Methods for Sampling Gas and Drill Cuttings," *SPEFE* (June 1989) 167.
- Low, J.W.: "Examination of Well Cuttings," *Quarterly*, Colorado School of Mines, Golden, Colorado (October 1951) 46, 1.
- Archie, G.E.: "Classification of Carbonate Reservoir Rocks and Petrophysical Considerations," *Bull. AAPG* (February 1952) 36, 278.
- Dunham, R.J.: "Classification of Carbonate Rocks According to Depositional Texture," *Classification of Carbonate Rocks*, W.E. Ham (ed.), Memoir 1, AAPG, Tulsa (1962) 108–121.
- Swanson, R.G.: *Sample Examination Manual*, American Assn. of Petroleum Geologists, Tulsa (1981).
- Pixler, B.O.: "Formation Evaluation by Analysis of Hydrocarbon Ratios," *JPT* (June 1969) 665.

19. Ferrie, G.H., Pixler, B.O., and Allen, S.: “Well-Site Formation Evaluation by Analysis of Hydrocarbon Ratios,” presented at the 1981 Annual Technical Meeting of the Petroleum Society of CIM, Calgary, 3–6 May.
20. Haworth, J.H., Sellens, M., and Whittaker, A.: “Interpretation of Hydrocarbon Shows Using Light (C1-C5) Hydrocarbon Gases from Mud-Log Data,” *AAPG Bulletin* (August 1985) **69**, 1305.
21. Whittaker, A. and Sellens, M.: “Analysis Uses Alkane Ratios from Chromatography,” *Oil & Gas J.* (18 May 1987) 42.
22. Whittaker, A. and Sellens, G.: “Normalization of Gas Shows Improves Evaluation,” *Oil & Gas J.* (20 April 1987) 53.
23. Amen, R.M.: “Technique Uses Reference Gas to Assess HC Shows,” *The American Oil & Gas Reporter* (April 1995) 57.
24. Wright, A.C.: “Estimation of Gas/Oil Ratios and Detection of Unusual Formation Fluids from Mud Logging Gas Data,” paper CC presented at the 1996 SPWLA Annual Logging Symposium, 16–19 June.
25. Delaune, P.L.: “Surface Techniques to Measure Oil Concentrations While Drilling,” paper KK presented at the 1992 SPWLA Annual Logging Symposium, June.
26. Delaune, P.L. *et al.*: “Enhanced Wellsite Technique for Oil Detection and Characterization,” paper SPE 56802 presented at the 1999 SPE Annual Technical Conference and Exhibition, Houston, 3–6 October.
27. Boone, D.E.: “Gas Volumetric Analysis,” *Petroleum Engineer Intl.* (August 1985).
28. Beeunas, M.A. *et al.*: “Application of Gas Geochemistry for Reservoir Continuity Assessment, Gulf of Mexico,” presented at the 1996 AAPG/EAGE Research Symposium on Compartmentalized Reservoirs: Their Detection, Characterization and Management, 20–23 October.
29. Ehrenberg, S.N. and Siring, E.: “Use of Bulk Chemical Analyses in Stratigraphic Correlations of Sandstones: An example from the Statfjord Nord Field, Norwegian Continental Shelf,” *J. of Sedimentary Petrology* (1992) **62**, 318.
30. Pearce, T.J. and Jarvis, I.: “Applications of Geochemical Data to Modeling Sediment Dispersal Patterns in Distal Turbidites: Late Quaternary of the Madeira Abyssal Plain,” *J. of Sedimentary Petrology* (1992) **62**, 1112.
31. Hall, D., Shentwu, W., and Sterner, M.: “Using Fluid Inclusions to Explore for Oil and Gas,” *Hart’s Petroleum Engineer Intl.* (1997) No. 11, 29.
32. Hall, D.L., Bigge, M.A., and Jarvie, D.M.: “Fluid Inclusion Evidence for Alteration of Crude Oils,” presented at the 2002 AAPG Annual Meeting, Houston, 10–13 March.
33. Barclay, S.A. *et al.*: “Assessment of Fluid Contacts and Compartmentalization in Sandstone Reservoirs Using Fluid Inclusions, An Example from the Magnus Oil Field, North Sea,” *AAPG Bull.* (April 2000) 489.
34. Bourgoyne, A.T. *et al.*: *Applied Drilling Engineering*, second edition, SPE, Richardson, Texas (1991) Chap. 6.
35. Rehm, W.A. and McClendon, R.: “Measurement of Formation Pressure From Drilling Data,” paper SPE 3601 presented at the 1971 SPE Annual Meeting, New Orleans, 3–6 October.
36. Naegel, M. *et al.*: “Cuttings Flow Meters Monitor Hole Cleaning in Extended Reach Wells,” paper SPE 50677 presented at the 1998 SPE European Petroleum Conference, The Hague, 20–22 October.
37. *Gas Detection: Theory and Practice*, training manual, Geoservices Inc. (1995).
38. Mercer, R.F. and McAdams, J.B.: “Standards for Hydrocarbon Well Logging,” presented at the 1982 SPWLA Annual Logging Symposium, 6–9 June.
39. *Mud Logging: Principles and Interpretation*, Exploration Logging Inc. (1979)
40. “Mud Logging: Methods and Interpretation Workshop,” workshop notes, 1989 SPWLA Annual Logging Symposium, 11 June.
41. Helander, D.P.: *Fundamentals of Formation Evaluation*, OGC Publications, Tulsa (1983).
42. “Advances in Mud Logging,” presented at the 1995 SPWLA/CWLS Symposium, 17 June.

SI Metric Conversion Factors

$$\text{ft} \times 3.048^* \qquad \text{E} - 01 = \text{m}$$

*Conversion factor is exact.

Chapter 3G

Specialized Well-Logging Topics

Paul F. Worthington, Gaffney, Cline, and Assocs.

3G.1 Introduction

This chapter describes three categories of specialized well logging: downhole measurements that are concerned with the geometry and integrity of the wellbore; acoustic and electrical imaging of the geological architecture and fabric of the rock system penetrated by the well; and downhole measurements that use the Earth's gravitational and magnetic fields to infer large-scale changes through density and magnetization, respectively. Although some of these technologies are applied beyond the petroleum industry (e.g., geotechnical studies and hydrogeology), this overview concentrates on their hydrocarbon applications. Each topic has a brief introduction, a description of the principles of each method, a discussion of its practical application, and, in selected cases, an illustrative case history. **Fig. 3G.1** summarizes how these specialized logging methods relate to reservoir characteristics and the techniques for measuring them, as presented in Chaps. 3B through 3F and Chap. 4 in this section and Chap. 15 in the Drilling Engineering section of this *Handbook*.

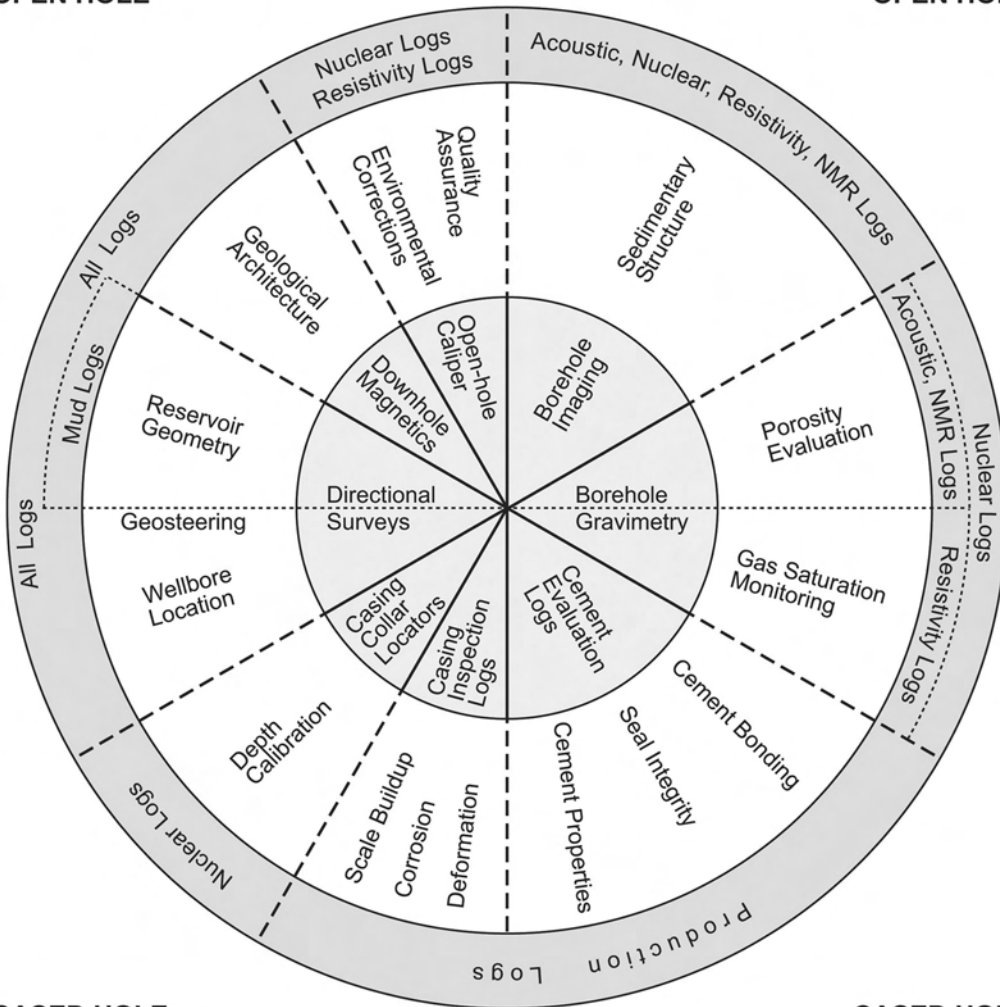
3G.2 Geometry and Integrity of the Wellbore

3G.2.1 Directional Surveys. Principles. With the growth in drilling deviated, extended-reach, and horizontal wells, the location of the wellbore is increasingly a 3D problem. It is encountered in one of two situations: to direct and define the trajectory of the well during the drilling process (geosteering) or to characterize the well path after drilling. The former has contributed to huge increases in well productivity. The latter is a vital element of integrated reservoir studies in which the aim is to generate a 3D model of the reservoir based on correct well locations. This discussion is set within the context of the latter. Geosteering is a benefit of logging-while-drilling technology (see Chap. 15 in the Drilling Engineering section of this *Handbook*).

In directional-survey terminology, the azimuth is the orientation of the wellbore to "north," which has been variously defined as magnetic north, geographic north (latitude and longitude), or grid north [e.g., the Universal Transverse Mercator (UTM) geographic coordinate system]. Azimuth is typically measured clockwise from north. The inclination is the deviation of the wellbore from the vertical. The azimuth and inclination define the coordinates of the wellbore along its length, usually relative to the location of the wellhead. Tool face quantifies the direction in which the tool is pointing. It is the angle between a reference direction on a downhole

OPEN HOLE

OPEN HOLE



CASED HOLE

CASED HOLE

Fig. 3G.1—This chart is separated into three concentric areas: the middle annular area indicates the subsurface properties to be evaluated, the innermost area indicates the specialized logging tools discussed here, and the outermost area indicates the logging tools discussed in other subchapters of this Handbook. The corresponding innermost and outermost areas show how the different tools complement each other in the investigation of particular subsurface properties.

tool and a fixed reference in space. For near-vertical wells, the fixed reference is magnetic north and the (magnetic) tool face is the angle between magnetic north and the projection of the tool's reference direction onto a horizontal plane. For more deviated wells, the fixed reference is the top of the hole and the (gravity or high side) tool face is the tool orientation with respect to the top of the hole. Directional surveys allow azimuth and inclination to be determined so that the coordinates of well location can be computed at each survey station.

Measurement. There are two types of directional surveys: magnetic and gyroscope surveys. Traditionally, each of these has been run using either single- or multishot tools. The tools are self-contained and can be powered from the surface or with downhole batteries. For a detailed description, see Bourgoyne *et al.*¹

Magnetic surveys can be run on the drillstring while tripping or on a wireline (conducting cable) after drilling. They are openhole measurements. In the simplest form, a magnetic-survey tool comprises a downhole inclinometer and a compass unit. More advanced tools comprise arrays of three-axis accelerometers (inclinometers) and magnetometers. A three-axis accelerometer measures three orthogonal components of gravity, which combine vectorially to give the direction of the Earth’s gravitational field relative to the axis of the tool and a reference position on its circumference. A three-axis magnetometer measures the direction of the Earth’s magnetic field relative to the tool axis. As **Fig. 3G.2** illustrates, by combining the accelerometer and magnetometer data, it is possible to calculate the inclination, I , and azimuth, A , of the tool. Through the tool face, it is then possible to calculate the inclination, α , and azimuth, β , of the wellbore itself. The magnetic measurements are impacted by short-term variations in the Earth’s magnetic field and by proximity to magnetic materials such as drillpipe and casing or to magnetic minerals such as pyrite and/or hematite, the latter also occurring as a mud additive. These problems can be mitigated through the use of nonmagnetic drill collars and repeat measurements with different alignments of the tool in the wellbore. It should be noted that even where magnetic-survey tools are run in long lengths of nonmagnetic drill collars, there can still be a significant effect from steel drillstring tools.³

One of the problems with gyroscope surveys is that the instrumentation is very sensitive and cannot withstand downhole vibrations and stresses. For this reason, gyroscope surveys have to be run on wireline, usually while entering the hole with a few additional checkshots on coming out. They interrupt the drilling process, and this adds to cost. However, they can be run in cased hole. In the simplest form, a gyro tool comprises a downhole inclinometer and gyroscope unit. Gyroscope surveys are usually mechanically driven, but other methods, which use a rotating beam of light, have been developed on the basis of fiber optics and laser technology. Mechanical gyroscopes are grouped in terms of their freedom of movement and the number of flywheels (between one and three). Three-axis systems (i.e., three orthogonal accelerometers and gyroscopes mounted on an inertial platform) have proved superior, especially in highly deviated and horizontal wells, where, for example, the axial component of the Earth’s gravity field is small. Here, the tool position is calculated from the accelerometer and gyroscope data through the tool’s inertial navigation system.

Fig. 3G.3 shows the reporting format of a typical directional survey. A synopsis of the errors associated with these measurements and their application has been provided by Theys.²

Processing. The results of directional surveying usually take the form of inclination, α , and azimuth, β , of a borehole at a sequence of survey stations. The only other information available is the difference in measured depths for two adjacent stations, but this does not describe the shape of the well path. Starting with the coordinates of the surface reference point, the actual distance between adjacent survey stations needs to be calculated so that the coordinates of any station can be found by addition and those of any intermediate point can be found by interpolation. There are several ways of doing this interpolation. The following account is based on Inglis’ work.⁴

The balanced tangential method assumes that the actual wellpath between two adjacent measurement stations can be approximated by two straight lines of equal length, $L/2$, shown as AX and BX in **Fig. 3G.4**. This leads to the following expressions for the incremental distances between adjacent survey stations in the vertical direction (ΔV), in the direction of the northing (ΔN), and in the direction of the easting (ΔE):

$$\Delta V = \Delta V_1 + \Delta V_2 = L/2(\cos \alpha_1 + \cos \alpha_2), \dots\dots\dots (3G.1)$$

$$\Delta N = \Delta N_1 + \Delta N_2 = L/2(\sin \alpha_1 \cos \beta_1 + \sin \alpha_2 \cos \beta_2), \dots\dots\dots (3G.2)$$

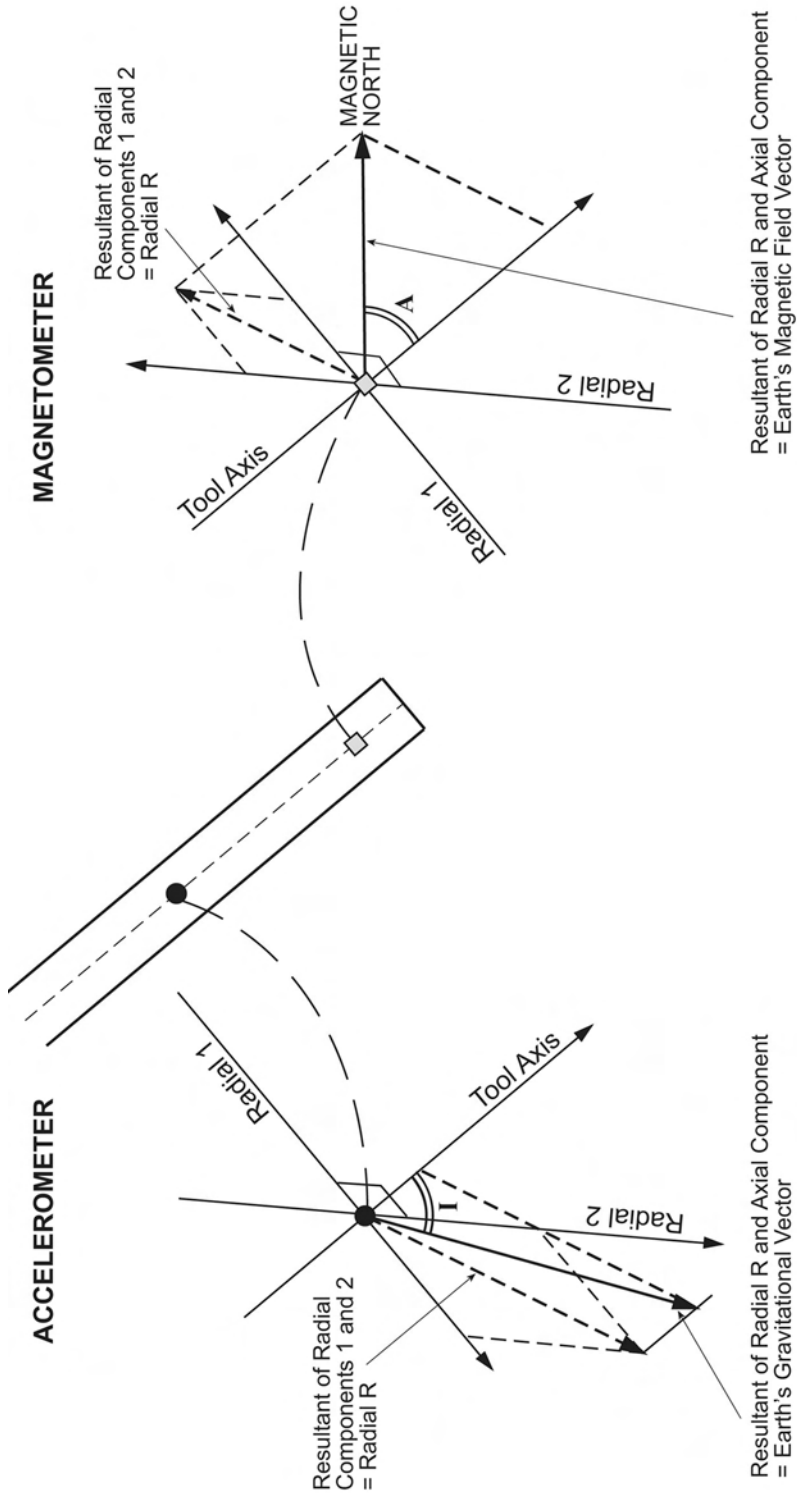
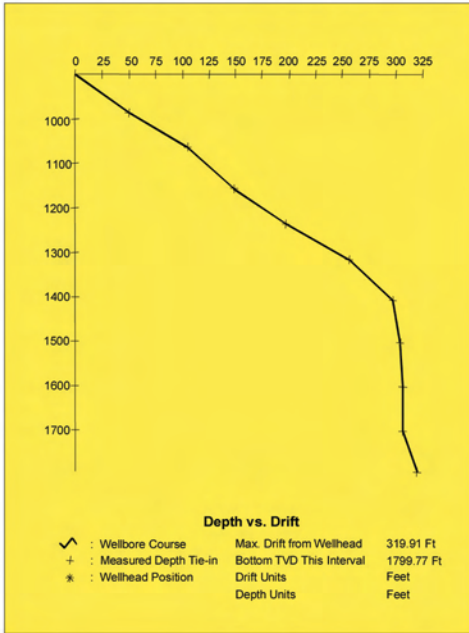
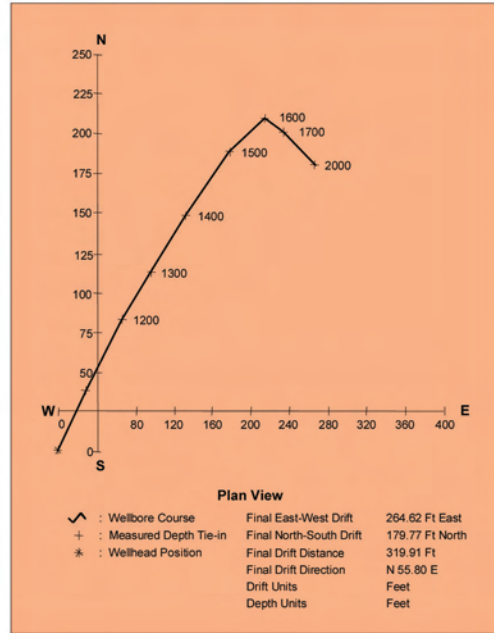


Fig. 3G.2—Vectorial illustration of the use of three-axis magnetometer and accelerometer data to calculate the inclination and azimuth of the directional-survey tool and of the wellbore itself.²

Well Path Plot



Plan View



Tabular Listing

COMPANY WELL				PAGE 1			
DEPTH	DEVIATION		TVD	DRIFT COORDINATES			TOTAL
	ANGLE	AZIMUTH		STATION	E-W	N-S	
1000.00	9.0	35.0	900.00	0.00N	0.00E	0.00N	0.00E
1100.00	50.0	37.0	985.19	38.66N	28.78E	38.66N	28.78E
1200.00	20.0	45.0	1066.17	43.70N	35.99E	82.37N	64.76E
1300.00	30.0	44.0	1156.69	30.15N	29.53E	112.52N	94.30E
1400.00	30.0	47.0	1243.29	35.04N	35.65E	147.55N	129.95E
1500.00	45.0	50.0	1322.40	40.01N	45.63E	187.56N	175.58E
1600.00	10.0	110.0	1409.73	20.63N	36.81E	208.19N	212.39E
1700.00	10.0	120.0	1508.21	7.31S	15.68E	200.88N	228.06E
1800.00	0.0	120.0	1607.70	4.35S	7.54E	196.53N	235.60E
1900.00	0.0	120.0	1707.70	0.00N	0.00E	196.53N	235.60E
2000.00	40.0	120.0	1799.78	16.76S	29.02E	179.77N	264.63E
THE FIRST POINT INFORMATION:							
1000.00	9.0	35.0	900.00	0.00N	0.00E	0.00N	0.00E
THE LAST POINT INFORMATION:							
2000.00	40.0	120.0	1799.78	16.76S	29.02E	179.77N	264.63E
FINAL EAST-WEST DRIFT = 264.63 E							
FINAL NORTH-SOUTH DRIFT = 179.77 N							
FINAL DRIFT DISTANCE = 319.91 FT							
FINAL DRIFT DIRECTION = N 55.81 E							

Fig. 3G.3—Example of the reporting format of a directional survey with depths in feet. Vertical scale on the Well Path Plot is true vertical depth (TVD). Depth markers on the Plan View trace are measured depths. The Tabular Listing links the two depth scales at measurement stations and contains the wellbore deviation, azimuth, and coordinates at the points of measurement. (Courtesy of Baker Atlas.)

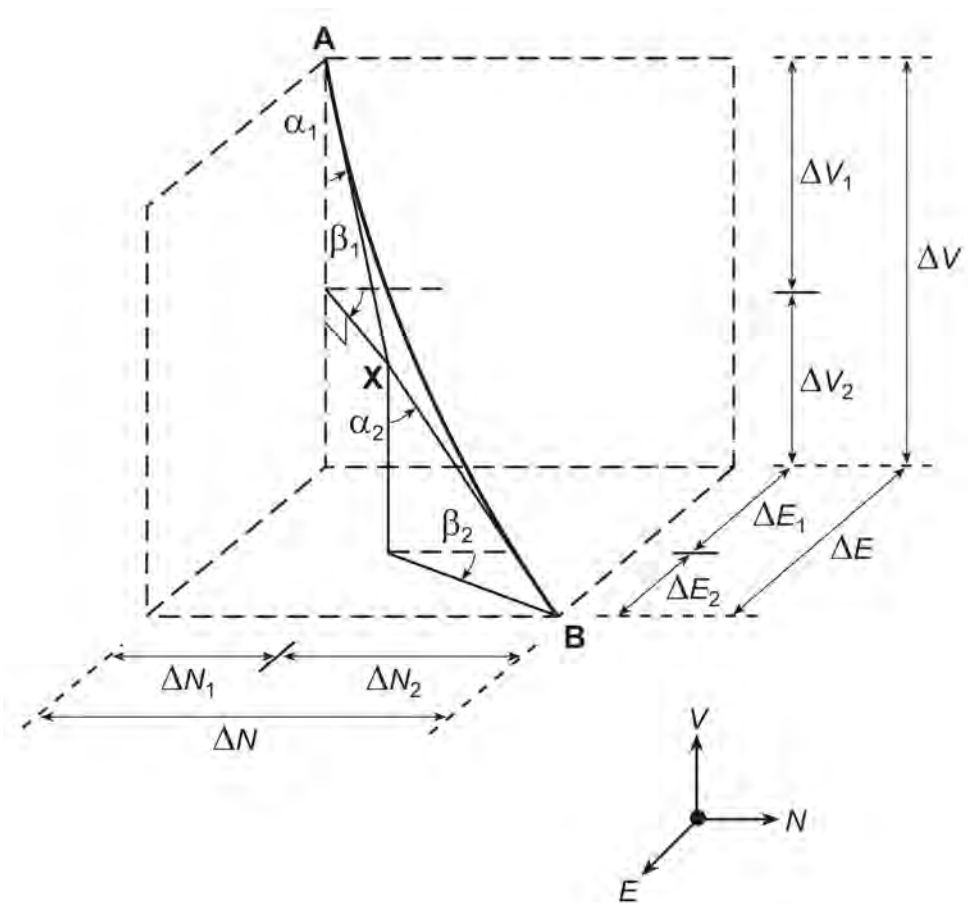


Fig. 3G.4—Principles of the balanced tangential method for modeling the well path between directional survey stations A and B.⁴

$$\text{and } \Delta E = \Delta E_1 + \Delta E_2 = L/2(\sin \alpha_1 \sin \beta_1 + \sin \alpha_2 \sin \beta_2), \dots\dots\dots (3G.3)$$

where the subscripts 1 and 2 denote the upper and lower survey stations, respectively.

An improvement on the balanced tangential method is the minimum curvature method, which replaces the two straight lines by an arc. The position of the arc is based on the amount of bending in the wellpath between the two survey stations. The amount of bending is described by a ratio factor, F_r , and quantified by a dogleg angle, ψ (Fig. 3G.5), so that:

$$F_r = (360 / \pi\psi) \tan (\psi / 2), \dots\dots\dots (3G.4)$$

where

$$\cos \psi = \cos \alpha_1 \cos \alpha_2 + \sin \alpha_1 \sin \alpha_2 \cos (\beta_2 - \beta_1) . \dots\dots\dots (3G.5)$$

The ratio factor is applied to each of the quantities ΔV , ΔN , and ΔE as calculated by the balanced tangential method (Eqs. 3G.1 through 3G.3). Thus, for example, Eq. 3G.1 becomes

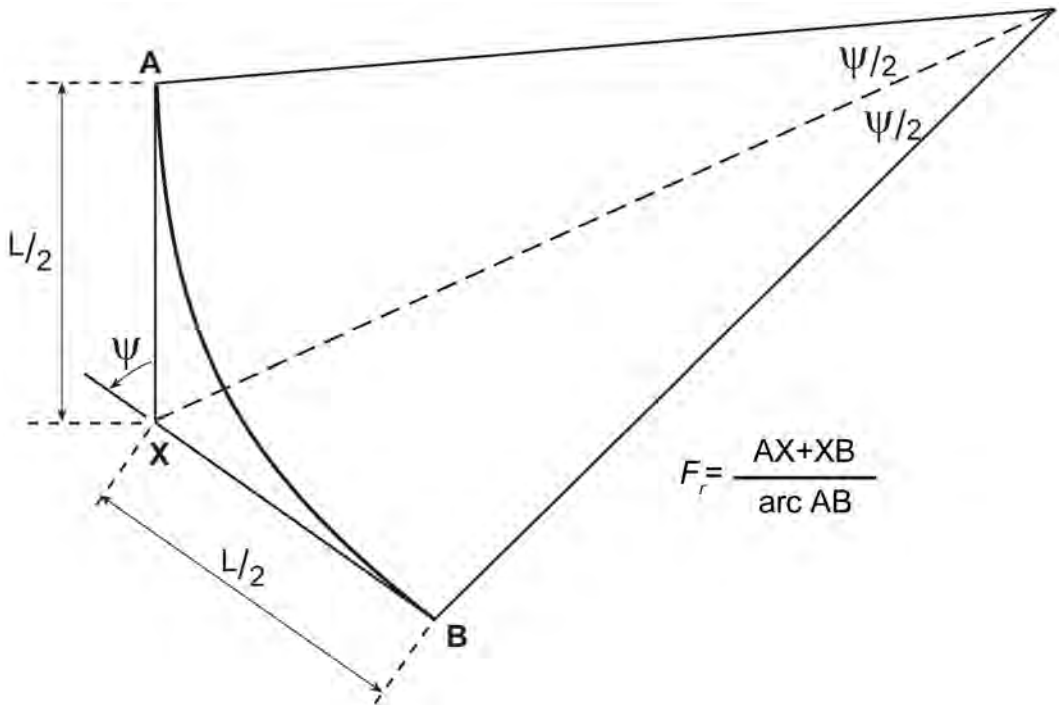


Fig. 3G.5—Principles of the minimum curvature method for modeling the well path between directional survey stations A and B, drawn in the plane of the wellbore.

$$\Delta V = F_r L / 2 (\cos \alpha_1 + \cos \alpha_2) \dots\dots\dots (3G.6)$$

The minimum curvature method is the most widely used for computing the coordinate deliverables of directional surveys. Inglis⁴ provided a detailed description of the calculations.

Applications. The uses of directional surveys include monitoring the actual wellpath to ensure that the drilling target has been reached, defining the X–Y coordinates of points in the wellbore, and determining the true vertical depth (TVD) for geological mapping. Other important operational objectives are to ensure that well paths do not collide (a noteworthy risk given that several production wells are drilled from the same platform) and that there are no changes in angularity (e.g., doglegs) that might impede tool deployment or production efficiency.

An important exercise for integrated reservoir studies is to use the TVD to evaluate the true stratigraphic thickness, h_{ts} , and the true vertical thickness, h_{tv} , of constituent reservoir beds.

Fig. 3G.6a shows a well with inclination or deviation, α , penetrating a bed with dip, ϕ , over a measured bed thickness, h_m , for the particular case in which the azimuths of the well and the dip are the same. Here, the values of h_{ts} and h_{tv} can be calculated as

$$h_{ts} = h_m \cos (\alpha + \phi) \dots\dots\dots (3G.7)$$

$$\text{and } h_{tv} = h_m \cos (\alpha + \phi) / \cos \phi \dots\dots\dots (3G.8)$$

In the more general case, for which the azimuth of the well, β , is not the same as the azimuth of the dip, β_d (Fig. 3G.6b), the equations are more complex:

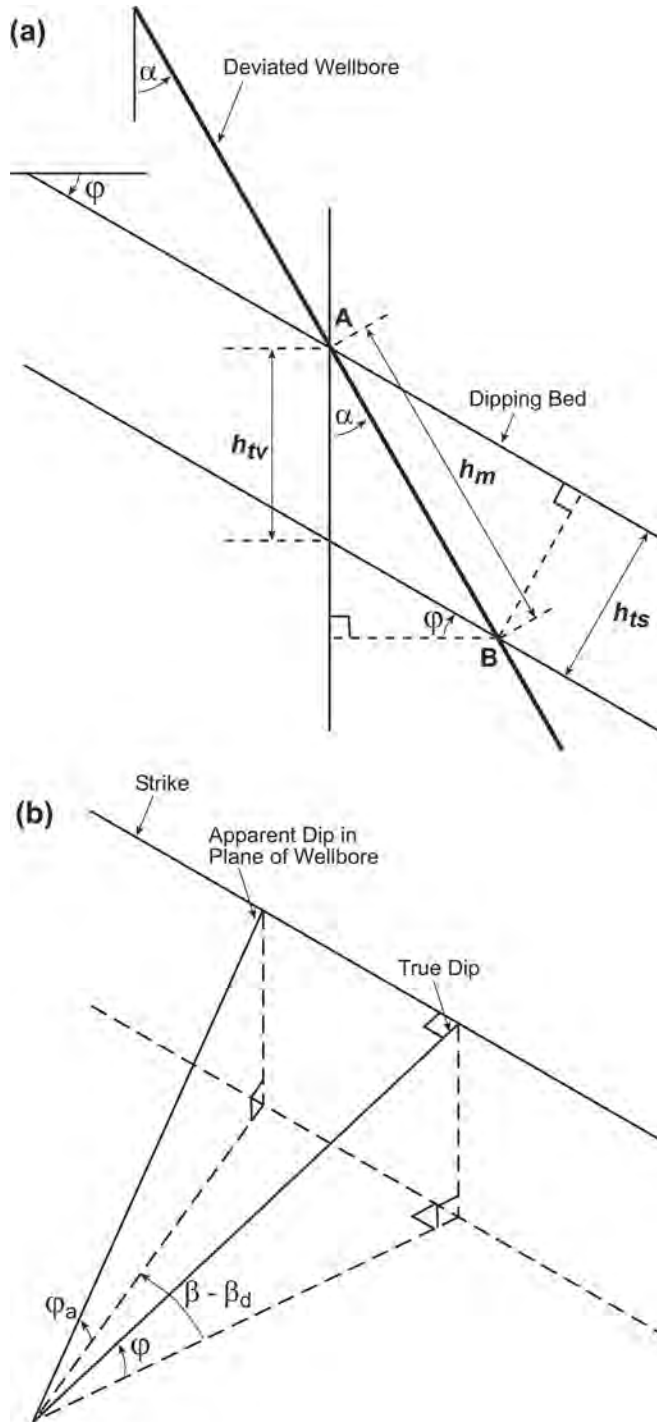


Fig. 3G.6—Basis for the evaluation of true stratigraphic thickness, h_{ts} , and true vertical thickness, h_{tv} , from processed directional-survey data using Eqs. 3G.9 and 3G.10, respectively. (a) The azimuths of the well and true dip are the same. (b) The azimuths of the well and true dip are not the same: the true dip is projected into the plane of the wellbore to become an apparent dip, so that the azimuths of the well and apparent dip are the same.

$$h_{ts} = h_m [\cos \alpha \cos \varphi - \sin \alpha \sin \varphi \cos (\beta - \beta_d)] \dots \dots \dots (3G.9)$$

$$\text{and } h_{tv} = h_m [\cos \alpha - \sin \alpha \tan \varphi \cos (\beta - \beta_d)] \dots \dots \dots (3G.10)$$

As an illustration of the derivation of these expressions, Eq. 3G.10 can be derived from Eq. 3G.8 by projecting the true angle of dip, φ , onto the vertical plane that contains the wellbore azimuth within the layer of interest (Fig. 3G.6b). This introduces an apparent dip, φ_a , which is related to the true dip by the relationship:

$$\tan \varphi_a = \tan \varphi \cos (\beta - \beta_d) \dots \dots \dots (3G.11)$$

If the apparent dip is used instead of the true dip in Eq. 3G.8, we have

$$h_{tv} = h_m \cos (\alpha + \varphi_a) / \cos \varphi_a \dots \dots \dots (3G.12)$$

Eq. 3G.12 will give the correct answer. If we now use Eq. 3G.11 to substitute for φ_a in Eq. 3G.12, we obtain Eq. 3G.10. Other derivations of Eq. 3G.10 are available (e.g., those that rotate the dip or deviation to zero to simplify the equations). Eqs. 3G.9 and 3G.10 can also be written in terms of wellbore coordinates.⁵

3G.2.2 Openhole Caliper Logs. Openhole calipers comprise up to six arms attached to the body of a sonde and held against the borehole wall by spring action. They provide a continuous measurement of borehole diameter. In general, one- and two-arm calipers measure only the maximum diameter where a hole is not circular. Four- and six-arm tools define the hole size and shape, and this is especially important in deviated wells and elliptically shaped wellbores. However, the size and pressure of the contacting arms also affect the measured data. This means that a caliper run with the density-log tool string (Chap. 3D in this section of the *Handbook*) might show a larger hole diameter than one run with the induction log (Chap. 3B in this section of the *Handbook*). This is because the density tool is a pad device, and the pad cuts through the mudcake to sense a larger diameter, whereas the induction tool is a mandrel device (i.e., it is essentially contained within a cylindrical housing). For these reasons, different openhole caliper logs should not be expected to show precise repeatability.

The movement of the caliper arms must be converted to something that is measurable at the surface. Most modern calipers use a potentiometer circuit connected to the caliper arms using transducers. The circuitry can use direct current or pulses. In the former case, the displacement of the arms translates directly to a voltage within the measuring circuit. Pulsed caliper tools use the potentiometer to deliver a variable voltage to a voltage-frequency circuit. The frequency of the pulse train is proportional to the extension of the caliper arm. A basic problem with armed calipers is that the extension of an arm is not directly proportional to the displacement of the transducer. This gives rise to a nonlinear response, which is linearized through data processing based on detailed calibration data. A caliper tool is designed to operate over a specified range of hole diameter. The design sets out to minimize nonlinearity of tool response over this range.

Openhole caliper data are used to estimate the volumes of gravel and cement needed for well-completion planning. Other openhole uses include providing information on the buildup of mudcake over permeable intervals and locating seats for packers (hydraulic seals used to isolate sections of the wellbore for flow-test purposes). They also indicate where boreholes are washed out or penetrate swelling clays as a result of rock/filtrate interaction. Yet again, calipers can be used to center or eccentric logging-tool strings. However, in a logging context,

the greatest application of caliper data is in environmental corrections to other logs such as natural gamma ray, density, and neutron logs (Chap. 3D in this section of the *Handbook*). It is this application that makes the calibration and depth matching of caliper data especially important. Calibration is carried out using rings or sleeves of known diameter. Depth matching is usually done by applying to caliper data those same depth shifts that were generated by comparing the gamma log on the same tool string with the depth-reference gamma log where this has been measured on a different logging run.

3G.2.3 Casing-Collar Locators. The casing-collar locator (CCL) is an important tool because it is used for depth control. When combined with a gamma ray log, it allows depth correlation of a cased-hole logging run with the openhole logs and, therefore, reservoir units or zones. This is essential for subsequent downhole operations such as perforating. Because it constitutes the primary depth control, the CCL is run on almost every cased-hole tool string. The tool comprises a coil-and-magnet arrangement with a downhole amplifier. The most sensitive of these arrangements is two like-facing magnetic poles positioned on either side of a central coil. The magnetic lines of flux are distorted when the tool passes a location at which the metallic casing is enlarged by a collar. This distortion gives rise to a classical change in the magnetic field around the conducting coil, within which current is induced. The signal is amplified and recorded at the surface in the form of a voltage spike known as a collar “kick.”

CCLs can be run in standard wireline logging mode or on a slickline (i.e., a nonconducting line).⁶ Pure-memory slickline CCLs record their data simultaneously with, for example, a full production logging suite, but these CCL data are not available until the memory section has been retrieved and downloaded at the surface. Real-time slickline tools convert the voltage spike to a tension spike by using spring-loaded electromagnets that increase the apparent drag through the greater attraction between the electromagnets and the casing at collar locations. The tension spike can be detected at the surface. CCLs have had to be modified for coiled-tubing applications. The primary difference arose because the heaviness of a coiled-tubing string did not allow relatively small tension spikes to be detected with confidence. For this reason, a solenoid/piston/valve arrangement is used to transmit pressure spikes through the fluid within the coiled tubing to the surface, where they can readily be detected. These tools have recently been improved for high-pressure/high-temperature applications.⁷ Some types of downhole tractor that are used to deploy tool strings in deviated wells also have the ability to produce a CCL during the tractor operation and thereby provide the same depth control.

3G.2.4 Casing Inspection Logs. There are four commonly used techniques for the inspection of casing: cased-hole calipers, flux-leakage tools, electromagnetic phase-shift tools, and ultrasonic tools.

Cased-Hole Calipers. Multifinger calipers are used to identify changes in casing diameter as indicators of wear and corrosion. They are also used to monitor casing deformation.⁸ They can have up to 80 spring-loaded feelers or fingers, depending on the nominal casing diameter (Fig. 3G.7). Different multifinger caliper tools can log casing sizes from 4 to 20 in. [100 to 500 mm]. Smaller tools are available for tubing inspection. Each hardened finger can measure the internal casing diameter with a radial resolution of a few thousandths of an inch and a vertical resolution of a few hundredths of an inch at a typical logging speed of 1800 ft/hr [550 m/h]. Measurements are taken many times per second for each finger, giving a typical spatial-sampling interval of approximately 0.15 in. [4 mm] as the tool travels up the borehole. A finger extends where it encounters a pit or hole and retracts where there is scale present or there has been partial collapse. A potential disadvantage is that the fingers can damage the casing, although modern electronic tools have a very low finger pressure to avoid this. The tool also indicates which finger is the one on the highest side of the well. Moreover, fingers can be grouped azimuthally. All these data can be combined with the measurements of diame-

ter to produce a 3D picture of the casing, including cross-sectional distortions and changes in the trajectory of the well axis as small as 0.01° . The data can be either transmitted to the surface where the tool is run on a wireline or stored downhole where the tool is deployed on a slickline.

There are two types of multifinger calipers, mechanical and electronic, although the distinction is misleading because all such calipers are mechanical in their deployment. The difference is in the way in which data are recorded. Older calipers were truly mechanical in that they were operated on a slickline and used a scribe chart for downhole data recording. These mechanical calipers have high temperature ratings because they are not limited by the ratings of downhole electronics [e.g., 600°F (315°C) for the Kinley caliper offered by the Expro Group]. Modern tools convert the mechanical data into electronic information for downhole memory storage or for transmittal uphole for real-time data display. Operating temperatures for these electronic tools are typically up to 350°F [177°C].

Multifinger tools contain an inclinometer so that tool deviation and orientation can be recorded. If these parameters are known, the high-quality output from modern multifinger calipers allows several image-based products to be generated. Deliverables include digital “maps” of the ovality of the casing and its internal diameter. The logs can be run and displayed in time-lapse mode to quantify the rates of corrosion or scale buildup. A digital image of variations in the inner diameter of the casing is the principal tool for identifying corrosion. In its basic form, this is an electronic version of what one might see using a downhole video camera; however, the electronic image can be rotated and inspected from any angle. Artificial colors are used to bring out anomalies.

Another processed product is the 3D shape of downhole tubulars to map the trajectory of the wellbore and to quantify casing deformation. An interesting example of the use of multifinger-caliper data to evaluate casing deformation in primary heavy-oil production in northeastern Alberta has been described by Wagg *et al.*⁹ (Fig. 3G.8). Several postulates for formation movement were modeled and compared with the observed casing deformations. In the end, it was concluded that sand production from an elongated disturbed zone caused reservoir shortening to an extent that could account for the wellbore observations. The use of casing-deformation logs as a tool in reservoir geomechanics leads to an improved knowledge base for well design.

Although they are intended for cased-hole application, it is possible to use multifingered calipers in open hole. The results are much more detailed than with a standard openhole caliper, and the output can be displayed as images similar to those obtainable with ultrasonic imaging tools (see the “Ultrasonic Tools” section below).

Flux-Leakage Tools. Flux leakage is a semiquantitative method that uses a strong magnetic field to identify and, to a certain extent, quantify localized corrosion on both the inner and the outer surfaces of the casing. A downhole electromagnet that fits snugly within the casing creates a low-frequency or a direct-current magnetic field. This can be a permanent magnet so it is possible to use this tool on a memory string for which battery power is at a premium. Magnetic flux is concentrated within the casing, which is close to magnetic saturation. The tool contains spring-loaded, coil-type, pad-mounted sensors that are pushed close to the casing during logging. Where casing corrosion is encountered, the lines of flux “bulge out” from the casing as though they were leaking from it. The primary sensors pass through this excluded flux and measure the induced voltage. The amplitude and spatial extent of the sensor response is related to the volume and shape of the corrosion metal loss, thereby allowing an estimate of the size of the defect. Because the primary measurement cannot distinguish between internal and external casing defects, many tools use an additional higher-frequency eddy-current measurement. This is a shallower measurement that responds only to casing flaws on the inner wall. It uses a separate transmitter coil. The flux-leakage and eddy-current signals are distinguished using frequency filters.



Fig. 3G.7—Multifingered caliper tool for deployment as a memory tool on slickline or as a surface-readout tool on monoconductor cable. This tool has 60 fingers, a 4-in. [100-mm] diameter, and a measurement range of 4.4 to 9.625 in. [114 to 245 mm]. It has a radial resolution of 0.005 in. [0.13 mm], a radial accuracy of ± 0.03 in. [0.75 mm], and a vertical resolution of 0.23 in. [5.84 mm] at a logging speed of 3,000 ft/hr [914 m/hr]. Pressure and temperature ratings are 15,000 psi [103 MPa] and 350°F [177°C], respectively. Note the tool centralizers. (Courtesy of Sondex.)

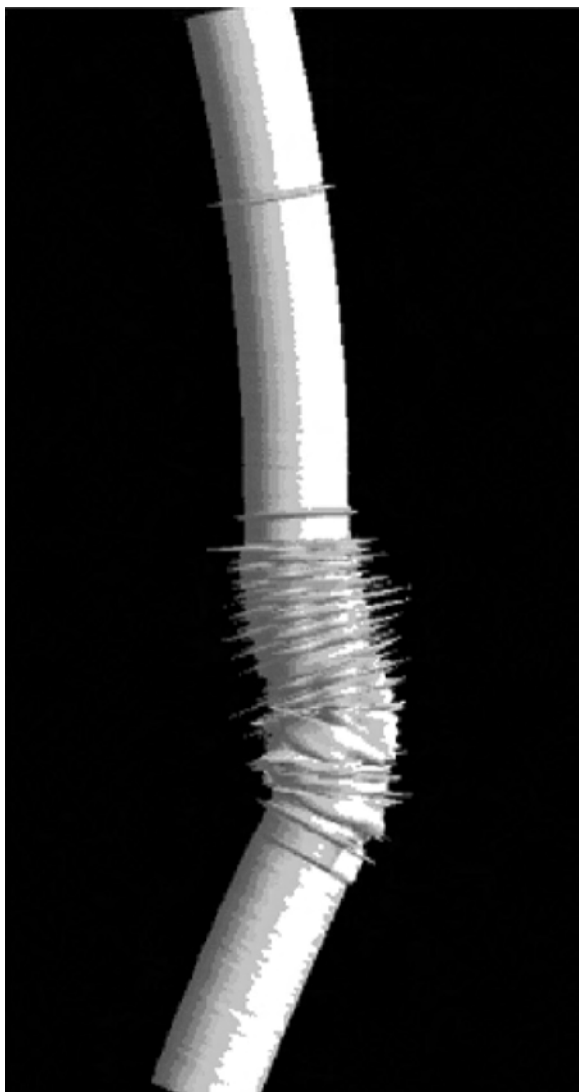


Fig. 3G.8—Digital image of casing deformation based on multifingered caliper data processed with C-FER Technologies' CalTran™ software. The "spikes" are indications of casing connections or perforations.⁹

The major advantage of flux-leakage tools is that they can identify localized casing defects such as corrosion patches, pits, and holes as small as 0.2 in. [5 mm] on both the inside and the outside of the pipe. A disadvantage is that the tool does not detect large areas of corrosion. It does not see nonmagnetic scale, which can degrade the sensor response. The tool is affected by changes in the electromagnetic properties of the casing. It is of limited accuracy, coverage, and resolution. The coil-sensor response is sensitive to logging speed, and this sensitivity makes quantitative interpretation more difficult.

Electromagnetic Phase-Shift Tools. The electromagnetic phase-shift technique provides an estimate of casing thickness across approximately 1 ft [300 mm] of casing length, so its spatial resolution is weaker than that of the first two methods. Electromagnetic phase-shift tools make measurements that are averages around the circumference of the pipe. They lack the localized investigative capability of flux-leakage tools and are best used to investigate larger-scale corro-

sion. Essentially, a transmitter coil generates a low-frequency alternating magnetic field, which couples to a receiver coil. It also induces eddy currents in the surrounding casing and formation. These eddy currents generate their own magnetic field, which is phase-shifted by the presence of casing. The phase-shifted field is superimposed on the transmitted field. This total field is detected by a receiver coil. The phase shift between the transmitted and received signals is related to the thickness, electrical conductivity, and magnetic permeability of the casing. If the last two are known, the casing thickness can be determined. Higher phase shifts indicate a higher casing thickness, all other things being equal. In practice, the electromagnetic properties of the casing can vary with composition, aging, and stress. To overcome this problem, modern tools comprise multiple sensor coils, which allow variations in the electromagnetic properties of the casing to be factored into the computation of casing thickness. Advantages are that the method is sensitive to large areas of corrosion and to gradual thinning of the casing. The sensors do not need to be in close proximity to the casing, so a single tool can examine a range of casing sizes. Disadvantages are the low spatial resolution and the lack of response to nonmagnetic scale. Moreover, the alternating-current magnet requires a relatively high power, which makes the tool difficult to deploy in memory mode.

Ultrasonic Tools. The ultrasonic method provides a full quantitative record of casing radius and thickness. The first ultrasonic casing-inspection tools were the borehole viewers, but these only “saw” the inner casing surface and their use is now mainly in open hole (see [Sec. 3G.3.2](#)). Later tools had fixed ultrasonic transducers, but these were principally directed at cement evaluation, and they provided an incomplete coverage of casing-thickness measurements. This problem was overcome by a rotating ultrasonic transducer that was initially directed at cement evaluation (see [Sec. 3G.2.5](#)).

More recently, tools have been designed for a better spatial resolution.¹⁰ Schlumberger’s Ultrasonic Corrosion Imager (UCI™) was designed with a short-pulse 2-MHz transducer, 0.5 in. [12.5 mm] in diameter, focused at a distance of 2 in. [50 mm] from its front face. The higher-frequency measurement sharpened the spatial resolution so that internal pits of diameter 0.16 in. [4 mm] could be defined quantitatively. The velocity of sound in the borehole fluid is measured using a built-in reflector at a known offset while running into the hole. The wellsite computer calculates the internal radius from internal echo time and the measured fluid velocity. Downhole processing extracts the time difference between the internal and external echoes for an improved determination of casing thickness using the velocity of sound in steel. This information allows external casing defects to be identified. Azimuthal sampling interval is 2°. Vertical sampling interval in high-resolution mode is 0.2 in. [5 mm] at a logging speed of 425 ft/hr [130 m/hr]. The signal is attenuated by the borehole fluid. Best results are achieved with brine, oil, or very light drilling muds. [Fig. 3G.9](#) shows UCI images of 2D percentage metal loss and 3D views of casing integrity in a 5.5-in. [140-mm] saltwater-injection casing in Canada.¹⁰

Frisch and Mandal¹¹ described a “new generation of ultrasonic tools” for use in large-diameter casings. Their (Halliburton) tool uses two ultrasonic transducers, one of which rotates while the other is fixed for real-time measurements of borehole-fluid velocity. The tool operates in image mode or cased-hole mode. In image mode, the tool can be operated in open hole or in cased hole, where it examines only the inner casing surface. In cased-hole mode, it determines the inner radius and the casing thickness, so that defects on the outer casing can be discerned. Waveform processing allows the evaluation of cement bonding from the same logging run.

3G.2.5 Cement-Evaluation Logs. Conventional cement-bond logs (CBLs) comprise a pulsed transmitter and several receivers of acoustic energy positioned as a vertical array of transducers. The acoustic signal travels through borehole fluid, casing, cement, and the formation itself. The signal is received, processed, and displayed as a microseismogram. The recorded wave-

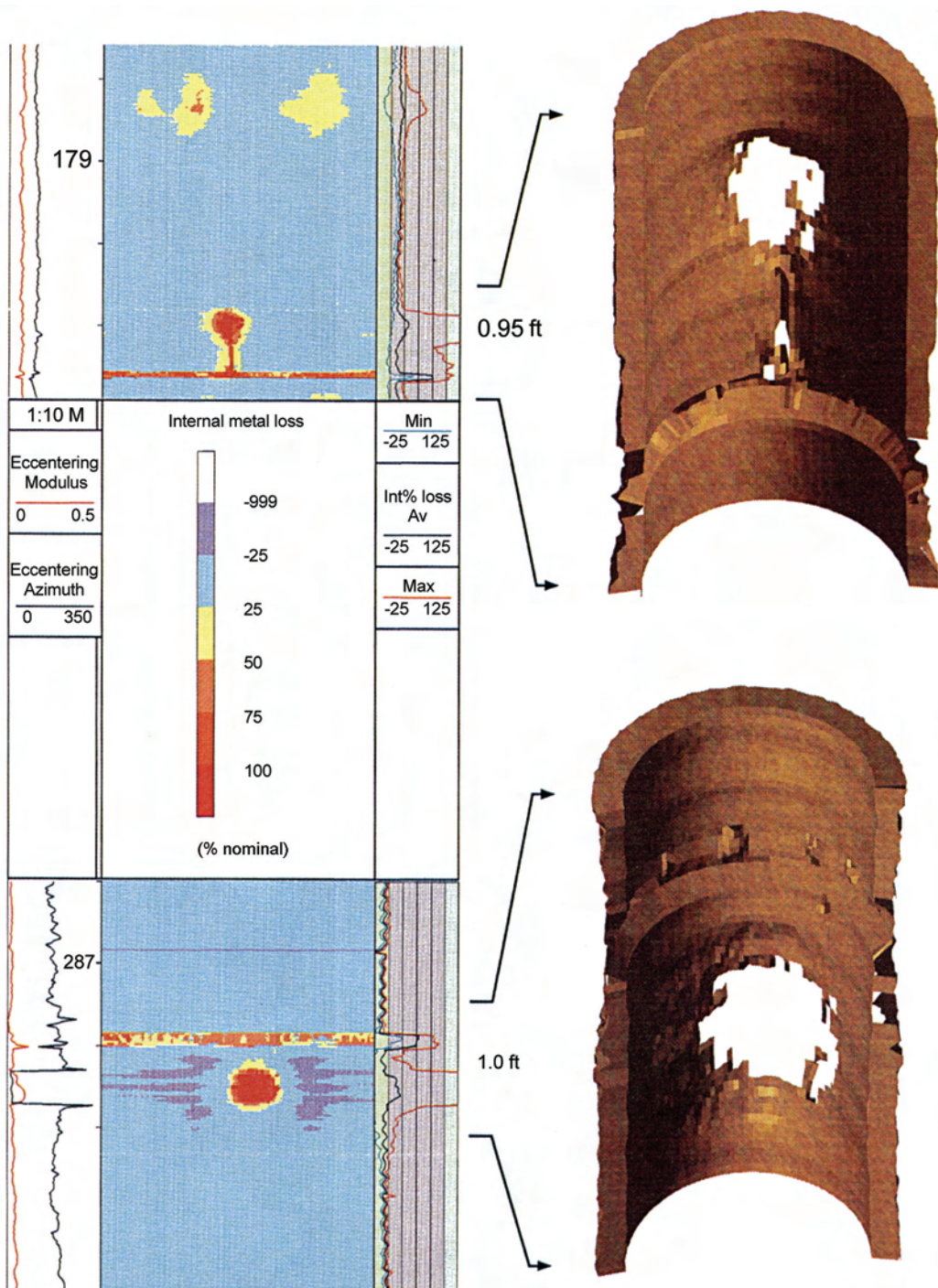


Fig. 3G.9—Example of casing inspection using the Ultrasonic Corrosion Imager (UCI™). The presentation includes digital 2D images of percentage metal loss, with good casing shown in light blue and holes indicated in red, together with 3D views of casing integrity. There are two holes in the 5.5-in. [140-mm] casing, each with a diameter of approximately 2 in. [50 mm]. In the upper image, note the deep groove from the casing hole down to the casing collar.¹⁰ [Courtesy of the Soc. of Petrophysicists and Well Log Analysts (SPWLA)].

forms are presented together with the travel time and a casing-amplitude curve, which displays the amplitude of the acoustic signal that has traveled through the casing but not through the cement and formation. The waveform and amplitude data allow two bonds to be investigated. These are the bond between casing and cement and, to a lesser extent, that between cement and formation. A “straight” waveform display is traditionally interpreted to mean no cement bonding. Variations in the acoustic display are interpreted as indicating the presence of bonded cement.¹² These displays have been enhanced by the application of statistical variance processing to ultrasonic data.¹³ CBLs clearly indicate the top of cement, where there is unbonded pipe, and they indicate where the pipe is well cemented (Fig. 3G.10). However, they are not reliable as indicators of hydraulic sealing by the cement, because they cannot detect small channels therein. Part of the problem is that conventional CBL transducer arrays are vertical, whereas bonding problems need to be investigated circumferentially.

Baker Atlas’ Segmented Bond Tool (SBT™) uses six pads, on each of which there is a transducer arrangement of receivers and transmitters of acoustic energy.¹⁴ The pads are in contact with the casing. Energy is transmitted at one pad and is received at an adjacent pad. The pad spacing is such that the first arrival is the wave that has passed through the casing. The rate of attenuation can be computed across each 60° segment of the casing circumference. A high rate of attenuation is indicative of a good cement bonding to the casing and an absence of channels within the cement. The method allows localized zones of good hydraulic seal to be identified in a way that is independent of borehole-fluid type. The bonding between cement and formation is investigated through a CBL-type receiver array for wave-train presentation (Fig. 3G.11).

Ultrasonic tools are superior to the acoustic CBLs, although they remain adversely affected by highly attenuating muds. They are often grouped as “cement evaluation tools.” One of the earlier ultrasonic tools was actually called the Cement Evaluation Tool (CET™). This Schlumberger tool comprised an array of eight ultrasonic transducers that allowed a limited radial inspection of the casing and its annulus. The most recent tools have a single rotating transducer that incorporates both the source and receiver of ultrasonic energy. The tool has to be centered. The data for circumferential inspection of the casing, as described above, and for the evaluation of cement bonding are obtained on the same logging pass. Acoustic energy is reflected at interfaces that correspond to changes in acoustic impedance (the product of acoustic velocity and density). The first reflection is at the casing itself. The second reflection may be at the outside of the casing. If cement is bonded to the casing, there will be a strong reflection. If there is unset cement or water behind the casing, there will be a weak reflection. The received waveform is the sum of the reflected waveform from the original burst and the exponentially decaying waveform from the resonant energy that is trapped between the inner and outer edges of the casing. By analyzing the entire waveform, an acoustic-impedance map of the cement can be constructed. This map can indicate the presence of channels and their orientations.

Schlumberger’s Ultrasonic Imager (USI™) is one such tool.¹⁵ It operates from 200 to 700 Hz and provides a full high-resolution coverage of the casing and cement integrity. Channels as narrow as 1.2 in. [30 mm] can be detected. It is used with a conventional CBL tool. An interesting example of the complementary nature of these data has been presented by De Souza Padilha and Da Silva Araujo.¹⁶ It deals with the problem of gas-contaminated cement, which has been a longstanding interpretation problem in the industry. Essentially, the CBL reads low-amplitude values in gas-contaminated cements. The USI cannot distinguish between gas-filled cement and fluids, but it can quantify the acoustic impedance of the cement. Therefore, the presence of gas-contaminated cement is indicated where the CBL reads low and the USI indicates fluids. If there is only gas behind the casing, the CBL reads high and the USI shows gas. The CBL and USI were used conjunctively to distinguish these cases. The application of statis-

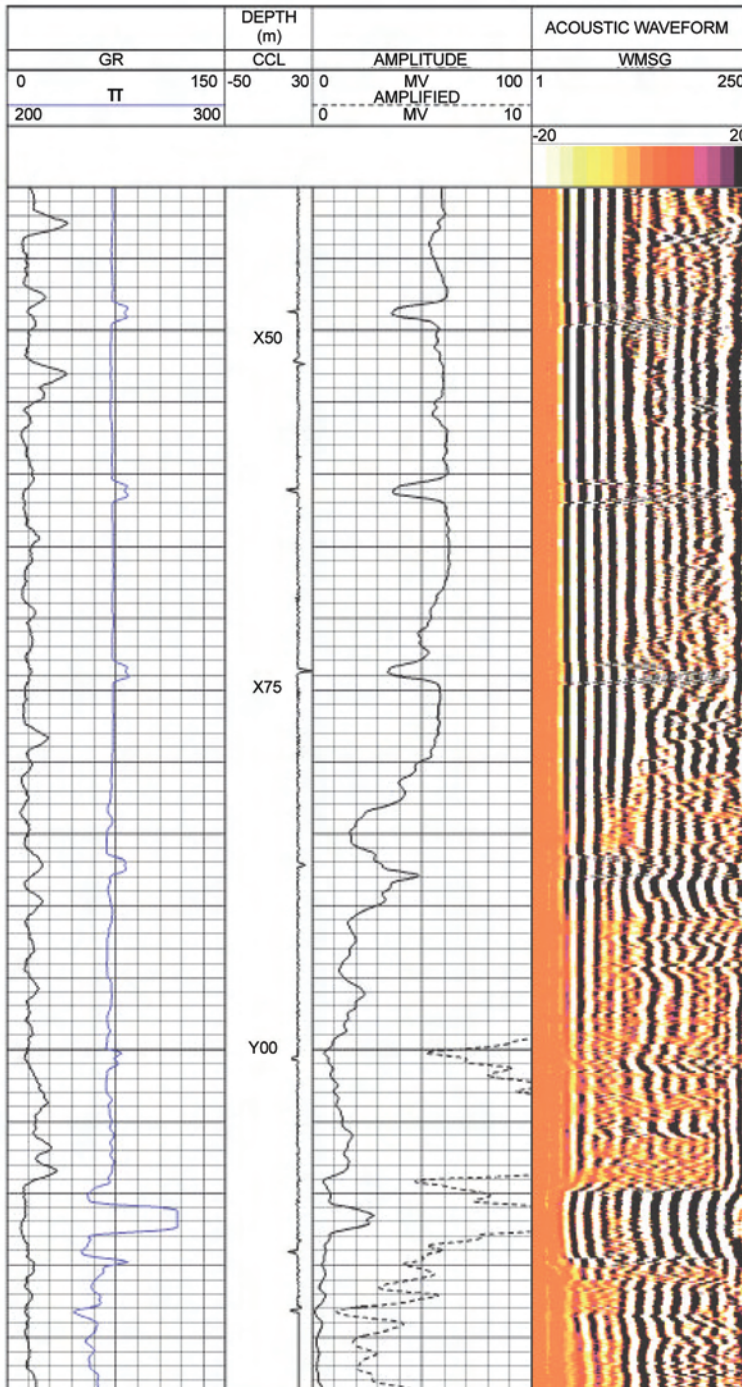


Fig. 3G.10—Example of a CBL. Track 1 contains the gamma ray (for correlation) and acoustic travel time (for quality control). Track 2 contains the amplitude curve and amplified amplitude, which indicates cement-to-casing bond. Track 3 contains the CBL waveform, which indicates cement-to-casing bond as well as cement-to-formation bond. Straight lines in the CBL waveform, along with high amplitude readings, indicate poor cement-to-casing bond. There is nearly free pipe above an apparent top of cement at a depth of approximately X80 depth units. At greater depths, the pipe is well bonded. (Courtesy of Halliburton.)

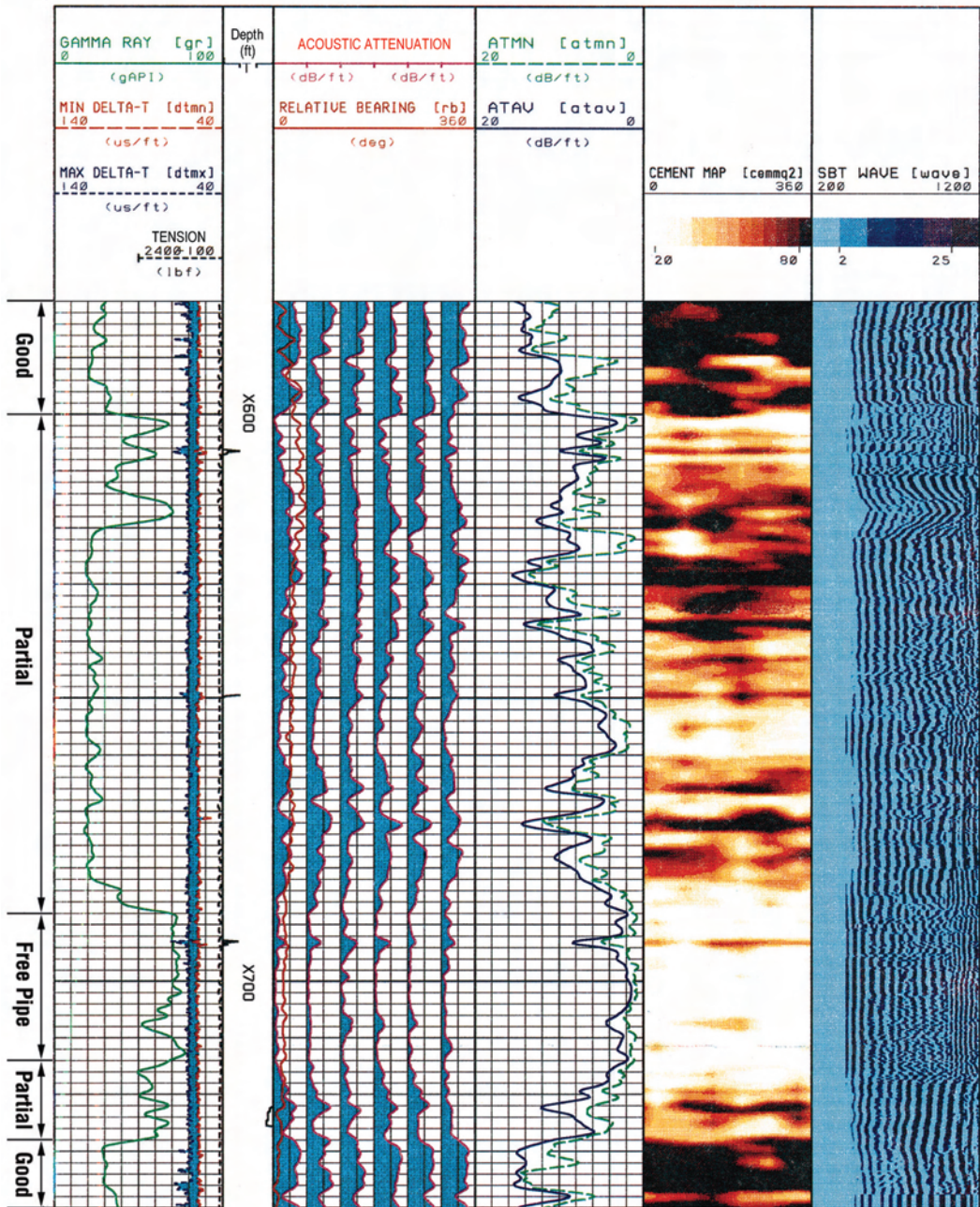


Fig. 3G.11—Example of cement evaluation using the Segmented Bond Tool (SBT™). Track 1 contains the gamma ray and two quality curves for pad contact with the borehole wall and for centralization, both of which are of high quality in this example. Track 2 contains the acoustic attenuation logs for the six pads. Track 3 shows the average and minimum attenuation at each sampling level. Track 4 presents a variable-attenuation log or cement map of the casing periphery vs. depth. Dark zones are the most strongly bonded. Track 5 is a CBL-type display. In this example, the partial bonding is sufficient to provide hydraulic isolation. There is poor cement condition between X688 and X714 depth units. Attempts to rectify this problem will be impeded by the hydraulic isolation above and below this interval. (Courtesy of Baker Atlas.)

tical variance processing to the conjunctive use of CBL and ultrasonic impedance data has led to an improved cement evaluation.¹⁷ The CBL is also discussed in the chapter on Acoustic

Logging in this volume of the *Handbook*.

3G.2.6 Simultaneous Casing Inspection and Cement Evaluation. As indicated above, the ultrasonic tools can be operated to address two objectives concurrently: casing integrity and cement evaluation. A further example is Halliburton's Circumferential Acoustic Scanning Tool—Visualization version (CAST-V™), which allows separate or simultaneous casing inspection and cement evaluation.¹⁸ The tool can operate in two modes: an image mode, whereby the scanner evaluates only the inner surface of the casing, or a cased-hole mode, whereby circumferential maps of casing thickness and acoustic impedance are used to assure casing integrity and to distinguish between fluids and cement in the annulus. **Figs. 3G.12 and 3G.13** show examples of CAST-V data displays. This tool can also operate in open hole as a formation imager (see **Sec. 3G.3**).

3G.3 Borehole Imaging

As introduced here, the term “borehole imaging” refers to those logging and data-processing methods that are used to produce centimeter-scale images of the borehole wall and the rocks that make it up. The context is, therefore, that of open hole, but some of the tools are closely related to their cased-hole equivalents. Borehole imaging has been one of the most rapidly advancing technologies in wireline well logging. The applications range from detailed reservoir description through reservoir performance to enhanced hydrocarbon recovery. Specific applications are fracture identification, analysis of small-scale sedimentological features, evaluation of net pay in thinly bedded formations, and the identification of breakouts (irregularities in the borehole wall that are aligned with the minimum horizontal stress and appear where stresses around the wellbore exceed the compressive strength of the rock).

The subject area can be classified into four parts: optical imaging, acoustic imaging, electrical imaging, and methods that draw on both acoustic and electrical imaging techniques using the same logging tool. Prensky¹⁹ has provided an excellent review of this important subject.

3G.3.1 Optical Imaging. Downhole cameras were the first borehole-imaging devices. Today they furnish a true high-resolution color image of the wellbore. The principal drawback is that they require a transparent fluid in liquid-filled holes. Unless transparent fluid can be injected ahead of the lens, the method fails. This requirement has limited the application of downhole cameras. The other major historic limitation, the need to wait until the camera is recovered before the images can be seen, has fallen away with the introduction of digital systems.

The principal application of downhole video has been in air-filled holes in which acoustic and contact electrical images cannot be obtained. Most applications described in the literature are directed at fracture identification or casing inspection.

3G.3.2 Acoustic Imaging. Acoustic borehole-imaging devices are known as “borehole televiewers.” They are mandrel tools and provide 100% coverage of the borehole wall. The first borehole televiewer, operating at a relatively high ultrasonic frequency of 1.35 MHz, was developed by Mobil Corp. in the late 1960s.^{20,21} Since then, a succession of improvements have been made, principally through advances in digital instrumentation and computer-image enhancement. Modern tools contain a magnetometer to provide azimuthal information.

The borehole televiewer operates with pulsed acoustic energy so that it can image the borehole wall in the presence of opaque drilling muds. Short bursts of acoustic energy are emitted by a rotating transducer in pulse-echo mode. These travel through the drilling mud and undergo partial reflection at the borehole wall. Reflected pulses are received by the transducer. The amplitudes of the reflected pulses form the basis of the acoustic image of the borehole wall. These amplitudes are governed by several factors. The first is the shape of the borehole wall itself: irregularities cause the reflected energy to scatter so that a weaker reflected signal is

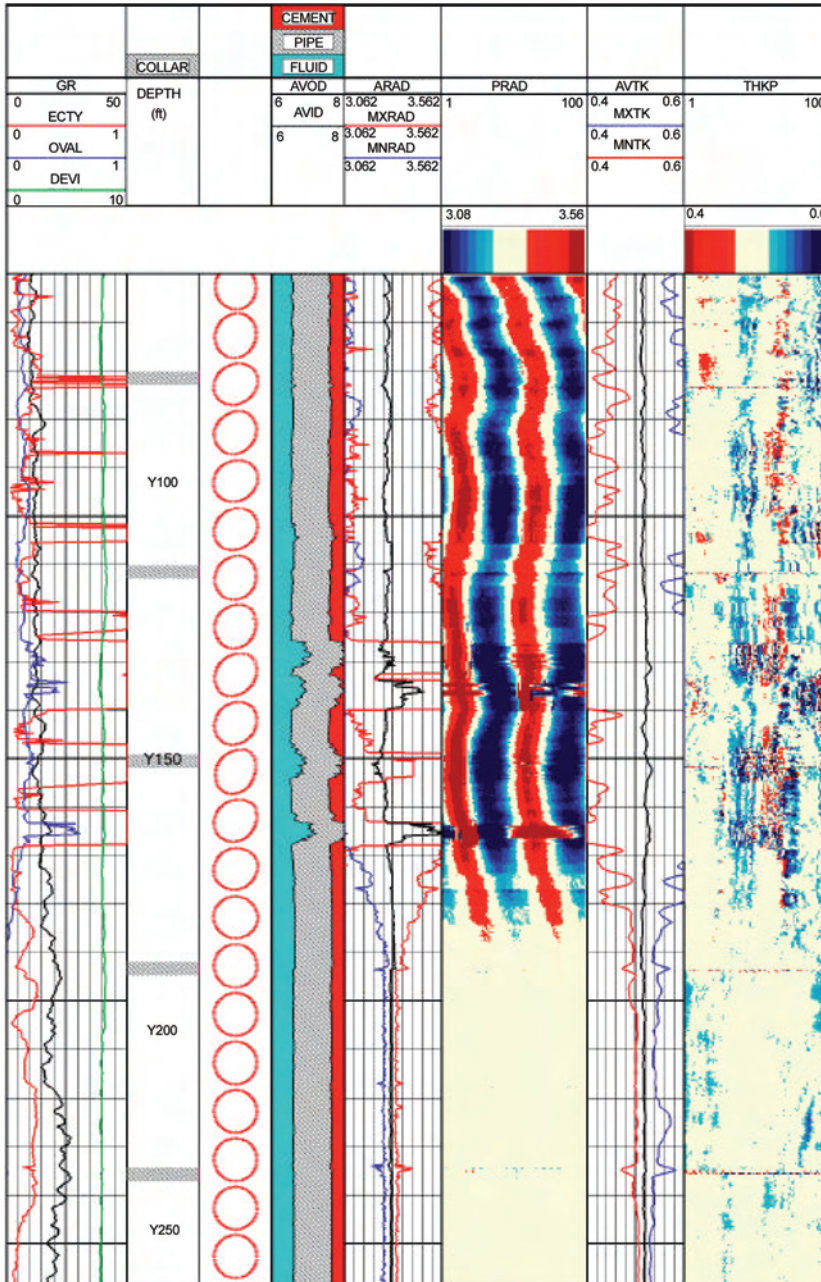


Fig. 3G.12—Example of casing inspection using the visualization version of the Circumferential Acoustic Scanning Tool (CAST-V™). The casing-evaluation presentation includes casing ovality, eccentricity, hole deviation, and gamma ray in Track 1. In this case, the eccentricity comprises both tool and casing eccentricity resulting from formation movement (salt flow). Track 2 shows a cross-sectional presentation of the pipe shape. Track 3 shows a cross section of the pipe wall. Track 4 provides the average, minimum, and maximum values of the pipe radius that is shown in Track 5. Track 6 provides the average, minimum, and maximum values of the pipe thickness that is the image shown in Track 7, where red indicates pipe thinning and blue indicates pipe thickening. (Courtesy of Halliburton.)

received by the transducer. Examples of these irregularities are fractures, vugs, and breakouts. Moreover, the reflected signal is degraded in elliptical and oval wellbores because of non-nor-

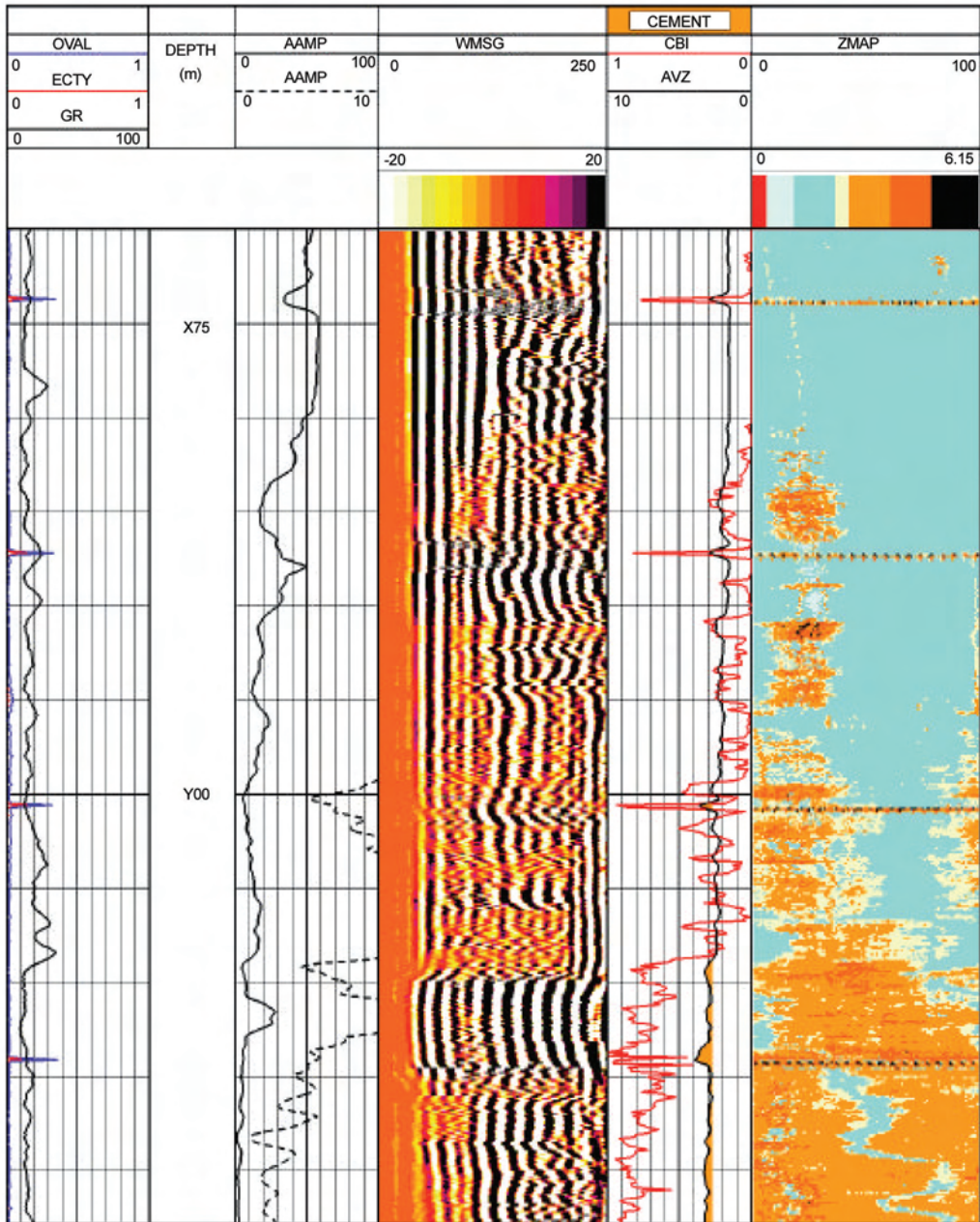


Fig. 3G.13—Example of cement evaluation using the visualization version of the Circumferential Acoustic Scanning Tool (CAST-V™). The data relate to an interval that overlaps with the conventional CBL in Fig. 3G.10. The cement-evaluation presentation includes casing ovality and tool eccentricity in Track 1. The conventional CBL output is shown in Tracks 2 and 3 as per Fig. 3G.10. Data from CAST-V are shown in Tracks 4 and 5. The image in Track 5 is an acoustic-impedance map from 0 to 360° (left to right) with 0° representing the high side of the hole. Track 4 contains the average impedance of the image in Track 5 and a cement-bond index (CBI) as a quick indication of the degree of bonding. Tracks 4 and 5 impart clarity to the interpretation of Fig. 3G.10 by more clearly showing no cement above X80 depth units, good cement below Y20 depth units and questionable bonding in between. (Courtesy of Halliburton.)

mal incidence. The second factor is the contrast in acoustic impedance between the drilling mud and the material that makes up the borehole wall. Acoustic impedance provides an acous-

tic measure of the relative firmness of the formations penetrated by the wellbore material and, thus, it has the capability of discriminating between different lithologies, with high acoustic impedance giving rise to high reflected amplitudes. Borehole televiewers work best where the borehole walls are smooth and the contrast in acoustic impedance is high. The third factor is the scattering or absorption of acoustic energy by particles in the drilling mud. This problem is more serious in heavily weighted muds, which are the most opaque acoustically, and it gives rise to a loss of image resolution.

The borehole televiewer can provide a 360° image in open or cased holes. It can operate in all downhole environments other than gas-filled holes. The travel time for the acoustic pulse depends on the distance between the transducer and the borehole wall, as well as the mud velocity. Modern televiewers allow some independent method of measuring the mud velocity. Thus, the borehole televiewer also operates as an acoustic caliper log. For best results, the tool should be centered, although correction algorithms have been developed for eccentered surveys.

An example of a modern ultrasonic imaging tool is Schlumberger's Ultrasonic Borehole Imager (UBI™), which is based on the cased-hole USI (see [Sec. 3G.2.5](#)) with two hardware modifications: a focused transducer was fitted for improved resolution, and an openhole centralizer was added.²² The tool incorporates a rotating transducer within a subassembly. The size of the subassembly is selected on the basis of the diameter of the hole that is to be logged. The direction of rotation of the subassembly governs the orientation of the transducer. There are two positional modes: the standard measurement mode with the transducer facing the borehole wall ([Fig. 3G.14](#)) and the fluid-property mode with the transducer facing a target within the tool. In standard mode, the tool measures both amplitude and transit time at one of two frequencies, 250 or 500 kHz, with recommended logging speeds of 800 ft/hr [244 m/hr] and 400 ft/hr [122 m/hr], respectively, where logging speed is primarily determined by vertical sampling density and the rate of transducer rotation. The higher frequency allows a sharper image resolution of 0.2 in. [5 mm], but it is less effective in highly dispersive muds where the lower frequency should be used. The tool can also be used for investigating the geometry of the inner surface of casing where it is not desired to measure resonant ringing as an indicator of cement integrity.

Baker Atlas' Circumferential Borehole Imaging Log (CBIL™) has a similar range of capability but is rated to 20,000 psi [138 MPa] and 400°F [204°C]. Halliburton's Circumferential Acoustic Scanning Tool (CAST™) additionally offers simultaneous casing inspection and cement evaluation. It is rated to 20,000 psi [138 MPa] and 350°F [177°C], as is Schlumberger's UBI. Both of these tools predated the UBI.^{23,24}

Data are usually presented as depth plots of enhanced images of amplitude and borehole radius. Applications include fracture detection, analysis of borehole stability, and identification of breakouts.

[Fig. 3G.15](#) shows an example of breakout identification using an ultrasonic borehole televiewer.²⁵ The data presented are from the Cajon Pass scientific borehole in southeastern California. The aim was to investigate the orientation and magnitudes of in-situ stresses using borehole-image data. The televiewer has superseded multiarm dipmeter calipers for these applications. Although the caliper can reveal the orientation of breakouts, the tool provides little information about their size and, more generally, about the overall shape of the borehole wall. The ultrasonic televiewer can detect much smaller features than the multiarm caliper and can distinguish between features that are stress induced and those that are drilling artifacts.

3G.3.3 Electrical Imaging. Microresistivity imaging devices were developed as an advancement on dipmeter technology, which they have mostly superseded. Traditionally, they have required a conductive borehole fluid, but it will be seen later that this requirement has been obviated by oil-based-mud imaging tools. Originally, in the mid-1980s, they comprised two high-resolution pads with 27 button electrodes distributed azimuthally on each. This arrangement

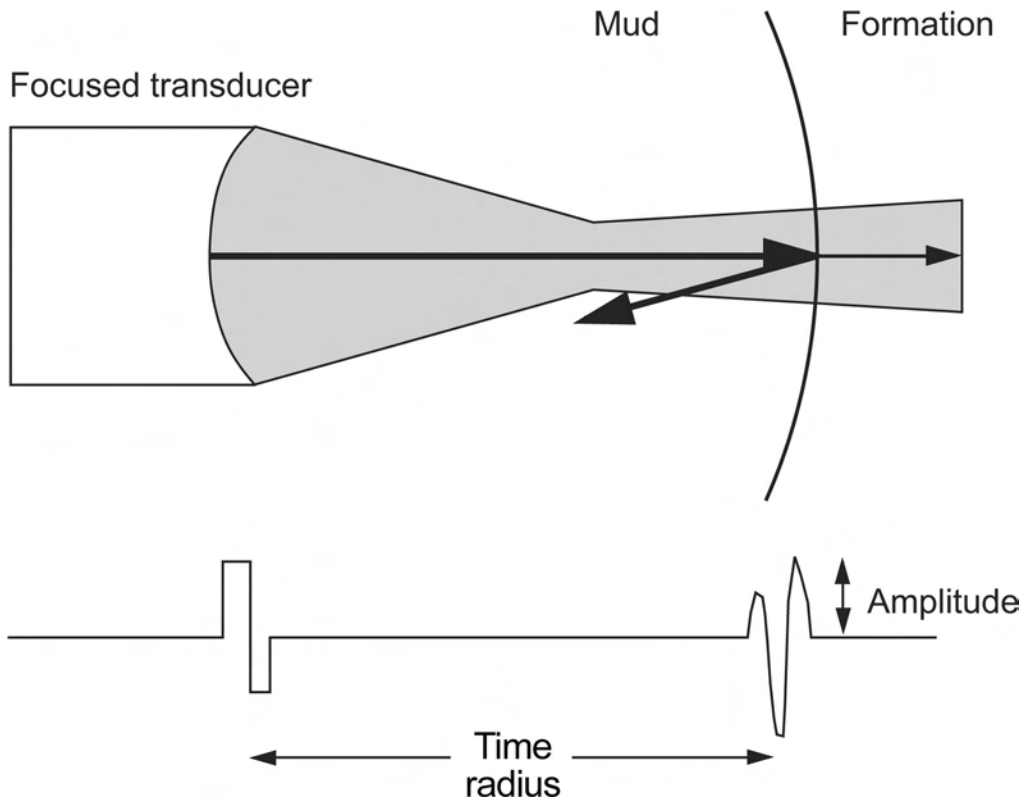


Fig. 3G.14—Principle of the Ultrasonic Borehole Imager (UBI™). The UBI measures reflection amplitude and radial distance using a direct measurement of mud velocity.²²

provided a coverage of 20% of an 8.5-in. [216-mm] wellbore in a single pass.²⁶ This coverage was doubled by the development of a four-pad microresistivity imaging tool, each with 16 button electrodes arranged azimuthally in two rows of eight. The number of electrodes was limited by tool-transmission electronics.²⁷ Coverage was increased still further through the use of pads with flaps that opened to give a borehole-wall coverage of 80% in an 8-in. [203-mm] hole.²⁸ In another approach, the six-arm dipmeter evolved into a six-pad microresistivity imager,²⁹ Halliburton's Electrical Micro-Imaging tool (EMIT™). Each pad contained 25 button electrodes also arranged azimuthally in two rows. With this arrangement, a 60% coverage was achieved in an 8-in. [203-mm] hole.

The measurement principle of the microresistivity imaging devices is straightforward. The pads and flaps contain an array of button electrodes at constant potential (Fig. 3G.16). An applied voltage causes an alternating current to flow from each electrode into the formation and then to be received at a return electrode on the upper part of the tool. The microelectrodes respond to current density, which is related to localized formation resistivity. The tool, therefore, has a high-resolution capability in measuring variations from button to button. The resistivity of the interval between the button-electrode array and the return electrode gives rise to a low-resolution capability in the form of a background signal. The tool does not provide an absolute measurement of formation resistivity but rather a record of changes in resistivity. The resolution of electrical microimaging tools is governed by the size of the buttons, usually a fraction of an inch. In theory, any feature that is as large as the buttons will be resolved. If it is smaller, it might still be detected. The tools can be run as dipmeters.

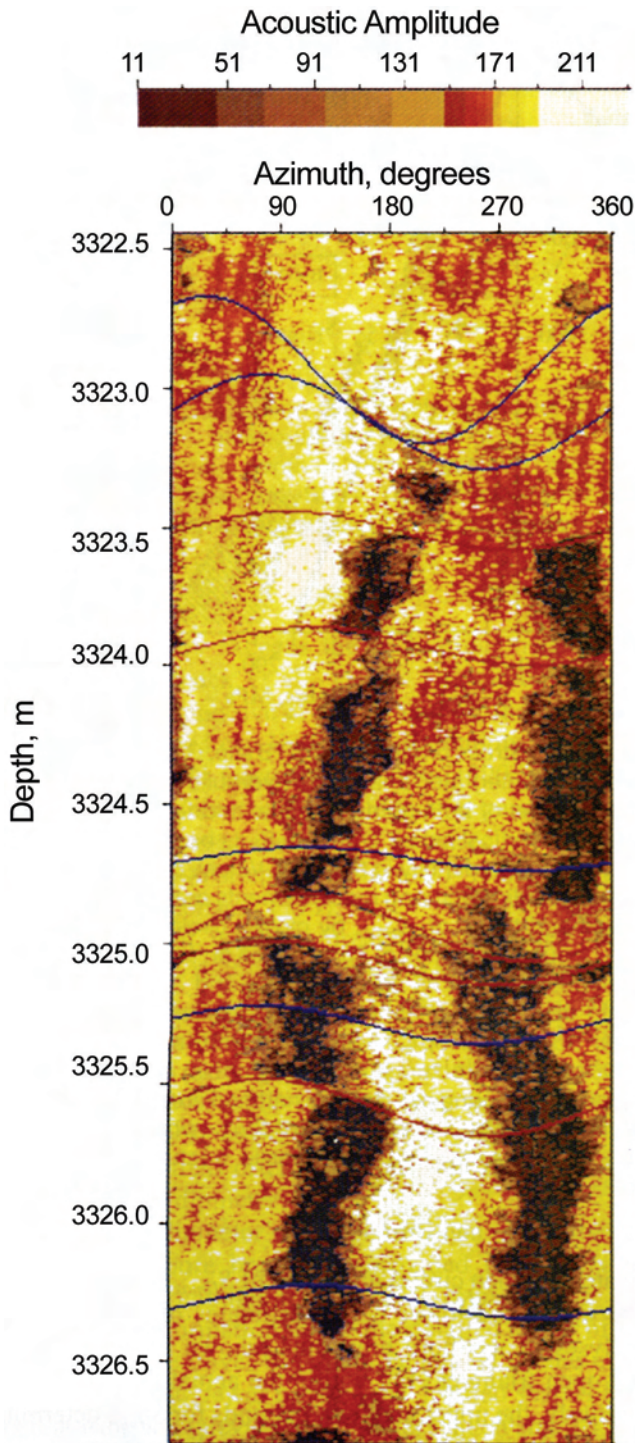


Fig. 3G.15—Example of breakout detection using an ultrasonic borehole televiewer. Breakouts are indicated by the low acoustic amplitude of the reflected signal, shown here as darker areas. The breakouts are rotated because of a drilling-induced slippage of localized faults.²⁵ (Courtesy of SPWLA.)

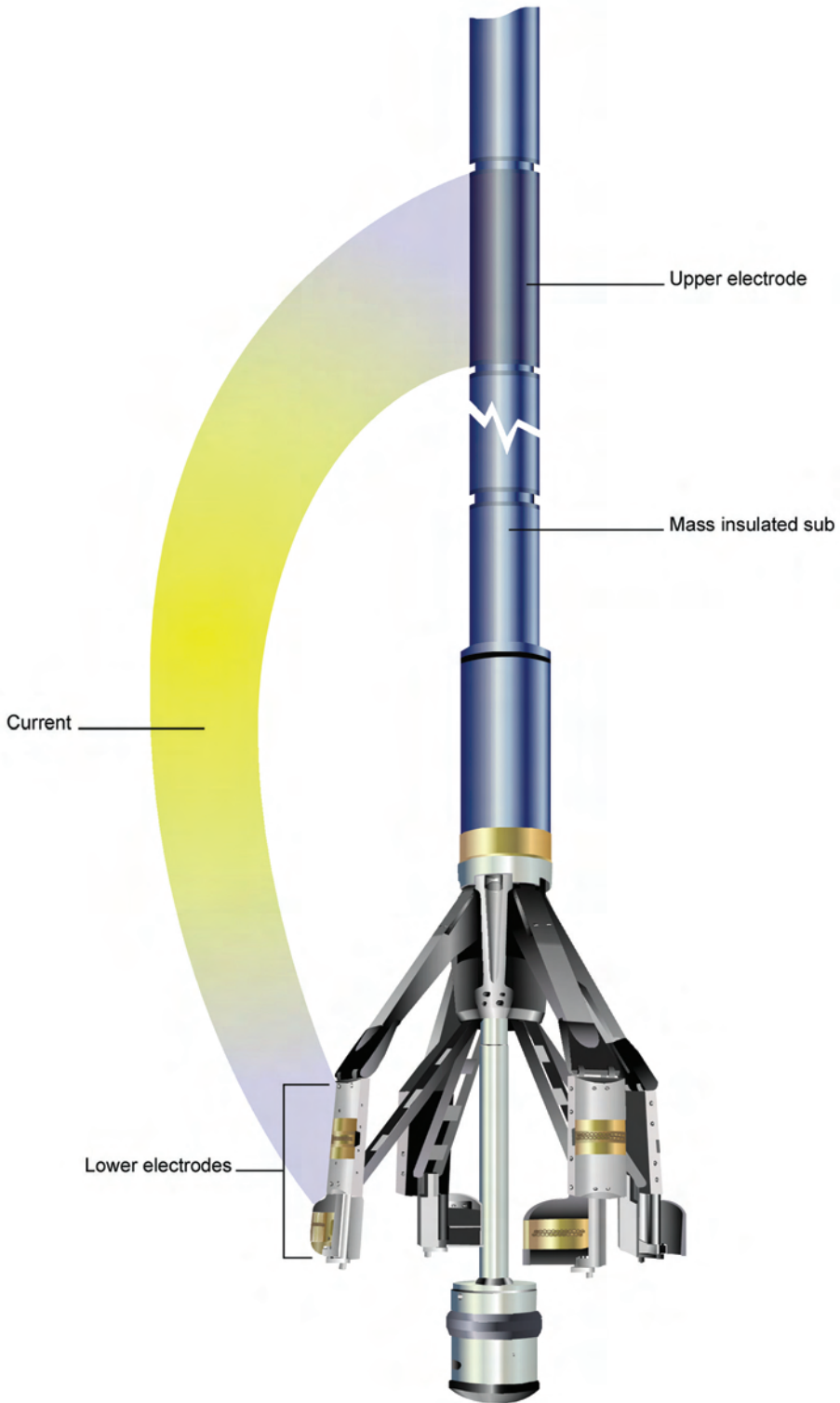


Fig. 3G.16—Measurement principle of microresistivity imaging devices illustrated by Schlumberger's Formation MicroImager (FMI™). (Courtesy of Schlumberger.)

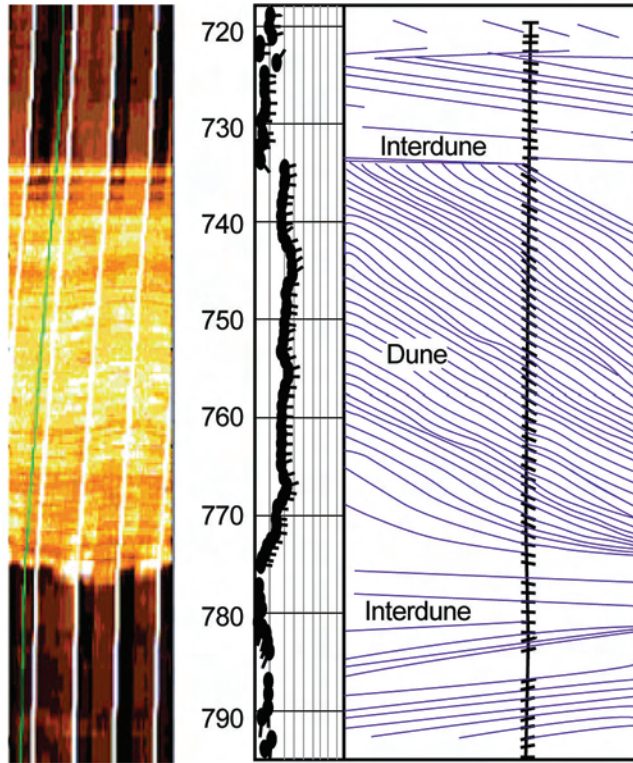


Fig. 3G.17—Recognition of sedimentary and structural features in microresistivity images. These Formation Microimager (FMI™) images have been used to generate the dip information in Track 2. The combination of FMI images and dip data clearly differentiates the eolian and interdune sands in this 8.5-in. [216-mm] borehole. (Courtesy of Schlumberger.)

Data are presented as orientated, juxtaposed pad outputs whereby the cylindrical surface of the borehole wall is flattened out. This has the effect of distorting quasiplanar features such as dipping layers or fractures, which appear as sinusoidal in the data display. **Fig. 3G.17** shows a typical data display and identifies some of the key features.

Electrical microimaging tools have proved superior to the ultrasonic viewers in the identification of sedimentary characteristics and some structural features such as natural fractures in sedimentary rocks. They are especially useful for net-sand definition in thinly laminated fluvial and turbidite depositional environments.

There are several microimaging tools available, each with similar capability. For example, Schlumberger's fullbore FMI™ has two horizontally offset rows of 24 button electrodes on each pad and each flap, making a total of 192 electrodes (**Fig. 3G.18**). The buttons have a diameter of 0.2 in. [5 mm], which determines the intrinsic spatial resolution of the tool. However, features as small as 50- μ fluid-filled fractures can be detected (but not fully resolved). Current is focused into the formation, where a depth of investigation of several tens of centimeters is claimed. However, the image probably relates to a depth of investigation of no more than 0.8 in. [20 mm]. The high-resolution image is normalized with respect to the low-resolution part of the signal or to another resistivity logging tool.

The conventional microresistivity imaging devices require a conductive mud in which to function. However, drilling with oil-based or synthetic muds has increased because of the improved drilling efficiency and greater borehole stability relative to water-based muds. Rather than have to change out the mud specifically for a microresistivity imaging survey, two other

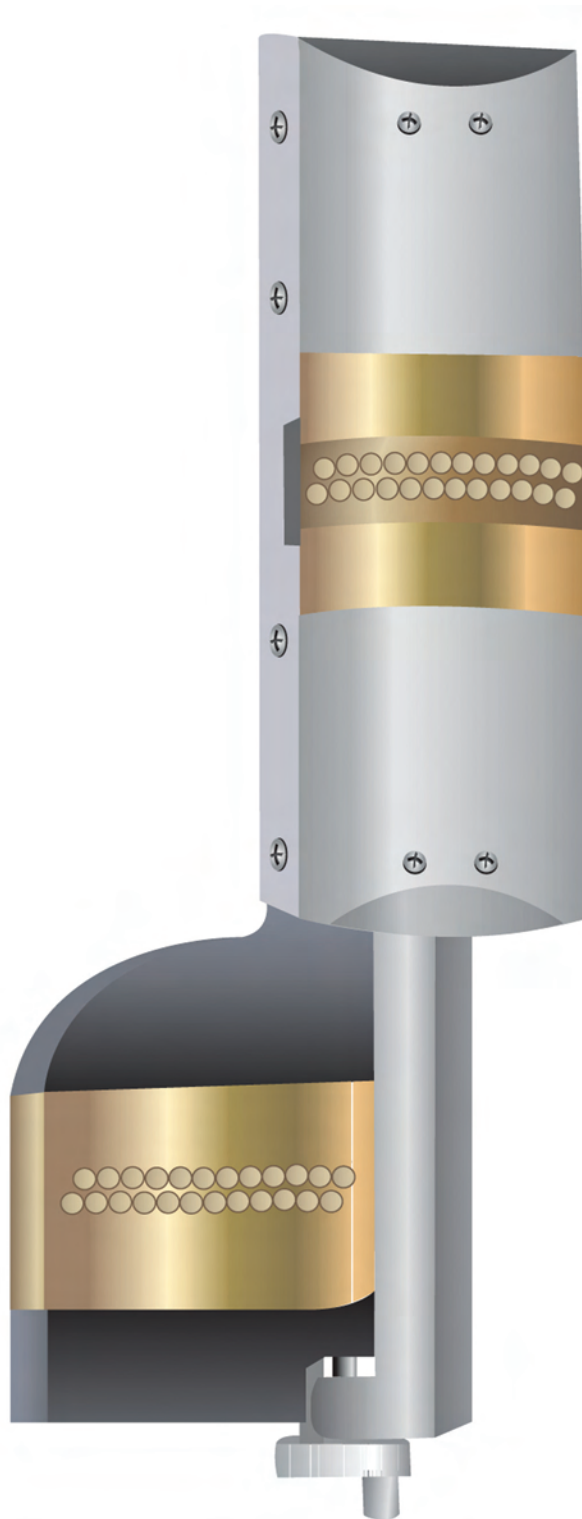


Fig. 3G.18—The Formation MicroImager (FMI™) pad and flap assembly with horizontally offset rows of electrode buttons. (Courtesy of Schlumberger.)

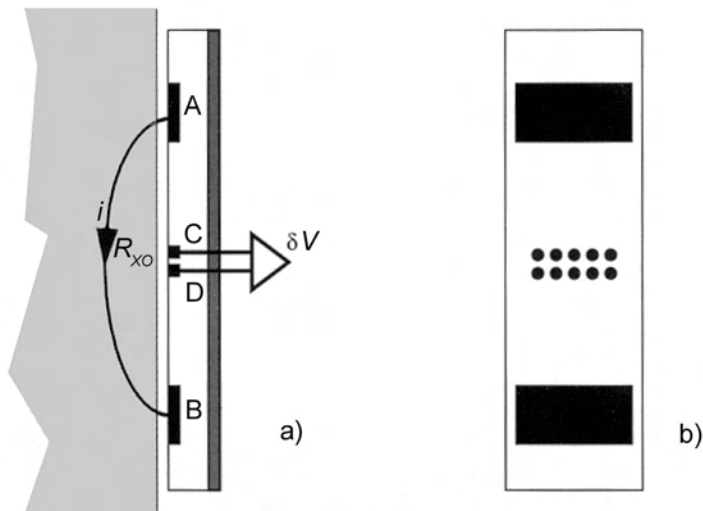


Fig. 3G.19—Principle of the Oil-Base MicroImager (OBMI™). A current, i , is applied between electrodes A and B. The potential difference, δV , is measured between electrodes C and D. An apparent formation resistivity, R_{xo} , is calculated using Ohm's law and an array geometry factor.³² (Courtesy of SPWLA.)

approaches have been pursued. The first has been to develop a new synthetic mud that retains all the stabilizing characteristics of conventional synthetic muds but is sufficiently conductive to permit microresistivity imaging measurements.³⁰ The second has been to develop an electrical imaging device that operates in oil-based muds. This problem was addressed by the so-called oil-based mud dipmeters. These are conventional four-arm dipmeters for which the four microelectrodes are replaced by microinduction sensors.³¹ More recently, contact resistivity methods have been applied in oil-based or synthetic muds.³² Schlumberger's Oil-Base MicroImager (OBMI™) uses four pads positioned at 90° to one another to achieve a 32% coverage of an 8-in. [203-mm] wellbore. Each pad contains two current electrodes and a set of five pairs of closely spaced potential electrodes positioned centrally between the current electrodes (Fig. 3G.19). The arrangement is reminiscent of the Schlumberger electrode array that is still used for surface resistivity sounding in geoelectrical prospecting. However, in this downhole case, the aperture of the sensor gives an intrinsic spatial resolution of 0.4 in. [10 mm] with a nominal depth of investigation of 3.5 in. [90 mm]. Although the OBMI tool is sensitive to borehole rugosity, it has performed well in oil-based and synthetic muds for which water content lies between 1 and 30%. Examples of microresistivity image displays are shown in Figs. 3G.20 and 3G.21.

3G.3.4 Conjunctive Acoustic and Electrical Imaging. To some extent, the ultrasonic and electrical images are complementary because the ultrasonic measurements are influenced more by rock properties, whereas the electrical measurements respond primarily to fluid properties. Another difference is that the ultrasonic image covers 360°, whereas the electrical image is somewhat less than 80% of the surface of an 8-in. [203-mm] wellbore. Ultrasonic measurements can be made using the same tool in all types of drilling mud, and this can facilitate interwell comparisons. On the other hand, most microresistivity imaging devices require a water-based mud; otherwise, an alternative tool, such as the OBMI, has to be used.

These differences can be accommodated through the combined use of electrical and acoustic imaging. As an example, Baker Atlas' Simultaneous Acoustic and Resistivity Imager (STAR™) uses a combination of a CBIL and a six-pad resistivity imager with 12 electrodes per pad. The tool delivers a more complete data set than is achievable using either of the com-

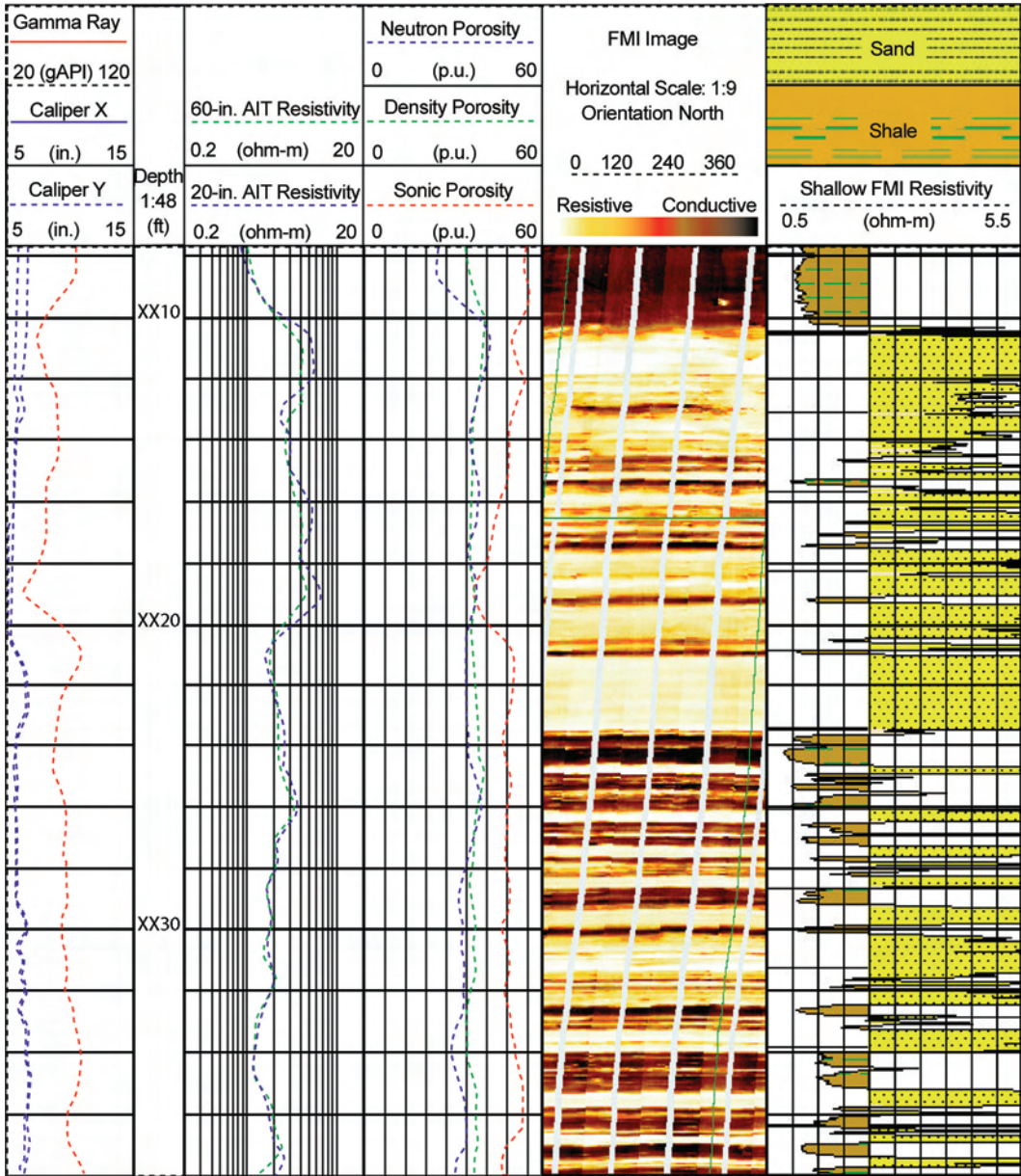


Fig. 3G.20—Example of the Formation Microlmager (FMI™) run in highly laminated sediments. The FMI tool is able to detect laminations as thin as 0.2 in. [5 mm]. In contrast, note the undiagnostic smoothed form of the conventional array induction logs around depth XX30 ft in Track 2. Microresistivity tools are able to detect pay in places where conventional log analysis might overlook it. Note the more complete description of borehole geometry afforded by the X and Y calipers in Track 1 (see [Sec. 3G.2.2](#)). (Courtesy of Schlumberger.)

ponents separately. The combined tool is 86 ft [26.2 m] in length with a diameter of 5.70 in. [145 mm]. It is rated to 20,000 psi [138 MPa] and 350°F [177°C].

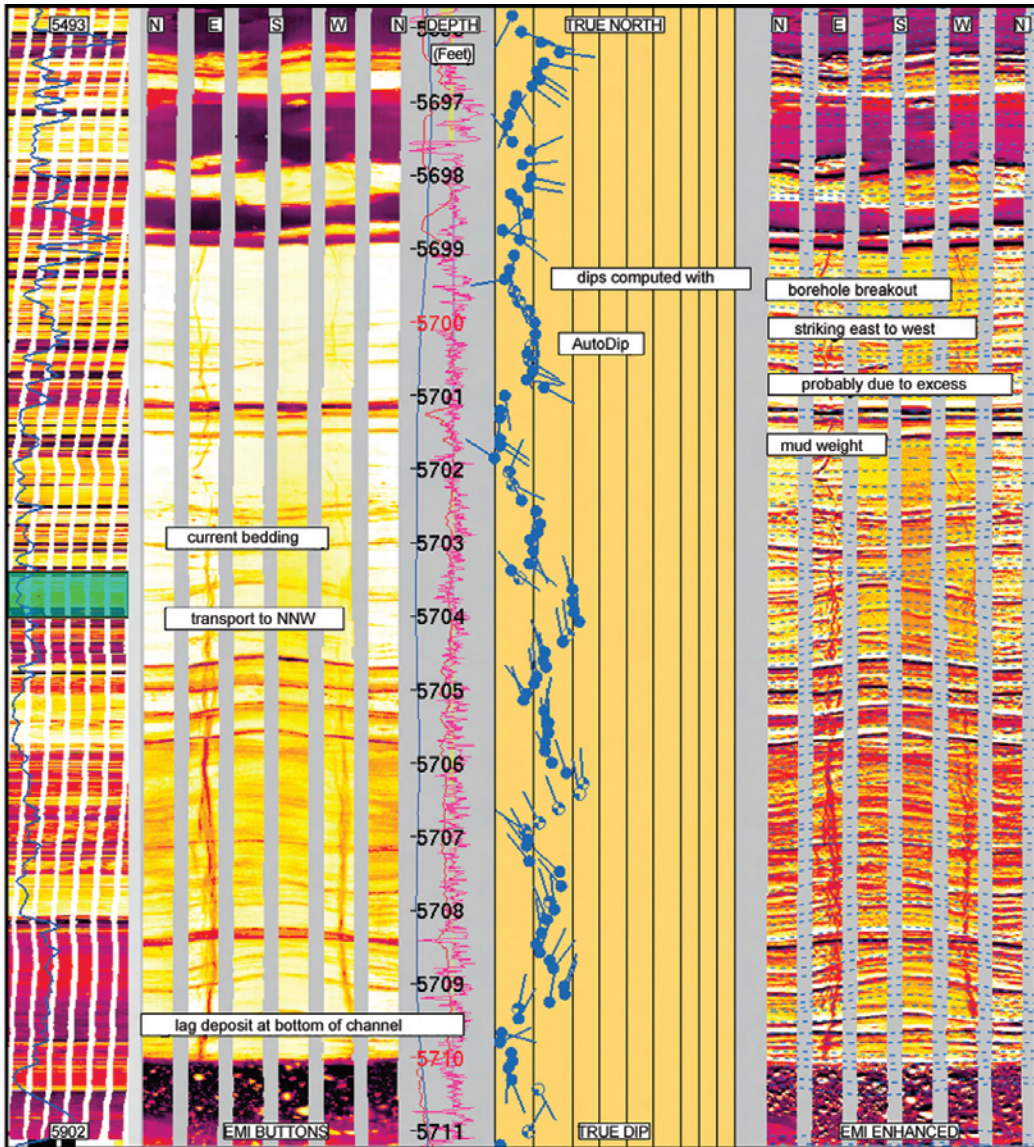


Fig. 3G.21—Example of an electrical microimage using the six-arm Electrical Micro-Imaging Tool (EMI™). Static (Track 2) and dynamic (Track 5) image enhancement has revealed a laminated sand/shale sequence and delivered computed dips (Track 4) of the sedimentary strata. The enhanced images also reveal drilling-induced fractures, which cut vertically across the bedding as sensed by Pads 2 and 5. (Courtesy of Halliburton.)

3G.4 Natural Field Methods

3G.4.1 Borehole Gravimetry. Borehole gravity was pioneered by Smith³³ and then applied to problems of reservoir evaluation by McCulloh *et al.*³⁴ The borehole gravity meter or gravimeter responds to variations in density. Modern instruments sense a rock volume that is approximately the same as that investigated by deep resistivity tools. Unlike the shallower-sensing density log, the borehole gravimeter is insensitive to wellbore conditions such as rugosity and the presence of casing. Its principal applications are (through-casing) time-lapse monitoring of

saturations/fluid contacts in gas reservoirs and downhole calibration of surface geophysical mapping of geological structures.

Theory. Any two masses, m_i and m_j , separated by a distance, r , experience a gravitational force of attraction, f , which is expressed as

$$f = Gm_i m_j / r^2, \dots\dots\dots (3G.13)$$

where G is the universal gravitational constant (6.6726×10^{-8} cgs units). More specifically, a mass, m , on the surface of the Earth would experience a gravitational force given by

$$f = GMm / R^2, \dots\dots\dots (3G.14)$$

where M is the mass of the Earth, R is its radius, and an acceleration due to gravity, g , is given by

$$g = GM / R^2 . \dots\dots\dots (3G.15)$$

Because the Earth is a rotating oblate spheroid, the quantity g at mean sea level varies with latitude, and it must be corrected for tidal effects. The unit of g is the Gal [1 cm/s^2]. Surface gravity surveys use the milliGal as the preferred unit. Borehole gravity surveys often use the microGal. The acceleration due to gravity, or just “gravity,” is measured with a gravimeter.

Measurement. A borehole gravimeter follows the same principles of operation as a surface gravity meter. It is essentially a very sensitive spring balance. The weight of a horizontal hinged beam with a small mass attached to its free end is balanced by a combination of the tension in a compensating spring and an electrostatic force (Fig. 3G.22). When the acceleration due to gravity increases, the weight of the beam increases, and there is a greater tension in the spring. The spring tension is directly related to the acceleration due to gravity. It is controlled by an adjusting screw for which the number of turns is calibrated in gravitational units. The electrostatic force brings the beam to a horizontal position for reading purposes. It, too, is calibrated in gravitational units. The gravity reading is the difference between the spring tension and the electrostatic force: a tidal gravity correction has to be applied. In this way, differences in gravity can be measured between two places (e.g., between two depth locations in a borehole). Downhole measurements are made by occupying selected gravity stations. They are not continuous measurements with depth.

It can be shown³⁵ that the difference in gravity, Δg (mGal), between two locations at the top and bottom of an infinite horizontal reservoir layer penetrated by a vertical well is related to the density, ρ (g/cm^3), and thickness, h_m (m), of that layer by the expression:

$$\Delta g = [F - (4\pi\rho G \times 10^5)]h_m, \dots\dots\dots (3G.16)$$

where F is the vertical gradient of gravity (mGal/m), and G is in cgs units. Eq. 3G.16 can be solved for the layer density so that

$$\rho = \frac{[F - (\Delta g / h_m)]}{4\pi G \times 10^5} . \dots\dots\dots (3G.17)$$

The gradient, F (mGal/m), is a function of latitude, λ (degrees), and elevation, h (m), as per the Intl. Gravity Formula of 1967, as follows:

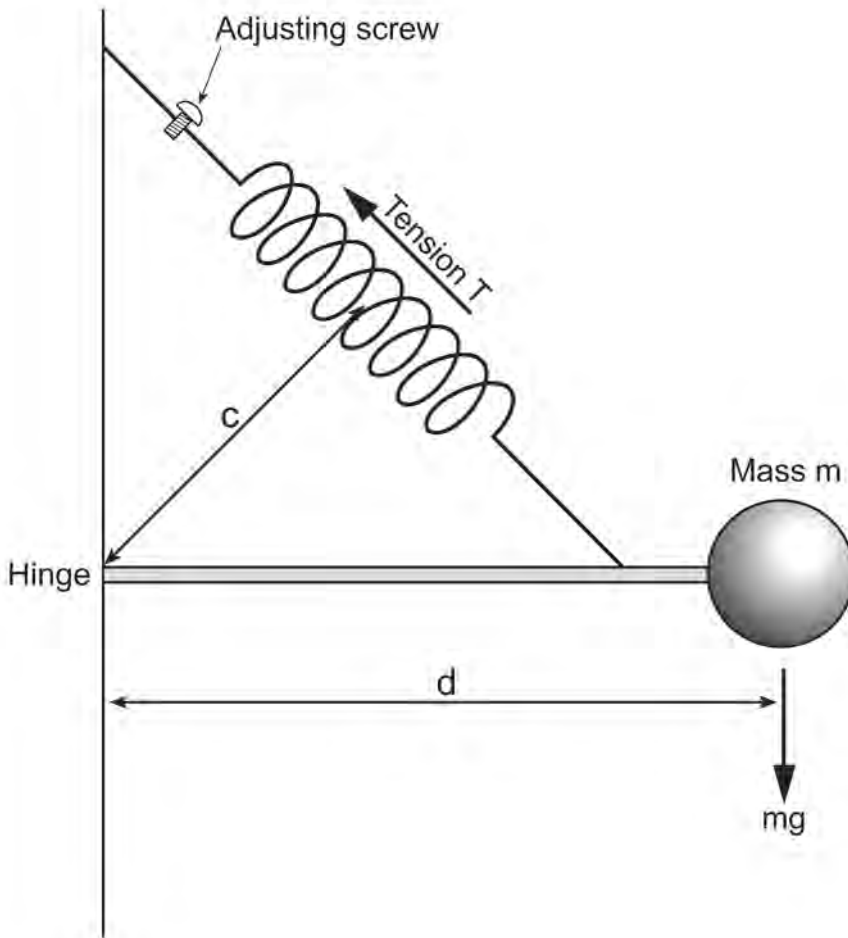


Fig. 3G.22—Principle of measurement of the borehole gravimeter. At equilibrium, the moments of force about the hinge are equal, so that $cT = mgd$. Because d , m , and c are design constants, g can be calculated if T is known.

$$F = 0.308768 - 0.000440\sin^2\lambda - 0.0000001442h \dots\dots\dots (3G.18)$$

By substituting for F in Eq. 3G.17, we have

$$\rho = 3.6827 - 0.00524\sin^2\lambda - 0.00000172\bar{h} - 11.926(\Delta g / h_m), \dots\dots\dots (3G.19)$$

where \bar{h} is the mean elevation of the layer (m), and $\Delta g/h_m$ is in mGal/m. Eq. 3G.19 is that most commonly used for deriving density from borehole gravity measurements. If the borehole is deviated at an angle, α , the measured depth interval has to be converted to a true stratigraphic thickness using a specific form of Eq. 3G.7 for zero dip. Corrections are needed where the model of an infinite layer breaks down because of the presence of structural discontinuities away from the wellbore. Modern borehole gravimeters can detect gravity differences of a few microGals.

The borehole gravity meter delivers an interval density. It is the only tool that can furnish through-casing density. Where the layer is heterogeneous, the computed density is an average

or apparent density. The error in density is a function of the layer thickness. With a LaCoste-Romberg borehole gravimeter, a single measurement of gravity above and below a layer of thickness 6.6 ft [2 m] should result in an error in apparent density of approximately $\pm 0.025 \text{ g/cm}^3$. This expected error can be reduced through repeat measurements and by selecting a larger depth interval. Turning this around, the spatial resolution of a borehole gravimeter is governed by the accuracy to which density is required. For example, an accuracy of $\pm 0.01 \text{ g/cm}^3$ would be achieved through three measurements of gravity at the top and at the base of the target layer, provided that the latter is at least 9 ft [2.7 m] thick.

Borehole gravity tools have different sizes for different hole conditions. For example, the EDCON tools range in diameter from 3.875 in. [98 mm] for low-temperature (110°C), low-pressure (8,000 psi) applications to 5.25 in. [133 mm] for high-temperature (204°C), high-pressure (20,000 psi) applications. The temperature range can be extended to 260°C with special ring seals. Because of the tool size, there are limits on the deviation of boreholes in which it can be deployed. The measurement stations are located relative to other logging runs by using the gamma log and the CCL (see [Sec. 3G.2.3](#)). The depth of investigation within a homogeneous layer is governed by the contrast between the mud filtrate and formation fluids. It is typically more than 23 ft [7 m]. A larger station spacing, h_m , will not increase this range. It will merely reduce the ability of the tool to see near-well density anomalies. Like surface gravity meters, the tool suffers from drift (of the spring tension), which makes accurate calibration difficult.

Application. Key thrusts in reservoir evaluation have been the sensing of vuggy, fractured, and heterogeneous reservoirs, in which a deep-sensing porosity measurement is needed to complement the volumetric-sensing capability of deep resistivity logs.^{36,37} More recent applications have been directed at through-casing monitoring of gas saturations.^{38,39} In this respect, it is noteworthy that the larger volumes sensed by the borehole gravity meter, relative to conventional density logs, are more closely associated with the simulator grid scale. Moreover, time-lapse gravity measurements are not degraded by structural anomalies.

As an example, time-lapse borehole gravimetry has been used to determine the residual oil saturation to gas within the oil rim of the onshore Rabi field in Gabon.³⁵ The reservoir comprises clean, coarse-grained sands with high-salinity formation water. The required accuracy for residual oil saturation was ± 10 saturation units. A baseline gravity survey was run over an undepleted oil-bearing interval near the gas/oil contact (GOC) (Run 1). As the reservoir is depleted, the GOC moves down and the oil saturation decreases toward its residual value. A second gravity survey (Run 2) allowed the change in gas saturation, ΔS_g , to be calculated from the change in measured density, $\Delta \rho_b$, porosity, ϕ , and the densities of oil, ρ_o , and gas, ρ_g .

$$\Delta S_g = \Delta \rho_b / \phi (\rho_g - \rho_o) . \dots\dots\dots (3G.20)$$

Once ΔS_g was known, the oil saturation could be calculated, assuming no change in connate-water saturation.

Three surveys were undertaken twelve months apart ([Fig. 3G.23](#)). All measurements were made in a data-dedicated borehole. Gravity was measured four to six times at each station, with station intervals as low as 3.3 ft [1 m]. Stations were reoccupied with a shuttle-based system for enhanced depth control. The overall accuracy of the density difference in [Eq. 3G.20](#) was 0.015 g/cm^3 . This accuracy corresponds to an accuracy of $0.7 \text{ } \mu\text{Gal}$ on the station-specific readings and an accuracy of $1.0 \text{ } \mu\text{Gal}$ on the gravity difference. The residual oil saturation was determined as 15 ± 10 saturation units. Of this uncertainty, eight saturation units could be ascribed to the borehole-gravity measurements and two saturation units to uncertainties in porosity and connate-water saturation. This study set new objectives and standards for borehole gravimetry.

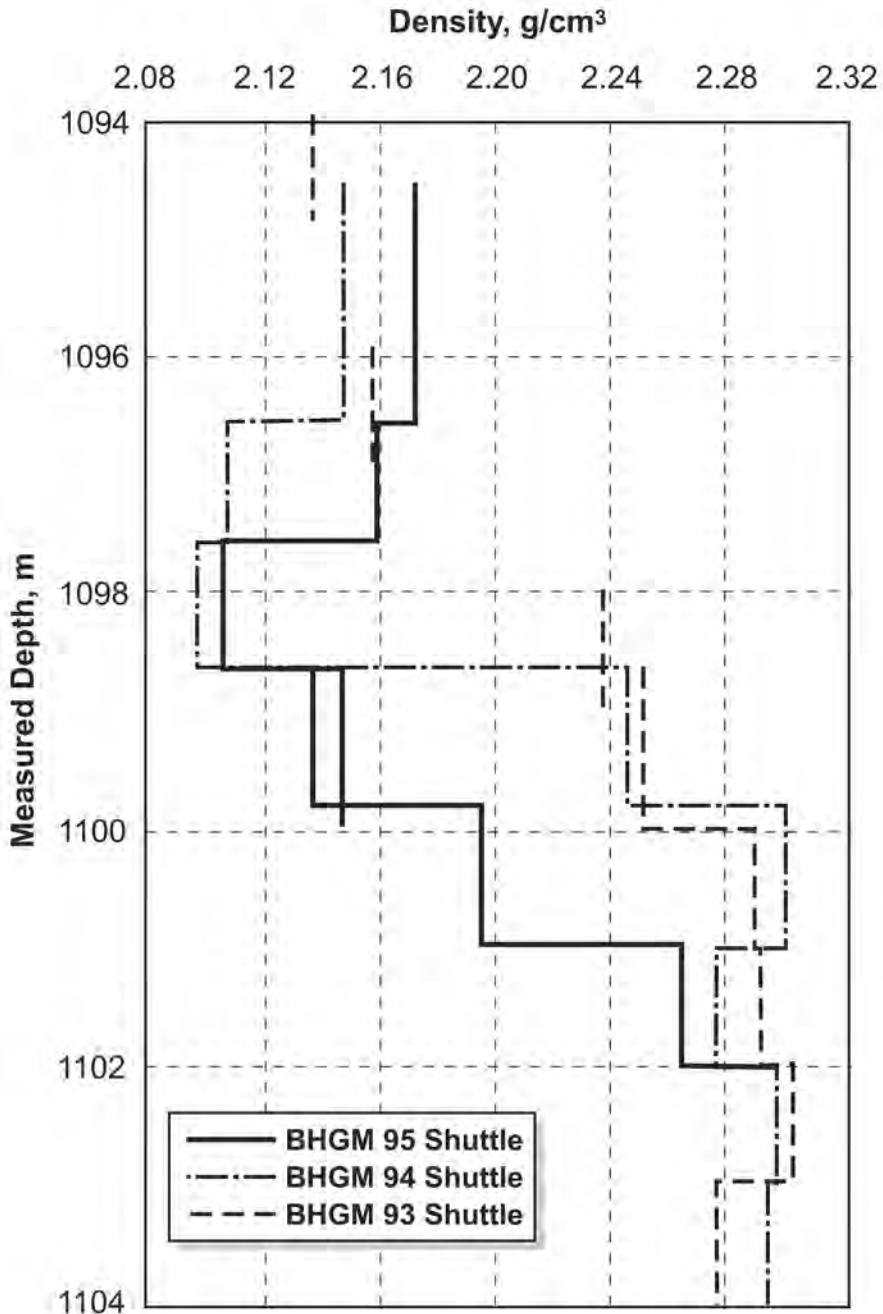


Fig. 3G.23—Time-lapse borehole gravimeter data around the GOC in the Rabi field, Gabon. Note the excellent repeatability of the 1995 shuttle data at approximately 1099 m measured depth. The density reduction caused by GOC movement is apparent between 1097 and 1101 m measured depth. The data recorded between 1098.5 and 1101 m measured depth were used to assess the remaining oil saturation to gas.³⁵

3G.4.2 Downhole Magnetics. Downhole magnetic surveys have been most commonly applied in highly magnetized igneous rocks, which have usually been studied within pure geoscience, especially beneath the ocean floor. These rocks preserve the direction of the Earth's field at the

time of their formation (i.e., the prevailing magnetic field is “frozen” in the rocks as they solidify, giving them a strong natural remnant magnetization). A primary application has been to identify points in time at which the Earth’s magnetic field has undergone a polarity reversal. These reversals have been dated globally (e.g., isotopically in the case of volcanic series or by correlation with biostratigraphy in the case of volcanoclastics) and have given rise to a geomagnetic polarity time scale (GPTS) that is based on laboratory measurements. This, in turn, has allowed dates to be assigned to a given magnetozone that is bounded by reversal phenomena. It has been possible to recognize these reversals through downhole measurements and, therefore, to date the rocks accordingly.

Sedimentary rocks have much weaker remnant magnetizations than igneous sequences, and it has been much more difficult to investigate their magnetic character. However, recent advances in instrumentation have led to progress in downhole magnetic measurements of sedimentary strata.⁴⁰

Theory. The following magnetic theory is extracted from Lalanne *et al.*⁴¹ The magnetic field measured downhole has three parts: the Earth’s magnetic field of the present day; the field that is induced in the rocks by the prevailing Earth’s field; and the remnant magnetic field, which is the preservation in the rocks of a paleomagnetic field. The effect of the Earth’s magnetic field can be accommodated during logging by extrapolating downhole the measurements made by a surface magnetometer that records diurnal variations in the Earth’s field and allows the downhole data to be corrected for these variations where they are significant. The induced field is proportional to the magnetic susceptibility of the rock, which is governed by (ferro-magnetic) mineralogy and fluid composition. The remnant magnetic field adopts the direction of the Earth’s field at the time that the rock was forming. For sediments, it is most pronounced in clays.

A measurement of magnetic induction or field strength, B_T , can be written as

$$B_T = B_o + B_i + B_r, \dots\dots\dots (3G.21)$$

where B_o is the magnetic induction associated with the present Earth’s field, B_i is the magnetic induction caused by the field induced in the rock, and B_r is the magnetic induction caused by the remnant field. Magnetic induction is measured in units of nanoTesla (nT). It is a measure of field strength expressed in terms of the field’s ability to induce magnetization. Typically, B_i and B_r are no more than a few tens of nanoTesla, and they have to be measured against a prevailing Earth’s field that is a thousand times greater. Therefore, the exercise becomes very much one of analyzing residuals. For this reason, the prevailing Earth’s field, B_o , is removed from the value of B_T , which then becomes a “net” field B_t .

$$B_t = B_i + B_r \dots\dots\dots (3G.22)$$

The induced magnetic field, B_i (nT), is proportional to the magnetic susceptibility, χ (units SI), of the rock:

$$B_i = \mu_o H_T \chi \times 10^6, \dots\dots\dots (3G.23)$$

where μ_o is the magnetic permeability of the void ($4\pi \times 10^{-1}$ μ H/m), and H_T is the Earth’s magnetic field (A/mm). Therefore, B_i can be evaluated if susceptibility can be measured.

If B_i and B_r can be determined, B_r can be quantified,

$$B_r = B_t - B_i \dots\dots\dots (3G.24)$$

If B_r is positive, the remnant magnetization and, therefore, the paleomagnetic field that caused it are aligned as per the present-day Earth's field, and B_r is described as "normal." Otherwise, its polarity is "reversed." The polarity of remnant magnetization is evaluated through a numerical comparison of B_i and B_r .

Measurement. A magnetic logging sonde developed for sedimentary rocks is Schlumberger's Geological High-Resolution Magnetic Tool (GHMT™). It actually comprises two tools: one to measure the total magnetic field and one to measure magnetic susceptibility. The tool housings are nonmagnetic and electrically insulating with a diameter of 4 in. [100 mm].

Because sedimentary rocks have a very low magnetization, a very high precision magnetometer is required. This requirement is satisfied by Schlumberger's Nuclear Magnetic Resonance Tool (NMRT™), which uses the principles of nuclear magnetic resonance whereby the frequency of precession of relaxing protons is proportional to B_T (see Chap. 3E in this section of the *Handbook*). The problem, therefore, reduces to a very precise measurement of frequency. The NMRT measurement has a sensitivity of 10^{-2} nT. Data are recorded at a logging speed of 1970 ft/hr [600 m/hr] with a sampling interval of 4 in. [100 mm].

A second tool measures the magnetic susceptibility of the rock, which is proportional to B_i (Eq. 3G.23). This tool, Schlumberger's Susceptibility Measurement Tool (SUMT™), uses the principles of electromagnetic induction. The voltage induced in the receiver coil increases with susceptibility, which is determined from the complex character of the induced signal. Susceptibility is dimensionless. The downhole measurement of susceptibility has a sensitivity of approximately 10^{-6} units SI. Data measured in sedimentary rocks are typically in the range 10^{-5} to 10^{-4} units SI. Data can be recorded at a logging speed of up to 3940 ft/hr [1200 m/hr] with a sampling interval of 6 in. [150 mm]. The tools are rated to a temperature of 257°F [125°C] and a pressure of 15,000 psi [103 MPa].

The key measurement deliverable from the combined use of these two integral tools is a depth record of the polarity of remnant magnetization based on the sign of B_r in Eq. 3G.24. This display is called the well magnetic stratigraphy (WMS).

Application. Fig. 3G.24 illustrates the application of the measured data. It shows how a magnetostratigraphic sequence was established for a well in the Paris basin using GHMT log data.⁴⁰ For dating purposes, this sequence has to be tied to the GPTS.

Fig. 3G.25 illustrates another example, this time from the Ocean Drilling Program (ODP). This example reveals some geomagnetic features that are not yet part of the global standard. Notwithstanding these disparities, this chonal benchmarking allows the absolute dating of much of the sedimentary succession.

Future applications will examine the direction of remnant magnetization to investigate the movement of fault blocks and enhancing the fieldwide correlation of the sedimentary column.

3G.5 Discussion

There are two principal drivers for the further advancement of the technologies that have been described here.

The first is the need for improved reservoir characterization to help us deal with problematic reservoirs that have low-permeability characteristics, thin beds, laminations, low-resistivity-contrast pay, and fracture networks. Fracture networks lead us to the question of carbonates and their petrophysical differences from clastic rocks. One might ask why it is that with so much technology available, the industry still perceives a shortfall in its interpretative capability. The reason is that recent attention has been directed at data acquisition and management rather than methods of interpreting the data themselves. Thus, for example, we have not yet succeeded in reconciling petrophysical data measured at different scales. The gap between our ability to measure and our ability to interpret the measurements widened still further during the 1990s, the decade of the horizontal well. This drove the analysis of downhole measurements further

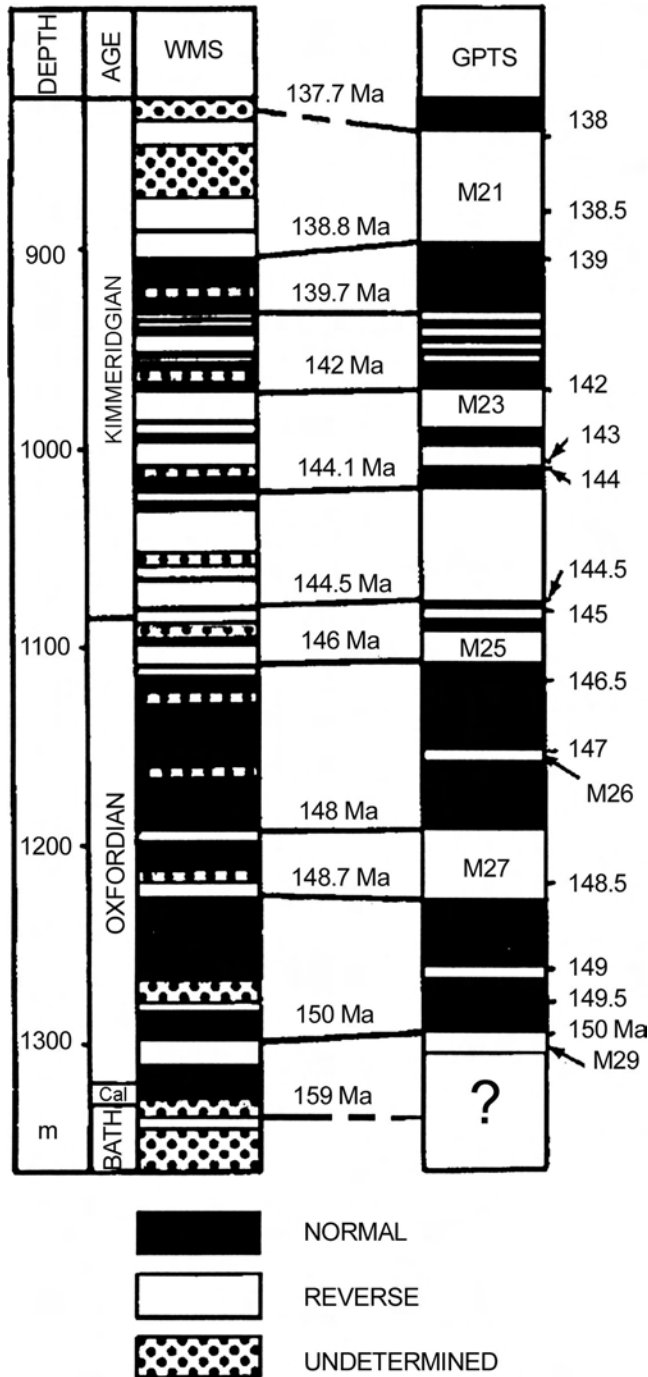


Fig. 3G.24—Comparison between the Geomagnetic Polarity Time Scale (GPTS) and the Well Magnetic Stratigraphy (WMS) for a borehole in the Paris basin. Normal polarity is black; reversed polarity is white. The GPTS and WMS are similar. This allows polarity to be correlated and absolute determinations of age to be made along the borehole column. In some places (e.g., at approximately 950 m depth), the detail of the GPTS is not reflected in the WMS, presumably because of low rock magnetization or, possibly, localized erosion. On the other hand, at approximately 1060 m, there are indications of detail that has yet to be accommodated within the GPTS.⁴⁰ (Courtesy of SPWLA.)

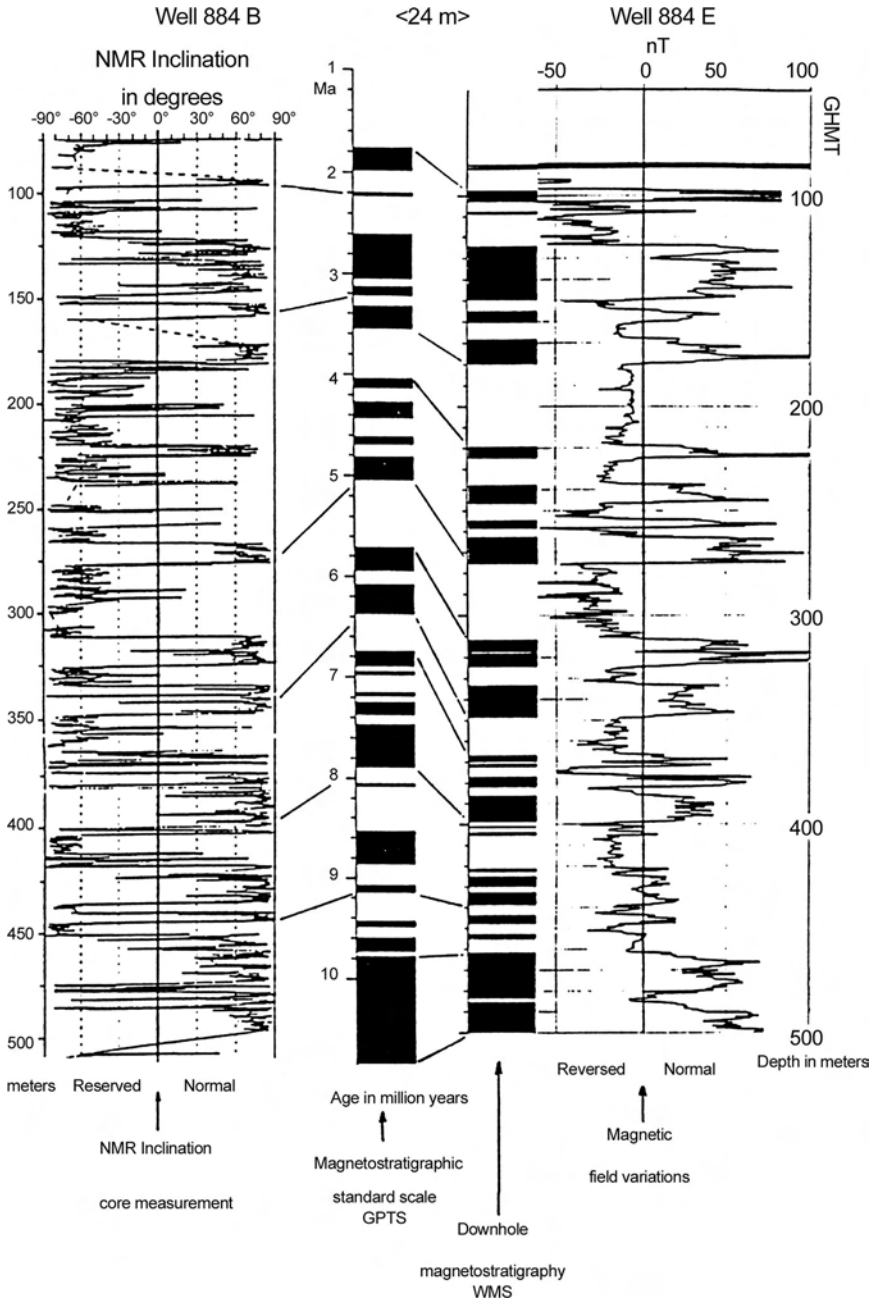


Fig. 3G.25—Geomagnetic data from Ocean Drilling Program (ODP) Leg 145. Wells 884B and 884E are 24 m apart. Normal polarity is black; reversed polarity is white. Well 884B was cored; core data have furnished the inclination of the remnant magnetization. These data have been correlated with the Geomagnetic Polarity Time Scale (GPTS). Well 884E was logged geomagnetically; log data have furnished the Well Magnetic Stratigraphy (WMS). The WMS shows detail that is not part of the GPTS. This could be highly significant because in these wells the susceptibility was very low indeed, so that the measured “net” field B_t was directly related to the remnant magnetization without being impacted by possible errors in susceptibility.⁴⁰ (Courtesy of SPWLA.)

into three dimensions and emphasized the need for us to get more out of our data if our reservoir models are to deliver the greatest benefit.

The second technology driver is the cost-effectiveness of multiwell platforms from which deviated, extended-reach, horizontal, and multilateral wells can be drilled to target hydrocarbon accumulations that have been identified in a reservoir model. This heralds a further thrust in the need to drill more difficult subsurface environments in a way that allows full control of the wellbore trajectory. This, in turn, will require a full casing- and cement-evaluation service, especially with regard to the monitoring of casing deformation. Only in this way can one be assured of an absence of flow constrictions or impediments to tool deployment.

Both reservoir characterization and the cost-effectiveness of multiwell platforms will continue to benefit from further developments in data recording, transmittal, processing, and visualization, which have underpinned the technical progress made to date.

3G.6 Summary

This chapter has addressed several specialized logging tools and the information they can provide in assessing borehole trajectory, wellbore conditions, and reservoir characteristics. Directional, caliper, and cement-bond surveys can be used to determine well location, the quality and condition of the open hole, the condition of the tubing, the presence of cement, the quality of the bond between tubing and cement, and, to a lesser extent, the degree of bonding between cement and formation. Borehole imaging can be used in open hole to picture the different strata encountered, and it is of particular use in detailing thinly bedded (sand/shale) intervals and identifying both natural and induced fractures. Finally, borehole gravimetry and downhole magnetics can be used to measure formation properties at a larger scale. Each of these specialized tools is experiencing a stronger application base as better sensor technology delivers the information needed for improved reservoir characterization and reservoir management.

Acknowledgments

The author is obliged to those oilfield service companies and petroleum technical societies who have granted permission for subject matter to be included here. Special mention is made of Baker Atlas, EDCON, Halliburton Energy Services, Schlumberger, and Sondex. This material has been included to give a balanced overview of the state of technology in this important subject area rather than to endorse any particular commercial service. In this rapidly changing world, the material is current as of June 2003.

Nomenclature

A	= tool azimuth relative to magnetic north, $-$, degrees
B_o	= magnetic induction associated with the present Earth's field, m/qt, nT
B_i	= magnetic induction due to the field induced in the rock, m/qt, nT
B_r	= magnetic induction due to the remnant field, m/qt, nT
B_t	= "net" field, m/qt, nT
c	= gravimeter design constant, L, m
d	= gravimeter design constant, L, m
f	= gravitational force of attraction, mL/t ² , N
F_r	= ratio factor for the minimum curvature method
F	= vertical gradient of gravity, 1/t ² , mGal/m
g	= acceleration due to gravity, L/t ² , mGal
G	= universal gravitational constant, L ³ /mt ² , dyne cm ² /g ²
h	= elevation, L, m
h_m	= measured bed thickness, L, m
h_{ts}	= true stratigraphic thickness, L, m
h_v	= true vertical thickness, L, m
H_T	= Earth's magnetic field, q/tL, A/mm

- i = current, q/t, A
 I = tool inclination relative to gravitational vector, –, degrees
 L = length of equal straight lines representing dogleg in wellbore, L, m
 m_i, m_j = any two gravitationally attracting masses, m, kg
 m = mass, m, kg
 M = mass of the Earth, m, kg
 r = distance between two gravitationally attracting masses, L, m
 R = Earth's radius, L, km
 R_{xo} = apparent formation resistivity, mL^3/qt^2 , Ωm
 T = tension, mL/t^2 , N
 \bar{h} = mean elevation of layer, L, m
 α = inclination or deviation of wellbore, –, degrees
 φ = dip, –, degrees
 φ_a = apparent dip, –, degrees
 β = azimuth of wellbore, –, degrees
 β_d = azimuth of dip, –, degrees
 δV = potential difference, mL^2/qt^2 , V
 ΔE = incremental distances between adjacent survey stations in the direction of the easting, L, m
 Δg = difference in gravity between two locations at the top and bottom of an infinite horizontal reservoir layer penetrated by a vertical well, L/t^2 , Gal
 ΔN = incremental distances between adjacent survey stations in the direction of the northing, L, m
 ΔS_g = time-lapse change in gas saturation
 ΔV = incremental distances between adjacent survey stations in the vertical direction, L, m
 $\Delta \rho_b$ = change in measured density, m/L^3 , g/cm^3
 λ = latitude, –, degrees
 μ_o = magnetic permeability of the void, mL/q^2 , $\mu H/m$
 ρ = density, m/L^3 , g/cm^3
 ρ_g = gas density, m/L^3 , g/cm^3
 ρ_o = oil density, m/L^3 , g/cm^3
 ψ = dogleg angle, –, degrees
 ϕ = porosity
 χ = magnetic susceptibility of the rock, –

Subscripts

- 1 = upper directional survey station
 2 = lower directional survey station

References

1. Bourgoyne, A.T. Jr. *et al.*: *Applied Drilling Engineering*, Textbook Series, SPE, Richardson, Texas (1991) **2**.
2. Theys, P.: *Log Data Acquisition and Quality Control*, Editions Technip, Paris (1999).
3. Thorogood, J.L.: "Directional Survey Operations Management," *JPT* (December 1989) 1250.
4. Inglis, T.: *Directional Drilling*, Graham & Trotman, London (1987).

5. Boak, J.M.: "Conversion of Well Log Data to Subsurface Stratigraphic and Structural Information," AAPG Methods in Exploration Series, No. 10, American Assn. of Petroleum Geologists, Tulsa (1992) 289–293.
6. Larimore, D.R., Fehrmann, G.Z., and White, S.: "Field Cases of Cost Efficient Well Interventions Performed With Advanced Slickline Technology," paper SPE 38097 presented at the 1997 SPE Asia Pacific Oil and Gas Conference, Kuala Lumpur, 14–16 April.
7. Connell, M.L. *et al.*: "High-Pressure/High-Temperature Coiled Tubing Casing Collar Locator Provides Accurate Depth Control for Single-Trip Perforating," paper SPE 60698 presented at the 2000 SPE/ICoTA Coiled Tubing Roundtable, Houston, 5–6 April.
8. Wagg, B. and Matthews, C.: "Evaluating Casing Deformation," *World Oil* (2000) **221**, No. 12, 44.
9. Wagg, B. *et al.*: "Evaluating Casing Deformation Mechanisms in Primary Heavy Oil Production," paper SPE 54116 presented at the 1999 SPE International Thermal Operations and Heavy Oil Symposium, Bakersfield, California, 17–19 March.
10. Hayman, A.J. *et al.*: "Developments in Corrosion Logging Using Ultrasonic Imaging," *Trans.*, Soc. of Professional Well Log Analysts 36th Annual Logging Symposium, Paris (1995) paper W.
11. Frisch, G.J. and Mandal, B.: "Advanced Ultrasonic Scanning Tool and Evaluation Methods Improve and Standardize Casing Inspection," *Trans.*, Soc. of Professional Well Log Analysts 42nd Annual Logging Symposium, Houston (2001) paper X.
12. Frisch, G.J., Graham, L., and Wyatt, D.: "Economic Evaluation of the Use of Well Logs for Diagnosing Conformance Problems," paper SPE 40036 presented at the 1998 SPE Gas Technology Symposium, Calgary, 15–18 March.
13. Harness, P.E., Sabins, F.L., and Griffith, J.E.: "New Technique Provides Better Low-Density-Cement Evaluation," paper SPE 24050 presented at the 1992 SPE Western Regional Meeting, Bakersfield, California, 30 March–1 April.
14. Bigelow, E.L., Domangue, E.J., and Lester, R.A.: "A New and Innovative Technology for Cement Evaluation," paper SPE 20585 presented at the 1990 SPE Annual Technical Conference and Exhibition, New Orleans, 23–26 September.
15. Hayman, A.J., Hutin, R., and Wright, P.V.: "High Resolution Cementation and Corrosion Imaging by Ultrasound," *Trans.*, Soc. of Professional Well Log Analysts 32nd Annual Logging Symposium, Midland, Texas (1991) paper KK.
16. De Souza Padilha, S.T.C. and Da Silva Araujo, R.G.: "New Approach on Cement Evaluation for Oil and Gas Reservoirs Using Ultrasonic Images," paper SPE 38981 presented at the 1997 SPE Latin American and Caribbean Petroleum Engineering Conference, Rio de Janeiro, 30 August–3 September.
17. Frisch, G., Graham, L., and Griffith, J.: "A Novel and Economical Processing Technique Using Conventional Bond Logs and Ultrasonic Tools for Enhanced Cement Evaluation," *Trans.*, Soc. of Professional Well Log Analysts 41st Annual Logging Symposium, Dallas (2000) paper EE.
18. Graham, W.L. *et al.*: "Cement Evaluation and Casing Inspection With Advanced Ultrasonic Scanning," paper SPE 38651 presented at the 1997 SPE Annual Technical Conference and Exhibition, San Antonio, Texas, 5–8 October.
19. Prensky, S.: "Advances in Borehole Imaging Technology and Applications," *Borehole Imaging: Applications and Case Histories*, M. Lovell, G. Williamson, and P. Harvey (eds.) Geological Soc., London, Special Publications (1999) **159**, 1–43.
20. Zemanek, J. *et al.*: "The Borehole Televiwer—A New Logging Concept for Fracture Location and Other Types of Borehole Inspection," *JPT* (June 1969) 762.
21. Zemanek, J. *et al.*: "Formation Evaluation by Inspection With the Borehole Televiwer," *Geophysics* (1970) **35**, 254.
22. Hayman, A.J. *et al.*: "Improved Borehole Imaging by Ultrasonics," paper SPE 28440 presented at the 1994 SPE Annual Technical Conference and Exhibition, New Orleans, 25–28 September.
23. Faraguna, J.K., Chace, D.M., and Schmidt, M.G.: "An Improved Borehole Televiwer System: Image Acquisition, Analysis and Integration," *Trans.*, Soc. of Professional Well Log Analysts 30th Annual Logging Symposium, Denver (1989) paper UU.
24. Seiler, D. *et al.*: "Field Performance of a New Borehole Televiwer Tool and Associated Field Processing Techniques," *Trans.*, Soc. of Professional Well Log Analysts 31st Annual Logging Symposium, Lafayette, Louisiana (1990) paper H.

25. Barton, C.A. *et al.*: “Utilizing Wellbore Image Data To Determine the Complete Stress Tensor: Application to Permeability, Anisotropy and Well Bore Stability,” *The Log Analyst* (1997) **38**, No. 6, 21.
26. Ekstrom, M.P. *et al.*: “Formation Imaging With Microelectrical Scanning Arrays,” *The Log Analyst* (1987) **28**, No. 3, 294.
27. Boyeldieu, C. and Jeffreys, P.: “Formation Microscanner: New Developments,” *Trans.*, Soc. of Professional Well Log Analysts 11th European Formation Evaluation Symposium, Paris (1988) paper X.
28. Safinya, K.A. *et al.*: “Improved Formation Imaging With Extended Microelectrical Arrays,” paper SPE 22726 presented at the 1991 SPE Annual Technical Conference and Exhibition, Dallas, 6–9 October.
29. Seiler, D., King, G., and Eubanks, D.: “Field Test Results of a Six Arm Microresistivity Borehole Imaging Tool,” *Trans.*, Soc. of Professional Well Log Analysts 35th Annual Logging Symposium, Tulsa (1994) paper W.
30. Laastad, H. *et al.*: “Water-Based Formation Imaging and Resistivity Logging in Oil-Based Drilling Fluids—Today’s Reality,” paper SPE 62977 presented at the 2000 SPE Annual Technical Conference and Exhibition, Dallas, 1–4 October.
31. Dumont, A., Kubacsi, M., and Chardac, J.L.: “The Oil-Base Mud Dipmeter Tool,” *Trans.*, Soc. of Professional Well Log Analysts 28th Annual Logging Symposium, London (1987) paper LL.
32. Cheung, P. *et al.*: 2001. “Field Test Results of a New Oil-Base Mud Formation Imager Tool,” *Trans.*, Soc. of Professional Well Log Analysts 42nd Annual Logging Symposium, Houston (2001) paper XX.
33. Smith, N.L.: “The Case for Gravity Data From Boreholes,” *Geophysics* (1950) **15**, 605.
34. McCulloh, T.H., Kandle, G.R., and Schoellhamer, J.E.: “Application of Gravity Measurements in Wells to Problems of Reservoir Evaluation,” *Trans.*, Soc. of Professional Well Log Analysts 9th Annual Logging Symposium, New Orleans (1968) paper O.
35. Alixant, J.-L. and Mann, E.: “In-Situ Residual Oil Saturation to Gas From Time-Lapse Borehole Gravity,” paper SPE 30609 presented at the 1995 SPE Annual Technical Conference and Exhibition, Dallas, 22–25 October.
36. Jageler, A.H.: “Improved Hydrocarbon Reservoir Evaluation Through Use of Borehole-Gravimeter Data,” *JPT* (1976) 709.
37. Gournay, L.S. and Lyle, W.D.: “Determination of Hydrocarbon Saturation and Porosity Using a Combination Borehole Gravimeter (BHGM) and Deep Investigating Electric Log,” *Trans.*, Soc. of Professional Well Log Analysts 25th Annual Logging Symposium, New Orleans (1984) paper WW.
38. Popta, J.V. *et al.*: “Use of Borehole Gravimetry for Reservoir Characterization and Fluid Saturation Monitoring,” paper SPE 20896 presented at the 1990 SPE European Petroleum Conference, The Hague, 22–24 October.
39. Brady, J.L., Wolcott, D.S., and Aiken, C.L.V.: “Gravity Methods: Useful Techniques for Reservoir Surveillance,” paper SPE 26095 presented at the 1993 SPE Western Regional Meeting, Anchorage, 26–28 May.
40. Pages, G. *et al.*: “Wireline Magnetostratigraphy: Principles and Field Results,” *Trans.*, Soc. of Professional Well Log Analysts 35th Annual Logging Symposium, Tulsa (1994) paper XX.
41. Lalanne, B. *et al.*: “Magnetic Logging: Borehole Magnetostratigraphy and Absolute Datation in Sedimentary Rocks,” paper SPE 21437 presented at the 1991 SPE Middle East Oil Show, Bahrain, 16–19 November.

SI Metric Conversion Factors

degree	× 1.745329	E - 02 = rad
dyne	× 1.0*	E - 05 = N
ft	× 3.048*	E - 01 = m
°F	(°F - 32)/1.8	= °C
Gal	× 1.0*	E - 02 = m/s ²
in.	× 2.54*	E + 00 = cm
psi	× 6.894 757	E + 00 = kPa

*Conversion factor is exact.

Chapter 3H

Petrophysical Applications

H.R. (Hal) Warner Jr., Warner Consulting Services and Richard Woodhouse, Independent Consultant

3H.1 Introduction

This chapter discusses the determination of lithology, net pay, porosity, water saturation, and permeability from wellbore core and log data. The chapter deals with “Development Petrophysics” and emphasizes the integration of core data with log data; the adjustment of core data, when required, to reservoir conditions; and the calibration and regression line-fitting of log data to core data. The goal of the calculations is to use all available data, calibrated to the best standard, to arrive at the most accurate quantitative values of the petrophysical parameters (i.e., lithology, net pay, porosity, water saturation, and permeability). Log analysis, cased-hole formation evaluation, and production logging are not covered here.

The following topics are covered in this chapter: petrophysical data sources and databases, lithology determination, net-pay (or pay/nonpay) determination, porosity determination, fluid-contacts identification, water-saturation determination, permeability calculations, case studies, other considerations in petrophysical calculations, and summary and conclusions. This chapter concerns the foot-by-foot calculations of the five petrophysical parameters at the wellbore. It does not cover the propagation of the wellbore values, or “populating” of static or dynamic reservoir models, vertically and areally over the whole of the reservoir volume. Because other chapters in this section of the *Handbook* discuss the technical details of various well logs and coring, these details are generally assumed as the basis for this chapter and are referenced accordingly.

In practical terms, petrophysics is used for two types of calculations: determination of original hydrocarbons in place [original oil in place (OOIP) or original gas in place (OGIP)] and their distribution, and reservoir-engineering dynamic flow calculations. For the development geoscientists (geologists, geophysicists, and geostatisticians), petrophysics means developing the detailed stratigraphic, depositional, and diagenetic descriptions of the reservoir, both vertically and areally. To make accurate calculations of OOIP or OGIP and the various flow calculations, accurate foot-by-foot calculations of lithology, net pay, porosity, water saturation, and permeability are necessary. These calculations need to be made not only as overall calculations, but also so that the variation and distribution of these parameters are determined appropriately.

Some of the petrophysical calculations can be made in several ways, particularly for porosity and water saturation. One key to arriving at an accurate petrophysical calculation is to obtain the same quantitative result with a variety of techniques. An important consideration is the acquisition and handling of the various types of petrophysical data and, for each reservoir, the preparation of its unique petrophysical database. Petrophysical data take many forms and, for many reservoirs, may not be as comprehensive as desired. The technical personnel working with these data have to review what data are available, their quality, and what additional data might be acquired from the existing wellbores and from preserved and unpreserved cores. Finally, if there are sufficient financial stakes, new wells might be drilled, cores cut, various additional sample measurements made, and both conventional and special logs run to obtain other desired petrophysical information.

As mentioned previously, this chapter does not deal with log analysis, the petrophysical evaluations made when no core, mud log, or tester data are available. Log analysis is used universally and is generally successful in the identification of oil and gas reservoirs and in the preliminary estimation of their volumes.¹⁻⁷ However, log analysis augmented and calibrated with core⁸ and other data provides the most accurate quantification of oil and gas volumes present in a well and best represents the practice of petrophysics.

This chapter is focused on petrophysical calculations at the reservoir level, where there are several to hundreds of wells with logs and significant amounts of core data that need to be integrated to develop the most accurate overall values for the petrophysical parameters over the whole of the reservoir. The techniques discussed also apply to single wellbores, but many of the complications are not a concern in single-well evaluation.

This chapter does not cover some special cases, such as oil shales, tight gas-sand reservoirs, or coalbed-methane reservoirs. Petrophysical calculations for tight gas-sand reservoirs and coalbed-methane reservoirs are discussed in separate chapters on these topics in the *Emerging and Peripheral Technologies* volume of this *Handbook*.

3H.2 Petrophysical Data Sources and Databases

In making the petrophysical calculations of lithology, net pay, porosity, water saturation, and permeability at the reservoir level, the development of a complete petrophysical database is the critical first step. This section describes the requirements for creating such a database before making any of these calculations. The topic is divided into four parts: inventory of existing petrophysical data; evaluation of the quality of existing data; conditioning the data for reservoir parameter calculations; and acquisition of additional petrophysical data, where needed. The overall goal of developing the petrophysical database is to use as much valid data as possible to develop the best standard from which to make the calculations of the petrophysical parameters.

3H.2.1 Inventory of Existing Petrophysical Data. To start the petrophysical calculations, the data that have been gathered previously from various wellbores throughout the reservoir must be identified, organized, and put into electronic form for future calculations.

In a typical reservoir, several “generations” of wells have been drilled. The exploration wells that discover and delineate the reservoir constitute the first generation of wells. These wells are usually drilled with scant knowledge of formation pressure, which results in deep mud-filtrate invasion in the reservoir interval for which there may be significant hole-washout problems. For this series of wells, the muds used may vary from one well to the next, and this phase may take from 1 to 10 years to complete. The second generation is the group of wells drilled during initial reservoir development. These wells are likely to be drilled with a common mud system, which might be either water-based or oil-based and will be tailored to help minimize the near-wellbore damage caused by detrimental mud-filtrate/reservoir-rock interactions. Third-generation wells may also be available. These wells would be those from later field-

development activities and may have been drilled 5 to 15 years after the initial development wells were drilled.

The logs from these various generations of wells can vary in several regards. First, the logs may have been run by various service companies and may not be directly comparable to each other, even if they were from the same time period. Secondly, if the logs were run by the same service company, they may still have significant differences because different generations of logging tools were used for each set of wells. An additional difference may be between logging-while-drilling (LWD) logs and those run on wireline. LWD logging is often associated with high-angle wells. This geometry can lead to significantly different responses from zones previously seen in vertical wells and may lead to petrophysical mapping issues for high-angle-well evaluations, if not correctly accounted for.

Many of these same caveats hold for core data. The early wells may or may not have been completely cored through the reservoir interval. Later wells are more likely to be fully cored, although some zones of particular interest may have a greater concentration of cores. The routine data acquisition from cores also may vary because of different laboratories performing the core analysis on each well and because of changes in laboratory procedures and equipment over the intervening years. Also, different portions of the reservoir interval may have been analyzed with different techniques because they differ in degree of consolidation or rock heterogeneity. Special-core-analysis (SCAL) data are likely to be a variety of information because the SCAL programs for each well's cores will be unique to the perceived data needs when each well was drilled. With respect to the geologists' core descriptions, there may be differences between wells because different individuals prepared the various core descriptions with different techniques and emphasis. The number of petrographic measurements on cores [e.g., thin sections, scanning electron microscope (SEM), and X-ray diffraction (XRD)] is likely to vary widely from well to well.

First, the technical team must prepare several spreadsheets tabulating the basic information about each of the drilled wells. **Tables 3H.1 through 3H.3** show templates for a spreadsheet for the log data and two for the core data, respectively. These spreadsheets provide quick access by the technical team to see what data are available, what form the data are in, how much of each type of data is available, and where gaps exist in the database. Separate sets of spreadsheets should be prepared for each of the reservoirs, if there are several separate reservoirs in a particular oil or gas field.

Next, as much as possible of these detailed log and core data should be obtained in electronic form. There are a number of commercially available software packages that are useful for this purpose and can be used to access the log data and the routine-core-analysis data. However, the routine-core-analysis data may also be entered into spreadsheet form for easy use by the engineers and geoscientists. To the extent possible, the geologists' core descriptions and petrographic measurements should be converted to electronic form for use with the other types of petrophysical data. The SCAL data will require special spreadsheet formats because each of these types of data is unique.

Core and log databases should be considered as a part of the overall reservoir database. In establishing and maintaining the overall reservoir database, controls should be in place to ensure high quality of the data and the timely inclusion of all data that are obtained.

3H.2.2 Evaluation of the Quality of Existing Data. The second step in working with the petrophysical data is to evaluate the quality of each of these types of data. This step requires that the data inventory and database preparation steps are completed first so that this second step can occur as a systematic and complete process. The evaluation process is a “compare and contrast” exercise.

TABLE 3H.1—LOG DATABASE FOR EXPLORATION AND DEVELOPMENT WELLS

Well	Resistivity	Sonic	Density	Neutron	Gamma	Tester	Dip/Image	Other
E1	DIL, DLL, IES	LSS, BHC	FDC	CNL	GR	RFT	HDT	VSP, CST
E2	DIL	DDBHC	LDL	CNL	NGS, GR		HDT	CST
E3	DIL, DLL	LSS, DDBHC	LDL	CNL	GR			BGT
E4	DIL	LSS	LDL	CNL	GR	RFT	SHDT	VSP, CST
E6	DIL	LSS	LDL	CNL	GR	RFT	SHDT	VSP, CST
E8	DIT	BHC	LDL	CNL	GR	RFT	SHDT	VSP, CST
D1	AIT	DSI	LDL	DNL	NGS	RFT	UBI, OBDT	VSP
D2	AIT	DSI	LDL	DNL	NGS	RFT	UBI	VSP
D3	AIT	DSI	LDL	DNL	NGS	RFT	UBI	CS
D4	AIT	DSI	LDL	DNL	NGS	RFT	UBI	
D5	AIT	DSI	LDL	DNL	NGS	RFT	UBI	
D6	AIT	DSI	LDL	DNL	NGS	RFT	UBI	CS
D7	AIT	DSI	LDL	CNL, APS	NGS	MDT		
D8	AIT, CDR	DSI	ADN	ADN	GR	MDT		
D9	AIT	DSI	LDL	APS	NGS	MDT	UBI	

Note: ADN=azimuthal density neutron (logging while drilling); AIT=array induction tool; APS=accelerator porosity sonde; CDR=compensated dual resistivity (logging while drilling); CNL=compensated neutron log; CS=checkshot survey; CST=chronological sample taker; DIL=dual induction log; DIT-E=phasor dual induction log; DLL=dual laterolog; DNL=dual detector (thermal-epithermal) compensated neutron log; DSI=dipole sonic imager; GR=gamma ray; HDT=high-resolution dipmeter tool; IES=induction electrical survey (deep induction only); LDL=lithodensity log; LSS=long-spaced sonic; MDT=multidynamic tester; NGS=natural gamma ray spectroscopy tool; OBDT=oil-based dipmeter tool; RFT=repeat formation tester; SHDT=stratigraphic high-resolution dipmeter tool; UBI=ultrasonic borehole imager; and VSP=vertical seismic profile.

Log Data. The evaluation of log-data quality has many aspects.⁷ First, the drilling-mud and hole-condition effects may lead to no valid readings being recorded on the logs. This should be noted in the petrophysical database. “Flags” of various types should be stored, for example, to denote intervals where the hole size exceeds some limit, or where there is cycle-skipping on the sonic logs. Logging tools sometimes become temporarily stuck as a log is being run. This results in constant readings on each of the several detectors on the tool string. When the tool is stationary, each detector on it becomes stuck at a different depth, so the interval of “stuck” log will vary for each log curve. For example, the neutron log typically sticks over an interval approximately 10 ft above the stuck interval on a density log. It may be possible to “splice” in a replacement section of log from a repeated log section, or the invalid readings may simply be deleted.

Second, each log is formally calibrated before the start of each logging run by various calibration standards. The logs are also checked again after the run. Calibration records may assist in determining the quality of the logs. Perhaps of equal importance are the written comments on the log heading made immediately after the job by the logging engineer.

Third, systematic influences on the quality of log readings should be corrected. For example, if some of the wells are drilled with water-based mud (WBM), the effect of WBM-filtrate invasion on various resistivity logs can be quantified. This is done by computations made using the various resistivity logs in the same wellbore; however, where deep invasion of WBM filtrate occurs, offsetting wells drilled with oil-based mud (OBM) give a good comparison. The induction logs in OBM wells can provide accurate true reservoir resistivity values in thick hydrocarbon zones. See the chapter on resistivity and SP logging in this volume of the *Handbook*

TABLE 3H.2—ROUTINE-CORE-ANALYSIS PROCEDURE BY WELL

Well	Plug Type	Laboratory No.	Net Confining Pressure (psi)	Porosity	Permeability	S_w
E2	H	1	350	Yes	Yes	No
E3	H,V	2	250	Yes	Yes	No
E3	H	1	350	Yes	Yes	No
E4	H,V	2	250	Yes	Yes	No
E5	H	2	250	Yes	Yes	No
D1	H	3	800 (CMS)	Yes	Yes	Yes
D3	H	3	800 (CMS)	Yes	Yes	Yes
D8	H	1	800 (CMS)	Yes	Yes	Yes
D9	H	1	800 (CMS)	Yes	Yes	Yes
D9	H	3	800 (CMS)	Yes	Yes	Yes

Note: H=horizontal core plugs, V=vertical core plugs, and CMS is an abbreviation for Core Measurement Systems.³

TABLE 3H.3—SUMMARY OF THE NUMBER OF ROUTINE CORE ANALYSES BY WELL AND BY ZONE

Well	E2	E3	E4	E5	D1	D3	D8	D9	Total
Reservoir No. 1 (by zone)									
1	0	47	18	35	14	117	0	0	231
2	0	0	0	49	91	108	0	136	384
3	70	0	0	52	99	96	0	0	317
4	53	0	121	56	123	136	0	0	489
5	0	0	0	88	94	108	0	0	290
6	0	59	116	12	43	92	0	0	322
Total	123	106	255	292	464	657	0	136	2033
Reservoir No. 2	0	0	0	0	0	0	177	0	177
Reservoir No. 3	0	0	44	0	0	42	0	0	86

Note: Tabulation is based on the number of horizontal core plugs and the number of porosity measurements.

for more information on how invasion effects can be handled. Boreholes are not always right cylinders. Holes sometimes become spiral shaped during the drilling process, and their logs show sinusoidal responses.

Routine-Core-Analysis Data. The evaluation of the quality of routine-core-analysis⁹⁻¹¹ data starts with crossplot comparisons of various wells' porosity, permeability, grain density, and saturation data on a reservoir or zone basis. With various wells' data presented on the same plot (permeability vs. porosity, grain density vs. porosity, S_w vs. permeability, or S_w vs. porosity), one can determine if there are significantly different trends from one well to the next. Differences may exist, and there may be good geologic reasons for such differences; however, some laboratory data may be of suspect quality and may require further review and inquiry.

With respect to core's fluid-saturation data, the evaluation process must be an end-to-end review process. This evaluation begins with knowledge of the drilling mud used and whether

the cores were specially cut and preserved to try to obtain undisturbed connate S_w . Second, review the core sampling and routine-core-analysis laboratory procedures to understand how those steps impacted the final fluid-saturation data reported. Well-preserved OBM cores that are analyzed using the Dean-Stark water-extraction procedure typically provide the most valid values for connate S_w in the hydrocarbon column above the mobile gas/water or oil/water transition zone. In aquifers and other mobile-water intervals, OBM-filtrate invasion displaces mobile water during core cutting, and fluid “bleeding” occurs during core surfacing. As a result, OBM-core water saturations are too low and not representative of true resident saturations. They may also be more uncertain in very poor quality, high- S_w rock intervals in which it is difficult to make accurate porosity and water-volume determinations.

WBM cores can provide a qualitative measure of residual-oil saturations in the oil column after accounting for oil shrinkage and bleeding.¹² WBM cores in oil reservoirs may also provide information about oil/water contacts (OWCs) and the S_w of low-quality rock intervals above the OWC into which oil has never entered because the entry capillary pressure, P_{ce} , has not been exceeded.

The OBM and WBM routine-core-analysis data should be compared and contrasted to identify how each alone, and in combination, can be used to answer certain petrophysical issues. Also, the trends of these sets of data (e.g., permeability vs. porosity) should be compared as one of the evaluation tools.

Coring in friable, uncemented, and unconsolidated sands demands special coring, handling, and analysis techniques so that the grain structure is not altered. Modern practice is to use rapid drilling rates and fiberglass or aluminum inner core barrels to minimize the friction as the core enters the barrel. The core is tripped to surface slowly and smoothly to allow dissolved gas to exit the core without disruption. The last two stands of drillpipe are the most critical because during this time the volume of gas doubles, then quadruples. During the laying down of the inner core barrel, precautions are needed to prevent bending and core deformation. For transporting the core, the inner core barrel can be cut into short (1-m/3-ft) lengths, the ends sealed with caps, then the voids between the core and the sections of the inner core barrel filled with resin. Freezing the cores in their segments before transportation is sometimes used to prevent damage, but is not very effective when there is little formation water. The costs are also higher. Cross-section X-raying of the tubes reveals which cores are damaged and which are suitable for measurements in the laboratory. See the American Petroleum Institute's (API) *RP 40 Recommended Practices for Core Analysis* for details about the various types of core analysis and details of the laboratory procedures.¹³

Special Core Analysis Laboratory Data. SCAL-data evaluation begins with a comparison of the same type of data from different laboratories and whether data from each laboratory are internally consistent. SCAL data are much more difficult to measure, and the procedures often differ from laboratory to laboratory. The challenge is to determine which of these data are more correct and should be used to make various petrophysical-parameter calculations. With SCAL data, the best approach is to have those individuals who are expert in taking and evaluating these types of data review the procedures of the various laboratories and the reported data and provide an opinion about which of these data should be used and which should be discarded.

Capillary pressure (P_c/S_w) data can be susceptible to not being taken to fully equilibrated conditions because it occasionally takes longer for equilibrium to occur than typical laboratory procedures require. This is because the relative permeability of the wetting phase becomes so low that equilibrium is very slowly reached. Additionally, the porous-plate method is susceptible to loss of capillary contact between the core plug and the porous plate. In both situations at higher capillary pressure, P_c , reported S_w values will be too high.¹⁴

For the rock electrical-property laboratory measurements and how they are reported, the raw laboratory data should be reviewed very carefully to ensure that the data are of high quality and are properly reported for later S_w calculations. These measurements, as a function of brine saturation, again have the potential problem of nonequilibrium saturation distributions. Sometimes the saturation exponent, n , is a function of brine saturation, but this nonlinear behavior is typically not reported as such by the reporting laboratory. Restoration of the in-situ brine-saturation distribution is absolutely required for making laboratory rock-electrical-property and P_c measurements that lead to accurate reservoir S_w calculations, so it is best if any restored-state core-plug measurements agree with similar measurements made on native-state core plugs. Finally, the resistivity index (I_R) vs. S_w data should be taken over a range of S_w values equivalent to those found in the particular reservoir. Sometimes these data are taken only down to 30% pore volume (PV) S_w , yet some of the in-situ S_w values may be in the 5 to 20% PV saturation range. If this is the case, laboratory electrical-property measurements may not lead to accurate in-situ S_w calculations from resistivity logs for the low S_w values.

Internal consistency in a laboratory's reported results is a very good "first test" to determine if some of the data are immediately suspect. For example, if the measurements of the reduction in porosity from surface to reservoir stress vary from one set of measurements to another for a particular laboratory, then those measurements must be discarded or used very carefully. As another example, with respect to P_c /saturation measurements, there is an immediate concern if the air/water and air/oil P_c /saturation measurements do not reasonably overlay after accounting for the interfacial-tension (IFT) and contact angle difference between these fluid pairs. There would be a similar concern when mercury-injection P_c data are available. Again, experts in taking and using these types of data should evaluate the quality of the various sets of laboratory measurements.

3H.2.3 Conditioning the Data for Reservoir Parameter Calculations. Conditioning the log and core data for calculations of the various petrophysical parameters includes adjustments from surface-to-reservoir conditions, normalization, and environmental-correction factors. The emphasis here is on obtaining, at reservoir conditions, a set of reliable petrophysical data that involve many wells with many sets of log data and a variety of routine and SCAL core measurements.

Log Data. Each type of log data may need to be conditioned in unique ways for the subsequent petrophysical-parameter calculations. The purpose of each of these preliminary sets of calculations is to put that portion of the overall petrophysical database on a common basis.

The log data, as a whole for each well, must be depth aligned so that the various log measurements at each depth refer, as closely as possible, to the same rock volume. Differences in log response characteristics and in each tool's path in the hole make this a complex task. Lining up the bed boundaries is particularly important. Some commercial software programs have automatic routines that perform the depth-alignment process, but, more often, shifts are made manually. Borehole-size corrections are required for most logs, while the readings of some tools require correction for other factors, such as temperature, mud density, and mud resistivity.

Histograms are often used to compare the log values of one well with the typical field values of the same log type. This process can identify logs that are miscalibrated, and it may indicate by how much they should be corrected. Bad logs that cannot be corrected by reasonable shifts should be discarded from the database.

Gamma Ray Logs. For reservoir-wide petrophysical calculations, gamma ray (GR) logs are often normalized to reduce the variation in their values from one well to the next in intervals that are considered to have the same rock properties, usually clean sands and specific thick shale intervals.

Density and Neutron Logs. Log calibrations³⁻⁷ can be checked in situ because they read nearly constant values in certain formations. Anhydrite has a density value of 2.98 g/cm³ and close to zero neutron porosity, while salt has a density value of 2.04 g/cm³ and zero neutron porosity. There are few “marker” beds in which higher neutron-log readings can be verified. (See the chapter on Nuclear Logging in this volume of the *Handbook*.)

Sonic Logs. Sonic logs read near-constant velocity values inside steel casing (57 μ sec/ft) and in evaporate formations such as anhydrite (50 μ sec/ft) and salt (67 μ sec/ft). Where they occur, these constant values are used to check the correct operation of the compressional-wave travel-time tool.

Resistivity (Laterolog and Induction) Logs. One of the main goals in developing the reservoirwide petrophysical database is to provide the most accurate true resistivity values for subsequent S_w calculations. (See the chapter on resistivity and SP logging in this section of the *Handbook* for information on electric logging.) Often there are several generations of laterolog and induction-logging devices that were run in the various wellbores, and this leads to a variety of data sources with different depths of investigation. Also, over the past two decades, various calculation techniques have been published to deconvolve the reported foot-by-foot resistivity values to obtain more-accurate estimates of true resistivity, R_t .^{15,16} Some of the more modern induction tools incorporate deconvolution into the wellsite processing.¹⁶

Routine-Core-Analysis and SCAL Data. To prepare the routine-core-analysis data for use in reservoir petrophysical calculations, most of these data require adjustment from surface to reservoir conditions.

One of the first steps is aligning core data to depth-aligned log data. Frequently, a GR log of the core is measured in the laboratory, and this is used to depth match the core to the in-situ GR log. Also, in a sandstone with occasional shale intervals of low permeability, the core-analysis data must be aligned with those obvious from the downhole GR log. The log data are often digitized on a half-foot basis, but the core data are typically on a one-foot basis. As these different types of data are included in the same electronic database, care must be taken to ensure that some of the individual data points are not lost. This is likely to require a significant degree of user intervention. The core data for a particular well are really several subsets of data, each of which comes from an individual core-barrel run. These subsets of data must be kept together, and each may need to be individually depth-shifted to the log data.

Porosity Data. For the routine-core-analysis porosity data, SCAL measurements of core samples' porosity at various confining-stress levels are used as the basis for making compaction corrections. Historically, routine-core-analysis porosity measurements were taken at low stress conditions, and SCAL measurements on a small set (10 to 30) of core plugs were made to determine the relationship of porosity to overburden-stress level. Stressed-porosity values are plotted vs. laboratory stressed-porosity values to determine the relationship between the two. Regression of the porosity difference vs. surface porosity gives the same result as regressing stressed porosity vs. surface porosity. Two factors are important to consider in analyzing these plots: whether or not there is a systematic “baseline” laboratory effect related to the equipment's coreholder tightening against the core plug at the start of the test procedure, and whether there is a systematic relationship. Theoretically, the change in porosity is a function of porosity level; however, many sets of SCAL experimental data indicate the “baseline” effect can dominate the second effect.

In the past decade, an unsteady-state style of equipment has come into fairly common usage in which routine porosity measurements can be made at both low-stress and high-stress conditions.⁹ With this equipment, reservoir-stress-level porosity measurements can be made on each and every core plug during the routine-core-analysis testing; however, typically, high-stress porosity measurements are made only on every fifth or tenth sample for later use in making the porosity adjustment from surface to reservoir conditions.

For some oil reservoirs, or OBM cores, there is a second adjustment that may need to be applied. This effect is that the routine-core-analysis procedures did not clean all of the heavy hydrocarbons from the pore space, and, hence, the measured porosity values are understated. This effect can be evaluated two ways: first, the measured grain densities may appear to be lower than expected for the particular rock type (i.e., grain densities of less than 2.65 g/cm³ for clean sandstones); and second, if some of the routine core plugs are retested later, the cleaning solvent is found to discolor, and subsequent porosity values are found to be systematically higher than the original values. This second effect [0.5 to 1.0% bulk volume (BV)] can be as large as the stress-related porosity-reduction effect discussed in the previous paragraphs.

Permeability Data. For the routine-core-analysis permeability data, SCAL measurements of core samples' permeability at various stress levels are used as the basis for making compaction corrections. Historically, routine-core-analysis permeability measurements were taken at low-stress conditions, and SCAL measurements on a small set (10 to 30) of core plugs were made to determine the relationship of permeability to stress level. The “permeability ratio” values (stressed permeability divided by surface permeability) need to be plotted vs. surface-permeability values to determine the relationship, likely to be nonlinear, between the two. Determination of permeability at reservoir conditions is especially important in rocks with air permeabilities of less than 20 md. For low-permeability samples (< 2 md), reductions in permeability of 1 to 2 orders of magnitude have been observed between values at ambient conditions and those at reservoir stress levels.

OBM S_w Data. For routine-core-analysis S_w data from OBM cores, the adjustment from the surface values to those at reservoir conditions requires the application of several factors. First, the pore-volume reduction, as a result of the porosity adjustment discussed previously and because of the change in size of the core plug at stressed conditions, must be applied to the S_w data. Second, the water volume and S_w must be increased because of the effects of reservoir temperature and pressure, salinity, and gas in solution.

Other SCAL Measurements. For other SCAL measurements, some conditioning of these data may be required. For example, for the P_c/S_w data, the data must be converted from surface to reservoir conditions and a height-above-the-OWC (H_{owc}) basis by accounting for the oil/water or gas/water density difference at reservoir conditions and the change in IFT and contact angle between surface and reservoir conditions.

The SCAL electrical-property measurements of a , m , and n (and possibly Q_v , a^* , m^* , and n^*) will need to be considered in the light of the theoretical model that will be used to make S_w calculations from resistivity-log data. Many shaly-sand relationships for estimating S_w from R_t have been proposed.^{3,8} These parameters are sometimes measured at overburden conditions.

Other Relevant Data. There are various other types of wellbore data that may need to be inventoried, organized, reviewed, and considered when making the various petrophysical calculations. Other wellbore data that can be particularly important include mud-log data, formation-pressure surveys, formation-tester fluid samples, drillstem-test fluid samples, and 3D-seismic data. Sections 3H.6 and 3H.7 discuss the uses of these data for the fluids-contact identification and for the S_w calculations.

3H.2.4 Acquisition of Additional Petrophysical Data, Where Critically Needed. Often when a new petrophysical evaluation of a reservoir is undertaken, there are significant gaps in the overall database after the existing data have been inventoried and evaluated. It is possible that an acceptable petrophysical evaluation can be completed within the constraints and limitations of the available data, but sometimes additional data are needed. These new data, typically additional SCAL data or possibly routine-core-analysis data, can be obtained from two sources: additional experimental measurements on core plugs taken from existing cores; and drilling,

logging, and coring new wells to obtain the needed data. The second approach is used only if such expensive data gathering is required and economically justified.

To obtain additional data from existing cores, geologists can redescribe existing cores as needed. Additional porosity and permeability measurements can be made on newly cut core plugs from any of these cores. Additional valid fluid-saturation measurements might be made on well-preserved core samples; however, such measurements have to be checked carefully because such core samples often dry out over the years. Samples can be cut for more SCAL measurements if the experts consider that the rock samples can be restored for such testing.

In some cases, the need for additional data can justify the drilling of one or more new wells in which cores are cut and routine and special logs are run. In certain equity-redetermination situations, additional wells at specific locations have been drilled to gather additional data about the reservoir interval to more accurately calculate net pay, porosity, and water saturation. For some proposed reservoir-development projects, expensive new data, often of a special nature, can be economically justified because a new well can reduce risk and improve the likelihood of project success.

3H.3 Lithology Determination

Understanding reservoir lithology is the foundation from which all other petrophysical calculations are made. To make accurate petrophysical calculations of porosity, S_w , and permeability, the various lithologies of the reservoir interval must be identified and their implications understood. Lithology means “the composition or type of rock such as sandstone or limestone.”¹⁷ These few words belie a host of details about reservoir rocks, their depositional and diagenetic history, pore structure, and mineralogy. Geologists are trained to describe rocks, based on outcrops, cuttings, cores, and more-detailed mineralogical measurements, and they identify certain log-curve characteristics related to particular depositional environments (i.e., coarsening upwards, fining upwards, massive bedding, and the scales of interbedding). For reservoir petrophysical evaluations, a geologist must be on the technical team, and there must be cooperation between the geologists and engineers.

The lithology of a new oil or gas reservoir is understood on a preliminary basis by the wellsite geologist’s description of mud-shaker cuttings and possibly by a few cores that are cut if the reservoir interval is sufficiently long. Lithology is also determined from the logs, because each main reservoir lithology has characteristic responses. Frequently, lithologies are derived by pattern recognition of the GR-, density-, and neutron-log responses.

Some subsequent delineation wells are likely to be cored over the entire of the reservoir interval. The geologist will make detailed descriptions of these cores and order a number of thin-section, SEM, XRD, and mercury-injection capillary pressure (MICP) or pore-size measurements on various rock types that have been identified. From these data and the routine-core-analysis data, geologists can construct their interpretation of the reservoir’s depositional environment and insights into the nature of its pore system and mineralogy. Geologists typically prepare reservoir cross sections with seismic traces, well logs, and core descriptions to illustrate the depositional environments, rock types, and internal geometries. See the chapter on Reservoir Geology in this volume of the *Handbook* for additional discussion of geologic aspects of oil and gas reservoirs.

The lithology of a reservoir impacts the petrophysical calculations in numerous ways. The depositional environment and sediments being deposited will define the grain size, its sorting, and its distribution within the reservoir interval. In most sandstone reservoirs, the depositional environment controls the porosity/permeability relationship (see the chapter on permeability in the General Engineering volume of this *Handbook* for additional details about the controls on the absolute permeability because of grain size and rock sorting).

The mineralogy of a reservoir results from a combination of its depositional and diagenetic histories. For a sandstone reservoir, the depositional environment controls the percentages of

quartz, chert, feldspar, and detrital clay-mineral grains and the other matrix material. These materials must be measured and their variations within the reservoir interval quantified. The diagenetic history determines the extent to which portions of the grains have been leached away; cements such as calcite, siderite, or pyrite have been deposited; and authigenetic clay minerals formed. The diagenetic history can be complicated and can be impacted by differences in burial history from one part of a reservoir to other parts, or by aspects of the hydrocarbon-filling history.

For carbonate reservoirs, most of the same factors as discussed for sandstones come into play, but the mineralogical considerations are different. For carbonate formations, the rock formations typically consist of interbedded sequences of carbonates, dolomites, anhydrite, salt, and shale layers. The keys to reservoir development within the carbonate layers are the original grain size and how it has been altered by chemical diagenetic processes. As these chemical reactions take place, the pore-size distribution and porosity level will change (e.g., by dolomitization). Carbonate-reservoir porosity is also greatly enhanced by weathering, dissolution, and fracturing.

As well as the basic mineralogy, clay-mineral properties are also of particular importance to the petrophysical calculations in the reservoir intervals. There are many types of clay minerals, and their impacts on well logs are quite different. Particularly, there may be differences between clay minerals that form shale layers and claystones and those that occur within sandstone intervals. While the detrital clay minerals in sandstones will likely be the same as the clay minerals in the shales, the authigenetic clay minerals in the sandstone pore system can be quite different. The types and amounts of the various clay minerals impact the rock pore system by affecting its electrical properties and permeability characteristics (see [Sec. 3H.3.1](#)). A few of the aspects of mineralogy that impact the petrophysical calculations are the extent to which various heavy minerals (e.g., anhydrite, calcite, dolomite, granites, pyrite, siderite) impact the density log; various light minerals (e.g., coal, halite salt) impact the density, neutron, and sonic logs; various radioactive minerals (e.g., uranium, thorium, and potassium salts such as K-feldspar) impact the GR log; and various electrically conductive minerals (e.g., clay minerals and pyrite) impact the resistivity logs.

3H.3.1 Clay-Mineral Properties. Clay minerals are, in general, composed of layered alumina and silicate molecules,^{8,18,19} and the properties of the various clay minerals vary widely. Some swell when wet, are plastic, and can easily deform, while others are hard and dense. Clay minerals are extremely fine-grained, and those with the smallest grain size have a very high surface-area-to-volume ratio. Clay minerals (e.g., chlorite, illite, kaolinite, smectites, and mixed-layer clays) generally impair the permeability and porosity of the pores in which they reside; the permeability is sometimes impacted by an order of magnitude or more. However, it is the smectites (one of which is montmorillonite) that often cause very significant effects on the petrophysical measurements of porosity and water saturation.

In smectites, exchange cations and adsorbed water molecules are loosely bound between the silicate layers. Dehydration occurs whenever there is low humidity or an elevated temperature (e.g., in a dried-up lakebed or in a brick kiln). Loss of this adsorbed water is even more rapid at temperatures above the boiling point of water. For smectites, this is a problem during core analysis because the extraction and drying of the core samples is an essential step in the measurement procedures.

For resistivity logging, smectite clay minerals pose a further problem. The exchange cations and adsorbed water molecules lead to smectite exhibiting excess electrical conductivity. This occurs as exchange cations (e.g., sodium, calcium) migrate from site to site on the clay surfaces. The clays thus exhibit a lower resistivity and, in most cases, depress the bulk resistivity

of reservoir rocks in which they reside. Cation exchange also occurs with the other clay minerals, but to a lesser extent.

Rock formations of pure clay minerals are rare. More typically, several species of clay mineral are associated together with clay-sized and silt-sized quartz, mica, and other rock grains. This association is known widely as “shale.” In sandstone reservoirs, clay-mineral content typically ranges from 0 to approximately 10% BV. In shales, clay minerals occupy approximately 20 to 40% BV, and the remainder is often very-fine-grained quartz, volcanic minerals, carbonates, and organic matter. Besides the adsorbed water on the clay minerals, shales and authigenic clay minerals also include additional formation water held in their micron-sized pore system by capillary retention. This water cannot be produced from the formation and is referred to as “capillary water.”

During the burial of the sediments over geological time, the overburden stress and the pore-fluid pressures increase. The net result is that water is expelled from the shale beds into surrounding permeable beds. Young clay-mineral-bearing sediments at shallow burial depths are likely to be smectites (e.g., gumbo shale in the submerged Mississippi delta of Louisiana, U.S.A.). Clay minerals in deeply buried shales become less hydrated, and their forms can be altered by higher temperatures and pressures. Low-salinity water is sometimes observed in reservoir-rock pores adjacent to the shales and where clay-mineral-expelled water cannot escape from the permeable bed. This formation may become overpressured and can cause severe problems during drilling if not predicted or detected in time to alter the drilling program.

Although shale formations are not usually of commercial importance, the measurement and evaluation of core and log data in partly shaly reservoirs presents many difficulties that are not present in clay-mineral-free (clean) formations. A large body of technical literature addresses shaly-formation analysis because the shale, to one degree or another, affects all log and core measurements. Because these shaly rocks are so variable, a single model usually cannot fully describe all of their behaviors.

Reservoirs with a fractional shale content, V_{sh} , are common, and the clay minerals/shales take several physical forms, including laminated, structural, and pore-filling.^{3,8} Laminated shales are thin detrital shale layers interbedded within a reservoir interval. Each represents short periods of deposition where the suspended finest sediments could settle out of the original sediment-rich river, lake, or seawater. Laminated shales may range from approximately one hundredth of a centimeter to 1 m thick. Shale deposits can be broken up and reworked after their original deposition and become “grains” in the same manner as quartz grains. Structural, or detrital, shale grains become a part of the grain composition of sandstone. As well as the clay minerals that are deposited directly as solids from lakes and marine environments, they also may be deposited from in-situ formation-water solutions that are rich in dissolved minerals. These clay minerals are called “authigenic.” By this mechanism, the pores of sandstone may become partly filled with various clay minerals and other minerals. Of this type, illite, kaolinite, chlorite, and smectite clays are most common. Each can take several physical and chemical forms within a pore. Several generations of pore-filling clay minerals may be present, representing different periods of geological time when changes occurred in formation-water composition or depth of burial.

3H.3.2 Evaluation of Shale Volume. Geological techniques, like XRD, are available to identify clay-mineral species and to quantify rock-component volumes in physical specimens. Such analyses can help calibrate the log-based methods for estimating V_{sh} , the bulk-volume fraction of shale. V_{sh} from the GR log is frequently used to determine nonpay.

Shale content can be estimated from well logs by many techniques, because shale affects the readings of most logs. The task for a particular field is to identify an evaluation technique that is reasonably accurate and as simple as possible. A method using a combination of the

neutron and density logs is often applied for practical log analysis. Modern optimized simultaneous-equations log solutions²⁰ attempt to identify individual clay species. Nevertheless, for petrophysical studies for field development, it is the GR log that is probably used most frequently to evaluate V_{sh} . The GR-log readings are normalized to reduce hole-size variations and mud effects and differences among the tools. Normalization is achieved by finding typical GR values in the 100% “clean” sand and 100% shale formations for each well. These different endpoint values in each well are then equalized. The GR values in between the sand and shale levels are scaled to give V_{sh} values. The scaling is often linear, but nonlinear alternatives are available, if appropriate. Occasionally the GR log is affected by radioactive components that are not shale, and these need to be identified and assigned a revised V_{sh} . Water-based drilling muds sometimes contain high concentrations of potassium salts, and these may also lead to GR interpretation problems, such as invasion of potassium salts into the near-wellbore region.

The uncertainty of V_{sh} log evaluations is moderate to high. At low values, less than 30% BV, the authors estimate that V_{sh} may typically be accurate to approximately $\pm 10\%$ BV at one standard deviation (SD). At values greater than 30% BV, the uncertainty increases. The uncertainties affect nonpay bed-boundary evaluations; however, the V_{sh} uncertainty also seriously impacts the accuracy of the effective-porosity and S_w estimates when smectites, with their high clay-mineral adsorbed-water fraction, are present. If the clay species is different (illite or chlorite with little or no adsorbed water), then the V_{sh} uncertainty has a much-reduced impact on porosity, as is discussed in [Sec. 3H.5.3](#).

3H.3.3 Reservoir Zonation or Layering. An important conclusion from the geologists’ technical studies is a definition of the extent to which the reservoir needs to be subdivided either vertically or areally. Besides all of the information developed by the geologists from the detailed core descriptions, the routine-core-analysis and SCAL data need to be analyzed for such effects. This is accomplished by preparing, for different possible layering within the reservoir interval, a variety of crossplots such as \log_{10} (permeability) vs. porosity and OBM-core S_w vs. porosity or \log_{10} (permeability) and comparing the data clouds and trends of those plots from one possible layer to the next. Significant differences should be expected between reservoir intervals with different depositional environments and differences in grain size and sorting. Areal variations may occur across a given vertical zone within the reservoir because of varying distances from the sediment source, differences in the depositional environment in various areas, or varying diagenetic effects.

For accurate petrophysical calculations, most large reservoirs will probably require a number of vertical subdivisions, usually termed zones or layers. Typical zones for a reservoir are 50 to 150 ft (15 to 45 m) thick. Areally, several square miles of reservoir can usually be included together; however, if the reservoir covers tens of square miles, it is likely to require some areal subdivision for accurate petrophysical calculations.

A second consideration is the amount of available data of various types. If a reservoir has a large database of log and core data from many wells, then the number of these subdivisions is not impacted by the quantity of data. However, if some types of data are very limited, then this consideration may control the degree of vertical and areal subdivision that can be used for various petrophysical calculations. The same degree of subdivision may not be required for net-pay calculations relative to porosity calculations or for porosity calculations relative to S_w calculations. In summary, more-accurate vertical and areal petrophysical calculations are made if the reservoir is appropriately subdivided.^{21,22} [Fig. 3H.1](#) shows the vertical zonation used for the Prudhoe Bay field’s Sadlerochit reservoir. [Figs. 3H.2 through 3H.4](#) are example plots based on real reservoir data that show how rock properties within the same field can vary from one reservoir to another and from one vertical portion of a reservoir interval to other parts.

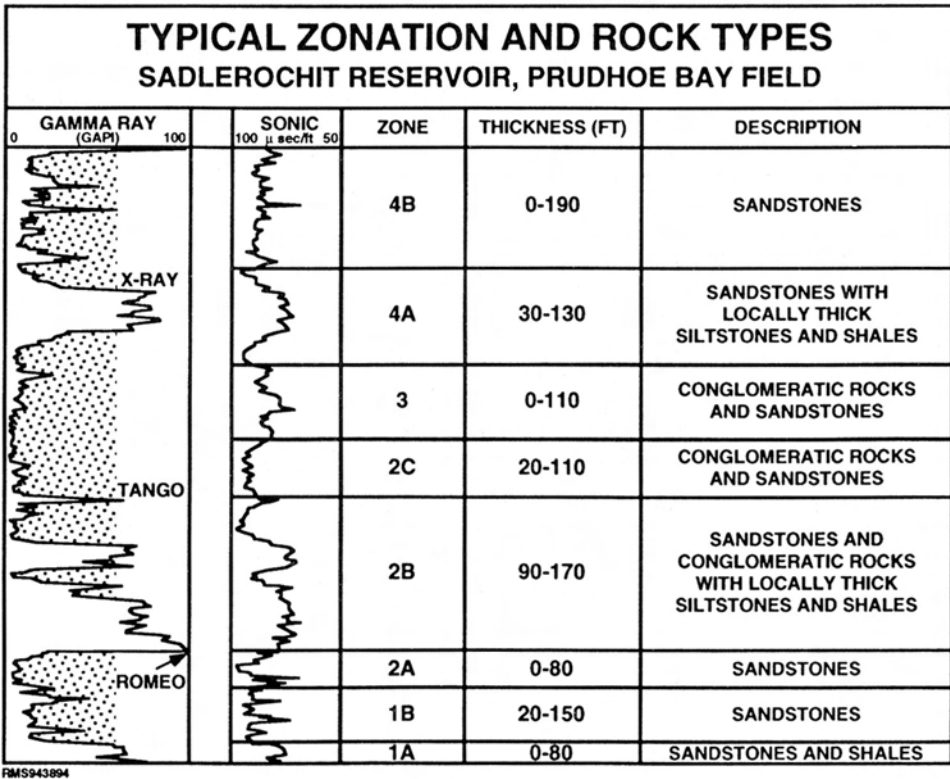


Fig. 3H.1—Reservoir zonation of the Sadlerochit reservoir, Prudhoe Bay field, Alaska, U.S.A.²¹

3H.4 Net-Pay (or Pay/Nonpay) Determination

The goal of the net-pay calculations is to eliminate nonproductive rock intervals and, from these calculations at the various wellbores, provide a solid basis for a quality 3D reservoir description and quantitative hydrocarbons-in-place and flow calculations. The determination of net pay is a required input to calculate the hydrocarbon pore feet, F_{HCP} , at a wellbore and its input to the overall reservoir OOIP or OGIP calculations. The total F_{HCP} at a well is the point-by-point summation over the reservoir interval with Eq. 3H.1. The top and base of the reservoir interval are defined by geologists on the basis of core descriptions and log characteristics.

$$F_{HCP} = \sum_{i=1}^{i=m} h_{ni} \phi_i (1 - S_w)_i \dots \dots \dots (3H.1)$$

In the F_{HCP} calculation, net pay, h_{ni} , at each data point has a value of either 1 (pay) or 0 (nonpay). The “net-to-gross ratio” or “net/gross” (N/G) is the total amount of pay footage divided by the total thickness of the reservoir interval (for simplicity, the well is assumed here to be vertical). A N/G of 1.0 means that the whole of the reservoir interval is pay footage. In this formula, any foot (or half foot) that is defined as nonpay contributes absolutely nothing to the subsequent reservoir-engineering OOIP (or OGIP) and reserves calculations, even if it contains some amount of hydrocarbons. The net-pay determination should be performed in a reasonable practical manner, but it should be recognized that when any cutoff is used, the result will, to

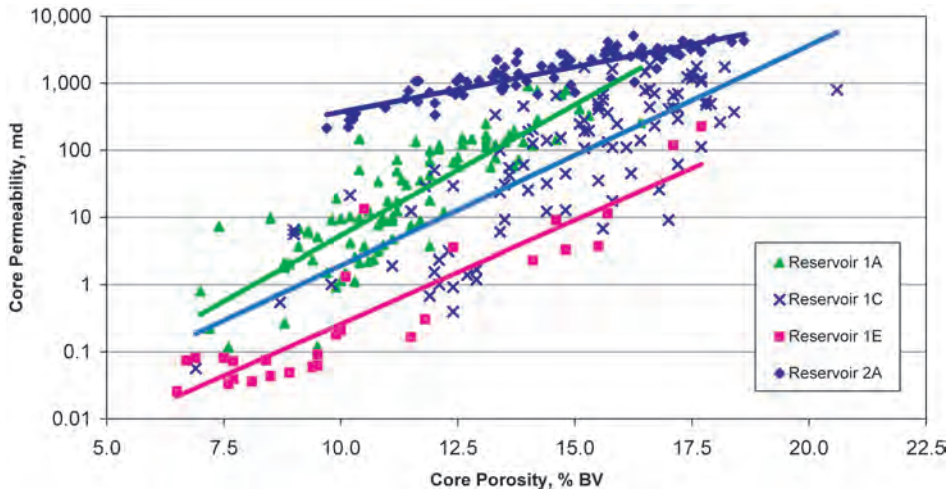


Fig. 3H.2—Typical reservoir permeability vs. porosity crossplot; data from an Asian gas field.

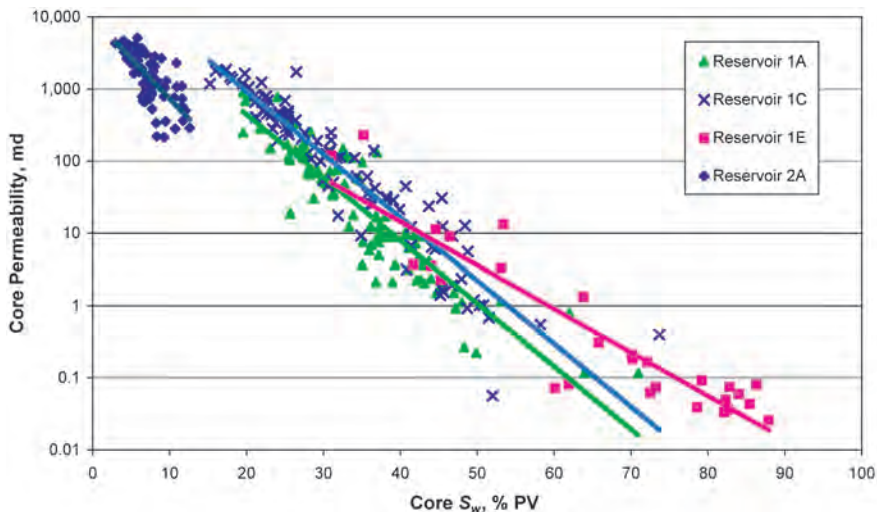


Fig. 3H.3—Typical reservoir permeability vs. S_w crossplot; data from an Asian gas field.

some extent, be arbitrary (see the chapter on reserves determination in this volume of the *Handbook*).

3H.4.1 Conceptual Bases for Net-Pay Calculations. Several conceptual bases for the petrophysical calculations of net pay are described here. At one limit, the whole of the reservoir interval can be treated as net pay (i.e., N/G equals 1.0). Another reasonable engineering approach is to define some lower limit on flow, below which each foot or half foot of the reservoir interval is deemed to be nonpay. A third approach is to use one or more log cutoffs that have been used historically within the petroleum industry. The advantages and disadvantages of these various approaches will be discussed in this section.

$N/G = 1.0$. One approach is to calculate the OOIP or OGIP assuming that all the reservoir interval is pay to determine the total volume of hydrocarbons present within the reservoir inter-

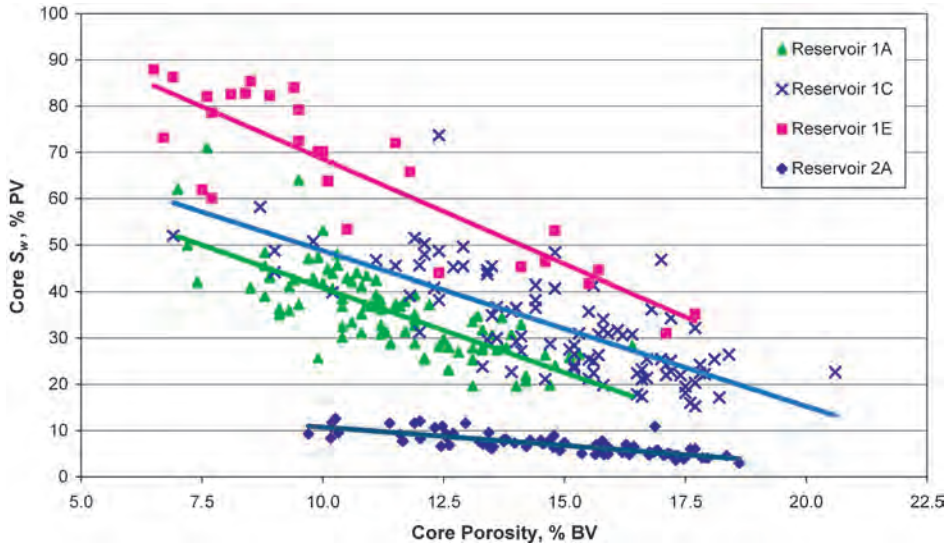


Fig. 3H.4—Typical reservoir S_w vs. porosity crossplot; data from an Asian gas field.

val. When using an $N/G = 1$ approach, the technical team needs to ensure that the calculations of porosity, permeability, and S_w are quantitatively reasonable over the whole range of values for each of these parameters. This calculation could be called a determination of the “total hydrocarbon resource” within the reservoir interval, and it provides a value for the total hydrocarbon potential of the reservoir. Some of these hydrocarbons will have low mobilities and will contribute little or nothing to hydrocarbon recovery. But, with this value available, the engineer has a measure of how well the reservoir is producing overall and what resources should be considered for improved-recovery-project evaluations. This value can be viewed as the ultimate “prize.”

Another reason for setting N/G to 1.0 is that, with modern reservoir-engineering tools, it is technically feasible to treat the entire reservoir interval as pay. For example, with modern reservoir-engineering tools, a million (or more) cell reservoir-simulation model can be constructed in which a very detailed description of the vertical and horizontal variations in the reservoir-rock properties are incorporated. In this approach, the very-poor-quality portions of the reservoir are assigned low porosities, low permeabilities, and higher water-saturation values. Then, in the OOIP or OGIP calculations, these portions contain only small volumes of hydrocarbons and will contribute their appropriate, albeit small, share to pressure maintenance and recoverable hydrocarbons. This is in contrast to defining these poor-quality intervals as nonpay and defining *a priori* that they contribute nothing to OOIP or OGIP or reserves.

Mobility or Permeability Cutoff Approach. From first-principle calculations using Darcy’s law, a reservoir engineer can define net pay by applying a fluid-flow cutoff. The choice of this cutoff would be related directly to the hydrocarbon mobility (rock permeability divided by hydrocarbon viscosity) in the different portions of the reservoir interval. With this approach, the net-pay permeability cutoff used in the point-by-point log calculations would be quite different between that for a gas reservoir (very low gas viscosity of approximately 0.02 cp), that for a light-oil reservoir (oil viscosity of 1 to 10 cp), and that for a heavy oil reservoir (oil viscosity of 10,000 cp or more).²³ Any portion of the reservoir interval that has a permeability at reservoir conditions below the cutoff would be defined to be nonpay. In the next section, the gas-reservoir situation is discussed separately from that for oil reservoirs.

The arbitrary nature of any net-pay cutoff is apparent when one notes the flow implications of using a permeability cutoff. If a rock interval has a permeability 1% greater than the cutoff value, it is included as net pay. However, if another rock interval has a permeability 1% less than the cutoff value, it is excluded as nonpay. The difference between the fluid-flow contributions from these two rock intervals is only 2%, yet one is allowed to contribute to the subsequent OOIP or OGIP and reserves calculations, while the other is not.

If a permeability cutoff is chosen, its application to the various wellbore data (cores and logs) generally takes three steps.²⁴ The first step is to apply the permeability cutoff to the routine-core-analysis permeability data. In this step, there are two checks that need to be made. First, a permeability/porosity plot needs to be prepared and outlier points identified. The outlier points need to be individually checked for validity. For example, a very-low-porosity shale sample may have dried out and a parting developed between the shale layers. This may lead to a very high permeability value that is not consistent with the rest of the rock characteristics. Bad routine-core-analysis data points should be excluded from the database. A second consideration is that often during the routine core analysis, the shale intervals are not sampled at the same frequency of core plugs as the other lithologies. This likelihood must be kept in mind in reviewing the routine-core-analysis database and in comparing the results of pay/nonpay calculations between cores and logs. The subsequent steps—the conversion of a permeability cutoff to a porosity or V_{sh} cutoff including the calibration of logs to the core standard, and the calculations from the logs of net pay for all wells over the reservoir interval—are discussed later in this section.

3H.4.2 Gas Reservoirs. For a gas reservoir being produced under pressure-depletion drive, any permeability cutoff applied should be very low. This is quite evident by the successful development of tight gas-sandstone reservoirs producing nearly 10 Bcf/D from 85,000 wells in the United States, some with average permeabilities in the microdarcy range (see the chapter on tight gas sands in the *Emerging and Peripheral Technologies* volume of this *Handbook* for additional details). In conventional gas reservoirs in which higher-quality rock intervals are interbedded with the poorer-quality ones, gas in the poorer-quality rocks will flow to the higher-quality rock intervals if there is any permeability between the two. An example calculation for gas flow from a 1-microdarcy layer with a pressure difference of 2,000 psi, over a thickness of 10 ft for an area of 10 acres, and for a period of 1 year shows that this layer would contribute 1 Bcf per year.

Because pressure-depletion-drive gas reservoirs are produced for decades and, if found at significant depths, have abandonment pressures less than 10% of their initial pressures, there are both long times and large pressure differentials to cause gas to flow from very-low-permeability and low-porosity rock intervals into higher-permeability conduits and on to the production wellbores. In many instances, the distance traveled to reach a higher-permeability layer is just a few feet vertically.

3H.4.3 Oil Reservoirs. For oil reservoirs, any permeability cutoff will be significantly higher than that for a gas reservoir, generally by a factor of 10 or 100 or more. A second aspect of oil reservoirs is that typically, only 10 to 20% of the OOIP will be produced by pressure-depletion drive (without assistance from gravity drainage) in which the pressure differential will affect all portions of the reservoir. However, during waterflooding, overall oil/water displacement efficiency will depend, in part, on how much of this displacement process occurs in poorer-quality oil-bearing rock intervals. Hence, the choice of oil-reservoir permeability cutoff needs to account for the oil/water relative permeability effects. Interwell injector/producer connectivity (or “floodability”) is not a topic of this chapter. Connectivity will affect recovery but is considered a separate issue apart from individual-wellbore calculations of net pay.

Any permeability cutoff cannot be directly applied to foot-by-foot log calculations of net pay because there is no log that quantitatively measures permeability. A permeability cutoff

typically is converted to a porosity cutoff and is subsequently applied to the logs through log porosity, bulk density, GR, or V_{sh} cutoffs. The procedures for applying a permeability cutoff to the logs are discussed later in this section.

3H.4.4 Other Historical Net Pay Cutoffs. The technical literature shows that a number of net-pay-cutoff approaches have been used over the years by petrophysicists, geologists, and reservoir engineers.^{23–26} These cutoffs are often simply stated as a particular value for porosity, V_{sh} , and/or S_w . The justification for those cutoffs is rarely stated. Geologists often provide their foot-by-foot pay/nonpay identifications (“picks”) with their detailed core descriptions.

In all cases, chosen cutoffs generally exclude poorer-quality rock intervals. The key issues become whether the cutoff is applied in an accurate, consistent, and systematic manner through net-pay calculations using log data and the volume of hydrocarbons that are excluded in the net-pay calculations. For example, geologists often define shales, and possibly siltstones and very shaly sandstones, as nonpay intervals; then the GR logs can be calibrated to this nonpay standard. A value of the geologists’ core descriptions in the net-pay determination is that core descriptions are generally more continuous than are the routine-core-analysis data.

Like the geologist’s criteria, porosity and V_{sh} cutoffs also exclude poorer-quality rocks because lower-porosity rocks also generally have lower permeability, higher water saturations, and little, if any, mobile oil. Higher V_{sh} values are generally indicative of more clay-mineral-rich rocks that also tend to have lower porosities, lower permeabilities, higher water saturations, and little, if any, mobile oil. If these two cutoffs are applied without consideration for flow implications, then some rock intervals containing significant volumes of hydrocarbons that can contribute significantly to production may be excluded before OOIP, OGIP, or reserves calculations.

An S_w cutoff is sometimes also used as a nonpay cutoff, often in addition to a porosity and/or V_{sh} cutoff. An S_w cutoff is typically justified on the basis that, at high S_w , gas or oil is immobile on the basis of relative permeability considerations. This approach does not account for, at original reservoir conditions, high- S_w rock intervals that contain lower hydrocarbon saturations but with those hydrocarbons in the larger pores of the rock. These hydrocarbons will have mobility and contribute to production, particularly for gas reservoirs in which, as the pressure declines, the gas phase expands (and gas saturation increases) and results in gas flow toward the production-well pressure sinks.

The difficulty with the use of porosity, V_{sh} , or S_w cutoffs, without reference to flow considerations, is that rock intervals evaluated to contain hydrocarbons may be excluded from the other reservoir-engineering calculations. Each of these approaches, when applied to the logs, requires that underlying physical relationships between log readings and these cutoffs be understood. Also, complications on logs (e.g., intervals of heavy minerals, radioactive minerals other than clay minerals, or hole washouts) need to be quantified and treated appropriately in net-pay calculations.

3H.4.5 Geologic Considerations in Net-Pay Determination. The primary geological considerations in determining pay and nonpay in the reservoir interval are depositional environment and hydrocarbon and structural history. The depositional environment provides a picture of whether the overall reservoir interval is sand rich (high N/G) or shale rich (low N/G) and the nature of the interbedding of high-quality rock with poor-quality rock. If the reservoir interval is quite interbedded with high-quality rock intimately layered with poor-quality rock on the scale of a few inches to a few feet, the poor-quality rock intervals, if they contain hydrocarbons, will likely contribute to production. However, if the layering is on a much larger scale with thick high-quality rock intervals separated from thick low-quality rock intervals, then the poor-quality rock intervals are much less likely to contribute significantly to production.

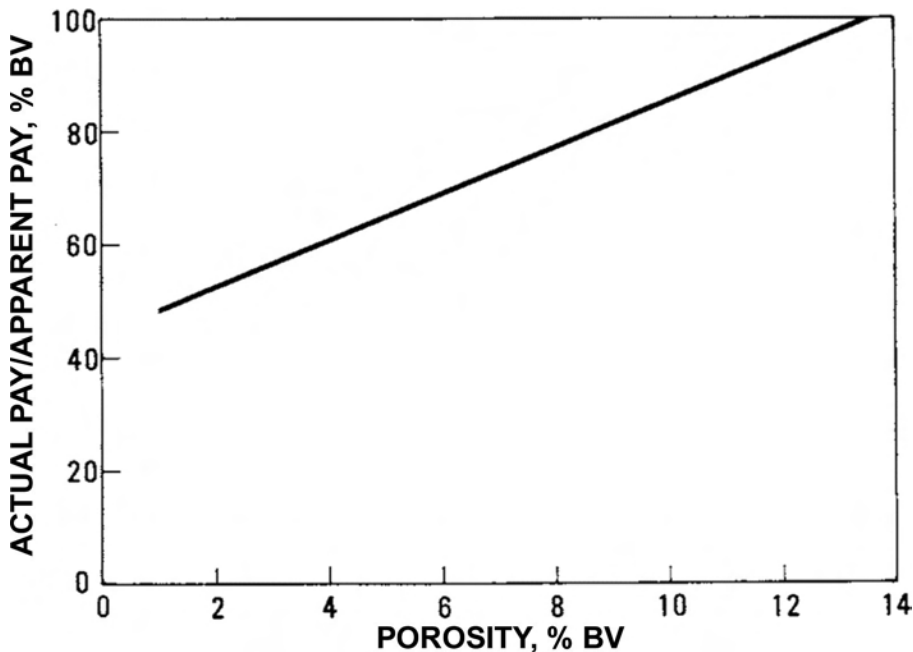


Fig. 3H.5—Apparent and actual pay for Robertson Upper Clearfork unit, west Texas, U.S.A.²⁶

Regarding hydrocarbon and structural history considerations in net pay calculations, several fields have relict-oil intervals below the current OWC (e.g., Prudhoe Bay, Alaska North Slope, U.S.A.; San Andres carbonate reservoirs, west Texas, U.S.A.)^{27–29} or relict-gas intervals below the current gas/water contact (GWC) (e.g., North Morecambe field, Irish Sea, U.K.).³⁰ These relict-oil columns would generally be considered to be nonpay intervals because of their high mobile-water saturations and lack of oil mobility. This is true for either primary production or waterflooding; however, for CO₂ enhanced oil recovery, the west Texas San Andres relict-oil intervals have been considered for development. A more significant situation is that of relict-gas saturations below the current GWC. This gas does not have immediate mobility; but if the aquifer is not strong, this gas will expand and can contribute to production as the reservoir pressure declines. Hence, a relict-gas interval should not necessarily be excluded in net-pay calculations.

George and Stiles²⁶ published an excellent example of the complications of net-pay calculations concerning the heterogeneous Clearfork carbonate oil reservoirs in west Texas, U.S.A. Their approach was to develop an empirical relationship between “actual pay” and “apparent pay” as a function of porosity in order to redetermine net pay to improve OOIP calculations and to obtain a reasonable distribution of net pay. They defined two net-pay cutoffs. The “actual pay” was defined as the net thickness of core samples with permeabilities greater than 0.1 md, and an “apparent pay” was defined as the net thickness of core samples with porosity greater than a specific cutoff. Fig. 3H.5 shows the relationship of actual pay to apparent pay as a function of porosity. On the basis of this analysis, at a porosity level of 8% BV, 75% of the rock samples would be pay, while at a porosity level of 1% BV, 50% of the rock samples would be pay. By this methodology, wells with low porosity levels will not be all nonpay, but will be given a limited amount of pay. The purpose of their method was “to achieve a better distribution of porosity-feet” and “both total original oil in place and distribution of PV throughout the field will be realistic.”²⁶

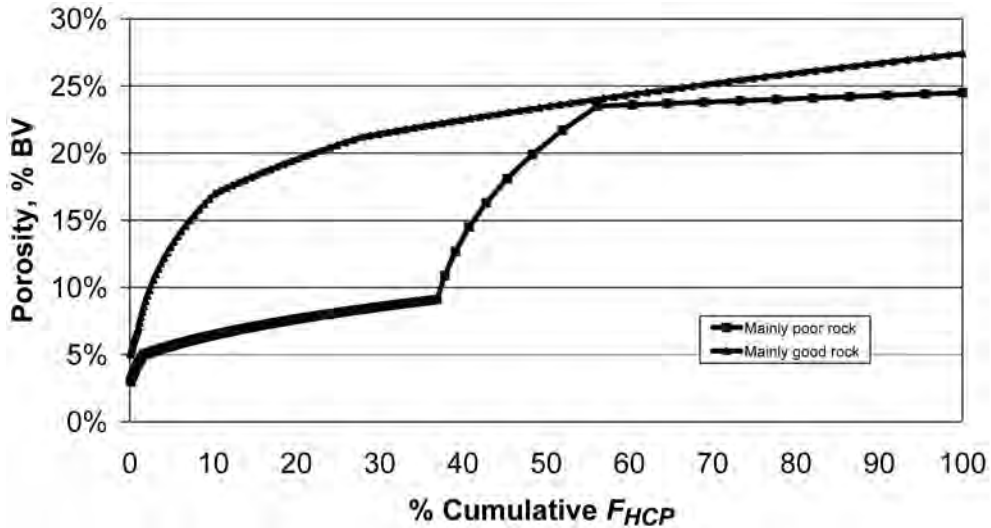


Fig. 3H.6—Illustrative plot of cumulative F_{HCP} vs. porosity for two types of reservoirs (one mainly good-quality rock, the other mainly poor-quality rock). The total F_{HCP} of the “good” reservoir is three times the total F_{HCP} of the “poor” reservoir.

Finally, the technical team needs to determine the implications of any net-pay cutoff. This is best done by plotting the cumulative hydrocarbon pore feet (F_{HCP}) percentage as a function of porosity and as a function of permeability (see Figs. 3H.6 and 3H.7 for respective examples of these two types of plots). In this way, it is possible to determine what percentage of the hydrocarbons within the reservoir interval would be excluded by any particular net-pay cutoff. While this net-pay sensitivity method is a logical approach, the evaluation of porosity and water saturation is more uncertain in low-porosity rocks. Log calculations may indicate hydrocarbon saturations in rocks where no hydrocarbon actually exists.

3H.4.6 Application of Net-Pay Cutoffs to Well Logs. The four main steps in the application of a net-pay cutoff to a particular reservoir interval are to establish a standard, calibrate one or more logs to the chosen standard, confirm that the calibration step produces results consistent with the standard, and apply the calibrated model to all wells.

Establish a Standard. As discussed previously, the choice of the standard for the net-pay calculations should be reasonable but is, to some degree, arbitrary. The choice should be a single concept, such as a permeability cutoff, a porosity cutoff, or geologists’ calls of pay/non-pay from core descriptions. The use of multiple cutoffs will lead to a very conservative result that eliminates rock intervals that are likely to contribute to production, particularly for gas reservoirs. This underestimation occurs because each of the individual cutoffs will, to some extent, define different datapoints as nonpay. Even after the best possible depth matching of the logs involved, remaining depth mismatches always occur, resulting in the double counting of nonpay at bed boundaries. The following discussion assumes that an air-permeability cutoff of 0.1 md has been chosen.

Calibrate One or More Logs to the Chosen Standard. Once the 0.1-md air-permeability cutoff has been chosen, it needs to be converted into a methodology that can be applied to foot-by-foot log calculations. Typically, this is done by converting the permeability-cutoff value into a porosity-cutoff value by a permeability-vs.-porosity semilog crossplot of routine-core-analysis data converted to reservoir conditions. Also, plots are made of the core permeability data vs. the various available log parameters to determine if there is a strong correlation that can be

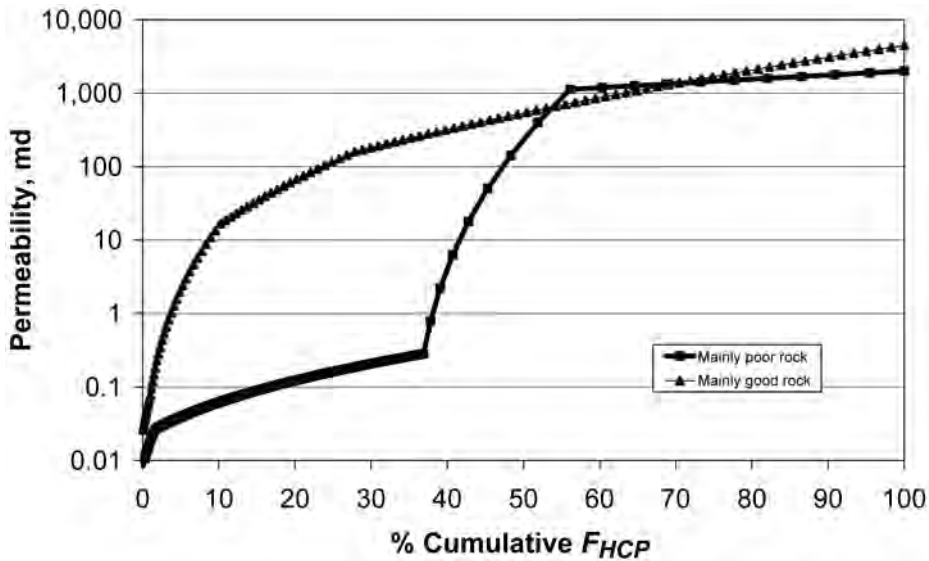


Fig. 3H.7—Illustrative plot of cumulative F_{HCP} vs. permeability for two types of reservoirs (one mainly good-quality rock, the other mainly poor-quality rock). The total F_{HCP} of the “good” reservoir is three times the total F_{HCP} of the “poor” reservoir.

used. Alternatively, a multivariate regression technique might be used to calibrate multiple logs to permeability. If a porosity cutoff is developed from the permeability cutoff, then it needs to be defined as a log-related cutoff, such as a log-derived porosity or density log cutoff, or a V_{sh} or GR-log cutoff. There are several variations on how this calibration step can be undertaken. The alternatives are not discussed here because each reservoir situation has unique characteristics.

Confirm That the Calibration Step Produces Results Consistent With the Standard. After the calibration step is completed, the resulting log calculations of pay/nonpay need to be checked against the core standard in the cored wells. This is needed to determine that the log calculations and their cutoffs do not overstate or understate the calibration standard of net pay of the reservoir interval. The goal is to develop the “best estimate” values in the reservoir-engineering calculations, not the “low estimate” or the “high estimate.”

Apply the Calibrated Model to All Wells Over the Reservoir Interval. After the first steps have been successfully completed, the finalized net-pay log model can be applied to all wells’ valid log data in the reservoir interval to develop point-by-point pay/nonpay determinations. For optimal results, it may be necessary to have different models in different areas of the reservoir. The results for each zone over the reservoir should be quality controlled. Maps should be examined looking for “bulls-eyes” that may represent either real geological effects, artifacts in the database, or bad calculations.

In the subsequent steps of calculating porosity, S_w , and permeability, those calculations will be made only for pay intervals. The nonpay intervals will be excluded from the core and SCAL database and the log database. In cases in which the depth matching of cores and logs presents difficulties, it is prudent to retain both core- and log-defined nonpay in the database. This will enable appropriate samples to be selected for various analyses, such as the evaluation of SCAL petrophysical properties.

3H.5 Porosity Determination

The accurate calculation of porosity at the wellbore is essential for an accurate calculation of OOIP or OGIP throughout the reservoir. The porosity and its distribution also need to be calcu-

lated as accurately as possible because they are almost always directly used in the S_w and permeability calculations and, possibly, in the net pay calculations. In most OOIP and OGIP studies, only the gross-rock-volume uncertainties have a greater influence on the result than porosity does. Occasionally, where porosity estimates are difficult, porosity is the leading uncertainty. Fractured and clay-mineral-rich reservoirs remain a challenge.

This section describes the methods that can be used to make porosity calculations at the wellbore with the available core and log data. For this discussion, it is assumed that the core data have been properly adjusted to reservoir conditions, that the data from various logs have been reviewed and validated as needed, and that all of the required depth-alignment work has been completed. [Sec. 3H.2](#) discusses the specifics of these topics. This section discusses the use of core porosity data, total and effective porosity, core-log calculation approaches, consistency of calculations, and uncertainty.

3H.5.1 Use of Core Porosity Data. There are a few preliminary steps in the use of routine core porosity data over the reservoir interval. First, this data set needs to be restricted to those porosity measurements made in pay intervals; the nonpay porosity measurements should be excluded from the porosity calculations. Second, if more than one type of porosity measurements are made, then a hierarchy of these measurements needs to be developed for use in subsequent log/core porosity calculations. For example, it is possible that whole-core Boyles-law porosity measurements, core-plug Boyles-law porosity measurements, and sum-of-fluids porosity measurements are made with several of these measurements made on the same feet of core.¹³ (See the chapter on petrophysical measurements in the General Engineering volume of this *Handbook*.) Also, if enough of two data types are taken for the same footage of cores, then these data need to be crossplotted to determine if there are any systematic differences between the various types of core porosity data. If more than one porosity measurement are available for a given depth, then only the highest priority in the hierarchy should be included in the log/core porosity calculations; otherwise, there will be unequal weighting in the statistical calculations.

The core porosity measured in shaly sands may include some volume that is associated with the dehydration of certain types of clay minerals (see [Sec. 3H.3.1](#)).^{10,11,18,19} When smectite (montmorillonite) clay mineral is present as a significant fraction [e.g., a V_{cl} (not V_{sh}) of 40% BV], the core porosity may be increased, by approximately 12% BV, solely because of the smectite present. However, when other species of clay are present that have much less clay-mineral physically bound water (e.g., chlorite, illite, kaolinite), the clay water will add little to the core porosity. The effects of the presence of shale and clay minerals must be understood to yield the correct evaluation of the hydrocarbon and water content of a reservoir's pore network.

3H.5.2 Total and Effective Porosity. The estimation of porosity and water saturation in shaly formations is, where possible, based on various types of laboratory core data. Where core measurements are not available, estimates based wholly on log measurements and selected interpretation models are widely used. Rock models are based on “total” or “effective” porosity and “total” or “effective” S_w definitions. Both definitions account for the usual grain volume and hydrocarbon and capillary-water volumes seen in the porosity of nonshaly sands, and both models include volumes for the clay-mineral physically adsorbed water (sometimes known as clay-bound water) and the volume of dry clay minerals. [Fig. 3H.8](#) is a schematic of a shaly-sand-reservoir model. It indicates the various solid and fluid volumes and pore networks to which core measurements, density, and neutron logs correspond.

Core Analysis. This discussion is restricted to siliciclastic rocks; carbonate rocks are not discussed. The porosity measured on core plugs containing clay minerals is dependent on the methods used to clean and dry the sample before it is measured. Cleaning removes oil from the pores. It is widely, if not universally, accepted that drying the core in a vacuum oven at temperatures just above the boiling point of water (110°C) will remove most, or all, of the clay-

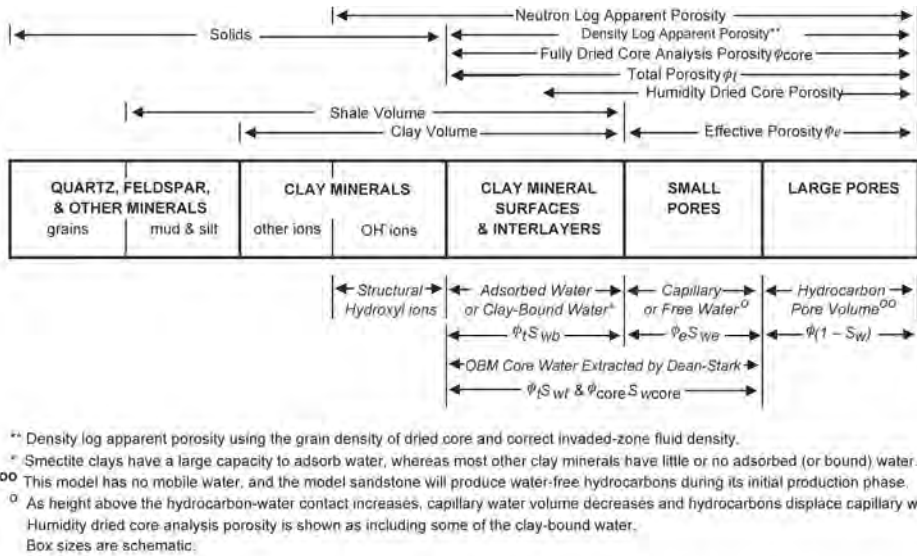


Fig. 3H.8—Total, effective, and core porosities and their associated water saturations in shaly sands (after Woodhouse and Warner³¹).

mineral adsorbed water and the capillary water, but not the chemically bonded hydroxyl groups within the clay minerals. The standard reported core porosity, ϕ_c , is, therefore, a total porosity including the effective porosity, ϕ_e , and the clay-mineral adsorbed water volume, $V_{cl}\phi_{cl}$ or $V_{sh}\phi_{sh}$.

$$\phi_c = \phi_e + V_{cl}\phi_{cl} = \phi_e + V_{sh}\phi_{sh} \dots\dots\dots (3H.2)$$

OBM-core S_w determined using Dean-Stark water-volume extraction is also accomplished with boiling toluene at approximately 110°C. Subsequent preparation of the OBM-core sample to measure porosity uses the same maximum temperature.

The core total porosity, ϕ_c , and core water saturation, S_{wc} , are, therefore, fully compatible with each other.³¹ They are used together to accurately quantify hydrocarbon pore volume (V_{HCP}) [the “core” $V_{HCP} = \phi_c \times (1 - S_{wc})$]. When smectite clays are present, the core total porosity will be higher than the effective porosity, ϕ_e , as defined in the previous paragraph. However, for the same sample, the core water saturation, S_{wt} (capillary water plus clay-mineral adsorbed water volumes as a fraction of ϕ_t), will also be greater than S_{we} (capillary water volume as a fraction of the effective porosity) and will fully compensate the V_{HCP} for the increased porosity.

V_{HCP} is used instead of F_{HCP} in the following discussion because the equalities apply at all scales.

$$V_{HCP} = \phi_t \times (1 - S_{wt}) = \phi_e \times (1 - S_{we}) = \phi_c \times (1 - S_{wc}) \dots\dots\dots (3H.3)$$

For porosity,

$$\phi_t \geq \phi_c \geq \phi_e \dots\dots\dots (3H.4)$$

For water saturation,

$$S_{wt} \geq S_{wc} \geq S_{we} \dots \dots \dots (3H.5)$$

“Humidity-dried” cores, extracted at temperatures lower than boiling water and partially dried, retain some, or all, of the clay-mineral physically bound water and, therefore, approximate the effective porosity. There is, however, no generally accepted way to measure accurately the values of effective porosity on shaly-formation cores. In smectite-rich shaly sands, humidity-dried porosity is incompatible with the Dean-Stark S_w , and, if combined, the result will understate V_{HCP} .

Cores extracted at much higher temperatures may give compatible porosity and S_w results, but other problems can sometimes occur. The mineral gypsum dehydrates between 110 and 120°C and must be corrected for in the retort method of water-volume measurements. At 110°C, the structural, chemically bound hydroxyl groups that are part of the clay-mineral lattice are not liberated.¹⁸ However, at very high temperature (500°C or more), these hydroxyl groups react to form water and condense as water in the collecting tubes of a high-temperature retort apparatus. This “structural water” is not captured during standard core analysis but is the hydrogen component of clay minerals that is detected by the neutron porosity log even though it is a part of the solid mineral (Fig. 3H.8).

Log Analysis. Log-interpretation methods for porosity and S_w all seek the same end result in terms of porosity and hydrocarbon volume. They are divided into methods that model the effective porosity and the clay-mineral adsorbed water separately and methods that model the total porosity containing both clay-mineral adsorbed water and capillary water. The total porosity is often calculated from the density log and the core grain density, as Fig. 3H.8 shows. Estimates of interconnected porosity (effective porosity) at reservoir conditions come from combinations of many different logs, but all of them attempt to quantify the clay-water volume fraction and subtract it from the total porosity.

3H.5.3 Core/Log Calculation Approaches. In calculating porosity values from the core and log data, the first step is to create depth plots and crossplots of the core data against the various log data, like those in Figs. 3H.9 and 3H.10, respectively. These crossplots visually show which of the logs has the strongest correlation with the core porosity measurements. For example, the density log readings vs. core porosity data may have a less-scattered data cloud than the sonic log vs. core porosity data, or, if there are heavy-mineral complications, the opposite may be the case. These crossplots show, and the correlation coefficient, r , of each correlation indicates which of the log/core combinations should be used for the log/core calibration step discussed next. Where possible, it is best to use a single-log porosity estimator because multiple-log estimators will have problems at bed boundaries because of imperfect depth matching. The volumes sampled by different logs also vary, with the neutron log “seeing” a larger volume than the density log.

The variance of core-plug data is always larger than the equivalent variance of a log because of the small plug volume compared with the larger volume seen by the running-average log reading. One way to reduce the core-plug variance is to create a modified core property curve that is the running average of the core data (a 1-2-1 filter may be appropriate). Core data modified in this way are considered by some to be a superior calibration standard.

Calibration Line-Fitting. The generally recommended method for obtaining a line-fit for porosity prediction is the “y-on-x” ordinary least-squares regression method.^{32,33} The recommendation presumes that the calibration data set has accurate depth adjustments and is fully representative in all respects of the environment of the equation’s future use. The dependent-variable calibration data, y , the values wanted in the future (e.g., core porosity), are regressed against the selected independent x -variable data [the values available to make the future prediction (e.g., the density log values)]. The same x -variable must be used when the calibration line

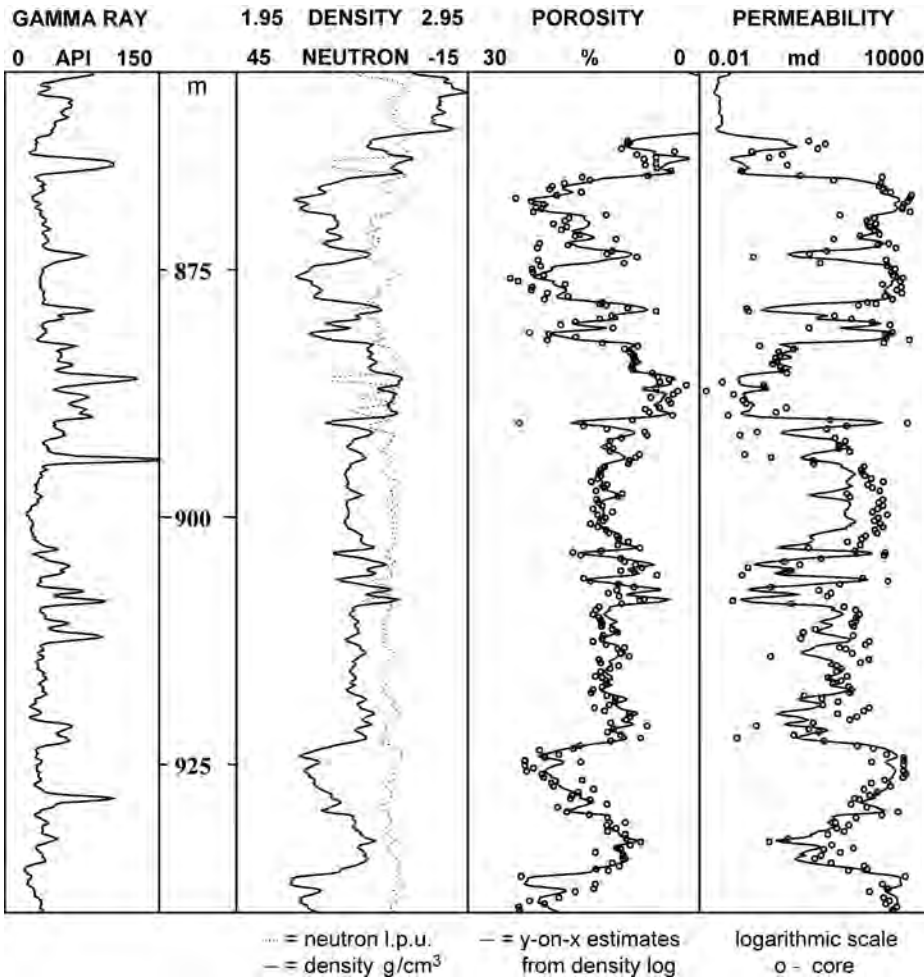


Fig. 3H.9—Well-log and core data from gas-bearing sandstone with predicted porosity and permeability (South Morecambe gas field, offshore U.K.). After Woodhouse.³²

is applied in the uncored wells. Multiple regression uses more than one independent variable (e.g., the density and GR logs).

For *y-on-x* regression lines, removal of *x-y* data outliers, far from the general trend, must be considered. The *y-on-x* method assumes that the *y* and *x* measurements apply to the same rock sample, so data pairs that are not likely to represent similar rocks must be edited from the data set.

Although straight (linear) regression lines are often created with the data in their original form, the regression method applies equally to curved relationships. These are achieved by transforming one or more of the variables. For example, it is common to transform permeability to a logarithm, thereby creating a \log_{10} (permeability) and linear porosity relationship. This transform preserves the geometric averages of the permeability. As an alternative, a permeability and exponential porosity relationship should be considered because this will preserve the arithmetic averages of permeability, instead of the geometric averages.

To some observers, the *y-on-x* line-fit initially is awkward and less central than some other line-fits. The reduced-major-axis (RMA) line-fit, for example, follows the intuitive middle

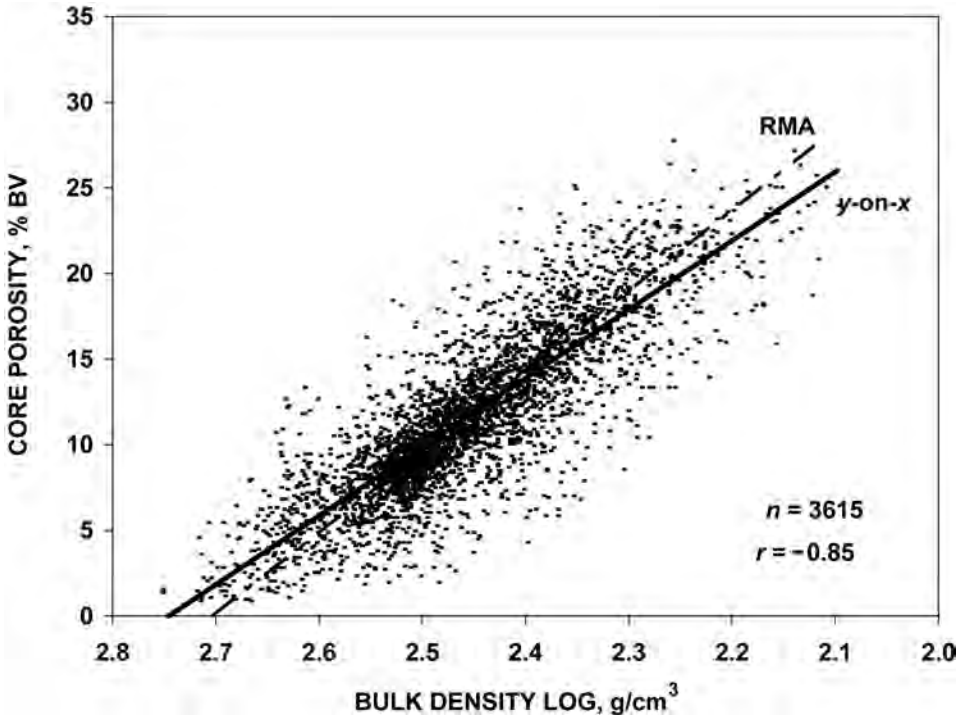


Fig. 3H.10—Core-plug porosity vs. well-log bulk density with *y-on-x* and RMA line fits (South Morecambe gas field, offshore U.K.) After Woodhouse.³²

ground along the major axis of the data cloud (see Fig. 3H.10). The “structural” line-fits estimate the relationship that would be observed if both the *y* and *x* variables were error-free. The RMA line provides this relationship for the particular case when *y* and *x* have equal fractional errors. These structural line-fits are not generally used in practice because, for their future use, they apply to error-free *x*-input data, not the real measured data. The RMA slope is defined by the ratio of the SDs of *y* and *x* together with the sign of *r*. The *y-on-x* slope is equal to the RMA slope multiplied by the correlation coefficient *r*.

The initial impression of *y-on-x* does not weaken its status as the method with the lowest overall residual error in the required *y* estimates. When viewed from any position on the *x*-axis, the *y-on-x* line is central within the *y*-data values near that *x*-position (see Fig. 3H.11). Providing average *y*-estimates from measured *x*-data is the main feature of *y-on-x* lines; however, the *y*-variance of the calibration data is not preserved by *y-on-x* predictions and the extremes of the *y*-range are averaged. The RMA line-fit does honor the *y*-variance; but if *y* and *x* are only moderately correlated, high porosity values are overestimated and low porosity values are underestimated (see Fig. 3H.12). The depths of the RMA-predicted high and low *y*-values will not be at the same depths as the core high and low values.

Cores are not always regularly sampled (e.g., at one per foot) and are typically sampled at a lower frequency in the shale intervals. In these cases, the plotted data can sometimes have no trend, for example, in a high-porosity reservoir. External information, not in the standard log/core variables, can be used to provide a useful line-fit. The zero-porosity end of the line might be derived from the core grain-density data. Calibration lines may be calculated by joining this grain density to the means (arithmetic averages) of the *x-y* data, or a fixed-point regression might be used.

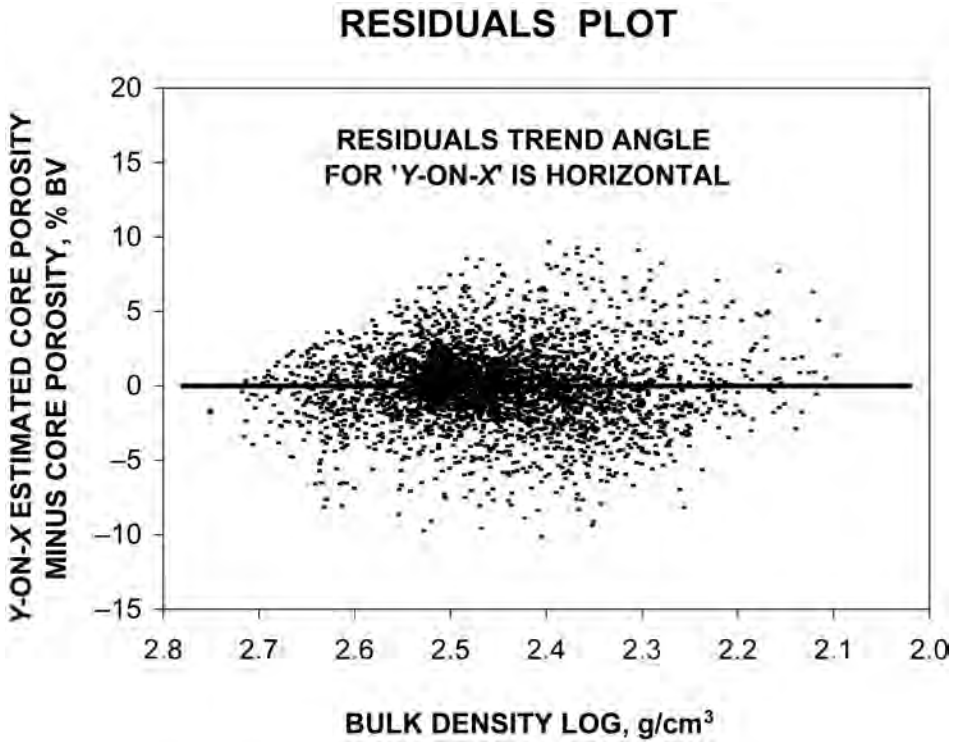


Fig. 3H.11—Residuals plot for y-on-x predicted porosity vs. well-log bulk density. Residuals are evenly distributed around zero (South Morecambe gas field, offshore U.K.). After Woodhouse.³²

There are circumstances when line-fits such as RMA should be considered. Some reservoirs (e.g., carbonates and finely laminated sandstones) are so heterogeneous that it is difficult, if not impossible, to make accurate core-to-log depth adjustments. In these cases, where the data pairs do not reliably sample similar rocks, core porosity vs. log plots have a poor correlation, and the y-on-x line-fit has a low slope. Here, the RMA line can be a better practical approximation of the underlying core/log relationship. If the core/log correlation is very poor, deterministic³ or simultaneous-equations log analysis²⁰—without using the core—remain useful options.

Calibration lines should be determined for a single population, not a mixture of two or more populations. For example, when density logs are used to predict porosity, if two zones in a well have significantly different lithologies or grain densities, they should, where possible, be separated into different population groups. Likewise, significant grain-density trends across the reservoir area should be honored; however, this process must not be taken to an extreme. Calibration lines with excellent apparent correlations can be achieved with very fine subdivisions of the calibration sample data. Unfortunately, when they are applied in prediction mode to the uncored wells, these “overfitted” calibrations will not yield robust and accurate porosity estimates.

Density Log. The density log is often the best log for making porosity estimates.³⁴ In their simplest form, the density-log readings are considered to be a linear relationship between the zero-porosity limit where the density log reads the rock-matrix density and the 100% BV porosity limit where the density log reads the fluid density.

$$\phi = \frac{\rho_{ma} - \rho_b}{\rho_{ma} - \rho_{fl}}, \dots\dots\dots (3H.6)$$

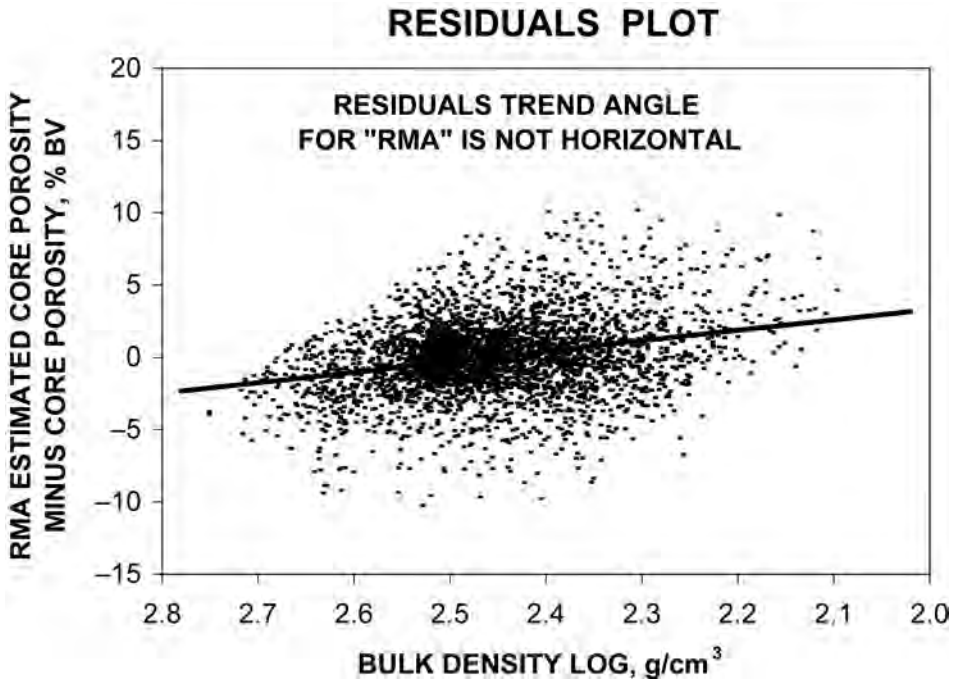


Fig. 3H.12—Residuals plot for RMA-predicted porosity. Residuals trend from negative at high densities to positive at low-density values (South Morecambe gas field, offshore U.K.). After Woodhouse.³²

where ϕ = porosity, ρ_{ma} = matrix density, ρ_b = formation bulk density, and ρ_{fl} = fluid density.

This physical relationship assumes constant matrix density and insignificant variation in the fluid saturation and fluid density within the pore system. These are not necessarily the case in real reservoirs. Where core measurements and regression analysis are used to quantify the relationship, the regression coefficients (slope and intercept) do not represent true matrix and fluid-density properties. The regression coefficients are “catch-all” fitted parameters without a physical meaning.

When using the density log for porosity calculations, it should be expected that a different log/core relationship will be found for the aquifer, the oil column, and the gas column because of the different fluid densities in these various fluid environments. Also, there may be curvature of the relationship if the near-wellbore gas saturations increase as porosity increases. This curvature does not always occur, and gas saturations “seen” by the density tool (up to 4 in. into the borehole wall) may be fairly constant. Differences in the core/log relationship are also expected for WBM vs. OBM wells.

In a density-log vs. core-porosity crossplot, the low-porosity portion of the data cloud needs to be handled carefully. Typically, these rocks have lower porosity because of either a much higher clay-mineral content or various cements filling some of the pore system, either of which is likely to alter the average matrix density. Also, the lower-porosity rocks within the hydrocarbon column will have significantly higher S_w . Hence, either of these effects can cause curvature of this crossplot that will need to be accounted for in the correlation of log and core data.

For reservoirs that are buried sufficiently deep and in which no smectite clay mineral is present, the sandstone and shale core grain densities are often similar, and the core porosity of the shale is low, less than approximately 5% BV. In these particular conditions, there are very small volumes of adsorbed water in the clay molecules, ϕ_{cl} and ϕ_{sh} in Eq. 3H.2 are low, and it is possible to use the density log alone to estimate effective porosity. Neutron logs usually

do not indicate such low apparent shale porosities because of chemically bound hydroxyl groups in clay-mineral structures and neutron-adsorbing elements. Sonic logs in shales usually read higher than quartz travel-time. The sonic and neutron are, therefore, not satisfactory single-log effective-porosity predictors in shaly sands.

Other Approaches. Evaluations based on the sonic log follow a logic similar to that of the density-log methods described previously. The sonic-derived porosities are particularly useful when conditions are adverse for the density log, such as in caved holes or when heavy minerals are present. See the chapter on acoustic logging in this volume of the *Handbook*.

Two-log combination solutions, such as density/neutron or density/GR, are useful in carbonate and siliciclastic reservoirs, including shaly sands. Gas-bearing sands may require multiple-log methods. Multiple-log and multivariate regression methods can be used but are often difficult to apply in practice. All multilog methods will have problems where one of the input logs reads incorrectly (e.g., hole washouts, tool sticking, cycle skipping, GR statistical variations, and poor depth alignment).

Some prefer to use core data for nonquantitative, visual comparison with log-analysis porosity developed from a variety of methods. When the volume of core data is low, making simple qualitative presentations of the measured core may be satisfactory. When there is sufficient core data to provide a representative sample of the formations in one or more wells, quantitative use will lead to more accurate OOIP and OGIP. It is not possible to provide strong guidance on the amount of core required, because the geological and engineering issues of each reservoir differ greatly. However, as a starting point, one might consider coring one well in approximately every 10 if this fits sensibly with the unique parameters of the reservoir under study.

3H.5.4 Consistency of Calculations and Uncertainty. Calculations of porosity and S_w must be compatible with each other. They must both be evaluated within the “total ϕ/S_w system,” or both be evaluated within the “effective ϕ/S_w system” (see the discussion in the following S_w section). When preserved OBM (“native”) core measurements of both porosity and water saturation are available, the core sample $F_{HCP} [= \phi \times (1 - S_w)]$ is, after a few small standard adjustments, usually the best estimate of the V_{HCP} at each cored depth. This core-based V_{HCP} can be used to validate, or calibrate, the V_{HCP} given by either the “effective” or the “total” ϕ/S_w evaluation systems, as calculated from the log data (see Eq. 3H.3).

The uncertainty of porosity evaluations varies from case to case. The porosity of a single cleaned core plug can be repeated to within approximately $\pm 0.2\%$ BV, where this uncertainty refers to one SD.¹³ This very small instrument-repeatability uncertainty does not, however, include the many other noninstrumental variables that affect the systematic uncertainty and overall accuracy. Before the measurement is made, there may be core-plug cleaning problems from native salt in the pore space and incomplete oil removal. The drying time of water-adsorbing clay minerals adds further uncertainty. Surface roughness causes the plug volume to be uncertain especially when there are large grains and vugs. The uncertainty of the average core porosity will be improved when many plugs are selected at approximately one per foot without regard for the rock quality (i.e., randomly). However, because of commercial pressures and common sense, plug samples are not always selected at random, so care must be exercised, especially concerning the porosity values predicted at depths where core is not available. It must also be remembered that 1-in. core-plug samples, taken from each foot of whole core, sample only approximately 2% of the whole core volume.

Log readings are also uncertain, and, for example, the bulk-density-log random uncertainty may be approximately ± 0.015 g/cm³ or approximately $\pm 1\%$ BV.⁷ Systematic errors, such as poor density-tool pad contact with the borehole wall, increase the uncertainty in some wells.

Further uncertainty in the final calculated porosity arises from the grain- and fluid-density values (or the related regression coefficients) and from mixed-mineral and shaly-sand effects.

The evaluations of zone-average porosity in the net-pay intervals in a single well that has relevant core control might have an accuracy of approximately $\pm 1.0\%$ BV. This is largely the result of systematic uncertainty because the random uncertainties will be very small for zone-average values. In other words, an average porosity of 20% BV has an uncertainty range of 19 to 21% BV. This is a one SD estimate. In 32% of cases, zone-average uncertainties of greater than $\pm 1.0\%$ BV are considered likely. Where core control is not available, these accuracy estimates should probably be doubled. Effective-porosity accuracy in very shaly sands is also more uncertain because of the associated V_{sh} estimates.

For fractured reservoirs, imaging tools now provide better visualizations of the borehole wall, but quantification of the open-fracture porosity, which may be approximately 0.1 to 1.0% BV, is highly uncertain. Production testing and test analysis are recommended to determine the nature and extent of any fracture system within the reservoir interval.

3H.6 Fluid-Contacts Identification

Defining the depths of the fluid contacts, GWC, OWC, and gas/oil contact (GOC), or defining both of the latter in some reservoir situations, is essential for volumetrics calculations and important for detailed petrophysical calculations. For example, for more-accurate porosity calculations, the reservoir's vertical interval needs to be subdivided by fluid type to account for differences in the average fluid saturation and, hence, differences in fluid density or sonic travel time in the various fluid intervals: gas cap, oil column, or aquifer. For the S_w calculations, the depth of the OWC or GWC, or more particularly the related free water level (FWL), is a required input for any S_w calculations using capillary pressure, P_c , data. These depths need to be defined in every wellbore, to the extent that they occur. This section addresses the methods used to make the most accurate determination of the GOC, OWC, and/or GWC depths at the wellbores. This section does not address the larger topic of how these fluid contacts may vary over the whole of the reservoir either because of faults, rock-quality variations, isolated sands, a reservoir's hydrocarbon-filling history, or hydrodynamics of the reservoir-aquifer system.

There are four types of data that can be used to define the fluid-contact depths in a wellbore: mud logs, cores (geologists' descriptions and routine-core-analysis data), resistivity and neutron logs, and formation-tester pressure surveys. These are listed approximately in the order in which these data are gathered from a wellbore. Each has its own strengths and weaknesses. Each is an independent source of information; therefore, the most accurate fluid contact is obtained by using all of the data available for a particular well. The first step in using any and all of these data sources is to align their depths as accurately as possible.

3H.6.1 Mud Logs. Mud logs record mud gas compositions and quantities and descriptions and analyses of drill cuttings. These provide information about the fluid content and lithology of the rock as it is drilled. These data have some depth uncertainty because of the lag time between a rock interval being drilled and the time the cuttings are recovered at the surface. The field personnel work to minimize this uncertainty by periodically dropping a bit of "carbide" into the drilling mud and then determining how long it takes for it to show up on the mud-returns gas-chromatograph output. The mud log gas-analysis data plotted vs. drilled depth, and adjusted for drilling rate, is a semiquantitative measure of the gas content over the reservoir interval. It can be used to determine a GWC or OWC because the background gas content per unit volume of aquifer brine is so low compared with that of free gas or gas dissolved in oil. The methane-concentration log is most useful for defining the top of the reservoir and the GWC for a gas reservoir, and the detailed gas analyses can also identify a GOC from increasing ratios of the heavier hydrocarbon components compared with methane as depth increases.

Direct observation of oil staining, and yellow or brown ultraviolet (UV) fluorescence on drill cuttings, identifies oil. When drill cuttings are crushed in solvents, mobile oil migrates to the solvent, which then fluoresces. Gas condensate has a bright white fluorescence. These characteristics assist in identifying oil and gas reservoirs, the top of the reservoir, GOC and OWC, and, possibly, the base of the reservoir.

3H.6.2 Water-Based-Mud Cores. WBM cores can provide direct observations of the OWCs and GOCs. Because of differences in the colors of the oil staining, the depths of gas, oil, tar, and relict-oil intervals can often be determined visually from the cores, especially when they are cut at a high rate of penetration. It is common practice to photograph cores in both white and UV light to provide an accessible, permanent visual record. These visual observations are typically complemented by the routine-core-analysis S_o data over the same depth ranges.⁸ Gas and aquifer intervals have low core oil saturations, and tar intervals often have high core oil saturations.

3H.6.3 Log-Based Methods. The use of resistivity-log data is another method of determining OWC and GWC depth in a wellbore.³ The resistivity logs are used to calculate S_w , and where there is a significant decrease in the S_w values (decreasing from near 100% PV as one moves up through the reservoir interval), that depth is defined as the fluid-contact depth. Also, the invasion profile of the shallow- vs. deeper-reading resistivity tools can be used to help define the depth interval in which the fluid contact occurs. This is true of either WBM- or OBM-drilled wells. Also in WBM-drilled wells, tar intervals can be defined by those depths over which the shallow- and deep-reading resistivity tools show a lack of oil-saturation change, which indicates that the hydrocarbons in the pore space are too viscous to be displaced by the WBM filtrate. If the reservoir is not too shaly, neutron logs can be one of the keys to identifying gas-bearing intervals.³ A GOC, or a GWC, can be defined at the depth at which the neutron porosity significantly decreases and the density and sonic porosities slightly increase as one moves up through the reservoir interval.

3H.6.4 Formation-Pressure Surveys. The best data from which to determine FWL fluid contacts are given by the formation-pressure-testing tools (e.g., RFT, formation multitester, MDT, and RCI) that measure pressure surveys over reservoir intervals.³⁵ In going vertically from the gas cap into the oil column, or from the hydrocarbon column into the aquifer, there will be breaks in the formation-pressure vs. depth trends as one moves from a very low gas pressure gradient (0.10 psi/ft or less) to the higher oil pressure gradient (typically 0.25 to 0.35 psi/ft) and then to the water pressure gradient (0.40 to 0.55 psi/ft). When adequate data can be collected, the fluid contacts can be determined very accurately by identifying the depths at which the characteristic pressure gradients change. See the chapter on reservoir pressure and temperature in this volume of the *Handbook* for additional information on fluid-contact depth determination using pressure information.

Overall, the formation-pressure-survey data should be the primary source of data for defining the FWL fluid contacts. The other data should be used to complement these pressure data, or should be used together to define the fluid contacts if no pressure-survey data are available. In reservoirs with sand/shale sequences, sometimes the fluid contact is determined to be within a shale interval, even if that interval is only 10 ft thick or less. If this is the case, the best estimate depth of the fluid contact is at the mid-depth of the shale interval (unless the pressure-survey data indicate otherwise). The fluid contact may be different from the FWL, and it is the FWL depth that is important commercially and important when making S_w calculations from P_c/S_w data.

Since the introduction of 3D-seismic surveys, acoustic-impedance contrasts between gas-, oil- and water-bearing formations are increasingly used. The impedance is dependent on the density and acoustic velocity of each fluid. Many reservoirs exhibit a significant change of acoustic impedance at the fluid contacts, allowing the contacts defined at the wells to be propagated, with data control, into the undrilled areas of the reservoir. These impedance maps show visual “haloes” around a GWC or OWC. These same impedance changes may also be seen in vertical seismic sections and assist in identifying the top of the reservoir, GOC, GWC, and OWC.

3H.7 Water-Saturation Determination

S_w determination is the most challenging of petrophysical calculations and is used to quantify its more important complement, the hydrocarbon saturation ($1 - S_w$). Complexities arise because there are a number of independent approaches that can be used to calculate S_w . The complication is that often, if not typically, these different approaches lead to somewhat different S_w values that may equate to considerable differences in the OOIP or OGIP volumes. The challenge to the technical team is to resolve and to understand the differences among the S_w values obtained using the different procedures, and to arrive at the best calculation of S_w and its distribution throughout the reservoir vertically and areally. In OOIP and OGIP calculations, it is important to remember the relative importance of porosity and S_w . A 10% PV change in S_w has the same impact as a 2% BV change in porosity (in a 20% BV porosity reservoir).

3H.7.1 Techniques for Calculating S_w . S_w in wellbores can be determined by the following primary methods:

- S_w calculations from resistivity well logs by application of a model relating S_w to porosity, connate-water resistivity, and various rock electrical properties.
- S_w calculations from laboratory capillary pressure/saturation (P_c / S_w) measurements by application of a model relating S_w to various rock and fluid properties and height above the free-water level.
- S_w calculations using OBM-core-plug Dean-Stark water-volume determinations.
- Combinations of these methods.

This listing is the chronological order in which data are likely to become available, not in a ranked order based on the accuracy of the various methods. In fact, the use of S_w values from properly handled and preserved OBM cores is superior to the other techniques in the oil (or gas) column above the mobile-water part of the oil/water (or gas/water) transition zone. The OBM cores are superior because the water-volume measurements on these core plugs are a direct determination of S_w . The extracted water is the reservoir's connate water. The resistivity-log data are inferential measurements that have to be converted to S_w values by a conceptual, theoretical, or empirical model. The use of P_c / S_w data requires other models and a number of input parameters whose values at reservoir conditions cannot be directly determined and, hence, must be estimated.

The choice of which S_w -calculation approach to use is often controlled by the availability of the various types of data. If no OBM cores have been cut, then this technique cannot be used unless funds are spent to acquire such data from one or more newly drilled wells. This is not a high incremental cost when OBM use is planned for other purposes. Resistivity logs are run in all wells, so these data are available for making standard-log-analysis S_w calculations. A key consideration when making calibrated S_w calculations is the availability of SCAL data on core samples from the particular reservoir; that is, the number of laboratory electrical-property and P_c / S_w core-plug measurements that have been made.

The technique chosen to calculate S_w is often a hybrid that combines the use of two of these basic data sources. For example, the OBM-core S_w data can be used in combination with the resistivity logs to expand the data set used to include all wells and the whole of the hydrocarbon column. Alternatively, the OBM-core S_w data can be used in combination with the $P_c /$

S_w data. In this way, the OBM-core S_w data define the S_w values for the majority of the reservoir, whereas the P_c/S_w data define the S_w values in the interval just above the fluid contact and perhaps in areas of the field where P_c data are available but OBM-core data are not.

3H.7.2 Data Availability and Data Quality. This section discusses the input-data availability and data-quality issues for each S_w technique. Details of the S_w physical-models equations are given in the next section. These considerations often control the initial choice of methodology to calculate S_w and need to be addressed at the start of the project to determine whether it is practically possible to fill gaps in the database in order to use a more accurate S_w -calculation approach. This discussion assumes that accurate porosity values are available from the routine-core-analysis database and that porosity is calculated point by point from the well logs. The discussion focuses on particular aspects that affect the choice of S_w methodology. Many of the database considerations were discussed in [Sec. 3H.2](#).

Resistivity Logs. Wells generally have one variety or another of laterolog or induction resistivity log because they are broadly useful and because government regulations typically demand that they be recorded. This generally provides point-by-point data from the top of the hydrocarbon column down through any aquifer intervals that are present. However, in many fields, the early wells are spread thinly over the reservoir area, but the later development wells are drilled only in areas chosen to maximize rate and recovery while minimizing costs. This means that, often, few wells are drilled downdip where the hydrocarbon column thins because of an underlying aquifer, or in the potentially thin updip limits of the reservoir. In such areas, there may, therefore, be few resistivity logs.

Laterologs are preferred to induction logs when the drilling mud has moderate to high salinity. This limitation of induction tools arises because of the excessive conductivity signal from the borehole and the mud-filtrate-invaded zone. Deep laterolog tools read too high when measuring immediately beneath anhydrite and salt,³ and alternative resistivity curves should be selected. When formation resistivity, R_t , is very high, previous generations of induction tools had limited accuracy, but current tools are much improved. Although the deep induction measurement is a running average over many vertical feet, modern tools include systems to deconvolve the raw log and provide a final log with a good vertical resolution.

Deep invasion of WBM filtrate affects all resistivity logs, and, in the extreme, the available resistivity log may be used only qualitatively. At the opposite extreme, when OBM filtrate invades a hydrocarbon reservoir, the invading OBM filtrate generally displaces only the reservoir oil and gas, leaving the S_w unchanged. Here, invasion of OBM does not usually change the deep-formation or the invaded-zone resistivity. For moderate invasion depths, the logging company charts are sometimes used to correct the deep-reading log to provide a better estimate of R_t .

Pad-mounted shallow-reading microresistivity logs measure R_{xo} , the resistivity of the mud-filtrate-invaded zone. When used together with the deeper-reading tools, these logs provide valuable information about the mobility of the reservoir fluids, including the presence of tar. In WBM wells, they also provide an estimate of the residual-hydrocarbon saturation, S_{orw} .

Connate-Brine Resistivity Data. An accurate value of connate-brine resistivity, R_w , or its values and distribution throughout the reservoir, are required for accurate S_w calculations using resistivity logs. Temperature estimates are also required.

A first check on the R_w of the aquifer is to back-calculate the apparent R_w with the Archie equation using the invasion-corrected resistivity logs and the best estimates of a and m parameters. Because S_w is typically 100% PV in the aquifer interval, the n value is not relevant here.

The spontaneous-potential (SP) log provides a second method to calculate R_w in wells drilled with WBM. Information on the mud-filtrate composition and temperature is used with the SP deflection to calculate R_w .^{3,5} The moderately accurate calculation process is valid in the aquifer but is also valid in the hydrocarbon column if high resistivity does not suppress the SP

response. When OBM-core salinity measurements are not available, the SP log provides the only evidence of possible R_w variations in the hydrocarbon column.

A third estimate of aquifer-water composition and R_w is often taken from samples recovered during flow tests of the aquifer interval; however, the R_w of the oil and/or gas column is not always the same as that of the aquifer interval.³⁶⁻³⁸ Aquifer-interval flow tests must be validated and checked for contamination from mud-filtrate invasion.

For the oil or gas column, the determination of the R_w value or values is far more of a challenge because the reservoir water will not flow. The typical, but not necessarily correct, first assumption is that the hydrocarbon-column R_w is the same as that of the underlying aquifer. If wells have been cored with OBM, core plugs from the hydrocarbon- and water-bearing intervals can be analyzed for both their water volume and their salt content, particularly the chloride ion that in almost all cases dominates the anion side of the salinity determination.³⁶

Fig. 3H.13 shows variation of chloride concentration with depth for a reservoir in Ecuador.³⁷ The chloride value can generally be used to quantify the reservoir-water salinity, from which the R_w at reservoir conditions can be calculated using standard water-resistivity vs. chloride charts or algorithms. For reservoirs in which there is a considerable CO₂ content (3+ mol%), the ion distribution at surface conditions will differ from that at reservoir temperature and pressure. Equilibrium ion-distribution calculations need to be made when adjusting the surface-salinity measurement to reservoir conditions.

Formation temperature affects the S_w estimates because, for constant formation-water composition, R_w varies with temperature.³ Maximum downhole temperature is measured with most log runs and drillstem-tool (DST) tests, and these are widely used to estimate a temperature vs. depth profile. It can be argued that the temperature required for resistivity-derived S_w estimates is the prevailing temperature in the rock volume seen by the tool at the time of logging. At this time, the relevant rock is likely to be cooler than the original formation temperature. The error induced by the usual maximum temperature simplification is not large, and the cooling issue is generally ignored.

Electrical-Property SCAL Data. The third aspect of making these S_w calculations is the choice of the model for the “electrical network” within the rock. These models relate S_w to several formation variables including the bulk-formation resistivity and the formation-water resistivity. A number of models have been published [e.g., Archie, Waxman-Smits-Thomas (WST), dual-water (DW), and Indonesia].^{16,31} Laboratory measurements of two or more types of electrical properties are taken. All of these models assume a homogeneous rock sample.

Archie Exponents.³⁹ First, a set of cleaned core plugs with a range of porosities are fully saturated with brine of known resistivity, and the bulk resistivity of each core plug is measured. For this simplest model, the slope of a line fitted to a log-log plot of the data set gives the cementation exponent, m , and the intercept is the cementation constant,³⁹ a (see **Fig. 3H.14**, where $a = 1$ and $m = 1.77$). These parameters are used to predict point-by-point F from porosity; leading to predictions of R_0 and S_w .

$$F = \frac{R_0}{R_w}, \dots\dots\dots (3H.7)$$

where F = formation factor, R_w = brine-water resistivity, and R_0 = rock resistivity with zero oil and gas saturation (100% PV S_w). The plotted logarithmic data ($\log_{10}F$ and $\log_{10}\phi$) are fitted with a linear model of the form,

$$F = \frac{a}{\phi^m}, \dots\dots\dots (3H.8)$$

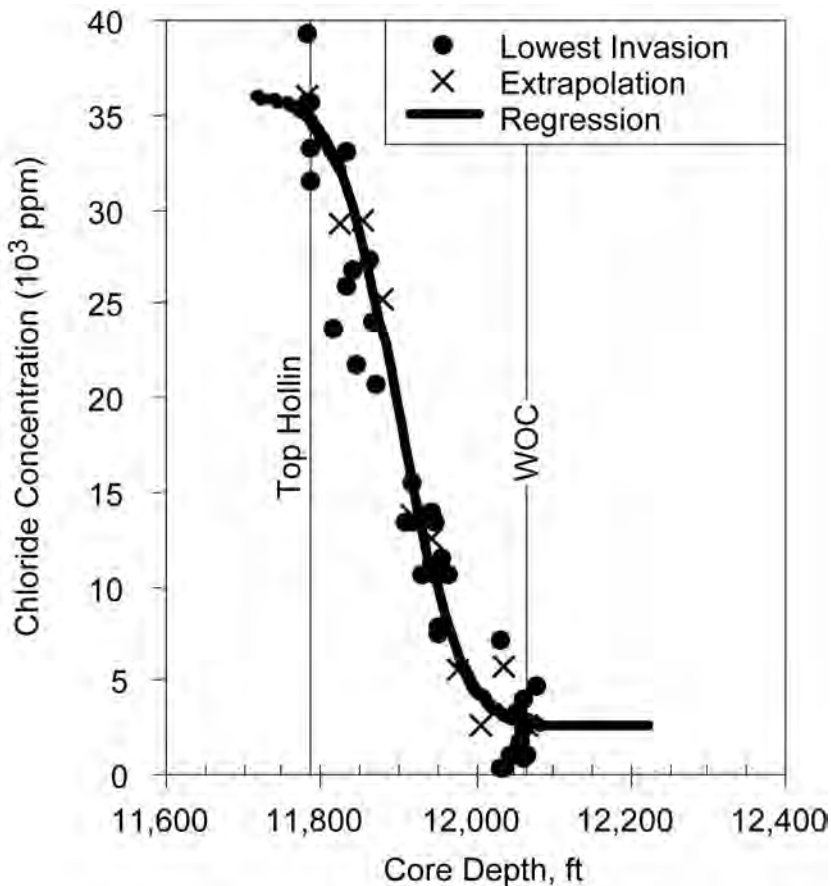


Fig. 3H.13—Formation-water salinity variation within the hydrocarbon column (Villano oil field, Ecuador).³⁷ Hollin is the name of the oil-reservoir formation, and WOC is the water/oil contact. Chloride concentration in the reservoir brine varies from approximately 2,000 to 35,000 ppm. Lowest invasion refers to limited OBM-filtrate invasion into the cores.

where ϕ = porosity, a = cementation constant, and m = cementation exponent. Therefore, $m = -\text{change in } \log_{10} F / \text{change in } \log_{10} \phi$ (the slope of the line-fit) and $a = F$ at 100% BV porosity (the line-fit intercept).

This model was developed by Archie,³⁹ who proposed $a = 1.0$ and $m = 1.8$ to 2.0 for his data set. Subsequent work by Exxon researchers for several sandstone rocks recommended $a = 0.61$ and $m = 2.15$ (the Humble formula).⁴⁰ Carbonates also have been studied and yielded a recommendation to use $m = 1.87 + 0.019/\phi$ below 9% BV (the Shell formula).³ However, carbonate pore and fracture networks vary greatly, and m values from 1.0 to 3.0 may be required. Clearly, m is not a constant, but varies with rock type.

When plotting these formation-factor data, it is typically assumed that the rock samples have similar pore geometry, but with differing levels of porosity and diagenesis. Reservoir-specific exponent values are likely to provide more-accurate S_w results than worldwide correlations. However, before reservoir-specific values are determined, descriptive and experimental data need to be studied to determine whether they need to be subdivided into various groupings that relate to distinct differences in lithological properties (grain size, sorting, or clay-mineral content).

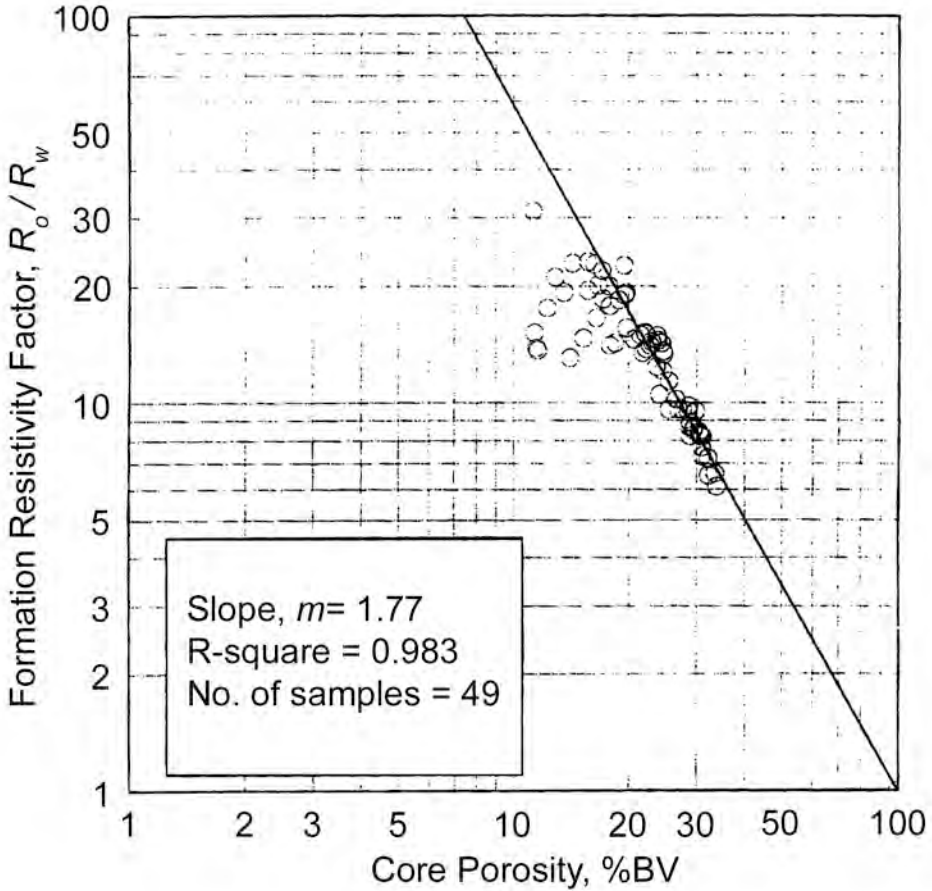


Fig. 3H.14—Laboratory-measured formation resistivity factor (F) vs. porosity for core plugs from Dulang field, Malaysia.⁵²

In partially brine-saturated rocks, a related experimental study involves measuring electrical properties as a function of water saturation. In these experiments, the resistivity index (I_R), the ratio of the desaturated-rock resistivity to the 100% PV brine-saturated rock resistivity (R_t/R_0), is measured as a function of brine saturation. For example, in a porous-plate apparatus, S_w is changed by increasing gas pressure, and therefore capillary pressure, at the gas/water interface in the pores. Brine flows from the base of the plug via a porous-plate. From the measurements on each core plug, a log-log plot of I_R vs. S_w is made (see Fig. 3H.15, where $n = 1.64$). The slope of the line (almost always forced through $I_R = 1.0$ at $S_w = 100\%$ PV) is the Archie saturation exponent n (see Eqs 3H.9 and 3H.10). On the basis of experimental data, Archie³⁹ recommended that $n = 2.0$, and this value is still widely used when no experimental data are available. Although cementation exponents can be determined from log analysis, saturation exponents cannot and, therefore, require external information from core data.

$$n = \frac{-\Delta \log_{10} I_R}{\Delta \log_{10} S_w}, \dots \dots \dots (3H.9)$$

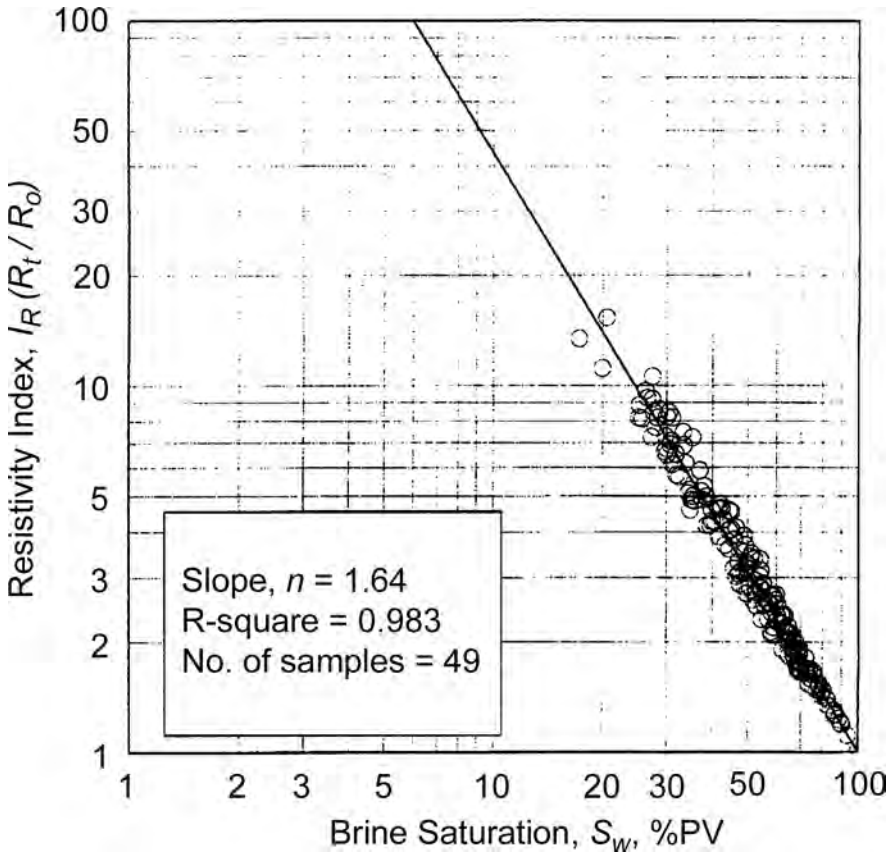


Fig. 3H.15—Laboratory-measured formation resistivity index (I_R) vs. brine saturation for core plugs from Dulang field, Malaysia.⁵²

$$\text{and } S_w = \left(\frac{1}{I_R}\right)^{1/n} = \left(\frac{R_0}{R_t}\right)^{1/n}, \dots\dots\dots (3H.10)$$

where n = saturation exponent, the slope from the origin of a line-fit of several data points; I_R = resistivity index; and S_w = fractional brine water saturation.

A straight line-fit is usually used, but curved line-fits can be considered where necessary. Curvature is often the result of the clay-mineral content but may also result from an inhomogeneous water distribution at the pore scale (e.g., when microporous rock grains are present). When significant amounts of clay minerals are present in the rocks, other models are required to extend the Archie relationships. The WST model, discussed next, is based on laboratory SCAL measurements including cation-exchange capacity (CEC).

Waxman-Smiths-Thomas Exponents and Cation-Exchange Capacity. WST cementation and saturation exponents (m^* and n^*) are required to apply the WST shaly-sand-model equation discussed in Sec. 3H.7.3. The quantity of cation-exchange sites per gram of rock sample (CEC) may be measured in the laboratory by several methods and, after converting to CEC per unit PV, is used as the model parameter Q_V .^{41,42} The most reliable measurement of Q_V involves carrying out bulk-rock resistivity, R_0 , tests at several brine resistivities and, therefore, is time consuming. The rock conductivity values ($1/R_0$) are plotted vs. brine conductivity ($1/R_w$) to identify the excess conductivity resulting from the shales and clay minerals. The slope of the fitted

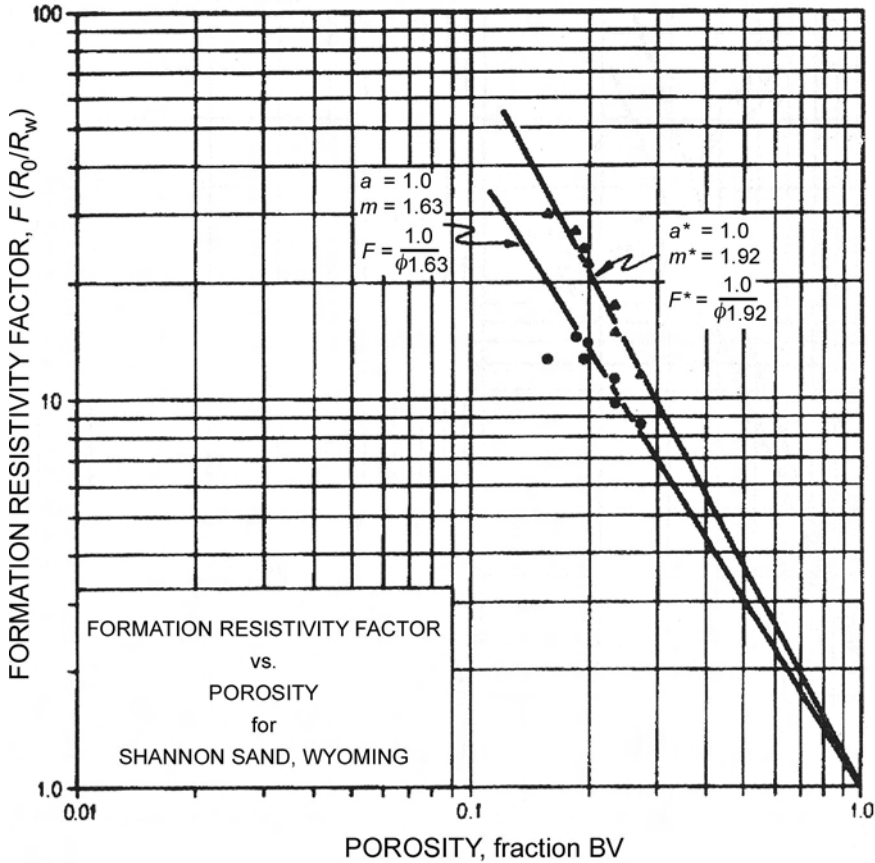


Fig. 3H.16—Laboratory-measured formation resistivity factor (F) vs. porosity for core plugs from the Shannon sand, Wyoming, U.S.A. (after Keelan and McGinley⁵⁴). F and m are Archie parameters, and F^* and m^* are Waxman-Smiths-Thomas parameters.

line is the reciprocal of F^* , the WST formation factor. The excess conductivity is modeled as being equal to BQ_v/F^* , and B is presumed in this model to be always positive. The parameter B is the equivalent counter-ion conductance,^{41,42} which is a function of temperature and the free-water resistivity. Q_v is estimated from the values of F^* and B . Core resistivities are also measured when S_w is less than 100% PV and both the WST exponents m^* and n^* are derived (see Fig. 3H.16 and Fig. 3H.17, respectively). It should be noted that $m^* > m$ and $n^* > n$, except in “clean” sands.

Other CEC methods require the breaking up, disaggregation, and consequent partial loss of the real geometry of the rock’s electrical network. These simpler methods, such as the ammonia method, use analytical-chemistry methods to measure CEC. After measuring porosity and grain density, this practical laboratory unit is converted to the required Q_v parameter.⁴³ These simpler CEC measurements are often made on sidewall cores and are used together with exponent values measured on cores from neighboring wells.

Numerous other shaly-sand models have been developed, and, unlike WST, many are calculated from effective porosity. These types of models are generally applied using Archie exponents. When using SCAL electrical-property data, there must be consistency between the electrical-network model used to derive the laboratory parameters and the model used in the

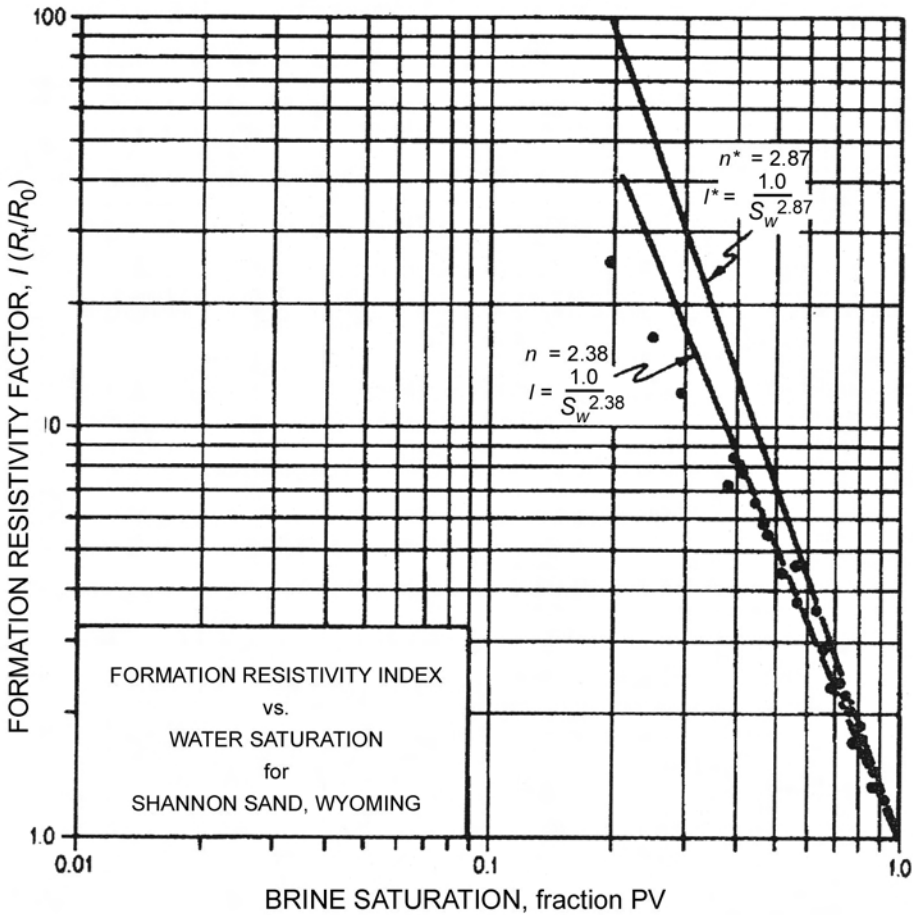


Fig. 3H.17—Laboratory-measured formation resistivity index (I_R) vs. brine saturation for core plugs from the Shannon sand, Wyoming, U.S.A. (after Keelan and McGinley⁵⁴). n is the Archie saturation exponent, and n^* the Waxman-Smiths-Thomas saturation exponent.

final S_w calculations from the porosity and the resistivity logs (e.g., if the laboratory provides standard Archie n values, these are not appropriate input to the WST equation).

Capillary Pressure SCAL Data. P_c data are a different type of SCAL data that can be taken experimentally in several ways. All P_c saturation tests respond to the pore-size distribution of the rock and the interfacial properties of the various solid/fluid systems. These data are obtained by desaturating core plugs, either using a centrifuge or a porous-plate apparatus. Initially, cleaned and dry plugs are saturated with either water or oil. The liquid is then displaced by air or nitrogen. Because air is very nonwetting compared with either water or oil, using these fluid pairs (air/water or air/oil) means that, as the P_c increases, the air will first occupy the largest pores. As the P_c and air saturation increase, the air will occupy smaller and smaller pores. The core plug begins the experiment saturated with the wetting phase, so the desaturation process provides data for the drainage P_c curve. After completing the drainage process, the core plug can be spun under the liquid in a centrifuge experiment, the liquid saturation will increase, and the imbibition P_c curve will be generated. Usually, only drainage P_c/S_w data are

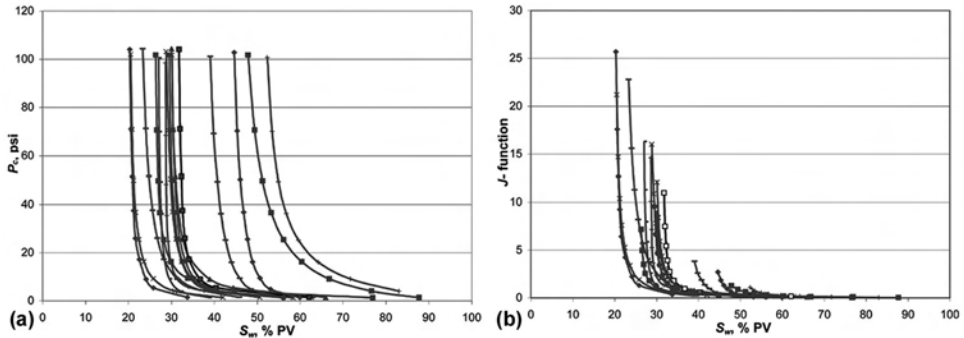


Fig. 3H.18—Example plots of centrifuge air/brine capillary pressure (P_c/S_w) data and its conversion to a J -function basis; data from an Asian gas field. The air/brine P_c value of 100 psi is equivalent to a height above free-water level of 200 to 350 ft, depending on the reservoir fluid’s properties and the temperature and pressure conditions.

taken, and for most reservoir situations, these are the relevant data because they correspond to the original oil (or gas) trap-filling process.

MICP data are taken on cleaned and dried irregular core pieces. The core pieces are evacuated to a low vacuum, and mercury is injected with increasing pressure, up to 20,000 psi and sometimes higher. Corrections for clay-mineral adsorbed-water removed during drying can be made with the Hill-Shirley-Klein method.⁴⁴ The MICP experiment has the advantage of being run rapidly but is not a true wetting/nonwetting system. The sample cannot be used for subsequent SCAL tests because some mercury is retained within the core pieces at the end of the testing sequence. MICP data are widely used to measure pore-size distribution, but, when considering whether they should be used for accurate S_w calculations, MICP should be compared with air/water or air/oil P_c/S_w data.

The P_c/S_w data are usually compared first on a Leverett “ J -function” basis.⁴⁵ The P_c data are converted to the J -function basis by multiplying each P_c value by the square root of its permeability divided by porosity and then dividing by the fluid-pair IFT multiplied by the contact angle (see Eq. 3H.11). J -function values differ depending on whether they are calculated in oilfield or metric units. The J -function approach assumes similar pore-size distribution in all cores tested. In this way, the various P_c/S_w data tend to converge when the underlying assumptions are met; however, there may still be enough scatter to suggest that the data need to be divided into two or more groupings (see Fig. 3H.18).

$$J(S_w) = \frac{P_c}{\sigma \times \cos \theta} \sqrt{\frac{k}{\phi}} \dots\dots\dots (3H.11)$$

From a J -function vs. S_w plot, the technical team can determine whether enough data have been obtained, whether new data need to be gathered to fill in portions of the data ranges, and whether the data indicate that subgroupings are appropriate and needed. Also, this plot indicates whether there are significant outliers that should be excluded or examined in more detail. A drawback to this averaging method is the introduction into S_w determination of four measured parameters and their associated errors (i.e., porosity, permeability, IFT, and contact angle).

Capillary pressure data may also be averaged by various models.^{46,47} The relationship of S_w with permeability, and then porosity, is examined and is followed by examination of the height dependency.

OBM-Core S_w Data. The last type of S_w data discussed here is that obtained from routine core analysis of core plugs cut from OBM cores, either preserved as whole cores or else with

core plugs cut at the wellsite and preserved individually. These data are taken foot-by-foot and are direct measurements of reservoir S_w values.^{37,38,48-51} Many fields may never have had any wells cored with OBM; others may have only one or two OBM-cored wells. Even a single OBM coring of the full reservoir interval offers significant data that may impact the technical team’s methodology for making the S_w calculations. It is better to have at least two wells fully cored with OBM from different areas of the reservoir.

To evaluate the OBM-core S_w data, they should be plotted as S_w vs. \log_{10} (permeability) or vs. porosity to identify outliers and trends in the data. Particularly, the low-porosity/low-permeability data range should be examined for potential measurement problems. Sometimes, the raw laboratory measurements of water volume and PV data need to be reviewed for problem points and recalculations made where appropriate. Finally, the data should be divided into various possible interval groupings so that any needed zonation can be identified.

If reservoir connate water has flowed out of the core plug at any stage before the laboratory measurement, the OBM-core S_w data are clearly not representative of the in-situ reservoir S_w . This certainly occurs in water-bearing formations and can also occur in the lowest intervals of the oil/water or gas/water transition zones. These lowest intervals, which may be a few feet to approximately 30-ft thick, are precisely the same intervals in which a water cut is expected with the initial oil production. The mobile-water intervals can be identified in OBM wells where the shallow-reading induction-log resistivity is higher than the deep-reading induction-log resistivity. This pattern indicates higher oil saturations in the invaded zone compared with the original oil saturations. Where mobile water is observed, the OBM-core S_w measurements do not represent in-situ S_w and are too low.

3H.7.3 Application of Each S_w Technique and Its Strengths and Weaknesses. Methodologies for quantifying S_w at the wellbore are discussed here. The main features of each approach are described; however, in some cases, there are variations that are not addressed. For each technique, its strengths and weaknesses are discussed.

Calculating S_w From Resistivity Well Logs by Applying a Model Relating S_w to Porosity, Connate-Water Resistivity, and Various Rock Electrical Properties. The most common technique for calculating S_w is the use of resistivity logs with a model (empirical or theoretical) that relates S_w to R_t , R_w , and porosity. As mentioned previously, a large number of R_t/S_w models have been published. The models are applied at every data point in the reservoir where deep resistivity, porosity, and shale-volume estimates, if required, are available. The evaluation of all other necessary parameters (constant or variable R_w values, a , m , n , Q_V , V_{sh} , $R_0 = F \cdot R_w$, etc.) has also been discussed previously. Several commercial software packages are available that perform these S_w calculations for a variety of log models.

Clean-Sand (Archie) Model.

$$S_w = \left(\frac{aR_w}{R_t \phi^m} \right)^{1/n}, \dots\dots\dots (3H.12a)$$

and, alternatively,

$$S_w = \left(\frac{R_0}{R_t} \right)^{1/n} \dots\dots\dots (3H.12b)$$

This model³⁹ is used for field studies in the many sandstone and carbonate reservoirs in which the clay-mineral content is low. This decision is strengthened after SCAL data have demonstrat-

ed that the simplest solution is satisfactory. When a significant fraction of smectite (montmorillonite) is present and where finely laminated sand and shale sequences occur, one of the shaly-sand models is very likely to be required. Low-resistivity pay is an issue in several oil-producing areas, such as the U.S. Gulf Coast, Egypt, and Indonesia, and hydrocarbon reserves can be missed and left undiscovered as a result of the resistivity suppression by clay minerals and shales.

Shaly-Sand Models. In the clean-sand model, the formation water is the only electrically conductive medium. In shaly rocks, R_t is suppressed and Archie S_w calculations are too high. As clay-mineral-rich rocks were studied and experimentally tested, more-complicated electrical models were developed to account for the effects of the geometries of conductive clay minerals and shale on rock resistivity. The primary goal of the shaly-sand models is to determine a working relationship between S_w using parameters similar to the Archie model, but also incorporating the quantity and specific electrical properties of the clay-mineral/shale. All of the shaly-sand models reduce to the Archie equation when the shale component is zero. For simplicity, in all of the shaly-sand models, the cementation constant, a , is taken to be 1.0 but, if required, can be easily associated again with the R_w term.

Laminated Sand/Shale Model. A parallel resistor model might be used for laminated sands, with multiple thin parallel layers of 100% shale interbedded with clean-sand layers. Thin, in this context, means that there are several beds within the vertical resolution of the resistivity-logging tool.

$$\frac{1}{R_t} = \frac{V_{sh}}{R_{sh}} + \frac{1 - V_{sh}}{R_{sd}}, \dots\dots\dots (3H.13)$$

where the clean-sand resistivity $R_{sd} = R_w / (\phi_{sd}^m S_{wsd}^n)$. For this laminated shale/sand model, effective porosity depends simply on the sand fraction of the bulk volume:

$$\phi_e = \phi_{sd}(1 - V_{sh}), \dots\dots\dots (3H.14)$$

$$\text{and } S_{we} = S_{wsd} \dots\dots\dots (3H.15)$$

The value of ϕ_{sd} may be assumed from neighboring thick sands, and all of the parameters, except the S_w of the sand, S_{wsd} , can be estimated.

Poupon-Leveaux (Indonesia) Model. The Indonesia model was developed by field observation in Indonesia rather than by laboratory experimental measurement support.⁵² It remains useful because it is based on readily available standard log-analysis parameters and gives reasonably reliable results. The formula was empirically modeled with field data in water-bearing shaly sands, but the detailed functionality for hydrocarbon-bearing sands is unsupported, except by common sense and long-standing use. S_w results from the formula are comparatively easy to calculate and, because it is not a quadratic equation, it gives results that are always greater than zero. Several of the other quadratic and iterative-solution models can calculate unreasonable negative S_w results.

$$\frac{1}{R_t} = S_w^n \left[\left(\frac{V_{sh}^{2-V_{sh}}}{R_{sh}} \right)^{1/2} + \left(\frac{\phi_e^m}{R_w} \right)^{1/2} \right]^2 \dots\dots\dots (3H.16)$$

$$S_w = \left\{ \left[\left(\frac{V_{sh}^{2-V_{sh}}}{R_{sh}} \right)^{1/2} + \left(\frac{\phi_e^m}{R_w} \right)^{1/2} \right]^2 R_t \right\}^{-1/n} \dots\dots\dots (3H.17)$$

The Indonesia model,⁵² and other similar models, are often used when field-specific SCAL rock electrical-properties data are unavailable but are also sometimes used where the SCAL exponents do not measure the full range of shale volumes. Although it was initially modeled on the basis of Indonesian data, the Indonesia model can be applied everywhere. The inputs are the effective porosity, ϕ_e , shale volume and resistivity (V_{sh} and R_{sh}), and water and deep resistivities (R_w and R_t). The S_w output is usually taken to be the water saturation of the effective porosity, but it has been recently suggested that the output is likely to estimate S_{wt} .³¹ Many other log-based shaly-sand models have been proposed⁵³ but, for brevity, are not discussed here.

Waxman-Smits-Thomas and Dual-Water Models. S_{wt} , the water saturation of the total porosity, is calculated at each reservoir data point by iterative solution of the complex multiparameter WST and DW equations (Eqs. 3H.18 and 3H.19). For brevity, the details^{3,41-43,54-56} of the solution methods are not presented here. The WST and DW models are total-porosity/ S_w system models.

The WST model is based on laboratory measurements of resistivity, porosity, and saturation of real rocks.^{41-43,54} Q_v is the CEC per unit PV.

$$\frac{1}{R_t} = \phi_t^{m^*} S_{wt}^{n^*} \left(\frac{1}{R_w} + \frac{BQ_v}{S_{wt}} \right), \dots\dots\dots (3H.18)$$

where S_{wt} = water saturation of the total porosity as shown schematically in Fig. 3H.8, B = specific cation conductance in (1/ohm*m)/(meq/mL), and Q_v = CEC in meq/mL of total PV. The exponents m^* and n^* apply to the total PV.

The DW model^{31,55,56} is also based on the WST data. It uses clay-bound-water conductivity instead of WST's BQ_v factor (see Eqs. 3H.18 and 3H.19) and an alternative shale-volume descriptor, S_{wb} , the saturation of physically bound water in the total PV (see Fig. 3H.8).^{3,43} When V_{sh} is zero, S_{wb} is zero; and when V_{sh} is 100% BV, S_{wb} and S_{wt} are also 100% PV.

$$\frac{1}{R_t} = \phi_t^{m_o} S_{wt}^{n_o} \left[\frac{1}{R_{wf}} + \frac{S_{wb}}{S_{wt}} \left(\frac{1}{R_{wb}} - \frac{1}{R_{wf}} \right) \right], \dots\dots\dots (3H.19)$$

where R_{wb} = resistivity of clay-bound water (= $R_t \phi_t^m$) in the shales, and R_{wf} = resistivity of free formation water (= $R_t \phi_t^m$) in the shale-free water zones. Because of the different model assumptions, DW exponents m_o and n_o must always be smaller than the WST exponents⁵⁵ and may be values similar to “clean” sand exponents. Where the WST and DW models have been properly applied, the V_{HCP} results should be equal. All S_{wt} calculations from the WST and DW methods must be checked to ensure that they are greater than S_{wb} . After this check, they are used with ϕ_t to obtain the V_{HCP} . For the DW model, when the outputs require conversion to effective porosity, ϕ_e , and effective water saturation, S_{we} , the properties are converted with Eqs. 3H.20 and 3H.21, respectively.

$$\phi_e = \phi_t (1 - S_{wb}), \dots\dots\dots (3H.20)$$

$$\text{and } S_{we} = \frac{S_{wt} - S_{wb}}{1 - S_{wb}} \dots\dots\dots (3H.21)$$

Strengths and Weaknesses of R_t -Based S_w Calculations. The greatest strength of S_w calculations from the R_t logs is that these calculations can be made at each net-pay depth with valid data for all wells within the log database. The calculations can account for any subsets of input parameters related to the individual zones.

The weaknesses of the R_t -based S_w calculations are that one has to select a model to describe the relationship of S_w to R_t , R_w , and a variety of other input parameters. Any model is an approximation to the real nature of the reservoir pore system and, typically, has limitations such as how the clay-mineral conductivity is modeled. Log-analysis estimates of V_{sh} are rather uncertain, so sands that are substantially free of clay minerals can easily, and incorrectly, be assigned significant clay volumes. In these circumstances, complex shaly-sand models may have been applied when it is more appropriate to model the sand as clean sand. Effective porosity is also impacted by the uncertain V_{sh} estimates. The R_w is often assumed to be constant within the hydrocarbon column, and usually there is little data regarding R_w other than from aquifer samples. In several cases in which the R_w distribution has been studied in depth, it was found to vary in systematic ways within the hydrocarbon column and not necessarily be the same as in the underlying aquifer.³⁶⁻³⁸

CEC can be measured in the laboratory, but in the reservoir it must be estimated by correlations with porosity or V_{sh} . For the laboratory CEC measurements, there are fundamental uncertainties such as the degree to which the clay-mineral geometry is altered by the disaggregation of the core. The total surface area and CEC may be enhanced by comminution (i.e., grinding to grain-size particles).⁵⁷

The other input parameters for the S_w/R_t models are either based on “worldwide experience” (such as default exponent parameters in commercial software packages) or developed from SCAL rock-electrical-property measurements on a relatively small number of core plugs from the reservoir interval. Hence, there are relatively few data determining the parameters that are used for the log point-by-point S_w calculations. It has to be assumed that the manner in which the water saturation is distributed in the core plugs during these laboratory experiments is like that of the real reservoir. Because water is present during the laboratory measurements, clay minerals are rehydrated at the time of the tests.

Calculating S_w From Laboratory Capillary-Pressure/Saturation Measurements. A second S_w method that is totally independent of the resistivity logs uses laboratory-measured P_c/S_w data. The underlying concept of the use of capillary pressure data is that the reservoir has come to capillary equilibrium over geologic time (the millions of years since hydrocarbons have entered and filled the reservoir trap). This equilibrium is reproduced in laboratory experiments using the centrifuge, porous-plate, and MICP methods. The P_c/S_w data are measured on a selected set of reservoir core plugs representing a range of porosity and permeability values (and possibly also lithologies).

Centrifuge experiments are typically made on 1-in. core plugs over a period of several days in the intense gravitational field (up to 1000 G) of the centrifuge and are assumed to be equivalent to what occurs in a hydrocarbon reservoir over millions of years in a 1-G gravitational field and over lengths of 10 to hundreds of feet. These assumptions are broadly accepted as being reasonable, provided that the samples are not damaged during testing in the centrifuge. The reported P_c/S_w values are not the raw laboratory data. In the laboratory, the average saturation is determined at each centrifuge speed, and those raw data are input to a mathematical model to convert them to a tabulation of endface saturations and P_c values.

Porous-plate P_c tests are made on core plugs at several different gas pressures and are generally carried out at the same time as the resistivity experiments. After reaching equilibrium with no further brine flow at each pressure, the S_w is constant along each plug and is calculated from its weight loss.

TABLE 3H.4—TYPICAL IFT AND CONTACT ANGLES AND APPROXIMATE CONVERSION FACTORS FROM P_c TO H_{hwc} (after *Fundamentals of Rock Properties*⁸)

Fluid-Pair Nonwetting/Wetting	Contact Angle (°)	IFT (dynes/cm)	Approximate Equivalent Vertical Height in Reservoir per psi of Laboratory P_c (ft per psi)
Laboratory P_c Pair			
Air/Brine	0	72	2 to 3.5
Oil/Brine	30	48	3.5 to 5
Mercury/Air	140	480	0.4 to 0.7
Air/Oil	0	24	6 to 11
Reservoir P_c Pair			
Oil/Brine	30*	30	
Gas/Brine	0*	50**	

*Typical contact angle for mainly water-wet system. **Pressure and temperature dependent. Approximate IFT value to depth of 5,000 ft. Note: These conversion-factor ranges apply in many gas and oil reservoirs, but conversion factors are larger for heavy-oil reservoirs. Assumes fluid density difference of 0.25 g/cm³ for oil/water and 0.75 g/cm³ for gas/water reservoirs. Eq. 3H.22 used to calculate height conversion factors.

MICP tests are made on dried core pieces and the volume of injected mercury, the nonwetting phase, is converted to an S_w value. This is considered to be total S_w if, at high enough pressures, mercury enters both the microporosity and dry clay-mineral porosity. Conversely, for centrifuge or porous-plate tests, where brine is present as the wetting phase, clay minerals probably hydrate, and their physically bound water is unlikely to be displaced during the test. Brine-related P_c/S_w measurements may give total or effective S_w , depending on the specific porosity measurement method used (i.e., whether the porosity occupied by the clay-mineral physically-bound water is included or excluded from the porosity calculation). Effective S_w values are always lower than total S_w values and should be very low at high capillary pressures if there is little nonclay-mineral-related microporosity.⁵⁸

The conversion of the laboratory P_c/S_w data to reservoir conditions requires knowledge of the IFT and contact angle of the fluid pair used in the laboratory and properties of the brine and hydrocarbon fluids at reservoir conditions. These are needed to calculate the density of each phase and to estimate the IFT between the fluid pair at reservoir conditions. The P_c values (in psi) are converted to vertical height above the hydrocarbon/water contact, H_{hwc} (in feet), with the following formula:

$$H_{hwc} = \frac{[(\sigma \times \cos \theta)_r \times P_c]}{[0.433 \times (\rho_w - \rho_h) \times (\sigma \times \cos \theta)_s]}, \dots\dots\dots (3H.22)$$

where fluid densities (ρ) are in g/cm³, and the subscripts are r = reservoir, s = surface, h = hydrocarbon, and w = water. **Table 3H.4** lists some typical values⁸ for IFT, σ , and contact angle, θ , used in **Eq. 3H.22** and provides approximate ranges for the factors for converting P_c -laboratory data to height above a reservoir free-water level. Height- P_c conversion factors are similar for many oil and gas reservoirs; the footnotes in **Table 3H.4** describe the values that were assumed to calculate these ranges. More details of correlations for brine/hydrocarbon IFT as a function of oil or gas gravity have been published.⁵⁹ The reservoir-condition contact angle, θ , is usually taken as 0 for gas reservoirs and 0 or 30° for oil reservoirs because, generally, data are not available at reservoir conditions.

The suite of P_c/S_w data is typically converted to a mathematical relationship between S_w as the dependent variable and the independent variables—porosity, permeability, and H_{owc} or H_{gwc} .^{46,47,60} Because permeability is usually determined as a function of porosity, it is often not included as an independent variable. Two of the mathematical forms that have been used are

$$S_w = A + B \times \phi + C \times \phi^2 + \frac{D}{H_{owc}} + \frac{E}{H_{owc}^2}, \dots\dots\dots (3H.23)$$

$$\text{and } \log_{10} S_w = A \times \log_{10}(H_{owc} + B) + C \times \phi + D, \dots\dots\dots (3H.24)$$

where A , B , C , D , and E are curve-fit constants. In Eq. 3H.24, B permits the removal of singularities at zero height.

In developing the coefficients for these relationships, any zonation of the reservoir intervals needs to be applied, and then separate sets of coefficients developed for each zone. The zonation can be based on geological interpretation of the reservoir depositional and diagenetic history and/or variation in the P_c/S_w curves for different parts of the reservoir interval.

The depth of the reservoir's OWC or GWC must be known in order to make S_w calculations using the P_c/S_w methodology. The calculations of S_w are made only above this depth. In reality, the H_{owc} or H_{gwc} is referenced to the FWL (i.e., the depth at which $P_c=0$ and which is deeper than the observed OWC or GWC). For a gas reservoir consisting of good-quality rocks, the difference between the FWL and the GWC is typically 1 ft or less. However, for an oil reservoir containing a heavier oil, this difference can be 10 feet or more, and, given four-way closure on an anticlinal structure, the impact on the OOIP volume between using the FWL vs. the observed OWC as the $H_{owc} = 0$ depth can equal a few percent of OOIP.

Once the various sets of coefficients have been developed and the P_c to H_{owc} (or H_{gwc}) conversion made, an S_w value can be calculated at each data point within the log database that has a valid porosity value and is above the OWC or GWC. Hence, there will be the same number of, or more, S_w values available from this S_w methodology as when using the R_i logs.

Strengths and Weaknesses of P_c/S_w -Based S_w Calculations. The strength of S_w calculations from P_c/S_w data is that, after making a correlation with porosity and height, a unique S_w value is available for all wells at all net-pay depths with valid porosity values in the log database. This also applies to the whole hydrocarbon column anywhere in the reservoir once the well-bore porosity values have been propagated into the full geocellular model grid. These calculations can account for any zonation and subsets of input parameters related to the individual zones.

A potential weakness in the P_c approach to S_w calculations is whether the laboratory measurements have been allowed sufficient time to reach equilibrium. If not, the S_w values, particularly at high P_c values, will be too high. Another potential weakness is the accuracy of the IFT value used in converting from surface to reservoir conditions; fortunately, these values vary over a limited range for most hydrocarbon/brine pairs. A third potential weakness is the definition of the FWL depth compared with the observed OWC or GWC. A fourth potential weakness is whether enough data have been taken to be representative, both vertically and areally, of the zones in the reservoir.¹⁴

The fifth potential weakness concerns the complexity of the reservoir's hydrocarbon-filling and structural history. In simple oil-reservoir situations and most gas-reservoir situations, this is not an issue. However, for oil reservoirs with tar mats and heavy-oil zones there is a complication because of the varying oil density near the OWC, including the possibility that the tar mat has a hydrocarbon density very close to that of the connate brine. Another aspect may be whether all or portions of the hydrocarbon column are on the imbibition cycle where imbibition P_c/S_w data are needed for the S_w calculations, not the typical drainage P_c/S_w data.¹⁴

Calculating S_w With OBM-Core-Plug Dean-Stark Water-Volume Determinations. The third method for determining the S_w in a reservoir's hydrocarbon column is to cut OBM cores and perform Dean-Stark water-volume determinations on the routine core plugs. Foot-by-foot S_w values can be calculated from these water volumes and the associated core-plug PVs. OBM cores are typically cut only in a few wells in a particular field. These S_w data can be applied to other, uncored wells in the reservoir if strong correlations between these values and porosity and/or permeability are identified. These data are not valid in the oil/water or gas/water transition zone or in the aquifer, intervals in which the connate brine is mobile. OBM-core S_w values may be found to be either higher or lower than those from the other two methods described previously.

Strengths and Weaknesses of OBM-Core S_w Values. The strength of S_w values from routine-core-analysis Dean-Stark S_w data is that these data are the most direct measure of reservoir connate S_w values above the oil/water or gas/water transition zone. Relative to the two methods discussed previously and the variations of these methods, the OBM-core S_w approach is a direct S_w determination and the other methods are indirect S_w -calculation approaches that require many more assumptions and inferences.

The weaknesses of the OBM S_w method are that it does not apply to the lowest parts of the oil/water or gas/oil transition zone where the brine phase has mobility and that, generally, the amount of OBM core S_w data is limited because the operator cuts cores with OBM only in a limited number of wells because of the expense. The first of these weaknesses can be overcome if the OBM S_w data are used in combination with either the resistivity logs or with P_c/S_w data.

Another consideration is that the whole project, from the mud formulation to the core-handling and -preservation procedures on through the routine-core-analysis measurements, needs to be monitored and reviewed in detail to ensure all steps were executed properly. This demands that considerable time and effort be spent by the technical team to ensure success; however, to some extent the same comment applies to the P_c/S_w and resistivity-log/ S_w calculation approaches discussed previously.

3H.7.4 Integration of S_w Data From the Different Methods. Depending on the data availability in a particular reservoir situation, a combination of the various S_w approaches may prove superior to the use of a single type of data. The first step in going to a combination approach is to review the reservoir's database to identify any significant gap in vertical, or areal, coverage. The most obvious gap often occurs near the fluid contact, because there is little reason to drill wells in downdip locations, particularly during a reservoir's development phase. Three examples of combination approaches are described here.

Resistivity-Log Data With P_c/S_w Data. Resistivity-log-derived S_w results may not be available throughout the hydrocarbon column of a reservoir. To fill gaps and average the point-by-point data set, it is common practice to plot S_w as a function of height, to omit nonpay points, and to identify various porosity ranges by coding the data points. Resistivity-log-derived S_w data frequently shows V- or U-shaped patterns on these plots because of the shoulder/bed effects near nonpay sections (shales). The most accurate S_w values in such patterns are usually at the lowest S_w values where the thin-bed correction is minimized. In a manner similar to that described in the previous P_c/S_w section, height/saturation curves are often fitted to these resistivity-log-derived S_w data to enable reservoir hydrocarbons-in-place volumes to be calculated. The function forms are similar to or are the same as those described in the P_c/S_w section.⁶⁰

Routine OBM Core S_w Data With P_c/S_w Data. Because there is a need to define the S_w characteristics of the oil/water or gas/water transition zone and because the OBM-core S_w data

can be incorrect and too low in this interval, one approach is to use P_c/S_w data in combination with the routine OBM-core S_w data. This can be done by first correlating the OBM-core S_w data to porosity and assuming that this relationship is valid above the oil/water or gas/water transition zone. The functional form of this first relationship might be

$$S_w = A + B \times \phi + C \times \phi^2 \dots\dots\dots (3H.25)$$

The second step is to create a tabular data set in which the S_w /porosity correlation is used to calculate an array of S_w values for large H_{owc} or H_{gwc} values and a range of porosity values. For this part of the data set, S_w is assumed to be independent of the H_{owc} or H_{gwc} values. The P_c/S_w data converted to reservoir conditions is used to provide data points for low H_{owc} or H_{gwc} values and various porosity values. Statistical calculations are applied to the whole of this data set. The functional form of this second relationship might be

$$S_w = A' + B' \times \phi + C' \times \phi^2 + \frac{D}{H_{owc}} + \frac{E}{H_{owc}^2} \dots\dots\dots (3H.26)$$

With this functional form, the boundary conditions of the first step are automatically met in the second step.

Routine OBM-Core S_w Data With Resistivity-Log Data. To address the lack of valid OBM-core S_w data in the oil/water or gas/water transition zone discussed previously, it is also possible to combine OBM-core S_w data with the resistivity-log data to develop an overall S_w methodology. This approach assumes that a number of wells have been drilled through the OWC or GWC so that there are log resistivity values through the oil/water or gas/water transition zone. In this approach, the OBM-core S_w data are used to back-calculate the saturation-exponent, n , values over each zone so that the core-based V_{HCP} value equals that calculated from the resistivity logs (see Eq. 3H.26). Then the core-based saturation-exponent, n , values are applied to the noncored well's resistivity logs to calculate S_w point-by-point throughout the reservoir interval in all wells.^{22,61} This approach assumes that the R_w , a , and m values have been determined from other experimental and fluid-sample data so that R_0 can be calculated.

$$n = \frac{\log_{10}R_0 - \log_{10}R_t}{\log_{10}S_{wc}} \dots\dots\dots (3H.27)$$

where R_0 is the bulk resistivity at $S_w = 100\%$ PV and is calculated with Eqs. 3H.7 and 3H.8. R_t is the deep-reading resistivity-log reading, and S_{wc} is the OBM-core S_w above the mobile-water transition zone. The resulting back-calculated n values at the core-plug depths are averaged for the zone. In some instances, n may be found to have an areal variation within a zone that should be taken into account in subsequent calculations.

Adjustments to S_w Data From Different Methods. In the previous section, a number of methodologies for S_w calculations have been described. These are basically three independent methods; hence, they can be used together to determine the accuracy of the S_w calculations throughout the hydrocarbon column. Because the methods are based on very different technical approaches and assumptions, if the different methods give essentially the same S_w answer, then it is highly likely that this is the correct S_w .

However, the challenge comes when, as is often the case, the different methods result in different S_w values and distributions. The OBM-core S_w values might be either higher or lower than those from the other two methods. The common misunderstanding that OBM-core S_w is likely to be too low is unsubstantiated. In a very large reservoir, it could go both ways depending on where one is in the reservoir.^{22,61} If the values are quite different, two aspects of the calculations need to be reviewed in depth. First, the quality of the input laboratory data needs to be checked and how it was converted from raw data into the input values to the S_w calculations needs to be reviewed. Second, the assumptions and models used for the S_w calculations need to be checked. For example, with the P_c/S_w data, the assumed oil/water density difference may be considerably in error, or the shaly-sand S_w model may be inappropriate for the particular reservoir. As well as the S_w averages, the zone-average V_{HCP} values from the various methods should be compared, which includes porosity in the comparison calculations.

Core, Total, and Effective Systems Compatibility. The Archie R_r -based S_w equation models “clean” sands. Various other shaly-sand models use either the effective or the total-porosity systems. It is well known that these basic models, if applied properly to the same formation, must produce the same final V_{HCP} from their different calculation procedures (see Fig. 3H.8 and Eqs. 3H.3 through 3H.5 in Sec. 3H.5).³ ϕ_t is greater than or equal to ϕ_e ; however, at the same time, S_{wt} is greater than or equal to S_{we} and, when used together, the appropriate combinations must give the same V_{HCP} result. For the total-porosity system, $V_{HCP} = \phi_t \times (1 - S_{wt})$, whereas for the effective-porosity system, $V_{HCP} = \phi_e \times (1 - S_{we})$.

The V_{HCP} can also be estimated from a combination of core porosity and Dean-Stark S_w measured on preserved OBM cores. The several systems—core, total, and effective—must all give the same fundamental results, and the most accurate of them (the OBM-core method) can be used to calibrate and test the less accurate methods. When properly adjusted and applied (e.g., by improving the V_{sh} estimates or IFT values), all three methods give the same final V_{HCP} . If they do not agree, the likely sources of uncertainty and error must be examined.

It is clearly inconsistent and incorrect to mix the systems by, for example, reporting an effective porosity with a total S_w , a total porosity with an effective S_w , or a standard-core porosity with an effective S_w . System compatibility must also be maintained by correct use of the SCAL measurements and log-analysis formulae, when these are used to calibrate the resistivity logs and P_c/S_w methods. The differences should be resolved as much as possible. To the extent that they are not, the differences can be considered to be a measure of the uncertainty in the S_w calculations.

3H.7.5 Uncertainties. It is the uncertainty of the hydrocarbon saturation ($1 - S_w$) that is economically important, not the absolute uncertainty in S_w . When uncertainties in S_w are evaluated, their importance in terms of S_o and S_g should be accounted for. The uncertainties of the several S_w -evaluation methods vary widely.

OBM-Core S_w Data. The water volume extracted from a single core plug may have a random and known systematic uncertainty of $\pm 0.05 \text{ cm}^3$, where each uncertainty refers to one SD. The PV of a typical 1-in. core plug is 4.0 cm^3 if the porosity is 20% BV. The water-volume uncertainty alone equates to an S_w uncertainty of $\pm 1\% \text{ PV}$ ($0.05/4.0$). The uncertainties in porosity have a further effect on this calculation.⁴⁸ An OBM-core S_w of 20% PV, therefore, has a combined 1-SD range from approximately 18 to 22% PV. At lower porosities and higher S_w values, the water-volume uncertainty may be $\pm 0.1 \text{ cm}^3$, leading to an S_w uncertainty of $\pm 3\% \text{ PV}$, when the porosity is 15% BV. As porosity decreases, the uncertainty grows. Before the measurements are made, any water in the toluene and the Dean-Stark apparatus must be removed, or the S_w values will be overstated. The extraction time required to recover the water adsorbed on the clay minerals adds to the uncertainty.

The uncertainty of the average core S_w will be improved when plugs are selected at one or two per foot with equal spacing and without regard for the rock quality. However, as discussed previously, plug samples are not always selected at random, so care must be exercised, especially regarding the S_w values predicted at depths where core is not available. From a broader perspective, it must also be remembered that 1-in. core plugs only sample approximately 2% of the full-core volume. Because of these many factors, the authors estimate that uncertainties similar to those given concerning porosity also propagate to the zone-average OBM-core S_w values. Measurements in which larger core plugs are analyzed will reduce several of the uncertainties.

Resistivity-Log-Derived S_w Values. The log readings, typical SCAL-derived Archie exponents, and all of the other associated parameters are uncertain. For example, the resistivity-log uncertainty may be $\pm 50\%$ when R_t is 500 ohm•m. The most important uncertainty contributors at low S_w values are likely to be R_t and n . S_w uncertainty in this circumstance is estimated at $\pm 5\%$ PV (i.e., if S_w is calculated as 10% PV, the 1-SD range is 5 to 15% PV).⁴⁸ At lower porosity values and higher water saturations, similar methods led to uncertainty estimates of $\pm 9\%$ PV. Given that further uncertainty in the final calculated S_w may arise from shaly-sand effects and many other sources, the authors believe that the ranges given apply equally to the overall systematic uncertainty of the S_w zone-average values. These estimates are all 1 SD; therefore, in 32% of cases, zone-average uncertainties are considered likely to be greater than the ranges given.

P_c -Derived S_w Values. The uncertainty estimates are the sum of several factors. Most of these factors have their greatest impact on the S_w calculations in the first 100 to 200 ft of the hydrocarbon column above the fluid contact. Therefore, because the transition zone is considerably longer in many oil reservoirs than in a gas reservoir, their impacts will be greater in most oil reservoirs. Above 200 ft, the S_w values are usually only changing slowly; hence, the primary consideration above the transition zone is whether the laboratory measurements are taken at equilibrium conditions.

The first factor in the uncertainty analysis is the fundamental assumption as to whether the drainage or imbibition P_c/S_w data should be used. In most cases, the drainage curves should be used, but, in a few situations, the reservoir may be on the imbibition cycle. In these situations, the improper choice of using the drainage P_c curve can lead to a +5 to 20% PV S_w error in the first 100 to 200 ft above the OWC.^{28,29}

The second factor concerns the laboratory P_c/S_w measurements. If the measurements are not taken to equilibrium, then the S_w values at a particular P_c value will be too high. This can be +1 to 10% PV effect for the large H_{owc} or H_{gwc} range. The other key aspects for reported centrifuge laboratory results are how the raw laboratory measurements of water volumes were determined and how these data have been converted to the reported endface saturations. The water-volume measurements have the same-size potential error as discussed for the OBM Dean-Stark S_w measurements (± 1 to 3% PV). Differences in the laboratory calculation procedures can result in further variations of ± 1 to 3% PV in reported P_c/S_w results when using the same raw laboratory data. For porous-plate tests and others, the repeated handling of poorly cemented or uncemented core plugs can cause grain loss, which, after the final calculations, translates into small errors in S_w .

The third factor is how the suite of raw laboratory data for a particular reservoir interval are curve-fitted and presented in the final laboratory report as tabulations of P_c/S_w values for each core plug. Uncertainty in the application arises from how these reported values are averaged for use in the S_w calculations over the full range of reservoir porosity and permeability values. This uncertainty includes how the data are weighted and whether some potential outlier data from one or two core plugs distorts the averaged P_c/S_w curves. These uncertainties primar-

ily affect the first 100 to 200 ft above the H_{owc} or H_{gwc} so that their impact depends on how thick the hydrocarbon column is and its distribution as a function of H_{owc} or H_{gwc} .

The final factor is the conversion of the averaged P_c/S_w curves (or equation) from surface to reservoir conditions, all of which affect the conversion of P_c values to H_{owc} or H_{gwc} values. This includes a number of subfactors, each with its own uncertainty level: IFT at surface and reservoir conditions, fluid-pair density difference at reservoir conditions, contact angles, and depth of the actual in-situ FWL compared with the OWC or GWC. The contact angles at surface and reservoir conditions are generally taken to be the same because no data are available to proceed otherwise. For these other factors, the uncertainty is considerably greater for an oil reservoir than for a gas reservoir; because the IFT values can be low and compared with those for a gas reservoir, the density differences are significantly less particularly if there is a vertical oil-gravity variation that results in a heavy-oil interval just above the OWC. All of these factors affect the H_{owc} or H_{gwc} values; therefore, their impact on the S_w calculations is predominantly in the first 100 to 200 ft above the fluid contact.

In summary, the use of P_c/S_w data can result in S_w uncertainty of ± 5 to 15% PV in the oil/water or gas/water transition zone. Above that transition zone, the uncertainty is related to whether the laboratory data were taken at equilibrium conditions and how the various P_c/S_w curves have been averaged together. In this range, the uncertainty is likely to be 3 to 10% PV.

3H.8 Permeability Determination

Point-by-point permeability values are needed over the reservoir interval at the wellbores for several purposes. First, the distribution and variation of the permeabilities are needed by the engineers to develop completion strategies. Second, this same information is needed as input to the geocellular model and dynamic-flow calculations (e.g., numerical reservoir-simulation models). For both of these, the first consideration is the location of shales and other low-permeability layers that can act as barriers or baffles to vertical flow. A second consideration is the nature of the permeability variation (i.e., whether the high-permeability rock intervals occur in specific layers and the low-permeability intervals occur in other layers, or that there is so much heterogeneity that the high- and low-permeability intervals are intimately interbedded with each other).

When good-quality core data are not available, estimates of permeability can be made from empirical equations. Permeability is controlled by such factors as pore size and pore-throat geometry, as well as porosity. To take some account of these factors, the widely used Timur equation⁶² relates permeability to irreducible S_w and porosity, and therefore can be applied only in hydrocarbon-bearing zones. This form of his equation applies to a medium-gravity oil zone:

$$k = \frac{10^4 \phi_e^{4.5}}{S_w^2}, \dots\dots\dots (3H.28)$$

where k = absolute permeability in millidarcies, ϕ_e = effective (not total) porosity as a bulk volume fraction, and S_w = effective water saturation above the transition zone as a fraction of PV. Estimates that are based only on porosity are likely to have large prediction errors, especially in carbonate reservoirs. Equations of the following form, or a logarithmic-linear form, are useful particularly in sandstones:

$$\log_{10} k = C \log_{10} \phi_e + D, \dots\dots\dots (3H.29)$$

where parameters C and D are very approximate and equal to about 7, and k and ϕ_e are as defined following Eq. 3H.28. They should be adjusted according to local knowledge.

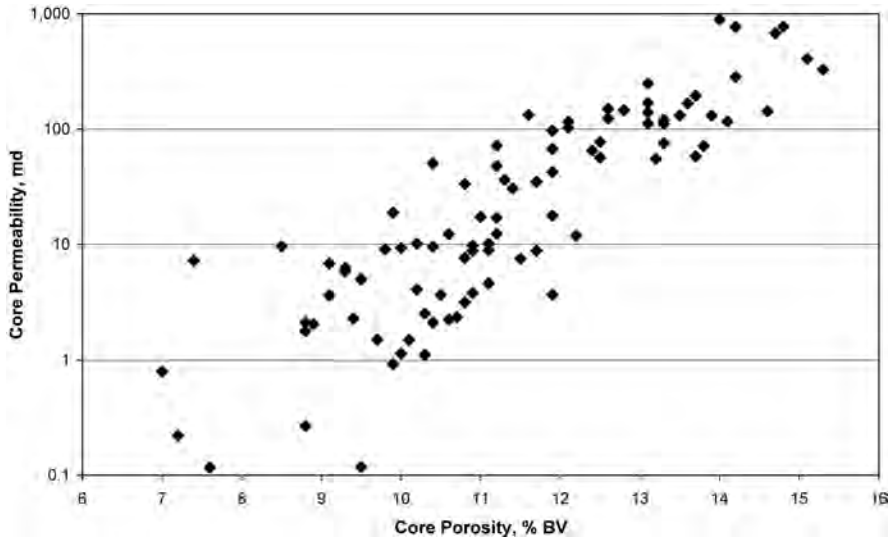


Fig. 3H.19—Core permeability vs. core porosity crossplot; data from an Asian gas field.

In field evaluation, the starting point for calculations of permeability is the routine-core-analysis data. These data, and the associated SCAL measurements of permeability and porosity as a function of overburden stress, are input to calculations to develop permeability values at reservoir conditions and the permeability vs. porosity correlation. The permeability vs. porosity correlation is often taken as semilogarithmic but usually with a steeper slope at low-porosity values. [Figs. 3H.19 and 3H.20](#) demonstrate the characteristics of these relationships. [Fig. 3H.19](#) presents a typical permeability vs. porosity relationship from routine-core-analysis data (the scatter in these data increases at the lower-porosity levels). [Fig. 3H.20](#) shows the permeability ratio (stressed permeability divided by unstressed permeability) vs. unstressed permeability. This ratio is much smaller for low-permeability values and approaches a value of 1.0 for the high-permeability values.

In developing the permeability vs. porosity relationships, the technical team needs to identify the extent to which the reservoir interval needs to be subdivided into zones or layers. The subdividing of the core data over the reservoir interval should be into logical subdivisions that are strongly influenced by the geologists' understanding of the depositional environment. This will naturally account for major differences in grain size, sorting, and key mineralogical factors. Alternatively, a sufficiently thick reservoir interval can be subdivided into layers of 50 to 100 ft each. A superior petrophysical methodology will be developed if a thick reservoir is appropriately subdivided, compared with treating the full reservoir interval with a single permeability vs. porosity correlation. A single permeability vs. porosity correlation for a reservoir interval with different depositional environments can lead to underprediction of permeability by an order of magnitude in an interval of better-sorted rocks compared with poorly sorted rocks (see [Fig. 3H.3](#)). Identifying the location and correct values of highest-permeability rocks is very important for reservoir flow modeling.

The result of modeling the relationship with the least-squares regression method is that the range of predicted permeability values is smaller than that of the original routine-core permeability data. This loss of range is made worse when the logarithm of permeability is used as the y -variable because the logarithmic model is a predictor of the geometric-average permeability.³² While the permeability vs. porosity relationship is developed from the routine and SCAL core-analysis data, the application to the point-by-point well-log database requires the use of porosity values calculated from the logs. It is preferable to model the prediction

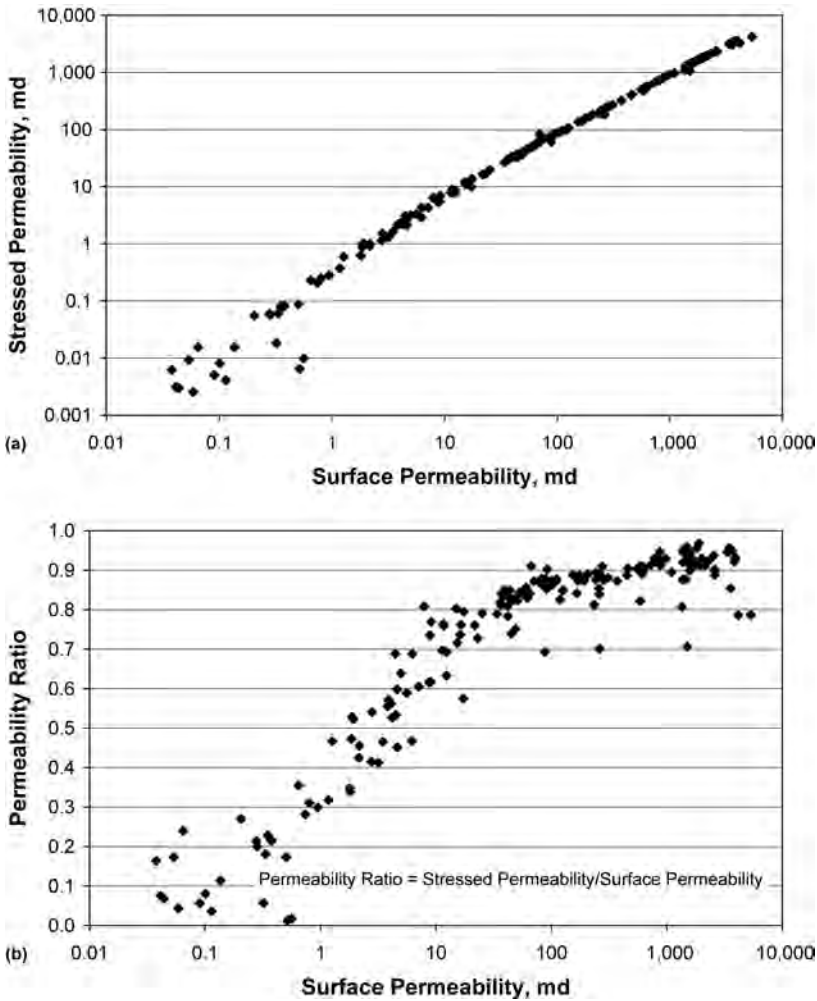


Fig. 3H.20—Crossplots of core permeability at stressed vs. surface conditions and core permeability ratio vs. core permeability at surface conditions; data from an Asian gas field. “Stressed” refers to the rock being subjected to simulated overburden pressure of approximately 4,500 psia. The permeability correction is larger at low permeabilities.

equation directly with core permeability and the basic log values³² (see **Fig. 3H.21** and the calibration line-fitting in **Sec. 3H.5.3**). The *y-on-x* (dashed) line-fit in **Fig. 3H.21** follows a curved trend on the logarithmic-linear plot and uses an arctangent function as the transformation. The solid line gives arithmetic average permeabilities at various bulk-density values. The arithmetic averages, which may be more appropriate in some reservoirs, are 2 to 3 times larger than the geometric averages. Alternative predictions of permeability may also be estimated using two-log or multiple regression analysis methods.

After the permeability values have been calculated point-by-point over the reservoir interval from the various wells’ logs, these permeability values need to be compared with those derived at each well from the pressure-transient analysis (PTA) of the pressure-buildup (PBU) or falloff data. The PBU permeability values are average values for the interval open to flow into the wellbore. The type of average (arithmetic, geometric, harmonic, or somewhere in between) to use with the point-by-point permeability values depends on the nature of the depositional envi-

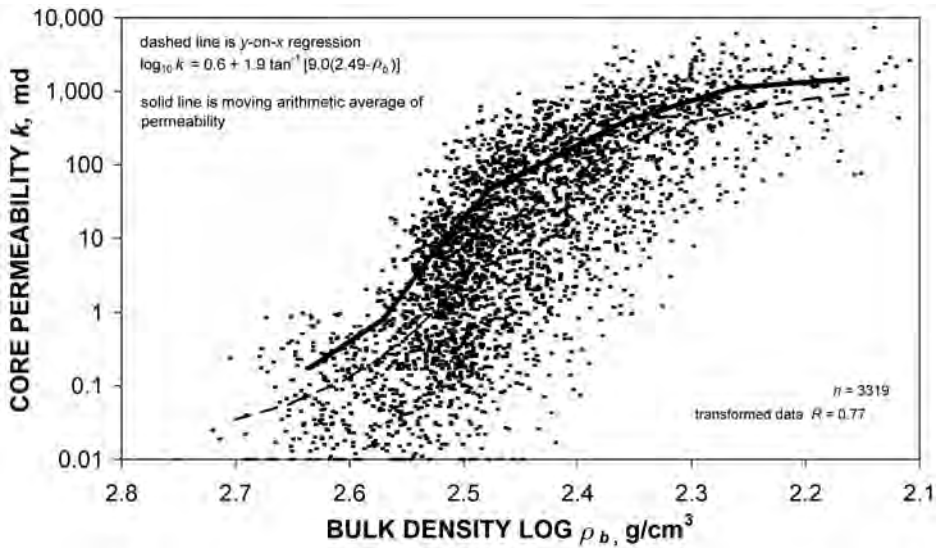


Fig. 3H.21—Nonlinear regression relationships for core permeability and bulk density log (South Morecambe gas field, offshore U.K.). After Woodhouse.³² The two lines illustrate the significant difference between geometric and arithmetic averages.

ronment and whether the perforated intervals are a small fraction of the full reservoir interval. If there are significant differences between the two sets of average permeability values, then the technical team needs to determine the likely cause of the differences—small-scale fractures, relative permeability effects, or some other geological factors. The point-by-point permeability values may need to be adjusted on the basis of the technical teams' conclusions.

3H.9 Petrophysical Case Studies

This section presents brief summaries of detailed petrophysical evaluations of several fields that have been described in the SPE and Soc. of Professional Well Log Analysts (SPWLA) technical literature. These case studies cover some of the complications that occur when making net-pay, porosity, and S_w calculations.

3H.9.1 Prudhoe Bay Field. Prudhoe Bay is the largest oil and gas field in North America with more than 20 billion bbl of OOIP and an overlying 30 Tscf gas cap. In the early 1980s, the unit operating agreement required that a final equity determination be undertaken. In the course of this determination, an extensive field coring program was conducted, which resulted in more than 25 OBM cores being cut in all areas of the field and some conventional WBM and bland-mud cores in other wells. Also, several major laboratory programs were run to address various technical issues regarding the correct approach to calculate porosity and water saturation. The background geologic understanding of the major reservoir, the Ivishak or Sadlerochit, and various technical studies have been presented in a number of technical papers.^{14,15,21,22,27,36,48,49,61,63,64}

Geologically, the Sadlerochit reservoir is a combination structural/stratigraphic trap consisting of a 500-ft reservoir interval covering an area of 15×35 square miles at a depth of 8,000 to 9,000 ft. This reservoir is mainly very high quality deltaic Permo-Triassic sandstones deposited in a braided stream environment, ranging from fine-grained to conglomeratic, with some limited intervals of shales found in various areas of the reservoir. The reservoir has been divided vertically into eight zones on the basis of differences in rock types (see Fig. 3H.1). The grains are primarily quartz, quartzite, and chert. Over geologic time, there have been significant leach-

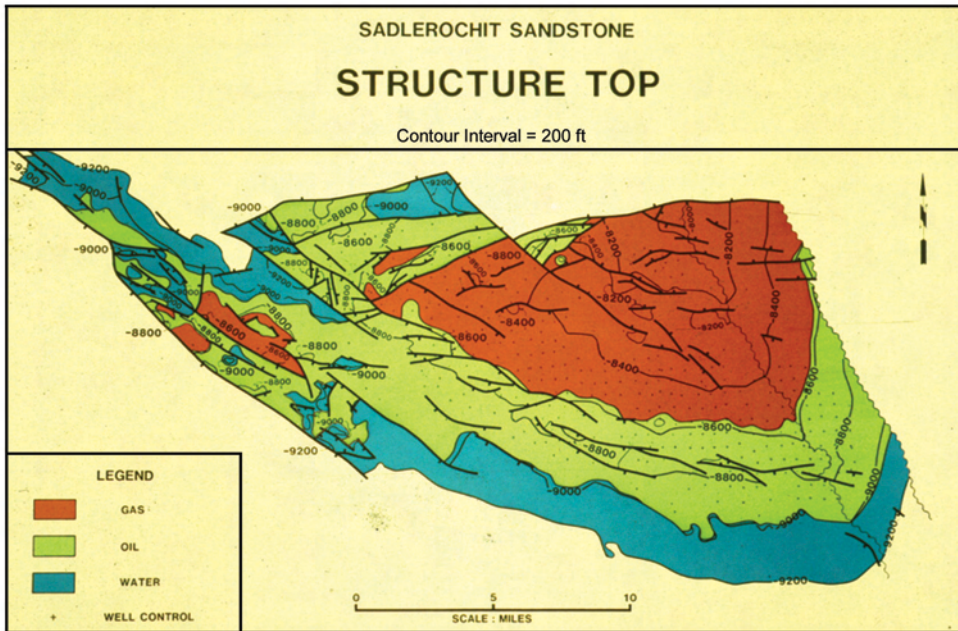


Fig. 3H.22—Areal structure map showing gas-cap and oil-column distribution in the Sadlerochit reservoir, Prudhoe Bay field, Alaska, U.S.A.²⁷

ing and cementation. The chert grains have been leached to varying degrees, resulting in a significant intragranular component (10 to 60%) of the pore system. There are considerable amounts of siderite and pyrite cementation, together with quartz overgrowth and kaolinite cementation.²¹

The structural and hydrocarbon-filling histories of Prudhoe Bay are very complicated; this is clearly evident from a visual examination of the cores, the routine-core-analysis fluid-saturation data, and an interpretation of the seismic data.²⁷ Oil initially filled this trap 40 million years ago. Since that time, because of differential burial, there has been a change in the configuration of the trap. Where there was previously a 2,000-ft closure, currently there is less than 1,000-ft maximum closure. The reservoir “tilting” resulted in a relict-oil zone systematically varying in thickness, which underlies the current oil column particularly to the southeast. At its base, the relict-oil zone had a flat OWC at the end of the original oil filling. Later, gas migrated into the trap creating a large gas cap over the main area of the field, but also smaller ones in the west-end area of the field. At discovery, a 40- to 60-ft heavy-oil-tar (HOT) layer was found above the current OWC with the oil gravity decreasing upwards from there. No relict-oil interval and essentially no HOT interval are found in the western part of the reservoir (see [Figs. 3H.22 and 3H.23](#)).

The net pay was based on defining the shale and siltstone intervals as nonpay.²¹ Except for the inclusion of a small number of highly cemented sandstone intervals, this is effectively equivalent to a permeability cutoff of 0.6 md on the basis of routine-core-analysis permeability data, unadjusted to reservoir conditions. The net pay was determined from geologists’ core descriptions. A GR-log model was used to define the pay/nonpay intervals within the Sadlerochit reservoir interval using the more than 450 logged wells’ normalized GR logs. Radioactive sandstone intervals had previously been edited out of the core-log database. This GR-log model had to account for both thick and thin shale intervals, which it did by using three parameters—GR-

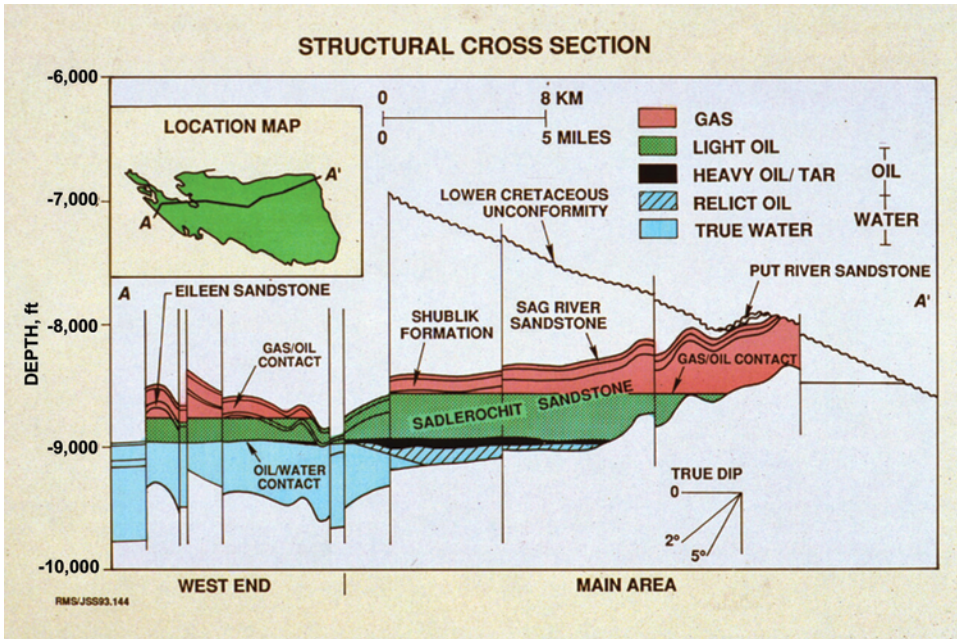


Fig. 3H.23—Cross section showing hydrocarbon distribution at discovery in the Sadlerochit reservoir Prudhoe Bay field, Alaska, U.S.A.²⁷

sand, GR-thin, and GR-thick. The reservoir area was subdivided to account for areal variations when calibrating the GR-log model to the geologists' core picks of shale and siltstone intervals.

Porosity in the Sadlerochit interval was based on use of routine-core-analysis porosity data and sonic logs. The density log was not used because of the heavy-mineral effects discussed previously. The porosity data were not adjusted for overburden stress at reservoir conditions because it was found that the highly asphaltic crude oil had not been thoroughly cleaned from the core plugs during the routine laboratory procedures. Because there were generally both full-diameter Boyles-law and sum-of-fluids porosity measurements on the pebbly-sandstone and conglomeratic intervals (and both core-plug Boyles-law and sum-of-fluids porosity measurements for the other intervals), a hierarchy of these data was used when preparing the core standard for use with the sonic logs. The sonic log was calibrated linearly to the core porosity data. The calculations were performed individually for each of the eight zones and the different fluid intervals (gas cap, oil column, and aquifer). Finally, the reservoirwide porosity solution for each of these zone/fluid combinations was arealized to account for remaining systematic differences.

The OBM cores indicated that there is a wide range of S_w values, from less than 5% PV in the updip oil column and its overlying gas cap to as high as 50 to 70% PV in the west-end and southwestern portions of the Sadlerochit reservoir. Conventional log-analysis and capillary pressure methods suggested a much narrower range of S_w values. For these reasons, major studies were undertaken to identify the reasons for these differences and to determine if the OBM-core S_w data were valid. The primary conclusions were as follows:

- The OBM-core S_w data are valid.^{22,48,49,61,63,64} This was confirmed by detailed observations and measurements at the wellsite at the time of coring some of the wells and at the commercial laboratory where the routine-core-analysis measurements were made.
- The centrifuge P_c data were found to agree with the OBM-core S_w data after the following effects were accounted for: the laboratory P_c/S_w measurements were run sufficiently long to reach equilibrium, it was recognized that various portions of the Sadlerochit reservoir were

on different drainage and imbibition cycles on the basis of either the ancient or the current OWC, and the vertical variation of oil densities and the effect of the HOT interval were accounted for.¹²

- The S_w calculations from the SCAL measurements of rock electrical properties agreed with the OBM-core S_w values after the following effects were included: native-state rock electrical properties were measured at the wellsite and restored-state rock electrical properties were measured in the same S_w range as found from the OBM cores; and the variations in the R_w in the oil column and gas cap were included in these S_w calculations.⁵⁹ The n parameter was found to vary significantly as a function of S_w because of the complicated intergranular/intra-granular (inhomogeneous) nature of the Sadlerochit pore system.²¹

- An independent in-situ measurement of S_w using the single-well chemical-tracer test produced results consistent with the OBM-core S_w at two updip well locations.⁶⁴

The S_w methodology for the Sadlerochit reservoir was a combined use of the OBM-core S_w data with R_i values from the deconvolved¹⁵ deep induction logs. Because of the low clay-mineral content of the Sadlerochit reservoir, an Archie S_w equation was used with n values derived for each zone at the OBM-cored wells and then trended over the reservoir. This results in foot-by-foot S_w calculations for the whole hydrocarbon column in the more than 450 logged wells. This very large database of S_w values was converted into a relationship involving porosity and H_{owc} and subdivided to account for systematic variations from one area to the next, before making the OOIP and OGIP calculations.

In summary, the Prudhoe Bay field shows that accurate petrophysical calculations can be complex, particularly in large reservoirs. If a typical approach had been used to make the various petrophysical calculations, the OOIP, OGIP, and the distribution of the hydrocarbons would have been significantly in error. Only through detailed core review by the geologists and by working through a number of complicated laboratory studies was closure reached. The same S_w values were then calculated using the various independent S_w methods.

3H.9.2 West Howard-Glasscock Unit Oil Field. This west Texas San Andres oil reservoir is an example of the petrophysical evaluation of a carbonate reservoir.⁶⁵ It is one of many San Andres oil reservoirs found in the Permian Basin of west Texas, U.S.A., and is presented to show that good-quality core/log petrophysical calculations can be undertaken even when a reservoir covers only a few square miles.

This study was performed in the 1970s after this unit was formed, and the waterflood of the San Andres reservoir was expanded. A total of 40 new wells was drilled with WBM and logged. Ten wells were extensively cored. The new wells were primarily for water injection and added to the existing 80 wells. This coring program was instituted because of the reservoir's complex and heterogeneous lithology and to aid log interpretation, geological mapping, and injection-well planning.

The routine-core-analysis measurements were primarily performed on whole core samples. **Fig. 3H.24** displays, through a permeability vs. porosity plot, the very heterogeneous nature of this reservoir. A number of plug samples (1.5 in. in diameter and 2 in. long) were cut for SCAL studies. **Figs. 3H.25 and 3H.26** show a comparison of the SCAL samples' permeability and porosity data with those from the adjacent whole-core data and show how heterogeneous this reservoir is. Previously published San Andres P_c/S_w correlations were used to calculate the irreducible S_w in the log calculations.⁶⁶

The reported SCAL measurements focused on lithology, grain-density, and electrical-property measurements. The grain densities of the vast majority of the tested samples (82%) were in the 2.84- to 2.86-g/cm³ range. The average m from tests on 32 core plugs was 2.1 (assuming $a = 1.0$). The average for n was 2.2; however, the data were quite scattered (see **Fig. 3H.27**).

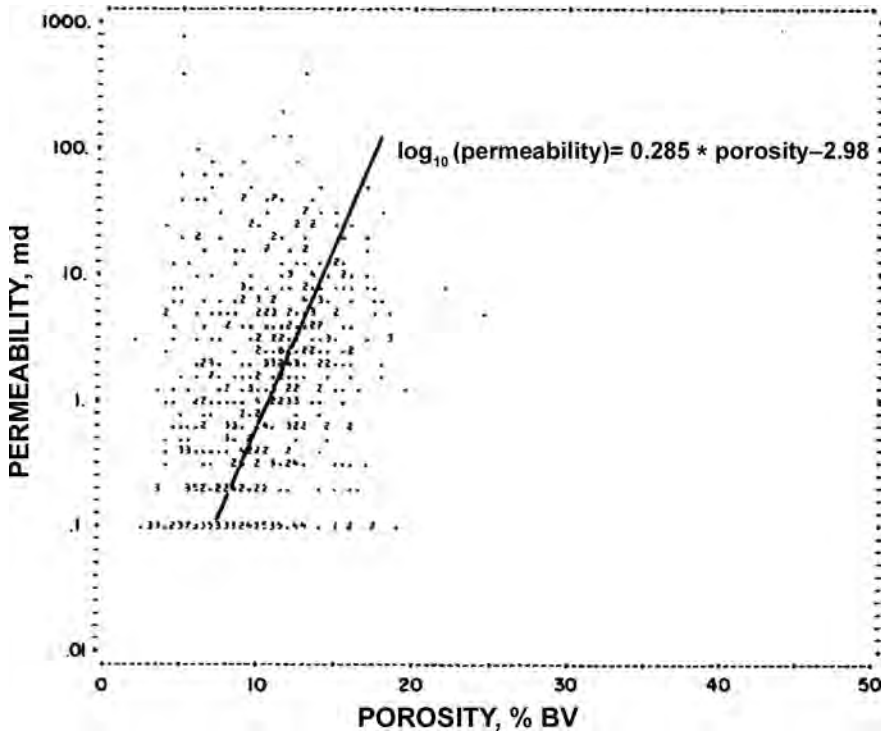


Fig. 3H.24—Core-permeability/core-porosity data for Zone D, West Howard-Glasscock Unit, west Texas, U.S.A.⁶⁵ The line fit is manually estimated.

Log computation software was used to calculate lithology and porosity. The volume of shale present was computed from the sonic and density logs because the GR log was not a good shale indicator because of the presence of many radioactive zones containing little or no shale. Variables calculated were primary porosity, secondary-porosity index, dolomite, sand, anhydrite, and shale. Fig. 3H.28 presents a comparison of the computed and the core porosity values. The permeability, S_w , and S_{wi} were calculated from the logs on the basis of relationships derived from core data.

3H.9.3 Oil Fields—Offshore Peninsular Malaysia. Several technical papers have been written about the combined use of core and log data to increase the reliability of the petrophysical calculations for the various oil reservoirs found in this basin.^{50,51} These papers particularly address how the calculations of fluid saturations were improved, and the uncertainty reduced, by a variety of coring and core-analysis studies. The bottom line to the technical work regarding the Dulang oil field was that the best estimate of OOIP was increased by approximately 30%, which led to management being more confident regarding further development.

The oil fields of the Malay basin consist of stacked sequences of laminated sands and shales. Dispersed clay minerals are present in the sands in the form of kaolinite, illite, and mixed-layer clays. The connate waters are generally of low salinity and impacted by the presence of meteoric (surface) waters. The resistivity-log readings in the sand intervals are suppressed because of the thin-bed effects.

For the reasons described in the previous paragraph, OBM- and bland-mud-coring programs were undertaken in the stacked oil reservoirs of several of these fields. These coring programs' design and execution paid great attention to all of the details before, during, and after the cor-

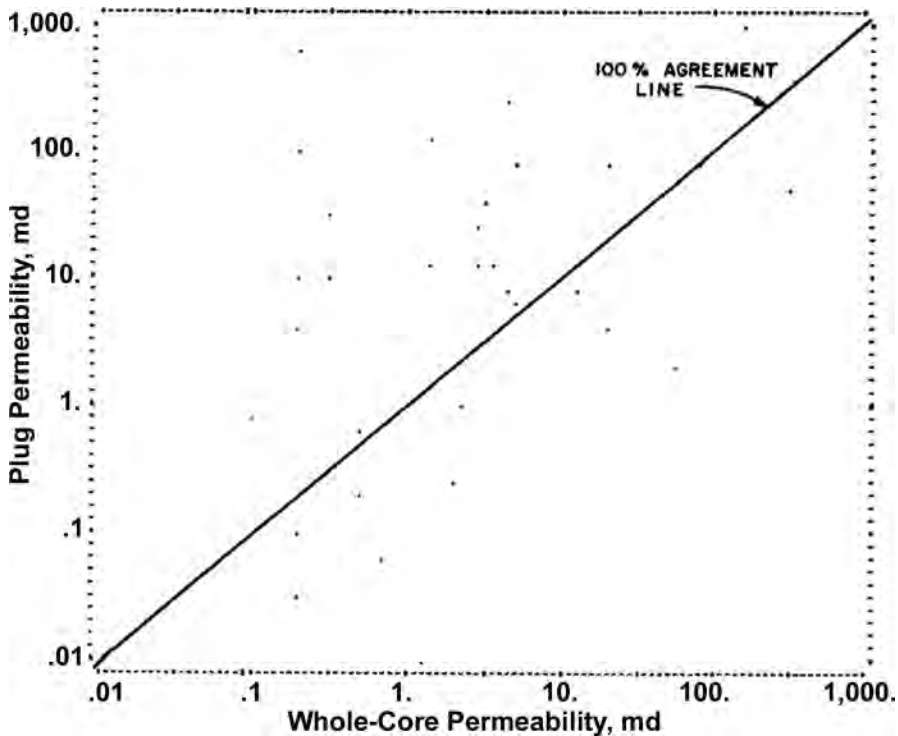


Fig. 3H.25—Comparison of whole-core permeability with core-plug permeability (West Howard-Glasscock unit, west Texas, U.S.A.).⁶⁵

ing operations. The cores were generally cut at high rates of penetration (60 to 90 ft/hr) and with low overbalance pressure (maximum of 200 psi). Because of the friable and unconsolidated nature of some of the sands, full-diameter cores were frozen in dry ice before plug cutting with liquid nitrogen. Special testing, including the use of mud-system tracers, was conducted to determine that OBM filtrate had not impacted the connate-water saturations. Because some unpublished studies suggested that some of the connate water might be displaced as far as 100 to 150 ft above the OWC, core-layering tests were run to determine the depth and concentration of mud tracers within the cross section of the core. The layering tests found that OBM-filtrate invasion was insignificant.

The routine-core-analysis measurements of OBM cores included Dean-Stark S_w determinations and water-salinity studies. Sponge cores were analyzed for residual-oil saturations. SCAL core samples were taken for rock electrical-property measurements. Fig. 3H.29 presents an example plot showing a comparison of the core results and the results calculated from the logs.⁵⁰

The results from the analysis of the Dulang field's various studies were as follows:⁵¹

- The Dulang reservoirs' connate S_w was found, from OBM cores, to range from 20.1 to 43.1% PV with an average of 33.6% PV, compared with the previous range of 19 to 61% PV with an average of 39% PV. Also, the S_w varies from reservoir to reservoir, as controlled by the reservoir quality and depositional environments.

- The measurements of water salinity and R_w indicated that R_w varied with reservoir depth and was not constant as previously assumed (see Table 3H.5).

- The rock electrical-property measurements indicated that m and n have values of 1.77 and 1.64, respectively (assuming $a = 1.0$). n was significantly lower than the previously used value of 1.89 (see Table 3H.5).

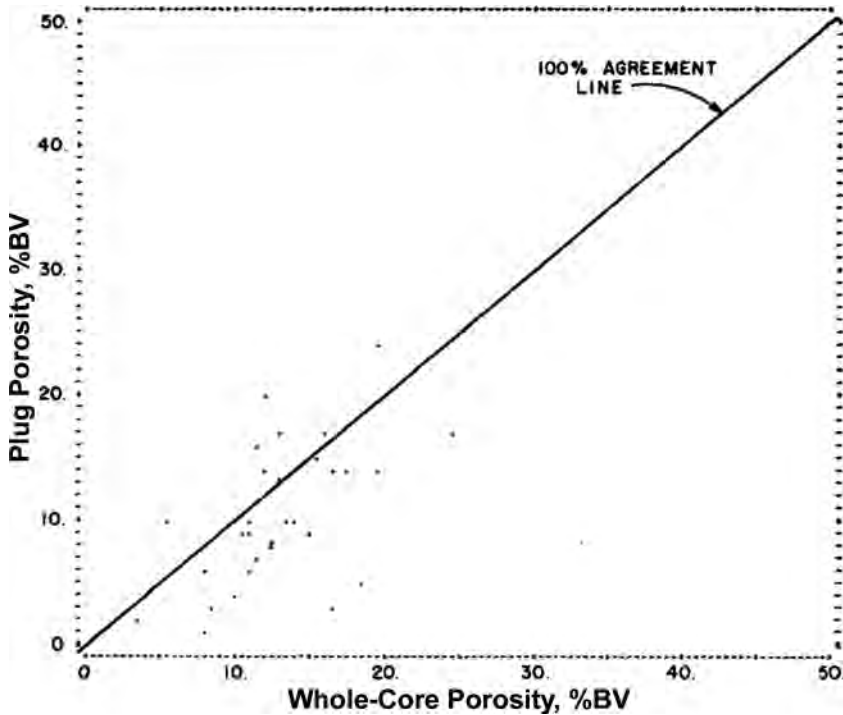


Fig. 3H.26—Comparison of whole-core porosity with core-plug porosity (West Howard-Glasscock unit, west Texas, U.S.A.).⁶⁵

- The authors used these core data to calibrate the DW model.
- The residual-oil saturation data indicated that S_{orw} ranged from 25.8 to 29% PV with an average of 27.5% PV. Recovery factors ranged from 37.8 to 49.4% for the various reservoirs.

The effect of these changes in the petrophysical calculations for the various reservoirs was that S_w had been previously overestimated. The impact of the revised calculations and new core data for the Dulang field's OOIP was that it increased from 550 to 685 million STB.

3H.9.4 Block A-18, Gas/Condensate Field, Malaysia-Thailand Joint Development Area.

This example used core P_c and log data to increase the reliability of the petrophysical calculations for gas/condensate reservoirs found offshore near the Thailand-Malaysia border.⁶⁷ It addresses how the S_w calculations were improved by the integrated use of resistivity logs in a shaly-sand model and P_c data measured on core plugs. The calibration method led to the resistivity model reproducing the S_w given by the core-measured P_c data. The end result of the work was a well-supported increase in OGIP estimates for the A-18 gas field, leading to a greater confidence in the development viability. The best estimate of gas reserves was increased by more than 20%.

In the first part of the calibration method, the shaly-sand sequence is classified into several facies according to the clay distribution. Initially, 10 facies are identified in the cores, but they are reduced to four petrophysical facies consisting of clean sands, sands with discontinuous clay, bioturbated and heterolithic, and poor reservoir mainly consisting of mudstones and coals. The electrical continuity of the shale components increases with each facies. Where core is not available, the facies type is estimated, preferably from resistivity imaging logs. P_c data were acquired on 1.5-in.-diameter plugs using the centrifuge method and spanned the full range

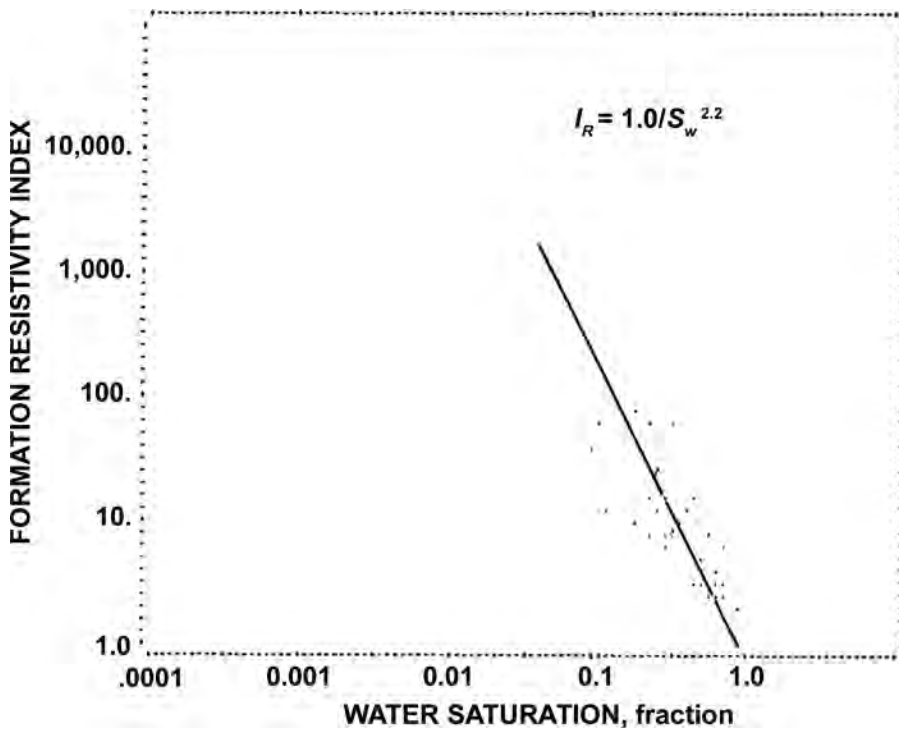


Fig. 3H.27—Laboratory-measured formation resistivity index (I_R) vs. brine saturation for core plugs from West Howard-Glasscock unit, west Texas, U.S.A.⁶⁵

of reservoir parameters. A multiple-linear-regression prediction of S_w from P_c , porosity, and permeability was used to estimate S_w at every routine-core-plug depth.

In the second part of the calibration, the P_c -predicted S_w values were correlated with the Waxman-Smiths shaly-sand model and the deep-resistivity log values at each foot of the core. The Waxman-Smiths model and the resistivity log were forced to match the P_c -based S_w by back-calculation of the n^* value at each foot in a way similar to that described for OBM cores in the main S_w section of this chapter (Sec. 3H.7). A mean back-calculated n^* is then determined for each of the four facies. Table 3H.6 gives the n^* mean values, along with the usual SCAL electrical-properties n^* values acquired by measuring core-plug resistivities in the laboratory. The P_c -calibrated n^* values are significantly lower than the SCAL electric-property n^* values, leading to significant increases in effective hydrocarbon column, especially in the bioturbated and heterolithic sands.

Total porosity at every logged foot was calculated from the density-log force fitting the line-fit through the core grain density. Fig. 3H.30 shows mainly raw data with the S_w results at the right side.

3H.9.5 Whitney Canyon—Carter Creek Gas Field. This Wyoming, U.S.A., gas field produces from a 1,000-ft-thick complex carbonate with a wide range of minerals including dolomite, anhydrite, limestone, and quartz.^{68,69} The study hoped to examine significant differences in well performance and to provide recommendations to increase recovery.

The main reservoir is in dolomitic rocks where there is a full continuum from slightly to fully dolomitized limestones. There is little or no relationship between permeability and porosity. Four rock types were identified by high-pressure mercury injection (HPMI) and, because

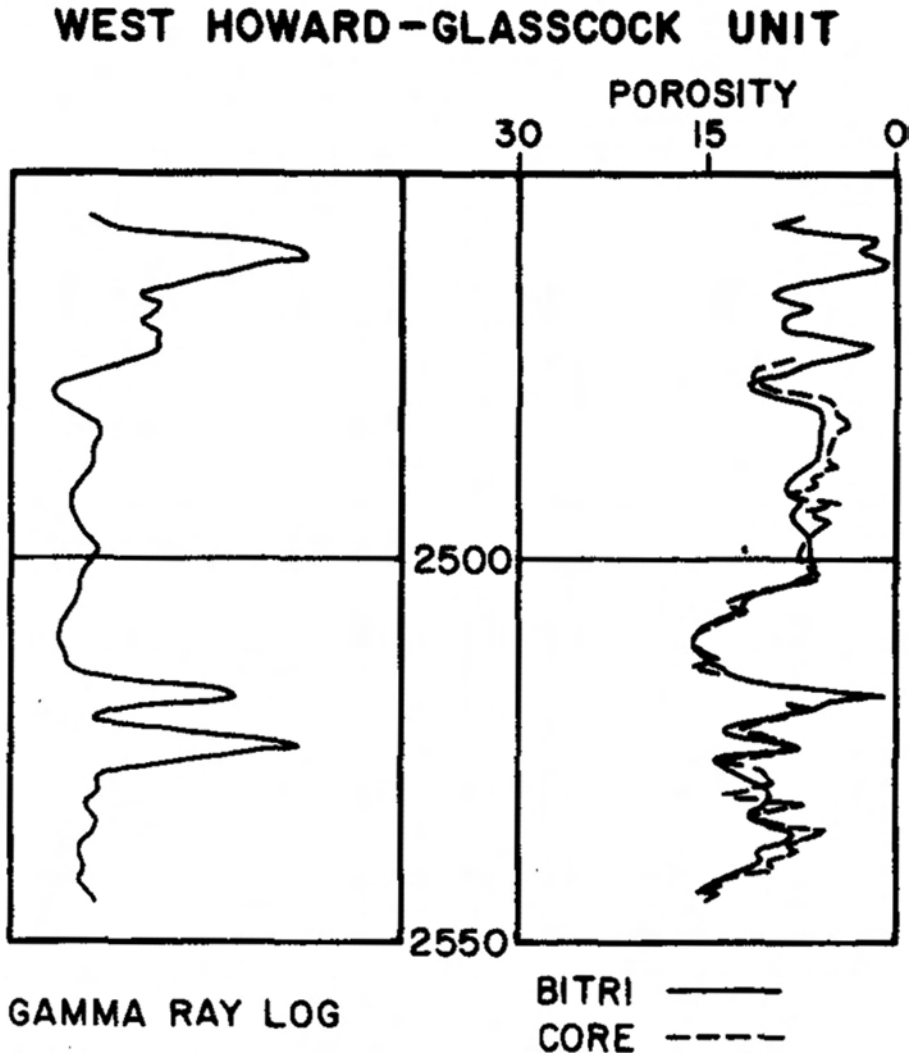


Fig. 3H.28—Agreement of core-analysis and Bitri-computed porosity for West Howard-Glasscock unit, west Texas, U.S.A.⁶⁵ “Bitri” refers to the log-response simultaneous-equations solution used to obtain porosity and rock-component volumes.

this reservoir has very high P_c (deriving from the 1,000-ft-thick gas column), even the poorest dolomitic rock has some gas saturation in the small pores. [Table 3H.7](#) gives a summary of the petrophysical properties of the four rock types.

Porosity and mineralogy were evaluated with a probabilistic simultaneous-equation method.²⁰ Gas corrections were required and had a significant effect on the results because, while the density-log reading is shallow, the neutron log is much deeper. Boron, a neutron absorber, is present in the dolomites and required a correction. S_w was calibrated to Dean-Stark initial S_w measurements and to the HPMI P_c measurements ([Fig. 3H.31](#)) because the laboratory Archie n measurements (1.1 to 1.5) were unreliable in the “tight” rocks. Force-fitted Archie exponents of $m = 2.18$ and $n = 2.0$ were used in the evaluations, and provided similar results to the OBM core S_w and HPMI P_c data.

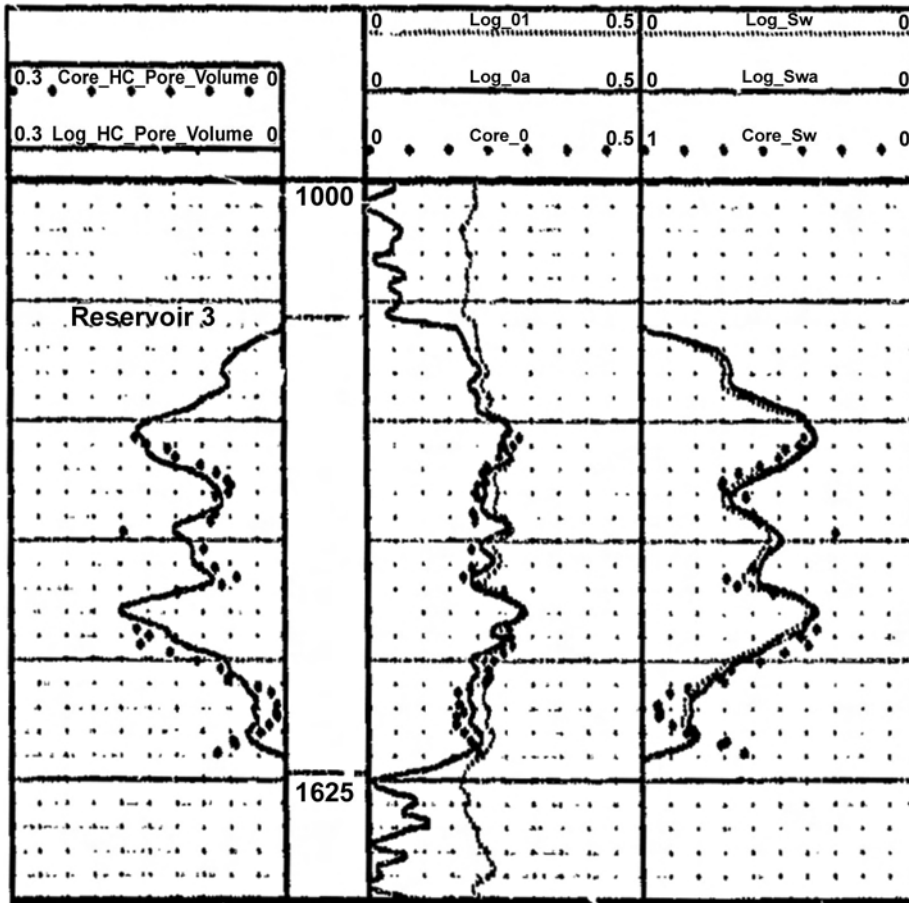


Fig. 3H.29—Plots of core- and log-calculated hydrocarbon pore volume, porosities, and S_w vs. depth for a Malaysian shaly-sandstone reservoir—Core #3.⁵¹

Gas saturations up to 75% PV were calculated for the poorest rock type and represented a significant prize for the production team. Positive steps were taken to ensure that this gas was accessed by production wells. The study determined that, as well as the usual acid stimulation of the higher-quality rock, the poorer rocks should also be separately stimulated with acid. Acid diversion to lower-permeability zones was used in new infill wells.

3H.10 Other Considerations in Petrophysical Calculations

While this chapter focuses on the calculations of various petrophysical properties using core and log data, there are other types of data obtained from oil and gas reservoirs that need to be considered when making petrophysical calculations. This section briefly discusses some of those data and how they can be used to improve the petrophysical evaluation. [Sec. 3H.6](#) discussed some of these data sources, as used for determining fluid-contact depths.

3H.10.1 Mud-Log Gas and Oil Shows. The information gathered by the mud logger regarding lithology, oil and gas shows, and gas composition should be integrated with the petrophysical calculations. In a gas reservoir, the mud log gas shows can be used to reasonably locate the GWC. In an oil reservoir, this same information can be used to identify the depth of the OWC.

TABLE 3H.5—EFFECT OF PETROPHYSICAL PARAMETERS R_w , m_i and n on S_w ⁶⁶

Petrophysical Parameters	1982 Values	1992 Values	Error in Parameter	ΔS_w (%)
Cementation exponent, m	1.72	1.77	0.05	3.4
Saturation exponent, n	1.89	1.84	-0.25	-13.9
Formation-water resistivity, R_w	0.185	0.150 (LD1)	-0.035	-10.0
		0.155 (LD2)	-0.030	-8.6
		0.155 (LD3)	-0.030	-8.6
		0.140 (E1)	-0.045	-12.9
		0.145 (E2)	-0.040	-11.4
		0.135 (E6)	-0.050	-14.3
		0.182 (E7)	-0.003	-0.9
		0.182 (E8)	-0.003	-0.9
		0.180 (E10/11)	-0.005	-1.4
		0.160 (E12/13)	-0.025	-7.2
		0.195 (E14)	0.010	2.9
		0.220 (E20/22)	0.035	10.0
		0.278 (E23)	0.093	26.6
		0.211 (E32*)	0.026	7.4
		0.211 (E34)	0.026	7.4
		0.205 (E36)	0.020	5.7
0.220 (E40/42)	0.035	10.0		
0.220 (E48*)	0.035	10.0		
0.220 (E50*)	0.035	10.0		
0.220 (E51*)	0.035	10.0		

*Estimated from nearby sands.

TABLE 3H.6—CHANGES IN EFFECTIVE HYDROCARBON COLUMN BY FACIES GROUP AS DETERMINED FROM SCAL ELECTRICAL-PROPERTY n^* VS. n^* BACK-CALCULATED FROM P_c and LOG DATA⁶⁷

Facies Group	SCAL n^*	Mean Core/Log n^*	% Change in EHC
1. Clean sands	1.76	1.53	9
2. Sand with discontinuous clay	1.93	1.55	16
3. Bioturbated and thin heterolithic sands	2.03	1.40	31
4. Poor reservoir	1.54	1.23	20

Note: EHC is equivalent to F_{HCP} .

These data are useful to determine whether there is a relict-gas or -oil interval below the current GWC or OWC.

3H.10.2 Pressure Measurements and Fluid Samples From Formation-Tester Logging Runs.³⁵ At the time wells are drilled, a suite of pressure measurements are often made over the reservoir interval, and sometimes, a few fluid samples are taken. These pressure data can aid the petrophysical interpretation by indicating whether the vertical pressures are in equilibrium throughout the reservoir interval. If not, then the reservoir may actually be several different

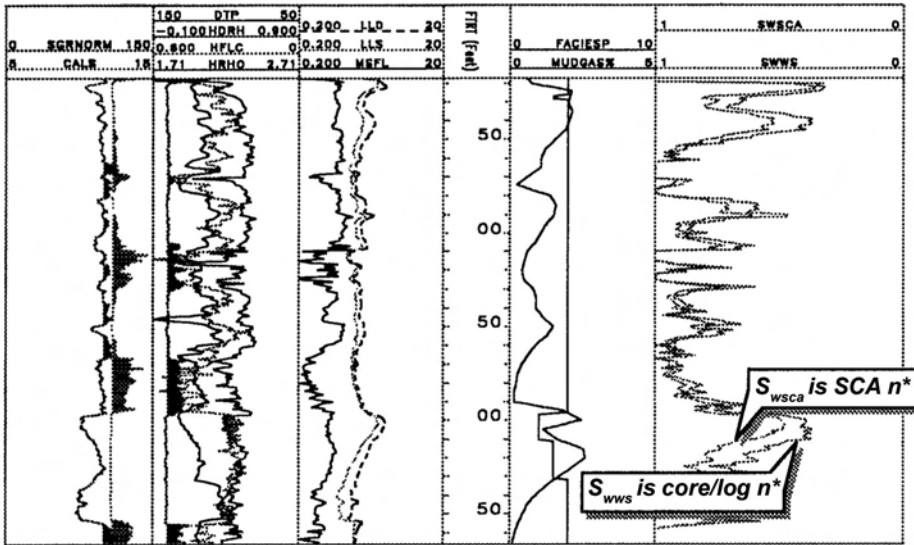


Fig. 3H.30—Water saturation S_{wsc} calibrated to capillary pressure P_c core data and S_{wsc} calibrated to standard core-electrical-properties n^* .⁶⁷ The P_c -based solution provides lower S_w results in this offshore gas field in the Malaysia-Thailand Joint Development Area. From left to right: Track 1 = GR log and caliper showing washouts; Track 2 = high resolution density log and other porosity logs; Track 3 = laterolog deep resistivity, shallow resistivity, and microspherically focused log; Track 5 = facies identifier and mud-gas log; and Track 6 = S_{wsc} , the P_c -calibrated core/log n^* -derived S_w and S_{wsc} , and the standard rock-electrical-properties n^* -derived S_w .

TABLE 3H.7—ROCK TYPE SUMMARY (after Gunter *et al.*⁶⁹)

Rock Type	Porosity Range (% BV)	Permeability Range (md air at 1,000 psi)	Irreducible S_w (% PV)	Equivalent P_{co} (ft)	Pore-Throat Radius (μm)	Pore-Throat Category
1	2 to 20	0.2 to 20	5 to 15	4 to 15	>1	meso/macro
2	2 to 18	0.1 to 4	10 to 20	10 to 30	0.5 to 1	meso
3	2 to 16	0.01 to 1	15 to 25	30 to 100	0.1 to 0.5	micro
4	0 to 12	0.001 to 0.01	25 to 50	100 to 300	<0.1	nano

compartments with different OWCs, GWCs, or GOCs. The fluid samples are useful in defining which fluid is flowing in each of the tested intervals and the extent of compositional differences. In addition to pressure data, modern wireline formation-tester tools can determine hydrocarbon type, GOR, and API gravity from spectroscopic measurements before taking fluid samples.⁷⁰

3H.10.3 Drillstem-Test Data. The pressure and flow data from DST tests must also be considered when performing a reservoir petrophysical evaluation. These tests provide information about the flowing fluids in different portions of the reservoir. Also, the pressure-transient-analysis calculations from the flow-rate and pressure data are used to calculate an average value for reservoir permeability. This needs to be compared with that calculated from the routine-core-analysis permeability data and the well logs. The permeability values determined from these two sources of data often disagree, with the value from the DST testing almost always taken to

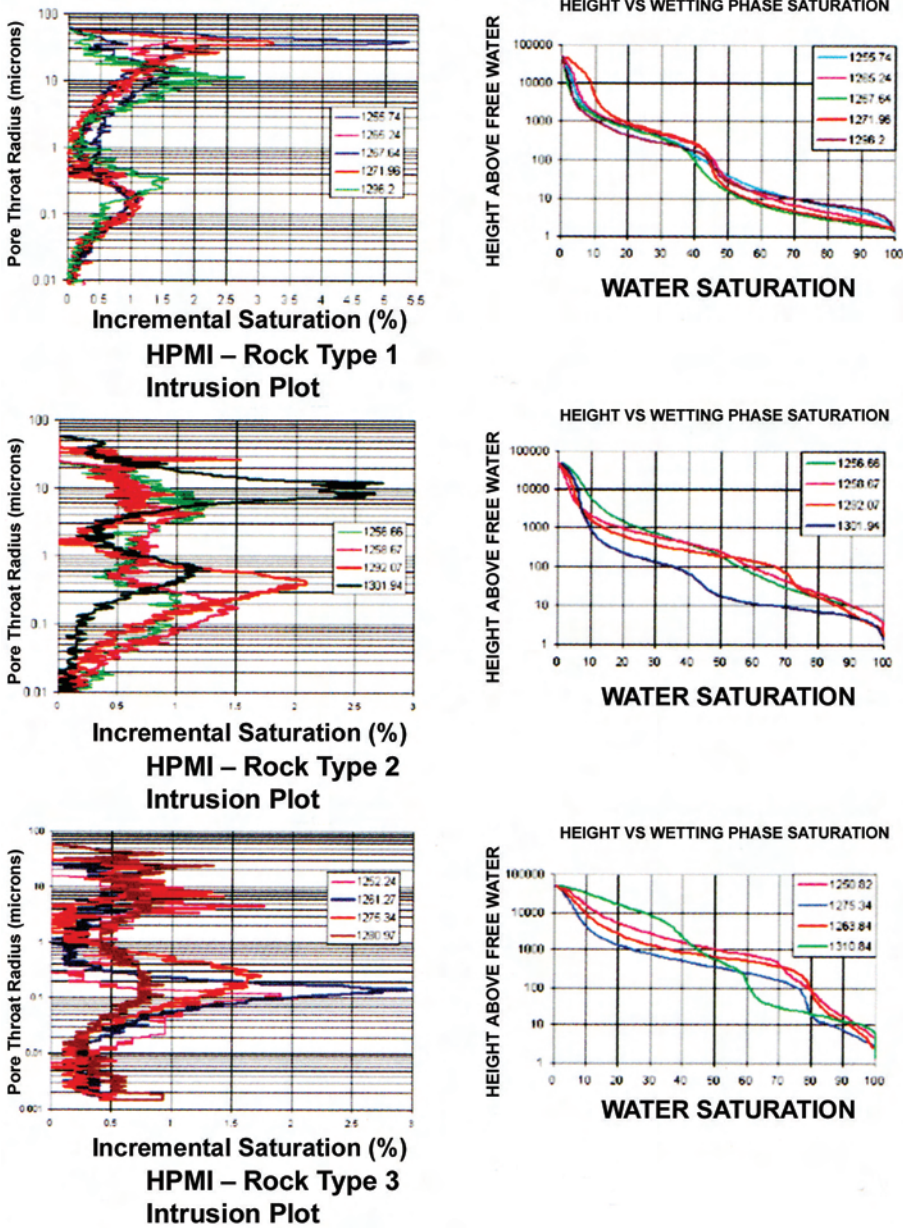


Fig. 3H.31—High pressure mercury injection (HPMI) plots for Whitney Canyon-Carter Creek field, Wyoming, U.S.A. for Rock Types 1, 2, and 3 (see Table 3H.6): (a) mercury intrusion as pore-throat radius changes and (b) wetting-phase saturation as height above free-water level (H_{GWC}) changes (after Gunter *et al.*⁶⁹). Each rock type is represented by 4 or 5 core samples. Plots for Rock Type 4 are not included because those are the poorest rocks with nano-sized pore throats.

be more correct. The DST results can be used to develop adjustments to the methodology for calculating permeability from core and log data, but also to determine the underlying technical reason for the need for the adjustments. If a DST is run long enough, it may yield information on the drainage limits of a reservoir.

3H.10.4 Three-Dimensional Seismic Data. The interpretation of the 3D-seismic data provides complementary data to that gathered at the wellbores and, with the rapidly improving data quality and interpretation techniques, can add significantly to reservoir-characterization calculations. The depositional, diagenetic, structural, and hydrocarbon-filling histories of a reservoir can be better understood by including the broad picture available from the 3D-seismic data. Locations of major faults that may compartmentalize the reservoir can be identified and the extent and location of channel-sand deposits is possible. Seismic attributes may be correlated with rock properties and fluid contents, allowing prediction of properties at proposed well locations.

3H.11 Summary and Conclusions

The purpose of this chapter is to acquaint the reader with the various aspects of the quantitative petrophysical determination of lithology, net pay, porosity, fluid contacts, water saturation, and permeability. To make these calculations as accurately as possible, core and log data need to be integrated. The routine-core-analysis data adjusted to reservoir conditions should be used to calibrate the logs for more-accurate calculations at the various wells. The conclusions of this chapter are as follows:

- Lithology is determined by geologists working with cores and rock cuttings. This information can be combined with log characteristics to identify depositional environments and characterize how these change vertically and areally throughout the reservoir.

- The clay minerals present in the shales and the sandstone intervals, both as detrital and authigenic components, must be identified and quantified so that their effects on the logs and routine-core-analysis data can be adequately understood. Radioactive components present in the reservoir rocks must be identified and quantified so that the clay-mineral volumes derived from the GR log are not overstated.

- Net pay calculations determine how much of the reservoir interval contributes to the technical calculations of in-place hydrocarbon volumes and fluid flow. With modern reservoir engineering tools, it is possible to set N/G to 1.0 and work the various engineering calculations from that basis. If some portion of the reservoir interval is to be excluded as nonpay, the choice of cutoff should be based on flow considerations with a systematic and consistent approach. Whatever nonpay cutoff is used, that cutoff will be somewhat arbitrary.

- Porosity can be computed from a variety of well logs (density, sonic, or neutron) in combination with routine-core data adjusted to reservoir conditions. In sandstones in which the mineralogy and the hole conditions permit, foot-by-foot porosity calculations from the density log, calibrated to core, are likely to be the most accurate. Correct fluid values are an integral part of the log evaluation. Porosity needs to be calculated accurately because, as well as its primary use, these values are also required for S_w and permeability estimates used directly in the volumetrics and flow calculations. Minerals that affect the porosity calculations, such as clay and heavy minerals, need to be identified as part of the lithology determination.

- Water saturation can be computed by a number of independent methods using routine-core-analysis OBM-core Dean-Stark S_w data, SCAL capillary pressure data, resistivity logs used in combination with SCAL rock electrical-property measurements, or some combination of these three datasets. Adjusted OBM-core Dean-Stark S_w data are likely to be the most accurate method. Integrated use of these various technical approaches will result in the most accurate S_w solution overall. The relevant uncertainty here is not in S_w itself; it is the uncertainty in the complement, the hydrocarbon saturation ($1 - S_w$), that is important.

- In the water-saturation calculation using resistivity logs, the connate-brine salinity and its resistivity, R_w , can vary within the hydrocarbon column, but the extent of this variation is often not measured. Also, the rock electrical properties may be a function of S_w . In most conventional S_w calculations using well logs, these are both assumed to be constant, and those assumptions can lead to significant errors in the calculated S_w values. The S_w calculations from the

resistivity logs and the various Archie parameters can be partially checked in aquifer intervals where S_w is known to be 100% PV.

- In the S_w calculation using P_c measurements, the laboratory tests are measurements of fluid volumes associated with cleaned and restored core plugs. For application, the reservoir values of the IFT, contact angle, and the wetting state of the reservoir generally must be estimated, along with several other factors. P_c laboratory tests do not always achieve the equilibrium water saturation, or the same water distribution within the pore network as is present in the real reservoir.

- Permeability is typically calculated from porosity logs through a permeability/porosity transform. Permeability values need to be adjusted to reservoir conditions. This adjustment is nonlinear, with poor-quality rocks having larger adjustments compared with those applied to high-quality rocks. Also, the calculated permeabilities at the wells should be compared with those obtained from PBU analysis of flow tests.

- The statistical correlation and calibration of core and log data requires that these data are properly depth aligned, have outliers deleted, and, if required, are mathematically transformed. A variety of line-fitting techniques are available, but the “y-on-x” approach generally results in the most accurate predictor, except in highly variable, heterogeneous rocks.

- In any reservoir with a thick hydrocarbon column and large areal extent, more accurate-petrophysical calculations are made if the reservoir is vertically zoned or layered. Different parameters for different areas of the reservoir may also be required for the most accurate solution.

Nomenclature

a	= Archie cementation constant
a^*	= Waxman-Smits cementation constant
A	= Coefficient in various equations of this chapter
A'	= Coefficient of term of Eq. 3H.26
B	= Specific cation conductance, [(1/ohm•m) / (meq/mL)]
B'	= Coefficient of term of Eq. 3H.26
C	= Coefficient in various equations
C'	= Coefficient of term in Eq. 3H.26
D	= Coefficient in various equations
E	= Coefficient in various equations
F	= Archie formation factor
F^*	= Waxman-Smits-Thomas formation factor
F_{HCP}	= hydrocarbon pore feet, L, ft [m]
H_{gwc}	= height above the gas/water contact, L, ft [m]
H_{hwc}	= height above the hydrocarbon/water contact, L, ft [m]
H_{owc}	= height above the oil/water contact, L, ft [m]
I_R	= resistivity index
$J(S_w)$	= Leverett J -function
k	= permeability, L ² , md [μm^2]
m	= Archie cementation exponent
m^*	= Waxman-Smits-Thomas cementation exponent
m_o	= dual-water cementation exponent
n	= Archie saturation exponent
n^*	= Waxman-Smits-Thomas saturation exponent
n_o	= dual-water saturation exponent
P_c	= capillary pressure, m/Lt ² , psi
P_{ce}	= entry capillary pressure, m/Lt ² , psi
Q_v	= cation-exchange capacity of total PV, meq/mL

r	= correlation coefficient
R_0	= rock resistivity with 100% PV water saturation, ohm•m
R_{sd}	= clean-sand resistivity, ohm•m
R_{sh}	= shale resistivity, ohm•m
R_t	= true resistivity of uninvaded, deep formation, ohm•m
R_w	= connate-brine resistivity, ohm•m
R_{wb}	= clay-bound water resistivity, ohm•m
R_{wf}	= free-formation-water resistivity, ohm•m
R_{xo}	= shallow-reading invaded-zone microresistivity, ohm•m
S_g	= gas saturation, %PV
S_o	= oil saturation, %PV
S_{orw}	= residual-oil saturation to water displacement, %PV
S_w	= water saturation, %PV
S_{wb}	= saturation of clay-bound water in the total porosity, %PV
S_{wc}	= connate water saturation, %PV
S_{wc}	= core water saturation, %PV
S_{we}	= water saturation of the effective porosity, %PV
S_{wsd}	= sand water saturation, %PV
S_{wt}	= water saturation of the total porosity, %PV
V_{cl}	= clay content, %BV
V_{HCP}	= hydrocarbon pore volume, L ³ , ft ³ [m ³]
V_{sh}	= shale content, %BV
θ	= contact angle, degrees
ρ_b	= formation bulk density, m/L ³ , g/cm ³
ρ_{fl}	= fluid density, m/L ³ , g/cm ³
ρ_h	= hydrocarbon density, m/L ³ , g/cm ³
ρ_{ma}	= matrix or grain density, m/L ³ , g/cm ³
ρ_w	= water density, m/L ³ , g/cm ³
σ	= interfacial tension, m/t ² , dynes/cm
ϕ	= porosity, %BV
ϕ_c	= core porosity, %BV
ϕ_{cl}	= clay porosity, %BV
ϕ_e	= effective porosity, %BV
ϕ_{sd}	= sand porosity, %BV
ϕ_{sh}	= shale porosity, %BV
ϕ_t	= total porosity, %BV

Subscripts

c	= connate
c	= core
e	= effective
h	= hydrocarbon
i	= initial
r	= reservoir
s	= surface
t	= total
w	= water

References

1. Crain, E.R.: *Log Analysis Handbook*, PennWell, Tulsa (1986).
2. Dewan, J.T.: *Essentials of Modern Openhole Log Interpretation*, PennWell, Tulsa (1983).
3. *Log Interpretation Principles/Applications*, Schlumberger, Houston (1989).
4. *Introduction to Wireline Log Analysis*, Baker Atlas, Baker Hughes Inc., Houston (2002).
5. *Log Interpretation Charts*, Schlumberger, Sugar Land, Texas (2000).
6. *Log Interpretation Charts*, Baker Atlas, originally published by Western Atlas, Houston (1995).
7. Theys, P.P.: *Log Data Acquisition and Quality Control*, second edition, Editions Technip, Paris (1999).
8. *Fundamentals of Rock Properties*, Core Laboratories UK Ltd., Aberdeen (2002).
9. Keelan, D.K.: "Automated Core Measurement System for Enhanced Core Data at Overburden Conditions," paper SPE 15185 presented at the 1986 SPE Rocky Mountain Regional Meeting, Billings, Montana, 19–21 May.
10. Keelan, D.K.: "Core Analysis Techniques and Applications," paper SPE 4160 presented at the 1972 SPE Eastern Regional Meeting, Columbus, Ohio, 8–9 November.
11. Keelan, D.K.: "Critical Review of Core Analysis Techniques," *J. Cdn. Pet. Tech.* (April 1972) 42.
12. Rathmell, J.J., Braum, P.H., and Perkins, T.K.: "Reservoir Waterflood Residual Oil Saturation From Laboratory Tests," *JPT* (February 1973) 175.
13. *RP 40 Recommended Practices for Core Analysis*, second edition, API, Washington, DC (February 1998).
14. Richardson, J.G. and Holstein, E.D.: "Comparison of Water Saturations from Capillary Pressure Measurements With Oil-Base-Mud Core Data Ivishak (Sadlerochit) Reservoir, Prudhoe Bay Field," paper SPE 28593 presented at the 1994 SPE Annual Technical Conference and Exhibition, New Orleans, 25–28 September.
15. Woodhouse, R., Greet, D.N., and Mohundro, C.R.: "Induction Log Vertical Resolution Improvement in Vertical and Deviated Wells Using a Practical Deconvolution Filter," *JPT* (June 1984) 993.
16. Barber, T.D.: "Introduction to the Phasor Dual Induction Tool," *JPT* (September 1986) 1699.
17. Hynes, N.J.: *Dictionary of Petroleum Exploration, Drilling, and Production*, PennWell, Tulsa (1991).
18. Hensel, W.M. Jr.: "An Improved Summation-of-Fluids Porosity Technique," *SPEJ* (April 1982) 193.
19. Brown, G.: *The X-Ray Identification and Crystal Structures of Clay Minerals*, Mineralogical Soc. Clay Minerals Group, London (1961).
20. Mezzatesta, A., Rodriguez, E., and Frost, E.: "Optima: A Statistical Approach to Well Log Analysis," *Geobyte* (August 1988).
21. Sneider, R.M. and Erickson, J.W.: "Rock Types, Depositional History, and Diagenetic Effects: Sadlerochit Reservoir, Prudhoe Bay Field," paper SPE 28575 presented at the 1994 SPE Annual Technical Conference and Exhibition, New Orleans, 25–28 September.
22. Holstein, E.D. and Warner, H.R. Jr.: "Overview of Water Saturation Determination for the Ivishak (Sadlerochit) Reservoir, Prudhoe Bay Field," paper SPE 28573 presented at the 1994 SPE Annual Technical Conference and Exhibition, New Orleans, 25–28 September.
23. Cobb, W.M. and Marek, F.J.: "Net Pay Determination for Primary and Waterflood Depletion Mechanisms," paper SPE 48952 prepared for presentation at the 1998 SPE Annual Technical Conference and Exhibition, New Orleans, 27–30 September.
24. *Oil Reservoir Engineering*, S.J. Pirson (ed.), McGraw-Hill Book Co. Inc., New York City (1958) 443–445.
25. *Determination of Oil and Gas Reserves*, Petroleum Soc. of the Canadian Inst. of Mining, Metallurgy, and Petroleum, Petroleum Soc. Monograph 1 (1994) 45–46.
26. George, C.J. and Stiles, L.H.: "Improved Techniques for Evaluating Carbonate Waterfloods in West Texas," *JPT* (November 1978) 1547.

27. Erickson, J.W. and Sneider, R.M.: "Structural and Hydrocarbon Histories of the Ivishak (Sadlerochit) Reservoir, Prudhoe Bay Field," paper SPE 28574 presented at the 1994 SPE Annual Technical Conference and Exhibition, New Orleans, 25–28 September.
28. Lucia, F.J.: "San Andres and Grayburg Imbibition Reservoirs," paper SPE 59691 presented at the 2000 SPE Permian Basin Oil and Gas Recovery Conference, Midland, Texas, 21–23 March.
29. Thai, B.N. *et al.*: "Denver Unit Infill Drilling and Pattern Reconfiguration Program," paper SPE 59548 presented at the 2000 SPE Permian Basin Oil and Gas Recovery Conference, Midland, Texas, 21–23 March.
30. Cowan, G. and Boycott-Brown, T.: "The North Morecambe Gas Field," *United Kingdom Oil and Gas Fields, Commemorative Millennium Volume*, Geological Soc., London (2003).
31. Woodhouse, R. and Warner, H.R. Jr.: "Improved Log Analysis in Shaly Sandstones—Based on S_w and HCPV Routine Measurements on Preserved Cores Cut in Oil-based Mud," *Petrophysics* (May 2004) **45**, No. 3, 281. [An improved version of this paper is SPE 96618, presented at the 2005 SPE Annual Technical Conference and Exhibition, Dallas, 9–12 October.]
32. Woodhouse, R.: *Statistical Regression Line-Fitting in the Oil and Gas Industry*, PennWell, Tulsa (2003).
33. Jensen, J.L. *et al.*: *Statistics for Petroleum Engineers and Geoscientists*, second edition, Elsevier (2000).
34. Patchett, J.G. and Coalson, E.B.: "The Determination of Porosity in Sandstones and Shaly Sandstones, Part One—Quality Control," *The Log Analyst* (Nov 1979) **20**, 6.
35. *Formation Multi-Tester (FMT) Principles, Theory and Interpretation*, Baker Atlas, originally published by Western Atlas, Houston (1987).
36. McCoy, D.D., Warner, H.R. Jr., and Fisher, T.E.: "Water-Salinity Variations in the Ivishak and Sag River Reservoirs at Prudhoe Bay," *SPEE* (February 1997) 37.
37. Rathmell, J.J., Atkins, L.K., and Kralik, J.G.: "Application of Low Invasion Coring and Outcrop Studies to Reservoir Development Planning for the Villano Field," paper SPE 53718 presented at the 1999 SPE Latin American and Caribbean Petroleum Engineering Conference, Caracas, 21–23 April.
38. Rathmell, J.J. *et al.*: "Low Invasion, Synthetic Oil-Base Mud Coring in the Yacheng 13-1 Gas Reservoir for Gas-in-Place Calculation," paper SPE 29985 presented at the 1995 SPE International Meeting on Petroleum Engineering, Beijing, 14–17 November.
39. Archie, G.: "The Electrical Resistivity Log as an Aid in Determining Some Reservoir Characteristics," *Trans., AIME* (1942) **146**, 54.
40. Winsauer, W.O., Shearin H.M., Masson P.H., and Williams M.: "Resistivity of Brine Saturated Sands in Relation to Pore Geometry," *AAPG Bull.* (February 1952) **36**, 2.
41. Waxman, M.H. and Smits, L.J.M.: "Electrical Conductivities in Oil-Bearing Shaly Sands," *SPEJ* (June 1968) 107.
42. Waxman, M.H. and Thomas, E.C.: "Electrical Conductivities in Sands—I. The Relation Between Hydrocarbon Saturation and Resistivity Index; II. The Temperature Coefficient of Electrical Conductivity," *SPEJ* (February 1974) 213.
43. Juhasz, I.: "The Central Role of Q_v and Formation Water Salinity in the Evaluation of Shaly Formations," *The Log Analyst* (June 1979) **20**, 4.
44. Hill, H.J., Shirley, O.J., and Klein, G.E.: "Bound Water in Shaly Sands—Its Relation to Q_v and Other Formation Properties," *The Log Analyst* (1979) **20**, No. 3, 3.
45. Leverett, M.C.: "Capillary Behavior in Porous Media," *Trans., AIME* (1941) **142**, 152.
46. Heseldin, G.M.: "A Method of Averaging Capillary Pressure Curves," *The Log Analyst* (1974) **4**, 3.
47. Johnson, A.: "Permeability Averaged Capillary Data: A Supplement to Log Analysis in Field Studies," paper EE presented at the 1987 SPWLA Annual Symposium, London, June.
48. Woodhouse, R.: "Accurate Reservoir Water Saturations from Oil-Mud Cores: Questions and Answers from Prudhoe Bay and Beyond," *The Log Analyst* (May–June 1998) 23.
49. Richardson, J.G. *et al.*: "Validation of As-Received Oil-Based-Core Water Saturations From Prudhoe Bay," *SPEE* (February 1997) 31.
50. Dawe, B.A. and Murdock, D.M.: "Laminated Sands: An Assessment of Log Interpretation Accuracy by an Oil-Base Coring Program," paper SPE 20542 presented at the 1990 SPE Annual Technical Conference and Exhibition, New Orleans, 23–26 September.

51. Egbogah, E.O. and Amar, Z.H.B.T.: "Accurate Initial/Residual Saturation Determination Reduces Uncertainty in Further Development and Reservoir Management of the Dulang Field, Offshore Peninsular Malaysia," paper SPE 38024 presented at the 1997 SPE Asia Pacific Oil and Gas Conference, Kuala Lumpur, 14–16 April.
52. Poupon, A. and Leveau, J.: "Evaluation of Water Saturations in Shaly Formations," *The Log Analyst* (July 1971) 3.
53. Worthington, P.F.: "The Evolution of Shaly-Sand Concepts in Reservoir Evaluation," *The Log Analyst* (January 1985) 23.
54. Keelan, D.K. and McGinley, D.C.: "Application of Cation Exchange Capacity in a Study of the Shannon Sand of Wyoming," paper KK presented at the 1979 SPWLA Annual Symposium, June.
55. Clavier, C., Coates, G., and Dumanoir, J.L.: "Theoretical and Experimental Bases for the Dual-Water Model for Interpretation of Shaly Sands," *JPT* (April 1984) 153.
56. Best, D.L., Gardner, J.S., and Dumanoir, J.L.: "A Computer-Processed Wellsite Log Computation," paper Z presented at the 1979 SPWLA Annual Symposium.
57. Huff, G.F.: "A Correction for the Effect of Comminution on the Cation Exchange Capacity of Clay-Poor Sandstones," *SPEFE* (September 1987) 338.
58. Bryant, W.T. and Truman, R.B. II: "Proper Core-Based Petrophysical Analysis Doubles Size of Ha'py Field," paper SPE 77638 presented at the 2002 SPE Annual Technical Conference and Exhibition, San Antonio, Texas, 29 September–2 October.
59. Katz, D.L. and Firoozabadi, A.: "Predicting Phase Behavior of Condensate/Crude-Oil Systems Using Methane Interaction Coefficients," *JPT* (November 1978) 1649.
60. Harrison, B. and Jing, X.D.: "Saturation-Height Methods and Their Impact on Volumetric Hydrocarbon-in-Place Estimates," paper SPE 71326 presented at the 2001 SPE Annual Technical Conference and Exhibition, New Orleans, 30 September–3 October.
61. McCoy, D.D. and Grieves, W.A.: "Use of Resistivity Logs to Calculate Water Saturations in the Prudhoe Bay Field," *SPEFE* (February 1997) 45.
62. Timur, A.: "An Investigation of Permeability, Porosity and Residual Water Saturation Relationships for Sandstone Reservoirs," *The Log Analyst* (July 1968) 9, 4.
63. Charlson, G.S. *et al.*: "Application of Oil-Based-Mud Pressure Coring to the Determination of In-Situ Water Saturations," *SPEDC* (June 1997) 105.
64. Deans, H.A. and Mut, A.D.: "Chemical Tracer Studies To Determine Water Saturation at Prudhoe Bay," *SPEFE* (February 1997) 52.
65. Wilson, D.A. and Hensel, W.M. Jr.: "Computer Log Analysis Plus Core Analysis Equals Improved Formation Evaluation in West Howard-Glasscock Unit," *JPT* (January 1978) 43.
66. Osborn, C.K. and Hogan, C.A.: "Corecom—A Practical Application of Core Analysis," Southwestern Petroleum Short Course, Texas Tech U., Lubbock, Texas (April 1972) 75.
67. Deakin, M. and Manan, W.: "The Integration of Petrophysical Data for the Evaluation of Low Contrast Pay," paper SPE 39761 presented at the 1998 SPE Asia Pacific Conference on Integrated Modelling for Asset Management, Kuala Lumpur, 23–24 March.
68. Logan, P.A. *et al.*: "Using Petrophysics to Improve Recovery: Whitney Canyon—Carter Creek Field, Western Wyoming Trust Belt, USA," paper W presented at the 1999 SPWLA Annual Symposium, Oslo, Norway, May.
69. Gunter, G.W. *et al.*: "Saturation Modeling at the Well Log Scale Using Petrophysical Rock Types and a Classic Non-Resistivity Based Method," paper Z presented at the 1999 SPWLA Annual Symposium, Oslo, Norway, May.
70. Hashem, M.N. *et al.*: "Determination of Producing Hydrocarbon Type and Oil Quality in Wells Drilled with Synthetic Oil-Based Muds," *SPEFE* (April 1999) 125.

SI Metric Conversion Factors

acre	× 4.046 856	E + 03 = m ²
bbl	× 1.589 873	E - 01 = m ³
Btu	× 1.055 056	E + 00 = kJ
cp	× 1.0*	E - 03 = Pa·s
dyne	× 1.0*	E - 02 = mN
ft	× 3.048*	E - 01 = m

$$\begin{array}{l} \text{°F} \quad (\text{°F} - 32)/1.8 \quad = \text{°C} \\ \text{in.} \times 2.54^* \quad \text{E} + 00 = \text{cm} \\ \text{mile} \times 1.609\,344^* \quad \text{E} + 00 = \text{km} \\ \text{psi} \times 6.894\,757 \quad \text{E} + 00 = \text{kPa} \end{array}$$

*Conversion factor is exact.

Chapter 4

Production Logging

R.M. McKinley, SPE, Consultant and Norman Carlson, Consultant

4.1 Introduction

This chapter consists of a general discussion of production logs, some misconceptions about what can be determined with these logs, and the requisite skills to obtain good results. Also included are discussions of practical matters such as required safety and environmental tips, sinker-bar weight, maximum tool length to pass through a bend, depth control, pricing, and record keeping. Attached as an Appendix is a set of tables prepared for readers that are consulting this text to find out quickly what type of production-logging tools are appropriate to a particular problem. These tables indicate what tools to use, how to use them, and what results (resolution) to expect. These tables were designed to be independent of the general discussion and can be used by themselves. The indexing scheme used in the tabulation is explained in the Appendix.

Production-logging tools find many applications from the time a well is drilled until abandonment and, occasionally, beyond. An appropriate categorization of production logs is by usage. This approach leads to the five distinct categories listed below that also represent a rough chronological order of tool evolution. Effective interpretation of the data from each type of log requires significant education and experience.

1. Diagnose production problems and allocate production.
2. Monitor cement placement.
3. Monitor corrosion.
4. Monitor reservoir fluid contacts.
5. Select zones for recompletion.

These are discussed as categories below.

4.1.1 Category One. Includes tools used to track movement of fluid either inside or immediately outside the casing of a well. The logs frequently used for such flow diagnosis and allocation include temperature surveys, mechanical flowmeter surveys, and borehole fluid-density or fluid-capacitance surveys. Each of these tools responds to fluid velocity or fluid type. The logs are run to determine if a production problem, such as excessive water or gas production, is the result of a completion problem or a reservoir problem. Their value thus resides in the guidance they give for continued expenditure on a well that is performing poorly. This type of application is largely responsible for the growth and evolution of modern production logging.

Also belonging in Category One are evaluations of the placement of acids or hydraulic-fracturing material and diagnoses of premature flow or lost circulation in a drilling well.

4.1.2 Category Two. There are two different objectives of cement-placement monitoring: to determine where the cement went (cement top) and to determine whether the cement provides zonal isolation. The logs used to locate the cement top include the temperature log, which responds to hydration heating; the unfocused gamma ray log, which responds to behind-pipe density; and the regular bond log, which measures the acoustical deadening of pipe.

Zonal isolation should be addressed when pressure imbalance causes crossflow through poorly cemented sections, leading to excessive production of unwanted fluids. The tools most often used for this purpose include cement-bond logs, temperature, noise, radioactive tracer, and neutron-activation logs. The temperature log detects alterations caused by flow, the noise log measures turbulent sound caused by flow, and the tracer log tracks tagged fluid behind casing. The neutron-activation log creates tracer in behind-pipe water.

4.1.3 Category Three. Corrosion-monitoring tools are specialized in nature and include mechanical caliper tools and electromagnetic casing-inspection tools. The mechanical caliper tools are used to assess corrosion internal to the casing and to measure the shape of casing as well as the amount of rod and drillpipe wear inside tubing or casing. The electromagnetic devices respond to changes in metal thickness either inside or outside the pipe containing the tool. These logging tools are either of the eddy-current type or of the flux-leakage type, or a combination of the two. The eddy-current devices measure the load on a coil resulting from eddy currents induced into the wall of the casing. This load increases with increases in wall thickness. The driven frequency of the coil determines the depth of penetration of the field into the casing wall. The flux-leakage devices measure, by means of pad-conveyed coils in contact with the pipe wall, the induced currents that result from magnetic field lines that escape at abrupt changes in metal-wall thickness. Both types of tools make indirect measurements that are then related to metal loss through calibration.

4.1.4 Categories Four and Five. The last two categories, monitoring of fluid contacts in formations and selection of recompletion zones, use the cased-hole nuclear logs such as the neutron, the pulsed-neutron, and the various spectral logs. Please refer to the chapter on nuclear logging in the Reservoir Engineering volume of this *Handbook* for information on these logs.

4.2 Misconceptions About Production Logging

There are three pervasive myths about production logging:

4.2.1 Anyone Can Run a Production Log. Quality control is paramount, and careful attention must be focused upon three parts of the logging operation: (1) procedure (this will usually determine the value of the resulting logs), (2) tool calibration, and (3) depth control.

4.2.2 Only One Logging Tool Is Needed. Just like openhole-logging tools, production-logging tools should be run in complementing suites so that one log can be compared with another. Seldom does a single log identify a problem sufficiently to prescribe a remedial action.

Table 4.1 lists the more common tool combinations used to diagnose problems and allocate flow. The Class A tools respond to flow either inside or outside the pipe containing the sonde and are usually employed for initial evaluation of a production problem. Class B tools respond to flow past the sensor and are used for detailed flow allocation from multiple entries into or exits from the pipe containing the sonde. The resolution of some of the Class A tools is actually better than some of the Class B members.

TABLE 4.1—LOGGING TOOLS FOR DIAGNOSING FLOW PROBLEMS AND ALLOCATING FLOW

Class A Tools		Class B Tools	
Behind/Within-Pipe Detectors		Within-Pipe Detectors	
<u>Flowmeters</u>		<u>Flowmeters</u>	
Temperature		Continuous spinners	
Noise		Diverting spinners	
Radioactive tracer		<u>Fluid Identifiers</u>	
Neutron activators (water)		Focused-gamma	
Fluid density (unfocused)		Ray-density	
Gamma-ray (gravel-pack logs)		Pressure-gradient	
Uncompensated neutron (gas holdup)		Density	
		Fluid-capacitance	
		Fluid-resistance	

4.2.3 The Answer (Anomaly) Will Jump Out From a Casual Scan of the Log. This myth is responsible almost entirely for the lack of adequate training in this area.

Production logs should be interpreted in a consistent fashion that first identifies normal or expected features. The abnormal portions can then be examined to determine which parts are pertinent to the problem and which parts are irrelevant. It is these irrelevant features that so often confound novices to the point that they delay or forego appropriate remedial action.

Once these three myths are set aside, the requisite skills, listed next, can be developed for use of production logs. In the authors' experience, a collaborative effort by service provider and client is needed to yield the most meaningful results. The effective user must be able to

1. Select the proper combination of tools.
2. Establish operating procedure.
3. Monitor data quality.
4. Interpret results.

4.3 Origin of Flow Problems

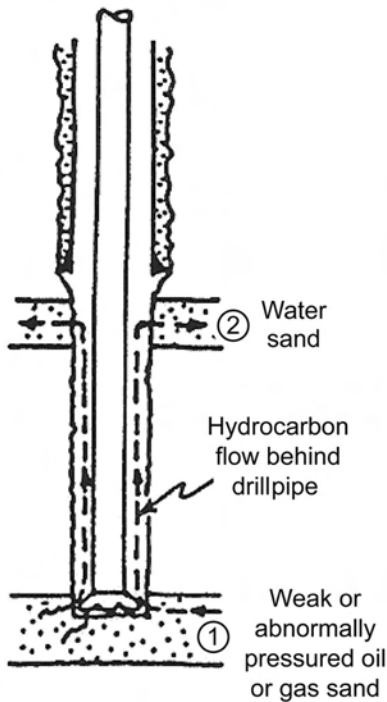
The more common types of flow problems associated with production-logging efforts are summarized in [Fig. 4.1](#). Side A shows a drilling well that has crossflow or an underground blowout. Such flow can start for two different reasons. First, the well may “take a kick”; that is, entry into an abnormally pressured zone may result in drilling mud being blown out of the hole. Even though the well may be successfully shut in at the surface, the culprit zone is still free to flow into lower-pressured strata. Second, the well may “lose returns”; that is, a zone may fracture and allow drilling mud to leave the wellbore faster than it is pumped down the drillpipe. The loss in mud pressure may allow hydrocarbon crossflow as shown. Such a flow must be stopped before drilling can be resumed to prevent an uncontrolled blowout with the potential for injuries and equipment loss, as illustrated in [Fig. 4.2](#).

Side B of [Fig. 4.1](#) illustrates why a well completed for production may flow excessive amounts of water or gas. Any combination of three reasons may account for the unwanted flow:

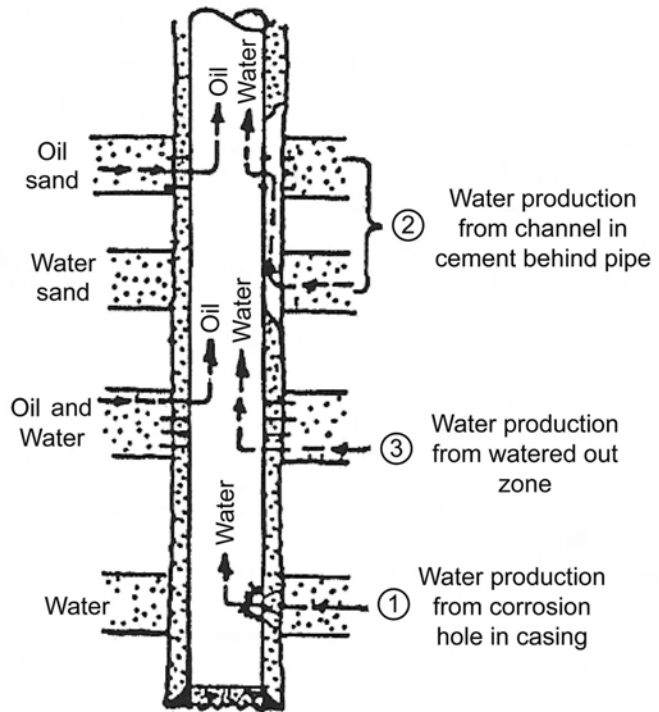
1. Casing failure by stress or corrosion.
2. Lack of cement integrity behind the casing.
3. Mobile gas or water in the completed zone.

The first two situations result from completion failures that can usually be remedied. The third situation is caused by reservoir performance and typically remains as long as the zone is produced.

(A) Well being drilled

*Flow Behind Drillpipe*

(B) Well on production

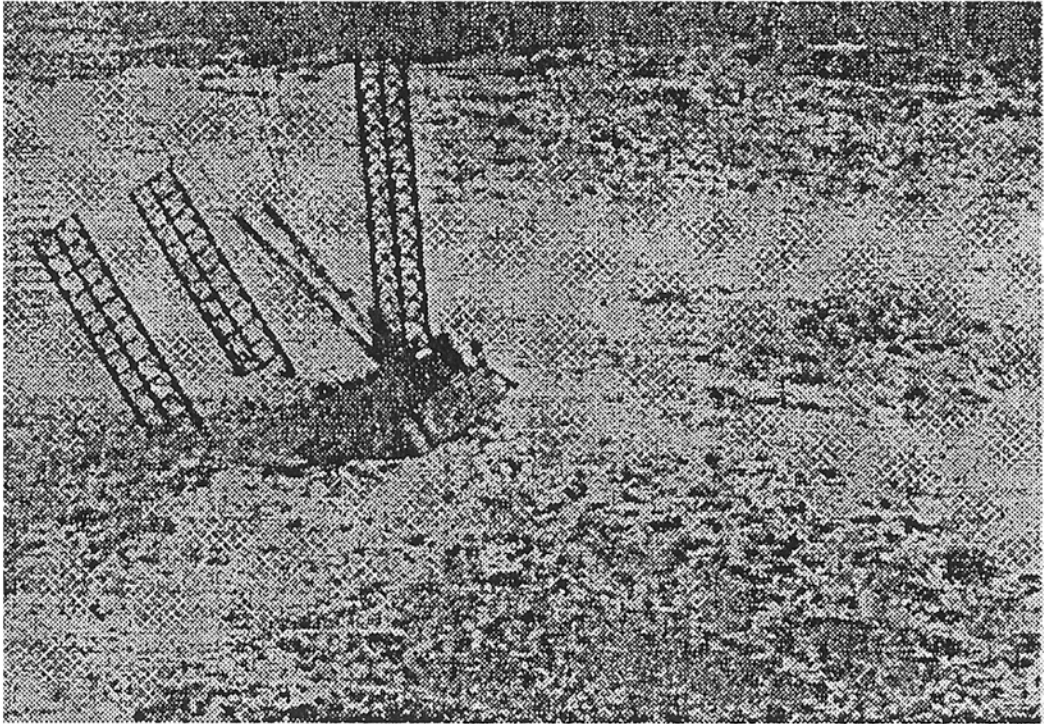
*Flow Either Behind Casing or Within Casing***Fig. 4.1—Origin of flow problems.**

All the problems illustrated in Fig. 4.1 have a common feature, namely the presence of flow either inside or outside the pipe or both. Those devices listed under Class A tools in Table 4.1 were selected because of their ability to respond to whatever situation exists in a particular well. The Class B tools were then selected as discriminators or as quantifiers for known flow conditions. The structure of Table 4.1 is a direct consequence of the situations illustrated in Fig. 4.1.

4.4 Safety and Environmental Tips

The following safety and environmental tips should be considered on every production-logging job:

1. All wireline units should be equipped with at least one 30-lbm dry chemical fire extinguisher.
2. Engines should be equipped with emergency shutoff devices on air intake (butterfly valve) and with spark-arrester-type mufflers.
3. Drip pans should be installed under all engines, pumps, oil reservoirs, and reels of skid-mounted units. Drip pans should be provided for trucks on barges.
4. Oil from the lubricator control head and oil from the line should not be permitted to drip into canals and streams.
5. Pieces of cut-off wireline or cable should be carried off by the wireline crew for disposal.



A Penrod Drilling Co. rig in the Gulf of Mexico sinks after the Exxon U.S.A. natural gas well it was drilling blew out, destroying the 147-ft-tall derrick and breaking one of the rig's three legs.

Fig. 4.2—Surface blowout of a gas well while drilling.

6. Bleeding of gas and oil into metal buckets should not be done. Use of a plastic bucket rather than a metal one will minimize the danger of a static-electricity spark.

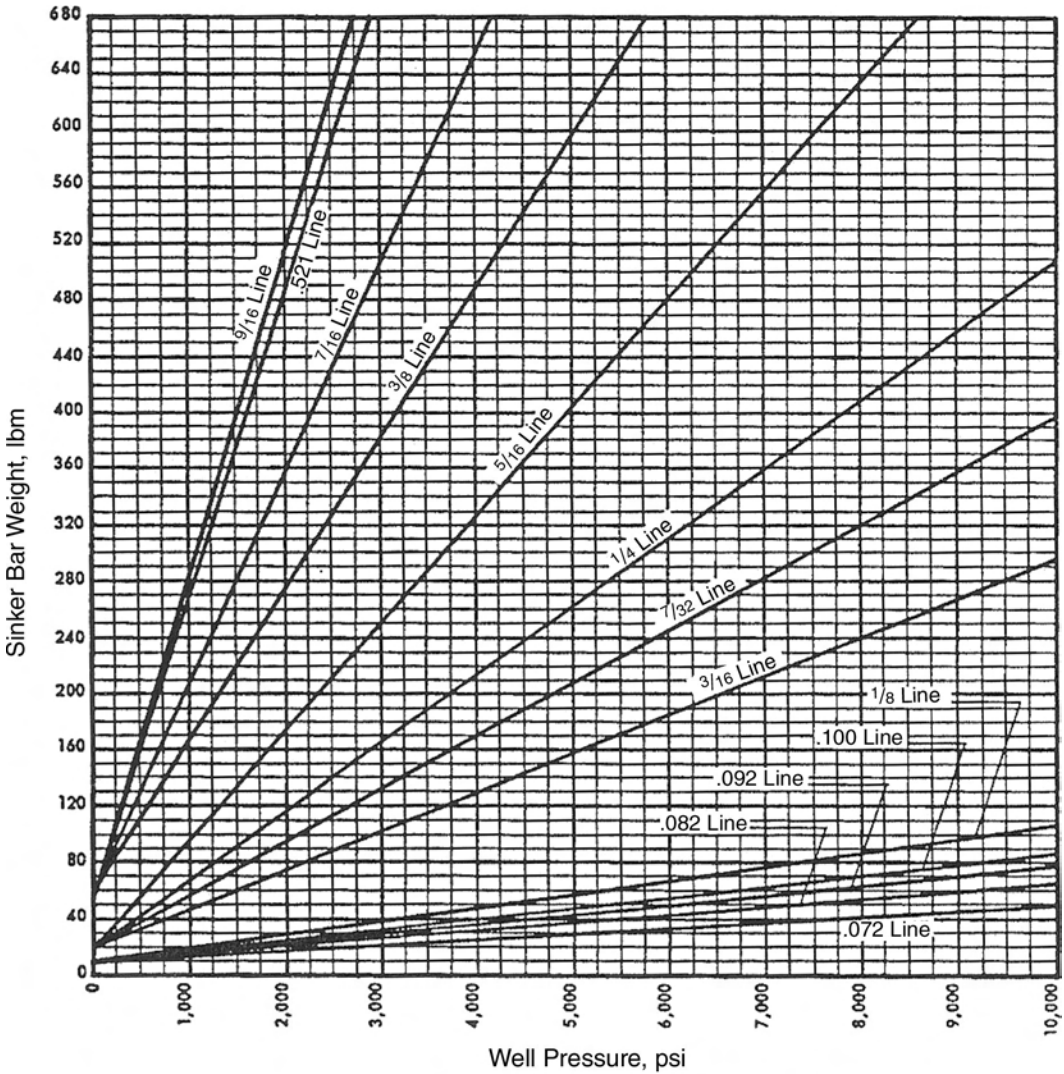
7. Truck-mounted units should not be positioned over tall grass in such a way that mufflers or power-generator engines could ignite the grass.

When a potential risk is identified, the purchaser of the logging should make all required operational changes. Because service companies perform most of the production logging, it is also the purchaser's responsibility to ensure that a system is in place for (1) contractor selection and evaluation; (2) defining, communicating, and stewarding performance requirements; (3) managing interfaces between the purchaser and the contractor; and (4) monitoring performance and correcting deficiencies.

4.5 Sinker Bar Weight

A dead weight (sinker bar) is necessary to overcome the force of the wellhead pressure acting on the cross-sectional area of the logging cable. [Fig. 4.3](#) shows the required sinker bar weight in relation to the shut-in wellhead pressure. The weight shown is just enough to balance the force of the well pressure acting on the wireline.

Additional weight above that which is indicated on the graph is needed to realize downward movement of the logging string. As the inclination angle of the wellbore increases, it becomes especially important to increase the sinker bar weight over the value specified by the vertical axis of the figure. When an inclination angle requires unreasonably long sinker bars, roller centralizers are required.



Note: Sinker bar weight given is at balance point.
 Add weight as desired to obtain downward movement

Fig. 4.3—Sinker bar weight to balance wellhead pressure (Courtesy Bowen Tool Co.).

Typical slickline diameters are represented by the group of lines at the bottom of Fig. 4.3. The low sinker-bar weight needed to carry out a slickline survey, even at high wellhead pressures, requires only a short lubricator. As a result, slickline services are enjoying a rebirth. New versions of these tools contain sufficient downhole memory to record what is essentially a continuous log.

4.5.1 Maximum Tool Length To Negotiate Bend. Fig. 4.4a illustrates the maximum length of a tool that can pass a bend. The ends of the tool contact the bottom of the borehole, and its middle touches the top.

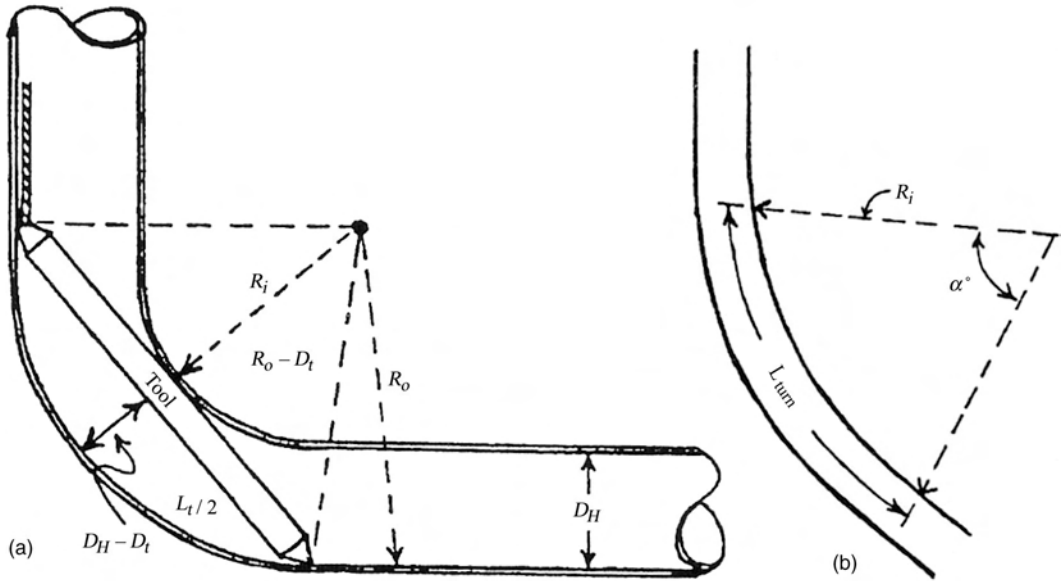


Fig. 4.4—(a) Tool limitations through a bend; (b) inside radius, bend angle, and distance to turn.

With the following equation, the maximum tool length that can pass through a bend can be calculated. While Fig. 4.4a shows a bend into a horizontal wellbore, the expression is valid for any bend and is independent of whether the final wellbore is horizontal.

$$L_t = 2(D_h - D_t)[1 + 2R_i / (D_h - D_t)]^{1/2} \dots\dots\dots (4.1)$$

The expression for L_t involves the hole and tool diameters, as well as the inside radius of the bend. The inside radius can be expressed in terms of the angle of the bend, and the distance to bend through the specified angle (see Fig. 4.4b):

$$R_i = L_{turn} / [(\alpha\pi) / 180] \dots\dots\dots (4.2)$$

An example of the use of the maximum-length equation:

$$D_h = 6 \text{ in.} = 0.5 \text{ ft}; D_t = 1.5 \text{ in.} = 0.125 \text{ ft}; \alpha = 90^\circ; L_{turn} = 30 \text{ ft}; (D_h - D_t) = 0.375 \text{ ft};$$

$$\text{and } R_i = 2 \times 30 / \pi = 19.098 \text{ ft} .$$

$$L_t = 2(0.375)(1 + 2 \times 19.098 / 0.375)^{1/2}; \text{ and } L_t = 7.61 \text{ ft} .$$

Any 1.5-in. OD tool 7.61 ft in length can pass through the bend. If longer tools are required, then the tool string must be segmented with “knuckle” joints.

4.6 Depth Control

The counter wheels on a production-logging unit measure the length of cable in the well to an accuracy of 5 out of 15,000 ft, provided that a great deal of back and forth travel (yo-yoing) is not required to work the tool string down the well. Better depth control is obtained by placing a casing collar locator (CCL) sub at the top of any production-logging tool string. See logging chapters in the Reservoir Engineering volume of this *Handbook* for more on this tool. This sub

generates a voltage spike as it moves past a change in metal thickness, particularly as it passes through the connection between joints of pipe. The resulting record of collars is the source of depth control.

Wells are perforated from a perforating depth control (PDC) log, a combination of a collar log and a cased-hole nuclear log such as a gamma ray log. The nuclear log is then depth correlated to a similar log run before the well was cased. This procedure ties the collar record into the depth scale on the openhole logs. Accuracy in this latter depth scale is maintained by means of magnetic flags placed at precise intervals—customarily, 100-ft intervals—along the openhole logging cable. The PDC log is a part of the file on a given well and provides the collar record that serves as the depth reference for subsequent production logging. A short joint of casing called a “pup” joint is often placed in the casing string as a depth marker. Otherwise, normal variations in length are used to correlate collar records.

Sometimes a radioactive collar that emits gamma rays is used as a marker for depth control. For flush-joint casing, collars are available that are strapped around the casing before it is run into the hole. Occasionally, radioactive bullets are fired into the formation before casing the well. Finally, it may become necessary to run a section of a nuclear log and to flag (mark) the logging cable on a particular operation to achieve the necessary depth control.

4.7 Pricing and Record Keeping

4.7.1 Pricing. An understanding of the price structure to perform production logging can help optimize data-acquisition costs. The total cost of a job is the sum of four separate charges:

1. **Set-Up Charge.** This is the amount the service company charges to bring their equipment to your well and “rig up” on it.

2. **Pressure Charge.** This charge is based on the surface pressure on the well and represents a rental fee on the equipment necessary to safely log the well.

3. **Depth Charge.** This is a charge based on the maximum depth reached in the well. It reflects the fact that at least three people are needed to rig up, to spool so much wireline off the drum of the logging unit, to reel this same amount of cable back onto the drum, and to rig down. It is the substitute for the familiar hourly charge.

4. **Logging Charge.** This is a per-foot charge for each tool run that reflects the length of interval actually logged by the tool.

From this structure, one can immediately see the potential savings to be had from being present during the logging operation. On-site changes in procedure to ensure the desired diagnostic logs can prevent having to start another day, resulting in incurring the first three charges again.

The footage-logging charge is often cited as the reason for running only one tool. This, however, is false economics because this charge, even for a three-tool suite, is usually no more than 40% of the total.

4.7.2 Record Keeping. Forward planning will ensure maximum long term use of log data. The log headings used by most service companies, while recording some specifics about the run itself, have little information on why and how the logs were run. Consequently, most professional loggers have their own forms to bridge this documentation gap. While the organization of these forms is a matter of personal preference, a good rule is to prepare a preliminary summary that specifies at least the following:

- Why the logging is undertaken.
- Previous production-logging summary.
- Current well-completion data with a wellbore sketch.
- Collars used for perforation.
- Depth reference point.

- Most recent well-test data.
 - Anticipated total depth, bottomhole pressure, and temperature.
- A second form completed at the time of logging is a chronology that lists
- Logs run and their order.
 - Run number.
 - String logged and its status for each run.
 - Status of other strings or annuli.
 - Logging direction and speed.
 - Tool calibration checks.
 - Intervals relogged.
 - A summary of conclusions.

4.8 Operating Principles and Performance of Production-Logging Tools

The following sections describe operating principles for each of the tools listed in [Table 4.1](#). The text will indicate applications for which a tool is best suited, those for which it is only partially suited and, when possible, those for which a tool is not suitable.

Some interpretive principles and recommended logging procedures will be presented in examples. However, the reader should refer to the Appendix for detailed information of this type. Oxygen-activation, cement-bond, and casing-inspection tools are not treated. These tools are, however, included in the application tables of the Appendix.

4.8.1 Temperature-Logging Tool. The tool includes a cage, which is open to the wellbore fluid, at the tool's bottom end. Inside the cage is a thermistor that senses the surrounding fluid temperature. The preferred sensor is a platinum element because the electrical resistance of the sensor varies linearly with temperature over a wide range and is stable over time. The circuitry of the tool is designed so that the voltage across the sensor is proportional to the sensor's electrical resistance.

In analog recording, the transmitted spikes per minute are converted to a voltage by a counting circuit. This voltage is recorded on a pen-and-ink strip chart recorded as the temperature (or gradient) trace. This is Trace 1 of [Fig. 4.5](#). The scale of this trace is in °F. A recording sensitivity of 1°F/in. across the chart is strongly recommended for production wells.

In analog recording, the voltage output of the counting circuit is also input to a differentiating amplifier. The output of the amplifier is recorded as Trace 2 (the differential trace or the derivative of the temperature), and is proportional to the depth-rate-of-change of the temperature curve. Although no absolute scale is associated with the differential trace, it is useful for highlighting important changes of the slope of the temperature curve.

On the log, the temperature trace warms abruptly below Depth B. Because the tool is logging down and the temperature is increasing, the depth-rate-of-change of temperature is positive. Consequently the differential trace shows a strong positive excursion at B, highlighting the change of the slope of the temperature trace at this depth. The differential trace, when properly amplified as on [Fig. 4.5](#), is easily worth the additional logging charge.

The flowing temperature Trace 1 in [Fig. 4.5](#) also provides information on the production profile. Production commences at Depth A, where the flowing trace “stands up” to separate to the warm side of static. This location is at the bottom of the bottom set of perforations. The middle set of perforations, on the other hand, contributes nothing to the production. The largest contribution comes from near the bottom of the top set of perforations at Depth B, where a large mixing signature is evident. The volumetric rate of entry here is so large that the mixture temperature is “pulled” almost back to static temperature (i.e., to the entry temperature for the stream). There is one additional smaller entry at Depth C, whose mixing signature is hardly recognizable on the flowing Trace 1 but is clearly evident on the differential Trace 2. The location of this entry suggests that it is composed primarily of oil. The temperature traces there-

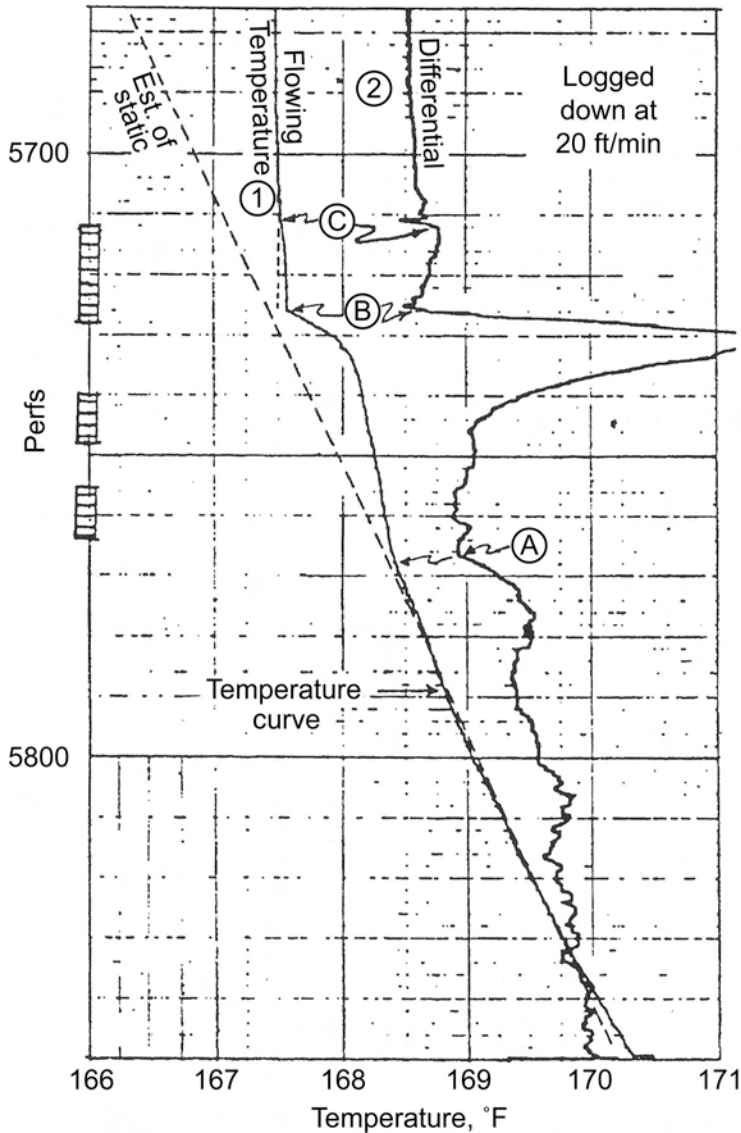


Fig. 4.5—Section of a temperature survey from a well flowing mainly water at 1,800 B/D.

fore show that the top set of perforations is responsible for the majority of both water (the major stream) and oil (the minor stream). The use of these mixing signatures to profile both single-phase and multiphase flow is described in detail in the Appendix under production-well profiling. The important point is that the size of a mixing signature relative to static temperature is dependent upon the thermal content (product of density, specific heat, and volumetric rate) both of the entry stream and of the stream in the casing immediately below the entry.

In digital recording, the spikes-per-minute from the logging cable are counted digitally at the surface, and the resulting count rate is converted to a temperature trace by the computer's program. Again, the temperature trace should be recorded at a sensitivity of 1°F across the chart. Digital recording degrades the sensitivity of the differential trace from that available with analog recording. Thus, the digitally determined differential trace is not as useful for highlighting important changes of the temperature curve's slope.

Depending on how carefully (or recently) a particular temperature tool was calibrated, there may be several °F difference between the recorded temperature and the true downhole temperature. However, the difference does not degrade the sensitivity of the differential trace. Provided that the temperature curve is recorded at the recommended sensitivity of 1°F/in. across the chart, and that the temperature log is carefully depth-correlated, the resulting temperature curve has more vertical resolution than does a curve from any other production-logging tools.

The temperature tool is most effective when located at the bottom of a tool string. In a production well, the tool should always be logged downward so as to enter undisturbed fluid. The log should be recorded at a constant logging speed not to exceed 30 ft/min. With digital recording, the maximum logging speed should be reduced to 20 ft/min.

Fig. 4.6 shows temperature logs from an exploration well that was perforated and acidized before the flow test. During the flow test, the surface rates were 2 MMscf/D gas and 500 B/D spent acid and formation water. The formation is gas-saturated limestone.

The temperature profile from the flow test is the solid trace; the line labeled “static” is a temperature log after a 6-day shut-in following the flow test. In the sump below the bottom perforation, there is no flow. The temperature here is approximately 6°F cooler than static. During drilling, mud circulation takes heat from the near-wellbore, leaving the near-wellbore below static temperature. Over time, heat flows from the formation farther away from the wellbore, where the temperature still is static. This heat flow, given enough time, restores the near-wellbore to static. In a no-flow interval, this heat flow is the only process for restoring the near-wellbore to static temperature.

At the time of the flow test, the near-wellbore temperature below the bottom perforation was still below static. The line labeled “cool temp” coincides with the flowing temperature profile below the bottom perforation and is parallel to the static temperature line determined subsequently. The cool temp line shows that, at the time of the flow test, the near-wellbore is below static throughout the perforated interval.

During the flow test, spent acid and formation water enter the wellbore at Depths 1, 2, 3, and 4. Each entry flow begins in the formation at static temperature. At Depth 1, the entry rate is small enough that the flow, after being cooled during passage through the cooler near-wellbore, enters the pipe at a flowing temperature that is considerably below static. Still, the entry causes an abrupt warming at Depth 1. Because the entry at this depth does not mix with a flow from below, the “entry temperature” (i.e., the temperature of the entry as it emerges into the wellbore) is the flowing temperature at the entry Location 1.

At Depth 2, additional liquid enters and mixes in the wellbore with the upward flow from Depth 1; the mixing of the two flows results in the abrupt warming at this depth. The flowing temperature at Location 2 is the final temperature after the mixing. The entry at Depth 2 comes into the wellbore at an entry temperature (before mixing) that exceeds the final temperature after mixing but is no greater than the static. Notice that the final temperature after mixing at Depth 2 is less reduced from static than is the entry temperature at Depth 1. Thus, the entry rate at Depth 2 exceeds that at Depth 1. The entry at 2 is cooled less by passage through the near-wellbore region than is the entry at 1, leaving the entry temperature at 2 higher than that at 1.

At Depth 3, liquid enters and mixes with the flow arriving from below. The mixing of the flows causes the abrupt warming at Depth 3. The flowing temperature at this depth is the final temperature after the mixing. The entry at Depth 3 comes into the wellbore at an entry temperature (before mixing) that exceeds the final temperature after mixing. However, this temperature is less reduced from static than is the final temperature at Depth 2. Thus, the entry rate at Depth 3 exceeds that at Depth 2. The entry at 3 is cooled less by the near-wellbore than the entry at 2, leaving the entry temperature at 3 higher than that at 2.

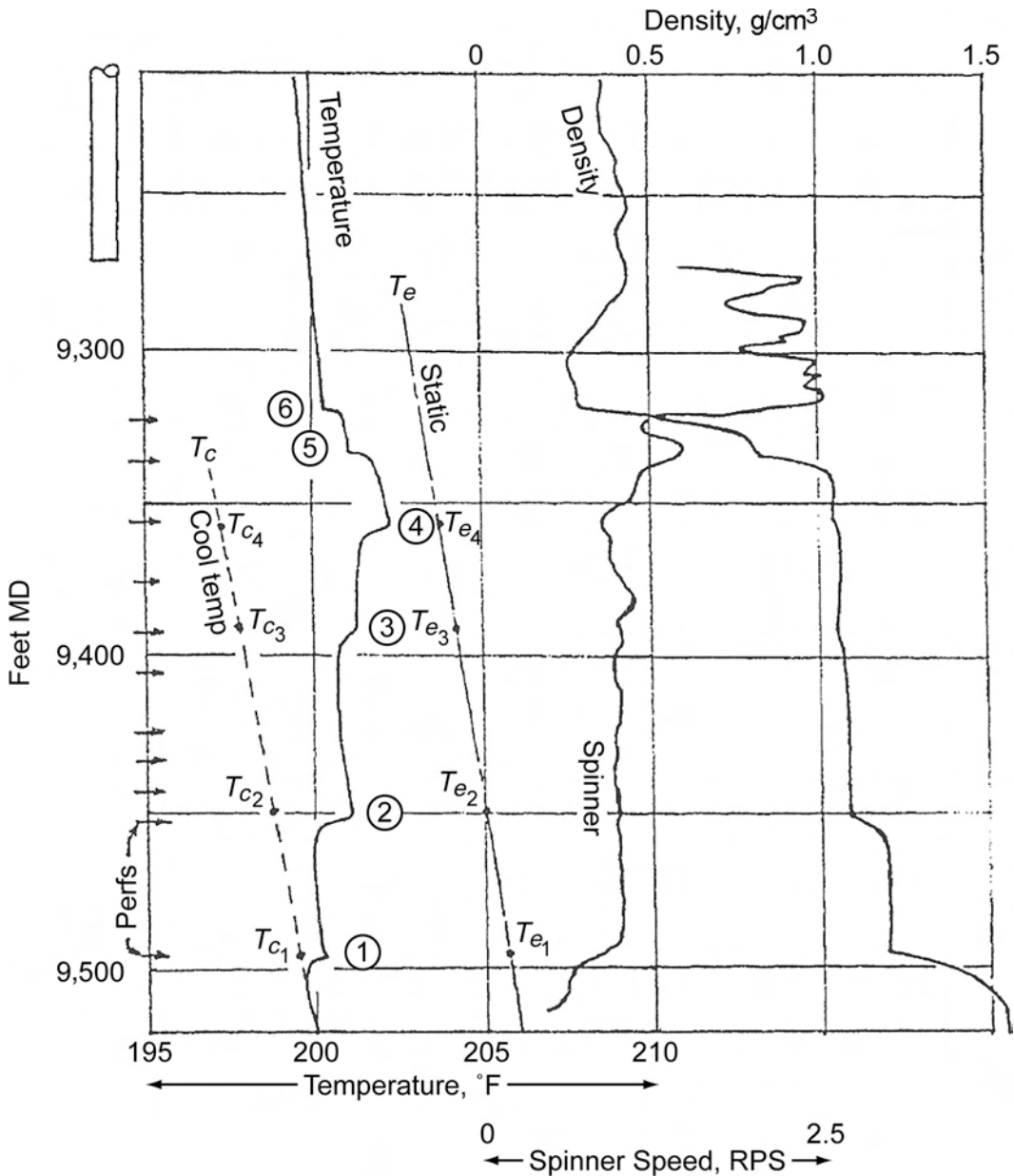


Fig. 4.6—Flowing logs from a new gas well flowing 2 MMcf/D.

By similar reasoning, the entry rate at Depth 4 is greater than the entry rate at Depth 3. In a recently drilled well or in an old gas well, provided that the near-wellbore is below static, the deepest entry, if it is a liquid, results in a warming signature. The warming is caused by the liquid's bringing of its warmer temperature into the wellbore itself. The contrast between the entry temperature and the cooler temperature of the wellbore below the entry is responsible for the warming signature. A common but mistaken view holds that the warming is caused by frictional heating of the liquid as it moves through the near-wellbore region and into the well. The fact that a water rate of only a few B/D is sufficient to produce a warm signature clearly refutes this "frictional" hypothesis. In a gas well, pressure loss in the near-wellbore and comple-

tion results in expansion of the gas during its passage into the wellbore. This expansion cools (or warms) the gas to a degree that depends on the flowing bottomhole pressure, temperature, and the amount of pressure loss. If the gas is cooled, it absorbs heat as it passes through the near-wellbore region before entry. Over time, the heat spreads up and down the near-wellbore, resulting in a below-static temperature in the near-wellbore region. Any subsequent liquid production produces the same warm signatures as described for a new well. In actual fact, the expanding gas warms at bottomhole pressures in excess of approximately 10,000 psi and cools at pressures lower than 5,000 or 6,000 psi. At intermediate pressures, the amount of cooling or warming is generally not significant.

In reference to the example of Fig. 4.6, the flowing bottomhole pressure and temperature are 1,325 psia and 200°F, respectively. The well flows at a drawdown in excess of 3,000 psia. At Depths 5 and 6, each temperature mixing signature is caused by expansion of a dry gas as it passes through the near-wellbore and completion. At Depth 5, the colder gas mixes in the wellbore with the warmer liquid arriving from below, giving the cooling signature at this depth. At Depth 6, the colder gas mixes with the warmer flow of gas and liquid arriving from below, giving the cooling signature at this depth. The next calculations focus again on the water entries.

Certain conventions apply to the volumetric rates q_i in the relationships to be discussed next. If water is produced, then the rates for all other phases are “water equivalent” rates that represent the multiplication of each actual rate by a ratio. The numerator in this ratio is the product of density and specific heat for the particular phase, whereas the denominator is the same product for water. If only gas and oil are produced, then the gas rate is presumed to be an “equivalent oil” rate obtained with a similar ratio for gas/oil. Once profiling is done by the following expressions, then the equivalent rates are converted to phase rates according to the equivalence ratios. Typically, 3 volumes of oil are the equivalent of 1 volume of water, whereas ~ 10 volumes of gas are the same equivalent.

The entry rates of the four liquid entries can be determined quantitatively from two relationships, a warming relationship where q_i ($i \geq 2$) refers to a given stream entering the wellbore at temperature T_i to mix with the total stream from below at temperature T_{i-1} and produce a mixture with temperature T_{mix} .

$$\left(\frac{q_i}{q_{i-1}} \right) = \left(\frac{T_{i-1} - T_{mix}}{T_{mix} - T_i} \right) \cdot \left(1 + \frac{q_2}{q_1} + \dots + \frac{q_{i-1}}{q_1} \right), \dots \dots \dots (4.3)$$

and a warming relationship,

$$\frac{q_i}{q_1} = \left(\frac{\ln R_1}{\ln R_i} \right), \dots \dots \dots (4.4)$$

where

$$R_i = \left(\frac{T_{geo} - T_{cool}}{T_i - T_{cool}} \right)_i \dots \dots \dots (4.5)$$

and q_i ($i \geq 2$) denotes any stream entering the bottom stream $- 1$. In the ratio for R_i , the temperature T_i refers to the temperature at which stream- i arrives at the wellbore, whereas T_{geo} indicates normal geothermal temperature at the depth of the entry, and T_{cool} is the cooler temperature of the stream coming from below entry- i . Usually, the entry temperature T_i for a given liquid stream will be the same as geothermal temperature T_{geo} and only the mixing relationship

Trial Value T_{in2}	Rate Ratio, q_2/q_1	
	Mixing	Warming
201.5	2.75	2.35
201.6	2.20	2.56
201.55	2.44	2.50
201.54	2.50	2.49

(Eq. 4.3) is required to determine the relative size of the rates. The warming relationship (Eq. 4.4) is required when the wellbore has been cooled below geothermal, and liquid entries arrive at the wellbore at some unknown temperature cooler than geothermal. In this situation, a succession of liquid entries moves the flowing temperature profile successively closer to the geothermal temperature line without bringing the two into coincidence. This is the temperature behavior at Depths 1 through 4 of Fig. 4.6. The left side of the relationship in Eq. 4.5 is the ratio q_i/q_1 ($i = 1$ to 4 in the present example), which is the ratio of the entry rate q_i to the entry rate at Depth 1. The right side of the relationship in Eq. 4.5 incorporates numerical values that are available from the “cool temp” and “static” lines in the figure. The remaining variable is T_i , which is the temperature of the i th entry as it emerges into the wellbore, before mixing with the flow from below. This is the same as the “entry temperature” used in the text above. T_1 is the temperature at the warming signature at Depth 1, because there is no flow below this depth. The value of T_i at higher depths must be determined along with the rate ratios.

On the left side of the mixing equation appears the ratio q_i/q_1 ; on the right side all numerical values are available from the temperature profiles of Fig. 4.6 with the exception of T_i . Thus, there are two unknowns: q_i/q_1 and T_i . Various trial values of T_i are entered into the warming and mixing relationships to give two values for q_i/q_1 . A solution for T_i is the trial value for which the two values of q_i/q_1 are substantially in agreement. A trial value for T_{in2} should exceed the final temperature after mixing at Depth i , but should be less than the static temperature at Depth i .

The process of using trial values is shown by Table 4.2, which relates to finding the value of q_2/q_1 and T_2 . As can be seen, the two values of the rate ratio are in close agreement at a trial temperature of 201.54°F.

From the same technique illustrated previously, the ratio of the third entry rate to the first is 4.65, and the ratio of the fourth entry rate to the first is 14.85. These ratios, along with a ratio of 1.00 for Entry 1, sum to 23.0 and provide the fractional value of each entry in the total liquid stream of 500 RB/D. Thus, Entry 1 amounts to $500 \times (1/23) = 22$ RB/D. Likewise, the entry rate at Depth 2 is 54 RB/D, at Depth 3, 101 RB/D, and at Depth 4, 323 RB/D. In Fig. 4.6, notice that the entry at Depth 4, with by far the largest rate, moves the temperature after mixing much closer to static than does any other entry, as expected. The density log of Fig. 4.6 shows that all four streams are composed primarily of water so that no phase conversion is needed.

4.8.2 Radioactive Tracer-Logging Tool. The tool has a reservoir to hold radioactive material and a pump section at the top. For injection-well logging, two gamma ray detectors below the reservoir and pump are preferable. Some tools employ only one detector, but this is less desirable. The tool includes the circuitry to amplify and transmit the detector counts to the surface, for recording.

Most natural radioactivity underground is from the decay of isotopes of potassium, thorium, and uranium. These materials concentrate in the shales, where they register approximately 100

API units on the gamma-ray log. Once downhole, a “slug” of tracer is ejected by the pump, under surface control. The activity owing to the ejected slug is much greater than the natural background activity. By tracking the progress of the slug down the wellbore, the exits of injected flow from the wellbore can be determined, as well as whether any of the injection, after exiting, passes through a channel close to the pipe.

There are two modes of logging: slug tracking and velocity shot. For slug tracking, the logging operator ejects a slug of tracer from the tool. After ejection, the tool is run up and down through the slug to ensure that the slug is uniformly mixed across the wellbore cross section. Then, the tool is lowered quickly and an upward logging pass is made at constant logging speed until the slug is detected. The time of detection of the peak and the depth of the peak are recorded. Then the tool is quickly lowered again, and another upward logging pass is made at the constant logging speed until the slug is detected again. Again, the time of detection of the peak and the depth of the peak are recorded. This process is repeated several times, resulting in a succession of detections of the same slug (see [Fig. 4.7](#)). As long as the peak progresses downward, there is flow in or near the wellbore. Once the peak stops, there is no flow in or near the wellbore below the stopping depth. For each detection, the area under the trace and above the common baseline of the traces is proportional to the percentage of injection still in or near the wellbore.

By visual inspection of the area under the traces in [Fig. 4.7](#), nearly all of the injection reaches Depth D, and the injection leaves the wellbore between D and the bottom of the perforation set. A convenient measure proportional to slug area is the product of the slug’s height, above a common baseline, and the slug’s width at half-height. Numbers from the areas agree with those shown on the left side of [Fig. 4.7](#) as derived from the travel times. Slug A is not yet mixed in the flow. Slug area has the advantage of being insensitive to variations in fluid velocity, allowing the approach to be extended to traced slugs moving behind casing. Notice in [Fig. 4.7](#) that activity also is detected below the perforations. A slug was ejected below the perforations. Upward logging passes showed that the peak of this slug was stationary. Therefore, there is no wellbore flow below the perforations, and the activity below the perforations is attributable to tracer channeling downward behind the pipe.

Generally, only one gamma-ray detector is used for slug tracking. Slug tracking gives the best overview of where injection leaves the wellbore and whether, after exiting, any injection travels in a channel close to the pipe. The upward logging passes are made at high line speed. A constant logging speed should be used, and the same speed should be used for all passes.

Provided the ejected slug is uniformly mixed in the flow by movement of the tool up and down through the slug after ejection, the vertical distance (ft) between two successive peaks in total flow divided by the time (minutes) between detection of the peaks provides an accurate estimate of the average flow velocity of total injection. Such velocities are listed on the left of [Fig. 4.7](#). The most frequently used tagging material for water is an aqueous solution of sodium iodide, which contains the isotope of iodine, I-131. The 8-day half-life is ideal. In solution, the iodine does not stick to rock surfaces; instead, with continued injection, the iodine is washed from the rock surfaces and carried away from the near-wellbore, beyond detection by the logging tool.

From inspection of slug spacing in [Fig. 4.7](#), it is evident that slug tracking has limited vertical resolution. Furthermore, because 90% of the detected gamma rays originate within 1 ft of the detector, the tracer tool’s depth of investigation is also limited and is much less than that of the temperature tool. Because of the limited depth of investigation, tracer that is channeling after exiting the wellbore must be close to the pipe to be detectable. Not all channels can be detected by the tracer tool. The same is true for fractures.

A velocity-shot survey is used in intervals where greater vertical resolution is desired. To perform a velocity shot, the logging operator stations the tool so that the detectors are at cho-

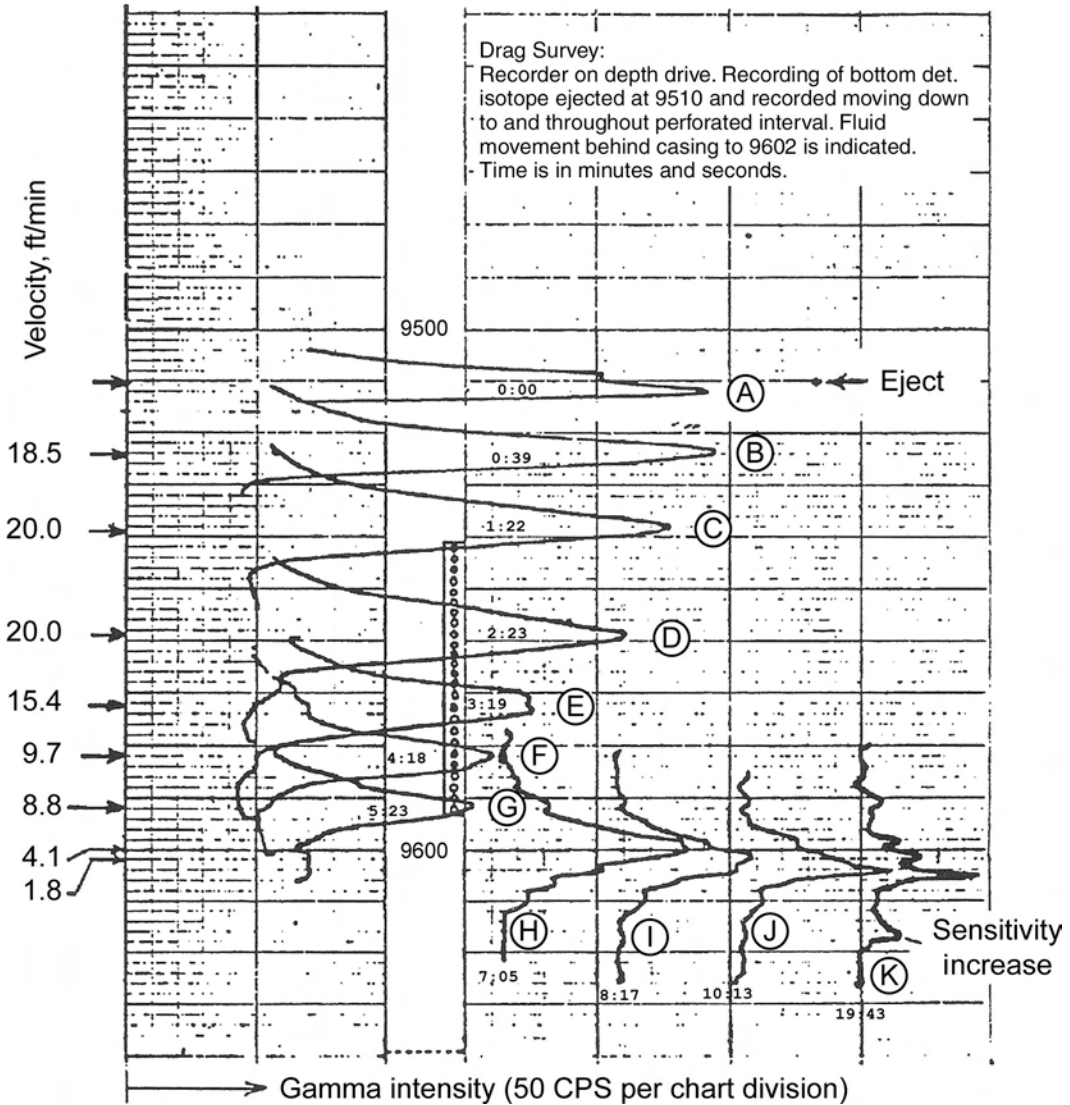


Fig. 4.7—A radioactive slug-tracking record from a water-injection well taking 600 BWPD.

sen locations. Then, with the tool stationary, a slug of tracer is ejected into the injection flow. As it passes downward, the slug is first detected by the top detector and then by the bottom detector, resulting in two traces on the log (see Fig. 4.8). On the chart, time increases from the bottom upward. Thus, the top detector gives the lower trace. The time interval between the two peaks (travel time) is inversely related to the velocity of the injection flow. The chart speed should be such that there are 5 to 10 vertical chart divisions between the peaks in total flow, although such is not the case in the figure.

The ratio of the travel time in total flow to the travel time at a selected position is the fraction of injection still in the wellbore at the selected position. However, dividing the separation between the detectors (ft) by the travel time (minutes) does not produce the average velocity of flow, as the slug cannot be uniformly mixed in the flow before it passes the detectors.

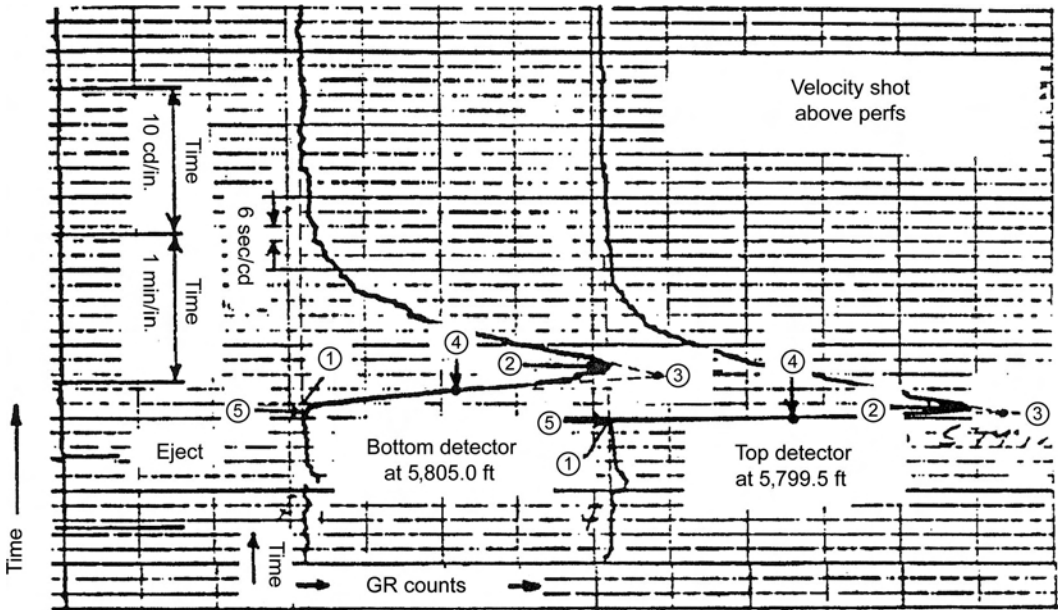


Fig. 4.8—Example of a radioactive tracer velocity-shot survey.

Two detectors are preferred for velocity shots. If there is only a single detector, there can be timing errors between initiating ejection of a slug and actual ejection downhole. These timing errors contaminate the measured travel times.

For detection of flow behind pipe, many logging operators prefer velocity shots. One detector is stationed within the perforations, while the other is stationed above or below the perforations to see if any flow channels up or down after exiting the wellbore. One difficulty with velocity shots is that they investigate only a very limited part of the total injection interval. In some circumstances, the results from velocity shots indicate the presence of a channel when in fact there is none. Whenever the results from velocity shots indicate an integrity problem, it is better to switch over to slug tracking, which investigates the overall injection interval as well as the wellbore above the interval.

Fewer applications of tracer logging occur in production wells. In a true single-phase flow, there is an appropriate tracer, whether the flow is water, oil, or gas. Because a slug is tracked for a while and then disappears uphole, multiple slugs are used, one for each producing interval under investigation. Usually, a well is logged from a bottom, no-flow interval up to an interval of total flow. Because of the unusual circulation patterns that can occur in multiphase flows, tracer results in these flows can be misleading.

4.8.3 Noise-Logging Tool. This tool “listens” passively to downhole noise, for example, from gas bubbling up through liquid in the wellbore. Behind pipe, a channeling flow often passes through cramped spaces and constrictions. These “tight spots” cause high velocities, sudden pressure reductions, and significant flow turbulence. The noise tool listens to the noise associated with the turbulence. Consequently, noise logging is an inexpensive way to investigate whether there is channeling in injection or production wells.

The tool includes piezoelectric crystals (transducers) which convert the oscillating pressure of wellbore sound to a corresponding oscillating voltage. At the surface, the oscillating voltage is applied to a speaker, permitting the logging operator to hear the downhole sound. The oscillating voltage also is applied to each of four high pass filters. A high pass filter is unrespon-

sive to frequency components of the oscillating voltage that are below the filter's "cutoff" frequency, while it generates an oscillating output signal whose amplitude represents the content of the oscillating voltage of frequencies in excess of the cutoff. The cutoff frequencies most often used are 200, 600, 1,000, and 2,000 Hz.

For quality measurements, the operator stops the tool at a selected depth and waits for extraneous noise, such as the noise generated by tool and logging-cable movement, to subside. Hurrying contaminates the measurements with extraneous noise. Then, a recording system averages and records the amplitude of each filter's oscillating output signal. Subsequently, the tool is moved to a new measurement depth; after waiting for the extraneous noise to subside, the operator initiates the averaging and recording of the amplitudes at the new depth. Thus, four values are recorded for each measurement depth. These are plotted in millivolts across the chart at a measurement depth. The amplitude of the 200-Hz filter output is the greatest; as the cutoff frequency increases, the amplitude correspondingly decreases, with the amplitude of the 2,000-Hz filter output being the least. To form a log, the plotted 200-Hz amplitudes are joined by line segments between successive measurement depths, as are the amplitudes for 600, 1000, and 2,000 Hz.

Because a filter's output signal is oscillatory, it consists of positive excursions from neutral alternating with negative excursions. There are two ways of measuring the amplitude of the output. One measures the amplitude from the peak of a positive excursion to the trough of the following negative excursion. The resulting amplitude is known as "peak to peak," and the recording is characterized as "standard gain" or "standard sensitivity." The other amplitude measurement is from the peak of a positive excursion to neutral, with the amplitude being characterized as "peak" and the recording sensitivity as "one-half standard gain." Other measures are sometimes used.

A single-station measurement typically lasts 3 to 4 minutes. Relocating the tool usually requires 1 minute. Thus, the logging rate is approximately 15 stations per hour. A 4-hour logging run accommodates 60 measurements. Thirty of these are used for a coarse-measurement grid, with successive measurements separated by one-thirtieth of the total survey interval. The remaining 30 measurements are used for detailing areas of interest, such as a noise peak identified by the coarse grid, a gas/liquid interface in the wellbore, a plug, or a packer. For detailing, the separation between successive measurements can be as little as 1 to 3 ft.

Fig. 4.9 shows the "dead-well" response recorded at one-half standard gain in a shut-in injection well. As expected, the 200-Hz amplitude is greatest, and the amplitudes progressively decrease as the frequency increases. Notice that the trace for one frequency never crosses the trace for another frequency. If such crossings occur, the log is faulty. If a dead-well response does not appear at all, the log is suspect. The figure is illustrative, and the amplitudes of the dead-well response in other wells may vary from those shown.

The cutoff frequencies were carefully determined from laboratory measurements. The 200-Hz cutoff rejects most logging-truck vibrations transmitted through the logging cable, while it is low enough to identify gas bubbling up through liquid. The 1,000-Hz cutoff permits identification of single-phase flow, the strongest frequencies of which occur at 1,000 Hz or higher. The determination of whether behind-pipe flow is single-phase or gas-through-liquid is facilitated by the 600- and 2,000-Hz cutoffs.

One service company uses software processing that implements four different *high*-cutoff frequencies with the same *low*-frequency cutoff of 100 Hz in all four instances. Thus, the computed amplitudes pertain to the frequency "bands" between 100 Hz and each of the high-cutoff frequencies. One difficulty is that the lower-frequency components of the sound, whatever their origin, have amplitudes more variable with time than those of the higher frequencies. Also, extraneous noise sources tend to be more intense at the lower frequencies. The result is that

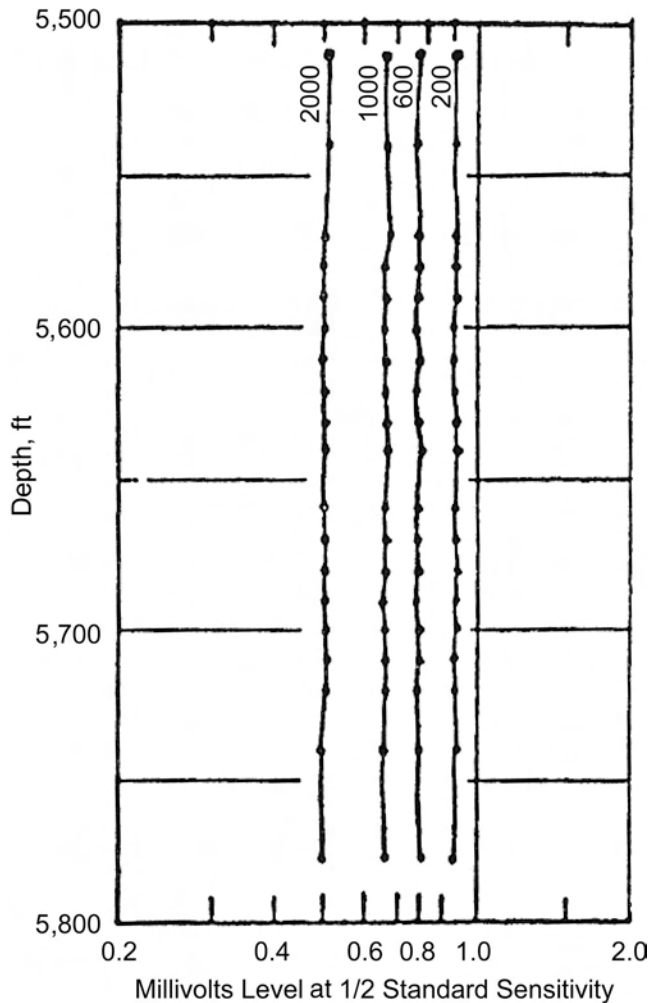


Fig. 4.9—Shut-in injection well.

each of the bandpass amplitudes can be contaminated by the variable amplitudes and the extraneous sources.

Noise can travel appreciable distances to the noise tool, both vertically and horizontally. The user must be sure that all extraneous noise from surface operations (with the exception of logging-truck vibrations) and flow in nearby wells is eliminated, so that the only noise recorded is that associated with the suspected well problem.

Fig. 4.10 pertains to a 20-B/D water flow behind pipe into a depleted gas zone. Only one noise peak occurs, corresponding to a single “tight spot” between the water sand and the gas sand. Almost 30 measurement stations were used. Farthest away from the peak, the spacing between measurements was greatest. Closer to the peak, the spacing was reduced. The measurements were densest in the locality of the peak for best detailing of the peak itself. The single-phase nature of the behind-pipe flow is evident from the “bunching” of the 200-, 600-, and 1,000-Hz traces at the peak. Gas-through-liquid flow would separate the 200- and 600-Hz traces, in addition to the separation of the 1,000- and 2,000-Hz traces.

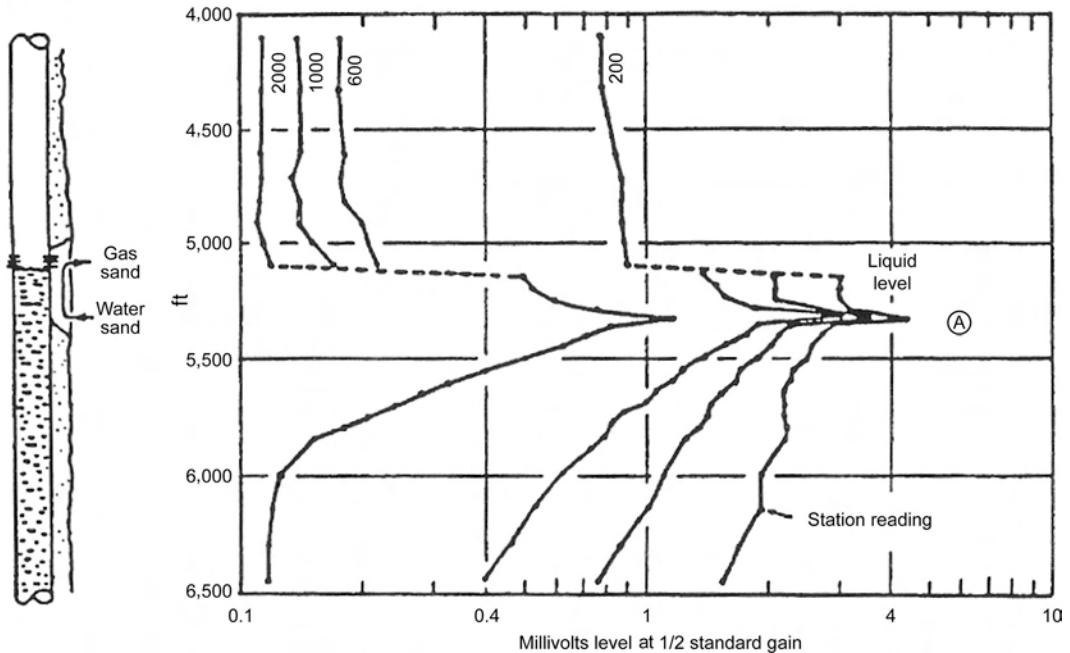


Fig. 4.10—Noise log format with a 20-B/D water flow behind pipe into a gas zone depleted by 250 psi.

Because there is no noise peak at the water or gas sand, the entry and exit of flow to and from the channel occur in absence of a tight spot at either sand. With the known 250-psi pressure drop between the sands confined to a single constriction, it is possible to estimate the flow rate of the channeling water from the pressure drop and the level of the 1,000-Hz trace at the peak (twice the level shown on the log, which was recorded at half-standard gain), yielding the 20-B/D rate. The rate equations are discussed in the appendix. If there were multiple tight spots, the estimate could still be made based upon total pressure drop and upon the sum of all the peak 1,000-Hz noise levels.

Above the gas/water interface in the wellbore, all four traces in Fig. 4.10 decline rapidly to dead-well response because of two attenuating factors. First, much of the sound reflects downward at the interface itself. Second, the tool sensor is constructed for coupling to liquid rather than to gas. In the water below the interface, only the 2,000-Hz trace, which attenuates the most rapidly with distance, reaches dead-well level. Because the water transmits sound at much less attenuation with distance than the gas, the 2,000-Hz trace requires almost 700 ft to reach the dead-well level in the water. In the gas, the dead-well level is reached in considerably less distance. In the water, the other traces show typical noise behavior; the attenuation with distance is least for the 200-Hz trace and increases with increasing frequency. In a production or injection well, it is not unusual to find a gas/liquid interface.

4.8.4 Focused Gamma-Ray Density-Logging Tool. The tool incorporates a compacted slug of Cesium-137 at the bottom of an open cage. The Cesium emits gamma rays, and a lead lens focuses gamma rays in a narrow beam parallel to the axis of the cage. Because the cage is open, wellbore fluid is present inside the cage, and the fluid is in the path of the focused beam. The gamma rays have an energy level low enough that the rays are deflected by the electron cloud surrounding the nucleus of any atom. Furthermore, the amount of backscatter (or absorption) is directly related to the density of the electron cloud and, therefore, to the density

of the wellbore fluid. Those gamma rays that are backscattered or absorbed do not emerge from the wellbore fluid at the top of the cage.

At the upper end of the tool cage, a gamma detector responds to the gamma rays that still remain when the beam emerges from the wellbore fluid. A counter determines the counts/min (intensity) of the gamma rays; this information is transmitted through the logging cable to the surface.

The preferred gamma-ray detector is a scintillation crystal because of its high sensitivity and short dead time (the interval required between detection of different gamma rays). Many tools use Geiger tubes as the gamma-ray detector. A Geiger tube has a much longer dead time than a scintillation crystal. It is necessary to use multiple Geiger tubes to ensure detection of all the gamma rays. Preferably, there are eight tubes, but tools of lesser quality may have as few as three.

Count rate is inversely related to the density of the fluid in the wellbore and is recorded in g/cm^3 vs. depth. The count-rate/density relationship is calibrated first with air in the open cage, yielding a count rate corresponding to a density of 0 g/cm^3 and then with tap water in the open cage, yielding a count rate corresponding to a density of 1 g/cm^3 . For some tools, there is an aluminum block of known density that can be placed in the open cage. There is enough nonlinearity in the relationship to justify a calibration with three known density values, but typical practice is to use only two. Often, the recording system is adjusted so that the range from 0 to 1 g/cm^3 spans the right-side track of a typical log. With 20 chart divisions in this track, the recorded log is shown at a sensitivity of 0.05 g/cm^3 . Attempts to increase the recording sensitivity appreciably over that used for the typical display result in a trace with many irregularities because of the statistical nature of nuclear events. The irregularities can make log interpretation difficult.

The advantage of the focused tool is that it measures only the density of the wellbore fluid. If an unfocused (gravel-pack) tool is used, the gamma rays investigate not only the density of the wellbore fluid, but also that of the pipe wall as well as the material and fluids that are close to the outside wall. The gamma tool can distinguish between the phases in a two-phase mixture, but it cannot distinguish among the phases of a three-phase mixture.

The tool should be logged downward at logging speeds between 15 and 30 ft/min in a flowing production well. A constant logging speed should be used, and the same speed should be used for all runs. It is best to log downward from a starting depth above all the perforations, and to log all the way to the deepest depth that can be surveyed. In a slugging or churning multiphase flow, the log may show variable behavior even in intervals that are not perforated. In that case, another logging run is advisable to establish the degree of repeatability. If the result is less than desirable, a stationary measurement can be time-averaged for each selected location. Usually a logging run is also made with the well shut-in. This log should be run after at least two or three hours of shut-in, to be sure that the fluid distribution is stable. If the well has been shut in overnight, a shut-in log can be recorded, but the well must flow for 2 or 3 hours before the first flowing log is recorded. If the tool is centralized, there is a tendency for the recorded density to be somewhat low in a multiphase flow relative to the average density across the wellbore cross section. This is because the lighter phase tends to rise through the center of the cross section, leaving the remainder of the cross section for the heavier phase.

Although the health, safety, and environmental risks are generally low, radiation safety procedures should be strictly followed when calibrating or running a gamma-ray density logger. Needless exposure to the radiation from the tool when it is at the surface should be avoided. Logging-company personnel should have current radiation training and certification. Because of the long half-life of Cesium-137, the legal restrictions on the use of the tool vary from state to state and country to country. If the tool is dropped in the well or becomes stuck, it must be retrieved or cemented over.

Another common density tool is the pressure-gradient instrument. As the name implies, this device determines density from a differential; pressure measurement across a spacing of a few feet along the wellbore. These instruments are often called “gradiomanometers” or “differential manometers.” Owing to their linearity, a two-point, air/water calibration is sufficient for such instruments. Furthermore, the resolution of the tools is higher than that of the gamma-ray densimeters. However, at high fluid velocities, the apparent density provided by these tools is corrupted by frictional losses in pressure and requires correction. Likewise, in wellbore intervals containing intense fluid turbulence, the apparent values are again corrupted and are uncorrectable. Finally, the apparent density must be corrected for deviation of the wellbore from the vertical.

A pressure-gradient density log is shown in Fig. 4.6. Near the top of the figure, about halfway across the chart, is a trace labeled “Density.” This trace is scaled from 0 to 1.5 g/cm³. Below the perforations, there is a stagnant mud column in the wellbore; the mud’s density is somewhat in excess of 1.5 g/cm³.

Spent acid and formation water enter the wellbore at the bottom perforation, Depth 1, where a density of approximately 1.2 g/cm³ is measured. This density continues to the perforations at Depth 2. At Depth 2, spent acid, water, and a small amount of gas enter the wellbore and mix with the flow from below. After mixing, the gas contributed at Depth 2 causes a density decrease from approximately 1.2 g/cm³ to approximately 1.1 g/cm³. The density remains at that level to Depth 3.

Additional entries of spent acid and gas at Depths 3 and 4 result in further, slight reductions in density.

Major gas entries at Depths 5 and 6 reduce the density to less than 0.3 g/cm³.

Redistribution of phases occurring in the 20 ft above 9,300 ft results in a density averaging approximately 0.4 g/cm³ below and within the tubing. The actual density of the gas/liquid mixture decreases significantly in the tubing stream relative to the mixture density in the casing just below the end of tubing. This happens because the gas holdup in the stream in the tubing increases in response to the increase in fluid velocity. This significant decrease is hidden on the density trace by the increased frictional loss associated with the increased velocity.

The four liquid entries and the two major gas entries correlate with the temperature behavior. Please refer to the discussion of the temperature-logging tool for a detailed interpretation of the temperature data.

4.8.5 Fluid-Capacitance-Logging Tool. The tool includes an inside dielectric probe located on the tool’s axis. The probe is surrounded by an outside housing that is open to the wellbore fluid. Together, the probe, the housing, and the fluid constitute an electrical capacitor, the capacitance level of which depends on the particular fluid, or fluids, within the capacitor.

Circuitry within the tool is connected to the electrical capacitor, with the result that the circuitry generates an oscillating signal that varies inversely with the capacitance level. Water has the greatest capacitive effect, resulting in the lowest frequency. Gas has the least capacitive effect, resulting in the highest frequency. The frequency with oil is intermediate to those of water and gas. However, the oil frequency is much closer to the gas frequency than to the water frequency. Consequently, the tool distinguishes principally between water and hydrocarbons.

Preferably, the tool is calibrated at the surface in produced water from the well, establishing the trace for water. Normally, the recording system is adjusted so that the water trace is at the left edge of the track. Air customarily establishes the trace for gas. Normally, the recording system is adjusted so that the air trace is at the right edge of the track. If the well produces any oil, the tool can be calibrated in produced oil, establishing the trace for oil. Sometimes tap water is used to establish the water trace.

Obviously, the tool poses no hazard to personnel who are exposed to it at the surface. If the tool is dropped into the well and it must be left there, it is not necessary to cement it over, as with a nuclear tool. Furthermore, the recording sensitivity can be greatly increased above normal sensitivity because the tool produces a signal that is “clean” (free of statistical events), unlike a nuclear tool. At such an increased sensitivity, the tool can detect the slightest “whiff” of hydrocarbon that passes close enough to its sensor. With the sensitivity increased, the tool also can detect very small amounts of water dispersed in oil.

A small gas entry into water looks to the fluid-capacitance tool just about the same as a small oil entry. Whereas the small oil entry, because of its low density contrast with water, changes the fluid density only slightly, the small gas entry, because of its low density relative to water, changes the density log significantly. Thus, by a comparison of the two log types, an analyst can fathom the nature of a hydrocarbon entry.

From the prior discussion, it is obvious that the fluid-capacitance tool can distinguish between water and the two hydrocarbons, but it cannot distinguish one hydrocarbon from the other. Also, the tool has a very nonlinear response over the range from water to hydrocarbon. During use downhole, there can be a calibration drift because of filming of the housing or the dielectric probe, or both. If the drift is severe, the film possibly can be removed with the tool pulled into the tubing, where the velocity of flow may be high enough to remove the film.

In a production well, the tool should be logged down at a logging speed between 20 and 30 ft/min. Maintain a constant logging speed, and use the same speed for all passes. The log should begin at a location above the perforations and end at the deepest depth that can be reached. In a slugging or churning multiphase flow, the log may show variable behavior, even in intervals that are not perforated. In that case, another logging run is advisable to establish the degree of repeatability. If results are less than desirable, a stationary measurement can be time-averaged at each selected location. Usually, a log is run with the well shut-in after flow. If the well has been shut in before logging, a shut-in log can be recorded, but the well must flow for 2 or 3 hours before the first flowing log.

Fig. 4.11 pertains to a well producing 3,520 RB/D at 68% oil and 32% water. Notice the shut-in log (left trace); at the bottom, below the perforations, the water response is near the left edge of the track. At 8,250 ft, the log shows a water/oil interface in the wellbore. In the oil above the interface, the response appears near the right edge of the track. In gas, the response would be approximately 2,350 Hz.

Below the perforations, the flowing log shows a water response indicating stagnant water. Across the bottom perforations, the log shifts somewhat to the right, indicating some contribution to the oil production.

At 8,420 ft, there is a spike in the oil direction caused by perforations which jet oil directly at the tool’s sensor. Just above the spike, the log is somewhat farther in the oil direction than it is just below, identifying the additional oil in the wellbore.

Near the top of the upper perforations (8,400 ft), there is a major shift in the oil direction. Moreover, the log response persists from this location to the end of tubing. This means that the major contribution to the oil production is from the top part of the upper perforations. Above 8,350 ft, the elevated fluid velocity within the tubing results in the oil being more effective at sweeping the water out of the pipe’s cross section than it is in the casing. The reduced presence of water across the tubing cross section results in a shift of the log in the oil direction. The presence of the water production is indicated because the log never shifts as far right as the oil response identified by the shut-in log.

Note that in **Fig. 4.11**, the flowing trace in the tubing crosses the oil/water contact on the shut-in trace at approximately 62% of the total deflection from water to oil. If the tool’s response was completely linear in holdup, then the flowing trace would cross at 68% of the total deflection (i.e., at a point slightly closer to the oil frequency). Unfortunately, the “calibration”

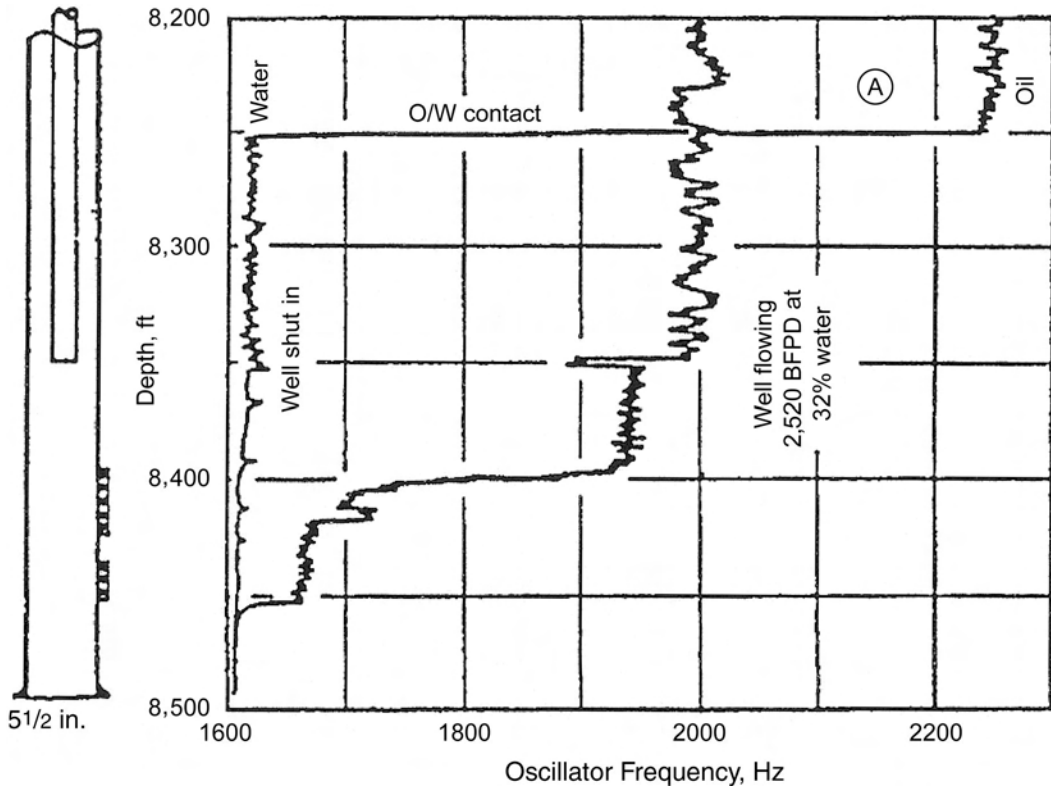


Fig. 4.11—Fluid-capacitance surveys from a well that produces 2,520 RB/D, 68% oil, 32% water.

for these instruments depends upon the viscosity of the oil owing to the filming of oil on the electrode. The smaller the diameter of the electrode, the larger this effect. In gas/water flows, water tends to film the electrode instead, which biases the “calibration” toward water.

4.8.6 Unfocused Gamma Ray (Gravel-Pack) Density Logger. The tool incorporates a compacted slug of Cesium-137 near the bottom of the device. A gamma-ray detector, located approximately 20 in. above the slug, responds to incident gamma radiation. A counter determines the counts/min (intensity) of the gamma rays; this information is transmitted through the logging cable to the surface, where the count rate is plotted against depth.

From the Cesium-137 source, some of the gamma rays are transmitted to the detector through the tool body (“direct” transmission), some by the wellbore fluid between the tool and the casing (“indirect” transmission), and some through the material outside the casing (also “indirect” transmission). Not all of the gamma rays from the source reach the detector because of backscattering by the wellbore fluid, but the majority of the detector’s response is attributable to this transmission.

As in the focused detectors, a scintillation crystal is preferable, but Geiger tubes are used in many tools. Preferably there are eight tubes, but tools of lesser quality may have as few as three.

When the tool is at the surface, radiation safety procedures should be strictly followed. Needless exposure to the radiation from the tool should be avoided. Logging-company personnel should have current radiation training and certification. Because of the long half-life of Cesium-137, the legal restrictions on the use of the tool vary from state to state and country to country. If the tool is dropped in the well or becomes stuck, it must be retrieved or cemented over.

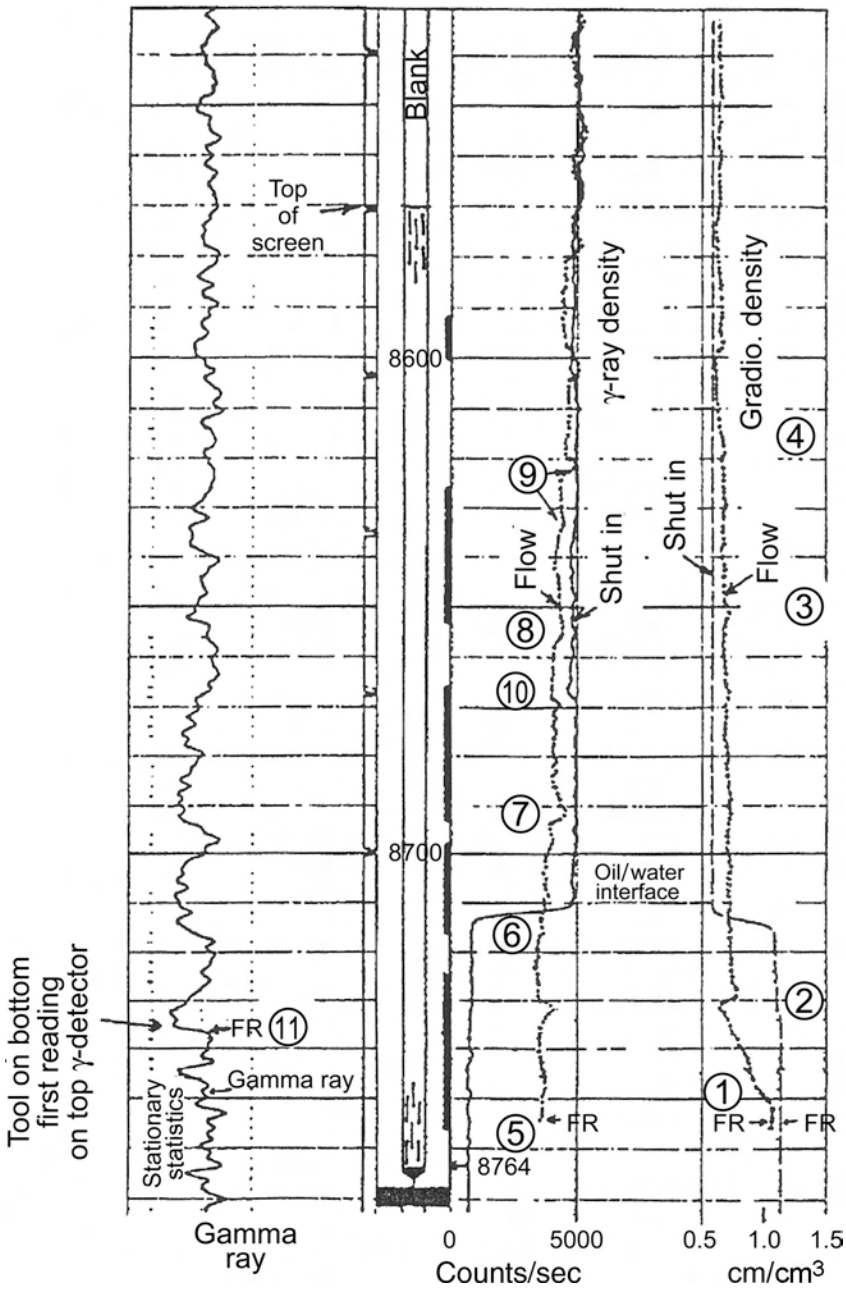


Fig. 4.12—Unfocused gamma-ray density (gravel-pack) log and gradiometer density log on a 2,264-BOPD cased gravel pack (well deviation 38°).

Logging-speed and shut-in times for a shut-in survey are the same as recommended for the focused tools.

An example of an unfocused gamma log appears in Fig. 4.12. A gradiometer (pressure-gradient) density log also is shown. Logs were recorded with the well flowing and shut-in.

During shut-in, both tools identify an oil/water interface at Depth 6. The gradio shows that the density of water in the screen below the interface is approximately 1.1 g/cm³. Although the

gradio responds only to fluid inside the screen, 1.1 g/cm^3 is also the density of the fluid in the porosity of the pack below the interface, because this porosity is water-filled during shut-in. Above the interface, the oil density in the screen is approximately 0.6 g/cm^3 ; although the gradio surveys only within the screen, the density of the fluid in the porosity of the pack is also 0.6 g/cm^3 , because this porosity is oil-filled during shut-in.

Because gamma-ray count rate is inversely related to density, the count rate on the shut-in unfocused log is lowest in the water below the interface. Whether the transmission is direct or indirect, the transmission is lower and the count rate is lower when the density of the fluid in the transmission path is higher.

Above the interface, the unfocused gamma ray shows its greatest count rate in the oil in the screen and pack.

During flow, the gradio shows essentially water in the screen below Depth 1. Farther down, at Depth 5, however, the unfocused gamma ray shows a much higher count rate than during shut-in. Because the screen at this depth is water-filled, as during shut-in, the increased response implies more transmission of gamma rays through the pack than during shut-in. More transmission through the pack is attributable to a lower density fluid in the pack. Thus, oil is present in the pack on the high side of the casing at Depth 5, but it is not in the screen. From Depths 1 to 2, the gradio shows decreasing density in the screen. This means that oil enters the stagnant water in the screen between Depths 1 and 2. Consequently, the oil in the pack at Depth 5 flows up the pack and enters the screen between Depths 1 and 2.

There is an oil-jet entry in the screen at Depth 2. Correspondingly, the gradio shows a slight spike toward lower density. The unfocused gamma ray shows a spike toward higher count rate because the oil jet lowers the density around the tool, causing more transmission of gamma rays to the detector.

At Depths 6, 7, 8, and 9, the unfocused gamma ray shifts somewhat toward higher count rate. From Depths 6 to 7, the gradio, however, shows no change of the density of the fluid in the screen. The same is true for Depths 10 to 9. Consequently, the shifts toward higher count rate of the unfocused log are attributable to increased transmission of gamma rays through the pack. Each shift, then, implies an increased presence of oil in the pack, and thus, an entry of oil to the pack at each of the four depths. At Depth 4, a slight decrease of the gradio response indicates that oil from the four entries flows up the pack and enters the screen over the 10 ft immediately above this depth.

Both logs show little or no contribution from the top, short interval at 8,600 ft. The gradio shows no change of the density of the fluid in the screen, and the unfocused gamma ray also shows no change, implying that no change occurs in the pack.

At Depth 10 (8,670 ft), the unfocused gamma ray response decreases on both the flowing and shut-in logs. During shut-in, the screen and the pack are both oil-filled above and below Depth 10; thus, the decrease during shut-in cannot be explained by a change of the density of the fluid, whether in the screen or in the pack. Also, the flowing gradio response is unchanged at Depth 10; thus, the decrease during flow cannot be attributed to a change of the density of the fluid within the screen. Instead, the decrease is attributable to a change in the porosity of the pack, with the porosity decreasing at Depth 10, resulting in an increased density of the pack above Depth 10, relative to the pack density below this depth. Above Depth 10, the increased pack density results in lower transmission of gamma rays through the pack and, thus, a lower count rate. Consequently, the decrease appears on both the flowing and shut-in logs.

In this example, it is important to note that the unfocused gamma ray, by itself, cannot distinguish between entries to the screen and entries to the pack. In addition to the unfocused gamma ray, this distinction requires a gradio log, as in this case, or a focused gamma-ray log.

The comparison of the two density logs has shown that, at least in the lower parts of the hole, oil moves upward as a separate layer on the high side of the hole. The discussion in the

Appendix shows that in such situations, the count rate from the unfocused density tool is linear in the fraction of water occupying the casing's cross-sectional area. If this concept is applied to the data in Fig. 4.12, then the two unfocused-density trace shows a constant water holdup of 28% below Depth 6 during flow. This quantitative feature of the tool can be exploited in the high-angle holes discussed in the next section of the text.

4.8.7 Special Logging Tools for Fluid Identification in High-Angle Wells. Layered flow often occurs in high-angle wells. (i.e., a water layer in the lower part of the wellbore cross-section, an oil layer above the water, and a gas layer at the upper part of the cross-section). While the tools used in vertical wells have proven effective in high-angle wells on most occasions, special tools have been developed for studying two- and three-phase flow. These tools make use of arms to position electrodes across the casing diameter. Consequently, they are “blind” to flow outside a screen or perforated liner. The brief descriptions of these tools that follow are based on the limited published information and personal discussions with suppliers.

Halliburton Gamma-Ray Backscatter Gas-Holdup Tool.* The purpose of this instrument is to distinguish liquid holdup (the percentage of the wellbore cross section occupied by liquid) from gas holdup (the percentage of the cross section occupied by gas) and provide a cross-sectional average for the mixture.

The gamma-ray source is the same Cesium-137 isotope used in the gamma-ray densimeters. A shielded scintillation crystal detector receives its signal from radiation backscattered by the density of material around the tool. The tool is used primarily to differentiate between gas and liquids. The contrast in density between gas and liquid causes a large change in signal level, while the small difference between oil and water densities causes a correspondingly small change in signal level. The value used for liquid density in the holdup calculation does not make much difference as long as it is in the range common to liquids. Thus, the corresponding error in holdup is at worst 10 to 15% and probably better because only backscattered radiation is involved. To compensate for pipe size, variable spacing between source and detector and/or shield should be used to eliminate backscatter from the formation outside the pipe.

For a limited range of gas-holdup values, flow-loop data for the backscatter tool show a linear response over the range of the data. Sensitivity to small gas concentrations is sufficient. These data do not shed any light on the matter of compensation for variable pipe size, however. If formation backscatter is high, then the gas point will show a much higher count rate and the small difference in liquid signal at zero gas holdup will become a relatively large difference. In-situ calibration in a shut-in well is therefore recommended for this tool if it is to function quantitatively.

Baker Atlas Multi-Capacitance Flowmeter. This centralized tool includes a spinner flowmeter at its bottom end. The wellbore cross section is considered as being divided into eight levels, and a positive orientation section of the tool ensures that the levels are perpendicular to true vertical.

Twenty-eight capacitance sensors are deployed on “wings” from the tool in such a way that there are capacitance sensors spanning each of the eight levels. An array of capacitance sensors spans levels at a first position along the tool's axis. Another array of sensors spans levels at a second axial position.

During logging, the various capacitance measurements for each level are recorded and converted to values for the gas, oil, and water holdups. An across-the-wellbore, bidirectional velocity profile is constructed from transit-time measurements of the capacitance sensors on Levels 1 and 2 (bottom levels) and 7 and 8 (top levels). The construction involves cross-corre-

*Personal communication, Halliburton (1993).

lation of some of the sensor responses. The spinner flowmeter provides velocity information related to the wellbore centerline. Stationary measurements can be made as well.

The holdups, the velocity profile, and the cross-sectional area of the wellbore are combined to determine the flow rate of each fluid as a function of the axial position along the wellbore.

A possible limitation is that capacitance sensors sometimes film in heavier oils; in turn, an oil film biases the capacitance measurements toward oil and gas and away from water. Another possible limitation is that the distinction between oil and gas may not be nearly as great as the distinction between oil and water. Finally, the concept of velocity determination from two measurements at the same radius along the axis supposes perfectly layered flow free of circulatory velocities. This condition, however, is at odds with the assumption of capacitive-event creation for cross-correlation.

Schlumberger Flowview. In a horizontal well, five types of segregated flow are usually defined. These are: stratified with a flat interface, stratified with a wavy interface, stratified with a bubbly interface, lighter phase slugging over the heavy phase, and one phase existing as bubbles in the other phase.

Because of segregated flow, the new tool string consists of both traditional and nontraditional sensors. Some of these sensors average over the entire cross section of the casing, whereas others make measurements at different locations in the cross section. The various sensor sections are referred to as “items” in the description that follows. The tool string described next is for mainly oil/water flow. For three-phase flow, a larger tool string, called the Flagship (Schlumberger), is available.

Item 1 is a full-bore spinner. This item gives information about composite fluid velocity, which in multiphase flow is difficult to relate to fluid-flow rates even after an image of the layers in the well has been generated by an imaging sensor such as the Flowview Plus (Schlumberger).

Item 2 is the Flowview Plus. The main results from this tool are eight-electrode measurements of water holdup to provide an approximate image of how the fluids are segregated in the cross section. The fluid image greatly aids in the interpretation of the spinner response.

This item consists of two Flowview tools, combined so that one is rotated 45° to the other and separated from it by at least 3 ft. Each Flowview makes four independent measurements of borehole fluid holdup and bubble counts, distributed in different quadrants of the pipe cross section. The tool is self-centralized and uses matchstick-sized electrical probes to measure the resistivity of the wellbore fluid—high for hydrocarbons and low for water. The probes are located inside the tool’s four centralizer blades to protect them from damage. The opening of the blades positions each probe at midradius in the casing. The tool can run up to 9⁵/₈-in. casing.

Each probe is sensitive to the resistivity of the fluid that impinges upon its sharp leading edge. If the fluids are distinct and not in a fine droplet emulsion form, and the bubble size is larger than the tip of the probe (less than 1 mm), then both water-holdup and bubble-count measurements may be obtained from the output of the probe. Local water holdup is equated to the fraction of the time that the probe is conductive, whereas bubble count comes from the average frequency of the output. The local water holdup from each of the eight probes is used to generate the water/hydrocarbon distribution in the well’s cross section.

Item 3 is the Reservoir Saturation Tool. This tool is a pulsed-neutron tool that can be operated in lifetime mode or spectral carbon/oxygen mode. Its main applications are for estimation of oil, gas, and water holdups and determination of water-phase velocity by oxygen activation.

Item 4 consists of pressure, temperature, and deviation sensors. In addition to the spinner, these are the sensors found on traditional production-logging tool strings. The new string, however, locates the temperature sensor nearly 15 ft from the end of the string, making the measurement subject to interferences from fluid mixing by tool movement.

From a combination of the holdups, the cross-sectional area of the wellbore, and the fluid velocities, the rates of the individual phases are estimated as a function of position along the wellbore's axis.

The small resistivity probes tend to film with oil when in use in heavier oils and with water in gas/water flow. In these cases, the measurements of the affected probes are biased toward the filming phase.

4.8.8 Diverting-Spinner Flowmeter. These are the most accurate of the spinner devices when low total rates and multiphase flows occur. The stream is diverted through the tool's barrel, thereby raising the velocity of flow and increasing the sensitivity to the point that diverting spinners can detect rates as low as 10 to 15 B/D. A typical $1\frac{1}{16}$ -in. tool has a barrel ID of approximately 1.45 in. A flow of 10 B/D results in a velocity of 3.4 ft/min inside the barrel. Because of the limited clearance between the spinner and the barrel, this velocity is enough to overcome friction and turn the spinner.

Furthermore, a flow of 100 B/D passes through the barrel at 34 ft/min, which is sufficient to start the homogenization of the flow, which eventually eliminates phase influence. In casing, a rate of 2,000 B/D is needed to have the same effect around a continuous spinner. Another benefit to multiphase-flow application is that the tool can be calibrated directly for such flow. As long as the diversion is effective, casing size is not a parameter in the calibration, and the tool can be calibrated in the low-rate range where phase bias is still important even inside the tool.

One type of diverting flowmeter is the hem-packer. The lower end of the diverter contains a coated fabric "skirt" with a 1-in. hem at the bottom. The skirt is opened by the metal struts to which it is attached, so that the momentum of the stream can effect a reasonable seal. A downhole pump inflates the hem with oil contained in the tool body, resulting in a seal that diverts practically the full stream through the barrel and past the spinner. A downhole motor expands and retracts the struts. The response of the tool to single-phase flow is nearly linear. Two interchangeable spinner elements are available—one with a small pitch for high sensitivity at low rates and a second with a larger pitch for rates up to approximately 2,400 RB/D. Because of its fragility, the tool never found widespread use, but is still available at some locations.

Another type of diverting flowmeter is the basket (metal-petal) flowmeter. On the lower end, the basket is opened by motorized compression of its several struts, each of which is tack-welded on its underside to a corresponding petal cut from sheet metal. As the struts are compressed to open the basket, the petals slip over each other so as to maintain some overlap even when the basket is fully opened. As the basket opens more to accommodate larger casing diameters, overlap between the petals decreases and leakage through the basket increases. Strut travel is limited to prevent excessive opening and leakage. Standard $1\frac{11}{16}$ -in. tools accommodate casings as large as 5.5 in. nominal. Some $1\frac{11}{16}$ -in. tools can accommodate 7-in. casing. This is an operational feature that should be checked carefully when ordering this service. Also, it is prudent to inquire whether the tool has been calibrated in a section of pipe of diameter close to the intended application. If not, the service company may not know the effect of leakage on spinner response.

At the point where the outside of the struts meets the casing's inside wall, the metal petals (which are attached to the inside of the struts) cannot deform enough to effect a complete seal. Because of leakage around the struts the low flow-rate response of the tool is nonlinear. Attaching the petals to the outside of the struts would improve the seal, but would wear the petals quickly during use, destroying the tool's main advantage, its ruggedness.

There is very small clearance between the spinner and the ID of the barrel. This feature assures almost no diversion of flow around the spinner. On the other hand, small particles of debris can plug the tool.

As the spinner turns, it generates a specific number of voltage pulses per revolution. Thus, the pulse rate from the tool can be transmitted through the logging cable for surface recording and determination of the corresponding revolutions per second. The number of pulses per revolution varies considerably from manufacturer to manufacturer. When ordering the service, it is recommended to inquire as to the number of pulses per revolution (more is better).

Typical basket flowmeters are rated for temperatures in the range of 320 to 350°F and for pressures in the range of 15,000 to 20,000 psia. The 1.70-in. tool typically accommodates 3,000 B/D (maximum); the 2.25-in. tool, 5,000 B/D; and the 3-in. tool, 8,000 B/D. In each case, the tool length is approximately 60 in.

Measurements are made with the tool stationary. In a production well, the tool is lowered to the deepest measurement depth and then opened. After recording the measurement at this depth, the tool is pulled up (while open) to the next measurement depth, and so on. When opened in a production well, the tool can be damaged considerably by movement downwards. When considering a diverting flowmeter for an injection well, the user should inquire of the service company whether its tool is capable of such operation.

The chance of having a diverting flowmeter stick in the hole is greater than with a continuous flowmeter. In a sandy flow, for example, the basket recesses may plug, in which case the basket cannot close downhole. If the tool is stuck, the cable can almost always be pulled loose from the cable head and retrieved. If the flowmeter is stuck in the casing, the least expensive approach may be to jar the tool to the bottom of the hole and leave it. If stuck in the tubing, it may be necessary to pull the tubing. Horizontal wells typically have dirt along the bottom of the wellbore; the flow carries the dirt into the diverting flowmeter, which usually plugs.

Diverting flowmeters are easily calibrated in a flow loop, in both single- and multiphase flows. While continuous spinner flow-loop calibrations require many correction factors for their use, such is not the case for the diverting flowmeter.

Only a few companies have extensive flow-loop facilities. If flow loops are not used for calibration, the customary approach is to apply the same calibration to all types of flow or, even worse, to use the same sensitivity coefficient for all situations. Flow-loop facilities at various universities do offer an alternative source of equipment.

Flow loops generally cannot be pressurized or heated, so the calibrations they produce for diverting flowmeters are not exactly correct for multiphase flows, especially gas/liquid. The error, however, is much less than with a corresponding calibration for a continuous flowmeter. Further, some degree of correction is possible for a diverting flowmeter calibration, because diversion of flow around the spinner element is not a problem.

A single-phase calibration of a packer flowmeter in liquid flow is linear, showing constant sensitivity (slope), with no change of the response because of casing size. The corresponding calibration of a basket flowmeter is nonlinear because of leakage around the struts and through the basket. Moreover, the degree of leakage increases with the casing size. For a packer tool in water flow, the RPS-flow rate relation involves a threshold rate (below which the spinner does not turn); for rates above the threshold spin rate, the spin rate increases linearly with rate. For a basket tool in water flow, the initial response (at lower rates) is nonlinear because of leakage around the struts. The final response (at rates approaching maximum) is nonlinear because of leakage through the overlap between petals (i.e., flow through the basket itself). Because of leakage around the struts at lower rates, the basket also has a threshold. Unlike the packer calibration, there is no single sensitivity to the basket flowmeter calibration. The sensitivity is lower at lower rates, then increases with rate until it reaches a maximum at midrange, after which it decreases with increasing rate.

For a packer flowmeter in air at atmospheric pressure, the earlier portion of the tool's response is nonlinear in gas rate. The lower the gas rate, the less the sensitivity because of the tendency of the gas to "spiral" through the spinner element rather than turn it. With increasing

rate, the response becomes linear (constant sensitivity). The value of this sensitivity, however, is approximately one-half the sensitivity in water because of the presence of spiral-velocity components in the low-pressure stream. At normal wellbore pressure, gas density is sufficient to largely eliminate these distortions; however, tool sensitivity remains slightly lower than that for liquid.

In a multiphase flow, the diverting flowmeter should be calibrated at light-phase cuts of 0, 20, 40, 60, 80, and 100%. For each cut, the total flow rate should vary from the minimum the tool can sense up to the maximum the tool can accommodate. This process generates a family of calibration curves, with the total flow rate on the horizontal axis, the light-phase cut as the parameter of the curves, and the RPS response on the vertical axis. The total flow rate should begin at minimum and then include 100, 200, 300, 400, 500, 700, and 1,000 B/D. Above 1,000 B/D, the total flow rate should increase in 500-B/D increments until the maximum is reached. The calibrations should be performed in a pipe size close to the user's intended application. The deviation angle is unimportant.

When requesting the diverting flowmeter, the user should verify that the service company has a calibration of the tool in the same phases as those that flow downhole in the user's well, and in a pipe size close to that in the user's intended application. Unfortunately, very few companies have such calibrations. If the calibration is at a different deviation angle than in the user's well, this difference is not important.

An example of the use of a diverting flowmeter appears in [Fig. 4.13](#), which also shows two temperature traces. A 24-hour shut-in temperature log, recorded before the flowing log, is dashed. A flowing temperature log, after 4 hours of flow, is solid. An open set of perforations is shown near the bottom of the figure. Six squeezed perforation sets are above the open set. The stationary measurements from the diverting flowmeter are shown at locations labeled A through D, top-to-bottom.

Above Depth F, the flowing temperature log is initially constant. A water flow of sufficient rate that the flow carries its temperature up with it originates at Depth F. At Depth D, the diverting flowmeter response is 7.1 RPS, showing that the water from F enters the pipe through the open perforations.

At Depth E, the flowing temperature log cools over a short interval, indicating that the water from F mixes with colder water entry at E. The size of the mixing signature at Depth E indicates that the entry accounts for 43% of the total flow, with the remaining 57% produced from the open perforations at Depth F. The flowmeter response at Depth C is 11.7 RPS, also showing that the colder water enters the pipe through squeezed perforations.

Above C, the flowmeter response is 11.5 RPS at Depth B and 11.6 RPS at Depth A. Thus, no more water enters the pipe above C. For a linear response from the diverting flowmeter, 7.1 RPS is 61% of 11.7 RPS; therefore, 61% of the water (approximately 610 BWPD) is from F, with the remaining 39% (approximately 390 BWPD) entering through the squeezed set. This is all the information the diverting flowmeter can yield, because the flowmeter responds only to flow in the pipe. On the basis of this information, one would assume that the 390 BWPD flow comes from the formation at E.

The flowing temperature log, which responds to flow within and behind the pipe, shows that the assumption just made is fallacious. Above depth G, the flowing temperature log is more constant (less slope) than it is below G. Above G the flowing temperature log responds to the full 1,000 B/D water flow inside the casing. At this rate, the stream cools slowly as it moves upward. Immediately below G, the temperature increases more rapidly with depth. This behavior is consistent with an "entry" at depth G that "pulls" the temperature toward its shut-in value. However, the spinner fails to show such an entry at this depth. Instead, the 390 B/D water flow channels down from G and enters the pipe through the squeezed set at Depth E, creating the mixing signature where it mixes with the flow from F. Therefore, the source of the

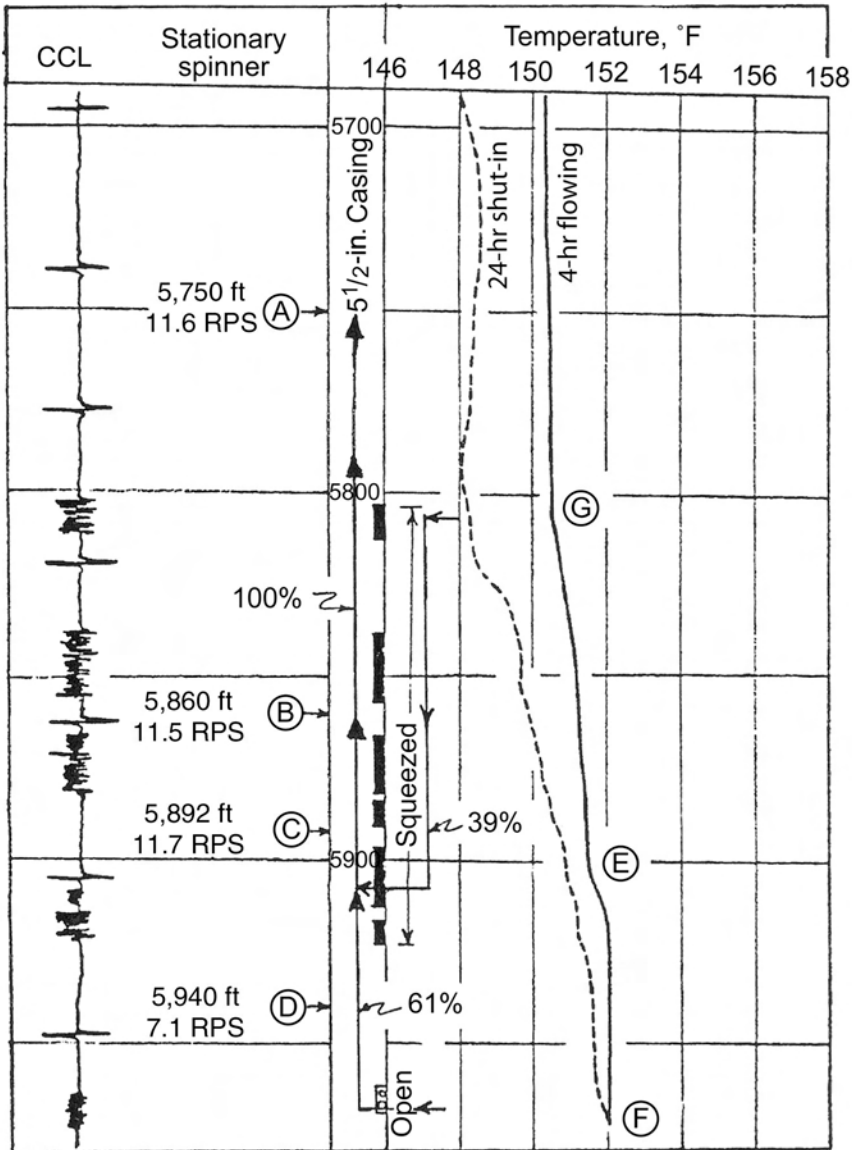


Fig. 4.13—Spinner and temperature survey in well producing 1,000 BWPD with minor oil cut.

colder water entering through the squeezed set is the formation at G, and not the formation at E. Between Depths E and G, water flows up inside the pipe at 1,000 B/D, while the 390 B/D water flow from G travels down behind the pipe. Because the net upward flow is less than 1,000 B/D and the temperature tool responds to the flow within and behind the pipe, the temperature trace between E and G cools more rapidly with decreasing depth than above G, where the net upward flow is 1,000 B/D.

4.8.9 Continuous and Fullbore Spinner Flowmeters. There is no generic difference between a “continuous” spinner and a “fullbore” spinner. In the case of the fullbore, the spinner element folds into a diameter no greater than that of the tool when in the tubing, but expands into

a larger diameter for surveying in the casing. The continuous spinner does not have this capability. The difference between the two is too small to justify a separate discussion of each.

The continuous meter derives its name from the need to move the tool fast enough to overcome frictional torque and start the spinner element rotating. It also derives its name from the in-situ calibration procedure that uses logging runs at several different cable speeds with the well shut-in at the surface. Neither continuous nor fullbore, however, can provide a log that is quantitative whenever the fluid velocity is sporadic, that is, changing in the logged interval.

The continuous and fullbore tools share three features. First, the spinner element on each is at the very bottom of the tool string. If the temperature tool is run in combination with the spinner, then the thermometer's sensor will usually be located in the tool string above the spinner. Thus, the sensor will be 4 to 6 ft above the bottom of the string. Moreover, this 4 to 6 ft will include at least one centralizer. The mixing caused by the passage of the centralizer in front of the temperature sensor will decrease the vertical resolution of the temperature log by a few ft. Even so, the vertical resolution of the temperature tool to localized entries is still far superior to that of the spinner tool, and the temperature tool should be included in the tool string.

The second common feature is the presence of at least two centralizers in any tool string containing the spinner flowmeter. The centralizers ensure that the spinner element samples the same location in the wellbore's cross section at each depth. This consistency is necessary for the same tool calibration to apply at each depth and for the relative profile to be representative of flow rates.

The third shared feature is that both tools use a four-blade propeller-type (or turbine-type) spinner element. Although the design of the spinner element may vary, the four-blade feature is retained.

The spinner element can rotate either clockwise or counterclockwise (as viewed down the tool barrel). The direction of rotation depends upon the movement of the fluid relative to the barrel of the tool, that is, upon the direction of fluid movement as seen by "rider" on the tool. Usually, the pitch of the spinner is such that relative movement of fluid up the barrel causes the spinner to turn clockwise, whereas relative movement of fluid down the barrel causes a counterclockwise rotation of the spinner. Consequently, movement of the tool downward in stagnant fluid causes relative movement of fluid up the barrel and rotates the spinner clockwise. Movement upward in a stagnant fluid causes relative fluid movement down the tool barrel and spins the element in a counterclockwise direction. Movement of the tool in a direction opposite to the direction of flow causes the spinner to turn in the same direction, clockwise or counterclockwise, throughout the logged interval including those intervals with stagnant fluid. Passes made downward in a production well therefore cause a clockwise rotation over the interval from 100% to 0% flow. Passes made upward in an injection well cause a counterclockwise rotation. On the other hand, movement of the tool in the direction of flow at a line speed less than full-steam velocity causes a reversal in the direction of spinner rotation at some depth within the flow interval. The spinner first loses speed as flow velocity approaches tool speed. It then stops when fluid velocity reaches tool speed less the frictional threshold speed for the tool. The spinner remains stopped until fluid velocity changes by an amount that equals two threshold values, at which point the spinner begins to turn again, but in a direction opposite the previous one. As fluid velocity changes further, the spinner maintains its opposite rotational direction. Such a pass should not be used for percentage flow profiling, because two threshold values are "lost" in the record of spin rate.

Many spinners, however, do not record the direction of rotation. Even worse, some spinners have lower sensitivities when rotating counterclockwise. In event the direction of rotation changes and the spinner does not record it, the change can be recognized from its signature: a drop of the RPS to zero, followed by a resumption of the RPS to above-zero values.

Both continuous and fullbore tools are intended for quantitative use only in flow streams having a single component of velocity directed along the axis of the tool. Furthermore, the stream should be a single-phase or a high-rate multiphase (10,000 B/D or more). In the multiphase case, the well should have low deviation angle. The meters are designed to function quantitatively in environments such as that indicated in [Fig. 4.14](#). This spinner pass downward is from a cased, vertical well producing single-phase gas from three isolated perforation sets, the deepest of which is a short interval at 11,700 ft. In the left track, the cable speed trace shows a logging speed of 56 ft/min. This speed produces the 1.2-RPS rate of spin below the deepest perforations. This part of the RPS trace is labeled “zero-flow reference” because the RPS response is caused by moving the tool downward through the stagnant fluid below the deepest set.

The completion in the figure has at least 50 ft of separation between successive perforation intervals. This is sufficient distance for any tangential velocity components associated with an entry at a given interval to die out before additional gas enters at the next interval above. Thus, the spinner attains a constant rotational rate above a given entry that reflects the axial velocity produced by the combined flow from that entry and all others below. In the figure, this constant rate is attained within approximately 10 ft above the entry. The amount of deflection to the right of the no-flow reference is proportional to the flow rate in the wellbore at the respective depth. Under these conditions, flow profiling is done simply from a determination of the fraction that a given stable deflection represents of the total stable deflection above all entries. Thus, the top set contributes approximately two-thirds of the total gas while the bottom set contributes only approximately 15% of the total.

The survey of the figure appears to show simple and direct a spinner record is to interpret. The validity of the interpretation, however, cannot be judged on the basis of the spinner log itself. Most wells that produce only oil or gas will have a stagnant column of mud or workover fluid standing to some depth in the wellbore unless the deepest entry is at a high rate. A wellbore-fluid density log for the present example could show a stagnant water column standing in the wellbore, at least to the bottom of the middle perforation set. If that is the case, then the spinner record above the bottom set is in response to lifting of water by the buoyant rise of gas through it and not a response to the single-phase velocity of gas flow upward. Then, if the response is assumed to be from single-phase gas flow, the contribution from the bottom set will be greatly exaggerated.

Furthermore, the type of completion in [Fig. 4.14](#) is seldom encountered. The type of completion more likely to be associated with spinner logs is shown in [Fig. 4.15](#). Here, there is a long bottom interval perforated over 65 ft and a short perforated interval only 5 ft above the bottom one. The figure shows a fullbore-spinner log on the right track and a wellbore-fluid density log on the left track. Both logs were run downward at a cable speed of 200 ft/min with the well producing at a combined rate of 10,000 B/D of oil and water at a 50% water cut. The objective of the logs was to profile the relative oil and water production within the long interval and to determine the relative contributions of each from the short interval.

Below the bottom of the long interval, the wellbore-fluid density is 1.0 g/cm³, identifying water. Above the bottom of the long interval, the fluid density decreases up to approximately Depth D because of the entry of oil. The increasing presence of oil in the water shows that the bottom interval is productive up to D. Above D, there is very little change of the fluid density, suggesting that the upper part of the long interval and the short interval are not significantly productive.

Below D, the RPS trace in the 7-in. casing is ever-changing. The trace never attains a stable RPS value, which is necessary for quantitative analysis of the flow velocity. This fact alone means that the production from the long part of the bottom interval cannot be profiled in the straightforward manner of [Fig. 4.14](#). Possibly, the absence of a stable RPS response is because

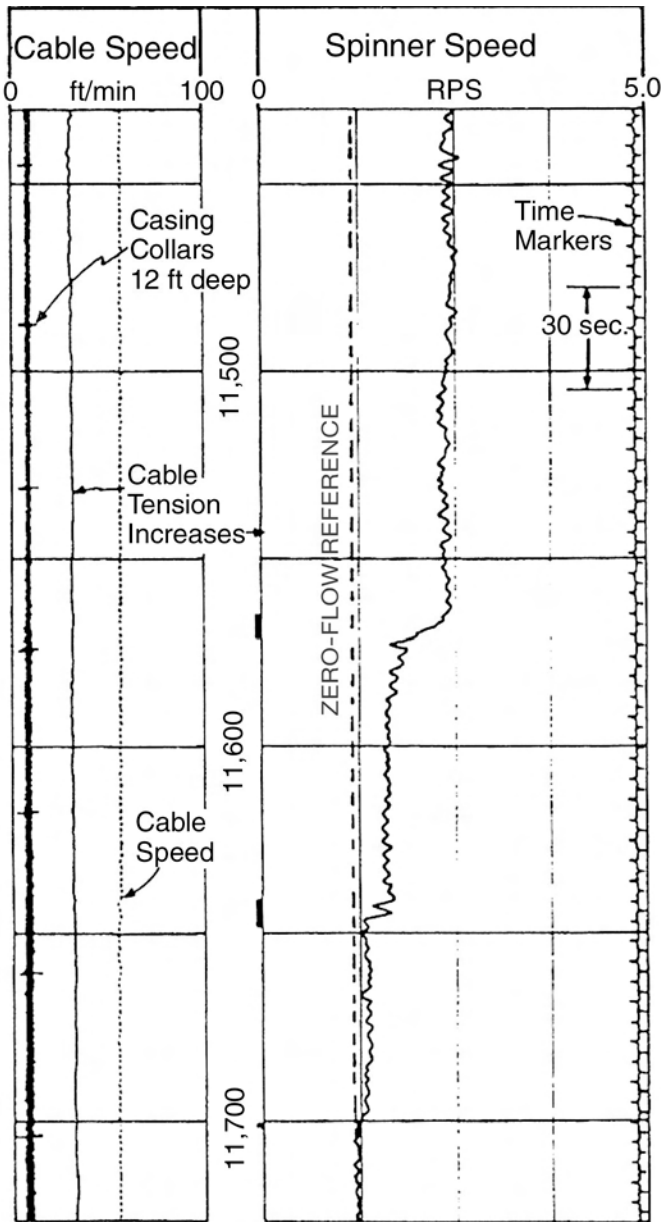


Fig. 4.14—Ideal completion for continuous flowmeter application (courtesy Schlumberger Wireline).

of the high logging speed, which raises the rotational inertia of the spinner element. Quantitative analysis also requires that the flow velocity be entirely axial. But such is not the case in this example. At Depth A, there is a jetting entry, the tangential velocity of which causes a spiked increase in the RPS response. The fluid-density log at this depth decreases for a short interval, identifying oil. At Depth C, the fluid-density trace spikes in response to a fluid jet that appears to put water between the sensor ports spaced 2 ft apart. If this is the case, then the rate is insignificant because the density is the same on either side of the spike. At D, there is a spiked increase in the RPS response resulting from the tangential velocity of a jet entry. This

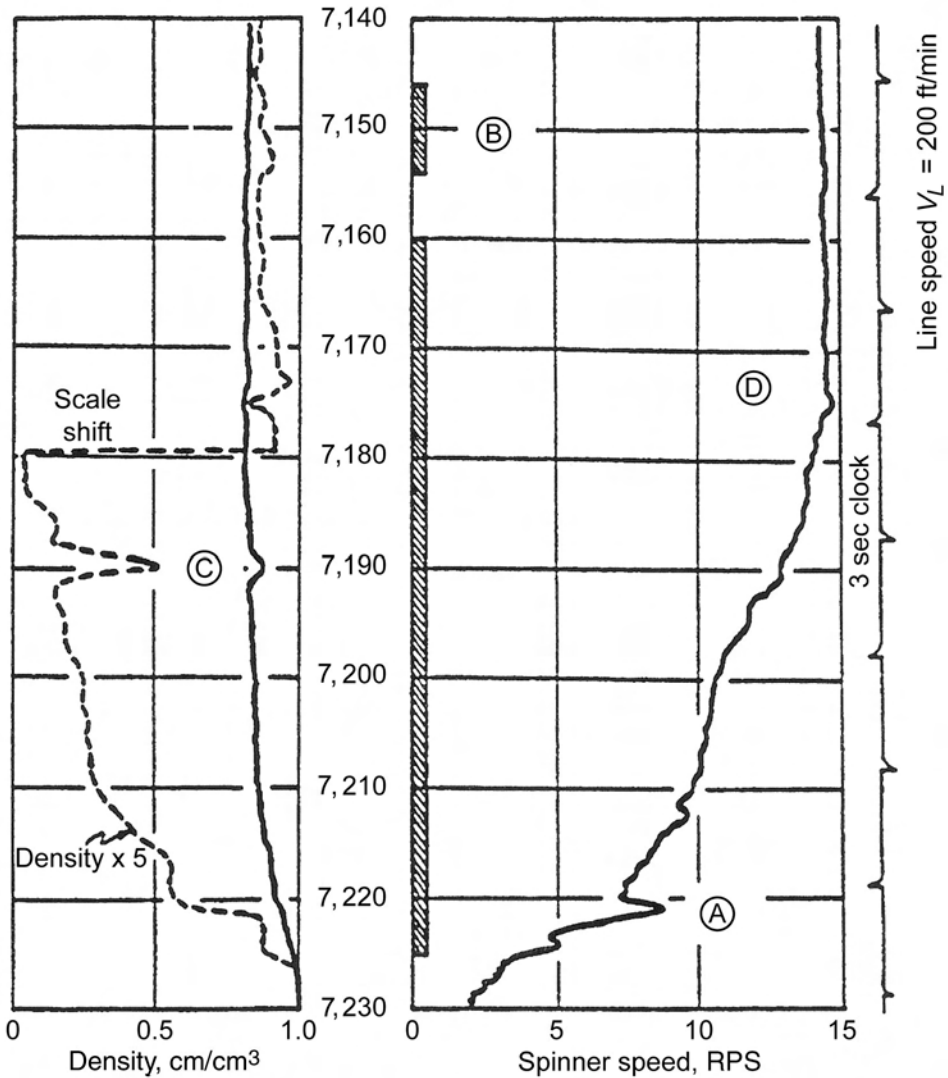


Fig. 4.15—A “fullbore” spinner and “gradiomanometer” density survey from a well flowing 10,000 B/D at 50% water cut.

is not to say that all perforation jets cause an increase of the RPS response. In other cases, a jet entry may have a tangential velocity that decreases the RPS trace. This happens at 7,211 ft, for example.

The density trace shows that essentially all the oil has entered the wellbore by a depth of 7,180 ft. The spinner shows that essentially all the flow is in the wellbore by this depth. Consequently, both oil and water enter below this depth. The reader can apply similar reasoning to conclude that approximately 70% of the flow enters below 7,200 ft, bringing with it a major part of the oil and water production.

Above D, the RPS trace slowly diminishes. This means that the flow at D has a swirling (tangential) component that dies away as the flow moves up. Swirls can require several hundred feet of travel to decay completely. At D, the swirl is contributing to the RPS response; as the swirl dies away, the contribution diminishes and the RPS decreases. In other cases, the swirl may detract from the RPS response; as the swirl decays, the RPS increases. Even if the

RPS trace were to show some evidence of production from the short interval, the presence of the swirl would preclude a quantitative analysis of the flow velocity.

The logging operator used the high logging speed in this example to minimize the distortion of the RPS trace by jet entries, as at Depth A. Actually, this procedure maximizes the distortion by biasing all fluctuations to the high side of their excursions rather than to their average.

The previous two examples should remind the reader that an apparently simple record from a direct measurement can have subtle meanings and may fail to present a complete accounting of the situation.

Continuous tools are available in a wide range of configurations, more so than the fullbore tools. The diameters range from 1 $\frac{3}{8}$ -in. to 2 $\frac{1}{8}$ -in. The 1 $\frac{3}{8}$ -in. versions, with centralizers, should pass through 2-in. tubing. If the tubing includes landing nipples, such as the 1.82-in. size, it is difficult to force the centralizers through the nipples. Safety considerations preclude even an attempt.

The centralizers also come in a variety of configurations. Powered centralizers offer the least problem to entry through tubing. These are closed by strong springs when in the tubing. In the casing, a downhole motor opens the centralizer against the spring force. In event of a failure of the motor downhole, the powered centralizer has a shearing mechanism so that the constriction at the tubing's end can be used to close the centralizer when re-entering the tubing. The chance of sticking a centralized string is greater than that for an uncentralized one.

Some continuous tools have the spinner element inside a bow-spring cage with no additional protection from damage. In others, the element is inside a rigid cage having the same diameter as the tool. Still others place the element inside a short section of tubing having the same diameter as the barrel. The latter are immune to the tangential velocity of a jet-entry; they are not immune to swirl, which has both axial and tangential components. If the flow is multiphase, the trace from such a tool is noisier because of the light phase's tendency to pass through the "chimney."

To measure the RPS of the spinner element, the most common means is a magnet and pickup coil. A narrow magnet is attached lengthwise to a section of the spinner shaft. The magnet rotates under the pickup coil, which is divided into independent segments so that the coil generates a number of inductive current spikes per revolution of the shaft. The resolution, however, does not approach that from tools utilizing an optical sensing assembly, which also detects the direction of rotation. Another variation uses a single sector of pickup coil with three bar magnets embedded in the rotor at unequal azimuth angles. While reducing the tool's resolution, this approach does detect the direction of rotation.

Magnets should be located inside the tool barrel so that iron particles in the wellbore fluid attach themselves to the outside of the tool and do not interfere with rotation of the spinner. Magnets located on the spinner shaft before it enters the barrel can attract iron particles and eventually make rotation impossible.

Most continuous spinners are rated for pressures in the range of 15,000 to 20,000 psi and temperatures of 350 to 400°F. Some tools can accommodate 500°F, but they employ vacuum flasks and thus have a diameter of at least 2.5 in.

Practically all fullbore spinners are copies of the original Schlumberger version with slight modifications here and there. Fullbore tool diameters range from 1 $\frac{1}{2}$ to 1 $\frac{1}{16}$ in.

These tools use specific diameter spinner elements to accommodate specific casing sizes. Typically, three different diameters are used to cover casings in the range of 4 to 9 $\frac{5}{8}$ in. Pressure and temperature ratings are the same as for the continuous spinners, which were stated previously.

The difference in resolution between continuous and fullbore spinners is small; the following comments apply to both types. Neither is very effective for quantitative resolution of low-

Type of Fluid in Wellbore	Typical Rate Resolution
Single-phase liquid	60 to 100 B/D
Single-phase gas	200 Mcf/D
Oil and water	300 B/D
Gas and liquid	600 B/D

rate, multiphase production. In the U.S., the spinners' greatest quantitative application is injection profiling. **Table 4.3** summarizes typical rate resolution under different flow conditions in vertical wellbores, although actual resolutions are quite dependent on flow conditions.

These numbers should be viewed in the sense that the given amount of flow is lost, even qualitatively, for entries above the deepest entry. The qualitative resolution of the deepest entry is better than the numbers in the table.

Refer to **Fig. 4.16**, which pertains to the record of a high-quality, high-resolution continuous tool that detects the spinner element's direction of rotation. The well, with three perforation sets, produces 1,800 B/D at 28% oil, 72% water, and no gas. The survey shows two logging runs, one up and one down, with each at 22 ft/min cable speed (left track). There are two respective RPS records (right track). Zero RPS is at the fifth chart division from the left, and 1 RPS is spread over four chart divisions (a sensitivity of 0.25 RPS per chart division), showing the tool's high resolution.

On the up run (dashed trace) in the stagnant fluid below the bottom perforation set, an imaginary observer riding on the tool would perceive the fluid velocity as down the barrel so that this trace records counterclockwise rotation (CCW) below the bottom set. On the down run through the stagnant fluid below the bottom set, the imaginary observer would perceive the fluid velocity as up the barrel; therefore, the rotation is clockwise (CW). Below the bottom set, the RPS of the up run is more irregular than on the down run, because the tool, when jerked off the bottom, requires some distance to reach a steady speed. Thus, the comments below pertain to the down run.

On the down run in the stagnant fluid (which is single-phase formation brine or workover fluid) below the bottom set of perforations, the RPS shows a very steady value of three chart divisions; that is, 0.75 RPS. The tool used for this survey has a threshold velocity of 5 ft/min. This amount of line speed in the stagnant fluid is required to overcome frictional torque and start the spinner rotating. Therefore, the velocity driving the spinner on the down run through the stagnant fluid is $22 - 5 = 17$ ft/min. The sensitivity of the tool is $17/0.75 = 22.67$ ft/min/RPS. In the stagnant fluid, a sustained deflection of 0.2 chart division would be recognizable on the RPS trace. The single-phase sensitivity of this tool is

$$0.2(\text{chart div}) \times 0.25(\text{RPS/chart div}) \times 22.67 \text{ ft/min/RPS} = 1.13 \text{ ft/min} .$$

The 7-in., 23-lbm/ft casing has a capacity of .0393 bbl/ft; thus, this velocity corresponds to a flow rate of

$$1.13(\text{ft/min}) \times 0.0393(\text{bbl/ft}) \times 1,440(\text{min/D}) = 64 \text{ B/D} .$$

This value is at the low end of the range listed in **Table 4.3** because the flowmeter in this case has very high resolution. On the down run, the flow from the bottom two sets causes an average deflection of 0.8 chart divisions to the right of the steady response in the stagnant fluid

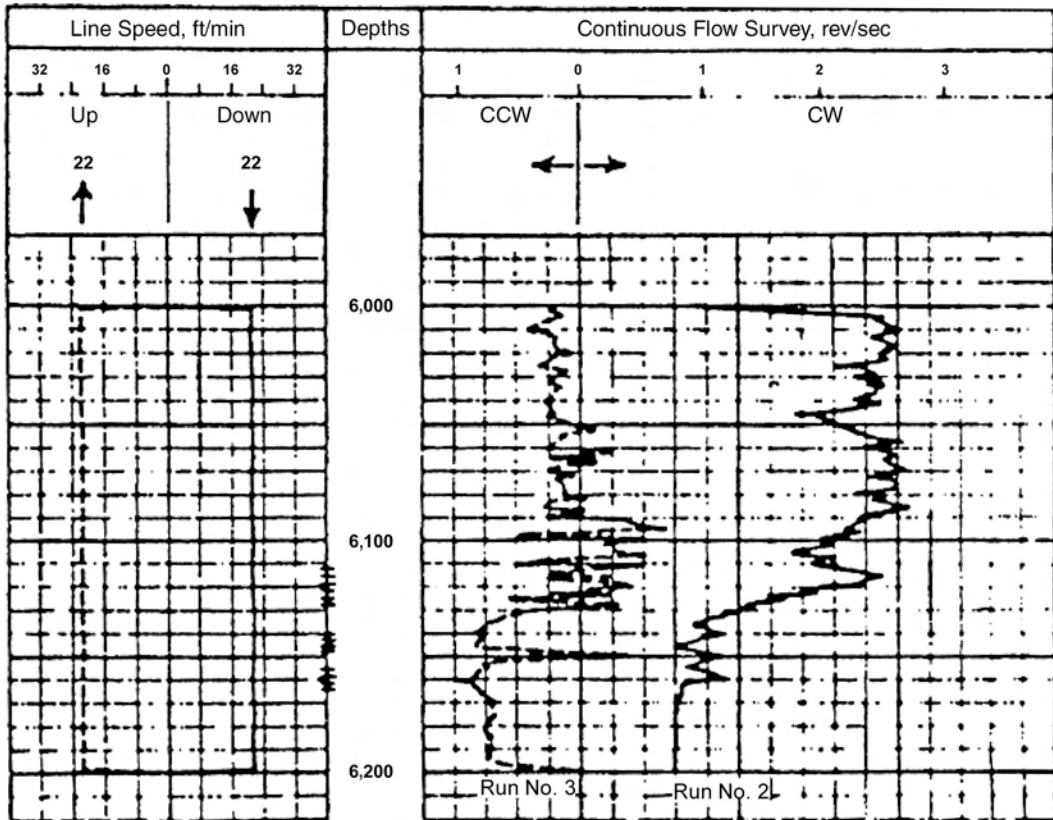


Fig. 4.16—High-resolution, continuous-spinner record from a production well.

below the bottom set (the no-flow reference). In full flow, the average deflection is 6.5 chart divisions to the right of reference. Thus, the relative contribution of the bottom two sets is $(0.8/6.5) \times 1,800 = 222$ B/D. A flowing temperature survey in the same well (not shown), analyzed separately, establishes a more reliable estimate of the contribution of the bottom two sets: 430 B/D. The flowmeter lost 200 B/D, which is consistent with the resolution stated for oil and water flows (see Table 4.3). As oil, because of its buoyancy, rises through water in the wellbore interval defined by the bottom two sets, the oil churns and circulates the water even if the water is flowing; in turn, this action in the heavy phase can either slow down or speed up the spinner element, depending upon what component of circulation in the heavy phase most affects the tool. On the down run, the spinner is slowed, diminishing the spinner-estimated relative contribution of these sets. On the other hand, the spinner element speeds up slightly on the up run in response to a circulation downward.

The calculation immediately preceding is an example of relative profiling; that is, using the flowmeter log to establish relative contributions, with the total flow rate known independently. When an absolute flow rate is needed, the method of downhole calibration can be used. Downhole calibration is appropriate for injection flows or single-phase production except for, perhaps, the deepest entry, which may be submerged in captive completion fluid.

To perform a downhole calibration, the well is shut in at the surface. Both up and down runs are made through the static fluid at various cable speeds. On the calibration plot, cable velocities appear on the horizontal axis, with downward logging speeds as positive velocities and upward speeds as negative velocities. Values of RPS appear on the vertical axis, with val-

ues positive for down runs and negative for up runs. For each run, a point is plotted that corresponds to the cable velocity and its respective RPS value. A “best-fit” straight line is constructed for the plotted points of the down runs; this line corresponds to clockwise rotation and is located in the first quadrant of the plot. A second best-fit straight line is constructed for the plotted points of the up runs; this line corresponds to counterclockwise rotation and appears in the third quadrant.

The line for the down runs intersects the cable velocity axis to the right of the origin, and the velocity value at this intersection is the ideal or extrapolated threshold velocity for down runs. This value is slightly less than the actual speed needed to overcome frictional torque and start the spinner element rotating. The slope of this line is the sensitivity of the tool during down runs. The line for the up runs intersects the cable velocity axis to the left of the origin, and the absolute velocity value at the intersection is the threshold velocity for up runs. The value of the slope of the line is the sensitivity of the tool during up runs. For a quality tool, the two threshold velocities are nearly the same, as are the two sensitivities.

As an example of the use of the downhole calibration, consider a down run with the well producing. The RPS value at a depth of interest is taken from the log and on the plot is projected horizontally onto the straight line for the down runs. The corresponding value on the velocity axis is the velocity that drives the spinner element at this location. From this velocity, subtract the cable speed to obtain the net velocity. This velocity value is the apparent flow velocity. Multiplication of the net velocity (ft/min) by the pipe capacity (bbl/ft), by $1,440$ (min/D) and by an independently determined calibration factor yields the desired flow rate. The calibration factor is needed because the apparent velocity as measured by a spinner is larger than the average or superficial velocity of the stream.

As another example, consider an up run with the well producing and with the spinner turning counterclockwise. The RPS value at a depth of interest is taken from the log and projected onto the line for the up runs. The corresponding value on the velocity axis is the velocity that drives the spinner element. From the absolute value of this velocity, subtract the positive value of the cable speed to obtain the net velocity. The rate is calculated from this net velocity in the same way. Had the spinner reversed to spin clockwise, the speed would be projected onto the calibration line for down runs and the cable speed added to the result to obtain the net velocity. An algebraic formulation of spinner speed as a function of cable and fluid velocities is given in the Appendix under the category of injection profiling.

Some additional comments are in order relative to the spinner traces in Fig. 4.16. Note first the pass upward at a line speed of 22 ft/min (the dashed-line trace). This line speed is close to the value of the upward superficial velocity for the full-flow stream (18 ft/min). Consequently, the spinner deflection is small approximately 0.25 rps counterclockwise above 6,050 ft. Below this depth, this low speed accentuates the fluid turbulence associated with the lifting and fall-back of water as oil moves through it. This churning and circulatory action causes the spinner speed to flip-flop across the zero-rps axis with a reversal in the direction of spin on each crossing. On the downward pass at 22 ft/min (the solid-line trace), the higher-frequency oscillations are much smaller than on the upward pass. With the relative speed of the fluid to the tool being approximately 10 times larger than on the up pass, the sample time is too small for the spinner response to mirror the full extent of the high-frequency fluctuations seen on the up pass. As a result, one sees on the downward pass primarily the occasional lower-frequency events associated with gross slugging or “heading” in the flow.

The reduced effect of turbulence on the pass downward illustrates an adage that one still finds repeated in the literature to the effect that a high logging speed should be used to “minimize” the effect of turbulence. Although the claim is true, the implication that the response is more accurate is not. The reduced sample time caused by high relative speed between fluid and tool introduces a “hidden” bias toward higher spinner speed in flows affected by multiphase

turbulence. The positive bias results from the greater influence of the life surges relative to the fallback flow along the casing wall. Such a bias is evident on the record from the upward pass, the dashed line in Fig. 4.16. An average value for the spinner speeds on the section of record in the interval of 6,090 to 6,130 ft is clearly to the clockwise side of the zero axis by approximately 0.25 rps, whereas the value above 6,050 ft is approximately 0.25 rps counterclockwise. The gross bias of approximately 0.5 rps represents a flow of 160 B/D in this example. The bias increases as the relative speed increases. Some spinner tools rectify the output pulses before conversions to rps values. On records from such tools, turbulence of any type produces a bias to higher speeds, owing to the interaction between sample time and spinner inertia.

4.9 Production-Logging Suite Examples

The earlier discussion emphasized the importance of using suites of production logs, rather than relying on a single log. In addition, the discussion indicated the applicability of production logs at various stages of a well's life, from drilling to abandonment, and even beyond. To further emphasize these points, four examples of production-logging suites (during drilling, during primary recovery, during tertiary recovery, and after abandonment) are described. These discussions include the objective of running a particular production-logging suite, stating why each log was used, and indicating what each log contributed toward achieving the objective of an understanding of the subject well's behavior.

4.9.1 Gas Kick While Drilling. In this development well, 10 $\frac{3}{4}$ -in. pipe is set to 3,500 ft, and 7 $\frac{5}{8}$ -in. casing is set to slightly below 14,000 ft. Behind the 7 $\frac{5}{8}$ -in. casing, the top of the cement is just below 6,000 ft. During the coring of a gas sand at 15,000 ft, a pressure kick occurred, gas pressure was then lost at the surface, and mud was added periodically to keep the drillpipe full.

On the day after the gas kick, noise and temperature logs were recorded during the same run inside the drillpipe with the well static. These logs were run to identify the flow path of a likely underground blowout. The temperature log is basic to understanding a well's behavior, and the noise log is particularly responsive to the movement of gas through liquid.

At 15,000 ft, the noise log (Fig. 4.17a) exhibits a nearly "dead-well" noise level, indicating no activity (i.e., no fluid movement). Above 15,000 ft, however, the noise log departs from dead-well response. This departure shows that the gas, which enters the wellbore just above 15,000 ft, moves uphole. Above 14,000 ft, the noise log decreases very rapidly to dead-well response, showing that the gas moving uphole enters a formation at 14,000 ft, approximately 100 ft above the 7 $\frac{5}{8}$ -in. casing shoe. The log thus shows a crossflow of gas (single-phase) from approximately 14,800 to 14,000 ft. The absence of gas pressure at the surface on the annulus between the drillpipe and the 7.625-in. casing means that the annulus is plugged by a bridge at some unknown depth above 14,000 ft.

A temperature log is quite sensitive to liquid flow and will reveal details regarding the flow path of any mud returns, which should move uphole in the annulus between the drillpipe and the 7 $\frac{5}{8}$ -in. casing, owing to the periodic addition of mud to the drillpipe at the surface. Each time mud is added at the surface, some hotter mud is pushed upward in the annulus. For a given length of wellbore, the volume of hotter mud in the annulus greatly exceeds the volume of cooler mud in the drillpipe. During the time between additions, the two volumes equate in temperature to a value warmer than static. The periodic addition of mud at the surface should therefore produce what appears to be a "production" profile on a temperature survey. The temperature log in Fig. 4.17b does indeed show such a profile below Depth C. From this depth downward to 14,000 ft, the temperature is warmer than static, indicating displacement of annular mud upward to Depth C. This depth happens to be the location of a zone that was fractured and used during drilling for disposal of sour mud from the mud pit. The log therefore shows the movement of mud from deep in the well upward and into the disposal zone at Depth C.

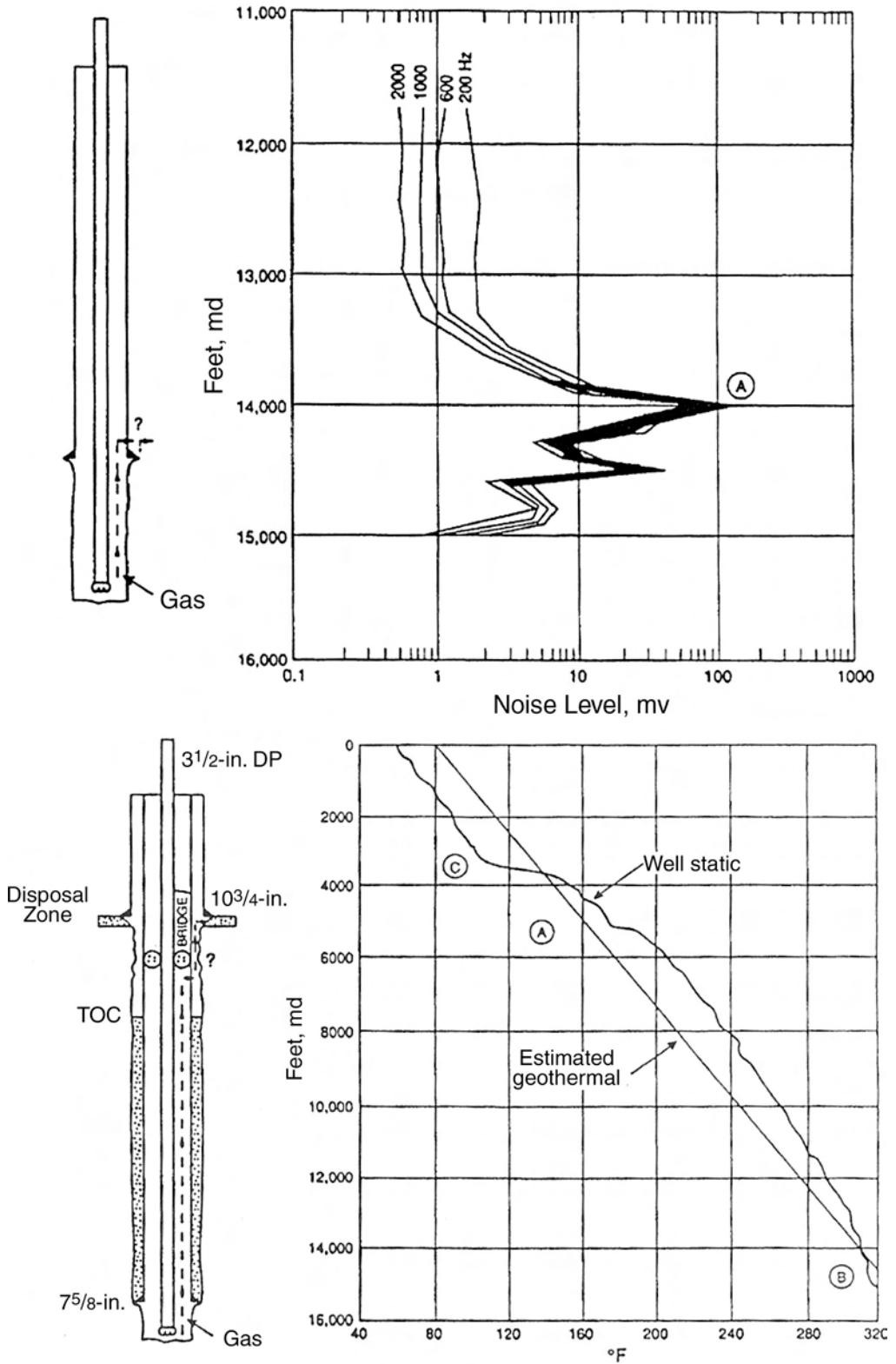


Fig. 4.17—(a) Noise log with well shut in at surface; (b) temperature log with well shut in at surface.

Above Depth C, the temperature trace lies to the cool side of static, reflecting the addition of cool mud to the drillpipe without displacement of warmer mud upward in the annulus.

For this flow path to exist, the 7.625-in. casing must also have failed at some depth. The temperature trace shows the location of this failure at Depth A just below 5,000 ft. Above this depth, the displaced mud moves behind the casing and loses heat to the formation at an increased rate. The corresponding mud temperature, although still warmer than static, is not as warm as the mud still in the annulus below Depth A. A mud path is therefore established as shown by the dashed line on the wellbore schematic on the left side of Fig. 4.17b. The only remaining task is the location of the depth of the failure in the drillpipe.

To investigate the mechanical integrity of the drillpipe, a radioactive tracer log was run, with the tracer tool stationary in the drillpipe at various depths while mud was pumped into the drillpipe continuously. The tracer traveled down the drillpipe with the mud flow, and the time lapse between its ejection and its subsequent detection by a detector below the ejector was measured. Time-lapse measurements made at various depths indicated a significant mud leak from the drillpipe in the interval between 12,800 and 12,900 ft. As further confirmation of the mud leak, tracer was ejected at 12,800 ft, and the tracer tool was quickly repositioned to 12,500 ft. While the logging tool was at 12,500 ft, the detector responded to the ejected tracer as it moved upward in the drillpipe-casing annulus. As a result of this survey, one can further conclude that the annulus is plugged to gas flow at some depth below the leaking joint of drillpipe at approximately 12,800 ft. The location of this bridge was determined from a free-point survey (see appendix), allowing a joint of split drillpipe to be replaced. The underground gas crossflow was then “killed” with mud.

Once the underground blowout was eliminated, the drillpipe was removed and the 7⁵/₈-in. casing string was examined with a casing collar locator to complete the investigation of mechanical integrity. The collar-locator log showed a 4-ft vertical separation in the casing string at Depth A because of a casing joint that was unscrewed from the collar above.

In this example, a careful analysis of a suite of inexpensive production logs yields definitive information of a diagnostic nature. Please note that the first suggestion of mechanical integrity problems resulted from a thorough examination of the temperature profile. Because the temperature profile was analyzed during the logging, the tracer and collar-locator logs were run while at the wellsite, avoiding the additional setup, pressure, and depth charges that would occur if the service company were to return for the tracer and collar-locator logs at a later date.

4.9.2 Profiling Commingled-Gas Production. This well produces gas from four perforated intervals; however, the bottom two intervals are in such close proximity that they are considered as one perforation set. Therefore, the perforations are referred to as the “top set” (A), the “middle set” (B), and the “bottom set” (C). The well produces 175 to 320 Mscf/D, with negligible water production. The objective of the production logs was to determine the fraction of total production contributed by each perforation set. With the well flowing, fluid density, temperature, and continuous-spinner flowmeter profiles were recorded. With the well flowing, a diverting flowmeter log was also recorded with the flowmeter stationary below and above each perforation set.

Viewed upward from the bottom, the fluid-density profile (Fig. 4.18) responds to a column of water below the bottom perforation set. Then it decreases above each of the three perforation sets, indicating that each set produces gas. Above the top perforation set, the measured density still exceeds the density of the gas, showing that water is present in the wellbore throughout the survey interval. Even though the water production is negligible, the gas rate is insufficient to lift water out of the wellbore.

Below the bottom perforation set, the temperature profile (Fig. 4.18) coincides with the estimated geothermal temperature profile. At each perforation set, the temperature profile shows cooling, which occurs because of the expansion of the produced gas as it passes through the near-

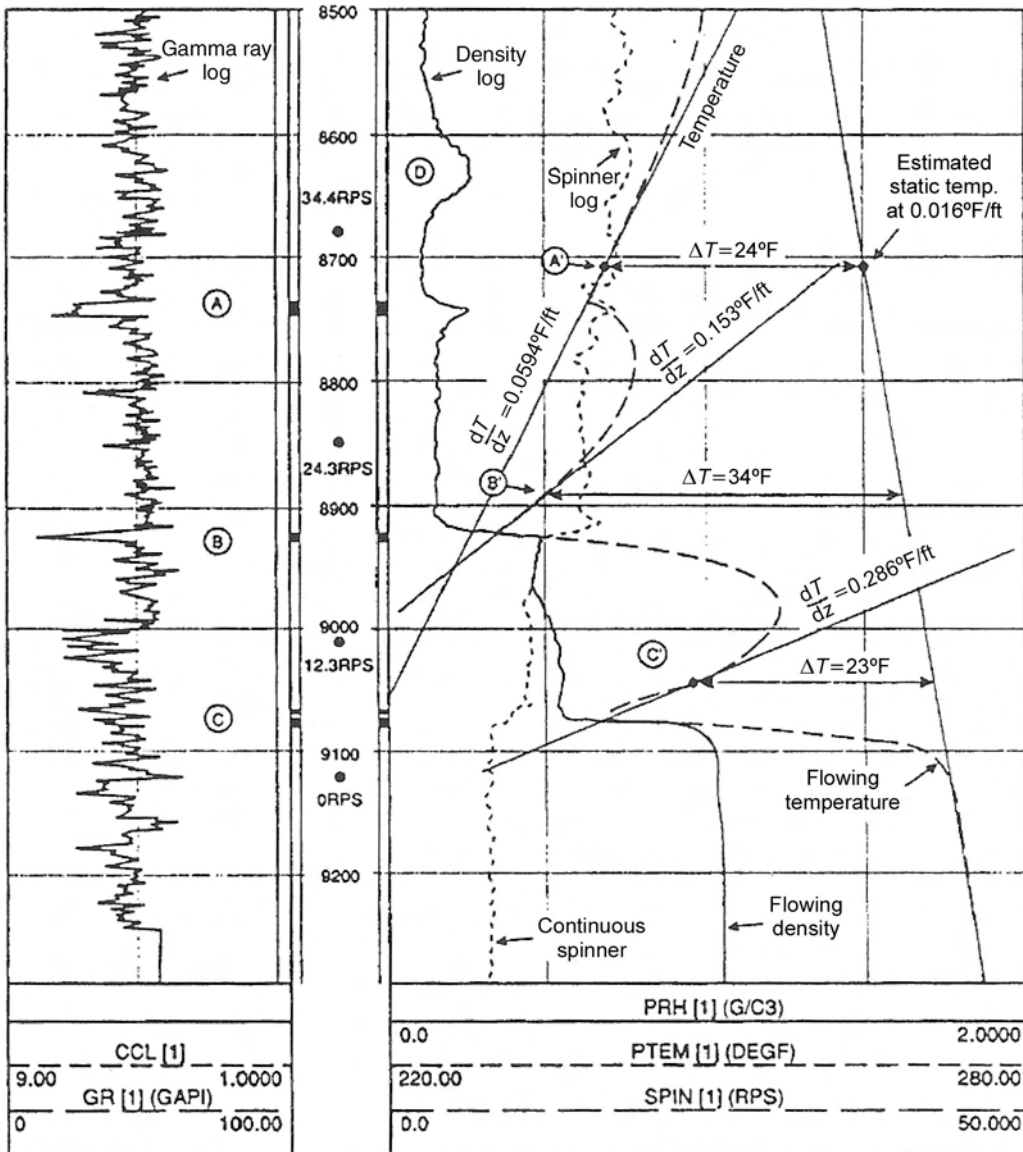


Fig. 4.18—Log suite in flowing gas well with commingled production from three zones.

wellbore region and the perforated completion. These cooling effects corroborate the gas production at each set indicated by the fluid-density profile. Between perforation sets, the temperature profile warms toward geothermal and then cools as it approaches the perforation set above. The tangent lines with their slopes illustrate the relative rates of warming of the stream above each perforation set.

Although there are two phases present in the wellbore (the produced gas and the captive water), the diverting flowmeter can respond to the gas flow rate at each measurement depth. This flowmeter was calibrated in a flow loop by measuring its response to a variety of air flows as they were passed through a column of stationary water. A “percolation calibration” was generated by plotting the diverting flowmeter’s responses to the various air-flow rates. With this percolation calibration, the flowmeter’s downhole measurements, shown in the depth

<u>Perforation Set</u>	<u>Fraction of Production</u>
Top	0.44
Middle	0.39
Bottom	0.17

<u>Perforation Set</u>	<u>Fraction of Production</u>
Top	0.45
Middle	0.35
Bottom	0.20

track, were interpreted to yield the profile in [Table 4.4](#), which shows the fraction of total gas production from each perforation set.

An independent analysis of the production profile was made from the temperature log by a profiling technique described in the Appendix under injection-well profiling. At a fixed distance above each perforation set, a tangent line was constructed to the temperature profile at a depth on its recovery toward geothermal. For each tangent, a determination was made of the slope of the tangent and the difference between the profile temperature at the depth of tangency and the corresponding geothermal temperature. By appropriately combining these data, the fractional contributions of the three perforation sets were obtained, as shown by [Table 4.5](#). The two analyses are in good agreement.

The fractional contributions of the three sets also were determined by a linear analysis of both the diverting-flowmeter log and the continuous-spinner-flowmeter log. With this approach, a perforation set's fractional contribution to production is determined as the ratio of the change of the flowmeter's response across the perforation set to the total change of response from below the bottom perforation set to above the top set. The linear analyses of the two flowmeter logs both erroneously indicate that only one-quarter of the total production is from the top set, as opposed to the correct contribution of nearly one-half. A linear analysis is appropriate when only one phase is present in the wellbore but not when there are two.

In this example, the production profiles based on the temperature log and a proper analysis of the diverting flowmeter log corroborate each other, showing the advantage of more than one log in the suite. Also, this example demonstrates that when reliable data are analyzed with an inappropriate method (the linear-flowmeter technique), appreciable errors can result.

4.9.3 Profiling Oil Production Under WAG Recovery. In this well, 5½-in. casing is set to 4,463 ft. Below the casing, oil is produced in the open hole under WAG (water-alternating-gas) recovery.

The well produces 1381 RB/D of water, 119 RB/D of oil, and 245 RB/D of CO₂. Carbon dioxide, CO₂, dissolves primarily in the oil and secondarily in the water. Water is the continuous phase in the wellbore. The produced oil, with CO₂ in solution, bubbles (or “percolates”) up through the flowing water. The logs in this suite were run with the objective of identifying the following:

1. Intervals in which water enters the wellbore.

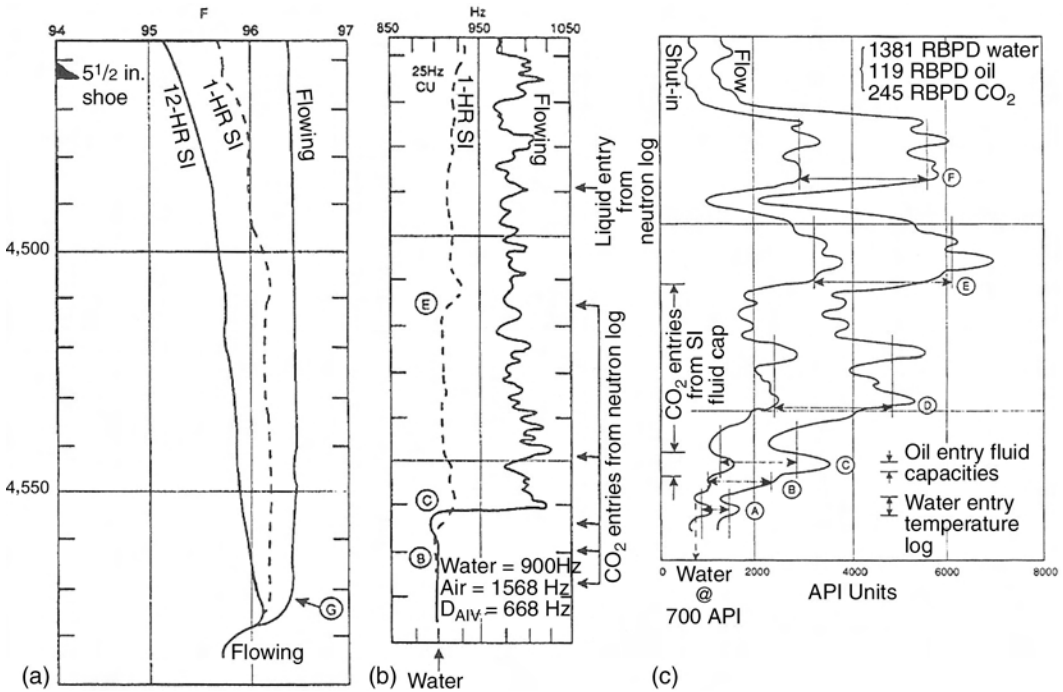


Fig. 4.19—(a) temperature logs; (b) fluid-capacitance logs; and (c) neutron logs.

2. Whether CO_2 is dissolved in the water.

3. Intervals in which oil (with CO_2 in solution) enters the wellbore.

The well was logged flowing, then shut in overnight. Shut-in logs were recorded the next morning. The following logs were run: fluid capacitance, fluid density, neutron, and temperature.

A comparison of flowing and shut-in temperature profiles (Fig. 4.19a) shows that the major production originates from a thin interval just above 4,575 ft (Depth G). Because the thermal content of the stream is essentially water, a thin interval at Depth G is therefore the source of water production. Injected water travels along a permeable streak known to exist at the based of the porous interval. This is not a good profile for oil recovery. The water is warm because warmer brine is being injected into a formation cooled by years of waterflooding.

The fluid-capacitance log (Fig. 4.19b) (well flowing) responds to the deepest oil entry at Depth C on an up run. However, fouling of the capacitance probe by the heavy oil renders the remainder of the up run useless for detecting additional oil entries. The probe was cleaned by stationing it in the tubing, where the elevated flow velocity removed the heavy oil film; however, it again fouled upon exit from the tubing. The shut-in capacitance profile, recorded later, reveals an additional oil entry at Depth E.

One usually depends on the response of the flowing fluid-capacitance log to determine whether an entering fluid is water or oil. In this example, the failure of the flowing capacitance log to respond to all oil entries with the exception of the deepest one (C) was anticipated in advance of logging and is not a problem because the water production is localized, and a comparison of flowing and shut-in neutron logs, which respond to a change of CO_2 concentration in the wellbore, can detect oil entries above Depth C.

The comparison of the separations between flowing and shut-in neutron logs (Fig. 4.19c) reveals the following:

1. CO_2 is dissolved in the water entering at (A).

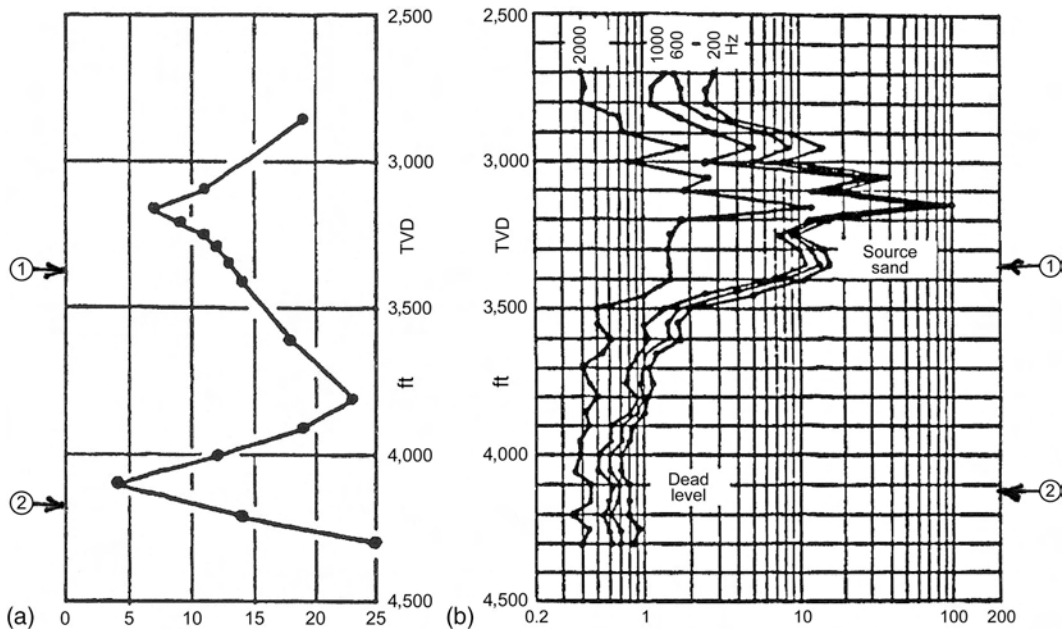


Fig. 4.20—(a) Magnetometer survey in relief well; (b) noise log in relief well.

2. CO_2 is dissolved in the water entering below (B), but at higher concentration than in the entry below (A).

3. CO_2 is dissolved in the oil entry at (C), which is the deepest oil entry according to the flowing capacitance log.

4. Oil with dissolved CO_2 enters just below (D).

5. CO_2 is dissolved in the fluid entering at (E), which is oil according to the shut-in capacitance log.

6. There is a fluid entry at (F), but with no CO_2 dissolved in the entering fluid. Because the water is produced below (C), the entering fluid is probably oil. The injected CO_2 is not reaching as far up the formation as Depth F. Still, the gravity migration of carbon dioxide upward in the formation above the bottom permeability streak is much better than one might suspect from the water production profile alone.

In this example, none of the three log types (temperature, fluid capacitance, and neutron) is capable of accomplishing the logging objective by itself. Moreover, no combination of two of the logs is capable of fulfilling the objective. Only a thorough analysis of the three logs taken together can accomplish the objective, showing the importance of a carefully selected, comprehensive suite of logs.

4.9.4 Gas Blowout After Abandonment. A well was drilled through two gas zones on the way to test a deeper oil zone. The well was abandoned and the wellhead cut at the seafloor.

Six months after abandonment, there was a gas blowout to the surface, causing the sea to churn. A relief well was drilled in order to flood the blowing zone. A magnetometer survey (Fig. 4.20a) shows the distance of the relief well from the original wellbore. The separation of the two wellbores “corkscrews” between approximately 5 and 25 ft, an effect caused by changes in the direction of the original wellbore. The two gas-zone locations are marked on the figure.

A noise log (Fig. 4.20b) was run in the relief well to identify which of the two gas zones was the source of the gas blowout. The noise log is applicable for this purpose because of its ability to “listen” to the sound in the original wellbore.

The dead-well noise levels in the interval of the relief well at the location of Gas Zone (2) shows it is not the source of the blowout. The noise-log response is elevated above the dead-well level in an interval of the relief well corresponding to the location of Gas Zone (1) showing that this gas zone is the source of the blowout. Above this location, the noise log exhibits several peak responses, two of which are larger than the response at the source of the gas blowout. The location of the largest corresponds to the location of least separation above Zone (1) in Fig. 4.20a. The other spikes are likely at locations of tight spots in the flow path.

It is also possible to estimate the distance between a blowing well and a relief well a point source of noise in the blowing well. This is done from the rate at which the noise level attenuates with distance along the relief wellbore from the peak noise location, and is possible because the noise level is inversely proportional to distance from the source. For example, the 200-Hz noise level at the location of zone (1) in Fig. 4.20b is 17 millivolts. By 3,500 ft, a distance of 140 ft in the relief well, this level has dropped to 2.0 millivolts. The separation between the wells at zone (1) is therefore estimated by the expression:

$$L_{\text{sep}} = \frac{140}{\sqrt{\left(\frac{17}{2}\right)^2 - 1}} = 16.6 \text{ ft.}$$

This value compares to the 13–14 distance indicated by the magnetometer survey. Likewise, the separation at the large peak at 3,150 ft is estimated from the decay at a value of 6.5 ft, which is the same distance as that shown on the magnetometer survey.

In this example, only two production logs were used. In considering this point, it is important to remember that the logging objective is quite limited: to determine which of the two known gas zones is the source of the blowout. Given that the logging is in the relief well, the noise log is better suited to this purpose than any other production log.

In aggregate, the previous four examples give the reader an appreciation of what can be accomplished with production logs during the entire life of a well.

4.10 Summary

This chapter describes the various tools used in production logging and provides insight on how to interpret results. In addition, the Appendix provides a “road map” of what logs to use for specific circumstances and what analysis methods apply. In particular, logging tools for making temperature surveys, several types of gamma-ray measurements, and spinner surveys are described. Examples are included for each tool and for four examples that illustrate why logging suites are needed to pinpoint what is happening in a well. Specific information is included on logging suites and skills needed to make successful surveys and meaningful interpretations. There are two specific recommendations that merit repeating: logging suites can be used to reduce ambiguous interpretations, and careful planning and documentation will ensure the current and future usability of production-logging results.

Nomenclature

- a = coefficient
- A = coefficient; also area, L^2
- B = coefficient
- C = casing capacity, bbl/ft
- C = count rate, counts/sec
- C_p = specific heat

- D_h = casing or hole diameter, ft
 D_t = tool diameter, ft
 f = frequency
 L_t = maximum tool length to pass through bend, ft
 L_{turn} = distance to bend, ft
 N = noise frequency
 N_p = number of pipe strings
 q = flow rate, B/D–scf/D
 R = ratio
 R_t = inside bend radius (or turning radius), ft
 S = spinner turn rate, RPS
 T = temperature, °F
 V = linear velocity
 y = holdup of a given phase
 z = distance in z vertical direction
 α = angle of bend, degrees
 Δ = difference in two values
 ρ = density, g/cm³

Subscripts

- 1 = reference to bottom set of perforations
 cool = area cooled below geothermal gradient
 flow = flowing condition
 g = gas
 geo = geothermal
 hc = hydrocarbon
 i = counter
 in = property of fluid flowing into wellbore from a set of perforations
 mix = mixture of flowing fluids
 rel = relative
 S = slippage
 shut-in = shut-in condition

Acknowledgments

The authors wish to express their appreciation to the ExxonMobil Co. for permission to use the information contained in this chapter. The information was extracted largely from an internal document that required many hours of preparation by the authors.

References

1. "Polaris-Production Optimization Log and Reservoir Information Solutions," Baker-Hughes Brochure, Houston (1999).
2. Hupp, D. and Schnorr, D.R.: "Evaluating High-Angle Wells With Advanced Production-Logging Technology," paper SPE 57690 presented at the 1999 SPE Annual Technical Conference and Exhibition, Houston, 3–6 October.

General References

The following brief collection of references to production-logging technology is definitely not intended to be comprehensive. Instead, the entries are chosen as being representative of the available literature within the constraint that each reference contains information of general in-

terest. The reader should be warned that some of the articles are strongly biased toward the tools offered by a particular company to the exclusion of other equally effective but usually older devices. The inclusion of such articles does not constitute an endorsement by us. Furthermore, the reader should know that log interpretations offered in some of the papers differ from those that would follow from the application of the interpretative guidelines presented in the Appendix to this chapter.

The references are organized into categories for ease of use. Within each category, articles are listed in alphabetical order according to the surname of the lead author without regard to the relative significance of the article.

Books

Bateman, R.M.: *Cased-Hole Log Analysis and Reservoir Performance Monitoring*, Intl. Human Resources Development Corp., Boston, Massachusetts (1985).

Carlson, N.R.: *Interpretative Methods for Production Well Logs*, Publication 9411, Dresser Atlas (Baker Hughes) Co., Houston (1982).

Hill, A.D.: *Production Logging—Theoretical and Interpretative Elements*, Monograph Series, SPE, Richardson, Texas (1990) **14**.

McKinley, R.M.: *Temperature, Radioactive Tracer and Noise Logging for Injection Well Integrity*, U.S. Environmental Protection Agency, Publication EPA/600/R-94/124, R.S. Kerr Research Laboratory, Ada, Oklahoma (1994).

Smolen, J.J.: *Production Log Interpretation*, Publication C-11811, Schlumberger Ltd., Houston (1973).

Smolen, J.J.: *Production Logging*, Reprint Series No. 19, SPE, Richardson, Texas (1985).

Smolen, J.J.: *Cased Hole and Production Log Evaluation*, PennWell Publishing Co., Tulsa (1996).

Survey Papers

Connolly, E.T.: "Resume and Current Status of the Use of Logs in Production," paper presented at the 1965 SPWLA Annual Well Logging Symposium, Dallas, 4–7 May.

Hill, A.D. and Oolman, T.: "Production Logging Tool Behavior in Two-Phase Inclined Flow," *JPT* (October 1982) 2432.

McKinley, R.M.: "Production Logging," paper SPE 10035 presented at the 1982 SPE International Petroleum Exhibition and Technical Symposium, Beijing, 17–26 March.

Petevello, B.G.: "Evaluation of Well Performance Through Production Logging," paper presented at the 1975 Formation Evaluation Symposium, Calgary, 5–7 May.

Wade, R.T. *et al.*: "Production Logging—The Key to Optimum Well Performance," *JPT* (February 1965) 137.

Operational Topics

Garwood, G.L.: "Equipment Selection for Sour Gas Condensate Wells," *The Drilling Contractor* (March–April 1974) 40.

Hammack, G.W., Myers, B.D., and Barcenas, G.H.: "Production Logging Through the Annulus of Rod-Pumped Wells to Obtain Flow Profiles," paper SPE 6042 presented at the 1976 SPE Annual Technical Conference and Exhibition, New Orleans, 3–6 October.

Howell, E.P., Smith, L.J., and Blount, C.G.: "Coiled-Tubing Logging System," *SPEFE* (March 1988) 37; *Trans.*, AIME, **285**.

Instrument Evolution

Anderson, R.A. *et al.*: "A Production Logging Tool With Simultaneous Measurements," *JPT* (February 1980) 191.

Brown, G.A., Kennedy, B., and Meling, T.: “Using Fiber-Optic Distributed Temperature Measurements to Provide Real-Time Reservoir Surveillance Data on Wytch Farm Field Horizontal Extended-Reach Wells,” paper SPE 62952 presented at the 2000 SPE Annual Technical Conference and Exhibition, Dallas, 1–4 October.

Dennis, B.R. *et al.*: “High-Temperature Borehole Instrumentation,” Report LA-10558-HDR, Los Alamos Natl. Laboratory, Los Alamos, New Mexico (1985).

Hupp, D. *et al.*: “Polaris—Production Optimization Log and Reservoir Information Solutions,” Brochure A99118, Baker-Atlas Div. of Baker Hughes, Houston (1999).

Hupp, D. *et al.*: “Evaluating High-Angle Wells With Advanced Production-Logging Technology,” paper SPE 56790 presented at the 1999 SPE Annual Technical Conference and Exhibition, Houston, 3–6 October.

Hupp, D. *et al.*: “Memory Pressure and Production Logging Tools,” Brochure, Sondex Ltd., Bramshill, U.K.

Tello, L.N. *et al.*: “A Dipole Array Sonic Tool for Vertical and Deviated Wells,” paper SPE 56790 presented at the 1999 SPE Annual Technical Conference and Exhibition, Houston, 1–4 October.

Papers Aimed at Computerized Interpretation

Catala, G.N., Torre, A.J., and Theron, B.E.: “An Integrated Approach to Production Log Interpretation,” paper SPE 25654 presented at the 1993 SPE Middle East Oil Show, Manama, Bahrain, 3–6 April.

Holm, W.H. *et al.*: “A Cased Hole Well Log Computer System,” paper presented at the 1983 SPWLA Annual Well Logging Symposium, Calgary, 27–30 June.

Nerby, G.: “A New Approach to Production Log Analysis,” *Graham and Trotman’s Proceedings*, 1989 North Sea Oil and Gas Reservoirs Conference II, Trondheim, Norway, May.

Nerby, G.: “Plato—The Answer to Your Production Logging Analysis,” Brochure, IPS Interpretative Software Products Co., Houston (2000).

Temperature Logging

Agnew, B.G.: “Evaluation of Fracture Treatments with Temperature Surveys,” *JPT* (July 1966) 892.

Carlson, N.R. *et al.*: “The Significance of the Temperature Log in Multiphase Flow,” paper presented at the 1986 SPWLA Annual Well Logging Symposium, Houston, 9–13 June.

Cooke, C.E. Jr.: “Radial Differential Temperature (RDT) Logging—A New Tool for Detecting and Treating Flow Behind Casing,” *JPT* (June 1979) 676.

Dobkins, T.A.: “Improved Methods to Determine Fracture Height,” *JPT* (April 1981) 719.

Jameson, L.R.: “Some Applications of Differential Temperature Logging,” paper SPE 1977 presented at the 1967 SPE Regional Secondary Recovery Symposium, Pampa, Texas, 26–27 October.

Millikan, C.V.: “Temperature Surveys in Oil Wells,” *Trans.*, AIME (1941) **142**, 15.

Pierce, A.E. *et al.*: “Temperature surveys spot well ills, solve operating problems,” *Oil & Gas J.* (June 1966) 96.

Ramey, H.J. Jr.: “Wellbore Heat Transmission,” *JPT* (April 1962) 427; *Trans.*, AIME, **225**.

Smith, R.C.: “Temperature Log Interpretation,” Publication L-36, The Welex (Halliburton) Co.

Smith, R.C. and Steffensen, R.J.: “Interpretation of Temperature Profiles in Water-Injection Wells,” *JPT* (June 1975) 777; *Trans.*, AIME, **259**.

Noise Logging

Enright, R.J.: “Sleuth for Down-Hole Leaks,” *Oil & Gas J.* (1955) **38**, 78.

Koerner, H.B. Jr. and Carroll, J.C.: "Use of the Noise Log as a Downhole Diagnostic Tool," paper SPE 7774 presented at the 1979 SPE Middle East Technical Conference and Exhibition, Manama, Bahrain, 25–29 March.

Korotaev, Y.P.: "Acoustic Method of Delineating Operating Intervals in Gas-Bearing Formations," *Gazovaya Prom.* (1970) No. 11, 14.

McKinley, R.M., Bower, F.M., and Rumble, R.C.: "The Structure and Interpretation of Noise From Flow Behind Cemented Casing," *JPT* (March 1973) 329; *Trans.*, AIME, **255**.

Myung, J.L.: "Fracture Investigation of the Devonian Shale Using Geophysical Well Logging Techniques," paper SPE 6366 presented at the 1976 SPE Eastern Regional Meeting, Columbus, Ohio, 18–19 May.

Pennebaker, E.S. Jr. and Woody, R.T.: "The Temperature-Sound Log and Borehole Channel Scans for Problem Wells," paper SPE 6782 presented at the 1977 SPE Annual Technical Conference and Exhibition, Denver, 9–12 October.

Rambow, F.H.K.: "Active Listening: An Alternative Method for Detecting Flow and Measuring Flow Velocity Behind Casing," *The Log Analyst* (November–December 1991) 645.

Robinson, W.S.: "Recent Application of the Noise Log," paper presented at the 1976 SPWLA Annual Well Logging Symposium, Dallas, June 9–12.

Shuck, L.V. *et al.*: "Noise Characteristics of Oil Wells and Reservoirs," paper SPE 5147-B presented at the 1974 SPE Annual Meeting, Houston, 6–9 October.

Stein, N. *et al.*: "Sand Production Determined From Noise Measurements," paper SPE 3498 presented at the 1971 SPE Annual Meeting, New Orleans, 3–6 October.

Radioactive-Tracer Logging

Akers, T.J. *et al.*: "Radioactive Tracer Logging in Laminar Flow," paper presented at the 1985 CWLS Formation Evaluation Symposium, Calgary, 29 September–2 October.

Anthony, J.L. and Hill, A.D.: "An Extended Analysis Method for Two-Pulse Tracer Logging," *SPEPE* (March 1986) 117; *Trans.*, AIME, **281**.

Bearden, W.G. *et al.*: "Interpretation of Injectivity Profiles in Irregular Bore Holes," *JPT* (September 1970) 1089.

Gadeken, L.L.: "The Interpretation of Radioactive-Tracer Logs Using Gamma-Ray Spectroscopy Measurements," *The Log Analyst* (January–February 1991) 24.

Hill, A.D. and Solares, J.R.: "Improved Analysis Methods for Radioactive Tracer Injection Profile Logging," *JPT* (March 1985) 511.

Hill, A.D., Boehm, K.E., and Akers, T.J.: "Tracer Placement Techniques for Improved Radioactive Tracer Logging," *JPT* (November 1988) 1484.

Kelldorf, W.F.N.: "Radioactive Tracer Surveying—A Comprehensive Report," *JPT* (June 1970) 661.

Killian, H.W.: "Fluid Migration Behind Casing Revealed by Gamma Ray Logs," *The Log Analyst* (January–March 1966) 46.

Lichtenberger, G.J.: "A Primer on Radioactive Tracer Injection Profiling," Southwestern Petroleum Short Course, Lubbock, Texas (1981) 251–263.

Roesner, R.E. *et al.*: "New Logging Instruments for Polymer and Water Injection Wells," paper presented at the 1983 SPWLA Annual Well Logging Symposium, Calgary, 27–30 June.

Self, C. and Dillingham, M.: "A New Fluid Flow Analysis Technique for Determining Bore Hole Conditions," paper SPE 1752 presented at the 1967 SPE Mechanical Engineering Aspects of Drilling and Production Symposium, Fort Worth, Texas, 5–7 March.

Simpson, G.A. and Gadeken, L.L.: "Interpretation of Directional Gamma Ray Logging Data for Hydraulic Fracture Orientation," paper SPE 25851 presented at the 1993 SPE Low Permeability Reservoirs Symposium, Denver, 26–28 April.

Small, G.P.: "Steam-Injection Profile Control Using Limited-Entry Perforations," *SPEPE* (September 1986) 388.

Wiley, R. and Cocanower, R.D.: “A Quantitative Technique for Determining Injectivity Profiles Using Radioactive Tracers,” paper SPE 5513 presented at the 1975 SPE Annual Technical Conference and Exhibition, Dallas, 28 September–1 October.

Oxygen-Activation Logging

Arnold, D.M. and Paap, H.J.: “Quantitative Monitoring of Water Flow Behind and in Wellbore Casing,” *JPT* (January 1979) 121; *Trans.*, AIME, **267**.

Hill, F.L. *et al.*: “New Instrumentation and Interpretive Methods for Identifying Shielded Water Flow Using Pulsed Neutron Technology,” paper presented at the 1989 CWLS Formation Evaluation Symposium, Calgary, September.

Ierubino, J.V. and Ginest, N.H.: “Use of Pulsed Neutron Logging Techniques to Prove Protection of Underground Sources of Drinking Water,” paper SPE 19616 presented at the 1989 SPE Annual Technical Conference and Exhibition, San Antonio, Texas, 8–11 October.

Lamb, G. *et al.*: “Measurement of Water Flow in Deviated Production Wells by Oxygen Activation Logging,” paper presented at the 1983 SPWLA Annual Well Logging Symposium, Calgary, 27–30 June.

Scott, H.D. *et al.*: “Applications of Oxygen Activation for Injection and Production Profiling in the Kuparuk River Field,” *SPEFE* (June 1993) 103.

Thornhill, J.T. *et al.*: “Injection Well Mechanical Integrity,” Publication EPA/625/9-87/007, U.S. Environmental Protection Agency, R.S. Kerr Research Laboratory, Ada, Oklahoma (1987).

Wydrinsky, R. and Katahara, K.W.: “Effects of Thermal Convection on Oxygen Activation Logs,” paper SPE 24739 presented at the 1992 SPE Annual Technical Conference and Exhibition, Washington, DC, 4–7 October.

Flowmeter Logging

Dale, C.R.: “Bottom Hole Flow Surveys for Determination of Fluid and Gas Movements in Wells,” *Trans.*, AIME (1949) **186**, 205.

Hess, A.E.: “A Heat-Pulse Flowmeter for Measuring Low Velocities in Boreholes,” Report 82-669 (Open File), U.S. Dept. of the Interior Geological Survey, Denver, Colorado (1982).

Hess, A.E.: “Identifying hydraulically conductive fractures with a slow-velocity borehole flowmeter,” *Canadian Geotechnical J.* (1986) **23**, No. 1, 69.

Kading, H.W.: “Horizontal Spinner, A New Production Logging Technique,” Southwestern Petroleum Short Course, Lubbock, Texas (1975).

Kragas, T.K. *et al.*: “Downhole Fiber-Optic Flowmeter: Design, Operating Principle and Testing,” paper SPE 77655 presented at the 2002 SPE Annual Technical Conference and Exhibition, San Antonio, Texas, 29 September–2 October.

Leach, B.C. *et al.*: “The Full Bore Flowmeter,” paper SPE 5089 presented at the 1974 SPE Annual Meeting, Houston, 6–9 October.

McBane, R.A., Campbell, R.L. Jr., and DiBello, E.G.: “Acoustic Flowmeter Field Test Results,” *SPEPE* (February 1991) 49.

Piers, G.E., Perkins, J., and Escott, D.: “A New Flowmeter for Production Logging and Well Testing,” paper SPE 16819 presented at the 1987 SPE Annual Technical Conference and Exhibition, Dallas, 27–30 September.

Rumble, R.C.: “A Subsurface Flowmeter,” *Trans.*, AIME (1955) **204**, 258.

Fluid-Capacitance Logging

Carlson, N.R. *et al.*: “Applications of the Fluid Capacitance Log in Multiphase Flows,” paper B presented at the 1986 Symposium of the Soc. of Aberdeen Well-Log Analysts, Aberdeen.

Carlson, N.R. *et al.*: “Water-Oil Flow Surveys with Basket Fluid Capacitance Tool,” paper F presented at the 1982 SPWLA Annual Well Logging Symposium, Corpus Christi, Texas, 6–9 July.

Carlson, N.R. *et al.*: “New Method for Accurate Determination of Water Cuts in Oil-Water Flows,” paper presented at the 1989 SPWLA Annual Well Logging Symposium, 22–25 June.

Guo, H. *et al.*: “The Design and Development of Microwave Holdup Meter and Application in Production Logging Interpretation of Multiphase Flows,” paper SPE 26451 presented at the 1993 SPE Annual Technical Conference and Exhibition, Houston, 3–6 October.

Knight, B.L.: “Flow-Loop Evaluation of Production Logging Holdup Meter,” *The Log Analyst* (July–August 1992) 412.

Multiphase Logging in Vertical Wellbores

Carlson, N.R. *et al.*: “Importance of Production Logging Suites in Multiphase Flows,” paper P presented at the 1983 SPWLA Annual Well Logging Symposium, Calgary, 27–30 June.

Cmelik, H.R.M.: “A Controlled Environment for Measurements in Multiphase Vertical Flow,” paper R presented at the 1979 SPWLA Annual Well Logging Symposium, Tulsa, 3–6 June.

Cmelik, H.R.M. and Sarabian, R.A.: “Quantitative Analysis of Production Logs in Two-Phase Gas-Liquid Systems,” paper SPE 8761 presented at the 1979 SPE Production Technology Symposium, Lubbock, Texas, 5–6 November.

Darvarzani, J.D.: “Investigation of the Flow of Oil and Water Mixtures in Large Diameter Vertical Pipes,” paper Q presented at the 1983 SPWLA Annual Well Logging Symposium, Calgary, 27–30 June.

Nicolas, Y. and Witterholt, E.J.: “Measurements of Multiphase Fluid Flow,” paper SPE 4023 presented at the 1972 SPE Annual Meeting, San Antonio, Texas, 8–11 October.

Multiphase Logging in Deviated and Horizontal Wellbores

Barnette, J.C., Copoulos, A.E., and Biswas, P.B.: “Acquiring Production Logging Data with Pulsed Neutron Logs in Highly Deviated Wells with Multiphase Flow in Prudhoe Bay, Alaska,” paper SPE 24089 presented at the 1992 SPE Western Regional Meeting, Bakersfield, California, 30 March–1 April.

Carlson, N.R. and Davarzani, M.J.: “Profiling Horizontal Oil-Water Production,” *JPT* (July 1991) 780.

Carnegie, A., Roberts, N., and Clyne, I.: “Application of New Generation Technology to Horizontal Well Production Logging—Examples from the North West Shelf of Australia,” paper SPE 50178 presented at the 1998 SPE Asia Pacific Oil and Gas Conference and Exhibition, Perth, Australia, 12–14 October.

Chauvel, Y. and Clayton, F.: “Quantitative Three-Phase Profiling and Flow Regime Characterization in a Horizontal Well,” paper SPE 26520 presented at the 1993 SPE Annual Technical Conference and Exhibition, Houston, 3–6 October.

Maher, T. and Trcka, D.: “Inflow Fluid Typing in Screened Horizontal Completions Using a Pulsed Neutron Holdup Imager,” paper SPE 56646 presented at the 1999 SPE Annual Technical Conference and Exhibition, Houston, 3–6 October.

Nice, S.B.: “Production Logging in Horizontal Wellbores,” paper presented at the 1992 *World Oil* Horizontal Well Conference, Houston, 9–11 November.

Roscoe, B.A.: “Three-Phase Holdup Determination in Horizontal Wells using a Pulsed-Neutron Source,” paper SPE 37147 presented at the 1996 SPE International Conference on Horizontal Well Technology, Calgary, 18–20 November.

SI Metric Conversion Factors

bbl × 1.589 873	E - 01 = m ³
ft × 3.048*	E - 01 = m
°F (°F - 32)/1.8	= °C
psi × 6.894 757	E + 00 = kPa

*Conversion factor is exact.

Appendix—Production-Logging Application Tables: Tool Selection, Operating Procedures, and Interpretation Aids

Introduction. This section of the chapter provides an extensive set of tables intended to aid in the practical application of production-logging technology. For a given problem, the reader is guided first in the selection of the set of logging tools most appropriate. Next, suggestions are given on the proper procedure for each tool's use. This is an important part of the guidance, because the way logging records are obtained is often the most important part of the operation. Finally, the user is provided with comments regarding what the records should show relative to the problem. Recognition of expected results is equally important because irrelevant features on a log can easily prevent its proper interpretation. The tables are independent of the preceding body of the text and presume that the user lacks detailed knowledge of the subject.

The tables are unique to the literature in their ability to provide the user with detailed guidance without the investment of extensive search time. This feature is a consequence of the indexing approach to the information in the tables. The first level in the classification system is the nature of the well and the type of completion in which the tools are to be run. This environmental factor is called the *Well Category*. The tools that are best for one type of completion may be completely inappropriate for another type. For a given *Well Category*, the second level is the type of problem of interest to the user. This level is called *Problem Type*. Its identification leads to the final or third level in the classification—namely, to a table of tools appropriate to the specific well category and problem type. This final table provides the information listed above. Such an approach leads to much duplication of material, but is the one most beneficial to the user. Available publications attempt the classification on the basis of problem type alone, but this approach leads to so many disclaimers “for this situation and for that situation” that the result is confusion rather than guidance.

To make use of the application tables, one therefore enters the compilation sequentially through two indexing tables, identified as **Table 4.A1: *Well Category*** and **Table 4.A2: *Problem Type***. Having selected a category number from **Table 4.A1** (Level 1), the user then locates this number in **Table 4.A2** (Level 2), where a listing of general problem types is associated with each category number. Each problem type is identified by its index number, made up of a category number followed by a capital letter. For example, the designation 1A identifies a well still being drilled (well category) but experiencing problems of pipe sticking (pipe manipulation) or cross-sectional constriction (problem type). Having selected an index number from **Table 4.A2**, the reader next locates the third-level table having this number/letter designation. This final table subdivides the general problem into more specific problems (where appropriate) and provides a listing of recommended logging tools along with suggestions concerning their proper use and comments on what one should expect to see in the records from each tool. The tools are listed in the order of their likelihood to resolve the reasons for a particular problem; consequently, tool exclusion for a particular job should start at the bottom of the list and work upward.

The well category, **Table 4.A1**, cannot include all possible combinations of tubing placement relative to casing. The user may therefore not find a single category that describes completely an unusual completion. Instead, the completion may have at certain locations features common to one particular listing, whereas, at other locations, the features may coincide with a different listing. In such a case, the user will need to digest the contents of several tool-selection tables to devise a tool string appropriate to the completion.

A general comment is in order relative to tool selection. Slickline or downhole-memory logging tools have evolved to the point that multiple traces can be recorded on a single pass. This gives the ability to record traces from depth-control sensors, such as a collar locator and a gamma-ray tool, simultaneously with traces from production-logging sensors. The previously limited quality in depth control has therefore been eliminated. Furthermore, sample rates can be

<u>Category No.</u>	<u>Well Type</u>
1	Well still being drilled
2	Newly cased, unperforated well
3	Well being stimulated, fractured, or gravel-packed
4	Injection well—cased or openhole without screen or liner (any deviation)
5	Injection well with screen or liner (any deviation)
6	Injection well with tubing across perforations (dual completions)
7	Production well—vertical, cased, or openhole without screen or liner
8	Production well—vertical with screen, liner, or dual completion
9	Production well—highly deviated without screen or liner
10	Production well—highly deviated with screen, liner, or dual completion
11	Production well shut in owing to annular pressure or to suspected crossflow behind casing
12	Well down for tubing and/or casing inspection

set sufficiently high (up to 5 samples per second) so that the tools produce traces with a quality equal to that from electric-line surveys. In fact, the newer sensors on slickline strings often provide better traces. A corresponding improvement in surface interrogation and processing hardware now makes it possible to prepare a log from a slickline string within a few hours after tool retrieval. Memory tools now have practically all the advantages of electric-line tools with the added potential for safer and less-expensive operation.

Despite the extensive nature of the tables, their primary function is to provide realistic information on the selection of logging tools for a particular environment and a specific problem. The tables cannot make the user proficient in the very important task of interpretation. Moreover, computer software cannot do this either; intervention by an expert analyst is still required to ensure correct interpretation. The user should not hesitate to seek such intervention, preferably from experts other than employees of the logging company involved.

Classification Tables. The two classification [Tables 4.A1](#) and [4.A2](#) are provided here. These tables are used sequentially to navigate the extensive set of tables devoted to tool selection. [Table 4.A1](#) is used to select a category number best describing the type of well to be logged. This numeral is then entered in [Table 4.A2](#) and associated with the capital letter best describing the type of problem to be resolved. The resulting *Index Number* identifies one of the *Tool-Selection Tables*. This final table provides the user with the information necessary to plan and conduct the logging operation.

Tool-Selection Tables. These guidance tables list recommended logging tools in order of general effectiveness, giving comments regarding procedures for tool use and indicating the normal features that should appear on the log traces. Each table is identified by an index code made up of a number and a capital letter, such as 2C. A specific index code is obtained through the use of [Tables 4.A1](#) and [4.A2](#). Each tool-selection table deals with a particular problem area for a particular well configuration.

TABLE 4.A2—PROBLEM TYPE

Category No.	Tool-Selection Table Number According to Problem
1	<u>Well Still Being Drilled</u> 1A: Pipe manipulation or constriction difficulties 1B: Lost returns 1C: Underground flow (blowout)
2	<u>Newly Cased, Unperforated Well</u> 2A: Cement placement 2B: Casing inspection for wear, collapse, and bends 2C: Annular pressure, crossflow behind casing, and well certification for hazardous injection
3	<u>Well Being Stimulated, Fractured, or Gravel-Packed</u> 3: Acid, fracture proppant, or gravel placement
4	<u>Injection Well—Cased or Openhole Without Screen or Liner</u> 4A: Demonstration of confinement 4B: Injection profile determination
5	<u>Injection Well With Screen or Liner</u> 5A: Demonstration of confinement 5B: Injection profile determination
6	<u>Injection Well With Tubing Across Perforations</u> 6A: Demonstration of confinement 6B: Injection profile determination
7	<u>Production Well—Vertical, Cased, or Openhole Without Screen or Liner</u> 7A: Tracking single-phase production 7B: Tracking two-phase production 7C: Tracking three-phase production
8	<u>Production Well—Vertical With Screen, Liner, or Dual Completion</u> 8A: Tracking single-phase production 8B: Tracking two-phase production 8C: Tracking three-phase production
9	<u>Production Well—Highly Deviated Without Screen or Liner</u> 9A: Tracking single-phase production 9B: Tracking two-phase production 9C: Tracking three-phase production
10	<u>Production Well—Highly Deviated With Screen, Liner, or Dual Completion</u> 10A: Tracking single-phase production 10B: Tracking two-phase production 10C: Tracking three-phase production
11	<u>Production Well Shut In Owing to Annular Pressure or to Suspected Crossflow Behind Casing</u> 11A: Location of source of annular pressure 11B: Detection of crossflow behind pipe
12	<u>Well Down for Tubing or Casing Inspection</u> 12A: Detection of corrosion or wear to string containing tool 12B: Detection of holes or parting in casing external to one containing tool

TABLE 4.A3—1A: DRILLPIPE MANIPULATION AND CONSTRICTION PROBLEMS (WELL STILL BEING DRILLED)

Problem	Recommended Logging Tools	Operational Tips and Expected Results
Stuck pipe	Stuck-pipe log (axial cement-bond log)	This log is the trace of the transmitted amplitude (millivolts) from an acoustical device having a transmitter and a receiver spaced approximately 3 ft apart. A large, nearly constant amplitude denotes free pipe. Intervals where pipe is stuck show small, irregular amplitude. Log is only qualitative in the degree of pipe immobility; consequently, a backoff operation should not be done on the basis of this log. Its advantage is that a long interval of pipe can be logged relatively quickly.
	Gamma-ray gravel-pack log (unfocused gamma-density log, not neutron gravel-pack log)	This device uses gamma-ray transmission to respond to the density of material within a radius of approximately 6 in. and should be run centralized. Count rate is related inversely and exponentially to density. Larger count rates correspond to lower density, whereas higher density produces lower count rates. Free pipe gives the highest and most constant count rate. Log is qualitative in degree of pipe mobility and should not be the basis of a backoff procedure. Its advantage is that a long interval of pipe can be logged quickly. Its disadvantage is that it contains radioactive material that must be cemented in place if the tool cannot be retrieved.
Free pipe location	Free-point indicator log	This device locates the depth above which pipe is free and should be used to plan a backoff job after a stuck-pipe survey. It uses an articulated, two-section tool with load cells in each part to make stationary measurements joint-by-joint. If the bottom section is anchored in a location where the pipe is stuck, whereas the top section is in free pipe, then the top section will stretch or rotate relative to the bottom in response to a pull or a torque on the pipe string at the surface. Free pipe will show little or no relative movement.
Pipe bend or kink	"Dog-leg" or kink-meter log	These tools make a nonoriented measurement of the angle of deviation of the pipe from the vertical. The typical sensor is a pendulum-type element. The device therefore responds only to bends in the pipe and not to pipe collapse.
Pipe collapse	X-Y caliper log	This is a simple caliper device that measures two pipe diameters oriented 90° to each other. The measurement is sufficient to detect changes from the round, but is not sufficient to define the shape of the pipe's cross section for collapse extent.
Casing external to drillpipe (dropped casing)	Gravel-pack log (see previous)	The same operational principles outlined previously also apply here. Interpretation of the log is greatly aided if it is possible to log across one end of the parted casing external to the drillpipe.
	Eddy-current wall-thickness log (an induction tool normally used for pipe inspection)	This is actually the best tool for this problem, but versions small enough to run in drillpipe are scarce. The instrument is a two-coil device having an active coil driven at a very low frequency (~1Hz) and a passive coil to detect the induced field. The phase lag of the induced signal behind the driven signal is the measured trace. This lag is directly proportional to the thickness of metal within the induced field. The interpretation is aided by the ability to log across one end of the parted casing. A multi-frequency tool should be operated at its lowest frequency for greatest depth of field penetration. The tool, of course, will not function in non-magnetic metal.

TABLE 4.A4—1B: LOST RETURNS (WELL STILL BEING DRILLED)

Problem	Recommended Logging Tools	Operational Tips and Expected Results
Losing returns while circulating	Temperature survey while pumping down drillpipe	At least 60 bbl of mud should be pumped prior to logging. One display should be at a relatively high sensitivity of 1°F/in. At the lost-returns zone, the temperature trace will show a step increase to a warmer value that is maintained below the zone if all or most of the injection enters the zone. Only an increase to larger gradient (slope) at and below the zone may be evident for partial loss of returns (small loss to zone). The temperature behavior is the result of the warmer temperature brought upward from the bottom of the hole by flow up the annulus on the outside of the drillpipe.
	Temperature survey with pumping down annulus (backside)	This approach to the problem requires the least amount of mud for its execution, but is often not feasible for reasons of well control. Circulation should be stopped for approximately 3 hours before this operation is commenced to allow some recovery in wellbore temperature. A base survey should then be recorded prior to the start of injection. One display should be at a sensitivity of at least 2°F/in. of chart. A logging pass downward can be commenced after approximately 10 minutes of injection. Below the injection zone, the injection temperature trace will show a rapid warming back to or slightly above the base temperature. If multiple injection zones are present, then the trace will show only partial recovery at each zone above the deepest.
	Radioactive tracer survey while pumping down the drillpipe	Tracer slug should be ejected in the drillpipe near the bit and subsequently followed as it travels up the annulus behind the pipe. Slug size should be tailored for the expected travel distance up the annulus. A 10-microcurie slug will survive for approximately 3,000 ft before dispersion causes the activity to be lost in background. Tracer adsorption on the borehole wall is generally not a problem for an Iodine-131 tracer. If loss is only partial, pumping should cease before the tracer is returned to the surface.
Location of lost-returns zone after occurrence	Activated oxygen survey with tool configured for upflow for injection down drillpipe and for downflow for annular injection.	Water-based mud must be used for this survey. The pulsed-neutron tool creates its own tracer through the activation of the oxygen in the water. The velocity of movement of the activated oxygen relative to the tool is then measured. Stationary measurements are therefore the easiest to interpret. The resolution of these tools is determined by fluid velocity and is generally in the range of 4 ft/min. Typical resolution rates for annular flow are therefore in the range of 300 B/D. The survey should not be attempted from vessels experiencing significant vertical motion. This survey is usually considerably more expensive than the other surveys, but is listed because radioactive tracer service offshore may not be available.
	Temperature survey	Cool "anomalies" identify those zones into which mud has been injected relative to inactive parts of the borehole. One display should be at a sensitivity of at least 1°F/in. of chart. Survey should be run within days of a mud loss of 100 bbl or less and within a week or two of larger losses. Owing to the character normally present on the temperature trace, expert interpretation is usually required to identify the lost-returns zones. Two surveys run at least 18 hours apart aids in the interpretation because injection zones warm slower than do inactive parts of the wellbore.

TABLE 4.A5—1C: UNDERGROUND FLOW (BLOWOUT) (WELL STILL BEING DRILLED)

Problem	Recommended Logging Tools	Operational Tips and Expected Results
Detection of flow underground	Temperature survey	<p>Because a base survey is generally unavailable under these circumstances, an absolute interpretation of the traces is required. One display at a sensitivity of at least 2°F per in. of chart is advisable. Two surveys recorded at least 8 hours apart aids this interpretation because any crossflow interval will change its temperature less than will inactive sections of hole. Liquid entry into the cooled wellbore will bring its warmer temperature with it to give a warm anomaly at the entry location. This temperature is carried away in the direction of flow in proportion to the rate. A rough rule of thumb for water is that the trace remains vertical for 20 ft for each 100 B/D rate (0.20 ft/B/D). The entire crossflow interval will either "stand up" more or parallel the gradient at inactive (static) locations. The warming makes this survey particular sensitive to liquid and able to detect rates of a few B/D. Annular liquid rates behind drillpipe can be estimated from the slope dT/dz, °F/ft, and amount of warming $\Delta T = T_{\text{flow}} - T_{\text{static}}$, °F, at a given location in the crossflow path from the expression:</p> $q \text{ (B/D)} = A \times \frac{\Delta T}{\left(\frac{dT}{dz}\right)}$ <p>where $A = 1.0$ for water flow and $A = 2.5$ for oil flow. The result is an approximation only.</p> <p>Gas entry will generally produce a cool anomaly at the point of entry. For dry gas, this cooling can amount to 1°F for each 50-psi drop in pressure experienced by the gas. If the flow path is short, then the entire section will be cooled. If, however, the path is over a long section of hole, then the trace will cross to the warm side of "static" at some point. The previously mentioned rate expression applies to downhole B/D of dry gas if $A = 10$.</p>

TABLE 4.A5—1C: UNDERGROUND FLOW (BLOWOUT) (WELL STILL BEING DRILLED) (Continued)

Problem	Recommended Logging Tools	Operational Tips and Expected Results
Detection of flow underground	Noise-log survey	<p>This device is a microphone that measures the amount of turbulent noise produced by the movement of fluids. It makes stationary measurements of the sound level, millivolts, above four high-pass cutoff frequencies, typically set at 200, 600, 1,000, and 2,000 Hz. Each reading includes levels at all frequencies above the cutoff values; consequently, the readings decrease with increasing cutoff frequency. The cutoff values are chosen so as to distinguish two flow conditions: single phase and gas movement through liquid. The movement of gas through liquid produces a high level of noise in the low-frequency range below 600 Hz. This fact makes the tool particularly sensitive to small gas flows through liquid, the application for which it was devised. Gas percolation at downhole rates as low as 10 ft³/d can be resolved. Below 400 ft³/d, gas rate behind drillpipe can be estimated from the millivolts of noise in the band N₂₀₀–N₆₀₀ from the relationship</p> $q_g (\text{ft}^3/\text{d}) = 0.35 \times (N_{200} - N_{600})$ <p>Higher rates are underestimated by this expression.</p> <p>Single-phase flow, by contrast, produces noise primarily in response to acceleration past tight spots in the flow path. The resulting sound is of relatively weak amplitude and has a frequency in the range of 1,000 Hz or higher. If a restriction holds a pressure drop Δ<i>p</i> psi in response to a rate <i>q</i> B/D, then the single-phase rate of either liquid or gas behind drillpipe can be estimated from the millivolt value of the noise cut at 1,000 Hz by the expression</p> $q \times \Delta p = 700 \times N_{1000}$ <p>If the total pressure drop over the entire flow path is used in this expression, then the summed noise levels at each constriction should also be used. Both of these flow expressions suppose that the tool is calibrated to read standard peak-to-peak millivolts.</p>
	Activated oxygen survey for water with tool configured for suspected direction of flow	<p>This tool activates the oxygen in water to create its own radioactive tracer, whose movement is then timed to provide a velocity of water with a resolution of approximately 4 ft/min. This device also takes stationary measurements. If the direction of flow is unknown, then two surveys may be necessary. The tool must be retrieved or cemented in place.</p>

TABLE 4.A6—2A: CEMENT PLACEMENT (NEWLY CASED, UNPERFORATED WELL)

Problem	Recommended Logging Tools	Operational Tips and Expected Results
Cement top location	Temperature survey	<p>Must be recorded within limited time frame, typically 12 to 24 hours, after cement is circulated into place. The cement company can usually provide the proper time for logging. Owing to the heat of hydration, temperature will increase at the top of the cement column and will remain warmer throughout the column. Below the cement top, temperature will be more "noisy" than above because the variations in caliper are accentuated by the heat of hydration. Display sensitivity should be such as to avoid "wraps" in the record for a few hundred feet on either side of the cement top so that the increase in both temperature and "noise" is evident. Highly retarded cements usually produce very little heat of hydration for such a survey. This approach has the advantage that, unlike cement-bond logs, it does not depend upon intimate contact between cement and the outside of the casing at the top of the column.</p>
	Axial (regular) cement-bond log	<p>This is an acoustical device having one transmitter and two receivers. The latter are 3 and 6 ft from the transmitter. The 3-ft receiver measures the signal amplitude at the start of the wave train and thus gives a millivolt reading of the transmission along the casing wall. Free pipe produces the highest and nearly constant amplitude on this "pipe signal" trace. Typical values are in the range of 5 to 100 millivolts. This constancy above the top of cement is the "calibration" feature to the log. At the top of cement, signal amplitude will usually decrease. The signal will drop to a few millivolts if the casing is in intimate contact with cement and will usually become more erratic with depth otherwise.</p> <p>The 6-ft receiver measures the entire wave train as a function of time since the transmitter was pulsed. It thus captures signal transmitted along all paths linking transmitter and receiver. It is best displayed on a black-and-white variable density format (VDL record) so that lines vertical with depth denote arrivals at a constant sonic velocity. Such lines at the front of the record denote transmission along the casing wall (Pipe Signal), whereas lines at the back of the record result from transmission through the liquid inside the casing itself (Borehole Fluid Signal). If nothing but mud is present in the annulus behind casing, then the VDL display will consist of little more than pipe signal over the first two-thirds of record merging into borehole fluid signal over the final third. Cement in the annulus will pass enough signal to the formation and on to the receiver to interfere with and to degrade the borehole fluid signal. Consequently, the VDL trace often locates the top of cement even in the absence of contact with the casing.</p>

TABLE 4.A6—2A: CEMENT PLACEMENT (NEWLY CASED, UNPERFORATED WELL) (Continued)

Problem	Recommended Logging Tools	Operational Tips and Expected Results
Cement top location	Axial (regular) cement-bond log	<p>The application of pressure to the casing at the surface generally improves the quality of a bond log through improved contact between casing and cement. Any pressure at all is beneficial, but values of 500 to 2,000 psi are typical. Pressure may not offer any improvement whenever pipe and cement are separated by a viscous film on the outside of the casing. This is a problem with oil-based mud and with polymer mud.</p> <p>For cement to provide support to the casing, it must be rigid (i.e., must have some compressive strength). Usually, a 3-day waiting period prior to logging is sufficient for the cement to cure to approximately 75% of its ultimate strength. This time should be verified with the cement company.</p> <p>Foamed and other light-weight (extended) cements never develop much rigidity and thus fail to dampen pipe signal significantly. Cement-top location is therefore a subtle determination made from the VDL display. The same approach must also be used for bond logs recorded in fiberglass casing, but for a different reason. Fiberglass does not transmit much pipe signal, whether free or in contact with cement.</p> <p>Compensated versions of the tool with dual transmitters should be used in wells that are intentionally deviated because of their tolerance to variations in offset between tool and casing. On the other hand, the use of radial (circumferential) tools is not necessary.</p>
Evaluation of cement placement	Axial (regular) cement-bond log in combination with radial (circumferential) -bond log	<p>The objective is to determine whether cement has displaced mud in the rugose annulus behind casing. The principal record is the one from the axial tool, whereas the radial record is primarily of value in the determination of why poor contact may exist between casing and cement. The operational principles of the axial tool are described previously. The logging should be done under surface pressure and the wave-train record should be of the black-and-white, VDL type.</p>

TABLE 4.A6—2A: CEMENT PLACEMENT (NEWLY CASED, UNPERFORATED WELL) (Continued)

Problem	Recommended Logging Tools	Operational Tips and Expected Results
Evaluation of cement placement	Axial (regular) cement-bond log in combination with radial (circumferential) -bond log	<p>Three types of radial tools are available. The simplest is an axial-transmission tool with a set of 8 button receivers arrayed at 45° increments around the circumference of the tool. The array is spaced approximately 1 to 3 ft from an omnidirectional transmitter. The display is a variable-density representation of the eight values for pipe-signal amplitude. White generally represents large pipe signal (poor contact), whereas black denotes small pipe signal and very good contact. The second type of radial tool contains six pads that are held in contact with the inside casing wall by bow springs. Each pad contains a transmitter crystal and a receiver crystal. The pads are aligned so as to make six measurements of the pipe-signal attenuation coefficient over a transmission of approximately 6 in, forming a saw-tooth pattern around the circumference of the casing. The six coefficients are displayed both as six curves and as a variable-density display. This is the radial tool of choice. The third type of radial tool is a reflection-type device operating in the ultrasonic range. It contains a single crystal that rotates as it is pulsed. Between pulses, the crystal records the wave train reflected from both the inside and the outside walls of the casing. These data are processed so as to measure the amplitude of the signal reflected from the outside wall under the premise that a large reflection means little solid support to the casing, whereas a small amplitude implies good support. As one would suspect, the signal range from "good-to-bad" is quite small. This amplitude signal is presented on a yellow-to-dark-brown-colored, variable-density display called a "cement map." The reflection from each pulse is affected by conditions immediately outside such a small segment of the circumference that the record indicates anomalies that often have little or no significance to effective placement.</p> <p>If the well is deviated, then the radial tools should be run in the "oriented" mode so as to distinguish the high side of the hole from the low side.</p> <p>The VDL display from the axial tool is used to determine whether the annulus is essentially filled with cement. For casing 5 in. in diameter or larger, a full annulus will allow sufficient signal to travel through the formation to interfere with and to usually obliterate the borehole fluid signals otherwise appearing at the end of the record. In 4.5-in. casing, formation signal may end soon enough to leave approximately 1 stripe of borehole signal at the end. For smaller casing, formation signal may cease before the last third of the record, leaving this part free for borehole fluid signal. The annulus may be filled even though the pipe-signal trace indicates free pipe. In those locations showing poor contact on the pipe-amplitude trace, the radial record is used to determine circumferential extent of the lost contact. This information along with porosity data from an included gamma log can help in distinguishing among the many conditions that can cause loss of contact.</p>

TABLE 4.A6—2A: CEMENT PLACEMENT (NEWLY CASED, UNPERFORATED WELL) (Continued)

Problem	Recommended Logging Tools	Operational Tips and Expected Results
Evaluation of cement placement	Axial (regular) cement-bond log in combination with radial (circumferential) -bond log	Bond logs measure acoustical coupling, a quantity only marginally related to the ability of the cement to seal against the movement of fluid behind casing. Many conditions can destroy coupling without allowing the transmission of fluid over any significant distance. The most that can be concluded from a bond log is that it shows no reasons to suspect that the cement should not seal. This does not mean that the cement will seal.
	Combination of openhole-caliper log and temperature survey after cement placement	This combination is actually the best way to determine how effectively cement has displaced mud from a rugose borehole. The temperature trace should be run according to the same time guidelines used for the location of the top of cement and should be displayed at a sensitivity sufficiently high to accentuate the "noise" arising from caliper variations below the top. If the placement is effective, then locations showing hole enlargements on the caliper trace will show as warm spots on the temperature trace owing to the increased volume of hydrating cement. Likewise, sections of hole with reduced caliper will appear as cooler spots on the temperature log. If such a calibration exists between the surveys, then the placement should be sufficient to seal the annulus.
	Gamma-ray gravel-pack log (unfocused gamma-ray) before and after cement is circulated in place	This device uses the transmission of gamma rays to respond to density within roughly a 6-in. radius around it. Higher count rate means lower density, whereas lower count rate signifies higher density. The dependence is exponential in density, giving it a resolution of approximately 0.03 g/cm ³ . For the approach to be effective, the difference in density between cement and displaced mud should be at least twice this amount, or 0.06 g/cm ³ . The advantage is that no waiting time is required after the cement slurry is circulated.

TABLE 4.A7—2B: CASING INSPECTION FOR WEAR, COLLAPSE, AND BENDS (NEWLY CASED, UNPERFORATED WELL)

Problem	Recommended Logging Tools	Operational Tips and Expected Results
Casing wear	Multifeeler, mechanical caliper survey with display for each feeler or for cluster of feelers	<p>These devices record the movement of anywhere from 16 to 84 individual feelers along the inside wall of the casing. The resolution to a change in offset between the centralized tool and the pipe wall is approximately 0.005 in. Earlier versions recorded only the minimum and maximum deflections. Modern versions record either the movement of each feeler or the average movement for each of several clusters of feelers along with traces for minimum and maximum excursions. Even a 16-arm log provides a reasonable depiction of the shape of the casing's cross section, thereby distinguishing wear from collapse. Drillpipe wear (increased diameter) is generally restricted to one side of the casing over long stretches of vertical intervals, whereas casing collapse produces either simple ovality in shape or ovality with flattening on one side of the casing. These devices have no orientation detectors; consequently, it may be difficult to track gradual wear along the casing length. Rotation of the tool as it moves upwards places first one set of feelers in the worn area and then another set. The traces from tools with 64-plus feelers are so closely spaced on the display that a "wave" of change in deflection will sweep across the record as the tool rotates. These waves identify locations where the deflections of individual feelers can be examined for circumferential detail.</p> <p>These devices also respond to bends in the casing, provided the radius of the bend is small enough to displace the tool body off the centerline of the casing as the instrument moves through the bend. The signature is a diameter with one radius smaller than normal and the other larger. Collapse and bending often occur in concert, so that a detailed picture of the cross-section is needed if the two affects are to be separated.</p>
	Reflection-type radial-bond log	<p>This device has a rotating transmitter crystal that is pulsed at ultrasonic frequency as it rotates. Between pulses, the crystal records the echo wave train from the casing wall. When operated in the casing-inspection mode, the device records first the transit time for the echo from the inside wall of the casing as well as the transit time through the wellbore liquid over a fixed distance. The two measurements provide a pipe radius corresponding to each pulse. These radii are presented as a colored, variable-density map over the circumference of the inside wall. In deviated wells, the tool provides an oriented display to remove the effects of tool rotation. Each reflected wave train is also processed to identify the resonant frequency, if present, in the portion following the echo from the inside wall. This frequency is inversely proportional to wall thickness. This information is displayed on a second colored, variable-density map of wall thickness over the circumference of the casing. This display can also be oriented to remove the effect of rotation. These displays of caliper and wall thickness are easy to interpret and are more reliable than results from operation in the cement-bond mode. Still, the accuracy is less than that provided by mechanical calipers. The thickness measurements are highly sensitive to small displacements of the tool off pipe center. In fact, at shallow depths, sufficient centralization sometimes cannot be maintained for the tool to even operate.</p>

TABLE 4.A7—2B: CASING INSPECTION FOR WEAR, COLLAPSE, AND BENDS (NEWLY CASED, UNPERFORATED WELL) (Continued)

Problem	Recommended Logging Tools	Operational Tips and Expected Results
Casing wear	Eddy-current wall-thickness log	This is an electromagnetic induction device having very high resolution to changes in wall thickness. The normal taper in a joint of seamless casing (~0.125 in. over 40 ft) can be spread easily over three or more chart divisions. The tool uses a coil driven at a very low frequency (~ 1 Hz) to induce a field throughout the thickness of the wall. A passive coil is used to measure the lag angle of the induced field behind the driven field. Ideally, this angle is directly proportional to wall thickness. Although included on the log, the "caliper" trace from a coil driven at high frequency is responsive primarily to sudden changes in internal radius. Normal taper is difficult to discern on this trace. Furthermore, the casing versions of this tool are too long and of too large a diameter to negotiate bends.
Casing collapse (or split or part)	Tight-spot survey	These are minimum caliper tools containing one set of centralizer arms hinged at center and whose maximum compression is recorded. The devices tend to remain on pipe center even in sections of collapsed casing. The tools are short and small in diameter, and are less likely to stick in the well while providing some idea of the severity of collapse.
	Multifeeler mechanical-caliper survey	As indicated previously, this is the best device available for defining the shape of the cross section of casing. In collapsed casing, the record will reveal an oval shape with perhaps flattening along one side of the casing. The tools are long and strongly centralized. Safety precautions may preclude their use until the severity of the problem is known.
	Acoustical caliper survey (radial, reflection-type bond log)	The "caliper" map provided by this "pulse-echo" tool is described in this table under Casing Wear. Because of its strong centralization and relatively large diameter (2 or more in.), the tool should only be run where severity of collapse is known.
	Casing-collar log	A simple collar record is usually sufficient to detect parted casing. The tool should be run with a decentralizing magnet on the bottom. Relative to a normal casing signal, a large deflection is induced as the tool passes across each end of the parted casing. The amount of part is determined by the spacing between the centers of the signal.

TABLE 4.A7—2B: CASING INSPECTION FOR WEAR, COLLAPSE, AND BENDS (NEWLY CASED, UNPERFORATED WELL) (Continued)

Problem	Recommended Logging Tools	Operational Tips and Expected Results
Casing bends (dog legs)	Kink-meter or dog-leg survey	These are relatively compact devices that measure the inclination of the tool's axis from the vertical. This measurement is typically made with a pendulum free to rotate around the tool axis. Passes upward and downward or successive passes in the same direction may produce different dog-leg angles because of the way the tool is displaced off casing center on a given pass. Despite this sensitivity to offset, the tool provides an estimate of radius of curvature in a relatively safe procedure. These devices should thus be the first ones run. However, they cannot detect the presence of collapsed casing in conjunction with a bend.
	Multifeeler mechanical-caliper survey	As described previously under Casing Wear, these devices respond to bends because of the displacement of the tool off pipe center as it navigates a bend. The classic signature of a pure bend is therefore a diameter with one radius too short and the other too long. A bend with collapse is therefore easily distinguished once the existence of the bend is established. The radius of the bend must be larger than ideal if the casing is also out of round.
Condition of external casing strings	Eddy-current wall-thickness survey	These tools are electromagnetic field induction devices. They utilize a coil driven at very low frequency (~1 Hz) to spread a magnetic field within a radius of 8 to 10 in. about the coil. A second sensing coil is used to detect the lag angle between the driven field and the induced field. This lag is proportional to the amount of metal within the induced field. The angle is therefore influenced by the first two casing strings external to the one containing the tool. Collars on the first string external to the string containing the device are clearly evident on the trace of phase lag. Accordingly, the trace is sensitive to parts in the casing external to the one containing the tool. Likewise, the trace will detect significant holes in the external string. However, it will not detect splits along the axis of the external string unless these have expanded into holes. Finally, the trace will usually detect an end to the second external string.

TABLE 4.A8—2C: ANNULAR PRESSURE, CROSSFLOW BEHIND CASING, AND CERTIFICATION FOR HAZARDOUS WASTE INJECTION (NEWLY CASED, UNPERFORATED WELL)

Problem	Recommended Logging Tools	Operational Tips and Expected Results
Location of source of annular pressure	Temperature surveys before and during (or after) annulus bleed	<p>The before and after traces should be merged on a display with a sensitivity of 1°F per in. of chart. A second display should be at a reduced sensitivity sufficient to prevent "wrapping" over the logged interval. Because the wellbore is new and cooler than normal geothermal temperature, any movement of liquid to the well will produce a warm signature at the source depth. This makes the survey quite sensitive to low rates. The warmer temperature will be carried upward from the source in proportion to the flow rate.</p> <p>For annular flow behind the string containing the tool, liquid rated can be estimated from the slope dT/dz, °F/ft, and amount of warming $\Delta T = T_{\text{flow}} - T_{\text{static}}$, °F, at a given location in the crossflow path from the Romero-Juarez expression:</p> $q \text{ (B/D)} = A \times \frac{\Delta T}{\left(\frac{dT}{dz}\right)},$ <p>where $A = 1.0$ for water flow and $A = 2.5$ for oil flow. The result is an approximation that supposes no cooling to the liquid as a result of the dissolution of gas from water or the flashing of gas from oil. The expression underestimates rates for short-time flow behind multiple strings.</p> <p>Expansion at a gas source usually produces a cool signature. For dry gas, this cooling amounts to approximately 1°F for each 50-psi drop in pressure. This cooler temperature is carried upward in proportion to the gas rate. This rate can be approximated from the previous expression with $A = 10$.</p>

TABLE 4.A8—2C: ANNULAR PRESSURE, CROSSFLOW BEHIND CASING, AND CERTIFICATION FOR HAZARDOUS WASTE INJECTION (NEWLY CASED, UNPERFORATED WELL) (Continued)

Problem	Recommended Logging Tools	Operational Tips and Expected Results
Location of source of annular pressure	Noise-logging surveys run in same way as temperature surveys	<p>This survey is particularly sensitive to the percolation of a small rate of gas into liquid, a condition where the temperature survey loses sensitivity. The tool is a microphone that measures the amount of turbulent noise produced by the movement of fluids. It makes stationary measurements of the sound level, in millivolts, above four high-pass cutoff frequencies, typically set at 200, 600, 1,000, and 2,000 Hz. Each reading includes levels at all frequencies above the cutoff values; consequently, the readings decrease with increasing cutoff frequency. The cutoff values are chosen so as to distinguish two flow conditions: single-phase and gas movement through liquid. The movement of gas through liquid produces a high level of noise in the low-frequency range below 600 Hz. This fact makes the tool particularly sensitive to small gas flows through liquid, the application for which it was devised. Gas percolation at downhole rates as low as 10 ft³/d can be resolved. Below 400 ft³/d, gas rate behind drillpipe can be estimated from the millivolts of noise in the band N_{200}–N_{600} from the relationship</p> $q_g (\text{ft}^3/\text{d}) = 0.35 \times N_p \times (N_{200} - N_{600}),$ <p>where N_p is the number of pipe strings between the source and the tool. Higher rates are underestimated by this expression.</p> <p>Single-phase flow, by contrast, produces noise primarily in response to acceleration past tight spots in the flow path. The resulting sound is of relatively weak amplitude and has a frequency in the range of 1,000 Hz or higher. If a restriction holds a pressure drop Δp psi in response to a rate q B/D, then the single-phase rate of either liquid or gas behind drillpipe can be estimated from the millivolt value of the noise cut at 1,000 Hz by the expression</p> $q \times \Delta p = 700 \times N_p \times N_{1000},$ <p>where the pressure drop Δp is in psi, the rate q is in B/D and N_p is the number of pipe strings between source and tool. If the total pressure drop over the entire flow path is used in this expression, then the summed noise levels at each constriction should also be used. Both of the previous flow expressions suppose that the tool is calibrated to read standard peak-to-peak millivolts.</p> <p>The tool makes stationary measurements, meaning that approximately 60 to 80 locations can be surveyed on a typical run. Sample density can be compressed at locations such as suspect zones, cement tops, and casing shoes. Otherwise, 50-ft increments are typical.</p>

TABLE 4.A8—2C: ANNULAR PRESSURE, CROSSFLOW BEHIND CASING, AND CERTIFICATION FOR HAZARDOUS WASTE INJECTION (NEWLY CASED, UNPERFORATED WELL) (Continued)

Problem	Recommended Logging Tools	Operational Tips and Expected Results
Location of source of annular pressure	Activated-oxygen survey for water movement	<p>The operating principles for this device are described previously in Table 1B under Lost Returns. Because the direction of flow is generally unknown, the tool must be configured for water movement either upward or downward. For some service companies, this may require two separate runs into the hole.</p> <p>The "calibration" feature is a measurement, preferably in a shale zone, in a location where flow behind casing is absent. This calibration is essential to the reliable detection of small crossflow rates near the tool's resolution (2 to 3 ft/min water velocity).</p>
Certification for annular disposal of mud and cuttings	Temperature surveys before and during the injection of mud or brine down the annulus	<p>This procedure is sometimes called a "pump-in test" to determine the base of injection. The two surveys should be merged on a common display at a sensitivity of approximately 2°F per in. of chart. The injection trace will separate, usually to the cool side, from the "before" trace down to the base of injection, where it will begin an exponential approach to the "before" trace. The coincidence of the two traces does not occur immediately below the base of injection owing to the combination of tool response time and thermal conduction along the wall of the casing containing the tool. Still, base detection is easy.</p>
	Radioactive tracer surveys during and after injection of tracer into annulus at surface	<p>Some states require this test for certification, although it is both expensive and often misleading unless conducted carefully. The cost arises from the use of two service companies, one to pump the tracer at the surface and another to do the logging. The potential for erroneous interpretation arises from the tendency for pockets of tracer to be trapped in pockets in the annular space and thereby move down the hole behind the main slug. To prevent this stringing out of tracer from clouding the interpretation, pumping should be continued after the main slug has been pumped away until all trailing slugs are also pumped away. A common failing is to stop the pumping too soon and then to detect tracer above the target zone, a condition often attributed to seal failure on the part of the external casing shoe above the zone.</p> <p>The injection of 5 to 10 millicuries of tracer at the surface is generally sufficient to track injection for approximately 5,000 ft down the annulus. Before injection commences, a section of gamma-ray log should be recorded past the target zone so as to define the normal gamma activity in the hole and the noise statistics for the tool.</p>

TABLE 4.A8—2C: ANNULAR PRESSURE, CROSSFLOW BEHIND CASING, AND CERTIFICATION FOR HAZARDOUS WASTE INJECTION (NEWLY CASED, UNPERFORATED WELL) (Continued)

Problem	Recommended Logging Tools	Operational Tips and Expected Results
Certification for the injection of hazardous waste	Activated-oxygen survey configured for flow upward	<p>Federal regulations require this survey in a well penetrating drinking-water sands even before the well is perforated for hazardous injection. This requirement is to insure that the wellbore does not allow crossflow of brine into depleted-water sands (so-called "Unrelated Flow"). Contemporary practice, however, is to delay the survey until the well is perforated and to make the measurements before and with the well on injection. The procedure is the same either way. Operational principles are described previously under Annular Pressure.</p> <p>"Calibration" measurements are first made in a deeper shale where crossflow is not expected. The tool is then positioned for measurements in first shale below the deepest drinking-water sand. The detection of water moving upward behind casing at a velocity in excess of 3 ft/min prevents certification. Precautions should be taken to prevent water circulation inside the logged string. For example, heavy mud should not be circulated out of the hole with brine before the test. This prevents the slumping of viscous layers of mud that have adhered to the casing wall.</p>
Detection of crossflow behind casing	See Table 4.A5 (1C): Detection of flow underground	<p>The tool preference carries over intact to this environment. Likewise, the features to expect are unchanged. Because the new wellbore is cooler than geothermal, the temperature surveys are the most sensitive to water crossflow because of water's ability to produce warm signatures at low rates. Likewise, the noise logger remains the most sensitive to small flows of gas upward through water behind casing. If the rate expressions are used, then the noise levels must be multiplied by N_p = number of pipe strings separating sensor from source. Table 4.A5 (1C) assumes this value is 1.</p>

**TABLE 4.A9—3: ACID, FRACTURE-PROPPANT, OR GRAVEL-PLACEMENT
(WELL BEING STIMULATED, FRACTURED, OR GRAVEL-PACKED)**

Problem	Recommended Logging Tools	Operational Tips and Expected Results
Single-stage acid placement	Temperature surveys before and after acid placement	This is listed as the prime survey because the injection of acid often fractures into locations not intended. The two surveys should be merged on a display scaled at least at 2°F per in. of chart. The "after" temperature survey will show cool signatures at locations into which the flush pad was injected. Locations where acid remains close to the wellbore will show warm signatures if acid reacts with formation or mud solids. Otherwise, cool anomalies will appear. The base of injection is located by the convergence of the "after" trace with the "before" trace. If ball diverters are used, the amount of acid injection is limited and may produce only small signatures.
	Radioactive tracer surveys before and after treatment	Both the acid and the flush liquid are tagged at the surface, typically with Iridium-192. The operation usually requires two contractors—one to pump tag at the surface, and one to do the logging. Interpretation of the records is simple but subject to certain peculiarities. First, if the tagged fluid is displaced more than approximately 2 ft away from the wellbore (in a fracture, for example), then tag activity approaches background level. Second, tagged fluid tends to hang in collars along the wellbore and in eddies formed at the end of the treatment string.
Multistage acid placement	Temperature surveys before and after treatment	Ideally, a survey would be recorded after each stage, but such a practice is usually impractical. Before and After surveys are subject to conditions listed previously.
	Radioactive-tracer spectral surveys before and after treatment	For all stages except the last, only the diverting fluid is usually tagged. A different tracer is used for each stage so that a spectral survey (gamma-ray energy survey) can identify subsequently the location of each tracer. Metal tracers such as antimony (Sb), scandium (Sc), silver (Ag), and gold (Au) are used commonly in the form of powders with neutral buoyancy. The final acid stage and its flush are tagged with Iridium-192. The use of a spectral log has an advantage over a normal gamma-ray log. The energy levels can be used to make an estimate of the distance from the tool to the tracer. Tracer hang-up in the wellbore can thus be distinguished from displaced tracer. Two contractors are again usually required—one to tag at the surface and one to log.
Single-stage fracture placement	Temperature surveys including a "before" log and at least one "after" log recorded 12 to 48 hours later	This is the best procedure for the determination of the vertical extent of a fracture so far as fluid communication is concerned. The large volumes of pumped fluid produce large cool signatures on the "after" log. However, the fracture wings continue to close on the proppant for typically 12 hours or longer. Unequal rates of closure pumps liquid from one wing to the other during this time. This return produces warm signatures at locations where the liquid passes through the wellbore. For surveys run shortly after a fracturing operation, a warm "nose" may mark the top of a fracture. This activity is usually over after 24 to 48 hours so that the size of the cold signatures can be used to assess relative degrees of treatment.

**TABLE 4.A9—3: ACID, FRACTURE-PROPPANT, OR GRAVEL-PLACEMENT
(WELL BEING STIMULATED, FRACTURED, OR GRAVEL-PACKED) (Continued)**

Problem	Recommended Logging Tools	Operational Tips and Expected Results
Single-stage fracture placement	Radioactive-tracer survey to locate tagged proppant	Special solids are available that can be made radioactive at location and added to the fracture proppant continuously. This approach avoids the transport of large amounts of precoated solids. If this is not a problem, then solids coated with resin containing Iridium-192 are available. The same interpretative restrictions mentioned previously for tagged acid apply here, particularly the problem of hang-up in collars. An additional problem is the inevitable settling of tagged sand to the bottom of the wellbore.
Multistage fracture placement	Temperature surveys before and 24 to 48 hours after treatment	Remarks concerning the long shut-in time for the "after" survey are given above for single-stage fracturing. The time is more critical here because the size of the cool signatures can be used to judge the relative effectiveness of each stage. The larger the cooling anomaly on the survey, the greater the displacement away from the wellbore.
	Spectral gamma-ray survey to locate radioactive tracers particular to each stage	The same metal tracers are used to tag solids as described previously for multistage acidization. The same contamination problems arise as for single-stage fracturing.
Gravel placement	Gravel-pack survey before and after placement	Most companies use an unfocused, gamma-ray tool for this survey. This device measures the gamma-ray transmission over 17 to 23 in. to determine the density of material in an 8- to 12-in. radius about the tool. Gravel behind the screen causes a large reduction in count rate relative to liquid. A uniformly low count rate is desired over the packed interval.
	Gravel-pack survey before and after placement	Some companies use a compensated neutron-porosity tool for this survey. Gravel behind the screen reduces the liquid porosity. Effective gravel placement will produce a relatively uniform porosity of approximately 40%.
	Gamma-ray survey to detect tagged gravel	Whatever the type, the tool contains a radioactive source. If lost in the hole, it must be either recovered or cemented in place.
		Modern practice has tended towards the use of prepacked screens, making these types of surveys unnecessary. However, the unfocused gamma tool has remained in widespread use as an "interface" device used to locate the hydrocarbon/brine interface in storage caverns.
		Tagged solids are added continuously at the surface to the gravel during its placement. The sole advantage to this approach is that some companies have gamma detectors that rotate to give an indication of the placement around the circumference of the screen. This type of information is useful for packs in holes having high deviation angles (horizontal wells).

TABLE 4.A10—4A: DEMONSTRATION OF CONFINEMENT (INJECTION WELL—CASED OR OPENHOLE WITHOUT SCREEN OR LINER)

Problem	Recommended Logging Tools	Operational Tips and Expected Results
Determination of extent of fluid injection	Three temperature surveys: One with well on injection and two, spaced approximately 12 hours apart, with the well shut in	<p>Temperature surveys are essential to this problem because the majority of wells on continuous injection fracture at some time in their history. Flow in these fractures, either above or below the target interval, is detected by the temperature surveys but may be missed by radioactive-tracer surveys. The three surveys should be merged and have one display at a sensitivity of 1°F per in. of chart and one display free of "wraps." The survey recorded with the well on injection shows those locations where fluid is lost from the vicinity of the wellbore. Below each such location, the injection trace will shift toward the shut-in traces. Depending upon the amount of loss, the shift may be a step change in temperature or simply an increase in gradient. The base of injection is at the location where the injection trace begins an uninterrupted, exponential-type return to shut-in temperature. Movement upward behind casing to a thief zone will produce on the injection trace at the zone the same type of shift as described previously but of less magnitude. This behavior is caused by the slightly warmer temperature carried upward by the stream.</p> <p>A shut-in survey recorded after a few hours of shut-in time will show cool signatures at all the porosity taking injection, provided the trace is not corrupted by backflow from the closure of unpropped fractures. It is not a good survey from which to judge relative amounts of injection, however. A survey after 12 to 48 hours is much better suited to this purpose. Those zones having received larger volumes of injection (farther displacement of fluid away from the wellbore) will remain cooler than those zones taking lesser volumes. This distinction persists after years of injection, but the contrast shrinks to a fraction of a degree after approximately 6 months.</p> <p>If the well is on gas injection, then expansion at each injection zone may produce a temperature at that zone that is cooler than the temperature above. Dry gas expanding adiabatically cools approximately 1°F for each 50-psi drop in pressure. Other than this localized cooling, the injection trace behaves in the same manner described previously. Whenever gas moves behind casing, however, the shut-in traces may also show localized cooling at tight spots in the path as well as at receptor porosity.</p>

TABLE 4.A10—4A: DEMONSTRATION OF CONFINEMENT (INJECTION WELL—CASED OR OPENHOLE WITHOUT SCREEN OR LINER) (Continued)

Problem	Recommended Logging Tools	Operational Tips and Expected Results
Determination of extent of water injection	Radioactive-tracer survey with the well on injection	<p>These surveys make use of a tool consisting of two or more gamma detectors along with a reservoir filled with 50 to 100 cm³ of field brine tagged with 5 to 10 microcuries of Iodine-131. A piston-type pump is operated at the surface to discharge discrete slugs of this tagged brine into the wellbore. The amount of tracer ejected on each "shot" is determined by the length of time the pump is on.</p> <p>For this particular problem, the best procedure is to eject a slug of tracer at least 50 ft above the target zone with the well on full injection. Successive logging runs are then made upward with one of the detectors active so as to locate the position of the slug at the time of each pass. These "chased-slug" passes are continued until the slug of tagged brine is pumped beyond recognition depth (~1 ft from tool). When merged, these successive records present a graphic picture of what happens to the slug as it moves down the wellbore. So long as the slug remains in the casing or open hole, it produces on the record a bell-shaped pattern of activity. However, as the leading edge of the slug moves into a confined space, such as the annulus behind casing, it begins to string out or unspool like a ribbon from the main slug. The "ribbon" will continue to unwind until the main slug passes the entry location. The signature of a "channel" (annular flow) is therefore unmistakably unique.</p> <p>The sensitivity of this survey to liquid movement immediately behind pipe is unsurpassed. A rate of only a few B/D can be detected in the manner described. The same sensitivity also prevails for the detection of crossflow in a shut-in wellbore. On the other hand, the tool may not detect flow in a fracture behind pipe unless the liquid remains in the immediate vicinity.</p> <p>The method suffers from two disadvantages. First, the steam can only be tagged while it is inside the wellbore. Second, the service is becoming difficult to obtain. Very few companies now run radioactive tracer surveys on offshore locations. Furthermore, tools for general use in gas wells are nonexistent except for certain special applications such as CO₂ injection (carbon-12) and steam injection (Xenon tag).</p>

TABLE 4.A10—4A: DEMONSTRATION OF CONFINEMENT (INJECTION WELL—CASED OR OPENHOLE WITHOUT SCREEN OR LINER) (Continued)

Problem	Recommended Logging Tools	Operational Tips and Expected Results
Demonstration of injection-packer seal	Radioactive-tracer survey with well on injection	<p>The same tracer tool as described above is best suited to this problem. However, the "chased-slug" approach described above is unsuitable because of the danger associated with the operation of pulling the tool into a tubing string at high logging speed.</p> <p>Instead, a stationary or "velocity-shot" approach is utilized. The tool is positioned according to the length of tailpipe extending below the packer. If the pipe is short, then the tool is placed in the tubing so that the top detector (usually located above the ejection sub) is approximately 3 ft above the packer-seal elements. A bottom detector (located below the ejector) should also be active for this procedure. Whether it is positioned in the tubing or below it is not important. With the tool stationary and the well on injection, a slug of tracer is ejected and records of activity made for each detector with the recorder on time drive. The record from the bottom detector should show the passage of tracer on its way down the hole. To satisfy regulatory constraints for hazardous liquids, the record should be continued for a time long enough to allow tracer to reach the top detector at a velocity of 1% of injection velocity. Typically, a 30-minute record satisfies this constraint.</p>
	Activated-oxygen survey with well on injection	<p>This is a pulsed-neutron tool that creates its own radioactive tracer (activated oxygen by bombardment of water) with neutrons and then times the passage of the tracer between two detectors. Stationary measurements give the best resolution. The device has two detectors spaced approximately 1 ft apart and 2 to 3 ft above the neutron source. On this test for flow upward, the detectors should be located above the source. Both detectors as well as the source should be inside the tubing string.</p> <p>With a tracer half-life of only 7.4 seconds, velocity resolution is poor compared to that for the chemical-tracer tool. However, some regulations allow the activation tool as a substitute for the latter.</p>
"Channel" check for annular seal above and below perforations	Radioactive-tracer surveys with well on injection	<p>If the chased-slug surveys described above under Injection Extent have been done, then this check has already been made. Otherwise, stationary velocity-shot records can be taken with the bottom detector positioned first above the perforations and then below (ejector in perforations). If tracer movement is detected below the perforations, then a slug should be ejected in the sump and logged on at least three passes.</p>

TABLE 4.A11—4B: INJECTION PROFILE DETERMINATION (INJECTION WELL—CASED OR OPENHOLE WITHOUT SCREEN OR LINER)

Problem	Recommended Logging Tools	Operational Tips and Expected Results
Determine injection profile	Three temperature surveys: One with well on injection and two, spaced approximately 8 hours apart, with well shut in	<p data-bbox="650 272 1184 446">Most wells that have been on continuous injection for any length of time are fractured. The distribution of the unpropped fractures along the borehole determines the locations where fluid exits the well. These locations, however, may not correspond to the locations of the porosity that ultimately stores the fluid. Temperature traces can detect this storage porosity.</p> <p data-bbox="650 471 1184 741">The trace with the well on injection shows the locations where fluid leaves the vicinity of the wellbore to enter porosity. At each location where fluid enters porosity or circulates in a fracture, the injection trace will exhibit a shift toward the shut-in traces. Depending upon the relative size of the loss, the shift may take the form of a step change (large loss) or a bend toward the shut-in traces (gradient increase at small loss). Starting at the top, one can examine the slope of the injection trace to identify the exit locations down to the base of injection where the trace returns to the shut-in traces.</p> <p data-bbox="650 767 1184 896">The volumetric rate remaining in the wellbore vicinity at any location is determined from the injection trace from its slope dT/dz and its displacement from the longest shut-in trace $\Delta T = T_{\text{flow}} - T_{\text{shut-in}}$ by the Romero-Juarez relationship</p> $q = A \frac{\Delta T}{\frac{dT}{dz}}$ <p data-bbox="650 987 1184 1232">The value of the constant A is not required for relative profiling. Values for the ratio on the right side of this expression are determined from the top in the full stream downward to a location above the last exit at the base of injection. The profile is then the ratio of each value to the value in the full stream. The slopes should be determined far enough below an exit to escape the effect of the associated shift. For many injection wells, the displacement is relatively constant, meaning that only values for reciprocal slopes are needed.</p> <p data-bbox="650 1257 1184 1406">The profile determined in this manner lacks the accuracy of one obtained from either tracer surveys or flowmeter survey, but is typically a better representation of the actual injection profile. In a fractured wellbore, the temperature-based profile is usually quite different from either a tracer or a flowmeter survey.</p> <p data-bbox="650 1431 1184 1624">The long-time shut-in trace defines true storage locations as either cool or warm anomalies depending upon which side of the shut-in traces the injection trace is located. The trace will allow the elimination of "exits" that cause only circulation patterns in fractures and "exits" that arise from slope changes because of variations in rate. This problem exists because multiple injection wells are often attached to a single supply header.</p>

TABLE 4.A11—4B: INJECTION PROFILE DETERMINATION (INJECTION WELL—CASED OR OPENHOLE WITHOUT SCREEN OR LINER) (Continued)

Problem	Recommended Logging Tools	Operational Tips and Expected Results
Determine injection profile	<p>Three temperature surveys: One with well on injection and two, spaced approximately 8 hours apart, with well shut in</p> <p>Radioactive tracer surveys with well on injection at rates no larger than approximately 5,000 B/D</p>	<p>When compared to the shorter-time shut-in trace, the long shut-in trace also allows an assessment of the historical progression of the injection program. Those zones that have taken a large volume of fluid will show anomalies whose sizes change more slowly with time than do the anomalies at zones that have received lesser volumes. This condition persists after years of injection, but the differences shrink quickly to fractions of a degree.</p> <p>This tool is one next most likely to detect flow in fractures as long as the stream remains within ± 1 ft of the tool. The device is described in Table 4.A10 (4A), to which the reader should refer before continuing here.</p> <p>A merged record of chased-slug surveys should be obtained first to obtain a graphic picture of the tracer slug as it moves down the hole. An exit profile can be derived from this record in two ways. The most common approach is to record the time at which the peak activity is attained on each pass through the ejected slug. An injection velocity is then determined from the difference in peak location and peak time for two adjacent slugs. These velocities are then proportioned for the profile. A second, preferred approach is the slug-area method that equates the area under the activity trace for a given slug to the volumetric rate in the hole at that location. A ratio of areas to that in total flow then provides the profile. This approach is unaffected by variations in rate and retains its accuracy for annular flow. Because only a ratio of areas is involved, one can determine quickly a value that is proportional to area by taking the product of slug height (in millimeters above base activity, for example) and the slug width at a distance above the base of one-half the peak height. If the curve is Gaussian, then this number is 14% smaller than the actual area.</p> <p>At injection rates greater than a few hundred B/D, the chased-slug approach gives a vertical resolution of only 10 to 20 ft. To supplement this data, approximately 10 to 12 stationary velocity-shot records should be made at different locations in the hole. A slug of tracer is ejected above two detectors spaced 4 to 10 ft apart with the recorder on time drive. A travel time between two detectors is determined from each shot record. These values are ratioed inversely for profiling. Vertical resolution less than detector spacing is obtained from measurements on closer stations. Such travel times are quite sensitive to variations in rate, however.</p>

TABLE 4.A11—4B: INJECTION PROFILE DETERMINATION (INJECTION WELL—CASED OR OPENHOLE WITHOUT SCREEN OR LINER) (Continued)

Problem	Recommended Logging Tools	Operational Tips and Expected Results
Determine injection profile	Diverting spinner-flowmeter surveys with well on injection at rates no larger than 2,000 B/D	<p>These are the most sensitive of the spinner-type flowmeters with a resolution in the range of 10 to 15 B/D. They make stationary measurements using either a packer or extended metal vanes to divert the flow past a spinner element contained in the barrel of the tool. Because of the limited clearance between tool wall and spinner element, these devices plug easily. They should not be run in highly deviated wells where debris tends to settle to the low side of the casing everywhere. Profiling from these stationary measurements is straightforward. The service company can also usually provide a calibration curve for single-phase flow giving rate as a function of spinner speed.</p> <p>The metal-petal devices have been known to stick in the end of tubing strings owing to a failure of the petals to close into the tool body. Furthermore, all spinner devices have the disadvantage of identifying only locations where fluid exits the casing or open hole.</p>
	Continuous or fullbore spinner surveys both with well on injection and shut-in	<p>These devices produce continuous traces of spinner speed, RPS, as a function of depth in the wellbore. Other than at very low spin rates, the speed is linearly related to fluid velocity relative to the tool. Profiling is therefore a simple matter of proportioning the changes in spinner speed from that speed induced by line speed.</p> <p>Continuous flowmeters have spinner elements whose diameter is slightly smaller than the diameter of the tool itself, whereas fullbore flowmeters have large-diameter elements hinged so as to open only when the tools emerge from the end of tubing. Both versions have poorer rate resolution than do the diverting types. Depending upon casing size, the resolution for either type is in the range of 70 to 200 B/D for liquid and 100 to 500 Mcf/D for gas.</p>

TABLE 4.A11—4B: INJECTION PROFILE DETERMINATION (INJECTION WELL—CASED OR OPENHOLE WITHOUT SCREEN OR LINER) (Continued)

Problem	Recommended Logging Tools	Operational Tips and Expected Results
Determine injection profile	Continuous or fullbore spinner surveys both with well on injection and shut-in	<p>The principal difference between the two types of spinners lies in the fluid velocity required to start the spinner turning with the tool stationary (i.e., in the threshold velocity). This value depends upon the density of the fluid, the frictional resistance in the tool bearings, and the amount of diversion of fluid around the element rather than past it. Fullbore spinners and high-sensitivity continuous spinners both have a threshold velocity in the range of 5 to 8 ft/min in liquid. In gas, however, the fullbore tools have a much smaller threshold velocity (10 to 15 ft/min) than do the continuous tools (25 to 50 ft/min). Both types typically use an element with a pitch of approximately 6 in. This is the distance fluid must move to turn the element one revolution. The corresponding theoretical sensitivity is 0.050 RPS per ft/min. Actual values are more like 0.044 RPS per ft/min.</p> <p>Values for sensitivity and threshold velocity are best determined by calibration in the well shut-in so as to avoid the influence of rate variations. At least three passes at sequentially doubled line speeds should be made for tool movement both upward and downward in the wellbore. The slowest line speed should be sufficient to turn the spinner at a speed of at least 1 RPS. Even after such a calibration, one must still have an independently determined tool factor to convert spinner speed into the superficial velocity required for rate calculation. This factor usually comes from flow-loop data.</p> <p>The most reliable injection profile is obtained from the pass made against flow (upward) at a line speed no greater than 30 ft/min in liquid and 50 to 70 ft/min in gas. Common practice, however, is to log in both directions at three line speeds.</p>

TABLE 4.A12—5A: DEMONSTRATION OF CONFINEMENT [INJECTION WELL WITH SCREEN OR SLOTTED (PERFORATED) LINER]

Problem	Recommended Logging Tools	Operational Tips and Expected Results
Determination of injection extent	Three temperature surveys: one with well on injection and two, spaced approximately 8 hours apart, with well shut in	This completion is just as subject to formation fracturing as is the completion described in Table 4.A10 (4A). The user should refer to Table 4.A10 (4A) for details of this procedure. Briefly, on the flowing trace, each exit will produce the normal shift back toward the shut-in traces, even though the exit is behind the screen or liner. One new feature is introduced by this completion. Because of a partially plugged screen or widely spaced holes in the liner, fluid may exit the screen or liner and then move upward to a higher receptor zone. In this case, one will observe what appears to be a normal exit signature at both the receptor and exit locations, but both are muted and, in fact, may appear only as "kinks" to an increased gradient between the receptor zone and the exit.
	Radioactive-tracer surveys with well on injection	The use of this tool is also described in Table 4.A10 (4A). The chased-slug approach is recommended for completion because of the variation in fluid velocity caused by changes in gravel porosity or hole size around a liner. Slug area is essentially preserved when the tracer passes into the annulus behind the screen or liner even though the slug may lose its "bell" shape. The chased-slug records will also reveal those locations where fluid exits the screen or liner and moves upward to a higher receptor zone.
Demonstration of packer seal	Radioactive-tracer surveys with well on injection	As described in Table 4.A10 (4A), the stationary, velocity-shot procedure should be used for this problem.
	Activated-oxygen survey with well on injection	The procedure is the same as that described in Table 4.A10 (4A). The tool is a substitute for the chemical-tracer device in those cases where the latter is unavailable. It provides only stationary, velocity-shot type data. Its velocity resolution, 2 to 3 ft/min, is not nearly as good as that of the chemical-tracer device.
"Channel" check for annular seal above and below perforations	Radioactive-tracer survey (activated-oxygen survey as substitute)	Same procedure as described in Table 4.A10 (4A).

TABLE 4.A13—5B: INJECTION PROFILE DETERMINATION [INJECTION WELL WITH SCREEN OR SLOTTED (PERFORATED) LINER]

Problem	Recommended Logging Tools	Operational Tips and Expected Results
Determine injection profile	Three temperature surveys: one with well on injection and two, spaced approximately 8 hours apart, with well shut in	The possibility of flow in fractures makes this the preferred initial approach. The procedure is the same as that described in Table 4.A11 (4B), to which the reader should refer. One new difficulty is introduced by this completion. Owing to plugged screens or to widely spaced holes in liner, flow may exit screen or liner and move back upwards to a higher receptor zone. Normal but muted exit signatures will appear both at the location of the receptor and at the location of the exit. However, the circulation gradient existing between these locations does not satisfy the rate-estimation expression given in Table 4.A11 (4B). Only qualitative assessments based on exit-signature size can be made for such rates from the flowing trace. The same sort of assessment can also be made from the trace made after the longest shut-in time.
	Radioactive-tracer surveys with well on injection at rates no larger than approximately 5,000 B/D	In the absence of flow in fractures, this is the most accurate method of profiling. The procedure is described in Table 4.A11 (4B). Because of the mixture of flow both inside and outside the screen/liner, the chased-slug approach should be used and the profiling should be based on slug area. This approach remains valid for slugs that exit the screen/liner and move "strung out" upward or downward in the annulus.
	Activated-oxygen surveys with well on injection	This tool is a pulsed-neutron device that creates its own tracer, activated oxygen, by neutron bombardment of water. It makes station measurements of the travel time of the tracer between detectors spaced approximately 1 ft apart. Hence, the device gives data corresponding to velocity-shot data from a chemical-tracer tool. However, the velocity resolution is much less at approximately 2-3 ft/min. The profile may also be only qualitative owing to distortion from variations in fluid velocity. The possibility for flow either upward or downward means that the tool must be configured for both cases. For some companies, this means separate trips into the hole. Furthermore, if lost in the hole, the tool must either be "fished" out or cemented in place.
	Continuous flowmeter surveys with well on injection	These devices are described in Table 4.A11 (4B). They respond only to flow inside the screen/liner. Consequently, the profile is qualitative at best.

TABLE 4.A14—6A: DEMONSTRATION OF CONFINEMENT [INJECTION WELL WITH TUBING ACROSS PERFORATIONS (DUAL COMPLETIONS, REGULATED INJECTION)]

Problem	Recommended Logging Tools	Operational Tips and Expected Results
Determine extent of injection	Three temperature surveys: One with well on injection and two, spaced about 8 hours apart, with well shut in	This type of completion is no less susceptible to formation fracturing than are the other types considered previously. Temperature surveys are therefore the preferred initial logging method. The procedure is described in Table 4.A10 (4A), to which the reader should refer. A new feature is introduced for wells with tailpipe extending across perforations and for wells injecting from a tubing string equipped with regulator valves. In such cases, fluid may exit the tubing and then flow back upward to receptor zones. These locations are recognized on the injection trace by the muted exit signatures (shifts in temperature or bending towards shut-in traces) that appear at both receptor and exit locations. The receptor zones are also evident on the shut-in traces.
	Radioactive tracer surveys with well on injection	This method is not suitable for dual completions for which logging must be done in the shut-in long string. The procedure is described in Table 4.A10 (4A). The chased-slug approach is recommended because of the likely presence of flow in both directions behind the tubing string.
	Activated-oxygen surveys with well on injection	This is the only tracer method possible for dual completions. The device creates its own tracer by the bombardment of water with pulsed neutrons. The passage of the tracer between detectors spaced approximately 1 ft apart is timed to give data comparable to velocity-shot data from a chemical-tracer survey. If flow upward as well as downward is possible, then the tool must be configured for both. For some companies, this requires separate trips into the hole. A lost tool must be fished out or cemented in place.
Demonstration of packer seals	Radioactive-tracer survey or activated-oxygen survey with the well on injection	Stationary velocity shots are used for this test. The procedure is described in Table 4.A10 (4A) for both tools. In dual completions, only the activated-oxygen survey is available. Its relatively low resolution of 2 to 3 ft/min velocity may not satisfy some regulations. A lost tool must be recovered or cemented in place.
"Channel" check for annular seal	Radioactive-tracer (or activated-oxygen surveys) on injection	See Table 4.A10 (4A) for procedure. In dual completions, only the activated-oxygen survey is available. Tool must be configured for annular flow both above and below perforations.

TABLE 4.A15—6B: INJECTION PROFILE DETERMINATION (INJECTION WELL WITH TUBING ACROSS PERFORATIONS (DUAL COMPLETIONS, REGULATED INJECTION))

Problem	Recommended Logging Tools	Operational Tips and Expected Results
Determine injection profile	Three temperature surveys: one with well on injection and two, spaced approximately 8 hours apart, with well shut in	Flow in unproped fractures is common to all injection wells; consequently, temperature surveys are the best approach initially. The procedure for flow profiling from the injection trace is described in Table 4.A11 (4B), to which the reader should refer. In a dual completion, the procedure is unchanged from that described in Table 4.A11 (4B). For injection through tubing-string regulator valves or into wells with tailpipe extending into the perforations or open hole, a new feature is present.
	Radioactive-tracer surveys with well on injection at rates no larger than approximately 5,000 B/D	Exits from the tubing may move upward, downward or in both directions as the stream splits. Those exits giving rise to flow upwards to a receptor zone cause, on the injection trace, normal but muted exit signatures at both exit location and receptor location. The circulation gradient existing between the two locations, however, does not satisfy the profiling expression given in Table 4.A11 (4B). The injection trace gives only a qualitative idea of the rates based on the relative size of the exit signatures. Similar information is available from the two shut-in surveys.
		This approach is not applicable to dual completions because the flow is entirely external to the long tubing string. In the other completions, the tool is the next one most likely to detect flow in fractures. The logging procedure is described in Table 4.A11 (4B), to which the reader should refer before going on to the special features unique to these completions. The chased-slug procedure is the appropriate approach because of flow both inside and outside the tubing string. Slug areas must be used for profiling.
		If the completion is one with a long tailpipe, then the slug should be injected inside the tubing string so that it can be captured just below its exit from the end of tubing. Such a record reveals any split into upward and downward-moving components and provides the area representative of the full stream.
		If the completion is one of regulator valves in a plugged tubing string, then the first slug should be ejected above the top valve and then chased past all deeper valves so as to determine the relative exits from each valve. Additional slugs should then be ejected above each regulator valve so as to capture the slug as it first passes into the annulus and on its subsequent travel to receptor zones. This approach provides a slug area that is compensated both for dispersion in the annulus and for the minor amount of attenuation offered by the tubing wall. The dispersion can affect the area significantly because it changes the distribution of tracer around the detector.

TABLE 4.A15—6B: INJECTION PROFILE DETERMINATION [INJECTION WELL WITH TUBING ACROSS PERFORATIONS (DUAL COMPLETIONS, REGULATED INJECTION)] (Continued)

Problem	Recommended Logging Tools	Operational Tips and Expected Results
Determine injection profile	Activated-oxygen survey with well on injection	<p>This is the only tracer survey available for a dual completion. In this case, the tool need be configured only for flow downward. The best resolution is achieved from stationary measurements. This device creates its own tracer by the bombardment of water with pulsed neutrons. For one version of the tool, the passage of the slug past two detectors spaced 1 ft apart is timed directly. A second version of the tool determines velocity from the decay in count rate as measured simultaneously at two detectors spaced approximately the same distance apart. Either way, the tool functions as a velocity-shot device for annular flow behind the long string. Tool resolution is approximately 2 to 3 ft/min.</p>
		<p>In wells with extended tailpipe, the tool must be configured for flow both upward and downward. Area corrections must be made to the velocities of flow upward behind the tailpipe relative to velocities measured below the end of the pipe.</p>
	Continuous-spinner surveys with well on injection	<p>The device is not suitable for use in wells on injection through regulator valves. Any flow downward behind tubing is obscured by the large signal from flow inside the tubing.</p>
		<p>Continuous-spinner flowmeters can be used to determine rates inside the tubing string of a well on injection through regulator valves. Of course, no information is provided relative to flow behind the tubing string. The device is described in Table 4.A11 (4B) where its calibration is discussed. This aspect is not important for use in a small tubing string because the diversion around the element is insignificant. Furthermore, the distinction between spinner-derived fluid velocity and superficial velocity is moot. The tool should operate at a sensitivity equal to the theoretical value for the element's pitch.</p>

TABLE 4.A16—7A: TRACKING SINGLE-PHASE PRODUCTION (PRODUCTION WELL—VERTICAL, CASED, OR OPENHOLE WITHOUT SCREEN OR PERFORATED LINER)

Problem	Recommended Logging Tools	Operational Tips and Expected Results
Profile production	Continuous or fullbore spinner flowmeter survey both with well on production and shut in	<p>Either type of device is suitable for liquid production, but the fullbore type is preferable for gas production. The continuous types have either propeller or turbine (screw thread) elements having a diameter slightly less than the diameter of the tool barrel. The fullbore types have four longer vanes that are hinged so as to open only when the tool emerges from the production tubing. Both devices are run continuously to give a record of spinner turn rate in RPS as a function of depth. Common practice is to log both upward and downward at three different line speeds in each direction. Actually, the most reliable profile is usually obtained from the pass made against the flow (downward) at a line speed of approximately 30 ft/min. This pass is least biased by variations in fluid velocity and gives the best vertical resolution. Depending upon casing size, both types of spinners have rate resolutions in the range of 70 to 200 B/D for liquid or 100 to 500 Mcf/D for gas.</p> <p>The principal difference between the two types lies in the amount of fluid that diverts around the spinner element without turning it. This effect is incorporated into a threshold velocity V_{th} (i.e., a velocity required to turn the element with the tool stationary). In liquid, both fullbore and high-sensitivity continuous tools have a threshold velocity in the range of 5 to 8 ft/min. In gas, however, the fullbore type has a lower threshold (10 to 15 ft/min) than does the continuous type (25 to 50 ft/min). Once the elements are turning at rates in excess of approximately 0.5 RPS, both types produce signals that are related linearly to flow velocity relative to the tool. Thus, spinner turn rate, S RPS, is proportional to relative velocity, V_{rel}.</p> $S = a \cdot (V_{rel} - V_{th}) = a \cdot (V_{line} + V_{fluid} - V_{th})$ <p>A relative velocity directed up the tool barrel turns the spinner in a clockwise direction. The sign conventions in the expression assign a + sign to both spinner speed and threshold velocity when the spinner turns clockwise. Both are negative for counterclockwise spin. Line speed is positive for downward logging and negative for upward passes. Fluid velocity is then positive for flow upward and negative for flow downward. On passes upward with the flow, the spinner first turns counterclockwise until fluid velocity increases to within threshold value of line speed and the spinner stops turning. An additional increase in fluid velocity equal to twice the threshold value starts the spinner turning again, but in a clockwise direction. The constant a is a sensitivity value for the element expressed in units of RPS per ft/min relative velocity.</p>

TABLE 4.A16—7A: TRACKING SINGLE-PHASE PRODUCTION (PRODUCTION WELL—VERTICAL, CASED, OR OPENHOLE WITHOUT SCREEN OR PERFORATED LINER) (Continued)

Problem	Recommended Logging Tools	Operational Tips and Expected Results
Profile production	Continuous or fullbore spinner flowmeter survey both with well on production and shut in	<p>This value is related to the pitch of the element, P_{inches}, as $a = 12/(60P)$. A common pitch is 4 in., corresponding to a sensitivity of 0.05 RPS/(ft/min). The actual value is approximately 0.044.</p> <p>Values for sensitivity and threshold velocity are best determined from calibration pass in a shut-in well. The well is logged both upward and downward, each at three progressively doubled line speeds, starting with a speed sufficient to turn the spinner no slower than 1 RPS. For these passes, the relative velocity is the line speed, which is given a + sign for travel down and a - sign for travel up. The threshold velocity is similarly signed.</p> <p>The number produced for fluid velocity by a spinner tool in casing is larger than the superficial velocity needed for volumetric rate calculation. The value of the reduction factor depends on the element size relative to casing size. It is usually determined for a given pipe size from measurements in a flow loop.</p> <p>Owing to tool inertia, both devices lack the vertical resolution needed to locate precisely entries within perforated intervals. A very localized entry can be smeared out over 10-20 ft. Within such intervals, the spin rate can either increase or decrease in response to lateral velocities from perforations. Furthermore, high rates can carry for over 100 ft up the well any swirl components induced by entries.</p>
	Diverting-spinner surveys for rates below 2,000 B/D	<p>The devices make station measurements using an inflated packer or extended metal vanes to divert flow past a turbine element inside the tool barrel. Consequently, their rate resolution, 10 to 15 B/D, is much better than that of the continuous devices. Packers usually provide complete diversion, so that spin rate is linear in B/D rate. A single calibration coefficient is therefore sufficient. The metal vanes, used more commonly, leak so that diversion is not complete. Calibration curves for specific casing sizes are therefore needed. The vanes sometimes jam open, sticking the tool as it enters the end of tubing.</p>
	Density survey	<p>Oil rates in excess of 400 B/D and gas rates in excess of 200 Mcf/D are required to remove completion liquid from a vertical wellbore. Productive locations below the depth at which such velocities are attained are therefore submerged in completion liquid. Hydrocarbon percolates upward through this liquid at "slippage" velocities in the range of 25 ft/min for oil in water and 45 ft/min for gas in water. In the process, the continuous-liquid phase is churned up and down at equivalent lift velocities. Spinner speeds tend to reflect these higher velocities and are thus not comparable to speeds measured higher in the hole. Instead, rates are typically determined from percolation theory. For a casing capacity C bbl/ft, a slippage velocity V_s ft/min and an hydrocarbon holdup y_{hc}, the B/D rate is</p> $q_{bc} = 1440 y_{hc} V_s C$

TABLE 4.A16—7A: TRACKING SINGLE-PHASE PRODUCTION (PRODUCTION WELL—VERTICAL, CASED, OR OPENHOLE WITHOUT SCREEN OR PERFORATED LINER) (Continued)

Problem	Recommended Logging Tools	Operational Tips and Expected Results
Profile production	Density survey	<p>The density survey not only identifies the depth below which percolation occurs, but also provides a value for hydrocarbon holdup from the density of the mixture as</p>
		$Y_m = \frac{\rho_{\text{liquid}} - \rho_{\text{mixture}}}{\rho_{\text{liquid}} - \rho_{H_2O}}$
	<p>Temperature surveys with the well on production and at least one with the well shut in for 1 to 6 hours</p>	<p>Two types of density tools are available. One is a differential pressure device that measures pressure gradient over a distance of approximately 2 ft. These devices are linear and need only two calibration points, air and water. The second type is a gamma-ray transmission device that uses a tightly focused chemical gamma source at the bottom of a cage approximately 6 in. in length, having detectors placed at its top. Owing to gamma scatter out of the cage, these devices are usually nonlinear, requiring three calibration points. Either type is suitable for this problem. However, if the gamma device is lost in the hole, then it must be fished out or cemented in place.</p>
		<p>The flowing and shut-in traces should be merged on a display of 1°F per in. of chart. Another display should be made at a reduced scale that eliminates "wraps." Even for single-phase production, temperature surveys are still valuable. In the first place, hydrocarbon can travel to perforations from locations behind casing. The base of production is at the location where the merged surveys begin to separate. For oil, the flowing trace "stands up" to the warm side of the shut-in trace(s). A gas source typically moves the flowing trace to the cool side of the shut-in owing to expansion cooling. If either oil or gas moves downward behind casing to perforations, then the flowing trace will show a "mixing" signature at the source in the form of a shift or a bend toward shut-in temperature. At the perforations, the temperature will warm upon shut in. Two shut-in traces best illustrate this direction.</p>
		<p>Second, the vertical resolution on a flowing temperature trace within a perforated interval is much superior to that of a trace from a spinner flowmeter. Over a productive interval, temperature traces invariably show a sequence of essentially "point" entries rather than the drawn-out change in spin rate typically exhibited on a spinner trace.</p>

TABLE 4.A16—7A: TRACKING SINGLE-PHASE PRODUCTION (PRODUCTION WELL—VERTICAL, CASED, OR OPENHOLE WITHOUT SCREEN OR PERFORATED LINER) (Continued)

Problem	Recommended Logging Tools	Operational Tips and Expected Results
Profile production	Temperature surveys with the well on production and at least one with the well shut in for 1 to 6 hours	<p>Finally, production can also be profiled from the temperature traces. Each entry above the bottom one normally produces, on the flowing trace, a mixing signature in the form of a step shift at the entry toward the shut-in traces. This signature is the result of the mixing of an entering stream at a temperature less than that of the stream arriving from below. This mixing is so rapid that it is essentially achieved under adiabatic conditions. The temperature of the mixture T_{mix} must conserve energy. If a stream enters at a volumetric rate q_{in} and temperature T_{in} and mixes with a stream from below at a rate q_b and temperature T_b, then energy conservation requires that</p> $(\rho C_p)_{in} q_{in} (T_{mix} - T_{in}) = (\rho C_p)_b q_b (T_b - T_{mix}),$ <p>where ρC_p is the product of density and specific heat capacity. Because this product is the same for both streams, the ratio of volumetric rates is given by</p> $\frac{q_{in}}{q_b} = \frac{T_b - T_{mix}}{T_{mix} - T_{in}} = \frac{\Delta T_b}{\Delta T_{in}}$ <p>This expression is applied to the second entry off bottom assuming a unit rate for bottom entry q_1, to establish a relative value for q_2. The process is continued for all higher entries. Oil-entry temperature for each stream can be taken as static temperature.</p> <p>A value for entry temperature at each depth can be found from the 6-hour shut-in trace. For gas, the entry temperature can be taken as the coolest temperature on either a 1-hour shut-in trace or on a 6-hour trace. Uncertainty in entry temperatures is greatly attenuated in the percentages for the production profile. As a result, a profile determined in this fashion is often more accurate within a perforated interval than is one derived from spinner deflections.</p> <p>If the completion is new, then there is a cooled zone around the wellbore at temperature T_{cool}. The presence of this zone is evidenced by the temperature in the sump. Liquid entries therefore show as warm signatures on the temperature traces. On the flowing trace, one may see from the bottom upward several steps to warmer temperature indicative of entries of liquid at progressively increasing rates. Liquid arrives at the outer edge of the cool zone at normal geothermal temperature T_{geo} but in moving through the zone cools to arrive at the wellbore at a temperature T_{in} that is warmer than the cool temperature T_{cool} but is cooler than geothermal. The flowing temperature trace provides an entry temperature only for the bottom entry. For all higher entries T_{in} is unknown.</p>

TABLE 4.A16—7A: TRACKING SINGLE-PHASE PRODUCTION (PRODUCTION WELL—VERTICAL, CASED, OR OPENHOLE WITHOUT SCREEN OR PERFORATED LINER) (Continued)

Problem	Recommended Logging Tools	Operational Tips and Expected Results
Profile production	Temperature surveys with the well on production and at least one with the well shut in for 1 to 6 hours	<p>The mixing equation thus contains another unknown besides q_{in}, meaning that another equation is needed to profile. If one supposes that the entry is a "point" entry and that the formation in the cool zone changes temperature slowly with time, then one can arrive at a second expression for the ratio of any higher rate to the bottom rate q_1:</p> $\frac{q_i}{q_1} = \frac{(\rho C_p)_i \ln(R_i)}{(\rho C_p)_1 \ln(R_1)},$ <p>where</p> $R_i = \frac{T_{cool+i} - T_{cool-i}}{T_{in+i} - T_{cool-i}}$ <p>for $i = 1, 2$, etc. The ratio of density-specific heat products is set equal to 1 to provide the second equation. Extrapolation of sump temperature gives values for T_{cool}.</p>
	Radioactive tracer surveys with well on production	<p>This is an approach that should be used only as a last resort because of the production of radioactive fluid at the surface. Dilution in the surface facilities must be sufficient to meet exposure regulations. Tracer surveying is discussed in detail in Table 4.A11 (4B), to which the user should refer. A stationary, velocity-shot approach is used with a progression from the top of production down. The flowing temperature trace is used to select locations for shots.</p> <p>On the other hand, the chased-slug procedure offers two advantages unique to the tracer tool. The first relates to a slug ejected in the full stream and tracked upward. With the tracer well mixed over the casing cross section, the centroid of the slug moves at a velocity equal to the superficial velocity required for calculation of volumetric rate. The tool is thus the only absolute flowmeter available. The second feature is the ability of the tool to measure very small rates of zonal crossflow in a shut-in well.</p>
Location of source of hydrocarbon behind casing	Temperature surveys both with well on production and shut in	<p>The merged surveys should be displayed on one scale at 1°F per in. of chart and another scaled to prevent wraps. The features to expect for flow behind casing from either above or below the perforations are described here under Profiling Production.</p>
	Noise-logging survey with well on production	<p>Single-phase flow inside casing produces such a low level of noise that the well can be logged while on production. The tool is described in detail in Table 4.A5 (1C) under Detection of Flow Underground, to which the user should refer. The expression given in this table for estimation of single-phase rate q_{in} B/D past a constriction with pressure drop Δp psi from the 1,000-Hz noise level N_{1000} is modified to include the number of pipe strings between flow and tool N_p to give</p> $\Delta p \times q = 700 \times N_p \times N_{1000}$ <p>The flow can be either gas or liquid as long as the gas is not mixed with liquid.</p>

TABLE 4.A17—7B: TRACKING TWO-PHASE PRODUCTION (PRODUCTION WELL—VERTICAL, CASED, OR OPENHOLE WITHOUT SCREEN OR PERFORATED LINER)

Problem	Recommended Logging Tools	Operational Tips and Expected Results
Profiling commingled oil/water production	Temperature survey with well on production followed by two shut-in surveys spaced 3 hours apart	<p>The traces should be merged on one display at 1°F per in. of chart. Another display should be at a scale that prevents wraps. Trace behavior is the same as described in Table 4.A16 (7A) under Profile Production. The user should refer to this table. The distinction for the oil/water case relates to the effect of the individual phases on the temperature traces. A unit volume of water affects the temperature trace more than does a unit volume of oil owing to its higher value for the product of density and specific heat. This product is approximately 2.5 times larger for water than for oil. If a stream has a volumetric composition that is 50% oil and 50% water, then the "thermal" barrels in 100 bbl of mixture is 50 bbl of water and $50/2.5 = 20$ bbl of oil as far as the temperature traces are concerned. The "thermal" composition is therefore approximately 29% oil and 71% water.</p>
	Fluid-capacitance surveys both with well on production and shut in	<p>Mixing signatures are used to profile by the method described in Table 4.A16 (7A) in detail for streams with equal values for the product of density and specific heat. This equality is retained here so that the relative rates so obtained are "thermal" rates rather than volumetric rates. The conversion to volumetric rates is obtained once the volumetric composition of the wellbore streams is determined from the fluid-identification traces described here. For a given stream, the volumetric composition is converted to a "thermal" composition as illustrated here. Each thermal rate is then decomposed into its oil and water thermal rates. These rates are then referenced to their corresponding thermal component in the full stream for volumetric percentages.</p> <p>This device is the best available for the detection of small oil entries into water or vice versa. The tool's electrode is exposed to wellbore fluid and acts as a capacitor that regulates the frequency output of an oscillatory circuit. In water, a polar compound, the effective capacitance is high and the output frequency is low. In oil, the capacitance is small and the output frequency is high. Likewise, the output frequency in gas is high at a value only slightly larger than that for oil. The device therefore basically distinguishes water from hydrocarbon. The spread in frequency between oil and water depends upon the tool's manufacturer, ranging from a low of 1,000 Hz to a high of 4,000 Hz. The spread measured at the surface between fresh water and any oil will be close to the downhole value. The effect of salinity is small, as the water readings downhole will show.</p>

TABLE 4.A17—7B: TRACKING TWO-PHASE PRODUCTION (PRODUCTION WELL—VERTICAL, CASED, OR OPENHOLE WITHOUT SCREEN OR PERFORATED LINER) (Continued)

Problem	Recommended Logging Tools	Operational Tips and Expected Results
Profiling commingled oil/water production	Fluid-capacitance surveys both with well on production and shut in	<p>The tool produces such a "clean" signal that, whatever the spread, the display sensitivity can be increased to the point that one chart division represents only 0.25% of the spread. This is the reason for the tool's ability to detect very small entries of oil into water.</p>
		<p>In theory, the output frequency should be inversely proportional to water holdup y_w in the wellbore. In fact, the relationship is quite nonlinear and is just as well represented as a function of frequency rather than its reciprocal. Flow-loop calibrations are needed to define the relationship for a particular tool. Furthermore, the electrode is subject to filming with oil in an oil/water environment and with water in a gas/water environment. One therefore needs calibrations both for light oil and for heavy oil. For oil viscosity greater than a few cp at downhole temperature, the first contact with oil films the electrode so severely that additional oil entries are hidden.</p>
		<p>On either end of the water holdup range, the tool is relatively linear. For $y_w < 0.30$, the water holdup can be represented as a linear function of frequency f as</p>
		$y_w = A \left(\frac{f_{oil} - f_{mix}}{f_{oil} - f_{water}} \right)$
		<p>The coefficient A typically lies in the range of 0.5 to 1.0. At the other end, for $y_w > 0.70$, the relationship is</p>
		$y_w = 1 - B \times \left(1 - \frac{f_{oil} - f_{mix}}{f_{oil} - f_{water}} \right)$
		<p>with B typically in the range of 1 to 3. If the full stream has water holdup in this range, then the tool response to this stream can be used as a calibration point to determine the value for the appropriate constant.</p>
	Fluid density surveys both with well on production and shut in	<p>Density tools are available in two versions as described in Table 4.A16 (7A) under Profile Production, to which the user should refer. The differential-pressure (gradient) types have a resolution of 0.01 g/cm³, whereas the gamma-transmission types are limited by gamma statistics to a resolution of 0.025 g/cm³ or less. Some companies "manufacture" their density traces from a pressure trace. This approach relies on two measurements taken at different times rather than simultaneously, making the result highly sensitive to tool flexure and to rate variations. The resolution for such traces is therefore much poorer than the previous values.</p>
		<p>Unlike the capacitance probe, a fluid density device produces a value that is linear in wellbore holdup. If a mixture density is measured at a value ρ_{mix}, then the oil holdup in the well is given by</p>
		$y_o = \frac{\rho_{water} - \rho_{mix}}{\rho_{water} - \rho_{oil}}$

TABLE 4.A17—7B: TRACKING TWO-PHASE PRODUCTION (PRODUCTION WELL—VERTICAL, CASED, OR OPENHOLE WITHOUT SCREEN OR PERFORATED LINER) (Continued)

Problem	Recommended Logging Tools	Operational Tips and Expected Results
Profiling commingled oil/water production	Fluid density surveys both with well on production and shut in	<p>The density for the pure phases can be determined usually from the shut-in survey. For a density difference between oil and water of 0.20 g/cm³, the resolutions given here amount to oil holdups of 5% for the differential-pressure (gradient) tools and 12.5% for the gamma-transmission devices. For heavy oil with a density of 0.9 g/cm³, the resolution for even for the gradient tools drops to an oil holdup of 10%.</p> <p>Oil holdup values are needed to determine the oil "cut" (volumetric percentage) of the stream in the wellbore at a given depth. The so-called slippage velocity V_s is defined such that the oil cut C_o is given by an expression also involving the average or superficial velocity V_{ave}.</p> $C_o = y_o \cdot \left[1 - (1 - y_o) \cdot \frac{P_o}{V_{ave}} \right]$ <p>This value is the number referred to under temperature surveys as being needed in order to convert thermal rates into volumetric rates. The expression, however, contains two unknowns, the slippage velocity and the average flow velocity. Numerous correlations exist to refine the approximate value of 25 ft/min mentioned in Table 4.A16 (7A) according to the type of flow regime and density difference. An initial estimate for average velocity can be made from spinner data if available. Otherwise, a value consistent with thermal rate is assumed. In either case, an iterative calculation must be made until the assumed average rate agrees with the value calculated from the thermal profile.</p>
	Diverting-spinner survey with production no greater than 2,000 B/D	<p>This device is described in Table 4.A16 (7A) under Profile Production, to which the user should refer. The tool has two distinct advantages for this problem. With the flow sped up, the oil and water phases tend to move together without slippage between the two. The tool can therefore be calibrated for two-phase flow in terms of total rate as a function of spinner speed with the light-phase cut (oil cut) as the parameter on a family of curves. Unfortunately, few service companies have such calibration data. The increased speed also means the oil holdup in the tool barrel is very nearly equal to the flowing cut. Most such devices are therefore also equipped with a fluid-capacitance probe in the barrel.</p>
	Continuous or fullbore-spinner surveys with the well on production and shut in	<p>These two types of spinner flowmeters are described in Table 4.A16 (7A) under Profile Production, to which the user should refer. Both devices are poorly suited to the quantification of multiphase flow of any type. The deflections tend to reflect the entries of the lightest phase, oil in this case, rather than average flow velocity. In fact, the traces can be used to obtain an approximate-percentage production profile for the light phase.</p>

TABLE 4.A17—7B: TRACKING TWO-PHASE PRODUCTION (PRODUCTION WELL—VERTICAL, CASED, OR OPENHOLE WITHOUT SCREEN OR PERFORATED LINER) (Continued)

Problem	Recommended Logging Tools	Operational Tips and Expected Results
Profiling commingled gas and water production (or gas and oil)	Temperature surveys both with well on production and after shut-in periods of 1 and ~4 hours	<p>The traces should be merged on one display scaled at 1°F per in. of chart and one scaled so as to avoid wraps. Gas wellbores are generally cooler than geothermal throughout. Consequently, water production warms the wellbore at the source. This makes the surveys particularly sensitive to low rates of water production. If warm signatures are not evident on the flowing trace, then the water enters commingled with a major part of the gas production and is hidden by expansion cooling. Even then, warm signatures are usually evident on the shut-in traces.</p>
		<p>Profiling is done from mixing signatures as described in Table 4.A16 (7A) under Profile Production, to which the user should refer. The distinction here is the effect that the individual phases have on the temperature traces. A unit volume of water has much more effect than does a unit volume of gas because the product of density and specific heat for water is much higher than that for gas. Typically, at least 10 volumes of gas are required to have the same effect as one volume of water, although the exact equivalency depends upon bottomhole temperature and pressure. The conversion of the thermal rates to volumetric rates for each phase is done as described above for oil/water.</p>
	Density surveys both with the well on production and shut in	<p>These surveys are identical to those of oil-water production described earlier. Gas holdup corresponding to a mixture density ρ_{mix} is given by</p>
		$y_g = \frac{\rho_{water} - \rho_{mix}}{\rho_{mix} - \rho_g}$
		<p>A typical value for density difference between water and gas is 0.80 g/cm³. For gradient-type density tools, a resolution of 0.01 g/cm³ corresponds to a gas holdup of 1.2%, whereas a resolution of 0.025 g/cm³ for gamma-transmission tools corresponds to a gas holdup of 3.1%. Both types of tools are therefore sensitive to small gas entries.</p>
		<p>The same comments apply to gas cut (volumetric percentage in stream) as made above for oil/water flow. The gas cut C_g is related to holdup, gas slippage velocity V_{sg} and average fluid velocity V_{ave} by the expression</p>
		$C_g = y_g \cdot \left[1 + (1 - y_g) \cdot \frac{V_{sg}}{V_{ave}} \right]$
		<p>The typical value of 45 ft/min for slippage velocity can be refined by reference to correlations. As explained above for oil/water production, the gas cut is used to decompose thermal rates into gas and water volumetric rates.</p>

TABLE 4.A17—7B: TRACKING TWO-PHASE PRODUCTION (PRODUCTION WELL—VERTICAL, CASED, OR OPENHOLE WITHOUT SCREEN OR PERFORATED LINER) (Continued)

Problem	Recommended Logging Tools	Operational Tips and Expected Results
Profiling commingled gas and water production (or gas and oil)	Back-scatter gamma-ray density surveys with well on production and shut in	<p>These devices are referred to as gas holdup meters because of their ability to distinguish gas from liquid. They are relatively insensitive to the density of the surrounding liquid. Like the gravel-pack device, they contain an unfocused, chemical source of gamma rays. The detector, however, is shielded from direct transmission of gamma rays to the point that it responds primarily to rays back-scattered from the material around the tool. The back-scatter from gas is insignificant relative to that from liquid. Normally the logarithm of the tool's count rate should be inversely proportional to the gas holdup around the tool, at least in the absence of layered flow. Some limited calibration data suggest the gas holdup may be more linearly related to count rate directly as in layered flow [Table 4.A23 (9B)]. At this point, gas holdup y_g is taken as a linear function of the logarithm of count rate C.</p> $y_g = 1 - \frac{\ln(C_{mix}) - \ln(C_{gas})}{\ln(C_{liquid}) - \ln(C_{gas})}$ <p>Calibration in the shut-in well is necessary because the pure-phase counts depend upon casing size. The devices retain their vitality in mixtures of water and completion fluid.</p>
	Diverting-spinner flowmeter survey	<p>Same comments as above for oil/water production. The distinction here is that gas leakage through the metal-vane type diverters is worse for gas/water production. Furthermore, calibration curves for this case are practically nonexistent.</p>
	Continuous or fullbore flowmeter surveys both flowing and shut in	<p>Same comments as above for oil/water production. Owing to the increased chaos in the wellbore, spinner speeds are even less related to average flow velocity than was the case for oil/water production. In fact, it is common to see the spinner turn backward above the deepest gas entry in response to circulation in the continuous water phase. This artifact is more pronounced for fullbore tools with their larger spinners. Generally, however, the spinner deflections indicate gas entries and can be used to profile relative gas rates approximately.</p> <p>Gas jetting from perforations into water tends to produce a relatively stable foam whenever a trace of condensate is present to act as a surfactant. The spinner sensitivity coefficient to foam flow is so small that the element can nearly cease to spin.</p>
	Noise-logging survey with well on production	<p>This tool is described in detail in Table 4.A5 (1C) under Detection of Underground Flow. The user should refer to this material.</p>

TABLE 4.A17—7B: TRACKING TWO-PHASE PRODUCTION (PRODUCTION WELL—VERTICAL, CASED, OR OPENHOLE WITHOUT SCREEN OR PERFORATED LINER) (Continued)

Problem	Recommended Logging Tools	Operational Tips and Expected Results
Profiling commingled gas and water production (or gas and oil)	Noise-logging survey with well on production	<p>The advantage of the device lies in its ability to detect very small gas entries into liquid, an ability that extends to the entry of occasional individual bubbles. For gas entry into a wellbore, the gas rate q_g in ft³/d at downhole conditions can be estimated for rates less than 200 ft³/d from the noise level in standard millivolts in the 200- to 600-Hz band from the expression</p> $q_g = 0.07 \times (N_{200} - N_{600}).$ <p>This device will also detect the creation of foam in the wellbore. Foam is an insulator to sound; consequently, the noise levels above a gas entry that foams are much less than the levels immediately below the entry.</p>
Location of water source behind casing	Temperature surveys: one with well on production and two, spaced approximately 4 hours apart, with well shut in	<p>The traces should be merged on one display scaled at 1°F per in. of chart. Another display should be scaled so as to avoid wraps. Temperature logging is recommended for this problem because the well must be flowed for the logging. This causes problems for other sensors of flow behind casing. Most oil wells produce a small amount of gas that, although insignificant volumetrically, creates a noisy environment for the noise logger. The production of multiple phases sets up a circulation pattern in the water phase that extends for great distances below the perforations. This circulation is detected by the oxygen-activation tools as water flow upward.</p> <p>A water source moving behind casing from below is detected as a base of production located below the deepest perforations. This base is the depth at which the flowing trace first "stands up" to separate to the warm side of the shut-in traces. The flowing trace will also show a normal mixing signature (a shift towards the shut-in traces) at the deepest entry from the perforated zone. At the base of perforations, temperature will decrease on the shut-in surveys. The two traces better illustrate this direction of change. A water source located above the top perforations will cause a normal mixing signature on the flowing trace at the source location and at the top of perforations, where the temperature will increase upon shut-in.</p> <p>Temperature surveys have the advantage that water, with its relatively large value for the product of density and specific, has a larger influence than does either oil or gas. Approximately 2.5 bbl of oil are required to give the same effect as 1 bbl of water. The disparity is even greater for gas. At least 10 bbl of gas are required to equal 1 bbl of water.</p>
	Flowing fluid-capacitance survey for oil detection and flowing density survey for gas	<p>These devices are described individually above. It is just as necessary to identify the source of hydrocarbon as it is to find the source of water. A workover that eliminates both water and hydrocarbon is certainly not desired.</p> <p>If the water is from a source external to the perforated zone, then it is highly unlikely that it will enter the wellbore commingled with hydrocarbon. The fluid-identifier traces are needed to establish qualitatively a separation between water and hydrocarbon sources.</p>

TABLE 4.A18—7C: TRACKING THREE-PHASE PRODUCTION (PRODUCTION WELL—VERTICAL, CASED, OR OPENHOLE WITHOUT SCREEN OR PERFORATED LINER)

Problem	Recommended Logging Tools	Operational Tips and Expected Results
Profile commingled gas, oil, and water production	Temperature surveys: one with well on production and two, spaced approximately 4 hours apart, with well shut in	<p>The traces should be merged with one display scaled at 1°F per in. of chart and another scaled so as to avoid wraps. Thermal profiling is done from mixing signatures as described in Table 4.A16 (7A) under Profile Production. The user should read this material. The distinction here is that water, with its relatively large product of density and specific heat, has the larger influence on the temperature traces. Approximately 2.5 bbl of oil are needed to equal the affect of 1 bbl of water. The equivalent for gas is at least 10 bbl.</p> <p>The thermal profile, assuming equal density-specific heat product for all phases, can be done quite accurately. To find individual phase rates, volumetric composition of the stream at various locations in the wellbore must be converted to "thermal" composition. For example, if a stream has a 50% water cut, a 25% oil cut, and a 25% gas cut, then 100 bbl of the mixture contains 50 "thermal" bbl of water, $25/2.5 = 10$ thermal bbl of oil, and $25/10 = 2.5$ "thermal" bbl of gas. The thermal composition is then 80% water, 16% oil, and 4% gas. The uncertainty is introduced in the determination of stream composition from the fluid-identifier traces. The determination of holdup values in the wellbore for a three-phase mixture is inaccurate. The conversion of these values to their corresponding stream compositions (cuts) introduces more error. Consequently, the resulting profiles tend to be only semiquantitative at best.</p>
	Fluid-capacitance surveys with well flowing and shut in	<p>These devices distinguish water from hydrocarbon. They are described in Table 4.A17 (7B) under Profiling. The user should refer to this material. The endpoint calibration expressions in this table are approximately valid for the determination of the water holdup in the liquid phase (i.e., in the mixture of oil and water). If this value is denoted by y_{wc}, then the water holdup in the wellbore is</p> $y_w = y_{wc} \cdot (1 - y_g)$ <p>where y_g is the gas holdup in the wellbore. The oil fraction $y_{oc} = 1 - y_{wc}$ is adjusted in the same manner to arrive at oil holdup in the wellbore. The chaos created in the wellbore by the flow of gas keeps the liquid phase mixed to the point that oil slippage relative to water is insignificant. The water and oil cuts (compositions) are the same as the holdup fractions in the wellbore.</p>
	Back-scatter gamma-ray density surveys with well both flowing and shut in	<p>This device is described in Table 4.A17 (7B) under Profiling. The user should read this material. It is the ideal tool for the determination of gas holdup y_g in the wellbore because of its insensitivity to the density of the surrounding liquid. Its output is typically scaled linearly in counts/seconds. For this application, the user should request that the output be calibrated in terms of gas holdup. Otherwise, a calibration equation is given in Table 4.A17 (7B).</p>

TABLE 4.A18—7C: TRACKING THREE-PHASE PRODUCTION (PRODUCTION WELL—VERTICAL, CASED, OR OPENHOLE WITHOUT SCREEN OR PERFORATED LINER) (Continued)

Problem	Recommended Logging Tools	Operational Tips and Expected Results
<p>Profile commingled gas, oil, and water production</p>	<p>Fluid density survey with well both flowing and shut in</p>	<p>These tools are described in Table 4.A17 (7B). Either type, differential-pressure or gamma-transmission, is suitable to this application. With a water holdup having been estimated from a fluid-capacitance survey, the measured value for mixture density can be converted to a value for gas holdup by the expression</p>
		$y_g = \frac{y_w \rho_w + (1 - y_w) \rho_o - \rho_{mix}}{\rho_o - \rho_g}$
		<p>where the subscripts <i>o</i>, <i>g</i>, and <i>w</i> refer to oil, gas, and water, respectively. Density for oil and water are determined from the shut-in traces, but gas density is usually estimated. Owing to uncertainty in the value for water holdup, this value may not agree with that obtained from the back-scatter density survey. Adjustments should be made to <i>y_w</i> to bring the two values into agreement. If the fluid-capacitance trace is not recorded, then the previous expression can be used to determine water holdup in the wellbore from the back-scatter gas holdup value</p>
		$y_w = \frac{\rho_{mix} - \rho_g y_g - (1 - y_g) \rho_w}{\rho_w - \rho_o}$
		<p>Hence, the water cut <i>C_w</i> in the well-mixed liquid phase as <i>C_w</i> = <i>y_w</i> / (1 - <i>y_g</i>). The corresponding oil cut is <i>C_o</i> = 1 - <i>C_w</i>.</p>
		<p>The chaos created by the gas flow keeps the oil and water sufficiently mixed that slippage between the two is minor. Only the gas phase need be corrected to obtain flowing gas cut <i>C_g</i> from the equation</p>
		$C_g = y_g \cdot \left[1 + (1 - y_g) \frac{V_g}{V_{sg}} \right]$
		<p>where the slippage velocity <i>V_g</i> ≅ 45 ft/min is the value appropriate to the rise of gas through water. An estimate of the average or superficial velocity is selected consistent with the thermal rate as an initial estimate, and then iterated upon until value calculated from the volumetric rate equals the assumed value.</p>
		<p>The three cut values are converted into "thermal" cuts as explained above under Temperature. The thermal phase components are then determined from the total thermal rate at depth. Each of these values is ratioed to the "thermal" cut in the full stream as a volumetric percentage of each phase (and, hence, a volumetric rate).</p>
	<p>Diverting-spinner flowmeter surveys with the well flowing at less than 2,000 B/D</p>	<p>As described in Table 4.A17 (7B), these devices are ideal for multiphase flow because they can be calibrated in terms of B/D vs. spinner speed to give a family of curves with gas cut as the parameter. Unfortunately, such calibration data are lacking, so the principal advantage offered by the device lies in the values for total rate and superficial velocity.</p>
	<p>Continuous or fullbore spinner surveys with well both on production and shut in</p>	<p>As discussed in Table 4.A17 (7B), the principal contribution from these devices is an approximate profile for the light phase—gas, in this case. The entry of this phase produces the major deflections on the trace.</p>
<p>Location of water water behind casing</p>		<p>This is the same problem covered at the end of Table 4.A17 (7B), to which the user is referred.</p>

**TABLE 4.A19—8A: TRACKING SINGLE-PHASE PRODUCTION
(PRODUCTION WELL—VERTICAL WITH SCREEN, PERFORATED LINER, OR DUAL COMPLETION)**

<u>Problem</u>	<u>Recommended Logging Tools</u>	<u>Operational Tips and Expected Results</u>
Profiling production	Temperature surveys with the well on production and at least one after 1 to 6 hours shut in	This is exactly the same problem described in Table 4.A16 (7A). The presence of flow both inside and outside the screen/liner has an effect on temperature traces. The flow profiling from mixing signature proceeds in the manner described in the table.
	Density surveys flowing and shut in (not for dual completions)	The principal distinction here is that the spinner surveys that occupied a top position in Table 4.A16 (7A) are relegated to secondary status for this completion, being superseded by temperature surveys.
	Gravel-pack (unfocused gamma transmission) survey in dual completion with well shut in	As explained in Table 4.A16 (7A), this survey is run to determine the depth below which hydrocarbon-productive zones are submerged in residual completion fluid. Although this condition has no effect on the profiling procedure from temperature surveys, it does influence the output of the flowmeters as well as the activated-oxygen tracer tool.
	Continuous spinner surveys with the well on production (not for dual completions)	This tool has a chemical source of gamma rays positioned approximately 17 to 23 in. below a detector. The gamma-ray transmission is influenced by the density of the material within approximately a 6-in. radius about the tool. The count rate is attenuated exponentially by the density. A high count rate indicates a low density and vice versa. This tool can easily locate the interface between hydrocarbon and workover fluid behind the long string in a dual completion.
	Activated-oxygen survey with well on production	These devices are described in Table 4.A11 (4B), to which the user may refer. Their contribution here is qualitative owing to the fact that fluid may enter at locations other than where it enters the screen/liner, and that fluid velocity will vary with conditions behind screen/liner.
Source of hydrocarbon behind casing	Same as listed in Table 4.A16 (7A)	This is the only tracer survey possible for a dual completion. This tool is described in Table 4.A13 (5B) under Injection Profiling, to which the user should refer. The tool is configured for flow upward. The apparent velocity is affected by swirl patterns in the annulus.

TABLE 4.A20—8B: TRACKING TWO-PHASE PRODUCTION (PRODUCTION WELL—VERTICAL WITH SCREEN, PERFORATED LINER, OR DUAL COMPLETION)

Problem	Recommended Logging Tools	Operational Tips and Expected Results
Profiling commingled production of oil and water	Temperature surveys with well on production followed by surveys after 3 and 6 hours shut in	<p>The profiling procedure is described in Table 4.A17 (7B), to which the reader should refer. As explained in that table, one must convert the "thermal" production profile, which is usually accurate, into a volumetric profile for each phase. This is done from phase "cuts" (compositions) as determined by fluid-identifier tools. These cuts are a source of error.</p>
	Gravel-pack (unfocused gamma transmission) surveys both flowing and shut in	<p>This device is described under Profiling in Table 4.A19 (8A). The distinction introduced for this problem is that any fluid identifier must give a cross-sectional average so as to sample fluid both inside and outside the liner/screen or in the annulus behind the long string in a dual completion. Furthermore, one should be able to estimate holdup values from the tool signal.</p>
		<p>In vertical wellbores, this tool's output, C counts/sec, is related exponentially to density (i.e., to holdup). Thus, water holdup y_w is approximated by the expression</p>
		$y_w = 1 - \frac{\ln\left(\frac{C_{\text{mix}}}{C_{\text{water}}}\right)}{\ln\left(\frac{C_{\text{oil}}}{C_{\text{water}}}\right)}$
		<p>The counts for the pure phases are taken from the shut-in survey.</p>
	Pulsed-neutron surveys both with well on production and shut in	<p>These surveys include the neutron lifetime log and the carbon/oxygen log. The lifetime survey provides an estimate for the capture cross section or Sigma value for the borehole fluids. In theory, this value is a holdup-weighted average of the Sigma values for the two phases. Water holdup in terms of Sigma for a mixture Σ_{mix} is therefore</p>
		$y_w = \frac{\Sigma_{\text{mix}} - \Sigma_{\text{oil}}}{\Sigma_{\text{water}} - \Sigma_{\text{oil}}}$
		<p>Values for pure-phase Sigma come from the shut-in surveys. The estimate for water holdup is less accurate than that from a gravel-pack survey owing to the higher noise level in the raw signal and to inaccuracy in processing the signal.</p>
		<p>A carbon/oxygen log is a spectral survey of induced gamma radiation. Energy levels are processed to give a volumetric ratio of carbon-to-oxygen in the material around the tool. This ratio is converted to a ratio of oil-to-water holdup, the sum of which is 1.0. The holdup estimates are even less accurate than are the ones from the lifetime log. The survey is therefore of qualitative value (comparison of flowing to shut-in traces).</p>
	Fluid-capacitance surveys both flowing and shut in (not for dual completions)	<p>This device is described under profiling in Table 4.A17 (7B). For this problem, its ability to detect very small oil entries is exploited in a qualitative manner. In a vertical wellbore, the light phase (oil) tends to move inside the screen/liner.</p>

TABLE 4.A20—8B: TRACKING TWO-PHASE PRODUCTION (PRODUCTION WELL—VERTICAL WITH SCREEN, PERFORATED LINER, OR DUAL COMPLETION) (Continued)

Problem	Recommended Logging Tools	Operational Tips and Expected Results
Profiling commingled production of oil and water	Continuous spinner surveys with well on production (not for dual completions)	These tools are described in Table 4.A11 (4B) under profiling. Their value to this problem is purely qualitative. The chaos caused by an oil entry into water manifests itself inside the screen/liner. The survey therefore serves to identify locations where oil enters.
Profiling commingled gas and water (or gas and oil)	Temperature surveys with well on production followed by surveys after 1 and 6 hours shut in	The traces are used exactly as described under gas/water profiling in Table 4.A11 (4B). The thermal profile from mixing signatures is more accurate than are the stream compositions determined from the fluid-identifier surveys and used to convert to a volumetric profile.
	Gravel-pack (unfocused gamma-transmission) density survey both flowing and shut in	This device is described in Table 4.A19 (8A). In a gas/water (oil) environment, the water (oil) holdup is a nonlinear function of logarithm of the count rate C . The calibration equation is of the form $y_w = a R_{mix} + (1 - a)(R_{mix})^2,$ where $a \geq 0.45$ and $R_{mix} = \frac{\ln(C_{gas}) - \ln(C_{mix})}{\ln(C_{gas}) - \ln(C_{water})}$
	Back-scatter gamma-ray survey with well on production and shut in	This is the "reflection" counterpart to a gravel-pack survey and is referred to as a gas-holdup survey. The tool is described in Table 4.A17 (7B) under Profiling Gas/Water. It functions in the same capacity as described in this table. However, the sensitivity to gas holdup outside the screen/liner or behind the long string of a dual completion is reduced by the presence of the intervening metal. Its advantage over the gravel-pack tool is that it may be more readily available and may be run in combination with other tools.
	Gradient density surveys flowing and shut in (not for dual wells)	The service company is unlikely to have a calibration for this environment.
	Gradient density surveys flowing and shut in (not for dual wells)	This tool is described under Profiling in Table 4.A16 (7A). Its value here is primarily as a qualitative trace that should corroborate the features evident on the gravel-pack log.
	Pulsed-neutron surveys both flowing and shut in	See previous discussion for oil/water profiling.

TABLE 4.A20—8B: TRACKING TWO-PHASE PRODUCTION (PRODUCTION WELL—VERTICAL WITH SCREEN, PERFORATED LINER, OR DUAL COMPLETION) (Continued)

Problem	Recommended Logging Tools	Operational Tips and Expected Results
Profiling commingled gas and water (or gas and oil)	Noise-logging survey with the well flowing	<p>This device is described in Table 4.A5 (1C) under Detection of Underground Flow. It is an excellent survey for the detection of gas entry into liquid, either inside pipe or outside. The expression giving an estimate of gas rate behind the long string of a dual completion in terms of the noise level difference between the 200- and 600-Hz cut is</p> $q_g = 0.35 \times (N_{200} - N_{600}),$ <p>where the rate is in downhole ft³/d and the noise levels are in standard millivolts. The companion expression for gas entry into a screen or liner is</p> $q_g = 0.07 \times (N_{200} - N_{600}).$ <p>Unfortunately, these linear expressions apply for relatively low rates no greater than approximately 200 ft³/d. At higher rates, the expressions become nonlinear. In fact, at locations where gas jets from perforations are fast enough to foam water, noise levels drop to very low values.</p>
	Neutron survey from a simple correlation tool with well flowing and shut in	<p>This is an inexpensive way to detect gas entry into a screen or behind the long string in a dual completion. The tool consists of a chemical neutron source and a single detector spaced 17 to 23 in. above the source. It has a small diameter (1.373 in.) and is widely available. Because the tool responds to formation porosity, the shut-in trace is essential to interpretation.</p> <p>The tool has the advantage that a gas entry causes the same response in either water or oil. Because gas, with its low hydrogen content, is an ineffective neutron attenuator, a gas entry causes the flowing trace to shift away from the shut-in trace toward higher count rates. The size of the shift is exponentially related to the change in gas holdup in the liquid. However, the calibration is even more nonlinear than that for the gravel-pack correlation given previously.</p>
Location of a water source behind casing		<p>This survey can also be used to detect the entry of oil containing dissolved CO₂, a situation encountered in locations with active carbon-dioxide injection projects.</p> <p>This is the same problem discussed at the end of Table 4.A11 (4B). The user should refer to this table.</p>

TABLE 4.A21—8C: TRACKING THREE-PHASE PRODUCTION (PRODUCTION WELL—VERTICAL WITH SCREEN, PERFORATED LINER, OR DUAL COMPLETION)

Problem	Recommended Logging Tools	Operational Tips and Expected Results
Profiling commingled gas, oil, and water production.	Temperature survey with well flowing and two after shut-in times of 3 and 6 hours	The traces should be merged on one display scaled at 1°F per in. of chart and another scaled so as to avoid wraps. The procedure is the same as that of Table 4.A17 (7B). Water has the greatest effect—approximately 2.5 bbl of oil and 10 bbl or more of gas equal 1 bbl of water. Although the thermal profile is accurate, the volumetric profile is likely to be mainly qualitative in this situation. The reason is that stream compositions are required to convert the thermal profile to a phase-volumetric profile. These compositions are almost impossible to obtain with any accuracy.
	Back-scatter gamma density survey both flowing and shut in	This "gas-holdup" device is described in Table 4.A17 (7B) under Profiling. Its advantage here is that its response to gas is relatively insensitive to liquid density. If the device is calibrated for this environment, then it provides a value for gas holdup y_g directly. The corresponding value $y_{liq} = 1 - y_g$ represents an oil/water mixture created by the chaos associated with gas flow in liquid. It is the density of this mixture that determines the response from the gravel-pack tool listed next.
	Gravel-pack (unfocused gamma transmission) density survey both flowing and shut in	This device is described in Table 4.A20 (8B), where its nonlinear calibration equation is given for a flow containing liquid and gas. In the case of three-phase flow, water holdup y_w becomes y_{liq} for the oil/water mixture. Likewise, the count rate C_{water} becomes C_{liq}^* for the oil/water mixture. This value is no longer a constant, but varies with location in the hole. If y_{liq} is known from the back-scatter survey, then a value for C_{liq}^* can be calculated from the gravel-pack log at any location in the well. For these values, one uses the linear expression
		$y_w^* = \frac{\ln\left(\frac{C_{liq}^*}{C_{water}}\right)}{\ln\left(\frac{C_{oil}}{C_{water}}\right)}$
		to obtain values of y_w^* and $y_o^* = 1 - y_w^*$. These are the compositions by which the flowing liquid cut must be multiplied by to arrive at the water and oil cuts, respectively. Under the assumption that the only slippage is between the gas and liquid phases, the gas cut is obtained from the expression
		$C_g = y_g \left[1 + (1 - y_g) \cdot \frac{V_s}{V_{ave}} \right]$
		where $V_s \cong 45$ ft/min is the value for gas slippage through water and V_{ave} as estimated from the thermal rate. The corresponding liquid cut is $C_{liq} = 1 - C_g$. The corresponding oil and water cuts are obtained from this last value to give the three cuts needed to convert the thermal profile to a volumetric profile. A check is available on the calculations from the fact that the actual water holdup is given by $y_w = y_w^* y_{liq}$ and oil holdup is $y_o = y_o^* y_{liq}$. The three holdups must sum to 1.

TABLE 4.A21—8C: TRACKING THREE-PHASE PRODUCTION (PRODUCTION WELL—VERTICAL WITH SCREEN, PERFORATED LINER, OR DUAL COMPLETION) (Continued)		
<u>Problem</u>	<u>Recommended Logging Tools</u>	<u>Operational Tips and Expected Results</u>
Profiling commingled gas, oil, and water production	Pulsed neutron surveys with well flowing and shut in	These surveys are described in Table 4.A9 (3) under oil/water profiling. Their use here is qualitative.
	Gradient-type density survey both flowing and shut in (not in duals)	Same comments as in Table 4.A20 (8B).
	Continuous-spinner surveys both flowing and shut in (not in duals)	These are described in Table 4.A17 (7B). Deflections are caused primarily by gas entries. Consequently, the trace can be used to profile gas production approximately.
	Noise-logging survey flowing	Same comments as in Table 4.A20 (8B).
Location of water source behind casing		This is the same problem discussed at the end of Table 4.A20 (8B).

**TABLE 4.A22—9A: TRACKING SINGLE-PHASE PRODUCTION
(PRODUCTION WELL—HIGHLY DEVIATED WITHOUT SCREEN OR LINER)**

Problem	Recommended Logging Tools	Operational Tips and Expected Results
Profiling production	Elevation survey for wells deviated at more than 85°	Attempts to drill a wellbore nearly horizontal result in delayed corrections that cause variations in elevation from a few ft up to 20 ft. It is virtually impossible to produce a well at rates high enough to displace residual workover liquids and/or mud from the low spots along the length of the wellbore over the long section intended to produce. During production, hydrocarbon moves in waves along the top of this trapped liquid at locations where inclines upward in the direction of flow are encountered. Logging values measured at such locations are accordingly distorted.
	Density survey with well shut in	These devices are described in Table 4.A16 (7A). The type of tool is unimportant for this application because they are run simply to verify the presence of trapped completion fluid or mud.
	Continuous or fullbore spinner surveys both flowing and shut in	The procedure for the use of these tools is described under Profiling in Table 4.A16 (7A). The distinction here is that spinner responses used to profile should be taken in relatively level sections of the hole or, if this is not possible, at the top of downslope locations. The devices tend to plug because of debris on the low side of the hole. Diverting-spinner tools should be avoided for this reason.
	Temperature surveys both flowing and shut in for 1 to 6 hours	For wellbores with deviation angles less than 75°, a merged display scaled at 1°F per in. of chart is sufficient to clearly define mixing signatures for profiling according to the method described in Table 4.A16 (7A). For wells approaching horizontal, the merged display should be at 1°F per 2.5 in. of chart or even at 1°F per 5 in. of chart. At this magnification, variations in elevation may appear as corresponding variations in temperature on the shut-in trace. Mixing signatures are accordingly affected.
Location of hydrocarbon source behind casing	Temperature survey flowing and shut in	In new wells, horizontals included, liquid flow to the wellbore will cause warm signatures because of cooling around the well residual from the drilling operations. Because of this effect, this is the time when profiles with the best accuracy will be obtained. The warm signatures have a size increasing with increasing rate in the manner described in Table 4.A16 (7A).
		At any time, a liquid rate of approximately 500 B/D is sufficient to remove the normal variations in temperature present on the shut-in traces. Active locations are therefore recognizable. Likewise, gas production usually creates cold signatures at entry locations with a size of approximately 0.02°F per psi drop in pressure. Temperature surveys remain a valuable source of information even in horizontal wells.
Location of hydrocarbon source behind casing	Temperature survey flowing and shut in	The traces should be treated in the manner described previously. The same features and behavior can be expected at the locations of the source. In particular, the comparison of flowing and shut-in traces is important.

**TABLE 4.A23—9B: TRACKING TWO-PHASE PRODUCTION
(PRODUCTION WELL—HIGHLY DEVIATED WITHOUT SCREEN OR LINER)**

Problem	Recommended Logging Tools	Operational Tips and Expected Results
	Elevation survey for wells deviated 80° or more	<p>In nearly horizontal wellbores, delayed corrections during drilling introduce changes in elevation ranging from a few to 20 ft. The resulting high and low spots appear all along the long interval in the productive zone. Water or completion fluid is trapped in the low spots and restricts the cross section of the hole. When the well is produced, the light phase moves on top of the heavy phase. In long, nearly horizontal sections of hole, the flow consists of well-defined layers, but in practice, these sections appear to be limited in number. When the stream encounters an upward-sloping section of hole, the heavy phase lags so that its layer thickness increases. The light phase then moves in waves or surges along the top of the hole. This action induces strong circulation velocities into the heavy phase to the extent that a device measuring the upward velocity of the heavy phase records an increase even though the cross-section occupied by the heavy phase increases. The behavior on a downward-sloping section is the reverse. The heavy phase races ahead and thins in the cross-sectional area. The resulting drag action induces circulation into the light phase.</p>
Profiling commingled oil and water production	Temperature surveys with the well flowing and after shut-in times of 3 and 6 hours	<p>One shut-in trace after approximately 3 hours suffices for horizontal completions. The merged surveys should be scaled and interpreted as described in Table 4.A22 (9A). The artifact added by this completion is related to the shut-in traces. Upon shut in, the heavy phase drops back down the wellbore into the productive interval. In wells deviated by approximately 10° or more, the heavy phase circulates on the low side of the hole, usually behind the liner or screen, bringing cooler temperature with it. Consequently, the shut-in traces in the sump may lie to the cool side of the flowing trace rather than coincide with it. The two traces, however, will parallel each other, indicating no net upward flow. The flowing chaos described above under elevation survey is an advantage to temperature surveys and a detriment to all others.</p>
	Fluid-capacitance surveys both flowing and shut in	<p>These devices are described in Table 4.A17 (7B). Any oil that enters the wellbore rises quickly to the high side of the hole. Unless entering on the high side, the oil still must pass through the well's cross section. Thus, very small entries are detectable. The sensor is essentially a "line-of-sight" element capable of revealing layered flow by pure-phase values.</p>

**TABLE 4.A23—9B: TRACKING TWO-PHASE PRODUCTION
(PRODUCTION WELL—HIGHLY DEVIATED WITHOUT SCREEN OR LINER) (Continued)**

Problem	Recommended Logging Tools	Operational Tips and Expected Results
Profiling commingled oil and water production	Differential-pressure (gradient-type) density surveys both flowing and shut in (for wells with 75° or less) (not for duals)	<p>These devices are described in Table 4.A16 (7A). For deviations of 75° or less, they seem to function quite well. When corrected for deviation, they yield holdup values that often agree much better with expected values than do values from the more elaborate multiarm devices described below. The reason for this is likely the result of circulatory chaos in the flow combined with a 2-ft sample interval.</p> <p>For this environment, the hydrocarbon holdup values seem to obey simple momentum-displacement relationships to either light-phase cut C_{hc} or light-phase rate q_{hc} so that</p>
		$C_{hw} = (y_{hw})^n \quad \text{or} \quad q_{hw} = (y)_{hw}^n$ <p>where the constant $n=1-z$ is established from full-stream values.</p>
	Gravel-pack (unfocused gamma-transmission) surveys both flowing and shut in	<p>This device is described in Table 4.A20 (8B), where its calibration equation is given for vertical wellbores. In layered flow, however, the logarithmic relationship no longer applies. Data from horizontal flow loops show that water holdup is linear in count rate C instead. The calibration equation thus becomes</p> $y = \frac{C_{oil} - C_{ms}}{C_{oil} - C_{water}}$
	Continuous spinner survey with well flowing (not for duals)	<p>Pure-phase count rates are provided by the shut-in survey.</p> <p>These devices are described in Table 4.A11 (4B). In horizontal wellbores, it is a struggle just to keep the element from plugging. Even if this does not happen, the trace shows activity primarily at locations where light phase enters. In lesser deviated wellbores, however, the spinner deflections can often provide an approximate production profile for the light phase.</p>
	Pulsed-neutron lifetime or spectral surveys flowing and shut in	<p>These logs are described in Table 4.A20 (8B). The behavior of neutron transmission in layered flows, however, is quite complicated. Certain relative locations between tool and interface can produce count rates higher than the highest pure-phase value. Consequently, these traces are at best qualitative in this environment.</p>
	Flowing surveys with radioactive or chemical tracers specific to each phase (not for duals)	<p>A variety of tracers have been proposed to track the movement of individual phases. These include radioactive tags for oil and for water, chemical tags that increase capture-cross-section of each phase and activation of oxygen in the water phase. All of this activity is motivated by the fact that a rate cannot be calculated from a holdup value without an associated velocity. The conclusion from these efforts is that tracers behave just as badly in this environment as they do in vertical wells. Circulation patterns cause the tracers to spread, split, disperse or move in the wrong direction. Most wellbores lack the long sections of purely horizontal hole required to complete the profile.</p>

**TABLE 4.A23—9B: TRACKING TWO-PHASE PRODUCTION
(PRODUCTION WELL—HIGHLY DEVIATED WITHOUT SCREEN OR LINER) (Continued)**

Problem	Recommended Logging Tools	Operational Tips and Expected Results
Profiling commingled oil and water production	Multiarm conductivity surveys both flowing and shut in (not for duals)	<p>The one device of this type available has conductivity electrodes on each of the four bow-spring centralizers that open the fullbore-spinner element. When opened, the centralizers position each electrode at the midpoint of four radii spaced on 90° angles. Conductivity is not measured directly owing to its strong dependency on salinity. Instead, the fraction of time that each probe conducts in a time sample is measured. During this fraction, the electrode is in contact with water. The assumption is then made that this time distribution of water equals its space distribution; that is, the time fraction equals the water holdup.</p> <p>On the display from the tool, the four holdup values are interpolated to provide a colored display of water distribution over the casing's cross section. A trace of average holdup is also presented. An orientation angle is presented for the arm at left of the display.</p> <p>The small diameter of the electrodes make them quite sensitive to oil films to the point that they can become nonconductive even though they are surrounded by water. Unlike the fluid-capacitance probe, there is no way to calibrate out the effect of filming on the average holdup value.</p>
	Multiarm fluid capacitance surveys both flowing and shut in (not for duals)	<p>These devices contain two or more bow springs with arrays of button electrodes attached fore and aft along each spring. The one tool of this type that is widely available has two opposing bow springs and contains a positioning arm that points the same spring downward as the springs open. The result is a high-density measurement of the distribution of oil and water along a diameter perpendicular to the bottom of the hole. The relatively small electrodes are more subject to interference from oil filming than is the larger-diameter regular fluid-capacitance probe.</p> <p>This tool also makes a cross-correlation in time of the fluctuations at similarly positioned arrays on each end of both springs to establish a travel time. A velocity distribution over the diameter is then derived from these travel times. From these data, an average velocity is estimated for each phase. In perfectly layered flow, this is a valid approach. In practice, however, the tool is unable to distinguish an event created by circulatory movement upward from any other.</p>
Profiling commingled gas and water production (or gas and oil)	Temperature surveys both flowing and shut in for periods of 1 and 4 hours	<p>A single shut-in survey will usually suffice for a horizontal well. The same comments apply as listed in Table 4.A22 (9A). The distinction here is that even in horizontal holes, gas expansion generally cools approximately 0.02°F per psi drop in pressure at entry locations. These cooled locations are easily identified on the shut-in survey.</p> <p>The thermal profile derived from mixing signatures as described in Table 4.A17 (7B) is relatively accurate. The volumetric profile derived with the aid of flowing cuts is likely to be only qualitative owing to error in the determination of composition from fluid-identifier traces.</p>

**TABLE 4.A23—9B: TRACKING TWO-PHASE PRODUCTION
(PRODUCTION WELL—HIGHLY DEVIATED WITHOUT SCREEN OR LINER) (Continued)**

Problem	Recommended Logging Tools	Operational Tips and Expected Results
Profiling commingled gas and water production (or gas and oil)	Back-scatter gamma density surveys both flowing and shut in	<p>This device is described in Table 4.A17 (7B), where a correlation equation is given for gas holdup independent of liquid density. In this environment, the tendency of the flow to layer means that the equation should be altered to replace logarithms by count rates directly</p> $y_g = 1 - \frac{C_{mix} - C_{gas}}{C_{liquid} - C_{gas}}$ <p>Shut-in traces give pure-phase counts.</p>
	Gravel-pack (unfocused gamma-transmission) density survey flowing and shut in	<p>This device is described in Table 4.A19 (8A). In layered flows with only one liquid phase present (water or oil), the water holdup becomes a nonlinear function of count rate according to</p> $y_w = aR_{mix} + (1-a)(R_{mix})^2 ; R_{mix} = \frac{C_{gas} - C_{mix}}{C_{gas} - C_{liquid}}$ <p>where the pure-phase counts come from the shut-in traces.</p>
	Gradient-type density surveys both flowing and shut in (not in duals)	See previous under profiling oil and water. This device is sensitive to small gas entries and will corroborate the back-scatter survey.
	Pulsed-neutron surveys both flowing and shut in	These surveys are described in Table 4.A20 (8B). The expressions given in that table for holdup do not apply to layered flows, making these surveys qualitative only.
	Flowing spinner surveys	See comments under oil/water above. May provide an approximate gas-rate profile.
	Neutron survey with a simple correlation tool both flowing and shut in	This tool is described in Table 4.A17 (7B). Like the back-scatter gamma tool, it is also able to distinguish gas from liquid irrespective of the type of liquid. In a highly deviated wellbore, the formation component in the signal is relatively constant. Furthermore, this tool has been calibrated for layered flows when centralized (U.S. Patent #5,708,203, 13-Jan-1998). The count-rate ratio in this patent is defined as R_{mix} above.
	Optical gas-detection surveys both flowing and shut in	One company runs an optical sensor that combines measurements of light reflection and transmission to arrive at a bubble "count rate" and an assumed bubble size to estimated gas holdup.
	Noise-logging survey with the well flowing	This survey is described in Table 4.A20 (8B). The same concepts apply to this environment at locations where gas enters liquid.
Water channeling		This is the same problem discussed at the end of Table 4.A17 (7B).

**TABLE 4.A24—9C: TRACKING THREE-PHASE PRODUCTION
(PRODUCTION WELL—HIGHLY DEVIATED WITHOUT SCREEN OR LINER)**

Problem	Recommended Logging Tools	Operational Tips and Expected Results
	Elevation survey	See Table 4.A23 (9B). The distinction in this environment is that low spots in the wellbore may contain a layer of oil on top of water whereas high spots will contain gas at top.
Profiling production of gas, oil, and water	Temperature surveys flowing and after shut-in times of 3 and 6 hours	See Table 4.A23 (9B) under profiling oil and water and profiling gas and water.
	Back-scatter gamma-ray density survey both flowing and shut in	See Table 4.A23 (9B) under profiling gas and water. This tool distinguishes gas from liquid. In this case, the liquid is a combination of oil and water. With wellbore deviations of no more than 75°, the two phases will be mixed together by lifting action of the gas. The calibration equation in Table 4.A23 (9B) for gas holdup y_g contains a liquid count rate, C_{liq} , that in theory changes with composition along the productive length of the wellbore. The same is true for horizontal wells with the additional complexity of changes in form from well-mixed to combined layers of oil on water. Fortunately, the tool is relatively insensitive to liquid density.
	Gravel-pack (unfocused gamma transmission) density survey both flowing and shut in	See Table 4.A23 (9B) under profiling gas and water. The nonlinear calibration equation in this table also contains a count rate for the oil/water mixture. Unfortunately, this device is sensitive to liquid density as the shut-in surveys will show. If the flowing trace is to give a value for water holdup y_w , then the method outlined in Table 4.A21 (8C) will have to be used with the logarithm of count rates replaced by count rates.
	Fluid capacitance surveys flowing and shut in (not in duals)	See Table 4.A23 (9B) under profiling oil and water. The tool functions just as well in this environment for the detection of small oil entries and for detection of layered flow. Its response is relatively insensitive to gas in the presence of oil.
	Gradient-type density surveys flowing and shut in (not in duals)	See Table 4.A23 (9B) under profiling oil and water and profiling gas and water. This device will detect very small gas entries and in conjunction with the fluid-capacitance trace will help distinguish gas entries from oil entries.
	Flowing spinner survey	See comments in Table 4.A23 (9B). This survey may provide an approximate gas-rate profile.
	Noise-logging survey with well flowing	See Table 4.A20 (8B). This tool is sensitive to small entries of gas into liquid. The gas-rate estimations in the table are valid at entry locations before gas rises to the top of the hole.
Neutron survey with simple correlation tool flowing and shut in	See Table 4.A23 (9B) under gas and water profiling. This tool detects gas holdup independent of liquid composition. It is one of the few tools that has been calibrated for layered flow.	

**TABLE 4.A24—9C: TRACKING THREE-PHASE PRODUCTION
(PRODUCTION WELL—HIGHLY DEVIATED WITHOUT SCREEN OR LINER) (Continued)**

Problem	Recommended Logging Tools	Operational Tips and Expected Results
Profiling production of gas, oil, and water	Multiarm fluid-conductivity surveys with well flowing (not for duals)	See Table 4.A23 (9B) under profiling oil and water. This tool can provide a value for water holdup provided oil does not film on the electrodes.
	Multiarm fluid-capacitance surveys with well both flowing and shut in (not for duals)	See Table 4.A23 (9B) under profiling oil and water. The tool provides a distribution profile of gas, water, and oil across a diameter perpendicular to the bottom of the casing in sections of the hole where flow is layered.
	Flowing surveys with radioactive or chemical tracers specific to individual oil and water phases (not for duals)	See Table 4.A23 (9B). These surveys are intended to provide velocities for the oil and the water phases. However, the chaos created by gas entries is so severe that the utility of the survey is restricted to horizontal sections of the hole free of gas entries.
	Pulsed-neutron surveys with well both flowing and shut in	See Table 4.A23 (9B). The chaos resulting from the presence of gas increases the noise level on these surveys greatly. Furthermore, their processing software was not intended to apply to layered flows.

**TABLE 4.A25—10A: TRACKING SINGLE-PHASE PRODUCTION
(PRODUCTION WELL—HIGHLY DEVIATED WITH SCREEN, LINER, OR DUAL COMPLETION)**

<u>Problem</u>	<u>Recommended Logging Tools</u>	<u>Operational Tips and Expected Results</u>
Profiling production	Elevation survey	See Table 4.A22 (9A). This survey identifies low spots that may contain trapped completion fluid
	Density survey with well shut in	These devices are described in Table 4.A16 (7A). The survey verifies the presence of trapped fluids.
	Temperature surveys both flowing and shut in for 1 to 6 hours	Table 4.A22 (9A) outlines the use of these devices even in horizontal holes. The mixing signature method of profiling is not affected by the presence of trapped liquids in low spots.
	Continuous spinner flowmeter survey both flowing and shut in (not for use in dual completions)	These devices are described in Table VIIA. Their use here, however, is purely qualitative owing to their response only to flow inside the screen/liner. The traces will identify the locations where velocity increases because of trapped completion fluids or changes in hole size.
Location of hydrocarbon source behind casing	Temperature surveys both flowing and shut in	These surveys should be scaled and interpreted in the manner described in Table 4.A22 (9A). A general discussion of the features to expect on the merged traces appears in Table 4.A16 (7A).
	Noise-logging survey with well shut in	The use of this device for detection of flow behind casing is described in Table 4.A8 (2C). A shut-in condition is chosen so as to detect continuing flow from above.

**TABLE 4.A26—10B: TRACKING TWO-PHASE PRODUCTION
(PRODUCTION WELL—HIGHLY DEVIATED WITH SCREEN, LINER, OR DUAL COMPLETION)**

Problem	Recommended Logging Tools	Operational Tips and Expected Results
	Elevation survey for well deviated 80° or more	See Table 4.A23 (9B), where the behavior of multiphase flow is discussed. The distinction to be made in this environment is that the light phase tends to move along the top of the hole and not enter the screen/liner completely until the top of the screen or the last hole in the liner. Likewise, the heavy phase moves along the low side of the hole until the top of the screen/liner.
Profiling commingled oil and water production	Temperature surveys both flowing and after shut-in times of 3 and 6 hours	See comments in Table 4.A23 (9B) and general behavior in Table 4.A16 (7A). The distinction for this environment is related to the merged traces. When the well is shut in, the heavy phase tends to flow back down the well on the low side of the casing and circulate all the way to the sump. Consequently, the shut-in traces in the sump may be located slightly to the cool side of the flowing trace; however, they will parallel the flowing trace owing to the lack of production in the sump.
	Fluid-capacitance traces both flowing and shut in	These devices are described in Table 4.A17 (7B) and their use in deviated wells is discussed in Table 4.A23 (9B). This device will also identify locations where flow is layered.
	Gravel-pack (unfocused gamma-transmission) density surveys both flowing and shut in	This device is described in Table 4.A17 (7B), where its calibration equation for water holdup in sections without layered flow is presented. The corresponding calibration for water holdup in layered flow appears in Table 4.A23 (9B).
	Continuous-spinner survey with well flowing (not for use in duals)	See comments in Table 4.A23 (9B). The survey may provide an approximate production profile for the oil phase.
	Pulsed-neutron lifetime or spectral surveys both flowing and shut in	The presence of the screen/liner does not prevent these devices, described in Table 4.A20 (8B), from providing values called "borehole fluid" that capture the cross section or "borehole carbon/oxygen" ratio. The software, however, was not written for layered flow [see comments in Table 4.A23 (9B)].
Profiling commingled gas and water production (or gas/oil)	Temperature surveys both flowing and after shut-in periods of 1 and 4 hours	See comments in Table 4.A23 (9B). As indicated in that table, cooling signatures at gas-entry locations are the distinctive feature. The distinction for this environment is the tendency for the gas to move along the top of the hole outside the screen/liner until its last chance for entry at the top of screen/liner. This does not interfere with profiling, but may produce an additional mixing signature at the top of the screen/liner.
	Back-scatter gamma-ray surveys both flowing and shut in (so-called gas-holdup surveys)	See comments in Table 4.A23 (9B), where the calibration equation for layered flow is given. This device should provide a value for gas holdup in the present environment if it is calibrated with the well shut-in at locations where only gas is present behind the screen/liner and at locations where only water (or oil) is present.

TABLE 4.A26—10B: TRACKING TWO-PHASE PRODUCTION (PRODUCTION WELL—HIGHLY DEVIATED WITH SCREEN, LINER, OR DUAL COMPLETION) (Continued)		
Problem	Recommended Logging Tools	Operational Tips and Expected Results
Profiling commingled oil and water production	Gravel-pack (unfocused gamma-transmission) both flowing and shut in	See comments in Table 4.A23 (9B), where the calibration equation is given for layered flow. The value of the survey in this environment lies in its ability to provide an independent value for water (oil) holdup and thereby check the accuracy of the gas holdup determined from the back-scatter survey. The two holdups should sum to 1.0.
	Gradient-type density surveys both flowing and shut in (not in duals)	Table 4.A23 (9B) explains why these devices remain useful in wells with no more than approximately 75° deviation. They function in this environment to detect small gas entries.
	Continuous-spinner survey with well flowing (not for use in duals)	See comments in Table 4.A23 (9B). In wells with no more than 75° deviation, the survey may provide an approximate rate profile for the gas.
	Neutron survey with simple correlation tool both flowing and shut in	This device is a backup for the back-scatter gamma-ray survey. It also provides a gas holdup that is independent of liquid type. Its calibration for layered flow is discussed in Table 4.A23 (9B).
	Optical gas-detection surveys	See comments in Table 4.A23 (9B). At gas entries other than at the top of the hole, the tool should provide gas-holdup data for comparison to back-scatter values.
	Noise-logging survey with well flowing	This survey is described in Table 4.A20 (8B). The same concepts and rate expressions apply to this environment at locations where gas enters liquid.
Water channeling		This is the same problem discussed at the end of Table 4.A17 (7B).

TABLE 4.A27—10C: TRACKING THREE-PHASE PRODUCTION (PRODUCTION WELL—HIGHLY DEVIATED WITH SCREEN, LINER, OR DUAL COMPLETION)		
<u>Problem</u>	<u>Recommended Logging Tools</u>	<u>Operational Tips and Expected Results</u>
	Elevation survey	See Table 4.A26 (10B). The distinction for this environment is that the low spots may have a layer of oil on top of water, whereas gas will be present at the top of high spots.
Profiling production of gas, oil, and water	Temperature surveys both flowing and after shut-in times of 3 and 6 hours	See Table 4.A26 (10B) under profiling both oil and water and gas and water.
	Fluid-capacitance surveys both flowing and shut in (not in duals)	See Table 4.A26 (10B) under profiling oil and water production. The distinction here is that the liquid phase is an oil/water mixture produced by gas lift (except in layered flow).
	Gradient-type density surveys with well flowing (not in duals)	See Table 4.A26 (10B) under profiling gas and water. They complement the fluid-capacitance survey in this environment to distinguish small gas entries from large oil entries.
	Continuous flowmeter survey with well flowing (not in duals)	See Table 4.A26 (10B) under profiling gas and water
	Gravel-pack density surveys both flowing and shut in	See Table 4.A26 (10B) under profiling oil and water production. The distinction here is that the liquid phase is a mixture of oil and water carried by gas lift (except in layered flow)
	Back-scatter gamma-ray surveys both flowing and shut in	See Table 4.A26 (10B) under profiling gas and water production. These devices are called gas-holdup meters and are relatively insensitive to liquid density.
	Neutron survey with simple correlation tool both flowing and shut in	See Table 4.A26 (10B) under profiling gas and water production. The device is a backup to the back-scatter gamma survey. It is totally independent of liquid density.
	Optical gas-detection surveys	See Table 4.A26 (10B).
	Noise-logging survey flowing	See Table 4.A26 (10B).
Water channeling		Same problem discussed at end of Table 4.A17 (7B).

TABLE 4.A28—11A: LOCATION OF ANNULAR PRESSURE SOURCE (PRODUCTION WELL SHUT IN OWING TO ANNULAR PRESSURE OR CROSSFLOW BEHIND CASING)		
<u>Problem</u>	<u>Recommended Logging Tools</u>	<u>Operational Tips and Expected Results</u>
Location of annular pressure source	See same problem in Table 4.A8 (2C)	<p>The location of the source is determined by a comparison of the "Before" and "After" annular bleed surveys.</p> <p>The distinction between this table and Table 4.A8 (2C) lies entirely in their environments. In this case, the logging will most likely be carried out in a tubing string under pressure from its hydrocarbon content. The tubing must be sealed to flow at the surface, meaning that wing valves must be checked for their ability to seal completely. Furthermore, careful attention must be paid to the seal on the lubricator provided by the grease-injection unit during logging.</p> <p>Because the well is not at geothermal temperature, this survey remains the most sensitive to water sources because of water's ability to warm or cool (depending upon shut-in temperature) at relatively low rates. Likewise, the noise logger remains the most sensitive to small gas sources that must move through liquid behind or in casing. If the tubing string contains gas, then the noise levels must be multiplied by a coupling factor $F \cong 2$ before application of the rate expressions in Table 4.A8 (2C).</p>

TABLE 4.A29—11B: DETECTION OF CROSSFLOW BEHIND PIPE (PRODUCTION WELL SHUT IN OWING TO ANNULAR PRESSURE OR CROSSFLOW BEHIND CASING)		
<u>Problem</u>	<u>Recommended Logging Tools</u>	<u>Operational Tips and Expected Results</u>
Detection of crossflow behind casing	See Table 4.A5 (1C)—detection of flow underground	<p>The environmental differences are the same ones listed in Table 4.A28 (11A). The procedures and expected features remain the same as those discussed in Table 4.A5 (1C). If the rate expressions given for the noise logger are used, then the noise levels must first be multiplied by N_p = Number of pipe strings between source and sensor and by a coupling factor $F = 2$ if the tool is in gas rather than liquid.</p>

**TABLE 4.A30—12A: DETECTION OF CORROSION OR WEAR TO STRING CONTAINING TOOL
(WELL DOWN FOR TUBING OR CASING INSPECTION)**

Problem	Recommended Logging Tools	Operational Tips and Expected Results
Corrosion detection	Multifeeler mechanical-caliper surveys for internal corrosion	<p>These devices are available for both tubing and casing inspection. They are described in detail in Table 4.A7 (2B) (Casing Wear), to which the user should refer before continuing here. Because a direct measurement is made, these tools are the best for the detection of internal pitting, which appears as high-frequency spiking to larger radii. This kind of "hash" is easily recognizable on the display of individual feeler records. However, scale buildup on the inside surface of the tubing or casing can also produce "hash" in the records with the spikes being toward smaller radii. It is therefore very helpful to have "min-max" traces (minimum and maximum deflections) on the display as well. These traces reveal immediately the direction of the spikes. Furthermore, the min-max traces are essential to the recognition of extended regions of wear or relatively uniform loss of wall from corrosion. Because of tool rotation, such regions are difficult to spot otherwise.</p>
	Eddy-current wall-thickness and caliper surveys for both internal and external corrosion	<p>These electromagnetic-induction devices are also available for both tubing and casing. Their description appears in Table 4.A7 (2B), to which the user should refer. These tools are the most sensitive available for the detection of external metal loss. The trace from the wall-thickness coils can be displayed easily at a sensitivity of 0.02 in. per chart division (i.e., at 4% normal wall thickness per chart division). In seamless tubing or casing, the normal taper (approximately 0.125 in. per 40 ft) can be used as a calibration point.</p> <p>Corrosion pits also appear as high-frequency spiking to lesser values of wall thickness on the display. Internal or external pitting produces equal effects on the trace. The two are distinguished by the caliper trace. This signal is the variation in voltage of a field induced by a coil driven at a high frequency to prevent penetration into the metal wall. This trace is displayed so as to spike to larger radii at internal pits. Of course, the tool does not function in nonmagnetic metals.</p>

**TABLE 4.A30—12A: DETECTION OF CORROSION OR WEAR TO STRING CONTAINING TOOL
(WELL DOWN FOR TUBING OR CASING INSPECTION) (Continued)**

Problem	Recommended Logging Tools	Operational Tips and Expected Results
Corrosion detection	Magnetic flux-leakage surveys for internal and external corrosion	<p>These are casing-inspection devices that use either a permanent magnet or an electromagnet to induce a magnetic field over the wall thickness of the casing. At locations where metal thickness changes abruptly, the magnetic field either expands out of (metal loss) or collapses into (metal gain) the wall. Either way, the field acquires a component perpendicular to the casing wall. Pads containing coils to cut this field are pressed tightly against the casing wall. Two rings, each containing between 6 and 12 pads, are used so that the pads can be staggered to sample more closely around the casing circumference. The polarity of the signal is displayed so that, with the tool moving upwards, the passage of a coil over a sudden decrease in wall thickness induces a spike to the right on the display from that coil. A sudden increase in wall thickness induces a "negative" spike (i.e., a deflection to the left). The polarity of a spike is used to distinguish, for example, the bands on centralizers or "scratchers" attached to the outside of the casing. The size of the induced spike is, of course, smaller for a change in thickness on the outside casing wall than for a change on the inside wall.</p> <p>On modern versions of this tool, the output from each of the 12 to 24 coils is displaced as a function of depth. Two additional traces display the maximum and the average spike size without regard to polarity. Pitting induces a swarm of spikes with positive polarity on the individual traces. The display of these traces, along with the average trace, shows the radial extent of the corrosion, whereas the maximum trace shows the severity of pitting.</p> <p>To be effective, the trace of maximum deflection is recorded at a sensitivity such that the "road noise" induced by tool motion corresponds to the signal produced by approximately 10% of internal thickness loss and approximately 30% external loss. The sparser the pitting density, the smaller the spikes. Casing strings external to the one being logged further decrease spike amplitude. Without calibration data, one can only use the response at collars ($\approx 100\%$ loss) as a relative guide.</p>

TABLE 4.A30—12A: DETECTION OF CORROSION OR WEAR TO STRING CONTAINING TOOL (WELL DOWN FOR TUBING OR CASING INSPECTION) (Continued)

<u>Problem</u>	<u>Recommended Logging Tools</u>	<u>Operational Tips and Expected Results</u>
Corrosion detection	Magnetic flux-leakage surveys for internal and external corrosion	Each pad also contains a pair of coils, one driven at high frequency and one to sample induced voltage, to examine the inside wall of the casing. This "caliper" trace is used to discriminate internal corrosion from external. These devices respond only to abrupt changes in wall thickness and, consequently, can miss severe wear or the equivalent from overlapping pits. It should therefore be run in conjunction with a mechanical caliper. This procedure also allows one to judge the percentage of spurious events to be expected on the maximum trace.
	Casing differential voltage survey	The device uses two (or more) contact electrodes to measure the difference in voltage, caused by galvanic currents, in sections along the casing wall. A section with a voltage swing, top-to-bottom, in the positive direction identifies an area losing metal ions to the earth. A current is calculated for such sections and converted into a rate of metal loss.
	Radial-type (pulse-echo) bond-logging survey for caliper and wall thickness	This device is described in Table 4.A7 (2B). It provides colored-density displays for wall thickness and for internal radius. It is an excellent tool for the detection of wear and its equivalent from overlapping pit-corrosion. It is less effective for high-frequency pitting that has yet to coalesce.
Casing collapse, part or split		See Tool Selection in Table 4.A7 (2B).
Bends or "dog-legs"		See Tool Selection in Table 4.A7 (2B).

TABLE 4.A31—12B: DETECTION OF HOLES OR PARTING IN CASING EXTERNAL TO THE ONE CONTAINING THE TOOL (WELL DOWN FOR TUBING OR CASING INSPECTION)

<u>Problem</u>	<u>Recommended Logging Tools</u>	<u>Operational Tips and Expected Results</u>
Holes or parts in external casing	Eddy-current wall-thickness surveys	See Tables 4.A7 (2B) and 4.A28 (12A).
	Gravel-pack (unfocused gamma-transmission) survey	See Table 4.A19 (8A).

Chapter 5

The Single-Well Chemical Tracer Test—A Method For Measuring Reservoir Fluid Saturations In Situ

Harry Deans and Charles Carlisle, Chemical Tracers, Inc.

5.1 Introduction

The single-well chemical tracer (SWCT) test is an in-situ method for measuring fluid saturations in reservoirs. Most often, residual oil saturation (S_{or}) is measured; less frequently, connate water saturation (S_{wc}) is the objective. Either saturation is measured where one phase effectively is stationary in the pore space (i.e., is at residual saturation) and the other phase can flow to the wellbore. Recently, the SWCT method has been extended to measure oil/water fractional flow at measured fluid saturations in situations in which both oil and water phases are mobile.

The SWCT test is used primarily to quantify the target oil saturation before initiating improved oil recovery (IOR) operations, to measure the effectiveness of IOR agents in a single well pilot and to assess a field for bypassed oil targets. Secondly, it is used to measure S_{wc} accurately for better evaluation of original oil in place (OOIP). Fractional flow measurement provides realistic input for simulator models used to calculate expected waterflood performance.

This chapter familiarizes the reader with the SWCT method, and offers guidelines for selecting suitable test wells and for planning and executing the field operations on the target well. Test interpretation is also discussed and illustrated with typical examples.

5.2 History

The first SWCT test for S_{or} was run in the East Texas Field in 1968.¹ Patent rights were issued in 1971.² Since then, numerous oil companies have used the SWCT method.³⁻⁷ More than 400 SWCT tests have been carried out, mainly to measure S_{or} after waterflooding.

The SWCT method has gained considerable recognition over the past few years because of increasing interest in the quantitative measurement of S_{or} . Some experts^{8,9} consider the SWCT test to be the method of choice because of its demonstrated accuracy and reasonable cost.

5.3 Measuring S_{or}

Accurate S_{or} measurement is important because of a combination of basic problems in oil recovery. The industry still produces less than half the oil in the reservoirs discovered, and nearly all that oil is produced using traditional primary and secondary recovery methods.¹⁰ Furthermore, as the cost of finding new reserves continues to increase, especially in the U.S.A., the oil re-

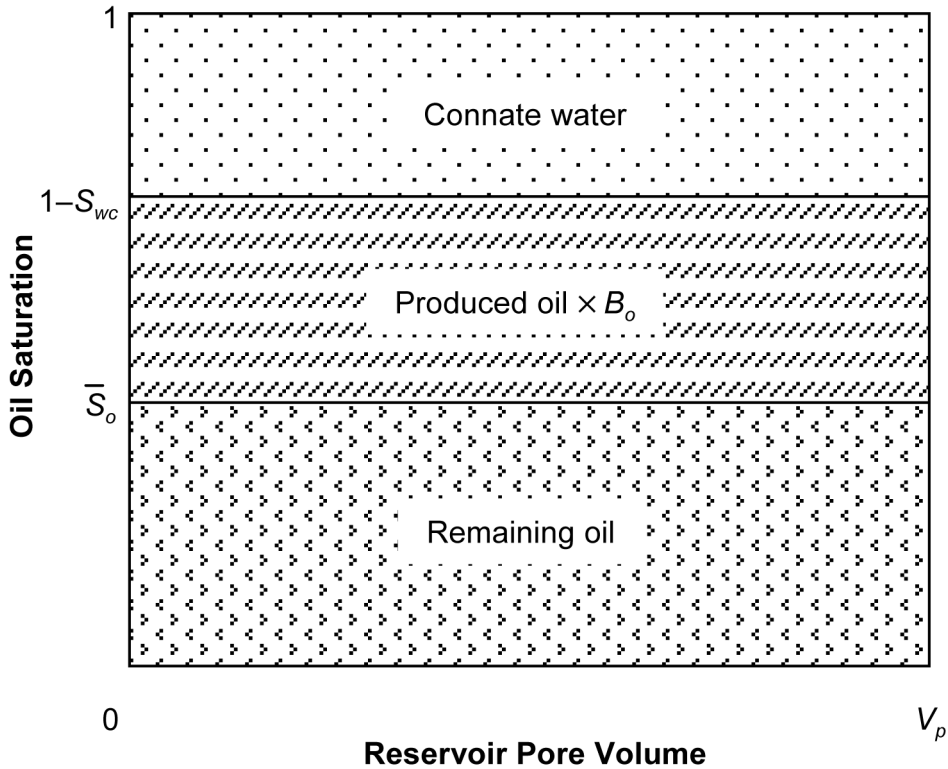


Fig. 5.1a—Reservoir evaluation by material balance alone in a waterflooded oil field. B_o = formation volume factor, oil RB/STB.

maining in old fields becomes a significant economic target for infill drilling and IOR projects. See Chaps. 12 through 17 in the Reservoir Engineering and Petrophysics volume of this *Handbook* for more detail on these methods.

In every target field, the quantity and location of the remaining oil must be determined. Fig. 5.1a illustrates the principle of material balance, as applied to an oil reservoir. The entire area of the graph represents the reservoir pore volume (V_p), which is known with varying degrees of uncertainty. The produced oil, corrected back to reservoir conditions, is the middle area; its accuracy, however, depends on how thoroughly the production records are kept.

The uppermost area is the connate water, which is known only as well as available methods and coverage of measurements allow. The lowermost area, the remaining oil, can be expressed as an average saturation of oil (\bar{S}_o), if we accept the total pore volume V_p , produced oil, and S_{wc} values as being accurate.

If a given field has been waterflooded, the fraction of the OOIP displaced by the water is a critical parameter. Testing for S_{or} in watered-out wells in the field can determine the maximum waterflood displacement efficiency. A significant difference between the material-balance S_o and the measured S_{or} would indicate the presence of bypassed oil. This would signify that parts of the reservoir had not been contacted by injected water, or had not received sufficient water throughput to reach S_{or} . This concept is shown in Fig. 5.1b.

A reliable in-situ measurement of S_{or} simultaneously defines the target for enhanced oil recovery (EOR) and allows estimation of the potential bypassed (mobile) oil in the field. This moveable oil is the target for infill drilling and/or flood sweep efficiency improvements.

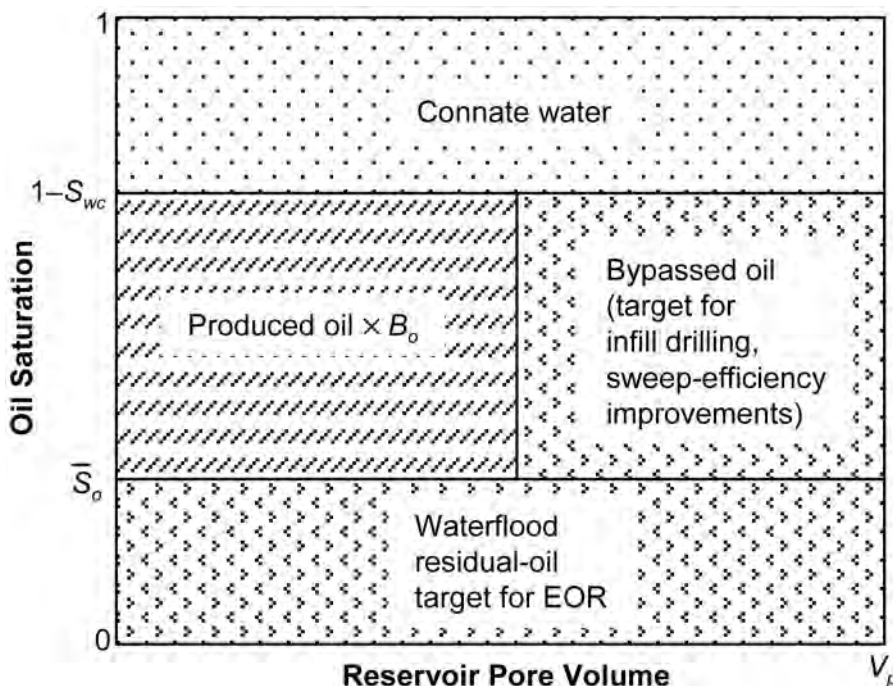


Fig. 5.1b—Reservoir evaluation by material balance with measured S_{or} .

Because S_{or} varies greatly with formation type, oil/water properties, and other variables that are not completely understood (e.g., wettability changes caused by water flood practices), S_{or} measurements range from $< 10\%$ to $> 45\%$. There is no reliable way to predict S_{or} with acceptable accuracy for most reservoirs. Furthermore, measuring residual oil is not easy. Laboratory corefloods performed at other than native state wettability are unreliable.¹¹

Well logs can give vertical profiles of S_{or} under optimal conditions, but their results are not absolute. Logs of all types require calibration by an independent method, which gives either a quantitative S_o at some point or an average S_o over some layer. Pressure cores or sponge cores can provide this calibration, but require a new well and are subject to saturation disturbances caused by mud filtrate invasion.

An advantage of the SWCT method is that it pushes tracers beyond damaged regions near the wellbore and into layers that are known to be at residual oil conditions. The tracers go where water is contacting the residual oil, as shown in Fig. 5.1b.

In an SWCT test, the formation volume sampled is large enough to be representative. A typical test quickly investigates hundreds of barrels of pore space in an existing watered-out well. The tracer-bearing fluids are produced back into the well without disturbing the formation, allowing further testing.

5.4 Measuring S_{wc}

Connate water saturation is more variable (and less predictable) than S_{or} , with S_{wc} measurements ranging from $> 50\%$ in certain rock types to $< 5\%$ in unusual reservoir situations. Large variations within the producing intervals of major reservoirs are well documented.⁹

As Figs. 5.1a and 5.1b show, estimates of recoverable oil depend fundamentally on knowing S_{wc} . Oil-based coring can provide reliable results and is an effective choice if its expense can be justified at the time a well is drilled. Electric logs can give vertical profiles, but as with S_{or} , require calibration for quantitative S_{wc} measurement.

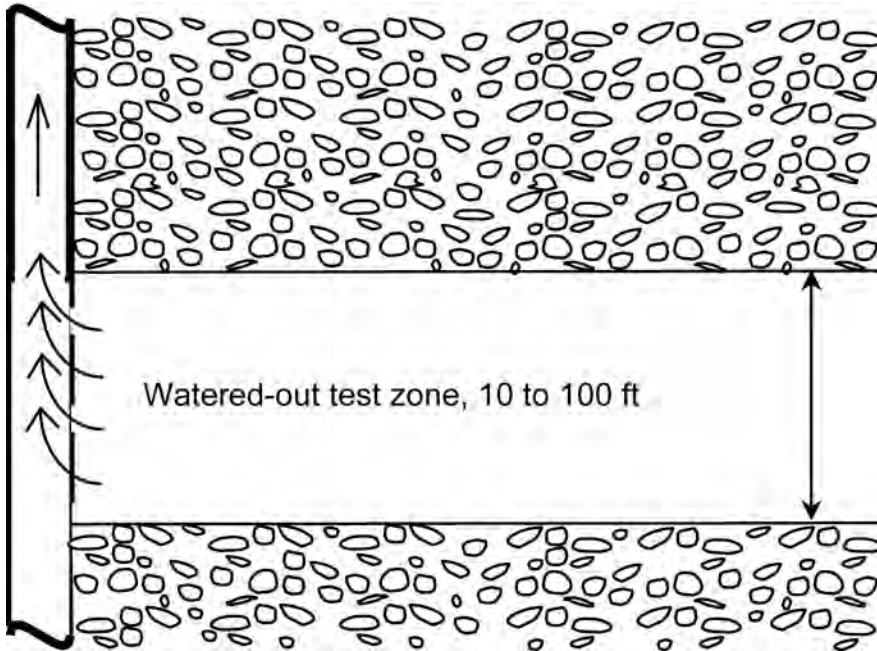


Fig. 5.2—Candidate SWCT test well.

Deans and Shallenberger¹² reported the first application of the SWCT method for measuring S_{wc} . As in the case when measuring S_{or} , the reservoir volume sampled is large and the test is nondestructive, which is especially important for a producing oil well. The tracers used in measuring S_{wc} are nonhazardous oxyhydrocarbons, so that no contaminated oil needs to be disposed of after the SWCT test. Most importantly, though, the test holds a high success rate—every known SWCT test for S_{wc} has yielded quantitative results.

5.5 SWCT S_{or} Tests

5.5.1 How the SWCT Test Works. The SWCT test for S_{or} uses only one well and involves the injection and back production of water carrying chemical tracers. A typical target interval for SWCT testing is shown in Fig. 5.2. The candidate well should be completed only to the watered-out zone of interest (zone at S_{or}). The water used normally is from the formation to be tested, and often is collected during the initial setup for the test.

The injected volume is divided into two parts: the partitioning tracer bank, which carries a small concentration of tracer (usually some type of ester) dissolved in water, and the push volume of water, which pushes the partitioning tracer bank away from the wellbore 10 to 20 ft. A material-balance tracer (normally a water-soluble alcohol) is added to the entire injected volume to differentiate it from the formation water being displaced. This injection step is shown in Fig. 5.3.

The primary tracer is an alkyl ester. The esters used in SWCT testing usually are more soluble in oil than in water. This solubility preference is expressed quantitatively by the ester's oil/water partition coefficient, K_e :

$$K_e = \frac{C_{eo}}{C_{ew}}, \dots\dots\dots (5.1)$$

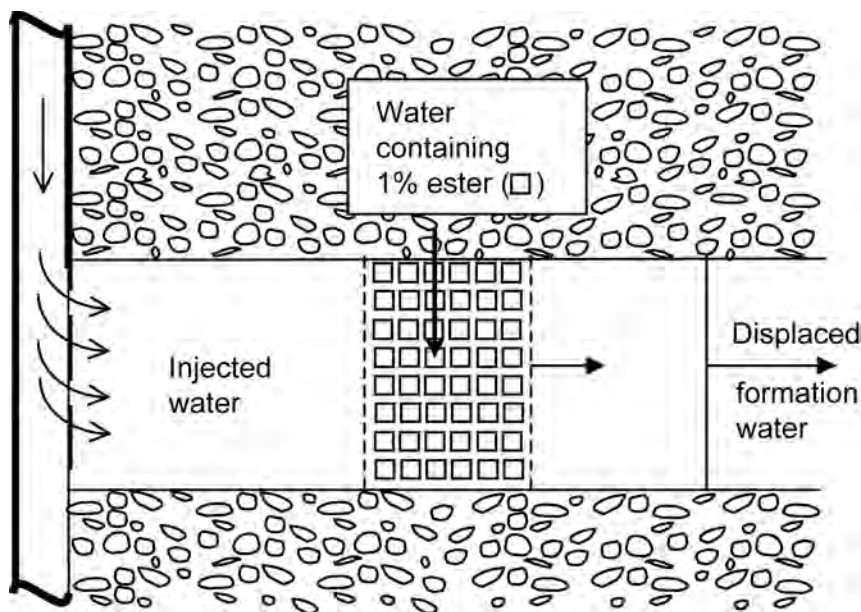


Fig. 5.3—Injection of ester tracer and push volume.

where C_{eo} = the concentration of ester in oil; C_{ew} = the concentration of ester in water; C_{eo} and C_{ew} are values at equilibrium.

For example, if the partition coefficient is four, the ester prefers the oil phase four times more than the water phase. For each tracer to be used in each test, the actual value of K_e must be measured in the laboratory at reservoir conditions. Oil and water samples are collected from the target formation for this purpose.

As the ester tracer enters the pore space containing the residual oil, it partitions between the oil and water phases. The ester maintains a local equilibrium concentration in the oil phase, controlled by the ester's partition coefficient, even though the water is flowing.

Because the oil is stationary and the water is moving, the ester tracer moves more slowly through the reservoir pore space than does the water with which it was injected. The ester's velocity thus is a function of the water velocity, the ester partition coefficient, and the S_{or} . Fig. 5.3 schematically shows the radial position of the injected ester and water. The material-balance tracer, normally an alcohol, is nearly insoluble in oil, so that it travels at approximately the same velocity as the water, reaching as far into the formation as the injected water.

For simplicity, Fig. 5.3 illustrates the no-dispersion case however, in real reservoirs, the tracers disperse significantly, though this effect does not alter the basic mechanism of retardation of ester velocity by the residual oil.

After the ester and push injections are completed, the well is shut in for one to ten days, depending on the reactivity of the ester and the reservoir temperature. This shut-in period allows some of the ester to react with water in the reservoir, which forms a new tracer in situ, the secondary (or "product") tracer.

Reacting an alcohol and an organic acid makes an alkyl ester. At reservoir temperature, however, when dissolved in water, this ester slowly breaks down again into the alcohol and acid: $\text{Ester} + \text{H}_2\text{O} = \text{Alcohol} + \text{Acid}$. The shut-in period must be long enough for measurable alcohol to form in situ by this reaction (Fig. 5.4).

It is the alcohol formed that makes the S_{or} measurement possible. The acid formed during the reaction is not observed because it is neutralized by the natural base components of the

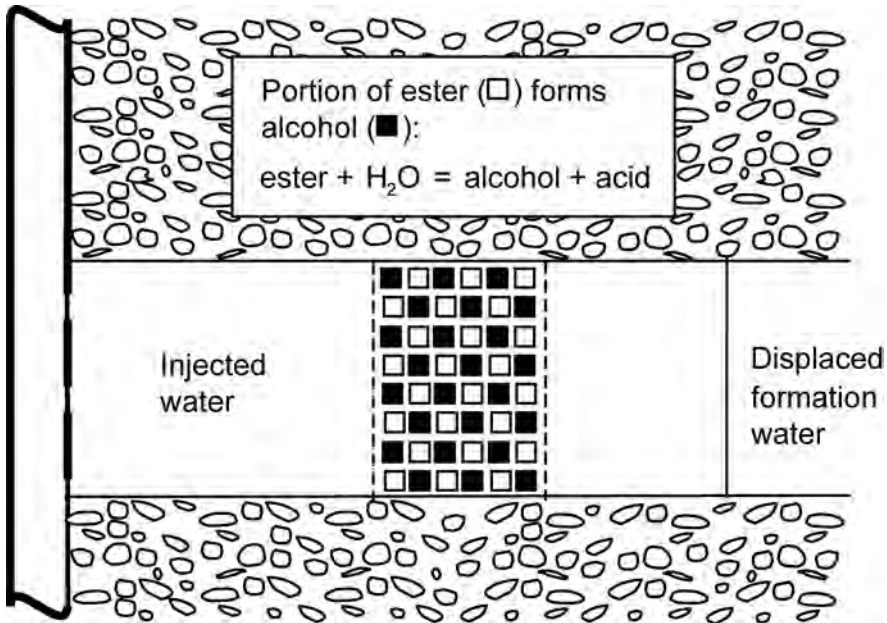


Fig. 5.4—Shut-in (reaction) period.

reservoir. The alcohol, however, is not in the original formation water, and can be detected at very low concentrations in the produced water, thus acting as a unique, secondary tracer.

At the end of the reaction period, the remaining ester and the product alcohol tracers are located together 10 to 20 ft from the wellbore. The tracers then are ready to be back produced to the wellbore and monitored at the surface in the produced water.

Fig. 5.5 shows the chromatographic separation of the product alcohol and ester tracers. This separation occurs because the product alcohol and water velocities are essentially the same, whereas the ester production velocity is slower because the ester must partition between the oil and water phases during production in the same manner described in the injection step. For an animation of the entire process, see <http://www.pe.utexas.edu/~castillo/lwl/> [CD edition includes video].

Throughout the production period, samples of the produced water are collected frequently at the surface. Total produced volume is measured at the time each sample is taken. At a portable laboratory at the wellsite, the samples are analyzed immediately for product alcohol and remaining ester tracer concentrations. A plot of concentration of tracers vs. total volume produced is developed during the production, as the samples are analyzed.

Fig. 5.6 shows a hypothetical example of typical tracer concentration profiles. All three tracer profiles show the effects of dispersion, which always occurs during flow in porous formations. The unreacted ester, for example, was injected as a square wave and returns as a Gaussian peak.

5.5.2 Summary of SWCT Test Features. The important SWCT test features are summarized below:

- The S_{or} measurement is made in situ in the waterflooded layers of the target formation. The tracers can go only where the injected water goes.
- Compared to coring or logging method results, the S_{or} results are from a relatively large reservoir volume.

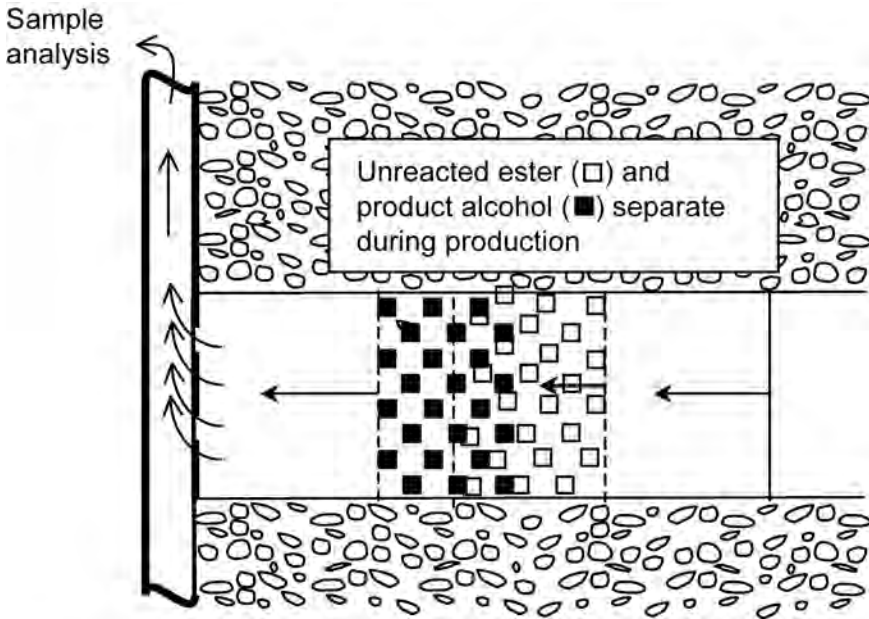


Fig. 5.5—Production period.

- The S_{or} measurement is carried out on an existing well, and usually in an existing completion, which can be perforated or openhole.
- Because the S_{or} measured actually is the volume fraction of oil in the pore space, the measurement is independent of porosity.

5.5.3 How the SWCT Test Works Quantitatively. Before discussing the design and interpretation of SWCT tests, we need to establish the quantitative relationship between tracer velocity, the tracer distribution coefficient, and S_{or} . Fig. 5.7 schematically shows a local population of ester tracer molecules in a control volume (V_c) of a pore. The tracer is assumed to be locally in equilibrium, even though the water phase is moving and the oil phase is fixed (residual oil conditions).

The number of ester molecules in the water (n_{ew}) is given by

$$n_{ew} = C_{ew}S_wV_c, \dots\dots\dots (5.2)$$

and the number of ester molecules in the oil (n_{eo}) is given by

$$n_{eo} = C_{eo}S_{or}V_c, \dots\dots\dots (5.3)$$

where C_{ew} and C_{eo} = the concentration of ester (molecules/unit volume) in water and oil, respectively; and S_w = saturation of water, in fraction of PV.

We determine the retardation factor for ester (β_e) by dividing these two equations:

$$\beta_e = \frac{n_{eo}}{n_{ew}} \dots\dots\dots (5.4)$$

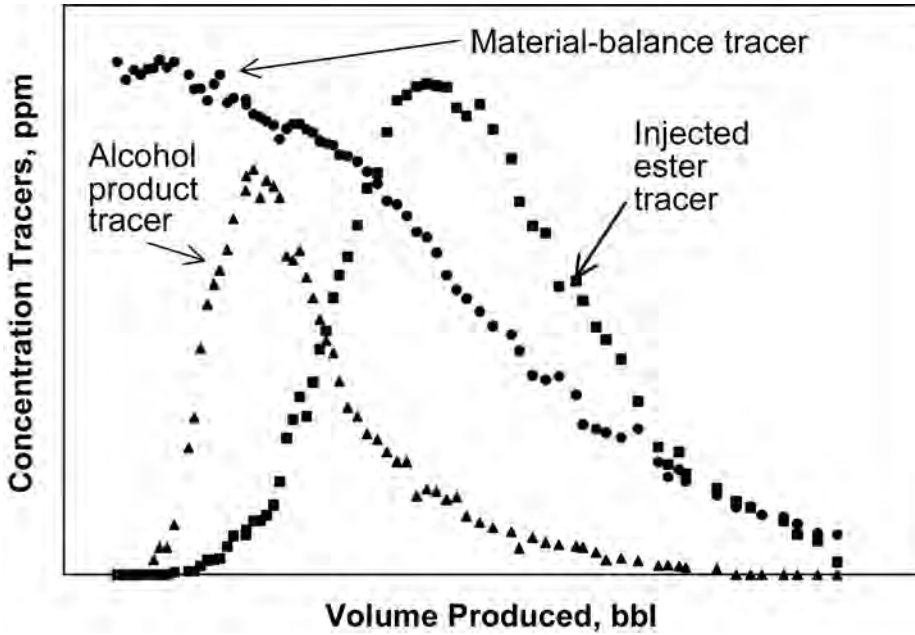


Fig. 5.6—Hypothetical SWCT test tracer-concentration profiles.

The larger β_e is, the more the ester tracer is retarded by the residual oil. Substituting in Eqs. 5.2 and 5.3 and canceling V_c yields:

$$\beta_e = \left(\frac{C_{eo}}{C_{ew}} \right) \left(\frac{S_{or}}{S_w} \right) \dots\dots\dots (5.5)$$

Because $C_{eo}/C_{ew} = K_e$ (see Eq. 5.1), the equilibrium distribution coefficient of ester between oil and water, and $S_w = 1 - S_{or}$, this becomes

$$\beta_e = K_e \left(\frac{S_{or}}{1 - S_{or}} \right) \dots\dots\dots (5.6)$$

The typical ester molecule spends a fraction of its time (f_i) in water and the rest of its time ($1 - f_i$) in oil. Elementary probability theory requires that

$$\frac{n_{eo}}{n_{ew}} = \frac{1 - f_t}{f_t} \dots\dots\dots (5.7)$$

The probable behavior of each ester molecule is the same as the behavior of a large population of identical molecules. From Eq. 5.6, then:

$$\frac{1 - f_t}{f_t} = \beta_e \dots\dots\dots (5.8)$$

Solving for f_i :

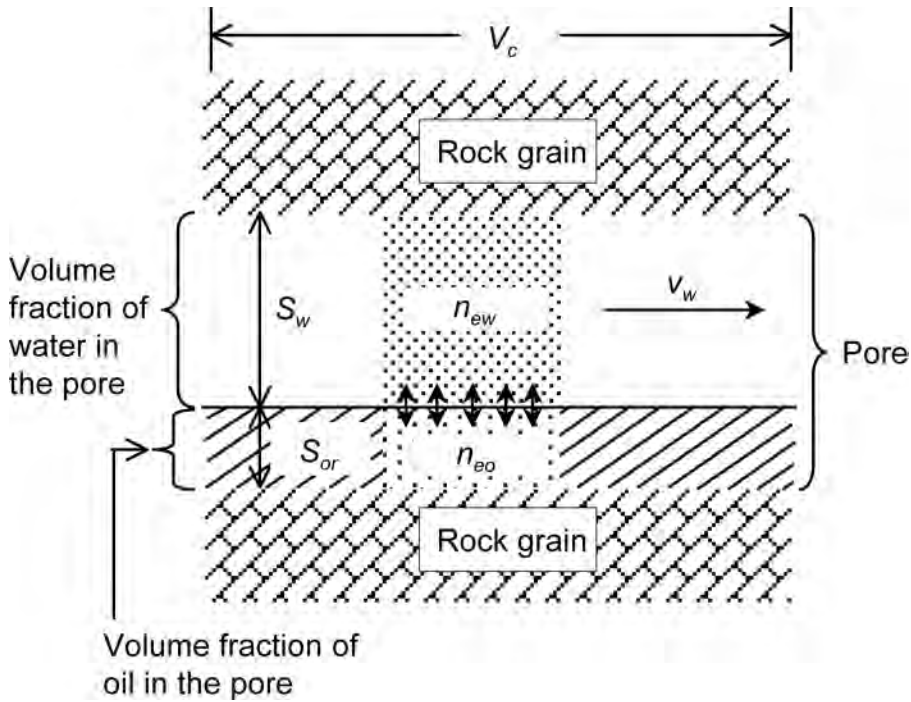


Fig. 5.7—Ester distribution between oil and water in a pore.

$$f_t = \frac{1}{1 + \beta_e} \dots \dots \dots (5.9)$$

The typical ester molecule will travel at the time-weighted average velocity:

$$v_e = f_t v_w + (1 - f_t) v_o, \dots \dots \dots (5.10)$$

where v_e , v_w , and v_o = the time-weighted velocities of the tracer molecule, water, and oil, respectively. Because $v_o = 0$ if oil is at residual saturation, the last two equations combine to give

$$v_e = \frac{v_w}{1 + \beta_e} \dots \dots \dots (5.11)$$

Eq. 5.11 is the fundamental equation for tracer chromatography in a porous medium. Solving Eq. 5.11 for β_e :

$$\beta_e = \frac{v_w}{v_e} - 1. \dots \dots \dots (5.12)$$

If we can develop a way to measure v_e and v_w using an in-situ test, then β_e can be evaluated. We then can measure K_e in the laboratory (at reservoir conditions) and substitute it into Eq. 5.6 to solve for S_{or} :

$$S_{or} = \frac{\beta_e}{\beta_e + K_e} \quad \dots\dots\dots (5.13)$$

Both the well-to-well flow of two tracers and the SWCT test are methods that have been used to measure v_e and v_w in the reservoir. Well-to-well was the first suggested of these¹³ and in it, tracers A and B are injected (dissolved in water) into Well 1, and water is produced from nearby Well 2 until the tracers arrive. Tracer A is a partitioning tracer, such as an ester, that has a partition coefficient ranging from 2 to 10. Tracer B is assumed to have an equilibrium distribution coefficient (K_B) of zero (insoluble in oil), so that its time-weighted velocity (v_B) = v_w . Tracer B arrives first, after time t_B , and tracer A later, after time t_A . Because the two tracers travel the same distance,

$$\frac{v_w}{v_A} = \frac{v_B}{v_A} = \frac{t_A}{t_B}, \quad \dots\dots\dots (5.14)$$

where v_A = the time-weighted velocity of tracer A. β_A then is determined from Eq. 5.12. Once the equilibrium distribution coefficient of tracer A (K_A) is measured, S_{or} follows from Eq. 5.13.

Often, the well-to-well method is impractical for determining S_{or} because well spacing is too large. At the velocities that can be achieved between such wells, t_A is months, or even years. Also, where different permeability layers exist, the different travel time in each layer causes excessive dispersion of tracers traveling from Well 1 to Well 2.

Chap. 6 in this volume presents the technology of well-to-well tracer tests and discusses where they can be beneficial to the management of a reservoir.

5.5.4 The SWCT Test. Using the SWCT test avoids the problems of too-wide well spacing and excessive tracer dispersion caused by layering. In the SWCT test, the tracer-bearing fluid is injected into the formation through the test well and then produced back to the surface through the same well. The time required to produce the tracers back can be controlled by controlling the injected volume on the basis of available production flow rate from the test well.

In a single-well test, tracers injected into a higher-permeability layer will be pushed farther away from the well than those in a lower-permeability layer, as indicated in Fig. 5.8a; however, the tracers in the higher-permeability layer will have a longer distance to travel when flow is reversed. As the tracer profiles in Fig. 5.8b show, the tracers from different layers will return to the test well at the same time, assuming that the flow is reversible in the various layers.

Flow reversibility in a single-well test is desirable for the reason just explained, but it complicates S_{or} measurement. The simple strategy of injecting two tracers with different partition coefficients does not work in this case. As Fig. 5.9 shows, tracers A and B separate during injection, just as in a well-to-well test, and at the end of injection, tracer B will be farther from the wellbore than tracer A because the presence of the residual oil retards A. During production, then, tracer B has farther to travel to return to the well. The separation achieved during injection is reversed during back production, so that A and B arrive back at the wellbore at the same time (if they were injected at the same time). No measurement of S_{or} is possible using Eqs. 5.12 and 5.13 because no information can be obtained about the ratio of velocities of A and B.

One possible way of avoiding this reversibility problem is to generate the second tracer in the formation instead of injecting it. The steps are: (1) Inject tracer A and push it into the target formation, as described above; (2) Stop flow to allow part of the injected A to react, forming tracer B in the same pore space where A is located, after the reaction time, A and B are together; (3) The fluid is then produced back into the test well; A and B must separate if

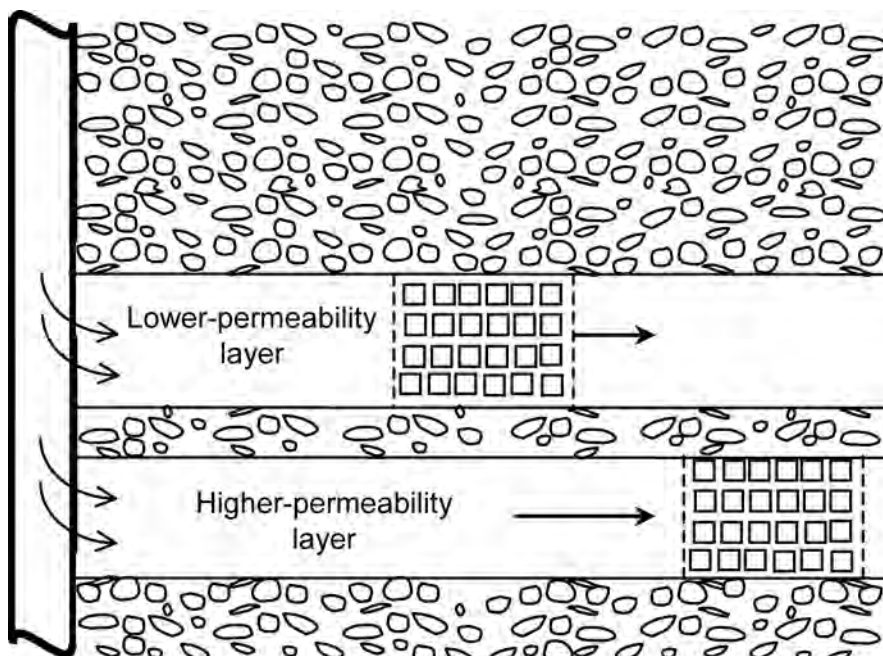


Fig. 5.8a—Injection of tracers into two layers of different permeability.

their equilibrium distribution coefficients (K_A and K_B) are different and if residual oil is present. This concept is the basis for the SWCT test patent.²

The practicability of this method depends on finding suitable tracers. The demands on partitioning tracer A are especially severe: inexpensive, available in reasonable quantities at high purity, nontoxic, not present in the reservoir fluids, and easily measured at low concentrations in water. It must have an appropriate K_A for the oil, water, and temperature of the target field, and, most importantly, it must react at a rate that allows formation of enough (but not too much) of a suitable tracer B. K_B must be different from K_A , and tracer B also must be measurable at low concentrations in the produced water, and not be present in the reservoir fluids.

A methyl, ethyl, or propyl ester of formic or acetic acid has proved suitable in every reservoir tested. These simple chemicals are sufficiently soluble in water, and have an appropriate range of K values and reaction rates. They are relatively inexpensive and nontoxic at the concentrations used, and they react with water to produce alcohols, which are not found in crude oils and can be detected readily in the produced fluid.

For best results,³ choose an ester with a retardation factor (β_e) in the optimum range ($0.5 < \beta_e < 1.5$). This requires that K_e be in the range $0.5(1.0 - S_{or})/S_{or} < K_e < 1.5(1.0 - S_{or})/S_{or}$. Use the best available estimate of S_{or} to fix this range. Then choose the optimum ester using available correlations¹⁴ for the dependence of K_e on temperature and water salinity.

In several past SWCT tests, two esters (e.g., methyl acetate and ethyl acetate) were used simultaneously to give two different depths of investigation for S_{or} in the same test. The multiple-ester test design has become increasingly popular in recent years.

5.5.5 Test Design. The design and implementation of a SWCT test for S_{or} is straightforward. Certain facts about the target formation are needed to begin test design. Some essential reservoir properties include oil cut of the test well; reservoir temperature; reservoir lithology; production rate; test interval size and average porosity; and formation water salinity.

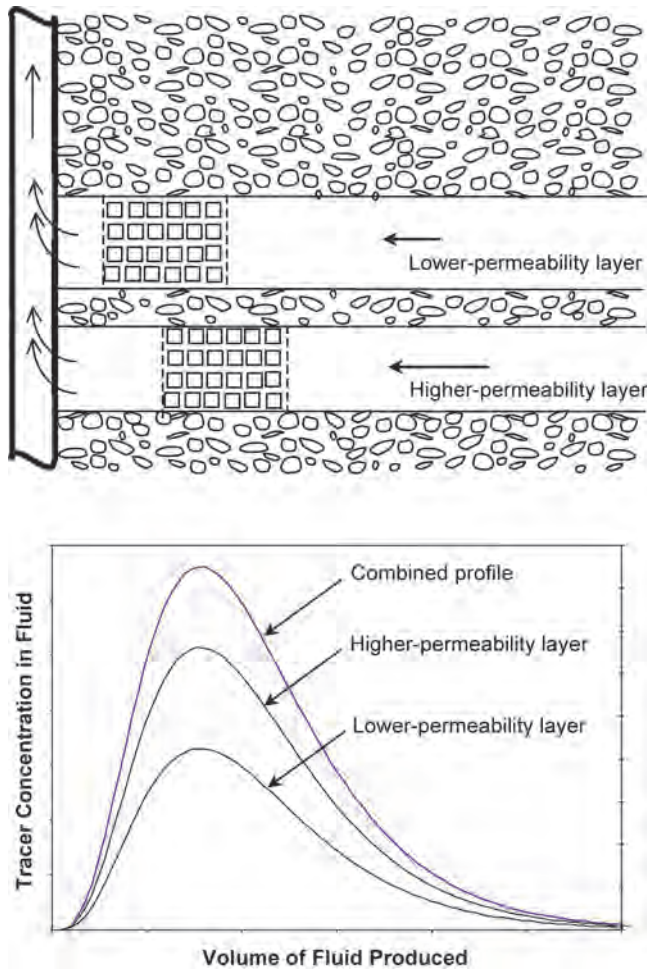


Fig. 5.8b—Production of tracers from two layers of different permeability.

Oil Cut of Test Well. Candidate wells for S_{or} measurement must be able to produce formation water to the surface. The produced fluid should be nearly all water to ensure that the test interval is at or near S_{or} . In cases where the test interval produces high oil cut, water can be injected into the test interval before testing to water-out the zone before tracers are injected.

Reservoir Temperature. Reservoir temperature dictates which esters are suitable for the SWCT test. The formate esters hydrolyze approximately 50 times faster than do the acetate esters, and are used in the reservoir temperature range of 70 to 135°F. The slower-reacting acetate esters generally are used in the 130 to 250°F range.

Reservoir Lithology. SWCT testing has been done in a variety of test conditions. In sandstone reservoirs, SWCT tests give satisfactory results for a wide range of test designs. Test timing, total injected volume, and the ester used can vary considerably for the same zone, with little effect on test interpretability.

However, SWCT tests in carbonate formations require much more precise design. In a given carbonate test zone, subtle changes in test design can cause significant variation in the tracer profile shapes. Each of our past carbonate test designs has required significant tailoring to overcome the dispersed nature of the production profiles generally present in carbonate test

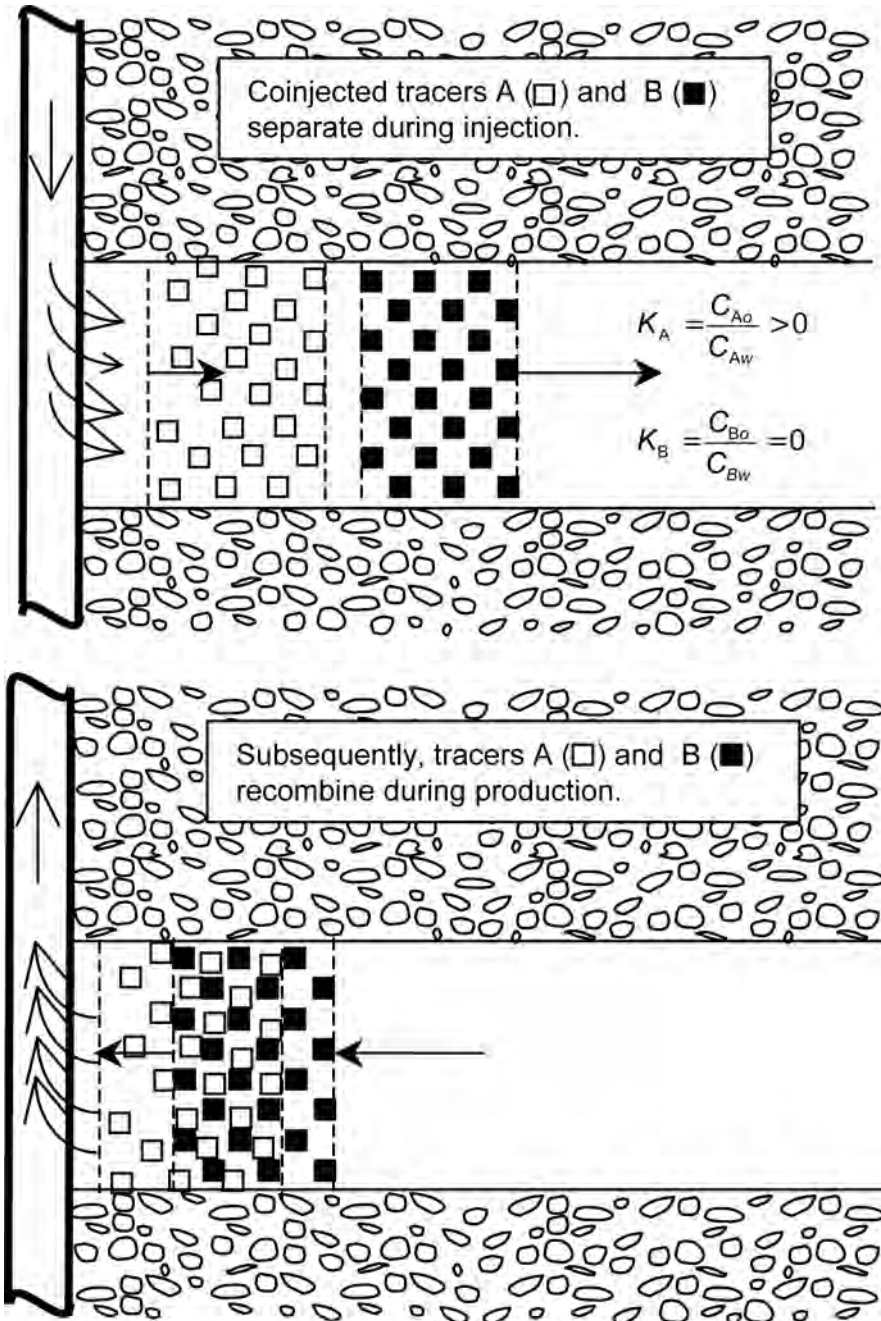


Fig. 5.9—Reversing composition profiles in a single-well injection/production test using tracers. C_{Ao} = concentration of tracer A in oil, C_{Aw} = concentration of tracer A in water, C_{Bo} = concentration of tracer B in oil, and C_{Bw} = concentration of tracer B in water.

results.¹⁵ The reason for this dispersed nature is that the assumption of local equilibrium is not always valid for carbonate reservoir tests. This problem is illustrated in Case 4 below.

Production Rate. The production rate of the candidate well controls the test size or volume to be injected. The amount of water that can be produced in one day is a normal test volume;

two days' production is a practical upper limit. In normal productivity reservoirs, the injection is sized to give a 15- to 20-ft depth of investigation into the formation. The injection rate of the SWCT test usually is approximately the same as the well's production rate. Care must be exercised to avoid fracturing the formation during test injection.

Test-Interval Size and Average Porosity. SWCT test can be carried out on cased and open-hole completions. Estimated interval size and porosity are used to calculate a theoretical radius of investigation for the design injection volume, although S_{or} results are not dependent on either. Interval sizes of from 1 to 100 ft have been tested with satisfactory results. Generally, testing on 10- to 50-ft zones generates more definitive results.

Formation-Water Salinity. Because it normally avoids chemical incompatibility, water that is produced from the test well generally is used to carry the chemical tracers into the reservoir. Because K_e depends on it, water salinity also is a factor in choosing the best ester for the SWCT test. To avoid difficulties during injection of the tracers, closely examine the water quality (especially suspended solids) and any precipitation tendencies.

5.5.6 Field Procedures. After selecting the ester and sizing the test volume, determine the field-test location, production method, and safety requirements. Then, schedule and implement the test.

Four lift methods have been used in SWCT testing. They are free flow, electric submersible pump, rod pump, and gas lift. These lift mechanisms are listed roughly in order of desirability, but all are satisfactory.

Before the field test, the candidate well should be produced long enough to establish the oil cut, measure the stabilized production rate, and clean up the tubular goods in the completion. Then accumulate produced water for the upcoming test in clean tanks near the well. Position the portable laboratory/pumping system near the test well.

Pure tracer chemicals usually are delivered to the wellsite in 55-U.S.-gal drums. The tracers either can be batch-mixed with formation water before injection, or continuously metered into the water during injection. Fig. 5.10 shows a schematic for a typical field setup for continuous metering of chemical in the injection water. For batch mixing, the tank can serve as the mixing vessels. With either batch-mixing or continuous metering, filter the water to one-micron or higher quality to prevent plugging when the fluids enter the reservoir.

After a short period for analytical equipment checkout, inject the chemical solution of ester and material-balance tracer and push it according to test design. Samples of the injection water should be analyzed periodically to verify tracer concentrations, and volume, rate, and pressure information should be monitored carefully throughout the injection. Be careful not to part the formation by exceeding the fracture gradient.

Once the injection is complete, the well is secured for the planned shut-in period. When the shut-in period is over, the well is placed on production. Fig. 5.11 shows a general schematic for the production phase of a SWCT test. The produced water flows through a portable separator (if necessary) to the storage tanks on location, where its volume is carefully measured. Production volume also can be measured using a field production test separator, if one is available.

During production, water samples should be taken near the wellhead and analyzed on location for tracer concentrations. On-site chemical analysis is necessary to gather data that are accurate for the time of production, whereas sending the samples to a service laboratory for analysis would allow additional hydrolysis of the ester to take place during transport. At the time each sample is taken, the total production volume is recorded and plots of tracer concentration vs. volume produced are generated. These tracer concentration profiles are the essential field data for the SWCT test.

Because of dispersion, the total produced volume required normally is two to three times the injected test volume. Injected volume usually is one day's production, and two to three days normally are required for the back-production phase of an SWCT test.

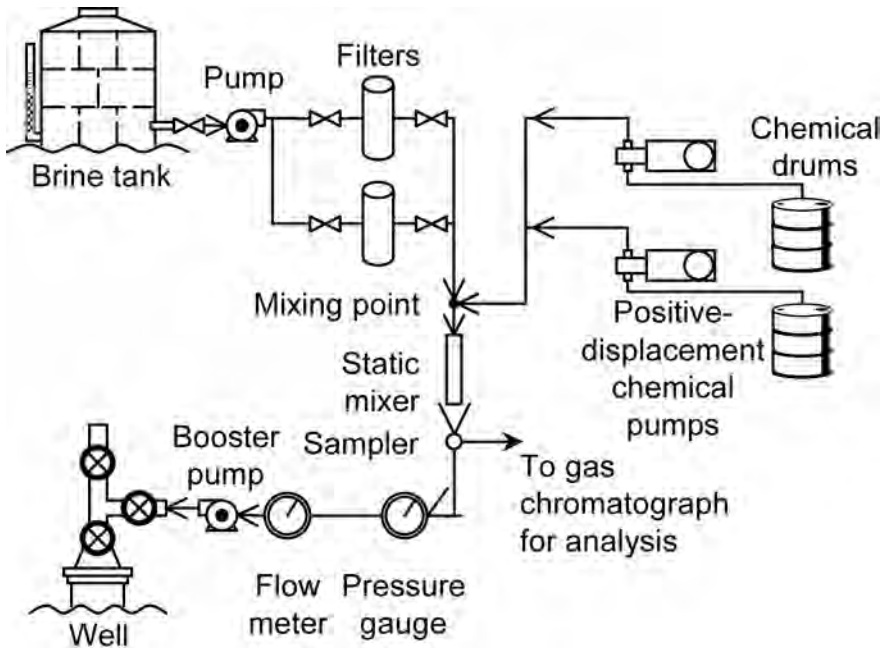


Fig. 5.10—Schematic of SWCT test injection step field setup.

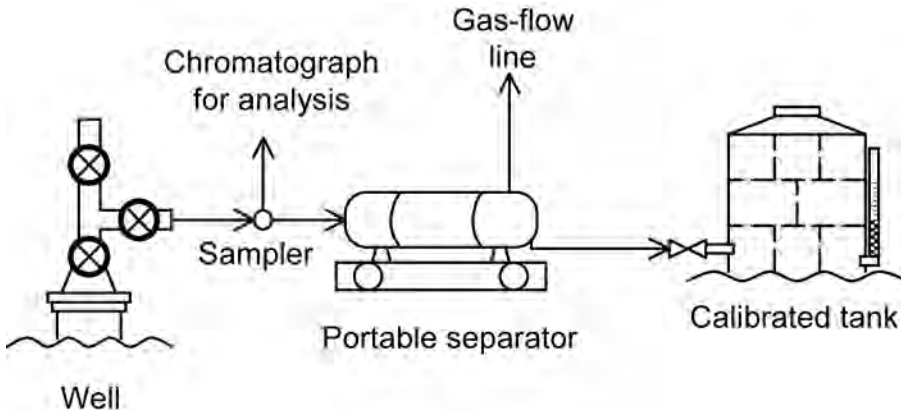


Fig. 5.11—Schematic of field setup for SWCT test production step.

5.5.7 Test Data Interpretation—Case 1. Tomich *et al.*¹ report one of the earliest SWCT tests, which was performed on a Frio Sandstone reservoir on the Texas Gulf Coast. The results of this test are used here to demonstrate the details of SWCT test interpretation for an ideal situation.

The test well in the Tomich *et al.*¹ report was in a fault block that had been depleted for several years. Because of the natural water drive and high permeability of the sand, the formation was believed to be near true S_{or} . When the well was returned to production (gas lift), it produced 100% water at a rate of 1,000 BWPD.

On the basis of observed reservoir temperature (160°F) and brine salinity [100,000 ppm total dissolved solids (TDS)], ethyl acetate was chosen as the primary tracer. Formation oil and

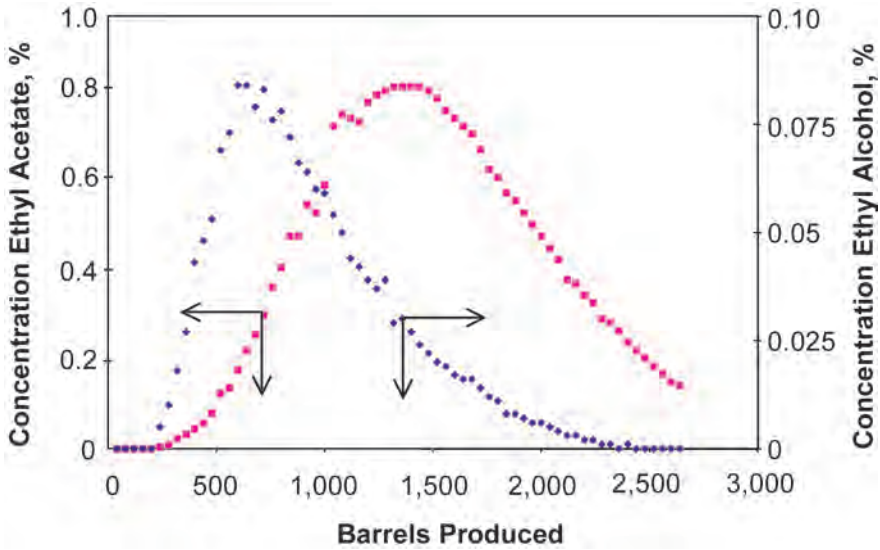


Fig. 5.12—SWCT test results from a Frio Sandstone well.

water samples were obtained for laboratory measurement of K at reservoir temperature conditions. The value of K_e measured for ethyl acetate was 6.5 at these conditions.

The test injection consisted of 1,000 bbl of formation water carrying ethyl acetate (13,000 ppm) and methyl alcohol (5,000 ppm), followed by a push bank of 1,000 bbl of formation water carrying methyl alcohol (5,000 ppm), injected over a period of two days. An eight-day shut-in period followed. During the production period, samples were collected regularly and analyzed on site using gas chromatography. The observed data are plotted as tracer concentration vs. produced volume in Fig. 5.12.

In ideal cases, when enough data have been gathered to define the tracer profiles, it is possible to use Eqs. 5.11 through 5.13 to approximate S_{or} in the field. If product tracer B and unreacted ester A begin together in the formation, the produced volume when A arrives back at the well (Q_{pA}) is related to the produced volume when B arrives (Q_{pB}) by the formula

$$Q_{pA} = Q_{pB}(1 + \beta_A), \dots\dots\dots (5.15)$$

where Q_{pA} and Q_{pB} are in bbl.

This suggests that if on the same graph we plot normalized concentration of A vs. volume produced (Q_p) and normalized concentration of B vs. $Q_p(1 + \beta_A)$, the two curves should coincide. Because we do not know β_A , this must be done by trial and error (i.e., β_A is adjusted until the best possible match of the two profiles is found).

Fig. 5.13 demonstrates this procedure. Profiles from the SWCT test (Fig. 5.12) first were normalized by dividing each observed concentration by the peak value measured for that tracer. β_A then was varied to obtain the plot shown. The best-fit value for β_A was 0.97.

Using Eq. 5.13, the S_{or} is approximated as

$$S_{or} = \frac{\beta_A}{\beta_A + K_A} = \frac{0.97}{0.97 + 6.5} = 0.13.$$

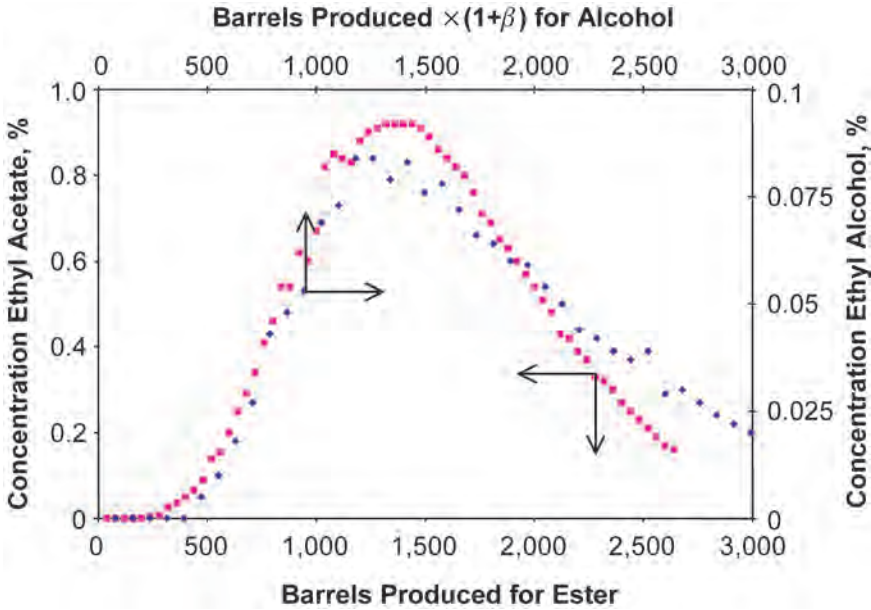


Fig. 5.13—Approximation of S_{or} using alcohol/ester superposition.

Agreement is only fair over the entire curve in Fig. 5.13; still, this result is quite close to the final interpreted result, obtained as described below under core/simulation. The approximated S_{or} depends on the validity of several idealized assumptions, which are rarely satisfied in practice:

- That no B is present in the injected A, and that most of the hydrolysis reaction occurs during shut-in (no flow), so that B and unreacted A are exactly together before backflow begins. In reality, some reaction takes place during injection and production, and there always is some B present in the A as purchased. These two sources explain the high ethyl alcohol “tail” observed in Fig. 5.13.

- That S_{or} is uniform throughout the formation tested. In practice, however, there often is evidence of several layers with different saturations in a given completion.

- That the injected tracer-carrying fluids are stationary in the reservoir throughout the shut-in period. Actually, fluids sometimes relocate during the shut-in period, because of pressure gradients across the field or pressure differences within subzones of the test completion.

- That the fluids inject uniformly into subzones and subsequently produce back to the test well reversibly. Total fluid flow reversibility is not observed in many tests.

Obtaining a more reliable answer for S_{or} requires a detailed simulation of the actual test procedure for a given SWCT test. Simulators are available to account for all the nonideal situations listed above. Simulation is time-consuming and is an added expense, but in our experience, it always is justifiable and its expense is small compared to that of field data acquisition.

Theory of Simulation. Mathematical modeling of the ideal SWCT test assumes that the carrier fluid flow is incompressible, pseudosteady state, single-phase, and radial only; that the formation is a homogeneous layer of thickness (h) and porosity (ϕ) extending from the wellbore radius (r_w) to an external boundary radius (r_e), where reservoir pressure is constant.

With these assumptions, the interstitial fluid velocity (v_{fi}) is given by

$$v_{fi} = \frac{q}{2\pi h \phi S_f r} \text{ for } r_w \leq r \leq r_e, \dots\dots\dots (5.16)$$

where r = radial position; q = fluid flow rate in the single well ($q > 0$ is injection and $q < 0$ is production); h = height of test zone; ϕ = porosity; and S_f = flowing fluid saturation, constant.

The additional assumptions regarding the tracers are:

- That K_A for tracer A is constant and that A is in local equilibrium between flowing fluid (saturation S_f) and residual fluid (saturation S_r). For Case 1, $S_r = S_{or}$ and $S_f = 1.0 - S_{or}$.
- That tracer A (primary) reacts in situ to form tracer B (product) at a rate given by

$$R_H = k_H C_A, \dots\dots\dots (5.17)$$


where R_H = hydrolysis reaction rate, in moles of A per vol-day; C_A = concentration of A, in mol/volume; and k_H = hydrolysis rate constant (days⁻¹) in the aqueous phase. Tracers are dispersed in the radial flow with an effective dispersion coefficient (D_a), given by


$$D_E = \alpha v_{fi}, \dots\dots\dots (5.18)$$


where α = dispersivity (ft).


The material balance for tracer A is the partial differential equation:

$$(1 + \beta_A) \frac{\partial C_A}{\partial t} + \frac{q}{2\pi h \phi (1.0 - S_{or})} \frac{1}{r} \frac{\partial C_A}{\partial r} + k_H C_A = \frac{1}{r} \frac{\partial}{\partial r} \left(r D_E \frac{\partial C_A}{\partial r} \right) \dots\dots\dots (5.19)$$


 (Accumulation of A
in both phases)


 (Convection (Reaction)
of A)


 (Reaction)


 (Dispersion)

Similar equations apply for product tracer B and the material-balance tracers.

SWCT test simulation requires the numerical solution of these equations for A, B, and the material-balance tracer. The equations first are converted to finite-differenced form, based on the perfectly mixed cell model.¹⁶ The simulation program then solves the finite-differenced equations for the concentrations of the tracers in a radial series of cells over the test time interval.

Input to the simulation program consists of:

- Known parameters, which are: q as a function of time (injection, shut-in, production), injected concentration of tracer A (C_A) and concentration of tracer B (C_B) as a function of time; r_w , h , ϕ ; K_A and K_B .
- Unknown (estimated) parameters, which are: k_H , S_{or} , and the radial dimension of the cells (ΔR). Note: according to the theory of the perfectly mixed cell model for small time intervals, $\Delta R = 2\alpha$.

5.5.8 Finding Best-Fit Parameters Using the Simulator—Case 1 Simulation. Simulation of a relatively ideal test now will be demonstrated using the tracer profiles of Case 1, shown in Fig. 5.12. The known parameters are input to the program, along with estimated values for ΔR , k_H , and S_{or} .

First, several runs are made with different ΔR values, keeping all other parameters constant. The simulation predicts values for tracer concentrations vs. volume produced. Fig. 5.14 shows the C_A results superimposed on the field data, for different values of ΔR . The best-fit value appears to be approximately 0.50 ft. (Further refinement, using least-squares criteria, yields a value of 0.52 ft.) Note that ΔR affects the shapes of the concentration peaks, not their average positions on the produced volume axis. The shapes of C_A and C_B peaks are similarly affected.

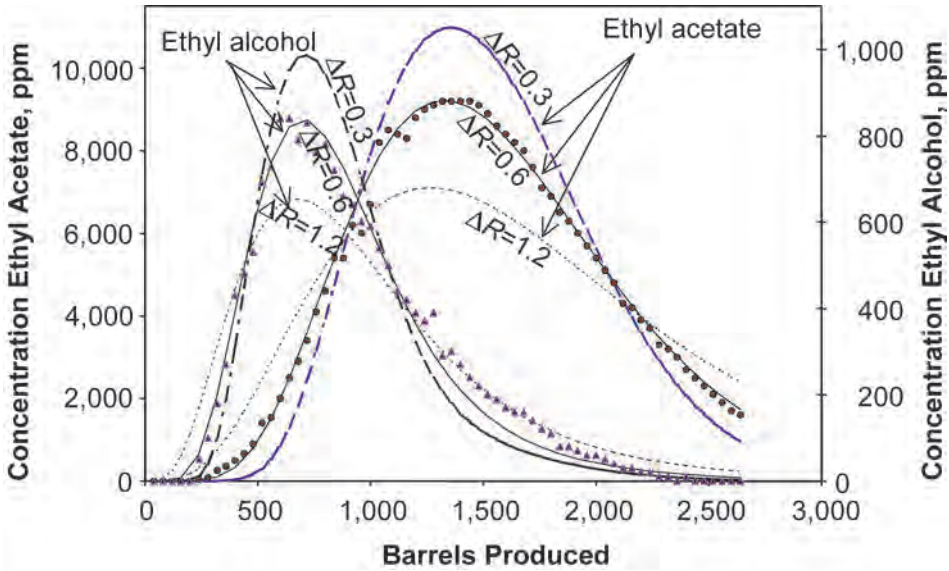


Fig. 5.14—Variation of ΔR shown for three cases.

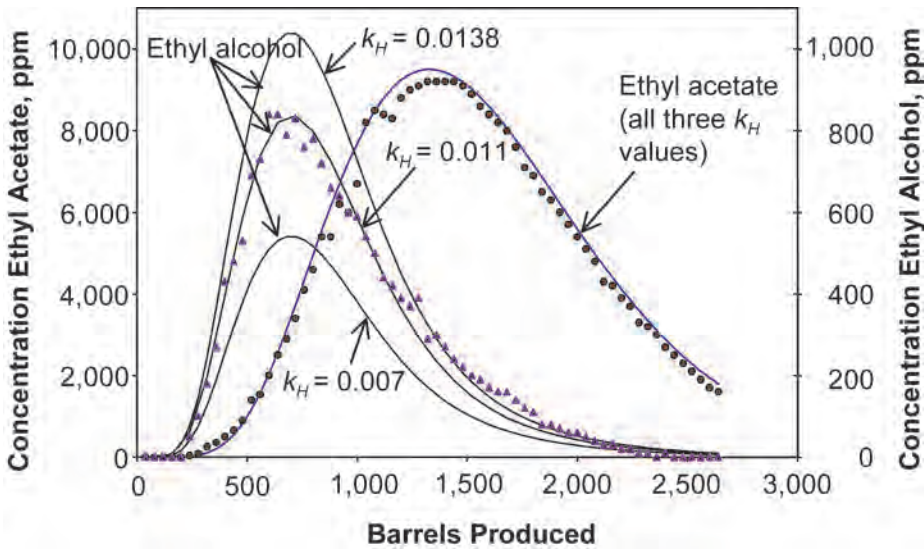


Fig. 5.15—Variation of k_H shown for three cases.

The next step is to find the best-fit value of k_H , which determines how much product tracer B will form. In Fig. 5.15, the simulated profiles for C_B are superimposed on the field data for C_B , for a range of values of k_H . Note that k_H affects the height of the C_B peak, but not its position. Because of the relatively small amount of hydrolysis in this case (less than 10% of the injected ester was hydrolyzed), the height of the simulated C_A peak changes very little when k_H is varied in this range of values.

Finally, the input value for S_{or} is varied. Minor adjustments are made in k_H to keep the height of the C_B peak constant. As Fig. 5.16 shows, changing the S_{or} moves the position of the product tracer peak on the “produced volume” axis. Changing the S_{or} does not affect the pre-

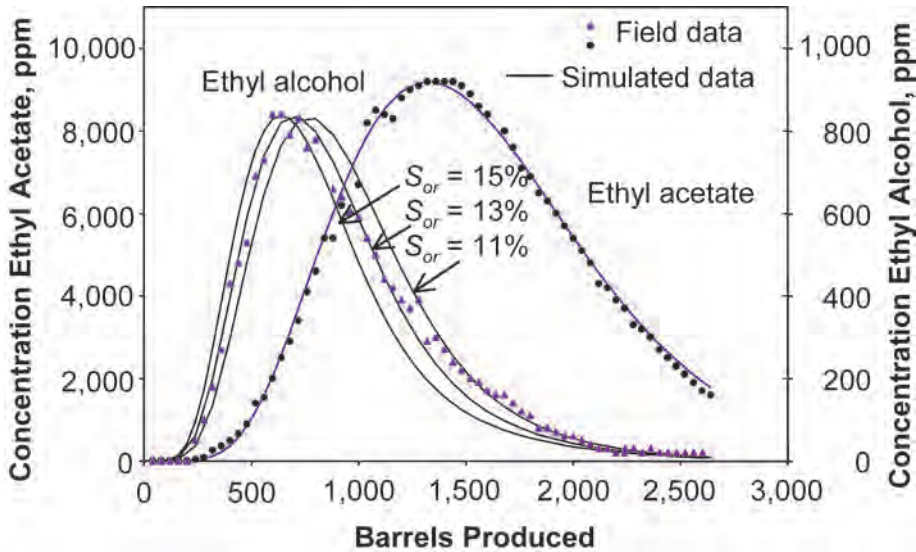


Fig. 5.16—Varying S_{or} to match the ethyl alcohol profile.

dicted position of the unreacted ester peak because of the reversibility effect that was discussed earlier.

The final best-fit simulation is shown with the field data in Fig. 5.16. The best-fit estimates of the unknown parameters for Case 1 are $\Delta R = 0.52$ ft, $k_H = 0.011$ days⁻¹, and $S_{or} = 0.13$. To indicate the level of precision expected in the test, simulated C_B peaks also are shown for $S_{or} = 0.11$ and $S_{or} = 0.15$. $S_{or} = 0.13 \pm 0.02$ is the best estimate for S_{or} for this reservoir, using the SWCT method.

5.5.9 How To Simulate Nonideal SWCT Tests. The 400+ SWCT tests performed to date have demonstrated that most cases are not ideal. Some reservoir factors cause the produced concentration profiles to have irregular shapes. The challenge to the test interpreter in those cases is to deduce what has caused the irregularities and to modify the simulation to obtain a credible match to the field profiles.

The three major nonideal conditions observed in SWCT tests, in order of their potential encounter, include fluid movement in the formation at the test site; in carbonates, a lengthy time required for local equilibrium to be achieved by diffusion in liquids, as compared to test duration; and in sandstones, nonreversing flow behavior in formation layers.

Fluid Movement. In active parts of a reservoir (i.e., when other producers or water injectors are close to the test well), there might be fluid movement in the formation at the test site. This is known as fluid drift. The tracers injected with the SWCT test fluids are subjected to a flow field that is not radial and reversible, as is assumed by the simulation theory above. Such was the situation during the first SWCT test.¹ A specialized simulator was developed to interpret that test.

The simulation theory assumes that a linear flow field with a fixed drift velocity, v_D , is superimposed on the radial flow at the test well. This requires the numerical solution of partial differential equations involving two space dimensions and time. Obtaining a best fit to field data involves varying drift velocity, v_D , in addition to the unknowns ΔR , k_H , and S_{or} . The drift velocity is caused by a regional pressure gradient in the formation, whereas the radial component of velocity is caused by injection or production at the test well. The original simulator is furnished to licensed users of the SWCT method.

Local Equilibrium Time Length. The pore geometry of most carbonates is such that the basic assumption of local equilibrium of partitioning tracers is not valid. A significant fraction of the pore space is not directly in the flow paths, but is only in diffusional contact with these paths. Because the time required for local equilibrium to be achieved by diffusion in liquids can be long compared to the duration of the SWCT test, dual-porosity models must be used to simulate SWCT tests in carbonates. In addition to ΔR , k_{H_2} , and S_{or} discussed earlier, several new unknown parameters must be added to the list:

- The fraction of the total PV that appears to be poorly connected for flow (dead-end fraction).
- The effective diffusion parameter for each tracer in the poorly connected fraction.
- S_{or} in the poorly connected pores.

The dual-porosity simulator has been used to interpret more than 30 tests to date. Case 3 below uses the dual-porosity simulation model.

For a summary of SWCT test experience in carbonate formations, see Deans and Carlisle.¹⁵

Nonreversing Flow. Interpretation of SWCT tests in sandstone formations has revealed a very common nonideality. The formations tested appear to consist of two or more layers, as might be expected, but reversing behavior is not observed. One likely explanation is the existence of local pressure differences between the layers, caused by activity at other wells in the reservoir. Qualitatively, the effects of such pressure differences on the SWCT test results are:

1. A layer at higher pressure accepts less fluid during injection and produces more fluid during production than a parallel layer at lower pressure. This results in a nonideal profile because the tracer bank from the higher-pressure layer will return earlier than it should and the tracer from the lower-pressure layer will be late.

2. During the shut-in period for ester hydrolysis, fluid will flow through the wellbore from the higher-pressure layer to the lower-pressure layer. One tracer bank moves back toward the well and the other moves away during the shut-in period. This special flow condition, called crossflow, adds to the separation caused by effect 1.

3. As mentioned earlier, apparent differences in S_{or} sometimes are observed in different layers in the same formation. Along with nonreversing flow, these differences require the use of a multilayer simulator program to interpret certain SWCT tests.

Once the specific nonideal conditions are recognized, the SWCT test simulation proceeds as before. The unknown parameter set now contains an estimate of the number of layers present, the fraction of total fluid injected/produced from each layer, the crossflow between layers, and the S_{or} for each layer. Because of the large number of adjustable parameters, semi-automated optimum-seeking subprograms have been developed help find the best fit. Seetharam and Deans¹⁷ demonstrate that an accurate flow-weighted S_{or} is obtainable using such a multilayer simulator to match field data, even though the layering parameters are not unique. Case 2 (below) presents an example of a SWCT test in a layered sandstone formation.

In all SWCT test simulations, the objective is to find the simplest simulator model that adequately matches the observed tracer profiles. The same model must match all tracers used in a given test (ester, product alcohol, and material-balance tracers). In some tests, one or more additional tracers may be used in different injection patterns to identify wellbore and/or formation flow irregularities. The more tracers that are used, the more difficult it is for the simulator to find a reasonable model to fit all field-measured tracer profiles. Our experience suggests, however, that several models can adequately describe a given set of profiles, and that the least-sensitive parameter to changing models is the main target, S_{or} .

5.5.10 Simulation of SWCT Tests in Layered Formations—Case 2. The second field test example is from a candidate test zone with the following characteristics:

- Produced water cut of 0% (100% oil).
- Reservoir temperature of 234°F.

- Lithology is sandstone.
- Produced by gas lift.
- Production rate of 500 B/D.
- Perforated interval of 45 ft.
- Average porosity of 22%.
- Brine salinity of 43,000 ppm.

No well was available in this field that produced water only. In this case, the test well initially produced 100% oil. To generate residual oil saturation near the well, 6,500 bbl of filtered water first was injected into the test zone. The waterflood injection took eight days to complete, after which the well produced 100% water during a short test.

Samples of produced oil and water were collected for ester K value measurement. Ethyl acetate was selected as a suitable partitioning tracer. Its K value was 3.65, based on laboratory measurements at reservoir conditions. With an assumed S_{or} of 25%, the corresponding value of β is 0.94, which is close to the optimum value of 1.0.

For the test that followed the waterflood, 135 bbl of formation water was injected containing ethyl acetate (7,000 ppm), normal propyl alcohol (NPA) (3,900 ppm), and isopropyl alcohol (IPA) (12,700 ppm). This was followed by 550 bbl of formation water carrying only isopropyl alcohol (12,700 ppm). The injection rate was 650 B/D and wellhead pressure was 1,200 psia during injection. Wellhead pressure was monitored carefully during injection to avoid fracturing the test zone.

The SWCT test injection required 1.15 days. The well then was shut in for five days to allow hydrolysis of a fraction of the ethyl acetate tracer. After hydrolysis, the gas lift system was turned on and the well was produced through a separator at an average rate of 500 B/D, with a stable gas lift ratio of 620 scf/bbl.

The production period was 2.7 days, throughout which samples of the produced water were taken at 5- to 15-minute intervals and analyzed immediately at the wellsite for tracer content. Total produced volume was carefully recorded at the time of each sampling. Total produced volume was 1,350 bbl. No oil cut was observed in the produced fluids at the end of the 1,350-bbl production period.

The field data from this test are plotted in **Figs. 5.17 and 5.18** as tracer concentration vs. total produced volume, along with simulation results. The best-fit simulation required four layers, with minor irreversible flow. The ethyl acetate contributions from the four layers are shown in **Fig. 5.17**, along with the composite concentration, which is the flow-weighted sum of the four layers. The two main layers accepted 73% of the injected tracer, and produced the same fraction. The early layer took 13% of the injection and gave back 19% of the production, and the late layer took 14% of the injected fluid, but only produced back 9%.

The predicted ethanol concentrations for the same four-layer model are shown in **Fig. 5.18**. To obtain the ethanol best fit, only the S_{or} was varied for the four layers. The two main layers have an S_{or} ranging from 22 to 28%. A radial gradient of oil saturation caused by the waterflood performed before the SWCT test would produce a similar effect.

On the basis of this model, the tracer-injection average S_{or} is calculated to be $26 \pm 2\%$. This is a permeability-thickness-weighted average for the PV accessed by the ethyl acetate, which is roughly the volume of a cylinder 8 ft in radius and 45 ft high.

5.5.11 Simulation of SWCT Tests in Dual-Porosity Media. Tracer test results from many carbonate formations seem far from ideal when compared to those from sandstone formations. One of the fundamental assumptions of the SWCT test—local equilibrium of tracer in all the available fluid—is invalid for carbonates. This also is the case with fractured sandstones.

Fig. 5.19 shows the assumed situation in these cases. Tracer material being transported through the well-connected pores can diffuse into the fluid in the dead-end pores. Depending

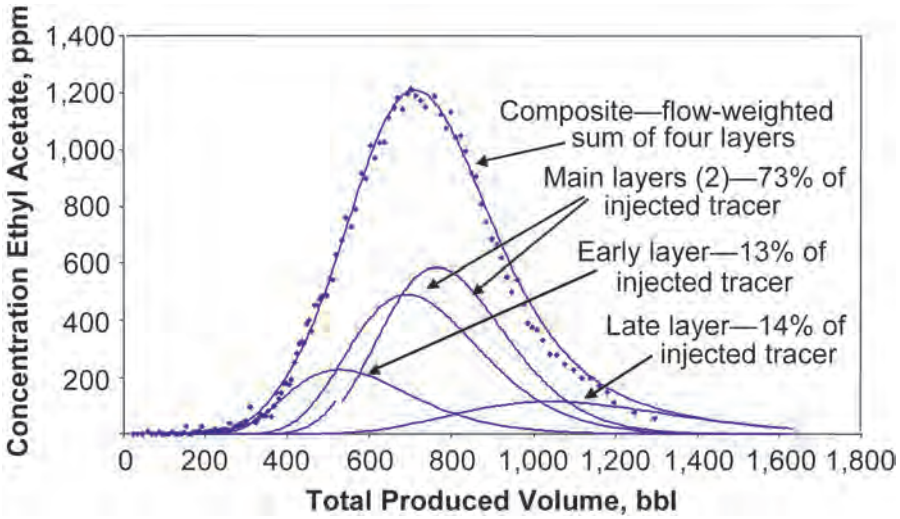


Fig. 5.17—Ethyl acetate field data and simulation, Case 2.

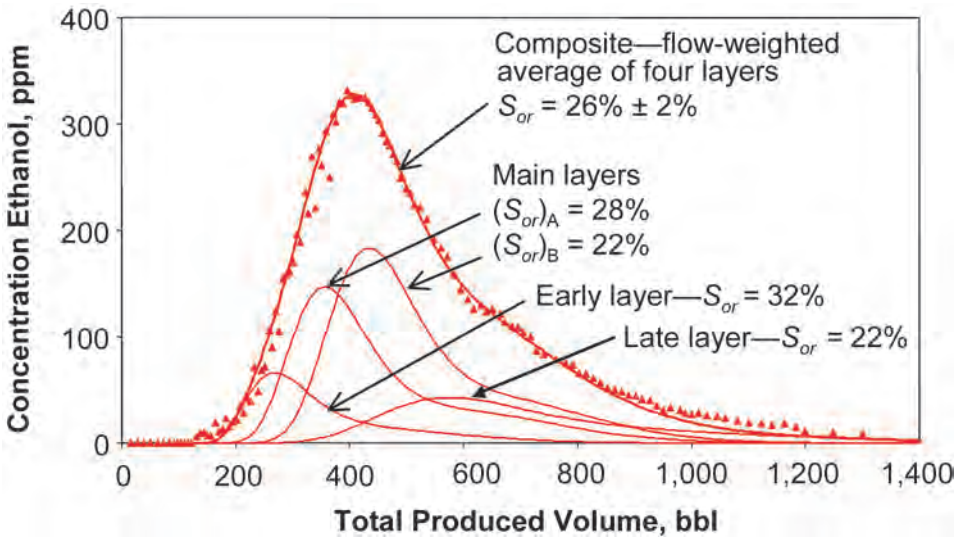


Fig. 5.18—Ethanol field data and simulation results, Case 2.

on the geometry of the pore system and the flow rates, however, the tracer might not have enough time to approach equilibrium by diffusion during the test.

A dual-porosity simulator accounts for this effect.¹⁵ First, a “source” term is added to each tracer material-balance equation, which now describes the flow of tracer in the well-connected pores. New material-balance equations then are written to describe the diffusion of each tracer in the local dead-end pores. The diffusion equations are connected to the flowing pore equations through the source term in the original material balances.

The new model introduces three new parameters:

- The S_{or} in the dead-end pores, which is not necessarily the same as S_{or} for the well-connected pore space.

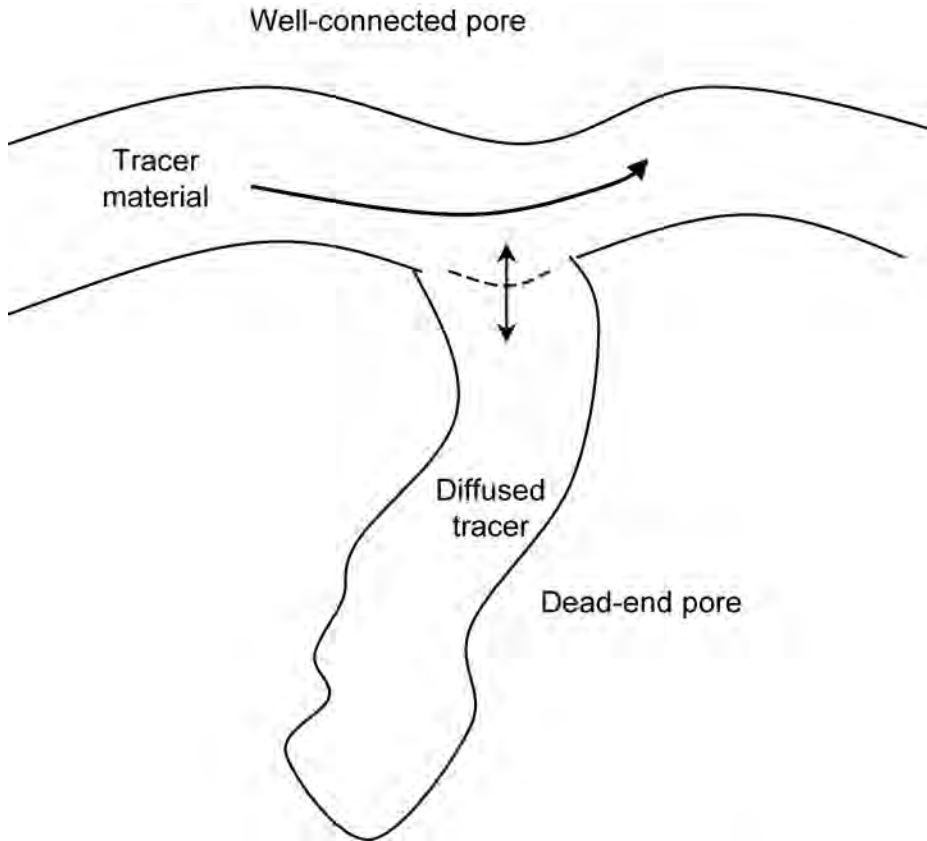


Fig. 5.19—Schematic of dual-porosity system.

- The fraction of total porosity that is in the dead-end pores.
- A diffusion parameter that controls the rate at which tracers diffuse in the dead-end pores (this parameter is smaller for long, thin pores and larger for short, fat pores).

For details on the numerical solution of the dual-porosity model equations, consult Deans and Carlisle.¹⁵

5.5.12 Simulation of SWCT Tests in Carbonate Formations—Case 3. The field test example for Case 3 demonstrates the extreme nonidealities that are possible in carbonate formations. The test well in this case was completed in a carbonate reef structure in Alberta, Canada. Test well characteristics were:

- Produced water cut of 99%.
- Reservoir temperature of 133°F.
- Lithology is vuggy carbonate.
- Production rate of 320 B/D.
- Perforated interval of 13 ft.
- Average porosity of 12.8%.
- Brine salinity of 113,000 ppm.
- S_{or} (anticipated) of 20%.

Because of the low reservoir temperature and high brine salinity, ethyl formate was chosen as the partitioning tracer for this test. This was designed to be a relatively small-volume test because previous large-volume tests in the same formation had not produced definitive results

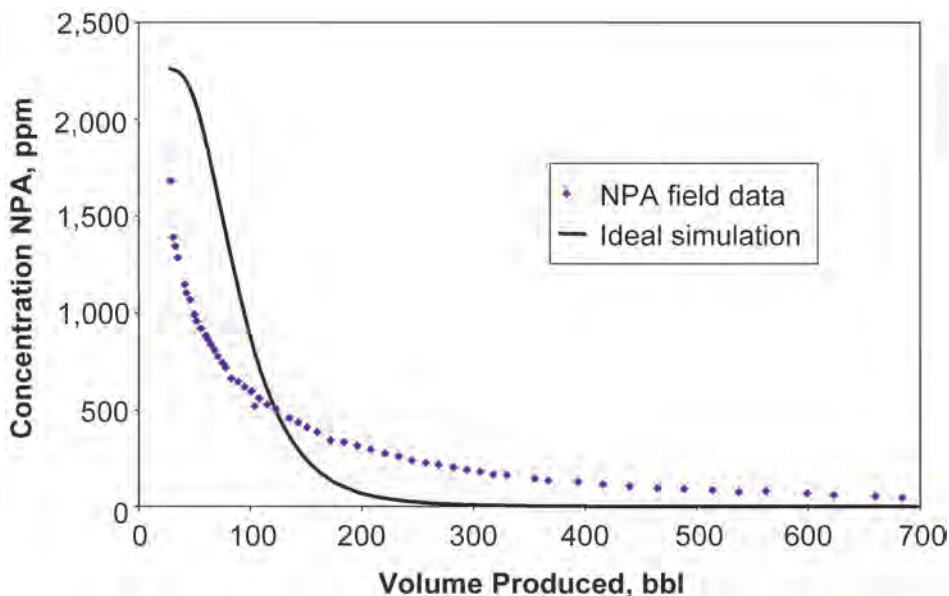


Fig. 5.20—NPA field data and ideal simulation, Case 3.

and had taken many days to complete production. Because ethyl formate is highly reactive, a decision was made to try to complete the test in less than 5 days. At an injection rate of approximately 300 B/D, 20 bbl of formation water was injected carrying ethyl formate (10,800 ppm), IPA (cover tracer) (4,700 ppm), and NPA (material-balance tracer) (2,300 ppm). This bank was followed with a net push injection of 50 bbl of water containing NPA (2,300 ppm).

The well was shut in for 1.3 days to allow part of the ethyl formate to hydrolyze, producing the secondary tracer, ethyl alcohol. The well then was produced at a rate of 300 B/D for 3.0 days. Samples were taken at regular intervals and analyzed at the wellsite for ethyl formate, ethyl alcohol, NPA, and IPA. These data are plotted as concentration vs. produced volume in **Figs. 5.20 through 5.24**.

Fig. 5.20 shows the simulation of the NPA material-balance tracer profiles with an ideal model that assumes local equilibrium. Several features are obvious:

- The ideal model is inadequate.
- Although all the injected water contained 2,300 ppm of NPA, the first returns from the formation contain significantly lower concentrations.
- The field data “tail” very badly—NPA is still being produced after 600 bbl, even though only 70 total bbl containing NPA were injected into the formation.

Figs. 5.21 through 5.24 show the dual-porosity test simulation results for each of the four tracers. The fraction of dead-end pores is 0.80 for all these simulated profiles. The S_{or} in both flowing and dead-end pores was 0.24. The dimensionless diffusion parameters ranged from 0.22 for ethyl formate to 0.28 for NPA and IPA.

5.5.13 Single-Well (One-Spot) Improved Oil Recovery (IOR) Pilot. The SWCT test can be used to evaluate an IOR process quickly and inexpensively. The one-spot procedure takes advantage of the nondestructive nature of the SWCT method.

The single-well (one-spot) pilot is carried out in three steps. First, S_{or} for the target interval is measured as described earlier. Then an appropriate volume of the IOR fluid is injected into the test interval and pushed away from the well with water. Finally, the SWCT test is repeated

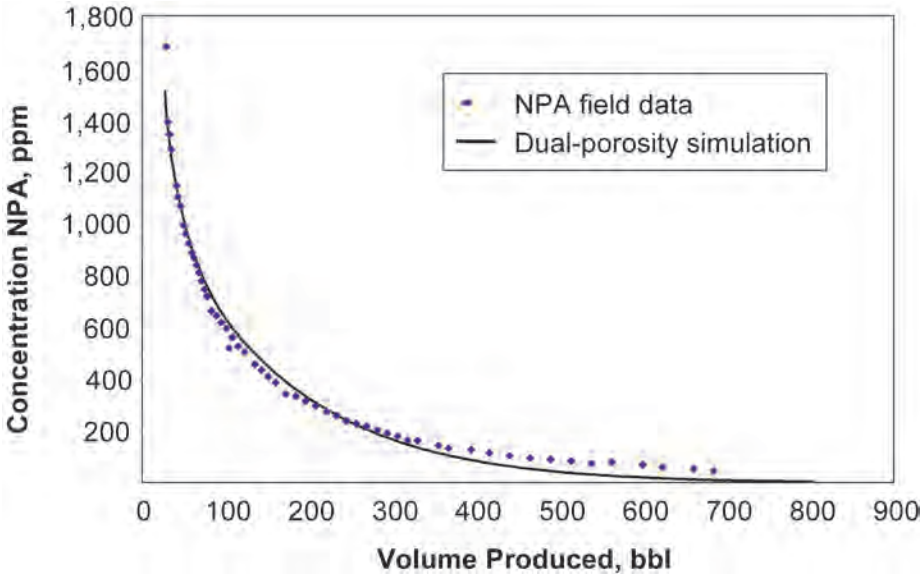


Fig. 5.21—NPA material-balance tracer simulation, dual-porosity model, Case 3.

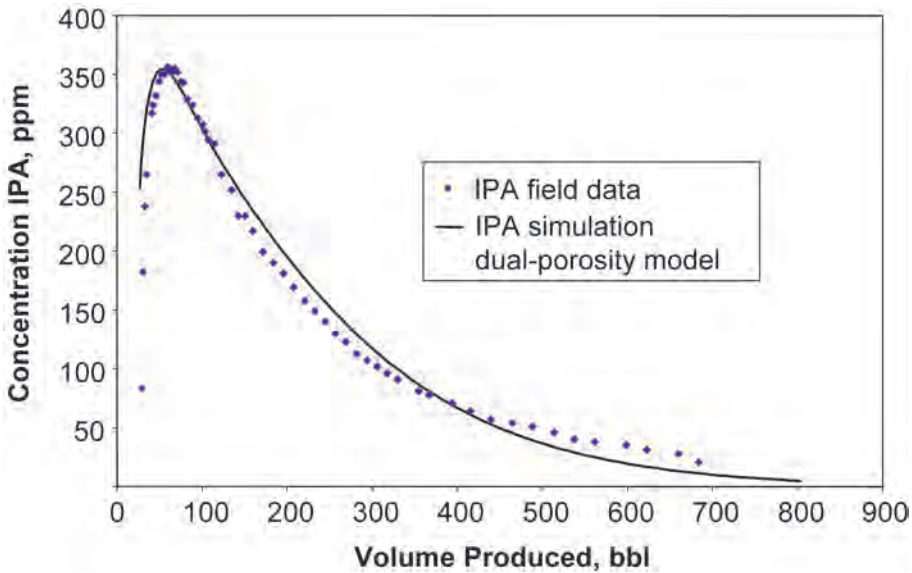


Fig. 5.22—IPA cover tracer simulation, dual-porosity model, Case 3.

within the treated region. Typically, the entire process is completed in a few weeks, as compared to the much longer duration of pilot programs, even small-patterned ones.

The reduction in S_{or} observed in the postflood SWCT test is a measure of the IOR flood performance. By using several esters with different partition coefficients, it is possible to measure S_{or} as a function of radial position from the test well. This procedure also can be used to evaluate the stability of the IOR process because tracer test volume is increased relative to the IOR displaced volume.

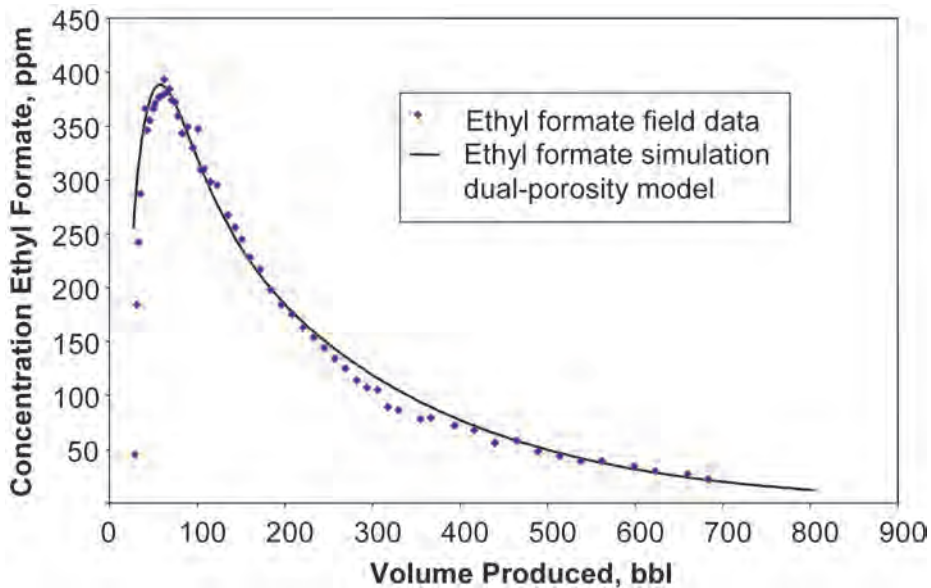


Fig. 5.23—Ethyl formate simulation, dual-porosity model, Case 3.

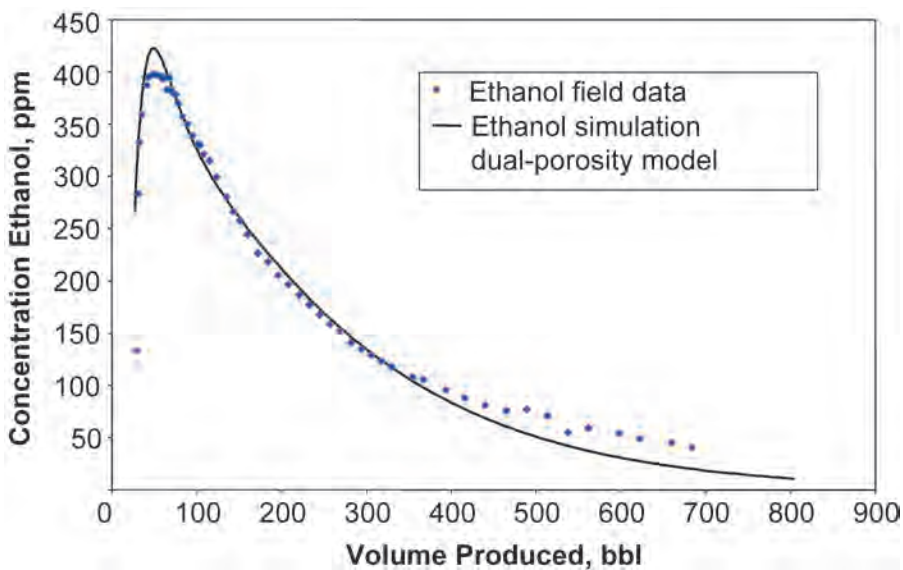


Fig. 5.24—Ethanol simulation, dual-porosity model, Case 3.

- The single-well IOR pilot concept has been applied in a number of different projects,^{18–21} in the course of which the following IOR processes have been evaluated:
 - Surfactant, surfactant-polymer, and alkaline-surfactant-polymer (ASP).
 - CO₂ miscible.
 - Caustic and caustic-polymer.
 - Hydrocarbon-miscible.

In every case, the process was evaluated successfully using the SWCT test. In most of these sequences, the IOR fluid injection and push steps were carried out by the SWCT test

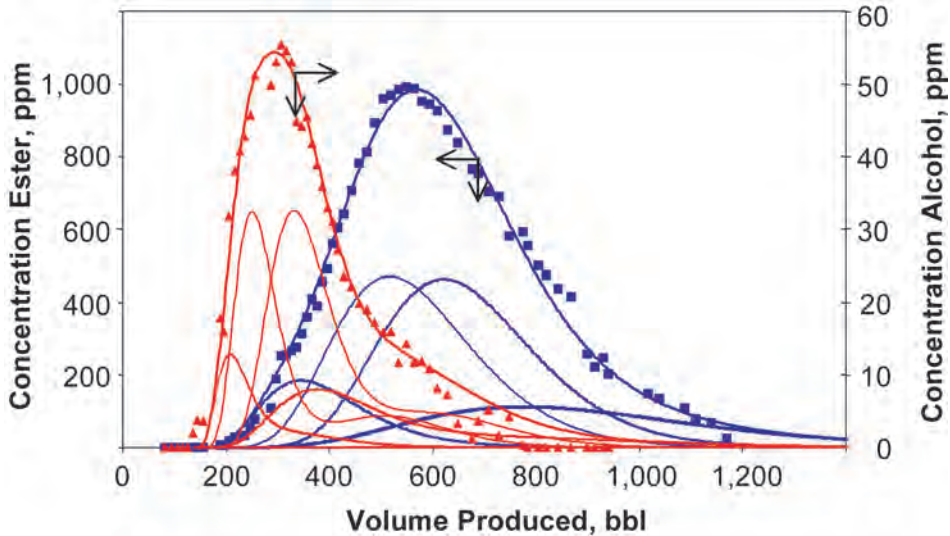


Fig. 5.25—One-spot pilot evaluation of hydrocarbon-miscible IOR before IOR bank.

field group as a part of the field test program. A typical single-well pilot evaluation of an IOR process requires four to six weeks to complete.

5.5.14 SWCT Tests for In-Situ Evaluation of Hydrocarbon-Miscible IOR—Case 4. A series of SWCT tests was performed in the Aurora Field on the Alaska North Slope,²² U.S.A., to provide an in-situ formation evaluation and to evaluate hydrocarbon-miscible IOR. The target well produced 100% oil.

The steps in the test sequence were:

1. An SWCT test for S_{wc} (see below under *Other Field Measurements*).
2. A multiple tracer test to determine oil/water fractional flow vs. saturation.
3. A waterflood to reduce the near-wellbore oil saturation to near-residual conditions.
4. An SWCT test for S_{or} .
5. Injection of a bank of hydrocarbon-miscible solvent.
6. A waterflood to displace the IOR bank away from the test well.
7. A second SWCT test for S_{or} , to determine the post-IOR oil saturation in the flooded region.

Steps 4 through 7 constitute the “one-spot” pilot for the hydrocarbon-miscible IOR process. The results of step 4 are shown in Fig. 5.25. The field data are plotted, along with the best-fit four-layer simulation model. Two nonideal effects are indicated by these data:

- Nonreversing flow is evidenced by the early hump and the extended tail on the tracer profiles.

- A radial gradient of oil saturation apparently was present in the formation because the waterflood of step 3 was not large enough to reduce the formation to true residual oil.

The four-layer model can account for both of these effects. The ester-weighted S_{or} measured in step 4 is $32 \pm 3\%$.

The field data and best-fit simulation of the aftertest (step 7) are shown in Fig. 5.26. Again, two distinct nonideal effects are apparent:

- Nonreversing flow again is a factor. An early hump and a tail indicate that small layers are needed to improve the fit of the simulation model.

- In this case, the late layer, which produces the tail, also is anomalous regarding oil saturation. Whereas both of the other layers require an S_{or} of 6% to produce the best fit, the late layer appears to have an S_{or} of 26%. A likely explanation for this remarkable difference is

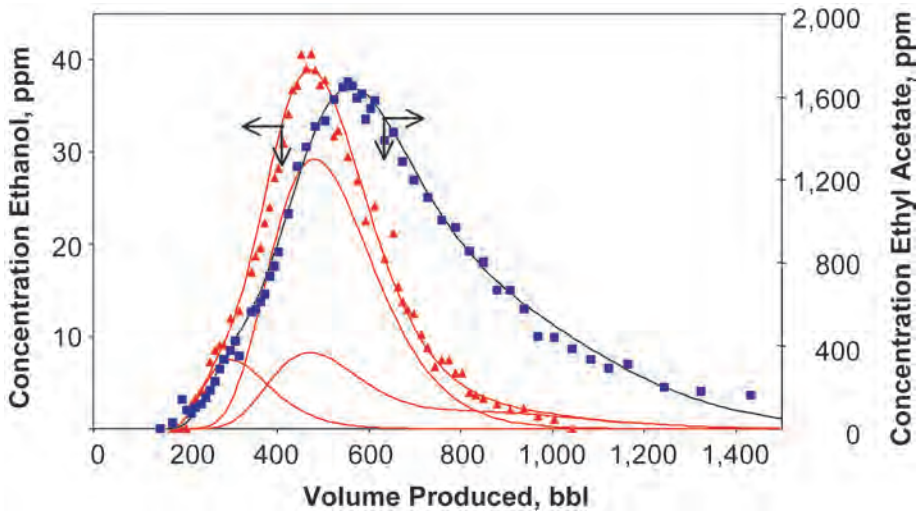


Fig. 5.26—One-spot pilot evaluation of hydrocarbon-miscible IOR after IOR bank.

gravity override by the miscible solvent bank. There appears to be a layer that was not contacted by the IOR bank.

5.6 Other Field Measurements

5.6.1 Connate Water Saturation Testing. In certain situations, it is necessary to obtain a reliable measurement for S_{wc} in an oil reservoir. The SWCT method has been used successfully for this purpose in six reservoirs.²³ The SWCT test for S_{wc} usually is carried out on wells that are essentially 100% oil producers. The procedure is analogous to the SWCT method for S_{or} , taking into account that oil is the mobile phase and water is stationary in the pore space.

Because oil is the mobile phase, it is used to carry the chemical tracers into and back out of the formation. The ester dissolved in oil is injected and then pushed away from the well. The first bank carries the ester plus material-balance tracer, as in the S_{or} test. The push bank contains only the material-balance tracer.

During the flow into the formation, the ester partitions between the oil and water phases. This partitioning slows the ester velocity only slightly because the ester is more soluble in the oil phase. After the push step, the ester bank is located 10 to 20 ft from the wellbore.

During the 2- to 10-day shut-in period, a portion of the ester hydrolyzes (reacts with the connate water) to form the alcohol product tracer. The product alcohol is much more soluble in the connate water than in the oil phase.

The well then is placed on production. Samples of the produced oil are taken frequently and analyzed for tracer content. The unreacted ester comes back first because it travels at nearly the same velocity as the carrier oil. The product alcohol is produced later because it travels more slowly than the oil. Because of its preferential solubility in the stationary water phase, the alcohol has a large β value compared to that of ester. The difference in arrival volumes between the ester and the delayed alcohol tracer thus is a function of S_{wc} .

As in the SWCT test for S_{or} , β can be calculated directly from the concentration vs. produced volume profiles. Using the partition coefficients measured in the laboratory, S_{wc} can then be calculated. However, the best-fit S_{wc} result actually is determined by matching the field tracer profiles using our multilayer simulator program for the connate water test.

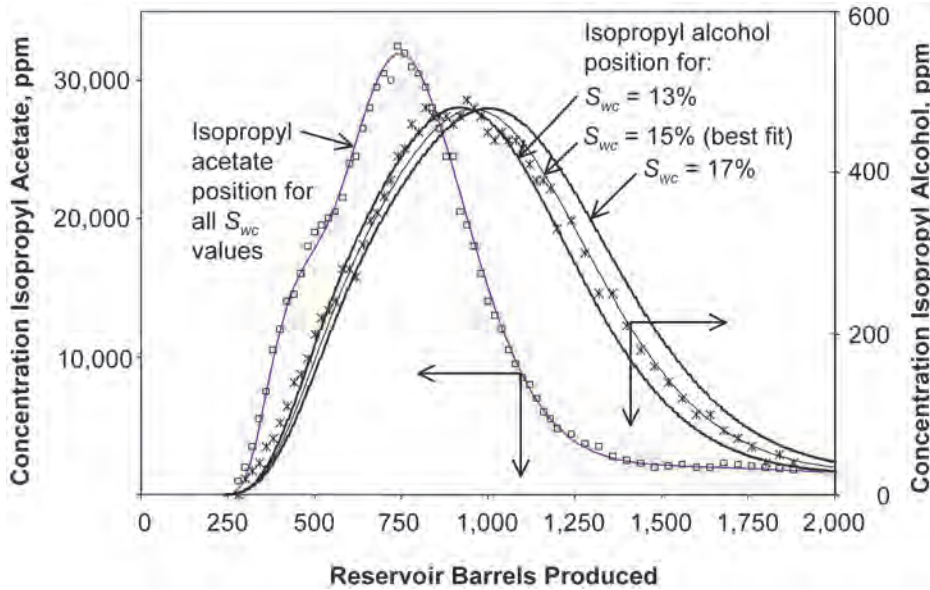


Fig. 5.27—Field data and simulated tracer profiles for an SWCT test for S_{wc} .

5.6.2 SWCT Test for Connate Water—Case 5. An example of a production profile from a SWCT test for connate water is shown in Fig. 5.27.²³ The target formation was in the Prudhoe Bay Field on the Alaska North Slope, U.S.A. The reactive ester injected was isopropyl acetate, which was dissolved in light diesel oil. The product tracer in this case was IPA.

The best-fit simulation model for this case used three layers, to account for the slightly nonreversing flow behavior. The injected ester-weighted average result was $S_{wc} = 0.15 \pm 2\%$. This is in close agreement with the average S_{wc} determined from oil-based cores on the same well.²³

5.6.3 Gas-Saturation Testing. In formations where the pore space is occupied by a stationary gas phase and a mobile water phase, such as in a watered-out gas reservoir, the residual gas saturation (S_{gr}) may need to be measured in situ. The S_{gr} also can be determined using a single-well injection/production test method.²⁴

S_{gr} measurement involves injecting and immediately producing a suitable volume of water. The water used for injection typically is produced from the target well before the test and stored in tanks on the surface. During production, the amount of gas dissolved in the water (R_{sw}) that is produced from the formation is measured.

The injected water is essentially free of dissolved hydrocarbon gases (i.e., it is “dead”). As the injected water enters the formation that contains residual gas, the water dissolves the gas, becoming saturated at the temperature and pressure in the reservoir. A region of increasing radius around the wellbore is stripped of gas. Injection continues until a volume (V_I) has entered the formation. A material-balance tracer such as methanol is added to all injected water.

At the end of the injection, the stripped region near the well is a volume of pore space that is filled with dead water (V_d). Just beyond this dead-water zone, the pore space contains the original gas saturation and gas-saturated injected water.

Immediately after injection, water is produced back from the formation through the well to the surface. The first volume of water produced is the V_d from the leached region, and so contains no dissolved gas. This dead water is followed by gas-saturated water from the region outside the stripped zone. The gas-saturated water is able to move through the stripped region

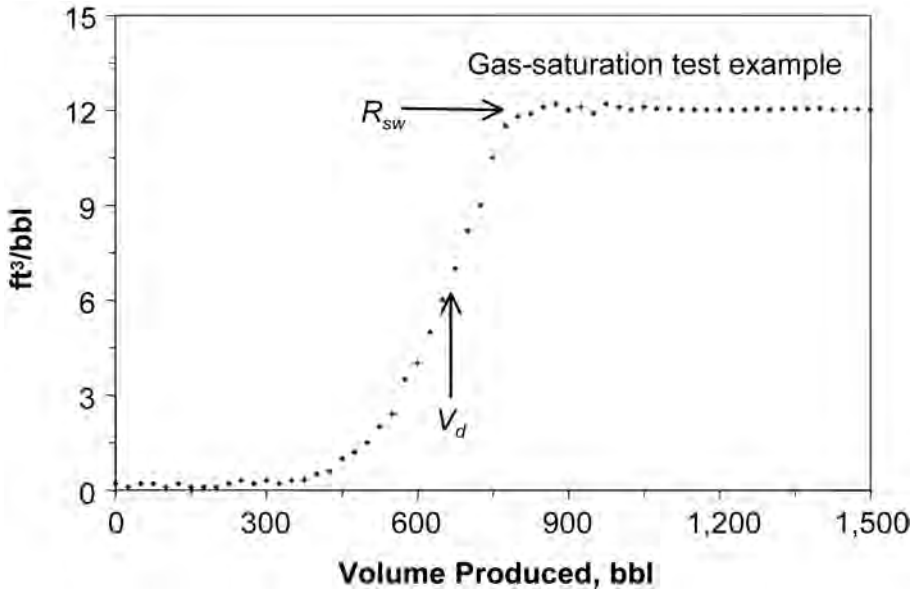


Fig. 5.28—Gas-saturation test example.

without giving up its dissolved gas to reform the original gas saturation. This nonreversing behavior is the reason the method works in a single well.

After the volume of dead water is produced, the observed gas content of the produced water rises to the solubility R_{sw} (scf/bbl) of gas at reservoir conditions. The volume of gas-saturated water $(V_I - V_d)$ produced after the dead water contains the gas that was dissolved from the stripped zone. Thus, if B_g is the gas formation volume factor at reservoir conditions, the reservoir volume of gas dissolved in this fluid (V_g) is:

$$V_g = (V_I - V_d)R_{sw}B_g \dots\dots\dots (5.20)$$

But this is just the volume of gas originally in the stripped zone, which is:

$$V_g = V_d S_{gr} \dots\dots\dots (5.21)$$

Equating the two and solving for S_{gr} :

$$S_{gr} = (V_I - V_d)R_{sw} \left(\frac{B_g}{V_d} \right) \dots\dots\dots (5.22)$$

Fig. 5.28 is a typical profile for gas content vs. produced water volume from a single-well injection test for S_{gr} . The volume required to produce the inflection point of the gas content profile is V_d . The final level of gas content is R_{sw} , the solubility of gas at reservoir conditions. These two values, along with the total injected volume V_I , are the only field data required to calculate S_{gr} . The procedure for measuring S_{gr} is described in detail by Bragg and Shallenberger.²⁴

Performing the S_{gr} test is relatively simple. The only operational requirements are that a method must be available to produce water from the formation in the test well and that there must be a way to measure the gas content of the water leaving the formation, with which the

fluid lifting mechanism does not interfere. Because of the nonreversing feature, the test cannot be repeated in a given completion. The gas that is dissolved from the near-well pore space is not replaced during the production step.

This method can be used to measure either hydrocarbon gas or carbon dioxide (CO₂) saturation after displacement by water, and in some cases where residual oil, residual gas, and mobile water all share the pore space (three-phase system), this test has been conducted in tandem with the SWCT test. The ester solution and push volume are added to the end of the dead-water injection. A shut-in period also is added. The S_{or} value measured by the SWCT test is for the two-phase (oil and dead water), gas-leached zone near the well. The S_{gr} obtained from the gas content profile represents the fraction of the near-well pore space filled with gas before the test injection.

5.7 Summary

This *Handbook* chapter has familiarized the reader with the SWCT method by presenting the essential details of its theory to establish its credibility. It also has covered the planning and execution of the field operations to show the practicality of the method, and has outlined the process of test data interpretation and applied it to real test data to demonstrate the SWCT method's sensitivity and accuracy. High-quality fluid-saturation data always have been essential to the reservoir engineer, and in today's challenging oil production operations, the information provided by SWCT testing methods is more important than ever before. In the coming years, this unique and intriguing method is likely to be used more widely in reservoir evaluation.

Nomenclature

B_o	= formation volume factor, oil, RB/STB
B_g	= formation volume factor, gas, RB/Mscf
C_A	= concentration of tracer A, mol/vol
C_{Ao}	= concentration of tracer A in oil
C_{Aw}	= concentration of tracer A in water
C_B	= concentration of tracer B, mol/vol
C_{Bo}	= concentration of tracer B in oil, mol/vol
C_{Bw}	= concentration of tracer B in water, mol/vol
C_{eo}	= concentration of ester in oil, mol/vol
C_{ew}	= concentration of ester in water, mol/vol
D_E	= effective dispersion coefficient, ft ² /D
f_i	= fraction of time
h	= thickness, ft
k_H	= hydrolysis rate constant (days ⁻¹) in the aqueous phase
K	= equilibrium partition coefficient
K_A	= equilibrium partition coefficient for tracer A
K_B	= equilibrium partition coefficient for tracer B
K_e	= oil/water partition coefficient for ester
n_{eo}	= number of ester molecules in oil
n_{ew}	= number of ester molecules in water
q	= fluid-flow rate in a single well, B/D
Q_p	= produced volume, bbl
Q_{pA}	= volume required to produce tracer A, bbl
Q_{pB}	= volume required to produce tracer B, bbl
r	= radial position, ft
r_e	= external boundary radius, ft

- r_w = wellbore radius, ft
 R_H = hydrolysis reaction rate, mol/vol-day
 R_{sw} = gas solubility in produced water at reservoir conditions, scf/bbl
 S_f = flowing fluid saturation, fraction of PV
 S_{gr} = residual gas saturation, fraction of PV
 S_o = oil saturation, fraction of PV
 \bar{S}_o = average oil saturation in the reservoir, fraction of PV
 S_{or} = residual oil saturation, fraction of PV
 S_r = residual fluid saturation fraction of PV
 S_w = saturation of water, fraction of PV
 S_{wc} = connate water saturation, fraction of PV
 t = time, day
 t_A = arrival time of tracer A, day
 t_B = arrival time of tracer B, day
 v_A = average velocity of tracer chemical A, ft/D
 v_B = average velocity of tracer chemical B, ft/D
 v_D = fluid drift velocity in the formation, ft/D
 v_e = time-weighted velocity of ester
 v_{fi} = interstitial fluid velocity, ft/D
 v_o = time-weighted velocity of oil
 v_w = time-weighted velocity of water
 V_c = control volume of a pore, bbl
 V_d = volume of dead (gas-free) water produced, bbl
 V_g = the reservoir volume of gas dissolved in gas-saturated water, scf/bbl
 V_I = volume of water injected, bbl
 V_p = total pore volume, bbl
 V_w = velocity of water
 α = dispersivity
 β = retardation factor
 β_A = retardation factor for tracer A
 β_e = retardation factor for ester
 ΔR = radial dimension (ft) of a cell
 ϕ = porosity

References

1. Tomich, J.F. *et al.*: "Single-Well Tracer Method to Measure Residual Oil Saturation," *JPT* (February 1973) 211.
2. Deans, H.A.: "Method of Determining Fluid Saturations in Reservoirs," U.S. Patent No. 3,623,842 (1971).
3. Deans, H.A. and Majoros, S.: "The Single-Well Chemical Tracer Method for Measuring Residual Oil Saturation," Final report, Contract No. DOE/BC20006-18, U.S. DOE, Washington, DC (October 1980).
4. O'Brien, L.J., Cooke, R.S., and Willis, H.R.: "Oil Saturation Measurements at Brown and East Voss Tannehill Fields," *JPT* (January 1978) 17.
5. Sheely, C.Q.: "Description of Field Tests to Determine Residual Oil Saturation by Single-Well Tracer Method," *JPT* (February 1978) 194.

6. Thomas, E.C. and Ausburn, B.E.: "Determining Swept-Zone Residual Oil Saturation in a Slightly Consolidated Gulf Coast Sandstone Reservoir," *JPT* (April 1979) 513.
7. Nute, A.J.: "Design and Evaluation of a Gravity-Stable, Miscible CO₂-Solvent Flood, Bay St. Elaine Field," paper SPE 11506 presented at the 1983 SPE Middle East Oil Technical Conference, Manama, Bahrain, 14–17 March.
8. Chang, M.M. *et al.*: "Evaluation and Comparison of Residual Oil Saturation Determination Techniques," *SPEFE* (March 1988) 251.
9. Donaldson, E.C. and Staub, H.L.: "Comparison of Methods for Measurement of Oil Saturation," paper SPE 10298 presented at the 1981 SPE Annual Technical Conference and Exhibition, San Antonio, Texas, 5–7 October.
10. Energy Information Administration (EIA). 1980. Annual Report to Congress, Volume 3, DOE/EIA-0173(79)/3. Washington, DC (July 1979).
11. Salathiel, R.A.: "Oil Recovery by Surface Film Drainage in Mixed-Wettability Rocks," *JPT* (October 1973) 1216; *Trans.*, AIME, **255**.
12. Deans, H.A. and Shallenberger, L.K.: "Single-Well Chemical Tracer Method to Measure Connate Water Saturation," paper SPE 4755 presented at the 1974 SPE Improved Oil Recovery Symposium, Tulsa, 22–24 April.
13. Cooke, C.E. Jr.: "Method of determining Residual Oil Saturation in Reservoirs," U.S. Patent No. 3,590,923 (1971).
14. Carlisle, C.T. *et al.*: "Development of a Rapid and Accurate Method for Determining Partition Coefficients of Chemical Tracers Between Oils and Brines (for Single-Well Tracer Tests)," Contract No. DOE/BC/10100-4, U.S. DOE, Washington DC (December 1982).
15. Deans, H.A. and Carlisle, C.T.: "Single-Well Tracer Test in Complex Pore Systems," paper SPE/DOE 14886 presented at the 1986 SPE/DOE Symposium on Enhanced Oil Recovery, Tulsa, 20–23 April.
16. Deans, H.A.: "A Mathematical Model for Dispersion in the Direction of Flow in Porous Media," *SPEJ* (March 1963) 49; *Trans.*, AIME, **228**.
17. Seetharam, R.V. and Deans, H.A.: "CASTEM-A New Automated Parameter-Estimation Algorithm for Single-Well Tracer Tests," *SPERE* (February 1989) 35.
18. Sheely, C.Q. Jr. and Baldwin, D.E.: "Single-Well Tracer Test for Evaluating Chemical Enhanced Oil Recovery Processes," *JPT* (August 1982) 1887.
19. Holland, K.M. and Porter, L.T.: "Single-Well Evaluation Program for Micellar/Polymer Recovery, Main and 99 West Pools, West Coyote Field, California," paper SPE 11990 presented at the 1983 SPE Annual Technical Conference and Exhibition, San Francisco, 5–8 October.
20. Edinga, K.J., McCaffery, F.G., and Wytrychowski, I.M.: "Cessford Basal Colorado A Reservoir—Caustic Flood Evaluation," *JPT* (December 1980) 2103.
21. Cockin, A.P. *et al.*: "Design, Implementation and Simulation Analysis of a Single-Well Chemical Tracer Test To Measure the Residual Oil Saturation to a Hydrocarbon Miscible Gas at Prudhoe Bay," paper 48951 prepared for presentation at the 1998 SPE Annual Technical Conference and Exhibition, New Orleans, 27–30 September.
22. Carlisle, C.T. *et al.*: "Aurora Single Well Tracer Test (SWTT) Results," poster presented at the 2002 SPE Western North American Region/Pacific Section AAPG Joint Meeting, Anchorage, 20–22 May.
23. Deans, H.A. and Mut, A.D.: "Chemical Tracer Studies To Determine Water Saturation at Prudhoe Bay," *SPERE* (February 1997) 52.
24. Bragg, J.R. and Shallenberger, L.K.: "In-Situ Determination of Residual Gas Saturation by Injection and Production of Brine," paper SPE 6047 presented at the 1976 SPE Annual Technical Conference and Exhibition, New Orleans, 3–6 October.

SI Metric Conversion Factors

bbl × 1.589 873	E – 01 = m ³
°F (°F – 32)/1.8	= °C
ft × 3.048*	E – 01 = m
ft ³ × 2.831 685	E – 02 = m ³
day × 1.0*	E – 00 = d

lbm mol × 4.535 924

psia × 6.894 757

res bbl × 1.689 873

*Conversion factor is exact.

E - 01 = kmol

E - 00 = kPa

E - 01 = res m³

Chapter 6

Well-To-Well Tracer Tests

Øyvind Dugstad, Inst. for Energy Technology

6.1 Introduction

Well-to-well tracer tests contribute significantly to the reservoir description, which is essential in determining the best choice of production strategy. Direct dynamic information from a reservoir may be obtained, in principle, from three sources: production history, pressure testing, and tracer testing.

The value and importance of tracer tests are broadly recognized. Tracer testing has become a mature technology, and improved knowledge about tracer behavior in the reservoir, improved tracer analysis, and reduction of pitfalls have made tracer tests reliable. Many tracer compounds exist; however, the number of suitable compounds for well-to-well tracers is reduced considerably because of the harsh environment that exists in many reservoirs and the long testing period. Radioactive tracers with a half-life of less than one year are mentioned only briefly in this chapter because of their limited applicability in long-term tests.

Tracers may be roughly classified as passive or active. In principle, a passive tracer blindly follows the fluid phase in which it is injected. Active tracers interact with the other fluids in the system or with the rock surface. Interpretation of tracer-production curves must account for this. The results from the application of active tracers may give information about fluid saturation and rock surface properties. This information is especially important when enhanced-oil-recovery techniques that use expensive fluids such as surfactants, micellar fluids, or polymers are considered.

In the last 50 years, many tracer studies have been reported and even more have been carried out without being published in the open literature. Wagner¹ pointed out six areas in which tracers could be used as a tool to improve the reservoir description.

- Volumetric sweep. The volume of fluid injected at an injection well until breakthrough of the traced fluid at an offset producer is a measure of the volumetric sweep efficiency between that pair of wells. Very small volumes injected before breakthrough [relative to the interwell pore volume (PV)] would indicate the existence of an interwell open fracture (or a very thin high-permeability stringer) and would give an idea of the volume of that channel. Knowledge of channels is important to the sizing of remedial treatment.
- Identification of offending injectors. Problem injection wells can be identified by associating the breakthrough of a specific tracer to its point of injection. At this well, a remedial treatment to seal a channel normally would be applied.

- **Directional flow trends.** When fluids are injected in a regular pattern (five-spot, nine-spot, line drive, etc.) and the fluids injected at each well tagged with a different tracer, directional flow trends will be obvious from the repeated early tracer breakthrough at producers in a preferential direction from the injectors. Where directional flow trends are prevalent, the interwell sweep efficiency often can be improved by altering the injection pattern and/or the injection and withdrawal rates at selected wells.

- **Delineation of flow barriers.** Faults with large displacement along the fault plane and permeability pinchouts can represent barriers to the flow of fluids perpendicular to their axis. Normally, such barriers are detected by bottomhole pressure buildup surveys run in nearby wells. However, the course of these barriers can be delineated further from the production well's response (or lack of it) to traced water injection at an array of wells surrounding the producer.

- **Relative velocities of injected fluids.** When different fluids are injected simultaneously, alternately, or sequentially in the same well with each fluid tagged with a different nonadsorbing tracer, the relative velocities of these fluids can be measured from the individual-tracer arrival time at offset producers. For example, assume that traced solvents and traced water are injected alternately in the same well. The early arrival of one of the traced fluids at the producing well would indicate that the early arriving fluid had contacted less of the reservoir than the slower fluid. This shows a need to alter one of the fluid injection cycles to achieve more uniform sweep of the reservoir. Similarly, in a micellar flood in which water is injected sequentially, the overrunning or fingering of one injected fluid through another points out the need for better fluid-mobility control to achieve more uniform sweep by the various injected fluids.

- **Evaluations of sweep-improvement treatments.** Remedial treatments to correct sweep problems can be evaluated by comparing the before-and-after-treatment interwell volumetric sweep as determined by tracing.

Many companies apply tracer on a routine basis. The reservoir engineer's problem generally is a lack of adequate information about fluid flow in the reservoir. The information obtained from tracer tests is unique, and tracer tests are a relatively cheap method to obtain this information. The information is an addendum to the general field production history and is used to reduce uncertainties in the reservoir model.

Tracer tests provide tracer-response curves that may be evaluated further to obtain relevant additional information. Primarily, the information gained from tracer testing is obtained simply by observing breakthrough and interwell communication. Adequate data presentation and simple hand calculation can give further knowledge about the flow behavior in the reservoir. More quantitative information can be obtained by fitting response curves obtained from numerical simulation to the observed response curves. Additional information also can be obtained by applying analytical procedures on the basis of generic or simplified reservoir models.

6.2 Types of Tracers Available

A passive tracer that labels gas or water in a well-to-well tracer test must fulfill the following criteria. It must have a very low detection limit, must be stable under reservoir conditions, must follow the phase that is being tagged and have a minimal partitioning into other phases, must have no adsorption to rock material, and must have minimal environmental consequences. The tracers discussed in the following sections have properties that make them suitable for application in well-to-well test in which dilution volumes are large. For small fields in which the requirement with respect to dilution is less important, other tracers can be applied.

6.2.1 Radioactive Water Tracers. In most field studies, the tracer is expected to behave exactly as the water it is going to trace. Very few compounds will behave as passive tracers in all situations, but near-passive tracers will, in many applications, work satisfactorily. If the objec-

TABLE 6.1—RADIOACTIVE WATER TRACERS USED IN OIL RESERVOIR EXAMINATIONS (after Bjørnstad and Maggio²)

Water Tracer Compound	Half-Life (year)	Main Radiation Characteristics (keV)	Comments
HTO	12.32	β^- (18)	Generally applicable
CH ₂ TOH ¹⁾	12.32	β^- (18)	Caution at $T > 100^\circ\text{C}$ (partition into gas phase), some biodegradation below 70 to 80°C
CH ₃ CTOHCH ₃	12.32	β^- (18)	Reasonably general application
C ₃ H ₇ CHTOH	12.32	β^- (18)	Reasonably general application, partition somewhat into oil
S ¹⁴ CN ⁻	5730	β^- (156)	For $T < 90$ to 100°C , long-term experiments
³⁶ Cl ⁻	3.10 ⁵	β^- (709)	High-temperature reservoirs, long term, EMS-analysis
²² Na ⁺	2.6	β^+ (545), γ (1274.5)	High-temperature tracer in saline reservoirs, long term, slight reversible sorption

tive is to measure fluid communication exclusively, a near-passive tracer may be as good as a true passive tracer. **Table 6.1** lists the most frequently applied radioactive tracers.

The compound that best fulfills the passive tracer requirements is tritiated water (HTO). The passive water tracer mimics all movements and interactions that the water molecules do in the traced water volume. For instance, HTO can track the free movement in and out of dead-end pores because it is insensitive to coulombic forces set up by negatively charged rock surfaces. Other interactions can exchange with connate water in the rock pores or exchange with crystal water molecules. Thus, HTO sometimes seems to lag behind the injection water breakthrough as measured, for instance, by a salt balance (ionic logging). This has sometimes been interpreted that HTO is unstable at reservoir conditions and that it may be subject to isotope-exchange reactions of tritium with hydrogen in neighboring hydrogen-containing compounds, some of which are stationary.² Isotopic exchange, however, is expected to be negligible.

Other noncharged tracers are methanol, CH₂TOH, and the other light alcohols. These tracers will behave qualitatively similar to HTO with respect to transport but have different interactions. Other organic molecules may be applied as radioactive water tracers and can be labeled either with tritium or with ¹⁴C. Larger alcohols, however, may have a partition coefficient that may cause a considerable retention.

Zemel³ measured partition coefficients of some alcohols. Over a limited range, the effect of temperature on the partition coefficient, K , can be represented by a semiempirical equation:

$$\ln K = A + \frac{B}{T}, \dots\dots\dots (6.1)$$

where T is the temperature in Kelvin, A is a constant related to the enthalpy, and B is a constant related to the entropy change. **Table 6.2** gives B and A values for some alcohols.

Anions are the more applicable electrically charged tracers; however, in laboratory experiments, clear evidence of ion exclusion can be seen (i.e., negatively charged species tend to be repelled from the negatively charged rock surfaces). As a result, the tracers tend to flow in the middle of the fluid-conducting pores and will not easily enter into dead-end pores or through

Tracer	K at 194°F	A	B
Isopropyl alcohol	0.26	2.15	-992.6
n-propyl alcohol	0.28	1.72	-883.1
n-butyl alcohol	1.23	2.52	-882.2

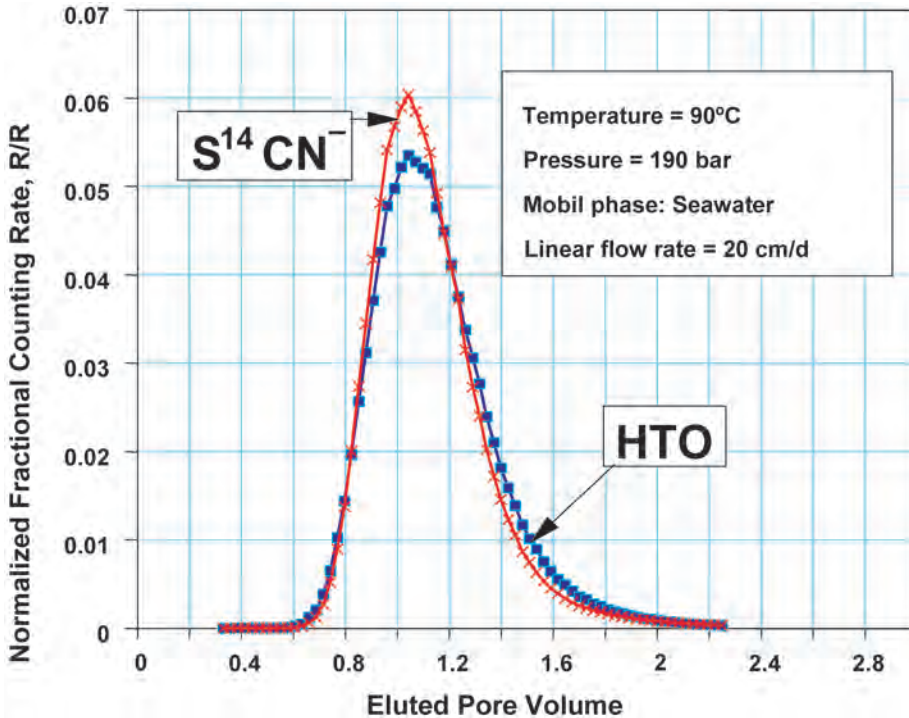


Fig. 6.1—Production curve of $S^{14}CN^-$ compared with the production curve of HTO in a dynamic flooding laboratory test (carbonate rock) (after Bjørnstad and Maggio²).

narrow pore throats, which results in a smaller available PV for anions than for noncharged species. The production profile differs in reproducible ways from that of HTO.

Anionic tracers are represented here by thiocyanate or $S^{14}CN^-$. Fig. 6.1 gives a typical production profile from flooding experiments. This profile is compared with the production profile of the simultaneously injected HTO. It is evident from the curve that the breakthrough of HTO occurs before that of $S^{14}CN^-$ and that the tail of the HTO profile is more pronounced. This profile difference is qualitatively the same for all near-passive anionic water tracers. The retention volume may be represented by the peak maximum value or the mass middle point (first moment, μ_1) for nonsymmetrical profiles. These values are found best by fitting the profile with an analytical function consisting of polynomials.

$^{35}SCN^-$ is applicable only to small reservoirs because the half-life of ^{35}S is only 87 days. $^{36}Cl^-$ has shown to be an excellent tracer. There are no possibilities for thermal degradation, and it follows the water closely. The $^{36}Cl^-$ is a long-lived nuclide (3×10^5 years), and the detec-

<u>Nonradioactive Water Tracers</u>	<u>Normal Abbreviation</u>	<u>Chemical Formula</u>
Thiocyanate	SCN ⁻	SCN ⁻
2-fluorobenzoic acid	2-FBA	C ₆ H ₄ FCOOH
4-fluorobenzoic acid	4-FBA	C ₆ H ₄ FCOOH
2,6-fluorobenzoic acid (FBA)	2,6-DFBA	C ₆ H ₃ F ₂ COOH
15-20 other FBAs	Other FBAs	C ₆ H _{5-x} F _x COOH, C ₆ H _{5-n} (CF ₃) _n COOH

tion method is atomic mass spectroscopy rather than radiation measurements. The disadvantage is that the analysis demands very sophisticated equipment and is relatively time consuming.

For mono-valent anions, the retention factors (see Eq. 6.2) are in the range of 0 to -0.03, which means that such tracers pass faster through the reservoir rock than the water itself (represented by HTO). A compound such as ³⁵SO₄²⁻ may be applied in some very specific cases but should be avoided normally because of absorption.

Some anionic tracers may show complex behavior. Radioactive iodine (¹²⁵I- and ¹³¹I-) breaks through before water but has a substantially longer tail than HTO. Both a reversible sorption and ion exclusion seem to play a role here. ¹²⁵I- and ¹³¹I- have half-lives of 60 and 8 days, respectively, which makes the compounds less attractive as tracers in large reservoir segments.

Cationic tracers are, in general, not applicable; however, experiments have qualified ²²Na⁺ as an applicable water tracer in highly saline (total dissolved solids concentration > seawater salinity) waters. In such waters, the nonradioactive sodium will operate as a molecular carrier for the tracer molecule. Retention factor has been measured in the range of 0.07 (see Eq. 6.2) at reservoir conditions in carbonate rock (chalk).⁴ Accordingly, the tracer is delayed somewhat by sorption and ion exchange to reservoir rock but in a reversible manner.

Wood⁵ reported the use of ¹³⁴Cs, ¹³⁷Cs, ⁵⁷Co, and ⁶⁰Co cations as tracers. The same cations also were injected as ethylene diamine tetra-acetic acid (EDTA) complex in a carbonate reservoir. The EDTA complexes were recovered completely in a 3-day push-and-pull test. For the cations, only the Cs⁺ were produced while the Co³⁺ never appeared in the producer; however, the Cs⁺ cations generally cannot be used. It will adsorb strongly on clay-containing rock.

⁵⁶Co(CN)₆³⁻ is a stable complex that has been tried as tracer. Not all trials have been successful, and the compound is not normally applied. Especially at temperatures greater than 90°C, they should be avoided.² The complex can be labeled with several isotopes of cobalt (⁵⁶Co, ⁵⁷Co, ⁵⁸Co, ⁶⁰Co) in addition to ¹⁴C.

6.2.2 Chemical Water Tracers. Application of several nonradioactive chemical tracers has been reported in the literature. Table 6.3 lists the most frequently used chemical water tracers. The most-applied nonradioactive anion is the thiocyanate anion. It has a low natural background in the reservoir, and a detection limit in the range of 1 µg/L (1 ppb) can be obtained by electrochemical detection after separation on a high-pressure liquid chromatograph. In the reservoir, this tracer will behave as the radioactive labeled S¹⁴CN⁻ or as the ³⁵SCN⁻.

Nitrate (NO₃⁻), bromide (Br⁻), iodide (I⁻), and hydrogen borate (HBO₃⁻) also have been applied as tracers.³ These can be analyzed by ion chromatography or by high-pressure liquid chromatograph. A minimum detection limit in the range of 25 to 1 ppb is reported for the different compounds. This detection limit will not be sufficient in many situations. It is also a problem for several of these compounds that the background concentration normally will be

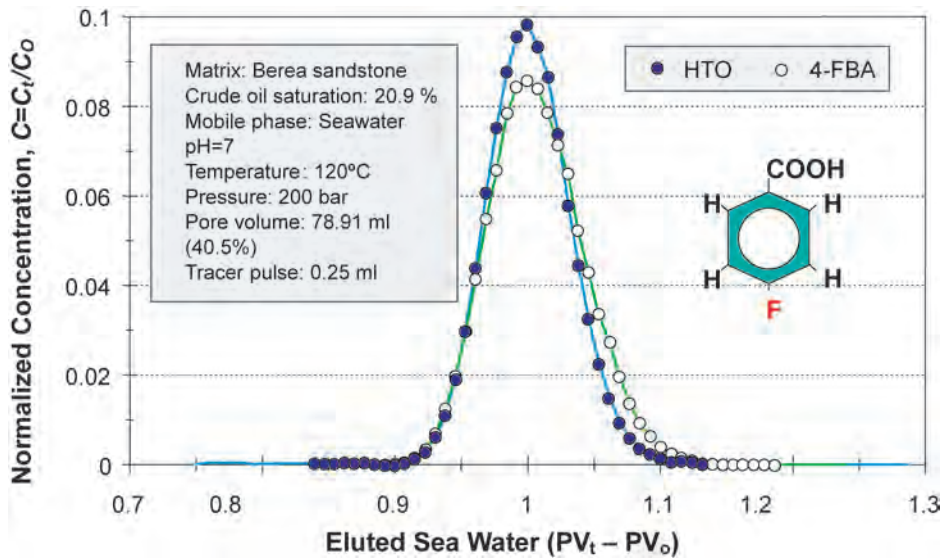


Fig. 6.2—Response curve of 4-FBA compared with the response curve of tritiated water in a laboratory flood (after Bjørnstad and Maggio²).

too high. Nitrate is the cheapest of the tracers, but its background may be in the range of 500 ppb, which means that an excessive amount of tracer is needed. Examples of organic molecules are fluorescein, rhodamine B, methanol, ethanol, and isopropanol.

The most-applied chemical water tracers are fluorinated benzoic acids. A large suite of mono-, di- and tri-fluorinated benzoic acids have been qualified as tracers. Because their thermal stability is variable, the compounds must be selected with care, especially for high-temperature reservoirs. Trifluoromethylbenzoic acids also may work as tracers; however, these compounds interact with the oil phase to a larger degree and retention of these compounds is observed.

The partitioning of acids to the oil phase is generally low. The partitioning will depend on the pH and at lower pH, when a larger portion of the compounds is in the undissociated form, higher partitioning can be expected. Fig. 6.2 shows laboratory test results in which the 4-FBA is compared with tritiated water in a packed-column flooding test. The two tracers are injected simultaneously and the residence time distribution measured. Both tracers are produced at the same time, and only a marginal retention of the 4-FBA is recorded. This experiment is performed by an oil saturation of approximately 20%. In most practical applications, this retention can be neglected.

There is active research to identify new tracers. Among the new tracers are deuterated compounds. Deuterated fatty acids probably will work well as tracers but, because of production costs, their applicability is limited. A new group of potential tracers are shorter DNA fragments. These compounds have two major advantages. They have an extremely low detection limit and exist in an almost unlimited number of distinguishable variations. It is, however, uncertain if it is possible to produce modifications that can be qualified with respect to flow behavior and stability.

6.2.3 Radioactive Gas Tracers. Several authors report the use of radioactive gas tracers in oilfield applications. The tracers most frequently applied have been tritiated methane, tritiated ethane, and ⁸⁵Kr.^{7,8,9} In addition, the use of tritiated butane, ¹²⁷Xe, ¹³³Xe, and tritiated hydrogen gas (HT) has been reported. Table 6.4 lists the most widely applied radioactive tracers.

Gas Tracer Compound	Half-Life	Main Radiation Characteristics (keV)
CH ₃ T*	12.32 years	β ⁻ (18)
CH ₂ TCH ₃ *	12.32 years	β ⁻ (18)
CH ₃ CHTCH ₃ *	12.32 years	β ⁻ (18)
⁸⁵ Kr	10.76 years	β ⁻ (687)
¹⁴ CO ₂	5,730 years	β ⁻ (156)
¹³³ Xe	5.25 days	β ⁻ (346) # (81)
¹²⁷ Xe	36.4 days	γ (202.9, 172.1, 375.0)

*These molecules may also be labelled by ¹⁴C.

The tritium-labeled compounds may be measured directly in the gas phase by proportional counter techniques. To obtain the low detection limit normally required in well-to-well tracer studies, it is normal to convert the gas to water by combustion. The produced water then is counted by a liquid scintillation technique. The detection limit of the water produced from this process depends on the instrumentation but can be less than 1 Bq/L. Typically, approximately 5 to 10 mL of water must be produced to obtain the low detection limits. The water, mixed with a liquid scintillator, is counted for a few hours. The same technique can be applied for the different tritium-labeled hydrocarbon gases. If several tritium-labeled compounds are present in the same sample, it will be necessary to perform a chemical separation of the compounds before oxidation to produce the water. This separation complicates the analysis considerably; therefore, it is not common to use several of these tritiated compounds in the same reservoir segment.

The chemical properties of tritium-labeled hydrocarbon compounds are equal to their nonlabeled homologues in almost all practical situations, which means that their behavior in the reservoir will be the same as the nonlabeled hydrocarbons. The partition coefficients of these compounds, therefore, can be found by ordinary pressure-volume-temperature (PVT) packages like those applied in phase-equilibria calculations. The partition coefficient will influence the residence time in the reservoir and the concentration of the tracer in the production line. It is important to take into account partitioning both in the evaluation of flow behavior in the reservoir and in the understanding of sampling quality. Because of partitioning to the oil phase, some of the tracers will be in the oil phase at the sampling point. Calculation of total recovery of the tracer then requires partition coefficient and gas/oil ratio (GOR) at sampling conditions. This problem will be more significant for heavier hydrocarbons than for the lighter ones.

All the hydrocarbons that are labeled with tritium can also be labeled with ¹⁴C. These molecules are, in general, more expensive and their analyses are more complicated. From a general demand for reducing the application of long-lived radioactive tracers, the ¹⁴C-labeled compounds are less attractive than the tritium-labeled compound.

Other alternatives are the noble gases. The noble gases are virtually inert against chemical reaction. ⁸⁵Kr has a half-life of 10.76 years and is a beta emitter with an energy of 687 keV. The two xenon isotopes, ¹²⁷Xe and ¹³³Xe, are also inert noble gases that may be applied in special situations in which rapid response is expected. The half-lives are 36.4 and 5.25 days, respectively.

TABLE 6.5—APPLICABLE CHEMICAL GAS TRACERS (after Bjørnstad *et al.*⁶)

Tracer Type	Common Abbreviation	Detection Method	Disadvantage
Perfluorocarbons	PDMCH, PMCP, PMCH, 1,2-PDMCH, 1,3-PDMCH	GC/MS or GC/ECD	High GWP
Sulfur hexafluoride	SF ₆	GC/MS or GC/ECD	High GWP
Freons	Freon-11, Freon-12, Freon-113	GC/MS or GC/ECD	Ozone depleting
Deuterated hydrocarbons	CD ₄ , C ₂ D ₆ , C ₃ D ₈	GC/MS	High cost

TABLE 6.6—PROPERTIES OF THE MOST FREQUENTLY APPLIED PERFLUOROCARBON GAS TRACERS (after Dugstad¹¹)

Perfluorocarbons Tracer	Abbreviation	Chemical Formula	Molecular Weight	Boiling Point
Perfluoromethylcyclopentane	PMCP	C ₆ F ₁₂	300	48
Perfluorodimethylcyclobutane	PDMCB	C ₆ F ₁₂	300	45
Perfluoromethylcyclohexane	PMCH	C ₇ F ₁₄	350	76
1,3 Perfluorodimethylcyclohexane	1,3-PDMCH	C ₈ F ₁₆	400	102

For CO₂ as injection gas, ¹⁴CO₂ will be an ideal tracer. CO₂ will interact with the formation water, which must be considered when ¹⁴CO₂ is used as a tracer. A few papers have reported application of HT.9 Hydrogen gas is reactive, and the tracer is lost in the reservoir.

6.2.4 Chemical Gas Tracers. As early as 1946, Frost¹⁰ reported the use of helium as a tracer under gas injection. The background of the noble gases in the reservoir is, however, generally too high, which makes nonradioactive noble gases unattractive as tracers. These gases can be applied only when the dilution volume is very small. [Table 6.5](#) lists the most frequently applied chemical gas tracers.

One group of tracers that has found wide application and has become the most widely applied of the chemical gas tracers today is the perfluorocarbon (PFC) group of molecules. PFCs have excellent tracer properties such as high stability, chemical inertness, and high detectability. The most frequently applied compounds are perfluorodimethylcyclobutane (PDMCB), perfluoromethylcyclopentane (PMCP), perfluoromethylcyclohexane (PMCH), and 1,2- and 1,3-perfluorodimethylcyclohexane (1,2-/1,3-PDMCH). [Table 6.6](#) lists some of their properties. PFCs are liquids with a density of approximately 1.8 g/mL at standard conditions; therefore, they can be injected into the reservoir with high-pressure liquid pumps.¹¹

One technique for analyzing PFCs is gas chromatography (GC) in combination with an electron-capture detector. The electron-capture detector is extremely sensitive to perfluorinated hydrocarbons and especially the cyclic compounds.

Senum¹² reported a method to analyze the PFC content in a hydrocarbon gas from a production stream. The gas contained in pressure bombs is flushed through a capillary absorption tube sampler (CATS) filled with activated carbon that absorbs the PFCs. The PFC-containing pellets are desorbed thermally, and the gas is directed through a combustion system composed of a precolumn, catalysts, and traps to remove the hydrocarbons before the PFCs enter the main separation column on the GC/electron-capture detector system to determine the amount of each tracer.

Another applicable technique is GC in combination with mass spectroscopy.^{13,14} This technique distinguishes tracers from other compounds not only by chromatographic separation but also by molecular mass. This reduces background noise, which is essential to obtaining a low limit of detection. The technique employing CATS has made the collection and logistics of gas samples much more efficient. Shipment and handling of high-pressure sampling cylinders are expensive and complicated. Sampling on CATS made a large improvement, making gas tracing on remote locations easier to operate. This technique allows analysis of tracer quantities in low 10^{-13} L/L concentrations. Because of the very sensitive analytical techniques, the amount of tracer needed even in large reservoirs is only a few kilograms. The CATS technology is applicable only to PFC tracers and has not been developed for the other gas tracers.

In addition to the PFC tracers, SF₆ is a frequently applied chemical tracer. SF₆ can be measured in very low concentration on electron-capture and mass-spectroscopy detectors. The tracer is stable at reservoir conditions, and it is relatively cheap. This compound is a gas at standard conditions and must be injected with gas booster pumps. The PFCs and SF₆ have a very high global-warming potential; therefore, finding an alternative tracer is needed.

Another group of compounds that have good tracer properties is freons; however, because of their ozone-depleting character, these compounds are rarely applied. Hydrocarbon gases, in which hydrogen is substituted with the deuterium isotope, will work as a tracer, but because of high production costs, these compounds are not in common use.

6.2.5 Health, Safety, and Environment Constraints. The regulations for the use of radioactive and chemical substances vary from country to country. The application of radioactivity is generally restricted, and it is important to plan the tracer test with the actual regulations in mind.

Radioactive tracers are either gamma emitters, beta emitters, or both. Tritium is a low-energy beta emitter. A sheet of paper stops this beta radiation, and it will not cause any harm to humans as long as it is kept outside the body. If spillage occurs, operators can be exposed to radiation because of direct contact with skin or because of evaporation and inhalation. Procedures must be followed carefully to ensure a safe operation.

Radioactive tracers such as ²²Na and ¹³¹I emit gamma radiation. This radiation penetrates steel walls, which means that an operator can be exposed to this radiation. The tracers are transported in lead containers and special handling procedures are needed to reduce the radiation exposure to a minimum. The activity, measured in becquerels, is normally 2 to 3 orders of magnitude less than the activity applied for tritium-labeled compounds.

Gas tracers like the PFCs have a high global-warming potential. Most of the back-produced gas will be burned in the end, and the tracers will decompose; therefore, the amount of PFCs entering the atmosphere is low. The tracers, however, may be banned in the future, and research activities are ongoing to identify new gas tracers that are more environmentally friendly.

6.3 Tracer Flow in Porous Reservoir Rock

6.3.1 Retention Caused by Partitioning Between Phases. When tracers are flowing in the reservoirs, it is normally a requirement that the compounds follow the phase they are going to trace. The best example of a passive water tracer is HTO. The HTO will, in all practical aspects, follow the water phase.

For gas tracers, there are no known passive tracers. All gas compounds will, to a certain degree, partition between the phases. The most ideal gas tracer is tritiated methane. This gas tracer follows the methane component in the gas phase closely, and the PVT properties of this gas tracer can be found with ordinary PVT calculations. The properties of the other radioactive hydrocarbon gas tracers may be found with the same PVT calculations by examining their respective nonradioactive homologues.

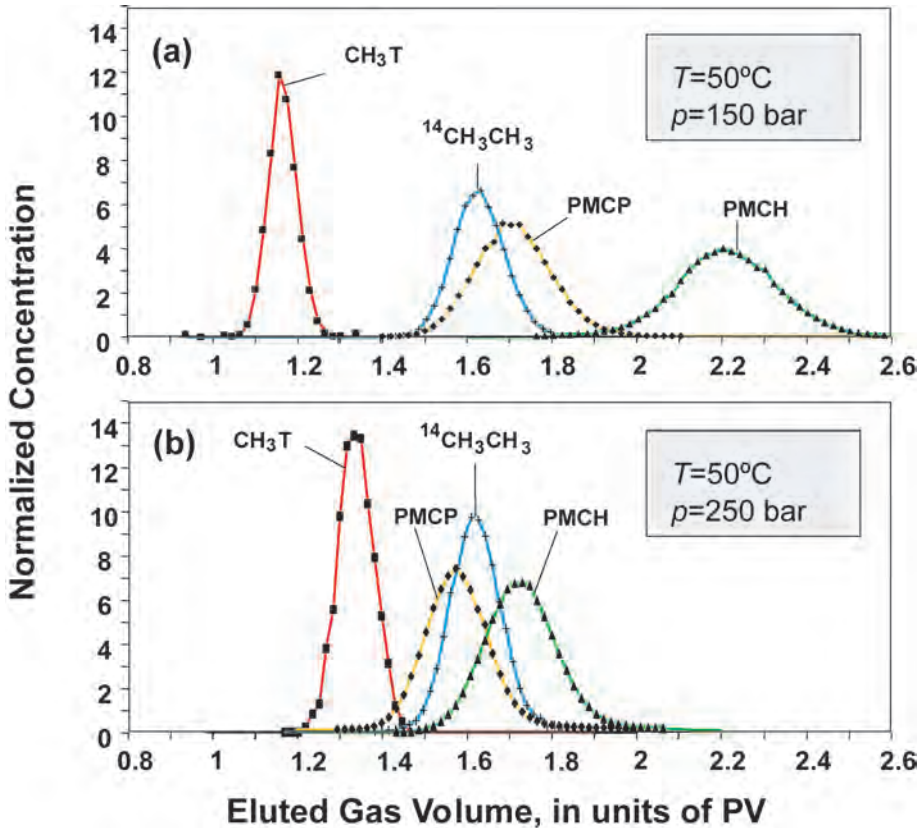


Fig. 6.3—Tracer-retention experiments in a packed column of Ottawa sand. Gas tracers are compared at two different conditions (after Dugstad¹¹).

In Fig. 6.3, the flowing properties of a selection of some gas tracers are compared. These tracers were tested in a 12-m-long slimtube with an inner diameter of 0.5 cm. The filling material was crushed Ottawa sand. Tritiated methane, CH_3T , was the reference tracer. The oil saturation in the experiments is 30% and the production curve, when a small slug of tracer is flowing through a porous medium, is measured. All tracers, even the tritiated methane, are delayed with respect to the average flow rate in the reservoir. A nonpartitioning tracer would have been produced after one PV (available gas volume) had been flushed through the system.

Normally, the K_C values (see Eq. 6.3) decrease and, thereby, the variations in retention time are reduced when the pressure is increased. The K_P value (see Eq. 6.4) converges to 1 for all compounds when miscible conditions are obtained. The separation of the tracer production curves is reduced considerably in Fig. 6.3b when the pressure increases from 150 to 250 bar. It also is observed that the ethane tracer, $^{14}\text{CH}_3\text{CH}_3$, is produced before that of the PMCP at 150 bar while, at 250 bar, PMCP is in front of ethane. The partitioning properties of the PFC have different characteristics than the partitioning properties of the hydrocarbons.

Water tracers, like gas tracers, may partition to the oil phase. Many water tracers exist that behave almost as ideal tracers. Fig. 6.4 shows laboratory tests in which some benzoic acid tracers are compared with the HTO. These experiments are carried out in a packed column of 2-m length. The packing material was crushed Berea sandstone. Other types of equipment also are used frequently. It is common to use cores of consolidated reservoir or reservoir-like rock (i.e., sandstones and/or carbonate material).

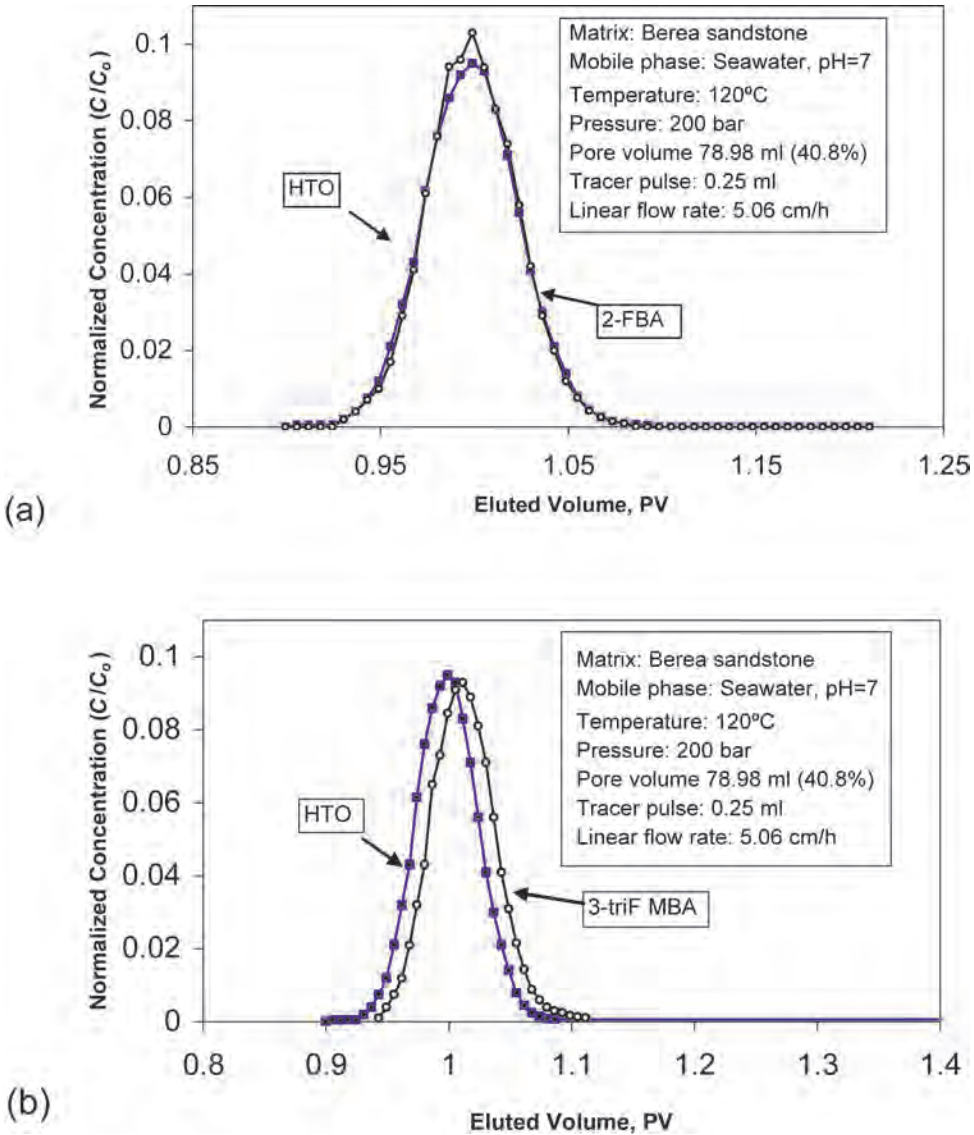


Fig. 6.4—Tracer-dispersion curves of (a) 2-fluorobenzoic acid and (b) 3-trifluoromethyl-benzoic acid compared with tritiated water from flooding experiments in sandstone (after Bjørnstad *et al.*⁶).

Retention factors, β , may be derived from Eq. 6.2 on the basis of the production profiles found by such experiments.

$$1 + \beta = \frac{V_T}{V_S}, \dots\dots\dots (6.2)$$

where V_T is the retention volume for the tracer candidate and V_S is the retention volume for the standard reference tracer. The retention volume for the standard reference tracer (nonpartitioning) may further be regarded as the volume of the mobile phase, V_M , in this system. If other retention effects can be excluded, the retention factor is an expression for the delay caused by partitioning the tracer between the mobile and the stationary phase.

Partition Coefficients. The partition coefficient depends on the temperature and pressure as well as the composition of the system. Unlike the radioactively labeled hydrocarbons, the partition coefficient of the PFC gas tracers are not easily obtained. The equation of state (EOS) used in PVT calculations is not optimized for these types of compounds, and lack of interaction parameters makes partition coefficient estimation on the basis of the EOS difficult. Normally, laboratory measurements are necessary.

When the composition, temperature, and pressure are given, each component will have a given partitioning coefficient at equilibrium. This component may be defined in different ways. Two different definitions are used frequently for gas/oil systems:

$$K_C \equiv \frac{C_O}{C_G} \dots\dots\dots (6.3)$$

$$\text{and } K_P \equiv \frac{y_i}{x_i} \dots\dots\dots (6.4)$$

C_O = the tracer concentration in the oil phase, and C_G = the tracer concentration in the gas phase. The partition coefficient, K_P , is calculated by dividing the mole fraction of the tracer in the gas phase, y_i , by the mole fraction of the tracer in the oil phase, x_i .

When the molar composition and the densities of the two phases are known, the relation between the two values can be expressed as

$$K_C = \frac{\delta_O \sum y_i M_W}{\delta_G \sum x_i M_W} \cdot \frac{1}{K_P} \dots\dots\dots (6.5)$$

For simple systems, partition coefficients can be found when the vapor pressure, p_v , of the tracer compound is known. At low pressure, the partitioning between the phases will obey Henry's law, and the Henry's law constant, H_C , is

$$H_C = \frac{p_i}{x_i} \dots\dots\dots (6.6)$$

In the case in which Raoult's law is valid (ideal behavior), the partial pressure, p_i , of the component in the gas phase is given as

$$p_i = x_i p_v \dots\dots\dots (6.7)$$

$$\text{and } y_i = \frac{p_i}{p}, \dots\dots\dots (6.8)$$

where p is the total pressure. Combining these two equations gives

$$\frac{y_i}{x_i} = \frac{p_v}{p} = K_P \dots\dots\dots (6.9)$$

The vapor pressure of the pure component divided by the total pressure gives the K_p value. This relation will normally be too simple to be accurate but may have sufficient validity to carry out a rough estimate.

Flow Equations When One Phase Is Mobile. The partition coefficient may be measured directly by measuring the concentration of the component in each of the two phases in an equilibrium system.

In a dynamic situation, the K_C value can be found by measuring the retention time of the actual component. K_C values can be calculated when the saturation and the retention time are known. In a dynamic column experiment in which the column contains only two phases (one stationary), the fraction of time, t_f , the tracer stays in the gas phase may be expressed as the number of tracer molecules in the gas phase in a reference block of the column divided by the total number of tracer molecules in the same reference block.

$$t_f = \frac{C_M V_M}{C_M V_M + C_S V_S} \dots\dots\dots (6.10)$$

Dividing by $C_M V_M$ above and below the fraction time and inserting Eq. 6.3 leads to

$$t_f = \frac{1}{1 + K_C \left(\frac{V_S}{V_M} \right)} \dots\dots\dots (6.11)$$

C_M and C_S are tracer concentrations in mobile and stationary phases, respectively. The tracer is produced when one retention volume, V_T , has been injected. This volume multiplied by the fraction of the time the tracer stays in the mobile phase is equal to the volume of the mobile phase, V_M , in the system.

$$t_f = \frac{V_M}{V_T} \dots\dots\dots (6.12)$$

A combination of Eqs. 6.11 and 6.12 gives

$$K_C = \frac{(V_T - V_M)}{V_S} \dots\dots\dots (6.13)$$

Assuming steady-state flow, V_T/V_S may be replaced by the t_T/t_S , where t_T and t_S are the retention time of the partitioning tracer and the nonpartitioning reference tracer, respectively. Applying Eqs. 6.14 and 6.15 and rearranging, the oil saturation in the flooded porous medium can be estimated (with retention factor β found in Eq. 6.2) by Eq. 6.16.

$$V_p = V_S + V_M, \dots\dots\dots (6.14)$$

$$S_o = \frac{V_S}{V_p}, \dots\dots\dots (6.15)$$

$$\text{and } S_o = \frac{1}{K_C/\beta + 1} \dots\dots\dots (6.16)$$

In Eq. 6.14, V_s is assumed to be the volume of the oil phase.

Flow Equations When Two Phases Are Mobile. Eqs. 6.10 through 6.16 assume one mobile and one stationary phase. For a generic two-phase case, the tracer flow equation may be expressed in a dimensionless form where S = saturation, C = concentration, K = partition coefficient, and f = fractional flow and when dispersion is neglected.

$$\frac{\partial}{\partial t^*} \{[S + (1 - S)K]C\} + \frac{\partial}{\partial x^*} \{[f + (1 - f)K]C\} = 0. \dots\dots\dots (6.17)$$

$x^* = x/L$ and $t^* = (q t) / (a L \phi)$ to obtain the dimensionless form of the system.

Assuming a two-phase gas/oil system in which the tracers are flowing partly in the gas phase and partly in the oil phase, the linear velocity of the gas and oil phases are given as¹⁵

$$\bar{U}_o = \left(\frac{f_o}{S_o}\right)\left(\frac{q}{a\phi}\right) \dots\dots\dots (6.18)$$

$$\text{and } \bar{U}_g = \left(\frac{f_g}{S_g}\right)\left(\frac{q}{a\phi}\right), \dots\dots\dots (6.19)$$

where f_o and f_g are the fractional flow of oil and gas, respectively, and q = volumetric flow rate, ϕ = porosity, and a = flow cross section. As previously shown, the fraction of time the tracer stays in the gas may be expressed by Eq. 6.10. The mean velocity of the tracer in a two-phase flow may be expressed by Eq. 6.20 when accepting that V_g/V_M is equal to S_o/S_g .

$$\bar{U}_{tr} = \left(\left(\frac{f_g}{S_g}\right) \frac{1}{1 + K_C \left(\frac{S_o}{S_g}\right)} + \left(\frac{f_o}{S_o}\right) \left[1 - \frac{1}{1 + K_C \left(\frac{S_o}{S_g}\right)} \right] \right) \left(\frac{q}{a\phi}\right) \dots\dots\dots (6.20)$$

Rearrangement gives

$$\bar{U}_{tr} = \left(\frac{f_g + K_C f_o}{S_g + K_C S_o}\right)\left(\frac{q}{a\phi}\right) = f_t \left(\frac{q}{a\phi}\right) \dots\dots\dots (6.21)$$

This tracer-flow-velocity model may be applied when the K_C values are known. Fig. 6.5 gives a graphical outline of f_t (based on Eq. 6.21) for five different partitioning coefficients. The fractional flow curve for the gas, f_g , is arbitrarily chosen. The f_t curves = 1 at the saturation where $f_o/S_o = f_g/S_g$ (i.e., when both phases are flowing with the same linear velocity). When the K_C value = 1, the tracer flow rate is independent of saturation and shape of the fractional flow curve. The f_t curves plotted in Fig. 6.5 show that the relative flow of the tracers depends strongly on the saturation. Below the gas saturation at which the two phases flow with the same linear velocity, the lower-partitioning tracers will be in front while above that saturation decreasing K_C value will give increasing flow rate.

Residual-Oil Measurements. Eqs. 6.10 through 6.21 give the basis for estimating remaining oil in the reservoir. In the most simple system, in which the oil saturation is stationary, S_o may be calculated from the knowledge of the partition coefficient of two tracers and the peak of the tracer-response curve by

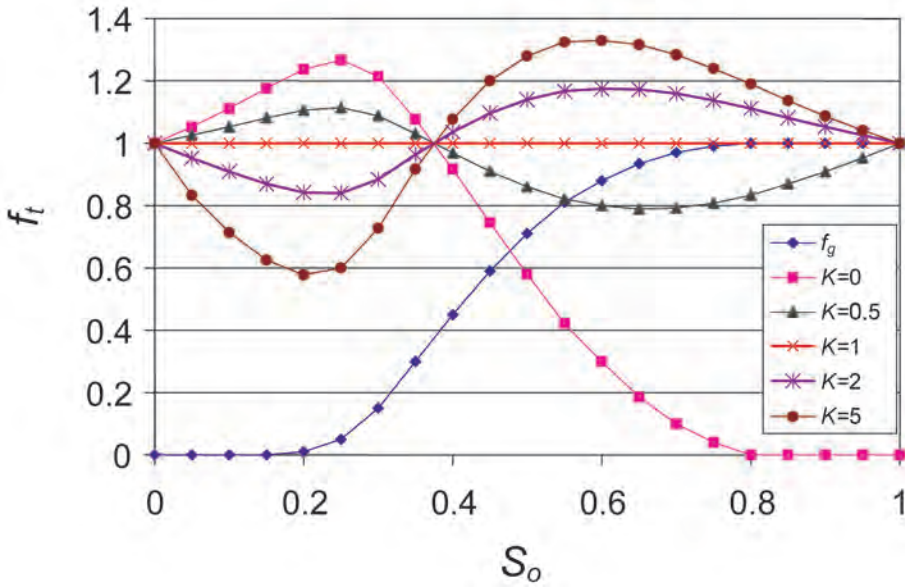


Fig. 6.5—Relative tracer flow rates in a two-phase system for a certain fractional flow curve (after Dugstad, Bjørnstad, and Hundere¹⁵).

$$S_o = \left[\left(\frac{V_{Ti}K_{ci} - V_{Tj}K_{cj}}{V_{Tj} - V_{Ti}} \right) + 1 \right]^{-1} \dots\dots\dots (6.22)$$

Under ideal conditions, V_T may be replaced by the retention time of the two tracers. There is always a question about which retention time to use in the calculations. Alternatives are breakthrough, production peak, moment (mass middle point), or other specific landmarks. The production curve is a superposition of contribution from individual streamtubes in the reservoir; therefore, the choice of retention time will reflect either saturations in certain streamtubes or an average value. A sensitivity evaluation of Eq. 6.22 shows that it is preferable to apply two tracers with K_C values far apart from each other. The most efficient would be to include one tracer that has no partitioning to the liquid phase. Eq. 6.22 then is simplified to Eq. 6.16.

One of the questions that may be raised against the method is the possibility for obtaining equilibrium between the phases. The calculations are based on a real equilibrium between the phases, which depends on saturation, diffusion rates, flow rates, pore structure, and partition coefficient.

To obtain reliable results, it is crucial to understand the flow situation. If the oil phase is stationary, Eq. 6.22 may give a satisfactory result. If two phases are flowing, it is important to know the fractional flow curves (i.e., relative permeability), and a reservoir simulator will be necessary to obtain a reliable result.

6.3.2 Biodegradation. Microbial stability of water tracers may be a problem. This problem will be less important at higher temperatures at which the microbial activity is lower. The problem, however, must be addressed in sample handling and storage. Some tracers, in special situations, may biodegrade after sampling. To avoid such degradation, a biocide may be added to the sample immediately after collection. Adding 0.1 ppm NaN_3 to the stock solution can prevent bacterial growth.

Fluorobenzoic acid tracers have been reported to biodegrade when exposed to seawater. The biodegradation has been measured for monofluorobenzoic acid and di- and tri-fluorobenzoic acid. No degradation was observed for the di- and tri-fluor compounds. Alcohols also may biodegrade under certain conditions. In general, the odd-carbon-number alcohols are more resistant to bacterial attack than the even-number ones.

6.3.3 Ion Exchange. Ions adsorbed on the reservoir surface are free to exchange with ions in the water. This ion exchange is a reversible process and tends to obtain equilibrium between surface concentration and the concentration in the water. Different adsorption isotherms may be used to describe this situation. In most cases, this ion exchange can be described by a Langmuir isotherm (Eq. 6.24).

The flow of the tracer through the reservoir may be influenced by adsorption to the grain surface. To come into contact with the grain surface, the gas tracer may need to diffuse through a film of oil, water, or both. The adsorption depends on the partitioning of the tracer into the two liquid phases in the reservoir. Different models are applied to describe the adsorption on the grains. The simplest form is the linear relation in which the adsorbed amount, a_c , is proportional to the concentration in the contacting phase C_c .

$$a_c = K \cdot C_c \quad \dots\dots\dots (6.23)$$

A tracer in a dynamic system will be retained independently of concentration. In many cases, however, the active adsorption sites on the surface will be saturated and the amount adsorbed will not increase linearly with the concentration. In some cases, a more accurate expression is the Langmuir isotherm,

$$a_c = \frac{U \cdot c}{1 + V \cdot c} \quad \dots\dots\dots (6.24)$$

U and V are two parameters that decide the shape of the curve for the actual system at a specific temperature. c = the concentration in the liquid phase caused by partitioning between the gas and liquid phase, and a_c = the amount of tracer adsorbed to the grain. At low concentration, which is the case when tracers are considered, this equation will be a straight line with slope U . Other isotherms also may be considered but are less likely to be needed. Different adsorption isotherms will influence the produced tracer peak.

If the tracer is positively charged, it can be exchanged with cations adsorbed to the reservoir surface. The affinity to the surface may vary, and some cations will be more tightly adsorbed than others. The effect on the tracer flow will be retention of the tracer. According to the most likely adsorption isotherm, the adsorption will be linear with the tracer concentration as long as the concentration is very low.

^{22}Na has shown to move through porous media with only minor delay caused by sorption and ion exchange to reservoir rock but in a reversible manner. Most other cations (Cs^+ , Co^{3+}) have shown strong adsorption and cannot be used as tracers.

6.4 Planning and Design of Tracer Tests

6.4.1 Timing of Tracer Programs. The timing for tracer injection depends on the information that is requested. Normally, it is desirable to inject the tracer early in the injection process to obtain information as soon as possible and be able to take the necessary actions to optimize the production strategy. However, it has been seen that water tracer is lost in the reservoir because of imbibition of water. Therefore, if there is large imbibition potential in the reservoir and water is trapped in volumes that do not contribute to the normal flow path, tracers can be trapped

and only minor tracer concentrations leak out in the flowing part of the reservoir. This information can be valuable on its own, but if the problem is not considered, it may contribute to wrong interpretation of the results. In this situation, water may break through from an injector that is traced without observing any positive detection of tracer. In general, injecting the tracer in the very front of an injection program is not recommended.

Tracers should not be injected until the pattern area has been pressured up with the injected fluid. If the traced injected fluid is spent in collapsing a gas phase or otherwise pressuring the reservoir, the volume injected to tracer breakthrough, which indicates the volumetric sweep to breakthrough, may be significantly larger than that determined after the pattern area has been pressured.

Well-to-well tracer tests may be performed, in principle, either as a pulse injection or as a continuous injection. The most often applied method is pulse injection. The continuous injection may be useful especially where unsaturated water-wet rock may absorb short tracer pulses by water imbibition from the injected waterfront edge. To obtain a constant concentration in the injected water, a constant recording of the water-injection rate is necessary. In general, continuous injection is more complicated and a tracer engineer must follow the injection for a long period. For pulse injection, however, the whole program can be carried out within a few hours.

6.4.2 Field-Test Design. The design of a field tracer test has two components: a tracer part and an analytical part. The tracer component includes choosing the tracer for each well, estimating the required amount of each tracer, dealing with the regulations, and planning for acquisition and injection of the tracer into the ground. The analytical part includes selecting an analytical strategy, setting up a sampling program, and determining the background realistic detection limits in the samples collected from the particular field.

Traditionally, two methods have been applied to determine how much tracer must be added to obtain a tracer-production response significantly above background. In general, it is desirable to inject as small an amount as possible to reduce environmental problems, contamination, and costs. Both radioactive- and chemical-tracer compounds are potentially harmful to the environment; therefore, the amount applied must be kept to a minimum. In some cases, the maximum permissible concentration of the tracer that may be released to the environment is limited by requirement from the authorities.

In many situations, produced gas containing tracer is reinjected into the reservoir. This has, in some cases, contaminated the whole reservoir and destroyed the possibility of applying the same tracers in another segment of the reservoir. If not considered, flow conditions can be misinterpreted because of positive identification of tracer originated from reinjection of tracer in uncontrolled conditions.

The third reason for the use of low concentrations is to reduce costs. In small reservoirs, the tracer cost is a minor part of the total cost connected to the test but, in larger reservoirs, the tracer costs may be significant, especially if exotic tracers are required.

One method to estimate the tracer concentration is to assume that the injected tracer is diluted uniformly by the entire swept volume when it is produced. Sufficient tracer is added to ensure detection at this dilution volume. The peak tracer concentration is presumed to be well above the average.

The first part of the calculation is to estimate a dilution volume, which is obtained by calculating the water- or gas-filled PV between the injector and the production wells. The first approximation is to assume radial flow from injector, but it usually is modified by any known reservoir conditions, such as known flow channels or barriers, large permeability variations, or other constraints causing nonradial pressure gradients. It is important to know porosity, net pay zone, and distances between wells for the calculation. Optimal design can be obtained by performing full-field simulations. The problem with this method is that many of the parameters are unknown, which again is the main reason for performing the tracer test.

The smallest injection pulse required is usually the amount of tracer needed to obtain an average concentration of 10 times the minimum limit of detection in the dilution volume. This is expected to give a peak production on the order of 100 times the detection limit. To be able to follow production curves reflecting the contribution from different layers and zones, it is important to have at least this amount of tracer injected.

In the ideal situation, the dilution volume, V_d , can be calculated with a radial approximation.

$$V_d = \pi \times r^2 \times h \times S_w \times \phi \times F, \dots\dots\dots (6.25)$$

where r = distance between the injector and the producer, h = height of the reservoir zone, ϕ = porosity, and S_w = water saturation. For a gas tracer, S_g should substitute for S_w . In addition, the expansion of the gas has to be taken into account. F is a correction factor that accounts for nonsymmetry caused by barriers, well location, and other restrictions causing changes in the drainage area.

An analytical method to determine tracer production curves in a layered system exists.¹⁶ The method assumes that the tracer pulse moves radially from the injector to the producers through homogeneous, noncommunicating layers with longitudinal dispersion in the direction of flow. The number of layers, their thickness, and their permeability are used to represent the reservoir heterogeneity. The tracer pulse moving through each layer is diluted at the producers by untagged water from other streamlines in the same layer. This dilution effect is a consequence of pattern geometry. Production of the combined tracer responses from all these layers makes up the response curve of tracer concentration as a function of the cumulative volume of water injected.

The model predicts peak height, breakthrough time, and shape of the produced tracer-response curve from the amount of tracer injected and the pattern geometry. The fundamental equation (Eq. 6.26) used to calculate tracer-pulse flow in a streamtube is further applied to give analytical expressions for pattern-breakthrough curves.¹⁷

$$\frac{C(\psi)}{C_o} = \frac{1}{2} \operatorname{erfc} \left(\frac{L - s_1}{\sqrt{2\sigma_1^2}} \right) - \frac{1}{2} \operatorname{erfc} \left(\frac{L - s_2}{\sqrt{2\sigma_2^2}} \right) \dots\dots\dots (6.26)$$

The concentration of a tracer at any location within the streamtube, ψ , is the difference between two terms, given by Eq. 6.26. L = the distance along a streamline, and s_1 and s_2 = the front and end location of the tracer pulse in the streamline, respectively. σ = the standard deviation that, in a radial system, can be found from

$$\sigma^2 = 2\alpha \frac{r}{3}, \dots\dots\dots (6.27)$$

where α = dispersivity and r = the radius at the front defined at a location corresponding to the 50%-concentration point. On the basis of these predictions, tracer amounts can be injected to ensure a peak concentration in the production well that is well above detection limits. In practice, however, such calculations are often based on so many unknown or estimated parameters that it is advisable to inject more tracer than these calculations predict.

A reservoir simulator probably can provide the best estimate for tracer amounts; however, these simulations are based on detailed reservoir description. At the stage of tracer injection, the reservoir model is generally uncertain and, again, it is advisable to inject more than these calculations predict. Sufficient tracer must be injected to enable measurement of unexpected flow behavior.

6.4.3 Collection of Samples for Tracer Analysis. Sampling frequencies will depend strongly on the field considered. Tracer tests are, in general, a method to verify proposed flow scenarios. To cover unexpected behavior, sampling should be started long before expected breakthrough. Sampling frequency should be highest at the start of the flood to avoid missing early breakthrough.

Water samples may be stored in bottles that normally are collected from the separator. Water sampling is cheap, and frequent sampling is advised. Initially, only some of the collected samples need be analyzed; intermediate samples can be discarded if no tracer is found. Once tracer is found, samples are analyzed backward until the tracer breakthrough is found. In certain situations, some tracers may biodegrade after sampling. To avoid this, a biocide may be added to the sample immediately after collection. Adding 0.1 ppm NaN_3 to the stock solution can prevent bacterial growth.

Samples can be collected at the wells or from a test separator shared by a number of wells, provided the stream is sampled only near the end of the test when the water is representative of the currently sampled well. Well sampling usually involves a water-separation problem, which can be avoided by sampling at the separator. The optimal situation is to have a dedicated separator for the particular well. New technology involving multibranching wells, horizontal wells with perforation in several reservoir compartments, subsea manifolds, or even subsea separators cause additional problems in providing relevant samples.

Gas tracers normally have been collected on pressure cylinders. The gas may be collected directly on the flowline or from a separator. The tracer content in the gas will depend on where the sample is collected. The partition coefficient of the tracer depends strongly on the pressure. A sample collected on the flowline at 100 bars and one collected at a separator at 30 bars will give different results. Further estimation of the total amount of tracer produced also will depend on the GOR at the sampling point. To calculate the produced-tracer amount in one particular well, it is necessary to know the pressure, temperature, and GOR at the sampling point. In addition, it is necessary to establish the partition properties of the tracer at these particular conditions. This can be done by measurement or by applying PVT models; however, existing PVT models will not treat all tracer types with the same accuracy.

Collection of gas tracers is more expensive than the collection of water tracers. When gas is collected on pressure cylinders, the cost of the cylinders will add considerably to the analysis cost. A new technology¹⁴ has been developed in which the tracers are absorbed by an activated carbon trap. These CATS are used for collection of PFC gas tracers. The tracer then is collected in these tubes in the field, and only small tubes, without any surplus pressure, are shipped to the laboratory. Special sampling equipment is available that ensures a reliable and reproducible sampling. The CATS method is applicable only for a limited number of tracers, and in many situations, it is still necessary to collect samples with pressure cylinders. The cylinder size and the amount of gas collected will depend on the tracers and the concentration expected in the produced gas. Normally, a 200-mL cylinder will be sufficient.

The laboratory applies a large variety of techniques to measure the concentrations of the tracers. The different techniques will have degrees of uncertainty and the differences between detection limit and quantification limit should be distinguished. At concentrations close to the detection limit, it may be very difficult to obtain accurate quantification of the tracer; therefore, some laboratories report only “detected” without quantification when the concentration is low.

The detection limit obtained by an analytical procedure will be influenced by the quality of the sample. In formation water, the detection limit may be different from the detection limit in production water that also contains emulsion breakers, scale inhibitors, corrosion inhibitors, and other additives. It is, therefore, important to have a good cooperation between the field operators and the laboratory to obtain the best quality on the field samples.

Because of the very sensitive analytical techniques needed, it is essential to avoid cross contamination. It is important to plan tracer operations carefully to avoid any possibilities of close contact between injection equipment and sampling equipment. For example, it might be a source of contamination if injection pumps or tracer containers are transported after injection in the same van or stored in the same building as sample bottles or sample equipment.

6.5 Interpretation of Field Data

6.5.1 Different Levels of Interpretation. To obtain high-quality tracer-response curves that are the basis for the further interpretation, a well-designed sampling program is needed. In general, more samples will give the potential for extraction of more information from field tests. Too often, interpretation is difficult because of limited tracer data.

The final objective of a well-to-well study is the interpretation of the response curves. A good analysis of the information given by the tracers, in combination with other available data, gives a better understanding of the flow in the reservoir, not just verification of communication between injector and producer.

The response curve can be analyzed from three different points of view or complexity levels. The simplest interpretation is the qualitative one. By observing the curves, the following pattern characteristics can be derived: injection-water arriving time (breakthrough); existence of high-permeability channels, barriers, and fractures between wells; communication between different layers; stratification in the same layer; and preferential flow directions in the reservoir. Furthermore, the cumulative response can be obtained by integrating the concentration vs. time curve if the production flow rate is known. From this new curve, the fraction of injection water reaching each producer is easily calculated. A common spreadsheet is the best way to make these calculations. This type of interpretation can be carried out without any advanced simulation. It is important to integrate the data obtained from the geological model, primary production data, 4D seismic data (if available), and tracer data in a systematic way.

The second level of analysis uses basic mathematical models to fit simple response curves by means of theoretical expressions and to decompose complex responses in several simpler functions. In this way, partial residence times, as well as other parameters, can be determined for each function. Mathematical models also allow for the evaluation of important parameters, such as permeability, and make it possible to predict the behavior of unknown patterns.

Finally, complex mathematical models like numerical finite-element simulators or stream-tube modeling can be used to achieve a deeper analysis. Most of the commercially available simulators have tracer options with varying degrees of complexity. Not all simulators include important physical effects like partitioning, dispersion, and adsorption. A tracer simulator that can be coupled to full-field reservoir simulators has been developed recently. Simulation is a tool to improve the existing reservoir model; therefore, it is crucial to have access to the best available model to enable an efficient optimization based on the tracer-production data.

6.5.2 Evaluation Based on Hand Calculation and Adequate Data Presentation. Qualitative interpretation of field data is illustrated by examples from the Snorre field in the North Sea. **Fig. 6.6** shows the segment of the field that was tested and the location of injectors (triangles) and producers (circles).¹⁸ A water-alternating-gas (WAG) injection program is being used in the field.

Fig. 6.7 shows a way to present field data for a gas-tracer program. The data are plotted as a time response. Alternatively, the data can be plotted as a volumetric response. To obtain a better understanding, it is important to plot gas-tracer-production data with GOR. The tracer data are plotted relative to the amount of tracer injected, which means that the concentrations presented for each individual tracer can be compared directly.

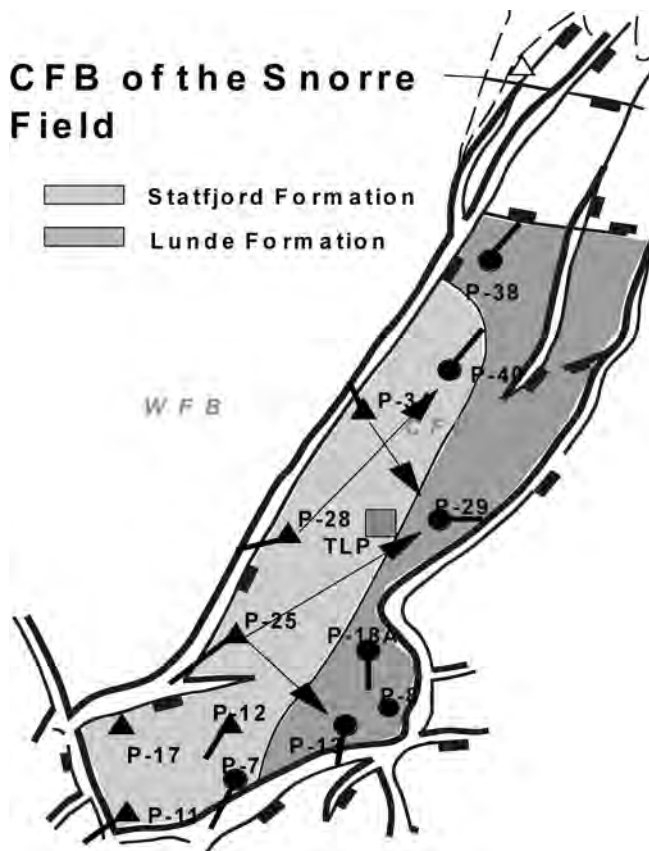


Fig. 6.6—Well location in the central fault block (CFB) of the Snorre field. Arrows indicate the main producers of injected tracers.¹⁸

From Fig. 6.7, it is possible not only to find communication but also to extract information about the prevailing flow regime. The gas tracer injected into Well P25 breaks through without any significant increase in GOR, which means that the gas has not followed a free gas layer but has been dissolved in the oil. Three different gas tracers were injected in Well P28 at three different times. These tracers were produced only after a significant GOR was recorded. All the tracers were produced at almost the same time. This shows that gas has been trapped and that the gas in the individual gas slugs has subsequently filled this trap. At a certain time, the gas trap has been filled and the gas moves on to the producers. When reaching the producer, the gas contains all three different tracers injected over a 3-year period.

From the data in Fig. 6.7, it is possible to carry out a spreadsheet calculation to estimate the recovery of the injected tracer in each individual production well. This shows that a large percentage of the injected gas has moved in different directions. Breakthrough time also may be estimated, either as the first sample that contains tracer above the detection limit or as an extrapolation backward of the initial phase of the production curve. However, the accuracy of this calculation is limited by the sampling frequency.

To fully understand the flow behavior, it is important to add all information available. The picture may be modified by the knowledge of injection rates and production rates in the neighboring wells.

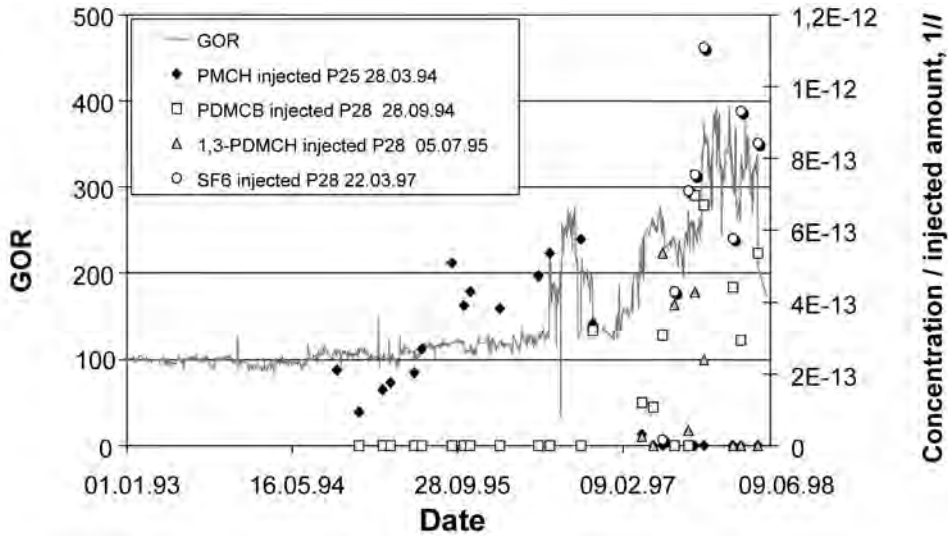


Fig. 6.7—Gas tracer data from the Snorre field in the North Sea.¹⁸

Because of maintenance and operational problems, production wells may be shut in for some periods. Because of fluid drift in the reservoir during shut-in, samples collected immediately after such periods may give unexpected results. This additional information can be exploited to better understand the pressure distribution in the field. Somaruga *et al.*¹⁹ used well shut-in in a systematic way to obtain additional information. If the changes that may occur during shut-in are not considered, it may cause misinterpretation of the tracer-response curves.

The water-tracer-response curves should be presented together with the water cut. Fig. 6.8 shows water-tracer-response curves in the same well as discussed previously. Initially, a small water-cut increase is recorded. The tracer injected in Well P34 follows this increase. When the water cut starts to increase more rapidly, one of the other tracers starts production while the concentration of the first tracer vanishes. This method of presentation increases the understanding of the flow behavior and the water contribution from the different injectors.

Response Curves. The time response is the graphic representation of the concentration of activity (after background subtraction and decay correction) as a function of time. Preprocessing the experimental data can smooth the response. From this curve, the cumulative response (recovered activity vs. time) is derived by a simple numeric integration.

Concerning the cumulative response, the Eq. 6.28 gives the cumulative tracer recovered up to an instant, t_i .

$$m_{t_i} = \int_0^{t_i} Q_{p_t} C_t dt, \dots\dots\dots (6.28)$$

where m_{t_i} = the total tracer recuperation up to t_i , Q_{p_t} = the production water flow rate as a function of time, C_t = tracer concentration as a function of time, and t_i = the elapsed time (days after the injection). Q_{p_t} often will be available as a discrete value representing each day. C_t will be available only as an individual measurement according to the sampling program. The accuracy of the total recovery will depend on the sampling frequency.

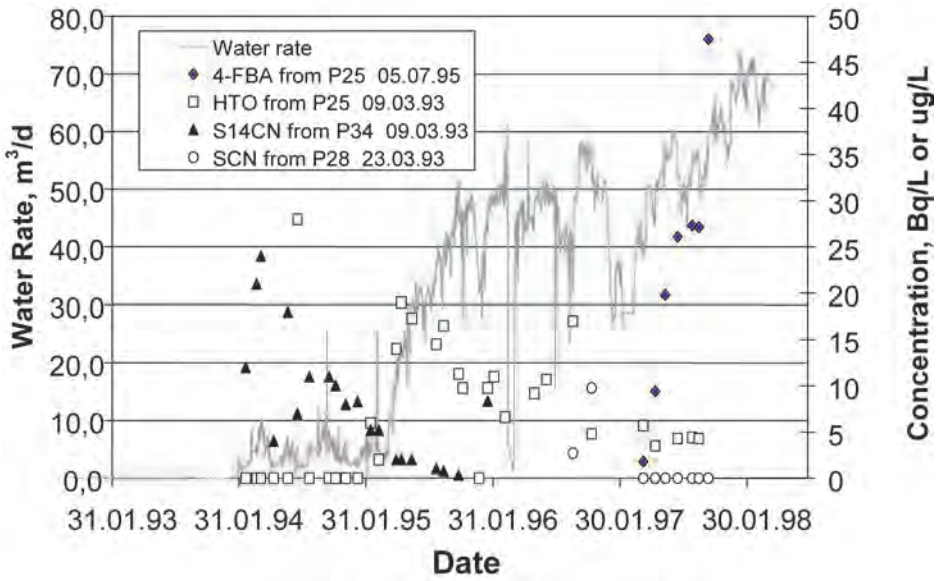


Fig. 6.8—Water-tracer-response curve from the Snorre field in the North Sea.¹⁸

Sweep Volume. Instead of the time-response curves, the data are often presented as volumetric-response curves. The presentation is especially convenient for estimating the swept volume between the particular injector and producer pair. Swept volume, V_s , can be estimated from the product of the mean produced volume, \bar{V} , and the ratio of the mean volumetric water rate between the injector and the producer, Q_m , to the mean volumetric water production rate, Q_p .³

$$V_s = \frac{Q_m \bar{V}}{Q_p} \dots\dots\dots (6.29)$$

\bar{V} is calculated from the first moment of the produced-tracer concentration, C .

$$\bar{V} = \frac{\int_0^\infty CV \, dV}{\int_0^\infty C \, dV} \dots\dots\dots (6.30)$$

Q_m , the flow rate between injector and producer, is estimated from the fraction of injected tracer produced at the well at the mean injection rate, Q_i .

$$Q_m = \frac{m}{M} Q_i \dots\dots\dots (6.31)$$

where m = the amount of tracer produced at a given well and M = the amount of tracer originally injected. The swept volume can be expressed in terms of the injected and produced flow rates and the fraction, m/M , of water going from the injector to the producer.

$$V_s = \frac{m}{M} \frac{Q_i}{Q_p} \bar{V} \quad \dots\dots\dots (6.32)$$

Because of limited data, the tracer-production curve is composed of a discontinuous set of points and, in practice, the integral in Eq. 6.30 is approximated by

$$\bar{V} = \frac{\sum_0^{\infty} CV \Delta V}{\sum_0^{\infty} C \Delta V} \quad \dots\dots\dots (6.33)$$

The calculation of swept volume often is complicated by a lack of data. The mean produced volume may need to be estimated on the basis of extrapolated tracer-production curves. In many cases, the sampling program is either not finished or it has been stopped without following the tail of the production curve. To fit the missing data in the tail of the production curve, an exponential decline approximation can be applied.

$$C = C_e \exp \left(-\frac{V - V_e}{a} \right) \quad \dots\dots\dots (6.34)$$

where C_e = the measured tracer concentration at the value of V_e from which the exponential fit starts. The slope of the line is represented by $1/a$. If Eq. 6.34 is substituted for C in Eq. 6.30 and the integral replaced by a finite sum, the following expression is valid:

$$\bar{V} = \frac{\sum_0^{V_e} CV dV + aC_e(a + V_e)}{\sum_0^{V_e} C dV + aC_e} \quad \dots\dots\dots (6.35)$$

To find the swept volume in an incomplete data set, this equation is used for \bar{V} in Eq. 6.32.

6.5.3 Evaluation Based on Analytical Solutions. Eq. 6.26 gives the fundamental equation for tracer breakthrough in a streamtube. A correlation into a single breakthrough curve for various repeated homogeneous-flooding patterns has been found.¹⁶ In a layered system, the overall tracer-response curve is a combination of responses from individual layers. The individual-layer responses are predictable from the correlated pattern-breakthrough curve; however, the tracer arrival time at the production well and the concentration contribution from each layer are functions of the porosity, permeability, and thickness of that layer. Conversely, the decomposition of an actual tracer-production curve from a multilayered system into the individual-layer responses can yield individual-layer parameters. Computer algorithms exist that deconvolve the overall tracer profile into the individual-layer responses and compute ϕh and $kh/\Sigma kh$ of the individual layers.

6.5.4 Evaluation of Tracer-Response Curves With Numerical Simulation. The most thorough analyses of tracer data are carried out in combination with a reservoir simulator applied for that particular field. Many of the applied reservoir simulators, based on numerical solution

of flow equations applying finite-difference methods, have options for handling tracers.²⁰ In addition, streamline models^{21,22} exist that handle tracer flow. However, normal simulators have limitations. One problem is the limited possibilities for including physical properties such as partitioning between phases and adsorption to grain surfaces. This problem is of special importance for gas tracers. There is also a problem connected to handling of dispersion because the tracer pulse is, in its initial phase, much smaller than a typical gridblock size.

To overcome some of these problems, Sagen *et al.*²³ developed a simulation module to improve the accuracy of the calculations. To resolve the influence of reservoir heterogeneities on the measured tracer response, an accurate numerical treatment of the tracer equation is needed. This is especially important when narrow tracer slugs are injected in a reservoir. This tracer module calculates tracer flow with an explicit method for integration of the convection part of the tracer equation. To reduce numerical smearing of the tracer pulses, the timestep for the tracer calculation is selected as large as possible but may still be much smaller than the timesteps of the host reservoir simulator, which most often uses an implicit formulation. In the tracer module, the main tool for reducing numerical dispersion is the use of a second-order numerical scheme for integrating the tracer equation. A separate grid-refinement option for tracer calculation is available. In combination, these methods lead to a good resolution of narrow slugs propagating through the reservoir. The method of separate grid refinement is far less time consuming than performing the whole reservoir simulation on a refined grid. This tracer simulation module has been coupled to some of the standard reservoir simulation tools.

6.6 Field Experience

Interwell tracer tests are widely used. This chapter reviews some of the studies reported in open literature. The selection introduces different problems to be addressed, but the original papers should be studied to obtain a more detailed description of the programs.

6.6.1 Tracers in WAG Programs. The Snorre field is a giant oil reservoir (sandstone) in the Norwegian sector of the North Sea. Injection water and gas were monitored with tracers,¹⁸ and the resulting tracer measurements are discussed in [Sec. 6.5.2](#).

The same tracers used in the Snorre field have been injected in the Gullfaks field²⁴ in the North Sea. The tracers identified unexpected communication paths between layers. The results contributed to methods for improving the WAG recovery performance.

6.6.2 Water and Gas Tracer Injection in Fractured Reservoir. A tracer test was carried out in the Spraberry trend in west Texas.²⁵ In this field, the oil was produced primarily from fractures and not from the matrix porous sandstone. To carry out the most efficient waterflooding strategy, the knowledge of fracture direction was imperative. Instead of a costly water-injection pilot project, natural gas with tracer was injected into a central well for 16 weeks to define the fracture pattern. The ⁸⁵Kr tracer applied was injected continuously with a concentration 28 times minimum detectability, which was 13,000 Bq/m³ (10⁻⁸ Ci/ft³) gas. The detector system applied was a thin-wall, beta-sensitive Geiger-Muller tube that records the tracer amount in the effluent gas continuously.

At the beginning of the thirteenth week, a 2-Ci slug was injected, and at the beginning of 14th week, a 1-Ci slug was injected. Radioactive gas was recorded only in two wells. No radioactivity increases were detected at any of the other 10 wells monitored, either continuously or intermittently, during the tracer survey. The cyclic nature of tracer appearance was attributed to the necessity for overcoming the varying hydrostatic head of oil in the well and to the appreciable difference in effective permeability of the principal and cross-fracture systems. Apparently, neither of the two wells in which tracer was recorded intersected the same fracture plane as the injection well. The tracer survey confirmed predictions about the general line of fracture orientation in the lower formation of the Spraberry trend.

6.6.3 Gas and Water Tracers in the El Furrial Field. Viela *et al.*²⁶ reported the application of both gas and water tracers in the El Furrial field. The radioactive water tracers applied were isopropyl alcohol, HTO, ²²Na, and thiocyanate. Breakthrough time recorded was between 1 and 3 years. In the same field, gas tracers also were added. The tracers applied were PMCP, PDMCB, and SF₆. The conclusion was that the tracer survey was important to verify expected flow behavior and to identify unexpected communication paths.

6.6.4 Tracers for Gas Injection. Welge²⁷ described one of the pioneering works of tracer application to follow injected gas. The communication between the wells in a small part of the Cromwell pool in central Oklahoma was investigated. The well spacing in the area was approximately 65 m. Three radioactive tracers were used: HT (only tritiated hydrogen is mentioned which may be either HT or T₂), CH₃T, and ⁸⁵Kr. One Ci of the tritiated compounds and 280 mCi of ⁸⁵Kr were injected into the same well. In the nearest well, the tracers were produced after 7 days, which indicates an average flow rate of 10 m/day or more than 1 ft/hr. The tracers were not injected simultaneously; therefore, a comparison of the response curves should be done with care. The curves show small variation with the methane peak produced a day or two later than tritium and ⁸⁵Kr. It also seems that the ⁸⁵Kr data are a bit more spread out than the other data. The test results were used to improve the knowledge about the sweep area and the volumetric flow in the different directions.

Calhoun²⁸ reported the use of several gas tracers in the Fairway field. The program consisted of three phases of injection. In the first phase, 10 Ci of tritiated hydrogen and ⁸⁵Kr were injected. Four months later, 10 Ci of tritiated methane, tritiated hydrogen, and ⁸⁵Kr were injected in a new set of injectors. In the third phase, 10 Ci of tritiated methane and ⁸⁵Kr were injected again in several wells. The extensive tracer program showed the source of gas breakthrough of 25 production wells. Continuous sampling of these wells after gas breakthrough has indicated a change in front configurations and fluid-migration pattern. Tracer responses proved the need for controlled injection and withdrawal to even out sweep configurations. Furthermore, tracers have indicated those areas in which injection rates and gas/water cycles should be changed to reduce fingering of the injected gas. This knowledge has been useful in alternating injection cycles and rates to control GORs at a reasonable level. Radioactive-tracer results also indicate that high-pressure gas injection at the Fairway is yielding additional oil recovery, either through swelling of the residual oil or by partial miscibility.

Tinker²⁹ reported the use of tritiated hydrogen and ⁸⁵Kr as tracers under methane injection in the Trembler zone II reservoir of the East Coalinga field, California. The tracers revealed that desaturated intervals were often continuous over wide areas of the field. Those intervals could greatly influence an injection project by acting as a thief zone for injection water. The tracer study suggested generally better reservoir-sand continuity than could be inferred from a related outcrop study.

6.6.5 Tracers in Enriched-Gas Injection. In the Prudhoe Bay field,³⁰ ⁸⁵Kr, tritiated methane, ethane, and propane have been used as tracers for an enriched-gas flooding. In the South Swan Hills unit, Alberta, Canada,³¹ tracers were applied to follow enriched gas in a water/solvent cyclic-injection program. This is a limestone reservoir, and the tracers applied were tritiated hydrogen gas, tritiated ethane, and ⁸⁵Kr.

To gain information about the interwell reservoir characteristics, relative fluid velocities, and volumetric sweep efficiency in the early life of this project, it was desirable to trace the interwell movement of both the injected solvent and water. Tracers were added in as many as 14 solvent and 14 water injectors. The tracer responses in the wells were applied to redesign the injection program to achieve better sweep efficiency. The results proved to be of value as a qualitative indication of sweep, showing water and solvent flowing together to the majority of

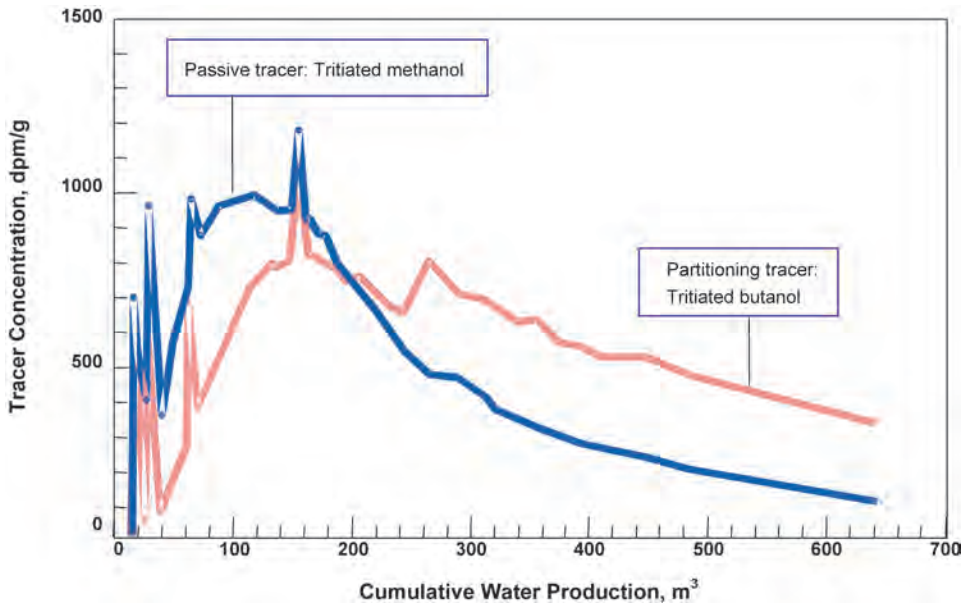


Fig. 6.9—Production curve of tritiated methanol and tritiated butanol in the Leduc field.³⁵

the offset wells. In some cases, unexpected flow paths were identified. No quantitative interpretation and information on project performance, however, have been derived from these data.

6.6.6 High-Pressure N₂ Miscible Injection. In the Jay/Little Escambia Creek field, five radioactive tracers and one chemical tracer were used to tag injected N₂.³² The radioactive tracers used were ⁸⁵Kr, tritiated hydrogen, methane, ethane, and propane. Sulfur hexafluoride was the lone chemical tracer. The N₂ was injected at a pressure of up to 7,600 psig for a period of 1 to 2 weeks before the well was switched over to water injection. The tracers produced are ⁸⁵Kr and tritiated propane. The main purpose of tracer injection was to determine the source of N₂ breakthrough. This knowledge enabled adjustment of injection rates and volumes to improve area convergence on the production wells.

Also in the Fordyce field,³³ ⁸⁵Kr, HT, CH₃T, and C₂H₅T were applied in a high-pressure (> 7,000 psig) miscible injection program. The gas injected was dry natural gas with an N₂ content of approximately 5%. The tracer-production data were used in a gas-sweep model to predict gas movement and to localize unswept areas.

6.6.7 Labeling of CO₂ Injection. Craig³⁴ reported the use of halogen compounds to trace injected CO₂. The compounds applied were freon-11, freon-12, freon-113, and sulfur hexafluoride. The halocarbons were reported to be detectable in concentrations down to 0.5 ppb in laboratory tests on produced fluids. The detection was carried out by separation through a GC column and registration by an electron-capture detector. These four tracers were injected in nine injection wells, and registration of the tracer content in the production was done from 23 production wells.

6.6.8 Residual-Oil Saturation in a Leduc Miscible Pilot.³⁵ Because of the large remaining oil in place, Leduc Woodbend D-2A had the potential to be an ideal miscible-flood candidate. Before the miscible injection, it was important to quantify the remaining oil. An injector/producer pair on 64-m spacing was chosen as a pilot for the tracer test. The partitioning tracer

applied was tritiated butanol. Fig. 6.9 shows the production curves of the tracers. On the basis of the retention of the butanol and methanol and the partition coefficient of these two tracers at the actual conditions, the residual oil between the two wells was measured. The tritiated methanol was regarded as a nonpartitioning tracer. The residual oil, S_{or} , was calculated on the basis of different arrival times of the two tracers, as shown in the production curve. The “peak,” “half-peak height,” and “breakthrough” gave the S_{or} at 34, 35, and 38%, respectively. The results were compared with the oil saturation obtained from sponge coring and single-well push-and-pull tracer tests. The sponge core gave an S_{or} at 33%, while the single-well tracer test gave a result from 35 to 40%, depending on the porosity model applied.

In summary, all field tracers, whether chemical or radioactive, are currently the only feasible, direct means of tracking the movement of injected fluids in a reservoir. In many fields, this information has been crucial for improving injection and production programs. Investments in new wells and equipment for injection programs are large and decisions should be based on the best possible data. A tracer test is a cost-efficient method to obtain important data that allow the analysis of injection and production options.

Nomenclature

- a = cross section, L²
- a_c = adsorbed amount
- A = constant related to the enthalpy
- B = constant related to the entropy change
- c = concentration in the liquid phase caused by partitioning between the gas and liquid phase
- C = concentration
- C_c = concentration in the contacting phase
- C_e = measured tracer concentration
- C_G = concentration of tracer in gas phase
- C_M = concentration of tracer in mobile phase
- C_O = concentration of tracer in oil phase
- C_S = concentration of tracer in stationary phase
- C_t = tracer concentration as a function of time
- f = fractional flow
- f_g = fractional flow for gas
- f_o = fractional flow for oil
- f_t = flow of tracer (see Eq. 6.21)
- F = correction factor
- h = height of reservoir zone, L
- H_C = Henry's law constant
- k = permeability, L²
- K = partition coefficient
- K_C = partition coefficient based on concentration
- K_{ci} = partition coefficient of component i
- K_{cj} = partition coefficient of component j
- K_P = partition coefficient based on mol fraction
- L = distance, L
- m = amount of tracer produced in a given well
- m_{t_i} = total tracer recuperation up to t_i
- M = amount of tracer originally injected

- M_W = molecular weight, m
 p = pressure, m/Lt²
 p_i = partial pressure, m/Lt²
 p_v = vapor pressure, m/Lt²
 q = volume flux, L³/t
 q_T = total volume flux, L³/t
 Q_i = mean volumetric injection rate, L³/t
 Q_m = mean volumetric water rate between injector and producer, L³/t
 Q_p = mean volumetric water production rate, L³/t
 Q_{p_t} = production-water flow rate as a function of time, L³/t
 r = radius of tracer front in radial system, L
 s = frontal location in streamtube, L
 s_1 = front location of tracer pulse in the streamline, L
 s_2 = end location of tracer pulse in the streamline, L
 S = saturation
 S_g = gas saturation
 S_o = oil saturation
 S_{or} = residual oil
 S_w = water saturation
 t = time, t
 t^* = dimensionless time
 t_f = fraction of time, t
 t_i = elapsed time for tracer i , t
 t_S = retention time of nonpartitioning reference tracer, t
 t_T = retention time of partitioning tracer, t
 T = temperature, T
 U = parameter that decides the shape of the curve for the actual system at a specific temperature
 \bar{U} = average linear flow rate of gas phase, L/t
 \bar{U}_L = average linear flow rate of liquid phase, L/t
 \bar{U}_{tr} = average velocity of tracer, L/t
 V = parameter that decides the shape of the curve for the actual system at a specific temperature
 \bar{V} = mean produced volume, L³
 V_d = dilution volume, L³
 V_e = produced volume from which the exponential fit starts, L³
 V_M = volume of mobile phase, L³
 V_p = pore volume, L³
 V_S = retention volume of standard reference tracer, L³
 V_T = retention volume of tracer candidate, L³
 V_{T_i} = retention volume of tracer candidate i , L³
 V_{T_j} = retention volume of tracer candidate j , L³
 x^* = dimensionless distance
 x_i = mole fraction of tracer i in liquid phase
 y_i = mole fraction of tracer i in gas phase
 α = dispersivity

- β = retention factor
 δ_G = density of gas, m/L³
 δ_O = density of oil, m/L³
 μ = viscosity, m/Lt
 μ_1 = first momentum
 σ = standard deviation
 ϕ = porosity
 ψ = streamtube

References

1. Wagner, O.R.: "The Use of Tracers in Diagnosing Interwell Reservoir Heterogeneities—Field Results," *JPT* (November 1977) 1410.
2. Bjørnstad, T. and Maggio, G.M.: "Radiotracer Applications in Industrial Processing, Oil & Geothermal Reservoirs," *IAEA Technical Report Series*, Intl. Atomic Energy Agency, Vienna, Austria (2002).
3. Reprinted from *Developments in Petroleum Science*, **43**, Zemel, B., "Tracers in the Oil Fields," 199 (1995) with permission from Elsevier.
4. Bjørnstad, T., Haugen, O.B, and Hundere, I.A.: "Dynamic Behaviour of Radio-Labelled Water Tracer Candidates for Chalk Reservoirs," *J. Petroleum Science Engineering* (1994) **10**.
5. Wood, K.N., Lai, F.S., and Heacock, D.W.: "Water Tracing Enhances Miscible Pilot," *SPEFE* (March 1993) 65.
6. Bjørnstad, T. *et al.*: "Interwell Tracer Technology in Oil Reservoirs: State-of-the-Art," *Tracing and Tracing Methods, Nancy, France, 2001, Recent Progress en Génie des Procédés* (May 2001) **15**, No. 79.
7. McIntyre, F.J. *et al.*: "Radioactive Tracers Monitor Solvent Spreading in Rainbow Vertical Hydrocarbon Miscible Flood," *SPEFE* (February 1988) 273.
8. Howell, W.D., Armstrong, F.E., and Watkins, W.: "Radioactive Gas Tracer Survey Aids Waterflood Planning," *World Oil* (1961) **41**, No. 2, 152.
9. Calhoun, T.G. and Tittle, R.M.: "Use of Radioactive Isotopes in Gas Injection," paper SPE 2277 presented at the 1968 SPE Annual Meeting, Houston, 29 September–2 October.
10. Frost, E.M.: "Helium Tracer Studies in the Elk Hills, California Field," BM-R1-3897, U.S. Bureau of Mines (June 1946).
11. Dugstad, Ø.: "An Experimental Study of Tracers for Labelling of Injection Gas in Oil Reservoirs," PhD dissertation, U. of Bergen, Norway (1992).
12. Senum, G.I. *et al.*: "Hydrocarbon Precombusting Catalyst Survey and Optimization for Perfluorocarbon Tracer Analysis in Subsurface Tracer Application," BNL 42769, Brookhaven Natl. Laboratories Report Series (May 1989) 34.
13. Galdiga, C.U. and Greibrokk, T.: "Ultra Trace Detection of Perfluorocarbon Tracers in Reservoir Gases by Absorption/Thermal Desorption in Combination with NICI-GC/MS," *Fresenius J. Analytical Chemistry* (May 2000) **367**, No. 1.
14. Galdiga, C.U. *et al.*: "Experience With the Perfluorocarbon Tracer Analysis by GC/NICI-MS in Combination With Thermal Desorption," *Tracing and Tracing Methods, Nancy, France, 2001, Recent Progress en Génie des Procédés* (May 2001) **15**, No. 79.
15. Dugstad, Ø., Bjørnstad, T., and Hundere, I.A.: "Measurement and Application of Partition Coefficients of Compounds Suitable for Tracing Gas Injected into Oil Reservoirs," *Revue de L'Institut Français du Pétrole* (March–April 1992) **15**, No. 79.
16. Abbazadeh-Dehghani, M. and Brigham, W.E.: "Analysis of Well-to-Well Tracer Flow to Determine Reservoir Layering," *JPT* (October 1984).
17. Abbazadeh-Dehghani, M. and Brigham, W.E.: "Computation of Tracer Production Curves from Various Flooding patterns," *Proc.*, Annual Heavy Oil/EOR Contractor Reports, U.S. DOE, San Francisco (1981) L-1,L-15.

18. Dugstad, Ø. *et al.*: “Application of Tracer to Monitor Fluid Flow in the Snorre Field: A Field Study,” paper SPE 56427 presented at the 1999 SPE Annual Technical Conference and Exhibition, Houston, 3–6 October.
19. Somaruga, C., Gazzera, C., and Wouterland, C.: “Application of ‘BIPI’ Tests Employing Natural and Artificial Tracers in Waterflooded Oil Fields of the Neuquina Basin (Argentina),” *Tracing and Tracing Methods, Nancy, France, 2001, Recent Progress en Génie des Procédés* (May 2001) **15**, No. 79.
20. Agca, C., Pope, G.A., and Sepehrmoori, K.: “Modelling and analysis of tracer flow in oil reservoirs,” *J. Petroleum Science and Engineering* (1990) **4**, 3.
21. Yoon, S. *et al.*: “In-Situ Characterization of Residual NAPL Distribution Using Streamline-Based Inversion of Partitioning Tracer Tests,” paper SPE 52729 presented at the 1999 SPE/EPA Exploration and Production Environmental Conference, Austin, Texas, 28 February–3 March.
22. King, M.J. and Datta-Gupta, A.: “Streamline Simulation: A Current Perspective,” *In-Situ* (1998) **22**, No. 1, 91.
23. Sagen, J. *et al.*: “Reservoir Chemical-Thermal Simulation with Tracers,” paper SPE 36921 presented at the 1996 SPE European Petroleum Conference, Milan, Italy, 22–24 October.
24. Kleven, R.: “Non-Radioactive Tracing of Injection Gas in Reservoirs,” paper SPE 35651 presented at the 1996 SPE Gas Technology Conference, Calgary, 28 April–1 May.
25. Armstrong, F.E.: “Field use of Radioactive Gas Tracers,” *Petroleum Engineer* (December 1960).
26. Vilela, M.A., Zerpta, L.B., and Mengual, R.: “Water and Gas at El Furrial Field,” paper SPE 53737 presented at the 1999 SPE Latin American and Caribbean Petroleum Engineering Conference, Caracas, 21–23 April.
27. Welge, H.J.: “Super Sleuths Tracer Flow of Injected Gas,” *Oil & Gas J.* (August 1955) 77.
28. Calhoun, T.G. and Hurford, G.T.: “Case History of Radioactive Tracers and Techniques in Fairway Field,” *JPT* (October 1970) 1217.
29. Tinker, G.E.: “Gas Injection with Radioactive Tracers to Determine Reservoir Continuity, East Coaling Field, California,” *JPT* (November 1973) 1251.
30. Rupp, K.A. *et al.*: “Design and Implementation of a Miscible Water-Alternating-Gas Flood at Prudhoe Bay,” paper SPE 13272 presented at the 1984 SPE Annual Technical Conference and Exhibition, Houston, 16–19 September.
31. Davis, J.A., Blair, R.K., and Wagner, O.R.: “Monitoring and Control Program for a Large Scale Miscible Flood,” paper SPE 6097 presented at the 1976 SPE Annual Technical Conference and Exhibition, New Orleans, 3–6 October.
32. Langston, E.P. and Shirer, J.A.: “Performance of Jay/LEC Fields Unit Under Mature Waterflood and Early Tertiary Operation,” *JPT* (February 1985) 261.
33. Mayne, C.J. and Pendleton, R.W.: “Fordoche: An Enhanced Oil Recovery Project Utilizing High-Pressure Methane and Nitrogen Injection,” paper SPE 14058 presented at the 1986 SPE International Meeting on Petroleum Engineering, Beijing, 17–20 March.
34. Craig, F.F.: “Field Use of Halogen Compounds To Trace Injected CO₂,” paper SPE 14309 presented at the 1985 SPE Annual Technical Conference and Exhibition, Las Vegas, Nevada, 22–25 September.
35. Wood, K.N., Tang, J.S., and Luckasavich, R.J.: “Interwell Residual Oil Saturation at Leduc Miscible Pilot,” paper SPE 20543 presented at the 1990 SPE Annual Technical Conference and Exhibition, New Orleans, 23–26 September.

SI Metric Conversion Factors

bar	× 1.0*	E + 05	= Pa
Ci	× 3.7*	E + 10	= Bq
ft	× 3.048*	E - 01	= m
°F	(°F - 32)/1.8		= °C
°F	(°F + 459.67)/1.8		= K
eV	× 1.602 19	E - 19	= J
mL	× 1.0*	E + 00	= cm ³
psi	× 6.894 757	E + 00	= kPa

*Conversion factor is exact.

Chapter 7

Reservoir Pressure and Temperature

David Harrison, Schlumberger, and Yves Chauvel, Gamma Experts

7.1 Introduction

The practice of using bottomhole pressure measurements to improve oil and gas production and solve problems of reservoir engineering began around 1930. Initially, pressures were calculated using fluid levels; a later method was to inject gas into the tubing until the pressure became constant. The earliest bottomhole pressure measurements were made with one-time-reading pressure bombs and maximum-indicating or maximum-recording pressure gauges that lacked the accuracy, reliability, or durability of present-day technology.

The varied uses of bottomhole pressure and temperature measurements have increased in scope during the past two decades as instrumentation technologies have produced more reliable and accurate tools. These advances have made more applications possible, including use in multilayer reservoirs, horizontal wells, interference testing, and drawdown test interpretation.

This chapter is focused mainly on the types of measurements made and the tools available. Some information is included on interpretation techniques to connect the data acquisition with its use in characterizing a reservoir and its contents. Detailed explanations of these interpretation techniques can be found in other chapters in this *Handbook*.

7.2 Reservoir Pressure

The measurement commonly referred to as “bottomhole pressure” is a measurement of the fluid pressure in a porous reservoir. The reservoir pore-fluid pressure is a fraction of the overburden pressure that is supported by the fluid system. The other portion is supported by the rock and generates the in-situ rock stress. The overburden pressure is created by the weight of the rocks composing the lithostatic column at the point of observation. Hence, the difference between the overburden pressure and the vertical rock stress can approximate the pore pressure.

At original, or virgin, conditions, the vertical pressure profile reflects the distribution of fluids in the reservoir and may also indicate compartmentalization resulting from fluid flow barriers. Within any reservoir compartment, the pressure gradient reflects the density of the continuous fluid phase in the reservoir, hence the position of fluid contacts. **Fig. 7.1** illustrates a typical pressure profile showing gas-, oil-, and water-bearing intervals of a reservoir at initial conditions.

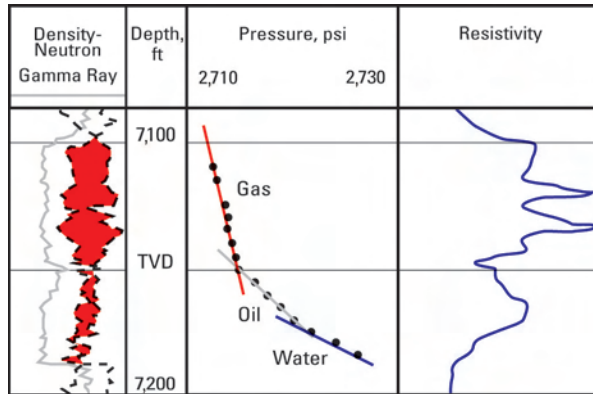


Fig. 7.1—Pressure gradients in a well drilled in a virgin reservoir.

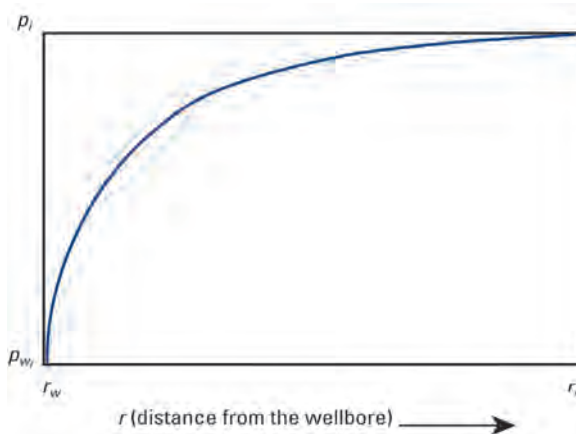


Fig. 7.2—Pressure profile away from the wellbore.

In a developed reservoir, differential depletion of lithostatic layers with various permeabilities and the movement of fluid contacts can change the pressure profile. Monitoring the static pressures vs. time in developed reservoirs is a crucial tool for reservoir management.

7.2.1 Pressure Distribution in the Reservoir During Fluid Flow. The Fluid Flow chapter in this volume of the *Handbook* explains the factors that govern the flow of fluids through porous media for steady-state, pseudosteady-state, and transient flow conditions.

Steady-State Flow. Steady-state flow is characterized by simultaneous constant pressure and flow rate. From the equation for steady-state radial flow,¹

$$p_i - p_{wf} = \frac{141.2qB\mu}{kh} \ln \left(\frac{r_e}{r_w} \right), \dots\dots\dots (7.1)$$

the pressure profile away from a producing well can be calculated. A typical result is shown in [Fig. 7.2](#).

Pseudosteady-State Flow. Pseudosteady-state flow behavior is observed when a well reaches stabilized production from a limited drainage volume. For constant-rate production under

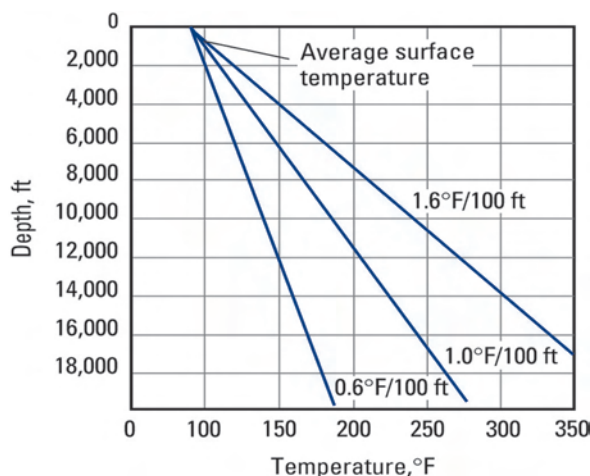


Fig. 7.3—Definition of an average geothermal gradient.

pseudosteady-state conditions, the difference between the flowing wellbore pressure and the average reservoir pressure in the drainage volume is constant, and the pressure drawdown is a linear function of time. The late-time buildup pressure will level off to the average reservoir pressure if the buildup duration is sufficiently long. Pressure depletion occurs with continued pseudosteady-state production.

Transient Flow. Transient flow is most often modeled with the radial diffusivity equation, which allows modeling pressure vs. time and pressure vs. distance from an observation point (typically, a well).

At a sufficiently large time, the pressure disturbance anywhere in the reservoir is proportional to the logarithm of the inverse square of the radius away from the origin of the disturbance. Thus, the magnitude of the disturbance is maximum near its origin (the wellbore) and rapidly terminates away from the wellbore. Because the pressure wave is affected by the reservoir fluid transmissibility, kh/μ , higher transmissibility results in smaller pressure differentials and vice versa. This effect explains why high-resolution pressure gauges are necessary to measure meaningful pressure differentials in reservoirs with high transmissibility. The radius of influence of a pressure disturbance is proportional to the square root of time. This is why the well testing time necessary to observe distant boundaries becomes prohibitively expensive, particularly in low-productivity reservoirs.

The variations of pressure as a function of time, which can be formulated by solving the radial diffusivity equation for specific cases, have given rise to well-testing applications.

7.3 Reservoir Temperature

Reservoir temperature is governed primarily by the reservoir's proximity to the earth's mantle, and by the relative heat exchange capacities and thermal conductivities of the formations forming the lithostatic sequence that includes the reservoir.

The geothermal gradient resulting from the heat-exchange process varies from basin to basin, but within a specific area the variations are small. In most hydrocarbon-producing areas, the gradient is usually in the range of 0.6 to 1.6°F per 100 ft of depth increase (Fig. 7.3). Areas where the earth's crust is thinner than average, such as volcanic and geothermal areas, have much higher gradients. In thin-crust areas the gradient change averages 4°F per 100 ft of depth increase. Local temperature gradients at depth have been reported as high as 10°F per 100 ft approaching singularities (e.g., major faults, areas of tectonic movement) in the earth's crust in geothermal areas.

To determine a precise geothermal gradient, the selected well must be shut in, without disturbance, for a period of time sufficient to let conduction effects equilibrate the temperatures. The temperature survey should be conducted from surface to bottom on the first descent into the well and at a slow speed (ideally, no more than 30 ft/min to accommodate the thermal inertia of the sensor). This procedure is necessary because the passage of the thermometer alters the static gradient. Even if a precise gradient is not required, following the procedure is still recommended for running temperature surveys in wells (shut-in, injecting, or flowing). Anomalies present during the first descent—whether observed or not—may disappear on subsequent surveys after disruption of the initial thermal equilibrium.

The virgin reservoir temperature may be determined when drilling initial exploration and appraisal wells by using the maximum temperatures recorded on successive logging runs or wireline sampling operations. The technique¹ calls for plotting T_{bh} vs. $(t_k + \Delta t_c)/\Delta t_c$ on a linear scale.

These data are interpreted in Horner analysis fashion by drawing a straight line through the data points and extrapolating to the reservoir temperature at $(t_k + \Delta t_c)/\Delta t_c = 1$, which corresponds to infinite shut-in time. Even though this approach is not mathematically rigorous, it provides reliable estimates of the static temperature when short circulation times are assumed. This technique is especially applicable to regions with high geothermal gradients, where the temperatures recorded at the time of logging runs can be significantly lower than the static temperature.

7.4 Metrology of Bottomhole Pressure and Temperature Gauges

Metrology is the science and process of ensuring that a measurement meets specified degrees of accuracy and precision. Bottomhole pressure-gauge and temperature-gauge performance depends on the static and dynamic metrological parameters described here. The pressure measurement equipment consists of the pressure transducer, associated electronics, and telemetry. Each component uniquely influences the measurement quality.

7.4.1 Static Metrological Parameters. The main static metrological parameters affecting gauge performance are accuracy, resolution, stability, and sensitivity.

Accuracy. Accuracy is the maximum pressure error exhibited by the pressure transducer under the following applied conditions: fitting error, pressure hysteresis, and repeatability. The fitting error, also called the mean quadratic deviation (MQD), is a measure of the quality of the mathematical fit of the sensor response at a constant temperature. Pressure hysteresis is the maximum discrepancy of the transducer signal output between increasing and decreasing pressure excursions. Repeatability is defined as the discrepancy between two consecutive measurements of a given pressure at the same temperature.

Resolution. Resolution is the minimum pressure change detected by the sensor. When referring to the resolution of a bottomhole pressure gauge, it is important to account for the associated electronics, because the gauge is always used in series with the electronics. Thus, the resolution of the measurement is the lower of the resolution of the gauge and its electronics. Another important consideration is that the resolution must be evaluated with respect to a specific sampling rate, because an increase of the sampling rate worsens the resolution. The electronic noise of strain-gauge transducers is often the major factor affecting resolution. Mechanically induced noise may further limit gauge resolution because some gauges behave like microphones or accelerometers. This effect may be significant during tests when there is fluid or tool movement downhole.

Stability. A pressure sensor is stable if it can retain its performance characteristics for a relatively long time period. Stability is quantified by the sensor mean drift (psi/D) at a given pressure and temperature. Three levels of stability can be defined: short-term stability for the

first day of a test, medium-term stability for the following 6 days, and long-term stability for a minimum of one month.

Sensitivity. Sensitivity is the ratio of the transducer output variation induced by a change in pressure to that change in pressure. The ratio represents the slope of the line produced by a plot of the transducer output vs. pressure input. The plotted sensitivity should be, but is not always, linear with respect to pressure.

7.4.2 Dynamic Metrological Parameters. Four aspects are used to evaluate the dynamic metrology of pressure gauges.

Transient Response During Temperature Variation. The sensor response is monitored under dynamic temperature conditions while holding the applied pressure constant. The transient response characterizes the time required to get a reliable pressure measurement for a given temperature variation. Peak error and stabilization time are calculated.

Transient Response During Pressure Variation. The sensor response is recorded before and after a pressure variation at a constant temperature. Peak error and stabilization time are calculated.

Dynamic Response During Pressure and Temperature Shock. The sensor response is recorded before and after a temperature shock.

Dynamic Temperature Correction on the Pressure Measurement. The most advanced quartz-gauge transducers are based on a single-crystal sensor design. The crystal is activated on two distinct resonating modes, which are sensitive to both pressure and temperature but with different sensitivities. An advantage of this design is that the measured temperature is the temperature of the crystal. “Dynamic temperature correction” is used to adjust the pressure measurement of single-crystal sensors in real time for any remnant temperature effect. The nonuniform temperature of the crystal, especially while undergoing strong pressure or temperature variations or both, may induce such effects.

7.5 Calibration and Standard Evaluation Tests for Pressure Gauges

Calibration is essential for obtaining good temperature and pressure data. To ensure that a pressure gauge gives a pressure as close as possible to the real pressure over its entire operating range, it must be calibrated. Calibration involves establishing transfer functions to convert raw output from the pressure and temperature data channels into scaled pressure and temperature readings. These transfer functions are 2D (in pressure and temperature) polynomial models—the degree of which is a function of the accuracy required for the measurement.

The calibration process consists of applying known pressures and temperatures to the desired operational ranges. The raw pressure and temperature output signals are received and entered into a polynomial optimization routine. Input pressures are applied with a dead-weight tester, and input temperatures are generated by an oil bath. The following steps are required for a complete master calibration.

7.5.1 Choosing the Pressure-Temperature Calibration Points. Clearly, more calibration points yield a more accurate calibration; however, the inertia in temperature equilibration is a limiting factor. The best practice is to never use fewer than 100 pressure-temperature calibration points and distribute the points in a scheduled time routine, such as shown in [Fig. 7.4](#).

7.5.2 Deriving the Pressure Calibration Function. The pressure calibration function is a polynomial of order N in pressures and order M in temperatures:

$$p_c = \sum_{i=0}^{i=N, j=M} A_{ij} (S_p - S_{p0})^i (S_t - S_{t0})^j, \dots \dots \dots (7.2)$$

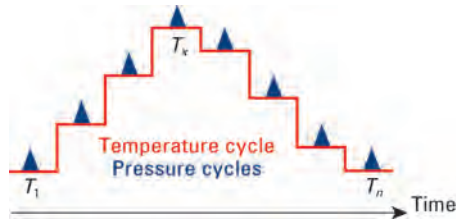


Fig. 7.4—Scheduled time routine for a pressure gauge calibration test.

in which the A_{ij} calibration coefficients are determined by a linear regression providing a least-squares minimization; S_p and S_t are the pressure and temperature outputs, respectively; and S_{po} and S_{to} are the corresponding offsets. Usually the number of A_{ij} coefficients can be limited to approximately 15. During this step, the peak error and MQD are determined.

7.5.3 Temperature Calibration Function. It is often useful, though not always necessary, to calibrate the transducer to output a scaled temperature measurement. The temperature calibration function is a polynomial of order N in temperatures and order M in pressures:

$$T_c = \sum_{i=j=0}^{i=N, j=M} A'_{ij} (S_t - S_{to})^i (S_p - S_{po})^j, \dots \dots \dots (7.3)$$

in which the A'_{ij} calibration coefficients are determined by a linear regression providing a least-squares minimization; S_p , S_t , S_{po} , and S_{to} are as described previously.

7.5.4 Determining Nonlinearity in Pressures and Temperatures. Several other tests supplement the master calibration.

Pressure Thermal Sensitivity. The pressure thermal sensitivity represents the error (psi) that results if the temperature measurement is in error 1°C.

Maximum Hysteresis During the Calibration Cycle. This test is determined from calibration data.

Calibration Check. A calibration check verifies the consistency of the sensor readings when the applied pressures and temperatures are different from those used during the calibration cycle. The calibration check is performed in the laboratory at the time the sensor is evaluated and is essentially a rerun of a master calibration.

Other Procedures and Tests. Standard procedures are typically used in evaluating pressure transducers to compare different technologies and certify the calibration parameters. The most commonly used standard procedures are as follows:

- Complete master calibration.
- Calibration check.
- Stability tests: middle term and long term.
- Repeatability test.
- Resolution test.
- Noise or short-term stability test.
- Dynamic tests: temperature shock, temperature transient, temperature response time, and pressure shock.

7.6 Metrology of Temperature Gauges

When the temperature is used to correct pressure gauge readings, it must come from the pressure-sensing element, not from the wellbore fluid. On the other hand, bottomhole-fluid temperature

measurements are performed with sensors that are in immediate contact with the wellbore fluid and have a minimum thermal inertia (1 or 2 seconds) to follow the variations of the fluid temperature as closely as possible. For this reason, temperature measurements available from pressure-gauge technology are rarely valid for traditional wellbore temperature profiling, which uses the wellbore fluid temperature as a diagnostic tool to detect anomalies in the expected flow patterns in and around the wellbore.

Typical wellbore-fluid temperature measurements have a resolution in the range of 0.05°F and accuracy in the range of 1°F. Accuracy in thermometry is not always a prerequisite because temperature measurements are often normalized between themselves—e.g., from pass to pass or from flowing run to shut-in run in production-logging applications. Accuracy is necessary, however, to compare absolute bottomhole temperatures to draw geothermal maps; to design temperature-sensitive operations, such as stimulation or drilling operations using temperature-sensitive chemicals; or to operate close to the limitations of equipment, such as in geothermal or other high-temperature oil and gas fields.

Resolution is of paramount importance for applications such as the diagnosis of flowing wells or when the measured temperature is the temperature of a pressure-sensing element—the reading of which is affected by minute changes in sensor temperature. High-resolution wellbore-fluid thermometry is also used in extremely slanted and horizontal wells, in which true vertical depth (TVD) variations, and therefore geothermal temperature variations, are small.

7.7 Pressure Transducer Technology

All pressure transducers operate on the principle of converting a pressure change into a mechanical displacement, or deformation. Deformation of the sensing element is then converted into an electrical signal that is processed by the measuring system. Types of pressure transducers available in the field, either individually or in combination, are mechanical, capacitance, strain gauge, and quartz gauge.

7.7.1 Mechanical Pressure Transducers. The first pressure transducers had mechanical-force-summing elements that converted energy into mechanical displacement, or deformation, and then coupled the generated force to a recording device. In the Amerada gauge, a popular mechanical pressure transducer, the pressure-sensing element is a helical Bourdon tube. The tube is of sufficient length to rotate a clock-driven stylus a full circumference inside the cylindrical chart holder. The chart, usually made of coated metal, is recovered at the end of the test, unfolded until flat, and read on a high-precision optical machine. The transducer also incorporates a vapor-type recording thermometer to make temperature corrections on the pressure measurements.

Mechanical transducers have largely been abandoned because of their obsolete metrological characteristics and lack of surface readout (SRO). They are still used occasionally for basic applications at the lower end of the economic spectrum, for some very high-temperature applications, or as backup for an electronic pressure gauge.

7.7.2 Capacitance Pressure Transducers. Capacitance transducers have a variable-gap capacitor in which the sensing element is formed by two metallic or quartz plates. As the external pressure increases, the deflection of the sensing plate creates a change in the capacitance that can be mathematically related to the applied pressure. Capacitance transducers have the advantages of good frequency response, low hysteresis, good linearity, and excellent stability and repeatability. The disadvantages are high sensitivity to temperature, acceleration, orientation, and mechanical noise.

Fused quartz has excellent elastic behavior (low hysteresis) and is chemically inert. These properties make it an almost ideal material for manufacturing small capacitor modules with a high temperature rating.

7.7.3 Strain Pressure Transducers. Many types of strain-gauge transducers are in use. Strain gauges have become very popular because of their ruggedness, low cost, and good dynamic behavior. Their metrological characteristics have greatly improved in recent years; gauges with an accuracy of a few psi and resolution as low as 0.05 psi are available. The primary limitation of strain gauges is their tendency to drift, although that aspect of the measurement has improved.

A strain gauge has a strain-sensitive resistor directly attached to a measuring sensor; when the sensor is subjected to pressure, it deforms. The resulting displacement changes the resistor length, hence its resistance. The applied pressure is calculated from a calibrated relationship to the change in resistance at a given temperature.

Bonded Wire Transducers. In this design, introduced by the Paine Corporation in the 1970s, two sets of wire, called the “active” windings, are wrapped around a cylindrically shaped tube-sensing member. As pressure increases, the tube bore is stretched, causing a change in the wire resistance. Another two sets of wire—the reference, or “passive,” windings—are wrapped on the upper part of the tube, which is not exposed to pressure. These four sets of wire form a Wheatstone bridge that allows the electrical output to be reduced to a pressure reading.

Thin-Film Transducers. The thin-film sensor consists of a resistor pattern that is vaporized or sputter-deposited onto the force-summing element (the measuring diaphragm). In some transducers the resistors are not directly mounted on the diaphragm but are on a beam linked to the diaphragm by a push rod.

Sapphire Transducer. In the Schlumberger improvement of the diaphragm-type thin-film transducer, the sensing resistors are mounted on a miniature substrate of industrial sapphire. The Sapphire* pressure-gauge system is vacuum-filled and the resistor pattern forms a Wheatstone bridge. This system benefits from the elastic performance of the sapphire and its stable deformation properties. The result is a sensor with good repeatability, good stability, low hysteresis, and low drift. A high-gauge factor improves the resolution over traditional designs. The main disadvantages are low output level and high cost.

7.7.4 Quartz Pressure Transducers. Quartz-crystal pressure transducers vibrate at their resonating frequency when excited by a suitable external energy source. The resonating frequency is affected by both the pressure and temperature to which the crystal is exposed. Because of the excellent gauge factor yielded by this physical process, quartz-crystal pressure transducers have exceptional accuracy, resolution, and long-term stability. The disadvantages are high cost and high sensitivity to temperature, although the most recent designs are much less temperature-sensitive.

Hewlett-Packard Design. The Hewlett-Packard (HP) design has been in use since the early 1970s. It features a two-crystal arrangement of a measure and a reference crystal. The measure crystal is exposed to both pressure and temperature. The reference crystal is exposed only to temperature and is used to compensate for temperature effects on the measure crystal. Both crystals are factory-matched so that their frequency characteristics in temperature are approximately the same. The measure crystal senses the pressure directly rather than through a mechanical linkage or other force-summing device. This has the effect of optimizing the metrology of the measurement.

The output from the crystal pair and associated electronics is calibrated to yield the measured pressure by means of a 2D cubic polynomial including 16 coefficients. The values of these coefficients are determined at least annually during the gauge master calibration.

* Mark of Schlumberger.

Quartzdyne Design. The Quartzdyne design features three resonating crystals: the measure crystal, which is exposed to both pressure and temperature, and the temperature and reference crystals, which are exposed only to temperature. The measure crystal is a thick-walled, hollow quartz cylinder closed at both ends. The resonating element is a disk placed in the center, which divides the cylinder into halves. Separate conductive plates are located on the front and back of the resonator disk. Fluid pressure on the exterior walls hydrostatically compresses the quartz cylinder, producing internal compressive stresses in the resonator. The oscillating frequency of the resonator changes in response to these internal stresses.

The reference crystal oscillates at a fixed high frequency, which is subtracted from both the measure crystal and temperature crystal resonating frequencies. The temperature compensation is performed based on these low-frequency signals. The calibration procedure involves a fourth-order polynomial.

Because of its small size, the Quartzdyne design provides good thermal performance and low cost, although somewhat at the expense of accuracy.

Schlumberger Design. In the Schlumberger CQG* Crystal Quartz Gauge design, the transducer features a single quartz crystal structure in which a resonator is coupled with a dual-mode oscillator. The resonant frequency of the first mode is highly sensitive to pressure, and that of the second mode is more sensitive to temperature. The sensor consists of a cylindrical quartz body fitted with two end caps. The end caps maintain a vacuum inside the sensor. The resonator is a plate etched out of the quartz cylinder that features shaped surfaces acting as vibrating lenses. The resonating frequency of the plate varies with changes in pressure and temperature.

From a static point of view, the main advantage of this design is that pressure and temperature are measured at the same location, which minimizes time and space delays for thermal corrections. From a dynamic point of view, this design leads to very small peak transient errors in the thermal response that can be further minimized by using real-time dynamic compensation. The calibration involves a fourth-order polynomial.

The main disadvantages of the CQG design are fragility and high cost.

Paroscientific Design. The Paroscientific design uses a quartz crystal operating in flexure mode to measure force. To derive a pressure output, a force-summing device such as a Bourdon tube or bellows must be used. Thus, the transducer senses pressure through the force-summing device and is not in direct contact with the wellbore fluid. This design tends to improve temperature characteristics but dampens the response and downgrades the measurement metrology. A temperature sensor comprising a quartz torsional tuning fork provides temperature compensation.

Quartztronics Design. The Quartztronics design is a modified HP design, with a specially cut resonator and a noncylindrical cell geometry. The result is a smaller, lower cost pressure transducer with a higher pressure range.

The transducer features a temperature-sensing crystal and a reference crystal, both located close to the measure crystal. This configuration provides improved pressure- and temperature-transient responses in comparison with the HP design. The two crystals are thermally matched to the measure sensor and within a pressure-proof package bonded to one of the end caps of the measure sensor.

7.8 Temperature Sensors

7.8.1 Mechanical Transducers. The first bottomhole thermometers were mechanical. They were identical to bottomhole mechanical pressure gauges, except that a thermometer sensor was substituted for the pressure sensor. This type of thermometer has been mostly replaced by sensors and recording elements that are easier to use and have higher precision and accuracy.

7.8.2 Thermistors. Thermistors are temperature-sensitive resistive elements made of semiconductor material with a negative coefficient of resistance. The physical effect governing a thermistor's change of resistance is the increased number of conducting electrons for a corresponding increase in temperature. Thermistors can be built up to 100 times more sensitive to temperature change, for the same resistivity change, than resistance temperature detectors (RTDs), which are described next. The main drawback of thermistors is their operating temperature limitation of approximately 300°F.

7.8.3 Resistance Temperature Detectors. RTDs rely on the increase in resistance of metals in response to increasing temperature. The resistor consists of a coil of fine metal wire or a film of pure metal deposited on a nonconductive surface. Different metals with different resistances are used, but platinum has become the most popular because of its excellent accuracy, large linear range of operation, and wide temperature range (higher than 1000°F is possible). The RTD is usually encased in a probe that is directly exposed to the well fluids. The RTD is commonly the active leg of a Wheatstone bridge.

7.9 Optical Fiber Measurement of Pressure and Temperature

Several systems are being developed to provide pressure and temperature measurements distributed over the length of an optical fiber that is permanently deployed in the completion. An advantage of fiber optic technology is that the sensors have no electronic components at depth, so they tend to be more reliable. Furthermore, optical sensors are immune to shock, not prone to electromagnetic interference, and operable at high temperatures.

Fiber optic technology is based on exposing the fiber to periodic ultraviolet (UV) light patterns that induce a "grating" on it. Pressure and temperature variations change the reflection wavelength of the gratings and can be decoded with respect to the fixed, incipient operating wavelength. The system is self-referencing.

Every point distributed along the length of the fiber has the potential to generate a different temperature measurement. The advantages are measurement of a permanent temperature gradient over the length of the fiber and the ability to select specific measurement points. Single-point and distributed temperature sensors have been reported to operate successfully in steamflood wells up to 575°F. In one reported case, temperature measurements taken along a horizontal wellbore at different times showed steamchests, water breakthrough, crossflow, and flow behind pipe.

Pressure is measured by sensors located at discrete, fixed points along the fiber. At the sensors, the fiber is cut, and its ends are placed face-to-face in a proximal arrangement. The face-to-face spacing is measured by successive reflections of the light wave. Changes in the value of the spacing reflect the environmental pressure around the fiber at that point. The self-referencing technique uses the distributed temperature measurement for suitable corrections.

7.10 Acquiring Bottomhole Pressure and Temperature Data

The acquisition of bottomhole pressure and temperature data can be planned and executed in a cost-effective manner with a minimum disruption to normal operating routines. In many cases, early on-site interpretation is useful in guiding decisions about continuing the acquisition program. Several questions should be answered at the design stage.

- What are the objectives of measurement: static pressure, reservoir dynamics, fluid characterization, vertical pressure and temperature profile, well flow characterization, or other?
- Is the environment openhole or cased hole? An exploration or development well?
- Is there a need for real-time SRO measurements or can the data be recorded downhole and reviewed later?
- What metrology is needed for the measurements (e.g., maximum temperature and pressure, measurement resolution and accuracy)?²

- How will the gauges be conveyed to the bottomhole measuring points?
- Is there a need to perform continuous or repeated measurements over months or years?
- What economics apply, and do they imply a possible tradeoff with the quality or quantity of the measurements?

This section addresses these issues within the categories of SRO vs. downhole recording (DHR), surface vs. downhole shut-in, mode of conveyance, drillstem tests (DSTs), openhole wireline formation testing, production logging, measurement while perforating, and permanent installations in “smart” completions.

7.10.1 Surface Readout vs. Downhole Recording. Measurements can be transmitted to the surface, usually via an electric cable, or recorded in downhole memory powered by batteries.

SRO has the obvious advantage of providing data in real time. Real-time readouts are especially beneficial for transient measurements that require time for the pressure to stabilize and radial flow to develop. Because stabilization times depend on reservoir and fluid properties and because the determination of these parameters is often the purpose of pressure measurements in well tests, predicting the duration of stabilization periods is often difficult. SRO is preferred in these cases.

Some applications, usually those in the lower economic tier, can be conducted without the need for SRO. The benefits include lower operating costs and a fixed operations schedule. The drawback is the difficulty of guaranteeing the quality of the acquired data, including the potential for significant operating losses if the bottomhole recording equipment malfunctions. For these reasons, DHR should be chosen only when the measurement target does not necessarily depend on stabilization times or when stabilization times are already known (e.g., to measure the average reservoir pressure in a reservoir of known mobility).

Many industry tools provide both SRO and DHR. The measuring section of these tools is common to both options. In the SRO option, the sensor electronics are coupled to a telemetry system for uphole transmission, and the cable supplies downhole power. In the DHR option, downhole batteries supply power, and the data are stored in memory boards for future readout or downloading to suitable computer systems.

7.10.2 Surface Shut-In vs. Downhole Shut-In. The practice of downhole shut-in during a buildup test as opposed to surface shut-in is discussed in “Pressure Transient Testing.” The advantages of downhole shut-in include control of the wellbore volume (afterflow), reduction of the duration of buildup tests, and choice on the recording mode (SRO or DHR).

Downhole shut-in can be performed during conventional DSTs or during tests performed on production wells. In a DST, the downhole shut-in valve is usually the main test valve. Shut-in is performed at the end of a flow period by actuating the test valve. Traditionally buildup pressures are recorded in DHR mode. Another procedure is to use the DST valve as the main shut-in valve while the DataLatch* electrical wireline downhole recorder/transmitter is used to observe pressures in real time during the buildup. DataLatch technology is described in “Drillstem Testing.”

In producing wells, downhole shut-in is performed by setting a valve assembly in the tubing before performing the test. The tubing must have been previously equipped with locator nipples so that the valve can be anchored at the appropriate depth. The valve is run on either a slickline carrying a DHR pressure gauge or an electric line equipped with an SRO recording gauge. The shut-in valve is actuated by a sequence of pulls and releases on the slickline or cable. Commonly operated shut-in valves can perform in the range of up to 12 open-close cycles, after which the valve assembly is released from the setting nipples by an appropriate pull on the line. Other versions of shut-in valves can be operated by a clock, small explosive squib, or battery.

7.10.3 Bottomhole Conveyance of Gauges. Pressure and temperature gauges can be conveyed to the downhole environment by a number of methods, possibly in tandem with other measurements. Several possibilities are discussed here.

Drillstem Test String. Refer to the DST subsection 7.10.4.

Electric Line. Electric line operations provide surface readout and can be conducted any time during the life of the well. In openhole, wireline pressure testing offers a unique opportunity to efficiently collect distributed pressure data on the entire stratigraphic sequence penetrated by the well. In cased holes, pressure and temperature measurements are taken repeatedly along with other production logging measurements to monitor well performance and diagnose flow and completion problems. In addition, pressure buildups and other transient tests are frequently conducted in producing wells, using production logging tools or with “hanging” gauges, to check for variations in the productivity index and for skin development and to monitor multilayer producing systems. In the exploration environment, however, electric lines are not typically used because of the risks associated with having cable in the well while flowing. These risks include difficulty closing safety valves or subsea trees with cable in the borehole and sticking of the cable because of sanding from unconsolidated formations or hydrate formation in subsea wells. The DataLatch electrical wireline downhole recorder/transmitter, introduced in the late 1980s, has largely mitigated this risk. The DataLatch system is briefly described in “Drillstem Testing.”

Slickline. Slickline pressure and temperature surveys are performed with hanging gauges in situations that do not require SRO. Slickline operations are more cost-effective than electric line operations; however, the data quality usually does not match that of SRO data. Depth control is one of the critical factors affecting data accuracy. On the other hand, surface pressure control is easier in slickline operations because of their smaller diameter, typically in the range of 0.1 in. in diameter. A promising development is the “slick conductor line,” a thin, hollow-core, 100% steel cable laid around an electric conductor to provide limited SRO capabilities.

Coiled Tubing. A popular alternative to drillpipe, coiled tubing is used to convey downhole gauges and other equipment in deviated holes when gravity is insufficient to pull the tools to the bottom of the well. Insufficient gravity occurs where well deviation exceeds values in the range of 60 to 70°, depending on tool weight and length, friction coefficients, pipe roughness, and the presence and type of completion components. In horizontal wells, the coiled tubing may not reach the toe of the completion because of a helical lockup of the coil inside the completion. Coiled tubing may be equipped with an internal electric cable running the length of the coil to support SRO operations.

Tractors. Tractors are an emerging technology that complements the use of coiled tubing in difficult, deviated completions. Tractors are self-powered and operated by electric line. They can negotiate bends, crawl up or down, and overcome the limitations of coiled tubing in long horizontal wells. Their main limitation is the large amount of cable power required for operation.

Wireless Transmission. Wireless transmission is a technique that has been in use since the late 1980s. It attempts to provide the advantages of SRO without using an electric line. The downhole tool, a sub that is part of a DST string, features a pressure gauge, battery pack, telemetry, recorder board, and antenna. The antenna sends the signals collected from the pressure recorder at a frequency suitable for transmission through the formation strata. At the surface, the signals are picked up by an array of suitably deployed stake antennae. This technique is limited to land operations and depths of approximately 8,000 ft.

7.10.4 Drillstem Testing. A DST string is a complex array of downhole hardware used for the temporary completion of a well. DSTs provide a safe and efficient method to control flow while gathering essential reservoir data in the exploration, appraisal, and development phases of a reservoir or to perform preconditioning or treatment services before permanent well completion. [Fig. 7.5](#) shows a typical DST string with its essential components. In exploration well

testing in particular, the DST string usually includes tubing-conveyed perforating (TCP) guns, which are shot underbalanced (i.e., wellbore pressure is less than reservoir pressure) at the initial well completion.

DST strings include gauge carriers, which are collars that normally contain up to four pressure gauges bundled together, affording redundancy in long tests in which one or more gauges are likely to fail. These gauges perform only DHR measurements.

Most modern DST strings are fullbore strings, which means they have a flush opening running completely through the string of tools. The opening enables running pressure gauges and other slim tools (typically 1¹¹/₁₆ in.) in SRO mode.

The DataLatch system is a DST string component that combines the advantages of DHR (typically during flow periods) with the advantages of SRO (typically during shut-in periods). Pressure data are recorded in the tool's memory boards. In suitable conditions, a LINC* Latched Inductive Coupling tool is run with an electric cable and latched into the DataLatch mandrel. This combination is used to read out the memories, reprogram the gauge acquisition schedule if necessary, and monitor the test in real time. The DataLatch system is unique for bottomhole pressure measurement applications. It allows simultaneous and continuous acquisition of three different measurements during the course of a DST test: rathole or reservoir pressure, cushion or tubing pressure, and annulus pressure.

7.10.5 Openhole Wireline Pressure Testing. Wireline pressure testing is conducted using tools lowered on an electric cable or coiled tubing in deviated wells. The tools consist of function-specific modules selected for a specific operation. Fig. 7.6 shows the modular arrangement of a modern wireline pressure tester.³ In a complete configuration, the tools may include a single-probe module for basic pressure testing and sampling, a dual-probe module for permeability applications, a flow-control module for flexible schedule testing, a fluid analyzer module for optical fluid properties monitoring in real time, multisample module for representative fluid sampling at reservoir pressure-volume-temperature (PVT) conditions, sample modules for large-volume fluid sampling, a pumpout module that can recirculate mud filtrate and other unrepresentative fluids out of the tool flow system before representative sampling, and a dual-packer module for very large area sampling, interference testing, and DST emulation.

Wireline pressure testing encompasses several applications described in “Specific Applications and Interpretations.” The applications include measuring static reservoir pressure, collecting representative fluid samples, determining anisotropic permeability, identifying reservoir permeability barriers, determining reservoir fluid gradients and densities, and determining rock stress components.

As in conventional well testing, a wireline sampling operation must be carefully designed beforehand to achieve the desired objectives. Key parameters that require special attention include the test type, fit of the probe type to the reservoir's mechanical and hydraulic deliverability characteristics, volumes to be withdrawn, type of pressure gauges for the expected reservoir permeability, test sequence, number of pressure points to be taken, and interpretation objectives. The actual downhole tool configuration and the test sequence directly reflect the design study that precedes the operation.

7.10.6 Production Logging. The uses, benefits, and interpretation techniques of production logging are discussed in another chapter in this section of the *Handbook*.

7.10.7 Measurements While Perforating. Pressure and temperature measurements may be performed concurrently with shaped-charge perforating. This technique, called measurement while perforating (MWP),⁴ includes the following applications:

- Before perforating, MWP verifies the completion fluid density, directly measures the wellbore pressure, and adjusts the perforating underbalance.

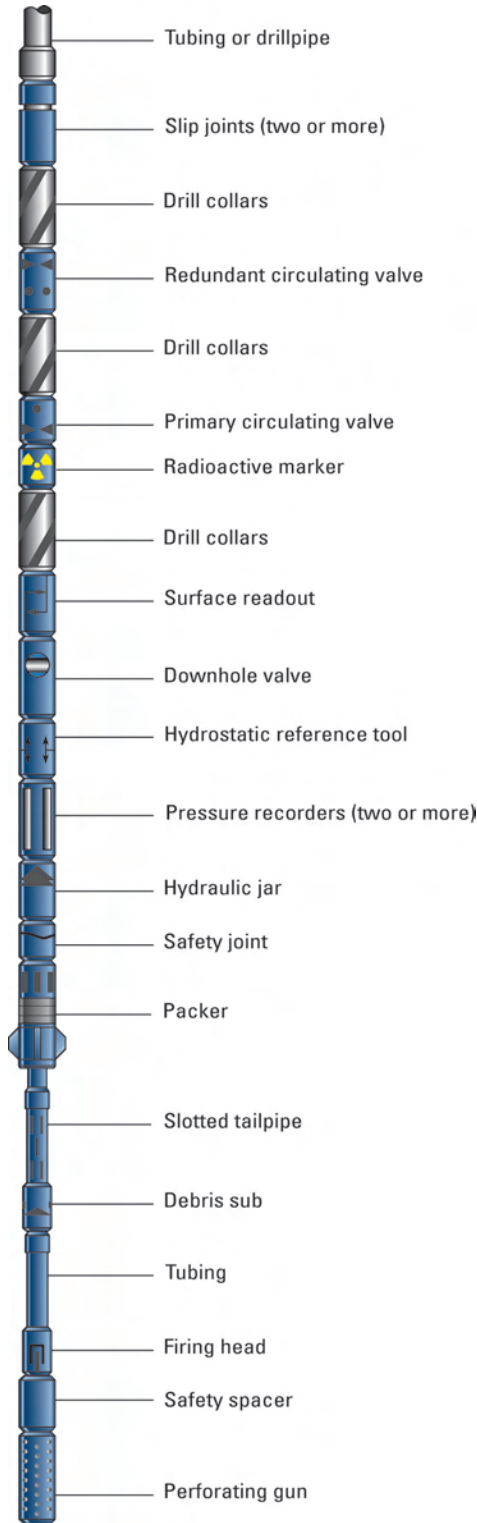


Fig. 7.5—Pressure-controlled DST string.

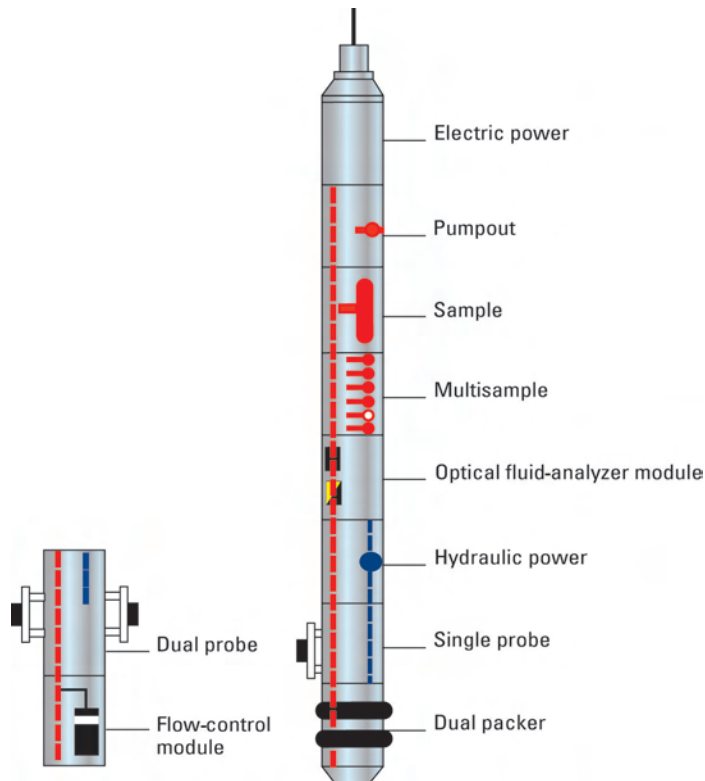


Fig. 7.6—Wireline tool components.

- During perforating, MWP positively detects the detonation of the perforating gun.
- After perforating, MWP observes the pressure responses and interprets them as a transient test, and it monitors the fluids produced by the perforation.

The MWP system is especially adapted to low-flow-rate or short-duration tests such as IMPULSE* measurement while perforating tests, closed-chamber tests, and slug tests. Flow tests can also be analyzed.

MWP must be performed in SRO mode; otherwise, the technique offers no benefit. An SRO tool such as the DataLatch recorder/transmitter or an electric line tool must be used. The production well environment is preferred for MWP, with the perforating guns conveyed on an electric line with the MWP sub above the guns. A typical MWP sub for pressure and temperature measurements incorporates a gamma ray detector and casing collar locator for depth control and suitable shock absorbers to mechanically decouple the guns from the measurement system. An optional bottom electric adapter can fire the guns electrically, which is often the procedure in non-TCP applications.

Because MWP also measures the wellbore fluid temperature, it is used for the same applications as production logging.

7.10.8 Permanent Pressure Measurement Installations. Permanent monitoring systems are placed downhole with the completion string near the depth of the reservoir to be monitored. They are connected to the surface by a cable that runs the full length of the completion string and exits the wellbore through suitable connectors crossing any subsurface safety systems and the wellhead. Advanced telemetry allows querying these sensors at any time throughout the life of the reservoir. Most systems in operation today record bottomhole pressure and temperature.

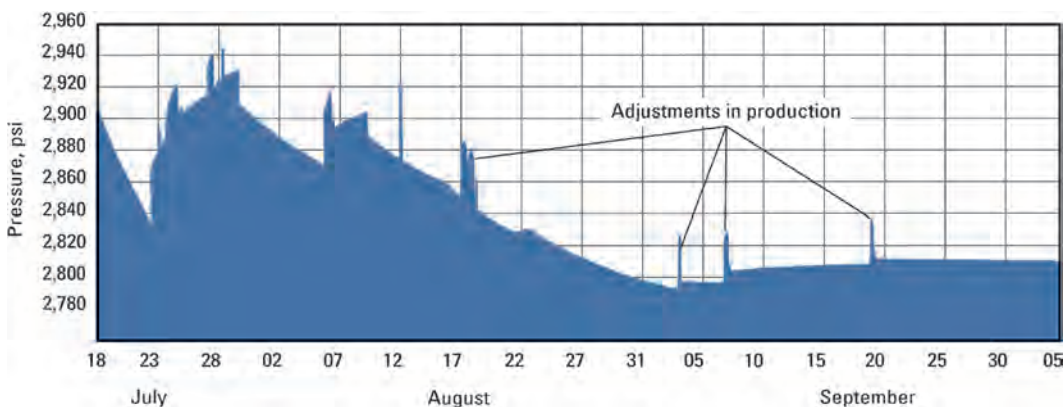


Fig. 7.7—Readout of a recording over an 80-day period from a permanent gauge.

Permanent systems⁵ are engineered specifically for monitoring applications and have a life expectancy of several years. The digital electronics within the gauges are designed for extended exposure to high temperature without required maintenance. The metrology characteristics emphasize long-term stability rather than fast dynamic response. Quartz crystals as well as sapphire-based sensors can be used.

The cables for permanent installations are designed to withstand pressure, temperature, and exposure to highly corrosive fluids. They must also be mechanically rugged to prevent damage during installation. Usually single conductor cables are used.

The connections are similarly designed for durability. They include bottomhole connectors (power and pressure) to the permanent gauge mandrel and uphole connectors that cross through the wellhead. The complexity of the surface installation varies, depending on whether the wellhead is located at the surface—as on a land well or wellhead exposed above the sea on a platform—or subsea. For subsea wells, the acquisition system is typically through existing data-gathering systems through umbilicals. On platforms, several permanent gauges may be connected to an autonomous surface unit that records the measurements and communicates with shore facilities through standard or advanced (satellite) transmission links.

Fig. 7.7 shows a continuous data stream from an 80-day recording in which the pressure measurement was used to optimize production. The surface production rate was repeatedly adjusted to yield an acceptable bottomhole flowing pressure.

7.11 Wellhead Environments

Although the focus of this chapter is bottomhole measurements, it is worthwhile to mention a few interesting points about the environments of surface and subsea measurements.

7.11.1 Surface Acquisition of Downhole Data. Current specifications of surface acquisition systems, sensors, umbilicals, and piping commonly used in the industry are 0 psi and -40°F for the lower range of pressures and temperatures, respectively. The temperature specification in particular presents no obstacle to testing operations in extremely cold areas, such as the Arctic and similar cold-weather territories.

7.11.2 Subsea Acquisition of Pressure and Temperature. Pressure and temperature measurements are sometimes required at the subsea tree level. The measurements are mainly used to monitor the operating conditions of the landing string near the ocean floor. Applications include ensuring that the maximum temperature rating of the elastomers in the blowout preventer

(BOP) is not exceeded, and providing data to help prevent hydrate formation during deep-sea cleanup and well testing operations.

7.12 Specific Applications and Interpretation

Bottomhole pressure data are vital for understanding reservoir performance and predicting future behavior. Applications include volumetric calculations (e.g., reserves), reservoir dynamic properties (e.g., permeability), drainage volumes (e.g., compartmentalization and flow barriers), fluid properties (e.g., density, phase behavior), well tubular and artificial lift design (e.g., size selection and lifting systems), evaluation of reservoir energy and fluid contacts with time, and input to numerical reservoir simulation models.

7.12.1 Depth Datum of Pressure. Static pressures should be corrected to a fixed depth datum to eliminate the influence of the fluid pressure gradient for building isobaric maps, using bottomhole pressure to calculate inflow performance relationship (IPR) diagrams for multilayer pressure data sets, or interpreting vertical permeability barriers from a pressure differential between two reservoir layers.

Pressures are adjusted to a fixed datum by calculating the hydrostatic potential (also called the datum-corrected pressure) as follows:

$$\Phi = p - 0.00135\rho_{fl}g(D - D_0) \cos \delta \dots\dots\dots (7.4)$$

The potentials (adjusted pressures) reflect the dynamics of fluid movement in the reservoir better than the raw pressure data can. Reservoir layers with different potentials flow into one another if put in communication (e.g., if they are completed in the same wellbore). Isobaric maps built on datum-depth-corrected pressures reveal flow within a specific reservoir layer if this layer shows different potentials in different regions of the reservoir. In addition, vertical permeability barriers are qualified in terms of potential differences between the two adjacent reservoir units separated by the barrier.

D_0 , the datum depth, can be arbitrary and has no influence on the interpretation of the hydrostatic potential, assuming a constant reservoir fluid density across the different wells or layers. Typically, a datum at the midpoint of the hydrocarbon column is selected to study pressure trends across the reservoir and phase behavior effects. A datum within a well may prove more useful for analyzing potential differences between multiple reservoir layers crossed by the well.

7.12.2 Static Pressure. Static pressure measurements always result from some form of transient test, in which a large or small amount of fluid is withdrawn from the well before the pressures are allowed to stabilize. Static pressures are acquired during wireline testing at the rate of approximately one measurement every few minutes because only very small amounts of fluid samples are withdrawn. Conversely, static pressures take much longer to stabilize in conventional well testing because the much larger fluid samples withdrawn create much greater pressure disturbances.

Static Pressure From Buildup Tests. The static pressure of a reservoir is one of the interpretation outputs of pressure transient tests. Many short-duration buildup tests (including wireline pressure “pretests”) are designed solely for measuring the static reservoir pressure. The interpretation of buildup tests to determine the static reservoir pressure is discussed in another chapter in this section of the *Handbook*.

Average Reservoir Pressure. The average reservoir pressure can be determined arithmetically by averaging the datum-corrected pressures of a given layer in all wells, with each pressure weighted by the net thickness of the reservoir at the well. A better average pressure is determined by recording the pressures, either actual or weighted, on a map of the area and drawing

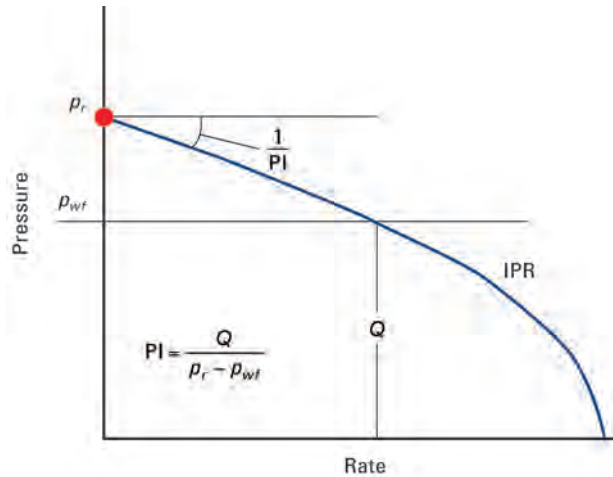


Fig. 7.8—PI of a reservoir with a single producing layer.

isobars from which the average pressure weighted for an area is determined by planimetry (or gridding) of the isobars.

Static Pressure Determined From the Productivity Index. The productivity index (PI) of a producing layer, J , is defined as the ratio of the downhole production rate of the layer to the pressure drawdown under which the layer produces:

$$J = \frac{Q}{(p_r - p_{wf})} \dots\dots\dots (7.5)$$

On a plot of bottomhole flowing pressure vs. downhole flow rate, the PI is represented by the inverse of the slope of the IPR line describing the pressure-rate characteristics of the producing layer (Fig. 7.8).

The static reservoir pressure and PI of a reservoir with a single producing layer can be determined with production logging measurements without the need to shut in the well. The well must be flowed at several different flow rates (typically three or four) and allowed to stabilize between successive rate changes. Bottomhole pressure and flow-rate measurements are performed for each value of the surface flow rate. The IPR is drawn through the data points on a pressure vs. rate plot, and extrapolation of the IPR line to a zero-flow condition gives the static pressure.

In most gas wells and in oil wells drawn below the bubblepoint pressure, the IPR may not be linear. Although the same procedure can be used, the IPR shape should fit the curved nature of the data (e.g., a quadratic fit if turbulence is the cause of the nonlinearity of the IPR). Once properly fitted, the y -axis intercept (zero flow) of the modeled IPR gives the static pressure, and the x -axis intercept (atmospheric pressure) gives the absolute open flow (AOF) potential. The AOF potential of a gas well is generally a better indicator of its performance than its PI because PI is not constant and the IPR is represented by a curved line. The AOF of a gas well is determined by plotting the gas potential, $m(p)$, as a function of the flow rate of each flow period of an isochronal test. In some cases of low reservoir pressure, Δp^2 can be used instead of $m(p)$. More information on determining gas flow potential and reserves is in another chapter in this *Handbook*.

The same procedure applies to multilayer completions—plotting bottomhole pressure vs. rate for each layer of the system. To interpret the pressure data of comparable layers, however,

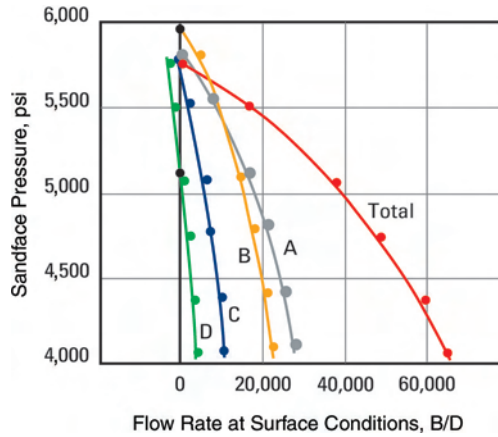


Fig. 7.9—SIP analysis of a four-layer commingled reservoir with crossflow.

the pressures must be corrected to a common arbitrary datum depth to readily differentiate whether the layers belong to the same hydraulic system. The results of the procedure, called selective inflow performance (SIP), include the static pressure and the PI per layer. The SIP procedure has become very popular for commingled producing systems, especially in gas wells because of the shorter stabilization times involved. SIP overcomes a fundamental limitation of commingled producing systems where the layer static pressures are not available by direct measurement, not even by shutting in the well, unless all the reservoir layers are in a strict hydraulic equilibrium.

Fig. 7.9 shows this technique applied to a multilayer reservoir comprising four layers: A, B, C, and D. The “Total” curve represents the global performance of the whole system, intersecting the pressure axis at a value that represents the wellbore pressure when shutting in the well. Obviously, this shut-in pressure differs from the pressure of each of the individual wells because the whole system is not at hydraulic equilibrium. Crossflows develop when shutting in this well, and high-pressure Layers A and B flow into depleted Layers C and D.

7.12.3 Pressure-Depth Plots. Vertically distributed wellbore and formation pressures, such as those measured by a wireline pressure tester, can be used to build mud and reservoir pressure profiles. If the measured interval is sufficiently thick, accurate pressure gradients may be established. As already mentioned, the gradients can in turn be used to spot permeability barriers and reservoir fluid contacts and to determine the reservoir fluid density.

Thick beds have a greater pressure change from top to bottom than thin beds. Therefore, the resolution of the pressure gauge becomes increasingly important the thinner the beds are. Another important factor is the number of pressure measurements taken within the bed of interest. Fig. 7.10 shows that increasing the number of pressure points greatly reduces the statistical error in determining the true gradient.

In some plots, the recorded pressures may not fall on a linear gradient. One example of this condition is when pressure points are not taken in a uniform depth-increasing or depth-decreasing sequence. This situation favors dispersion of the pressure measurements because of gauge hysteresis and lack of temperature stabilization. A procedure to help determine the reservoir fluid density consists of comparing the fluid density with the mud density over a set of tests taken with a wireline tester. As shown in Fig. 7.11, if the fluid pressures vary by Δp_f and the mud pressures vary by Δp_m over the depth interval ΔD and a vertical well is assumed, then the following can be written:

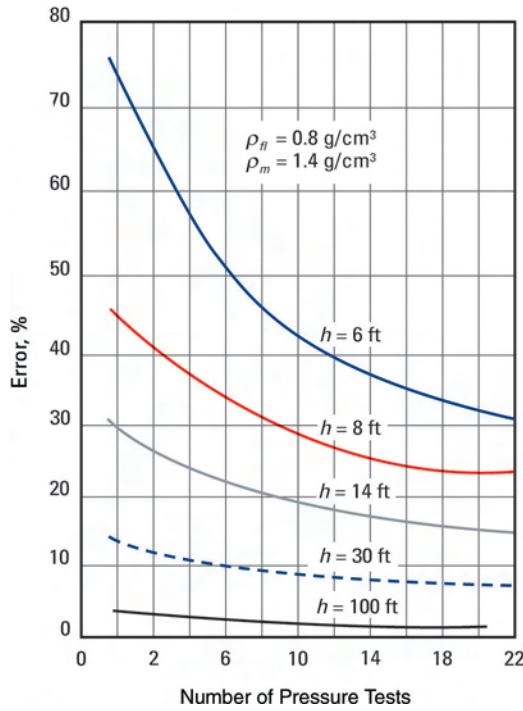


Fig. 7.10—Gradient accuracy vs. bed thickness.

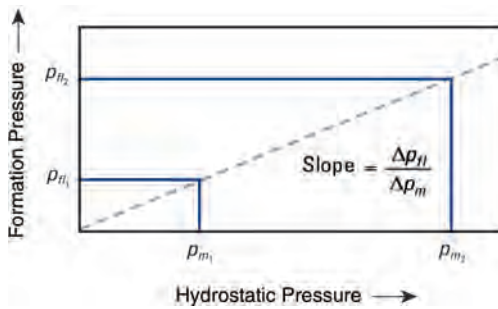


Fig. 7.11—Plot of reservoir (formation) pressure vs. mud (hydrostatic) pressure.

$$\Delta p_m = 0.00135 \rho_m g \Delta D, \dots\dots\dots (7.6)$$

$$\Delta p_{fl} = 0.00135 \rho_{fl} g \Delta D, \dots\dots\dots (7.7)$$

then by elimination:

$$\rho_{fl} = \rho_m \left(\frac{\Delta p_{fl}}{\Delta p_m} \right) \dots\dots\dots (7.8)$$

Because mud pressures are consistent over greater depth intervals, ρ_m is usually known. Eq. 7.8 then can be used to improve the reservoir fluid density determination.

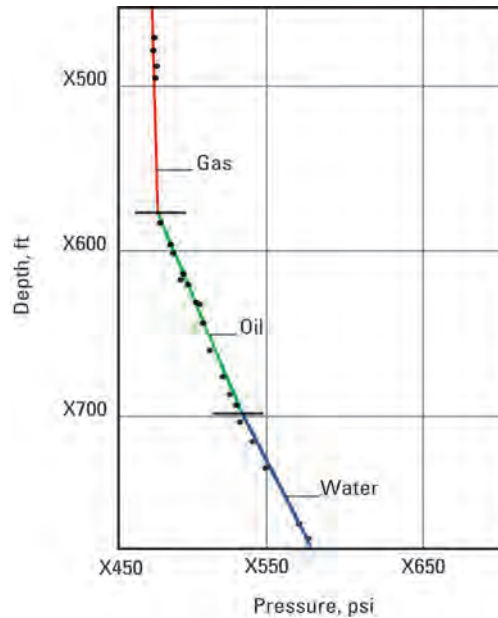


Fig. 7.12—Fluid types and contacts in a virgin reservoir.

Virgin Reservoirs. In virgin reservoirs, the static reservoir pressures are unaffected by fluid withdrawal and the observed gradients therefore reflect the density of the original fluids. The “breaks,” where the slope changes in the gradient, reflect the original fluid contacts as illustrated in Fig. 7.12.

Permeability barriers can also be identified as illustrated in Fig. 7.13. The barrier is indicated in Fig. 7.13a by the hydrostatic potential difference between the layers above and below the detected permeability barrier of approximately 20 psi. The line with a gradient of 0.497 psi/ft represents the mud pressure, which was measured in the same trip in the well while acquiring the formation pressure. In Fig. 7.13b, the reservoir fluid gradients differ across the permeability barrier. Nevertheless, a potential difference of approximately 140 psi across the barrier is interpreted as indicating a no-flow barrier. Zero permeability is implied. Otherwise, the pressure would have equilibrated on both sides of the barrier over geologic time.

Sometimes the gradients must be extrapolated to confirm fluid contacts. The gas/water contacts in Fig. 7.14 cannot be identified by the pressure profile of Well 1 or Well 2. By extrapolating the water gradient of Well 1 and the gas gradients of Well 2, however, it is possible to determine the position of the gas/water contacts in three zones. This extrapolation shows that pressure readings taken near the wellbore in this case reflect pressures that exist deep within the formation. From the gradient interpretation, the fluid in the upper formation is water, and there are two gas/water contacts in the lower formation.

It is important to note when extrapolating gradients from reservoir pressures in low-permeability reservoirs that the pressures may be affected by supercharging. Supercharging is caused by the nonzero, small value of the mudcake permeability. This permeability allows a finite continuous flow of filtrate across the mudcake. In a low-permeability formation, the resistance to fluid flow created by the mudcake can be on the same order of magnitude as the resistance of the formation to accepting fluid. A standard wireline pressure measurement is therefore insufficient to measure the pressure of the virgin formation because a residual finite pressure difference remains between the formation at the mudcake interface and the virgin formation some distance away. Supercharged points plot to the right of a normal fluid gradient line.

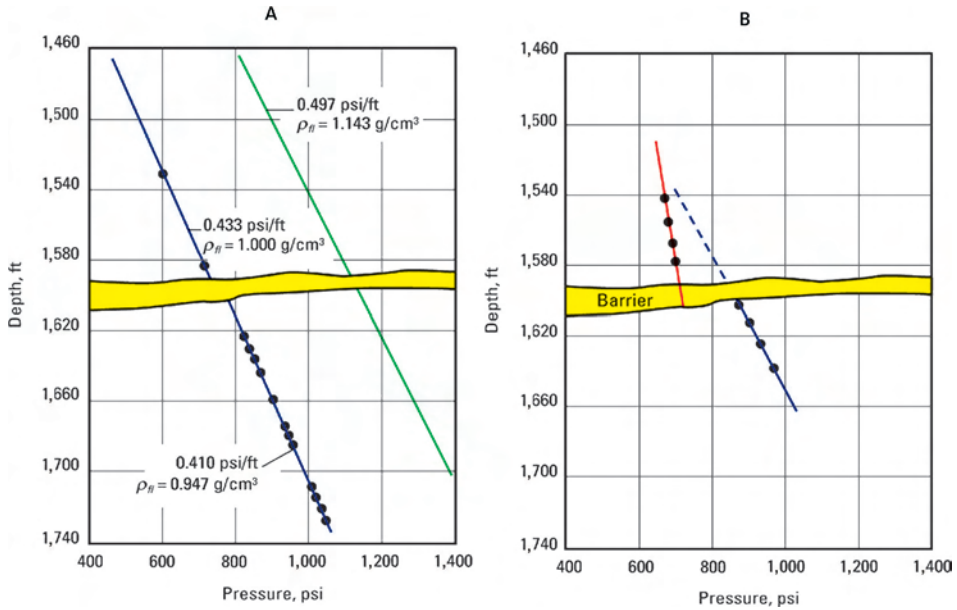


Fig. 7.13—Detecting permeability barriers.

Developed Reservoirs. Differential depletion is most likely to occur in developed reservoirs, destroying the original gradients. In addition, differential depletion generates vertical flow in the reservoir. Vertical flow may also result from partial completion effects that superimpose the corresponding pressure gradients on the fluid density gradients. A typical pressure-depth profile in a well drilled in a field under production is in Fig. 7.15. The well was completed in an interval in Zone 1. The pressure profile taken some time after initial completion clearly shows that the pressure in Zone 1 has been drawn down by fluid withdrawal. The pressure in Zones 2, 3, 4, and 5, which were not perforated, has also been affected by vertical flow through the reservoir. The measured gradients reflect the pressure drop created by vertical flow. The sharp pressure drop across Zone 2 reflects the very low permeability of this zone.

In spite of the blurring of fluid gradients in developed reservoirs, vertically distributed reservoir pressures are still useful for correlating formations hydraulically from well to well. The initial correlation made on the basis of openhole logs (left side) in Fig. 7.16 had to be modified because of the reservoir pressure data. Although time equivalent and present in both Wells 1 and 2, Zones A and B show different pressure regimes in the two wells and are not in hydraulic communication (right side).

7.12.4 Pressure Probes in Duplex or Triplex. Taking pressure points with a multiple-probe wireline tester eliminates the uncertainty of the depth measurement for the set of points taken at a tool station. Modern wireline testers include a multiple-probe system that can measure pressure at a sink, or flowing, probe, at the same depth at a “horizontal probe” opposite the sink probe, and at a “vertical probe” at some vertical distance on a generatrix (i.e., parallel to the tool axis) with the sink probe. Both data density and data consistency increase greatly when this probe arrangement is used.

7.12.5 Effect of Capillary Pressure. Several studies have shown that a wireline formation tester actually measures the pressure of the continuous phase in the invaded region around a wellbore; typically this is the drilling fluid filtrate. The measured tester pressure is thus differ-

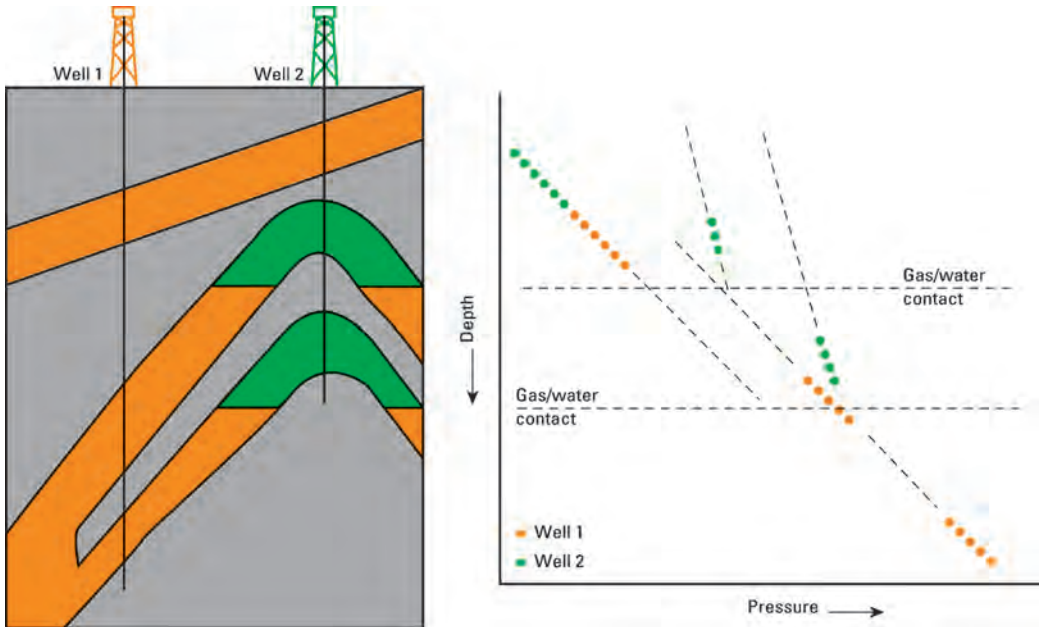


Fig. 7.14—Extrapolation of pressure gradients to fluid contact levels.

ent from the reservoir pressure by the amount of capillary pressure. The capillary pressure affects the saturation of the wetting phase in the reservoir. The combined effects of rock wettability and capillary pressure can be reflected as changes in the pressure gradient, fluid contact level, or both on pressure-depth profiles, especially those recorded with oil-base mud in the borehole.^{6,7}

The principles, measurement techniques, and applications of capillary pressure measurements are discussed in another chapter in this *Handbook*. Refer to that chapter for information on the variation of water saturation with height, entry or threshold pressure, free-water level (FWL), and oil/water contact (OWC).

The first and most conspicuous effect of capillary pressure on wireline tester pressure gradient profiles is the creation of a break in the gradient at the FWL that may not coincide with the OWC interpreted from other measurements such as resistivity logs. The depth difference increases as the displacement pressure (a function of pore-throat diameter) increases. Fine-grained reservoirs with small pore throats are most likely to exhibit potentially large depth differences between the OWC and FWL.

The second, potentially more deleterious effect of capillary pressure on wireline tester pressure gradient profiles is that the measured pressure may differ from the true formation pressure. The difference results in an unrecognized shift of the gradient to the right or left of the true reservoir fluid gradient. The effect of the gradient shift, which is equal to the amount of capillary pressure, is to displace the observed break in the gradient. Interpreting this break as the FWL yields an erroneous depth, located either above or below the true FWL, depending on the conditions described next.

Fig. 7.17 presents pressure-depth plots and capillary pressure profiles in a water-wet reservoir drilled with water-base mud and oil-base mud. **Fig. 7.17c** shows the capillary pressure profile expected in a water-wet oil-bearing section of the reservoir. The capillary pressure is greater in the virgin zone because oil is the nonwetting fluid. The wireline tester measures a filtrate pressure in the invaded zone that is lower because of the absence of capillary pressure.

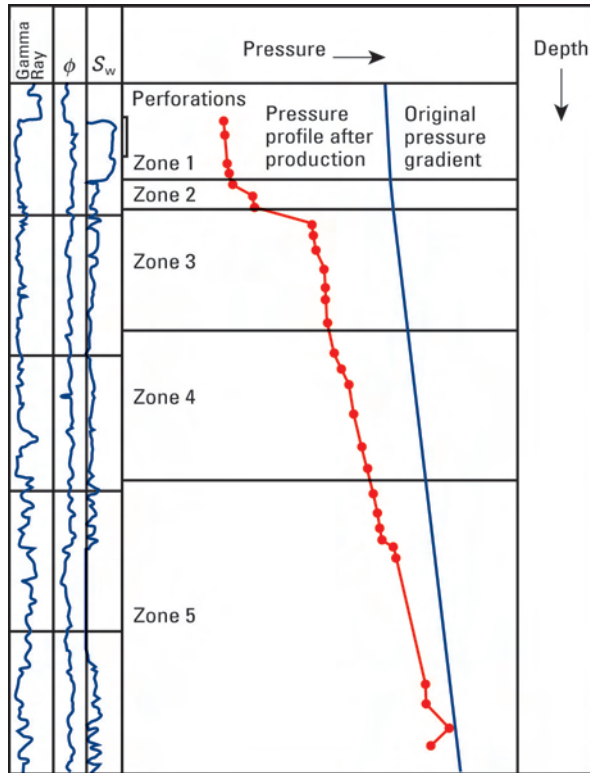


Fig. 7.15—Pressure profile of a well in a developed field.

The result is a gradient shift to lower pressure values and the FWL is interpreted above its true location. There is no shift in the water-bearing section of the reservoir because the capillary pressure is zero in both the virgin zone and invaded zone.

When oil-base mud is used in a water-wet reservoir, the effect of the capillary pressure causes the measured pressures to differ from the true formation pressures only in the water-bearing section of the reservoir (Fig. 7.17b). Fig. 7.17d shows the capillary profile in the water-bearing section of the reservoir for this case.

Similar data and effects for water- and oil-base muds used in oil-wet reservoirs are shown in Fig. 7.18.

One possible method to correct for wettability and capillary pressure effects on wireline formation tester pressures is the Leverett J-function⁸:

$$J(S_w) = p_c \frac{\sqrt{k/\phi}}{\sigma \cos \delta} \dots\dots\dots (7.9)$$

Laboratory measurements of p_c , k , and Φ are used to develop a relationship for a reservoir. The amount of capillary pressure determined by the J-function is added to the measured pressure:

$$p_{\text{corrected}} = p_{\text{measured}} + p_c(S_{xo}), \dots\dots\dots (7.10)$$

where $p_c(S_{xo})$ is the capillary pressure in the filtrate-invaded zone, for which the water saturation is traditionally called S_{xo} .

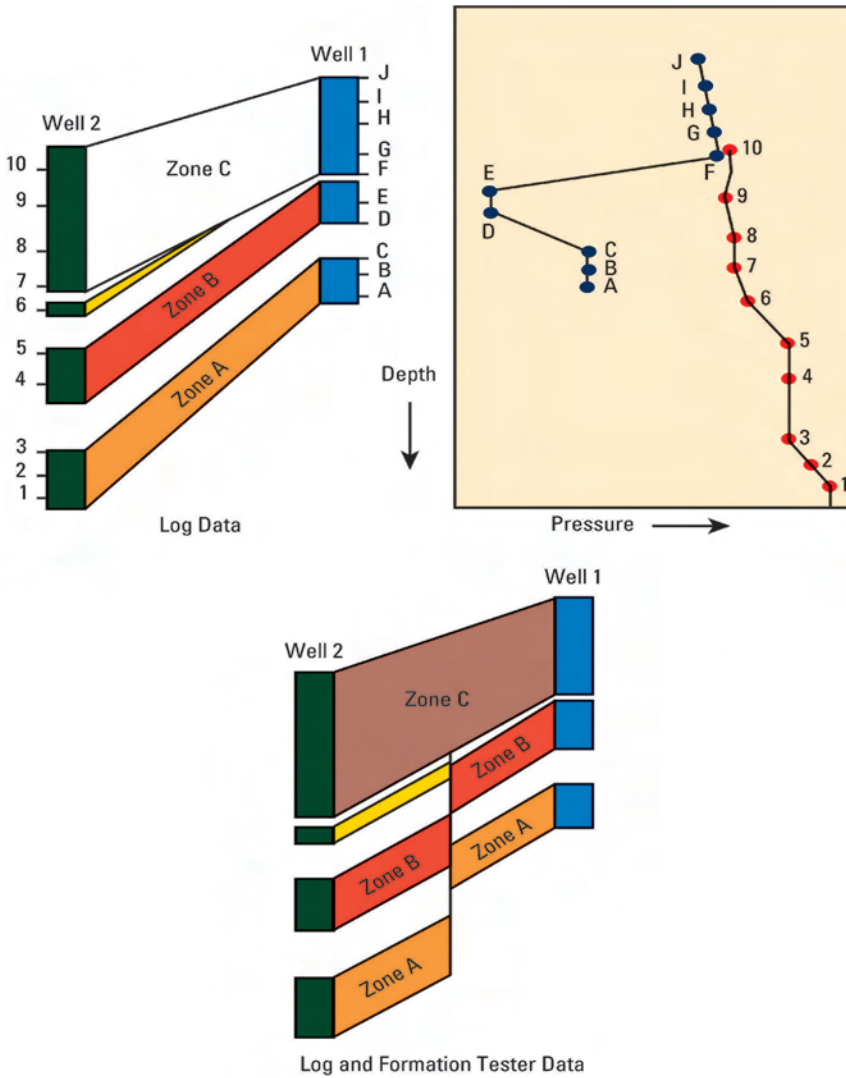


Fig. 7.16—Hydraulic correlation between two wells.

Alternatively, if a nuclear magnetic resonance log (NMR) is available, the in-situ capillary pressure correction can be performed directly. NMR logs have the capability to model the pore-size distribution. The method also makes use of laboratory experiments on cores to calibrate the correction.^{9,10}

7.13 Pressure Transient Testing

The interpreted pressure transient test is a primary source of dynamic reservoir data. Tests on oil and gas wells are performed at various stages of drilling, completion, and production. The test objectives at any stage range from simple measurement of reservoir pressure to complex characterization of reservoir features. Most pressure transient tests can be classified as either single-well productivity tests or descriptive reservoir tests.

Productivity tests are conducted to determine well deliverability, characterize formation damage and other sources of skin effect, identify produced fluids and determine their respective

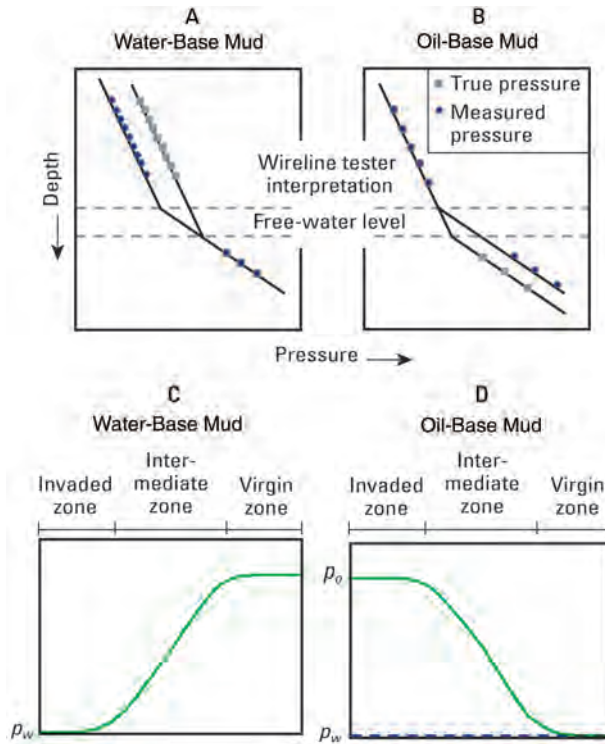


Fig. 7.17—Pressure-depth plots and capillary pressure profiles—water-wet reservoirs.

volume ratios, measure reservoir pressure and temperature, obtain representative fluid samples suitable for PVT analysis, evaluate completion efficiency, and evaluate workover or stimulation treatments.

Descriptive reservoir tests are conducted to assess reservoir extent and geometry, determine hydraulic communication between wells, characterize reservoir heterogeneities, and evaluate reservoir parameters.

Detailed information on the use and interpretation of transient pressure data is presented in another chapter in this *Handbook*. Some special analytical techniques follow.

7.13.1 Pressure Flow Convolution and Deconvolution. The pressure-flow convolution involves simultaneous bottomhole flow rate and pressure measurements to correct for the variations of bottomhole pressure caused by flow rate fluctuations during drawdown tests.¹¹

The bottomhole pressure and flow rate are mathematically convolved (coupled) as follows:

$$p_D(t_D) = \int_0^{t_D} q_D(\tau) p'_D(t_D - \tau) d\tau, \dots\dots\dots (7.11)$$

where p_D , the pressure function equivalent to a constant flow rate situation, is obtained by mathematical deconvolution of the pressure from the flow-rate fluctuations. When software deconvolution operators are used, trial and error is required to convolve a flow-rate schedule with a pressure function that approximates the true constant rate-equivalent pressure function, thus reproducing the measured pressures. The process can be made to converge rather rapidly for a

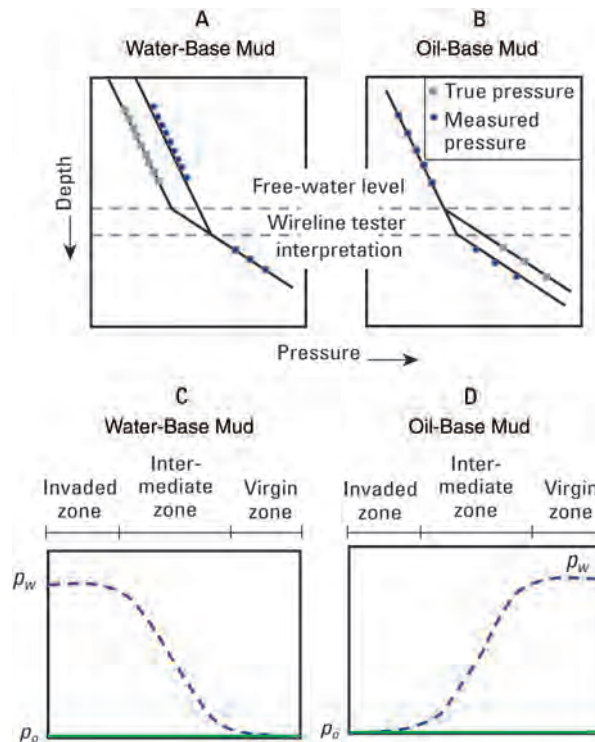


Fig. 7.18—Pressure-depth plots and capillary pressure profiles—oil-wet reservoirs.

pressure measurement of a given resolution, as long as the results allow for an acceptable margin of error.

Fig. 7.19 shows an example in which the transient consists of a step-rate change from a high value with a downhole spinner flowmeter rotation rate of approximately 17 revolutions per second (rps) to a lower value with a flowmeter response of approximately 7 rps. Clearly, the pressure and flow-rate data mirror each other, which is precisely the effect of the convolution. A constant flow-rate function was sought to interpret this test. The technique used here makes use of semilog analysis, in which rate-normalized pressures are plotted vs. the “sandface convolution time” (a time function akin to a generalized superposition function). The result (Fig. 7.20) is a straight line on the semilog plot, which in turn can be interpreted to yield the test objectives of the permeability and skin effect.

7.13.2 Benefits of Downhole Shut-In. Fig. 7.21 shows superimposed log-log plots for two buildup tests run on the same well. The surface shut-in test barely reaches radial flow after 200 hours. However, a large fraction of the wellbore volume is eliminated in the downhole shut-in test, and consequently radial flow is detected almost as early as the first minute after shut-in, and confirmed after 1 hour. This test, which lasts 100 hours, could well have been aborted after a maximum of 5 hours without any loss of information.

7.13.3 Multilayer Tests. To interpret tests when several layers are producing in a commingled environment, a generalization of the pressure-flow convolution is used. Conventional well tests performed on commingled multilayer reservoir systems normally do not yield interpretable data. The different dynamic reservoir parameters (i.e., kh , skin effect, static pressure, boundary condition, heterogeneity) of each layer induce off-phase flow rate events in the layer that do

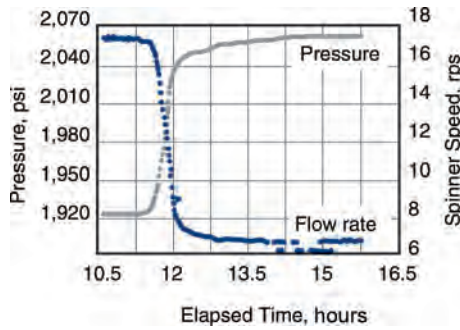


Fig. 7.19—Pressure and spinner data in a step-rate change test.

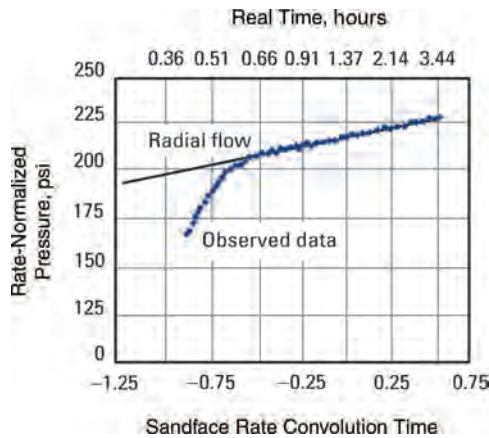


Fig. 7.20—Interpretation of test data in Fig. 7.19.

not superimpose themselves to yield a predictable sandface pressure response. By using simultaneous bottomhole pressure and flow rate measurements and designing the drawdown test as a succession of step-rate tests (Fig. 7.22), a rigorous solution to deriving the dynamic reservoir parameters can be obtained for each layer.^{12,13}

The following steps describe a typical design for a three-layer multirate test:

1. The well is shut in, and the pressure and flow sensors (typically conveyed by a production logging tool) are positioned above the top of the uppermost layer. The well is opened to the smallest choke opening, and the ensuing transients of rate and pressure are recorded until stabilization occurs. Finally, a continuous flow profile is recorded across the set of producing layers.
2. The pressure and flow sensors are repositioned above the top of the middle layer. The well is opened to the intermediate choke opening, and the ensuing transients of rate and pressure are recorded until stabilization occurs. A second continuous flow profile is recorded across the set of producing layers.
3. The pressure and flow sensors are repositioned above the top of the lowermost layer. The well is opened to the largest choke opening, and the ensuing transients of rate and pressure are recorded until stabilization occurs. A third continuous flow profile is recorded across the set of producing layers.

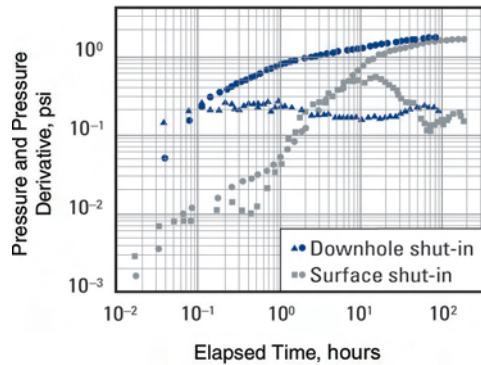


Fig. 7.21—Compared pressures of a surface shut-in and downhole shut-in test.

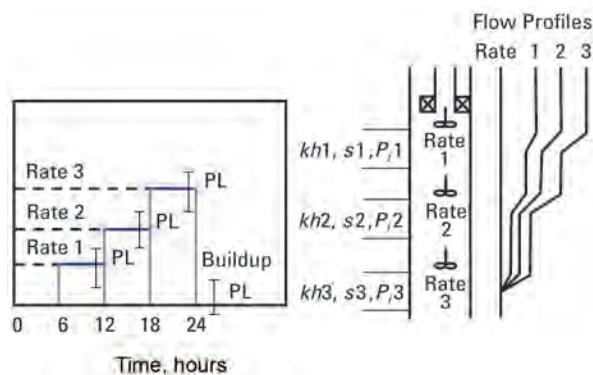


Fig. 7.22—Typical design for a three-layer multirate test (PL = production logging).

4. In a last, optional step, the pressure and flow sensors are repositioned above the top of the uppermost layer and the well is shut in again. The observed transients of rate and pressure are recorded as in a traditional buildup test.

The interpretation of this data set (which includes SIP data) makes extensive use of the pressure-flow convolution to extract the individual layer parameters. After the results are obtained, it is advised to verify their quality by forward-simulating the commingled pressure and flow response of the layered system and by matching the simulated responses to the measured data. A single-well numerical simulator is used with the layered system described by the interpreted values of permeability and skin effect for each layer. The surface flow rate schedule is input, and the simulator predicts the commingled pressure response of the system as well as the individual layer flow history for the entire test, which must match the measured downhole pressure and flow rate records.

7.13.4 Wireline Pressure Transient Tests. Some interpretation techniques are unique to wireline testers because of the specific hardware used to perform the tests. Wireline testers investigate a smaller region around the wellbore because of the smaller volumes flowed. Wireline pressure testing offers unique advantages over drillstem testing, however, because of the variety of options available in the downhole hardware configuration, multiprobe arrangements, and packer devices. Stewart and Wittmann first described some salient techniques specific to wireline pressure testing in 1979.¹⁴

In wireline pressure testing, the static pressure is measured by shutting in the sampling system after retrieving a small sample, typically 5 to 20 cm³. The subsequent buildup duration is short, and the stabilized static pressure is typically obtained within a few seconds to a maximum of approximately 30 minutes.

In low-permeability situations, the buildup may take much longer. Continued testing with the tool hanging stationary at the same depth, firmly seated against the formation, may be impractical. In addition, pressure measurements may be affected by the supercharging phenomenon as described previously, resulting in understated pressures.

Packer Probe Tests: Small-Scale Drillstem Testing. A packer probe fitted into the string of a modern wireline tester increases the area of the formation open to the flow during formation sampling, typically by a factor of up to several thousand. This increase multiplies flow rates by the same factor, which in turn greatly increases the depth of investigation. In some cases, a packer probe test has a depth of investigation similar to that of a small-scale DST.

Packer and Multiple-Probe Tests for Vertical Interference Testing. A packer probe can be used in tandem with a vertical probe to test for vertical permeability.¹⁵ The vertical probe is located on a generatrix (parallel to the tool axis) with the sink (packer) probe of the downhole tool. The distance of the vertical probe from the sink probe is adjustable. Whereas the pressure response at the sink probe depends on the local values of the permeability tensor, called k_x , k_y , and k_z , which are the permeabilities along arbitrary axes x , y , and z , respectively, the pressure response at the vertical probe (which is considered an observation probe) is a function of both the horizontal permeability at the vertical probe and the vertical permeability being measured. Thus, both pressure responses must be modeled simultaneously by a numerical parameter estimator.

Fig. 7.23 depicts the results of a tandem test. The dots are pressure measurements and the dashed curves are the pressures reconstructed from probe responses calculated from the interpretation results. **Fig. 7.23a** shows the response at the sink (packer) probe, and **Fig. 7.23b** shows the response at the vertical probe, which was set approximately 1 hour after the packer was set. The test sequence included a number of open-close cycles generated at the sink probe by the use of a flow-control module. A sample was also taken between times 2,800 and 3,800 seconds. The vertical probe response clearly shows the delayed interference response that occurred after that probe was set. From this data set, the horizontal mobility k_h/μ was calculated as 1.0 md/cp, and the vertical mobility k_v/μ was calculated as 0.3 md/cp. **Fig. 7.24** shows the log-log plot of the buildup between times 3,800 and 4,700 seconds that occurred after the sample was taken.

7.13.5 NODAL Analysis. The techniques and uses of NODAL* production system analysis are explained in another chapter in this *Handbook*. The objective of NODAL analysis is to predict well-productivity characteristics, also referred to as vertical lift properties (VLP), for various tubular and pressure configurations. If the pressure data are limited to sandface and wellhead measurements, the normal procedure is to generate several sets of VLP characteristics and select the one that best represents the measured pressure data. There may not be a unique solution. Recording a continuous profile of pressure vs. depth can alleviate nonuniqueness because the profile constitutes a precise measurement of the multiphase pressure losses that take place in a well. Using a continuous profile for input leads to better optimization of production rates with NODAL analysis.

NODAL analysis, aided by distributed pressure measurements, is the best way to design gas-lift systems. Gas-lift valve placement involves matching the pressure drop in the valves with the amount of pressure available in the well above the valve opening pressure. The pressure drop in the tubing, in turn, depends on the location and flow capacity of the valves.

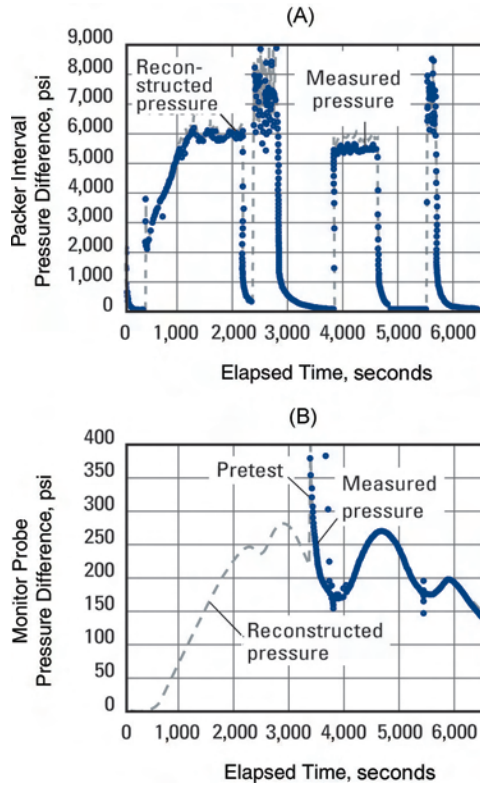


Fig. 7.23—Sink probe (a) and vertical probe (b) pressure responses during a vertical interference test conducted with wireline tester.

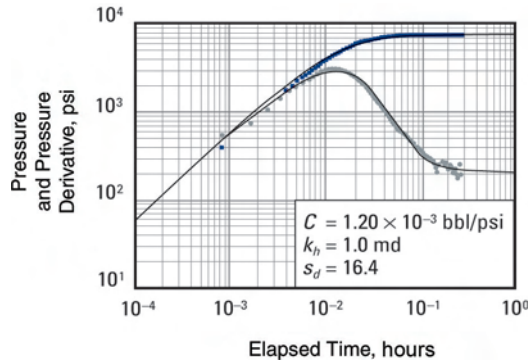


Fig. 7.24—Log-log plot of post-sampling buildup from the vertical interference test of Fig. 7.23.

7.13.6 Using Pressure To Characterize Reservoir Fluids. Pressure and temperature provide important information about the phase behavior and calibration of the equation-of-state for a fluid and average fluid density in flowing wells.

The average fluid density can be calculated by differentiating the pressure measurement vs. depth. In the absence of fluid friction on pipes, the acceleration and kinetic terms can be written as follows:

$$\frac{dp}{dD} = 0.00135\rho_f g \cos \delta \dots\dots\dots (7.12)$$

In a well flowing above the bubblepoint, the bubblepoint pressure can be inferred from a plot of the fluid density in the tubing. At the depth where the pressure reaches bubblepoint pressure, gas starts evolving from solution, and the density of the fluid shows a break to lower values. Density can be measured by differential pressure measurements.

Similarly, the pressure gradient in wet gas wells shows a break when the dewpoint is reached and condensate forms.

7.13.7 Temperature Profiles in Production and Injection Wells. All the mass-transfer processes taking place in and around a wellbore produce changes in the wellbore temperature. Measuring the wellbore temperature is a good diagnostic tool for applications such as identifying fluid entries into and exits from the wellbore, monitoring exothermic reactions such as cement hydration, determining the effects of temperature change on compression or decompression (Joule-Thompson effects), detecting the movement of fluids behind the casing, and identifying nongeothermal fluid entries into the wellbore. Another chapter in this section of the *Handbook* explains the use and interpretation of these data.

Recommendations for Temperature Profiling. To obtain good-quality temperature profile data, the following procedures are recommended.

1. Record a complete profile from surface to total depth (bottom of the well) on the first descent into the well. If the well is shut in, the thermal equilibrium becomes disrupted after the first passage of the temperature sensor, and unrecorded temperature anomalies may be lost forever. If the well is flowing, the first descent is a unique opportunity to diagnose leaks, spurious flow, or loss of completion integrity.
2. It may be possible to record a representative geothermal gradient if the well is shut in.
3. Record shut-in profiles if possible. Always compare shut-in profiles with the flowing profiles.
4. Repeat all runs.
5. In dual completions, run the temperature log in both tubing strings because the two logs are not identical.
6. Use short depth scales for presentation. They highlight temperature anomalies better than large depth scales.
7. Always interpret temperature logs together with flowmeter data.

Detecting Cement Tops. Cement hydration is an exothermic reaction that generates sufficient heat for determining the presence of cement behind a casing string by a temperature survey up to several days after cementing. The character of the anomaly above the cement top may be a large, sharp increase, in some cases up to 50°F, or a very slight increase in gradient.

The principal influence on the survey is the time elapsed between placing the cement and running the survey. Other influential conditions include cement texture, chemical composition, rate of hydration, mass of cement in place, and the thermal conductivity of the adjacent formation. The maximum temperature usually occurs 4 to 9 hours after cementing, but reliable data can be determined in most areas after 48 hours. The rate of hydration affects temperature change more than the total amount of heat liberated. Although hydration continues indefinitely, the rate decreases rapidly from the peak. A washed-out section of hole may be responsible for a large, sharp increase in temperature that falsely indicates a cement top. A small temperature change or slight change in gradient could be caused by a small annular area or dilution of the cement with drilling mud. These factors, which influence the size of the temperature anomaly at the top of the cement in a well, vary widely in their effect. Even for an unfavorable combination of factors, however, sufficient heat is typically generated to determine the cement top.

Vertical Extent of Fracturing and Detecting Lost Circulation. The temperature of fluids and solids injected during a frac job is low relative to that of the formation which causes anomalies in the geothermal profile. This effect also applies to lost circulation zones that receive excessive amounts of drilling mud. Diagnosis of these anomalies with temperature surveys can supply quantitative data on the fracture size and amount of mud lost.

Nomenclature

- A_{ij} = pressure calibration coefficient of orders i and j , dimensionless
 A_{ij}' = temperature calibration coefficient of order i and j , dimensionless
 B = formation volume factor, RB/STB
 C = wellbore storage coefficient, bbl/psi
 D = depth along the wellbore, ft
 D_0 = depth along wellbore of the reference datum, ft
 g = acceleration of earth's gravity, ft/sec²
 h = reservoir thickness, ft
 J = productivity index, B/D/psi
 $J(S_w)$ = Leverett J-function, dimensionless
 k = reservoir permeability, md
 k_h = reservoir horizontal permeability, md
 k_x = permeability along arbitrary axis x , md
 k_y = permeability along arbitrary axis y , md
 k_z = permeability along arbitrary axis z , md
 $m(p)$ = real gas pseudopressure, psi²/cp
 p = pressure, psi
 p_c = pressure calibration function, dimensionless
 $p_c(S_{xo})$ = capillary pressure in filtrate invaded zone, psi
 p_D = observed pressure response at the wellbore, dimensionless
 p_D' = derivative of the sought constant rate pressure response, dimensionless
 p_{fl} = fluid pressure, psi
 p_i = original reservoir pressure, psi
 p_m = mud pressure, psi
 p_o = oil-phase pressure, psi
 p_r = reservoir pressure, psi
 p_w = water-phase pressure, psi
 p_{wf} = bottomhole flowing pressure, psi
 q = flow rate, STB/D
 $q_D(\tau)$ = variable sandface flow rate, dimensionless
 Q = downhole flow rate, B/D
 r = distance from wellbore axis, ft
 r_e = external boundary radius of the well, ft
 r_w = wellbore radius, ft
 s = skin effect, dimensionless
 s_d = skin effect due to damage, dimensionless
 S_p = pressure output of a pressure gauge, psi
 S_{po} = pressure output offset of a pressure gauge, psi
 S_f = temperature output of a pressure gauge, °F
 S_{to} = temperature output offset of a pressure gauge, °F
 S_w = water saturation, fraction

t_D	= dimensionless time
t_k	= circulation time, hr
T_{bh}	= observed temperature in a well, °F
T_c	= temperature calibration function, dimensionless
δ	= deviation of the well, assumed constant between D and D_0 , deg
ΔD	= vertical depth differential, ft
Δp	= pressure change, psi
Δp_{fl}	= fluid pressure differential, psi
Δp_m	= mud pressure differential, psi
Δt_c	= time after circulation, hr
μ	= fluid viscosity, cp
ρ	= reservoir fluid density, g/cm ³
ρ_{fl}	= reservoir fluid density, g/cm ³
ρ_m	= mud density, g/cm ³
σ	= surface tension, psi.ft
τ	= integration variable, dimensionless
ϕ	= reservoir porosity, fraction
Φ	= hydrostatic potential, psi

References

1. Dowdle, W.L. and Cobbs, W.M.: "Static Formation Pressure From Well Logs—An Empirical Method," *JPT* (November 1975) 1326.
2. Veneruso, A., Ehlig-Economides, C.A., and Petitjean, L.: "Pressure Gauge Specification Considerations in Practical Well Testing," paper SPE 22752 presented at the 1991 SPE Annual Conference and Exhibition, Dallas, 6–9 October.
3. Colley, N. *et al.*: "The MDT Tool: A Wireline Testing Breakthrough," *Schlumberger Oilfield Review* (April 1992) 58.
4. Davies, J. *et al.*: "Spinners Run While Perforating," paper SPE 38549 presented at the 1997 SPE Offshore Europe Conference, Aberdeen, 9–12 September.
5. Eck, J. *et al.*: "Downhole Monitoring: The Story So Far," *Schlumberger Oilfield Review* (Winter 1999) 20.
6. Elshahawi, H., Fathy, K., and Hiekal, S.: "Capillary Pressure and Rock Wettability Effects on Wireline Formation Tester Measurements," paper SPE 56712 presented at the 1999 SPE Annual Technical Conference and Exhibition, Houston, 3–6 October.
7. Elshahawi, H., Samir, M., and Fathy, K.: "Correcting for Wettability and Capillary Pressure Effects on Formation Tester Measurements," paper SPE 63075 presented at the 2000 SPE Annual Technical Conference and Exhibition, Dallas, 1–4 October.
8. Leverett, M.C.: "Capillary Behavior in Porous Solids," *Trans.*, AIME (1941) **142**, 152.
9. Lowden, B.: "Some Simple Methods for Refining Permeability Estimates From NMR and Generating Capillary Pressure Curves," *DiaLog*, *The On-Line Newsletter of the London Petrophysical Society* (March 2000) **8**, No. 1, http://www.lps.org.uk/site_pages/dialog.htm#top.
10. Marschall, D. *et al.*: "Method for Correlating NMR Relaxometry and Mercury Injection Data," *Trans.*, Intl. Symposium of the SCA, San Francisco, 12–15 September.
11. Joseph, J., Ehlig-Economides, C.A., and Kuchuk, F.: "The Role of Downhole Flow and Pressure Measurements in Reservoir Testing," paper SPE 18379 presented at the 1988 SPE European Petroleum Conference, London, 16–18 October.
12. Kuchuk, F., Karakas, M., and Ayestaran, L.: "Well Test Analysis of Commingled Zones Without Crossflow," paper SPE 13081 presented at the 1984 SPE Annual Technical Conference and Exhibition, Houston, 16–19 September.

13. Ayestaran, L. *et al.*: “Layered Reservoir Testing,” *Schlumberger Technical Review* (October 1987) **35**, No. 4, 4.
14. Stewart, G. and Wittmann, M.: “Interpretation of the Pressure Response of the Repeat Formation Tester,” paper SPE 8362 presented at the 1979 SPE Annual Technical Conference and Exhibition, Las Vegas, Nevada, 23–26 September.
15. Head, E.L. and Bettis, F.E.: “Reservoir Anisotropy Determination With Multiple Probe Pressures,” *JPT* (December 1993) 1177.

SI Metric Conversion Factors

bbl × 1.589 873	E - 01 = m ³
cp × 1.0*	E - 03 = Pa·s
ft × 3.048*	E - 01 = m
°F (°F - 32)/1.8	= °C
in. ³ × 1.638 706	E + 01 = cm ³
psi × 6.894 757	E + 00 = kPa
psi ² × 4.753 8	E + 01 = kPa ²

*Conversion factor is exact.

Chapter 8

Fluid Flow Through Permeable Media

John Lee, Texas A&M U.

8.1 Overview

This chapter discusses fluid flow in petroleum reservoirs. Basic concepts, which include flow equations for unsteady-state, pseudosteady-state, and steady-state flow of fluids, are discussed first. Various flow geometries are treated, including radial, linear, and spherical flow. The pseudosteady-state equations provide the basis for a brief discussion of oil well productivity, and the unsteady-state equations provide the basis for a lengthy discussion of pressure-transient test analysis. For pressure-transient test analysis, semilog techniques, type curves, damage and stimulation, modifications for gases and multiphase flow, the diagnostic plot, bounded reservoirs, average pressure in the drainage area, hydraulically fractured wells, and naturally fractured reservoirs are included. The chapter also discusses transient and stabilized flow in horizontal wells and gas-well deliverability tests. It concludes with considerations of coning in vertical and horizontal wells.

8.2 Basic Concepts

8.2.1 The Ideal Reservoir Model. Many important applications of fluid flow in permeable media involve 1D, radial flow. These applications are based on a model that includes many simplifying assumptions about the well and reservoir. These assumptions are introduced as needed to combine the law of conservation of mass, Darcy's law, and equations of state to achieve our objectives.

Consider radial flow toward a well in a circular reservoir. Combining the law of conservation of mass and Darcy's law for the isothermal flow of fluids of small and constant compressibility yields the radial diffusivity equation,¹

$$\frac{\partial^2 p}{\partial r^2} + \frac{1}{r} \frac{\partial p}{\partial r} = \frac{\phi \mu c}{0.0002637k} \frac{\partial p}{\partial t} \quad \dots\dots\dots (8.1)$$

In the derivation of this equation, it is assumed that compressibility of the total system, c_t , is small and independent of pressure; permeability, k , is constant and isotropic; viscosity, μ , is independent of pressure; porosity, ϕ , is constant; and that certain terms in the basic differential

equation (involving pressure gradients squared) are negligible. The grouping $0.0002637k/\phi\mu c_t$ is called the hydraulic diffusivity and is given the symbol η .

8.2.2 Line-Source Solution to the Diffusivity Equation. Assume that a well produces at constant reservoir rate, qB ; the well has zero radius; the reservoir is at uniform pressure, p_i , before production begins; and the well drains an infinite area (i.e., that $p \rightarrow p_i$ as $r \rightarrow \infty$). Under these conditions, the solution to Eq. 8.1 is¹

$$p = p_i + 70.6 \frac{qB\mu}{kh} Ei \left(\frac{-948\phi\mu c_t r^2}{kt} \right), \dots\dots\dots (8.2)$$

where p is the pressure at distance r from the well at time t , and

$$Ei(-x) = - \int_x^\infty \left(\frac{e^{-u}}{u} \right) du, \dots\dots\dots (8.3)$$

the Ei function or exponential integral.

The Ei -function solution is an accurate approximation to more exact solutions to the diffusivity equation (solutions with finite wellbore radius and finite drainage radius) for $3.79 \times 10^5 \phi\mu c_t r_w^2/k < t < 948\phi\mu c_t r_e^2/k$. For smaller times, the assumption of zero well size (line source or sink) limits the accuracy of the equation; for larger times, the reservoir's boundaries affect the pressure distribution in the reservoir, so that the reservoir is no longer infinite acting.

For the argument, x , of the Ei function less than 0.01, the Ei function can be approximated with negligible error by

$$Ei(-x) = \ln(1.781x) . \dots\dots\dots (8.4)$$

For $x > 10$, the Ei function is zero for practical applications in flow through porous media. For $0.01 < x < 10$, Ei functions are determined from tables or subroutines available in appropriate software.⁴

8.2.3 Altered Zone and Skin Factor. In practice, most wells have reduced permeability (damage) near the wellbore resulting from drilling or completion operations. Many other wells are stimulated by acidization or hydraulic fracturing. Eq. 8.2 fails to model such wells properly. Its derivation includes the explicit assumption of uniform permeability throughout the drainage area of the well up to the wellbore. Hawkins² pointed out that if the damaged or stimulated zone is considered equivalent to an altered zone of uniform permeability, k_s , and outer radius, r_s , the additional pressure drop, Δp_s , across this zone can be modeled by the steady-state radial flow equation

$$\begin{aligned} \Delta p_s &= 141.2 \frac{qB\mu}{k_s h} \ln \left(\frac{r_s}{r_w} \right) - 141.2 \frac{qB\mu}{kh} \ln \left(\frac{r_s}{r_w} \right) \\ &= 141.2 \frac{qB\mu}{kh} \left(\frac{k}{k_s} - 1 \right) \ln \left(\frac{r_s}{r_w} \right) . \dots\dots\dots (8.5) \end{aligned}$$

Eq. 8.5 states that the pressure drop in the altered zone is inversely proportional to k_s rather than to k and that a correction to the pressure drop in this region must be made. Combining Eqs. 8.2 and 8.5, we find that the total pressure drop at the wellbore is

$$\begin{aligned}
 p_i - p_{wf} &= -70.6 \frac{qB\mu}{kh} Ei \left(-\frac{948\phi\mu c_t r_w^2}{kt} \right) + \Delta p_s \\
 &= -70.6 \frac{qB\mu}{kh} \left[Ei \left(-\frac{948\phi\mu c_t r_w^2}{kt} \right) - 2 \left(\frac{k}{k_s} - 1 \right) \ln \left(\frac{r_s}{r_w} \right) \right] \dots \dots \dots (8.6)
 \end{aligned}$$

For $r = r_w$, the argument of the Ei function is sufficiently small after a short time that we can use the logarithmic approximation; thus, the drawdown is

$$p_i - p_{wf} = -70.6 \frac{qB\mu}{kh} \left[\ln \left(\frac{1688\phi\mu c_t r_w^2}{kt} \right) - 2 \left(\frac{k}{k_s} - 1 \right) \ln \left(\frac{r_s}{r_w} \right) \right] \dots \dots \dots (8.7)$$

We can conveniently define a dimensionless skin factor, s , in terms of the properties of the equivalent altered zone:

$$s = \left(\frac{k}{k_s} - 1 \right) \ln \left(\frac{r_s}{r_w} \right) = \frac{kh\Delta p_s}{141.2qB\mu} \dots \dots \dots (8.8)$$

Thus, the drawdown is

$$p_i - p_{wf} = -70.6 \frac{qB\mu}{kh} \left[\ln \left(\frac{1688\phi\mu c_t r_w^2}{kt} \right) - 2s \right] \dots \dots \dots (8.9)$$

Eq. 8.9 provides some insight into the physical significance of the algebraic sign of the skin factor. If a well is damaged ($k_s < k$), s will be positive, and the greater the contrast between k_s and k and the deeper into the formation the damage extends, the larger the numerical value of s , which has no upper limit. Some newly drilled wells will not flow before stimulation; for these wells, $k_s = 0$ and $s \rightarrow \infty$. If a well is stimulated ($k_s > k$), s will be negative, and the deeper the stimulation, the greater the numerical value of s . Rarely does a stimulated well have a skin less than -7 , and such skin factors arise only for wells with deeply penetrating, highly conductive hydraulic fractures. If a well is neither damaged nor stimulated ($k = k_s$), $s = 0$.

The altered zone near a well affects only the pressure near that well; that is, the pressure in the unaltered formation away from the well is not affected by the existence of the altered zone. Thus, use Eq. 8.9 to calculate pressures at the sandface of a well with an altered zone, and Eq. 8.2 to calculate pressures beyond the altered zone in the formation surrounding the well. See Sec. 8.4 for more information on damage and stimulation.

8.2.4 Inertial-Turbulent Flow and Rate-Dependent Skin. The diffusivity equation, Eq. 8.1, assumes that Darcy’s law represents the relationship between flow velocity and pressure gradients in the reservoir, an assumption that is adequate for low-velocity or laminar flow. However, at higher flow velocities, deviations from Darcy’s law are observed as a result of inertial effects or even turbulent flow effects. In 1D radial flow, these inertial/turbulent effects (often

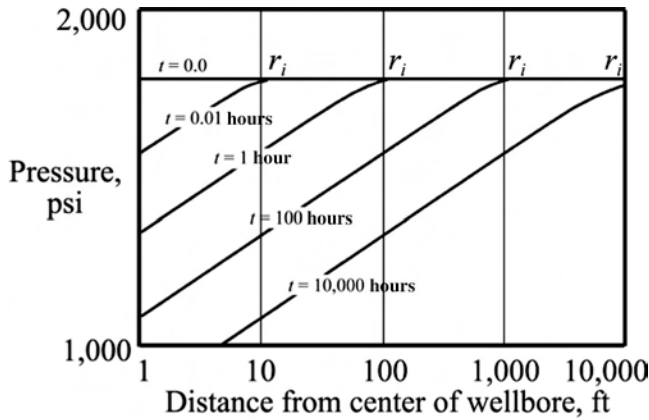


Fig. 8.1—Pressure distributions at increasing times.

called non-Darcy flow effects) are confined to the region near the wellbore in which flow velocities are largest. This results in an additional pressure drop similar to that caused by skin, but the additional pressure drop is proportional to flow rate. The apparent skin, s' , for a well with non-Darcy flow near the wellbore is given by³

$$s' = s + Dq, \dots\dots\dots (8.10)$$

where D is the non-Darcy flow factor for the system. D can be regarded as constant, although, in theory, it depends slightly on near-well pressure. In practice, non-Darcy flow is ordinarily important only for gas wells, which have high-flow velocities near the wellbore, but it can be important for oil wells with high-velocity flow in some situations.

8.2.5 Radius of Investigation and Stabilization Time. Radius of investigation is the distance a pressure transient has moved into a formation following a rate change in a well. This distance is related to formation rock and fluid properties and time elapsed since a rate change in the well. Consider this concept by visualizing the pressure distributions at increasing times as Fig. 8.1 shows for a well producing at constant rate from a reservoir initially at uniform pressure. (These pressure distributions were calculated using the Ei -function solution to the diffusivity equation.)

Important observations about this figure include the following:

- The pressure in the wellbore, at $r = r_w$, decreases steadily as flow time increases; likewise, pressures at other fixed values of r also decrease as flow time increases.
- The pressure drawdown (or pressure transient) caused by producing the well moves further into the reservoir as flow time increases. For the range of flow times shown, there is always a point beyond which the drawdown in pressure from the original value is negligible. This time-dependent point of “negligible drawdown” can be considered to be a radius of investigation.

Analysis shows that the time, t , at which a pressure disturbance reaches a distance, r_i , which is called the radius of investigation, is given by the equation⁴

$$r_i = \sqrt{\frac{kt}{948\phi\mu c_t}} \dots\dots\dots (8.11)$$

Investigators differ on the numerical constant in Eq. 8.11, but this difference is of little practical importance if the radius of investigation is used as a semiquantitative indicator of the distance into the reservoir to which formation properties have influenced the response of a well in a pressure-transient test.

The radius of investigation has several applications in pressure-transient test analysis and design. A qualitative use is to help explain the shape of a pressure buildup or drawdown curve. For example, a buildup test plot may have a complex shape at early times when the radius of investigation is in the altered zone near the wellbore, where the permeability is different from formation permeability. Or a buildup test plot may change shape at long times when the radius of investigation reaches the general vicinity of a reservoir boundary.

The radius-of-investigation concept provides a guide for well-test design. For example, you may want to sample reservoir properties at least 1,000 ft from a test well. The radius of investigation concept allows you to estimate the time required to achieve the desired depth of investigation.

Eq. 8.11 also provides a means to estimate the time required to achieve “stabilized” flow; that is, the time required for a pressure transient to reach the boundaries of a tested reservoir. For example, if a well is centered in a cylindrical drainage area of radius r_e , then the time required for stabilization, t_s , is

$$t_s = \frac{948\phi\mu c_t r_e^2}{k} \dots\dots\dots (8.12)$$

For other drainage shapes, the time to stabilization can be quite different, as discussed later.

8.2.6 Pseudosteady-State Flow. The *Ei*-function solution to the radial diffusivity equation is valid only while a reservoir is infinite-acting; that is, until boundaries begin to affect the pressure drawdown at the well. For the constant rate flow of a well centered in its drainage area of radius, r_e , and modeled by the *Ei*-function solution, these effects begin at $t = 948 \phi\mu c_t r_e^2/k$. Before these boundary effects, the regime is called unsteady-state flow. After boundary effects are felt fully, the solution to the radial diffusivity equation for a well centered in a cylindrical drainage area and producing at constant rate is⁴

$$p_{wf} = p_i - 141.2 \frac{qB\mu}{kh} \left[\frac{0.000527kt}{\phi\mu c_t r_e^2} + \ln\left(\frac{r_e}{r_w}\right) - \frac{3}{4} \right] \dots\dots\dots (8.13)$$

This equation for calculating pressure in the wellbore becomes valid for $t > 948 \phi\mu c_t r_e^2/k$ at the same time at which the *Ei*-function solution becomes invalid.

Another form of Eq. 8.13 is useful for some applications. It involves replacing original reservoir pressure, p_i , with average pressure, \bar{p} , within the drainage volume of the well. The volumetric average pressure within the drainage volume of the well can be found from material balance. The pressure decrease ($p_i - \bar{p}$) resulting from removal of qB RB/D of fluid for t hours (a total volume removed of $5.615qBt/24$ ft³) is

$$p_i - \bar{p} = \frac{\Delta V}{c_t V} = \frac{5.615qB(t/24)}{c_t(\pi r_e^2 h \phi)} = \frac{0.0744qBt}{\phi c_t h r_e^2} \dots\dots\dots (8.14)$$

Substituting in Eq. 8.13, the time-dependent terms cancel, and the result is

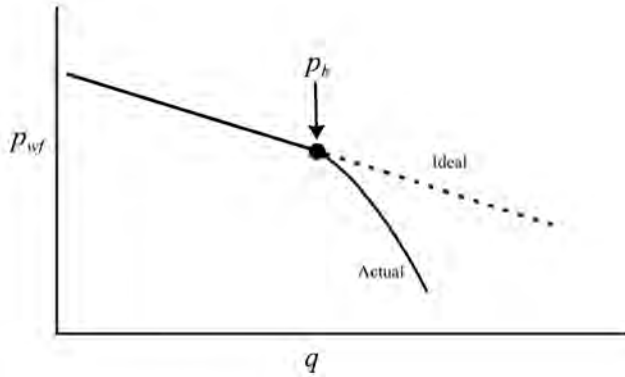


Fig. 8.2—Field data drop below idealized straight line at pressures below bubblepoint.

$$p_{wf} = \bar{p} - 141.2 \frac{qB\mu}{kh} \left[\ln \left(\frac{r_e}{r_w} \right) - \frac{3}{4} \right] \dots\dots\dots (8.15)$$

Eqs. 8.13 and 8.15 are more useful in practice if they include skin factors to account for damage or stimulation. In Eq. 8.15,

$$\bar{p} - p_{wf} = 141.2 \frac{qB\mu}{kh} \left[\ln \left(\frac{r_e}{r_w} \right) - \frac{3}{4} \right] + (\Delta p)_s \dots\dots\dots (8.16)$$

$$\bar{p} - p_{wf} = 141.2 \frac{qB\mu}{kh} \left[\ln \left(\frac{r_e}{r_w} \right) - \frac{3}{4} + s \right] \dots\dots\dots (8.17)$$

$$\text{and } p_i - p_{wf} = 141.2 \frac{qB\mu}{kh} \left[\frac{0.000527kt}{\phi\mu c_t r_e^2} + \ln \left(\frac{r_e}{r_w} \right) - \frac{3}{4} + s \right] \dots\dots\dots (8.18)$$

8.2.7 Productivity Index. The productivity index, *J*, of an oil well is the ratio of the stabilized rate, *q*, to the pressure drawdown, ($\bar{p} - p_{wf}$), required to sustain that rate. For flow from a well centered in a circular drainage area, Eq. 8.17 allows us to relate productivity index to formation and fluid properties:

$$J \equiv \frac{q}{\bar{p} - p_{wf}} = \frac{kh}{141.2B\mu \left[\ln \left(\frac{r_e}{r_w} \right) - \frac{3}{4} + s \right]} \dots\dots\dots (8.19)$$

Thus, if a well is tested at several different stabilized rates and the stabilized flowing bottomhole pressure (BHP), p_{wf} , is measured at each rate (that is, if pseudosteady-state is attained at each rate), Eq. 8.19 implies that a plot of test data should produce a straight line with slope *J* and intercepts $q = 0$ when $p_{wf} = \bar{p}$ and $q = J\bar{p}$ when $p_{wf} = 0$. (See Fig. 8.2.) In practice, actual field data will fall below the theoretical straight line for pressures below the bubblepoint pressure of the oil because of increasing gas saturations and oil viscosities that increase the resistance to flow.

8.2.8 Generalized Drainage Area Shapes. Eq. 8.17 is limited to a well centered in a circular drainage area. A similar equation models pseudosteady-state flow in more general reservoir shapes⁴:

$$\bar{p} - p_{wf} = 141.2 \frac{qB\mu}{kh} \left[\frac{1}{2} \ln \left(\frac{10.06A}{C_A r_w^2} \right) - \frac{3}{4} + s \right], \dots\dots\dots (8.20)$$

where A is the drainage area in square feet, and C_A is the dimensionless shape factor for a specific drainage-area shape and configuration. Table 8.A-1 (Appendix) gives values of C_A .

The productivity index, J , can be expressed for general drainage-area geometry as

$$J = \frac{q}{\bar{p} - p_{wf}} = \frac{0.00708kh}{B\mu \left[\frac{1}{2} \ln \left(\frac{10.06A}{C_A r_w^2} \right) - \frac{3}{4} + s \right]} \dots\dots\dots (8.21)$$

Other numerical constants tabulated in Table 8.A-1 allow us to calculate the maximum elapsed time during which a reservoir is infinite-acting (so that the Ei -function solution can be used), the time required for the pseudosteady-state solution to predict pressure draw-down within 1% accuracy, and time required for the pseudosteady-state solution to be exact. For a given reservoir geometry, the maximum time a reservoir is infinite acting can be determined using the entry in the column “Use Infinite System Solution With Less Than 1% Error for $t_{DA}<$.” This t_{DA} is defined as $0.0002637kt/\phi\mu c_t A$, so this means that the time in hours is calculated from

$$t = \frac{\phi\mu c_t A t_{DA}}{0.0002637k} \dots\dots\dots (8.22)$$

Time required for the pseudosteady-state equation to be accurate within 1% can be found from the entry in the column titled “Less Than 1% Error for t_{DA} .” Finally, the time required for the pseudosteady-state equation to be exact is found in the entry in the column “Exact for $t_{DA}>$.”

Figs. 8.3 and 8.4 show the flow regimes that occur at various times. These figures show p_{wf} in a well flowing at constant rate, plotted as a function of time on both logarithmic and linear scales. In the transient region, the reservoir is infinite acting and is modeled by Eq. 8.9, which implies that p_{wf} is a linear function of $\log t$. In the pseudosteady-state region, the reservoir is modeled by Eq. 8.20 in the general case or Eqs. 8.15 or 8.13 for the special case of a well centered in a cylindrical drainage area. Eq. 8.13 shows a linear relationship between p_{wf} and t during pseudosteady-state flow. This linear relationship also exists in generalized reservoir geometries.

At times between the end of the transient region and the beginning of the pseudosteady-state region, there is a transition region, sometimes called the late-transient region. This region is, for practical purposes, nonexistent for wells centered in circular, square, or hexagonal drainage areas, as Table 8.A-1 indicates. However, for a well off-center in its drainage area, the late-transient region can span a significant time region, as Table 8.A-1 also indicates.

8.2.9 Steady-State Flow. Pseudosteady-state flow describes production from a closed drainage area (one with no-flow outer boundaries, either permanent and caused by zero-permeability rock or “temporary” and caused by production from offset wells). In pseudosteady-state, reser-

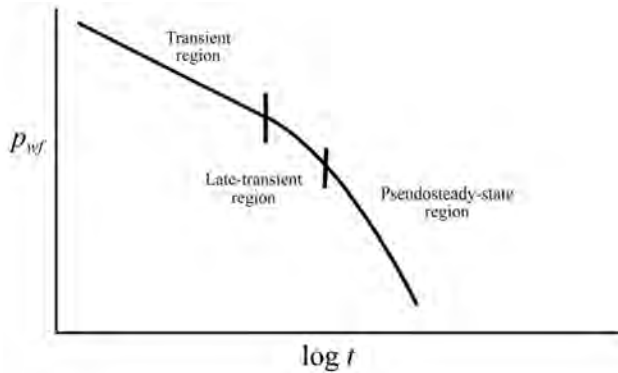


Fig. 8.3—Flow regions on semilogarithmic coordinates.

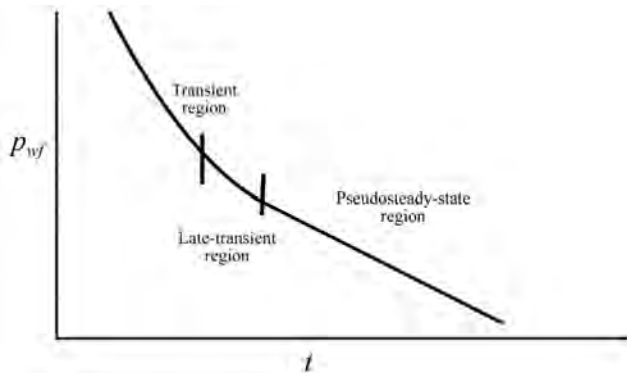


Fig. 8.4—Flow regions on Cartesian coordinates.

voir pressure drops at the same rate with time at all points in the reservoir, including at the reservoir boundaries. Ideally, true steady-state flow can occur in the drainage area of a well, but only if pressure at the drainage boundaries of the well can be maintained constant while the well is producing at constant rate. While unlikely, steady-state flow is conceivable for wells with edgewater drive or in repeated flood patterns in a reservoir. The solution to the radial diffusivity equation is based on a constant-pressure outer boundary condition, instead of a no-flow outer boundary condition. The steady-state solution, applicable after boundary effects have been felt, is

$$p_i - p_{wf} = 141.2 \frac{qB\mu}{kh} \left[\ln \left(\frac{r_e}{r_w} \right) + s \right] \dots\dots\dots (8.23)$$

8.2.10 Constant Pressure in the Well. Both the steady-state solution (constant pressure at the outer boundaries) and the pseudosteady-state solution (no-flow at the outer boundaries) assume constant rate production in the well. A well is actually more likely to be produced at something close to constant flowing BHP than constant rate. When pressure transients reach no-flow drainage area boundaries, the flow regime is not pseudosteady state; instead, it is more correctly called boundary-dominated flow. If the drainage boundaries are maintained at constant pressure, however, steady-state flow is achieved when the pressure transient reaches the reservoir boundaries.

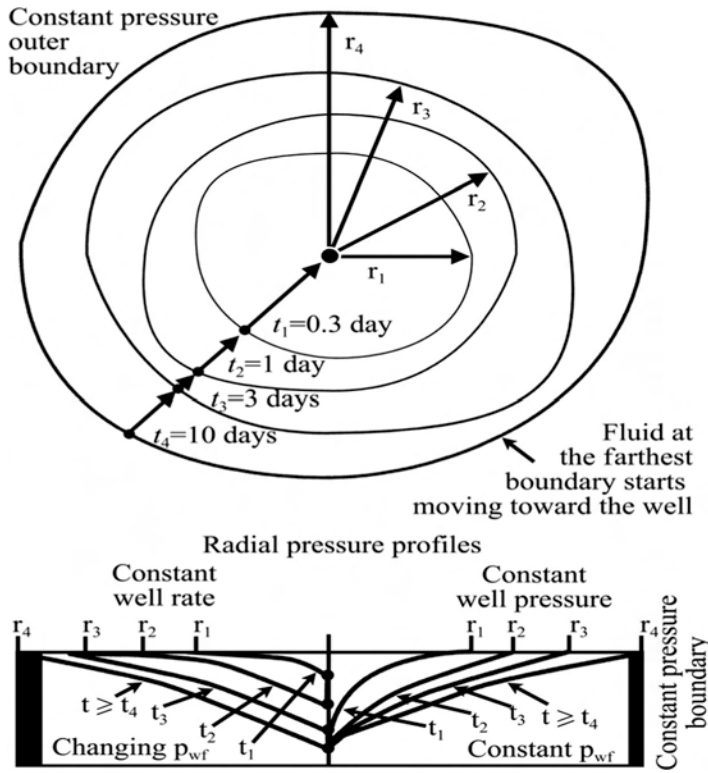


Fig. 8.5—Flow regimes with constant well flow rate or constant well pressure and constant-pressure outer boundaries.

These different flow regimes are clarified with figures showing pressure distributions in the drainage area of wells with constant flow rate and constant-pressure outer boundaries (Fig. 8.5); constant BHP and constant-pressure outer boundaries (also Fig. 8.5); constant flow rate and no-flow outer boundaries (Fig. 8.6); and constant BHP and no-flow outer boundaries (also Fig. 8.6).

8.2.11 Wellbore Storage. The *Ei*-function solution to the diffusivity equation assumes constant flow rate in the reservoir, starting at time zero. In practice, only the rate at the surface can be controlled. Under ideal conditions, a constant surface rate can be maintained, but the first fluid produced will be fluid that was stored in the wellbore, and, at first, the flow rate from the reservoir into the wellbore will be zero. As the wellbore is unloaded, the reservoir rate approaches the surface rate (Fig. 8.7). Only as the reservoir and surface rates become approximately equal does the *Ei*-function solution become valid. This wellbore unloading during flow tests is a special case of a general phenomenon called wellbore storage.

For a pressure buildup test, the surface rate is zero starting at the instant of shut-in. However, fluid continues to flow into the wellbore from the reservoir because of existing pressure gradients. Idealized models of pressure buildup tests assume a reservoir rate of zero starting at the time of shut-in for the test. This assumption is obviously violated because of the afterflow into the wellbore. As the afterflow rate diminishes, the downhole rate approaches the surface rate (zero), and only as the afterflow rate approaches zero closely can the idealized models closely approximate actual well behavior (Fig. 8.8). Afterflow during buildup tests is another special case of wellbore storage.

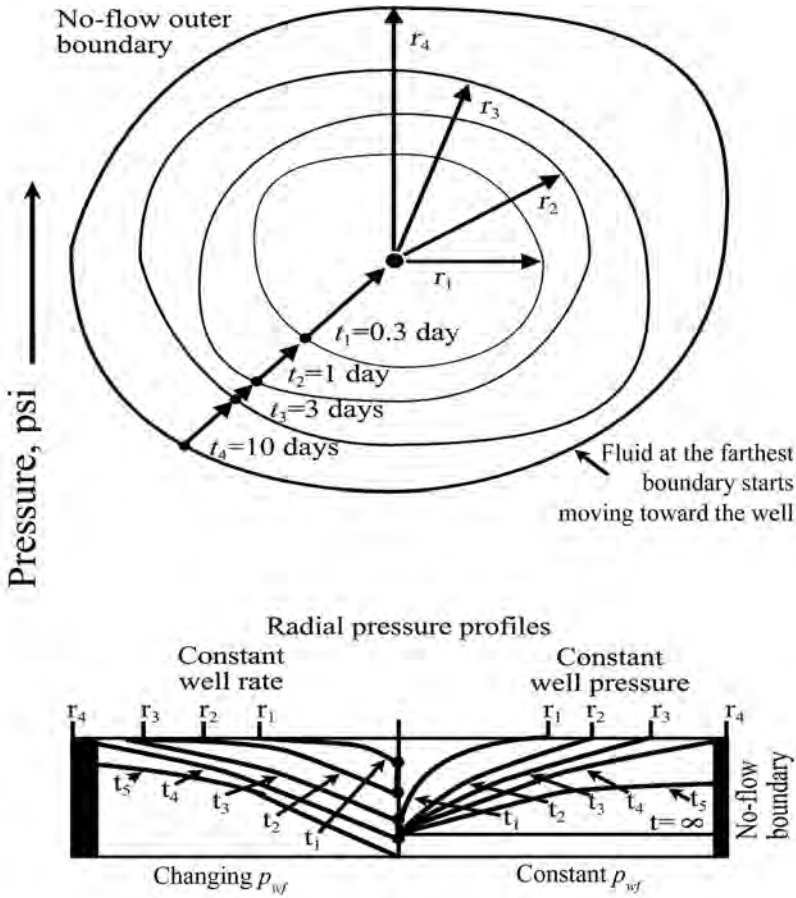


Fig. 8.6—Flow regimes with constant well flow rate and no-flow outer boundaries.

The relationship between changes in bottomhole pressure and wellbore unloading or after-flow rates can be modeled with mass balances on the wellbore. There are two special cases of interest: a wellbore completely filled with a single-phase fluid (Fig. 8.9, usually gas in practice) and a wellbore with a rising or falling liquid/gas interface in the well (Fig. 8.10).

For the wellbore filled with a single-phase fluid,⁴

$$q_{sf} = q + \frac{24V_{wb}c_{wb}}{B} \frac{dp_w}{dt} \dots\dots\dots (8.24)$$

For a well with a rising or falling liquid/gas interface,⁴

$$\frac{(24)(144)}{5.615\rho_{wb}} \frac{g_c}{g} A_{wb} \frac{d(p_w - p_l)}{dt} = (q_{sf} - q)B \dots\dots\dots (8.25)$$

In most applications, p_l is assumed to be constant, a convenient but frequently inaccurate simplification. Both equations can be written in the general form

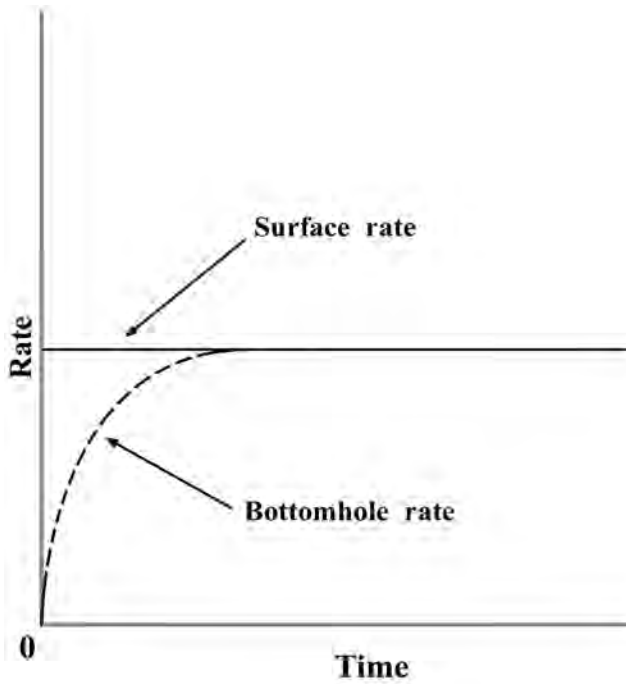


Fig. 8.7—Reservoir rate approaches surface rate as the wellbore is unloaded.

$$q_{sf} = q + \frac{24C}{B} \frac{dp_w}{dt}, \dots\dots\dots (8.26)$$

where, for a fluid-filled wellbore,

$$C = c_{wb}V_{wb}, \dots\dots\dots (8.27)$$

and, for a moving liquid/gas interface with unchanging surface pressure,

$$C = \frac{25.65A_{wb}}{\rho_{wb}} \dots\dots\dots (8.28)$$

C is called the wellbore storage coefficient.

For special cases in which, at earliest times for a flowing well, all the production is coming from fluid stored in the wellbore and none is entering the wellbore from the formation (or, for a shut-in well, the rate of afterflow is equal to the rate before shut in), the integration of Eq. 8.26 yields

$$\Delta p = \frac{qB\Delta t}{24C}, \dots\dots\dots (8.29)$$

where Δp is the pressure change in the time because either the start of flow or shut in and Δt is the elapsed time. On a log-log plot of Δp vs. Δt during these early times, a straight line with a slope of unity will result. For any point on this unit slope line, the wellbore storage coeffi-

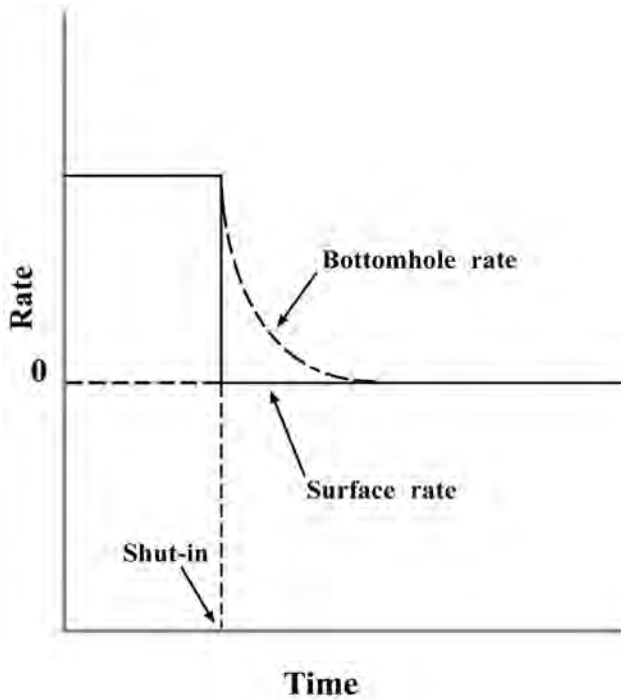


Fig. 8.8—Downhole rate approaches surface rate as afterflow rate diminishes.

cient, C , can be found from any point on the line (Δt , Δp) and Eq. 8.29 (Fig. 8.11). Alternatively, the slope ($qB/24C$) of a plot of Δp vs. Δt on Cartesian coordinates also leads to an estimate of the wellbore-storage coefficient.

8.2.12 Linear Flow. Linear flow occurs in some reservoirs with long, highly conductive vertical fractures; in relatively long, relatively narrow reservoirs (channels, such as ancient stream beds); and near horizontal wells during certain times. For unsteady-state linear flow in an unbounded (infinite-acting) reservoir,⁴

$$p_{wf} = p_i - 16.26 \frac{qB\mu}{kA} \left(\frac{kt}{\phi\mu c_t} \right)^{\frac{1}{2}} - 70.6 \frac{qB\mu}{kh} s_f \dots \dots \dots (8.30)$$

8.2.13 Spherical Flow. Spherical flow occurs in wells with limited perforated intervals and into wireline formation test tools. The solution to the spherical/cylindrical, 1D form of the diffusivity equation, subject to the initial condition that pressure is uniform before production and the boundary conditions of constant flow rate and an infinitely large drainage area, is⁵

$$p_{wf} = p_i - \frac{70.6qB\mu}{k_s r_s} + \frac{2456\sqrt{\phi\mu c_t} qB\mu}{k_{sp}^{3/2}} \frac{1}{\sqrt{t}} - \frac{70.6qB\mu}{k_{sp} r_{sp}} s, \dots \dots \dots (8.31)$$

$$\text{where } k_{sp} = (k_r k_z^{1/2})^{2/3}, \dots \dots \dots (8.32)$$

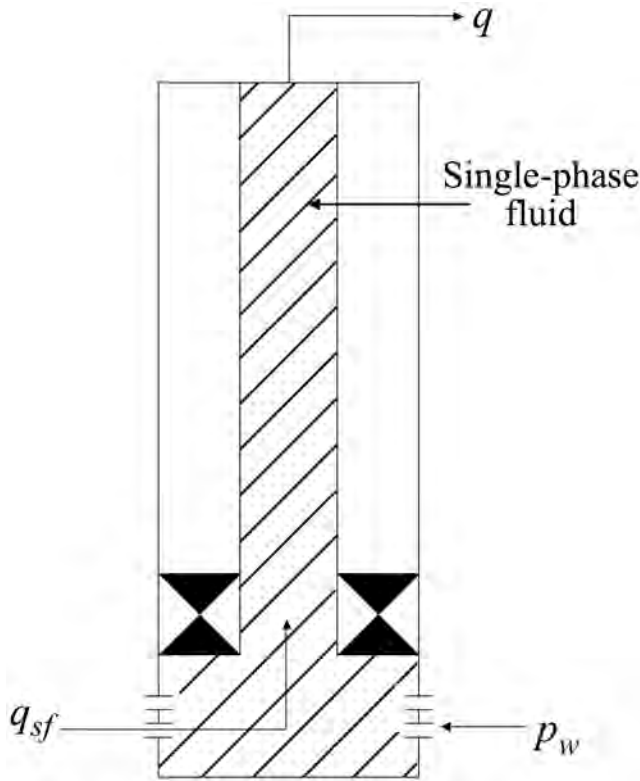


Fig. 8.9—Schematic of wellbore containing single-phase liquid or gas.

and r_{sp} = the radius of the sphere into which flow converges.

8.2.14 Superposition. The principle of superposition indicates that the total pressure at any point in a reservoir is the sum of the pressure drops at that point caused by flow in each of the wells in the reservoir. A simple illustration of this principle is the case of three wells in an infinite reservoir. Consider wells A, B, and C, that start to produce at times t_A , t_B , and t_C in an infinite-acting reservoir (Fig. 8.12). Application of the principle of superposition shows that⁴

$$(p_i - p_{wf})_{\text{total at Well A}} = (p_i - p)_{\text{due to A}} + (p_i - p)_{\text{due to B}} + (p_i - p)_{\text{due to C}} \cdot \dots \quad (8.33)$$

For an infinite-acting reservoir, use the Ei -function solutions, including the logarithmic approximation at Well A:

$$\begin{aligned} & (p_i - p_{wf})_{\text{total at Well A}} \\ &= -70.6 \frac{q_A B \mu}{kh} \left[\ln \left(\frac{1,688 \phi \mu c_t r_{wA}^2}{k(t - t_A)} \right) - 2s_A \right] \\ & \quad -70.6 \frac{q_B B \mu}{kh} Ei \left(\frac{-948 \phi \mu c_t r_{AB}^2}{k(t - t_B)} \right) \end{aligned}$$

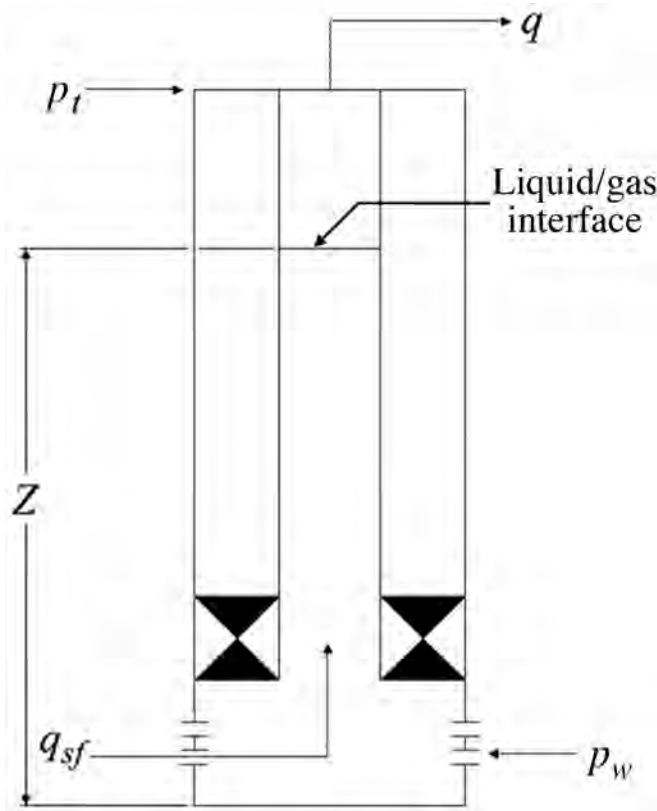


Fig. 8.10—Schematic of wellbore with moving liquid/gas interface.

$$-70.6 \frac{q_C B \mu}{kh} Ei \left(\frac{-948 \phi \mu c_t r_{AC}^2}{k(t-t_C)} \right), \dots\dots\dots (8.34)$$

where t_A , t_B , and t_C are times at which wells A, B, and C will begin to produce. The skin factor for Well A is included in Eq. 8.29. The skin factors for other wells are not, because skin factors for individual wells affect only pressures measured inside altered zones for those wells.

Next, consider the use of superposition to model the effects of boundaries in bounded reservoirs. Consider the well in Fig. 8.13, a distance L from a single no-flow boundary (such as a sealing fault). Mathematically, this problem is identical to the problem of a well at distance $2L$ from an “image” well; that is, a well that has the same production history as the actual well. The reason that the two-well system simulates the behavior of a well near a boundary is that a line equidistant between the two wells can be shown to be a no-flow boundary. That is, along this line the pressure gradient is zero, which means that there can be no flow. Thus, this problem is a simple problem of two wells in an infinite reservoir:

$$p_i - p_{wf} = -70.6 \frac{q B \mu}{kh} \left(\ln \frac{1,688 \phi \mu c_t r_w^2}{kt} - 2s \right) - 70.6 \frac{q B \mu}{kh} Ei \left(\frac{-948 \phi \mu c_t (2L)^2}{kt} \right). \dots\dots\dots (8.35)$$

The drawdown term of the image well does not include a skin factor.

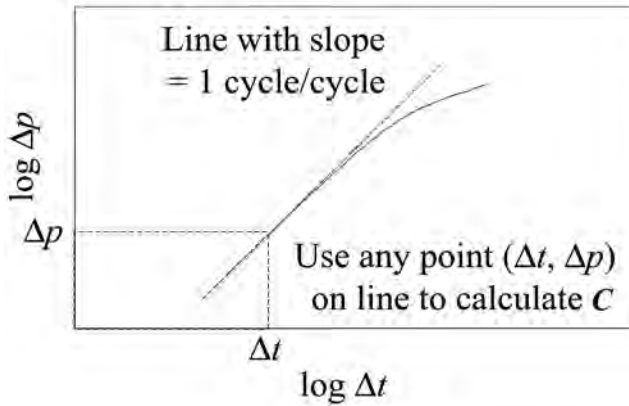


Fig. 8.11—Unit slope line on a log-log plot of Δp vs. Δt .

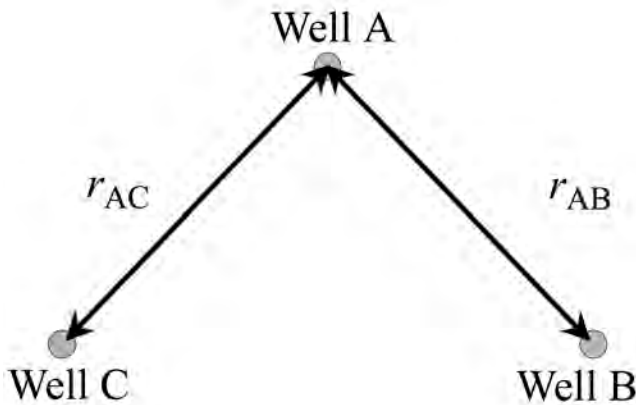


Fig. 8.12—Multiple-well system in infinite reservoir.

As examples, extend the imaging technique to model wells between boundaries intersecting at 90° (Fig. 8.14); wells between two parallel boundaries (Fig. 8.15); wells near single constant-pressure boundaries (Fig. 8.16); and wells at various locations in closed reservoirs (Fig. 8.17).

One of the most frequently used applications of superposition is to model variable-rate production. Consider Fig. 8.18, in which a well in an infinite-acting reservoir produces at rate q_1 from time 0 to time t_1 ; q_2 from t_1 to t_2 , and q_3 for times greater than t_2 . To model the total drawdown for $t > t_2$, add three drawdowns: the drawdown because of a well producing at rate q_1 starting at time zero and continuing to produce to time t ; the drawdown because of a well producing at rate $(q_2 - q_1)$, starting at time t_1 and continuing to time t ; and the drawdown because of a well producing at rate $(q_3 - q_2)$ starting at time t_2 and continuing to time t . The total drawdown is thus

$$p_i - p_{wf} = (\Delta p)_1 + (\Delta p)_2 + (\Delta p)_3 = -70.6 \frac{\mu q_1 B}{kh} \left[\ln \left(\frac{1,688 \phi \mu c_t r_w^2}{kt} \right) - 2s \right]$$

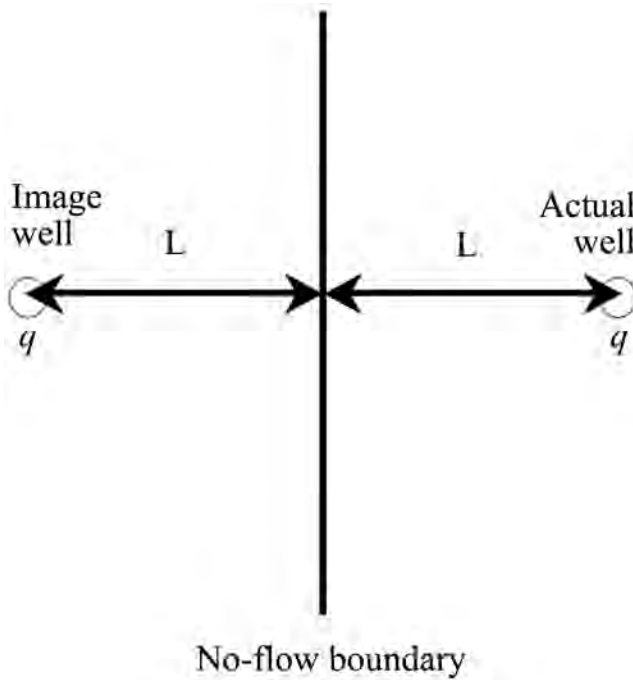


Fig. 8.13—Well near no-flow boundary illustrating use of imaging.

$$\begin{aligned}
 & -70.6 \frac{\mu(q_2 - q_1)B}{kh} \cdot \left\{ \ln \left[\frac{1,688\phi\mu c_t r_w^2}{k(t - t_1)} \right] - 2s \right\} \\
 & -70.6 \frac{\mu(q_3 - q_2)B}{kh} \cdot \left\{ \ln \left[\frac{1,688\phi\mu c_t r_w^2}{k(t - t_2)} \right] - 2s \right\} \dots\dots\dots (8.36)
 \end{aligned}$$

Horner⁶ proposed a convenient alternative to superposition to model the many changes in rate in the history of a typical well. With this approximation, the sequence of *Ei* functions reflecting rate changes can be replaced with a single *Ei* function that contains a single producing time and a single producing rate. The single rate is the most recent nonzero rate at which the well has produced, q_n . The single producing time, called t_p , is the ratio of cumulative production, N_p , to q_n .

$$t_p = \frac{N_p}{q_n} \dots\dots\dots (8.37)$$

This approximation preserves the material balance in the drainage area of the well and properly gives greatest weight to most recent rate (as opposed to average rate), which dominates the pressure distribution near a well out to the radius of investigation achieved while the well was produced at rate q_n . The approximation is particularly useful for hand calculations. Given the widespread availability of computer software for analyzing flow and buildup tests on well, the use of more rigorous superposition to model variable-rate production histories is generally more appropriate.

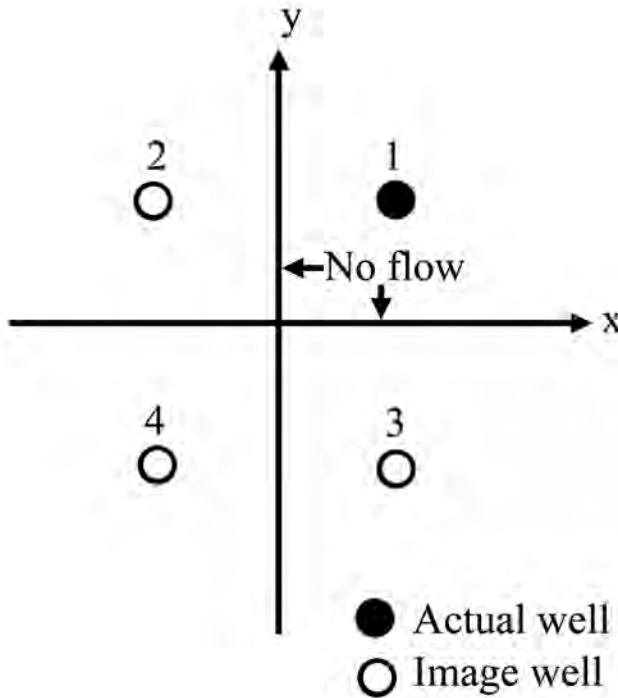


Fig. 8.14—Image-well locations for two intersecting no-flow boundaries.

8.2.15 Semilog Methods for Flow Tests. The logarithmic approximation to the *Ei*-function solution can be used as a basis for analysis of an ideal constant-rate flow test in a well. Written in terms of \log_{10} , this equation, which models the BHP for a well in a homogeneous-acting formation with an infinite-acting drainage area and, in absence of wellbore unloading, becomes

$$p_{wf} = p_i - 162.6 \frac{qB\mu}{kh} \left[\log_{10}(t) + \log_{10} \left(\frac{k}{\phi \mu c_t r_w^2} \right) - 3.23 + 0.869s \right] \dots (8.38)$$

This expression has the same form as the equation of a straight line, $y = mx + b$, with the analogies

$$p_{wf} \sim y, \dots (8.39)$$

$$\log_{10}(t) \sim x, \dots (8.40)$$

$$-162.6qB\mu / kh \sim m, \dots (8.41)$$

$$\text{and } p_i - m \left[\log_{10} \left(\frac{k}{\phi \mu c_t r_w^2} \right) - 3.23 + 0.869s \right] \sim b \dots (8.42)$$

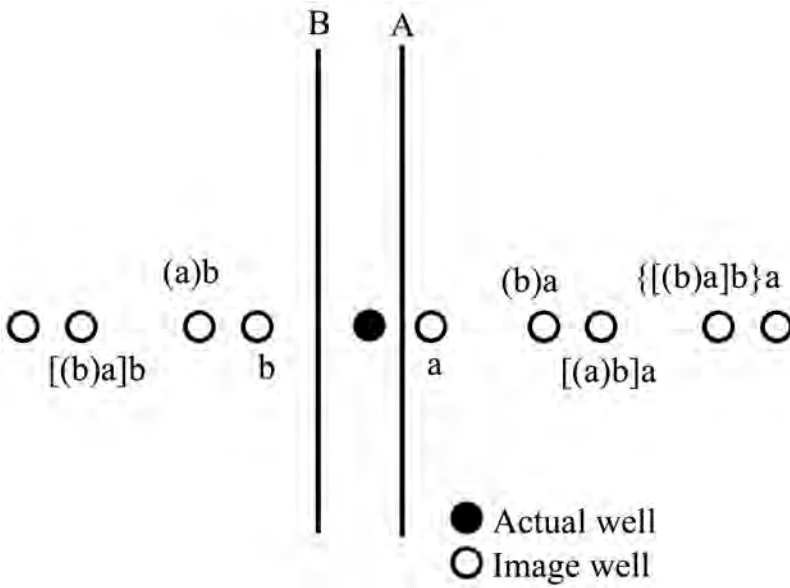


Fig. 8.15—Image-well locations for well between parallel faults.

These analogies suggest a graphical method of analysis. Eq. 8.38 indicates that a plot of p_{wf} vs. $\log_{10}(t)$ should be a straight line with slope m that will allow an estimate of effective permeability to the single liquid phase flowing. (See Fig. 8.19.)

$$k = \frac{162.6qB\mu}{(-m)h} \dots\dots\dots (8.43)$$

From the intercept, b , at $t = 1$ hr [$\log_{10}(1) = 0$], p_{1hr} , calculate the skin factor.

$$s = 1.151 \left[\frac{p_i - p_{1hr}}{-m} - \log_{10} \left(\frac{k}{\phi \mu c_t r_w^2} \right) + 3.23 \right] \dots\dots\dots (8.44)$$

In these equations, the slope, m , is given by

$$m = \frac{(p_{wf2} - p_{wf1})}{[\log_{10}(t_2) - \log_{10}(t_1)]} = \frac{(p_{wf2} - p_{wf1})}{[\log_{10}(t_2/t_1)]} \dots\dots\dots (8.45)$$

Eq. 8.45 indicates that m is most easily determined by choosing values of times t_1 and t_2 that differ by powers of 10 and is especially easy if t_1 and t_2 differ by one log cycle. The intercept, p_{1hr} , is the pressure at a time of 1 hour on the best straight line through the data. It may be necessary to extrapolate the straight line to a time of one hour to read the intercept.

8.2.16 Semilog Methods for Pressure Buildup Test. Consider the rate history for an idealized pressure test shown in Fig. 8.20. A well is produced at constant rate q for a time t_p , and then the well shut in ($q = 0$) for a pressure buildup test. The rate history is modeled as the sum of two constant flow rate periods, one at rate q , beginning at $t = 0$, and the other at rate $-q$,

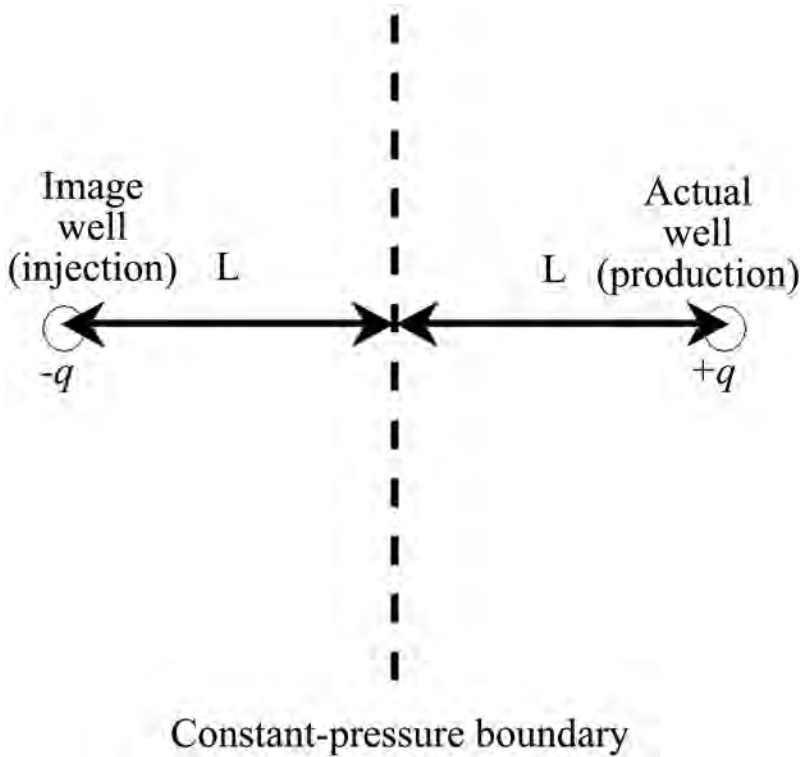


Fig. 8.16—Well near single constant-pressure boundary.

beginning at $t = t_p$, at which the time elapsed since shut-in, Δt , is zero. Use the log approximation to the *Ei*-function solution to model the drawdown, and sum them as Fig. 8.21 shows. Represented mathematically, the superposition process is

$$\begin{aligned}
 p_{ws} = p_i - 162.6 \frac{qB\mu}{kh} & \left[\log_{10}(t_p + \Delta t) + \log_{10} \left(\frac{k}{\phi \mu c_t r_w^2} \right) - 3.23 + 0.869s \right] \\
 - 162.6 \frac{(-q)B\mu}{kh} & \left[\log_{10}(\Delta t) + \log_{10} \left(\frac{k}{\phi \mu c_t r_w^2} \right) - 3.23 + 0.869s \right] \dots \dots \dots (8.46)
 \end{aligned}$$

This can be simplified to

$$p_{ws} = p_i - 162.6 \frac{qB\mu}{kh} \log_{10} \left(\frac{t_p + \Delta t}{\Delta t} \right) \dots \dots \dots (8.47)$$

Like the drawdown equation, Eq. 8.43 can be interpreted as the equation of a straight line. The analogies are

$$p_{ws} \sim y, \dots \dots \dots (8.48)$$

$$\log_{10}(t) \sim x, \dots \dots \dots (8.49)$$

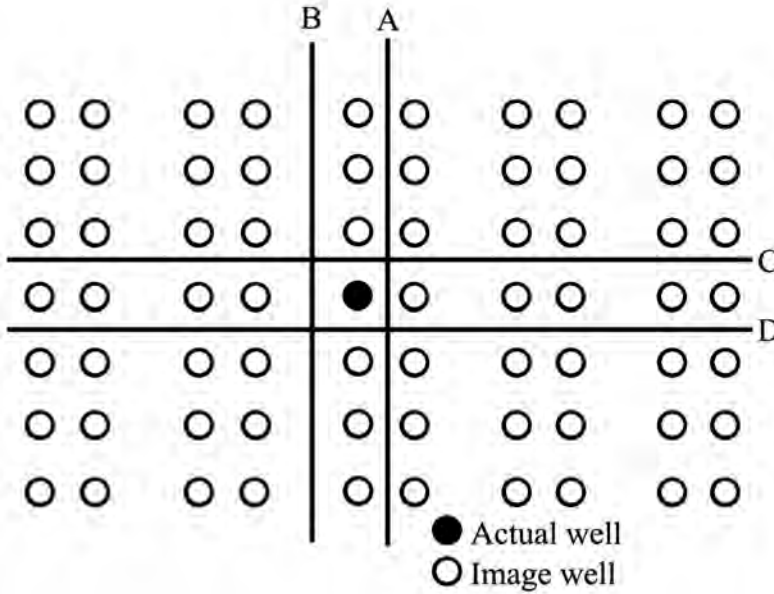


Fig. 8.17—Image-well locations for well between parallel boundaries.

$$-162.6qB\mu/kh \sim m, \dots\dots\dots (8.41)$$

$$\text{and } p_i \sim b . \dots\dots\dots (8.50)$$

The group $[(t_p + \Delta t)/\Delta t]$ is called the Horner time ratio (HTR) or sometimes simply the Horner time. Our simple model, which describes a buildup test in a homogeneous, infinite-acting reservoir, a well with one constant rate before shut in and without afterflow (wellbore storage), indicates that a graph of p_{ws} vs. the HTR should fall on a straight line. From the slope, m , of this line, the permeability to the single-phase liquid flowing into the wellbore can be estimated. The intercept, b , at $\log_{10}[(t_p + \Delta t)/\Delta t] = 0$ or $[(t_p + \Delta t)/\Delta t] = 1$ provides an estimate of original drainage area pressure, p_i .

Obtain the slope, m , from

$$\frac{P_{ws2} - P_{ws1}}{\log_{10}\left(\frac{t_p + \Delta t}{\Delta t}\right)_2 - \log_{10}\left(\frac{t_p + \Delta t}{\Delta t}\right)_1}, \dots\dots\dots (8.51)$$

where $\{[(t_p + \Delta t)/\Delta t]_1, p_{ws1}\}$ and $\{[(t_p + \Delta t)/\Delta t]_2, p_{ws2}\}$ are any two points on the straight-line (Fig. 8.22). Normally, choose $[(t_p + \Delta t)/\Delta t]_1$ and $[(t_p + \Delta t)/\Delta t]_2$ to be powers of 10.

In Fig. 8.22, which is called a Horner plot, the HTR on the horizontal axis decreases from left to right, so that shut-in time increases from left to right. In some Horner plots, the HTR increases from left to right; in that case shut-in time increases from right to left.

Skin factor can be estimated from a pressure buildup test, even though the skin factor does not appear in the buildup equation, Eq. 8.47. Simultaneously solve the equation modeling the drawdown at the instant of shut in (at time t_p) with Eq. 8.47, discard terms that are ordinarily negligible, and arrive at the result

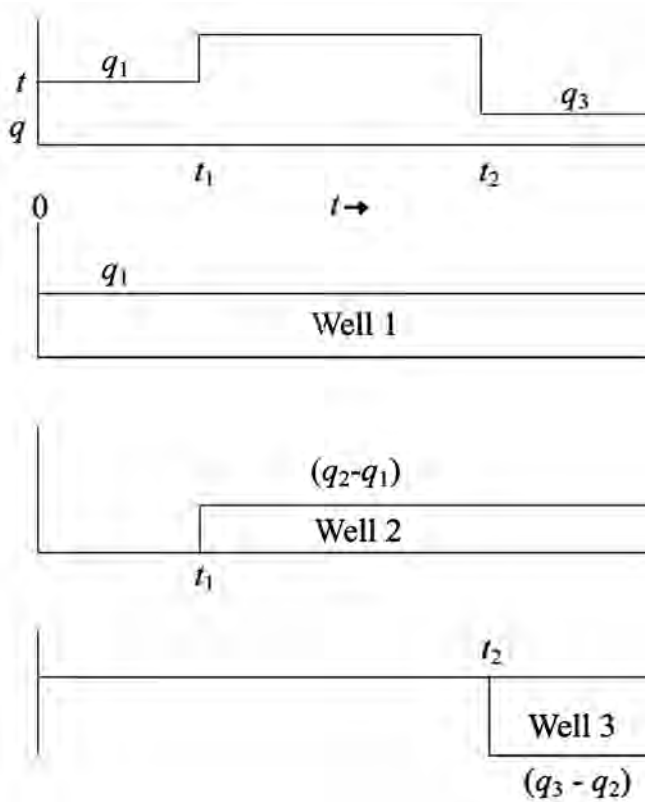


Fig. 8.18—Production schedule for variable-rate well.

$$s = 1.151 \left[\frac{p_{1hr} - p_{wf}}{-m} - \log_{10} \left(\frac{k}{\phi \mu c_t r_w^2} \right) + 3.23 \right] \dots \dots \dots (8.52)$$

The radius-of-investigation concept is also useful for pressure buildup tests, as Fig. 8.23 illustrates. The approximate position of the point at which the pressure has built up to a uniform level intersects the region in which the pressure is little affected by the shut-in is given by Eq. 8.11, with elapsed time, *t*, interpreted as shut-in time, Δ*t*.

8.3 Type Curves

Type curves provide a powerful method for analyzing pressure drawdown (flow) and buildup tests. Fundamentally, type curves are preplotted solutions to the flow equations, such as the diffusivity equation, for selected types of formations and selected initial and boundary conditions. Because of the way they are plotted (usually on logarithmic coordinates), it is convenient to compare actual field data plotted on the same coordinates to the type curves. The results of this comparison frequently include qualitative and quantitative descriptions of the formation and completion properties of the tested well.

8.3.1 Dimensionless Variables. The solutions plotted on type curves are usually presented in terms of dimensionless variables. To review dimensionless variables, consider the *Ei*-function solution to the flow equation, Eq. 8.2, presented in terms of dimensional variables:

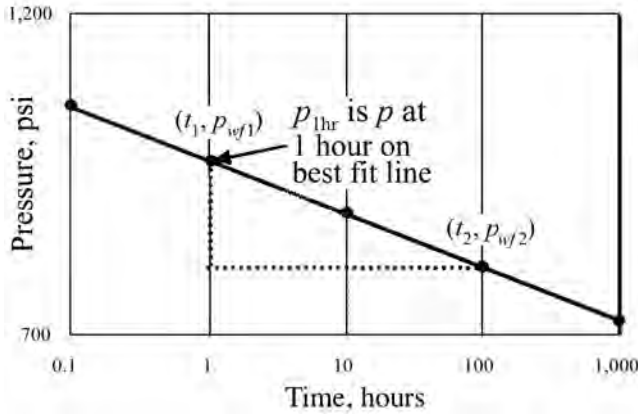


Fig. 8.19—Straight line with slope m allows us to estimate effective permeability to the single liquid phase flowing.

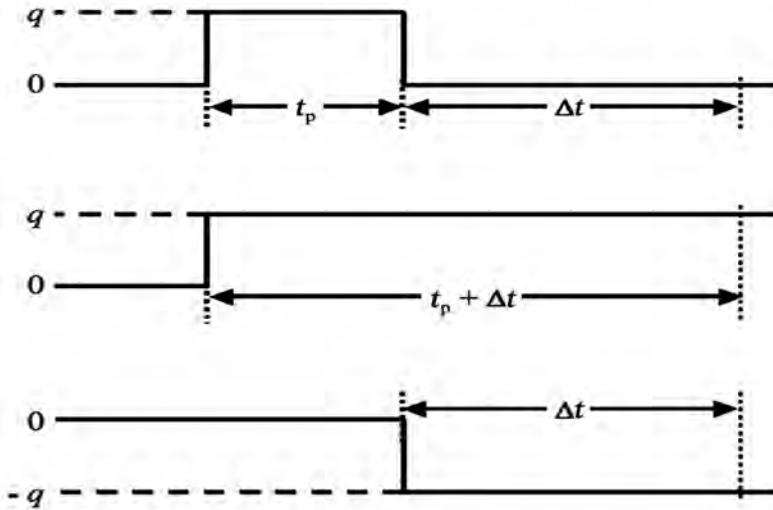


Fig. 8.20—Rate history for an idealized pressure buildup test.

$$p = p_i + 70.6 \frac{qB\mu}{kh} Ei \left(\frac{-948\phi\mu c_i r^2}{kt} \right) \dots\dots\dots (8.2)$$

Eq. 8.2 can be rewritten in terms of conventional definitions of dimensionless variables. (Variables that when the parameters are expressed in terms of the fundamental units of mass, length, and time, have no dimensions are sometimes said to have dimensions of zero.)

$$p_D = -\frac{1}{2} Ei \left(-\frac{r_D^2}{4t_D} \right) \dots\dots\dots (8.53)$$

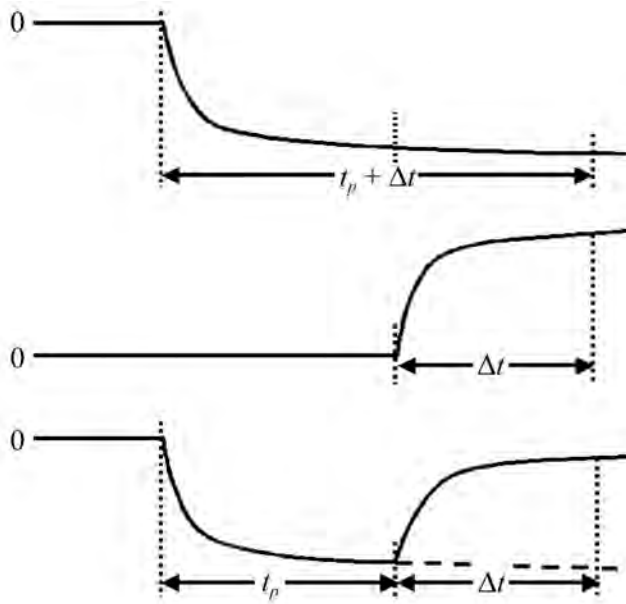


Fig. 8.21—Sum of *Ei*-function solutions to model pressure buildup test.

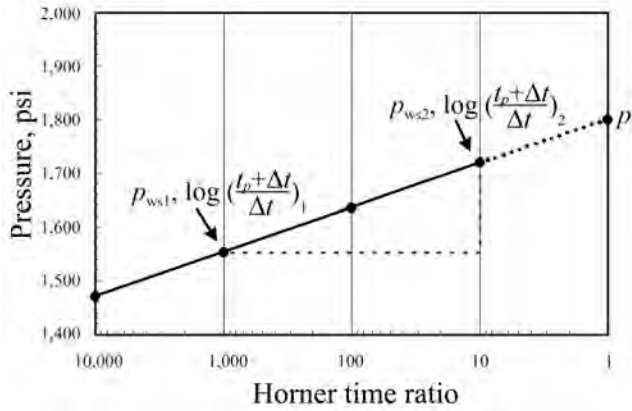


Fig. 8.22—Horner plot.

In Eq. 8.53, the definitions of the dimensionless variables are

$$p_D \equiv \frac{kh(p_i - p)}{141.2qB\mu}, \dots\dots\dots (8.54)$$

$$t_D \equiv \frac{0.0002637kt}{\phi\mu c_t r_w^2}, \dots\dots\dots (8.55)$$

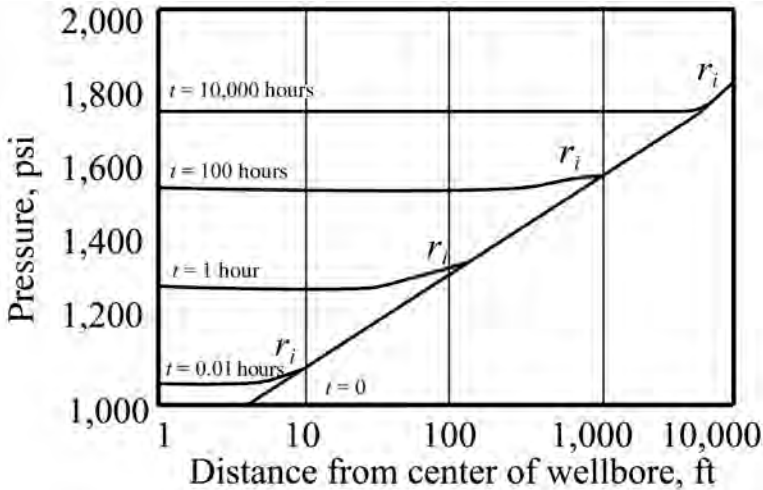


Fig. 8.23—Radius of investigation in pressure buildup tests.

$$\text{and } r_D \equiv \frac{r}{r_w} \dots\dots\dots (8.56)$$

The dimensionless form of Eq. 8.2 has the advantage that this solution, p_D , to the diffusivity equation can be expressed in terms of a single variable, t_D , and single parameter, r_D . This leads to much simpler graphical or tabular presentation of the solution than would direct use of Eq. 8.2. Solutions to the diffusivity equation for more realistic reservoir models also include the dimensionless skin factor, s , and wellbore storage coefficient, C_D , where

$$C_D = \frac{0.8936C}{\phi c_t h r_w^2} \dots\dots\dots (8.57)$$

8.3.2 Gringarten Type Curve. Gringarten *et al.*⁷ presented a type curve, commonly called the Gringarten type curve, that achieved widespread use. It is based on a solution to the radial diffusivity equation and the following assumptions: vertical well with constant production rate; infinite-acting, homogeneous-acting reservoir; single-phase, slightly compressible liquid flowing; infinitesimal skin factor (thin “membrane” at production face); and constant wellbore-storage coefficient. These assumptions indicate that the type curve was developed specifically for drawdown tests in undersaturated oil reservoirs. The type curve is also useful to analyze pressure buildup tests and for gas wells.

In the Gringarten type curve, p_D is plotted vs. the time function t_D/C_D , with a parameter $C_D e^{2s}$ (Fig. 8.24). Each different value of $C_D e^{2s}$ describes a pressure response with a shape different (in theory) from the responses for other values of the parameter. However, adjacent pairs of curves can be quite similar, and this fact can cause uncertainty when trying to match test data to the “uniquely correct” curve.

8.3.3 Derivative Type Curve. The derivative type curve proposed by Bourdet *et al.*⁸ eliminates the ambiguity in the Gringarten type curve. The “derivative” referred to in this type curve is the logarithmic derivative of the solution to the radial diffusivity equation presented on the Gringarten type curve. Two limiting forms of this solution help illustrate the nature of

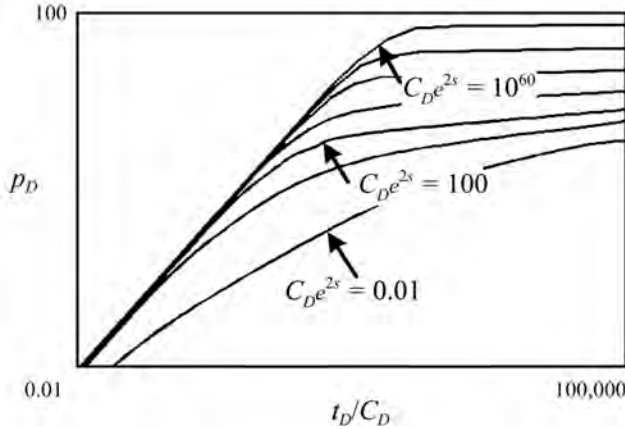


Fig. 8.24—Gringarten type curve with parameter $C_D e^{2s}$.

the derivative type curve. First, consider that part of a test response where the distorting effects of wellbore storage have vanished. This portion of the test is described by the logarithmic approximation to *Ei*-function solution, Eq. 8.9:

$$p_i - p_{wf} = -70.6 \frac{qB\mu}{kh} \left[\ln \left(\frac{1688\phi\mu c_t r_w^2}{kt} \right) - 2s \right] \dots\dots\dots (8.9)$$

The derivative of $(p_i - p_{wf})$ with respect to $\ln(t)$, expressed more simply as $t\partial\Delta p/\partial t$, is $70.6qB\mu/kh$, a constant. In terms of dimensionless variables, $t_D(\partial p_D/\partial t_D) = 0.5$. Thus, when the distorting effects of wellbore storage have disappeared, the pressure derivative will become constant in an infinite-acting reservoir, and, in terms of dimensionless variables, will have a value of 0.5.

When wellbore storage completely dominates the pressure response (all produced fluid comes from the wellbore, none from the formation),

$$\Delta p = \frac{qB\Delta t}{24C} \dots\dots\dots (8.29)$$

The derivative, $t\partial\Delta p/\partial t$, is $qBt/24C$, the same as the pressure change itself. In terms of dimensionless variables, the derivative becomes

$$p'_D = t_D(\partial p_D/\partial t_D) = t_D/C_D \dots\dots\dots (8.58)$$

The implication of Eq. 8.58 is that, on logarithmic coordinates, graphs of p_D and $t_D(\partial p_D/\partial t_D)$ vs. t_D/C_D will coincide and will have slopes of unity.

For values of $t_D(\partial p_D/\partial t_D)$ between the end of complete wellbore storage distortion and the start of infinite-acting radial flow, no simple solutions are available to guide us, but Fig. 8.25 shows the derivatives, including those times. Note the unit slope lines at earliest times and the horizontal derivative at later times. The shapes of the derivative stems are much more distinctive than those for the pressure-change type curve.

For test analysis, we plot pressure change, p_D , and pressure derivative $[t_D(\partial p_D/\partial t_D)]$ on the same graph (Fig. 8.26). On this graph, a specific value of the parameter $C_D e^{2s}$ refers to a pair

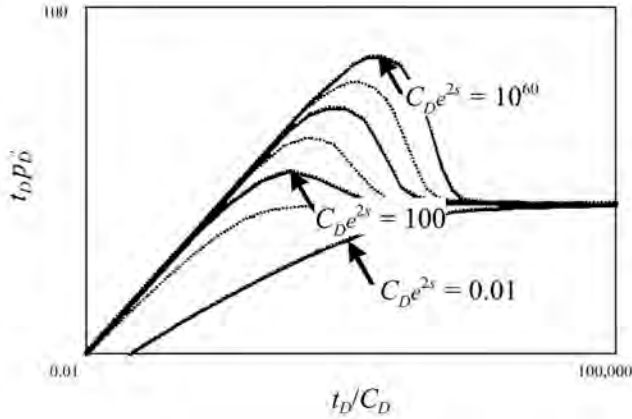


Fig. 8.25—Bourdet's derivative type curves.

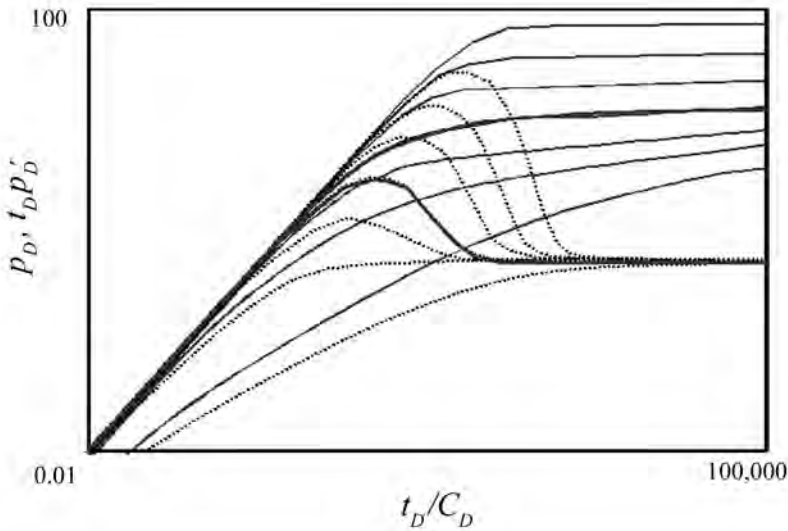


Fig. 8.26—Combined pressure change, pressure derivative curves.

of curves—one pressure-change curve and one pressure-derivative curve. Time regions can be defined conveniently on the basis of the combined pressure (Fig. 8.27) and pressure derivative type curves.

The shape of the pressure- and pressure-derivative type curves provides a qualitative estimate of skin factor (Fig. 8.28). For a well with a large skin factor, the derivative rises to a maximum and then falls sharply before flattening out for the middle-time region (MTR). The pressure change curve rises along the unit-slope line and then flattens quickly. The pressure-change and pressure-derivative curves are separated by approximately two log cycles when wellbore storage (WBS) ends.

When the skin is near zero, the pressure derivative rises to a maximum and then falls only slightly before flattening for the MTR. The pressure change and pressure derivative are separated by approximately one log cycle when WBS ends. When the skin factor is negative, the pressure derivative approaches a horizontal line from below. The pressure change and pressure

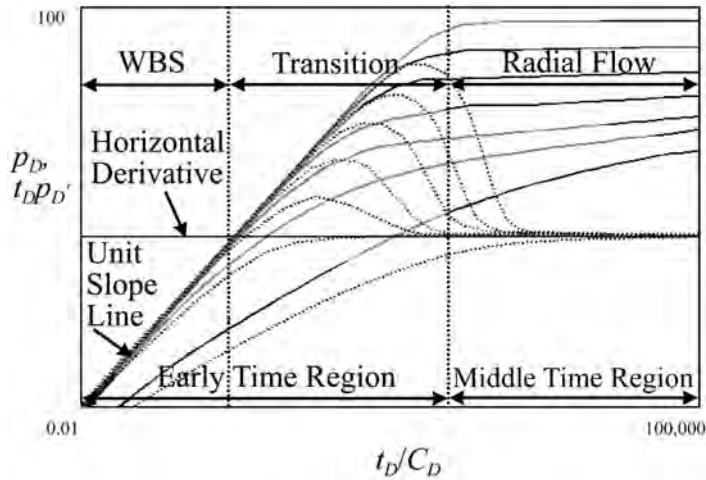


Fig. 8.27—Combined pressure-change/pressure-derivative type curves define time regions conveniently.

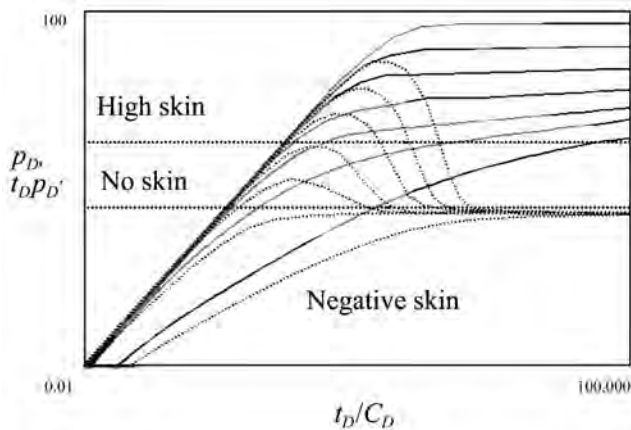


Fig. 8.28—Shape of the type curves provides a qualitative estimate of skin factor.

derivative curves leave the unit slope line at relatively early times and take a relatively long time to reach the MTR.

8.3.4 Differences in Drawdown and Buildup Test Type Curves. The shapes of drawdown and buildup type curves are different, as Fig. 8.29 illustrates. In this simplified case, in which wellbore storage distortion is absent, a well has produced for a dimensionless producing time, t_{pD} , of 10^5 , before shut-in. In the figure, note that, on a plot of p_D and p_D' (the derivative) vs. t_D (dimensionless time since each test began), the shapes of the buildup and drawdown curves for infinite-acting radial flow coincide up to $t_D = 10^4$ and then begin to deviate. The buildup pressure-change curve is “flatter” than the drawdown curve at later times in an infinite-acting reservoir, and thus the slope of the buildup curve (the derivative) tends to deviate from the drawdown derivative. For many years, test analysts used a rule of thumb that buildup tests could be analyzed on a drawdown type curve only up to a maximum time of one-tenth the producing time before shut-in. That rule of thumb is appropriate for the conditions in Fig. 8.29.

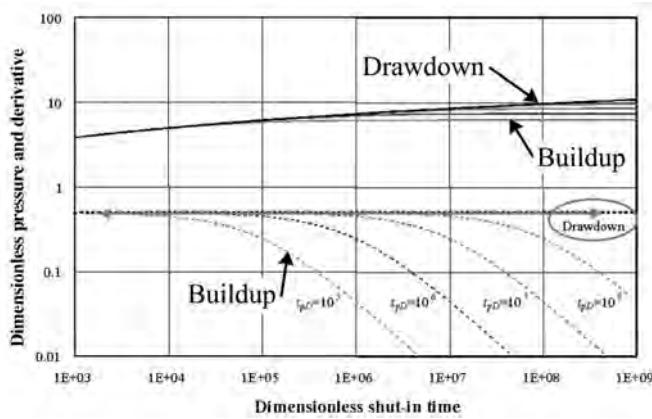


Fig. 8.29—Buildup and drawdown type curves have different shapes.

8.3.5 Equivalent Drawdown Time. Agarwal⁹ suggested a method of plotting pressure change data from a buildup test on a logarithmic graph that alters the shape so that it corresponds to that of a constant rate flow test during infinite-acting radial flow. The basis for Agarwal’s “equivalent time” is a combination of logarithmic approximations to *Ei*-function solutions to the diffusivity equation. The equation modeling the drawdown at the instant of shut-in is

$$p_i - p_{wf} = 162.6 \frac{qB\mu}{kh} \left[\log_{10}(t_p) + \log \left(\frac{k}{\phi \mu c_t r_w^2} \right) - 3.23 + 0.869s \right] \dots\dots\dots (8.59)$$

We model a buildup test with

$$p_i - p_{wf} = 162.6 \frac{qB\mu}{kh} \left[\log_{10}(t_p + \Delta t) + \log \left(\frac{k}{\phi \mu c_t r_w^2} \right) - 3.23 + 0.869s \right] - 162.6 \frac{qB\mu}{kh} \left[\log_{10}(\Delta t) + \log \left(\frac{k}{\phi \mu c_t r_w^2} \right) - 3.23 + 0.869s \right] \dots\dots\dots (8.60)$$

Combining Eqs. 8.59 and 8.60 and simplifying,

$$p_i - p_{wf} = + 162.6 \frac{qB\mu}{kh} \left[\log_{10}(t_p) + \log \left(\frac{k}{\phi \mu c_t r_w^2} \right) - 3.23 + 0.869s \right] - 162.6 \frac{qB\mu}{kh} \left[\log_{10}(t_p + \Delta t) + \log \left(\frac{k}{\phi \mu c_t r_w^2} \right) - 3.23 + 0.869s \right] + 162.6 \frac{qB\mu}{kh} \left[\log_{10}(\Delta t) + \log \left(\frac{k}{\phi \mu c_t r_w^2} \right) - 3.23 + 0.869s \right], \dots\dots\dots (8.61)$$

which can be rewritten as

$$p_{ws} - p_{wf} = 162.6 \frac{qB\mu}{kh} \left[\log_{10} \left(\frac{t_p \Delta t}{t_p + \Delta t} \right) + \log \left(\frac{k}{\phi \mu c_t r_w^2} \right) - 3.23 + 0.869s \right] \dots\dots\dots (8.62)$$

The forms of Eqs. 8.62 and 8.59 are the same; thus Eq. 8.62 is an “equivalent” drawdown equation, with the equivalent pressure change, $(p_{ws} - p_{wf})$, a function of equivalent time, $\Delta t_e = t_p \Delta t / (t_p + \Delta t)$. The analogies between these equations suggest that, just as $\Delta p = p_i - p_{wf}$ vs. t were plotted for drawdown tests, $\Delta p = p_{ws} - p_{wf}$ vs. Δt_e can be plotted for buildup tests and achieve the same shapes on logarithmic graphs. However, the theoretical basis for this radial-equivalent time indicates that the equivalence exists only for infinite-acting radial flow and not for data influenced by wellbore storage or by effects of boundaries or other conditions that cause the flow pattern to deviate from radial. In practice, buildup test data for infinite-acting radial flow, including data distorted by wellbore storage, are transformed to the same shape as drawdown test data. However, data affected by boundaries or by linear flow (as in wells with hydraulic fractures) may not be transformed accurately.

Radial equivalent time has the properties

$$\begin{aligned} \Delta t_e &= \frac{t_p \Delta t}{t_p + \Delta t} \\ &= \frac{t_p}{t_p + \Delta t} \Delta t \approx \Delta t, \Delta t \ll t_p \\ &= \frac{\Delta t}{t_p + \Delta t} t_p \approx t_p, \Delta t \gg t_p \dots\dots\dots (8.63) \end{aligned}$$

8.3.6 Type-Curve Matching. The steps in type-curve matching for wells with infinite-acting radial flow are outlined here. Details vary for more complex reservoirs, but the general procedure is similar to that for infinite-acting reservoirs.

- Plot field data on log-log coordinates with the same size log cycles as the type curve.
- Align the horizontal sections of the field data and the type curve.
- Align unit slope regions on the field data and the type curve.
- Select the value of $C_D e^{2s}$ that best matches the field data.
- Select pressure and time match points (corresponding values of real and dimensionless variables from field data and type curve plots) from anywhere on the plot.
- Calculate permeability from the pressure match-point ratio,

$$(\Delta p / \Delta p_D)_{MP} = kh / 141.2qB\mu, \dots\dots\dots (8.64)$$

$$\text{or } k = 141.2(qB\mu / h)(\Delta p / \Delta p_D)_{MP} \dots\dots\dots (8.65)$$

- Calculate C_D from the time match-point ratio,

$$\left[t / (t_D / C_D) \right]_{MP} = (\phi \mu c_t r_w^2 / 0.0002637k) C_D, \dots\dots\dots (8.66)$$

$$\text{or } C_D = (0.0002637k / \phi \mu c_t r_w^2) \left[t / (t_D / C_D) \right]_{MP} \dots\dots\dots (8.67)$$

- Calculate s from the matching stem value, $C_D e^{2s}$:

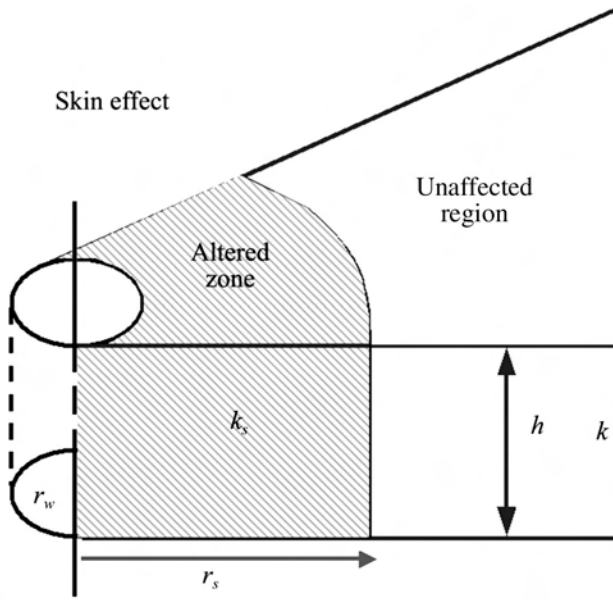


Fig. 8.31—Two-region reservoir model with altered zone around wellbore and unaltered formation permeability beyond.

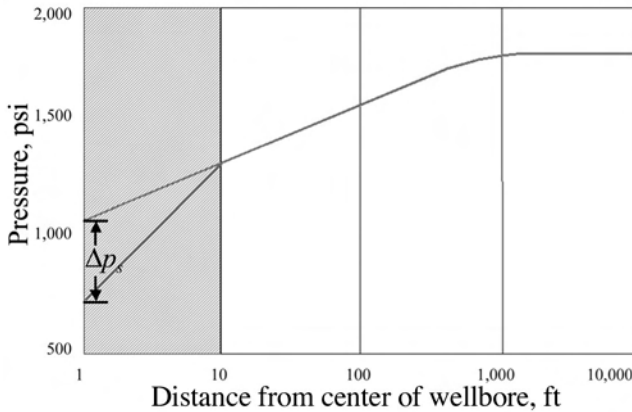


Fig. 8.32—Additional pressure drop in damaged well is caused by reduced permeability in altered zone.

For a damaged well, the reduced permeability in the altered zone causes an additional pressure drop, Δp_s (Fig. 8.32). The dimensionless skin factor, s , and the additional pressure drop across the altered zone are related by

$$\Delta p_s = \frac{141.2qB\mu}{kh} s \dots\dots\dots (8.69)$$

For a well with a known skin factor, s , Eq. 8.69 provides a method of translating the somewhat abstract dimensionless skin factor into a more concrete characterization of the practical effect of damage or stimulation.

In a two-region reservoir model, the skin factor, s , is related to the properties of the altered zone:

$$s = \left(\frac{k}{k_s} - 1 \right) \ln \left(\frac{r_s}{r_w} \right) \dots\dots\dots (8.70)$$

Rearrange Eq. 8.70 and solve for the permeability of the altered zone:

$$k_s = \frac{k}{1 + \frac{s}{\ln(r_s/r_w)}} \dots\dots\dots (8.71)$$

Rearrangements of Eq. 8.70 provide a second method of translating skin into a more concrete characterization of a well with altered permeability near the wellbore. If the depth of damage can be estimated for a well with a known skin factor, s , the permeability of the altered zone can be estimated. Even if the depth of permeability alteration, r_s , is estimated Eq. 8.71 can still provide a reasonable estimate of altered zone permeability because r_s appears in a logarithmic term. Alternatively, an estimate of the permeability reduction ratio (for example, from laboratory tests on cores) can produce an estimate of the depth of damage from another rearrangement of Eq. 8.70,

$$r_s = r_w \exp \left[s k_s / (k - k_s) \right] \dots\dots\dots (8.72)$$

8.4.3 Apparent Wellbore Radius. A third method of translating skin to a more concrete characterization of near-well conditions is to calculate apparent or effective wellbore radius, r_{wa} . Apparent wellbore radius is defined as

$$r_{wa} = r_w e^{-s} \dots\dots\dots (8.73)$$

$$\text{or } s = - \ln (r_{wa} / r_w) \dots\dots\dots (8.74)$$

For a stimulated well, the pressure drawdown at the wellbore is the same as it would be in a formation with unaltered permeability but with wellbore radius equal to the apparent wellbore radius. This concept has value in some simulation applications. Note that r_{wa} can be calculated from the actual wellbore radius and skin factor.

Eqs. 8.73 and 8.74 are also useful to illustrate the minimum (i.e., the most-negative possible) skin factor. This minimum skin, s_{\min} , occurs when the apparent wellbore radius is equal to the drainage radius of the well:

$$s_{\min} = - \ln (r_e / r_w) \dots\dots\dots (8.75)$$

For a well with a circular drainage area of 40 acres for which r_e is 745 ft and a wellbore radius of 0.3 ft, the minimum skin (maximum stimulation) is $s_{\min} = - \ln (r_e / r_w) = -(745/0.3) = -7.82$. Such a skin implies increasing the permeability throughout the entire altered zone to infinity—clearly an idealistic “upper limit.” More realistically, research¹⁰ has shown that the half-length, L_f , of a highly conductive vertical fracture is related to r_{wa} by

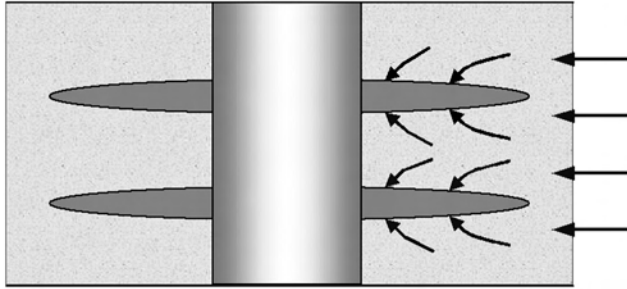


Fig. 8.33—When perforation spacing is large, converging flow results in positive skin factor.

$$r_{wa} = \frac{L_f}{2} = r_w e^{-s}, \dots\dots\dots (8.76)$$

$$\text{or } s = - \ln \left(\frac{L_f}{2r_w} \right) \dots\dots\dots (8.77)$$

Thus, for $L_f = r_e = 745$ ft, $s = -7.12$ is a more realistic minimum (for the given drainage radius and wellbore radius).

8.4.4 Flow Efficiency. A fourth way to characterize a well with nonzero skin is to calculate the flow efficiency of the well. Flow efficiency, E_f , is defined as the ratio of the actual productivity index of the well (including skin) to the ideal productivity index if the skin factor were zero. Because the productivity index is the ratio of stabilized flow rate to pressure drop required to sustain that stabilized rate,

$$J_{\text{actual}} = \frac{q}{(\bar{p} - p_{wf})}, \dots\dots\dots (8.78)$$

$$J_{\text{ideal}} = \frac{q}{(\bar{p} - p_{wf} - \Delta p_s)}, \dots\dots\dots (8.79)$$

$$\text{and } E_f \equiv \frac{J_{\text{actual}}}{J_{\text{ideal}}} = \frac{\bar{p} - p_{wf} - \Delta p_s}{\bar{p} - p_{wf}} \dots\dots\dots (8.80)$$

For a well with neither damage nor stimulation, $E_f = 1$; for a damaged well, $E_f < 1$; and for a stimulated well, $E_f > 1$.

8.4.5 Geometric Skin. When the area open to flow decreases, the pressure drop is greater than when the area is unchanged all the way to the formation face. Examples include flow converging to perforations (Fig. 8.33), partial penetration (Fig. 8.34), and an incompletely perforated interval (Fig. 8.35).

Fig. 8.33 illustrates flow converging into perforations. When the perforation spacing is too large, this converging flow results in a positive skin factor. The skin increases as vertical permeability decreases and increases as shot density decreases.

Partial Penetration. Fig. 8.34 illustrates flow converging into an interval that is only partly penetrated by perforations. When a well is completed in only a fraction of the productive inter-

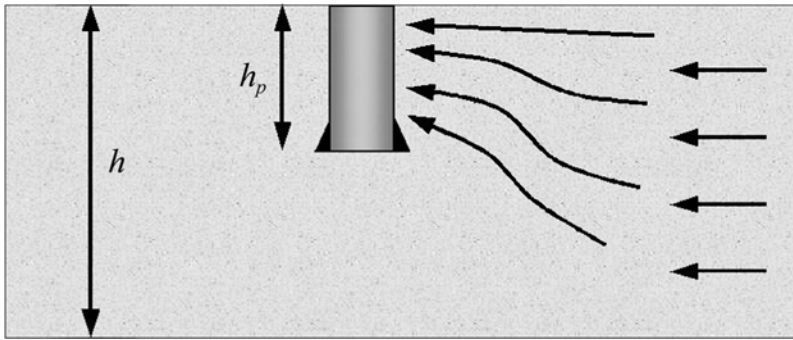


Fig. 8.34—When interval is only partially penetrated by perforations, flow converges through small area, increasing pressure drop near the well.

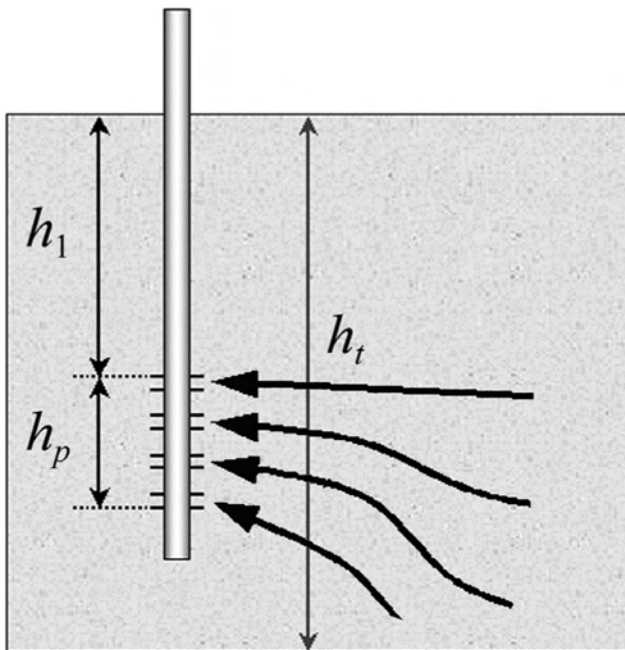


Fig. 8.35—In an incompletely penetrated well, only a portion of the total productive interval (h) is perforated, increasing pressure drop and skin.

val, the flow must converge through a smaller area, increasing the pressure drop near the well (compared to a fully completed interval). The additional pressure drop near the well results in a more positive skin. It increases as the vertical permeability decreases and as the perforated interval as a fraction of the total interval decreases. Formation damage (reduced permeability) near the completion face can significantly increase the additional pressure drop and thus the calculated skin factor.

Incompletely Perforated Interval. Partial penetration is a special case of an incompletely perforated interval (Fig. 8.35). In the general case, the well is perforated starting at a distance h_1 from the top of the productive interval and has perforations extending over a distance, h_p , in an interval of total thickness, h . The total skin for the well in this general situation is

$$s = (h/h_p)s_d + s_p \tag{8.81}$$

In Eq. 8.81, s_d is the skin caused by formation damage, and s_p is the skin resulting from an incompletely perforated interval. This equation is not valid for a stimulated well.

The skin factor for an incompletely perforated interval, s_p , can be quantified by¹¹

$$s_p = \left(\frac{1}{h_{pD}} - 1 \right) \ln \frac{\pi}{2r_D} + \frac{1}{h_{pD}} \ln \left[\frac{h_{pD}}{2 + h_{pD}} \left(\frac{A-1}{B-1} \right)^{1/2} \right] \tag{8.82}$$

$$\text{where } h_{1D} = h_1/h, \tag{8.83}$$

$$h_{pD} = h_p/h, \tag{8.84}$$

$$A = \frac{1}{h_{1D} + h_{pD}/4}, \tag{8.85}$$

$$r_D = \frac{r_w}{h} \left(\frac{k_v}{k_h} \right)^{1/2}, \tag{8.86}$$

$$\text{and } B = \frac{1}{h_{1D} + 3h_{pD}/4}. \tag{8.87}$$

The most significant limitation in applying Eq. 8.82 in practice is the difficulty in estimating accurately the vertical-to-horizontal-permeability ratio, k_v/k_h . Fortunately, this ratio appears only in a logarithmic term in Eq. 8.82, so errors will not seriously distort the calculated value of s_p .

Deviated Well. For a deviated well (Fig. 8.36), which penetrates the formation at an angle other than 90°, more surface is in contact with the formation. This introduces a negative skin factor, s_θ , which makes the total skin factor, s , more negative.

$$s = s_d + s_\theta \tag{8.88}$$

The effect increases as the vertical permeability increases and increases as the angle from the vertical, θ_w , increases. The deviated well skin factor, s_θ , is given by a correlation of simulated results¹² (valid for $\theta_w < 75^\circ$):

$$s_\theta = - \left(\frac{\theta'_w}{41} \right)^{2.06} - \left(\frac{\theta'_w}{56} \right)^{1.865} \log \left(\frac{h_D}{100} \right), \tag{8.89}$$

$$\text{where } \theta'_w = \tan^{-1} \left(\sqrt{\frac{k_v}{k_h}} \tan \theta_w \right), \tag{8.90}$$

$$\text{and } h_D = \frac{h}{r_w} \sqrt{\frac{k_h}{k_v}}. \tag{8.91}$$

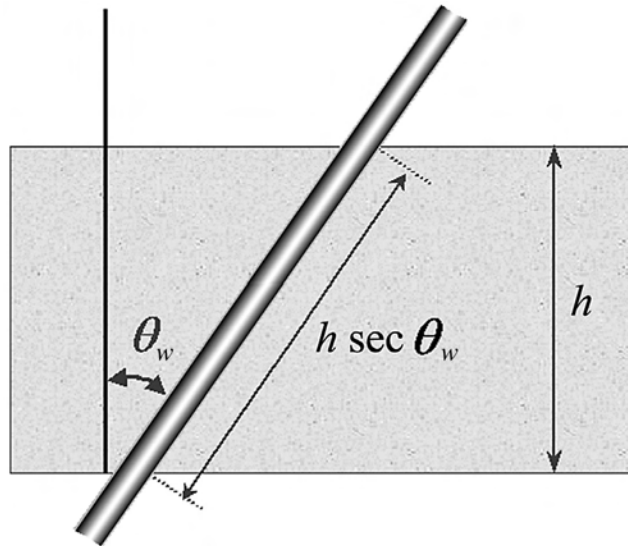


Fig. 8.36—More surface of a deviated well is in contact with formation, introducing a negative skin factor.

Gravel-Pack Skin. When a well is gravel packed (Fig. 8.37), there is a pressure drop through the gravel pack within the perforations, given by¹³

$$s_{gp} = \frac{khL_g}{2nk_{gp}r_p^2}, \dots\dots\dots (8.92)$$

where s_{gp} is the skin factor because of Darcy flow through the gravel pack; h , the net pay thickness, ft; k_{gp} , the permeability of the gravel in the gravel pack, md; k , the reservoir permeability, md; L_g , the length of the flow path through the gravel pack, ft; n , the number of perforations open; and r_p , the radius of the perforation tunnel, ft. Eq. 8.92 does not include the effects of non-Darcy flow, which may be extremely important in high-rate gas wells.

Completion Skin. For a perforated well, any reduced permeability, k_{dp} , in the zone surrounding the perforations (Fig. 8.38) introduces an additional pressure drop. The additional skin is¹⁴

$$s_{dp} = \left(\frac{h}{L_p n} \right) \left(\ln \frac{r_{dp}}{r_p} \right) \left(\frac{k}{k_{dp}} - \frac{k}{k_d} \right), \dots\dots\dots (8.93)$$

$$\text{and } s = s_p + s_d + s_{dp}, \dots\dots\dots (8.94)$$

where s_p is the geometric skin from flow converging to the perforations; s_d , the damage skin; s_{dp} , perforation damage skin; k_d , permeability of the damaged zone around the wellbore, md; k_{dp} , permeability of the damaged zone around perforation tunnels, md; k , reservoir permeability, md; L_p , length of perforation tunnel, ft; n , number of perforations; h , formation thickness, ft; r_d , radius of the damaged zone around the wellbore, ft; r_{dp} , radius of the damages zone around the perforation tunnel, ft; r_p , radius of the perforation tunnel, ft; and r_w , wellbore radius, ft. Eq. 8.94 does not include the effects of non-Darcy flow.

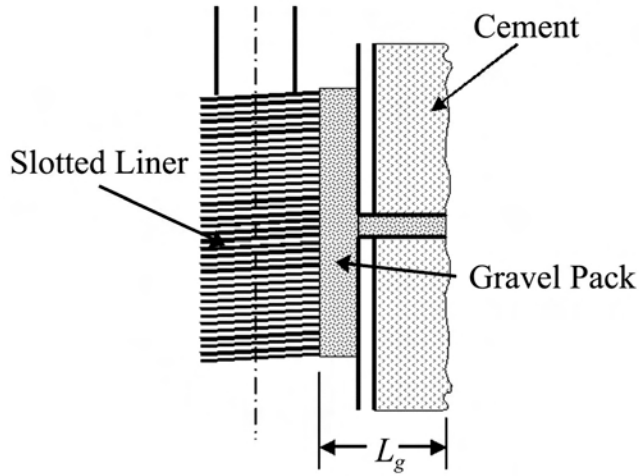


Fig. 8.37—Pressure drop in a gravel-packed well includes the skin effect in perforations.

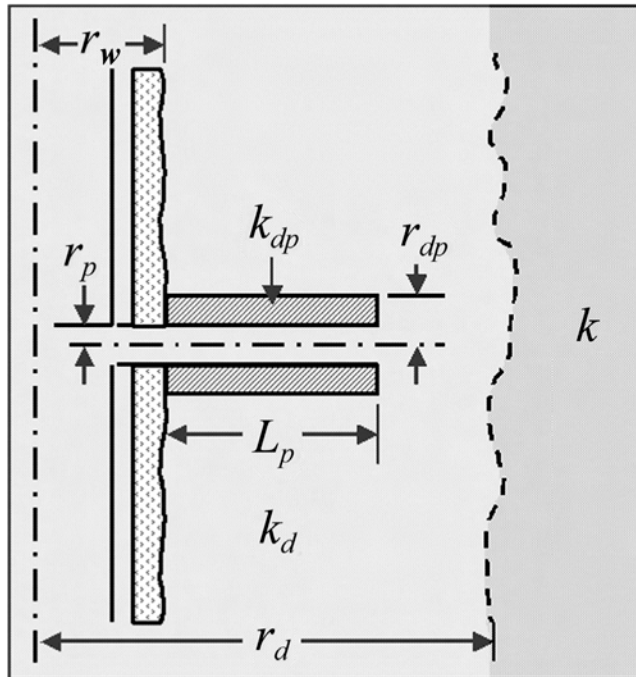


Fig. 8.38—Reduced permeability in damaged zone surrounding perforations introduces additional pressure drop and skin.

Hydraulically Fractured Wells. Wells are frequently fractured hydraulically to improve their productivity, especially in low-permeability formations where fractures increase the effective drained area and in high-permeability formations where they penetrate near-well damage or promote sand control. These fractures, almost always vertical (Fig. 8.39), are high-conductivity paths between the reservoir and the wellbore. If the fracture conductivity is large enough relative to the formation permeability and fracture length, the pressure drop within the fracture

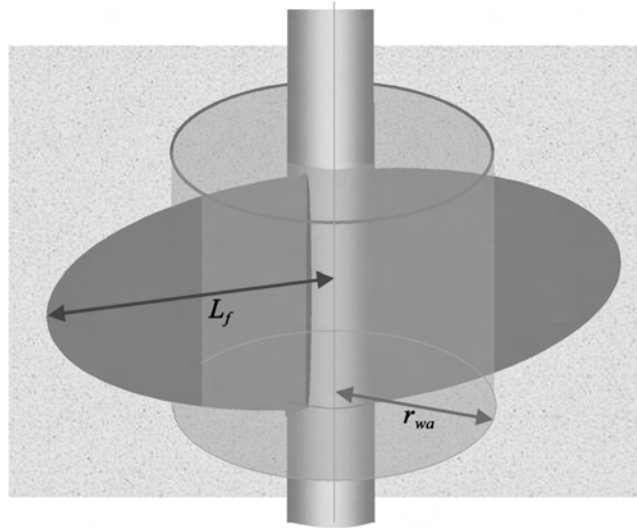


Fig. 8.39—Hydraulic fractures change the flow pattern in a reservoir and introduce a negative geometric skin effect.

will be negligible. This distributes the pressure drop caused by fluid influx into the wellbore over a much larger area, resulting in a negative skin factor, which is interpreted as a geometric skin.

Dimensionless fracture conductivity, C_r , is defined by

$$C_r = \frac{w_f k_f \pi}{k L_f}, \dots\dots\dots (8.95)$$

where w_f is the fracture length, ft; k_f the permeability of the proppant in the fracture; k , the formation permeability, md; and L_f the fracture half-length, ft. Pressure drop in the fracture is negligible for $C_r > 100$.

8.5 Modifications for Gases and Multiphase Flow

8.5.1 Diffusivity Equation for Gas Flow. The diffusivity equation for liquids, Eq. 8.1,

$$\frac{1}{r} \frac{\partial}{\partial r} \left(r \frac{\partial p}{\partial r} \right) = \frac{\phi \mu c_t}{0.0002637k} \frac{\partial p}{\partial t}, \dots\dots\dots (8.1)$$

was derived from three principles: conservation of mass, the equation of state for slightly compressible liquids, and Darcy’s law. This form of the diffusivity equation is linear, which makes solutions (such as the *Ei*-function solution) much easier to find and which allows us to use superposition in time and space to develop solutions for complex flow geometries and for variable rate histories from simple, single-well solutions.

8.5.2 Pseudopressure. Other forms of the equation for flow of gases must be developed because the equation of state for a slightly compressible liquid will not be applicable. First, introducing the real gas law,

$$pV = znRT, \dots\dots\dots (8.96)$$

to replace the slightly compressible equation of state results in a more complex, nonlinear partial differential equation. This equation can be partially linearized by introducing the pseudo-pressure transformation,¹⁵

$$p_p(p) = 2 \int_{p_o}^p p dp / \mu z, \dots\dots\dots (8.97)$$

where p_0 is an arbitrary “base” pressure, frequently chosen to be zero psia. The resulting form of the diffusivity equation is

$$\frac{1}{r} \frac{\partial}{\partial r} \left(r \frac{\partial p_p}{\partial r} \right) = \frac{\phi \mu c_t}{0.0002637k} \frac{\partial p_p}{\partial t} \dots\dots\dots (8.98)$$

Eq. 8.98 has the same form as the diffusivity equation for slightly compressible liquids, with pressure replaced by pseudopressure, p_p . However, this equation is nonlinear because the product μc_t is a strong function of pressure. Fortunately, research has shown that the equation can be treated as linear, and the *Ei*-function is valid for gases if μc_t is evaluated at the pressure at the beginning of a flow period until the time when boundaries begin to have a significant influence on the pressure drop at the well; that is, as long as the reservoir is infinite-acting.

8.5.3 Pressure-Squared and Pressure Approximations. By assuming that the product μz is constant, then, from Eq. 8.97, pseudopressure becomes

$$p_p(p) = \frac{1}{\mu z} (p^2 - p_0^2), \dots\dots\dots (8.99)$$

and the diffusivity equation becomes

$$\frac{1}{r} \frac{\partial}{\partial r} \left(r \frac{\partial p^2}{\partial r} \right) = \frac{\phi \mu c_t}{0.0002637k} \frac{\partial p^2}{\partial t} \dots\dots\dots (8.100)$$

The independent variable has become p^2 , and, in terms of this variable, the *Ei*-function solution is valid when the assumption that μz is constant is valid. This is true (based on empirical evidence) even though Eq. 8.100 is nonlinear (pressure-dependent μc_t), but it is valid only for an infinite-acting reservoir.

Fig. 8.40 shows the range of validity of this assumption for a reservoir temperature of 200°F and several different gas gravities. The μz product is fairly constant at pressures below approximately 2,000 psia (the shaded area in the figure). Conclusions are similar at other temperatures from 100 to 300°F.

By assuming that the group $p/\mu z$ is constant, from Eq. 8.97, pseudopressure becomes

$$p_p(p) = (p / \mu z)(p - p_0), \dots\dots\dots (8.101)$$

and the diffusivity equation becomes

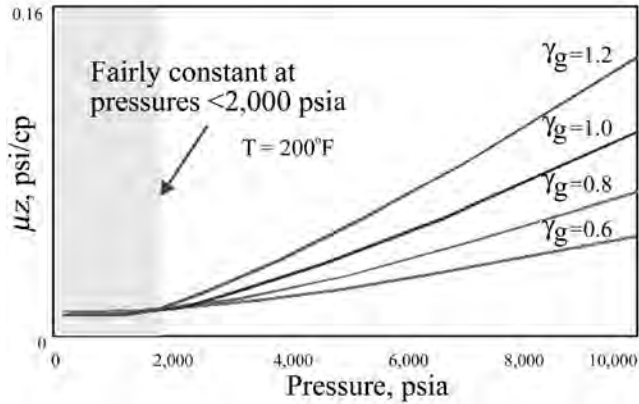


Fig. 8.40— μz product is fairly constant at low pressures. Shaded area indicates pressure range in which μz is constant.

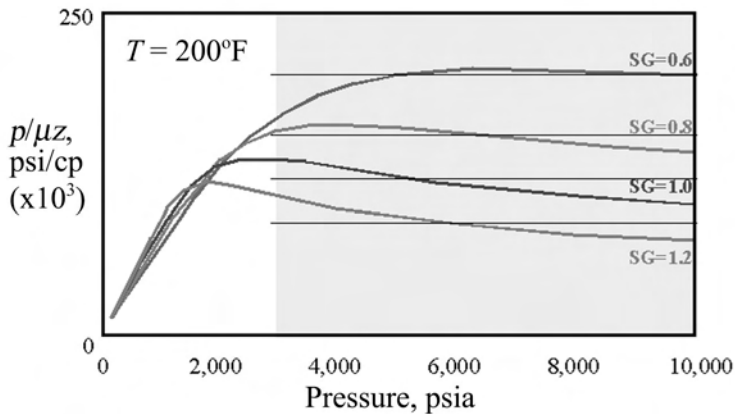


Fig. 8.41— $p/\mu z$ product is fairly constant for high pressures ($p > 3,000$ psia). Shaded area indicates pressure range in which μz is constant.

$$\frac{1}{r} \frac{\partial}{\partial r} \left(r \frac{\partial p}{\partial r} \right) = \frac{\phi \mu c_t}{0.0002637k} \frac{\partial p}{\partial t} \dots\dots\dots (8.102)$$

The independent variable has become p , and, in terms of pressure, the Ei -function is valid (from empirical evidence) when the assumption that $p/\mu z$ is constant is valid. This is true even though Eq. 8.102 is nonlinear (pressure-dependent μc_t), but is valid only for an infinite-acting reservoir.

Fig. 8.41 shows the range of validity of this assumption (shaded area in the figure) for a reservoir temperature of 200°F and several different gas gravities. The group $p/\mu z$ is fairly constant at pressures above approximately 3,000 psia as it is at other temperatures from 100 to 300°F .

The implication of these results is that the choice of variable for gas well-flow equations depends on the situation. The pressure-squared approximation is valid only for low pressures ($p < 2,000$ psia), the pressure approximation is valid only for high pressures ($p > 3,000$ psia), and the pseudopressure transformation is valid for all pressure ranges. For pressure transient test

analysis using software, the pseudopressure is almost always the optimal variable to use. For hand analysis, only pressure or pressure-squared approaches are feasible.

8.5.4 Pseudotime. Although the diffusivity equation written for gas flow has the same form as the diffusivity equation for slightly compressible liquids, with pressure replaced by pseudopressure, it is a nonlinear equation because the product, μc_i , is strongly pressure dependent. In some cases, the remaining nonlinearity cannot be ignored. To solve this problem, Agarwal¹⁶ introduced the pseudotime transformation to further linearize the diffusivity equation for gas. (The linearization is not rigorous, but is adequate for many practical purposes.¹⁷) The definition of pseudotime is

$$t_{ap} \equiv \int_0^{\Delta t} \frac{dt}{\mu(p)c_i(p)} \dots\dots\dots (8.103)$$

In terms of pseudotime, t_{ap} , the diffusivity equation becomes

$$\frac{1}{r} \frac{\partial}{\partial r} \left(r \frac{\partial p_p}{\partial r} \right) = \frac{\phi}{0.0002637k} \frac{\partial p_p}{\partial t_{ap}} \dots\dots\dots (8.104)$$

Subsequent studies¹⁸ have shown that the pseudotime transformation is particularly useful for analysis of flow and buildup tests distorted by wellbore storage when using type curves designed to model flow of slightly compressible liquids.

Because the pressure in the integrand of Eq. 8.103 is a function of position in the reservoir, it is not obvious where the pressure is to be evaluated. Empirical observations¹⁸ indicate that the pressure should be evaluated at BHP during wellbore storage distortion for both buildup and flow tests. During the middle time region for buildup tests, it should be evaluated at BHP, and, for flow tests, at the average reservoir pressure at the start of the test. For flow tests in infinite-acting reservoirs, this is equivalent to using ordinary time as the independent variable.

8.5.5 Normalized Transformed Variables. The pseudopressure and pseudotime transformations provide excellent results when used as part of the analysis procedure for gas well tests. However, they are inconvenient for two reasons: the values of both variables will often be in the range of 10^5 to 10^9 , and they do not have units of actual pressure and time. Thus, the intuitive “feel” for the transformed variables is lost, and they may tend to be regarded as “black box” output—never helpful in test analysis. The use of pseudopressure and pseudotime require different test interpretation equations for oil wells than for gas wells.

These difficulties are overcome by normalizing pseudopressure and pseudotime by multiplying them by constants¹⁹:

$$p_a(p) \equiv \left(\frac{\mu z}{p} \right)_i \int_{p_0}^p \frac{p dp}{\mu z} = \left(\frac{\mu z}{2p} \right)_i p_p(p), \dots\dots\dots (8.105)$$

$$\text{and } \Delta t_a \equiv (\mu c_i)_i \int_0^{\Delta t} \frac{dt}{\mu(p)c_i(p)} = (\mu c_i)_i \Delta t_{ap} \dots\dots\dots (8.106)$$

TABLE 8.1—PLOTING METHODS AND INTERPRETATION EQUATIONS FOR WELL TESTS		
Oil		
	Flow Test	Buildup Test
Semilog graph variables	p_{wf} vs. t	p_{ws} vs. $(t_D + \Delta t)/\Delta t$
Permeability	$k = \frac{162.6q_o B_o \mu_o}{-mh}$	$k = \frac{162.6q_o B_o \mu_o}{-mh}$
Skin factor	$s = 1.151 \left[\frac{p_i - p_{1hr}}{-m} - \log \left(\frac{k}{\phi \mu_o c_t r_w^2} \right) + 3.23 \right]$	$s = 1.151 \left[\frac{p_{1hr} - p_{wf}}{-m} - \log \left(\frac{k}{\phi \mu_o c_t r_w^2} \right) + 3.23 \right]$
Definition of $p_{MBH,D}$	NA	$\frac{kh(p^* - \bar{p})}{70.6q_o B_o \mu_o}$
Gas, Using Adjusted Variables		
	Flow Test	Buildup Test
Semilog graph variables	$p_{a,wf}$ vs. t	$p_{a,ws}$ vs. $(t_a + \Delta t_a)/\Delta t_a$
Permeability	$k = \frac{162.6q_g B_{gi} \mu_i}{-mh}$	$k = \frac{162.6q_g B_{gi} \mu_i}{-mh}$
Skin factor	$s^i = 1.151 \left[\frac{p_{a,i} - p_{a,1hr}}{-m} - \log \left(\frac{k}{\phi \mu_i c_{it} r_w^2} \right) + 3.23 \right]$	$s^i = 1.151 \left[\frac{p_{a,1hr} - p_{a,wf}}{-m} - \log \left(\frac{k}{\phi \mu_i c_{it} r_w^2} \right) + 3.23 \right]$
Definition of $p_{MBH,D}$	NA	$\frac{kh(p_o^* - \bar{p}_o)}{70.6q_g B_{gi} \mu_i}$
Gas, Using Pressure and Time		
	Flow Test	Buildup Test
Semilog graph variables	p_p vs. t	p_{ps} vs. $(t_p + \Delta t)/\Delta t$
Permeability	$k = \frac{162.6q_g \bar{B}_g \bar{\mu}}{-mh}$	$k = \frac{162.6q_g \bar{B}_g \bar{\mu}}{-mh}$
Skin factor	$s^i = 1.151 \left[\frac{p_i - p_{1hr}}{-m} - \log \left(\frac{k}{\phi \bar{\mu} c_t r_w^2} \right) + 3.23 \right]$	$s^i = 1.151 \left[\frac{p_{1hr} - p_{wf}}{-m} - \log \left(\frac{k}{\phi \bar{\mu} c_t r_w^2} \right) + 3.23 \right]$
Definition of $p_{MBH,D}$	NA	$\frac{kh(p^* - \bar{p})}{70.6q_g \bar{B}_g \bar{\mu}}$

This normalization, or multiplication by appropriate constants, gives the new variables the same units—and similar ranges—as pressure and time, respectively. With these transformations, the equations for analysis of gas wells in terms of normalized pseudopressure and pseudotime, which are called adjusted pressure and adjusted time, are obtained from the equations for analysis of oil well tests by simple substitution. Of course, the transformations require the computer. Commercial well-test analysis software often provides these transformations.

Table 8.1 summarizes plotting methods and interpretation equations for oil well tests. It also presents information for gas well tests analyzed with ordinary pressure and time, adjusted pressure and time, pressure squared and time, and, finally, pseudopressure and time. The table includes a definition of p_{DMBH} , a dimensionless pressure defined by Matthews, Brons, and Hazebroek²⁰ that is useful in estimating current average drainage pressure. See this topic in [Section 8.8](#).

TABLE 8.1—PLOTING METHODS AND INTERPRETATION EQUATIONS FOR WELL TESTS (continued)		
Gas, Using Pressure Squared and Time		
	Flow Test	Buildup Test
Semilog graph variables	p_{wf}^2 vs. t	p_{ws}^2 vs. $(t_p + \Delta t)/\Delta t$
Permeability	$k = \frac{1637q_g T \bar{\mu}}{-mh}$	$k = \frac{1637q_g T \bar{\mu}}{mh}$
Skin factor	$s' = 1.151 \left[\frac{p_i^2 - p_{wf}^2}{-m} - \log \left(\frac{k}{\phi \bar{\mu} \bar{c}_i r_w^2} \right) + 3.23 \right]$	$s' = 1.151 \left[\frac{p_{ihr}^2 - p_{wf}^2}{-m} - \log \left(\frac{k}{\phi \bar{\mu} \bar{c}_i r_w^2} \right) + 3.23 \right]$
Definition of $p_{MBH,D}$	NA	$\frac{kh(p^{*2} - \bar{p}^2)}{711q_g T \bar{\mu}}$
Gas, Using Pseudopressure and Time		
	Flow Test	Buildup Test
Semilog graph variables	p_p vs. t	p_p vs. $(t_p + \Delta t)/\Delta t$
Permeability	$k = \frac{1637q_g T}{-mh}$	$k = \frac{1637q_g T}{-mh}$
Skin factor	$s' = 1.151 \left[\frac{p_{p,i} - p_{p,ihr}}{-m} - \log \left(\frac{k}{\phi \bar{\mu} \bar{c}_i r_w^2} \right) + 3.23 \right]$	$s' = 1.151 \left[\frac{p_{p,ihr} - p_{p,wf}}{-m} - \log \left(\frac{k}{\phi \bar{\mu} \bar{c}_i r_w^2} \right) + 3.23 \right]$
Definition of $p_{MBH,D}$	NA	$\frac{kh(p_p^* - \bar{p}_p)}{711q_g T}$

In Table 8.1, the HTR for gas well buildup tests is best estimated to be simply $(t_p + \Delta t_a)/\Delta t_a$. This conclusion is based on the findings of Spivey and Lee.¹⁸ Thus, when using adjusted pressure and time, the HTR is calculated using the actual producing time, t_p .

8.5.6 Non-Darcy Flow. The flow equations shown to this point assume that Darcy’s law is an appropriate model for gas flow into wells. However, as the flow velocity and Reynolds number near the well increase, the result is a transition from laminar and turbulent flow and then to turbulent flow. This transitional (and possibly turbulent) flow is called non-Darcy (non-laminar) flow. The high velocities at which the flow is transitional occur in the immediate vicinity of the well, and the additional pressure drop caused by this transitional flow is similar to a zone of altered permeability that is characterized with a skin factor. In the case of non-Darcy flow, however, the additional “skin effect” caused by the deviations from Darcy’s law is rate dependent.

An adequate model for the apparent skin factor, s' , determined from a flow or buildup test is

$$s' = s + D \left| q_g \right| \dots \dots \dots (8.107)$$

In Eq. 8.107, s is the “true” skin because of damage or stimulation; D is a non-Darcy flow coefficient (assumed constant), with units of D/Mscf; and q_g is the gas flow rate with units of Mscf/D. The absolute value of the gas rate is used because the contribution to the skin is positive regardless of whether the gas well is a producer or an injector.

The true skin for a gas well cannot be obtained from information in a single test conducted at constant rate (including a buildup test following constant-rate production). However, skin calculated from tests conducted at several different rates (for example, associated with a multi-

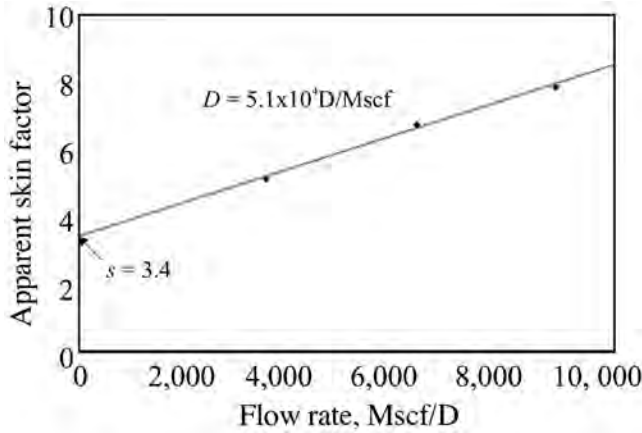


Fig. 8.42—Process to obtain true skin from rate-dependent skin factor.

point deliverability test on a well) can be used to determine the true skin and the non-Darcy flow coefficient. Fig. 8.42 illustrates the process for a well tested at three different rates, with an apparent skin factor determined at each rate.

The apparent skin factor extrapolated to zero rate is the true skin (in this case, 3.4), and the slope of the curve is the non-Darcy flow coefficient, D (in this case, 5.1×10^{-4} D/Mscf). When this method is used, take care to ensure that the permeabilities obtained from the different tests are the same; otherwise, the skin factors will be inconsistent and erroneous.

Often, only one test is available. In this case, the non-Darcy flow coefficient, D , can be estimated from³

$$D = \frac{2.715 \times 10^{-15} \beta k_g M p_{sc}}{h r_w T_{sc} \mu_{gwf}} \dots\dots\dots (8.108)$$

The turbulence parameter, β , can be estimated from²¹

$$\beta \approx 1.88 \times 10^{10} k^{-1.47} \phi^{-0.53} \dots\dots\dots (8.109)$$

The correlation represented by Eq. 8.109 will provide only a crude estimate of the turbulence parameter, β . Further, the correlation assumes that the non-Darcy flow occurs in the formation near the wellbore rather than through the perforations. In a gravel-packed well, the most significant additional pressure drop caused by non-Darcy flow may occur in the perforation channels through the casing.

8.5.7 Multiphase Flow. The equations modeling flow in reservoirs can be modified to include multiphase flow. Perrine²² suggested simple and easily applied modifications and Martin²³ gave them a theoretical basis. These modifications are based on the simplifying assumption that the saturation gradients in the drainage area of the tested well are small. Thus, as examples, the modifications may lead to reasonable approximations for solution-gas drive reservoirs and are inappropriate for water-drive reservoirs with a water bank (and saturation discontinuity) in the drainage area of the tested well. The Perrine-Martin modification for constant-rate flow in an infinite-acting reservoir is

$$p_{wf} = p_i + 162.6 \frac{q_{Rt}}{\lambda_t h} \left[\log \left(\frac{1,688 \phi c_t r_w^2}{\lambda_t t} \right) - 0.868s \right], \dots\dots\dots (8.110)$$

and the Horner equation modeling a buildup test in an infinite-acting reservoir becomes

$$p_{ws} = p_i - 162.6 \frac{q_{Rt}}{\lambda_t h} \log \frac{t_p + \Delta t}{\Delta t} . \dots\dots\dots (8.111)$$

In Eqs. 8.110 and 8.111, q_{Rt} represents the total reservoir flow rate (RB/D) and is given by

$$q_{Rt} = q_0 B_0 + \left(q_g - \frac{q_o R_s}{1,000} \right) B_g + q_w B_w, \dots\dots\dots (8.112)$$

and λ_t represents the total mobility, given by

$$\lambda_t = \frac{k_o}{\mu_o} + \frac{k_w}{\mu_w} + \frac{k_g}{\mu_g} . \dots\dots\dots (8.113)$$

The total mobility, λ_t , can be determined from a pressure buildup test run on a well that produces two or three phases simultaneously. Because Eq. 8.111 implies that λ_t is related to the slope, m , of a Horner plot of p_{ws} vs. $\log(t_p + \Delta t)/\Delta t$ by

$$\lambda_t = \frac{-162.6 q_{Rt}}{mh} . \dots\dots\dots (8.114)$$

The slope, m , of a plot of p_{wf} vs. $\log(t)$ data from a constant-rate flow test has the same interpretation. Perrine²² also showed that the permeability to each phase flowing can be estimated from the relations

$$k_o = -162.6 \frac{q_o B_o \mu_o}{mh}, \dots\dots\dots (8.115)$$

$$k_g = -162.6 \frac{\left(q_g - \frac{q_o R_s}{1,000} \right) B_g \mu_g}{mh}, \dots\dots\dots (8.116)$$

$$\text{and } k_w = -162.6 \frac{q_w B_w \mu_w}{mh} . \dots\dots\dots (8.117)$$

The quantity $(q_g - q_o R_s / 1,000) B_g$ in Eqs. 8.112 and 8.116 is the free-gas flow rate in the reservoir; that is, the difference in the total gas rate, q_g , and the dissolved gas rate, $q_o R_s / 1,000$. Skin factor for multiphase flow test analysis using semilog plots is calculated from

$$s = 1.151 \left[\frac{\Delta p_1 \text{ hr}}{-m} - \log \left(\frac{\lambda_t}{\phi c_t r_w^2} \right) + 3.23 \right] . \dots\dots\dots (8.118)$$

For analysis of tests using type curves, note that the pressure match point on a type curve is related to total and individual phase mobilities and rates by

$$\begin{aligned} \frac{\lambda_t}{q_{Rt}} &= \frac{k_o}{\mu_o q_o B_o} = \frac{k_w}{\mu_w q_w B_w} \\ &= \frac{k_g}{\mu_g [(q_g - q_o R_s) / 1,000] B_g} = \left(\frac{141.2}{h} \right) \left(\frac{P_D}{\Delta p} \right)_{MP}, \dots\dots\dots (8.119) \end{aligned}$$

and the time match point is related to the dimensionless storage coefficient by

$$\begin{aligned} C_D &= [0.0002637 \phi c_t (t C_D / t_D)_{MP} / r_w^2] \lambda_t \\ &= [0.0002637 (t C_D / t_D)_{MP} / r_w^2] (k_o / \mu_o) (q_{Rt} / q_o B_o) \\ &= [0.0002637 (t C_D / t_D)_{MP} / r_w^2] (k_w / \mu_w) (q_{Rt} / q_w B_w) \\ &= [0.0002637 (t C_D / t_D)_{MP} / r_w^2] (k_g / \mu_g) \left[q_{Rt} / \left(q_g - \frac{q_o R_s}{1,000} \right) B_g \right]. \dots\dots\dots (8.120) \end{aligned}$$

The practical implication of Eqs. 8.119 and 8.120 is that total mobility and individual phase permeability are determined from the pressure-match point on a type-curve match. The dimensionless storage coefficient is determined from the time-match point resulting in the calculation of skin factor from

$$s = 0.5 \ln (C_D e^{2s} / C_D), \dots\dots\dots (8.121)$$

just as for single-phase flow. When the conditions for applicability of the Perrine-Martin approximations (small saturation gradients in the drainage area of the tested well) are not satisfied, use of a reservoir simulator for test analysis is an appropriate alternative.

8.6 Diagnostic Plot

8.6.1 Introduction. The diagnostic plot is a log-log plot of the pressure change and pressure derivative (vertical axis) from a pressure transient test vs. elapsed time (horizontal axis). Fig. 8.43 shows an example. The diagnostic plot can be divided into three time regions: early, middle, and late. At the earliest times on a plot (the early-time region), wellbore and near-wellbore effects dominate. These effects include wellbore storage, formation damage, partial penetration, phase redistribution, and stimulation (hydraulic fractures or acidization). At intermediate times (the middle-time region), a reservoir will ordinarily be infinite acting. For a homogeneous reservoir, the pressure derivative will be horizontal during this time region. Data in this region lead to the most accurate estimates of formation permeability. At the latest times in a test (the late-time region), boundary effects dominate curve shapes. The types of boundaries that may affect the pressure response include sealing faults, closed reservoirs, and gas/water, gas/oil, and oil/water contacts. Several common flow regimes and the diagnostic plots associated with these flow regimes are discussed in the remainder of Section 8.6.

8.6.2 Volumetric Behavior. Volumetric behavior is defined as that pressure response time dominated by the wellbore, reservoir, or part of the reservoir acting like a uniform-pressure “tank” with fluid entering or leaving the tank. The most common example of volumetric behav-

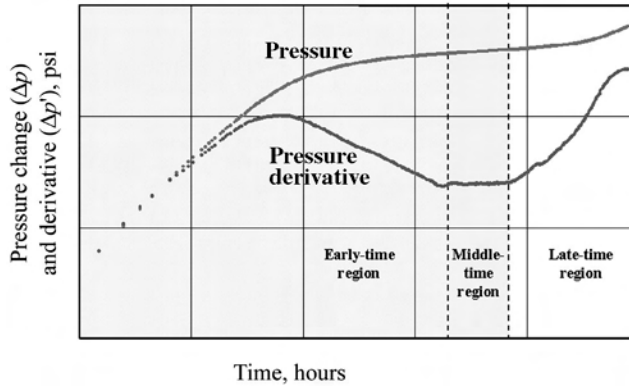


Fig. 8.43—Diagnostic plot showing time regions.

ior is wellbore storage, which dominates during the early-time region. The “tank” is the wellbore, in which the pressure is uniform. Fluid either leaves this tank (earliest times in a flow test, before the reservoir begins to respond) or enters the tank (earliest times in a buildup test). Another example is pseudosteady-state (boundary-dominated) flow in a closed reservoir during constant-rate production. In this case, the reservoir is the tank; pressure is changing at the same rate throughout (although it is not the same at all points), and fluid is leaving the reservoir through the producing well. As a final example, in a test the reservoir may behave like a tank with recharge (fluid influx) entering from a secondary source of pressure support, such as a large supply of hydrocarbons in a lower-permeability medium in pressure communication with the reservoir being tested.

The equation modeling wellbore storage (derived from a mass balance on the wellbore) is

$$\Delta p = \frac{qBt}{24C} \dots\dots\dots (8.29)$$

The equation modeling pseudosteady-state flow in a cylindrical drainage area is

$$p_i - p_{wf} = \frac{0.0744qBt}{\phi c_t h r_e^2} + \frac{141.2qB\mu}{kh} \left[\ln \left(\frac{r_e}{r_w} \right) - \frac{3}{4} + s \right] \dots\dots\dots (8.18)$$

The general form is

$$\Delta p = m_V t + b_V \dots\dots\dots (8.122)$$

The derivative of the general form is

$$t \frac{\partial \Delta p}{\partial t} = t \frac{\partial (m_V t + b_V)}{\partial t} = m_V t \dots\dots\dots (8.123)$$

The implication is that the derivative plot will have unit slope (up one log cycle as it moves over one log cycle) on log-log coordinates, and the pressure change plot will approach unity at long times when b_v is not equal to zero (Fig. 8.44). In wellbore storage, b_v is zero, and

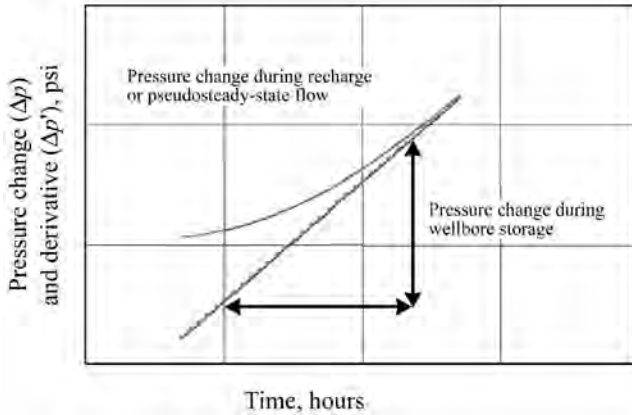


Fig. 8.44—Volumetric flow produces derivative with unit slope.

the derivative and pressure change plots will lie on top of one another. During pseudosteady-state flow or recharge, the pressure change and pressure derivative plots will not coincide.

8.6.3 Radial Flow. Infinite-acting radial flow is common in reservoirs, and data in the radial flow regime can be used to estimate formation permeability and skin factor. Common situations in which radial flow occurs include flow into vertical wells after wellbore storage distortion has ceased and before boundary effects, hydraulically fractured wells after the transient has moved well beyond the tips of the fracture, horizontal wells before the transient has reached the top and bottom of the productive interval, and horizontal wells after the transient has moved beyond the ends of the wellbore.

The equation used to model radial flow for a well producing at constant rate is the familiar logarithmic approximation to the line-source solution,

$$\Delta p = \frac{162.6qB\mu}{kh} \left[\log \left(\frac{kt}{\phi\mu c_t r_w^2} \right) - 3.23 + 0.869s \right] \dots\dots\dots (8.124)$$

Equations modeling radial flow have the general form

$$\Delta p = m \log (t) + b, \dots\dots\dots (8.125)$$

with derivative

$$t \frac{\partial \Delta p}{\partial t} = \frac{m}{2.303} \dots\dots\dots (8.126)$$

On the diagnostic plot (Fig. 8.45), radial flow is indicated by a horizontal derivative.

8.6.4 Linear Flow. Linear flow is also common and occurs in channel reservoirs, hydraulically fractured wells, and horizontal wells. Data from linear flow regimes can be used to estimate channel width or fracture half-length if an estimate of permeability is available. In horizontal wells, an estimate of permeability perpendicular to the well can be made if the productive well length open to flow is known.

An equation that models linear flow in a channel reservoir of width *w* is

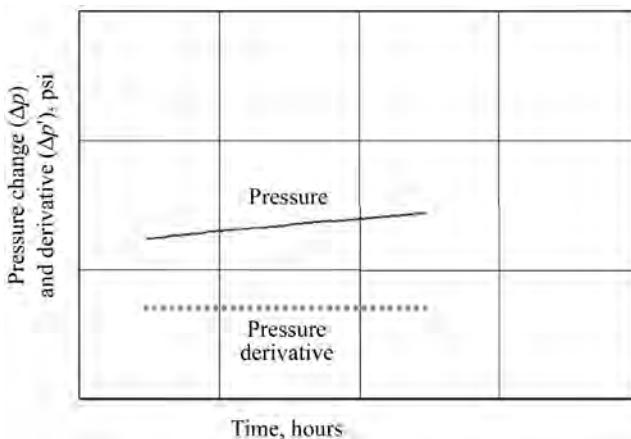


Fig. 8.45—Radial flow appears as a horizontal derivative on the diagnostic plot.

$$\Delta p = \frac{16.26qB\mu}{khw} \left(\frac{kt}{\phi\mu c_t} \right)^{1/2} + \Delta p_s \dots\dots\dots (8.127)$$

For a hydraulically fractured well with fracture half-length L_f ,

$$\Delta p = \frac{4.064qB\mu}{khL_f} \left(\frac{kt}{\phi\mu c_t} \right)^{1/2} + \Delta p_s \dots\dots\dots (8.128)$$

The general form is

$$\Delta p = m_L t^{1/2} + b_L \dots\dots\dots (8.129)$$

The derivative is

$$t \frac{\partial \Delta p}{\partial t} = \frac{1}{2} m_L t^{1/2} \dots\dots\dots (8.130)$$

Linear flow on the diagnostic plot is indicated when a derivative follows a half-slope line—that is, a line that moves up vertically by one log cycle for each two cycles of horizontal movement (Fig. 8.46). The pressure change may or may not also follow a half-slope line. In a hydraulically fractured well, the pressure change will follow a half-slope line unless the fracture is damaged. In a channel reservoir, a hydraulically fractured well with damage, or a horizontal well, the pressure change will approach the half-slope line from above.

8.6.5 Bilinear Flow. Bilinear flow occurs primarily in wells with low-conductivity hydraulic fractures. Flow is linear within the fracture to the well, and also linear (normal to fracture flow) from the formation into the fracture. Estimates of fracture conductivity, $w_f k_f$, can be made with data from this flow regime when estimates of formation permeability are available.

For a hydraulically fractured well, an equation that models bilinear flow is

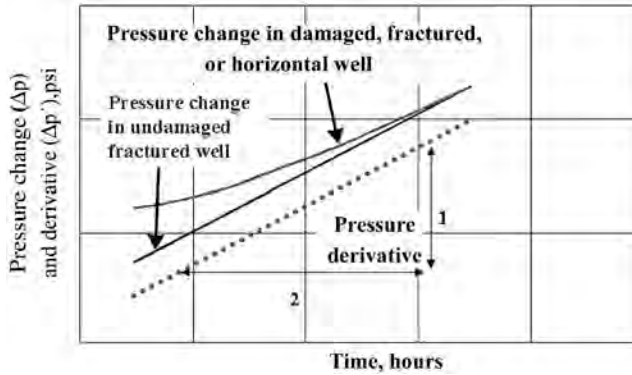


Fig. 8.46—Linear flow derivative follows a half-slope line on a diagnostic plot.

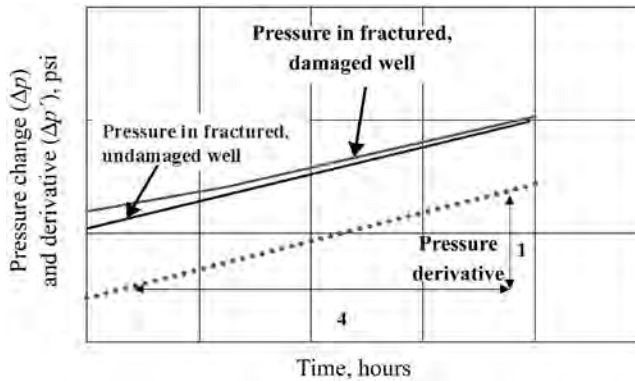


Fig. 8.47—Bilinear flow derivative follows a quarter-slope line on the diagnostic plot.

$$\Delta p = \frac{44.1qB\mu}{h} \left(\frac{1}{w_f k_f} \right)^{1/2} \left(\frac{t}{\phi \mu c_t k} \right)^{1/4} + \Delta p_s \dots \dots \dots (8.131)$$

The general form is

$$\Delta p = m_B t^{1/4} + b_B \dots \dots \dots (8.132)$$

The derivative is

$$t \frac{\partial \Delta p}{\partial t} = \frac{1}{4} m_B t^{1/4} \dots \dots \dots (8.133)$$

Bilinear flow derivatives plot as a quarter-slope line on the diagnostic plot (Fig. 8.47). The quarter-slope line moves up one log cycle as it moves over four log cycles. The pressure change does not necessarily follow a quarter-slope line. In a damaged, hydraulically fractured well, the pressure change curve will approach the quarter-slope line from above; in an undamaged hydraulically fractured well ($\Delta p_s = 0$), the pressure change will typically follow the quarter-slope line when the effects of wellbore storage have ended.

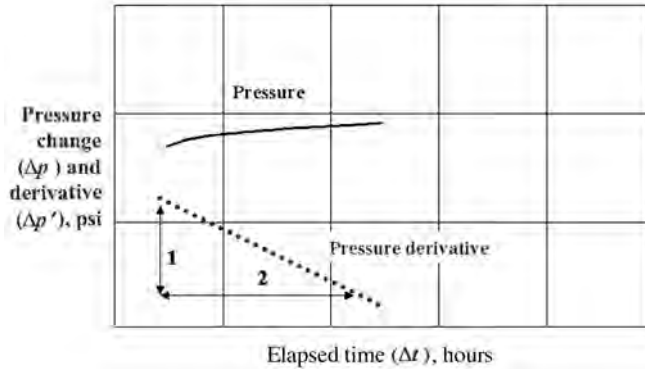


Fig. 8.48—Spherical flow derivative has slope of $-1/2$.

8.6.6 Spherical Flow. The flow pattern is spherical when the pressure transient can propagate freely in three dimensions and converge into a “point.” This can occur for wells that penetrate only a short distance into the formation (actually hemispherical flow), wells that have only a limited number of perforations open to flow, horizontal wells with inflow over only short intervals, and during wireline formation tests. Data in the spherical-flow regime can be used to estimate the mean permeability,

$$k_s = (k_h k_z^{1/2})^{2/3} \dots\dots\dots (8.134)$$

An equation that models spherical flow is

$$p_{wf} = p_i - \frac{70.6qB\mu}{k_s r_s} + \frac{2456\sqrt{\phi\mu c_t}qB\mu}{k_{sp}^{3/2}} \frac{1}{\sqrt{t}} - \frac{70.6qB\mu}{k_{sp} r_{sp}} s, \dots\dots\dots (8.31)$$

$$\text{where } k_{sp} = [k_r k_z^{1/2}]^{2/3}, \dots\dots\dots (8.32)$$

and r_{sp} is the radius of the sphere into which flow converges. The general form is

$$\Delta p = -m_s t^{-1/2} + b_s, \dots\dots\dots (8.135)$$

and the derivative is

$$\frac{\partial \Delta p}{\partial t} = \frac{1}{2} m_s t^{-1/2} \dots\dots\dots (8.136)$$

Spherical flow on the diagnostic plot produces a derivative line with a slope of $-1/2$. The pressure change during spherical flow approaches a horizontal line from below, and never exhibits a straight line with the same slope as the derivative (Fig. 8.48). Spherical flow can occur during either buildup or drawdown tests.

8.6.7 Flow Regimes on the Diagnostic Plot. A major application of the diagnostic plot is the potential that it provides in identifying the flow regimes that appear in a logical sequence during a buildup or flow test. For example, consider Fig. 8.49. At early times, the unit slope line

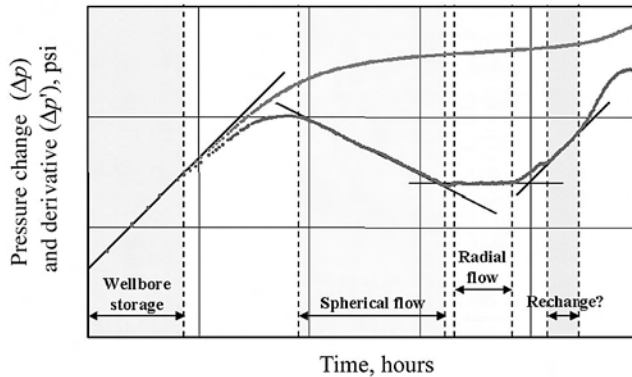


Fig. 8.49—Well test diagnostic plot indicating several flow regimes.

on both derivative and pressure change, indicating wellbore storage. Later, a derivative with a slope of $-1/2$, indicating possible spherical flow, followed by a horizontal derivative, indicating infinite-acting radial flow. Boundary effects, including a unit-slope line, follow, indicating possible recharge of the reservoir pressure.

8.7 Behavior of Bounded Reservoirs

8.7.1 Introduction. Reservoir boundaries have significant influences on the shape of the diagnostic plot. The effects of boundaries appear following the middle-time region (infinite-acting radial flow) in a test. Recognizing the influence of boundaries can be as important as analyzing the test quantitatively. However, a problem in recognition is that many reservoir models may produce similar pressure responses. The model selected to interpret the test quantitatively must be consistent with geological and geophysical interpretations. Once the proper reservoir model has been determined, test analysis may be relatively straight-forward type-curve matching or regression analysis using modern well-test analysis software.

The shapes of the diagnostic plots for a buildup test and a drawdown test are essentially identical during the early- and middle-time regions for most tests. However, boundary effects can cause quite different shapes for a given reservoir model at late times in buildup and drawdown tests. This problem is augmented by the common use of “equivalent time” functions to analyze buildup tests on drawdown type curves. (There are different equivalent time functions for radial flow, linear flow, and bilinear flow, as discussed in more detail in the section on analysis of hydraulically fractured wells.)

Basically, equivalent time functions apply rigorously only to situations where either the producing time and the shut-in time both lie within the middle-time region or, as is commonly the case, the shut-in time is much less than the producing time before shut in.

To further complicate matters for buildup test analysis, the shape of the derivative curve depends on how the derivative is calculated and plotted. The derivative of pressure change may be taken with respect to the logarithm of either shut-in time or equivalent time. The derivative may then be plotted vs. either of these time functions, and the shape differs for each plotting function. Some pressure transient test analysis software allows the user a choice in the time function used in taking the derivative and another choice in time plotting function; for other software, the time functions used are “hard-wired.” The results can be bewildering.

8.7.2 Well in an Infinite-Acting Reservoir. Infinite-acting, radial flow reservoirs were described in the previous section. Figs. 8.50 and 8.51 show their diagnostic curves. For these plots, the derivative was taken with respect to shut-in time and derivative and pressure change

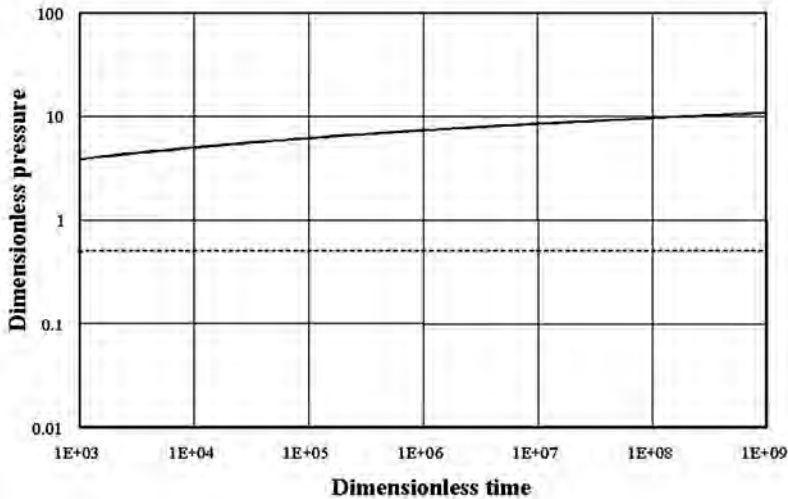


Fig. 8.50—Diagnostic plot for constant-rate drawdown test in an infinite-acting reservoir.

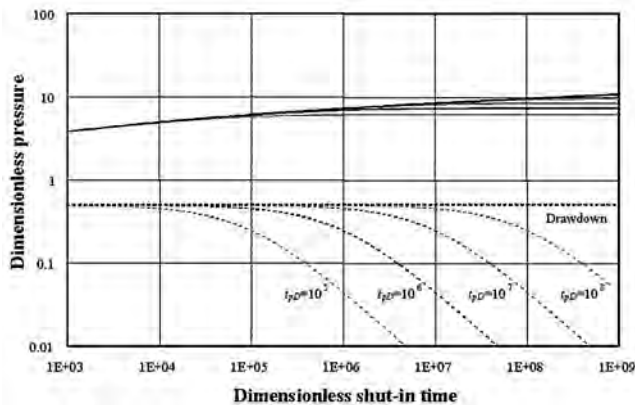


Fig. 8.51—Diagnostic plot for buildup test.

curves are plotted vs. shut-in time. Both pressure and time are in terms of dimensionless variables. Wellbore storage distortion is not included in any of the diagnostic plots in this section.

Notice the significant difference in the shapes of both the derivative and pressure change curves for buildup and drawdown tests, with the pressure change curves flattening for buildup tests and the derivatives moving downward with an ultimate slope of -1 . The time at which the flattening of the pressure change curve (and corresponding downward movement of the derivative) becomes apparent is a function of the producing time before shut-in. The longer the producing time, the longer the flattening is delayed and the longer the time the buildup diagnostic plot is essentially identical to the drawdown diagnostic plot.

Fig. 8.52 is the diagnostic plot that results when the derivative is taken with respect to radial equivalent time and the time-plotting function is radial equivalent time. The drawdown and buildup curves appear to be identical for all times. However, the radial equivalent time has a maximum value of the producing time before shut-in, so, for the buildup plots, the curves terminate at these maximum values of the time plotting function, and all points “stack up” at these limiting values of the plotting function. Our conclusion is that radial equivalent time is

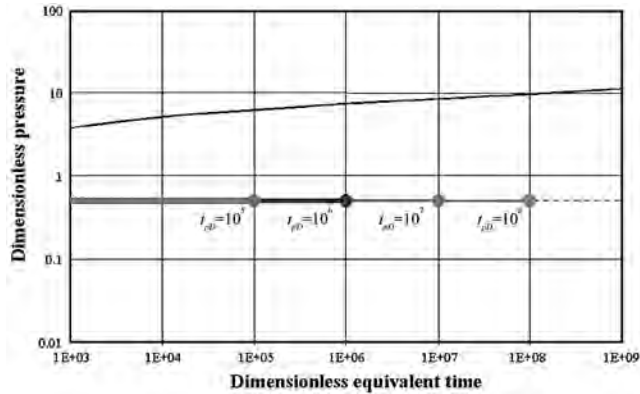


Fig. 8.52—Diagnostic plot when derivative is taken with respect to and plotted against radial equivalent time.

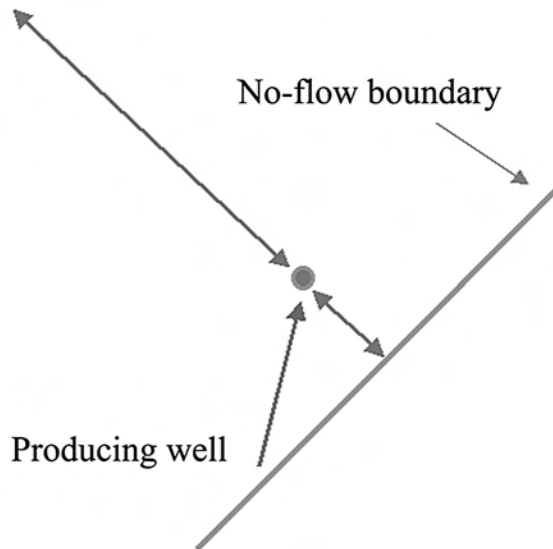


Fig. 8.53—Well near a single no-flow boundary.

more satisfactory as a variable for taking the derivative and as a plotting function for an infinite-acting reservoir because the shape of the diagnostic plot is the same as for a constant-rate drawdown test.

8.7.3 Linear No-Flow Boundary. When a well is near a single no-flow boundary (Fig. 8.53) or, as a practical matter, much closer to one boundary than to any other, and when sufficient time has elapsed for the boundary to have an influence on the pressure response during the test, the characteristic diagnostic plot, as Fig. 8.54 shows, results for a constant-rate drawdown test. (Wellbore storage may distort some of the earlier data on this diagnostic plot.) The derivative will double in value over approximately $1\frac{1}{2}$ log cycles (from 0.5 to 1.0 on a plot of dimensionless variables). Similar responses occur in naturally fractured reservoirs with transient flow from the matrix to the fractures.

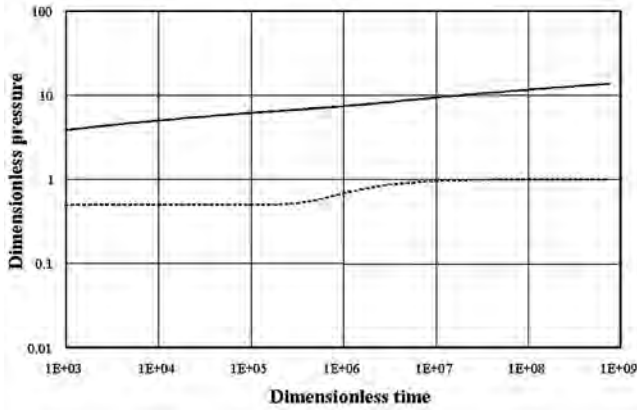


Fig. 8.54—Diagnostic plot for constant-rate drawdown test influenced by a single no-flow boundary.

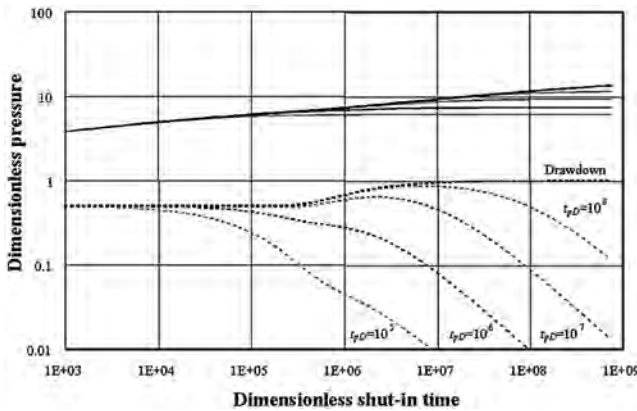


Fig. 8.55—Diagnostic plot for buildup test with derivative taken with respect to shut-in time. Long producing time before shut-in produces curve resembling plot for drawdown test.

Fig. 8.55 is the diagnostic plot for a buildup test with the derivative taken with respect to shut-in time and plotted vs. shut-in time. (Wellbore storage may distort some of the earlier data on this plot.) The longer the producing time before shut-in, the more nearly the shape of the diagnostic plot for a buildup test resembles the diagnostic plot for a drawdown test. The derivative has a slope of -1 for shut-in times much longer than producing time before shut-in.

Fig. 8.56 is the diagnostic plot for a buildup test with derivative taken with respect to radial equivalent time and plotted vs. equivalent time. Derivatives double over a small fraction of a log cycle for short producing times and, in general, the shapes of the diagnostic plots for buildup tests are similar to drawdown diagnostic plots only for longer producing times before shut-in.

Fig. 8.57 is the diagnostic plot for a buildup test, with derivative taken with respect to radial equivalent time and plotted vs. shut-in time. In this case, the diagnostic plot is similar to the drawdown response, but the plots are not identical. Notice that the derivative doubles over approximately $1\frac{2}{3}$ log cycle. This procedure for taking the derivative and preparing the diagnostic plot is the most satisfactory of the alternatives considered.

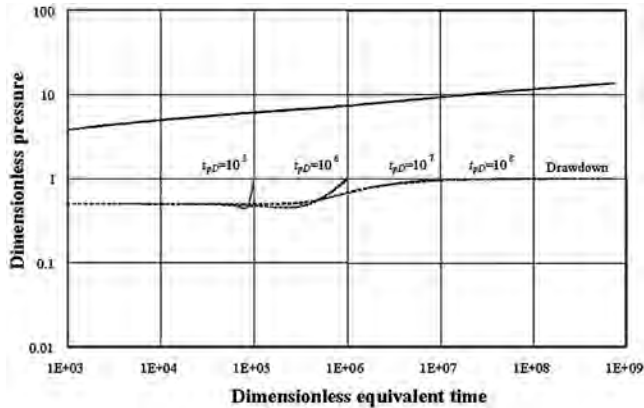


Fig. 8.56—Diagnostic plot for buildup test with derivative taken with respect to and plotted against equivalent time shows that derivative doubles over small fraction of log cycle for short producing times.

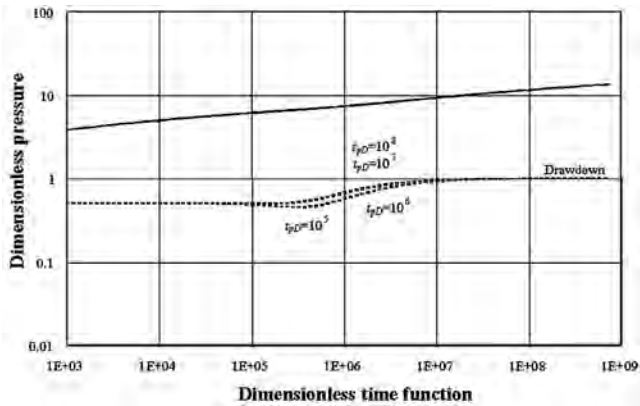


Fig. 8.57—Diagnostic plot for buildup test with derivative taken with respect to radial equivalent time and plotted vs. shut-in time resembles drawdown response.

8.7.4 Linear Constant-Pressure Boundary. When a well is much nearer a single boundary (similar to Fig. 8.53) but with a constant-pressure at that boundary and boundary effects are encountered during the test, the diagnostic plot shown in Fig. 8.58 will result in a constant-rate drawdown test. (Wellbore storage effects could also occur early in the test.) The derivative has a slope of -1 at late times on the diagnostic plot.

Fig. 8.59 is the diagnostic plot for a buildup test, with derivative taken with respect to shut-in time and plotted vs. shut-in time. This diagnostic plot is identical to the drawdown plot if steady state was achieved during the flow period preceding the buildup test. For other cases, with shorter producing times, the derivative has a slope steeper than the drawdown slope of -1 .

Fig. 8.60 is the diagnostic plot for a buildup test, with derivative taken with respect to radial equivalent time and plotted vs. equivalent time. For short producing times, the derivative falls precipitously.

Fig. 8.61 is the diagnostic plot for a buildup test, with derivative taken with respect to radial equivalent time and plotted vs. shut-in time. The shapes of the diagnostic plots are similar to, but not identical to, the drawdown diagnostic plot for all producing times before shut-in. The diagnostic plot prepared in this way is the most satisfactory of the alternatives considered.

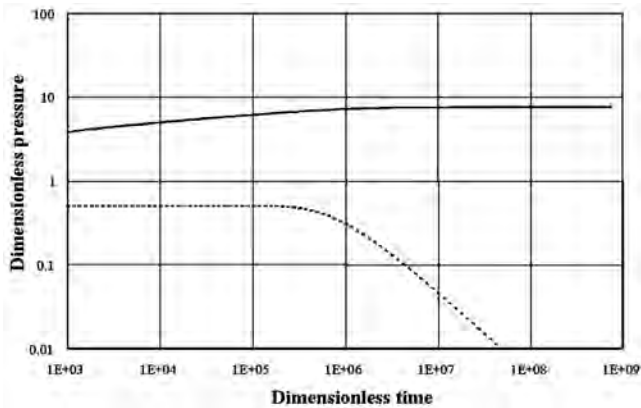


Fig. 8.58—Derivative has a slope of -1 for well located near a single, constant-pressure boundary.

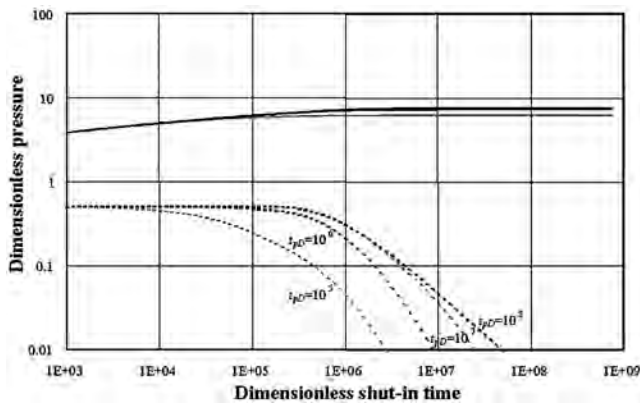


Fig. 8.59—Diagnostic plot for buildup test with derivative taken with respect to and plotted vs. shut-in time is similar to drawdown plot if steady state achieved during flow period preceding buildup test.

8.7.5 Well in a Channel. When a well is between two parallel no-flow boundaries and the pressure transient encounters both during a test long before the ends of the reservoir influence the test data, the diagnostic plot in Fig. 8.62 results for a constant-rate drawdown test. Before the boundary effects, with characteristic derivative slope of $1/2$, wellbore storage, radial flow (or hemiradial flow if the well is much nearer one boundary than the other) will usually appear on the diagnostic plot. Diagnostic plots with similar shapes occur for a well between two sealing faults, a hydraulically fractured well with a high-conductivity fracture, and a horizontal well during early linear flow.

Fig. 8.63 is the diagnostic plot for a buildup test, with derivative taken with respect to shut-in time and plotted vs. shut-in time. The longer the producing time before shut-in, the more similar the curve shape is to the drawdown-test diagnostic plot. The derivative has a slope of $-1/2$ when shut-in time is much larger than producing time.

Fig. 8.64 is the diagnostic plot for a buildup test with derivative taken with respect to radial equivalent time and plotted vs. equivalent time. This plot is not particularly useful for test analysis. However, linear equivalent time produces a more useful diagnostic plot as long as channel ends do not affect the pressure response.

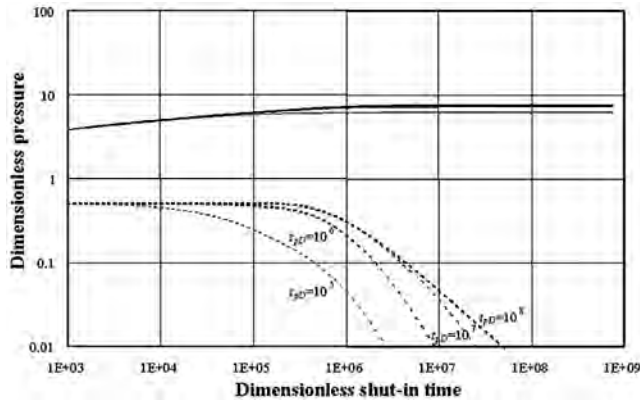


Fig. 8.60—Diagnostic plot for buildup test with derivative taken with respect to and plotted against equivalent time shows that derivative falls precipitously for short producing times.

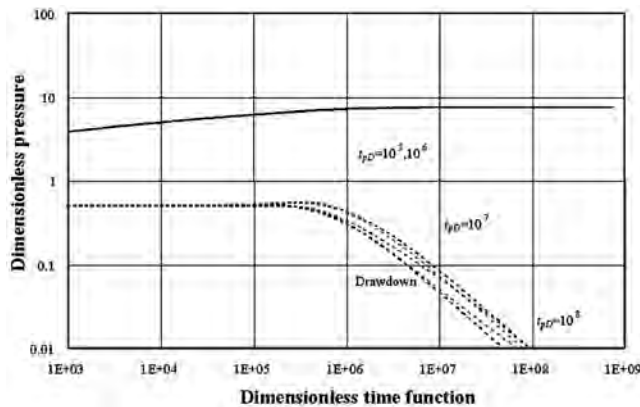


Fig. 8.61—Diagnostic plot for buildup test with derivative taken with respect to and plotted against shut-in time resembles drawdown diagnostic plot of all producing times before shut-in.

Fig. 8.65 is the diagnostic plot for a buildup test with derivative taken with respect to radial equivalent time and plotted vs. shut-in time. The derivative is similar to, but not identical to, the drawdown response. This method is the most useful for test analysis among the alternatives discussed.

8.8 Estimating Average Reservoir Pressure

Two different method types, one using data from the middle-time region and the second using data from the late-time region (LTR), are commonly applied in estimating average reservoir pressure. The middle-time region methods are the Matthews-Brons-Hazebroek (MBH) method²⁰ and the Ramey-Cobb method.²⁴ The LTR methods are the modified Muskat method²⁵ and the Arps-Smith method.²⁶

8.8.1 Middle-Time Region Methods. The MTR methods are based on extrapolation of the middle-time region and the correction of the extrapolated pressure. The advantage of these methods is that they use pressure data only from the middle-time region, which means they require relatively short tests. The disadvantages are the need for accurate fluid property estimates, a known drainage area shape and size, and the location of the well within the drainage area.

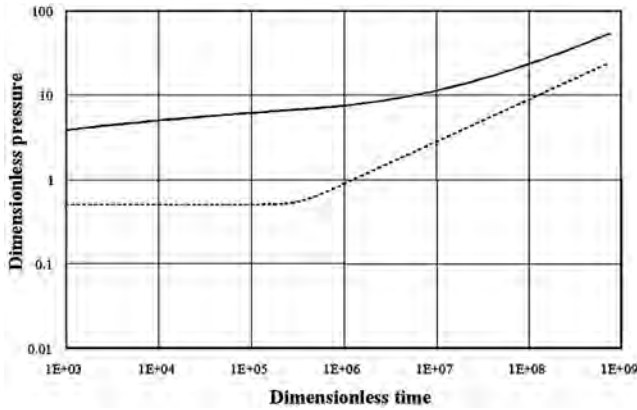


Fig. 8.62—Constant-rate drawdown diagnostic plot, well between two no-flow boundaries, characteristic derivative slope of 1/2.

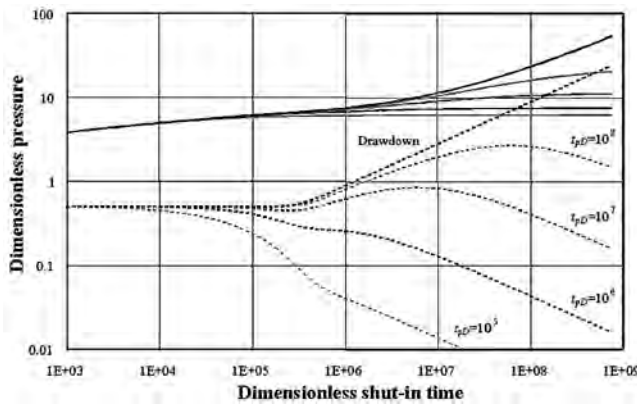


Fig. 8.63—Diagnostic plot for buildup test in well between two boundaries with derivative taken with respect to shut-in time. Longer producing time results in curve more similar to drawdown-test diagnostic plot. (Derivative has a slope of -1/2 when shut-in time is much longer than producing time.)

Drainage Area Shapes. The MTR methods depend on the shape of the drainage area. Matthews-Brons-Hazebroek²⁰ developed a series of curves that model buildup tests in many shapes. As a matter of interest, these graphs were generated using image wells to simulate boundaries.

Figs. 8.66 through 8.68 illustrate representative dimensionless pressures as calculated by the MBH method. Fig. 8.66 is a plot of dimensionless pressure as defined by the MBH method plotted against dimensionless producing time calculated using the drainage area. Dimensionless pressure is defined as

$$p_{DMBH} = \frac{kh}{70.6qB\mu}(p^* - \bar{p}) = \frac{2.303}{m}(p^* - \bar{p}), \dots\dots\dots (8.137)$$

and dimensionless time is

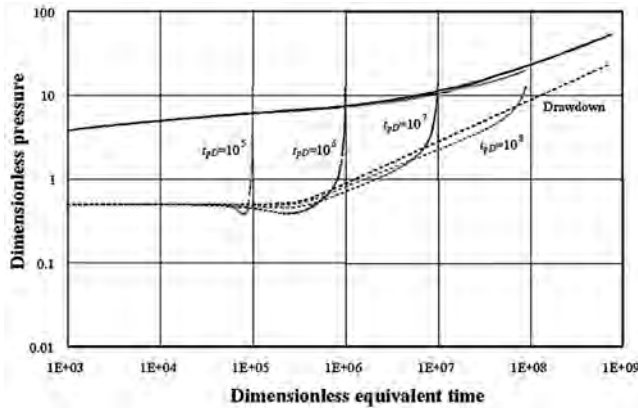


Fig. 8.64—Diagnostic plot for buildup test with derivative taken with respect to and plotted against equivalent time is not particularly useful for test analysis.

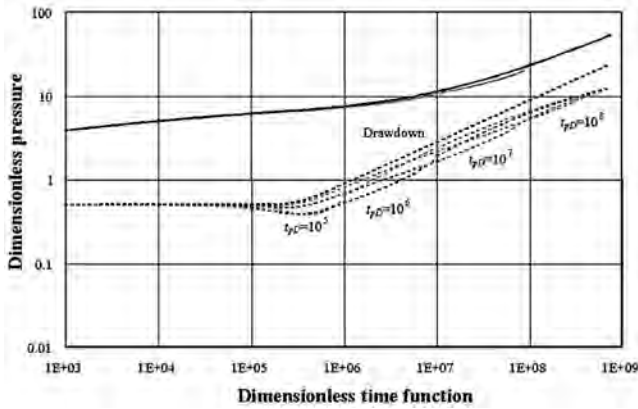


Fig. 8.65—Diagnostic plot for buildup test in well between two flow barriers. Derivative taken with respect to equivalent time and plotted against shut-in time resembles drawdown response.

$$t_{pAD} = \frac{0.0002637kt_p}{\phi\mu c_t A} \dots\dots\dots (8.138)$$

In Eq. 8.137, p^* = the extrapolated pressure at a HTR of unity, \bar{p} = the current average drainage area pressure, and m = the slope of the MTR straight line on a Horner plot. In Eq. 8.138, t_p = the producing time before shut-in, and A = the well’s drainage area expressed in square feet.

The four different curves in Fig. 8.66 represent four different locations of a well within a square drainage area. On this plot of dimensionless pressure on a linear scale vs. dimensionless time on a logarithmic scale, these curves eventually become straight lines. For example, for a well centered in a square drainage area, the line becomes straight at a dimensionless time of approximately 0.2. The time at which the line becomes straight is an indication that a well has reached pseudosteady-state flow at that dimensionless time.

Fig. 8.67 shows the Matthews-Brons-Hazebroek correlations for a well in the various positions in a 2×1 rectangle. The wells eventually reach pseudosteady state and the lines become

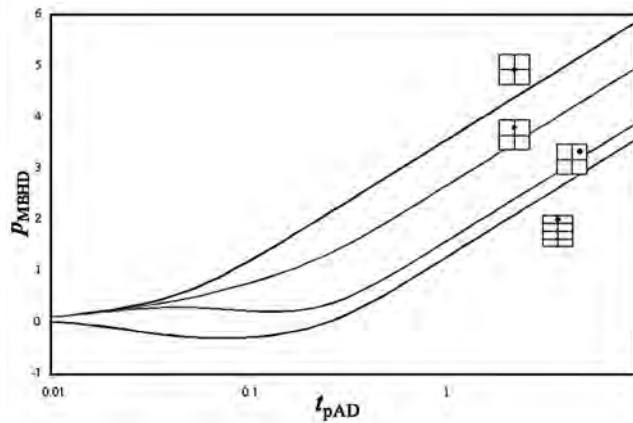


Fig. 8.66—MBH pressures for wells in square drainage area.

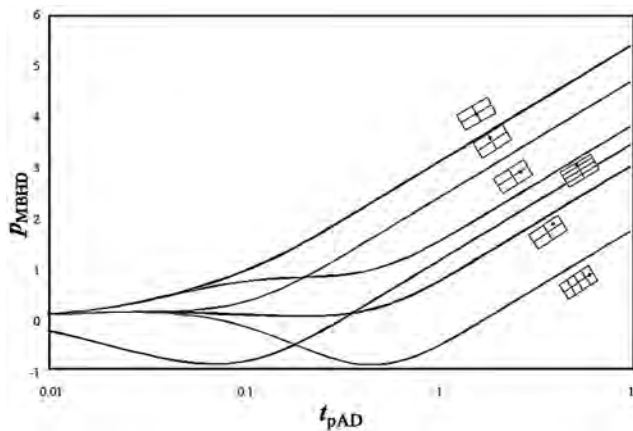


Fig. 8.67—MBH pressures for wells located in a 2×1 rectangular reservoir.

straight, but, in general, the time to reach pseudosteady state is longer for the 2×1 rectangle than it was for the square rectangle. Furthermore, the farther the well is off center within the drainage area, the longer the time required to reach pseudosteady state. The difference is on the order of one full log cycle between the case in which the well is centered in the drainage area and that for a well most off-centered in the drainage area, which is the lowest curve on this plot. Fig. 8.68 shows the MBH pressures for wells in various positions in a 4×1 rectangle. Matthews-Brons-Hazebroek generated many similar graphs for other drainage-area shapes.

Example of the Matthews-Brons-Hazebroek Method. This method will be applied to a well in a reservoir with the following properties: $t_p = 482$ hours, $\phi = 0.15$, $\mu = 0.25$ cp, $c_t = 1.615 \times 10^{-5}$, and $A = 1,500 \times 3,000$ ft (a 2 × 1 reservoir, well centered).

First, plot well shut-in pressure against the HTR on semilog coordinates. In Fig. 8.69, which is an ordinary HTR plot, the wellbore storage affects the data at large values of HTR, followed by the straight-line middle-time region, in turn followed by a deviation of the curve as it begins moving toward a fully built-up pressure.

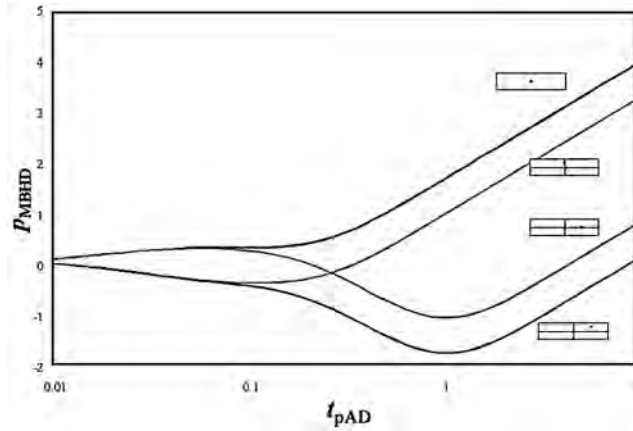


Fig. 8.68—MBH pressures for wells located in a 4×1 rectangular reservoir.

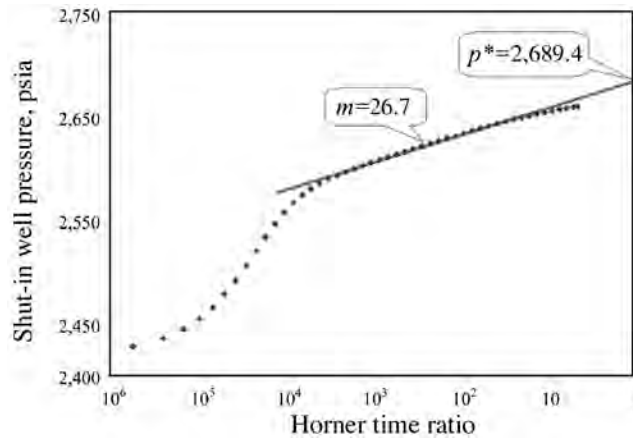


Fig. 8.69—Horner plot yields slope, Horner time ratio, and extrapolated pressure.

The MTR straight line on this Horner graph is extrapolated to a HTR of 1 to determine p^* . In this case, $p^* = 2,689.4$ psi. From the slope of the semilog straight line, 26.7 psi/cycle, we calculate $k = 7.5$ md.

Next, calculate the dimensionless producing time, t_{pAD} , with Eq. 8.138.

$$\begin{aligned}
 t_{pAD} &= \frac{0.0002637kt_p}{\phi\mu c_t A} \\
 &= \frac{(0.0002637)(7.5)(482)}{(0.15)(0.25)(1.615 \times 10^{-5})(1,500)(3,000)} = 0.35.
 \end{aligned}$$

To calculate dimensionless production time, use the same producing time used in preparing the Horner graph. If the actual producing time is quite long, replace it with the time required to reach pseudosteady state, but remember to use the same producing time in the HTR and in calculating the dimensionless time for the MBH function. The time to reach pseudosteady state

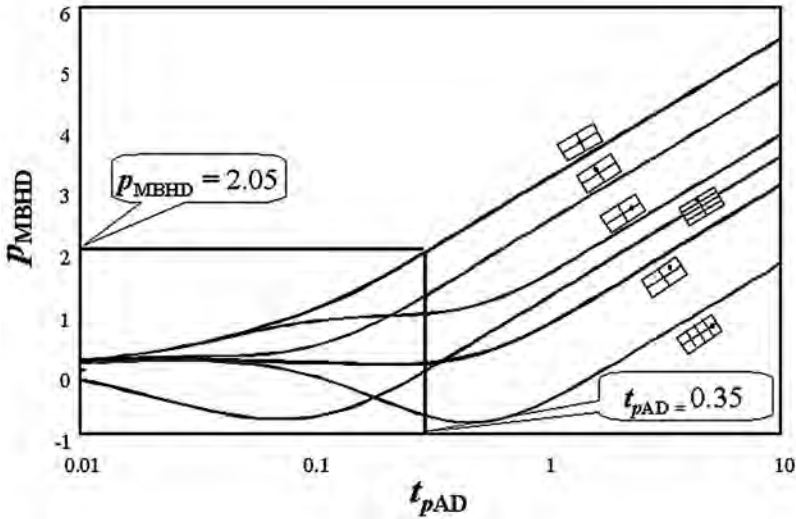


Fig. 8.70—Entering chart at producing time yields MBH pressure.

is determined by observing the appropriate MBH graph and finding when the dimensionless pressure vs. time becomes a straight line.

The next step is to select the appropriate MBH chart for the drainage area shape and well location being evaluated. Because the example well is centered in a 2×1 rectangle, choose Fig. 8.67. On this chart, enter the graph at a dimensionless producing time of 0.35, as illustrated in Fig. 8.70, and read across to find the dimensionless pressure, p_{MBHD} , which has a value of 2.05.

The next step is to calculate the average reservoir pressure, \bar{p} . From rearrangement of Eq. 8.137,

$$\bar{p} = p^* - \frac{m}{2.303} p_{MBHD} \dots\dots\dots (8.139)$$

In this case, the extrapolated $p^* = 2,689.4$ psi, the slope of the MTR = 26.7, and the dimensionless pressure = 2.05. Thus,

$$\bar{p} = 2689.4 - \frac{26.7}{2.303}(2.05) = 2665.6 \text{ psi.}$$

Ramey-Cobb Method. The Ramey-Cobb method²⁴ also uses information from a Horner plot of buildup test data. After determining permeability from the Horner plot, dimensionless producing time, t_{pAD} , can be calculated.

The third step differs from the MBH method in that the Dietz shape factors, C_A , from Table 8.A-1 for the drainage-area shape and well location that best describes the tested well are used. (For the physical significance of the shape factor, see Ramey and Cobb.²⁴) For the example well, the drainage area is a 2 × 1 rectangle, and the shape factor is 21.8369. Ramey and Cobb found a relationship between shape factor and the HTR at which the pressure on the MTR is current average drainage area pressure, \bar{p} . The relationship is

$$\left(\frac{t_p + \Delta t}{\Delta t} \right)_{\bar{p}} = C_A t_{pAD} \dots\dots\dots (8.140)$$

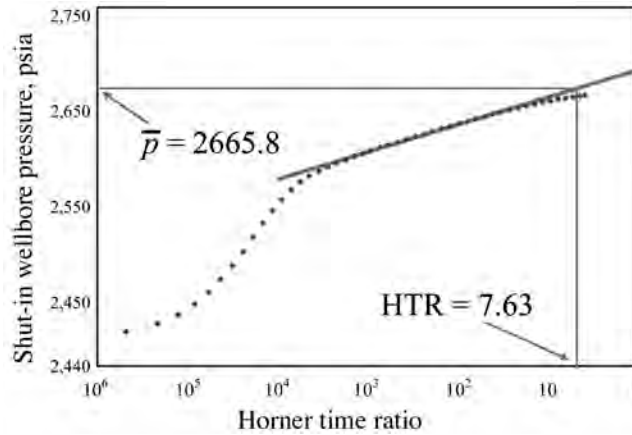


Fig. 8.71—Ramey-Cobb results replicate those of MBH method.

In the example test, the dimensionless producing time is 0.35, so the HTR that corresponds to the average reservoir pressure is 7.63.

$$\left(\frac{t_p + \Delta t}{\Delta t} \right)_{\bar{p}} = C_{AD} t_{pAD} = (21.8)(0.35) = 7.63.$$

Enter the Horner plot at a HTR of 7.63, read up to the extrapolated MTR straight line, then read across to the vertical axis. The resulting average reservoir pressure is 2,665.8 (Fig. 8.71). The result, for practical purposes, is identical to the result obtained using the MBH method.

The MBH and Ramey-Cobb methods use only data in the MTR. Once enough data is available to identify the MTR, the test can be terminated, which reduces test costs. The disadvantages of these methods are the need to know the drainage area size, shape, location of the well within that drainage area, and an accurate measurement of fluid properties. In the MBH method, the well can be in transient flow at the time of shut-in, but in the Ramey-Cobb method, the well must have reached pseudosteady state before shut-in. Results for the two methods should be identical, because they are based on the same theory. When it is applicable (pseudosteady state before shut-in), the Ramey-Cobb method is preferred because it is easier to apply.

8.8.2 Late-Time Region Methods. Methods using LTR data are based on extrapolation of the post-middle-time region data trend. The advantages of these methods are that they require neither accurate fluid property estimates nor the drainage area size and shape. They do require that the well be reasonably centered within its drainage area. The disadvantage is that they require the post-middle-time region transient data. Thus, they require longer and more expensive shut-in tests to provide the data required for analysis.

Modified Muskat Method. The modified Muskat method is based on the theoretical observation first published by Larsen²⁵ that, for late-time data (after boundary effects have appeared), the difference between current average reservoir pressure, \bar{p} , and shut-in BHP, p_{ws} , declines exponentially. In equation form,

$$\bar{p} - p_{ws} = Ae^{bt}, \dots\dots\dots (8.141)$$

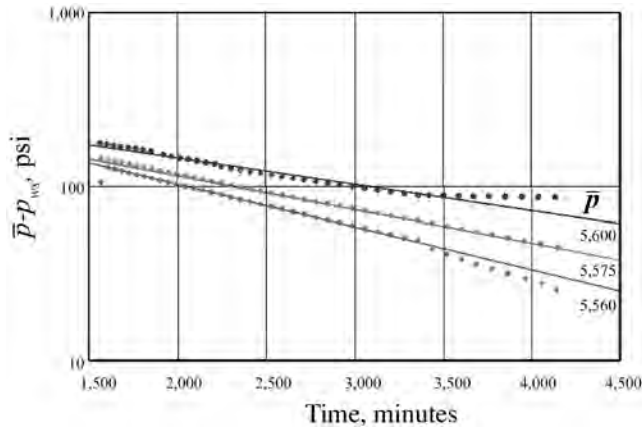


Fig. 8.72—Trial-and-error plot identifies best value of average pressure.

$$\text{or } \ln(\bar{p} - p_{ws}) = \ln(A) - bt \dots\dots\dots (8.142)$$

Eq. 8.142 leads to a procedure for estimating average drainage-area pressure, \bar{p} . This method requires a trial-and-error approach. To select data suitable for analysis with this method, use the diagnostic plot to determine the start of boundary effects. Then assume a value for \bar{p} , and plot $\log(\bar{p} - p_{ws})$ vs. time. If the curve is concave downward, the assumed pressure is too low; if the curve is concave upward, the assumed pressure is too high. Try different values for \bar{p} until the graph is a straight line, as predicted by theory.

On the example (Fig. 8.72), once the data begin to fall on a straight line, they tend to remain on that straight line. Shown are curves for assumed values of $\bar{p} = 5,600$; $5,575$; and $5,560$. On the first curve, for $\bar{p} = 5,600$, the final data points are trending above the straight line. For the lower curve, with $\bar{p} = 5,560$, the last few data points are trending below the straight line. For the assumed value $\bar{p} = 5,575$, all of the data points fall on a straight line making this assumption the right estimate of \bar{p} . The advantage to this method is that it is very easy to apply. It works best with a well reasonably centered within a drainage area.

The weaknesses of this method are that it is more sensitive to estimates that are too low rather than to estimates that are too high and that it is not easily automated and, therefore, not as widely incorporated into well-test analysis software as some other methods.

Arps-Smith Method. This is an alternative method for analyzing LTR data.²⁶ The theoretical basis for this originally empirical method is also Eq. 8.141. Differentiating Eq. 8.141 with respect to time,

$$\frac{dp_{ws}}{dt} = A b e^{-bt} = b(\bar{p} - p_{ws}) \dots\dots\dots (8.143)$$

To apply this method, plot the change in BHP with time, dp_{ws}/dt vs. p_{ws} , on Cartesian coordinates. On such a plot, data for the LTR should fall on a straight line, and extrapolation of that line to $dp_{ws}/dt = 0$ provides an estimate of the average drainage area pressure, \bar{p} .

In Fig. 8.73, the final points from an example test fall on a straight line. Extrapolating the straight line to the horizontal axis gives the average pressure at the intercept. For this example, which is the same test illustrated with the modified Muskat method, the average pressure is 5,575 psi, which is the same value found with the Muskat method.

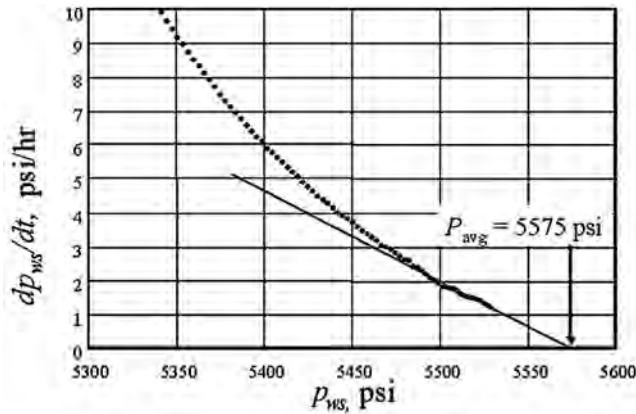


Fig. 8.73—Extrapolation of straight line to x-axis yields average pressure.

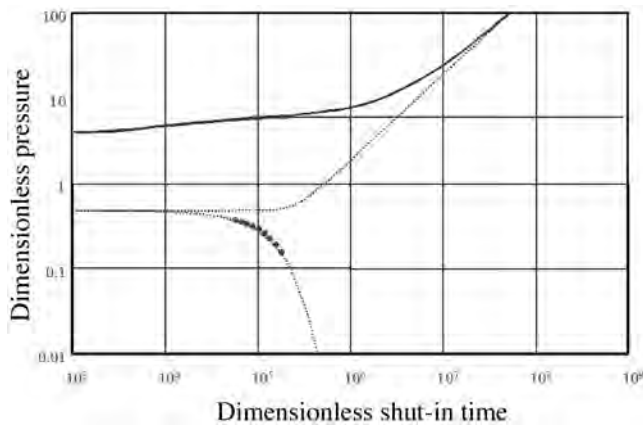


Fig. 8.74—Darker dots represent data in range of Muskat, Arps-Smith methods.

The advantages of the Arps-Smith method are that it is simple to apply and easily automated (which means that it is easily implemented into well-test analysis software or into spreadsheets). The disadvantages are that it requires data in the LTR, which means that it requires longer, more expensive tests. It assumes that shut-in pressure approaches average pressure exponentially, which is most nearly true for wells centered in the drainage area, and it requires numerical differentiation of pressure with respect to time, which tends to magnify any noise that may be present in the data.

The modified Muskat and Arps-Smith methods actually apply for shut-in times in the range,

$$\frac{250\phi\mu c_t r_e^2}{k} \leq \Delta t \leq \frac{750\phi\mu c_t r_e^2}{k} \dots\dots\dots (8.144)$$

In Fig. 8.74, the data points with darker dots are on the type curve for the derivative. These are the data in the range for which the modified Muskat and Arps-Smith methods work.

Fig. 8.74 illustrates one of the disadvantages of these two methods. Many other reservoir models will exhibit similar diagnostic plots, but data like that shown with the dark dots in this figure will not extrapolate to the correct average reservoir drainage area pressure. Examples of

these other cases include dual-porosity reservoirs during the early transition from fracture flow to total system flow, layered reservoirs, and composite reservoirs with an inner zone mobility much lower than the outer zone mobility.

8.9 Hydraulically Fractured Wells

Many wells—particularly gas wells in low-permeability formations—require hydraulic fracturing to be commercially viable. Interpretation of pressure-transient data in hydraulically fractured wells is important for evaluating the success of fracture treatments and predicting the future performance of fractured wells. This section includes graphical techniques for analyzing post-fracture pressure transient tests after identifying several flow patterns that are characteristic of hydraulically fractured wells. Often, identification of specific flow patterns can aid in well test analysis.

8.9.1 Flow Patterns in Hydraulically Fractured Wells. Five distinct flow patterns (Fig. 8.75) occur in the fracture and formation around a hydraulically fractured well.²⁷ Successive flow patterns, which often are separated by transition periods, include fracture linear, bilinear, formation linear, elliptical, and pseudoradial flow. Fracture linear flow (Fig. 8.75a) is very short-lived and may be masked by wellbore-storage effects. During this flow period, most of the fluid entering the wellbore comes from fluid expansion in the fracture, and the flow pattern is essentially linear.

Because of its extremely short duration, the fracture linear flow period often is of no practical use in well test analysis. The duration of the fracture linear flow period is estimated by²⁷

$$t_{L_f D} \cong \frac{0.1 C_r^2}{\eta_{fD}^2}, \dots\dots\dots (8.145)$$

where $t_{L_f D}$ is dimensionless time in terms of fracture half-length,

$$t_{L_f D} \cong \frac{0.0002637 k_t}{\phi \mu c_t L_f^2} \dots\dots\dots (8.146)$$

The dimensionless fracture conductivity, C_r , is

$$C_r = \frac{w_f k_f}{\pi k L_f}, \dots\dots\dots (8.147)$$

and η_{fD} is dimensionless hydraulic diffusivity defined by

$$\eta_{fD} = \frac{k_f \phi c_t}{k \phi_f c_{ft}} \dots\dots\dots (8.148)$$

Bilinear flow (Fig. 8.75b) evolves only in finite-conductivity fractures as fluid in the surrounding formation flows linearly into the fracture and before fracture tip effects begin to influence well behavior. Fractures are considered to be finite conductivity when $C_r < 100$. Most of the fluid entering the wellbore during this flow period comes from the formation. During the bilinear flow period, BHP, p_{wf} , is a linear function of $t^{1/4}$ on Cartesian coordinates.

A log-log plot of $(p_i - p_{wf})$ as a function of time exhibits a slope of $1/4$ unless the fracture is damaged. The pressure derivative also has a slope of $1/4$ during this same time period. The

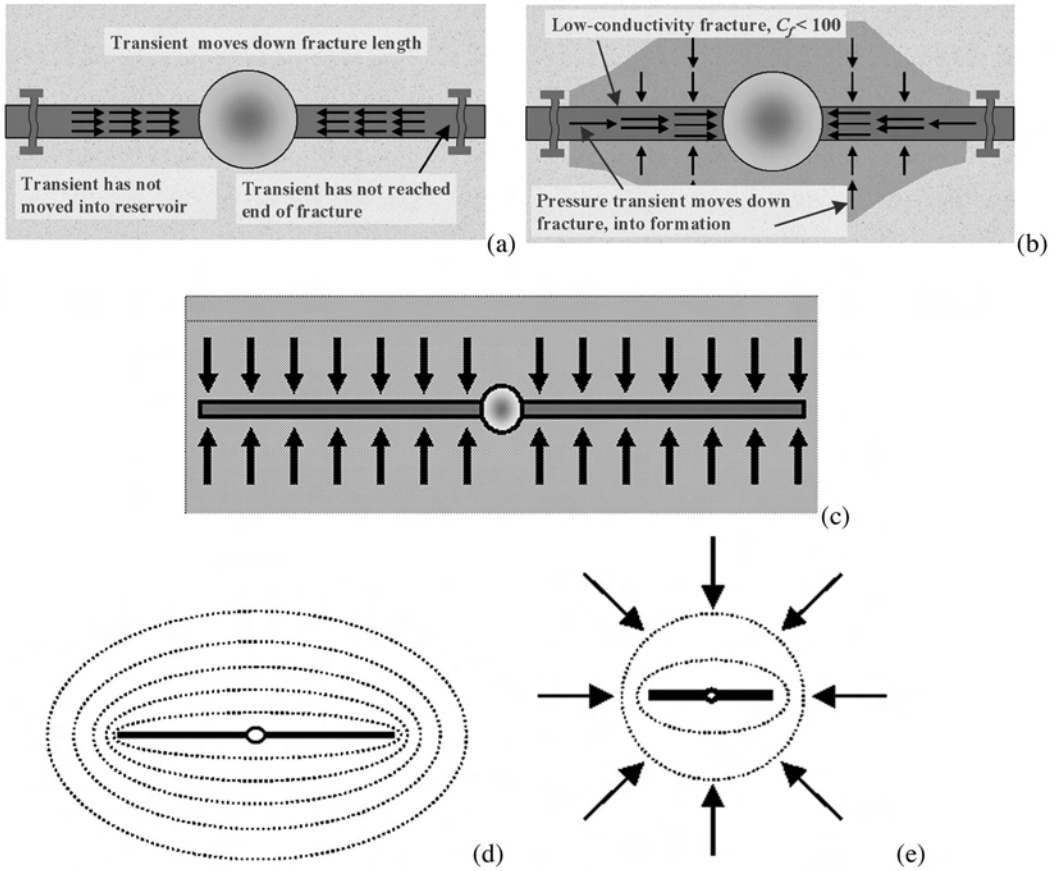


Fig. 8.75—Flow periods in a vertically fractured well.²⁷

duration of bilinear flow depends on dimensionless fracture conductivity and is given by Eqs. 8.149a through 8.149c²⁷ for a range of dimensionless times and fracture conductivities:

$$t_{L_f D} \cong \frac{0.01}{C_r^2} \text{ for } C_r > 3, \dots\dots\dots (8.149a)$$

$$t_{L_f D} \cong 0.0205(C_r - 1.5)^{-1.53} \text{ for } 1.6 \leq C_r \leq 3, \dots\dots\dots (8.149b)$$

$$\text{and } t_{L_f D} \cong \left(\frac{4.55}{\sqrt{C_r}}\right)^{-4} \text{ for } C_r < 1.6 \dots\dots\dots (8.149c)$$

Formation linear flow (Fig. 8.75c) occurs only in high-conductivity ($C_r \geq 100$) fractures. This period continues to a dimensionless time of $t_{L_f D} \cong 0.016$. The transition from fracture linear flow to formation linear flow is complete by a time of $t_{L_f D} = 10^{-4}$. On Cartesian coordinates, p_{wf} is a linear function of $t^{1/2}$, and a log-log plot of $(p_i - p_{wf})$ has a slope of $1/2$ unless the fracture is damaged. The pressure derivative plot exhibits a slope of $1/2$. Elliptical flow (Fig.

TABLE 8.2—DATA FOR EXAMPLE 8.1

Case No.	L_f (ft)	k (md)	Time to End of Linear Flow (hours)	Time to Start of Pseudoradial Flow (hours)
1	100	1.00	0.273	51.2
2	100	0.01	27.3	5,120 (213 days)
3	1,000	0.01	2,730 (114 days)	512,000 (58 years)

Other data: $\phi = 0.15$, $\mu = 0.03$ cp, $C_r = 100$, $c_r = 1 \times 10^{-4}$ psi⁻¹

8.75d) is a transitional flow period that occurs between a linear or near-linear flow pattern at early times and a radial or near-radial flow pattern at late times.

Pseudoradial flow (Fig. 8.75e) occurs with fractures of all conductivities. After a sufficiently long flow period, the fracture appears to the reservoir as an expanded wellbore (consistent with the effective wellbore radius concept suggested by Prats *et al.*¹⁰). At this time, the drainage pattern can be considered as a circle for practical purposes. (The larger the fracture conductivity, the later the development of an essentially radial drainage pattern.) If the fracture length is large relative to the drainage area, then boundary effects distort or entirely mask the pseudoradial flow regime. Pseudoradial flow begins at $t_{L,D} \cong 3$ for high-conductivity fractures ($C_r \geq 100$) and at slightly smaller values of $t_{L,D}$ for lower values of C_r .

These flow patterns also appear in pressure-buildup tests and occur at approximately the same dimensionless times as in flow tests. The physical interpretation is that the pressure has built up to an essentially uniform value throughout a particular region at a given time during a buildup test. For example, at a given time during bilinear or formation linear flow, pressure has built up to a uniform level throughout an approximately rectangular region around the fracture. At a later time during elliptical flow, pressure has built up to a uniform level throughout an approximately elliptical region centered at the wellbore. At a given time during pseudoradial flow, pressure has built up to a uniform level throughout an approximately circular region centered at the wellbore. The area of the region and the pressure level within that area increase with increasing shut-in time. Example 8.1 illustrates how to estimate the duration of flow periods for hydraulically fractured wells.

Example 8.1: Estimating Duration of Flow Periods in a Hydraulically Fractured Well. For each case, estimate the end of the linear flow period and the time at which pseudoradial flow period begins. Assume that pseudoradial flow begins when $t_{L,D} = 3$. Table 8.2 gives the data for each case.

Solution. The end of the linear flow regime occurs at a dimensionless time of $t_{L,D} \cong 0.016$ or, using Eq. 8.146,

$$t = \frac{\phi \mu c_r L_f^2 t_{L,D}}{0.0002637k} = \frac{(0.15)(0.03)(1 \times 10^{-4})L_f^2(0.016)}{0.0002637k} = \frac{2.73 \times 10^{-5}L_f^2}{k}$$

Similarly, the time to reach pseudoradial flow is $t_{L,D} \cong 3$, or

$$t = \frac{\phi \mu c_r L_f^2 t_{L,D}}{0.0002637k} = \frac{(0.15)(0.03)(1 \times 10^{-4})L_f^2(3)}{0.0002637k} = \frac{5.12 \times 10^{-3}L_f^2}{k}$$

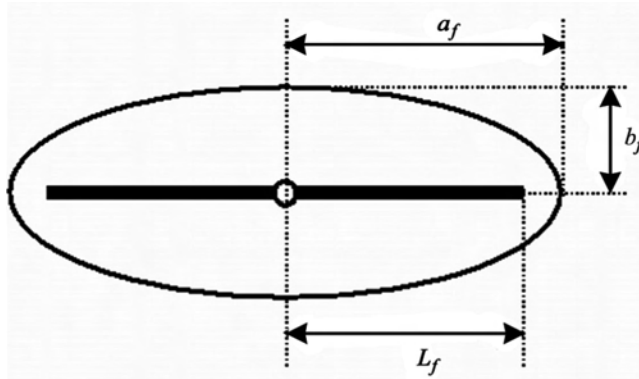


Fig. 8.76—Elliptical flow pattern around a vertically fractured well.

Table 8.2 summarizes the results.

8.9.2 Flow Geometry and Depth of Investigation of a Vertically Fractured Well. Fluid flow in a vertically fractured well has been described using elliptical geometry.²⁸ The equation for an ellipse with its major axis along the x -axis and minor axis along the y -axis is

$$\frac{x^2}{a_f^2} + \frac{y^2}{b_f^2} = 1, \dots\dots\dots (8.150)$$

where the endpoints of the major and minor axes are $(\pm a_f, 0)$ and $(0, \pm b_f)$, respectively. The foci of the ellipse are $\pm c_f$ where $c_f^2 = a_f^2 - b_f^2$. In terms of a well with a single vertical fracture with two wings of equal length, L_f , the relation becomes $L_f^2 = a_f^2 - b_f^2$, where L_f is the focal length of the ellipse. Fig. 8.76 shows the elliptical geometry of a vertically fractured well.

Hale and Evers²⁸ defined a depth of investigation for a vertically fractured well. Their definition is based on a definition of dimensionless time at a distance b_f , the length of the minor axis:

$$t_{bD} = \frac{0.0002637kt}{\phi \mu c_t b_f^2} \dots\dots\dots (8.151)$$

Solving for the length of the minor axis,

$$b_f = \left(\frac{0.0002637kt}{\phi \mu c_t b_D} \right)^{1/2} \dots\dots\dots (8.152)$$

Assuming that pseudosteady-state flow exists out to distance, b_f , at dimensionless time $t_{bD} = 1/\pi$ as in linear systems, Eq. 8.152 becomes

$$b_f = 0.0002878 \left(\frac{kt}{\phi \mu c_t} \right)^{1/2}, \dots\dots\dots (8.153)$$

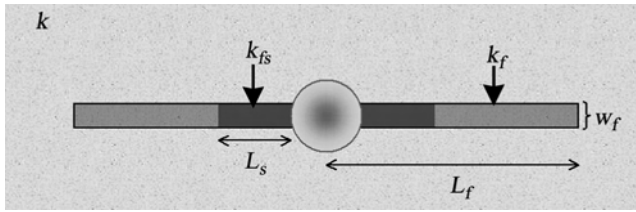


Fig. 8.77—Permeability differs between propped and near-wellbore portions of fracture.

which represents the depth of investigation in a direction perpendicular to the fracture at time, t , for a vertically fractured well. In gas wells, the terms μ and c_t should be $\bar{\mu}$ and \bar{c}_t , evaluated at average drainage-area pressure, \bar{p} .

The elliptical pattern of the propagating pressure transient can be fully described in terms of the lengths of the major axis, a_f , the minor axis, b_f , and the focus, L_f . Using the estimate of b_f from Eq. 8.153 and an estimate of L_f obtained by one of the methods described in sections that follow, the length of the major axis can be estimated from

$$a_f = \sqrt{L_f^2 + b_f^2} \dots\dots\dots (8.154)$$

Given values of a_f and b_f , the depth of investigation at a particular time, t , in any direction from the fracture can be calculated using Eq. 8.150. Furthermore, the area, A , enclosed by the ellipse at time, t (the area of the reservoir sampled by the pressure transient), is given by

$$A_f = \pi a_f b_f \dots\dots\dots (8.155)$$

The coefficient 0.0002878 in Eq. 8.153 is strictly correct only for highly conductive fractures ($C_r \geq 100$). As C_r becomes smaller, the ratio a_f/b_f also becomes smaller. The lower bound of a_f/b_f is 1 (a circle) as C_r approaches 0.

8.9.3 Fracture Damage. Two major types of fracture damage are frequent: choked fracture damage and fracture-face damage. The choked-fracture damage means that the fracture has a reduced permeability in the immediate vicinity of the wellbore (Fig. 8.77). In this case, k_f is used for the permeability in the propped portion of the fracture farther along the wellbore, and k_{fs} for reduced permeability near the wellbore, out to a length, L_s , in the fracture.

The choked-fracture skin factor, s_f , is²⁹

$$s_f = \frac{\pi k L_s}{k_{fs} w_f} \dots\dots\dots (8.156)$$

Fracture face damage in a hydraulically fractured well (Fig. 8.78) is a permeability reduction around the edges of the fracture, usually caused by invasion of the fracture fluid into the formation or an adverse reaction with the fracturing fluid. The equation for fracture face skin is²⁹

$$s_f = \frac{\pi w_s}{2 L_f} \left(\frac{k}{k_s} - 1 \right) \dots\dots\dots (8.157)$$

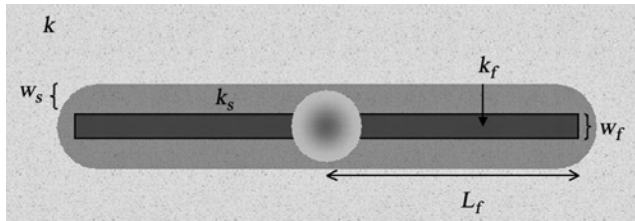


Fig. 8.78—Permeability reduction around edges of fracture represents fracture face damage.

8.9.4 Specialized Methods for Post-Fracture Well-Test Analysis. Generally, the objectives of post-fracture pressure-transient test analysis are to assess the success of the fracture treatment and to estimate the fracture half-length, fracture conductivity, and formation permeability. Three specialized methods of analyzing these post-fracture transient tests are included in this section: pseudoradial flow, bilinear flow, and linear flow.

Bilinear Flow Method. The bilinear flow method³⁰ applies to test data obtained during the bilinear flow regime in wells with finite-conductivity vertical fractures. Bilinear flow is indicated by a quarter-slope line on a log-log graph of pressure derivative vs. t or Δt_e .

During bilinear flow,

$$p_D = \frac{1.38}{\sqrt{C_r}} t_{L_f D}^{1/4} + s_f, \dots\dots\dots (8.158)$$

$$\text{and } t_{L_f D} \frac{dp_D}{dt_{L_f D}} = \frac{0.345}{\sqrt{C_r}} t_{L_f D}^{1/4} \dots\dots\dots (8.159)$$

The following procedure is recommended for analyzing test data obtained in the bilinear flow regime (that is, data in the time range with quarter slope on the diagnostic plot). In Step 1, note the use of “bilinear equivalent time,” Δt_{Be} . Radial equivalent time is rigorously correct as a plotting function only for infinite-acting radial flow.

1. For a constant-rate flow test, plot p_{wf} vs. $t^{1/4}$ on Cartesian coordinates. For a buildup test, plot p_{ws} vs. $\Delta t_{Be}^{1/4}$, where

$$\Delta t_{Be}^{1/4} = [t_p^{1/4} + \Delta t^{1/4} - (t_p + \Delta t)^{1/4}] \dots\dots\dots (8.160)$$

2. Determine the slope, m_B , of the straight line region of the plot.
3. Determine the pressure extrapolated to time zero, p_o , and the fracture skin, s_f , from

$$s_f = \frac{0.00708kh}{qB\mu} (p_i - p_o) \text{ or } \frac{0.00708 kh}{qB\mu} (p_o - p_{wf}) \dots\dots\dots (8.161)$$

for drawdown and buildup tests, respectively.

4. From independent knowledge of k (for example, from a prefracture well test), estimate the fracture conductivity, $w_f k_f$, using m_B and the relationship

$$w_f k_f = \left(\frac{44.1qB\mu}{hm_B} \right)^2 \left(\frac{1}{\phi \mu c_t k} \right)^{0.5} \dots\dots\dots (8.162)$$

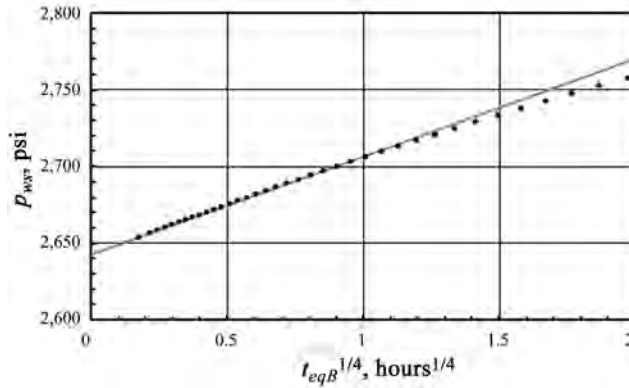


Fig. 8.79—Bilinear flow analysis.

where $\bar{\mu}$ and \bar{c}_p , evaluated at \bar{p} , are used for a gas well test.

Fig. 8.79 is an example of bilinear flow analysis. The bilinear flow analysis method has the following important limitations.

- No estimate of fracture half-length, L_f .
- In wells with low-conductivity fractures, wellbore storage frequently distorts early test data for a sufficient length of time so that the quarter-slope line characteristic of bilinear flow may not appear on a log-log plot of test data.
- An independent estimate of k is required. This suggests that prefracture well tests should be conducted before fracturing the well, thus obtaining independent estimates of formation properties.

Linear Flow Method. The linear flow method³⁰ applies to test data obtained during formation linear flow in wells with high-conductivity fractures ($C_r \geq 100$). After wellbore storage effects have ended, formation linear flow occurs up to a dimensionless time of $t_{L,D} = 0.016$, which means that a log-log plot of pressure derivative against time will have a slope of one-half. The plot of pressure change vs. time, however, will have a half-slope only if the fracture skin is zero. The pressure and pressure derivative are

$$p_D = (\pi L_{fD})^{1/2} + s_f, \dots\dots\dots (8.163)$$

$$\text{and } t_{LfD} \frac{dp_D}{dt_{LfD}} = \frac{1}{2} (\pi t_{LfD})^{1/2}, \dots\dots\dots (8.164)$$

so that

$$\log \left(t_{LfD} \frac{dp_D}{dt_{LfD}} \right) = \frac{1}{2} \log (t_{LfD}) + \frac{1}{2} \log (\pi), \dots\dots\dots (8.165)$$

which indicates that a log-log plot of the derivative against time will have a slope of one-half. Radial equivalent time applies rigorously only for radial flow in an infinite-acting reservoir. When linear flow is the flow pattern occurring at both times ($t_p + \Delta t$) and Δt , a more useful equivalent time function is the linear equivalent time, Δt_{eL} .

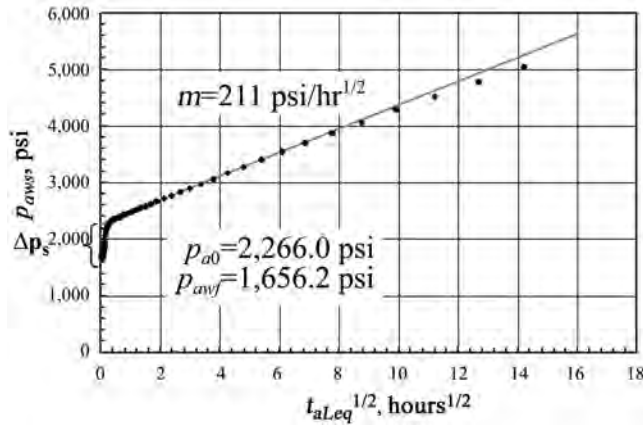


Fig. 8.80—Plot used in linear flow analysis.

$$\sqrt{\Delta t_{eL}} = \sqrt{t_p} + \sqrt{\Delta t} - \sqrt{t_p + \Delta t} \dots\dots\dots (8.166)$$

Test conditions in which linear flow occurs at both $(t_p + \Delta t)$ and Δt are rare, and, consequently, Eq. 8.166 is not necessarily rigorously correct for well-test analysis. Fortunately, when $t_p \gg \Delta t_{max}$, $\Delta t_{eL} \approx \Delta t$. Fig. 8.80 is an example of a plot used in linear flow analysis.

The linear flow analysis method also has limitations.

- The method applies only for fractures with high conductivities. Strictly speaking, linear flow occurs for the condition of uniform flux into a fracture (same flow rate from the formation per unit cross-sectional area of the fracture at all points along the fracture) rather than for infinite fracture conductivity. Therefore, only very early test data ($t_{L,D} \leq 0.016$) exhibit linear flow in a high-conductivity fracture.

- Some or all of these early data may be distorted by wellbore storage, further limiting the amount of linear-flow data available for analysis.

- Estimating fracture half-length requires an independent estimate of permeability, k , which suggests the need for a prefracture well test.

Pseudoradial Flow Method. The pseudoradial flow method applies when a short, highly conductive fracture is created in a high-permeability formation, so that pseudoradial flow develops in a short time. The time required to achieve pseudoradial flow for an infinitely conductive fracture ($C_r \geq 100$) in either a flow test or a pressure buildup test is estimated by

$$t_{L_f D} = \frac{0.0002637kt}{\phi \mu c_t L_f^2} \cong 3 \dots\dots\dots (8.167)$$

The beginning of pseudoradial flow is characterized by the flattening of the pressure derivative on a log-log plot and by the start of a straight line on a semilog plot. Hence, when the pseudoradial flow regime is reached, conventional semilog analysis can be used to calculate permeability and skin factor. For a highly conductive fracture, skin factor is related to fracture half-length by¹⁰

$$L_f \cong 2r_w e^{-s} \dots\dots\dots (8.168)$$

Fig. 8.81 shows an example.

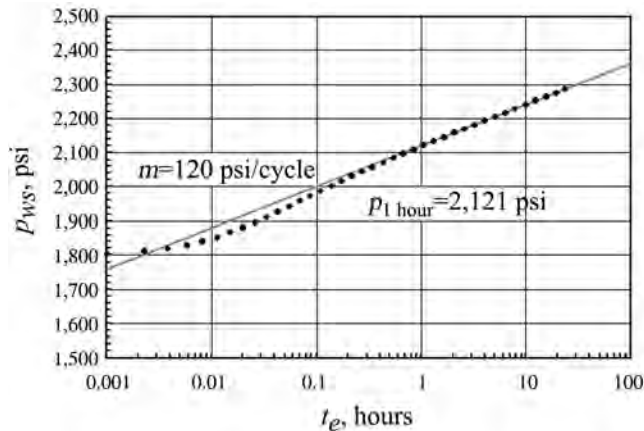


Fig. 8.81—Pseudoradial flow analysis.

A recommended procedure for analyzing test data from the pseudoradial flow regime is as follows.

- For a drawdown test, plot p_{wf} vs. $\log t$. For a buildup test, plot p_{ws} vs. the HTR.
- Determine the position and slope, m , of the semilog straight line and the intercept, p_{1hr} on the line.
- Using m , calculate values of k and s (or s' for a gas well).
- Calculate the fracture half-length, L_f , using Eq. 8.168.

The pseudoradial flow method has the following limitations that seldom make it applicable in practice.³⁰

- The conditions that are most favorable for the occurrence of pseudoradial flow are short, highly conductive fractures in high-permeability formations. These formations, however, are rarely fractured. The most common application of hydraulic fractures—wells with long fractures in low-permeability formations—require impractically long test times to reach pseudoradial flow.

- For gas wells, the apparent skin factor, s' , calculated from test data is often affected by non-Darcy flow.

- The pseudoradial method applies only to highly conductive ($C_r \geq 100$) fractures. For lower conductivity fractures, fracture lengths calculated using the skin factor (Eq. 8.168) will be too low.

8.9.5 Using Type Curves for Hydraulically Fractured Wells. Type curves are the most common method of analyzing hydraulically fractured wells. The independent variable for most type curves for analyzing hydraulically fractured wells is the dimensionless time based on hydraulic fracture half-length, $t_{L_f D}$. The dependent variable is usually the dimensionless pressure, p_D .

For type curves used for manual type-curve matching, most vary only one parameter. The Cinco type curve²⁷ is obtained for zero $C_{L_f D}$ and s_f ; the only parameter is dimensionless fracture conductivity, C_r or F_{cD} (where $F_{cD} = \pi c_r$). The choked-fracture skin is analyzed by assuming $C_{L_f D}$ and infinite C_r with single parameter s_f . The wellbore-storage type curve³¹ sets s_f to 0 and C_r (F_{cD}) to infinity and varies the coefficient $C_{L_f D}$.

When using type curves in commercial software, the computer can set any two of the three parameters to fixed values (other than their limiting values) and vary the third parameter to obtain the matching stems.

Procedures for Analyzing Fractured Wells With Type Curves. The following steps outline the procedure for analyzing fractured wells with type curves.

- Graph field data pressure change and pressure derivatives.
- Match field data to the appropriate type curve.
- Find the match point and matching stem.
- Calculate the formation permeability from the pressure match point.
- Calculate L_f from the time match point.
- Interpret the matching stem value appropriate for a given type curve. For one type curve, this can be $w_f k_f$, which will provide an estimate of fracture conductivity. For another, it can be s_f , the choked-fracture skin, or, for a third, it can be C , the wellbore-storage coefficient.

To interpret the match points for a test with unknown permeability, use Eqs. 8.169 and 8.170. The formation permeability, k , is determined from the pressure match point; that is, the relationship between the pressure derivative and pressure change found at a match point given by

$$k = \frac{141.2qB\mu}{h} \left(\frac{P_D}{\Delta p} \right)_{MP} \dots\dots\dots (8.169)$$

From the time match point, calculate the fracture half-length:

$$L_f = \sqrt{\frac{0.0002637k \left(\frac{\Delta t}{t_{L_f D}} \right)_{MP}}{\phi \mu c_t}} \dots\dots\dots (8.170)$$

Matching can be ambiguous for hydraulically fractured wells; the data can appear to match equally well in several different positions. The ambiguity can be reduced or eliminated if a prefracture permeability is determined, and the post-fracture test data forced to match the permeability.

Type Curves Used for Analysis in Fractured Wells. Cinco Type Curve. The Cinco type curve (Fig. 8.82),²⁷ assumes that $C_{L_f D} = 0$ and $s_f = 0$. The type-curve stems on this curve are obtained by varying values of C_r or F_{cD} . With the Cinco type curve, the fracture conductivity, $w_f k_f$, can be determined from the matching parameter:

$$w_f k_f = \pi k L_f C_r \dots\dots\dots (8.171)$$

Choked-Fracture Type Curve. Fig. 8.83 shows the choked-fracture type curve.²⁹ The choked-fracture type curve is generated with wellbore-storage coefficient, $C_{L_f D}$, of zero and infinite fracture conductivity, C_r . On this type curve, the stems represent different values of the fracture skin, s_f . The fracture skin, s_f , can be used to find the additional pressure drop from

$$\Delta p_s = \frac{141.2qB\mu}{kh} s_f \dots\dots\dots (8.172)$$

Wellbore-Storage Type Curve. The wellbore-storage type curve (Fig. 8.84) takes into account the possibility of wellbore storage. The wellbore-storage type assumes $s_f = 0$ and $C_r = \infty$. To interpret a best-fitting stem for this type curve, use the following:

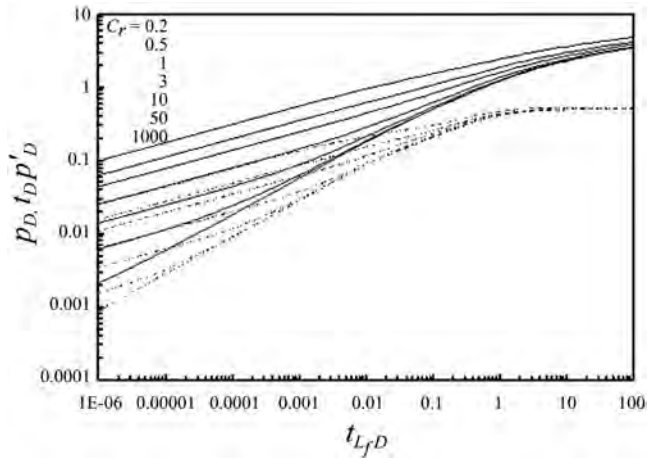


Fig. 8.82—Cinco type curve.

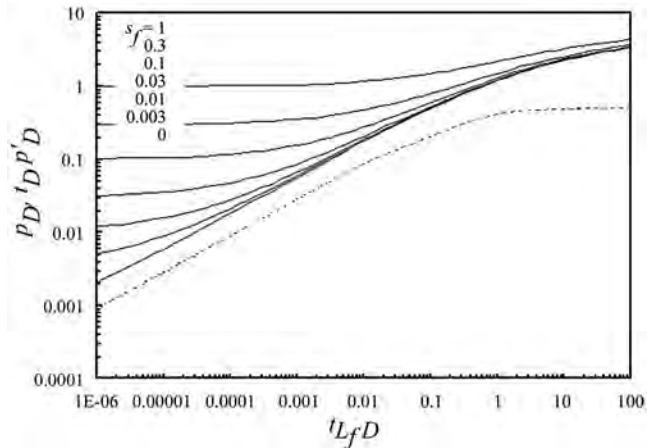


Fig. 8.83—Choked-fracture type curve.

$$C = \frac{\phi c_t h L_f^2}{0.8936} C_{L_f D} \dots\dots\dots (8.173)$$

8.9.6 Limitations of Type-Curve Analysis in Hydraulically Fractured Wells. Although it is the most common methodology for analyzing hydraulically fractured well, type-curve analysis still has some limitations.

First, type-curves for analysis of hydraulically fractured wells are usually based on solutions for constant-rate drawdown tests. For buildup tests, shut-in time itself may possibly be used as a plotting function in those cases in which producing time is much greater than the shut-in time. Equivalent time can be used in some cases, but equivalent time has different definitions depending on the flow regime: radial, linear, and bilinear flow. Another possibility is to use a “superposition” type curve, which depends on the specific durations of flow and buildup periods. Superposition type curves can be readily generated with computer software.

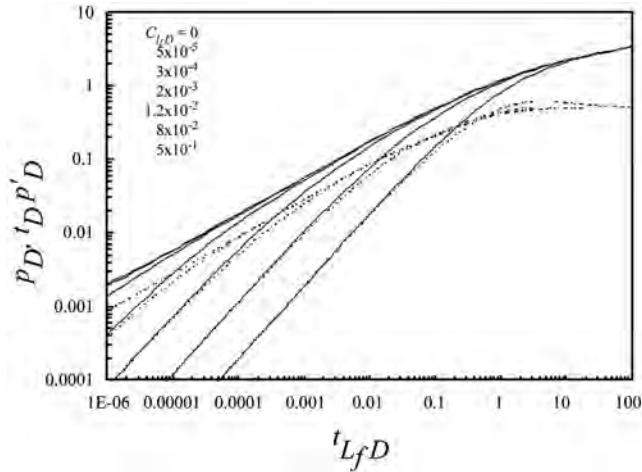


Fig. 8.84—Wellbore-storage type curve.

Another problem with type curves is that they may ignore important behavior. The type curve that takes into account wellbore storage does not consider a variable wellbore storage coefficient. This can be caused by phase redistribution in the wellbore, for example. The widely available type curves that have been discussed do not include boundary effects. With gas wells, the probability of non-Darcy flow is high, but available type curves don't take this into account.

An independent estimate of permeability may also be needed. A number of different type curves or a variety of stems on a given type curve may seem to match test data equally well. To remove this ambiguity, the best solution is to have an independent estimate of permeability.

8.10 Naturally Fractured Reservoirs

This section focuses on interpretation of well test data from wells completed in naturally fractured reservoirs. Because of the presence of two distinct types of porous media, the assumption of homogeneous behavior (discussed in previous sections) is no longer valid in naturally fractured reservoirs. This section includes two naturally fractured reservoir models, the physics governing fluid flow in these reservoirs and semilog and type-curve analysis techniques for well tests in these reservoirs.

8.10.1 Naturally Fractured Reservoir Models. Naturally fractured reservoirs are characterized by the presence of two distinct types of porous media: matrix and fracture. Because of the different fluid storage and conductivity characteristics of the matrix and fractures, these reservoirs often are called dual-porosity reservoirs. Fig. 8.85 illustrates a naturally fractured reservoir composed of a rock matrix surrounded by an irregular system of vugs and natural fractures. Fortunately, it has been observed that a real, heterogeneous, naturally fractured reservoir has a characteristic behavior that can be interpreted using an equivalent, homogeneous dual-porosity model such as that shown in the idealized sketch.

Several models have been proposed to represent the pressure behavior in a naturally fractured reservoir. These models differ conceptually only in the assumptions made to describe fluid flow in the matrix. Most dual-porosity models assume that production from the naturally fractured system comes from the matrix, to the fracture, and then to the wellbore (i.e., that the matrix does not produce directly into the wellbore). Furthermore, the models assume that the matrix has low permeability but large storage capacity relative to the natural fracture system,

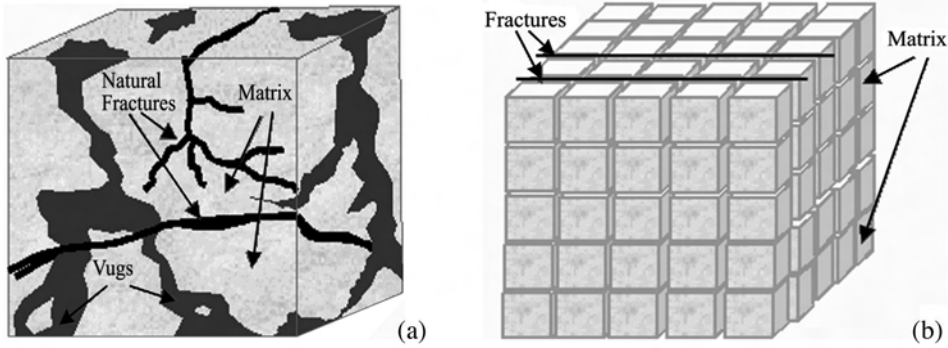


Fig. 8.85—Actual (a) and idealized (b) dual-porosity reservoir model.³²

while the fractures have high permeability but low storage capacity relative to the natural fracture system. Warren and Root³² introduced two dual-porosity parameters, in addition to the usual single-porosity parameters, which can be used to describe dual-porosity reservoirs.

Interporosity flow is the fluid exchange between the two media (the matrix and fractures) constituting a dual-porosity system. Warren and Root³² defined the interporosity flow coefficient, λ , as

$$\lambda = \alpha r_w^2 \frac{k_m}{k_f}, \dots\dots\dots (8.174)$$

where k_m is the permeability of the matrix, k_f is the permeability of the natural fractures, and α is the parameter characteristic of the system geometry.

The interporosity flow coefficient is a measure of how easily fluid flows from the matrix to the fractures. The parameter α is defined by³³

$$\alpha = \frac{4j(j+2)}{L^2}, \dots\dots\dots (8.175)$$

where L is a characteristic dimension of a matrix block and j is the number of normal sets of planes limiting the less-permeable medium ($j = 1, 2, 3$). For example, $j = 3$ in the idealized reservoir cube model in Fig. 8.85. On the other hand, for the multilayered or “slab” model shown in Fig. 8.86,³⁴ $j = 1$. For the slab model, letting $L = h_m$ (the thickness of an individual matrix block), λ becomes

$$\lambda = 12r_w^2 \frac{k_m}{k_f h_m^2} \dots\dots\dots (8.176)$$

The storativity ratio,³³ ω , is defined by

$$\omega = \frac{(\phi V c_t)_f}{(\phi V c_t)_{f+m}} = \frac{(\phi V c_t)_f}{(\phi V c_t)_f + (\phi V c_t)_m}, \dots\dots\dots (8.177)$$

where V is the ratio of the total volume of one medium to the bulk volume of the total system and ϕ is the ratio of the pore volume of one medium to the total volume of that medium.

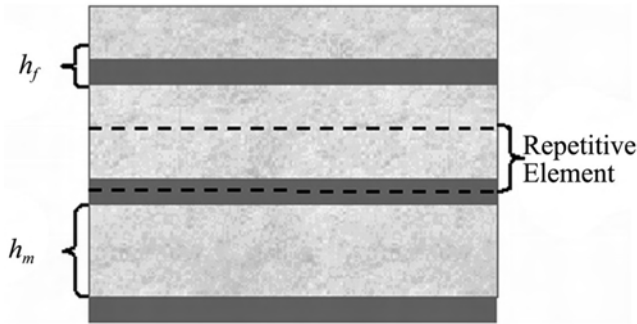


Fig. 8.86—Schematic reservoir with rectangular matrix elements.³⁴

Subscripts f and $f + m$ refer to the fracture and to the total system (fractures plus matrix), respectively. Consequently, the storativity ratio is a measure of the relative fracture storage capacity in the reservoir.

Many models have been developed for naturally fractured reservoirs. Two common models, pseudosteady-state and transient flow, that describe flow in the less-permeable matrix are presented here. Pseudosteady-state flow was assumed by Warren and Root³² and Barenblatt *et al.*³⁵; others, notably deSwaan,³⁶ assumed transient flow in the matrix. Intuition suggests that, in a low-permeability matrix, very long times should be required to reach pseudosteady-state and that transient matrix flow should dominate; however, test analysis suggests that pseudosteady-state flow is quite common. A possible explanation of this apparent inconsistency is that matrix flow is almost always transient but can exhibit a behavior much like pseudosteady-state, if there is a significant impediment to flow from the less-permeable medium to the more-permeable one (such as low-permeability solution deposits on the faces of fractures).

8.10.2 Pseudosteady-State Matrix Flow Model. The pseudosteady-state flow model assumes that, at a given time, the pressure in the matrix is decreasing at the same rate at all points and, thus, flow from the matrix to the fracture is proportional to the difference between matrix pressure and pressure in the adjacent fracture. Specifically, this model, which does not allow unsteady-state pressure gradients within the matrix, assumes that pseudosteady-state flow conditions are present from the beginning of flow.

Because it assumes a pressure distribution in the matrix that would be reached only after what could be a considerable flow period, the pseudosteady-state flow model obviously is oversimplified. Again, this model seems to match a surprising number of field tests. One possible reason is that damage to the face of the matrix could cause the flow from matrix to fracture to be controlled by a sort of choke (the thin, low-permeability, damaged zone) and, therefore, is proportional to pressure differences upstream and downstream of the choke. In the next two sections, semilog and type-curve analysis techniques are presented for well tests in naturally fractured reservoirs exhibiting pseudosteady-state flow characteristics.

Semilog Analysis Technique. The pseudosteady-state matrix flow solution developed by Warren and Root³² predicts that, on a semilog graph of test data, two parallel straight lines will develop. Fig. 8.87 shows this characteristic pressure response.

The initial straight line reflects flow in the fracture system only. At this time, the formation is behaving like a homogeneous formation with fluid flow originating only from the fracture system with no contribution from the matrix. Consequently, the slope of the initial semilog straight line is proportional to the permeability-thickness product of the natural fracture system, just as it is for any homogeneous system. Following a discrete pressure drop in the fracture

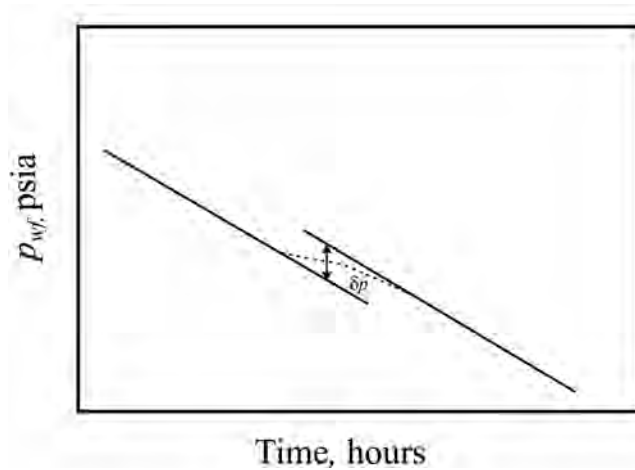


Fig. 8.87—Characteristic pressure response of flow test exhibiting pseudosteady-state matrix flow.

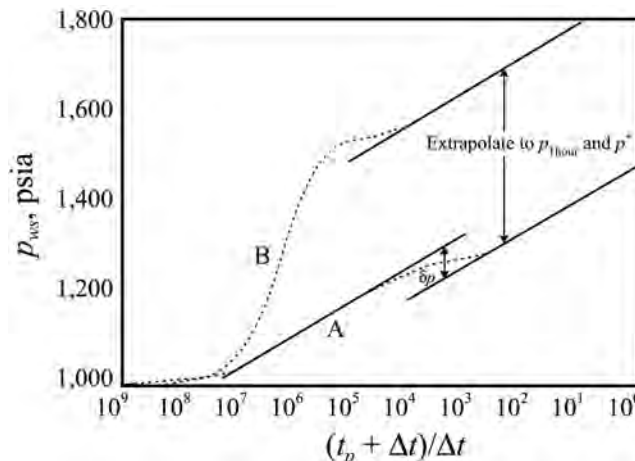


Fig. 8.88—Characteristic buildup pressure response predicted by the Warren and Root³² pseudosteady-state model.

system, the fluid in the matrix begins to flow into the fracture, and a rather flat transition region appears.

Finally, the matrix and the fracture each reach an equilibrium condition, and a second straight line appears. At this time, the reservoir again is behaving like a homogeneous system, but now the system consists of both the matrix and the fractures. The slope of the second semilog straight line is proportional to the total permeability-thickness product of the matrix/fracture system. Because the permeability of the fractures is much greater than that of the matrix, the slope of the second line is almost identical to that of the initial line.

Similar shapes are predicted for pressure buildup tests (Fig. 8.88). The lower curve, *A*, represents the ideal buildup test plot predicted by Warren and Root.³² The shape of a semilog plot of test data from a naturally fractured reservoir is almost never the same as that predicted by Warren and Root's model. Wellbore storage almost always obscures the initial straight line and often obscures part of the transition region between the straight lines. The upper curve, *B*, in Fig. 8.88 shows a more common pressure response.

The reservoir permeability-thickness product, kh [actually the kh of the fractures, or $(kh)_f$, because $(kh)_m$ is usually negligible], can be obtained from the slope, m , of the two semilog straight lines. Storativity, ω , can be determined from their vertical displacement, δp . The interporosity flow coefficient, λ , can be obtained from the time of intersection of a horizontal line, drawn through the middle of the transition curve, with either the first or second semilog straight line.³³

When semilog analysis is possible (i.e., when the correct semilog straight line can be identified), the following procedure is recommended for semilog analysis of buildup or drawdown test data from wells completed in naturally fractured reservoirs. Although presented in variables for slightly compressible fluids (liquids), the same procedure is applicable to gas well tests when the appropriate variables are used.

- From the slope of the initial straight line (if present) or final straight line (more likely to be present), determine the permeability-thickness product, kh . In either case, the slope, m , is related to the total kh of the system, which is essentially all in the fractures. The permeability-thickness product is given by

$$(kh)_f = \bar{k}h = \frac{162.6qB\mu}{|m|}, \dots\dots\dots (8.178)$$

where \bar{k} is equal to $(kh)_f/h$. Strictly speaking, the slope of the second straight line is related to $[(kh)_f + (kh)_m]$, but $(kh)_m$ ordinarily is negligible compared to $(kh)_f$.

- If both initial and final straight lines can be identified (or the position of the initial line can at least be approximated) and the pressure difference, δp , established, then the storativity ratio, ω is calculated from

$$\omega = 10^{-\delta p/m} \dots\dots\dots (8.179)$$

If the times of intersection of a horizontal line drawn through the midpoint of the transition data with the first and second semilog straight lines are denoted by t_1 and t_2 , respectively, the storativity ratio may also be calculated from

$$\omega = \frac{t_1}{t_2} \dots\dots\dots (8.180)$$

For a buildup test, where the times of intersection of a horizontal line drawn through the midpoint of the transition data with the first and second semilog straight lines are denoted by $[(t_p + \Delta t)/\Delta t]_1$ and $[(t_p + \Delta t)/\Delta t]_2$, respectively, the storativity ratio may be calculated from

$$\omega = \frac{[(t_p + \Delta t)/\Delta t]_2}{[(t_p + \Delta t)/\Delta t]_1} \dots\dots\dots (8.181)$$

- The interporosity flow coefficient, λ , is calculated³³ for a drawdown test by

$$\lambda = \frac{(\phi Vc_t)_f \mu r_w^2}{\gamma \bar{k} t_1} = \frac{(\phi Vc_t)_{f+m} \mu r_w^2}{\gamma \bar{k} t_2}, \dots\dots\dots (8.182)$$

or for a buildup test by

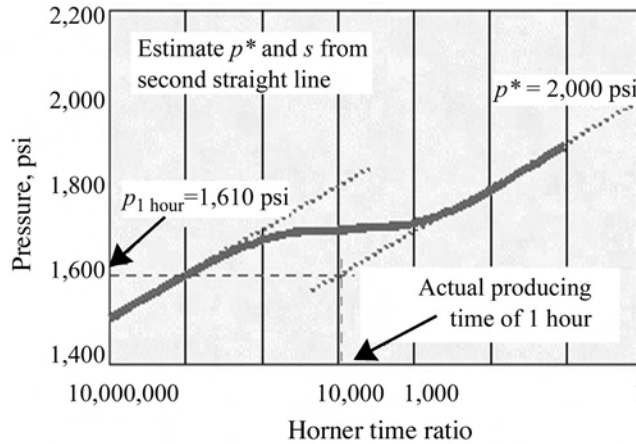


Fig. 8.89—Extrapolation of second semilog straight line to p^* .

$$\lambda = \frac{(\phi V c_t)_f \mu r_w^2}{\gamma \bar{k} t_p} \left(\frac{t_p + \Delta t_1}{\Delta t_1} \right) = \frac{(\phi V c_t)_{f+m} \mu r_w^2}{\gamma \bar{k} t_p} \left(\frac{t_p + \Delta t_2}{\Delta t_2} \right), \dots\dots\dots (8.183)$$

where $\gamma = 1.781$.

The terms $(\phi V)_m$ and $(c_t)_m$ in Eq. 8.183 are obtained by conventional methods. A porosity log usually reads only the matrix porosity (not the fracture porosity) and thus gives ϕ_m , while $(c_t)_m$ is the sum of $c_o S_o$, $c_g S_g$, $c_w S_w$, and c_f . V_m usually can be assumed to be essentially 1.0. From the definition of ω in Eq. 8.177,

$$(\phi V c_t)_f = (\phi V c_t)_m \left(\frac{\omega}{1 - \omega} \right). \dots\dots\dots (8.184)$$

- The second semilog straight line should be extrapolated to p_{1hr} , and the skin factor is

$$s = 1.151 \left[\frac{\Delta p_{1 \text{ hr}}}{|m|} - \log \left(\frac{\bar{k}}{\phi \mu c_t r_w^2} \right) + 3.23 \right], \dots\dots\dots (8.185)$$

where $\Delta p_{1 \text{ hr}}$ is equal to $(p_i - p_{1 \text{ hr}})$ for a drawdown test or $[p_{1 \text{ hr}} - p_{wf}(\Delta t = 0)]$ for a buildup test.

- The second semilog straight line should be extrapolated to p^* (Fig. 8.89). From p^* , \bar{p} can be found using conventional methods (such as the Matthew-Brons-Hazebroek p^* method).

Type Curve Analysis Technique. Particularly because of wellbore-storage distortion, type curves are quite useful for identifying and analyzing dual-porosity systems. Fig. 8.90 shows an example of the Bourdet *et al.*³⁷ type curves developed for pseudosteady-state matrix flow. Initially, test data follow a curve for some value of $C_D e^{2s}$ where C_D is the dimensionless wellbore storage coefficient. In Fig. 8.90, the earliest data for the well follow the curve for $C_D e^{2s} = 1$. The data then deviate from the early fit and follow a transition curve characterized by the parameter λe^{-2s} . In Fig. 8.90, the data follow the curve for $\lambda e^{-2s} = 3 \times 10^{-4}$. When equilibrium is reached between the matrix and fracture systems, the data then follow another $C_D e^{2s}$ curve. In the example, the later data follow the $C_D e^{2s} = 0.1$ curve.

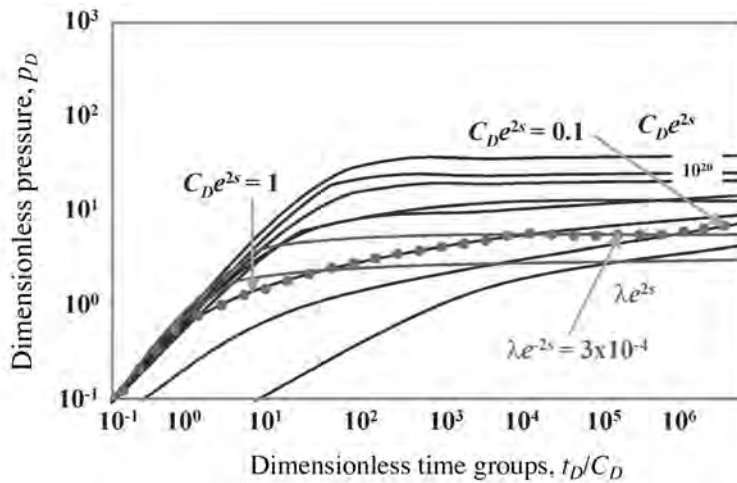


Fig. 8.90—Type curves for pseudosteady-state matrix flow. (After Bourdet et al.³⁷)

At earliest times, the reservoir is behaving like a homogeneous reservoir with all fluid originating from the fracture system. During intermediate times, there is a transition region as the matrix begins to produce into the fractures. At later times, the system again is behaving like a homogeneous system with both matrix and fractures contributing to fluid production.

Fig. 8.91 illustrates the derivative type curves for a formation with pseudosteady-state matrix flow.³⁷ The most notable feature, characteristic of naturally fractured reservoirs, is the dip below the homogeneous reservoir curve. The curves dipping downward are characterized by a parameter $\lambda C_D / \omega (1 - \omega)$, while the curves returning to the homogeneous reservoir curves are characterized by the parameter $\lambda C_D / (1 - \omega)$. Test data that follow this pattern on the derivative type curve can reasonably be interpreted as identifying a dual-porosity reservoir with pseudosteady-state matrix flow (a theory that needs to be confirmed with geological information and reservoir performance). Pressure and pressure derivative type curves can be used together for analysis of a dual-porosity reservoir. The pressure derivative data are especially useful for identifying the dual-porosity behavior. Manual type-curve analysis for well in naturally fractured reservoirs is tedious, and the interpretation involved is difficult. Most current analysis uses commercial software.

Transient Matrix Flow Model. The more probable flow regime in the matrix is unsteady-state or transient flow; that is, flow in which an increasing pressure drawdown starts at the matrix/fracture interface and moves further into the matrix with increasing time. Only at late times should pseudosteady-state flow be achieved, although a matrix with a thin, low-permeability damaged zone at the fracture face may behave as predicted by the pseudosteady-state matrix flow model even though the flow in the matrix is actually unsteady-state.

A semilog graph of test data for a formation with transient matrix flow has a characteristic shape different from that for pseudosteady-state flow in the matrix. Three distinct flow regimes have been identified that are characteristic of dual-porosity reservoir behavior with transient matrix flow. Fig. 8.92 illustrates these flow regimes on a semilog graph as regimes 1, 2, and 3.

Flow regime 1 occurs at early times during which all production comes from the fractures. Flow regime 2 occurs when production from the matrix into the fracture begins and continues until the matrix-to-fracture transfer reaches equilibrium. This equilibrium point marks the beginning of flow regime 3, during which total system flow, from matrix to fracture to wellbore, is dominant. The same three flow regimes appear when there is pseudosteady-state matrix flow.

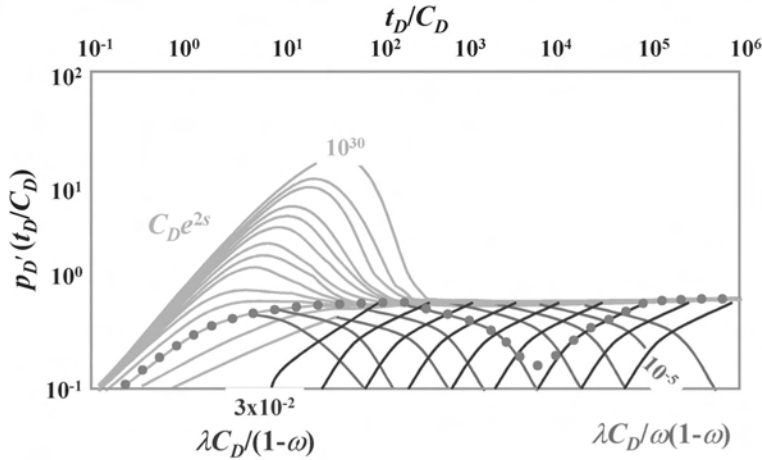


Fig. 8.91—Derivative type curves for pseudosteady-state matrix flow. (After Bourdet *et al.*³⁷)

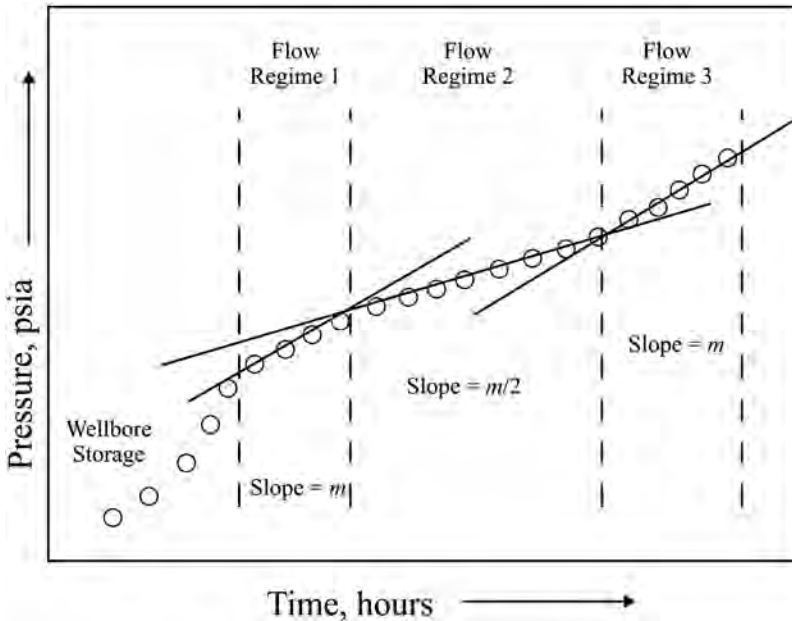


Fig. 8.92—Flow regimes in a dual-porosity reservoir with transient matrix flow.³⁴

The duration and shape of the transition flow regimes, however, is considerably different for the two matrix flow models.

Serra *et al.*³⁴ observed that pressures from each of these flow regimes will plot as straight lines on conventional semilog graphs. Flow regimes 1 and 3, which correspond to the classical early- and late-time semilog straight-line periods, respectively, have the same slope. Flow regime 2 is an intermediate transitional period between the first and third flow regimes. The semilog straight line of flow regime 2 has a slope of approximately one-half that of flow regimes 1 and 3. If all or any two of these regimes can be identified, then a complete analysis is possible using semilog methods alone. Certain nonideal conditions, however, may make this analysis difficult to apply.

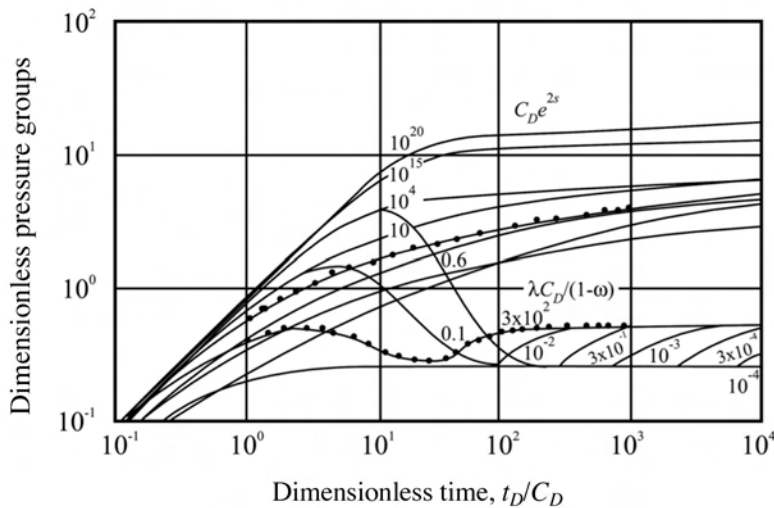


Fig. 8.93—Type curves for transient matrix flow.³⁷

Flow regime 1 often is distorted or obscured by wellbore storage, which often makes this flow regime difficult to identify. Flow regime 2, the transition, also may be obscured by wellbore storage. Flow regime 3 sometimes requires a long flow period followed by a long shut-in time to be observed, especially in formations with low permeability. Furthermore, boundary effects may appear before flow regime 3 is fully developed.

Semilog Analysis Techniques. Serra *et al.*³⁴ presented a semilog method for analyzing well test data in dual-porosity reservoirs exhibiting transient matrix flow (Fig. 8.92). They found that the existence of the transition region, flow regime 2, and either flow regime 1 or flow regime 3 is sufficient to obtain a complete analysis of drawdown or buildup test data. Further, they assumed unsteady-state flow in the matrix, no wellbore storage, and rectangular matrix-block geometry, as Fig. 8.86 shows. The rectangular matrix-block geometry is adequate, although different assumed geometries can lead to slightly different interpretation results.

The major weakness of the Serra *et al.* method is that it assumes no wellbore storage. In many cases, flow regimes 1 and 2 are partially or even totally obscured by wellbore storage, making analysis by the Serra *et al.* method impossible or difficult. Despite this limitation, the Serra *et al.* method has great practical value when used in conjunction with type-curve methods. These calculations of the Serra *et al.* method apply to both buildup and drawdown test data and are applicable for well test analysis of slightly compressible liquids and gas well tests.

Type Curve Analysis Technique. Bourdet *et al.*³⁷ presented type curves for analyzing well tests in dual-porosity reservoirs including the effects of wellbore storage and unsteady-state flow in the matrix. The type curves are useful supplements to the Serra *et al.* semilog analysis. Fig. 8.93 gives an example of the pressure and pressure derivative type curves for transient matrix flow. Early (fracture-dominated) data are fit by a $C_D e^{2s}$ value indicative of homogeneous behavior. Data in the transition region are fit by curves characterized by a parameter β' . Finally, data in the homogeneous-acting, fracture-plus-matrix flow regime are fit by another $C_D e^{2s}$ curve.

On the derivative type curve, early data also are fit by a derivative curve reflecting homogeneous behavior. Fig. 8.94 shows an actual example. If wellbore-storage distortion ceases before the transition region begins (which did not happen in the example but is possible in other cases), the derivative data will be horizontal and should be aligned with the $(t_D/C_D)p_D' = 0.5$

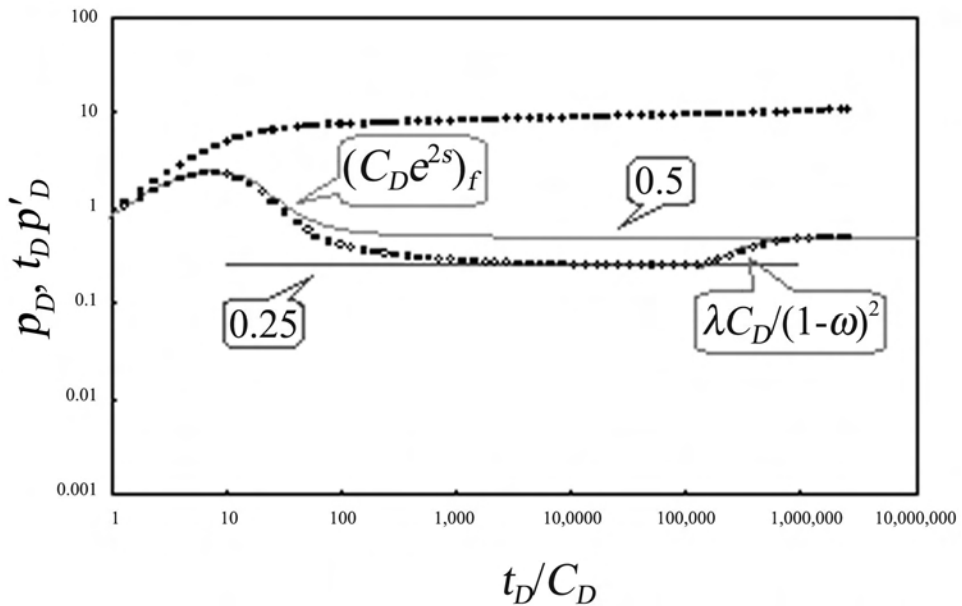


Fig. 8.94—Example of using type curves for transient matrix flow.³⁷

curve. However, if the transition region is present (recall that its semilog slope is half that of the middle-time straight line), the derivative curve will flatten and should be aligned with the $(t_D/C_D)p'_D = 0.25$ curve as shown in this example. The homogeneous (fracture-plus-matrix) data should, after wellbore distortion has ceased and before boundary effects have appeared, be horizontal on the derivative type curve and should be aligned with the $(t_D/C_D)p'_D = 0.5$ curve as this example shows.

Manual type-curve matching is tedious and difficult, especially with the interpolation involved. Analysis ordinarily uses commercially available software to analyze these kinds of tests after the reservoir model has been identified.

8.11 Horizontal Well Analysis

Productivity estimates in horizontal wells are subject to more uncertainty than comparable estimates in vertical wells. Further, it is much more difficult to interpret well test data because of 3D flow geometry. The radial symmetry usually present in a vertical well does not exist. Several flow regimes can potentially occur and need to be considered in analyzing test data from horizontal wells. Wellbore storage effects can be much more significant and partial penetration and end effects commonly complicate interpretation.

In vertical wells, variables such as average permeability, net vertical thickness, and skin are used. Horizontal wells need more detail. Not only is vertical thickness important, but the horizontal dimensions of the reservoir, relative to the horizontal wellbore, need to be known.

8.11.1 Steps in Evaluating Horizontal Well-Test Data. There are three basic steps in evaluating pressure-transient data from a horizontal well. First, identify the specific flow regimes in the test data. Second, apply the proper analytical and graphical procedures to the data. Finally, evaluate the uniqueness and sensitivity of the results to properties derived from analysis or simply assumed.

Identify Flow Regimes. As discussed in previous sections, evaluation of data from a vertical wellbore will generally center on a single flow regime, such as infinite-acting radial flow,

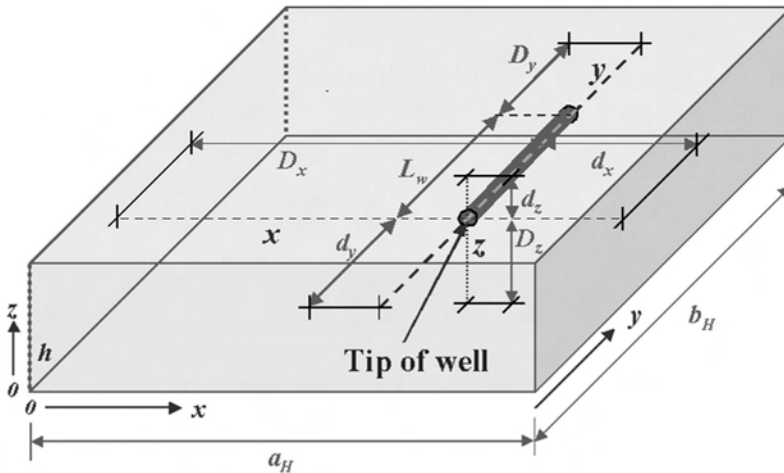


Fig. 8.95—Well and reservoir geometry and nomenclature for a horizontal well.

known as the MTR. However, a pressure-transient test in a horizontal well can involve as many as five major and distinct regimes that need to be identified. These regimes may or may not occur in a given test and may or may not be obscured by wellbore storage effects.

Apply the Proper Procedures. Each flow regime can be modeled by an equation that can be used to estimate important reservoir properties. At best, only groups of analytical parameters can be determined directly from equations. It is imperative that the proper analytical and graphical procedures be applied to the data. In many cases, when solving for specific parameters, the application of these analytical expressions may involve a complex iterative procedure.

Evaluate Uniqueness and Sensitivity. Experience indicates that results of horizontal well test analysis are seldom unique, so it is important that the uniqueness and sensitivity of the results to assumed properties be evaluated. Simulation of the test using properties that have been determined from the test can confirm that at least the analysis is consistent with the test data. A simulator can also determine whether other sets of formation properties will also lead to a fit of the data.

8.11.2 Horizontal Well Flow Regimes. Different formation properties can be calculated from the data in each of the five different flow regimes. Any flow regime may be absent from a plot of test data because of geometry, wellbore storage, or other factors. Nor does the fact that they can appear mean that they do appear. The five different flow regimes that can occur are early radial, hemi-radial, early linear, late pseudoradial, and late linear.

Fig. 8.95 shows a horizontal well with length, L_w , within a reservoir that is assumed to be a rectangular parallelepiped or a “box reservoir” drainage area. In this discussion, it is assumed that the axes of the coordinate system coincide with the direction of principal permeability and the well produces over its entire length, L_w .

The axes for this box are the usual x -, y -, and z -axes. Notice that the x -axis is measured along the bottom edge of the reservoir, going from left to right in the direction perpendicular to the well. The y -axis lies along the axis from front to back of the reservoir, parallel to the wellbore. The z -axis is oriented in the direction of reservoir thickness.

The total width of the reservoir perpendicular to the wellbore is a_H , the total length in a direction parallel to the wellbore is b_H , and the total height of the reservoir is the net pay thickness, h . Notice the parameters for the distance from the well to the various borders. Along the axis of the well, the shortest distance from the end of the well to a boundary is d_y , and the

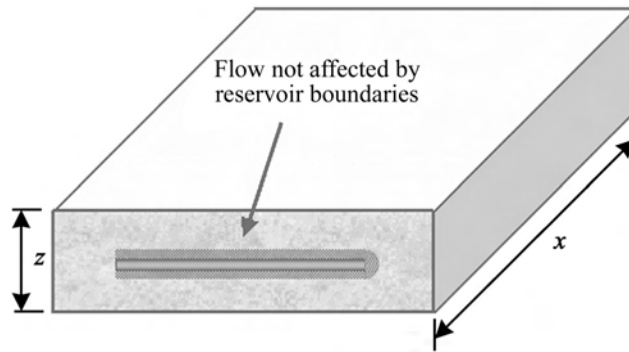


Fig. 8.96—Early-radial flow is not influenced by reservoir boundaries.

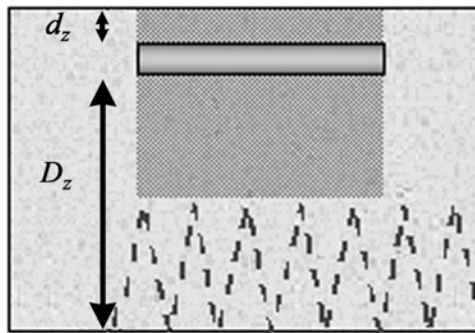


Fig. 8.97—Hemiradial flow occurs when effects of one vertical boundary are felt before the effects of the other.

longest distance from the other end of the well to the boundary is D_y . In the vertical direction, the shortest distance to a vertical boundary is d_z , and the longest distance to a vertical boundary is D_z .

Characteristics of Flow Regimes. Consider a well producing at a constant rate. The early radial flow regime occurs before the area drained or the pressure transient caused by this production encounters either of the vertical boundaries of the reservoir. Fig. 8.96 shows a radial flow pattern penetrating out into the reservoir. Actually, however, this flow pattern is likely to be elliptical, moving further into the reservoir at a given time in the higher-permeability x -direction than in the lower-permeability z -direction. This phenomenon causes no significant complications in our analysis.

When the wellbore is much nearer one vertical boundary than the other, another flow regime, called half-radial or hemiradial flow (Fig. 8.97) may exist. Hemiradial flow can occur immediately following the early radial flow regime, if the well is much nearer one of the vertical boundaries than the other. Eventually, the area affected by the production will include the entire thickness of the reservoir. When that happens, a linear flow pattern may develop, as Fig. 8.98 shows.

Eventually, flow will begin to come into the wellbore from beyond the ends of the well. Until these end effects become important, early linear flow continues. Once end effects become important a transition period is followed by a later pseudoradial flow regime, as Fig. 8.99 illustrates.

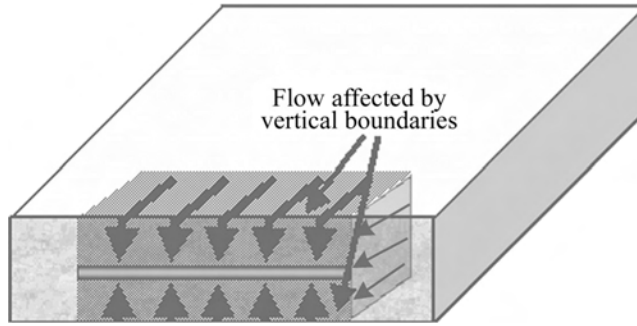


Fig. 8.98—Early-linear flow may develop after both vertical boundaries are encountered.

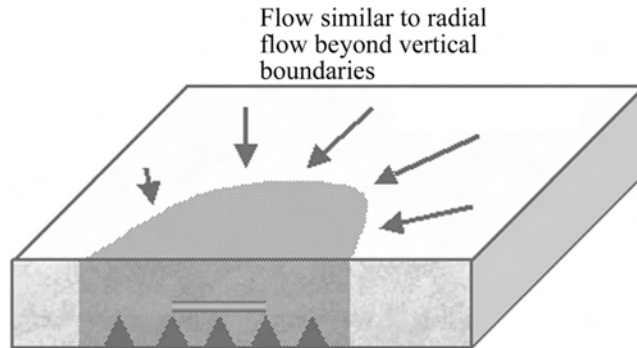


Fig. 8.99—Late pseudoradial flow begins after flow enters wellbore from beyond ends of well.

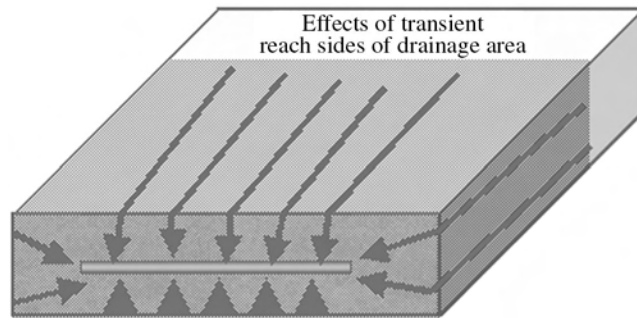


Fig. 8.100—Late-linear flow includes flow from the drainage volume perpendicular to the well.

This flow regime continues until the area affected by the production reaches one of the sides of the reservoir. Once the area affected is the entire width of the reservoir (that is, the pressure transient has reached both sides of the reservoir), then the late-linear flow regime begins (Fig. 8.100).

8.11.3 Identifying Flow Regimes in Horizontal Wells. All of these flow regimes in a test can be identified on a diagnostic log-log plot of the pressure change, Δp , and pressure derivative, p' , against the logarithm of time (Fig. 8.101).

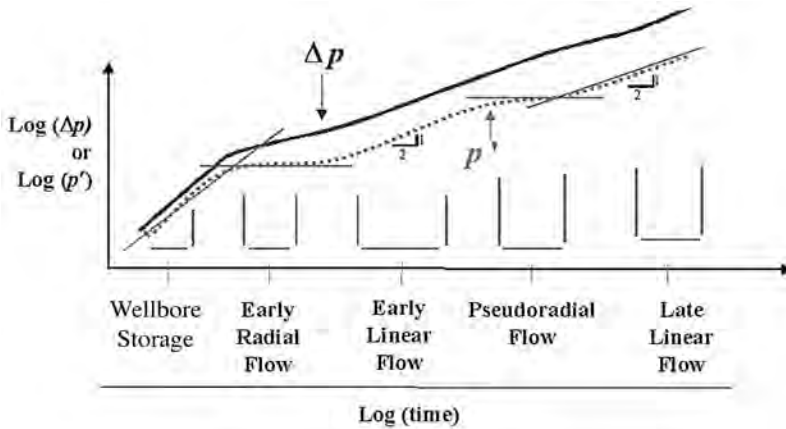


Fig. 8.101—Idealized diagnostic plot identifies all normally expected flow regimes.

A unit-slope line appears during wellbore storage; a horizontal derivative during early radial flow, and then, later, in pseudoradial flow; and a half-slope line in early-linear flow and then in late-linear flow. (These half-slope lines appear on the derivative but not on the pressure-change curves.) This does not imply that all these flow regimes will appear in any given test; in fact, that would be rare. But these are the shapes that identify the flow regimes that may appear in the test being analyzed.

The shapes that may appear in a drawdown test (which is the basis of Fig. 8.101) may not appear in a buildup test because of the complex superposition of flow regimes. For example, a test would have to be in linear flow both at time $(t_p + \Delta t)$ and at time Δt to ensure appearance of a derivative with half-slope; this is highly unlikely. The best way to solve the problem is to ensure that a buildup test on a horizontal well is run with a producing time, t_p , much greater than the maximum shut-in time in the test (that is, $t_p > 10 \Delta t_{max}$).

Table 8.A-2 (see Appendix) summarizes the working equations for permeability, skin, and start and end of each of the recognized flow regimes. Different investigators have found different equations for start and end of various flow regimes, especially linear flow regimes. This is partly because of a difference of assumptions about flow into the wellbore. Uniform flux or infinite conductivity models are common; neither is rigorously applicable in practice.³⁸ In this section, the equations for duration of flow regimes derived by Odeh and Babu³⁹ are used. This model assumes uniform flux into the wellbore.

Early-Radial Flow. Early-radial flow is similar to the radial flow period in a vertical well (Fig. 8.96). The governing equation for this flow regime is

$$p_i - p_{wf} = \frac{162.6qB\mu}{\sqrt{k_x k_z} L_w} \left[\log_{10} \left(\frac{\sqrt{k_x k_z} t}{\phi \mu c_t r_w^2} \right) - 3.227 + 0.868s_d \right] \dots\dots\dots (8.186)$$

Data for this period may be masked by wellbore storage effects, but, when present, they may be analyzed on a semilog plot.

The early-radial flow regime may in theory start at time zero, in absence of wellbore storage effects. The end of the early-radial flow regime may occur when the transient reaches a vertical boundary or when flow comes from beyond the end of the wellbore. The end of the period is the smaller of these two values.

Eq. 8.187³⁹ says that the period must end when the transient reaches the nearest boundary, d_s , from the well. This equation includes the permeability in the vertical direction:

$$t_{E\text{erf}} = \frac{1,800d_z^2\phi\mu c_t}{k_z} \dots\dots\dots (8.187)$$

The radial flow regime may also end when flow from beyond the end of the wellbore becomes important. Eq. 8.188 gives the time by

$$t_{E\text{erf}} = \frac{125L_w^2\phi\mu c_t}{k_y} \dots\dots\dots (8.188)$$

L_w is the completed length of the well, and k_y is the permeability in the direction parallel to the wellbore. The actual end is the lesser of the two times calculated from Eqs. 8.187 and 8.188. It is helpful to check the expected duration of the early-radial flow regime after estimating the parameters necessary to make these calculations.

Eq. 8.186 suggests that possible radial flow on the diagnostic plot be identified and then bottomhole flowing pressure be plotted against time during the appropriate time range on semilog coordinates. The slope of the straight line that results is

$$|m_{\text{erf}}| = \frac{162.6qB\mu}{L_w\sqrt{k_xk_z}} \dots\dots\dots (8.189)$$

The group $\sqrt{k_xk_z}$ can be found from the slope, m_{erf} :

$$\sqrt{k_xk_z} = \frac{162.6qB\mu}{|m_{\text{erf}}|L_w} \dots\dots\dots (8.190)$$

Effective completed length of the well must be known to make this calculation. This is not necessarily the same as the perforated or completed length of the well. Some sections of the well may not produce at all.

The equation for calculating the altered permeability skin, s_d , for early-radial flow is

$$s_d = 1.151 \left[\frac{\Delta p_{1\text{hr}}}{|m_{\text{erf}}|} - \log \left(\frac{\sqrt{k_xk_z}}{\phi\mu c_t r_w^2} \right) + 3.23 \right] \dots\dots\dots (8.191)$$

When analyzing a buildup test rather than a constant-rate flow test, plot the HTR or equivalent time on the horizontal axis of the semilog plot, and then plot shut-in or equivalent time on the vertical axis. Note that this plotting is correct only if $(t_p + \Delta t)$ and Δt appear in this time period simultaneously; that is, radial flow must exist at both time $(t_p + \Delta t)$ and time Δt . This is unlikely because radial-flow regime may exist at time Δt , but a different flow regime is likely at time $(t_p + \Delta t)$.

Example 8.2: Well Erf-1. For drawdown test data from Well Erf-1,³⁹ the diagnostic plot indicates the data from approximately 0.24 to 24 hours may be in early-radial flow. The following information is available for this well: $q = 800$ STB/D, $\mu = 1$ cp, $B = 1.25$ RB/STB, $r_w = 0.25$ ft, $\phi = 0.2$, $c_t = 15 \times 10^{-6}$ psi⁻¹, centered in box-shaped drainage area, $h = 200$ ft, $b_H = 4,000$ ft, and $a_H = 2,000$ ft, $L_w = 1,000$ ft, and, from analysis of data in early linear flow regime, $k_x = 200$ md. Table 8.3 shows the pressure change data for 0.24 to 24 hours.

Plot $(p_i - p_{wf}) = \Delta p$ vs. t on semilog coordinates (Fig. 8.102). The plot results in a straight line with a slope of 8 psi/cycle. In Fig. 8.102, at $t = 2.4$ hours, the points begin to deviate from the straight line, as expected from calculations for flow regime duration that follow. The pressure change at 1 hour is 39 psia. Using the slope of 8 and Eq. 8.190,

$$\begin{aligned}\sqrt{k_z k_x} &= \frac{162qB\mu}{|m_{\text{erf}}| L_w} \\ &= \frac{162.6(800)(1.23)(1)}{|8| 1000} \\ &= 20.3 \text{ md} \\ \text{and } k_x k_z &= 412 \text{ md}^2.\end{aligned}$$

Thus, because $k_x = 200$ md, $k_z = 2$ md. Using the value of 39 for $\Delta p_{1\text{hr}}$ from Fig. 8.102, skin from Eq. 8.191 is

$$\begin{aligned}s_d &= 1.151 \left[\left(\frac{\Delta p_{1 \text{ hr}}}{|m_{\text{erf}}|} \right) - \log \left(\frac{\sqrt{k_x k_z}}{\phi \mu c_t r_w^2} \right) + 3.23 \right] \\ &= 1.151 \left[\left(\frac{39}{8} \right) - \log \left(\frac{20.3}{(0.2)(1)(15 \times 10^{-6})(0.25)^2} \right) + 3.23 \right] = 0.0812.\end{aligned}$$

The start of the early-radial flow regime is controlled by wellbore storage, which appears to have vanished at times earlier than 0.24 hours in this example. The end of the early radial flow regime is expected at the lesser of the two values derived from Eqs. 8.187 and 8.188. For a centered well, $d_z = h/2 = 100$ ft, and Eq. 8.187 gives

$$\begin{aligned}t_{\text{Erf}} &= 1,800 d_z^2 \phi \mu c_t / k_z \\ &= (1,800)(100)^2 (0.2)(1)(1.5 \times 10^{-5}) / 2 = 27 \text{ hours}.\end{aligned}$$

Assuming $k_y = k_x = 200$ md, Eq. 8.188 gives

$$\begin{aligned}t_{\text{Erf}} &= 125 L_w^2 \phi \mu c_t / k_y \\ &= (125)(1000)^2 (0.2)(1)(1.5 \times 10^{-5}) / 200 = 1.875 \text{ hours}.\end{aligned}$$

Thus, expect the early-radial flow regime to end at approximately 1.875 hours, which is the smaller value and is consistent with observed test data.

8.11.4 Hemiradial Flow. The hemiradial flow period (Fig. 8.97) will occur only when the well is close to one of the vertical boundaries (either the upper or the lower boundaries) and is analogous to a vertical well near a fault. The governing equation is³⁸

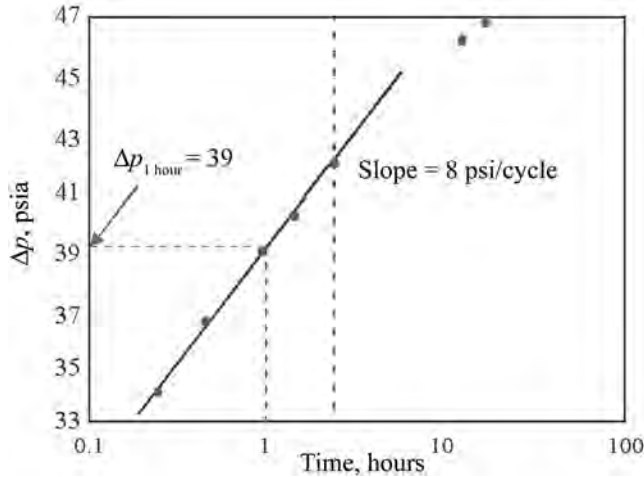


Fig. 8.102—Early-radial flow is indicated by semilog straight line for well Erf-1.

TABLE 8.3—PRESSURE CHANGE DATA FOR WELL Erf-1	
Time (hours)	$\Delta p=(p_i-p_w)$ (psi)
0.24	33.96
0.48	36.41
0.96	38.85
1.44	40.26
2.40	41.96
12.50	46.23
16.80	46.91
24.00	47.65

$$p_i - p_{wf} = \frac{325.2qB\mu}{\sqrt{k_x k_z} L_w} \left[\log_{10} \left(\frac{\sqrt{k_x k_z} t}{\phi \mu c_t r_w^2} \right) - 3.227 + 0.868s_d \right] \dots\dots\dots (8.192)$$

A horizontal derivative on the diagnostic plot identifies hemiradial flow. If data appear to fall into this flow regime, a straight line on a semilog plot would provide more confidence that radial flow has been identified. Consistency checks in the analysis coupled with a well survey will be required to distinguish hemiradial flow from early radial flow.

The time range in which the analysis for hemiradial flow is valid begins after the closest vertical boundary, d_z , affects the data and before the farthest boundary, D_z , affects them. In the absence of wellbore storage, the start of hemiradial flow is given by

$$t_{Shrf} \cong \frac{1,800d_z^2 \phi \mu c_t}{k_z} \dots\dots\dots (8.193)$$

Note that the start of the hemiradial flow regime involves the shortest distance to a vertical boundary and the permeability in the vertical direction. However, wellbore storage will most likely determine the actual start of hemiradial flow.

The end of hemiradial flow occurs when pressure is affected by the farther vertical boundary or flow from beyond the ends of the wellbore, whichever occurs first. It is the smaller of the times calculated using Eqs. 8.194 and 8.195. If the hemiradial flow regime ends when pressure reaches the farthest vertical boundary, it depends on the distance, D_z , and the vertical permeability, k_z :

$$t_{Ehrf} = \frac{1800D_z^2\phi\mu c_t}{k_z} \dots\dots\dots (8.194)$$

When the appearance of end effects—flow from beyond the ends of the wellbore—causes the end of the hemiradial flow regime to appear, the end of the flow regime occurs when

$$t_{Ehrf} = \frac{125L_w^2\phi\mu c_t}{k_y} \dots\dots\dots (8.195)$$

The completed length of the well, L_w , and the permeability k_y , parallel to the wellbore appear in this equation. These parameters determine when enough flow has come from beyond the ends of the wellbore to distort the radial flow pattern that appeared earlier.

$$\left| m_{hrf} \right| = \frac{325.2qB\mu}{L_w\sqrt{k_xk_z}} \dots\dots\dots (8.196)$$

gives the slope of the semilog straight line for semiradial flow, m_{hrf} . The multiplier, 325.2, is twice the multiplier for early-radial flow. The equation to estimate the damage skin factor is also similar to that for radial flow but has a multiplier that differs by a factor of two.

$$s_d = 2.303 \left[\frac{\Delta p_{1hr}}{\left| m_{hrf} \right|} - \log \left(\frac{\sqrt{k_xk_z}}{\phi\mu c_t r_w^2} \right) + 3.23 \right] \dots\dots\dots (8.197)$$

The equations relating slope and permeability and the equation for skin are similar in a buildup test to those for a drawdown test. The pressure change in the equation for skin is [$p_{1hr} - p_{wf}(\Delta t = 0)$]. Semilog plots of buildup test data from the hemiradial flow regime cannot be analyzed rigorously using data from a Horner plot unless the pressure data at ($t_p + \Delta t$) and at time Δt are simultaneously in this flow regime. As a practical matter, the hemiradial flow regime is likely to appear clearly in the buildup test only when the producing time is much greater than the shut-in time.

8.11.5 Early Linear Flow. The governing equation for early-linear flow is³⁸

$$p_i - p_{wf} = \frac{8.128qB}{L_w h} \sqrt{\frac{\mu t}{k_x\phi c_t}} + \frac{141.2qB\mu}{L_w\sqrt{k_xk_z}}(s_c + s_d) \dots\dots\dots (8.198)$$

The “convergence skin,” s_c , is discussed later in this section. The start of the early-linear flow regime (Fig. 8.98) depends on the farthest distance to a vertical boundary, D_z , and the vertical permeability, k_z .³⁹

$$t_{Self} = \frac{1,800D_z^2\phi\mu c_t}{k_z} \dots\dots\dots (8.199)$$

Not until flow reaches that farthest vertical boundary can a linear flow pattern begin toward the well. This flow period ends when fluids flow from beyond the ends of the wellbore. Thus,

$$t_{Eelf} = \frac{160L_w^2\phi\mu c_t}{k_y} \dots\dots\dots (8.200)$$

Notice that the end depends on the effective completed length of the well, L_w , and on the permeability in the direction parallel to the well. This is the time in which end effects—flow beyond the ends of the well—begin to significantly distort the linear flow pattern.

The early-linear flow regime is identified in a drawdown test with a half-slope for the derivative. (Because of the skin effect, the pressure change curve on the diagnostic plot will only approach a half-slope asymptotically.) For data identified as being in this flow regime, plot pressure against the square root of time.

The slope of the straight line on such a plot, m_{elf} , can be used to estimate the square-root of k_x , the horizontal permeability perpendicular to the well:

$$\sqrt{k_x} = \frac{8.128qB}{|m_{elf}| L_w h} \sqrt{\frac{\mu}{\phi c_t}} \dots\dots\dots (8.201)$$

To calculate the damage skin,

$$s_d = \frac{L_w \sqrt{k_x k_z}}{141.2qB\mu} \Delta p_{t=0} - s_c \dots\dots\dots (8.202)$$

This equation includes a convergence skin, s_c , which is³⁹

$$s_c = \ln\left(\frac{h}{r_w}\right) + 0.25 \ln\left(\frac{k_x}{k_z}\right) - \ln\left[\sin\left(\frac{\pi d_z}{h}\right)\right] - 1.838 \dots\dots\dots (8.203)$$

This convergence skin is an additional pressure drop that acts like a skin effect caused by flow moving from throughout the entire formation until it converges down to the small wellbore in the middle of the formation (**Fig. 8.103**). This convergence skin is defined in terms of the ratio of the permeability in the x -direction, which is perpendicular to the wellbore, to the vertical permeability. It also involves the distance to the nearest vertical boundary, d_z , and the net pay thickness, h .

Kuchuk⁴⁰ derived a different equation for convergence skin. As a practical matter, the Odeh-Babu and Kuchuk equations lead to the same result. When there has been a single rate preceding shut-in during early-linear flow, the buildup pressure is plotted against $\sqrt{t_p + \Delta t} - \sqrt{\Delta t}$ on a Cartesian plot, which is sometimes called a tandem root plot. The permeability, k_x , is calculated from the slope, m_{elf} , of the plot and **Eq. 8.201**. k_x has the same relationship to the slope that existed in a drawdown test. Skin for this flow regime is calculated with **Eqs. 8.202** and **8.203**.

Plots of buildup data from the early-linear flow regime cannot be analyzed rigorously with a plot of p_{ws} vs. $\sqrt{t_p + \Delta t} - \sqrt{\Delta t}$ (that is, the tandem-root plot) unless data at $(t_p + \Delta t)$ and Δt

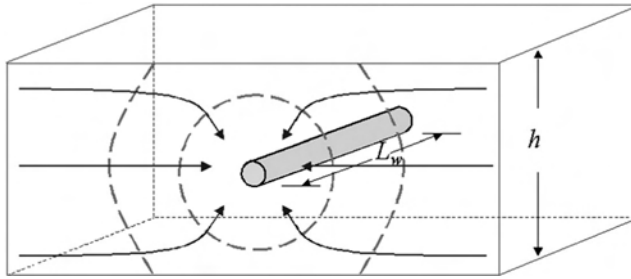


Fig. 8.103—Convergence skin accounts for increased pressure drop as flow deviates from the full vertical thickness of the reservoir into a radial pattern as it enters the well.

are simultaneously in this flow regime—highly unlikely—or unless t_p is much greater than Δt , in which case simply plot p_{ws} vs. $\sqrt{\Delta t}$. Little error results from ignoring the $(t_p + \Delta t)$ term, which is essentially constant.

Example 8.3: Well Elf-2. The diagnostic plot for a drawdown test from Well Elf-2³⁹ indicates data in the early-linear flow regime because the derivative has a half-slope. The following data apply to this well: $q = 800$ STB/D; $\mu = 1$ cp; $B = 1.25$ RB/STB; $r_w = 0.25$ ft; $\phi = 0.2$; $c_t = 15 \times 10^{-6}$ psi⁻¹; centered in box-shaped drainage area 100 ft thick, 4,000 ft long, 4,000 ft wide; $L_w = 2,500$ ft; and, from early radial-flow regime data, $k_x k_z = 8,000$ md². In addition, **Table 8.4** shows the pressure-change data for this well.

A plot of pressure change vs. the square root of time (**Fig. 8.104**) indicates early linear flow. The final point on the straight line is at a time of approximately 24 hours, but there may have been some deviation from the straight line by this time. From the slope of the straight line, $m_{\text{elf}} = 0.934$ psi/hr^{1/2} and **Eq. 8.201**, calculate the permeability in the horizontal plane perpendicular to the wellbore.

$$\begin{aligned} \sqrt{k_x} &= \frac{8.13qB}{|m_{\text{elf}}| L_w h} \sqrt{\frac{\mu}{\phi c_t}} \\ &= \frac{(8.13)(800)(1.25)}{(0.934)(2,500)(100)} \sqrt{\frac{1}{(0.2)(15)(10^{-6})}} \\ &= 20.10 \text{ md}^{1/2}, \end{aligned}$$

or $k_x = (20.1)^2 = 404$ md.

Analysis of data from the early radial flow regime indicated that $k_x k_z$ is 8,000 md²; thus, k_z is approximately 19.8 md. To calculate s_d , use **Eqs. 8.202** and **8.203**, noting that the value for $(p_i - p_{wf}) = 3.1$ at $t = 0$.

$$\begin{aligned} s_d &= \frac{L_w \sqrt{k_x k_z}}{141.2qB\mu} \Delta p_{t=0} - s_c \\ &= \frac{(2,500) \sqrt{(8,000)(3.10)}}{(141.2)(800)(1.25)(1)} - s_c = 4.91 - s_c. \end{aligned}$$

$$\begin{aligned}
 s_c &= \ln\left(\frac{h}{r_w}\right) + 0.25 \ln\left(\frac{k_x}{k_z}\right) - \ln\left[\sin\left(\frac{\pi d_z}{h}\right)\right] - 1.838 \\
 &= \ln\left(\frac{100}{0.25}\right) + 0.25 \ln\left(\frac{404}{19.8}\right) - \ln\left[\sin\left(\frac{\pi(50)}{100}\right)\right] - 1.838 = 4.91.
 \end{aligned}$$

Then, $s_d = 4.91 - 4.91 = 0$.

Check the expected time range for the early-linear flow regime.

Using $D_z = h/2 = 50$ ft and $k_z = 20$ md, calculate the beginning of linear flow with Eq. 8.199:

$$\begin{aligned}
 t_{Self} &= \frac{(1,800)D_z^2 \phi \mu c_t}{k_z} \\
 &= \frac{(1,800)(50)^2(0.2)(1)(1.5 \times 10^{-5})}{20} = 0.675 \text{ hours.}
 \end{aligned}$$

Assuming $k_y = k_x$ at 400 md, use Eq. 8.200 to find the end of early linear flow.

$$\begin{aligned}
 t_{Eelf} &= \frac{160L_w^2 \phi \mu c_t}{k_y} \\
 &= \frac{(160)(2,500)^2(0.2)(1)(1.5 \times 10^{-5})}{400} = 7.5 \text{ hours.}
 \end{aligned}$$

These limits are reasonably consistent with the time range analyzed assuming early linear flow.

8.11.6 Late Pseudoradial. The governing equation for late-pseudoradial flow is³⁸

$$p_i - p_{wf} = \frac{162.6qB\mu}{\sqrt{k_y k_x} h} \left[\log_{10}\left(\frac{k_y t}{\phi \mu c_t L_w^2}\right) - 2.303 \right] + \frac{141.2qB\mu}{L_w \sqrt{k_x k_z}} (s_c + s_d). \dots\dots\dots (8.204)$$

The late-pseudoradial flow period occurs only if³⁹

$$\frac{L_w}{b_H} < 0.45. \dots\dots\dots (8.205)$$

Here, b_H is the dimension of the reservoir parallel to the wellbore. As long as the completed length of the well is relatively short compared with the length of the drainage area late-pseudoradial flow can occur.

The start of this flow period occurs when fluid flows from well beyond the ends of the wellbore (Fig. 8.99). It is approximated with³⁹

$$t_{Sprf} = \frac{1,480L_w^2 \phi \mu c_t}{k_y} \dots\dots\dots (8.206)$$

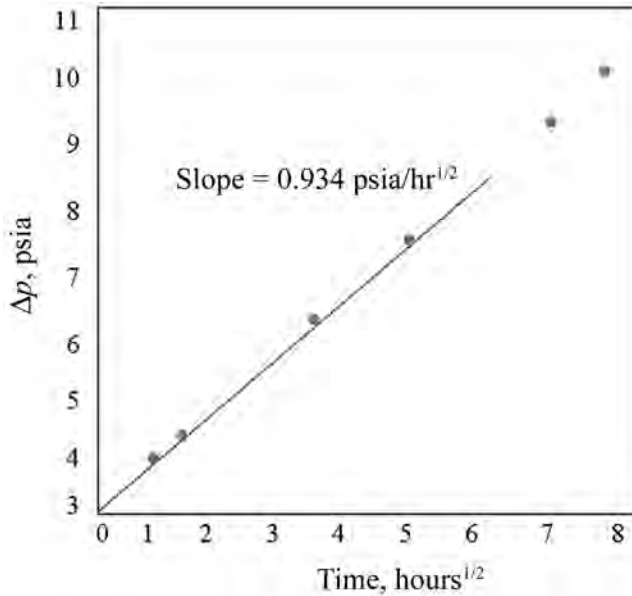


Fig. 8.104—Early-linear flow is indicated by straight line on square-root-of-time plot for well Elf-2.

TABLE 8.4—PRESSURE CHANGE DATA FOR WELL Elf-2	
Time (hours)	Δp = (p _i - p _{wf}) (psi)
1.2	4.11
2.4	4.54
12.0	6.33
24.0	7.65
48.0	9.49
60.0	10.26

This starting time depends on the completed length of the well, L_w , and on the permeability in the direction of the well, k_y . The end of this period, like others in this section, is approximated by the minimum of the results of two calculations. The first,

$$t_{Eprf} = \frac{2,000\phi\mu c_t(L_w/4 + d_y)^2}{k_y}, \dots\dots\dots (8.207)$$

depends on d_y and the length of the wellbore along with k_y , the permeability in the direction parallel to the wellbore. This is the time at which horizontal boundary effects first appear.

The other equation gives a time at which the radial-flow pattern begins to be distorted depending on the shortest distance, d_x , from the well to a boundary perpendicular to the wellbore and on k_x , the permeability in that direction.

$$t_{E\text{prf}} = \frac{1,650\phi\mu c_t d_x^2}{k_x} \dots\dots\dots (8.208)$$

Whenever boundary effects first appear, whether in a direction that is parallel to the well or perpendicular to the axis of the well, the late-pseudoradial flow period will end.

The diagnostic plot helps identify the late-pseudoradial flow regime with the characteristic horizontal derivative. For data in the appropriate time range, prepare a semilog plot of pressure against time for a drawdown test. The slope of this plot will be m_{prf} and the relationship between that slope and the square root of $k_x k_y$, or the permeabilities in the horizontal plane, is given by

$$\sqrt{k_x k_y} = \frac{162.6qB\mu}{|m_{\text{prf}}| h} \dots\dots\dots (8.209)$$

The skin equation is similar in form to those seen before:

$$s_d = \left(1.151\sqrt{\frac{k_z}{k_y}} \frac{L_w}{h} \right) \left[\frac{\Delta p_{1\text{hr}}}{|m_{\text{prf}}|} - \log \left(\frac{k_y}{\phi\mu c_t L_w^2} \right) + 1.76 \right] - s_c \dots\dots\dots (8.210)$$

Again, the total skin depends on $\Delta p_{1\text{hr}}$. The convergence skin (Eq. 8.203) is subtracted from the “total” skin to determine the damage skin.

For a buildup test preceded by production at a single rate, plot pressure against the HTR on a semilog graph. Permeability is calculated from Eq. 8.209, the same as for a drawdown test. The skin equation is basically the same as for a drawdown test, except that the $\Delta p_{1\text{hr}}$ is now $p_{1\text{hr}} - p_{\text{wf}}$. To obtain p^* , the extrapolated pressure, extrapolate the semilog straight line to a HTR of unity.

Semilog plots of buildup test data from the late-pseudoradial flow regime cannot be analyzed rigorously using a Horner plot unless pressures at $(t_p + \Delta t)$ and at time Δt are simultaneously in the pseudoradial flow regime, which is highly unlikely. However, little error appears if the producing time before shut-in is much greater than the maximum shut-in time achieved in the buildup test.

Example 8.4: Well Prf-3. The diagnostic plot suggests that a constant-rate drawdown test from Well Prf-3³⁹ includes data in the late-pseudoradial period. The following data are available from the test: $q = 800$ STB/D, $\mu = 1$ cp, $B = 1.25$ RB/STB, $r_w = 0.25$ ft, $\phi = 0.2$, $c_t = 15 \times 10^{-6}$ psi⁻¹, $h = 150$ ft, $L_w = 900$ ft, $a_H = 5,280$ ft, $b_H = 5,280$ ft, well centered in drainage volume, $k_x = 100$ md (from analysis of early linear flow), $k_x k_z = 1,000$ md², and $k_z = 10$ md (from analysis of early radial flow). **Table 8.5** gives the pressure change, $\Delta p = p_i - p_{\text{wf}}$ vs. time.

A plot of pressure change vs. the logarithm of time (**Fig. 8.105**) confirms pseudoradial flow. A straight line fits all the data from 192 to 432 hours; the slope of the line, m_{prf} , is 15.3 psi/cycle, and $\Delta p_{1\text{hr}} = 18.94$ psi (extrapolated). Then, from Eq. 8.209,

$$\sqrt{k_x k_y} = \frac{162.6qB\mu}{|m_{\text{prf}}| h} = \frac{(162.6)(800)(1.25)(1.0)}{(15.3)(150)} = 70.8 \text{ md.}$$

Thus, $k_y = \frac{\sqrt{k_x k_z}}{k_x} = \frac{(70.8)^2}{100} = 50.2 \text{ md.}$

From Eqs. 8.210 and 8.203,

$$s_d = 1.151 \sqrt{\frac{k_z}{k_y}} \frac{L_w}{h} \left[\frac{\Delta p_1 \text{ hr}}{|m_{\text{prf}}|} - \log \left(\frac{k_y}{\phi \mu c_t L_w^2} \right) + 1.76 \right] - s_c,$$

$$\text{and } s_c = \ln \left(\frac{h}{r_w} \right) + 0.25 \ln \left(\frac{k_x}{k_z} \right) - \ln \left[\sin \left(\frac{\pi d_z}{h} \right) \right] - 1.838.$$

Here,

$$s_c = \ln \left(\frac{150}{0.25} \right) + 0.25 \ln \left(\frac{100}{10} \right) - \ln \left[\sin \left(\frac{\pi(75)}{150} \right) \right] - 1.838 = 5.13,$$

$$\text{and } s_d = 1.151 \sqrt{\frac{10}{50.2}} \frac{(900)}{(150)} \left[\frac{18.94}{15.3} - \log \left(\frac{50.2}{(0.2)(1)(1.5 \times 10^{-5})(900)^2} \right) + 1.76 \right] - 5.13 = 0.057.$$

The pseudoradial flow regime should start at the time given by Eq. 8.206:

$$t_{S\text{prf}} = \frac{1,480 L_w^2 \phi \mu c_t}{k_y} = \frac{(1,480)(900^2)(0.2)(1)(1.5 \times 10^{-5})}{50.2} = 71.6 \text{ hours.}$$

It should end at a time given by the lesser of values from Eqs. 8.207 and 8.208. From Eq. 8.207,

$$t_{E\text{prf}} = \frac{2,000 \phi \mu c_t (L_w/4 + d_y)^2}{k_y} = \frac{(2,000)(0.2)(1)(1.5 \times 10^{-5})(900/4 + 2,190)^2}{50.2} = 697 \text{ hours,}$$

where $d_y = \frac{1}{2}(5,200 - 900) = 2,190$ ft for this centered well. From Eq. 8.208,

$$t_{E\text{prf}} = \frac{1,650 \phi \mu c_t d_x^2}{k_x} = \frac{(1,650)(0.2)(1)(1.5 \times 10^{-5})(2,640)^2}{(100)} = 344 \text{ hours.}$$

The smaller of these two values is 344 hours, which is thus the expected end of pseudoradial flow. The data on the figure that lie on the straight line show the time range from 192 to 432 hours, which is generally consistent with the expected duration of the flow regime.

8.11.7 Late-Linear Flow. The governing equation for late-linear flow is^{38,39}

$$p_i - p_{wf} = \frac{8.128qB}{b_H h} \sqrt{\frac{\mu t}{k_x \phi c_t}} + \frac{141.2qB\mu}{b_H \sqrt{k_x k_z}} \left(s_p + s_c + \frac{b_H}{L_w} s_d \right). \dots\dots\dots (8.211)$$

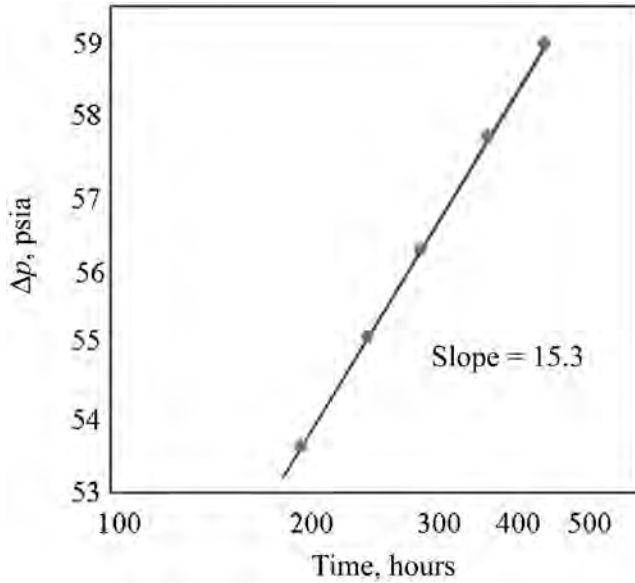


Fig. 8.105—Pseudoradial flow indicated by semilog straight line for well Prf-3.

TABLE 8.5—PRESSURE CHANGE DATA FOR WELL Prf-3	
Time (hours)	Δp = (p _r - p _{wf}) (psi)
192	53.69
240	55.13
288	56.32
360	57.81
432	59.05

The late-linear flow regime starts after the pressure transient has reached the boundaries in the *z*- and *y*-directions, and the flow behavior with regard to these directions has become pseudosteady state, as Fig. 8.100 shows.

The start of this time period is the maximum of two equations.³⁹ The first depends on the time to reach the boundary, *D_y*, beyond the end of the horizontal well. It also depends on the permeability, *k_y*, in the direction parallel to the wellbore.

$$t_{\text{SIlf}} = \frac{4,800\phi\mu c_t(D_y + L_w/4)^2}{k_y} \dots\dots\dots (8.212)$$

Another requirement for the start of the late-linear flow regime is the time to reach the maximum vertical distance, *D_z*, divided by the vertical permeability:

$$t_{\text{SIlf}} = \frac{1,800\phi\mu c_t D_z^2}{k_z} \dots\dots\dots (8.213)$$

Usually, the start of the late-linear flow regime is dictated by the time to reach the boundaries in the y -direction. The end of this period is given by the equation

$$t_{E\text{llf}} = \frac{1,650\phi\mu c_t d_x^2}{k_x} \dots\dots\dots (8.214)$$

The end of the late-linear flow regime depends on reaching the nearest boundary in the direction perpendicular to the wellbore, which is the distance, d_x , away, and on the permeability k_x in that direction.

Identify the late-linear flow regime by a half-slope on the derivative in the diagnostic plot of drawdown test data. (The pressure change may approach a half-slope asymptotically.) For data that appear to be in this flow regime, plot pressure against the square root of time. From the slope m_{llf} of the plot, estimate permeability in the x -direction from

$$\sqrt{k_x} = \frac{8.128qB}{|m_{\text{llf}}| b_H h} \sqrt{\frac{\mu}{\phi c_t}} \dots\dots\dots (8.215)$$

Alternatively, if k_x is known from an early-linear flow regime, estimate b_H , the length of the drainage area, from

$$b_H = \frac{8.128qB}{|m_{\text{llf}}| h} \sqrt{\frac{\mu}{\phi c_t k_x}} \dots\dots\dots (8.216)$$

This late-linear flow regime is the only period that provides the data to calculate the total skin, s , including the partial-penetration skin, s_p , and the convergence skin, s_c . To calculate the damage skin, s_d , use

$$s_d = \frac{L_w}{b_H} \left(\frac{b_H \sqrt{k_x k_z} (\Delta p_{t=0})}{141.2qB\mu} - s_p - s_c \right) \dots\dots\dots (8.217)$$

The total skin depends on $\Delta p_{t=0}$. Subtracting the partial penetration skin, s_p , and the convergence skin, s_c , from the total skin yields the damage skin.

The partial-penetration skin is a complex function that is calculated with Eqs. A-25 through A-35 in Table 8.A-2. For a buildup test, plot pressure against the HTR. From the slope, m_{llf} , calculate k_x with Eq. 8.215, exactly the same as for drawdown tests. Or, if k_x is known, estimate the length, b_H , of the drainage area with Eq. 8.216. Calculate the damage skin, s_d , from a pressure buildup test from Eq. 8.217, where $\Delta p_{t=0} = (p_{t=0})_{\text{ext}} - p_{wf(t=0)}$.

Note that the same difficulty arises in using superposition to find plotting functions plots of buildup data from the late-linear flow regime as existed with the previous flow regimes. Pressures at both time ($t_p + \Delta t$) and time Δt must be in the late linear flow regime for a tandem-root plot to be valid. However, if $t_p \gg \Delta t_{\text{max}}$, there is little error.

Example 8.5: Well Llf-4. The diagnostic plot for a drawdown test from Well Llf-4³⁹ appears to include data in the late-linear flow regime (derivative with half-slope). The following data applies to this well: $q = 800$ STB/D, $\mu = 1$ cp, $B = 1.25$ RB/STB, $r_w = 0.25$ ft, $\phi = 0.2$, $c_t = 15 \times 10^{-6}$ psi⁻¹, $h = 150$ ft, $L_w = 1,000$ ft, $b_H = 2,000$ ft (well centered), $a_H = 6,968$ ft (well centered), $D_z = 85$ ft, $d_z = 65$ ft, $k_x k_z = 1,000$ md² (from analysis of early-radial flow),

and $k_x k_y = 5,000 \text{ md}^2$ (from analysis of pseudoradial flow). **Table 8.6** gives pressure change, $\Delta p = p_i - p_{wf}$, data vs. time.

Fig. 8.106 is a plot of pressure change vs. the square root of time. The straight line on this plot for the entire time range (60 to 240 hours) confirms late-linear flow for this range. The slope of the line is $1.56 \text{ psi/hr}^{1/2}$, and the intercept is $\Delta p_{t=0} = 28.4 \text{ psi}$.

From **Eq. 8.215**,

$$\sqrt{k_x} = \frac{8.128qB}{|m_{\text{lf}}| b_H h} \sqrt{\frac{\mu}{\phi c_t}} = \frac{(8.128)(800)(1.25)}{(1.56)(2,000)(150)} \sqrt{\frac{1}{(0.2)(1.5 \times 10^{-5})}} = 10.0.$$

Then, $k_x = 100 \text{ md}$. Because $k_x k_z = 100 \text{ md}^2$, $k_z = 10 \text{ md}$. Also, because $k_x k_y = 5,000 \text{ md}^2$, $k_y = 50 \text{ md}$. From **Eq. 8.217**,

$$\begin{aligned} s_d &= \frac{L_w}{b_H} \left(b_H \frac{\sqrt{k_x k_z} \Delta p_{t=0}}{141.2qB\mu} - s_c - s_p \right) \\ &= \frac{(1,000)\sqrt{1,000}(28.4)}{(141.2)(800)(1.25)(1)} - \frac{1,000}{2,000} (s_p + s_c) = 6.36 - 0.5(s_c + s_p). \end{aligned}$$

From **Eq. 8.203**,

$$\begin{aligned} s_c &= \ln \left(\frac{h}{r_w} \right) + 0.25 \ln \left(\frac{k_x}{k_z} \right) - \ln \left[\sin \left(\frac{\pi d_z}{h} \right) \right] - 1.838 \\ &= \ln \left(\frac{150}{0.25} \right) + 0.25 \ln \left(\frac{100}{10} \right) - \ln \left[\sin \left(\frac{65\pi}{150} \right) \right] - 1.838 = 5.16. \end{aligned}$$

Calculate the partial penetration skin, s_p , using the appropriate equation from among Eqs. A-25 through A-35 in **Table 8.A-2**. First, calculate

$$\frac{a_H}{\sqrt{k_x}}, \frac{b_H}{\sqrt{k_y}}, \text{ and } \frac{h}{\sqrt{k_z}}$$

to determine whether “Case 1” or “Case 2” applies:

$$\begin{aligned} \frac{a_H}{\sqrt{k_x}} &= \frac{6,968}{\sqrt{100}} = 696.8, \\ \frac{b_H}{\sqrt{k_y}} &= \frac{2,000}{\sqrt{50}} = 283; \quad \frac{0.75b_H}{\sqrt{k_y}} = 212, \\ \text{and } \frac{h}{\sqrt{k_z}} &= \frac{150}{\sqrt{10}} = 47.4; \quad \frac{0.75}{\sqrt{k_z}} = 35.6. \end{aligned}$$

Because

$$\frac{a_H}{\sqrt{k_x}} > \frac{0.75b_H}{\sqrt{k_y}} \gg \frac{0.75h}{\sqrt{k_z}},$$

this is Case 1 (Eq. A-26). Use Eqs. A-25 through A-31 from the table. From Eq. A-27, $s_p = p_{xyz} + p'_{xy}$. From Eq. A-25,

$$\begin{aligned} p_{xyz} &= \left(\frac{b_H}{L_w} - 1 \right) \left\{ \ln \left(\frac{h}{r_w} \right) + 0.25 \ln \left(\frac{k_x}{k_z} \right) - \ln \left[\sin \left(\frac{\pi d_z}{h} \right) - 1.838 \right] \right\} \\ &= \left(\frac{2,000}{1,000} \right) \left\{ \ln \left(\frac{150}{0.25} \right) + 0.25 \ln \left(\frac{100}{10} \right) - \ln \left[\sin \left(\frac{65\pi}{150} \right) - 1.838 \right] \right\} = 5.16. \end{aligned}$$

From Eq. A-28,

$$p'_{xy} = \frac{2b_H^2}{L_w h} \sqrt{k_z / k_y} \left\{ F \left(\frac{L_w}{2b_H} \right) + 0.5 \left[F \left(\frac{4y_m + L_w}{2b_H} \right) - F \left(\frac{4y_m - L_w}{2b_H} \right) \right] \right\}.$$

Here, from Eq. A-29,

$$y_m = d_y + \frac{L_w}{2} = 500 + \frac{1,000}{2} = 1,000.$$

The well is centered, so $d_y = D_y = 500$ ft.

$$\frac{L_w}{2b_H} = \frac{1,000}{(2)(2,000)} = 0.25.$$

From Eq. A-30,

$$\begin{aligned} F(u) &= -u \left[0.145 + \ln(u) - 0.137(u)^2 \right], \quad u < 1. \\ F \left(\frac{L_w}{2b_H} \right) &= -(0.25) \left[0.145 + \ln(0.25) - 0.137(0.25)^2 \right] = 0.313. \end{aligned}$$

Also,

$$\begin{aligned} \frac{4y_m + L_w}{2b_H} &= \frac{(4)(1,000) + 1,000}{(2)(2,000)} = 1.25, \\ \text{and } \frac{4y_m - L_w}{2b_H} &= 0.75. \end{aligned}$$

From Eq. A-31,

$$\begin{aligned} F(u) &= (2 - u) \left[0.145 + \ln(2 - u) - 0.137(2 - u)^2 \right], \quad u > 1, \\ F \left(\frac{4y_m + L_w}{2b_H} \right) &= (2 - 1.25) \left[0.145 + \ln(2 - 1.25) - 0.137(2 - 1.25)^2 \right] = -0.165, \end{aligned}$$

and

$$F(u) = -u[0.145 + \ln(u) - 0.137(u)^2], \quad u < 1,$$

$$F\left(\frac{4y_m - L_w}{2b_H}\right) = -0.75[0.145 + \ln(0.75) - 0.137(0.75)^2] = 0.165.$$

Then,

$$p'_{xy} = \frac{(2)(2,000)^2}{(1,000)(150)} \sqrt{\frac{10}{100}} \{0.313 + 0.5[-0.165 - 0.165]\} = 2.50.$$

Then,

$$s_p = 5.16 + 2.50 = 7.66.$$

Thus, $s_d = 6.36 - 0.5(7.66 + 5.16) = -0.05$.

Now check the expected duration of the late-linear flow regime. The start is the larger of values from Eqs. 8.212 and 8.213. From Eq. 8.212,

$$t_{SIIF} = \frac{4,800\phi\mu c_t(D_y + L_w/4)^2}{k_y}$$

$$= \frac{4,800(0.2)(1)(1.5 \times 10^{-5})\left(500 + \frac{1,000}{4}\right)^2}{50} = 162 \text{ hours.}$$

From Eq. 8.213,

$$t_{SIIF} = \frac{1,800\phi\mu c_t D_z^2}{k_z}$$

$$= \frac{1,800(0.2)(1)(1.5 \times 10^{-5})(85)^2}{10} = 3.90 \text{ hours.}$$

Thus, the start is expected to be at approximately 162 hours. Eq. 8.214 gives the end of the flow regime.

$$t_{EIIF} = \frac{1,650\phi\mu c_t d_x^2}{k_x}$$

$$= \frac{1,650(0.2)(1)(1.5 \times 10^{-5})(3,484)^2}{100} = 601 \text{ hours.}$$

The data in this example spanned the time range from 60 to 240 hours. Some of the data that fall on the straight line are, in theory, from times before the start of the late-linear flow regime, but they appear to cause no problem in determining the slope of the line.

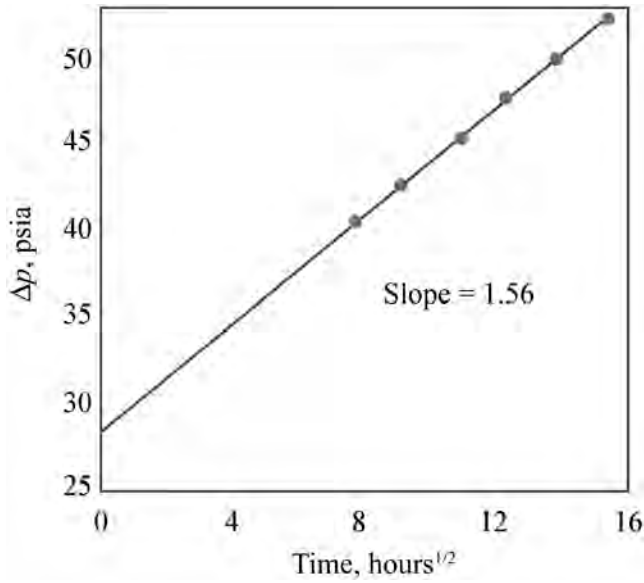


Fig. 8.106—Late linear flow indicated by straight line on square-root-of-time plot for well LIF-4.

Time (hours)	$\Delta p = (p_i - p_{wf})$ (psi)
60	40.50
84	42.72
120	45.25
156	47.92
192	50.07
240	52.65

8.11.8 Field Examples.⁴¹ The following field examples illustrate the procedures used in analyzing horizontal well-test data.

Field Example Well A. Table 8.7 summarizes the reservoir and completion properties for Well A. The target for Well A, a horizontal exploration well, was vertical tectonic fracture development in a low-permeability shale. Because of the fractures, the permeability is assumed to be isotropic ($k_h = k_z$) and a result of the fractures. Fig. 8.107 is a diagnostic plot for Well A and includes a history match using an analytical model.

During the early part of the test there is a unit-slope line representing wellbore storage. Following that wellbore storage, there is a transition to radial flow. The final few data points may be in radial flow. On the Horner plot (Fig. 8.108), the last few data points fall on a straight line. From the slope of the straight line, the apparent permeability is 0.011 md and the altered zone skin is 2.9. There is no evidence of boundary effects on this Horner plot. The existence of the semilog straight line is not assured, but the data are at least on the verge of reaching it.

Guided by the Horner analysis results, engineers simulated these data with an analytical horizontal well model. The initial match was poor. The match was improved considerably by

L_{di} , ft	2,470
L_{wi} , ft	-
r_{wi} , ft	0.25
ϕ , %	5
h , ft	150
q , STB/D	104
B_{oi} , RB/STB	1.40
μ , cp	0.45
t_p , hours	238

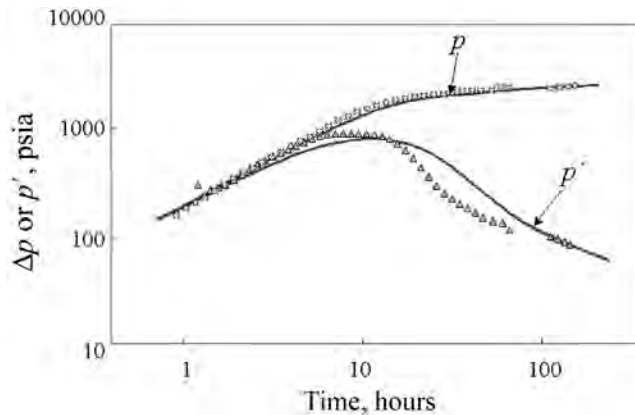


Fig. 8.107—Diagnostic plot for Well A.

introducing a no-flow boundary approximately 16 ft above the wellbore, which led to a permeability estimate of 0.027 md and an apparent skin of 11.5. It was concluded that the flow regime observed in the test was hemiradial flow.

The final match, shown on the type-curve plot in Fig. 8.107, is still not a good match at all times, but the author stated that the poor match in the transition region could be the result of phase-redistribution effects in the wellbore. The distance to the no-flow boundary that led to the best match compared favorably with well survey data, which indicated that the well was drilled approximately 20 ft below the upper limit of the productive horizon.

Field Example Well B. Well B is in a west Texas carbonate formation. It was expected to have isotropic permeability caused by fracturing and dissolution. Table 8.8 gives the field data for this well.

Fig. 8.109 is the diagnostic plot for this well. After wellbore storage, a short period of radial flow appears to be followed by the onset of linear flow, because p' approaches a slope of 0.5. In the time region where the derivative is horizontal, a straight line on the Horner plot (Fig. 8.110) yields $k = 0.14$ md. Using these results in the analysis shows that the end of radial flow occurs at $t_{Erf} = 165$ hours.

A tandem-root plot (Fig. 8.111) indicates linear flow and also suggests a distance to the nearest boundary of 29 ft. This is in good agreement with geological observations and helps to verify the assumption of isotropic permeability. The history match with an analytical horizontal well model, shown in Fig. 8.109, confirms the results of the Horner and tandem-root plots.

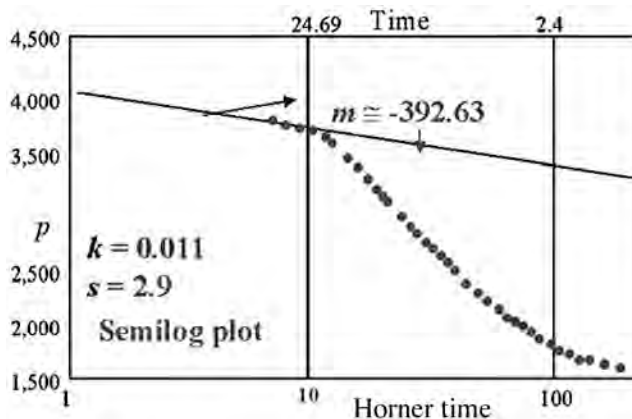


Fig. 8.108—Horner plot suggests beginning of middle-time region appears in test data.

TABLE 8.8—PARAMETERS FOR EXAMPLE WELL B	
L_{di} , ft	2,000
L_{wi} , ft	—
r_{wi} , ft	0.30
ϕ , %	17
h , ft	75
q , STB/D	200
B_{oi} , RB/STB	1.60
μ , cp	1.80
t_{pi} , hours	1,320

Field Example Well C. Well C data are from a buildup test of a horizontal well in a high-permeability sandstone where a 54-ft oil column overlies an extensive aquifer estimated to be approximately 180 ft thick. Table 8.9 shows the available data.

The diagnostic plot (Fig. 8.112) shows essentially no wellbore storage and a constant derivative, indicating radial, hemiradial, or elliptical flow at early times. The rapid decline of the derivative at the end of the test is caused by the aquifer underlying the oil column, which is acting like a constant-pressure boundary. A history match with an analytical horizontal well model with one no-flow and one constant-pressure boundary (the lower boundary), yielded $k_h = 313$ md, $k_z = 7.5$ md, $s_a = 1.5$, and $L_w = 356$ ft. The no-flow boundary was estimated to be approximately 112 ft below the wellbore.

The time at which the early radial flow regime ends—the time where the derivative ceases to be flat on the diagnostic plot—is approximately 1.5 hours. For a wellbore with a volume of 130 bbl filled with a fluid of compressibility of 3.5×10^{-6} psi, the duration of wellbore storage (the unit-slope line) is estimated to be 0.0005 hours. With the gauge sampling rate set at 0.017 hours, the wellbore-storage unit slope simply could not be detected and does not appear at all on this plot. Fig. 8.113 is the Horner plot for this test. A straight line appears in the same range as the flat derivative on a diagnostic plot. From the slope of the line, the permeability is estimated to be 53 md, close to the regression analysis match value of 48 md.

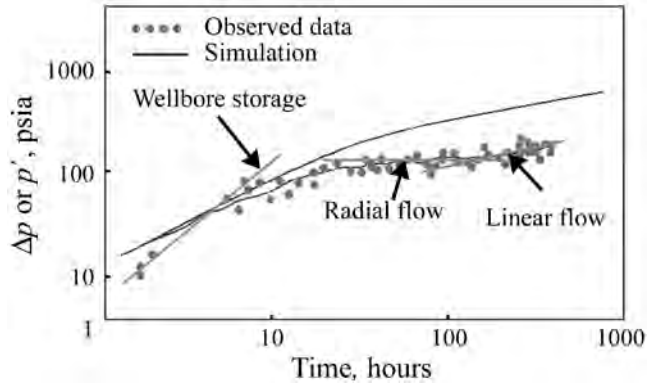


Fig. 8.109—Diagnostic plot for Well B indicates radial and linear flow regimes.

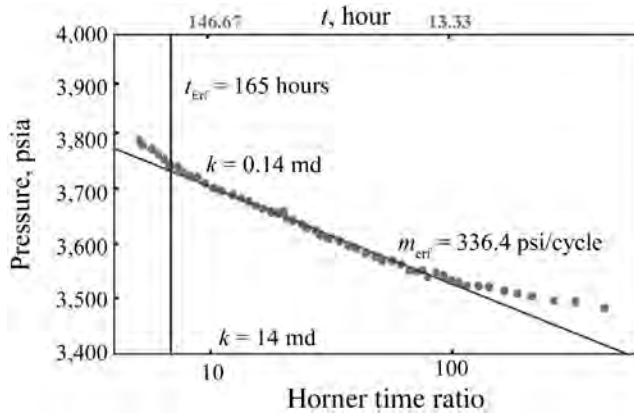


Fig. 8.110—Horner plot confirms early-radial flow.

8.11.9 Running Horizontal Well Tests. The measurements in horizontal wells are usually made above the wellbore with the pressure gauge still in the vertical section.

The test string may often be too rigid to pass through the wellbore. However, in most cases, conventional hardware can be used for horizontal well tests. With longer horizontal wellbores, wellbore storage is an inherent problem for testing, even for buildup tests with downhole shut-in. As mentioned previously, problems arise in conducting buildup tests with short-duration production periods because superposition is inappropriate; therefore, Horner plots and tandem-root plots, which depend on superposition being applicable, are often inappropriate.

Another problem in conducting buildup test following a short production period is that significant pressure gradients along the length of the wellbore may cause crossflow within the wellbore during shut-in, so fluid may flow from one region to another in the wellbore. These gradients can be removed and this crossflow eliminated by a longer-duration flow period preceding a buildup test.

Factors That Affect Transient Responses. A number of factors may affect the transient response of a horizontal well test: horizontal permeability (normal and parallel to well trajectory), vertical permeability, drilling damage, completion damage, producing interval that may be effectively much less than drilled length, and variations in standoff along length of well.

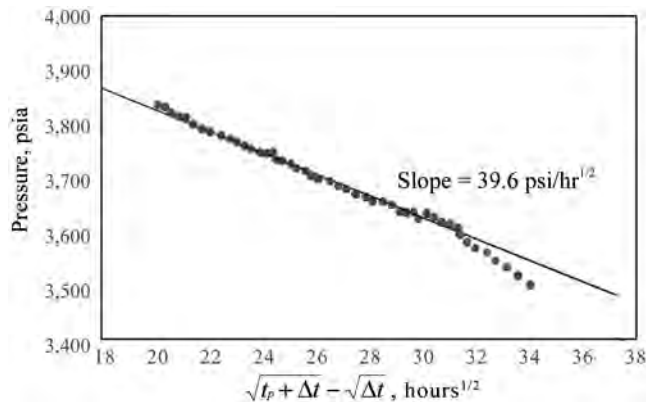


Fig. 8.111—Tandem-root plot confirms linear flow.

L_{d1} , ft	1,400
L_w , ft	484
r_w , ft	0.41
ϕ , %	17
h , ft	54
q , STB/D	2,760
B_{oi} , RB/STB	1.10
μ , cp	4.88
t_p , hours	36

In summary, seven or more factors may affect interpretation for horizontal wells in homogeneous reservoirs before the effects from boundaries. The problem is complex, so test results are frequently inconclusive. Furthermore, wellbore storage inhibits determination of properties associated with early-time transient behavior such as vertical permeability and damage from drilling and completion. Middle- and late-time behavior may require several hours, days, or months to appear in transient data.

Some practical steps will help ensure interpretable test data. First, it is helpful to run tests in the pilot hole before kicking off to drill the horizontal borehole section. From a test in the vertical section, it is possible to get usable estimates of horizontal and vertical permeabilities using modern wireline test tools. Second, a good directional drilling survey can frequently provide an adequate estimate of standoff. A production-log flow survey conducted with coiled tubing can determine what part of the wellbore is actually producing and, therefore, help provide an estimate of effective productive length. Wells in developed reservoirs should be flowed long enough to bring pressures along the wellbore to equilibrium and thus minimize crossflow. For high-rate wells, continuous borehole pressure and flow-rate measurements acquired during production can be used to interpret the pressure-drawdown transient response. If the downhole rates are not measured, the buildup test should be conducted with downhole shut-in to minimize wellbore storage distortion of test data.

8.11.10 Estimating Horizontal Well Productivity. Because of two fundamental problems, estimating the productivity of a horizontal well accurately is even more difficult than estimating

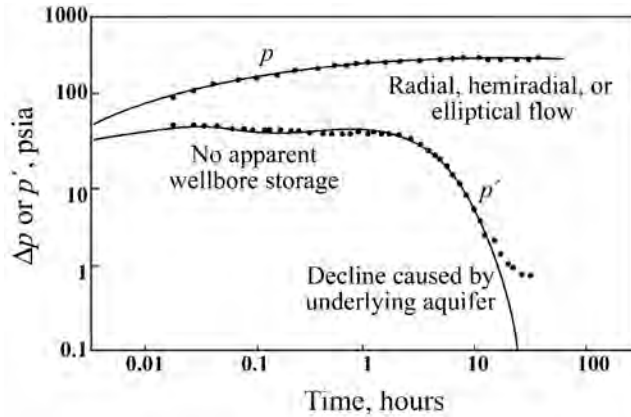


Fig. 8.112—Diagnostic plot for Well C shows no wellbore storage and constant derivative, with aquifer underlying oil column.

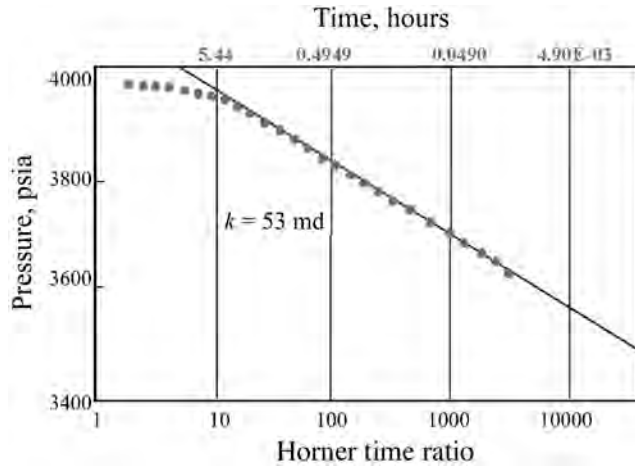


Fig. 8.113—Horner plot gives permeability of 5.3 md, close to that from regression analysis.

the productivity of a vertical well. The theoretical models available have a number of simplifying assumptions and the data required for even these simplified models are not likely to be available. Still, we must make estimates and decisions based on those estimates. In this section, two productivity models that have proved useful in practice are discussed. The first, published by Babu and Odeh⁴² in 1989, is limited to single-horizontal wells. The second, published by Economides, Brand, and Frick⁴³ in 1996, is more general and is useful for multilateral wells.

Babu-Odeh Method. Babu and Odeh⁴² obtained a rigorous solution to the diffusivity equation for a well in a box-shaped reservoir, subject to certain limiting assumptions. The assumptions include the following:

- Fluid flows to the well uniformly at all points along the wellbore (uniform flux) and the well is completed uniformly.
- The sides of the drainage volume are aligned with the principal permeability direction.
- The wellbore is parallel to the sides of the drainage area and is oriented parallel to one direction of principal permeability and perpendicular to the other two.

- The boundaries of the reservoir are all no-flow boundaries and the well reaches stabilized, pseudosteady-state flow.

- The formation damage around the wellbore is uniform at all points along the wellbore.

Fig. 8.95 introduces the nomenclature in the Babu and Odeh solution. The solution is quite complex but is approximated accurately with an equation written in the same form as the pseudosteady-state flow equation for a vertical oil well producing a single-phase, slightly incompressible liquid.

$$q = \frac{0.00708 b_H \sqrt{k_x k_z} (\bar{p} - p_{wf})}{B\mu \left[\ln \left(\frac{A^{1/2}}{r_w} \right) + \ln C_H - 0.75 + s_p + \left(\frac{b_H}{L_w} \right) s_d \right]} \dots\dots\dots (8.218)$$

$$J = \frac{q}{(\bar{p} - p_{wf})} = \frac{0.00708 b_H \sqrt{k_x k_z}}{B\mu \left[\ln \left(\frac{C_H A^{1/2}}{r_w} \right) - 0.75 + s_p + \left(\frac{b_H}{L_w} \right) s_d \right]} \dots\dots\dots (8.219)$$

Table 8.A-2 gives equations to estimate C_H and s_p . Two examples adapted from Babu and Odeh⁴² illustrate the application of these equations.

Example 8.6. A horizontal well 1,000 ft long (L_w) is drilled in a box-shaped drainage volume 4,000 ft long (a_H), 2,000 ft wide (b_H), and 100 ft thick (h). The well is off-center in the y -direction (parallel to the well), so $d_y = 250$ ft and $D_y = 750$ ft. The well is also off-center in the x -direction so that $d_x = 1,000$ ft and $D_x = 3,000$ ft. Finally, the well is centered in the z -direction so that $d_z = D_z = 50$ ft. The wellbore radius is 0.25 ft; $k_x = k_y = 200$ md and $k_z = 50$ md. Fluid properties are $B_o = 1.25$ RB/STB and $\mu = 1$ cp. Calculate the productivity index.

Solution.

From Eq. A-38,

$$\begin{aligned} \ln C_H &= 6.28 \frac{a_H}{h} \sqrt{\frac{k_z}{k_x}} \left[\frac{1}{3} - \frac{d_x}{a_H} + \left(\frac{d_x}{a_H} \right)^2 \right] - \ln \left(\sin \frac{\pi d_z}{h} \right) - 0.5 \ln \left[\left(\frac{a_H}{h} \right) \sqrt{\frac{k_z}{k_x}} \right] - 1.088 \\ &= \frac{(6.28)(4,000)}{(100)} \sqrt{\frac{50}{200}} \left[\frac{1}{3} - \frac{1,000}{4,000} + \left(\frac{1,000}{4,000} \right)^2 \right] - \ln \left[\sin \left(\frac{50\pi}{100} \right) \right] - 0.5 \ln \left[\left(\frac{4,000}{100} \right) \sqrt{\frac{50}{200}} \right] - 1.088 \\ &= 15.73 \end{aligned}$$

and $\frac{a_H}{\sqrt{k_x}} = \frac{4,000}{\sqrt{200}} = 283$; $\frac{0.75 b_H}{\sqrt{k_y}} = \frac{(0.75)(2,000)}{\sqrt{200}} = 106$; and $\frac{0.75 h}{\sqrt{k_z}} = \frac{(0.75)(100)}{\sqrt{50}} = 10.6$. Thus, use Case 1 equations (Eqs. A-26 through A-31) to calculate s_p .

$$\begin{aligned}
 s_p &= p_{xyz} + p'_{xy} \\
 p_{xyz} &= \left(\frac{b_H}{L_w} - 1 \right) \left\{ \ln \left(\frac{h}{r_w} \right) + 0.25 \ln \left(\frac{k_x}{k_z} \right) - \ln \left[\sin \left(\frac{\pi d_z}{h} \right) \right] - 1.838 \right\} \\
 &= \left(\frac{2,000}{1,000} - 1 \right) \left\{ \ln \left(\frac{100}{0.25} \right) + 0.25 \ln \left(\frac{200}{50} \right) - \ln \left[\sin \left(\frac{50\pi}{100} \right) \right] - 1.838 \right\} = 4.50.
 \end{aligned}$$

To calculate p'_{xy} , determine y_m , $L_w/2b_H$, $(4y_m - L_w)/2b_H$, and $(4y_m + L_w)/2b_H$.

$$\begin{aligned}
 y_m &= d_y + L_w/2 = 2.50 + 1,000 = 750 \text{ ft}, \\
 L_w/2b_H &= (1,000)/(2)(2,000) = 0.25, \\
 (4y_m - L_w)/2b_H &= [(4)(750) - 1,000]/(2)(2,000) = 0.5, \\
 \text{and } (4y_m + L_w)/2b_H &= [(4)(750) + 1,000]/(2)(2,000) = 1.0.
 \end{aligned}$$

Thus,

$$\begin{aligned}
 F(L_w/2b_H) &= F(0.25) = -(0.25)[0.145 + \ln(0.25) - 0.137(0.25)^2] = 0.313, \\
 F[(4y_m - L_w)/2b_H] &= F(0.5) = -(0.5)[0.145 + \ln(0.5) - 0.137(0.5)^2] = 0.291, \\
 \text{and } F[(4y_m + L_w)/2b_H] &= F(1.0) = -(1.0)[0.145 + \ln(1.0) - 0.137(1.0)^2] = -0.008.
 \end{aligned}$$

Then,

$$\begin{aligned}
 p'_{xy} &= \frac{2b_H^2}{L_w h} \sqrt{k_z/k_y} \left\{ F\left(\frac{L_w}{2b_H}\right) + 0.5 \left[F\left(\frac{4y_m + L_w}{2b_H}\right) - F\left(\frac{4y_m - L_w}{2b_H}\right) \right] \right\} \\
 &= \frac{(2)(2,000)^2}{(1,000)(100)} \sqrt{\frac{50}{200}} [0.313 + 0.5(-0.008 - 0.291)] = 6.54.
 \end{aligned}$$

Then, $s_p = p_{xyz} + p'_{xy} = 4.50 + 6.54 = 11.0$, and

$$\begin{aligned}
 J &= \frac{q}{(\bar{p} - p_{wf})} = \frac{0.00708 b_H \sqrt{k_x k_z}}{B\mu \left[\ln \left(\frac{C_H A^{1/2}}{r_w} \right) - 0.75 + s_p + \left(\frac{b_H}{L_w} \right) s_d \right]} \\
 &= \frac{(7.08 \times 10^{-3})(2,000) \sqrt{(50)(200)}}{(1.25)(1) \left\{ \ln \left[\frac{[(4,000)(100)]^{1/2}}{0.25} \right] + 15.73 - 0.75 + 11.0 \right\}} = 33.5 \text{ STB/D/psi.}
 \end{aligned}$$

Example 8.7. A horizontal well is drilled in a box-shaped reservoir with the following characteristics: $L_w = 1,000$ ft, $a_H = 2,000$ ft long, $b_H = 4,000$ ft wide, and $h_w = 2,000$ ft thick. The well is off-center in the y -direction ($d_y = 1,000$ ft; $D_y = 2,000$ ft), centered in the x -direction ($d_x = D_x = 1,000$ ft), and off-center in the z -direction ($d_z = 50$ ft; $D_z = 150$ ft).

Permeabilities are $k_x = k_y = 100$ md and $k_z = 20$ md. Wellbore radius is 0.25 ft, $B_o = 1.25$ RB/STB, $\mu = 1$ cp, and $s_d = 0$. Find the productivity index, J .

Solution.

From Eq. A-38 (Table 8.A-2),

$$\begin{aligned}\ln C_H &= 6.28 \frac{a_H}{h} \sqrt{\frac{k_z}{k_x}} \left[\frac{1}{3} - \frac{d_x}{a_H} + \left(\frac{d_x}{a_H} \right)^2 \right] - \ln \left(\sin \frac{\pi d_z}{h} \right) - 0.5 \ln \left[\left(\frac{a_H}{h} \right) \sqrt{\frac{k_z}{k_x}} \right] - 1.088 \\ &= \frac{(6.28)(2,000)}{(200)} \sqrt{\frac{20}{100}} \left[\frac{1}{3} - \frac{1,000}{2,000} + \left(\frac{1,000}{2,000} \right)^2 \right] - \ln \left[\sin \left(\frac{50\pi}{200} \right) \right] - 0.5 \ln \left[\left(\frac{2,000}{200} \right) \sqrt{\frac{20}{100}} \right] - 1.088 \\ &= 0.850.\end{aligned}$$

Note that

$$\frac{b_H}{\sqrt{k_y}} = \frac{4,000}{\sqrt{100}} = 400; \quad \frac{1.33a_H}{\sqrt{k_x}} = \frac{(1.33)(2,000)}{\sqrt{100}} = 266; \quad \text{and} \quad \frac{h}{\sqrt{k_z}} = \frac{(200)}{\sqrt{20}} = 44.7.$$

Thus, use Case 2 equations to calculate s_p .

$$\begin{aligned}s_p &= p_{xyz} + p_y + p_{xy}. \\ p_{xyz} &= \left(\frac{b_H}{L_w} - 1 \right) \left\{ \ln \left(\frac{h}{r_w} \right) + 0.25 \ln \left(\frac{k_x}{k_z} \right) - \ln \left[\sin \left(\frac{\pi d_z}{h} \right) \right] - 1.838 \right\} \\ &= \left(\frac{4,000}{1,000} - 1 \right) \left\{ \ln \left(\frac{200}{0.25} \right) + 0.25 \ln \left(\frac{100}{20} \right) - \ln \left[\sin \left(\frac{50\pi}{200} \right) \right] - 1.838 \right\} = 16.79.\end{aligned}$$

To calculate p_y , determine y_m . From Eq. A-29 (Table 8.A-2),

$$\begin{aligned}y_m &= d_y + \frac{L_w}{2} = 1,000 + \frac{1,000}{2} = 1,500 \text{ ft.} \\ p_y &= \frac{6.28b_H^2}{a_H h} \sqrt{\frac{k_x k_z}{k_y}} \left[\left(\frac{1}{3} - \frac{y_m}{b_H} + \frac{y_m^2}{b_H^2} \right) + \frac{L_w}{24b_H} \left(\frac{L_w}{b_H} - 3 \right) \right] \\ &= \frac{6.28(4,000)^2}{(2,000)(200)} \sqrt{\frac{(100)(20)}{100}} \left[\left(\frac{1}{3} - \frac{1,500}{4,000} + \left(\frac{1,500}{4,000} \right)^2 \right) + \frac{1,000}{(24)(4,000)} \left(\frac{1,000}{4,000} - 3 \right) \right] = 7.90.\end{aligned}$$

From Eq. A-35 (Table 8.A-2),

$$\begin{aligned}p_{xy} &= \left(\frac{b_H}{L_w} - 1 \right) \left(\frac{6.28a_H}{h} \sqrt{\frac{k_z}{k_x}} \right) \left(\frac{1}{3} - \frac{d_x}{a_H} + \frac{d_x^2}{a_H^2} \right), \quad d_x \geq 0.25a_H \\ &= \left(\frac{4,000}{1,000} - 1 \right) \left(\frac{(6.28)(2,000)}{200} \sqrt{\frac{20}{100}} \right) \left(\frac{1}{3} - \frac{1,000}{2,000} + \left(\frac{1,000}{2,000} \right)^2 \right) = 7.02.\end{aligned}$$

Thus, $s_p = 16.79 + 7.90 + 7.02 = 31.7$. Then, from Eq. A-37 (Table 8.A-2),

$$\begin{aligned}
 J &= \frac{q}{(\bar{p} - p_{wf})} = \frac{0.00708b_H\sqrt{k_x k_z}}{B\mu \left[\ln \left(\frac{C_H A^{1/2}}{r_w} \right) - 0.75 + s_p + \left(\frac{b_H}{L_w} \right) s_d \right]} \\
 &= \frac{(7.08 \times 10^{-3})(4,000)\sqrt{(100)(200)}}{(1.25)(1) \left[\ln \left(\frac{\sqrt{(200)(2,000)}}{0.25} \right) + 0.850 - 0.75 + 31.7 + 0 \right]} = 25.6 \text{ STB/D/psi.}
 \end{aligned}$$

Economides et al. Method. Economides *et al.*⁴⁵ presented a more general method to estimate productivity index for a horizontal well. The method has the advantage that it is applicable to multilateral wells in the same plane and is not limited to wells aligned with principal permeabilities. It includes solutions for wells with no pressure drop in the wellbore (infinite conductivity, as opposed to wells with uniform flux). It has the disadvantage that it requires interpolation in a table in which only certain drainage area shapes are given.

The basic working equation for the productivity index in this method is

$$J = \frac{\bar{k} b_H}{887.22 B\mu \left(p_D + \frac{b_H}{2\pi L_w} \Sigma s \right)}, \dots\dots\dots (8.220)$$

where Σs refers to damage skin, turbulence, and other pseudoskin factors. In Eq. 8.220,

$$p_D = \frac{b_H C_H}{4\pi h} + \frac{b_H}{2\pi L_w} s_c, \dots\dots\dots (8.221)$$

where

$$s_c = \ln \left(\frac{h}{2\pi r_w} \right) - \frac{h}{6L_w} + s_e, \dots\dots\dots (8.222)$$

and s_e , describing eccentricity effects in the vertical direction, is

$$s_e = \frac{h}{L_w} \left[\frac{2d_z}{h} - \frac{1}{2} \left(\frac{2d_z}{h} \right)^2 - \frac{1}{2} \right] - \ln \left[\sin \left(\frac{\pi d_z}{h} \right) \right]. \dots\dots\dots (8.223)$$

$s_e = 0$ when a well is centered in the vertical plane. This convergence skin differs only slightly from that used by Babu and Odeh. The difference is $0.25 \ln(k_x/k_z) + h/L_w [2d_z/h - 1/2(2d_z/h)^2 - 2/3]$, which is usually small (< 0.5). Table 8.10 gives values of C_H for several drainage areas and multilateral configurations. The equations as written are for isotropic reservoirs. Certain variable transformations are required before substituting into the working equation:

$$L' = L_w \alpha^{-1/3} \beta. \dots\dots\dots (8.224)$$

$$r'_w = r_w \frac{\alpha^{2/3}}{2} \left(\frac{1}{\alpha\beta} + 1 \right), \dots\dots\dots (8.225)$$

where

$$\alpha = \sqrt{\frac{(k_x k_y)^{1/2}}{k_z}}, \dots\dots\dots (8.226)$$

$$\text{and } \beta = \left(\sqrt{\frac{k_x}{k_y}} \cos^2 \phi + \sqrt{\frac{k_y}{k_x}} \sin^2 \phi \right)^{1/2} \dots\dots\dots (8.227)$$

ϕ is the azimuth of the well trajectory (relative to the y-axis). Reservoir dimensions:

$$x' = x \frac{\sqrt{k_y k_z}}{\bar{k}}, \dots\dots\dots (8.228)$$

$$y' = y \frac{\sqrt{k_x k_z}}{\bar{k}}, \dots\dots\dots (8.229)$$

$$z' = z \frac{\sqrt{k_x k_y}}{\bar{k}}, \dots\dots\dots (8.230)$$

$$\text{and } \bar{k} = \sqrt[3]{k_x k_y k_z} \dots\dots\dots (8.231)$$

Two examples, one from an isotropic reservoir and one from an anisotropic reservoir, illustrate this method.

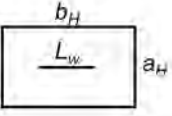
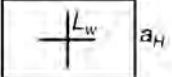
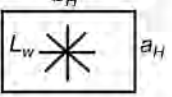
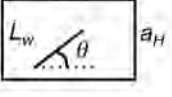
Example 8.8. Economides *et al.*⁴³ provide this example. Consider a horizontal well 1,500 ft long in a reservoir with $b_H = 2,000$ ft, $a_H = 4,000$ ft, $h = 20$ ft, $r_w = 0.4$, $k_x = k_y = k_z = 10$ md, $B_o = 1.25$ RB/STB, and $\mu = 1$ cp. Assume that the well is centered vertically so that $s_e = 0$. Also, assume $\Sigma_S = 0$.

Solution.

From Eq. 8.223,

$$\begin{aligned} s_c &= \ln \left(\frac{h}{2\pi r_w} \right) - \frac{h}{6L_w} + s_e \\ &= \ln \left(\frac{20}{2\pi(0.4)} \right) - \frac{20}{(6)(1,500)} + 0 = 2.07. \end{aligned}$$

(As a matter of interest, the Babu and Odeh s_c for this case is also 2.07.) From Table 8.10, for $2b_H = a_H$ and $L_w/b_H = 1,500/2,000 = 0.75$, $C_H = 2.53$. From Eq. 8.221,

TABLE 8.10—HORIZONTAL PLANE SHAPE FACTORS		L_w/b_H	C_H
	$b_H = 4a_H$	0.25	3.77
		0.5	2.09
		0.75	1.00
		1	0.26
	$b_H = 2a_H$	0.25	3.19
		0.5	1.80
		0.75	1.02
		1	0.52
	$b_H = a_H$	0.25	3.55
		0.5	2.21
		0.75	1.49
		1	1.04
$2b_H = a_H$	0.25	4.59	
	0.5	3.26	
	0.75	2.53	
	1	2.09	
$4b_H = a_H$	0.25	6.69	
	0.5	5.35	
	0.75	4.63	
	1	4.18	
	$b_H = a_H$	0.25	2.77
	0.5	1.47	
	0.75	0.81	
	1	0.46	
	$b_H = a_H$	0.25	2.66
	0.5	1.36	
	0.75	0.69	
	1	0.32	
	$b_H = a_H$	0	1.49
	$L_w/b_H = 0.75$	30	1.48
		45	1.48
		75	1.49
		90	1.49

$$\begin{aligned}
 P_D &= \frac{b_H C_H}{4\pi h} + \frac{b_H}{2\pi L_w} S_c \\
 &= \frac{(2,000)(2.53)}{(4\pi)(20)} + \frac{(2,000)(2.07)}{(2\pi)(1,500)} = 20.58.
 \end{aligned}$$

Then, from Eq. 8.220,

$$J = \frac{\bar{k}b_H}{887.22B\mu\left(p_D + \frac{b_H}{2\pi L_w}\Sigma s\right)}$$

$$= \frac{(10)(2,000)}{(887.22)(1.25)(1)(20.58 + 0)} = 0.876 \text{ STB/D/psi.}$$

Example 8.9. Rework the Babu-Odeh [Example 8.7](#) using the Economides *et al.* method.
Solution.

First transform the variables. From [Eqs. 8.226](#) and [8.227](#),

$$\alpha = \sqrt{\frac{(k_x k_y)^{1/2}}{k_z}} = \sqrt{\frac{[(100)(100)]^{1/2}}{(20)}} = 2.236.$$

Because the well is parallel to the x -axis, $\phi = 0$, and

$$\beta = \left(\sqrt{\frac{k_x}{k_y}}\right)^{1/2} = 1.$$

From [Eq. 8.231](#),

$$\bar{k} = \sqrt[3]{k_x k_y k_z} = 58.5 \text{ md.}$$

From [Eq. 8.224](#),

$$L' = L_w \alpha^{-1/3} \beta = (1,000)(2.236)^{-1/3}(1) = 765 \text{ ft.}$$

From [Eq. 8.225](#),

$$r'_w = r_w \frac{\alpha^{2/3}}{2} \left(\frac{1}{\alpha\beta} + 1\right) = (0.25) \frac{(2.236)^{2/3}}{2} \left[\frac{1}{(2.236)(1)} + 1\right] = 0.309 \text{ ft.}$$

From [Eqs. 8.228](#) through [8.230](#),

$$a'_H = a_H \frac{\sqrt{k_y k_z}}{\bar{k}} = \frac{2,000\sqrt{(100)(20)}}{58.5} = 1,529 \text{ ft,}$$

$$b'_H = b_H \frac{\sqrt{k_x k_z}}{\bar{k}} = \frac{4,000\sqrt{(100)(20)}}{58.5} = 3,058 \text{ ft,}$$

$$h' = h \frac{\sqrt{k_x k_y}}{\bar{k}} = \frac{200\sqrt{(100)(100)}}{58.5} = 342 \text{ ft,}$$

$$\text{and } d'_z = d_z \frac{\sqrt{k_x k_y}}{\bar{k}} = \frac{(50)\sqrt{(100)(100)}}{58.5} = 85.5 \text{ ft.}$$

Thus, the equivalent system is a rectangular-shaped drainage area twice as long parallel to the wellbore (3,050 ft) as perpendicular, with $L'/b'_H = 765/3,058 = 0.25$. In the original example, the well was off-center in the horizontal plane; here, assume that a centered well is an adequate approximation. From Table 8.10, $C_H = 3.19$.

From Eq. 8.223,

$$s_e = \frac{h'}{L'_w} \left[\frac{2d'_z}{h'} - \frac{1}{2} \left(\frac{2d'_z}{h'} \right)^2 - \frac{1}{2} \right] - \ln \left[\sin \left(\frac{\pi d'_z}{h'} \right) \right]$$

$$= \frac{342}{765} \left[\frac{(2)(85.5)}{342} - \frac{1}{2} \left(\frac{(2)(85.5)}{342} \right)^2 - \frac{1}{2} \right] - \ln \left[\sin \left(\frac{85.5\pi}{342} \right) \right] = 0.291.$$

Then,

$$s_c = \ln \left(\frac{h'}{2\pi r'_w} \right) - \frac{h'}{6L'_w} + s_e$$

$$= \ln \left(\frac{342}{2\pi(0.309)} \right) - \frac{342}{(6)(765)} + 0.291 = 5.39.$$

(The Babu-Odeh s_c is 5.60 for this case.) Then, from Eq. 8.221,

$$p_D = \frac{b'_H C_H}{4\pi h'} + \frac{b'_H}{2\pi L'_w} s_c$$

$$= \frac{(3,050)(3.14)}{4\pi(342)} + \frac{(3,050)(5.39)}{2\pi(765)} = 5.70.$$

Finally, from Eq. 8.220,

$$J = \frac{\bar{k} b'_H}{887.22 B \mu \left(p_D + \frac{b'_H}{2\pi L'_w} \Sigma s \right)}$$

$$= \frac{(58.5)(3,058)}{(887.22)(1.25)(1.0)(5.70 + 0)} = 28.3 \text{ STB/D/psi.}$$

The result is slightly larger than the result using the Babu-Odeh method ($J = 25.6$ STB/D/psi). At least part of the reason for the difference is that, in this example, it was necessary to assume that the well was centered in its drainage volume, which was not true in the original example. The optimal location of a horizontal well to maximize productivity is to center it within its drainage volume.

Comparison of Recent and Older Horizontal Well Models. Ozkan⁴⁴ compared “contemporary” (generally 1990s) and “conventional” horizontal well models in a paper published in 2001. He pointed out that the older models are used for both pressure-transient test analysis and for estimating well productivity. Ozkan stressed three limitations of the conventional models, which include the Babu-Odeh model and other pioneering work.

Conventional models usually assume that the horizontal well is parallel to one of the principal permeability directions (preferably the minimum permeability direction in the horizontal plane). In many cases, this is not true. In fact, in many cases the principal permeability directions are unknown. When the principal permeability directions are known, corrections to length are possible (as in the Economides *et al.* model); if they are not known, there is no way to correct the analysis. Contemporary models show that the error in permeability estimates approaches 50% when the deviation angle exceeds 50°. Unfortunately, the models also indicate that there is nothing in a well’s response that provides any indication that the assumption that the well is parallel to a principal permeability direction is incorrect.

Ozkan pointed out that the damaged region around a horizontal well probably is nonuniform with distance (perhaps with the greatest damage near the heel of the well and the least near the toe, because filtrate invasion is of much longer duration near the heel). If there is variable permeability along the path of the well, the situation is even more complicated. Some contemporary models can take this variation into account; however, most conventional models cannot. Conventional models usually assume (implicitly) uniform skin effect along the wellbore. However, the contemporary models will not be helpful if the skin distribution along the length is unknown.

Ozkan notes that it is a common practice to complete horizontal wells selectively. Also, in other cases, some segment of the well may not be open to flow of reservoir fluids because of relatively low permeabilities or relatively large local skin effects. The absolute amount of the well that is open to flow and the location of the open intervals affect the pressure response in the well. Some contemporary well models can take these effects into account, but, again, the capabilities of the newer models may be limited if the location and length of the open intervals is unknown.

Many models assume negligible pressure drop in the wellbore (infinite conductivity). Others assume the same flow rate per unit length at all points along the well bore (uniform flux). In fact, there is likely to be finite pressure drop in the wellbore, resulting in neither uniform flow nor infinite conductivity. Contemporary models in which a reservoir model is coupled to a wellbore model can take these effects into account.

Unfortunately, contemporary horizontal well models have not led to simple, easily applied methods of well-test analysis or of predicting well productivity. Further, their full utility depends on availability of detailed well and reservoir description data. At present, the major use of such models may be to quantify the possible errors that arise from uncertainty and to be used to history-match observed information when sufficient data are available.

8.12 Deliverability Testing of Gas Wells

8.12.1 Introduction. This section discusses the implementation and analysis of the four most common types of gas-well deliverability tests: flow-after-flow, single-point, isochronal, and mod-

ified isochronal tests. A summary of the fundamental gas-flow equations, both theoretical and empirical, used to analyze deliverability tests in terms of pseudopressure is followed by a focus on specific tests and testing procedures, advantages and disadvantages of each testing method, and common analysis techniques. Examples illustrating deliverability tests analyses are included.

8.12.2 Types and Purposes of Deliverability Tests. Deliverability testing refers to the testing of a gas well to measure its production capabilities under specific conditions of reservoir and bottomhole flowing pressures (BHFPs). A common productivity indicator obtained from these tests is the absolute open flow (AOF) potential. The AOF is the maximum rate at which a well could flow against a theoretical atmospheric backpressure at the sandface. Although in practice the well cannot produce at this rate, regulatory agencies sometimes use the AOF to allocate allowable production among wells or to set maximum production rates for individual wells.

Another application of deliverability testing is to generate a reservoir inflow performance relationship (IPR) or gas backpressure curve. The IPR curve describes the relationship between surface production rate and BHFP for a specific value of reservoir pressure (that is, either the original pressure or the current average value). The IPR curve can be used to evaluate gas-well current deliverability potential under a variety of surface conditions, such as production against a fixed backpressure. In addition, the IPR can be used to forecast future production at any stage in the reservoir's life.

Several deliverability testing methods have been developed for gas wells. Flow-after-flow tests are conducted by producing the well at a series of different stabilized flow rates and measuring the stabilized BHP. Each flow rate is established in succession without an intermediate shut-in period. A single-point test is conducted by flowing the well at a single rate until the BHFP is stabilized. This type of test was developed to overcome the limitation of long testing times required to reach stabilization at each rate in the flow-after-flow test.

Isochronal and modified isochronal tests were developed to shorten tests times for wells that need long times to stabilize. An isochronal test consists of a series of single-point tests usually conducted by alternately producing at a slowly declining sandface rate without pressure stabilization and then shutting in and allowing the well to build to the average reservoir pressure before the next flow period. The modified isochronal test is conducted similarly, except the flow periods are of equal duration and the shut-in periods are of equal duration (but not necessarily the same as the flow periods).

8.12.3 Theory of Deliverability Test Analysis. This section summarizes the theoretical and empirical gas-flow equations used to analyze deliverability tests. The theoretical equations developed by Houpeurt⁴⁵ are exact solutions to the generalized radial-flow diffusivity equation, while the Rawlins and Schellhardt⁴⁶ equation was developed empirically. All basic equations presented here assume radial flow in a homogeneous, isotropic reservoir and therefore may not be applicable to the analysis of deliverability tests from reservoirs with heterogeneities, such as natural fractures or layered pay zones. These equations should not be used to analyze tests from hydraulically fractured wells during the fracture-dominated linear or bilinear flow periods. Finally, these equations assume that wellbore-storage effects have ceased. Unfortunately, wellbore-storage distortion may affect the entire test period in short tests, especially those conducted in low-permeability reservoirs.

Theoretical Deliverability Equations. The early-time transient solution to the diffusivity equation for gases for constant-rate production from a well in a reservoir with closed outer boundaries, written in terms of pseudopressure, p_p ,⁴⁷ is

$$p_p(p_s) - p_p(p_{wf}) = \frac{1.422 \times 10^6 qT}{k_g h} \times \left[1.151 \log \left(\frac{k_g t}{1,688 \phi \bar{\mu}_g \bar{c}_i r_w^2} \right) + s + Dq \right], \dots\dots\dots (8.232)$$

where p_s is the stabilized shut-in BHP measured before the deliverability test. In new reservoirs with little or no pressure depletion, this shut-in pressure equals the initial reservoir pressure, $p_s = p_i$, while in developed reservoirs, $p_s < p_i$.

The late-time or pseudosteady-state solution is

$$p_p(\bar{p}) - p_p(p_{wf}) = \frac{1.422 \times 10^6 qT}{k_g h} \times \left[1.151 \log \left(\frac{10.064A}{C_A r_w^2} \right) - \frac{3}{4} + s + Dq \right], \dots\dots\dots (8.233)$$

where \bar{p} is current drainage-area pressure. Gas wells cannot reach true pseudosteady state because $\mu_g(p)c_i(p)$ changes as \bar{p} decreases. Note that, unlike \bar{p} , which decreases during pseudosteady-state flow, p_s is a constant.

Eqs. 8.232 and 8.233 are quadratic in terms of the gas flow rate, q . For convenience, Houpeurt⁴⁵ wrote the transient flow equation as

$$\Delta p_p = p_p(p_s) - p_p(p_{wf}) = a_t q + b q^2, \dots\dots\dots (8.234)$$

and the pseudosteady-state flow equation as

$$\Delta p_p = p_p(\bar{p}) - p_p(p_{wf}) = a q + b q^2, \dots\dots\dots (8.235)$$

where

$$a_t = \frac{1.422 \times 10^6 T}{k_g h} \left[1.151 \log \left(\frac{k_g t}{1,688 \phi \bar{\mu}_g \bar{c}_i r_w^2} \right) + s \right], \dots\dots\dots (8.236)$$

$$a = \frac{1.422 \times 10^6 T}{k_g h} \left[1.151 \log \left(\frac{10.064A}{C_A r_w^2} \right) - \frac{3}{4} + s \right], \dots\dots\dots (8.237)$$

$$\text{and } b = \frac{1.422 \times 10^6 TD}{k_g h} \dots\dots\dots (8.238)$$

The coefficients of q (a_t for transient flow and a for pseudosteady-state flow) include the Darcy flow and skin effects and are measured in (psia²/cp)/(MMscf/D) when q is in MMscf/D. The coefficient of q^2 represents the inertial and turbulent flow effects and is measured in (psia²/cp)/(MMscf/D)² when q is in MMscf/D.

The Houpeurt equations also can be written in terms of pressure squared and are derived directly from the solutions to the gas-diffusivity equation, assuming that $\mu_g z$ is constant over the pressure range considered. For transient flow,

$$\Delta p^2 = p_s^2 - p_{wf}^2 = a_t q + b q^2, \dots\dots\dots (8.239)$$

and for pseudosteady-state flow,

$$\Delta p^2 = \bar{p}^2 - p_{wf}^2 = aq + bq^2 \dots\dots\dots (8.240)$$

The flow coefficients are

$$a_t = \frac{1.422 \times 10^6 \bar{\mu}_g \bar{z} T}{k_g h} \left[1.151 \log \left(\frac{k_g t}{1.688 \phi \bar{\mu}_g \bar{c}_t r_w^2} \right) + s \right] \dots\dots\dots (8.241)$$

$$a = \frac{1.422 \times 10^6 \bar{\mu}_g \bar{z} T}{k_g h} \left[1.151 \log \left(\frac{10.06 A}{C_A r_w^2} \right) - \frac{3}{4} + s \right] \dots\dots\dots (8.242)$$

$$\text{and } b = \frac{1.422 \times 10^6 \bar{\mu}_g \bar{z} T D}{k_g h} \dots\dots\dots (8.243)$$

When the Houpeurt equation is presented in terms of pressure squared, the coefficients of q are measured in $\text{psia}^2/(\text{MMscf}/\text{D})$ when q is in MMscf/D , while the coefficient of q^2 is measured in units of $\text{psia}^2/(\text{MMscf}/\text{D})^2$ when q is in MMscf/D . For convenience, all equations and examples in this section are presented with q measured in MMScf/D .

The pressure-squared form of the equation should be used only for gas reservoirs at low pressures (less than 2,000 psia) and high temperatures. To eliminate doubt about which equations to choose, use of the pseudopressure equations, which are applicable at all pressures and temperatures, is recommended. Consequently, all the analysis procedures in this section are presented in terms of pseudopressure.

An advantage of the pseudopressure form of the theoretical deliverability equation is that the flow coefficients are independent of the average reservoir pressure and, therefore, do not change as \bar{p} decreases during a flow test conducted under pseudosteady-state flow unless s , k , or A changes. Because the non-Darcy flow coefficient is a function of $\mu_g(p_{wf})$, the coefficient b will change slightly if the BHFP is changed. In contrast, because of the pressure dependency of the gas properties on average reservoir pressure, the flow coefficients for the pressure-squared form of the deliverability equation must be recalculated for every new \bar{p} value. When s , k , or A changes with time, the only way to update the deliverability curve is to retest the well.

Empirical Deliverability Equations. In 1935, Rawlins and Schellhardt⁴⁶ presented an empirical relationship that is used frequently in deliverability test analysis. The original form of their relation, given by Eq. 8.244 in terms of pressure squared, is applicable only at low pressures:

$$q = C(\bar{p}^2 - p_{wf}^2)^n \dots\dots\dots (8.244)$$

In terms of pseudopressure, Eq. 8.244 becomes

$$q = C[p_p(\bar{p}) - p_p(p_{wf})]^n \dots\dots\dots (8.245)$$

which is applicable over all pressure ranges. In Eqs. 8.244 and 8.245, C is the stabilized performance coefficient and n is the inverse slope of the line on a log-log plot of the change in pressure squared or pseudopressure vs. gas flow rate. Depending on the flowing conditions, the theoretical value of n ranges from 0.5, indicating turbulent flow throughout a well's drainage

area, to 1.0, indicating laminar flow behavior modeled by Darcy’s law. The value of C changes depending on the units of flow rate and whether Eq. 8.244 or 8.245 is used. All equations and examples in this section are presented with q measured in MMscf/D.

Houpeurt proved that neither Eq. 8.244 nor Eq. 8.245 can be derived from the generalized diffusivity equation for radial flow of real gas through porous media. Although the Rawlins and Shellhardt equation is not theoretically rigorous, it is still widely used in deliverability analysis and has worked well over the years, especially when the test rates approach the AOF potential of the well and the extrapolation from test rates to AOF is minimal.

8.12.4 Stabilization Time. Unlike pressure-transient tests, the analysis techniques for conventional flow-after-flow and single-point tests require data obtained under stabilized flowing conditions. Although isochronal and modified isochronal tests were developed to circumvent the requirement of stabilized flow, they may still require a single, stabilized flow period at the end of the test. Consequently, there is a need to understand the meaning of stabilization time and have a method to estimate its value.

Stabilization time is defined as the time when the flowing pressure is no longer changing or is no longer changing significantly. Physically, stabilized flow can be interpreted as the time when the pressure transient is affected by the no-flow boundaries, either natural reservoir boundaries or an artificial boundaries created by active wells surrounding the tested well. Consider a graph of pressure as a function of radius for constant-rate flow at various times since the beginning of flow. As Fig. 8.1 shows, the pressure in the wellbore continues to decrease as flow time increases. Simultaneously, the area from which fluid is drained increases, and the pressure transient moves farther out into the reservoir.

The radius of investigation, the point in the formation beyond which the pressure draw-down is negligible, is a measure of how far a transient has moved into a formation following any rate change in a well. The approximate position of the radius of investigation at any time for a gas well is estimated by Eq. 8.246⁴⁸:

$$r_i = \sqrt{\frac{k_g t}{948 \phi \bar{\mu}_g \bar{c}_t}} \dots\dots\dots (8.246)$$

Stabilized flowing conditions occur when the calculated radius of investigation equals or exceeds the distance to the drainage boundaries of the well (i.e., $r_i \geq r_e$). Substituting r_e and rearranging Eq. 8.246, yields an equation for estimating the stabilization time, t_s , for a gas well centered in a circular drainage area:

$$t_s = \frac{948 \phi \bar{\mu}_g \bar{c}_t r_e^2}{k_g} \dots\dots\dots (8.247)$$

As long as the radius of investigation is less than the distance to the no-flow boundary, stabilization has not been attained and the pressure behavior is transient. To illustrate the importance of stabilization times in deliverability testing, stabilization times were calculated as a function of permeability and drainage area for a well producing a gas with a specific gravity of 0.6 from a formation at 210°F and an average pressure of 3,500 psia ($\bar{\mu}_g = 0.02$ cp and $\bar{c}_t = 2.468 \times 10^{-4}$ psia⁻¹), with a porosity of 10%. **Table 8.11** shows that, for wells completed in low-permeability reservoirs, several days—or even years—are required to reach stabilized flow, while wells completed in high-permeability reservoirs stabilize in a short time.

A more general equation for calculating stabilization time is

TABLE 8.11—EFFECTS OF PERMEABILITY AND DRAINAGE AREA ON STABILIZATION TIME

<i>k</i> (md)	A = 40 acres		A = 640 acres	
	<i>t_s</i> (hours)	<i>t_s</i> (days or years)	<i>t_s</i> (hours)	<i>t_s</i> (days or years)
0.01	25,953	3 years	415,242	47 years
0.1	2,595	108 days	41,524	4.7 years
1.0	259.5	10.8 days	4,152.4	173 days
10.0	25.95	1.1 days	415.2	17.3 days
100.0	2.59	0.11 days	41.52	1.73 days
1000.0	0.259	0.011 days	4.15	0.173 days

TABLE 8.12—EFFECTS OF PERMEABILITY AND HYDRAULIC FRACTURE HALF-LENGTH ON TIME TO REACH PSEUDORADIAL FLOW

Case	<i>k</i> (md)	<i>L_f</i> (ft)	<i>t_{prf}</i> (hours)
1	1	100	51.2
2	0.01	100	5,120 (213 days)
3	0.01	1,000	512,000 (58 years)

$$t_s = \frac{\phi \bar{\mu}_g \bar{c}_t A t_{DA}}{0.0002637 k_g}, \dots\dots\dots (8.248)$$

where *t_{DA}* is dimensionless time for the beginning of pseudosteady-state flow. Values for *t_{DA}* are given in Table 8.A-1 for various reservoir shapes and well locations.⁴⁹ The time required for the pseudosteady-state equation to be exact is found from the entry in the column “Exact for *t_{DA}* >.”

The Rawlins-Schellhardt and Houpeurt deliverability equations assume radial flow. If pseudoradial flow has been achieved, however, these analysis techniques can be used for hydraulically fractured wells. The time to reach the pseudoradial flow regime, *t_{prf}*, occurs³⁰ at *t_{L_fD}* = 3 and is estimated with

$$t_{prf} = \frac{11,400 \phi \bar{\mu}_g \bar{c}_t L_f^2}{k_g} \dots\dots\dots (8.249)$$

To illustrate the importance of achieving pseudoradial flow during a deliverability test, values of *t_{prf}* were calculated for a hydraulically fractured well completed in a reservoir with $\phi = 0.15$, $\bar{\mu}_g = 0.03$ cp, and $\bar{c}_t = 1 \times 10^{-4}$ psia⁻¹ and with the range of permeabilities and hydraulic fracture half-lengths in Table 8.12. The results illustrate that a well with a long fracture in a low-permeability formation will take far too long to stabilize for conventional deliverability testing.

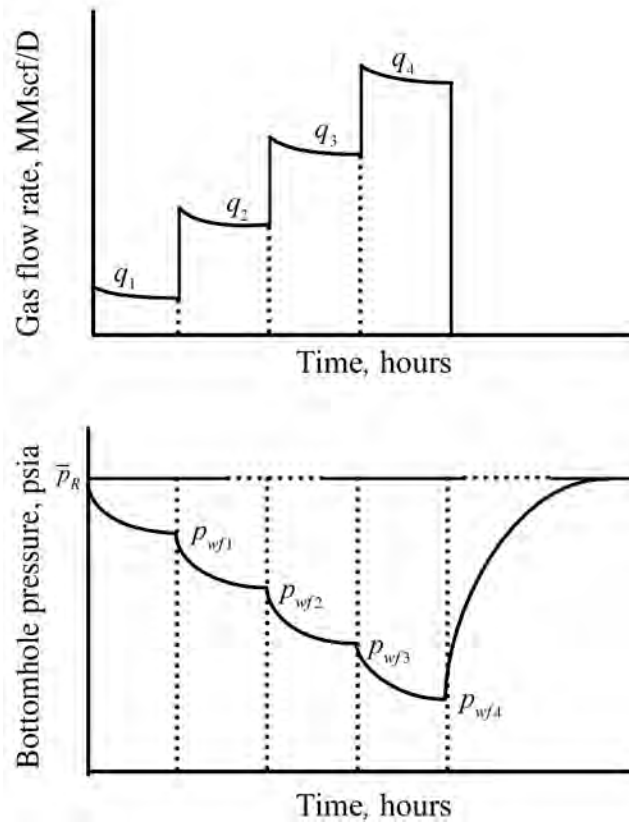


Fig. 8.114—Pressure and flow rate history of a typical flow-after-flow test.

8.12.5 Analysis of Deliverability Tests. This section discusses the implementation and analysis of the flow-after-flow, single-point, isochronal, and modified isochronal tests. Both the Rawlins and Schellhardt and Houpeurt analysis techniques are presented in terms of pseudopressures.

Flow-After-Flow Tests. Flow-after-flow tests, sometimes called gas backpressure or four-point tests, are conducted by producing the well at a series of different stabilized flow rates and measuring the stabilized BHFP at the sandface. Each different flow rate is established in succession either with or without a very short intermediate shut-in period. Conventional flow-after-flow tests often are conducted with a sequence of increasing flow rates; however, if stabilized flow rates are attained, the rate sequence does not affect the test.⁴⁶ The requirement that the flowing periods be continued until stabilization is a major limitation of the flow-after-flow test, especially in low-permeability formations that take long times to reach stabilized flowing conditions. Fig 8.114 illustrates a flow-after-flow test.

Rawlins-Schellhardt Analysis Technique. Recall the empirical equation that forms the basis for the Rawlins-Schellhardt analysis technique:

$$q = C [p_p(\bar{p}) - p_p(p_{wf})]^n \dots\dots\dots (8.245)$$

Taking the logarithm of both sides of Eq. 8.245 yields the equation that forms the basis for the Rawlins-Schellhardt analysis technique:

$$\log(q) = \log(C) + n \left\{ \log \left[p_p(\bar{p}) - p_p(p_{wf}) \right] \right\} \dots\dots\dots (8.250)$$

The form of Eq. 8.250 suggests that a plot of $\log(\Delta p_p)$ vs. $\log(q)$ will yield a straight line of slope $1/n$ and an intercept of $\{-1/n[\log(C)]\}$. The AOF potential is estimated from the extrapolation of the straight line to Δp_p evaluated at p_{wf} equal to atmospheric pressure (sometimes called base pressure). This analysis technique is illustrated with Example 8.10.

Houpeurt Analysis Technique. Flow-after-flow tests require stabilized data or data measured during pseudosteady-state flow. Houpeurt⁴⁵ gives the theoretical equation for pseudosteady-state flow, which was derived from the gas-diffusivity equation, as

$$\Delta p_p = p_p(\bar{p}) - p_p(p_{wf}) = aq + bq^2 \dots\dots\dots (8.235)$$

The coefficients a and b have theoretical bases and can be estimated if reservoir properties are known or they can be determined from flow-after-flow test data. Dividing both sides of Eq. 8.235 by the flow rate, q , and rearranging yields the equation that is the basis for the Houpeurt analysis technique:

$$\frac{\Delta p_p}{q} = \frac{p_p(\bar{p}) - p_p(p_{wf})}{q} = a + bq \dots\dots\dots (8.251)$$

The form of Eq. 8.251 suggests that a plot $\Delta p_p/q$ vs. q will yield a straight line with a slope b and an intercept a . The AOF is estimated in the Houpeurt deliverability analysis by solving Eq. 8.235 for $q = q_{\text{AOF}}$ at $p_{wf} = p_b$.

Example 8.10: Analysis of a Flow-After-Flow Test. Estimate the initial stabilized AOF potential of a well⁵⁰ with the well and reservoir properties listed. Use both the Rawlins-Schellhardt and the Houpeurt analysis techniques. In addition, estimate the AOF potential 10 years later when the static drainage area pressure has decreased to 350 psia. Evaluate the AOF potential at $p_b = 14.65$ psia. Table 8.13 summarizes the flow-after-flow test data. $L = 3,050$ ft, $r_w = 0.5$ ft, $M_a = 20.71$ lbm/lbm-mole, $T = 90^\circ\text{F} = 555^\circ\text{R}$, $A = 640$ acres, $\phi = 0.25$, $C_A = 30.8828$, and $h = 200$ ft.

Current $\bar{p} = 407.6$ psia, $p_p(\bar{p} = 407.6) = 1.617 \times 10^7$ psia²/cp. \bar{p} after 10 years = 350 psia, $p_p(\bar{p} = 350) = 1.2239 \times 10^7$ psia²/cp. $p_b = 14.65$ psia, $p_p(p_b) = 2,674.8$ psia²/cp.

The pseudopressure in this example (and all others in this section) were calculated using the methods suggested by Al-Hussainy *et al.*¹⁵ These methods, which involve numerical evaluation of the integral in Eq. 8.97 and which require computational routines to estimate gas viscosity, μ , and deviation factor, z , are widely available in basic reservoir fluid flow analysis software.

Solution.

Rawlins-Schellhardt Analysis. Plot Δp_p vs. q on log-log graph paper (Fig. 8.115). Table 8.14 gives the plotting functions. Construct the best-fit line through the data points. All data points lie on the best-fit line and will be used for all subsequent calculations.

Next, determine the deliverability exponent using least-squares regression analysis. Alternatively, because Points 1 and 4 both lie on the perceived “best” straight line through the test data, the reciprocal slope is estimated to be

TABLE 8.13—FLOW-AFTER-FLOW TEST DATA, EXAMPLE 8.10			
q (MMscf/D)	p_{wf} (psia)	p_{wf} (psia)	$p_p (p_{wf})$ (psia ² /cp)
0	375.2	407.60	1.6173×10^7
4.288	371.2	403.13	1.5817×10^7
9.265	361.3	393.03	1.5032×10^7
15.552	343.8	375.79	1.3736×10^7
20.177	327.1	359.87	1.2591×10^7

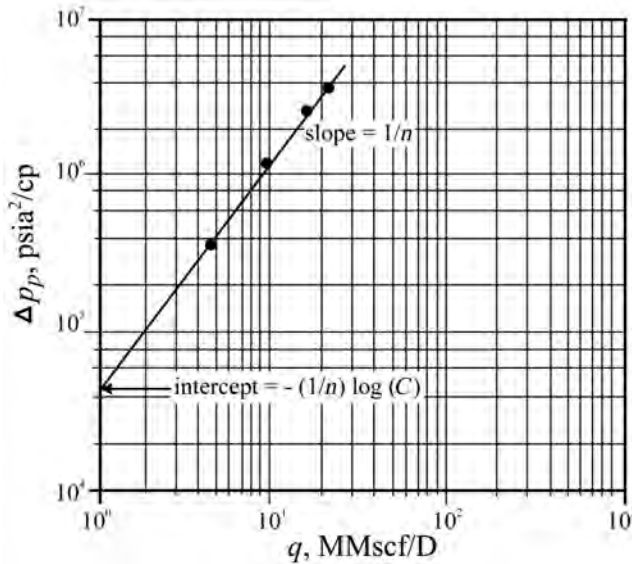


Fig. 8.115—Rawlins-Schellhardt analysis, Example 8.10.

$$n = \frac{\log(q_4/q_1)}{\log(\Delta p_{p4}/\Delta p_{p1})} = \frac{\log(20.177/4.28)}{\log(3.582 \times 10^6/3.560 \times 10^5)} = 0.671.$$

Now, calculate the AOF of the well. Because $0.5 \leq n \leq 1.0$, calculate C using either regression analysis or a point from the best-fit straight line through the test data. Estimating C with regression analysis results in $\log(C) = \alpha = -3.09$. Thus,

$$C = 10^\alpha = 10^{(-3.09)} = 8.13 \times 10^{-4}.$$

Estimating C using Point 4 from the best-fit line and Eq. 8.245:

$$C = \frac{q_4}{(\Delta p_{p4})^n} = \frac{20.177}{(3.582 \times 10^6)^{0.671}} = 8.07 \times 10^{-4}.$$

Therefore, the AOF potential of this well is

q (MMscf/D)	$\Delta p_p = p_p(p) - p_p(p_{wi})$ (psia ² /cp)
4.288	3.560×10^5
9.265	1.1416×10^6
15.552	2.437×10^6
20.177	3.582×10^6

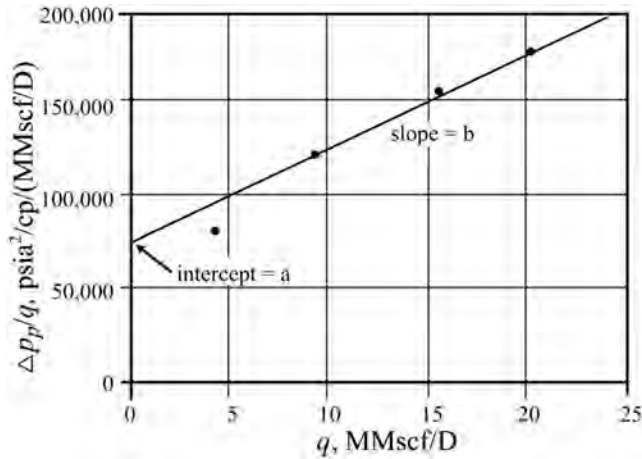


Fig. 8.116—Houpeurt analysis, Example 8.10.

$$q_{\text{AOF}} = C [p_p(\bar{p}) - p_p(14.65)]^n$$

$$= 8.13 \times 10^{-4} (1.6173 \times 10^7 - 2.6738 \times 10^3)^{0.67} = 55.0 \text{ MMscf/D at } \bar{p} = 407.6 \text{ psia.}$$

To update the AOF to a new average reservoir pressure, recall that for pseudopressure analysis, neither C nor n changes as drainage area pressure decreases. The AOF for the new drainage area pressure becomes

$$q_{\text{AOF}} = C [p_p(\bar{p}) - p_p(14.65)]^n$$

$$= 8.13 \times 10^{-4} (1.2239 \times 10^7 - 2.6748 \times 10^3)^{0.67} = 45.6 \text{ MMscf/D at } \bar{p} = 350 \text{ psia.}$$

Houpeurt Analysis. Plot $\Delta p_p/q$ vs. q on Cartesian graph paper (Fig. 8.116). Table 8.15 gives the plotting functions. Construct the best-fit line through the last three data points. The first point, corresponding to the lowest flow rate, does not follow the trend and will be ignored in subsequent analyses.

Determine the deliverability coefficients, a and b , from a least-squares regression analysis, excluding the first point. The result is

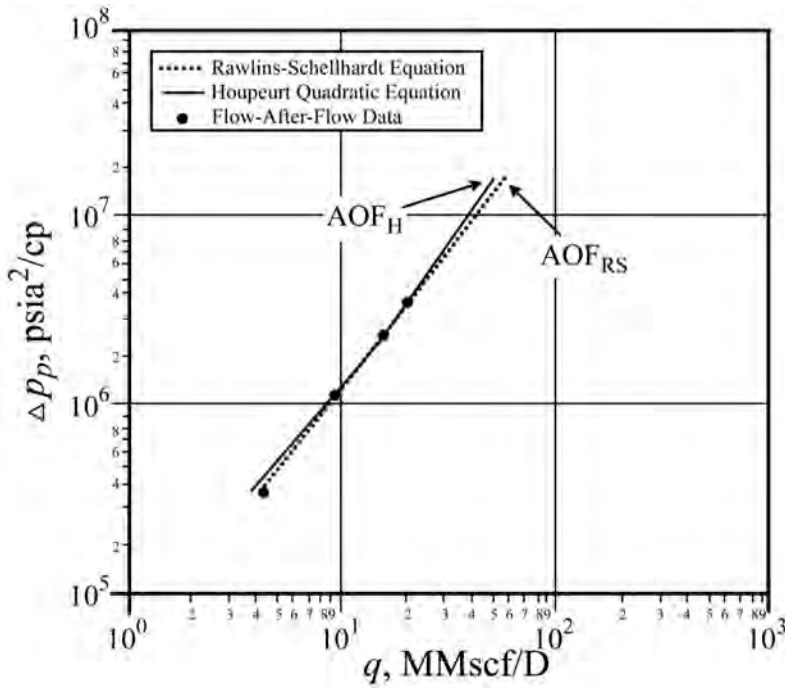


Fig. 8.117—Comparison of Rawlins-Schellhardt and Houpeurt methods.

TABLE 8.15—PLOTING FUNCTIONS FOR THE HOUPEURT ANALYSIS, EXAMPLE 8.10	
q (MMscf/D)	$\frac{\Delta p_p/q = [p_o(p) - p_o(p_w)]/q_i}{[(psia^2/cp)/(MMscf/D)]}$
4.288	0.8302×10^5
9.265	1.232×10^5
15.552	1.567×10^5
20.177	1.775×10^5

$$a = 7.75 \times 10^4 \text{ psia}^2 / \text{cp} / (\text{MMscf} / \text{D})$$

$$\text{and } b = 5.00 \times 10^3 \text{ psia}^2 / \text{cp} / (\text{MMscf} / \text{D})^2 .$$

Alternatively, use Points 2 and 4 from the line drawn through the test data to calculate a and b :

$$b = \frac{\left(\frac{\Delta p_p}{q}\right)_4 - \left(\frac{\Delta p_p}{q}\right)_2}{q_4 - q_2}$$

$$= \frac{1.775 \times 10^5 - 1.232 \times 10^5}{20.177 - 9.265} = 4.976 \times 10^3 \text{ psia}^2 / \text{cp} / (\text{MMscf} / \text{D})^2 .$$

$$\begin{aligned}
 a &= \left(\frac{\Delta p_p}{q_1} \right)_1 - b q_1 \\
 &= 1.775 \times 10^5 - (4,976)(20.177) = 7.71 \times 10^4 \text{ psia}^2 / \text{cp} / (\text{MMscf}/\text{D})^2 .
 \end{aligned}$$

Then,

$$\begin{aligned}
 q_{\text{AOF}} &= \frac{-a + \sqrt{a^2 + 4b[p_p(\bar{p}) - p_p(14.65)]}}{2b} \\
 &= -(7.75 \times 10^4) \\
 &+ \frac{\sqrt{(7.75 \times 10^4)^2 + 4(5.00 \times 10^3)[(1.62 \times 10^7) - 2,674.8]}}{2(5.00 \times 10^3)} = 49.7 \text{ MMscf}/\text{D} \text{ at } \bar{p} = 407.6 \text{ psia}.
 \end{aligned}$$

To update the AOF, note that for pseudopressure analysis neither a nor b changes as drainage area pressure changes. Therefore, the AOF for the new drainage area pressure is

$$\begin{aligned}
 q_{\text{AOF}} &= \frac{-a + \sqrt{a^2 + 4b[p_p(\bar{p}) - p_p(14.65)]}}{2b} \\
 &= \frac{-(7.75 \times 10^4) + \sqrt{(7.75 \times 10^4)^2 + 4(5.00 \times 10^3)[(1.2239 \times 10^7) - 2,674.8]}}{2(5.00 \times 10^3)} \\
 &= 42.2 \text{ MMscf}/\text{D} \text{ at } \bar{p} = 350 \text{ psia} .
 \end{aligned}$$

A comparison (**Fig. 8.117**) of the results from the two parts of **Example 8.10** shows that the Rawlins-Schellhardt equation appears to be valid for this range of test data; however, the line representing the Houpeurt equation deviates from the Rawlins-Schellhardt equation as BHFP decreases. Although the Rawlins-Schellhardt method is valid under many testing conditions, this deviation suggests that extrapolating the empirical equation over a large interval of pressure may not predict well behavior correctly.

Single-Point Tests. A single-point test is an attempt to overcome the limitation of long test times. A single-point test is conducted by flowing the well at a single rate until the sandface pressure is stabilized. One limitation of this test is that it requires prior knowledge of the well's deliverability behavior, either from previous well tests or possibly from correlations with other wells producing in the same field under similar conditions. Ensure that the well has flowed long enough to be out of wellbore storage and in the boundary-dominated or stabilized flow regime. Similarly, for hydraulically fractured wells, the well must be flowed long enough to be in the pseudoradial flow regime and then stabilized.

To analyze a single-point test with the Rawlins-Schellhardt method, n must be known or estimated. An estimate of n can be obtained either from a previous deliverability test on the well or from correlations with similar wells producing from the same formation under similar conditions. The calculation procedure is similar to that presented for flow-after-flow tests. The AOF can be estimated graphically by drawing a straight line through the single flow point with

a slope of $1/n$ and extrapolating it to the flow rate at $\Delta p_p = p_p(\bar{p}) - p_p(p_b)$. The AOF can also be calculated with

$$q_{\text{AOF}} = C [p_p(\bar{p}) - p_p(p_b)]^n,$$

where C is estimated with

$$C = q / [p_p(\bar{p}) - p_p(p_{wf})]^n .$$

To use the Houpeurt analysis technique, the slope, b , of the line on a plot of

$$\Delta p_p / q = [p_p(\bar{p}) - p_p(p_{wf})] / q \text{ vs } q$$

must be known. If a value of b is unavailable, estimate b using Eq. 8.238. Note that estimates of the formation properties are necessary to use Eq. 8.238. The remaining analysis procedure is similar to that for flow-after-flow tests.

Isochronal Tests. The isochronal test⁵¹ is a series of single-point tests developed to estimate stabilized deliverability characteristics without actually flowing the well for the time required to achieve stabilized conditions at each different rate. The isochronal test is conducted by alternately producing the well then shutting it in and allowing it to build to the average reservoir pressure before the beginning of the next production period. Pressures are measured at several time increments during each flow period. The times at which the pressures are measured should be the same relative to the beginning of each flow period. Because less time is required to build to essentially initial pressure after short flow periods than to reach stabilized flow at each rate in a flow-after-flow test, the isochronal test is more practical for low-permeability formations. A final stabilized flow point often is obtained at the end of the test. Fig. 8.118 illustrates an isochronal test.

The isochronal test is based on the principle that the radius of drainage established during each flow period depends only on the length of time for which the well is flowed and not the flow rate. Consequently, the pressures measured at the same time periods during each different rate correspond to the same transient radius of drainage. Under these conditions, isochronal test data can be analyzed using the same theory as a flow-after-flow test, even though stabilized flow is not attained. In theory, a stabilized deliverability curve can be obtained from transient data if a single, stabilized rate and the corresponding BHP have been measured and are available.

The transient flow regime is modeled by

$$p_p(p_s) - p_p(p_{wf}) = \frac{1.422 \times 10^6 qT}{k_g h} \times \left[1.151 \log \left(\frac{k_g t}{1,688 \phi \bar{\mu}_g \bar{c}_t r_w^2} \right) + s + Dq \right], \dots\dots (8.232)$$

where p_s is the stabilized BHP measured before the test. The transient equation can be rewritten in a form similar to the stabilized equation for a circular drainage area. To start this process, write

$$p_p(p_s) - p_p(p_{wf}) = \frac{1.422 \times 10^6 qT}{k_g h} \times \left[\ln \left(\frac{1}{r_w} \right) + \ln \left(\frac{k_g t}{377 \phi \bar{\mu}_g \bar{c}_t} \right)^{1/2} - \frac{3}{4} + s + Dq \right] . \dots (8.252)$$

Further, a transient radius of drainage is defined as

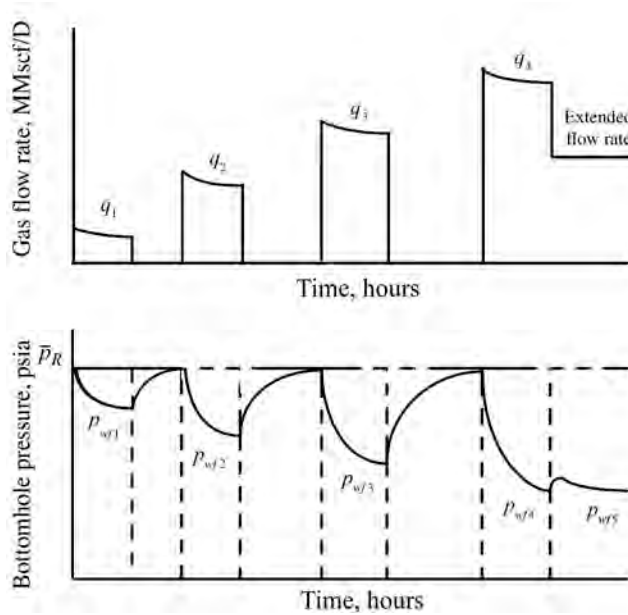


Fig. 8.118—Pressure and flow rate history of a typical isochronal test.

$$r_d = \sqrt{\frac{k_g t}{377 \phi \bar{\mu}_g \bar{c}_t}} \dots\dots\dots (8.253)$$

By substituting Eq. 8.253 into Eq. 8.252 and rearranging, the transient solution becomes

$$p_p(p_s) - p_p(p_{wf}) = \frac{1.422 \times 10^6 qT}{k_g h} \times \left[\ln \left(\frac{r_d}{r_w} \right) - \frac{3}{4} + s + Dq \right], \dots\dots\dots (8.254)$$

which is valid at any fixed time because r_d is a function of time and not of flow rate. r_d has no rigorous physical significance. It is simply the radius that forces the transient equation to resemble the pseudosteady-state equation. In addition, do not confuse r_d with r_i , which is the transient radius of investigation given by Eq. 8.246.

Similar to Houpeurt’s equations, rewrite Eq. 8.254 as

$$p_p(p_s) - p_p(p_{wf}) = a_t q + b q^2, \dots\dots\dots (8.255)$$

where

$$a_t = \frac{1.422 \times 10^6 T}{k_g h} \left[\ln \left(\frac{r_d}{r_w} \right) - \frac{3}{4} + s \right] \dots\dots\dots (8.256)$$

$$\text{and } b = \frac{1.422 \times 10^6 DT}{k_g h} \dots\dots\dots (8.238)$$

b is not a function of time and will remain constant. Similarly, the intercept a_t is constant for each fixed time line or isochron.

The theory of isochronal test analysis implies that the transient pressure drawdowns corresponding to the same elapsed time during each different flow period will plot as straight lines with the same slope b . The intercept a_t for each line will increase with increasing time. Therefore, draw a line with the same slope, b , through the final, stabilized data point, and use the coordinates of the stabilized point and the slope to calculate a stabilized intercept, a , independent of time, where (for radial flow) the stabilized flow coefficient is defined by

$$a = \frac{1.422 \times 10^6 T}{k_g h} \left[\ln \left(\frac{r_e}{r_w} \right) - \frac{3}{4} + s \right] \dots\dots\dots (8.257)$$

Rawlins-Schellhardt Analysis. In logarithmic form, the empirical equation introduced by Rawlins and Schellhardt for analysis of flow-after-flow test data is

$$\log (q) = \log (C) + n \left\{ \log \left[p_p(\bar{p}) - p_p(p_{wf}) \right] \right\} \dots\dots\dots (8.250)$$

For isochronal tests, plot transient data measured at different flow rates but taken at the same time increments relative to the beginning of each flow period. The lines drawn through data points corresponding to the same fixed flow time prove to be parallel, so the value of n is constant and independent of time. However, the intercept, $\log (C)$, is a function of time, so a different intercept must be calculated for each isochronal line. This “transient” intercept is $\log (C_t)$. In terms of this transient intercept, Eq. 8.248 becomes

$$\log (q) = \log (C_t) + n \left\{ \log \left[p_p(p_s) - p_p(p_{wf}) \right] \right\} \dots\dots\dots (8.258)$$

\bar{p} is replaced by p_s in the modified equation.

The conventional Rawlins-Schellhardt method of isochronal test analysis is to plot

$$\log \left[\Delta p_p = p_p(p_s) - p_p(p_{wf}) \right] \text{ vs } \log (q)$$

for each time, giving a straight line of slope $1/n$ and an intercept of

$$\left\{ -1/n \left[\log (C_t) \right] \right\} .$$

Houpeurt Analysis. Recall that the Houpeurt equation for analyzing flow-after-flow tests is

$$\frac{\Delta p_p}{q} = \frac{p_p(\bar{p}) - p_p(p_{wf})}{q} = a + bq \dots\dots\dots (8.251)$$

Eq. 8.251 assumes stabilized flow conditions; however, in isochronal testing, measured transient data are being recorded. Consequently, for each isochronal (or fixed time) line, the equation for transient flow conditions is

$$\frac{\Delta p_p}{q} = \frac{p_p(p_s) - p_p(p_{wf})}{q} = a_t + bq, \dots\dots\dots (8.259)$$

where

$$a_t = \frac{1.422 \times 10^6 T}{k_g h} \left[\ln \left(\frac{r_d}{r_w} \right) - \frac{3}{4} + s \right], \dots\dots\dots (8.256)$$

$$\text{and } b = \frac{1.422 \times 10^6 DT}{k_g h} \dots\dots\dots (8.238)$$

The form of Eq. 8.259 suggests that a plot of $\Delta p_p/q = [p_p(p_s) - p_p(p_{wf,s})]/q$ vs. q will yield a straight line with slope b and intercept a_t . This theory can then be extended to the stabilized point and calculate a stabilized intercept, a , using the coordinates of the stabilized point. The slope b remains the same.

Example 8.11: Analysis of Isochronal Tests. Estimate the AOF of this well⁵¹ using both the Rawlins and Schellhardt and the Houpeurt analyses. Table 8.16 summarizes the isochronal test data. Assume $p_b = 14.65$ psia.

$$\bar{p} \approx p_s = 352.4 \text{ psia, } p_p(\bar{p}) \approx p_p(p_s) = 9.9715 \times 10^6 \text{ psia}^2/\text{cp} .$$

$$p_b = 14.65 \text{ psia, } p_p(p_b) = 2,098.7 \text{ psia}^2/\text{cp} .$$

Solution.

Rawlins-Schellhardt Analysis Technique. First, plot $\Delta p_p = p_p(p_s) - p_p(p_{wf})$ vs. q on log-log coordinates (Fig 8.119) and include the single stabilized, extended flow point. Table 8.17 gives the plotting functions.

Calculate the deliverability exponent, n , for each line or isochron using least-squares regression analysis. Note that, because the first data point for each isochron does not align with the data points at the last three flow rates (Fig. 8.119), the first data point is ignored in all subsequent calculations.

Table 8.18 summarizes the deliverability exponents determined with a least-squares regression analysis for each isochron. The arithmetic average of the n values in Table 8.18 is 0.89.

Because $0.5 \leq \bar{n} \leq 1.0$, AOF can be calculated or determined graphically using Fig. 8.120. AOF will be calculated in this example. First, determine the stabilized performance coefficient using the coordinates of the stabilized, extended flow point and $n = \bar{n}$:

$$C = \frac{q_s}{[p_p(p_s) - p_p(p_{wf, s})]^n} = \frac{1.156}{(2.443 \times 10^6)^{0.89}} = 2.39 \times 10^{-6} .$$

Then calculate the AOF potential:

$$q_{\text{AOF}} = C [p_p(\bar{p}) - p_p(p_b)]^n$$

$$= 2.39 \times 10^{-6} (9.9715 \times 10^6 - 2,098.7)^{0.89} = 4.04 \text{ MMscf/D} .$$

To determine the AOF graphically, first calculate the pseudopressure at p_b and compute

$$\Delta p_p = p_p(p_s) - p_p(p_b) = 9.9715 \times 10^6 - 2,098.7 = 9.969 \times 10^6 .$$

Then, draw a line of slope $1/\bar{n}$ through the stabilized flow point, extrapolate the line to the flow rate at $\Delta p_p = p_p(p_s) - p_p(p_b)$, and read the AOF directly from the graph. The result is $q_{\text{AOF}} = 4.04 \text{ MMscf/D}$.

Houpeurt Analysis Technique. Plot $\Delta p_p/q = [p_p(p_s) - p_p(p_{\text{wf}})]/q$ vs. q on Cartesian graph paper (**Fig. 8.121**). **Table 8.19** gives the plotting functions. Construct best-fit lines through the isochronal data points for each time. Note that, for each flow time, the point corresponding to the lowest rate does fit on the same straight line, so all four data points will be used for the analysis of each isochron.

Next, determine the slope b of each line or isochron. Values of b from least-squares regression analysis are summarized in **Table 8.20**. The arithmetic average value of the slopes in **Table 8.20** is $2.074 \times 10^4 \text{ psia}^2/\text{cp}/(\text{MMscf/D})^2$.

Calculate the stabilized isochronal deliverability line intercept using $\Delta p_p/q = 2.113 \times 10^6 \text{ psia}^2/\text{cp}/(\text{MMscf/D})$ at the extended, stabilized point.

$$\begin{aligned} a &= (\Delta p_p/q) - bq \\ &= 2.113 \times 10^6 - (2.074 \times 10^4)(1.156) = 2.109 \times 10^6 \text{ psia}^2/\text{cp}/(\text{MMscf/D}) . \end{aligned}$$

Calculate the AOF potential using the average value of b and the stabilized value of a .

$$\begin{aligned} q_{\text{AOF}} &= \frac{-a + \sqrt{a^2 + 4b[p_p(p_s) - p_p(p_b)]}}{2b} \\ &= \frac{-(2.109 \times 10^6) + \sqrt{(2.109 \times 10^6)^2 + 4(2.074 \times 10^4)(9.97 \times 10^6)}}{2(2.074 \times 10^4)} = 4.53 \text{ MMscf/D} . \end{aligned}$$

Fig. 8.122 illustrates the results.

Modified Isochronal Tests. The time to build up to the average reservoir pressure before flowing for a certain period of time still may be impractical, even after short flow periods. Consequently, a modification of the isochronal test was developed⁵² to shorten test times further. The objective of the modified isochronal test is to obtain the same data as in an isochronal test without using the sometimes lengthy shut-in periods required to reach the average reservoir pressure in the drainage area of the well.

The modified isochronal test (**Fig. 8.123**) is conducted like an isochronal test, except the shut-in periods are of equal duration. The shut-in periods should equal or exceed the length of the flow periods. Because the well does not build up to average reservoir pressure after each flow period, the shut-in sandface pressures recorded immediately before each flow period rather than the average reservoir pressure are used in the test analysis. As a result, the modified isochronal test is less accurate than the isochronal test. As the duration of the shut-in periods increases, the accuracy of the modified isochronal test also increases. Again, a final stabilized flow point usually is obtained at the end of the test but is not required for analyzing the test data.

The well does not build up to the average reservoir pressure during shut-in; the analysis techniques for the modified isochronal tests are derived intuitively. Recall the transient flow equation, expressed in terms of the reservoir pressure at the start of flow, on which isochronal testing is based:

TABLE 8.16—ISOCRONAL TEST DATA, EXAMPLE 8.11

Time (hours)	<i>q</i> (MMscf/D)	<i>p_{wf}</i> (psia)	<i>p_p</i> (<i>p_{wf}</i>) (psia ² /cp)
0.5	0.983	344.7	9.6386×10 ⁶
1.0	0.977	342.4	9.5406×10 ⁶
2.0	0.970	339.5	9.4179×10 ⁶
3.0	0.965	337.6	9.3381×10 ⁶
0.5	2.631	329.5	9.0027×10 ⁶
1.0	2.588	322.9	8.7351×10 ⁶
2.0	2.533	315.4	8.4371×10 ⁶
3.0	2.500	310.5	8.2458×10 ⁶
0.5	3.654	318.7	8.5674×10 ⁶
1.0	3.565	309.5	8.2071×10 ⁶
2.0	3.453	298.6	7.7922×10 ⁶
3.0	3.390	291.9	7.5435×10 ⁶
0.5	4.782	305.5	8.0534×10 ⁶
1.0	4.625	293.6	7.6136×10 ⁶
2.0	4.438	279.6	7.0990×10 ⁶
3.0	4.318	270.5	6.7797×10 ⁶
214 (Extended Flow Point)	1.156	291.6	7.5285×10 ⁶

TABLE 8.17—PLOTING FUNCTIONS FOR RAWLINS-SHELLHARDT ANALYSIS, EXAMPLE 8.11

<i>t</i> (hours)	<i>q</i> (MMscf/D)	Δp_p (psia ² /cp)	<i>t</i> (hours)	<i>q</i> (MMscf/D)	Δp_p (psia ² /cp)
0.5	0.983	0.3329×10 ⁶	2.0	3.654	1.4041×10 ⁶
	0.977	0.4309×10 ⁶		3.565	1.7644×10 ⁶
	0.970	0.5536×10 ⁶		3.453	2.1793×10 ⁶
1.0	0.965	0.6334×10 ⁶	3.0	3.390	2.4280×10 ⁶
	2.631	0.9688×10 ⁶		4.782	1.9181×10 ⁶
	2.588	1.2364×10 ⁶		4.625	2.3579×10 ⁶
	2.533	1.5344×10 ⁶		4.438	2.8725×10 ⁶
	2.500	1.7257×10 ⁶		4.318	3.1918×10 ⁶
			214	1.156	2.443×10 ⁶

$$p_p(p_s) - p_p(p_{wf}) = \frac{1.422 \times 10^6 q T}{k_g h} \left[\ln \left(\frac{r_d}{r_w} \right) - \frac{3}{4} + s + Dq \right] \dots\dots\dots (8.254)$$

In new reservoirs with little or no pressure depletion, *p_s* equals the initial reservoir pressure (*p_s* = *p_i*); in developed reservoirs, *p_s* < *p_i*. In addition, the transient drainage radius, *r_d*, in Eq. 8.254 is defined as

TABLE 8.18—DELIVERABILITY EXPONENTS FOR VARIOUS FLOWING TIMES, EXAMPLE 8.10

t (hours)	n
0.5	0.88
1.0	0.91
2.0	0.89
3.0	0.88

TABLE 8.19—PLOTING FUNCTIONS FOR HOUPEURT ANALYSIS, EXAMPLE 8.11

t (hours)	q (MMscf/D)	$\Delta p_r/q$ (psia ² /cp/MMscf/D)	t (hours)	q (MMscf/D)	$\Delta p_r/q$ (psia ² /cp/MMscf/D)
0.5	0.983	3.387×10^5	2.0	0.970	5.707×10^5
	2.631	3.682×10^5		2.533	6.058×10^5
	3.654	3.843×10^5		3.453	6.311×10^5
	4.782	4.011×10^5		4.438	6.473×10^5
1.0	0.977	4.410×10^5	3.0	0.965	6.564×10^5
	2.588	4.777×10^5		2.500	6.903×10^5
	3.565	4.949×10^5		3.390	7.162×10^5
	4.625	5.098×10^5		4.318	7.392×10^5

TABLE 8.20—SLOPES, b , OF THE ISOCHRONS, EXAMPLE 8.11

t (hours)	b [psia ² /cp/(MMscf/D) ²]
0.5	1.644×10^4
1.0	1.904×10^4
1.5	2.255×10^4
2.0	2.492×10^4

$$r_d = \sqrt{\frac{k_g t}{377 \phi \mu_g \bar{c}_t}} \dots\dots\dots (8.253)$$

Because r_d is a function of time and not of flow rate, Eq. 8.254 is valid at any fixed time. For modified isochronal tests, use Eq. 8.254, in which the stabilized shut-in BHP, p_s , is replaced with shut-in BHP, p_{ws} , measured before each flow period, where $p_{ws} \leq p_s$,

$$p_p(p_{ws}) - p_p(p_{wf}) = \frac{1.422 \times 10^6 q T}{k_g h} \left[\ln \left(\frac{r_d}{r_w} \right) - \frac{3}{4} + s + Dq \right] \dots\dots\dots (8.260)$$

Eq. 8.260 can be rewritten as

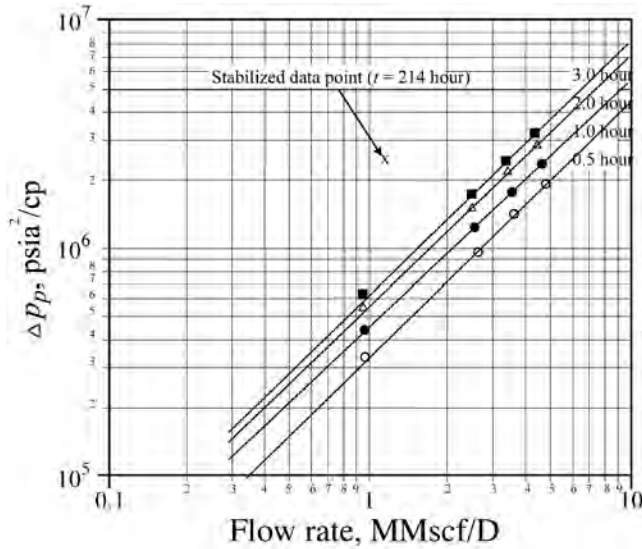


Fig. 8.119—Rawlins-Schellhardt analysis, Example 8.11.

$$p_p(p_{ws}) - p_p(p_{wf}) = a_t q + b q^2, \dots\dots\dots (8.261)$$

$$\text{where } a_t = \frac{1.422 \times 10^6 T}{k_g h} \left[\ln \left(\frac{r_d}{r_w} \right) - \frac{3}{4} + s \right] \dots\dots\dots (8.256)$$

$$\text{and } b = \frac{1.422 \times 10^6 DT}{k_g h} \dots\dots\dots (8.238)$$

Eq. 8.238 indicates that *b* is independent of time and will remain constant during the test. Similarly, Eq. 8.256 indicates that *a_t* is constant for a fixed time. The similarity of Eqs. 8.254 and 8.260 for the isochronal and modified isochronal tests, respectively, suggests that the modified isochronal test data can be analyzed like those from an isochronal test.

The theory developed for the modified isochronal test implies that, if the intuitive approximation of using *p_{ws}* instead of *p_s* is valid, the transient data will plot as straight line for each time with the same slope, *b*. The intercept, *a_t*, will increase with increasing time. By drawing a line with slope *b* through the stabilized data point and using the coordinates of the stabilized point and the slope, a stabilized intercept, *a*, that is independent of time can be calculated, where

$$a = \frac{1.422 \times 10^6 T}{k_g h} \left[\ln \left(\frac{r_e}{r_w} \right) - \frac{3}{4} + s \right] \dots\dots\dots (8.257)$$

To calculate the AOF of the well, use the average reservoir pressure, *p_s*, measured before the test instead of the *p_{ws}* value, or

$$q_{\text{AOF}} = \frac{-a + \sqrt{a^2 + 4b[p_p(p_s) - p_p(p_b)]}}{2b} \dots\dots\dots (8.262)$$

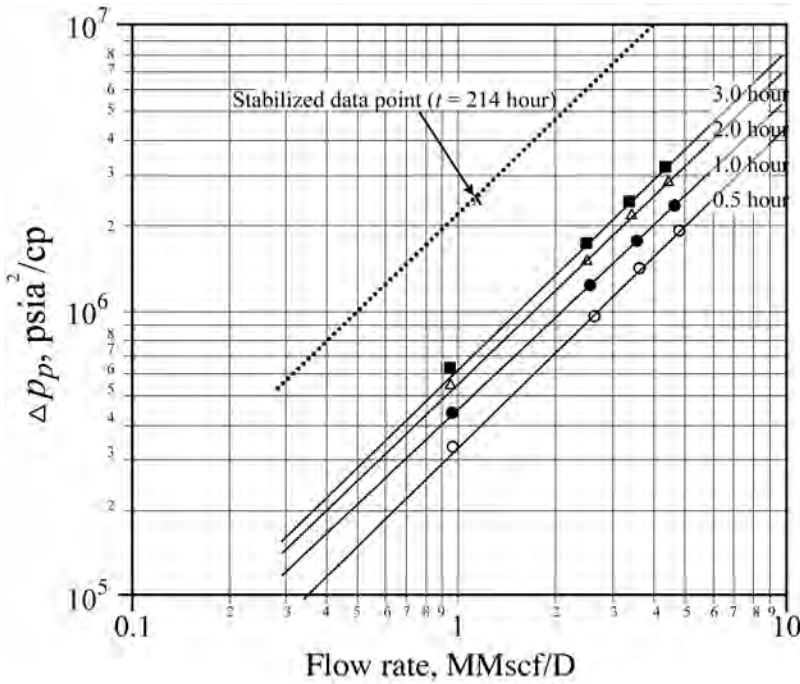


Fig. 8.120—Rawlins-Schellhardt analysis result, Example 8.11.

Two variations of the modified isochronal test are considered: tests with a stabilized flow point obtained at the end of the test and tests run without that final point.

Modified Isochronal Tests With a Stabilized Flow Point. Rawlins-Schellhardt Analysis. Recall the empirical Rawlins and Schellhardt equation in terms of transient isochronal test data:

$$\log (q) = \log \left(C_t \right) + n \left\{ \log \left[p_p \left(\bar{p}_s \right) - p_p \left(p_{wf} \right) \right] \right\} \dots \dots \dots (8.258)$$

As in the graphical analysis techniques for isochronal tests, plot several trends of data taken at different times during a modified isochronal test. The slope n of each line through points at equal time values will be constant. However, the intercept, $\log(C_t)$, is a function of time but not flow rate. Therefore, a different intercept should be calculated for each isochronal test. Use $p_p(p_{ws})$ instead of $p_p(p_s)$ in Eq. 8.258, which gives

$$\log (q) = \log \left(C_t \right) + n \left\{ \log \left[p_p \left(p_{ws} \right) - p_p \left(p_{wf} \right) \right] \right\} \dots \dots \dots (8.263)$$

The conventional analysis technique for modified isochronal test data is to plot $\log [p_p(p_{ws}) - p_p(p_{wf})]$ vs. $\log (q)$ for each time, giving a straight line of slope $1/n$ and an intercept of $\{-1/n [\log(C_t)]\}$. The Rawlins-Schellhardt analysis procedure for modified isochronal tests with a stabilized flow point is similar to that presented for isochronal tests, except the plotting functions are developed in terms of the shut-in pressure measured immediately before the next flow period. Only the stabilized, extended flow point is plotted in terms of the average reservoir pressure measured before the test, p_s . Example 8.12 illustrates the procedure.

Houpeurt Analysis. As shown previously, the Houpeurt deliverability equation in terms of transient isochronal test data is

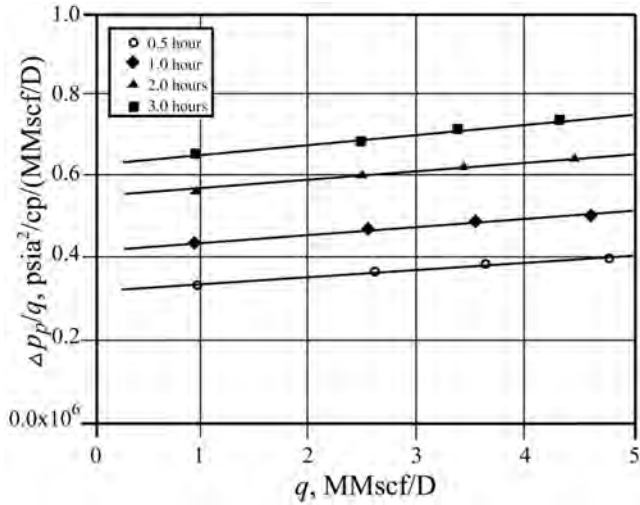


Fig. 8.121—Houpeurt analysis of isochronal test data, Example 8.11.

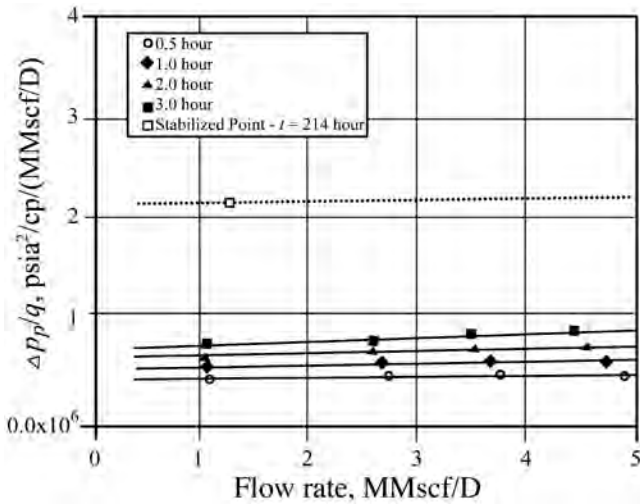


Fig. 8.122—Houpeurt analysis of isochronal test data result, Example 8.11.

$$\frac{\Delta p_p}{q} = \frac{p_p(p_s) - p_p(p_{wf})}{q} = a_t + bq \dots\dots\dots (8.259)$$

For modified isochronal test data, Eq. 8.259 should be modified with the assumption that p_p (p_{ws}) can be used instead of $p_p(p_s)$. With this assumption, Eq. 8.259 becomes

$$\frac{\Delta p_p}{q} = \frac{p_p(p_{ws}) - p_p(p_{wf})}{q} = a_t + bq, \dots\dots\dots (8.264)$$

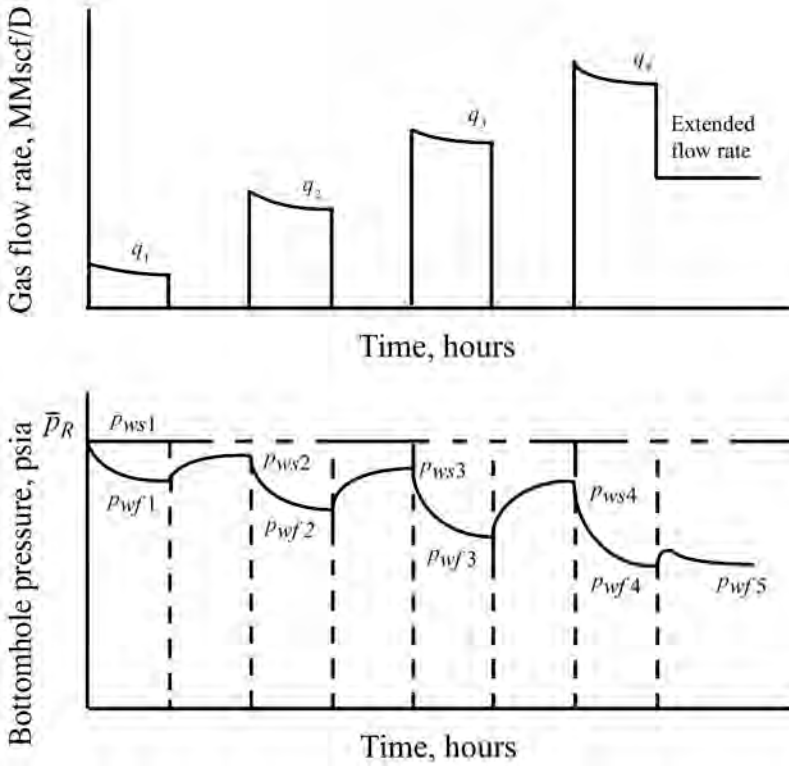


Fig. 8.123—Pressure and flow rate history of a typical modified isochronal test.

$$\text{where } a_t = \frac{1.422 \times 10^6 T}{k_g h} \left[\ln \left(\frac{r_d}{r_w} \right) - \frac{3}{4} + s \right], \dots\dots\dots (8.256)$$

$$\text{and } b = \frac{1.422 \times 10^6 D T}{k_g h} \dots\dots\dots (8.238)$$

The form of Eq. 8.264 suggests that a plot of

$$\Delta p_p / q = [p_p(p_{ws}) - p_p(p_{wf})] / q \text{ vs. } q$$

will be a straight line with a slope b and intercept a_t . This theory can be extended to the stabilized point, and we can calculate a stabilized intercept, a , using the coordinates of the stabilized point, or

$$a = \frac{[p_p(p_s) - p_p(p_{wf}, s)]}{q_s} - b q_s = \frac{\Delta p_p}{q_s} - b q_s \dots\dots\dots (8.265)$$

The slope b of the line through the stabilized point should remain the same. In addition, the average reservoir pressure, which is measured before the test, must be used to evaluate the pseudopressure, $p_p(p_s)$ in Eq. 8.265. Example 8.12 illustrates the Houpeurt analysis procedure

for modified isochronal tests with a stabilized flow point, which is similar to that presented for isochronal tests.

Example 8.12: Analysis of a Modified Isochronal Test With a Stabilized Flow

Point. Using the following data taken from Well 4,⁵³ calculate the AOF using both Rawlins and Schellhardt and Houpeurt analysis techniques. Assume $p_b = 14.65$ psia, where $p_p(p_b) = 5.093 \times 10^7$ psia²/cp. **Table 8.21** gives the test data. $h = 6$ ft, $r_w = 0.1875$ ft, $\phi = 0.2714$, $T = 540^\circ\text{R}$ (80°F), $\bar{p} \approx p_s = 706.6$ psia, $\bar{\mu}_g = 0.015$ cp, $\bar{z} = 0.97$, $\bar{c}_g = 1.5 \times 10^{-3}$ psia⁻¹, $\gamma_g = 0.75$, $S_w = 0.30$, $c_f = 3 \times 10^{-6}$ psia⁻¹, and $A = 640$ acres (assume that the well is centered in a square drainage area).

Solution.

Rawlins-Schellhardt Analysis. Plot

$$\Delta p_p = p_p(p_{ws}) - p_p(p_{wf}) \text{ vs. } q$$

on log-log graph paper (**Fig. 8.124**). **Table 8.22** gives the plotting functions. In addition, plot on the same graph the values of Δp_p that corresponds to the stabilized, extended flow point evaluated at p_s .

$$\begin{aligned} \Delta p_p &= p_p(p_s) - p_p(p_{wf}) \\ &= 5.093 \times 10^7 - 3.276 \times 10^7 = 1.817 \times 10^7 \text{ psia}^2/\text{cp} . \end{aligned}$$

For each time, construct the best-fit line through the data points. Because the first data points for each isochron do not follow the trend of the higher rate points, they will be ignored for all subsequent calculations.

Calculate the deliverability exponent, n , for each line or isochron. For this example, use least-squares regression analysis. For example, at $t = 0.5$ hours, $n_1 = 0.72$. **Table 8.23** summarizes the deliverability exponents.

The arithmetic average of the values in **Table 8.23** is

$$\bar{n} = \frac{n_1 + n_2 + n_3 + n_4}{4} = \frac{0.72 + 0.74 + 0.74 + 0.78}{4} = 0.74.$$

Because $0.5 \leq \bar{n} \leq 1.0$, determine the stabilized performance coefficient, C , using the coordinates of the stabilized, extended flow point and $n = \bar{n}$. Note that the pseudopressure used to calculate the stabilized C value is evaluated at p_s , measured at the beginning of the test, rather than p_{ws} . From **Eq. 8.245**,

$$C = \frac{q}{[p_p(p_s) - p_p(p_{wf})]^n} = \frac{2.665}{(5.093 \times 10^7 - 3.276 \times 10^7)^{0.74}} = 1.132 \times 10^{-5} .$$

Then,

$$\begin{aligned} q_{\text{AOF}} &= C [p_p(p_s) - p_p(p_b)]^n \\ &= 1.132 \times 10^{-5} (5.0935 \times 10^7 - 2,766.6)^{0.74} = 5.7 \text{ MMscf/D} . \end{aligned}$$

To determine the AOF graphically draw a line of slope $1/\bar{n}$ through the extended flow point, extrapolate the line to the flow rate at $\Delta p_p = p_p(p_s) - p_p(p_b)$, and read the AOF directly from the graph (**Fig. 8.125**).

Houpeurt Analysis. Plot

$$\Delta p_p / q = [p_p(p_{ws}) - p_p(p_{wf})] / q \text{ vs. } q$$

on Cartesian coordinates (**Fig. 8.126**). In addition, plot the $\Delta p_p / q$ value that corresponds to the stabilized, extended flow point. **Table 8.24** gives the plotting functions. Construct best-fit lines through the modified isochronal data points for each time. The first data point at the lowest rate for each isochron does not fit on the same straight line as the last three rate points and is ignored in subsequent calculations.

Determine the slopes of the lines, b , for each isochron by least-squares regression analysis of the best-fit lines through the data points. For example, at $t = 0.5$ hours, $b_1 = 9.654 \times 10^5 \text{ psia}^2/\text{cp}/(\text{MMscf}/\text{D})^2$. **Table 8.25** summarizes the slopes of the isochrons. The average arithmetic values of the slopes in **Table 12.15** is

$$\bar{b} = \frac{b_2 + b_3 + b_4}{3} = \frac{(8.678 + 8.711 + 8.780) \times 10^5}{3} = 8.723 \times 10^5 \text{ psia}^2/\text{cp}/(\text{MMscf}/\text{D})^2.$$

Calculate the stabilized isochronal deliverability line intercept, a :

$$\begin{aligned} a &= \left[\frac{p_p(p_s) - p_p(p_{wf})}{q} \right] - bq \\ &= \frac{1.817 \times 10^7}{2.665} - (8.732 \times 10^5)(2.665) = 4.493 \times 10^6 \text{ psia}^2/\text{cp}/(\text{MMscf}/\text{D}). \end{aligned}$$

Calculate the AOF potential using \bar{b} and the stabilized a value:

$$\begin{aligned} q_{\text{AOF}} &= \frac{-a + \sqrt{a^2 + 4b[p_p(\bar{p}) - p_p(14.65)]}}{2b} \\ &= \frac{-(4.493 \times 10^6) + \sqrt{(4.493 \times 10^6)^2 + 4(8.723 \times 10^5)[5.093 \times 10^7 - 2,766.6]}}{2(8.723 \times 10^5)} = 5.5 \text{ MMscf}/\text{D}. \end{aligned}$$

Fig. 8.127 shows the data for this example.

Modified Isochronal Tests Without a Stabilized Flow Point. Because the well is not required to build up to the average reservoir pressure between the flow periods, the modified isochronal approximation shortens test times considerably. However, the test analysis relies on obtaining one stabilized flow point. Under some conditions, environmental or economic concerns prohibit flaring produced gas to the atmosphere during a long production period, thus preventing measurement of a stabilized flow point. These conditions often occur when new wells are tested before being connected to a pipeline.

TABLE 8.21—MODIFIED ISOCHRONAL TEST DATA, EXAMPLE 8.12

Time (hours)	p_{wf} (psia)			
	$q = 1.520$ MMscf/D	$q = 2.041$ MMscf/D	$q = 2.688$ MMscf/D	$q = 3.122$ MMscf/D
0 (p_{ws})	706.6	706.6	703.5	701.2
0.5	655.6	724.5	578.5	541.7
1.0	653.6	620.7	573.9	537.8
1.5	652.1	619.9	572.3	536.3
2.0	651.3	619.1	570.8	534.7
	p_D (p_{wf}) (psia)			
0 [p_D (p_{ws})]	5.093×10^7	5.093×10^7	5.093×10^7	5.015×10^7
0.5	4.379×10^7	3.970×10^7	3.403×10^7	2.979×10^7
1.0	4.352×10^7	3.922×10^7	3.348×10^7	2.936×10^7
1.5	4.332×10^7	3.911×10^7	3.330×10^7	2.919×10^7
2.0	4.321×10^7	3.901×10^7	3.312×10^7	2.902×10^7
Extended Flow Point				
$p_{wf} = 567.7$ psia $t = 24$ hours				
$p_s = 706.6$ psia		$q = 2.665$ MMscf/D		
p_D (p_{wf}) = 3.276×10^8 psia ² /cp		$p_D = (14.65) = 2,766.6$ psia ² /cp		

TABLE 8.22—PLOTING FUNCTIONS FOR RAWLINS-SHELLHARDT ANALYSIS, EXAMPLE 8.12

Time (hours)	Δp_D (psia ² /cp)			
	$q = 1.520$ (MMscf/D)	$q = 2.041$ (MMscf/D)	$q = 2.688$ (MMscf/D)	$q = 3.122$ (MMscf/D)
0.5	0.714×10^7	1.123×10^7	1.645×10^7	2.039×10^7
1.0	0.714×10^7	1.171×10^7	1.700×10^7	2.082×10^7
1.5	0.761×10^7	1.182×10^7	1.718×10^7	2.099×10^7
2.0	0.772×10^7	1.192×10^7	1.736×10^7	2.113×10^7

Two methods have been developed to analyze modified isochronal tests without a stabilized flow point. The Brar and Aziz method⁵³ was developed for the Houpeurt analysis, while the stabilized C method⁵⁴ was developed for the Rawlins and Schellhardt analysis. The stabilized C method requires prior knowledge of permeability and skin factor or determination of these properties using the methods Brar and Aziz proposed for analyzing modified isochronal tests. Both methods require knowledge of the drainage area shape and size.

Brar and Aziz Method—Houpeurt Analysis. The Brar and Aziz method⁵³ is based on the transient Houpeurt deliverability Eqs. 8.234, 8.236, 8.238, and p_s , the stabilized BHP measured before the deliverability test.

Rewriting Eq. 8.236 as

$$a_t = m' \log(t) + c', \dots\dots\dots (8.266)$$

TABLE 8.23—SLOPES, *n*, OF ISOCHRONS, EXAMPLE 8.12

<i>t</i> (hours)	<i>n</i>
0.5	0.72
1.0	0.74
1.5	0.74
2.0	0.78

TABLE 8.24—PLOTING FUNCTIONS FOR HOUPEURT ANALYSIS, EXAMPLE 8.12

Time (hours)	$\frac{\Delta p_p}{q}$ (psia ² /cp/MMscf/D)			
	<i>q</i> = 1,520 (MMscf/D)	<i>q</i> = 2,041 (MMscf/D)	<i>q</i> = 2,688 (MMscf/D)	<i>q</i> = 3,122 (MMscf/D)
0.5	0.470×10^7	0.550×10^7	0.612×10^7	0.653×10^7
1.0	0.488×10^7	0.574×10^7	0.632×10^7	0.667×10^7
1.5	0.501×10^7	0.579×10^7	0.639×10^7	0.672×10^7
2.0	0.508×10^7	0.584×10^7	0.646×10^7	0.678×10^7

TABLE 8.25—SLOPES, *b*, OF ISOCHRONS, EXAMPLE 8.12

<i>t</i> (hours)	<i>b</i> (psia ² /cp/(MMscf/D) ²)
0.5	9.654×10^5
1.0	8.678×10^5
1.5	8.711×10^5
2.0	8.780×10^5

$$\text{where } m' = \frac{1.632 \times 10^6 T}{k_g h} \dots\dots\dots (8.267)$$

$$\text{and } c' = \frac{1.422 \times 10^6 T}{k_g h} \times \left[1.151 \log \left(\frac{k_g}{1,688 \phi \bar{\mu}_g \bar{c}_l r_w^2} \right) + s \right] \dots\dots\dots (8.268)$$

m' and *c'* can be calculated using regression analysis of Eq. 8.266. Alternatively, these variables can be computed directly from the slope and the intercept of a plot of *a_i* vs. log *t*. Then calculate the permeability from the slope,

$$k_g = \frac{1.632 \times 10^6 T}{m' h} \dots\dots\dots (8.269)$$

Combining Eqs. 8.267 and 8.268 yields an equation for the skin factor,

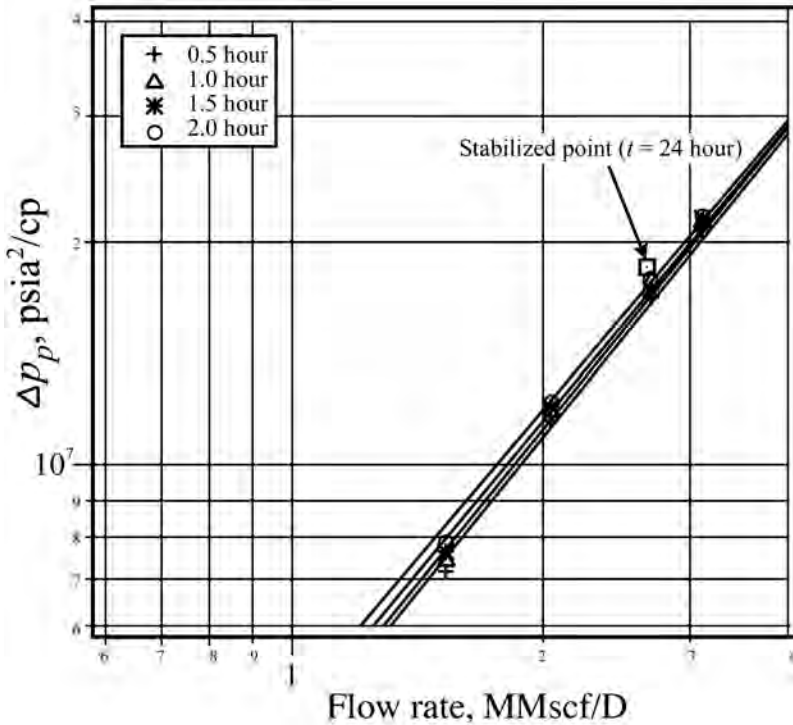


Fig. 8.124—Rawlings-Schellhardt plot of modified isochronal test data, Example 8.12.

$$s = 1.151 \left[\left(\frac{c'}{m} \right) - \log \left(\frac{k_g}{\phi \bar{\mu}_g \bar{c}_t r_w^2} \right) + 3.23 \right] \dots \dots \dots (8.270)$$

Estimating the AOF potential of the well requires a stabilized value of *a*. If the drainage area size and shape are known, the gas permeability calculated from Eq. 8.269 and the skin factor from Eq. 8.270 can be used to calculate *a*:

$$a = \frac{1.422 \times 10^6 T}{k_g h} \left[1.151 \log \left(\frac{10.06 A}{C_A r_w^2} \right) - \frac{3}{4} + s \right] \dots \dots \dots (8.271)$$

Table 8.A-1 gives shape factors for various reservoir shapes and well locations. The stabilized value of *a* then is used in Eq. 8.262 to calculate the AOF of the well:

$$q_{\text{AOF}} = \frac{-a + \sqrt{a^2 + 4b[p_p(p_s) - p_p(p_b)]}}{2b} \dots \dots \dots (8.262)$$

Stabilized C Method—Rawlings-Schellhardt Analysis. Although the Houpeurt equation has a theoretical basis and is rigorously correct, the more familiar but empirically based Rawlings and Schellhardt equation continues to be used and is indeed favored by many in the natural gas industry. The Houpeurt and Rawlings-Schellhardt analysis techniques are combined here to develop a version of the Rawlings-Schellhardt method for analyzing modified isochronal tests.

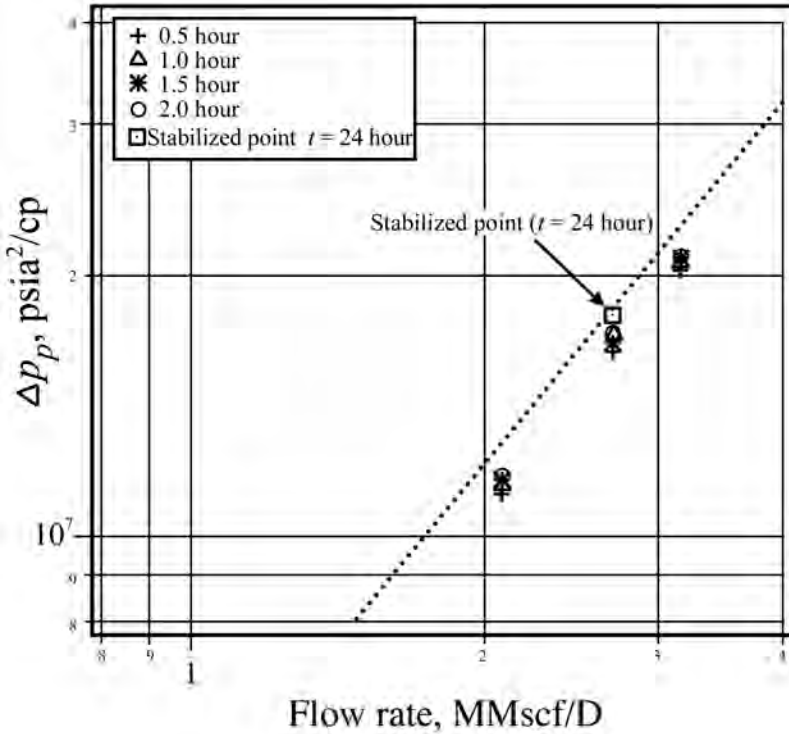


Fig. 8.125—Rawlins-Schellhardt analysis of modified isochronal test, Example 8.12.

This analysis technique, called the “Stabilized C” method,⁵⁴ is derived by equating the stabilized Rawlins and Schellhardt empirical backpressure equation with the stabilized theoretical Houpeurt equation to obtain equations for the deliverability exponent, n , and the stabilized flow coefficient, C , in terms of the Houpeurt flow coefficients, a and b .

To obtain an equation for the exponent n , take the logarithm of both sides of the stabilized Rawlins and Schellhardt empirical backpressure equation (Eq. 8.245).

$$\ln q = n \ln (\Delta p_p) + \ln C . \dots\dots\dots (8.272)$$

n is the slope of a plot of $\ln(q)$ vs. $\ln(\Delta p_p)$. Alternatively, note that n can be expressed as the derivative of $\ln(q)$ with respect to $\ln(\Delta p_p)$:

$$\frac{d \ln q}{d \ln (\Delta p_p)} = \frac{1}{q} \frac{dq}{d[\ln (\Delta p_p)]} = n . \dots\dots\dots (8.273)$$

Similarly, take the logarithms of both sides of the Houpeurt Eq. 8.235

$$\ln \Delta p_p = \ln [aq + bq^2], \dots\dots\dots (8.274)$$

and, thus,

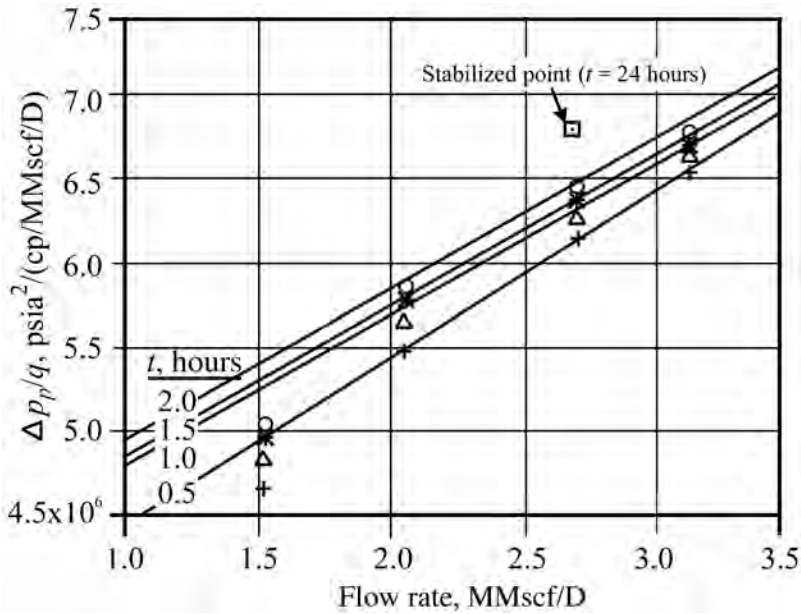


Fig. 8.126—Houpeurt plot of modified isochronal test data, Example 8.12.

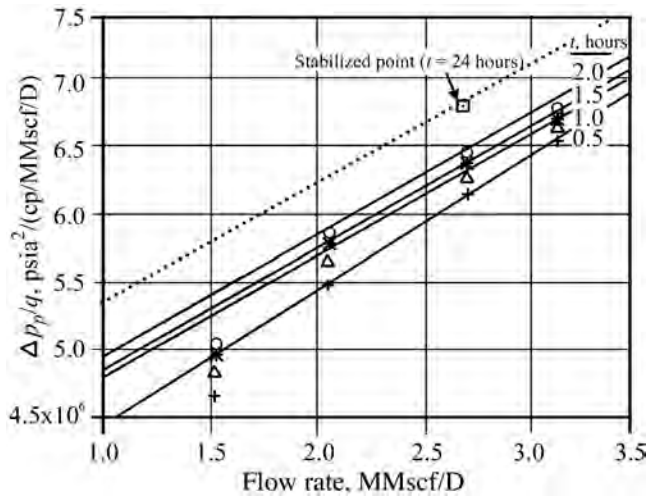


Fig. 8.127—Houpeurt analysis of modified isochronal test data, Example 8.12.

$$\frac{d \ln (\Delta p_p)}{dq} = \frac{(a + 2bq)}{aq + bq^2}, \dots\dots\dots (8.275)$$

$$\text{or } \frac{dq}{d(\ln \Delta p_p)} = \frac{aq + bq^2}{a + 2bq} = qn \dots\dots\dots (8.276)$$

$$\text{and } n = \frac{a + bq}{a + 2bq} \dots\dots\dots (8.277)$$

In Eq. 8.277, let q be the unique value q_e at which the $d \ln (\Delta p_p) / dq$ values from the Rawlins-Schellhardt and Houpeurt equations are identical. Solving Eq. 8.277 for this value of $q = q_e$,

$$n = \frac{a + bq_e}{a + 2bq_e} \dots\dots\dots (8.278)$$

$$\text{and } q_e = \frac{a(1 - n)}{b(2n - 1)} \dots\dots\dots (8.279)$$

Substituting in the Rawlins-Schellhardt equation and noting that, from the Houpeurt equation $(\Delta p_p)_e = aq_e + bq_e^2$,

$$q_e = C(\Delta p_p)_e^n = C(aq_e + bq_e^2)^n \dots\dots\dots (8.280)$$

Rearranging,

$$C = \frac{q_e}{(aq_e + bq_e^2)^n} \dots\dots\dots (8.281)$$

To apply the stabilized C method, it is necessary to assume that the slope, n , of the Rawlins-Schellhardt deliverability plot is constant. This assumption implies that if values of a and b can be calculated for given reservoir properties, a flow rate can be calculated from Eq. 8.279, at which the change in pseudopressures calculated by the Rawlins-Schellhardt equation is equal to the change in pseudopressure calculated by the Houpeurt equation. The substitution this flow rate into Eq. 8.281 allows calculation of a stabilized value of C and this value of C can be used to calculate a value of AOF:

$$q_{\text{AOF}} = C[p_p(\bar{p}) - p_p(p_b)]^n \dots\dots\dots (8.282)$$

The stabilized C method is limited by the need for values of reservoir properties determined separately from the deliverability test analysis. These properties can be estimated either from drawdown or buildup test analysis or from the Brar and Aziz method.

Example 8.13: Analysis of Modified Isochronal Test Without a Stabilized Data Point.

The purpose of this example is to compare results obtained from the analysis of a modified isochronal test (see Table 8.26) with and without an extended, stabilized data point. Calculate the AOF for the following modified isochronal test data without the extended flow point. Use both the Brar and Aziz and the stabilized C methods. Compare these results with the results obtained by using the extended flow point. This example is Well 8.⁵³ Only the last four flow points from the test are used in the analysis. Reservoir data are summarized here: $h = 454$ ft, $r_w = 0.2615$ ft, $\phi = 0.0675$, $T = 718^\circ\text{R}$ (258°F), $p_s \cong 4,372.6$ psia, $\mu = 0.023$ cp, $z = 0.87$, $c_g = 1.69 \times 10^{-4}$ psia⁻¹, $\gamma_g = 0.65$, $S_w = 0.3$, $A = 640$ acres. $C_A = 30.8828$ (assume that the well is centered in a square drainage area). In addition, the results from a drawdown test in this well indicate $k_g = 4.23$ md and $s = -5.2$.

The Rawlins and Schellhardt analysis with extended flow point gave $C = 2.426 \times 10^{-3}$, $n = 0.54$ and $q_{\text{AOF}} = 180.1$ MMscf/D. The Houpeurt analysis with extended flow point gave $a =$

1.455×10^6 psia²/cp/MMscf/D, $b = 1.774 \times 10^4$ psia²/cp/(MMscf/D)², and $q_{\text{AOF}} = 205.6$ MMscf/D.

Solution.

Brar and Aziz Method.

Step 1—Plot

$$\Delta p_p / q = [p_p(p_{ws}) - p_p(p_{wf})] / q \text{ vs. } q$$

on Cartesian coordinates (**Fig. 8.128**). **Table 8.27** gives the plotting functions. Construct best-fit lines through the modified isochronal data points for each time. Although the data are scattered, all flow rates were used for each isochron.

Step 2—Determine the slopes of the lines, b , for each time by least-squares regression analysis. For example, at $t = 3.0$ hours, $b_1 = 1.823 \times 10^4$ psia²/cp/(MMscf/D)². **Table 8.28** summarizes the slopes for all isochrons. The arithmetic average value of the b values in **Table 8.28** is

$$\begin{aligned} \bar{b} &= \frac{b_1 + b_2 + b_3 + b_4}{4} \\ &= \frac{(1.823 + 1.870 + 1.881 + 1.939) \times 10^4}{4} = 1.878 \times 10^4 \text{ psia}^2 / \text{cp} / (\text{MMscf} / \text{D}) . \end{aligned}$$

Step 3—Using least-squares regression analysis, calculate the transient deliverability line intercepts for each isochronal line. For example, at $t = 3.0$ hours,

$$a_t = 5.677 \times 10^5 \text{ psia}^2 / \text{cp} / \text{MMscf} \cdot \text{D} .$$

Table 8.29 gives the intercepts for each isochron.

Step 4—Prepare a graph of a_t vs. $\log t$ (**Fig. 8.129**) and draw the best-fit line through data. Using all four data points, calculate m' and c' of the best-fit line of the plot of a_t vs. $\log t$ using least-squares regression analysis. The result is $m' = 3.871 \times 10^5$ psia²/(cp-MMscf/D)/cycle and $c' = 3.909 \times 10^5$ psia²/(cp-MMscf/D).

Step 5—Calculate the formation permeability to gas using the slope of the semilog straight line.

$$k_g = \frac{1.632 \times 10^6 T}{m'h} = \frac{1.632 \times 10^6 (718)}{(3.871 \times 10^5)(454)} = 6.6 \text{ md},$$

which compares with $k_g = 4.23$ md estimated from the drawdown test analysis.

Step 6—Calculate the skin factor with **Eq. 8.270**.

$$\begin{aligned} s &= 1.151 \left[\left(\frac{c'}{m'} \right) - \log \left(\frac{k_g}{\phi \mu_g c' r_w^2} \right) + 3.23 \right] \\ &= 1.151 \left\{ \left(\frac{3.909 \times 10^5}{3.871 \times 10^5} \right) - \log \left[\frac{6.6}{(0.0675)(0.023)(0.000169)(0.2615)^2} \right] + 3.23 \right\} = -5.0. \end{aligned}$$

This value agrees with $s = -5.2$ estimated from the drawdown test analysis.

Step 7—Calculate the stabilized flow coefficient, a . Assume that the well is centered in a square drainage area with $C_A = 30.8828$.

$$\begin{aligned} a &= \frac{1.422 \times 10^6 r}{k_g h} \left[1.151 \log \left(\frac{10.06A}{C_A r_w^2} \right) - \frac{3}{4} + s \right] \\ &= \frac{(1.422 \times 10^6)(718)}{(6.6)(454)} \left\{ 1.151 \log \left[\frac{(10.06)(640)(43,560)}{(30.8828)(0.2615)^2} \right] - \frac{3}{4} + (-5.0) \right\} \\ &= 1.227 \times 10^6 \text{ psia}^2 / \text{cp} / (\text{MMscf} / \text{D}) . \end{aligned}$$

Now, calculate the AOF potential using \bar{b} from Step 2 and the stabilized a value calculated in Step 7.

$$\begin{aligned} q_{\text{AOF}} &= \frac{-a + \sqrt{a^2 + 4b[p_p(\bar{p}) - p_p(14.65)]}}{2b} \\ &= \frac{-(1.277 \times 10^6) + \sqrt{(1.277 \times 10^6)^2 + 4(1.878 \times 10^4)[(1.049 \times 10^9) - 2,003.8]}}{2(1.878 \times 10^4)} = 205.9 \text{ MMscf} / \text{D} . \end{aligned}$$

Stabilized C Method.

Step 1—Plot

$$\Delta p_p = p_p(p_{ws}) - p_p(p_{wf})$$

vs. q on log-log coordinates (**Fig. 8.130**). **Table 8.30** gives the plotting functions. Construct best-fit lines through the data.

Step 2—Calculate the deliverability exponent, n , for each line. For this example, use the least-squares regression analysis of all points for each isochron. For example, for $t = 3.0$ hours, $n = 0.63$. **Table 8.31** summarizes values of the deliverability exponent for each isochron. The arithmetic average slope of the values in **Table 8.31** is

$$\bar{n} = \frac{0.63 + 0.64 + 0.65 + 0.65}{4} = 0.64.$$

Step 3—Calculate the theoretical value of the Houpeurt coefficient, a , using the permeability and skin factor values calculated previously with the Brar and Aziz analysis (i.e., $k_g = 6.6$ md, $s = -5.0$).

$$\begin{aligned} a &= \frac{1.422 \times 10^6 r}{k_g h} \left[1.151 \log \left(\frac{10.06A}{C_A r_w^2} \right) - \frac{3}{4} + s \right] \\ &= \frac{(1.422 \times 10^6)(718)}{(6.6)(454)} \left\{ 1.151 \log \left[\frac{(10.06)(640)(43,560)}{(30.8828)(0.2615)^2} \right] - \frac{3}{4} - 5.0 \right\} \\ &= 1.227 \times 10^6 \text{ psia}^2 / \text{cp} / (\text{MMscf} / \text{D}) . \end{aligned}$$

Use the average value for the coefficient, $b = 1.878 \times 10^4$ psia²/(cp-MMscf/D), obtained from the Brar and Aziz analysis.

Step 4—Calculate the rate at which the change in pseudopressure determined with Rawlins-Schellhardt equation equals the change in pseudopressure determined with the Houpeurt equation. Use the average value for the coefficient, $b = 1.878 \times 10^4$ psia²/(cp-MMscf/D), obtained from the Brar and Aziz analysis, and the a coefficient from Step 3.

$$q_e = \frac{a(1-n)}{b(2n-1)} = \frac{1.227 \times 10^6(1-0.64)}{1.878 \times 10^4[2(0.64)-1]} = 84.2 \text{ MMscf/D.}$$

Step 5—Calculate the stabilized C value.

$$C = \frac{q_e}{(aq_e + bq_e^2)^n} \\ = \frac{84.2}{[(1.227 \times 10^6)(84.2) + (1.878 \times 10^4)(84.2)^2]^{0.64}} = 3.69 \times 10^{-4}.$$

Step 6—Calculate the AOF potential of the well using \bar{n} from Step 2.

$$q_{\text{AOF}} = C[p_p(\bar{p}) - p_p(p_b)]^n \\ = 3.69 \times 10^{-4}(1.049 \times 10^9 - 2,003.8)^{0.64} = 218.7 \text{ MMscf/D.}$$

Table 8.32 compares the results of the analyses with and without the extended, stabilized flow points. In general, the results are comparable and illustrate the validity of the Brar and Aziz and the stabilized C methods for modified isochronal tests with no extended, stabilized flow point.

8.13 Coning

Coning is the production of an (usually) unwanted second phase simultaneously with a desired hydrocarbon phase in reservoirs with fluid contacts near the wellbore throughout much of the drainage area of a well. The term coning is used because, in a vertical well, the shape of the interface when a well is producing the second fluid resembles an upright or inverted cone (**Fig. 8.131**). Important examples of coning include production of water in an oil well with bottomwater drive, production of gas in an oil well overlain by a gas cap, and production of bottom water in a gas well.

In a horizontal well, the cone becomes more of a crest (**Fig. 8.132**), but the phenomenon is still customarily called coning. In a given reservoir, the amount of undesired second fluid a horizontal well produces is usually less than for a vertical well under comparable conditions. This is a major motivation for drilling horizontal wells, for example, in thin oil columns underlain by water.

Coning is a problem because the second phase must be handled at the surface in addition to the desired hydrocarbon phase, and the production rate of the hydrocarbon flow is usually dramatically reduced after the cone breaks through into the producing well. Produced water must also be disposed of. Gas produced from coning in an oil well may have a market, but

TABLE 8.26—MODIFIED ISOCHRONAL TEST DATA, EXAMPLE 8.13

Time (hours)	p_{wf} (psia)			
	$q = 31.612$ (MMscf/D)	$q = 44.313$ (MMscf/D)	$q = 56.287$ (MMscf/D)	$q = 70.26$ (MMscf/D)
0 (p_{wh})	4,372.6	4,3756.0	4,344.3	4,343.6
3.0	4,274.1	4,206.5	4,111.8	3,994.6
4.0	4,266.8	4,199.3	4,103.3	3,973.3
5.0	4,262.5	4,192.0	4,097.0	3,959.6
6.0	4,258.3	4,190.4	4,093.5	3,951.9
0 [p_p (p_{ws})]	p_{ii} (p_{wi}) (psia ² /cp)			
	1.049×10^9	1.042×10^9	1.038×10^9	1.037×10^9
3.0	1.011×10^9	9.848×10^8	9.488×10^8	9.047×10^8
4.0	1.008×10^9	9.821×10^8	9.456×10^8	8.968×10^8
5.0	1.006×10^9	9.793×10^8	9.433×10^8	8.916×10^8
6.0	1.005×10^9	9.787×10^8	9.419×10^8	8.888×10^8
Extended Flow Point				
$p_{wf} = 3,794$ psia		$t = 72$ hours		
$p_s = 4,372.6$ psia		$q = 77.346$ MMscf/D		
$p_{ii}(p_{wi}) = 8.303 \times 10^8$		$p_{ii}(14.65) = 2,003.8$ psia ² /cp		

TABLE 8.27—PLOTING FUNCTIONS FOR BRAR AND AZIZ ANALYSIS, EXAMPLE 8.13

Time (hours)	$\Delta p_p/q$ (psia ² /(cp/MMscf/D))			
	$q = 31.612$ (MMscf/D)	$q = 44.313$ (MMscf/D)	$q = 56.287$ (MMscf/D)	$q = 70.265$ (MMscf/D)
3.0	1.202×10^6	1.291×10^6	1.585×10^6	1.883×10^6
4.0	1.297×10^6	1.352×10^6	1.642×10^6	1.995×10^6
5.0	1.360×10^6	1.415×10^6	1.682×10^6	2.069×10^6
6.0	1.392×10^6	1.428×10^6	1.707×10^6	2.121×10^6

also may not. In any event, production of gas in an oil well after the cone breaks through can rapidly deplete reservoir pressure and, for that reason, may force shut in of the oil well.

Several strategies may apply to wells with a potential to cone. One is to try to predict the rate at which a well will cone and produce at a lower rate as long as possible. Or, optimal economics may result by producing at a much higher rate, causing the well to cone, but increasing the cumulative hydrocarbon volume produced (and present value) at any future date. A horizontal well may be preferred to a vertical well.

Most prediction methods for coning predict a “critical rate” at which a stable cone can exist from the fluid contact to the nearest perforations. The theory is that, at rates below the critical rate, the cone will not reach the perforations and the well will produce the desired single phase. At rates equal to or greater than the critical rate, the second fluid will eventually be produced and will increase in amount with time. However, these theories based on critical rates do not predict when breakthrough will occur nor do they predict water/oil ratio or gas/oil ratio (GOR) after breakthrough. Other theories predict these time behaviors, but their accuracy is limited because of simplifying assumptions.

Time (hours)	b (psia ² /cp/MMscf/D)
3	1.823×10^4
4	1.870×10^4
5	1.881×10^4
6	1.939×10^4

Time (hours)	a_t (psia ² /MMscf/D)
3.0	5.677×10^5
4.0	6.247×10^5
5.0	6.794×10^5
6.0	6.807×10^5

Time (hours)	Δp_p (psia ² /cp)			
	$q = 31.612$ (MMscf/D)	$q = 44.313$ (MMscf/D)	$q = 56.287$ (MMscf/D)	$q = 70.265$ (MMscf/D)
3.0	3.800×10^7	5.720×10^7	8.920×10^7	1.323×10^8
4.0	4.100×10^7	5.990×10^7	9.240×10^7	1.402×10^8
5.0	4.300×10^7	6.270×10^7	9.470×10^7	1.454×10^8
6.0	4.400×10^7	6.330×10^7	9.610×10^7	1.490×10^8

Time (hours)	n_t
3.0	0.63
4.0	0.64
5.0	0.65
6.0	0.65

The calculated critical rate is valid only for a certain fixed distance between the fluid contact and the perforations. With time, that distance usually decreases (for example, bottom water will usually tend to rise toward the perforations). Thus, the critical rate will tend to decrease with time, and the economics of a well with a tendency to cone will continue to deteriorate with time.

Whether a cone will move toward perforations depends on the relative significance of viscous and gravitational forces near a well. The pressure drawdown at the perforations tends to

Parameter	Without Stabilized Data		With Stabilized Data	
	Stabilized C Method	Brar and Aziz Method	Rawlins-Schellhardt	Houpeurt
n	0.64	—	0.54	—
$C, (\text{MMscf/D})/(\text{psia}^2/\text{cp})^n$	3.60×10^{-4}	—	2.426×10^{-3}	—
$a, \text{psia}^2/(\text{cp-MMscf/D})$	1.227×10^6	1.227×10^6	—	1.455×10^6
$b, \text{psia}^2/(\text{cp-MMscf/D}^2)$	1.878×10^4	1.878×10^4	—	1.744×10^4
AOF, MMscf/D	218.7	205.9	180.1	205.6

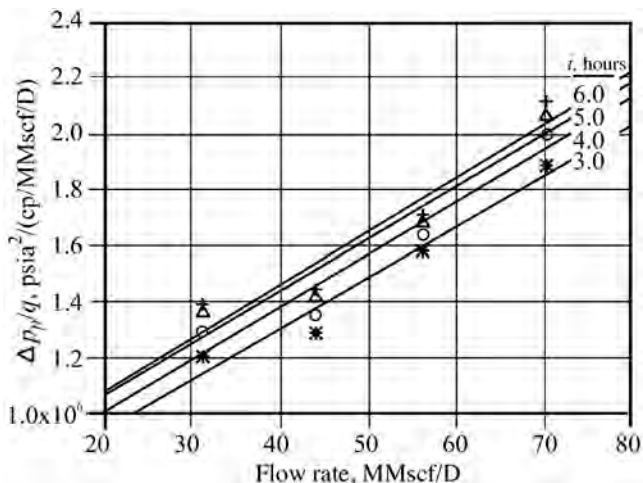


Fig. 8.128—Brar-Aziz analysis of modified isochronal test data, Example 8.13.

cause the undesired fluid to move toward the perforations. Gravitational forces tend to cause the undesired fluid to stay away from the perforations. Coning occurs when viscous forces dominate.

The variables that could affect coning are density differences between water and oil, gas and oil, or gas and water (gravitational forces); fluid viscosities and relative permeabilities; vertical and horizontal permeabilities; and distances from contacts to perforations. Coning tendency turns out to be quite dependent on some of these variables and insensitive to others.

A number of prediction methods have been published. There is no guarantee of great accuracy when using any of these methods because they all contain significant simplifying assumptions. In particular, areal and vertical variations in vertical permeability (because of flow barriers of varying extent) can cause the prediction methods to differ significantly from what actually happens in the field. Accordingly, the prediction methods are best used for quick approximations, screening, and comparison of alternatives. Reservoir simulations, based on accurate reservoir characterization, will ultimately be required.

The coning prediction method proposed by Chaperon⁵⁵ is of particular interest because of the variables it includes and because variations of the method are applicable to gas and water coning in both vertical and horizontal wells. For vertical wells, the Chaperon method calculates the critical rate for coning from the expression

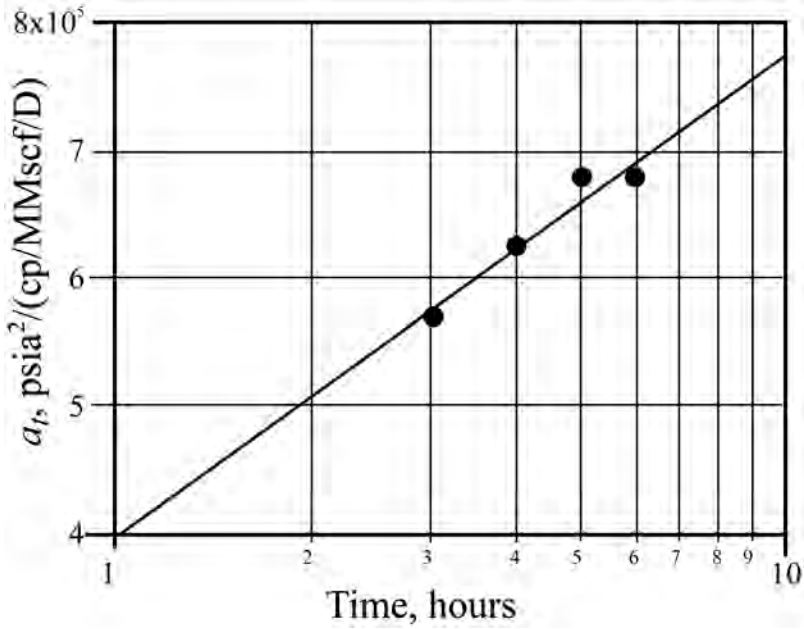


Fig. 8.129—Brar-Aziz plot of a_t vs. t .

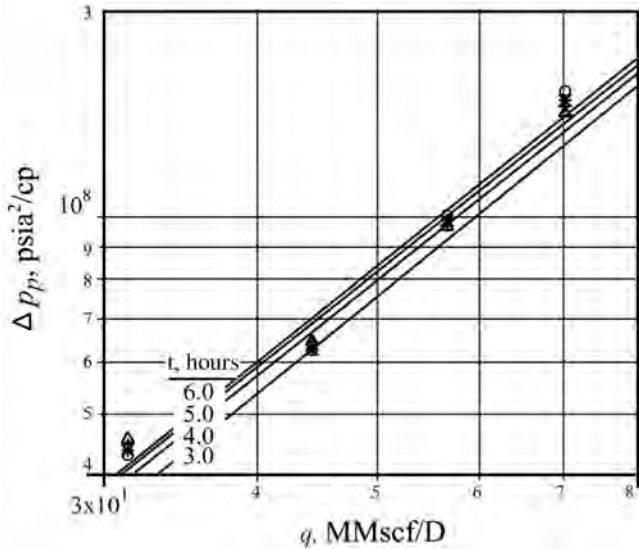


Fig. 8.130—Stabilized C analysis of modified isochronal test data, Example 8.13.

$$q_c = \frac{4.888 \times 10^{-4} k_h h_c^2 \Delta \rho q_{cD}}{B_o \mu_o}, \dots\dots\dots (8.283)$$

where

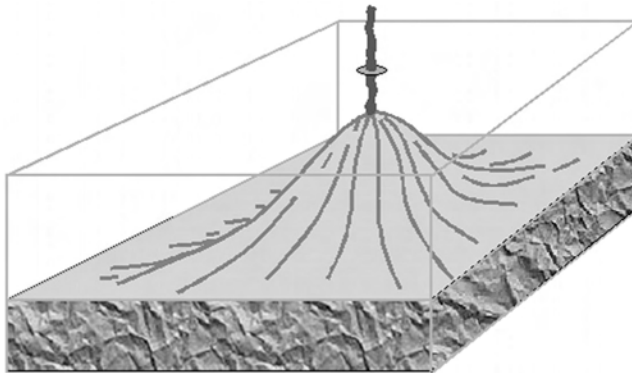


Fig. 8.131—Coning in a vertical well.

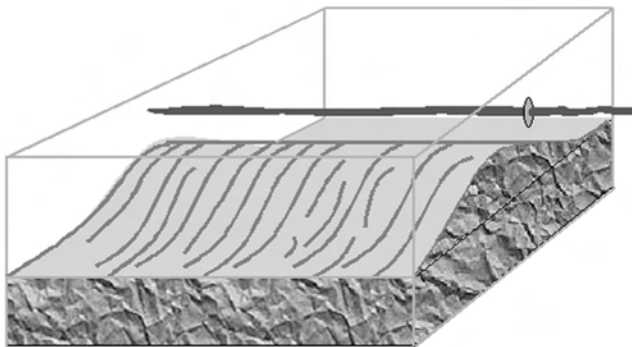


Fig. 8.132—Coning in a horizontal well.

$$q_{cD} = 0.7311 + \frac{1.843 / r_{rD}}{\sqrt{k_v / k_h}}, \dots\dots\dots (8.284)$$

$$r_{rD} = (r_e / h_c) \sqrt{k_v / k_h}, \dots\dots\dots (8.285)$$

$$\Delta\rho = \rho_w - \rho_o \text{ or } \rho_o - \rho_g, \text{ density difference, g/cm}^3, \dots\dots\dots (8.286)$$

and h_c = distance from perforations to fluid contact, ft. For horizontal wells, the critical rate is given by

$$q_c = \frac{4.888 \times 10^{-4} L_w \Delta\rho (k_h h^2)}{(a_H / 2) \mu_o B_o} F, \dots\dots\dots (8.287)$$

where

$$F = 3.964 + 0.0616 a_{HD} - 0.000540 a_{HD}^2, \dots\dots\dots (8.288)$$

and

$$a_{HD} = \left(\frac{a_H}{2h_c} \right) \sqrt{\frac{k_v}{k_h}} \dots\dots\dots (8.289)$$

Example 8.14. Consider a square, 160-acre drilling unit in an oil reservoir overlain by a gas cap. To determine the critical production rate (at or above which coning is likely to occur) for both horizontal and vertical well alternatives, assume the following well and formation properties: $k_h = 80$ md, $a_H = 2,640$ ft, $\mu_o = 0.5$ md, $\rho_o = 0.8$ g/cm³, $\rho_g = 0.3$ g/cm³, $L_w = 1,500$ ft, $h = 90$ ft, $B_o = 1.2$ RB/STB, $r_w = 0.33$ ft, distance from top of perforations in vertical well to GOC = 80 ft, and distance from horizontal well to GOC = 80 ft. Consider two cases: Isotropic Reservoir A, where $k_v = k_h = 80$ md, and Anisotropic Reservoir B, where $k_v = 8$ md and $k_h = 80$ md.

Solutions.

Isotropic Reservoir A ($k_v = k_h = 80$ md). For a horizontal well,

$$q_c = \frac{4.888 \times 10^{-4} L_w \Delta\rho (k_h h^2)}{(a_H/2) \mu_o B_o} F$$

Here,

$$a_{HD} = \left(\frac{a_H}{2h_c} \right) \sqrt{\frac{k_v}{k_h}} = \frac{2,640}{(2)(80)} \left(\sqrt{\frac{1}{1}} \right) = 16.5$$

$$\begin{aligned} \text{and } F &= 3.964 + 0.0616a_{HD} - 0.000540a_{HD}^2 \\ &= 3.964 + (0.0616)(16.5) - (0.000540)(16.5)^2 = 4.83. \end{aligned}$$

Then,

$$q_c = \frac{(4.888 \times 10^{-4})(1,500)}{(2,640/2)} \frac{(0.8 - 0.3)(80)(80)^2}{(0.5)(1.2)} (4.83) = 1,145 \text{ STB/D.}$$

For a vertical well, note that $r_e = \sqrt{\frac{(160)(43,560)}{\pi}} = 1,489$ ft.

$$q_c = \frac{4.888 \times 10^{-4} k_h h_c^2 \Delta\rho q_{cD}}{B_o \mu_o},$$

$$\text{where } r_{rD} = \left(\frac{r_e}{h_e} \right) \sqrt{\frac{k_v}{k_h}} = \frac{(1,489)}{(80)} \sqrt{\frac{1}{1}} = 18.61$$

and

$$q_{cD} = 0.7311 + \frac{1.843/r_{rD}}{\sqrt{k_v/k_h}} = 0.7311 + \frac{1.843}{18.61} = 0.830.$$

Then,

$$q_c = \frac{(4.888 \times 10^{-4})(80)(80)^2(0.8 - 0.3)(0.830)}{(1.2)(0.5)} = 173 \text{ STB/D.}$$

Anisotropic Reservoir B ($k_v = 8$ md and $k_h = 80$ md). For a horizontal well,

$$a_{HD} = \frac{2,640}{(2)(80)} \sqrt{\frac{8}{80}} = 5.22,$$

$$F = 3.964 + (0.616)(5.22) - (0.000540)(5.22)^2 = 4.27,$$

$$\text{and } q_c = (1,145) \left(\frac{4.27}{4.83} \right) = 1,012 \text{ STB/D.}$$

For a vertical well,

$$r_{rD} = \frac{1,489}{80} \sqrt{\frac{8}{80}} = 5.89,$$

$$q_{cD} = 0.7311 + \frac{1.843}{5.89} = 1.044,$$

$$\text{and } q_c = (173) \left(\frac{1.044}{0.830} \right) = 217 \text{ STB/CD.}$$

The important conclusions and lessons from this example are:

- Vertical permeability has only a modest influence on critical coning rate, at least for this situation.
- The advantage of a horizontal well over a vertical well is substantial for both isotropic and anisotropic reservoirs in this situation.
- The same sorts of calculations could be made for an oil well coning water or a gas well coning water.
- These calculations give us no information on time at which the cone will break through to the producing well nor on GOR and oil production rate following breakthrough.

While these types of simple calculations can provide some insight on the potential for coning, a finely grided simulator model could be used to more effectively predict coning behavior including timing and the benefits of a horizontal well over a vertical one.

Nomenclature

$$a = \frac{1.422 \times 10^6}{k_g h} \left[1.151 \log \left(\frac{10.06A}{C_A r_w^2} \right) - \frac{3}{4} + s \right], \text{ stabilized deliverability}$$

coefficient, psia²-cp/MMscf-D

a = total length of reservoir perpendicular to wellbore, ft

a_h = length of reservoir perpendicular to horizontal well, ft

$a_f = \sqrt{L_f^2 + b_f^2}$, depth of investigation along major axis in fractured well, ft

$$a_t = \frac{1.422 \times 10^6 T}{k_g h} \left[1.151 \log \left(\frac{k_g t}{1,688 \phi \bar{\mu}_g \bar{c}_t r_w^2} \right) + s \right], \text{ transient deliverability}$$

coefficient, psia²-cp/MMscf-D

a_H = total width of reservoir perpendicular to the wellbore, ft

- a_H' = modified total width of reservoir perpendicular to the wellbore, ft
 A = drainage area, sq ft
 $A = \pi a_f b_f$, area of investigation in fractured well, ft²
 A_f = cross-sectional area perpendicular to flow, sq ft
 A_{wb} = wellbore area, sq ft
 $b = \frac{1.422 \times 10^6 TD}{kgh}$ (gas flow equation)
 $b_f = 0.02878 \left[\frac{kt}{\phi \mu c_t} \right]^{1/2}$, depth of investigation of along minor axis in fractured well, ft
 b_B = intercept of Cartesian plot of bilinear flow data, psi
 b_H = length in direction parallel to wellbore, ft
 b_H' = modified length in direction parallel to wellbore, ft
 b_L = intercept of Cartesian plot of linear flow data, psi
 b_V = intercept of Cartesian plot of data during volumetric behavior, psi
 B = formation volume factor, res vol/surface vol
 B_g = gas formation volume factor, RB/STB
 B_{gi} = gas formation volume factor evaluated at p_i , RB/Mscf
 B_o = oil formation volume factor, RB/Mscf
 \underline{B}_w = water formation volume factor, RB/STB
 \overline{B}_g = gas formation volume factor evaluated at average drainage area pressure, RB/Mscf
 $B_{ND} = 1,422 \mu z TD/kh$, non-Darcy flow coefficient
 c = compressibility, psi⁻¹
 c_f = formation compressibility, psi⁻¹
 c_g = gas compressibility, psi⁻¹
 c_o = oil compressibility, psi⁻¹
 $c_t = S_o c_o + S_w c_w + S_g c_g + c_f$ = total compressibility, psi⁻¹
 c_w = water compressibility, psi⁻¹
 \overline{c}_t = total compressibility evaluated at average drainage area pressure, psi⁻¹
 c_{yf} = total compressibility of pore space and fluids in fracture porosity, psi⁻¹
 c_{im} = total compressibility of pore space and fluids in matrix porosity, psi⁻¹
 c_{wb} = compressibility of fluid in wellbore, psi⁻¹
 C = performance coefficient in gas-well deliverability equation, or wellbore storage coefficient, bbl/psi
 C_A = shape factor or constant
 $C_D = 0.8936 C / \phi c_i h r_w^2$, dimensionless wellbore storage coefficient
 $(C_D e^{2s})_f$ = type-curve parameter value for the formation
 $(C_D e^{2s})_{f+m}$ = type-curve parameter value for the formation plus the matrix
 $C_{LD} = 0.8936 C / \phi c_i h L_f^2$, dimensionless wellbore storage coefficient in fractured well
 $C_r = w_f k_f / \pi k L_f$, fracture conductivity, dimensionless
 d_x = shortest distance between horizontal well and x boundary, ft
 d_y = shortest distance between tip of horizontal well and y boundary, ft
 d_z = shortest distance between horizontal well and z boundary, ft
 D_x = longest distance between horizontal well and x boundary, ft
 D_y = longest distance between tip of horizontal well and y boundary, ft

- D_z = longest distance between horizontal well and z boundary, ft
 D = non-Darcy flow constant, D/Mscf
 e^{-bt} = exponential decline with a constant b and elapsed time, t
 E_f = flow efficiency, dimensionless
 $Ei(-x) = \int_x^\infty (e^{-u}/u)du$, the exponential integral
 $F(u)$ = function used in horizontal well analysis
 $F_{CD} = w_f k_f / k L_f$, fracture conductivity, dimensionless
 g = acceleration due to gravity, ft/sec²
 g_c = gravitational units conversion factor, 32.17 (lbm/ft)(lbf-s²)
 h = net formation thickness, ft
 $h_D = (h/r_w)(k_h/k_v)^{1/2}$, dimensionless
 h_f = fracture height, ft
 h_m = thickness of matrix, ft
 h_p = perforated interval thickness, ft
 $h_{pD} = h_p/h_t$
 h_t = total formation thickness, ft
 h_l = distance from top of formation to top of perforations, ft
 $h_{lD} = h_l/h_t$
 HTR_{avg} = HTR at average drainage area pressure
 J = productivity index, STB/D, psi
 J_{actual} = actual well productivity index, STB/D-psi
 J_{ideal} = ideal productivity index ($s = 0$), STB/D-psi
 k = matrix permeability, md
 \bar{k} = average permeability, md
 k_f = permeability of the proppant in the fracture, md
 k_{fs} = permeability near the wellbore, md
 k_g = permeability to gas, md
 k_{gp} = permeability of the gravel in the gravel pack, md
 k_h = horizontal permeability, md
 k_m = matrix permeability, md
 k_o = permeability to oil, md
 k_r = permeability in horizontal radial direction, md
 k_s = permeability of altered zone, md
 k_w = permeability to water, md
 k_x = permeability in x -direction, md
 k_y = permeability in y -direction, md
 k_z = permeability in z -direction, md
 L = distance from well to no-flow boundary, ft
 L_d = drilled length of horizontal well, ft
 L_f = fracture half length, ft
 L_g = length of flow path through gravel pack, ft
 L_m = length of matrix, ft
 L_p = length of perforation tunnel, ft
 L_s = length of damaged zone in fracture, ft
 L_w = completed length of horizontal well, ft

- L_x = distance from boundary, ft
 m = $162.2 qB\mu/kh$ = slope of middle-time line, psi/cycle
 m_B = slope of bilinear flow graph, psi/hr^{1/4}
 m_L = slope of linear flow graph, psi/hr^{1/2}
 m_s = $\frac{2456\sqrt{\phi\mu c_p qB\mu}}{k_{sp}^{3/2}}$, slope of spherical flow plot, psi-hr^{1/2}
 m_V = slope of volumetric flow graph, psi/hr
 m_{hrf} = slope of semilog plot for hemiradial flow, psi/log cycle
 m_{elf} = slope of square-root-of-time plot for early linear flow, psi/ $\sqrt{\text{hr}}$
 m_{erf} = slope of semilog plot of early radial flow, psi/log cycle
 m_{lfr} = slope of square-root-of-time plot for late linear flow, psi/ $\sqrt{\text{hr}}$
 m_{prf} = slope of semilog plot for pseudoradial flow, psi/log cycle
 M = Molecular weight of gas
MTR = middle-time region
 n = inverse slope of the line on a log-log plot of the change in pressure squared or pseudopressure vs. gas flow rate
 p = pressure, psi
 p_{avg} = average pressure, psi
 p_b = base (atmospheric) pressure, psia
 p_0 = arbitrary reference or base pressure, psi
 \bar{p} = volumetric average or static drainage-area pressure, psi
 p_a = adjusted or normalized pseudopressure, $(\mu z/p)p_p$, psia
 p_{awf} = adjusted flowing bottomhole pressure, psia
 p_{aws} = adjusted shut-in bottomhole pressure, psia
 p_f = formation pressure, psi
 p_i = original reservoir pressure, psi
 p_m = matrix pressure, psi
 p_p = pseudopressure, psia²/cp
 p_s = stabilized shut-in BHP measured just before start of a deliverability test, psia
 p_{sc} = standard-condition pressure, psia
 p_t = surface pressure in tubing, psi
 p_w = BHP in wellbore, psi
 p_{wf} = flowing BHP, psi
 p_{ws} = shut-in BHP, psi
 p_{xy} = parameter in horizontal well analysis equations
 p_{xyz} = parameter in horizontal well analysis equations
 p_y = parameter in horizontal well analysis equations
 p_{1hr} = pressure at 1-hour shut-in (flow) time on MTR line or its extrapolation, psi
 p' = pressure derivative
 p^* = MTR pressure trend extrapolated to infinite shut-in time, psi
 p_D = $0.00708 kh(p_i - p)/qB\mu$, dimensionless pressure as defined for constant-rate production
 p_{MBHD} = Matthews-Brons-Hazebroek pressure, dimensionless
 $(p_D)_{MP}$ = dimensionless pressure at match point
 q = flow rate at surface, STB/D
 q_{AOF} = absolute-open-flow potential, MMscf/D

- q_g = gas flow rate, Mscf/D
 q_o = water flow rate, STB/D
 q_{Rt} = total flow rate at reservoir conditions, RB/D
 q_{sf} = flow rate at formation (sand) face, STB/D
 q_w = water flow rate, STB/D
 r = distance from the center of wellbore, ft
 r_a = radius of altered zone (skin effect), ft
 r_d = effective drainage radius, ft
 r_{dp} = radius of damage zone around perforation tunnel, ft
 r_e = external drainage radius, ft
 r_i = radius of investigation, ft
 r_p = radius of perforation tunnel, ft
 r_s = outer radius of the altered zone, ft
 r_{sp} = radius of source or inner boundary of spherical flow pattern, ft
 r_w = wellbore radius, ft
 r_{wa} = apparent or effective wellbore radius, ft
 r_D = r/r_w , dimensionless radius
 R_s = dissolved GOR, scf/STB
 s = skin factor, dimensionless
 s_a = skin caused by alteration of permeability around wellbore, dimensionless
 s_c = convergence skin, dimensionless
 s_d = skin caused by formation damage, dimensionless
 s_e = skin caused by eccentric effects, dimensionless
 s_{dp} = perforation damage skin, dimensionless
 s_f = skin of hydraulically fractured well, dimensionless
 s_{gp} = skin factor from to Darcy flow through gravel pack, dimensionless
 s_{min} = minimum skin factor, dimensionless
 s_p = skin resulting from an incompletely perforated interval, dimensionless
 s_t = total skin, dimensionless
 s_θ = skin factor resulting from well inclination, dimensionless
 s' = $s + Dq$ = apparent skin factor, dimensionless
 S_g = gas saturation, fraction of pore volume
 S_o = oil saturation, fraction of pore volume
 S_w = water saturation, fraction of pore volume
 t = elapsed time, hours
 t_a = $\mu c_t t_{ap}$, adjusted or normalized pseudotime, hours
 t_{ap} = pseudotime, hours
 t_{bD} = dimensionless time in linear flow, hours
 t_D = $0.0002637 kt / \phi \mu c_r r_w^2$, dimensionless time
 t_{DA} = $0.0002637 kt / \phi \mu c_r A$ = dimensionless time based on drainage area, A
 t_{eqB} = equivalent time for bilinear flow, hours
 t_e = equivalent time, hours
 t_{LrD} = $0.0002637 kt / \phi \mu c_r L_f^2$, dimensionless time for fractured wells
 t_p = pseudoproducing time, hours
 t_{pD} = pseudoproducing time, dimensionless

- t_{prf} = time required to reach the pseudoradial flow regime, hours
 t_{Eelf} = end of early linear flow, t, hours
 t_{Eerf} = end of early radial flow, t, hours
 t_{Elf} = end of linear flow, hours
 t_{Ellf} = time to end of late linear flow regime, hours
 t_{Ehrf} = end of hemiradial flow, hours
 t_{Erf} = end of early radial flow, hours
 t_{Eprf} = end of pseudoradial flow, hours
 t_p = constant-rate production period, t, hours
 t_{pAD} = dimensionless producing time, hours
 t_{pss} = time required to reach pseudosteady state, hours
 t_{Self} = start of early linear flow, hours
 t_{Sllf} = start of late linear flow, hours
 t_{Shrf} = start of hemiradial flow, t, hours
 t_{Sprf} = start of pseudoradial flow, t, hours
 t_s = time required for stabilization, hours
 T = reservoir temperature, °R
 T_{sc} = standard condition temperature, °R
 u = dummy variable
 V = volume, bbl
 V_f = fraction of bulk volume occupied by fractures
 V_m = fraction of bulk volume occupied by matrix
 $V_w = V_{wb}$ = wellbore volume, bbl
 w = width of channel reservoir, ft
 w_f = fracture width, ft
 wk_f = fracture conductivity, md-ft
 w_s = width of damaged zone around fracture face, ft
WBS = wellbore storage
 z = gas-law deviation factor, dimensionless
 \bar{z} = gas-law deviation factor at average reservoir pressure, dimensionless
 Δp = pressure change since start of transient test, psi
 $(\Delta p)_{MP}$ = pressure change at match point
 Δp_D = dimensionless pressure change
 Δp_p = pseudopressure change since start of test, psia²/cp
 Δp_s = additional pressure drop due to skin, psi
 $\Delta p_{t=0}$ = pressure drop at time zero, psi
 Δp_{1hr} = pressure change from start of test to one hour elapsed time, psi
 Δt = time elapsed since start of test, hours
 $\Delta t_a = \bar{\mu} \bar{c}_t \Delta t_{ap}$, normalized or adjusted pseudotime, hours
 $\Delta t_{ap} = \int_0^{\Delta t} \frac{dt}{\mu(p)c_t(p)}$, pseudotime, hr-psia/cp
 Δt_{Be} = bilinear equivalent time, hours
 Δt_e = radial equivalent time, hours
 Δt_{Le} = linear equivalent time, hours
 Δt_{max} = maximum shut-in time in pressure buildup test, hours
 ΔV = change in volume, bbl

- $\eta = 0.0002637 k/\phi\mu c_i$, hydraulic diffusivity, ft²/hr
 η_{fD} = hydraulic diffusivity, dimensionless
 λ = interporosity flow coefficient
 $\lambda_t = \frac{k_0}{\mu_0} + \frac{k_w}{\mu_w} + \frac{k_g}{\mu_g}$, total mobility, md/cp
 α = exponent in deliverability equation
 α = parameter characteristic of system geometry in dual-porosity system
 β = turbulence factor
 β' = transition parameter
 γ = Euler's constant, = 1.781, dimensionless
 γ_g = gas gravity (air = 1.0)
 γ_m = matrix density
 ω = storativity ratio in dual porosity reservoir
 μ = viscosity, cp
 μ_i = viscosity evaluated at p_i , cp
 μ_g = gas viscosity, cp
 μ_o = oil viscosity, cp
 μ_w = water viscosity, cp
 $\bar{\mu}_g$ = gas viscosity evaluated at average pressure, cp
 μ_{gwf} = gas viscosity evaluated at p_{wf} , cp
 $\bar{\mu}$ = viscosity evaluated at \bar{p} , cp
 ρ = density, lbm/ft³ or g/cm³
 ρ_{wb} = density of liquid in wellbore, lbm/ft³
 ϕ_f = fraction of fracture volume occupied by pore space, $\cong 1$
 ϕ_m = fraction of matrix volume occupied by pore space
 $(\phi V)_f$ = fraction of bulk volume occupied by pore space in fractures
 $(\phi Vc_i)_f$ = fracture "storativity" for dual porosity reservoir
 $(\phi Vc_i)_{f+m}$ = total "storativity" for dual porosity reservoir
 $(\phi V)_m$ = fraction of bulk volume occupied by pore space in matrix
 ϕ = porosity, dimensionless
 Σs = sum of damage skin, turbulence, and other pseudoskin factors

References

1. Matthews, C.S. and Russell, D.G.: *Pressure Buildup and Flow Tests in Wells*, Monograph Series, SPE, Richardson, Texas (1967) **1**.
2. Hawkins, M.F. Jr.: "A Note on the Skin Effect," *Trans.*, AIME (1956) **207**, 356–357.
3. Wattenbarger, R.A. and Ramey, H.J. Jr.: "Gas Well Testing With Turbulence, Damage, and Wellbore Storage," *JPT* (August 1968) 877; *Trans.*, AIME, **243**.
4. Lee, W.J.: *Well Testing*, Textbook Series, SPE, Dallas (1982).
5. Joseph, J.A. and Koederitz, L.F.: "Unsteady-State Spherical Flow With Storage and Skin," *SPEJ* (December 1985) 804.
6. Horner, D.R.: "Pressure Buildup in Wells," *Proc.*, Third World Pet. Cong., The Hague (1951) Sec. II, 503–523; also *Pressure Analysis Methods*, Reprint Series, SPE, Richardson, Texas (1967) **9**, 25–43.
7. Gringarten, A.C. *et al.*: "A Comparison Between Different Skin and Wellbore Storage Type-Curves for Early-Time Transient Analysis," paper SPE 8205 presented at the 1979 SPE Annual Technical Conference and Exhibition, Las Vegas, Nevada, 23–26 September.

8. Bourdet, D. *et al.*: “A New Set of Type Curves Simplifies Well Test Analysis,” *World Oil* (May 1983) 95.
9. Agarwal, R.G.: “A New Method To Account for Producing Time Effects When Drawdown Type Curves Are Used To Analyze Pressure Buildup and Other Test Data,” paper SPE 9289 presented at the 1980 SPE Annual Technical Conference and Exhibition, Dallas, 21–24 September.
10. Prats, M., Hazebroek, P., and Strickler, W.R.: “Effect of Vertical Fractures on Reservoir Behavior—Compressible Fluid Case,” *SPEJ* (June 1962) 87; *Trans.*, AIME, **225**.
11. Papatzacos, P.: “Approximate Partial-Penetration Pseudoskin for Infinite-Conductivity Wells,” *SPEERE* (May 1987) 227.
12. Cinco, H., Miller, F.G., and Ramey, H.J. Jr.: “Unsteady-State Pressure Distribution Created by a Directionally Drilled Well,” *JPT* (November 1975) 1392; *Trans.*, AIME, **259**.
13. Brown, K.E.: *The Technology of Artificial Lift Methods*, PennWell, Tulsa (1984) **4**, 134.
14. McLeod, H.O. Jr.: “The Effect of Perforating Conditions on Well Performance,” *JPT* (January 1983).
15. Al-Hussainy, R., Ramey, H.J. Jr., and Crawford, P.B.: “The Flow of Real Gases Through Porous Media,” *JPT* (May 1966) 624; *Trans.*, AIME, **237**.
16. Agarwal, R.G.: “Real Gas Pseudo-Time—A New Function for Pressure Buildup Analysis of MFH Gas Wells,” paper SPE 8279 presented at the 1979 SPE Annual Technical Conference and Exhibition, Las Vegas, Nevada, 23–26 September.
17. Lee, W.J. and Holditch, S.A.: “Applications of Pseudotime to Buildup Test Analysis of Low Permeability Gas Wells with Long-Duration Wellbore Storage Distortion,” *JPT* (December 1982) 2877.
18. Spivey, J.P. and Lee, W.J.: “The Use of Pseudotime: Wellbore Storage and the Middle Time Region,” paper SPE 15229 presented at the 1986 SPE Unconventional Gas Technology Symposium, Louisville, Kentucky, 18–21 May.
19. Meunier, D.F., Kabir, C.S., and Wittmann, M.J.: “Gas Well Test Analysis: Use of Normalized Pressure and Time Functions,” *SPEFE* (December 1987) 629.
20. Matthews, C.S., Brons, F., and Hazebroek, P.: “A Method for Determination of Average Pressure in a Bounded Reservoir,” *Trans.*, AIME (1954) **201**, 182–191.
21. Jones, S.C.: “Using the Inertial Coefficient, β , To Characterize Heterogeneity in Reservoir Rock,” paper SPE 16949 presented at the 1987 SPE Annual Technical Conference and Exhibition, Dallas, 27–30 September.
22. Perrine, R.L.: “Analysis of Pressure Buildup Curves,” *Drill. and Prod. Prac.*, API, Dallas (1956) 482.
23. Martin, J.C.: “Simplified Equations of Flow in Gas Drive Reservoirs and the Theoretical Foundation of Multiphase Pressure Buildup Analyses,” *JPT* (October 1959) 309; *Trans.*, AIME, **216**.
24. Ramey, H.J. Jr. and Cobb, W.M.: “A General Pressure Buildup Theory for a Well in a Closed Circular Drainage Area,” *JPT* (December 1971) 1493; *Trans.*, AIME, **251**.
25. Larsen, V.C.: “Understanding the Muskat Method of Analysing Pressure Build-Up Curves,” *J. Cdn. Pet. Tech.* (Fall, 1963) **2**, No. 136.
26. Arps, J.J. and Smith, A.E.: “Practical Use of Bottom Hole Pressure Build-Up Curves,” Reprint Paper No. 851-23-I, Tulsa Meeting, API (March 1949).
27. Cinco-Ley, H. and Samaniego-V., F.: “Transient Pressure Analysis for Fractured Wells,” *JPT* (September 1981) 1749.
28. Hale, B.W. and Evers, J.F.: “Elliptical Flow Equations for Vertically Fractured Gas Wells,” *JPT* (December 1981) 2489.
29. Cinco-Ley, H. and Samaniego-V., F.: “Transient Pressure Analysis: Finite Conductivity Fracture Case Versus Damaged Fracture Case,” paper SPE 10179 presented at the 1981 SPE Annual Technical Conference and Exhibition, San Antonio, Texas, 5–7 October.
30. Lee, W.J.: “Postfracture Formation Evaluation,” *Recent Advances in Hydraulic Fracturing*, J.L. Gidley, S.A. Holditch, D.E. Nierode, and R.W. Veatch Jr. (eds.), Monograph Series, SPE, Richardson, Texas (1989) **12**.
31. Ramey, H.J. Jr. and Gringarten, A.C.: “Effect of High Volume Vertical Fractures on Geothermal Steam Well Behavior,” *Proc.*, Second United Nations Symposium on the Use and Development of Geothermal Energy, San Francisco (1975).

32. Warren, J.E. and Root, P.J.: "The Behavior of Naturally Fractured Reservoirs," *SPEJ* (September 1963) 245.
33. Gringarten, A.C.: "Interpretation of Tests in Fissured and Multilayered Reservoirs With Double-Porosity Behavior: Theory and Practice," *JPT* (April 1984) 549.
34. Serra, K., Reynolds, A.C., and Raghavan, R.: "New Pressure Transient Analysis Methods for Naturally Fractured Reservoirs," *JPT* (December 1983) 2271.
35. Barenblatt, G.E., Zheltov, I.P., and Kochina, I.N.: "Basic Concepts in the Theory of Homogeneous Liquids in Fissured Rocks," *J. Appl. Math. Mech.* (1960) **24**, 1286.
36. de Swann, A.: "Analytical Solutions for Determining Naturally Fractured Reservoir Properties by Well Testing," *SPEJ* (June 1976) 117-122.
37. Bourdet, D. *et al.*: "New Type Curves Aid Analysis of Fissured Zone Well Tests," *World Oil* (April 1984).
38. Goode, P.A. and Thambynayagam, R.K.M.: "Pressure Drawdown and Buildup Analysis of Horizontal Wells in Anisotropic Media," *SPEFE* (December 1987) 683; *Trans.*, AIME, **283**.
39. Odeh, A.S and Babu, D.K.: "Transient Flow Behaviour of Horizontal Wells: Pressure Drawdown and Buildup Analysis," *SPEFE* (March 1990) 7; *Trans.*, AIME, **289**.
40. Kuchuk, F.J.: "Well Testing and Interpretation for Horizontal Wells," paper SPE 25232 available from SPE, Richardson, Texas (1995).
41. Lichtenberger, G.J.: "Data Acquisition and Interpretation of Horizontal Well Pressure-Transient Tests," *JPT* (February 1994) 157.
42. Babu, D.K. and Odeh, A.S.: "Productivity of a Horizontal Well," *SPEFE* (November 1989) 417.
43. Economides, M.J., Brand, C.W., and Frick, T.P.: "Well Configurations in Anisotropic Reservoirs," *SPEFE* (December 1996) 257.
44. Ozkan, E.: "Analysis of Horizontal-Well Responses: Contemporary vs. Conventional," *SPEFE* (August 2001) 260.
45. Houpeurt, A.: "On the Flow of Gases in Porous Media," *Revue de L'Institut Francais du Petrole* (1959) **14**, No. 11, 1468.
46. Rawlins, E.L. and Schellhardt, M.A.: *Backpressure Data on Natural Gas Wells and Their Application to Production Practices*, Monograph Series, USBM (1935) 7.
47. Al-Hussainy, R., Ramey, H.J. Jr., and Crawford, P.B.: "The Flow of Real Gases Through Porous Media," *JPT* (May 1966) 624; *Trans.*, AIME, **237**.
48. Lee, W.J.: *Well Testing*, Textbook Series, SPE, Richardson, Texas (1977) **1**.
49. Earlougher, R.C. Jr.: *Advances in Well Test Analysis*, Monograph Series, SPE, Richardson, Texas (1977) 5.
50. Jennings, J. W. *et al.*: "Deliverability Testing of Natural Gas Wells," prepared for the Texas Railroad Commission, Texas A&M U., College Station, Texas (August 1989).
51. Cullender, M.H.: "The Isochronal Performance Method of Determining the Flow Characteristics of Wells," *Trans.*, AIME (1955) **204**, 137.
52. Katz, D.L. *et al.*: *Handbook of Natural Gas Engineering*, McGraw-Hill Publishing Co., New York City (1959).
53. Brar, G.S. and Aziz, K.: "Analysis of Modified Isochronal Tests To Predict the Stabilized Deliverability Potential of Gas Wells Without Using Stabilized Flow Data," *JPT* (February 1978) 297; *Trans.*, AIME, **265**.
54. Johnston, J.L., Lee, W.J., and Blasingame, T.A.: "Estimating the Stabilized Deliverability of a Gas Well Using the Rawlins and Schellhardt Method: An Analytical Approach," paper SPE 23440 presented at the 1991 SPE Eastern Regional Meeting, Lexington, Kentucky, 22–25 October.
55. Chaperon, I.: "Theoretical Study of Coning Toward Horizontal and Vertical Wells in Anisotropic Formations: Subcritical and Critical Rates," paper 15377 presented at the 1986 SPE Annual Technical Conference and Exhibition, New Orleans, 5–8 October.

SI Metric Conversion Factors

acre	×	4.046 873	E + 03	=	m ²
bb1	×	1.589 873	E - 01	=	m ³
cp	×	1.0*	E - 03	=	Pa·s
ft	×	3.048*	E - 01	=	m
ft ²	×	9.290 304*	E - 02	=	m ²
ft ³	×	2.831 685	E - 02	=	m ³
°F		(°F - 32)/1.8		=	°C
in. ³	×	1.638 706	E + 01	=	cm ³
lbf	×	4.448 222	E + 00	=	N
lbm	×	4.535 924	E - 01	=	kg
psi	×	6.894 757	E + 00	=	kPa

*Conversion factor is exact.

Appendix





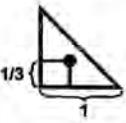
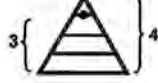
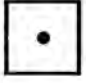
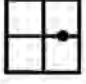
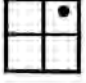

TABLE A-1—SHAPE FACTORS AND DURATIONS OF FLOW REGIME ⁴⁹				
Reservoir Shape	C _A	Pseudosteady-State System		Infinite System
		Exact for t _{DA} >	Less Than 1% Error for t _{DA} >	Less than 1% Error for t _{DA} <
	31.62	0.1	0.06	0.10
	31.6	0.1	0.06	0.10
	27.6	0.2	0.07	0.09
	27.1	0.2	0.07	0.09
	21.9	0.4	0.12	0.08
	0.098	0.9	0.60	0.015
	30.8828	0.1	0.05	0.09
	12.9851	0.7	0.25	0.03
	4.5132	0.6	0.30	0.025
	3.3351	0.7	0.25	0.01

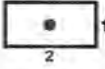
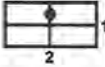

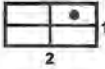

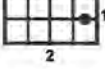
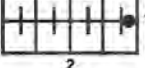




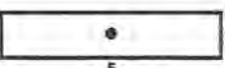
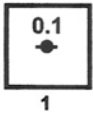
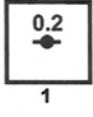
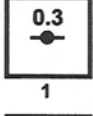
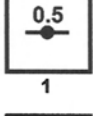
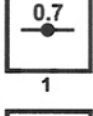
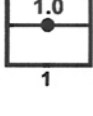


TABLE A-1—SHAPE FACTORS AND DURATIONS OF FLOW REGIME ⁴⁹ (continued)				
Reservoir Shape	C_A	Pseudosteady-State System		Infinite System
		Exact for $t_{DA} >$	Less Than 1% Error for $t_{DA} >$	Less than 1% Error for $t_{DA} <$
	21.8369	0.3	0.15	0.025
	10.8374	0.4	0.15	0.025
	4.5141	1.5	0.50	0.06
	2.0769	1.7	0.50	0.02
	3.1573	0.4	0.15	0.005
	0.5813	2.0	0.60	0.02
	0.1109	3.0	0.60	0.005
	5.3790	0.8	0.30	0.01
	2.6896	0.8	0.30	0.01
	0.2318	4.0	2.00	0.03
	0.1155	4.0	2.00	0.01
	2.3606	1.0	0.40	0.025

TABLE A-1—SHAPE FACTORS AND DURATIONS OF FLOW REGIME ⁴⁹ (continued)					
Reservoir Shape	C _A	Pseudosteady-State System		Infinite System	
		Exact for t _{DA} >	Less Than 1% Error for t _{DA} >	Less than 1% Error for t _{DA} <	
 1 1 =X _f /X _e	2.6541	0.175	0.08	cannot use	
 1 1	2.0348	0.175	0.09	cannot use	
 1 1	1.9886	0.175	0.09	cannot use	
 1 1	1.6620	0.175	0.09	cannot use	
 1 1	1.3127	0.175	0.09	cannot use	
 1 1	0.7887	0.175	0.09	cannot use	
In waterdrive reservoirs					
	19.1	--	--	--	
In reservoirs of unknown production character					
	25.0	--	--	--	

**TABLE A-2—EQUATIONS FOR ANALYZING FLOW IN
HORIZONTAL WELLS WITH UNIFORM FLUX**

Wellbore Storage

$$t_{Ews} = \frac{(4,000 + 240s_d)C}{\sqrt{k_x k_z} L_w / \mu} \quad (A-1)$$

$$C = V_{wb} c_{wb} \quad (A-2)$$

$$C = \frac{25.65 A_{wb}}{\rho_{wb} \cos \theta} \quad (A-3)$$

$$C = qBt / 24\Delta p \quad (A-4)$$

Early Radial Flow

$$\sqrt{k_x k_z} = \frac{162.6qB\mu}{|m_{erf}| L_w} \quad (A-5)$$

$$s_d = 1.151 \left[\frac{\Delta p_{1hr}}{|m_{erf}|} - \log \left(\frac{\sqrt{k_x k_z}}{\phi \mu c_t r_w^2} \right) + 3.23 \right] \quad (A-6)$$

$$t_{Eerf} = 1,800 d_z^2 \phi \mu c_t / k_z \quad (A-7)$$

$$t_{Eerf} = 125 L_w^2 \phi \mu c_t / k_y \quad (A-8)$$

Hemiradial Flow

$$\sqrt{k_x k_z} = 2 \left(\frac{162.6qB\mu}{|m_{hrf}| L_w} \right) \quad (A-9)$$

$$s_d = 2.303 \left[\frac{\Delta p_{1hr}}{|m_{hrf}|} - \log \left(\frac{\sqrt{k_x k_z}}{\phi \mu c_t r_w^2} \right) + 3.23 \right] \quad (A-10)$$

$$t_{Ehrf} \approx 1,800 D_z^2 \phi \mu c_t / k_z \quad (A-11a)$$

$$t_{Ehrf} = 125 L_w^2 \phi \mu c_t / k_y \quad (A-11b)$$

Early Linear Flow

$$\sqrt{k_x} = \frac{8.13qB}{|m_{elf}| L_w h} \sqrt{\frac{\mu}{\phi c_t}} \quad (A-12)$$

$$s_d = \frac{L_w \sqrt{k_x k_z}}{141.2qB\mu} \Delta p_{t=0} - s_c \quad (A-13a)$$

$$\text{where } s_c = \ln \left(\frac{h}{r_w} \right) + 0.25 \ln \left(\frac{k_x}{k_z} \right) - \ln \left[\sin \left(\frac{\pi d_z}{h} \right) \right] - 1.838 \quad (A-13b)$$

$$t_{Self} = \frac{1,800 D_z^2 \phi \mu c_t}{k_z} \quad (A-14a)$$

$$t_{Eelf} = 160 L_w^2 \phi \mu c_t / k_y \quad (A-14b)$$

**TABLE A-2—EQUATIONS FOR ANALYZING FLOW IN
HORIZONTAL WELLS WITH UNIFORM FLUX (continued)**

Late Pseudoradial Flow (requires $L_w/b_H < 0.45$)

$$\sqrt{k_x k_y} = \frac{162.6qB\mu}{|m_{prf}|h} \quad (\text{A-15})$$

$$s_d = 1.151 \sqrt{\frac{k_z L_w}{k_y h}} \left[\frac{\Delta p_{1hr}}{|m_{prf}|} - \log \left(\frac{k_y}{\phi \mu c_t L_w^2} \right) + 1.76 \right] - s_c \quad (\text{A-16})$$

Note that s_c is defined by Eq. 8.13b.

$$t_{Sprf} = \frac{1,480 L_w^2 \phi \mu c_t}{k_y} \quad (\text{A-17})$$

$$t_{Eprf} = \frac{2,000 \phi \mu c_t (L_w/4 + d_y)^2}{k_y} \quad (\text{A-18})$$

$$\text{or } t_{Eprf} = \frac{1,650 \phi \mu c_t d_x^2}{k_x} \quad (\text{A-19})$$

Late-Linear Flow

$$\sqrt{k_x} = \frac{8.128qB}{|m_{llf}|b_H h} \sqrt{\frac{\mu}{\phi c_t}} \quad (\text{A-20})$$

$$s_t = \frac{L_w}{b_H} \left(\frac{b_H \sqrt{k_x k_z} \Delta p_{l=0}}{141.2qB\mu} - s_p - s_c \right) \quad (\text{A-21})$$

where s_p , the partial penetration skin given in Eqs. 8.25 to 8.35, is due to the convergence skin, s_c .

$$t_{Sllf} = \frac{4,800 \phi \mu c_t (D_y + L_w/4)^2}{k_y} \quad (\text{A-22})$$

$$\text{or } t_{Sllf} = \frac{1,800 \phi \mu c_t D_z^2}{k_z} \quad (\text{A-23})$$

$$t_{Ellf} = \frac{1,650 \phi \mu c_t d_x^2}{k_x} \quad (\text{A-24})$$

Calculating Partial Penetration Skin in Late-Linear Flow and Productivity Equations

$$p_{xyz} = \left(\frac{b_H}{L_w} - 1 \right) \left\{ \ln \left(\frac{h}{r_w} \right) + 0.25 \ln \left(\frac{k_x}{k_z} \right) - \ln \left[\sin \left(\frac{\pi d_z}{h} \right) \right] - 1.838 \right\} \quad (\text{A-25})$$

$$\text{Case 1, } \frac{a_H}{\sqrt{k_x}} \geq \frac{0.75b_H}{\sqrt{k_y}} \gg \frac{0.75h}{\sqrt{k_z}} \quad (\text{A-26})$$

$$s_p = p_{xyz} + p'_{xy} \quad (\text{A-27})$$

TABLE A-2—EQUATIONS FOR ANALYZING FLOW IN HORIZONTAL WELLS WITH UNIFORM FLUX (continued)

$$p'_{xy} = \frac{2b_H^2}{L_w h} \sqrt{k_z/k_y} \left\{ F\left(\frac{L_w}{2b_H}\right) + 0.5 \left[F\left(\frac{4y_m + L_w}{2b_H}\right) - F\left(\frac{4y_m - L_w}{2b_H}\right) \right] \right\} \quad (\text{A-28})$$

$$\text{where } y_m = d_y + \frac{L_w}{2} \quad (\text{A-29})$$

$$F(u) = -u[0.145 + \ln(u) - 0.137(u)^2], \quad u < 1 \quad (\text{A-30})$$

$$F(u) = (2-u)[0.145 + \ln(2-u) - 0.137(2-u)^2], \quad u > 1 \quad (\text{A-31})$$

$$\text{Case 2, } \frac{b_H}{\sqrt{k_y}} > \frac{1.33a_H}{\sqrt{k_x}} \gg \frac{0.75h}{\sqrt{k_z}} \quad (\text{A-32})$$

$$s_p = p_{xyz} + p_y + p_{xy} \quad (\text{A-33})$$

$$p_y = \frac{6.28b_H^2}{a_H h} \frac{\sqrt{k_x k_z}}{k_y} \left[\left(\frac{1}{3} - \frac{y_m}{b_H} + \frac{y_m^2}{b_H^2} \right) + \frac{L_w}{24b_H} \left(\frac{L_w}{b_H} - 3 \right) \right] \quad (\text{A-34})$$

$$p_{xy} = \left(\frac{b_H}{L_w} - 1 \right) \left(\frac{6.28a_H}{h} \sqrt{k_z/k_x} \right) \left(\frac{1}{3} - \frac{d_x}{a_H} + \frac{d_x^2}{a_H^2} \right), \quad d_x \geq 0.25a_H \quad (\text{A-35})$$

Productivity and Productivity Index (Uniform Flux Solutions)

$$q = \frac{0.00708b_H \sqrt{k_x k_z} (\bar{p} - p_{wf})}{B\mu \left[\ln\left(\frac{A^{1/2}}{r_w}\right) + \ln C_H - 0.75 + s_p + \left(\frac{b_H}{L_w}\right) s_d \right]} \quad (\text{A-36})$$

$$J = \frac{q}{(\bar{p} - p_{wf})} = \frac{0.00708b_H \sqrt{k_x k_z}}{B\mu \left[\ln\left(\frac{C_H A^{1/2}}{r_w}\right) - 0.75 + s_p + \left(\frac{b_H}{L_w}\right) s_d \right]} \quad (\text{A-37})$$

$$\ln C_H = 6.28 \frac{a_H}{h} \frac{\sqrt{k_z}}{\sqrt{k_x}} \left[\frac{1}{3} - \frac{d_x}{a_H} + \left(\frac{d_x}{a_H}\right)^2 \right] - \ln\left(\sin \frac{\pi d_z}{h}\right) - 0.51 \ln\left[\left(\frac{a_H}{h}\right) \sqrt{k_z/k_x}\right] - 1.088 \quad (\text{A-38})$$

Chapter 9

Oil Reservoir Primary Drive Mechanisms

Mark P. Walsh, Consultant

9.1 Introduction

Muskat defines primary recovery as the production period “beginning with the initial field discovery and continuing until the original energy sources for oil expulsion are no longer alone able to sustain profitable producing rates.”¹ Primary recovery is also sometimes referred to as pressure depletion because it necessarily involves the decline of the reservoir pressure. Primary recovery should be distinguished clearly from secondary recovery. Muskat defines secondary recovery as “the injection of (fluids) after the reservoir has reached a state of substantially complete depletion of its initial content of energy available for (fluid) expulsion or where the production rates have approached the limits of profitable operation.”¹ One of the most popular secondary-recovery methods is waterflooding. Because primary recovery invariably results in pressure depletion, secondary recovery requires “repressuring” or increasing the reservoir pressure.

Primary recovery includes pressure-maintenance methods. Muskat defines pressure maintenance as “the operation of (fluid) injection into a reservoir during the course of its primary-production history.”¹ The main effect of pressure maintenance is to mitigate the reservoir’s pressure decline and conserve its energy. The purpose of pressure maintenance is ultimately to improve oil recovery. The most common injected fluids for pressure maintenance are water and separator or residue gas. “Partial” and “complete” pressure maintenance describe the general effectiveness of a given pressure-maintenance operation to retard the rate of pressure decline. Partial pressure maintenance refers to fluid injection while a general state of pressure decline still exists. Full or complete pressure maintenance refers to fluid injection while the reservoir pressure remains essentially constant.

According to Muskat’s definition of pressure maintenance, secondary-recovery methods such as waterflooding are not strictly pressure-maintenance operations because they begin after pressure depletion. However, if water injection takes place before the end of pressure depletion, which is not uncommon, it is considered a pressure-maintenance method. If water is injected before the end of primary recovery, the reservoir is classified as an artificial water-drive. Since Muskat first proposed his definition, others have loosely applied the term pressure maintenance to include any fluid-injection strategy at any stage in the reservoir’s production.

Oil reservoirs are classified according to their fluid type. There are three broad oil classes. In order of increasing molecular weight, they are volatile oil, black oil, and heavy oil. Heavy-

oil reservoirs are of minor interest during pressure depletion because they typically yield only marginal amounts of oil because of their low dissolved-gas contents and high fluid viscosities. Although heavy-oil reservoirs are not addressed specifically in this chapter, the methods of analysis presented here are equally applicable to them. The distinguishing characteristic between volatile and black oils is the stock-tank-oil content of their equilibrium gases. Equilibrium gases liberated from volatile oils contain appreciable stock-tank or condensable liquids whereas the gases from black oils contain negligible stock-tank liquids. While this distinction leads to only slightly different recovery strategies, it leads to very different methods of analysis and mathematical modeling requirements.

9.2 Volatile- and Black-Oil Fluid Characteristics

The petroleum fluid spectrum is gradational. There is no strict definition of volatile and black oils; there are only general guidelines and characteristics. Despite this lack of precision and the occasional confusion it brings, classification is quite useful and popular.

Molecular weight is a useful yardstick. Black oils typically range from 70 to 150 in molecular weight but may range as high as 190 to 210. In contrast, volatile oils are lower in molecular weight than black oils and typically range from 43 to 70. Oils with molecular weights greater than 210 usually are classified as heavy oils. Fluids with molecular weights of less than 43 are generally gases, which include gas condensates, wet gases, and dry gases. A molecular weight of 43 marks the lower molecular-weight limit of volatile oils.

Black and volatile oils are sometimes subdivided into different fluid types. For instance, volatile oils include near-critical fluids and high-shrinkage oils. Near-critical fluids represent light volatile oils and can include some very rich condensates. High-shrinkage oils represent the high-molecular-weight end of volatile oils and can include some light black oils.

Volatile and black oils are characterized in terms of a number of different properties. **Table 9.1** summarizes their characteristics. This table includes the properties of the full range of petroleum fluids, including gases.

The defining property that distinguishes black and volatile oils is the volatilized-oil content of their equilibrium gases. The volatilized-oil content of a gas represents its condensable liquid portion. Condensable refers to the portion that condenses or “drops out” during pressure reduction and ultimately results as stock-tank liquid. Condensation may take place within the reservoir as the gas passes through the lease separators. Physically, intermediate-hydrocarbon components, typically C_2 through C_7 , dominate this fraction. Volatilized oil also is called lease condensate or distillate. Gas condensates and wet gases also contain volatilized oil. Volatilized oil is reported conventionally as part of the crude-oil reserves and production. It should not be confused with and is distinctly different from natural-gas liquids. Natural-gas liquids are derived from the gas-processing plant and are called plant products.

The volatilized-oil content of gases is quantified in terms of their volatilized-oil/gas ratio, typically expressed in units of STB/MMscf or stock-tank m^3 per std m^3 of separator gas. The volatilized-oil/gas ratio of equilibrium gases of black oils is usually less than 1 to 10 STB/MMscf (approximately 0.04 to 0.4 gal/Mscf). The volatilized-oil content of these gases is so low that it usually is ignored. In contrast, the volatilized-oil content of gases from volatile oils is much greater. Their volatilized-oil/gas ratio typically ranges from 10 to 300 STB/MMscf or 0.4 to 8 gal/Mscf.

Several benchmark properties can be correlated with the reservoir fluid's initial molecular weight. **Fig. 9.1** plots the initial formation volume factor (FVF) and initial dissolved gas/oil ratio (GOR) as a function of reservoir-fluid molecular weight for 36 reservoir fluids. The abscissa in **Fig. 9.1** spans from a molecular weight of 15 to 180. This range of molecular weights covers the full spectrum of petroleum fluids ranging from dry gases to heavy oils.

Volatile oils exhibit an initial oil FVF in the range of 1.5 to 3.0. Black oils exhibit an initial oil FVF in the range of 1.1 to 1.5. Volatile oils exhibit an initial GOR in the range of

TABLE 9.1—PETROLEUM FLUIDS AND THEIR CHARACTERISTICS

Characteristic	Oils			Gases	
	Heavy Oils and Tars	Black Oils	Volatile Oils	Gas Condensates	Wet and Dry Gases
Initial fluid molecular weight	210+	70 to 210	40 to 70	23 to 40	<23
Stock-tank-oil color	black	brown to light green	greenish to orange	orange to clear	clear
Stock-tank oil-gravity, °API	5 to 15	15 to 45	42 to 55	45 to 60	45+
C7-plus fraction, mol%	>50	35 to 50	10 to 30	1 to 6	0 to 1
Initial dissolved GOR, scf/STB	0 to 200	200 to 900	900 to 3,500	3,500 to 30,000	30,000+
Initial FVF, B_{oi} , RB/STB	1.0 to 1.1	1.1 to 1.5	1.5 to 3.0	3.0 to 20.0	20.0+
Typical reservoir temperature, °F	90 to 200	100 to 200	150 to 300	150 to 300	150 to 300
Typical saturation pressure, psia	0 to 500	300 to 5,000	3,000 to 7,500	1,500 to 9,000	—
Volatile-oil/gas ratio, STB/MMscf*	0	0 to 10	10 to 200	50 to 300	0 to 50
Maximum vol% liquid during CCE**	100	100	100	0 to 45	0
OOIP, STB/acre-ft (bulk)	1,130 to 1,240	850 to 1,130	400 to 850	60 to 400	0 to 60
OGIP, Mscf/acre-ft (bulk)	0 to 200	200 to 700	300 to 1,000	500 to 2,000	1,000 to 2,200

*At bubblepoint pressure. **Constant composition expansion of reservoir fluid.

900 to 3,500 scf/STB. Black oils exhibit an initial GOR in the range of 200 to 900 scf/STB. These relations establish molecular weight as a credible correlating parameter. McCain² has found success in the use of the heptanes-plus content as a correlating parameter.

The inverse of the oil FVF yields a measure of the original oil in place (OOIP) per unit volume of reservoir pore space. Because the oil FVF is greater for volatile oils than black oils, the latter yield greater OOIP per unit volume. Black-oil reservoirs contain 850 to 1130 STB/acre-ft (bulk) while volatile-oil reservoirs contain less, typically 400 to 850 STB/acre-ft.

Although volatile-oil reservoirs contain less oil per unit volume, they typically yield slightly higher oil recoveries than black-oil reservoirs because of their higher dissolved-gas content and lower oil viscosity. Ultimately, volatile-oil reservoirs may yield greater oil reserves than black-oil reservoirs. Light black oils and heavy volatile oils are among the most economically attractive reservoir fluids.

There has been no systematic study to determine the relative percentage of black-oil and volatile-oil reservoirs; however, an examination of the world's 500 largest reservoirs reveals that black-oil reservoirs overwhelmingly dominate the group.³ One reason there are more black-oil than volatile-oil reservoirs is that the latter are characteristically located at greater depths than the former. As exploration continues to go deeper, more volatile-oil reservoirs can be expected to be discovered.

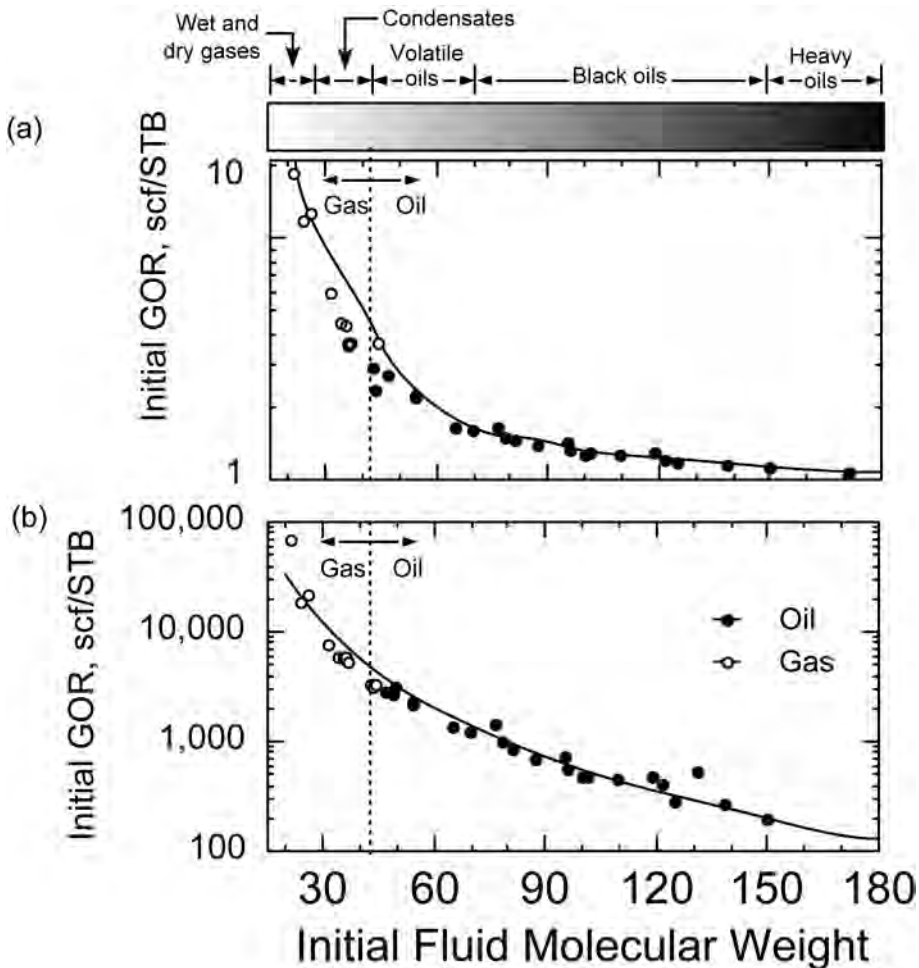


Fig. 9.1—(a) Initial formation volume factor (FVF) and (b) initial dissolved GOR as a function of initial fluid molecular weight.

9.3 Types of Reservoir Energy

The following list outlines the major types of energy available for petroleum production.

- The energy of compression of the water and rock within the reservoir.
- The energy of compression of oil within the reservoir.
- The energy of compression of gas within the reservoir.
- The energy of compression of waters contiguous to and in communication with the petroleum reservoir.
- The gravitational energy that causes the oil and gas to segregate within the reservoir.

Water within the reservoir refers to the water that is originally present within the reservoir at the time of discovery. Oil within the reservoir refers to the oil phase that is originally present at discovery or that may form from the condensation of volatilized oil upon pressure release. Likewise, gas within the reservoir refers to the gas phase that is originally present at discovery or that may form subsequently from the liberation of dissolved gas upon pressure release.

As mechanisms of energy release are provided by the drilling and operation of wells, reservoir pressure declines, fluids expand, flow is induced, and fluids are produced. The net volume

of expansion of rock and fluids within the reservoir results in an equal volume of expelled fluids. The water-bearing reservoirs that adjoin petroleum reservoirs are called aquifers. The expansion of water from the aquifer results in an overflow of water from the aquifer into the petroleum reservoir. The net overflow of water into the petroleum reservoir, in turn, results in an equal volume of fluid expulsion from the petroleum reservoir. Gravity segregation does not directly result in fluid expulsion but causes oil to settle to the bottom and gas to migrate to the top of the reservoir. By producing from only the lower reaches of the reservoir, this process affords a skilled operator a means to recover oil selectively and possibly recover more oil than would otherwise be recovered.

In ranking the types of energy in order of least importance to oil recovery, the energy of the compressed water and rock originally within the reservoir is probably the least important because of the relatively low compressibilities of water and rock. Of equal unimportance is the energy of the compressed oil, although the effects of compressed oil are slightly greater than the effects of compressed water and rock, as evidenced by the slightly greater compressibility of oil (10^{-5} per psi) than water (3×10^{-6} per psi) and rock (6×10^{-6} per psi). Of the energies of the compressed fluids, the effects of compressed gas are undoubtedly the most important because of the greater compressibility of gas. The effects of compressed gas are important even if there is not much free gas initially present, as in the case of an initially undersaturated oil reservoir. In these cases, gas will appear naturally during the course of pressure depletion because of the release of dissolved gas from the oil once the pressure falls below the bubblepoint pressure.

Gravitational forces can be a major factor in oil recovery if the reservoir has sufficient vertical relief and vertical permeability. The effectiveness of gravitational forces will be limited by the rate at which fluids are withdrawn from the reservoir. If the rate of withdrawal is appreciably greater than the rate of fluid segregation, then the effects of gravitational forces will be minimized.

The energy from the compressed waters of aquifers also can be a major factor even though the water has a low compressibility because the size of most aquifers tends to be much larger than the petroleum reservoir. Most oil fields have areas of less than 10 sq mile (6,400 acres), whereas aquifers often have areas of more than 1,000 sq mile.¹

The energies discussed thus far represent “internal” reservoir energies (i.e., energies originally present within the reservoir and its adjoining geological units at the time of discovery). In addition to these energies, there may be important “external” energies (i.e., energies that originate from outside the reservoir). External energies imply the practice of injecting fluids into the reservoir to augment the reservoir’s natural energies. This practice is called pressure maintenance. The two most important injection fluids are compressed water and gas. The resultant action of injected fluids once inside the reservoir is much the same as the fluids originally present. The overall intention of injecting fluids is to add energy to the reservoir to recover more oil or gas than would otherwise be recovered. If gas is injected, it is clear that the intention is to recover more oil than otherwise would be recovered. In addition, the economic attractiveness of this practice relies on the expectation that the additional income derived from the increased oil production will more than offset the additional expenditures and lost or deferred revenues incurred by gas injection. The most common source of gas for gas injection is the gas produced from the reservoir. The chapters on Water Injection and Immiscible Gas Injection in this volume discuss these subjects further.

9.4 Producing Mechanisms

The general performance characteristics of hydrocarbon-producing reservoirs are largely dependent on the types of energy available for moving the hydrocarbon fluids to the wellbore. The predominate energy forms give rise to distinct producing mechanisms. These producing mechanisms are used to help classify petroleum reservoirs.

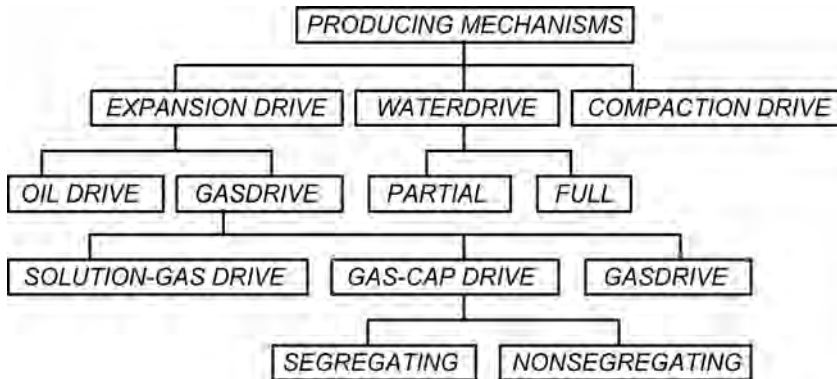


Fig. 9.2—Classification of reservoir-producing mechanisms.

In this section, these producing mechanisms are defined and delineated, although there is not a well-established consensus for some of these definitions. A petroleum reservoir rarely can be characterized throughout its pressure-depletion life by any single producing mechanism. A petroleum reservoir usually is subject to several producing mechanisms over its lifetime; nevertheless, the practice of describing a petroleum reservoir by its predominant producing mechanism is helpful.

Broadly, all commercially productive petroleum reservoirs are divided into either expansion-drive, compaction-drive, or waterdrive reservoirs. An expansion- or compaction-drive reservoir is a predominantly sealed reservoir in which the expansion of fluids and rock originally within the reservoir is responsible for petroleum expulsion from the reservoir. Fig. 9.2 shows the producing-mechanism system of classification.

In contrast, a waterdrive reservoir is an unsealed petroleum reservoir in communication with water-bearing reservoirs and in which there is appreciable movement of water from the water-bearing reservoir to the petroleum reservoir. If the rate of water intrusion into the reservoir is equal to the volumetric rate of fluid withdrawal from the reservoir, then the reservoir is more descriptively referred to as a complete-waterdrive reservoir. A complete-waterdrive reservoir often experiences, but does not necessarily imply, very little pressure decline. Complete-waterdrive reservoirs may require substantial pressure decline before the water-delivery rate can balance the production rate.

If the rate of water intrusion into the reservoir is substantial but substantially less than the volumetric rate of fluid withdrawal from the reservoir, then the reservoir is referred to as a partial-waterdrive reservoir. In all cases, when a waterdrive is the major producing mechanism, the reservoir pressure will be sensitive to the producing rate. If the reservoir-producing rate is too high relative to the water-influx rate, the waterdrive will lose its effectiveness and the reservoir pressure will decline.

Waterdrives are also classified as edgewater or bottomwater drives, depending on the nature and location of the water encroachment into the reservoir. Fig. 9.3 shows a schematic of a bottomwater-drive reservoir. Because waterdrive reservoirs experience increasing water content and decreasing hydrocarbon content, they are referred to as nonvolumetric reservoirs. More generally, nonvolumetric reservoirs are reservoirs in which hydrocarbon pore volume (PV) changes during pressure depletion. Conversely, volumetric reservoirs are reservoirs in which hydrocarbon PV does not change during pressure depletion. Because waterdrive reservoirs involve water influx into the reservoir, they also are referred to as water-influx reservoirs.

Pressure depletion causes the internal stress within the reservoir rock to increase. This change produces changes in the grain arrangement and other phenomena that ultimately cause the pore volume of the rock to decrease. The contraction of the reservoir pore volume aids in

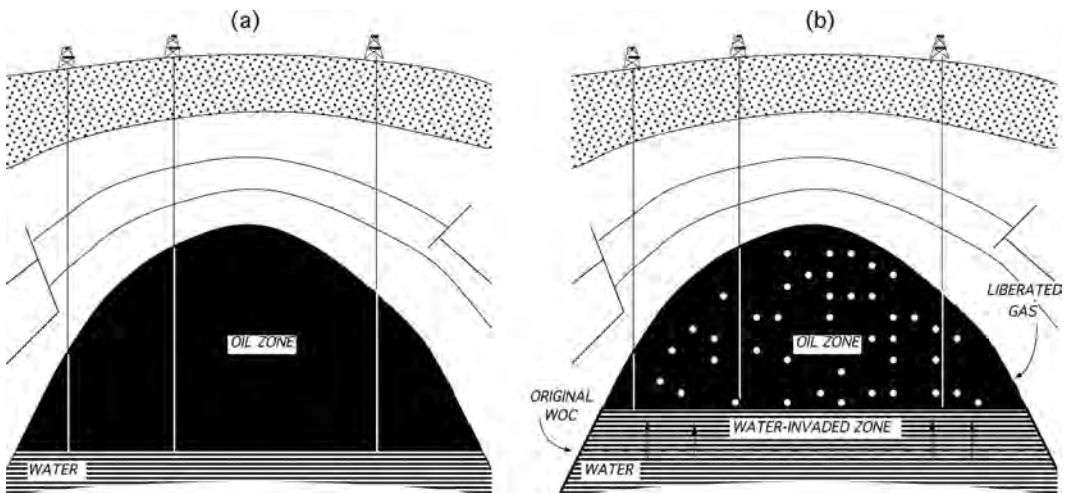


Fig. 9.3—Distribution of water and oil and position of water/oil contact (WOC) in a waterdrive reservoir (a) before production and (b) during depletion.

expelling fluids from the reservoir. The terms “pore-volume contraction” and “rock expansion” are used interchangeably in this chapter to describe this phenomenon, even though very little grain expansion usually takes place. If this phenomenon is a major producing mechanism, the reservoir is a compaction-drive reservoir. Compaction-drive reservoirs are rare because the PV compressibility is usually less than the oil compressibility.

Expansion-drive reservoirs are further classified as oil- or gas-expansion-drive reservoirs depending on whether the oil or gas expansion is the predominant producing mechanism. Dry- and wet-gas reservoirs are gas-expansion-drive reservoirs because they do not contain any free oil at reservoir conditions. More descriptively, a gas-drive reservoir is one in which the expansion of free gas is the predominant producing mechanism. The expanding free gas may originate as initial free gas or as dissolved gas. An oil-drive reservoir, on the other hand, is one in which the expansion of free oil is the predominant producing mechanism.¹ According to these definitions, black-oil and volatile-oil reservoirs are not likely to be oil-drive reservoirs but gas-drive reservoirs because the expansion of gas is ultimately much greater than the expansion of oil. The oil in saturated, black-oil and volatile-oil reservoirs does not expand but contracts during pressure depletion because of the release of dissolved gas. Because the overwhelming majority of expansion-drive reservoirs are gas-drive reservoirs, the term oil-drive reservoir is rarely used. An oil-drive producing mechanism dominates in oil reservoirs only while they are undersaturated.

Gas-drive reservoirs are further subdivided into either solution-gas-drive or gas-cap expansion-drive reservoirs. A gas-cap expansion-drive reservoir is a gas-cap reservoir in which the expanding gas cap is responsible for the majority of the gas expansion. A gas cap is a free-gas zone that overlies an oil zone. The free-gas zone may be pre-existing or may form during the depletion process. Pre-existing gas caps are called primary gas caps. Gas caps that are not originally present but that develop during the depletion process are called secondary or developed gas caps. Secondary gas caps can form from the upward migration of either liberated dissolved gas or from reinjected gas. **Fig. 9.4** shows a schematic of a gas-cap expansion-drive reservoir.

Gas caps are also classified according to their displacement efficiency. At the most favorable extreme, the expanding gas displaces oil in a piston-like manner. At the other limit, the expanding gas displaces oil in a totally diffuse manner. The former are segregation-drive or gravity-drainage gas caps; the latter are nonsegregation-drive gas caps. The boundary between

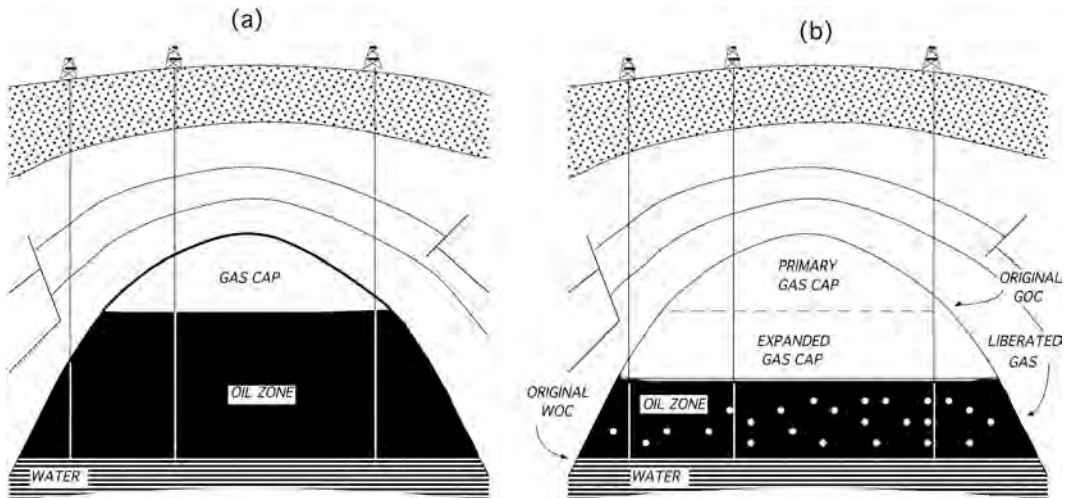


Fig. 9.4—Distribution of water, oil, and gas and position of gas/oil contact (GOC) in a segregating-gas-cap reservoir: (a) before production and (b) during depletion.

the gas-cap zone and oil zone is the gas/oil contact (GOC). Segregation-drive gas caps exhibit a GOC that moves progressively downward during depletion. In contrast, nonsegregation-drive gas caps exhibit a GOC that appears stationary. The gas-cap displacement efficiency depends on the producing rate and vertical permeability. Segregation-drive gas caps tend to have high vertical permeability, while nonsegregation-drive gas caps tend to have low vertical permeability. These two types of gas caps represent limiting cases. In reality, there is a continuum of character between these limits. The exact gas-cap character depends on the actual conditions.

Gas-drive reservoirs that are not gas-cap reservoirs but are dominated by the expansion of solution gas are called solution-gas-drive or dissolved-gas-drive reservoirs. Fig. 9.5 shows a schematic of a solution-gas-drive reservoir. Gas-drive reservoirs that are neither gas-cap nor solution-gas-drive reservoirs are called gas-drive reservoirs. For example, dry-gas reservoirs are gas-drive reservoirs because they do not qualify as solution-gas-drive or as gas-cap reservoirs. The practice of reinjecting dry gas into and producing wet gas from gas/condensate reservoirs is called gas cycling or cycling.

9.4.1 Recovery Ranges. Table 9.2 lists the approximate primary-recovery range for the different producing mechanisms. The ranges reflect the rank of the reservoir energies. Black-oil reservoirs that exclusively produce by solution-gas-drive mechanism typically recover 10 to 25% of the OOIP by pressure depletion. The American Petroleum Inst. reports an average primary oil recovery of 20.9% for 307 solution-gas-drive reservoirs.⁴ In contrast, primary oil recovery from waterdrive, black-oil reservoirs typically ranges from 15 to 50% or higher of the OOIP. Waterdrive, black-oil reservoirs have yielded some of the highest recoveries ever recorded. The primary oil recovery from gas-cap, black-oil reservoirs varies widely depending on whether there is significant gravity drainage. The primary oil recovery from nongravity-drainage, gas-cap, black-oil reservoirs ranges from 15 to 40% of the OOIP. In contrast, the primary oil recovery from gravity-drainage, gas-cap, black-oil reservoirs ranges from 15 to 80% of the OOIP. Primary oil recoveries from gravity-drainage, black-oil reservoirs are among the highest of any black-oil reservoir. Pressure maintenance by gas reinjection is practiced commonly in black-oil reservoirs to improve oil recovery. Black-oil reservoirs subject to gas reinjection without gravity drainage typically recover 15 to 45% of the OOIP. If gas is reinject-

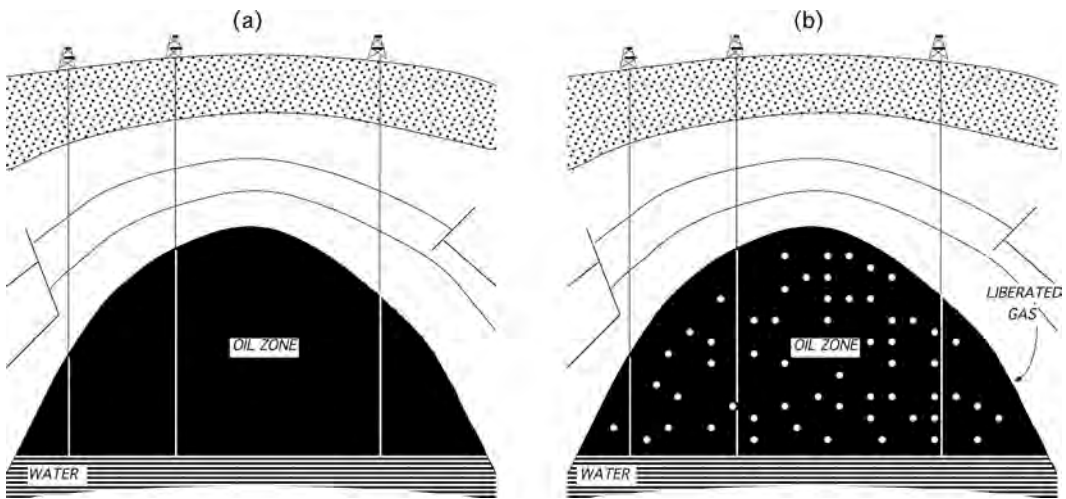


Fig. 9.5—Distribution of water, oil, and gas in a solution-gas-drive reservoir: (a) before production and (b) during depletion.

Producing Mechanism	Oil Recovery Range (% OOIP)
Solution-gas drive	10 to 25%
Gas-cap drive without gravity drainage	15 to 40%
Gas-cap drive with gravity drainage	15 to 80%
Gas reinjection with gravity drainage	15 to 80%
Gas reinjection without gravity drainage	15 to 45%
Waterdrive	15 to 60%

ed in a reservoir with active gravity drainage, the primary oil recovery typically ranges from 15 to 80%.

9.5 Fluid Properties

Black and volatile oils, as well as other petroleum fluids, are characterized routinely in terms of their standard pressure/volume/temperature (PVT) parameters: oil FVF (B_o), gas FVF (B_g), dissolved GOR (R_s), and volatilized oil/gas ratio (R_v). These fluid properties, in addition to some others, are prerequisites for a wide variety of reservoir-engineering calculations, including estimating the OOIP and original gas in place (OGIP) and material-balance calculations.

Table 9.3 tabulates and Fig. 9.6 plots the standard PVT parameters as a function of pressure for a black oil from a west Texas reservoir located at a depth of 6,700 ft with an initial pressure of 3,100 psia and a temperature of 131°F. Only the PVT properties below 2,000 psia are listed. The fluid exhibited a bubblepoint at approximately 1,688 psia and had a molecular weight of 81. Table 9.4 summarizes its compositional analysis. The fluid has an initial oil FVF of 1.467 RB/STB and dissolved GOR of 838 scf/STB. The equilibrium gas contains negligible volatilized oil. Fig. 9.7 plots the oil and gas viscosities as a function of pressure.

p (psia)	B_o (RB/STB)	B_g (RB/Mscf)	R_s (scf/STB)	μ_o (cp)	μ_g (cp)	Volume Fraction Liquid*
2,000	1.467		838.5	0.3201		1.0000
1,800	1.472		838.5	0.3114		1.0000
1,700	1.475		838.5	0.3071		1.0000
1,640	1.463	1.920	816.1	0.3123	0.0157	0.9780
1,600	1.453	1.977	798.4	0.3169	0.0155	0.9600
1,400	1.408	2.308	713.4	0.3407	0.0140	0.8670
1,200	1.359	2.730	621.0	0.3714	0.0138	0.7540
1,000	1.322	3.328	548.0	0.3973	0.0132	0.6440
800	1.278	4.163	464.0	0.4329	0.0126	0.5130
600	1.237	5.471	383.9	0.4712	0.0121	0.3750
400	1.194	7.786	297.4	0.5189	0.0116	0.2320
200	1.141	13.331	190.9	0.5893	0.0108	0.0970

*From constant composition expansion.

Table 9.5 tabulates and **Fig. 9.8** plots the standard PVT parameters for a volatile oil from a north-central Louisiana reservoir located at a depth of approximately 10,000 ft with an initial pressure of 5,070 psia and a temperature of 246°F.^{5,6} The fluid exhibited a bubblepoint at approximately 4,677 psia and had a molecular weight of 47. **Table 9.6** summarizes the initial fluid composition. The fluid has an initial oil FVF of 2.704 RB/STB and dissolved GOR of 2,909 scf/STB. The bubblepoint gas had a volatilized-oil/gas ratio of approximately 120 STB/MMscf. The volatilized-oil/gas ratio decreases with pressure until a pressure of 998 psia is reached. At pressures between 998 and 598 psia, the volatilized-oil/gas ratio increases slightly.

The standard PVT parameters of volatile and black oils are determined experimentally with different laboratory procedures. Black oils are evaluated with a differential-vaporization (DV) experiment;^{7,8} in contrast, volatile oils are evaluated with constant volume depletion (CVD).^{9,10} Sometimes, however, volatile oils use a specialized DV experiment¹¹ instead of a CVD experiment. The specialized DV experiment includes a step to measure the volatilized-oil content of equilibrium gases.

The standard PVT parameters for black oils are specified routinely in commercial PVT reports. McCain provides some example PVT reports.¹² The reported PVT parameters, however, may or may not be adjusted for the effects of surface separators. Surface separators maximize the stock-tank liquid yield as fluids pass through them. The oil FVF and dissolved GOR of adjusted properties are characteristically less than unadjusted properties. If the PVT report specifies the adjusted parameters, then no further adjustment is required. If only the raw parameters are specified, then adjustment is needed.

Various empirical methods are used to correct the standard PVT parameters for the effects of separators.^{7,13,14} Generally, correction is very important. For example, the unadjusted bubblepoint oil FVF and the dissolved GOR for the example black oil in **Table 9.3** are 1.584 RB/STB and 1,007 scf/STB, respectively. On adjustment for separators at 100 psia, the corresponding oil FVF and dissolved GOR are 1.467 RB/STB and 838.5 scf/STB, reflecting increased stock-tank-liquid recovery. Failure to correct the standard PVT parameters for separators can lead to substantial errors in subsequent reservoir-engineering calculations including the volumetric OOIP and OGIP calculations. Volatile oils are even more sensitive to the effects of separators

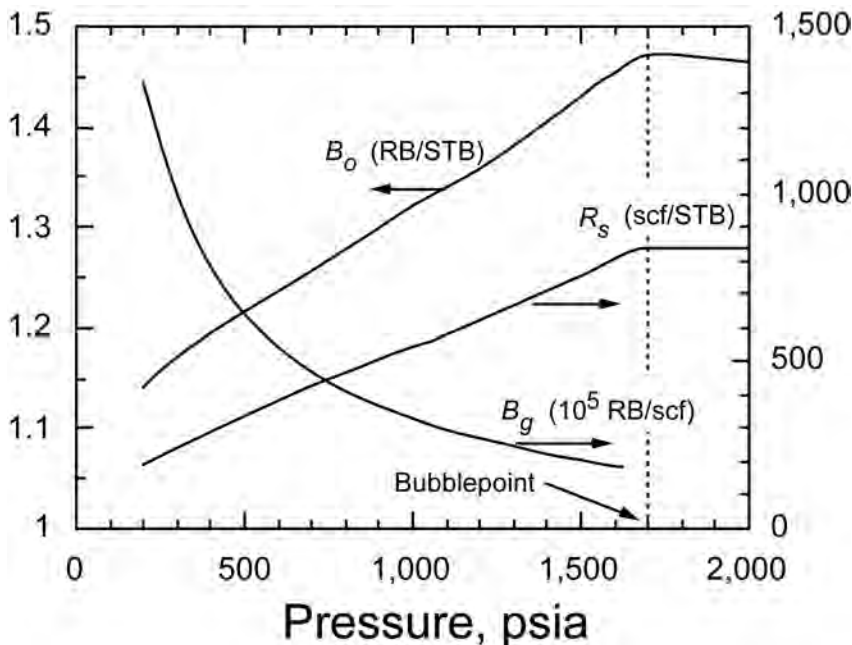


Fig. 9.6—Standard PVT properties as a function of pressure for a west Texas black oil.

than black oils. Volatile oils, however, are subjected to an entirely different laboratory procedure for measurement.

The standard PVT parameters for volatile oils rarely are given in commercial PVT reports. They must be calculated from CVD measurements. In order of increasing complexity, the three methods to calculate standard PVT parameters are the Walsh-Towler algorithm,¹⁵ the Whitson-Torp method,⁹ and the equation-of-state (EOS) method.^{16,17} The Walsh-Towler algorithm uses recovery data directly from the CVD measurement and computes the corresponding properties. This method is suited for spreadsheet calculation and is fast and simple. The Whitson-Torp method, in contrast, uses equilibrium gas-composition data and computes the properties with Standing's¹⁸ low-pressure K -values and a stock-tank-liquid density correlation such as the Alani-Kennedy EOS.¹⁹ This method requires iterative, K -value flash calculations. Although this method is more computationally intensive than the Walsh-Towler algorithm, it is more versatile because it allows for arbitrary separator conditions. The EOS method is much more computationally intensive than the other methods. This method tunes a cubic EOS to the attending phase behavior and then uses the EOS to simulate the CVD numerically and estimate the PVT parameters. This method regularly uses commercial software. The methods yield virtually identical results despite their differences.

9.6 Material Balance

The material-balance equation is the simplest expression of the conservation of mass in a reservoir. The equation mathematically defines the different producing mechanisms and effectively relates the reservoir fluid and rock expansion to the subsequent fluid withdrawal. The applicable equation for initially saturated volatile- and black-oil reservoirs is²⁰⁻²³

TABLE 9.4—COMPOSITIONAL ANALYSIS OF WEST TEXAS BLACK OIL	
Component	Mol%
N ₂	0.28
C ₁	28.98
CO ₂	0.20
C ₂	10.34
C ₃	12.03
i-C ₄	0.56
n-C ₄	6.02
i-C ₅	1.47
n-C ₅	2.93
C ₆	3.42
C ₇₊	33.15
Total	100.00
Fluid molecular wt.	81.2

$$\begin{aligned}
 & \underbrace{G_{fgi}E_g}_{\text{free-gas expansion}} + \underbrace{N_{foi}E_o}_{\text{free-oil expansion}} + \underbrace{WE_w}_{\text{free-water expansion}} + \underbrace{V_{pi}E_f}_{\text{pore-volume contraction}} + \underbrace{W_e}_{\text{water influx}} \\
 & = \underbrace{(G_p - G_I) \left(\frac{B_g - B_o R_v}{1 - R_v R_s} \right)}_{\text{net gas withdrawal}} + \underbrace{N_p \left(\frac{B_o - B_g R_s}{1 - R_v R_s} \right)}_{\text{oil withdrawal}} + \underbrace{(W_p - W_I) B_w}_{\text{net water withdrawal}}, \dots \dots \dots (9.1)
 \end{aligned}$$

where G_{fgi} , N_{foi} , and W are the initial free gas, oil, and water in place, respectively; G_p , N_p , and W_p are the cumulative produced gas, oil, and water, respectively; G_I and W_I are the cumulative injected gas and water, respectively; and E_g , E_o , E_w , and E_f are the gas, oil, water, and rock (formation) expansivities. Most of the equations in this chapter apply to any consistent set of units. A few equations, however, are written assuming English or customary units. Those equations are expressed in SI units in the [Appendix](#).

N_{foi} and G_{fgi} are related to the total OOIP and OGIP, N and G , according to $N = N_{foi} + G_{fgi}R_{vi}$ and $G = G_{fgi} + N_{foi}R_{si}$.

The expansivities are defined as

$$E_o = B_{to} - B_{toi}, \dots \dots \dots (9.2)$$

$$E_g = B_{tg} - B_{tgi}, \dots \dots \dots (9.3)$$

$$E_w = B_w - B_{wi}, \dots \dots \dots (9.4)$$

and $E_f = \frac{V_{pi} - V_p(p)}{V_{pi}}$, where B_{to} and B_{tg} are the two-phase FVFs,

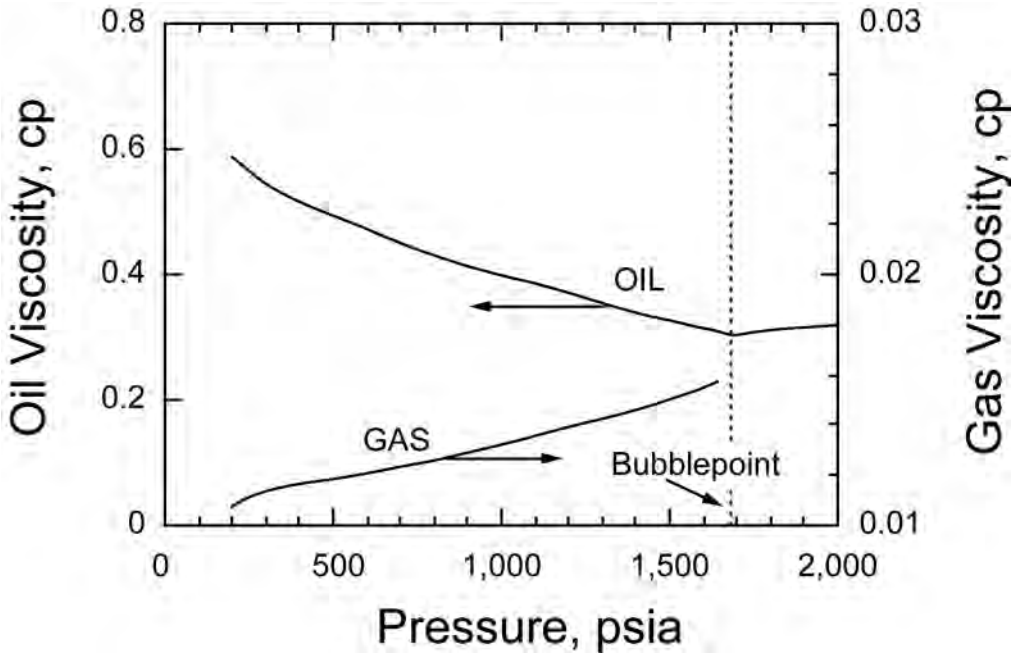


Fig. 9.7—Oil and gas viscosities as a function of pressure for west Texas black oil.

$$B_{to} = \frac{B_o(1 - R_{si}R_v) + B_g(R_{si} - R_s)}{1 - R_vR_s}, \dots\dots\dots (9.5)$$

$$\text{and } B_{tg} = \frac{B_g(1 - R_{vi}R_s) + B_o(R_{vi} - R_v)}{1 - R_vR_s} \dots\dots\dots (9.6)$$

The rock expansivity is obtained from direct measurement. See [Sec. 9.10](#) for a greater discussion.

Physically, the two-phase FVF is the total hydrocarbon volume per unit volume of oil or gas at standard conditions. The two-phase FVF mimics the observations noted during a constant-composition expansion test. For instance, the two-phase oil FVF is the total hydrocarbon (oil + gas) volume of a saturated oil sample per unit volume of oil at standard conditions. In contrast, the two-phase gas FVF is the total hydrocarbon volume of a saturated gas sample per unit volume of gas at standard conditions. B_{to} and B_{tg} typically are expressed in units of RB/STB and RB/Mscf, respectively. For undersaturated oils, the two-phase oil FVF is equal to the oil FVF; for undersaturated gases, the two-phase gas FVF is equal to the gas FVF.

[Eqs. 9.5](#) and [9.6](#) account for volatilized oil in the equilibrium gas phase. If volatilized oil is negligible, these equations are simplified. For instance, $B_{to} = B_o + B_g (R_{si} - R_s)$ and $B_{tg} = B_g$. These equations apply for black oils. [Eq. 9.4](#) ignores dissolved gas in the aqueous phase.

[Eq. 9.1](#) broadly states that net expansion equals net withdrawal. More specifically, it shows the different forms of expansion and withdrawal. The different forms of expansion such as gas expansion are responsible for the different producing mechanisms.

For the sake of simplicity, [Eq. 9.1](#) is often written in the abbreviated form of

$$G_{fgi}E_{gwf} + N_{foi}E_{owf} + W_e = F, \dots\dots\dots (9.7)$$

TABLE 9.5—PVT PARAMETERS FOR LOUISIANA VOLATILE OIL

p (psia)	B_o (RB/STB)	B_g (RB/Mscf)	R_s (scf/STB)	R_v (STB/MMscf)	μ_o (cp)	μ_g (cp)	Volume Fraction Liquid*
5,070	2.704		2,909		0.0742		1.000
4,998	2.713		2,909		0.0735		1.000
4,798	2.740		2,909		0.0716		1.000
4,698	2.754		2,909		0.0706		1.000
4,658	2.707	0.830	2,834	116.0	0.0718	0.0375	0.967
4,598	2.631	0.835	2,711	111.0	0.0739	0.0367	0.847
4,398	2.338	0.853	2,247	106.0	0.0847	0.0350	0.747
4,198	2.204	0.874	2,019	94.0	0.0906	0.0327	0.683
3,998	2.093	0.901	1,828	84.0	0.0968	0.0306	0.630
3,798	1.991	0.933	1,651	74.0	0.1028	0.0288	0.584
3,598	1.905	0.970	1,500	66.0	0.1104	0.0271	0.544
3,398	1.828	1.015	1,364	60.0	0.1177	0.0255	0.508
3,198	1.758	1.066	1,237	54.0	0.1242	0.0240	0.471
2,998	1.686	1.125	1,111	49.0	0.1325	0.0227	0.433
2,798	1.632	1.196	1,013	44.0	0.1409	0.0214	0.402
2,598	1.580	1.281	918	39.0	0.1501	0.0203	0.368
2,398	1.534	1.380	833	36.0	0.1598	0.0193	0.336
2,198	1.490	1.498	752	33.0	0.1697	0.0184	0.305
1,998	1.450	1.642	677	30.0	0.1817	0.0175	0.271
1,798	1.413	1.819	608	28.0	0.1940	0.0168	0.239
1,598	1.367	2.035	524	26.0	0.2064	0.0161	0.209
1,398	1.333	2.315	461	25.0	0.2223	0.0155	0.177
1,198	1.305	2.689	406	24.1	0.2438	0.0150	0.146
998	1.272	3.190	344	23.9	0.2629	0.0146	0.117
798	1.239	3.911	283	24.4	0.2882	0.0142	0.089
598	1.205	5.034	212	26.4	0.3193	0.0138	0.063

*From constant composition expansion.

where F = total net fluid withdrawal or production, E_{gwf} = composite gas expansivity, and E_{owf} = composite oil expansivities. F , E_{gwf} , and E_{owf} are defined in

$$F = G_{ps} \left(\frac{B_g - B_o R_v}{1 - R_v R_s} \right) + N_p \left(\frac{B_o - B_g R_s}{1 - R_v R_s} \right) + (W_p - W_I) B_w, \dots (9.8)$$

$$E_{owf} = E_o + \frac{B_{oi}}{(1 - S_{wi})} \left(\frac{S_{wi} E_w}{B_{wi}} + E_f \right), \dots (9.9)$$

$$\text{and } E_{gwf} = E_g + \frac{B_{gi}}{(1 - S_{wi})} \left(\frac{S_{wi} E_w}{B_{wi}} + E_f \right). \dots (9.10)$$

The composite expansivities include the connate-water and rock expansivities. Eq. 9.8 includes G_{ps} , which is the cumulative produced sales gas and is defined as $(G_p - G_I)$. F is expressed in reservoir volume units (e.g., RB or res m³), E_{gwf} is expressed in reservoir volume units per standard unit volume of gas (e.g., RB/scf), and E_{owf} is expressed in reservoir volume units per standard unit volume of oil (e.g., RB/STB).

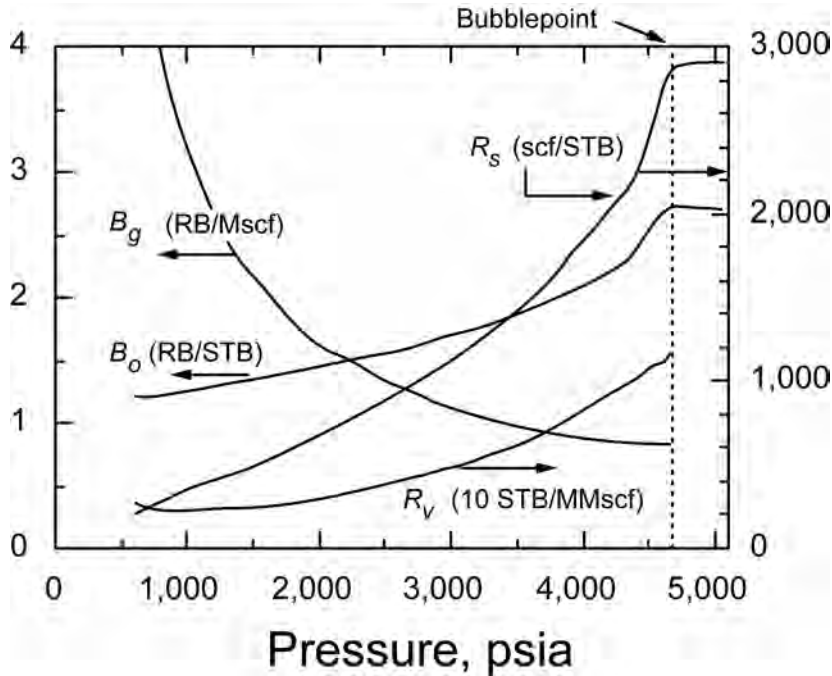


Fig. 9.8—Standard PVT properties as a function of pressure for a Louisiana volatile oil.

TABLE 9.6—COMPOSITIONAL ANALYSIS OF LOUISIANA VOLATILE OIL	
Component	Mol%
N ₂	1.67
C ₁	60.51
CO ₂	2.18
C ₂	7.52
C ₃	4.74
i-C ₄	0.00
n-C ₄	4.12
i-C ₅	0.00
n-C ₅	2.97
C ₆	1.38
C ₇₊	14.91
Total	100.00
Fluid molecular wt.	46.69

For strictly undersaturated oil reservoirs, no free gas exists (i.e., $G_{fgi} = 0$) and the initial free oil in place is equal to the OOIP (i.e., $N_{foi} = N$) and Eqs. 9.1, 9.7, and 9.8 simplify, respectively, to^{20,23,24}

$$\underbrace{NE_o}_{\text{free-oil expansion}} + \underbrace{WE_w}_{\text{free-water expansion}} + \underbrace{V_{pi}E_f}_{\text{pore-volume contraction}} + \underbrace{W_e}_{\text{water influx}}$$

$$= \underbrace{N_p B_o}_{\text{oil withdrawal}} + \underbrace{(W_p - W_I) B_w}_{\text{net water withdrawal}}, \dots\dots\dots (9.11)$$

$$N E_{owf} + W_e = F, \dots\dots\dots (9.12)$$

$$\text{and } F = N_p B_o + (W_p - W_I) B_w. \dots\dots\dots (9.13)$$

Eqs. 9.11 through 9.13 ignore gas reinjection.

The material-balance equation also helps explain most oil-recovery strategies. If the material-balance equation is solved for the produced fraction of the original free oil in place, then

$$\frac{N_p}{N_{foi}} = \frac{\frac{(W_I - W_p) B_w + W_e}{N_{foi}} + E_{owf} + \frac{G_{fgi} E_{gwf}}{N_{foi}}}{\frac{(B_o - B_g R_s) + \frac{G_{ps}}{N_p} (B_g - B_o R_v)}{(1 - R_v R_s)}}. \dots\dots\dots (9.14)$$

Eq. 9.14 succinctly shows that oil recovery increases with water influx (W_e), initial free-gas-cap volume (which is proportional to G_{fgi}), surface water injection (W_I), and surface gas injection (by minimizing gas sales through G_{ps}). It also shows that oil recovery increases by minimizing water production (W_p).

The material-balance equation and its many different forms have many uses including confirming the producing mechanism, estimating the OOIP and OGIP, estimating gas-cap sizes, estimating water-influx volumes, identifying water-influx model parameters, and estimating producing indices.

9.7 Solution-Gas Drives

Oil reservoirs that do not initially contain free gas but develop free gas on pressure depletion are classified as solution-gas drives. The solution-gas-drive mechanism applies once the pressure falls below the bubblepoint. Both black- and volatile-oil reservoirs are amenable to solution-gas drive. Other producing mechanisms may, and often do, augment the solution-gas drive. Solution-gas-drive reservoir performance is used as a benchmark to compare other producing mechanisms.

9.7.1 Stages of Production. Pure solution-gas-drive reservoirs are subject to four stages of idealized production. In chronological order, the four stages are: (1) production while undersaturated; (2) production while saturated but the free gas is immobile; (3) production while saturated and the free gas is mobile and the producing GOR is increasing; and (4) production while saturated and the free gas is mobile and the producing GOR is decreasing. Not all these stages are necessarily realized. For instance, Stage 4 may not be realized if primary recovery is terminated during Stage 3.

The key characteristics of each stage are outlined here.

Stage 1.

- No free gas.
- Producing GOR is equal to initial dissolved GOR.
- Fractional oil and gas recoveries are small and approximately equal.
- Reservoir pressure drops rapidly.

- Duration of stage depends on degree of initial undersaturation. The greater the initial undersaturation, the longer the duration of Stage 1. The stage duration is generally short.

Stage 2.

- Reservoir pressure is less than bubblepoint.
- Free gas appears, but the saturation is small and immobile.
- Producing GOR is slightly less than initial dissolved GOR.
- Rate of pressure decline is mitigated.

Stage 3.

- Free gas becomes mobile.
- Producing GOR increases steadily.
- Fractional gas recovery exceeds fractional oil recovery.
- Longest of all stages; typically consumes 85 to 95% of primary recovery.
- Primary recovery may be terminated during this stage.

Stage 4.

- Reservoir pressure is very low, typically less than 100 to 400 psia.
- Producing GOR decreases.
- Primary recovery often terminated before this stage is realized.

This chronology and these characteristics are an idealization and oversimplification of actual behavior; nevertheless, they are instructive and provide a preliminary basis for understanding scenarios that are more complicated.

9.7.2 Performance. To illustrate solution-gas-drive performance, tank model predictions of a west Texas black-oil reservoir are presented. Though idealized, these simulations, which are from a commercial simulator,^{25,26} capture the main features and establish the theory of solution-gas drives.

For the sake of simplicity, the simulations consider the depletion of only a single well in an 80-acre closed area. **Table 9.7** summarizes some of the reservoir and fluid properties. The simulations assume that the PVT parameters in **Table 9.3** apply.

Fig. 9.9 shows the performance in terms of pressure, producing GOR, and gas saturation as a function of cumulative produced oil. The four stages of production are depicted. During Stage 1, less than 1% of the OOIP is produced. The pressure decreases from the initial pressure of 2,000 psia to the bubblepoint pressure of 1,688 psia. The producing GOR remains constant and equal to the initial dissolved GOR of 838 scf/STB; no free gas evolves.

During Stage 2, the pressure falls below the bubblepoint; solution gas is liberated; and low, immobile gas saturations form. The cumulative oil recovery reaches approximately 4.5% of the OOIP. The pressure decreases from the bubblepoint to approximately 1,550 psia. The gas saturation increases to approximately 5% PV. The producing GOR actually decreases slightly, but this change is barely noticeable.

During Stage 3, the gas saturation increases to the point at which gas is mobile. Free-gas production begins, and the producing GOR rises steadily. By the end of Stage 3, the cumulative oil recovery is 28% of the OOIP, the pressure has decreased to 200 psia, the gas saturation reaches approximately 35% PV, and the producing GOR reaches approximately 6,700 scf/STB.

During Stage 4, the pressure has reached such a low level that the expansion of gas from reservoir to surface conditions is minimal. Consequently, the producing GOR decreases. By the time the pressure reaches 50 psia, the GOR is only 2,000 scf/STB and the total oil recovery is 32% of the OOIP.

Fig. 9.10 shows reservoir performance as a function of time. This figure plots the pressure, instantaneous producing GOR, cumulative producing GOR, gas saturation, oil rate, gas rate, and fraction of OOIP and OGIP recovered as a function of time. Stage 1 is very short and lasts

TABLE 9.7—RESERVOIR AND FLUID PROPERTIES FOR BLACK-OIL SIMULATIONS

Property	Value
Pattern area, acres	80
Depth, ft	6,700
Number of wells	1
Horizontal permeability, md	5.0
Pay thickness, ft	20
Average porosity, %	31
Connate-water saturation, % PV	20
Temperature, °F	131
Initial pressure, psia	2,000
Bubblepoint pressure, psia	1,688
Initial producing GOR, scf/STB	838.5
Bottomhole pressure, psia	199
Residual-oil saturation to water, % PV	25
Residual-oil saturation to gas, % PV	20
Critical gas saturation, % PV	5
Initial fluid molecular weight	81.2
Initial oil FVF, RB/STB	1.466
Separator pressure, psia	100
Stock-tank-oil density, lbm/ft ³	53.10
Stock-tank-oil molecular weight	151.5
Separator-gas molecular weight	30.7
OOIP, million STB	2.10
OGIP, Bscf	1.76

less than one month. The oil and gas producing rates and pressure decline sharply. The producing rates decline if the bottomhole pressure (BHP) is restricted. The producing rates can remain constant, but only if the minimum BHP is not yet reached.

Stage 2 also is relatively brief, lasting only several months. The reservoir pressure and producing rates also decline sharply but not as quickly as during Stage 1. The decline rate dampens because solution gas is liberated. The producing rates decline if the BHP is restricted. Constant producing rates can be realized only if the minimum BHP is not yet reached.

Stage 3 starts before one year of depletion and continues until the economic limit is reached. In this example, the limit is reached after 13.5 years when the oil-producing rate reaches 20 STB/D. The length of pressure depletion depends strongly on the reservoir permeability and on the prevailing economic conditions. For instance, lower permeabilities will decelerate recovery and protract depletion. The final pressure is 613 psia. This pressure is not low enough to realize Stage 4; therefore, this stage of depletion is not portrayed in Fig. 9.10. The absence of Stage 4 in field cases is not uncommon. The marked increase in the GOR from 838 to 4,506 scf/STB during Stage 3 coincides with marked increase in the gas saturation from 5 to 28.7% PV. At the economic limit, these simulations predict final oil and gas recoveries of 24.2% of the OOIP and 53.1% of the OGIP. Stage 3 clearly dominates the depletion life of a solution-gas-drive reservoir.

The results of this simulation are an oversimplification and idealization of actual performance. Oversimplification stems from the fact that the tank model ignores many important

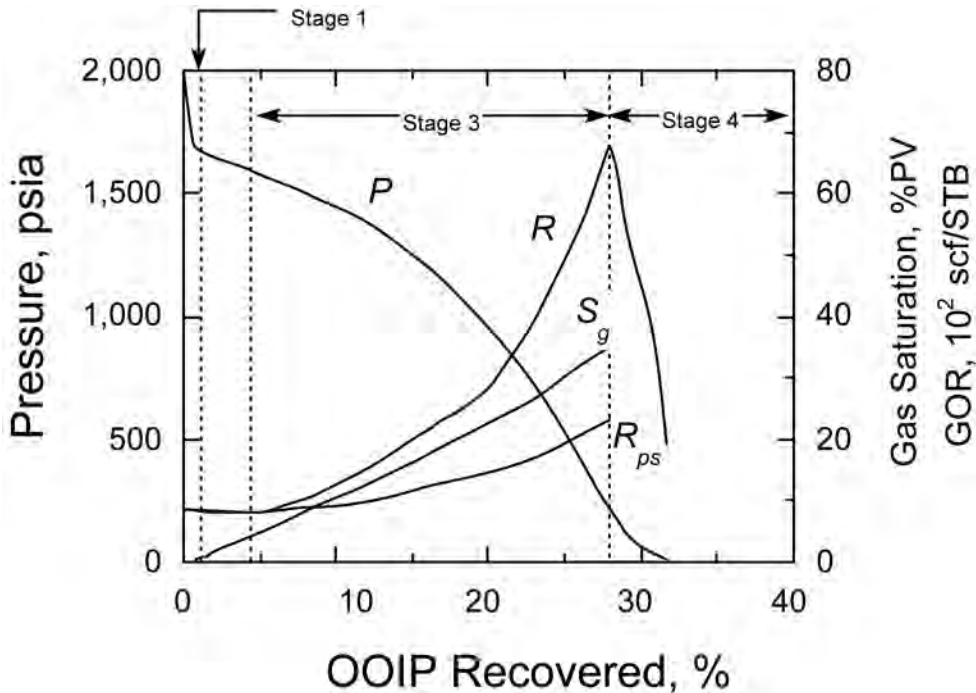


Fig. 9.9—Pressure (p), gas saturation (S_g), producing GOR (R), and cumulative producing GOR (R_{ps}) as a function of OOIP recovered for a solution-gas-drive, black-oil reservoir.

secondary phenomena. For example, the simulations ignore reservoir heterogeneity, which can be expected to reduce the recoveries by approximately 20 to 50% depending on the degree of heterogeneity. For instance, if a volumetric recovery efficiency of 80% is applied, then the idealized oil recovery of 24.2% corresponds to an adjusted oil recovery of 19.4%. Also, the simulations ignore spatial effects.

Qualitatively, solution-gas-drive, volatile-oil reservoirs act very similarly to their black-oil counterparts. One pronounced quantitative difference, however, is that volatile-oil reservoirs exhibit much greater peak producing GORs. The field example in [Sec. 9.7.3](#) illustrates this difference. This example considers a volatile-oil reservoir that exhibits a peak GOR of approximately 29,000 to 32,000 scf/STB. This GOR is considerably greater than the peak GOR for the example black oil of 6,700 scf/STB. Another difference between volatile- and black-oil reservoirs is that the former often exhibit slightly greater oil recoveries; however, there are numerous exceptions to this trend.

9.7.3 Field Example. Cordell and Ebert⁵ report the performance of a volatile-oil reservoir located in north-central Louisiana. [Table 9.8](#) summarizes some of the pertinent reservoir data. This reservoir produced from the Smackover lime located at an approximate depth of 10,000 ft. The field was discovered in 1953 and was developed with 11 wells on 160-acre spacing. Jacoby and Berry⁶ report on the fluid properties of this volatile oil. The standard PVT parameters in [Table 9.5](#), which were developed from laboratory data with the EOS method, are applicable.

[Table 9.9](#) summarizes the reservoir performance in terms of the cumulative oil production, cumulative gas production, and instantaneous producing GOR as a function of pressure. [Table 9.9](#) includes the oil and gas recoveries as a percent of the OOIP and OGIP. These recoveries

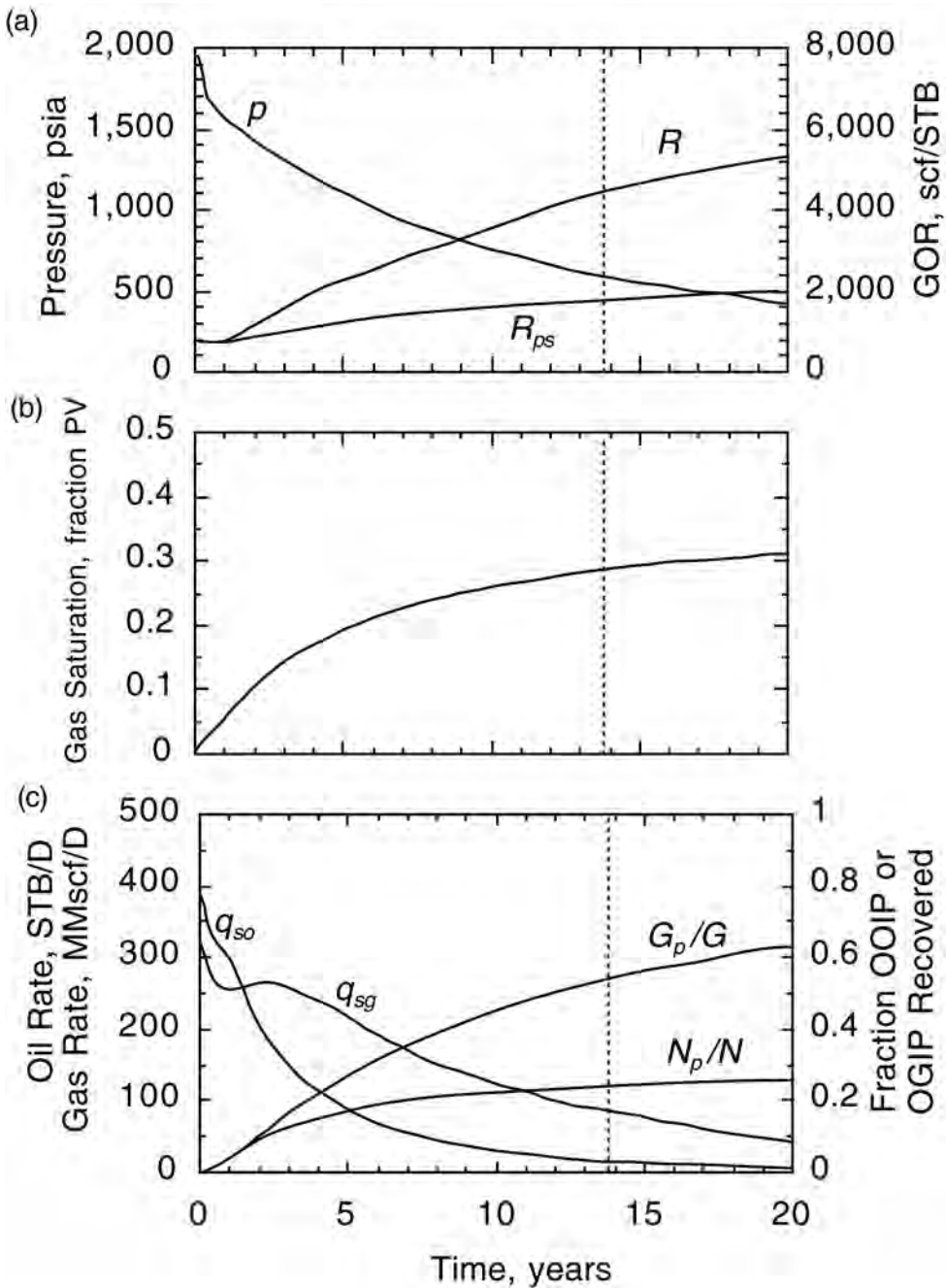


Fig. 9.10—Performance of a solution-gas-drive reservoir: (a) pressure, p , instantaneous producing GOR, R , and cumulative producing GOR, R_{ps} , histories; (b) gas-saturation history; (c) oil-rate, q_{so} , gas-rate, q_{sg} , oil-recovery, N_p/N , and gas-recovery, G_p/G , histories.

were based on the volumetric OOIP and OGIP estimates of 10.7 million STB and 31.1 Bscf, respectively.

TABLE 9.8—SELECTED RESERVOIR AND FLUID PROPERTIES FOR LOUISIANA VOLATILE-OIL RESERVOIR	
Property	Value
Discovery year	1953
Location, state	Louisiana
Formation	Smackover
Lithology	Limestone
Area, acres	80
Depth, ft	10,000
Number of wells	11
Well spacing, acres	160
Horizontal permeability, md	174
Pay thickness, ft	24.4
Average porosity, %	13.6
Connate-water saturation, % PV	28.3
Temperature, °F	246
Initial pressure, psia	5,070
Bubblepoint pressure, psia	4,698
Initial producing GOR, scf/STB	2,909
Initial fluid molecular weight	47
Initial oil FVF, RB/STB	2.703
OOIP, million STB*	10.7
OGIP, Bscf*	31.1

*Volumetric estimate.

Fig. 9.11 shows the reservoir performance in terms of pressure and producing GOR as a function of cumulative oil recovery. This figure qualitatively agrees with the theoretical results for the black oil in **Fig. 9.9**. A comparison confirms that volatile-oil reservoirs experience much higher producing GORs. For example, this volatile-oil reservoir reaches a peak GOR of 29,000 scf/STB (compared with 6,700 scf/STB for the black oil). This reservoir was produced to a low enough pressure to exhibit Stage 4, which is the period of declining GOR. The GOR began to decline at a reservoir pressure of approximately 800 psia.

9.7.4 Material-Balance Analysis. A material-balance analysis is performed routinely to confirm the suspected producing mechanism and to estimate the OOIP independently. The applicable material-balance equation for a solution-gas-drive reservoir is^{20,23,24,27}

$$F - W_e = NE_{owf} \dots\dots\dots (9.15)$$

Eq. 9.15 is a simplification of **Eq. 9.7** and assumes no initial free gas ($G_{fgi} = 0$). Because there is no initial free gas, $N_{foi} = N$. If free gas is present initially, the material-balance methods for gas-cap reservoirs should be applied (see **Section 9.8.2**). **Eq. 9.15** also applies to waterdrives; however, if the following methods are applied to waterdrives, the water-influx history must be reliably known. If the water-influx history is not known, then the methods in **Section 9.9.8** regarding waterdrives must be applied. If there is no water influx, then $W_e = 0$.

If a reservoir produces exclusively by solution-gas drive with only supplemental connate-water expansion and pore-volume contraction, then **Eq. 9.15** dictates that a plot of F vs. E_{owf} is a straight line, emanates from the origin, and has a slope equal to N . This observation is used to confirm the producing mechanism. If water influx exists and if W_e is known, then an F -vs.- E_{owf} plot is replaced by a $(F - W_e)$ -vs.- E_{owf} plot. **Fig. 9.12** shows a $(F - W_e)$ -vs.- E_{owf} plot for a volatile-oil reservoir. Once the OOIP is determined, the OGIP is given by $G = R_{st}N$. If an F -vs.-

TABLE 9.9—PRODUCTION HISTORY OF LOUISIANA VOLATILE-OIL RESERVOIR

<i>p</i> (psia)	<i>N_p</i> (million STB)	<i>G_{ps}</i> (Bscf)	<i>R</i> (scf/STB)	<i>N_p</i> (%OOIP)	<i>G_{ps}</i> (%OGIP)
5,070	0.000	0.000	2,909	0.00	0.00
4,998	0.036	0.105	2,909	0.34	0.34
4,798	0.130	0.388	2,909	1.22	1.25
4,698	0.184	0.539	2,909	1.72	1.73
4,658	0.227	0.657	2,834	2.13	2.11
4,598	0.302	0.872	2,749	2.83	2.80
4,398	0.582	1.657	2,914	5.44	5.33
4,198	0.808	2.366	3,256	7.55	7.61
3,998	1.022	3.140	4,026	9.56	10.10
3,798	1.227	4.032	5,087	11.48	12.96
3,598	1.388	4.967	6,494	12.98	15.97
3,398	1.528	5.988	8,068	14.29	19.25
3,198	1.646	7.062	9,541	15.40	22.71
2,998	1.764	8.223	11,290	16.50	26.44
2,798	1.861	9.405	13,093	17.41	30.24
2,598	1.947	10.652	15,248	18.21	34.25
2,398	2.022	11.909	17,340	18.91	38.29
2,198	2.097	13.199	19,738	19.62	42.44
1,998	2.151	14.542	22,595	20.12	46.76
1,798	2.215	15.886	24,433	20.72	51.08
1,598	2.269	17.337	26,574	21.23	55.74
1,398	2.323	18.723	27,913	21.73	60.20
1,198	2.366	20.109	29,090	22.13	64.66
998	2.420	21.539	29,491	22.63	69.26
798	2.463	22.979	29,191	23.04	73.89
598	2.527	24.505	27,534	23.64	78.79

E_{owf} plot is not a straight line, then another producing mechanism, such as a waterdrive or an initial gas cap, exists. The shape of the nonlinearity is important in diagnosing the true producing mechanisms. For instance, if the *F*-vs.-*E_{owf}* plot curves upward, this suggests that a waterdrive or an initial gas cap exists. Fig. 9.13 shows the effect of water influx or an initial gas cap on an *F*-vs.-*E_{owf}* plot.

The number of data points in an *F*-vs.-*E_{owf}* plot is usually limited by the number of average-reservoir-pressure measurements. Recall that *F* and *E_{owf}* are functions of pressure by means of the standard PVT parameters. If two or more data points (other than the origin) exist, then a mathematical criterion must be adopted to determine the “best” line through the data or the “best” estimate of *N*. If a least-squares criterion is adopted, then the OOIP estimate is²⁸

$$N = \frac{n \sum_{j=1}^n (F)_j (E_{owf})_j - \sum_{j=1}^n (F)_j \sum_{j=1}^n (E_{owf})_j}{n \sum_{j=1}^n (E_{owf})_j^2 - \sum_{j=1}^n (E_{owf})_j \sum_{j=1}^n (E_{owf})_j}, \dots \dots \dots (9.16)$$

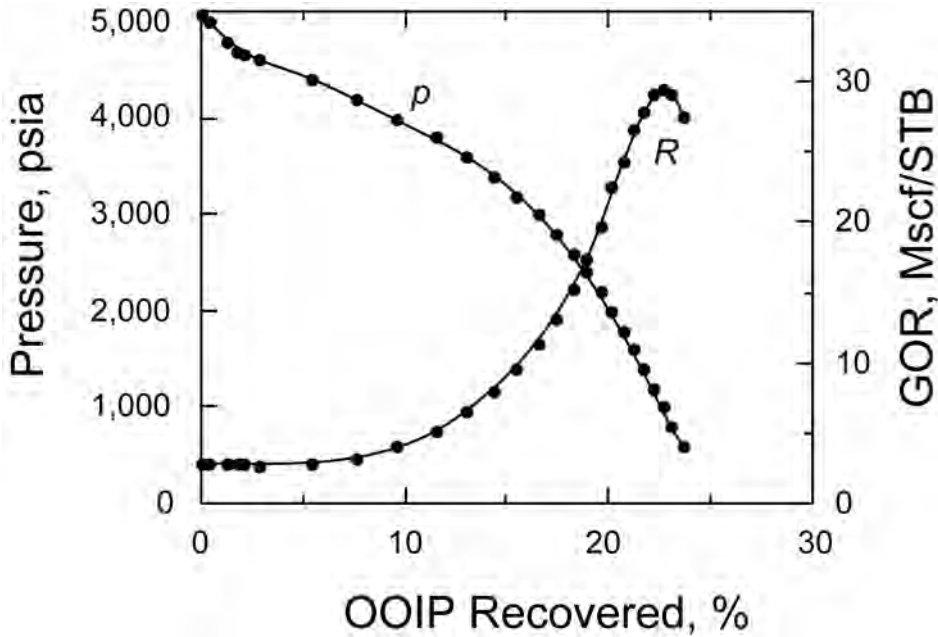


Fig. 9.11—Pressure and producing GOR as a function of OOIP recovered for a Louisiana volatile-oil reservoir.

where subscript j denotes the value at pressure p_j and n is the total number of data points. Eq. 9.16 offers a strictly mathematical means to estimate the OOIP without constructing an F -vs.- E_{ovf} plot. In general, however, a plot is recommended because it provides a visual means to assess the scatter of the data. The straightness of the data points is a measure of material balance and confirmation of the solution-gas-drive mechanism.

The composite expansivity E_{ovf} implicitly includes and accounts for rock and connate-water expansion. Thus, the methods offered here are applicable equally to reservoirs in which rock and connate-water expansion are important. In practice, rock and connate-water expansion cannot be neglected unless the reservoir is saturated and the pressure is less than approximately 1,500 psia. These phenomena cannot be neglected while the reservoir is undersaturated because their combined effects are not negligible compared to oil expansion. For instance, the relative expansion of oil, rock, and water in an undersaturated west Texas black-oil reservoir was 72, 25, and 3%, respectively. This example also demonstrates that the connate-water expansion is normally insignificant and can be ignored. Not until the pressure falls below the bubblepoint and approximately 1,500 psia will the rock expansion be negligible compared to the net hydrocarbon expansion. If doubt persists as to whether it is safe to ignore rock and connate-water expansion, the safest approach is to include them. To include these phenomena, the rock and connate-water expansivities, E_f and E_w , must be calculated. Sec. 9.10 discusses experimental and empirical methods to estimate E_f . The connate-water expansivity is calculated from Eq. 9.4. This equation ignores dissolved hydrocarbon gases in the water. To include dissolved gases, the water expansivity is calculated from

$$E_w = B_{tw} - B_{twi} \dots\dots\dots (9.17)$$

where B_{tw} is the two-phase water FVF and is given by

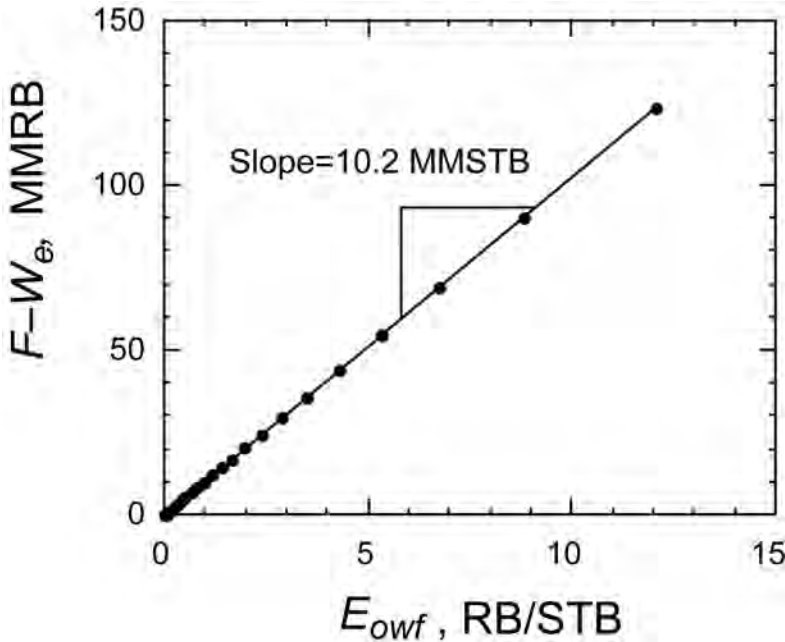


Fig. 9.12— $(F - W_e)$ -vs.- E_{owf} plot for a volatile-oil reservoir.

$$B_{tw} = B_w + B_g(R_{swi} - R_{sw}), \dots\dots\dots (9.18)$$

where R_{sw} is the dissolved gas/water ratio.²⁷

Two common errors occur when applying a material-balance analysis to volatile-oil reservoirs. First, an incorrect set of PVT parameters is used. This occurs if the volatile oil is subjected to a conventional DV test instead of a CVD or a specialized DV experiment that measures volatilized oil. The resulting set of PVT parameters will not reflect the true phase behavior. If this mistake occurs, the volatilized oil/gas ratio, R_v , will be omitted altogether and the resulting values of B_o and R_s will be erroneous and overestimated. Significant errors in these fluid properties will occur if appreciable volatilized oil exists. For example, the volatile oil in Table 9.5 yielded an erroneous initial oil FVF of 3.379 RB/STB and a dissolved GOR of 3,636 scf/STB (errors of approximately 25%) when it was subjected to a standard DV instead of a CVD. The second error commonly occurs if the conventional or black-oil material-balance equation^{29,30} is applied instead of the generalized equation in Eq. 9.1. The conventional material balance inherently ignores R_v . Both of these errors will cause the OOIP to be underestimated, which can be quite serious if the volatilized-oil content is appreciable.

Example 9.1: Material-Balance Analysis of a Volatile-Oil Reservoir. Perform a material-balance analysis on the Louisiana volatile-oil reservoir in Sec. 9.7.3. Use the production data in Table 9.9 and the PVT data in Table 9.5 as necessary. Estimate the OOIP (million STB) and confirm the suspected solution-gas-drive producing mechanism if possible. Compare your OOIP estimate to the volumetric estimate of 10.7 million STB reported by Cordell and Ebert.⁵

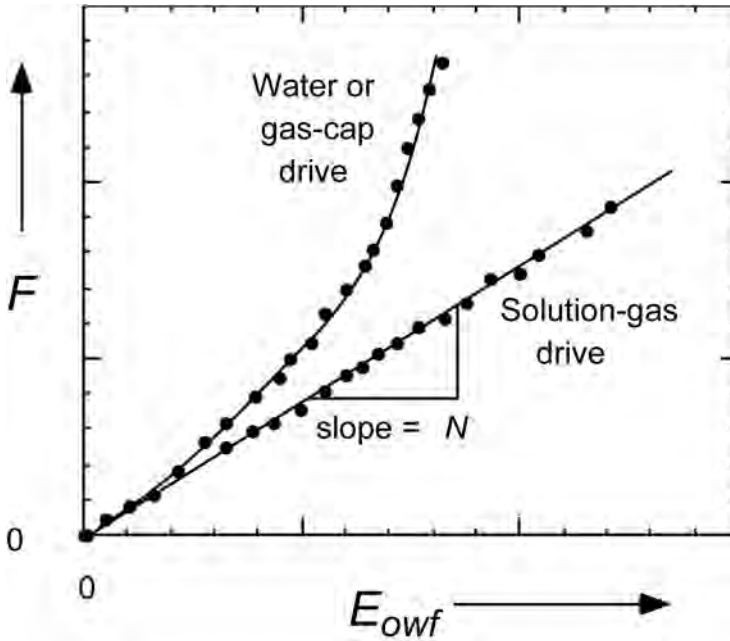


Fig. 9.13—Effect of water influx or an initial gas cap on an F -vs.- E_{owf} plot.

Solution. To confirm the producing mechanism and estimate the OOIP, construct an F -vs.- E_{owf} plot. Because the lower pressure in Table 9.9 is less than 1,500 psia and below the bubblepoint, connate-water expansion and pore-volume contraction can be ignored. Thus, E_{owf} can be replaced by E_o , where $E_o = B_{to} - B_{oi}$ and B_{to} is given by Eq. 9.5. Table 9.10 tabulates the results of B_{to} and E_o as a function of pressure. For example, at $p = 4,398$ psia, evaluating Eqs. 9.5 and 9.2 yields

$$B_{to} = \frac{\left(2.338 \frac{\text{RB}}{\text{STB}}\right) \left[1 - \left(2,909 \frac{\text{scf}}{\text{STB}}\right) \left(106 \times 10^{-6} \frac{\text{STB}}{\text{scf}}\right)\right] + \left(0.000853 \frac{\text{RB}}{\text{scf}}\right) \left(2,909 - 2,247 \frac{\text{scf}}{\text{STB}}\right)}{1 - \left(106 \times 10^{-6} \frac{\text{STB}}{\text{scf}}\right) \left(2,247 \frac{\text{scf}}{\text{STB}}\right)}$$

$$= 2.864 \frac{\text{RB}}{\text{STB}}$$

and $E_o = 2.864 - 2.704 = 0.160$ RB/STB.

F is given by Eq. 9.8 when the reservoir is saturated and by Eq. 9.13 when the reservoir is undersaturated. For example, at $p = 4,398$ psia, evaluating Eq. 9.8 yields

$$F = \left(1.657 \times 10^9 \text{ scf}\right) \left[\frac{0.000853 \frac{\text{RB}}{\text{scf}} - \left(2.338 \frac{\text{RB}}{\text{STB}}\right) \left(106 \times 10^{-6} \frac{\text{STB}}{\text{scf}}\right)}{1 - \left(106 \times 10^{-6} \frac{\text{STB}}{\text{scf}}\right) \left(2,247 \frac{\text{scf}}{\text{STB}}\right)} \right]$$

$$+ \left(0.582 \times 10^6 \text{ STB}\right) \left[\frac{2.338 \frac{\text{RB}}{\text{STB}} - \left(0.000853 \frac{\text{RB}}{\text{scf}}\right) \left(2,247 \frac{\text{scf}}{\text{STB}}\right)}{1 - \left(106 \times 10^{-6} \frac{\text{STB}}{\text{scf}}\right) \left(2,247 \frac{\text{scf}}{\text{STB}}\right)} \right] = 1.638 \text{ million RB.}$$

Table 9.10 tabulates the results at other pressures and the cumulative GOR, $R_{ps} = G_{ps} / N_p$.

TABLE 9.10—MATERIAL-BALANCE CALCULATIONS FOR LOUISIANA VOLATILE OIL

p (psia)	B_{10} (RB/STB)	E_o (RB/STB)	R_{ps} (scf/STB)	F (million RB)
5,070	2.704	0.000	2,906.0	0.000
4,998	2.713	0.010	2,906.0	0.098
4,798	2.740	0.037	2,976.6	0.366
4,698	2.754	0.051	2,925.1	0.510
4,658	2.765	0.061	2,891.9	0.625
4,598	2.785	0.081	2,883.3	0.836
4,398	2.864	0.160	2,847.0	1.638
4,198	2.936	0.233	2,929.7	2.385
3,998	3.019	0.316	3,070.6	3.229
3,798	3.117	0.413	3,286.6	4.238
3,598	3.225	0.522	3,578.6	5.347
3,398	3.351	0.648	3,919.6	6.642
3,198	3.498	0.794	4,291.1	8.124
2,998	3.668	0.965	4,661.5	9.879
2,798	3.863	1.159	5,054.5	11.885
2,598	4.098	1.394	5,471.7	14.287
2,398	4.369	1.666	5,890.0	17.066
2,198	4.695	1.991	6,293.6	20.391
1,998	5.092	2.388	6,761.0	24.471
1,798	5.578	2.875	7,170.6	29.449
1,598	6.202	3.498	7,640.1	35.834
1,398	6.984	4.280	8,060.2	43.843
1,198	8.023	5.319	8,499.8	54.479
998	9.444	6.740	8,901.7	69.044
798	11.501	8.797	9,331.1	90.124
598	14.772	12.068	9,696.9	123.619

Fig. 9.12 shows a plot of F vs. E_o . The slope of this plot is 10.2 million STB, which is an estimate of the OOIP. This estimate agrees closely with the volumetric estimate of 10.7 million STB. The agreement of the volumetric and material-balance OOIP estimates, together with the straightness of the F -vs.- E_o plot, is strong evidence that this reservoir is producing exclusively by a solution-gas-drive mechanism.

If the volatilized oil was ignored and standard PVT parameters based on a conventional DV test were used, the material balance would yield an OOIP estimate of 8.2 million STB, or an error of 23%. Alternatively, if the volatilized oil was ignored and the conventional (black oil) material-balance equation were used instead of the generalized equation defined by Eqs. 9.7 through 9.10, the material balance would yield an OOIP of 9.09 million STB, or an error of 15%.

9.8 Gas-Cap Drives

In some instances, oil reservoirs are discovered with a segregated-gas zone overlying an oil column. The overlying gas zone is referred to as a primary gas cap. In addition to free gas, gas caps usually contain connate water and residual oil. The underlying oil column is sometimes referred to as an oil leg. In other instances, as reservoir pressure declines with production, gas evolves in the reservoir (see Sec. 9.7) and migrates to the top of the structure to add to an existing primary gas cap or to form a gas cap. If properly harnessed, gas caps can enhance oil recovery considerably. The degree with which they improve recovery depends mainly on their size and on the vertical permeability and/or formation dip. Producing wells usually are complet-

TABLE 9.11—GAS-CAP CHARACTERISTICS	
<u>Segregating Gas Caps</u>	
•	Forms expanded gas-cap zone
•	Downward-moving GOC
•	Segregation mechanisms
•	Active segregation—oil-leg gas migrates to gas cap and oil drains downward; and/or
•	Passive segregation—gas-cap gas expands and displaces oil at GOC
•	High vertical permeability
•	High vertical relief
•	Rate sensitive
•	High oil recovery
<u>Nonsegregating Gas Caps</u>	
•	No expanded gas-cap zone
•	Stationary GOC
•	Gas-cap gas diffuses into oil leg
•	Low vertical permeability
•	Moderate oil recovery

ed only in the oil leg to minimize gas production. Broadly, gas caps are classified as segregating or nonsegregating. **Table 9.11** summarizes the distinguishing characteristics of each.

Segregating gas caps are gas caps that grow and form an enlarged gas-cap zone. **Fig. 9.4** shows a schematic of a segregation-drive reservoir. Two different segregation mechanisms are possible: (1) expansion of and frontal displacement by pre-existing gas-cap gas and (2) upward migration of oil-column gas as solution gas is liberated and a free-gas phase forms. The second mechanism involves the simultaneous downward movement of oil to balance the upward flow of gas. This diametric flow pattern is referred to as counterflow.³¹ Pirson³² refers to the first mechanism as passive segregation and the latter mechanism as active segregation. Hall³¹ refers to the first mechanism as segregation drive without counterflow and the second mechanism as segregation drive with counterflow. Both mechanisms are time-dependent, and their displacement efficiency depends on the gas/oil density difference, the producing rate, and the vertical permeability.

Both segregation mechanisms yield a progressively descending GOC. The segregation-drive mechanisms can be augmented by crestal gas injection.

If neither of these segregation mechanisms is present, the gas cap is called a nonsegregating gas cap. Nonsegregating gas caps do not form an enlarged gas-cap zone, and their GOC appears stationary. The gas-cap gas expands but the displacement efficiency is so poor that the expanding gas appears to merely diffuse into the oil column. **Fig. 9.14** illustrates the distribution of water, oil, and gas in a nonsegregation-drive gas-cap reservoir.

Broadly, gas caps act to mitigate the pressure decline, extend the life of the reservoir, and ultimately improve the oil recovery. The degree of oil-recovery improvement depends on the size of the gas cap and whether it is a segregation-drive or nonsegregation-drive gas cap.

To understand the mechanics of gas-cap reservoirs, numerical simulation results of segregating and nonsegregating gas caps are presented. Each example uses the fluid-property data in **Table 9.3**. Each example also uses the reservoir data summarized in **Table 9.7**, except that the initial pressure is 1,640 psia instead of 2,000 psia and the gas-cap thickness is 10 ft. The gas, oil, and water saturations in the gas cap are 60, 20, and 20%, respectively. The gas cap initial-

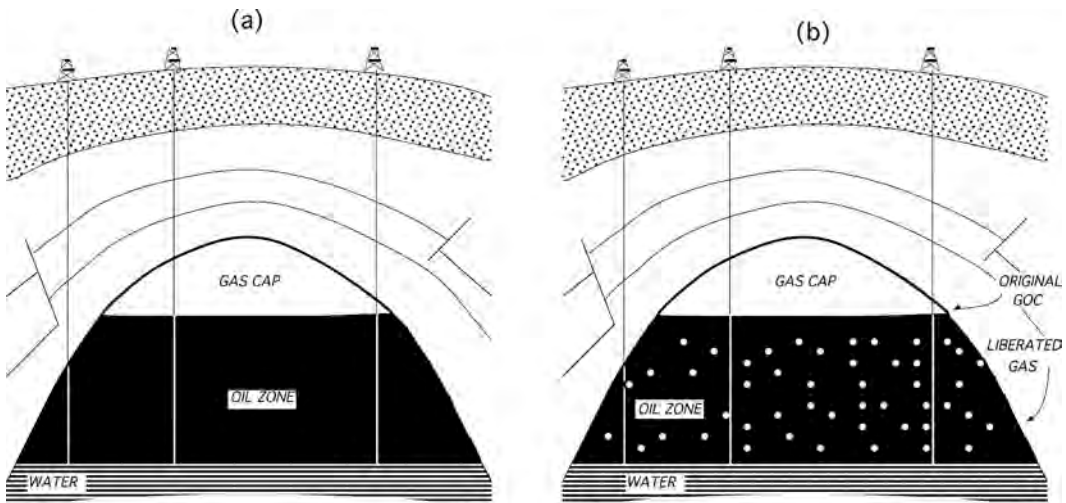


Fig. 9.14—Distribution of water, oil, and gas in a nonsegregating-gas-cap reservoir: (a) at discovery and (b) during depletion.

ly contains 270,000 STB of oil and 816 MMscf of gas; the oil leg initially contains 210 million STB of oil and 1.718 Bscf of gas. The total OOIP = 2.37 million STB, and OGIP = 2.534 Bscf, and $m = 0.33$. For reference, the segregating- and nonsegregating-gas-cap cases are compared with an identical reservoir without a gas cap (base case).

9.8.1 Performance. Nonsegregation-Drive Gas Caps. Fig. 9.15 plots pressure as a function of cumulative oil recovery for a nonsegregation-drive gas-cap reservoir. For comparison, this figure includes the results of the no-gas-cap (base) case. This figure also includes the results of other cases, which are discussed later in this section. All recoveries are reported as a fraction of the original oil-leg OOIP to make direct comparisons valid. The nonsegregation-drive gas-cap case consistently yields higher oil recoveries at a given pressure than the no-gas-cap case, which illustrates the superior recovery performance of gas caps. Viewed another way, the nonsegregation-drive gas-cap case consistently yields a higher pressure at a given oil recovery than the no-gas-cap case, which illustrates the superior pressure-maintenance ability of gas caps.

Fig. 9.16 is a composite figure and shows the performance as a function of time. This figure includes the GOR, gas saturation, oil rate, and oil-recovery histories. The GOR history shows that nonsegregating gas caps eventually yield higher producing GORs than the no-gas-cap reservoir. The higher GOR is caused by higher gas saturation in the oil leg. The higher gas saturation is caused by the gas-cap gas migrating from the gas cap into the oil leg as the pressure declines.

Fig. 9.16 also shows the effect of a nonsegregating gas cap on the oil-rate history. The nonsegregating gas cap consistently yields higher oil rates than without the gas cap. If an economic limit corresponding to a minimum oil rate of 20 STB/D is arbitrarily assumed, then the no-gas-cap case is terminated after 13.8 years while the nonsegregation-drive gas-cap case is terminated after 15.2 years. This comparison shows that the presence of a gas cap extends the primary-recovery life of the reservoir. The curve endpoints denote the time of termination. The no-gas-cap case is slightly different from the black oil case discussed earlier due to the assumed lower original pressure.

Fig. 9.16 includes the fractional oil-recovery history; Fig. 9.17 shows the gas-recovery history. The curve endpoints denote the time of the economic limit. Table 9.12 summarizes the

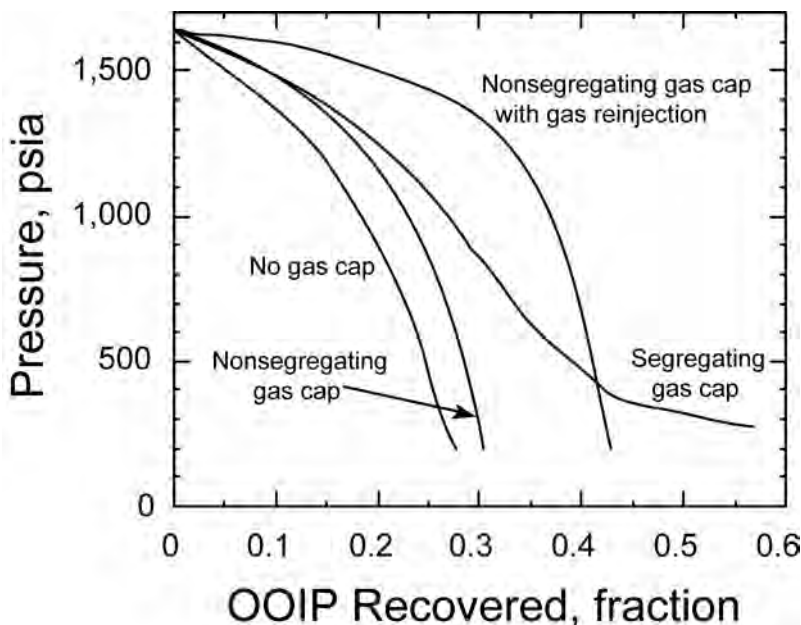


Fig. 9.15—The effect of gas cap and gas reinjection on oil recovery as a function of pressure for a west Texas black-oil reservoir.

conditions at the economic limit. The no-gas-cap and nonsegregation-drive gas-cap cases recover 23.7% and 26.8% of the oil-leg OOIP, respectively. Thus, the nonsegregating gas cap recovers more oil than without the gas cap. The nonsegregating gas cap also is terminated at a higher pressure, producing GOR, gas saturation, and gas rate than without the gas cap. The nonsegregating gas cap recovers 74.9% of the oil-leg OGIP while the no-gas-cap case recovers 52.3% of the oil-leg OGIP. The nonsegregating gas cap recovers more gas because some of the gas-cap gas infiltrates the oil leg and is produced. In conclusion, the presence of a nonsegregating gas cap yields higher ultimate oil and gas recoveries, accelerates recovery, and extends the primary-recovery life of a reservoir.

The effect of a gas cap on oil recovery is related directly to its size relative to the size of the oil leg. The size of the gas cap is described effectively in terms of the dimensionless variable m , which is defined as the ratio of the initial free-gas and free-oil phase volumes (see Eq. 9.23). If all the free gas is located in the gas cap, all the free oil is located in the oil leg, and the oil-leg and gas-cap porosities and connate-water saturations are the same, then m represents the ratio of the gas-cap and oil-leg PV. Fig. 9.18 shows the effect of m on the final fractional oil recovery for a nonexpanding-gas-cap reservoir. The results in Fig. 9.18 use the same reservoir data as in the previous simulations except different gas-cap sizes are considered. Other reservoir conditions may yield slightly different results. The most noticeable improvement in oil recovery comes as m increases from 0 to 2.0.

The gas-cap size also affects the peak GOR. As the gas cap increases, the peak GOR increases. Fig. 9.18 shows the peak GOR as a function of m for the west Texas reservoir properties. The peak GOR increases with the gas-cap size because more gas-cap gas migrates into the oil column as the gas cap increases. In summary, nonsegregation-drive gas-cap reservoirs tend to yield final fractional oil recoveries in the range of 15 to 40% of the OOIP. Segregation-drive gas-cap reservoirs tend to yield even higher final oil recoveries.

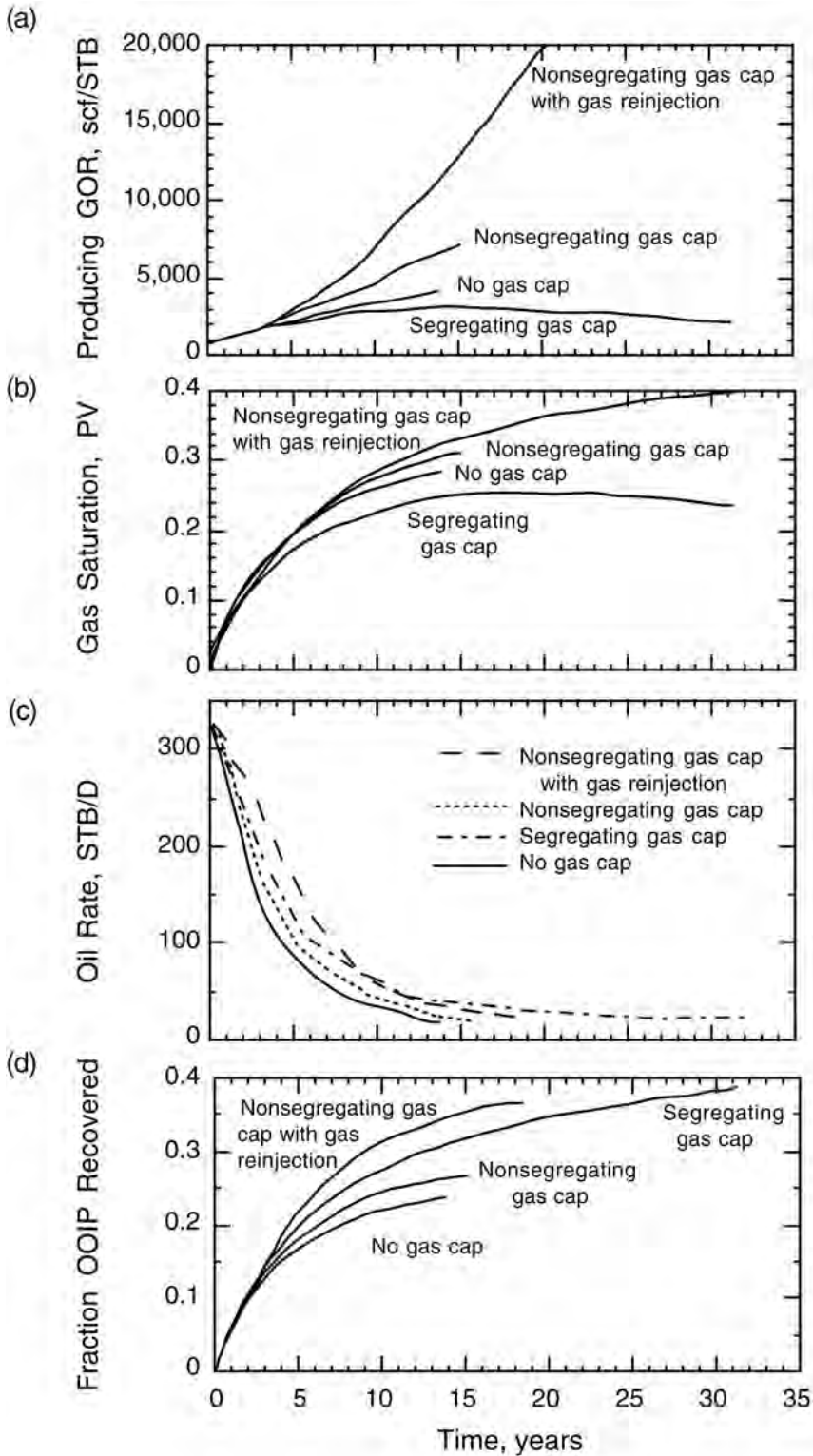


Fig. 9.16—Performance of a gas-cap reservoir: (a) instantaneous producing GOR, (b) gas-saturation, (c) oil-rate, and (d) oil-recovery histories for a west Texas black-oil reservoir.

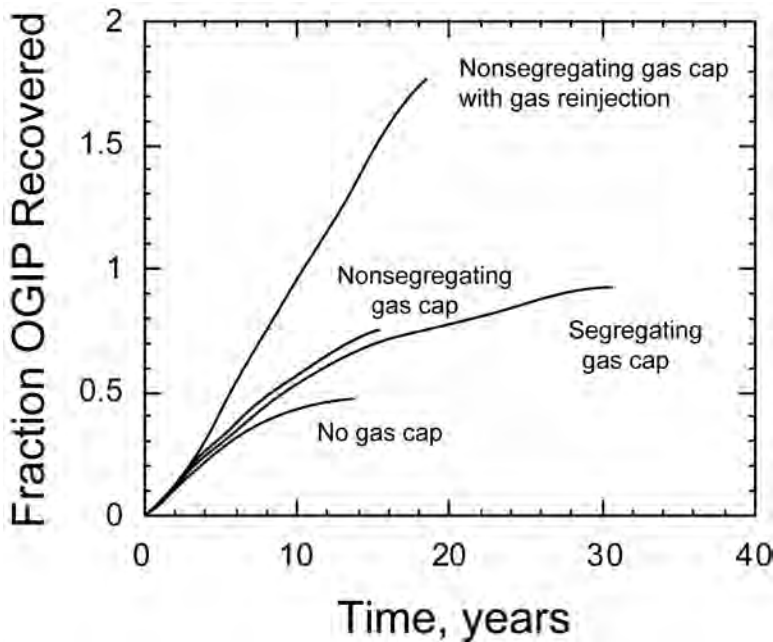


Fig. 9.17—The effect of gas cap and gas reinjection on gas-recovery history for a west Texas black-oil reservoir.

Case	Time (years)	p (psia)	Recovery		R (scf/STB)	S_g (% PV)	Gas Rate (Mscf/D)
			Oil (%)	Gas* (%)			
No gas cap (base case)	13.8	605	23.7	52	4,218	28.3	84
Nonsegregating gas cap	15.2	690	26.8	75	7,055	31.2	132
Gas reinjection, nonexpanding gas cap	18.5	993	36.7	177	17,904	35.3	352
Segregating gas cap	31.3	508	38.7	91	2,173	23.5	46

*Expressed as a percent of original oil-leg GIP.

Segregation-Drive Gas Caps. Segregating gas caps are characterized by progressively descending GOCs. The movement of the GOC is caused by active or passive gravity segregation. Active gravity segregation is the simultaneous migration of gas upward and drainage of oil downward. Passive segregation is the natural expansion of the gas-cap gas. Both of these processes involve frontal displacement of oil at the GOC. Frontal displacement helps drive oil to the producing wells. Frontal displacement does not dominate in nonsegregation-drive gas-cap reservoirs. The extent to which gravity segregation occurs depends on the vertical permeability and the rate at which fluids are withdrawn from the reservoir. The greater the vertical permeability and slower the fluid withdrawal, the more pronounced the effects of gravity segregation.

Figs. 9.15 through 9.17 include simulation results of a segregation-drive gas-cap reservoir. These simulations assume properties identical to those of the nonsegregation-drive gas-cap sim-

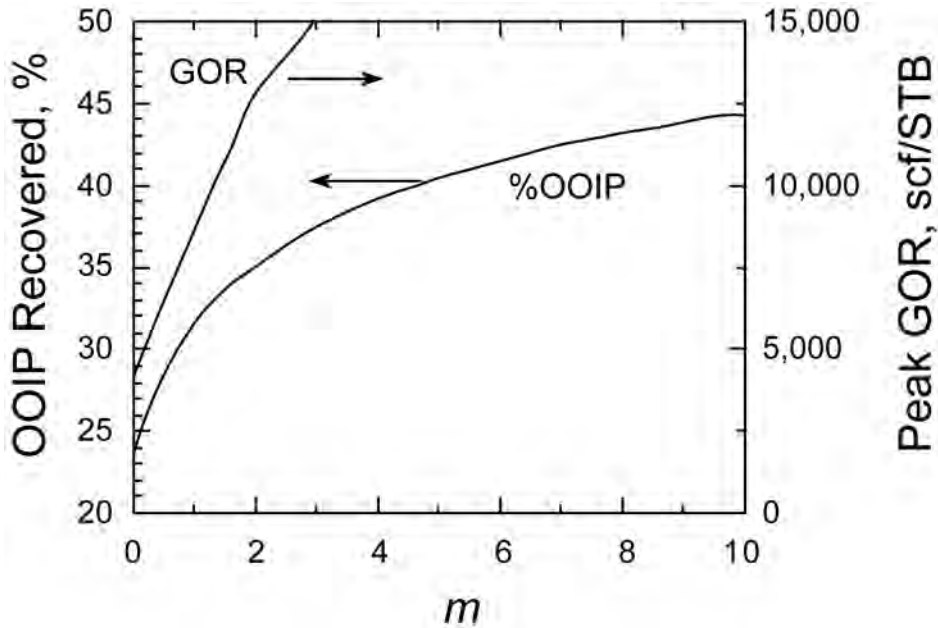


Fig. 9.18—The effect of dimensionless gas-cap size (m) on final primary oil recovery and peak producing GOR for a west Texas black-oil reservoir. Recoveries reported as percent of oil-leg OOIP.

ulations except gravity segregation is included. The simulations assume no free-gas production from the gas cap.

Fig. 9.15 shows the pressure as a function of cumulative oil recovery. This figure shows that oil recovery in a segregation-drive gas-cap reservoir at a given pressure is consistently greater than that in a nonsegregation-drive gas-cap or nongas-cap reservoir, especially at low pressures when the effects of gas expansion become pronounced. The oil recovery performance is discussed below.

Fig. 9.16 shows the effect of a segregating gas cap on the GOR history. Only a marginal increase in the GOR is noted; after 15 years, the GOR actually decreases slightly. This type of GOR behavior is characteristic of segregation-drive gas-cap reservoirs.^{1,33,34} The segregating gas cap effectively drives and concentrates oil into the shrinking oil leg. The oil leg shrinks as the GOC descends; thus, the segregating gas cap minimizes the gas saturation in the oil leg. The GOR reversal coincides with a reversal in the gas saturation. Fig. 9.16 includes the gas saturation history. The gas saturation steadily increases until it peaks at approximately 0.25 PV; then it decreases. The GOR and gas saturation reversals occur at a moderate to low pressure when the expansion of the gas-cap gas becomes pronounced. The change in the position of the GOC yields a measure of the oil-leg shrinkage. At termination, the GOC has descended approximately 9.3 ft into the original 20-ft oil column.

Fig. 9.16 includes the oil-rate history. The oil rate for the segregating gas cap is consistently higher than for the nonsegregating gas cap or without the gas cap. The oil rate eventually flattens out to between 20 and 50 STB/D and stays within this range for 15 to 31 years. This moderate but steady oil rate explains the superior performance and long life of segregation-drive gas-cap reservoirs. Table 9.12 summarizes and compares the primary-recovery lifetimes of the various cases: the segregating gas cap has a life of 31.3 years; the nonsegregating gas cap has a life of 15.2 years; and the solution-gas drive (base case) has a life of 13.8 years.

Fig. 9.16 includes the cumulative-oil-recovery history. The segregating-gas-cap reservoir recovers 38.7% of the oil-leg OOIP while the nonsegregating-gas-cap and solution-gas-drive reservoirs recover 26.8 and 23.7% of the OOIP, respectively. Such a high recovery level for a segregation-drive reservoir is not uncommon. It is not uncommon for gravity-drainage reservoirs to realize recoveries as high as 60 to 70% of the OOIP; however, they generally require a long time to do so. The curve endpoints in Fig. 9.16 denote the time of the economic limit. The segregating-gas-cap reservoir terminates at a pressure of 508 psia.

Fig. 9.17 shows the gas-recovery history. The segregating-gas-cap reservoir recovers 91.1% of the oil-leg OGIP. This recovery level is considerably greater than the nonsegregating-gas-cap or solution-gas-drive reservoirs (74.9 and 52.3%, respectively). One reason segregating-gas-cap reservoirs tend to yield such high gas recoveries is that they often recover some of the original gas-cap gas, which migrates into the oil leg. In addition, they generally realize lower termination pressures.

The final fractional oil recovery in a segregating-gas-cap reservoir is a strong function of the vertical communication within the reservoir. Vertical communication dictates the extent of segregation. If vertical communication is good, then most of the gas-cap gas will be available for segregation. It will also be available to help drive oil through frontal displacement to the producing wells. If vertical communication is poor, then very little, if any, of the gas-cap gas will segregate. In summary, segregation is controlled principally by three variables: the vertical reservoir permeability, the producing rate, and well spacing. As well spacing and vertical permeability increase and as the producing rate decreases, the effect of gravity segregation increases. For the effects of gravity segregation to be important, however, the well spacing may need to be prohibitively large or the producing rate may need to be prohibitively low. In such reservoirs, the vertical permeability is not high enough to permit much gravity segregation.

The likely role of gravity segregation can be measured in terms of a gravity number, N_g . N_g is defined as the ratio of the time it takes a fluid to move from the drainage radius to the wellbore to the time it takes a fluid to move from the bottom of the reservoir to the top. In oilfield units, the gravity number is

$$N_g = \frac{2.46 \times 10^{-5} k_v \Delta \rho r_e^2}{\mu_o q}, \dots\dots\dots (9.19)$$

where k_v = vertical permeability, md; $\Delta \rho$ = density difference, lbm/ft³; r_e = drainage radius, ft; q = producing rate at reservoir conditions, RB/D; and μ_o = oil viscosity, cp.

Gravity segregation is likely pronounced if $N_g > 10$; gravity segregation is likely unimportant if $N_g < 0.10$. For example, if $k_v = 10$ md, $\Delta \rho = 50$ lbm/ft³, $r_e = 930$ ft, $q = 500$ RB/D, and $\mu_o = 1$ cp, then $N_g = 21.3$ and the effects of gravity segregation are likely important. If the vertical permeability is $k_v = 0.10$ md instead of 10.0 md, then $N_g = 0.21$ and the effects of gravity segregation are relatively unimportant.

Gas Reinjection. One method for improving oil recovery is to reinject a portion of the produced gas. The reinjected gas helps maintain reservoir pressure. One obvious drawback of gas reinjection is that gas sales revenues are reduced or delayed. The overall intention of gas reinjection is to increase the net profit despite lower gas sales. When there is no sales outlet for produced gas, reinjection can improve oil recovery until a sales outlet is established. Regulations may require reinjection until sales are possible. Inert gases such as nitrogen or carbon dioxide also could be used to supplement or replace natural-gas reinjection.

Figs. 9.15 through 9.17 present simulation results of a gas-reinjection scenario. In this scenario, 70% of the produced wellhead gas is reinjected into the gas cap, and the gas cap is nonsegregating. This means that only 30% of the produced wellhead gas is available for sales. The non-reinjected gas is referred to as sales gas. This term is sometimes a misnomer because

not all of the non-reinjected gas is necessarily sold. In practice, some of the sales gas is used routinely as fuel for power or utility requirements.

Fig. 9.15 shows the effect of gas reinjection on pressure as a function of oil recovery. Oil recovery at a given pressure is consistently higher for the gas-reinjection case than for the other cases in Fig. 9.15, except at very low pressures at which the segregating-gas-cap case yields superior performance. Gas reinjection leads to higher oil recoveries because the compressed reinjected gas effectively adds extra energy to the reservoir.

Fig. 9.16 shows the effect of gas reinjection on the GOR history. Gas reinjection leads to very high producing GORs, significantly higher than the other cases. The GOR is higher because the gas saturation is higher. The gas saturation is higher because reinjected gas and initial gas-cap gas migrate into the oil leg during pressure depletion. This occurs because the gas cap is nonsegregating. High producing GORs are a characteristic feature of reservoirs subject to gas reinjection if there is little or no active gravity drainage. High producing GORs mean that large volumes of produced gas will have to be handled and processed at the surface.

Fig. 9.16 includes the effect of gas reinjection on the oil-rate history. This figure shows that the oil rate is higher for the first 8½ years for the gas-reinjection case than for any of the other cases. After 8½ years, the oil rate for the segregating-gas-cap case is slightly greater than the oil rate for the gas-reinjection case. These results demonstrate that gas reinjection is an effective means to arrest the normal oil-rate decline dramatically.

Fig. 9.16 also shows the effect of gas reinjection on the fractional oil-recovery history and that the gas-reinjection case is superior to the other cases. The gas-reinjection case recovers 36.7% of the original oil-leg OOIP at its economic limit of 18½ years. Only the segregating-gas-cap reservoir recovers more oil (38.7%); however, the segregating-gas-cap reservoir requires more time to recover the additional oil.

Fig. 9.17 shows the effect of gas reinjection on the fractional gas-recovery history. The fractional gas recovery is the cumulative produced wellhead gas normalized by the original oil-leg OGIP. The gas-reinjection case recovers 177% of the oil-leg OGIP (see Table 9.12). More than 100% of the oil-leg OGIP is produced because some of the reinjected gas is produced. Because 30% of the produced gas is not reinjected, 0.30×177 or 53.1% of the oil-leg OGIP is available for gas sales. This sales-gas recovery is comparable to the case without gas reinjection (52% OGIP).

Reservoirs subject to gravity drainage are especially attractive for gas reinjection. Crestal gas injection into the developing gas cap is the preferred strategy because gravity drainage helps control the movement of the injected gas. Excellent sweep and displacement efficiencies and high oil recoveries can be realized. The Tensleep pool in the Elk Basin field in Wyoming is a good example.^{35–37} This pool was projected to recover approximately 64% of the OOIP. See the chapter on Immiscible Gas Injection in Oil Reservoirs in this volume of the *Handbook* for more information on gravity drainage.

9.8.2 Material-Balance Analysis. The purpose of a material-balance analysis includes confirming the producing mechanism and estimating the OOIP, OGIP, and size of the gas cap. The applicable material-balance equation for initially saturated oil reservoirs is^{20,22,23}

$$F - We = G_{fgi} E_{gwf} + N_{foi} E_{owf} \quad (9.20)$$

This equation is applicable to all initially saturated reservoirs regardless of the distribution of the initial free gas. For example, this equation is applicable to reservoirs whether the initial free gas is segregated into a gas cap or uniformly dispersed throughout the reservoir. Eq. 9.20 also applies to waterdrives; however, if the following methods are applied to waterdrives, the

water-influx history must be reliably known. If the water-influx history is unknown, then the methods [Section 9.9.8](#) must be applied.

The quantities G_{fgi} and N_{foi} are related to N (OOIP) and G (OGIP) by the following equations:

$$G = G_{fgi} \left(1 + \frac{R_{si} B_{gi}}{m B_{oi}} \right) \dots\dots\dots (9.21)$$

$$\text{and } N = N_{foi} \left(1 + \frac{m B_{oi} R_{vi}}{B_{gi}} \right), \dots\dots\dots (9.22)$$

where m is the ratio of the free-gas-phase and free-oil-phase volumes and is defined by

$$m = \frac{V_{fgi}}{V_{foi}} = \frac{G_{fgi} B_{gi}}{N_{foi} B_{oi}} \dots\dots\dots (9.23)$$

The dimensionless variable m is sometimes called the dimensionless gas-cap volume.

Because G_{fgi} and N_{foi} are independent, they must be determined simultaneously. At least two sets of the independent variables (F , W_e , E_{gwf} , E_{owf}) must be known at two or more pressures (other than the initial pressure) to determine the set (G_{fgi} , N_{foi}). If three or more sets (F , W_e , E_{gwf} , E_{owf}) are known, then multiple sets (G_{fgi} , N_{foi}) can be determined. The optimal set is determined by one of two least-squares solution techniques: iterative or direct methods.

In the iterative method, [Eq. 9.20](#) is expressed as

$$F - W_e = N_{foi} E_t(m), \dots\dots\dots (9.24)$$

where E_t is the total expansivity expressed per unit volume of stock-tank oil and is defined by

$$E_t(m) = E_{owf} + m E_{gwf} \left(\frac{B_{oi}}{B_{gi}} \right) \dots\dots\dots (9.25)$$

The solution procedure to estimate the OOIP and OGIP involves the following steps:

1. Compute F , E_{gwf} , and E_{owf} for each data point (i.e., average reservoir-pressure measurement).
2. Guess m .
3. Compute $E_t(m)$ with [Eq. 9.25](#).
4. Estimate N_{foi} with a least-squares analysis using [Eq. 9.26](#).

$$N_{foi} = \frac{n \sum_{j=1}^n (F - W_e)_j (E_t)_j - \sum_{j=1}^n (F - W_e)_j \sum_{j=1}^n (E_t)_j}{n \sum_{j=1}^n (E_t)_j^2 - \sum_{j=1}^n (E_t)_j \sum_{j=1}^n (E_t)_j}, \dots\dots\dots (9.26)$$

where j denotes the data point index and n is the total number of data points.

5. Compute the residual R for each data point with

$$R_j = (F - W_e)_j - N_{foi} (E_t)_j \dots\dots\dots (9.27)$$

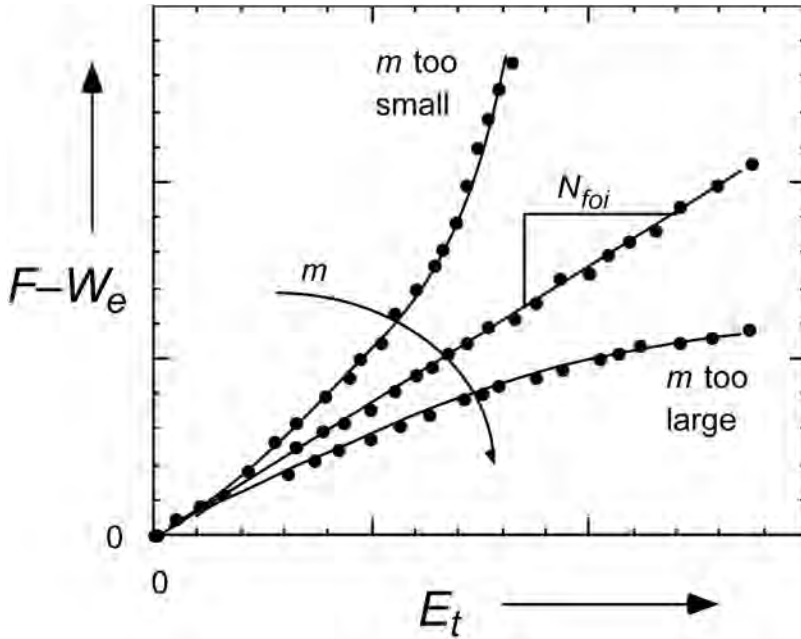


Fig. 9.19—The effect of m on a plot of $(F - W_e)$ vs. E_t .

6. Compute sum of the squares of residual, R_{ss} , as

$$R_{ss} = \sum_{j=1}^n R_j^2 \dots\dots\dots (9.28)$$

7. Return to Step 2 and repeat until R_{ss} is minimized.

8. Compute G , N , and G_{fgi} from Eqs. 9.21 through 9.23.

Minimization algorithms speed solution. This procedure is ideally suited for spreadsheet calculation, especially spreadsheet programs that contain minimization algorithms.

The use of Eq. 9.26 in Step 4 to determine N_{foi} is equivalent to the slope of a $(F - W_e)$ -vs.- $E_t(m)$ plot. This graphical solution method can be substituted for Eq. 9.26 in Step 4 if desired. Overall, Steps 2 through 7 are equivalent to the graphical procedure of varying m until the straightest possible $(F - W_e)$ -vs.- $E_t(m)$ plot is realized.³⁸ Fig. 9.19 shows the qualitative effect of m on the shape of the $(F - W_e)$ -vs.- E_t plot. If m is too small, the plot curves upward slightly; if m is too large, the plot curves downward slightly.

Once m is determined, the final $(F - W_e)$ -vs.- E_t plot is used to confirm the producing mechanism. The linearity of the plot is a measure of material balance and the applicability of the presumed producing mechanism. If the plot exhibits considerable curvature, then either the presumed mechanism is incorrect or additional producing mechanisms are active. If curvature exists, the shape of the curvature provides insight into the true producing mechanism. For instance, if the plot curves upward, this indicates that net withdrawal exceeds net expansion and that water influx, for example, has been ignored or is possibly underestimated.

As an alternative to the iterative method, Walsh^{23,28} presented a direct method. This method is based on least-squares multivariate regression. The least-squares equations are simple but lengthy. The technique is ideally suited for spreadsheet calculation. Walsh's method is especial-

ly attractive because it avoids iteration and the complications of attaining and judging convergence.

Havlena and Odeh³⁸ proposed another solution method in which $(F - W_e)/E_{owf}$ is plotted vs. (E_{gwf}/E_{owf}) ; the slope of the plot is equal to G_{fgi} and the y -intercept is equal to N_{foi} . This method is popular and attractive because it yields a direct solution. In theory, this method is perfectly acceptable. In practice, however, it has shown to be unreliable because it suffers from hypersensitivity to pressure uncertainty.^{28,39} The method has been shown to yield highly erroneous G_{fgi} and N_{foi} estimates in the presence of only small amounts of uncertainty. For instance, Walsh²⁸ shows that only a 5-psi pressure uncertainty yielded an error of more than 150% in N_{foi} and an error of more than 250% in G_{fgi} . The hypersensitivity is caused by the fact that the divisor (E_{owf}) approaches zero as the pressure approaches the initial pressure. Small errors in E_{owf} in turn, produce large errors in the quotients $(F - W_e)/E_{owf}$ and (E_{gwf}/E_{owf}) . Tehrani⁴⁰ calls this problem a “loss in resolving power.” Because of this hypersensitivity, this method should be used cautiously.

Walsh²⁸ tested the direct and iterative methods for their tolerance to uncertainty. He observed sensitivity, but the degree of sensitivity was less than the method of plotting $(F - W_e)/E_{owf}$ vs. (E_{gwf}/E_{owf}) . He concluded that material-balance methods for gas-cap reservoirs should be used cautiously.

9.9 Waterdrives

Waterdrive petroleum reservoirs are characteristically bounded by and in communication with aquifers. As pressure decreases during pressure depletion, the compressed waters within the aquifers expand and overflow into the petroleum reservoir. The invading water helps drive the oil to the producing wells, leading to improved oil recoveries. Like gas reinjection and gas-cap expansion, water influx also acts to mitigate the pressure decline. The degree with which water influx improves oil recovery depends on the size of the adjoining aquifer, the degree of communication between the aquifer and petroleum reservoir, and ultimately the amount of water that encroaches into the reservoir. Some of the most prolific oil fields in the world are waterdrive reservoirs. Perhaps the most celebrated example is the East Texas field. The final oil recovery in the East Texas field is projected to be approximately 79%.⁴¹ As this example shows, water influx has the potential to improve oil recovery considerably.

Once a water-influx mechanism has been identified, it is important to monitor the producing wells closely and to minimize water production. Minimizing water production in “edgewater drives” may require systematically shutting in flank wells once the advancing water reaches them. Minimizing water production in “bottomwater drives” may require systematically cementing in lower perforations as the bottom water slowly rises.

An integral part of reservoir surveillance for waterdrives is an active assessment program. The first phase of assessment includes diagnosis, classification, and characterization. The second phase identifies mathematical models that effectively simulate the aquifer, especially its deliverability. This phase includes reliably estimating aquifer model parameters. The third and final phase includes combining aquifer and reservoir models into a common model that can be used to forecast future recovery effectively and to identify optimal depletion strategies. The success of the third phase depends heavily on the success of the preceding two phases.

9.9.1 Waterdrive and Aquifer Classification. Waterdrives are classified in several ways. First, they are classified according to the location of the aquifer relative to the reservoir. If the aquifer areally encircles the reservoir, either partially or wholly, the waterdrive is called a peripheral waterdrive. If the aquifer exclusively feeds one side or flank of the reservoir, the waterdrive is called an edgewater drive. If the aquifer underlays the reservoir and feeds it from beneath, the waterdrive is called a bottomwater drive.

Waterdrives also are classified according to the aquifer's strength and to how well the aquifer delivers recharge water to the reservoir. The aquifer strength also refers to how well the aquifer mitigates the reservoir's normal pressure decline. A strong aquifer refers to one in which the water-influx rate approaches the reservoir's fluid withdrawal rate at reservoir conditions. These reservoirs also are called complete waterdrives and are characterized by minimal pressure decline. Strong aquifers are generally very large in size and highly conductive. A moderate or weak aquifer is one in which the water recharge rate is appreciably less than the reservoir's fluid withdrawal rate. These reservoirs are called partial waterdrives and they are characterized by pressure declines greater than a complete waterdrive but less than a volumetric reservoir. An aquifer's weakness is related directly to its lack in size or conductivity.

9.9.2 Waterdrive Diagnosis. There are several diagnostic indicators to help identify or discount a possible active aquifer.

First, an understanding of the reservoir's geology is important. The entire outer surface of the reservoir must be scrutinized carefully to identify communicating and noncommunicating pathways; communicating pathways represent possible water entry points. Geological maps should be consulted to identify the type of reservoir trap and the trapping surfaces. Trapping surfaces represent impenetrable surfaces and are discounted automatically as possible water-entry points. The remaining outer surfaces need to be evaluated and classified. If no communicating pathways exist, then the reservoir can be confidently discounted as a possible waterdrive; however, if communicating pathways exist, then the reservoir remains a candidate waterdrive.

Second, and perhaps most importantly, the water-cut history of all producing wells should be recorded and regularly monitored. A steady rise in a well's water cut is a good indicator of an active aquifer. Although this is among the best indicators, it is not foolproof. For instance, an increasing water cut might be caused by water coning instead of an active waterdrive. Special precautions need to be exercised to avoid water coning. A rising water/oil contact (WOC) is a good indicator of a bottomwater drive. Special attention should be paid to the location of high-water-cut wells. Their location will help define the position of the reservoir/aquifer boundary in peripheral and edgewater drives.

Third, the change in reservoir pressure also can be a helpful indicator. Strong-waterdrive reservoirs are characterized by a slow or negligible pressure decline. Thus, a slower-than-expected pressure decline can help indicate a waterdrive. Material-balance calculations are important to help identify and confirm a slower-than-expected pressure decline.

The reservoir pressure distribution also can help diagnose an active aquifer. For peripheral-water and edgewater drives, higher pressures tend to exist along the reservoir/aquifer boundary while lower pressures tend to exist at locations that are more distant. A pressure contour map is sometimes helpful to identify pressure disparities.

Fourth, the producing GOR can be a helpful indicator. Strong waterdrives are characterized by small changes in the producing GOR. The small GOR change is directly related to the small pressure decline. [Sec. 9.9.3](#) discusses this and other performance features characteristic of waterdrive reservoirs.

Fifth, a material-balance analysis can help diagnose water influx. Several different types of material-balance analyses such as the McEwen⁴² analysis can identify water influx. [Sec. 9.9.8](#) discusses these methods.

9.9.3 Performance. To illustrate the performance of waterdrives, simulation results of an 80-acre segment of a west Texas black-oil reservoir are presented. The segment is assumed to be surrounded by an infinite radial-flow aquifer. The reservoir properties in [Table 9.7](#) apply. The aquifer permeability and porosity are 37 md and 27%, respectively.

Fig. 9.20 shows the effect of water influx on a plot of pressure vs. fractional oil recovery. The initial reservoir pressure is 2,000 psia. Waterdrive and solution-gas-drive performances are

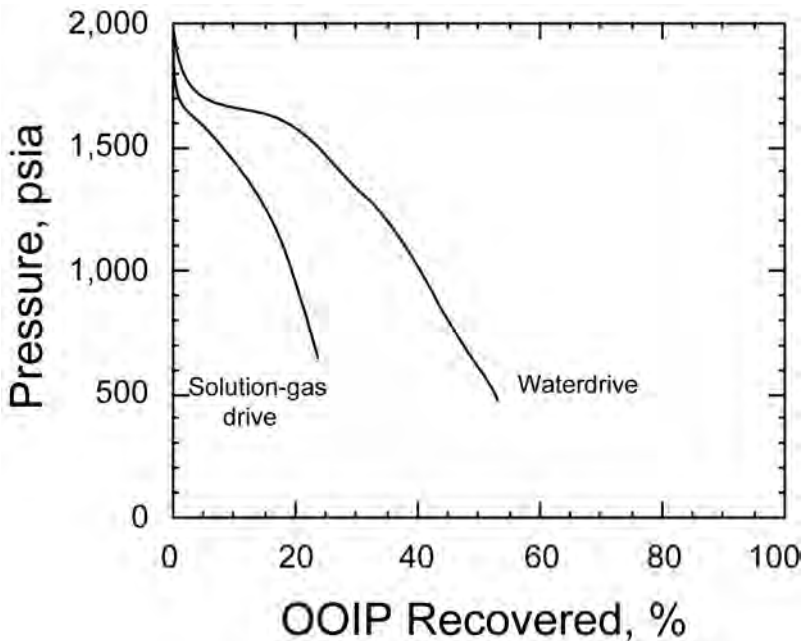


Fig. 9.20—The effect of water influx on pressure vs. percent OOIP recovered at a west Texas black-oil reservoir.

compared. This figure shows that water influx consistently improves the fractional oil recovery at a given pressure. Alternatively, the waterdrive maintains a higher pressure at a given recovery.

Fig. 9.21 shows the reservoir performance with time. This figure contains four separate plots: GOR, saturation, oil-recovery, and pressure histories. Waterdrives typically yield a characteristic GOR history. After a brief increase, the GOR typically levels off. This behavior is explained by the gas-saturation history. The gas saturation increases as soon as the pressure falls below the bubblepoint. After a brief increase, the gas saturation also levels off. The gas saturation levels off because the invading water drives the oil toward the producers. The oil is concentrated in a nonswept region or shrinking oil zone. Without oil displacement, the gas saturation and GOR would rise unabated. The solution-gas drive yields a final GOR of 4,506 scf/STB and gas saturation of 0.287 PV, while the waterdrive yields 1,323 scf/STB and 0.19 PV, respectively. The GOR for the water drive in Fig. 9.21 actually peaks after approximately 10 years and then decreases slightly. A decrease in the GOR reflects good displacement efficiency of oil by water.

As expected, the waterdrive yields a substantially higher recovery. The waterdrive also lengthens the productive life of the reservoir considerably. In this example, the waterdrive recovers 53.2% of the OOIP after 32.6 years, while the solution-gas drive recovers 24.2% of the OOIP after 13.5 years. Both cases assume a terminal oil rate of 20 STB/D. This recovery level indicates a relatively moderate to strong waterdrive. The waterdrive also yields a higher gas recovery (80.5 vs. 53.1%). The water-influx history basically mimics the incremental oil-recovery history. The cumulative encroached water is 58% hydrocarbon pore volume (HCPV) or 0.46 PV. This translates to approximately 1% OOIP incremental recovery for each 0.16 PV (or 2.0% HCPV) of encroached water. The waterdrive in Fig. 9.21 consistently yields higher producing rates than solution-gas drive.

Also as expected, the waterdrive consistently yields a higher pressure at a given time. The waterdrive yields a lower terminal pressure because lower gas saturations are realized at a giv-

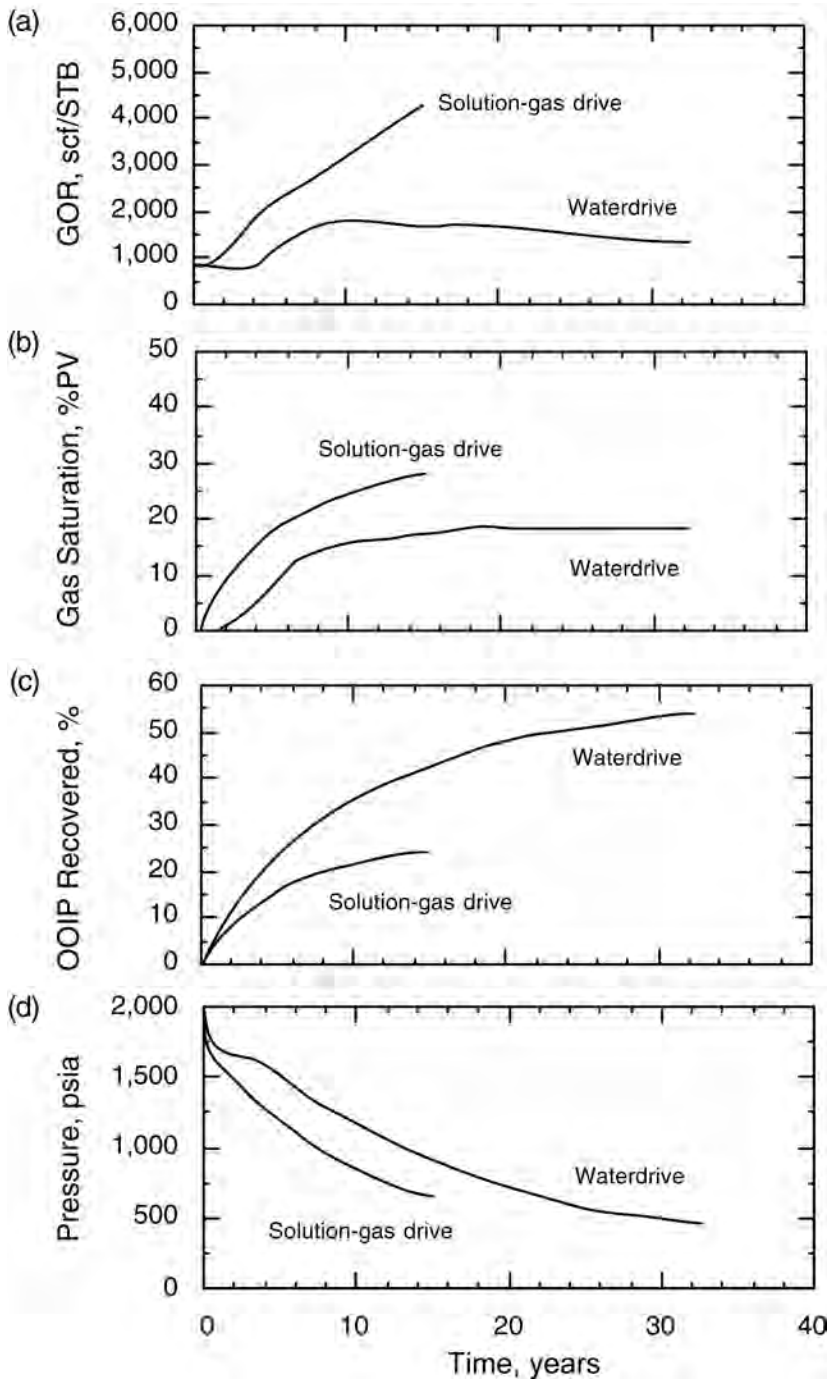


Fig. 9.21—Effect of water influx on (a) GOR, (b) gas-saturation, (c) oil-recovery, and (d) pressure histories for a west Texas black-oil reservoir.

en pressure. The example water and solution-gas drives yield final pressures of 471 and 613 psia, respectively.

The performance trends noted in Figs. 9.20 and 9.21 are not without exception. Waterdrive performance is strongly influenced by the displacement efficiency of oil by water. Figs. 9.20 and 9.21 are representative of moderate-to-good displacement efficiency. If displacement efficiency is poor, lower oil recovery will occur. A less obvious result, however, is that the GOR history will exhibit much different character than already discussed. Instead of rising slightly and leveling off, the GOR acts much like solution-gas drive; namely, the GOR steadily and monotonically increases. This difference occurs because the invading water bypasses substantial oil and fails to drive enough oil toward the producers to arrest the natural increase in the gas saturation. The GOR of a waterdrive can even exceed the GOR of the solution-gas drive if the displacement efficiency is poor enough. Peripheral waterdrives do not tend to be as efficient as bottomwater drives.

In summary, water influx can markedly improve oil recovery in oil reservoirs. The final oil recovery in a waterdrive reservoir depends largely on the net volume of influxed water. The net volume of influxed water is defined as the volume of influxed water less the volume of produced water. As the net volume of influxed water increases, the oil recovery increases. The volume of the influxed water depends mainly on the size of the aquifer and the communication between the aquifer and the reservoir. The maximum possible net volume of influxed water expressed as a fraction of the reservoir PV is

$$(1 - S_{orw} - S_{grw} - S_{wi}), \dots\dots\dots (9.29)$$

where S_{orw} is the residual oil saturation to water, S_{grw} is the residual gas saturation to water, and S_{wi} is the initial water saturation. As this equation shows, the residual saturations directly affect oil recovery by limiting the net volume of water that can influx into the reservoir. The residual saturations are a direct measure of the displacement efficiency of water. Lower residual oil saturations are preferred over lower residual gas saturations to promote oil production over gas production. The maximum fractional oil recovery for an initially undersaturated black-oil reservoir is

$$E_v(1 - S_{orw} - S_{grw} - S_{wi}) / (1 - S_{wi}), \dots\dots\dots (9.30)$$

where E_v is the volumetric sweep efficiency of the invading water. This equation assumes a complete waterdrive (i.e., no pressure depletion).

9.9.4 Water-Influx Models. Water-influx models are mathematical models that simulate and predict aquifer performance. Most importantly, they predict the cumulative water-influx history. When successfully integrated with a reservoir simulator, the net result is a model that effectively simulates waterdrive performance.

There are several popular aquifer models: the van Everdingen-Hurst (VEH) model,⁴³ the Carter-Tracy model,⁴⁴ the Fetkovich model,⁴⁵ the Schilthuis model,²⁹ and the small- or pot-aquifer model.⁴⁶ The first three models are unsteady-state models and are the most realistic. They attempt to simulate the complex pressure changes that gradually occur within the aquifer and between the aquifer and reservoir. As pressure depletion proceeds, the pressure difference between the reservoir and aquifer grows rapidly and then abates as the aquifer and reservoir eventually equilibrate. This pressure interaction causes the water-influx rate to start at zero, grow steadily, reach a maximum, and then dissipate. This particular water-influx-rate history behavior applies to initially saturated oil reservoirs; the behavior for initially undersaturated oil reservoirs is often slightly but distinctly different. The effects of undersaturation on the water-influx performance are discussed in Sec. 9.9.7. The unsteady-state models are far more successful at capturing the real dynamics than other models. In contrast, Schilthuis' steady-state model

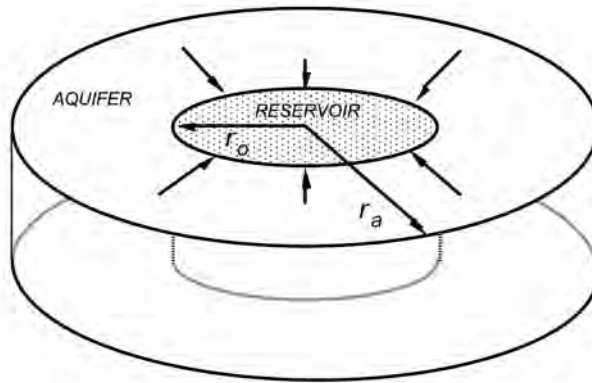


Fig. 9.22—Radial aquifer model.

assumes the aquifer pressure remains constant. The small-aquifer model, however, assumes the aquifer and reservoir pressures are equal.

The VEH model is the most sophisticated of all these models. Its main advantage is its realism. Originally, its main disadvantage was its cumbersome nature. Charts or tables had to be consulted repeatedly to execute a single calculation. To address this limitation, the Carter-Tracy and Fetkovich models were alternatives that were free of tables and charts. These models, however, were only approximations to and simplifications of the VEH model. Since the VEH charts and tables were digitized,^{47–49} the need for alternatives has diminished.

Allard and Chen⁵⁰ proposed an aquifer model specifically for bottomwater drives. This model included 2D flow. In comparison, the VEH model considered only 1D flow. Simulation practitioners, however, have found that the VEH model is satisfactory in simulating bottomwater drives.⁵¹

9.9.5 van Everdingen-Hurst (VEH) Model. van Everdingen and Hurst considered two geometries: radial- and linear-flow systems. The radial model assumes that the reservoir is a right cylinder and that the aquifer surrounds the reservoir. Fig. 9.22 illustrates the radial aquifer model, where r_o = reservoir radius and r_a = aquifer radius. Flow between the aquifer and reservoir is strictly radial. This model is especially effective in simulating peripheral and edgewater drives but also has been successful in simulating bottomwater drives.⁵⁰

In contrast, the linear model assumes the reservoir and aquifer are juxtaposed rectangular parallelepipeds. Fig. 9.23 shows examples. Flow between the aquifer and reservoir is strictly linear. This model is intended to simulate edgewater and bottomwater drives. The model definition depends on the application. For edgewater drives, the thicknesses of the reservoir and aquifer are identical; the widths of the reservoir and aquifer are also the same, and the aquifer and reservoir lengths are L_a and L_r , respectively (Fig. 9.23a). For bottomwater drives, the width of the reservoir and aquifer are identical; the length (L) of the reservoir and aquifer are also the same; the aquifer depth is L_a , and the reservoir thickness is h (Fig. 9.23b).

van Everdingen and Hurst solved the applicable differential equations analytically to determine the water-influx history for the case of a constant pressure differential at the aquifer/reservoir boundary. This case assumes the reservoir pressure is constant. They called this case the “constant terminal pressure” and reported their results in terms of tables and charts. This solution is not immediately applicable to actual reservoirs because it does not consider a declining reservoir pressure. To address this limitation, van Everdingen and Hurst applied the superposition theorem to a specific reservoir pressure history. This adaptation usually requires

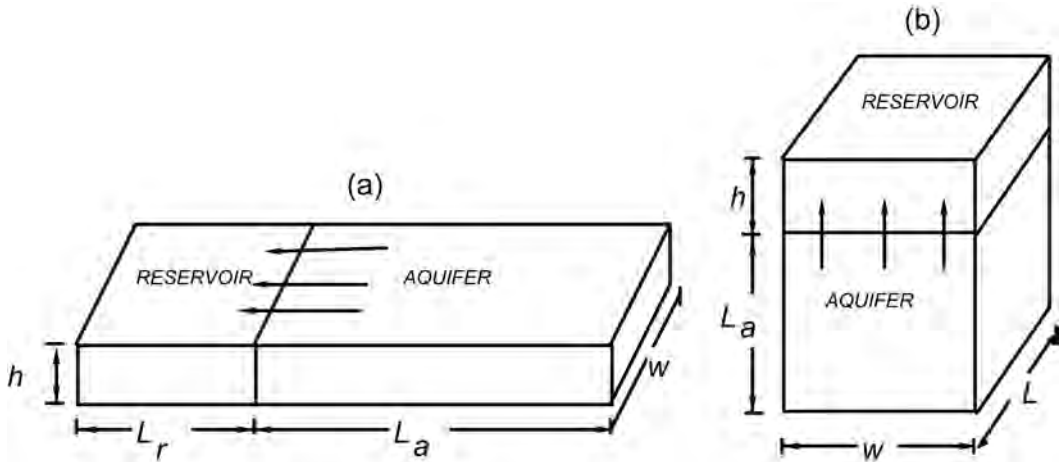


Fig. 9.23—Linear aquifer model for (a) an edgewater drive and (b) a bottomwater drive.

TABLE 9.13—TIME- AND PRESSURE-DOMAIN DISCRETIZATION FOR VEH MODEL					
j	t	t_D	\bar{p}	\tilde{p}	Δp
0	$t_0=0$	t_{D0}	$\bar{p}_0 = p_i$	$\tilde{p}_0 = \bar{p}_0 = p_i$	n/a
1	t_1	t_{D1}	\bar{p}_1	$\tilde{p}_1 = (\bar{p}_0 + \bar{p}_1)/2$	$\Delta p_1 = (\bar{p}_0 - \bar{p}_1)$
2	t_2	t_{D2}	\bar{p}_2	$\tilde{p}_2 = (\bar{p}_1 + \bar{p}_2)/2$	$\Delta p_2 = (\bar{p}_1 - \bar{p}_2)$
...
n	t_n	t_{Dn}	\bar{p}_n	$\tilde{p}_n = (\bar{p}_{n-1} + \bar{p}_n)/2$	$\Delta p_n = (\bar{p}_{n-1} - \bar{p}_n)$

that the reservoir’s pressure history be known. The first step in applying their model is to discretize the time and pressure domains.

Discretization. The time domain is discretized into $(n + 1)$ points $(t_0, t_1, t_2, \dots, t_n)$, where $t_0 < t_1 < t_2 < \dots < t_n$ and t_0 corresponds to $t = 0$. The average reservoir pressure domain also is discretized into $(n + 1)$ points $(\bar{p}_0, \bar{p}_1, \bar{p}_2, \dots, \bar{p}_n)$, where \bar{p}_0 is the initial pressure p_i . The time-averaged pressure between levels j and $j - 1$ is

$$\tilde{p}_j = \left(\frac{\bar{p}_{j-1} + \bar{p}_j}{2} \right) \text{ for } j = 1, 2, \dots, n \dots\dots\dots (9.31)$$

The time-averaged pressure at level $j = 0$ is defined as the initial pressure p_i . **Table 9.13** shows discretization of t , \bar{p} , and \tilde{p} . The time-averaged pressure decrement between levels j and $j - 1$ is

$$\Delta p_j = \tilde{p}_{j-1} - \tilde{p}_j \text{ for } j = 1, 2, \dots, n \dots\dots\dots (9.32)$$

No value is defined for $j = 0$. **Table 9.13** shows the complete discretization of t , \bar{p} , \tilde{p} , and Δp .

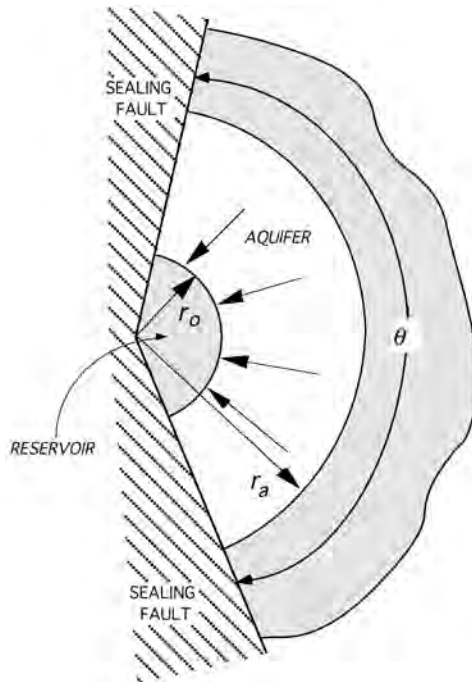


Fig. 9.24—Definition of angle, θ , for radial aquifer model.

Cumulative Water Influx. The cumulative water influx at k th level is

$$W_{ek}(t) = U \sum_{j=0}^{k-1} \Delta p_{j+1} W_D(t_{Dk} - t_{Dj}) \quad \text{for } k = 1, 2, \dots, n, \dots \quad (9.33)$$

where U is the aquifer constant and W_D is the dimensionless cumulative water influx. This equation is based on the superposition theorem. The term $W_D(t_{Dk} - t_{Dj})$ is not a product but refers to the evaluation of W_D at a dimensionless time difference of $(t_{Dk} - t_{Dj})$. If we apply Eq. 9.33 for $k = 1, 2$, and 3 , we obtain

$$\begin{aligned} W_{e1}(t) &= U \Delta p_1 W_D(t_{D1} - t_{D0}), \\ W_{e2}(t) &= U \Delta p_2 [W_D(t_{D2} - t_{D0}) + W_D(t_{D2} - t_{D1})], \\ \text{and } W_{e3}(t) &= U \Delta p_3 [W_D(t_{D3} - t_{D0}) + W_D(t_{D3} - t_{D1}) + W_D(t_{D3} - t_{D2})]. \end{aligned}$$

The length of the equation grows with the time. The aquifer constant, U , and the dimensionless cumulative water influx, $W_D(t_D)$, depend on whether the radial or linear model is applied.

Radial Model. The radial model is based on the following equations. The effective reservoir radius is a function of the reservoir PV and is

$$r_o = \sqrt{\frac{5.6146 V_{pr}}{\pi \phi_r h f}}, \dots \quad (9.34)$$

where r_o is expressed in ft, V_{pr} is the reservoir PV expressed in RB, ϕ_r is the reservoir porosity (fraction), and h is the pay thickness in ft. The constant f is $\theta/360$, where θ is the angle that defines the portion of the right cylinder. **Fig. 9.24** illustrates the definition of θ for a radial aquifer model. The dimensionless time is

$$t_D = \frac{2.309k_a t}{\phi_a \mu_w c_t r_o^2}, \dots\dots\dots (9.35)$$

where k_a = aquifer permeability (md), μ_w = water viscosity (cp), c_t = total aquifer compressibility (psi^{-1}), ϕ_a = aquifer porosity (fraction), and t is expressed in years. The total aquifer compressibility is the sum of the aquifer and rock compressibilities. The aquifer constant is

$$U = 1.19hf r_o^2 \phi_a c_t, \dots\dots\dots (9.36)$$

where U is in units of RB/psi if h is in ft, r_o is in ft, and c_t is in psi^{-1} .

The dimensionless aquifer radius is

$$r_{eD} = \frac{r_a}{r_o} \dots\dots\dots (9.37)$$

The dimensionless water influx, W_D , is a function of t_D and r_{eD} and depends on whether the aquifer is infinite acting or finite.

Infinite, Radial Aquifer. The aquifer is infinite acting if r_e approaches infinity or if the pressure disturbance within the aquifer never reaches the aquifer’s external boundary. If either of these conditions is met, then W_D is

$$W_D = 2\sqrt{\frac{t_D}{\pi}} + \frac{t_D}{2} - \frac{t_D}{6}\sqrt{\frac{t_D}{\pi}} + \frac{t_D^2}{16} \text{ for } t_D < 1, \dots\dots\dots (9.38)$$

$$\text{or } W_D = a_7 t_D^7 + a_6 t_D^6 + a_5 t_D^5 + a_4 t_D^4 + a_3 t_D^3 + a_2 t_D^2 + a_1 t_D^1 + a_0 \text{ for } 1 < t_D < 100, \dots\dots\dots (9.39)$$

where $a_7 = 4.8534 \times 10^{-12}$, $a_6 = -1.8436 \times 10^{-9}$, $a_5 = 2.8354 \times 10^{-7}$, $a_4 = -2.2740 \times 10^{-5}$, $a_3 = 1.0284 \times 10^{-3}$, $a_2 = -2.7455 \times 10^{-2}$, $a_1 = 8.5373 \times 10^{-1}$, $a_0 = 8.1638 \times 10^{-1}$, or

$$W_D = \frac{2t_D}{\ln t_D} \text{ for } t_D > 100. \dots\dots\dots (9.40)$$

Marsal⁴⁸ presented **Eqs. 9.38** and **9.40**. Walsh^{23,49} presented **Eq. 9.39**.

Finite, Radial Aquifer. For finite aquifers, **Eqs. 9.38** through **9.40** apply if $t_D < t_D^*$, where

$$t_D^* = 0.4(r_{eD}^2 - 1) \dots\dots\dots (9.41)$$

$$\text{and } r_{eD} = \frac{r_a}{r_o} \dots\dots\dots (9.37)$$

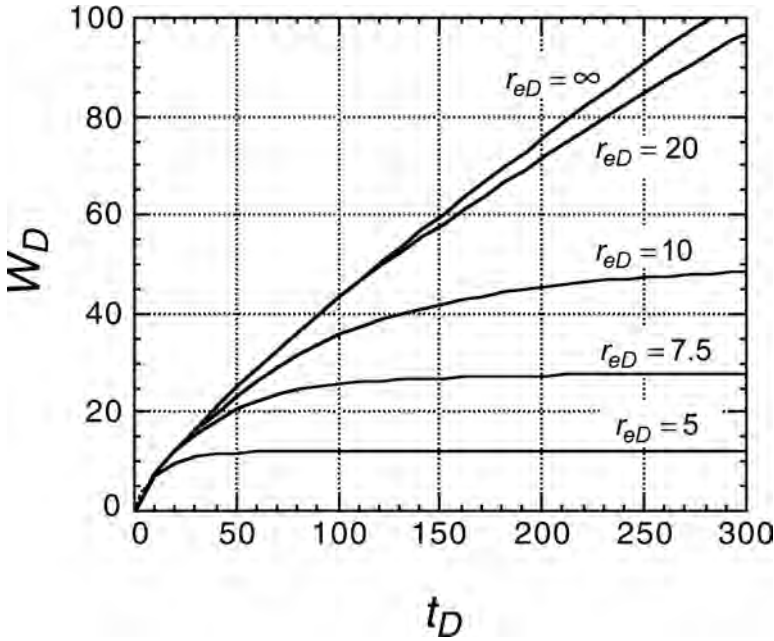


Fig. 9.25— W_D vs. t_D for radial aquifer model.

If $t_D > t_D^*$, then

$$W_D = 0.5(r_{eD}^2 - 1) \left[1 - \exp\left(-\frac{2t_D}{J^*}\right) \right] \text{ for } t_D > t_D^* , \dots\dots\dots (9.42)$$

$$\text{where } J^* = \frac{r_{eD}^4 (\ln r_{eD})}{(r_{eD}^2 - 1)} + 0.25(1 - 3r_{eD}^2) . \dots\dots\dots (9.43)$$

Marsal⁴⁸ gave Eqs. 9.41 through 9.43. These equations are effective in approximating the charts and tables by van Everdingen and Hurst. Minor discontinuities exist at some of the equation boundaries. A slightly more accurate but much more lengthy set of equations has been offered by Klins *et al.*⁴⁷ Fig. 9.25 shows W_D as a function of t_D for $r_{eD} = 5, 7.5, 10, 20$, and ∞ . These equations simplify the application of the VEH model enormously.

A finite aquifer can be treated effectively as an infinite aquifer if

$$t_{Dmax} \leq 0.4(r_{eD}^2 - 1) \dots\dots\dots (9.44)$$

$$\text{or } r_{eD} \geq \sqrt{\frac{t_{Dmax}}{0.4} + 1} , \dots\dots\dots (9.45)$$

where t_{Dmax} is the maximum value of t_D . These equations follow from Eq. 9.41. For example, if t_{Dmax} is 540 and corresponds to a time of 8 years, then Eq. 9.45 yields $\geq r_{eD} = 38$. Therefore, if the aquifer has a dimensionless radius greater than 38, then the aquifer acts indistinguishably from and equivalent to an infinite aquifer at all times less than 8 years.

Linear Aquifer. The aquifer size in the linear model is given in terms of the aquifer/reservoir pore-volume ratio, V_{pa}/V_{pr} .

$$V_{pa} = \left(\frac{V_{pa}}{V_{pr}}\right)V_{pr} \dots\dots\dots (9.46)$$

The aquifer constant is

$$U = V_{pa}c_t \dots\dots\dots (9.47)$$

For edgewater drives, the aquifer length is

$$L_a = L_r \left(\frac{V_{pa}}{V_{pr}}\right) \left(\frac{\phi_r}{\phi_a}\right) \dots\dots\dots (9.48)$$

where L_a and L_r are defined in Fig. 9.23a. For bottomwater drives, the aquifer depth is

$$L_a = h \left(\frac{V_{pa}}{V_{pr}}\right) \left(\frac{\phi_r}{\phi_a}\right) \dots\dots\dots (9.49)$$

where L_a is defined in Fig. 9.23b. The dimensionless time is

$$t_D = \frac{2.309k_a t}{\phi_a \mu_w c_t L_a^2} \dots\dots\dots (9.50)$$

Eqs. 9.50 and 9.35 use the same units except L_a is given in ft. One difference between the linear and radial models is that t_D is a function of the aquifer size for the linear model, whereas t_D is independent of the aquifer size for the radial model. This difference forces a recalculation of t_D in the linear model if the aquifer size is changed. The dimensionless cumulative water influx is

$$W_D = 2\sqrt{\frac{t_D}{\pi}} \text{ for } t_D < 0.47 \dots\dots\dots (9.51)$$

$$\text{and } W_D = 1 - 0.065807t_D^{-1.6512} \text{ for } t_D > 0.47 \dots\dots\dots (9.52)$$

Eq. 9.51 is by Marsal,⁴⁸ and Eq. 9.52 is by Walsh.^{23,49} Fig. 9.26 shows W_D as a function of t_D . The aquifer can be treated as infinite if the aquifer length is greater than the critical length.

$$L_{ac} = \sqrt{\frac{2.309k_a t_{max}}{0.5\phi_a \mu_w c_t}} \dots\dots\dots (9.53)$$

where t_{max} is the maximum time expressed in years and L_{ac} is in units of ft. Eqs. 9.50 and 9.53 use the same units. Alternatively, the aquifer is infinite-acting if $t_D \leq 0.50$. If infinite-acting and an edgewater drive, W_e can be evaluated directly without computing W_D and is

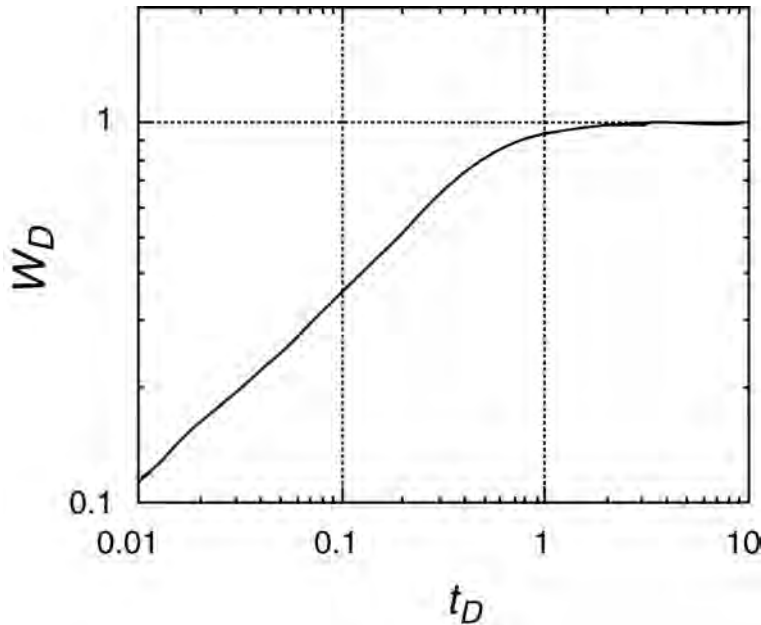


Fig. 9.26— W_D vs. t_D for linear aquifer model.

$$W_e = 0.3054hw\Delta p\sqrt{\frac{\phi k_d c_t t}{\mu w}}, \dots\dots\dots (9.54)$$

where the units in Eq. 9.35 apply, and W_e is in units of RB and h and w are in units of ft.

Calculation Procedure. The calculation requires historical average reservoir-pressure data. Given this data, the following procedure is used to compute the water-influx history. This method applies for radial and linear models, except where noted:

1. Discretize the time and average reservoir-pressure domains and define t_j and \bar{p}_j for ($j = 0, 1, \dots, n$) according to Table 9.13.
2. Compute the time-averaged reservoir pressure \tilde{p}_j for ($j = 1, 2, \dots, n$) with Eq. 9.31. Note that $\tilde{p}_0 = p_i$.
3. Compute the time-averaged incremental pressure differential Δp_j for ($j = 1, 2, \dots, n$) with Eq. 9.32.
4. Compute t_{Dj} for ($j = 0, 1, \dots, n$) with Eq. 9.35 for radial aquifers or with Eq. 9.50 for linear aquifers.
5. Steps 5 through 9 create a computational loop that is repeated n times. The loop index is k , where $k = 1, \dots, n$. For the k th time level, compute $(t_{Dk} - t_{Dj})$ for ($j = 0, \dots, k - 1$).
6. For the k th time level, compute $W_D(t_{Dk} - t_{Dj})$ for ($j = 0, \dots, k - 1$).
7. For the k th time level, compute $\Delta p_{j+1}W_D(t_{Dk} - t_{Dj})$ for ($j = 0, \dots, k - 1$).
8. For the k th time level, compute W_{ek} with Eq. 9.33.
9. Increment the time from level k to $k + 1$, and return to Step 5 until $k > n$.

This procedure is highly repetitive and well suited for spreadsheet calculation. Example 9.2 illustrates the procedure.

9.9.6 Determining Water-Influx Model Parameters. The minimum parameters that need to be specified in the radial model are the aquifer constant, U , the time constant, k_t , and the dimen-

sionless aquifer radius, r_{eD} . The time constant combines a number of constants, is the proportionality constant between the dimensionless and real time, and is defined by

$$t_D = k_t t \dots\dots\dots (9.55)$$

Physically, the time constant represents the aquifer conductivity. In summary, U and k_t are defined as

$$U = 1.19hf r_o^2 \phi_a c_t = \frac{2V_{pr} \phi_a c_t}{\phi_r} \dots\dots\dots (9.56)$$

$$k_t = \frac{2.309k_a}{\phi_a \mu_w c_t r_o^2} \dots\dots\dots (9.57)$$

$$\text{and } r_{eD} = r_e / r_o \dots\dots\dots (9.37)$$

Eq. 9.56 assumes the same units as Eq. 9.36, and V_{pr} is given in res bbl. Eq. 9.57 assumes the same units as Eq. 9.35.

The minimum parameters that need to be specified in the linear model are the aquifer constant, time constant, and aquifer/reservoir PV ratio (V_{pa} / V_{pr}). The aquifer constant and time constant are

$$U = V_{pa} c_t \dots\dots\dots (9.58)$$

$$\text{and } k_t = \frac{2.309k_a}{\phi_a \mu_w c_t L_a^2} \dots\dots\dots (9.59)$$

Eq. 9.59 assumes the same units as Eq. 9.35.

There are three common methods to estimate model parameters: direct measurement, history matching, and material balance. The first two methods are described in the following sections. The material-balance method, through the McEwen method,⁴² is described in Section 9.9.8.

Direct Measurement. This method estimates model parameters from direct measurement of the independent constants. Though ideally preferred, this method is rarely possible because of the uncertainty of some of the constants.

For the radial model, the model parameters (U , k_t , and r_{eD}) are a function of the following constants: r_e , r_o , k_a , h , f , ϕ_a , c_t , and μ_w . These constants follow from inspection of Eqs. 9.36, 9.37, and 9.57. The uncertainty among these constants varies. Of these constants, r_e , r_o , and k_a are perhaps the most uncertain. Qualitatively, these constants are related to the aquifer size, reservoir size, and aquifer conductivity (i.e., V_{pa} , V_{pr} , and k_t).

For the linear model, the model parameters (U , k_t , and V_{pa} / V_{pr}) are a function of the following constants: V_{pa} , V_{pr} , k_a , ϕ_a , c_t , μ_w , and L_a . This list follows from inspection of Eqs. 9.47 and 9.59. Of these constants, V_{pa} , V_{pr} , L_a , and k_a are the most uncertain. If h is approximately known, then V_{pa} and L_a are not independent but related through Eqs. 9.48 or 9.49. Thus, V_{pa} , V_{pr} , and k_a are the most uncertain independent constants. Qualitatively, these constants are related to the aquifer size, reservoir size, and aquifer conductivity (i.e., V_{pa} , V_{pr} , and k_t , respectively). Note the similarity between the radial and linear models.

TABLE 9.14—RESERVOIR PERFORMANCE DATA FOR EXAMPLE 9.2

<i>j</i>	Time (years)	<i>p</i> (psia)	Cumulative Water Influx (million RB)
1	0.000	1,640	0.000
2	0.368	1,600	0.062
3	2.439	1,400	1.272
4	4.957	1,200	4.156
5	7.732	1,000	8.455
6	11.926	800	15.494
7	18.126	600	26.014
8	30.044	400	42.243

In summary, because of the uncertainty of the aquifer size and conductivity and reservoir size, it is difficult to estimate reliably the water-influx model parameters. Nevertheless, every attempt should be made to estimate the median, variance, and range of each constant and the model parameters. This information is helpful in the history-matching method.

History Matching. If the water-influx history can be estimated, then model parameters can be estimated from history matching. When history matching is used, only the most uncertain constants should be treated as adjustable parameters: preferably only r_e , r_o , and k_a for the radial model or V_{pa} , V_{pr} , and k_a for the linear model. Unless only one adjustable parameter exists, history matching is usually complicated by nonuniqueness.^{40,42,52–54} Nonuniqueness, however, can be minimized by limiting the range of parameter adjustment to realistic ranges. **Example 9.2** illustrates the history-matching procedure.

Example 9.2: History Matching Water Influx. **Table 9.14** summarizes the cumulative water influx and average reservoir pressure as a function of time for an initially saturated, black-oil reservoir. Areally, the reservoir is approximately semicircular, bounded on one side by a sealing fault and the other side by an aquifer. **Fig. 9.27a** shows a schematic representation of the reservoir. Assume the reservoir and aquifer properties in **Table 9.15** apply.

Assume a radial-flow aquifer with $f = 0.50$. Find the optimal aquifer size (V_{pa} and r_{eD}) that best simulates the water-influx performance. Plot and compare the actual and predicted water-influx histories.

Find the optimal aquifer size (V_{pa}/V_{pr} and L_a) that best matches the water-influx performance assuming a linear-flow aquifer. Assume the reservoir width is $w = 2r_o$ and length is $L_r = \pi r_o/4$, where r_o is given by **Eq. 9.34**. **Fig. 9.27b** schematically shows the areal interpretation. Plot and compare the actual and predicted water-influx histories. Which model (linear or radial) best matches the data?

Solution. Compute the effective reservoir radius from

$$r_o = \sqrt{\frac{5.6146V_{pr}}{\pi\phi_r h f}} = \sqrt{\frac{(5.6146 \text{ ft}^3/\text{bbl})(385 \times 10^6 \text{ RB})}{\pi(0.31)(20 \text{ ft})(0.5)}} = 14,892 \text{ ft}, \dots\dots\dots (9.34)$$

where $f = 0.50$. The total compressibility is the sum of the rock and water compressibilities or $c_t = 5.88 \times 10^{-6} \text{ psi}^{-1}$. The time constant, k_t , is given by **Eq. 9.57** and is $k_t = 0.8682 \text{ years}^{-1}$. U is given by **Eq. 9.56** and is 3,955 RB/psi. **Table 9.16** tabulates t_D , \tilde{p} , and Δp .

The solution procedure varies r_{eD} until the best match is obtained. **Tables 9.17 through 9.19** give the details of the calculation for $r_{eD} = 5.0$. **Table 9.17** tabulates $(t_{Dk} - t_{Dj})$ for k and j

TABLE 9.15—RESERVOIR AND FLUID PROPERTIES FOR EXAMPLE 9.2	
Property	Value
Reservoir pore volume, million RB	385
Reservoir porosity, %	31
Reservoir permeability, md	5
Pay thickness, ft	20
f	0.50
Initial water saturation, %	20
Temperature, °F	131
Water viscosity, cp	0.48
Water compressibility, 1/psi	2.88
Rock compressibility, 10^{-3} PV/PV/psi	3.0
Aquifer porosity, %	27
Aquifer permeability, md	64.2
Aquifer thickness, ft	20
Water salinity, ppm	20,000

= 0, 1, ..., 7. **Table 9.18** tabulates $W_D(t_{Dk} - t_{Dj})$ for k and $j = 0, 1, \dots, 7$. **Table 9.19** tabulates $\Delta p_{j+1} W_D(t_{Dk} - t_{Dj})$ for k and $j = 0, 1, \dots, 7$. **Table 9.16** tabulates $\Sigma \Delta p_{j+1} W_D(t_{Dk} - t_{Dj})$ for $k = 1, 2, \dots, 7$ for $r_{eD} = 5$ and W_{ej} for $j = 0, 1, \dots, 7$ for $r_{eD} = 5$. **Fig. 9.28** plots W_e vs. t and compares model and actual results; excellent agreement is noted. These calculations were repeated for other values of r_{eD} but $r_{eD} = 5.0$ was found to give the best fit of the actual and model water-influx histories. Notice how well the radial model matches the history. A dimensionless aquifer radius of $r_{eD} = 5.0$ corresponds to $V_{pa}/V_{pr} = 20.8$. This means that the aquifer is 20.8 times larger than the reservoir.

To determine whether this aquifer can be treated as infinite acting, we evaluate **Eq. 9.45** with $t_{Dmax} = 26.08$. This calculation yields $r_{eD} = 8.1$. Because this value of r_{eD} is greater than the history-matched value of $r_{eD} = 5.0$, this aquifer cannot be treated as infinite.

For the linear aquifer model, the geometry dictates that $L_r = 11,696$ ft if $L_r = \pi r_o/4 = \pi (14,892)/4$. With the same trial-and-error procedure as used for the radial aquifer, the linear aquifer yields $V_{pa}/V_{pr} = 12$ for the best match between the actual and predicted water-influx data. This value of V_{pa}/V_{pr} yields $L_a = 161,145$ ft, $U = 27,271$ RB/psi, and $k_t = 0.0074$ years⁻¹. **Fig. 9.28** compares the predicted and actual data and shows that the match is poor. This comparison reveals that the linear model is not preferable to simulate water influx for this reservoir.

9.9.7 Aquifer Performance. The aquifer performance is described in terms of the delivery rate, average aquifer pressure, and cumulative water-influx volume as a function of time. The aquifer pressure characteristically lags behind the reservoir pressure and is estimated by

$$\bar{p}_a = p_i - \frac{W_e(t)}{c_t V_{pa}} \dots \dots \dots (9.60)$$

The aquifer delivery rate is $q_w = \partial W_e(t)/\partial t$, which is determined from the slope of the W_e vs. t curve.

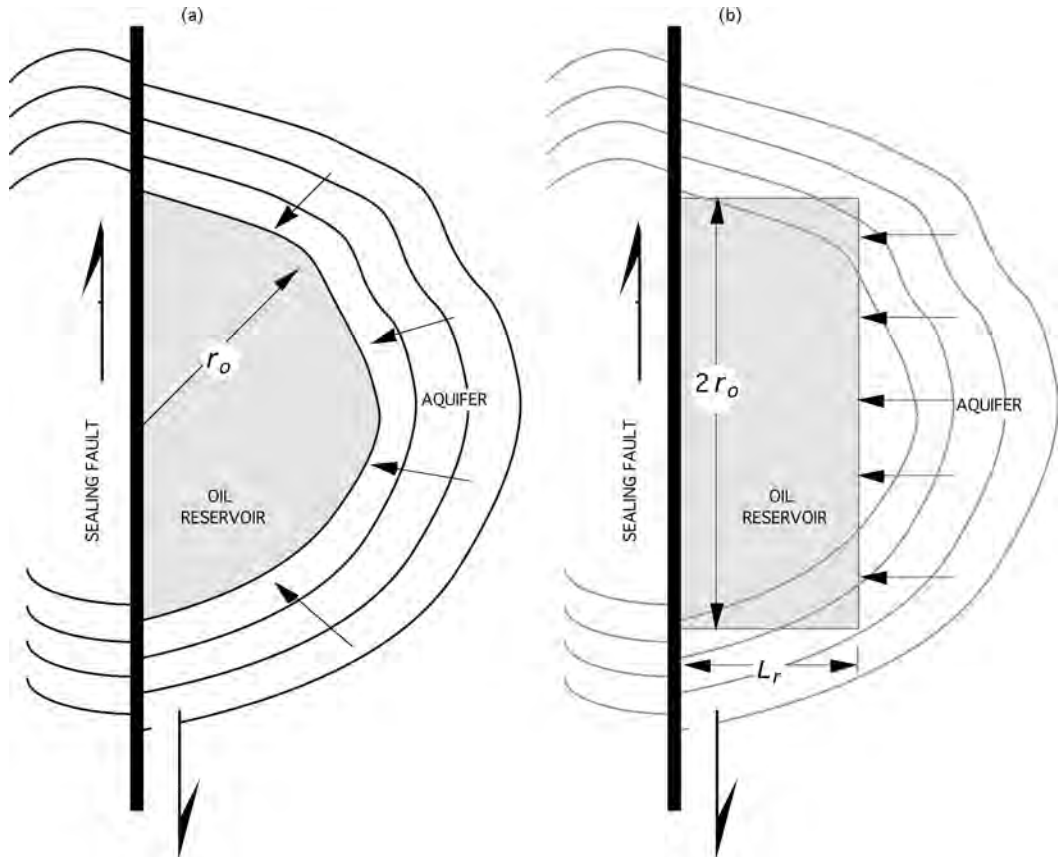


Fig. 9.27—(a) Areal schematic of a reservoir partially surrounded by a radial aquifer; (b) interpretation of reservoir geometry when linear aquifer model is applied.

Fig. 9.29 shows the aquifer pressure and delivery-rate history for the data in [Example 9.2](#). This figure includes the reservoir pressure history for comparison. The qualitative results in [Fig. 9.29](#) are representative of many aquifers. The water-delivery rate is initially zero and increases rapidly. It peaks after approximately 12 to 14 years and then slowly decreases. The aquifer and reservoir pressures start at equivalent values. The reservoir pressure declines more quickly than the aquifer pressure. The pressure differential between the aquifer and reservoir grows and is approximately 250, 350, and 500 psia, respectively, after 2, 5, and 10 years. The pressure differential peaks after 12 to 14 years and then begins to dissipate. The pressure differential and delivery rate decline together.

The aquifer performance noted in [Fig. 9.29](#) is not without exception. The qualitative performance in [Fig. 9.29](#) is characteristic of an initially saturated reservoir. Aquifers feeding initially undersaturated reservoirs may behave quite differently. The difference stems from the difference in the reservoir pressure histories. The reservoir pressure in initially undersaturated oil reservoirs initially declines much more quickly than in initially saturated reservoirs. Consequently, initially undersaturated reservoirs create a substantial pressure differential between the reservoir and aquifer much sooner than initially saturated reservoirs. Of course, this distinction depends on the degree of undersaturation. If the reservoir is significantly undersaturated, a large pressure differential between the reservoir and aquifer is quickly established. This large pressure differential, in turn, promotes water influx; consequently, the water-influx rate increas-

TABLE 9.16—PREDICTED WATER-INFLUX HISTORY FOR RADIAL AQUIFER IF $r_{eD}=5.0$

j	t (years)	\bar{p} (psia)	t_D	\bar{p} (psia)	Δp (psi)	$\Sigma \Delta p W_D$ (psi)	W_e (million RB)
0	0	1,640	0	1,640		0	0
1	0.368	1,600	0.32	1,620	20	16	0.062
2	2.439	1,400	2.12	1,500	120	322	1.275
3	4.957	1,200	4.30	1,300	200	1,054	4.170
4	7.732	1,000	6.71	1,100	200	2,147	8.491
5	11.926	800	10.35	900	200	3,939	15.580
6	18.126	600	15.74	700	200	6,620	26.182
7	30.044	400	26.08	500	200	10,735	42.460

TABLE 9.17—SUMMARY OF $(t_{Dk}-t_{Dj})$ CALCULATIONS FOR RADIAL AQUIFER

k	t_{Dk}	$t_{Dk}-t_{Dj}$						
		$j=0$	$j=1$	$j=2$	$j=3$	$j=4$	$j=5$	$j=6$
0	0.00	0.00	0.00	0.00	0.00	0.00	0.00	0.00
1	0.32	0.32	0.00	0.00	0.00	0.00	0.00	0.00
2	2.12	2.12	1.80	0.00	0.00	0.00	0.00	0.00
3	4.30	4.30	3.98	2.19	0.00	0.00	0.00	0.00
4	6.71	6.71	6.39	4.60	2.41	0.00	0.00	0.00
5	10.35	10.35	10.03	8.24	6.05	3.64	0.00	0.00
6	15.74	15.74	15.42	13.62	11.43	9.02	5.38	0.00
7	26.08	26.08	25.76	23.97	21.78	19.37	15.73	10.35

es more rapidly in initially undersaturated reservoirs than initially saturated reservoirs. Once the bubblepoint is reached, the pressure differential between the aquifer and reservoir may decline temporarily. Later, the pressure differential may increase, reminiscent of an initially saturated reservoir, as in Fig. 9.29. The net effect is that water recharge rate may oscillate in an initially undersaturated oil reservoir.

9.9.8 Material-Balance Analysis. The objectives of a material-balance analysis include confirming the producing mechanism, estimating the OOIP, estimating the water-influx history, and estimating the water-influx model parameters. The water-influx model parameters are needed to forecast future water influx and oil recovery.

The analysis depends on the known and unknown constants and variables. Three scenarios are considered: the water-influx history is known but the OOIP is unknown, the water-influx history is unknown but the OOIP is known, and both the water-influx history and the OOIP are unknown.

Water Influx Known, OOIP Unknown. If the water-influx history is known and the OOIP unknown, the material-balance methods in the previous sections are directly applicable. For instance, if the reservoir is initially undersaturated, then an $(F - W_e)$ -vs.- E_{owf} plot can be used

TABLE 9.18—SUMMARY OF $W_D(t_{Dk}-t_{Dj})$ CALCULATIONS FOR RADIAL AQUIFER

k	t_{Dk}	$W_D(t_{Dk}-t_{Dj})$						
		$j=0$	$j=1$	$j=2$	$j=3$	$j=4$	$j=5$	$j=6$
0	0.00	0.00	0.00	0.00	0.00	0.00	0.00	0.00
1	0.32	0.79	0.00	0.00	0.00	0.00	0.00	0.00
2	2.12	2.51	2.27	0.00	0.00	0.00	0.00	0.00
3	4.30	4.06	3.84	2.56	0.00	0.00	0.00	0.00
4	6.71	5.24	5.39	4.25	2.73	0.00	0.00	0.00
5	10.35	7.05	6.91	6.06	5.18	3.61	0.00	0.00
6	15.74	8.87	8.78	8.25	7.48	6.45	4.76	0.00
7	26.08	10.71	10.67	10.45	10.13	9.71	8.87	7.04

TABLE 9.19—SUMMARY OF $\Delta p_{j+1}W_D(t_{Dk}-t_{Dj})$ CALCULATIONS FOR RADIAL AQUIFER

k	t_{Dk}	$\Delta p_{j+1}W_D(t_{Dk}-t_{Dj})$						
		$j=0$	$j=1$	$j=2$	$j=3$	$j=4$	$j=5$	$j=6$
0	0.00	0.00	0.00	0.00	0.00	0.00	0.00	0.00
1	0.32	15.70	0.00	0.00	0.00	0.00	0.00	0.00
2	2.12	50.20	272.20	0.00	0.00	0.00	0.00	0.00
3	4.30	81.10	461.00	512.30	0.00	0.00	0.00	0.00
4	6.71	104.70	646.40	850.10	545.60	0.00	0.00	0.00
5	10.35	140.90	829.00	1,212.50	1,035.30	721.30	0.00	0.00
6	15.74	177.40	1,054.20	1,650.20	1,496.30	1,289.70	951.80	0.00
7	26.08	214.10	1,280.60	2,090.20	2,026.60	1,941.30	1,773.90	1,408.40

to confirm the mechanism and estimate the OOIP. The water-influx model parameters can be determined by history matching.

Water Influx Unknown, OOIP Known. If the OOIP is known and the water-influx history is unknown, then the material-balance equation can be used to estimate the water-influx history. Solving Eq. 9.7 for W_e yields

$$W_e = G_{f_{gi}}E_{gwf} + N_{f_{oi}}E_{owf} - F \dots\dots\dots (9.61)$$

If the OOIP (N) and OGIP (G) are known, $G_{f_{gi}}$ and $N_{f_{oi}}$ are computed from Eqs. 9.21 and 9.22. Eq. 9.61 is applied for each historical average pressure measurement to compute the cumulative water influx. Example 9.3 illustrates this method. Once the water-influx history is estimated, the aquifer parameters can be estimated from history matching.

Water Influx Unknown, OOIP Unknown. This case simultaneously determines the OOIP, water-influx history, and water-influx model parameters. This is a challenging problem. Woods and Muskat⁵² were among the first to study this problem and they noted that the solution was complicated by nonuniqueness. Others, too, have noted nonuniqueness.^{40,42,53,54} Despite these complications, certain techniques have proved useful and some approaches are better than others are. The solution method is based on the work of McEwen⁴² and depends on whether the radial or linear version of the VEH model is applied.

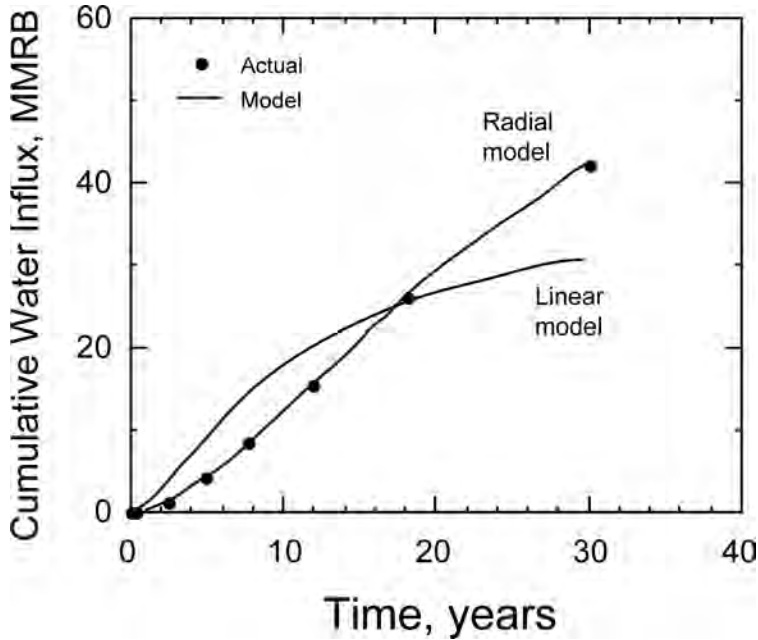


Fig. 9.28—Comparison of actual and predicted water-influx histories for Example 9.2.

Radial Aquifer. This method simultaneously determines the OOIP, water-influx history, and model parameters r_{eD} and k_t . The aquifer constant U is then subsequently determined. The water influx is

$$W_e = U \Sigma \Delta p W_D \dots\dots\dots (9.62)$$

This equation is an abbreviation of Eq. 9.33. The summation $\Sigma \Delta p W_D$ is a function of only r_{eD} and k_t . McEwen noted that U is related to N_{foi} and G_{fgi} through

$$U = \frac{2(N_{foi} B_{oi} + G_{fgi} B_{gi}) c_t \left(\frac{\phi_a}{\phi_r} \right)}{(1 - S_{wi})} \dots\dots\dots (9.63)$$

Substituting this equation into Eq. 9.62 and substituting this result into Eq. 9.7 yields

$$F = N_{foi} E_{ow} + G_{fgi} E_{gw} \dots\dots\dots (9.64)$$

where

$$E_{ow} = E_{owf} + \frac{2 B_{oi} c_t \Sigma \Delta p W_D (k_t, r_{eD}) \left(\frac{\phi_a}{\phi_r} \right)}{(1 - S_{wi})} \dots\dots\dots (9.65)$$

$$\text{and } E_{gw} = E_{gwf} + \frac{2 B_{gi} c_t \Sigma \Delta p W_D (k_t, r_{eD}) \left(\frac{\phi_a}{\phi_r} \right)}{(1 - S_{wi})} \dots\dots\dots (9.66)$$

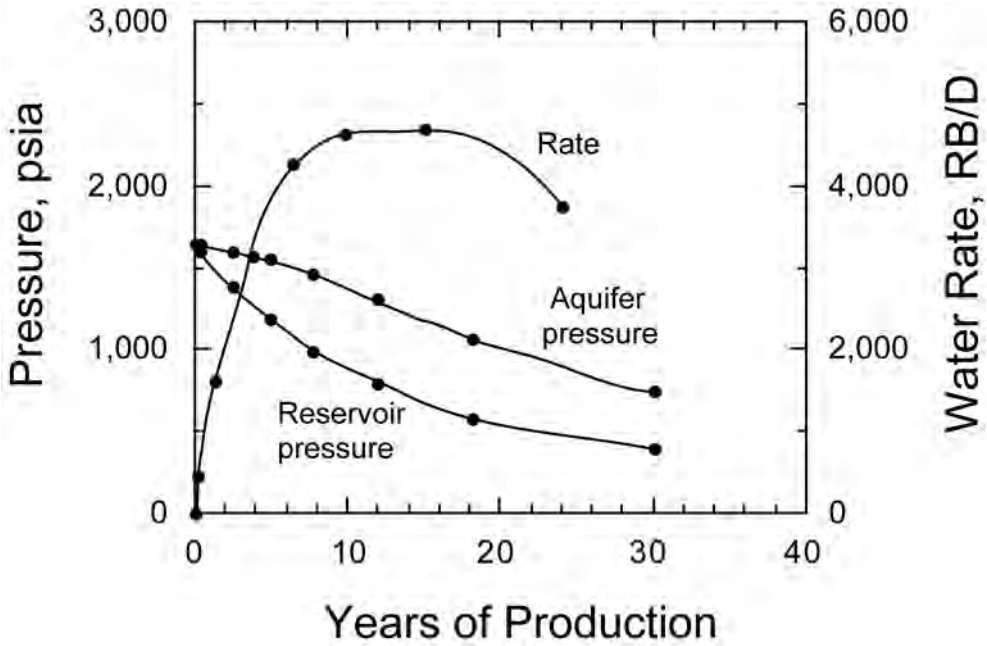


Fig. 9.29—Predicted aquifer pressure and water-influx rate histories for Example 9.2.

For the case of an initially undersaturated oil reservoir,

$$F = NE_{ow} \dots\dots\dots (9.67)$$

This equation shows that a plot of F vs. E_{ow} is a straight line, emanates from the origin, and has a slope equal to N , the OOIP. This observation provides a means to confirm the producing mechanism.

E_{ow} , however, is a function of k_t and r_{eD} , and these parameters are unknown *a priori*. Thus, the problem reduces to one of finding the optimal k_t and r_{eD} that minimizes the material-balance error. Graphically, this is equivalent to varying k_t and r_{eD} until the straightest possible line is realized. The slope of the line equals the OOIP, and the OGIP is the product NR_{si} if the reservoir is initially undersaturated. Mathematically, the material-balance error is minimized when the sum of the squares of the residual is minimized. The residual for point i is

$$R_i = (F)_i - N(E_{ow})_i \dots\dots\dots (9.68)$$

The sum of the squares of the residual is

$$R_{ss} = \sum_{i=1}^n (R_i)^2, \dots\dots\dots (9.69)$$

where n is the total number of data points.

In summary, the McEwen method to simultaneously estimate N , r_{eD} , and k_t is as follows:

1. Estimate a limited range of realistic values for k_t if possible.
2. Compute F for each data point with Eq. 9.8 if saturated or Eq. 9.13 if undersaturated.
3. Guess k_t and r_{eD} .

4. Compute E_{ow} for each data point with Eq. 9.65.
5. Compute N with least-squares linear regression or graphically from the slope of an F -vs.- E_{ow} plot.
6. Compute R_i for each data point with Eq. 9.68.
7. Compute R_{ss} with Eq. 9.69.
8. If the R_{ss} is minimized, then go to Step 9; otherwise, return to Step 3.
9. Compute the aquifer constant with Eq. 9.63.
10. Compute the water influx for each data point with Eq. 9.62.

If least-squares linear regression is used to compute N in Step 5, an equation analogous to Eq. 9.16 is used (where E_{ow} is substituted for E_{owf}). This solution method is iterative because the material-balance error must be minimized. This calculation is carried out with a trial-and-error method or a minimization algorithm. Least-squares linear regression and minimization algorithms have become standard features in commercial spreadsheets.

McEwen’s method also can be applied to initially saturated reservoirs; however, the solution procedure must be expanded and modified slightly. More specifically, the solution procedure is the same as for initially undersaturated reservoirs except Steps 5 and 6. Step 5 must be modified to include the simultaneous calculation of N_{foi} and G_{fgi} by multivariate, least-squares (planar) regression.^{23,28} Step 6 must be modified, and the residual for point i is computed with $R_i = (F)_i - G_{fgi}(E_{gw})_i - N_{foi}(E_{ow})_i$.

Linear Aquifer. McEwen’s method for linear aquifers is very similar to the radial model. The method simultaneously determines the OOIP, water-influx history, and the model parameters [(V_{pa}/V_{pr}) and k_t].

The aquifer constant U is related to V_{pa} through

$$U = \left(\frac{V_{pa}}{V_{pr}}\right) \frac{(N_{foi}B_{oi} + G_{fgi}B_{gi})c_t}{(1 - S_{wi})} \dots\dots\dots (9.70)$$

Substituting this equation into Eq. 9.62 and substituting the result into Eq. 9.7 gives Eq. 9.64, where

$$E_{gw} = E_{gwf} + \left(\frac{V_{pa}}{V_{pr}}\right) \frac{B_{gi}c_t \Sigma \Delta p W_D(k_t)}{(1 - S_{wi})}, \dots\dots\dots (9.71)$$

$$E_{ow} = E_{owf} + \left(\frac{V_{pa}}{V_{pr}}\right) \frac{B_{oi}c_t \Sigma \Delta p W_D(k_t)}{(1 - S_{wi})}, \dots\dots\dots (9.72)$$

and $\Sigma \Delta p W_D$ is a function of only k_t and not (V_{pa}/V_{pr}) . Eqs. 9.71 and 9.72 are analogous to Eqs. 9.65 and 9.66 in the radial model.

The solution procedure for the linear model is identical to that of the radial model except that k_t and V_{pa}/V_{pr} are optimized to minimize the material-balance error. Once V_{pa}/V_{pr} is determined, the aquifer constant U is determined from Eq. 9.70 and W_e is determined from Eq. 9.62. Example 9.4 illustrates an example of the McEwen method.

Numerous alternative material-balance methods have been proposed to analyze waterdrive reservoirs. Some are very popular and widely used. While most are theoretically valid, most are also unreliable. van Everdingen *et al.*,⁵⁵ for instance, proposed plotting F/E_o vs. $(\Sigma \Delta p W_D)/E_o$. The slope of this plot equals U and the y -intercept equals N . van Everdingen *et al.* proposed varying k_t until the straightest possible line was obtained. Later, Havlena and Odeh³⁸ popularized this method and modified it to include the aquifer size (r_{eD}) as an additional un-

known and determinable parameter. Dake³⁰ also advocated this method. Chierici *et al.*⁵³ proposed a variation of this method with a $F/(\Sigma\Delta pW_D)$ vs. $E_o/(\Sigma\Delta pW_D)$ plot. McEwen⁴² studied the method of van Everdingen *et al.* and noted hypersensitivity to pressure uncertainty. He observed unacceptably large errors and deemed the method unreliable. Later, Tehrani⁴⁰ presented a systematic analysis of these methods and confirmed McEwen’s conclusions. Wang and Hwan³⁹ confirmed Tehrani’s findings. Sills⁵⁴ presents a review and comparison of the McEwen, Havlena-Odeh, and van Everdingen-Timmerman-McMahon methods.

To help diagnose waterdrives, Campbell⁵⁶ proposed plotting F/E_{owf} vs. N_p for initially undersaturated oil reservoirs. This method is analogous to Cole’s⁵⁷ popular method of plotting F/E_{gwf} vs. G_p for gas reservoirs. In theory, an active waterdrive is indicated if the plot varies appreciably from a horizontal line. The degree of curvature is a qualitative measure of the waterdrive strength. The curve emanates from a y -intercept equal to the OOIP. The shape of the curve mimics and is related to the attending water recharge rate history. Cole and Campbell plots are attractive because of their simplicity and are widely reported. Unfortunately, in practice, they are not always reliable because of hypersensitivity caused by uncertainty. The origin of the hypersensitivity is analogous to the problems noted by McEwen,⁴² Tehrani,⁴⁰ Wang and Hwan,³⁹ and Walsh²⁸ for other types of material-balance plots. The quotient F/E_{owf} approaches infinity initially because the E_{owf} approaches zero. A systematic reservoir pressure error of only 1 to 2%, for instance, can lead to erroneous conclusions regarding water-influx diagnosis. These facts complicate the interpretation. For these reasons, Campbell plots should be used cautiously to diagnose water influx and used very cautiously to estimate the OOIP. If they are used, the early-time data should be weighted minimally. The reliability of these plots increases with pressure depletion; however, water influx mitigates pressure depletion and delays reliability. Unfortunately, water-influx diagnoses are sought as early as possible, which further complicates and compromises the use of these plots.

Example 9.3: Estimating Water Influx With Material Balance. Table 9.20 summarizes the cumulative oil and gas production as a function of time and average reservoir pressure for a black-oil reservoir. The discovery (initial) pressure is 1,640 psia, and production data are tabulated through a pressure of 800 psia.

Volumetric measurements estimate an OOIP of 210,420 thousand STB with no initial free gas. Estimate the cumulative water influx (RB) at each pressure in Table 9.20 with material balance. Assume that the standard PVT parameters in Table 9.3 apply.

Solution. Eq. 9.61 gives the cumulative water influx. Because there is no initial free gas, $G_{fgi} = 0$, $N_{foi} = N$, and Eq. 9.61 simplifies to

$$W_e = NE_o - F, \dots\dots\dots (9.73)$$

where rock and water expansion are ignored and F and E_o are given by Eqs. 9.8 and 9.2, respectively. E_o is a function of B_{to} , which is given by Eq. 9.5.

Table 9.21 tabulates the results. Fig. 9.30 plots the water-influx history.

Example 9.4: Determining Water-Influx Parameters and OOIP. van Everdingen *et al.*⁵⁵ studied water influx in an initially undersaturated oil reservoir located in the Wilcox formation at a depth of 8,100 ft subsea. The accumulation covered approximately 1,830 acres. The maximum gross and net thicknesses were 37 and 26 ft, respectively. The reservoir fluid exhibited an initial oil FVF of 1.538 RB/STB and a GOR of 900 scf/STB. Table 9.22 reports the reservoir and aquifer properties.

**TABLE 9.20—RESERVOIR PERFORMANCE DATA
FOR EXAMPLE 9.3**

Time (years)	p (psia)	Cumulative Oil Recovery (million STB)	Cumulative Gas Recovery (Bscf)
0.000	1,640	0.000	0.000
0.368	1,600	3.619	2.921
2.439	1,400	19.938	19.208
4.957	1,200	32.262	38.535
7.732	1,000	40.399	56.131
11.926	800	47.873	75.978

**TABLE 9.21—SUMMARY OF WATER-INFLUX CALCULATIONS
FOR EXAMPLE 9.3**

p (psia)	B_{to} (RB/STB)	E_o (RB/STB)	F (million RB)	Cumulative Water Influx (million RB)	Time (years)
1,640	1.4630	0.0000	0.00	0.00	0.000
1,600	1.4880	0.0250	5.32	0.062	0.368
1,400	1.6450	0.1820	39.57	1.270	2.439
1,200	1.8916	0.4286	94.34	4.150	4.957
1,000	2.2142	0.7512	166.53	8.450	7.732
800	2.7438	1.2808	285.00	15.500	11.926

van Everdingen *et al.*⁵⁵ estimated the OOIP at 24 to 25 million STB from volumetric measurement. From the oil, gas, and water production data and standard PVT properties, they computed F and E_o as a function of pressure. Production took place from 1942 through 1950. Approximately 6.965 million STB of oil and 7.1 Bscf of gas were produced during this period. **Table 9.23** gives the average reservoir pressure, total fluid withdrawal, and oil-phase expansivity as a function of time.

Use McEwen's method to find the optimal dimensionless aquifer radius, r_{eD} , and the aquifer time constant, k_t (years⁻¹). Plot F vs. E_{ow} . Also, compute the aquifer constant, U (RB/psi). Estimate the OOIP (million STB). Estimate the water delivery rate (RB/D) and average aquifer pressure (psia), and plot the histories.

Solution. Though the time constant, k_t , is unknown, first estimate a realistic range of values based on reservoir and aquifer properties. The time constant is given by Eq. 9.57. The total compressibility is the sum of the rock and water compressibility or 6.8×10^{-6} psi⁻¹. The aquifer porosity is 20.9%. The water viscosity is 0.25 cp. The aquifer permeability is 275 md. The only unspecified quantity on the right side of Eq. 9.57 is the effective reservoir radius. Although this quantity is unknown because the size of the reservoir is uncertain, it can be estimated from

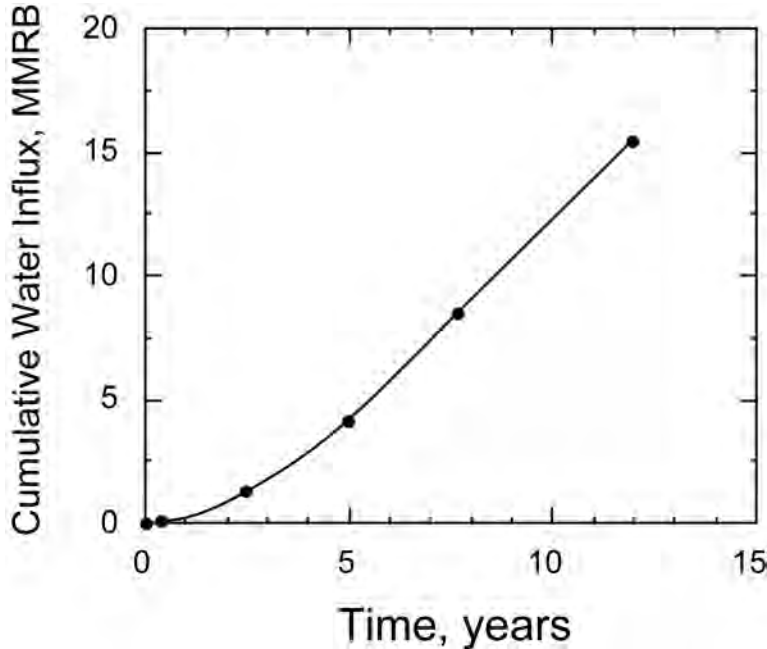


Fig. 9.30—Computed water-influx history for Example 9.3.

$$r_o = \sqrt{\frac{5.6146V_{pr}}{\pi\phi_r hf}} \dots\dots\dots (9.34)$$

To use this equation, estimate the reservoir PV, which is given by

$$V_{pr} = \frac{N_{foi}B_{oi} + G_{fgi}B_{gi}}{(1 - S_{wi})} \dots\dots\dots (9.74)$$

Evaluating this equation on the basis of $N_{foi} = 25$ million STB yields $V_{pr} = 45.23$ million RB. Evaluating Eq. 9.34 for $f = 1$, $h = 26$ ft, and $\phi_r = 19.9\%$ yields $r_o = 3,951$ ft. Evaluating Eq. 9.57 yields $k_t = 116$ years⁻¹. Thus, a liberal range for k_t is 10 to 1,000 years⁻¹.

Next, compute E_{ow} from Eq. 9.65. This equation requires computing $\Sigma\Delta pW_D$, which is a function of r_{eD} and k_t . The overall solution procedure contains the following steps:

1. Assume values of r_{eD} and k_t .
2. Compute t_D for each historical data point with Eq. 9.35.
3. Compute $\Sigma\Delta pW_D$ for each historical data point with the VEH model.
4. Compute E_{ow} for each historical data point with Eq. 9.65.
5. Plot F vs. E_{ow} .
6. Determine the OOIP from the slope.
7. Compute the residual, R_s , for each data point with Eq. 9.68 and compute R_{ss} with Eq. 9.69.
8. Change r_{eD} and k_t and return to Step 1 until a minimum R_{ss} is obtained.

Table 9.24 summarizes the results for the case of $r_{eD} = 20$ and $k_t = 17$ years⁻¹. The step-by-step calculations to compute $\Sigma\Delta pW_D$ are omitted for the sake of brevity. Example 9.2 illustrates these calculations.

TABLE 9.22—RESERVOIR AND AQUIFER PROPERTIES FOR WILCOX FORMATION BLACK OIL	
Reservoir Properties	
Property	Value
Porosity, %	19.90
Permeability, md	236
Initial water saturation, %	15
Temperature, °F	240
Initial pressure, psia	3,793
Bubblepoint pressure, psia	3,690
Aquifer Properties	
Porosity, %	20.90
Permeability, md	275
Water compressibility, 10^{-6} PV/PV/psi	3.3
Rock compressibility, 10^{-6} PV/PV/psi	3.5
Water viscosity, cp	0.25
Water salinity, ppm	20,000

Fig. 9.31 plots F vs. E_{ow} for $r_{eD} = 20$ and $k_t = 17 \text{ years}^{-1}$. The slope of this plot is 18.7 million STB, which is an estimate of the OOIP. The material-balance error is given by the R_{ss} , which is 0.015 million res bbl.

The values of r_{eD} and k_t were varied until a minimum R_{ss} was realized. **Table 9.25** summarizes the results for the following values of r_{eD} : 10, 15, 20, and 30. No values greater than $r_{eD} = 30$ were considered because they yielded identical results and were equivalent to an infinite-acting aquifer.

The results in **Table 9.25** are summarized graphically in **Fig. 9.32**. This figure plots the standard error vs. the time constant for $r_{eD} = 10, 20,$ and 30 . The standard error is defined as the square root of R_{ss}/n , where n is the total number of data points. These results show that a minimum error is realized for the following range of properties: $r_{eD} = 20$ to 30 and $k_t = 16$ to 17 years^{-1} . **Table 9.26** summarizes the range of constants yielded by this range of values.

The material-balance OOIP estimate (18.7 to 20.3 million STB) approximately agrees with the volumetric estimate (24 to 25 million STB). Technically, $r_{eD} = 20$ and $k_t = 17 \text{ years}^{-1}$ yields a minimum error; however, comparable errors are realized for the stated range of r_{eD} and k_t . The boundary between infinite- and noninfinite-acting aquifers occurs at $r_{eD} = 20.1$. Thus, an aquifer with $r_{eD} = 20$ is not quite but very nearly an infinite-acting aquifer. These observations help explain why values of r_{eD} in the range 20 to 30 yield virtually identical errors and similar results. On the basis of simulating reservoir performance through 9 years, selecting any value of r_{eD} greater than 20 is practically acceptable. A value of $r_{eD} = 30$, however, yields an OOIP estimate (20.2 million STB) slightly closer to the volumetric OOIP estimate than the OOIP estimate (18.8 million STB) for $r_{eD} = 20$. On this basis, $r_{eD} = 30$ may be preferable. Without additional historical data and history matching, a more conclusive determination of r_{eD} beyond the stated range is not possible.

Fig. 9.31 includes an F -vs.- E_{ow} plot for $r_{eD} = 10$ and $k_t = 11 \text{ years}^{-1}$. The F vs. E_{ow} plots for $r_{eD} = 20$ and $r_{eD} = 30$ are virtually indistinguishable. The plot for $r_{eD} = 10$ exhibits appreciable curvature; in contrast, the plot for $r_{eD} = 20$ is linear. The degree of curvature is a measure of the lack of material balance. The upward curvature of the former plot indicates that water influx is underpredicted.

Fig. 9.33 shows the predicted water-influx history. This figure assumes $r_{eD} = 20$. A cumulative water-influx volume of 14.83 million res bbl is predicted after 9 years. This amount of

j	t (quarters of years)	\bar{p} (psia)	Total Fluid Withdrawal F (million RB)	Oil-Phase Expansivity E_o (RB/STB)
1	0	3,800	0.000	0.00000
2	2	3,768	0.075	0.00075
3	4	3,699	0.266	0.00267
4	6	3,613	0.831	0.01296
5	8	3,511	1.690	0.02725
6	10	3,444	2.600	0.03731
7	12	3,375	3.656	0.04827
8	14	3,309	4.770	0.05936
9	16	3,277	5.813	0.06497
10	18	3,263	6.790	0.06747
11	20	3,230	7.914	0.07348
12	22	3,174	9.138	0.08409
13	24	3,116	10.499	0.09564
14	26	3,057	11.949	0.10801
15	28	3,015	13.455	0.11721
16	30	3,040	14.533	0.11169
17	32	3,062	15.497	0.10693
18	34	3,060	16.547	0.10736
19	36	3,060	17.576	0.10736

water influx equates to 46.0% of the (reservoir) HCPV (assuming an OOIP of 18.7 million STB and a HCPV of 33.83 million res bbl). This substantial amount of water influx, together with the relatively small pressure decline (from 3,800 to 3,060 psia), suggests a moderate to strong waterdrive.

The pressure data in Table 9.23 show that the reservoir pressure actually increased after 7 years. This example illustrates another consequence of the VEH model; namely, the model can treat pressure increases as well as pressure decreases. The operators offered no explanation regarding why the reservoir pressure began to increase after seven years. It was noted that the pressure remained approximately constant and increased during periods of marked GOR decline. It was suspected that a secondary gas cap formed as the reservoir pressure declined below the bubblepoint. Upstructure wells reportedly began producing free gas as the gas cap formed and grew. The GOR grew as the free-gas production grew. The GOR declined when production from the high-GOR wells was curtailed. Though this scenario explains the GOR behavior and some of the pressure behavior, it does not explain why the reservoir pressure actually increased slightly during the last two years of production.

9.10 Compaction Drives

If pore-volume contraction contributes prominently to overall expansion while the reservoir is saturated, then the reservoir is classified as a compaction drive. Compaction-drive oil reservoirs are supplemented by solution-gas drive if the reservoir falls below the bubblepoint; they may or may not be supplemented by a water or gas-cap drive.

Compaction drives characteristically exhibit elevated rock compressibilities, often 10 to 50 times greater than normal. Rock compressibility is called PV, or pore, compressibility and is expressed in units of PV change per unit PV per unit pressure change. Rock compressibility is a function of pressure. Normal compressibilities range from 3 to 8×10^{-6} psi⁻¹ at pressures

TABLE 9.24—PREDICTED WATER-INFLUX HISTORY FOR RADIAL AQUIFER IF $r_{e0}=20$ and $k_r=17$ years⁻¹

<i>j</i>	<i>t</i> (years)	\bar{p} (psia)	<i>t_D</i>	\hat{p} (psi)	Δp (psi)	$\Sigma \Delta p W_D$ (psi)	E_{cw} (RB/STB)	$W_e(f)$ (million RB)	Average Water Rate (RB/D)	Time at Rate (years)
0	0.0	3,800	0	3,784		0	0.000	0.000	0	0
1	0.5	3,768	9	3,734	16.0	106	0.003	0.049	589	0.25
2	1.0	3,699	18	3,656	50.5	509	0.016	0.233	2,241	0.75
3	1.5	3,613	27	3,562	77.5	1,300	0.047	0.596	4,401	1.25
4	2.0	3,511	36	3,478	94.0	2,507	0.092	1.151	6,718	1.75
5	2.5	3,444	45	3,410	84.5	4,009	0.141	1.840	8,357	2.25
6	3.0	3,375	54	3,342	68.0	5,698	0.196	2.616	9,398	2.75
7	3.5	3,309	63	3,293	67.5	7,599	0.256	3.488	10,572	3.25
8	4.0	3,277	72	3,270	49.0	9,586	0.313	4.400	11,057	3.75
9	4.5	3,263	81	3,247	23.0	11,529	0.366	5.292	10,808	4.25
10	5.0	3,230	90	3,202	23.5	13,498	0.423	6.195	10,955	4.75
11	5.5	3,174	99	3,145	44.5	15,643	0.489	7.180	11,937	5.25
12	6.0	3,116	108	3,087	57.0	18,007	0.562	8.265	13,152	5.75
13	6.5	3,057	117	3,036	58.5	20,569	0.640	9.441	14,252	6.25
14	7.0	3,015	126	3,028	50.5	23,262	0.719	10.677	14,985	6.75
15	7.5	3,040	135	3,051	8.5	25,821	0.780	11.852	14,235	7.25
16	8.0	3,062	144	3,061	-23.5	28,120	0.835	12.907	12,791	7.75
17	8.5	3,060	153	3,060	-10.0	30,282	0.891	13.899	12,029	8.25
18	9.0	3,060	162	900	1.0	32,315	0.944	14.832	11,309	8.75

greater than approximately 1,000 psia. In contrast, elevated rock compressibilities can reach as high as 150×10^{-6} psi⁻¹ or higher at comparable pressures.⁵⁸

In general, compaction-drive reservoirs are rare; however, strong compaction drives do exist. The Ekofisk field in the Norwegian sector of the North Sea, with reserves in excess of 1.7 billion bbl, lies at a depth of 9,300 ft below sea level in 235 ft of water. The reservoir is a chalk formation that exhibits porosities in the range of 25 to 48%.⁵⁹ The operators reported rock compressibilities as high as 50 to 100×10^{-6} psi⁻¹.⁶⁰ Extreme compressibilities such as these can account for 70 to 80% of the expansion above the bubblepoint and 20 to 50% or more of the expansion below the bubblepoint.

9.10.1 Performance. Compaction-drive oil reservoirs act like their noncompaction counterparts except that they exhibit enhanced recoveries. For instance, a solution-gas-drive, compaction-drive reservoir will act qualitatively like a normal solution-gas-drive reservoir except the oil recovery will be greater. The enhanced recoveries are a direct consequence of the extra rock expansion that compaction-drive reservoirs naturally possess.

The excessive compaction noted in compaction-drive reservoirs has contributed to some production problems. For example, the compaction has been linked to a decline in reservoir permeability, fracture closure, and subsidence.⁵⁸⁻⁶⁰ In most cases, however, these problems have been manageable, and the net result of compaction has been very favorable.

9.10.2 Material-Balance Analysis. The material-balance methods discussed in the previous sections are equally applicable to compaction drives. The only difference is that rock expansion cannot be ignored. Including rock expansion requires evaluating the rock expansivity, E_f .

The most accurate and reliable method is to measure E_f as a function of pressure. This method is strongly recommended if a compaction-drive mechanism is suspected because of the sensitivity of the analysis to E_f . Table 9.27 summarizes the experimental results for a high-pressure Gulf Coast gas reservoir.⁶¹ The initial reservoir and hydrostatic pressure was 9,800

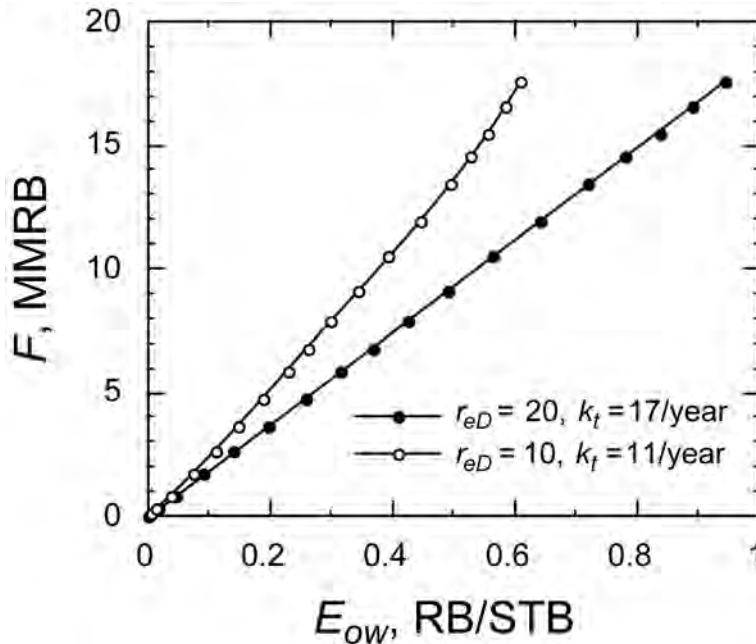


Fig. 9.31— F -vs.- E_{ow} plot for Example 9.4.

TABLE 9.25—MATERIAL-BALANCE ERROR AS A FUNCTION OF r_{eD} and k_t

k_t (year ⁻¹)	$r_{eD}=10$		$r_{eD}=15$		$r_{eD}=20$		$r_{eD}=30$	
	Standard Error (million RB)	N (million STB)	Standard Error (million RB)	N (million STB)	Standard Error (million RB)	N (million STB)	Standard Error (million RB)	N (million STB)
1	1.220	76.7	1	1.220	76.7	1	1.220	76.7
5	0.591	41.3	3	0.729	51.9	5	0.485	40.7
10	0.403	29.0	10	0.229	27.5	10	0.189	27.4
11	0.397	27.7	20	0.115	18.2	15	0.046	21.1
20	0.579	20.8	23	0.102	16.7	17	0.029	18.7
50	1.295	15.5	30	0.133	14.2	20	0.040	17.5
100	1.860	14.0	100	0.900	8.1	30	0.064	13.4
1,000	2.436	13.1	300	1.897	6.6	50	0.070	9.5
			1000	2.395	6.2	100	0.256	6.3
						500	1.740	3.9

psia. The rock expansivity ranged between 0 and 8.07%. The porosity decreased from 16.7 to 15.5% over the course of the test. This particular sample exhibited higher than normal expansion.

The rock expansivity and compressibility are related through

$$E_f(p) = \int_p^{p_i} c_f dp, \dots\dots\dots (9.75)$$

where c_f is the rock compressibility. This equation assumes that the fractional change in PV is small. Physically, the rock expansivity represents the fractional change in PV while, in con-

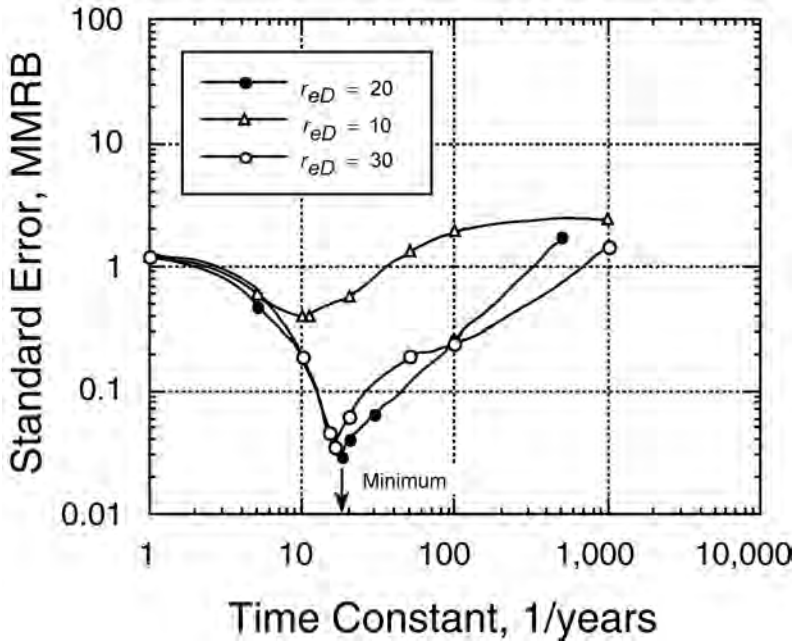


Fig. 9.32—Material-balance error vs. time constant for several values of r_{eD} for Example 9.4.

TABLE 9.26—RANGE OF CONSTANTS	
OOIP, million STB	18.7 to 20.2
OGIP, Bscf	16.8 to 18.2
U , RB/psi	459 to 477
Standard error, million RB	0.029 to 0.035

trast, the rock compressibility represents the rate of change in fractional PV with pressure. While the former is more pertinent to material-balance calculation, experimental data are often reported in terms of the latter. Table 9.27 includes rock-compressibility measurements. If c_f is known as a function of pressure, then the integral on the right side of Eq. 9.75 can be evaluated numerically to determine $E_f(p)$. If c_f is relatively independent of pressure, then Eq. 9.75 can be simplified to

$$E_f(p) = c_f(p_i - p) \dots\dots\dots (9.76)$$

This method of estimating E_f is not usually preferable because c_f is rarely constant. Fig. 9.34 illustrates a case and plots the rock compressibility as a function of pressure from the data in Table 9.27. Several features are worth noting, and many of these features are characteristic of compaction drives. First, the rock compressibility ranges between 4 to 21×10^{-6} psi⁻¹, which is a greater-than-normal range. Second, the rock compressibility clearly is not independent of pressure. Third, the compressibility declines sharply as the pressure first declines below the initial pressure. This phenomenon is largely attributed to grain rearrangement. Fourth, the rock com-

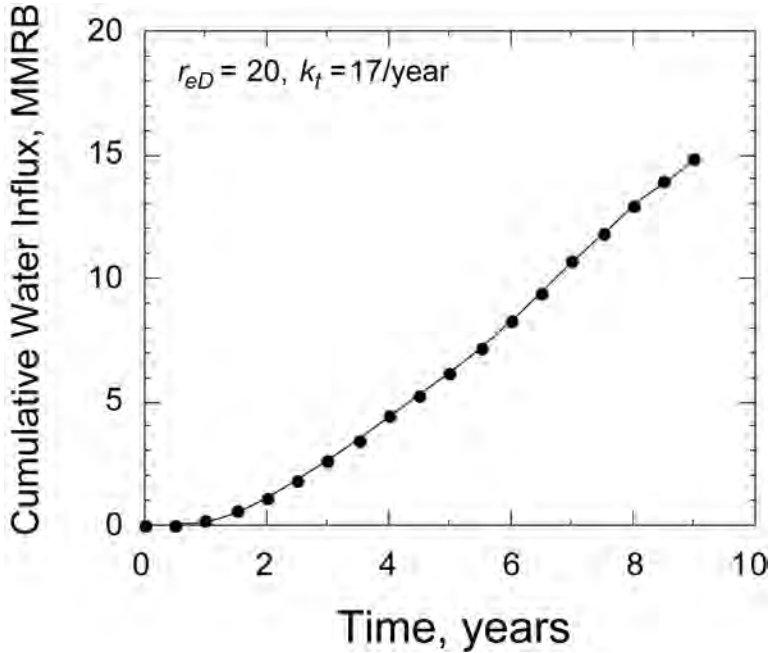


Fig. 9.33—Predicted water-influx history for Example 9.4.

Overburden Pressure (psia)	PV (cm ³)	Bulk Volume (cm ³)	Porosity (%)	Pressure (psia)	Rock Expansivity	Rock Compressibility (10 ⁻⁶ PV/PV/psi)
200	3.420	20.530	16.66	9,800	0.0000	15.1
1,000	3.379	20.498	16.48	9,000	0.0120	12.5
2,000	3.337	20.447	16.32	8,000	0.0243	10.2
3,000	3.303	20.413	16.18	7,000	0.0342	8.2
4,000	3.276	20.382	16.07	6,000	0.0421	5.8
5,000	3.257	20.367	15.99	5,000	0.0477	4.3
6,000	3.243	20.353	15.93	4,000	0.0518	4.0
7,000	3.230	20.340	15.88	3,000	0.0556	5.3
8,000	3.213	20.323	15.81	2,000	0.0605	11.3
9,000	3.177	20.329	15.63	1,000	0.0711	20.9
9,500	3.144	20.254	15.52	500	0.0807	

compressibility increases at pressures below 4,000 psia. This phenomenon is attributed to pore collapse.

Once $E_f(p)$ is estimated, the material-balance methods in the previous sections can be applied to estimate the OOIP and confirm the producing mechanism.

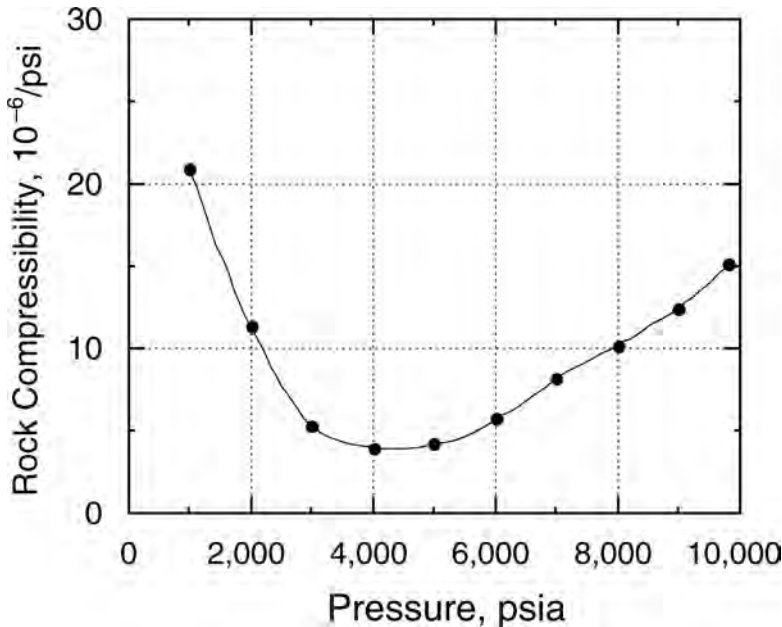


Fig. 9.34—Rock compressibility as a function of pressure for a Gulf Coast reservoir.

9.11 Water and Gas Coning

Coning is a production problem in which gas-cap gas or bottomwater infiltrates the perforation zone in the near-wellbore area and reduces oil production. Gas coning is distinctly different from, and should not be confused with, free-gas production caused by a naturally expanding gas cap. Likewise, water coning should not be confused with water production caused by a rising WOC from water influx. Coning is a rate-sensitive phenomenon generally associated with high producing rates. Strictly a near-wellbore phenomenon, it only develops once the pressure forces drawing fluids toward the wellbore overcome the natural buoyancy forces that segregate gas and water from oil.

Under ideal conditions in which no coning exists, flow is principally horizontal and mainly oil is produced. Fig. 9.35 illustrates a producing well with no coning. When coning exists, however, the overlying gas is drawn downward or bottomwater is drawn upward and into the oil column. Coning trades oil production for gas or water production. Fig. 9.36 illustrates a producing well subject to gas and water coning.

Two strategies commonly are used to minimize coning. One approach is partial perforation or penetration. In this approach, only a limited portion of the pay thickness is perforated. If gas coning is anticipated, the pay thickness near the GOC is not perforated. If water coning is anticipated, the pay thickness near the WOC is not perforated. In instances in which severe coning is expected, only a small portion of the pay thickness may be perforated. The variables in Fig. 9.37 define the length of the perforation interval, b , and its position within the pay thickness, h . The distance L_g is the distance between the top of the pay and the uppermost perforation, and the distance L_w is the distance between the bottom of the pay and the lowest perforation. The quotient b/h is the partial perforation fraction. Although this strategy will reduce and can eliminate coning problems, it suffers an obvious drawback; namely, it temporarily reduces oil production in the hope of eventually avoiding coning.

A second remedial strategy is based on the observation that there is a critical producing rate below which the cone stabilizes and will not reach the perforations. This critical rate is a

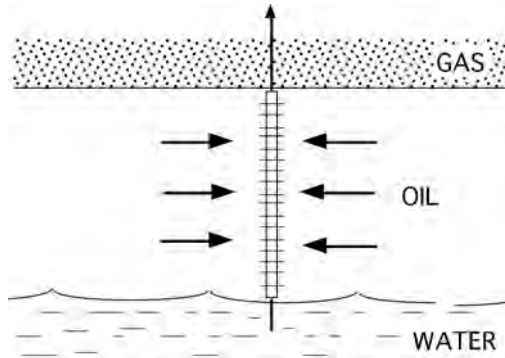


Fig. 9.35—A producing well with no coning.

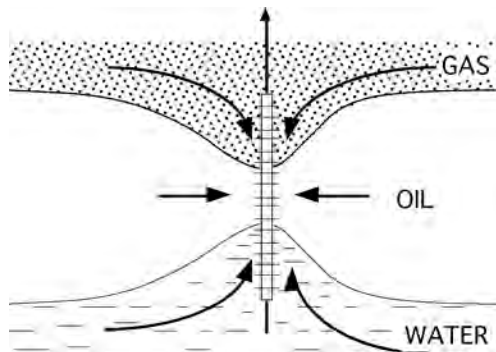


Fig. 9.36—A producing well subject to gas and water coning.

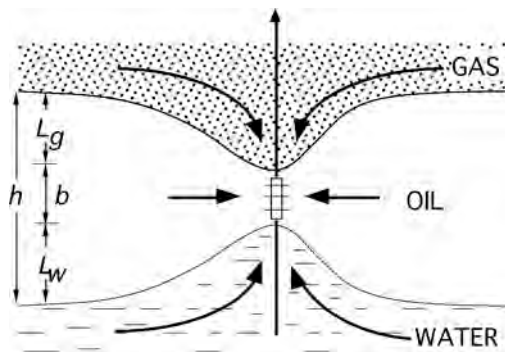


Fig. 9.37—Definition of variables for a partially perforated producing well.

function of the perforation length. As the perforation length increases, the critical producing rate decreases. Often, the critical producing rate is much less than the possible producing rate. This difference creates an operational decision: produce at a rate greater than the critical and eventually risk coning, or produce at a rate less than the critical and temporarily sacrifice oil production. If the critical rate is less than the minimum economic rate, then the operator has no choice but to produce above the critical rate or abandon the well.

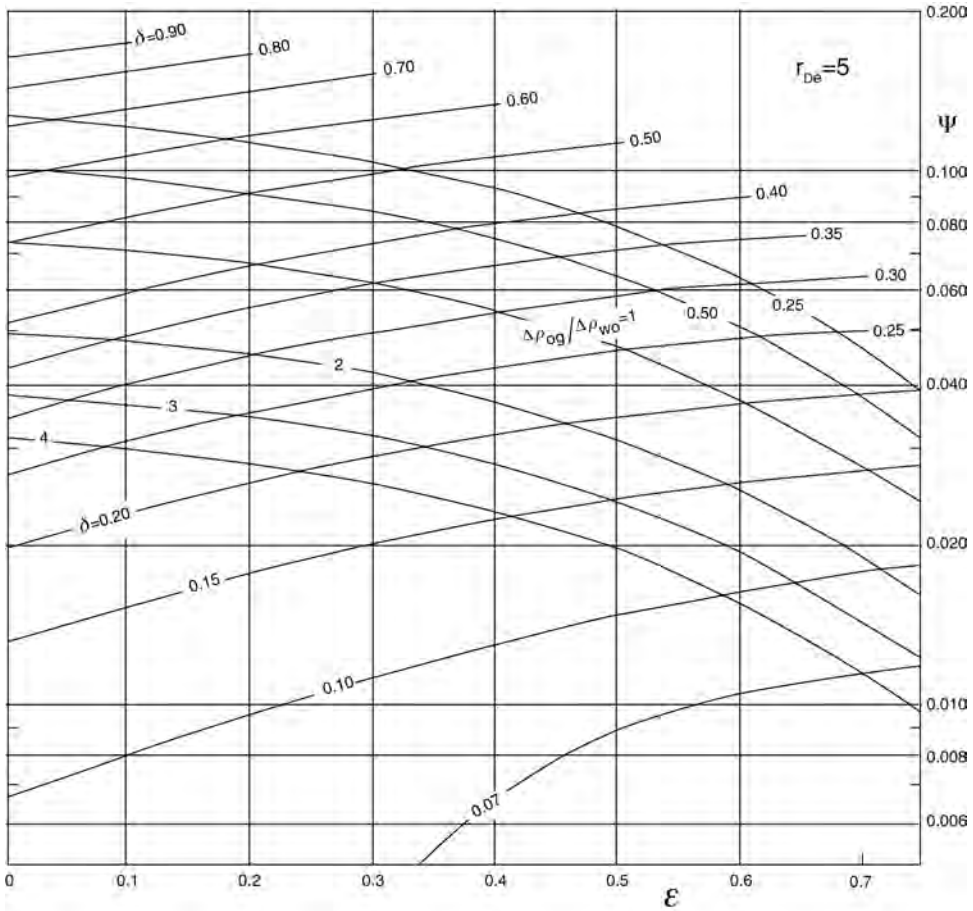


Fig. 9.38— ψ as a function of ϵ , δ , and $\Delta\rho_{og}/\Delta\rho_{wo}$ for $r_{De}=5$.⁶⁶

To combat coning, a hybrid strategy is often used whereby a combination of partial perforation and a reduced producing rate is used. One especially unattractive consequence of gas coning is that it prematurely depletes the gas-cap gas and diminishes the gas-cap producing mechanism. Fortunately, gas coning is not as problematic as water coning because the density difference between oil and gas is greater than the difference between water and oil. This density difference through gravity segregation helps mitigate coning.

To develop an effective remedial strategy against coning, certain theoretical aspects regarding coning must be understood. Mathematically, coning is a challenging problem because of its complexity. To develop tractable analytical solutions, tenuous assumptions must be invoked. These assumptions limit the practical applicability of these solutions. The most reliable way to study coning is with a specially designed finite-difference simulator.^{61,62,63} Nevertheless, certain analytical solutions and empirical correlations can be helpful and serve as a preliminary guide.

Muskat and Wyckoff⁶⁴ and Chaney *et al.*⁶⁵ were among the first to contribute substantively to this problem. Since their efforts, several other authors have contributed to the body of literature.⁶⁶⁻⁷³ Many of these works have led to similar correlations. Wheatley⁷² presented a comparison of some popular correlations. As a representative sample, the correlations of Schols⁷¹ and Chierici *et al.*⁶⁶ are presented here. Both works apply to both water and gas coning. Both efforts also use the following equation to compute the critical producing rate:

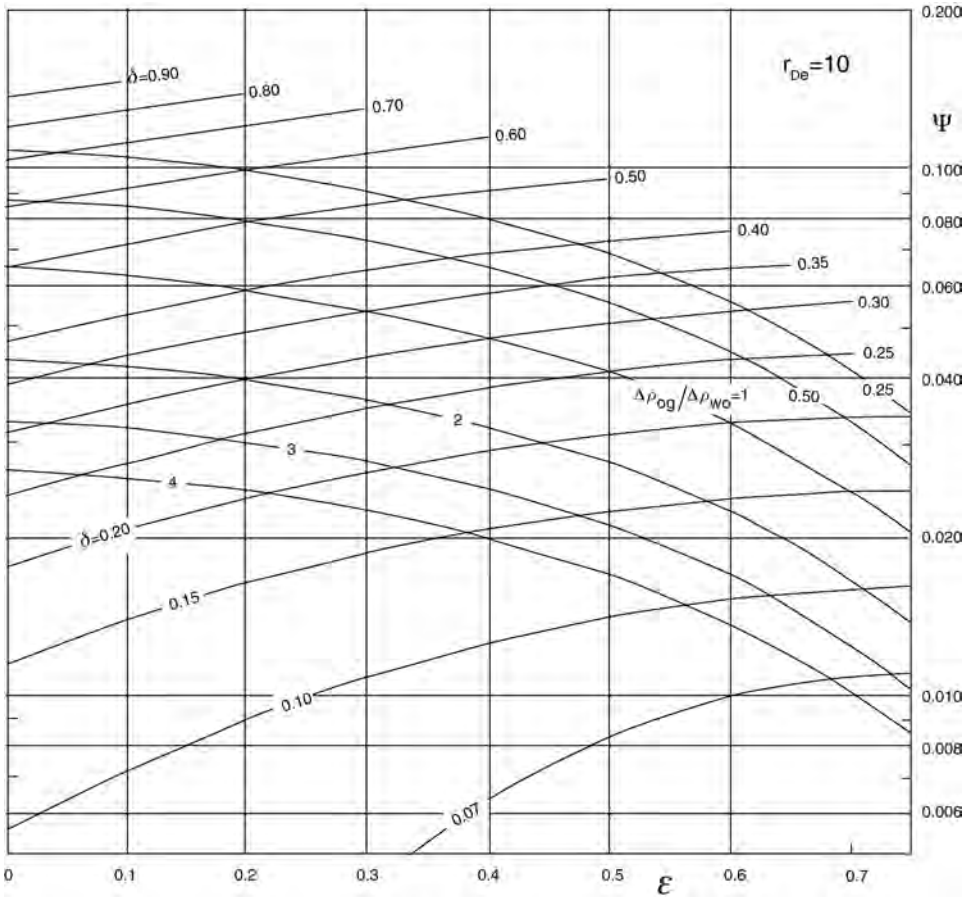


Fig. 9.39— ψ as a function of ϵ , δ , and $\Delta\rho_{og}/\Delta\rho_{wo}$ for $r_{De} = 10$.⁶⁶

$$q_c = \frac{0.003073k_o h^2 \Delta\rho}{\mu_o B_o} q_{Dc}, \dots\dots\dots (9.77)$$

where $\Delta\rho$ = density difference (g/cm³), B_o = average oil FVF, μ_o = average oil viscosity (cp), k_o = oil permeability (md), q_{Dc} = dimensionless critical producing rate, h = pay thickness (ft), and q_c is given in STB/D. The oil permeability, k_o , is the product of the horizontal permeability and the oil relative permeability. The dimensionless critical rate, q_{Dc} , is specified by correlation.

9.11.1 Schols' Correlation. Schols' correlation⁷¹ is based on a numerical simulation study. The dimensionless critical producing rate is

$$q_{Dc} = \frac{1}{2\pi} \left[0.432 + \frac{\pi}{\ln\left(\frac{r_e}{r_w}\right)} \right] \left[1 - \left(\frac{b}{h}\right)^2 \right] \left(\frac{r_e}{h}\right)^{-0.14}, \dots\dots\dots (9.78)$$

where b is the length of the perforation interval and r_e is the drainage radius.

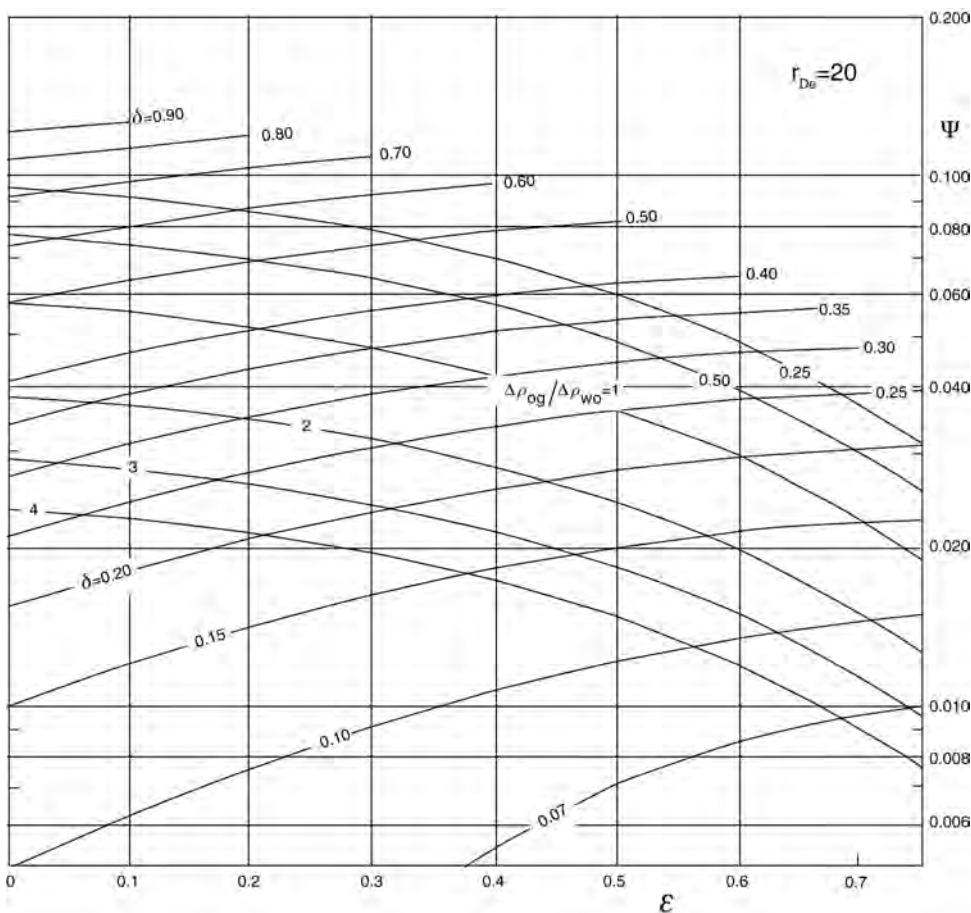


Fig. 9.40— ψ as a function of ϵ , δ , and $\Delta\rho_{og}/\Delta\rho_{wo}$ for $r_{De} = 20$.⁶⁶

This correlation applies to both water and gas coning; however, it directly applies only to cases in which water or gas coning exist separately. In other words, it does not directly apply to cases in which water and gas coning act simultaneously. The correlation can be used to predict the critical rate for a pre-existing completion or to predict the optimum perforation length for a future completion. In this latter application, the optimum perforation length is defined as the length at which the critical and theoretical producing rates are equal. The theoretical producing rate of a partially penetrating well is computed in Section 9.11.3. Example 9.5 illustrates the former application while Example 9.6 illustrates the latter application.

9.11.2 Chierici *et al.* Correlation. The correlation by Chierici *et al.*⁶⁶ was based on a potentiometric study. This was one of the most sophisticated correlations. It allows the vertical permeability to differ from the horizontal permeability. This can be an important factor because coning vanishes as the vertical permeability approaches zero. This correlation also treats the problem of simultaneous gas/water coning. This is important in situations in which a gas cap and bottomwater coexist.

The correlation of Chierici *et al.* was specified in terms of a series of charts. The charts used the following nomenclature. The dimensionless critical rate is denoted as ψ (previously defined as q_{Dc}) and the following dimensionless variables are defined as

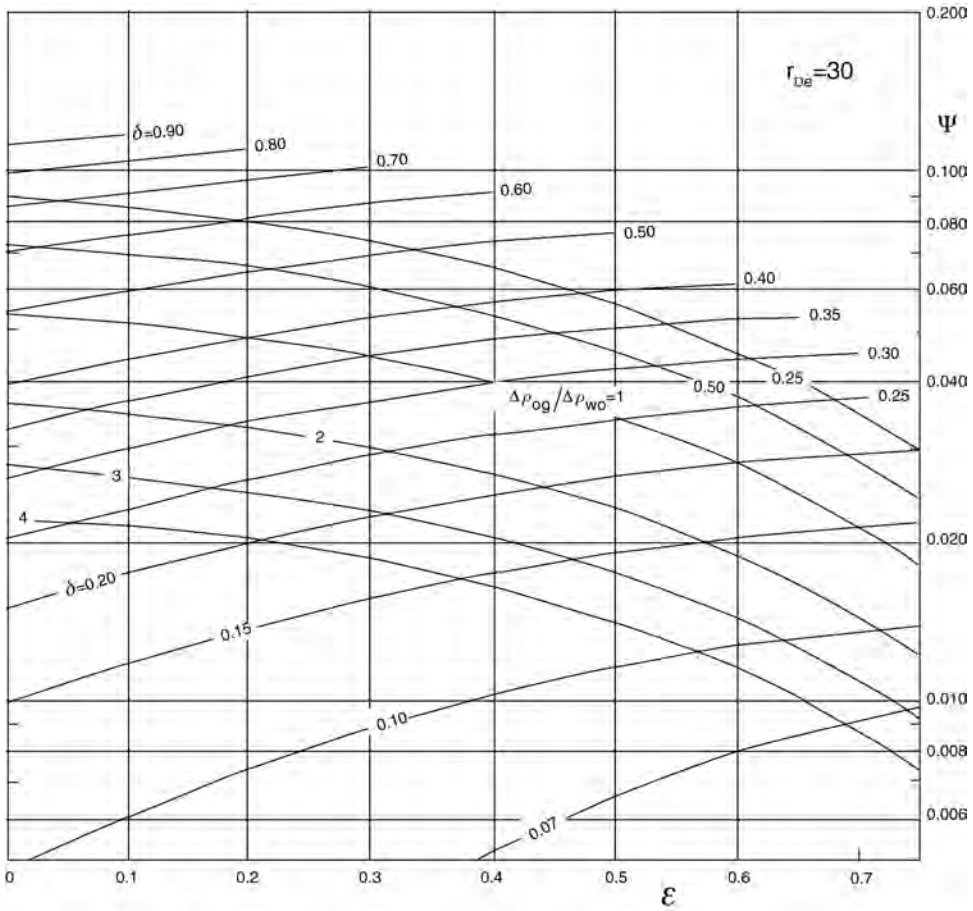


Fig. 9.41— ψ as a function of ϵ , δ , and $\Delta\rho_{og}/\Delta\rho_{wo}$ for $r_{De} = 30$.⁶⁶

$$\delta_g = L_g / h, \dots\dots\dots (9.79)$$

$$\delta_w = L_w / h, \dots\dots\dots (9.80)$$

$$\epsilon = b / h, \dots\dots\dots (9.81)$$

$$\text{and } r_{De} = (r_e / b)(k_v / k_H)^{1/2} . \dots\dots\dots (9.82)$$

The dimensionless critical rate, ψ , is a function of r_{De} , ϵ , and δ . **Figs. 9.38 through 9.44** show the charts. Each chart corresponds to a different value of r_{De} . Specific charts exist for $r_{De} = 5, 10, 20, 30, 40, 60,$ and 80 .

The charts are used differently depending on whether they are used to compute the critical rates or optimize the perforation length. The problem of optimizing the perforation length for simultaneous gas and water coning is more complicated than separate water or gas coning. The charts simplify the problem; however, the solution procedure depends on the application.

Calculating Critical Rates. For a pre-existing perforation length, b , the critical rates are computed with the following procedure:

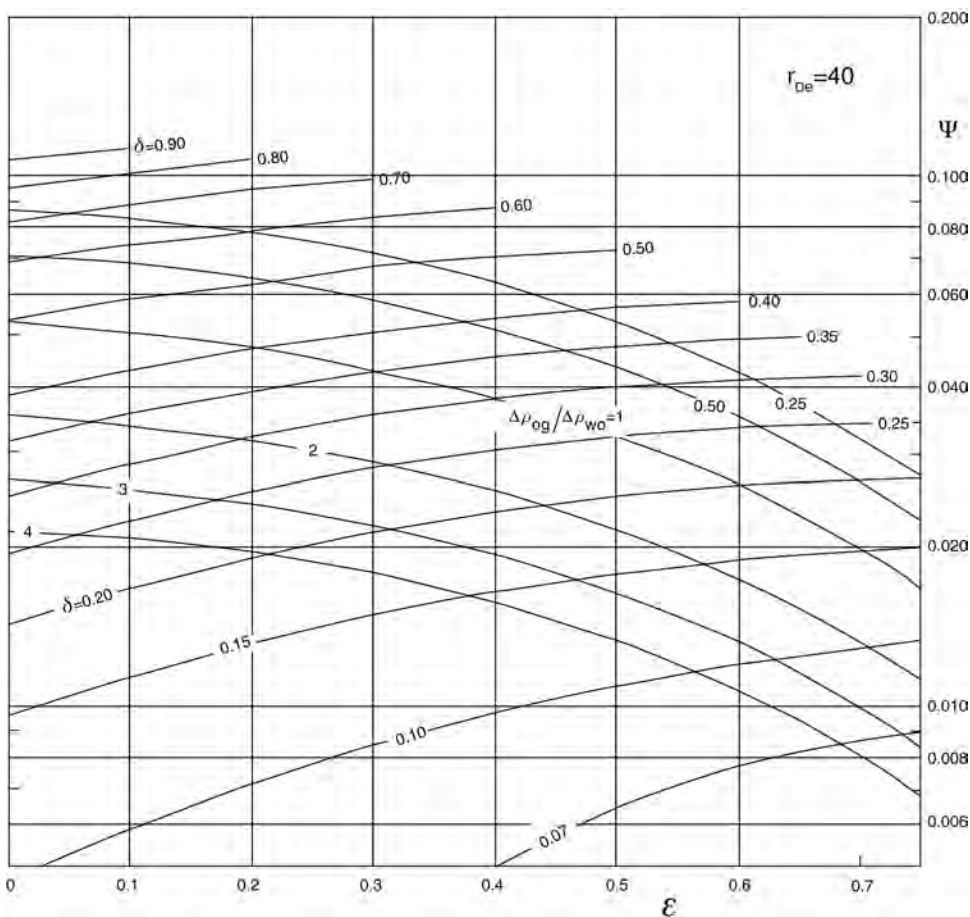


Fig. 9.42— ψ as a function of ϵ , δ , and $\Delta\rho_{og}/\Delta\rho_{wo}$ for $r_{De} = 40$.⁶⁶

1. Compute δ_g , δ_w , ϵ , and r_{De} with Eqs. 9.79 through 9.82.
2. Locate the correct chart or charts, depending on the value of r_{De} . Interpolation between two charts may be required.
3. Compute ψ_g from the charts based on r_{De} , ϵ , and δ_g ; then, compute ψ_w from the charts based on r_{De} , ϵ , and δ_w .

4. Compute the critical rates to avoid water and gas coning with Eq. 9.77.

This procedure ignores the curves labeled $\Delta\rho_{og}/\Delta\rho_{wo}$. The calculation procedure is simplified if only bottomwater or a gas cap exists. If no bottomwater exists, then the calculation of ψ_w and δ_w can be ignored. Conversely, if no gas cap exists, then the calculation of ψ_g and δ_g can be ignored. Example 9.5 illustrates an application.

Calculating Optimum Perforation Length. For a bottomwater, gas-cap reservoir, the procedure to calculate the optimum perforation (length and position) uses the curves labeled $\Delta\rho_{og}/\Delta\rho_{wo}$ and is as follows:

1. Compute r_{De} with Eq. 9.82. Also, compute $\Delta\rho_{og}/\Delta\rho_{wo}$.
2. Assume a value of ϵ .
3. Compute ψ and δ with the charts. These values correspond to ψ_g and δ_g .
4. Compute $L_g = h\delta_g$ and $L_w = h(1 - \epsilon) - L_g$.

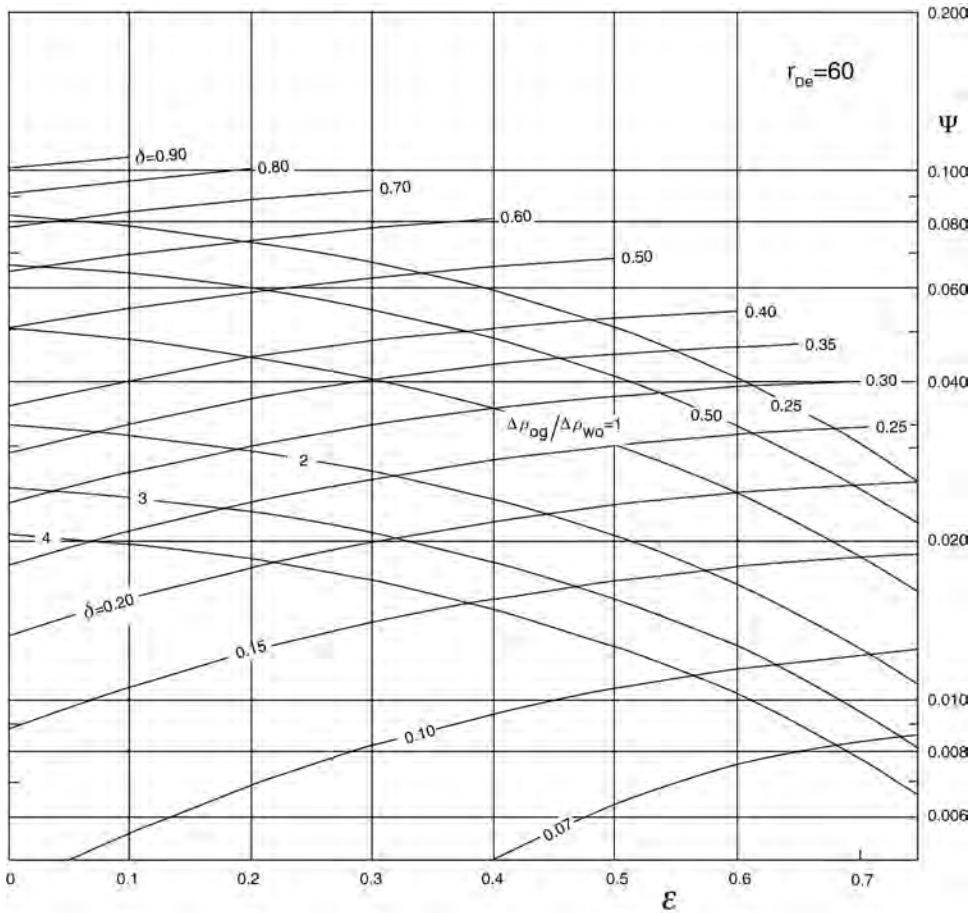


Fig. 9.43— ψ as a function of ε , δ , and $\Delta\rho_{og}/\Delta\rho_{wo}$ for $r_{De} = 60$.⁶⁶

5. Compute the critical rate from Eq. 9.77. Only one critical rate is needed because the procedure assumes equal critical rates for gas and water coning.

6. Return to Step 2. Assume a new value of ε , and repeat the calculation until an adequate range of ε is covered.

7. Compute the theoretical producing rate of a partially penetrating well as a function of ε with Eq. 9.83. (See Section 9.11.3 below).

8. Plot the critical and theoretical producing rates as a function of ε . The value of ε at which the critical and producing rates intersect yields the optimal perforation interval.

This procedure is simplified if only a gas cap or bottomwater exists. The same procedure applies except $\Delta\rho_{og}/\Delta\rho_{wo}$ is not calculated and $\delta_g = 1 - \varepsilon$ (if there is no bottomwater and only gas coning is a problem) or $\delta_w = 1 - \varepsilon$ (if there is no gas cap and only water coning is a problem). ψ is computed for a range of ε until an optimal value of ε is identified. Example 9.6 illustrates this procedure for a gas-cap reservoir. Example 9.7 illustrates an application for a gas-cap, bottomwater reservoir.

9.11.3 Partially Penetrating Wells. The theoretical producing rate of a partially penetrating well is needed to compute the optimum perforation length. Partially penetrating wells are wells that do not fully penetrate or are not fully perforated throughout the pay thickness. If vertical

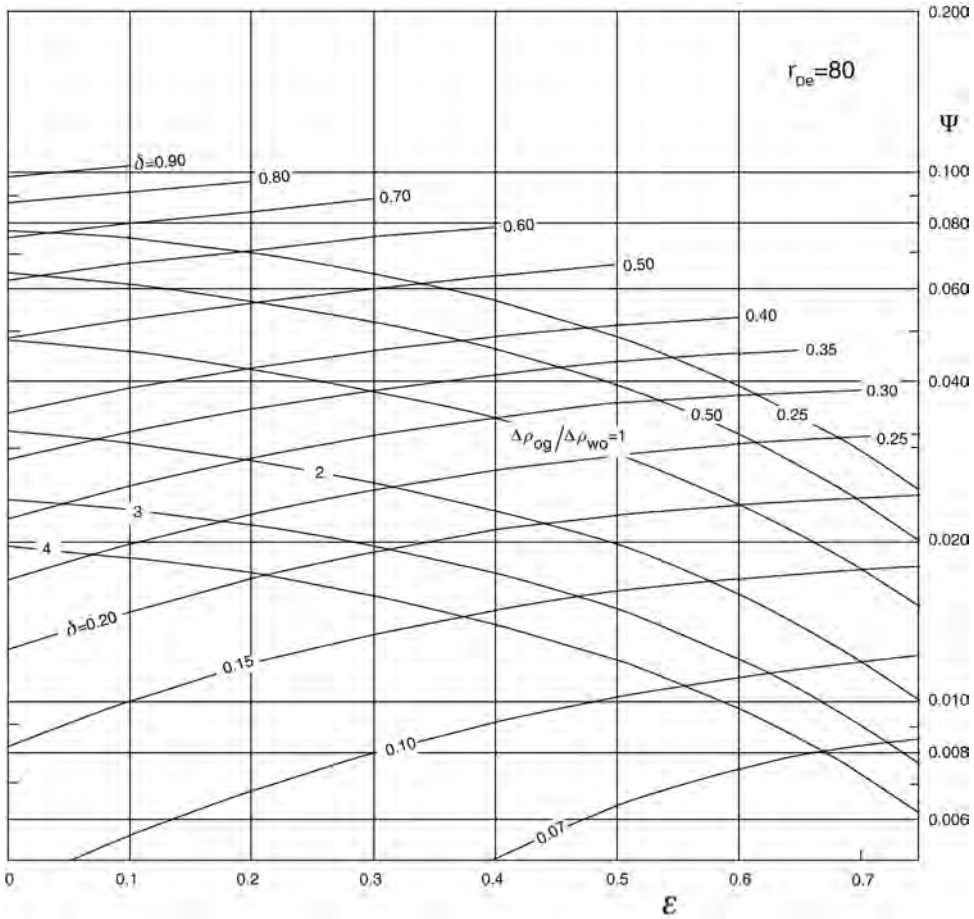


Fig. 9.44— ψ as a function of ϵ , δ , and $\Delta\rho_{og}/\Delta\rho_{wo}$ for $r_{De} = 80$.⁶⁶

permeability exists, these wells will produce fluids from above and below the perforations. Fig. 9.45 illustrates fluid delivery into a partially penetrating producing well. Under these circumstances, fluid flow is obviously not strictly horizontal. The producing rate in partially penetrating wells with nonzero vertical permeability is greater than the rate with no vertical permeability.

Partially penetrating wells commonly are used to minimize coning. The critical rate gives a producing rate below which no coning will occur. Often, however, the critical flow rate is much less than maximum possible flow rate. To judge the difference, estimates for the flow rate of a partially penetrating well are needed. Several authors have offered analytical expressions to estimate the flow rate.^{1,74,75} Most efforts yield estimates within a few percent of one another. The Kozeny expression,⁷⁵ for example, is

$$q = \frac{0.00708k_H b(p_e - p_w)}{\mu_o B_o \left[\ln \left(\frac{r_e}{r_w} \right) + s \right]} \left[1 + 7 \sqrt{\frac{r_w}{2b}} \sqrt{\frac{k_v}{k_H}} \cos \left(\frac{\pi b}{2h} \right) \right], \dots \dots \dots (9.83)$$

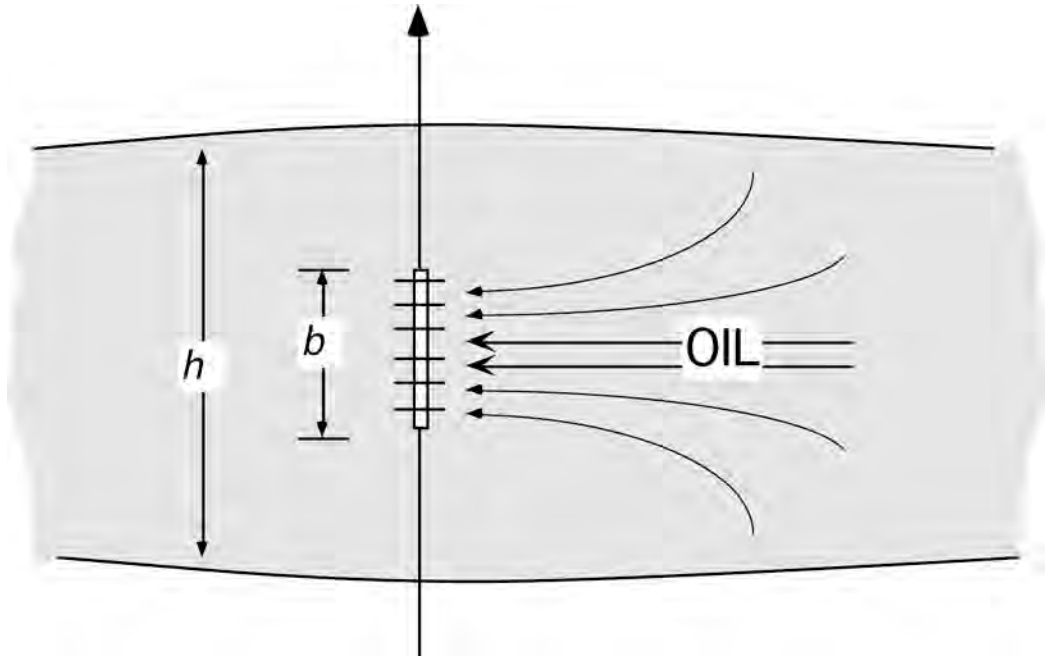


Fig. 9.45—Fluid delivery into a partially penetrating producing well.

where k_H = horizontal permeability, k_v = vertical permeability, p_e = pressure at drainage radius, p_w = wellbore pressure, s = skin factor, q = oil producing rate, and the argument of the cosine assumes radians. This equation assumes units of md, ft, psi, cp, and STB/D. This equation also assumes steady-state flow in a circular drainage area, where r_e and r_w are the drainage and wellbore radii, respectively. Eq. 9.83 gives the Kozeny equation in SI units.

9.11.4 Variables Affecting Coning. The ratio of q_c/q is a measure of the tendency not to cone. As q_c increases or q decreases, the likeliness to avoid increases. According to Eqs. 9.77 and 9.83, the ratio q_c/q is proportional to

$$\frac{q_c}{q} \propto \frac{h^2 \Delta \rho \left[\ln \left(\frac{r_e}{r_w} \right) + s \right]}{b} \dots\dots\dots (9.84)$$

This expression shows that the likeliness to control coning increases as the penetration interval b decreases. Eq. 9.84 also shows that the likeliness to control coning increases as the pay thickness increases, density difference increases, well spacing increases, and perforation length decreases. Horizontal permeability does not affect the likelihood of success. This expression also suggests that controlling coning in a thin reservoir may be difficult.

9.11.5 Additional Measures To Control Coning. Other techniques have been applied to control coning. These include placing an artificial barrier above or below the pay to suppress vertical flow,⁷⁶ injecting oil to control gas coning,⁷⁷ or the use of horizontal wells. Barriers composed of cement and high-molecular-weight polymers have been tried. Another, although expensive, technique is to drill additional wells and produce them at the critical rate.

Example 9.5: Computing Critical Rate To Prevent Coning. Compute the critical rate (STB/D) for a well in a gas-cap reservoir with the following characteristics: $k_H = 60$ md, $k_v = 39$ md, $h = 150$ ft, $r_e = 933$ ft (80-acre well spacing), $r_w = 0.5$ ft, $B_o = 1.25$ RB/STB, $\mu_o = 1.11$ cp, $\rho_o = 0.714$ g/cm³, and $\rho_g = 0.098$ g/cm³. The well is completed in only the lower 60 ft of the pay thickness.

Solution. Schols' Correlation. With Eq. 9.78, compute q_{Dc} . This yields

$$q_{Dc} = \frac{1}{2\pi} \left(0.432 + \frac{\pi}{\ln \frac{933}{0.5}} \right) \left[1 - \left(\frac{60}{150} \right)^2 \right] \left(\frac{933}{150} \right)^{-0.14} = 0.0879.$$

The critical rate is then computed with Eq. 9.77, which yields

$$q_c = \frac{0.003073(60 \text{ md})(150 \text{ ft})^2(0.714 - 0.098 \text{ g/cm}^3)}{(1.11 \text{ cp})(1.25 \text{ RB/STB})} (0.0879) = 161.9 \text{ STB/D}.$$

Chierici *et al.* Correlation. First, evaluate $L_g = 90$ ft, $\delta_g = 90/150 = 0.60$, $\varepsilon = 60/150 = 0.40$, and $r_{De} = 5.01$. With the chart for $r_{De} = 5$, obtain $\psi = 0.120$. Evaluating Eq. 9.77 yields

$$q_c = \frac{0.003073(60 \text{ md})(150 \text{ ft})^2(0.714 - 0.098 \text{ g/cm}^3)}{(1.11 \text{ cp})(1.25 \text{ RB/STB})} (0.120) = 221 \text{ STB/D}.$$

Example 9.6: Computing Optimum Perforation Length To Prevent Coning. For an uncompleted well in the gas-cap reservoir in Example 9.5, compute the optimum perforation length at a reservoir pressure of 1,800 psia. Assume a wellbore pressure of 1,500 psia and a skin factor of 10.

Solution. Schols' Correlation. Compute the dimensionless critical rate and critical rate as a function of b/h . Table 9.28 summarizes the results for $b/h = 0$ to 1.

Next, estimate the theoretical producing rate for a partially penetrating well. With Eq. 9.83 for $b = 60$ ft yields

$$q = \frac{0.00708(60 \text{ md})(60 \text{ ft})(1,800 - 1,500 \text{ psi})}{(1.11 \text{ cp})(1.25 \text{ RB/STB}) \left(\ln \frac{933}{0.5} + 10 \right)} \left(1 + 7 \sqrt{\frac{(0.5 \text{ ft})}{2(60 \text{ ft})}} \sqrt{\frac{39}{60}} \cos \left(\frac{\pi(60 \text{ ft})}{2(150 \text{ ft})} \right) \right) = 430 \text{ STB/D}.$$

Table 9.28 summarizes the results at other values of b . The rate varies from 0 to 808 STB/D, depending on the length of the perforation interval. The optimum perforation length corresponds to the value of b at which the critical and theoretical producing rates are equal. Fig. 9.46 shows a plot of q and q_c vs. b/h . The curves intersect at approximately $b/h = 0.15$. This corresponds to $b = 22.5$ ft, $L_g = 127.5$ ft, and $q = 187$ STB/D. In conclusion, only the lower 22.5 ft of the pay thickness should be perforated to avoid gas coning.

Chierici *et al.* Correlation. First, compute $\delta_g = 1 - b/h$ for a range of b/h . Next, compute r_{De} . From Example 9.5, $r_{De} = 5$. With the appropriate chart, compute ψ for the range of b/h . The charts use b/h as ε . Then compute the critical rate with Eq. 9.77. Table 9.29 summarizes the results. Fig. 9.46 plots q_c vs. b/h .

TABLE 9.28—SUMMARY OF CALCULATIONS WITH THE SCHOLS ⁷¹ CORRELATION			
b/h	q_{Dc}	q_c (STB/D)	Oil-Producing Rate (STB/D)
0	0.1046	192.7	0.0
0.1	0.1036	190.8	145.7
0.2	0.1004	185.0	250.1
0.3	0.0952	175.4	344.0
0.4	0.0879	161.9	429.8
0.5	0.0785	144.5	508.2
0.6	0.0670	123.3	579.9
0.7	0.0534	98.3	645.1
0.8	0.0377	69.4	704.5
0.9	0.0199	36.6	758.8
1	0.0000	0.0	808.9

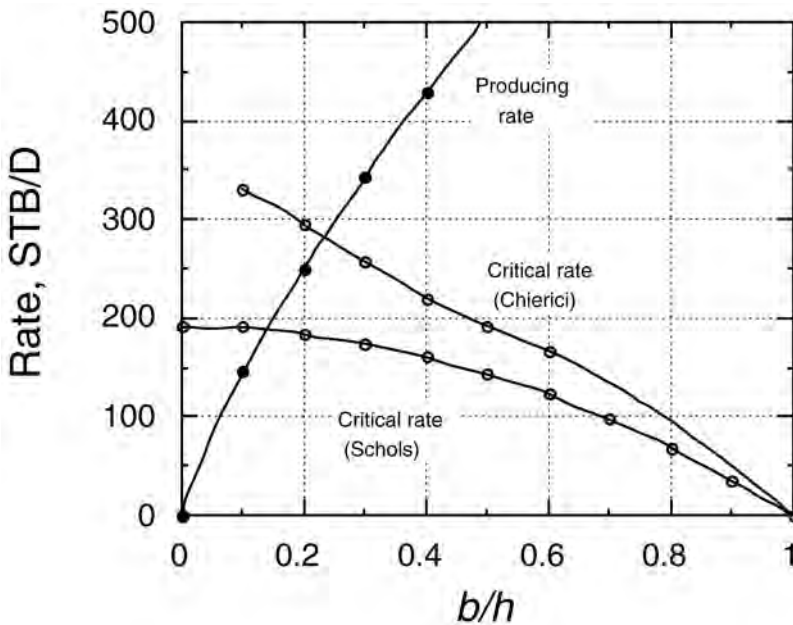


Fig. 9.46—Producing and critical rates as a function of b/h .

The optimal perforation length corresponds to the value of b/h at which the critical and producing rates are equal. This approximately occurs for $b/h = 0.25$. This corresponds to $b = 37.5$ ft, $L_g = 112.5$ ft, and $q = 275$ STB/D. In conclusion, only the lower 37.5 ft of the pay should be perforated. The method of Chierici *et al.* yields a wider perforation interval than the method of Schols (37.5 vs. 22.5 ft). The Chierici *et al.* method is consistently more liberal than Schols' method.

Example 9.7: Optimum Perforation Length To Prevent Coning in a Bottom-Water, Gas-Cap Reservoir. Assume the gas-cap reservoir in Examples 9.5 and 9.6 is

**TABLE 9.29—SUMMARY OF CALCULATIONS WITH THE
CHIERICI *et al.*⁶⁶ CORRELATION**

b/h	δ_g	$\psi = q_{Dc}$	q_c (STB/D)	Oil-Producing Rate (STB/D)
0	1			0.0
0.1	0.9	0.180	331.5	145.7
0.2	0.8	0.160	294.7	250.1
0.3	0.7	0.140	257.9	344.0
0.4	0.6	0.120	221.0	429.8
0.5	0.5	0.105	193.1	508.2
0.6	0.4	0.090	165.8	579.9

TABLE 9.30—RESULTS FOR EXAMPLE 9.7

b/h	δ_g	$\psi = q_{Dc}$	q_c (STB/D)	Oil-Producing Rate (STB/D)
0				0.0
0.05	0.40	0.059	108.7	86.7
0.10	0.37	0.058	106.8	145.7
0.20	0.33	0.055	101.3	250.1
0.30	0.28	0.048	88.4	344.0
0.40	0.24	0.040	73.7	429.8

underlain by water. The water density is 1.092 g/cm^3 . Compute the optimum perforation length and position of the perforation interval with the Chierici *et al.* correlation.

Solution. First, compute $\Delta\rho_{og}/\Delta\rho_{wo}$. This yields $(0.741 - 0.098)/(1.092 - 0.741) = 1.83$. Next, determine δ_g and ψ from the charts for a range of ε . If $\varepsilon = 0.40$, for example, use the chart corresponding to $r_{De} = 5$ to determine that $\delta_g = 0.24$ and $\psi = 0.040$. **Table 9.30** summarizes the results for a range of ε values from 0.05 to 0.40. Next, compute the critical rate for each value of ψ with **Eq. 9.77**. Finally, compute the theoretical producing rate with **Eq. 9.83**.

An examination of **Table 9.30** shows that the critical and producing rates are equal at $\varepsilon = b/h = 0.075$. This value of b/h corresponds to $L_g = (0.385)(150) = 57.8 \text{ ft}$, $b = (0.075)(150) = 11.3 \text{ ft}$, and $L_w = 150 - 57.8 - 11.3 = 81 \text{ ft}$. In conclusion, the well should be perforated with an 11.3-ft interval located 57.8 ft below the GOC and 81 ft above the WOC.

Nomenclature

- a = constant
- b = perforation length, L, ft
- B_g = gas FVF, RB/scf
- B_o = oil FVF, RB/STB
- B_{ig} = two-phase gas FVF, RB/scf
- B_{io} = two-phase oil FVF, RB/STB
- B_{iw} = two-phase water/gas FVF, RB/STB
- B_w = water FVF, RB/STB
- c_f = rock compressibility, L^2/m , 1/psi

- c_t = total aquifer compressibility, Lt^2/m , 1/psi
 E_f = rock (formation) expansivity
 E_g = gas expansivity, RB/scf
 E_{g_w} = expansivity for McEwen method, RB/scf
 $E_{g_{wf}}$ = composite gas/water/rock FVF, RB/scf
 E_o = oil expansivity, RB/STB
 E_{o_w} = expansivity for McEwen method, RB/STB
 $E_{o_{wf}}$ = composite oil/water/rock FVF, RB/STB
 E_t = total expansivity, RB/STB
 E_v = volumetric sweep efficiency, fraction
 E_w = water expansivity, RB/STB
 f = reservoir angle
 F = total fluid withdrawal, L^3 , RB
 G = total original gas in place, L^3 , scf
 G_{fgi} = initial free gas in place, L^3 , scf
 G_i = cumulative gas injected, L^3 , scf
 G_p = cumulative produced gas, L^3 , scf
 G_{ps} = cumulative produced sales gas, L^3 , scf
 h = pay thickness, L, ft
 J^* = constant
 k = permeability, L^2 , md
 k_a = aquifer permeability, L^2 , md
 k_H = horizontal permeability, L^2 , md
 k_t = time constant, 1/t, 1/years
 k_v = vertical permeability, L^2 , md
 K = gas/oil equilibrium ratio or constant
 L_a = aquifer length, L, ft
 L_g = perforation gap between uppermost perforation and GOC, L, ft
 L_r = reservoir length, L, ft
 L_w = perforation gap between lowermost perforation and WOC, ft, L
 m = initial free-gas-phase to free-oil-phase volume ratio (gas-cap size)
 n = total number of data points
 N = total original oil in place, L^3 , STB
 N_{foi} = initial free oil in place, L^3 , STB
 N_g = dimensionless gravity number
 N_p = cumulative produced oil, L^3 , STB
 p = pressure, m/Lt^2 , psi
 \tilde{p} = time-averaged pressure, m/Lt^2 , psi
 \bar{p} = average reservoir pressure, m/Lt^2 , psi
 \bar{p}_a = average aquifer pressure, m/Lt^2 , psi
 p_e = pressure at drainage radius, m/Lt^2 , psi
 p_w = wellbore pressure, m/Lt^2 , psi
 q = producing rate at reservoir conditions (RB/D) or surface conditions (STB/D), L^3/t
 q_c = critical coning rate, STB/D, L^3/t
 q_{Dc} = dimensionless critical coning rate

- q_{sg} = surface producing gas rate, L³/t, scf/D
 q_{so} = surface producing oil rate, L³/t, STB/D
 q_w = aquifer delivery rate, L³/t, RB/D
 r_a = aquifer radius, L, ft
 r_{De} = dimensionless radius including vertical permeability
 r_e = reservoir drainage radius
 r_{eD} = ratio of reservoir to aquifer radii
 r_o = effective reservoir radius, L, ft
 r_w = wellbore radius, L, ft
 R = instantaneous producing GOR, scf/STB
 R_j = residual for point j , L³, RB
 R_p = cumulative GOR, scf/STB
 R_{ps} = cumulative sales GOR, scf/STB
 R_s = dissolved GOR, scf/STB
 R_{ss} = sum of squares of the residual, L⁶, RB²
 R_{sw} = dissolved-gas/water ratio, scf/STB
 R_v = volatilized-oil/gas ratio, STB/MMscf
 s = skin factor
 S_g = gas saturation, fraction
 S_{grw} = residual gas saturation to water flow, fraction
 S_{orw} = residual oil saturation to water flow, fraction
 S_{wi} = initial water saturation, fraction
 t = time, t, years
 t_{max} = maximum time, t, years
 t_D = dimensionless time
 t_{D*} = dimensionless time boundary between infinite-acting and finite aquifers
 t_{Dmax} = maximum dimensionless time
 U = aquifer constant, L⁴t²/m, RB/psi
 V_{fgi} = initial volume of free gas, L³, RB
 V_{foi} = initial volume of free oil, L³, RB
 V_p = reservoir PV, L³, RB
 V_{pa} = aquifer PV, L³, RB
 V_{pi} = initial reservoir PV, L³, RB
 V_{pr} = reservoir PV, L³, RB
 w = reservoir width, L, ft
 W = initial water in place, L³, STB
 W_D = dimensionless cumulative water influx
 W_e = cumulative water influx, L³, RB
 W_I = cumulative injected water, L³, STB
 W_p = cumulative produced water, L³, STB
 δ_g = dimensionless perforation gap below GOC
 δ_w = dimensionless perforation gap above WOC
 Δp = difference of time-averaged pressure, m/Lt², psi
 $\Delta \rho$ = density difference, m/L³, lbm/ft³ and g/cm³
 $\Delta \rho_{og}$ = oil/gas density difference, m/L³, g/cm³
 $\Delta \rho_{wo}$ = water/oil density difference, m/L³, g/cm³

- $\varepsilon = b/h$
 $\phi_a =$ aquifer porosity, fraction
 $\phi_r =$ reservoir porosity, fraction
 $\theta =$ angle
 $\mu_g =$ gas viscosity, m/Lt, cp
 $\mu_o =$ oil viscosity, m/Lt, cp
 $\mu_w =$ water viscosity, m/Lt, cp
 $\rho_g =$ gas density, m/L³, g/cm³
 $\rho_o =$ oil density, m/L³, g/cm³
 $\rho_w =$ water density, m/L³, g/cm³
 $\psi =$ dimensionless critical rate
 $\psi_g =$ dimensionless critical gas coning rate
 $\psi_w =$ dimensionless critical water coning rate

Subscripts

- $i =$ initial condition
 $j =$ index
 $k =$ index

References

1. Muskat, M.: *Physical Principles of Oil Production*, McGraw-Hill Book Co. Inc., New York City (1949).
2. McCain, W.D. Jr.: "Heavy Components Control Reservoir Fluid Behavior," *JPT* (September 1994) 746.
3. Carmalt, S.W. and St. John, B.: "Giant Oil and Gas Fields," *Future of Petroleum Provinces of the World*, M.T. Halbouty (ed.), American Assn. of Petroleum Geologists (1984).
4. *Bull. D-14, Statistical Analysis of Crude Oil Recovery and Recovery Efficiency*, second edition, API, Dallas (1984).
5. Cordell, J.C. and Ebert, C.K.: "A Case History—Comparison of Predicted and Actual Performance of a Reservoir Producing Volatile Crude Oil," *JPT* (November 1965) 1291.
6. Jacoby, R.H. and Berry, V.J. Jr.: "A Method for Predicting Depletion Performance of a Reservoir Producing Volatile Crude Oil," *Trans.*, AIME (1957) **210**, 27.
7. Amyx, J.W., Bass, D.M., and Whiting, R.L.: *Petroleum Reservoir Engineering—Physical Properties*, McGraw-Hill Book Co. Inc., New York City (1960).
8. Dodson, C.R., Goodwill, D, and Mayer, E.H.: "Application of Laboratory PVT Data to Reservoir Engineering Problems," *Trans.*, AIME (1953) **198**, 287.
9. Whitson, C.H. and Torp, S.B.: "Evaluating Constant-Volume Depletion Data," *JPT* (March 1983) 610.
10. Ahmed, T.: *Hydrocarbon Phase Behavior*, Gulf Publishing Co., Houston (1989).
11. Reudelhuber, F.O. and Hinds, R.F.: "A Compositional Material Balance Method for Prediction of Recovery from Volatile Oil Depletion Drive Reservoirs," *Trans.*, AIME (1957) **210**, 19.
12. McCain, W.D.: *The Properties of Petroleum Fluids*, PennWell Publishing Co., Tulsa (1990).
13. Poettmann, F.H. and Thompson, R.S.: "Discussion of Engineering Applications of Phase Behavior of Crude Oil and Condensate Systems," *JPT* (November 1986) 1263.
14. Moses, P.L.: "Engineering Applications of Phase Behavior of Crude Oil and Condensate Systems," *JPT* (July 1986) 715.
15. Walsh, M.P. and Towler, B.F.: "Method Computes PVT Properties for Gas Condensates," *Oil & Gas J.* (31 July 1995) 83.
16. Coats, K.H. and Smart, G.T.: "Application of Regression-Based EOS PVT Program to Laboratory Data," *SPE* (May 1986) 277.

17. Cook, R.E., Jacoby, R.H., and Ramesh, A.B.: "A Beta-Type Reservoir Simulator for Approximating Compositional Effects During Gas Injection," *SPEJ* (October 1974) 471.
18. Standing, M.B.: "A Set of Equations for Computing Equilibrium Ratios of a Crude Oil/Natural Gas System at Pressures Below 1,000 psia," *JPT* (September 1979) 1193.
19. Alani, G.H. and Kennedy, H.T.: "Volumes of Liquid Hydrocarbons at High Temperatures and Pressures," *Trans.*, AIME (1960) **219**, 288.
20. Walsh, M.P.: "A Generalized Approach to Reservoir Material Balance Calculations," *J. Cdn. Pet. Tech.* (January 1995) 55–63.
21. Walsh, M.P.: "New, Improved Equation Solves for Volatile Oil and Condensate Reserves," *Oil & Gas J.* (22 August 1994) 72.
22. Walsh, M.P., Ansah, J., and Raghavan, R.: "The New, Generalized Material Balance as an Equation of a Straight Line: Part 2—Applications to Saturated and Non-Volumetric Reservoirs," paper SPE 27728 presented at the 1994 SPE Permian Basin Oil and Gas Recovery Conference, Midland, Texas, 16–18 March.
23. Walsh, M.P. and Lake, L.W.: *A Generalized Approach to Primary Hydrocarbon Recovery*, Elsevier, Amsterdam (2003).
24. Walsh, M.P., Ansah, J., and Raghavan, R.: "The New, Generalized Material Balance as an Equation of a Straight Line: Part 1—Applications to Undersaturated, Volumetric Reservoirs," paper SPE 27684 presented at the 1994 SPE Permian Basin Oil and Gas Recovery Conference, Midland, Texas, 16–18 March.
25. Society of Petroleum Engineers: *QUICKSIM—A Modified Black-Oil Tank Model, User's Guide*, SPE Software Catalog, Richardson, Texas (2001).
26. Walsh, M.P.: "QUICKSIM—A Modified Black-Oil Tank Model," Version 1.6, Petroleum Recovery Research Inst., Austin, Texas (2000).
27. Walsh, M.P.: "Discussion of Application of Material Balance for High-Pressure Gas Reservoirs," *SPEJ* (December 1998) 402.
28. Walsh, M.P.: "Effect of Pressure Uncertainty on Material-Balance Plots," paper SPE 56691 presented at the 1999 SPE Annual Technical Conference and Exhibition, Houston, 3–6 October.
29. Schilthuis, R.J.: "Active Oil and Reservoir Energy," *Trans.*, AIME (1936) **118**, 33.
30. Dake, L.P.: *Fundamentals of Reservoir Engineering*, Elsevier Scientific Publishing Co., Amsterdam (1978).
31. Hall, H.N.: "Analysis of Gravity Drainage," *JPT* (September 1961) 927; *Trans.*, AIME, **222**.
32. Pirson, S.J.: *Oil Reservoir Engineering*, McGraw-Hill Book Co. Inc., New York City (1958).
33. Katz, D.L.: "Possibilities of Secondary Recovery for the Oklahoma City Wilcox Sand," *Trans.*, AIME (1942) **146**, 28.
34. Hill, H.B. and Guthrie, R.K.: "Engineering Study of the Rodessa Oil Field in Louisiana, Texas, and Arkansas," Report Investigation 3715, U.S. Bureau of Mines, Washington, DC (August 1943) 87.
35. Garthwaite, D.L. and Krebill, F.K.: "Supplement 1962: Pressure Maintenance by Inert Gas Injection in the High Relief Elk Basin Field," *Field Case Histories, Oil Reservoirs*, Reprint Series, SPE, Richardson, Texas (1962) **4**.
36. Garthwaite, D.L.: "Supplement, 1975: Pressure Maintenance by Inert Gas Injection in the High Relief Elk Basin Field," *Field Case Histories, Oil and Gas Reservoirs*, Reprint Series, SPE, Richardson, Texas (1975) **4a**.
37. Stewart, F.M., Garthwaite, D.L., and Krebill, F.K.: "Pressure Maintenance by Inert Gas Injection in the High Relief Elk Basin Field," *Trans.*, AIME (1955) **204**, 49.
38. Havlena, D. and Odeh, A.S.: "The Material Balance as an Equation of a Straight Line," *JPT* (August 1963) 896; *Trans.*, AIME, **228**.
39. Wang, B. and Hwan, R.R.: "Influence of Reservoir Drive Mechanism on Uncertainties of Material Balance Calculations," paper SPE 38918 presented at the 1997 SPE Annual Technical Conference and Exhibition, San Antonio, Texas, 5–8 October.
40. Tehrani, D.H.: "An Analysis of a Volumetric Balance Equation for Calculation of Oil In Place and Water Influx," *JPT* (September 1985) 1664.
41. Roadifer, R.E.: "Size Distributions of World's Largest Known Oil, Tar Accumulations," *Oil & Gas J.* (24 February 1986) 93.

42. McEwen, C.R.: "Material Balance Calculations with Water Influx in the Presence of Uncertainty in Pressures," *SPEJ* (June 1962) 120.
43. van Everdingen, A.F. and Hurst, W.: "The Application of the Laplace Transformation to Flow Problems in Reservoirs," *Trans.*, AIME (1949) **186**, 305.
44. Carter, R.D. and Tracy, G.W.: "An Improved Method for Calculating Water Influx," *Trans.*, AIME (1960) **219**, 415.
45. Fetkovich, M.J.: "A Simplified Approach to Water Influx Calculations—Finite Aquifer Systems," *JPT* (July 1971) 814.
46. Coats, K.H.: "Mathematical Methods for Reservoir Simulation," presented by the College of Engineering, U. of Texas at Austin, 8–12 June 1970.
47. Klins, M.A., Bouchard, A.J., and Cable, C.L.: "A Polynomial Approach to the van Everdingen-Hurst Dimensionless Variables for Water Encroachment," *SPERE* (February 1988) 320.
48. Marsal, D.: "Topics of Reservoir Engineering," Course Notes, Delft U. of Technology (1982).
49. Walsh, M.P.: *A Generalized Approach to Petroleum Reservoir Engineering*, Petroleum Recovery Research Inst., Austin, Texas (1996).
50. Allard, D.R. and Chen, S.M.: "Calculation of Water Influx for Bottomwater Drive Reservoirs," *SPERE* (May 1988) 369.
51. Field, M.B., Givens, J.W., and Paxman, D.S.: "Kaybob South—Reservoir Simulation of a Gas Cycling Project with Bottom Water Drive," *JPT* (April 1970) 481.
52. Woods, R.W. and Muskat, M.M.: "An Analysis of Material-Balance Calculations," *Trans.*, AIME (1945) **160**, 124.
53. Chierici, G.L., Pizzi, G. and Ciucci, G.M.: "Water Drive Gas Reservoirs: Uncertainty in Reserves Evaluation From Past History," *JPT* (February 1967) 237.
54. Sills, S.R.: "Improved Material-Balance Regression Analysis for Waterdrive Oil and Gas Reservoirs," *SPERE* (May 1996) 127.
55. van Everdingen, A.F., Timmerman, E.H., and McMahon, J.J.: "Application of the Material Balance Equation to a Partial Water-Drive Reservoir," *Trans.*, AIME (1953) **198**, 51.
56. Campbell, R.A. and Campbell, J.M.: *Mineral Property Economics, Vol. 3: Petroleum Property Evaluation*, Campbell Petroleum Series, Norman, Oklahoma (1978).
57. Cole, F.W.: *Reservoir Engineering Manual*, Gulf Publishing Co., Houston, (1969).
58. Cook, C.C. and Jewell, S.: "Simulation of a North Sea Field Experiencing Significant Compaction Drive," *SPERE* (February 1996) 48.
59. Sulak, R.M.: "Ekofisk Field: The First 20 Years," *JPT* (October 1991) 1265.
60. Sulak, R.M., Thomas, L.K., and Boade, R.R.: "3D Reservoir Simulation of Ekofisk Compaction Drive," *JPT* (October 1991) 1272.
61. Fetkovich, M.J., Reese, D.E., and Whitson, C.H.: "Application of a General Material Balance for High-Pressure Gas Reservoirs," *SPEJ* (March 1998) 3.
62. Letkeman, J.P. and Ridings, R.L.: "A Numerical Coning Model," *SPEJ* (December 1970) 418.
63. MacDonald, R.C. and Coats, K.H.: "Methods for Numerical Simulation of Water and Gas Coning," *SPEJ* (December 1970) 425.
64. Muskat, M. and Wyckoff, R.D.: "An Approximate Theory of Water-Coning in Oil Production," *Trans.*, AIME (1935) **114**, 144.
65. Chaney, P.E. *et al.*: "How to Perforate Your Well to Prevent Oil and Gas Coning," *Oil & Gas J.* (7 May 1956) 108.
66. Chierici, G.L., Ciucci, G.M., and Pizzi, G.: "A Systematic Study of Gas and Water Coning By Potentiometric Models," *JPT* (August 1964) 923.
67. Bournazel, C. and Jeanson, B.: "Fast Water-Coning Evaluation Method," paper SPE 3628 presented at the 1971 SPE Annual Meeting, New Orleans, 3–6 October.
68. Hoyland, L.A., Papatzacos, P., and Skjaeveland, S.M.: "Critical Rate for Water Coning: Correlation and Analytical Solution," *SPERE* (November 1989) 495.
69. Kuo, M.C.T. and DesBrisay, C.L.: "A Simplified Method for Water Coning Predictions," paper SPE 12067 presented at the 1983 SPE Annual Technical Conference and Exhibition, San Francisco, 5–8 October.
70. Meyer, H.I. and Garder, A.O.: "Mechanics of Two Immiscible Fluids in Porous Media," *J. of Applied Physics* (November 1954) 1400.

71. Schols, R.S.: "An Empirical Formula for the Critical Oil Rate," *Erdöl Erdgas, Zeitschrift* (January 1972) 6–11.
 72. Sobocinski, D.P. and Cornelius, A.J.: "A Correlation for Predicting Water Coning Time," *JPT* (May 1965) 594.
 73. Wheatley, M.J.: "An Approximate Theory of Oil/Water Coning," paper SPE 14210 presented at the 1985 SPE Annual Technical Conference and Exhibition, Las Vegas, Nevada, 22–25 September.
 74. Saidikowski, R.M.: "Numerical Simulations of the Combined Effects of Wellbore Damage and Partial Penetration," paper SPE 8204 presented at the 1979 SPE Annual Technical Conference and Exhibition, Las Vegas, Nevada, 23–26 September.
 75. Kozeny, J.: *Wasserkraft and Wasserwirtschaft* (1933) **28**, 101.
 76. Howard, G.C. and Fast, C.R.: "Squeeze Cementing Operations," *Trans.*, AIME (1950) **189**, 53.
 77. Richardson, J.G. and Blackwell, R.J.: "Use of Simple Mathematical Models for Predicting Reservoir Behavior," *JPT* (September 1971) 1145.
-

General References

- Amyx, J.W., Bass, D.M., and Whiting, R.L.: *Petroleum Reservoir Engineering—Physical Properties*, McGraw-Hill Book Co. Inc., New York City (1960).
- Archer, J.S. and Wall, P.G.: *Petroleum Engineering: Principles and Practice*, Graham and Trotman, London (1992).
- Bradley, H.B.: *Petroleum Engineering Handbook*, SPE, Richardson, Texas (1987).
- Calhoun, J.C. Jr.: *Fundamentals of Reservoir Engineering*, U. of Oklahoma Press, Norman, Oklahoma (1951).
- Caudle, B.H.: *Fundamentals of Reservoir Engineering—Parts 1 and 2*, SPE, Richardson, Texas (1967).
- Clark, N.J.: *Elements of Petroleum Reservoirs*, Society of Petroleum Engineers of AIME, Dallas (1960).
- Craft, B.C. and Hawkins, M.F. Jr.: *Applied Petroleum Reservoir Engineering*, Prentice-Hall Inc., Upper Saddle River, New Jersey (1959).
- Craft, B.C., Hawkins, M.F. Jr., and Terry, R.E.: *Applied Petroleum Reservoir Engineering*, second edition, Prentice-Hall Inc., Upper Saddle River, New Jersey (1991).
- Dake, L.P.: *Fundamentals of Reservoir Engineering*, Elsevier Scientific Publishing Co., New York City (1978).
- Guerrero, E.T.: *Practical Reservoir Engineering*, Petroleum Publishing Co., Tulsa (1951).
- Hagoort, J.: *Fundamentals of Gas Reservoir Engineering*, Elsevier, New York City (1988).
- Katz, D.L. *et al.*: *Handbook of Natural Gas Engineering*, McGraw-Hill Book Co. Inc., New York City (1959).
- Koederitz, L.F., Harvey, A.H., and Honarpour, M.: *Introduction to Petroleum Reservoir Analysis*, Gulf Publishing Co., Houston (1989).
- Muskat, M.: *Physical Principles of Oil Production*, McGraw-Hill Book Co. Inc., New York City (1949) National Human Resources Development Corp., reprinted (1981).
- Pirson, S. J.: *Oil Reservoir Engineering*, McGraw-Hill Book Co. Inc., New York City (1958).
- Smith, C.R., Tracy, G.W., and Farrar, R.L.: *Applied Reservoir Engineering—Vols. 1 and 2*, Oil and Gas Consultants Intl., Tulsa (1992).
- Standing, M.B.: *Volumetric and Phase Behavior of Oil Field Hydrocarbon Systems*, SPE, Dallas (1951).
- Timmerman, E.H.: *Practical Reservoir Engineering—Parts 1 and 2*, PennWell Books, Tulsa (1982).
- Walsh, M.P. and Lake, L.W.: *A Generalized Approach to Primary Hydrocarbon Recovery*, Elsevier, Amsterdam (2003).

Appendix—Key Equations in SI Units

$$N_g = \frac{2.63 \times 10^{-3} k_v \Delta \rho r_e^2}{\mu q}, \dots\dots\dots (9.19)$$

$$t_D = \frac{0.03110 k_a t}{\phi_a \mu_w c_t r_o^2}, \dots\dots\dots (9.35)$$

$$U = 4.89 \times 10^{-3} h f r_o^2 \phi_a c_t, \dots\dots\dots (9.36)$$

$$t_D = \frac{0.03110 k_a t}{\phi_a \mu_w c_t L_a^2}, \dots\dots\dots (9.50)$$

$$L_{ac} = \sqrt{\frac{0.03110 k_a t_{max}}{2 \phi_a \mu_w c_t}}, \dots\dots\dots (9.53)$$

$$q_c = \frac{5.256 \times 10^{-3} k_o h^2 \Delta \rho}{\mu_o B_o} q_{Dc}, \dots\dots\dots (9.77)$$

$$\text{and } q = \frac{5.35 \times 10^{-4} k_H b (p_e - p_w)}{\mu_o B_o \left(\ln \frac{r_e}{r_w} + s \right)} \left[1 + 7 \sqrt{\frac{r_w}{2b}} \sqrt{\frac{k_v}{k_H}} \cos \left(\frac{\pi b}{2h} \right) \right], \dots\dots\dots (9.83)$$

where the following units apply: *k* is given md; $\Delta \rho$ is in g/cm³; *b*, *h*, *r*, and *L_a* are in m; *q* is in std m³/day; μ is in mPa·sec or cp; *t* is in years; *c* is in 1/kPa; *U* is in m³/kPa; and *k_t* is in 1/years.

SI Metric Conversion Factors

acre × 4.046 856	E + 03 = m ²
acre-ft × 1.233 489	E + 03 = m ³
bbl × 1.589 873	E - 01 = m ³
cp × 1.0*	E - 03 = Pa·s
ft × 3.048*	E - 01 = m
°F (°F - 32)/1.8	= °C
gal × 3.785 412	E - 03 = m ³
lbm × 4.535 924	E - 01 = kg
psi × 6.894 757	E + 00 = kPa
sq mile × 2.589 988	E + 00 = km ²
std ft ³ × 2.831 685	E - 02 = m ³

*Conversion factor is exact.

Chapter 10

Gas Reservoirs

Mark A. Miller, Consultant and E.D. Holstein, Consultant

10.1 Introduction

This chapter addresses the flow characteristics and depletion strategies for gas reservoirs. The focus will be primarily on nonassociated accumulations, but much of the fluid behavior, flow regimes, and recovery aspects are also applicable to gas caps associated with oil columns.

In this chapter, gas reservoirs have been divided into three groups; dry gas, wet gas, and retrograde-condensate gas. A dry-gas reservoir is defined as producing a single composition of gas that is constant in the reservoir, wellbore, and lease-separation equipment throughout the life of a field. Some liquids may be recovered by processing in a gas plant. A wet-gas reservoir is defined as producing a single gas composition to the producing well perforations throughout its life. Condensate will form either while flowing to the surface or in lease-separation equipment. A retrograde-condensate gas reservoir initially contains a single-phase fluid, which changes to two phases (condensate and gas) in the reservoir when the reservoir pressure decreases. Additional condensate forms with changes in pressure and temperature in the tubing and during lease separation. From a reservoir standpoint, dry and wet gas can be treated similarly in terms of producing characteristics, pressure behavior, and recovery potential. Wellbore hydraulics may be different. Studies of retrograde-condensate gas reservoirs must consider changes in condensate yield as reservoir pressure declines, the potential for decreased well deliverability as liquid saturations increase near the wellbore, and the effects of two-phase flow on wellbore hydraulics.

A comprehensive discussion of gas and condensate properties and phase behavior can be found in several chapters of the General Engineering section of this *Handbook*. Aspects of predicting wellbore hydraulics are covered in the Production Operations Engineering section of this *Handbook*. Lease equipment for processing gas and pipelining considerations are covered in several chapters of the Facilities Engineering section of this *Handbook*. The reader may want to refer to these chapters to understand some of the nomenclature and concepts referred to in the present chapter.

10.2 Properties of Natural Gases

Natural petroleum gases contain varying amounts of different (primarily alkane) hydrocarbon compounds and one or more inorganic compounds, such as hydrogen sulfide, carbon dioxide,

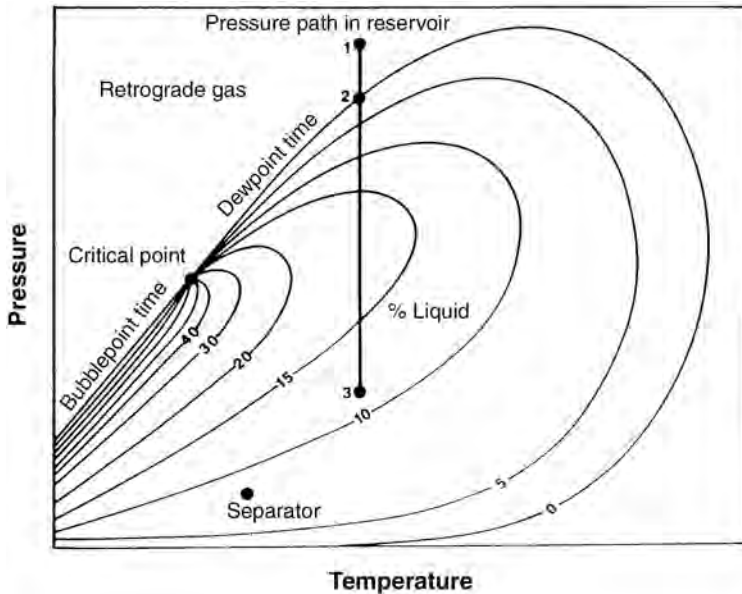


Fig. 10.1—Phase diagram of a retrograde-condensate gas.¹ (Source: *The Properties of Petroleum Fluids*, second edition, by William D. McCain Jr. Copyright PennWell Books, 1990.)

nitrogen (N_2), and water. Characterizing, measuring, and correlating the physical properties of natural gases must take into account this variety of constituents.

10.2.1 Phase Behavior of Natural-Gas Reservoirs. A widely accepted system for categorizing petroleum reservoir fluids is based on five classes: low-shrinkage (crude) oils, high-shrinkage (volatile) oils, retrograde-condensate gases, wet gases, and dry gases. Typical phase diagrams for the gas categories are shown in Figs. 10.1 through 10.3.

A retrograde-condensate fluid has a phase envelope such that reservoir temperature lies between the critical temperature and the cricondentherm (Fig. 10.1). As a result, a liquid phase will form in the reservoir as pressure declines, and the amount and gravity of produced liquids will change with time. Condensate liquids are generally “water white” or light in color (brown, orange, or greenish), with gravities typically between 40 and 60°API. Producing-liquid yields can be as high as 300 STB/MMscf. McCain¹ suggests that when yields are below approximately 20 STB/MMscf, even though phase-behavior considerations may show retrograde behavior, the amount of liquid dropout in the reservoir is insignificant. The primary difficulties in producing condensate reservoirs are as follows: (a) liquid deposition near the wellbore causes a decrease in gas deliverability that can approach 100% in a reservoir with less than 50-md permeability, and (b) a large amount of the most valuable hydrocarbon components is left in the reservoir rather than produced.

In a wet-gas reservoir, temperature is higher than the cricondentherm (Fig. 10.2). Therefore, a liquid phase never forms in the reservoir. Considerable liquid can still form (condense) at surface conditions or even in the wellbore. The term “condensate” is often applied to any light hydrocarbon liquid produced from a gas well. However, the term “condensate reservoir” should be applied only to situations in which condensate is actually formed in the reservoir because of retrograde behavior. Wet-gas reservoirs can always be treated as containing single-phase gas in the reservoir, while retrograde-condensate reservoirs may not. Wet-gas reservoirs generally produce liquids with gravities similar to those for retrograde condensates, but with yields less than approximately 20 STB/MMscf.¹

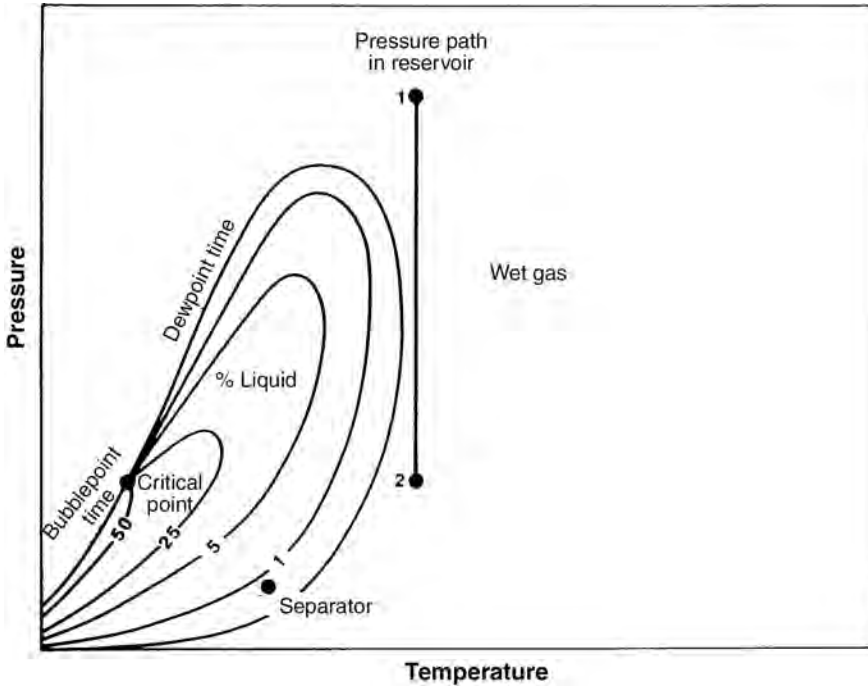


Fig. 10.2—Phase diagram of a wet gas.¹ (Source: *The Properties of Petroleum Fluids*, second edition, by William D. McCain Jr. Copyright PennWell Books, 1990.)

In a dry-gas reservoir, the cricondentherm is much lower than the reservoir temperature (Fig. 10.3), resulting in little or no liquid production at the surface. A somewhat arbitrary cut-off liquid yield of 10 STB/MMscf is sometimes used to distinguish dry-gas reservoirs.

While the difference between retrograde-condensate and wet gases is notable, there is much less distinction between wet and dry gases. For both wet and dry gases, reservoir engineering calculations are based on a single-phase reservoir gas. The only issue is whether there is a sufficient volume of produced liquid to be considered in such calculations as material balance or wellbore hydraulics. Retrograde systems require more-complex calculations using equations of state (EOSs) and other advanced engineering methods.

10.2.2 Pressure/Volume/Temperature (PVT) Behavior. The chapters on Fluid Sampling, Gas Properties, and Thermodynamics and Phase Behavior in the General Engineering section of this *Handbook* contain a detailed explanation of PVT and thermodynamic relationships for ideal and real gases. Some fundamental relations are repeated here as background for the remainder of this chapter.

The basis of gas PVT behavior is the ideal gas law, and by extension the real gas law:

$$pV_m = zRT \dots\dots\dots (10.1)$$

The universal gas constant in practical units is

$$R = 10.7315 \frac{\text{psia} \cdot \text{ft}^3}{\text{lb mol} \cdot ^\circ\text{R}} = 1.98586 \frac{\text{btu}}{\text{lb mol} \cdot ^\circ\text{R}}$$

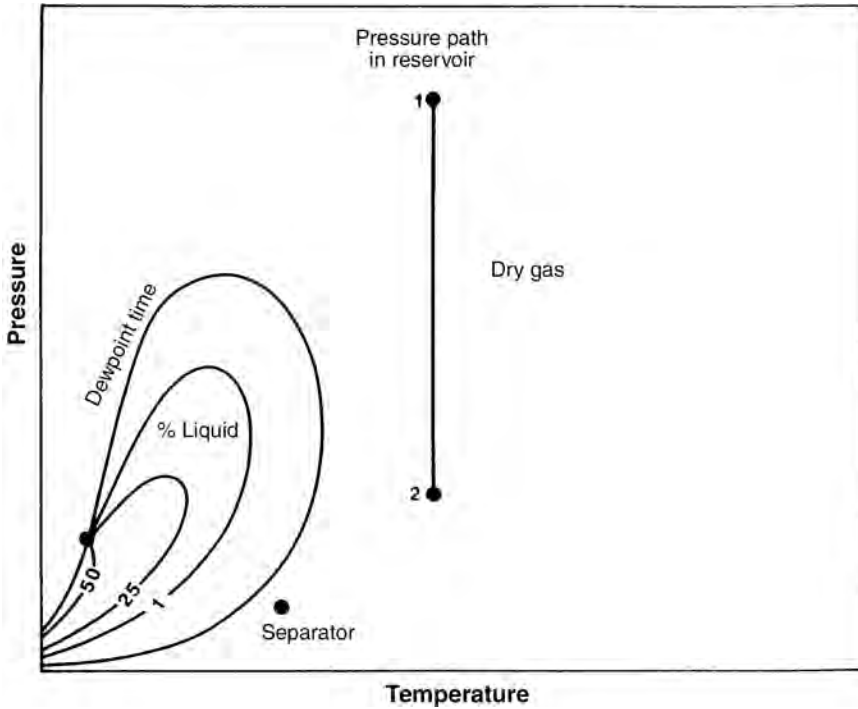


Fig. 10.3—Phase diagram of a dry gas.¹ (Source: *The Properties of Petroleum Fluids*, second edition, by William D. McCain Jr. Copyright PennWell Books, 1990.)

$$= 8.31441 \frac{\text{kPa} \times \text{m}^3}{\text{kmol} \times \text{K}} = 8.31441 \frac{\text{kJ}}{\text{kmol} \cdot \text{°R}} \dots\dots\dots (10.2)$$

For economic reasons, most (but not all) pressure gauges read zero pressure when pressure is equal to the ambient atmospheric pressure. Therefore, atmospheric pressure must be added to gauge pressures to convert them to an absolute basis. For most engineering purposes, atmospheric pressure is usually taken to be 14.7 psia (101 kPa). For precise scientific and engineering applications, actual atmospheric pressure (i.e., barometric pressure, which varies with both location and time) should be used. Standard temperature and pressure are set by different governmental agencies and should be determined for a specific field or reservoir to be sure that reserves and produced quantities are reported with the correct bases. The SPE standard temperature is 59°F (15°C), and the standard pressure is 14.696 psia (101.325 kPa).

Application of Eq. 10.1, in a practical sense, must consider how to determine the various factors for petroleum gases that are mixtures of several components. Such determinations would include apparent molecular weight and *z* (using pseudoreduced pressure and temperature and corrections for nonhydrocarbon components).

10.2.3 Gas Density and Formation Volume Factor. The density of a gas can be calculated from the real-gas law once a *z* factor has been determined. For pressure in psia and temperature in °R, density in lbm/ft³ is given by

$$\rho_g = 2.6988 \frac{p\gamma_g}{zT} \dots\dots\dots (10.3)$$

For pressure in kPa, temperature in K, and density in kg/m³,

$$\rho_g = 3.4834 \frac{p\gamma_g}{zT} \dots\dots\dots (10.4)$$

The gas formation volume factor is defined as the volume occupied by a gas at reservoir conditions divided by the volume at standard conditions:

$$B_g = \frac{P_{sc}}{T_{sc}} \frac{zT}{p}$$

$$= 28.279 \frac{zT}{p} \text{ft}^3 / \text{Mscf} = 5.0368 \frac{zT}{p} \text{bbl} / \text{Mscf} \dots\dots\dots (10.5)$$

The second and third lines of Eq. 10.5 give B_g using standard pressure of 14.696 psia and standard temperature of 60°F.

In SI units using SPE standard pressure and temperature,

$$B_g = 2.8438 \frac{zT}{p} \text{m}^3 / \text{std m}^3 \dots\dots\dots (10.6)$$

10.2.4 Viscosity. Most gas viscosities range from 0.01 to 0.03 cp, making them difficult to measure accurately. Accurate determination of gas viscosities has low economic value. Instead, values are normally determined from one of two correlations.

The first one in common use today, from Lee *et al.*,² is given in equation form as

$$\mu_g = K \times 10^{-4} \exp(X\rho_g^Y), \dots\dots\dots (10.7)$$

where $K = \frac{(9.4 + 0.02M_g)T^{1.5}}{209 + 19M_g + T}$, $X = 3.5 + \frac{986}{T} + 0.01M_g$, $Y = 2.4 - 0.2X$, and

$$\rho_g = \frac{1}{669.95} \frac{pM_g}{zT} = \frac{1}{23.132} \frac{p\gamma_g}{zT}$$

The gas density in Eq. 10.7 is in g/cm³ when p and T are in oilfield units (psia, °R). The equivalent formula for SI units (pressure and temperature in kPa and K, respectively) is

$$\rho_g = \frac{1}{8314.4} \frac{pM_g}{zT} = \frac{1}{287.08} \frac{p\gamma_g}{zT} \dots\dots\dots (10.8)$$

Fig. 10.4 shows gas viscosities generated from this correlation for a 0.80-gravity natural gas.

Another common correlation³ entails a two-step graphical process and is cumbersome for computer applications. Because gas viscosities are seldom needed with great accuracy, the Lee *et al.*² correlation is most applicable for modern reservoir-engineering practice.

10.2.5 Determining Reservoir-Fluid Properties. Condensation of liquids from wet-gas and retrograde-condensate fluids in the production system means that gas produced from separation equipment may be significantly different from the gas that flows into the wellbore from the reservoir. In general, separator gas will be lower in gravity and will have fewer high-molecular-weight hydrocarbons present in the mixture.

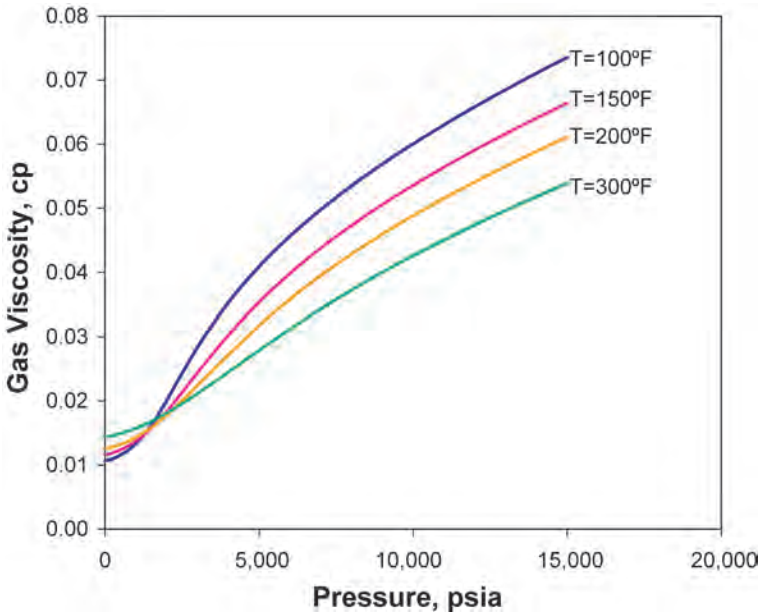


Fig. 10.4—Viscosity of 0.80-gravity natural gas vs. pressure and temperature according to the Lee *et al.*² correlation.

For proper laboratory measurements, a bottomhole sample should be collected. An alternative is a reconstituted sample that is created by mixing the separator-produced gas and liquid in proportion to their relative production rates. When the compositions of liquid and gaseous streams have both been measured, the composition of the mixture can be determined from

$$z_j = x_j \tilde{n}_o + y_j \tilde{n}_g \dots\dots\dots (10.9)$$

Note that

$$\sum_{j=1}^{n_c} x_j = \sum_{j=1}^{n_c} y_j = \sum_{j=1}^{n_c} z_j = 1 \dots\dots\dots (10.10)$$

$$\tilde{n}_o + \tilde{n}_g = 1 \dots\dots\dots (10.11)$$

Relative molar amounts can be determined by converting measured produced volumes either to moles or to equivalent standard cubic feet. For a gas phase, conversion of a produced volume referenced to standard conditions to moles is

$$n_g = \frac{p_{sc} V_g^{sc}}{RT_{sc}} = \frac{V_g^{sc}}{V_{msc}} \dots\dots\dots (10.12)$$

For a liquid, conversion of a volume to moles is

$$n_o = V_o \frac{\rho_o}{M_o} \dots\dots\dots (10.13)$$

If liquid volume is measured at standard conditions, density can be calculated from specific gravity or API gravity. If liquid molecular weight is not measured, it can be approximated with the Gold *et al.*⁴ correlation:

$$M_o = \frac{5,954}{^\circ\text{API} - 8.8} = \frac{42.43\gamma_o}{1.008 - \gamma_o} \dots\dots\dots (10.14)$$

An alternative to converting measured volumes to moles is to convert all measured volumes to equivalent standard volumes because standard volume is directly proportional to moles (through the value of the standard molar volume). This procedure has the advantage that measured gas volumes need not be converted (this is necessary only for liquid volumes).

Liquid volumes are converted to equivalent gas standard volumes using a parameter called the gas equivalent of oil. This parameter represents the effective standard volume occupied by hydrocarbons that are liquid at surface conditions but are in the gas phase at downhole conditions. This parameter is calculated by

$$GE_o = R\rho_{\text{H}_2\text{O}}^{sc} \frac{T_{sc}}{p_{sc}} \frac{\gamma_o}{M_o} \dots\dots\dots (10.15)$$

GE_o is calculated with oilfield units in Mscf/STB (the second term below uses standard conditions of 14.696 psia and 60°F) by

$$GE_o = 3.7615 \frac{T_{sc}}{p_{sc}} \frac{\gamma_o}{M_o} = 133.01 \frac{\gamma_o}{M_o} \dots\dots\dots (10.16)$$

In SI units, GE_o in std m³/std m³ is (using standard conditions of 101.325 kPa and 15°C)

$$GE_o = 8,314.4 \frac{T_{sc}}{p_{sc}} \frac{\gamma_o}{M_o} = 23,645 \frac{\gamma_o}{M_o} \dots\dots\dots (10.17)$$

Liquid-production volumes are multiplied by GE_o to determine the equivalent standard volume as gas in the reservoir; that is,

$$V_{o, \text{eq}}^{sc} = GE_o V_o^{sc} \dots\dots\dots (10.18)$$

where V_o^{sc} is the actual oil volume measured at stock-tank conditions, and $V_{o, \text{eq}}^{sc}$ is the gas-equivalent volume of the oil.

These equations also can be used to determine the equivalent gas production of pure hydrocarbons separated from gas in a processing plant. Values of specific gravity and molecular weight for pure components can be found from standard sources such as the Gas Processors Suppliers Assn. (GPSA) Handbook.⁵ In addition, if liquid production is measured at separator, rather than stock-tank, conditions, Eq. 10.16 or Eq. 10.17 can be used with separator temperature and pressure rather than standard temperature and pressure.

Relative volumes of gas and liquid phases can then be calculated as

$$\begin{aligned} \tilde{n}_g &= \frac{n_g}{n_g + n_o} = \frac{V_g^{sc}}{V_g^{sc} + V_{o, eq}^{sc}} \\ \tilde{n}_o &= 1 - \tilde{n}_g = \frac{n_o}{n_g + n_o} = \frac{V_{o, eq}^{sc}}{V_g^{sc} + V_{o, eq}^{sc}} \end{aligned} \quad \dots\dots\dots (10.19)$$

When wellstream composition is unavailable, correlations must be used to determine gas properties, requiring the calculation of the wellstream (mixture) gravity on the basis of the gravity of the separator gas (often called dry gas) and the specific gravity of the produced liquid (condensate or oil):

$$\gamma_{wg} = \frac{\gamma_g + \frac{V_{msc} \rho_{H_2O}^{sc}}{M_{air}} \gamma_o Y}{1 + V_{msc} \rho_{H_2O}^{sc} \frac{\gamma_o}{M_o} Y} \quad \dots\dots\dots (10.20)$$

where the subscript g refers to the separator-gas gravity, wg refers to the wellstream gas, and o refers to the produced condensate (oil). Y is the produced condensate yield. Gold’s correlation can be used to estimate condensate molecular weight.

In oilfield units with yield in STB/MMscf,

$$\gamma_{wg} = \frac{\gamma_g + \frac{1}{7707.2} \frac{T_{sc}}{p_{sc}} \gamma_o Y}{1 + \frac{1}{266.11} \frac{T_{sc}}{p_{sc}} \frac{\gamma_o Y}{M_o}} = \frac{\gamma_g + \frac{\gamma_o Y}{217.95}}{1 + \frac{\gamma_o Y}{7.5254 M_o}} \quad \dots\dots\dots (10.21)$$

In SI units with yield in std m³/std m³,

$$\gamma_{wg} = \frac{\gamma_g + 286.80 \frac{T_{sc}}{p_{sc}} \gamma_o Y}{1 + 8,306.4 \frac{T_{sc}}{p_{sc}} \frac{\gamma_o Y}{M_o}} = \frac{\gamma_g + 815.61 \gamma_o Y}{1 + 23,622 \frac{\gamma_o Y}{M_o}} \quad \dots\dots\dots (10.22)$$

10.2.6 Measuring Retrograde Behavior. When a liquid phase begins to form in the reservoir, the produced stream is no longer representative of the reservoir-fluid composition, but rather only the composition of the fluids entering the wellbore. Situations in which the liquid content of gases is high require the use of advanced laboratory tests and/or equation-of-state modeling to measure and predict these multiphase effects.

Laboratory measurements of the PVT behavior of condensate systems are similar to tests used for black oils; however, the primary interest becomes the measurement of relatively small amounts of condensed liquid. In general, systems with producing gas/oil ratios of 15,000 scf/STB (67 STB/scf) have a liquid dropout of approximately 4 to 6% by volume, while reservoirs with ratios around 50,000 scf/STB ordinarily have liquid dropouts of less than 1% by volume.¹

Two types of tests are generally run on retrograde fluids: constant-composition expansion (CCE) and constant-volume depletion. For examples refer to **Tables 10.1 through 10.3**.

Table 10.1 gives the compositions of separator gas and liquid streams and other data used in making a recombined sample for analysis of reservoir-fluid composition.

TABLE 10.1—EXAMPLE FIELD AND ANALYSIS DATA FOR RETROGRADE-FLUID STUDY⁶

Field data and analyses for condensate well No. 7 (courtesy of Core Lab Inc.)					
Original reservoir pressure at 11,300 ft, 7,000 psig					
Reservoir temperature, 256°F (398 K)					
At sampling bottomhole pressure 1,505 psig (10.4 MPa), tubing rd. 780 psig (5.5 MPa)					
Separator liquid, 185 B/D (46.5°API)					
Primary separator gas, 869 Mcf/day (gravity 0.699)					
Gas/liquid ratio, 4,697 scf/bbl, 212.9 bbl/MMcf					
Component	Separator liquid, mol%	Separator Gas		Wellstream	
		Mol%	Gallons per thousand ft ³ , GPM	Mol%	GPM
Hydrogen sulfide	0.00	0.00		0.00	
Carbon dioxide	0.00	0.01		0.01	
Nitrogen	0.01	0.13		0.11	
Methane	10.76	83.01		68.93	
Ethane	6.17	9.23	2.454	8.63	2.295
Propane	-8.81	4.50	1.231	5.34	1.461
iso-butane	2.85	0.74	0.241	1.15	0.374
n-Butane	7.02	1.20	0.376	2.33	0.730
iso-pentane	3.47	0.31	0.113	0.93	0.338
n-Pentane	3.31	0.25	0.090	0.85	0.36
Hexanes	8.03	0.21	0.085	1.73	0.702
Heptanes plus	49.57	0.41	0.185	9.99	6.006
	100.00	100.00	4.775	100.00	12.212
<u>Properties of Heptane Plus</u>					
API gravity at 60°F	39.0				
Density, g/cm ³ at 60°F	0.8293				
Molecular weight	160	103		158	
Calculated separator-gas gravity = 0.699					
Calculated gross heating value for separator gas = 1,230 Btu/ft ³ of dry gas at 14.65 psia and 60°F					
Primary separator gas collected at 440 psig and 87°F					
Primary separator liquid collected at 440 psig and 87°F					
Primary-separator-gas/separator-liquid ratio = 3,944 scf/bbl at 60°F					
Primary-separator-liquid/stock-tank-liquid ratio = 1.191 bbl/bbl at 60°F					
Primary-separator-gas/wellstream ratio = 805.19 Mcf/MMcf					
Stock-tank-liquid/wellstream ratio = 171.4 bbl/MMcf					
From Katz, D.L., <i>Handbook of Natural Gas Engineering</i> , © The McGraw-Hill Companies Inc. (1990)					

A CCE using a visual cell furnishes the dewpoint of the reservoir fluid at reservoir temperature and the total volume of the reservoir fluid as a function of pressure. The volume of liquid formed at pressures below the dewpoint can also be measured. Table 10.2 shows the results of such a test. The term “relative volume” refers to the volume of gas plus liquid compared to the dewpoint volume. Retrograde-liquid volume is given as a percent of pore space,

TABLE 10.2—EXAMPLE VOLUMETRIC BEHAVIOR OF CONDENSATE WELL FLUID ^a		
Volumetric and retrograde-liquid measurements on condensate well fluid, well No. 7 (courtesy of Core Lab Inc.)		
Pressure, psig	Relative Volume	Retrograde-Liquid Volume, percent of pore space
7,500	0.9341	
7,000 (reservoir pressure)	0.9523*	
6,500	0.9727	
6,300	0.9834	
6,200	0.9891	
6,100	0.9942	
6,010 (dewpoint pressure)	1.0000 [†]	0.0
5,950	1.0034	Trace
5,900	1.0076	0.1
5,800	1.0138	0.2
5,600	1.0267	0.5
5,300	1.0481	2.0
5,000 (first depletion level)	1.0749	7.8
4,500	1.1268	—
4,000	1.2024	21.3
3,500	1.3096	—
3,000	1.4689	25.0
2,500	1.7169	—
2,100	2.0191	24.4
1,860	2.2747	—
1,683	2.5150	—
1,460	2.9087	—
1,290	3.3173	—
1,200	—	22.5
1,160	3.7153	—
1,050	4.1342	—
700	—	21.0
0	—	17.6

*Gas expansion factor = 1.545 Mcf/bbl
[†]Gas expansion factor = 1.471 Mcf/bbl

From Katz, D.L.: *Handbook of Natural Gas Engineering*. © 1990 The McGraw-Hill Companies Inc. (1990)

which essentially shows how the average condensate saturation changes with average reservoir pressure. **Fig. 10.5** is a graphical representation of the relative condensate volume.

Visual cells also can be used to simulate pressure depletion. The validity of these tests is based on the assumption that the retrograde liquid that condenses in the reservoir will not be mobile. This assumption is valid except for very rich gas/condensate reservoirs. If significant retrograde liquid becomes mobile and migrates to producing wells, gas/liquid relative permeability data should be measured and used to adjust the predicted recovery.

Table 10.3 is an example of a visual-cell depletion study on the same retrograde gas for which properties are shown in **Tables 10.1** and **10.2**.

TABLE 10.3—DEPLETION STUDY AT 256°F								
Component	Reservoir Pressure (psig)							
	6,010	5,000	4,000	3,000	2,100	1,200	700	700*
	Composition of Produced Well Stream (mol%)							
Inerts	0.12	0.13	0.13	0.14	0.14	0.13	0.12	0.01
C ₁	68.93	70.69	73.60	76.60	77.77	77.04	75.13	11.95
C ₂	8.63	8.67	8.72	8.82	8.96	9.37	9.82	4.10
C ₃	5.34	5.26	5.20	5.16	5.16	5.44	5.90	4.80
<i>i</i> -C ₄	1.15	1.10	1.05	1.01	1.01	1.10	1.26	1.57
<i>n</i> -C ₄	2.33	2.21	2.09	1.99	1.98	2.15	2.45	3.75
<i>i</i> -C ₅	0.93	0.86	0.78	0.73	0.72	0.77	0.87	2.15
<i>n</i> -C ₅	0.85	0.76	0.70	0.65	0.63	0.68	0.78	2.15
C ₆	1.73	1.48	1.25	10.80	1.01	1.07	1.25	6.50
C ₇₊	9.99	8.84	6.48	3.82	2.62	2.25	2.42	63.02
MW C ₇₊	158	146	134	123	115	110	109	174
Density C ₇₊	0.827	0.817	0.805	0.794	0.784	0.779	0.778	0.837
Z								
Equil Gas	1.140	1.015	0.897	0.853	0.865	0.902	0.938	
Two-Phase	1.140	1.016	0.921	0.851	0.799	0.722	0.612	
G _p % of G	0	6.6	17.5	32.9	49.9	68.1	77.9	

* Equilibrium liquid phase

The depletion study begins by expanding the reservoir fluid in the cell until the first depletion pressure is reached (5,000 psig in this example). The fluid in the cell is brought to equilibrium, and the volume of retrograde liquid is observed. Gas is removed from the top of the cell while a constant pressure is maintained until the hydrocarbon volume of the cell is the same as when the test began. The gas volume removed is measured at the depletion pressure and reservoir temperature, analyzed for composition, and measured at atmospheric pressure and temperature.

The ideal-gas law can be used to calculate the “ideal volume” at the depletion pressure and reservoir temperature of the gas withdrawn from the cell. Dividing the ideal volume by the actual volume yields the deviation factor, *z*, for the produced gas. This is listed in **Table 10.4** under *z* for the equilibrium gas. The actual volume of gas remaining in the cell at this point is the gas originally in the cell at the dewpoint pressure minus the gas produced at the first depletion level. Dividing the actual volume remaining in the cell into the calculated ideal volume remaining in the cell at this first depletion pressure yields the two-phase deviation factor shown. The two-phase *z* factor is an equivalent *z* factor that includes the total volume of gas plus liquid:

$$z_{2\phi} = \frac{p(V_g + V_l)}{(n_g + n_l)RT} \dots\dots\dots (10.23)$$

The two-phase *z* factor is the correct value to apply to such things as *p/z* analysis of retrograde-condensate reservoirs.

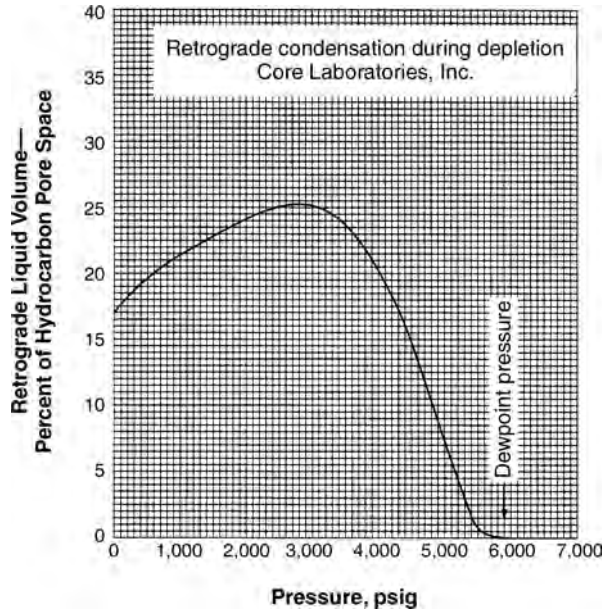


Fig. 10.5—Example retrograde-liquid volume vs. pressure.⁶

A series of expansions and constant-pressure displacements is repeated at each depletion pressure until an arbitrary abandonment pressure is reached. The abandonment pressure is considered arbitrary because no engineering or economic calculations have been made to determine this pressure for the purpose of the reservoir-fluid study.

At the final depletion pressure, the compositions of both the produced well stream and the retrograde liquid are measured. These data are included as a control composition in the event that the study is used for compositional material-balance purposes.

The composition data can be used with equilibrium constants (determined by either laboratory measurements or general correlations) to determine recovery at the various stages of pressure depletion represented by the laboratory measurements. In this case, initial condensate content was 181.74 STB/Mrcf (213 STB/Mscf), and the amount recovered from the dewpoint to 700 psig was 51.91 STB/Mrcf. The gas formation volume factor was determined to be 0.6472 RB/Mscf at initial conditions and 0.6798 RB/Mscf at the dewpoint. If a hydrocarbon pore space of 500×10^6 ft³ were determined from volumetric calculations, then from these data and those presented in Table 10.3, recoveries by pressure depletion would be

$$\begin{aligned}
 G &= (500 \text{ MMcf})(178.1) / (0.6472) = 137 \text{ Bscf} \\
 G_p &= G \left(\frac{B_{gdp} - B_{gi}}{B_{gdp}} \right) + G \left(\frac{B_{gi}}{B_{gdp}} \right) (0.779) = 108 \text{ Bscf (79 \% OGIP)} \\
 N_p &= G \left(\frac{B_{gdp} - B_{gi}}{B_{gdp}} \right) (181.74)(1,000) + G \left(\frac{B_{gi}}{B_{gdp}} \right) (51.91)(1,000) \\
 &= 8 \text{ MMSTB (33 \% OOIP)} . \dots\dots\dots (10.24)
 \end{aligned}$$

These calculations indicate the large amount of liquid remaining in the reservoir at depletion even with excellent drainage to the wells. Further reductions in recovery would be expected because of areas of the reservoir inadequately drained with existing wells.

TABLE 10.4—DEFINITIONS OF A “GENERIC” POTENTIAL DIFFERENCE $\Delta\psi$ FOR DIFFERENT FLUIDS			
	$\Delta\psi$	Oilfield Units	SI Units
Liquids	Δp	psia	kPa
Real gases	$\Delta m(p)$	psia ² /cp	GPa/s
High-pressure gases (approximate)	Δp	psia	kPa
Low-pressure gases (approximate)	Δp^2	psia ²	kPa ²

To deal with such phase-behavior effects in more than an empirical manner requires the use of PVT simulators. These simulators are based on EOSs that describe the phase volumes and compositions of liquid and gaseous phases as functions of pressure and temperature. Because hydrocarbon molecules interact with each other in solution, the coefficients in an EOS are not always adequately known. PVT tests such as those described in this section, along with the known composition of the original fluid, can be used to “tune” an appropriate EOS to achieve results that nearly match the measurements. Once this tuning process is complete, those coefficients can then be used to make predictions under differing operating conditions with some degree of reliability.

10.2.7 EOSs. When the effects of complex phase behavior on phase compositions and physical properties cannot be calculated accurately with simple approaches, it is often desirable to use an EOS. An EOS approach is often necessary when dealing with volatile oils and retrograde-condensate gases.

EOSs provide a numerical method for calculating both composition and relative amount for each phase present in the system. In reservoir simulation, EOS calculations are typically restricted to two hydrocarbon phases: a liquid (oleic) phase and a gaseous phase. However, there are situations in which an aqueous phase is included in the EOS calculations, or even in which a third hydrocarbon-containing phase may be present (e.g., in CO₂ flooding). These are generally done in more advanced compositional simulators.

The two most common EOSs used in petroleum engineering applications are the Peng-Robinson and Soave-Redlich-Kwong equations, which historically were derived from van der Waals’ equation. These three equations are called “cubic” because they result in a cubic representation for the molar volume. The basic equations are as follows:

Ideal Gas

$$pV_m = RT \dots\dots\dots (10.25)$$

van der Waals

$$\left(p + \frac{a_c}{V_m^2} \right) (V_m - b) = RT \dots\dots\dots (10.26)$$

Soave-Redlich-Kwong

$$\left[p + \frac{a_c a(T)}{V_m(V_m + b)} \right] (V_m - b) = RT \dots\dots\dots (10.27)$$

Peng-Robinson

$$\left[p + \frac{a_c \alpha(T)}{V_m(V_m + b) + b(V_m - b)} \right] (V_m - b) = RT \dots\dots\dots (10.28)$$

The parameters a_c , $\alpha(T)$, and b are determined empirically from experimental data (for pure components, the data are critical temperature and pressure and a specified point on the vapor-pressure curve), $\alpha(T)$ being a function of temperature and having a value of 1 at the critical temperature. Note that the parameters have different values depending on the equation.

The reader is referred to texts such as those by Ahmed,⁷ Pedersen *et al.*,⁸ McCain,¹ and Whitson and Brule.⁹

10.3 Petrophysical Properties

Petrophysical properties required for typical reservoir engineering purposes include porosity, pore-volume compressibility, permeability, relative-permeability-vs.-saturation curves, capillary-pressure-vs.-saturation curves, and liquid saturations. Additional data are sometimes required as well, but typically not for natural-gas reservoirs.

An extensive discussion of the methods for measuring, analyzing, and interpreting petrophysical data on these and other petrophysical properties can be found in several chapters of the General Engineering section of this *Handbook* and in subchapters of this section.

Two petrophysical properties of interest in gas engineering work are the Klinkenberg effect and non-Darcy flow.

10.3.1 Klinkenberg Effect. Low-pressure (i.e., laboratory) measurements give rise to what is termed the Klinkenberg¹⁰ or “slippage” effect because the mean free path of gas molecules is approximately the same size as the pores in a reservoir rock, meaning that gas molecules are so far apart that the gas does not behave as a continuum fluid, resulting in erroneously high apparent permeability. At low pressures, measured gas permeabilities can be empirically related to effective liquid (or high-pressure gas) permeabilities by

$$k_g = k_l \left(1 + \frac{b}{p} \right) \dots\dots\dots (10.29)$$

The effective liquid permeability can be determined in the laboratory by measuring gas permeabilities at different average core pressures. A plot of k_g vs. $1/\bar{p}$ yields an intercept equal to k_l (**Fig. 10.6**) of 24 md compared with 48 md at low pressure. The Klinkenberg effect is unimportant at reservoir pressures.

10.3.2 Non-Darcy Flow. At high fluid velocities, Darcy’s law may not always be accurate. An additional energy loss is often apparent above that predicted from the laminar-flow relationship suggested by Darcy’s law. This effect has sometimes been called *turbulence* or *inertial turbulence* based on analogies with pipe flow. The effect, however, is probably caused by multiple factors, including pore-scale as well as reservoir-scale phenomena. Because of the lack of understanding of the fundamental nature of such phenomena, it is usually simply referred to as non-Darcy flow.

The most common expression of the non-Darcy effect is through the Forchheimer¹¹ equation:

$$-\nabla p = \frac{\mu}{k} \vec{u} + \beta \rho |u| \vec{u}, \dots\dots\dots (10.30)$$

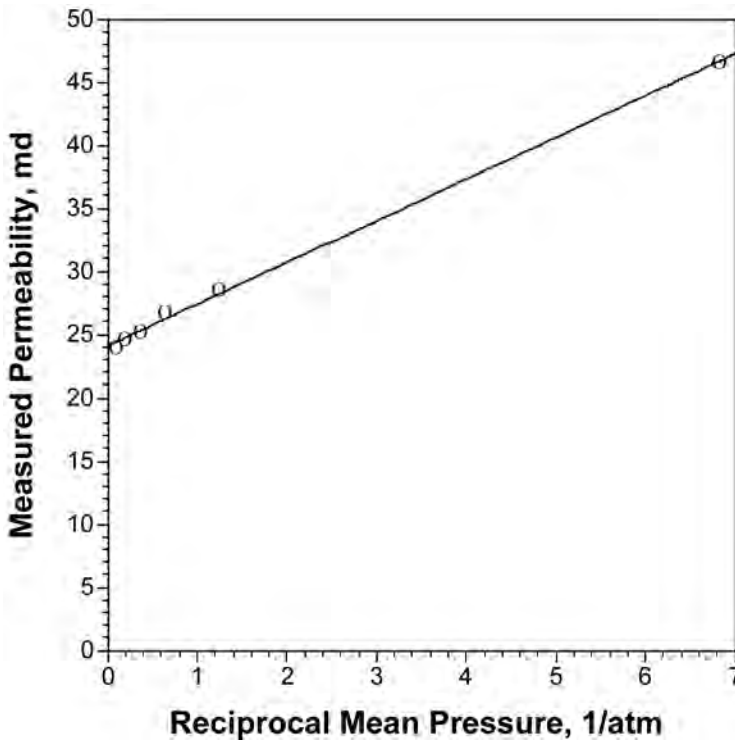


Fig. 10.6—Example of Klinkenberg¹⁰ permeability correction.

where β is called the non-Darcy velocity coefficient, having units of L^{-1} , and u is the volumetric flux (q/A) through the rock.

Note that Eq. 10.30 introduces a velocity-squared term into Darcy's law. This effect shows up as a flow-rate-squared term in flow relationships (e.g., well-deliverability equations) that involve Darcy's law.

Although non-Darcy flow can occur at all points in a reservoir, in practice it is only significant in the near-well region, where gas velocities are highest owing to radial-flow effects and expansion of gas volume at low pressure. For this reason, non-Darcy flow is incorporated primarily as a flow-rate-dependent skin factor and is seldom, if ever, incorporated to calculate flow away from the wellbore. The magnitude of the non-Darcy effect must generally be measured empirically at reservoir conditions using well tests.

10.4 Well Performance

This section deals with methods for analyzing and predicting the performance of producing natural-gas wells. Steady-state-, pseudosteady-state-, and transient-flow concepts are developed, resulting in a variety of specific techniques and empirical relationships for both testing wells and predicting their future performance under different operating conditions. The information included here is a condensation of the concepts and equations developed in detail in the chapter on fluid flow and well analysis in this section as they apply to gas reservoirs.

10.4.1 Basic Equations. The basis for all well-performance relationships is Darcy's law, which in its fundamental differential form applies to any fluid—gas or liquid. However, different forms of Darcy's law arise for different fluids when flow rates are measured at standard conditions. The different forms of the equations are based on appropriate equations of state (i.e., density as a function of pressure) for a particular fluid. In the resulting equations, present-

ed next, flow rate is taken as being positive in the direction opposite to the pressure gradient, thus dropping the minus sign from Darcy’s law. When multiple-line equations are presented, the first will be in fundamental units, the second in oilfield units, and the third in SI units.

Four different fluid representations are considered: (1) liquid (small and constant compressibility), (2) real gas, (3) approximate high-pressure gas, and (4) approximate low-pressure gas. Because this chapter is devoted to well performance, radial forms of the flow equations are presented. Linear and spherical forms follow a similar development.

Steady-State Radial Horizontal Liquid Flow.

$$q_o = \frac{2\pi kh}{\ln(r_2/r_1)} \int_{p_1}^{p_2} \frac{d\tilde{p}}{B_o(\tilde{p})\mu_o(\tilde{p})} \dots\dots\dots (10.31)$$

Steady-State Radial Horizontal Gas Flow.

$$q_g = \frac{2\pi khT_{sc}}{p_{sc}T \ln(r_2/r_1)} \int_{p_1}^{p_2} \frac{\tilde{p}d\tilde{p}}{\mu_g(\tilde{p})z(\tilde{p})} \dots\dots\dots (10.32)$$

For liquids, the product of $B_o\mu_o$ is approximately constant over a fairly wide pressure range so that for practical purposes, Eq. 10.31 can be written as

$$q_o \approx \frac{2\pi kh\Delta p}{\bar{B}_o\bar{\mu}_o \ln(r_2/r_1)} \dots\dots\dots (10.33)$$

where $\Delta p = p_2 - p_1$ and $\bar{B}_o\bar{\mu}_o$ is evaluated at some average pressure between p_1 and p_2 . The exact pressure at which the oil formation volume factor and viscosity are evaluated is not critical because the product of $B_o\mu_o$ is approximately constant.

Because this approximation is not generally valid for gases, the steady-state radial gas-flow equation is written as

$$q_g = \frac{\pi khT_{sc} \Delta m}{p_{sc}T \ln(r_2/r_1)} \dots\dots\dots (10.34)$$

where the real-gas potential Δm^{12} is defined by

$$\Delta m = m(p_2) - m(p_1) = 2 \int_{p_1}^{p_2} \frac{\tilde{p}d\tilde{p}}{\mu_g(\tilde{p})z(\tilde{p})} \dots\dots\dots (10.35)$$

Fig. 10.7 shows a typical plot of $p/\mu z$ vs. p . Twice the area under the curve between any two pressures represents the real-gas potential difference. Note that at high pressures, $p/\mu z$ is approximately constant. Also, although it is not readily apparent from the plot, at low pressures the product μz is approximately constant.

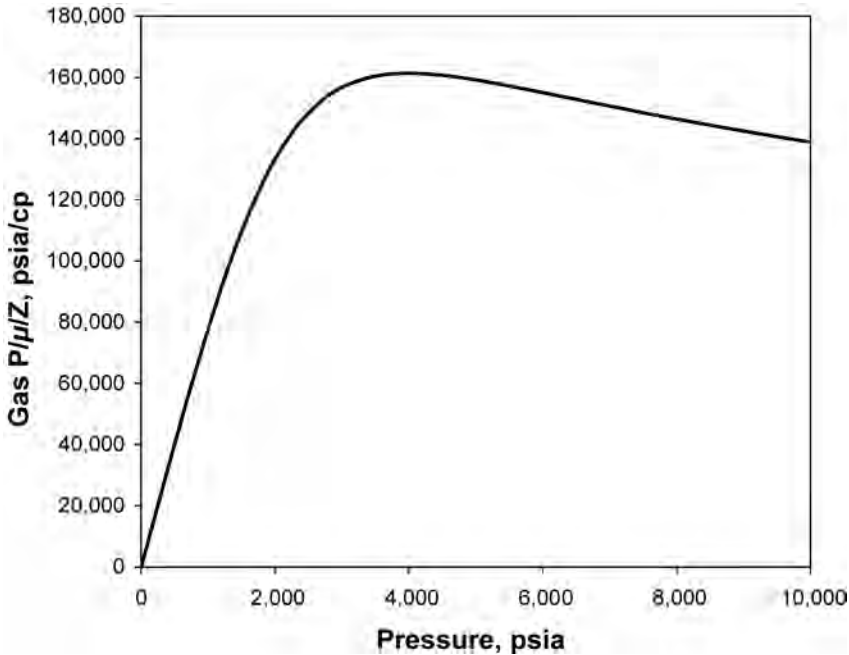


Fig. 10.7—Typical plot of $p/\mu z$ vs. p .

Values for Δm are usually determined by numerically integrating Eq. 10.35 using gas viscosity and z -factor data from measurements or correlations. Typical results are shown in Fig. 10.8.

Note that for ideal gases, $z = 1$ and does not vary with pressure, resulting in the identity $\Delta m = \frac{p_1^2 - p_2^2}{\mu_g}$. The steady-state radial-flow equation for an ideal gas is thus

$$q_g = \frac{\pi k h \Gamma_{sc} \Delta p^2}{\mu_g p_{sc} T \ln(r_2/r_1)}, \dots\dots\dots (10.36)$$

where $\Delta p^2 = p_2^2 - p_1^2$.

To avoid numerical evaluation of Δm , which can be time-consuming if done by hand, it is sometimes useful to have two other approximate real-gas forms of each of the flow equations. These approximate forms are derived by noting that for most natural gases at low pressures (i.e., less than approximately 2,000 psia, or 14 MPa), the product $\mu_g z$ is approximately constant. Under these conditions,

$$\Delta m = 2 \int_{p_1}^{p_2} \frac{\tilde{p} d\tilde{p}}{p_1 \mu_g(\tilde{p}) z(\tilde{p})} dp \approx \frac{\Delta p^2}{\bar{\mu}_g \bar{z}} \dots\dots\dots (10.37)$$

Both μ_g and z should be evaluated at some average pressure between the two pressures. The specific value of average pressure used is not very significant because the product $\mu_g z$ is relatively constant, as demonstrated in Fig. 10.9.

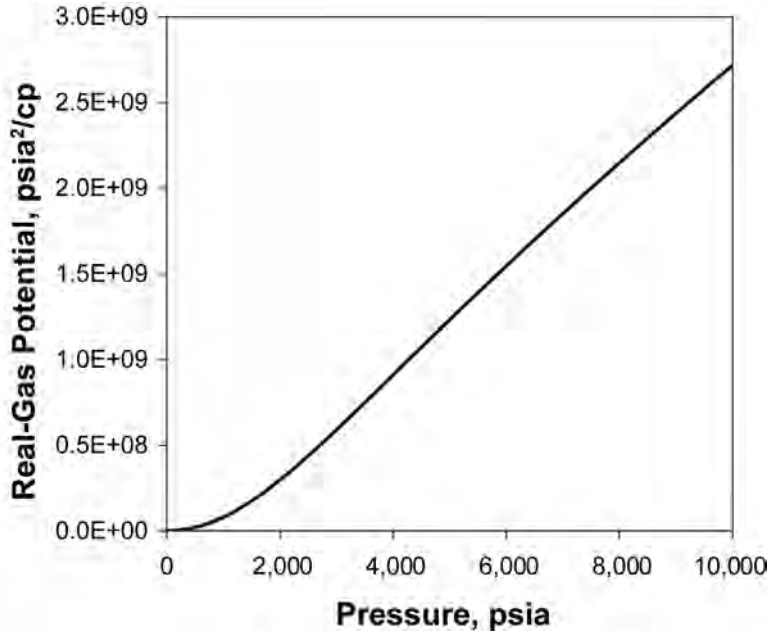


Fig. 10.8—Example graph of real-gas potential vs. pressure.

At high pressures (i.e., greater than approximately 2,000 psia, or 14 MPa), for most natural gases the product of $\mu_g \beta_g$ is relatively constant (see Fig. 10.10 for an example).

This means that

$$\Delta m = 2 \int_{p_1}^{p_2} \frac{\tilde{p} d\tilde{p}}{\mu_g(\tilde{p})z(\tilde{p})} = 2 \frac{p_{sc} T}{T_{sc}} \int_{p_1}^{p_2} \frac{\tilde{p} d\tilde{p}}{\mu_g(\tilde{p})B_g(\tilde{p})} \approx 2 \frac{p_{sc} T}{T_{sc}} \frac{\Delta p}{\bar{\mu}_g \bar{B}_g} \dots (10.38)$$

Note that the conversion between the real-gas potential in oilfield vs. SI units is

$$\left[\Delta m(p) - \frac{\text{GPa}}{\text{s}} \right] = 47.538 \left[\Delta m(p) - \frac{\text{psia}^2}{\text{cp}} \right] \dots (10.39)$$

So that one simplified set of equations can be used throughout the remainder of the chapter, some additional parameters will be defined. First, a “generic” potential difference, $\Delta\psi$, can be expressed for each of the fluid cases according to Table 10.4.

A general radial-flow equation can then be expressed for all cases as

$$q_{sc} = \frac{kh}{\beta \ln(r_2/r_1)} \Delta\psi, \dots (10.40)$$

where β is given by the following expressions, which include the unit conversions necessary to apply Eq. 10.40. The first line of each equation is in fundamental units, the second in oilfield units, and the third in SI units.

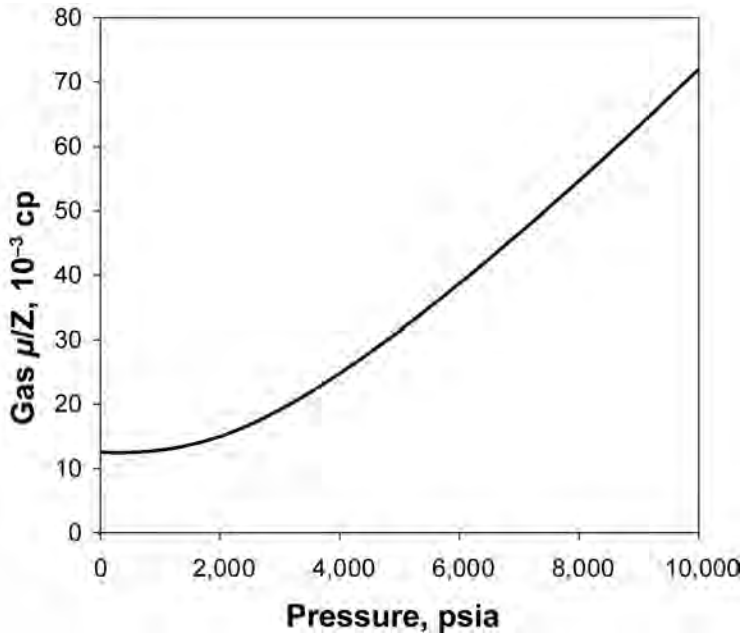


Fig. 10.9—Example showing that $\mu_g z$ is approximately constant at < 2,000 psia.

Liquids (β units are psi-md-ft-D/STB, kPa·m²·m-d/std m³).

$$\begin{aligned} \beta &= \frac{\bar{B}\bar{\mu}}{2\pi} \\ &= 141.21\bar{B}\bar{\mu} = 1.8421\bar{B}\bar{\mu} \dots\dots\dots (10.41) \end{aligned}$$

Real Gases (β units are psi²-md-ft-D/Mscf/cp, kPa²·m²·m-d/std m³/mPa·s).

$$\begin{aligned} \beta &= \frac{p_{sc}T}{\pi T_{sc}} \\ &= 50,300 \frac{p_{sc}T}{T_{sc}} = 1422.4T \\ &= 3.6841 \frac{p_{sc}T}{T_{sc}} = 1.2955T \dots\dots\dots (10.42) \end{aligned}$$

High-Pressure Gases (approximate) (β units are psi-md-ft·D/Mscf, kPa·m²·m-d/std m³).

$$\begin{aligned} \beta &= \frac{\bar{B}_g \bar{\mu}_g}{2\pi} \\ &= 25.150\bar{B}_g \bar{\mu}_g = 1.8421\bar{B}_g \bar{\mu}_g \dots\dots\dots (10.43) \end{aligned}$$

Low-Pressure Gases (approximate) (β units are psi²-md-ft-D/Mscf, kPa²·m²·m-d/std m³).

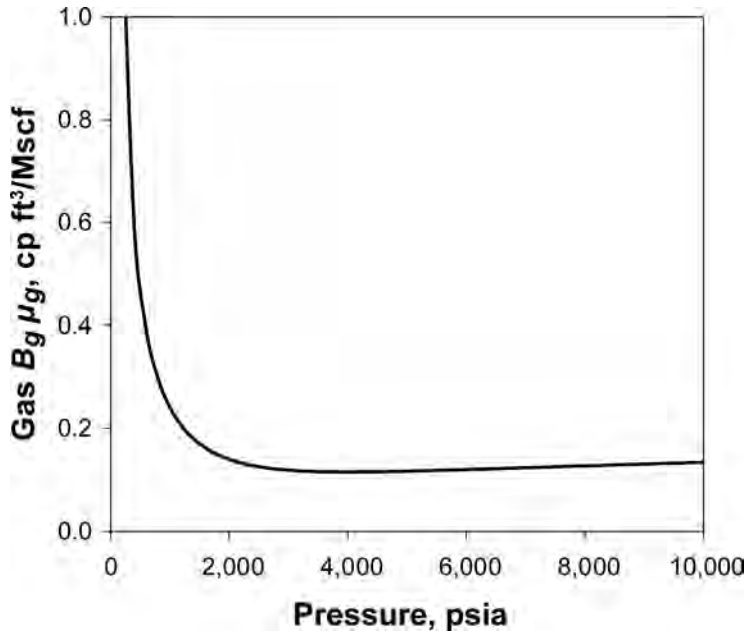


Fig. 10.10—Example graph showing that the product $\mu_g B_g$ is approximately constant for gases at pressures greater than approximately 2,000 psia.

$$\begin{aligned}
 \beta &= \frac{p_{sc} T \bar{\mu}_g \bar{z}}{\pi T_{sc}} \\
 &= 50,300 \frac{p_{sc} T \bar{\mu}_g \bar{z}}{T_{sc}} = 1422.4 T \bar{\mu}_g \bar{z} \\
 &= 3.6841 \frac{p_{sc} T \bar{\mu}_g \bar{z}}{T_{sc}} = 1.2955 T \bar{\mu}_g \bar{z} \dots\dots\dots (10.44)
 \end{aligned}$$

To concentrate on the specifics of well flow, in the remainder of the chapter the subscript *e* will refer to an external drainage radius, and the subscript *wf* will refer to pressure at the inlet sandface of a flowing well.

10.4.2 Skin. Sometimes wells experience near-wellbore phenomena (e.g., fractures and mud-filtrate damage) that cause production to be different from that calculated by Darcy’s law. These near-wellbore effects are often very complex. Their total effect is normally characterized with the use of a skin factor, *S*, which appears in the steady-state radial-flow equation as

$$q_{sc} = \frac{k h \Delta \psi}{\beta [\ln (r_e / r_w) + S]} \dots\dots\dots (10.45)$$

Skin is a dimensionless parameter treated mathematically as an infinitely thin damaged or stimulated zone, regardless of the actual dimensions of the altered zone. Positive values indicate well damage (decreased productivity). Negative values indicate well stimulation (increased productivity). Fig. 10.11 shows a typical pressure profile for a well with a positive skin. Wells with formation damage, partially penetrating wells, and wells with significant pressure drops in

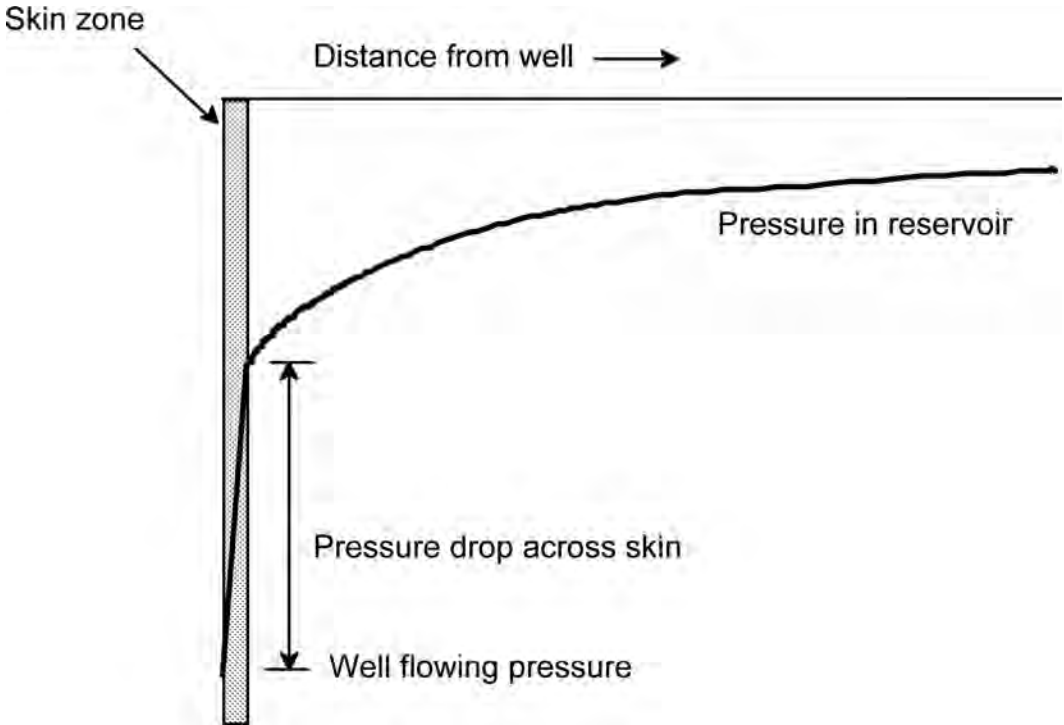


Fig. 10.11—Pressure distribution in a reservoir with a positive skin.

their completions have positive skins. Hydraulically fractured wells have negative skins. In general, skin must be determined empirically, usually from pressure-transient tests. Further discussion of the physical meaning of skin is given in the section on pressure-transient analysis.

10.4.3 Non-Darcy Flow. In gas wells, there may be a significant non-Darcy component of flow that results in an additional potential difference that depends on the square of the flow rate. The non-Darcy effect appears in well-deliverability equations as a flow-rate-dependent skin,

$$S' = S + Dq_g, \dots\dots\dots (10.46)$$

where S is the fixed or “mechanical” skin, and S' represents the total apparent skin including non-Darcy effects. D is called the non-Darcy-flow coefficient, having units of D/Mscf or d/std m³. Although the non-Darcy coefficient may be calculated from laboratory measurements of the non-Darcy coefficient, it is typically determined in the field from well tests.

10.4.4 Transient Flow. At early times after a well has been put on production and at early times after a well has been shut in, flow occurs in a transient mode, making the steady-state forms of Darcy’s law inappropriate. To mathematically represent transient flow, the relationship between density and pressure and material-balance (continuity) relationships must also be considered. When combined with Darcy’s law, the result is the diffusivity equation, which in radial coordinates is

$$\frac{1}{r} \frac{\partial}{\partial r} \left(r \frac{\partial \psi}{\partial r} \right) = \frac{\phi \mu c_t}{k} \frac{\partial \psi}{\partial t} \dots\dots\dots (10.47)$$

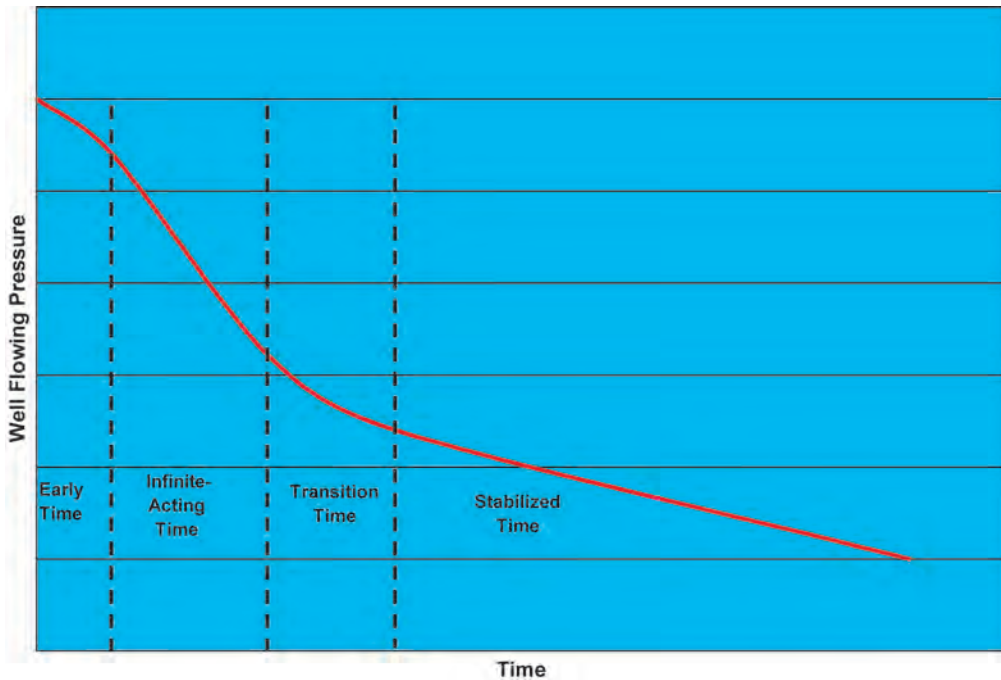


Fig. 10.12—Pressure/time history for a well produced at constant rate. Stabilized time occurs after all drainage-volume boundaries are fully “felt” and the well enters either steady-state or pseudosteady-state flow.

Note that the generic potential ψ is used in Eq. 10.47. This will be discussed further with regard to transient solutions for different fluid systems.

It is useful to distinguish between four different time periods when dealing with solutions to Eq. 10.47: (1) early time, (2) infinite-acting time, (3) transition time, and (4) stabilized time (Fig. 10.12).

Early time is dominated by wellbore, rather than reservoir, effects. During this time, little can be determined about the reservoir. This time may last from a few minutes to a few days.

During infinite-acting time, however, well response is the same as a well being produced from an infinite reservoir. Most pressure-transient tests analyze data during this time period. Because all reservoirs are finite, however, this time must end. It does so when the well response is affected by a part of the outer boundary of the well’s drainage volume.

Steady-state flow is characterized by pressures being constant with time, requiring that the outer boundary of the system be maintained at constant pressure and the well be kept at either constant pressure or constant rate. This flow regime applies to certain water-influx situations or fluid-injection projects.

Pseudosteady-state flow occurs at late time in closed systems with a well produced at constant rate. Although pressures still change with time in pseudosteady state, all pressures everywhere in the reservoir decline at the same rate. This means that the pressure profile reduces uniformly throughout the reservoir.

Transition time occurs between infinite-acting and late time. During the transition period, the outer drainage boundaries are being felt in succession, causing the shift from infinite-acting to late time to occur over some length of time. In regularly shaped drainage areas (e.g., circles and squares), transition time may not exist. In irregularly shaped drainage areas, particularly with a well placed off-center, transition time can be quite long.

Infinite-Acting Flow. The time of primary interest in pressure-transient testing is the infinite-acting period, the mathematical solution for which comes from the diffusivity equation, expressed with the following dimensionless variables.

$$r_D = \frac{r}{r_w} \dots\dots\dots (10.48)$$

$$t_D = \frac{kt}{\phi\mu c_t r_w^2}$$

$$= \frac{1}{3,792.5} \frac{kt}{\phi\mu c_t r_w^2} = \frac{1}{277.78} \frac{kt}{\phi\mu c_t r_w^2} \dots\dots\dots (10.49)$$

$$\psi_D = \frac{kh\Delta\psi}{q_{sc}\beta}$$

$$\Delta\psi = \psi_i - \psi(r, t) \dots\dots\dots (10.50)$$

The subscript *i* refers to the initial conditions of the well’s drainage volume. Time is in hours for both dimensionless-time equations.

At sufficiently large values of t_D/r_D^2 , which are typical for most reservoir conditions, the solution can be mathematically approximated by

$$\psi_D(t_D, r_D) = \frac{1}{2} \left[\ln \left(\frac{t_D}{r_D^2} \right) + 0.80908 \right] = 1.1513 \log \left(\frac{2.2458t_D}{r_D^2} \right) \dots\dots\dots (10.51)$$

This approximation is good to within 2% accuracy for $t_D/r_D^2 > 5$, within 1% accuracy for $t_D/r_D^2 > 8.5$, and essentially identical to $t_D/r_D^2 > 100$.¹³

Noting that the dimensionless potential at the well differs from the dimensionless potential at the wellbore radius ($r_D = 1$) by the skin factor, the basic radial well flow equation used for most well-testing purposes is

$$\psi_{Dw} = 1.1513 \log (2.2458t_D) + S' \dots\dots\dots (10.52)$$

A graph of ψ_{wf} vs. the logarithm of time is a straight line. This slope is the basis for much pressure-drawdown and -buildup testing.

When predicting well performance, it is important to recognize when data are being collected during transient flow and to take into account the continuing decline in well deliverability until a steady-state or pseudosteady-state condition is established.

Pseudosteady State. In a closed drainage volume, once all the outer boundaries have been fully felt, a constant-rate well will experience pseudosteady-state flow. Because all pressures in the reservoir decline at the same rate during pseudosteady-state flow, the difference between reservoir pressures and the well pressure remains constant, even though both individually are changing with time. Because the resulting equation does not explicitly show a time dependence, the term *pseudosteady state* is used. Some authors also refer to this time period as “semisteady state.”

Because pressure differences remain constant during pseudosteady-state flow, the following equations can be written to represent well performance during this period.¹³

$$\psi_{Dw} - \bar{\psi}_D = \frac{1}{2} \ln \left(\frac{2.2458A}{C_A r_w^2} \right) + S' = \ln \left(\sqrt{\frac{2.2458A}{C_A r_w^2}} \right) + S', \dots\dots\dots (10.53)$$

where C_A is the Dietz shape factor, dimensionless.

Because $\psi_{Dw} - \bar{\psi}_D = \frac{kh}{q_{sc}\beta} (\bar{\psi} - \psi_{wf})$, Eq. 10.53 can also be written in a more usable engineering form as

$$q_{sc} = \frac{kh}{\beta} \frac{\Delta\psi}{\ln \left(\sqrt{\frac{2.2458A}{C_A r_w^2}} \right) + S'}, \dots\dots\dots (10.54)$$

where $\Delta\psi = \bar{\psi} - \psi_{wf}$.

The shape factor can be determined empirically from mathematical solutions to the diffusivity equation in closed systems. Tables 10.5 and 10.6 provide a list of shape factors for different drainage shapes and well placements.

For a well in a closed circle, the pseudosteady-state equation can also be written as follows, which is equivalent to having a shape factor of 31.62.

$$\psi_{Dw} - \bar{\psi}_D = \ln \left(\frac{r_e}{r_w} \right) - \frac{3}{4} + S' = \ln \left(\frac{0.472r_e}{r_w} \right) + S'. \dots\dots\dots (10.55)$$

This equation also works for a well in the center of a closed square or other regular shape by calculating an equivalent-radius circle:

$$r_e = \sqrt{\frac{A}{\pi}} \dots\dots\dots (10.56)$$

Transient Drainage Radius. To simplify the flow equations, it is sometimes useful to use what has been called a transient drainage radius, defined by

$$\ln \left(\frac{r_d}{r_w} \right) = \psi_D(r_D = 1) - \bar{\psi}_D \dots\dots\dots (10.57)$$

This drainage radius is defined so that it represents the radius out to which there is a significant pressure drop.







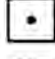
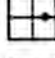
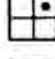

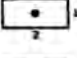
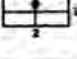
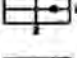
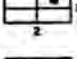

During infinite-acting time, $\bar{\psi}_D \approx 0$ because there has been little withdrawal from the reservoir, which means that

$$\ln \left(\frac{r_d}{r_w} \right) \approx \frac{1}{2} (\ln t_D + 0.80908), \dots\dots\dots (10.58)$$

or, equivalently,

$$r_d = 1.4986 \sqrt{t_D r_w^2} \dots\dots\dots (10.59)$$

TABLE 10.5— PSEUDOSTEADY-STATE SHAPE FACTORS FOR VARIOUS RESERVOIR SHAPES¹³

IN BOUNDED RESERVOIRS	C_A	$\ln C_A$	$\frac{1}{2} \ln \left(\frac{2.2458}{C_A} \right)$	EXACT FOR $t_{DA} >$	LESS THAN 1% ERROR FOR $t_{DA} >$	USE INFINITE SYSTEM SOLUTION WITH LESS THAN 1% ERROR FOR $t_{DA} >$
	31.62	3.4538	-1.3224	0.1	0.06	0.10
	31.6	3.4532	-1.3220	0.1	0.06	0.10
	27.6	3.3178	-1.2544	0.2	0.07	0.09
	27.1	3.2995	-1.2452	0.2	0.07	0.09
	21.9	3.0865	-1.1387	0.4	0.12	0.08
	0.098	-2.3227	+1.5659	0.9	0.60	0.015
	30.8828	3.4302	-1.3106	0.1	0.05	0.09
	12.9851	2.5638	-0.8774	0.7	0.25	0.03
	4.5132	1.5070	-0.3490	0.6	0.30	0.025
	3.3351	1.2045	-0.1977	0.7	0.25	0.01
	21.8369	3.0836	-1.1373	0.3	0.15	0.025
	10.8374	2.3830	-0.7870	0.4	0.15	0.025
	4.5141	1.5072	-0.3491	1.5	0.50	0.06
	2.0769	0.7309	+0.0391	1.7	0.50	0.02
	3.1573	1.1497	-0.1703	0.4	0.15	0.005

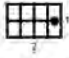
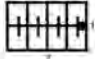
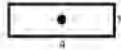

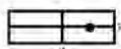
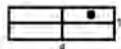




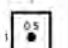




From Katz, D.L.: *Handbook of Natural Gas Engineering*, © The McGraw-Hill Companies Inc. (1990).

Note that the product $t_D r_w^2$ is simply dimensionless time without the wellbore radius in the denominator.

During pseudosteady-state time,

$$r_d = 1.4986 \sqrt{\frac{A}{C_A}} \dots\dots\dots (10.60)$$

TABLE 10.6—MORE PSEUDOSTEADY-STATE SHAPE FACTORS FOR VARIOUS RESERVOIR SHAPES¹³

	C_A	$\ln C_A$	$\frac{1}{2} \ell n \left(\frac{2.2458}{C_A} \right)$	EXACT FOR $t_{DA} >$	LESS THAN 1% ERROR FOR $t_{DA} >$	USE INFINITE SYSTEM SOLUTION WITH LESS THAN 1% ERROR FOR $t_{DA} >$
	0.5813	-0.5425	+0.6758	2.0	0.60	0.02
	0.1109	-2.1991	+1.5041	3.0	0.60	0.005
	5.3790	1.6825	-0.4367	0.8	0.30	0.01
	2.6896	0.9894	-0.0902	0.8	0.30	0.01
	0.2318	-1.4619	+1.1355	4.0	2.00	0.03
	0.1155	-2.1585	+1.4838	4.0	2.00	0.01
	2.3606	0.8589	-0.0249	1.0	0.40	0.025
IN VERTICALLY FRACTURED RESERVOIRS						
USE $(x_e/s_i)^2$ IN PLACE OF A/r_w^2 FOR FRACTURED SYSTEMS						
	2.6541	0.9761	-0.0835	0.175	0.08	CANNOT USE
	2.0348	0.7104	+0.0493	0.175	0.09	CANNOT USE
	1.9986	0.6924	+0.0583	0.175	0.09	CANNOT USE
	1.6620	0.5080	+0.1505	0.175	0.09	CANNOT USE
	1.3127	0.2721	+0.2685	0.175	0.09	CANNOT USE
	0.7887	-0.2374	+0.5232	0.175	0.09	CANNOT USE
IN WATER-DRIVE RESERVOIRS						
	19.1	2.95	-1.07	-	-	-
IN WATERS OF UNKNOWN INFILTRATION CHARACTER						
	25.0	3.22	-1.20	-	-	-

From Katz, D.L.: *Handbook of Natural Gas Engineering*, © The McGraw-Hill Companies Inc. (1990)

For a circular or equivalent square drainage area, it can be shown that

$$r_d = 0.472r_e \dots\dots\dots (10.61)$$

The deliverability equation for wells can then be written in the following simplified form for all times:

$$q_{sc} = \frac{kh}{\beta} \frac{\bar{\psi} - \psi_{wf}}{\ln\left(\frac{r_d}{r_w}\right) + S'} \dots\dots\dots (10.62)$$

Note that pressures decline in proportion to the logarithm of time during infinite-acting time, while in pseudosteady state, pressures decline approximately in direct proportion to time.

Another way to determine the onset of pseudosteady state is through knowledge of the drainage shape and reservoir parameters. Tables 10.5 and 10.6 give times for the end of the infinite-acting period and for the beginning of time when the pseudosteady-state equation can be used. These tables use a dimensionless time based on drainage area,

$$\begin{aligned} t_{DA} &= \frac{kt}{\phi \mu c_t A} = t_D \frac{r_w^2}{A} \\ &= \frac{1}{3,792.5} \frac{kt}{\phi \mu c_t A} = \frac{1}{277.78} \frac{kt}{\phi \mu c_t A} \dots\dots\dots (10.63) \end{aligned}$$

10.4.5 Estimating Drainage Shapes. With little effort, it is possible to make a reasonable approximation of well drainage volumes and shapes. The process is based on the following assumptions:

1. The volume drained by an individual well is proportional to its flow rate.
2. Distance to a “no-flow” boundary between pairs of wells is proportional to each competing well’s flow rate.

The following technique can then be used to estimate the drainage area at a given time. Assign a flow rate to each well based on an average production over some reasonable time period.

1. Using Assumption 2 above, assign no-flow points between pairs of wells.
2. Sketch no-flow lines by connecting up no-flow points.
3. Adjust the lines near reservoir boundaries to ensure that Assumption 1 is satisfied. Make adjustments for variations in thickness and known geologic features (e.g., faults).

Although this process is fairly rough, it can give a reasonable estimate of the drainage areas of each well in a reservoir.

10.4.6 Radius of Investigation. Tables 10.5 and 10.6 list times for the end of the infinite-acting-flow period and the beginning of the pseudosteady-state-flow period. These times can be used to define a “radius of investigation.” The physical meaning of the radius of investigation is that it represents the minimum radius at which a boundary could exist, but which has not yet been “felt” at a given time (usually meaning the time at the end of a drawdown test that has not yet been affected by a reservoir boundary).

Thus, if t_{DA}^* is the area-based dimensionless time that defines the end of the infinite-acting period for a circular drainage area,

$$r_{inv} = \frac{1}{\sqrt{\pi t_{DA}^*}} \sqrt{t_D r_w^2} \dots\dots\dots (10.64)$$

Depending on the level of precision that would define the end of the infinite-acting period, the radius of investigation would have different values. If a 1% criterion is used, t_{DA}^* is equal to 0.06, and

$$r_{inv} = 2.3\sqrt{t_D r_w^2} \dots\dots\dots (10.65)$$

Another common cutoff criterion is a t_{DA}^* of 0.1, after which the pseudosteady-state solution is listed by Earlougher¹³ as being “exact” (probably to within the number of significant digits of one’s computer). With this criterion,

$$r_{inv} = 1.8\sqrt{t_D r_w^2} \dots\dots\dots (10.66)$$

For practical purposes, it is reasonable to use what many authors recommend for the radius of investigation,

$$r_{inv} = 2\sqrt{t_D r_w^2} \dots\dots\dots (10.67)$$

10.4.7 Pressure-Transient Testing of Gas Wells. Refer to the chapter on well testing in this section of the *Handbook* for detailed discussions of interpreting pressure-transient tests of gas wells.

10.4.8 Deliverability Testing. Gas wells have historically been tested at a series of bottom-hole pressures and rates to develop stabilized-deliverability relationships. One of the reasons for this is the importance of the non-Darcy flow contribution to well performance. A single-rate test cannot address this contribution. This section describes the types of tests typically run, along with their appropriate analysis techniques.

Stabilized-Deliverability Test. A stabilized deliverability, sometimes called a four-point or backpressure test, is conducted by producing a well at four rates (Fig. 10.13). In this test, each rate is run long enough to reach stabilized conditions. To be theoretically valid, “stabilized” should mean to pseudosteady state, although in practice tests are sometimes run only until little variation in well flowing pressure is observed.

The most widely used method of presenting such data was first suggested by Rawlins and Schellhardt.¹⁵ This method is not based on the pseudosteady-state-flow equations but is based on an empirical observation that Δp^2 vs. q_g plotted on a log-log graph typically lies on a straight line (Fig. 10.14). The equation for a straight line on a log-log graph is

$$q_g = C(\bar{p}^2 - p_{wf}^2)^n = C(\Delta p^2)^n \dots\dots\dots (10.68)$$

The slope of the straight line on a log-log graph is $1/n$. The easiest way to determine slopes on a log-log graph is to recall that differences in the run and rise of the line must be taken in terms of logarithms, so that if $(q_{g1}, \Delta p_1^2)$ and $(q_{g2}, \Delta p_2^2)$ are two points on the straight line,

$$\text{Slope} = \frac{\log \Delta p_2^2 - \log \Delta p_1^2}{\log q_{g2} - \log q_{g1}} = \frac{\log (\Delta p_2^2 / \Delta p_1^2)}{\log (q_{g2} / q_{g1})} \dots\dots\dots (10.69)$$

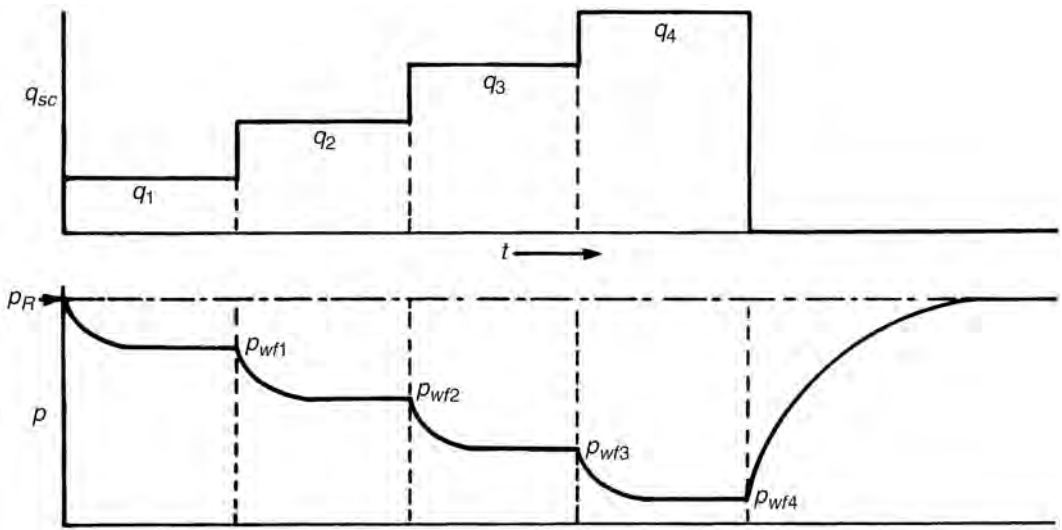


Fig. 10.13—Rate vs. time history of a stabilized deliverability test.¹⁴

A value of $n = 1$ corresponds to Darcy (laminar) flow, while $n = 0.5$ (slope = 2) corresponds to completely turbulent flow.

A parameter usually presented with this data is the absolute open flow (AOF) potential. The AOF may be found by extrapolating the log-log plot and reading the flow rate at a value of $\Delta p^2 = \bar{p}^2$ (i.e., $p_{wf} = 0$). The value of C is calculated from any point on the straight line but is perhaps easiest to calculate as

$$C = \frac{\text{AOF}}{\bar{p}^{2n}} \dots\dots\dots (10.70)$$

An alternative is to write the deliverability equation in terms of AOF instead of the parameter C :

$$q_g = \text{AOF} \left(1 - \frac{p_{wf}^2}{\bar{p}^2} \right)^n \dots\dots\dots (10.71)$$

The AOF is sometimes used as a measure of a well’s potential flow capacity for regulatory and other purposes.

A more accurate way to analyze the stabilized deliverability test is to use the following equation, which is simply an alternative algebraic form of Eq. 10.62.

$$\begin{aligned} \Delta\psi &= \bar{\psi} - \psi_{wf} = a q_g + b q_g^2, \\ a &= \frac{\beta}{kh} \left[\ln \left(\frac{r_d}{r_w} \right) + S \right], \\ b &= \frac{\beta}{kh} (D) \dots\dots\dots (10.72) \end{aligned}$$

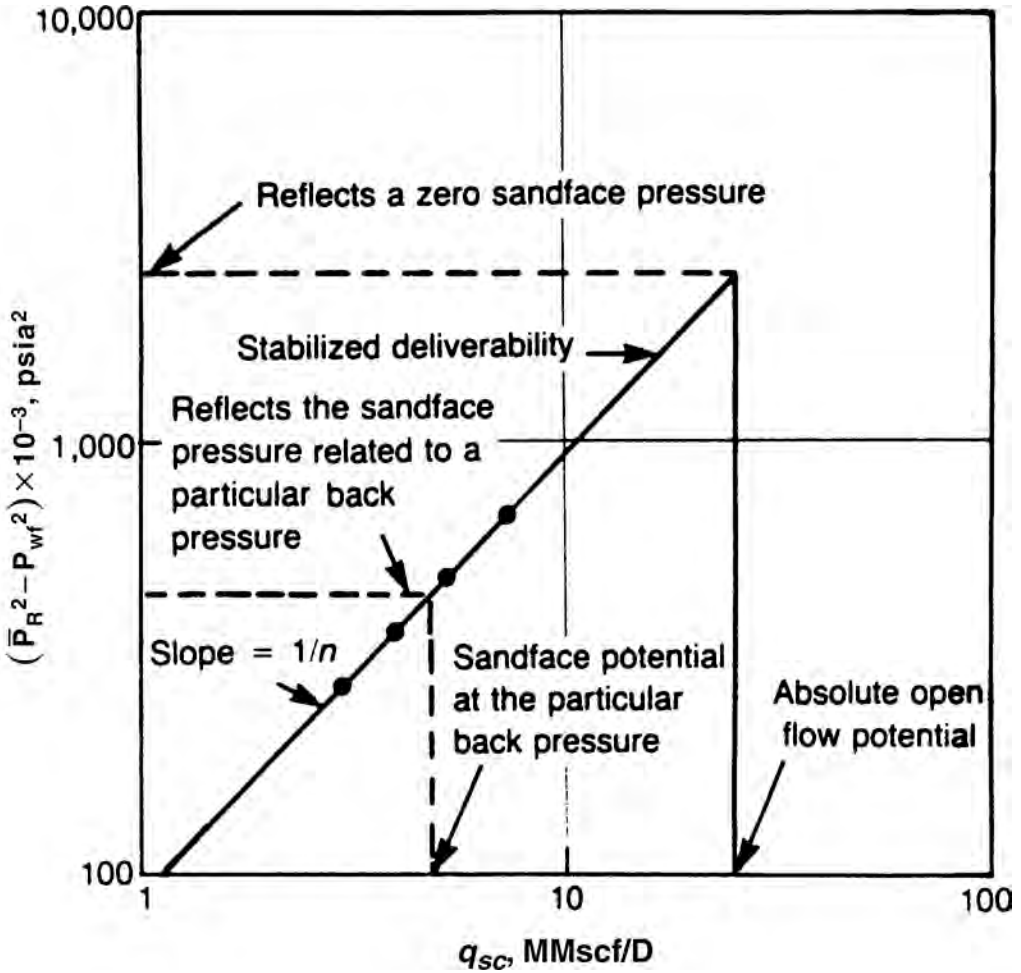


Fig. 10.14—Typical gas-well stabilized-deliverability plot.¹⁴

A Cartesian plot of $\Delta\psi/q_g$ vs. q_g will yield a slope of b and an intercept of a (Fig. 10.15). The advantage of this approach is that a and b have physical meaning based on reservoir parameters and thus can be compared to what is known about well and reservoir properties. C and n , on the other hand, have no such physical meanings. One disadvantage of this approach is that it is often more difficult to find a good straight line. However, this is a vagary of using Cartesian rather than log-log plots and does not represent any actual degradation of the data.

Once a and b are determined from the graph, the AOF using this approach is calculated by

$$\text{AOF} = \frac{\bar{\psi}}{a} \frac{2}{1 + \sqrt{1 + 4b\bar{\psi}/a^2}} \dots\dots\dots (10.73)$$

The second factor in Eq. 10.73 represents the reduction in the AOF caused by non-Darcy effects. The AOF determined from the a/b approach is usually lower than that calculated from the C/n approach.

Isochronal Tests. Another type of test often run on gas wells is the isochronal test. The difference between an isochronal test and a stabilized-deliverability test is that the flow periods

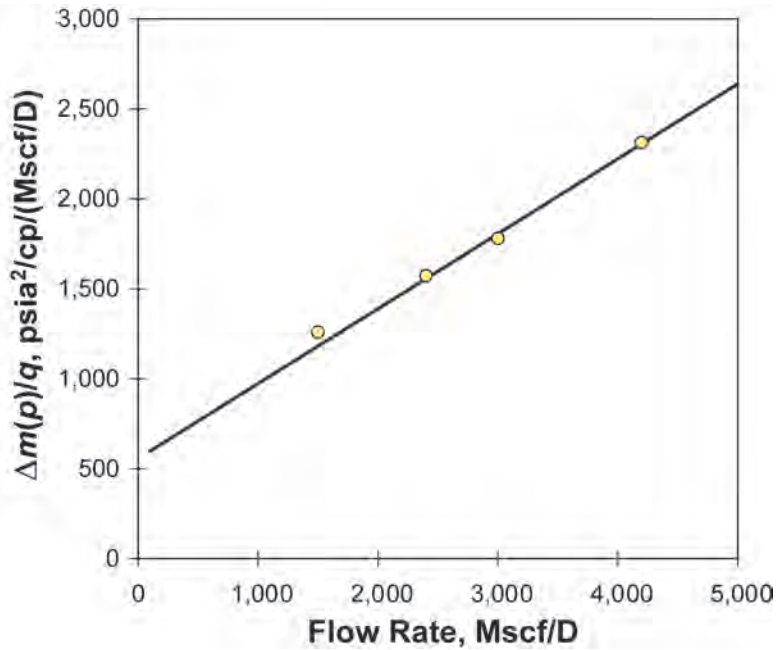


Fig. 10.15—Theoretical gas-well stabilized-deliverability plot.

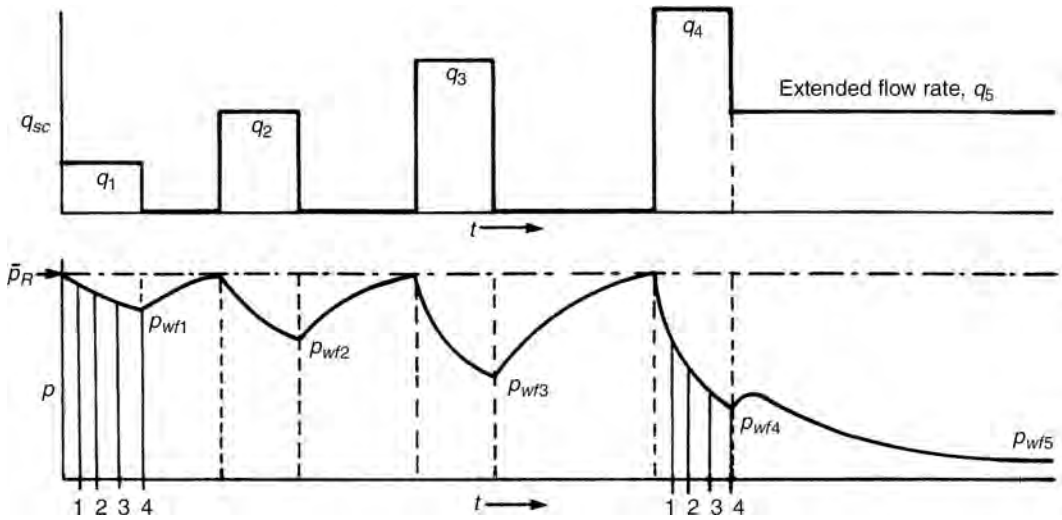


Fig. 10.16—Rate-vs.-time history for a typical isochronal test.¹⁴

are not run long enough to reach stabilized flow. This is done to shorten testing time and to conserve gas, particularly where no pipeline is available. Fig. 10.16 shows a rate-vs.-time history for a typical isochronal test. Note that although the shut-in times are sufficiently long to approach initial reservoir pressure, the producing times are not long enough to reach pseudosteady state.

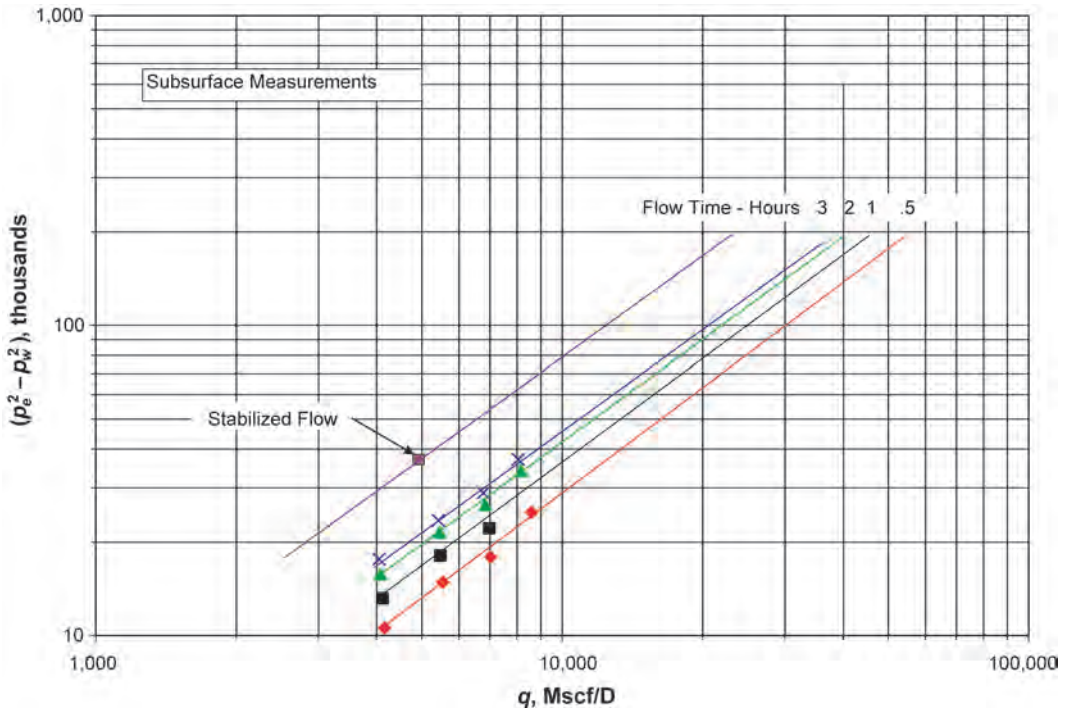


Fig. 10.17—Results of a typical isochronal test.

Lines are drawn through a Δp^2 -vs.- q_g (Fig. 10.17) or $\Delta\psi/q_{sc}$ -vs.- q_{sc} plot (Fig. 10.18) at common producing times; that is, during each flowing period, pressures are read at fixed times since the initiation of flow.

For a given producing time, a line through the data should have a constant slope. This slope should be the same no matter what the producing time because the transient drainage radius does not depend on flow rate. Thus, from each flow period, data are plotted for identical producing times (Fig. 10.17 or Fig. 10.18).

Finally, an extended flow period (to stabilization) is run at one rate. A line is passed through this single stabilized point, with the same slope as the other isochronal lines. If properly conducted, this test has been shown to give results comparable to a stabilized-deliverability test.

A modified isochronal test is also sometimes run in which the shut-in times are also shortened (Fig. 10.19). This type of test also works well if the value of pressure at the end of the last shut-in period is used in place of the average reservoir pressure.

10.4.9 Using Gas-Well Deliverability Relationships. Single-well deliverability equations can be used for a variety of purposes, including the following:

- Prediction of flow-rate changes caused by changing reservoir pressure (i.e., during reservoir depletion over time).
- Prediction of flow-rate changes caused by changing well flowing pressure resulting from production-equipment changes (e.g., compression).
- Prediction of bottomhole-flowing-pressure changes caused by changing well rates.

In general, the most theoretically valid deliverability equation should be used:

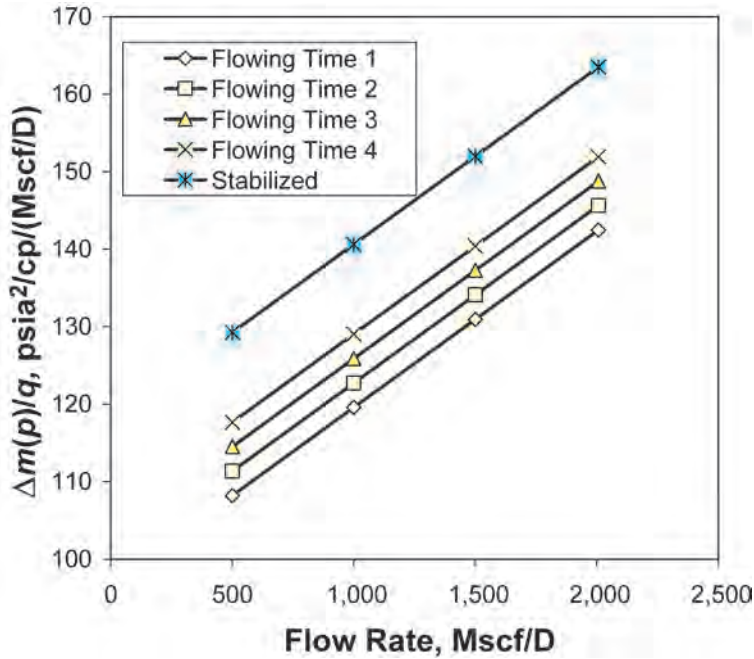


Fig. 10.18—Modified isochronal test analyzed by *a/b* analysis.

$$\bar{\psi} - \psi_{wf} = a q_g + b q_g^2 \dots \dots \dots (10.74)$$

The use of Eq. 10.74 to solve for well flowing pressure is straightforward, except for the requirement to convert the generic potential ψ to actual pressure when using the real-gas potential $m(p)$. The conversion of $m(p)$ to p can be done either graphically or numerically with a computational algorithm (preferred).

Eq. 10.74 is a quadratic equation in flow rate, so when flow rate is being calculated from known pressures, the following can be used.

$$q_g = \frac{(\bar{\psi} - \psi_{wf})}{a} \frac{2}{1 + \sqrt{1 + 4b(\bar{\psi} - \psi_{wf})/a^2}} \dots \dots \dots (10.75)$$

In some circumstances, it may be desirable to use either the *C/n* equation,

$$q_g = C(\bar{p}^2 - p_{wf}^2)^n = C(\Delta p^2)^n, \dots \dots \dots (10.76)$$

or a productivity index (PI) equation,

$$q_g = PI(\bar{\psi} - \psi_{wf}), \dots \dots \dots (10.77)$$

for deliverability calculations. Both can be used in a similar manner, as described above.

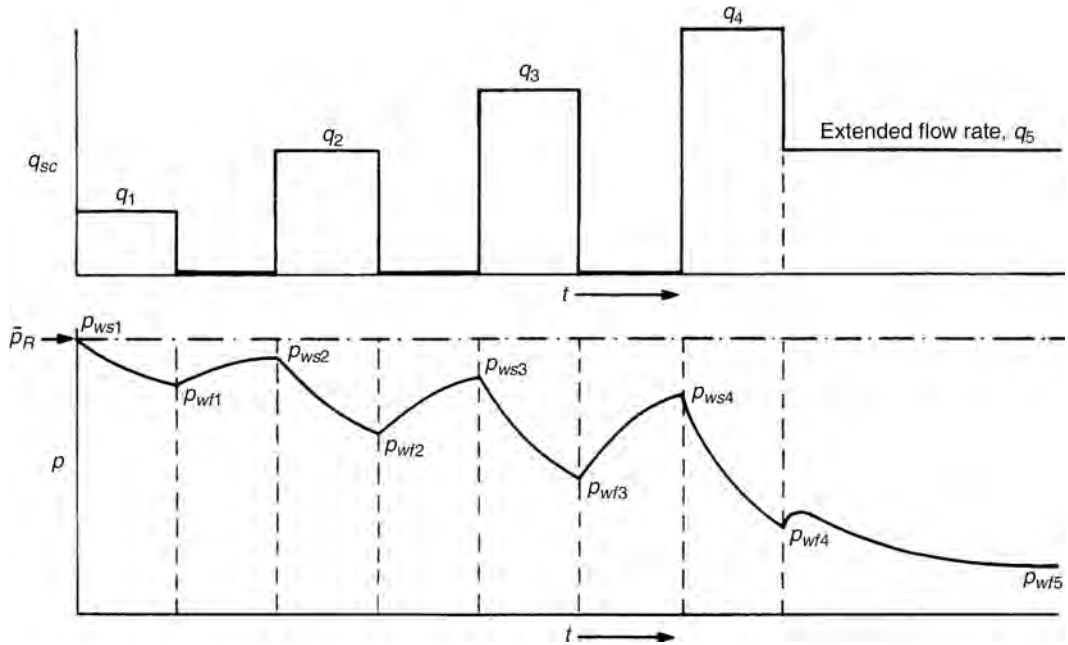


Fig. 10.19—Rate vs. time history for a typical modified isochronal test.¹⁴

10.4.10 Effects of Skin. There are several ways to look at the physical effects attributable to skin. The first is in terms of a flow efficiency (FE), which is defined as the well productivity with skin compared to the no-skin case:

$$FE = \frac{\ln(r_d/r_w)}{\ln(r_d/r_w) + S'} \dots\dots\dots (10.78)$$

The effective potential drop caused by skin also can be calculated as

$$\Delta\psi_{skin} = \frac{S'm}{1.1513} \dots\dots\dots (10.79)$$

Some prefer to consider skin in terms of an effective wellbore radius,

$$r'_w = r_w e^{-S} \dots\dots\dots (10.80)$$

It should be remembered that the skin in these equations is rate-dependent because of the non-Darcy effect. To determine the two different components of skin, mechanical-vs.-non-Darcy pressure-buildup or -drawdown tests must be run at more than one rate. If multirate transient tests are run, a simple plot of S' vs. q_g will yield a slope of D and an intercept of S .

10.5 Volumes and Recovery

This section discusses various aspects of gas reservoir performance, primarily to determine initial gas in place and how much is recoverable. The equations developed in this section also will be used to form the basis of forecasting future production rates by capturing the relationship between cumulative fluid production and average reservoir pressure.

10.5.1 Gas in Place. Volumetric Determination. Original gas in place (OGIP) can be estimated volumetrically with geological and petrophysical data:

$$G = \frac{Ah\phi S_{gi}}{B_{gi}} \dots\dots\dots (10.81)$$

In oilfield units with gas measured in Bscf and B_{gi} in ft³/Mscf,

$$G = \frac{1}{22.957} \frac{Ah\phi S_{gi}}{B_{gi}}$$

$$= \frac{1}{22,957} \frac{T_{sc}}{p_{sc}} \frac{Ah\phi S_{gi}(p/z)_i}{T} = \frac{1}{649.21} \frac{Ah\phi S_{gi}(p/z)_i}{T} \dots\dots\dots (10.82)$$

In SI units with gas measured in std m³ and A in m²,

$$G = \frac{Ah\phi S_{gi}}{B_{gi}}$$

$$= \frac{T_{sc}}{p_{sc}} \frac{Ah\phi S_{gi}(p/z)_i}{T} = 2.8438 \frac{Ah\phi S_{gi}(p/z)_i}{T} \dots\dots\dots (10.83)$$

Material-Balance Determination of OGIP. Material-balance equations provide a relationship between original fluids in place, cumulative fluid production, and average reservoir pressure. For many gas reservoirs, a simple material-balance equation can be derived on the basis of the following assumptions:

- The gas-filled pore volume is constant.
- Gas dissolved in water or liberated from the rock is negligible.
- Reservoir temperature is uniform and constant.

With these assumptions, the real-gas law can be used to derive

$$V_g = \frac{RT}{V_{msc} p_i} z_i G = \frac{RT}{V_{msc} p} z (G - G_p) \dots\dots\dots (10.84)$$

This equation can be rearranged to get the usual volumetric gas material-balance equation,

$$\frac{G_p}{G} = 1 - \frac{p/z}{p_i/z_i} \dots\dots\dots (10.85)$$

This equation is the basis for the p/z -vs.- G_p graph used to analyze gas reservoirs.

10.5.2 Determining Average Reservoir Pressure. Reservoir engineers have often used pressure contour maps or some approximate methods to determine field average reservoir pressure for p/z analysis. Usually, however, individual well pressures are based on extrapolation of pressure buildup tests or from long shut-in periods. In either case, the average pressure measured does not represent a point value, but rather is the average value within the well’s effective drainage volume (see [Sec. 10.4.5](#)).

By combining the assumptions used to assign drainage shapes and considerations of the gas law, the following procedure could be used for developing an average reservoir pressure at any point in time.

1. Be certain to determine average reservoir pressure accurately. Sometimes, shut-in times are inadequate to achieve complete buildup. When this occurs, one way to approximate reservoir pressure from a long shut-in is to use the Matthew-Brons-Hazebroek method¹⁶ estimating the semilog straight-line slope from reservoir properties rather than a buildup test. Of course, buildup tests are the preferable way to determine average reservoir pressure when economically feasible. An alternative way to ramp up an incomplete buildup is to run a buildup test early in the life of a well, noting the time to complete buildup and the percentage buildup at shorter times. Then, these percentages can be used in subsequent shut-in tests of shorter times than those required for full buildup.

2. For each well, make a graph of p/z vs. G_p . In general, these graphs will not necessarily yield a straight line. If the well's drainage volume is changing with time, these will be curves. Either way, pass a smooth curve (not necessarily straight) through the data points.

3. To estimate the average p/z for a given well's drainage volume at a given point in time, first determine the cumulative gas produced for that well at the desired time, then use the value of G_p to get a value of well p/z from the graphs created in Step 2.

4. Estimate the average production rate for each well at the desired time. This should be some reasonable average "eye-balled" from production curves, and not necessarily a specific daily rate.

5. Determine the reservoir average p/z as the average of the individual-well values (Step 2), weighted by their production rate:

$$(p/z)_{\text{res}} = \frac{\sum_{j=1}^{n_w} (p_j/z_j)q_j}{\sum_{j=1}^{n_w} q_j}, \dots\dots\dots (10.86)$$

where n_w is the number of active producing wells. This procedure works reasonably well and is straightforward.

Accurate determination of average reservoir pressure is particularly difficult in tight gas sands. Shut-in pressures may not be near average reservoir pressure for several months or years, obviously too long to be of any value. In addition, low-permeability reservoirs can have significant pressure differences across the field because certain areas can be drained more effectively than others.

Poston and Berg¹⁷ discuss methods for adjusting p/z plots for the lack of sufficient buildup time in determining average reservoir pressures. Although these methods have some validity, they also are prone to large errors because of data uncertainties. A recommended practice is, where feasible, to perform advanced pressure-transient-analysis methods on pressure-buildup tests to provide the means to extrapolate to expected values of average reservoir pressure. Such methods rely on the extrapolation of buildup pressures followed by a correction that incorporates drainage shape and volume. The problem with these techniques is that the correction for drainage shape and volume can be very significant (because of low reservoir permeabilities), and these techniques are highly uncertain, given the extent of heterogeneities and compartmentalization in typical tight gas reservoirs. Calibration of pressure-buildup analyses against actual well responses and reservoir simulation history-match studies can be helpful.

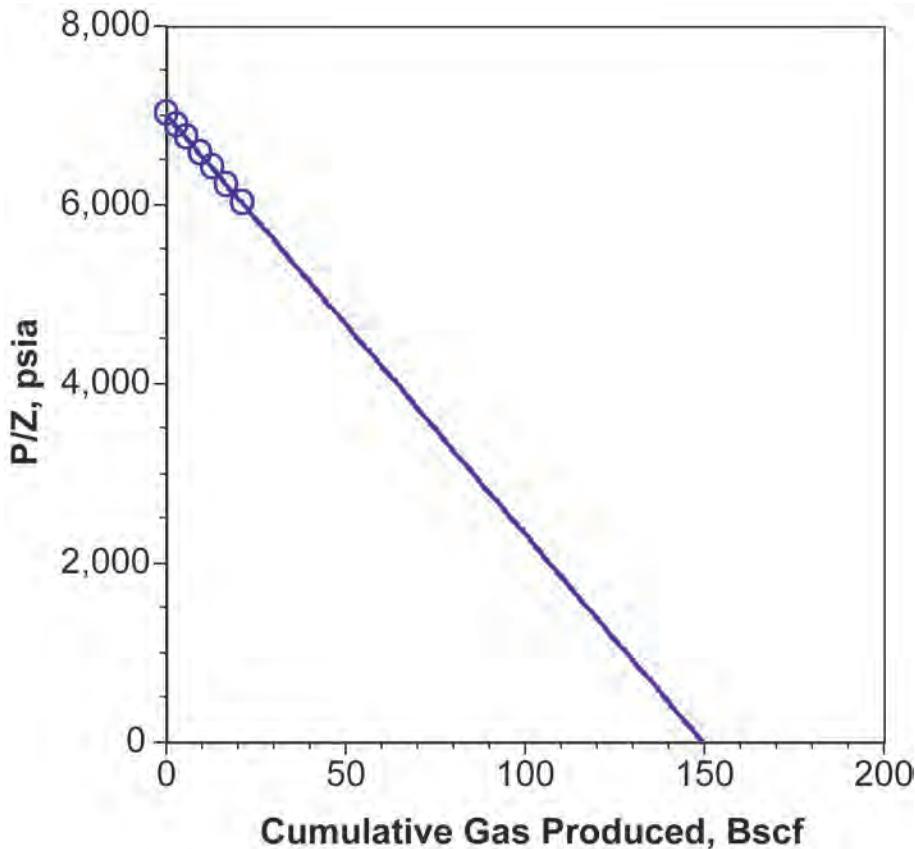


Fig. 10.20—Example p/z -vs.- G_p curve for a volumetric gas reservoir.

Another problem in tight reservoirs is the variation in average reservoir pressure across the field, both because of reservoir compartmentalization and because of low permeabilities. In higher-permeability gas reservoirs, this problem is generally not so severe, meaning that the average reservoir pressure needs to be measured only in a few wells to generate accurate p/z analyses. When variations in average reservoir pressure are large, however, methods need to be used to account for differences across the field.

Although reservoir simulation is one possibility to deal with this problem, it is also possible to use a “compartmentalized-reservoir model”¹⁸ to incorporate these effects. This model treats the reservoir as a set of communicating “tanks.” The technique is basically a history-matching process that uses compartment volumes and compartment-to-compartment transmissibilities as tuning parameters. This method is important and has technical value, although it does not address the problem of required long shut-in times. The method has been applied to several reservoirs with very good results; hence, its use is recommended.

10.5.3 Volumetric Reservoirs. In volumetric dry- and wet-gas reservoirs, p/z vs. cumulative gas production will be a straight line intercepting the gas-production axis at the OGIP. An example is given in Fig. 10.20. The intercept ($G_p = 0$) on the p/z axis is p_i/z_i , and the intercept on the G_p axis ($p/z = 0$) is G . This graph provides a convenient method of using average-reservoir-pressure data to estimate OGIP and recoverable reserves once an abandonment p/z is established. When these plots are applicable, results for OGIP are generally considered very accurate after approximately 10% of gas reserves have been produced (sometimes a bit earlier).

When only a small amount of early data is available, the OGIP can be determined from any point ($G_p, p/z$) by

$$G = \frac{G_p}{1 - \frac{p/z}{p_i/z_i}} \dots\dots\dots (10.87)$$

When placing the straight line through p/z data, it is usually prudent to consider the first point (i.e., at field discovery pressure) as more accurate than others. Because there has been little field depletion and there has been sufficient time for pressures to return to stabilized conditions, discovery-pressure measurements are generally reliable. Regression approaches to placing the p/z -vs.- G_p line should take this into consideration.

Volumetric estimates based on cores, well logs, fluid analyses, and geological estimates of reservoir size provide a “rock-based” estimate of gas in place, while material-balance relationships provide a “fluids-based” or “pressure-based” estimate. These two types of estimates are essentially independent (except for the use of consistent values of B_{gi}). Thus, when the two estimates are comparable, there is greater certainty in the OGIP estimate. It is now a common practice to develop geologic and simulation models of a reservoir to determine reserves and depletion strategies and to evaluate alternative development scenarios. Acquisition of p/z data can provide another measure of the volume being drained by a well or set of wells in what is thought to be a common reservoir. Differences between models and p/z data can be a valuable tool in managing a reservoir and detecting opportunities for additional development or deferral of expenditures that become unnecessary because of a change in the size of a resource.

Well-deliverability forecasts can be used to predict the economic limit of production for a field (income = costs) and the resulting p_a/z_a . Recoverable reserves then become

$$G_{pa} = G \left(1 - \frac{p_a/z_a}{p_i/z_i} \right) \dots\dots\dots (10.88)$$

10.5.4 Highly Compressive Reservoirs. For some high-pressure gas reservoirs (e.g., geopressed or abnormally pressured reservoirs), the combined rock and water compressibility can result in a nonlinear p/z plot (**Fig. 10.21**). Ignoring this effect can lead to large overestimates of the OGIP. Local knowledge is the best source of information about whether these effects should be considered. Such performances usually should be suspected for geopressed reservoirs.

If the pore volume and water can be considered to have constant compressibility, then the change of gas-filled pore volume with pressure is

$$\frac{V_g}{V_{gi}} = \frac{e^{c_f \Delta p} - S_{wi} e^{-c_w \Delta p}}{1 - S_{wi}} \dots\dots\dots (10.89)$$

Using the first two terms in a Taylor series expansion for the exponential function,

$$\frac{V_g}{V_{gi}} \approx 1 - c_e \Delta p, \dots\dots\dots (10.90)$$

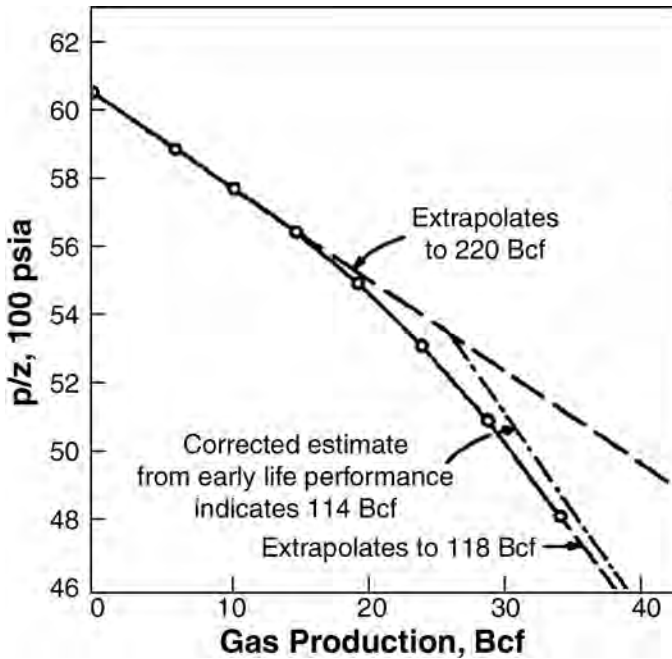


Fig. 10.21— p/z vs. cumulative production, North Ossum field, Lafayette Parish, Louisiana, NS2B reservoir.¹⁹

$$\text{where } c_e = \frac{c_f + S_{wi}c_w}{1 - S_{wi}} \dots\dots\dots (10.91)$$

The material-balance equation for a compressive reservoir then becomes

$$\frac{G_p}{G} = 1 - (1 - c_e \Delta p) \frac{p/z}{p_i/z_i} \dots\dots\dots (10.92)$$

Eq. 10.92 suggests that if the effective reservoir compressibility, c_e , can be estimated, then the p/z plot for such reservoirs can be linearized by multiplying the p/z values by $1 - c_e \Delta p$. However, there is typically very little knowledge of the effective system compressibility, meaning that this relationship is of limited practical use for reservoir engineering purposes. In addition, the effective system compressibility may even change with time, typically becoming smaller as reservoir pressure declines and the reservoir rocks compact.

There is sometimes a change in the slope of the p/z plot when an abnormally pressured gas reservoir reaches normal pressure, as shown in Fig. 10.21. Approaches suggested for analyzing geopressed gas reservoirs include methods to account for some unusually high apparent values of the effective pore-volume compressibility. Soft-sediment compaction, shale dewatering, and limited aquifer influx are among the physical effects proposed by various authors. For further information on this topic, the reader is referred to papers by Hammerlindl,¹⁹ Roach,²⁰ Prasad and Rogers,²¹ Bernard,²² Fetkovich *et al.*,²³ Ambastha,²⁴ Yale *et al.*,²⁵ El Sharkawy,²⁶ and Gan and Blasingame.²⁷ Poston and Berg¹⁷ also provide an evaluation of different methods of accounting for pressure support experienced in geopressed reservoirs.

Many overpressured reservoirs, however, do not demonstrate the change in slope, as illustrated by Fig. 10.22. These data are from four wells in a common reservoir with an initial

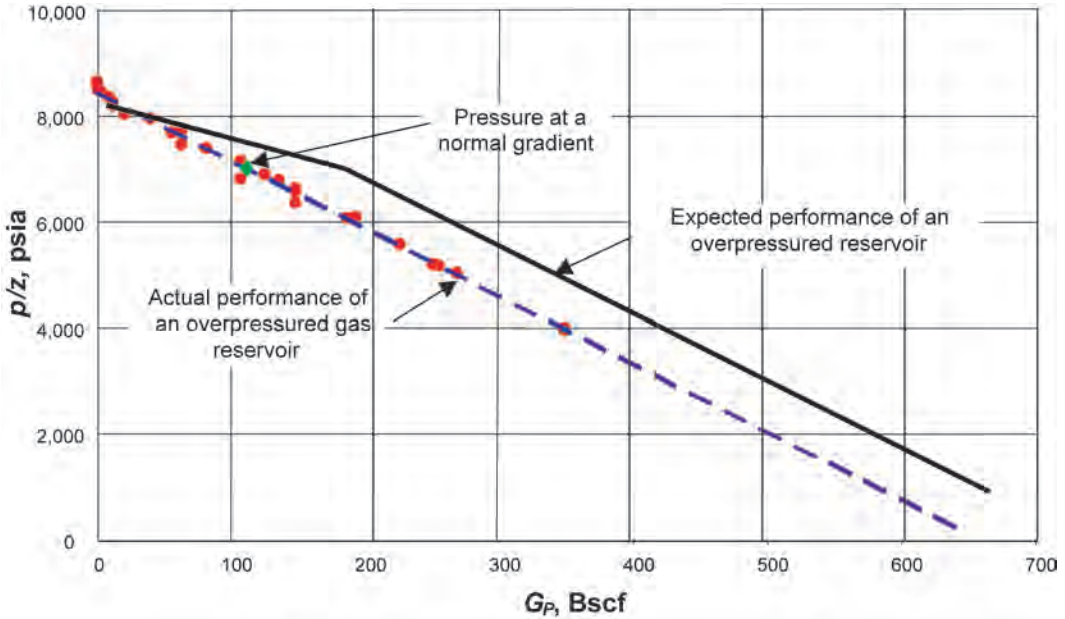


Fig. 10.22—Actual vs. expected p/z curves for an overpressured gas reservoir.

pressure gradient >0.65 psi/ft. As indicated, there was no change in slope when the reservoir pressure reached a normal gradient. The reservoir consists of a competent sandstone that may have a low effective compressibility.

Considering the previous discussions, using early p/z has many uncertainties. Best practices would suggest that early-time analyses use ranges for effective pore-volume compressibility based (where possible) on analogous or similar regionally located reservoirs to reduce the high uncertainty in early data and its potential dramatic effect on estimates of OGIP.

Abandonment conditions for highly compressive reservoirs are determined in the same manner as those for volumetric reservoirs.

10.5.5 Waterdrive Reservoirs. Fig. 10.23 shows a typical p/z plot for a gas reservoir with an active waterdrive. Note that for a given value of cumulative gas production, pressures are higher than for a volumetric reservoir.

The material-balance equation for a waterdrive reservoir is

$$\frac{G_p}{G} = 1 - \left[1 - \frac{(W_e - W_p B_w)}{GB_{gi}} \right] \frac{p/z}{p_i/z_i} \dots\dots\dots (10.93)$$

If it can be assumed that volumetric estimates of G are accurate, then Eq. 10.93 can be rearranged to calculate a water-influx history for comparison against contact mapping.

$$W_e = W_p B_w + GB_{gi} \left[1 - \left(1 - \frac{G_p}{G} \right) \frac{p_i/z_i}{p/z} \right] \dots\dots\dots (10.94)$$

This can be used with different aquifer models to determine how to predict future water influx. This will be discussed further in the next section.

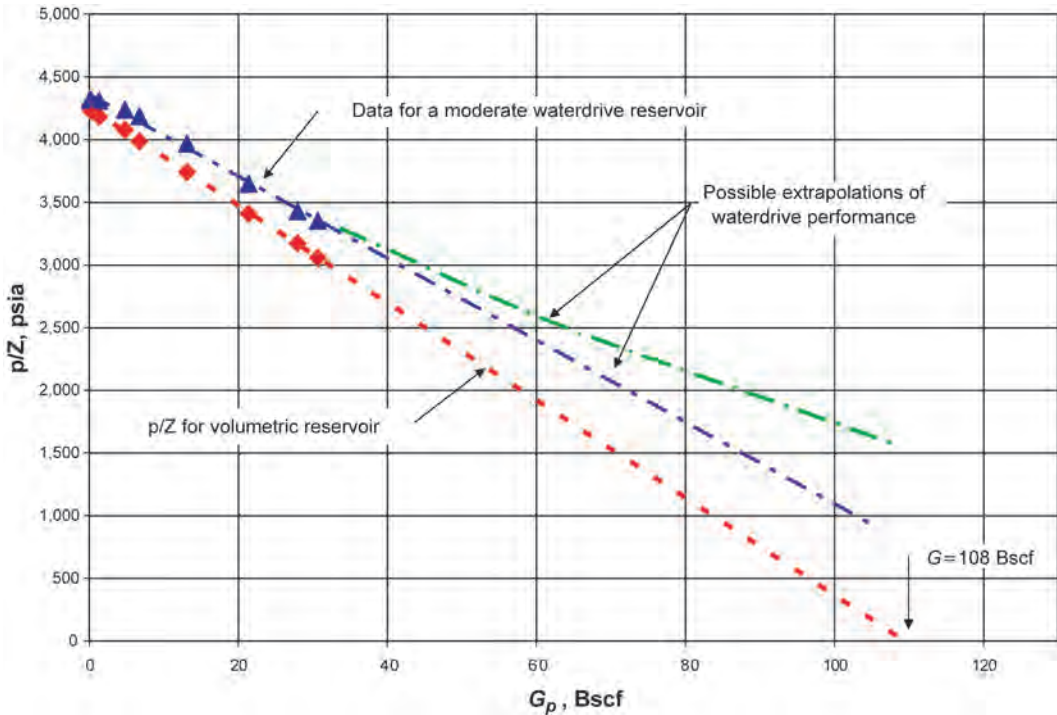


Fig. 10.23—Volumetric-vs.-waterdrive *p/z* trends.

Using Eq. 10.93 to estimate *G* requires information about the cumulative water influx. Estimates may be obtained by mapping water movement using watered-out wells, logging surveys, or data from infill wells.

By writing Eq. 10.93 in terms of a volumetric sweep efficiency, *E_v*, and the residual gas saturation to water displacement, *S_{gr}*, the material-balance calculation can then be written as

$$\frac{G_p}{G} = 1 - \left[1 - E_v \left(1 - \frac{S_{gr}}{S_{gi}} \right) \right] \frac{p/z}{p_i/z_i} \dots\dots\dots (10.95)$$

If *E_v* is taken to be the estimated volumetric sweep efficiency at abandonment, then this equation represents all possible abandonment conditions regardless of the rate of water influx. An abandonment line can then be drawn on the *p/z* plot, the bottom point of which is at *p/z* = 0, *G_p* = *G*, and the top point of which is at *p/z* = *p_i/z_i*. A straight line connecting these two points is the locus of all possible abandonment points. The intersection of this abandonment line and the actual *p/z*-vs.-*G_p* line, as illustrated in Fig. 10.24, gives an estimate of ultimate recovery.

Many factors affect gas-recovery potential when a waterdrive is active. The main considerations are how much of the reservoir will be invaded by water, what the pressure decline will be, and what the trapped-gas saturation will be behind the waterfront. Simple 3D simulations can be used to study the strength of an aquifer based on its size relevant to the gas volume and the variation in rock quality. A good reservoir description is the key to a successful prediction. How the reservoir is affected is also a function of withdrawal rates. Strong aquifers can sustain reservoir pressure and result in low recoveries. Gas saturations trapped behind the invading water are typically about one-third of the initial hydrocarbon saturation. If volumetric sweep is

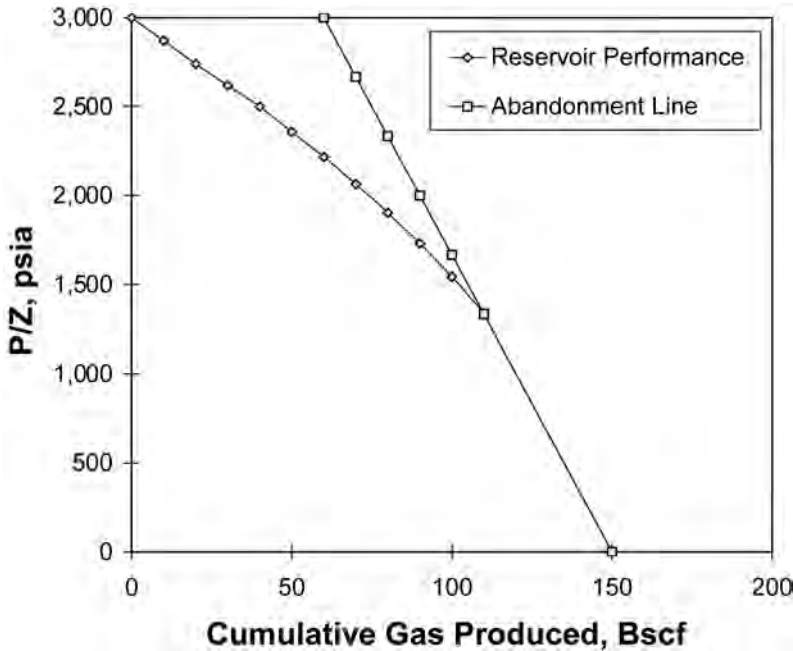


Fig. 10.24—Typical p/z plot for a waterdrive gas reservoir.

high and there is little pressure depletion ($B_{ga} \approx B_{gi}$), then a reservoir with S_{wi} equal to 25% of pore volume would experience a recovery of

$$E_{Rg} = \left(\frac{1 - S_{wi} - S_{gr}}{1 - S_{wi}} \right) \frac{B_{gi}}{B_{ga}} E_v = \left(\frac{1 - 0.25 - 0.25}{1 - 0.25} \right) 0.9 = 0.6 \dots\dots\dots (10.96)$$

Recoveries as low as 50% of OGIP can occur in adverse circumstances, but more often recoveries exceed 70% of OGIP owing to partial pressure depletion. There are documented cases^{28,29} in which a significant increase in offtake rate has resulted in pressure depletion of a waterdrive reservoir when withdrawal rates were sufficient to outrun invading water. Recovery from reservoirs that exceed 1 Tcf OGIP with permeabilities greater than 250 md will normally be unaffected by an aquifer of any size if field depletion occurs over a 20-year period or less. Again, a simple simulation model will confirm how potentially effective an aquifer may be.

The effect of a weak to moderate waterdrive is often difficult to detect with a simple p/z plot. Often, a straight-line plot will occur (Fig. 10.23) and will lead to incorrect estimates. Cole³⁰ has suggested an improved method. If the expansibility of water is small compared to gas expansibility, then the material balance can be arranged as

$$\frac{G_p B_g}{B_g - B_{gi}} = G + \frac{W_e - W_p B_w}{B_g - B_{gi}} \dots\dots\dots (10.97)$$

Cole’s methodology is to plot the left side of the equation against G_p . The shape of the resulting plot will vary depending on the existence and strength of a waterdrive, as illustrated by Fig. 10.25.

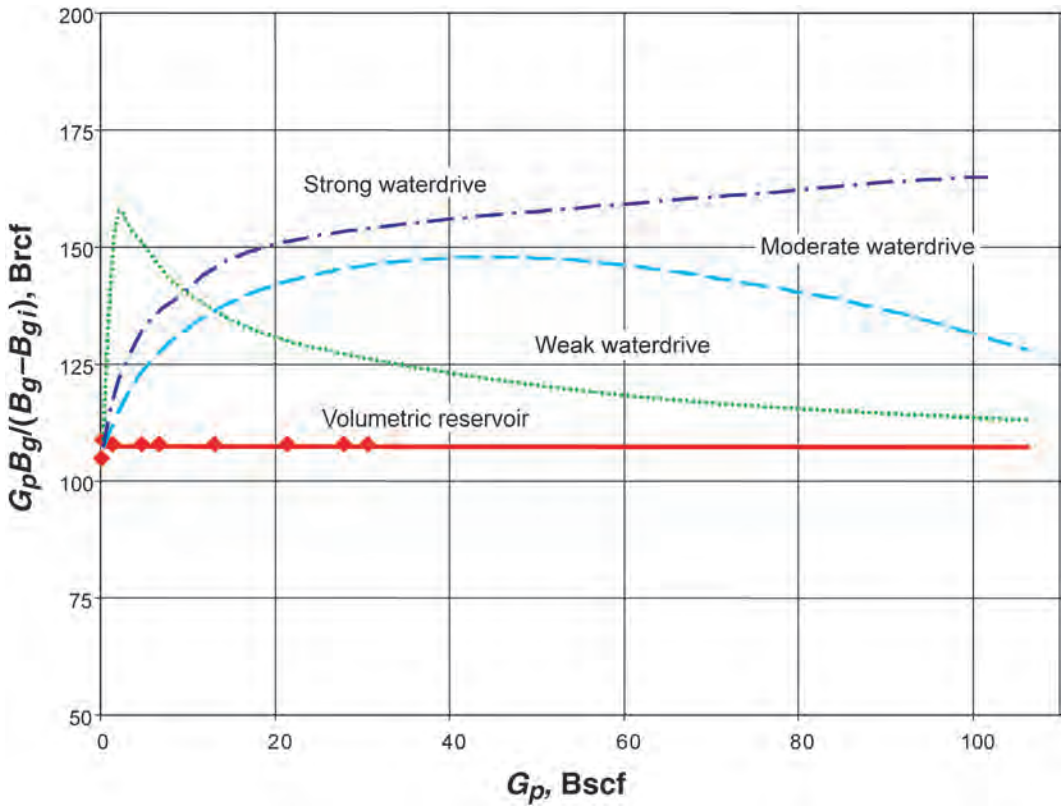


Fig. 10.25—Plot for volumetric and waterdrive gas reservoirs (after Cole³⁰).

Data from a volumetric reservoir will plot as a horizontal line. A weak waterdrive yields an early increase in ordinate values followed by a negative slope. The initial increase may not be detected because many pressure measurements are needed very early in the producing life of the reservoir. Moderate to strong waterdrives give overstated OGIP values. This plot is very sensitive to the effects of water influx and is a good qualitative tool. Back extrapolating the plot to OGIP has been suggested. In practice, the slope usually changes with each pressure measurement, and extrapolation is difficult to impossible.

Pletcher³¹ has suggested a further modification to the Cole plot to account for rock and water compressibility. In doing so, Eq. 10.97 becomes

$$\frac{F}{E_t} = G + \frac{W_e}{E_t}, \dots\dots\dots (10.98)$$

where $F = G(E_g + E_{fw}) + W_e$,

$$E_g = B_g - B_{gi}$$

$$E_{fw} = \frac{(B_{gi})(S_{wi}c_w + c_f)(p_i - p)}{(1 - S_{wi})}$$

and $E_t = E_g + E_{fw} \dots\dots\dots (10.99)$

The shapes of the resulting plots are the same as those in Fig. 10.25, but they do avoid the negative slope of a Cole plot that results from an abnormally pressured reservoir with no water influx.

10.5.6 Retrograde-Condensate Reservoirs. Depletion behavior of retrograde-condensate reservoirs can be handled through the p/z analyses discussed previously, with the caveat that the z factor must be the two-phase z factor (see Sec. 10.2). Two-phase z factors either may be obtained from laboratory tests or predicted from composition with an EOS. In wet-gas and retrograde-condensate reservoirs, cumulative gas produced must include both gas and liquid (as equivalent gas) production. This is particularly important for high-liquid-yield gases.

In the calculation of future reserves for planning purposes, it is usually necessary to break out gas and liquid reserves separately, perhaps even by individual gas component. For wet-gas reservoirs, liquid yields from a particular gas can be expected to remain constant with time, so long as the gas is processed in the same manner. Changes in separator conditions and/or gas-processing facilities could result in changing liquid yields, however.

Retrograde-condensate reservoirs, on the other hand, will produce at a variable yield as the reservoir pressure declines. Determination of the expected yields can be based on laboratory tests and/or EOS calculations. The PVT test presented in Sec. 10.2 shows how yields of the various gas components can vary over time.

10.5.7 Pressure Maintenance and Cycling Operations. Pressure maintenance of a retrograde-condensate gas reservoir can exist by virtue of an active waterdrive, water-injection operations, gas-injection operations, or combinations of all of these. Certain reservoirs may contain fluids near their critical points and are thereby candidates for special recovery methods, such as the injection of specially tailored gas compositions to provide miscibility and phase-change processes that could improve recovery efficiency. These usually are not regarded as gas/condensate cases. All these improved-recovery methods are best studied with simple-to-complex computer models. Simple models can be used initially to screen prospects, and then more-detailed studies including compositional considerations can be conducted.

Waterdrive and Water-Injection Pressure Maintenance. Recovery from retrograde-condensate gas reservoirs with a waterdrive or water injection is subject to the same considerations as described in the chapter on Waterflooding (in the Reservoir Engineering and Petrophysics section of this *Handbook*) for water injection into oil reservoirs. To make a recovery assessment, the first requirement is a good description of the rock and fluid characteristics of the reservoir and the aquifer. Variations in the permeability of various strata, mobility ratios, and gravity-stable advance of the water front will affect the volumetric sweep. S_{gr} should be approximately the same as described earlier for dry- and wet-gas displacements by water. The favorable mobility ratio can result in a high volumetric sweep. There is strong evidence, however, that displacement efficiency by water is not high. While Buckley *et al.*³² indicated that the displacement efficiency of water displacement of gas can be as high as 80 to 85%, experiments and field observations by Geffen *et al.*³³ indicate that it may be as low as 50%. All things considered, the recovery of gas condensate in the vapor phase by water injection is likely to be appreciably lower than by cycling, and any consideration of water injection for gas/condensate recovery should be accompanied by detailed experimental work on cores from the specific reservoir involved. This will help to determine whether water can, in fact, accomplish a high-enzyme displacement efficiency to justify its use.

Premature water breakthrough can, and often does, result in “load up” and loss of the ability of a well to flow. It is difficult to obtain economical flow rates by artificial lift. This loss of productivity may result in premature abandonment of the project. The problems would be particularly serious for deeper reservoirs in which the cost of removing water would be a

significant factor. Yuster³⁴ discusses possible remedial methods for drowned gas wells. Bennett and Auvenshine³⁵ discuss dewatering gas wells. Dunning and Eakin³⁶ describe an inexpensive method to remove water from drowned gas wells with foaming agents.

Generally, the use of water injection for maintaining pressure in a gas/condensate reservoir will be unattractive where a wide range of permeabilities exists in a layered reservoir and selective breakthrough of large volumes occurs early in the life of the reservoir.

Dry-Gas Injection. Comparative economics determine whether a gas/condensate reservoir should be produced by pressure depletion or by pressure maintenance (i.e., does the additional condensate recovery justify the cost of compressing, injecting, and processing the injected gas?). Delayed gas sales also may be a factor. The objective of using dry-gas injection is to maintain the reservoir pressure usually above or near the dewpoint to minimize the amount of retrograde condensation. Dry field gases are miscible with nearly all reservoir gas/condensate systems; methane normally is the primary constituent of dry field gas. Dry-gas cycling of gas/condensate reservoirs is a special case of miscible-phase displacement of hydrocarbon fluids for improving recovery. Experimentation has shown that the displacement of one miscible fluid by another that is miscible is highly efficient on a microscopic scale; usually, the efficiency is considered 100% or very nearly so. Cycling does result in liquid recoveries at economical rates while avoiding waste of the produced gas when a market for that gas is not available.

Inert-Gas Injection. The use of inert gas to replace voidage during cycling of gas/condensate reservoirs can be an economical alternative to dry natural gas. One of the first successful inert-gas-injection projects was in 1949 at Elk Basin, Wyoming,³⁷ where stack gas from steam boilers was used for injection. In 1959, the first successful use of internal-combustion-engine exhaust was seen in a Louisiana oil field.³⁸ The first use of pure cryogenically produced N₂ to prevent the retrograde loss of liquids was in the Wilcox 5 sand in the Fordoche field located in Pointe Coupee Parish, Louisiana.³⁹ In the Fordoche field, the N₂ amounted to approximately 30% of the natural-gas/N₂ mixture injected.

Studies by Moses and Wilson⁴⁰ confirmed that the mixing of N₂ with a gas/condensate fluid elevated the dewpoint pressure. Moses and Wilson also presented data to show that the mixing of a lean gas with a rich-gas condensate would result in a fluid with a higher dewpoint pressure. The increase in dewpoint pressure was greater with N₂ than with the lean gas. In the same study, results are presented from slimtube displacement tests of the same gas/condensate fluid both by pure nitrogen and by a lean gas. In both displacements, more than 98% recovery of reservoir liquid was achieved. These results also were observed by Peterson⁴¹ using gas-cap gas material from the Painter field located in southwest Wyoming. The authors concluded that the observed results were obtained because of multiple-contact miscibility.

Cryogenic-produced N₂ possesses many desirable physical properties.⁴² Those that make nitrogen most useful for a cycling fluid are that it is totally inert (noncorrosive) and that it has a higher compressibility factor than lean gas (requires less volume). The latter advantage is partially offset by increased compression requirements when compared with lean gas.

The use of inert gas as a cycling fluid offers both advantages and disadvantages. The major advantages are early sale of residue gas and liquids and a higher recovery of total hydrocarbons because the reservoir contains large volumes of inert gas rather than hydrocarbons at abandonment. Disadvantages are production problems and increased operating costs caused by corrosion if combustion or flue gas is used, possible additional capital investments and operating costs to remove inert gas from the sales gas (a condition aggravated by early breakthrough of inerts), and potential costs to pretreat before compression and/or to fund reinjection facilities.

10.6 Forecasting

This section explores the fundamental relationships underlying gas-reservoir performance and presents some simple techniques for forecasting production rate vs. time.

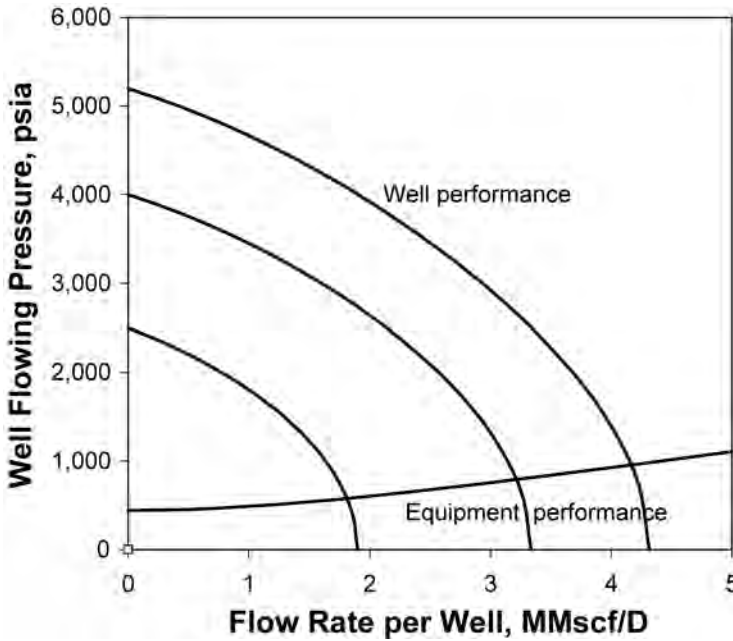


Fig. 10.26—Example well- and equipment-performance curves.

10.6.1 System Performance. One way to envision the different factors affecting the performance of a gas reservoir is to define the production “system” with three components: (1) well deliverability (developed in [Sec. 10.4](#)), (2) wellbore hydraulics, and (3) production-equipment constraints. Rate-vs.-time behavior is governed by the combined effect of these three parts, which in turn have performance characteristics that vary with pressure and production rate. Wellbore and system constraints include

- Tubing and choke sizes.
- Amount of entrained liquids (condensate and water).
- Accumulation of sand or debris in the wellbore.
- Flowline pressure drops.
- Compression ratios across compressors.
- Pressure losses in separators.

If these relationships are plotted on the same presentation, the resulting graph will look like [Fig. 10.26](#).

At low flow rates, the equipment-performance curve is nearly horizontal, reflecting the small flowing frictional pressure drops in the system. If there is liquid holdup in the production tubing, multiphase-flow calculations can show the curve bending upward at low production rates.

The curves represent maximum performance with existing completion, well, and equipment configurations. At any time, of course, it is possible to operate a well below its maximum performance characteristics by adjusting such things as a choke size at the wellhead. Because this is effectively a “zero-expense” change, it represents how a system is “tuned” to operate at some predetermined rate or other operating condition. Perforating additional producing intervals, using stimulation treatments, lowering separator pressure, or installing compressors, larger flowlines, and/or production tubing can change the performance curves.

The concave downward lines (flow rate increasing with decreasing well pressure) are the well-performance curves for different average reservoir pressures. Note that the value of well flowing pressure at zero flow rate is the average reservoir pressure and that the value of flow

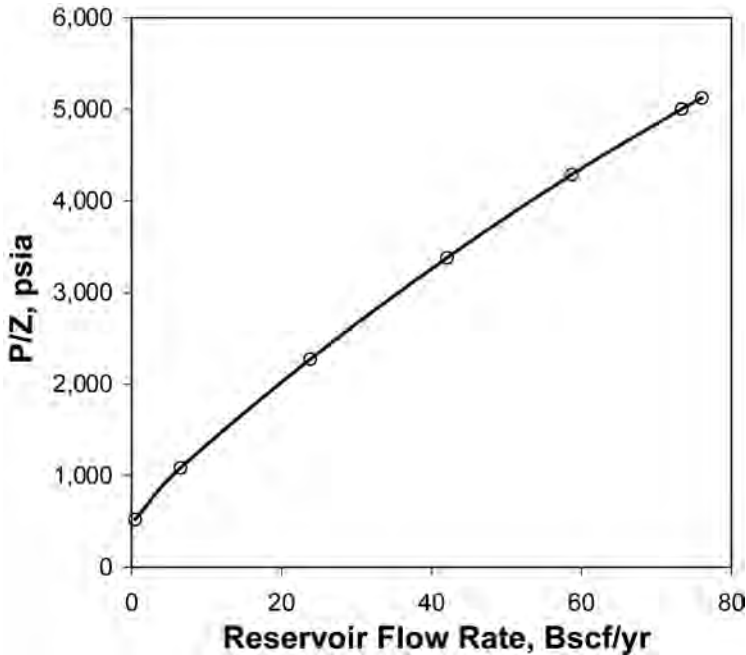


Fig. 10.27—Example reservoir-deliverability curve.

rate at zero well flowing pressure is the AOF. As reservoir pressure declines, of course, the well-performance curves move down and to the left. These curves may be altered by operational changes that affect well deliverability. Such processes as hydraulic fracturing, acidizing, or reperforating will increase well productivity and move up the AOF point.

The intersection of the equipment- and well-performance curves represents the operating point of the well at a given value of average reservoir pressure. Note that if the equipment-performance curve represents maximum (full-open choke) performance, then the intersection point also represents maximum rate performance.

10.6.2 Reservoir Deliverability. The intersection points of the well- and equipment-performance curves can be used to construct a relationship between average reservoir p/z and maximum well deliverability such as that shown in Fig. 10.27. This curve represents the rate that the combined well and equipment design is capable of delivering at any particular average reservoir pressure. Note that this curve can be used to determine the abandonment p/z by knowing the economic limit (i.e., the minimum economic rate).

For the purposes of forecasting total reservoir performance, it is necessary to develop a graph such as Fig. 10.27 for the reservoir and not just for an individual well. One way to do this is to construct individual graphs for each well and then to add up the flow rates for each well at a given value of average reservoir p/z . Alternatively, one could construct the graph for an average well in the reservoir and then simply multiply by the total number of wells.

Another method would be to first determine reservoir deliverability constants a and b (that is, a and b should represent the following deliverability equation for the reservoir):

$$\bar{\psi} - \psi_{wf} = a q_R + b q_R^2 \dots\dots\dots (10.100)$$

where q_R is the total reservoir production rate.

There are many ways to develop this sort of relationship, including an analysis of reservoir performance in the same manner as well performance with techniques explained in [Sec. 10.4](#). A simple way would be to obtain \bar{a} and \bar{b} for the individual wells in the reservoir, and then, by assuming that the average well produces at the total reservoir rate divided by the number of wells, n_w ,

$$\bar{\psi} - \psi_{wf} = \frac{\bar{a}}{n_w} q_R + \frac{\bar{b}}{n_w^2} q_R^2 \dots\dots\dots (10.101)$$

This equation could then be used with an average well-equipment-performance curve.

10.6.3 Forecasting Methods. It was seen in [Sec. 10.5](#) that through material-balance relationships, it is possible to evaluate expected reservoir pressures knowing cumulative production. The material-balance equation combined with the reservoir-deliverability relationship thus leads to a set of two relationships that must hold simultaneously:

$$q = \text{Function}(\bar{p}) \dots\dots\dots (10.102)$$

$$\text{and } \bar{p} = \text{Function}(G_p) = \text{Function} \left[\int_0^t q(t) dt \right] \dots\dots\dots (10.103)$$

For simple gas-reservoir situations, it is possible to solve these two relationships either graphically or computationally.

Consider, for example, a typical gas-reservoir production scenario in which the reservoir is first put on production at some fixed reservoir rate for an extended period of time. This fixed rate may result from sales-contract considerations or limitations on processing equipment and pipelines. Let q_c denote the fixed initial reservoir production rate and t_c denote the time of the fixed-rate period.

It is possible to use the reservoir-deliverability and p/z material-balance curves to determine the length of the constant-rate period given the rate or vice versa. First, consider how to determine the time.

For a given rate, the reservoir-deliverability curve can be used to determine the lowest reservoir p/z that will deliver this rate. Because the reservoir-deliverability curve represents the maximum reservoir deliverability before the end of the constant-rate period, the reservoir will be produced at less-than-maximum rates. The value of p/z at the end of the constant-rate period can be entered into the p/z material-balance plot to determine G_{pc} at the end of the constant-rate period. The constant-rate time period is then

$$t_c = \frac{G_{pc}}{q_c} \dots\dots\dots (10.104)$$

For instance, refer to [Fig. 10.28](#), where reservoir deliverability and G_p vs. p/z are plotted. If rates from the field were limited to 40 Bscf/yr by contract, equipment, or pipeline limitations, then the lowest p/z that will support this rate is equivalent to a cumulative production of 400 Bscf. The period of constant production would be 10 years.

Similarly, other rates can be selected and equivalent periods of production calculated to develop the inset curve in [Fig. 10.28](#).

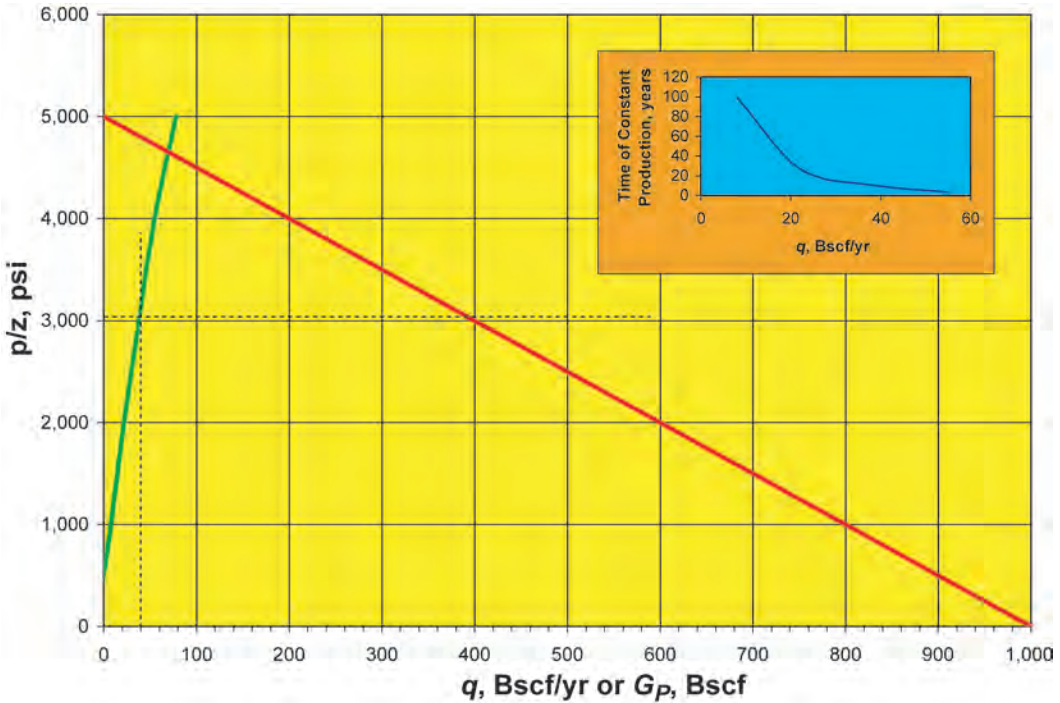


Fig. 10.28—Example reservoir-deliverability and material-balance curves.

These procedures should be based on average sustainable rates that account for down time and other factors that reduce the composite well deliverability. Care also should be taken to account for the normal “ramp-up” of production that occurs during development drilling.

At the end of the constant-rate period, the reservoir will, barring well or equipment changes, go on decline. At this point, the reservoir will produce at its maximum rate according to the reservoir-deliverability curve. A simple procedure can be used to forecast this period as well by discretizing future production into increments.

Consider that a prediction will be made by discretizing the future cumulative gas produced in an increment ΔG_p . Over the time period that this amount of gas is to be produced, there will be some average flow rate \bar{q} . The time to produce the incremental gas production can be approximated by

$$\Delta t = \frac{\Delta G_p}{\bar{q}} \dots\dots\dots (10.105)$$

Assume that q_j is the flow rate at the end of the time increment, and q_{j-1} is the flow rate at the beginning of the time increment. Approximating the average flow rate during flow period j as

$$\bar{q}_j = \frac{q_j + q_{j-1}}{2}, \dots\dots\dots (10.106)$$

$$\text{then } \Delta t_j = \frac{\Delta G_{pj}}{\bar{q}_j} = \frac{2\Delta G_{pj}}{q_j + q_{j-1}} \dots\dots\dots (10.107)$$

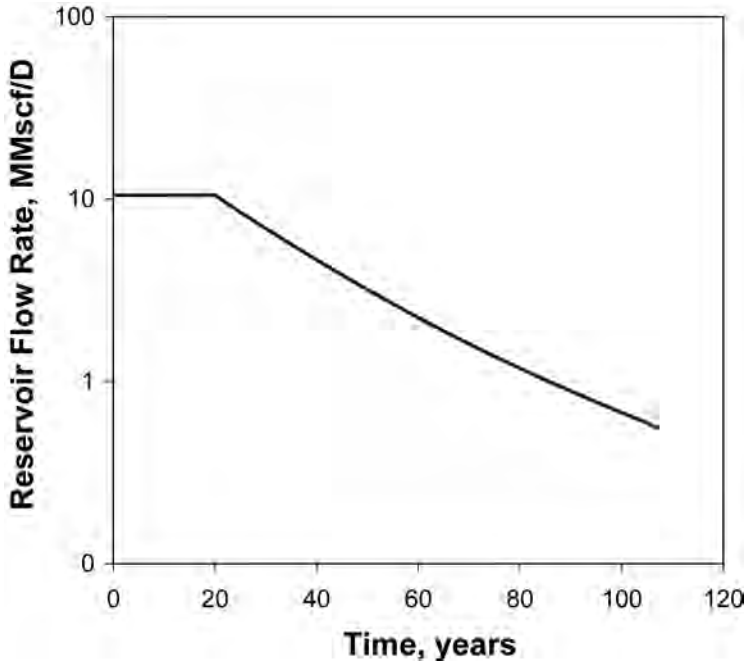


Fig. 10.29—Example production rate-vs.-time curve for a gas reservoir.

Total time since the beginning of the decline period is determined by

$$t_j = t_{j-1} + \Delta t_j \quad \text{..... (10.108)}$$

A plot of q_j (not \bar{q}_j) vs. t_j is the desired forecast. Improved accuracy may be achieved by using smaller values of ΔG_p . An example decline graph can be seen in [Fig. 10.29](#).

The above procedures can be used to evaluate different reservoir-development scenarios. For example, infill drilling or adding compressors would improve the reservoir-deliverability relationship (and thus change the forecast) by sustaining or increasing early-time production but causing the reservoir to have a steeper decline. Whether this would be desirable would depend on economic considerations.

These procedures also suggest ways that past reservoir performance may be evaluated. For example, a historical reservoir-deliverability curve can be generated by plotting reservoir p/z vs. q_R during the decline period. This curve could then be adjusted for changes in operating equipment to determine future performance characteristics.

10.6.4 Water Influx. If a gas reservoir is under waterdrive conditions, there is an additional requirement to forecast the amount of water influx to be expected. The difficulty in performing water-influx calculations for most reservoir situations is in knowing the performance characteristics of the aquifer. As mentioned before, computer models ranging from simple to very complex are now available for general use and represent the best method of predicting the amount and timing of water influx. The models also allow investigation of the effects of varying aquifer size and rock characteristics. Matching of performance data will significantly improve the reliability of model projections.

10.6.5 Retrograde-Condensate Reservoirs. The options discussed before for depleting retrograde-condensate reservoirs are:

- Produce by depletion.
- Recycle processed produced gas.
- Recycle processed produced gas plus other makeup gas.
- Inject N_2 or other inert gas.
- Waterdrive or injected water.

With straight depletion, a considerable amount of the heaviest and most valuable hydrocarbons will be left in the reservoir. Also, reservoir fluids passing through the low-pressure region around the wellbore experience retrograde condensation, resulting in a large liquid saturation buildup and a significant decrease in gas permeability. This is important from at least two standpoints. First, the composition history of produced fluids early in the life of the reservoir may diverge from predictions that assume uniform pressure in the reservoir at any instant of time. Second, and more importantly, well deliverability will be decreased significantly, affecting both timing and ultimate recovery. Wells can even cease to produce in reservoirs with permeabilities less than 10 md. The effects of liquid buildup on well deliverability need special consideration in low-permeability environments.

Recycling of gas aids recovery from condensate reservoirs in two ways. First, reservoir pressure is maintained, if not above the dewpoint, at least at pressures that minimize liquid deposition. If makeup gas is injected, it is, of course, possible to never go below the dewpoint pressure. The economics of recycling produced gas must weigh the additional recovery benefits against the additional handling and injection costs, the deferred revenue of recovered injected gas, and the lost revenue of injected gas that will remain in the reservoir. These factors make most hydrocarbon gas-injection schemes uneconomical if a gas sale is possible. But where gas sales are to be delayed for many years (e.g., Prudhoe Bay), the resulting economics support a cycling program.

If, however, reservoir pressure has dipped below the dewpoint pressure, injected lean gas can also serve to revaporize a significant part of the deposited condensate because of phase-behavior effects. There has been some interest in the use of N_2 as an injected gas for condensate reservoirs. There is evidence that phase behavior is nearly equivalent to methane injection, and costs may be somewhat lower.

These effects, however, are complex. Injected gas may sweep inefficiently between injection and production wells, causing poor economics. Because of the complexities of this process, cycling operations should not be undertaken without the aid of reservoir-simulation studies. Compositional reservoir-simulation models are available that can easily handle the thermodynamics and fluid-flow characteristics of a recycling project. Characterization of phase behavior is generally done through an EOS, which can be tuned to laboratory PVT tests.

Gas Requirements in Cycling Operations. Miller and Lents⁴³ expected to cycle the equivalent of approximately 115% of the gas in place to recover some 85% of the wet-gas reserves of the Cotton Valley Bodcaw reservoir. Brinkley⁴⁴ indicated cycling-gas volumes of as much as 130% of original wet gas in place for various reservoirs. The requirements for a given reservoir will be driven mostly by economic considerations. The makeup gas needed for constant-pressure cycling is mainly the volume required to replace shrinkage by liquid recovery and the amount consumed for various fuel needs. For some composition, temperature, and pressure ranges, the removal of high-molecular-weight constituents from the produced wet gas may result in a higher compressibility factor for the injected dry gas; hence, the greater volume per mole injected may require little or no makeup gas for constant-pressure cycling.

The amount of gas not available for injection because of consumption for operating needs should be taken into account when determining makeup-gas requirements if pressure is to be maintained. The amount of fuel for compression and treatment plants depends mainly on the total amount of gas to be returned to the reservoir and the discharge pressure for the plant. Discharge pressure, in turn, depends on the total rate of injection demanded, the number of

injection wells, and their intake capacities throughout the life of the operation. Other factors affecting the amount of gas required for overall operations are type of plant, type of liquid-recovery system used, and auxiliary field requirements (such as for drilling, completion, and well testing; camp fuel and power for maintenance shops, general service facilities, and employee housing; and other factors that vary from one case to another).

Moore⁴⁵ reports that fuel consumption for the compression plant alone varies from 7 to 12 ft³/bhp-hr; this is probably for gases with heat values of approximately 1,000 Btu/scf.

If the fuel consumption is 8 ft³/bhp-hr and the compression ratio is 15 (compressing from, say, 461 to 7,000 psia), fuel requirements would be 34.4 Mscf/MMscf injected. For an example reservoir originally containing 131 Bscf of wet gas, which might be cycled the equivalent of 1.25 times, the approximate compressor fuel consumption would be 5.6 Bscf, or approximately 3% of the gas handled through the plant.

Treatment-plant fuel and other plant needs added to compressor fuel bring the range of consumption inside the plant fence to 3 to 7% of the gas handled by a cycling plant. In addition to these needs and others mentioned earlier, possible gas losses that can occur in a cycling operation are: gas used in “blowing down” wells, should this be necessary for cleaning or treating purposes; small gas leaks at compressor plants and in field lines; and gas leaks resulting from imperfect seals or corrosion in well tubing, casing, and cement jobs. Remedial workover operations should be planned immediately when there is evidence of appreciable loss of gas between the compression plant and the reservoir sandface or between the outflow-well sandface and the plant intake.

10.7 Summary

The study of gas reservoirs must consider the unique nature of gaseous fluids and their behavior in the reservoir and during production. This chapter has provided methods for characterizing gas reservoirs and their contents, including deliverability calculations, OGIP determination, and recovery potential. Differences in phase behavior between dry, wet, and retrograde-condensate gases result in different depletion schemes that may need additional altering if a strong waterdrive exists. Recycling of produced hydrocarbon gases or injection of nonhydrocarbon fluids may be justified in retrograde-condensate gas reservoirs, particularly if gas sales will be delayed for several years.

Nomenclature

a	= empirical constant
A	= drainage area, reservoir area, L ²
AOF	= absolute open flow potential, std L ³ /t
b	= empirical constant
B	= formation volume factor, L ³ /std L ³
B_{gi}	= initial gas formation volume factor, L ³ /std L ³
c	= compressibility, Lt ² /m
c_f	= pore-volume compressibility, Lt ² /m
c_w	= water compressibility, Lt ² /m
C	= constant in gas-deliverability equation
C_A	= Dietz shape factor, dimensionless
D	= non-Darcy-flow coefficient, t/std L ³
E_{fw}	= cumulative formation and water expansion, L ³
E_g	= cumulative gas expansion, L ³
E_R	= recovery efficiency, fraction
E_t	= total cumulative expansion, L ³
E_v	= volumetric sweep efficiency, fraction

- F = cumulative reservoir voidage, L^3
 G = original gas in place, std L^3
 GE = gas equivalent, std L^3 /std L^3
 G_{pc} = cumulative gas production during a period of constant rate, std L^3
 h = average reservoir thickness, L
 k_g = measured gas permeability, L^2
 k_l = effective liquid permeability, L^2
 K = parameter in Lee *et al.*² viscosity correlation
 m = real-gas potential, m/Lt^2
 M = molecular weight
 n = number of moles of gas or exponent in gas-deliverability equation
 n_c = total number of components in gas mixture
 n_w = number of wells
 \tilde{n}_g = relative number of total moles in gaseous phase, fraction
 \tilde{n}_o = relative number of total moles in oil phase, fraction
 N_p = cumulative condensate production, std L^3
 p = pressure, m/Lt^2
 \bar{p} = average pressure, m/Lt^2
 \tilde{p} = variable of integration in real-gas potential equation, m/Lt^2
 PI = productivity index, std $L^3/t/m/Lt^2$
 q = production rate, std L^3/t
 q_c = production rate during period of constant rate, std L^3/t
 q_R = total reservoir gas production rate, std L^3/t
 r_1 = radial distance at which pressure p_1 is measured, L
 r_2 = radial distance at which pressure p_2 is measured, L
 R = universal gas constant, mL^2/nt^2T
 S = mechanical skin, dimensionless
 S' = total skin, dimensionless
 S_{gi} = initial average gas saturation, fraction
 S_{wi} = initial water saturation, fraction
 t = time, t
 t_c = time of constant-rate production, t
 T = temperature, T
 u = volumetric flux (q/A), $L^3/t/L^2$
 V = volume, L^3
 V_m = molar volume, L^3/n
 W_e = cumulative water influx, L^3
 W_p = cumulative water produced, std L^3
 x_j = mole fraction of component j in liquid phase
 X = parameter in Lee *et al.*² viscosity correlation
 y_j = mole fraction of component j in gaseous phase
 Y = produced condensate yield, std L^3 /std L^3
 z = gas deviation factor, dimensionless
 z_j = mole fraction of component j in mixture
 α = cubic equation-of-state parameter
 α_c = empirical constant
 β = defined in Eq. 10.41

- ρ = density, m/L³
 ϕ = porosity, fraction
 γ = specific gravity (air = 1.0 for gas)
 μ = viscosity, cp
 ψ = generic potential
 $\Delta\psi$ = generic-potential difference

Subscripts

- 2ϕ = two-phase
 a = abandonment
 D = dimensionless
 e = at the drainage radius
 g = gas
 i = initial
 inv = investigation
 l = liquid
 m = molar
 o = oil
 p = produced
 r = residual
 sc = standard conditions
 t = total
 v = vertical
 w = well or wellbore
 wf = wellbore face
 wg = wellstream gas

References

- McCain, W.D. Jr.: *The Properties of Petroleum Fluids*, PennWell, Tulsa (1990).
- Lee, A.L., Gonzalez, M.H., and Eakin, B.E.: "The Viscosity of Natural Gases," *JPT* (August 1966) 997; *Trans.*, AIME, **237**.
- Carr, N.L., Kobayashi, R., and Burrows, D.B.: "Viscosity of Hydrocarbon Gases Under Pressure," *Trans.*, AIME (1954) **201**, 264.
- Gold, D.K., McCain, W.D. Jr., and Jennings, J.W.: "An Improved Method for the Determination of the Reservoir-Gas Specific Gravity for Retrograde Gases," *JPT* (July 1989) 747; *Trans.*, AIME, **287**.
- Engineering Data Book*, Gas Processors Suppliers Assn., Tulsa (1987).
- Katz, D.L. and Lee, R.L.: *Natural Gas Engineering—Production and Storage*, McGraw-Hill, New York City (1990).
- Ahmed, T.: *Hydrocarbon Phase Behavior*, Gulf Publishing Co., Houston (1989).
- Pedersen, K.S., Fredenslund, A., and Thomassen, P.: *Properties of Oils and Natural Gases*, Gulf Publishing Co., Houston (1989).
- Whitson, C.H. and Brule, M.R.: *Phase Behavior*, Monograph Series, SPE, Richardson, Texas (2000) **20**.
- Klinkenberg, L.J.: "The Permeability of Porous Media to Liquids and Gases," *Drill. & Prod. Prac.*, API (1941) 200.
- Forchheimer, P.: "Wasserbewegung durch Boden," *Zeitz ver deutsch Ing.* (1901) **45**, 1731.
- Al-Hussainy, R., Ramey, H.J. Jr., and Crawford, P.B.: "The Flow of Real Gases Through Porous Media," *JPT* (May 1966) 637.
- Earlougher, R.C. Jr.: *Advances in Well Test Analysis*, Monograph Series, SPE, Dallas (1977) **5**.
- Beggs, H.D.: *Gas Production Operations*, OGI Publications, Tulsa (1984).

15. Rawlins, E.L. and Schellhardt, M.A.: *Backpressure Data on Natural Gas Wells and Their Application to Production Practices*, U.S. Bureau of Mines Monograph 7 (1936).
16. Matthews, C.S., Brons, F., and Hazebroek, P.: "A Method for Determination of Average Reservoir Pressure in a Bounded Reservoir," *Trans.*, AIME (1954) **201**, 182.
17. Poston, S.W. and Berg, R.R.: *Overpressured Gas Reservoirs*, SPE, Richardson, Texas (1997).
18. Payne, D.A.: "Material-Balance Calculations in Tight-Gas Reservoirs: The Pitfalls of p/z Plots and a More Accurate Technique," *SPE* (November 1996) 260.
19. Hammerlindl, D.J.: "Predicting Gas Reserves in Abnormally Pressured Reservoirs," paper SPE 3479 presented at the 1971 SPE Annual Meeting, New Orleans, 3–6 October.
20. Roach, R.H.: "Analyzing Geopressured Reservoirs—A Material Balance Technique," paper SPE 9968 available from SPE, Richardson, Texas (1981).
21. Prasad, R.K. and Rogers, L.A.: "Superpressured Gas Reservoirs: Case Studies and a Generalized Tank Model," paper SPE 16861 presented at the 1987 SPE Annual Technical Conference and Exhibition, Dallas, 27–30 September.
22. Bernard, W.J.: "Gulf Coast Geopressured Gas Reservoirs: Drive Mechanism and Performance Prediction," paper SPE 14362 presented at the 1985 SPE Annual Technical Conference and Exhibition, Las Vegas, Nevada, 22–25 September.
23. Fetkovich, M.J., Reese, D.E., and Whitson, C.H.: "Application of a General Material Balance for High-Pressure Gas Reservoirs," *Gas Reservoir Engineering*, Reprint Series, SPE, Richardson, Texas (1999) **52**, 48.
24. Ambastha, A.K.: "Evaluation of Material Balance Analysis Methods for Volumetric, Abnormally-Pressured Gas Reservoirs," *J. Cdn. Pet. Tech.* (October 1993) **32**, 8, 19.
25. Yale, D.P. *et al.*: "Application of Variable Formation Compressibility for Improved Reservoir Analysis," paper SPE 26647 presented at the 1993 SPE Annual Technical Conference and Exhibition, Houston, 3–6 October.
26. El Sharkawy, A.M.: "Analytical and Numerical Solutions for Estimating the Gas In-Place for Abnormal Pressure Reservoirs," paper SPE 29934 presented at the 1995 SPE International Meeting on Petroleum Engineering, Beijing, 14–17 November.
27. Gan, R.G. and Blasingame, T.A.: "A Semianalytical p/z Technique for the Analysis of Reservoir Performance From Abnormally Pressured Gas Reservoirs," paper SPE 71514 presented at the 2001 SPE Annual Technical Conference and Exhibition, New Orleans, 30 September–3 October.
28. Brinkman, F.P.: "Increased Gas Recovery From a Moderate Water Drive Reservoir," *JPT* (December 1981) 2475.
29. Moltz, A.K.: "Modeling a Repressured Waterdrive Gas Reservoir," paper SPE 22936 presented at the 1991 SPE Annual Technical Conference and Exhibition, Dallas, 6–9 October.
30. Cole, F.W., *Reservoir Engineering Manual*, Gulf Publishing Co., Houston (1969) 285.
31. Pletcher, J.L.: "Improvements to Reservoir Material-Balance Methods," *SPE* (February 2002) 49.
32. *Petroleum Conservation*, S.E. Buckley *et al.* (eds.), AIME, New York City (1951).
33. Geffen, T.M. *et al.*: "Efficiency of Gas Displacement From Porous Media by Liquid Flooding," *Trans.*, AIME (1952) **195**, 29.
34. Yuster, S.T.: "The Rehabilitation of Drowned Gas Wells," *Drill. & Prod. Prac.*, API (1946) 209–16.
35. Bennett, E.N. and Auvenshine, W.L.: "Dewatering of Gas Wells," *Drill. & Prod. Prac.*, API (1956) 224–30.
36. Dunning, H.N. and Eakin, J.L.: "Foaming Agents Are Low-Cost Treatments for Tired Gassers," *Oil and Gas J.* (2 February 1959) **57**, No. 6, 108.
37. Bates, G.O., Kilmer, J.W., and Shirley, H.T.: "Eight Years of Experience with Inert Gas Equipment," paper S7-PET-34 presented at the 1957 ASME Petroleum Mechanical Engineering Conference, September.
38. Barstow, W.F.: "Fourteen Years of Progress in Catalytic Treating of Exhaust Gas," paper SPE 4574 presented at the 1973 SPE Annual Meeting, Las Vegas, Nevada, 30 September–3 October.
39. Eckles, W.W. and Holden, W.W.: "Unique Enhanced Oil and Gas Recovery Project for Very High Pressure Wilcox Sands Uses Cryogenic Nitrogen and Methane Mixture," paper SPE 9415 presented at the 1980 SPE Annual Technical Conference and Exhibition, Dallas, 21–24 September.

40. Moses, P.L. and Wilson, K.: "Phase Equilibrium Considerations in Utilizing Nitrogen for Improved Recovery From Retrograde Condensate Reservoirs," paper SPE 7493 presented at the 1978 SPE Annual Technical Conference and Exhibition, Houston, 1–3 October.
41. Peterson, A.V.: "Optimal Recovery Experiments with N₂ and CO₂," *Pet. Eng. Intl.* (November 1978) 40.
42. *Physical Properties of Nitrogen for Use in Petroleum Reservoirs, Bull.*, Air Products and Chemical Inc., Allentown, Pennsylvania (1977).
43. Miller, M.G. and Lents, M.R.: "Performance of Bodcaw Reservoir, Cotton Valley Field Cycling Project, New Methods of Predicting Gas-Condensate Reservoir Performance Under Cycling Operations Compared to Field Data," *Drill. & Prod. Prac.*, API (1946) 128–49.
44. Brinkley, T.W.: "Calculation of Rate and Ultimate Recovery from Gas Condensate Reservoirs," paper IO28-G presented at the 1958 SPE Petroleum Conference on Production and Reservoir Engineering, Tulsa, 20–21 March.
45. *Proc.*, Ninth Oil Recovery Conference Symposium on Natural Gas in Texas, College Station, Texas (1956).

SI Metric Conversion Factors

°API	141.5/(131.5 + °API)	= g/cm ³
bbl ×	1.589 873	E - 01 = m ³
Btu ×	1.055 056	E + 00 = kJ
cp ×	1.0*	E - 03 = Pa·s
ft ×	3.048*	E - 01 = m
ft ³ ×	2.831 685	E - 02 = m ³
°F	(°F + 459.67)/1.8	= K
in. ³ ×	1.638 706	E + 01 = cm ³
lbm ×	4.535 924	E - 01 = kg
psi ×	6.894 757	E + 00 = kPa
psi ² ×	4.753 8	E + 01 = kPa ²

*Conversion factor is exact.

Chapter 11

Waterflooding

H.R. (Hal) Warner Jr., SPE, Warner Consulting Services

11.1 Introduction

This chapter concerns the use of water injection to increase the production from oil reservoirs, and the technologies that have been developed over the past 50+ years to evaluate, design, operate, and monitor such projects. Use of water to increase oil production is known as “secondary recovery” and typically follows “primary production,” which uses the reservoir’s natural energy (fluid and rock expansion, solution-gas drive, gravity drainage, and aquifer influx) to produce oil.

The principal reason for waterflooding an oil reservoir is to increase the oil-production rate and, ultimately, the oil recovery. This is accomplished by “voidage replacement”—injection of water to increase the reservoir pressure to its initial level and maintain it near that pressure. The water displaces oil from the pore spaces, but the efficiency of such displacement depends on many factors (e.g., oil viscosity and rock characteristics). In oil fields such as Wilmington (California, U.S.A.) and Ekofisk (North Sea), voidage replacement also has been used to mitigate additional surface subsidence. In these cases, the high porosity of the unconsolidated sandstones of the Wilmington oil field’s reservoirs and of the soft chalk reservoir rock in the Ekofisk oil field had compacted significantly when the reservoir pressure was drawn down during primary production.

This chapter discusses various aspects of waterflooding briefly, and it mainly covers the fundamental considerations involved when engineering, designing, operating, and monitoring a waterflood. Waterflooding technology is a large and well-covered topic in the literature, and the ability of this chapter to cover all aspects of these technologies is limited. Over the past 40 years, SPE has published three significant and in-depth books written by Craig,¹ Willhite,² and Rose *et al.*³ that address waterflooding technology.

SPE Reprint Series Vol. 2a⁴ contains the most significant SPE technical papers that describe waterflooding technology as of 1973. A recent search of the SPE eLibrary using keyword “waterflood” identified more than 5,500 SPE technical papers, including 650+ whose titles contain “waterflood.”

11.1.1 Historic Context. In the early days of the oil industry, saline water or brine frequently was produced from a well along with oil, and as the oil-production rate declined, the water-production rate often would increase. This water typically was disposed of by dumping it into

nearby streams or rivers. In the 1920s, the practice began of reinjecting the produced water into porous and permeable subsurface formations, including the reservoir interval from which the oil and water originally had come. By the 1930s, reinjection of produced water had become a common oilfield practice.

Reinjection of water was first done systematically in the Bradford oil field of Pennsylvania, U.S.A.⁵ There, the initial “circle-flood” approach was replaced by a “line flood,” in which two rows of producing wells were staggered on both sides of an equally spaced row of water-injection wells. In the 1920s, besides the line flood, a “five-spot” well layout was used (so named because its pattern is like that of the five spots on a die).

Much of waterflooding’s technology and common practice developed in the U.S. between 1940 and 1970. By the mid-1940s, the onshore U.S. oil industry was maturing and primary production from many of its reservoirs had declined significantly, whereas most reservoirs elsewhere in the world were in the early stages of primary production. Also, in the U.S., thousands of wells had been drilled that were closely spaced, so that the effects of water injection were more obvious and so were more quickly understandable.

In addition to the need to dispose of saline water that was produced along with the oil, several other factors made waterflooding a logical and economical method for increasing recovery from oil fields. Very early on, it was recognized that in most reservoirs, only a small percentage of the original oil in place (OOIP) was being recovered during the primary-production period because of depletion of the reservoirs’ natural energy. Additional recovery methods were needed to produce the large quantity of oil that remained. Water injection’s early success in lengthening the oil-production period by years made waterflooding the natural step after primary production to recover additional oil from reservoirs whose oil-production rate had declined to very low levels.

Other key factors that drove waterflooding’s development and increasing use were that water is inexpensive; that water generally is readily available in large quantities from nearby streams, rivers, or oceans, or from wells drilled into shallower or deeper subsurface aquifers; and that water injection effectively made production wells that were near the water-injection wells flow or be pumped at higher rates because of the increased reservoir pressure. Concurrently, the scientific reasons behind waterflooding’s success were identified (i.e., that water has viscosity, density, and wetting properties, compared to oil, that affect how efficiently it will displace various oils from reservoir rock).

By the 1970s, most onshore oil fields in the U.S., USSR, and China, for which waterflooding was the logical recovery process, were being produced by use of this technology in various well-pattern arrangements. Some U.S. offshore oil fields and oil fields elsewhere in the world were receiving water injection as deemed appropriate by their owners and operators. Since then, many large-scale water-injection projects have been applied to oil reservoirs in locations ranging from far offshore in the North Sea to the Arctic regions to desert areas.

11.1.2 Chapter Topics. This chapter presents the subject of waterflooding in nine sections and follows the logic sequence used by Willhite²:

- Microscopic efficiency of immiscible displacement.
- Macroscopic displacement efficiency of a linear waterflood.
- Reservoir-geology considerations in the design and operation of waterfloods.
- Immiscible displacement in two dimensions—areal.
- Vertical displacement in linear and areal models.
- Waterflood design.
- Waterflood monitoring.
- Field case studies: waterflood examples.
- Summary and conclusions.

The sections begin with a discussion of unit-displacement efficiency, which is how water displaces oil from a porous and permeable reservoir rock on a microscopic scale. This is the level of analysis that is applied when water-/oil-flow measurements are made on small core-plug samples in a laboratory. Calculations for determining how well waterflooding will work on a reservoir scale must include the effects of geology, gravity, and geometry (vertical, areal, and well-spacing/-pattern arrangement). The formula for overall waterflood oil-recovery efficiency E_R might be simply stated as the product of three independent terms:

$$E_R = E_D E_I E_A, \dots\dots\dots (11.1)$$

where E_D = the unit-displacement efficiency, E_I = the vertical-displacement efficiency, and E_A = the areal-displacement efficiency. Of course, assuming independence of these three factors is not valid for real oil reservoirs.

Also, a waterflood is a dynamic process that lasts for several decades; hence, after the project has been initiated, there are opportunities to modify the original waterflood design and operating guidelines on the basis of analysis of the actual field production data. This is why real-time monitoring of waterflood performance is required, both at the injection wells and at the production wells.

Throughout this chapter, keep in mind that the most important aspect of evaluating a field waterflooding project is understanding the reservoir rocks. This understanding begins with knowing the depositional environment at the pore and reservoir levels and possibly also several levels in between. Second, the diagenetic history of the reservoir rocks must be ascertained. Then, the structure and faulting of the reservoir must be determined to understand the interconnectivities among the various parts of the reservoir, particularly the injector/producer connectivity. Finally, the water/oil/rock characteristics need to be understood because they control wettability, residual oil saturation to waterflooding, and the oil relative permeability at higher water saturations. Because of these needs, there always should be a developmental geologist on the waterflood-evaluation team.

This chapter does not include a separate section on oil properties and their impact on waterflooding recovery efficiency, but oil properties are important to technical and economic success and are discussed as appropriate throughout this chapter. The key oil properties are viscosity and density at reservoir conditions. In a porous medium, the mobility of a fluid is defined as its endpoint relative permeability divided by its viscosity; hence, a fluid with a low viscosity (≤ 1 cp) has a high mobility unless its relative permeability is very low. Similarly, a low-API crude oil ($\leq 20^\circ\text{API}$) has a high viscosity and a very low mobility unless it is heated to high temperatures. Because water's viscosity at reservoir temperatures generally is much lower than or, at best, equal to that of the reservoir oil, the water-/oil-viscosity ratio is generally much greater than 1:1. As discussed in some detail later in this chapter, the water-/oil-mobility ratio is a key parameter in determining the efficiency of the water/oil displacement process, with the recovery efficiency increasing as the water-/oil-mobility ratio decreases.

11.1.3 Topics Covered Elsewhere in This *Handbook*. Topics that concern typical water-injection operations but that are not discussed in this chapter are (1) aquifer or bottomwater drives with water injected into underlying aquifer intervals; (2) use of numerical reservoir simulators to analyze waterflood performance; and (3) enhanced-oil-recovery (EOR) methods that involve either continuous or alternating water injection. Discussions of these and other aspects of waterflooding technologies can be found elsewhere in this *Handbook*, including in the numerical-reservoir-simulation chapter in the Reservoir Engineering and Petrophysics volume, in the General Engineering volume chapters about crude-oil properties and water properties, in the Production Operations Engineering volume chapters about handling of oil and water production

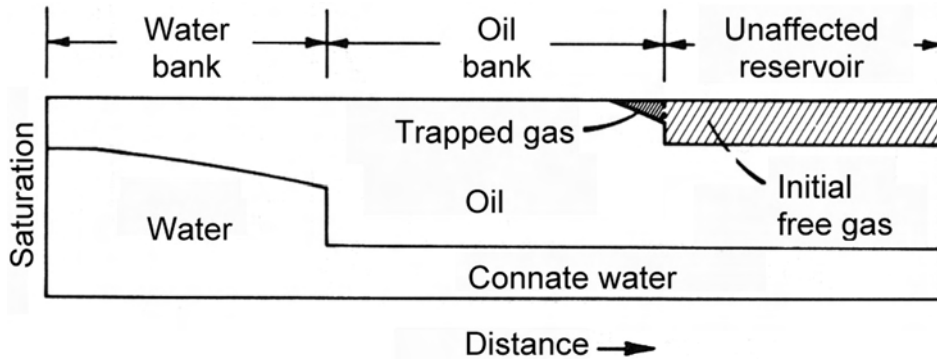


Fig. 11.1—Saturation profile during a waterflood.¹

during waterflooding operations, and in the Facilities and Construction Engineering volume chapters about surface facilities that are required for waterflood operations.

11.1.4 Limitations of Waterflood Technology. Waterflooding can increase the volume of oil recovered from a reservoir; however, it is not always the best technology to use and it can have complicating factors. When evaluating how best to produce a particular oil reservoir, a petroleum engineer should include waterflooding in the options that are analyzed, both technically and economically. Those evaluations should include such potentially complicating factors as compatibility of the planned injected water with the reservoir's connate water; interaction of the injected water with the reservoir rock (clay sensitivities, rock dissolution, or generally weakening the rock framework); injection-water treatment to remove oxygen, bacteria, and undesirable chemicals; and the challenges involved in separating and handling the produced water that has trace oil content, naturally occurring radioactive materials (NORMs), and various scale-forming minerals.

11.2 Microscopic Efficiency of Immiscible Displacement

This section discusses the conceptual aspects of the displacement of oil by water in reservoir rocks. Fig. 11.1 is a schematic diagram of the water/oil displacement process. At the pore level (i.e., where the water and oil phases interact immiscibly when moving from one set of pores to the next), wettability and pore geometry are the two key considerations. The interplay between wettability and pore geometry in a reservoir rock is what is represented by the laboratory-determined capillary pressure curves and water/oil relative permeability curves that engineers use when making OOIP and fluid-flow calculations. The sections below discuss these basic concepts and their implications for initial water- and oil-saturation distribution, for relative permeability, and for how initial gas saturation will affect water/oil flow behavior.

11.2.1 Wettability. Wettability is defined in terms of the interaction of two immiscible phases, such as oil and water, and a solid surface, such as that of the pores of a reservoir rock. For understanding wettability concepts and for simple laboratory determinations, the solid surface is taken as a smooth flat surface. Fig. 11.2 illustrates two styles of wettability: water-wet and oil-wet. Eq. 11.2 describes the force relationship that is in balance for the drop of water that is on the solid surface and is surrounded by oil. The interfacial tension (IFT) between the oil and water phases varies depending on the compositions of the phases but generally is relatively high, in the 10- to 30-dyne/cm range. The contact angle θ is used to define which fluid phase is more wetting—for low contact angles, the water phase is more wetting, whereas for high contact angles, the oil phase is more wetting.

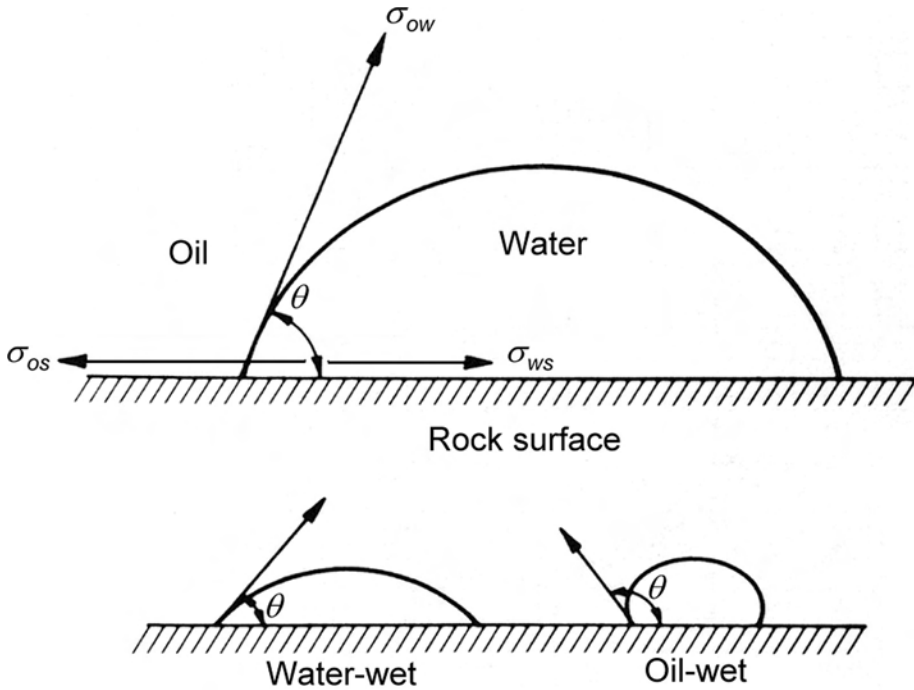


Fig. 11.2—Wettability of oil/water/solid system.²

$$\sigma_{os} - \sigma_{ws} = \sigma_{ow} \cos \theta, \dots\dots\dots (11.2)$$

where σ_{os} = the IFT between the oil and solid phases, σ_{ws} = the IFT between the water and solid phases, and σ_{ow} = the IFT between the oil and water phases.

The particular contact angle depends on many variables, including the composition of the crude oil and the amount of gas in solution; the salinity and pH of the connate brine; the mineralogy of the rock surfaces; and the salinity and pH of the injected water that is used for waterflooding. The concentration of surface-active components (e.g., asphaltenes) that are in the crude oil and that can adsorb on the rock surfaces affects wettability.

Reservoir rocks typically are described as being water-wet, oil-wet, or intermediate-wet. A water-wet rock surface is one that has a strong preference to be coated, or “wetted,” by the water phase, so that there will be a continuous water phase on the rock surfaces. Oil-wet rocks prefer to be coated with oil instead of water. Strongly oil-wet rocks have been created for laboratory studies but, as discussed below, are unlikely to exist in real reservoirs. Intermediate-wet reservoir rocks have been found in several oil reservoirs. The term “dalmatian wetting” describes reservoir rocks that have both oil-wet and water-wet surfaces. Fig. 11.3 illustrates two styles of intermediate-wetting.

Two types of laboratory measurements commonly are used to estimate wettability. First, the crude-oil/brine IFT values can be measured on smooth rock surfaces of various mineralogies. Second, Amott tests can be run on the reservoir rock to determine the extents to which it imbibes oil and brine. When running the Amott tests, it is critical to initialize the core plugs as close to original reservoir conditions as possible either by using well-preserved core samples or by aging the core plugs in the presence of reservoir crude oil. High-quality water/oil capillary-pressure (P_c) and water/oil relative permeability (k_{rwo}) data, both of which are strongly affected

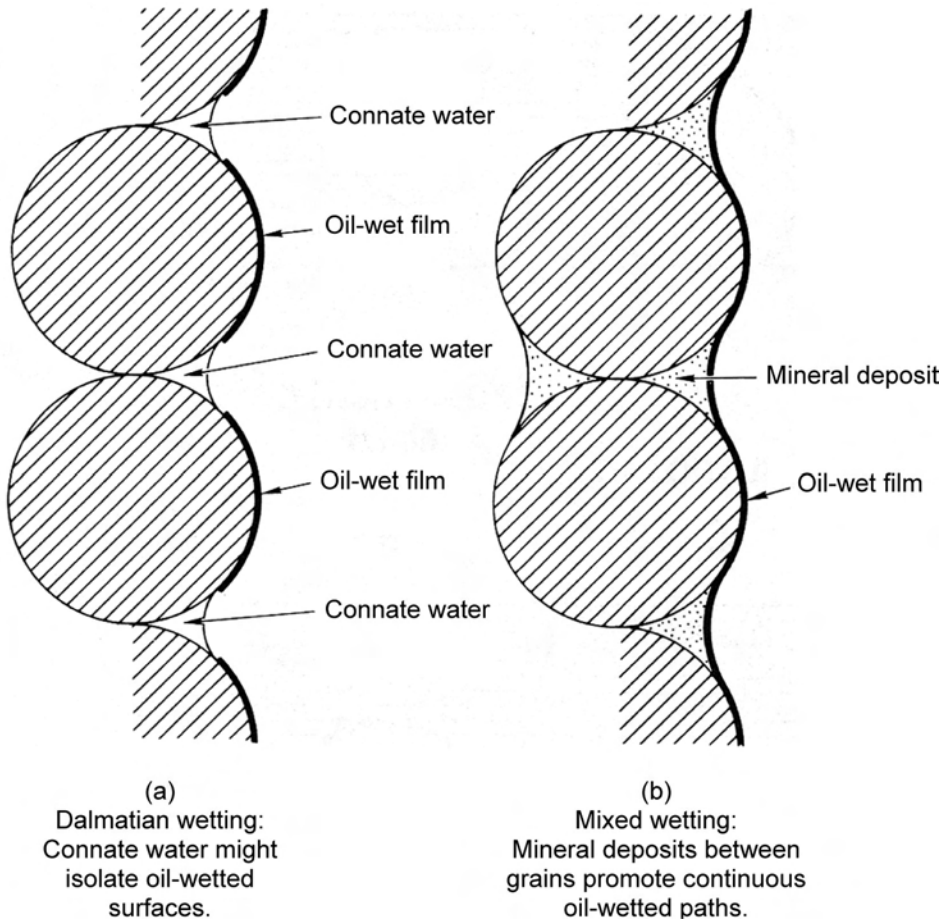


Fig. 11.3—Relationship of mineralogy to wetting conditions: (a) dalmatian wetting and (b) mixed wetting.²

by rock wettability, are needed as input to waterflood calculations, whether using simple engineering methods or complex numerical reservoir simulators.

11.2.2 Pore Geometry. The pore geometry for any reservoir rock is the result of its depositional and diagenetic history. The depositional environment determines a rock's grain size and sorting. Post-depositional diagenetic changes caused by various types of cementation, leaching, and clay alteration will impact a rock's pore characteristics whether the rock is primarily silica or carbonate. A chapter in the General Engineering volume of this *Handbook* discusses many of these factors and how they affect the single-phase permeability of a reservoir rock.

Figs. 11.4 and 11.5 show photomicrographs and k_{rwo} curves for a sandstone with large, well-connected pores and for one with small, well-connected pores, respectively. These illustrate just one of many possible differences in pore geometry. Pore distributions in carbonate rocks often are more complicated because of vug networks and fractures. Also, there are many scales of pore-geometry heterogeneities; a core plug has one scale of pore-size variation, but other important variations are found at each higher scale.

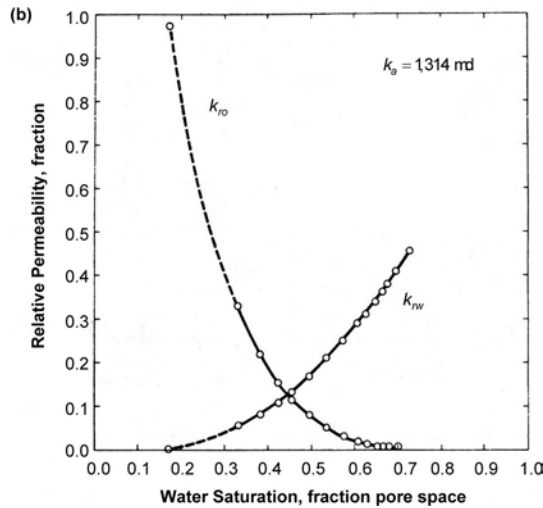
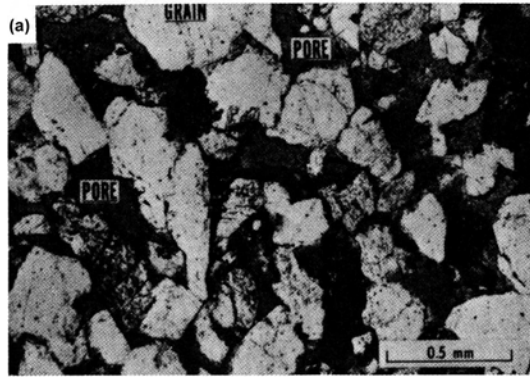


Fig. 11.4—Photomicrograph (a) and water/oil relative permeability curve (b) for a sandstone with large, well-connected pores. k_a = air permeability, md; k_{ro} = relative permeability to oil, fraction; and k_{rw} = relative permeability to water, fraction.²

11.2.3 Capillary Pressure. Capillary-pressure concepts are discussed in detail in a chapter of the General Engineering volume of this *Handbook*. This chapter considers the characteristics of and differences between the drainage and imbibition capillary-pressure/water-saturation (P_c/S_w) curves. Capillary pressure affects waterflood performance and engineering calculations because the extent to which the water/oil flood front is vertically and horizontally “smeared out” during the waterflood is controlled by the P_c/S_w imbibition curve.

Reservoir rocks are considered to be water-wet initially because all reservoir rocks were deposited in water-filled environments or were immersed in water soon after deposition, when their overlying sediments were deposited. The drainage P_c/S_w curve describes the drainage process, or the P_c/S_w relationship while the nonwetting-fluid phase (oil) displaces the wetting-fluid phase (brine) from various parts of the pore system, thus decreasing the wetting-phase saturation. If during the displacement process the process is reversed and the wetting-phase saturation increases, it is known as imbibition (the imbibing of the wetting phase).

Fig. 11.6 shows the drainage and imbibition P_c/S_w characteristics of a strongly water-wet rock. The minimum wetting or water saturation from the drainage process is termed the con-

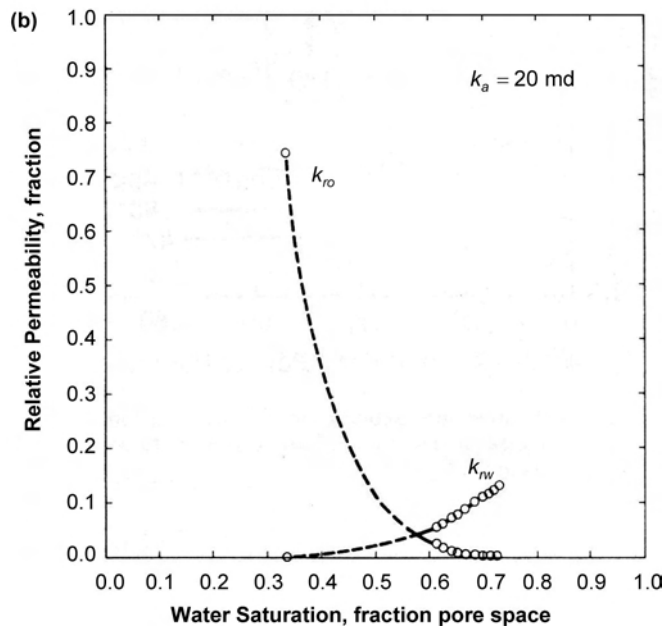
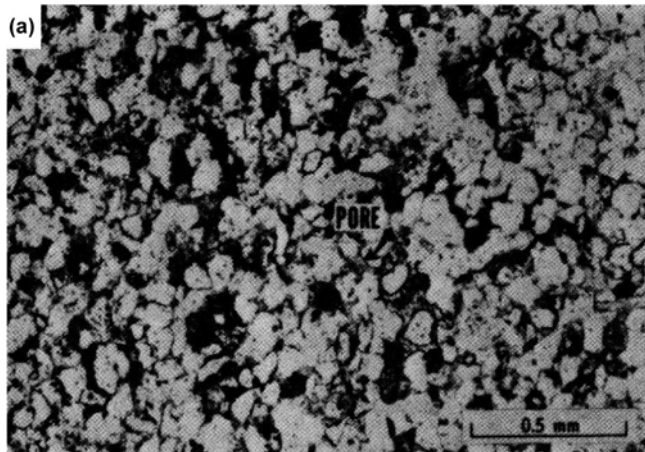


Fig. 11.5—Photomicrograph (a) and water/oil relative permeability curve (b) for a sandstone with small, well-connected pores.²

nate (or irreducible) water saturation. The maximum water saturation from the imbibition process defines the minimum nonwetting-phase saturation, or (for waterflooding considerations) the residual oil saturation to waterflooding S_{orw} . Figs. 11.7 and 11.8 show the drainage and imbibition P_c/S_w curves from the laboratory tests of an oil-wet rock and a rock with intermediate wettability, respectively. Fig. 11.8 includes both the spontaneous (number 2 on curve) and the forced (number 3 on curve) portions of the imbibition curve. Spontaneous imbibition occurs without any pressure being applied to the test apparatus, whereas obtaining the forced imbibition portion of the curve requires an external pressure to be applied. Note that $P_c = 0$ does not define the S_{orw} .

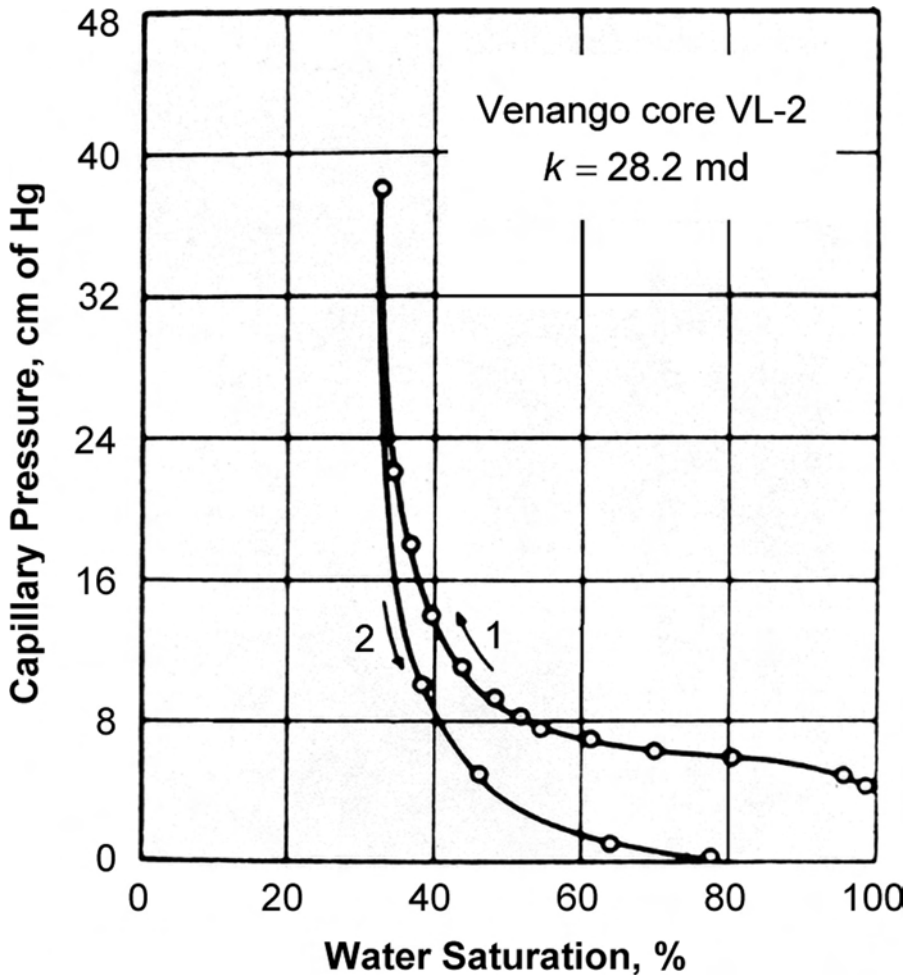


Fig. 11.6—Capillary pressure characteristics for a strongly water-wet rock. Curve 1 represents drainage, and Curve 2 represents imbibition.²

11.2.4 Initial Water-/Oil-Saturation Distribution. An oil field's initial water-/oil-saturation distribution depends on its hydrocarbon history and has a significant effect on its waterflooding potential. The pore system in a reservoir rock contains a very large number of pore bodies whose filling by oil is controlled by the diameters of the pore throats that link them.

During the oil-filling process, the oil first enters through the largest pore throats, and all other parts of the pore system remain filled with connate brine. As more oil enters the reservoir trap, the oil column lengthens downward. Just above the oil/water contact, only the pores that are accessible from the largest pore throats fill with oil. At the top of the oil column, where the capillary pressure is greatest, not only the largest pores are oil-filled, but also some that have smaller pore throats. The very fine pore spaces remain filled with connate brine.

This process continues until the oil column reaches its maximum length. This whole process is the drainage cycle of the P_c/S_w curves. At this point in the process, oil is filling the largest pores and water is filling the smallest pores; however, the P_c/S_w drainage curve governs the percentage of each. Connate brine will remain as films on the surfaces of the largest

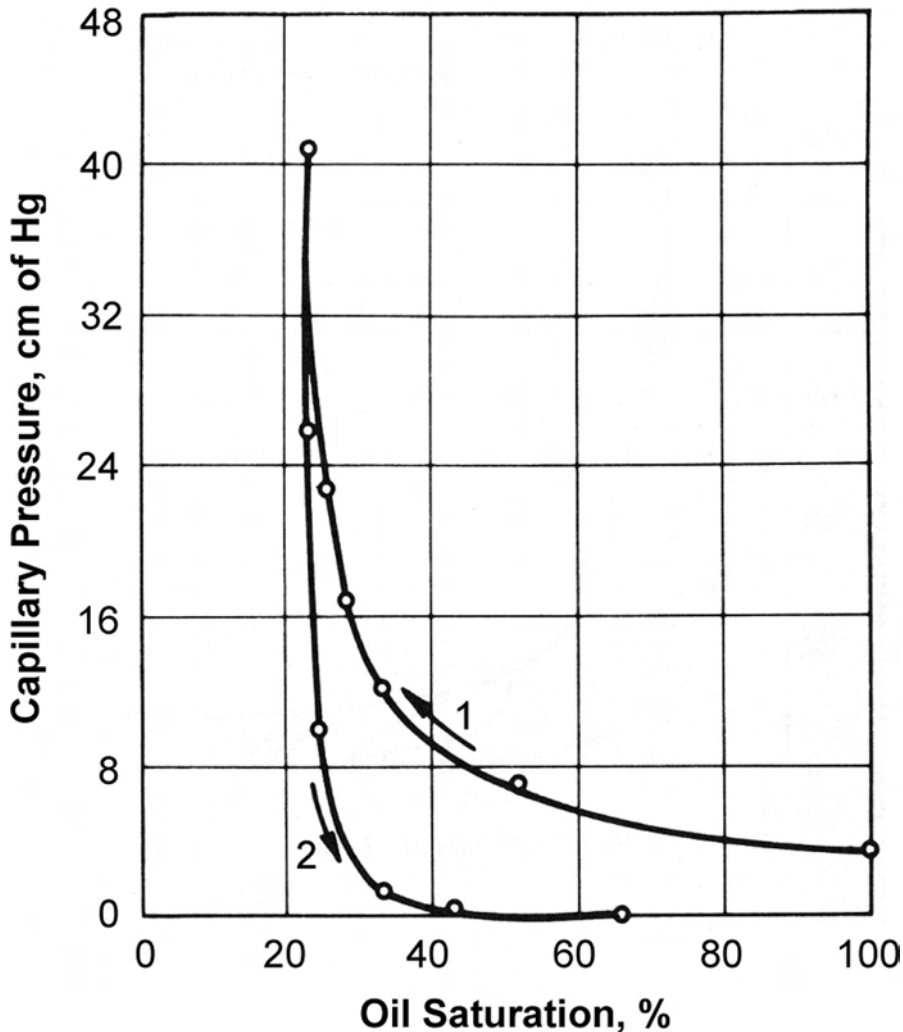


Fig. 11.7—Water/oil capillary pressure characteristics for Tensleep Sandstone oil-wet rock. Curve 1 represents drainage, and Curve 2 represents imbibition.²

pores, but surface-active components of the crude oil might adsorb on some of the pore surfaces, rendering them oil-wet. Hence, the overall system can have mixed-wet characteristics.

There are oil fields that, although initially filled through a drainage process, when discovered were on the imbibition cycle because of a complicated hydrocarbon or structural history. Portions of several west Texas San Andres carbonate reservoirs and the Prudhoe Bay field of Alaska are examples of such oil fields.

This original water-/oil-saturation distribution is important to understand for waterflooding because it controls the efficiency of the waterflood in portions of the reservoir. It also relates directly to the residual oil saturation that can be achieved at the end of a waterflood.

11.2.5 Relative Permeability. Relative permeability (k_r) concepts are discussed in detail in a chapter of the General Engineering volume of this *Handbook*. For the purposes of this chapter, their important aspect is the characteristics of imbibition oil/water k_r curves because these gov-

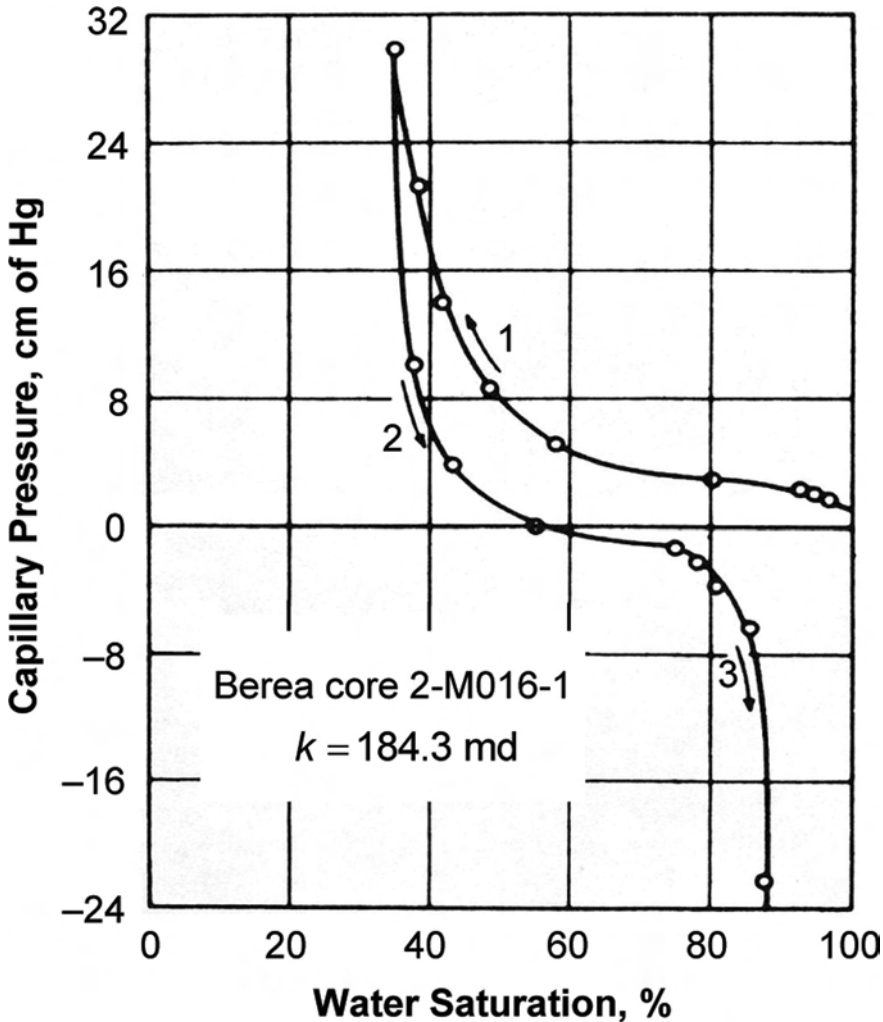


Fig. 11.8—Water/oil capillary-pressure characteristics for intermediate wettability. Curve 1 represents drainage, Curve 2 represents spontaneous imbibition, and Curve 3 represents forced imbibition.²

ern the nature and efficiency of the waterflood displacement and how much of the OOIP will be recovered before the waterflood economic limit is reached.

The shapes of the imbibition water/oil k_r curves depend on pore geometry and wettability. As noted earlier, Figs. 11.4 and 11.5 show the differences between these curves for a sandstone with large, well-connected pores and one with small, well-connected pores. The k_{rw} is greatly reduced for the sandstone with small pores at all saturation levels. Fig. 11.9 shows the effect of wettability, as measured by the U.S. Bureau of Mines (USBM) Amott wettability index, on the water/oil k_r curves. As is expected for a change from water-wet to oil-wet in such laboratory tests, the water k_r curve rises with increasing oil-wetness and the oil k_r curve decreases.

Most importantly, laboratory-determined water/oil k_r data should be obtained at the best approximation of reservoir conditions. Salathiel describes the importance of this to actual field oil/water displacement.⁶ Fig. 11.10 shows the results of Salathiel's laboratory experiments that relate to the East Texas oil field. These curves show that the oil relative permeability for water-wet conditions is significantly different than for mixed-wet conditions. In water-wet conditions,

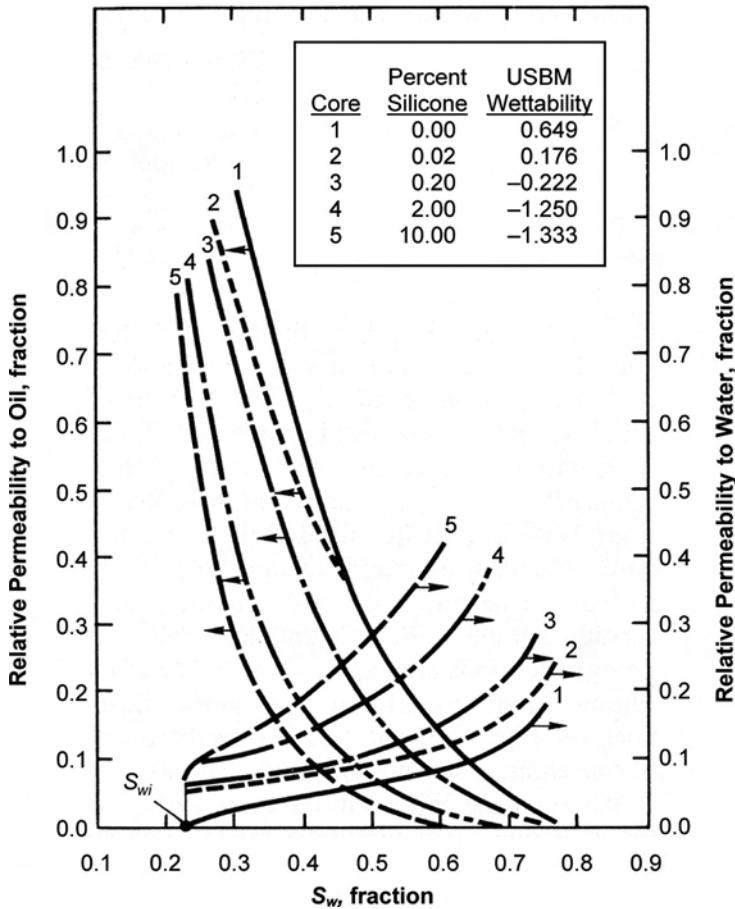


Fig. 11.9—Oil and water relative permeabilities for Squirrel-sandstone cores for water-wet and oil-wet conditions.²

the oil phase becomes discontinuous and loses its mobility quickly. In mixed-wet conditions, the oil maintains phase continuity by means of the oil-wetted rock surfaces and slowly drains to significantly lower oil saturations. The comparison of the laboratory results to the actual field production data and the residual-oil-saturation-pressure core data showed that the reservoir had mixed-wettability, yielding S_{orw} values of < 10% PV in many portions of the reservoir.

11.2.6 Residual Oil Saturation. For waterflooding, the two most important numbers for a reservoir rock are the connate-water saturation S_{wc} and the S_{orw} . The S_{wc} determines how much oil initially is in each unit volume of rock when the reservoir is discovered. The S_{orw} is how much of the OOIP will remain in rock that will be well swept by injected-water volumes. Assuming that the oil-formation-volume factor is the same at the beginning and the end of the waterflood, the equation for the unit-displacement efficiency is:

$$E_D = 1 - \frac{S_{orw}}{S_{oi}}, \dots\dots\dots (11.3)$$

where S_{oi} = initial oil saturation ($1 - S_{wc}$).

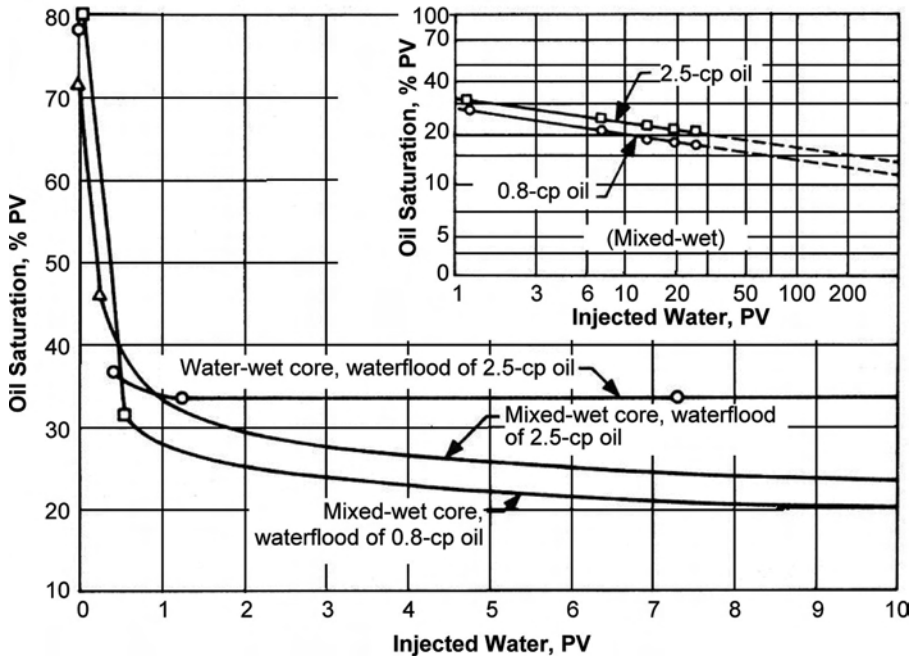


Fig. 11.10—Comparison of waterflood behavior for mixed-wet and water-wet cores. Insert shows extension of mixed-wet-core flooding data.² PV = pore volume.

Rock Sample	Permeability, md	Porosity, % BV	S_w at Time of “Contact,” % PV	S_o After 25 PV of Waterflooding	
				Water-Wet	Mixed-Wet
Boise (sandstone)	1,094	29.3	13.5	33.5	20.5
Upper Austin (sandstone)	596	28.0	20.0	30.0	22.9
Woodbine Outcrop (sandstone)	690	33.0	17.0	27.3	30.7
Upper Noodle (limestone)	620	21.2	18.9	40.5	28.1
Lissie (sandstone)	536	21.9	7.2	42.5	29.1

The S_{orw} is the endpoint of the water/oil imbibition k_{ro} curve, which was discussed above; however, for simple waterflood calculations this value is the most critical one. Table 11.1 compares Salathiel’s S_{orw} results for the water-wet conditions to those for the mixed-wet conditions.⁶ The S_{orw} for the mixed-wet samples generally was 10% PV lower than for the water-wet samples. In the water-wet conditions, more of the oil phase gets “snapped off” and therefore trapped and immobilized as isolated oil globules by the increasing water saturation. Jerauld and Rathmell⁷ found similar results for the Prudhoe Bay field.

S_{orw} can be measured several ways. It can be determined as part of all relative permeability laboratory studies. Historically, short core-plug “floodpot” tests have been run in the laboratory, and only the rock sample’s porosity, absolute air permeability, S_{wc} , S_{orw} , and permeability at the two endpoint saturations have been reported. It is important to ensure that these laboratory tests are conducted long enough for the displacement to be taken to its true endpoint. They can

be performed either as displacement tests or by using a centrifuge to measure these data. Displacement tests historically have been used, but because of improvements in centrifuge technology, the centrifuge approach is becoming more common. Usually, floodpot-test times are inadequate to reach a true S_{orw} . Imbibition capillary pressure measurements obtain more-reliable values for water-wet porous media.

Generally, S_{orw} is inversely related to S_{wi} . This can be understood in terms of the pore spaces that become filled with water and oil. While the S_{wi} decreases (or the S_{oi} increases), the oil phase occupies more of the pores and fills more of the smaller pore spaces. When water displaces the oil, the advancing water front traps more of the oil, especially if the rock is water-wet.

The performance of a waterflood depends on the impact of viscous and capillary forces on S_{orw} and k_r . At reservoir flow rates, the viscous forces do not vary enough to make a significant difference in k_r and S_{orw} ; however, under laboratory conditions, viscous and capillary forces are major considerations because short core-plug displacement tests actually measure pressure drops and fluid-production volumes as a function of time that include large capillary end effects. These data must be entered into interpretative calculations to derive the water/oil P_c/S_w and k_r curves that are used later in field waterflood calculations. The laboratory personnel must choose what length of core plugs to test, what flow rates and pressure drops to apply, whether to make the measurements at steady-state or unsteady-state conditions, and how to interpret these data.

11.2.7 Initial Gas Saturation S_{gi} . In many oil reservoirs, a free-gas saturation formed during the early production period because the waterflood was not initiated before the reservoir pressure had dropped through the oil bubblepoint pressure. For many years, the effect of this gas saturation on S_{orw} has been a subject of considerable technical interest. **Fig. 11.11** summarizes the experimental results of several investigators and shows the impact of S_{gi} on S_{orw} for water-wet rocks. The S_{orw} decreased as S_{gi} increased. Because gas is the most nonwetting of the fluid phases, the residual gas phase occupies the center of the pore bodies and hence can reduce the volume of oil that is trapped.

11.2.8 Other Considerations. Historically, most laboratory tests have been run at surface temperature and pressure conditions using dead crude oils and constant brine salinity when measuring water/oil P_c/S_w and k_r data. Over the past decade, U.S. researchers at the U. of Wyoming and the U. of Texas have published papers concerning studies of the effect of temperature, salinity, and oil composition on wettability and waterflood oil recovery.^{8,9} Those studies show that oil recovery increases with higher temperature, and generally also with variation in salinity.

11.2.9 Mobility Ratio. The mobility of a phase (Eq. 11.4) is defined as its relative permeability divided by its viscosity. Hence, mobility combines a rock property (relative permeability) with a fluid property (fluid viscosity). The water/oil relative permeability is assumed to depend only on the saturations of the two fluid phases.

$$\lambda_i = \left(\frac{k_i}{\mu_i} \right), \dots\dots\dots (11.4)$$

where λ_i = mobility of fluid phase i , k_i = relative permeability of fluid phase i , and μ_i = viscosity of fluid phase i . Mobility relates to the amount of resistance to flow through a reservoir rock that a fluid has at a given saturation of that fluid. Because viscosity is in the denominator

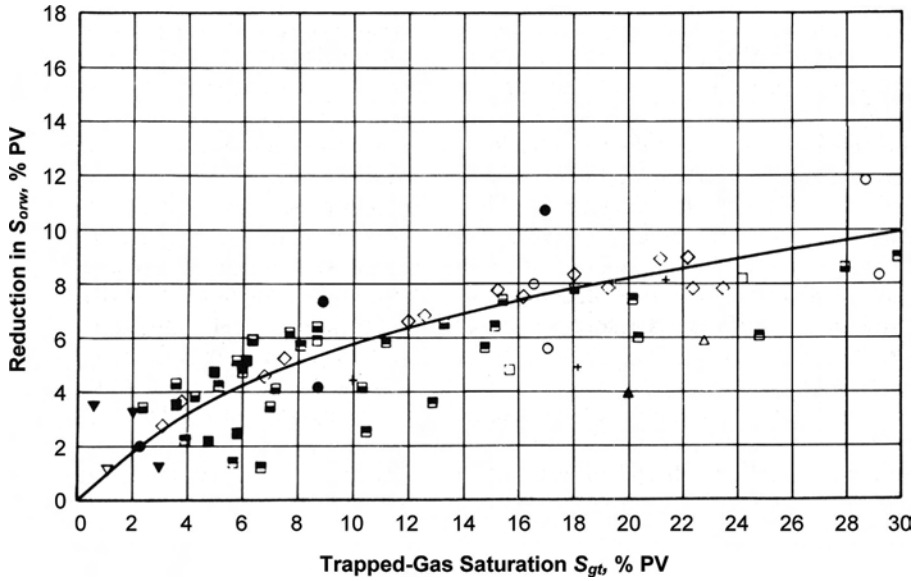


Fig. 11.11—Effect of trapped-gas saturation on waterflood oil recovery for preferentially water-wet rocks.²

of this equation, low-viscosity fluids generally have high mobility and high-viscosity fluids generally have low mobility.

The mobility ratio M generally is defined as the mobility of the displacing phase (for waterflooding, water) divided by the mobility of the displaced phase (oil). Eqs. 11.5 and 11.6 present two forms of the mobility-ratio equation:

$$M = \frac{k_{rw} \mu_o}{\mu_w k_{ro}}, \dots\dots\dots (11.5)$$

where μ_w = viscosity of water, cp; μ_o = viscosity of oil, cp; k_{rw} = relative permeability to water; and k_{ro} = relative permeability to oil.

The mobility ratio also can be expressed as the product of the two fluids' relative permeability and viscosity ratios.

$$M = \frac{k_{rw} \mu_o}{k_{ro} \mu_w} \dots\dots\dots (11.6)$$

Mobility ratios are considered to be either “favorable” or “unfavorable.” A favorable mobility ratio is a low value (≤ 1); this means that the displaced phase (oil) has a higher mobility than does the displacing phase (water). An unfavorable mobility ratio (> 1) is the other way around. In practical terms, a favorable mobility ratio means that the displaced oil phase can move more quickly through the reservoir rock than can the displacing water phase.

For simple waterflooding calculations, the mobility ratio is calculated at the endpoint relative permeability values for the two phases. Hence, the equation to be used for the waterflood mobility ratio is:

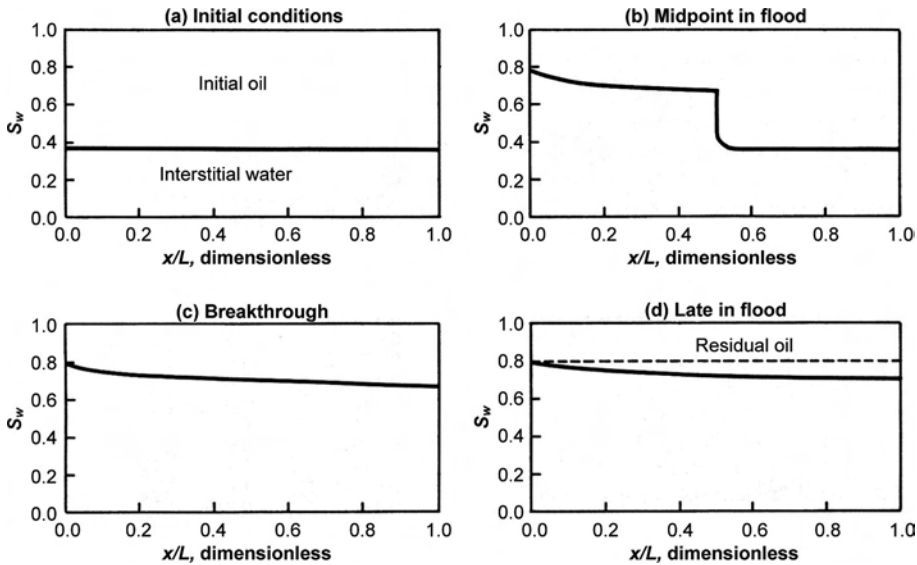


Fig. 11.12—Saturation distribution during different stages of a waterflood.² L = length, ft; x = x -direction length, ft; and x/L is dimensionless and varies from 0 to 1.

$$M = \frac{k_{rwe} \mu_o}{k_{roe} \mu_w}, \dots\dots\dots (11.7)$$

where k_{rwe} = relative permeability to water at the endpoint (S_{orw}) and k_{roe} = relative permeability to oil at the endpoint (S_{wi}). This mobility ratio assumes a plug-like displacement between the oil phase at connate-water saturation before the flood front and the water phase at residual oil saturation behind the flood front.

Because, in most reservoir situations, water’s viscosity is lower than oil’s, the viscosity ratio is unfavorable for water to displace oil efficiently; however, as Figs. 11.4, 11.5, and 11.9 show, the relative permeability of water at residual oil saturation is lower by a factor of two to eight than that of oil at connate-water saturation. Hence, for many reservoirs, the mobility ratio is close to unity (favorable) if the oil viscosity is greater than the water viscosity at reservoir conditions only by a factor of five.

11.3 Macroscopic Displacement Efficiency of a Linear Waterflood

This section discusses the mathematical aspects of water/oil displacement for homogeneous linear systems. The presentation here is brief and does not include the intermediate steps of the mathematical derivation of the key equations. The details of these mathematical derivations are available in Willhite.²

The displacement of oil by water from a porous and permeable rock is an unsteady-state process because the saturations change with time and distance from the injection point (see schematic diagram of Fig. 11.1). These saturation changes cause the relative permeability values and pressures to change as a function of time at each position in the rock. Fig. 11.12 illustrates the various stages of an oil/water displacement process in a homogeneous linear system.

The mathematical derivation of fluid-flow equations for porous media begins with the simple concept of a material-balance calculation: accumulation equals fluid in minus fluid out. This equation is written for the whole system and for each of the phases: water, oil, and gas. Eqs. 11.8 and 11.9 are the equations for the conservation of mass for a water/oil homogeneous linear system:

$$-\frac{\partial}{\partial x}(\rho_o u_{ox}) = \frac{\partial}{\partial t}(\rho_o S_o \phi) \dots\dots\dots (11.8)$$

and

$$-\frac{\partial}{\partial x}(\rho_w u_{wx}) = \frac{\partial}{\partial t}(\rho_w S_w \phi), \dots\dots\dots (11.9)$$

where x = position in x -coordinate system, ft; ρ_o = oil density, lbm/ft³ or g/cm³; u_{ox} = oil velocity in the x direction, ft/day; t = time, days; S_o = oil saturation, fraction PV; ϕ = porosity, fraction BV; ρ_w = water density, lbm/ft³ or g/cm³; u_{wx} = water velocity in the x direction, ft/day; and S_w = water saturation, fraction.

Assuming that the oil and water are incompressible and that the porosity is constant, these equations become:

$$-\frac{\partial q_o}{\partial x} = A\phi \frac{\partial S_o}{\partial t} \dots\dots\dots (11.10)$$

and

$$-\frac{\partial q_w}{\partial x} = A\phi \frac{\partial S_w}{\partial t}, \dots\dots\dots (11.11)$$

where q_o = oil-production rate, B/D; A = cross-sectional area available for flow, ft²; and q_w = water-production rate, B/D.

Next, the equations for fractional flow of oil and water are incorporated into these equations. The three fractional-flow equations are:

$$f_o = \frac{q_o}{q_t} = \frac{q_o}{q_w + q_o}, \dots\dots\dots (11.12)$$

$$f_w = \frac{q_w}{q_t} = \frac{q_w}{q_w + q_o}, \dots\dots\dots (11.13)$$

and

$$f_o + f_w = 1.0, \dots\dots\dots (11.14)$$

where f_o = fractional flow of oil; q_t = the total production rate, B/D; and f_w = fractional flow of water.

Substituting Eq. 11.13 into Eq. 11.11 yields:

$$-\frac{\partial f_w}{\partial x} = \frac{\phi A}{q_t} \frac{\partial S_w}{\partial t} \dots\dots\dots (11.15)$$

11.3.1 Buckley-Leverett Solution. Further mathematical manipulation of these equations obtains the Buckley-Leverett equation (Eq. 11.16), or frontal-advance equation. To derive this

equation, it is assumed that the fractional flow of water is a function only of the water saturation and that there is no mass transfer between the oil and water phases.

$$\left(\frac{dx}{dt}\right)_{S_w} = \frac{q_t}{\phi A} \left(\frac{\partial f_w}{\partial S_w}\right)_t \dots\dots\dots (11.16)$$

This equation shows that in a linear displacement of water displacing oil, each water saturation moves through the rock at a velocity that is computed from the derivative of the fractional flow with respect to water saturation.

The general form of the fractional-flow equation for water is:

$$f_w = \frac{1}{1 + \left(\frac{k_o}{k_w}\right)\left(\frac{\mu_w}{\mu_o}\right)} + \frac{\frac{k_o A}{\mu_o q_t} \left[\frac{\partial P_c}{\partial x} + (\rho_o - \rho_w)g \sin \alpha \right]}{1 + \left(\frac{k_o}{k_w}\right)\left(\frac{\mu_w}{\mu_o}\right)} \dots\dots\dots (11.17)$$

where k_o = permeability to oil, darcies; g = gravity constant; α = reservoir dip angle, degrees; and k_w = permeability to water, darcies. This equation includes terms for capillary pressure variation (as a function of saturation) in the linear direction and for the linear system possibly dipping at angle α .

Assuming that the gradient in P_c with position is very small and that the linear system is horizontal reduces Eq. 11.17 to:

$$f_w = \frac{1}{1 + \left(\frac{k_o}{k_w}\right)\left(\frac{\mu_w}{\mu_o}\right)} \dots\dots\dots (11.18)$$

Fig. 11.13 presents a typical fractional-flow curve that would be calculated from Eq. 11.18. This figure also shows a tangent to the fractional-flow curve that originates at the initial water saturation. The tangent point defines the “breakthrough” or “flood-front” saturation S_{wf} . This saturation is equivalent to the saturation that Buckley and Leverett obtained through intuitive arguments.¹⁰ It subsequently was recognized that this tangent intersects the fractional-flow curve at the saturation that is common to the stabilized and the nonstabilized zones.¹¹

The frontal-advance equation (Eq. 11.16) cannot predict the saturation profile between the connate-water saturation and the breakthrough saturation. An approximation that was developed from the Buckley-Leverett solution considers the saturation change to be a step increase (“shock”) from the connate-water saturation S_{wc} to the flood-front saturation S_{wf} . **Fig. 11.14** shows this saturation profile. The shock occurs because all saturations that are less than S_{wf} travel at the velocity of the flood front. Saturations that are greater than S_{wf} travel at velocities that are determined from Eq. 11.16 by calculating the derivative of the fractional-flow curve at each S_w value.

That the Buckley-Leverett solution is reasonable has been experimentally verified. **Fig. 11.15** compares experimental results with calculated values for two oils that have nearly a hundred-fold difference in viscosity.

Fig. 11.16 shows the viscosity ratio’s effect on the water fractional-flow behavior. The viscosity ratio is a key parameter; the efficiency of the linear displacement process of water displacing oil changes and is substantially different when the oil’s and the water’s viscosity is the same compared to when the oil’s viscosity is much higher than the water’s.

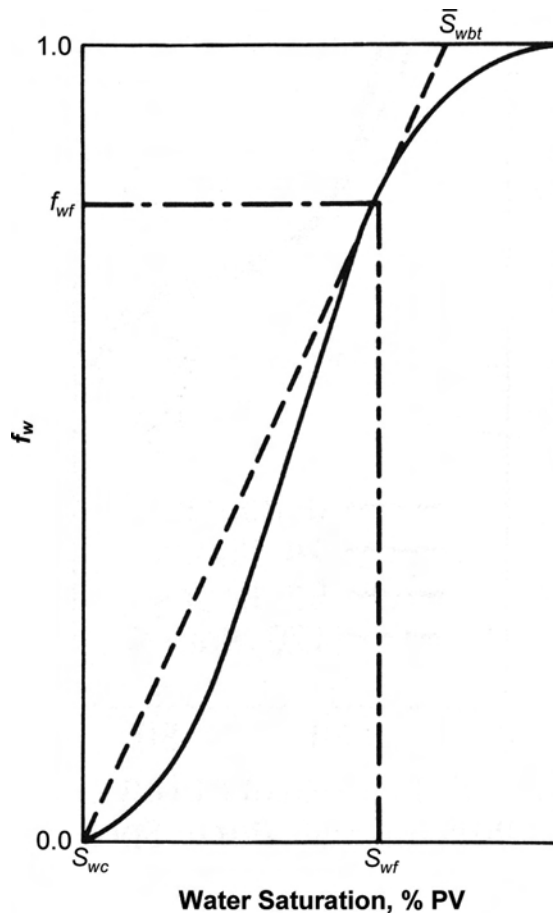


Fig. 11.13—Determination of flood-front saturation.² f_{wf} = fractional flow of water at the flood front, \bar{S}_{wbt} = average water saturation behind the flood front at water breakthrough, and S_{wf} = water saturation at the flood front.

11.4 Reservoir-Geology Considerations in the Design and Operation of Waterfloods

This section briefly discusses the geologic considerations in assessing waterflood performance and then describes the areal and vertical aspects of waterflood performance and analysis. (See Chap. 1 in this volume of the *Handbook* for a review of the geologic factors required for detailed reservoir engineering of oil and gas fields.) This section considers the macroscopic aspects of the geology that affects waterfloods; the microscopic aspects were discussed earlier in [Sec. 11.2](#).

All oil reservoirs are heterogeneous rock formations. The primary geological consideration in waterflooding evaluation is to determine the nature and degree of heterogeneities that exist in a particular oil field. Reservoir heterogeneities can take many forms, including

- Shale, anhydrite, or other impermeable layers that partly or completely separate the porous and permeable reservoir layers.
- Interbedded hydrocarbon-bearing layers that have significantly different rock qualities—sandstones or carbonates.
- Varying continuity, interconnection, and areal extent of porous and permeable layers throughout the reservoir.

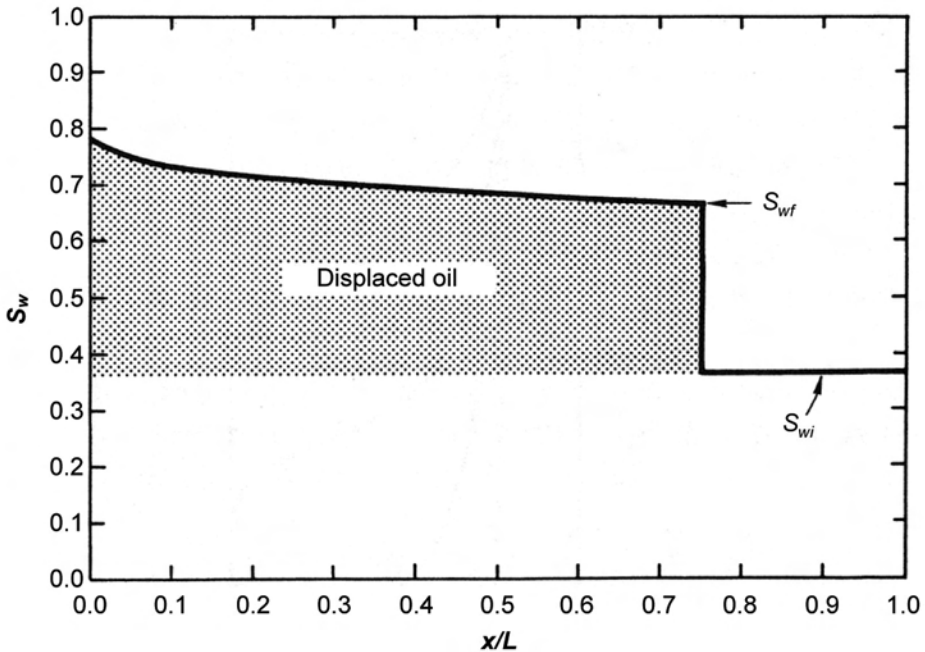


Fig. 11.14—Saturation profile computed from Buckley-Leverett solution.²

- Directional permeability trends that are caused by the depositional environment or by diagenetic changes.
- Fracture trends that developed because of regional tectonic stresses on the rock and the effects of burial and uplift on the particular rock layer.
- Fault trends that affect the connection of one part of an oil reservoir to adjacent areas, either because they are flow barriers or because they are open conduits that allow unlimited flow along the fault plane.

The structure of the reservoir and how it affects waterflood performance is another geological consideration. Structure creates dipping beds that dip at various angles. The interplay between the bed angle, gravity, and the oil/brine density difference at reservoir conditions significantly affects the relative vertical and horizontal flow behaviors. Structural considerations also can include whether the oil column has an underlying aquifer or an overlying gas cap, either of which can significantly affect the likelihood of successfully waterflooding the oil column.

Geologists and geophysicists must assess such geological and structural aspects of a reservoir. Geologists use cores and routine-core-analysis data to develop an understanding of the depositional environment and post-depositional diagenesis and to characterize the reservoir's internal architecture. Using seismic data, geophysicists can discern the major faults, as well as trends in rock quality, since cores and well logs are essentially pin pricks into the overall reservoir.

The technical team that is evaluating and monitoring waterflood performance should include a geologist and a geophysicist. Including a geostatistician on the technical team, as well, will help to ensure that the geoscientists' reservoir description is properly translated into engineering calculations, whether those are simpler calculations or are detailed numerical reservoir simulations.

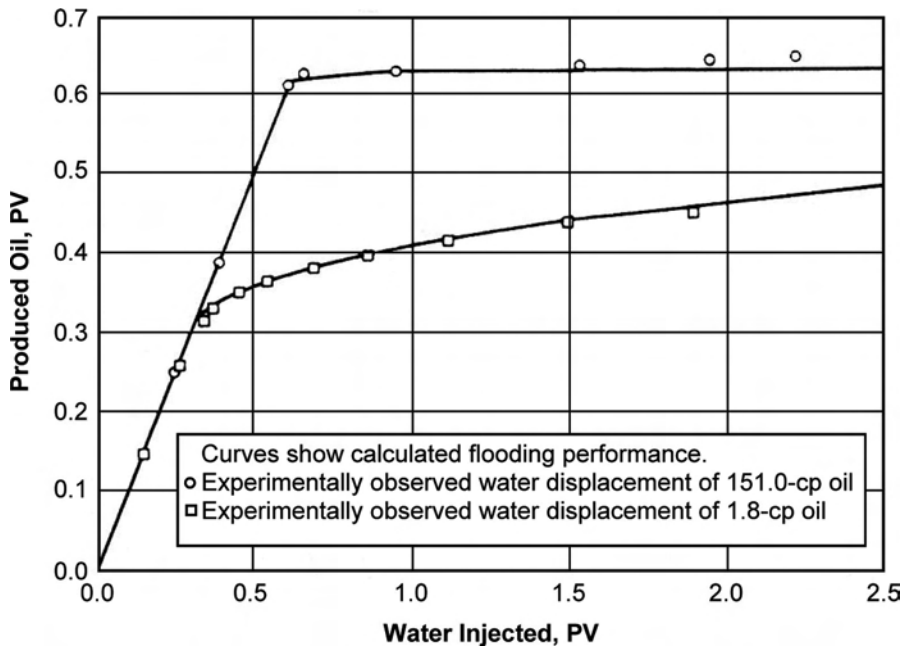


Fig. 11.15—Comparison of waterflooding response with results calculated from frontal-advance equation.²

For a waterflood, the reservoir description must be developed on the scale that is required for the quantitative evaluation (i.e., it must be “fit-for-purpose”). A variety of approaches (e.g., object- and pixel-based techniques) can be used.¹² The “flow unit” is a concept that frequently is used by geologists and that would be useful to engineers. “A flow unit is a volume of the total reservoir rock within which geological and petrophysical properties that affect fluid flow are internally consistent and predictably different from properties of other rock volumes (e.g., flow units).”¹³

The process of evaluating a reservoir’s geology begins when the reservoir is discovered and is placed on primary production. After a waterflood has been initiated, the production- and injection-well data provide additional insight into the internal characteristics of the rock volume that is being flooded. In fact, the waterflood production-well data (the water and oil rates as a function of time) are critical because they are the first data that relate directly to the interwell connectivity within the reservoir and that validate or cause modification of the geoscientists’ concepts of the various levels of reservoir heterogeneities.

During a waterflood, tracers can be injected to track which injector/producer pairs are well connected and which are poorly connected. (See the chapter on tracers in this volume of the *Handbook*.) Other monitoring techniques include the use of specially drilled observation wells and 4D-seismic interpretations to track the directionality and shape of the higher-pressure water-swept reservoir areas that are centered on the injection wells.

11.5 Immiscible Displacement in Two Dimensions—Areal

Historically, when computer capabilities were limited, the 3D aspects of a waterflood evaluation were simplified so that the technical problem could be treated as either a 2D-areal problem or a 2D-vertical problem. This section reviews the methods for treating the waterflood analysis as a 2D-areal technical problem. To simplify 3D to 2D areal, either the reservoir must be assumed to be vertically a thin and homogeneous rock interval (hence having no gravity

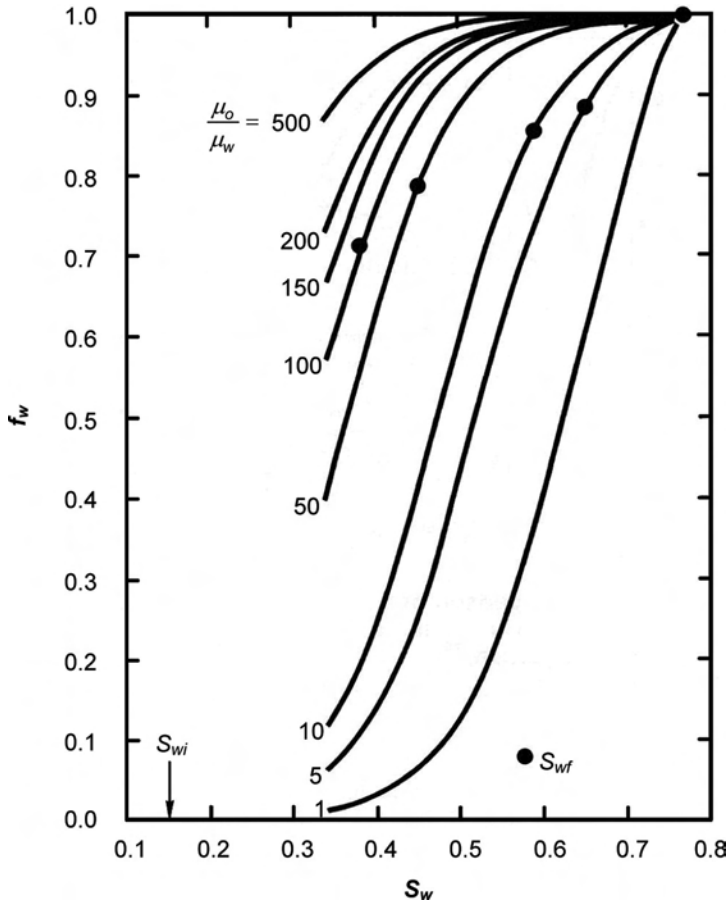


Fig. 11.16—Effect of viscosity ratio on fractional flow.²

considerations) or one of the published techniques to handle the vertical heterogeneity and expected gravity effects within the context of a 2D-areal calculation must be used.

The primary areal considerations for a waterflood involve the choices of the pattern style (see Fig. 11.17) and the well spacing. Maximizing the ultimate oil recovery and economic return from waterflooding requires making many pattern- and spacing-related decisions when secondary recovery is evaluated. This has been particularly true for onshore oil fields in the U.S. in which a significant number of wells were drilled for primary production. Many SPE technical papers have been published addressing these issues. (Sec. 11.9.4 West Texas Carbonate Waterfloods discusses these topics further and references several relevant papers.) For offshore oil fields where the maximum number of wells is limited, the optimal waterflood injection-well/production-well layout is best determined by the use of 3D numerical reservoir simulation.

The discussion below describes various factors that affect waterflood performance and discusses some of the 2D-areal calculation methodologies that have been developed. This discussion does not cover the use of modern numerical reservoir-simulation models in a 2D mode for analyzing a reservoir's waterflood performance, either for history matching or for future-performance projections. See Chap. 17 in this volume of the *Handbook* for a review of numerical reservoir simulation.

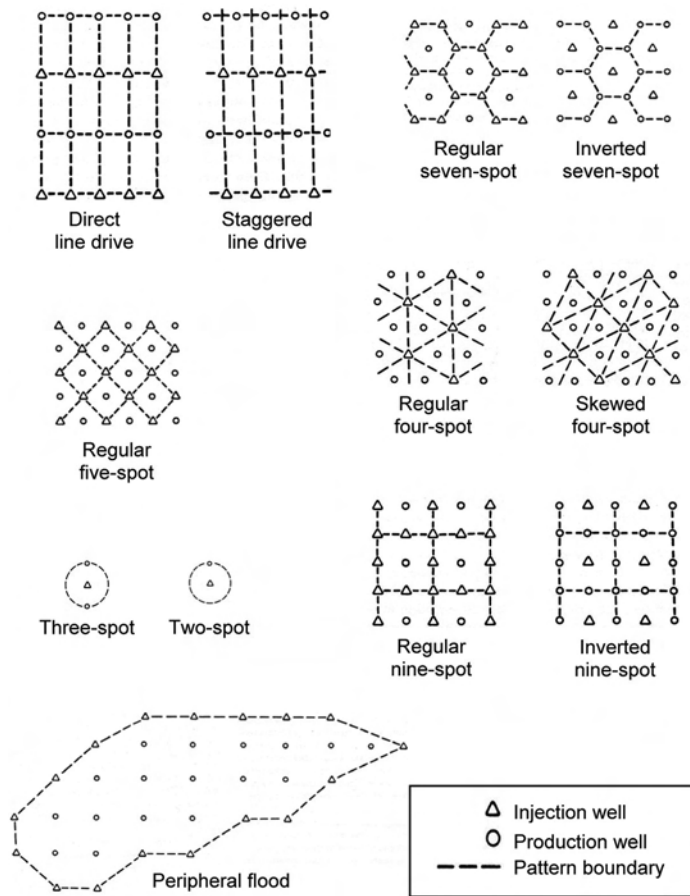


Fig. 11.17—Common waterflood-pattern configurations.³

11.5.1 Waterflood Displacement in a Five-Spot Pattern. Because it has been studied extensively, taking a look at the five-spot pattern (Fig. 11.17) provides an effective review of the areal aspects of waterflooding. Fig. 11.18 plots the waterflood performance of a five-spot experimental homogeneous sandpack for range of water/oil viscosity ratios from 0.83 (slightly favorable) to 754.0 (very unfavorable). Fig. 11.19 shows the X-ray shadowgraphs of a waterflood of two five-spot homogeneous sandpacks, one whose mobility ratio is favorable ($M = 0.40$) and one whose mobility ratio is unfavorable ($M = 1.43$). Fig. 11.20 plots the breakthrough areal-sweep efficiency as a function of M for a five-spot-pattern flood.

Figs. 11.18 through 11.20 show that the water/oil viscosity ratio is critical to the efficiency of the waterflood displacement. When the oil is more viscous than the water, the water areally displaces the oil less efficiently. When the oil is less viscous than the water, the water areally displaces the oil very efficiently.

11.5.2 Streamtube Waterflood Calculations. In the 1960s, Higgins and Leighton published a technique for analyzing waterfloods using what has been termed streamtubes, or stream channels, and using the concept of streamlines.^{14,15} Streamlines are the paths that fluid particles follow when they move from the injector to the producer; a streamtube is the region between two streamlines. The Higgins and Leighton technique approximates the displacement problem by use of a set of streamtubes in which fluid flows from the injection well to the production

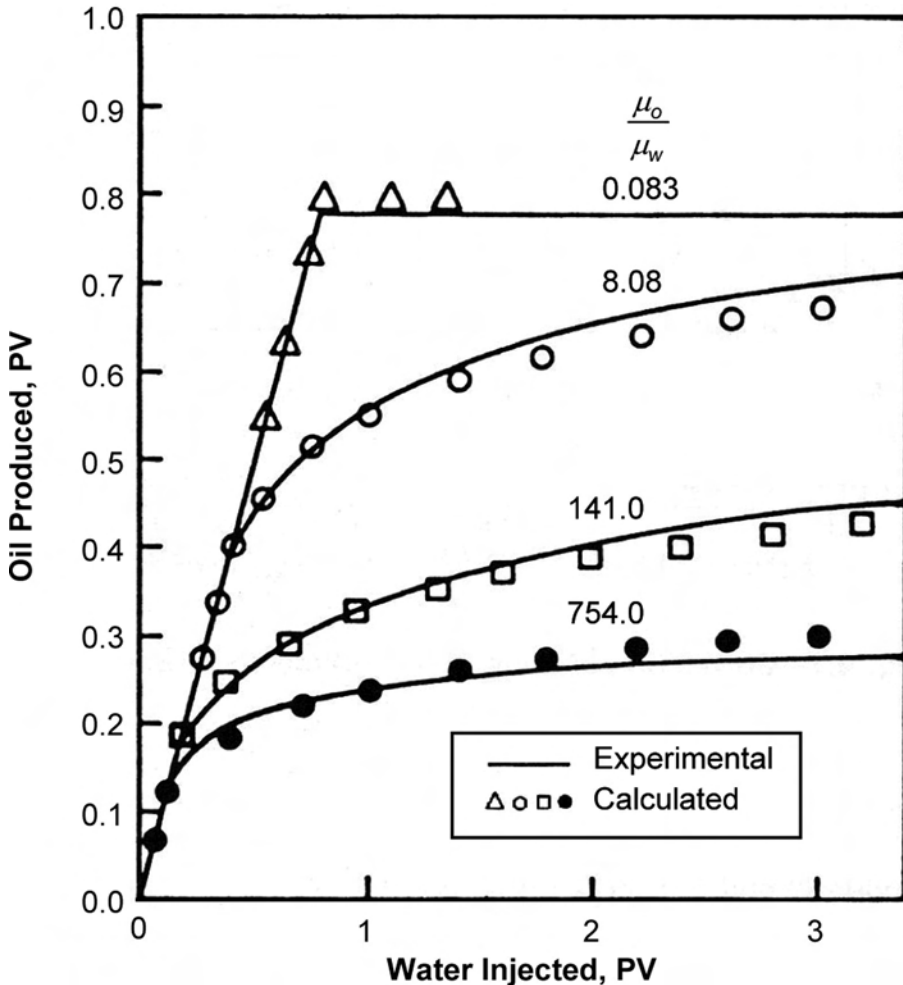


Fig. 11.18—Oil recovery from waterflooding five-spot pattern models.²

well and in which no fluid flows perpendicular to the streamlines (Fig. 11.21). Streamlines for the steady flow of a single phase (unit mobility ratio) have been determined for regular displacement patterns. Streamlines for arbitrary arrangements of injection and production wells can be determined by superposition of numerical solutions (see Fig. 11.22).¹⁶

Streamtube techniques originally were developed for areal waterflood analysis. These techniques have continued to be popular with advancements in the mathematical techniques and computing power. (Also see the discussion about streamtube techniques in the Simulation chapter in this volume of the *Handbook*). The more advanced streamtube models can handle stratified-layer systems. Many universities and oil companies have developed sophisticated streamtube models and applied them to waterflood calculations. Such models also are available from commercial software providers to the oil industry.¹⁷

Any 2D approach to waterflood analysis is an approximation. How accurate an approximation it is will depend on how vertically stratified the reservoir is and how significant the gravity considerations are in the real reservoir compared to what the numerical modeling assumes about them. For many situations, 2D-streamtube models have been used successfully to model historic waterflood performance and to project future waterflood performance.¹⁸

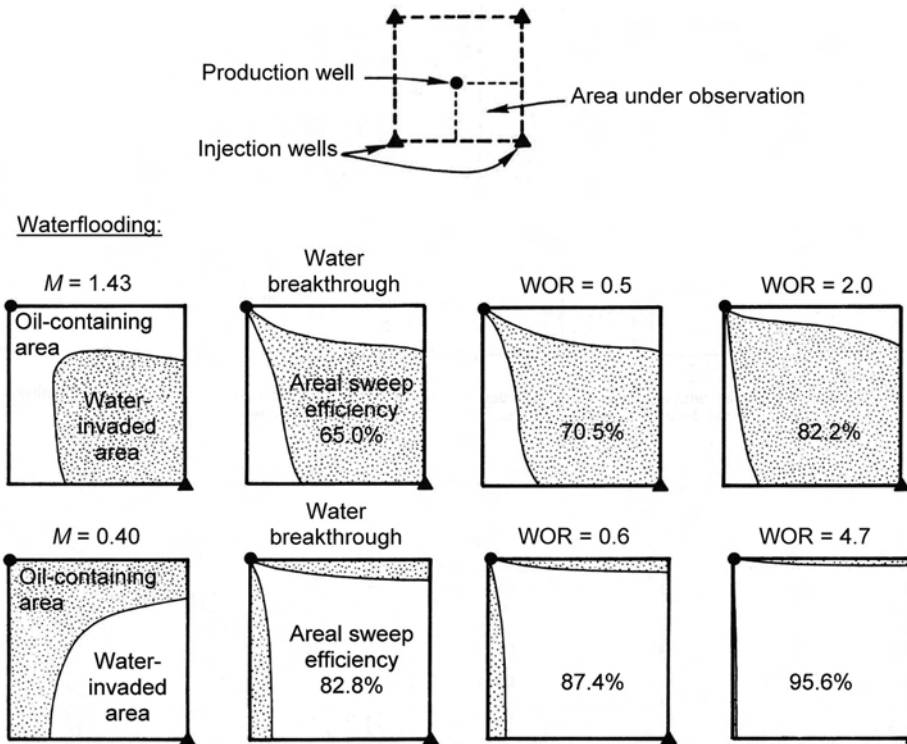


Fig. 11.19—X-ray shadowgraphs of flood progress in experimental scaled five-spot pattern models.² (WOR = instantaneous producing water/oil ratio.)

11.5.3 Waterflood-Pattern and Well-Spacing Considerations. As Fig. 11.17 shows, a variety of geometric injector/producer pattern layouts can be used when waterflooding an oil reservoir. These geometric layouts are designed to produce an efficient waterflood for the whole of the reservoir, assuming the rock is homogeneous. The producer/injector ratio typically is chosen on the basis of the expected injection rates for the water injectors and the total fluid-production rates for the production wells. The goal is to have voidage replacement, with the injected volume equal to the produced volume. Injection and produced volumes will depend on the transmissibility of the system, the maximum pressure that can be applied at the injector, and the minimum pressure that can be achieved at the producer. It has been customary to limit injection pressures to lower than what would cause fracturing. As will be discussed later, this guideline can be relaxed in some circumstances.

Other considerations with the injector/producer-pattern layout are the anisotropic permeability in the reservoir and the orientation of any natural-fracture systems that are within the reservoir interval. Fig. 11.23 shows the correct and incorrect orientation of lines of injectors and producers in this respect. The goal is to make these natural aspects of the reservoir improve the areal sweepout as the water displaces the oil, rather than allowing them to affect it negatively.

The choice of waterflood well spacing is primarily a function of four considerations: incremental oil recovery; increased oil-production rate; reduced operating costs (producing more of the oil at lower water cuts); and costs to drill additional wells, including additional platform space at offshore locations. The initial well spacing typically is chosen on the basis of engineering studies, assuming that there will be a logical phased-development plan for the oil field,

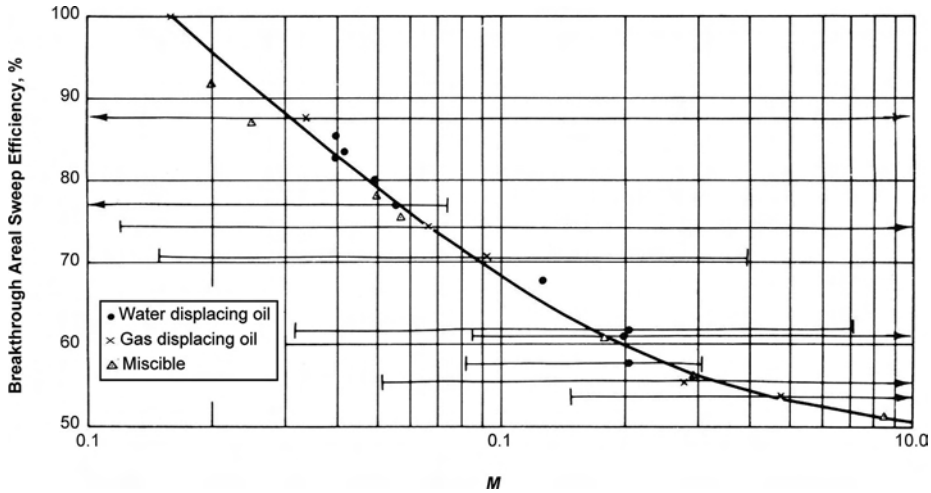


Fig. 11.20—Correlation of areal sweep efficiency at breakthrough with mobility ratio for miscible and immiscible displacement in five-spot-pattern floods.² On this figure, the mobility M has been calculated using the average water saturation in the water-contacted portion of the reservoir. The horizontal lines indicate what the range of mobility ratios M would be if it were calculated using the water mobility at floodout conditions (the right extremity of the horizontal bar) or using the water mobility at the flood front (the left extremity of the bar), with the arrows indicating that the values were off the scale of this plot.

including possibilities for various levels of infill drilling and pattern realignments. Low-permeability reservoirs typically have closer well spacings than do high-permeability ones because of their reduced ability to move fluids rapidly between widely spaced injectors and producers. The initial well spacing usually is somewhat wider than what is likely to be used toward the end of field life. The number of injection and production wells also is tied to the capacity of the injection facilities and production-fluid-separation facilities.

The incremental oil recovery can be a function of the well spacing and depends on the continuity of the porous and permeable reservoir-rock layers. If the reservoir layers are highly continuous, then reducing the well spacing will not have much effect on the ultimate oil recovery by waterflooding; however, for layers that are discontinuous over the reservoir, closer well spacing will provide more reservoir continuity between injector/producer pairs. This aspect of waterflooding has been studied in depth for a variety of U.S. oil fields, mainly west Texas carbonate reservoirs, in which reservoir-layer continuity is a major issue. Many papers have been published on this topic.

For example, Barber *et al.*¹⁹ reviewed nine sandstone and carbonate reservoirs' responses to infill drilling. **Figs. 11.24 and 11.25** show aspects of reservoir discontinuity in west Texas Clearfork and San Andres carbonate reservoirs. **Fig. 11.25** shows that the San Andres reservoirs have significantly greater reservoir continuity at a 10-acre well spacing than at 20- and 40-acre well spacings. For these reservoirs, “[c]ontinuity calculations made after infill drilling indicated the pay zones to be more discontinuous than when calculations were made before infill drilling.”¹⁹ From the experience in those nine fields, the authors concluded that “the ultimate well density in any given field can be determined only after several years of field performance provide sufficient information on reservoir continuity and recovery efficiencies.”¹⁹

Another paper on this topic is by researchers at Texas A&M U.,²⁰ who spent several years analyzing the impact of well-spacing reduction on west Texas Clearfork and San Andres waterflood performance from various geographic areas of the Permian Basin. The authors found infill drilling to be more effective for the San Andres units than for the Clearfork units. In the San Andres units, they determined the infill drilling to be more effective for the units in the

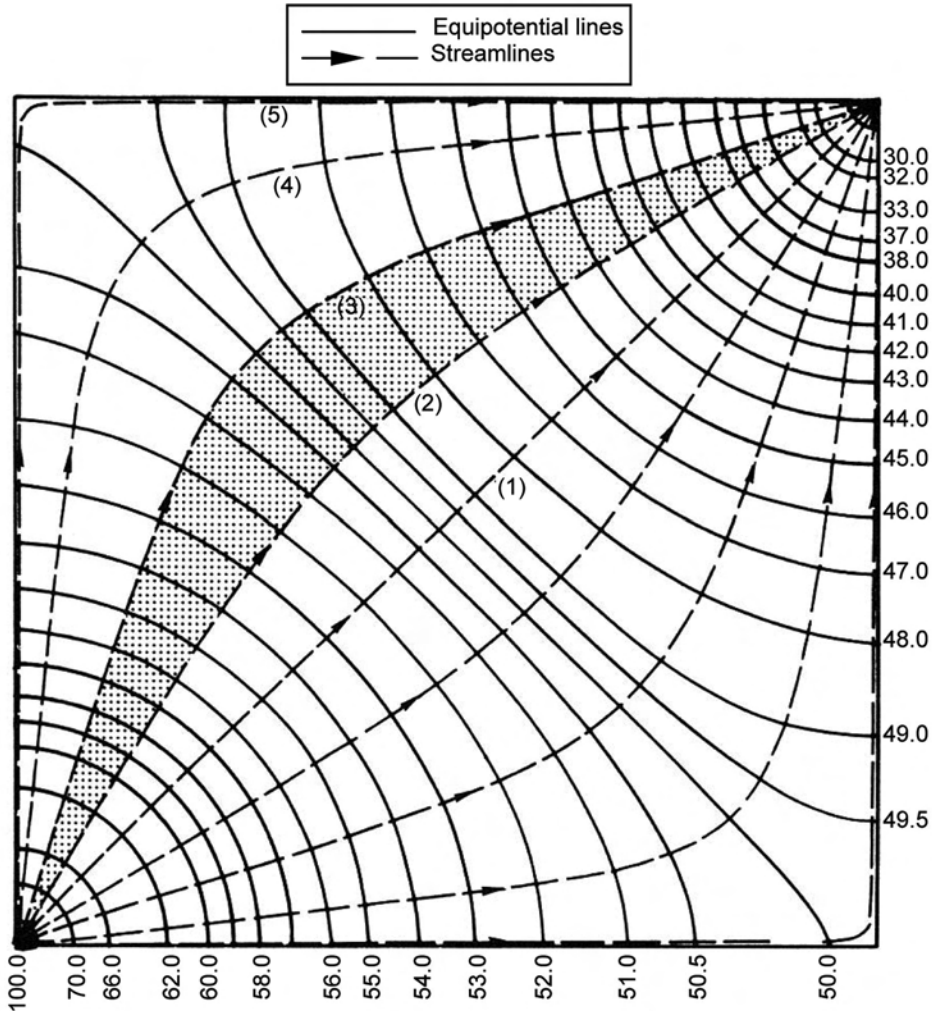


Fig. 11.21—Streamlines and equipotential lines for single-phase flow in a quadrant of a five-spot pattern.² For illustrative purpose, for this homogeneous quarter-of-a-five-spot pattern and single-phase flow, a set of streamlines has been shown as (1) through (5); the numbers along the axes are lines of equal potential scaled from 100 at the injection point to zero at the production point. By definition, streamlines are perpendicular to lines of equal potential.

Northern Shelf area than for those in the Central Basin Platform area. In those analyses, they calculated a 2 to 5% additional recovery of OOIP for a 9-acre well spacing, compared to a 22-acre well spacing.²⁰

As noted above, many more papers have been published on this topic, but these two papers identify the key well-spacing issues. As both studies conclude, one does not know *a priori* what the optimal well spacing will be. The technical team must analyze the available data before starting a waterflood, then continue to evaluate the production and injection data to determine the waterflood's efficiency and the extent to which infill-well locations should be drilled or patterns realigned.

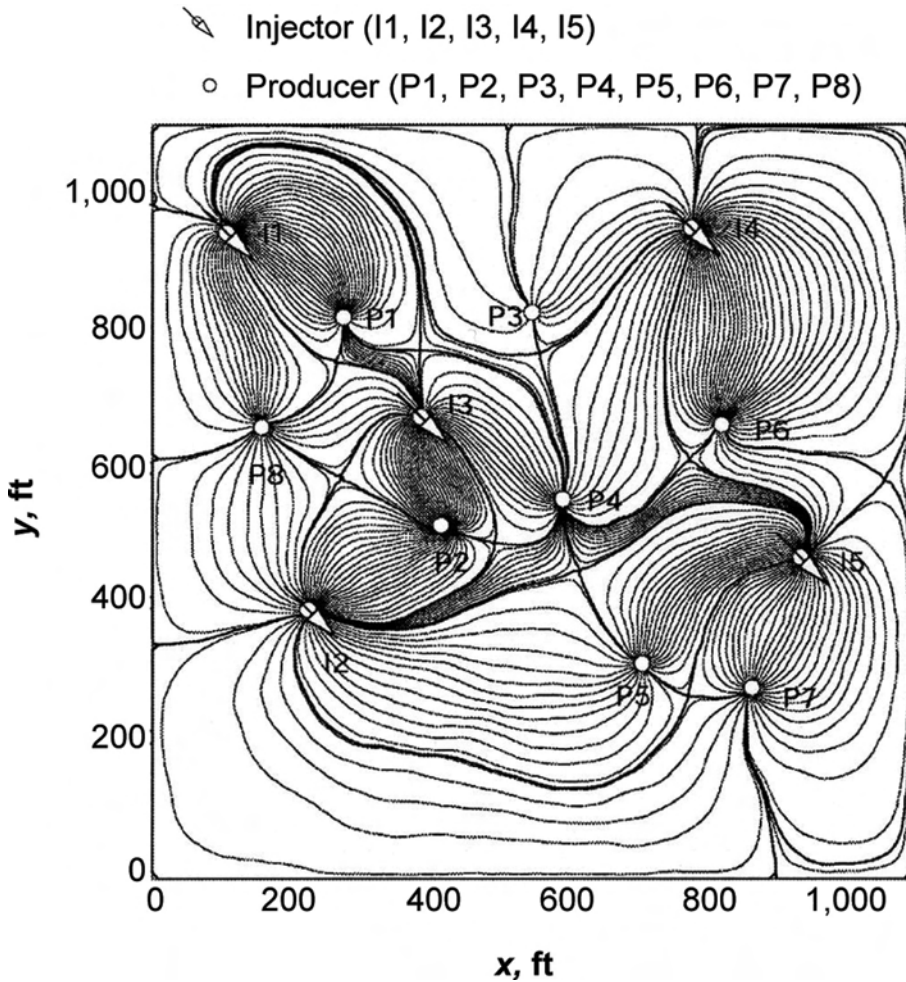


Fig. 11.22—Geometries of streamtubes of a heterogeneous multiwell case (113 × 113 grid, heterogeneous, $M = 10$).¹⁶

11.5.4 Horizontal Wells, Multilateral Wells, and Fracture Orientation. Until the 1980s, all waterflood analysis assumed that the wellbores would penetrate the reservoir vertically and that water should not be injected above the formation parting pressure. Accordingly, mathematical formulations assumed areally that injection and production wells were point sources and sinks. This style of analysis is evident in the streamline patterns in Fig. 11.22.

The advent of horizontal-well and multilateral-well technologies has brought with it the ability to create line injection-well sources and line production-well sinks, which has changed how a waterflood pattern might be developed. Theoretical calculations show that parallel lines of horizontal injectors and horizontal producers will increase oil recovery and in the limit are the perfect line-drive pattern arrangement.

When fracturing injection wells, a concern has been that a fracture might extend from the oil-reservoir intervals into adjacent porous and permeable layers, into which considerable injection brine could be lost (i.e., thief zones); however, given that the principal orientation of any hydraulic fracture is known and that the fractures can be restricted to the oil-reservoir interval, hydraulic fractures can improve the areal sweepout during waterflooding in much the same

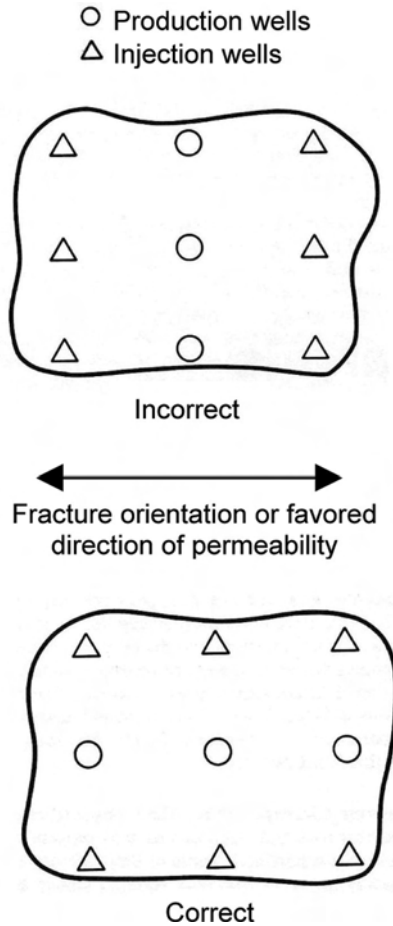


Fig. 11.23—Correct and incorrect pattern alignment with anisotropic permeability, or an oriented fracture system.³

way that horizontal wells can. This is true of fractures from the injection wells and the production wells, given that an appropriate pattern style is used. On the other hand, if they are oriented so that the fracture tips are significantly closer to each other than the vertical wellbores are, hydraulic fractures from the injectors and producers will yield poorer areal sweepout of the reservoir during waterflooding than would unfractured vertical wells.

An excellent example of a situation in which fracturing was needed is the waterflooding of diatomite reservoirs in California, U.S.A. These reservoirs have high porosity, but permeabilities of 0.1 md or less. Conventional injection methods yielded uneconomic rates; however, positioning the injectors and producers normal to the induced-fracture orientation established reasonable rates without significant loss of injected water to adjacent porous and permeable intervals and without premature water breakthrough.^{21,22}

11.6 Vertical Displacement in Linear and Areal Models

The previous section’s discussion of waterflood displacement behavior assumed that the vertical saturation distribution was homogeneous at all areal locations. This section discusses the impact of vertical variations in permeability and the effect of gravity on simple 2D reservoir situations in which the areal effects are ignored. Gravity effects always are present because for

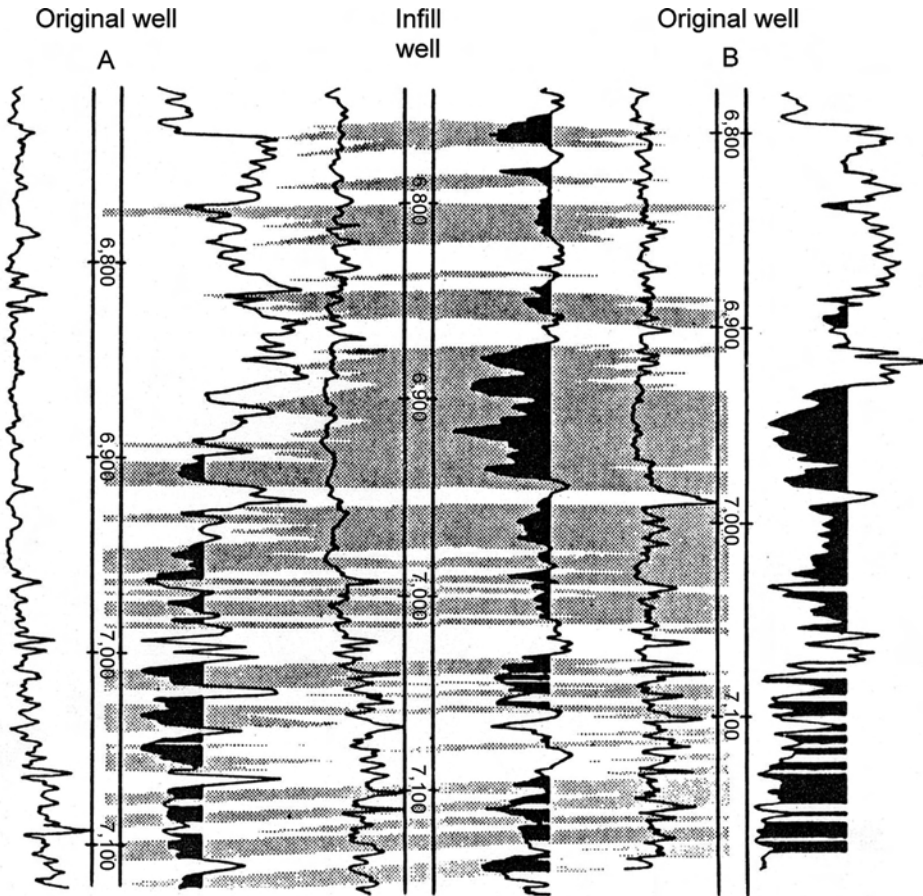


Fig. 11.24—Type cross section for Fullerton Clearfork reservoir.¹⁹

any potential waterflood project, oil always is less dense than water, even more so after the gas is included that is dissolved in the oil at reservoir conditions.

Three particular situations are discussed here:

- Stratified systems with noncommunicating layers for various mobility ratios.
- Homogeneous systems with gravity (including dipping beds).
- Stratified systems with communicating layers and assumed vertical fluid equilibrium.

The discussion below does not include the P_c effects on vertical saturation distributions. Through countercurrent imbibition, P_c effects help to counteract nonequilibrium water/oil saturation distributions. The mathematics of including P_c effects makes the problems too complicated for inclusion in this chapter. Standard numerical reservoir simulators—which are needed for a complete analysis of real reservoir situations—account for the effects of countercurrent imbibition caused by P_c effects, as well as for the water/oil density and viscosity differences that lead to injection-water gravity underrunning and the layer-by-layer permeability variations, with or without communicating layers.

Before presenting some of the technical-literature techniques for studying the vertical displacement characteristics of water/oil displacement, one must first define some measure of the vertical permeability variations. Dykstra and Parsons²³ developed a method that is based on routine-core-analysis data. In that approach, the routine-core-analysis permeability data for the pay intervals are arranged in descending order, and the percent of the total number of values

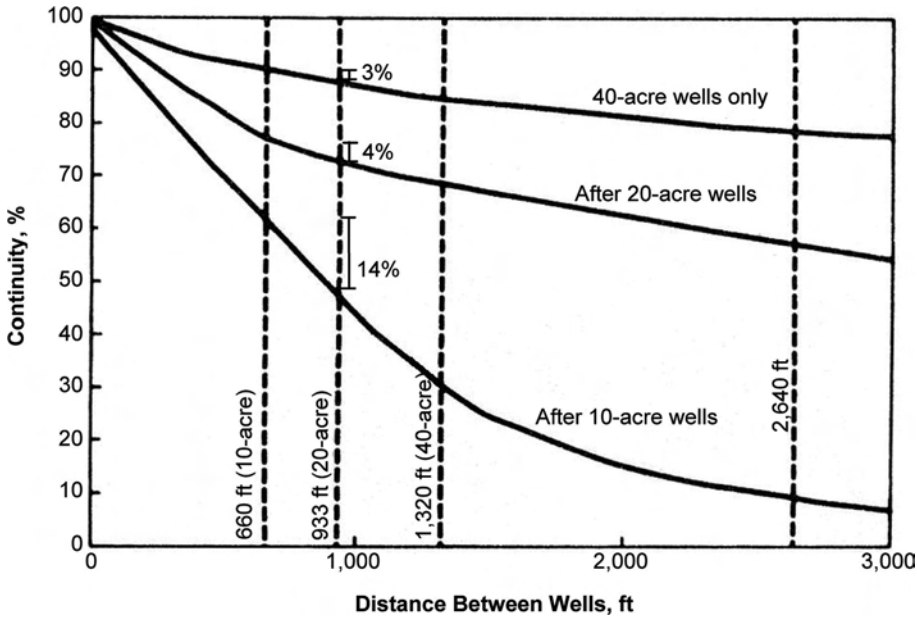


Fig. 11.25—Continuity progression for Means San Andres unit.¹⁹ The lines on this plot show the estimated percent continuity before drilling infill wells. After each set of infill wells was drilled, the actual reservoir continuity was found to be less than predicted. This is why the “After 10-acre wells” line is the lowest of the three lines. The 3, 4, and 14% vertical bars indicate the expected increase in percent continuity estimated for a 10-acre well spacing from the 40-acre well-spacing data (3%) and from the 20-acre well-spacing data (4%), compared to what actually was found after the 10-acre infill wells were drilled (14%).

that exceeds each entry is calculated. The values then are presented as a log-probability plot (see Fig. 11.26). A reasonably straight line is drawn through the data, with the points in the 10-to-90% range being more heavily weighted. This straight line is a measure of the dispersion and the heterogeneity of the reservoir rock. What has come to be known as the “Dykstra-Parsons coefficient of permeability variation” V is defined as:

$$V = \frac{k_{50} - k_{84.1}}{k_{50}}, \dots\dots\dots (11.19)$$

where k_{50} = median permeability value, md, and $k_{84.1}$ = permeability at 84.1% probability (one standard deviation), md.

Fig. 11.27 shows the relationship of the Dykstra-Parsons V values to varying degrees of rock heterogeneity. Note that in Fig. 11.27, the V for most reservoirs ranges from 0.5 to 0.9.

11.6.1 Stratified Systems With Noncommunicating Layers. Over the years, several waterflood prediction methods have been proposed and published that account for the vertical variations in rock properties, particularly permeability. These simple methods assumed that every rock layer acts independently of all other rock layers (even at 1-ft increments in the reservoir) and that each rock layer is continuous from the injection well to the production well. These early methods were developed when the ability to make detailed, complicated engineering calculations was limited. They focused on how to account for (1) the effect of the vertical permeability variation with minimal consideration of the mobility ratio and (2) the effect of

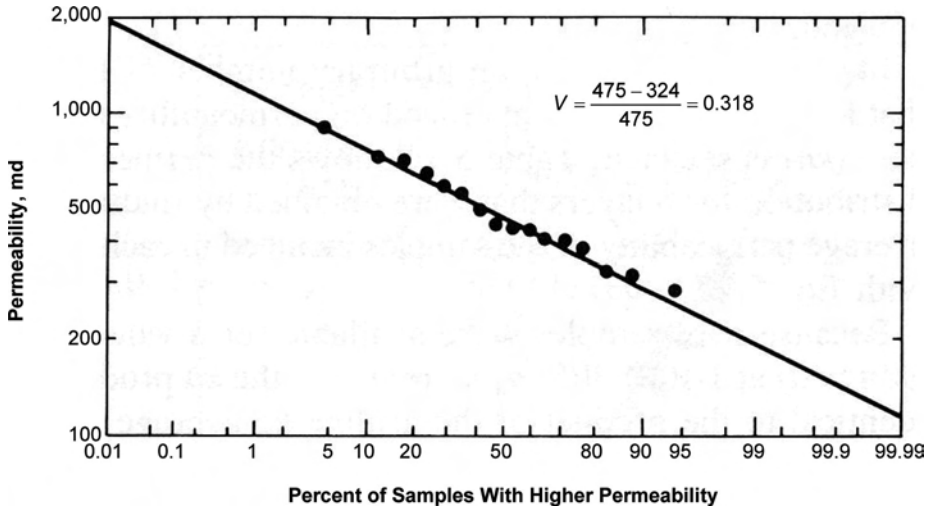


Fig. 11.26—Plot of permeability data on log-normal paper.²

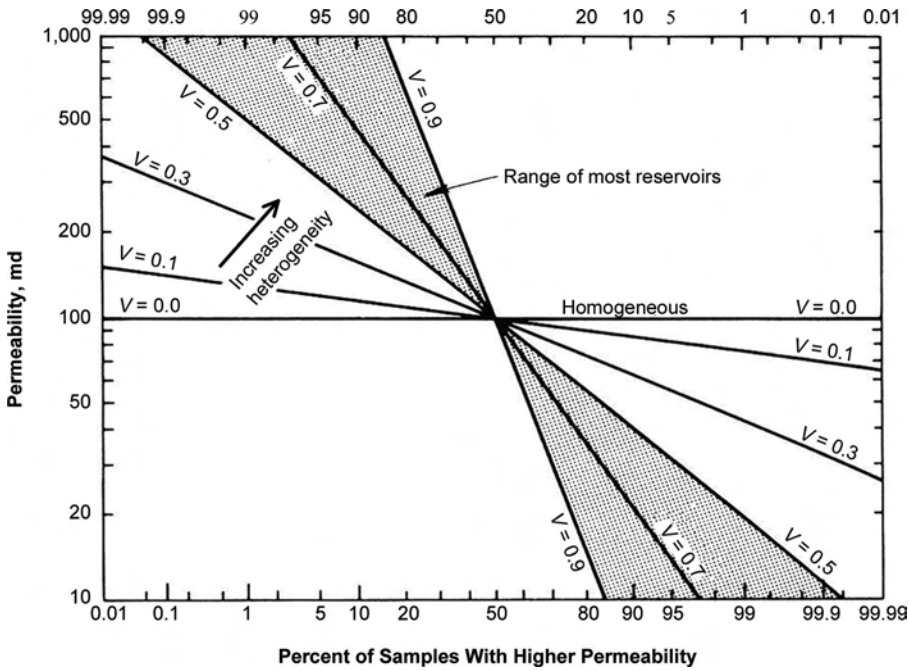


Fig. 11.27—Characterization of reservoir heterogeneity by permeability variation V .²

vertical permeability variation and mobility ratio, assuming constant pressure at the injection and production wells.

Stiles²⁴ developed one of the earliest methods, for which only the permeability-thickness (kh) distribution of the vertical reservoir interval and the mobility ratio at endpoint conditions need to be known (see Eq. 11.6). The water/oil ratio (WOR) F_{wo} after water breakthrough as a function of the fraction of the total flow capacity C represented by layers having water breakthrough is defined as:

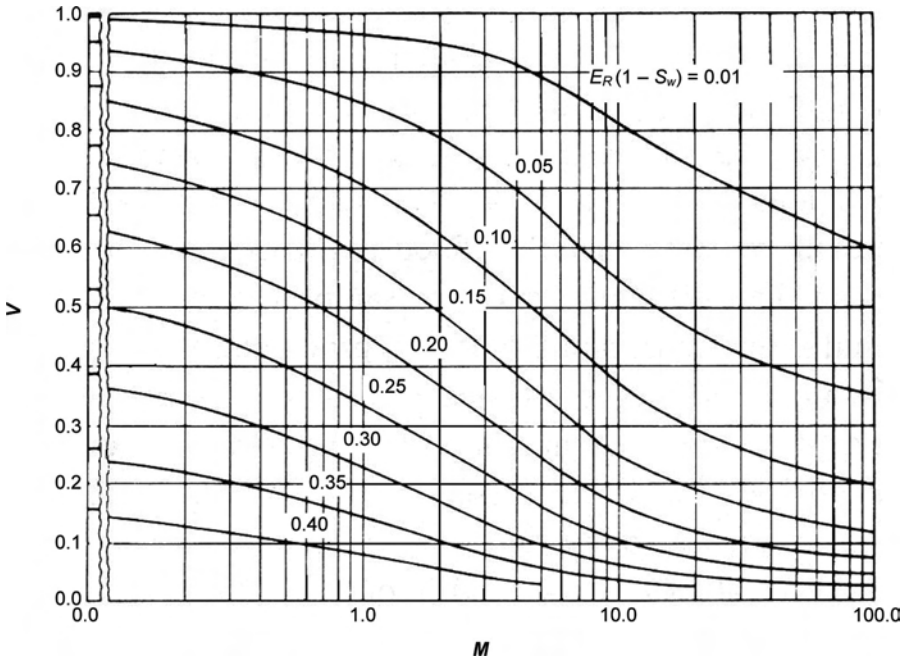


Fig. 11.28—Permeability variation plotted against mobility ratio, showing lines of a constant $E_R(1 - S_w)$ for a producing WOR of 1.1

$$F_{wo} = \frac{C}{1 - C} \frac{k_{rw} \mu_o}{\mu_w k_{ro}} B_o, \dots\dots\dots (11.20)$$

where B_o = the oil formation-volume factor, RB/STB.

A more sophisticated method that is widely used is that of Dykstra and Parsons.²³ Their method is based on calculations for linear layered models and assumes no crossflow and the use of the results of more than 200 floodpot tests that were performed on more than 40 California oil-reservoir core samples. This Dykstra-and-Parsons method takes into account initial fluid saturations, mobility ratios, producing WORs, and fractional oil recoveries. The permeability variation was taken into account by use of V , as defined in Eq. 11.19 above. Figs. 11.28 through 11.31 plot the results of the Dykstra-and-Parsons technique as V vs. M for four WOR levels (1, 5, 25, and 100).

11.6.2 Homogeneous Reservoirs Subject to Gravity Effects. In essentially all reservoirs, even those with close well spacings, the horizontal distance between an injector well and a producer well is very long relative to the vertical thickness of the reservoir pay interval. This means that gravity plays a major role in the water/oil-displacement process, given that the fluids can move vertically within the pay interval. For conceptual and calculation purposes, the limiting case is to assume that gravity forces dominate the water/oil-displacement process, that gravity segregation of the oil and water is complete, and that the system is in “vertical equilibrium.” This means that vertically the gravity and capillary forces are in balance and that the vertical saturation distribution is governed by the P_c/S_w function.

The first and simplest homogeneous reservoir situation described here is a reservoir whose permeability is constant throughout the pay interval. Craig¹ studied a set of scaled laboratory vertical models experimentally and developed a correlation between the sweep efficiency at breakthrough and the values of the scaling parameter:

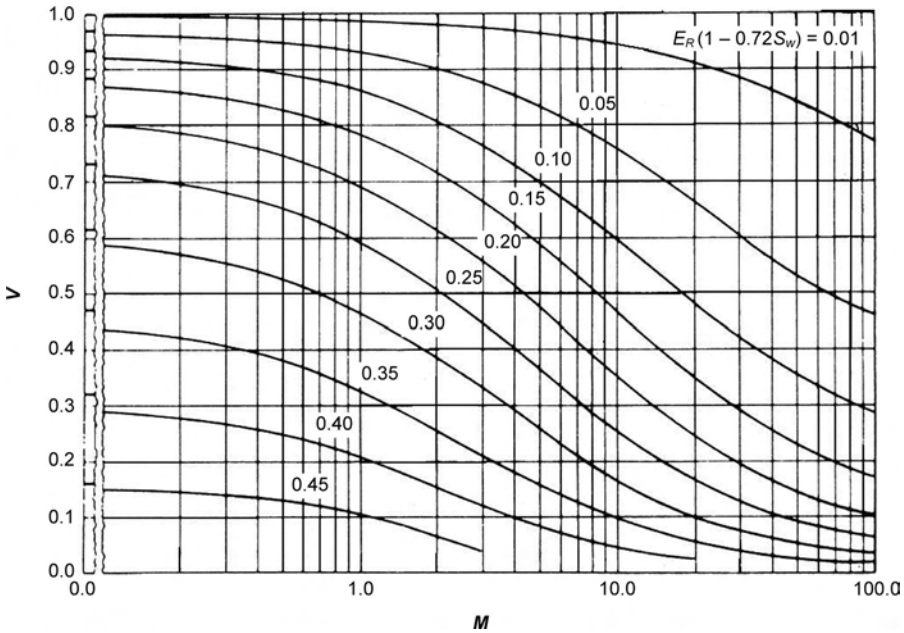


Fig. 11.29—Permeability variation plotted against mobility ratio, showing lines of a constant $E_R(1 - 0.72S_w)$ for a producing WOR of 5.¹

$$\frac{(\Delta p)_h}{(\Delta p)_V} = \frac{u_t \mu_o L}{k_x g \Delta \rho h}, \dots\dots\dots (11.21)$$

where $(\Delta p)_h$ = pressure difference in the horizontal direction, psi; $(\Delta p)_V$ = pressure difference in the vertical direction, psi; u_t = horizontal Darcy velocity, ft/D; k_x = permeability in the x direction, darcies; and $\Delta \rho$ = water/oil density difference, lbm/ft³.

As Fig. 11.32 shows, the sweep efficiency as it is related to the scaling parameter is a strong function of mobility ratio. Fig. 11.33 compares the fractional flow of water for a homogeneous system with vertical equilibrium to the fractional flow of water calculated from the original laboratory water/oil relative permeability curves. The effect of the water moving along the base of the reservoir interval because of the gravity effects—but with the P_c/S_w curve controlling the vertical distribution of the water and oil saturations—is that the water breaks through earlier and the WOR rises more slowly.

Another reservoir situation that involves gravity effects is a homogeneous reservoir with dipping beds. If the rate of water injection in a waterflood is too low for vertical equilibrium to occur, there will be gravity-stabilized flow between the water and the oil. Dietz²⁵ has derived a relationship to predict the critical velocity q_c required to propagate a stable interface through a linear system in which gravity forces dominate, but in which pistonlike displacement occurs and P_c effects are neglected:

$$q_c = \frac{(4.9 \times 10^{-1}) k k_{rw} A (\rho_w - \rho_o) \sin \alpha}{\mu_w (M - 1)}, \dots\dots\dots (11.22)$$

where ρ_o = oil density, lbm/ft³; ρ_w = water density, lbm/ft³; and α = dip angle, degree.

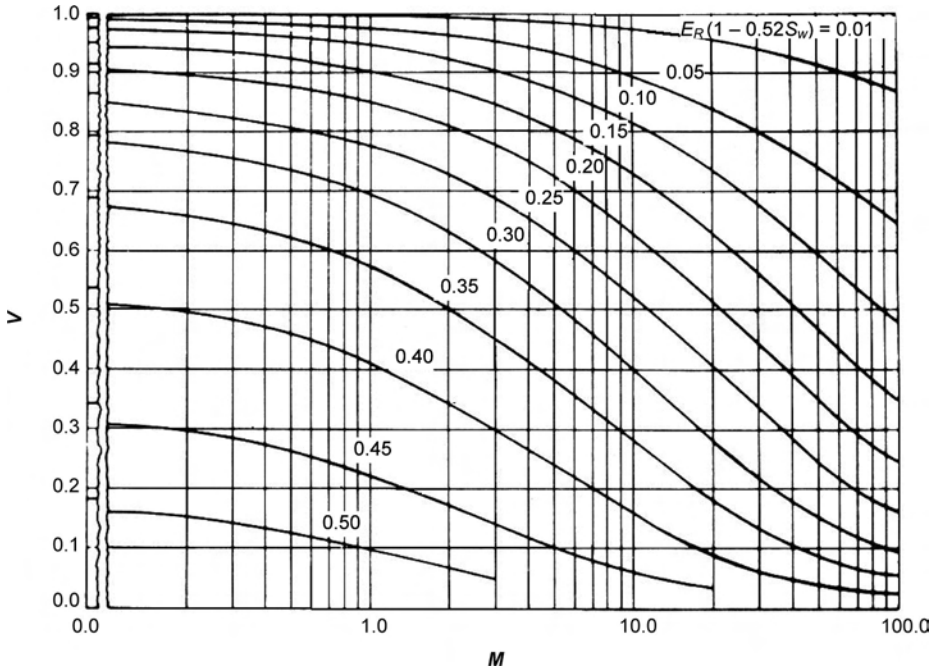


Fig. 11.30—Permeability variation plotted against mobility ratio, showing lines of a constant $E_R(1 - 0.52S_w)$ for a producing WOR of 25.¹

When the oil/water interface is stable, the velocities of oil and water are equal at every point in the interface. The interface is linear and will move at a constant velocity through the system as long as $q < q_c$. The stable linear interface will not necessarily be flat; however, it will be stable with a slope β , as defined by Eq. 11.23:

$$\frac{dy}{dx} = - \tan \beta = \frac{(M - 1 - G)}{G} \tan \alpha, \dots\dots\dots (11.23)$$

where y = the position in y -coordinate system, ft, and G is dimensionless and defined by Eq. 11.24:

$$G = \frac{(4.9 \times 10^{-1}) k k_{rw} A (\rho_w - \rho_o) \sin \alpha}{\mu_w q_t} \dots\dots\dots (11.24)$$

Figs. 11.34a and 11.34b depict gravity-stable situations for two different mobility ratios.²⁶ Fig. 11.34c depicts the unstable situation for an unfavorable mobility ratio where the displacement rate is too high for the water and oil to maintain vertical equilibrium.

11.6.3 Stratified Systems With Communicating Layers and Assumed Vertical Equilibrium.

One of the systems that have been analyzed with simple calculations is that of water/oil displacement with vertical permeability variations and gravity effects, but with capillary pressure neglected. Dake²⁶ explores this in his reservoir-engineering textbook. Dake’s illustrative example assumes a three-layer system. He assumes the permeability variation to be highest to lowest from top to bottom, and then compares those results with results from assuming the reverse,

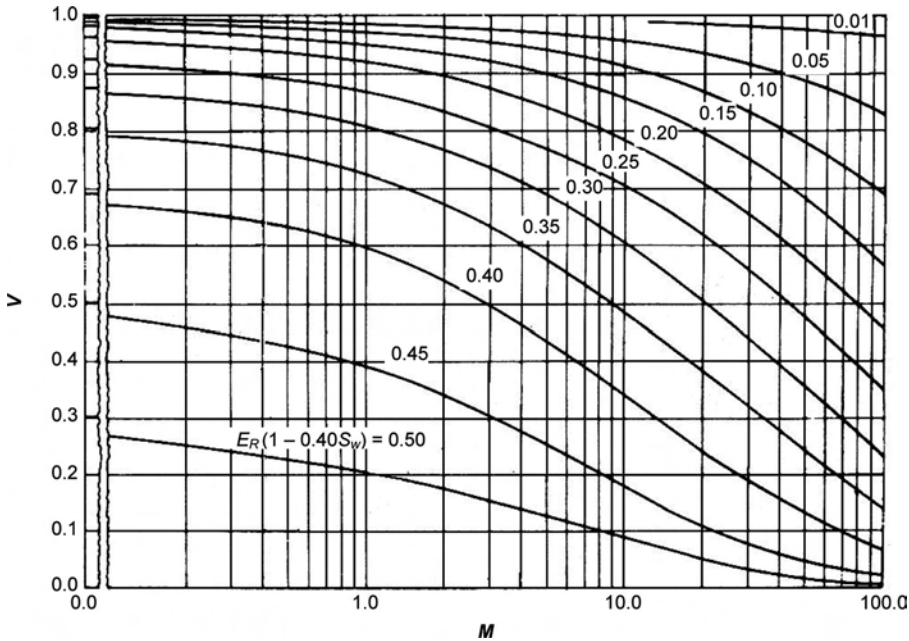


Fig. 11.31—Permeability variation plotted against mobility ratio, showing lines of a constant $E_R(1 - 0.40S_w)$ for a producing WOR of 100.¹

the layer with highest permeability variation then on the bottom. Fig. 11.35 lists the properties of the three layers, and Fig. 11.36 presents the averaged relative permeability curves. Fig. 11.37 shows the pseudocapillary pressure (a) and fractional-flow curves (b). Note that Fig. 11.37b includes smoothed and unsmoothed versions of the fractional-flow curve. The smoothed version is the curve that would be used for a Welge-type fractional-flow calculation.

Dake's example shows that in waterflooding where gravity effects are significant, having the high-permeability layers at the top of the reservoir interval allows a much more efficient oil displacement than when the high-permeability layers are at the bottom of the reservoir interval. This is because gravity causes the water to slump, and when the lower-permeability layers are the base, the water must move more slowly than the oil from the injector to the producer.

So far, the chapter discussions have highlighted the development of techniques for understanding and analyzing key aspects of oil/water displacement. These techniques predate modern computers; hence, they were developed to simplify the real reservoir problem sufficiently to allow various engineering calculations to be made.

Of course, the availability of modern computers and advanced numerical-reservoir-simulation software has rendered many of these simplifying assumptions unnecessary when quantifying waterflood-type water/oil displacements in real reservoirs. Nevertheless, these historic techniques have been discussed here to provide an understanding of the dynamics of the water/oil-displacement process and the primary variables that influence the recovery efficiency, as background to the discussion of waterflood design in the next section.

11.7 Waterflood Design

The design of a waterflood has many phases. First, simple engineering evaluation techniques are used to determine whether the reservoir meets the minimum technical and economic criteria for a successful waterflood. If so, then more-detailed technical calculations are made. These include the full range of engineering and geoscience studies. The geologists must develop as

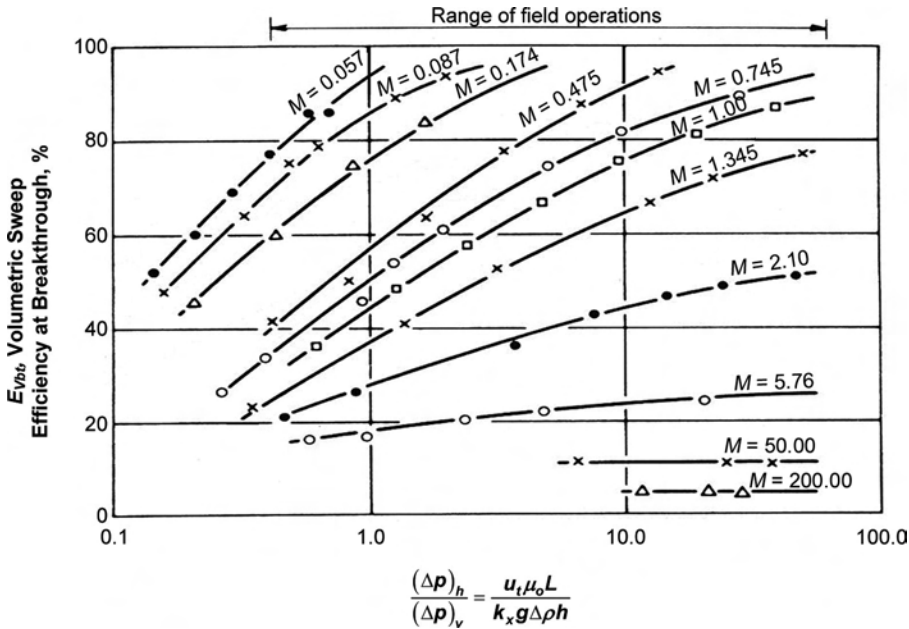


Fig. 11.32—Correlation of scaled-model experiments to determine the effect of gravity segregation on volumetric sweep efficiency in uniform linear systems.²

complete an understanding as possible of the internal character of the pay intervals and of the continuity of nonpay intervals. This pre-flood understanding often is limited because the injector/producer wells' connectivity has not been determined quantitatively. Interference testing can provide insight into connectivity when its cost is justifiable. Data gathered from smart wells can be particularly helpful in determining connectivity in high-cost environments where there is a limited number of wellbores. Analogs also can prove useful. Otherwise, little definitive data will be available until after there has been significant fluid movement from the injectors toward the producers.

The engineer will make a number of reservoir calculations to determine the well spacing and pattern style that will be used in a particular flood. These choices are based on the available understanding of the reservoir geology, the proposed design of surface facilities (particularly water-injection volumes), and any potential limits on the numbers of injectors and producers. Such factors are interrelated in terms of capital and operating costs and oil-, water-, and gas-producing rates to define the overall economics of the project. In making these preliminary calculations, facility capacities need to be flexible because as the waterflood progresses, there almost certainly will be modifications to the original designs and operating plans.

Fig. 11.17 shows a variety of injector/producer pattern layouts that can be considered. In reality, the existing wellbore locations might limit the pattern layout to a nonsymmetrical arrangement like that shown in Fig. 11.38. Also, as shown in Fig. 11.23, the orientation of the rows of producers and injectors must take into account any permeability anisotropy and natural-fracture orientation. At offshore locations, the number of well slots on the drilling platforms limits the number of producers and injectors and their layout.

In this section, a number of waterflood design considerations will be discussed briefly. (Rose *et al.*³ is entirely devoted to this topic.) The design aspects discussed below include

- Injection-water sensitivity studies.
- Injection wells, injectivity, and allocation approaches, including well fracturing.

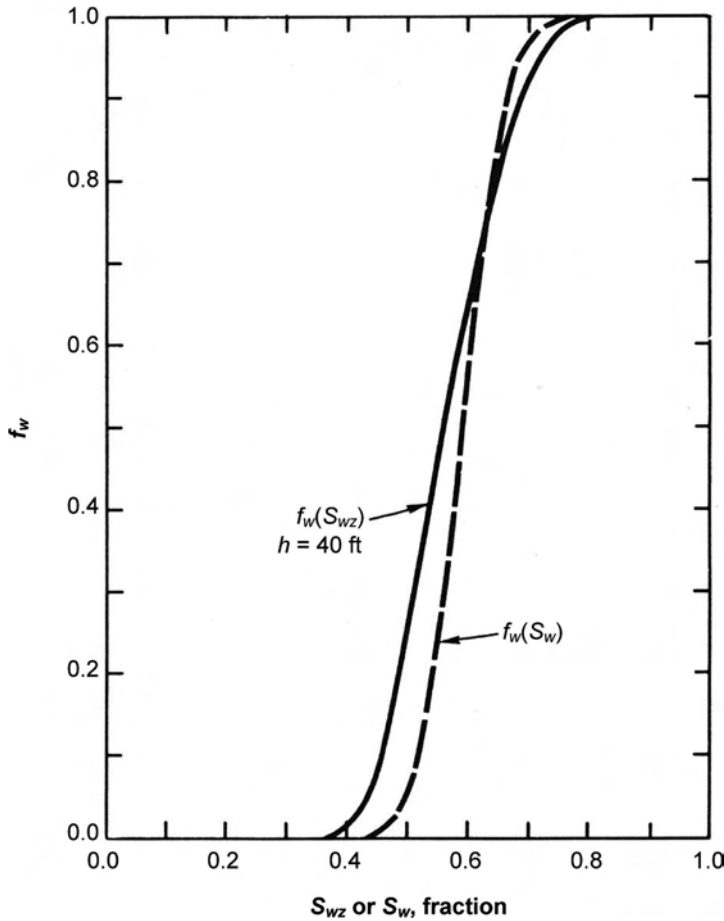


Fig. 11.33—Comparison of the fractional-flow curve for vertical equilibrium with the fractional-flow curve obtained from fluid and rock properties.² (h = reservoir thickness, ft, and S_{wz} = thickness-averaged water saturation for vertical equilibrium case with $h = 40$ ft, fraction PV.)

- Pilot waterflooding.
- Production wells.
- Surface facilities for injection water.
- Surface facilities for produced fluids.

11.7.1 Injection-Water-Sensitivity Studies. The factors to which injection-water-sensitivity studies relate are water-source and -volume options, source-water/connate-water compatibility, and source-water/reservoir-rock interactions. After the preliminary reservoir evaluation indicates that waterflooding is likely to be economically justified and that it will increase significantly the volume of oil recovered, the next consideration is to find an acceptable source from which to obtain enough water for the proposed waterflood project. Fig. 11.39 schematically shows the variety of natural sources for such water. Onshore locations typically obtain injection water from subsurface aquifer intervals or nearby streams or rivers. Nearshore and offshore waterflood projects typically use seawater.

Source-water/connate-water compatibility mainly concerns whether mixing the two waters causes any precipitation of insoluble carbonate or sulfate compounds that might impair reservoir permeability. Although permeability impairment typically is not a major consideration,

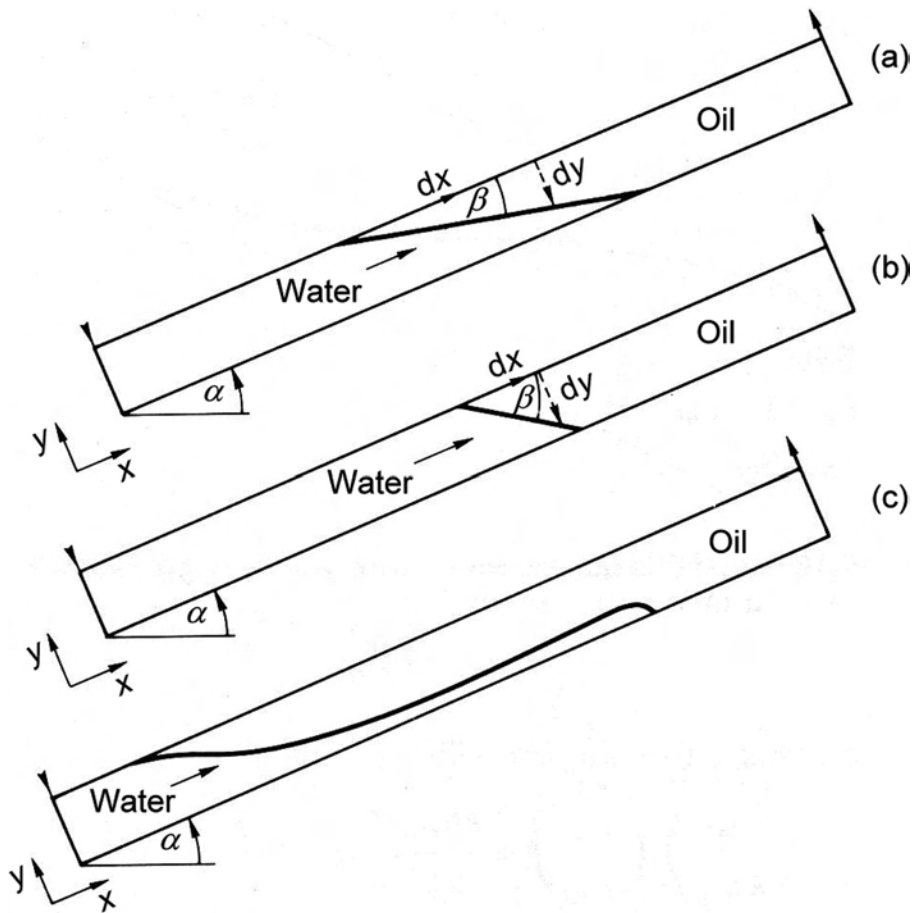


Fig. 11.34—Stable [(a) and (b)] and unstable (c) displacement in gravity-segregated displacement.² For (a), $G > M - 1$, $M > 1$, and $\beta > \alpha$. For (b), $G > M - 1$, $M < 1$, and $\beta > \alpha$. For (c), $G < M - 1$.

precipitation and scale buildup in pumps and other surface water-handling equipment can cause costly downtime and repairs.

Potential sensitivity of the reservoir pay intervals to the injection water is a major consideration. For sandstone reservoirs that contain various types of clay, the key consideration is whether there exists clay sensitivity to the difference between the connate-water salinity and the injection-water salinity, particularly for freshwater injection-water sources. Such sensitivity can occur either as clay swelling or as mobilization of clay fines, both of which can reduce reservoir permeability significantly. For high-porosity chalk reservoirs, the injection-water/reservoir-rock interaction might weaken the rock framework and cause pore collapse and surface subsidence.²⁷

Another aspect of injection-water sensitivity is the amount and size of suspended particulate being carried by the injection water. This is a concern mainly when using surface water sources for the injection water. An example of where this is a significant consideration is the Kuparuk oil field on the North Slope of Alaska, U.S.A., where nearshore ocean water is the waterflood injection water. There, the spring runoff down the rivers from the Brooks Mountains can cause the nearshore ocean water to contain unacceptable amounts of solid particulate for several weeks of the year. Similar problems occur in the Gulf of Mexico in fields near the

Layer 3	$h = 10$ ft, $k = 200$ md, $\phi = 0.20$, $k_{rw} = 0.4$, and $k_{ro} = 0.8$
Layer 2	$h = 20$ ft, $k = 100$ md, $\phi = 0.17$, $k_{rw} = 0.3$, and $k_{ro} = 0.6$
Layer 1	$h = 10$ ft, $k = 50$ md, $\phi = 0.15$, $k_{rw} = 0.25$, and $k_{ro} = 0.5$

Fig. 11.35—Individual layer properties for a three-layer example (after Ref. 26). (ϕ = porosity, fraction BV.)

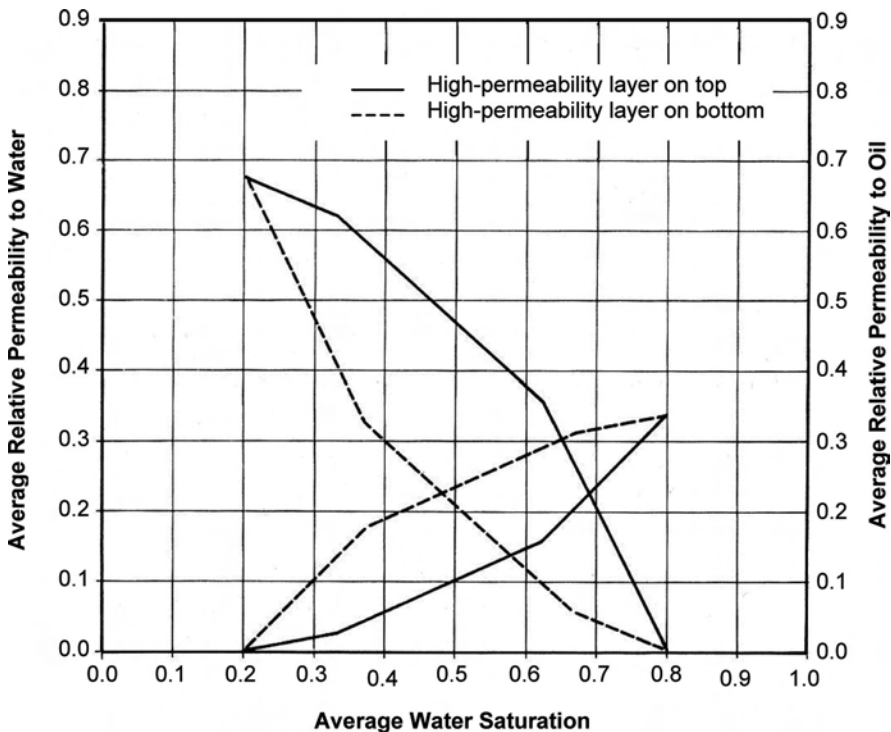


Fig. 11.36—Averaged relative permeability curves for a three-layer example (after Ref. 26).

mouth of the Mississippi River. Also in the Gulf of Mexico, water that is drawn from too near the surface often contains organic matter that can reduce injectivity.

11.7.2 Injection Wells, Injectivity, and Allocation Approaches, Including Well Fracturing.

Several aspects of the design and operation of water-injection wells are critical to their success. The first is that these wells must have sufficient injectivity to flow the desired volume of water into the reservoir each day. The expected injectivity can be calculated on the basis of routine core analysis, special core analysis and/or log data, and the existing production wells' productivity; however, well injectivity often is not known until water actually is injected into the reservoir interval. This is because the near-wellbore "skin" (a rock volume of reduced permeability around the wellbore) is not known until an actual well test is conducted. Injection wells

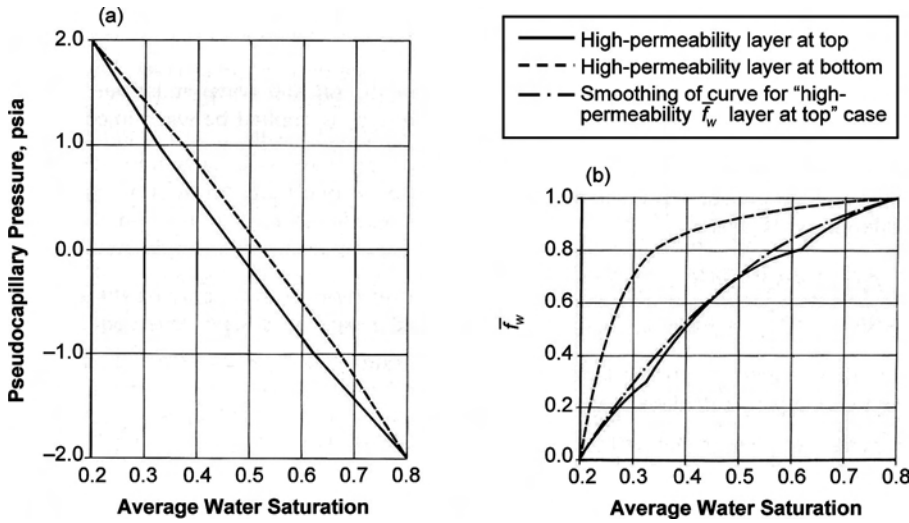


Fig. 11.37—Pseudocapillary pressures (a) and fractional-flow curves (b) for a three-layer example (after Ref. 26).

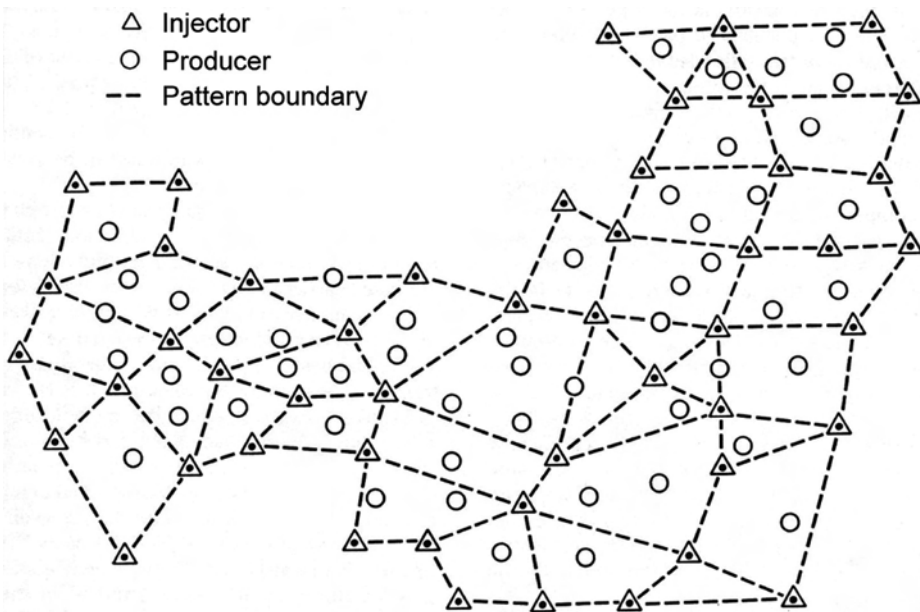


Fig. 11.38—Irregular five-spot pattern layout.³

can be fractured to eliminate positive skin in the near-wellbore region; however, fracturing must be done carefully to avoid fracturing out of the reservoir interval and into adjacent porous and permeable intervals into which injection water can be lost.

An aspect of well injectivity that has been studied during the last 20 years is the change in rock stresses that is caused by the cooling effect of the injection water on the near-wellbore region around injectors. This happens particularly in Arctic and offshore waterflood operations, where the injection-water temperatures can be considerably below the reservoir temperature

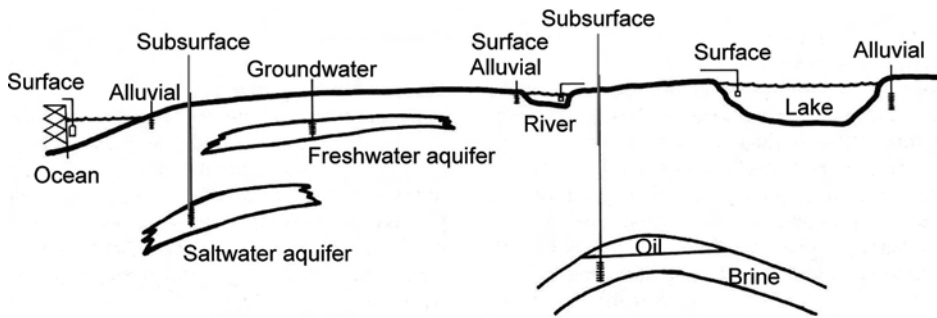


Fig. 11.39—Possible injection-water sources.³

(i.e., more than 100°F difference). Perkins and Gonzalez²⁸ have studied this phenomenon and found that the cooling effect reduces the earth stresses by several hundred psi. Hence, in the reservoir, a small area around water injectors' wellbores will fracture more easily, giving that area enhanced permeability (or negative skin).²⁸ For the Prudhoe Bay field on the North Slope of Alaska, U.S.A., the fracture gradient was reduced to as low as 0.50 psi/ft from the original fracture gradient of 0.60 to 0.70 psi/ft.²⁹

Another critical aspect of water-injection-well design and operation is the allocation of water to zones being waterflooded. Having the ability to allocate injection water as desired to the various waterflooded intervals is important for waterflood success because the overall waterflood is controlled primarily at the injection wells, not at the production wells. This is not an issue if there is only one reservoir interval, but in many oil fields, there are multiple reservoir intervals being waterflooded at the same time. If possible, the injection-well bottomhole-tubing, packer, and perforation configuration should be designed to allow control of the relative volumes of water that are injected into the various intervals being waterflooded. This can be accomplished if each injection well is perforated in only one reservoir interval, but one reservoir interval per injector is unlikely to be cost-effective compared to the alternative of fewer wells with more-complicated arrangements of chokes, tubing strings, and packers, particularly if there are multiple pay intervals stacked on top of each other.

Optimum completion design is site-specific and must be based on mechanical and reservoir characteristics for the project at hand.

11.7.3 Pilot Waterflooding. Pilot waterfloods seldom are used today because of the wealth of experience in waterflooding; however, in many situations, they have been conducted to provide more quantitative data on the potential for successful waterflooding on a fieldwide scale.³⁰ Such pilot waterfloods definitely provide useful data concerning water injectivity, tendencies for early water breakthrough, and additional recovery potential. Determining recovery potential requires a pilot waterflood that is designed to represent what will happen in a full-scale application. Too often, one-pattern pilot waterfloods have been conducted that do not represent the confined injection/production relationship that is needed. Also, if the pilot waterflood is conducted on a well spacing that is considerably smaller than that used for the full-field waterflood (so that injector/producer connectivity data can be obtained sooner), the information it provides might be misleading about the injector/producer connectivity on the larger well spacing of the full-field waterflood. Thus, definitive objectives of a pilot waterflood should be established, and the pilot project should be designed and operated accordingly.

11.7.4 Production Wells. In many cases, the water-injection wells are drilled as new wells; however, the production wells typically are those that already are producing from the oil field. For waterflooding, producers should be completed in the same intervals in which the injection

wells are completed. If the production wells are completed in several reservoir intervals, it is best to have sufficient length between the perforated reservoir intervals to allow workover operations to shut off those intervals that are producing much water and little oil by either cement-squeeze operations or by setting a packer in the production tubing.

11.7.5 Surface Facilities for Injection Water. Maintaining high water quality is important for sustaining injectivity, reducing corrosion-related costs, and minimizing equipment plugging. The American Petroleum Institute (API) has published recommendations for analysis of oilfield waters³¹ and for biological analysis of injection waters.³² The industry also has adopted standardized procedures for membrane/filterability tests.³³

The water-injection surface facilities prepare the water chemically for injection and pressure the water to the desired wellhead injection pressure. Depending on the source of the injection water, the water might need treatment to remove oxygen, prevent scale and corrosion, and chelate the iron. It also might need microbiological treatment and to be filtered to remove particulates.^{34,35} What injection-water preparation techniques are used will vary from one waterflood project to the next. (See chapters in the Facilities and Construction Engineering volume for extensive information on preparing water for injection.) This section specifically discusses surface and produced waters, but the techniques that are covered here also are applicable to water that is produced from aquifers.

One major consideration in injection-water treatment is to prevent the reservoir from being “inoculated” with sulfate-reducing bacteria that can cause a reservoir to develop an in-situ H_2S concentration during the waterflood. This particularly is a problem when using ocean water, which contains both the sulfate-reducing bacteria and the sulfate ions that are their food supply. Once the sulfate-reducing bacteria have been introduced into a reservoir, they are essentially impossible to kill; however, they can be controlled with the injection of bactericides such as formaldehyde.^{36,37}

Pressuring water to the desired injection pressure is the final step before it is piped to the injection wells. Chapters in the Facilities and Construction Engineering volume of this *Handbook* cover the types of equipment required for increasing the pressure of the injected water. The wellhead injection pressure is calculated by subtracting the weight of the injection-water column from the desired bottomhole pressure, and then adding friction-flow pressure losses down the wellbore.

In a few reservoir situations, “dumpflooding” has been practiced. This is where a water-bearing formation above or below the oil reservoir is perforated, as is the oil-reservoir interval in those same wellbores. Water then is allowed to flow directly from the water-bearing formation into the oil-bearing formation, without ever bringing that water to the surface for any treating or pumping. This is a very simple approach to waterflooding, but generally it has been unsuccessful because the rate of water injection is uncontrolled and limited to the pressure difference between the two formations, which decreases with time as the water-bearing interval is depleted, particularly near the wellbore, and as the oil reservoir interval near the wellbore pressures up.

11.7.6 Surface Facilities for Produced Fluids. The facilities for handling produced fluids for a waterflood must be designed with considerable flexibility. These facilities must handle a wide range of gas-, oil-, and water-production rates over the course of the waterflood, typically a period of several decades. Several chapters in the Facilities and Construction Engineering volume of this *Handbook* cover these issues in detail.

Initially, the production wells are likely to handle only oil and gas, without water production. When water breakthrough occurs, the water volumes will increase and, over time, water will become the great majority of the produced fluids. Accordingly, a variety of water issues must be considered. First is whether the produced fluids can be separated easily or must be

treated with heat and/or chemicals in the surface equipment to achieve the desired level of separation. Second is whether the precipitation of scale in the producing wells or the production surface facilities is causing complications. Regarding scaling tendencies and because of increasing environmental concerns, the handling of NORMs has become an issue with respect to produced-water discharges.³⁸

Over the duration of a waterflood and as produced-water volumes increase, there is likely to be the need and desire to reinject the produced water. In this situation, the produced water must be treated so that its oil and particulate content is sufficiently small that, when the water is reinjected, these very small oil droplets will not reduce the injectivity of the water injectors.³⁹ Oil fields in the North Sea and on Alaska's North Slope have had to reinject large volumes of produced water.^{40,41} Regarding injectivity losses, experimental coreflood data tend to be more pessimistic than is actual injector performance in the field.³⁷ In all cases, to reinject produced water successfully, that water must be treated to meet specifications determined to minimize those injectivity losses.⁴¹

11.8 Waterflood Monitoring

Because a waterflood project spans several decades, it is monitored continuously and routinely by engineers who are responsible for its operations, as well as periodically using more-detailed and specialized technical studies (e.g., full-field numerical-reservoir-simulation studies). There are many opportunities to modify and improve the waterflood as data are acquired and analyzed.

The basics of a waterflood analysis center on material-balance concepts. Applying material-balance concepts means that initially there is “reservoir fill-up” if the reservoir previously had some years of primary production. During this period, the reservoir is repressured to its original reservoir pressure because the injected-water volumes will be substantially greater than the produced-fluid volumes. Thereafter, the waterflood will be operated as a voidage-replacement process.

The earliest waterflood-monitoring techniques were developed soon after the first field applications of waterflooding; they were based on simple plots, maps, and calculations. Among these were the plots published by Dyes *et al.*⁴² that estimated the water breakthrough and post-breakthrough behavior of various waterflood pattern configurations. **Figs. 11.40 and 11.41** are examples of these plots for a five-spot pattern and a direct-line-drive pattern, respectively, and can be used to make “first-estimate” waterflood calculations.

In this section, the aspects of waterflood monitoring that are discussed are

- Data acquisition: routine data gathering.
- Special-data acquisition: infill and observation wells and 4D-seismic data.
- Simple waterflood-analysis techniques: X -plot, $\log(\text{WOR})$ vs. cumulative-oil-production plots, and decline curves.
- Sophisticated waterflood-monitoring techniques.

11.8.1 Data Acquisition—Routine-Data Gathering. Waterflood monitoring begins with the acquisition of the routine data that are necessary for engineering calculations. The routine data include well-by-well daily oil-, gas-, and water-production rates; well-by-well water-injection rates; injection wellhead pressures; and production-well pressure data. Often, the well-by-well daily rate data are back-calculated from the gathering center's total produced volumes of these three phases, and then are allocated back to the individual wells on the basis of periodic individual well tests.

Next, the production- and injection-well data are allocated to the individual reservoir intervals, if multiple reservoir intervals are commingled. This well-by-well data allocation requires that spinner surveys (or their equivalent) be run periodically in the individual wells to determine how much of the fluid is coming from each of the perforated intervals. The spinner surveys should be run both with the well flowing and with the well shut in. Data from these

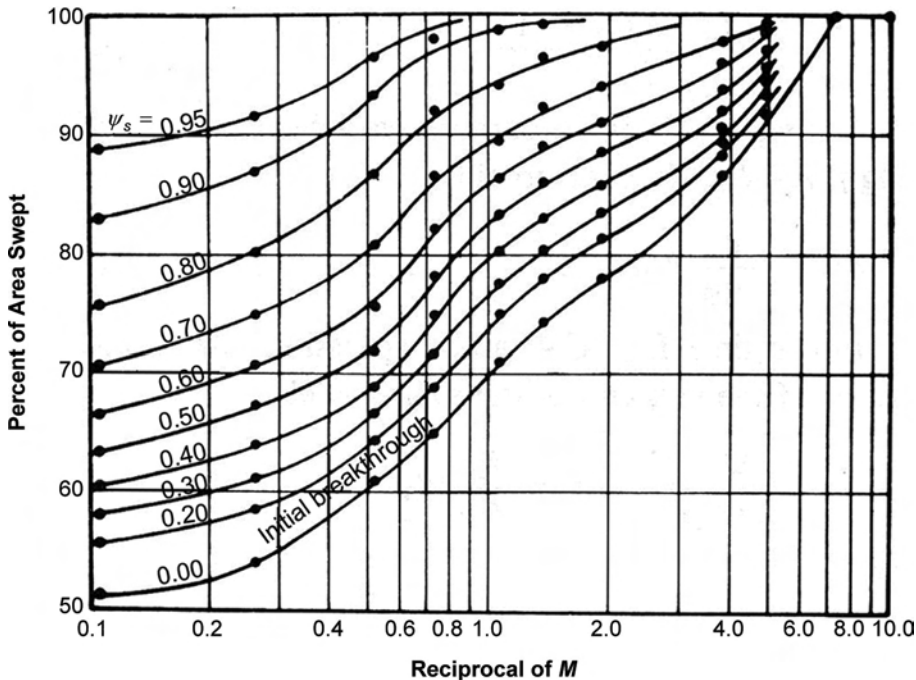


Fig. 11.40—Effect of mobility ratio on oil production for five-spot pattern.¹ (ψ_s = fraction of total flow coming from the swept portion of the pattern.)

surveys, along with pressure-buildup and -falloff data, help in the estimation of the reservoir pressure in the various reservoir intervals. Also, a variety of production logs should be run to estimate changes in fluid saturations in the near-wellbore region as the waterflood progresses.

The field engineers can use all these data in the types of calculations that are described below.

11.8.2 Special-Data Acquisition: Infill and Observation Wells and 4D-Seismic Data. During the waterflood, there are likely to be opportunities to gather additional data away from the injection and production wellbores. These data can take several forms.

Infill wells are likely to be drilled in locations where oil should not have been displaced by the injected water. Consequently, these locations are not good locations for determining how effectively the various portions of the reservoir intervals are being swept by injected water. After drilling, the hydrocarbon distribution actually present at an infill-well location is evaluated using openhole or cased-hole logging. Where formation waters have a sufficiently high salinity, pulsed-neutron thermal-decay time and resistivity logging may be used to evaluate the residual oil saturations. In lower-water-salinity conditions, carbon/oxygen and resistivity logging are used. Using these techniques, the locations of fully flooded, partly flooded, and unflooded reservoir intervals can be determined in new wells and in existing producing wells. Multiple logging runs over time in a producing well allow the monitoring and management of a waterflood. If wells are drilled later during the waterflood, then the residual-oil-saturation distribution can be obtained by use of special coring procedures or special tracer tests, as described elsewhere in this volume of the *Handbook*.

Special observation wells sometimes are drilled at a location in the oil reservoir where the water/oil flood front should be detectable as it passes. Historically, most of these wells were cored but had steel casing, such that standard logging methods could not be used; however, before the development of through-steel-casing resistivity logging, fiberglass casing together

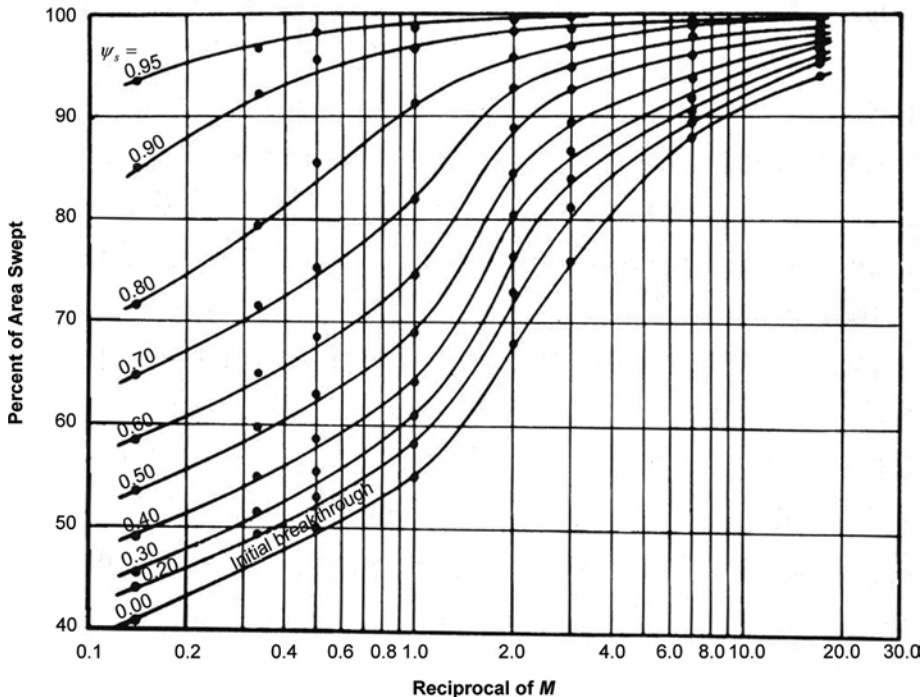


Fig. 11.41—Effect of mobility ratio on oil production for the direct-line-drive (square pattern). In this case, the distance between adjacent rows of wells is equal to the distance between like wells in a row.

with induction-resistivity logging occasionally were used to observe the water/oil displacement process over time.

Recently, the 4D-seismic technique has been developed to determine in what directions the water is moving from the injection wells.^{43,44} The 4D-seismic technique compares 3D-seismic data that were obtained before the start of waterflooding to a second or third 3D survey that was conducted some years later. This allows an areal visualization of where there are high-pressure areas caused by water injection and where there are low-pressure areas caused by production (typically from the presence of some free-gas saturation near the production wellbores). Also, the 4D picture might show which portions of the reservoir pay intervals are well connected and which are not.

11.8.3 Simple Waterflood-Analysis Techniques: X-Plot, Log(WOR) vs. Cumulative-Oil-Production Plots, and Decline Curves. The initial engineering analysis of waterflood performance is done to ensure that the water is being injected into the wells at the desired well-by-well rates and, if several oil-reservoir intervals are perforated in each injector, that each of those reservoir intervals is taking its appropriate share of the injected water from each of the injection wells. This may appear trivial, but many waterfloods have had significant problems in this regard. Before the waterflood begins, the engineers must estimate how much water should be flowing into each injector. Those estimates are based on fill-up and voidage-replacement calculations for that area of the oil reservoir and for the reservoir as a whole.

A “bubble map” can be used for visualizing the advance and relative volumes of the injected water. Fig. 11.42 shows the injection wells’ bubble map for one of the staggered line-drive pattern elements of one of the oil-reservoir intervals of the Long Beach Unit (LBU) area of the Wilmington oil field in California, U.S.A.⁴⁵ Bubble maps are created for each injector by dividing the volume of water injected by the movable oil per vertical reservoir interval [thickness ×

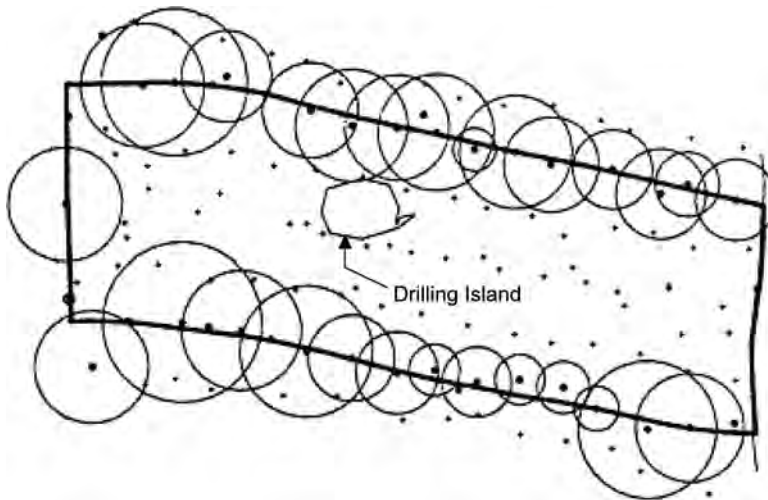


Fig. 11.42—Layer injection-bubble map for Voidage Block 3 FO sand interval—LBU of the Wilmington oil field in California, U.S.A.⁴⁵

porosity $\times (1 - S_{wc} - S_{orw})$] to calculate the area that should have been swept by that volume of injected water; then presenting these areas on a map as circles of various sizes centered on each of the injection-well locations.

Another aspect of waterflood monitoring is to track the performance of the production wells. As noted earlier, some oil reservoirs will have had a considerable period of primary production during which the reservoir pressure was drawn down below the bubblepoint pressure and a gas saturation developed. These reservoirs first will “fill up,” which means that they will go through a period during which the injection water displaces mobile gas and increases the reservoir pressure to force free gas back into solution in the oil. During the early part of the fill-up period, the production wells will see minimal response because of water injection. When the reservoir pressure has returned to its original value, the water injection becomes a voidage-replacement operation. During the voidage-replacement period, the engineer must make sure (1) that the volume of injected water equals the reservoir voidage of oil, gas, and water production, and (2) that the various areas or patterns of the reservoir are being balanced to maximize the oil recovery and to minimize water-handling operating costs.

A number of graphs of the production and injection data can be prepared to help analyze the waterflood performance. For example, a conformance plot is a plot of cumulative oil recovery (or oil-recovery efficiency) vs. net displaceable hydrocarbon PV injected. A waterflood-performance envelope is defined by drawing an obtuse triangle that is bounded by recovery at the start of waterflooding, the maximum oil recovery at 100% of the x-axis, and a third point, F_{pvg} , which is related to the net injection required to displace the existing gas saturation at the start of the waterflood and is defined as:

$$F_{pvg} = S_g / (1 - S_{wi} - S_{orw}), \dots\dots\dots (11.25)$$

where S_g = gas saturation, fraction.

Because actual performance cannot fall outside the performance envelope, this plot is a check on fluid allocation for a pattern. This plot also can indicate when injection water is being lost to thief zones. When slope changes are noted in this plot, the possible causes should be investigated. **Fig. 11.43** is a conformance plot for the Kuparuk River oil field on Alaska’s North Slope.⁴⁶

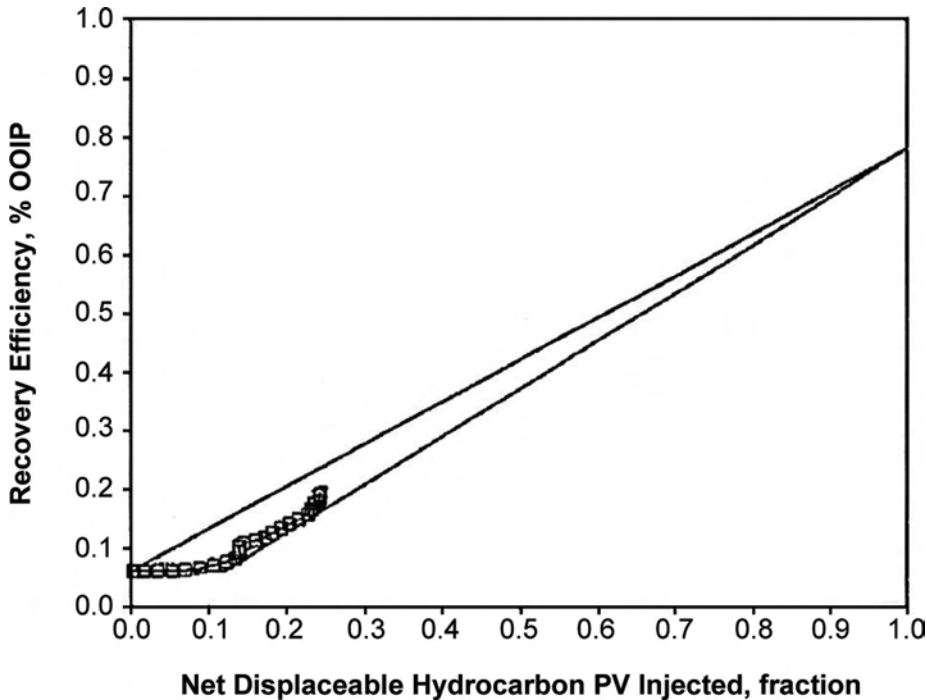


Fig. 11.43—Example of a conformance plot.⁴⁶

Other plots that typically are made after water breakthrough are the X -plot and its close cousin, the $\log(\text{WOR})$ vs. cumulative-oil-production plot. The X -plot technique, developed by Ershaghi and coworkers, is based on the leaky-piston-displacement concepts of Buckley and Leverett⁴⁷ and assumes that the plot of $\log(k_{rw}/k_{ro})$ vs. S_w is a straight line.^{48,49} The X -plot is a graph of recovery, E_R vs. X , where $X = \ln\left(\frac{1}{f_w} - 1\right) - \frac{1}{f_w}$. This plot's underlying assumption suggests that its usefulness theoretically is limited to higher water cuts.

The “cut-cum” plot, or plot of $\log(\text{WOR})$ vs. cumulative oil production, easily can be made using production data for each well and for reservoirs as a whole. These plots generally are useful predictors of future waterflood performance because there is a considerable period of straight-line behavior on these plots for many wells and reservoirs when the waterflood is fully developed without major variations in field operations. Analysis of $\log(\text{WOR})$ vs. cumulative-oil-production plots for waterflood analysis has been conducted using numerical reservoir simulation. These simulations show that the linear trends on this type of plot are found even at low WOR values and also are found for a variety of reservoir layering, flood configurations, and operational changes.⁵⁰

Decline curves also have been used for waterflood analysis. Where waterfloods were initiated in depleted sandstone reservoirs, empirical correlations were developed to estimate the likely oil-rate increases during fill-up and while the oil bank moves toward the production wells, and then to estimate the oil-rate declines as the WOR increased later in the life of the waterflood.⁵¹ Fig. 11.44 shows the production response for this situation. For the oil-rate-increase and -decline periods, the plot has exponential oil-rate-vs.-time characteristics.

Hall plots and Hearn plots often are used to monitor injection wells. Use of these plots helps to maximize water-injection rates, which accelerates oil production from offsetting producers. On a Hall plot, the bottomhole injection pressure is plotted vs. cumulative water injection

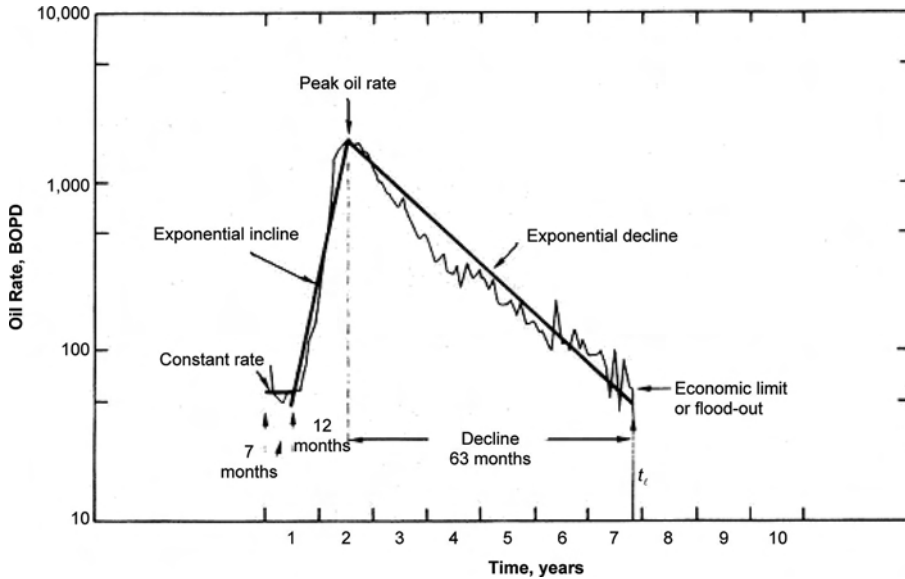


Fig. 11.44—Production response of a fully developed waterflood with water input to all injection wells at the beginning of the flood.²

to monitor reservoir fill-up and average-reservoir-pressure increase. On a Hearn plot, the inverse injectivity index is plotted vs. cumulative water injection. Both types of plots also can be used to determine whether the water-injection rates are being kept below those allowed by the fracture-parting pressure.⁵²

A combination of these simple plot and calculation techniques typically is used for waterflood analysis. By plotting both oil rate vs. time and $\log(\text{WOR})$ vs. cumulative oil, the engineer can better understand how well the waterflood is performing compared to original estimates and can determine what changes, if any, are needed.

Keep in mind that most of these techniques are premised on continued current operations. If there are significant changes in the allocation of injection water or if there are well workovers or pattern realignments, then the trends on these plots might not remain straight lines from which future waterflood performance is easy to predict.

11.8.4 Sophisticated Waterflood-Monitoring Techniques. The modern numerical reservoir simulator is the best tool for performing waterflood analysis, including history matching of past performance and projection of future performance for continued current operations or for various operational and well changes. However, this tool generally is used with an updated history match only every 5 to 10 years.

Between major studies, the field engineers typically use simpler surveillance methods that have been upgraded by the availability of the notebook computers that have sizeable hard disks and rapid computing capabilities. New software packages have been developed that analyze trends and can handle large amounts of electronically acquired data.

One example of the use of this approach is the set of techniques used for the LBU area of the Wilmington oil field, which has 1,200 wells, multiple oil reservoirs, and 27 years of waterflood history.⁴⁵ Fig. 11.45 shows the logic used for the surveillance calculations. As Fig. 11.45 shows, a large waterflood involves massive amounts of data that must be handled logically and consistently so that the engineers can obtain useful results.

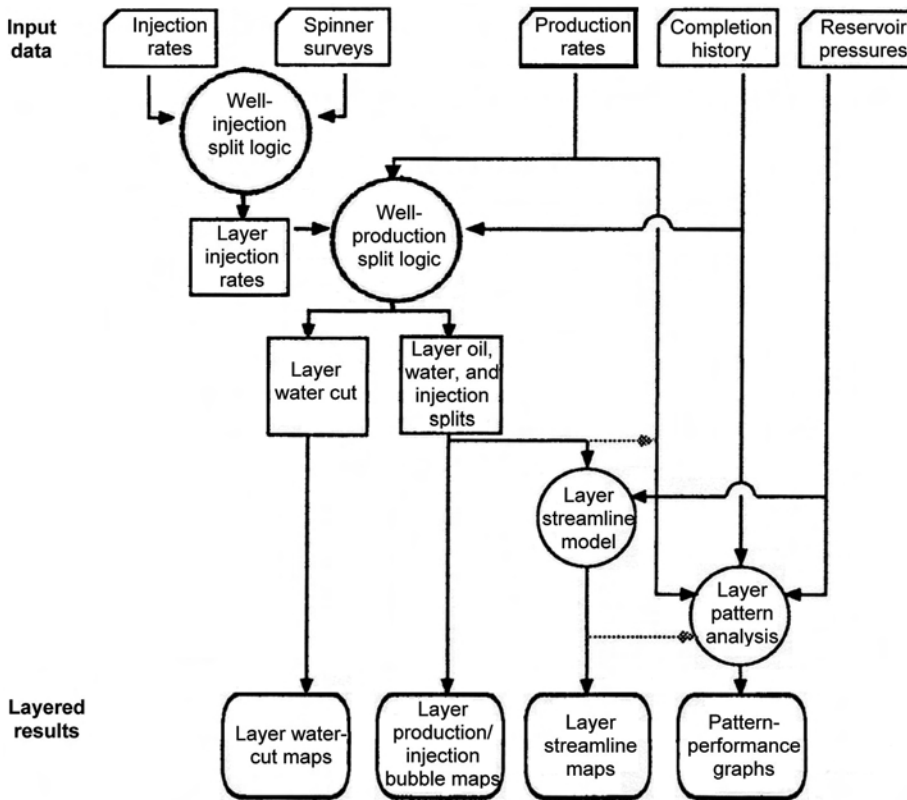


Fig. 11.45—Surveillance-overview logic for a layered waterflood.⁴⁵

The routine waterflood-analysis calculations that are used for the Kuparuk River oil field^{46,53,54} are another example of this approach. The Kuparuk River oil field covers more than 200 square miles and contains 600 patterns, with two separate reservoir intervals. Again, a massive amount of well data has been gathered over more than a decade of waterflooding and primary production. All of the simple calculation procedures that were discussed in earlier sections of this chapter [decline curves, $\log(\text{WOR})$ vs. cumulative-oil-production plots, and X -plots] are used to evaluate well-by-well and pattern performance. Figs. 11.46 and 11.47 show relationships among the various calculation and database modules within the material-balance shell and the object relationships.⁵⁴

These two examples are of very large oil fields. Oil fields with fewer injection and production wells will require less-extensive waterflood-monitoring calculations; however, all the types of material-balance calculations will be required to determine whether the waterflood is performing as expected and whether significant operational changes are needed.

Also keep in mind that the usefulness of all these calculations depends greatly on the quality of the input data. The original field data must be reviewed for completeness and accuracy before entering them to these types of calculations. Where gaps in the data or clearly erroneous numbers are found, the engineers must judge how to edit the data or adjust calculations for such data problems. Where total field data has been allocated to the individual wells, the allocation procedures should be checked, including whether they have changed over time and thus caused changes in the slopes of some of plotted data—changes that are not real, but that are artifacts of the data-allocation procedures.

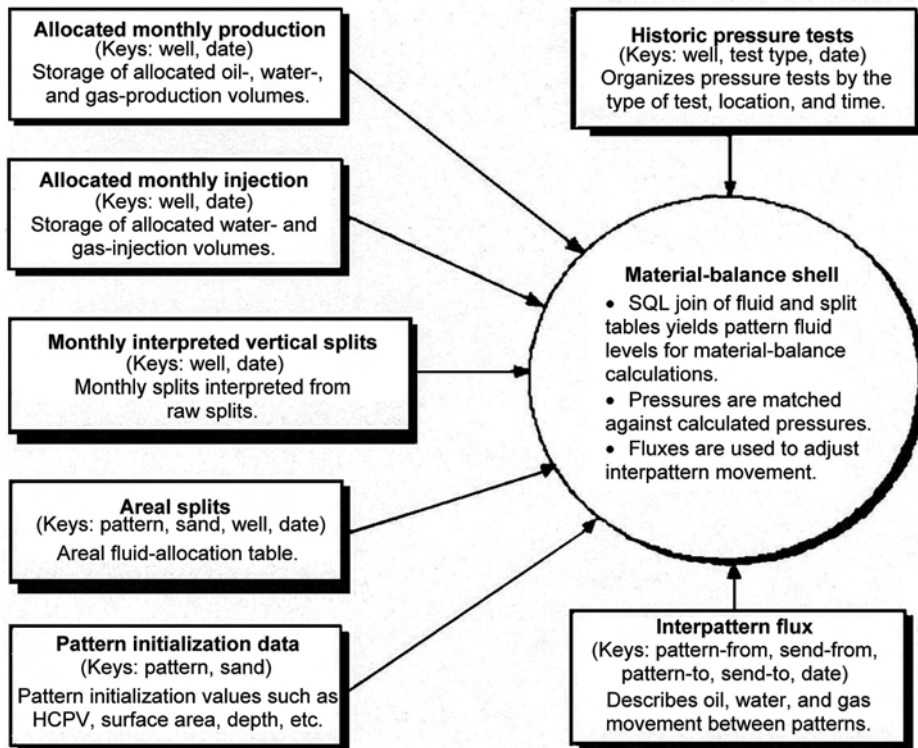


Fig. 11.46—Relationship of relational database management system (RDBMS) tables to material-balance shell logic.⁵⁴ (HCPV = hydrocarbon pore volume, and SQL = structured query language.)

11.9 Waterflood Field-Case-Studies Examples

Several oil fields have been discussed in this chapter as examples of the use of various waterflood concepts and calculation procedures. The SPE technical literature contains many papers about major fields that have been waterflooded for a decade or more. In this section, a few of these oil fields are described briefly to highlight these waterflooding projects from their inception to the present, including how they were modified as they proceeded and as detailed engineering analyses were completed, and what complications were encountered. As noted earlier, many technical papers are available on these topics, but here only one to three publications are referenced for each oil field.

The waterfloods in these examples involve oils that range from light (30 to 40°API, with reservoir viscosities of 0.2 to 0.4 cp) to heavy (15 to 20°API, with reservoir viscosities of 30 to 70 cp). In all cases, the waterfloods have maintained reservoir pressure and increased oil recovery very successfully. A few other waterfloods also will be discussed briefly to highlight additional waterflooding considerations. The fields and waterfloods that are discussed here are Ekofisk (North Sea, offshore Norway), Wilmington (southern California, U.S.A.), Kuparuk River (Alaska North Slope, U.S.A.), west Texas carbonate waterfloods (U.S.A.), and Kirkuk (Iraq).

Three of these fields are various types of carbonate, and two are sandstone. Geographically, one is in the North Sea; one in the Long Beach, California, harbor area; one in the Arctic on Alaska's North Slope; and two are in onshore oilfield areas. In some of these oil fields, the waterflood has been followed by EOR that uses miscible- or immiscible-gas injection in which some water injection has been continued to provide mobility control.

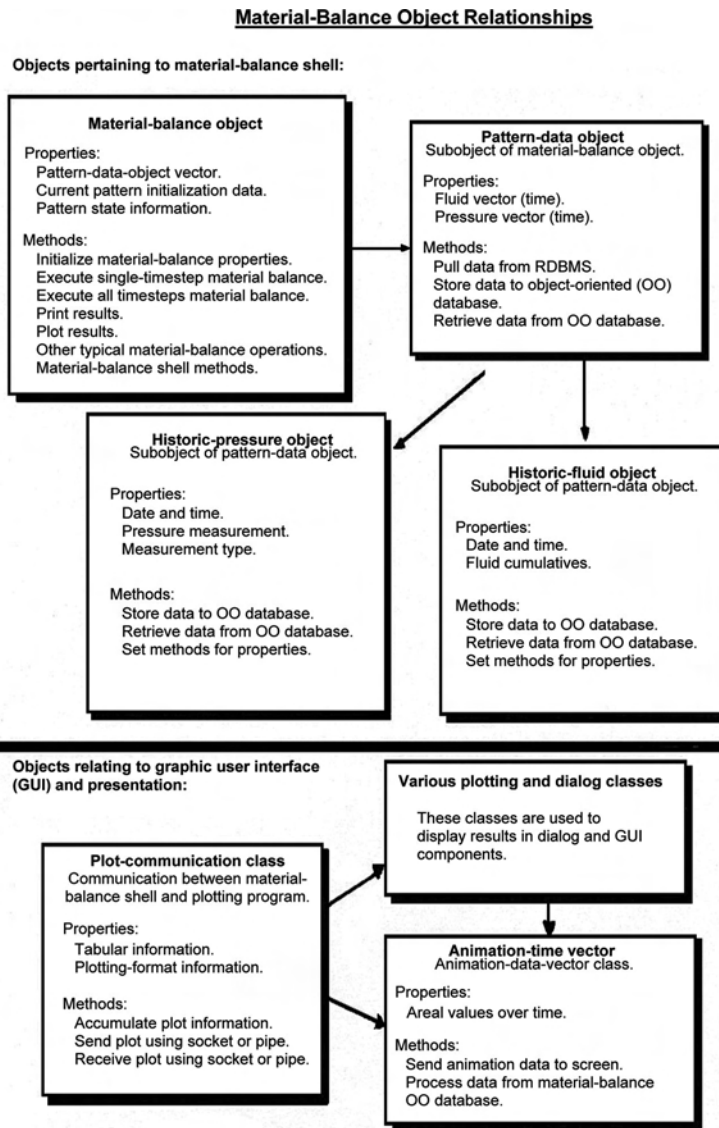


Fig. 11.47—Material-balance object relationships.⁵⁴

The reservoir-management chapter in this volume of the *Handbook* also describes the performance of several fields that are being waterflooded. That discussion's emphasis is on reservoir management; however, it does include some information on recovery performance and depletion strategies.

11.9.1 Ekofisk (North Sea).⁵⁵⁻⁵⁷ The Ekofisk oil field is in the North Sea, south of Norway. It is a large, carbonate reservoir [(6.4 billion bbl stock tank original oil in place (STOOIP)] that has two zones, Ekofisk and Tor, that are high-porosity, fractured chalks with matrix permeabilities of approximately 1 md and effective permeabilities that range from 1 to 50 md. Discovered in 1969, the Ekofisk field was found at very high pressure [7,120 psia at 10,400 ft true vertical depth subsea (TVDSS)] but with an initial bubblepoint pressure that was 1,600 psi below initial reservoir pressure. Ekofisk's oil is 38°API, has a viscosity of approximately 0.25

cp, and has a solution gas/oil ratio (GOR) of more than 1,500 scf/STB. Primary production began in June 1971 and peaked in 1976 at 350,000 BOPD from 30 production wells (with 8 gas reinjection wells). Fig. 11.48 shows the structure of the Ekofisk field and its injection- and production-well locations as of early 2003. Laboratory-test results indicated that waterflooding by water imbibition into the low-permeability chalk was favorable for the Tor formation, but the laboratory results for the Ekofisk formation were variable.⁵³ A waterflood pilot of the Tor formation was initiated in 1981, and favorable results were obtained by 1983. A 30-slot water-injection platform with an injection capacity of 375,000 BWPD started up in 1987. A second waterflood pilot was run in the lower Ekofisk formation from 1985 to 1987, and its results were positive.³⁰ Further laboratory studies of the upper Ekofisk formation were somewhat negative, but a water-injection test into this zone and a coring of a sidetrack well 6 months later indicated that the upper Ekofisk formation also could be waterflooded successfully. By the early 1990s, all three intervals were receiving injected water.

Surface subsidence was a major issue at Ekofisk. By 1984, the seabed had subsided approximately 10 ft, prompting a major project to jack up the offshore platforms. A major field study in 1992 concluded that using water-injection pressure maintenance to arrest the reservoir pressure decline could minimize future seabed subsidence. Voidage replacement was achieved in 1993. Additional laboratory studies found that water injection had induced shear in the chalk. Shear failure and water-weakening of the rock matrix causes additional deformation of the chalk, even under conditions of constant or decreasing stress levels. Despite the use of voidage-replacement waterflooding, seabed subsidence continued until 1998, when the subsidence rates slowed dramatically because the water-weakening effect was expended and the reservoir pressure had increased.

In 1997, production began from the 50-slot production platform 2/4 X, and in 1998 full processing of the Ekofisk fluids was handled by the 2/4 J processing platform. These new “Ekofisk II” facilities replaced the aging original facilities and were designed to increase operational efficiency and to allow safe and economical production until at least 2028, the end of the current license period. The current best estimate of the ultimate recovery factor from the start of production through waterflooding is 44% of OOIP.

During the past 20 years of waterflooding, many operational changes have been made at Ekofisk. The changes were a logical progression that was based on laboratory studies, field pilot tests, and engineering analyses of field production and pressure data. All of this has led to a very successful waterflood project, but with a few unexpected complications that the engineers had to handle in the course of the waterflood project.

11.9.2 Wilmington Oil Field (California). The LBU area of the Wilmington oil field (southern California, U.S.A.) is mainly under the Long Beach harbor and contains more than 3 billion bbl of OOIP.^{45,58,59} This oil field is a large anticline that is crosscut by several faults with displacements of 50 to 450 ft. It consists of seven zones between 2,500 and 7,000 ft TVDSS, the upper six of which are turbidite deposits of unconsolidated to poorly consolidated sandstone (1 to 1,000 md and 20 to 30% BV porosity) interbedded with shales. The gross thickness of 3,300 ft contains 900 ft of sandstone. In the largest zone, the Ranger (> 2 billion bbl of OOIP), the oils range from 14 to 21°API gravity and from 20- to 70-cp viscosity; hence, any waterflood would operate under a very unfavorable mobility ratio, and early water breakthrough would be expected.

From its discovery in 1936 to the 1950s, most of the onshore portion of this oil field (the non-LBU area of the Wilmington oil field) was produced using the pressure-depletion oil-recovery mechanism. Because of this, there was significant surface subsidence—up to 29 ft, with some areas dropping from several feet above sea level to below sea level (but protected by dikes). Development of the LBU area was delayed until an agreement with the government

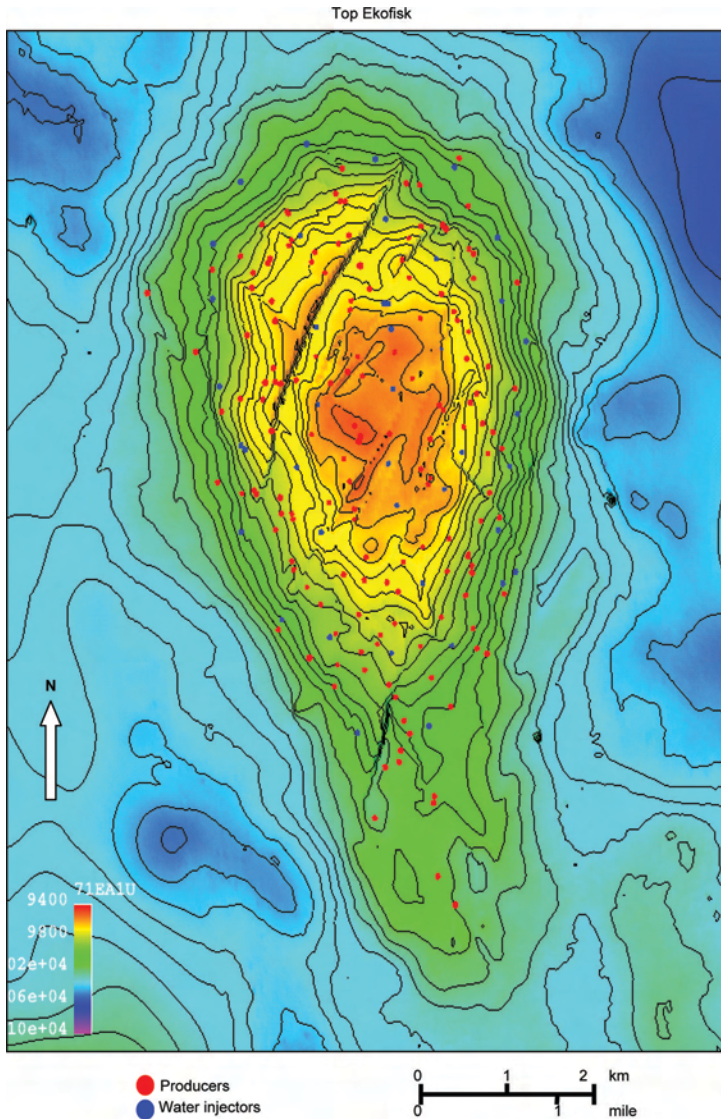


Fig. 11.48—Areal map of Ekofisk field with injection- and production-well locations (image provided courtesy of ConocoPhillips).

was reached that required voidage-replacement waterflooding to be implemented from its beginning to prevent further subsidence. LBU was developed in the mid-1960s, with the directional drilling of more than 1,000 wells from four artificial islands and from the nearby pier area. The early completions consisted of gravel-packed slotted liners that were up to 1,000 ft long in the injectors and the producers.

The LBU Ranger-zone waterflood was a 3:1 staggered line drive on a 10-acre well spacing (see [Fig. 11.49](#)); peripheral waterflooding has been used in the other zones. Oil production peaked in 1969 at 150,000 BOPD. The oil production has declined slowly since then, and the water production rate has increased steadily over the years. Water has been injected at rates of up to 1 million BWPD. Current oil production is approximately 32,000 BOPD at an average water cut of approximately 96%. To date, total production is > 940 million bbl of oil.

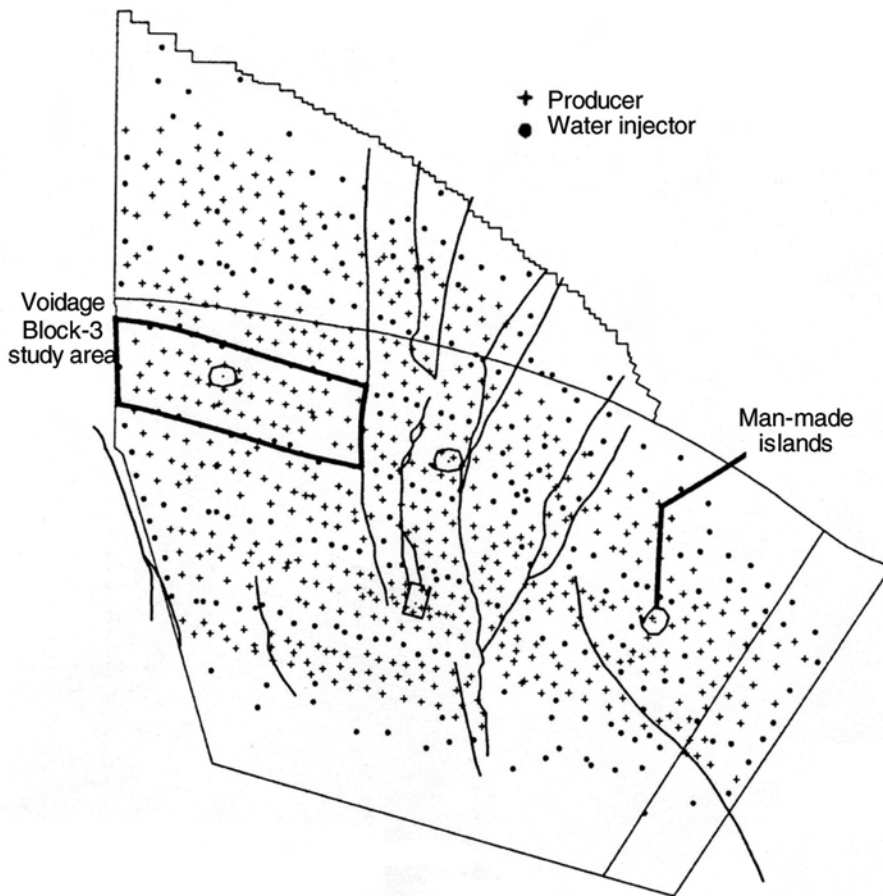


Fig. 11.49—Areal map of injection and production wells in the Ranger-zone waterflood, LBU, Wilmington oil field.⁴⁵

As years of oil-production and water-production and -injection data were acquired, the field engineers determined that some of the initial well-completion practices needed to be changed. The early completion techniques caused thief zones to develop in the higher-permeability sands, so that the deeper sands could not be pumped off. Between 1979 and 1986, by the drilling of 450 new wells into the lower portions of the Ranger and Terminal zones, this massive interval was redeveloped as two or three separate intervals.⁵⁸ This subzoning added 160 million bbl of oil reserves and increased the field rate by 30,000 BOPD.

In 1991, an optimized waterflood program was undertaken to reduce the volume of produced water, recomplete wells in sands that were not being well swept by the waterflood, and drill new wells in selected locations to improve the performance of the waterflood.⁵⁹ Pattern surveillance was used to quantify areas with low water throughputs and to guide the selection of new well locations. To aid the optimization studies, detailed studies of the geology of the field were undertaken and some 3D-seismic data were acquired and interpreted. The 3D-seismic data significantly changed the understanding of orientation of some of the faulting patterns within the field area; the previous fault patterns had been developed from the data gathered during drilling of 1,200 directional wells and from interpretation of early 2D-seismic data. Also in thicker sands, more than 50 horizontal wells have been drilled to capture bypassed “attic”

TABLE 11.2—ESTIMATED ULTIMATE-RECOVERY FACTORS FOR THE LBU PORTION OF THE WILMINGTON OIL FIELD

Zone	OOIP, million bbl oil	Recovery Factor, % OOIP
Ranger West	1,335	38
Ranger East	875	29
Terminal (upper and lower)	415	35

oil and banked oil along faults. This optimized waterflood program has added 125 million bbl of oil reserves and has the potential to add another 90 million bbl of reserves.

Over the past 30 years, the field engineers have monitored and modified the original waterflood design using the full variety of waterflood-analysis techniques, including bubble maps, log (WOR) vs. cumulative-oil–production plots, *X*-plots, streamtube models, and numerical reservoir simulation for selected intervals within the Ranger zone over most of the LBU area.

One last point: Because of its very unfavorable mobility ratio, the LBU waterflood has undergone several decades of water injection and production with 80 to 97% water cuts (5 to 25 bbl water produced per bbl oil). The injected water has stripped considerable amounts of the dissolved solution gas from the oil in the reservoir sands. This is observed in the producing GORs, which—if all the gas were assumed to be from the oil—would indicate that free gas is being produced along with the oil and water. Instead, what is happening is that each barrel of “dead” injected water that cycles through the reservoir sands is extracting 5 to 10 scf of gas per STB of reservoir oil. This causes the reservoir oil to contain less solution gas and to increase in viscosity as the waterflood progresses.

Estimated ultimate-recovery factors for the LBU as of 2005 are shown in [Table 11.2](#).

Overall, the LBU area of the Wilmington oil field has been a very successful waterflood of a lower-API-gravity, more-viscous oil. For much of the waterflood period, the water cuts have been high, 80 to 97%. The LBU waterflood has successfully prevented further surface subsidence.

11.9.3 Kuparuk River (Alaska North Slope). The Kuparuk River oil field is west of the supergiant Prudhoe Bay oil field on Alaska’s North Slope and was discovered in 1969.^{12,46,50,54} It has approximately 5.9 billion bbl of STOOIP and covers more than 200 sq. miles (see [Fig. 11.50](#)). The sandstone reservoir consists of two zones [A (62% of STOOIP) and C (38% of STOOIP)] that are separated by impermeable shales and siltstones. Sales oil is approximately 24°API with a viscosity at reservoir conditions of approximately 2.5 cp. The reservoir oil was approximately 300 to 500 psi undersaturated at the original reservoir pressure of approximately 3,300 psia. The reservoir is broken into segments by several north-to-south faults (density of approximately three faults per mile) that have sufficient throw to totally offset adjacent portions of the reservoir. The two major stratigraphic flow units exhibit considerably different properties, with the lower A zone having lower permeability, the C zone having considerably higher permeability, and the difference between them being approximately an order of magnitude.

The oil field was developed in stages, starting with the initially discovered eastern portion. Initial development was on 160-acre well spacing, and production started in 1981. The waterflood began in 1983. Expansion of the water-handling and -injection facilities led to full-field waterflooding in 1985. To date, more than 600 patterns have been developed with approximately 850 wells from 42 drillsites. The pattern style—a 320-acre, nominally 1:1 east/west line drive—takes into consideration the fault alignment. Annual average production peaked at more than 320,000 BOPD in 1992. Water production began in 1983, and the WOR slowly but steadily increased over the years to a value > 1 by 1990. The two intervals have been flooded at differ-

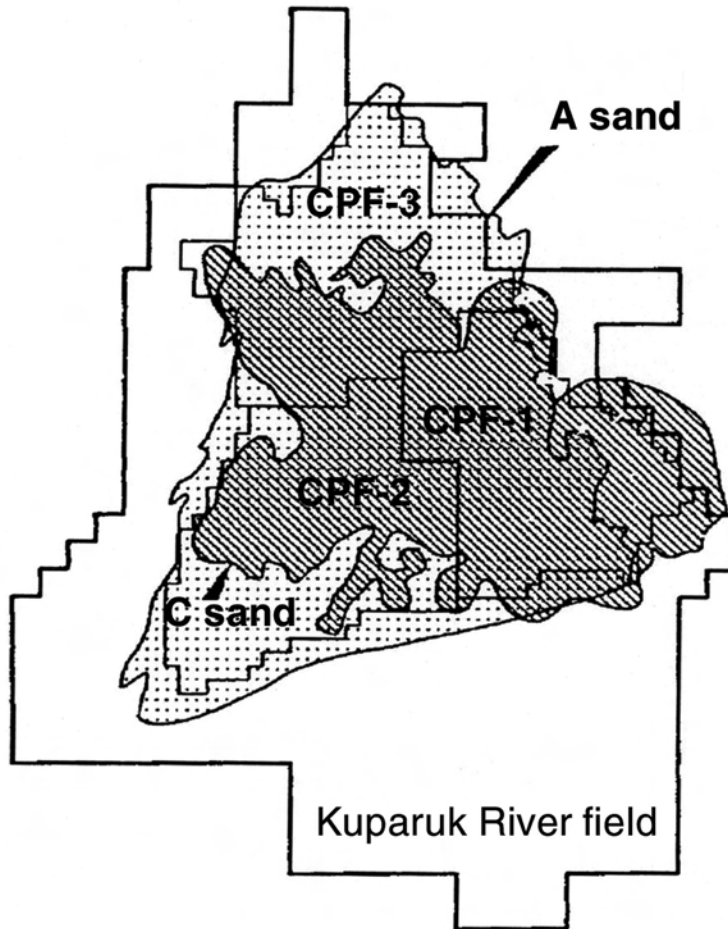


Fig. 11.50—Areal map of reservoir sands, Kupařuk River oil field.⁵³ (CPF = central production facility. On this map, CPF 1, CPF 2, and CPF 3 refer to the areas of the Kupařuk River field that are producing into these three sets of facilities.)

ent rates because of their different reservoir properties. Practically all of the wells have been hydraulically fractured to enhance well productivity and injectivity.

The most significant aspects of the Kupařuk River waterflood are the field pattern development taking into account the reservoir-fault alignment, the allocation of water injection into the dually completed water-injection wells, and the souring of what was originally an H₂S-free oil reservoir. Produced water is treated and reinjected with make-up seawater to balance pattern withdrawals. During the waterflood, the reservoir became inoculated with sulfate-reducing bacteria.^{33,34} Because of the sulfate content of the seawater, these bacteria flourished and multiplied at reservoir conditions, so that the produced gas began to contain H₂S.

Estimated ultimate-recovery factors for the Kupařuk River oil field are given in [Table 11.3](#).

The Kupařuk River waterflood has been very successful because of the field engineers' constant monitoring and active intervention over the past two decades. Over the years, EOR by immiscible water-alternating-gas (IWAG) and miscible water-alternating-gas (MWAG) injection has been used in various areas of the oil field to gain additional oil recovery (10% for Zone C

TABLE 11.3—ESTIMATED ULTIMATE-RECOVERY FACTORS FOR THE KUPARUK RIVER OIL FIELD

Zone	OOIP, million bbl oil	Recovery Factor, % OOIP
C	3,700	40
A	2,200	41

and 6% for Zone A). Large-scale MWAG injection started in 1996 and has expanded to include more than 50% of the patterns.

11.9.4 West Texas Carbonate Waterfloods. San Andres and Clearfork are two carbonate reservoir intervals that are present over a considerable area of the Permian Basin in west Texas. These reservoirs (e.g., Wasson, Slaughter, Seminole) contain several billion bbl of approximately 30°API oil. They are very-layered, heterogeneous carbonates and dolomites that have large variation in permeability from layer to layer. Interestingly, because of the complex hydrocarbon-accumulation history of this basin, much of this area has an underlying interval that contains residual oil saturation.

Most of these reservoirs were discovered in the late 1930s and the 1940s. Even where both the San Andres and the Clearfork were found to be oil-bearing, surface-lease and unitization considerations required the reservoirs to be developed by drilling separate sets of wells. These reservoirs had approximately two decades of primary production.

From the 1960s through the 1980s, almost all of these reservoirs underwent waterflooding. During this period, many SPE technical papers addressed aspects of these waterfloods. Of particular interest was the continuity, or discontinuity, of the pay intervals and the extent to which infill drilling from 40-acre well spacing to 20 acres, and possibly to 10 acres, could be economically justified by increased oil recovery.^{19,20,60} Another issue was what pattern style was the best to use.⁶¹ The recovery factors for the sum of primary production and waterflooding ranges from 25 to 60% of OOIP; the variation is caused mainly by geological factors in these different geographical areas and by differences between the San Andres and Clearfork reservoirs.²⁰

Pressure coring and sponge coring are technologies that were developed specifically for these waterfloods to determine the residual oil saturation to waterflooding in these carbonate reservoirs.⁶² These techniques were used to determine the variation in oil saturation from well-swept higher-permeability layers to poorly swept lower-permeability layers.

The west Texas carbonate waterfloods have proved quite successful and have recovered significant additional oil. Also, the San Andres reservoirs' waterfloods have provided much of the data and related technical studies that were needed to justify implementation of EOR by using CO₂ injection. During the tertiary EOR projects, water injection in the WAG mode has continued to control the mobility of the low-viscosity CO₂.

11.9.5 Kirkuk (Iraq). There is only one SPE technical paper about the supergiant reservoir, the Kirkuk oil field of Iraq. This field is given as an example here because its reservoir's geology is quite different from the other reservoirs discussed above.⁶³

The primary pay interval for the Kirkuk field is the 1,200-ft-thick Main Limestone. This interval consists of a series of extensively fractured limestones, some porcelaneous and some dolomitized. These limestones were deposited in a variety of environments—back-reef/lagoon-al, fore-reef, and basinal—and have a wide range of porosity and permeability properties. The oil is contained both in an extensive, extremely permeable but low-capacity fracture system and in a low-permeability but high-capacity, matrix-pore system. Also, the reservoir is under-

lain by a fieldwide aquifer. The oil gravity is approximately 36°API and was approximately 500 psi undersaturated at the original reservoir pressure of 1,100 psia.

Kirkuk began production in 1934, and 2 billion bbl of oil were produced before water injection was implemented in 1961. From 1961 to 1971, 3.2 billion bbl of oil were produced under pressure maintenance by waterdrive using river water. The 1971 production rate was approximately 1.1 million BOPD. Since then, the field has continued to produce large volumes of oil by voidage-replacement water injection; however, few production details for recent years appear in the technical literature.

The interesting technical aspects of this type of reservoir are the determination of the ultimate oil recovery from the matrix and the time scale of matrix oil recovery. Laboratory experiments can be run using matrix rock samples to determine the water/oil imbibition behavior; however, what matters is the actual reservoir's matrix/fracture interaction because the fracture density varies considerably. The early water injection showed that within the fracture network there was rapid communication over a distance of more than 20 miles. Water injection initially was peripheral; however, because of low injectivity caused by lack of down-dip fracturing, injection was shifted to seven injection wells in the saddle area between the two principal domes of this oil field, one of which had an injection capacity of more than 400,000 BWPD.

A 90-day temporary production stoppage in 1967 allowed unique field data to be acquired regarding the matrix/fracture interaction because of the observed changes in the oil/water contact (OWC). It was observed that the OWCs fell in the areas where they were the highest and rose in the areas where they were the lowest. These OWC changes were the result of the counter-current imbibition process between the fracture network and matrix pore system. From these data, the time-delay function could be calculated on the basis of observed field data. Depending on the assumptions, the half-life was estimated to be 3 to 5 years and the ultimate recovery was estimated at 30 to 45% of the OOIP.

11.10 Summary and Conclusions

This chapter has described the technical aspects of waterflooding, but only briefly compared to the vast amount of SPE technical literature on this subject. It also presented several field case studies for a few very large oil fields. Note, though, that reservoirs of all sizes have been waterflooded: very large fields having hundreds to 1,000+ wells; medium-sized fields; and small fields, for which the total waterflood is only a few patterns.

The conclusions concerning waterflooding are:

- Waterflooding is the most commonly used secondary-oil-recovery method. This is because water is inexpensive and readily available in large volumes and because water is very effective at substantially increasing oil recovery.

- The level of effectiveness of a waterflood depends on the mobility ratio between the oil and water, and the geology of the oil reservoir. Waterflooding is effective because almost all reservoir rocks are either water-wet or mixed-wet. The depositional and diagenetic characteristics of a reservoir control major aspects of the water/oil displacement process. These characteristics can either enhance waterflood performance or have detrimental effects on the WOR as a function of time. Often, the details of a reservoir's internal geology are not known until production wells start producing injected water.

- Gravity effects—i.e., the interplay between the gravity/density effects and the geologic layering of a reservoir—are important in waterfloods because at reservoir conditions, oil always is less dense than connate brine or injected water. This interplay can either help or hurt waterflood performance relative to a homogeneous system.

- Waterflooding is a process that typically takes several decades to complete. Hence, continuous, routine field production and pressure data must be taken for monitoring and analyzing waterflood performance. Occasionally, more-expensive, special-data acquisition programs (i.e., 3D- or 4D-seismic data) are run to assist the evaluation process. A variety of engineering tools

have been developed to analyze waterflood performance, ranging from simple plots of field production data to full-field numerical-reservoir-simulation models.

- Waterfloods are dynamic processes the performance of which, as production wells respond to the injection of water, can be improved by modification of operations by the technical team. Such modifications include changing the allocation of injection water among the injection wells and the waterflooded intervals, drilling additional wells at infill locations, and/or modifying the pattern style.

- Waterflooding has been used successfully in oil fields of all sizes and all over the world, in offshore and onshore oil fields.

Nomenclature

A	= cross-sectional area available for flow, ft ²
B_o	= oil formation-volume factor, RB/STB
C	= total flow capacity
E_A	= areal displacement efficiency
E_D	= unit-displacement efficiency
E_I	= vertical displacement efficiency
E_R	= waterflood oil-recovery efficiency
E_V	= volumetric sweep efficiency
E_{Vbt}	= volumetric sweep efficiency at breakthrough
f_o	= fractional flow of oil
f_w	= fractional flow of water
\bar{f}_w	= average fractional flow of water
f_{wf}	= fractional flow of water at flood front
F_{wo}	= water/oil ratio
F_{pvg}	= fraction of displaceable pore volume that is gas saturated
g	= gravity constant
G	= value as defined by Eq. 11.24, dimensionless
h	= reservoir thickness, ft
i	= fluid phase i
k	= absolute permeability, darcies
k_{50}	= median permeability value, md
$k_{84.1}$	= permeability at 1 standard deviation above mean value, md
k_a	= air permeability
k_i	= permeability of fluid phase i , darcies
k_o	= permeability to oil, darcies
k_r	= relative permeability
k_{ro}	= relative permeability to oil, fraction
k_{roe}	= relative permeability to oil at endpoint (S_{wi})
k_{rw}	= relative permeability to water, fraction
k_{rwe}	= relative permeability to water at endpoint (S_{orw})
k_{rwo}	= water/oil relative permeability
k_w	= permeability to water, darcies
k_x	= permeability in the x direction, darcies
L	= length, ft
M	= mobility ratio
P_c	= capillary pressure, psia
q_c	= critical rate, B/D
q_o	= oil-production rate, B/D
q_t	= total production rate, B/D

- q_w = water-production rate, B/D
 S_{gi} = initial gas saturation, fraction PV
 S_{gt} = trapped gas saturation, fraction PV
 S_o = oil saturation, fraction PV
 S_{oi} = initial oil saturation or $(1 - S_{wc})$, fraction PV
 S_{orw} = residual oil saturation to waterflooding, fraction PV
 S_w = water saturation, fraction PV
 S_{wbt} = averaged water saturation behind the flood front at breakthrough, fraction PV
 S_{wc} = connate-water saturation, fraction PV
 S_{wf} = breakthrough or flood-front water saturation, fraction PV
 S_{wi} = initial water saturation, fraction PV
 S_{wz} = thickness-averaged water saturation for vertical equilibrium, fraction PV
 t = time, days
 u_{ox} = oil Darcy velocity in the x direction, ft/day
 u_t = total Darcy velocity, ft/day
 u_{wx} = water Darcy velocity in the x direction, ft/day
 V = Dykstra-Parsons coefficient of permeability variation
 x = position in x -coordinate system, ft
 X = the X -plot value X , which is $\ln\left(\frac{1}{f_w} - 1\right) - \frac{1}{f_w}$
 y = position in y -coordinate system, ft
 α = reservoir dip angle, degrees
 β = slope, degrees
 $(\Delta p)_h$ = pressure difference in horizontal direction, psi
 $(\Delta p)_V$ = pressure difference in vertical direction, psi
 $\Delta\rho$ = water/oil density difference, lbm/ft³ or g/cm³
 θ = contact angle, degrees
 λ_i = mobility of fluid phase i , darcies/cp
 μ_i = viscosity of fluid phase i , cp
 μ_o = oil viscosity, cp
 μ_w = water viscosity, cp
 ρ_o = oil density, lbm/ft³ or g/cm³
 ρ_w = water density, lbm/ft³ or g/cm³
 σ_{os} = interfacial tension between the oil phase and solid phase, dyne/cm
 σ_{ws} = interfacial tension between the water phase and solid phase, dyne/cm
 σ_{ow} = interfacial tension between the oil phase and water phase, dyne/cm
 ϕ = porosity, fraction BV
 ψ_s = fraction of total flow coming from the swept portion of the pattern

Acknowledgments

SPE members have published numerous papers concerning waterflood technology over the past 60 years. SPE has several major publications about waterflood technology, including two monographs,^{1,3} one textbook,² and one *Reprint Series* volume⁴. I have relied on these major publications and on a number of these technical papers in preparing this waterflood chapter for SPE's *Petroleum Engineering Handbook*. I have particularly relied on Willhite's *Waterflooding* textbook.² From the outset, I recognized that much of the summary of waterflood technologies presented here could only paraphrase portions of Willhite's textbook. Willhite describes the waterflood technical calculations in much more detail than is appropriate for this *Handbook* chapter. Also, I have used a number of the same figures as Willhite did; for the reader's conve-

nience, I have referenced them to his textbook and not to the many SPE technical papers of the past 50 years in which they originally were published. **Appendix A** cross-references to Willhite² all the tables, figures, and equations from it that are used in this chapter.

References

1. Craig, F.F. Jr.: *Reservoir Engineering Aspects of Waterflooding*, Monograph Series, SPE, Richardson, Texas (1980) **3**.
2. Willhite, G.P.: *Waterflooding*, Textbook Series, SPE, Richardson, Texas (1986) **3**.
3. Rose, S.C., Buckwalter, J.F., and Woodhall, R.J.: *Design Engineering Aspects of Waterflooding*, Monograph Series, SPE, Richardson, Texas (1989) **11**.
4. *Waterflooding*, SPE Reprints Series, SPE, Richardson, Texas (1973) **2a**.
5. Fettke, C.R.: "The Bradford oil field, Pennsylvania and New York," Mineral Resources Report M21, Pennsylvania Geological Survey, Harrisburg, Pennsylvania (1938) 298–301.
6. Salathiel, R.A.: "Oil Recovery by Surface Film Drainage in Mixed-Wettability Rocks," *JPT* (October 1973) 1216; *Trans.*, AIME, **255**.
7. Jerauld, G.R. and Rathmell, J.J.: "Wettability and Relative Permeability of Prudhoe Bay: A Case Study in Mixed-Wet Reservoirs," *SPERE* (February 1997) 58.
8. Sharma, M.M. and Filoco, P.R.: "Effect of Brine Salinity and Crude-Oil Properties on Oil Recovery and Residual Saturations," *SPEJ* (September 2000) 293.
9. Zhou, X., Morrow, N.R., and Shouxiang, M.: "Interrelationship of Wettability, Initial Water Saturation, Aging Time, and Oil Recovery by Spontaneous Imbibition and Waterflooding," *SPEJ* (June 2000) 199.
10. Buckley, S.E. and Leverett, M.C.: "Mechanism of Fluid Displacement in Sands," *Trans.*, AIME (1942) **146**, 107.
11. Terwilliger, P.L. *et al.*: "An Experimental and Theoretical Investigation of Gravity Drainage Performance," *Trans.*, AIME (1951) **192**, 285.
12. Scheihing, M.H., Thompson, R.D., and Seifert, D.: "Multiscale Reservoir Description Models for Performance Prediction in the Kuparuk River Field, North Slope of Alaska," paper SPE 76753 presented at 2002 SPE Western Regional/AAPG Pacific Section Joint Meeting, Anchorage, 20–22 May.
13. Ebanks, W.J., Scheihing, M.H., and Atkinson, C.D.: "Flow Units for Reservoir Characterization," *AAPG Methods in Exploration, No. 10*, D. Morton-Thompson and A.M. Woods (eds.), AAPG, Tulsa (1993) 282–285.
14. Higgins, R.V. and Leighton, A.J.: "Computer Prediction of Water Drive of Oil and Gas Mixtures Through Irregularly Bonded Porous Media Three-Phase Flow," *JPT* (September 1962) 1048; *Trans.*, AIME, **225**.
15. Higgins, R.V. and Leighton, A.J.: "Matching Calculated With Actual Waterflood Performance by Estimating Some Reservoir Properties," *JPT* (May 1974) 501.
16. Baek, M. and Hewett, T.A.: "A Hybrid Streamtube Simulator Using a Semianalytical Method," paper SPE 63151 presented at the 2000 SPE Annual Technical Conference and Exhibition, Dallas, 1–4 October.
17. Emanuel, A.S. and Milliken, W.J.: "The Application of Streamtube Techniques to Full-Field Waterflood Simulation," *SPERE* (August 1997) 211.
18. Grinestaff, G.H. and Caffrey, D.J.: "Waterflood Management: A Case Study of the Northwest Fault Block Area of Prudhoe Bay, Alaska, Using Streamline Simulation and Traditional Waterflood Analysis," paper SPE 63152 presented at the 2000 SPE Annual Technical Conference and Exhibition, Dallas, 1–4 October.
19. Barber, A.H. *et al.*: "Infill Drilling to Increase Reserves—Actual Experience in Nine Fields in Texas, Oklahoma, and Illinois," *JPT* (August 1983) 1530.
20. Lu, G.F., Brimhall, R.M., and Wu, C.H.: "Geographical Distribution and Forecast Models of Infill Drilling Oil Recovery for Permian Basin Carbonate Reservoirs," paper SPE 26503 presented at the 1993 SPE Annual Technical Conference and Exhibition, Houston, 3–6 October.

21. Fast, R.E., Murer, A.S., and Zambrano, L.G.: “Lost Hills Diatomite Simulation Study: Predicting Waterflood Performance in a Low-Permeability, Compacting Reservoir,” paper SPE 26627 presented at the 1993 SPE Annual Technical Conference and Exhibition, Houston, 3–6 October.
22. Wright, C.A. and Conant, R.A.: “Hydraulic Fracture Reorientation in Primary and Secondary Recovery from Low-Permeability Reservoirs,” paper SPE 30484 presented at the 1995 SPE Annual Technical Conference and Exhibition, Dallas, 22–25 October.
23. Dykstra, H. and Parsons, R.L.: “The Prediction of Oil Recovery by Water Flood,” *Secondary Recovery of Oil in the United States, Principles and Practice*, second edition, API, Washington, DC (1950) 160–174.
24. Stiles, W.E.: “Use of Permeability Distribution in Water Flood Calculations,” *Trans.*, AIME (1949) **186**, 9.
25. Dietz, D.N.: “A Theoretical Approach to the Problem of Encroaching and By-Passing Edge Water,” *Proc.*, Akad. Wetenschappen, Amsterdam, (1953) **56** (1), series B, 83.
26. Dake, L.P.: *Fundamentals of Reservoir Engineering*, Elsevier Scientific Publishing Co., New York City (1978) 399–413.
27. Teufel, L.W. and Rhett, D.W.: “Failure of Chalk During Waterflooding of the Ekofisk Field,” paper SPE 24911 presented at the 1992 SPE Annual Technical Conference and Exhibition, Washington, DC, 2–4 October.
28. Perkins, T.K. and Gonzalez, J.A.: “The Effect of Thermoelastic Stresses on Injection Well Fracturing,” *SPEJ* (February 1985) 78.
29. Garon, A.M., Lin, C.Y., and Dunayevsky, V.A.: “Simulation of Thermally Induced Waterflood Fracturing in Prudhoe Bay,” paper SPE 17417 presented at the 1988 SPE California Regional Meeting, Long Beach, California, 23–25 March.
30. Sylte, J.E., Hallenbeck, L.D., and Thomas, L.K.: “Ekofisk Formation Pilot Waterflood,” paper SPE 18276 presented at the 1988 SPE Annual Technical Conference and Exhibition, Houston, 2–5 October.
31. *RP 45, Recommended Practice for Analysis of Oilfield Waters*, second edition, API, Washington, DC (1968, reissued 1981, third edition 1 August 1998).
32. *RP 38, Recommended Practice for Biological Analysis of Subsurface Injection Waters*, third edition, API, Washington, DC (1975, reissued 1982).
33. *TM0173-2005, Methods for Determining Quality of Subsurface Injection Water Using Membrane Filters*, NACE, Houston (1973, reaffirmed 2005).
34. Mitchell, R.W.: “The Forties Field Sea-Water Injection System,” *JPT* (June 1978) 877.
35. Hamouda, A.A.: “Water Injection Quality in Ekofisk—UV Sterilization and Monitoring Techniques,” paper SPE 21048 presented at the 1991 SPE International Symposium on Oilfield Chemistry, Anaheim, California, 20–22 February.
36. Kriel, B.G. *et al.*: “The Efficacy of Formaldehyde for the Control of Biogenic Sulfide Production in Porous Media,” paper SPE 25196 presented at the 1993 SPE International Symposium on Oilfield Chemistry, New Orleans, 2–5 March.
37. Frazer, L.C. and Bolling, J.D.: “Hydrogen Sulfide Forecasting Techniques for the Kuparuk River Field,” paper SPE 22105 presented at the 1991 International Arctic Technology Conference, Anchorage, 29–31 May.
38. Hart, A.D., Graham, B.D., and Gettleson, D.A.: “NORM Associated with Produced Water Discharges,” paper SPE 29727 presented at the 1995 SPE/EPA Exploration and Production Environmental Conference, Houston, 27–29 March.
39. Hjelmas, T.A. *et al.*: “Produced Water Reinjection: Experiences from Performance Measurements on Ula in the North Sea,” paper SPE 35874 presented at the 1996 SPE Conference on Health, Safety, and Environment in Oil and Gas Exploration and Production, New Orleans, 9–12 June.
40. Hsi, C.D. *et al.*: “Formation Injectivity Damage Due to Produced Water Reinjection,” paper SPE 27395 presented at the 1994 SPE Formation Damage Control Symposium, Lafayette, Louisiana, 7–10 February.
41. Martins, J.P. *et al.*: “Produced-Water Reinjection and Fracturing in Prudhoe Bay,” *SPERE* (August 1995) 176.
42. Dyes, A.B., Caudle, B.H., and Erickson, R.A.: “Oil Production after Breakthrough—as Influenced by Mobility Ratio,” *Trans.*, AIME (1954) **201**, 201.

43. O'Donovan, A.R., Smith S.G., and Kristiansen, P.: "Foinaven 4D Seismic—Dynamic Reservoir Parameters and Reservoir Management," paper SPE 63294 presented at the 2000 SPE Annual Technical Conference and Exhibition, Dallas, 1–4 October.
44. Staples, R. *et al.*: "Integrating 4D seismic to optimize production," paper SPE 78346 presented at the 2002 SPE European Petroleum Conference, Aberdeen, 29–31 October.
45. Woodling, G.S. *et al.*: "Layered Waterflood Surveillance in a Mature Field: The Long Beach Unit," paper SPE 26082 presented at the 1993 SPE Western Regional Meeting, Anchorage, 26–28 May.
46. Chapman, L.R. and Thompson, R.R.: "Waterflood Surveillance in the Kuparuk River Unit With Computerized Pattern Analysis," *JPT* (March 1989) 277.
47. Buckley, S.E. and Leverett, M.C.: "Mechanisms of Fluid Displacement in Sands," *Trans., AIME* (1942) **146**, 107–116.
48. Ershaghi, I. and Omorigie, O.: "A Method for Extrapolation of Cut vs. Recovery Curves," *JPT* (February 1978) 203.
49. Ershaghi, I. and Abdassah, D.: "A Prediction Technique for Immiscible Processes Using Field Performance Data (includes associated papers SPE 13392, 13793, 15146 and 19506)," *JPT* (April 1984) 664.
50. Lo, K.K., Warner, H.R. Jr., and Johnson, J.B.: "A Study of the Post-Breakthrough Characteristics of Waterfloods," paper SPE 20064 presented at the 1990 SPE California Regional Meeting, Ventura, California, 4–6 April.
51. Bush, J.L. and Helander, D.P.: "Empirical Prediction of Recovery Rate in Waterflooding Depleted Sands," *JPT* (September 1968) 933.
52. Jarrell, P.M. and Stein, M.H.: "Maximizing Injection Rates in Wells Recently Converted to Injection using Hearn and Hall Plots," paper SPE 21724 presented at the 1991 SPE Production Operations Symposium, Oklahoma City, Oklahoma, 7–9 April.
53. Currier, J.H. and Sindelar, S.T.: "Performance Analysis in an Immature Waterflood: The Kuparuk River Field," paper SPE 20775 presented at the 1990 SPE Annual Technical Conference and Exhibition, New Orleans, 23–26 September.
54. Hedges, P.L. and Scherer, P.W.: "Group Oriented Software Solution for Pattern Material Balance of an Areally Extensive Field, Kuparuk River Field, Alaska," paper SPE 35987 presented at the 1996 SPE Petroleum Computer Conference, Dallas, 2–5 June.
55. Torsaeter, O.: "An Experimental Study of Water Imbibition in Chalk From the Ekofisk Field," paper SPE 12688 presented at the 1984 SPE Enhanced Oil Recovery Symposium, Tulsa, 15–18 April.
56. Hermansen, H. *et al.*: "Twenty Five Years of Ekofisk Reservoir Management," paper SPE 38927 presented at the 1997 SPE Annual Technical Conference and Exhibition, San Antonio, Texas, 5–8 October.
57. Agarwal, B. *et al.*: "Reservoir Characterization of Ekofisk Field: A Giant, Fractured Chalk Reservoir in the Norwegian North Sea—History Match," *SPEE* (December 2000) 534.
58. James, D.M., Mayer, E.H., and Scranton, J.M.: "Use of Economic and Reservoir Models in Planning the Ranger Zone Flood, Long Beach Unit, Wilmington Field," paper SPE 1855 presented at the 1967 SPE Annual Meeting, New Orleans, 1–4 October.
59. Robertson, J.A., Blesener, J.A., and Soo Hoo, S.: "Subzone Redevelopment of the Long Beach Unit, Wilmington Oil Field: A Case Study," *JPT* (October 1987) 1229.
60. Maguson, W.L. and Knowles, J.D.: "Denver Unit 10-Acre Infill Pilot Test and Residual Oil Testing," paper SPE 6385 presented at the 1977 SPE Permian Basin Oil and Gas Recovery Conference, Midland, Texas, 10–11 March.
61. Christman, P.G.: "Modeling the Effects of Infill Drilling and Pattern Modification in Discontinuous Reservoirs," *SPEE* (February 1995) 4.
62. Bilhartz, H.L. Jr. and Charlson, G.S.: "Coring for In-Situ Saturations in the Willard Unit CO₂ Flood Mini-Test," paper SPE 7050 presented at the 1978 SPE Symposium on Improved Methods of Oil Recovery, Tulsa, 16–17 April.
63. Al-Naqib, F.M. *et al.*: "Water Drive Performance of the Fractured Kirkuk Field of Northern Iraq," paper SPE 3437 presented at the 1971 SPE Annual Meeting, New Orleans, 3–6 October.

TABLE 11A.1—CHAPTER TABLES, FIGURES, AND EQUATIONS CROSS-REFERENCED TO WILLHITE²

<u>This chapter's:</u>	<u>Is or is modified from Willhite's:</u>	<u>This chapter's:</u>	<u>Is or is modified from Willhite's:</u>
Table 11.1	Table 2.5	Fig. 11.33	Fig. 5.15
Fig. 11.2	Fig. 2.5	Fig. 11.34	Fig. 5.19
Fig. 11.3	Fig. 2.9	Fig. 11.44	Fig. 6.24
Fig. 11.4	Fig. 2.33	Eq. 11.2	Eq. 2.1
Fig. 11.5	Fig. 2.34	Eq. 11.3	Eq. 2.17
Fig. 11.6	Fig. 2.19	Eq. 11.4	Eq. 3.205
Fig. 11.7	Fig. 2.23	Eq. 11.7	Eq. 3.207
Fig. 11.8	Fig. 2.24	Eq. 11.8	Eq. 3.46
Fig. 11.9	Fig. 2.37	Eq. 11.9	Eq. 3.47
Fig. 11.10	Fig. 2.52	Eq. 11.10	Eq. 3.5
Fig. 11.11	Fig. 2.58	Eq. 11.11	Eq. 3.51
Fig. 11.12	Fig. 3.6	Eq. 11.12	Eq. 3.54
Fig. 11.13	Fig. 3.9	Eq. 11.13	Eq. 3.55
Fig. 11.14	Fig. 3.10	Eq. 11.14	Eq. 3.56
Fig. 11.15	Fig. 3.38	Eq. 11.15	Eq. 3.57
Fig. 11.16	Fig. 3.39	Eq. 11.16	Eq. 3.63
Fig. 11.18	Fig. 4.5	Eq. 11.17	Eq. 3.73
Fig. 11.19	Fig. 4.6	Eq. 11.18	Eq. 3.79
Fig. 11.20	Fig. 4.8	Eq. 11.19	Eq. 5.178
Fig. 11.21	Fig. 4.11	Eq. 11.21	Eq. 5.136
Fig. 11.26	Fig. 5.44	Eq. 11.22	Eq. 5.75
Fig. 11.27	Fig. 5.45	Eq. 11.23	Eq. 5.76
Fig. 11.32	Fig. 5.25	Eq. 11.24	Eq. 5.72

Appendix A—Cross-Referencing to Willhite²

Table 11A.1 cross-references to Willhite² all the tables, figures, and equations from it that are used in this chapter.

SI Metric Conversion Factors

acre	× 4.046 873	E + 03 = m ²
°API	141.5/(131.5 + °API)	= g/cm ³
bbl	× 1.589 873	E - 01 = m ³
cp	× 1.0*	E - 03 = Pa·s
dyne	× 1.0*	E - 02 = mN
dyne/cm	× 1.0*	E - 00 = mN/m
°F	(°F - 32)/1.8	= °C
ft	× 3.048*	E - 01 = m
ft/D	× 3.527 778	E - 03 = mm/s
ft ²	× 9.290 304	E - 02 = m ²
ft ³	× 2.831 685	E - 02 = m ³
in.	× 2.54*	E - 00 = cm
in. ²	× 6.451 6*	E + 00 = cm ²

in. ³ ×	1.638 706	E + 01 =	cm ³
lbm ×	4.535 924	E - 01 =	kg
lbm/ft ³ ×	1.601 846	E + 01 =	kg/m ³
mile ×	1.609 344*	E - 00 =	km
psi ×	6.894 757	E - 00 =	kPa
psi/ft ×	2.262 059	E + 01 =	kPa/m
scf/STB ×	1.801 175	E - 01 =	std m ³ /m ³
sq mile ×	2.589 988	E + 00 =	km ²

*Conversion factor is exact.

Chapter 12

Immiscible Gas Injection in Oil Reservoirs

H.R. (Hal) Warner Jr., Warner Consulting Services and
E.D. Holstein, Consultant

12.1 Introduction

This chapter concerns gas injection into oil reservoirs to increase oil recovery by immiscible displacement. The use of gas, either of a designed composition or at high-enough pressure, to result in the miscible displacement of oil is not discussed here; for a discussion of that topic, see the chapter on miscible flooding in this section of the *Handbook*. A variety of gases can and have been used for immiscible gas displacement, with lean hydrocarbon gas used for most applications to date. Historically, immiscible gas injection was first used for reservoir pressure maintenance. The first such projects were initiated in the 1930s and used lean hydrocarbon gas (e.g., Oklahoma City field and Cunningham pool in the United States¹ and Bahrain field in Bahrain^{2,3}). Over the decades, a considerable number of immiscible gas injection projects have been undertaken, some with excellent results and others with poor performance. Reasons for this range of performance are discussed in this chapter. At the end of this chapter, a variety of case studies are presented that briefly describe several of the successful immiscible gas injection projects.

Gas injection projects are undertaken when and where there is a readily available supply of gas. This gas supply typically comes from produced solution gas or gas-cap gas, gas produced from a deeper gas-filled reservoir, or gas from a relatively close gas field. Such projects take a variety of forms, including the following:

- Reinjection of produced gas into existing gas caps overlying producing oil columns.
- Injection into oil reservoirs of separated produced gas for pressure maintenance, for gas storage, or as required by government regulations.
- Gas injection to prevent migration of oil into a gas cap because of a natural waterdrive, downdip water injection, or both.
- Gas injection to increase recoveries from reservoirs containing volatile, high-shrinkage oils and into gas-cap reservoirs containing retrograde gas condensate.
- Gas injection into very undersaturated oil reservoirs for the purpose of swelling the oil and hence increasing oil recovery.

The primary physical mechanisms that occur as a result of gas injection are (1) partial or complete maintenance of reservoir pressure, (2) displacement of oil by gas both horizontally

and vertically, (3) vaporization of the liquid hydrocarbon components from the oil column and possibly from the gas cap if retrograde condensation has occurred or if the original gas cap contains a relict oil saturation, and (4) swelling of the oil if the oil at original reservoir conditions was very undersaturated with gas. Gas injection is particularly effective in high-relief reservoirs where the process is called “gravity drainage” because the vertical/gravity aspects increase the efficiency of the process and enhance recovery of updip oil residing above the uppermost oil-zone perforations.

The decision to apply immiscible gas injection is based on a combination of technical and economic factors. Deferral of gas sales is a significant economic deterrent for many potential gas injection projects if an outlet for immediate gas sales is available. Nevertheless, a variety of opportunities still exist. First are those reservoirs with characteristics and conditions particularly conducive to gas/oil gravity drainage and where attendant high oil recoveries are possible. Second are those reservoirs where decreased depletion time resulting from lower reservoir oil viscosity and gas saturation in the vicinity of producing wells is more attractive economically than alternative recovery methods that have higher ultimate recovery potential but at higher costs. And third are reservoirs where recovery considerations are augmented by gas storage considerations and hence gas sales may be delayed for several years.

Nonhydrocarbon gases such as CO₂ and nitrogen can and have been used.⁴ In general, calculation techniques developed for hydrocarbon-gas injection and displacement can be used for the design and application of nonhydrocarbon, immiscible gas projects. Valuing the use of such gases must include any additional costs related to these gases, such as corrosion control, separating the nonhydrocarbon components to meet gas marketing specifications, and using the produced gas as fuel in field operations.

The sections in this chapter are presented in the following order:

- Microscopic and Macroscopic Displacement Efficiency of Immiscible Gas Displacement
- Gas/Oil Compositional Effects During Immiscible Gas Displacement
- Reservoir Geology Considerations Regarding Immiscible Gas Displacement
- General Immiscible Gas/Oil Displacement Techniques
- Vertical or “Gravity Drainage” Gas Displacement
- Calculation Methods for Immiscible Gas Displacement
- Immiscible Gasflood Monitoring
- Field Case Studies: Immiscible Gas Injection Examples
- Miscellaneous Topics
- Summary and Conclusions

The purposes of this chapter include listing the physical criteria that separate the successful gas injection operations from the unsuccessful ones, describing the reservoir and process variables that must be defined and quantified, and demonstrating some of the simple techniques available for predicting and evaluating field performance. Some of these calculations can be performed with spreadsheets or, more tediously, with hand-held calculators. Modern numerical reservoir simulators are commonly used to calculate the projected performance of applying immiscible gas injection to a particular reservoir. For reservoirs with several years of immiscible gas injection, these same simulators can be used to history match past performance and to project future performance under various scenarios (e.g., continuing current operations, evaluating various new producing wells options, or comparing surface facility operational alternatives). See the chapter on reservoir simulation in this section of the *Handbook*.

Specifically not included in this chapter is any discussion of the factors to consider in implementing a gas injection project, such as gas compression needs, gas distribution systems, wellbore configurations, and vessel selection and sizing for handling produced fluids. These subjects are covered in various chapters in the Production Operations Engineering and Facilities and Construction Engineering sections of the *Handbook*.

TABLE 12.1—COMPARISON OF MEASURED AND COMPUTED SURFACE TENSIONS OF VARIOUS RESERVOIR FLUID SYSTEMS^a

Reservoir Fluid	Pressure, psia	Surface Tension, dynes/cm	
		Measured	Computed
Asphalt-free oil system at 73°F	2,275	2.7	2.6
Asphalt-free oil and rich gas at 73°F	2,275	0.55	0.52
Asphalt-free oil and lean gas at 73°F	2,275	4.1	3.8
Equilibrium liquid and gas phases of Oil A at 130°F	2,150	5.5	4.7
	1,650	6.7	7.4
	1,150	10.1	10.3
	185	19.5	18.7
Equilibrium liquid and gas phases of Oil C at 180°F	2,815	1.3	1.2
	3,315	2.3	2.1
	2,815	3.3	3.1
	2,315	4.6	4.8
Equilibrium liquid and gas phases of Oil D at 170°F	2,010	6.0	5.6
	1,610	8.5	8.1
	1,110	10.3	11.5

12.2 Microscopic and Macroscopic Displacement Efficiency of Immiscible Gas Displacement

The conceptual aspects of the displacement of oil by gas in reservoir rocks are discussed in this section. There are three aspects to this displacement: gas and oil viscosities, gas/oil capillary pressure (P_c) and relative permeability (k_r) data, and the compositional interaction, or component mass transfer, between the oil and gas phases. The first two topics are discussed in this section; the third is discussed in the next section.

12.2.1 Gas/Oil Viscosity and Density Contrast. One must first understand the viscosity and density differences between gas and oil to appreciate why the gas/oil displacement process can be very inefficient. Gases at reservoir conditions have viscosities of ≈ 0.02 cp, whereas oil viscosities generally range from 0.5 cp to tens of centipoises. Gases at reservoir conditions have densities generally one-third or less than that of oil. Thus, gas is generally one to two orders of magnitude less viscous than the oil it is trying to displace. Regarding the fluid density difference, gas is always considerably “lighter” than the oil; hence, gas, when flowing, will segregate by gravity to the top of the reservoir or zone and oil will “sink” simultaneously to the bottom of the reservoir or zone.

Another gas/oil property that must be known for calculations at reservoir conditions is the interfacial tension (IFT) between the oil and gas fluid pair. This value is needed at reservoir conditions for the conversion of gas/oil capillary pressure data from surface to reservoir conditions. A number of technical papers discuss the calculation of IFT from compositional information about the oil and gas phases.⁵⁻⁹ Table 12.1 from Firoozabadi *et al.*⁸ shows several reservoir oil-gas fluid-pair IFT values (measured and calculated) as a function of temperature and pressure. As the pressure increases, the IFT values decrease, although not low enough for miscible displacement to occur. Although not illustrated in the table, it should be noted that the IFT between nitrogen and oil is higher than that between a lean natural gas and the same oil.

12.2.2 Gas/Oil Capillary Pressure and Relative Permeability. The gas/oil capillary pressure and relative permeability data are typically measured by commercial laboratories using routine

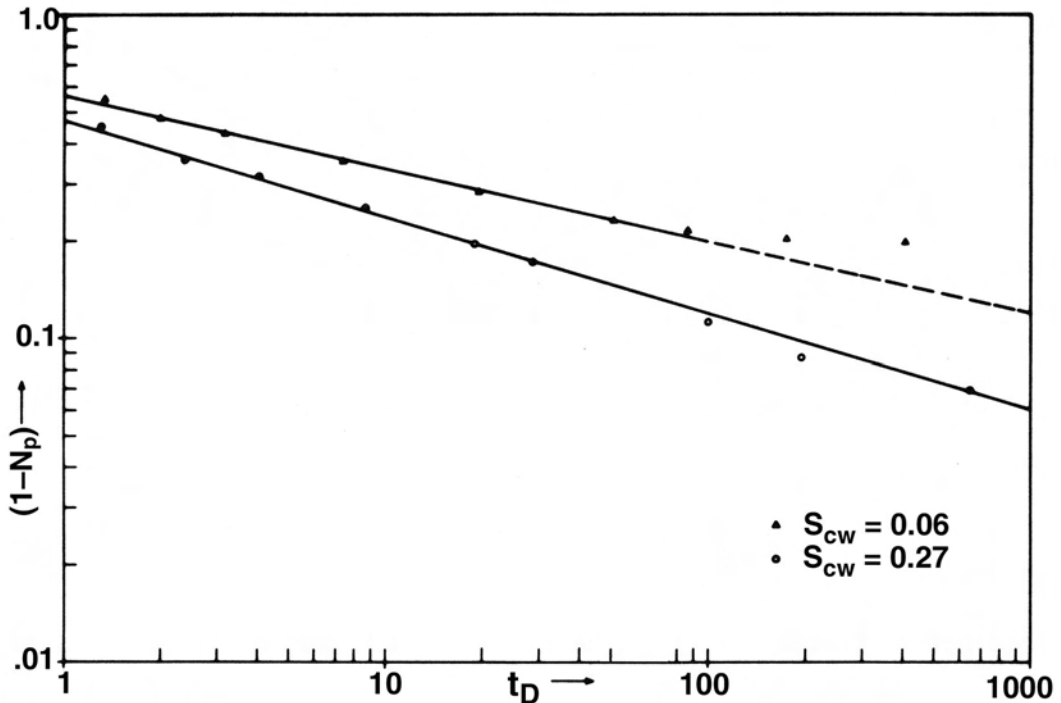


Fig. 12.1—Gas/oil displacement results for Berea cores; oil production as a function of time. This figure shows that long drainage times are required for displacement of oil to low saturation values.¹⁰

special core analysis procedures. Gas-oil capillary pressure data can be measured with either porous-plate or centrifuge equipment. One approach for obtaining gas/oil relative permeability data is the viscous displacement method in which gas displaces oil. A second method is the centrifuge method, which is generally used to obtain capillary pressure and relative permeability information simultaneously.

In all cases, gas is the nonwetting phase in this displacement; hence, it will preferentially flow through the largest pores first. However, what is very important in the determination of the oil relative permeability is the distribution of the oil phase in the core sample because in real reservoirs connate water occupies the smallest pores. As shown by Hagoort,¹⁰ initial water saturation has a significant effect on oil relative permeability during the gas/oil displacement (centrifuge experiments). The water phase will occupy a greater percentage of the smaller pore spaces as the connate water saturation increases. As a result, the pore structure appears more streamlined to the oil and gas phases. The oil relative permeability at higher connate water saturations is considerably higher (see Fig. 12.1 and the discussion of capillary pressure and relative permeability concepts in the chapter on those topics in the General Engineering Section of the *Handbook*).

The other key aspect of the oil relative permeability (k_{ro}) is the determination of its value as the oil saturation decreases. Because oil relative permeability becomes quite low but nonzero, the time to reach equilibrium in laboratory core plug measurements can be very long. Fig. 12.1 presents experimental results for cumulative oil recovery as a function of drainage time and shows that the oil continues to flow but more and more slowly (linearly as a function of the logarithm of t_D); Hagoort¹⁰ found similar behavior for the four different rock types he tested.

If the gas/oil relative permeability data were measured with the viscous displacement technique (the extended Welge technique as described by Johnston *et al.*),¹¹ extra care is needed in

applying these data. First, the displacement of oil by gas is at an unfavorable mobility ratio (see discussion below) that makes the process unstable. Second, a displacement is adversely affected by capillary end effects that, for the gas/oil system, cannot be overcome by high gas throughput rates. At low oil saturations, the region of most interest, the capillary end effect is the greatest.¹⁰

Finally, one method developed to affect the gas/oil relative permeability and to reduce gas mobility is to inject water alternately with gas (WAG). This procedure was proposed by Caudle and Dyes.¹² Although the method was proposed for use in miscible gasfloods, the concept applies equally to immiscible gas displacements. This technique has been used in many west Texas CO₂ miscible gas projects, in the Prudhoe Bay miscible flood,¹³ and in the Kuparuk immiscible and miscible gas injection processes.^{14,15} The three-phase gas, oil, and water relative permeabilities are calculated in numerical reservoir simulators with algorithms developed over the past several decades.¹⁶

12.2.3 Mobility Ratio. The mobility of a fluid (Eq. 12.1) is defined as its relative permeability divided by its viscosity. Mobility combines a rock property, permeability, with a fluid property, fluid viscosity. Gas-oil relative permeabilities are assumed to be dependent on the saturations of the two fluid phases and independent of fluid viscosity:

$$M_i = (k k_{r_i} / \mu_i) \dots\dots\dots (12.1)$$

A fluid's mobility relates to its flow resistance in a reservoir rock at a given saturation of that fluid. Because viscosity is in the denominator of this definition, gases, which are very-low-viscosity fluids, have very high mobility.

Mobility ratio is generally defined as the mobility of the displacing phase (in the gas/oil case, gas) divided by the mobility of the displaced phase, which is oil. Eq. 12.2 presents two forms of the mobility ratio equation:

$$M = \frac{k_{rg}}{\mu_g} \bigg| \frac{k_{ro}}{\mu_o} = \frac{k_{rg}\mu_o}{k_{ro}\mu_g} \dots\dots\dots (12.2)$$

Eq. 12.2 can also be written in more familiar engineering terms as the ratio of the two fluids' relative permeability values multiplied by the ratio of the two fluids' viscosities.

$$M = \left(\frac{k_{rg}}{k_{ro}} \right) \left(\frac{\mu_o}{\mu_g} \right) \dots\dots\dots (12.3)$$

For simple calculations, the mobility ratio is calculated at the endpoint relative permeability values for the two phases. Hence, the equation that practical engineers use for the gas/oil mobility ratio is

$$M = \frac{k_{g@Sorg} \mu_o}{k_{o@Swi} \mu_g} \dots\dots\dots (12.4)$$

All displacements of oil by gas are at “unfavorable” mobility ratios, with typical values of 10 to 100 or more.

12.2.4 Gas/Oil Linear Displacement Efficiency. The equations that characterize the mechanics of oil displacement by an immiscible fluid were developed by Buckley and Leverett¹⁷ using

relative permeability concepts and Darcy’s law describing steady-state fluid flow through porous media. The resulting fractional flow equation describes quantitatively the fraction of displacing fluid flowing in terms of the physical characteristics of a unit element of porous media. Assumptions inherent in their work are steady-state flow, constant pressure, no compositional effects, no production of fluids behind the gas front, no capillary effects, movement of advancing gas parallel to the bedding plane, immobile water saturation, and uniform cross-sectional flow (no gravity segregation of fluids within the element). Subsequent work by Welge¹⁸ made solving the displacement equations easier.

The Welge equation for the fractional flow of gas at any gas saturation (S_g) is calculated as follows:

$$f_g = \frac{1 + \left(\frac{0.0444 k k_{ro} \Delta \rho A \sin \alpha}{q_T \mu_o} \right)}{1 + 1/M}, \dots\dots\dots (12.5)$$

where

- A = area of cross section normal to the bedding plane, ft²,
- f_g = fraction of flowing stream that is gas,
- k = permeability, darcies,
- k_{ro} = relative permeability to oil, fraction,
- k_{rg} = relative permeability to gas, fraction,
- M = mobility ratio, $\frac{k_{rg} \mu_o}{k_{ro} \mu_g}$,
- q_T = total flow rate through area A , res ft³/D,
- α = angle of dip, positive downdip, degrees,
- $\Delta \rho$ = density difference, $\rho_g - \rho_o$, lbm/ft³,
- μ_o = viscosity of oil, cp, and
- μ_g = viscosity of gas, cp.

When gravity is negligible, this equation becomes the more familiar Buckley-Leverett equation:

$$f_g = \frac{1}{1 + 1/M} \cdot \dots\dots\dots (12.6)$$

Fig. 12.2 is a typical plot resulting from these calculations. The importance of the gravity term is indicated.

To relate the fraction of gas flowing to time, Buckley and Leverett developed the following material-balance equation:

$$L = \frac{q_T t}{\phi A} \left(\frac{df_g}{dS_g} \right), \dots\dots\dots (12.7)$$

where

- L = length, ft,
- S_g = gas saturation, fraction,
- t = time, days, and
- ϕ = porosity, fraction.

The value of the derivative df_g/dS_g may be obtained for any value of gas saturation by determining slopes at various points on the f_g vs. S_g curve. These slopes can be determined manually or, more precisely, using the method presented by Kern¹⁹ for computer spreadsheets.

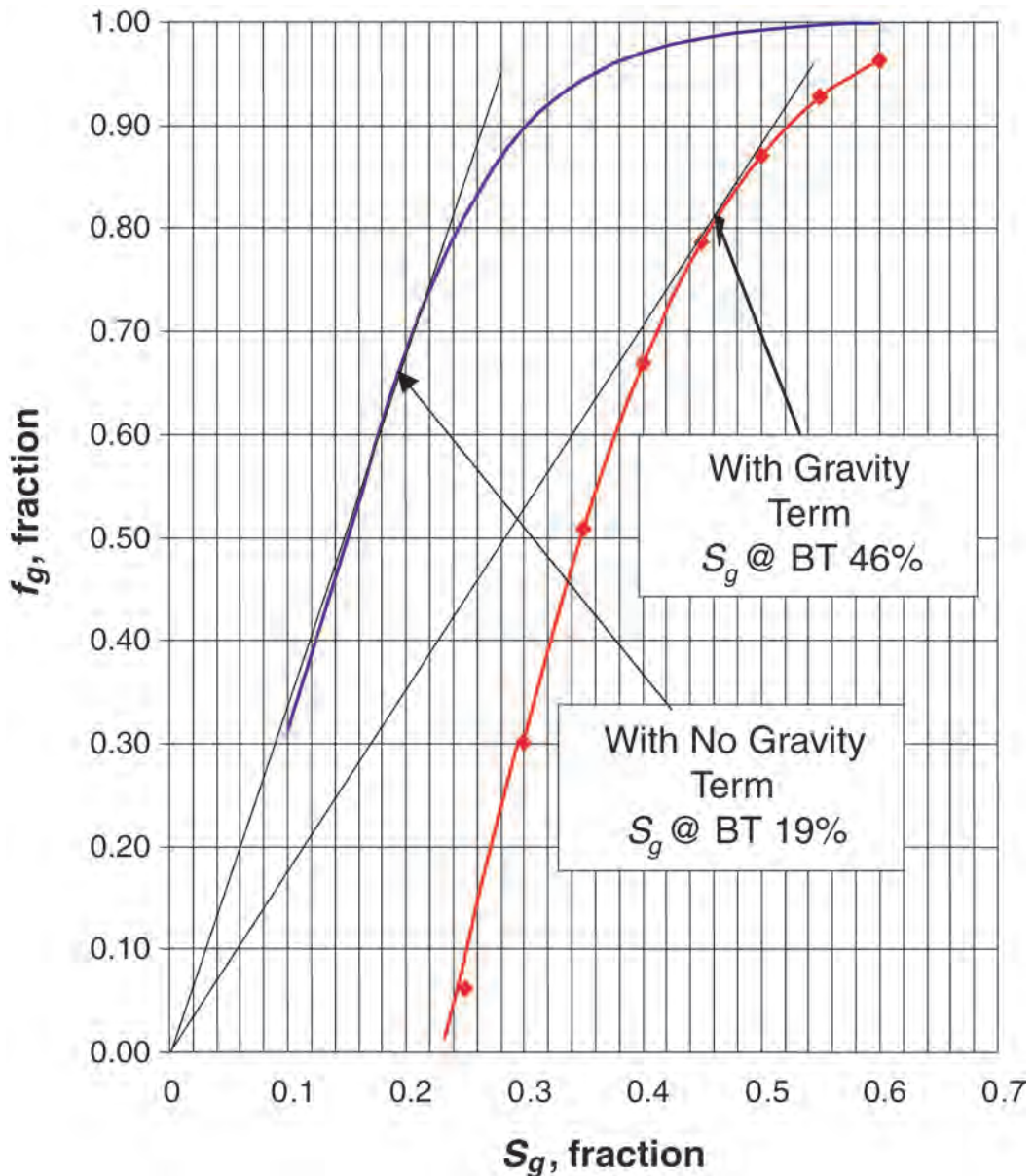


Fig. 12.2—Buckley-Leverett fractional gas flow plot (based on data from the Hawkins field).

Fig. 12.3 illustrates calculated gas-saturation distributions derived from the no-gravity and with-gravity fractional flow curves shown in Fig. 12.2. The area beneath each curve represents the gas-invaded zone. The saturation profile calculation results in lengths that first increase as saturation decreases and then decrease at lower saturations. While correct from a material-balance standpoint, it has been customary to square off the leading edge of the curve at the breakthrough saturation to account for capillary pressure that was neglected in the original derivation of the equation.

The gas/oil displacement efficiency, the percent of the oil volume that has been recovered, can be calculated for any period of gas injection by integrating the volume of the gas-invaded

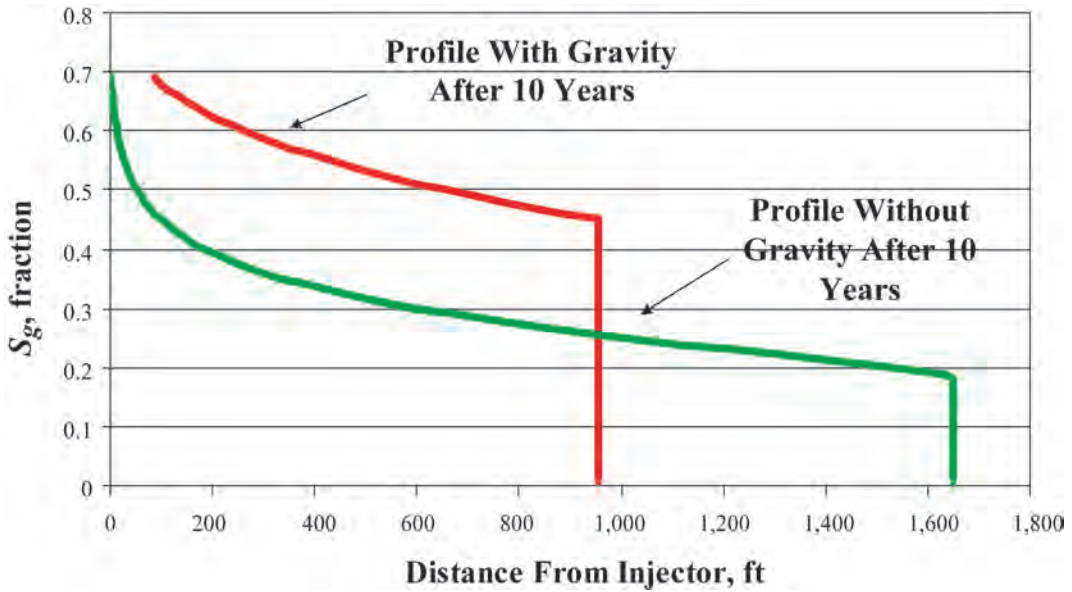


Fig. 12.3—Typical Buckley-Leverett saturation profiles.

zone as a function of gas saturation (S_g). Hence, the fractional flow curves (Fig. 12.2) are used to generate saturation profiles (Fig. 12.3) that lead to values for the gas/oil displacement efficiency. In the next section, several of the factors affecting this efficiency are discussed.

12.2.5 Factors Affecting Gas/Oil Displacement Efficiency. The fractional-flow and material-balance equations discussed above are important for understanding the effects on the efficiency of the gas/oil displacement process of (1) initial saturation conditions, (2) fluid viscosity ratios, (3) relative permeability ratios, (4) formation dip, (5) capillary pressure, and (6) factors of permeability, density difference, rate of injection, and cross section open to flow.

Initial Saturation Conditions. If gas injection is initiated after reservoir pressure has declined below the bubblepoint, the gas saturation will decrease the amount of displaceable oil. If the free gas saturation exceeds the breakthrough saturation, no oil bank will be formed. Instead, oil production will be accompanied by immediate and continually increasing gas production. Laboratory investigations and mathematical analyses have demonstrated this influence of gas saturation on gas displacement performance.²⁰

S_{wi} has been shown to have no influence on displacement efficiency at gas breakthrough, but it directly affects the displaceable oil volume.²¹ If S_{wi} is mobile, the displacement equations are not directly applicable because they were developed for two-phase flow. Approximations of gas displacement performance can usually be made when three phases are mobile by treating the water and oil phases as a single liquid phase. Displacement calculations can then be made with k_{rg} and k_{ro} data determined from core samples containing an immobile water saturation. Oil recovery can be differentiated from total liquid recovery on the basis of material balance calculations incorporating an estimated minimum interstitial water saturation.

Fluid Viscosities. The effect of oil viscosity on fractional flow is illustrated in Fig. 12.4. In this plot, the S_g at breakthrough increases from 12 to 38% with a 10-fold decrease in oil viscosity.

Relative Permeability Ratios. The concepts of relative permeability can be applied equally well to complete or partial pressure-maintenance operations. Relative permeability, a character-

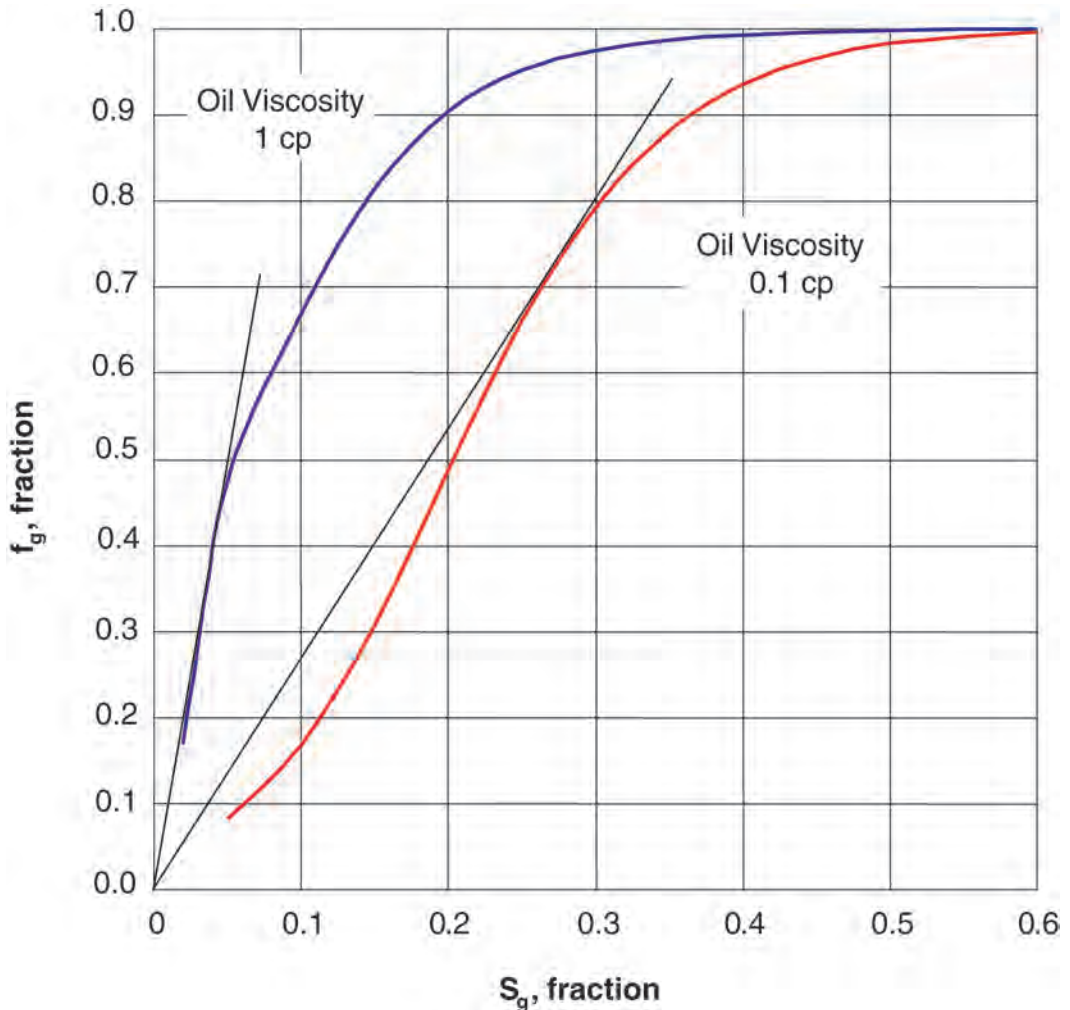
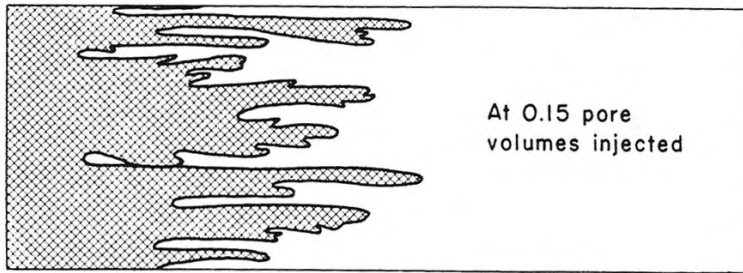


Fig. 12.4—Effect of viscosity on gas/oil fractional flow.

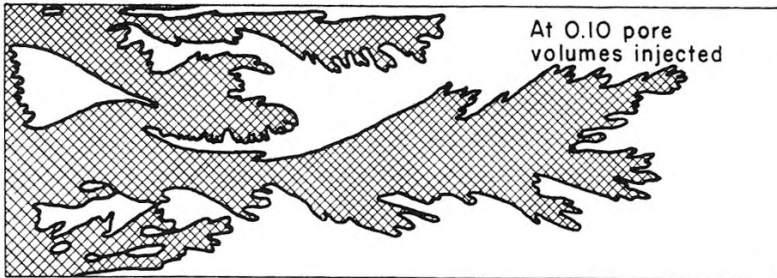
istic of the reservoir rock, is a function of fluid saturation conditions. It is important that calculations be based on dependable data obtained by laboratory analyses at reservoir conditions using representative core samples. If possible, the laboratory-determined data should be supplemented by relative permeabilities calculated from field performance data.

Formation Dip. When formation dip aids gravity, as illustrated in Fig. 12.2, fractional flow behavior is significantly improved if permeability is high enough and withdrawal rates do not exceed gravity-stable conditions. Gravity drainage is discussed later in this chapter.

Capillary Pressure. Capillary forces are opposite gravity drainage forces and directionally decrease displacement efficiency. However, capillary forces can often be ignored as insignificant for projects with rates of displacement normally used. Only at extremely low rates of displacement, where viscous forces become negligible, is the saturation distribution controlled to a significant extent by the balance between capillary and gravitational forces. Another place where capillary forces are considered important is many of the large carbonate reservoirs of the Middle East where the matrix-blocks/fracture-system interaction can significantly affect overall reservoir performance.



(a) Displacement front for mobility ratio of 20.



(b) Displacement front for mobility ratio of 383.

Fig. 12.5—Cross-sectional view of gas/oil displacement front [at 0.15 pore volumes injected (PVI)] for mobility ratios of (a) 20 and (b) 383 at 0.10 and 0.15 PVI, respectively.²²

Other Factors. Higher permeability, greater density difference between oil and gas, and a lower displacement rate all improve the displacement efficiency.

12.2.6 Unfavorable Mobility Ratio Causes Viscous Flow Instabilities. Displacements that take place at very unfavorable mobility ratios are unstable, and viscous fingering occurs. This is the situation for essentially all gas/oil displacements, especially if the displacement is occurring horizontally. The impact of such instabilities is illustrated in Figs. 12.5 and 12.6.^{22,23} Both figures were drawn from technical literature concerning miscible displacement laboratory experiments using homogeneous sandpacks, but the observed effects would be the same for immiscible gas displacing oil at very unfavorable mobility ratios. Fig. 12.5 shows, in cross-sectional view, the nature of viscous fingering for two highly unfavorable mobility ratios (the two fluids have equal densities). The flood front in both cases is very unstable. Fig. 12.6 shows, in areal view, the effect of mobility ratio on the displacement process in a quarter of a five-spot pattern for mobility ratios from 0.151 to 71.5. For mobility ratios from 4.58 to 71.5 (cases D through F), the flood front is very unstable, and breakthrough occurs via narrow fingers of the injected fluid; these cases show how the process of gas displacing oil would occur.

In both of these illustrations, the cause of the viscous fingering was a slight perturbation in the flow field that grew into the viscous finger once the perturbation occurred. In real reservoir situations, there are two physical aspects that enhance the viscous-fingering phenomenon. First, real reservoirs are very heterogeneous, so a variety of styles of permeability heterogeneities can initiate viscous fingering. Second, in a cross-section immiscible gas/oil displacement process, gas is always less dense than oil. Hence, there is a gas/oil density difference, and the force of gravity causes the gas to override the oil and initiate a viscous finger of the high-mobility gas phase along the top of the reservoir interval.

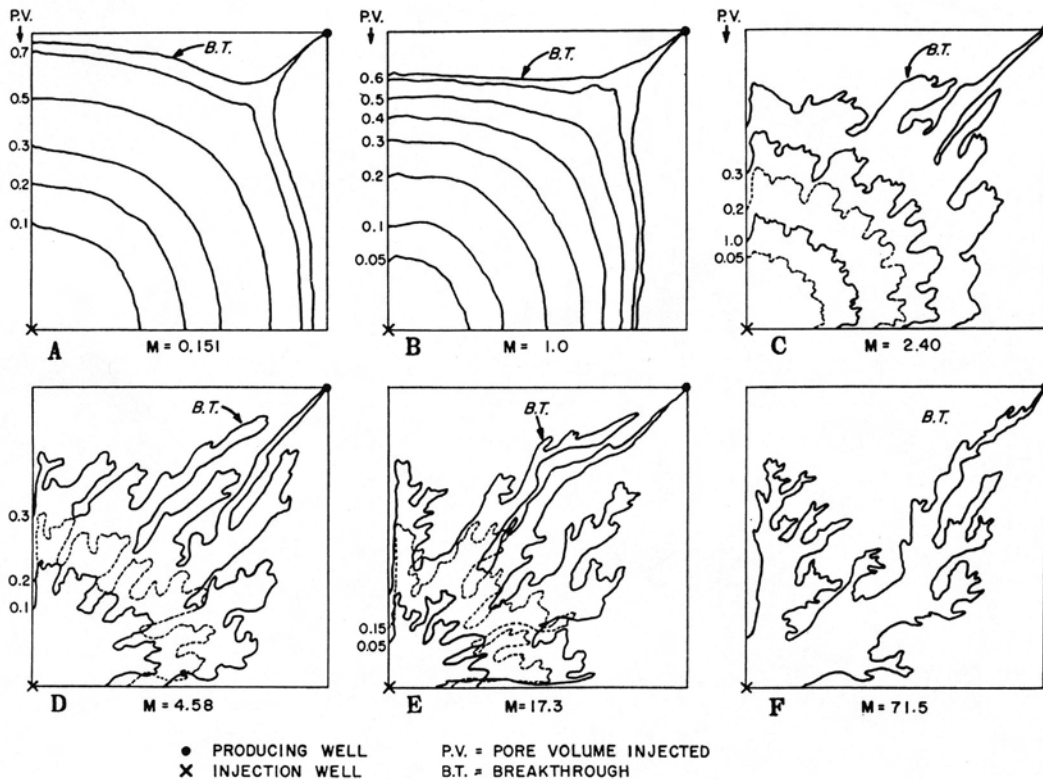


Fig. 12.6—Gas/oil displacement fronts for various mobility ratios (0.151 to 71.5) and PVI until breakthrough, quarter of a five-spot pattern.²³

If the gas/oil displacement is occurring vertically with gas generally displacing oil downward, gravity will work to stabilize the flood front between the gas and oil, although if the rate is too high, instabilities in the form of gas cones or tongues can occur.

12.3 Gas/Oil Compositional Effects During Immiscible Gas Displacement

This section briefly discusses the various mass transfer compositional aspects of the immiscible gas/oil displacement process. The implications of these compositional effects are very dependent on the oil composition, the composition of the injected gas, and the surface facilities and pipelines available in a particular field situation. The injected gas/oil composition interactions can be categorized as either swelling effects (gas dissolving into the oil phase) or stripping effects (various components from the oil transferring to the gas phase).

12.3.1 Swelling Compositional Effects. The most obvious compositional effect in the immiscible gas/oil displacement process is that, if the oil is not saturated with gas at the reservoir pressure or if the reservoir pressure is increased as a result of the gas injection, the volume of gas dissolved in the oil will increase until the oil is saturated at that pressure. At the same time and because of the increased volume of gas in solution in the oil, the oil formation volume factor (FVF) will increase. This phenomenon, commonly called swelling, can increase the efficiency of the gas/oil displacement process.

The significance of the swelling effect is dependent on the oil reservoir situation. For an oil reservoir in which there is a gas cap, the underlying oil column will already be fully or nearly saturated with gas at the reservoir pressure. Hence, there will be very little impact on the gas/

oil displacement process as a result of the interaction between the reservoir oil and injected gas. However, for an oil reservoir in which there is no gas cap and where the oil bubblepoint pressure is very low compared with the original reservoir pressure, the swelling effect can be a very significant part of the gas/oil displacement process. The Swanson River field (Cook Inlet, Alaska) is an example of this latter situation (original reservoir pressure, 5,580 psi; oil bubblepoint pressure, 1,350 psi).²⁴ The change in oil FVF from a bubblepoint of 1,350 psi to being saturated at 5,580 psi is from 1.21 to ≈ 1.80 RB/STB. The application of immiscible gas injection to the Swanson River field is discussed in the Case Studies section of this chapter.

In some of the simple calculation techniques discussed below, the swelling effect is included. In a “black oil” type of numerical reservoir simulator, the swelling effect is taken into account because, although there are only two hydrocarbon components (gas and oil) for the two hydrocarbon phases, the swelling effect is incorporated by means of the entered table of oil pressure/volume/temperature (PVT) properties (e.g., FVF, gas in solution, oil viscosity) as a function of pressure. In other words, in this type of reservoir simulator, the gas hydrocarbon component exists either as a free-gas phase or as gas dissolved in the oil; the oil hydrocarbon component exists only as part of the liquid phase. A compositional numerical reservoir simulator will automatically take the swelling phenomenon into account in its equation-of-state phase-behavior calculations. See the chapter on numerical simulation in this section of the *Handbook* for detailed discussion of the various types of numerical reservoir simulators and their applications.

12.3.2 Stripping Compositional Effects. The other key compositional aspect of the immiscible gas/oil displacement process is the vaporizing (or stripping) by the lean injected gas of some hydrocarbon components of the oil, particularly the intermediate hydrocarbon components (C_3 through C_8). In most cases, the injected gas is very lean natural gas that is the residue gas from a nearby gas processing plant and composed primarily of methane. At such gas processing plants, the propane and heavier hydrocarbon components typically have been condensed from the entering produced gas; in some cases, ethane is also extracted from the gas. Such a lean injected gas will, when in contact with the oil at reservoir conditions, vaporize various hydrocarbon components from the oil until the gas and oil phases have reached compositional equilibrium.

In immiscible gas/oil displacements using nitrogen (N_2), carbon dioxide (CO_2), or some combination of these gases (such as flue gas, 88% N_2 , 12% CO_2), these nonhydrocarbon injected gases can also vaporize various hydrocarbon components until gas/oil equilibrium is reached at reservoir conditions. This phenomenon has been observed in the Hawkins nitrogen injection project. Nitrogen is not as efficient as methane at stripping hydrocarbon components from the oil. Carbon dioxide, because its phase behavior is much like that of propane, can vaporize a considerable amount of hydrocarbon components from the oil at reservoir conditions.

The significance of the stripping effect depends on the oil composition. Immiscible gas/oil injection projects have been applied to reservoirs with oil gravities from 24 to 43°API or more.^{14,25,26} In all cases, the stripping effect increases the recovery of hydrocarbons from the oil reservoir, but lighter oils have a much greater percentage of their components vaporized by cycling gas through the reservoir and operating at higher gas/oil ratios (GORs).

In some of the simple calculation techniques discussed below, aspects of the stripping of oil by lean injected gas can be approximated. Black-oil numerical reservoir simulators cannot handle the vaporization of hydrocarbon components from the oil into the gas phase. A compositional numerical reservoir simulator must be used to quantify this effect for a particular oil/injected-gas reservoir situation. These calculations are based on the use of an equation-of-state fluid characterization that is “tuned” to PVT laboratory data for the particular oil and potential

injected-gas compositions. The compositional simulator also can quantify the effects of various surface facility configurations, including associated gas plants.

Calculation Methods. These compositional effects are too complicated to be quantified with hand-calculation methods. The black-oil numerical reservoir simulator can be used in limited ways to make these calculations. The black-oil model can reasonably handle the swelling effect, but it cannot handle the stripping effect at all.

The compositional effects of immiscible gas injection are best calculated using a compositional numerical reservoir simulator. To use such a model most accurately, considerable gas/oil PVT data need to be taken with the reservoir oil mixed with a range of gas compositions. These measurements should include a variety of special measurements, such as swelling experiments and stripping experiments, that can be used to develop a more accurate equation-of-state fluid characterization. Then the reservoir model can be used to quantify the performance of possible immiscible gas injection projects and associated surface facilities that might be built.

Surface Facility Considerations. In most applications of immiscible gas injection, during the early years of the projects, hydrocarbons are produced at about the original solution GOR. During this period, the impact of surface-facility design on the volume of produced hydrocarbon liquids is relatively limited. Later in the life of the projects when the producing GOR rises, the surface facilities are far more important in terms of both the volume of gas that can be handled and the extent to which this gas is processed. During this late period, the rate of oil production will be limited by the surface facilities' gas-handling capacity.²⁷

The gas recovered from the typical series of oilfield separators will contain a large amount of ethane through butane components and decreasing but significant amounts of the various heavier hydrocarbon components. Early generations of gas-processing plants were capable of separating out components that would condense down to temperatures of -10 to -20°F. Modern gas-processing plants operate at temperatures of -40°F or considerably lower; at these low temperatures, essentially all the ethane and heavier hydrocarbons are recovered, leaving a residue gas consisting primarily of methane. See the chapters in the Facilities and Construction Engineering section of the *Handbook* for additional discussion of oilfield surface separators and gas-processing plants.

Another related factor is the type of pipeline networks available to transport the hydrocarbon products to market. In some geographical areas, only those hydrocarbon components that can be stabilized in a crude oil stream can be transported and sold because there are only crude oil pipelines in that area. In much of the United States and Canada, a variety of crude oil and natural gas liquid (NGL) pipelines have been built so that the lighter, liquefied hydrocarbon components can also be marketed, particularly to the petrochemical industry of the U.S. Gulf Coast. In other parts of the world, as the number of liquefied petroleum gas tankers has increased, worldwide markets for the lighter hydrocarbons have developed. As a result, more oil fields have had large-scale gas-processing projects built to recover and market propane and heavier hydrocarbons from the produced gas streams.

12.4 Reservoir Geology Considerations Regarding Immiscible Gas Displacement

Many aspects of reservoir geology interplay with the immiscible gas/oil displacement process to determine overall recovery efficiency. Because there is always a considerable density difference between gas and oil, the extent to which vertical segregation of the fluids occurs and can be taken advantage of or controlled is critical to the success of gas displacing oil. See the reservoir geology chapter in this section of the *Handbook* for considerably more discussion of this topic.

12.4.1 General Geological Considerations. As with any oil recovery process involving the injection of one fluid to displace oil in the reservoir, the internal geometries of the reservoir interval have a controlling effect on how efficiently the injected fluid displaces the oil from the

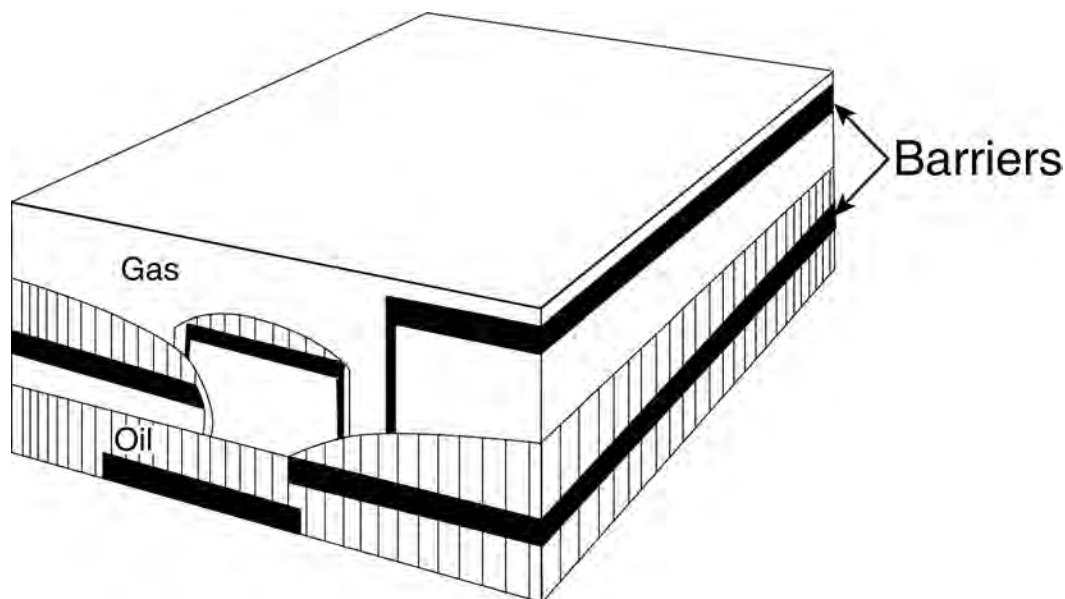


Fig. 12.7—Schematic of oil draining off small vertical flow barriers.²⁸

whole of the reservoir. For the immiscible gas/oil displacement process, the key factors are stratigraphy and structure.

Stratigraphy. The stratigraphy of a reservoir is determined primarily by its depositional environment. First and foremost is how layered the reservoir is in terms of both how heterogeneous the various sand intervals are and the scale at which shales or other barriers to vertical flow are interbedded with the sands. Another very important aspect is how continuous the shale intervals are. With fully continuous shales, a reservoir interval should be divided into compartments that will not interact with each other. Unless the reservoir has a steep dip, such shales will negatively affect the gas/oil displacement process.

Less continuous shales can result in better distribution of injected gas without a strong negative impact on the gas/oil gravity drainage process (see Fig. 12.7 for an illustrative cross-sectional view of sands interbedded with discontinuous shales). Richardson *et al.*²⁸ analyzed the effects of such limited-size shales. First, they determined geologic factors that control shale dimensions and continuity for sandstone deposits. There is a wide range of shales whose dimensions depend on the depositional environment, with marine shales being the most extensive and flood-plain and interdistributary shales being of smaller areal dimensions (1,300 to 5,250 ft wide by 5,250 to 10,500 ft long). Next, simple 2D calculations of oil drainage off small shales were made, assuming that the various beds were horizontal. They concluded that, “The time required for oil drainage from a barrier is proportional to its width squared and viscosity, and inversely proportional to the horizontal permeability and density difference. Lateral drainage off small barriers can be rapid, and recoveries may be reduced only slightly.”²⁸

Structure. The structural aspects of a particular reservoir consist of several parts: the closure or vertical thickness of the hydrocarbon column, dip angle of the beds, and size and relative thickness of the gas cap compared with the oil column. Thick reservoirs (> 600 ft of oil column) are the best for application of the immiscible gas/oil drainage process with gas injection at the crest of the structure and oil production from as far downdip as possible. Dip angle is important to the efficiency of the displacement process because a higher dip angle generally means that the effective vertical permeability is increased.

The relative size of the oil column compared with the gas cap affects the performance of a particular reservoir. The gas/oil gravity drainage process has been applied to reservoirs that have, relative to the size of the oil column, very small gas caps²⁶ and to some with very large gas caps.²⁹ Success has been achieved over the full range of ratios of gas cap to oil column size. The advantage of having a large initial gas cap is that the reservoir pressure drops very slowly as the oil is produced compared with a situation with a relatively small gas cap in which the reservoir pressure falls quite rapidly until the secondary gas cap grows sufficiently.

Other Geological Factors. Within the reservoir sandstone layers, the nature of the sand layering can strongly affect the efficiency of the gas/oil displacement. In those depositional environments in which the highest-permeability sands are on the bottom of the reservoir interval, the gas/oil displacement process will be far more efficient, especially compared with the situation in which the depositional environment results in the highest permeability toward the top of the reservoir interval. The reason is that, in the first situation, the gravity override of the gas is slowed by the vertical distribution of permeability, but in the latter situation, the gas gravity override is enhanced.

Even if the reservoir were totally homogeneous, a horizontal gas/oil displacement process would not be very efficient because the gas will strongly override the oil and, because of its high mobility, will rapidly travel from the injection wells to the production wells. For reservoirs with many “random” heterogeneities, the gas/oil displacement process will be aided because heterogeneities inhibit growth of low-viscosity fingers by forcing them to travel a more circuitous path between the injector and producer.

Vertical Permeability at Various Scales. The challenge in making calculations for the immiscible gas/oil displacement process at the reservoir scale is to quantify properly the vertical permeability of the reservoir as a whole. There are several scales at which vertical permeability affects the gas/oil displacement process. The engineer has quantitative data on the vertical permeability from routine core analysis performed foot by foot on small core plugs from the reservoir interval. The next larger scale concerns the areal extent of any impermeable layers observed in the cores, be they 1 in., 6 in., or several feet thick. Geologists typically estimate the areal dimensions of these impermeable layers from their training, experience, and studies of outcrops from similar depositional environments.

Despite all the technical work performed before this process is applied to a particular reservoir, the actual effective vertical permeability and its distribution will not be fully known until some years later. The vertical permeability can be quantified by observing reservoir performance. Typically, gravity-drainage immiscible gas/oil displacements are undertaken with the assumption of good vertical permeability so that if actual reservoir performance matches the projections, then the vertical permeability is as high as previously assumed. However, if the reservoir performance is poorer than expected, a likely cause is lower vertical permeability and/or heterogeneities in the vertical permeability distribution over the reservoir.

Carbonate Reservoirs. The geologic discussion above primarily concerns sandstone reservoirs, although many of the general concepts also apply to carbonate reservoirs. Because diagenetic changes often alter the original framework of a carbonate reservoir far more than what occurs in sandstone reservoirs and because some types of carbonate reservoirs do not have sandstone equivalents, this section briefly discusses some differences in carbonate reservoirs.

One type of carbonate deposits that results in reservoirs with thick vertical dimensions, especially compared with their areal dimensions, is the carbonate reef deposit. The style of this deposit with the greatest vertical-to-horizontal aspect is called a pinnacle reef. Reef deposits typically contain large vugs. The key question is, How interconnected are these vugs? Diagenetic processes can isolate these vugs or can provide various types of pore-to-pore interconnections. For example, in New Mexico, the Abo reef trend developed on the northern margin of

the Delaware basin. The original reef framework of hydrocorals, sponges, and algae has been totally dolomitized to create a pore system consisting only of vugs, fractures, and fissures.²⁶

In carbonate reservoirs, the diagenetic process includes both chemical alteration, such as dolomitization, and cementing and leaching processes. Cementation with calcite, anhydrite, or other insoluble chemicals can have a significant negative impact on the reservoir's pore system. Leaching has the opposite effect and generally enhances the reservoir quality, although leaching may increase the range of heterogeneities and lead to some superconductive flow paths in portions of a reservoir. As carbonate rocks become more brittle because of chemical alteration, fracturing commonly occurs. The geologist and petrographer must examine the cores in great detail to determine the number and sequence of cementation, leaching, and fracturing events that have altered a particular rock interval over geologic time.

Middle East Carbonate Matrix/Fracture-System Reservoirs. A particular style of reservoir in which a considerable number of immiscible gas/oil gravity drainage projects have been applied is the Middle East carbonate matrix-block/fracture-system reservoirs. Most of these reservoirs are very large folded anticlinal structures with dimensions of tens of miles long by several miles wide and with hydrocarbon columns hundreds of feet to several thousand feet thick.

In these carbonate reservoirs, the matrix is high porosity but low permeability (generally ≤ 1 md), and the fracture system created matrix blocks with dimensions ranging from a few feet to > 10 ft.^{30,31} The fractures can be up to a tenth of an inch wide, so the effective interwell permeabilities are very high.

The geologic complications of these matrix-block/fracture-system reservoirs concern the way that the matrix and fractures are interconnected and fluid is transferred between these two portions of the pore system. This combines (1) the interaction of the fractures with the matrix along the faces of vertical fractures, (2) the interaction of one matrix block with its neighboring matrix blocks if capillary continuity exists along such surfaces (see [Fig. 12.8](#) for the schematic oil saturation profiles for cases without and with capillary continuity), and (3) possible fluid transfer along matrix/fracture surfaces if portions of the fracture system are inclined planes and neither vertical nor horizontal. Also, the presence of cementation along some of the fracture surfaces is very important to fluid transfer because the fractures will rapidly transport fluid, but for overall high recovery efficiency, the matrix blocks must exchange oil and gas with the surrounding fracture system. The geological aspects of such matrix-block/fracture systems are difficult to quantify because their dimensions and fracture characteristics cannot be easily discerned from cores and logs. Descriptions of nearby outcrops of the reservoir formation can often be helpful in understanding the macrodimensions of the matrix-block/fracture system.

A number of technical papers have explored aspects of the geology/fluid-flow interactions of such matrix-block/fracture network carbonate reservoirs. Firoozabadi and coworkers³²⁻³⁷ have developed theories, made calculations, and performed experiments to explore aspects of these types of reservoirs. Saidi³⁰ has discussed the physical phenomena affecting the performance of the Haft Kel field (Iran) and analyzed its performance; more discussion of the Haft Kel field is found in the Case Studies section of this chapter.

12.5 General Immiscible Gas/Oil Displacement Techniques

In this section, the general technical features of the various immiscible gas injection projects are discussed.

12.5.1 Types of Gas-Injection Operations. Immiscible gas injection is usually classified as either crestal or pattern, depending on the location of the gas injection wells. The same physical principles of oil displacement apply to either type of operation; however, the overall objectives, type of field selected, and analytical procedures for predicting reservoir performance vary considerably by gas injection method.

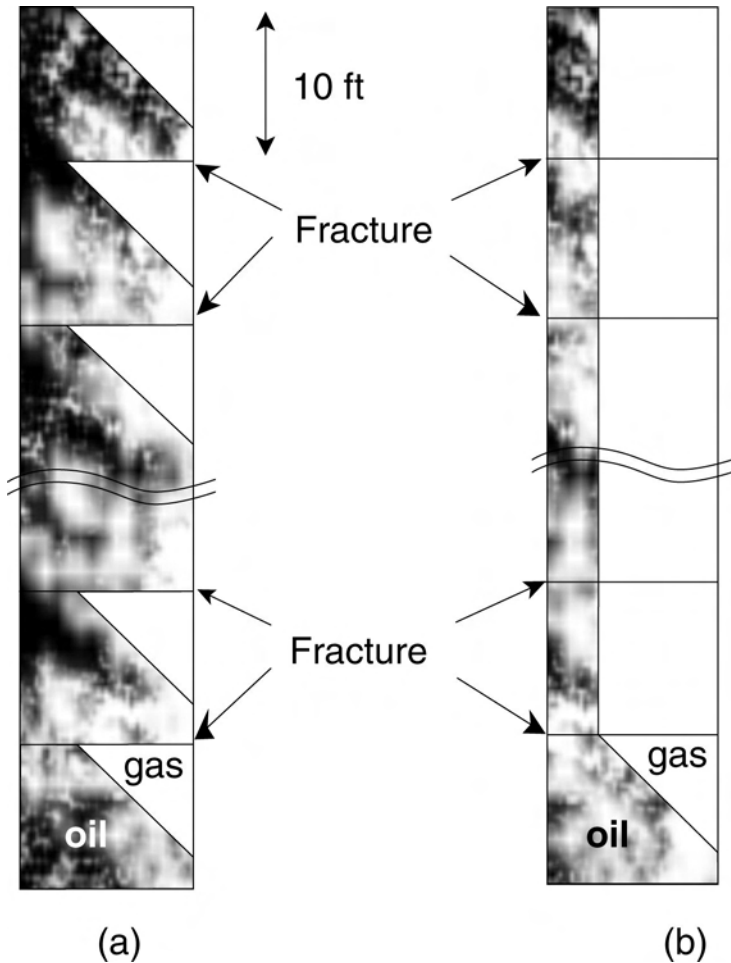


Fig. 12.8—Schematic of oil saturation profiles (dark shading) from stacks of matrix blocks: (a) without capillary continuity and (b) with capillary continuity bounded by vertical and horizontal fractures.³⁰

Crestal Gas Injection. Crestal gas injection, sometimes called external or gas-cap injection, uses injection wells in higher structural positions, usually in the primary or secondary gas cap. This manner of injection is generally used in reservoirs with significant structural relief or thick oil columns with good vertical permeability. Injection wells are positioned to provide good areal distribution and to obtain maximum benefit of gravity drainage. The number of injection wells required for a specific reservoir depends on the injectivity of individual wells and the distribution needed to maximize the volume of the oil column contacted.

Crestal injection, when applicable, is superior to pattern injection because of the benefits of gravity drainage. In addition, crestal injection, if conducted at gravity-stable rates—e.g., less than the critical rate (see Eq. 12.8 later in this chapter)—will result in greater volumetric sweep efficiency than pattern injection operations. There are many examples of ongoing crestal injection projects throughout the world, including some very large projects in the Middle East.

Pattern Gas Injection. Pattern gas injection, sometimes called dispersed or internal gas injection, consists of a geometric arrangement of injection wells for the purpose of uniformly distributing the injected gas throughout the oil-productive portions of the reservoir. In practice, injection-well/production-well arrays often vary from the conventional regular pattern configurations—e.g., five-spot, seven-spot, nine-spot (see the chapter on waterflooding in this section for

more description of these patterns)—to irregular injection-well spacing. The selection of an injection arrangement is a function of reservoir structure, sand continuity, permeability and porosity levels and variations, and the number and relative locations of existing wells.

This method of injection has been applied to reservoirs having low structural relief, relatively homogeneous reservoirs with low permeabilities, and reservoirs with low vertical permeability. Many early immiscible gas-injection projects were of this type. The greater injection-well density results in pattern gas injection, rapid pressure and production response, and shortened reservoir depletion times.

There are several limitations to pattern-type gas injection. Little or no improvement in recovery is derived from structural position or gravity drainage because both injection and production wells are located in all areas of the reservoir. Low areal sweep efficiency results from gas override in thin stringers and by viscous fingering of gas caused by high flow velocities and adverse mobility ratios. High injection-well density increases installation and operating costs. Typical results of applying pattern injection in low-dip reservoirs are rapid gas breakthrough, high producing GORs, significant gas compression costs to reinject the gas into the reservoir, and an improved recovery of < 10% of original oil in place (OOIP). Note that gas inefficiently displaces oil in gas-swept areas. Attempts to subsequently waterflood such areas result in rapid water breakthrough and little, if any, additional oil displacement.

Few pattern gas injection projects have been implemented in recent years because this method is not as attractive economically as alternative methods for increasing oil recovery.

12.5.2 Optimum Time To Initiate Gas Injection Operations. The optimum time to begin gas injection is site specific and depends on a balance of risks, gas market availability, environmental considerations, and other factors that affect project economics. When only oil recovery and improvements in reservoir producing characteristics are considered, reservoir conditions for gas injection operations are usually more favorable when the reservoir is at or slightly below the oil bubblepoint pressure, unless the bubblepoint pressure is low compared with the initial reservoir pressure. Near the oil bubblepoint pressure, nonrecovered oil represents the smallest volume of stock-tank oil, oil relative permeability is high, and oil viscosity is low.

12.5.3 Efficiencies of Oil Recovery by Immiscible Gas Displacement. It is customary in most displacement processes to relate recovery efficiency to displacement efficiency and volumetric sweep efficiency. The product of these factors provides an estimate of recoverable oil expressed as a percentage of OOIP. Analytical procedures are available for evaluating each efficiency factor. For the purposes of this chapter, the two components describing the overall recovery efficiency are defined as follows:

1. Displacement efficiency is the percentage of oil in place within a totally swept reservoir rock volume that is recovered as a result of viscous displacement and gravity drainage processes.
2. Volumetric sweep efficiency is the percentage of the total rock or PV that is swept by gas. This factor is sometimes divided into horizontal and vertical components, with the product of the two components representing the volumetric sweep.

Recovery efficiencies increase with continued gas injection, but the rate of recovery diminishes after gas breakthrough occurs as the GOR increases. The overall result is that the ultimate oil recovery efficiency is a function of economic considerations, such as the cost of gas compression and the volume and availability of lean residue gas or potentially more expensive alternatives like N₂ from a nitrogen rejection plant.

12.6 Vertical or Gravity Drainage Gas Displacement

In this section, the primary manner in which the immiscible gas/oil displacement process has been used is discussed in qualitative terms. This is the use of gas injection high on structure to displace oil downdip toward the production wells that are completed low in the oil column. In

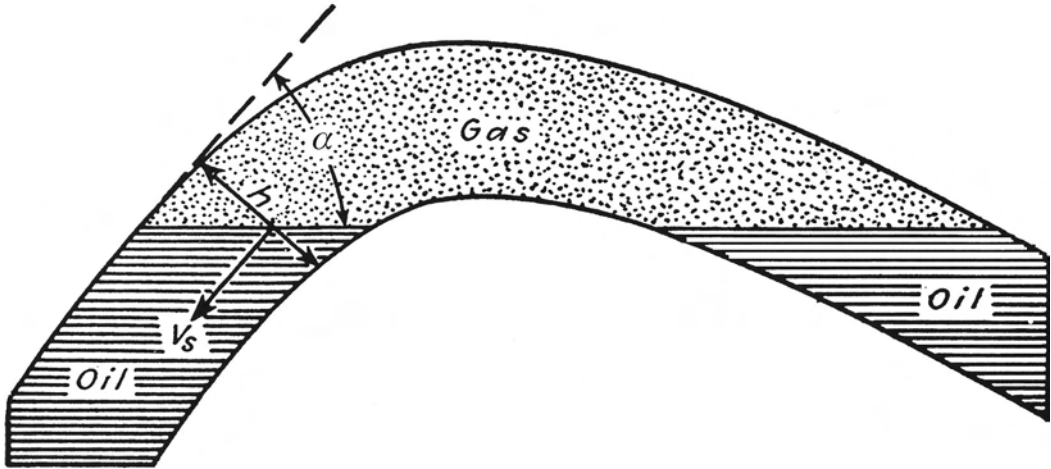


Fig. 12.9—Schematic cross-sectional view of anticlinal reservoir of thickness h and dip angle α with gas cap overlying oil column.¹

many cases, an original gas cap was present, so the gas was injected into that gas-cap interval (see Fig. 12.9 for cross-sectional view of anticlinal reservoir with gas cap over oil column with dip angle α and thickness h). In this situation, the force of gravity is at work, trying to stabilize the downward gas/oil displacement process by keeping the gas on top of the oil and counteracting the unstable gas/oil viscous displacement process. If the oil production rate is kept below the critical rate, then the gas/oil contact (GOC) will move downward at a uniform rate. In the next section, the simple engineering calculation techniques for estimating the rate for stable gravity drainage for a gas/oil system are discussed.

In normal oilfield operations, producing wells are drilled and perforated as far as possible from the gas cap, both vertically and laterally. Hence, many production wells may not have any of the gas cap directly over them initially. Until the gas cap extends over the whole of the oil column and its producing wells, because of the pressure differential between the gas cap and the area around the producing wells, the downdip oil production will result in the gas cap moving rapidly along the top of the structure to provide pressure support to the whole oil column. When this happens, if the reservoir is a dipping structure, the gas cap is described as “draping” over the oil column. If the oil reservoir is an anticlinal structure, then this process is often described as the gas cap having expanded to form an “umbrella” over the whole oil column. Once the gas-cap drape or umbrella has formed, the continued downward movement of the gas cap at each location can be stabilized. Fig. 12.10 shows views of the Prudhoe Bay oil field (Alaskan North Slope) in which the original gas cap was offset to the northeast of most of the oil column and where there has been gas cap underrunning of the top of structure until it draped over much of the downdip oil column where the hundreds of producing wells were located.

There are likely to be local variations in the GOC caused by reservoir heterogeneities and near-wellbore pressure gradients. The most notable of these results in gas coning caused by high pressure gradients around the perforated interval of each wellbore. Here, the controlling factors are the oil and gas production rates, the distance from the top of the perforations to the overlying GOC, and the horizontal and vertical permeabilities.³⁸ In this situation, the presence of a small shale interval between the GOC and the top of the perforated interval can have a very beneficial effect on the maximum oil production rate before gas coning occurs (see Fig. 12.11). For a particular reservoir situation, gas-coning calculations are best made with a numerical reservoir simulation model.^{38,39}

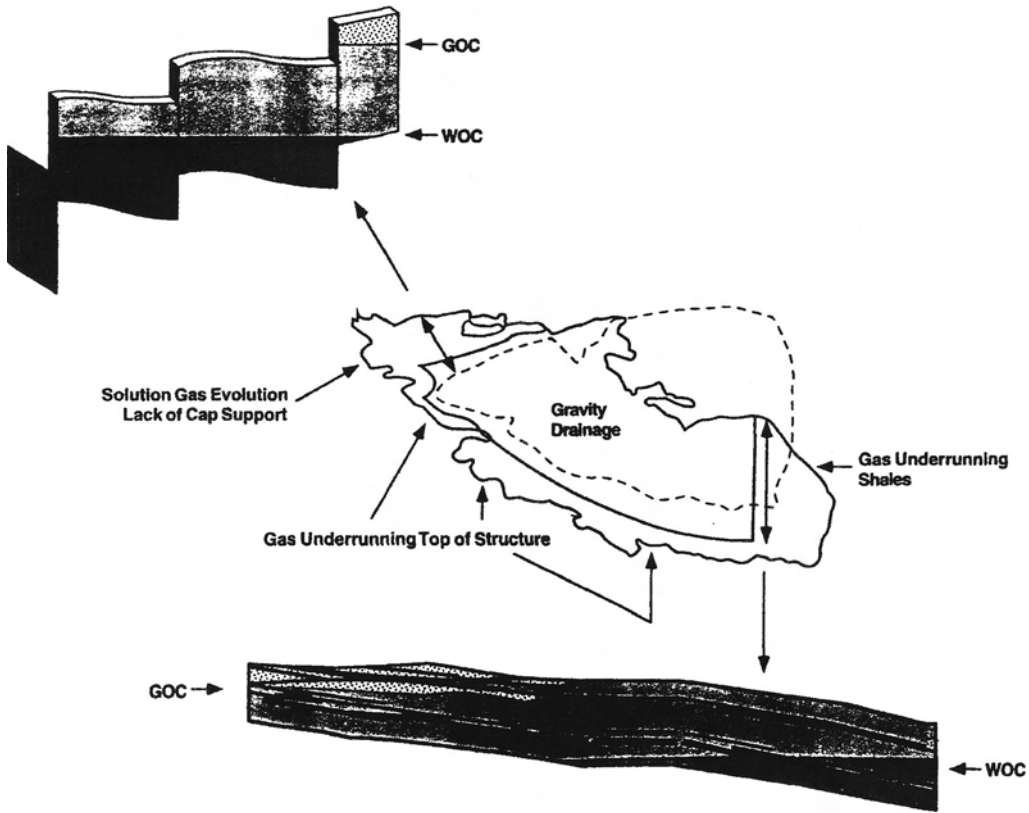


Fig. 12.10—Prudhoe Bay field: different natural depletion producing mechanisms in various areas of the Sadlerochit reservoir.¹³

The gas/oil gravity drainage process is complicated if the oil column is underlain by an aquifer because the aquifer will provide pressure support to the oil column in response to any decrease from original reservoir pressure caused by oil production. If the aquifer is very strong, it will invade the lower portions of the oil column and may provide almost barrel-for-barrel voidage replacement. In this case, the original gas cap may not expand much. If the aquifer is weak or if there is a tar mat at the oil/water contact (OWC) inhibiting water influx, then the gas cap will be the primary means of pressure support for the oil column and the reservoir will perform almost as if there were no aquifer present. A problem sometimes experienced with oil reservoirs with both overlying gas caps and underlying aquifers is that the near-wellbore coning behavior is more complicated. The reason is that gas-cap gas is coning downward toward the perforated interval and aquifer water is trying to cone upward toward the same perforated interval. If water cones first into the perforated interval, then the gas coning will be more severe because, with three-phase relative permeability effects, the near-wellbore pressure gradients are greater, which causes gas coning to occur at lower oil production rates.

12.7 Calculation Methods for Immiscible Gas Displacement

Techniques described in this chapter are classic methods for describing immiscible displacement assuming equilibrium between injected gas and displaced oil phases while accounting for differing physical characteristics of the fluids, the effects of reservoir heterogeneities, and injection/production well configurations. The reservoir is treated in terms of average properties for volume of rock, and production performance is described on the basis of an average well. Black-

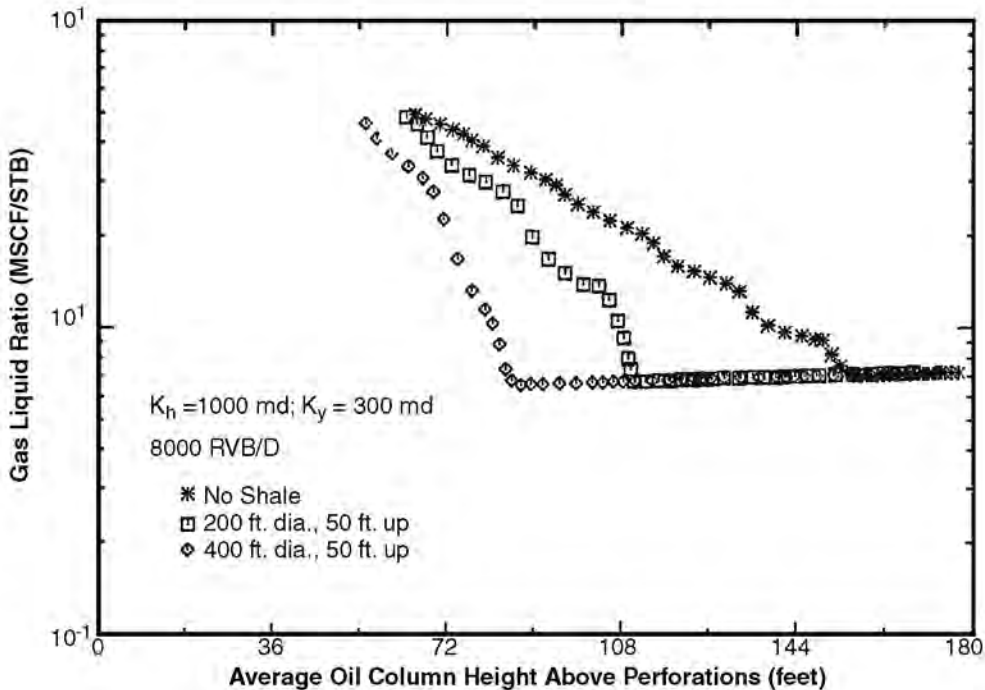


Fig. 12.11—Numerical simulation results of the effects of small shales on near-wellbore gas coning behavior.³⁸

oil-type reservoir simulation models use essentially these same techniques but, by means of 1D, 2D, or 3D cell arrays, account for areal and vertical variations in rock and fluid properties, well-to-well gravity effects, and individual well characteristics. More complex compositional models account for nonequilibrium conditions between injected and displaced fluids and can be used to describe individual well streams in terms of the compositions of the produced fluids.

The increasing capability of desktop computers and the growing amount of affordable simulation software are making it possible to use numerical reservoir simulation more often. However, results obtained from simulation will be directly dependent on the quality of data to describe the reservoir rocks and fluids. It is also important to comprehend the physics of displacement to understand the simulation results and to identify incorrect results. The fundamentals of the displacement process presented in this section are intended to provide the background needed to produce good-quality predictions of oil recoveries.

12.7.1 Modifications of Displacement Equations. Applicability of the basic displacement equations to a given reservoir is governed by whether the underlying assumptions are reasonable. Several authors have reported modifications that eliminate the need to make certain assumptions. Modifications that take into consideration the swelling effects experienced from injection into an undersaturated reservoir and production of fluids from behind the gas front have been presented by Welge,¹⁸ Kern,¹⁹ Shreve and Welch,⁴⁰ and others. Jacoby and Berry,⁴¹ Attra,⁴² and others have presented equations and simple analytical procedures for calculating performance to account for some of the compositional interchange between the displacing gas and the reservoir oil.

These works are mentioned for completeness. If significant deviations from the basic assumptions of the Buckley-Leverett method are a concern, the more practical approach is to use numerical reservoir simulation to account for reservoir heterogeneities and gravity, capillary,

and compositional effects. These simulators are discussed in the numerical simulation chapter in this section of the *Handbook*.

12.7.2 Methods for Evaluating Sweep Efficiency. Some techniques for estimating the volumetric, vertical, and areal sweep efficiency of an immiscible gas/oil displacement are discussed below.

History Matching. If there are sufficient data concerning the location of the gas front and oil recovery as a function of time, past reservoir performance can be used to calculate the volumetric sweep efficiency by dividing observed recovery at various times by the theoretical recovery determined from displacement efficiency calculations.

If there are adequate data to reliably describe spatial variations in reservoir rock and fluid characteristics, numerical reservoir simulation is the best way to predict sweep efficiency, particularly after the historical production and pressure data are matched. If data or sufficient economic justification to undertake a full numerical reservoir simulation study is lacking, the following methods are presented as useful for screening studies and in situations when more detailed studies are inappropriate.

Vertical Sweep Efficiency. Several authors have presented methods for determining vertical sweep efficiency based on statistical treatments of routine core analysis data. Some of the most frequently used methods are adaptations of the Stiles⁴³ method for evaluating the effect of permeability variations on waterflood performance. The same assumptions and calculation procedures may be used for immiscible gas/oil displacements. The relative permeability ratio used in such calculations is considered to be a constant equal to the relative permeability to gas at residual oil saturation ($k_{rg@Sor}$) divided by the relative permeability to oil at initial gas saturation ($k_{ro@Sgi}$).

Areal Sweep Efficiency. Several investigators have shown that areal sweep efficiency is primarily a function of injection/production well pattern arrangement, mobility ratio, and volume of displacing phase injected. Various studies have confirmed what would be expected intuitively, that areal sweep efficiency increases with the volume injected and with a lower mobility ratio. Data from model studies that show the influence of mobility ratio and displacement volume on areal sweep efficiency in a regular five-spot pattern are illustrated in [Fig. 12.12](#).⁴⁴

Thin models containing miscible fluids of varying viscosity were used to develop these area sweepout curves. These data are considered applicable to either water/oil or gas/oil displacement. These data are presented to aid in the understanding of the effect of some factors on the gas displacement mechanism and may prove useful in preliminary studies of a potential gas injection project to predict volumetric sweep. However, the quantitative applicability of laboratory data is inherently questionable because of uncertainties in model scaling, laboratory techniques, and associated simplifying assumptions regarding no vertical gas override effects or reservoir heterogeneities. The instability of the very unfavorable mobility ratio gas/oil displacement is most difficult to quantify in laboratory experiments. All these effects can cause a smaller sweepout efficiency than presented in [Fig. 12.12](#). Nevertheless, laboratory model studies do offer a convenient means of making quantitative estimates when simulation is not practical or justified and injected gas remains dispersed in the reservoir.

When the laboratory data are used, the common practice is to calculate a mobility ratio using the viscosity and relative permeabilities of the oil ahead of the gas front and of the gas at the average saturation behind the displacing front.

12.7.3 Calculating Immiscible Gas Injection Performance. Numerical simulation represents the best way to predict the performance of immiscible gas injection if there are sufficient data to characterize the reservoir rocks and fluids adequately. Even simple 2D and 3D black-oil models provide insight into the more important aspects of oil recovery for reservoirs in which

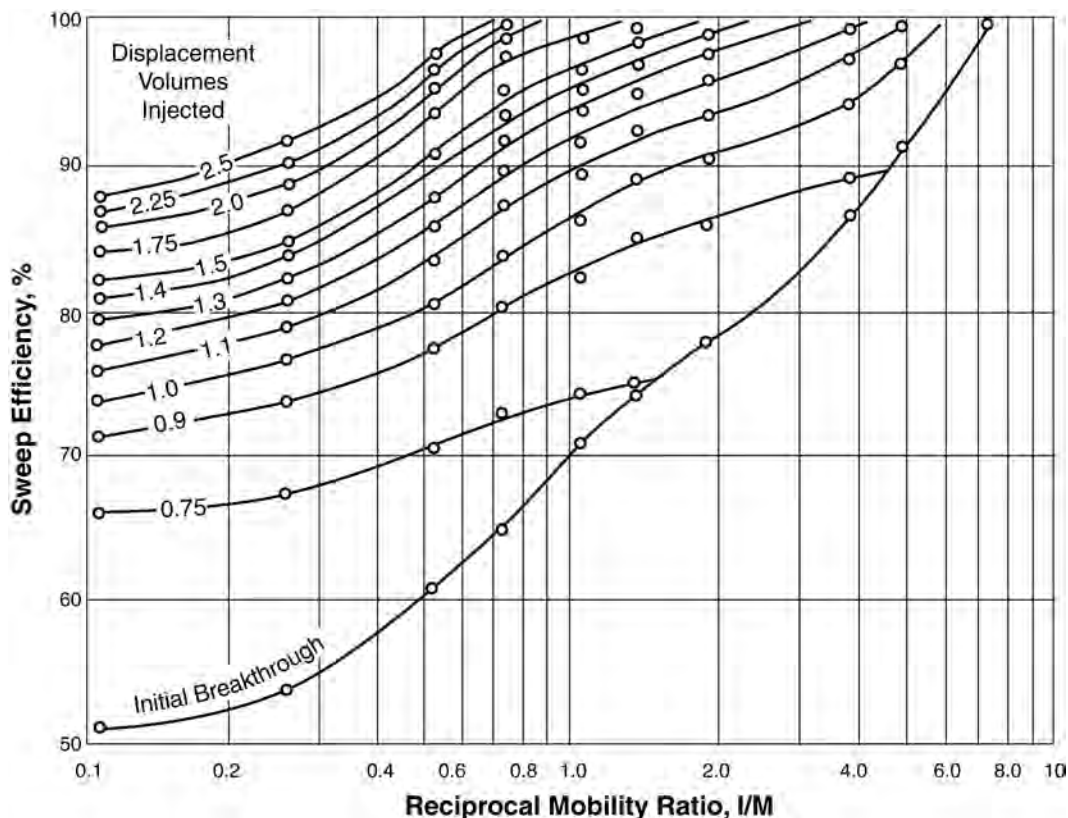


Fig. 12.12—Sweep efficiency as a function of mobility ratio.⁴⁴

compositional effects are not a major concern. When adequate data are unavailable or when screening work is being done, simple models may suffice.

The immiscible displacement of oil by gas is described with fractional flow theory. Muskat¹ presented the basics of this theory more than 60 years ago. Since then, additional work has been done to develop various mathematical calculation methods based on fractional flow theory. A few of the more recent papers discussing these techniques are listed in the References section.⁴⁵⁻⁵¹

As discussed above, pattern gas injection is seldom used now because waterflooding performance is much better in those types of reservoirs where pattern gas injection has historically been tried. Therefore, the remainder of this section discusses a simple model used for reservoirs in which stabilized gravity drainage controls the gas/oil displacement process and increases the ultimate oil recovery.¹³

Viscous, gravitational, and capillary forces and diffusion are involved in the displacement of oil by gas, complicating technical analysis of a particular reservoir if each of these forces and flow in all three dimensions are important. Fortunately, there are instances in which one force is dominant and only one dimension is involved in the rate-limiting step. In these circumstances, engineering solutions can be direct and simple. One such circumstance is that of thick reservoirs with high permeabilities.

In steeply dipping oil reservoirs containing sands with high vertical permeabilities, gravity drainage of the oil can be more effective than is calculated from the Buckley-Leverett assumptions alone, as illustrated in Fig. 12.13.⁵² When sufficient vertical permeability exists, even at lower oil saturations, oil behind the gas front can continue to flow vertically downward

For vertical drainage of oil, the rate is given by Darcy's law, with the driving force proportional to the density difference between gas and oil. The assumption is made that resistance to flow of gas and capillary effects are negligible⁵³:

$$u_{ov} = \frac{-0.044k k_{ro} \Delta\rho}{\mu_o}, \dots\dots\dots (12.9)$$

where u_{ov} = vertical oil flow per unit area, res ft³/ft²-D.

From continuity considerations,

$$\left(\frac{dz}{dt}\right)_{S_o} = \frac{1}{\phi} \left(\frac{du_{ov}}{dS_o}\right), \dots\dots\dots (12.10)$$

where z = vertical distance, ft; t = time, days; ϕ = porosity, fraction; and S_o = oil saturation, fraction.

The rate of movement of a particular saturation, $(dz/dt)_{S_o}$, can be determined by plotting u_{ov} calculated from Eq. 12.9 vs. saturation, taking the slope to determine du_{ov}/dS_o and dividing by porosity, as indicated in Eq. 12.10. The amount of oil drained from each region since passage of the gas front can be calculated by graphical integration of the height vs. saturation plot.

As a first approximation, the time for oil to flow downdip in the thin layer along the base of the reservoir interval can be neglected, as can the volume of oil in this layer. If the displacement rate exceeds one-half the critical rate, oil tends to accumulate rather than flow away along the bottom of the reservoir. More accurate calculations also include consideration of the thickness of the gas/oil transition zone arising from capillary effects above this layer of oil, especially if the transition zone is < 10 ft thick.

Recoveries calculated by this technique are quite sensitive to the values of k_{ro} at low oil saturations.¹⁰ Ways to extrapolate measured information are discussed next. First, conventional laboratory data can be extended to low oil saturations by plotting measured values of k_{ro} vs. $(S_o - S_{org}^*)/(1 - S_{wi} - S_{org}^*)$, in which S_{org}^* is the irreducible oil saturation in the presence of gas and connate water. S_{org}^* can be calculated by material balance for areas of a reservoir that have been invaded by gas if good data are available on GOC movement and oil recovery from the area. A second source is the oil saturation in an associated gas cap as determined in cores from that region. If the gas cap was originally filled with oil, drainage of oil over geologic time as gas migrates into the reservoir establishes an endpoint relict oil saturation. For instance, the Prudhoe Bay Sadlerochit reservoir was originally filled with oil. Gas then migrated into the reservoir several million years later, creating the gas cap.⁵⁴ Water-based mud cores from the gas cap interval showed an average routine core analysis oil saturation at discovery of 7% PV. The dip of the reservoir is 1 to 3°, but vertical permeabilities throughout the gas and oil columns are generally very high. Interestingly, oil saturations above small shale lenses in the gas cap averaged more than 7% PV, indicating that more time may be required to reach irreducible oil saturations when oil drainage is limited by the dip of this reservoir. A third source is drainage capillary pressure vs. saturation measurements. Experience has indicated that S_{org}^* should be < 10% PV and sometimes approaches zero. Although these endpoint saturations are seldom realized in the depletion time of a reservoir, it is important to have the correct value for predicting flow behavior and ultimate oil recovery. A benefit of even simple, multidimensional simulation models is that the inclusion of capillary effects controls the oil flow rate and conditions under which irreducible saturations are approached.

If a measured value of S_{org}^* is unavailable, a value is chosen to yield a straight line through the data, so for

TABLE 12.2—AVERAGE RESERVOIR PROPERTIES, HAWKINS FIELD	
k , darcies	3.4
K_v , darcies	2.38
ϕ , fraction	0.279
S_{wi} , %	8
Dip angle, degrees	6
h_v , ft	49
L (along bedding planes), ft	3,500
p_r , psi	1,500
μ_o , cp	4.45
μ_g , cp	0.0185
ρ_o , lbm/ft ³	51.7
ρ_g , lbm/ft ³	5.35
u per unit area, ft ³ /ft ² -D	0.0365

$$k_{rr} = \left(\frac{S_o - S_{org}^*}{1 - S_{wi} - S_{org}^*} \right)^n, \dots\dots\dots (12.11)$$

the slope of the line n should be ≈ 4 according to the theory of Corey *et al.*⁵⁵ but may be as large as 6 and as small as 2. Recovery data can be correlated by the dimensionless parameter $\frac{q_T \mu_o h_v}{k_v \Delta \rho L A}$, which is derived by dividing the time required for vertical drainage,

$$t_v = \frac{h_v}{\frac{k_v \Delta \rho}{\mu_o}}, \dots\dots\dots (12.12)$$

by the time required for flow along the bedding plane,

$$tu = \frac{LA}{q_T}, \dots\dots\dots (12.13)$$

where k_v = vertical permeability, darcies, and h_v = vertical thickness, ft.

Example Gas/Oil Gravity-Drainage Problem. The utility of this simple model can be illustrated by predicting recovery by gas drive and gravity drainage for an actual reservoir, in this case the Hawkins field in east Texas.⁵⁶

Given: Average Hawkins Woodbine reservoir properties as presented in **Table 12.2** and **Fig. 12.14**.

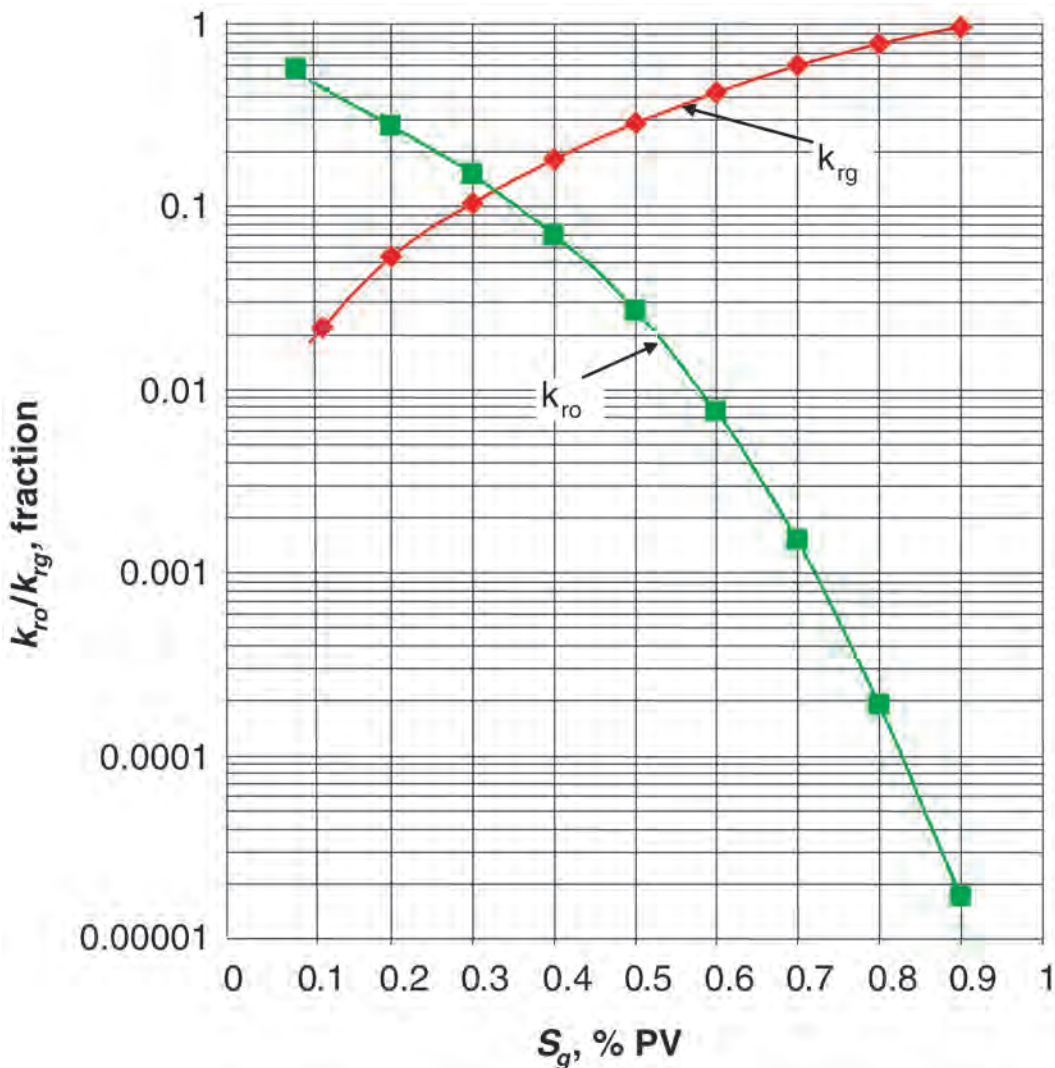


Fig. 12.14—Gas/oil relative permeability for Hawkins field.

Solution: With Eq. 12.8, the critical rate for the Hawkins field is calculated to be 0.173 ft³/D-ft². The average actual rate, q_T/A , of 0.0365 ft³/D-ft² (see Table 12.2) is 21% of the critical rate, and the simplified model should apply. With Eq. 12.5, the average gas saturation just above the GOC is found to be 46% PV by the Welge procedure, as shown in Fig. 12.2. The rate of frontal movement is

$$u_{\text{actual}} = \frac{q_T}{A\phi\Delta S} = \frac{(0.0365 \text{ ft}^3 / \text{D} - \text{ft}^2)(365 \text{ D/yr})}{(0.279)(0.46\text{FracPV})} = 104 \text{ ft/yr} . \dots\dots\dots (12.14)$$

Time to gas breakthrough is 3,500/104 = 34 years. Recovery at breakthrough may now be estimated by dividing the reservoir into seven blocks, each 500 ft long and 49 ft thick. The average vertical movement of saturations in each block can be calculated from Eqs. 12.9 and 12.10. The relative permeability data for oil were extrapolated to low S_o values using the corre-

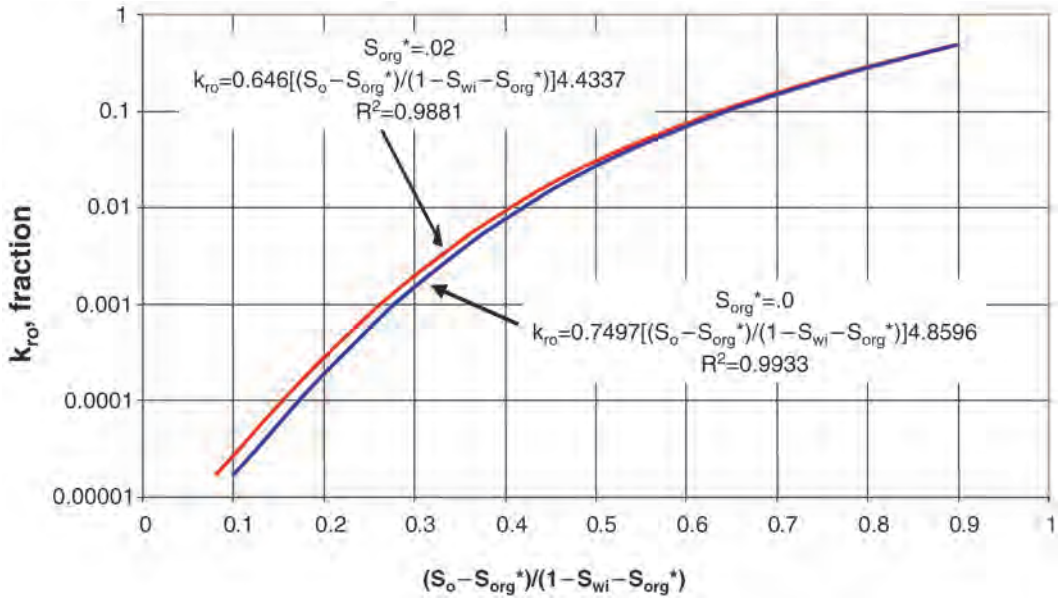


Fig. 12.15—Curve fit of laboratory k_{ro} vs. S_o data, Hawkins field.

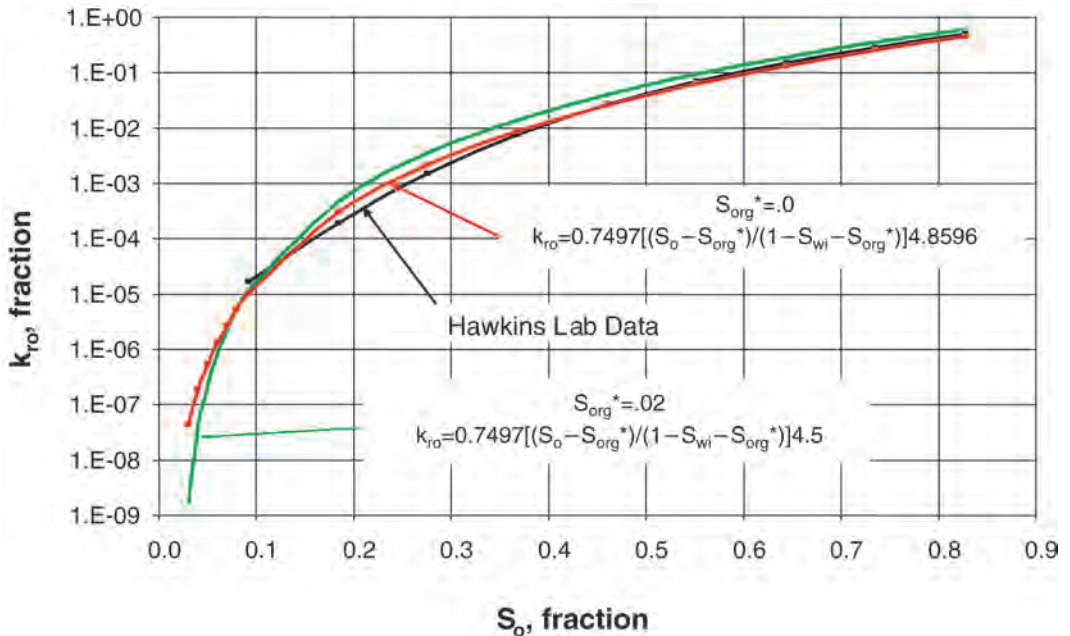


Fig. 12.16—Oil relative permeability projected to low S_o values, Hawkins field.

lation term $(S_o - S_{org}^*) / (1 - S_{wi} - S_{org}^*)$ discussed above. The resulting plots for two S_{org}^* assumptions are shown in Fig. 12.15.

In this case, $S_{org}^* = 0$ gave a slightly better fit. The resulting plot of k_{ro} vs. S_o is shown in Fig. 12.16. The laboratory data and a plot resulting from use of an S_{org}^* of 2% PV and an n of 4.5 are also shown to indicate the differences in k_{ro} at low S_o that result.

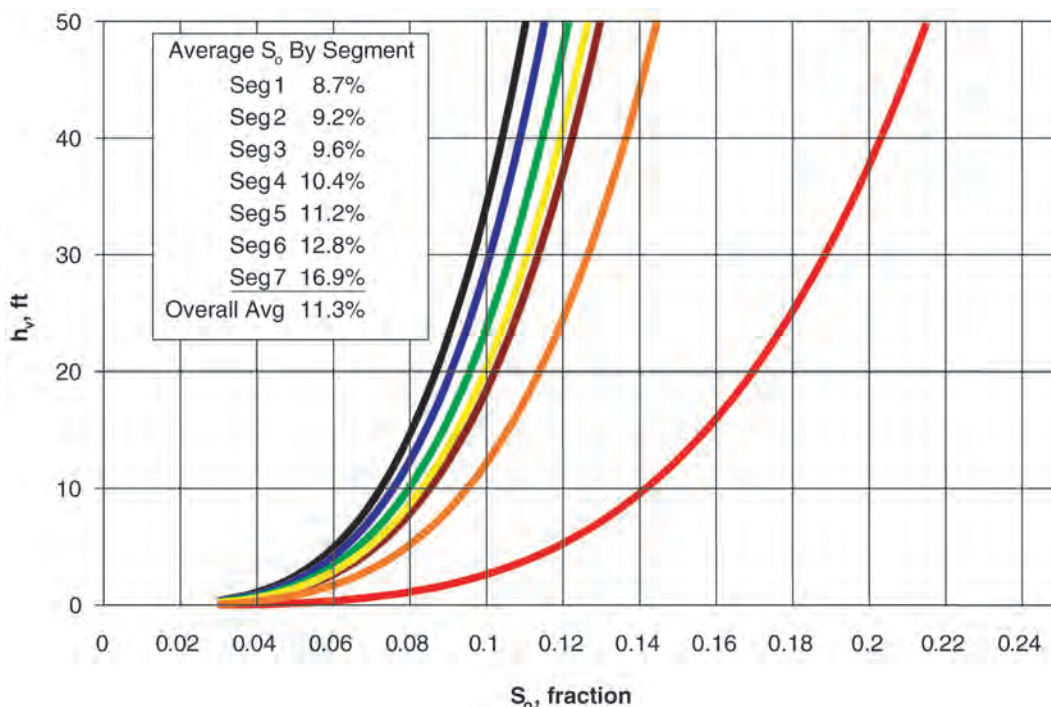


Fig. 12.17—Oil saturation profiles for different blocks, Hawkins field example problem.

The average time interval since passage of the gas front is calculated from the calculated rate of frontal movement of 104 ft/yr. The residual oil left in each block is determined by graphical integration of a plot of S_o vs. height, such as the ones shown in Fig. 12.17. Results of these calculations are shown in Table 12.3.

$$\text{Oil recovery to gas breakthrough} = \left[\frac{(1 - S_{wi} - S_{or})}{(1 - S_{wi})} \right] = \frac{1 - 0.080 - 0.113}{1 - 0.080} = 88 \% \text{ of OOIP.}$$

Comparisons With Field Data. A recovery of 87% of OOIP was observed in the Hawkins field for an area affected by an expanding gas cap.⁵⁶ The calculated recovery of 88% compares very favorably. A 2D two-phase reservoir simulation using similar relative permeabilities predicted 87% recovery at breakthrough. The recoveries observed in the field and predicted by models that permit flow in two dimensions are > 15% greater than those calculated by conventional 1D techniques that assume flow only along the bedding planes.

Model Summary. This section has shown how a simple gravity drainage model can be readily applied to predict recoveries by gas drive and gravity drainage when flow rates are less than one-half the critical rate and permeabilities in the vertical direction are high. Some applications of the model have been unsuccessful because of lower-than-expected vertical permeabilities. As a practical matter, the simple model should be used to predict reservoir behavior only when it can be shown to match history or when applied to a field analogous to one that the model fits.

TABLE 12.3—AVERAGE S_o IN EACH CALCULATION SEGMENT

Segment	End Location, ft	Breakthrough to Segment End, yr	Average Drain Time, yr	Days	Average S_o , %
1	3,500	33.7	31.3	11,406	8.7
2	3,000	28.8	26.4	9,651	9.2
3	2,500	24	21.6	7,897	9.6
4	2,000	19.2	16.8	6,142	10.4
5	1,500	14.4	12	4,387	11.2
6	1,000	9.6	7.2	2,632	12.8
7	500	4.8	2.4	877	16.9
				Average	11.3

12.8 Immiscible Gasflood Monitoring

There are a variety of methods for monitoring immiscible gas injection projects. Some apply both to the pattern type of gas injection projects and to the vertical gravity-drainage type of gas injection projects; others apply only to the gravity-drainage projects. In all cases, individual well production and pressure performance as a function of time must be recorded.

The most obvious monitoring method is to track the GORs of the individual production wells as a function of time. The GOR will be approximately flat at the oil's solution GOR until there is gas breakthrough. Then the GOR will climb. The timing of gas breakthrough and the rate of GOR climb will indicate how efficiently, or inefficiently, the gas/oil displacement is progressing. Field engineers should have made preliminary calculations, possibly using a numerical reservoir simulator, so that they have projections of what should be expected regarding gas breakthrough timing and GOR increases at the individual well locations (and as a function of the volume of gas injected at the individual injection wells).

The other methods concern primarily the monitoring of the vertical movement of the gas/oil interface (the current GOC) in gravity-drainage-type projects. Two techniques are generally used: cased-hole logging programs and monitor-well observations. Both help track the GOC movement as a function of time. By mapping the GOCs from the individual wells, engineers can determine whether the GOC is staying reasonably horizontal. By comparing the GOC movement as a function of time to the projected GOC behavior, engineers can determine how efficient the gas/oil displacement is and whether the project's expectations are being met.

For some reservoirs, other unique techniques can be used. For example, if a reservoir has a natural oil gravity variation as a function of depth, then the production wells' oil gravity can be tracked as a function of time.

Another technique is to take periodic gas samples and perform gas chromatograph analyses to determine the produced gas composition. To use this technique, baseline gas samples should be taken early and periodically from all wells. There are two circumstances in which gas chromatography is a useful tool for gas-injection project monitoring. The first is those projects in which flue gas (88% N_2 , 12% CO_2) or pure N_2 is injected. In that type of project, it is important to track the BTU value of the gas from each well and how the nonhydrocarbon content of the produced or residue gas changes as a function of time. This is important with respect to the use of that gas for field fuel and the marketability of the residue gas stream.

Second, this technique can be important late in the life of a gas-injection project when wells are operating at very high GORs. This technique is useful for determining whether some of the very lean injection gas is breaking through into some of the wells without becoming

saturated with light and intermediate hydrocarbon components from the residual oil phase in the gas-swept region above the current GOC. Such lean gas can actually strip intermediate hydrocarbon components from the produced oil in the field gas/oil separators. If there is no gas plant as part of the field facilities, then those hydrocarbons will be lost to the downstream owner of the gas plant that processes the field gas.

One other aspect of the monitoring activities is to track from which of the perforated intervals most of the gas flow is entering the wellbores. This can be accomplished with periodic spinner or temperature surveys. Depending on the nature of the reservoir interval, it may be possible to temporarily plug off some of the perforations to reduce wells' producing GOR.

The purpose of all these monitoring activities is to perform real-time analysis of reservoir performance and to consider any remedial actions. These actions include such alternatives as rebalancing the gas rates into the various injectors, rebalancing the flow rates of the various producers, and potentially drilling a few new injection or production wells into areas of the reservoir determined to require more drainage points or to improve the overall sweep efficiency.

12.9 Field Case Studies: Immiscible Gas Injection Examples

In this section, a number of field applications of immiscible gas injection are briefly reviewed. In each case, the following facts will be listed, to the extent that they are available.

- Field name.
- Structural closure.
- Rock type.
- Nature of pore system
- Average permeability.
- Source of injected gas.
- Field size.
- Presence of initial gas cap.
- Oil gravity.
- Initial reservoir pressure.
- Oil bubblepoint pressure.

Both successful and unsuccessful immiscible gas injection projects are discussed. A number of early successful and unsuccessful gas injection projects are summarized by Muskat in his 1949 classic book *Physical Principles of Oil Production*.¹ Most of this section describes successful projects because those have been presented in a number of SPE technical papers. Immiscible gas injection has been used in oil fields with a wide range of characteristics.

12.9.1 Early Successful and Unsuccessful Immiscible Gas Injection Projects. Muskat discusses four gas injection projects in the United States from the 1930s and 1940s.¹ Two of these projects were termed successes, and two were viewed as having poor response.

Cunningham Pool (Kansas). This 1,400-acre anticlinal 31 to 36°API oil field had a maximum closure of 75 ft and 53 producing wells. The reservoir is an oolitic limestone and had an initial gas cap. Field discovery was in 1932, and gas injection began in 1936 into three to five wells after the reservoir pressure had declined from 1,115 to 424 psi. The average reservoir properties were as follows: net thickness, 8 ft; porosity, 11% BV; and permeability, 105 md. Muskat termed this project a success because of its GOR history and concluded that “in spite of the thin pay section there has been effective gas segregation, so that the injected gas largely remained trapped in the reservoir and helped to sustain the oil saturation within the oil zone.”¹

Schuler Field (Arkansas). This 3,000-acre anticlinal 34°API oil field had a maximum closure of 135 ft and 146 wells drilled on 20-acre well spacing. This sandstone reservoir had a small initial gas cap. Field discovery was in 1937; gas injection began in 1941 into six wells at the crest of the structure and after the reservoir pressure had declined from 3,520 to about 1,550 psi. The average reservoir properties were as follows: net thickness, 0 to 70 ft; porosity,

17.6% BV; and permeability, 0 to 4,000 md (355-md average). Success was achieved because the reservoir pressure was stabilized, producing GORs were decreased, and produced gas was reinjected instead of flared. Because of proration limits on production, the allowed oil rate was being produced from a few optimally located down-dip wells.

Grayburg Lime (West Texas). This 750-acre section of a west Texas anticlinal reservoir is a sandy dolomite and had an average net pay of 18 ft (in a gross thickness of 130 ft). Pay porosity ranged from 8 to 14% BV, and permeabilities ranged from 2 to 10 md. Oil gravities were in the 33 to 37°API range. In 1942, 1 of the 26 producing wells was converted to gas injection after the reservoir pressure had declined from 1,800 to 1,275 psi. Approximately a year after the start of gas injection, there was a sharp rise in the producing GOR. Because the oil production rate was considerably increased at about the same time as the GOR rise, Muskat reasons that, although the gas may have traveled rapidly through “a substantially continuous and intercommunicating fracture system,” the GOR rise may have resulted from the inability of the reservoir matrix to supply oil to the fracture system at the higher oil rate.

Canal Field (California). This 1,100-acre dome oil field had a maximum closure of 150 ft with wells drilled on 20-acre well spacing. The reservoir is a sand of variable character with silt/shale streaks. There was no original gas cap; the original reservoir pressure was 3,550 psi, and the oil bubblepoint pressure was 2,800 psi. Porosity ranged from 15 to 32% BV with an average of 22% BV, and permeability ranged from 10 to 1,000 md with an average of 200 md. Field discovery was in 1937. Gas injection began in 1942 into a single crestal well, but within a year, two other injection wells located down the flanks of the structural axis were added. Within 6 months, the ethyl mercaptan tracer was spotted in one well, and within a year, two other wells showed tracer responses. It was concluded that “the appearance of the tracer at the producing wells definitely proves gas channeling through high-permeability streaks, rather than a uniform drive through the sand as a whole.”¹

In these four situations, the first two were deemed successful applications of immiscible gas injection; the last two were deemed failures. All these fields were relatively small compared with those discussed below. In small fields, there is less opportunity to optimize well placement and make changes in the course of the project life.

Hawkins Field (East Texas).^{4,25,56,57} The Hawkins field contains > 1.3 billion bbl OOIP and 430 Bcf gas in the original gas cap. The reservoir consists of two high-quality sandstone intervals (27% BV porosity and 1- to 3-darcy permeability), the Lewisville and the Dexter; the Dexter, the better-quality sandstone, contains 70% of the oil. The structure caused by a deep-seated salt dome has 1,200 ft of closure and is extensively faulted (see structure map in [Fig. 12.18](#)). The reservoir is divided into two areas separated by a major fault. The eastern area contains 20% of the OOIP and 7% of the original gas cap gas and is underlain by the active Woodbine aquifer that covers much of east Texas. The western area contains the rest of the oil and gas. The western area has a tar mat that varies in thickness from 50 ft on the north to 100 ft on the south. This tar mat impeded aquifer influx until a decline in reservoir pressure resulted in water influx in the north that constituted a strong waterdrive that tilted the gas cap to the south, where aquifer influx did not occur. The average formation dip is 6 to 8°. Oil gravity averages 24.2°API gravity and varies somewhat vertically (21 to 26°API range). Oil viscosity averages about 3.7 cp (with values as high as 15 cp observed near the OWC on the east side), and its FVF is 1.22 RB/STB.

The 10,000-acre field, discovered in 1940, was developed on 20-acre well spacing. Unitization was completed on 1 January 1 1975 after 536×10^6 bbl of oil production. Before unitization, oil production was supported by gas-cap expansion and aquifer influx in the east. A small gas injection project was used in the west to stabilize the GOC and to prevent oil migration into the gas cap because of the aquifer influx from the north.

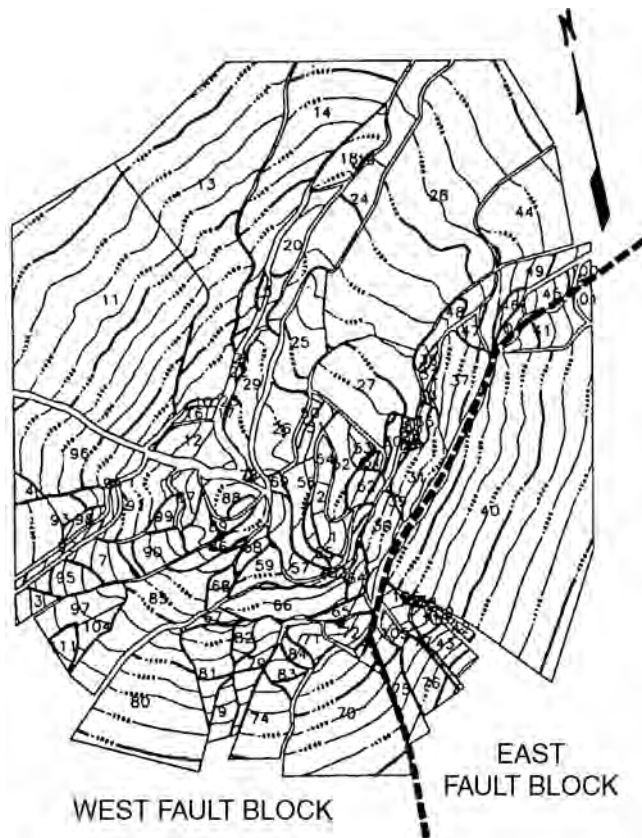


Fig. 12.18—Areal view of the Hawkins field. Top of reservoir structure showing major fault patterns.²⁵

Extensive laboratory testing was conducted on reservoir core samples to quantify the ability of both water and gas to displace oil.²⁵ The results of these tests are shown in [Table 12.4](#). These tests showed that gas was more efficient at displacing oil from the reservoir rock than water and that gas would recover at least 10% PV more oil. From the laboratory data, engineers calculated that, in the field, waterdrive would leave a residual oil saturation of 35% PV, whereas gas drive would leave an average residual oil saturation of 12% PV; the difference results from the lower density difference between the oil and water.

The field was unitized to facilitate the implementation of a gravity drainage project using crestal gas injection. Gas injection began in 1975. Two types of gases were injected. All produced gas, less fuel and shrinkage, was reinjected into the gas cap areas, and beginning in 1977, 120 MMcf/D of flue gas (88% N₂, 12% CO₂) generated at a nearby plant was also injected.⁴ More recently, pure nitrogen from a cryogenic nitrogen rejection plant has been injected.

In 1987, a tertiary immiscible gas-drive process was started in the East Fault Block where the aquifer had invaded a large portion of the oil column. This tertiary process has been called the double displacement process (DDP).^{25,57} In this process, the invading aquifer is being displaced to the original OWC so that the gas-drive gravity drainage process can remobilize much of the waterflood residual oil all the way down to this depth. Although the DDP is working, it is working more slowly than expected because of “higher viscosity oil (note the higher viscosity oil downdip discussed above), significant targeted oil volume found in lower-quality rock (in bypassed-oil zones), and lower-than-expected oil relative permeability.”⁵⁷ With the success of the DDP in the east, a similar project was implemented in the west.

TABLE 12.4—SUMMARY OF LABORATORY TEST RESULTS ON HAWKINS FIELD CORE SAMPLES²⁵

Plug	Porosity, % BV	Permeability, md		Water Imbibition, % PV	Gas/Liquid Drainage, % PV
		k_g	k_{ocw}		
1	27.1	1,330	1,270	22.2	8.8
2	24.7	1,230	155	21.0	13.4
3	26.9	6,210	729	14.4	3.8
4	28.9	7,450	2,210	22.8	7.9
5	27.9	5,680	1,510	23.9	9.3
6	25.8	4,420	1,800	16.3	4.2
7	25.4	2,310	1,310	19.4	8.3
8	26.0	2,790	1,160	15.2	5.4
9	22.6	2,240	1,380	21.5	8.9
10	24.0	1,720	720	18.8	11.6
11	27.5	4,470	658	9.5	6.2
12	27.1	3,340	907	15.3	11.6
			Mean	18.4	8.3
			<u>Gas/Liquid Drainage Only</u>		
1	23.2	2,300	842		8.8
2	28.0	5,460	2,420		5.4
3	25.7	3,060	1,200		6.9
4	26.0	3,050	1,000		8.5
			Mean		7.4

Overall Hawkins' recovery efficiency from the gas-drive mechanism is about 87% in the gas-swept areas or > 20% better than estimated for the waterdrive process. Overall reservoir performance resulting from immiscible gas injection is considered excellent.

Prudhoe Bay Field (North Slope, Alaska).^{13,27,38,54,58} The Prudhoe Bay field, the largest oil and gas field in North America, was discovered in 1968. The main Permo-Triassic reservoir is a thick deltaic high-quality sandstone deposit about 500 ft thick with porosities of 15 to 30% BV and permeabilities ranging from 50 to 3,000 md. The field contains > 20×10^9 bbl of oil overlain by a 35-Tcf gas cap. The reservoir, a monocline structure dipping 1 to 2° to the south and southwest, is bounded on the north by major faults and on the east by a major lower Cretaceous truncation. The oil averages 27.6°API gravity and has an original solution GOR of about 735 scf/STB. Under much of the oil column area, there is a 20- to 60-ft-thick tar mat located above the OWC.

Because of its remote location, first production did not begin until 1977 after an oil pipeline across Alaska to the southern port of Valdez was built and extensive oilfield facilities were installed. The initial facilities had a gas-handling capacity of about 2 Bcf/D to separate and compress the produced gas for reinjection into the updip gas cap. For the regulated oil production rate of 1.2×10^6 BOPD, this was sufficient for more than the first decade of field operations. As of 2004, no gas pipeline has been built from the North Slope of Alaska.

Immiscible gas/oil displacement has been the production mechanism at work over much of the Prudhoe Bay oil column (Fig. 12.10), and waterflooding and miscible WAG processes have been used in the very downdip portions of the oil column. More recently, horizontal wells are

being used nearer the GOC to exploit the thin oil columns that cannot be drained with existing wells. During the first decade of operations, the original gas cap had expanded to drape over much of the oil column area, but the producing GOR was kept low by perforating the production wells as far as possible, both vertically and laterally, from the gas cap. By the mid-1980s the engineers determined that maintaining the oil production rate depended on expanding the field's gas-handling capacity. Two major projects were undertaken. First, a central gas facility was constructed to strip the produced gas of many of the hydrocarbon components for sale as blendable NGLs and for use as miscible injectant. This project also increased the field gas handling capacity to 3.3 Bcf/D. The second project was a sequence of gashandling facility expansions that increased overall capacity to > 7.5 Bcf/D.

The reinjection of residue gas served two purposes. First, it maintained reservoir pressure, which helped increase oil recovery; the reservoir pressure declined only by $\approx 1,000$ psi (from 4,300 to 3,300 psi) during the production of the first 10×10^9 bbl of oil. Second, the very lean residue gas has vaporized large amounts of hydrocarbon components from the relict oil saturation in the original gas cap⁴⁴ and from the remaining oil behind the gas/oil front. Simulations showed that the vaporization mechanism would contribute recovery of an additional 4 to 6 STB/MMcf of additional gas produced.¹³ During the past 15 years, the average API gravity of the marketed Prudhoe Bay hydrocarbon liquids has increased by $> 5^\circ\text{API}$.

Haldorsen *et al.*⁵⁸ have studied the efficiency of the Prudhoe Bay gravity drainage mechanism by means of laboratory experiments and field cased-hole log evaluations. They concluded, "The 'most likely' displacement efficiency, through the stochastic approach, was 68 percent after three years and 76 percent after 30 years of gravity drainage."

The ultimate Prudhoe Bay oil recovery has increased from initial estimates of 9.6 to 13×10^9 bbl oil, much of which is related to exploiting the immiscible gas/oil gravity drainage and oil stripping mechanisms. This has been accomplished by massive expansions of the gas handling facilities and extraction of the maximum volume of blendable NGLs from the produced gas stream. Application of the immiscible gas processes at Prudhoe Bay has been aided by the lack of alternative uses or markets for the produced gas.

Empire Abo Field (New Mexico).^{26,39} Another example of the application of the immiscible gas/oil gravity drainage process is found at the Empire Abo field. This field covers $\approx 11,000$ acres (12.5 miles long by 1.5 miles wide) and contains approximately 380 million STB of OOIP. This reservoir is a dolomitized reef structure (Fig. 12.19) with a dip angle of 10 to 20° from the crest toward the fore reef. The oil column is approximately 900 ft thick, but the average net pay is only 151 ft thick. The pore system of this reservoir is a network of vugs, fractures, and fissures because the primary pore system has been so altered by dolomitization; the average log-calculated porosity was 6.4% BV. Numerical simulations of field performance and routine core analysis data have indicated that the horizontal and vertical permeabilities are about equal. The Empire Abo field has a small initial gas cap ($< 1\%$ of the hydrocarbon PV), so the oil was gas saturated at the original reservoir pressure of 2,360 psia. The oil gravity was 43°API , and viscosity at reservoir conditions was approximately 0.4 cp.

The field was discovered in 1957 and unitized in 1973. At that time, high-GOR back-reef wells were shut in, only the downdip solution-GOR wells continued to produce, and gas-plant residue gas was reinjected into some of the former crestal production wells. The unit added 56 infill producers on 20-acre well spacing in the downdip area during the mid-1970s (see structure map in Fig. 12.20). In the late 1970s, 100 additional producers on 10-acre well spacing in the downdip area were drilled.

Because of the concentration of producing wells downdip, the gas cap draped downdip along the top of the reservoir. The Empire Abo field overall performance was excellent because of its very high vertical permeability; however, gas coning was a major issue, with the overall relatively low reservoir permeability of approximately 50 md. In 1979, Empire Abo

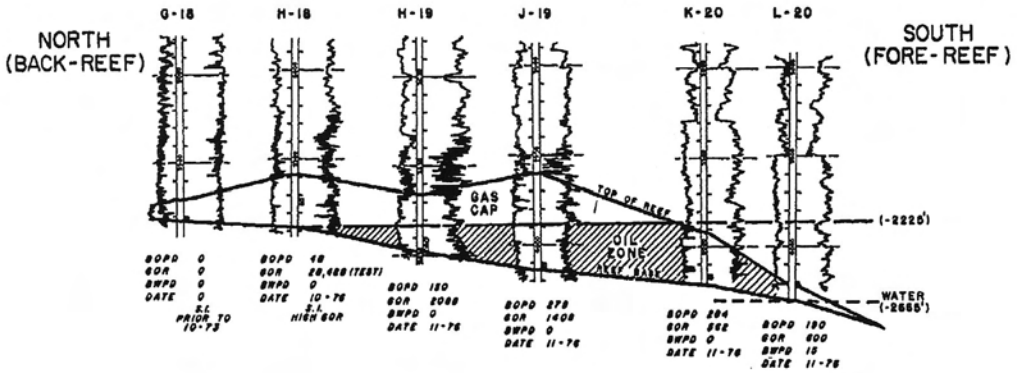


Fig. 12.19—Empire Abo field. Typical back-reef to fore-reef cross section, with openhole gamma ray/neutron logs.²⁶

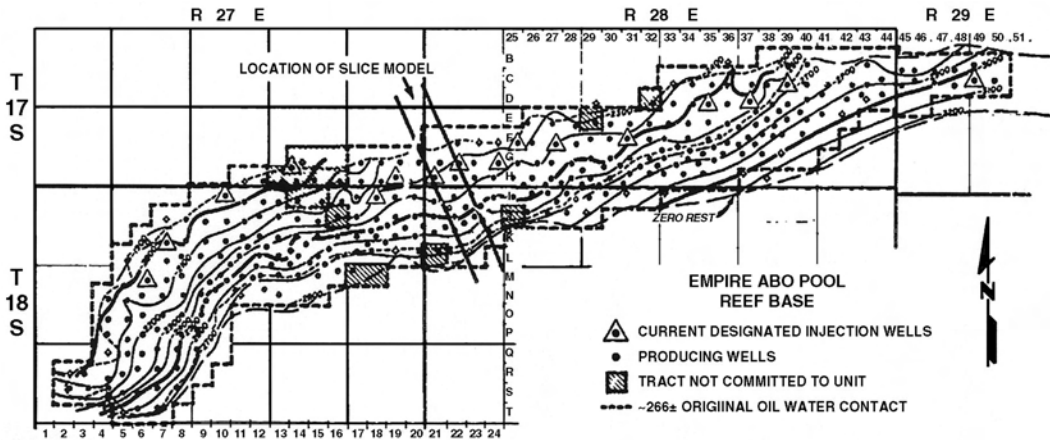


Fig. 12.20—Empire Abo field. Structure map on the base of the Abo reef.²⁶

was the site of one of the first applications of horizontal wellbores to minimize gas coning.⁵⁹ The field is currently being blown down to recover as much gas as possible. On the basis of production data through 2002, on a stock-tank-oil basis, approximately 74% of the OOIP has been recovered from this field by application of the immiscible gas/oil gravity drainage process.

Heft Kel Field (Iran).³⁰ An example of the application of immiscible gas/oil displacement in a large Middle East matrix-block/fracture-system reservoir is the Heft Kel field. Its Asmari reservoir structure is a strongly folded anticline that is 20 miles long by 1.5 to 3 miles wide with an oil column thickness of approximately 2,000 ft. The most probable OOIP was slightly $> 7 \times 10^9$ STB with about 200 million STB in the fissures; numerical model history matching resulted in a value of 6.9×10^9 STB. The matrix block size determined from cores and flowmeter surveys varied from 8 to 14 ft. The numerical simulation model considered matrix permeabilities from 0.05 to 0.8 md. The overall horizontal and vertical permeabilities are approximately equal. There was an initial gas cap on the oil column. The oil gravity is approximately 37°API. The IFT at the bubblepoint pressure (1,412 psi and 116°F) is approximately 9 dynes/cm.

The field was discovered and put on production in 1928. It was produced on primary production from then until 1976 with a plateau rate of 200,000 BOPD for several early years. In 1976, gas injection began at a rate of 400 MMcf/D using gas from the nearby NIS gas dome. Recently, the field has been producing at approximately 35,000 BOPD.

Saidi³⁰ describes the many oil recovery mechanisms at work in this oil-wet reservoir as gravity drainage at constant IFT and reservoir pressure; oil swelling in the present gas-invaded zone because of the increase in reservoir pressure; oil swelling in the present oil zone through thermal convection/diffusion process; oil imbibition within the oil column; oil gravity drainage from the partially saturated blocks within the gas-invaded zone; and oil gravity drainage from the fully oil-saturated block in the oil zone and the blocks between that and the present GOC.

The flow behavior developed from the history match is that the oil-drainage performance follows that of stacks of discontinuous blocks, supporting practically no vertical capillary continuity between the matrix blocks (see Fig. 12.8).

By going to immiscible gas injection, oil recovery is increased by about 500×10^6 bbl by returning to the original reservoir pressure and could be increased by another 100×10^6 bbl if the reservoir pressure is increased an additional 100 psi because of the reduction in gas/oil IFT with increasing reservoir pressure.

Overall, the application of immiscible gas injection to the Haft Kel field has been considered a success. The estimated displacement efficiency by water was 17%, whereas that estimated for immiscible gas displacement was 32%.

Swanson River Field (Cook Inlet, Alaska).²⁴ A very different style of successful immiscible gas/oil displacement project is that applied to the Swanson River field's Hemlock reservoir. Figs. 12.21 and 12.22 show an areal view of this reservoir and a type log through the Hemlock formation, respectively. This field is a north/south-trending anticlinal flexure about 6 miles long by 1 to 3 miles wide with as much as 600 ft of closure. The Hemlock formation consists of interbedded fine- to coarse-grained sandstone, conglomerate, siltstone, and coal, with numerous thin, impermeable, calcareous stringers of somewhat limited areal extent. Field experience has confirmed that these calcareous stringers are effective barriers to the vertical migration of fluids in the vicinity of producing wells. There are 10 Hemlock intervals, and the H1 through H5, H8, and H10 intervals have been engineered and managed separately (see Fig. 12.22).

The OOIP of this field is 435 million STB. This oil was very undersaturated at discovery in 1957, with an original reservoir pressure of 5,580 psi but with a bubblepoint pressure of only 1,350 psi. The oil is 37°API gravity, had an initial FVF of 1.21, and had a viscosity of 1.1 cp.

From these reservoir characteristics, it was clear that at the start of production the reservoir pressure would fall rapidly and that some form of pressure maintenance needed to be applied quickly. Fortunately for this very undersaturated oil field, a Tcf-sized dry gas field was discovered nearby for which there was no immediate or large outlets for its gas. A gas rental contract was signed between the two fields owners, and starting in 1966, 400 MMcf/D of gas was delivered for injection into crestal wells in the Swanson River Hemlock reservoir.

Laboratory studies indicated that a number of mechanisms were at work when methane gas displaced the low-bubblepoint-pressure Swanson River oil. First, if operating at a 5,000-psi pressure, the oil would swell from an FVF of 1.21 to an FVF of 1.80 on contact with the injected gas. Second, free gas would become saturated with intermediate hydrocarbon components from the fairly light (37°API) reservoir oil. Laboratory experiments show that breakthrough recovery efficiency exceeded 60%.

Although the Swanson River field has operated at high GORs (> 10 Mscf/STB) after the first several years of production, reservoir performance has been excellent, with 38% of the OOIP recovered through the first 10 years of gas injection. To show that the oil vaporization

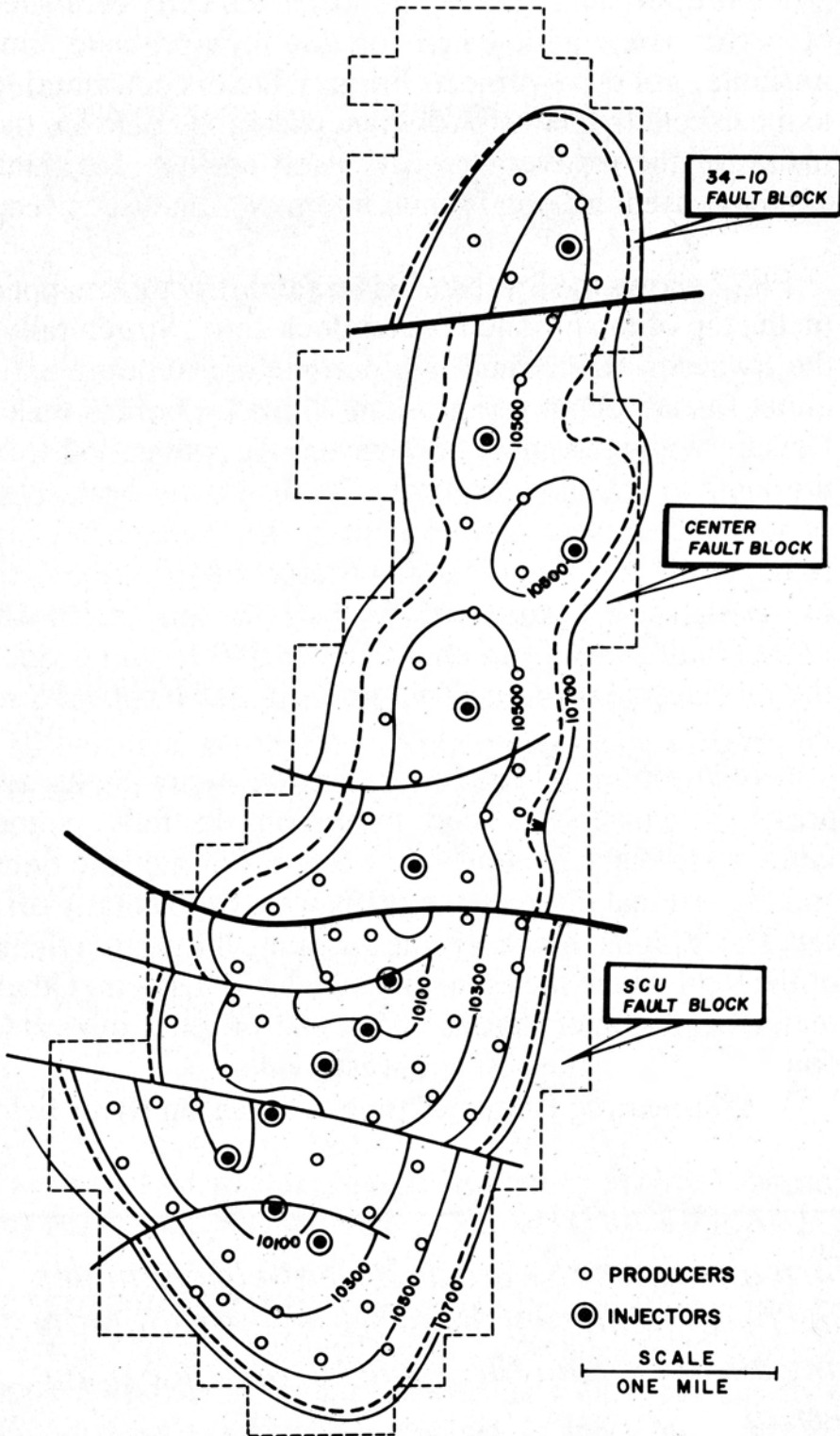


Fig. 12.21—Swanson River field. Contour map of top of Hemlock structure.²⁴

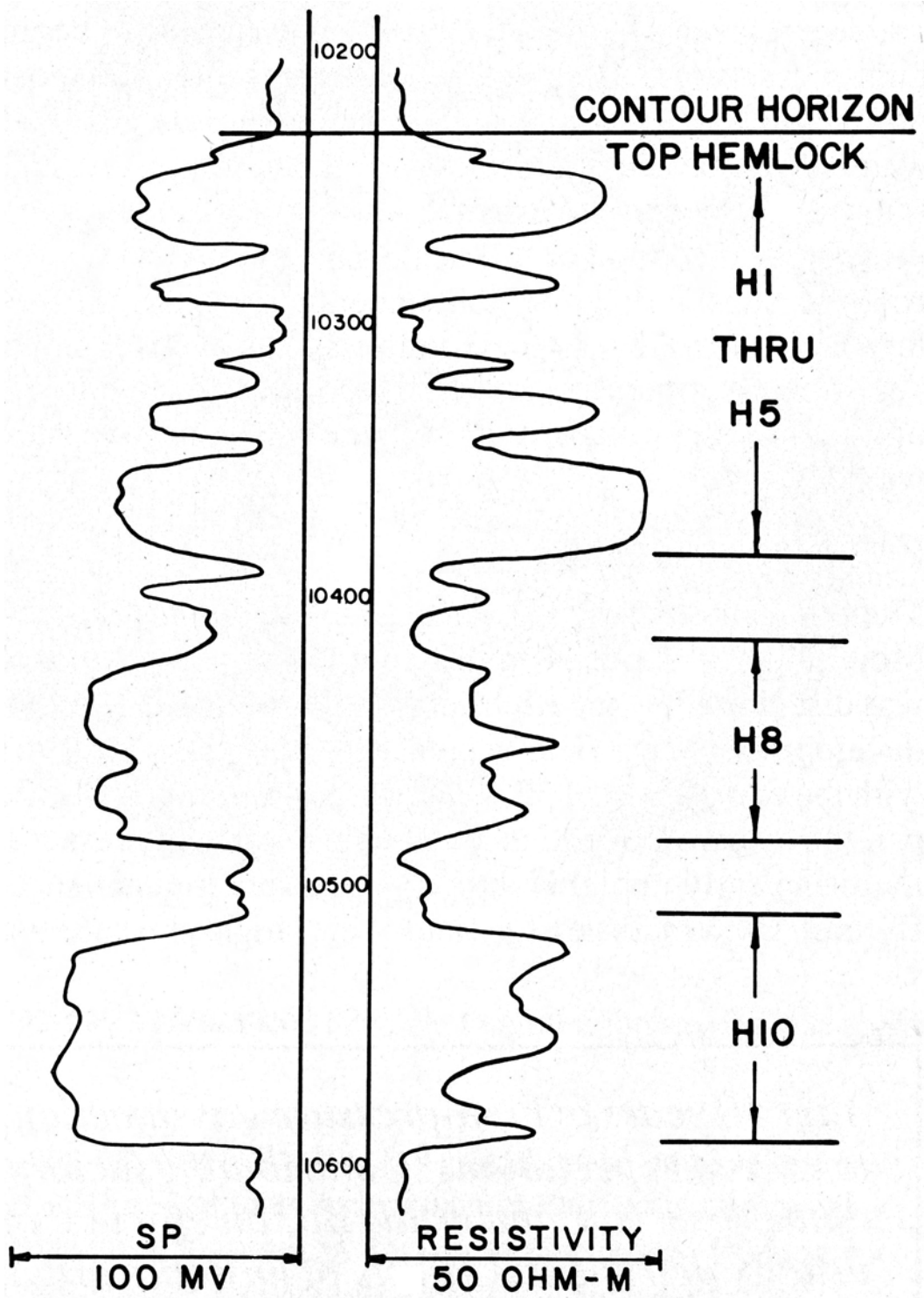


Fig. 12.22—Swanson River field. Typical electric log through Hemlock reservoir interval.²⁴

mechanism is also at work in this reservoir, during these first 10 years of production after the start of gas injection, the produced oil gravity increased from 37 to 40°API.

The Swanson River field is currently being blown down to recover as much remaining gas as possible. From production statistics through 2002 and an updated OOIP of 390×10^6 bbl, ultimate recovery from application of immiscible gas/oil displacement to this field is nearly 58% of OOIP. This has been achieved primarily through oil swelling and oil stripping, not vertical gas/oil gravity drainage.

Kuparuk River Field, Alaskan North Slope.^{14,15} Another type of immiscible gas/oil project is that applied to some areas of the Kuparuk River oil field. The Kuparuk River field contains approximately 5.9×10^9 bbl of 24°API oil in two producing zones (zones A and C). The oil was slightly undersaturated at discovery (3,300-psi original reservoir pressure, with oil 300 to 500 psi undersaturated). The shallower C sand is more permeable than the A sand, but the A sand contains approximately 62% of the OOIP. The reservoir covers > 200 sq miles.

The field was discovered in the late 1960s and went on production in 1981. The maximum rate has exceeded 300,000 BOPD, producing from 42 drillsites with wells on 160-acre well spacing. The challenges in this field were that there was no initial gas cap on the reservoir into which to reinject the produced gas; the reservoir dip is very slight, and the reservoir intervals were not very thick, so gas/oil gravity drainage could not efficiently occur; the gas could not be flared; and there was no off-site location to which the residue gas could be sent. For these reasons, the gas had to be reinjected into one of the reservoir intervals for storage and to maintain the oil production rates. The challenge for the field engineers was how to reinject the residue gas in the most efficient way, given the various constraints.

After a few years of gas injection into the A sand in one area of the field in which the offsetting producers soon experienced rapidly increasing GORs, the engineers decided to go to an immiscible WAG injection process.¹⁴ WAG could be applied at minimal cost and with few operational complications because most of the field was already being waterflooded. Calculations indicated that there were three beneficial effects to this approach. First, there would be some swelling of the oil because of the free gas. Second, the residual oil saturation could potentially be reduced by the presence of trapped gas. Third, WAG injection was used to reduce the high mobility of the gas by means of three-phase relative permeability effects (simultaneously having mobile gas, oil, and water in the pore system); also, a tapered WAG scheme helped in this regard. The overall effect was that oil recovery could potentially be increased by 1 to 3% of OOIP without resulting in significant gas cycling problems. To date, immiscible WAG injection has worked as expected and has been a satisfactory solution to the Kuparuk River gas disposal problem.

12.10 Miscellaneous

12.10.1 Gas Sources for Immiscible Gas Injection Projects. The first consideration in any immiscible gas injection project is where to get the volume of gas necessary for the project. Historically, produced and processed residue gas from that particular oil field has been used. This is the most satisfactory solution if the economics of the additional oil recovery justify deferred gas sales. In some locations, this is not an issue because there is no current market outlet for the produced gas. Generally, reinjection of this local gas supply is sufficient to nearly maintain the current reservoir pressure.

The next best alternative in some locations is to develop deeper gas horizons as a gas supply. This is particularly true in the Middle East where massive volumes of gas are often found in the deeper formations, such as the Khuff, underlying some major oil reservoirs. The third alternative is to look to nearby fields for a source of gas; this alternative has been used at the Swanson River field in Alaska²² and the Heft Kel and other Iranian fields.³⁰

If there is no source for lean hydrocarbon gas, then possibly flue gas (88% N₂, 12% CO₂) or nitrogen might be used. Both of these options require that a plant be constructed at the field to generate these gases in the large volumes needed. This approach requires the economics of the project to justify the large capital expenditure for such facilities, additional operating costs, and future impact of the produced gas becoming increasingly contaminated with nonhydrocarbon components with time.

Sometimes, the solution to the gas supply problem is to use a combination of sources to provide the required volume of gas. At the Hawkins field, both residue hydrocarbon gas and flue gas initially were injected. More recently, nitrogen from a cryogenic nitrogen rejection plant has been injected.^{4,25,57}

12.10.2 Use of Horizontal Wells in Immiscible Gas Injection Projects. Horizontal wells have not been discussed in this chapter because the technology to drill horizontally has developed rapidly since the mid-1980s and such wells have not had widespread use in historic immiscible gas injection projects. Horizontal wells are particularly suited for use in gravity drainage immiscible gas injection projects because they maximize the distance between the producing wells' perforations and the overlying gas cap and because such wells minimize the pressure gradients in the near-wellbore region (the cause of near-wellbore gas coning). At the Prudhoe Bay field, a large number of horizontal wells have been drilled for a variety of purposes, including the two mentioned above. For these reasons, in future immiscible gas gravity drainage projects, it is logical to consider using horizontal production wells. The chapter on fluid flow and well analysis in this section of the *Handbook* shows how to predict and to interpret the performance of horizontal wells.

12.10.3 Operating Procedures for Thin Oil Columns. One consideration in immiscible gas gravity drainage projects is the challenge of maximizing oil recovery from thin oil columns. The thin oil column may be what is found initially,²⁹ or in most cases, as the gas cap expands, it is all that is left to produce late in the life of the project. The field engineers have to monitor individual well performance and overall reservoir performance closely to optimize production under these circumstances. Obviously, if new wells are drilled, they should be either carefully targeted horizontal wells or wells with very limited perforated intervals.

A related consideration is when there is a thin oil column sandwiched between the expanding gas cap and the underlying aquifer.²⁹ In this situation, well perforations must be chosen to maximize recovery and to minimize the production of both gas and water. Although coning simulations with numerical reservoir simulators will provide insights into the best approach for a particular reservoir situation, actual field experience is necessary to optimize the operations.

12.11 Summary and Conclusions

In this chapter, the technical aspects of immiscible gas/oil displacement have been described, and several field case studies have been presented. The conclusions concerning immiscible gas/oil displacement are listed below:

1. Immiscible gas/oil viscous displacement is an inefficient oil displacement process because gas is a highly mobile fluid.
2. Gas-oil capillary pressure data indicate that in many situations the residual oil saturation to gas displacement is significantly lower than the residual oil saturation to water displacement.
3. The immiscible gas/oil process becomes efficient and desirable when gravity works to keep the very-low-density gas on top of the higher-density oil and/or there is significant mass transfer of components from the oil to the gas.
4. The most successful immiscible gas/oil injection projects are the vertical gravity drainage projects in which gas is injected into the crestal primary or secondary gas cap, with the oil wells producing from as far downdip as possible to maximize this distance from the gas cap

both vertically and laterally. To maximize the efficiency of this approach, the overall oil production rate has to be restricted to the critical displacement rate.

5. One gas/oil compositional mass-transfer effect is oil swelling. If an oil field contains a very undersaturated oil, then oil swelling by contact with the injected gas can be a very significant effect. However, if a reservoir has an original gas cap, the oil swelling effect is minimal because the oil is already fully saturated or nearly saturated with gas.

6. The other gas/oil compositional mass-transfer effect is stripping or vaporization of intermediate hydrocarbon components from the oil by the lean injected gas. The importance of this effect increases as the producing GOR rises. Toward the end of the life of an immiscible gas injection project, the stripping effect can contribute many of the liquid hydrocarbons produced in the surface facilities and associated gas plants. This effect occurs with all types of oils but is more significant for lighter, or higher API gravity, oils.

7. A few immiscible gas injection field projects have been undertaken that are not vertical gas/oil gravity drainage projects but in which compositional effects have led to project success. An excellent example of this approach is the Swanson River field in Alaska.

8. Gas coning into producing wellbores' perforated intervals occurs with thin oil columns or as the gas/oil interface moves downward. Horizontal wells are a method of further reducing the height of the remaining oil column by lowering pressure drawdown and thus minimizing the effects of gas coning.

9. Numerical reservoir simulators are the best tool to evaluate all the technical aspects of an immiscible gas injection project, either historical performance and/or projections of future performance. Simple mathematical techniques have been developed to analyze some types of immiscible gas/oil displacements.

Nomenclature

A	= cross-sectional area, ft ²
F_g	= fractional gas flow, fraction
h	= thickness of oil zone normal to direction of dip, ft
h_v	= vertical thickness, ft
k	= permeability, darcies
k_h	= permeability in horizontal direction, darcies
k_{ro}	= relative permeability to oil, fraction
k_{rg}	= relative permeability to gas, fraction
k_v	= permeability in vertical direction, darcies
L	= distance along the bedding plane, ft
M	= mobility ratio, $k_{rg}\mu_o/k_{ro}\mu_g$
N_g	= oil production, fraction
P_c	= gas/oil capillary pressure, psi
q_T	= total flow rate through area A , ft ³ /D
S_{cw}	= connate water saturation, fraction PV
S_g	= gas saturation, fraction PV
S_o	= oil saturation, fraction PV
S_{org}^*	= irreducible oil saturation in presence of gas, fraction PV
S_{wi}	= initial water saturation, fraction PV
t	= time, days
t_D	= dimensionless time
t_v	= time for vertical drainage, days
t_u	= time for drainage along bedding plane, days
u	= flow per unit area, ft ³ /ft ² -D

- v_s = downdip free fall of oil, ft/D
 V = volume of gas injected, res bbl
 z = vertical distance, ft
 α = angle of dip (positive downdip), degrees
 μ_g = gas viscosity, cp
 μ_o = oil viscosity, cp
 ρ_g = gas density, lbm/ft³
 ρ_o = oil density, lbm/ft³
 ϕ = porosity, fraction

References

1. Muskat, M.: *Physical Principles of Oil Production*, McGraw-Hill Book Co. Inc., New York City (1949) 470–502.
2. Cotter, W.H.: “Twenty-Three Years of Gas Injection Into a Highly Undersaturated Crude Reservoir,” *JPT* (April 1962) 361.
3. Shehabi, J.A.N.: “Effective Displacement of Oil by Gas Injection in a Preferentially Oil-Wet, Low-Dip Reservoir,” *JPT* (December 1979) 1605.
4. Kuehm, H.G.: “Hawkins Inert Gas Plant: Design and Early Operation,” paper SPE 6793 presented at the 1977 SPE Annual Technical Conference and Exhibition, Denver, 9–12 October.
5. Katz, D.L., Monroe, R.R., and Tanner, R.P.: “Surface Tension of Crude Oils Containing Dissolved Gases,” *Pet. Tech.* (September 1943) 1.
6. Hough, E.W. and Warren, H.G.: “Correlation of Interfacial Tension of Hydrocarbons,” *SPEJ* (December 1966) 345.
7. Katz, D.L. and Firoozabadi, A.: “Predicting Phase Behavior of Condensate/Crude-Oil Systems Using Methane Interaction Coefficients,” *JPT* (November 1978) 1649–1655.
8. Firoozabadi, A. *et al.*: “Surface Tension of Reservoir Crude-Oil/Gas Systems Recognizing the Asphalt in the Heavy Fraction,” *SPEJ* (February 1988) 265.
9. Broseta, D. and Ragil, K.: “Parachors in Terms of Critical Temperature, Critical Pressure and Acentric Factor,” paper SPE 30784 presented at the 1995 SPE Annual Technical Conference and Exhibition, Dallas, 22–25 October.
10. Hagoort, J.: “Oil Recovery by Gravity Drainage,” *SPEJ* (June 1980) 139.
11. Johnston, E.F., Bossler, C.P., and Naumann, V.O.: “Calculation of Relative Permeability From Displacement Experiments,” *Trans.*, AIME (1959) **216**, 61.
12. *Miscible Processes*, Reprint Series, SPE, Richardson, Texas (1957) **8**, 111–114.
13. Simon, A.D. and Petersen, E.J.: “Reservoir Management of the Prudhoe Bay Field,” paper SPE 38847 presented at the 1997 SPE Annual Technical Conference and Exhibition, San Antonio, Texas, 5–8 October.
14. Ma, T.D. and Youngren, G.K.: “Performance of Immiscible Water-Alternating-Gas (IWAG) Injection at Kuparuk River Unit, North Slope, Alaska,” paper SPE 28602 presented at the 1994 SPE Annual Technical Conference and Exhibition, New Orleans, 25–28 September.
15. Stoitsits, R.F., Scherer, P.W., and Schmidt, S.E.: “Gas Optimization at the Kuparuk River Field,” SPE 28467 presented at the 1994 SPE Annual Technical Conference and Exhibition, New Orleans, 25–28 September.
16. Aziz, K. and Settari, A.: *Petroleum Reservoir Simulation*, Applied Science Publishers Ltd., London (1979) 30–38.
17. Buckley, S.E. and Leverett, M.C.: “Mechanism of Fluid Displacement in Sands,” *Trans.*, AIME (1942) **146**, 107.
18. Welge, H.J.: “A Simplified Method for Computing Oil Recovery by Gas or Water Drive,” *Trans.*, AIME (1952) **195**, 91.
19. Kern, L.R.: “Displacement Mechanism in Multi-well Systems,” *Trans.*, AIME (1952) **195**.
20. Craft, B.C. and Hawkins, M.F.: *Applied Petroleum Reservoir Engineering*, Prentice-Hall Inc., Englewood Cliffs, NJ (1959) 370.

21. Anders, E.L. Jr.: "Mile Six Pool: An Evaluation of Recovery Efficiency," *JPT* (November 1953) 279; *Trans.*, AIME, **198**.
22. *Miscible Processes*, Reprint Series, SPE, Richardson, Texas (1965) **8**, 197.
23. *Miscible Processes*, Reprint Series, SPE, Richardson, Texas (1965) **8**, 205.
24. Young, R.E., Fairfield, W.H., and Dykstra, H.: "Performance of a High-Pressure Gas Injection Project, Swanson River Field, Alaska," *JPT* (February 1977) 99.
25. Carlson, L.O.: "Performance of Hawkins Field Unit Under Gas Drive—Pressure Maintenance Operations and Development of an Enhanced Oil Recovery Project," paper SPE 17324 presented at the 1988 SPE/DOE Enhanced Oil Recovery Symposium, Tulsa, 17–20 April.
26. Christianson, S.H.: "Performance and Unitization of the Empire Abo Pool," paper SPE 6384 presented at the 1977 Permian Basin Oil and Gas Recovery Conference, Midland, Texas, 10–11 March.
27. Metz, W.P. and Elliott, R.A.: "Gas Handling Expansion Facilities at Prudhoe Bay, Alaska," paper SPE 22113 presented at the 1991 SPE International Arctic Technology Conference, Anchorage, 29–31 May.
28. Richardson, J.G., *et al.*: "The Effect of Small, Discontinuous Shales on Oil Recovery," *JPT* (November 1978) 1531.
29. Selamat, S., Goh, S.T., and Lee, K.S.: "Seligi Depletion Management," paper SPE 57251 presented at the 1999 SPE Asia Pacific Improved Oil Recovery Conference, Kuala Lumpur, 25–26 October.
30. Saidi, A.M.: "Twenty Years of Gas Injection History Into Well-Fractured Haft Kel Field (Iran)," paper SPE 35309 presented at the 1996 SPE International Petroleum Conference and Exhibition, Villahermosa, Mexico, 5–7 March.
31. O'Neill, N.: "Fahud Field Review: A Switch From Water to Gas Injection," *JPT* (May 1988) 609.
32. Horie, T., Firoozabadi, A., and Ishimoto, K.: "Laboratory Studies of Capillary Interaction in Fracture/Matrix Systems," *SPEE* (June 1990) 784.
33. Firoozabadi, A. and Hauge, J.: "Capillary Pressure in Fractured Porous Media," *JPT* (August 1990) 353.
34. Firoozabadi, A., Ishimoto, K., and Dindoruk, B.: "Theory of Reinfiltration in Fractured Porous Media: Part 2—Two-Dimensional Model," paper SPE 21798 presented at the 1991 SPE Rocky Mountain Regional Meeting and Low-Permeability Reservoirs Symposium, Denver, 15–17 April.
35. Dindoruk, B. and Firoozabadi, A.: "Crossflow in Fractured/Layered Media Incorporating Gravity, Viscous, and Phase Behavior Effects: Part I—Formulation and Features in Layered Media," paper SPE 35457 presented at the 1996 SPE/DOE Symposium on Improved Oil Recovery, Tulsa, 21–24 April.
36. Dindoruk, B. and Firoozabadi, A.: "Crossflow in Fractured/Layered Media Incorporating Gravity, Viscous, and Phase Behavior Effects: Part II—Features in Fractured Media," paper SPE 35458 presented at the 1996 SPE/DOE Symposium on Improved Oil Recovery, Tulsa, 21–24 April.
37. Ghorayeb, K. and Firoozabadi, A.: "Numerical Study of Natural Convection and Diffusion in Fractured Porous Media," *SPEJ* (March 2000) 12.
38. Addington, D.V.: "An Approach to Gas Coning Correlations for the Prudhoe Bay Field," *JPT* (November 1981) 2267.
39. Killough, J.E. and Foster, H.P. Jr.: "Reservoir Simulation of the Empire Abo Field: The Use of Pseudos in a Multilayered System," *SPEJ* (October 1979) 279.
40. Shreve, D.R. and Welch, L.W. Jr.: "Gas Drive and Gravity Drainage Analysis for Pressure Maintenance Operations," *JPT* (June 1956) 136; *Trans.*, AIME, **207**.
41. Jacoby, R.H. and Berry, V.J. Jr.: "A Method for Predicting Pressure Maintenance Performance for Reservoirs Producing Volatile Crude Oil," *JPT* (March 1958) 59; *Trans.*, AIME, **213**.
42. Attra, H.D.: "Nonequilibrium Gas Displacement Calculation," *SPEJ* (September 1961) 130; *Trans.*, AIME, **222**.
43. Stiles, W.E.: "Use of Permeability Distribution in Water Flood Calculations," *Trans.*, AIME (1949) **186**, 9.
44. Dyes, A.G., Caudle, B.H., and Erickson, R.A.: "Oil Production After Breakthrough—As Influenced by Mobility Ratio," *Trans.*, AIME (1954) **201**, 81.
45. Johns, R.T.: "Analytical Theory of Multicomponent Gas Drives with Two-Phase Mass Transfer," PhD dissertation, Stanford U., Palo Alto, California (1992).

46. Jessen, K., *et al.*: “Fast, Approximate Solutions for 1D Multicomponent Gas Injection Problems,” paper SPE 56608 presented at the 1999 SPE Annual Technical Conference and Exhibition, Houston, 3–6 October.
47. Falls, A.H. and Schulte, W.M.: “Features of Three-Component, Three-Phase Displacement in Porous Media,” *SPE* (November 1992) 426.
48. Lake, L.W.: *Enhanced Oil Recovery*, first edition, Prentice-Hall Inc., Englewood Cliffs, NJ (1989).
49. Juanes, R. and Patzek, T.W.: “Relative Permeabilities in Co-Current Three-Phase Displacements with Gravity,” paper SPE 83445 presented at the 2003 SPE Western Regional/AAPG Pacific Section Joint Meeting, Long Beach, California, 19–24 May.
50. Azevedo, A.V. *et al.*: “Nonuniqueness of Riemann Problems,” *Zeitschrift für angewandte Mathematik und Physik* (1997) **47**, No. 6, 977.
51. Marchesin, D., Plohr, B., and Schechter, S.: “An Organizing Center for Wave Bifurcation in Multiphase Flow Models,” *SIAM J. Appl. Math.* (October 1997) **57**, No. 5, 1189.
52. Richardson, J.G. and Blackwell, R.J.: “Use of Simple Mathematical Models for Predicting Reservoir Behavior,” *JPT* (September 1971) 1145.
53. Cardwell, W.T. Jr. and Parsons, R.L.: “Gravity Drainage Theory,” *Trans.*, AIME (1949) **179**, 199.
54. Erickson, J.W., and Sneider, S.M.: “Structural and Hydrocarbon Histories of the Ivishak (Sadlerochit) Reservoir, Prudhoe Bay Field,” paper SPE 28574 presented at the 1994 SPE Annual Technical Conference and Exhibition, New Orleans, 25–28 September.
55. Corey, A.T. *et al.*: “Three-Phase Relative Permeability,” *Trans.*, AIME (1956) **207**, 349.
56. King, R.L., Stiles, J.H. Jr., and Waggoner, J.M.: “A Reservoir Study of the Hawkins Woodbine Field,” SPE 2972 presented at the 1970 SPE Annual Meeting, Houston, 4–7 October.
57. Langenberg, M.A., Henry, D.M., and Chlebana, M.R.: “Performance and Expansion Plans for the Double-Displacement Process in the Hawkins Field Unit,” *SPE* (November 1995) 301.
58. Haldorsen, H.H. *et al.*: “An Evaluation of the Prudhoe Bay Gravity Drainage Mechanism by Complementary Techniques,” paper SPE 13651 presented at the 1985 SPE California Regional Meeting, Bakersfield, California, 27–29 March.
59. Stramp, R.L.: “The Use of Horizontal Drainholes in the Empire Abo Unit,” paper SPE 9221 presented at the 1980 SPE Annual Technical Conference and Exhibition, Dallas, 21–24 September.

SI Metric Conversion Factors

acre	× 4.046 863	E + 03 = m ²
bbl	× 1.589 873	E – 01 = m ³
cp	× 1.0*	E – 03 = Pa·s
dyne	× 1.0*	E – 05 = N
ft	× 3.048*	E – 01 = m
ft ²	× 9.290 304*	E – 02 = m ²
ft ³	× 2.831 685	E – 02 = m ³
°F	(°F – 32)/1.8	= °C
in.	× 2.54*	E + 01 = cm
lbm	× 4.535 924	E – 01 = kg
psi	× 6.894 757	E + 00 = kPa

*Conversion factor is exact.

Chapter 13

Polymers, Gels, Foams, and Resins

Robert D. Sydansk, Sydansk Consulting Services

13.1 Introduction

This chapter provides an overview of selected chemical systems and technologies that promote improved conformance during light oil-recovery operations. These conformance-improvement systems and technologies include fluid systems for use during oil-recovery flooding operations in which the fluids promote sweep improvement and mobility control (e.g., polymer waterflooding) and oilfield conformance-improvement treatment systems (e.g., “small-volume” gel treatments). A conformance-improvement fluid system for promoting flood sweep improvement and mobility control involves injecting a volume of an oil-recovery fluid that constitutes a significant fraction of the reservoir pore volume. The volume of an oil-recovery flooding system that is applied for sweep improvement is usually greater than 5% of the reservoir and/or well-pattern pore volume. Conformance-improvement treatment systems normally are of a relatively small volume and usually are used to treat the near-wellbore region or a relatively small fracture volume within the reservoir.

This chapter provides an overview of the following conformance-improvement systems: polymer waterflooding and treatments, gel treatments, foam flooding and treatments, and resin treatments. This chapter does not discuss improving conformance during oilfield drilling and stimulations operations for which the application of conformance-improvement technologies also can be quite advantageous.

Conformance is a measure of the uniformity of the flood front of the injected drive fluid during an oil-recovery flooding operation and the uniformity vertically and areally of the flood front as it is being propagated through an oil reservoir. If there were perfect conformance in a perfect regular five-spot well pattern during an oil-recovery flooding operation, the flood front would reach all four of the offset producers at the same time, and the flood front would reach the entire vertical interval of all four of the producing wells at the same time. Of course, there never has been a reservoir that has exhibited perfect conformance during an oil-recovery flooding operation. The issues that must be considered are how imperfect is the conformance for a given flooding operation in an oil field, and what is the economic or other beneficial rate of return if a conformance-improvement flood or treatment is implemented.

Improved conformance during an oil-recovery operation will result in incremental and/or accelerated oil production and/or will result in reduced oil-production operating costs. Properly designed and executed conformance-improvement flooding or treatments will improve the effec-

tiveness, efficiency, and profitability of an oil-recovery operation, regardless of whether the oil-recovery operation is primary production, secondary waterflooding, or tertiary-mode flooding.

This chapter contains seven major sections. [Sec. 13.2](#) discusses conformance improvement and the benefits imparted by the technologies and treatment systems reviewed in this chapter and imparted during light oil-recovery flooding operations. [Sec. 13.3](#) provides an overview of the conformance problems that flooding technologies and treatment systems are intended to reduce or eliminate. [Sec. 13.4](#) briefly discusses disproportionate permeability reduction. [Secs. 13.5](#) through [13.8](#) review, respectively, polymer waterflooding and treatments, gel treatments, foam flooding and treatments, and resin treatments.

13.2 Conformance Improvement

Improving conformance, in its original and most limited definition, is synonymous with improving the drive-fluid sweep efficiency during an oil-recovery flooding operation. Improving the conformance and/or sweep efficiency for any given oil-recovery drive fluid during a reservoir flooding operation involves improving one, or both, of two components of flood sweep efficiency: vertical and areal sweep efficiency.

The volumetric sweep efficiency of a given oil-recovery drive fluid during a flooding operation within a reservoir or well pattern is defined as

$$E_V = E_A E_I, \dots\dots\dots (13.1)$$

where E_A is the areal sweep efficiency, and E_I is the vertical sweep efficiency.^{1,2} For [Eq. 13.1](#) to be strictly correct, the geological layers or strata of the reservoir must be uniform in terms of porosity, thickness, and oil saturation.²

Strictly speaking for a real reservoir, volumetric sweep efficiency is more precisely defined as

$$E_V = E_p E_I, \dots\dots\dots (13.2)$$

where E_p is the pattern sweep efficiency,² which is the areal sweep efficiency for a reservoir with variations in thickness, porosity, and oil saturation. Areal sweep efficiency is defined as

$$E_A = \frac{A_f}{A_t}, \dots\dots\dots (13.3)$$

where A_f is the area contacted by the oil-recovery displacement fluid, and A_t is the total reservoir area under consideration.

Vertical sweep efficiency is defined as

$$E_I = \frac{A_V}{A_{tV}}, \dots\dots\dots (13.4)$$

where A_V is the reservoir vertical cross section contacted by the oil-recovery displacement fluid, and A_{tV} is the total reservoir vertical cross section.

For any given oil-recovery drive/displacement fluid, poor sweep efficiency often results primarily from spatial variation and/or heterogeneity in the permeability (fluid flow capacity) of the reservoir rock. Poor vertical conformance and poor vertical sweep efficiency in matrix rock (unfractured) reservoirs usually result primarily from geological strata of differing permeability overlying one another in a reservoir. Conformance treatments to improve poor vertical sweep

profiles and/or to shut off competing water or gas production, emanating from a subset of geological strata, are referred to as profile modification treatments. The Dykstra-Parsons coefficient is a widely used measure of the vertical permeability heterogeneity of an oil-producing reservoir and is discussed in Ref. 1.

For any given oil reservoir, poor sweep efficiency that results from flooding with an oil-recovery drive fluid is aggravated as the viscosity of the drive fluid decreases. Within any reservoir with a given degree of permeability heterogeneity, as the viscosity of the drive/displacement fluid of an oil-recovery flooding operation decreases, the degree of viscous fingering and the associated poor sweep efficiency increases. The mathematical and engineering term that relates the viscosity of the oil-recovery drive fluid to conformance and sweep efficiency is “mobility ratio.”

Mobility ratio is defined as

$$M = \frac{\lambda_D}{\lambda_d}, \dots\dots\dots (13.5)$$

where λ_D is the mobility of the oil-recovery displacement fluid phase, and λ_d is the mobility of displaced fluid phase. In this chapter, the mobility of the displaced fluid phase is the mobility of the reservoir oil phase. Eq. 13.5 holds for a piston-like oil-recovery flooding operation in which the flood front is sharp. Mobility is defined as

$$\lambda_i = \frac{k_i}{\mu_i}, \dots\dots\dots (13.6)$$

where k_i is the permeability to phase i , and μ_i is the viscosity of phase i .² Thus, as the viscosity of the oil-recovery displacement/drive fluid is increased in a reservoir with a given degree of permeability heterogeneity, the sweep efficiency and the degree of the oil-recovery flood conformance are improved. See Ref. 3 for the definition of mobility ratio in the case in which a waterflood does not exhibit piston-like displacement.

When the sweep efficiency and the degree of conformance are improved during an oil-recovery flooding operation, the rate at which the reservoir oil is recovered is increased, and the amount of oil-recovery drive fluid, which must be coproduced for a given oil recovery factor, is decreased. Reducing the amount of oil-recovery drive fluid (e.g., water) that must be coproduced for the attainment of a given oil-recovery factor reduces the operating and production costs associated with producing a given amount of oil. It also often reduces certain environmental liabilities, including the production of excessive and unnecessary amounts of saline reservoir brines that can contain toxic heavy-metal ions and the production of excessive and unnecessary volumes of possibly environmentally unfriendly secondary or tertiary flooding oil-recovery drive fluids.

For the most part, conformance-improvement flooding operations and treatments do not decrease residual oil saturation. However, there has been a contention made in the literature that polymer flooding can reduce residual oil saturation under certain circumstances. This contention is discussed briefly later in this chapter. Also, by virtue of the fact that surfactants are incorporated into foams of foam-flooding operations, foam flooding can, in principle, reduce residual oil saturation. However, oilfield foams that are applied for mobility control are believed to function primarily by improving flood sweep efficiency. For the most part, conformance-improvement treatments accelerate oil production and/or delay premature economic abandonment of wells, well patterns, and fields, and can do so while conducting normal primary, secondary, or tertiary oil-production operations.

As previously noted, conformance-improvement floods and treatments do not normally promote reductions in residual oil saturation. Therefore, conformance-improvement operations should be limited to well patterns or reservoirs with a substantial and economically viable amount of moveable oil that can be recovered as a result of conducting the conformance flood or treatment.

As originally and purely defined, conformance-improvement flooding operations and treatments involve improving the uniformity of the flood front of an injected drive fluid during an oil-recovery flooding operation. In addition to the original definition, the working definition of conformance-improvement treatments now includes treatments applied to production wells to shut off excessive, deleterious, and competing coproduction of water or gas coming from a source other than the producing oil-formation interval. Examples of such coproduction are the coning of water from an underlying aquifer and the coning of gas from an overlying gas cap. Thus, using this expanded working definition of conformance-improvement treatments, conformance treatments can include water or gas shutoff treatments that are applied to production wells during primary oil-recovery operations. In this chapter, we use the modern and expanded definition of conformance improvement. Ref. 4 presents a high-level overview of the use of polymers, gels, foams, and resins as water and gas shutoff treatments.

The vast majority of conformance-improvement treatments function by reducing the permeability and fluid-flow capacity of the offending and treated reservoir high-permeability flow paths, channels, and conduits. The only practical exception to this is acid stimulation treatments to improve the wellbore flow profiles in injection or production wells. Discussion of near-wellbore conformance-improvement treatments using acid stimulation is beyond the scope of this chapter. Although this chapter is focused primarily on conformance improvement for application to light oil reservoirs, many of the conformance-improvement technologies discussed can be applied during gas and heavy-oil recovery operations (i.e., gel and resin water-shutoff treatments).

In summary, conformance improvement facilitates improved sweep efficiency of an oil-recovery flooding operation and/or reduces the coproduction of water and gas, which impede the full production potential of any given production well. All the polymers, gels, foams, and resins discussed in this chapter are used for conformance improvement in oil or gas producing operations.

13.3 Conformance Problems

Conformance problems can be divided into six categories:

- Poor sweep efficiency and/or excessive coproduction of the oil-recovery drive fluid in a relatively homogeneous matrix-rock (unfractured) reservoir resulting from poor mobility control and/or oil-recovery drive-fluid fingering.
- Poor sweep efficiency and/or excessive coproduction of the oil-recovery drive fluid in a matrix-rock reservoir resulting from substantial permeability variation and heterogeneity.
- Poor sweep efficiency and/or excessive coproduction of the oil-recovery drive fluid occurring in a naturally fractured reservoir.
 - Water or gas coning.
 - Excessive and competing water or gas production emanating from a casing leak.
 - Excessive and competing water or gas production emanating from flow behind pipe.

The remediation, or partial remediation, of the first conformance problem is exemplified by a mobility-control polymer flood conducted in a reservoir containing a viscous oil and/or a reservoir that is characterized as being relatively homogeneous.

13.3.1 Key Distinctions. The first of two key distinctions relating to conformance problems is to differentiate between vertical conformance problems and areal conformance problems.⁵ Vertical conformance problems, which are probably the most pervasive and most easily remedied

conformance problems in matrix-rock (unfractured) reservoirs, are commonly manifested by geological strata of differing permeability overlying one another. In matrix-rock (unfractured) reservoirs, areal conformance problems, also referred to as “directional” high-permeability trends, can exist. Such conformance problems, which as a whole are usually less often treated by the technologies discussed in this chapter, are normally best addressed (by technologies of this chapter) through the application of a mobility-control flood such as a polymer waterflood. Areal conformance problems in matrix rock oil reservoirs are often more effectively remedied through well-pattern alignment strategies, which are beyond the scope of this chapter.

Within the conformance-problem category involving vertical matrix-rock problems and involving reservoir geological strata of differing permeabilities, there exists another aspect of this critical conformance-problem distinction that needs to always be made when considering technologies for reducing vertical conformance problems. This distinction is whether the geological strata of differing permeability are in fluid and pressure communication with each other.⁵⁻⁷ That is, is there vertical permeability communication between the zones or are there impermeable layers (e.g., a shale layer) separating the geological strata? If these geological strata are not in vertical fluid communication throughout the reservoir or the well pattern to be treated, then this conformance problem can be remedied or alleviated simply by reducing the injectivity into the high-permeability strata at the injection well or by reducing the productivity from the high-permeability strata at the production well. This problem can often be treated cost effectively in the wellbore or the near-wellbore environment with mechanical packer systems, tubing patches, sandpacks, squeeze cementing, near-wellbore polymer-gel treatments, or resins. When such a treatment involves the placement of a chemical fluid-flow shutoff material (e.g., a gel or resin) in the offending strata surrounding a radial-flow well of a matrix-rock reservoir, then it is imperative (as is discussed in more detail in [Sec. 13.6](#)) that the treatment be placed selectively only in the offending geological strata and that none of the treatment shutoff material be placed in the oil-producing strata.⁶⁻⁸ This type of treatment for improving vertical conformance is referred to by some as a profile modification treatment.

If vertical pressure communication and fluid crossflow exists between the geological strata, then the oil-recovery sweep efficiency problem and/or the associated excessive drive-fluid production problem cannot be remedied effectively with a wellbore operation or by a near-wellbore blocking agent treatment.⁵⁻⁷ As [Fig. 13.1](#) shows, when a conformance-treatment blocking agent is placed near wellbore in the high-permeability geological strata at either the production or injection well, the conformance-improvement gains are short lived in terms of improved sweep efficiency and/or reduced rate of the excessive oil-recovery drive fluid (e.g., water during waterflooding) production. If the blocking agent is placed selectively in the high-permeability strata near wellbore to the injection well, the subsequently injected oil-recovery drive fluid will be injected into, and flow through, the low-permeability strata for a relatively short distance until it flows beyond the radius of the blocking agent. At this point, the oil-recovery drive fluid will tend to rapidly crossflow into the high-permeability strata where the fluid flow resistance is less. Other than very early in the life of a flooding operation, the near-wellbore volume of the low-permeability strata is likely already swept of its mobile oil saturation. In this case, little, or often no, sweep improvement or incremental oil production is gained from the placement of the blocking agent in the near-wellbore volume of the high-permeability strata.

If the blocking agent is placed selectively in the high-permeability strata near wellbore to the production well when crossflow between the reservoir strata occurs, a relatively small, and often uneconomic, volume of incremental oil production and a short-lived reduction in the undesirable high rate of the oil-recovery drive fluid production are realized after the treatment. After placing the blocking agent near wellbore in the high-permeability strata, the oil-recovery drive fluid will flow from the high-permeability strata to the low-permeability strata at a point just beyond the outer radius of the emplaced blocking agent.

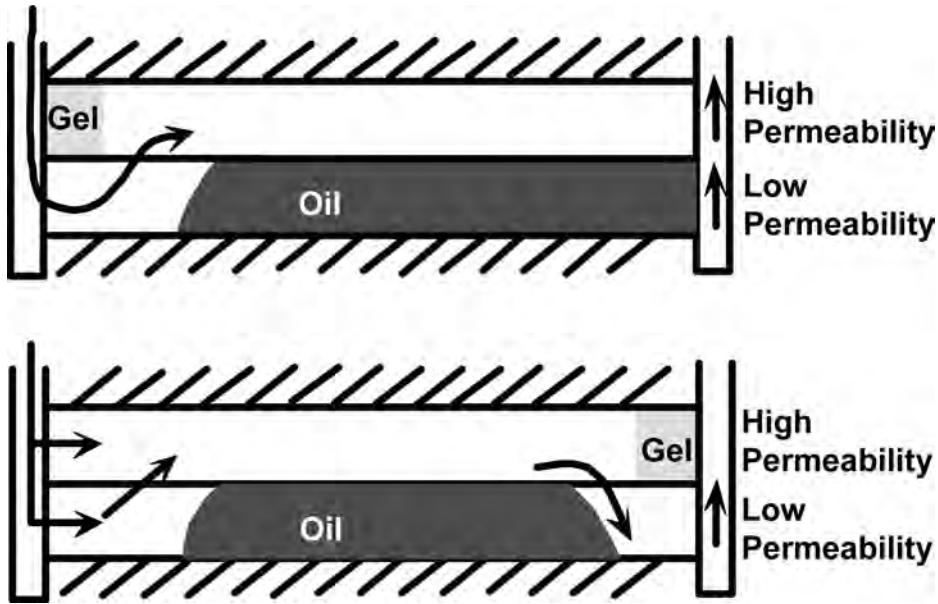


Fig. 13.1—Near-wellbore blocking agent placed in the high-permeability strata of a matrix rock reservoir exhibiting crossflow and suffering from a conformance problem.

Thus, when crossflow exists between the geological strata, when radial flow exists, and when the reservoir is undergoing an oil-recovery flooding operation, the selective placement of a blocking agent at, or near, the wellbore in the high-permeability strata of a matrix-rock reservoir renders little or no significant sweep improvement or reduction in the deleterious coproduction of the oil-recovery drive fluid (e.g., water during waterflooding).

If a matrix-rock reservoir with crossflow between geological strata and with radial-flow production is to be treated successfully with a blocking-agent conformance treatment, it must be treated such that the blocking agent is placed selectively deep in the reservoir in the high permeability strata.⁶ The technical and economic feasibility of successfully applying water-shutoff treatments to this type of conformance problem has been questioned.⁷ On the other hand, there are some reports in the literature, as exemplified by Ref. 9, that certain specialized polymer microgels have been applied through injection wells in the form of large volume conformance-improvement gel treatments that are intended to treat deeply into “matrix rock” reservoirs with crossflow between the reservoir geological strata.

A better strategy for rendering conformance improvement in layered reservoirs of matrix rock reservoirs where crossflow exists would be to use a mobility-control flood, such as a polymer flood. When flooding with a viscosity-enhancing mobility-control drive fluid, more of the injected drive fluid will be injected into, and flow through, the lower permeability and more poorly sweep geological reservoir strata. In this case, the strategy will result in accelerated oil production and reduced production of the oil-recovery drive fluid.

The second key conformance-problem distinction is whether the high-permeability flow path of the conformance problem is simply a high-permeability flow path through unfractured matrix rock or is a high-permeability anomaly, such as a fracture.⁵ For this chapter, the cut off between a high-permeability flow path in matrix reservoir rock and a high permeability anomaly is the equivalent of about two Darcies in a sandstone reservoir.⁵ High-permeability anomalies within a reservoir can include fractures (both natural and hydraulically induced), fracture networks, faults, joints, solution channels, interconnected vugular porosity, caverns, cobble layers, coarse sand strata, rubblized zones, and localized matrix reservoir rock with permeabilities

greater than two Darcies. Reservoir fractures tend to be the most often encountered high-permeability anomaly. At depths greater than about 4,000 ft, fractures tend to be vertical in orientation and promote areal conformance problems.¹⁰ At depths less than about 2,000 ft, fractures tend to be horizontal in orientation and can cause serious vertical conformance problems.

The distinction between conformance problems involving high-permeability flow paths through matrix reservoir rock and high-permeability anomalies is very important to the successful application of a number of technologies used to improve conformance. As discussed in [Sec. 13.6](#), differentiating between these two conformance-problem regimes is critical to the success of the most widely applied polymer-gel treatment technologies because different versions of these polymer-gel technologies are normally required to treat these two different problems successfully. A polymer flood, which is applied to conformance problems involving solely matrix-rock permeability variation within a given well pattern or reservoir, is more likely to be successful than the same polymer flood that is applied to a similar well pattern or reservoir in which the conformance problem is dominated by high-permeability anomalies such as a carbonate well pattern or reservoir with numerous and extensive large solution channels. Classical mobility-control foam flooding is an inefficient option for use in a reservoir with high-permeability anomalies, such as an extensive and highly conductive fracture network.

Because the true nature of vugular-porosity conformance problems has often not been fully appreciated by many petroleum engineers, there have been a number of polymer-gel conformance treatment failures when treating vugular-porosity conformance problems. As [Fig. 13.2](#) depicts, the true and original definition of vugular porosity is relatively small voids (smaller than caverns) that exist randomly in matrix reservoir rock (especially carbonate reservoirs) where the vugular voids are not interconnected. If this is truly the vugular-porosity conformance problem that has been encountered in a given instance, then a matrix-rock conformance treatment is normally required. If, however, the conformance problem is dominated by large and extensive solution channels in the matrix reservoir rock (i.e., tubular flow pathways of often greater than 1/8-in. diameter), a high-permeability anomaly type of conformance treatment is required. The chances that a matrix-rock type of polymer-gel conformance treatment will be successful are remote when encountering reasonably large solution channels. As is often the case when vugular-porosity conformance problems are encountered, the vugular porosity is actually vugs that are interconnected with solution channels.⁵ If this is the actual nature of the vugular-porosity conformance problem, a high-permeability anomaly polymer-gel treatment is required. Failure to make the proper distinction between these two types of vugular-porosity problems can spell doom for a polymer-gel conformance-improvement treatment that is applied to such a vugular-porosity problem. When vugular-porosity conformance problems are encountered in those situations that the vugs are not interconnected, then a high-permeability anomaly polymer-gel treatment will not perform as expected and will not remedy this particular vugular-porosity conformance problem. Likewise, when vugular-porosity conformance problems are encountered in those situations that the vugs are interconnected, the application of a matrix rock polymer-gel conformance treatment will not be well suited for remedying such a vugular-porosity conformance problem.

13.3.2 How Conformance Problems Are Manifested. An alternate means of categorizing oil-field conformance problems is by the way conformance problems manifest themselves, such as by poor sweep efficiency during oil-recovery flooding operations, excessive and deleterious competing water coproduction, excessive and deleterious competing gas coproduction, coning and cusping, casing leaks, or water or gas flow behind pipe.

Two distinct types of water production exist. The first type, usually occurring later in the life of a waterflood, is water that is coproduced during oil/water fractional flow in reservoir matrix rock. When the production rate of this water is reduced, there will be a proportional reduction in the oil-production rate. The second type of water production directly competes with oil

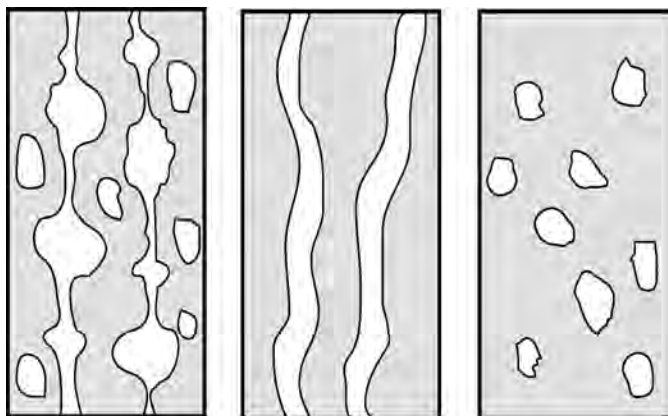


Fig. 13.2—Vugular porosity and solution channels.

production. This water often flows to the production wellbore via a flow path separate from that of the oil (e.g., water coning or a fracture emanating directly from a water injection well to the production well). For the second type of water-production problem, reducing water production can often lead to a greater pressure drawdown and/or an increase in the oil production rate. Thus, reducing the production of the second type of water production should be the objective of conformance-improvement floods and of water-shutoff treatments with gels, foams, and resins.⁷

A number of sources/causes of excessive and deleterious coproduction of water or gas exist:

- Early water or gas breakthrough during flooding operations resulting from poor sweep efficiency caused by vertical permeability variation in matrix-rock reservoirs (i.e., geological stratification).
- Early water or gas breakthrough during flooding operations resulting from poor sweep efficiency caused by variation in areal permeability in matrix-rock reservoirs.
- Early water or gas breakthrough caused by poor sweep efficiency that results from oil-recovery drive-fluid viscous fingering, where the viscous fingering is caused by an unfavorable mobility ratio between the oil-recovery displacement fluid and the reservoir oil.
- Fracture communication between the injector and producer (either extending fully or partially between wells).
 - Fracture networks (with and with out directional trends).
 - 2D coning via fractures.
 - 3D coning via unfractured matrix reservoir rock.
 - Cusping.
 - Flow behind pipe.
 - Casing leaks.

Coning and cusping can involve either water or gas. Cusping involves the production of aquifer water that flows to the production well through an inclined geological strata or zone, or gas-cap gas that flows to the production well through an inclined geological strata. In large part because of the relatively low viscosity and associated high mobility of gas, gas cusping tends to occur more easily than water cusping.

There are two distinctly different types and mechanisms of coning as it relates to conformance treatments such as water or gas shutoff coning treatments with gels. 2D coning occurs when water cones up, or gas cones down, to the production well's producing interval through vertical fractures or a fracture network. Conformance-treatment blocking agents, such as gels, can be used effectively and profitably to reduce such water or gas coning. 3D coning occurs

when water cones up or gas cones down through matrix reservoir rock to the production well's producing interval. The use of conformance-treatment blocking agents, such as gels, has a very low probability of success when applied to a 3D coning problem.⁷

When large flow conduits with apertures substantially greater than approximately $1/16$ in. are the cause of flow behind pipe and the cause of the deleterious water or gas production, then the use of Portland cement is often favored for remedying such problems. The use of Portland cement for these purposes is beyond the scope of this chapter.

13.3.3 Implementing Conformance Treatments and Diagnosing Conformance Problems. In general, a conformance-improvement treatment (e.g., a gel treatment) to improve sweep efficiency and to generate incremental oil production is applied most effectively from the injection well side. When implementing a conformance-improvement treatment to reduce production operating costs by reducing the rate of competing water or gas production, these treatments usually are applied most effectively from the production well side. Treatments for both improving sweep and reducing excessive water and/or gas coproduction during gas or supercritical-liquid (e.g., CO₂) flooding operations in naturally fractured reservoirs normally are applied most effectively from the injection well side.⁵

The nature of the reservoir conformance problem to be addressed through the application of polymers, gels, foams, or resins needs to be diagnosed or deduced correctly or substantial negative consequences can occur.^{5,7} A detailed discussion of how to properly and effectively diagnose and/or deduce reservoir conformance problems and flood sweep-efficiency problems is beyond the scope of this chapter. Refs. 5, 7, and 11 enumerate a number of techniques for diagnosing conformance problems and excessive water- and gas-production problems. Among the techniques discussed in these references are the use of interwell chemical and radioactive tracers, simple injectivity/productivity calculations to determine if fluid flow around a wellbore is radial or linear in nature, wellbore production and injection logs, various other logging tools, and pulse and pressure transient testing. An important element in successfully implementing a water or gas shutoff treatment is to determine at the onset, or at least hypothesize, the “plumbing” of the reservoir flow path of the excess water or gas production from its source to the production wellbore.⁵ Production water/oil ratio (WOR) diagnostic plots¹¹ have also been used to help diagnose conformance problems. WOR diagnostic plots should be used in conjunction with another independent conformance-problem diagnostic tool, because many diagnostic plots can be interpreted in more than one way.

There historically has been a trend whereby petroleum engineers, when first considering the application of a conformance-improvement treatment in a new field, tend to underestimate the permeability and fluid-flow capacity of the high-permeability channels and flow paths within the reservoir to be treated.⁵ This has contributed significantly to the low success rate of first-time conformance-improvement treatments being applied in a new field by an inexperienced petroleum engineer.

13.4 Disproportionate Permeability Reduction

Disproportionate permeability reduction (DPR) is a phenomenon whereby many water-soluble polymers and many polymer gels reduce the permeability to water flow to a greater extent than to oil or gas flow.¹²⁻²⁶ Most of the early work on, and application of, DPR involved fluid flow in reservoir matrix rock. More recently, water-shutoff chromium(III)-carboxylate/acrylamide-polymer (CC/AP) gels for use within fractures have been reported to impart DPR in gel-filled fractures.²⁷ However, because these relatively strong fracture-problem gels significantly reduce simultaneously the permeability to oil flow in fractures, these gels are better characterized as total-fluid-flow-shutoff gels and not DPR water-shutoff gels.

DPR is also referred to as relative permeability modification (RPM). However, some practitioners of this technology make the following subtle distinction. They tend to reserve the term

DPR for relatively strong polymer gels that impart a large degree of disproportionate permeability reduction and a relatively large reduction in water permeability. These practitioners reserve the term RPM for systems, such as solutions of water-soluble polymers or relatively weak gels, that impart more subtle disproportionate permeability reduction and more subtle reductions in water permeability. As used in this chapter when referring to water-shutoff treatments, the terms DPR and RPM are synonymous.

Alternatively, DPR conformance-improvement treatments, which involve relatively strong gels, can be successfully applied in hydraulically or naturally fractured reservoirs. In this case, the gel is placed and functions within the matrix rock that is adjacent to the fractures.²⁸

DPR has the most value when used in water-shutoff/reduction treatments that are applied to production wells. DPR has little or no value for use during sweep-improvement treatments that are applied from the injection-well side.

A distinction needs to be made regarding classical and relatively strong (not DPR) polymer-gel water-shutoff (total-fluid-flow-shutoff) treatments that are placed within fractures that surround production wells. Such gel treatments tend to be placed, or place themselves, so that they will selectively reside in the water-producing fractures where the gels effectively block water flow. Such gel treatments (when properly designed and executed) tend to reduce water production without substantially reducing oil production. Here, the selective water shutoff results from selective placement of the gel in the water-producing fractures and not by the DPR mechanism.

The ability of acrylamide polymers to impart DPR to water flow in porous media was recognized as early as 1964 by Sandiford²⁶ and in 1973 by White *et al.*¹² The mechanism by which polymers and gels impart DPR and RPM effects has been the subject of a number of investigations. Refs. 29 through 39 are representative of these investigations. More recently, a set of plausible mechanisms have been proposed that explain how CC/AP polymer gels impart DPR.⁴⁰

The application of DPR conformance-improvement technologies for water-shutoff (and/or water-reduction) purposes is not a panacea.^{4,23,24,41–44} The successful application of bullheaded DPR long-term water-shutoff/reduction treatments, which involve radial flow in matrix reservoir (unfractured) rock and where the drawdown pressure on the producing interval is not increased after the gel treatment, is limited to when the following conditions are met:

- A conformance problem exists in a matrix rock reservoir involving differing geological strata.
- No fluid crossflow can occur within the reservoir between the water and the oil or gas producing geological strata.⁴⁴
- The water strata is producing at an undesirably high water cut, and the oil or gas strata will produce for the economic life of the water-shutoff treatment at 100% oil or gas cut.

Possible exceptions to these limitations are as follows. First, if the DPR treatment induces an increase in the drawdown pressure on the producing interval, the DPR treatment may promote increased oil production. Second, if the DPR treatment material in the presence of oil flow breaks down, or is otherwise inactivated (with respect to its water-blocking ability), then selective water shutoff can occur over a wider range of excessive water-production problems.

For applications in radial-flow matrix-reservoir rock, commercially available DPR water-shutoff/reduction treatments usually attempt to reduce the permeability to oil or gas flow by a factor of two or less in the treated reservoir volume and reduce the permeability to water flow by a factor on the order of ten or more. Variability in performance of these systems has often led to erratic results when trying to accomplish this objective. To date, commercially available DPR water-shutoff/reduction treatments for application in radial-flow matrix-rock reservoirs have been based, almost exclusively, on the use of either solutions of water-soluble polymers or relatively “weak” gels.

For application to fractured wells, a DPR scheme for treating excess water production is discussed in the DPR subsection of [Sec. 13.6.1](#). This scheme relies on placing a relatively strong DPR water-shutoff gel in the matrix rock that is adjacent to the fractures.²⁸

DPR water-shutoff treatments are of no practical value [in terms of providing long-term (i.e., years) water shutoff] when applied to a single zone reservoir that is producing at a high water cut in the radial flow mode from a matrix rock reservoir. This is because a relative-permeability water block will form just beyond the outermost radial penetration of the DPR water-shutoff treatment.⁴⁴ What is less obvious is that for the same basic reason when producing from matrix rock reservoirs in the radial flow mode, DPR water-shutoff treatments are not effective at promoting long-term water shutoff/reduction anytime the oil-producing zones are producing at a finite water cut or crossflow exists between the oil- and water-producing zones.

Another issue with DPR water-shutoff treatments is that for such treatments, which are based on the use of solutions of water-soluble polymers or relatively “weak” gels, their water-shutoff performance is erratic and not highly reproducible in both the laboratory and field settings.⁴⁵ For DPR water-shutoff treatments, the restoration (or near restoration) of the oil permeability following the placement of the treatment in matrix reservoir rock can be quite slow.⁴⁵ An important point regarding DPR water-shutoff treatments is that DPR imparted in the treated volume of the matrix reservoir rock does not necessarily correspond in the field to a proportionate reduction in the water production rate.

An additional important distinction that needs to be made is to whether the DPR treatment is being applied for long-term (i.e., years) or short-term (i.e., hours to months) water-shutoff purposes. For the relative-permeability water-block reason discussed previously, many DPR water-shutoff treatments will render short-term or transient water-shutoff/reduction during treatments that are applied in the field. The water-block problem goes a long way in explaining why so many DPR water-shutoff treatments have failed to provide long-term water shutoff and have tended to render only short-term water shutoff. There are scenarios for limited reservoir conditions, where DPR treatments that render only transient water shutoff, can be engineered to be economically attractive and profitable.

The reason that bullheadable DPR water-shutoff treatments have created such a great interest in the oil industry is that they do not require the use of mechanical zone isolation when applied to layered matrix-rock reservoirs. Mechanical zone isolation often requires costly workover operations. Use of mechanical zone isolation during water-shutoff-treatment placement is not normally feasible when the well possesses a slotted-liner or gravel-pack completion or when the well involves a subsea tieback flow line.

Historically, a large number of ineffective DPR (RPM) water-shutoff treatments have been conducted. The high failure rate of DPR water-shutoff/reduction treatments has resulted from a combination of overexpectations by operators regarding DPR water-shutoff treatments, overselling of DPR water-shutoff treatments by oilfield service companies, and failure to recognize the constraints to the successful application of DPR water-shutoff treatments within matrix-rock (unfractured) reservoirs. However, DPR treatments remain one of the few options available to successfully treat excessive water-production problems in matrix rock reservoirs for which mechanical zone isolation is not possible or practical during treatment fluid placement. At the time of the writing of this chapter, the investigation, development, and exploitation of DPR conformance-improvement technologies were being actively pursued by petroleum industry R&D efforts.

13.5 Polymers

Early application of polymers for use during oilfield conformance-improvement operations was focused on improving volumetric sweep efficiency of waterfloods. More recently, polymers have been used extensively in DPR and RPM treatments for water shutoff and in conformance-improvement polymer-gel treatments. Most of this section focuses on the use of polymers in

polymer waterflooding operations. [Sec. 13.5.8](#) reviews the use of polymers in DPR and RPM treatments that are applied for “selective” water-shutoff/reduction.

13.5.1 Polymer Fundamentals. Polymers are large molecules and chemical entities referred to as macromolecules. Polymer molecules are the resultant chemical specie when a large number of relatively small and repeating molecular entities, called monomers, are joined together chemically. The chemical process of joining together the monomers and forming polymer molecules is referred to as the polymerization reaction process. Polymers, both natural and man made, have numerous beneficial uses and applications in modern society (everything from wood, to plastics, to man-made thickening agents added to milk shakes). Polymers can come in pure solid and liquid forms. Some polymers can be dissolved in liquids. This chapter is limited to polymers that can be dissolved (or dispersed) in an aqueous solution and that usually increase the viscosity of the aqueous solution.

Basic Oilfield Polymer Types. There are two fundamentally different types of water-soluble and viscosity-enhancing polymer chemistries that have been used during polymer waterflooding and conformance-improvement treatments. The first type is biopolymers, such as Xanthan gum polymer. The second type is man-made synthetic polymers, such as acrylamide-based polymers.

Biopolymers of the type used in conformance improvement are polysaccharides (poly sugars) in which the monomer chemical linkages of the polymer backbone are glycoside linkages, involving carbon-oxygen-carbon chemical bonds. In aqueous solution, the multistranded molecular complexes of xanthan polymer are fairly rigid molecular species, causing the polymer molecules to take on an extended molecular conformation.

Synthetic polymers of the type used in conformance improvement are usually highly flexible molecules in which the polymer backbone consists of a relatively chemically stable carbon molecular chain with single and flexible carbon-carbon bonds. Pendant water-soluble chemical groups (e.g., amide groups) on the molecule render the polymer molecule to be soluble in water.

Synthetic polymers have emerged to become the predominant and preferred polymer type for use in commercial oilfield conformance-improvement operations because of the inherent chemical and biological stability of synthetic polymers, along with injectivity and cost issues.

Historically, the two types of biopolymers primarily used in polymer waterflooding have been xanthan and scleroglucan polymers. The only synthetic polymers that have been used extensively during polymer waterflooding (and in polymer-gel conformance treatments) are those based on acrylamide-polymer chemistry.

Viscosity Enhancement and Permeability Reduction. Water-soluble polymers used in conformance-improvement operations operate by reducing fluid mobility by increasing viscosity of the oil-recovery drive fluid (primarily the flood water) and/or by reducing permeability, by which the polymers, directly or indirectly, act as a fluid-flow blocking agent. Reducing permeability is the conformance-improvement mechanism by which conformance treatments operate when polymers and polymer gels are used for imparting DPR. Polymers used in waterfloods often have a secondary component in their conformance-improvement mechanism that involves permeability reduction within the flooded volume of a matrix rock reservoir.

Chemistry of Polymers Used in Conformance Improvement. The chemistry of polymers used in conformance improvement is reviewed before discussing polymer waterflooding and DPR polymer treatments because several of the polymer chemistries that are reviewed are used in both of these oilfield conformance-improvement applications. In fact, some of the polymer chemistries discussed in this section are also used in conformance-improvement polymer gels (see [Sec. 13.6](#)).

Biopolymers. In addition to being environmentally friendly and readily available, advantages of biopolymers are their relative insensitivity to salinity and mechanical shear degradation. The two major concerns relating to the use of biopolymers are their susceptibility to biological and chemical degradation, and injectability issues resulting from cell debris that usu-

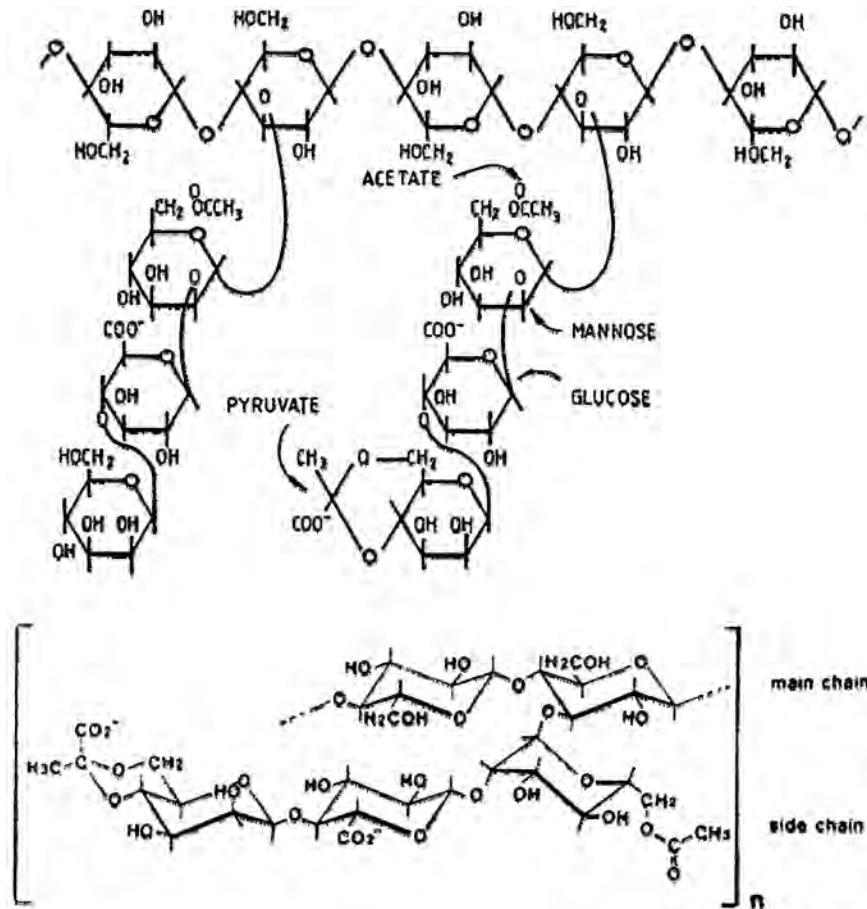


Fig. 13.3—Chemical structure of a xanthan polymer molecule.

ally remain in the biopolymer solutions that are derived from microorganism fermentation processes.

Xanthan⁴⁶ has been the most widely used biopolymer for polymer waterflooding. Fig. 13.3 shows the chemical structure of the xanthan biopolymer molecule.⁴⁶ For a xanthan molecule with a molecular weight of 4 million daltons (atomic mass units), the xanthan molecule comprises on the order of 20,000 repeating sugar monomer units. Xanthan polymer is derived from a microorganism fermentation process that usually leaves a substantial amount of cell debris in the final polymer solution.

Flooding reservoir matrix rock with fully filtered xanthan polymer solutions tends to result in much less permeability reduction than the comparable flooding with appropriate acrylamide-polymer solutions. Xanthan polymers and the resultant solution viscosity are relatively insensitive to the salinity of the brine into which the Xanthan polymers are dissolved, and Xanthan polymers tend to be relatively insensitive to mechanical shear degradation. Xanthan polymers are quite susceptible to biological degradation.

Scleroglucan, with a triple-stranded molecular configuration, has been suggested to be a biopolymer possessing more favorable stability and performance properties for use during high-temperature polymer waterflooding (e.g., 195°F).^{47,48}

Synthetic Polymers. Acrylamide polymers have emerged to be the most widely used synthetic polymer family for application in polymer flooding and in polymer and polymer-gel confor-

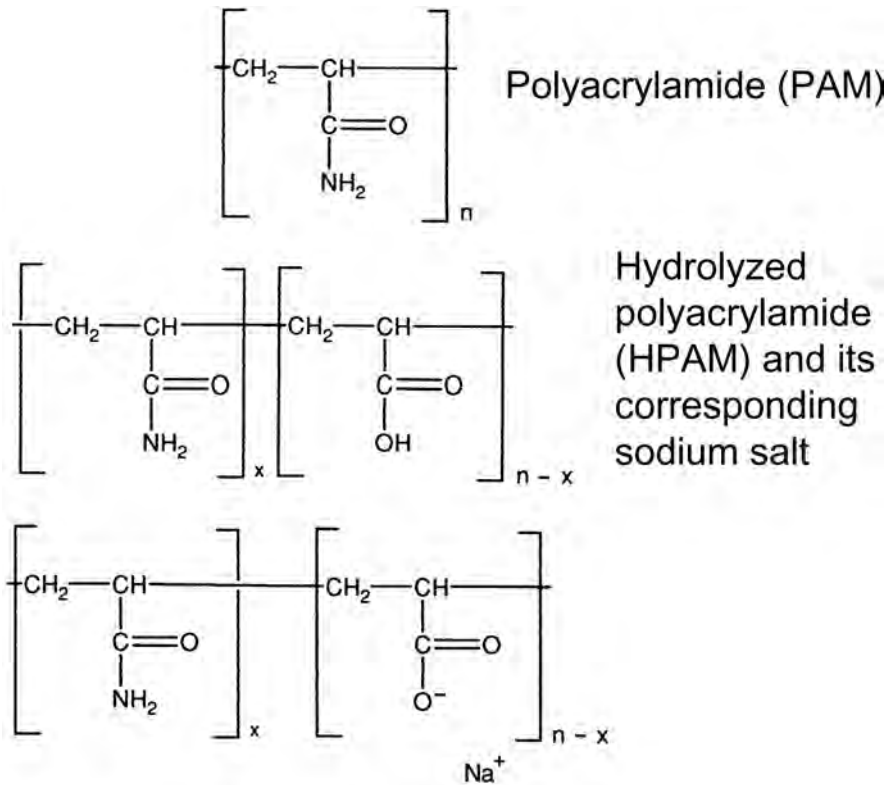


Fig. 13.4—Chemical structure of PAM and HPAM polymer molecules.

mance-improvement treatments. This has come about in large part because of cost and availability issues and because of the favorable chemical robustness and biological stability.

Polyacrylamide (PAM) is the simplest and most basic form of acrylamide polymers. Fig. 13.4 shows the chemical structure of polyacrylamide and partially hydrolyzed polyacrylamide. For polyacrylamide with a molecular weight of 7 million daltons (a representative molecular weight of an acrylamide polymer to be used in polymer waterflooding), the value of n in Fig. 13.4 and the number of repeating monomer units is on the order of 100,000. When all other factors are equal and when dissolved in brine with a relatively low salinity, polyacrylamide is not as good a viscosity-enhancing agent and is not propagated as well through sand reservoirs when compared to partially hydrolyzed polyacrylamide (HPAM). Because pure polyacrylamide is slightly positively charged (cationic) in an acidic or “neutral” pH environment, polyacrylamide tends to adsorb onto reservoir rock surfaces, especially sands and sandstone pore surfaces. For these reasons, partially HPAM is most often favored for use in polymer flooding.

When polyacrylamide is manufactured commercially, it normally contains 1 to 2 mole percent hydrolyzed (carboxylate) content that is inadvertently imparted during the manufacturing process. This carboxylate “impurity” in many of the commercial polyacrylamide polymers is enough carboxylate content to render such polyacrylamide to be a good candidate for use in conformance-improvement polymer gels that involve chemical crosslinking reactions occurring through the polymer’s carboxylate groups. A specialized polyacrylamide polymer is available commercially that contains essentially no carboxylate groups (less than 1 carboxylate groups in 1,000 acrylamide groups). Such polyacrylamide is referred to as ultra-low hydrolysis polyacrylamide. To manufacture ultra-low-hydrolysis polyacrylamide, normal acrylamide monomer feed stock is polymerized as usual, except the polymerization conditions (pH and temperature) are

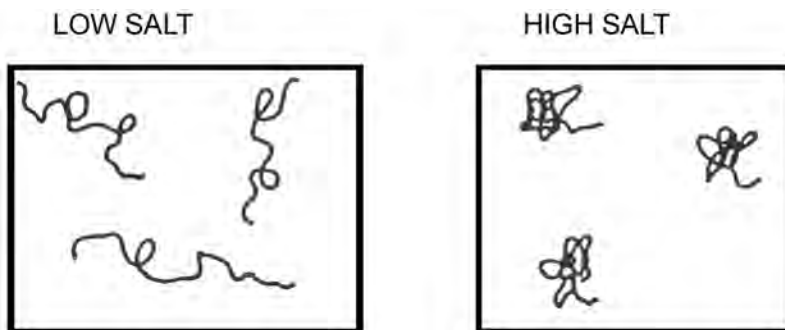


Fig. 13.5—Schematic of the effect of solution ionic strength on the molecular conformation of flexible coil polyelectrolyte molecules such as HPAM.

more tightly controlled. Polyacrylamide is normally not referred to as HPAM until the carboxylate content exceeds approximately 2 mole percent.

HPAM is the most widely employed water-soluble polymer for use in both polymer waterflooding and in oilfield conformance polymer-gel treatments. As mentioned previously and as compared with polyacrylamide, HPAM polymer tends to be a better viscosity-enhancing agent in low-salinity brines and tends to adsorb less onto the rock surfaces of reservoirs that are good polymer-waterflooding candidates. Thus, the use of the salt form of HPAM is favored over the use of straight polyacrylamide in most polymer-flooding applications. A number of practitioners of polymer flooding believe that because of the salt sensitivity of HPAM, this polymer performs best during polymer flooding conducted in reservoirs with low-salinity reservoir brines. However, there have been some instances in which HPAM, when dissolved in a fresh flooding brine, has performed well when flooded in a reservoir with a saline brine. [Ref. 49](#) cites such an example.

A 30% hydrolysis level within polyacrylamide is near the optimum in terms of simultaneously promoting maximum viscosity enhancement of the polymer solution and minimizing polymer adsorption onto reservoir rock surfaces during most polymer waterfloods. For crosslinked polymer gels, the optimum hydrolysis level of 5 to 10 mole percent (in this case) simultaneously maximizes gel strength and minimizes unproductive intramolecular crosslinking.

As [Fig. 13.4](#) shows, HPAM can come in two forms as it relates to the chemistry of the carboxylate groups. The carboxylate groups can be in the acid or salt form. For use in polymer waterflooding and in polymer gels, HPAM is almost always used in the sodium salt form. Unless specifically stated otherwise in this chapter, when referring to HPAM, we are referring to HPAM with its carboxylate groups in the sodium salt form.

In low salinity brines, the electrostatic charge repulsion between carboxylate groups of HPAM molecule tends to cause the flexible-backbone polymer to assume a distended tertiary conformational form that is a more effective for enhancing aqueous-solution viscosity than is the more balled-up form occurring for such polymers dissolved in a high salinity brine and the balled-up molecular conformational form of unhydrolyzed polyacrylamide. [Fig. 13.5](#) depicts the stretched out and more effective viscosity-enhancing molecular form of HPAM that exists in a low-salinity aqueous environment. [Fig. 13.5](#) also shows the balled-up conformational form that HPAM assumes in a high salinity brine environment. High salinity causes the electrostatic fields around the carboxylate groups to shrink substantially and allows the HPAM molecule to assume a more balled-up form because of the elimination of a high degree of electrostatic repulsion between the negatively charged carboxylate groups on the polymer's backbone. The balled-up polymer form does not generate nearly as much viscosity as the distended form in otherwise comparable polymer-waterflood solutions.

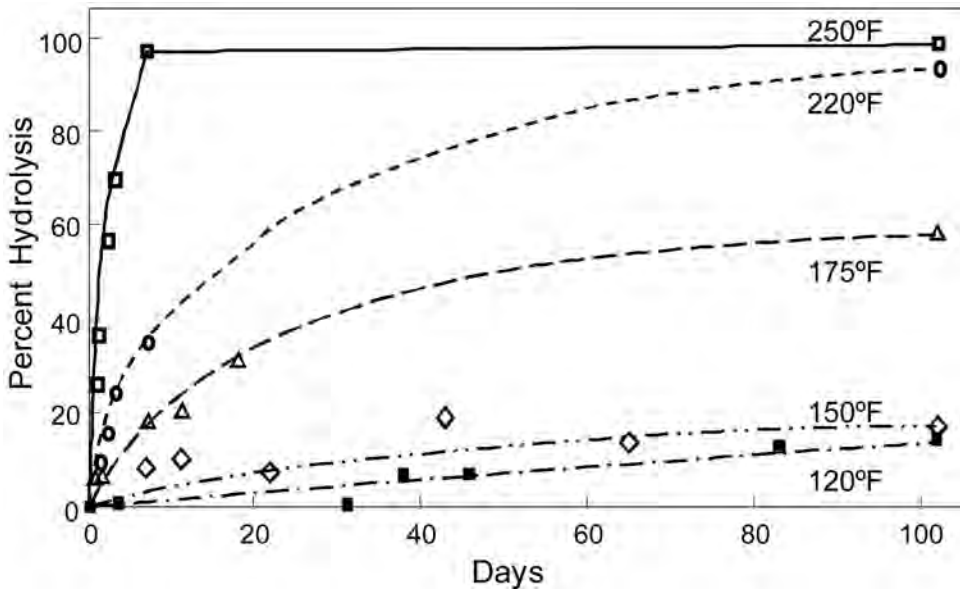


Fig. 13.6—Degree of hydrolysis vs. time at various temperatures for 1,000 ppm unhydrolyzed PAM in 5% salinity.

Hydrolyzed acrylamide groups, or equivalently termed carboxylate groups, can be introduced into polyacrylamide polymers by several means. First, polyacrylamide that is dissolved in aqueous solution can be reacted with caustic material, such as sodium hydroxide, to convert a portion of the polymer's pendant amide groups to carboxylate groups. This form of HPAM is referred to as partially hydrolyzed polyacrylamide. Second, during the polymerization process, acrylamide monomers can be copolymerized with acrylate monomers to form HPAM. This form of HPAM is referred to as being a copolymer of acrylamide and acrylate. All polyacrylamides and all commercially available HPAMs, when heated in aqueous solution, slowly undergo an autohydrolysis reaction in which a portion of the acrylamide polymer's pendant amide groups spontaneously hydrolyzes to carboxylate groups. The final degree of carboxylate content that is attainable within a polyacrylamide molecule increases with temperature, but does not reach 100 mole% carboxylate groups. That is, the acrylamide polymer cannot be converted in aqueous solution at high temperature (under reservoir conditions) to pure polyacrylate by means of the autohydrolysis reaction. The autohydrolysis reaction of acrylamide polymers is both acid and base catalyzed.

In high-temperature reservoirs after polyacrylamides or HPAMs autohydrolyze to sufficiently high levels, hardness ions, such as calcium or magnesium, in the reservoir brine cause the polymer to undergo a phase change, precipitate, and cause the polymer to lose most of its viscosity-enhancing function.^{46,50} This outcome is the major limitation of acrylamide-polymer flooding in high temperature reservoirs. Fig. 13.6 shows the degree of polymer hydrolysis vs. time at various selected temperatures for 1,000 ppm PAM polymer dissolved in a brine of 5% salinity.⁴⁶

Copolymers containing 2-acrylamido-2-methyl-propanesulfonic acid (AMPS) monomers and acrylamide monomers have been suggested to form acrylamide polymers for use in polymer waterflooding of high-temperature (e.g., 200°F) and high-salinity reservoirs where the AMPS copolymer's performance and stability will be somewhat better than comparable HPAM.

Copolymers of vinylpyrrolidone and acrylamide, along with ter-polymers of vinylpyrrolidone, acrylamide, and acrylate, have been reported to be candidate polymers for use in

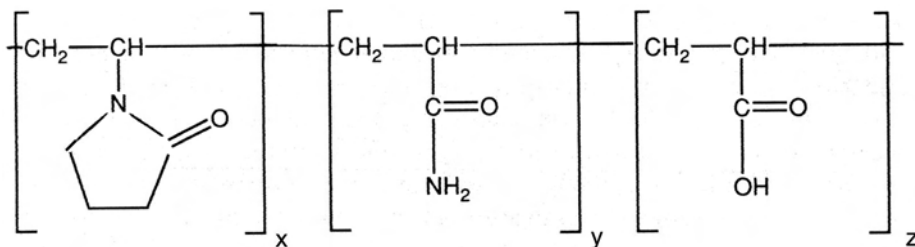


Fig. 13.7—Chemical structure of a ter-polymer poly (vinylpyrrolidone-acrylamide-acrylate) molecule.

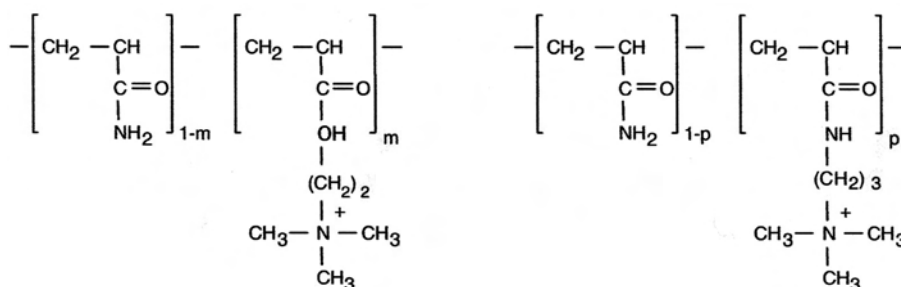


Fig. 13.8—Chemical structure of two cationic acrylamide polymers for possible use in the bridging-adsorption selective placement process for conformance gel treatments.⁵³

polymer floods and conformance polymer-gel treatments that are to be applied to high-temperature reservoirs with harsh environments. Certain vinylpyrrolidone polymers were reported to not precipitate from seawater after aging for six years at 250°F.⁵¹ Potential concerns regarding these co- and ter-polymers of vinylpyrrolidone are their relatively high cost as compared with more conventional acrylamide polymers and the relatively low molecular weight of the commercially available forms of these co and ter polymers.

Fig. 13.7 shows the general chemical structure of ter-polymers of vinylpyrrolidone, acrylamide, and acrylate. The primary beneficial function of the incorporated vinylpyrrolidone monomer into an acrylamide polymer is that it prevents the acrylamide monomer content of the polymer from autohydrolyzing at high temperatures to the excessively high levels of hydrolysis whereby the polymer would become susceptible to precipitating out of solution when the polymer encounters hardness divalent ions.

Cationic polyacrylamides are acrylamide polymers that have positively charged chemical groups attached to at least some of the polymer's pendant amide groups or acrylamide polymers that have been copolymerized with monomers containing positively charged pendant groups. These polymers have an exceptionally strong tendency to adsorb onto reservoir rock surfaces, especially sand and sandstone surfaces.

Cationic acrylamide polymers find specialized applications in conjunction with a variety of conformance-improvement treatments. These applications include use as polymer-anchoring agents to help promote conformance polymer-gel adsorption onto reservoir rock surfaces,⁵² “bridging-adsorption”⁵³ and/or “flow-induced-adsorption”⁵⁴ polymers for injection before a conformance gel treatment to purportedly promote the selective placement of the gel treatment during the bullheaded treatment-placement mode, and polymer for use in certain polymer DPR conformance treatments.⁴² Water-soluble cationic acrylamide polymers come in a wide variety of forms and chemistries. Fig. 13.8 shows the chemical structure of two cationic acrylamide polymers that have been studied for use in the bridging-adsorption phenomenon.⁵³

13.5.2 Benefits of Applying Conformance-Improvement Polymer Technologies. The application of oilfield polymer technologies, in the form of polymer waterflooding and polymer DPR treatments (and as polymer-gel treatments), can promote conformance improvement during oil-recovery-flooding and oil-production operations. They do so by the following means.

- Improve sweep efficiency—The application of polymer waterflooding and polymer DPR treatments promote more effective economic use of injected oil-recovery drive fluids, such as water during waterflooding. DPR treatments can also be used to reduce the amount of injected oil-recovery drive fluid that must be coproduced to yield a given oil-recovery factor.

- Accelerate production—Successful polymer waterflooding and polymer DPR treatments accelerate oil production during a waterflood or other oil-recovery flooding operations by reducing the amount of injected oil-recovery drive fluid that must be coproduced to attain a given level of oil recovery.

- Promotes incremental oil production—Polymer waterflooding and DPR treatments rarely reduce waterflood residual oil saturations. However, they do promote incremental oil recovery by increasing the amount of oil production before reaching the economic WOR limit of a production well, well pattern, or field during a waterflood or other oil-recovery flooding operation.

- Extend economic lives—Polymer waterflooding and DPR treatments can extend the economic lives of production wells, well patterns, and fields by increasing oil cuts as a function time and deferring the time when the economic WOR limit of a well, well pattern, or field is reached.

13.5.3 Polymer Waterflooding. When conducting a polymer waterflood, a high-molecular-weight and viscosity-enhancing polymer is added to the water of the waterflood to decrease the mobility of the flood water and, as a consequence, improve the sweep efficiency of the waterflood. The primary purpose of adding polymer to most polymer waterfloods is to increase the viscosity of the flood water; however, polymer addition to the flood water in many instances also imparts a secondary permeability-reduction component. Polymer waterflooding is normally applied when the waterflood mobility ratio is high or the heterogeneity of the reservoir is high. [Fig. 13.9](#) shows the polymer waterflooding process.⁵⁵

How Polymer Flooding Improves Recovery. Polymer waterflooding promotes improved sweep efficiency by improving the mobility ratio. Improved sweep efficiency imparted during polymer flooding is primarily accomplished by increasing the viscosity of the waterflood drive fluid. Conventional wisdom states that polymer waterflooding does not reduce irreducible oil saturation (residual oil saturation to waterflooding);^{46,55,56} however, at least one paper⁵⁷ has called this contention into question when flooding with selected acrylamide polymers.

Polymer Solutions. The principal beneficial property of polymer solutions for use in flooding oil reservoirs is the aqueous solution's enhanced viscosity. Aqueous polymer solutions that are used for conformance-improvement flooding normally exhibit non-Newtonian viscosity properties.

Viscosity of Polymer Solutions. The viscosity of a polymer solution is a measure of how “thick” a fluid is. For example, molasses is characterized as being “thicker” and more viscous than water. The viscosity of a fluid or solution may, in general terms, be defined as the solution's resistance to being sheared or as the resistance of a fluid mass to change its form.

Fluid viscosity, μ , is defined as

$$\mu = \frac{\tau}{\dot{\gamma}}, \dots\dots\dots (13.7)$$

where τ is shear stress and $\dot{\gamma}$ is shear rate.

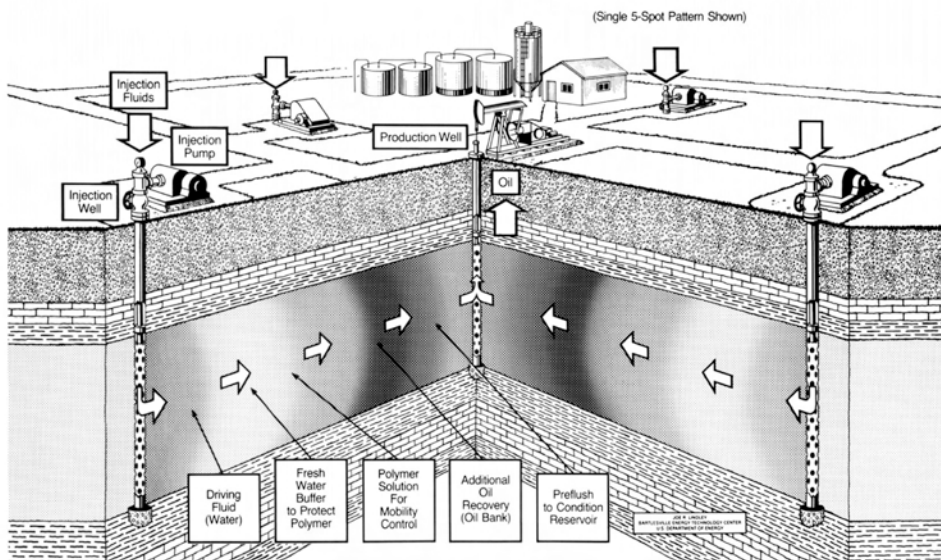


Fig. 13.9—Schematic of the polymer waterflooding process. The method shown requires a preflush to condition the reservoir, the injection of a polymer solution for mobility control to minimize channeling, and a driving fluid (water) to move the polymer solution and resulting oil bank to production wells. Mobility ratio is improved and flow through more permeable channels is reduced, resulting in increased volumetric sweep.⁵⁵

Many common fluids, such as water and motor oils, exhibit Newtonian viscosity. For fluids with Newtonian viscosities, the fluid’s viscosity is independent of the shear rate that the fluid is experiencing. That is, the value of the viscosity of a Newtonian fluid at a given temperature is a single value that is independent of shear rate.

The viscosity-enhancing power of a polymer is related to the size and extension of the polymer molecule in a particular aqueous solution.⁴⁶ For a number of reasons, the viscosity of a polymer solution that is measured in a viscometer and the effective viscosity of the polymer solution that is measured during flow through porous reservoir matrix rock often have different values.

To predict the viscosity-enhancing power of a polymer in a given solution, the polymer’s intrinsic viscosity, $[\eta]$, can be measured by

$$[\eta] = \lim_{c \rightarrow 0} \frac{\eta - \eta_s}{c\eta_s}, \dots\dots\dots (13.8)$$

where c is polymer concentration, η is polymer solution viscosity, and η_s is solvent viscosity. Intrinsic viscosity is obtained by determining the value $\lim_{c \rightarrow 0} (\eta - \eta_s)/c\eta_s$ that is obtained from the plot of $(\eta - \eta_s)/c\eta_s$ vs. polymer concentration and extrapolating the plotted data back to zero polymer concentration. See Chap. 3 of Ref. 46 for more details regarding intrinsic viscosity of polymer solutions. For a given polymer in an aqueous solution, the intrinsic viscosity for the polymer increases with polymer molecular weight (MW) according to the Mark-Houwink equation:

$$[\eta] = K'Mp^a, \dots\dots\dots (13.9)$$

where K' and a are polymer-specific constants, and M_p is the polymer molecular weight. See Chap. 3 of Ref. 46 for more details regarding the Mark-Houwink equation.

The empirical Flory equation⁵⁸ can be used to estimate the mean end-to-end distance of a polymer in solution. The Flory equation is

$$d_p = 8(M_p[\eta])^{1/3}, \dots\dots\dots (13.10)$$

where d_p is in Angstroms (10^{-10} m), and $[\eta]$ is in dl/g.

MW and Size. When all other factors are equal (such as polymer type and the brine solution into which the polymer is dissolved), as the MW of the polymer increases, the size of the polymer increases. As the size of the polymer increases, so does the polymer's viscosity enhancing ability when dissolved in a given brine. On the negative side, as the MW of a polymer increases, the propensity for the polymer to be retained during transport through matrix reservoir rock is increased, and the propensity for the polymer to exhibit injectivity problems is increased.

Because polymers used in polymer waterflooding are polydispersed in MW, polymer MW distribution is an important factor relating to how a given polymer will function during a polymer flood. Unfortunately, good MW distribution data are not readily and widely available for the polymers that are normally used in polymer flooding, because the determination of a polymer's MW distribution is relatively expensive and time consuming.

Fig. 13.10 shows the MW distribution for a typical HPAM polymer sample used in polymer flooding. The high MW tail of the MW distribution is quite significant. The small number of polymer molecules in the polymer's MW distribution have a disproportionately large effect on the viscosity-enhancing power of the polymer; are the polymer molecules that are first and most easily degraded by mechanical shear under intermediate- to high-shear flow conditions; are the polymer molecules that will be first and most easily retained during polymer transport through reservoir matrix rock; and are the polymer molecules that are most prone to causing injectivity damage.

Fig. 13.11 shows a series of MW distributions for a family of HPAM polymer samples. MAR-1 through MAR-9 denote sample numbers 1 through 9. When applied in a relatively high-permeability reservoir in which polymer retention during polymer transport and polymer injectivity are not major issues, polymers with higher molecular weights and narrower MW weight distributions perform relatively more effectively as viscosity-enhancing agents during a polymer waterflood.^{46,59}

For a polymer that is dissolved in a given solvent, polymer MW is proportional to molecular size. For several illustrative polymers used in polymer waterflooding, their molecular size, as related to MW, is as follows. A 30% HPAM polymer of approximately 4×10^6 dalton (atomic mass units) MW dissolved in a good solvent is expected to be fibril in form and to have a diameter of 0.7 to 2.5 μm and a backbone chain length greater than 10 μm .^{46,60} The hydrodynamic length of a xanthan molecule commonly used in polymer flooding has been reported to be approximately 1.5 μm .^{46,61} The MW of such a xanthan molecule is approximately 4×10^6 daltons.

Rheology. The non-Newtonian viscosity of polymer solutions used in polymer waterflooding normally exhibit shear-thinning behavior when subjected to sufficiently high shear rates (but not at low shear rates). The viscosity of a Newtonian fluid does not vary with the shear rate to which the fluid is subjected. For a shear-thinning fluid, the apparent viscosity of the fluid decreases as the fluid experiences increasing shear rates.

Figs. 13.12 and 13.13 show the shear-thinning viscosity behavior of two polymers of the type used in polymer flooding. In **Fig. 13.12**, at low shear rates ($< 0.1 \text{ s}^{-1}$), the viscosity behav-

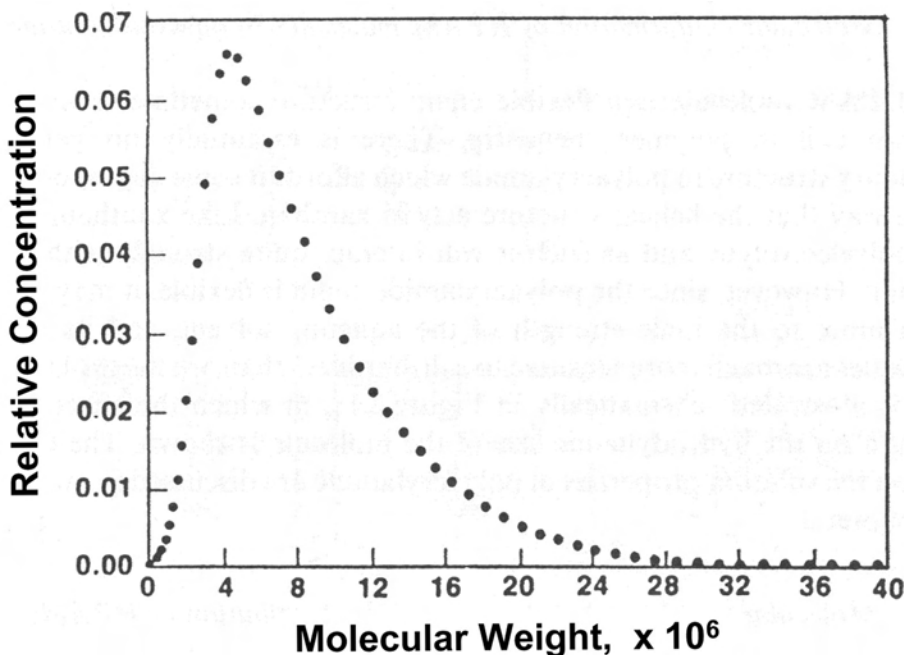


Fig. 13.10—Molecular weight distribution of a typical HPAM polymer used in polymer flooding.

ior of the polymer solutions at all polymer concentrations is invariant with shear rate and, thus, is Newtonian. At shear rates exceeding 1.0 s^{-1} , the viscosity of the polymer solutions decreases with increasing shear rate, thereby exhibiting shear-thinning viscosity behavior. The shear-thinning viscosity behavior of the polymer in Fig. 13.12 becomes relatively less pronounced as the concentration of the polymer in solution decreases. This trend is observed for all polymers that are used in polymer flooding. The shear-thinning viscosity reduction behavior results from the water-soluble high-MW polymers becoming uncoiled and unentangled when they are aligned and elongated in the fluid-flow shear field under sufficiently high shear-rate (~ 1 to 100 s^{-1}) conditions. When the polymers are aligned and unentangled by the shear field in this shear-rate range, the polymers become less effective viscosity enhancing agents. At the low shear rates of Fig. 13.12 ($< 0.1 \text{ s}^{-1}$), the shear field is not strong enough to appreciably uncoil and untangle the polymer molecules. The viscosity is invariant over this shear-rate range, and the viscosity behavior is characterized as being Newtonian over this shear-rate range.

As expected, the apparent viscosity at any given shear rate increases as polymer concentration increases. For the studied AMPS polymer, Fig. 13.13 shows the dramatic and undesirable effect that increasing the salt concentration in the makeup water has on reducing the viscosity of the polymer solution at any given shear rate. Similar detrimental effects of increasing salt concentration are observed in polymer solutions of high-MW HPAM.⁵⁵ Note also the trend, which is quite generalized, that as the salt concentration of the polymer solution increases, the degree of shear thinning of the polymer solution decreases.

The shear-thinning viscosity behavior of these polymer solutions is favorable because the shear rate experienced by the polymer in the vast majority of the reservoir is usually quite low (approximately 1 to 5 s^{-1}) and is a shear rate at which the polymer exhibits near maximum viscosity.⁵⁵ In the near-wellbore region, shear rates are often in the shear-thinning range for the polymer (e.g., 1 to 100 s^{-1}). This polymer shear thinning is fortuitous because the viscosity reduction improves the injectivity of the polymer solution.

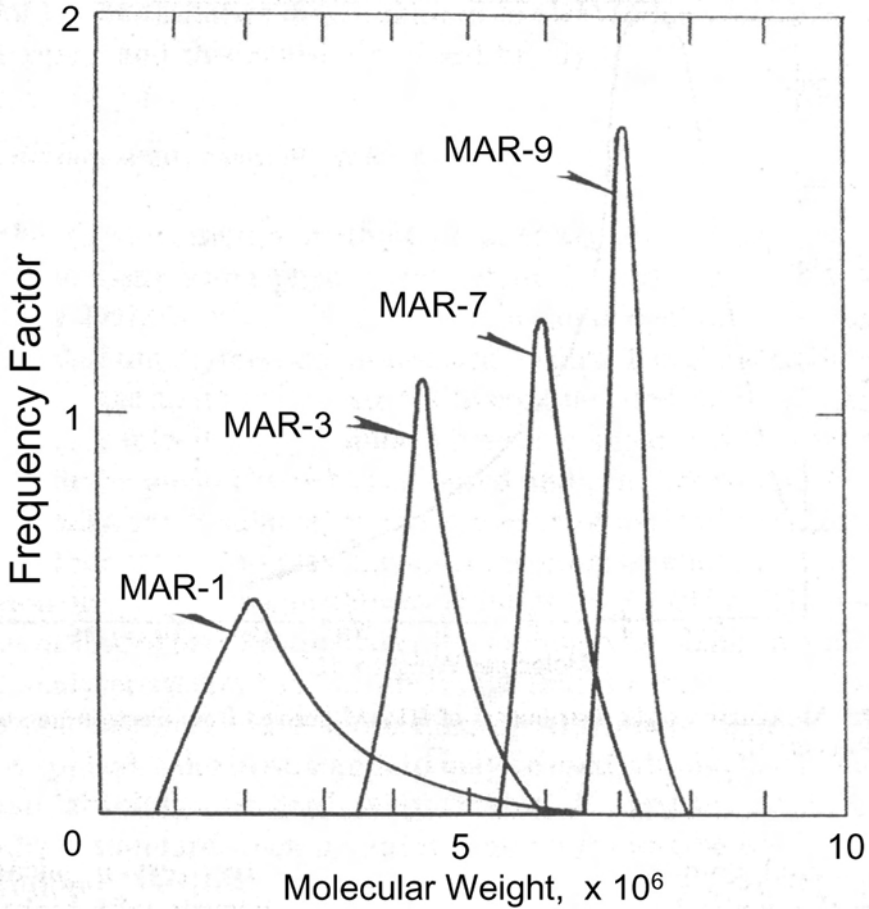


Fig. 13.11—Molecular weight distribution of a series of HPAM polymer samples.

The mathematical equation that describes the viscosity vs. shear-rate behavior (of the type of Figs. 13.12 and 13.13) for oilfield polymer solutions over the shear-rate range of approximately 1 to 100 s⁻¹ is the power-law model that takes the form of

$$\eta = K(\dot{\gamma})^{n-1}, \dots\dots\dots (13.11)$$

where *K* and *n* are, respectively, the power-law coefficient and exponent, and $\dot{\gamma}$ is shear rate. For polymer-flood fluids that are shear thinning, the value of the power-law coefficient, *n*, ranges between 0 and 1 and equals 1 for these fluids when they are Newtonian. The viscosity behavior of a polymer solution becomes more shear thinning as the value of the power-law exponent, *n*, decreases. The numerical value of the viscosity and the power-law constant, *K*, become equal when the value of the shear rate, $\dot{\gamma}$, equals 1.

As it relates to polymer solutions of polymer flooding, the power-law viscosity model is only applicable over a limited range of shear rates. For a description of other analytical mathematical expressions for describing polymer-solution viscosity vs. shear rate, especially expressions covering a wider range of shear rates, and for discussions on the viscoelastic properties and the extensional and elongational flow properties of high-MW polymer solutions, see Chap.

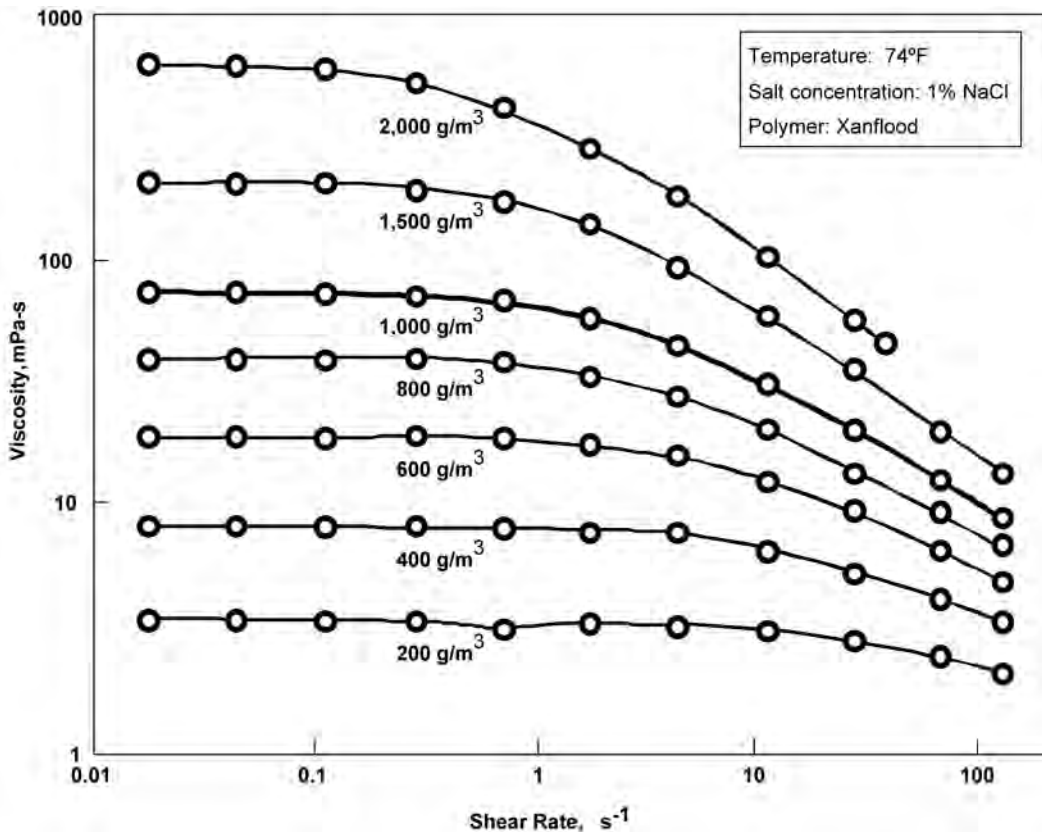


Fig. 13.12—Polymer solution viscosity vs. shear rate as a function of xanthan polymer concentration.

3 in Ref. 46. Extensional viscosity, which occurs under very high shear-rate conditions, can lead to pronounced increases in the apparent viscosity of polymer solutions and often leads to mechanical shear degradation of high-MW water-soluble polymers. The only location in a reservoir that a polymer solution is likely to experience extensional-viscosity conditions of any consequence is near wellbore to an injection or production well.

“Apparent viscosity” or “effective viscosity” refers to the viscosity of a polymer solution for which the viscosity is determined during flow of the polymer solution through porous media. This is discussed further later in this section.

Measuring Viscosity. When measuring the viscosity of polymer solutions to be used in polymer waterflooding, the use of standard laboratory steady-shear viscometers is often quite satisfactory. In addition to the use of conventional viscometers, the screen factor (SF) device has been used extensively to measure viscosity properties of polymer solutions that are used in polymer flooding. Fig 13.14 shows the SF device. The SF “viscometer” consists of a small fluid reservoir in the glass unit that is in fluid communication above several wire-mesh screens, often three to five 100-mesh stainless-steel screens. A fluid sample of fixed volume is placed in the fluid reservoir, and the time is recorded for the fixed volume of fluid to flow through the screens under the influence of gravity. The SF value for a given polymer is the time it takes the fixed volume of polymer solution to flow through the screen viscometer divided by the time it takes the fixed volume of the solvent brine to flow through the screen viscometer. The SF value of a polymer solution is quite sensitive to the nature of the high-MW tail of the polymer’s MW distribution. Some practitioners suggest that the SF value better correlates with

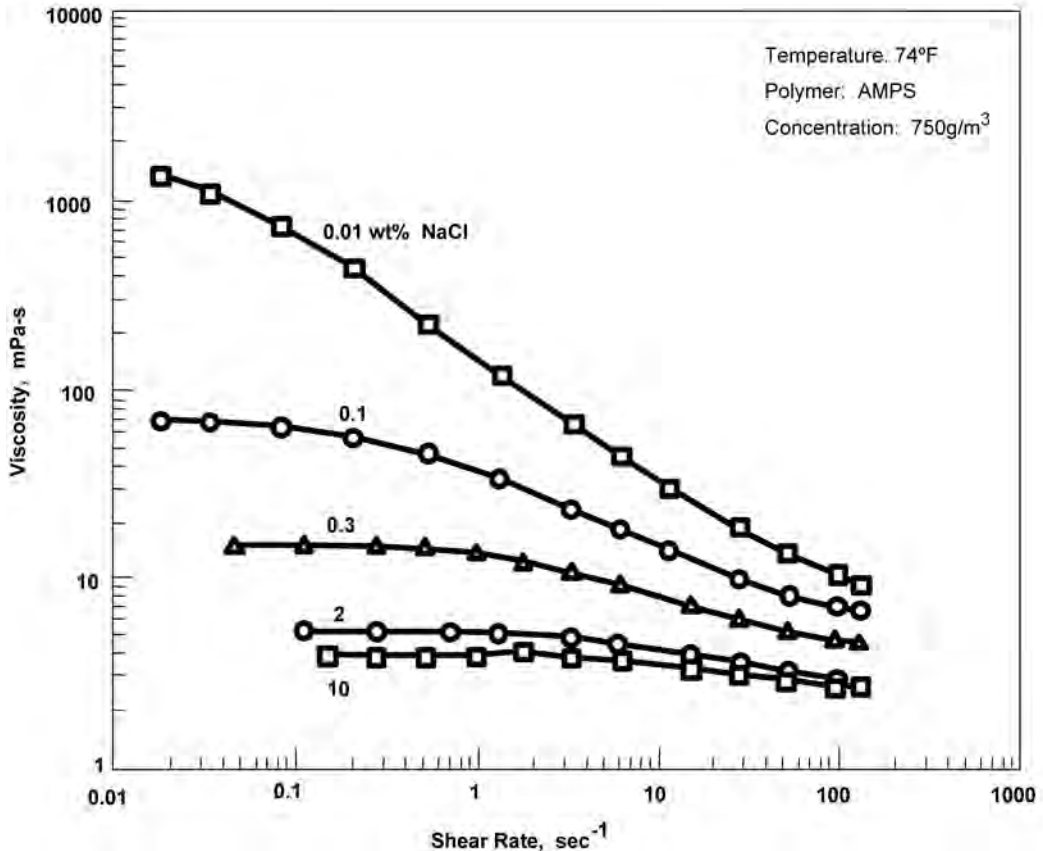


Fig. 13.13—Polymer solution viscosity vs. salinity as a function of AMPS polymer concentration.

mobility and permeability reduction exhibited by the polymer solution as it is propagated through matrix reservoir rock. However, this contention is not universally agreed on. The SF measurement is a simple, straightforward, and useful qualitative viscosity characterization of polymer solutions for use in polymer flooding.^{46,51}

Effects of Salt, Hardness, and pH. The effects of salt and hardness on polymer-flood biopolymers are of relatively small consequence at lower temperatures (< 170°F), as compared with the effects on HPAMs polymers that are used in polymer flooding at the same reservoir temperature. Salt insensitivity is one of the attractive features of polymer-flood biopolymers such as xanthan. Likewise, pH within the range likely to be encountered in low-temperature (< 140°F) oil reservoirs is of relatively small consequence to the viscosity and mobility-control properties of xanthan polymer.

The effect of salt and hardness on the viscosity and mobility-control function of polymer-flood HPAM, and similar and related synthetic polymers, is quite significant and can be very deleterious. Cations of dissolved salts reduce the electrostatic repulsion of the negatively charged hydrolyzed carboxylate pendant groups on the polymer backbone of HPAM. Cations do this by screening and collapsing the local negatively charged double layer formed around the carboxylate species. The degree of collapse of the negatively charged electrostatic fields surrounding the polymer's carboxylate groups increases with increasing salt concentrations; and at constant salt concentration, with increasing charge of the cations of the salt. As the electrostatic fields surrounding the polymer's carboxylate groups collapse, the electrostatic repulsive

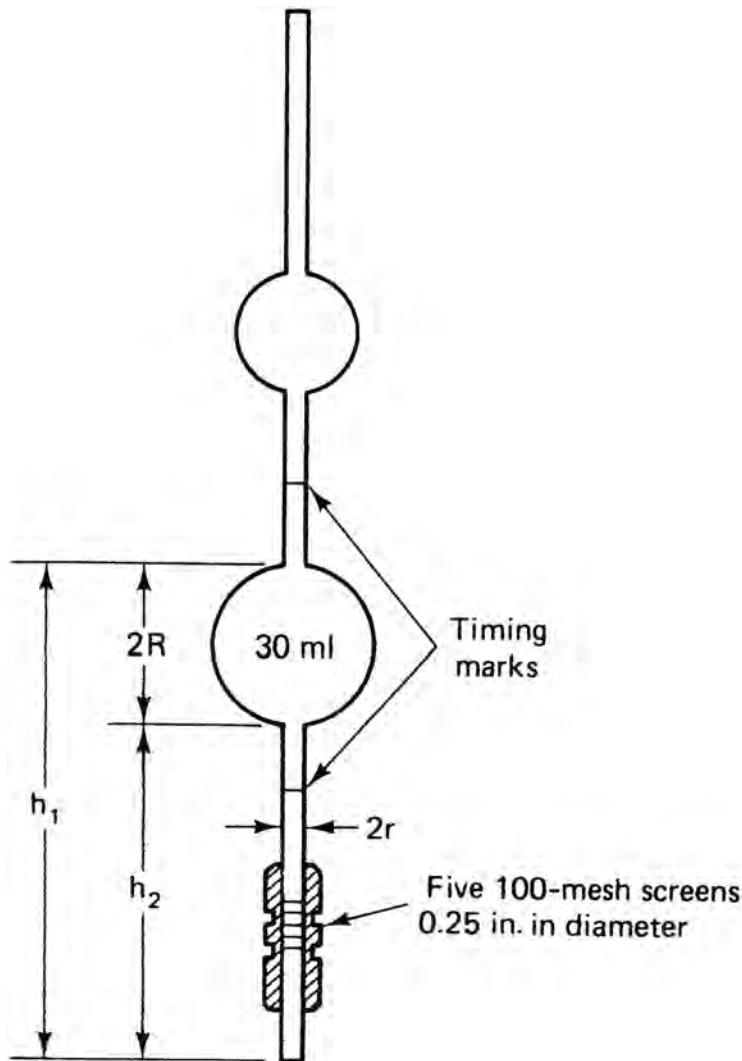


Fig. 13.14—Screen factor device.

forces that promote polymer backbone-chain distension decrease. As Fig. 13.13 shows, this leads to substantial reduction in polymer-solution viscosity. As a rule of thumb, the polymer-solution viscosity decreases by a factor of 10 for every factor of 10 increase in NaCl concentration.⁵⁵ The negative impact of divalent hardness ions, such as Ca^{++} and Mg^{++} , are much more deleterious at the same concentration than monovalent ions, such as Na^+ and K^+ .

As the concentration hardness cations, such as Ca^{++} , in the brine of a HPAM solution increases, the polymer becomes relatively more sensitive to mechanical shear degradation. The effect of pH on the viscosity of ionic HPAM can be significant. Decreasing the solution pH tends to convert the ionic salt form of the polymer's carboxylate groups to the relatively non-ionic carboxylic acid form of carboxylate groups. This diminishes the electrostatic repulsion of the ionic carboxylate groups along the polymer's backbone and leads to less distention of the polymer molecule and to less viscosity-enhancing power for the polymer in a low pH solution. For a studied hydrolyzed-polyacrylamide polymer solution, its viscosity decreased by a factor of approximately four when the pH of the polymer solution was decreased from 9.8 to 4.⁴⁶

Flow in Porous Media. Polymer solutions used in waterfloods must be able to be transported successfully and effectively through the reservoir. Thus, the manner in which polymer solution flows through porous rock and the associated polymer interaction with the pore walls of matrix reservoir rock are important aspects regarding the attainment of the technical and economic success of a polymer flood.

Polymer Transport. Polymer retention during flow through reservoir matrix rock is discussed in an upcoming subsection. Polymer retention by adsorption and entrapment retards the rate of polymer propagation.

Inaccessible and Excluded Pore Volume. Accelerating the rate of polymer propagation, as compared with the rate of an inert chemical tracer dissolved in the injected polymer solution, is the inaccessible pore volume (IPV) phenomenon. Two explanations for, and contributions to, the IPV phenomenon have been reported. The first IPV explanation is that the large size of the polymer molecules prevents entry into smaller and dead-end pores. This promotes propagation of the polymer molecules faster than an inert chemical tracer because the polymer flows only through the larger-pore flow paths.

The second IPV explanation is the wall-exclusion effect. It is hypothesized that polymer molecules flow and concentrate in the center of the pore-level flow channels of matrix reservoir rock because the polymer molecule flow and the free tumbling of the polymer molecules are excluded from the near-surface volume of the pore walls. Such flow behavior accelerates the rate of polymer propagation through the porous media relative to the rate of propagation of an inert chemical tracer.^{46,55,62}

Mobility Reduction. When polymer in solution flows through reservoir matrix rock, it imposes a mobility reduction that is the primary conformance-improvement benefit of polymer waterflooding. The mobility reduction can be imparted by one of two distinctly different mechanisms. First, the polymer can cause an increase in the viscosity of the brine being flooded through the porous media. This is normally the desired effect when flooding with polymer solutions for mobility control. The second mechanism reduces the permeability of the reservoir matrix rock. One measure of mobility reduction imparted by polymer-solution flow is the resistance factor, R_f , which is defined as

$$R_f = \frac{\lambda_w}{\lambda_p}, \dots\dots\dots (13.12)$$

where λ_w is the mobility of the solvent of the polymer solution, and λ_p is the mobility of the polymer solution. When the polymer solution imparts no permeability reduction and for measurements made at ambient temperature,

$$R_f = \mu_{\text{eff}}, \dots\dots\dots (13.13)$$

where μ_{eff} is the effective viscosity of the polymer solution as it flows through the reservoir matrix rock. Alternatively, for a single-phase polymer solution flowing through matrix reservoir rock at a given temperature and there is no imparted permeability reduction,

$$R_f = \frac{\mu_{\text{eff}}}{\mu_w}, \dots\dots\dots (13.14)$$

where μ_w is the viscosity of the brine in which the polymer is dissolved.

Permeability Reduction. Polymer flow through reservoir matrix rock can cause permeability reduction. A measure of the polymer-induced permeability reduction is the residual resistance factor, R_{rf} :

$$R_{rf} = \frac{k_b}{k_a}, \dots\dots\dots (13.15)$$

where k_b is brine permeability measured before polymer flooding, and k_a is brine permeability measured after polymer flooding.

Permeability reduction induced by polymers tends to be greater in lower permeability reservoir rock. This is, in general, counterproductive. Polymers, especially HPAMs, that undergo even a small amount of mechanical shear degradation often lose much of their permeability reduction propensity because the relatively small number of exceptionally large molecules of a given polymer MW distribution (especially for many HPAMs) are the first polymer molecules to be shear degraded. These large molecules contribute disproportionately to permeability reduction.

Extensional Flow. As mentioned in the discussion on rheology, when flexible, coiled, high-MW polymers, such as HPAM, are forced to flow through matrix reservoir rock at exceptionally high rates and experience exceptionally high-flow shear fields, the polymer can enter extensional and elongational flow at which point the polymer solution's apparent viscosity can rise rapidly. In this flow regime, the polymer is also often mechanically shear degraded. Solutions of well-designed polymer floods are likely to experience extensional flow of noticeable consequence only in certain instances in the very near-wellbore region adjacent to the injection or production well.

Polymer Retention. Polymer retention will often profoundly affect the technical and economic success of a polymer-flooding project. The amount of oil that will be recovered per pound of polymer injected is inversely related to polymer retention.

Retention for a given polymer during a polymer flood increases as the permeability decreases, increases as the polymer molecular weight increases, increases as the clay content in the reservoir rock increases, usually decreases as oil wetness increases, tends to increase in sand and sandstone reservoirs with decreasing anionic charge and increasing cationic charge of the polymer's pendant groups, and has been reported to increase at times in the presence of crude oil.

Polymer retention should be determined carefully, or at least estimated carefully, before initiating a polymer waterflood. Polymer retention for a given polymer flood is normally best estimated by conducting flooding experiments in reservoir rock with reservoir fluids at reservoir temperature.

"Field-measured values of retention range from 7 to 150 μg of polymer per cm^3 of bulk volume, with a desirable retention level being less than approximately 20 $\mu\text{g}/\text{cm}^3$."⁴⁶ Laboratory measurements of polymer retention in reservoir rock are usually reported as mass of polymer adsorbed per unit mass of rock, Γ , and is usually reported as $\mu\text{g}/\text{g}$ of polymer adsorbed onto reservoir rock. Frequently, it is preferred to have polymer retention reported in terms of mass of polymer adsorbed per unit volume of reservoir rock, Γ_v , or, more specifically, in terms of pounds of polymer adsorbed per acre-foot of reservoir, $\text{lbm}/\text{acre-ft}$. To convert from Γ to Γ_v ,

$$\Gamma_v = 2.7194\Gamma(1 - \phi)\rho_{RG}, \dots\dots\dots (13.16)$$

where ϕ is porosity, ρ_{RG} is the density of the reservoir rock grains (no pore space included), Γ_v is in units of lbm/acre-ft, and Γ is in units of $\mu\text{g/g}$.⁴⁶ Polymer retention, as measured during field projects, has been reported to range from 20 to 400 lbm polymer/acre-ft bulk volume, with desirable retention reported to be less than 50 lbm/acre-ft.⁶³

Adsorption. Polymer adsorption results primarily from physical adsorption and not chemisorption.⁴⁶ Polymer adsorption is often the major cause of polymer retention.⁴⁶

Mechanical Entrapment. Mechanical entrapment of polymer during propagation through reservoir porous media results from the larger polymer molecules becoming lodged in narrow flow channels (e.g., pore throats). Gogarty found that the HPAM polymers, under the conditions of his flooding experiment studies, had an effective size between 0.4 and 2 μm .⁶⁴ There are several significant consequences of mechanical entrapment:⁴⁶ permeability reduction, loss of the entrapped polymer's favorable viscosity enhancing functionality beyond the point of entrapment, loss of the largest of the polymer molecules first has a disproportionately large negative impact during the remainder of the polymer flood on viscosity and mobility-control properties, and loss of a disproportionately large portion of its viscosity and mobility control functionality relatively soon after the polymer solution is injected into a reservoir.

Hydrodynamic Retention. Hydrodynamic retention is the least understood and least well defined retention mechanism.⁴⁶ Polymer retention can increase as the flow rate of the polymer solution through reservoir matrix rock increases.⁴⁶ Hydrodynamic retention is thought to normally be a relatively small contributor to the total polymer retention during a polymer flood.⁴⁶ This retention mechanism is more significant in lower permeability reservoir rock. Hydrodynamic retention is thought to result from polymer molecules becoming temporarily trapped in stagnant flow regimes by hydrodynamic drag forces.⁴⁶

Precipitation. Polymer precipitation from solution, especially in the presence of high reservoir brine salinity, is another source of polymer retention. Precipitation is especially problematic when flooding with HPAM in high-temperature reservoirs with formation waters containing hardness divalent cations.

Polymer Degradation. A decrease in the average molecular weight of the polymer can be caused by chemical, biological, mechanical, or thermal degradation.^{46,55} Polymer stability, the inverse of degradation, should be evaluated and quantified under reservoir conditions in terms of a time span relevant to the lifetime of the polymer flood in question.

Chemical. Chemical free-radical species will degrade both biopolymers and synthetic polymers of polymer flooding. Free radicals cause chemical backbone scission of the polymer. Examples of free-radical sources that can be problematic for flooding and conformance-treatment polymers are free oxygen (O_2), hydrogen peroxide, sodium hypochlorite or bleach, and gel breakers such as ammonium peroxide. The combination of free oxygen and ferric ions is particularly problematic in causing oxygen free-radical degradation of polymer-flood polymers, especially of acrylamide polymers. Another source of polymer-degrading free radicals is free-radical or free-radical-precursor impurities within the polymer that are induced, in this case, during the manufacturing process. Polymer-degradation problems, caused by low levels of free radicals, are most problematic when conducting high-temperature ($> 150^\circ\text{F}$) polymer-flooding experiments, especially during the high-temperature laboratory evaluation of polymers for high-temperature flooding. A countervailing phenomenon relating to free-radical chemical degradation is that oil reservoirs tend to quite rapidly neutralize and consume chemical free-radical species.

Two procedures are recommended for removing free oxygen from polymer-solution samples to be used during laboratory evaluation of polymer solutions for high-temperature applications. The first procedure uses a glass ampoule, which is glass-blown sealed after oxygen removal, and high-quality vacuum to reduce oxygen content to < 10 ppb. The second procedure consists of bubbling high-purity argon gas through the polymer solution. The need to

deoxygenate polymer-solution samples in the laboratory during high-temperature testing is an aboveground laboratory artifact because polymer solutions that exist in most reservoirs are in an anaerobic and chemically reducing environment.

Hydrolysis reactions are important degradation reactions for both biopolymers and synthetic polymers; however, the hydrolysis reaction degrades the polymers in a much different manner for each of these two polymer types. Both acid- and base-catalyzed hydrolysis of the carbon-oxygen-carbon bonds of the backbone monomer chemical linkages of polysaccharide biopolymers cause polymer backbone scission and serious polymer MW degradation. The pH sensitivity of a biopolymer being used in a polymer flood needs to be considered. Serious polymer hydrolysis questions are raised if an acid-stimulation treatment contacts a previously placed conformance-improvement biopolymer gel treatment.

Hydrolysis (autohydrolysis) reactions of the amide pendant groups of the acrylamide polymers are of significant concern when such polymer is being flooded through a high-temperature reservoir that contains a significant concentration of hardness divalent ions in the formation water. If an acrylamide polymer, which is dissolved in a hardness-containing brine, autohydrolyzes to excessively high levels at high temperatures, the acrylamide polymer will undergo a phase change to an undissolved solid state that causes the polymer to precipitate. When this happens, the polymer loses its viscosity-enhancing properties. Technically, this type of acrylamide-polymer autohydrolysis is not polymer degradation, but simply leads to a phase change of the polymer from being dissolved in solution to being an undissolved solid specie.

Biological. Biological degradation is a serious potential problem for biopolymers, especially for use in shallow reservoirs and for the biopolymer as it resides in surface tanks and tubulars. For a properly designed acrylamide-polymer flood that uses solid polymer as the polymer source, potential biological degradation is essentially not an issue.

Mechanical. The form of mechanical degradation that is of most concern for polymers of polymer waterflooding is shear degradation. All dissolved polymers mechanically degrade if subjected to a sufficiently high-flow shear rate. During polymer flooding, deleteriously high-flow shear rates can exist in surface-injection equipment (valves, orifices, pumps, and tubing), at downhole constrictions (tubing orifices, perforations, or screens), and at the formation face of the injection well.

Xanthan biopolymer is usually not mechanically shear degraded under polymer-flood injection conditions. Under most radial-flow injection conditions, high-MW acrylamide polymers are quite susceptible to mechanical shear degradation. This is especially true if the flooding brine is high in hardness and salinity. When a water-soluble polymer encounters a sufficiently high-velocity flow field, both shear and elongational stress destroy the polymer solution's viscosity.⁵⁵ Maeker⁶⁵ and Seright⁶⁶ correlated permanent viscosity loss of a polymer solution to the product of the elongational stretch rate multiplied by the stretch length. The higher the MW of a given polymer, the more sensitive it is to mechanical shear degradation.

Thermal. All waterflooding polymers have an upper temperature limit above which they are no longer chemically stable, both with and without the addition of an appropriate thermal stabilizer package. This upper temperature limit varies with water chemistries of the polymer-dissolution and reservoir brines, polymer chemistry, manufacturer, and polymer lots from a given manufacturer. For the most part, the upper limit of thermal stability is fixed for a waterflood polymer obtained from a given manufacturer. It must be determined if the polymer to be used is thermally stable under reservoir conditions at the reservoir temperature of the polymer flood and that it will be sufficiently stable for the life of the polymer flood.

Stabilizers. Although once popular, the addition of chemical, biological, and thermal stabilizers to polymer-waterflooding solutions has lost a lot of its original attractiveness because of toxicity, environmental concern, effectiveness, and cost issues. A stabilizer that historically has been used widely as both a biological and thermal stabilizer for polymer-flood polymers is

formaldehyde. Formaldehyde is now considered highly toxic and is highly regulated. Also, a number of the stabilizers used to protect against free-radical degradation can become, in themselves, polymer-degrading free radicals at high temperatures. In addition, early practitioners of chemical stabilizers did not fully appreciate chemical loss and chromatographic separations issues. If a chemical stabilizer is to be considered, it is prudent to proceed cautiously.

Polymer Injectivity. Polymer-solution injectivity is an important consideration for several reasons. First, the rate at which the polymer solution can be injected directly impacts the economics of a polymer-flood project. Second, routine injection-well cleanup jobs may be required if polymer or polymer-microgel damages injectivity. These cleanup jobs can detract from the polymer flood's economics and effectiveness. Injectivity decreases as polymer MW increases. Polymer-solution injectivity is more favorable when the polymer solution exhibits shear-thinning viscosity behavior.

13.5.4 When and Where Applicable. The following screening guidelines can be used to determine where polymer waterflooding is most applicable, in terms of reservoir properties.^{46,67}

- Oil viscosity < 150 cp (preferably < 100 and > 10 cp) and API gravity > 15.
- Matrix-rock permeability > 10 md, with no maximum.
- Reservoir temperature: low temperatures are best (best at < 176°F; maximum of approximately 210°F).
- Water injectivity should be good with some spare capacity (hydraulic fracturing of injection wells may help).
- Reservoir clay content should be low.
- Low salinity of the injection and reservoir brines are preferable.

Polymer waterflooding has been conducted successfully in sandstone and carbonate matrix-rock reservoirs, fractured reservoirs, and in water-wet, mixed-wetting, and oil-wet reservoirs. For example, see [Ref. 68](#).

13.5.5 Field Implementation. The following subsections focus on the field implementation of a polymer waterflood.

Flood Design. Working up a flood design is one of the first steps when implementing a polymer-waterflooding project.

Selecting a Polymer. When selecting a polymer for a polymer-waterflooding project, one should try to maximize, as best as possible, all the following polymer attributes. The polymer should⁵⁵

- maximize the amount of viscosity enhancement and/or mobility reduction per unit cost.
- readily dissolve.
- propagate well and have low retention as transported through the reservoir.
- exhibit good shear stability.
- possess good chemical stability.
- have good biological stability.
- be thermally stable at reservoir temperature.
- possess acceptable injectivity properties.

Polymer Concentration. The optimum concentration of the polymer to be injected is a critical parameter in the design of an effective polymer-waterflooding project. The concentration of the injected polymer profoundly affects the cost, economics, and performance of a polymer-flooding project. The optimum concentration is a function of reservoir properties, the nature of the reservoir's conformance problems, and the business objective of the polymer flood. Business objectives of a polymer flood can include maximizing oil recovery, maximizing the rate of return on the cost of the polymer-flooding project, and minimizing the cost of the polymer flood.

Ref. 69 provides a literature review of 12 international polymer-flooding projects conducted between 1975 and 1992. The projects included both pilot and fieldwide projects. Ten of the polymer-flooding projects involved the use of acrylamide polymers, and two projects involved the use of xanthan polymers. All the flooding projects were conducted in reservoirs with temperatures less than 140°F. For the 12 international polymer-flooding projects, the median incremental oil recovery, as calculated from data in the paper, was 13% original oil in place (OOIP), and the range of incremental oil recoveries was reported to be 6 to 52% OOIP. The average pore volume (PV) of the polymer slug injected was calculated to be 51%, with the range of PVs being 21 to 100%.

These flooding parameter values are noteworthy when viewed in terms of comparable values reported in the paper, or calculated from data presented in the paper, for 128 polymer floods performed in the U.S. between 1980 and 1993. The median incremental oil production for the U.S. polymer floods was 4.9% OOIP. The average concentration of polymer injected in the U.S. projects was 460 ppm vs. 920 ppm for the international polymer floods. Ref. 69 states that it appears the amount of incremental oil production for the 12 international projects best correlates with the numerical value that is obtained from multiplying the PV of the polymer slug injected by the average concentration of the polymer injected during the polymer-flooding project.

On the basis of the 12 international polymer-flooding projects, 900-ppm polymer concentration in the polymer slug would be a good starting value in designing a polymer-waterflooding project. Working from this initial concentration, it should be determined, using appropriate engineering and evaluation tools, whether the optimum polymer concentration for the proposed polymer flood is actually higher or lower.

Sizing Volume Injected. At this writing, optimum sizing of the polymer-solution slug to be injected was one of the most controversial aspects of designing a polymer-waterflooding project. This design parameter profoundly affects the cost, economics, and performance of a polymer-flooding project. Underdesigning the size of the polymer slug injected has been thought to be a major cause for the disappointing performance of many polymer floods conducted in the U.S. Using the general arguments made in previous subsections, the optimum size of the polymer-solution slug during polymer flooding is a function of reservoir properties, nature of the reservoirs conformance problems, and the business objective of the polymer flood. Business objectives of a polymer flood can include maximizing oil recovery, maximizing the rate of return on the cost of the polymer-flooding project, or minimizing the cost of the polymer flood.

On the basis of 12 international polymer-flooding projects, a 50% PV slug of polymer solution would be a good starting value to use in designing a polymer-waterflooding project.⁶⁹ Working from this initial polymer-solution slug size, it should be determined, using appropriate engineering and evaluation tools, whether the optimum polymer-solution slug size for the proposed polymer flood is actually higher or lower. When attempting to design the optimum size of the polymer-solution slug, two important parameters that need to be accounted for are polymer retention and the rate and nature of the viscous fingering of the polymer-slug chase drive water into the polymer-solution slug.

Grading of Polymer Concentration. To overcome, or substantially reduce, the problem of viscous fingering of the polymer-slug chase drive water into the polymer slug, most polymer floods are designed with a tapered, decreasing-polymer-concentration chase slug beginning at or near the end of the design volume of the primary polymer-solution slug.

Timing. There is general agreement that, when all other factors are held constant, the earlier in the life of a waterflood that a polymer flood is initiated, the relatively more effective the polymer flood will be. Two factors offset the benefits of an early start. First, it is more difficult to definitively assess the oil-recovery potential and economic effectiveness of a polymer

flood until definitive waterflood performance has been established. Second, reservoir description and associated reservoir conformance problems are often less well defined, especially in a new reservoir.

Suggested Steps for Designing a Polymer Flood. Lake⁵⁵ and Sorbie⁴⁶ suggest that the design and planning procedure for a polymer waterflood should entail the following elements.

- Screen the candidate reservoirs for both the technical and economic feasibility of performing a successful polymer waterflooding project.
- If appropriate and needed, improve the reservoir description.
- Select the polymer that should be used in the flooding project.
- When and where cost-effective, conduct laboratory studies under reservoir conditions to perform screening and compatibility tests on the polymer and polymer-solution core-flooding tests to determine polymer-solution flow properties and to estimate incremental oil recovery (on the scale of the core size used).
- Estimate the amount of polymer that will be required for the polymer flood.
- Design the polymer-injection facilities.
- When and where cost-effective, conduct a polymer-injectivity test and a field polymer-flood pilot test.
- If feasible and cost-effective, conduct reservoir simulation studies.
- Optimize the reservoir, operational, and economic performance of the polymer waterflooding project, such as optimizing well and pattern spacing, completion strategies, and injection rates.

One of the primary causes of failure for polymer-flood projects is that the reservoir description used was inaccurate.⁴⁶

Polymer Injection. The polymer-injection facilities and the actual injection of the polymer solution are important aspects of a successful polymer-waterflooding operation.

Polymer Degradation. If the polymer is allowed to become mechanically shear degraded during surface mixing and pumping operations or during injection into the reservoir, the polymer will have lost a substantial amount, if not most, of its viscosity-enhancing and mobility-reducing power before leaving the injection-well near-wellbore region. The higher the rate that a polymer solution is injected across a unit area of injection surface, the greater the propensity for mechanical shear degradation of the polymer. It is most often the goal to inject the polymer solution as rapidly as possible without exceeding reservoir parting pressure. The strategy usually implemented is to use injection equipment and well completions that permit desired injection rates without substantial mechanical degradation.

To minimize mechanical shear degradation, the operator needs to use specialized pumping equipment, be sure that the polymer solution is not passed through any valves or orifices that cause high and damaging shear fields, and use special mixing and dilution equipment, such as the use of static mixers, to not shear degrade the polymer during mixing and dilution operations.

Well Completion. Injection wells of polymer floods are often openhole or gravel-packed completions. Hydraulically fracturing the injection well with short, wide fractures has been reported to have been used successfully to aid in injecting HPAM without excessive shear degradation.⁶⁸ The injection of polymer solutions through mandril completions, with associated flow of the polymer solution through mandril orifices, has proved to be detrimental in several instances.

Polymer Dissolution. Historically, the polymer, as supplied to (or near) the final wellsite, must be dissolved and/or diluted to some degree. The polymer dissolution or dilution process needs to be implemented so that the polymer is fully dissolved, at the proper concentration before injection into the reservoir, and dissolved or diluted in a manner that does not mechanically shear degrade the polymer. The dissolution or dilution process can range from a fairly simple process for broths of xanthan polymer to a quite difficult and technically challenging

process for ultra-high-MW solid HPAM. A long dissolution time is an economic deterrent for a polymer flood, because it requires extra equipment and extra polymer-solution holding tanks.

Polymer Filtration. The polymer solution normally should be filtered before injection to ensure that it is readily injectable and does not unduly damage injectivity. This is a particularly critical and challenging issue when injecting biopolymer solutions, such as xanthan solutions, that are notorious for containing substantial amounts of cell debris from the polymer's fermentation process and cell debris that are difficult to remove fully with filters.

HPAM polymer, when obtained in the solid form and then dissolved in the field, should normally be filtered to remove microgels or undissolved "fisheyes." The amount of microgel and fisheye material in a given hydrolyzed acrylamide polymer varies from manufacturer to manufacturer and even with manufacturing lots from the same polymer manufacturer. These microgels and fisheyes of partially hydrated solid HPAM in solution often largely result from the final drying process in the manufacturing of the polymer, in which overheating, overdrying, and other factors cause some of the polymer molecules to crosslink together chemically during the drying process.

Parting Pressure. Downhole injection pressure should normally be kept below formation fracturing and parting pressures. If injection-well fracturing is required to obtain adequate polymer solution injectivity or to eliminate mechanical shear degradation, the injection wells are normally appropriately hydraulically fractured during a separate hydraulic fracturing operation.

Pilot Testing. It is recommended that a pilot test of a polymer-waterflooding design be implemented in one or several injection wells before a polymer-waterflooding project is implemented field wide and/or before implementing an expensive polymer-flood project. The primary objective of a pilot test is to assure that there will be adequate injectivity and that there will be no substantial injectivity issues. The polymer-solution injectivity trial can be as short as several days. Proper interpretation of a single-well polymer injectivity test can be difficult. If time and economics permit, a secondary objective of the pilot test is to demonstrate that the polymer flood will perform in the reservoir as expected in terms of mobilizing and recovering incremental oil. If it proves to be cost-effective, observation wells can be drilled near the injection well to observe, in a relatively short time frame, how the polymer flood can be expected to perform in the reservoir.

Issues Regarding Manufacturing of Polymers. Polymers used in polymer waterflooding can be manufactured and provided to the end user in one of four forms. First, polymers in solid particle form, the oldest form, are readily transported and stored. Polymers supplied in solid particles are a challenge to dissolve properly and fully. In addition, the polymer of solid particle polymers can be damaged in the drying process during polymer manufacturing, may contain undesirable chemicals that coat the polymer particles, and often contain undissolvable microgels that are not injectable into matrix reservoir rock and that damage the injectivity of the polymer-solution injection wells. The second form, concentrated (~10%) broths of aqueous polymer (especially biopolymers), is more easily dissolved in the field, but is more costly per pound of polymer to transport to the field. The third form is either aqueous emulsions that contain up to 35% or more active polymer or hydrocarbon-fluid suspensions/dispersions that contain ~50% active polymer. The challenge in using polymers supplied in this form is to routinely and consistently fully invert the emulsion/suspension in the field to permit the polymer to be dissolved fully in the flood water and to be fully effective during the polymer waterflood. Fourth, where economic and project scale permit, field-manufactured polymer, especially field-manufactured partially hydrolyzed polyacrylamide, can be an attractive option for providing polymer of high quality and exceptional performance characteristics.^{59,68}

Quality Control. Quality control is an essential element for the successful implementation of a polymer-waterflooding project. A quality control program should include, but not be limited to, the following elements:

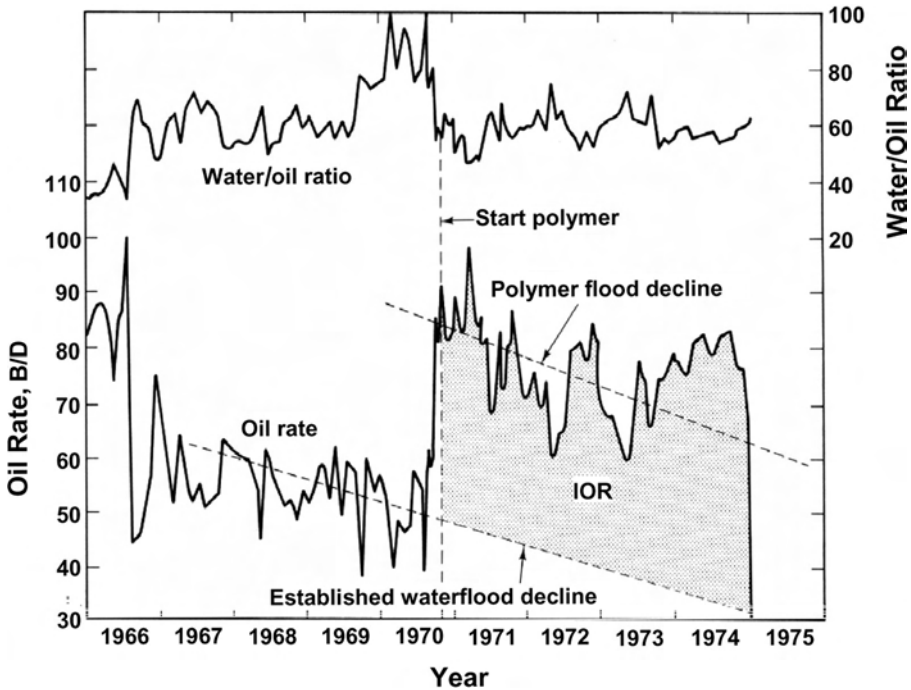


Fig. 13.15—Tertiary polymer flood response at the North Burbank unit, Osage County, Oklahoma.⁵⁵

- Routine verification of the polymer concentration in the polymer as supplied and in the polymer solution injected.
- Routine determination of the viscosity and SFs of the injected polymer solution.
- Check of the filterability of the polymer solution to be injected.
- Check of the dissolution-rate properties of the polymer as supplied.
- Check of the polymer to be injected for complete dissolution.
- Periodical check of the thermal and chemical stability of the polymer by measuring the viscosity and SF of wellhead polymer samples that have been aged for appropriate periods of time at reservoir temperature under scrupulous anaerobic conditions in sealed glass ampoules. (See the recommended polymer-solution-sample deoxygenation procedure discussed previously in Sec. 13.5.3.)

13.5.6 Illustrative Field Results and Trends. This section provides a brief review of illustrative field applications of polymer waterflooding, along with a very brief discussion of trends in the field application of polymer waterflooding in the U.S.

Comprehensive Manning Survey. In 1983, Manning *et al.*⁷⁰ published a comprehensive and classic summary of the field results and performance of more than 250 polymer waterflooding projects and provided information relating to the early field applications of polymer waterflooding.

North Burbank Unit Flood. Fig. 13.15 shows the incremental oil production response for the North Burbank polymer flood.⁵⁵

Wyoming Polymer Floods. A polymer-waterflooding project that involved a large full-field flooding project at the North Oregon Basin field in Wyoming's mature Big Horn Basin oil-producing area was reported in 1986 to be producing 2,550 BOPD of incremental oil production. It was reported that this polymer-flooding project would recover ultimately more than 10 million bbl of incremental reserves from the mature North Oregon Basin field. The field

project involved the flooding of both a fractured carbonate formation and a fractured sandstone formation with a polymer flood using partially hydrolyzed polyacrylamide. The polymer used in this flooding project was field manufactured at the North Oregon Basin field in a plant with a capacity of 23 million pounds of polymer per year.⁶⁸ This is an example of a successful polymer-flooding project using HPAM and conducted in naturally fractured sandstone and carbonate reservoirs where both the polymer dissolution brine and the reservoir brine were relatively saline and relatively hard (relatively high concentrations of divalent cations and anions).

Chinese Polymer Floods. The Chinese have reported on a number of polymer-flooding projects. During a pilot test of polymer flooding with HPAM in the 167°F Shuanghe reservoir of the Henan oil field in China, the incremental oil production was expected to approach 9.8% OOIP, and the polymer flood was expected to recover 0.7 bbl of oil per pound of polymer injected.⁷¹

It has been reported that polymer waterflooding, using HPAM, in the Daqing field in China has recovered cumulatively more than 300 million bbl of oil. This polymer waterflooding project was reported to be producing 70 million bbl/yr of oil in 2001. The cost of the oil from the polymer waterflooding project was stated to be U.S. \$6.60/bbl. The field was reported to be producing at a rate 310% greater than that expected for waterflooding alone. Incremental oil production attributed to the Daqing polymer waterflood is projected to be in the range of 12% to 15% of the OOIP.

French Polymer Flood. In 1995, an update was reported on the French Courtenay polymer flood that was conducted in the secondary recovery mode in a shallow sand reservoir with a 40 cp viscosity oil and 86°F reservoir temperature. Waterflooding was not conducted in this reservoir because of the combination of thin, high-permeability sand channels and an unfavorable mobility ratio. Oil recovery for the polymer flood was 6.6% PV. The total cost of oil production from this polymer flood project was U.S. \$12/bbl.⁷²

Canadian Rapdan Polymer Flood. A 13-producer and 5-injector pilot of polymer waterflooding was conducted in 1986 in the 130°F and 110 md average permeability Upper Shaunavon formation of the Rapdan Unit in Saskatchewan, Canada. The polymer-flood pilot consisted of injecting 17% PV of 1,100 to 1,500 ppm polyacrylamide polymer solution. Polymer flooding was started after waterflooding. As a result of polymer flooding, oil production was reported to have increased from 410 BOPD at 18% oil cut to peak production of 1,100 BOPD at 36% oil cut.⁷³

Review of Worldwide Polymer Floods. As [Sec. 13.5.5](#) describes, a literature review was conducted on twelve international polymer floods, both pilots and fieldwide projects, that were conducted between 1975 and 1992.⁶⁹ All floods were conducted in reservoirs with a reservoir temperature of less than 140°F. In ten of the floods, partially hydrolyzed polyacrylamide was used as the polymer, and, in two of the floods, xanthan was used as the polymer. The international polymer floods recovered between 6 and 52% of the OOIP, compared with the medium recovery of 4.9% OOIP for 128 U.S. polymer floods. The general conclusion of [Ref. 69](#) was that there tended to be a correlation between the polymer-flood incremental oil production and the total amount of polymer used in the polymer floods, as defined by PV of polymer injected multiplied by the average concentration of polymer injected.

Survey of U.S. Polymer-Flood Project Production. [Ref. 74](#) reported the total U.S. enhanced oil recovery (EOR) oil production from polymer-waterflooding projects in 1998 was only 139 BOPD. This production figure was down from 21,000 BOPD in 1988 for U.S. EOR oil production resulting from polymer-waterflooding projects. In the same survey in 2000,⁷⁵ EOR production for polymer and chemical flooding were combined so that the EOR production figure for polymer flooding alone was not discernable. The reported combined U.S. oil production in 2000 resulting from chemical and polymer flooding was 1,600 BOPD.

In 2002,⁷⁶ EOR production from polymer flooding was reported to have fallen to zero, and it was reported that the number of polymer-flooding projects in the U.S. had fallen from 178 in 1986 to 4 in 2002. In the 2002 survey, 20 polymer-flooding projects that were being conducted outside the U.S. and Canada were listed. There is, at this writing, a trend in the U.S. toward less EOR polymer-flood oil production.

13.5.7 Additional Reading. Polymer waterflooding is thoroughly documented in [Ref. 46](#) and nicely reviewed in Chap. 8 of [Ref. 55](#). Also, see Chap. 5 of [Ref. 2](#).

13.5.8 Polymers for Imparting DPR and RPM. In [Sec. 13.4](#), a review was presented of the concepts, applicability, limitations, and desirability of the DPR phenomenon as it applies to conformance-improvement water-shutoff (and/or water-reduction) treatments.

As early as 1964, certain polymer-flood water-soluble polymers were known to impart DPR to water flow in reservoir rock that had been previously flooded with the polymer.²⁶ Although, in concept, water-soluble permeability-reducing polymers can be injected (using appropriate polymers and conditions) into matrix rock to reduce the absolute permeability to all fluids (including water, oil, and gas), the injection of water-soluble permeability-reducing polymers into matrix rock is most often performed to impart DPR.

Advantages and Issues. Bullhead injection of a simple aqueous solution containing a water-soluble polymer to treat conformance problems, such as excessive water production, in matrix rock (unfractured) reservoirs is a highly appealing concept. Most DPR polymers (also known as RPM polymers) are not usually highly exotic or costly. Thus, polymer-alone DPR treatments for reducing excessive water production are much simpler and less risky, in concept, than conducting the same task using a relatively strong total-shutoff gel, particularly a “strong” crosslinked polymer gel. A polymer solution alone poses less risk of totally sealing off the treated reservoir volume compared with injecting a water-shutoff gel. The chemical and operational aspects of injecting a polymer solution for water-shutoff/reduction purposes are substantially less complicated than injecting a comparable polymer gel.

However, polymer DPR water-shutoff and/or water-reduction treatments do have a number of significant limitations, in addition to those already discussed in [Sec. 13.4](#). First, how fast will the treatment polymer be desorbed and flow back to the production well? Second, DPR polymer treatments for conformance improvement are normally successful only when applied to matrix rock oil reservoirs with a relatively low permeability (usually less than 1 Darcy). In addition, many existing DPR polymer conformance-improvement treatments are only applicable to sand and sandstone reservoirs. DPR polymer conformance-improvement treatments are not directly applicable within fractures and other high-permeability anomalies. Third, the amount of DPR, which is imparted by polymer systems available at this writing, is often quite small as compared with the amount of DPR that can be imparted by DPR polymer gels. [Ref. 42](#) provides guidelines for well-candidate and chemical selection for use when considering the application of polymer DPR water-shutoff/reduction treatments. Fourth, the performance of polymer DPR treatments has been erratic in both the laboratory and field setting.

Mechanism for Imparting DPR. Although the mechanism by which polymers impart DPR to water flow in reservoir porous media is currently under active study, the basic mechanism is thought to involve polymer adsorption onto the pore body walls and/or retention at the pore throats.^{31–36} In most cases, DPR polymers tend to decrease the relative permeability to water with little effect on the oil or gas relative permeability curve.^{35,77,79}

Fig. 13.16, taken from [Ref. 35](#), depicts the DPR and RPM effect on relative permeability curves imparted in a 4.8 Darcy sand pack that was flooded at 140°F with a 10 g/L solution of biopolymer Polysaccharide G in 10 g/L KCl brine. The figure shows, as a result of flooding the sand pack with the biopolymer solution, how the relative permeability curve to water was substantially reduced while the relative permeability curve to oil was relatively unaffected.

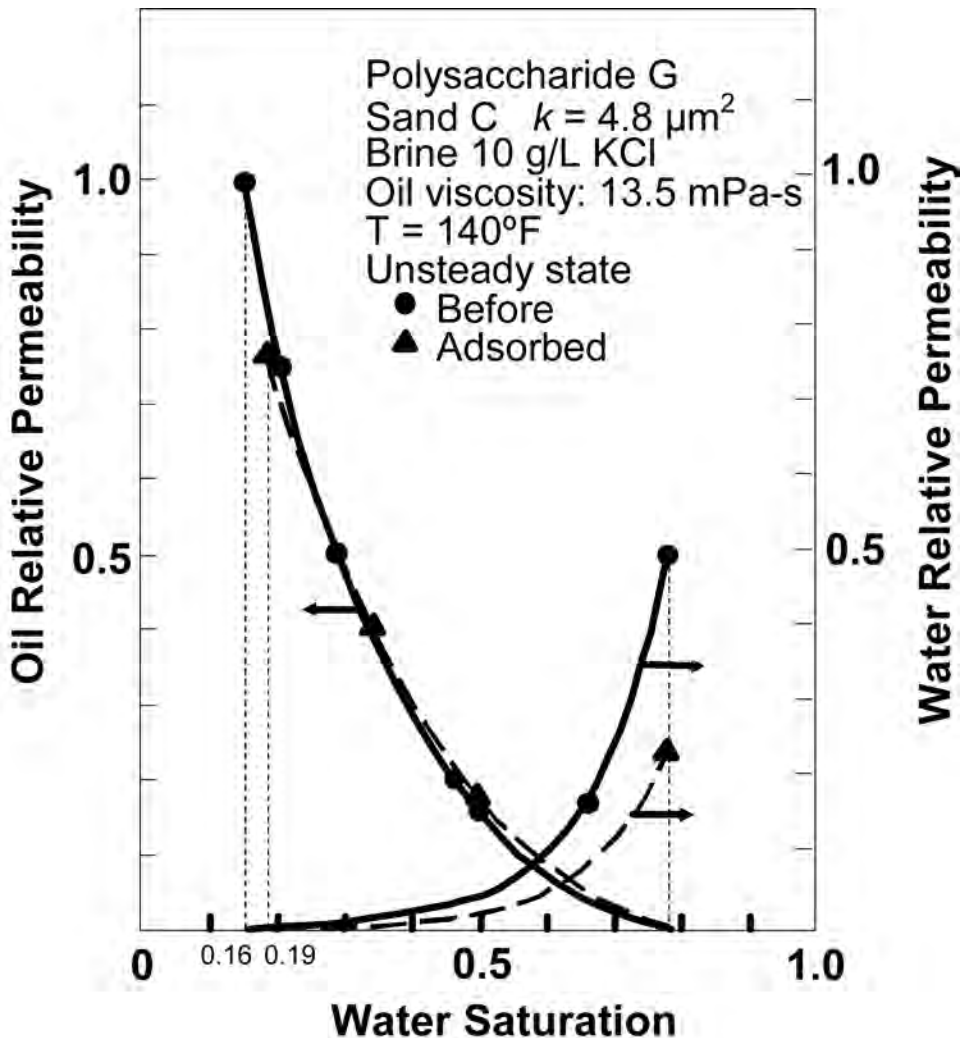


Fig. 13.16—Relative permeability modification effect induced in a sand pack by Polysaccharide G.³³

Range of Applicability of DPR Polymer Treatments. While DPR polymer systems for imparting conformance improvement have been targeted primarily at sand and sandstone reservoirs, presumably being water wet, favorable DPR polymer effects have been observed when nonionic polyacrylamide was placed in various carbonate rocks with either water-wet and oil-wet conditions.³⁶ DPR polymer treatments have been applied to reservoirs with temperatures up to 225°F;²² however, DPR polymer systems for use in conformance-improvement treatments are only applicable over a limited lower permeability range (approximately 5 md to hundreds of md in most cases). Because the upper permeability limit varies with the specific DPR polymer system and with specific reservoir rock lithologies, it is difficult to provide a universal upper permeability limit for the successful application of DPR polymer systems. The upper permeability limit for the successful application of any specific DPR polymer system is a treatment variable that should be scrutinized closely. The application of polymer DPR treatments to reservoir conformance problems involving flow channels with permeabilities exceeding the upper permeability limit of a DPR polymer is a major cause of failures for such polymer conformance treatments.

Illustrative Technologies and Field Applications. The earliest polymers (uncrosslinked) reported to have DPR properties used in water-shutoff/reduction treatments applied to production wells were polyacrylamides,^{12,13,26} which is the same general type of water-soluble polymer that has been used extensively in polymer flooding for mobility-control and sweep-improvement purposes. In 1973, SPE literature reported on a proprietary and commercially available “brush” polymer for “selectively reducing water production.”¹⁴

In 1988, Zaitoun and Kohler reported on how the adsorption of, respectively, polyacrylamide and a polysaccharide onto water-wet sand and sandstone promotes DPR to water flow. Also, it was reported how the adsorption of these polymers increase the irreducible water saturation.³⁵ The same research group reported on the development of two polyacrylamide-based DPR water-shutoff processes and the field application of one of the processes in an underground gas-storage facility.^{77,79}

Gruenenfelder *et al.*⁸⁰ reported on the application of DPR polymer water-shutoff/reduction treatments to two gravel-packed wells of high-temperature (190 to 200°F) sand reservoirs of the U.S. Gulf Coast. The DPR polymer treatments involved the use of a nonionic triple-stranded polysaccharide biopolymer.

The application of DPR polymer water-shutoff/reduction treatments, involving an amphoteric polymer material, to five wells in a high-permeability and high-temperature (up to 225°F) sandstone reservoir in Indonesia has been reported.²²

Refs. 34 and 42 discuss the use of cationic polyacrylamide as a candidate polymer for use in polymer DPR treatments to impart conformance improvement.

In 2001, Eoff *et al.* reviewed the structure and process optimization of a commercial “brush” polymer that has been used since 1973 in various forms and under various trade names as a RPM polymer in conjunction with conformance-improvement treatments.¹⁷

13.6 Gels

Gels are a fluid-based system to which, at least, some solid-like structural properties have been imparted. In other words, gels are a fluid-based system within which the base fluid has acquired at least some 3D solid-like structural properties. These structural properties are often elastic in nature. All of the conformance-improvement gels discussed in this section are aqueous-based materials. The term “gel” as used in this chapter (unless specifically noted otherwise) refers to classical, continuous, bulk, and “relatively strong” gel material and does not refer to discontinuous, dispersed, “relatively weak,” microgel particles in an aqueous solution. Gels discussed in this chapter, when formed in a beaker for example, constitute a single and continuous gel mass throughout its entire volume within the beaker. The term “gelant” refers to a gel fluid before any appreciable crosslinking of the gel’s chemical building blocks has occurred. The term gel refers to a gel fluid that has attained either partial or full chemical-crosslinking maturation. This chapter discusses polymer gels, as well as inorganic gels and monomer gels. Sec. 13.8 briefly discusses a conformance-improvement plugging material (i.e., a resin) that involves an organic-fluid-based gel.

An older definition of gel is “a jelly-like substance formed by the coagulation of a colloidal solution into a semisolid phase.” In modern oilfield and technical literature, the term gel includes the elastic and semisolid material that results from chemically crosslinking together water-soluble polymers in an aqueous solution. Crosslinked-polymer gels can possess rigidity up to, and exceeding that of, Buna rubber. They contain polymer concentrations in the 150 to 100,000 ppm range (but more commonly 2,000 to 50,000 ppm and most commonly 3,000 to 12,000 ppm). Gels are often formulated with relatively inexpensive commodity polymers.

Gels have found broad application as oilfield fluid-flow blocking agents because gels are often an exceptionally cost-effective plugging and/or permeability-reducing agent for use in a number of different conformance-improvement treatments. Conformance-improvement gels are,

for the most part, essentially nothing but water (often produced brine) with the remainder of the gel constituents incorporated as low concentrations of relatively inexpensive polymers and chemical crosslinking agents.

The use of conformance-improvement gels is an emerging technology that, at this writing, is still not well understood by petroleum engineers nor widely applied. Conformance-improvement gels are another conformance technology and engineering tool that should be added to the “petroleum engineering toolbox.” However, gels are not a panacea for remedying reservoir and flooding conformance problems, but rather simply another tool that can be used to alleviate conformance problems when there is a good match between a conformance problem and the application of a particular gel technology.

13.6.1 Gel Conformance-Improvement Treatments. Gels operate, for the most part, either by diverting fluid flow from high-permeability, low-oil-saturation reservoir flow paths to low-permeability, high-oil-saturation flow paths, and thereby promoting improved flood sweep efficiency and incremental oil production, or by reducing oil-production operating costs by reducing excessive, deleterious, and competing coproduction of water or gas.

Oilfield gel conformance treatments can be applied in a number of forms including sweep improvement treatments, water shutoff treatments, gas shutoff treatments, zone abandonment treatments, squeeze and recompletion treatments, and water and gas coning treatments involving fractures and other linear-flow high-permeability reservoir anomalies. Gels are particularly effective for treating oil-production coning problems when the coning is occurring via linear flow in “vertical” fractures.^{5,7}

When there is a good match between a given conformance problem and a particular gel technology, relatively large volumes of incremental oil production and/or substantial reductions in oil-production operating costs, by means of the shutting off of excessive, deleterious, and competing coproduction of water or gas, can be achieved profitably. Gel treatments are usually applied in the course of normal and ongoing primary, secondary, or tertiary oil-recovery operations, just as an operator would apply an acid or scale-inhibition treatment. Gel treatments are an emerging oilfield technology that can help extend the life of maturing oil reservoirs that are approaching their economic limit.

Background and Historical Information. Although conformance-improvement gel treatments have existed for a number of decades, their widespread use has only begun to emerge. Early oilfield gels tended to be stable and function well during testing and evaluation in the laboratory, but failed to be stable and to function downhole as intended because they lacked robust chemistries. Also, because of a lack of modern technology, many reservoir and flooding conformance problems were not understood, correctly depicted, or properly diagnosed. In addition, numerous individuals and organizations tended to make excessive claims about what early oilfield gel technologies could and would do. The success rate of these gel treatments was low and conducting such treatments was considered high risk. As a result, conformance-improvement gel technologies developed a somewhat bad reputation in the industry. Only recently has this reputation begun to improve. The information presented in this chapter can help petroleum engineers evaluate oilfield conformance gels and their field application on the basis of well-founded-scientific, sound-engineering, and field-performance merits.

How Gel Treatments Function. Gels used in conformance-improvement treatments reduce permeability in the reservoir treatment volume in which the gels are ultimately placed. Conformance gels do not function as viscosity-enhancing agents during oil-recovery flooding operations.

Although microgels (discussed in a later subsection of this section), which are colloidal-sized aggregates of suspended and noncontinuous gel particles, have, at times, been claimed to be viscosity-enhancing agents during their “propagation” through reservoir flow paths possessing high permeabilities, there is no substantiation in the petroleum engineering literature of any microgels substantially enhancing the viscosity of an aqueous oil-recovery drive fluid beyond

the viscosity of the gel's polymer solution alone. In fact, microgel-gel-containing aqueous solutions tend to have lower viscosities than the polymer solutions from which they were derived. Permeability reduction is the dominant mechanism by which microgels impart conformance improvement. Oilfield microgels are also referred to, at times, as colloidal dispersion gels.

The more widely applied conformance-improvement gels are characterized as being bulk gels that function as permeability-reducing agents. Bulk gels have a continuous chemically crosslinked polymer network structure throughout the entire macroscopic scale of the gel. These gels are blocking and plugging agents to fluid flow in the reservoir volume in which they have been placed. For example, gels used in near-wellbore water-shutoff treatments of producing wells are selectively placed in a high-permeability strata (that are not in fluid or pressure communication with the other reservoir strata) to function purely as a plugging and blocking agents to fluid flow.

If a gel is placed some significant distance into the fractures of a naturally fractured reservoir surrounding an injection well, the gel not only functions as a blocking agent, but also as a diverting agent. These gels divert injected oil-recovery drive fluid from predominantly flowing through the high-permeability, low-oil-content fractures to predominantly flowing through the relatively low-permeability, high-oil-saturation matrix reservoir rock adjacent to the gel-filled and gel-treated fractures.

What Benefits Can Be Expected. For good gel-treatment well and well-pattern candidates, the following is a partial list of benefits that can be achieved.

- Generate incremental oil production through conformance improvement, and possibly generate large volumes of incremental oil production per unit cost of chemical expended.
- Substantially reduce oil-production operating expenses per unit cost of chemical expended.
- Reduce competing water production that can be unproductive, costly, and environmentally unfriendly.
- Reduce competing gas production that can be unproductive, excessive, and economically detrimental.
- Improve the performance of an ongoing oil-recovery operation.
- Reduce certain environmental liabilities by reducing the amount of excessive and unnecessary coproduction of environmentally unfriendly fluids, such as highly saline and hard reservoir brines.
- Extend the economic lives of marginal wells, well patterns, and oil fields.

Properties of an Ideal Gel System. An ideal conformance-improvement gel technology should be applicable as injection and production well treatments, as sweep improvement treatments, and as water and gas shutoff treatments. It should also be applicable to all reservoir mineralogies and lithologies and to a wide variety of reservoir and flooding-operation conformance problems. The ideal gel technology should be a single-fluid system and should possess a robust gel chemistry, which requires that it be insensitive to oilfield and reservoir environments and chemical interferences (especially H_2S and CO_2); be insensitive to all reservoir minerals and fluids; and be applicable over a broad pH range.

An ideal conformance-improvement gel technology should also involve a simple and straightforward gel-forming chemical system; be applicable over a broad range of reservoir temperatures; be stable over the long term; provide for a broad range of gel strengths, including rigid gels, and provide highly controllable and predictable gelation-delay onset times. For matrix-rock reservoir treatments, an ideal gel technology must include gelant solutions that are readily injectable into matrix reservoir rock. An ideal gel must be environmentally acceptable and friendly, be formulated with low concentrations of relatively inexpensive chemicals, and be formulated with readily available (preferably commodity) chemicals. Finally, it should reduce the permeability to water flow in matrix rock more than the permeability to oil and gas flow.

<u>Inorganic Gels</u>	Silicate based Al (III) based Hydroxides of selected divalent and trivalent cations		
<u>Organic polymer gels</u>	Biopolymer gels Synthetic (usually acrylamide-based) polymers	Metal crosslinking agents	Cr (VI) redox Cr (III) inorganic Cr (III) complex Al (III) Zr (IV)
		Organic crosslinking agents	Aldehydes Phenol-formaldehyde and derivatives Polyethyleneimine
	Monomer gels	Acrylamide monomer Acrylate monomers Phenolics	
	Lignosulfonate gels Polymer self-induced gels		

Gel Systems and Chemistries. Oilfield conformance-improvement gels come in a wide range of forms and chemistries.⁴ Table 13.1 provides an overview of various conformance-improvement gels.

Chromium (III)-Carboxylate/Acrylamide-Polymer Gels. Widely applied as sweep-improvement treatments and as water and gas shutoff treatments, chromium (III)-carboxylate/acrylamide-polymer (CC/AP) gels^{5,81–83} are aqueous acrylamide-polymer gels in which the chemical crosslinking agent is a chromium (III) carboxylate complex. CC/AP gels have an exceptionally robust gel chemistry and are highly insensitive to oilfield and reservoir interferences and environments. They are also applicable over an exceptionally broad pH range.⁵ As a result, these gels, when properly formulated, are applicable to the acidic conditions associated with CO₂ flooding for which most earlier oilfield polymer gels did not function well. The chromium (III), as used in the crosslinking agent of this gel technology, is relatively nontoxic,⁸⁴ but it is highly regulated. This single-fluid gel technology provides a wide range of gel strengths and a wide range of controllable gelation-onset delay times. The gel technology is applicable over a broad range of reservoir temperatures and applicable to a broad range of conformance problems and reservoir mineralogies and lithologies. Chromic triacetate (CrAc₃) is the often-preferred crosslinking agent used with the CC/AP gel technology. A chemical gelation-rate-acceleration additive package, involving chromic trichloride, has been developed for use with the CC/AP gel technology. Two chemical means are available to retard the rate of gelation of CC/AP gels that are applied to high-temperature reservoirs. The first involves the use of low or ultra-low hydrolysis polyacrylamide and capitalizes on the slow formation of the required chemical crosslink sites on the polymer by means of autohydrolysis. The second chemical means is the addition of relatively strong carboxylate ligands, such as lactate or malonate, to the gelant solution.

Chromium (VI) Redox Gels. One of the early conformance-improvement gel technologies involved acrylamide polymers that were chemically crosslinked together using a chromium (VI) redox system.⁸⁵ This oilfield gel system has largely fallen from favor because of issues relating to the use of a crosslinking agent that contains toxic and carcinogenic chromium (VI) and because the crosslinking chemistry is rather complicated and subject to a number of oil-field interferences.

Aluminum Crosslinked Gels. Although other aluminum crosslinking agents have been developed and used in conformance-improvement gels, aluminum-citrate-crosslinked gels have historically been the most widely applied. The early widespread application of the aluminum-citrate gel technology was conducted in the sequential-injection mode, involving the repeated sequential injection of aqueous slugs containing, respectively, the polymer and the aluminum-citrated crosslinking agent. Sequential-injection aluminum-citrate gel technology is discussed in more detail later in this section. The application of conformance-gel treatments, involving the sequential injection of aqueous slugs containing the different chemicals that are required to form the gel in the reservoir, have largely fallen from favor.

More recently, aluminum-citrate acrylamide-polymer gels, which are formulated with low concentrations (200 to 1,200 ppm) of polymer and which are referred to as colloidal dispersion gels (CDGs), have been somewhat widely used as large-volume treatments applied through injection wells to “matrix rock” for improvement of waterflood sweep efficiency.^{9,86} CDGs are a form of discontinuous microgel particles. The mechanism and means by which this particular gel technology generates incremental oil production is not fully understood.

Published laboratory studies have reported the following regarding aluminum-citrate CDGs. First, CDGs of acrylamide polymers crosslinked with aluminum citrate are not readily injectable into, and propagatable through, matrix rock of normal permeabilities (e.g., sandstone of < 1,000 md).^{87,88} Ref. 88 discusses an experimental flooding study where an aluminum-citrate CDG was observed to not be readily propagatable, after two hours of aging, through matrix rock during a flooding experiment involving the injection of an aluminum-citrate colloidal dispersion gelant solution, containing 300 ppm high-MW HPAM, into a 700 md Berea sandstone core plug at 105°F and at a superficial velocity through the sandstone of 16 ft/d. Second, aluminum does not readily propagate through reservoir matrix rock.⁸⁷ Third, aluminum crosslinking of the polymer of CDGs normally occurs within several hours.⁸⁸ Fourth, aluminum-citrate CDGs do not preferentially enter high-permeability zones any more selectively than is dictated by Darcy’s law. Fifth, aluminum-citrate CDGs do not viscosify water more than do the gel’s polymer without the addition of the crosslinking chemical.⁸⁸ If aluminum-citrate CDGs are not readily injectable into and propagatable through matrix reservoir rock of normal permeabilities (sub-Darcy permeabilities), there are two possible explanations for the apparent success of a number of large-volume aluminum-citrate CDG treatments in terms of generating conformance improvement and generating incremental oil production when treating “matrix-rock conformance problems.” First, the successfully treated “matrix rock” reservoirs may actually have been at least somewhat naturally or otherwise fractured. Second, the offending high-permeability strata within the successfully treated matrix-rock reservoirs may have possessed multi-Darcy permeabilities.

Gels Crosslinked With an Organic Crosslinker. There has been a long-standing desire within the oil industry to develop effective conformance-improvement polymer-gel technologies using benign organic chemical crosslinking agents that would impart carbon-carbon-bond chemical crosslinks between the gel polymer molecules. This would avoid the use of metal crosslinking agents and would result in exceptionally strong and stable polymer gels. However, with the possible exception of the polyethyleneimine-crosslinked gel technology briefly discussed later in this section, no such gel technology has been developed and reduced to commercial practice.

The majority of organically crosslinked polymer-gel technologies developed to date have been based on phenol-formaldehyde chemistries. These gels either use phenol and formaldehyde as the chemical crosslinking agent or use derivatives or precursors to phenol and formaldehyde. There have been attempts to identify and use less toxic and more environmentally friendly derivatives of phenol and formaldehyde as the crosslinking agents.⁸⁹

Some of the most thermally stable polymer gels for use in high-temperature conformance-improvement treatments have been formulated with acrylamide polymers that are chemically crosslinked with organic crosslinking agents that are based on phenol-formaldehyde type chemistry.⁹⁰

At this writing, an organically crosslinked gel technology that does not involve a phenol-formaldehyde type crosslinking chemistry was somewhat recently developed. The gel technology involves the use of a specially manufactured and derivatized acrylamide polymer and the use of polyethyleneimine as the crosslinking agent.⁹¹ This gel technology is most readily applicable to reservoirs with temperatures exceeding approximately 180°F, and reports regarding the field application of this conformance polymer-gel technology have been favorable overall.

Biopolymer Gels. Gels based on the crosslinking of biopolymers with organic or inorganic crosslinking agents have been pursued. A popular conformance biopolymer-gel technology in the 1970s and early 1980s was based on gels of xanthan polymer crosslinked with an inorganic chromium (III) crosslinking agent.⁹²

Monomer Gels. Conformance-improvement gels based on the in-situ polymerization of organic monomers to form polymers with and without the inclusion of crosslinking monomers have been developed and successfully applied. Early monomer-gel treatments were often based on the in-situ polymerization of the acrylamide monomer; however, this is seldom practiced currently because of toxicity and environmental concerns. Most modern monomer-gel technologies for oilfield application are based on the in-situ polymerization of less toxic acrylate monomers.⁹³

An advantage of monomer gel technologies is the low water-like viscosity of the gelant solution. Disadvantages include cost and the sensitivity of the polymerization reaction to oilfield interference and environments. Care also needs to be taken to carefully distinguish between “linear” (uncrosslinked) and crosslinked oilfield monomer gels.

An older monomer gel technology involved gels formed from the reaction of formaldehyde with phenol.⁹⁴ A modern day concern with this gel technology is the toxicity and environmental issues associated with the use and handling in the field of formaldehyde, phenol, and/or their chemical derivatives.

Polymer Self-Induced Gels. A conformance-improvement biopolymer gel system has been reported that involves the injection of the polymer into the treated reservoir volume in the form of an alkaline high-pH solution. Once emplaced in the reservoir rock, the pH of the polymer solution is reduced by spontaneous or induced means. Following the reduction in the polymer solution’s pH, the polymer solution spontaneously forms a gel.⁹⁵

Inorganic Gels. A variety of inorganic gel technologies have been developed and applied over the years. These include gels based on, respectively, silicate or aluminum ion chemistries, along with gels of hydroxides of iron and magnesium.

Gels based on silicate chemistries were some of the earliest gel technologies applied for conformance improvement. A silicate gel is formed when a relatively high-pH aqueous solution, containing a sufficient concentration orthosilicate monomers or oligomers of orthosilicate, has its pH reduced or is exposed to hardness cations. Aqueous-based conformance-improvement silicate gels can be formed in a petroleum reservoir by either “internally catalyzed” or “externally catalyzed” means. Internally catalyzed silicate gels are formed by including in the aqueous gelant solution an acid-generating chemical that will spontaneously decrease the pH of the gelant solution when it is placed in the reservoir. Externally catalyzed silicate gels are usu-

ally formed by contacting the orthosilicate monomer or oligomer solution with a brine (e.g., reservoir brine) that contains a high level of harness cations (e.g., Ca^{++}). Internally catalyzed silicate gels are often favored for use in conformance-improvement treatments during oil-recovery operations. Externally catalyzed silicate gels are often used during drilling operations for lost circulation applications. Several potential concerns should be noted. Solution-aging, filterability, and quality-control issues can be a concern for silicate gelant solutions that are to be injected into matrix-rock reservoirs. There can be safety and environmental issues associated with the acid-generating chemical used in internally catalyzed silicate gel systems.

Silicate-based gels of conformance-improvement treatments have been applied successfully in Hungary.⁹⁶ A large-volume sodium-silicate gel treatment was reported to have been applied to an offshore Norwegian oil production well.⁹⁷ A large number of silicate-based conformance-improvement gel treatments have been applied worldwide.

The main advantage of inorganic gels is their environmentally friendly nature. Disadvantages historically have been that many of the inorganic gels were relatively weak gels, and a number of the inorganic gels do not provide good long-term fluid-shutoff performance. The latter is especially true for inorganic hydroxide “gels” that tend to convert over time to solutions containing ineffective oxide solids.

Gels Formulated With Synthetic Organic Polymers. Although a number of the early conformance-improvement gel technologies were based on inorganic gels and biopolymer gels, the recent trend has been toward the application of oilfield polymer gels based on the use and crosslinking of synthetic organic polymers, primarily acrylamide polymers.

Classification of Gel Treatment Types. Conformance-improvement gels can be classified in several manners. First, conformance-improvement gels can be classified as to whether they are intended to treat matrix-rock conformance problems, involving permeabilities less than roughly two Darcies, or treat reservoir high-permeability anomalies (usually fractures), involving permeabilities greater than roughly two Darcies. A subcategory of this classification is whether the gel treatments for treating matrix-rock conformance problems are to be placed in the near-wellbore environment (radial penetration of less than ~15 ft) or to be placed deeply in the far-wellbore environment (radial penetration of greater than ~15 ft). Although this classification scheme was originally developed for the CC/AP polymer-gel technology, the classification scheme is also generally applicable to all other conformance-improvement polymer-gel technologies.

Gels used to treat high-permeability-anomaly conformance problems are often treating fluid-flow problems involving linear flow, such as that occurring into fractures. Near-wellbore gel treatments placed in unfractured matrix rock are usually used to block radial fluid flow. Near-wellbore gel treatments that are placed in matrix rock are of relatively small volume, are often total-fluid-shutoff gel treatments, and are often relatively simple and straightforward to apply. These gel treatments usually have a relatively low risk factor if they can be placed properly and if the conformance problem is correctly diagnosed. In addition, these gel treatments can have high payout-to-cost ratios. Gels placed deep in matrix rock are large volume treatments that can be relatively costly and technically complex. In addition, these gel treatments can have a relatively high risk factor associated with them and tend to render a relatively low payout-to-cost ratio. The application of low-concentration aluminum-citrate CDG treatments that are applied via injection wells has been cited as a possible exception to this trend.

Second, the widely applied form of conformance-improvement gel treatments, namely crosslinked organic-polymer bulk gel treatments, can be classified as to whether when being injected from the wellbore into the reservoir, the gel fluid is a gelant solution or is a preformed or partially preformed gel fluid. In most instances, such as with the CC/AP gel technology, the polymer-gel fluid must be in its gelant form (i.e., before any initial microgels form) for the gel fluid to be readily injectable into matrix reservoir rock (such as sandstone having a permeabili-

ty less than 1,000 md). However, for polymer gels to be selectively placed in high-permeability anomalies such as fractures, the gel should be designed so at least some initial gelation has occurred when the gel leaves the wellbore to assure that the gel will not substantially leak off from the high-permeability anomaly (e.g., a fracture) into the adjacent matrix reservoir rock. This is the key to properly formulated polymer gel being able to selectively treat fracture conformance problems, without substantially damaging the adjacent matrix reservoir rock.

Third, conformance-improvement organic-polymer gels are classified as to whether they are the more widely applied bulk gels possessing relatively high polymer concentration with a continuous crosslinked polymer-gel structure on the macro scale or they are microgels, alternately known as colloidal dispersion gels. Microgels have been purportedly used to treat deeply in matrix reservoir rock. Microgel solutions contain low polymer concentrations (usually < 1,300 ppm) and do not have a continuous crosslinked polymer gel structure on the macro scale. Examples of conformance-improvement microgels are low concentrations of acrylamide polymer crosslinked with aluminum citrate^{9,86} and low concentrations of acrylamide polymer crosslinked with zirconium lactate.^{98,99} As mentioned previously, the conformance-improvement mechanism by which microgels function when treating “matrix-rock” reservoirs is not fully understood.

The fourth classification relates to the injection mode of the gel chemicals. Early oilfield conformance gel technologies tended to be based on the sequential injection of fluids containing, respectively, two of the reactive chemicals of the gel’s chemical make up. For example, the polymer would be injected in one aqueous fluid followed by injection of the crosslinking agent in a second fluid. This was done at that time because the gelation-delay onset time could not then be controlled and/or delayed sufficiently to permit the gel to be injected into the reservoir as desired and required. This strategy is flawed for two reasons. First, operational constraints almost always require a substantial inert fluid spacer be placed between the two reactive gel-forming solutions to prevent mixing of the reactive chemicals in the injection tubing. This practice essentially precludes formation of a gel in the near-wellbore region. Second, when the second reactive fluid begins to diffuse and/or finger into the first reactive fluid in the reservoir, gel will begin to form and tend to divert the second reactive fluid from further mixing. In general, this outcome leads to the highly inefficient use of injected chemicals. Most current oilfield gel technologies do not involve the sequential injection mode. Essentially all current technologies involve the injection of a single gelant solution that contains all of the gel chemical constituents. State-of-the-art single-fluid gel technologies have sufficient chemical gelation-onset-delay-time chemistries to allow proper placement.

A popular early polymer-gel technology for improving conformance within matrix rock reservoirs was the repeated sequential injection of aqueous slugs containing, respectively, HPAM and aluminum-citrate crosslinking agent.^{100,101} The mechanism by which the sequential-injection aluminum-citrate gel treatments were originally purported to operate was the so-called “layering mechanism.” This mechanism envisioned that repeated sequential injection of the gel-forming aqueous slugs would result in alternate adsorbed layers of crosslinking agent and polymer that would crosslink to form gel that would build out from the pore walls of matrix reservoir rock.¹⁰² The layering mechanism was later recanted by its original proponents. Today, most polymer-gel treatments involving acrylamide polymers crosslinked with aluminum citrate are injected as a single-fluid.

Gel Parameters and Evaluation. This section focuses on important formula parameters and on temperature effects as they relate to gelation rate and gel strength of conformance-treatment polymer gels. Similar relationships often hold for other gel technologies. **Figs. 13.17 through 13.20** relate to gel formula parameters and the effect of temperature for a specific CC/AP gel formula. Other oilfield polymer-gel technologies tend to follow similar relationships. The gel formula of **Figs. 13.17 through 13.21** is a fracture-problem fluid-shutoff gel that has a rigid and soft Buna rubbery consistency. The gel was formulated in fresh water and contained

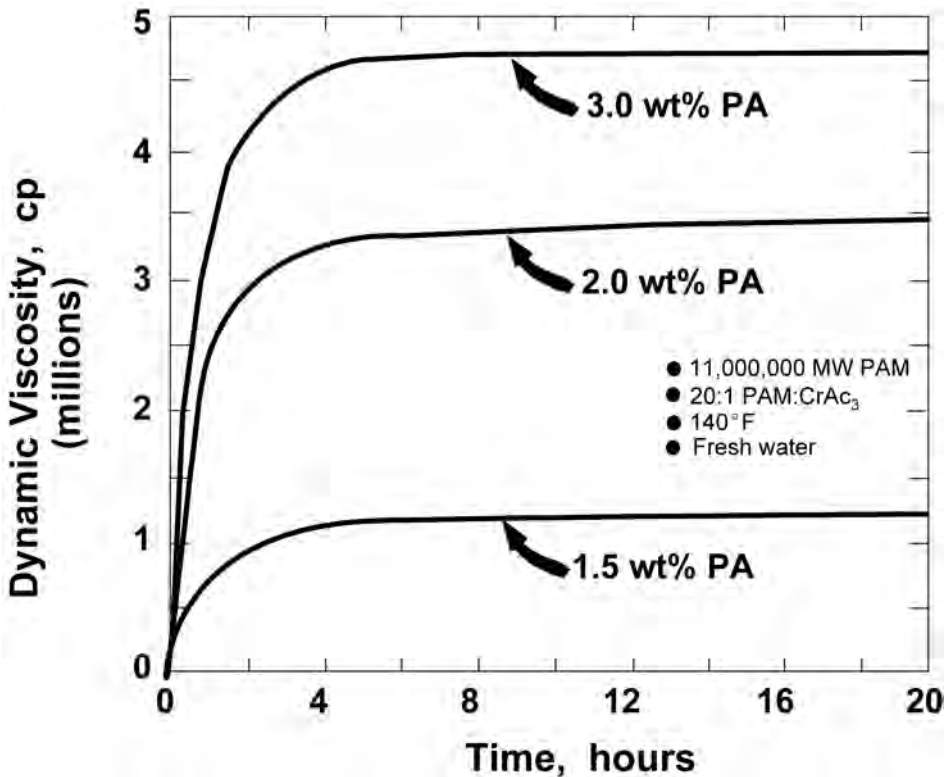


Fig. 13.17—Varying polymer concentration in a CC/AP gel.

2.0 wt% active polyacrylamide (PAM) polymer possessing 11 million MW and 2% hydrolysis. The polymer was chemically crosslinked together to form the gel using chromic triacetate (CrAc₃) as the crosslinking agent.

In **Figs. 13.17 through 13.22**, dynamic oscillatory viscometry was used to measure the elastic strength of the gel sample¹⁰³ as a function of aging time during the gel maturation process following the addition of the crosslinking agent to the gelant solution. The dynamic oscillatory viscosities were measured at an oscillation frequency of 0.1 radians per second.

These plots of dynamic oscillatory viscosity vs. gel aging time can be used to discern two important properties of any given gel sample. First, the equilibrium dynamic-oscillatory viscosity value that is eventually obtained for a given gel sample is a measure of the elastic strength of the gel. Second, the rate at which the dynamic oscillatory viscosity of the gel sample reaches the equilibrium viscosity value is a reflection of the gelation rate of the sample.

Polymer Concentration. As **Fig. 13.17** shows, gel strength increases with polymer concentration when all other gel formula parameters are held constant. For the gels of this figure, the crosslinker loading was held constant at a 20:1 weight ratio of weight active polymer to weight active CrAc₃ crosslinking agent. The gel samples were aged at 140°F. The trend shown is a near universal relationship for all gel technologies. As the concentration is increased of the polymer, monomer, or fundamental chemical building block of the gel's solid-like structure (up to its solubility limit), gel strength increases.

Polymer Molecular Weight. When all other gel formula parameters are held constant, polymer-gel strength increases as the polymer molecular weight (MW) is increased. For **Fig. 13.18**, which depicts this trend, the crosslinking agent concentration within the gel samples was 1,000

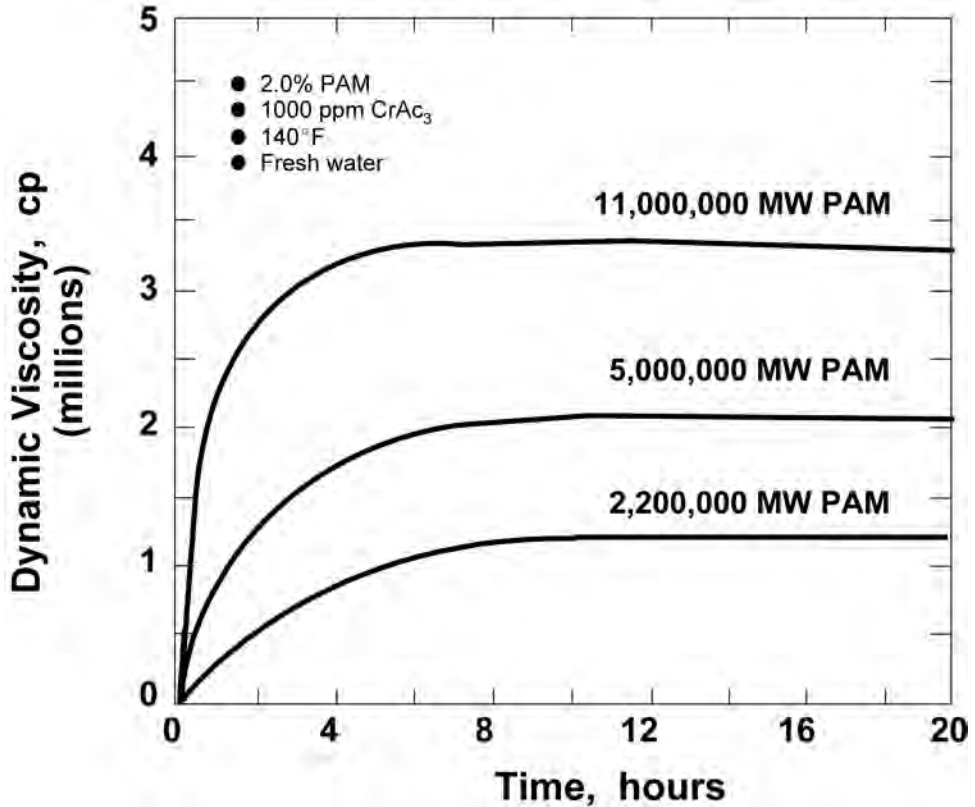


Fig. 13.18—Varying polymer MW in a CC/AP gel.

ppm CrAc₃. The trend shown explains why a gel formulated with a low-MW polymer needs a higher concentration of polymer to obtain the same strength of a comparable fracture-problem gel formulated with high-MW polymer. Comparable gels formulated with higher-MW polymers tend to be more elastic in nature.

Crosslinker Concentration. As Fig. 13.19 shows, when all other polymer-gel formula parameters are held constant, increasing the crosslinking agent concentration increases gel strength. Although not readily apparent in this figure, in general, increasing the crosslinking agent concentration also increases the gel's rate of gelation.

It should be emphasized that, for a given polymer gel, there usually is an optimum concentration for the crosslinking agent. For the samples of Fig. 13.19, that concentration is approximately 1,000 ppm CrAc₃ (or alternatively stated as a weight ratio of 20:1 active polymer to active crosslinking agent). The optimum crosslinking agent concentration is often specified in terms of the ratio of weight of active polymer to weight of active crosslinking agent (or, alternatively, in terms of the weight of the active polymer to the weight of metal ion in the crosslinking agent). Above a gel's optimum crosslinking-agent concentration, syneresis (expulsion of water from the gel) will occur. Below the optimum concentration, the gel is underoptimum in terms of gel strength. For most oilfield applications, the petroleum engineer wants to maximize effective gel strength to maximize economic performance per pound of polymer used in a given gel formula.

Syneresis results from shrinkage of the gel volume. Syneresis, a thermodynamic equilibrium phenomenon, results from excessive chemical attractive forces within the gel structure.

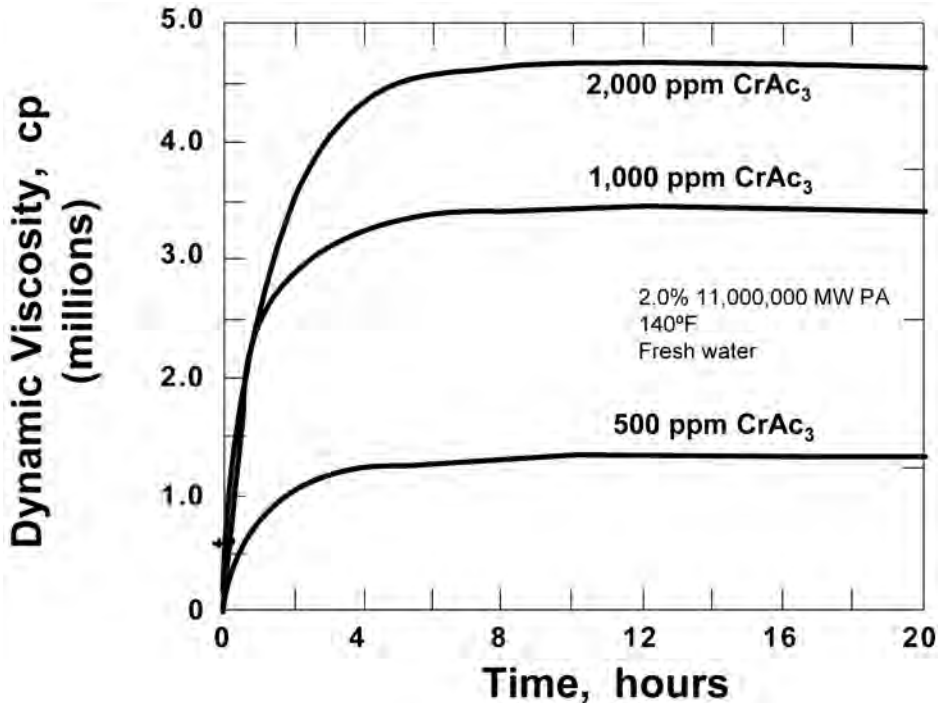


Fig. 13.19—Varying crosslinking agent concentration in a CC/AP gel.

Syneresis of a given polymer-gel formula usually results from one of two causes. First, syneresis for a given polymer-gel formula (fixed salinity and pH) can result from excessive crosslinking agent being incorporated into the gel formula. The second cause results from additional and excessive crosslinking chemical sites developing on the polymer over time, as exemplified by autohydrolysis of acrylamide polymers of CC/AP gels at high temperatures.

Syneresis is usually considered undesirable and unacceptable for gels to be used in near-wellbore treatments that are applied in matrix-rock reservoirs for total-fluid-shutoff purposes or in gels for sealing fluid flow in fractures. However, for gels, especially microgels, that are to be used in deeply placed gel treatments of matrix-rock reservoirs and to function where the microgel particles act as check valves in pore throats, gel syneresis may not be of significant concern.¹⁰⁴ Gel syneresis and gel degradation/degelation can be, and often are, distinctly different phenomena; however, both of these phenomena can result in expulsion of water from a gel.

The optimum concentration of the crosslinking agent for a given CC/AP polymer-gel formula decreases as the MW of the polymer increases, decreases proportionally with increasing polymer concentration (i.e., less pounds of crosslinker per pound of polymer), and increases with increasing temperature.

Temperature. Fig. 13.20 shows how the rate of gelation substantially increases with increasing temperature. For the CC/AP gel technology, the rate of gelation for a given gel formula approximately doubles with every 10°C increase in temperature.

Gelation Rate Acceleration. There are instances when applying conformance-improvement gel treatments that the optimum treatment design will call for the acceleration of the gelation rate of a given gel formula. This is especially true for gel treatments applied to low-temperature (e.g., subambient temperature) reservoirs. For example, for the CC/AP gel technology, a chemical gelation-rate-acceleration additive package involving the use as chromic trichloride as

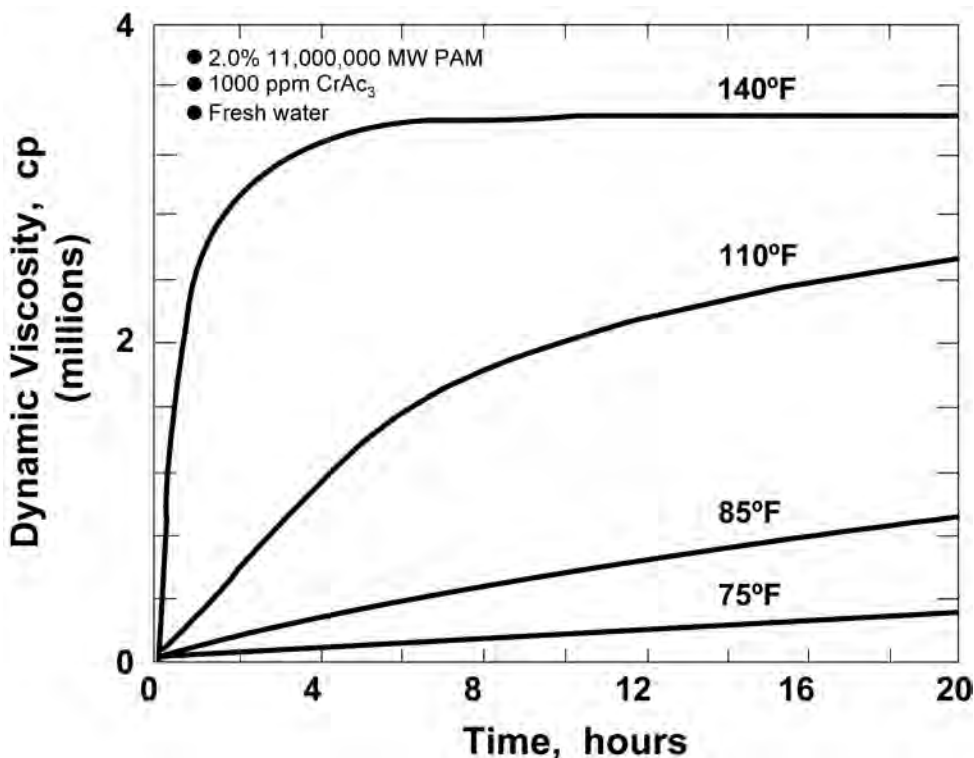


Fig. 13.20—Temperature effect on the gelation rate of a CC/AP gel.

the accelerating agent has been developed. Fig. 13.21 illustrates the use of this acceleration package with the CC/AP gel technology.

Gelation Rate Retardation. There are instances when applying oilfield gel treatments that the optimum treatment design will call for the retardation of the gelation onset time of a given gel formula. This is especially true for gel treatments that are to be applied to high-temperature reservoirs.

For example, for the CC/AP gel technology, a chemical gelation-rate-retardation additive package has been developed involving the use of strong carboxylate ligands as the gelation-rate retardation agent. Fig. 13.22 illustrates the use of this chemical gelation-rate-retardation additive package with the CC/AP gel technology. In the study of Fig. 13.22, the gel being investigated was a gel formula that was intended to impart total near-wellbore fluid shutoff in matrix-rock reservoirs at elevated temperatures. The gel was formulated in fresh water and contained 5.0 wt% active polyacrylamide (PAM) having a MW of ~250,000 daltons. Two versions of the PAM polymer were used in the study. The first PAM was 1.9 mole% hydrolyzed. The second PAM was ultra-low-hydrolysis PAM that had a hydrolysis level of < 0.1 mole%. The gelation-rate retardation agent used in the study of Fig. 13.22 was sodium lactate (NaLac). As the figure shows, the gelation rate was nearly instantaneous at 248°F when the gel was formulated with normal polyacrylamide (1.9% hydrolyzed) and no gelation-rate retardation agent was used. By using various combinations of gelation-rate chemical retarder addition and ultra-low-hydrolysis PAM in appropriately formulated gel recipes, the gelation onset delay time at 248°F could be extended in increments out to 23 hours. As the figure also shows, if the near-wellbore reservoir rock is cooled to 212°F (as can normally be easily done near wellbore through the use of ambient-temperature water injection), the gelation onset time could be extended to 68

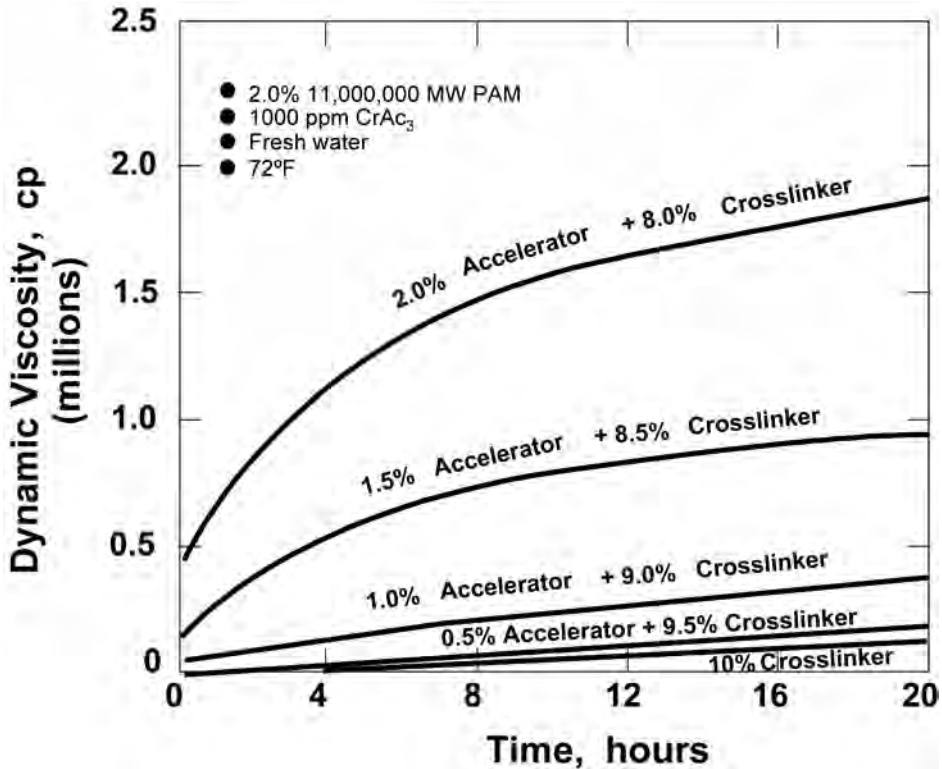


Fig. 13.21—Accelerating the gelation rate of a CC/AP gel.

hours. Appropriately formulated lactate-retarded CC/AP gels usually contain somewhat higher loadings of polymer and/or crosslinking agent. These increased gel chemical loadings are incorporated to counteract the slight weakening and destabilization of the gel that is imparted by the lactate addition.

Gel Strength. There are several different measurements of polymer-gel strength.⁸¹ These gel strengths have at least some analogous correlations in most other gel technologies.

The first measurement is elastic strength. As discussed previously, dynamic oscillatory viscosity can be used to measure the elastic strength of a gel. In practical oilfield terms, the measure of the elastic strength of a gel relates to the resistance to physical deformation that a gel will exhibit while extruding through a constriction in its flow path, such as a constriction in a fracture flow path.

The second measurement is yield or failure strength. When this strength is exceeded, portions of the chemical gel structure are broken. An example of exceeding the gel yield or failure strength is the rupturing of the chemical bonds of the polymer's backbone structure of a shear-non-rehealable gel. This gel strength is measured by placing a mature gel sample in a large container and increasing container pressure until there is flow through a small orifice in the testing container. The yield or failure strength of a total-fluid-flow-shutoff and shear-non-rehealing gel formed and residing in a sandpack is measured by the differential pressure required to make the gel flow from the sandpack. The yield or failure strength of a polymer gel is often much larger than its elastic strength.

The third measurement is compressive strength. Polymer gels do not possess large compressive strengths compared to Portland cement. Thus, polymer gels should not be applied as

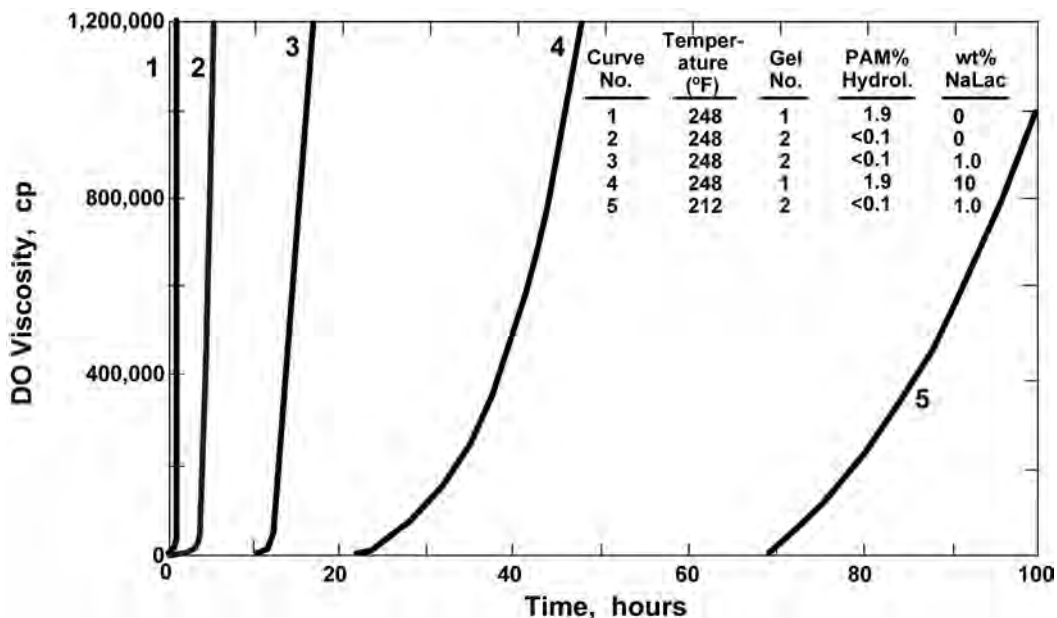


Fig. 13.22—Retarding the gelation rate of a CC/AP gel.

plugging material where substantial compressive strength is required. Adding solids to a polymer gel can greatly increase its compressive strength, especially at high solids loading.

The relative effectiveness of gels for plugging fluid flow through flow channels and flow paths, as measured by the differential pressure that causes the gel to breakdown and flow, increases as the size of the flow channel decreases. Gels that are placed as clear-fluid gelant solutions are particularly effective and strong plugging agents for use when plugging or reducing the fluid-flow capacity in microflow paths, such as is pores of matrix reservoir rock. Gels are especially effective at plugging small fluid-flow paths where solids-containing plugging agents, such as cement or even “microfine” cement, cannot be readily placed.

Gel Onset Time. There have been many and, at times, apparently conflicting means proposed to define and measure gelation onset times. There are two distinctly different and important times in the gel maturation process. The first is the initial onset of gel formation. The second is the time required to reach full gel strength. Because the time required to attain full gel strength is often reached asymptotically, pragmatically it is often better to measure the attainment of “near full gelation,” where “near full gel strength” is quantitatively defined.

When determining the time of initial onset of gelation for a classical bulk polymer gel to be used to treat matrix reservoir rock, the investigator needs to determine when the first onset of microgel particle formation occurs. It is at this point that the gelant usually ceases to be readily injectable into sandstone of less than 1,000 md. Filtration testing, core flooding injectivity experiments, bottle testing, and dynamic oscillatory viscosity techniques have all been used successfully to determine the first onset of such gelation. For a bulk polymer gel, microgel formation usually occurs at a time just before the onset of first being able to visually detect any gel structure in the gelant solution. For classical bulk polymer gels, initial microgel formation constitutes the formation on a colloidal scale of the first discrete crosslinked polymer aggregates that are the precursor to the formation of the continuous macro-scale crosslinked polymer network of the bulk gel.

For crosslinked polymer gels, there are several different modes of the gelation onset delay and different ways these modes manifest themselves. First, there can be a substantial induction

time before any gel formation, including microgel formation, can be detected. Second, and not mutually exclusive of the first mode, there can be “right angle gelation onsets.” Here, once the gelation process starts, the final gel strength is reached very rapidly (almost instantaneously). Third, the gelation begins as soon as the crosslinking agent is added and proceeds over a protracted period of time. CC/AP gels widely applied to treat fracture conformance problems in reservoirs with temperatures $< 150^{\circ}\text{F}$ are of the third gelation-delay type mode.

Gel Bottle Testing. Although not a highly sophisticated and exacting quantitative technique, bottle testing (ampoule testing at high temperatures) has been used widely in both the laboratory R&D setting and the field quality-control setting to test and evaluate gels, especially polymer gels.

Bottle testing provides a highly cost-effective and straightforward technique to obtain a semi-quantitative measure of gel strength and a semiquantitative measure of gelation rate. It is also a convenient means to evaluate the long-term stability of gels at a given test temperature. Bottle testing is often relatively easy to conduct in the field setting. Bottle testing in the laboratory provides a means to screen rapidly the performance of a large number of gel samples before selecting a few of the gels samples for more costly and rigorous testing, such as dynamic-oscillatory-viscosity and core-flooding experimental testing.

A polymer-gel bottle-test gel strength code has been developed and is now widely used (at times in various forms and with various modifications) for visually determining and evaluating, in a semiquantitative manner, the strength of polymer gels.⁸¹ **Table 13.2** shows the gel strength code. The gel strength code is set up such that two observers, who view the same gel sample, could possibly assign to the sample a gel strength code that differs by one letter code. However, the gel strength code is designed such that it is “virtually not possible” for two reasonable observers to view the same gel sample and assign the gel sample a gel strength code that differs by two letter codes. The comparison of the strength of different gels using this bottle-testing gel-strength-code scheme should only be made when the same volume of gel sample is placed in a bottle or ampoule with the same size and geometric shape. When quoting a gel strength code, the size of the gel sample and the size of the bottle should be provided. Bottle testing at low to intermediate temperatures is often conducted with a 50 cm^3 gel sample placed in a 120 cm^3 (4 oz) wide-mouth bottle.

When conducting polymer-gel bottle testing, there are several pitfalls to avoid. When performing field quality control work involving polymer gels containing H_2S , a nitrogen blanket should be applied to prevent the H_2S from reacting with atmospheric oxygen and forming intermediate free-radical chemical species that attack and degrade the polymer gel. This deleterious reaction with free oxygen does not occur in anaerobic oil reservoirs (most oil reservoirs are anaerobic). Free oxygen in the injected water of the gel formula tends to be chemically reduced and deactivated quickly in the chemically reducing environment of most oil reservoirs. Consumption of free oxygen in the chemically reducing reservoir environment is generally much faster than the oxygen-induced gel degradation reaction.

When conducting high-temperature ampoule testing of this bottle-testing scheme, the gelant solutions need to be scrupulously deoxygenated to less than 10 ppb free O_2 . There are two recommended procedures to deoxygenate the gelant solution of polymer-gel samples for high-temperature testing in the laboratory setting. The first procedure involves vacuum degassing to the point that the aqueous solution boils (ebulantes) for a minute or so and then glassblowing the ampoule shut under vacuum. It is highly recommended that properly tempered heavy-walled ($\sim 4\text{ mm}$ thick) glass ampoules be used for this purpose and that the glass ampoules be placed in appropriate transparent safety containers when the gel samples are aged in an oven at the test temperature. The second effective procedure for effectively deoxygenating gelant samples (to $< 10\text{ ppb O}_2$) for high-temperature laboratory testing is to bubble high purity argon gas through the gelant solution. The need to deoxygenate gel samples during high-temperature test-

A	No detectable gel formed. The gelant solution appears to have the same viscosity (fluidity) as the original polymer solution, and no gel structure is visually detectable.
B	Highly flowing gel. The gel appears to be only slightly more viscous than the initial polymer solution.
C	Flowing gel. Most of the obviously detectable gel flows to the bottle cap on inversion of the bottle.
D	Moderately flowing gel. A small portion (approximately 5 to 15%) of the gel does not readily flow to the bottle cap on inversion—usually characterized as a "tonguing" gel (i.e., after hanging out of the bottle, the gel can be made to flow back into the bottle by slowly turning the bottle upright).
E	Barely flowing gel. The gel slowly flows to the bottle cap and/or a significant portion (>15%) of the gel does not flow to the bottle cap on inversion.
F	Highly deformable nonflowing gel. The gel does not flow to the bottle cap on inversion (gel flows to just short of reaching the bottle cap).
G	Moderately deformable nonflowing gel. The gel flows approximately halfway to the bottle cap on inversion.
H	Slightly deformable nonflowing gel. Only the gel surface slightly deforms on inversion.
I	Rigid gel. There is no gel-surface deformation on inversion.
J	Ringing rigid gel. A tuning-fork-like mechanical vibration can be felt after the bottle is mechanically tapped.

ing is a laboratory artifact because gels existing in a reservoir will normally be in an anaerobic environment.

Flow and Placement Considerations. The flow properties of a gelant or gel as it is being placed are important parameters.

Gelant and Gel Flow and Placement in Matrix Rock. To date, for all known gelant solutions used in conformance-improvement treatments (including polymer gelant solutions), these gelant solutions place themselves in all matrix-rock geological strata according to Darcy flow considerations and do so without any special selective placement in only the high-permeability strata and flow paths.

Mechanical Zone Isolation. Any placement of gel into, and the associated permeability reduction of, a low-permeability and/or high-oil-saturation strata in the near-wellbore region surrounding a radial-flow matrix-rock-reservoir well will almost always be counter productive to improving the conformance of that well.^{7,8} Thus, when applying a gel treatment, especially a near-wellbore gel treatment, to treat a vertical conformance problem of a radial-flow well in a matrix rock reservoir, mechanical zone isolation must be used to assure that the gelant is injected only into the high-permeability and/or low-oil-saturation geological strata to be treated.^{7,8}

Gel Treatments When Matrix Crossflow Exists. For a gel treatment to be successful when treating vertical conformance problems in matrix-rock reservoirs in which there is fluid-flow and pressure crossflow communication between geological strata of differing permeabilities, the gel treatment must be selectively placed deeply in the reservoir.^{6,7} In addition, the gelant solution should approach unit mobility, or stated another way, the resistance factor equals 1.0 (i.e., the gelant solution should approach the viscosity of water).⁶ The successful treatment of verti-

cal conformance problems in matrix rock reservoirs of normal permeabilities (permeabilities < 1,000 md), where there is crossflow between the geological strata, requires the application of large-volume gel treatments for which the economic risks can be relatively high and the rates of returns can be relatively low. The large volume of gelant solution that needs to be injected begins to approach the volume of a traditional chemical flood, such as a polymer conformance-improvement waterflood. In addition, the requirement of being able to successfully propagate the gelant solution, or possibly microgels, deep into a matrix-rock reservoir (especially without damaging oil-productive zones) is a challenging task.

Gel Placement in Fractures. While no gel treatment fluid is available for the selective placement of gels (beyond Darcy flow considerations) into high-permeability flow channels of matrix reservoir rock of normal permeabilities, gels, especially polymer gels, can be routinely formulated for selective placement into fractures or into other high-permeability anomalies within a reservoir—such as fractures, solution channels, cobble packs, and rubblized zones. Such a polymer gel is normally designed so that the gelant solution is at least partially gelled when it leaves the wellbore, and initial microgels have formed. This initial gelation and the formation of microgel particles prevent the gel from substantially invading and damaging the matrix rock adjacent to high-permeability anomalies.¹⁰⁵ The next subsection of this chapter discusses a gel fluid-loss mechanism involving gel dehydration and expulsion of water from the gel into matrix reservoir rock adjacent to the gel-filled fracture. This gel dehydration does not involve the loss of gel from the fracture. For a properly designed polymer-gel treatment, gel leakoff from treated fractures is most often insignificant in terms of gel-treatment functionality. CC/AP fracture-problem polymer gels that are placed in such a manner are capable of selectively plugging the treated fracture volume effectively.¹⁰⁵

Gel Extrusion Through Fractures. Because many of the most successful gel treatments have been applied as large-volume treatments to naturally fractured reservoirs and because the injection times of such gel treatments often exceed the injected gel's gelation onset time (often by a factor of 10 or more), much of these gels must be flowing and extruding through the fractures in a mature gel state.^{106–108} Polymer gels used to treat fracture conformance problems have been shown, while extruding through fractures, to exhibit shear-thinning rheological behavior that correlates with gel superficial velocity and fracture width.¹⁰⁷ When extruding these gels through fractures at high velocities, the resultant pressure gradients within the fractures are insensitive to flow rate. This is a partial explanation for why these polymer gels have exhibited unexpectedly good injectivity into fractured formations. This explanation is not intuitive to many petroleum engineers.

Fracture-problem polymer gels of the type that are widely applied as sweep-improvement and water-shutoff treatments have a minimum pressure gradient that is required to mobilize the flow of the gel. This minimum pressure gradient for gel flow is proportional, over a broad range of fracture widths and differential pressures, to the inverse of the square of the fracture width.^{107–109} The implications of this observation are extremely significant. One implication is that these polymer gels will tend to be selectively placed in the widest and most offending fractures when treating fracture conformance problems in naturally fractured reservoirs. A second implication is that fracture-problem gel water-shutoff treatments, which are applied to a naturally fractured reservoir, should be designed so that the drawdown pressure of normal production operations does not exceed minimum pressure gradient for gel flow. If the drawdown pressure exceeds the minimum pressure gradient for gel flow, any gel experiencing drawdown exceeding the minimum pressure gradient for gel flow will be mobilized and back produced. Of note, the pressure gradient in the intermediate- and far-wellbore region of most naturally fractured reservoirs during oil-recovery operations is quite small (often less than 5 psi/ft). For a widely applied fracture-problem CC/AP gel formula under the studied experimental conditions,

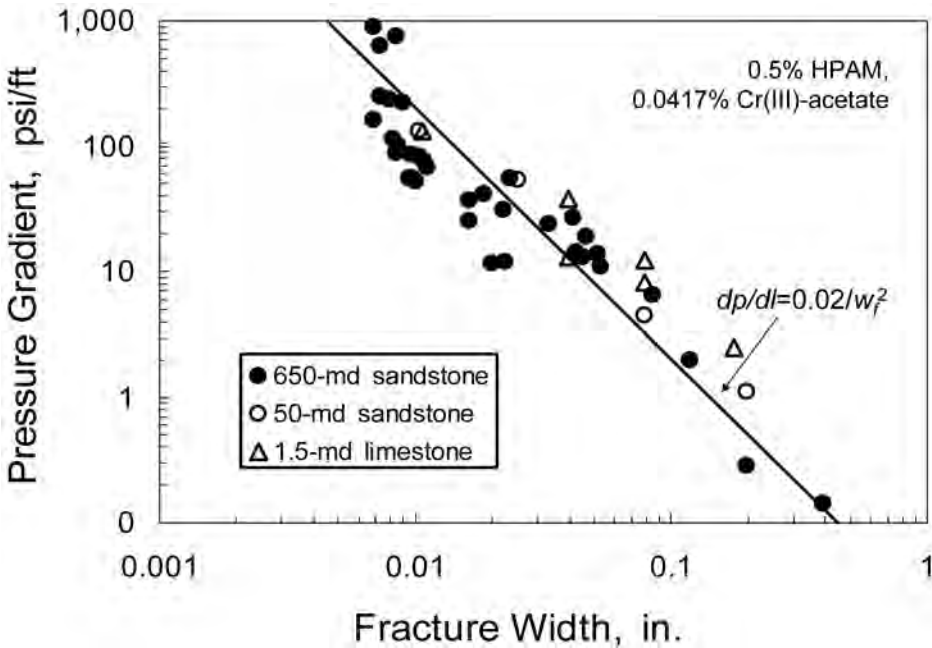


Fig. 13.23—Pressure gradients required to extrude a gel through open fractures.

the pressure gradient, dp/dl , required to extrude the gel from the studied fractures is described by the following mathematical equation:

$$dp/dl = 0.02/w_f^2, \dots\dots\dots (13.17)$$

where w_f is the fracture width.^{108,109} (See Fig. 13.23.) The data of Fig. 13.23 involved fracture widths ranging from 0.008 to 0.4 in. (0.2 to 10 mm) and pressure gradients from 0.1 to 1,000 psi/ft.

Aqueous polymer gels, being sponge like, can undergo dehydration while being propagated through fractures. Gel dehydration can occur any time a fracture-problem polymer gel experiences a differential pressure between the gel in the fracture and the adjacent permeable matrix reservoir rock. The rate of dehydration is not necessarily directly proportional to the differential pressure.^{108,109} This gel dehydration is loss of water from the gel and not leakoff of the gel itself. Gel dehydration decreases the rate at which the gel propagates through a given fracture and strengthens the gel that resides within the fracture. As previously noted, polymer-gel strength increases as the concentration of polymer and crosslinking agent increases within the gel. For a fracture-problem CC/AP gel formula that has been widely applied in the field and under experimental conditions simulating such field applications, the gel dehydration rate, μ_1 in ft/D (or alternatively $\text{ft}^3/\text{ft}^2/\text{D}$), has been described, as Fig. 13.24 shows, by the empirical equation:

$$\mu_1 = 0.05t^{-0.55}, \dots\dots\dots (13.18)$$

where t is time in days.¹⁰⁸ During the laboratory flooding-experiment study of Fig. 13.24, the fracture width was 0.04 in. (1 mm), fracture lengths varied from 0.5 to 4 ft, fracture heights varied from 1.5 to 12 in., and injection fluxes in the fracture varied from 130 to 33,000 ft/D.

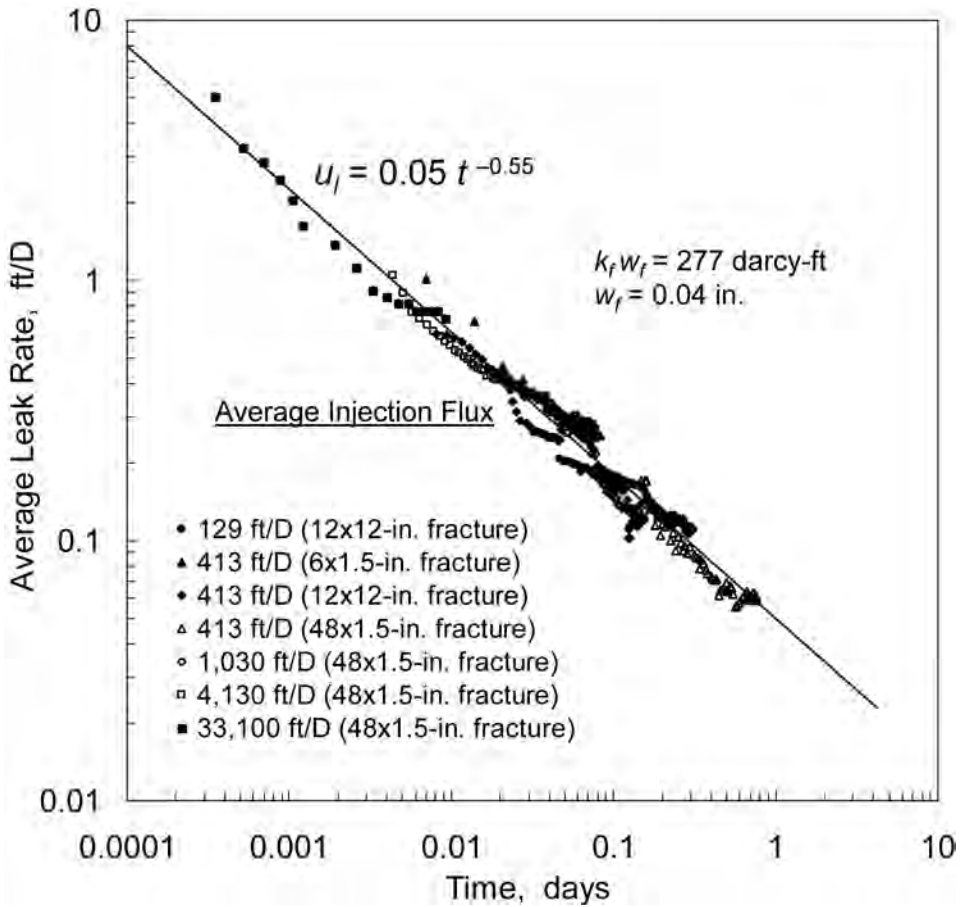


Fig. 13.24—Average gel-dehydration leakoff rate from seven fracture flooding experiments at different velocities.

The dehydration of fracture-problem polymer gels is the reason why if the objective is to inject the fracture-problem gel as deeply into a reservoir as possible, the gel should be injected as rapidly as feasible (without exceeding formation parting pressure). Conversely, to maximize the strength of the emplaced gel, the gel should be injected as slowly as feasible.

Gel Shear Rehealing. When a mature gel is exposed to a high shear-rate field and the gel structure is sheared, the gel may or may not be able to spontaneously reheal. Most polymer gels of the type used in hydraulic fracturing operations employ polymer crosslinking chemistries that impart shear-rehealing properties into the gel. That is, if the gel is subjected to a sufficient intensity shear flow field, the gel will temporarily shear degrade. The polymer chemical crosslinks will be temporarily broken, and the chemically crosslinked polymer molecules will temporarily separate in solution. However, on termination of the shear flow field, the gel and its chemical crosslinks of the polymer molecules will spontaneously reheal (for the most part). As a result, the gel will regain all (or nearly all) of its original gel strength. However, these gels are not normally good plugging agents for use in conformance-improvement treatments, especially for placement under high differential pressure conditions surrounding production wells. These gels, just like the “linear gels” resulting from high concentrations of uncrosslinked water-soluble polymers alone, tend to “slowly” flow under high differential pressure conditions. This is one possible shortcoming of the use of in-situ polymerization of

monomers for conformance-improvement purposes when no crosslinking monomer is incorporated into the in-situ polymerization process.

Many conformance-treatment polymer-gel technologies, such as CC/AP gels, use polymer-crosslinking and polymer chemistries that do not lend themselves to shear rehealing. These gels have effectively no tendency to flow through constricting microflow paths, such as pore throats, when subjected to differential pressure. When these gels are subjected to even very high shear-rate fields, the gel crosslinking sites and/or multiplicity of crosslinked sites on any given polymer molecule do not permit the crosslinked polymer molecules to separate at the crosslinking sites. If the shear-rate flow or shear-stress conditions become exceptionally high, the gel's polymer backbone begins to experience scissions caused by mechanical shear degradation, which results in irreversible shear damage and mechanical degradation of the polymer gel.

Injection Pressure. As a general rule, the reservoir fracture and/or parting pressure should not be exceeded during the injection of the gel treatment fluid. If reservoir fracture or parting pressure is unexpectedly and/or inadvertently exceeded when performing a gel treatment involving a relatively strong gel, normal practice calls for going to water injection at the same rate and pressure until the gel solution is displaced from the tubing. At worst in this situation, a minifracture will be created in the reservoir. On cessation of gel injection, the fracture will close, the gel will mature and should seal the fracture, and there will be little damage to the reservoir.

Hall Plots. Hall plots are often generated and analyzed during real-time placement of gel conformance-improvement treatments. At times, Hall plots of gel treatment placement have been creatively and unscientifically interpreted. The Hall plot was originally developed to analyze steady-state injectivity data for waterflood injection wells that are injecting into a single zone.¹¹⁰⁻¹¹² As normally used in conjunction with gel treatments and gel injection, $\Sigma p_{if} \Delta t$ is plotted vs. cumulative gel volume injected W_i , where p_{if} is the flowing wellhead pressure in psi, Δt is time in days, and W_i is cumulative injection volume in barrels. Under steady-state conditions, the slope of the Hall plot is

$$M_H = \frac{141.2\mu[\ln(r_e/r_w)] + s}{kh}, \dots\dots\dots (13.19)$$

where μ is viscosity in cp, r_e is the external reservoir radius in feet, r_w is the wellbore radius in feet, s is the skin factor, k is permeability in md, and h is formation height in feet. If a change in slope occurs in a Hall plot, all that the slope change can indicate, in the absence of some other and independent data, is that there has been a change in the well's injectivity. Without having other independent data, when a change occurs in the slope of a Hall plot, one cannot tell if the slope change was caused by a change in the well's skin factor, a change in the mobility (k/μ), or a change in the effective height of the well interval accepting the injection fluid.

Fig. 13.25 is a Hall plot illustrating an injectivity reduction after 5,000 bbl cumulative injection. In themselves, Hall plots, and any changes in their slopes, do not indicate selective placement of the gel in high-permeability channels during a gel treatment.¹¹²

Temperature Considerations and Limits. All gels, especially polymer gels, have a finite upper temperature limit above which the gels are not stable or functional. Significant progress has been made over the past two decades in increasing the upper temperature limit for the successful application of conformance-improvement gels. A continuation of this trend can be reasonably expected.

For CC/AP gel technology, the reservoir temperature limit for applying matrix-rock, near-wellbore total-shutoff treatments is reported to be 300°F.⁵ Ref. 5 reported that the upper temperature limit for treating high-permeability-anomaly conformance problems (e.g., fractures)

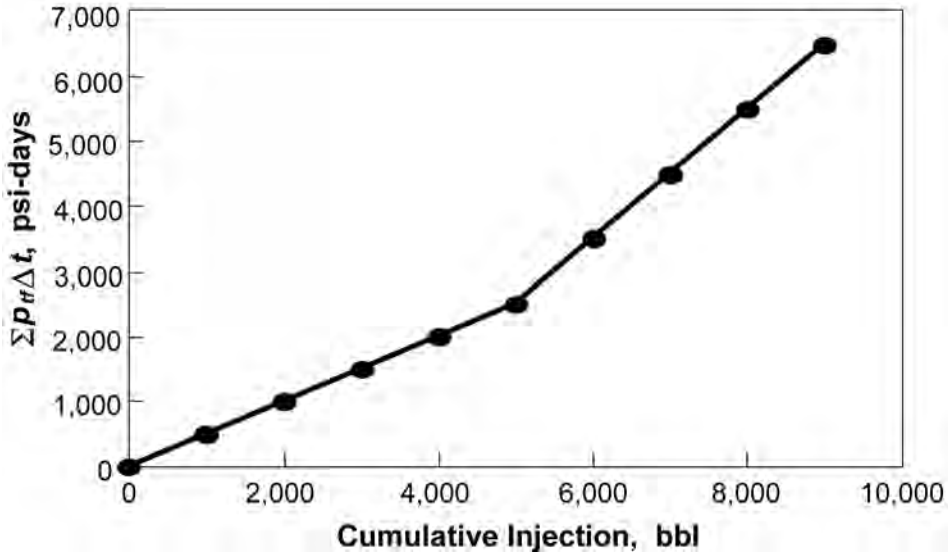


Fig. 13.25—Hall plot illustrating an injectivity decrease after 5,000 bbl cumulative injection.

with this gel technology can be up to approximately 270°F. Ref. 5 also discusses laboratory testing at 300°F that demonstrate how appropriately formulated CC/AP gels can essentially totally block flow to water in sandstone at high differential pressure conditions (1,000 psi per 3 in.) for an extended period of time (testing conducted for 23 days). Fig. 13.26 is a photo of a CC/AP gel that remained stable, rigid, and clear after aging for 2.5 years at 300°F. This CC/AP gel is used for near wellbore, total-fluid-shutoff purposes in high-temperature matrix-rock reservoirs. For most polymer-gel technologies, such as the CC/AP gel technology, it is necessary to increase the polymer concentration within a given formula as temperature increases to maintain gel stability, performance, and strength similar to that of the gel formula at lower temperatures.

Conformance-improvement gels, consisting of an acrylamide polymer crosslinked with a set of organic crosslinking agents, have been reported to form strong and stable gels up to 350°F.⁹⁰ This is an interesting observation because, in both this and the CC/AP conformance gel technology, it is believed that it is not the crosslinking chemistry that is limiting high-temperature gel stability, but limitations in the thermal stability of the gel's organic polymer. Thus, one interpretation of these observations is that the acrylamide polymer used in the organic-crosslinked acrylamide-polymer gels was of a purer and more stable form.

The upper reservoir temperature limit, at which a given gel technology is stable and functional, is an interrelated function of polymer concentration and chemistry used in the gel, hardness divalent-ion concentrations within the gel's makeup water, polymer purity, and, if used, the chemical stabilizer package.⁵ For organic polymer gels, stability is, in part, a function of the level of free-radical and free-radical-precursor chemical impurities in the polymer material itself. Free radicals cause organic-polymer backbone scission and associated polymer-gel degelation.

It is imperative to truly know what the upper reservoir temperature limit is for a conformance gel technology that is to be applied to a high-temperature reservoir and to not apply such a treatment at a temperature exceeding the temperature rating of the gel being used.

Treatable Conformance Problems. Table 13.3 provides guidelines as to which conformance problems are attractive and unattractive to treat with polymer gels.

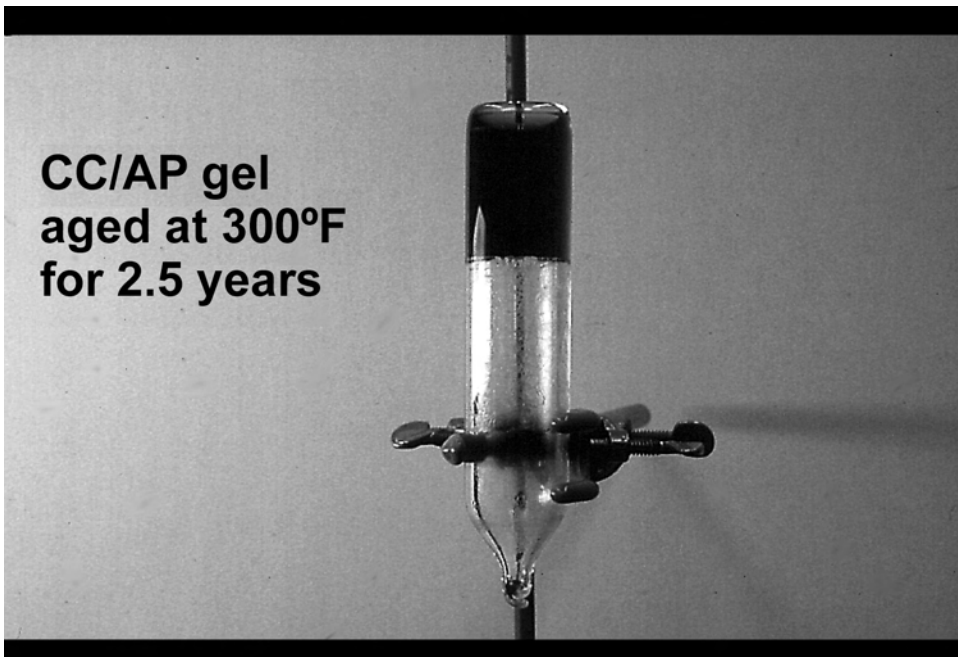


Fig. 13.26—CC/AP gel aged for 2.5 years at 300°F.

TABLE 13.3—CONFORMANCE PROBLEMS THAT ARE ATTRACTIVE TO TREAT WITH POLYMER GELS	
<u>Matrix Conformance Problems</u>	
Without crossflow	Yes
With crossflow	Challenging—must place very deeply
<u>Fracture Conformance Problems</u>	
Simple	Depends—case-by-case basis
Network—intermediate intensity and directional trends	Yes
Network—highly intense	Often not
Hydraulic	Yes
<u>Coning</u>	
Water and gas via fractures	Yes
Water and gas via matrix reservoir rock	No
<u>Behind Pipe Channeling</u>	Yes, for microflow channels
<u>Casing Leaks</u>	Yes, for microflow channels

Gel Treatment Design. The first step in designing a gel treatment is to correctly identify the nature of the conformance problem to be treated. This includes, during water- or gas-shut-off treatments, identifying the flow path of excessive water or gas production from its source to the production wellbore.

Gel Technology Selection. The following procedure for gel technology selection is highly generalized, and the procedure should be modified as dictated by the actual reservoir confor-

mance problem to be treated. If a service company or a company specializing in conformance-treatment gels is to be involved, they should be consulted during each step of the selection process. A prerequisite is to eliminate all gel technologies, if any, that are prohibited by locally applicable safety or environmental regulations.

First, determine the type of problem that is to be treated. That is, whether it is a matrix-rock problem or a high-permeability-anomaly problem, such as fractures. If treating a matrix-rock problem, decide if you need a gel for treating near-wellbore or deeply in the reservoir. Determine how strong the gel needs to be. If the gel must be placed deep in the reservoir, economic constraints on the unit volume cost of gel pumped need to be carefully factored into the gel technology selection process. If the gel treatment will require a shut-in time following gel placement, decide on the shut-in strategy (i.e., what shut-in time range is acceptable) and chose a gel technology accordingly. Then, begin to select a gel technology that will function as required at the reservoir temperature being treated.

Next, if treating a high-permeability-anomaly (> 2 Darcy) conformance problem, select a gel-treatment fluid that can be injected into the reservoir in a mature or partially mature state. If treating matrix-rock conformance problems for which all the permeabilities are less than approximately 2 Darcy, select a gel technology that can be injected in the gelant state. After completing these steps in the gel-selection process, decide what the initial and near-full gelation times should be. Depending on the exact needs of the treatment design so far, predict the thermal history that the gelant will experience as it is being injected. If a precise thermal history for the gelant as it is being injected is required, computer thermal-simulation work may be needed.

Based on the outcome of the gel technology selection process so far, numerous conformance gel technologies may have already been ruled out. If so, the remaining selection process may be simpler. Next, the remaining gel technologies, which fit all the gel technology selection criteria, should be sorted through to select the gel technology that will perform the most effectively in treating the reservoir conformance problem and will meet the specialized needs of the operator who is applying the gel treatment. At this point, if economically justified, comparative laboratory studies may be conducted to help select with more certainty which of several gel technologies will perform most effectively in treating the reservoir conformance problem that is to be remedied.

Treatment Sizing. At this writing, technical sophistication relating to the method used to size the volumes of various conformance-improvement gel treatments needs improvement. The encouraging news is that there are active R&D programs that are specifically pursuing the development of a more rigorous scientific and engineering basis for use in the sizing of conformance-improvement gel treatments. Ref. 28 reports on a sound engineering basis for the sizing of polymer-gel treatments, injected as gelants, for treating excessive water production that results when a hydraulic fracture inadvertently extends down into an aquifer or into some other type of water-bearing geological strata. Ref. 28 also references a user-friendly computer program for use in sizing such gelant treatments and provides information on how the computer program can be downloaded.

Unfortunately, sizing of gel treatments remains highly empirical and is often based on the experience of operators and gel service companies. There are a number of empirical guidelines for sizing conformance gel treatments. When conducting near-wellbore gel treatments in matrix-rock reservoirs for total shutoff purposes, such as when using a CC/AP gel treatment for zone-abandonment or squeeze-and-recompletion treatment purposes, the rule of thumb is to inject a gel treatment volume that extends, on the average, 6 to 9 ft radially from the wellbore. This is a good guideline when treating reservoirs with elevated temperatures ($> 150^{\circ}\text{F}$) and large drawdown pressures (> 300 psi). For lower temperatures and lower drawdown pressures, this rule of thumb can be relaxed somewhat. The depth of gel placement must be increased for gel tech-

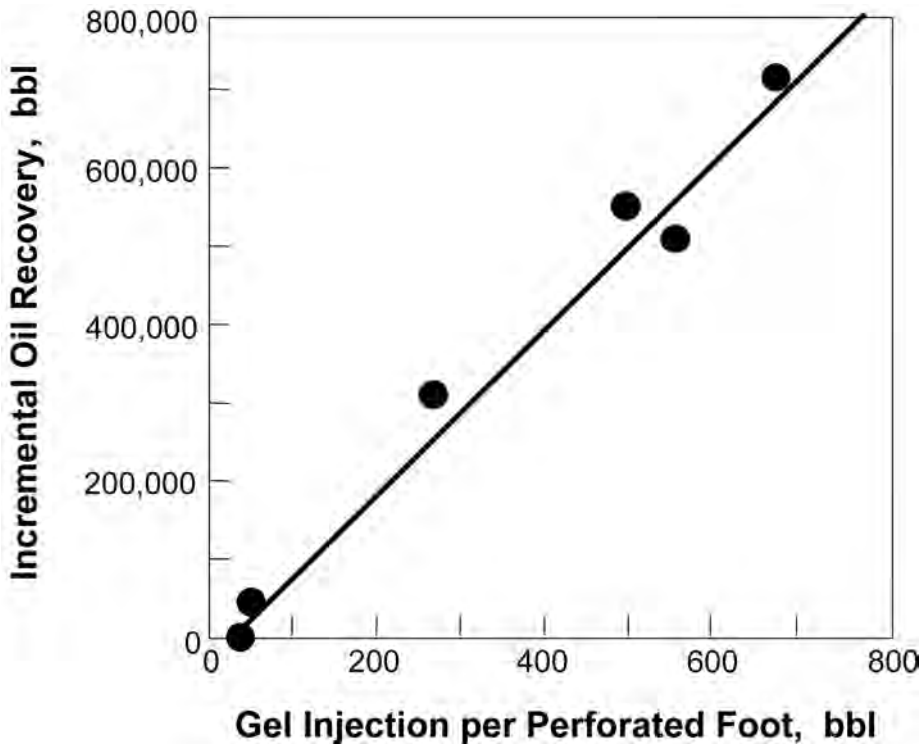


Fig. 13.27—Incremental oil production vs. volume of gel injected for CC/AP gel treatments applied to a series of fractured injection wells.

nologies that produce relatively weaker gel strengths. For any given gel treatment applied for total-fluid-shutoff application in the near-wellbore region in matrix reservoir rock, as the gel chemical loading is increased, the rule of thumb can again be relaxed (but do not treat, on the average, less than 3 ft radially). When using such higher chemical loadings in the gelant formula, the required depth of treatment penetration can be reduced, in part, because more chemical is available on the leading edge of gelant volume to be consumed and lost to the reservoir rock in the treated reservoir volume.

A series of CC/AP gel treatments were applied in an economically attractive manner as sweep-improvement treatments to waterflood injection wells of carbonate and sandstone reservoirs possessing fracture networks of intermediate intensity with directional trends. Gel treatment volumes ranged between 50 to 700 bbl of gel injected per perforated foot of reservoir pay zone.¹⁰⁶ Fig. 13.27 shows how the incremental oil production for these treatments increased as the amount of gel injected per perforated foot increased. Gel treatment volumes for this series of treatments ranged up to 37,000 bbl of gel injected. The trend depicted in Fig. 13.27 cannot be extrapolated to an infinite volume of incremental oil production. This curve must eventually bend over and not exceed the recoverable amount of oil in any given reservoir. However, for the volumes of gel injected for this series of gel treatments, the volume of gel injected had not yet begun to approach the volume of gel required to cause the curve to bend over.

Gel treatment volumes of 25 to 50 bbl (100 bbl in specialized cases) of gel injection per perforated foot of reservoir producing interval have been reported to have been injected during successful CC/AP gel water-shutoff treatments of production wells of naturally fractured reservoirs.⁵ One to two barrels of gel per foot of treated wellbore interval were injected during a series of total-shutoff CC/AP gel treatments that were successfully applied as chemical liner

completions to the curved section of openhole short-radius horizontal wellbores.¹¹³ These gel chemical-liner treatments were applied during the drilling of short-radius horizontal wells in a thin oil column. The gel chemical-liner treatments were applied to the curved section of the openhole borehole. Without the application of these chemical-liner gel treatments, excessive and uneconomic volumes of gas would have been produced into the short interval of openhole curved section of the borehole that extended up into the gas cap. For gel water-shutoff treatments to be applied to a vertical fracture that intersects a horizontal wellbore, it has been suggested that the gel needs to be placed only deep enough so that the gel will be able to prevent direct water entry into the borehole at the point of the fracture intersection.¹¹⁴

In general, an acceptable design strategy for sizing the volume of gel treatments applied to matrix rock (unfractured) reservoirs is to specify the radial distance that a gel treatment will extend, on the average, from the treated wellbore. The exact values of the required gel radial-penetration distance will be a strong function of, and vary widely with, the nature of the specific gel to be used, the nature of the reservoir-conformance problem, the nature of the reservoir properties, and the well's drawdown pressure. When conducting a gel treatment in a reservoir with a significant amount of fracturing, discussing radial depth of gel penetration into the reservoir from the wellbore is near meaningless, unless the fracture reservoir plumbing is quantitatively well characterized.

Injection Rate. When injecting fracture-problem gels, especially polymer gels that undergo gel dehydration during placement, the gel should be injected as rapidly as practical (without exceeding parting or fracture pressure) if the objective is to place the gel as deeply as possible into the fracture or fracture network. If the objective is to maximize the strength of the placed fracture-problem gel, then the gel should be injected as slowly as is feasible.¹¹⁵

In general, gel treatments should be injected as rapidly as feasible without exceeding reservoir parting or fracture pressure. For a gel with a given gelation onset time and gel that is to be injected into a matrix rock reservoir and for the situation of the gel-treatment pumping time possibly exceeding the gelation-onset time, maximizing the injection rate will maximize the amount of gel that can be injected within the gelation-onset-time constraint. Maximizing the injection rate will also reduce pumping time and costs.

A special word of caution needs to be made. If while pumping a gel treatment unexpectedly high or rapidly increasing injection pressure is encountered, normally a poor option to choose is to cut the pumping rate. When injecting a gel treatment, cutting the injection pump rate increases the residence time of the gel in the injection tubulars and results in a more structured gel being injected into the reservoir. Both of these outcomes are the opposite of what is needed if excessive injection pressure is being encountered. Also, many polymer-gel solutions are shear-thinning fluids. Thus, reducing the rate at which these gel solutions are being pumped results in a more viscous gel solution being pumped and injected. Again, this is the opposite of what is needed if excessive injection pressure is being encountered. The better options are to either stop gel injection and immediately clear the injection tubulars with water or reduce chemical loading in the injected gel.

Overdisplacement. The importance of the overdisplacement fluid itself and the volume of the overdisplacement fluid can range from negligible to profound. For example, the nature of the switch over to injecting water immediately following a large-volume weak gel treatment that is applied to an injection well as a sweep-improvement treatment is normally very straightforward and noncrucial. However, when applying a polymer-gel water-shutoff treatment to a naturally fractured reservoir surrounding a production well for which the excessive water production results from fracture channeling during a waterflood, the choice of the fluid and the volume injected of the overdisplacement fluid following gel injection is a crucial element of the treatment design and can have a major effect on treatment performance.

Balancing the following three (often opposing) requirements is critical to the success of this type of gel water-shutoff treatment. The first requirement is to displace the gel deep enough into the formation so that when the well is put back on normal production, the large near-wellbore drawdown differential pressure does not overlap some of the emplaced gel volume such that the large differential pressure will exceed the critical differential pressure for gel flow and, in turn, cause such emplaced gel to be back produced. The second requirement is that the gel is not excessively overdisplaced from the most offending and troublesome of fracture flow paths so as to permit undesired water production. The third requirement is that the gel is sufficiently overdisplaced so that the gel will not excessively block desired oil production through the fracture network to the production well. Many such successful polymer-gel water-shutoff treatments require post-treatment oil flow through fractures to the wellbore. At this writing, a lot of art is used in the selection of the overdisplacement fluid and its volume for this type of fracture-problem water-shutoff gel treatment.

The three basic varieties of overdisplacement fluids are water or brine (usually injection or produced water), a polymer solution (often the polymer solution of the gel without the addition of the crosslinking agent), and a hydrocarbon liquid (such as diesel or the reservoir crude oil). For water-shutoff gel treatments, the use of a liquid hydrocarbon has been advocated as a means to establish favorable relative permeability to oil flow in the near-wellbore environment. The pros and cons of the use of a hydrocarbon overdisplacement fluid during water-shutoff gel treatments have been vigorously debated among experts. The bottom line of these debates is that whether the use of a hydrocarbon fluid is favorable is reservoir specific and is relatively more advantageous when treating matrix-rock reservoirs. The use of a viscous polymer solution as the overdisplacement fluid helps to mitigate (or completely mitigates) the problem of a non-viscous brine overdisplacement fluid fingering into the gelant solution in the wellbore and near-wellbore environment, especially in a near-wellbore fracture environment. Additionally, there are numerous gel-treatment cases for which the use of a brine overdisplacement fluid is favored for functional, operational, safety, environmental, and/or economic reasons.

For total-fluid-flow-shutoff purposes in matrix rock, both the type of overdisplacement fluid used during a water- or gas-shutoff gel treatment and how much the gelant solution is over- or underdisplaced from the wellbore are critical. Gel will be left in the wellbore if underdisplaced. Overdisplacement can result in near-wellbore flow paths being opened to flow and essentially negating the value of the entire treatment. In general, the gel is underdisplaced, and some gel is left in the wellbore downhole near the production interval when treating matrix rock problems. Gel left in the wellbore will often spontaneously clean up during normal post-gel-treatment production, but, if not, can be cleaned/jetted out of the wellbore using coiled tubing.

Shut-in Time. After the placement of many gel treatments, the well needs to be shut in to allow the gelant solution to mature and set up. Post-treatment well shut in is mandatory following fluid-shutoff gel treatments applied to production wells in matrix rock reservoirs. Usually, the well needs to be shut in for the length of time it takes the gelant to reach near-full gel strength under the conditions encountered within the treated reservoir volume.

Returning a Well to Production. During the application of gel treatments to production wells for water- and gas-shutoff purposes, the manner in which the well is returned to production can have a major impact on the performance of the gel treatment. It is generally recommended to slowly return a gel-treated production well back to full production over a period of a day to several days. Obviously, the exact manner in which a production well should be slowly returned to full production is a strong function of the nature and the strength of the particular gel used and the nature of the reservoir being treated.

Injection Mode. There are two major modes of injecting conformance polymer-gel treatments. The single-fluid injection mode involves incorporating all the chemical components required to form the gel into a single gelant (pregel) solution. Essentially all modern conformance-

improvement polymer-gel treatments are injected in this mode. As discussed in the Classification of Gel Treatment Types subsection of [Sec. 13.6.1](#), many early polymer-gel treatments were pumped using the sequential-fluid injection mode.

Disproportionate Permeability Reduction. [Sec. 13.4](#) reviewed the applicability, limitations, desirability, and fundamental concepts of DPR as it applies to conformance-improvement (including water and gas shutoff) treatments. It focused on the application of radial-flow DPR conformance-improvement treatments that are applied in matrix rock (unfractured) reservoirs. The development and successful application of conformance-improvement DPR gels is of substantial interest to the petroleum industry, as indicated in [Refs. 4, 19 through 21, and 37 through 39](#). Gels that are used in matrix-rock radial-flow DPR gel treatments are typically characterized as being relatively weak gels.

A DPR gel treatment scheme exists²⁸ that often favors the use of relatively strong DPR polymer gels, for treating excessive water or gas production problems that occur in wells producing from a fractured oil-bearing formation. Such DPR fracture-problem gel treatments, which are conducted for water-shutoff purposes, are applied in the situation in which the oil-producing layer (producing 100% oil) is underlain or overlain by a water-producing zone and the vertical fractures provide the conduit for the undesired water production. The scheme was originally developed for, and is most directly applicable to, a production well that has been hydraulically fractured, where the hydraulic fracture has inadvertently extended down into, or up into, a water zone. Such gel DPR water-shutoff treatments require that the gel be placed in the matrix reservoir rock that is adjacent to water-producing fracture. A publicly available computer program can help design and size such a DPR water-shutoff gel treatment.²⁸ A strong CC/AP gel would be a good candidate for use in this type of DPR fluid-shutoff treatment. This DPR gel treatment scheme for imparting water-shutoff/reduction in fractured reservoirs is also applicable as production-well water-shutoff treatments that are applied to naturally fractured reservoirs in which the oil zone overlies or underlies a water zone or aquifer and when hydraulically fracturing through thin interbedded oil- and water-bearing geological strata.

13.6.2 Illustrative Field Results. The following examples illustrate field applications of various types of conformance-improvement gel treatments.

Fracture Problem Sweep-Improvement Treatments. [Fig. 13.28](#)^{5,106} shows the type of production response that is possible when applying a polymer-gel treatment to a waterflood injection well to improve sweep efficiency. The sweep-improvement treatment involved the application of a CC/AP gel treatment. The figure shows the combined production-response of the four direct offsetting production wells to the gel-treated injection well. The gel treatment was applied for waterflood sweep-improvement purposes to the naturally fractured Embar carbonate formation surrounding Well O-7 of the highly mature SOB field in the Big Horn basin of Wyoming. The wide variations in WOR and oil production rate are quite common in many of the well patterns of this highly fractured reservoir. [Ref. 106](#) provides more details regarding the 20,000 bbl gel treatment. The economics of applying this gel treatment were exceptionally good.

[Fig. 13.29](#)^{5,116} shows seven years of incremental-oil-production response for the combined direct offset producing wells to CC/AP gel-treated injection well O-17 of the SOB field. This figure illustrates the type of treatment longevity that can be expected from CC/AP gel treatments. Well O-17 was treated in approximately the same manner and as part of the same gel treatment series cited for the Well O-7 gel treatment in [Fig. 13.28](#).

Water Shutoff Treatments. [Fig. 13.30](#) shows the production response type that can occur when a gel treatment is applied to a production well to reduce excessive water production. In this case, a CC/AP gel treatment was applied to a production well for water-shutoff purposes. The gel treatment was applied to the 145°F fractured carbonate reservoir surrounding produc-

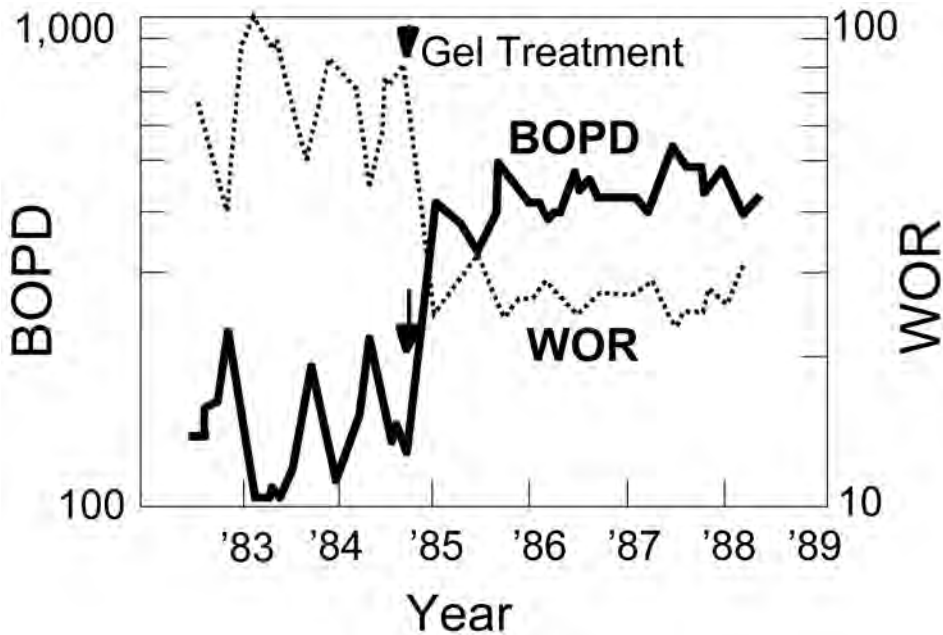


Fig. 13.28—Production response to the CC/AP gel treatment applied to injector O-7 in the SOB field.

tion well LSD N-17P in a field in Wyoming's Big Horn basin. The excessive water production, which was occurring during primary production, was thought to be edge water encroaching through fractures from a strong aquifer. Water production before the gel treatment was 5,000 BWPD. Following the treatment, the water production was reduced to 1,000 BWPD.⁵ There was a short-lived (several months) modest oil-production increase following the treatment that paid out the cost of the gel treatment. The primary objective and benefit was the water shutoff.

More recently, a large number of CC/AP gel water-shutoff treatments have been successfully applied to often old and highly marginal production wells of the dolomitic Arbuckle formation in Kansas. The excessive and detrimental water production is believed to be aquifer water coning up to the production wells via fractures or some other type of high-permeability anomaly. Successful Kansas Arbuckle CC/AP gel water-shutoff treatments often reduce the water production rate by more than 90%.

Willhite and Pancake reported in 2004 that more than 250 CC/AP water-shutoff treatments had been applied to Kansas Arbuckle wells.¹¹⁷ Their paper reported that incremental oil production was, in general, the business driver for conducting these gel treatments. The focus of their paper was on seven of these gel treatments that were studied in detail, where downhole pressure data was obtained before, during, and after the gel treatments. Highlights relating to these seven Arbuckle gel water-shutoff treatments are as follows:

- Water production was reduced in every well by 53 to 90%.
- Incremental oil production was obtained for 5 out of the 6 wells that were produced for 6 months after the gel treatment.
- Oil productivity indexes increased following the gel treatments.
- Incremental oil production increased with increasing volume of the gel treatment for the wells that were completed open hole.
- The duration of the treatment response is expected to be a function of the volume of the gelant injected.

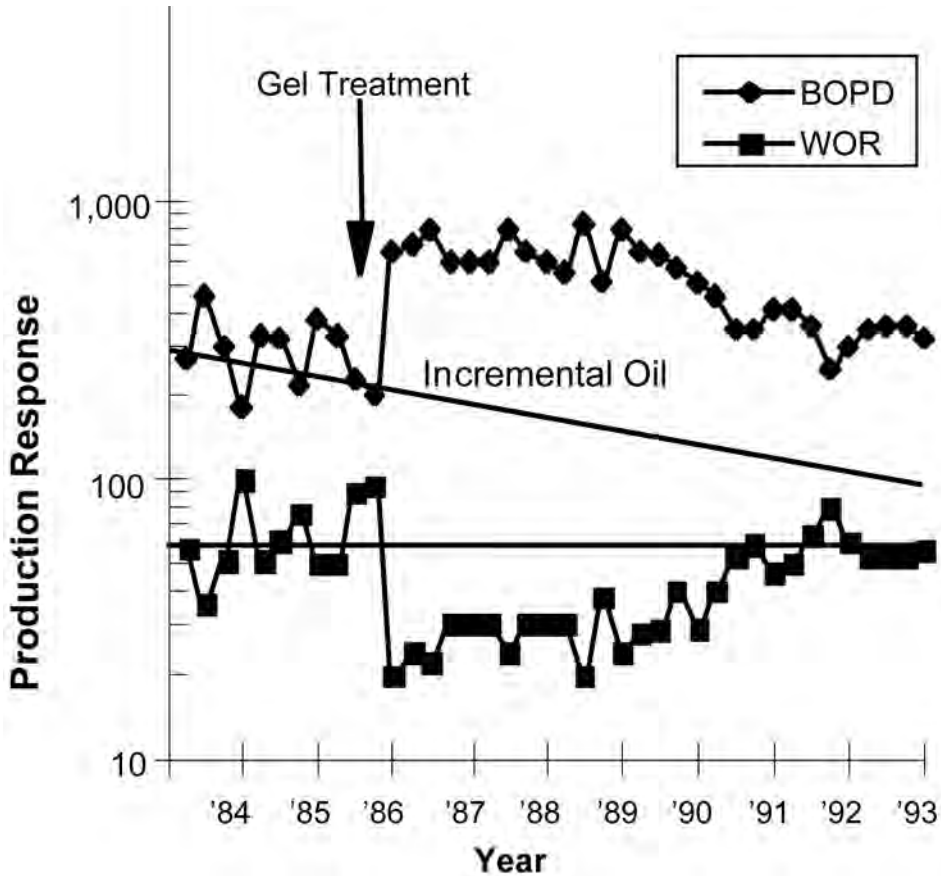


Fig. 13.29—Production response to the CC/AP gel treatment applied to injector O-17 in the SOB field (after Ref. 5 and Southwell¹¹⁶).

Rodney Reynolds reported on the performance of 300 CC/AP gel water-shutoff treatments that were applied in the Arbuckle formation of Kansas by more than 30 different operators.¹¹⁸ The 250 CC/AP gel water-shutoff treatments of Ref. 117 are likely a subset of these 300 gel treatments. The following analyses are based on performance data that were obtained from 95 of the 300 treatments and then factored/proportioned up to the 300 CC/AP gel water-shutoff treatments. Reynolds reported the following performance attributes for the 300 Arbuckle water-shutoff treatments (based on the 95 gel treatments analyzed):

- Shut off 110,000,000 bbl of excessive and undesirable water production.
- Generated 1,600,000 bbl of incremental oil from these, in general, old and marginal wells.
- Cost of the gel pumped ranged from approximately U.S. \$10 to \$15 per bbl.
- Average treatment size was 2,600 bbl of gel fluid injected.
- For gel treatments with “average performance,” payout times ranged from 3 to 6 months (based on incremental oil production only).
- Average incremental oil production from these “marginal” production wells was 5,500 bbl of oil.
- Operators reported reserve development costs for the incremental oil of U.S. \$2 to \$7 per bbl.

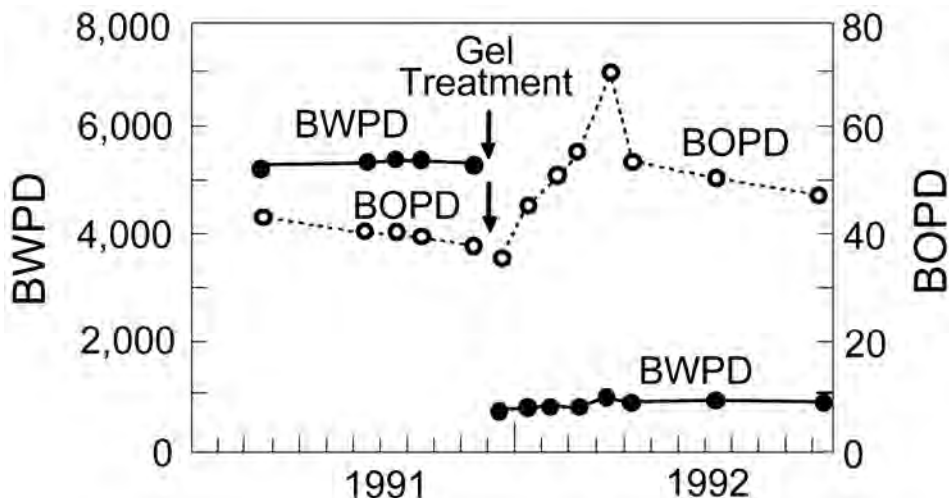


Fig. 13.30—Production response to the CC/AP gel water-shutoff treatment applied to production well LSD N-17P.

Gas Shutoff Treatments. Ref. 119 reported on 37 CC/AP gel gas-shutoff treatments that were applied to 31 production wells in the 190 to 220°F reservoir of Alaska’s Prudhoe Bay field. It reported that these gas-shutoff gel squeeze treatments cost 75% of comparable Portland cement gas-shutoff squeeze treatments in this field and afforded a higher success rate. Ref. 119 also reported that these gel gas-shutoff treatments had been credited with a gross initial (one month of production) incremental-oil-production rate of 22,000 BOPD and that these gel treatments reduced gas production to 213 MMscf/D. Ref. 119 stated that “squeeze longevity has been greater than one year [to date] in some cases with drawdown pressures exceeding 1,500 psi.”

Microgel Sweep-Improvement Treatments. Colloidal dispersion gels of acrylamide polymer crosslinked with aluminum citrate have been applied somewhat extensively in the U.S. Rocky Mountain region, especially in the Minnelusa sand formation. These large-volume gel treatments were applied to secondary and tertiary projects to promote in-depth permeability modification in highly heterogeneous “matrix” sandstone reservoirs. Ref. 9 reviews the recovery and economics of 29 such aluminum-citrate colloidal dispersion gel treatments. The polymer concentration of the aluminum-citrate colloidal dispersion gels was typically in the 200 to 1,200 ppm range. The mechanism by which these aluminum-citrate colloidal dispersion gel treatments function is not well understood, and technical issues relating to this technology are being debated.

Fractures Intersecting a Horizontal Well. Ref. 115 reviews the successful design and application of polymer-gel water-shutoff treatments that were applied using bullhead placement for treating excess water production from horizontal wellbores into which the excessive and competing water production was emanating from a “vertical” natural fracture that intersected the horizontal borehole and extended into an underlying aquifer. This is an emerging gel water-shutoff technology that is creating substantial interest because of the large number of expensive multilateral and/or subsea horizontal wells for which any water-shutoff treatments to be applied through these horizontal wells must be bullheaded due to their often openhole, multilateral, and/or subsea completions that do not readily permit the use of mechanical zone isolation.

Use During CO₂ Flooding. Borling¹²⁰ reported on successful conformance-improvement CC/AP gel treatments that were applied at the Wertz field CO₂ tertiary water alternating gas (WAG) flooding project in Wyoming’s Wind River basin. He reviewed 10 injection-well gel treatments applied to a 165°F naturally fractured Tensleep sandstone reservoir. The following

Reservoir lithology	Carbonate	Sandstone
Number of treatments	11	6
Average incremental oil recovery per treatment, STBO	261,000	129,000
Average incremental oil recovery per unit of polymer injected, STBO/lbm	17.5	7.6

benefits were reported to have been derived from applying these gel treatments during the Wertz CO₂ flooding project in this naturally fractured reservoir. The gel treatments promoted incremental oil recoveries of up to 140,000 barrels per well pattern and increased oil production rates by 100 to 300 BOPD per well pattern. The gel treatments extended the economic lives of marginal well patterns by nearly two years. They reduced GORs and WORs, reduced gas and water cycling, reduced gas and water breakthrough times, and improved water and gas injection profiles. The CC/AP gel treatments reduced operating expenses, contributed substantially to the fieldwide decline-rate reduction in 1992 from 24 to 9%, were effective where conventional oilfield foams had failed, and had rapid payout times of often less than three months. The Wertz conformance-improvement gel treatments were responsible for recovering substantial reserves that would not have been otherwise recovered.

Hild and Wackowski¹²¹ reported on 44 injection-well CC/AP gel treatments that were applied during 1994 through 1997 at the CO₂ miscible WAG flooding project of the Rangely Weber Sand unit in northwestern Colorado. These injection well treatments (average size ~10,000 bbl) had an 80% success rate and rendered an economic rate of return of 365%.

Gas Shutoff in an Openhole Gravel-Pack Completion. A “successful and selective” gas-shutoff treatment, using an organically crosslinked acrylamide-polymer gel, has been documented.¹²² The gel treatment was applied to an offshore well in the Norwegian North Sea. The gel treatment was applied to a gravel-packed well penetrating a multilayer reservoir containing shaley sandstone strata. A temporary blocking gel of crosslinked hydroxypropyl guar was selectively placed to temporarily seal and protect the upper producing portion of the well, while the organically crosslinked acrylamide-polymer gel for shutting off the lower gas-producing strata was being injected.

Carbonate vs. Sandstone Reservoirs. Table 13.4 shows a comparison of the production response and the economic performance of a series of large-volume (4,000 to 37,000 bbl) CC/AP gel treatments that were applied, between 1985 and 1988, as sweep-improvement treatments to naturally fractured injection wells in Wyoming’s Big Horn basin. The averaged combined production responses of the four direct offsetting production wells to the treated injection wells are shown. For this set of treatments, 11 of the gel treatments were applied to the naturally fractured Embar carbonate formation and six of the gel treatments were applied to the naturally fractured Tensleep sandstone formation. The gel treatments performed well in both the carbonate and sandstone reservoirs. The difference in performance of the gel treatments in the two sets of reservoir mineralogies is believed to have resulted mostly from differences in fracture characteristics and not from differences in gel performance in the two types of mineralogical formations. The fracture network of the carbonate formation in this instance is believed to be more conducive to being successfully treated with gel sweep-improvement treatments.

Chemical Liner Completions. More than 100 successful CC/AP gel gas-shutoff treatments were applied as chemical liner completions and were performed during a drilling program involving the drilling of short-radius horizontal wellbores in the Yates field of Pecos County, Texas.^{5,123,124} The gel chemical liner completions were applied to the openhole curved section

of the horizontal wellbores. The lateral borehole of these wells penetrates a relatively thin oil column in a fractured dolomitic reservoir, where the oil column is overlain by a substantial gas cap. The openhole curved section of the short-radius borehole partially extended up into the gas cap. If the curved section of the boreholes were not sealed, the horizontal wells would produce excessive, and often uneconomic, high GORs. In 1995, the first 80 of these horizontal wellbores, which had been treated with the gel chemical liner treatments, were producing 12,500 BOPD and had recovered approximately six million cumulative barrels of crude oil.⁵

13.6.3 Miscellaneous Gel-Treatment Issues. *Gels Complement Portland Cement.* A number of petroleum engineers believe that oilfield gel treatments are a competing technology to Portland cement. Gels of oilfield conformance-improvement treatments are, in reality, a complementary technology to Portland cement. Where Portland cement functions well, oilfield gels do not, and vice versa.

Gels are effective plugging agents for use in blocking fluid flow in flow channels with small apertures, such as pore-level flow paths in matrix reservoir rock and in microannulae behind pipe, where such microannulae often exist between a primary cement job and the adjacent geological formation material.

However, the solids contained within Portland cement prevent cement slurries from penetrating any significant distance into matrix reservoir rock or other similar small-channel flow paths. In fact, squeeze cement water-shutoff treatments function primarily by squeezing off perforations or by breaking down the formation rock and placing the cement into the newly formed reservoir partings. Even so-called microfine cement does not propagate any significant distance into oil-reservoir matrix rock of normal permeabilities, such as sandstone formations with permeabilities less than 1,000 md.

If the goal is to treat to any significant depth into matrix reservoir rock or other small flow channels such as microannulae behind pipe, the placement and maturation of a solids-free gelant solution of an appropriate gel is the preferred technique for shutting off fluid flow in such instances. However, if the goal is to plug large flow channels, such as a perforation, a large void space behind pipe, or oilfield tubulars, then the use of cement is the preferred technology. Oilfield gels, in general, simply do not have the favorable compressive strength characteristics of Portland cement that are required to plug such large flow channels, especially if there is any significant differential pressure involved in the fluid flow to be blocked. However, if solids are incorporated into the gelant solution of an oilfield gel, especially a polymer gel, the compressive strength of the resultant gel can be dramatically increased. When the solids loading is significantly increased in the gel or a local volume of the gel, the compressive strength of the gel can approach that of Portland cement.

A problem faced by petroleum engineers is determining the size of the fluid-flow channels to be plugged and whether they should pump an appropriate gel treatment or a Portland cement squeeze job. When conducting a gel production-well water- or gas-shutoff treatment for which there may be a significant distribution in the size of the offending flow channels, there may be uncertainty in the size of the problematic flow channels or significant drawdown pressures involved. In these instances, a good strategy is to cap off a gel treatment with Portland cement.¹²⁵ The reverse order of first injecting cement and then gel is not recommended. The cement cap should not be pumped at rates that will exceed the downhole reservoir parting or fracture pressure.

Historical Trends. Part of the explanation for the historically low success rate of gel treatments applied for the first time in a new field by inexperienced petroleum engineers is that the permeability of offending reservoir flow channels tend to have permeabilities higher than initially anticipated.⁵ Several reasons for this are the tendency to average permeabilities over relative-

ly long logging intervals, ignoring what unrecovered core intervals might be suggesting during coring operations, and incomplete core, borehole, and reservoir volumetric sampling.

The success of gel-conformance treatments tends to be proportional to the involvement of the field operator in the well-candidate selection, the treatment design, execution, and quality control. This is especially true for first-time treatments in a new field by an operator who is not highly familiar with oilfield gel treatments.⁵ An important aspect in explaining this observation is that the success of conformance-improvement and fluid-shutoff treatments is highly dependent on properly understanding and diagnosing the conformance and excess-fluid coproduction problems. These conformance problems are often best addressed and determined by the operator; however, the experience and capabilities of an oilfield-gel service company in determining and deducing the reservoir conformance problems for an operator should not be overlooked and underused.

Gel Treatment Elements That Must Be Successfully Executed. The successful application and execution of a sweep-improvement or fluid-shutoff gel treatment requires that all five of the following treatment elements be simultaneously implemented, otherwise, there is a high probability of failure.

- The conformance problem must be correctly identified.
- A proper and effective gel system must be selected.
- The gel treatment must be properly designed and sized.
- The gelant solution and/or gel must be properly applied and placed.
- The gel must function as intended downhole.

The success rate of any given gel sweep-improvement or fluid-shutoff treatment is often directly proportional to the operator's involvement in all the gel treatment elements. The implementation of successful gel treatments for sweep-improvement and fluid-shutoff purposes requires a high degree of teamwork between the field's operator and the service and technology providers.⁵

Prerequisites of Good Candidate Wells and Well Patterns. Because polymer-gel conformance treatments that are applied during oil-recovery production operations are, in fact, just treatments, the well or well pattern to be treated must be suffering from a treatable conformance sweep problem or suffering from a treatable excessive fluid coproduction problem. Because gel treatments alone do not reduce microscopic-displacement residual oil saturation, any well pattern to be treated successfully must contain sufficient remaining recoverable oil to make the treatment economical. When performing a fluid-shutoff treatment, the production well must be producing an excessive amount of unproductive competing water or gas.

Attributes of Good Well Candidates. Good well candidates for the application of gel conformance-improvement treatments during oil-recovery operations⁵ have the following attributes. Good injection-well candidates have some combination of early injectant breakthrough, an excessive injection capacity, a substantial movable oil saturation within the well pattern, and unexpectedly low oil recovery within the well pattern. Good production well candidates are characterized by some combination of high WOR or gas/oil ratio (GOR), excessive competing water or gas coproduction, a substantial movable oil saturation within the well pattern, unexpectedly low oil recovery, early water or gas breakthrough, and high producing levels within wells that are being pumped.

Quality Control Is Critical. There is a strong correlation between service companies and operators who conduct and/or insist on a strong quality control and quality assurance program during the application of conformance-improvement gel treatments and the success rate and the degree of benefits derived from the applied gel treatments.⁵

It is important for the operator to request, and to closely monitor and/or actually participate in, the quality control program for polymer-gel conformance treatments (or for any gel technology) if the operator expects to enjoy a high success rate for such chemical treatments.⁵ This is

especially true for the first application of a gel treatment in any given field. The quality control program should include, but not necessarily be limited to, assuring that the proper chemicals are being used in the actual gel formula of the treatment; before pumping the gel, formulating and testing the gel with the actual chemicals and water to be used; assuring complete dissolution of the gel chemicals before injection; when conducting matrix rock treatments, assuring that the gelant solution is injectable into the matrix reservoir rock without face plugging occurring; and taking gelant/gel solution samples regularly at or near the wellhead as the treatment is being pumped.

When performing nonroutine gel treatments using any gel, particularly for a new application or during a first-time treatment in a field, properly executed bottle testing, which is conducted in the field or at a nearby laboratory using actual field gel-formula chemicals and gel make-up water and which is conducted at reservoir temperature, is an especially powerful and effective quality control and quality assurance tool. Such testing provides a semiquantitative check on gelation rate, a semiquantitative check on final gel strength, and an indication of gel stability. In addition, such testing provides a degree of assurance that the proper chemicals are being used in the actual field gel formula, and that there are no chemical interferences involving the field make-up water that will interfere with the gel. Furthermore, such testing can provide a degree of assurance that the actual field recipe being used is the correct formula.

When conducting “bottle testing” of polymer gels at high temperatures (greater than ~180°F), the use of glass-blown sealed glass ampoules and appropriate associated safety procedures are recommended for both short-term and long-term testing. For such high-temperature gel ampoule testing, the gelant solution needs to be scrupulously deoxygenated (described in the Gel Bottle Testing subsection of [Sec. 13.6.1](#)) before placing the gel samples in the oven.

Limitations, Constraints, Pitfalls, and Risks. Polymer-gel treatments are not a panacea for rendering conformance improvement, but polymer gel treatments for sweep improvement and water and gas shutoff are a relatively new, emerging, and promising technology that should be added to the petroleum engineer’s toolbox. An important constraint is that, unfortunately, gel sweep-improvement and fluid-shutoff treatments tend to be highly well, well pattern, and reservoir specific. An improperly designed or executed gel conformance-improvement treatment can reduce oil or gas production rates, reduce ultimate oil or gas recovery from the treated well or well pattern, cause injection or production operational problems, and, following poorly designed producing-well treatments, result in excessive back production of gel.

Common pitfalls of oilfield sweep-improvement and fluid-shutoff treatments include improper diagnosis of the conformance problem to be treated with gel; applying a gel treatment to a radial-flow matrix rock reservoir suffering from a vertical conformance problem without selectively placing the gel in only the high-permeability geological strata; inadequate and improper quality control; applying a gel treatment designed for matrix rock application to a high-permeability anomaly conformance problem, such as a fracture problem; and failure to use a chemically robust and adequately thermally stable gel technology or a sufficiently strong gel formula. Additional pitfalls include the use of too small of a gel-treatment volume, insufficient involvement by the technical staff of the field operator in the well-candidate selection and in the design and execution of the gel treatment, overexpectations of what DPR and RPM gel treatments can do, an incomplete understanding of how microgels function, incomplete dissolution of all the gel’s makeup chemicals before gel-fluid injection, and failure to properly design production-well gel treatments, thereby encountering excessive back-production of the fluid-shutoff gel.

Guidelines for Most Effective Application. In general, gel sweep-improvement treatments for promoting incremental oil production are most advantageously applied to injection wells. Water coning through vertical fractures is a problem that often can be treated successfully with polymer gels. On the other hand, water coning through matrix reservoir rock is very difficult to

TABLE 13.5—EXCESS WATER PRODUCTION PROBLEMS AND TREATMENT CATEGORIES^{*7}
<p>Category A—Conventional treatments normally are an effective choice</p> <ol style="list-style-type: none"> 1. Casing leaks without flow restrictions (apertures greater than approximately $\frac{1}{16}$ in.) 2. Flow behind pipe without flow restrictions (apertures greater than approximately $\frac{1}{16}$ in.) 3. Unfractured wells (injectors or producers) with effective barriers to crossflow <p>Category B—Treatments in which gelants normally are an effective choice</p> <ol style="list-style-type: none"> 4. Casing leaks with flow restrictions (apertures less than approximately $\frac{1}{16}$ in.) 5. Flow behind pipe with flow restrictions (apertures less than approximately $\frac{1}{16}$ in.) 6. 2D coning through a hydraulic fracture from an aquifer <p>Category C—Treatments in which preformed or partially formed gels are injected</p> <ol style="list-style-type: none"> 7. Natural-fracture system in communication with an aquifer 8. Faults or fractures crossing a deviated or horizontal well 9. Single fracture causing channeling between wells 10. Natural fracture system allowing channeling between wells <p>Category D—Difficult problems in which gel treatments should not be used</p> <ol style="list-style-type: none"> 11. 3D matrix rock coning 12. Cusping 13. Channeling through strata (no fractures) with crossflow <p><small>*Categories are listed roughly in order of treatment difficulty.</small></p>

treat successfully with gels. Generally, gel treatments that are applied for water and gas shutoff purposes are usually most advantageously applied to production wells, except as noted below. When applying gel-conformance treatments in conjunction with gas flooding (e.g., CO₂ flooding) in naturally fractured reservoirs, whether for sweep improvement or fluid shutoff, they are usually more advantageously applied to injection wells. When treating naturally fractured reservoirs with gels for sweep improvement or water shutoff, the best reservoir candidates are found when a fracture network exists of intermediate intensity (fracture spacing) with a directional trend for the most problematic fractures.

List of Water Shutoff Problems By Increasing Difficulty to Treat. Ref. 7 proposed a straightforward strategy for the use of polymer-gel treatments to solve excess water-production problems.⁷ The strategy advocates that the easiest excess water-production problems to remedy should normally be attacked first. The paper advocates that conventional water-shutoff methods (e.g., cement and mechanical devices) should normally be applied first, where applicable. **Table 13.5⁷** provides a general ranking of water-production problems and treatment categories in order of increasing difficulty to treat successfully.

13.6.4 Emerging Trends and Issues. At this writing, there are a number of significant emerging trends and issues relating to gel treatments. An important emerging trend is the attempt to effectively exploit and capitalize on the DPR and RPM properties exhibited by many polymer gels. This emerging trend was discussed in a previous section and, in general terms, early in the chapter. Five other important emerging trends are discussed next.

Selective Placement. High on the oil industry wish list in the area of conformance-improvement treatments is to be able to bullhead treatments during gel injection, especially polymer-gel treatments when treating matrix-rock-strata (unfractured) radial-flow conformance problems, particularly when fluid crossflow between the strata does not occur. To do this, the gelant must

be injected into and/or function selectively in only the high-permeability and/or water-bearing strata. Three of the more promising selective placement strategies under study are described here.

The use of bridging-adsorption and/or flow-induced-adsorption properties of certain water-soluble polymer macromolecules are being studied as a means to promote the selective placement of conformance-improvement gels into high-permeability reservoir geological strata and selectively into water-producing strata.^{53,54,126} This scheme involves the pretreatment injection, under appropriate conditions, of a solution containing such polymers. The use of water-reactive diverting agents has been suggested as a means to selectively plug water-bearing strata.¹²⁷

Dual injection of two fluids to impart selective gel placement has been suggested and applied in pilot tests; however, it is not yet a routine practice, except possibly by a few large service companies. The dual-injection scheme is as follows. One of the injected fluids is a nongel, nonreactive, and nondamaging fluid that is injected into the low-permeability geological strata. The second fluid is the gelant solution that is simultaneously injected into the strata to be treated. The two fluids must be pumped down the well via isolated flow conduits, such as being pumped down two separate tubing stings or being pumped down a tubing string and the tubing annulus. When mechanical zone isolation can be used effectively (e.g., a mechanical packer), this version of the dual injection scheme is readily applicable with existing technology. The real “plum” and emerging technology in this area is to be able to dual inject the gelant and the protecting fluid without the use of mechanical-zone isolation and without performing a well-workover operation. The fluid-injection rates must be precisely controlled and selected so that the two fluids are injected only into the targeted strata. In this case, the nongelant and protective fluid that is being injected into the high-oil-saturation geological strata is often a hydrocarbon fluid, such as diesel or crude oil. The application of dual injection of fluids, which is to be applied without the use of mechanical-zone isolation, is an advanced and sophisticated technique. Such dual injection is custom designed for the well to be treated and often requires substantial computer simulation during the design phase. In addition, sophisticated downhole-pressure monitoring and computer-aided fluid-injection control will likely be required.

Selective Stimulation of Low-Permeability Strata. Another strategy being developed for treating matrix-rock vertical conformance problems is to conduct a bullhead treatment followed by selective stimulation of the damaged high-oil-saturation strata. Methods of stimulation being considered and developed are ultradeep perforation techniques, hydraulic fracturing, and, in certain and limited instances, the use of a gel chemical breaker.

Foamed Gels. Foamed gels^{4,83,128,129} provide the possibility of reducing the unit-volume cost of a given oilfield gel by replacing the bulk of the volume of the relatively expensive liquid phase of a gel with a relatively inexpensive gas phase. Foamed gels, in principal, would combine desirable features of foam-blocking agents and classical gels for use in conformance-improvement treatments, especially for use in the far-wellbore environment in which differential pressures are relatively low. The low density of foamed gels provides a driving force during placement in the reservoir for foamed gels to seek out different and, at times, more favorable flow paths than denser fluids, such as conventional aqueous gel fluids. This would be especially true when foamed gels are placed in highly conductive vertical fractures. Such selective placement could be particularly effective in reducing gas override, as occurs during CO₂ flooding in naturally fractured reservoirs of the U.S. Permian Basin and the Rocky Mountain region. Two countervailing issues relating to conformance foamed gels are that foamed gels are relatively more complex chemically and operationally compared with conventional gels, and their low density requires more pump horsepower to be expended during injection than conventional aqueous-based gelants of the same viscosity. Foamed gel has been applied as a conformance-improvement technology at the Rangely field CO₂ flooding project.^{130,131}

Solids Addition. One of the drawbacks of many gels is their low compressive strengths that prevent effective use when encountering large differential pressures in large-aperture reservoir

fluid-flow conduits, such as centimeter aperture fractures or solution channels. When solids are added to polymer gels, the compressive strength of the gel can be greatly increased and increased up to that of Portland cement when the gel is fully loaded with an appropriate solid.

There are numerous near-wellbore conformance problems that are best treated with gel. A small minority of these wells randomly and “unpredictably” require a plugging material with more compressive strength than the gel alone can provide. Previously when such unexpected well and conformance problems were encountered and detected during a gel treatment, a separate cement job had to be called out after, or during, the gel job. When an unexpected well and conformance problem is now encountered, appropriate solids can be added to the gel fluid as it is being pumped and only needs to be added near the end of gel fluid injection to be able to cost effectively plug the flow conduits that have unexpectedly wide apertures. This can be done cost effectively on the fly without the need to subsequently conduct an additional cement squeeze treatment. One of the keys to the effective addition of solids to conformance-improvement gels is to know how to precisely control the screen out of such solids addition during the placement of the gel treatment.

Gels Functional Only in the Presence of Water. Attempts have been made in the past to develop conformance-improvement gel technologies that are functional and active only in the presence of water, but inactive or inactivated in the presence of oil. There has been revived interest in developing such a gel technology.¹²⁷ One of the technical challenges that has to be overcome is that even when there is 100% oil flow in a matrix-rock, connate water also exists.

13.6.5 Gel Breakers. When an aqueous gel is contacted under appropriate conditions, chemical breakers can degrade the gel back to a low-viscosity and watery solution. Two possible reasons to use a breaker after a conformance-improvement gel treatment are to remove gel from the wellbore or perforations and to undo a gel treatment in the near-wellbore region if it was determined after its placement that the emplaced gel was not beneficial.

There are several reasons why a chemical breaker cannot be used to successfully and fully degrade a gel that has been placed deeply in either a matrix-rock or a fractured reservoir. First, successfully delivering the chemically reactive gel-breaker solution deeply in an oil reservoir is a daunting task. Second, and more fundamentally problematic, even if a chemical breaker solution could be 100% effective in the reservoir during its entire gel-breaking life, once injected into the reservoir, the gel-breaker solution would tend to wormhole through the emplaced gel. Thus, the chemical breaker would only be able to regain a small fraction of the pregel-treatment fluid-flow capacity within the gel-treated reservoir volume.

Many biopolymer gels and freshly placed inorganic gels can be chemically broken and reversed by contacting them with a strong acid solution. However, acids are usually ineffective at chemically breaking down metal-crosslinked synthetic-organic-polymer gels, such as metal-crosslinked acrylamide-polymer gels. Acrylamide-polymer gels can be chemically degraded back to a watery solution by contacting them with a free-radical chemical breaker, such as hydrogen peroxide, sodium hypochlorite or bleach, and ammonium peroxide. Free radicals chemically degrade polymer gels by a polymer-backbone scission mechanism.

Hydrogen peroxide is, in many instances, the most chemically powerful of the gel chemical breakers commercially available. However, its decomposition is catalyzed by tubular rust and many other oilfield substances, such that the injected hydrogen peroxide can be rendered essentially spent before it can be delivered to the downhole gel. The use of hydrogen peroxide may be favored when plastic-coated well tubulars have been used. Hydrogen peroxide is an extremely reactive chemical. It is advised to not inject concentrations exceeding 10% hydrogen peroxide; however, a concentration of less than 5% is ill advised, because ineffectively low concentration of hydrogen peroxide will often result downhole. Hydrogen peroxide decomposes to water and free oxygen during the gel-degradation process. The creation of oxygen in the

wellbore and/or the reservoir after the hydrogen peroxide is injected raises safety issues that need to be addressed as part of the hydrogen peroxide selection process.

Bleach (containing sodium hypochlorite) is probably the most widely used material to chemically breakdown acrylamide-polymer gels. It is more chemically robust downhole than hydrogen peroxide. A note of caution: when hydrogen peroxide or bleach is used to break gels crosslinked with a chromium (III)-containing crosslinking agent, some of the chromium (III) will be converted, at least temporarily, to chromium (VI). Because any Cr (VI) that might be formed in the chemically reducing reservoir environment is rapidly converted back to relatively nontoxic Cr (III), field experience has shown that this is often only a theoretical concern. Most oil reservoirs are characterized as having a chemically reducing environment. It should be noted that certain types of metal-crosslinked polymer gels, under certain conditions, can be degelled when contacted with an aqueous solution containing a high concentration of either a caustic chemical (e.g., sodium hydroxide) or a strong ligand (e.g., oxalate).

If an effective delayed and single-fluid reversible-gel technology, especially a reversible-polymer-gel technology, were to be developed in which the gel chemical breaker or gel-breaking mechanism were chemically built directly into the gel structure itself, there would be numerous oilfield applications for such reversible gels. The delayed gel reversal/degelation time would need to be controllable.

If a water-soluble chemical breaker (breaker not built into the gel structure itself) were incorporated into an aqueous gel formula and the gel were placed downhole under a differential pressure (as usually is the case), then as the chemical breaker begins to break down the gel, the differential pressure would begin to squeeze water, including the dissolved breaker, out of the gel. Unfortunately, increasing breaker concentration is required as the concentration of the polymer increases in the gel. When a water-soluble breaker is being squeezed out of the partially broken gel, the opposite trend is occurring. Thus, the use of water-soluble chemical breakers incorporated into a single-fluid aqueous gel under differential pressure always results in an incomplete gel break and always leaves a significant gel residue. To date, the addition of a water-soluble chemical breaker into a single-fluid aqueous gel formula has not proven effective in fully degrading a gel when the gel is broken under differential pressure.

13.7 Foams

Currently, the three major applications of conformance-improvement oilfield foams are as a mobility-control agent during steamflooding, a mobility-control agent during CO₂ flooding, and gas-blocking/plugging agents placed around production wells, often applied in conjunction with a gas-flooding project.

Although the use of foams for oil-recovery applications has been actively considered and studied for more than forty years, widespread application of foams for improving oil recovery has not occurred to date. In the pioneering work of the late 1950s and through the early 1970s, foam was identified to be a promising candidate for improving mobility control and sweep efficiency of oil-recovery drive fluids, especially gas-drive fluids.¹³²⁻¹³⁸ Early R&D personnel observed the following foam characteristics:

- Foams can be quite effective at reducing gas mobility.
- On the microscopic scale, the gas and liquid phases of foam flow separately through porous media with the liquid usually flowing as thin films or lamellae that are separated by gas bubbles.
- The pressure gradient during foam flow is proportional to the liquid flow rate, but quite independent of the gas flow rate.
- The macroscopic effective viscosity of foam during its flow in porous media is a function of the number and strength of the lamellae (alludes to the importance of foam texture and bubble size).

- Foams, at times, tend to promote larger mobility reductions in high-permeability porous media, as compared with lower-permeability porous media (an attractive property for improving conformance and reducing channeling).

- Foams might be good candidates for use as gas-flow blocking agents.

These early workers also noted that oil in porous media often tends to destabilize most aqueous foams and tends to harm oilfield foam performance. A number of the earliest oil-industry proponents of the use of foam hoped that foams would eventually lead to routine “air flooding” of reservoirs. This has not come to fruition.

The earliest study of foams for use during oil-recovery flooding operations attempted to capitalize on the ability of numerous aqueous-based foams to significantly reduce the mobility of gas flow during gas flooding and to be able to substantially improve oil-recovery flood sweep efficiency when flooding with a gas. In concept, foam flooding offers an alternative to polymer flooding. That is, foams can also provide mobility control during oil-recovery flooding operations. Early study and development focused on foam use for mobility-control purposes during oil-recovery flooding projects, especially during gas-flooding operations.

The focus of foam development and application has changed in more recent years. Two major factors have been largely responsible for promoting this change. First, it is unclear if foams (especially steam and natural gas foams) can be propagated distances of more than 100 ft in an oil reservoir because of the substantial minimum pressure gradient required for foam propagation and in view of the small pressure gradients that exist in most of the volume of matrix rock reservoirs. Second, economics now tend to favor small-volume chemical treatments (e.g., gel conformance-improvement treatments) over chemical-based improved oil-recovery flooding operations. Thus, the focus of oilfield foam development and application has shifted somewhat toward the use of foams as blocking/plugging agents that are part of relatively small volume treatments applied through production wells, especially for use as blocking agents to gas flow. The fluid-flow-blocking and permeability-reducing propensity of foams is one of the major factors hampering effective application of mobility-control foams (especially steam and natural gas foams) in the far-wellbore environment. The significant negative impact that crude oil often exerts on the desired performance of foams during mobility-control flooding also helped to shift the focus of oilfield foam use from mobility-control applications to fluid-flow-blocking treatments.

Conventional foams (i.e., not polymer-enhanced foams and foamed gels) are considered effective only when placed in matrix reservoir rock and are not applicable when placed in reservoir fracture channels with aperture widths on the order of greater than 0.5 mm. The application of foams for sweep-improvement and gas/water-blocking purposes is considered to be an advanced and nonroutine form of an oilfield conformance-improvement operation. It is recommended that the average petroleum engineer not undertake a foam conformance-improvement operation without in-house or commercially available technical support and/or without support from an organization that has expertise in conformance-improvement foam technologies. In addition, before implementing a foam conformance-improvement operation, it is usually necessary to perform a laboratory evaluation of the proposed foam formulation and the actual foam process to be used in the field.

13.7.1 Fundamentals and Science of Foams. *General Nature of Foams.* Bulk foam, as found in the head of a glass of beer or as found in association with cleaning solutions, is a metastable dispersion of a relatively large volume gas in a continuous liquid phase that constitutes a relatively small volume of the foam. An alternate definition of bulk foam is an “agglomeration of gas bubbles separated from each other by thin liquid films.”¹³⁹ In most classical foams, the gas content is quite high (often 60 to 97% volume). In bulk form, such as in oilfield surface facilities and piping, foams are formed when gas contacts a liquid in the pres-

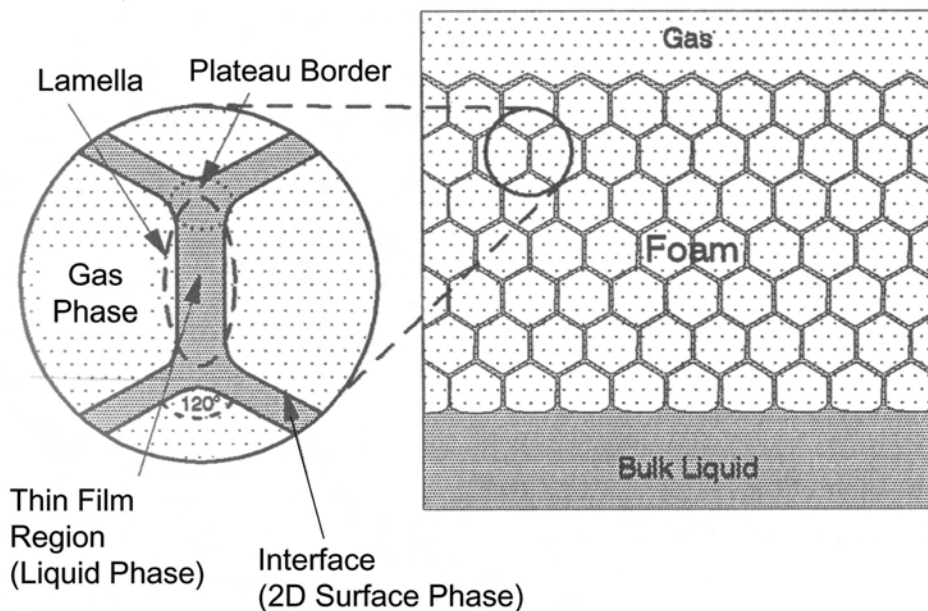


Fig. 13.31—Generalized 2D slice of a bulk foam system.

ence of mechanical agitation. As used herein, bulk foams are foams that exist in a container (e.g., a bottle or pipe) for which the volume of the container is much larger than the size of the individual foam gas bubbles.

Capillary processes control the formation and properties of foams in porous media. Foams for use in conformance improvement are dispersions of microgas bubbles usually with diameters/lengths ranging between 50 and 1000 μm . Foam in porous media exists as individual microgas bubbles in direct contact with the wetting fluid of the pore walls. These microgas bubbles are separated by liquid lamellae that bridge the pore walls and form a liquid partition on the pore scale between gas bubbles. Foam propagates in most matrix reservoir rock as a bubble train in which each gas bubble is separated from the next by a liquid lamellae film. In many instances, individual foam bubbles in reservoir matrix rock can be many pore bodies in length. Gauglitz *et al.* have defined foam structure in porous media as “a dispersion of gas in a continuous liquid phase with at least some gas flow paths made discontinuous by thin liquid films called lamellae.”¹⁴⁰

All foams discussed in this chapter and all foams that are used for conformance improvement have surfactants dissolved in the foam’s liquid phase to stabilize the gas dispersion in the liquid. The gas phase of a foam can include both a classical gas and a supercritical gas, such as supercritical/dense CO_2 . Except as specially noted, all foams discussed in this chapter that are used to impart oilfield conformance improvement are aqueous-based foams. This chapter is limited primarily to the discussion of surfactant-stabilized aqueous-based foams for use in improving conformance during oil-recovery operations.

Fig. 13.31 shows a 2D slice of a generalized bulk foam system.¹⁴¹ The thin liquid films separating the foam gas bubbles are defined to be foam lamellae. The connection of the three lamellae of a gas bubble at a 120° angle is referred to as the Plateau border. In persistent bulk foams, spherical foam gas bubbles become transformed into foam cells, polyhedra separated by nearly flat thin liquid films. Such a foam is referred to as a dry foam. The polyhedra foam cells are almost, but not quite, regular dodecahedra. In three dimensions, four Plateau borders of a foam cell meet at a point at a tetrahedral angle of approximately 109° .¹⁴¹

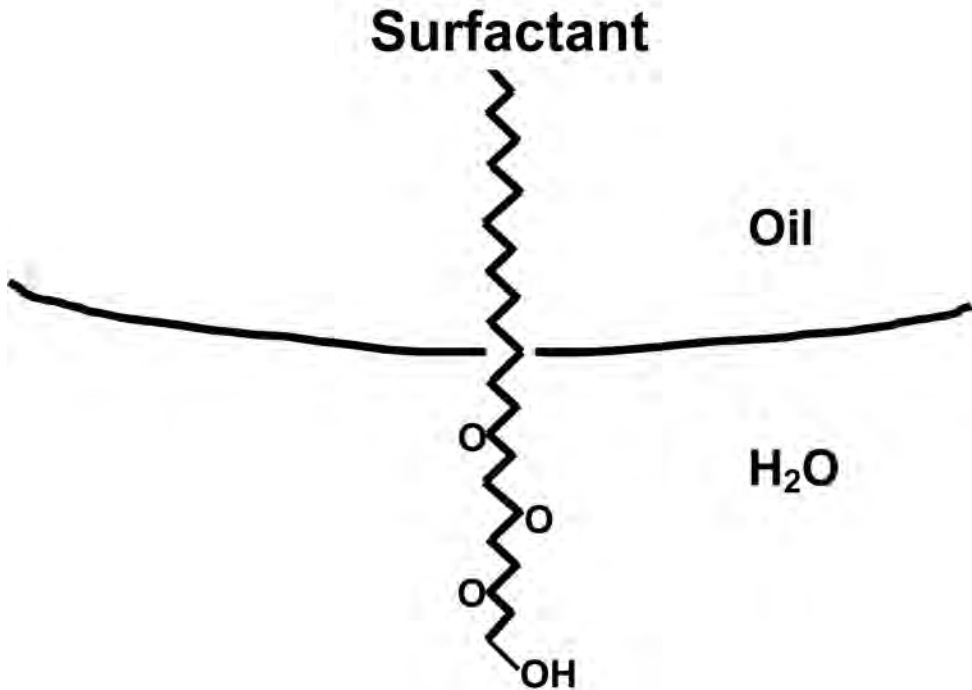


Fig. 13.32—Depiction of a polymer molecule residing at an oil/water interface.

Foams in porous media generally have bubbles that are as large as, or larger than, the pore bodies. Foam exists in reservoir-rock porous media as bubble trains where the Plateau border of the foam lamellae is formed at the pore wall and has, for static nonflowing foam in the pore body, an angle of about 90° between the liquid lamellae and the pore wall.

Foaming Agents. Surfactants are the necessary third ingredient required for the formation of the foams discussed in this chapter. An understanding of basic surfactant chemistry is essential when selecting a proper surfactant for a given oilfield foam application.

A surfactant molecule contains, within the same molecule, both a polar and nonpolar segment. The polar or hydrophilic segment of a surfactant molecule has a strong chemical affinity for water. The nonpolar or lipophilic segment has a strong chemical affinity for nonpolar hydrocarbon molecules. When water and oil or water and gas are in contact, surfactant molecules tend to partition to the oil/water or gas/water interface and reduce the interfacial tension of the interface. **Fig. 13.32** depicts a surfactant molecule residing at an oil/water interface. The partitioning of the surfactant molecule to the gas/water interface and the ensuing reduction of the interfacial tension is the primary mechanism through which surfactants stabilize dispersions of gas in water to form metastable foam.

Surfactants are classified into four types that are distinguished by the chemistry of the surfactant molecule's polar group.

- **Anionics**—The polar group of an anionic surfactant is a salt (or possibly an acid) where the polar anionic group is directly attached to the surfactant molecule and the counter and surface-inactive cation (often sodium) is strongly partitioned into the aqueous side of an oil/water or gas/water interface. Anionic surfactants are often used in oilfield foams because they are relatively good surfactants, generally resistant to retention, quite chemically stable, available on a commercial scale, and fairly inexpensive.

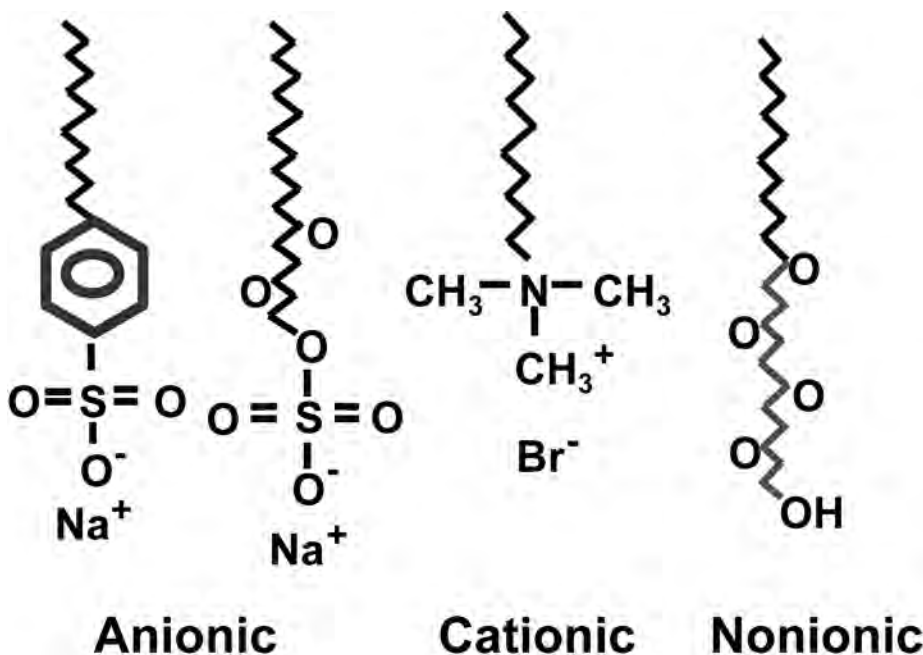


Fig. 13.33—Surfactant chemistry types.

- **Cationics**—The polar group of a cationic surfactant is a salt where the polar cationic group is directly attached to the surfactant molecule and the counter and surface-inactive anion is strongly partitioned into the aqueous side of an oil/water or gas/water interface. Cationic surfactants are infrequently used in oilfield foams because they tend to strongly adsorb on the surfaces of clays and sand and are relatively expensive.

- **Nonionics**—The polar group of a nonionic surfactant is not a salt, but rather a chemical specie, such as an alcohol, ether, or epoxy group, which promotes surfactant properties by imposing electronegativity contrast. Nonionic surfactants are less sensitive to high salinities and can be relatively inexpensive.

- **Amphoterics**—Amphoteric surfactants contain two or more characteristics of the previously listed chemical types of surfactants.

Fig. 13.33 illustrates the chemical structure of selected surfactants. Within any of the surfactant types, there can be substantial variations in their chemistries and performance. The chemistry, size, and degree of branching of the lipophilic segment of a surfactant molecule can have a major impact on foam-surfactant performance, just as the chemistry of the hydrophilic portion of a surfactant molecule can have. Even small and subtle differences in the lipophilic segment can alter surfactant properties dramatically. Most commercial surfactant products contain a distribution of surfactant types and sizes that adds further complexity of the surfactants used in conformance-improvement foams.

When using foam in conjunction with steam flooding or any elevated-reservoir-temperature application, it is important to choose a surfactant that will be thermally stable over the needed life of the foam in the reservoir. Historically, alpha-olefin surfactants and petroleum sulfonate surfactants have been most widely used in foams applied to high-temperature ($> 170^\circ\text{F}$) reservoirs. Sulfate surfactants have been used at times in low-temperature ($< 120^\circ\text{F}$) reservoirs.

Alpha-olefin sulfonates have emerged to be one of the most popular and widely employed surfactant chemistries for use in foams. This has resulted in large part because of their combined good foaming characteristics, relatively good salt tolerance, good thermal stability,

availability, and relatively low cost. Mixtures of different surfactant chemistries have been suggested to provide advantages when formulating conformance foams.¹⁴²

The use of fluorinated surfactants in foam formulas has shown some promise.¹⁴³ Fluorinated surfactants used with other surfactants have been reported to often improve the tolerance of the foam to oil.¹⁴⁴ Fluorinated surfactants have not been widely used in field applications of oilfield foams largely because of their relatively high cost.

Foam Properties. Several properties important to the characterization of bulk foam, as might exist in a bottle, are foam quality, foam texture, bubble size distribution, foam stability, and foam density. Foam quality is the volume percent gas within foam at a specified pressure and temperature. Foam qualities can exceed 97%. Bulk foams, having sufficiently high foam quality such that the foam cells are made of polyhedra liquid films, are referred to as dry foams.¹⁴¹ Oilfield conformance-improvement foams typically have foam qualities in the range of 75 to 90%. When propagated through porous media, the mobility of many foams decreases as foam quality increases up to the upper limit of foam stability in terms of foam quality (an upper limit of often > 93% foam quality). When dealing with oilfield steam foams, steam quality refers to the mass fraction of water that is converted to steam.

Foam texture is a measure of the average gas bubble size. In general, as a foam texture becomes finer, the foam will have greater resistance to flow in matrix rock.

Bubble size distribution is a measure of the gas bubble size distribution in a foam. When holding all other variables constant, a bulk foam with a broad gas-bubble size distribution will be less stable because of gas diffusion from small to large gas bubbles. The imparted resistance to fluid flow in porous media by a foam will be higher when the bubble size is relatively homogeneous.¹⁴¹

Stability of an aqueous-based foam is dependent on the chemical and physical properties of the surfactant-stabilized water film separating the foam's gas bubbles. Foams are metastable entities; therefore, all foams will eventually break down. Foam breakdown is a result of the foam liquid films excessively thinning and rupturing with time and a result of gas diffusing from smaller bubbles into the larger bubbles, thus coarsening the foam's bubble size. External effects, such as contact with a foam breaker (e.g., oil or adverse salinities), contact with a hydrophobic surface, and local heating can break foam structure.

Factors affecting foam lamellae stability include gravity drainage, capillary suction, surface elasticity, viscosity (bulk and surface), electric double-layer repulsion, and steric repulsion.¹⁴¹ The stability of foam residing in porous media evokes a whole series of additional considerations that are addressed in the next subsection of this chapter.

One of the attractive features of foams for use with gas-flooding operations is the relatively low effective density of foams. (As a countervailing note of reference, conformance-improvement foams formulated with supercritical CO₂ can attain densities exceeding the density of some crude oils.) The low-density feature has positive ramifications for foams used in both mobility-control flooding and for blocking fluid-flow. The low effective density causes the foam to be selectively placed higher in the reservoir interval where gas-flooding flow or gas production is most likely occurring.

For technical clarification, foam flow in porous media actually occurs as bubble trains of gas bubbles separated by liquid lamellae. Thus, strictly speaking, foam flow in porous media occurs as two phase flow—namely, gas bubble flow and liquid lamellae flow. In this more technically correct view, it is really the low density of the gas phase that promotes favored placement of the foam higher in the reservoir. During gas flooding, such as steam or CO₂ flooding, low-density foams used for mobility control are well suited to address and reduce the common problem of gas override that often precludes injectant oil-recovery gas from contacting the oil saturation lower in the reservoir vertical interval. Selective mobility-control by low-

density foams in the upper portion of the reservoir will force more displacing fluid gas to contact oil-saturated sections lower in the reservoir.

The low density of foam used during a gas-blocking treatment will tend to drive the placement of the foam higher up in the reservoir interval where the offensive gas flow and production is most likely occurring. In this respect, foams for use in blocking-agent treatments are well suited to treat gas coning and gas cusping problems occurring at production wells. Also, gas override in a relative homogeneous reservoir with good vertical permeability causes excessive gas production in the upper interval of production wells. Low density gas-blocking foam helps favorable placement around such problem wells.

When considering the potential benefit of low density during foam placement of a conformance-improvement operation, the relative effects of gravity forces vs. viscous forces that are operating during the foam placement need to be carefully considered. That is, the horizontal differential pressure gradient vs. vertical differential pressure gradient that the foam will experience during its flow and/or placement in the reservoir needs to be evaluated.

Foams in Porous Media. Understanding how foams behave and perform in porous media is critical to the effective application of foams for conformance-improvement applications in matrix-rock reservoirs. How foam exists and functions in porous media is not always intuitively obvious on the basis of how foam behaves in bulk form (e.g., when existing in a bottle).

Properties. In addition to the properties of bulk foams, which for the most part, are applicable to foam that resides in porous media, there are two specialized properties of foams that reside in porous media.

In general, foams in matrix rock pores do not exist as a continuous interconnected liquid/film structure that contains gas bubbles, as is the case for a bulk foam. Foam in porous media exists as individual gas bubbles that are in direct contact with the wetting fluid of the pore walls. These in-situ microgas bubbles are separated by liquid lamellae that bridge the pore walls and form a liquid partition on the pore scale between the in-situ foam gas bubbles. Foam propagates in most matrix reservoir rock as a bubble train, where each gas bubble is separated from the next gas bubble by a liquid lamellae film. The length of a foam gas bubble in porous media is on the order of, or exceeds, one pore length.¹³⁹

See the subsection on General Nature of Foams in [Sec. 13.7.1](#) for additional discussion of the nature of foams in porous media. Foam stability and performance in porous media is strongly influenced by lamellae/pore-wall interactions. Foam texture in porous media is believed to most often be controlled by the porous media.

Mobility Reduction. Compared with the mobility of the gas phase from which a foam is formulated, the mobility of the resultant foam is dramatically reduced. Often, the mobility of the foam in foam-saturated reservoir matrix rock is less than the mobility of the aqueous phase alone that is used in the foam formula. For a given foam formula, there often is a general trend of decreasing foam mobility with increasing foam quality (gas content) up to the upper foam-quality stability limit.

Foam mobility reduction results from a combination of foam-induced permeability reduction and, on the macro scale, apparent foam-induced viscosity enhancement. Foam-induced mobility reduction is caused by at least two different mechanisms: the formation of, or an increase in, the trapped residual gas saturation; and increased resistance to flow of the gas phase resulting from the drag of propagating the foam-lamellae aqueous films through constricting pore bodies and, especially, through constricted pore throats.

As the texture of a foam becomes finer, the apparent viscosity of the foam increases, and the foam mobility decreases. This occurs because the number of foam lamellae films within a given volume of the porous rock has increased; thus, foam texture is an important variable in determining the amount of mobility reduction that will occur during foam flow.

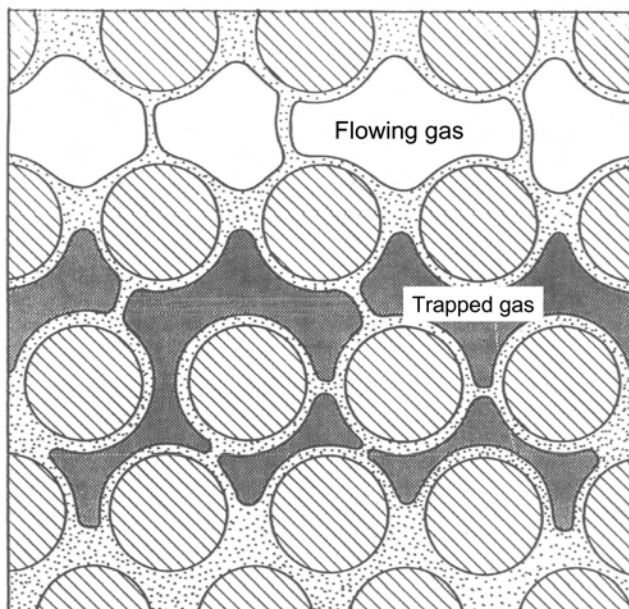


Fig. 13.34—Pore-level schematic of a flowing gas-bubble train and the trapped gas saturation during foam flooding in porous media. Flowing gas bubbles are unshaded; trapped gas is darkly shaded; liquid phase is dotted; and solid phase is hatched.

Rheology, Flow, and Transport. The apparent viscosity of foam (on the macro scale), as it is being propagated through porous media, frequently exhibits shear-thinning behavior. Such foams on the macro scale are a pseudoplastic fluid in porous media. Foams used in oilfield conformance treatments usually exhibit a yield stress. That is, the shear rate remains zero until a threshold stress and/or pressure gradient is reached, and, thereafter, foam flow begins.

Foam placement and saturation in water-wet reservoir matrix rock with normal permeabilities greatly reduces permeability to subsequent flow of gas. The reduction in gas permeability can be on the order of several hundred-fold. Following such foam placement in matrix reservoir rock, the relative permeability to water has often experienced little change.¹⁴⁵ The substantial selective reduction of the gas permeability has been attributed, in part, to a higher trapped gas saturation than occurred before foam flooding. Such foam trapped gas saturations have been reported to range between 10 and 70% PV, depending on surfactant type and the presence of oil during the foam flood.¹⁴⁵

It is the drag and the resistance to flow of the lamellae through the pore structure that imparts much of the mobility reduction of foam flow. **Fig. 13.34** shows a schematic drawing of a flowing train of foam gas bubbles and the trapped gas saturation during foam flow through a foam-saturated porous media. Only a small percentage, typically 1 to 15%, of the foam gas saturation actually flows. The stationary portion of the foam blocks gas flow in intermediate and small-sized flow paths and lowers the effective permeability to gas flow. In the flowing portion of the foam, interactions of the foam gas bubbles and the interspaced lamellae determine the effective foam viscosity of the foam that flows in the largest pore flow paths. The resultant effective foam viscosity is most often larger than the effective viscosity of the water when water alone saturates the same flow channels.¹⁴⁵

The rheology of flowing foam in porous media is controlled by the dynamics of foam generation and decay, in combination with the resulting foam texture and bubble size distribution of the equilibrium in-situ foam.¹⁴⁵ Foam flow in porous media is a complex process that in-

volves a number of interacting microscopic foam events. Macroscopic manifestations of foam flow in porous media are the result of the combination of many pore-scale events that involve foam bubble evolution and foam bubble/lamellae pore-wall interactions during multiphase flow. Fully understanding the macroscopic manifestation of foam flow in porous media requires understanding the pore-level phenomena of foam flow.

Foam lamellae formation during foam flow in porous media results from a combination of three foam-generation mechanisms: snap off, division, and leave behind.¹⁴⁵ The snap-off mechanism is believed to be the dominant foam-generation mechanism during foam flow and transport in porous media.

During foam flow through porous media, foam destruction (decay and coalescence) is primarily brought on by capillary suction and gas diffusion. In certain instances, gravity can also contribute to foam decay when there is a significant density difference between the gas and liquid phases of the foam. The gas diffusion mechanism leads to coarsening of the flowing foam and is normally of minor consequence for foam flow in porous media. Capillary suction coalescence is the dominant mechanism for lamellae breakage during foam flow in porous media and is strongly affected by the surfactant used in the foam.¹⁴⁵ If the lamellae of a foam can withstand the imposed capillary suction pressure, such a foam is termed a “strong foam.”

Coalescence of flowing foam bubbles in porous media is more complicated than the coalescence of static bulk foam. A limiting capillary pressure, P_c^* , exists above which foam coalescence is significant and below which coalescence is minimal. Limiting capillary pressure varies with gas flow rate, absolute permeability, and the surfactant used in the foam. The limiting capillary pressure of flowing foam in porous media is typically on the order of 0.44 psi (3 kPa).¹⁴⁵

Many foams flowing in matrix sand-reservoir rock do so under steady flow at, or near, P_c^* . Such foam flow occurs when the gas fractional flow rate is in the high range (i.e., high foam quality) and when the gas and liquid flow rates are fixed. In the P_c^* foam-flow regime, the wetting-liquid (usually water) saturation is nearly constant and is independent of gas and liquid velocities over a wide range. This limiting wetting-phase saturation is thought to result from the constant P_c^* .¹⁴⁵

Foam flow in the limiting capillary pressure (P_c^*) regime is quite interesting. When the liquid (water) velocity is held constant and the gas velocity is varied, the pressure drop is highly independent of the gas flow rate. Increasing the liquid velocity while holding the gas velocity constant usually results in a linearly increasing pressure drop. Increasing both the liquid and gas velocities, while holding the fractional flow constant, produces a linear response of pressure drop vs. total flow rate. Steady-state liquid and gas saturations are independent of gas fractional flow.¹⁴⁵

Foam flow in the P_c^* regime has a number of important ramifications. Under such foam-flow conditions, the aqueous phase saturation remains constant, as does the relative permeability of the water phase.¹⁴⁵

However, not all foam flow occurs under the limiting-capillary-pressure regime. The P_c^* regime for foam flow does not necessarily apply for low gas fractional flow (i.e., flow of low-quality foams). Osterloh and Jante¹⁴⁶ studied a wide range of flow rates and fractional flows (foam qualities) for foam flow in a 6,200 md sand pack at 302°F. During their flooding experiments involving a nitrogen foam and an alpha olefin-sulfonate-surfactant foam formula, they observed two foam-flow regimes when varying the foam quality. During flow of foam with foam qualities exceeding 94%, the pressure gradient was quite independent of gas velocity at a fixed liquid velocity and varied with liquid velocity to approximately the 0.33 power. The liquid saturation remained nearly constant. During flow of foam with lower foam qualities (< 94%), the opposite behavior was noted. The pressure gradient increased little with increased liquid velocities, but increased with gas velocity to the 0.31 power. It was suggested that the

transition between these two foam flow regimes occurred at the point where the limiting capillary pressure was attained. Subsequently, Alvarez *et al.*¹⁴⁷ reported on what is described to be a unified model for steady-state foam flow at both high and low foam qualities and a model that helps reconcile apparently contradictory foam flow data for foam flow occurring in reservoir-rock porous media. The unified model is predicated on the contention that, in the high-foam-quality flow regime of Osterloh and Jante, foam flow behavior is dominated by capillary pressure and coalescence and that, in the low-foam-quality flow regime, foam flow behavior is dominated by bubble trapping and mobilization.

Steady-state foam flow refers to foam flow in a given length of porous media after foam has been propagated and formed throughout the entire length of the porous media in question, and the liquid saturation profile is nearly uniform throughout the entire length of the porous media. Transient foam flow in a given length of porous media refers to foam flow as foam is progressively being formed and propagated along the length of the porous media and, as the liquid saturation profile varies from low to high along the length of the porous media, in the direction of flow.

An alternative definition for “strong foam” to the one given previously is based on the continuity of foam within porous media. For a given volume of porous media that contains foam, a “continuous gas foam” exists when there is at least one continuous flow path along the length of the porous media that is uninterrupted by the existence of a foam lamellae. A “discontinuous gas foam” exists when there is at least one foam lamellae along all the gas flow paths over the entire length of the porous media volume. Thus, when gas must flow through a discontinuous gas foam in a given porous media, the gas must mobilize and propagate (or possibly rupture) at least one foam lamellae. A strong foam is said to exist when a discontinuous gas foam occurs. A weak foam is said to exist when a continuous gas foam occurs.¹³⁹

Chang and Grigg¹⁴⁸ have studied and reported on the effect of foam quality and flow rate on the imparted mobility reduction resulting from the steady state flow of dense CO₂ foam in porous media at reservoir-like temperature and pressure conditions. Over the range of foam qualities normally used in oil reservoirs and for the studied conditions and foam formula, CO₂ foam mobility was observed to increase with increasing flow rate and to decrease with increasing foam quality.

Magnetic resonance imaging has been reported to be a useful tool for high-resolution viewing of foam flow in selected porous media.¹⁴⁹

Foams have been reported to have the very desirable feature, under certain conditions, of being able to reduce mobility to a greater extent in high-permeability porous media, as compared with lower-permeability porous media.¹⁵⁰⁻¹⁵⁴

Questions persist about the ability to propagate and place foams deep within matrix rock. One aspect of this concern is the often destabilizing effect of oil on foam transport. The next subsection discusses the effect of the presence of oil. Another aspect of this concern is the pressure gradient that is normally required for initiating and maintaining foam flow. Can foam flow be maintained in the far-wellbore regime where pressure gradients are inherently low?¹⁵⁵⁻¹⁵⁷

As a result, in part, of the low surface tension of CO₂, CO₂ foam is more easily propagated (than nitrogen, steam, and natural-gas foams) at the relatively small pressure gradients that exist in the far-wellbore region of most reservoirs.¹³⁹ Ref. 140 reports on laboratory results and literature references indicating that for dense/supercritical CO₂ foams, minimum pressure gradients in porous media of less than 1 psi/ft can exist for foam flow when flooding with strong CO₂ foams. However, under similar conditions, the minimum pressure gradients for the formation and flow of strong nitrogen foams are reported to be a factor of 20 psi/ft or greater. Viewed conversely, the relatively high minimum pressure gradient for foam flow in many instances can be advantageously used as the basis for foam treatments to block gas flow.

Another important aspect of the problem of deep foam placement is surfactant adsorption/retention. The upcoming subsection Surfactant Adsorption/Retention discusses adsorption and retention of surfactant during foam transport through matrix reservoir rock.

Effects of Oil and Wetting. Much has been published on the interaction of crude oil and foam within porous media—with much of this literature discussing negative interactions.^{150,157–174} When oil contacts a foam, the oil often has a destabilizing effect.¹⁴¹ The probability that oil will destabilize foams has been a major impediment to the widespread use of foams for oilfield conformance-improvement applications. The destabilizing effects of oil can range from minor to very deleterious. Ref. 159 reviews the mechanisms by which crude oil can destabilize foam in porous media. Foams are more stable in the presence of some crude oils as compared to others. In general, foams are more highly destabilized when contacted with lighter, lower viscosity crude oils.

The degree of sensitivity of foam to oil as foam flows through matrix reservoir rock depends on both the nature of the foam and the nature of the crude oil. Although many conformance-improvement foams are sensitive to oil contact, some foam formulas are quite resistant to destabilization by crude oil.

It has been suggested that even foams sensitive to crude oil can still be effective in matrix reservoir rock if the residual oil saturation is < 10%.¹⁵⁹ On the other hand, oil-sensitive foams will be significantly destabilized by the contact with the crude oil at higher oil saturations (e.g., 20% oil saturation). It has also been suggested that foam sensitivity to oil might be advantageously exploited. That is, by using foams to selectively reduce gas or water mobility in high-gas or water-saturation flow paths within an oil reservoir where the oil saturation is low, while the foam is simultaneously being destabilized and unable to reduce the oil mobility and productivity in the high-oil-saturation flow paths within the reservoir.

The general consensus of several investigators is that oil wetting is detrimental to foam stability and propagation in matrix reservoir rock; however, there is not universal agreement on this point.^{139,159–162}

Surfactant Adsorption/Retention. The degree of surfactant adsorption/retention often can “make or break” the oil-recovery performance and the economics of a foam application. “Retention” is the combination of all other mechanisms, other than adsorption, that retards surfactant propagation during foam propagation through reservoir matrix rock.

Surfactant adsorption/retention under reservoir conditions should be one of the key factors considered and is one of the first parameters that should be examined and/or estimated when considering the application of foam injection for mobility-control purposes during a gas flooding operation.

The use of low-cost adsorption/retention sacrificial agents in the foam or such agents injected before the foam have been proposed as a means to alleviate the adsorption/retention problem.¹⁷⁵ Surfactant adsorption is often lower when foam is transported through an oil-wet reservoir.

Injection Mode. One of three distinctly different modes is used for injecting conformance-improvement foams: sequential injection, coinjection, or preformed foam created on the surface before injection. Sequential injection involves the alternate injection into the oil reservoir of the foam’s gas and aqueous phases. Coinjection involves the coinjection into the reservoir of the foam’s gas and liquid phases. Because of the substantial effective viscosities of foams and the associated poor injectivity of preformed foams, early applications of conformance-improvement foams tended to involve the sequential-injection or coinjection mode. Also, sequential-injection and coinjection are substantially simpler to implement in the field. Sequential injection also avoids tubular corrosion problems if the gas and the foaming-solution form a corrosive mixture, such as found in CO₂ foams.

The concept, which is supported by laboratory evidence, is that during the sequential or coinjection mode, foam will form in situ in the matrix reservoir rock. Supporting this contention is the expectation that low-viscosity and high-mobility gas will tend to finger into the aqueous foaming solution and generate the foam in situ.

However, there are two significant countering concerns. First, as the gas begins to finger into the aqueous solution and form foam in situ, the newly formed foam will substantially reduce subsequent gas fingering and divert subsequent gas flow away from the remaining aqueous foaming solution residing just ahead of the initially formed foam. This phenomenon results in ineffective and inefficient use of the injected foam chemicals and fluids in generating foam. Second, in intermediate and far wellbore locations, there may not be enough mechanical energy and/or differential pressure to generate foam in situ when using common foaming solutions. This is especially of concern for steam, nitrogen, and natural-gas foams.

Krause *et al.*¹⁷⁶ reported on relatively near-wellbore production-well foam treatments that were applied at the Prudhoe Bay field to reduce excessive GOR emanating from the production of reinjected natural gas. The first treatment involved the injection of the foaming solution into the reservoir, followed by a series of overflushes. It was thought that the subsequent production of gas through the emplaced foaming solution, in a similar manner to the sequential injection mode, would cause the generation of a gas-blocking foam in situ. The second foam gas-blocking treatment involved the sequential injection of the foaming solution and a slug of nitrogen. Neither of these first two foam gas-blocking treatments showed any post-treatment GOR decline. The third foam gas-blocking treatment was a nitrogen foam of 65% quality that was preformed at the surface before injection. This treatment significantly reduced GOR at the treated production well for several weeks. These results suggest that, for many applications of natural-gas and nitrogen conformance-improvement foams, foam injection using the preformed mode, as compared to the sequential injection or coinjection mode, will result in superior performance of the foam within the oil reservoir when conducting “near-wellbore” treatments. Unless compelling arguments for a specific application can be made to the contrary, foams for most applications of near and intermediate wellbore conformance-improvement treatments should be preformed at the surface before injection.

The sequential process, alternately known as the WAG process, of injecting sequentially and repeatedly alternating slugs of CO₂ and aqueous foaming solution is often favored when using CO₂ foam for mobility-control purposes during CO₂ flooding. This is because CO₂ dissolved in an aqueous surfactant solution forms carbonic acid that is corrosive to steel tubulars. Because of the low surface tension of CO₂, foam generation and propagation is much more feasible (than steam, nitrogen, or natural-gas foams) at realistic field pressure gradients that occur throughout the reservoir.¹³⁹

Computer simulation studies have been reported to show that the optimal injection strategy for overcoming gas override during gas-flooding operations is the alternate/sequential injection of separate large slugs of gas and the foaming liquid at the maximum allowable fixed injection pressure.¹⁷⁷ This study was limited to foam injection into a homogeneous reservoir and did not account for any foam interactions with oil. The surfactant-alternating-gas-ameliorated (SAGA) injection mode for forming in situ mobility-control foam has been proposed for use when conducting large-volume WAG flooding projects in North Sea reservoirs.¹⁷⁸

13.7.2 When, Where, and Why to Use Foams. The use of foams is most advantageously applied during gas flooding or for reducing gas coning and cusping in one of two manners. First, foams can be used to improve sweep efficiency and improve oil recovery during gas flooding (e.g., steam, CO₂, and hydrocarbon-miscible flooding). Such mobility-control foam is usually injected from the injection well side. Second, foams can be used as gas-blocking agents to reduce excessive, deleterious, and competing gas production. Such gas-blocking foam is most

often placed from the production well side. Foams for use as both mobility-control and gas-blocking agents are attractive because they are relatively inexpensive on a unit-volume basis. The low unit-volume cost results from the combination of the bulk of the foam volume usually being a relatively low-cost gas, and the surfactant chemicals for the foaming solution are relatively inexpensive and used at relatively low concentrations.

13.7.3 Advantages and Disadvantages of Foams. There are a number of somewhat contrasting advantages and disadvantages for the use of foams for improving conformance during oil-recovery operations.

Advantages. The following is a list of the advantages of the use of foams.

- Foams are exceptionally effective in reducing gas mobility during gas flooding.
- Foams can be an effective gas-blocking agent.
- Foams are a conformance-improvement material that has the tendency, in numerous instances, to reduce permeability and mobility to a greater degree in higher permeability matrix reservoir rock.
- Foams are shear-thinning fluids resulting in relatively good injectivity and in more effective mobility control in the far-wellbore region where such mobility control is most needed.
- Foams possess low effective density that can often be exploited to help selectively place foams high in a reservoir thereby impeding problematic gas flow where it is most likely to occur.
- Foams are considered, in general, to be an environmentally friendly material for use in conformance-improvement operations.

Disadvantages. The following is a list of the disadvantages of the use of foams.

- Foams are a relatively complex technology, both chemically and operationally, to apply successfully.
- Oil tends to destabilize and deactivate many conformance-improvement foams.
- Many mobility-control foams (e.g., steam and natural gas foams) are difficult or impossible to propagate in the intermediate- to far-wellbore environment under the differential-pressure conditions encountered in most reservoirs.
- Surfactant adsorption/retention has a substantial negative impact on the performance and economics of mobility-control foams.
- Fluid-blocking (e.g., gas-blocking) foams used in production-well treatments have limited strength under high differential pressure conditions.
- Fluid-blocking (e.g., gas-blocking) foams are also limited by the inherent lack of long-term stability and the associated lack of long-term treatment effectiveness.
- The high viscosity and poor injectivity of preformed foams limit the application of this otherwise often favored foam-injection mode.
- The limited and sometimes poor ability to effectively form foam in situ in matrix reservoir rock during the coinjection or sequential injection of the foam's gas and liquid phases limit the effectiveness and the efficiency of the coinjection and sequential-injection modes for foam formation and placement in a reservoir.

13.7.4 Foams for Mobility Control. Foams, as a conformance-improvement technology for use during gas flooding (e.g., steam, CO₂, and miscible-gas flooding), have historically been most widely studied and applied when the foams are to be used in the form of a “viscosity-enhancing” mobility-control agent that is injected from the injection-well side. Because relatively large volumes of foam are required and because the foam must be propagated significant distances in the reservoir, applying foams for mobility control have proved technically and economically challenging.

Reducing Gas Channeling and Override. As initially discussed in the Foam Properties subsection of [Sec. 13.7.1](#), the low effective density of most mobility-control foams, which are

used during a gas flood such as a steam or CO₂ flood, provides a driving force for the foam to flow and be desirably placed in the upper reservoir vertical interval where the offending gas override is occurring and where the foam will be most effective at countering the negative impact of the gas override. Ref. 179 describes an “improved” surfactant-alternating-gas foam injection process to control gravity override during gas flooding projects.

Applications. CO₂ Flooding. CO₂ foams are considered to be an effective mobility-control agent candidate for use during CO₂ flooding to improve CO₂ sweep efficiency.^{150,152,180–184} This includes the use of “foams” formulated with supercritical and dense CO₂. Surfactant selection and surfactant adsorption/retention losses are particularly critical parameters to the successful economic application of CO₂ foams during CO₂ flooding operations. The exploitation of relatively low-cost CO₂ foams formulated with surfactant concentrations below the critical micelle concentration has been suggested.¹⁸⁴ As discussed in the Injection Mode subsection of Sec. 13.7.1, the sequential or WAG injection of the CO₂ and the foaming solution is often preferred for the injection of mobility-control CO₂ foam.

Steam Flooding. Use of steam foams has been studied extensively and has been reduced to field practice as a technique to improve vertical and areal sweep efficiency and to reduce steam channeling and override during steam flooding that is being applied to shallow heavy-oil reservoirs. The steam foam process consists of adding surfactant, with and without the addition of a noncondensable gas, to the injected steam.^{158,185} Based on the combined findings of theory, laboratory studies, and field performance, it has been determined that steam foams are normally more effective when a small amount of a noncondensable gas, such as nitrogen, is incorporated into a steam-foam formula. Steam foams have been used in conjunction with both continuous and cyclic steam injection.

As with foams for CO₂ flooding, the effectiveness and the economics of the steam-foam process are critically dependent on surfactant adsorption and retention. Unlike CO₂ foams, surfactant thermal stability is also a critical issue. Alpha-olefin sulfonates, along with petroleum sulfonates, are the surfactants that have been favored for use in conformance-improvement steam foams.¹⁷⁴ Borchardt and Strycker¹⁸⁶ have studied commercial olefin sulfonate surfactants to determine what the optimum chemistry should be in terms of favorable surfactant performance in foams for steam-flooding applications.

To mitigate the destabilizing effect of oil on steam foam, one proposed strategy is to inject a prefoam surfactant slug to mobilize the residual oil ahead of the steam foam.¹⁸⁵ Steam foams have been extensively applied in conjunction with the heavy-oil production operations in Kern County, California. The application of steam foam in Kern County, California has been considered a technical success, but its economic success is suspect.¹⁸⁵

Miscible Gas Flooding. Although it would appear that foams would be well suited to impart mobility control and to improve sweep efficiency during miscible gas flooding (in a similar manner as during CO₂ and steam flooding), relatively few papers have appeared in the literature about this application of conformance-improvement foams, especially the actual field application of foams for use in conjunction with miscible-gas flooding. Mannhardt and Novosad¹⁸⁷ studied the adsorption of foaming surfactants to be used with hydrocarbon-miscible flooding in reservoirs with high salinities. Refs. 188 and 189 discuss the application of foams for use during hydrocarbon-miscible flooding in Canada.

Sizing Volume Injected. The volume of foam that should be injected during application, as a mobility-control agent in conjunction with gas flooding, is a subject that lacks good and sound engineering guidelines. Thus, the sizing of such foam applications must be a custom design based on previous experience with similar applications, and/or be based on empirical guidelines. It does not make sense to design the depth of foam placement to be greater than the distance the foam can propagate through the reservoir.

Polymer-Enhanced Foams. The addition of a water-soluble polymer to the foaming solution has been suggested as a means to increase stability of the foam, increase the effective viscosity and structure of foams, and improve the oil tolerance of foams.^{4,157,190–193} The possible use of polymer-enhanced foams to treat fracture conformance problems has been suggested.¹⁹⁰ Polymer-enhanced foams formulated with high-MW acrylamide polymers have been noted to be rheologically shear-thinning fluids that substantially aid in the injectivity of preformed polymer-enhanced foams.

Potential disadvantages of the use of polymer-enhanced foams are reduced injectivity of preformed polymer-enhanced foams as compared with conventional foams, possible increased difficulty in propagating the polymer-enhanced foam through matrix reservoir rock, and somewhat increased operational and chemical complexity in applying polymer-enhanced foams as compared with conventional foams.

13.7.5 Foams as Blocking Agents. Because foam applications for mobility-control during gas flooding have proven technically challenging and marginally attractive, the recent focus has shifted somewhat to the application of relatively small volumes of foam that are placed as gas-blocking agents from the production well side. The application of foams as gas-blocking agents has been discussed and reviewed numerous times in the literature.^{4,139,155,156,194,195}

Concept. Because foams are exceptionally effective at reducing gas permeability, they are good candidates for use in gas-blocking treatments that are placed relatively near to producing wellbores. The foam's low effective density results in the tendency for selective placement in the upper sections of the reservoir where gas, especially coning and cusping, is entering the wellbore. The obvious and major challenges that must be overcome to successfully apply foams as a gas-blocking agents are to assure that the emplaced blocking foam will have adequate strength and that the metastable foam will be stable long enough to result in attractive economics.

Laboratory Studies and Treatment Design. Treatment design and laboratory studies in support of applying foam gas-blocking treatments need to assure the following.

- The foam has adequate strength to function as intended under actual reservoir conditions, including adequate strength within the maximum permeability rock to be blocked/sealed and adequate strength to withstand the maximum differential pressure that will be encountered.
- The foam has adequate durability and stability to function as intended under actual reservoir conditions for at least the minimum intended economic life of the foam gas-blocking treatment, including adequate thermal stability, adequate stability to the reservoir oil and to the salinity of the reservoir brine, and adequate stability in the presence of the reservoir minerals and lithologies to be encountered.
- The foam can be emplaced and/or generated in the desired reservoir volume to be treated.

Foams for Reducing Gas Coning. The use of foams as blocking agents to reduce or eliminate gas coning in matrix-rock reservoirs has long been studied. One concept is to inject a foaming solution at, or near, the gas/oil contact (GOC). As gas cones down through the foaming solution, it is proposed that gas-blocking foam will form in situ and reduce or eliminate gas coning. More recently, it has been proposed that the foaming solution in this case should be a hydrocarbon solution. For a properly designed treatment, gravity forces will tend to promote the selective placement of the hydrocarbon foaming solution at the GOC, just as desired. Dalland and Hanssen reported on a laboratory study of this concept.¹⁴⁵

Sizing Volume Injected. The volume of the emplaced foam required to successfully function as a gas-blocking treatment is smaller than the foam volume required for mobility-control purposes. In concept, the volume of the foam placed through a production well needs only be large enough to provide sufficient strength and durability to assure effective gas blockage. The volume and depth of foam placement for such a treatment will vary substantially with the foam

formula used, the permeability and mineralogical nature of the reservoir volume being treated, and the drawdown pressure that the foam gas-blocking treatment will experience. At this writing, no exact treatment size guidelines for foam gas-blocking treatments can be provided. The sizing of such foam treatments needs to be determined on a well-by-well and treatment-by-treatment basis.

Polymer-Enhanced Foams and Foamed Gels. A trend, which has often occurred when applying foams as gas- or water-blocking treatments from the production well side, is that the initial application of a conventional foam resulted in some blocking of gas or water flow that lasted for only a relatively short time. Encouraged by the initial favorable gas- or water-blocking performance of conventional foam treatments, but pursuing and needing longer-term gas- or water-blocking performance, the application and exploitation of polymer-enhanced foams were next pursued.^{4,191,192,196–201} Again encouraged by the improved gas- and water-flow blocking performance of the polymer-enhanced foam treatments, but still pursuing and needing even longer-term gas- and water-blocking performance, foamed gels were subsequently pursued.^{4,197,200,201} The application of foamed gels as a blocking-agent material for use across a broad spectrum of conformance treatments has been suggested and studied.^{4,83,129,201}

Ref. 131 reports on three large-volume (~40,000 res bbl) foamed-gel treatments that were applied for conformance-improvement purposes to injection wells of the Rangely field miscible CO₂ WAG project in northwestern Colorado. The three foamed-gel treatments were reported to have generated an incremental oil production rate of 155 BOPD. Each of the foamed-gel treatments induced stabilization in the pattern oil rate. The cost of the foamed-gel treatments was said to be 40 to 50% below that of comparable polymer-gel treatments that would have been conducted at the Rangely field.

13.7.6 Design Strategies for Field Application. Rossen¹³⁹ suggests the following design strategies for the field application of conformance-improvement foams. The initial steps are to characterize the field and its conformance problem; determine that there is sufficient recoverable oil to render the foam process economic; determine process goals (e.g., increase oil recovery or recovery rate, or reduce operating costs); and perform a preliminary economic evaluation of the foam project. Next, the surfactant to be used should be chosen by conducting wet-chemistry testing, conduct foam-property testing in porous media, and determining surfactant retention with reservoir core material, if possible. Finally, determine the injection strategy to be used.

13.7.7 Outlook. At this writing, the outlook for the use of foams extensively and routinely is not as encouraging as it was during the past two decades. Petroleum industry R&D was diminishing. The original interest in foams as mobility control agents has faded somewhat and interest in the use of conventional foams as fluid-flow blocking agents was also fading because foam fluid-flow blocking treatments are operationally and chemically relatively complex and polymer gels are considered by many petroleum engineers to be more effective, durable, and stronger.

13.7.8 Illustrative Field Results. The following are a series of illustrative field applications of foams for conformance-improvement purposes and/or a series of references to papers discussing such foam applications.

Foams Used During Steamflooding. In 1989, Hirasaki¹⁵⁸ reviewed early steam-foam-drive projects. In 1996, Patzek²⁰³ reviewed the performance of seven steam-foam pilots conducted in California. Early and delayed production responses were discussed for these pilots. Ref. 204 reviews a steam-foam trial conducted at the Midway-Sunset field of California.

Foams Used During CO₂ Flooding. The design, results, and analysis of a two-year CO₂ foam field trial at the North Ward-Estes field in Texas have been documented.²⁰⁵ The alternate injection of CO₂ and surfactant foaming solution was reported to have reduced injectivities by 40 to 85%. Gas production at an offset problematic production well decreased dramatically, while gas and oil production at the other offset producers increased, indicating favorable areal diversion. CO₂ foam application during this field trial was reported to have significantly improved CO₂ sweep efficiency and to have been economically successful.

Stephenson *et al.*²⁰⁶ reported that a foam bank could only be propagated several meters from the wellbore during an extended foam test at the Joffre Viking miscible CO₂ flood in Canada, where the foaming aqueous solution and the CO₂ were coinjected.

Hoefner and Evans²⁰⁷ reviewed four pattern-scale CO₂-foam field trials to determine the technical and economic potential for reducing channeling during CO₂ flooding. The field trials involved two different foaming surfactants, alternating and coinjection of the CO₂ and the aqueous foaming solution, and two field trials each in a San Andres carbonate reservoir of West Texas and one trial in a platform carbonate formation in southeast Utah. In all, 161,000 lbm of active foaming surfactant were injected, with one of the field trials lasting 18 months. The CO₂ foam treatments resulted in reduced CO₂ production and indications of increased oil production.

Ref. 208 reports on a 3,000-reservoir-bbl CO₂ foam treatment that was applied to reduce CO₂ channeling in the Wasson ODC Unit in Texas. The foam treatment was reported to have been a technical success, but an economic failure. Foam performance was noted to decrease with time and to be a treatment success issue.

Ref 182 provides a review of a four-year CO₂ foam mobility-control pilot test conducted in a dolomitic carbonate reservoir of the East Vacuum Grayburg/San-Andres Unit in New Mexico. During the CO₂ foam pilot, CO₂ mobility of the ongoing CO₂ WAG flooding operation was reduced, incremental oil production was noted at three of the eight offsetting producers, and gas cycling was significantly reduced.

Foam Gas-Blocking Treatments. Eight production wells in Nigeria were treated with foam gas-blocking treatments to reduce gas coning or cusping and to reduce excessive GOR.¹⁹⁶ The producing formation was thin and overlain by a gas gap. The reported set of applied nitrogen foam gas-blocking treatments included the use of polymer-enhanced foams, sequential and coinjection of the gas and foamer solution, and fluorosurfactants. The treatments were designed to place the foam barrier 5 to 10 m radially from the wellbore. A volume of 600 to 800 bbl of foam solution was injected per treatment. The success rate of the foam gas-blocking treatments was reported to be 50+%. Results ranged from significant reductions in GOR that lasted for twelve months (reduced GOR from 7,000 to 2,000 scf/bbl and increased the oil production rate from 340 to 450 BOPD) to minor reductions in GOR that lasted only for a few weeks. The foam treatments were said to be easy to apply and relatively inexpensive. The preliminary conclusion based on this set of foam gas-blocking treatments is that for this type of foam treatment, the sequential injection mode is preferred over the coinjection mode. Four out of six foam gas-blocking treatments that used the polymer-enhanced foam formulas were successful, while neither of the foam gas-blocking treatments using the fluoro-surfactant foam formula were successful.

Ref. 209 presents a review of the application of two foam gas-blocking treatments that were applied to high GOR problems occurring at production wells in the North Sea. The first foam pilot test was applied to a sandstone formation of a production well in the Oseberg field in the Norwegian North Sea, where the high GOR production problem involved gas coning. The upper producing interval was selectively treated with a strong and “oil-resistant” foam. This Norwegian foam pilot was reported to have been successful (at a minimum, technically successful) and delayed the onset of gas coning by several months.

Foam ASP. The reported use in China of foamed alkaline-surfactant-polymer (ASP) flooding is noteworthy for several reasons.²¹⁰ First, the field trial of foam flooding in this manner was reported to be both a technical and economic success with the reported economics being quite attractive. Second, definitive positive reservoir and flooding responses were noted during this foam pilot test. Positive responses included substantial incremental oil production; substantial increases in the injection pressure; significantly lower GOR indicating reduced gas mobility, fingering, and channeling; and favorable changes in the produced water salinity which indicated improved sweep efficiency. Third (and of significant importance), substantial increases in injection pressure occurred during the pilot test.

The implications of the higher injection pressures are three fold. First, for an older waterflood operation in a mature field, this situation may require installing relatively expensive high-pressure injection equipment, injection lines, and wellheads. Second, even if the foam should happen to have an effective viscosity identical to water, it will require substantially more horsepower to inject the foam at the same rate as compared to waterflooding because of the lower density and lower wellbore hydrostatic pressure of the foam. Third, if the previous waterflood injection pressure was just below reservoir parting pressure, any increase in injection pressure would require lower injection rates that might pose a possible negative impact on the economics of the project.

On the positive side (although, at first, a foam-ASP flood may appear to be quite complex), if an oil operator is conducting either an ASP or a WAG flood and if the operator has excess natural gas being produced in the field, then flooding in the WAG mode, using the ASP solution as the water phase of the WAG flood, could prove to be relatively easy to implement and relatively attractive if the conformance of the flooding operation could be improved in a similar fashion as reported for the Chinese foam-ASP pilot test.

13.7.9 Suggested Additional Reading. The subject of foam use in the petroleum industry is covered in depth in Refs. 211 and 139. Ref. 212 provides a more recent review of experimental and modeling studies of conformance-improvement foam flow through porous media. Ref. 213 provides a review of published field experience relating to 30 applications of foam for conformance improvement in North Sea reservoirs. Ref. 202 presents an overview of the field application of foam for improved sweep efficiency and control of produced gas in the United States, the North Sea, and the Former Soviet Union.

13.8 Resins

The term “resin,” as used in this chapter, refers to an organic, polymer-based, solid plastic material. Resins do not contain a significant amount of a solvent phase (as do gels), and resins are placed downhole in a liquid monomeric (or oligomeric) state and polymerized in situ to the mature solid state.

13.8.1 Oilfield Resins and Resin Treatments. Oilfield resins are exceptionally strong materials for use in blocking and plugging fluid flow in the wellbore and/or the very near-wellbore region.⁴ The three classical oilfield resins discussed here have exceptionally good compressive strengths. Also, these three resins usually have good bonding strength to oil-free rock surfaces. Resins for fluid-shutoff purposes during squeeze treatments can normally only be placed in the wellbore, perforations, gravel packs, and other near-wellbore multi-Darcy flow channels.

Solid fillers, such as silica flour and calcium carbonate, are sometimes added to fluid-shutoff resin formulas to reduce cost, increase resin specific gravity, and/or provide higher temperature stability. If solid fillers are added to a fluid-shutoff resin formula, the solids should normally be added at the wellsite just before resin placement. The exception to this is solids addition to epoxy resins that is often conducted at the resin manufacturing facility. This is

done because of the need for a high level of agitation while mixing the solids into the viscous immature epoxy-resin fluid.

In addition to resin treatments applied during a well's production phase, resin treatments have been successfully used as part of well completion strategies to improve conformance during the subsequent oil-recovery production phase of the well's later life. The use of resins for water control dates back at least to 1922.²¹⁴ The vast majority of the resin field applications, involving the use of the fluid-shutoff resins technologies that are described next, have used treatment volumes on the order of one to five barrels. At this writing, resin fluid-shutoff treatments were available from relatively few oilfield service companies.

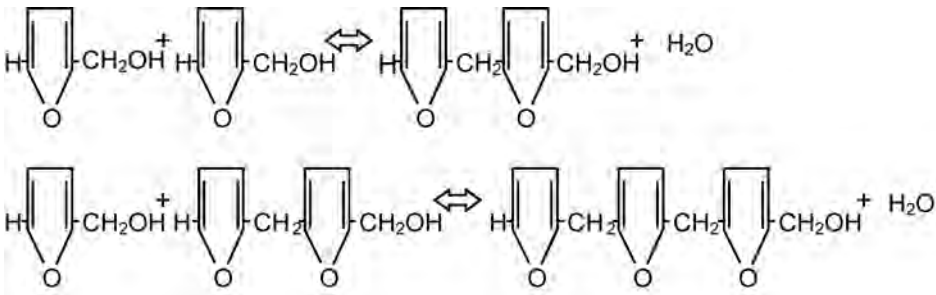
Types and Chemistries. There are three resin chemistry types that have been studied and applied for use as fluid-shutoff treatments in wellbores and the very near-wellbore region. A fourth fluid-shutoff "resin" technology involves a blocking agent that is a cross between a resin and a gel.

Epoxies. Epoxy resins have been favored for use in conjunction with CO₂ flooding. Many of the early epoxy resin technologies were extremely sensitive to water and were "deactivated" while being placed. Wiper plugs are often placed in the tubing at the beginning and the end of the injected resin material. Some of the newer oilfield epoxy resin technologies are much less sensitive to water contact. In general, epoxy resins are the strongest (especially in terms of bonding strength) of the three oilfield resins discussed here. The kinetic rate of maturation of epoxy resins is somewhat touchy and subject to numerous possible interferences during resin placement as a consequence of the epoxy-resin maturation chemistry being based on free-radical chemistries.

Oilfield epoxy resins commercially available are applicable over a downhole temperature range (downhole temperature possibly attained by cooling) of 80 to 130°F and have an ultimate temperature stability of up to 400°F. Placement outside the wellbore is limited to fractures, behind-pipe channels, large vugs, and multi-Darcy matrix rock. Epoxy resins are applicable for shutting off fluid flow involving water, CO₂, and hydrocarbon gases. Epoxy resins are also applied for casing repair purposes. In general, epoxy resins have better bonding properties and strengths than phenolic or furan resins. The relatively fast curing times of epoxy resins result in more restrictive placement times than those of the other two fluid-shutoff resins.

Phenolics. Phenolic resins are well suited for use during steamflooding operations because of their good thermal stability. Phenolic resin treatments have been used to improve steam injection profiles by blocking near-wellbore steam thief zones. During resin treatment placement, immature phenolic resins are not highly sensitive to water and will not be deactivated by limited contact with water. The high viscosity of immature phenolic resins suppresses excessive mixing with water in the wellbore. The maturation chemical kinetics of phenolic resins is not highly subject to interferences during resin placement. Two types of catalysts/activators, caustic and acid, can be used to initiate the polymerization reaction. The maturation chemical kinetics for the more commonly used base-catalyzed phenolic resins is primarily a function of the amount of hydroxide ion incorporated into the resin formula. Phenolic resin maturation involves a chemical condensation polymerization reaction. Commercial base-catalyzed phenolic resins that were available at this writing were applicable over a downhole temperature range (downhole temperature possibly attained by cooling) of 90 to 170°F and applicable to an ultimate downhole temperature of up to 450°F. Acid-catalyzed phenolic resins are considered to be most ideally applied over a downhole temperature range of 100 to 130°F.

Primary uses of phenolic resins are for near-wellbore applications involve the plugging of perforations, behind pipe channels, gravel packs, and fractures. Phenolic resins are applicable for shutting-off fluid flow involving water, steam, CO₂, and hydrocarbon gases. In general, fluid-shutoff phenolic resins have slower maturation chemical-reaction (polymerization) rates than



Repeated until obtained polymer

Fig. 13.35—Polymerization of furfuryl alcohol.

fluid-shutoff epoxy resins have. The bonding properties of phenolic resins are not as good as those of cement or epoxy resin.

Toxicity, safety, and environmental issues and regulations need to be carefully considered and reviewed before applying a phenolic resin treatment. The fundamental chemistry of phenolic resins is based on phenol/formaldehyde chemistry. Phenol and formaldehyde are both toxic. The use of phenolic resin treatments for oilfield fluid-shutoff purposes goes back to the 1960s.

Furans. Oilfield furan resins are, in general, weaker resins than epoxy and phenolic resins. Commonly available commercial furan resins are applicable over a downhole temperature range (downhole temperature possibly attained by cooling) of 60 to 350°F and are applicable to an ultimate downhole temperature of up to 700°F.^{215,216} The penetration of furan resins into an oil reservoir is limited to fracture channels, vugs, and multi-Darcy matrix rock. Furan resins are applicable for shutting off fluid flow involving water, steam, CO₂, and hydrocarbon gases. Furan resins are also applicable for casing repair purposes. Primary uses of furan resins are for near-wellbore plugging of perforations, behind pipe channels, and fractures, along with their use for casing repairs. The use of furan resins is reported to be environmentally friendly.²¹⁶

Oilfield furan resins are derived from the condensation polymerization reaction of furfuryl alcohol, as Fig. 13.35 shows.^{215,217} The polymerization reaction of furfuryl alcohol is acid catalyzed. Typically, furfuryl alcohol is obtained from the destructive distillation of corncobs. Furfuryl alcohol polymerizes to form a hard, black, chemically resistant, and thermally stable polymer resin.²¹⁷ Hardened furan resins have, in general, lower compressive strengths than epoxy and phenolic resins.

Modern oilfield furan resin treatments start with use and placement of furan oligomers or prepolymer chemical species (not the monomer specie). Use of oligomers of furfuryl alcohol reduces the reactivity of the polymerization reaction and greatly increases the controllability of the furan resin polymerization reaction.²¹⁵ Modern furan resin fluid-shutoff treatments are a single-fluid process in which an organic acid and an ester have been included in the resin formula.^{215–217} The ester reacts with, and absorbs, the water formed during the condensation reaction of the furan resin polymerization process. The uptake of the water rendered by the condensation reaction drives the polymerization reaction further to completion and, thus, renders a more effective and stronger final furan resin. Some of the currently used furan resin fluid-shutoff formulas contain a small amount of a water-swelling polymer to prevent shrinkage of the furan resin after it is polymerized.

In general, furan resins provide better control over the resin maturation time and do so over a larger temperature range compared with the epoxy resin technology. The lower viscosity, in general, of immature furan resins, as compared with epoxy and phenolic resins, permits better

penetration of furan resins, especially into reservoir matrix rock. Although not common, furan resins have been placed using coiled tubing.

Common Properties. The three resin technologies discussed previously have a number of features in common. They are all thermosetting and applicable to both sandstone and carbonate reservoirs. None of the three resin technologies are highly sensitive to the pH in the wellbore during resin placement or sensitive to H₂S. All three are not substantially degraded by conventional acid treatments performed after resin treatment placement. The three resins are more stable to acid than conventional Portland cement. Resins without solid fillers can flow into small flow channels where conventional Portland cement cannot.

All three resin types have good mechanical, bonding, and compressive strengths. Most fluid-shutoff resins have compressive strengths exceeding 1,000 psi, with some of these resins possessing compressive strengths up to, and exceeding, 20,000 psi.

The treatment volume of a high percentage of resin fluid-shutoff treatments placed downhole has only been in the range of one to five barrels (and most of these in the one to two barrel range). For all three of these resin technologies, the immature resin solution, as it is being placed downhole, is quite viscous (often qualitatively described as having approximately the consistency of molasses).

Crosslinked Styrene-Butadiene Block Copolymers. There is a conformance-improvement technology that involves a fluid-shutoff plugging agent that is a cross between a resin and a gel. The mature plugging agent contains approximately 10 to 20% styrene-butadiene block copolymer dissolved in an aromatic solvent, such as xylene, and the polymer has been chemically crosslinked using a peroxide free-radical crosslinking agent.²¹⁹

This plugging-agent material is an example of a crosslinked polymer gel in which the gel solvent is an organic fluid. However, this plugging-agent technology also has the attributes of a resin that contains a substantial amount of added organic solvent. Because this plugging technology has many of the functional attributes of a resin (both in terms of application and final physical form) and because, like the three resins described previously, the crosslinked styrene-butadiene block copolymer gel technology is essentially an organic and nonaqueous blocking-agent technology, it is included in this resin technology section.

Crosslinked styrene-butadiene block copolymer gels/resins, as reported in the petroleum literature,²¹⁹ are not a fully rigid material. However, crosslinked styrene-butadiene block copolymer gels/resins are an effective “resin” material for use in correcting steam injection profiles during steamflooding.²¹⁹ This blocking-agent material is reportedly stable to 500°F. The thermally activated chemical crosslinking of the styrene-butadiene block copolymer is imparted by a peroxide agent that starts a free-radical crosslinking chemical chain reaction. Control of the gelation onset time at various temperatures is achieved by the proper selection of the chemistry of the peroxide crosslinking agent such that the chosen peroxide chemical decomposes to free radicals in an appropriate time frame at a specified temperature.

13.8.2 Problem Identification and Temperature Issues. Because of the limited and relatively small volumes of resin that are placed during a typical resin fluid-shutoff treatment, the correct identification of both the nature and location of the fluid-flow path to be shut off are critical to the successful application of resin conformance-improvement treatments.

There are three reasons that resin jobs are inherently small-volume treatments. First, the immature resin fluid as it is being placed downhole is quite viscous, so that, at best, the immature resin can only be placed very slowly into matrix reservoir rock. This situation is compounded by the fact that the resin fluid has a relatively short maturation time. Second, because of the highly reactive nature of the immature resin solutions, they cannot be propagated any significant distance into or through porous reservoir rock or any other type of restricted flow path

without encountering serious chemical interferences to the resin polymerization reaction. Third, the high unit-volume cost usually precludes the application of large-volume resin treatments.

Temperature issues and the thermal history that a resin experiences during its placement to the final downhole location are critical to the successful application of resin fluid-shutoff treatments. Thermosetting resins have maturation/polymerization rates that are highly sensitive to temperature. If a resin were to inadvertently set up (as has occurred at times) in the dump bailer during placement or in an injection tubing string, this will be a costly outcome. If the resin sets up in an injection string, normally that injection string will have to be decommissioned.

Thus, it is critical that the temperature of the reservoir volume to be treated at the time of initial resin placement be known. It is also critical to know how the temperature of the resin will change with time during its placement downhole. Not correctly identifying the downhole temperature where the resin is to be placed and not knowing the thermal history of the resin while it is being placed are major causes of resin treatment failures.

13.8.3 Well Selection. The process of well-candidate selection for resin squeeze treatments is an important aspect of successfully applying resin fluid-shutoff treatments, and a resin treatment aspect that needs careful attention. In particular, the conformance problem of the well to be treated must be a problem for which only a few barrels of successfully placed resin will be sufficient to create the necessary flow barrier.

13.8.4 Placement. Originally, because of the small-volume of resin treatments, wireline dump bailers were widely used for placement. More recently, the majority of resin treatments have been placed through clean, uncorroded injection tubing. The advantages of using injection tubing are faster placement and the ability to attain large differential pressures during placement.

When treating reservoirs with elevated temperatures, the downhole target zone is often pre-cooled. For phenolic and furan resin treatments, the injected cooling fluid is usually water. However, when performing a water-intolerant epoxy resin treatment, the bulk of the injected cooling fluid is usually water that is followed by a hydrocarbon fluid spacer (often xylene). If prerésin-treatment cooling-fluid injection is conducted, it is critical to accurately know to what degree the downhole target zone has been cooled and how rapidly the downhole treatment volume will heat back up. The determination of such thermal information often requires the running of appropriate computer thermal-simulation programs and/or a high degree of experience with applying resins to the well type to be treated.

When placing fluid-shutoff resins using an injection string, wiper plugs are usually placed in the injection tubing at the beginning and the end of the resin injection. Historically, clean, uncorroded production or drill strings have been used. The use of such a relatively large internal-diameter injection string during resin injection has often been considered necessary because of the high viscosity of the resin material being injected. More recently, the use of coiled tubing has been successfully used in limited instances.²¹⁸

It is mandatory that the resin be placed only in the wellbore interval intended for the resin treatment. As a result, the resin must normally be placed with the use of mechanical zone isolation (e.g., use of mechanical packers). In the event any resin left in the wellbore needs to be removed, the resin material is usually drilled out using special drill bits. A major cause of failures for resin fluid-shutoff treatments is the improper placement downhole.²¹⁷

13.8.5 Wellbore and Injection-String Condition. For several reasons, the condition of the wellbore and the injection string is a critical parameter to the success of resin fluid-shutoff treatments.

First, if the surfaces of the wellbore or the near-wellbore reservoir material to be contacted with the resin have a substantial oil-coating film, the resin will fail to bond to the reservoir material or wellbore hardware, and much of the resin treatment effectiveness is lost. For this

reason, if oily solid surfaces are expected, a hydrocarbon-wash preflush is often performed. The hydrocarbon fluid used in such a preflush is usually xylene.

Second, corroded placement equipment or injection tubular strings can play havoc with the kinetics of the resin polymerization reaction, especially for epoxy resins.

Third, an oil-coated injection string can be detrimental to the polymerization reaction product of some resin formulas.

Fourth, when placing the resin through liners, screens, or coarse sands where these flow paths have previously become partially plugged with organic debris (e.g., asphaltenes) and inorganic debris (e.g., formation fines and scale), such previous plugging can prevent the resin from being fully placed into the desired treatment volume. These plugging materials should be removed before placing the resin treatment material. Jet washing is a common technique used to remove plugging material.

Fifth, in addition to water interfering with the maturation chemistry of certain oilfield resins, water in the injection string can cause physical problems during resin placement. Water can lead to “clumping” in which water becomes interspersed between blobs of resin material. The resulting coarse emulsion will often not flow readily and the ultimate strength of the placed resin will be decreased.

13.8.6 Advantages and Disadvantages. The advantages and disadvantages of the use of resins as small-volume fluid-shutoff treatments to remedy oilfield conformance problems are as follows.

Advantages. Resins possess good mechanical strength, good bonding strength, good thermal stability, and good chemical inertness (e.g., can acidize over resins).

Disadvantages. Resin fluid-shutoff treatments are constrained by limited resin penetration distances into the reservoir formation (because of a combination of high viscosity, being highly chemically reactive, and cost issues); are operationally and chemically relatively complicated; are somewhat tricky to successfully apply; are constrained by placement techniques and issues; are costly on a unit volume basis; have, in practice, usually been limited to shallow reservoir applications; and are considered to be a niche conformance-treatment technology.

13.8.7 Dos and Don'ts. The following items are a partial list of “do's” and “don'ts” as they apply to resin fluid-shutoff treatments.

Dos.

- Test the resin maturation and hardening rate onsite using the actual resin chemicals to be used and simulating the thermal history that the resin will experience during its placement.
- Before initiating a resin treatment, understand and be able to fully predict how the rate of resin maturation and hardening varies with the amount of catalyst and/or activator that is added to the resin formula.
- Know the age of the resin as it is received from the supplier. Older resins will often react faster than fresh ones because of an increased level of “self-polymerization” that occurs while the resin sits on the shelf during storage. (This is largely a concern for phenolic and furan resins.)
- Know, with a high degree of certainty, the thermal history that the resin will experience as it is placed and the rate at which the resin will mature and harden under this thermal history.
- Know, with a high degree of certainty, the exact location of the problem to be treated. (This is important because of the limited volume of resin that is to be placed.)
- Ensure that the injection tubing and placement equipment are free of rust and oil.
- Clean oil from the wellbore and reservoir location where the resin is to be placed and function.
- If economics permit, perform laboratory testing in reservoir or gravel-pack sandpacs if the resin is to be placed in such sands. Such testing, among other purposes, assures that the sands will not chemically interfere with the expected performance of the emplaced resin.

- Conduct, or have conducted, a good quality control and quality assurance program in conjunction with the application of resin squeeze treatments.

Don'ts.

- For most common epoxy resins, make sure water does not contact the epoxy resin while it is being placed and matured.
- For most common epoxy resins, don't inject the epoxy resin through injection tubing without the use of wiper plugs.
- Don't store the resin material above the recommended storage temperature before its use.
- Don't use aged resin material—always use fresh resin material.

13.8.8 Illustrative Field Results. *Water-Encroachment Treatments.* Ref. 215 reports on 26 production wells of the Kern River and San Ardo fields that were treated in 1990 and 1991 with furan resin jobs in which the treated production wells were suffering from water-encroachment problems. Most (24) of the wells were in the heavy-oil Kern River field of the Lower San Joaquin Valley in California. When the furan resin treatments were applied, the Kern River field was undergoing steamflooding. Of the production wells treated, 79% showed significant reductions in water production after the treatments. After drilling out the resin plug in the wellbore, the resin remaining in the treated perforations and in the treated formation was of a sufficient amount and strength to prevent water entry into the production wells.

Gravel Pack Resin Treatments. Phenolic-resin plugback treatments were applied to 32 wells with openhole gravel pack completions in the Midway-Sunset field in 1987.²²⁰ These resin treatments were reported to have decreased water production by 5,900 BWPD and increased oil production by 256 BOPD. Total revenue and savings from the resin treatments were estimated to be U.S. \$1 million, and the resin treatment project was reported to have paid out in 120 days. The phenolic resin treatments were applied successfully to downhole temperatures ranging from 100 to 200°F at this California cyclic-steam injection project.

Furan Resin Treatments in California. In 1980, Hess provided a brief review of 36 small-volume (1 to 5 bbl) furan resin treatments applied for a variety of purposes in California.²¹⁷ Of these 36 furan resin treatments, 27 were reported to have achieved “permanent” downhole plugging. The furan resin treatments were applied for a variety of purposes, including shutting off undesirable steam breakthrough in production wells, plugging thief zones in water and steam injection wells, shutting off bottomwater entry, and repairing casing and liner damage. The furan resin used in treating steam-stimulated and steamflood injection wells was reported to have held up through two years of service.

Epoxy Resin Treatment. A three-barrel epoxy resin treatment was applied to a Green Canyon production well in the Gulf of Mexico. The objective of this treatment was to shut off the lower perforated interval of the gravel-packed well. The temperature of the sand to be treated was 139°F. The wellbore had a deviation angle of 60° across the treated interval. The epoxy resin formula used was designed for a 4- to 6-hour pump time through coiled tubing and required a 24- to 48-hour shut-in time. Following the epoxy resin fluid-shutoff treatment, oil production increased from 240 BOPD before the resin job to 470 BOPD following the resin job. Following the resin treatment, the flowing tubing head pressure was reported to have increased dramatically.²¹⁸

Steam Injector Profile Correction. More than 40 crosslinked styrene-butadiene block copolymer resin/gel treatments of approximately four-barrel volume have been successfully applied as injection-well profile correction treatments in conjunction with the steamflood conducted at the Kern River field in California.²¹⁹ It was reported that none of the resin/gel treatments showed any steam entry into the treated wellbore intervals after the steam-shutoff resin treatments. Pay-out times for these resin steam-shutoff treatments, based on steam cost savings alone, were

reported to have averaged less than two months. These resin/gel treatments were applied with conventional oilfield surface and downhole equipment.

13.8.9 Historical Trend. Resin conformance fluid-shutoff treatments had been somewhat widely applied in previous years and had been relatively popular at that time. However, at the time of writing this chapter, relatively few resin fluid-shutoff treatments were being applied.

13.9 Summary

Conformance improvement encompasses improving drive-fluid sweep efficiency during oil-recovery flooding operations and the shutting off of excessive, deleterious, and competing coproduction of an extraneous fluid, such as water or gas. Conformance problems occur because of heterogeneity of reservoir permeability and/or viscosity and mobility-control attributes of the oil-recovery drive and reservoir fluids. A number of conformance problems and a number of key distinctions relating to conformance problems were discussed. Failure to correctly identify/diagnose the nature of an offending oilfield conformance problem and failure to adequately account for the key distinctions relating to the various conformance problems are major contributors to failures of conformance-improvement floods and treatments.

DPR is a phenomenon whereby a substantial number of, respectively, polymers and polymer gels of conformance-improvement treatments reduce the permeability to water flow to a greater extent than they reduce the permeability to oil and gas flow. The application of DPR technologies for water-shutoff purposes is not a panacea. The successful application of bullheaded DPR water-shutoff/reduction treatments (which are to be applied through production wells, involve radial flow in matrix rock, and for which the well's drawdown pressure is not increased post-treatment) is limited to the following conditions:

- A conformance problem exists in a matrix rock reservoir involving differing geological strata.
- No fluid crossflow exists within the reservoir between the water and the oil or gas producing geological strata.
- The water strata are producing at an uneconomically high water cut.
- The oil or gas strata is producing and will produce for the economic life of the water-shutoff treatment at 100% oil or gas cut.

Early use of water-soluble and viscosity-enhancing polymers during conformance-improvement operations was primarily for improving mobility control during waterflooding. Such polymer flooding was, and is, applied to improve the flood volumetric sweep efficiency of a waterflood by increasing the viscosity of the oil-recovery drive fluid. More recently, polymer application during conformance-improvement operations has additionally been used extensively in polymer-gel treatments and DPR polymer treatments for water-shutoff/reduction purposes. The science, technology, engineering, historical trends, and field application of polymers used in conformance improvement were reviewed.

Gels are a fluid-based system (usually relatively inexpensive) to which solid-like structural properties have been imparted. Gels, especially crosslinked-polymer gels, are effective, widely applied permeability-reducing and blocking/plugging agents for use in conformance-improvement treatments. Conformance-improvement gels are used to reduce or eliminate the fluid-flow capacity of high-permeability and/or water-producing flow paths within an oil or gas reservoir. Organic- and inorganic-based gels and the when, where, and how of successfully applying gel treatments were reviewed. The economics of polymer-gel treatments can be exceptionally attractive.

The use of conformance-improvement foams as mobility-control agents and as gas-flow blocking/plugging agents was reviewed. Foams are primarily used as mobility-control agents during gas-flooding operations or as gas-shutoff treatments. The fundamentals, history, science, technology, engineering, trends, and field application and performance of foams for confor-

mance improvement were reviewed. There are some significant distinctions between foam properties and performance as they exist in bulk foam (e.g., foam in a bottle) and foam as it exists in reservoir-rock porous media. Foam flow in porous media tends to occur as gas-bubble trains, in which the individual gas bubbles are separated by thin-film liquid lamellae. An important aspect of foams in porous reservoir rock is the increased trapped gas saturation that the foams impart. Polymer-enhanced foams and foamed gels for conformance improvement were briefly discussed.

Resins for use in conformance-improvement treatments are an organic polymer-based plastic solid material. Such resin material normally does not contain a significant amount of a solvent phase. Resins are placed downhole in a liquid monomeric (or oligomeric) state and then polymerized to the mature solid resin state. Resins are an exceptionally strong material and an exceptionally chemically and thermally stable material for use in blocking and plugging fluid flow in the wellbore and/or the very near-wellbore region. The chemistry, technology, engineering, limitations, trends, cost concerns, special issues, and field applications of resins for use in conformance-improvement treatments were reviewed. Resin treatments have been used successfully in conjunction with steam flooding. Volumes of resin placed during a conformance treatment are typically on the order of one to five barrels.

Nomenclature

- a = polymer-specific constant of the Mark-Houwink equation
- A_f = area contacted by oil recovery displacement fluid, L^2
- A_t = total reservoir area under consideration, L^2
- A_V = reservoir vertical cross section contacted by oil recovery displacement fluid, L^2
- A_{iV} = total reservoir vertical cross section, L^2
- c = polymer concentration
- d_p = mean end-to-end distance or size of a polymer molecule dissolved in solution, L
- E_A = areal sweep efficiency
- E_I = vertical sweep efficiency
- E_P = pattern sweep efficiency
- E_V = volumetric sweep efficiency
- h = formation height, L, ft
- k = permeability, L^2 , md
- K = power-law coefficient
- K' = polymer-specific constant of the Mark-Houwink equation
- k_a = permeability measured after polymer flooding, L^2
- k_{av} = average permeability, L^2
- k_b = permeability measured before polymer flooding, L^2
- k_{hi} = high permeability, L^2
- k_i = permeability of phase i
- M = mobility ratio
- M_p = polymer molecular weight
- M_H = Hall plot slope
- n = power-law exponent
- P_c^* = limiting capillary pressure, m/Lt^2
- p_{wf} = flowing wellhead pressure, m/Lt^2 , psi
- R_f = resistance factor
- R_{rf} = residual resistance factor

r_e	= external radius, L, ft
r_w	= wellbore radius, L, ft
s	= skin factor
t	= time, t, days
w_f	= fracture width/aperture, L
W_i	= cumulative volume injected, bbl
ϕ	= porosity
Γ	= polymer retention in $\mu\text{g/g}$
Γ_v	= polymer retention in lbm/AF
$\dot{\gamma}$	= shear rate
η	= viscosity of the polymer solution
η_s	= viscosity of the solvent
$[\eta]$	= intrinsic viscosity
ρ_{RG}	= density of reservoir rock (no porosity included)
μ	= viscosity
μ_{eff}	= effective viscosity of a polymer solution
μ_i	= viscosity of phase i
μ_i	= average rate of gel dehydration
μ_w	= viscosity of the brine into which polymer is dissolved
λ_D	= mobility of the displacement phase
λ_d	= mobility of the displaced phase
λ_i	= mobility of phase i
λ_p	= mobility of the polymer solution
λ_w	= mobility of the brine solution
τ	= shear stress

Abbreviations and Acronyms

AMPS	= 2-acrylamido-2-methyl-propanesulfonic acid
ASP	= alkaline surfactant polymer
BOPD	= barrels oil per day
BWPD	= barrels water per day
CC/AP	= chromium (III)-carboxylate/acrylamide-polymer
CDG	= colloidal dispersion gels
DPR	= disproportionate permeability reduction
EOR	= enhanced oil recovery
GOC	= gas/oil contact
GOR	= gas/oil ratio
HPAM	= hydrolyzed polyacrylamide
IPV	= inaccessible pore volume
MW	= molecular weight
OOIP	= original oil in place
PAM	= polyacrylamide
PV	= pore volume
RPM	= relative permeability modification
SF	= screen factor
WAG	= water alternating gas
WOR	= water/oil ratio

Acknowledgments

Special thanks to Craig Phelps, who provided much of the information on which the Resins section is based. The following individuals contributed significantly to the writing of this chapter by providing reviews of the chapter or selected sections of the chapter: Randy Seright, Paul Willhite, Malcolm Pitts, Bill Rossen, Jim Mack, Dwyann Dalrymple, Craig Phelps, Reid Grigg, Larry Eoff, and Ed Holstein.

References

1. Lake, L.W.: *Enhanced Oil Recovery*, Prentice Hall, Englewood Cliffs, New Jersey (1989) 189–200.
2. Green, D.W. and Willhite, G.P.: *Enhanced Oil Recovery*, Textbook Series, SPE, Richardson, Texas (1998) **6**, 73–75.
3. Willhite, G.P.: *Waterflooding*, Textbook Series, SPE, Richardson, Texas (1986) **3**, 87–89.
4. Kabir, A.H.: “Chemical Water & Gas Shutoff Technology—An Overview,” paper SPE 72119 presented at the 2001 SPE Asia Pacific Improved Oil Recovery Conference, Kuala Lumpur, 8–9 October.
5. Sydansk, R.D. and Southwell, G.P.: “More Than 12 Years’ Experience With a Successful Conformance-Control Polymer-Gel Technology,” *SPEPF* (November 2000) 270.
6. Sorbie, K.S. and Seright, R.S.: “Gel Placement in Heterogeneous Systems with Crossflow,” paper SPE 24192 presented at the 1992 SPE/DOE Symposium on Enhanced Oil Recovery, Tulsa, 22–24 April.
7. Seright, R.S., Lane, R.H., and Sydansk, R.D.: “A Strategy for Attacking Excess Water Production,” paper SPE 70067 presented at the 2001 SPE Permian Basin Oil and Gas Recovery Conference, Midland, Texas, 15–16 May.
8. Seright, R.S.: “Placement of Gels To Modify Injection Profiles,” paper SPE 17332 presented at the 1988 SPE/DOE Enhanced Oil Recovery Symposium, Tulsa, 17–20 April.
9. Mack, J.C. and Smith, J.E.: “In-Depth Colloidal Dispersion Gels Improve Oil Recovery Efficiency,” paper SPE 27780 presented at the 1994 SPE/DOE Symposium on Improved Oil Recovery, Tulsa, 17–20 April.
10. Martinez, S.J., Steanson, R.E., and Coulter, A.W.: “Formation Fracturing,” *Petroleum Engineering Handbook*, H.B. Bradley (ed.), SPE, Richardson, Texas (1987) Chap. 55, 55–2.
11. Chan, K.S.: “Water Control Diagnostic Plots,” paper SPE 30775 presented at the 1995 SPE Annual Technical Conference and Exhibition, Dallas, 22–25 October.
12. White, J.L., Goddard, J.E., and Phillips, H.M.: “Use of Polymers To Control Water Production in Oil Wells,” *JPT* (February 1973) 143.
13. Sparlin, D.D.: “An Evaluation of Polyacrylamides for Reducing Water Production,” *JPT* (August 1976) 906.
14. Weaver, J.D.: “A New Water-Oil Ratio Improvement Material,” paper SPE 7574 presented at the 1978 SPE Annual Technical Conference and Exhibition, Houston, 1–3 October.
15. VanLandingham, J.V.: “Laboratory & Field Development of Dispersed Phase Polymer Systems for Water Control,” paper SPE 8423 presented at the 1979 SPE Annual Technical Conference and Exhibition, Las Vegas, Nevada, 23–26 September.
16. Dunlap, D.D., Boles, J.L., and Novotny, R.J.: “Method for Improving Hydrocarbon/Water Ratios in Producing Wells,” paper SPE 14822 presented at the 1986 SPE Symposium on Formation Damage Control, Lafayette, Louisiana, 26–27 February.
17. Eoff, L. *et al.*: “Structure and Process Optimization for the Use of a Polymeric Relative-Permeability Modifier in Conformance Control,” paper SPE 64985 presented at the 2001 SPE International Symposium on Oilfield Chemistry, Houston, 13–16 February.
18. Schneider, F.N. and Owens, W.W.: “Steady-State Measurements of Relative Permeability for Polymer/Oil Systems,” *SPEJ* (February 1982) 79.
19. Kohler, N. *et al.*: “Weak Gel Formulations for Selective Control of Water Production in High-Permeability and High-Temperature Production Wells,” paper SPE 25225 presented at the 1993 SPE International Symposium on Oilfield Chemistry, New Orleans, 2–5 March.

20. Dovan, H.T. and Hutchins, R.D.: "New Polymer Technology for Water Control in Gas Wells," *SPEPF* (November 1994) 280.
21. Seright, R.S.: "Reduction of Gas and Water Permeabilities Using Gels," *SPEPF* (May 1995) 103.
22. Stanley, F.O. *et al.*: "Amphoteric Polymer Improves Hydrocarbon/Water Ratios in Producing Wells—An Indonesian Case Study," *SPEPF* (August 1997) 181.
23. Ligthelm, D.J.: "Water Shut Off in Gas Wells: Is There Scope for a Chemical Treatment?" paper SPE 68978 presented at the 2001 SPE European Formation Damage Conference, The Hague, 21–22 May.
24. Zaitoun, A. *et al.*: "Water Shutoff by Relative Permeability Modifiers: Lessons from Several Field Applications," paper SPE 56740 presented at the 1999 SPE Annual Technical Conference and Exhibition, Houston, 3–6 October.
25. Faber, M.J. *et al.*: "Water Shut-Off Field Experience With a Relative Permeability Modification System in the Marmul Field (Oman)," paper SPE 39633 presented at the 1998 SPE/DOE Improved Oil Recovery Symposium, Tulsa, 19–22 April.
26. Sandiford, B.B.: "Laboratory and Field Studies of Water Floods Using Polymer Solutions to Increase Oil Recovery," *JPT* (August 1964) 917.
27. Sydansk, R.D. *et al.*: "Characterization of Partially Formed Polymer Gels for Application to Fractured Production Wells for Water-Shutoff Purposes," *SPEPF* (August 2005) 240.
28. Seright, R.S., Liang, J., and Seldal, M.: "Sizing Gelant Treatments in Hydraulically Fractured Production Wells," *SPEPF* (November 1998) 223.
29. Seright, R.S. *et al.*: "Characterizing Disproportionate Permeability Reduction Using Synchrotron X-Ray Computed Microtomography," paper SPE 71508 presented at the 2001 SPE Annual Technical Conference and Exhibition, New Orleans, 30 September–3 October.
30. Nilsson, S., Stavland, A., and Jonsbraten, H.C.: "Mechanistic Study of Disproportionate Permeability Reduction," paper SPE 39635 presented at the 1998 SPE/DOE Improved Oil Recovery Symposium, Tulsa, 19–22 April.
31. Barreau, P. *et al.*: "Water Control in Producing Wells: Influence of an Adsorbed-Polymer Layer on Relative Permeabilities and Capillary Pressure," *SPERE* (November 1997) 234.
32. Mennella, A. *et al.*: "Pore-Scale Mechanism for Selective Permeability Reduction by Polymer Injection," paper SPE 39634 presented at the 1998 SPE/DOE Improved Recovery Symposium, Tulsa, 19–22 April.
33. Zitha, P.L.J., Vermolen, F.J., and Bruining, H.: "Modification of Two Phase Flow Properties by Adsorbed Polymers and Gels," paper SPE 54737 presented at the 1999 SPE European Formation Damage Conference, The Hague, 31 May–1 June.
34. Al-Sharji, H.H. *et al.*: "Disproportionate Permeability Reduction Due to Polymer Adsorption Entanglement," paper SPE 68972 presented at the 2001 SPE European Formation Damage Conference, The Hague, 21–22 May.
35. Zaitoun, A. and Kohler, N.: "Two-Phase Flow Through Porous Media: Effect of an Adsorbed Polymer Layer," paper SPE 18085 presented at the 1988 SPE Annual Technical Conference and Exhibition, Houston, 2–5 October.
36. Elmkie, P. *et al.*: "Further Investigations on Two-Phase Flow Property Modification by Polymers: Wettability Effects," paper SPE 64986 presented at the 2001 SPE International Symposium on Oilfield Chemistry, Houston, 13–16 February.
37. Thompson, K.E. and Fogler, H.S.: "Pore-Level Mechanisms for Altering Multiphase Permeability with Gels," *SPEJ* (September 1997) 350.
38. Liang, J.T., Sun, H., and Seright, R.S.: "Why Do Gels Reduce Water Permeability More Than Oil Permeability?" *SPERE* (November 1995) 282.
39. Grattoni, C.A., Jing, X.D., and Zimmerman, R.W.: "Disproportionate Permeability Reduction When a Silicate Gel Is Formed In-Situ to Control Water Production," paper SPE 69534 presented at the 2001 SPE Latin American and Caribbean Petroleum Engineering Conference, Buenos Aires, 25–28 March.
40. Seright, R.S., Prodanovic, M., and Lindquist, W.B.: "X-Ray Computed Microtomography Studies of Disproportionate Permeability Reduction," paper SPE 89393 presented at the 2004 SPE/DOE Symposium on Improved Oil Recovery, Tulsa, 17–21 April.
41. Stavland, A. *et al.*: "Disproportionate Permeability Reduction Is Not a Panacea," *SPEREE* (August 1998) 359.

42. Mennella, A. *et al.*: “Candidate and Chemical Selection Guidelines for Relative Permeability Modification (RPM) Treatments,” *SPEPF* (August 2001) 181.
43. Liang, J.T., Lee, R.L., and Seright, R.S.: “Gel Placement in Production Wells,” *SPEPF* (November 1993) *Trans., AIME*, **295**.
44. Botermans, C.W., Van Batenburg, D.W., and Bruining, J.: “Relative Permeability Modifiers: Myth or Reality?” paper SPE 68973 presented at the 2001 SPE European Formation Damage Conference, The Hague, 21–22 May.
45. Seright, R.S.: “‘Clean’ Up of Oil Zones after a Gel Treatment,” paper SPE 92772 presented at the 2005 SPE International Symposium on Oilfield Chemistry, Houston, 2–4 February.
46. Sorbie, K.S.: *Polymer-Improved Oil Recovery*, Blackie, Glasgow and London (1991).
47. Davison, P. and Mentzer, E.: “Polymer Flooding in North Sea Reservoirs,” *SPEJ* (June 1982) 353.
48. Rivenq, R.C., Donche, A., and Nolk, C.: “Improved Scleroglucan for Polymer Flooding Under Harsh Reservoir Conditions,” *SPEPE* (February 1992) 15.
49. Sohn, W.O., Maitin, B.K., and Votz, H.: “Preconditioning Concepts in Polymer Flooding in High-Salinity Reservoirs: Laboratory Investigations and Case Histories,” *SPEPE* (November 1990) 503.
50. Moradi-Araghi, A. and Doe, P.H.: “Hydrolysis and Precipitation of Polyacrylamides in Hard Brines at Elevated Temperatures,” *SPEPE* (May 1987) 189.
51. Stahl, G.A., Moradi-Araghi, A., and Doe, P.H.: “High Temperature and Hardness Table 14. Copolymers of Vinylpyrrolidone and Acrylamide,” *Water-Soluble Polymers for Petroleum Recovery*, G.A. Stahl and D.N. Schulz (eds.), Plenum Press, New York and London (1988) 121–130.
52. Mack, J.C.: “Improved Oil Recovery—Product to Process,” paper SPE 7179 presented at the 1978 SPE Rocky Mountain Regional Meeting, Cody, Wyoming, 17–19 May.
53. Denys, K., Fichen, C., and Zaitoun, A.: “Bridging Adsorption of Cationic Polyacrylamides in Porous Media,” paper SPE 64984 presented at the 2001 SPE International Symposium on Oilfield Chemistry, Houston, 13–16 February.
54. Chauveteau, G., Denys, K., and Zaitoun, A.: “New Insight on Polymer Adsorption Under High Flow Rates,” paper SPE 75183 presented at the 2002 SPE/DOE Improved Oil Recovery Symposium, Tulsa, 13–17 April.
55. Lake, L.W.: *Enhanced Oil Recovery*, Prentice Hall, Englewood Cliffs, New Jersey (1989) 314–353.
56. *Improved Oil Recovery*, Interstate Oil Compaction Commission, Oklahoma City, Oklahoma (1983) 36.
57. Demin, W. *et al.*: “Viscous-Elastic Polymer Can Increase Microscale Displacement Efficiency in Cores,” paper SPE 63227 presented at the 2000 SPE Annual Technical Conference and Exhibition, Dallas, 1–4 October.
58. Flory, P.J.: *Principles of Polymer Chemistry*, Cornell U. Press, Ithaca, New York (1953).
59. Argabright, P.A., Rhudy, J.S., and Phillips, B.L.: “Partially Hydrolyzed Polyacrylamides of Superior Flooding and Injection Properties,” paper SPE 11208 presented at the 1982 SPE Annual Technical Conference and Exhibition, New Orleans, 26–29 September.
60. Herr, J.W. and Routson, W.G.: “Polymer Structure and Its Relationship to the Dilute Solution Properties of High Molecular Weight Polyacrylamide,” paper SPE 5098 presented at the 1974 SPE Annual Meeting, Houston, 6–9 October.
61. Whitecombe, P.J. and Macosko, C.W.: *J. Rheology* (1978) **22**, 493.
62. Duda, J.L., Klaus, E.E., and Fan, S.K.: “Influence of Polymer-Molecule/Wall Interactions on Mobility Control,” *SPEJ* (October 1981) 613.
63. Lake, L.W.: “Chemical Flooding,” *Petroleum Engineering Handbook*, H.B. Bradley (ed.), SPE, Richardson, Texas (1987) Chap. 47.
64. Gogarty, W.B.: “Mobility Control with Polymer Solutions,” *SPEJ* (June 1967) 161.
65. Maerker, J.M.: “Mechanical Degradation of Partially Hydrolyzed Polyacrylamide Solutions in Unconsolidated Porous Media,” *SPEJ* (August 1976) 172.
66. Seright, R.S.: “The Effects of Mechanical Degradation and Viscoelastic Behavior on Injectivity of Polyacrylamide Solutions,” *SPEJ* (June 1983) 475.
67. Taber, J.J., Martin, F.D., and Seright, R.S.: “EOR Screening Criteria Revisited—Part 2: Applications and Impact of Oil Prices,” *SPEPE* (August 1997) 199.

68. DeHekker, T.G. *et al.*: "A Progress Report on Polymer-Augmented Waterflooding in Wyoming's North Oregon Basin and Byron Fields," paper SPE 14953 presented at the 1986 SPE/DOE Symposium on Enhanced Oil Recovery, Tulsa, 20–23 April.
69. De Bons, F.E. and Braun, R.W.: "Polymer Flooding: Still Viable IOR Technique," paper presented at the 1995 European IOR Symposium, Vienna, Austria, 15–17 May, 57–65.
70. Manning, R.K., Pope, G.A., and Lake, L.W.: "A Technical Survey of Polymer Flooding Projects," U.S. Department of Energy DOE/BETC/10327-19, Bartlesville, Oklahoma (September 1983).
71. Tielong, C. *et al.*: "A Pilot Test of Polymer Flooding in an Elevated-Temperature Reservoir," *SPEREE* (February 1998) 24.
72. Putz, A., Pedron, B., and Bazin, B.: "Commercial Polymer Injection in the Courtenay Field, 1993 Update," Geological Soc. Special Publication No. 84, New Developments in Improved Oil Recovery, H.J. De Haan (ed.), The Geographical Soc., London (1995) 239–249.
73. Pitts, M.J. *et al.*: "Polymer Flood of the Rapdan Pool," *SPEERE* (August 1995) 183.
74. Moritis, G.: "EOR Production Up Slightly," *Oil & Gas J.* (20 April 1998) 49.
75. Moritis, G.: "EOR Weathers Low Oil Prices," *Oil & Gas J.* (20 March 2000) 39.
76. Moritis, G.: "Special Report—Enhanced Oil Recovery," *Oil & Gas J.* (15 April 2002) 43.
77. Zaitoun, A., Kohler, N., and Guerrini, Y.: "Improved Polyacrylamide Treatments for Water Control in Producing Wells," *JPT* (July 1991) 862.
78. Stavland, A. and Nilsson, S.: "Segregated Flow Is the Governing Mechanism of Disproportionate Permeability Reduction in Water and Gas Shutoff," paper SPE 71510 presented at the 2001 SPE Annual Technical Conference and Exhibition, New Orleans, 30 September–3 October.
79. Zaitoun, A. and Pichery, T.: "A Successful Polymer Treatment For Water Coning Abatement in Gas Storage Reservoir," paper SPE 71525 presented at the 2001 SPE Annual Technical Conference and Exhibition, New Orleans, 30 September–3 October.
80. Gruenenfelder, M.A. *et al.*: "Implementing New Permeability Selective Water Shutoff Polymer Technology in Offshore, Gravel-Packed Wells," paper SPE 27770 presented at the 1994 SPE/DOE Symposium on Improved Oil Recovery, Tulsa, 17–20 April.
81. Sydansk, R.D.: "A Newly Developed Chromium(III) Gel Technology," *SPEERE* (August 1990) 346.
82. Sydansk, R.D.: "Acrylamide-Polymer/Chromium(III)-Carboxylate Gels for Near Wellbore Matrix Treatments," *SPE Advanced Technology Series* (April 1993) **1**, No. 1, 146–152.
83. Sydansk, R. D.: "Foam for Improving Sweep Efficiency in Subterranean Oil-Bearing Formations," U.S. Patent No. 5,105,884 (1992).
84. "Toxicological Profile for Chromium," U.S. Dept. of Health and Human Services, Public Health Service, Agency for Toxic Substances and Disease Registry, NTIS Report PB93-182434 (April 1993).
85. Purkale, J.D. and Summers, L.E.: "Evaluation of Commercial Crosslinked Polyacrylamide Gel Systems for Injection Profile Modification," paper SPE 17331 presented at the 1988 SPE/DOE Enhanced Oil Recovery Symposium, Tulsa, 17–20 April.
86. Smith, J.E.: "Performance of 18 Polymers in Aluminum Citrate Colloidal Dispersion Gels," paper SPE 28989 presented at the 1995 SPE International Symposium on Oilfield Chemistry, San Antonio, Texas, 14–17 February.
87. Ranganathan, R. *et al.*: "An Experimental Study of the In Situ Gelation Behavior of a Polyacrylamide/Aluminum Citrate 'Colloidal Dispersion' Gel in a Porous Medium and Its Aggregate Growth During Gelation Reaction," paper SPE 37220 presented at the 1997 SPE International Symposium on Oilfield Chemistry, Houston, 18–21 February.
88. Seright, R.S.: "Improved Techniques for Fluid Diversion in Oil Recovery," second annual report, Contract No. DE-AC22-92BC14880, U.S. DOE, Washington, DC (March 1995).
89. Moradi-Araghi, A.: "Application of Low-Toxicity Crosslinking Systems in Production of Thermally Stable Gels," paper SPE 27826 presented at the 1994 SPE/DOE Symposium on Improved Oil Recovery, Tulsa, 17–20 April.
90. Dovan, H.T., Hutchins, R.D., and Sandiford, B.B.: "Delaying Gelation of Aqueous Polymers at Elevated Temperatures Using Novel Organic Crosslinkers," paper SPE 37246 presented at the 1997 SPE International Symposium on Oilfield Chemistry, Houston, 18–21 February.

91. Hardy, M. *et al.*: “The First Carbonate Field Application of a New Organically Crosslinked Water Shutoff Polymer System,” paper SPE 50738 presented at the 1999 SPE International Symposium on Oilfield Chemistry, Houston, 16–19 February.
92. Avery, M.R., Burkholder, L.A., and Gruenenfelder, M.A.: “Use of Crosslinked Xanthan Gels in Actual Profile Modification Field Projects,” paper SPE 14114 presented at the 1986 SPE International Meeting of Petroleum Engineering, Beijing, 17–20 March.
93. Dalrymple, D., Tarkington, J.T., and Hallock, J.: “A Gelation System for Conformance Technology,” paper SPE 28503 presented at the 1994 SPE Annual Technical Conference and Exhibition, New Orleans, 25–28 September.
94. Jones, P.W. and Baker, R.O.: “Profile Control in Virginia Hills EOR Injectors,” paper SPE 24193 presented at the 1992 SPE/DOE Symposium on Enhanced Oil Recovery, Tulsa, 22–24 April.
95. Vossoughi, S. and Buller, C.S.: “Polymer Modification by In-Situ Gelation With a Newly Discovered Biopolymer,” *SPEPE* (November 1991) 485.
96. Lakatos, I. *et al.*: “Application of Silicate-Based Well Treatment Techniques at the Hungarian Oil Fields,” paper SPE 56739 presented at the 1999 SPE Annual Technical Conference and Exhibition, Houston, 3–6 October.
97. Rolfsvag, T.A. *et al.*: “Thin Gel Treatment of an Oil Producer at the Gullfaks Field: Results and Evaluation,” paper SPE 35548 presented at the 1996 SPE European Production Operations Conference and Exhibition, Stavanger, 16–17 April.
98. “Controlling Gelation Time and Microgel Size for Water Shutoff,” *JPT* (March 2001) 51.
99. Moffitt, P.D. *et al.*: “Development and Field Testing of a New Low Toxicity Polymer Crosslinking System,” paper SPE 35173 presented at the 1996 SPE Permian Basin Oil and Gas Recovery Conference, Midland, Texas, 27–29 March.
100. Trantham, J.C. and Moffitt, P.D.: “North Burbank Unit 1,440-Acre Polymer Flood Project Design,” paper SPE 10717 presented at the 1982 SPE/DOE Symposium on Enhanced Oil Recovery, Tulsa, 4–7 April.
101. Mack, J.C. and Warren, J.: “Performance and Operation of a Crosslinked Polymer Flood at Sage Spring Creek Unit A, Natrona County, Wyoming,” *JPT* (July 1984) 1145.
102. Needham, R.B., Threlkeld, C.B., and Gall, J.W.: “Control of Water Mobility Using Polymers and Multivalent Cations,” paper SPE 4747 presented at the 1974 SPE Improved Oil Recovery Symposium, Tulsa, 22–24 April.
103. Sydansk, R.D.: “A New Conformance-Improvement-Treatment Chromium(III) Gel Technology,” paper SPE 17329 presented at the 1988 SPE/DOE Enhanced Oil Recovery Symposium, Tulsa, 17–20 April.
104. Bryant, S.L., Rabaioli, M.R., and Lockhart, T.P.: “Influence of Syneresis on Permeability Reduction by Polymer Gels,” *SPEPF* (November, 1996) 209.
105. Seright, R.S.: “Gel Placement in Fracture Systems,” *SPEPF* (November 1995) 241.
106. Sydansk, R.D. and Moore, P.E.: “Gel Conformance Treatments Increase Oil Production in Wyoming,” *Oil & Gas J.* (20 January 1992) 40.
107. Seright, R.S.: “Use of Preformed Gels for Conformance Control in Fractured Systems,” *SPEPF* (February 1997) 59.
108. Seright, R.S.: “Gel Propagation Through Fractures,” *SPEPF* (November 2001) 225.
109. Seright, R.S.: “Mechanism for Gel Propagation Through Fractures,” paper SPE 55628 presented at the 1999 SPE Rocky Mountain Regional Meeting, Gillette, Wyoming, 15–18 May.
110. Hall, H.N.: “How to Analyze Waterflood Injection Well Performance,” *World Oil* (October 1963) 128.
111. Earlougher, R.C. Jr.: *Advances in Well Test Analysis*, SPE, Richardson, Texas (1997) 85–87.
112. Seright, R.S.: “First Annual Technical Progress Report—Improved Techniques for Fluid Diversion in Oil Recovery,” DOE/BC/14880-5, U.S. DOE, Bartlesville, Oklahoma (December 1993) Chap. 6.
113. Southwell, G.P. and Posey, S.M.: “Application and Results of Acrylamide-Polymer/Chromium (III) Carboxylate Gels,” paper SPE 27779 presented at the 1994 SPE/DOE Symposium on Improved Oil Recovery, Tulsa, 17–20 April.
114. O’Brien, W.J., Stratton, J.J. Jr., and Lane, R.H.: “Mechanistic Reservoir Modeling Improves Fissure Treatment Gel Design in Horizontal Injectors, Idd El Shargi North Dome Field, Qatar,”

- paper SPE 56743 presented at the 1999 SPE Annual Technical Conference and Exhibition, Houston, 3–6 October.
115. Lane, R.H. and Seright, R.S.: “Gel Water Shutoff in Fractured and Faulted Horizontal Wells,” paper SPE 65527 presented at the 2000 SPE/Petroleum Society of CIM International Conference on Horizontal Well Technology, Calgary, 6–8 November.
 116. Southwell, G.P.: “Marathon Oil Company’s Experience with Produced Water Control and Conformance Improvement Using Polymer Gels,” *Proc., Forty-Sixth Annual Southwestern Petroleum Short Course*, Texas Tech U., Lubbock, Texas (April 1999) 353–365.
 117. Willhite, G.P. and Pancake, R.E.: “Controlling Water Production Using Gelled Polymer Systems,” paper SPE 89464 presented at the 2004 SPE/DOE Symposium on Improved Oil Recovery, Tulsa, April 17–21.
 118. Reynolds, R.R.: “Gelled Polymer Treatments in Kansas Arbuckle Wells,” Petroleum Technology Transfer Council—Technology Connections website http://www.nmcpttc.org/Case_Studies/GelPolymer/index.html (accessed February 2003).
 119. Sanders, G.S., Chambers, M.J., and Lane, R.H.: “Successful Gas Shutoff With Polymer Gel Using Temperature Modeling and Selective Placement in the Prudhoe Bay Field,” paper SPE 28502 presented at the 1994 SPE Annual Technical Conference and Exhibition, New Orleans, 25–28 September.
 120. Borling, D.C.: “Injection Conformance Control Case Histories Using Gels at the Wertz Field CO₂ Tertiary Flood in Wyoming,” paper SPE 27825 presented at the 1994 SPE/DOE Symposium on Improved Oil Recovery, Tulsa, 17–20 April.
 121. Hild, G.P. and Wackowski, R.K.: “Results of the Injection Well Polymer Gel Treatment Program at the Rangely Weber Sand Unit, Rangely, Colorado,” paper SPE 39612 presented at the 1998 SPE/DOE Improved Oil Recovery Symposium, Tulsa, 19–22 April.
 122. Bach, T. *et al.*: “Polymer Sealant for Unwanted Gas in Openhole Gravel-Pack Completion,” paper SPE 68975 presented at the 2001 SPE European Formation Damage Conference, The Hague, 21–22 May.
 123. Southwell, G.P. and Posey, S.M.: “Applications and Results of Acrylamide-Polymer/Chromium (III)-Carboxylate Gels,” paper SPE 27779 presented at the 1994 SPE/DOE Symposium on Improved Oil Recovery, Tulsa, 17–20 April.
 124. Odorisio, V.G. and Curtis, S.C.: “Operational Advances From Field Application of Short-Radius Horizontal Drilling in the Yates Field Unit,” paper SPE 24612 presented at the 1992 SPE Annual Technical Conference and Exhibition, Washington, DC, 4–7 October.
 125. Lai, Q.J. *et al.*: “Gel-Cement Combination Squeezes For Gas Shutoff,” paper SPE 54596 presented at the 1999 SPE Western Regional Meeting, Anchorage, 26–28 May.
 126. Zitha, P.L.J. and Botermans, C.W.: “Bridging Adsorption of Flexible Polymers in Low-Permeability Porous Media,” *SPEPF* (February 1998) 15–20.
 127. Thompson, K.E. and Fogler, H.S.: “A Study of the Diversion Mechanisms by Reactive Water Diverting Agent,” *SPEPF* (May 1995) 130.
 128. Wassmuth, F.R. *et al.*: “Screening and Coreflood Testing of Gel Foams To Control Excessive Gas Production in Oil Wells,” *SPEREE* (June 2001) 187.
 129. Miller, M.J. and Fogler, H.S.: “A Mechanistic Investigation of Waterflood Diversion Using Foamed Gels,” *SPEPF* (February 1995) 62.
 130. Friedmann, F. *et al.*: “Development and Testing of a Foam-Gel Technology to Improve Conformance of the Rangely CO₂ Flood,” *SPEREE* (February 1999) 4.
 131. Hughes, T.L. *et al.*: “Large-Volume Foam-Gel Treatments to Improve Conformance of the Rangely CO₂ Flood,” *SPEREE* (February 1999) 14.
 132. Fried, A.N.: “The Foam-Drive Process for Increasing the Recovery of Oil,” Report of Investigation 5866, USBM (1961).
 133. Bernard, G.G. and Holm, L.W.: “Effect of Foam on Permeability of Porous Media to Gas,” *SPEJ* (September 1964) 267.
 134. Bernard, G.G. and Holm, L.W.: “Effect of Foam on Trapped Gas Saturation and on Permeability of Porous Media to Water,” *SPEJ* (December 1965) 295.
 135. Bernard, G.G. and Holm, L.W.: “Model Study of Foam as a Sealant for Leaks in Gas Storage Reservoirs,” *SPEJ* (March 1970) 9.

136. Holm, L.W.: "The Mechanism of Gas and Liquid Flow Through Porous Media in the Presence of Foam," *SPEJ* (December 1968) 359.
137. Holm, L.W.: "Foam Injection Test in the Siggins Field, Illinois," *JPT* (December 1970) 1499.
138. Mast, R.F.: "Microscopic Behavior of Foam in Porous Media," paper SPE 3997 presented at the 1972 SPE Annual Meeting, San Antonio, Texas, 8–11 October.
139. Rossen, W.R.: "Foams in Enhanced Oil Recovery," *Foams—Theory, Measurement, and Applications*, R.K. Prud'homme and S.A. Khan (ed.), Marcel Dekker Inc., New York (1996) 413–464.
140. Gauglitz, P.A. *et al.*: "Foam Generation in Porous Media," paper SPE 75177 presented at the 2002 SPE/DOE Improved Oil Recovery Symposium, Tulsa, 13–17 April.
141. Schramm, L.L. and Wassmuth, F.: "Foams: Basic Principles," *Foams: Fundamentals and Applications in the Petroleum Industry*, L.L. Schramm (ed.), Advances in Chemistry Series 242, American Chemical Soc., Washington, DC (1994) 3–45.
142. Llave, F.M. and Olsen, D.K.: "Use of Mixed Surfactants To Generate Foams for Mobility Control in Chemical Flooding," *SPEE* (May 1994) 125.
143. Dalland, M. and Hanssen, J.E.: "GOR-Control Foams: Demonstration of Oil-Based Foam Process Efficiency in a Physical Flow Model," paper SPE 50755 presented at the 1999 SPE International Symposium on Oilfield Chemistry, Houston, 16–19 February.
144. Mannhardt, K., Novosad, J.J., and Schramm, L.L.: "Comparative Evaluation of Foam Stability to Oil," *SPEE* (February 2000) 23.
145. Kovscek, A.R. and Radke, C.J.: "Fundamentals of Foam Transport in Porous Media," *Foams: Fundamentals and Applications in the Petroleum Industry*, L.L. Schramm (ed.), Advances in Chemistry Series 242, American Chemical Soc., Washington, DC (1994) 115–163.
146. Osterloh, W.T. and Jante, M.J. Jr.: "Effects of Gas and Liquid Velocity on Steady-State Foam Flow at High Temperature," paper SPE 24179 presented at the 1992 SPE/DOE Symposium on Enhanced Oil Recovery, Tulsa, 22–24 April.
147. Alvarez, J.M., Rivas, H.J., and Rossen, W.R.: "Unified Model for Steady-State Foam Behavior at High and Low Foam Qualities," *SPEJ* (September 2001) 325.
148. Chang, S.-H. and Grigg, R.B.: "Effects of Foam Quality and Flow Rate on CO₂-Foam Behavior at Reservoir Temperature and Pressure," *SPEE* (June 1999) 248.
149. Wassmuth, F.R., Green, K.A., and Randall, L.: "Details of In-Situ Foam Propagation Exposed With Magnetic Resonance Imaging," *SPEE* (April 2001) 135.
150. Casteel, J.F. and Djabbarah, N.F.: "Sweep Improvement in CO₂ Flooding by Use of Foaming Agents," *SPEE* (November 1988) 1186.
151. Llave, F.M. *et al.*: "Foams as Mobility Control Agents for Oil Recovery by Gas Displacement," paper SPE 20245 presented at the 1990 SPE/DOE Symposium on Enhanced Oil Recovery, Tulsa, 22–25 April.
152. Tsau, J.-S., Yaghoobi, H., and Grigg, R.B.: "Smart Foam to Improve Oil Recovery in Heterogeneous Porous Media," paper SPE 39677 presented at the 1998 SPE/DOE Improved Oil Recovery Symposium, Tulsa, 19–22 April.
153. Tsau, J.-S., and Heller, J.P.: "How Can Selective Mobility Reduction of CO₂-Foam Assist in Reservoir Floods?" paper SPE 35168 presented at the 1996 SPE Permian Basin Oil and Gas Recovery Conference, Midland, Texas, 27–29 March.
154. Lee, H.O., Heller, J.P., and Hoefler A.M.W.: "Change in Apparent Viscosity of CO₂ Foam with Rock Permeability," *SPEE* (November 1991) 421.
155. Albrecht, R.A. and Marsden, S.S.: "Foams as Blocking Agents in Porous Media," *SPEJ* (March 1970) 51.
156. Rossen, W.R.: "Theories of Foam Mobilization Pressure Gradient," paper SPE 17358 presented at the 1988 SPE/DOE Enhanced Oil Recovery Symposium, Tulsa, 17–20 April.
157. Minssieux, L.: "Oil Displacement by Foams in Relation to Their Physical Properties in Porous Media," *JPT* (January 1974) 100.
158. Hirasaki, G.J.: "The Steam-Foam Process," *JPT* (May 1989) 449.
159. Schramm, L.L.: "Foam Sensitivity to Crude Oil in Porous Media," *Foams: Fundamentals and Applications in the Petroleum Industry*, L.L. Schramm (ed.), Advances in Chemistry Series 242, American Chemical Soc., Washington, DC (1994) 165–197.

160. Kanda, M. and Schechter, R.S.: "On the Mechanism of Foam Formation in Porous Media," paper SPE 6200 presented at the 1976 SPE Annual Technical Conference and Exhibition, New Orleans, 3–6 October.
161. Suffridge, F.E., Raterman, K.T., and Russell, G.C.: "Foam Performance Under Reservoir Conditions," paper SPE 19691 presented at the 1989 SPE Annual Technical Conference and Exhibition, San Antonio, Texas, 8–11 October.
162. Sanchez, J.M. and Hazlett, R.D.: "Foam Flow Through an Oil-Wet Porous Medium: A Laboratory Study," *SPE* (February 1992) 91.
163. Raza, S.H.: "Foam in Porous Media: Characteristics and Potential Applications," *SPEJ* (December 1970) 328.
164. Friedmann, F. and Jensen, J.A.: "Some Parameters Influencing the Formation and Propagation of Foams in Porous Media," paper SPE 15087 presented at the 1986 SPE California Regional Meeting, Oakland, California, 2–4 April.
165. Jensen, J.A. and Friedmann, F.: "Physical and Chemical Effects of an Oil Phase on the Propagation of Foam in Porous Media," paper SPE 16375 presented at the 1987 SPE California Regional Meeting, Ventura, California, 8–10 April.
166. Lau, H.C. and O'Brien, S.M.: "Effect of Spreading and Nonspreading Oils on Foam Propagation Through Porous Media," *SPE* (August 1988) 893.
167. Raterman, K.T.: "An Investigation of Oil Destabilization of Nitrogen Foams in Porous Media," paper SPE 19692 presented at the 1989 SPE Annual Technical Conference and Exhibition, San Antonio, Texas, 8–11 October.
168. Schramm, L.L. and Novosad, J.J.: "Micro-Visualization of Foam Interactions with a Crude Oil," *Colloids and Surfaces* 46 (1990) 21.
169. Kuhlman, M.I.: "Visualizing the Effect of Light Oil on CO₂ Foams," *JPT* (July 1990) 902.
170. Manlowe, D.J. and Radke, C.J.: "A Pore-Level Investigation of Foam/Oil Interactions in Porous Media," *SPE* (November 1990) 495.
171. Hornbrook, J.W., Castanier, L.M., and Pettit, P.A.: "Observation of Foam/Oil Interactions in a New, High-Resolution Micromodel," paper SPE 22631 presented at the 1991 SPE Annual Technical Conference and Exhibition, Dallas, 6–9 October.
172. Kristiansen, T.S. and Holt, T.: "Properties of Flowing Foam in Porous Media Containing Oil," paper SPE 24182 presented at the 1992 SPE/DOE Symposium on Enhanced Oil Recovery, Tulsa, 22–24 April.
173. Law, D.H.-S., Yang, Z.-M., and Stone, T.W.: "Effect of the Presence of Oil on Foam Performance: A Field Simulation Study," *SPE* (May 1992) 228.
174. Hamida, F.M. *et al.*: "Further Characterization of Surfactants as Steamflood Additives," *In Situ* (1992) 16, No. 2, 137.
175. Tsau, J.-S., Syahputra, A.E., and Grigg, R.B.: "Economic Evaluation of Surfactant Adsorption in CO₂ Foam Application," paper SPE 59365 presented at the 2000 SPE/DOE Improved Oil Recovery Symposium, Tulsa, 3–5 April.
176. Krause, R.E. *et al.*: "Foam Treatment of Producing Wells to Increase Oil Production at Prudhoe Bay," paper SPE 24191 presented at the 1992 SPE/DOE Symposium on Enhanced Oil Recovery, Tulsa, 22–24 April.
177. Shan, D. and Rossen, W.R.: "Optimal Injection Strategies for Foam IOR," paper SPE 75180 presented at the 2002 SPE/DOE Improved Oil Recovery Symposium, Tulsa, 13–17 April.
178. Hanssen, J.E. *et al.*: "SAGA Injection: A New Combination IOR Process for Stratified Reservoirs," *New Developments in Improved Oil Recovery*, H.J. De Haan (ed.), Geological Soc. Special Publication (1995) 84, 111.
179. Shi, J.-X. and Rossen, W.R.: "Improved Surfactant-Alternating-Gas Foam Process to Control Gravity Override," paper SPE 39653 presented at the 1998 SPE/DOE Improved Oil Recovery Symposium, Tulsa, 19–22 April.
180. Heller, J.P.: "CO₂ Foams in Enhanced Oil Recovery," *Foams: Fundamentals and Applications in the Petroleum Industry*, L.L. Schramm (ed.), Advances in Chemistry Series 242, American Chemical Soc., Washington, DC (1994) 201–234.
181. Di Jullo, S.S. and Emanuel, A.S.: "Laboratory Study of Foaming Surfactant of CO₂ Mobility Control," *SPE* (May 1989) 136.

182. Martin, F.D., Stevens, J.E., and Harpole, K.J.: "CO₂-Foam Field Test at the East Vacuum Grayburg/San Andres Unit," *SPE* (November 1995) 266.
183. Prieditis, J. and Paulett, G.S.: "CO₂-Foam Mobility Tests at Reservoir Conditions in San Andres Cores," paper SPE 24178 presented at the 1992 SPE/DOE Symposium on Enhanced Oil Recovery, Tulsa, 22–24 April.
184. Kuhlman, M.I. *et al.*: "CO₂ Foam With Surfactants Used Below Their Critical Micelle Concentrations," *SPE* (November 1992) 445.
185. Isaacs, E.E., Ivory, J., and Green, M.K.: "Steam-Foams for Heavy Oil and Bitumen Recovery," *Foams: Fundamentals and Applications in the Petroleum Industry*, L.L. Schramm (ed.), Advances in Chemistry Series 242, American Chemical Soc., Washington, DC (1994) 235–258.
186. Borchardt, J.K. and Strycker, A.R.: "Olefin Sulfonate for High Temperature Steam Mobility Control: Structure—Property Correlations," paper SPE 37219 presented at the 1997 SPE International Symposium on Oilfield Chemistry, Houston, 18–21 February.
187. Mannhardt, K. and Novosad, J.J.: "Adsorption of Foam-Forming Surfactants for Hydrocarbon-Miscible Flooding at High Salinities," *Foams: Fundamentals and Applications in the Petroleum Industry*, L.L. Schramm (ed.), Advances in Chemistry Series 242, American Chemical Soc., Washington, DC (1994) 259–316.
188. Chad, J., Matsalla, P., and Novosad, J.J.: "Foam Forming Surfactants in Pembiana/Ostracod 'G' Poll," paper CIM 88-39-40 presented at the 1988 CIM Petroleum Soc. Technical Meeting, Calgary, 12–16 June.
189. Liu, P.C. and Besserer, G.J.: "Application of Foam Injection in Triassic Pool, Canada: Laboratory and Field Test Results," paper SPE 18080 presented at the 1988 SPE Annual Technical Conference and Exhibition, Houston, 2–5 October.
190. Sydansk, R.D.: "Polymer-Enhanced Foams Part 1: Laboratory Development and Evaluation," *SPE Advanced Technology Series* (April 1994) 2, No. 2, 150–159.
191. Zhu, T. *et al.*: "Foams for Mobility Control and Improved Sweep Efficiency in Gas Flooding," paper SPE 39680 presented at the 1998 SPE Improved Oil Recovery Symposium, Tulsa, 19–22 April.
192. Ye, Z. *et al.*: "Laboratory Study on Profile Modification by Foamed Polymer Solution," paper CIM 97-128 presented at the 1997 Petroleum Soc. Annual Technical Meeting, Alberta, Canada, 8–11 June.
193. Romero, C., Alvarez, J.M., and Muller, A.J.: "Micromodel Studies of Polymer-Enhanced Foam Flow Through Porous Media," paper SPE 75179 presented at the 2002 SPE/DOE Improved Oil Recovery Symposium, Tulsa, 13–17 April.
194. Hanssen, J.E. and Dalland, M.: "Gas-Blocking Foams," *Foams: Fundamentals and Applications in the Petroleum Industry*, L.L. Schramm (ed.), Advances in Chemistry Series 242, American Chemical Soc., Washington, DC (1994) 319–353.
195. Hanssen, J.E. and Dalland, M.: "Foam Barriers for Thin Oil Rims: Gas Blockage at Reservoir Conditions," paper presented at the 1991 European IOR Symposium, Stavanger, 21–23 May.
196. Chukwueke, V.O., Bouts, M.N., and van Dijkum, C.E.: "Gas Shut-Off Foam Treatments," paper SPE 39650 presented at the 1998 SPE Improved Oil Recovery Symposium, Tulsa, 19–22 April.
197. Wassmuth, F.R. *et al.*: "Screening and Coreflood Testing of Gel Foams to Control Excessive Gas Production in Oil Wells," *SPE* (June 2001) 187.
198. Dalland, M. and Hanssen, J.E.: "Enhanced Foams for Efficient Gas Influx Control," paper SPE 37217 presented at the 1997 SPE International Symposium on Oilfield Chemistry, Houston, 18–24 February.
199. Aarra, M.G., Ormehaug, P.A., and Skauge, A.: "Foams for GOR Control – Improved Stability by Polymer Additives," paper 010 presented at the 1997 SPE European Symposium on Improved Oil Recovery, The Hague, 20–22 October.
200. Thach, S. *et al.*: "Matrix Gas Shut-Off in Hydraulically Fractured Wells Using Polymer-Foams," paper SPE 36616 presented at the 1996 SPE Annual Technical Conference and Exhibition, Denver, 6–9 October.
201. Zhdanov, S.A. *et al.*: "Application of Foam for Gas and Water Shut-Off: Review of Field Experience," paper SPE 36914 presented at the 1996 SPE European Petroleum Conference, Milan, Italy, 22–24 October.

202. Isaacs, E.E. *et al.*: “Conformance Improvement by Using High Temperature Foams and Gels,” paper SPE 23754 presented at the 1992 SPE Latin America Petroleum Engineering Conference, Caracas, 8–11 March.
203. Patzek, T.W.: “Field Applications of Steam Foam for Mobility Improvement and Profile Control,” *SPE* (May 1996) 79.
204. Gauglitz, P.A. *et al.*: “Field Optimization of Steam/Foam for Profile Control: Midway-Sunset 26C,” paper SPE 25781 presented at the 1993 SPE International Thermal Operations Symposium, Bakersfield, California, 8–10 February.
205. Chou, S.I. *et al.*: “CO₂ Foam Field Trial at North Ward-Estes,” paper SPE 24643 presented at the 1992 SPE Annual Technical Conference and Exhibition, Washington, DC, 4–7 October.
206. Stephenson, D.J., Graham, A.G., and Luhning, R.W.: “Mobility Control Experience in the Joffre Viking Miscible CO₂ Flood,” *SPE* (August 1993) 183.
207. Hoefner, M.L. and Evans, E.M.: “CO₂ Foam: Results From Four Development Field Trials,” *SPE* (November 1995) 273.
208. Henry, R.L. *et al.*: “Field Test of Foam to Reduce CO₂ Cycling,” paper SPE 35402 presented at the 1996 SPE/DOE Symposium on Improved Oil Recovery, Tulsa, 21–24 April.
209. Surguchev, L.M. and Hanssen, J.E.: “Foam Application in North Sea Reservoirs, I: Design and Technical Support of Field Trials,” paper SPE 35371 presented at the 1996 SPE/DOE Symposium on Improved Oil Recovery, Tulsa, 21–24 April.
210. Demin, W. *et al.*: “First Ultra-Low Interfacial Tension Foam Flood Test Is Successful,” paper SPE 71491 presented at the 2001 SPE Annual Technical Conference and Exhibition, New Orleans, 30 September–3 October.
211. *Foams: Fundamentals and Applications in the Petroleum Industry*, L.L. Schramm (ed.), Advances in Chemistry Series 242, American Chemical Society, Washington, DC (1994).
212. Nguyen, Q.P. *et al.*: “Experimental and Modeling Studies of Foam in Porous Media: A Review,” paper SPE 58799 presented at the 2000 SPE International Symposium on Formation Damage Control, Lafayette, Louisiana, 23–24 February.
213. Hanssen, J.E., Holt, T., and Surguchev, L.M.: “Foam Processes: An Assessment of Their Potential in North Sea Reservoirs Based on a Critical Evaluation of Current Field Experience,” paper SPE 27768 presented at the 1994 SPE/DOE Symposium on Improved Oil Recovery, Tulsa, 17–20 April.
214. Barnes, R.M.: “Notes on the Use of Resin for Excluding Water From Oil Wells,” *Annual Report of the State Oil and Gas Supervisor of California*, California Division of Oil and Gas (1922–1923) **12**, 3.
215. Littlefield, B.A., Fader, P.D., and Surles, B.W.: “Case Histories of New Low-Cost Fluid Isolation Technology,” paper SPE 24802 presented at the 1992 SPE Annual Technical Conference and Exhibition, Washington, DC, 4–7 October.
216. Fader, P.D. *et al.*: “New Low-Cost Resin System for Sand and Water Control,” paper SPE 24051 presented at the 1992 Western Regional Meeting, Bakersfield, California, 30 March–1 April.
217. Hess, P.H.: “One-Step Furfuryl Alcohol Process for Formation Plugging,” *JPT* (October 1980) 1834.
218. “Coiled-Tubing Resin Squeeze to Mitigate Water Production,” *JPT* (June 1998) 41.
219. Morgenthaler, L.N. and Schultz, H.A.: “A Novel Process for Profile Control in Thermal Recovery Projects,” paper SPE 28504 presented at the 1994 SPE Annual Technical Conference and Exhibition, New Orleans, 25–28 September.
220. Peavy, M.A.: “Successful Water Control in Openhole Gravel-Packed Completions Within a TEOR Environment,” paper SPE 22778 presented at the 1991 SPE Annual Technical Conference and Exhibition, Dallas, 6–9 October.
221. Demin, W. *et al.*: “Experience Learned After Producing More Than 300 Million Barrels of Oil by Polymer Flooding in Daqing Oil Field,” paper 77693 presented at the 2002 Annual Technical Conference and Exhibition, San Antonio, Texas, 29 September–2 October.

SI Metric Conversion Factors

acre-ft	× 1.233 489	E + 03	= m ³
Å	× 1.0*	E - 01	= nm
bbl	× 1.589 873	E - 01	= m ³
cp	× 1.0*	E - 03	= Pa·s
ft	× 3.048*	E - 01	= m
ft ²	× 9.290 304*	E - 02	= m ²
ft ³	× 2.831 685	E - 02	= m ³
°F	(°F - 32)/1.8		= °C
in.	× 2.54*	E + 00	= cm
in. ³	× 1.638 706	E + 01	= cm ³
lbm	× 4.535 924	E - 01	= kg
psi	× 6.894 757	E + 00	= kPa

*Conversion factor is exact.

Chapter 14

Miscible Processes

E.D. Holstein, Consultant and Fred I. Stalkup, PetroTel Inc.

14.1 Introduction

Miscible injection is a proven, economically viable process that significantly increases oil recovery from many different types of reservoirs. Fieldwide projects have been implemented in fields around the world, with most of these projects being onshore North American fields. Many of these projects are quite mature, making the recovery and production-rate benefits well established. As a result, the ability to predict recovery levels, rate improvements, costs, and resulting economics can now be considered proven and reliable. The purpose of this chapter is to introduce some fundamental concepts about miscible displacement, suggest some methods of predicting the benefits of miscible injection, and present a few field examples that demonstrate what has been accomplished with miscible injection.

14.2 Introductory Concepts

To put miscible flooding into perspective, it is instructive to compare the performance of a miscible flood to that of a waterflood. Although it is impossible to define a “typical” flood, the simplistic example shown in [Fig. 14.1](#) introduces the physics of the process and illustrates the level of incremental recovery and sweep often achieved with miscible flooding. This example is based on simulation results for the Means Lower San Andres reservoir in west Texas.¹

The upper diagram in [Fig. 14.1](#) shows a pattern element in the reservoir (with an injector on the left and a producer on the right) near the end of a waterflood. The initial average oil saturation, S_{oi} , of 70% at the start of the waterflood was reduced to an average of 44%, S_{orwf} , at the end. The 44% accounts for much higher saturations near the edges of the pattern and in lower-permeability strata not contacted by water. The waterflood recovers 37% of the original oil in place (OOIP) and sweeps approximately 80% of the reservoir.

The average S_{orwf} in those regions swept by water is 38%. The oil that remains in the water-swept part of the reservoir is trapped as a discontinuous phase within the pore space. The primary goal of a miscible flood is to recover part of this trapped residual oil. However, solvent can sometimes also displace oil from upper regions of the reservoir not swept or poorly swept by water because of gravity-driven water “slumping.”

The lower diagram in [Fig. 14.1](#) shows the same reservoir element near the completion of a miscible flood started near the end of the waterflood. In practice, a solvent flood is often initiated before completing the waterflood—or, in some cases, even before starting the waterflood.

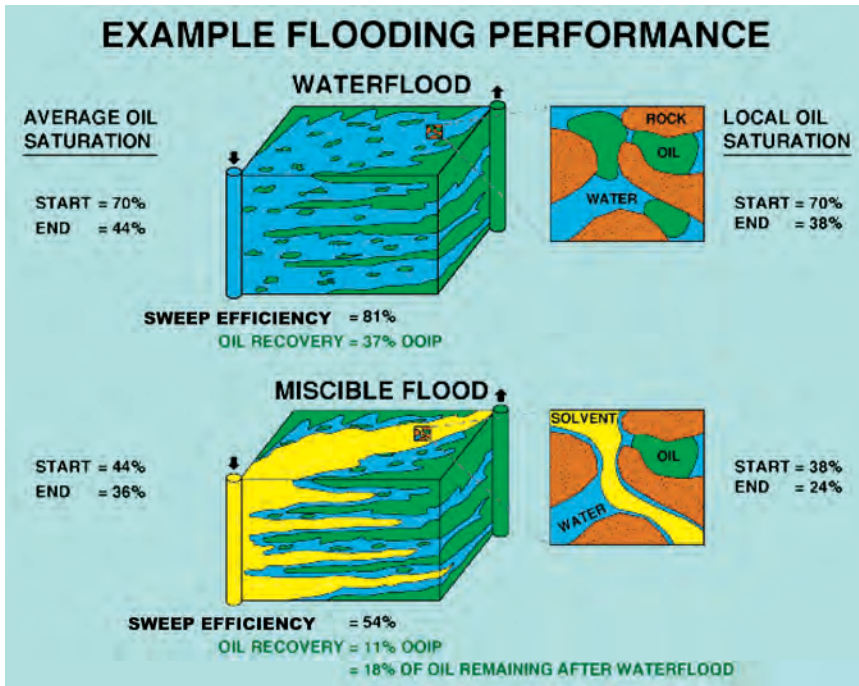


Fig. 14.1—Example flooding performance.²

The schematic shows that solvent sweeps only part of the reservoir previously swept by water, and only a portion of the residual oil in the solvent-swept regions is recovered. The average oil saturation after the miscible flood (S_{orm}) of 36% includes (1) higher oil saturations remaining in regions near the edge of the pattern element and in lower-permeability strata bypassed by both water and solvent and (2) residual oil in that part of the reservoir swept by water but not by solvent. The miscible flood recovered an incremental 11% OOIP over and above waterflooding results. Expressed another way, the incremental recovery was 18% of the oil remaining after waterflooding.

The solvent sweeps approximately 50% of the pattern, compared to approximately 80% for water. In regions swept by solvent, oil saturation is reduced from an average value of 38% to 24%. The average oil saturation of 24% in solvent-swept regions accounts for oil saturations lower than 24% near the injector, as well as higher saturations near the producer. At the pore level, solvent displaces some, but not all, of the waterflood residual oil.

Three solvent-injection strategies commonly used in commercial miscible-flooding applications are slug injection, water-alternating-gas (WAG) injection, and gravity-stable injection. The slug process usually involves continuous injection of approximately 0.2 to 0.4 hydrocarbon pore volumes (HCPV) of solvent that, in turn, is displaced by water or dry solvent.² The WAG process involves alternately injecting small volumes (0.01–0.04 HCPV) of water and solvent.² The total amount of solvent injected usually ranges from 0.2 to 0.6 HCPV.³ As with the slug process, the final drive fluid is usually water or dry solvent. It is commonly accepted that alternate injection of small slugs of water decreases solvent mobility and leads to increased solvent sweep efficiency.⁴ Experience with many projects has indicated that field-management processes improve with time, and additional volumes of injectant can be justified to further increase recovery.

For some pinnacle reefs and steeply dipping reservoirs with high vertical communication, it is advantageous to inject less-dense solvent at the top of the reservoir in a gravity-stable dis-

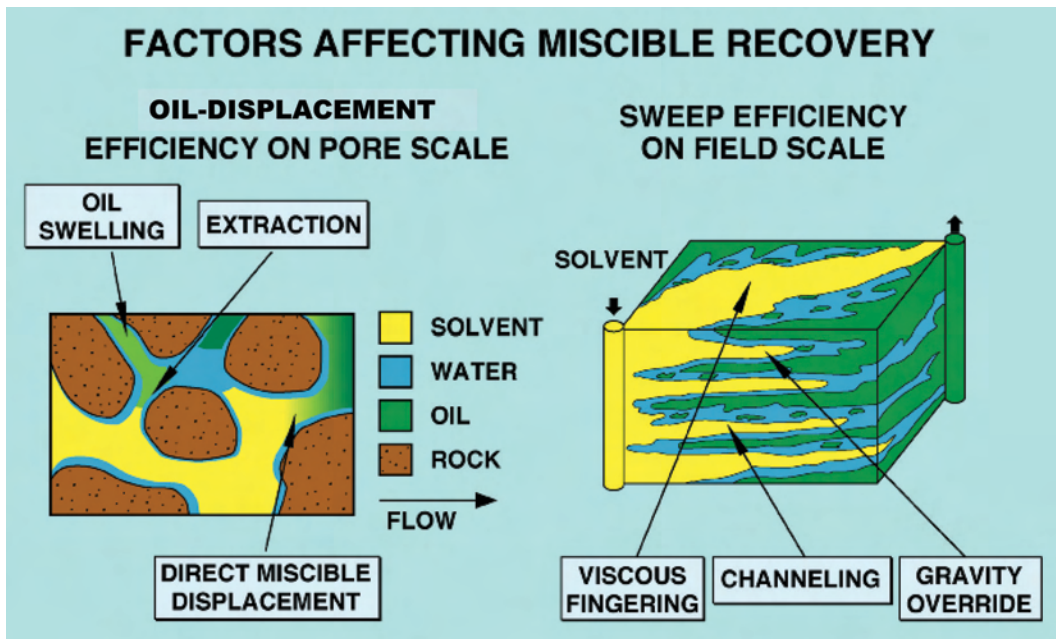


Fig. 14.2—Factors affecting miscible recovery.²

placement process. Solvent sweep efficiency and oil recovery are quite high, provided that there is sufficient vertical continuity.⁵⁻⁹

The two major factors that affect the performance of a miscible flood are oil-displacement efficiency at the pore level and sweep efficiency on the field scale. Oil displacement can be explained using the schematic on the left side of Fig. 14.2, which shows solvent flowing from left to right through a pore space. The displacement process involves several mechanisms.^{2,10,11} One is direct miscible displacement of oil by solvent along higher-permeability pore paths. Additionally, part of the oil initially bypassed (on the pore level) by solvent can later be recovered through oil swelling that occurs as solvent dissolves in the oil, or by extraction of oil into solvent. Swelling and extraction take place as solvent continues to flow past the initially bypassed oil. These can be significant mechanisms in field processes and together may account for as much as 20 to 30% of the total incremental recovery. Oil-displacement efficiency is affected by solvent composition and pressure. Solvents can be designed that give very high displacement efficiencies at the pore level.^{1,12-17}

The right side of Fig. 14.2 shows that, on a field scale, sweep efficiency is affected by viscous fingering and solvent channeling through high-permeability streaks. Gravity override can sometimes occur because solvent is usually less dense than the oil it is displacing.^{18,19} When vertical communication is high, solvent tends to gravity segregate to the top of a reservoir unit and sweep only the upper part of that zone. Although gravity override can be a problem in reservoirs having good vertical communication (such as Judy Creek²⁰ and Prudhoe Bay²¹), it is not usually a serious problem for west Texas carbonates,²² which tend to be more stratified and have poor vertical communication.

As discussed in specific field examples, sweep efficiency on the field scale is usually the single most important factor affecting performance of a miscible flood. Sweep efficiency can be increased to some extent by reducing well spacing, increasing injection rate, reconfiguring well patterns, increasing solvent-bank sizes, and modifying the ratio of injected water to injected solvent (WAG ratio).

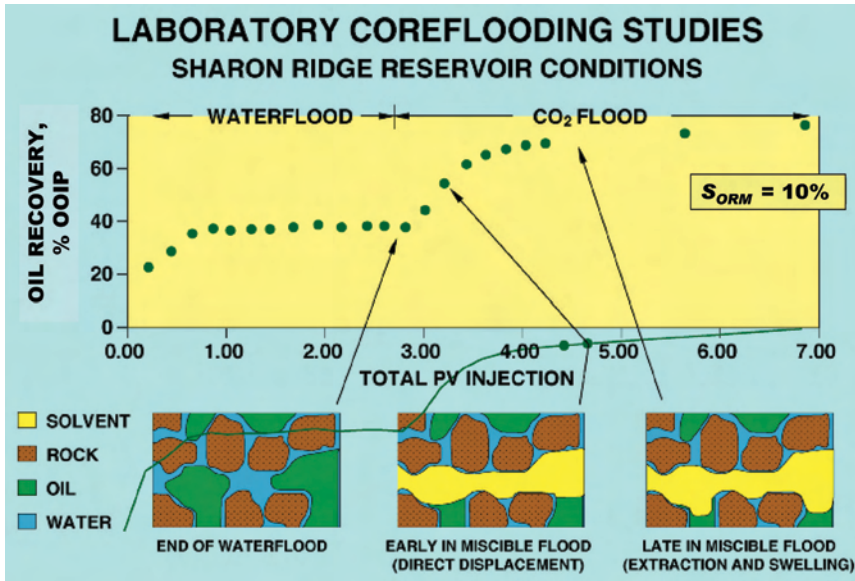


Fig. 14.3—Laboratory coreflooding studies.²

Fig. 14.3 presents part of a considerable body of laboratory evidence that solvent effectively displaces oil from contacted regions of the reservoir. The graph of oil recovery as a function of total pore volumes of fluid injected shows the results of a laboratory coreflood conducted at conditions corresponding to the Sharon Ridge reservoir in west Texas. The waterflood recovered approximately 40% OOIP. A CO₂ flood that followed increased oil recovery to approximately 80% OOIP, demonstrating that CO₂ can displace a large portion of the residual oil remaining after a waterflood. S_{orm} was 10%; the WAG ratio for the miscible flood was 1.

The schematics at the bottom of Fig. 14.3 illustrate the pore-level recovery mechanisms discussed earlier (Fig. 14.2). At the end of the waterflood, residual oil is a discontinuous phase that occupies approximately 40% of the pore space. Early in the miscible flood [3.0 to 3.5 total pore volumes (PV) injected], some of this oil has been miscibly displaced by solvent from the higher-permeability flow path (on the pore scale). However, some oil also has been initially bypassed by solvent. Note that this bypassing at the pore level is much different from solvent bypassing, which can occur at the field scale because of larger-scale reservoir heterogeneities. As depicted in the schematic corresponding to late in the flood (to 7.0 total PV injected), part of this locally bypassed oil is subsequently recovered by extraction and swelling that takes place as solvent continues to flow past the bypassed oil. In this case, approximately 30% of the total amount of oil recovered by the CO₂ flood was recovered by extraction and swelling.

14.3 Designing a Miscible Flood

14.3.1 Determining Miscibility. True miscible displacement implies that injected and displaced phases mix in all proportions without forming interfaces or two phases. The single-phase condition also implies that the solvent eventually displaces all resident oil from the pore space that it invades. Although some fluids, such as propane, fulfill this definition, most solvents available for oilfield use form two distinct phases over a broad range of mixtures and pressures when combined with reservoir oils. However, when the same solvent displaces oil at reservoir temperature and above a suitably high pressure in a long, small-diameter (slim) sand-

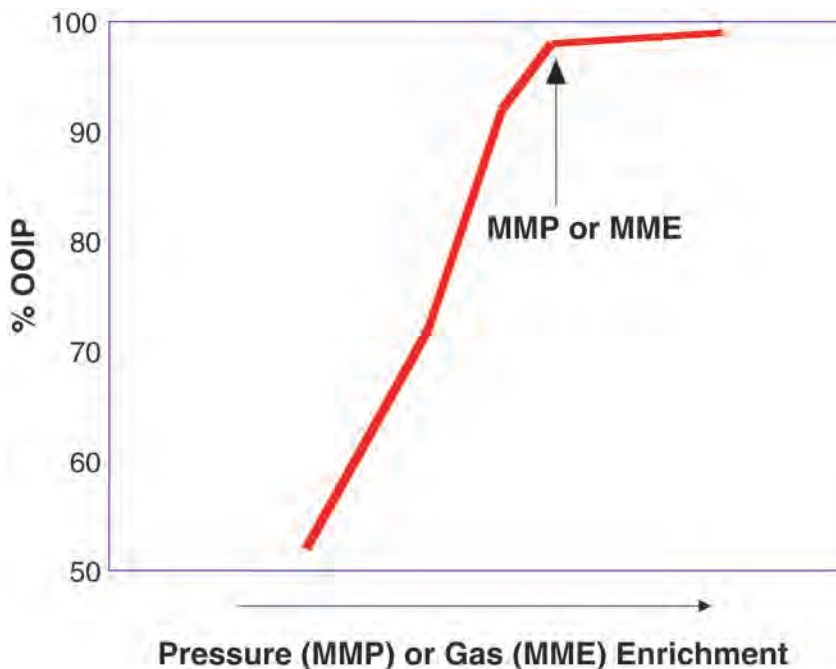


Fig. 14.4—Slimtube displacements used to determine MMP or MME.

packed tube, a miscible-like displacement occurs. Slimtube experiments are designed to make the displacement essentially 1D with 100% volumetric sweep by the solvent front.

Fig. 14.4 shows a series of hypothetical slimtube experiments. In these experiments, the solvent displaces oil from the fully oil-saturated slimtube at several pressures. Oil recovery is shown after 1.2 PV of injection for each pressure. Oil recovery increases with pressure up to approximately 95 to 98% and then increases very little thereafter. The pressure at which the break in the recovery curve occurs is said to be the minimum miscibility pressure (MMP). If the displacements had been conducted at constant pressure and with increasing enrichment by components such as ethane, propane, and butane, the break over would have been at the minimum miscibility enrichment (MME). Above the MMP or MME, the displacement is said to be “multiple-contact” or “dynamically” miscible. The increasing recovery with pressure or solvent enrichment results from in-situ mass transfer of components between solvent and resident oil. Each pressure increase produces an equilibrium mixture that becomes compositionally similar at the MMP or MME. Methane, methane enriched with C_2 – C_4 hydrocarbons, CO_2 , N_2 , and flue solvent will all give compositionally enhanced displacements under the right conditions of pressure, temperature, and oil composition. The MMP or MME can be significantly different for each of these solvents.

A slimtube is not representative of the performance in reservoir rock because it does not account for the effects of factors such as gravity segregation and reservoir heterogeneity on volumetric sweep. Fig. 14.5 shows how ethane enrichment of methane affected oil recovery in an experiment conducted by Chang *et al.*²³ with live reservoir fluid in a 34.6-in.-long, relatively homogeneous Bentheimer sandstone core. The experimental conditions resulted in a single, gravity-overriding tongue of solvent in the core.²³ Oil recovery continued to increase from enrichment levels well below to well above the MME determined from slimtube displacements without evidencing a pronounced break over. In other words, compositional enhancement continued to increase recovery well above the slimtube MME for this gravity-dominated displacement.

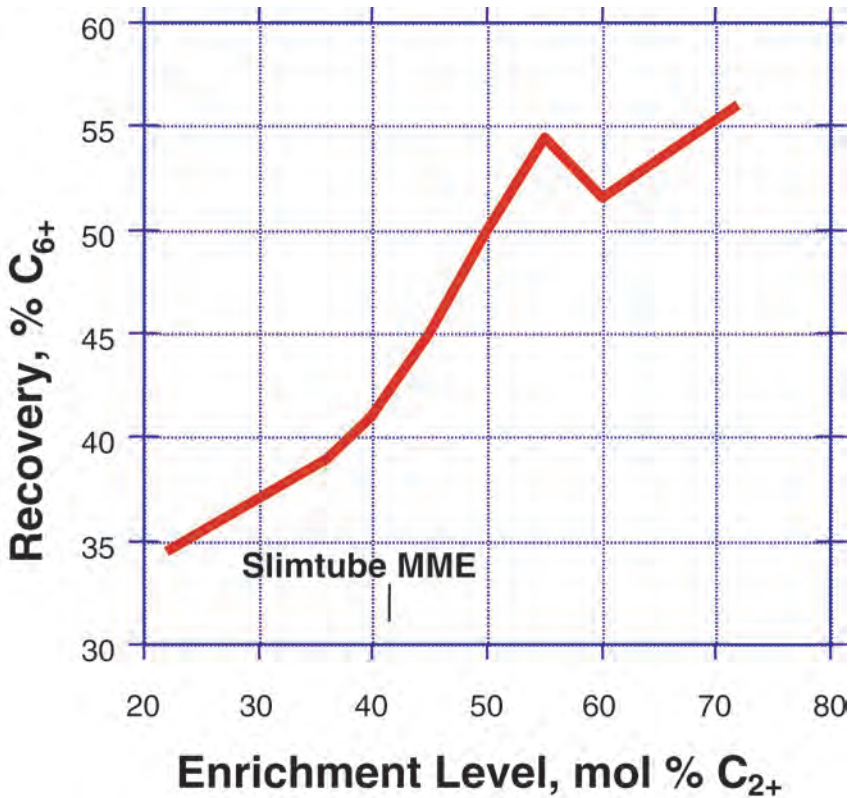


Fig. 14.5—Enriched gasflood with gravity tongue in outcrop core (after Ref. 23).

Jerauld²⁴ reported a similar finding by use of a compositional reservoir simulation of a one-fourth nine-spot pattern element (Fig. 14.6). Recovery continued to increase from well below to well above the simulator-predicted MME of 0.65.

14.3.2 Choosing a Candidate. A decision to implement a miscible flood in a particular field will usually consist of a sequential approach.

First is the screening stage. Data in the literature allow a reasonable estimate of MMP or MME, S_{orm} , amount of solvent required, and operating costs. This information is adequate to determine if a reservoir is a candidate.

MMP and MME Guidelines and Correlations. Table 14.1 gives some rough guidelines for achieving MMP or MME with different injection solvents. For hydrocarbon solvent enriched with the C₂–C₄ hydrocarbons, MMP in the range 1,500 to 3,000 psi might be expected for mid-API-gravity oils, depending on oil and solvent compositions and reservoir temperature.

The vaporizing-solvent process (see later sections) is applicable to high-gravity oils. MMP typically is greater than 3,500 psi and is usually greater than 4,500 psi (and can be much greater).

CO₂ flooding is applicable with medium-gravity oils. At temperatures less than approximately 125°F, MMP can be as low as 1,200 psi. MMP increases with temperature.

Fig. 14.7²⁵ shows an approximate correlation for CO₂ flooding MMP. Fig. 14.8¹⁴ shows one graph for a similar correlation that was developed for condensing-solvent-drive MMP. It also appears to be useful for condensing/vaporizing drives. Other graphs are given in Ref. 14.

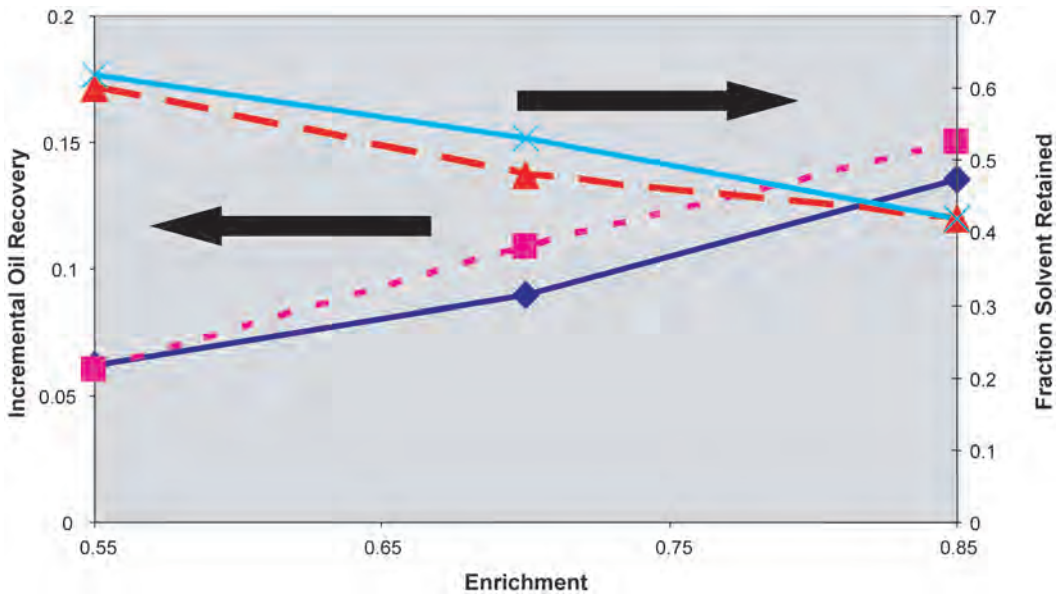


Fig. 14.6—Effect of enrichment on recovery in a reservoir study. After Jerauld (solid lines are the reference model, and dashed lines are the scaleup model).²⁴

Process	Injection Gas	Miscibility Pressure (psi)	Typical Depth (ft)
Enriched gas	Natural gas enriched with C ₂ , C ₃ , C ₄	1,500–3,000; >26°API	>2,000
Vaporizing gas	Natural gas; nitrogen; flue gas	>3,500; >40°API	>5,000
Carbon dioxide	CO ₂	>1,200; >26°API	>2,000

In field projects in which the displacement was above either the MMP or the MME, residual oil saturation determined by coring behind the solvent front varied from approximately 3 to 10% PV.²⁶

Second, a more thorough assessment may require acquiring laboratory data on S_{orwf} , S_{orm} , and MMP or MME. Analog data from nearby fields may be adequate for these values and may indeed be adequate for evaluating a project without additional work. Occasionally, some type of field pilot may be thought necessary to address such questions as displacement and sweep efficiencies (most small pilots do not produce results to reliably predict these factors), injectivity of miscible fluids, and existence of fractures or very-high-permeability layers that would prevent the miscible fluids from contacting a significant volume of the reservoir.

Third, some type of simulation will normally be done to incorporate reservoir and fluid characteristics unique to the field in question. The type of simulator used will depend on the

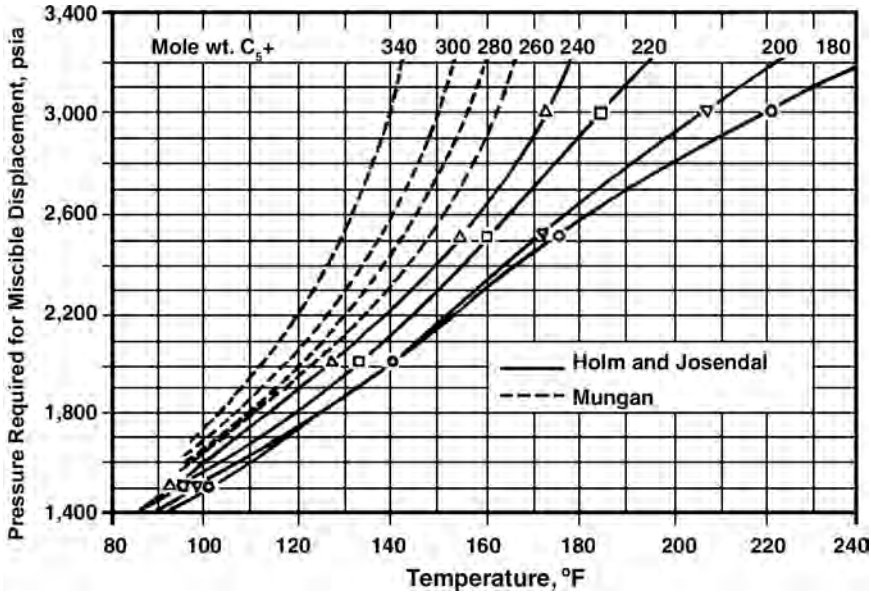


Fig. 14.7—Correlation for CO₂-flood MMP (after Refs. 25 and 26).

amount and quality of the characterization data available and the perceived risks of the project that justify the costs of the various types of simulation that can be done.

Several factors should be considered in assessing the economic viability of a miscible project:

- What miscible fluids are available, and what is the corresponding MMP or MME?
- Miscible fluids commonly considered are hydrocarbon solvents such as enriched methane, CO₂, N₂, and, less often, exhaust or flue gases. Assessments of hydrocarbon solvents should include near-term lost revenue because of delays in sales (if any) and the ultimate amount of solvent that will remain in the reservoir at abandonment. MMP and MME will also narrow the number of solvents that may be applicable to a specific field.

- Is the MMP sufficiently below overburden pressure, or are adequate enrichment fluids available for the field in question?

- In many instances, the MMP for a given solvent may exceed the overburden pressure of a formation. Where MMP is less than overburden, the question becomes whether a high-enough injection rate can be achieved to satisfy a reasonable project life.

- Are near-miscible recoveries high enough to support a project?

- As discussed earlier, significant additional recovery may be possible without reaching the slimtube MMP.

- What is the incremental recovery vs. the solvent slug size (Fig. 14.9)?

- Numerical simulations can provide sufficient insight to evaluate the economics of a project. For most projects, slug size can be refined further during the actual flood (usually increased) when actual performance can be used to modify initial projections.

- Which WAG ratio will be most effective?

- Simulations can give a good initial estimate and will be good enough for defining the costs of a WAG project. Several different WAG schemes have been used in practice. These include:

- An initial slug of miscible solvent followed by a low WAG ratio tapering to a high ratio.

- A constant WAG ratio that tapers to a high ratio near the end of the project.

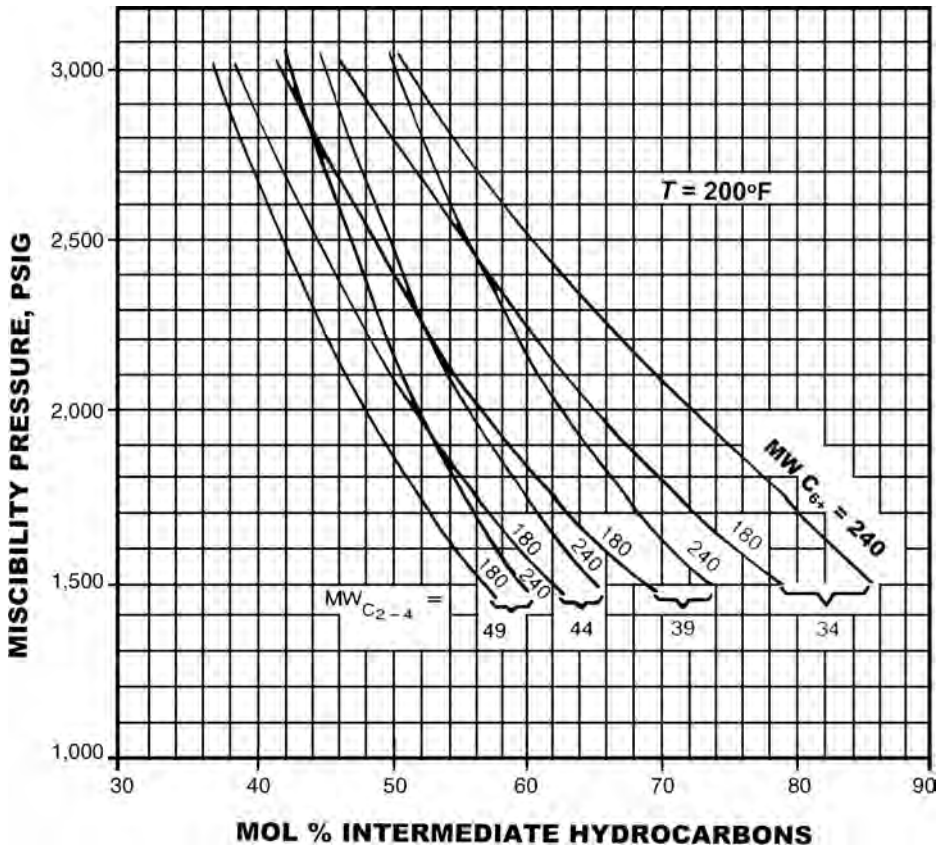


Fig. 14.8—Correlation for enriched-gas-drive MMP (after Ref. 14).

- Monthly adjustments in individual-pattern WAG ratios based on the observed performance of offset producers.
- In all cases, surveillance practices after the start of a project include periodic (monthly to quarterly) studies of the gas/oil-ratio (GOR) and water/oil-ratio (WOR) trends in producing wells and the indicated adjustments needed in WAG ratios in offsetting injectors to achieve desired performance.
 - Will water- and solvent-injection rates change?
 - Several projects have experienced reduced water injectivity (20% or more) after the WAG process was started.²⁷
 - Some projects have experienced solvent injectivity higher than water, while others have seen significant decreases.²⁷
 - Such decreases in injectivity may significantly affect project economics.
 - Will separation of the solvent from produced fluids be necessary?
 - This is a problem usually associated with CO_2 and N_2 projects. Breakthrough of solvents (which occurs early and grows with time) will contaminate produced hydrocarbon gases. Separation is required to remove contaminants before sale. The investment and operating cost of separation facilities and compression for reinjecting the recovered miscible materials should be included in the economic assessment of the project.
 - In some instances, the amount of hydrocarbon gases produced may not justify its recovery, and reinjection of the total solvent stream may be a more practical solution.

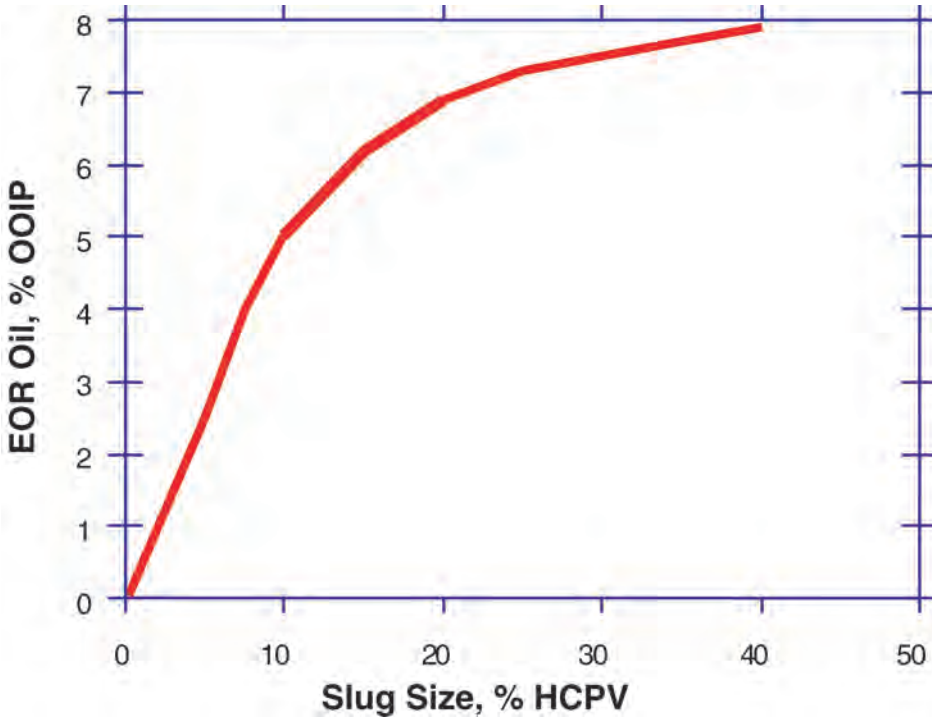


Fig. 14.9—Example of the relationship between incremental oil and slug size.

- How much solvent must be purchased, and how much should be recycled?
- Simulation results should provide sufficient insight on the rates of solvent breakthrough to answer this question. Predicted purchased volumes are generally in the 40 to 50% range of the total injection required, with the remainder being recycled solvent.
 - Initial estimates of solvent needs are usually in the 40 to 60% range of HCPV. This figure tends to increase over the project life as reservoir management practices improve sweep and reduce costs, thus sustaining the economic viability of the project longer than originally forecast.
 - What is the time from first expenditure to first incremental production ([Fig. 14.10](#))?
 - Capital outlays for equipment, drilling, and modifications to existing facilities will be made before the project start.
 - In addition, experience shows that there is a delay from the time solvent injection starts to the first significant production response. This delay roughly corresponds to injection of 0.05 to 0.1 HCPV of solvent. In most cases, most of the purchased solvent is injected before significant recovery of incremental oil. Such a delay, of course, is inevitable because waterflood residual oil that is displaced by the solvent front has to travel from injector to producer. Often, there is no delay because incremental increases in oil production result from immediate improvements made to operations. There also can be a substantial delay before the peak incremental oil rate is attained, amounting very roughly to 0.1 to 0.2 HCPV of solvent injected. Project economics should include the impact of this timing.
 - Another important feature of field tests that is consistent with mechanistic concepts and simulations is that solvent breakthrough usually occurs concurrently with the first production of the incremental-process oil or shortly thereafter. This signifies only a small, clean oil bank ahead of the advancing solvent front because of solvent fingering caused by adverse mobility ratios, gravity override, or permeability stratification. Much of the banked-up oil is located

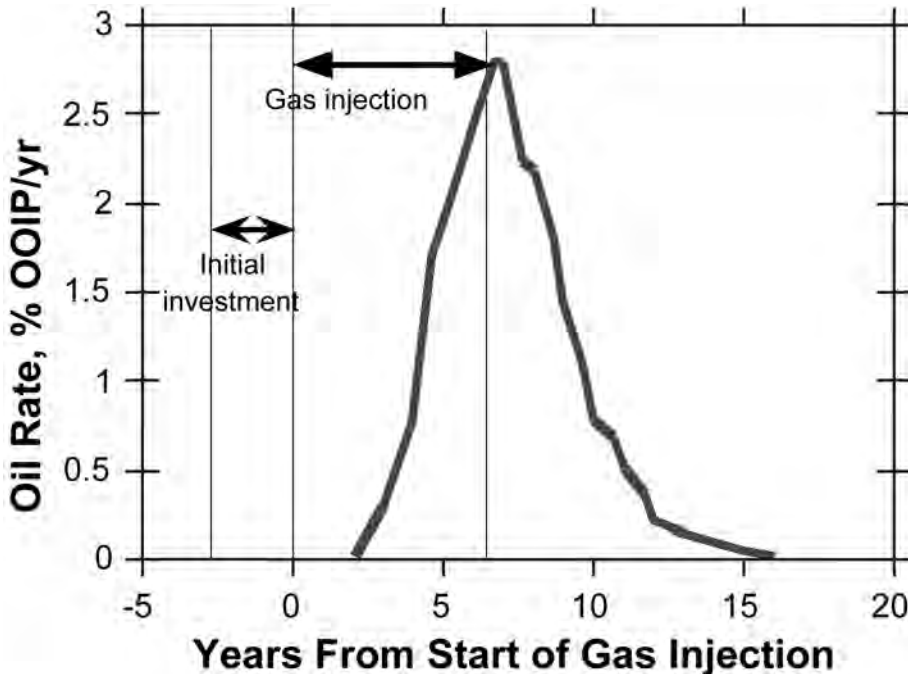


Fig. 14.10—Example of the relationship between initial investments, start of gas injection, and incremental oil production.

around the sides of these fingers and will be recovered with additional solvent injection (see Figs. 14.1 and 14.2).

- Are additional wells needed?
- Many projects have included the drilling of infill wells to provide more effective injectors, better volumetric sweep, and the productivity needed for good project economics. This applies to relatively low-cost environments in mature operating areas and has not been necessary or practical when wellbores are in good condition; in other, higher-cost operating areas; or where the reservoir characteristics did not require additional development.

14.4 Compositional Numerical Simulation

Prediction of a miscible flood is best done with a compositional reservoir simulator. The simulation must be able to predict the phase behavior as well as the sweep behavior in the reservoir to forecast such quantities as incremental oil recovery, miscible-solvent requirement, and solvent utilization efficiency and to optimize such variables as solvent composition, operating pressure, slug size, WAG ratio, injection-well placement, and injection rate. These topics are discussed in more detail in subsequent sections.

14.4.1 Phase Behavior. Methods for characterizing the reservoir and injected fluids vary from several approximation methods to rigorous component analysis.

Representation of Phase Behavior With Ternary and Pseudoternary Diagrams. Ternary diagrams and pseudoternary diagrams have been used for decades to visualize conceptually the phase behavior of injection-fluid/crude-oil systems. This is done by representing multicomponent fluids or mixtures by three pseudocomponents and then plotting fluid compositions in the interior of an equilateral triangle with apexes that represent 100% of each pseudocomponent and where the side opposite an apex represents 0% of that pseudocomponent. Usually, the three pseudocomponents represent a fraction of low-molecular-weight materials, a fraction of

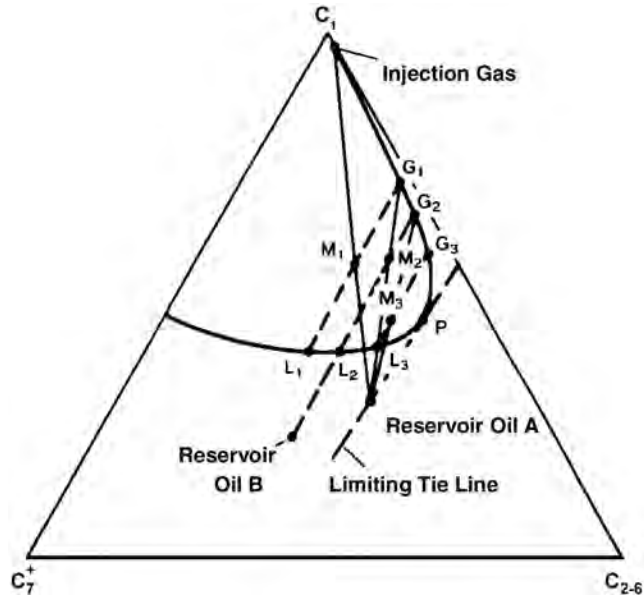


Fig. 14.11—The vaporizing-gas-drive process (after Ref. 4).

intermediate-molecular-weight materials, and a fraction of the higher-molecular-weight materials. For example, the low-molecular-weight fraction might include methane and nitrogen and perhaps CO_2 if CO_2 is the primary injection solvent. The intermediate-molecular-weight pseudocomponent might include the C_2 – C_6 hydrocarbons and perhaps CO_2 if the CO_2 is a constituent of an otherwise hydrocarbon injection solvent. The higher-molecular-weight pseudocomponent in this scheme would be the leftover C_{7+} fraction. There is no particularly “right” way to divide a fluid into three pseudocomponents. Different injection processes may be better represented by one type of grouping vs. another, and different groupings may give somewhat different insights into phase-behavior mechanisms.

Pseudoternary diagrams apply rigorously only to true ternary systems, and a strictly ternary analogy may give a somewhat misleading view of the mass-transfer mechanisms that result in compositional enhancement. Even so, a pseudoternary diagram is still a useful way to represent some complex phase-behavior concepts that are not so easily visualized otherwise.

A ternary diagram represents phase behavior at a constant temperature and pressure. Fig. 14.11 is a traditional pseudoternary-diagram representation of phase behavior for the pseudocomponents C_1 , C_{2-6} , and C_{7+} . It has the following characteristics.

There is a bubblepoint curve representing oil mixtures at their bubblepoint and a dewpoint curve representing solvent mixtures at their dewpoint. These curves come together at a critical composition. The dashed lines, called tie lines, connect liquid and solvent compositions that are in equilibrium. All mixtures inside the region bounded by the bubblepoint and dewpoint curves consist of two phases. The tie line that passes through a given mixture composition gives the equilibrium solvent and liquid compositions for this mixture where it intersects the dewpoint and bubblepoint curves. The tie line that just passes through the critical composition is called the critical tie line. All mixtures outside the region bounded by the dewpoint and bubblepoint curves are single phase.

The Vaporizing-Solvent-Drive Process. Fig. 14.11 shows how compositions change in situ when a lean injection solvent displaces an oil represented by point A, whose composition lies just to the right of the limiting tie line.

The injection solvent identified on the C_1 – C_{2-6} side of the triangle has a high methane content. When this solvent mixes with the reservoir fluid, an overall composition such as M1 may result. M1 is in the two-phase region of the diagram and consists of dewpoint solvent G1 and bubblepoint liquid L1. As more solvent is injected, solvent G1, formed in the first contact, is pushed ahead, where it contacts fresh reservoir fluid. Upon mixing, solvent G1 and the reservoir fluid form another overall mixture, M2, which consists of dewpoint solvent, G2, and bubblepoint liquid, L2. Solvent G2 then flows ahead and contacts fresh reservoir fluid, forming an overall mixture M3, which consists of dewpoint solvent G3 and bubblepoint liquid L3. In this way, solvent at the displacing front is progressively enriched to the critical composition P, which is first-contact miscible with the reservoir fluid.

In the vaporizing-solvent-drive process, compositional enhancement occurs by the injection solvent vaporizing intermediate-molecular-weight hydrocarbons from the oil and enriching the composition at the solvent front. For pseudoternary phase behavior, as long as the reservoir-fluid composition lies to the right of the limiting tie line through the critical point, multiple-contact miscibility can be achieved. If oil composition should lie to the left of the critical tie line, solvent enrichment can occur only to the composition of dewpoint solvent lying on the tie line that can be extended to pass through the oil composition. For example, if reservoir oil B were being displaced by the injection solvent, enrichment of the solvent front could occur only up to dewpoint solvent G2. Although multiple-contact miscibility is not achieved, efficient immiscible vaporization may still occur (depending on the compositions actually achieved) and should be evaluated for effectiveness.

The mechanism for compositional enhancement described above can be effective for other solvents besides lean hydrocarbon solvent. N_2 and flue-gas solvent can give compositionally enhanced displacements by this mechanism, although with different MMPs. CO_2 also achieves compositionally enhanced displacement by a similar mechanism, although for lower temperatures the mechanism may be one of liquid/liquid extraction rather than vaporization.

The conceptual argument given above indicates that compositions in the solvent/oil transition zone lie along the dewpoint curve until the critical composition is reached so that no transition-zone compositions lie inside the two-phase region. Because of mixing caused by diffusion and reservoir flow mechanisms, this is not the case in practice. Transition-zone compositions cut into the two-phase region, causing some solvent-flood residual oil to be left behind the solvent front.

The Condensing-Solvent-Drive Process. **Fig. 14.12** shows another mechanism whereby compositional enhancement can occur in a solvent flood. The oil is a bubblepoint liquid lying on the bubblepoint curve. For this phase behavior, an injection solvent that has composition A on the C_1 – C_{2-6} side of the triangle is completely miscible with the oil because the line connecting oil with composition A passes through only the single-phase region. However, according to the traditional ternary-diagram view of phase behavior, solvents that have compositions between A and B can develop multicontact miscibility in the following manner.

Solvent B lies just to the right of the critical tie line. When this solvent mixes with the original oil, an overall composition such as M1 may result, which is in the two-phase region. M1 consists of dewpoint solvent G1 and bubblepoint liquid L1, which are in equilibrium. Injection of fresh injection solvent B pushes the equilibrium solvent G1 ahead and contacts residual oil around the injector that now has composition L1. B mixes with L1 and forms a new overall composition in the two-phase region, M2, which splits into a new equilibrium solvent G2 and equilibrium liquid L2. Continued injection of solvent B pushes the new solvent G2 out of the way, and B mixes with liquid L2 to form a new overall mixture M3. Thus, solvent B successively contacts oil around the injector and enriches the oil along the bubblepoint curve by condensation of the intermediate-molecular-weight hydrocarbons that were used to enrich C_1 – C_{2-6} mixtures to composition B. This enrichment of the oil proceeds until the enriched oil reach-

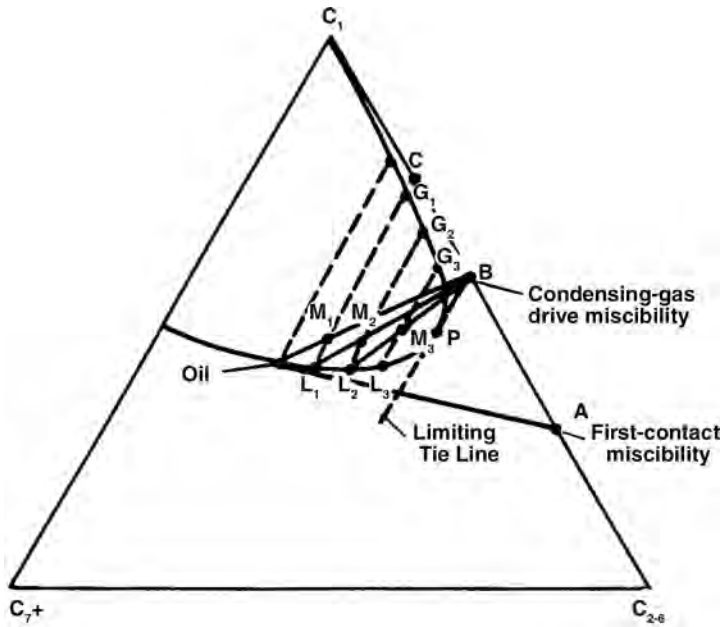


Fig. 14.12—The condensing-gas-drive process (after Ref. 4).

es the critical composition P at the critical point. Composition P is then first-contact miscible with solvent B. According to this concept, there is a transition zone of contiguously miscible liquid compositions from the original oil composition to the critical composition.

This method of solvent flooding historically was called the condensing-solvent-drive process because condensation of the intermediate-molecular-weight hydrocarbons into the oil was thought to be the mechanism responsible for the development of multicontact miscibility. In this process, miscibility is generated and propagated through the porous medium at the rear of the transition zone.

According to the pseudoternary diagram of Fig. 14.12, if the composition of injection solvent were to the left of the critical tie line, the displacement would be immiscible because the oil could never be enriched to the critical composition. For example, if solvent C were injected, the oil could be enriched only to composition L1 on the tie line that passes through C when the tie line is extended. Further contact of L1 with C only gives new overall mixtures that are on the tie line, so equilibrium solvent G1 on the tie line ends up displacing oil L1, and G1 and L1 are immiscible. The criterion for condensing-solvent-drive multiple-contact miscibility is that the injection-solvent composition must lie to the right of the critical tie line on the ternary diagram.

For most oils, however, the mechanism described previously for an enriched-solvent displacement is too simplified. Compositional enhancement occurs by a mixed mechanism that has both vaporizing and condensing features, as described below.

The Condensing/Vaporizing Process. Fig. 14.13 shows a pseudoternary diagram for a condensing/vaporizing displacement in which the equilibrium vapor and liquid compositions were calculated for a simulated slimitube displacement with a compositional simulator. The two-phase region has an hourglass shape. There is what looks like a condensing lobe in which vapor and liquid are trying to come together at a critical composition similar to condensing-solvent drive. However, before this happens, vapor and liquid compositions begin to diverge at the trailing part of the displacement.

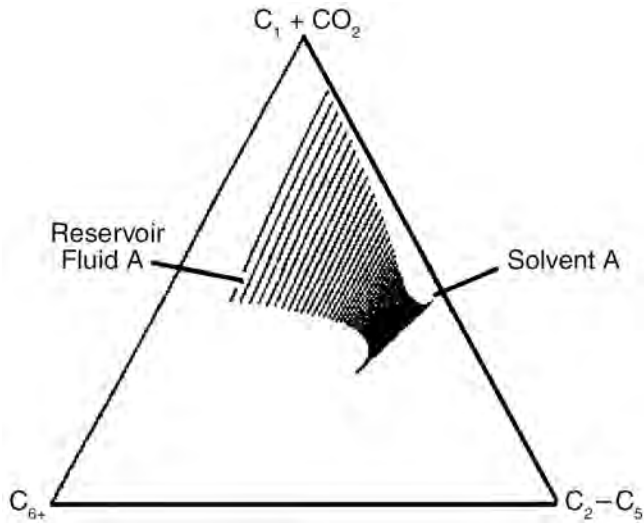


Fig. 14.13—The condensing/vaporizing process (after Ref. 27).

Zick¹⁶ was first to explain this behavior. He deduced that in addition to condensation of intermediate-molecular-weight hydrocarbons from the injection solvent, vaporization of mid-range hydrocarbons from the oil also played an important role. Zick explained this mechanism in the following way:

The easiest way to understand the condensing/vaporizing mechanism is to consider an oil/solvent system composed of essentially four groups of components. The first group consists of the lean components, such as methane, nitrogen, and carbon dioxide, which usually have equilibrium K-values greater than one. The second group consists of the light intermediate components, such as ethane, propane, and butane, which are the enriching components present in the injection solvent. The third group contains the middle intermediates, which are present in the oil but not significantly present in the injection solvent. These are components that can be vaporized from the oil. The lightest component in this group typically ranges from butane to decane, depending on the injection solvent composition. The heaviest component in this group cannot be defined precisely, but it might be around C_{30} . The fourth group consists of everything else, i.e., those heavy components in the oil which are very difficult to vaporize.¹⁶

When the enriched solvent comes into contact with the oil, the light intermediates condense from the solvent into the oil, making the oil lighter. The equilibrium solvent is more mobile than the oil, so it moves ahead and is replaced by fresh injection solvent, from which more light intermediates condense, making the oil even lighter. If this kept occurring until the oil was light enough to be miscible with the injection solvent, it would constitute the condensing-solvent-drive mechanism. However, this is unlikely to occur within a real reservoir oil. As the light intermediates are condensing from the injection solvent into the oil, the middle intermediates are being stripped from the oil into the solvent. Because the injection solvent contains none of these middle intermediates, they cannot be replenished in the oil. After a few contacts between the oil and the injection solvent, the oil becomes essentially saturated in the light intermediates, but it continues to lower the middle intermediates, which are stripped out and carried ahead by the mobile solvent phase. The light intermediates of the injection solvent cannot substitute for the middle intermediates the oil is losing. So after the first few contacts make the oil lighter by net condensation of intermediates, subsequent contacts make the oil heavier by net vaporization of intermediates. Once this begins to occur, the oil no longer has a chance of becoming miscible with the solvent. Ultimately, all the middle intermediates are removed, and

the residual oil will be very heavy, containing only the heaviest, nonvolatile fraction and the components present in the injection solvent.

If the mechanism stopped there, a considerable amount of oil would remain unrecovered. However, there are further steps to the mechanism. Consider the oil in place slightly downstream from the injection point. The first solvent it will see will not be the injection solvent, but the equilibrium solvent. This relatively lean solvent essentially will be injection solvent that has lost most of its light intermediates and picked up a very small amount of middle intermediates. There will be very little mass transfer between this solvent and the fresh oil. The solvent that follows, however, will be richer. Eventually, the solvent that comes through will be solvent that has passed over oil that was saturated in the light intermediates. Therefore, this solvent will have approximately the same amount of light intermediates as the injection solvent. However, it will also contain a small amount of middle intermediates that it stripped from the oil over which it passed. Thus, it actually will be a little richer than the original injection solvent. The oil that sees this solvent will receive slightly more condensable intermediates than did the oil just upstream. Before the vaporization process takes over and again makes it heavier, this oil will become slightly lighter than the upstream oil had become.

This process continues farther downstream. The farther downstream, the richer the solvent that eventually comes through because it will have passed over an increasing amount of residual oil, allowing it to pick up increasing amounts of middle intermediates. This is beginning to sound like the vaporizing-solvent-drive mechanism, in which a lean injection solvent passes over an oil rich in intermediates, vaporizing the intermediates and becoming richer and richer until it becomes rich enough to be miscible with the original oil. There is a significant difference, however. The solvent in the condensing/vaporizing mechanism does not become rich enough to be miscible with the original oil. The original oil does not have to be rich in intermediates, nor does it even have to be undersaturated, both of which are necessary conditions for developing a vaporizing-solvent-drive mechanism. Instead, the solvent develops only enough richness by the vaporization part of the mechanism so that it nearly generates a condensing-solvent-drive mechanism with the original oil. The intermediates that were originally present in the solvent, plus those that were stripped from the oil, condense when the solvent encounters fresh oil downstream. This condensation proceeds in a manner very much like the condensing-solvent-drive mechanism. A sharp transition zone develops and propagates, and multicontact miscibility is almost achieved before the condensation process reverts to the vaporization process. The vaporization results in a trail of residual oil being left behind the moving transition zone, although the saturation level of the residual oil supplies subsequent solvent with the middle intermediates necessary to continue the propagation of the transition zone. The intermediates are vaporized from the residual oil, carried upstream into and beyond the transition zone, condensed there, and again become part of the residual oil after the transition zone has passed.

The condensing region is at the leading edge of the enriched-solvent displacement. The vaporizing region, with a small saturation of residual oil, is at the trailing end. In between is the sharp, two-phase transition zone, the two phases of which are almost—but not quite—miscible. The propagation of the sharp transition zone results in a very efficient, “apparently miscible” displacement, even though miscibility is not actually developed (except possibly, and only speculatively, as the displacement front travels to infinite distances, relative to dispersion length scales, downstream of the injection point). The sharpness of the transition zone deteriorates rapidly as either the pressure or the enrichment of the injection solvent falls below some critical value, resulting in the reduced displacement efficiencies typical of immiscible displacements.

Mixing by diffusion and flow mechanisms affects how close the mixed mechanism gets to multicontact miscibility. The greater the mixing, the farther vapor and liquid compositions remain apart in the neck of the hourglass, which results in larger solvent-flood residual oil.

In all the processes just described, equilibrium solvent and oil properties become more similar as compositions become more similar and approach the critical composition. This causes the interfacial tension between the solvent and oil to decrease as the solvent and oil compositions become more alike. This in turn causes the capillary number for oil displacing solvent to increase.

The capillary number is defined as

$$N_{ca} = \frac{k |\Delta p_g|}{\sigma}, \dots\dots\dots (14.1)$$

where k = permeability, Δp_g = pressure gradient through the displacing phase, and σ = interfacial tension.

Below a threshold value of capillary number, solvent-flood residual oil and solvent/oil relative permeability remain unchanged. Above the threshold, residual oil begins to decrease with increasing capillary number, and the solvent and oil relative permeability curves begin to straighten, ultimately becoming straight lines at very high values of the capillary number. These changes may have contradictory effects on a displacement. For a given equilibrium oil and solvent composition near the critical composition, solvent-flood residual oil saturation may be a bit lower than it would because of phase-behavior effects alone. However, solvent mobility may be higher because of the more favorable solvent relative permeability, which may result in somewhat poor sweep. The overall effect needs to be evaluated with a simulator that accounts for changing capillary number.

Prediction of Phase Behavior With Equations of State. In practice, vapor/liquid reservoir phase behavior is calculated by an equation of state (EOS). Refer to the chapter on Thermodynamics and Phase Behavior in the General Engineering section of this *Handbook* for more detail on EOSs. The two most common EOSs that have been used for oil-recovery solvent-injection processes are the Peng-Robinson EOS²⁸ and the Soave-Redlick-Kwong EOS.²⁹ Of the two, the Peng-Robinson EOS seems to be the one most often cited in the literature and is the one discussed in some detail in the remainder of this section. The Soave-Redlick-Kwong EOS is used in a similar manner to predict solvent/oil phase behavior.

Peng and Robinson originally proposed the two-parameter EOS shown next for a pure component:

$$P = \frac{RT}{v-b} - \frac{a(T)}{v(v+b) + b(v-b)}, \dots\dots\dots (14.2)$$

$$a(T) = 0.45724 \left(\frac{R^2 T_C^2}{p_C} \right) \left[1 + \kappa \left(1 - \sqrt{\frac{T}{T_C}} \right) \right]^2, \dots\dots\dots (14.3)$$

$$\kappa = 0.37464 + 1.54226\omega - 0.26992\omega^2, \dots\dots\dots (14.4)$$

$$\text{and } b = 0.07780 \frac{RT_C}{p_C}, \dots\dots\dots (14.5)$$

where ω = the component acentric factor, T_c = component critical temperature, and p_c = component critical pressure.

For heavier components, where $\omega > 0.49$, the following equation is recommended:

$$\kappa = 0.3796 + 1.485\omega - 0.1644\omega^2 = 0.01667\omega^3 \quad (14.6)$$

The constants in Eqs. 14.3 and 14.5 are often designated Ω_a and Ω_b .

Eq. 14.2 represents continuous fluid behavior from the solvent to liquid state, and it can be rewritten as

$$Z^3 - (1 - B)Z^2 + (A - 3B^2 - 2B)Z - (AB - B^2 - B^3) = 0, \quad (14.7)$$

$$\text{where } A = 0.45724 \frac{P}{P_C} \left(\frac{T_C}{T} \right)^2 \left[1 + \kappa \left(1 - \sqrt{T/T_C} \right) \right]^2 \quad (14.8)$$

$$\text{and } B = 0.07780 \left(\frac{P}{P_C} \right) \left(\frac{T_C}{T} \right) \quad (14.9)$$

Jhaveri and Youngren³⁰ adapted a procedure used by Peneloux *et al.*³¹ and modified the original Eq. 14.2 to include a third parameter to allow more-accurate volumetric predictions, which is recommended for solvent/oil simulations. The third parameter does not change the vapor/liquid equilibrium conditions determined by the unmodified, two-parameter equation. Instead, it modifies the phase volumes by making a translation along the volume axis. Eqs. 14.10 and 14.11 give the modified three-parameter equation:

$$(Z + C)^3 - (1 - B)(Z + C)^2 + (A - 3B^2 - 2B)(Z + C) - (AB - B^2 - B^3) = 0, \quad (14.10)$$

$$C = sB, \quad (14.11)$$

where s is the volumetric shift parameter.

For mixtures:

$$A = \sum_{i=1}^n \sum_{j=1}^n x_i x_j A_{ij}, \quad (14.12)$$

$$A_{ij} = (1 - \delta_{ij}) \sqrt{A_i A_j}, \quad (14.13)$$

$$B = \sum_{i=1}^n x_i B_i, \quad (14.14)$$

$$\text{and } C = \sum_{i=1}^n x_i C_i \quad (14.15)$$

In Eq. 14.13, δ_{ij} is the binary interaction coefficient that characterizes the binary formed by components i and j . Eqs. 14.11 through 14.14 apply both to pure components and to lumped pseudocomponents that represent two or more pure components in complex mixtures.

The following expression derived from thermodynamic relationships and the EOS allows calculation of the fugacity, f_j , of component j in a mixture:

$$\ln\left(\frac{f_j}{x_j P}\right) = \frac{B_j}{B}(Z-1) - \ln(Z-B) - \frac{A}{2B\sqrt{2}}\left(\frac{2\sum_i x_i A_{ij}}{A} - \frac{B_j}{B}\right) \ln\left(\frac{Z+2.414B}{Z-0.414B}\right) \dots \quad (14.16)$$

Thus, by satisfying the equilibrium condition $f_j^L = f_j^V$, vapor/liquid equilibrium ratios can be calculated, and flash calculations can be made to calculate the compositions of vapor and liquid in equilibrium, molar splits, and volumes.

Solution of the EOS does not calculate phase viscosities directly. This is done from some external calculation once the phase compositions and densities are known. A commonly used calculation for liquid-mixture viscosity is the Lohrenz-Bray-Clark method, which requires the critical volumes of each component or pseudocomponent in the mixture.³² Refer to chapters in the General Engineering section for more information on estimating viscosities for gas and oil.

To use Eqs. 14.2 through 14.16 for calculating the phase behavior and properties of solvent compositional processes in oil recovery, the following steps must be taken to “characterize” the fluid system in question:

- Analyze the oil composition. This can be done by distillation or chromatographic methods. An extended analysis through at least C_{25+} is preferred. The advantage of distillation is that molecular weight, boiling point, and density can be measured on the distillation cuts.
- Represent the multicomponent reservoir fluid by an appropriate division into pure components and pseudocomponents. Pure components through C_5 plus three to five pseudocomponents usually will suffice. It may be possible to reduce the number of pure components and pseudocomponents further by combining similar components.
- Make an initial assignment of critical pressure and temperature, acentric factor, critical volume (or critical compressibility), volumetric shift parameter, and interaction parameters for each component and pseudocomponent.
- Tune the above properties for the pseudocomponents by comparing predicted phase behavior and properties with suitable experimental data.

Methods for dividing into pseudocomponents and estimating critical properties, shift parameters, and binary interaction coefficients are described in detail in Ref. 33.

Because of the approximations inherent in an EOS as well as the approximations required to represent a multicomponent reservoir fluid in a tractable form, it should be expected that phase-behavior properties and equilibrium compositions predicted with an EOS will depart from measured values over the range of composition and pressure conditions anticipated in a reservoir simulation. For this reason, additional adjustment of EOS parameters will be required for predictions to represent experimental measurements adequately. These adjustments usually are made by regression.

Reservoir oils usually are subjected to routine pressure/volume/temperature (PVT) experiments that give the volumetric and phase-behavior information necessary for predicting conventional recovery methods such as solution solvent drive or waterflooding. Experiments such as constant-composition expansion, differential liberation, constant-volume depletion, and separator tests provide black-oil properties. Other PVT experiments are more specific for solvent injection. These include swelling tests and multiple-contact experiments.

The swelling experiment is sometimes called a pressure-composition diagram determination. Injection solvent is added to reservoir oil in increments to give mixtures that contain increasing amounts of injection solvent. After each addition of solvent, the saturation pressure is measured at reservoir temperature. Overall composition of these mixtures ranges from that of black oil to compositions up to and beyond near-critical conditions (i.e., overall compositions that traverse a range from bubblepoint to dewpoint mixtures at reservoir temperature). Thus, the swelling experiment provides some PVT and phase-equilibrium information on mixture ranges that

might reflect compositions as solvent displaces oil through the reservoir. It provides information on the saturation pressure of injection-solvent/oil mixtures, the swelling or increase in oil formation volume factor as solvent is added, the composition of the critical mixture, and the liquid saturation vs. pressure in the two-phase region of the diagram.

Multiple-contact tests seek to simulate the solvent/oil multiple contacting that occurs in a reservoir. A forward multicontact experiment tries to simulate multicontacting in a vaporizing-solvent drive. A reverse multicontact experiment tries to simulate the multicontacting that occurs in a purely condensing-solvent drive. The experiments give information concerning equilibrium-phase volumes and compositions.

In a reverse-contact experiment, the PVT cell is charged with the reservoir fluid at the desired pressure and temperature, and an increment of injection solvent is added sufficient to form a two-phase mixture (or a three-phase mixture in some tests). The phases are allowed to equilibrate, and phase volumes are measured. The solvent phase is then displaced from the cell, and oil and solvent compositions are measured. The procedure is repeated, with injection of a new increment of injection solvent introduced into the cell to contact equilibrium oil left after the first contact.

In the forward-contact experiment, the oil phase is displaced after the first contact, and the remaining equilibrium-solvent phase in the cell is contacted with a fresh increment of reservoir oil.

The objective of tuning is to ensure that the EOS predicts fluid properties and phase equilibrium compositions accurately over the range of pressure, temperature (if this varies), and composition that one expects to encounter in a simulation. If the simulation is for a solvent compositional process, then at a minimum the EOS should predict properties and phase equilibrium for the range of injection-solvent/oil mixtures and pressures encountered in the simulation study. It also should predict adequately for any black-oil conditions expected in the simulation (e.g., waterflooding or pressure depletion before solvent injection) and for the separator conditions expected.

Pedersen *et al.*³⁴ observed that an EOS tuned to match a specific set of data may not give reliable predictions for other data not included in the tuning process. However, when both sets of data are included in the tuning process, the prediction for either one may not be quite as good as for tuning against these data individually.

It seems prudent that at a minimum, there should be differential depletion data, separator tests, and swell data to tune an EOS against for making solvent-compositional simulations. Swelling tests are necessary when near-critical compositions are expected in the simulation, and it is necessary for the swell tests to explore this composition region. Swell tests with several different injected-solvent compositions might be warranted if optimization of the solvent composition is an objective of the simulation study.

The value added by multiple-contact tests is unclear. These are the most difficult and expensive of the experiments discussed earlier, yet they provide direct measurements of vapor/liquid equilibrium compositions and molar splits for a composition path that at least crudely mimics the development of compositions at the leading or trailing edges of the solvent/oil transition zone, which is, of course, what the simulator is trying to calculate. However, for the condensing/vaporizing process, multiple-contact experiments do not give compositions that are very near the critical point.

Although they are difficult and expensive to run, slimtube tests give a direct verification of the ability of the EOS to predict MMP or MME. If the EOS after regression of parameters does not predict slimtube MMP or MME, further adjustment of parameters is required.

For additional information on EOS, refer to the chapter on Phase Behavior in the General Engineering section of this *Handbook*.

14.5 Prediction of Compositionally Enhanced Solvent Flood Behavior

The compositional reservoir simulator is the preferred simulator for predicting compositionally enhanced solvent flood reservoir behavior. This simulator calculates the flow in up to three dimensions of solvent, oil, and water phases as well as n components in the solvent and oil phases. It also computes the phase equilibrium of the oil and solvent phases (i.e., the equilibrium compositions and relative volumes of the solvent and oil phases) in each gridblock of the simulator. In addition, it computes solvent- and oil-phase densities. The equilibrium compositions and densities are calculated with an EOS. From knowledge of the phase compositions and densities, solvent and oil viscosity and other properties such as interfacial tension are estimated from correlations. See the chapter on Reservoir Simulation in the Reservoir Engineering and Petrophysics section for more information on compositional reservoir simulation.

A compositional simulator is the most mechanistically accurate simulator for solvent compositional processes. When the EOS is tuned properly to appropriate experimental data, it computes realistic phase behavior. Thus, the appropriate phase behavior for flooding with enriched hydrocarbon solvent, lean hydrocarbon solvent, N_2 , and CO_2 all can be taken into account. Compositional simulators predict the effect of changing pressure and injection-solvent composition on a displacement without the need to enter approximations into the simulator for these effects (except as the EOS itself is an approximation). The compositional simulator is capable of computing realistic behavior when pressure is well below the MMP of the injection solvent, is near but still below the MMP, or is well above the MMP. For this reason, it is ideally suited to study optimum operating conditions.

In addition to these advantages, a compositional simulation, to a large degree, removes the need for a user-defined miscible-flood residual oil saturation, as it naturally computes the amount of residual oil left after the interaction of phase behavior and dispersion and distributes this residual saturation realistically as a varying saturation instead of an input, constant saturation.

A compositional simulation can have other aspects of mechanistic reality besides phase behavior. The mechanisms of molecular diffusion and convective dispersion may be included in the equations solved by the simulator. Although grid-refinement sensitivity (described later), or numerical dispersion, may dwarf the effects of these mechanisms in many simulations, they may be important to include in the finely gridded reference simulations (also described later).

Another physical mechanism that can be included in compositional simulations is the effect of interfacial tension (IFT) on solvent/oil relative permeability and capillary pressure. Although one cannot readily foresee the impact of a particular mechanism in the complex compositional simulation of solvent flooding, inclusion of the IFT mechanism seems prudent.

When an appropriate relative permeability treatment is included, compositional simulation predicts realistic solvent trapping, especially the trapping of solvent by crossflowing oil. Oil crossflow into a solvent-swept zone immiscibly displaces the solvent in a compositional simulation and leaves the solvent as a residual saturation consistent with the phase behavior.

The primary disadvantages of a compositional simulator are the degree of grid refinement often required to compute oil recovery with satisfactory accuracy and the computing time required for fine-grid simulations. These factors generally preclude using a compositional simulator directly for full-field simulations unless some kind of scaling-up technique is used to transfer the information developed from fine-grid reference-model simulations on a limited reservoir scale to coarse-grid simulations on the full-field-model scale. The predicted benefit of compositionally enhanced solvent flooding can be substantially in error if the simulation is made directly with a full-field model with typical coarse grids. This is illustrated by [Fig. 14.14](#), which shows the results of an enriched-solvent-drive reservoir study.²⁴ In this figure, simulations were made for two one-fourth nine-spot models that represented the same reservoir description. One model had a fine grid ($30 \times 30 \times 31$ cells in the x -, y -, and z - directions); the other had the same grid as that used in the full-field model ($5 \times 5 \times 17$). The incremental recov-

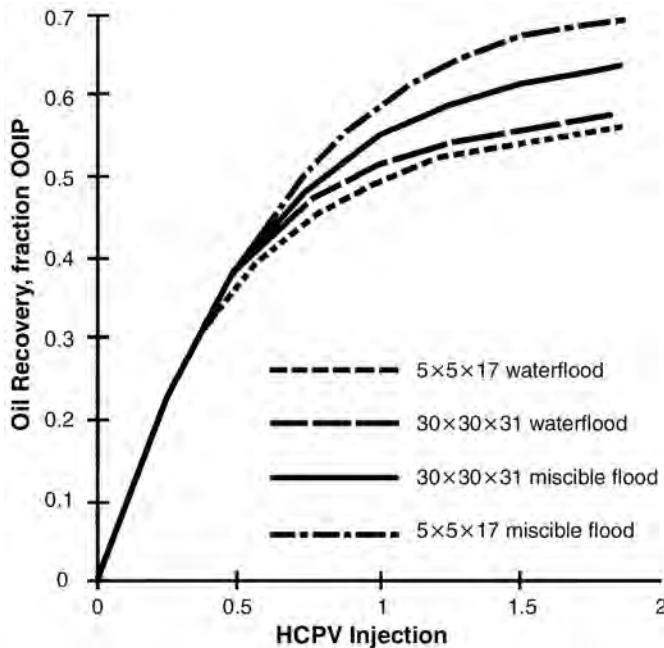


Fig. 14.14—Predictions with reference model and corresponding model with full-field grid size (after Ref. 24).

ery in this figure is the difference between solvent-flood and waterflood simulations in each model. The direct full-field simulation overpredicted incremental recovery by a factor of two.

There also are some additional data requirements for predicting solvent trapping and solvent relative permeability hysteresis that are not found in black-oil waterflood simulations. Solvent trapping, reference models, and scaleup are discussed next.

14.5.1 Solvent Trapping and Solvent Relative Permeability Hysteresis. In most compositionally enhanced solvent displacements, some of the solvent will be trapped permanently in the reservoir and will not be produced. This happens when water is used to drive a solvent slug and the oil displaced by the solvent. Solvent is trapped by advancing water much like oil is left as a residual in a waterflood. Solvent also can be trapped by oil that crossflows into a previously solvent-swept zone.

Laboratory data indicate that there is little dependence of the trapped solvent saturation on whether water or oil is the trapping phase.³⁵ These data also show that the magnitude of the trapped solvent saturation is insensitive to whether the measurement is made at reservoir or ambient conditions, on core plugs or composites of core plugs, or on native state or extracted cores.

The magnitude of the trapped-solvent saturation depends on the magnitude of the maximum solvent saturation present when the solvent is trapped. This is illustrated in Fig. 14.15, which shows data for Prudhoe Bay cores.³⁵ In these experiments, various initial solvent saturations were established before the cores were flooded with either water or oil. There is a substantial degree of scatter in the data, but the trapped-solvent saturation clearly depends on the initial solvent saturation. Moreover, within the data scatter, the trapping is nearly independent of the liquid phase doing the trapping and even independent of a small oil saturation if it should happen to be present as a third phase.

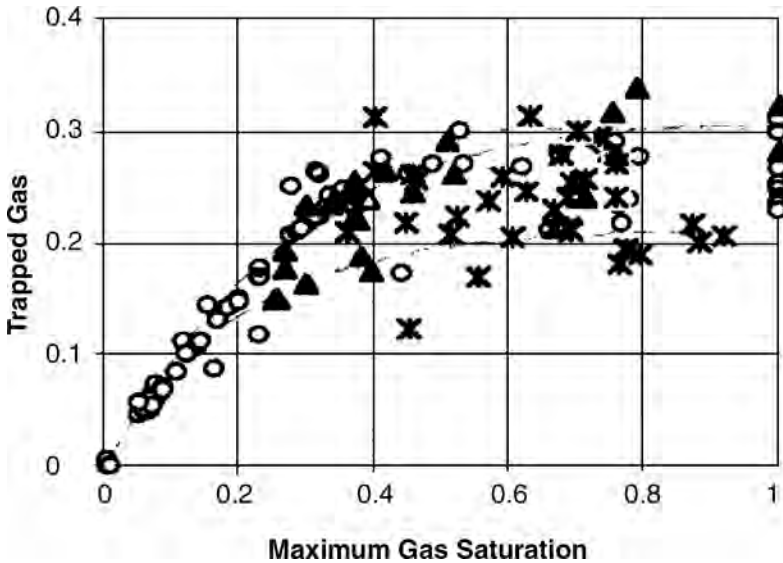


Fig. 14.15—Trapped-gas saturation in Prudhoe Bay cores (after Ref. 35).

According to Jerauld,³⁵ the relationship between trapped-solvent saturation and the maximum solvent saturation at the location at which trapping occurs is generally well represented by a “zero slope” adaptation of the Land curve:

$$S_{gr} = \frac{S_g^{\max}}{1 + (1/S_{gr}^{\max} - 1)(S_{gr}^{\max})^{1/(1 - S_{gr}^{\max})}} \dots\dots\dots (14.17)$$

In this equation, S_{gr}^{\max} is the solvent trapped when the rock is 100% solvent saturated, and S_g^{\max} is the maximum solvent saturation at the location where trapping occurs. According to Eq. 14.17, if solvent subsequently is mobilized from this location only to be trapped again when the flowing saturation is lower, the retrapped solvent still attains the trapped saturation achieved at the previous maximum saturation. If on subsequent remobilization the solvent saturation should reach a higher value than the previous maximum, the trapped saturation will attain a new and higher value, according to Eq. 14.17.

The maximum trapped-solvent saturation, S_{gr}^{\max} , when the rock initially is 100% solvent saturated depends strongly on both porosity and clay content, or microporosity. This is illustrated in Fig. 14.16 for data from various sandstones, which show a generally increasing trend for S_{gr}^{\max} with decreasing porosity.³⁵

Because of the nature of solvent trapping, an important mechanism to be accounted for in WAG flooding is solvent relative permeability hysteresis. This is illustrated in Fig. 14.17. Consider solvent injection for the first WAG cycle. Solvent is the nonwetting phase, and solvent injection is a drainage process. The solvent relative permeability depends only on the solvent saturation. The solvent may be displacing only oil in the presence of connate water for a secondary flood, only water in the presence of waterflood residual oil for a tertiary flood, or both oil and water for a partially waterflooded reservoir. All these situations are approximated by the same solvent primary-drainage curve, and on the first WAG cycle the solvent relative permeabilities follow the primary-drainage curve AE. If at the end of the first solvent cycle a

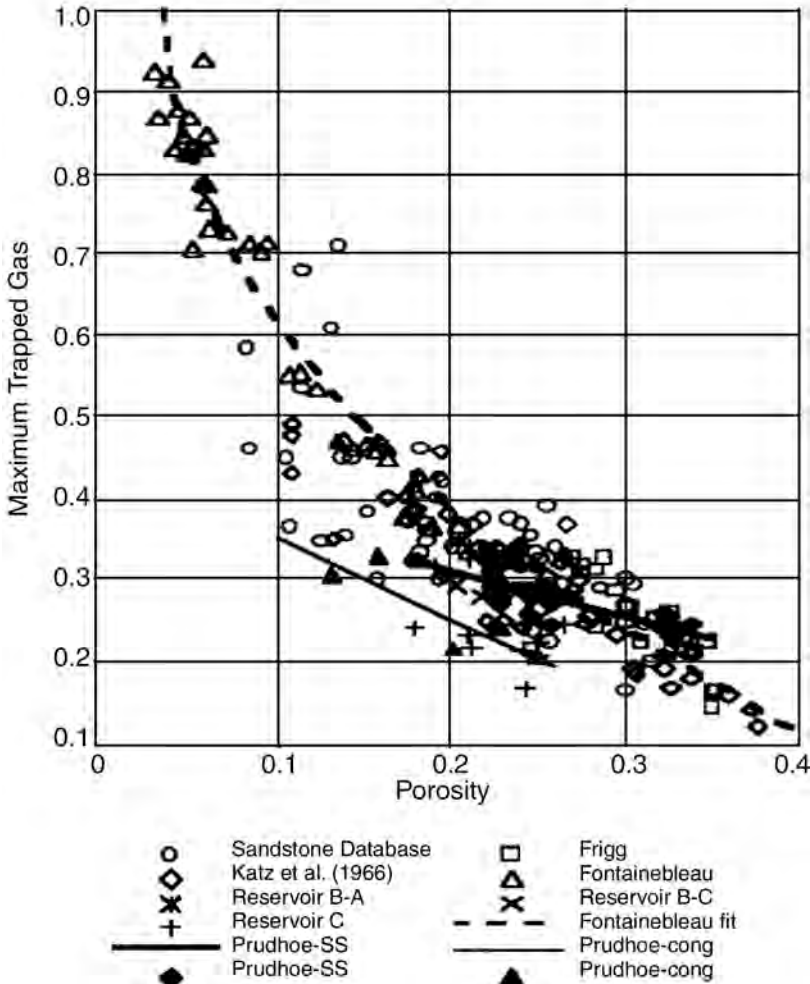


Fig. 14.16—Maximum trapped-gas saturation for different sandstones (after Ref. 35).

volume of solvent has been injected so that point B on the primary-drainage curve has been reached at a given location in the reservoir, the solvent saturation at this location will be S_{gB} .

Now consider water injection on the first WAG cycle. Assume that the solvent saturation at the location in question remains S_{gB} . (Actually, the saturation may increase somewhat as water at first displaces solvent past this location.) When water reaches this location, it will drive the solvent down to a trapped saturation, S_{gTD} , at point D according to the trapped-solvent- vs. maximum-solvent-saturation relationship for the rock. This is an imbibition process, and the solvent relative permeability follows the curve BD.

When solvent is injected on the second WAG cycle, the solvent relative permeability follows the curve DB because Land's evidence demonstrates that imbibition relative permeability often is nearly reversible.³⁶ It is important to take this hysteresis into account in a WAG simulation because the imbibition relative permeability is substantially less than the primary-drainage relative permeability and will cause the mobility ratio to be lower and the displacement more effective than would be the case with primary-drainage relative permeability only.

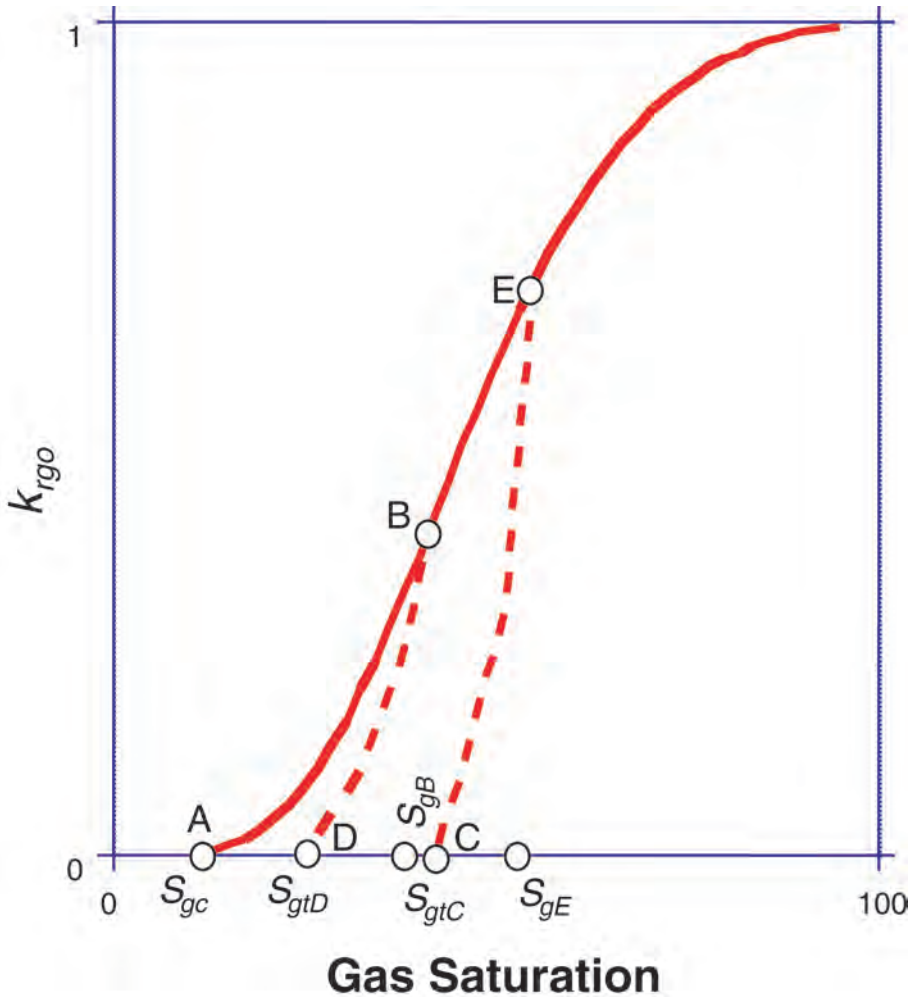


Fig. 14.17—Gas relative permeability hysteresis.

If the solvent saturation at the location in question never reaches S_{gB} , solvent relative permeability will stay on the curve BD during the subsequent second-WAG-cycle water slug. If such a large solvent slug is injected that S_{gB} is exceeded at this location, solvent relative permeability will once again follow the primary-drainage curve, perhaps to point E, and attain a new maximum solvent saturation at this location, S_{gE} . Then, on the subsequent water cycle, the solvent relative permeability will follow a new imbibition curve, EC, and solvent will be trapped at a new trapped-solvent saturation, S_{gtC} , according to the trapped-solvent- vs. maximum-solvent-saturation relationship.

14.5.2 Fine-Grid Reference Models. Grid-refinement sensitivity is an extremely troublesome problem in many compositionally enhanced solvent simulations. The problem manifests itself by the predicted behavior changing as the grid is refined (i.e., as the gridblocks become smaller and smaller). This behavior can be caused by truncation error or numerical dispersion that results from representing derivatives by finite differences; by the inability to accurately resolve the size of solvent tongues or fingers with large gridblocks; and by the inability to represent

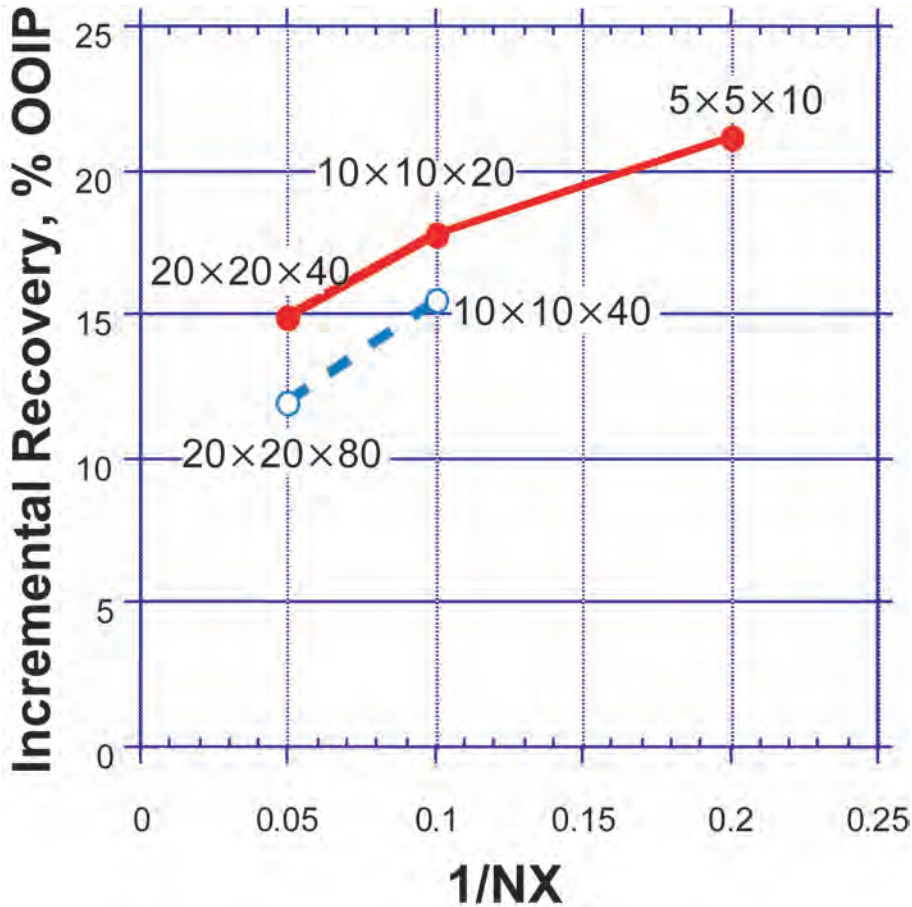


Fig. 14.18—Example of grid-refinement sensitivity.

with large gridblocks some features of reservoir description that have an important effect on solvent sweep, such as discontinuous shales, thin high-permeability strata, or thief zones.

Fig. 14.18 shows the incremental recovery computed for two different 3D models, one representing one-eighth of a nine-spot pattern, the other representing one-fourth of a nine-spot. Each model had a different geostatistical distribution of correlated permeability with scattered, discontinuous shales represented by zero vertical permeability between gridblocks. Permeability and porosity were scaled up by the renormalization method from the model with the smallest gridblocks to the other models.³⁷

The base model for the one-eighth nine-spot has a grid of 20×20×40. Gridblocks were 93 ft on a side and 1 ft thick. The gridding of the one-fourth nine-spot model was 20×20×80, with gridblocks also 93 ft on a side and 1 ft thick.

Incremental recovery in this figure is plotted vs. 1/NX, where 1/NX is the dimensionless x -direction gridblock size. However, in this problem the dimensionless gridblock sizes in the other two directions also vary directly with the x -direction gridblock size. It is apparent that as the gridblock size is refined, the predicted incremental recovery decreases for what is supposed to be the same reservoir problem.

Fig. 14.18 illustrates the importance of minimizing grid-refinement error and explicitly including reservoir-description details that affect flow in an important way. Generally, minimizing the error from grid refinement and accounting for important reservoir-description details

adequately requires small gridblocks. Layers that are 1 ft or no more than a few feet thick and have at least 20 to 40 lateral gridblocks between wells are desirable. Unfortunately, such fine gridding is not feasible for full-field simulations, for most 3D simulations of a single pattern, or perhaps even for some 3D repeating elements of a pattern. Because of this, field predictions need to be made in two steps—with reference models that can be gridded finely enough to accomplish the objectives summarized above, and with scaleup models that incorporate the information derived from reference models into field predictions that account for fieldwide reservoir description, multiple patterns, and operating realities and constraints.

Although it is desirable to make 3D reference-model simulations gridded so finely that the computed answer is adequately close to the converged answer, the discussion above shows that in general, it may not be feasible to do this. A reasonable alternative may be to make finely gridded 2D cross-section simulations to study the grid-refinement issue because for many problems, grid refinement has a larger effect on the computed outcome than the areal effects captured by a coarser-gridded 3D model. Variable-width 2D cross sections sometimes adequately represent the behavior of 3D pattern-segment models with the same fine gridding. In these cross sections, the width is smaller near the injector and producer and increases in the interwell region. This causes flow rate to be greatest near the wells and lowest midway between wells, as it would in a 3D displacement. Even when a fine-grid cross section does not realistically model a fine-grid 3D displacement, it still may predict incremental recovery better than a simulation in a more coarsely gridded 3D model. Moreover, 2D cross-section simulations are well suited for scaleup with the segment and streamline/streamtube models discussed in the next section.

A potential procedure for developing a 3D reference model is first to make a 3D simulation of a pattern element with the finest-grid refinement that is practical. Then, well-to-well cross sections are taken from this model, and the cross sections are refined further. Pseudoproperties are developed for the original cross sections (see [Sec. 14.5.4](#)) that predict the performance of the more finely gridded cross sections. Then, these pseudoproperties are used in the moderately gridded 3D model to approximate the effect of further grid refinement.²⁴

14.5.3 Scaleup To Predict Full-Field Behavior. The objective of scaleup is to take the behavior predicted from detailed, fine-grid reference models that at best represent only a few wells and a tiny part of the reservoir and transfer it to a model that attempts to represent many wells and the integrated behavior of the entire compositionally enhanced solvent flood (or at least a significant portion of it). Three scaleup methods are (1) development of pseudorelative permeability relations and pseudoproperties for use in coarse-grid, full-field, numerical reservoir simulators; (2) development of segment models that estimate the behavior of pattern-repeating elements and add up the behavior of all the segments of a pattern, as well as the behavior of all the patterns; and (3) development of areal streamtube or streamline models that incorporate 2D vertical cross-section solutions into the streamtubes or streamlines and integrate behavior for all the streamtubes or streamlines.

14.5.4 Pseudorelative Permeability Relations and Pseudoproperties. [Ref. 24](#) is a good example of the application of this method. Several reference models describe different areas of the field. Water/oil, solvent/oil, and solvent/water pseudorelative permeability relations are developed, along with pseudotrapped-solvent and solvent-flood residual oil values, so that the relevant behavior of the reference models is reproduced by corresponding models that have the same coarse grids as the full-field model. The coarse-grid models, of course, represent the same parts of the full-field model that the reference models represent. The pseudorelative permeability relations may be developed by trial and error, or they may be estimated by various methods from the fluid-flow and saturation values in the reference-model gridblocks.

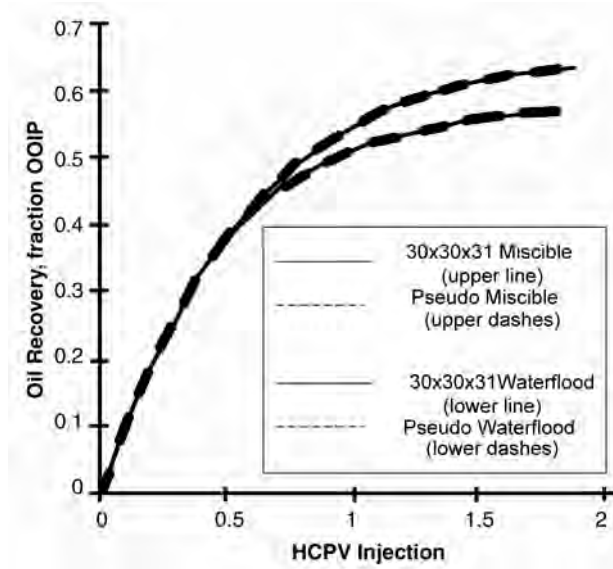


Fig. 14.19—Example of predicting reference-model behavior in a corresponding model with full-field-model grid size using pseudorelative permeability and pseudoproperties (after Ref. 24).

In practice, the pseudorelative permeability relations and pseudoproperties reproduce behavior of one particular fine-grid simulation (e.g., a particular slug size, WAG ratio, injection-solvent composition, start of injection relative to waterflooding, etc.). Of course, an objective of full-field-model simulations is to study different operating scenarios to optimize the flood; to have much utility, the pseudoproperties must predict behavior for conditions other than those of the particular fine-grid simulation that was used to derive them.

Fig. 14.19 shows how well behavior in one of the coarse-grid models of Ref. 24 reproduced the behavior of the corresponding fine-grid model for both the waterflood and the compositionally enhanced solvent flood. The fine-grid and corresponding coarse-grid models represented one-fourth of a nine-spot pattern. The grid of the reference model was $30 \times 30 \times 31$, which contained layers that ranged from 4 to 8 ft thick. This 3D reference model already contained pseudorelationships that had been derived from cross sections with 1-ft layers by the method described previously. The grid of the coarse-grid model was $5 \times 5 \times 17$. Both the timing and level of waterflood and WAG-flood oil recovery are predicted very well.

Although the pseudorelations were developed for a single slug size, WAG ratio, and solvent composition in the reference-model simulation, they reproduced the effect of these variables surprisingly well in subsequent coarse-grid simulations, as seen in **Figs. 14.6 and 14.20**. The reader is cautioned that this degree of predictability of the pseudorelations may result from the fact that the coarse-grid model still has a relatively large number of gridblocks, especially in the vertical direction, for a full-field model, and thus still retains a large degree of description detail and ability to resolve solvent tongues.

14.5.5 Scaleup With Segment Models. When there are too many patterns to allow a sufficient number of gridblocks between wells for adequate scaleup and predictions by the pseudofunction method, segment-model scaleup may be a suitable choice. This was the case for the enriched-solvent flood at Prudhoe Bay, where there are more than 200 enhanced oil recovery (EOR) and waterflood patterns.^{38–40}

The segment model is best suited for regular, repeating patterns. Segment-model scaleup divides each pattern into injector/producer segments, as illustrated in **Fig. 14.21**, for a nine-spot

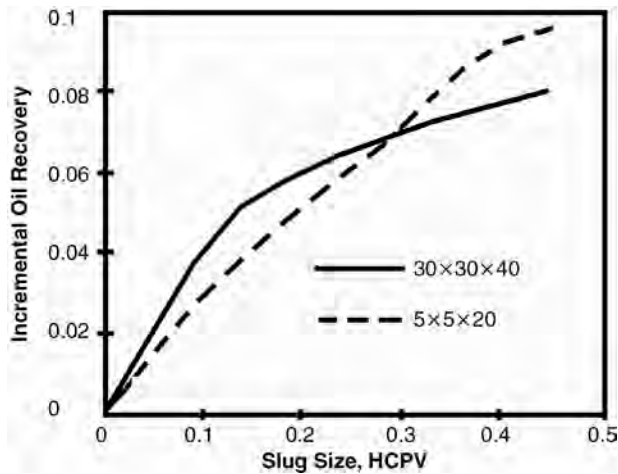


Fig. 14.20—Comparison of reference-model and full-field-model predictions (after Ref. 24).

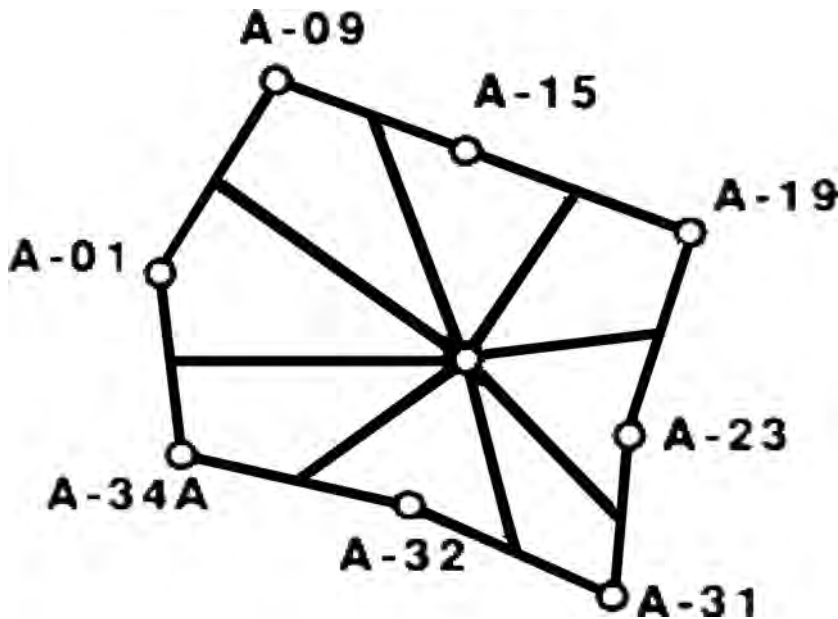


Fig. 14.21—Dividing a pattern into segments (after Ref. 42).

pattern. The dimensionless behavior of each segment is computed using information from suitable reference-model simulations (e.g., dimensionless recovery and solvent production vs. dimensionless injection such as HCPV or displaceable pore volumes). Time rating is accomplished with assumed rates, rates calculated by some other model, or actual injection and production data.

The preferred method for dividing the patterns into segments is with a streamline model that honors actual injection and production rates. Such a model calculates the streamline pattern from injectors to producers, and from this the no-flow boundaries can be determined. Typically, the streamlines for a waterflood are used. Such a model does not assume a balanced,

closed boundary system and is able to account for the effects of unbalanced patterns, reservoir heterogeneities, and faulting.

Of course, in an actual flood, the streamlines change with time as they are influenced by injection and production rates and fluid-mobility changes, and dividing a pattern into segments on the basis of a snapshot of streamline distribution is an approximation. It also may be prudent to adjust segments further according to engineering judgment.

A simpler, and more approximate, method for dividing into segments is by geometric construction. Segments are constructed by bisecting the area surrounding the producing wells and connecting these segments to the appropriate injector.

Using the reference-model curves directly can become cumbersome quickly because of such factors as different solvent slug sizes injected into each segment (because of different degrees of throughput into each segment), different amounts of water preinjection, and differing WAG ratios. Reference simulations need to be run for all these variations, and schemes must be developed to interpolate between the various reference curves.

Wingard and Redmond⁴¹ proposed a novel way of transforming the dimensionless performance computed by the reference model by making an analogy with the behavior of a series of stirred tanks. In their procedure, segment performance is calculated over a series of timesteps. The solvent injected during a given timestep mobilizes a given amount of incremental oil and creates a given amount of returned solvent that was not effective in mobilizing oil. The incremental oil mobilized during each timestep and the returned solvent are then produced from each segment according to the dimensionless performance of the reference model. The Wingard and Redmond method calculates the incremental oil recovered by solvent injection vs. time. The total recovery is obtained by superimposing this incremental recovery on a water-flood calculation.

Wingard and Redmond⁴¹ give equations that (1) represent the type of information shown in Fig. 14.9 and derived from reference-model simulations for incremental recovery vs. slug size, (2) represent the increment of returned solvent for each increment of solvent slug injected, and (3) represent the production of each mobilized-oil increment according to the dimensionless injection vs. production performance derived from the reference-model simulations.

The advantage of the segment model is its simplicity and tractability for a large number of patterns. Its major drawback is the inflexibility in accounting for drastic changes in streamline patterns and, thus, changing segment volumes and creation of new segments as wells are converted from producer to injector (or vice versa), as patterns are reconfigured, as wells are recompleted or shut in, or as new wells are drilled. Wingard and Redman discuss these issues and propose approximations to make.

In addition, if solvent-flood performance depends on factors other than just slug size, such as throughput rate, WAG ratio, degree of prior waterflooding, and changing pressure level, approximations must be made to account for these factors.

14.5.6 Scaleup With Streamtube and Streamline Models. In many respects, scaleup with areal streamtube models is similar to scaleup with segment models. First, segments are assigned from injectors to producers—in this case, the streamtubes. The streamtubes are defined with a special model that calculates streamlines.^{42–44} Typically, the pressure distribution is solved on an underlying grid for a given distribution of total mobility, and the streamlines are calculated for that pressure distribution. Fig. 14.22 illustrates streamlines calculated for 2D areal flow, no-flow boundaries between wells, and the resulting streamtubes for several wells. Refer to the chapter on Reservoir Simulation in the Reservoir Engineering and Petrophysics section for more information on streamtube models.

Emanuel *et al.*⁴⁵ describe a procedure for superimposing fine-grid reference-model solvent-flood simulations on 2D areal streamtubes as follows:

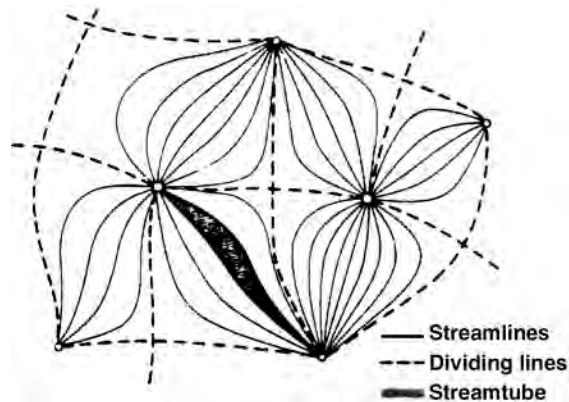


Fig. 14.22—Scaleup with streamtube or streamline models.

- Construct a detailed fine-grid geostatistical cross-section reference model that characterizes the permeability and porosity heterogeneity and correlation between wells in the reservoir area of interest. The wells chosen should typify the flow path of the displacing fluid. This selection is judgmental and will depend on reservoir characteristics. The reference model should be highly detailed in the vertical direction to represent measured log or core data as closely as possible. Layers should be 1 or 2 ft thick. The number of gridblocks between wells should be 20 to 100 depending on computational tractability. Although only one gridblock wide, the cross section should be of variable width to represent the shape of the streamtube. This geometry is intended to model the transition from radial flow near the wells to more linear flow midway through the pattern.

- Simulate the behavior of the process of interest in the reference model. The results of these simulations are reduced to correlations of phase fractional flow at the producer and the total mobility vs. distance from injector to producer as a function of pore volumes or HCPV injected.

- Map the fractional-flow solution onto each streamtube by (a) determining the total mobility in each tube for the cumulative HCPV injected into each tube, (b) allocating injected volume to each streamtube according to its total mobility (the fluid rate for each injection well can be specified or calculated from the imposed pressure drop and total resistance to flow of all the streamtubes), (c) calculating the incremental HCPV injected into each streamtube for the timestep selected, (d) determining the fractional phases of the produced fluid for the cumulative HCPV injected according to correlations, and (e) summing up the contributions from all the tubes connected to a producing well.

The primary advantage of streamtube models over segment models is that the effect of well-rate changes and changing mobility on the streamlines and resulting areal sweep can be accounted for, provided that the streamlines and streamtubes are updated with time. Even if they are not updated, such a model still gives an estimate of the effect of short streamlines and long streamlines on areal sweep, provided that areal sweep is dominated by viscous forces (i.e., a sufficiently high viscosity/gravity ratio) or by areal heterogeneity. In addition, throughput rates can be estimated from the total mobility of the streamtubes rather than being assumed as in segment models. Otherwise, limitations are similar to those encountered with segment models.

Giordano *et al.*⁴⁶ propose a novel method of mapping the behavior computed by a reference model directly on the streamlines. Their method makes an analogy between oil mobilization and solvent trapping with tracer adsorption and desorption. They convert the incremental solvent EOR performance computed for a 2D cross-section reference model to 1D tracer-model equations that represent adsorption and desorption of the tracer as it flows through the reservoir:

$$\frac{\partial(C_i + D_i)}{\partial t} + \frac{v_{xs}}{\phi_i} \left(\frac{\partial F_i}{\partial x_s} \right) = 0, \dots\dots\dots (14.18)$$

where C_i and A_i are the flowing and adsorbed concentrations of component i , x_s is the distance along the streamline from the injection well, and ϕ_i is the accessible pore volume of component i , which is used as a parameter to scale breakthrough times.

Giordano *et al.*⁴⁶ present equations that, for a series of timesteps, (1) calculate the solvent that is effective in mobilizing incremental oil and leaves it trapped according to an adsorption curve; (2) calculate additional ineffective solvent that is left trapped according to another adsorption curve; (3) calculate production of the remaining solvent that is not adsorbed; and (4) calculate the oil mobilized by a given increment of solvent injected according to a desorption curve. Injected water is calculated as the difference between the total injection rate and the injected-solvent rate; produced water is the difference between the total production rate and the sum of the produced solvent, EOR oil, and waterflood oil.

The power of the Giordano *et al.*⁴⁶ method is its ability to account for the effect of well conversions and shut-ins, infill drilling, and changing well rates on streamline patterns, as well as its ability to avoid the complications of having to recalculate streamtubes. Its limitations, similar to those for streamtube models, are in the complexity of accounting for changes in performance caused by changes in WAG ratio, throughput rate, pressure level, injected-solvent composition, and other operating conditions.

14.6 Field Examples

References included in this chapter^{19-21,38-40,47-75} present performance information on many different miscible projects. A few examples of these projects are included in this section to illustrate the types of performances that have been observed with the use of CO₂, hydrocarbon, and N₂ solvents in varying types of reservoirs.

14.6.1 CO₂ Projects. There have been more CO₂ projects than any other type of miscible flood. The three examples reviewed in this section are considered typical of such applications.

SACROC Four-Pattern Flood.^{1,47} This project has been completed. It was thoroughly waterflooded before starting miscible injection. This sequence allows a straightforward evaluation of increased recovery because of miscible displacement.

Fig. 14.23 shows the oil-production rate for the end of the waterflood and the miscible flood. Actual field data are represented by the solid curve, and the forecast decline curve for a continuing waterflood is shown as the dotted curve. The difference between the actual field rate and the forecast waterflood decline represents increased recovery resulting from the miscible project (shaded area); the amount is given in MMSTB. Additional reservoir performance data, including primary plus secondary (P + S), miscible, and total recovery, are given in the upper-right-hand box as a percent OOIP. These data are given in terms of cumulative recovery to date as well as projected ultimate recovery.

After completing the waterflood in 1981, the CO₂ flood was initiated with the same wells and injection patterns. The four-pattern area encompasses 600 acres and 19 MMSTB (3.0 million m³) OOIP. The well pattern is an inverted nine-spot with 40-acre well spacing. Shortly after starting CO₂ injection, there was an increase in oil-production rate. The EOR of 1.7 MMSTB (0.3 million m³) is equivalent to 9% OOIP, which, when added to primary plus secondary recovery (57% OOIP), gives a total recovery of 66% OOIP. Net CO₂ use was 3.2 Mscf/STB of increased recovery (570 std m³/m³).

This project demonstrated that incremental oil can be recovered by a miscible flood after an efficient waterflood. In this case, water injectivity after CO₂ injection was higher than during the waterflood, thus enabling oil to be recovered more quickly.

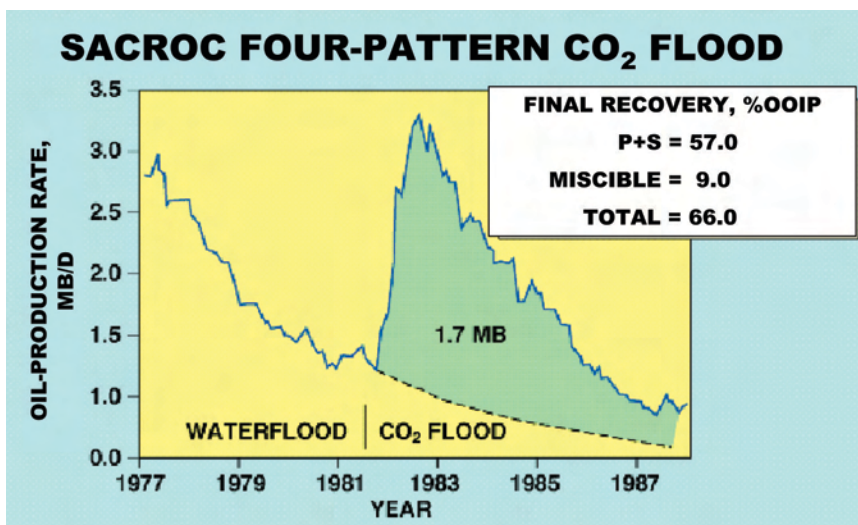


Fig. 14.23—Production history, SACROC four-pattern pilot. (From Healy, Holstein, and Batycky: “Status of Miscible Flooding Technology,” *Proc.*, 14th World Petroleum Congress, Improved Recovery and Heavy Oil, 1994. © John Wiley & Sons Limited. Reproduced with permission.)

Fig. 14.24 illustrates the comparison of actual miscible flood performance to that predicted with a four-component compositional simulator. The Todd-Longstaff mixing model⁶⁷ was used to account for viscous fingering, and phase behavior was represented by a pseudoternary diagram. Two major empirically based physical parameters, S_{orm} and a viscous-fingering parameter, were used to model local displacement and sweep efficiencies. S_{orm} was based on laboratory displacement tests using representative samples of reservoir rock and fluids. The first step in simulation was to history match the waterflood. This enabled fine-tuning of the reservoir-description model. The compositional simulator was then used to calculate performance of the miscible flood without further adjustment to any match parameters.

As shown in Fig. 14.24, the simulation of cumulative oil recovery vs. cumulative injection for the miscible flood agrees reasonably well with actual field results. The produced water/oil ratio from the simulation is also in reasonable agreement with field results. Waterflood sweep efficiency was 74%, and the miscible flood sweep efficiency was 44%. These sweep efficiencies were determined from analysis of the simulation studies.

Means San Andres Unit.^{1,7,12,21,48} This field, located in the eastern edge of the Central Basin Platform of the Permian Basin, produces primarily from the Permian-aged San Andres formation. It was discovered in 1934; waterflooding began in 1963. The field was developed initially on 40-acre spacing and subsequently drilled to 20-acre spacing after the start of waterflooding. The flooding pattern was first peripheral, then a three-to-one line drive, and finally an inverted nine-spot that proved most efficient for this reservoir. Reservoir characteristics are porosity of 9%, permeability of 20 md, S_{wi} of 35%, T_r of 95°F, net-to-gross ratio of 0.18, oil gravity of 29°API, and μ_{oi} of 6 cp.

An oil viscosity of 6 cp makes the waterflood mobility ratio relatively high. From pressure cores and laboratory corefloods, waterflood residual oil saturation was estimated to be 34% of pore volume. A CO₂ miscible project was evaluated with laboratory investigations, field pilots, and reservoir simulations. The pilot tests indicated that CO₂ could successfully mobilize the waterflood residual oil. Even though it is difficult to determine the governing mechanisms for

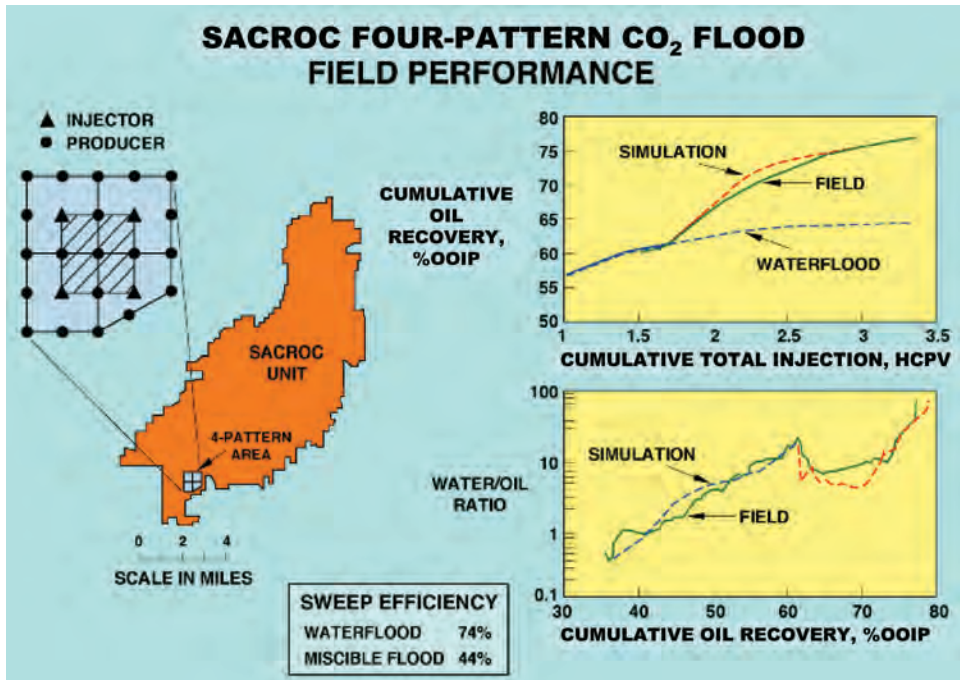


Fig. 14.24—SACROC pattern area, performance, and simulator match. (From Healy, Holstein, and Batycky: "Status of Miscible Flooding Technology," *Proc.*, 14th World Petroleum Congress, Improved Recovery and Heavy Oil, 1994. © John Wiley & Sons Limited. Reproduced with permission.)

improved oil recovery, it appears that after the initial direct displacement of oil by the solvent bank, lighter components of the remaining oil are recovered by extraction.

The original CO₂ project of 167 patterns on approximately 6,700 acres (which contained 82% of OOIP) was expanded to 7,830 acres as evaluation of performance indicated additional prospective areas. Factors affecting process design were the oil viscosity of 6 cp, high MMP, and low formation parting pressure that make operating pressure a critical factor. On the basis of the MMP estimation of 1,850 to 2,300 psi by slimtube experiments and the formation parting pressure of approximately 2,800 psi, a 2,000-psi operating pressure was selected.

Assessment of the economic viability of CO₂ miscible flooding was based on pattern-element simulations for representative project areas that were then used in a scaleup program to forecast total project incremental recovery. A 2:1 WAG ratio and primary CO₂ slug size of 0.40 HCPV were selected as optimum. Updated simulations after gaining operating experience indicated that a CO₂ slug size of 0.60 HCPV was better.

Results of the infill-drilling program and CO₂ flood combined for a total unit oil production increase from approximately 8,500 B/D in 1983 to approximately 16,000 B/D in 1987, as illustrated in Fig. 14.25. Much effort has been made to distinguish between the contributions of infill drilling, improved waterflooding, and miscible displacement. Originally incremental oil recovery resulting from infill drilling was projected to be 5.3% OOIP, while the incremental recovery resulting from CO₂ flooding was to be 7.1% OOIP. These recovery estimates have increased over time as a result of an effective reservoir-management program. Current estimates of recovery resulting from primary and waterflooding methods exceed 30% of OOIP, and incremental recovery resulting from the miscible CO₂ flood is more than 15% of the OOIP.

Utilization of new infill wells for injectors helped minimize downhole mechanical problems. A continuous injection-well profiling program is maintained for flood-management pur-

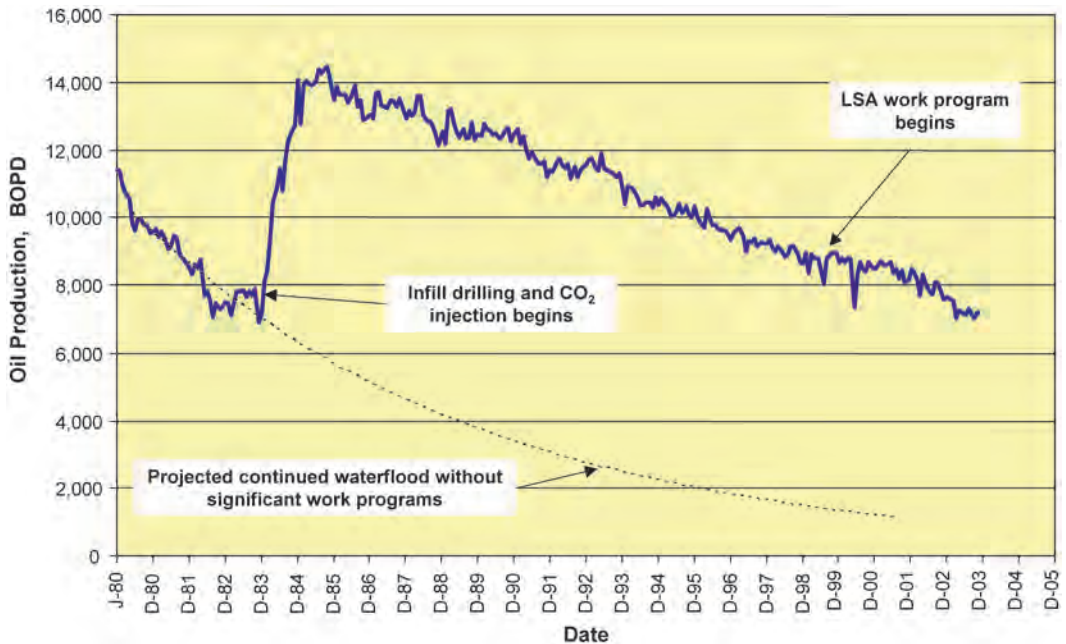


Fig. 14.25—Means San Andres miscible project performance.

poses. Increasing the WAG frequency minimized gas breakthrough between some WAG injectors and offsetting producers experiencing rapid gas breakthrough. While a detailed history-matching simulation of the test did not indicate solvent channeling through known, high-permeability leached layers to be a problem, all other indicators suggested otherwise. Dealing with leached pathways continues to be a challenge. History matching also indicated some loss of CO_2 into the basal water zone.

Several production enhancements have improved field and miscible project performance. First, a 360-acre, nine-pattern pilot was implemented in the North Dome to evaluate the Lower San Andres (LSA) potential. Results showed that additional reserves could be captured from this deeper horizon, although produced-water volumes exceeded initial projections and limited near-term LSA development because of facility constraints. Once water-handling issues were addressed, 59 additional wells were deepened to the LSA in 1992. Performance of these wells provided more insight into factors affecting reservoir performance and resulted in the deepening of an additional 81 injectors and producers and upgrading of facilities to handle more water and gas. As of this writing, the deepening of 97 production wells to the LSA has resulted in a 75% increase in unit oil production and a significant increase in reserves.

Several different types of profile modifications were attempted throughout the 1990s. Early foam and polymer treatments were discontinued because of limited, short-term benefits. Preliminary results from a recent conformance program indicate the possibility to mechanically isolate mature intervals and redirect CO_2 into oil-bearing intervals that would otherwise remain uncontacted.

The miscible-project performance is exceeding previous recovery projections. To better characterize the reservoir and improve business decisions for the asset, a detailed geologic study incorporating engineering and geologic data was used to provide the framework for 3D, three-phase reservoir simulation. Benefits of the study include increasing OOIP by 40%, identifying the potential in the residual oil zone found below the observed oil/water contact in the LSA,

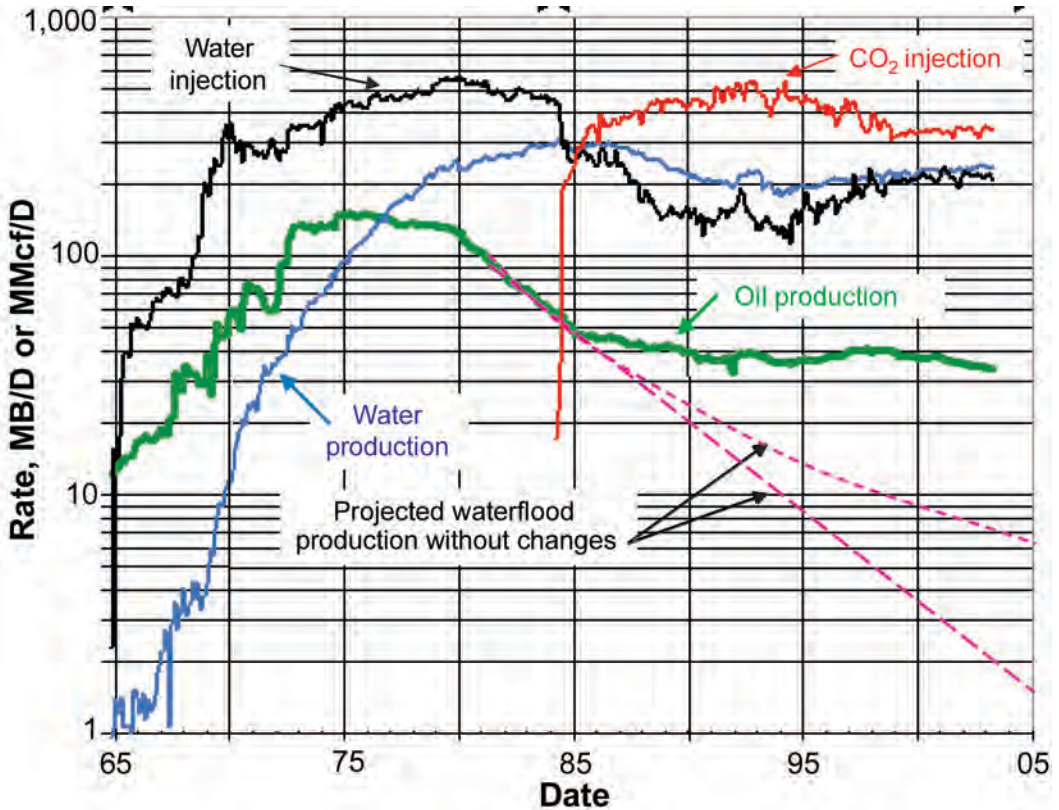


Fig. 14.26—Production performance of the Denver Unit miscible project.

and gaining a better understanding of reservoir continuity using flow units identified with sequence stratigraphy.

Future possibilities for the miscible project include expanding the CO₂-flood project on the basis of the geologic study, continuing the mechanical-isolation program to maximize sweep efficiency, and fine tuning other programs such as varying WAG ratios to further optimize flood performance and enhance profitability.

Denver Unit.^{1,49–52} The Wasson Denver Unit CO₂ flood, started in 1983, is one of the larger industry CO₂ projects [28,000 acres, 2.1 BSTB (0.33 billion m³) OOIP]. No new wells were drilled initially for this project; however, there was significant reconfiguration of the inverted nine-spot patterns (20-acre well spacing) being used in the waterflood preceding miscible injection. Unit performance is shown in Fig. 14.26 for the period beginning with the waterflood through the first 19 years of miscible CO₂ injection. The reservoir was depressured from 3,200 to 2,200 psi to reduce the amount of trapped CO₂. Oil response occurred after approximately 6 to 8 months. Unit oil-production rates have been sustained since the start of CO₂ injection as a result of response to miscible injection and to the continuing efforts of reservoir-management practices that identify more patterns to miscible flood and ways to improve volumetric sweep with well workovers and conversions. The first CO₂ production occurred almost simultaneously with incremental oil production.

There are uncertainties in the continued waterflood curve because of the usual difficulties in estimating waterflood decline and additional uncertainties introduced as a result of pattern

reconfiguration and other modifications that may have affected future waterflood performance as well as miscible recovery.

WAG Ratio. Different WAG ratios were implemented in different areas of the field to determine the most effective method. In the “Continuous Area,” CO₂ was injected continuously for approximately 7 years, and then some patterns were converted to 1:1 WAG to reduce CO₂ producing rates. Oil rates were sustained after WAG started.

In the “WAG Area,” HCPV injection rate was maintained at a level comparable to the Continuous Area. The WAG ratio was approximately 1:1. Incremental production response was poorer than in the Continuous Area, with a maximum of only about 17% of the waterflood oil rate at the start of CO₂ injection. In addition, there was about a 30% loss of water injectivity, and injection pressures exceeded fracturing pressure on water cycles. The area was converted to a line drive in 1988.

As a result of the experience described above, a “Hybrid Process” was applied in a final area of the field to capture the early response of continuous injection and the long-term gas management of WAG. In this process, CO₂ is injected continuously for 4 to 6 years, followed by 1:1 WAG, until a 60% (or larger) HCPV volume of CO₂ is injected. The final phase will be continuous water injection.

The project has performed well overall. There were a few problems in the western part of the field, where the WAG process was used. Water injection at the desired rates was difficult, and solvent was lost to the gas cap in a limited portion of the reservoir. Neither of these was a complete surprise because the operator recognized both as potential problems during the design phase of the project. The slug process used in the eastern part of the field has performed well, and an increase in the CO₂ slug size is being considered.

A fully compositional, fieldwide simulation model is being used to match field and individual-well performance. The simulator is then used to identify locations (which may require infill drilling or horizontal wells) for project expansion, which wells to shut in or return to production, where solvent losses are occurring, and needed changes in WAG ratios. Opportunities for infill drilling and pattern conversion were implemented and added several million barrels of recoverable oil.

The original estimated CO₂ slug size of 0.4 to 0.6 HCPV has now been increased to 0.72%. The current estimated ultimate EOR is 16.7% OOIP. Continued improvements in reservoir management may improve this outlook.

14.6.2 Enriched-Hydrocarbon Projects. While applied less frequently, these types of projects have been very successful when adequate supplies of methane and enriching fluids are available and profitable to inject.

Prudhoe Bay Field.^{20,35,38–41,68–73} The permotriassic-aged Ivishak (also known as Sadlerochit) reservoir, the largest producing horizon in the field, is a series of clastic zones ranging from near-shore marine deposits in the lower sections to sandstones and conglomeratic braided-stream deposits in the remaining, more productive units that contain most of the OOIP. The productive area is 225 square miles. Production began in 1977.

The reservoir is a structural stratigraphic trap consisting of a faulted, south- and southwestward-dipping, 1 to 2° homocline. The main and western areas contain gas caps with different gas/oil contacts (GOCs). Both have an oil/water contact (OWC). The reservoir has an average thickness of more than 500 ft (1600 m). Average rock and fluid properties include a porosity of 22%, S_{wi} of 35%, a net-to-gross ratio of 0.87, an oil gravity of 28°API, and an oil viscosity of 0.8 cp. Permeability averages 500 md and ranges from <100 md in the western area and the deeper deltaic sands up to several darcies in some of the open-framework conglomerate deposits. While the reservoir is connected to a sizeable aquifer, rock properties degrade rapidly

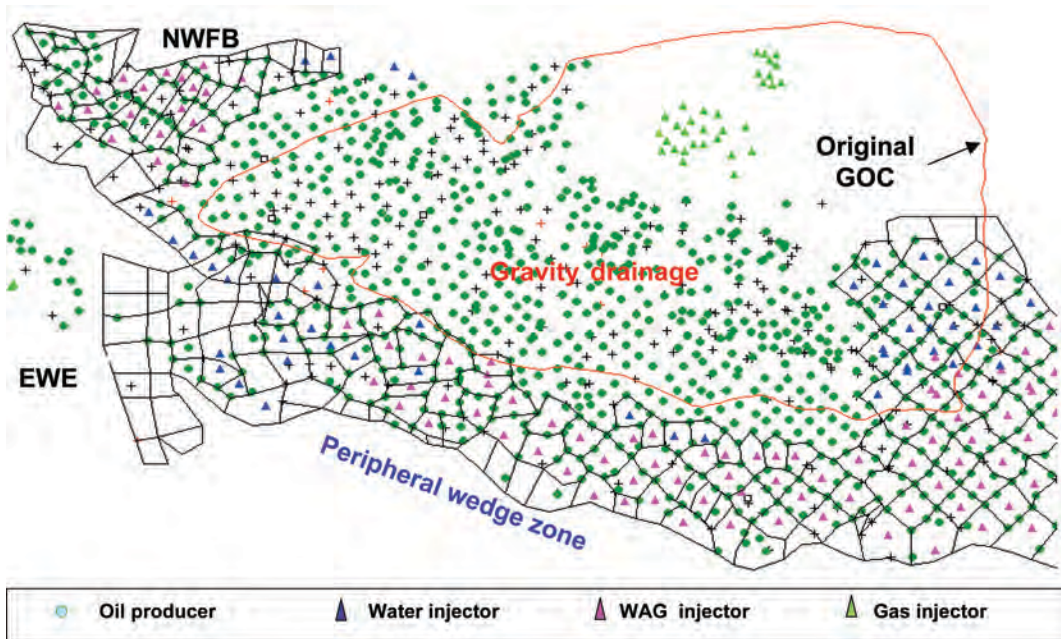


Fig. 14.27—Prudhoe Bay field project areas and recovery processes.

off structure, and the light oil column is separated from the aquifer in portions of the field by a heavy-oil tar mat.

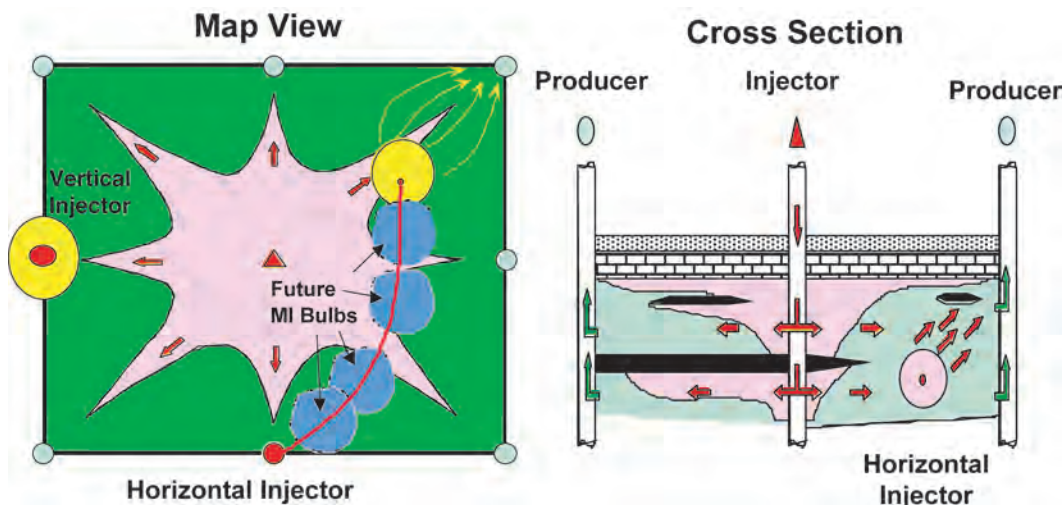
The primary-depletion mechanisms were gravity drainage below the sizable gas cap, a very weak waterdrive, and a potential solution-gas drive. The initial spacing of 320 acres per well was quickly reduced to 160 acres per well and then further reduced to 80 acres per well to sustain production levels and contact more of the reservoir.

Waterflooding (planned as part of the original development plan) was started in conjunction with the 80-acre infill-drilling program. Source water was obtained from the Beaufort Sea. Inverted seven- and nine-spot injection patterns were used in areas of the oil column not overlain by the gas cap.

The gas-cap cycling project was begun in 1977. Gas-handling facilities subsequently were expanded three times and reached a capacity throughput of 8.0 Bcf/D by the late 1990s.

An enriched-hydrocarbon miscible (methane with propane and butane added) WAG injection project was initiated in 1983 with the Flowstation 3 Injection Project. This was expanded to additional areas of the field in 1987. Fig. 14.27 shows the type of recovery mechanisms being managed in various parts of the field.

Miscible Flood Specifics. The method for optimizing the WAG ratio has shifted with time. Initially, all patterns received a solvent injection (miscible injectant, or MI) of 1% of total pore volume per year. This scheme was changed to a tiered allocation process whereby the more efficient patterns received more MI. When implementation of most miscible-injection patterns (149) was completed, the allocation scheme was changed again to direct MI to the most-efficient patterns (on the basis of a detailed analysis of field-performance data) using a binary method. All patterns are ranked in order of efficiency (production per volume of returned MI, or RMI), and solvent is allocated on a WAG ratio of 1 based on a pattern's throughput until available MI is assigned. The less-efficient patterns are shut in until another reallocation is made. A workover to correct well problems such as flow behind pipe or to open new zones or decline in another pattern's performance can result in a shut-in pattern being ranked higher and

Fig. 14.28—MIST concept.⁷³

placed on the active list. Gas samples are routinely collected from production wells to measure RMI as part of the MI allocation process.

Estimated ultimate recovery in the main part of the field is more than 60% OOIP and 80% original condensate in place. Of the total oil recovery, the miscible contribution is 10% OOIP in affected areas. Because the miscible project was started early in field history, a primary-waterflood base production curve was not established to provide an estimate of incremental recovery because of miscible injection. The miscible contribution is based on saturation changes measured by logs run in observation wells and simulations that match actual performance. Also, both tracer and log-inject-log tests have been conducted, and specialized core data have been obtained to measure and improve the effectiveness of the WAG miscible project.

Waterflood and WAG pattern recoveries can be improved with more focus on the management of individual injector/producer pairs within the floods. The objective is to ensure better vertical and areal distribution of the injectant. Patterns with the best performance have recovered in excess of 70% of the OOIP, while the poorer patterns have recovered less than 50% OOIP.

Miscible Injectant Stimulation Treatment (MIST) Concept.⁷² As would be anticipated in a high-quality sand with good vertical permeability, the miscible-recovery process has been dominated by gravity forces. Rapid gravity segregation of MI away from the injection well prevents the MI from contacting a significant portion of the target waterflood residual oil, as illustrated in Fig. 14.28. As shown on the right, only a small portion of the reservoir is contacted in clean sand intervals typical of much of the miscible flood area. As shown on the left, shale lenses tend to mitigate gravity override, resulting in more of the reservoir being contacted. Both vertical and lateral MIST processes are being implemented to improve volumetric sweep. A vertical MIST process involves completing a production well at the bottom of a thick, continuous, watered-out interval. A large slug of solvent is injected, followed by a small slug of chase water. The solvent sweeps rock not contacted by previous solvent injection.

In the lateral MIST process, horizontal wells are placed in the bottom of the overridden portion of the oil column to distribute injectant laterally (Fig. 14.29). A series of injection cycles (referred to as MI bulbs) can be scheduled along the horizontal wellbore to sweep more of the oil column in the pattern. After an MI bulb is complete, the perforations are isolated with a packer or sand, and new perforations are added for the next bulb.

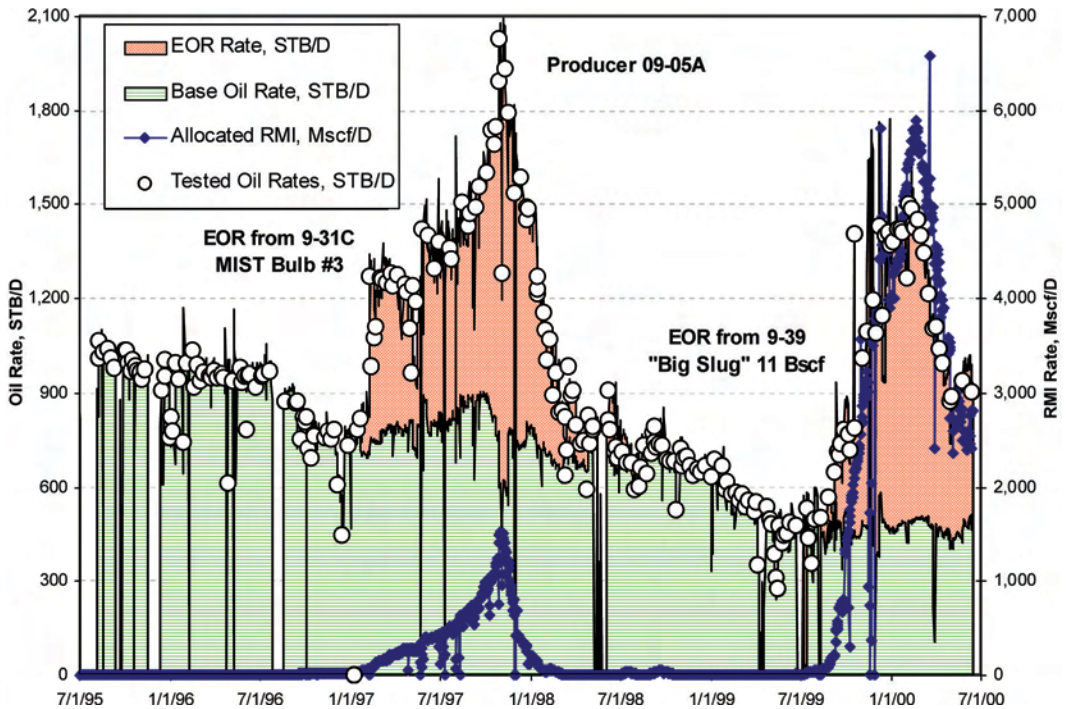


Fig. 14.29—Results of MIST injection.⁷³

Fig. 14.29 shows the production history of one producer in a lateral MIST pattern. There are distinctly recognizable production increases because of miscible injection. The first response was injection in MIST injector 9-31C, where production doubled above the base rate. The second response was injection in conventional WAG injector 9-39.

The correlation between response and RMI is consistent with compositional-simulation runs that show that the rapid response is caused by vapor-phase transport. The more subdued response that occurs when liquid oil is displaced and banked by MI is more difficult to discern from other factors affecting producing rate.

Piercement Salt Dome Field. This field is composed of upper- and lower-faulted, unconsolidated sands that dip away from the salt dome at 65 to 85°. Porosity averages 26.5%, and permeability is 1.3 darcies. Oil gravity is 38°API.

This project is operated as a gravity-stable hydrocarbon miscible flood. The injection rate corresponds to a velocity of roughly one-half the critical velocity required for gravity-stable operations. A volume, corresponding to 17% PV, of enriched gas [natural-gas liquids (NGLs) plus solution gas] was injected, followed by injection of solution gas alone. When injection is completed, blowdown of the gas cap is expected to recover approximately 90% of the enriched gas and a significant portion of the injected solution gas, thus reducing the effective cost of the solvent.

Constant pressure is being maintained to improve recovery by eliminating shrinkage of oil over the course of displacement. Coreflood experiments gave recoveries similar to those predicted by the simulations. Miscible residual oil saturation in corefloods was 7% of PV. Slimtube experiments also were carried out to determine the MME required to achieve miscibility at a given pressure level. An MMP was then selected consistent with the volume of enriching NGL available for the project.

Primary production occurred through gas-cap expansion. Miscible-gas injection began after a short primary-production period. Estimated ultimate recovery is 50% of OOIP for primary recovery in both sands, 74% for total recovery after miscible flood in the lower sand, and 86% total recovery after miscible flood in the upper sand. These recovery levels were determined by tracking gas fronts with pulsed neutron capture (PNC) logging and performing material-balance calculations. These recovery levels are consistent with predictions based on simulations. To date, conformance has been excellent, with field recoveries quite similar to those seen in core-floods.

Routine pressure measurements, PNC logs, and pressure-transient testing are used to monitor reservoir performance and contact movements and to identify areas of good and poor communication. Pressure was initially allowed to decline to slightly above the MMP and was then maintained by scheduling injection volumes equal to production. Pressure maintenance became a challenge because of increasing gas/oil ratio (GOR) that resulted in water-cut increases and reservoir pressures below the MMP in some areas. Pressures were increased and maintained by curtailing production from high-GOR wells.

Pressure communication between injectors and producers has been good in the upper reservoir. In the lower reservoir, pressure communication between wells has been sporadic because of faults and shale barriers that act as baffles between injectors and producers.

14.6.3 Nitrogen Projects. *Jay Field.*^{74,75} Discovered in 1970, this field produces primarily from a Jurassic-aged Smackover carbonate that is heavily dolomitized and has complex lithology. The entire pay interval was cored in virtually all the wells to provide an accurate geologic description and aid in unitization efforts. The productive area is 14,415 acres, average depth is 15,400 ft subsea (SS), porosity is 14%, permeability is 35 md, S_{wi} is 12.7%, oil gravity is 51° API, oil viscosity is 0.18 cp, P_{ri} is 7,850 psi, T_r is 285°F, and net-to-gross ratio is 0.27. The dip is 3°.

The field was unitized in 1973, and waterflooding began 4 days later to arrest pressure decline. Miscible N_2 injection was started in 1981. The MMP for many solvents and the light oil in this reservoir is well below 7,000 psi. N_2 was selected over methane and CO_2 because of cost and supply considerations. Delay in methane sales was unattractive. Using CO_2 would have required a long pipeline from central Mississippi with accompanying costs and right-of-way complications.

The field was developed initially with 89 wells on 160-acre spacing. Selective infill drilling later in poorer sections of the reservoir (both areally and vertically) improved the sweep of injected water. This reduced the average spacing to 140 acres per well.

The waterflood was implemented with a 3-to-1 line-drive pattern using low-salinity water from a water-source well. As-produced water is also injected. Peak water-injection rates reached 250,000 B/D.

Nitrogen is produced by three air-separation units. Produced nitrogen is recovered with cryogenic units and reinjected. The injection rate peaked at 86 MMcf/D. WAG injection is used; the WAG ratio varies by pattern, as dictated by ongoing surveillance of producer oil rate and GOR performance. Current plans call for the injection of a 0.4 HCPV bank.

The oil-production rate reached 100,000 BOPD in 1973 and was sustained at or above that level through 1979. Currently, the field is producing 10,500 BOPD at a 95% water cut. The gas production of 80 Mcf/D is approximately 75% N_2 . Reservoir pressure has been maintained at 7,500 psi. At this pressure, even high-water-cut wells continue to flow, negating the need for artificial lift.

Estimated ultimate recovery is 60% of OOIP, with recoveries approaching 70% in the upper section of the reservoir. Primary recovery resulting from fluid expansion and solution-gas drive was projected to be 17% of OOIP. Waterflooding increased this by 60%, and the misci-

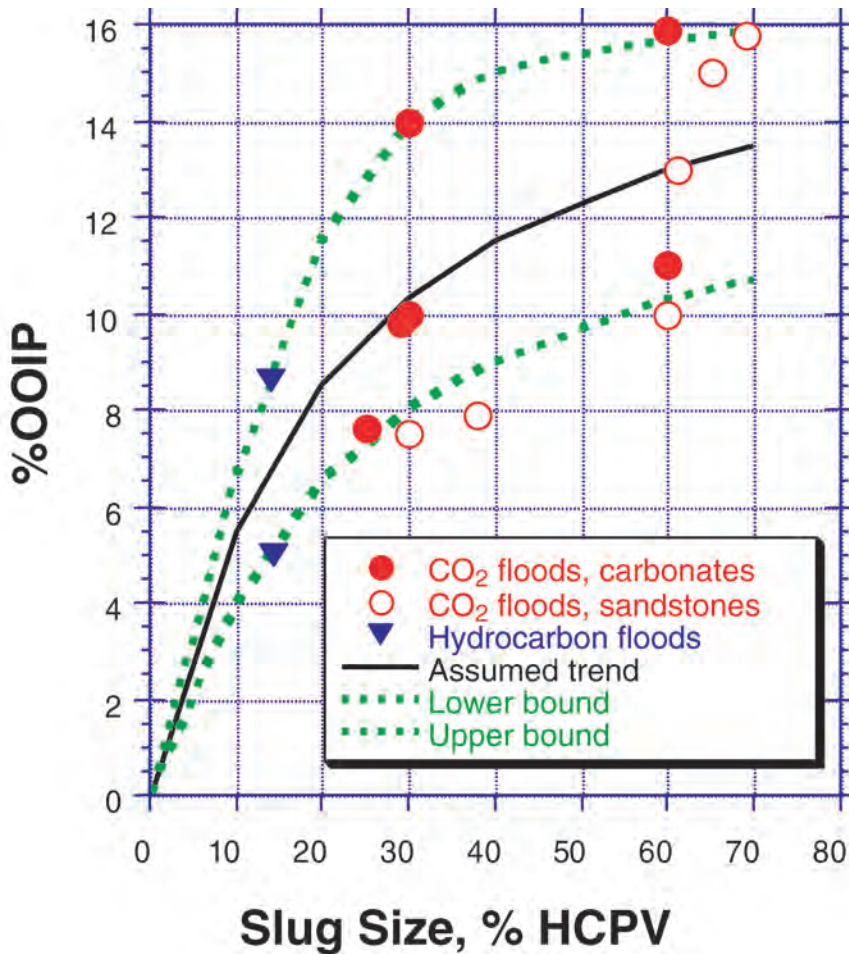


Fig. 14.30—Expected incremental ultimate recovery in selected field projects.

ble project will add another 7 to 10% of OOIP, with recovery in the upper part of the reservoir approaching 13%.

The reservoir surveillance program includes monitoring the WAG ratios, injection-to-withdrawal ratios, and profitability of each pattern. Tools used in the surveillance processes include a history-matched, fully compositional fieldwide simulation model based on an updated geologic model that includes sequence stratigraphy, geostatistical methods, and a strolite model. This finely gridded model includes an updated fluid characterization. These refinements enabled well-by-well matches of production and pressure data for all 137 wells in the field. The updated model has been used to optimize N₂ distribution and investigate several operational changes that are scheduled for implementation and will extend field life by more than 10 years.

14.6.4 Overall Industry Experience. Fig. 14.30 shows how incremental ultimate recovery increased with total solvent slug size for a few projects for which these data were available. The interpretations given in this figure are the author's and are not necessarily those of the project operators. Many of the projects represented in this figure are ongoing, and the ultimate incremental recovery is an estimate.

The contribution of incremental oil production from gas-injection projects (mostly miscible) has continued to grow since 1984, as reported biennially by the *Oil & Gas Journal*. Fig. 14.31

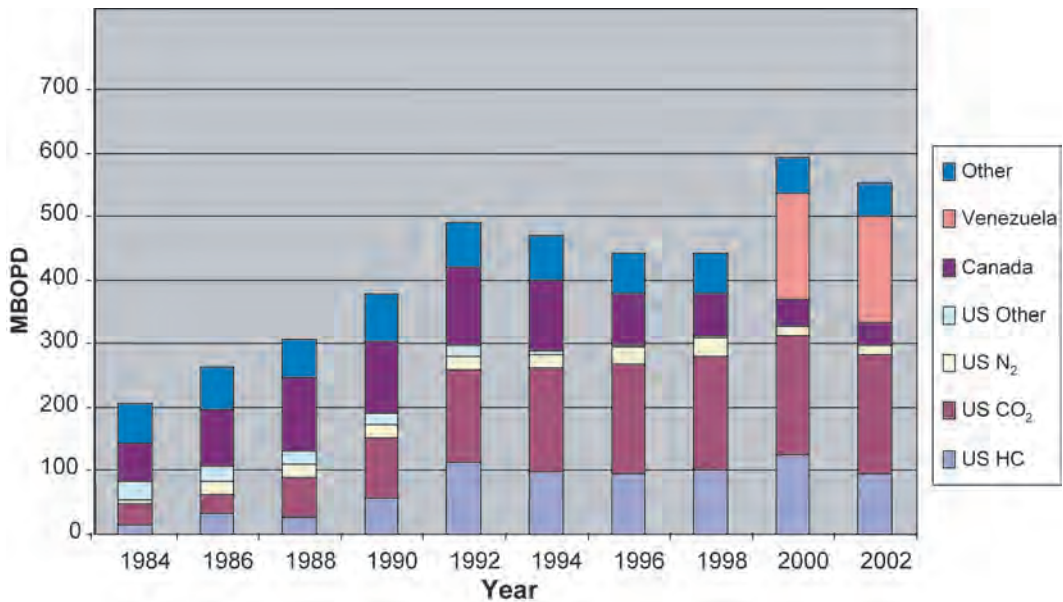


Fig. 14.31—World incremental oil production caused by gas injection (adapted from biennial reports, *Oil & Gas J.*).

shows the volumes reported in this reference. In 2002, total incremental production was nearly 550,000 BOPD. Approximately 60% of the total comes from hydrocarbon miscible projects, and most of the remainder comes from CO₂ miscible projects in the U.S. The advent of the significant contributions from the projects (hydrocarbon miscible) in Venezuela beginning in 2000 indicates an ongoing effort to identify and implement miscible projects around the world.

14.7 Summary

Miscible injection has been applied successfully in many reservoirs. The resulting experience has made it possible to reliably predict the economic viability of new projects in other reservoirs. This chapter contains some general guidelines that should suffice in screening studies of the applicability of a miscible process to a given reservoir or field. In addition, more-detailed information on phase behavior and compositional simulation has been discussed to provide guidance on how to make a more-detailed assessment of miscible flooding. Several field examples are presented to illustrate how CO₂, enriched hydrocarbons, and N₂ solvents have been used to increase oil recoveries significantly. Finally, proper assessment of the application of a miscible project should include the timing of capital outlays for project implementation, the timing of solvent injection and production response, changes in injectivity, and the costs and need to reinject produced solvent.

Nomenclature

- a = constant
- A = defined with Eq. 14.8
- b = constant
- B = defined with Eq. 14.9
- C = defined with Eq. 14.11
- D = adsorbed concentration
- f = fugacity
- f_j^L = fugacity of component j in the liquid phase, psi

- f_j^V = fugacity of component j in the vapor phase, psi
 F = flowing concentration
 g = gas
 i = component i
 j = component j
 k = permeability, md
 n = number of components
 N_{ca} = capillary number, dimensionless
 Δp_g = pressure gradient through the displacing phase, psi
 p_c = component critical pressure, psia
 P = pressure, psia
 P_{ri} = initial reservoir pressure, psi
 R = universal gas constant, units consistent with other equation parameters
 s = volumetric shift parameter, dimensionless
 S = saturation, fraction of pore volume
 S_g^{\max} = maximum solvent saturation, fraction of pore volume
 S_{gr}^{\max} = solvent trapped when rock is 100% solvent saturated
 S_{gt} = trapped gas saturation, fraction of pore volume
 S_{oi} = initial oil saturation, fraction of pore volume
 S_{orm} = miscible flood residual oil saturation, fraction of pore volume
 S_{orwf} = final waterflood residual oil saturation, fraction of pore volume
 S_{wi} = initial water saturation, fraction of pore volume
 t = trapped
 T = temperature, °R
 T_c = critical temperature, °R
 T_r = reduced temperature, T/T_c
 v = volume, cubic ft
 v_{xs} = fluid velocity along a streamline, ft/sec
 x = distance along the streamline, ft
 x,y,z = simulator grid directions
 Z = fluid compressibility factor, dimensionless
 ω = component acentric factor, dimensionless
 ϕ = accessible pore volume
 κ = define by [Eq. 14.6](#)
 σ = interfacial tension, dynes/cm
 ∂_{ij} = binary interaction coefficient
 μ_{oi} = oil viscosity, cp
 Ω_a = constant in [Eq. 14.3](#)
 Ω_b = constant in [Eq. 14.5](#)

Acknowledgments

The authors would like to express their appreciation to members of ExxonMobil Production Co. for their help in describing the performance of the Means San Andres Unit miscible flood performance and the members of Oxy Petroleum for their help in describing the Denver Unit miscible flood performance.

References

1. Healy, R.N., Holstein, E.D., and Batycky, J.P.: "Status of Miscible Flooding Technology," *Proc.*, 14th World Petroleum Congress, Improved Recovery and Heavy Oil, John Wiley and Sons, Vol. 7, No. 3, 407–16.
2. Hadlow, R.E.: "Update of Industry Experience with CO₂ Injection," paper SPE 24928 presented at the 1992 SPE Annual Technical Conference and Exhibition, Washington, DC, 4–7 October.
3. Brock, W.R. and Bryan, L.A.: "Summary Results of CO₂ EOR Field Tests, 1972–1987," paper SPE 18977 presented at the 1989 SPE Joint Rocky Mountain Regional/Low Permeability Reservoirs Symposium, Denver, 6–8 March.
4. Young, M.N. and Martin, W.E.: "The Wizard Lake D-3A Pool Miscible Floods," *J. Cdn. Pet. Tech.* (April–June 1980) 65.
5. Backmeyer, L.A. et al.: "The Tertiary Extension of the Wizard Lake D-3A Pool Miscible Flood," paper SPE 13271 presented at the 1984 SPE Annual Technical Conference and Exhibition, Houston, 16–19 September.
6. DaSie, W.J. and Guo, D.S.: "Assessment of a Vertical Hydrocarbon Miscible Flood in the Westpem Nisku D Reef," *SPE* (May 1990) 147; *Trans.*, AIME, **289**.
7. Johnston, J.R.: "Weeks Island Gravity Stable CO₂ Pilot," paper SPE/DOE 17351 presented at the 1988 SPE/DOE Enhanced Oil Recovery Symposium, Tulsa, 17–20 April.
8. Tiffin, D.L. and Kremesec, V.J.: "A Mechanistic Study of Gravity-Assisted CO₂ Flooding," paper SPE 14895 presented at the 1986 SPE/DOE Symposium on Enhanced Oil Recovery, Tulsa, 20–23 April.
9. Shyeh-Yung, J.-G.J.: "Mechanisms of Miscible Oil Recovery: Effects of Pressure on Miscible and Near-Miscible Displacements of Oil by Carbon Dioxide," paper SPE 22651 presented at the 1991 SPE Annual Technical Conference and Exhibition, Dallas, 6–9 October.
10. Stern, D.: "Mechanisms of Miscible Oil Recovery: Effects of Pore-Level Fluid Distribution," paper SPE 22652 presented at the 1991 SPE Annual Technical Conference and Exhibition, Dallas, 6–9 October.
11. Koch, H.A. and Hutchinson, C.A. Jr.: "Miscible Displacements of Reservoir Oil Using Flue Gas," *Trans.*, AIME (1958) **213**, 7.
12. Clark, N.J. et al.: "Miscible Drive—Its Theory and Application," *JPT* (June 1958) 11.
13. Hutchinson, C.A. Jr. and Braun, P.H.: "Phase Relations of Miscible Displacement in Oil Recovery," *AIChE J.* (1961) **7**, No. 1, 64.
14. Benham, A.L., Dowden, W.E., and Kunzman, W.J.: "Miscible Fluid Displacement—Prediction of Miscibility," *Trans.*, AIME (1960) **219**, 229.
15. Wu, R.S. et al.: "Enriched Gas Displacement: Design of Solvent Compositions," *J. Cdn. Pet. Tech.* (May–June 1986) 55.
16. Zick, A.A.: "Combined Condensing/Vaporizing Mechanism in the Displacement of Oil by Enriched Gases," paper SPE 15493 presented at the 1986 SPE Annual Technical Conference and Exhibition, New Orleans, 5–8 October.
17. Stone, H.L.: "Vertical Conformance in an Alternating Water-Miscible Gas Flood," paper SPE 11130 presented at the 1982 SPE Annual Technical Conference and Exhibition, New Orleans, 26–29 September.
18. Jenkins, M.K.: "An Analytical Model for Water/Gas Miscible Displacements," paper SPE/DOE 12632 presented at the 1984 SPE/DOE Symposium on Enhanced Oil Recovery, Tulsa, 15–18 April.
19. Pritchard, D.W.L. et al.: "Reservoir Surveillance Impacts Management of the Judy Creek Hydrocarbon Miscible Flood," paper SPE/DOE 20228 presented at the 1990 SPE/DOE Enhanced Oil Recovery Symposium, Tulsa, 22–25 April.
20. Dawson, A.G., Jackson, D.D., and Buskirk, D.L.: "Impact of Solvent Injection Strategy and Reservoir Description on Hydrocarbon Miscible EOR for the Prudhoe Bay Unit, Alaska," paper SPE 19657 presented at the 1989 SPE Annual Technical Conference and Exhibition, San Antonio, Texas, 8–11 October.

21. Magruder, J.B., Stiles, L.H., and Yelverton, T.D.: "Review of the Means San Andres Unit CO₂ Tertiary Project," *JPT* (May 1990) 638; *Trans.*, AIME, **289**.
22. Moritis, G.: "EOR Increases 24% Worldwide; Claims 10% of U.S. Production," *Oil & Gas J.* (20 April 1992) 51.
23. Chang, H.L. *et al.*: "The Effects of Injectant-Enrichment Level on Oil Recovery in Horizontal, Gravity-Tongue-Dominated Enriched-Gas Drives," paper SPE 26084 presented at the 1993 SPE Western Regional Meeting, Anchorage, 26–28 May.
24. Jerauld, G.R.: "A Case Study in Scaleup for Multicontact Miscible Hydrocarbon Gas Injection," *SPEREE* (December 1998) 575.
25. Mungan, N.: "Carbon Dioxide Flooding—Fundamentals," *J. Cdn. Pet. Tech.* (January–March 1981) 87.
26. Stalkup, F.I.: *Miscible Displacement*, Monograph Series, SPE, Dallas (1983) **8**.
27. Rogers, J.E. and Grigg, R.B.: "A Literature Analysis of the WAG Injectivity Abnormalities in the CO₂ Process," *SPEREE* (October 2001) 375.
28. Peng, D.Y. and Robinson, D.B.: "A New Two-Constant Equation of State," *Ind. Eng. Chem. Fundam.* (1976) **15**, No. 1, 59.
29. Soave, G.: "Equilibrium Constants from a Modified Redlich-Kwong Equation of State," *Chem. Eng. Sci.* (1972) **27**, 1197.
30. Jhaveri, B.S. and Youngren, G.K.: "Three-Parameter Modification of the Peng-Robinson Equation of State To Improve Volumetric Predictions," *SPEERE* (August 1988) 1033.
31. Peneloux, A., Rauzy, E., and Freze, R.: "A Consistent Correction for Redlich-Kwong-Soave Volumes," *Fluid Phase Equilibria* (1982) **8**, 7.
32. Lohrenz, J., Bray, B.G., and Clark, C.R.: "Calculating Viscosities of Reservoir Fluids From Their Composition," *JPT* (October 1964) 1171; *Trans.*, AIME, **231**.
33. Whitson, C.H. and Brule, M.R.: *Phase Behavior*, Monograph Series, SPE, Richardson, Texas (2000) **20**.
34. Pedersen, K.S., Thomassen, P., and Fredenslund, A.: "Thermodynamics of Petroleum Mixtures Containing Heavy Hydrocarbons. 1. Phase Envelope Calculations by Use of the Soave-Redlich-Kwong Equation of State," *Ind. Eng. Chem. Process Des. Dev.* (1984) **23**, No. 1, 163.
35. Jerauld, G.R.: "Gas-Oil Relative Permeability of Prudhoe Bay," paper SPE 35718 presented at the 1996 SPE Western Regional Meeting, Anchorage, 22–24 May.
36. Land, C.S.: "Comparison of Calculated with Experimental Imbibition Relative Permeability," *Trans.*, AIME (1971) **251**.
37. Christie, M.A. *et al.*: "A Renormalisation-Based Upscaling Technique for WAG Floods in Heterogeneous Reservoirs," paper presented at the 1995 SPE Symposium on Reservoir Simulation, San Antonio, Texas, 12–15 February.
38. Simon, A.D. and Petersen, E.J.: "Reservoir Management of the Prudhoe Bay Field," paper SPE 38847 presented at the 1997 SPE Annual Technical Conference and Exhibition, San Antonio, Texas, 5–8 October.
39. Szabo, J.D. and Meyers, K.O.: "Prudhoe Bay: Development History and Future Potential," paper SPE 26053 presented at the 1993 SPE Western Regional Meeting, Anchorage, 26–28 May.
40. McGuire, P.L. and Stalkup, F.I.: "Performance Analysis and Optimization of the Prudhoe Bay Miscible Gas Project," paper SPE 22398 presented at the 1992 SPE International Meeting on Petroleum Engineering, Beijing, 24–27 March.
41. Wingard, J.S. and Redman, R.S.: "A Full-Field Forecasting Tool for the Combined Water/Miscible Gas Flood at Prudhoe Bay," paper SPE 28632 presented at the 1994 SPE Annual Technical Conference and Exhibition, New Orleans, 25–28 September.
42. Martin, J.C. and Wegner, R.E.: "Numerical Solution of Multiphase, Two-Dimensional Incompressible Flow Using Stream-tube Relationships," *SPEJ* (October 1979) 313; *Trans.*, AIME, **267**.
43. Thiele, M.R., Blunt, M.J., and Orr, F.M. Jr.: "A New Technique for Predicting Flow in Heterogeneous Systems Using Streamtubes," paper SPE/DOE 27834 presented at the 1994 SPE/DOE Symposium on Improved Oil Recovery, Tulsa, 17–20 April.
44. Batycky, R.P., Blunt, M.J., and Thiele, M.R.: "A 3D Field-Scale Streamline-Based Reservoir Simulator," *SPEERE* (November 1997) 246.

45. Emanuel, A.S. *et al.*: “Reservoir Performance Prediction Methods Based on Fractal Geostatistics,” *SPE* (August 1991) 311.
46. Giordano, R.M., Redman, R.S., and Bratvedt, F.: “A New Approach to Forecasting Miscible WAG Performance at the Field Scale,” paper SPE 36712 presented at the 1996 SPE Annual Technical Conference and Exhibition, Denver, 6–9 October.
47. Langston, M.V., Hoadley, S.F., and Young, D.N.: “Definitive CO₂ Flooding Response in the SACROC Unit,” paper SPE/DOE 17321 presented at the 1988 SPE/DOE Enhanced Oil Recovery Symposium, Tulsa, 17–20 April.
48. Stiles, L.H. and Magruder, J.B.: “Reservoir Management in the Means San Andres Unit,” *JPT* (April 1992) 469; *Trans.*, AIME, **293**.
49. Tanner, C.S. *et al.*: “Production Performance of the Wasson Denver Unit CO₂ Flood,” paper SPE/DOE 24156 presented at the 1992 SPE/DOE Symposium on Enhanced Oil Recovery, Tulsa, 22–24 April.
50. Kittridge, M.G.: “Quantitative CO₂ Flood Monitoring, Denver Unit, Wasson (San Andres) Field,” paper SPE 24644 presented at the 1992 SPE Annual Technical Conference and Exhibition, Washington, DC, 4–7 October.
51. Hsu, C.-F., Morell, J.I., and Falls, A.H.: “Field-Scale CO₂ Flood Simulations and Their Impact on the Performance of the Wasson Denver Unit,” paper SPE 29116 presented at the 1995 SPE Symposium on Reservoir Simulation, San Antonio, Texas, 12–15 February.
52. Thai, B.N. *et al.*: “Denver Unit Infill Drilling and Pattern Reconfiguration Program,” paper SPE 59548 presented at the 2000 SPE Permian Basin Oil and Gas Recovery Conference, Midland, Texas, 21–23 March.
53. Harpole, K.J. and Hallenbeck, L.D.: “East Vacuum Grayburg San Andres Unit CO₂ Flood Ten Year Performance Review: Evolution of a Reservoir Management Strategy and Results of WAG Optimization,” paper SPE 36710 presented at the 1996 SPE Annual Technical Conference and Exhibition, Denver, 6–9 October.
54. Ring, J.N. and Smith, D.J.: “An Overview of the North Ward Estes CO₂ Flood,” paper SPE 30729 presented at the 1995 SPE Annual Technical Conference and Exhibition, Dallas, 22–25 October.
55. Brokmeyer, R.J., Borling, D.C., and Pierson, W.T.: “Lost Soldier Tensleep CO₂ Tertiary Project, Performance Case History: Bairoil, Wyoming,” paper SPE 35191 presented at the 1996 SPE Permian Basin Oil and Gas Recovery Conference, Midland, Texas, 27–29 March.
56. Flanders, W.A. and DePauw, R.M.: “Update Case History: Performance of the Twofreds Tertiary CO₂ Project,” SPE 26614 presented at the 1993 SPE Annual Technical Conference and Exhibition, Houston, 3–6 October.
57. Reinbold, E.W. *et al.*: “Early Performance and Evaluation of the Kuparuk Hydrocarbon Miscible Flood,” paper SPE 24930 presented at the 1992 SPE Annual Technical Conference and Exhibition, Washington, DC, 4–7 October.
58. Winter, B.T. and Edwards, K.A.: “Reservoir Management and Optimization of the Mitsue Gilwood Sand Unit #1 Horizontal Hydrocarbon Miscible Flood,” paper SPE 30725 presented at the 1995 SPE Annual Technical Conference and Exhibition, Dallas, 22–25 October.
59. Pritchard, D.W.L. and Nieman, R.E.: “Improving Oil Recovery Through WAG Cycle Optimization in a Gravity-Override-Dominated Miscible Flood,” paper SPE/DOE 24181 presented at the 1992 SPE/DOE Symposium on Enhanced Oil Recovery, Tulsa, 22–24 April.
60. Hoolahan, S.P. *et al.*: “Kuparuk Large Scale Enhanced Oil Recovery Project,” paper SPE 35698 presented at the 1996 SPE Western Regional Meeting, Anchorage, 22–24 May.
61. Bellavance, J.F.R.: “Dollarhide Devonian CO₂ Flood: Project Performance Review 10 Years Later,” paper SPE 35190 presented at the 1996 SPE Permian Basin Oil and Gas Recovery Conference, Midland, Texas, 27–29 March.
62. Pittaway, K.R. and Rosato, R.J.: “The Ford Geraldine Unit CO₂ Flood—Update 1990,” *SPE* (1991) 410.
63. Reitzel, G.A. and Callow, G.O.: “Pool Description and Performance Analysis Leads to Understanding Golden Spike’s Miscible Flood,” *J. Cdn. Pet. Tech.* (April–June 1977) **16**, No. 2, 39.

64. Lee, K.H. and El-Saleh, M.M.: "A Full-Field Numerical Modeling Study for the Ford Geraldine Unit CO₂ Flood," paper SPE/DOE 20227 presented at the 1990 SPE/DOE Symposium on Enhanced Oil Recovery, Tulsa, 22–25 April.
65. Phillips, L.A., McPherson, J.L., and Leibrecht, R.J.: "CO₂ Flood: Design and Initial Operations, Ford Geraldine (Delaware Sand) Unit," paper SPE 12197 presented at the 1983 SPE Annual Technical Conference and Exhibition, San Francisco, 3–5 October.
66. Pittaway, K.R. and Runyan, E.E.: "The Ford Geraldine Unit CO₂ Flood: Operating History," *SPEPE* (August 1990) 333.
67. Todd, M.R. and Longstaff, W.J.: "The Development, Testing, and Application of a Numerical Simulator for Predicting Miscible Flood Performance," *JPT* (July 1972) 874; *Trans.*, AIME, **253**.
68. Erickson, J.W. and Sneider, R.M.: "Structural and Hydrocarbon Histories of the Ivishak (Sadlerochit) Reservoir, Prudhoe Bay Field," paper SPE 28574 presented at the 1994 SPE Annual Technical Conference and Exhibition, New Orleans, 25–28 September.
69. Sneider, R.M. and Erickson, J.W.: "Rock Types, Depositional History, and Diagenetic Effects—Sadlerochit Reservoir, Prudhoe Bay Field," paper SPE 28575 presented at the 1994 SPE Annual Technical Conference and Exhibition, New Orleans, 25–28 September.
70. Weaver, J.W. and Uldrich, D.O.: "Optimizing Solvent Allocation in the Prudhoe Bay Miscible Gas Project," paper SPE 54615 presented at the 1999 SPE Western Regional Meeting, Anchorage, 26–28 May.
71. Cockin, A.P. *et al.*: "Analysis of a Single-Well Chemical Tracer Test To Measure the Residual Oil Saturation to a Hydrocarbon Miscible Gas Flood at Prudhoe Bay," *SPEEE* (December 2000) 544.
72. McGuire, P.L., Spence, A.P., and Redman, R.S.: "Performance Evaluation of a Mature Miscible Gasflood at Prudhoe Bay," *SPEEE* (August 2001) 318.
73. McGuire, P.L. and Holt, B.M.: "Unconventional Miscible EOR Experience at Prudhoe Bay: A Project Summary," *SPEEE* (February 2003) 17.
74. Langston, E.P. and Shirer, J.A.: "Performance of Jay/LEC Fields Unit Under Mature Waterflood and Early Tertiary Operations," *JPT* (February 1985) 261.
75. Lawrence, J.J. *et al.*: "Jay Nitrogen Tertiary Recovery Study: Managing a Mature Field," paper SPE 78527 presented at the 2002 Abu Dhabi International Petroleum Exhibition and Conference, Abu Dhabi, UAE, 13–16 October.

SI Metric Conversion Factors

acre	× 4.046 873	E + 03	= m ²
°API	141.5/(131.5 + °API)		= g/cm ³
barrel	× 1.589 873	E - 01	= m ³
cp	× 1.0*	E - 03	= Pa·s
dyne	× 1.0*	E - 02	= mN
ft	× 3.048*	E - 01	= m
ft ³	× 2.831 685	E - 02	= m ³
°F	(°F - 32)/1.8		= °C
in.	× 2.54*	E + 00	= cm
psi	× 6.894 757	E + 00	= kPa

*Conversion factor is exact.

Chapter 15

Thermal Recovery by Steam Injection

Jeff Jones, SPE, Nations Petroleum

15.1 Steam

The most common method used to enhance oil production over primary rates is water injection, commonly referred to as secondary oil recovery. Common practice in the industry is to refer to all other methods as tertiary enhanced oil recovery. According to Prats,¹ thermal enhanced oil recovery (TEOR) is a family of tertiary processes defined as “any process in which heat is introduced intentionally into a subsurface accumulation of organic compounds for the purpose of recovering fuels through wells.” By far, the most common vehicle used to inject heat is saturated steam. Hot water and heated gasses have been tried, but none are as effective as quality steam. According to a 2000 *Oil and Gas Journal* survey,² steam enhanced oil recovery projects account for 417,675 barrels of oil per day (BOPD), or 56% of the total for all tertiary enhanced recovery methods. That production rate has been essentially flat for more than 15 years. Hydrocarbon gas injection and CO₂ gas injection are the only other significant contributors and amount to only 17 and 24%, respectively. This chapter refers to the general process as steam enhanced oil recovery (SEOR).

15.1.1 Properties of Saturated Steam. Like other substances, water can exist in the form of a solid (ice), as a liquid (water), or as a gas (loosely called steam). SEOR processes are concerned with the liquid and gas phases, and the change from one phase to the other. The phase change region, in which water coexists as liquid and gas, is where our interest lies when considering steam for use in the oil field. The term “steam” is an imprecise designation because it refers to a water liquid/gas system that can exist from 32°F to any higher temperature; from 0.1 psia to any higher pressure; and from nearly all liquid to 100% gas. Steam quality refers to the phase change region of liquid to gas and is defined as

$$f_s = \frac{m_v}{m_v + m_l} \dots\dots\dots (15.1)$$

Heat capacity is expressed in units of Btu/(lbm-°F). A “Btu” is defined as the amount of heat required to raise 1 lbm of water from 60 to 61°F. All liquids and solids are compared to pure water, which has the highest heat capacity of any substance at 1 Btu/(lbm-°F). By calculating a

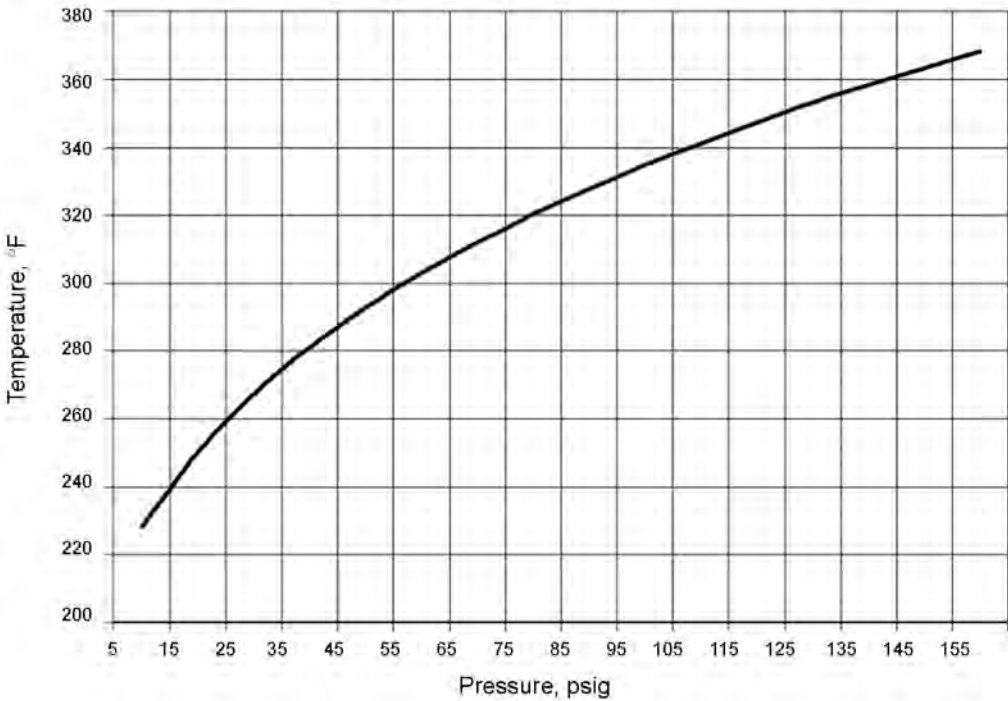


Fig. 15.1—Saturation steam temperature and pressure.

ratio of the heat capacity of water divided by that of another substance, a convenient fraction called “specific heat” is obtained. Notice that petroleum has a specific heat of 0.5, or half that of water, and sandstone is only 20% of water on a per pound basis. No other liquid or gas carries as much heat per pound as water. Also, the temperature range at which this high heat carrying performance is achieved, 34 to 700°F, is ideal for many processes, including SEOR.

Enthalpy is a useful property defined by an arbitrary combination of other properties and is not a true form of energy. The absolute value of enthalpy is of no practical value. Changes in enthalpy are extremely useful, however, and are the basis for SEOR energy calculations. The total enthalpy held by each pound of liquid water at any temperature is called sensible heat, h_f . The heat input, which produces a change of state from liquid to gas without a change of temperature, is called the “latent heat of evaporation” and is shown by h_{fv} . The total heat, h_v , in each pound of 100% quality or saturated steam is the sum of these two, $h_v = h_f + h_{fv}$.

In the phase change or “saturation” region, steam can only exist at one temperature for a given pressure regardless of quality or latent heat content, as shown in Fig. 15.1. Steam increases in volume as latent heat increases, as in Fig. 15.2. This is a useful property in displacing oil in an SEOR process. The volume occupied by 1 lbm of steam at any pressure is its specific volume in ft³/lbm and is represented by v_s . Values for these thermal properties of water are published widely.^{3,4} Fig. 15.3 is a chart of the phase change region. Equations have been derived that approximate the values to acceptable accuracy for most SEOR calculations.

Simple versions that are accurate to within a few percent in the normal pressure ranges encountered in SEOR projects are

$$T_s = 116.79p_s^{0.2229}, \text{ } ^\circ\text{F} ; \dots\dots\dots (15.2)$$

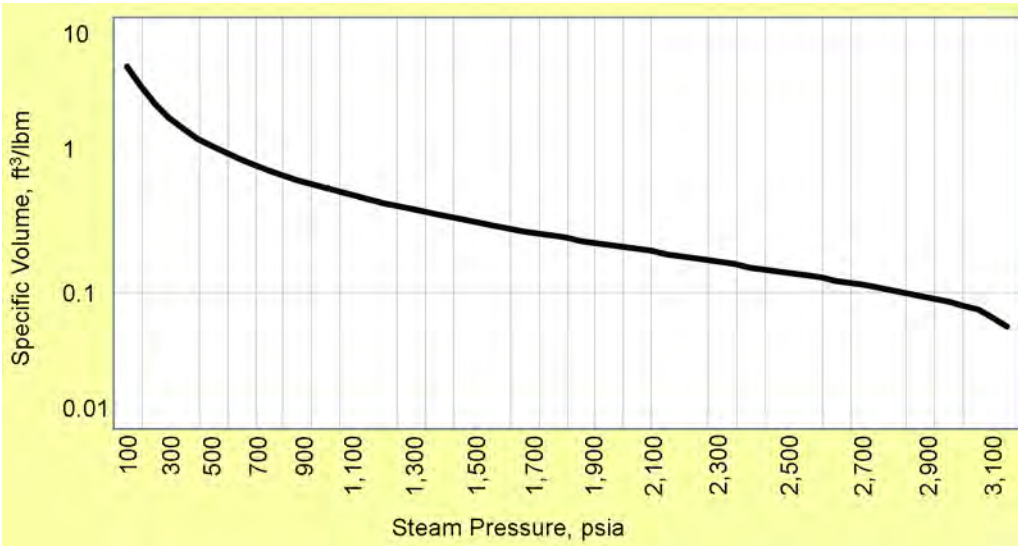


Fig. 15.2—Steam specific volume vs. saturation pressure.

$$v_s = 0.02 + f_s \left(\frac{443}{p_s} - 0.02 \right), \text{ ft}^3 / \text{lbm} ; \dots\dots\dots (15.3)$$

$$\rho_s = 5.06e^{0.000359 p_s} - 5, \text{ lbm} / \text{ft}^3 ; \dots\dots\dots (15.4)$$

$$h_f = 91 p_s^{0.2574}, \text{ Btu} / \text{lbm} ; \dots\dots\dots (15.5)$$

$$h_{fv} = 1,318 p_s^{-0.08774}, \text{ Btu} / \text{lbm} ; \dots\dots\dots (15.6)$$

$$h_v = 1,119 p_s^{0.01267}, \text{ Btu} / \text{lbm} ; \dots\dots\dots (15.7)$$

and

$$h_{fs} = \frac{f_s(1,318)}{p_s^{0.08774}} + 91 p_s^{0.2574}, \text{ Btu} / \text{lbm} . \dots\dots\dots (15.8)$$

These are recommended for hand calculations or simple analytical equations. There are more precise versions in the literature⁴, but for most purposes, Eqs. 15.2 through 15.8 are more accurate than any other available information that goes into SEOR calculations and are more than adequate for most calculations. The more accurate equations are cumbersome and lend themselves to computer applications. However, in a computer application, a lookup table is easy to create and is much more accurate than even the advanced analytical equations.

15.2 Reservoir Heating

The basis for reservoir heat-transfer calculations is traced back to the published solution⁵ to a mechanical engineering problem. Marx and Langenheim⁶ were the first to publish an adaptation of this solution to an SEOR process. They assumed that the equations for temperature response

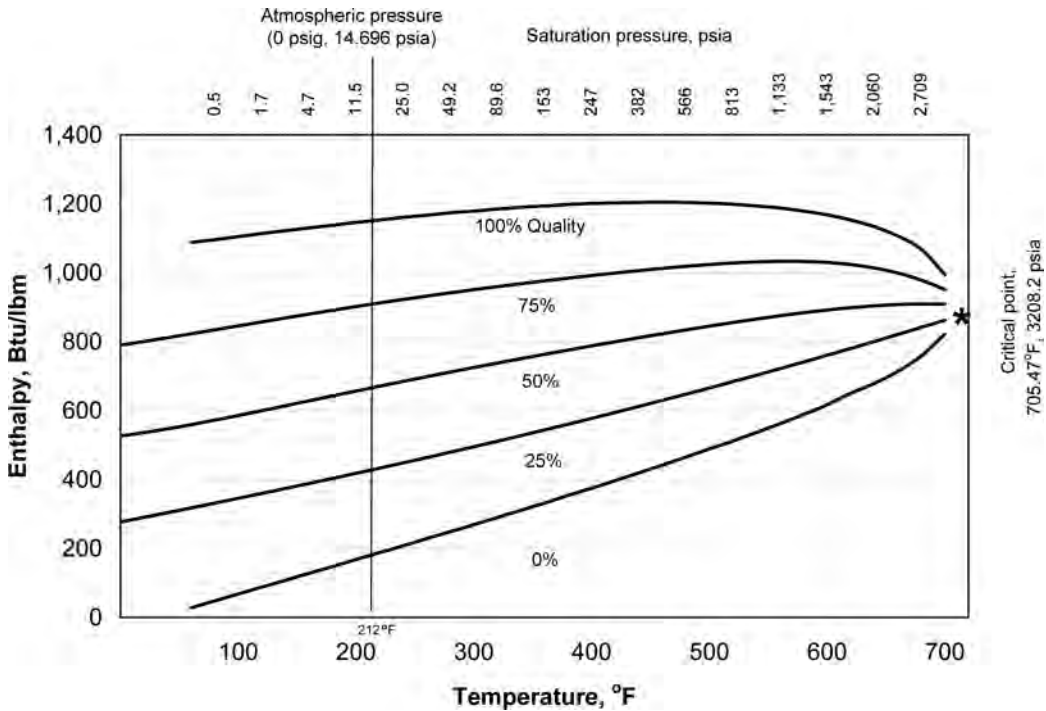


Fig. 15.3—Enthalpy of wet steam as a function of saturation pressure, temperature, and steam quality.

in a thin plate, backed in perfect contact to a semi-infinite solid after sudden exposure to constant-heat input, were analogous to steam injection into an oil-bearing reservoir.

Fig. 15.4 shows the temperature distribution anticipated in this model. The entire flood zone is at steam temperature upstream of the steam front, and the reservoir downstream of the steam front is at initial reservoir temperature. The true temperature profile is much less defined.

Their equation for the heated area, A_t , over time, t , is

$$A_t = \left[\frac{\dot{Q}_i M_R h_i \alpha}{4\lambda_S^2 \Delta T} \right] G(t_D), \text{ ft}^2 \dots\dots\dots (15.9)$$

$G(t_D)$ from the mechanical engineering problem is a function of dimensionless time, t_D .

$$G(t_D) = e^{-t_D} \operatorname{erfc} \sqrt{t_D} + 2\sqrt{\frac{t_D}{\pi}} - 1, \dots\dots\dots (15.10)$$

where t_D is time of injection, t , multiplied by a few reservoir properties.

$$t_D = 4 \left(\frac{M_S}{M_R} \right)^2 \frac{\alpha_S}{h^2} t, \dots\dots\dots (15.11)$$

and the complementary error function, $\operatorname{erfc}(x)$, is common in heat conduction calculations. Several publications have tables of values for $G(t_D)$ vs. time, but van Lookeren⁷ offers a simple equation with sufficient accuracy for most calculations, which is written as

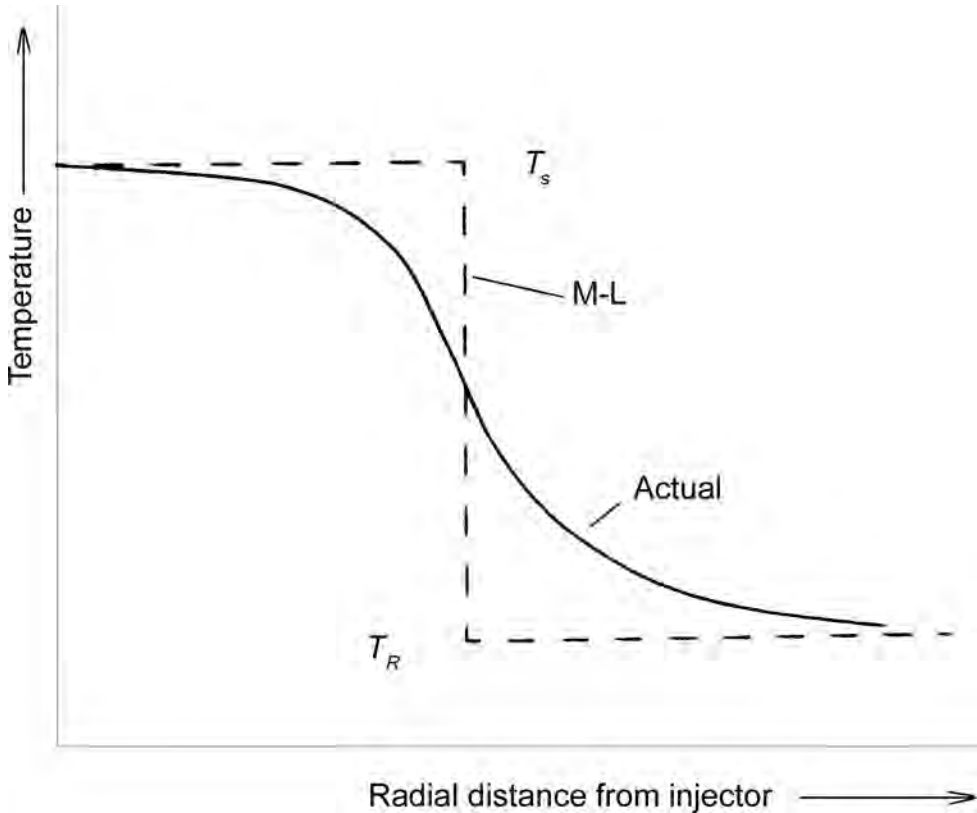


Fig. 15.4—Temperature profile resulting from convection and conduction caused by piston displacement of steam (after Marx and Langenheim⁶).

$$G(t_D) = \frac{1}{(1 + 0.85\sqrt{t_D})} \dots\dots\dots (15.12)$$

Other useful relationships derived from the Marx and Langenheim equations are heat loss to the adjacent formations,

$$\dot{Q}_l = \dot{Q}_i \left[2\sqrt{\frac{t_D}{\pi}} - G(t_D) \right]; \dots\dots\dots (15.13)$$

rate of heated zone growth,

$$\frac{dA}{dt} = \frac{\dot{Q}_i}{43,560\Delta T_i M_R h_t} \left[G(t_D) - 2\sqrt{\frac{t_D}{\pi}} + 1 \right]; \dots\dots\dots (15.14)$$

heat remaining in the reservoir,

$$Q = \frac{\dot{Q}_i M_R^2 h_t^2}{4\alpha_s M_S^2} G(t_D); \dots\dots\dots (15.15)$$

cumulative heat loss to the adjacent formations,

$$Q_l = \dot{Q}_i t - Q ; \dots\dots\dots (15.16)$$

and reservoir efficiency or fraction of injected heat remaining in the reservoir,

$$E_h = \frac{Q}{\dot{Q}_i t} = \frac{G(t_D)}{t_D} . \dots\dots\dots (15.17)$$

Two constants appear in the equations that need definitions. M_R is the volumetric heat capacity of the composite formation including rock and fluids.

$$M_R = (1 - \phi)M_\sigma + \phi S_o M_o + \phi S_w M_w + \phi S_g \left[f_s M_g + (1 + f_s) \left(\frac{\rho_s}{\Delta T} + \rho_s C_w \right) \right] . \dots\dots\dots (15.18)$$

Note that there are two gas components: inert gas represented by the volumetric heat capacity, M_g , and steam represented by two terms, one owing to the latent heat of vaporization and one to the sensible heat.

Thermal diffusivity, α , is the ratio of the thermal conductivity to the volumetric heat capacity,

$$\alpha = \frac{\lambda}{\rho C} . \dots\dots\dots (15.19)$$

Farouq Ali⁸ showed it is appropriate to use average values for M and α when the thermal properties of various layers of formation and over/underburden differ significantly.

Ramey⁹ and Prats¹⁰ showed that Eq. 15.17, reservoir heating efficiency, E_h , is independent of reservoir and steam zone geometry. Further the relationships apply to any form of heat transport (convection, conduction, or even radiation) in the plane of the reservoir and when the heat transport to adjacent formations is three-dimensional (3D). Assuming the reservoir properties are constant and vary little with changing temperature, E_h is solely a function of dimensionless time.

15.3 Steam Zone Growth

Reservoir heating by steam injection translates into the formation of a swept zone of some shape and an oil bank consisting of a migrating zone containing the displaced oil. Two general concepts have been proposed to describe this process.

15.3.1 Viscous Displacement. This is an extension of early water flooding concepts in which the displacement front is considered to be an advancing vertical front, the plane of which is normal to the bedding plane and extending vertically from the top to the bottom of a homogeneous flow section. Displacement of oil in this model is piston-like and is directly proportional to injection rate. The equations in the Reservoir Heating section, Sec. 15.2, have been used to calculate steamfloods as frontal advance floods.

Mandl and Volek,¹¹ followed by a slight modification by Myhill and Stegemeier,¹² contributed the concept of a critical time beyond which the vapor front stagnates and heat is carried only by hot water traveling through the condensation front. Dimensionless critical time, t_{cD} , is defined by

$$e^{t_{cD}} \operatorname{erfc} \sqrt{t_{cD}} \equiv 1 - f_{hv}, \dots\dots\dots (15.20)$$

where f_{hv} is the fraction of heat injected as latent heat.

$$f_{hv} = \left(\frac{1 + C_w \Delta T}{f_s h_{fv}} \right)^{-1}, \dots\dots\dots (15.21)$$

and f_s and h_{fv} are at reservoir conditions.

$$E_h = \frac{1}{t_D} \left\{ G(t_D) + (1 - f_{hv}) \frac{U(t_D - t_{cD})}{\sqrt{\pi}} \left[2\sqrt{t_D} - 2(1 - f_{hv})\sqrt{t_D - t_{cD}} - \int_0^{t_{cD}} \frac{e^x \operatorname{erfc} \sqrt{x} dx}{\sqrt{t_D - x}} - \sqrt{\pi} G(t_D) \right] \right\} \dots\dots\dots (15.22)$$

The Marx and Langenheim equation (Eq. 15.10) is an upper bound to Eq. 15.22, as shown in Fig. 15.5.

15.3.2 Bypass. These models address the severe buoyancy forces that pertain when steam vapor, a gas, is injected into a liquid filled reservoir. In bypass models, the fronts are not vertical; the steam migrates quickly to the top of the reservoir. Van Lookeren⁷ describes the severity of this override with a buoyancy factor.

$$A_{RD} = \left(\frac{\mu_s w_s}{\pi(\rho_o - \rho_s) g h_n^2 k k_s \rho_s} \right)^{0.5} \dots\dots\dots (15.23)$$

Average steam zone thickness is

$$h_s \cong 0.5 h_n A_{RD} \dots\dots\dots (15.24)$$

The shape of the steam zone is described by

$$h_s \cong h_n A_{RD} \left(\ln \frac{r_e}{r} - 0.5 + 0.5 \frac{r^2}{r_e^2} \right)^{0.5} \dots\dots\dots (15.25)$$

Note that steam zone thickness is not dependent on net zone thickness in Eqs. 15.24 and 15.25.

Fig. 15.6 shows the calculated injector liquid level as a function of time and five values of A_{RD} . A_{RD} is normally smaller than 0.6 in field projects; thus, the steam zone does not cover the vertical zone except for very thin reservoirs.

Neuman¹³ addresses the bypass or steam override concept by basically assuming that injected steam quickly rises to the top of the zone and spreads out evenly. Thickness of the steam zone, h_s , is related to

$$\Delta h_s = \frac{4(M\sqrt{\alpha})_s C_w \Delta T}{h_v M_s} \sqrt{\frac{\Delta t}{\pi}} \dots\dots\dots (15.26)$$

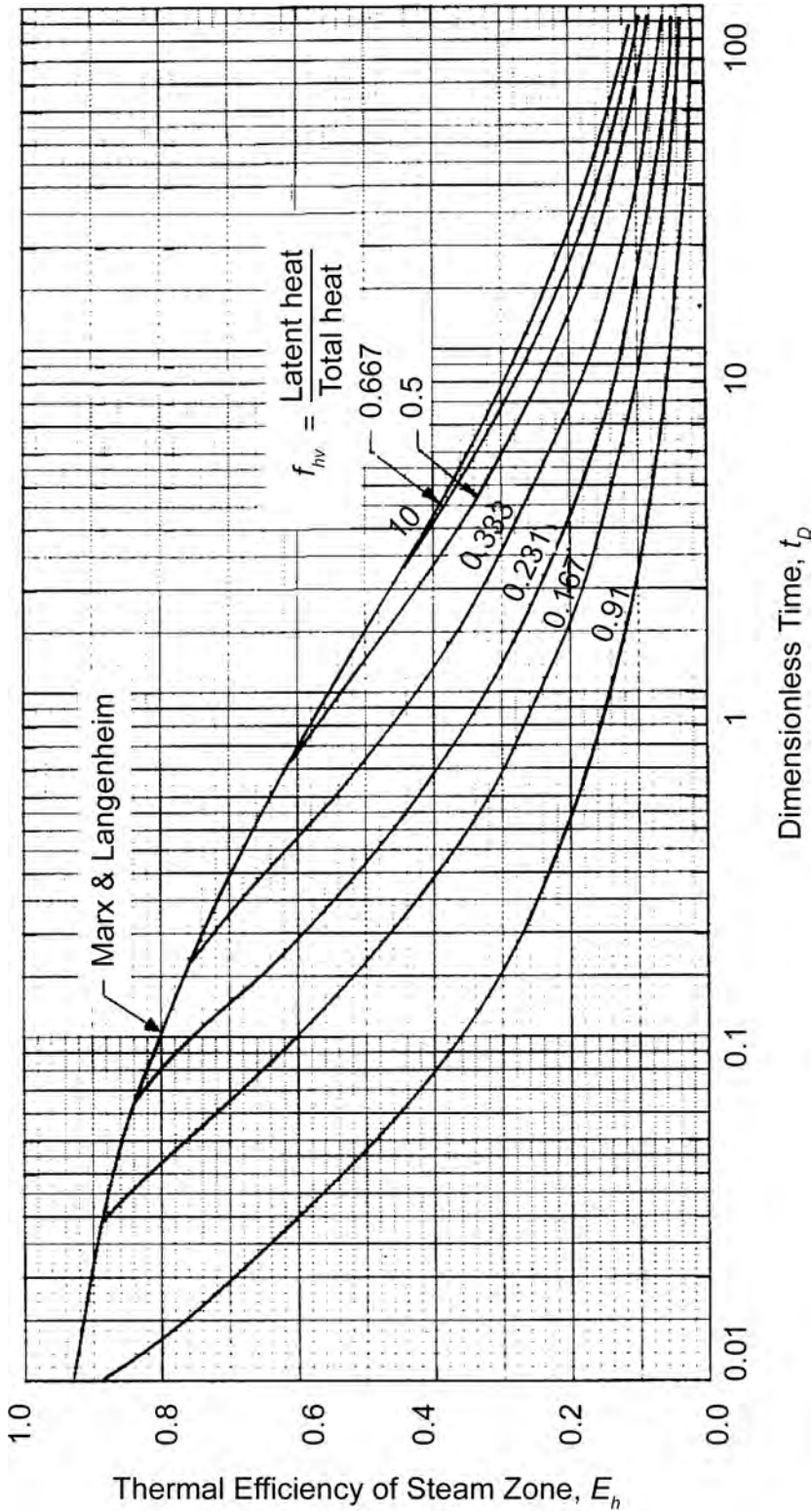


Fig. 15.5—Fraction of injected steam remaining in steam zone.¹¹

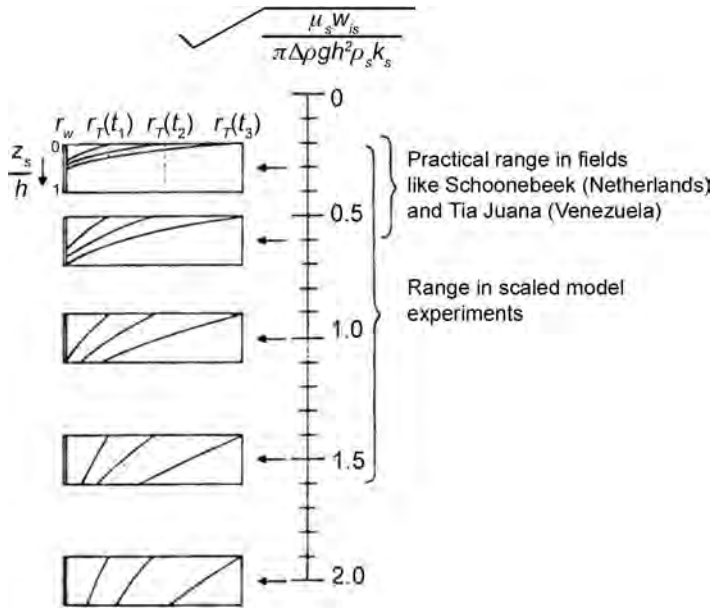


Fig. 15.6—Effect of the ratio of viscous to gravity forces on the location of steam displacement fronts.⁷

15.3.3 Combination. Field projects usually include features of both frontal advance and bypass processes. Owens and Ziegler¹⁴ propose an analytical model that calculates the contribution of each process. They calculate total oil rate, q_o , as the sum of gravity drainage oil rate, q_{og} , after Clossman,¹⁵ and viscous oil rate, q_{ov} , as

$$q_{ot} = q_{ov} + q_{og}, \dots\dots\dots (15.27)$$

$$q_{ov} = \frac{\frac{X}{Y} \left(\exp^{(-q_{ot} Y h_e)} - 1 \right) (p_e - p_w)}{q_{ot}}, \dots\dots\dots (15.28)$$

and

$$q_{og} = \frac{\frac{X}{Y} (h_e (0.433 \Delta \gamma)) \left\{ 1 + \left(\frac{1}{Y q_{ot} h_e} \right) \left(\exp^{(-Y q_{ot} h_e)} - 1 \right) \right\}}{q_{ot}}, \dots\dots\dots (15.29)$$

where

$$X = \frac{0.001127(2\pi)k\rho_s}{\mu_s \rho_o \left(\ln \frac{r_e}{r_w} - 0.5 \right)}, \dots\dots\dots (15.30)$$

$$Y = \frac{m^*}{\alpha A \phi (S_{oi} S_{or})}, \dots\dots\dots (15.31)$$

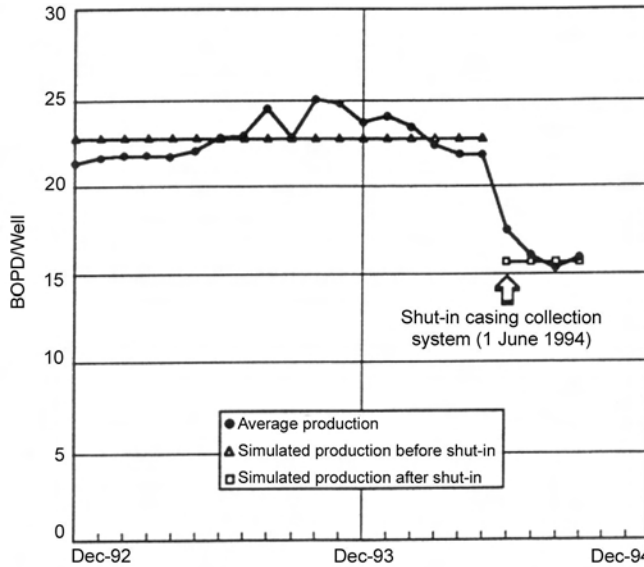


Fig. 15.7—Effect of shutting in casing vapor recovery system on a selected steamflood project.¹⁴

$$h_{e(n+1)} = h_{e(n)} \frac{q_o \Delta t}{7,758 m^* A \phi (S_{oi} - S_{or})}, \dots\dots\dots (15.32)$$

and

$$m^* = \frac{1}{2} \left\{ 1 + \left[1 - \frac{1}{2 \ln \left(\frac{r_e}{r_w} \right) - 1} \right]^{0.5} \right\} \dots\dots\dots (15.33)$$

This series of equations can be solved in a computer spreadsheet. The authors report that the viscous component of oil rate in the Kern River Ten-Pattern is significant and varied from 66% early in the project to 53% later. The method is also used to show the effect of operating with (supporting q_{ov}) and without (inhibiting q_{ov}) a casing vapor recovery system. Fig. 15.7 shows the impact of shutting in the casing vapor recovery on a selected project. This is not to say that shutting in casing vapor recovery will have this profound negative impact on every steamflood. Notice that this method does not account for steam injection rate. A project that is significantly over-injected (high-pressure drawdown) would be expected to respond as in Fig. 15.7, while a project with more controlled steam rate (modest-pressure drawdown) may show little, if any, reduction in production rate.

Kimber *et al.*¹⁶ found with a physical model that there is a viscous component of steam-flooding that has potential to add significant oil recovery. Fig. 15.8 shows that there is an optimal steam quality for a steamflood and that some amount of overinjection may be beneficial also. Ward and Sharpe¹⁷ studied the subject at the Kern River field using a numerical simulator and found that shutting in the casing vents resulted in a permanent 18% loss in oil production rate as shown in Fig. 15.9. Oil production could be restored if either the vents were reopened or a depleted zone in the wellbore were perforated, allowing the excess steam to vent by crossflow.

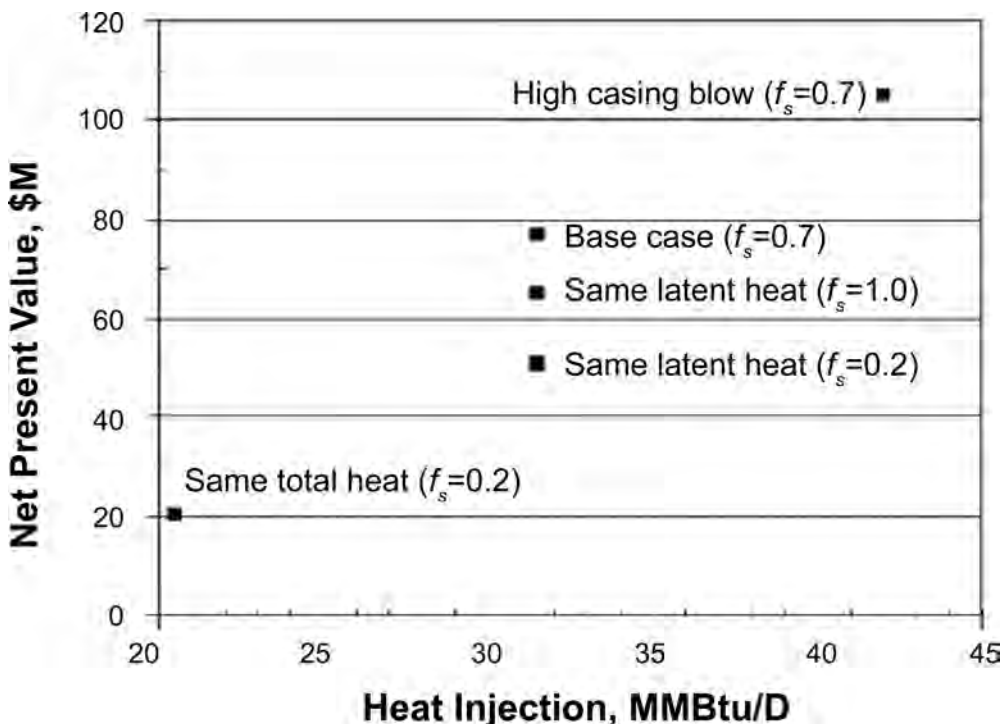


Fig. 15.8—The effect of latent heat injection rate on strategy economics.¹⁶

15.4 Steamflood Design

15.4.1 Candidate Selection. Screening criteria for identification of steamflood candidates have been published for many years. Table 15.1 shows the screening guides from five different sources.¹⁸⁻²²

It is obvious from Table 15.1 that there is a finite envelope of properties that define successful candidates. However, within that envelope there is a relatively wide spread of values for the indicators. The reason for this is that each reservoir is unique and success is a function of a combination of all of the screening criteria plus a myriad of other considerations. The authors of the papers (Refs. 18 through 22) typically offer linear regression equations to generate an indicator for a specific reservoir. The most recent version is by Donaldson,²³ which is written as

$$F_{os} = 0.0384 + 0.643\phi S_o + 6.48 \times 10^{-6} \left(\frac{kh_n}{\mu_{oi}} \right) D / (q_i A^{0.5}) \dots\dots\dots (15.34)$$

Doscher and Ghassemi²⁴ showed that there is an upper oil viscosity barrier that makes economic recovery of very viscous oils very difficult by conventional SEOR methods. Using scaled physical models, they found that for oils with a viscosity much greater than that in the Kern River or Midway Sunset fields in California, the steam/oil ratio for conventional steamflood or cyclic steam stimulation was uneconomic. The 14 and 12° API lines on Fig. 15.10 show the general upper bound range for oil viscosity in a successful conventional steamflood. They proposed a correlation equation to estimate the limiting viscosity. The correlation is a function of steam and oil viscosities.

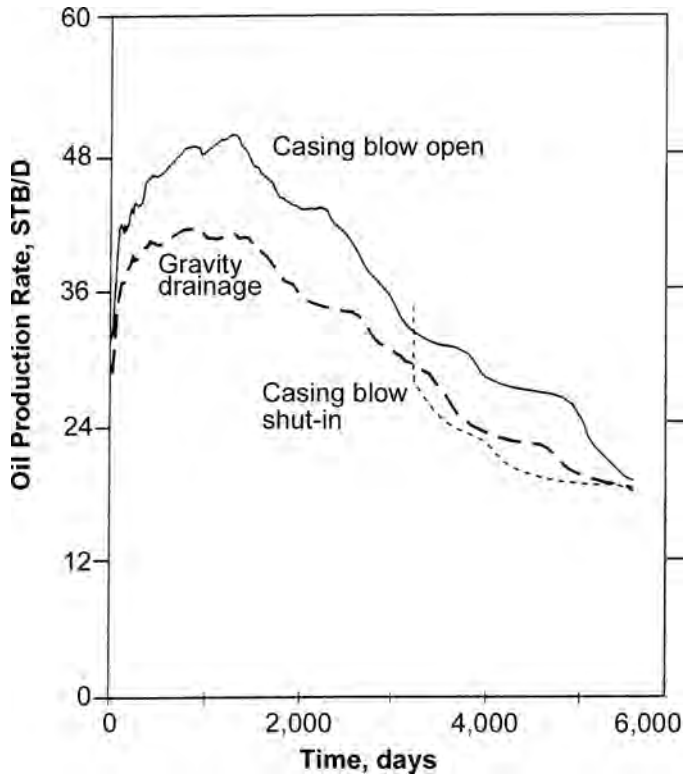


Fig. 15.9—Results of a numerical simulation showing 18% loss in production resulting from shutting in casing vapor recovery.¹⁷

TABLE 15.1—SEOR PROJECT SCREENING CRITERIA ²³					
Reference	Ref. 18	Ref. 19	Ref. 20	Ref. 21	Ref. 22
Depth, ft	<3,000	<2,500	<3,000	>20	>400
Net thickness, <i>h</i> , ft	>20	>30	>30	>20	>10
Porosity, ϕ	>0.2	>0.3	>0.3		>0.2
Oil saturation, S_o		>0.5			>0.4
$\phi \times S_o$	>0.1		0.15–0.22	>0.0	>0.8
Oil gravity, API	10–34	8–40	12–15	<25	<36
Permeability, <i>k</i> , md	>250	>1,000	>1,000		
Oil viscosity, μ , cp	<15,000	200–1000	<1,000	>20	
Transmissibility, <i>hk</i> / μ , md-ft/cp	>5	>50			
Initial pressure, psia	<1,500				
Pattern size, acre		<10			

$$F_{os} = 5.12 \left[f_s \left(\frac{\mu_s}{\mu_{oi}} \right) \right]^{0.57} \dots \dots \dots (15.35)$$

Other critical requirements exist such as reservoir continuity between injector and producer and barriers to contain steam from uncontrolled migration to nonsteam-bearing intervals. Qualitatively, one looks for relatively shallow, low pressure, low temperature, thick, high porosity, highly permeable reservoirs with medium to high saturation of high viscosity liquid oil.

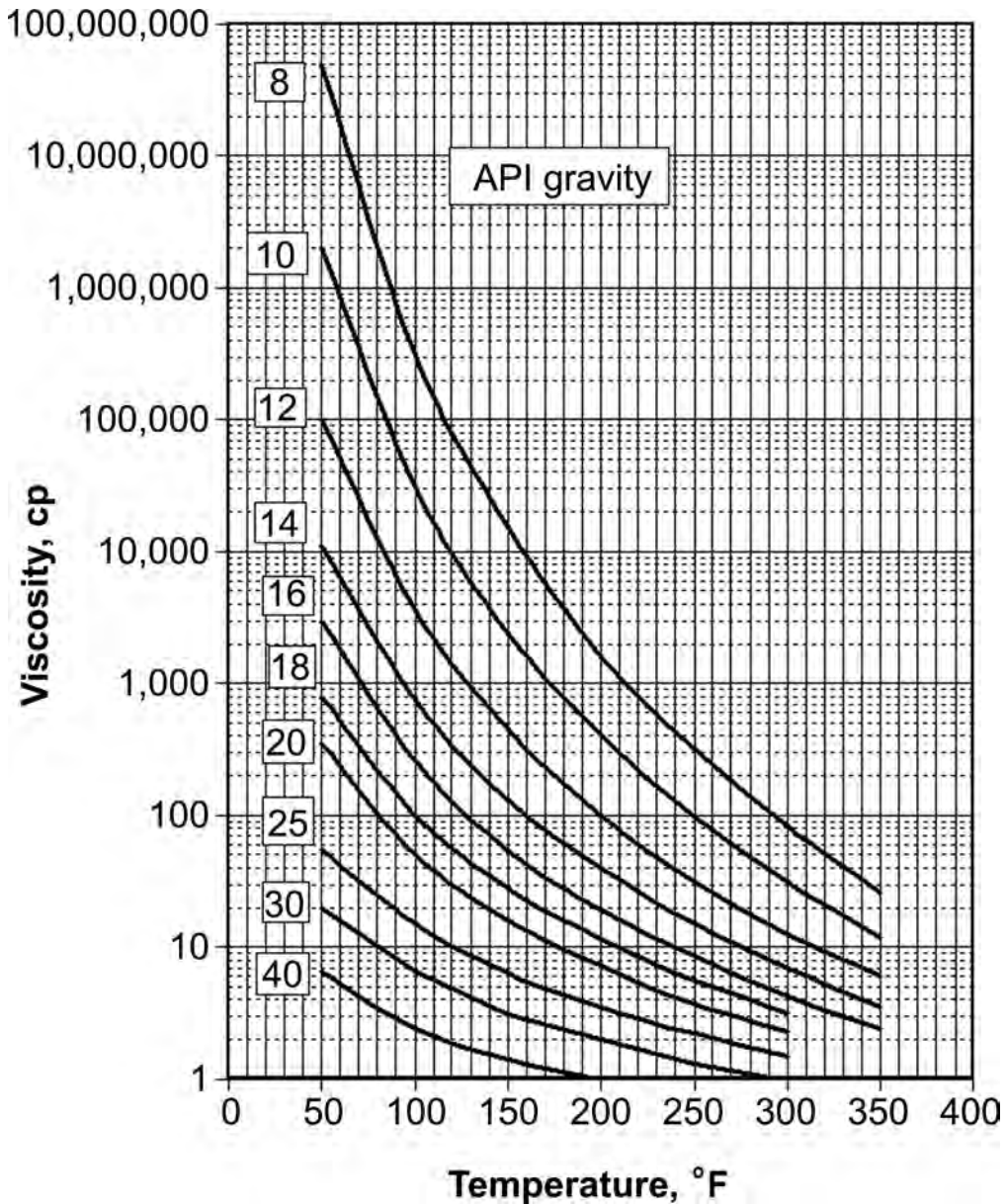


Fig. 15.10—Temperature dependence of viscosity for crude oils.

All of the following applies to oil sands with mobile oil. The SEOR process in reservoirs that are fractured during the steam injection process are too complicated to be calculated with analytical models.

15.4.2 Analogy. The simplest way to design an SEOR project is by analogy. If there is an analogous project in the same field or in a field with enough similarities to the one in question, simply using the design and results from the former may be adequate. Fig. 15.11 from a paper by Greaser *et al.*²⁵ in the Kern River field, California is an example of the use of analogy. In that project there are thousands of steamflood injection zones. Texaco made good use of the

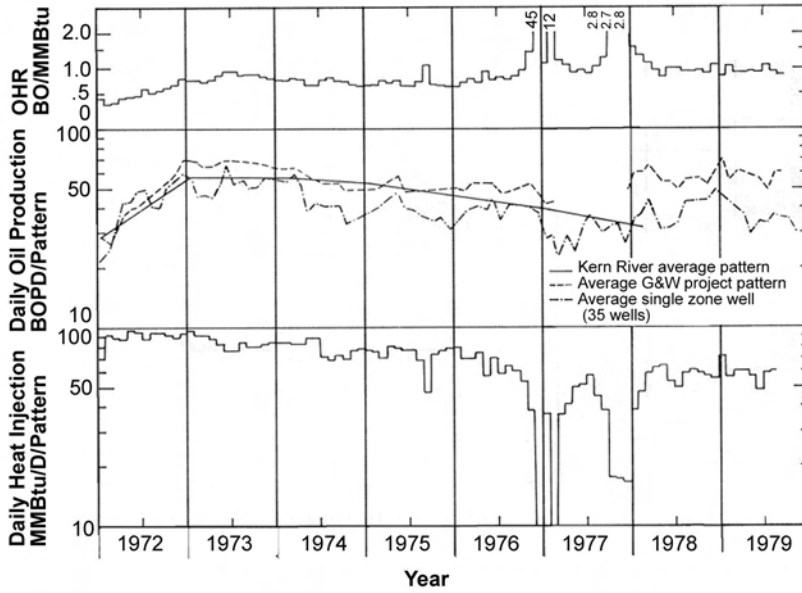


Fig. 15.11—Kern River “average pattern” used as an analogy to evaluate field performance.²⁵

huge amount of steamflood performance data by calculating an “average pattern response” and using that as the standard to design and monitor future flood patterns.

15.4.3 Recovery Mechanisms. Waterflooding, successful in reservoirs with low viscosity/high mobility crude oil, is extremely inefficient in reservoirs with low mobility/high viscosity crude oil. Three dimensionless flow parameters help us understand the problem.

$$\frac{Lg\Delta\rho \cos \theta}{\Delta p}, \frac{\sigma \cos \theta_c}{\sqrt{k\Delta p}}, \text{ and } \frac{k\Delta p}{\mu Lu} \dots\dots\dots (15.36)$$

These are, respectively, the ratio of gravity forces to applied pressure; the ratio of capillary forces to applied pressure; and the ratio of applied pressure to viscous forces. The ability to modify the variables in the above relationships is indicative of the potential success of extracting oil from the reservoir.

In the gravity ratio, the main controllable parameter is the distance between the injector and producer. The only other potential variable is density difference between injectant and the crude oil, which is large but does not change appreciably.

$\sigma \cos\theta_c$ in the capillary pressure-applied pressure ratio represents the interfacial tension of the crude oil in the rock pore and can be varied. The obvious goal is to reduce it to zero. Several approaches have been tried, including adding emulsified chemicals in the steam to form a single-phase water/oil emulsion, which has lower viscosity and lower interfacial tension than the crude alone. Many field trials have been tried over the years but have yet to prove economical.

The viscosity parameter in the third ratio has been the most important in designing a successful SEOR project. Other methods of reducing oil viscosity, such as miscible solvent injection, have been tried but have proven to be far inferior to heat injection. Fig. 15.10 shows the viscosity vs. temperature relationship for a few representative crude oils. Raising the temperature of the oil from the typical reservoir temperature of less than 100°F to approximately

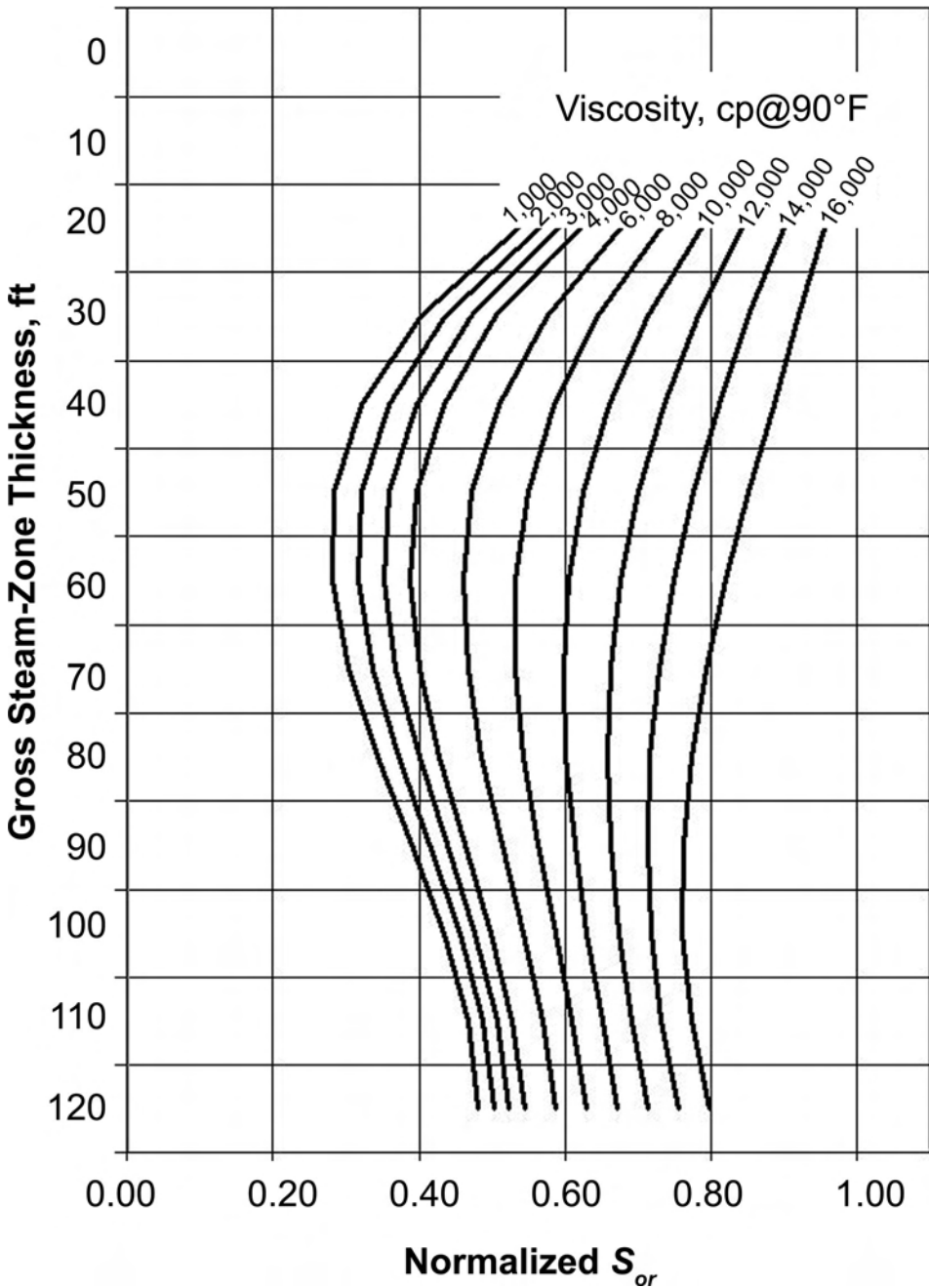


Fig. 15.12—Graph of a dimensionless function F_{Sor} , which relates residual oil saturation to gross section thickness and presteam oil viscosity.

300°F gives a viscosity reduction of orders of magnitude. Of all of the potential heat-carrying media, water-based steam is inexpensive and universally available and has the highest heat-carrying capacity of any compound; it exists at the ideal 300 to 500°F temperature range to achieve optimal oil viscosity reduction.

Texaco²⁶ published a correlation that estimates the residual oil saturation to steam based on the huge database generated over the decades of steamflood in the Kern River field. They found the residual saturation is a function of gross zone thickness and presteam oil viscosity. There appears to be an optimal zone thickness, above and below, where residual oil is less attractive. Residual oil saturation continuously increases for increasing viscosity, reaching a point of immobile oil at some high value. Their data was based on an average initial oil saturation of 55%. Fig. 15.12 shows their correlation, normalized for any initial oil saturation. Short of actual core or laboratory data, that figure can be used to estimate residual oil saturation by finding the value of the factor for the desired initial oil saturation and zone thickness and then multiplying that factor by initial oil saturation. The equations presented next provide an alternative method for obtaining the same information.

$$S_{or} = F_{s_{or}} S_{oi}, \dots\dots\dots (15.37)$$

where

$$S_{or_b} = \frac{(49.9876 - 1.626h_t + 0.02155h_g^2 - 0.0000823h_t^3)}{50}, \dots\dots\dots (15.38)$$

$$S_{or_a} = \frac{(50.5357 - 0.20877h_t - 0.000260989h_t^2 + 0.00000991h_t^3)}{50}, \dots\dots\dots (15.39)$$

and

$$F_{s_{or}} = S_{or_a} + S_{oi} \left(S_{or_b} - S_{or_a} \right) \left(\frac{\mu_{oi}}{15,000} \right), \dots\dots\dots (15.40)$$

This is instructive as to the qualitative relationships between the parameters, but caution should be used when applying it quantitatively outside of the Kern River field. Also, the authors explain that they had no information for zones thicker than 120 ft or oil viscosity greater than 16,000 cp.

Other mechanisms include formation compaction, in-situ steam distillation generated solvent banks, and formation and fluid heat-induced swelling, but they are rarely necessary to supplement the previous ones in adequately describing the SEOR process. Of these secondary mechanisms, compaction has had the most significant impact on SEOR. The most notable regions to benefit are the Bolivar Coast, western Venezuela, and the Long Beach area near Los Angeles, California. The Bolivar Coast has been using cyclic steam stimulation (CSS) since the early 1960s. Rattia and Farouq Ali²⁷ published a study that concluded that formation compaction enhanced process efficiency in CSS but harmed process efficiency in steamflood.

15.5 Design Calculations: Viscous Displacement Models

15.5.1 The Marx-Langenheim⁶ and Mandl-Volek¹¹ (M-V) Models. These steam zone growth models have often been used to calculate cumulative oil recovery and steam zone size over time. They are a simple way to get a quick estimate of project viability. Volume of steam zone is proportional to the fraction of heat remaining in the steam zone, E_h .

$$V_s = \frac{Q_i E_h}{43,560 M_R \Delta T} \dots\dots\dots (15.41)$$

It follows that oil displaced from the steam zone is

$$N_d = 7,758 \phi \frac{h_n}{h_t} (S_{oi} - S_{or}) E_c V_s \dots\dots\dots (15.42)$$

E_c is an arbitrary “capture” factor that is inserted to “scale” invariably optimistic oil volume to realistic values. This factor is best determined by history matching the equation to field project and normally has a value from 0.7 to 1.0. This represents a serious limitation in calculating oil recovery because the calculation predicts the highest oil production rate at the beginning of the project.

This method is most useful in calculating steam zone size and extent. It is less useful for calculating oil rates and recovery because it does not account for the terms in the ratios in Eq. 15.36.

The calculation allows any value for steam injection rate and calculates oil rate. Information on practical steam rates must be found before practical results can be derived. Either method can be done by hand or in a computer spreadsheet.

15.5.2 The Jones²⁸ Model. The Jones model extended the M-V model by accounting for the third dimensionless factor in Eq. 15.2 and by honoring the oil in place. The model modifies the former model by calculating the delayed oil response to a growing steam chest using the third term in Eq. 15.36, which shows that well spacing and oil viscosity are important parameters. Also addressed is the often-present depletion in the form of in-situ gas and depletion gas cap, both of which must be filled with steam before oil can be displaced. M-V steam zone growth rate is converted to an oil production rate by multiplying by three dimensionless factors.

$$q_{o_h} = q_{oD} A_{cD} V_{oD} V_{pD} \dots\dots\dots (15.43)$$

where

$$q_{oD} = \frac{N_{d(n)} - N_{d(n-1)}}{\Delta t} \dots\dots\dots (15.44)$$

$$A_{cD} = \left\{ \frac{A_t}{A \left[0.11 \ln \left(\frac{\mu_{oi}}{100} \right) \right]^{0.5}} \right\}^2 \dots\dots\dots (15.45)$$

$$V_{oD} = \left(1 - \frac{N_p S_{oi}}{N(S_{oi} - S_{ors})} \right)^{0.5} \dots\dots\dots (15.46)$$

$$V_{pD} = \left(\frac{5.62 V_s}{43,560 h_s \phi S_g} \right)^2 \dots\dots\dots (15.47)$$

$$N = \frac{43,560 Ah_n \phi S_{oi}}{5.62}, \dots\dots\dots (15.48)$$

and

$$N_p = \sum_{t=0}^{t=n} q_{oh} \dots\dots\dots (15.49)$$

The method can be calculated in a spreadsheet by first calculating a displaced oil rate from Eq. 15.44 for a time period, Δt ; 1/12 year is convenient. That volume is then multiplied by the dimensionless modifiers in Eqs. 15.45 through 15.47.

A_{cD} accounts for the viscosity of the oil and the size of the well spacing and has these restrictions: $0 \leq A_{cD} \leq 1.0$, and $A_{cD} = 1.0$ at $\mu_{oi} \leq 100$ cp.

V_{pD} accounts for reservoir fill-up that must occur because of in-situ gas saturation or depleted gas zones before steam zone growth can begin to displace oil. Restrictions are $0 \leq V_{pD} \leq 1.0$, and $V_{pD} = 1.0$ at $S_g = 0$.

The M-V method allows the steam zone to grow to an indefinite size for an indefinite time. Oil recovery can amount to more than original oil in place. V_{oD} is used to limit predicted oil recovery to some fraction of the original oil in place with this limit; $0 \leq V_{oD} \leq 1.0$.

Fig. 15.13 shows the results of the M-S viscous displacement model with and without the Jones corrections for a hypothetical steamflood. In this example Kern River California reservoir properties were used. A small pattern size was chosen to illustrate that the M-V displacement rate is independent of oil in place and pattern size. At 75 months, the M-V displacement was 132% of original oil in place, while the Jones model corrected it to 91%. This calculation was done to an unrealistic terminal point, but if the flood were terminated at 48 months when instantaneous oil/steam ratio had fallen to below 0.2 then recovery calculated by Jones would be 77%.

This method is very good for estimating oil rates, especially early in a steamflood and for incremental recovery. It has been used in many projects worldwide with success. As with the M-V method, this calculation allows any value for steam injection rate and calculates oil rate. Information on practical steam rates must be found before practical results can be derived. Because this method produces best results if calculated in small time steps (i.e., 10 days), it is best programmed on a computer.

15.6 Design Calculations: Gravity Drainage Models

15.6.1 The Neuman¹³ Model. The Neuman method is very useful for calculating post-steam breakthrough performance and for heat management in calculating required steam injection rates. It does not address the presteam breakthrough period. Van der Knaap²⁹ shows that the Neuman method can be derived from the Mandl-Volek method, and they are completely compatible. Note that Neuman’s paper¹³ contains typographical errors in Eqs. D-2 and D-3. They are corrected next.

Steam-zone thickness is calculated as a function of the time lapse between the time of prediction, t , and the time when the location reached steam temperature, τ .

$$h_s = \left(\frac{4k C_w \Delta T}{M_s h_{fv}} \right) \sqrt{\frac{t - \tau}{\pi \alpha_s}} \dots\dots\dots (15.50)$$

An estimation of the steam-injection rate and the time required to achieve the required complete coverage of the project area with a steam zone is given by

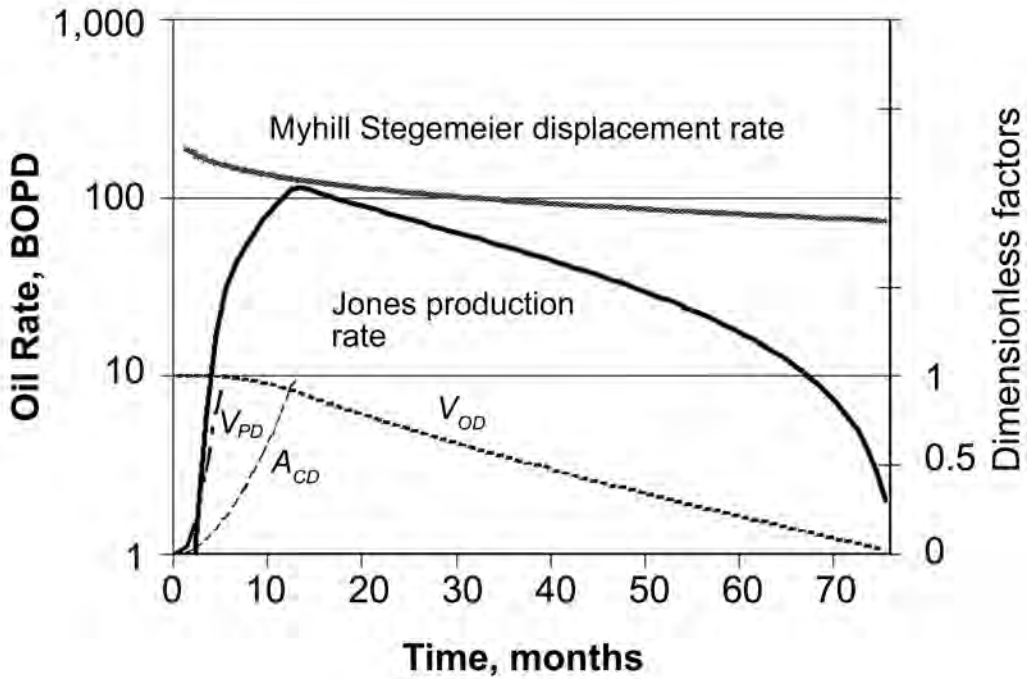


Fig. 15.13—Graphical presentation of Eq. 15.39.²⁸

$$q_{i_s} = \frac{Ak\Delta T}{5.615\rho_w h_{fv} f_s (1 - f_p) \sqrt{\frac{\alpha_s t}{\pi}}} \dots\dots\dots (15.51)$$

Because everything in Eq. 15.51 is a constant except time (*t*), an estimate of required rate is easy to derive by simply changing the time. Caution should be used because this time/rate is divorced from reservoir reaction, primarily to viscous forces during these early stages of a flood; therefore, impractical results are easily obtained.

The steam-zone volume is

$$V_{sz} = f_s (1 - f_p) q_{i_s} \frac{\rho_w C_w}{M_s} t \dots\dots\dots (15.52)$$

Oil displaced from both the steam zone and the adjacent hot-water zone, heated by condensate convection and by conductive heat lost from the steam zone, is

$$V_o = (1 - f_b) \phi (S_o - S_{ors}) f_s (1 - f_p) q_{i_s} \frac{\rho_w C_w}{M_s} t \dots\dots\dots (15.53)$$

where oil rate from the hot-water zone is expressed as a fraction (*f_b*) of the oil from the steam zone.

$$f_b = \frac{f(T)\sqrt{\pi(S_o - S_{orw})M_s h_{fv}}}{2(S_o - S_{ors})M_w C_w \Delta T}, \dots\dots\dots (15.54)$$

and

$$f(T) = 0.8864 - 0.9288 \left(\frac{T^* - T_R}{\Delta T} \right) + \frac{0.333}{\left(\frac{T^* - T_R}{\Delta T} \right)}. \dots\dots\dots (15.55)$$

Once steam covers the entire area, steam injection can be reduced by

$$\dot{Q}_i(n = t^*) = \dot{Q}_i(n = 0) \frac{2}{\pi} \sin^{-1} \left(\frac{t^*}{t} \right)^{0.5}, \dots\dots\dots (15.56)$$

where

$$\dot{Q}_i(n) = 350q_{i_s}(n)f_s(1 - f_p). \dots\dots\dots (15.57)$$

This method can be done by hand but is easier to use if programmed on a computer spreadsheet.

15.6.2 The Vogel³⁰ Model. Similar to the Neuman method, the Vogel method is very useful for post-steam breakthrough heat-management calculations. It does not address early steam-flood performance. Vogel first postulates that a producing well in a California-type reservoir with thick, dipping zones and gas caps that are incapable of maintaining pressure will produce at a maximum rate regardless of excess steam injection over some optimal rate. Thus, the steam rate can be calculated to maintain a steam chest by replacing lost heat and the voidage left by produced fluids. To use this method, a good estimate of a hot well producing rate is necessary, but it is very useful for optimizing existing projects with established producing rates.

A modified interpretation of the M-V method is used to calculate heat necessary to overcome reservoir heat loss. Vogel uses the following equations to calculate the steam injection rate in barrels per day.

$$q_{i_s} = (q_{l_s} + q_{p_s})h_{f_s} + q_{\text{excess}_s}, \dots\dots\dots (15.58)$$

where

$$q_{l_s} = \frac{2A\lambda_s\Delta T}{0.319 \times 10^6 \sqrt{\pi\alpha_s t}}, \dots\dots\dots (15.59)$$

and

$$q_{p_s} = \frac{(5.615)M_s\Delta T(q_{oh} + q_{oc})}{0.319 \times 10^6 \phi(S_{oi} - S_{or})}. \dots\dots\dots (15.60)$$

q_{excess_s} is a value added that accounts for surface and wellbore and miscellaneous heat losses.

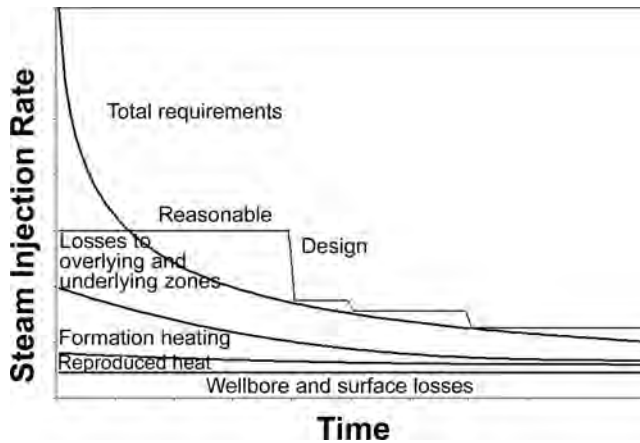


Fig. 15.14—Typical steam-injection rate schedule for gravity-dominated steam displacement.³⁰

Fig. 15.14 shows the main benefit provided by the Neuman and Vogel methods. They are very useful in managing steam-injection requirements that continuously reduce as the project matures.

These equations apply only after steam has overlaid the reservoir and oil production has peaked because oil rate is known and steam rate is unknown in the equations. This method is easily done by hand but can also be programmed on a computer spreadsheet.

15.6.3 Discussion of Steam Rate Reduction. Kumar and Ziegler³¹ investigated the issue of steam rate reduction schedule using a numerical reservoir simulator. The Neuman and Vogel methods previously described are based on analytical heat balances and do not directly predict oil production rates. Fig. 15.15 shows the effect on oil production rate determined using the simulator as a result of three steam-injection schedules: constant rate, linear constant reduction, and Neuman reduction schedule. Fig. 15.16 shows the steam injection for each of these schedules. The constant rate schedule results in the highest oil-production rate but at the cost of high late-steam rates. The linear reduction schedule yields nearly the same oil for a lot less steam. Neuman results in arrested steam-zone growth, but the severe early reduction in steam results in an equally severe loss in oil rate.

Table 15.2 shows that the linear rate-reduction compromise is economically superior to either of the other two schedules. Because the injection rate reduction changes net salable oil at various times in the project life, the authors used discount factors to properly value the oil production stream for each case. They termed this time-weighted oil volume “discounted net present barrels of oil.”

15.7 Design Calculations: Other Models

15.7.1 The Gomaa³² Model. Gomaa approached the problem by first doing a history match on a Kern River field steamflood using a numerical simulator then extracting an analytical solution from the simulator results.

Because the method is totally a function of a history match to the Kern River field, caution must be used in applying it to other projects. However, because it is a graphical method with few calculations, it offers ease in estimating project performance. After achieving a history match, Gomaa did several parametric simulations that allowed generation of several graphs that are, in turn, used to estimate project performance. Important parameters for the method are initial reservoir pressure (< 100 psia); steam injection pressure (< 200 psia); reservoir thickness

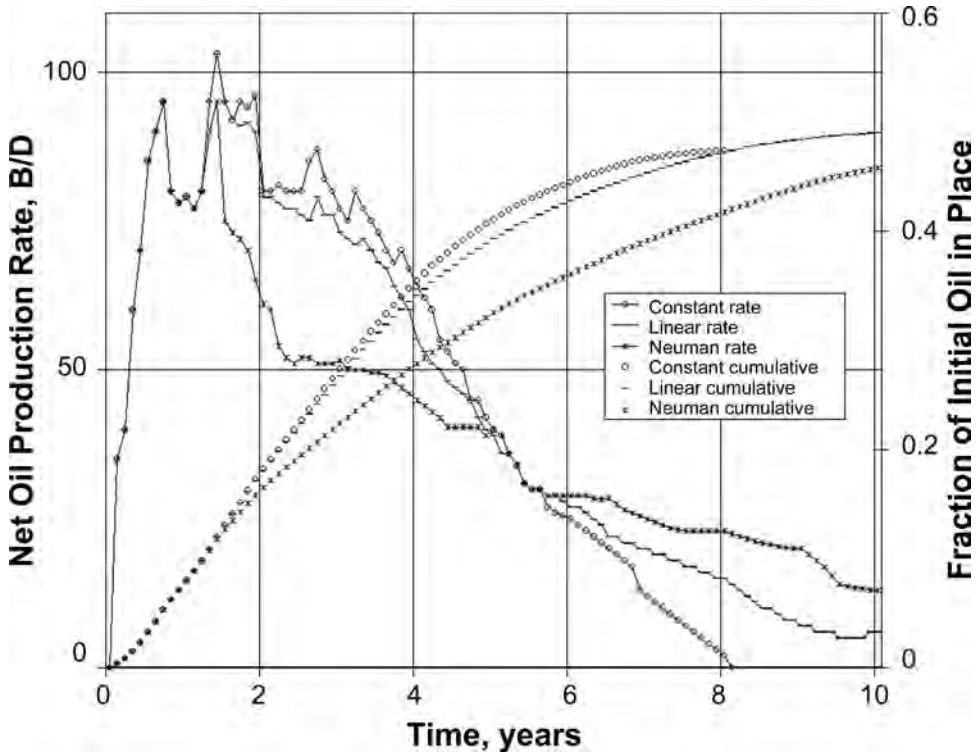


Fig. 15.15—Effect of steam injection schedule on oil production.³¹

(10 to 300 ft); mobile oil saturation (0.05 to 0.60); porosity (0.21 to 0.35); and heat injection rate (0.05 to 0.6 MM Btu/D/acre-ft). The steps for the procedure are outlined next.

- Provide downhole steam quality, pressure, and injection rate and determine enthalpy, h_s .
- Calculate the heat injection rate,

$$\dot{Q}_{s_v} = 350 \times 10^{-6} \frac{q_i h_s f_s}{A h_t} \dots\dots\dots (15.61)$$

- Determine vertical heat loss, Q_b , from Fig. 15.17.
- Determine the heat utilization factor from

$$f_h = 0.793 + 1.074 f_s - 1.737 f_s^2 + 0.628 f_s^3 \dots\dots\dots (15.62)$$

For a series of time steps (t , days), calculate the effective heat injection rate and the cumulative heat injected with

$$Q = \Delta t \dot{Q}_{s_v} f_h (1 - \dot{Q}_l) \dots\dots\dots (15.63)$$

and

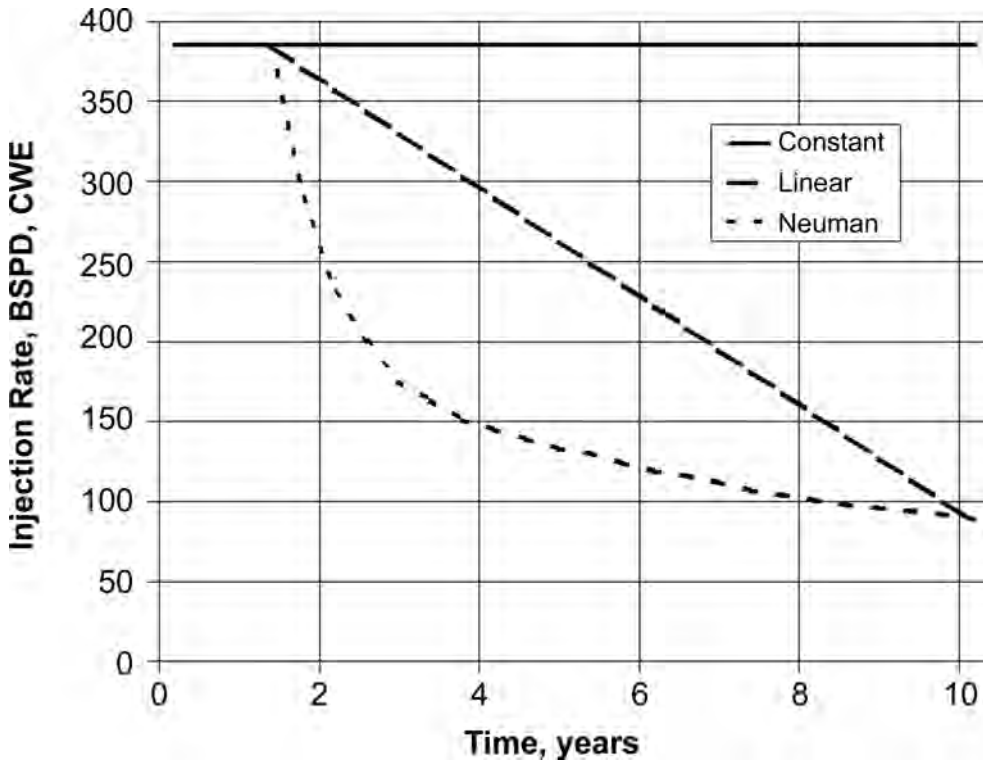


Fig. 15.16—Steam injection schedule.³¹

Injection Schedule	Discount Rate		
	0%	5%	10%
Constant rate	19,290	16,780	14,690
Linear reduction	19,770	16,960	14,690
Neuman reduction	18,360	15,410	13,120

$$\sum Q = \sum_n \dot{Q}_{s_{vn}} f_{hn} (1 - \dot{Q}_{ln}) \Delta t_n \dots (15.64)$$

- Estimate the mobile oil saturation,

$$S_{om} = S_{oi} - S_{ors} \dots (15.65)$$

- Use Fig. 15.18 to determine the oil recovery factor, f_R .
- Calculate the initial mobile oil in place with

$$N_m = \frac{7,758 \phi S_{om} h_n A}{B_o} \dots (15.66)$$

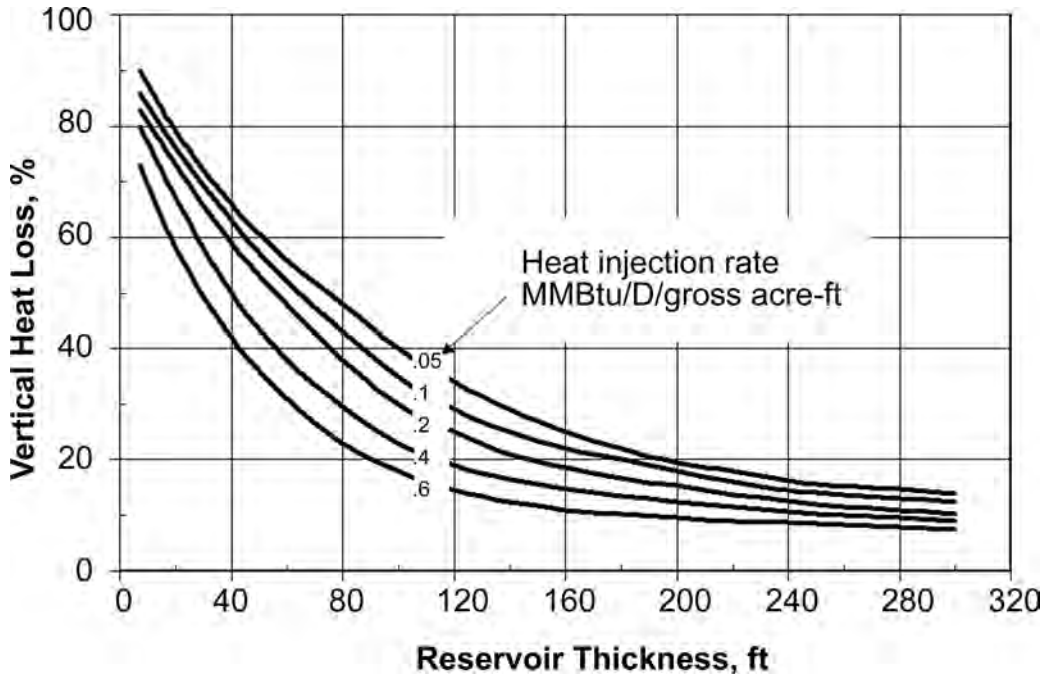


Fig. 15.17—Heat loss to overlying and underlying strata.³²

- Calculate the oil recovery at time (*t*),

$$N_p = N_m f_R \dots\dots\dots (15.67)$$

- Calculate the cumulative oil/steam ratio,

$$F_{os} = \frac{N_p}{\Delta t q_i} \dots\dots\dots (15.68)$$

Repeat these steps for a period equal to the expected life of a steamflood in convenient time steps (i.e., 365 days) to estimate steamflood performance. This calculation method is easily done by hand but can be programmed in a computer spreadsheet.

15.8 Cyclic Steam Stimulation Design

Prats¹ defines stimulation as “any operation (not involving perforating or recompleting) carried out with the intent of increasing the post-treatment production rate without changing the driving forces in the reservoir.” Periodic injection of steam into a producing well, alternating with a production cycle, has many features of this definition but also has many features that distinguish it as a true enhanced recovery mechanism. The primary benefit of the process is true stimulation—near wellbore reduction of flow resistance, viscosity reduction. However, there are EOR benefits of high-temperature gas dissolution, wettability changes, and relative permeability hysteresis (water flows into the reservoir easier than it flows out). Fortunately, calculating the temperature history of the wellbore, tracking the water/oil saturation history and the oil viscosity reduction is adequate to estimate the oil production response to the process.

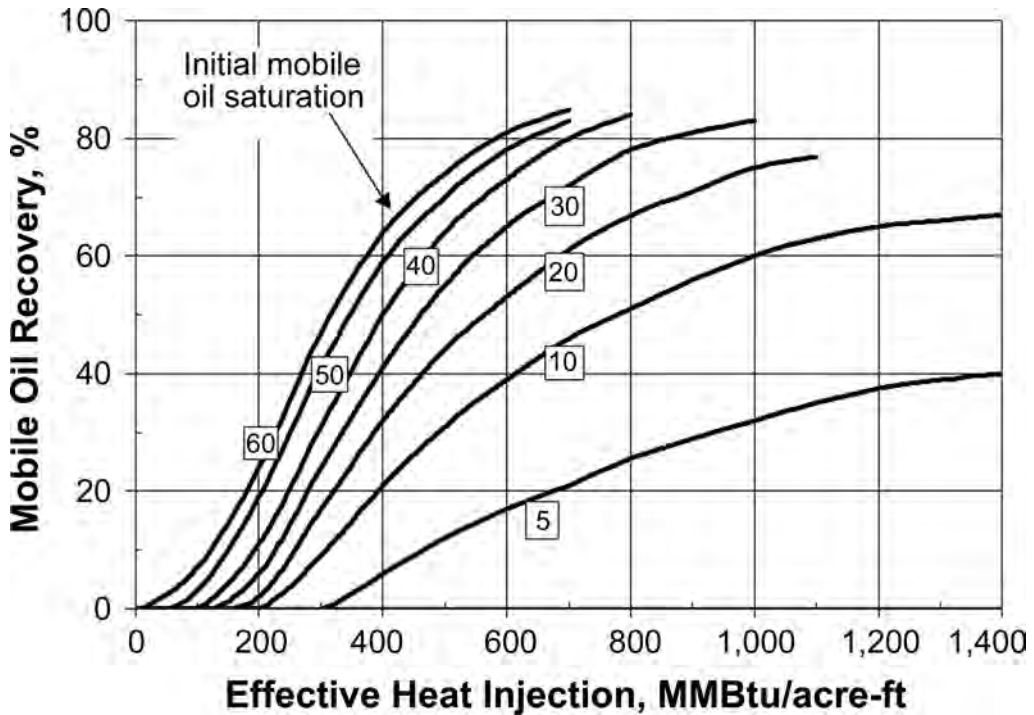


Fig. 15.18—Steamflood oil recovery as a function of effective heat injected and mobile oil saturation.³²

15.9 Design Calculations

Steamflood design is simple compared to cyclic steam stimulation (CSS) design. Whereas steamflood reaches equilibrium and can be represented by a set of steady-state equations for much of its life, the CSS process is one of constantly changing conditions. First there is the injection phase, which is relatively so short that it is a total transition period. Then during the soaking period, steam vapor condenses and temperature begins to fall. The producing period is in a constant state of flux as testified by the constantly changing producing rates. Relative permeability curves, which can typically be ignored in steamflood calculations, become very important to CSS.

In spite of these problems, there are several desktop calculations that give a good representation of what can be expected from CSS. Probably the simplest representation of the process is by Owens and Suter,³³

$$\frac{q_{oh}}{q_{oi}} = \frac{\mu_{oi}}{\mu_{oh}} \dots\dots\dots (15.69)$$

This simply indicates the productivity ratio resulting from steam temperature-induced oil-viscosity reduction. No attempt was made to calculate how the reservoir got the peak temperature, but once the well is steamed and placed on production, the authors propose that the operator can simply watch leadline temperature and accurately predict the production history of the production period prior to the next cycle.

15.9.1 The Boberg and Lantz³⁴ Method. The referenced paper describes the definitive work that serves as the basis of virtually all subsequent analytical analyses of CSS. They first calcu-

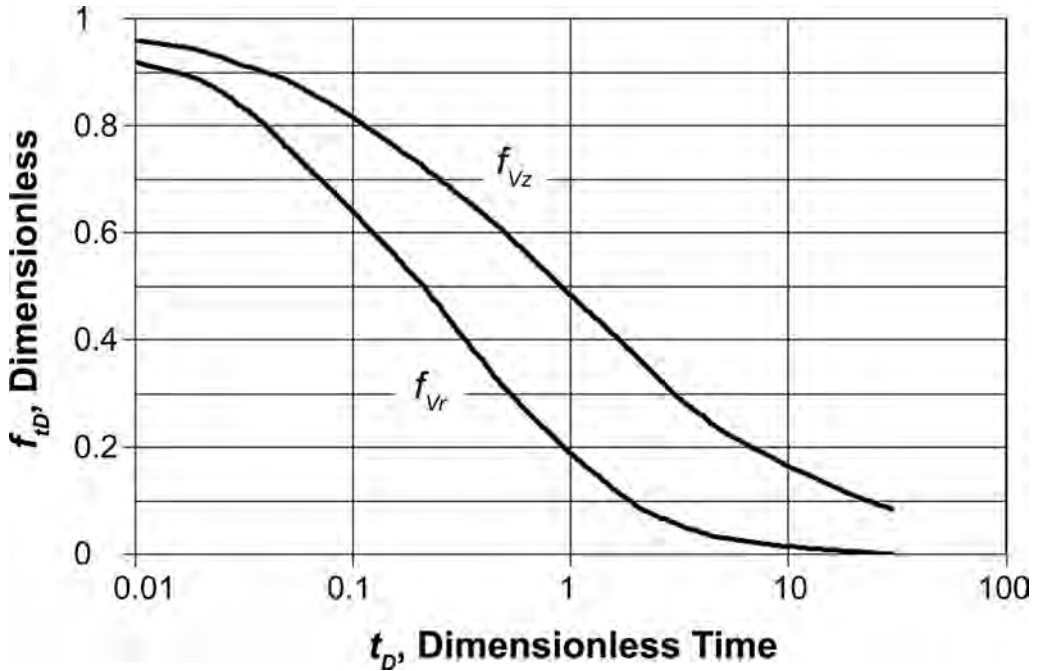


Fig. 15.19—Vertical and radial heat-loss factors for Eq. 15.65.³⁴

late the reservoir temperature distribution resulting during the injection period. Eq. 15.9 is used to calculate the area of the processed zone that is heated to T_i . Then, the well is placed on production and temperature of the heated volume, which is assumed to remain constant and begins to fall by conduction to the surrounding cold reservoir rock and by hot fluid production. The average temperature in the hot zone is

$$\bar{T} = T_R + \Delta T [f_{Vr} f_{Vz} (1 - f_{pD}) - f_{pD}], \dots\dots\dots (15.70)$$

where f_{Vr} and f_{Vz} are unit solutions of component conduction in the radial and vertical directions, respectively. They can be estimated from Fig. 15.19 or from

$$f_{Vr} = 0.92e^{\frac{(\ln t_D + 4.6)^2}{-13.5}}, \dots\dots\dots (15.71)$$

and

$$f_{Vz} = 0.96e^{\frac{(\ln t_D + 4.4)^2}{-27}}. \dots\dots\dots (15.72)$$

The term f_{pD} accounts for heat removed with produced fluids.

$$f_{pD} = \frac{1}{2Q} \int_0^t \dot{Q}_p dt, \dots\dots\dots (15.73)$$

TABLE 15.3—BOBERG AND LANTZ ³³ RADIAL FLOW FACTORS		
Flow Conditions	F_1	F_2
Steady state	$\frac{\ln\left(\frac{r_h}{r_w}\right) + S_h}{\ln\left(\frac{r_e}{r_w}\right) + S}$	$\frac{\ln\left(\frac{r_e}{r_w}\right)}{\ln\left(\frac{r_e}{r_w}\right) + S}$
Semisteady state	$\frac{\ln\left(\frac{r_h}{r_w}\right) - \frac{r_h^2}{2r_e^2} + S_h}{\ln\left(\frac{r_e}{r_w}\right) - \frac{1}{2} + S}$	$\frac{\ln\left(\frac{r_e}{r_h}\right) - \frac{1}{2} + \frac{r_h^2}{2r_e^2}}{\ln\left(\frac{r_e}{r_w}\right) - \frac{1}{2} + S}$

and

$$\dot{Q}_p = \left[5.615 \left(q_o M_o + q_{wh} M_w + q_s M_w + \frac{q_s \rho_w h_{fv}}{\Delta T} \right) + (10^3 q_{gh} M_g) \right] \Delta T \dots (15.74)$$

The subscript, *h*, indicates that the properties should be for fluids from the hot zone at the sand face. The model does not predict steam, gas, or water producing rates, which must be estimated from some other source. Oil production rates are given by a method similar to Eq. 15.69, which is written as

$$\frac{q_{oh}}{q_{oi}} = \frac{J_h}{J}, \dots (15.75)$$

and

$$\frac{J_h}{J} = \frac{1}{(\mu_{oh} / \mu_{oi}) F_1 + F_2} \dots (15.76)$$

F_1 and F_2 are radial flow factors for which Boberg and Lantz give expressions in Table 15.3. Note that the production rate is a function of only two variables—oil viscosity and the heated radius.

The method can be calculated by hand for a very few time steps, but it is much easier to use if programmed into a spreadsheet.

15.9.2 The Towson and Boberg³⁵ Model. The Boberg and Lantz method assumes that there is significant reservoir energy to produce oil under primary conditions. Because many CSS candidates have only gravity forces and initial viscosity is high, there is no significant primary production. Many California reservoirs have free liquid surfaces in the oil zones with a gas oil interface at atmospheric pressure. Towson and Boberg extended the former work to cover this situation. Eq. 15.70 is used to calculate the heated zone temperature from which oil viscosity is estimated. Then, gravity drainage oil rate may be calculated.

$$q_{oh} = \frac{\pi(1.127)\rho_o g k k_{ro} (h_h^2 - h_w^2)}{\mu_{oh} \left(\ln \frac{r_e}{r_w} - \frac{1}{2} \right)} \dots\dots\dots (15.77)$$

h_h must be computed for each time step during the production cycle by first calculating the average hot-zone fluid level.

$$\Delta h_h = \frac{\dot{Q}_o \Delta t (5.615)}{\pi (r_h^2 - r_w^2) \phi (S_{oi} - S_{or})} \dots\dots\dots (15.78)$$

Now the fluid level at the heated zone radius is

$$h_h = 4\Delta h_h \left(\ln \frac{r_h}{r_w} - \frac{1}{2} \right) - \sqrt{16(\Delta h_h)^2 \left(\ln \frac{r_e}{r_w} - \frac{1}{2} \right)^2 - h_w^2 - 8(\Delta h_h)^2 \left(\ln \frac{r_e}{r_w} - \frac{1}{2} \right)} \dots\dots (15.79)$$

This procedure can be hand calculated but is much easier to use if a computer spreadsheet is used.

15.9.3 The Jones³⁶ Method. Jones took a similar approach to Towson and Boberg³⁵ in calculating oil rates as a function of gravity forces alone. He extended the model by also calculating heated-zone water rate. Information on relative permeability is necessary to accomplish this. Further, recognizing that Towson and Boberg and other similar models commonly over-predict oil production, he limited the vertical size of the zone that is invaded with steam using a version of Eq. 15.24. This phenomenon is easily demonstrated by running a downhole temperature survey following a steam cycle. Then, because cold oil sand is still exposed in the wellbore, another set of equations similar to Eq. 15.77 is used to calculate oil and water from the cold zone. Using this modification, fluid rates can be matched quite well without need of a scaling factor to reduce predicted oil rates to realistic levels.

A convenient parameter to track, when trying to history-match a field steam cycle with this model, is produced fluid temperature that represents a combination of cold/hot oil and water.

$$T_p = \frac{T_R(q_{oc}C_o + q_{wc}C_w) + T_h(q_{oh}C_o + q_{wh}C_w)}{(q_{oc} + q_{oh})C_o + (q_{wc} + q_{wh})C_w} \dots\dots\dots (15.80)$$

This method does not lend itself to hand calculation and should be programmed on a computer.

Because steam only enters a small fraction of the sandface in a thick interval as in California oil fields, there is opportunity to improve performance of a steam cycle by using packers or other methods to divert steam into more of the oil zone.

15.10 Process Optimization

There are always the operational questions of how much steam should be injected during a cycle; what rate should steam be injected; when should a well be resteamed; etc. Jones³⁶ reported the results of the use of the model previously described to history-match a massive 20-year, 1,500-well cyclic steam project in the Potter Sand in the Midway Sunset field, California. He then used the history-match information to do a long-life parametric study of the process. **Table 15.4** lists the conclusions for this particular application. This is, however, not a common practice. There are so many variables that the results from a single well or even a small group of wells cannot be used for a meaningful history match. Further, cyclic steam is easy to apply

<u>Parameter</u>	<u>Model Results</u>
Cycle life	150–180 days
Cycle size	9,000 bbl
Injection rate	1,000 B/D
Well spacing	5/8 acre/well
Soak time	Short as possible
Steam quality	High as possible

in the field and is relatively inexpensive, so most operators simply start immediately with a field trial. Very little is published on optimizing CSS.

It is generally true of CSS that soak time should be as short as possible and that steam quality should be as high as possible. Further, efforts should be made to divert steam out of depleted zones and gas caps and into as much good oil-saturated sand as possible.

There are generally two reasons to apply CSS. First, there is the obvious stimulation of economic oil production immediately from the well. Second, because of the time delay in oil response from the initiation of steam injection into a continuous steam injector in a steamflood project, CSS concentrated in the steamflood zone is often used to accelerate project response.

15.10.1 Cumulative Average Daily Profit Method. Because process optimization is ultimately an economic decision, a restreaming decision can be based on the Rivero and Heintz³⁷ cumulative average daily profit (CADP) method. Fig. 15.20 shows a graphical representation of how to use this method. When steam is injected into a producer, profits of the cycle are driven negative because of the cost of the steam, costs to prepare the well for steaming, and lost production as a result of the well being shut down. Once the well is put back on production, the oil rate will peak, and daily cash flow will be at a relative high. Concurrently, CADP for the cycle will begin to increase as the daily production begins to pay for the injection costs. As the well continues to produce, the oil rate gradually falls, as does daily profit. CADP hopefully soon becomes positive, then continues to increase until it reaches a value equal to the daily cash flow. It is at this point that the well should be recycled because cash flow for the next day's production will fall below the CADP.

Although instructive as a concept for picking restreaming time, actual field application of the method is practically impossible because of ever-present problems in gathering precise enough well production gauges and in collecting all of the necessary economic data in a timely manner. Also, because the method is divorced from the reservoir process, it may lead to short-term economic decisions that damage the reservoir.

15.10.2 Sequential CSS Method. In a large CSS project, one needs a way to decide which well to steam and in what sequence. McBean³⁸ and Jones and Cawthon³⁹ presented a sequential CSS method that ensures that all wells will be stimulated in a timely manner and takes advantage of the interwell stimulation often observed.

By steaming wells in a sequential manner from downdip to updip as shown in Fig. 15.21, they observed not only the oil response from the steamed wells but also some response from offset wells caused by a mini-steamflood. Kuo *et al.*⁴⁰ found in numerical simulations that small cycles in closely spaced wells are preferable in this process. Field experience in the sequential CSS project confirmed that finding with wells drilled on $\frac{5}{8}$ acre (0.25 ha) spacing.

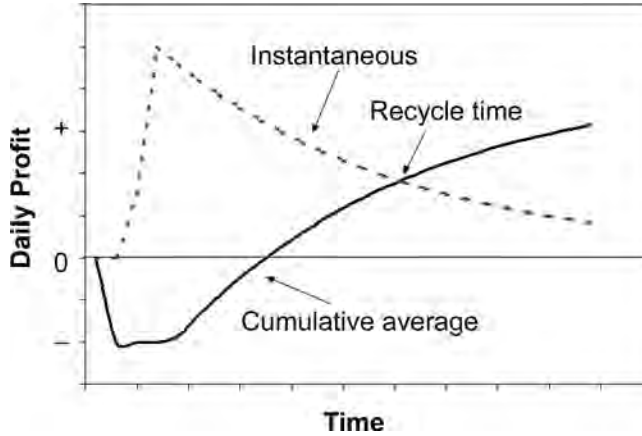


Fig. 15.20—Graphical representation of the cumulative average daily profit method of the recycle determination method.³⁷

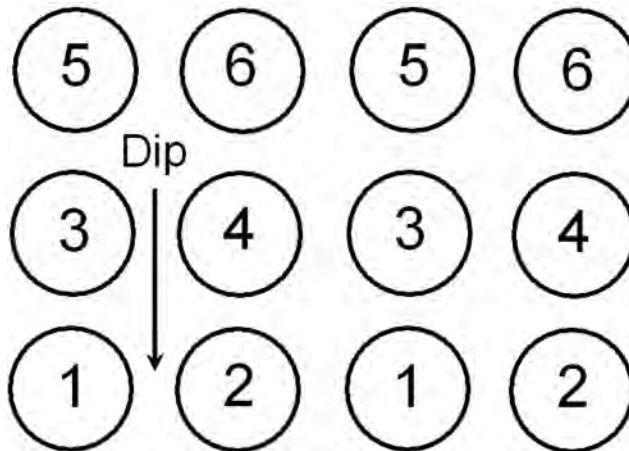


Fig. 15.21—Well steaming schedule for the sequential steam method of cyclic steam design.³⁹

15.11 Steam Delivery Systems

15.11.1 Heat Loss in Surface Distribution Piping. For any SEOR process, no matter how efficient, the major cost is always that of generating the process steam. Whether the product of oilfield steam generators, industrial boilers, or electrical/steam cogeneration plants, steam must be delivered through a network of pipes and through pipes down a wellbore to the oil-bearing formation. It is imperative that the unavoidable heat losses in this distribution system be minimized with some type of insulating system.

The basic equation for heat loss is

$$\dot{Q}_{ls} = \frac{(T_s - T_A)}{R_h} \dots\dots\dots (15.81)$$

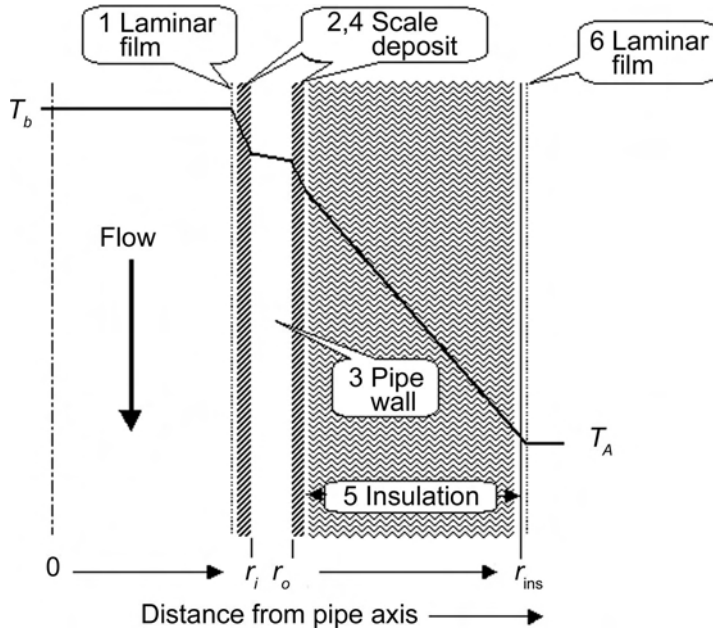


Fig. 15.22—Schematic diagram of resistance to heat transfer and of temperature profile in a suspended surface pipe.

The rate of heat loss in surface lines is usually calculated at steady-state conditions because transients disappear quickly in surface pipes. Thermal resistance to heat loss for that system is

$$R_h = \frac{1}{2\pi} \left[\frac{1}{h_f r_i} + \frac{1}{h_p r_i} + \frac{1}{\lambda_p} \ln \frac{r_o}{r_i} + \frac{1}{h_{p_o} r_o} + \frac{1}{\lambda_{ins}} \ln \frac{r_{ins}}{r_o} + \frac{1}{(h_{fc} + h_r) r_{ins}} \right] \dots (15.82)$$

The terms in Eq. 15.82 are the coefficients of heat transfer for each of the layers of an insulated pipe as shown in Fig. 15.22. They are, from left to right: conduction in the laminar layer in contact with the pipe wall; conduction in the scale or other solid coating on the inside pipe wall; conduction in the pipe wall; conduction in the scale or other coating on the outside pipe wall; conduction in the insulation; and convection and radiation from the outer surface of the insulation. Table 15.5 shows thermal conductivity for various materials. Refer to appropriate textbooks^{41,42} for more in depth information.

In the previous calculation, h_r is the coefficient of radiant heat transfer for the outermost surface of the system; in this case, it is for the insulation. It is common practice to cover insulation with a thin sheath of bright aluminum, mainly for protection from weather and from mechanical abuse. A side benefit is that the bright surface has low radiant emissivity that, combined with low surface temperature, results in negligible radiant heat loss, so this term is often ignored. If the pipe is uninsulated, the term applies.

Note that for every system there is an optimum insulation thickness. Adding more insulation above this optimum will not result in more heat savings. This is because there are two competing effects; the rate of heat loss decreases with increasing insulation thickness, but heat loss increases as the exposed surface area increases.

Coefficients of Heat Transfer. The following are useful in most cases, but the reader should refer to appropriate^{41,42} texts for more complicated systems.

Value of h_f . For condensing steam, the coefficient is large, and it is generally adequate to use

TABLE 15.5—THERMAL PROPERTIES FOR SELECTED MATERIALS			
Material	λ , Btu/(hr-ft-°F)	ϵ , Dimensionless	Surface Temp., °F
Black body emitter		1.00	all
Aluminum, polished	118	0.040–0.060	20–1,000
Carbon steel	28		
Rusty, mill finish		0.55–0.60	200–1,000
Stainless steel	9.4		
316, mill finish		0.28–0.66	100–1,000
Earth, wet	1.5		
Earth, dry	0.30		
Silica	0.83		
Concrete	1.05		
Glass wool insulation	0.022		

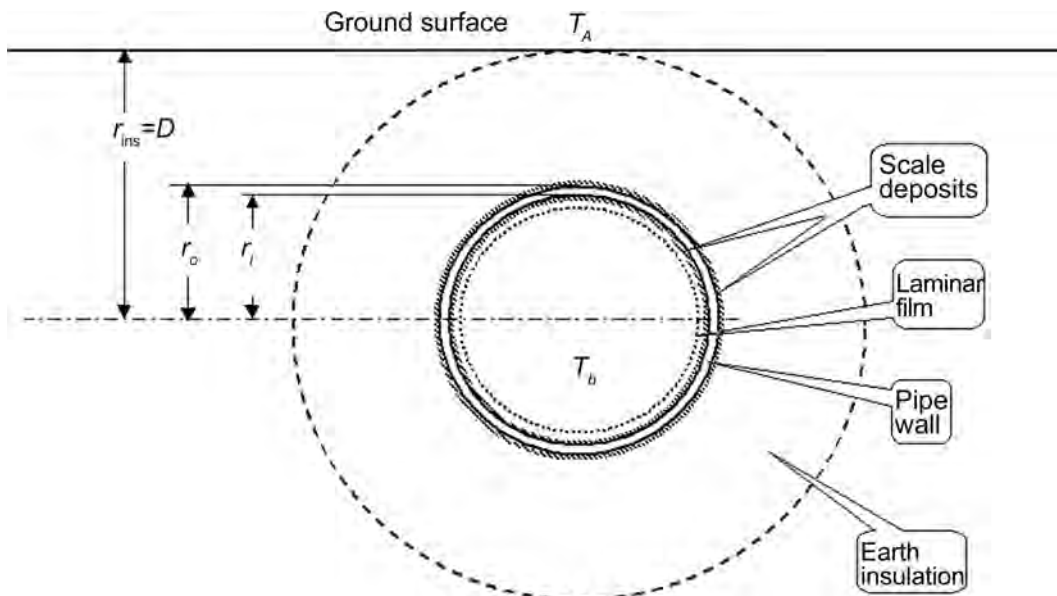


Fig. 15.23—Schematic diagram of idealized thermal resistances in buried surface lines.

$$h_f = 48,000, \dots \dots \dots (15.83)$$

when flow is turbulent (which is most of the time) and is determined by

$$N_{Re} > 2,100, \dots \dots \dots (15.84)$$

where

$$N_{Re} = \left[\frac{\pi}{2} (0.0616) \right] \frac{2i_w \rho_{w,sc}}{\pi \mu_s r_i} \dots \dots \dots (15.85)$$

Because $\mu_s \sim 0.018$ cp for typical oilfield steam temperatures, turbulence will prevail at

$$i_w > 9.85r_i \tag{15.86}$$

Value of h_{pi} and h_{po} . These are seldom known, and the terms are usually ignored for steam distribution lines. Actually, these deposits outside and, if not too thick and firmly attached, inside the pipe are desirable because they result in resistance to heat conduction. If they are present but no values are known, McAdams⁴¹ recommends a value of 48,000 Btu/(ft²-D-°F).

Value of h_{fc} . McAdams⁴¹ offers the next equation to calculate the coefficient of forced convection at the outer surface of a pipe system in air.

$$h_{fc} = \frac{0.12\lambda_a}{r_e} N_{Re}^{0.6} \tag{15.87}$$

for $1,000 < N_{Re} < 50,000$, where

$$N_{Re} = 4,364 \frac{r_e v_w \rho_{a,sc}}{\mu_a} \tag{15.88}$$

Value of h_r . In the following relationship for the coefficient of radiant heat transfer, temperatures must be expressed in °Rankine, which is °F + 460.

$$h_r = 1.712 \times 10^{-9} \varepsilon (920 + T_o + T_a) [(T_o + 460)^2 + (T_a + 460)^2] \tag{15.89}$$

Emissivity, ε , of various materials is listed in [Table 15.5](#).

Buried Lines. A special case of insulated lines is pipes buried in the earth. See [Fig. 15.23](#). [Eq. 15.82](#) applies, except for two modifications,⁴³ which are

$$\ln \left(\frac{r_{ins}}{r_o} \right) = \cos h^{-1} \left(\frac{D}{r_o} \right) \tag{15.90}$$

and

$$h_{fc} = \infty \tag{15.91}$$

Heat loss rate is very high for short-term injection for buried pipes, even in dry soil, so this is not recommended in cyclic steam projects. If the soil contains moisture, the losses are even greater.

15.11.2 Heat Loss in Wells. Heat loss in wells never reaches a steady-state condition. It begins at a very high rate when the well casing is suddenly heated by initial steam injection, then continually decreases in rate as the surrounding earth is heated. For long term continuous steam injection over a period of years, wellbore heat loss becomes relatively small. Conversely, for intermittent cyclic steam injection, the heat-loss rate will always be relatively high because the surrounding earth is never appreciably heated. [Eq. 15.82](#) still applies but is complicated by the ambient (earth) temperature increasing with depth because of geothermal gradient and by the “insulation,” earth again, having high conductivity and practically infinite thickness. The latter property results in the thermal resistance being time dependent. [Fig. 15.24](#) is a schematic depiction of typical elements that contribute to the resistance to heat flow which is described by

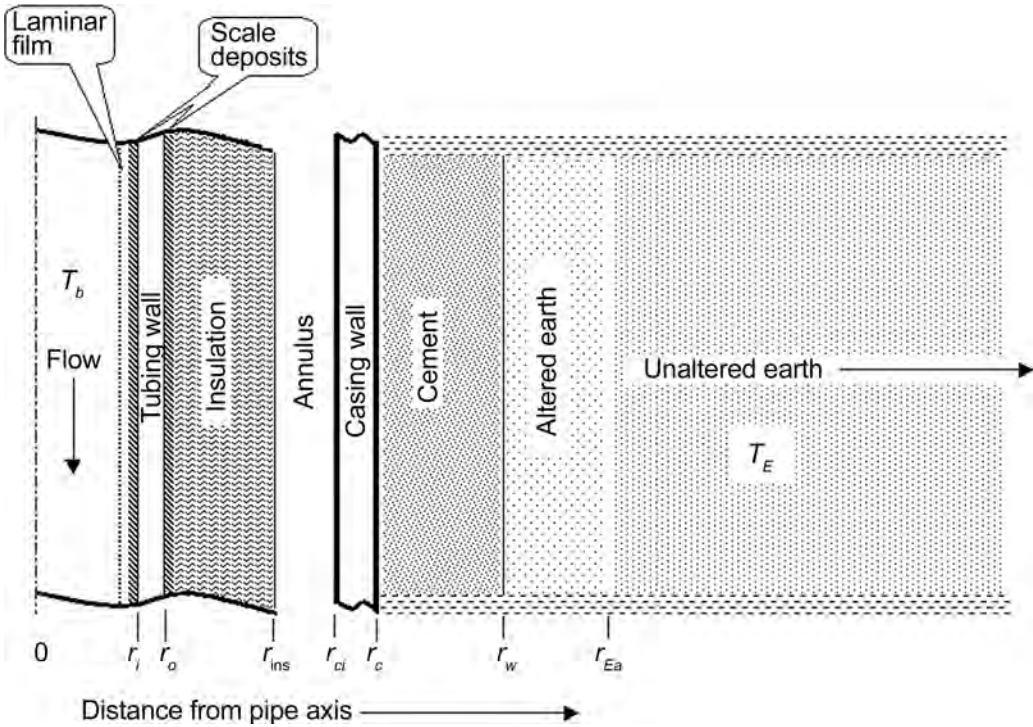


Fig. 15.24—Schematic diagram of resistance to heat transfer in wellbores.

$$R_h = \frac{1}{2\pi} \left[\frac{1}{h_{fi}r_i} + \frac{1}{h_{pi}r_i} + \frac{1}{\lambda_p} \ln \frac{r_o}{r_i} + \frac{1}{h_{po}r_o} + \frac{1}{\lambda_{ins}} \ln \frac{r_{ins}}{r_o} + \frac{1}{h_{rc,an}r_{ins}} + \frac{1}{\lambda_p} \ln \frac{r_{co}}{r_{ci}} \right. \\ \left. + \frac{1}{\lambda_{cem}} \ln \frac{r_w}{r_{co}} + \frac{1}{\lambda_{Ea}} \ln \frac{r_{Ea}}{r_w} + \frac{f(t_D)}{\lambda_E} \right], \dots \dots \dots (15.92)$$

where the first five terms are similar to those in Eq. 15.82. The last five terms are the resistances in radiation and convection in the casing annulus, in the casing, in the cement, in the altered earth zone (dried earth because of high temperatures), and in the time dependent loss to the earth. If other resistance zones can be identified, such as coatings in the casing or scale deposits, etc., terms should be added for them. Every system should be analyzed according to the elements included, such as wells with no insulation on the tubing, wells with no tubing at all, or simply injection down the casing. All of the additional terms can be determined with equations previously presented except for the coefficient of heat transfer in the annulus, $h_{rc,an}$ and f_{iD} .

Heat loss is a serious problem in cyclic steam stimulation because the wellbore and surface lines are never heated to steady-state conditions. Fig. 15.25 shows the results of Eq. 15.92 for several steam-injection rates in a typical Kern River field producer. It demonstrates that because steam is at a relatively constant temperature heat loss rate, it is a constant and injection should be done at the highest practical rate. Fig. 15.26 shows the benefit of insulating the casing from contact with steam for short duration injection as in a steam cycle. Conversely, Fig. 15.27⁴⁴ shows that for long-term injection, as in a steamflood injector, and for shallow wells, as encountered in the San Joaquin Valley oil fields, there is no benefit from insulating the

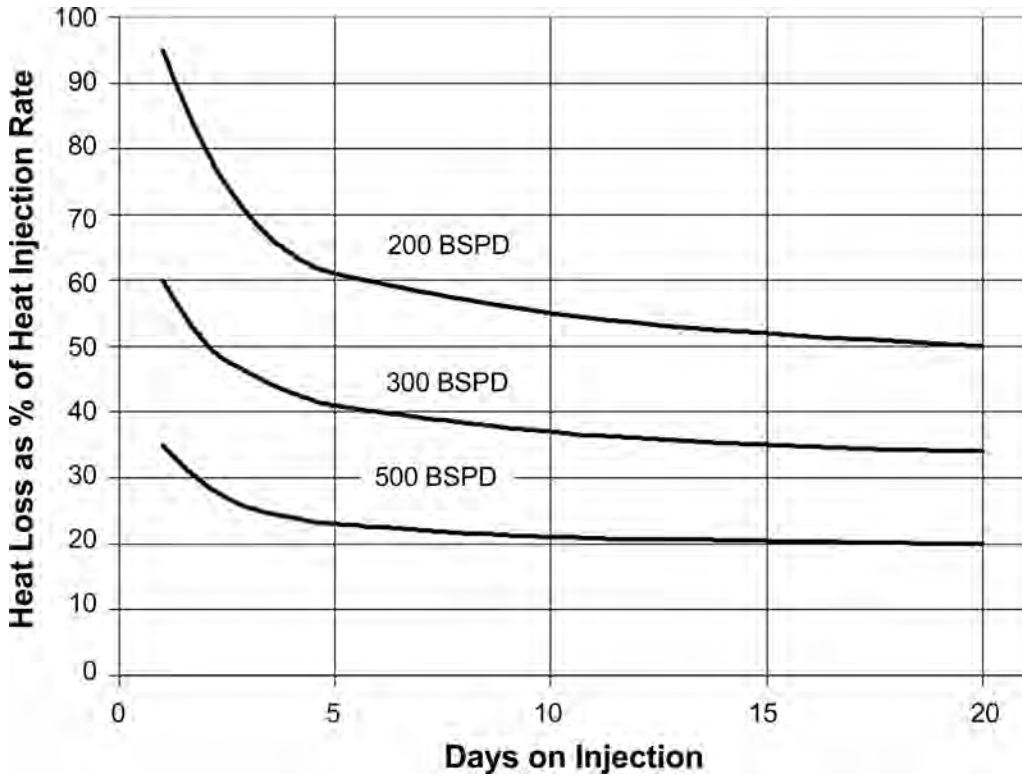


Fig. 15.25—Heat loss for several steam-injection rates in a typical California cyclic steam well. Rate should be as high as possible to minimize heat loss.

casing. Thus, it is possible to drill inexpensive slimhole injectors, completed simply with a tubing string, and not appreciably increase heat loss over the life of a project.

Value of $h_{rc,an}$ In an air-filled annulus operating under free convection, the coefficient of heat transfer for radiation and convection is given by Willhite.⁴³

$$h_{rc, an} = 4.11 \times 10^{-8} \left[\frac{1}{\epsilon_{ins}} + \frac{r_{ins}}{r_{ci}} \left(\frac{1}{\epsilon_{ci}} - 1 \right) \right] \cdot F(T_{ins}, T_{ci}) + \frac{1}{r_e} \frac{\lambda_{a, a}}{\ln \left(\frac{r_{ci}}{r_{ins}} \right)}, \dots (15.93)$$

where

$$\lambda_{a, a} = 0.049 \lambda_a NGr^{0.333} NPr^{0.047} \dots (15.94)$$

The Grashof number is

$$N_{Gr} = \left[7.12 \times 10^7 \frac{g_c}{g} \right] \cdot \frac{(r_{ci} - r_{ins})^3 g \rho_{an}^2 \beta_{an} (T_{ins} - T_{ci})}{g_c \mu_{an}^2}; \dots (15.95)$$

the Prandtl number is

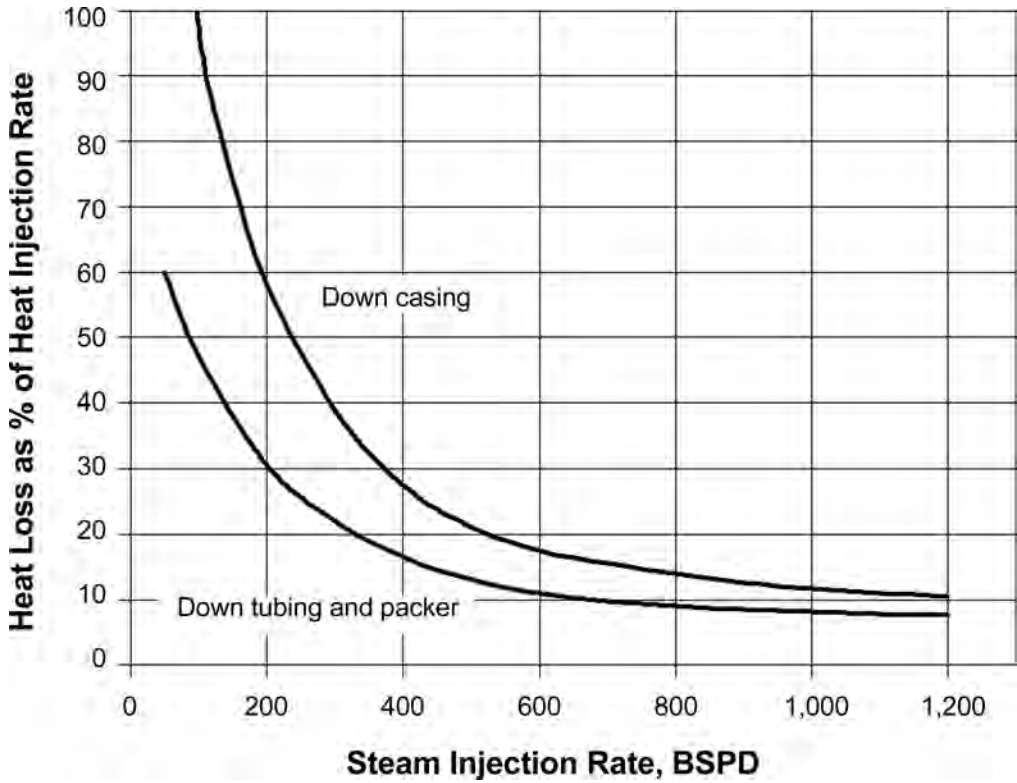


Fig. 15.26—Heat loss for cyclic steam in a typical California cyclic steam well after 10 days with and without tubing and a packer.

$$N_{Pr} = 58.1 \frac{C_{an} \mu_{an}}{\lambda_{an}} ; \dots\dots\dots (15.96)$$

and the temperature function is

$$F(T_{ins}, T_{ci}) = [(T_{ins} + 460)^2 + (T_{ci} + 460)^2] \cdot (920 + T_{ins} + T_{ci}) . \dots\dots\dots (15.97)$$

The temperatures for use in Eq. 15.97 are proportional to the fractional thermal resistance between the outer tubing surface, in this case the insulation, T_{ins} , and the casing inner wall, T_{ci} . They can be estimated by

$$T_{ins} = T_b \frac{T_b T_A}{2\pi R_h} \frac{1}{h_{fi} r_i} + \frac{1}{h_p r_i} + \frac{1}{\lambda_p} \ln \frac{r_o}{r_i} + \frac{1}{h_{po} r_o} + \frac{1}{\lambda_{ins}} \ln \frac{r_{ins}}{r_o} , \dots\dots\dots (15.98)$$

and

$$T_{ci} = T_A - \frac{T_b - T_A}{2\pi R_h} \left[\frac{1}{\lambda_p} \ln \frac{r_{co}}{r_{ci}} + \frac{1}{\lambda_{cem}} \ln \frac{r_w}{r_{co}} + \frac{1}{\lambda_{Ea}} \ln \frac{r_{Ea}}{r_w} + \frac{f(t_D)}{\lambda_E} \right] . \dots\dots\dots (15.99)$$

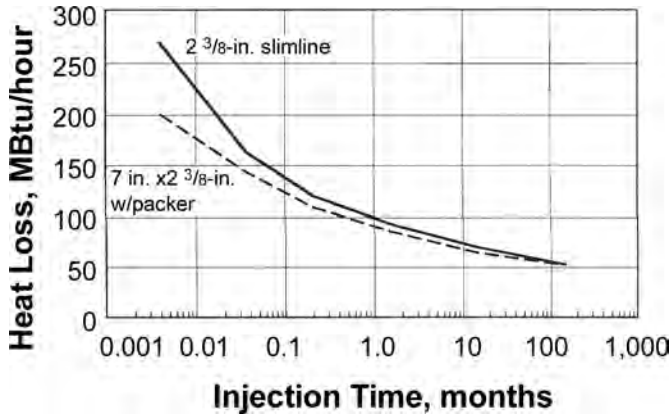


Fig. 15.27—Heat loss for a steamflood injector with a conventional casing, tubing, and packer completion compared to a slimhole completion.⁴⁴

Value of $f(t_D)$. This is a function of dimensionless time.

$$t_D = \frac{\alpha_E t}{r_{Ea}^2} \dots\dots\dots (15.100)$$

The radius in the denominator is the radius of the outermost element in contact with the reservoir, which is the heat altered zone in this case. Willhite⁴³ gives a table of values for $f(t_D)$, for $t_D < 100$. A reasonable estimate can be derived from

$$f(t_D) \cong 3.53e^{\frac{(\ln(t_D) - 7.66)^2}{-44.85}} \dots\dots\dots (15.101)$$

Ramey⁴⁴ gives a calculation of $f(t_D)$, for $t_D \geq 100$.

$$f(t_D) \cong 0.5 \ln(t_D) + 0.403 \dots\dots\dots (15.102)$$

Because R_h , T_{ins} , T_{cb} , and $f(t_D)$ are interrelated by nonlinear expressions, they must be solved by an iterative trial-and-error procedure.⁴³

15.12 Heat Management

While always an implicit goal in SEOR processes, overall process heat management became a topic in the literature in the mid-1980s. The growth of the discipline has closely followed the development of the personal computer and computer applications. Fig. 15.28⁴⁶ is a graphical representation of the major components of a heat balance that must be performed to properly manage a SEOR process. Ziegler *et al.*⁴⁷ published a very good summary of a method of implementing the principle. In essence, the operator must establish an iterative process that continues for the duration of the project and that continuously collects and analyzes pertinent data. Based on that analysis, the operator then makes appropriate midcourse adjustments to optimize the project. The process is actually a complete project optimization method but has adopted the name “heat management” because steam generating costs tower over any other cost and are

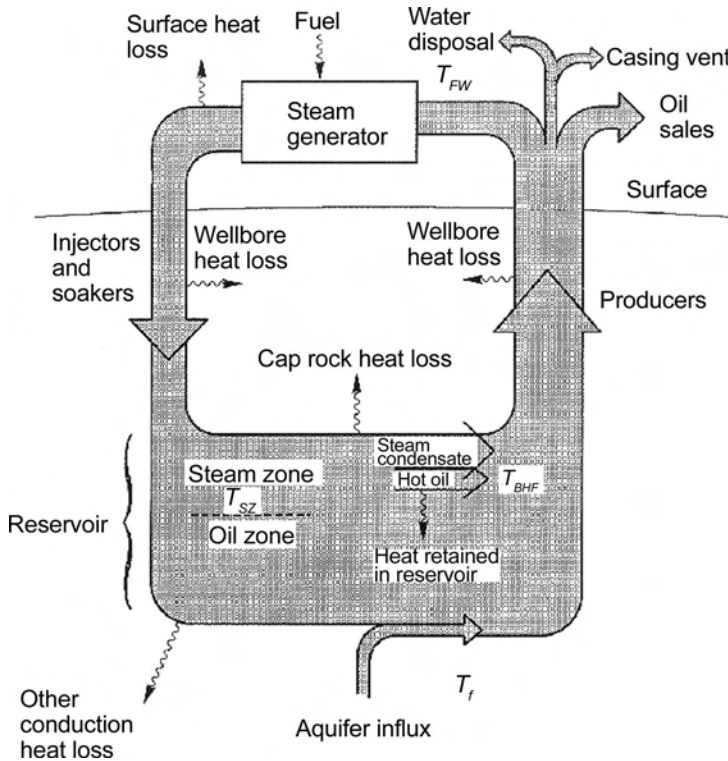


Fig. 15.28—Schematic diagram of the components of heat management for SEOR projects.⁴⁶

even several times larger than the initial substantial capital investment in a steamflood. There are three basic parts of the method, as shown in Fig. 15.29,⁴⁷ which are data gathering, data monitoring, and adjustments to the process.

15.12.1 Data Gathering. As its name implies, data gathering consists of compiling regular and typically large amounts of information on the operation. Data from producing wells, injection wells, observation wells, and surface facilities are compiled and stored in computer databases. Table 15.6 was derived from Ziegler⁴⁷ and indicates the information currently considered necessary for California steamfloods. In addition to the types of data collected, the operator must also specify a regular schedule for collection.

All of the data are from existing and necessary components of the system except for the observation wells. Although it is tempting to economize by eliminating them, that is false economy. Information they provide on the change in temperature and gas/oil saturation over time is critical in maintaining process efficiency. The data must be stored in computer databases that are accessible to desktop PCs.

15.12.2 Data Monitoring. As with any oil production operation, there are daily and weekly tasks that must be done. However, in heat management, the operator must schedule formal project reviews on a much longer term such as a semiannual or annual basis. Table 15.7⁴⁶ is an example review schedule. During these reviews, the project performance data is compared to the original design (using methods described in previous sections in this chapter), and adjustments are made accordingly.

Key calculations are heat and mass balances to quantify the terms shown in Fig. 15.28.

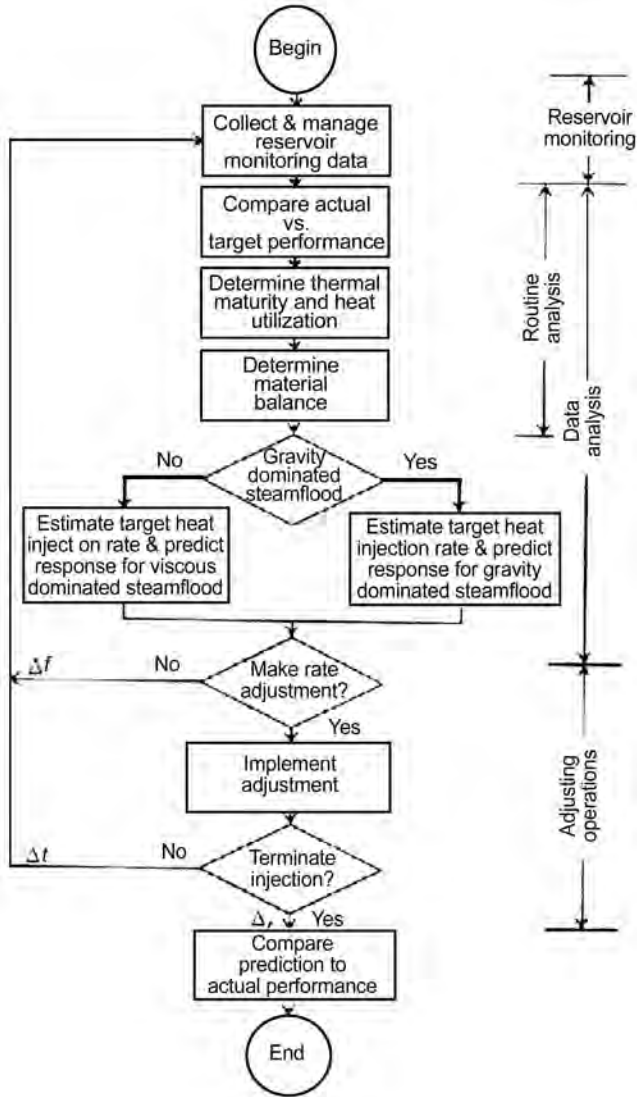


Fig. 15.29—Heat management flowchart.⁴⁷

$$m_i + m_{(o/w)\text{influx}} = m_{(o/w)\text{prod}} + m_{\text{casing_blow}} + m_{\text{influx}} + m_{z(\text{accumulation})} \dots\dots\dots (15.103)$$

and

$$Q_i + Q_{(o/w)\text{influx}} = Q_{(o/w)\text{prod}} + Q_{\text{casing_blow}} + Q_{\text{loss}} + Q_{\text{influx}} + Q_{z(\text{accumulation})} \dots\dots (15.104)$$

Table 15.8⁴⁷ is an example of a list of metrics that should be established to aid in making heat management decisions. Note the use of the term “produced oil/fuel” ratio, F_{of} , in the metrics table. This is in place of the more common “produced oil/steam injected” ratio, F_{os} . The reason for using the former is that steamfloods often are operated at steam qualities that vary significantly from the normal 70 to 80%. In these cases, F_{os} would be a misleading indicator,

TABLE 15.6—EXAMPLE STEAMFLOOD MONITORING DATA PLAN FOR HEAT MANAGEMENT⁴⁷

Source	Data Type	Collection Frequency	Presentation Format for Routine Analysis	Derived Information for Data Analysis
Injection wells	Rate	Bi-weekly	Rate, bubble, contour plots	Performance update, energy, material balance
	Quality	Annual, selected wells	Heat-injection map	Steam quality distribution, energy balance
	RA and spinner profiles	1–3 years	Injection profile	Remedial potential, compliance
	Shut-in pressure	6 months–1 year	Depth vs. pressure, areal map	Steam-zone pressure trends, maximum heating
	PNC log	Nonroutine	Saturation, shale maps	Screening for VE potential
	Pressure/temperature profile	Nonroutine	Heat injection log	Zonal heat allocation
	Pressure transient	Nonroutine	Log/log analysis	P , k , skin, steam-zone volume, boundary
Observation wells	Temperature profile	1–2 months	Temperature profile, average temperature map	Average temperature, heat rate, steam zone
	PNC log	6 months–1 year	Gas saturation trace, x-sections	S_g -sweep efficiency, steam-zone growth
	C/O log	Annual	Oil saturation trace	S_o , S_w recovery factor, allocation
Producing wells	Liquid rates	1–2 months	Rate, bubble, contour map	Performance update, material balance
	Effluent rate	Annual, selected wells	Bubble map	Steam breakthrough, energy balance
	Casing pressure	Monthly	Bubble, contour map	Steam breakthrough, pressure drawdown
	Flowline temperature	Monthly	Bubble, contour map	Steamflood response, steam-zone temperature
	Lead-line temperature	Annual, selected wells	Bubble, contour map	Reservoir heating, steam breakthrough
	F-Scott	Quarterly, if applicable	Zone rate, bubble, contour map	Zonal oil-production allocation
	Isolation test	Nonroutine	Performance x-section	Zonal oil/water/gas allocation
	Tracers	Nonroutine	Areal sweep map	Reservoir heterogeneity, areal sweep efficiency
Casing collection settings	Liquid rates	Daily	CCS effluent vs. steam injection rate	Energy balance
	Setting pressure	Daily	Pressure vs. oil rate plot	Effect of casing pressure on oil production
	Gas composition	Nonroutine	Lap report	Steam, reservoir interaction
Steam generator	Water rate	Daily		Mass delivery
	Steam quality	Daily		Heat delivery
	Fuel rate	Daily		Fuel consumption

Steps	Data Requirements	Evaluation Methods	Evaluation Outcomes	Possible Adjustments
1. Compare actual performance to prediction	Oil/water/steam rates, OFR, steam production, flowline temperature, current OPEX, oil price, TOW surveys	Compare actual and predicted reservoir performance and profitability	Identify gaps between actual and predicted	
2. Determine heat balance, thermal maturity and heat utilization	Heat injected: rate, quality, temperature, pressure and wellbore profiles	Comparison of actual vs. target injection	Estimate steamfront geometry	Changes to delivery system
	Heat stored in reservoir: temperature profile and PNC logs	Gravity, viscous-force ratio	Estimate process efficiency	Adjust injection intervals in injection wells
	Heat produced: oil/water rates, casing effluent, flowline temperature	Thermal maturity Heat utilization	Estimate process efficiency	Change cyclic steam frequency in pattern producers
3. Determine material balance	Production data: oil, water, and steam	Liquid balance vs. time	Voidage and influx estimates	Increase well productivity
	Injection data: steam and water	Material balance		Infill drilling Control Influx
4. Determine target heat injection rate	Reservoir properties	A. Neuman and Vogel analogy simulation	Current steam injection requirement	A. Steam rates
	Fluid properties	B. Mandl-Volek and Jones analogy, simulation	Steam-injection schedule	B. Steam rates and qualities
	OPEX forecast		Production forecast	Return to step one in six months
	Oil price forecast		Profitability forecast	

and an in/out energy factor would be a better benchmark to use.⁴⁸ Either of these is useful as a project metric, but the user must be aware of the limitations. Fig. 15.30 shows the F_{of} for three different steam injection schedules.³¹ Using only F_{of} as the criteria, The Neuman steam-injection schedule (Fig. 15.15) seems to be far superior to the other two. However, Fig. 15.14 shows that the linear steam rate reduction probably gives the best overall economic performance. The Neuman reduction rate is designed to optimize F_{of} , but severe early steam reduction results in lower oil rates and cumulative production.

15.12.3 Adjustments to the Process. Once the project has been reviewed and compared to the various benchmarks, it is either on or ahead of schedule, thus requiring no changes, or is not performing as expected and is in need of a midcourse correction. Table 15.7 lists common changes. There are only a few operational areas that can be changed.

Economic Metrics	Tracking Frequency	Internal Data Source	External Data Source
Oil production rate	Monthly	Company database	Commercial production data service
Instantaneous oil/fuel ratio	Monthly	Company database	Commercial production data service (with steam quality estimate)
Cumulative oil recovery	Monthly	Company database	Commercial production data service (with OOIP estimate)
Fuel cost: \$/bbl produced oil	Monthly	Company database	Commercial oil industry reporting service
Total operating cost: \$/bbl produced oil	Monthly	Company database	Commercial oil industry reporting service
Process Metrics	Tracking Frequency	Recommended Goal	
Status of company database	Quarterly	100%	
Number of heat analyses per year per project	Quarterly	Measured against target set by team	
Percentage of time on heat management	Quarterly	An initial increase at startup of project declining as project matures	

Fig. 15.31³⁰ is an example of a Midway Sunset, California, steamflood that benefited from heat management. The operator determined that the wells were producing at their maximum rate but that steam injection was much higher than required. Based on this analysis, the steam rate was redirected and then reduced with improved oil production, thus greatly improving project economics and ultimate recovery.

Fig. 15.32⁴⁷ is another example of heat management techniques being used to improve an in-progress steamflood. This Kern River, California, project was found to be overinjected, and some producers were not completed in the proper zones. Steam rate was redirected in new injectors, and some producing wells were recompleted; later, steam rate was reduced, resulting in lower steam cost, increased oil production, and reduced water production. At the time of publication, the operator was faced with an apparent opportunity for another heat management study and adjustment to the process.

15.13 Horizontal Well Applications in Steam Injection—S. M. Farouq Ali, Consultant and Jeff Jones

Horizontal wells are being employed in innovative ways in steam injection operations to permit commercial exploitation of reservoirs that are considered unfavorable for steam, such as very viscous oils and bitumen and heavy oil formations with bottomwater, etc. Numerous papers have explored steam injection using horizontal-vertical-well combinations by use of scaled physical models or numerical simulators. For example, Chang, Farouq Ali, and George⁴⁹ used scaled models to study five-spot steamfloods, finding that for their experimental conditions, a horizontal steam injector and a horizontal producer yielded the highest recovery. **Fig. 15.33** shows a comparison of oil recoveries for various combinations of horizontal and vertical wells and for four different cases: homogeneous formation, 10% bottomwater (% of oil zone thickness), 50% bottomwater, and homogeneous formation with 10% pore volume solvent injection before steam. Huang and Hight⁵⁰ carried out numerical simulations of a variety of hypothetical

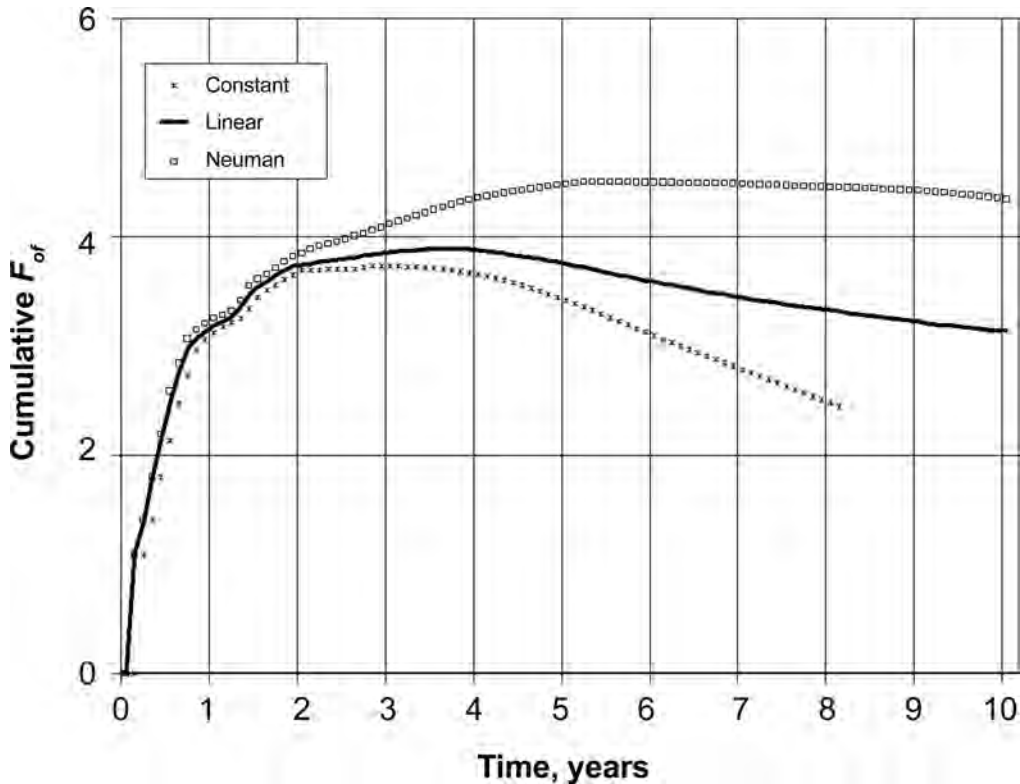


Fig. 15.30—Produced oil/fuel burned ratio for three steam-injection scenarios.³¹

situations involving horizontal and vertical wells. A few field-tested applications of horizontal wells are briefly described next.

15.13.1 Vertical Injectors, Multilateral Producer: Kern Hot Plate Test. Dietrich⁵¹ described the Kern Horizontal-Well Pilot, in a high viscosity (about 5,000 cp) oil reservoir, shown in Fig. 15.34. Key data are given in Table 15.9. Eight vertical injectors were used to inject steam at an average rate of 1,900 B/D (CWE). The producer consisted of 8 branches of ultra-short radius horizontal wells. The project operated for about 14 months. The production response from the wells averaged 120 B/D. The project was not economic (steam-oil ratio of 15) because of unfavorable placement of the horizontal producer and other factors.

15.13.2 Vertical Injectors and Horizontal Producer With Bottomwater: Tangleflags Project. Jespersen and Fontaine⁵² described the Tangleflags project that utilizes a system of vertical injectors and horizontal producers. There are 11 producers. Table 15.9 gives the key data for the project. Fig. 15.35 shows the first well, together with the estimated sizes of the steam zones around the vertical injectors at three different times. The original horizontal well (400 m [1,312 ft] in length, but only 107 m [351 ft] were open to flow) was drilled for primary production, but the water cut became prohibitive within months, at which time it was decided to inject steam into the offset vertical wells. As a result, the water cut declined rapidly and stayed at a low value. The well produced almost 2.5 million bbl of oil. It should be noted that a small, discontinuous primary gas cap is present over the field. Temperature surveys showed that the injected steam migrated into the gas cap and during the early part of the project, exerted a

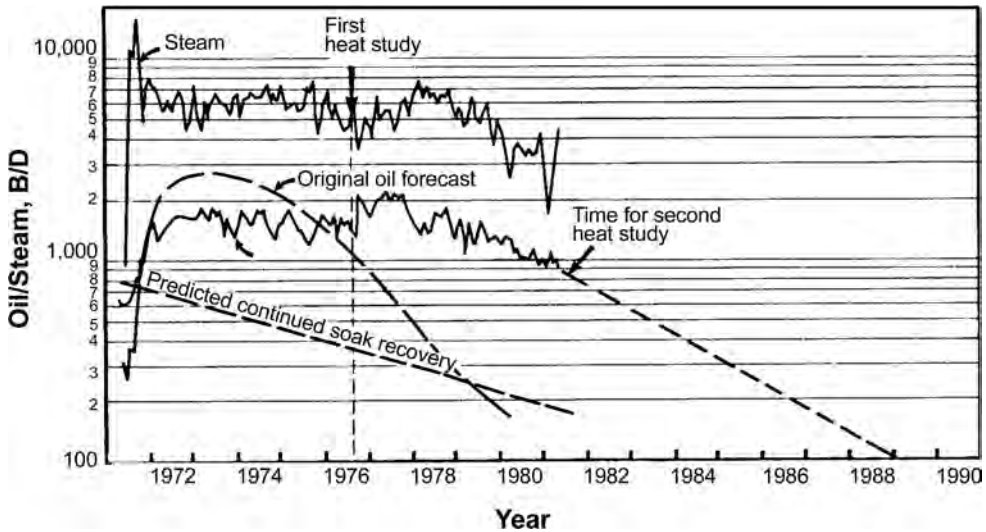


Fig. 15.31—Midway Sunset field example of heat management results on an in-progress steamflood.³⁰

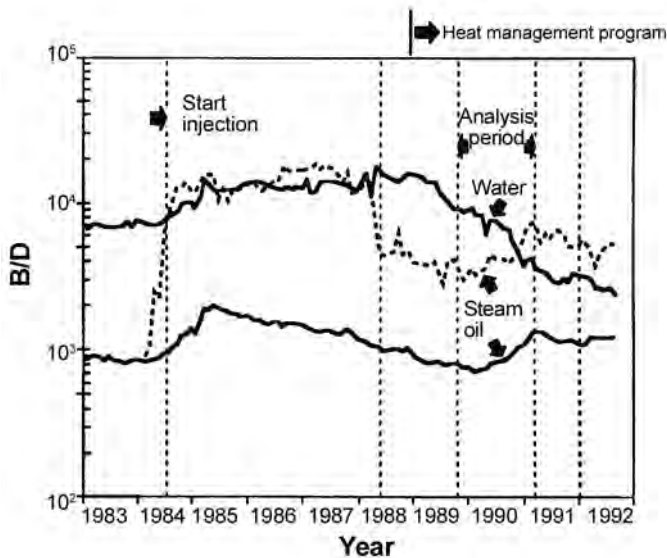


Fig. 15.32—Kern River field example of heat management results on an in-progress steamflood.⁴⁷

downward drive, restricting the advance of the oil/water contact. At a later stage, steam injection rate was decreased and fluid flow was gravity controlled.

There are several other steam injection operations like Tangleflags. If the vertical permeability is high, and gas cap absent or small, an operation utilizing horizontal producers and vertical injectors may be viable.

15.13.3 Steam-Assisted Gravity Drainage (SAGD). SAGD is an outstanding example of a steam injection process devised for a specific type of heavy oil reservoir utilizing horizontal wells. Several variations of the basic process have been developed, and are being tested. The

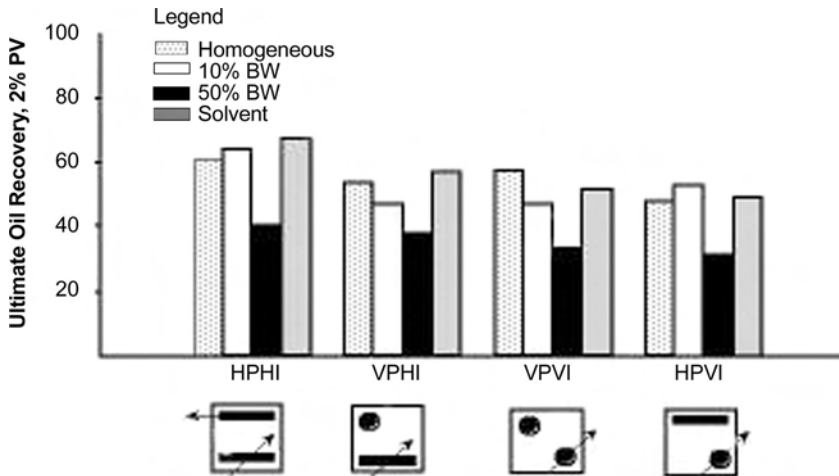


Fig. 15.33—Comparison of the various injection-production strategies on ultimate oil recovery, for the different bottomwater cases investigated (after Chang, George, and Farouq Ali⁴⁹).

Project	Kern	Tangleflags	Midway Sunset Monarch	Cymric/McKittrick Tulare	Duri
Depth, ft	500	1,475	1,000–1,400	900	450–700
Average thickness, ft	77	89	20–300	40	>40
Reservoir dip, degrees			60–70	20–65	10–15
Oil gravity, °API	18–20		14	10–14	21
Oil viscosity, cp	5,000	13,000	6,000	3,000–10,000	400
Reservoir temperature, °F	110	66	Mature cyclic ~150	Mature flood ~150	Mature flood ~150
Porosity, %	26	33	30	32–34	32
Horizontal permeability, md	300–700	~4000	200–1,500	400–7,000	500–2,000
Vertical permeability, md	60–470				
Oil saturation, %	50	50	80	55–65	55
Initial pressure, psig		591		75–150	
Solution gas/oil ratio, scf/STB		62			

original process, as developed by Butler, McNab, and Lo⁵³ in 1979, utilizes two parallel horizontal wells in a vertical plane: the injector being the upper well and the producer the lower well (Fig. 15.36, taken from Butler⁵⁴). If the oil/bitumen mobility is initially very low, steam is circulated in both wells for conduction heating of the oil around the wells. Steam is then injected into the upper well, while producing the lower well. As a result, steam rises forming a steam chamber with oil flowing at the sides of the chamber and condensate flowing inside the chamber, as shown in Fig. 15.36. This is an idealized situation. Other flow regime may occur depending on the oil and formation properties. For the simplest case, the oil production rate q_{oh} , in B/D per ft well length, is given by (multiplier “2” indicates flow from two sides of the steam chamber)

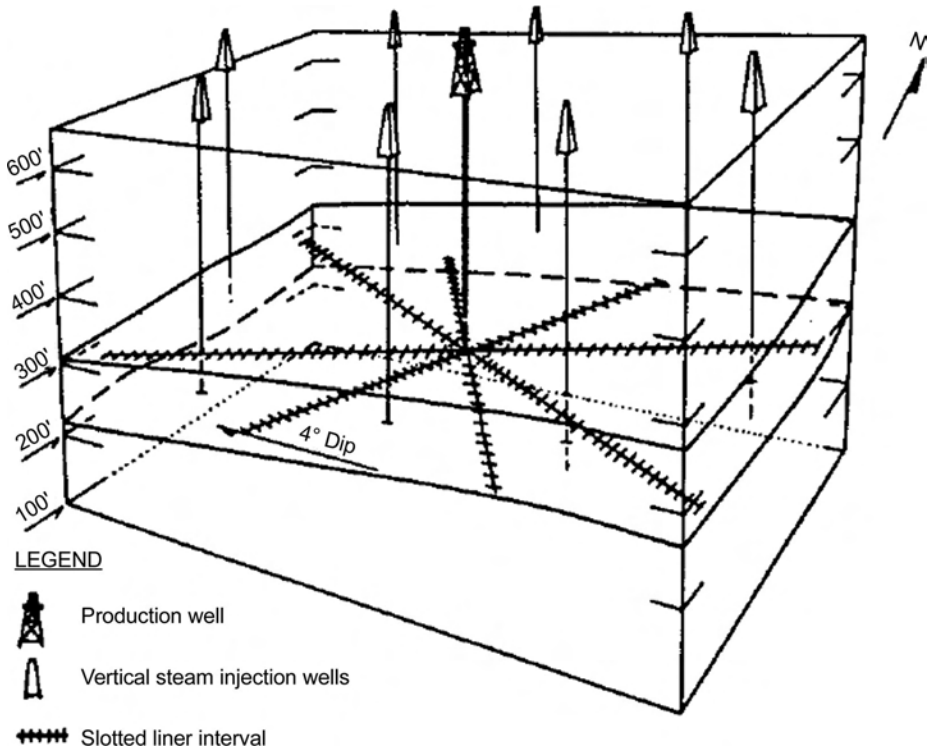


Fig. 15.34—Schematic of Kern River Hot Plate pilot injection and production wells.⁵¹

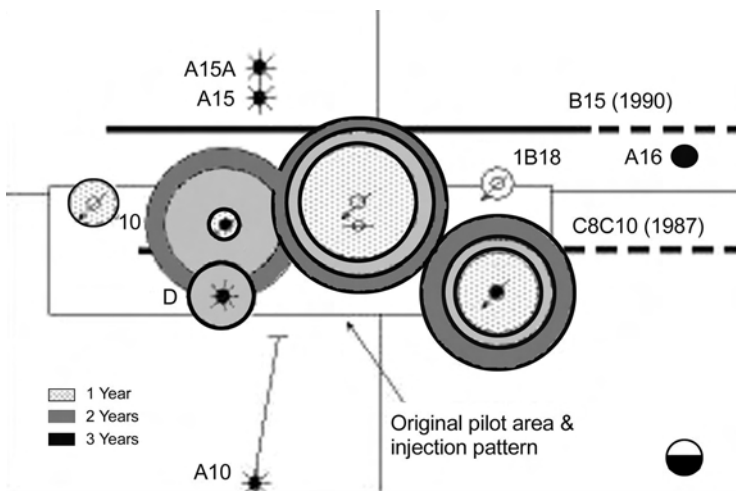


Fig. 15.35—Tangleflags project bubble map showing horizontal producer and vertical injectors and the growth of the steam zone over time (after Jespersen and Fontaine⁵²).

Mechanism:

- Steam condenses at interface
- Oil and condensate drain to well at bottom
- Flow is caused by gravity
- Chamber grows upwards and sideways

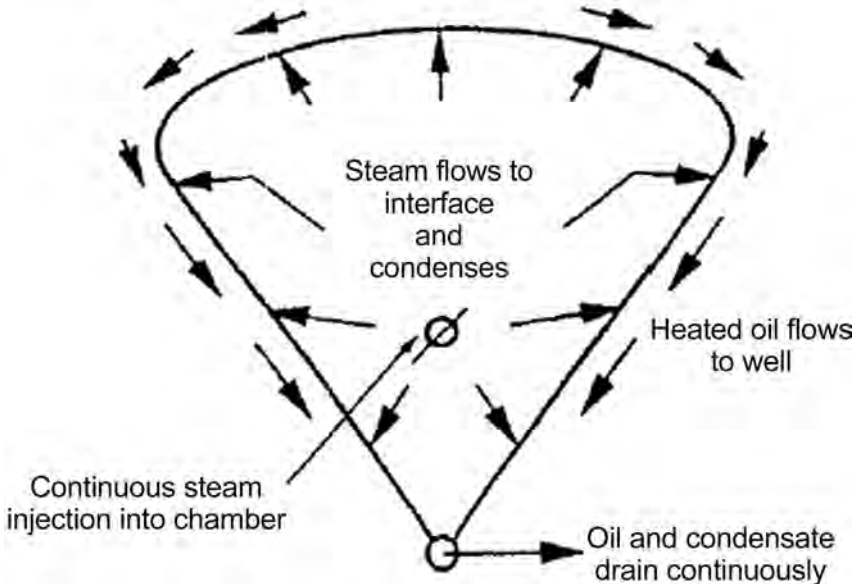


Fig. 15.36—Conceptual diagram of the SAGD process (after Butler⁵⁴).

$$q_{oh} = 2(0.295) \sqrt{\frac{2kk_{ro}\alpha\phi(S_o - S_{ors})h_h}{m^* v_{os}}}, \dots\dots\dots (15.105)$$

where the kinematic viscosity of oil (in centistokes) at the steam temperature, T_s , is given by v_s , and that at any other temperature, T , is given by

$$\left(\frac{v_{os}}{v}\right) = \left(\frac{T - T_R}{T_s - T_R}\right)^m, \dots\dots\dots (15.106)$$

where m is derived from the viscosity-temperature relationship of the oil.

Eq. 15.106 predicts rates of 0.1 to 0.7 B/D per ft for a horizontal well for an oil viscosity of 100,000 cp. For example, a 2,000-ft long well may be expected to produce about 800 B/D at a steam temperature of 400°F. The theory has been verified by laboratory experiments. Field results to-date have been encouraging. One commercial project (EnCana’s Foster Creek Project), consisting of 22 well pairs, has been in operation since October 2001. The current steam/oil ratios are averaging 2.5 bbl oil/bbl of steam. Earlier field tests of SAGD in Athabasca tar sands were successful at a depth of about 600 ft, which is too deep for surface mining and not deep enough for high-pressure steam injection.

SAGD is a complex process because gravity flow strongly relies on a high vertical permeability. The initial oil mobility determines the vertical spacing of the two wells. In a million cp

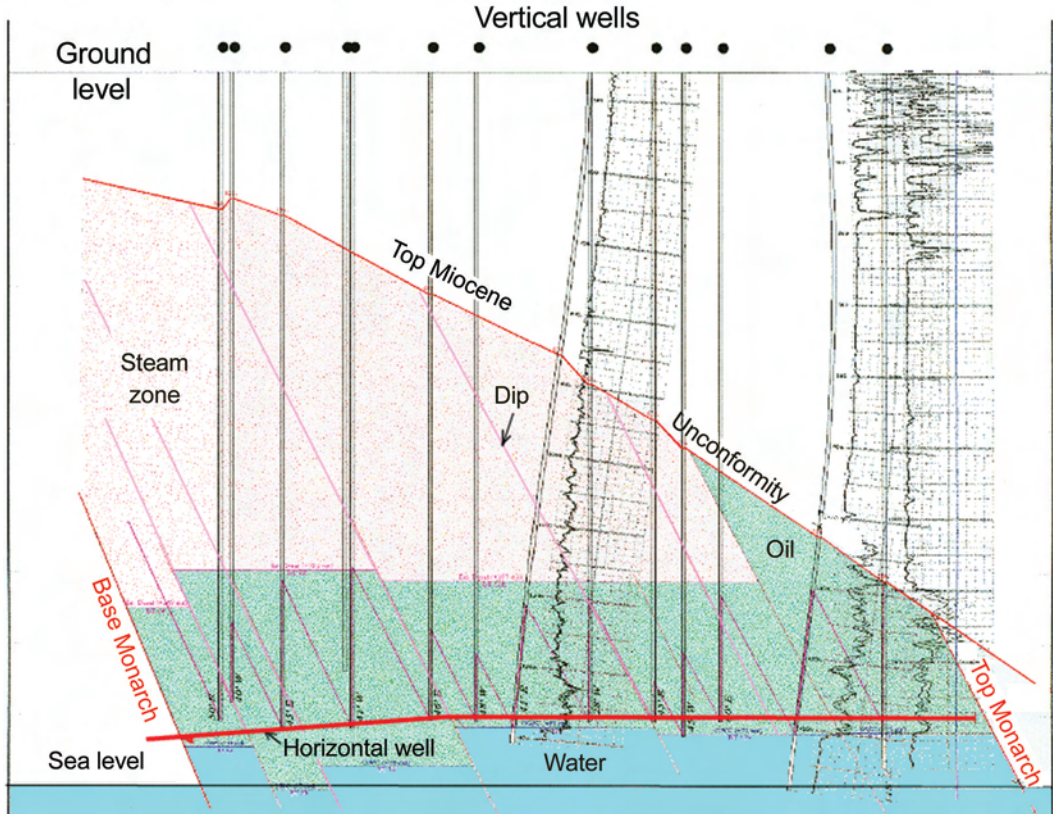


Fig. 15.37—Cross section of Midway Sunset Monarch sand cyclic steam project showing oil in bottom zone wedges bypassed by vertical wells but recovered by horizontal well.

tar sand, the spacing would be 5 to 6 m [16 to 20 ft]. It is also important that the steam chamber be sealed. There is no steam migration to offset vertical wells. In California, SAGD failed to achieve commercial success because of relatively high initial mobility of oil, as well as other reasons.

One variation of SAGD is known as single-well SAGD. Here, insulated tubing is used to inject steam into a single horizontal well, with production from the annulus. This process was successful in a few cases but generally failed. Another variation (Vapex) utilizes a suitable solvent (such as ethane, propane, etc.) instead of steam and is being field tested.

15.13.4 Cyclic Steam Stimulation and Other Uses of Horizontal Wells. Horizontal wells are being used for cyclic steam stimulation, much in the same manner as vertical wells, in Cold Lake, Alberta, and in Eastern Venezuela. In Cold Lake, horizontal well lengths are of the order of 3,000 ft, and steam slugs are very large (100,000 to 200,000 bbl). The resulting steam/oil ratios are 2 to 4, and performance is superior to SAGD continuous steamflood.⁵⁵ In Venezuela, wells are around 1,000 ft in length, and the steam slugs are of the order of 50,000 bbl. Response is good, with average stimulation ratios of 2 to 4 over a production period of 6 months.

In California, horizontal wells have been used sparingly in thermal projects, mainly because of sand control problems but also because of the fact that vertical wells are very cost effective, and it is difficult for horizontal wells to be competitive. Horizontal wells have successfully been incorporated into existing thermal projects to supplement conventional vertical-well performance for both Midway Sunset field cyclic steam^{56,57} and Cymric/McKittrick field

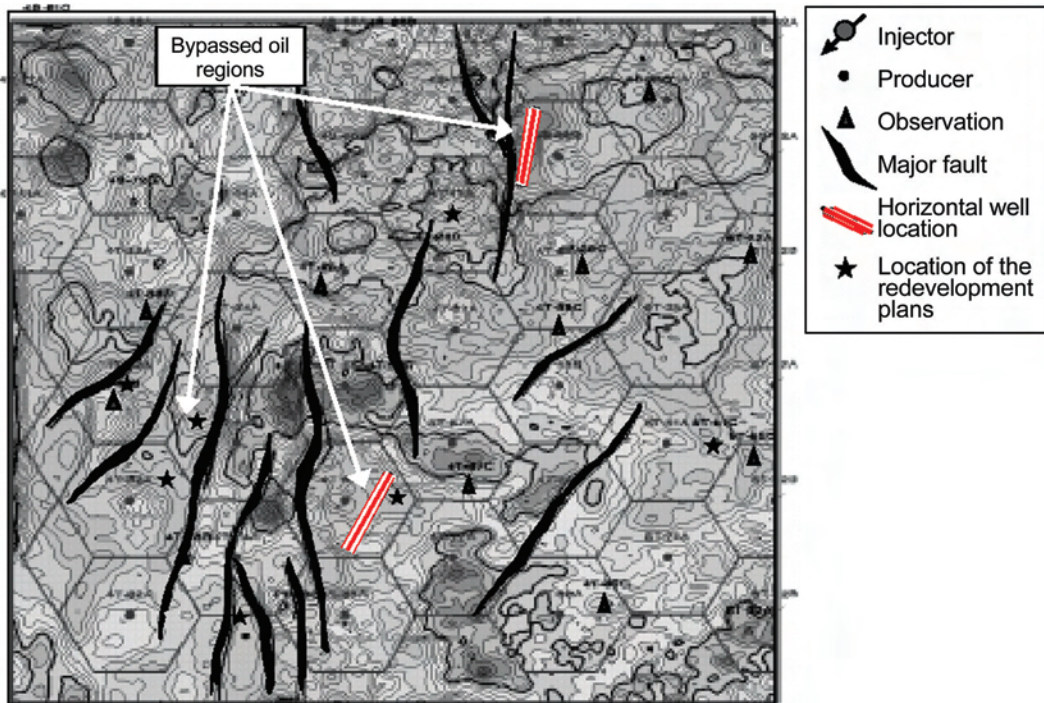


Fig. 15.38—Bypassed oil map of a zone in the Duri field and possible horizontal well locations.⁵⁹

steamfloods.⁵⁸ In the Duri field, Indonesia, horizontal wells are also being used to supplement conventional vertical-well steamflood.⁵⁹ Table 15.9 shows reservoir data for these three areas. All of these latter applications are accessing bypassed oil in mature projects for which vertical wells would be impractical. Fig. 15.37 is a schematic drawing showing the wedges of oil sand in the Midway Sunset cyclic steam project at the very bottom of the zones that cannot be accessed by the existing vertical wells but will be drained by the horizontal wells. Fig. 15.38⁵⁹ shows the result of a seismic study of the mature Duri steamflood. Highlighted on the map are pockets of oil that were bypassed by the flood because of proximity to a fault. The operators are strongly considering a suite of horizontal wells to access these reserves.

Nomenclature

- A = area, sq ft [m²]
- A_{cD} = dimensionless factor defined by Eq. 15.45
- A_{RD} = dimensionless buoyancy defined in Eq. 15.23
- A_t = time-dependent heated area, sq ft [m²]
- B_o = oil formation volume factor, RB/STB [res m³/stock-tank m³]
- C = isobaric specific heat
- C_{an} = isobaric specific heat of annular fluid, Btu/(lbm-°F) [kJ/kg·K]
- C_o = isobaric specific heat of oil, Btu/(lbm-°F) [kJ/kg·K]
- C_w = isobaric specific heat of water, Btu/(lbm-°F) [kJ/kg·K]
- D = depth below surface, ft [m]
- $erfc(x)$ = complementary error function
- E = efficiency
- E_c = fraction of oil displaced that is produced
- E_h = heat efficiency—fraction of injected heat remaining in reservoir

- f = volumetric fraction of noncondensable gas in vapor phase
 f_b = hot-water zone oil-rate factor defined by Eq. 15.54
 f_h = heat utilization factor defined by Eq. 15.55
 f_{hv} = fraction of heat injected as latent heat
 f_p = fraction of heat injected that is produced
 f_{pD} = heat loss factor caused by hot fluid production
 f_R = oil recovery factor defined by Eq. 15.14
 f_s = steam quality
 $f_{(tD)}$ = function of dimensionless time defined by Eq. 15.102
 $f(T)$ = temperature function defined in Eq. 15.56
 f_{Vr} = conductive heat loss factor caused by radial conduction
 f_{Vz} = conductive heat loss factor caused by vertical conduction
 F_1, F_2 = constants defined in Table 15.2
 F_{fo} = ratio of fuel burned to produced oil, B/B [m^3/m^3]
 F_{of} = produce oil/fuel burned ratio, B/B [m^3/m^3]
 F_{os} = produce oil/injected steam ratio, B/B [m^3/m^3]
 F_{Sor} = residual oil factor used in Eq. 15.37
 $F(T_{ins}, T_{ei})$ = temperature function defined by Eq. 15.97
 g = gravity acceleration constant, 32.174 ft/sec² [9.8067 m/s²]
 g_c = conversion factor in Newton's second law of motion, 32.174 lbf-ft/lbf-s² [$1.0 \text{ kg}\cdot\text{m}/\text{N}\cdot\text{s}^2$]
 $G(t_D)$ = function defined by Eq. 15.10
 h = enthalpy per unit mass, Btu/lbm [kJ/kg]
 h_e = fluid level in reservoir at external boundary, ft [m]
 h_f = enthalpy of liquid portion of saturated steam, Btu/lbm [kJ/kg]
 h_{fc} = forced convection coefficient of heat transfer, Btu/(sq ft-D-°F) [$\text{kJ}/\text{m}^2\cdot\text{d}\cdot\text{K}$]
 h_{fs} = enthalpy of < 100% quality saturated steam, Btu/lbm [kJ/kg]
 h_{fi} = film coefficient of heat transfer, Btu/(sq ft-D-°F) [$\text{kJ}/\text{m}^2\cdot\text{d}\cdot\text{K}$]
 h_{fv} = enthalpy of vapor portion of saturated steam, Btu/lbm [kJ/kg]
 h_h = fluid level in stimulated reservoir, ft [m]
 h_n = net reservoir thickness, ft [m]
 h_{pi} = film coefficient of heat transfer at pipe inner radius, Btu/(sq ft-D-°F) [$\text{kJ}/\text{m}^2\cdot\text{d}\cdot\text{K}$]
 h_{po} = film coefficient of heat transfer at pipe outer radius, Btu/(sq ft-D-°F) [$\text{kJ}/\text{m}^2\cdot\text{d}\cdot\text{K}$]
 h_r = coefficient of radiant heat transfer for the outermost surface, Btu/(sq ft-D-°F) [$\text{kJ}/\text{m}^2\cdot\text{d}\cdot\text{K}$]
 $h_{rc,an}$ = radiant/convection heat transfer coefficient in well annulus, Btu/(sq ft-D-°F) [$\text{kJ}/\text{m}^2\cdot\text{d}\cdot\text{K}$]
 h_s = steam zone thickness, ft [m]
 h_t = gross reservoir thickness, ft [m]
 h_v = enthalpy of 100% quality (saturated) saturated steam, Btu/lbm [kJ/kg]
 h_w = fluid level in cold wellbore, ft [m]
 i_w = cold water equivalent steam injection rate, B/D [m^3/d]
 J = productivity of a cold well, B/psi-D [$\text{m}^3/\text{kPa}\cdot\text{d}$]
 J_h = productivity of a stimulated well, B/psi-D [$\text{m}^3/\text{kPa}\cdot\text{d}$]

- k = reservoir permeability, md [μm^2]
 k_{ro} = relative permeability to oil
 k_{rs} = relative permeability to steam
 L = distance between wells, ft [m]
 m = mass, lbm [kg]
 m^* = exponent in Eqs. 15.33, 15.105, and 15.106
 $m_{\text{casing_blow}}$ = mass (gas) extracted from system, lbm [kg]
 m_i = mass injection, lbm [kg]
 m_{influx} = mass exiting system, lbm [kg]
 m_l = mass of liquid, lbm [kg]
 $m_{(o/w)\text{influx}}$ = mass flowing into system, lbm [kg]
 $m_{(o/w)\text{prod}}$ = mass (fluid) extracted from system, lbm [kg]
 m_v = mass of vapor, lbm [kg]
 $m_{Z(\text{accum})}$ = mass accumulating in system, lbm [kg]
 M_g = volumetric heat capacity of gas, Btu/(ft³-°F) [kJ/m³·K]
 M_o = volumetric heat capacity of oil, Btu/(ft³-°F) [kJ/m³·K]
 M_R = volumetric heat capacity of the reservoir, Btu/(ft³-°F) [kJ/m³·K]
 M_s = volumetric heat capacity of steam zone, Btu/(ft³-°F) [kJ/m³·K]
 M_S = volumetric heat capacity of surrounding formation, Btu/(ft³-°F) [kJ/m³·K]
 M_w = volumetric heat capacity of water, Btu/(ft³-°F) [kJ/m³·K]
 M_o = volumetric heat capacity of reservoir rocks, Btu/(ft³-°F) [kJ/m³·K]
 n = index of time increment
 N = initial oil in place, B [m³]
 N_d = oil displacement rate, B/D [m³/d]
 N_{Gr} = Grashof number
 N_m = initial mobile oil in place, B [m³]
 N_p = cumulative oil produced, B [m³]
 N_{Pr} = Prandtl number
 N_{Re} = Reynolds number
 p = atmospheric pressure, psia [kPa]
 p_e = external boundary pressure, psia [kPa]
 p_s = steam pressure, psia [kPa]
 p_w = wellbore pressure, psia [kPa]
 q_{excess} = steam injection rate to make up for surface heat losses, B/D [m³/d]
 q_{gh} = hot gas production rate, Mcf/D [std m³/d]
 q_{is} = reproduced steam rate, B/D [m³/d]
 q_{iso} = initial steam injection rate, B/D [m³/d]
 q_{ls} = steam injection rate to make up for reservoir heat losses, B/D [m³/d]
 q_{oc} = cold oil production rate, B/D [m³/d]
 q_{oD} = displaced oil rate defined in Eq. 15.49, B/D [m³/d]
 q_{og} = oil production rate owing to gravity displacement, B/D [m³/d]
 q_{oh} = hot oil production rate, B/D [m³/d]
 q_{oi} = initial oil production rate, B/D [m³/d]
 q_{ot} = total oil production rate, B/D [m³/d]
 q_{ov} = oil production rate because of viscous displacement, B/D [m³/d]
 q_{ps} = steam rate to replace reservoir volume of produced oil, B/D [m³/d]

- q_{wc} = cold water production rate, B/D [m^3/d]
 q_{wh} = hot water production rate, B/D [m^3/d]
 Q = amount of injected heat remaining in reservoir, Btu [kJ]
 $Q_{\text{casing_blow}}$ = heat removed with produced gas, Btu [kJ]
 Q_i = total heat injected, Btu [kJ]
 Q_{influx} = heat leaving system, Btu [kJ]
 Q_l = heat lost in reservoir, Btu [kJ]
 Q_{ls} = surface piping heat loss/unit length, Btu/ft [kJ/m]
 Q_{ot} = cumulative oil recovery at time (t), B/D [m^3/d]
 $Q_{(o/w)\text{influx}}$ = heat flowing into system, Btu [kJ]
 $Q_{(o/w)\text{prod}}$ = heat removed with produced liquids, Btu [kJ]
 $Q_{z(\text{accum})}$ = heat accumulating in system, Btu [kJ]
 \dot{Q}_i = heat injection rate, Btu/D [kJ/d]
 \dot{Q}_l = heat loss rate, Btu/D [kJ/d]
 \dot{Q}_p = heat removed with produced fluids, Btu/D [kJ/d]
 \dot{Q}_{sv} = volumetric heat injection rate, MMBtu/D/acre-ft [kJ/ m^3]
 r = radius of reservoir, ft [m]
 r_{ci} = casing internal radius, ft [m]
 r_{co} = outer casing radius, ft [m]
 r_e = external radius of heated zone, ft [m]
 r_{Ea} = altered radius in earth around wellbore, ft [m]
 r_h = radius of heated or steam zone, ft [m]
 r_i = inside pipe radius, ft [m]
 r_{ins} = insulation external radius, ft [m]
 r_o = outside pipe radius, ft [m]
 r_w = radius of well, ft [m]
 R_h = overall specific thermal resistance, °F-ft-D/Btu [$\text{K}\cdot\text{m}\cdot\text{d}/\text{kJ}$]
 S = skin factor before stimulation
 S_g = gas saturation fraction
 S_h = skin factor after stimulation
 S_o = oil saturation
 S_{oi} = initial oil saturation fraction
 S_{om} = mobile oil saturation fraction
 S_{or} = residual oil saturation fraction
 S_{oras}, S_{orb} = terms used in Eq. 15.40
 S_{ors} = residual oil saturation to steam fraction
 S_{orw} = residual oil saturation to water fraction
 S_w = water saturation fraction
 t = time, D [d]
 t^* = time at which steam injection rate reduction is to begin, D [d]
 t_{cD} = critical dimensionless time
 t_D = dimensionless time
 T = average temperature in heated reservoir, °F
 T^* = temperature above which oil saturation is reduced to S_{orw} , °F
 T_a = air temperature, °F
 T_A = ambient temperature, °F

- T_b = bulk fluid temperature, °F
 T_{BHF} = bottomhole fluid temperature, °F
 T_{ci} = temperature of casing wall, °F
 T_E = temperature of earth, °F
 T_{FW} = steam generator feedwater temperature, °F
 T_h = temperature in stimulated zone, °F
 T_i = influx water temperature, °F
 T_o = temperature of outer surface, °F
 T_p = produced fluid temperature, °F
 T_R = unaffected reservoir temperature, °F
 T_s = steam temperature, °F
 T_{SZ} = steam zone temperature, °F
 u = volumetric flux, ft³/sq ft-D [m/d]
 U = unit function equals 1 for $t_D - t_{cD} > 0$, 0 for $t_D - t_{cD} < 0$ in Eq. 15.22
 V_{oD} = dimensionless factor defined by Eq. 15.42
 V_{pD} = dimensionless factor defined by Eq. 15.43
 V_s = steam zone volume, acre ft [m³]
 V_{sz} = steam zone volume per Neuman in Eq. 15.52, B [m³]
 w_{st} = mass flow rate of dry steam, lbm/D [kg/d]
 x = distance along the x ordinate
 X = factor defined in Eq. 15.30
 Y = factor defined in Eq. 15.31
 α = thermal diffusivity of reservoir, ft²/D [m²/d]
 α_E = thermal diffusivity of earth, ft²/D [m²/d]
 α_s = thermal diffusivity of surrounding formation, ft²/D [m²/d]
 β_1 = thermal volumetric expansion coefficient, 1/°F [1/K]
 β_{an} = volumetric thermal expansion coefficient of gas in annulus, 1/°F [1/K]
 γ = specific gravity
 Δ = increment or decrement
 Δh_h = change in stimulated zone fluid level, ft [m]
 Δt = time steps, D [d]
 ΔT = steam temperature/reservoir temperature, T_s/T_R , °F
 $\Delta\gamma$ = oil/steam specific gravity difference
 $\Delta\rho$ = density difference between water and oil, lbm/ft³ [kg/m³]
 ε = emissivity
 ε_{ci} = radiant emissivity of casing wall
 ε_{ins} = radiant emissivity of insulation outer surface
 θ_c = wetting contact angle, deg (°) [rad]
 θ = formation dip angle, deg (°) [rad]
 λ = thermal conductivity, Btu/(ft-D-°F) [kJ/m·d·K]
 λ_a = thermal conductivity of air, Btu/(ft-D-°F) [kJ/m·d·K]
 $\lambda_{a,a}$ = thermal conductivity of air in well annulus, Btu/(ft-D-°F) [kJ/m·d·K]
 λ_E = thermal conductivity of unaltered earth, cp [Pa·s]
 λ_{Ea} = thermal conductivity of altered earth, cp [Pa·s]
 λ_{ins} = thermal conductivity of insulation, cp [Pa·s]
 λ_p = thermal conductivity of pipe, cp [Pa·s]

- λ_s = thermal conductivity of surrounding formation, cp [Pa·s]
 μ = viscosity, cp [Pa·s]
 μ_a = viscosity of air, cp [Pa·s]
 μ_{an} = viscosity of well annulus gas, cp [Pa·s]
 μ_{oh} = hot oil viscosity, cp [Pa·s]
 μ_{oi} = initial oil viscosity, cp [Pa·s]
 μ_s = steam viscosity, cp [Pa·s]
 π = constant pi, 3.141
 ρ = density, lbm/ft³ [kg/m³]
 $\rho_{a,sc}$ = density of air, lbm/ft³ [kg/m³]
 ρ_{an} = density of well annulus gas, lbm/ft³ [kg/m³]
 ρ_o = density of oil, lbm/ft³ [kg/m³]
 ρ_s = density of dry steam, lbm/ft³ [kg/m³]
 ρ_w = density of water, lbm/ft³ [kg/m³]
 $\rho_{w,sc}$ = density of water at standard conditions, 62.4 lbm/ft³ [662.69 kg/m³]
 σ = interfacial tension, oil/water, dyne/cm [mN/m]
 τ = time since location in reservoir reached steam temperature, D [d]
 v_s = steam specific volume, ft³/lbm [m³/kg]
 v_w = wind velocity, miles/hr [km/h]
 ϕ = porosity

Subscripts

- a = air
 cem = cement
 d = displaced
 ins = insulation
 o/w = oil/water
 prod = production

Superscripts

- * = special value as in t^* and T^*
 x = integration variable in [Eq. 15.22](#)

References

1. Prats, M.: *Thermal Recovery*, Monograph Series, SPE, Richardson, Texas (1982) 7, 1.
2. Moritis, G.: "EOR Weathers Low Oil Prices," *Oil & Gas J.* (March 2000) 39.
3. Keenan, J.H. et al.: *Steam Tables—Thermodynamic Properties of Water Including Vapor, Liquid, and Solid Phases*, John Wiley & Sons Inc., New York City (1969) 2.
4. Chien, S.: "Empirical Correlations of Saturated Steam Properties," paper SPE 20319 presented at the 1991 SPE Asia-Pacific Conference, Perth, Australia, 4–7 November.
5. Carslaw, H.S. and Jaeger, J.C.: *Conduction of Heat in Solids*, Oxford U. Press, Amen House, London (1950) 373.
6. Marx, J.W. and Langenheim, R.H.: "Reservoir Heating by Hot Fluid Injection," *Trans., AIME* (1959) **216**, 312.
7. van Lookeren, J.: "Calculation Methods for Linear and Radial Steam Flow in Oil Reservoirs," *SPEJ* (June 1983) 427.
8. Farouq Ali, S.M.: *Oil Recovery by Steam Injection*, Producers Publishing Co., Bradford, Pennsylvania (1970) 51.

9. Ramey, H.J. Jr.: "Discussion of Reservoir Heating by Hot Fluid Injection," *Trans.*, AIME (1959) **216**, 364.
10. Prats, M.: "The Heat Efficiency of Thermal Recovery Processes," *JPT* (March 1969) 323; *Trans.*, AIME, **246**.
11. Mandl, G. and Volek, C.W.: "Heat and Mass Transport in Steam Drive Processes," *SPEJ* (March 1969) 59; Reprint Series, SPE, Richardson, Texas (1972) **10**, 27.
12. Myhill, N.A. and Stegemeier, G.L.: "Steamdrive Correlation and Prediction," *JPT* (February 1978) 173.
13. Neuman, C.H.: "A Gravity Override Model of Steamdrive," *JPT* (January 1985) 163.
14. Owens, B.K. and Ziegler, V.M.: "An Oil Production Model for a Well Producing by Both Gravity Drainage and Viscous Flow From a Mature Steamflood," paper SPE 29656 presented at the 1995 SPE Western Regional Meeting, Bakersfield, California, 8–10 March.
15. Closmann, P.J.: "A Simplified Gravity Drainage Oil Production Model for Mature Steamdrives," paper SPE 25790 presented at the 1993 SPE International Thermal Operations Symposium, Bakersfield, California, 8–10 February.
16. Kimber, K.D. *et al.*: "The Role of Latent Heat in Heat Management of Mature Steamfloods," paper SPE 29659 presented at the 1995 SPE Western Regional Meeting, Bakersfield, California, 8–10 March.
17. Ward, R.C. and Sharpe, H.N.: "Mechanistic Modeling of Casing Blow Shut-In Effects and Strategies for the Recovery of Lost Production," paper SPE 37561 presented at the 1997 SPE International Thermal Operations Symposium, Bakersfield, California, 10–12 February.
18. Hayes, H.J. *et al.*: *Enhanced Oil Recovery*, National Petroleum Council, Industry and Advisory to the U.S. Department of the Interior, Washington DC (1984).
19. Iyoho, A.W.: "Selecting Enhanced Oil Recovery Processes," *World Oil* (November 1978) 61.
20. Farouq Ali, S.M.: "Current Status of Steam Injection as a Heavy Oil Recovery Method," *J. of Canadian Petroleum Technology* (January–March 1974) 1.
21. Venkatesh, E.S., Venkatesh, V.E., and Menzie, D.E.: "PDS Data Base Aids Selection of EOR Method," *Oil & Gas J.* (June 1998) 63.
22. Chu, C.: "State-of-the-Art Review of Steamflood Field Projects," paper SPE 11733 presented at the 1983 SPE California Regional Meeting, Ventura, California, 23–25 March.
23. Donaldson, A.B. and Donaldson, J.E.: "Dimensional Analysis of the Criteria for Steam Injection," paper SPE 38303 presented at the 1997 SPE Western Regional Meeting, Long Beach, California, 25–27 June.
24. Doscher, T.M. and Ghassemi, F.: "Limitations on the Oil/Steam Ratio for Truly Viscous Crudes," *JPT* (July 1984) 1123.
25. Greaser, G.R. and Shore, R.A.: "Steamflood Performance in the Kern River Field," paper SPE 8834 presented at the 1980 SPE/DOE Symposium on Enhanced Oil Recovery, Tulsa, 20–23 April.
26. Restine, J.L.: "On the Effect of Viscosity and Sand Thickness on Kern River Field, Single-Zone, Steamflood Performance," paper SPE 21526 presented at the 1991 SPE International Thermal Operations Symposium, Bakersfield, California, 7-8 February.
27. Rattia, A. and Farouq Ali, S.M.: "Effects of Formation Compaction on Steam Injection Response," paper SPE 10323 presented at the 1981 SPE Annual Technical Conference and Exhibition, San Antonio, Texas, 5–7 October.
28. Jones, J.: "Steamdrive Model for Hand-Held Programmable Calculators," *JPT* (September 1981) 1583; *Trans.*, AIME, **271**.
29. van der Knaap, W.: "Physical Aspects of Some Steam Injection Theories, an Application," paper SPE 26293 available from SPE, Richardson, Texas (1993).
30. Vogel, J.V.: "Simplified Heat Calculations for Steamfloods," *JPT* (July 1984) 1127.
31. Kumar, M. and Ziegler, V.M.: "Injection Schedule and Production Strategies for Optimizing Steamflood Performance," *SPEJ* (May 1993) 101.
32. Gomaa, E.E.: "Correlations for Predicting Oil Recovery by Steamflood," *JPT* (February 1980) 325.
33. Owens, W.D. and Suter, V.E.: "Steam Stimulation—Newest Form of Secondary Petroleum Recovery," *Oil & Gas J.* (April 1965) **90**, 82.
34. Boberg, T.C. and Lantz, R.B.: "Calculation of the Production Rate of a Thermally Stimulated Well," *JPT* (December 1966) 1613; *Trans.*, AIME, **237**.

35. Towson, D.E. and Boberg, T.C.: "Gravity Drainage in Thermally Stimulated Wells," *J. of Canadian Petroleum Technology* (October–December 1967) 130.
36. Jones, J.: "Why Cyclic Steam Predictive Models Get No Respect," *SPE* (February 1992) 67.
37. Rivero, R.T. and Heintz, R.C.: "Resteaming Time Determination—Case History of a Steam-Soak Well in Midway Sunset," *JPT* (June 1975) 655.
38. McBean, W.N.: "Attic Oil Recovery by Steam Displacement," paper SPE 4170 presented at the 1972 SPE California Regional Meeting, Bakersfield, California, 8–10 November.
39. Jones, J. and Cawthon, G.J.: "Sequential Steam: An Engineered Cyclic Steaming Method," *JPT* (July 1990) 848–853, 901.
40. Kuo, C.H., Shain, S.A., and Phocas, D.M.: "A Gravity Drainage Model for the Steam-Soak Process," *SPEJ* (June 1970) 119; *Trans., AIME*, **249**.
41. McAdams, W.H., Williams, G.C., and Smith, K.A.: "Standard Handbook for Mechanical Engineers," *Transmission of Heat by Conduction and Convection*, T. Baumeister and L. Marks (eds.), seventh edition, McGraw-Hill Book Co. Inc., New York City (1967) Chap. 4, 92.
42. Rohsenow, W.M. and Hartnett, J.P.: *Handbook of Heat Transfer*, McGraw-Hill Book Co. Inc., New York City (1973) 3.
43. Willhite, G.P.: "Overall Heat Transfer Coefficients on Steam and Hot Water Injection Wells," *JPT* (May 1967) 607.
44. Dennis, E.L.: "Project Design for Slimhole Steam Injectors in Thermal Recovery Projects as Compared to Conventional Steam Injectors," paper SPE 29629 presented at the 1995 SPE Western Regional Meeting, Bakersfield, California, 8–10 March.
45. Ramey, H.J. Jr.: "Wellbore Heat Transmission," *JPT* (April 1962) 427; *Trans., AIME*, **225**.
46. van Dorp, J.J. and Roach, R.H.: "Steam Management in Composite Mature Steamfloods—Midway Sunset Field," paper SPE 29658 presented at the 1995 SPE Western Regional Meeting, Bakersfield, California, 8–10 March.
47. Ziegler, V.M. *et al.*: "Recommended Practices for Heat Management of Steamflood Projects," paper SPE 25808 presented at the 1993 SPE International Thermal Operations Symposium, Bakersfield, California, 8–10 February.
48. Jones, J.A.: "Discussion of Simulating a Steamflood at the Georgsdorf Field, Federal Republic of Germany," *JPT* (June 1985) 1069.
49. Chang, H.L., George, A.E., and Farouq Ali, S.M.: "Performance of Horizontal-Vertical Combinations for Steamflooding Bottomwater Formations," *J. Cdn. Pet. Tech.* (May 1992) 41.
50. Huang, W.S. and Hight, M.A.: "Evaluation of Steamflood Processes With Horizontal Wells," *SPE* (February 1989) 69.
51. Dietrich, J.K.: "The Kern River Horizontal-Well Steam Pilot," *SPE* (August 1988) 935.
52. Jespersen, P.J. and Fontaine, T.J.C.: "The Tangleflags North Pilot: A Horizontal Well Steamflood," *J. Cdn. Pet. Tech.* (May 1993) 52.
53. Butler, R.M., McNab, G.S., and Lo, H.Y.: "Theoretical Studies on the Gravity Drainage of Heavy Oil During In-Situ Steam Heating," *Cdn. J. of Chem. Eng.* (August 1981) **59**, 455 (paper presented in 1979).
54. Butler, R.M.: "A New Approach to the Modeling of Steam-Assisted Gravity Drainage," *J. Cdn. Pet. Tech.* (May/June 1985) 42.
55. Scott, G.R.: "Comparison of CSS and SAGD Performance in the Clearwater Formation at Cold Lake," paper SPE 79020 presented at the 2002 SPE International Thermal Operations and Heavy Oil Symposium and International Horizontal Well Technology Conference, Calgary, 4–7 November.
56. Chona, R.A. *et al.*: "Evaluation of a Horizontal Infill Well in a Mature Cyclic-Steam Project," paper SPE 37087 presented at the 1996 SPE International Conference on Horizontal Well Technology, Calgary, 18–20 November.
57. McKay, C., Jones, J., and Pomerene, J.: "Successful Horizontal Producers in Midway Sunset Thermal Operations," paper SPE 83479 presented at the 2003 SPE Western Regional/AAPG Pacific Section Meeting, Long Beach, California, 19–24 May.
58. Cline, V.J. and Basham, M.: "Improving Project Performance in a Heavy Oil Horizontal Well Project in the San Joaquin Valley, California," paper SPE 78981 presented at the 2002 SPE International Thermal Operations and Heavy Oil Symposium and International Horizontal Well Technology Conference, Calgary, 4–7 November.

59. Sigit, R. *et al.*: “Seismically Guided Bypassed Oil Identification in A Mature Steamflood Area,” paper SPE 57261 presented at the 1999 SPE Asia Pacific Improved Oil Recovery Conference, Kuala Lumpur, 25–26 October.

General References

- Prats, M.: *Thermal Recovery*, Monograph Series, SPE, Richardson, Texas (1982) **7**.
 Green, D.W. and Willhite, G.P.: *Enhanced Oil Recovery*, Textbook Series, SPE, Richardson, Texas (1998) **6**, 301.
 Hong, K.C.: *Steamflood Reservoir Management Thermal Enhanced Oil Recovery*, PennWell Books, Tulsa (1994).
Thermal Recovery Processes, Reprint Series, SPE, Richardson, Texas (1965) **7**.
Thermal Recovery Processes, Reprint Series, SPE, Richardson, Texas (1985) **7**.
Thermal Recovery Techniques, Reprint Series, SPE, Richardson, Texas (1972) **10**.
 Lake, L.W.: *Enhanced Oil Recovery*, Prentice Hall, Indianapolis, Indiana (1989).

SI Metric Conversion Factors

acre	× 4.046 856	E - 01 = ha
acre-ft	× 1.233 489	E + 03 = m ³
°API	141.5/(131.5 + °API)	= g/cm ³
B	× 1.590	E - 01 = m ³
B/D	× 1.590	E - 01 = m ³ /d
Btu	× 1.055 056	E + 00 = kJ
Btu/(ft-D-°F)	× 6.231	E + 00 = kJ/m·d·K
Btu/hr	× 2.930 711	E - 01 = W
Btu/lbm	× 2.326	E + 01 = kJ/kg
Btu/(lbm-°F)	× 4.187	E + 00 = kJ/kg·K
cp	× 1.0*	E - 03 = Pa s
D	× 1.0	E + 00 = d
ft	× 3.048*	E - 01 = m
ft ²	× 9.290 304*	E - 02 = m ²
ft ³	× 2.831 685	E - 02 = m ³
°F	(°F - 32)/1.8	= °C
lbm	× 4.536	E - 01 = kg
lbm/ft ³	× 1.062	E + 01 = kg/m ³
MM Btu/D/acre-ft	× 8.556	E + 02 = kJ/m ³
psi	× 6.894 757	E + 00 = kPa
psia	× 6.895	E + 00 = kPa

*Conversion factor is exact.

Chapter 16

In-Situ Combustion

William E. Brigham and Louis Castanier, Stanford U.

16.1 Introduction

In-situ combustion (ISC) is the oldest thermal-recovery technique. It has been used for more than nine decades with many economically successful projects. Nevertheless, it is regarded as a high-risk process by many primarily because of the many failures of early field tests. Most of those failures came from the application of a good process (ISC) to the wrong reservoirs or the poorest prospects. An objective of this chapter is to clarify the potential of ISC as an economically viable oil-recovery technique for a variety of reservoirs. This chapter is a summary containing a description of ISC, a discussion of laboratory screening techniques, an illustration of how to apply laboratory results to field design, a review of performance-prediction methods, a discussion of operational practices and problems, and an analysis of field results. For a more complete review, the work of Sarathi,¹ Prats,² and Burger *et al.*³ should be consulted.

16.2 Process Description

ISC is basically injection of an oxidizing gas (air or oxygen-enriched air) to generate heat by burning a portion of resident oil. Most of the oil is driven toward the producers by a combination of gasdrive (from the combustion gases), steam, and waterdrive. This process is also called fire flooding to describe the movement of a burning front inside the reservoir. Based on the respective directions of front propagation and air flow, the process can be forward (when the combustion front advances in the same direction as the air flow) or reverse (when the front moves against the air flow).

16.2.1 Reverse Combustion. This process has been studied extensively in laboratories and tried in the field. The idea is that it could be a useful way to produce very heavy oils with high viscosity. In brief, it has not been successful economically for two major reasons.

First, combustion started at the producer results in hot produced fluids that often contain unreacted oxygen. These conditions require special, high-cost tubulars to protect against high temperatures and corrosion. More oxygen is required to propagate the front compared to forward combustion, thus increasing the major cost of operating an ISC project.

Second, unreacted, coke-like heavy ends will remain in the burned portion of the reservoir. At some time in the process, the coke will start to burn, and the process will revert to forward

combustion with considerable heat generation but little oil production. This has occurred even in carefully controlled laboratory experiments.

In summary, reverse combustion has been found difficult to apply and economically unattractive.

16.2.2 Forward Combustion. Because only forward combustion is practiced in the field, we will only consider this case. Forward combustion can be further characterized as “dry” when only air or enriched air is injected or “wet” when air and water are coinjected.

Dry Combustion. The first step in dry forward ISC is to ignite the oil. In some cases, autoignition occurs when air injection begins if the reservoir temperature is fairly high and the oil is reasonably reactive. This often occurs in California reservoirs. Ignition has been induced with downhole gas burners, electrical heaters, and/or injection of pyrophoric agents or steam injection; it will be discussed in more detail later.

After ignition, the combustion front is propagated by a continuous flow of air. Rather than an underground fire, the front is propagated as a glow similar to the hot zone of a burning cigarette or hot coals in a barbecue. As the front progresses into the reservoir, several zones exist between injector and producer as a result of heat, mass transport, and chemical reactions. [Fig. 16.1⁴](#) is an idealized representation of the various zones and the resulting temperature and fluid-saturation distributions. In the field, there are transitions between zones; however, the concepts illustrated provide insight on the combustion process.

Zone Definitions. Starting from the injector, seven zones have been defined.

- A—The burned zone is the volume already burned. This zone is filled with air and may contain small amounts of residual unburned organic solids. Because it has been subjected to high temperatures, mineral alterations are possible. Because of the continuous airflow from the injector, the burned-zone temperature increases from injected-air temperature at the injector to combustion-front temperature at the combustion front.

- B—The combustion front is the highest temperature zone. It is very thin, often no more than several inches thick. It is in this region that oxygen combines with the fuel and high-temperature oxidation occurs. The products of the burning reactions are water and carbon oxides. The fuel is often misnamed coke. In fact, it is not pure carbon but a hydrocarbon with H/C atomic ratios ranging from approximately 0.6 to 2.0. This fuel is formed in the thermal-cracking zone just ahead of the front and is the product of cracking and pyrolysis, which is deposited on the rock matrix. The amount of fuel burned is an important parameter because it determines how much air must be injected to burn a certain volume of reservoir.

- C/D—The cracking/vaporization zone is downstream of the front. The crude is modified in this zone by the high temperature of the combustion process. The light ends vaporize and are transported downstream, where they condense and mix with the original crude. The heavy ends pyrolyze, resulting in CO₂, CO, hydrocarbon gases, and solid organic fuel deposited on the rock.

- E—The steam plateau. This is the zone in which some of the hydrocarbon vapors condense. Most of those condense further downstream as the steam condenses. The steam plateau temperature depends on the partial pressure of the water in the gas phase. Depending on the temperature, the original oil may undergo a mild thermal cracking, often named visbreaking, that usually reduces oil viscosity.

- F—A water bank exists at the leading edge of the steam plateau, where the temperature is less than steam saturation temperature. This water bank decreases in temperature and saturation downstream, with a resulting increase in oil saturation.

- G—The oil bank. This zone contains most of the displaced oil, including most of the light ends that result from thermal cracking.

- H—Beyond these affected areas is the undisturbed original reservoir. Gas saturation will increase slightly in this area because of the high mobility of combustion gases.

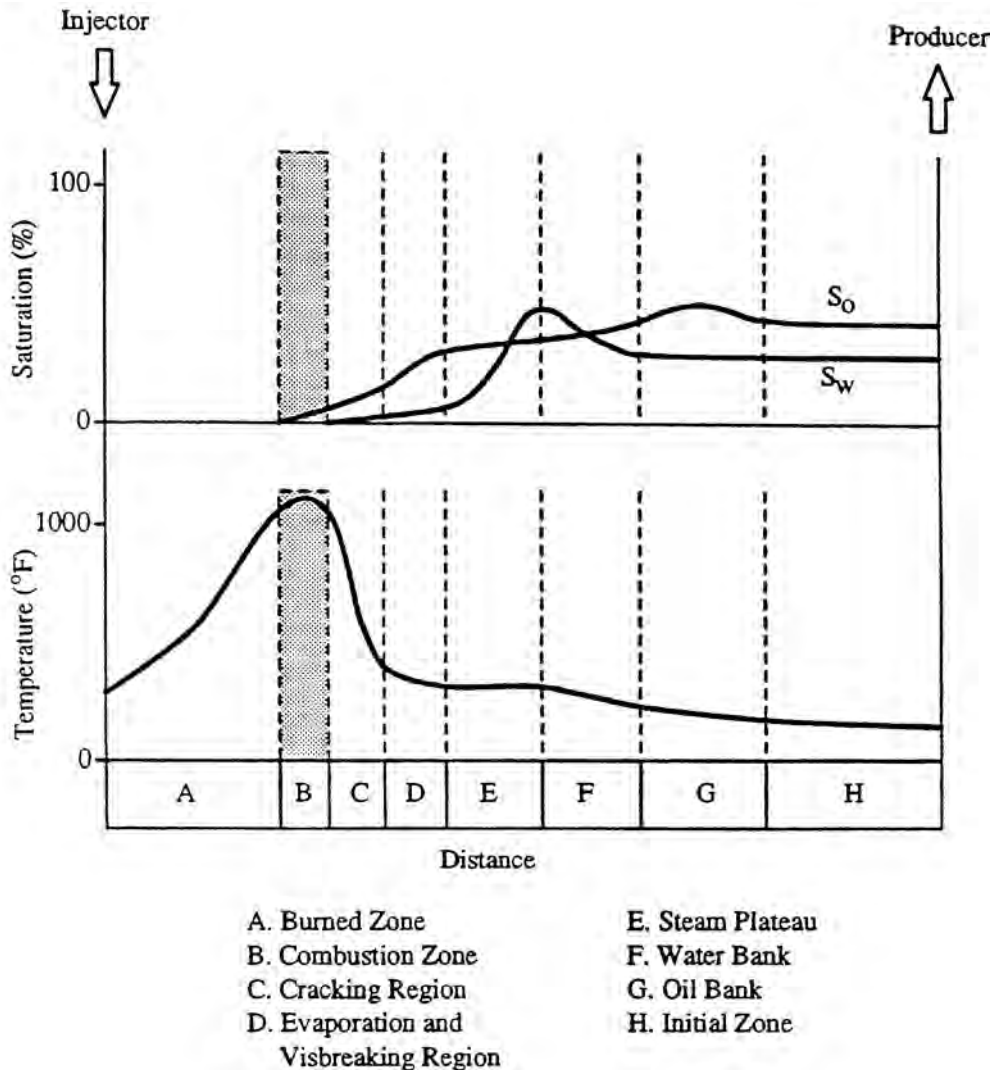


Fig. 16.1—Schematic diagram of temperature and saturation profiles and zones in ISC.⁴

Wet Combustion. A large amount of heat is stored in the burned zone during dry forward ISC, (Fig. 16.1) because the low heat capacity of air cannot transfer that heat efficiently. Water injected with the air can capture and advance more heat stored in the burned zone.

During the wet combustion process, injected water absorbs the heat from the burned zone, vaporizes, moves through the burning front, and expands the steam plateau. As a result, the steam plateau is extended. This results in faster heat movement and oil displacement.

Depending on the water/air ratio, wet combustion is classified as (1) incomplete when the water is converted into superheated steam and recovers only part of the heat from the burned zone, (2) normal when all the heat from the burned zone is recovered, and quenched or (3) super wet when the front temperature declines as a result of the injected water.

When operated properly, water-assisted combustion reduces the amount of fuel needed, resulting in increased oil recovery and decreased air requirements to heat a given volume of reservoir. Up to a 25% improvement in process efficiency can be achieved.⁵ Determination of the optimum water/air ratio is difficult because of reservoir heterogeneities and gravity override

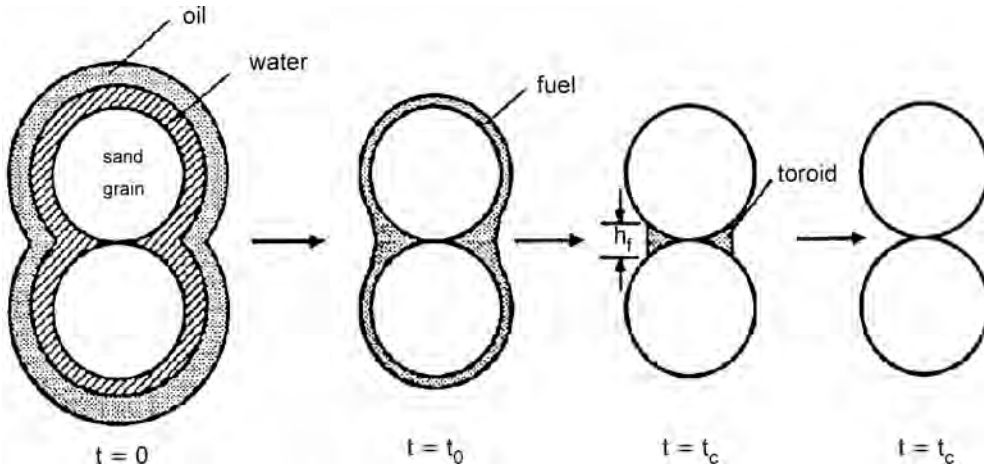


Fig. 16.2—Schematic diagram of varying fuel geometry.⁶

that can affect fluid movement and saturation distributions. Injecting too much water can result in an inefficient fire front, thus losing the benefits of the process.

Some authors recommend, as a best practice, injecting water at high rates to achieve “partially quenched combustion.” This method has limited application. A high-temperature burn is preferred but is difficult to achieve with oils that are not highly reactive. Injecting large amounts of water can lower combustion temperatures, resulting in a greater fraction of oil burned and higher costs for oxygen. At the same time, these types of burns only partially oxidize the oil. This partial oxidation results in a much more viscous liquid, which in turn lowers the flow rate. So, in brief, if water injection is used, great care should be taken to assure that liquid water never reaches the high-temperature combustion front. A discussion of heat- and material-balance calculations that includes chemical reactions and the effect of injected air and water is presented later in some detail.

16.3 Laboratory Studies

ISC processes are largely a function of oil composition and rock mineralogy. The extent and nature of the chemical reactions between crude oil and injected air, as well as the heat generated, depend on the oil-matrix system. Laboratory studies, using crude and matrix from a prospective ISC project, should be performed before designing any field operation.

16.3.1 The Reactions. The chemical reactions associated with ISC are complex and numerous. They occur over a broad temperature range. Most researchers group them into three classes in ascending temperature ranges:

- Low-temperature oxidation (LTO)—heterogeneous gas/liquid reactions producing partially oxygenated compounds and few carbon oxides.
- Medium-temperature reactions—cracking and pyrolysis of hydrocarbons to form fuel.
- High-temperature oxidation (HTO)—heterogeneous H/C bond breaking reactions in which the fuel reacts with oxygen to form water and carbon oxides.

A more recent and more accurate kinetics model has been developed.⁶ Only two reactions are used, but in addition, the geometry of the reacting residual fuel in the pore spaces is taken into account, as indicated in Fig. 16.2. The crude-oil oxidation consists of two stages: LTO forming an oxygenated hydrocarbon fuel, and high-temperature combustion of this fuel. A detailed description of the different reaction regimes is outside the scope of this *Handbook*; some practical comments on the role of LTO, however, are appropriate at this stage.

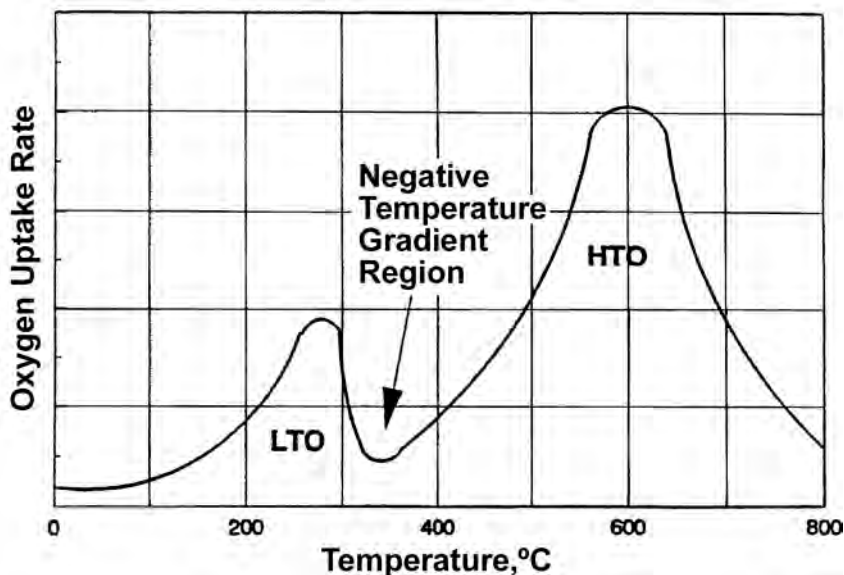


Fig. 16.3—Schematic of dry combustion temperature profile showing the general effect of temperature on oxygen uptake rate for heavy oils and the negative temperature gradient region.⁸

LTO can be described as oxygen addition to the crude oil. LTO yields water and oxygenated hydrocarbons such as ketones, alcohols, and peroxides. A good description of LTO can be found in Burger.⁷ LTO generally increases original oil viscosity, boiling range, and density. LTO increases the amount of fuel and is promoted by low air flux in the oxidation zone. Poor crude oxidation characteristics can also play a role. In heavy-oil reservoirs (API gravity < 20°), LTO tends to be more pronounced when oxygen (rather than air) is injected in the reservoir.⁸

A U. of Calgary research team has shown that, for heavy oils, LTO reactions must be minimized. Fig. 16.3 shows the oxygen uptake as the temperature of a typical heavy oil is raised linearly with time. Notice the negative temperature-gradient region, that is, the region in which oxygen-rate uptake decreases with temperature increase. If the temperature of the ISC process stays at or below the negative temperature-gradient region, the oil displacement efficiency will be very low. This is because LTO increases the oil viscosity and fuel content. The injected-air flux in a heavy-oil project should be maintained at a value well above the value needed to maintain the reactions in the high-temperature oxidation regime. LTO generally has almost no effect on light oils in terms of mobility or recovery despite the fact that light oils are more susceptible to LTO than heavy oils.

Fuel deposition determines the feasibility and economic success of a combustion project. It occurs at intermediate temperatures after the LTO reactions. Numerous studies have been conducted in an attempt to understand fuel formation and deposition at intermediate temperatures. The oil type and chemical structure determine the rate and extent of the different reactions. Catalytic effects from the matrix and/or injected solutions of metals may affect the type and amount of fuel formed. Again, all laboratory experiments must include not only the crude to be tested but also representative core material from the reservoir of interest.

16.3.2 Kinetics. Kinetics of combustion reactions can be defined by how fast the chemical reactions occur and how much of the oil is affected. It is important to study kinetics for several reasons:

- Characterization of oil reactivity.
- Determination of ignition conditions.

- Insight on the nature of the fuel and its combustion characteristics.
- Use of kinetic parameters as input for possible numerical simulation of the process.

Because crude oils contain hundreds of different compounds, it is impossible to accurately represent all the reactions occurring during ISC. Even if it were possible to detail all the reactions, the use of such information in numerical models would be impossible because of cost and computer limitations. Consequently, we will concentrate on useful simple models describing ISC reaction kinetics that have been published in the literature. Most studies use the Arrhenius expressions defined as follows. The model assumes a functional dependency on fuel concentration and oxygen partial pressure. It is given by

$$R_c = \frac{dC_f}{dt} = K p_{O_2}^a C_f^b, \dots\dots\dots (16.1)$$

where R_c = reaction rate of the crude, kg/m³s; C_f = concentration of fuel, kg/m³; and p_{O_2} = oxygen partial pressure, Pa.

The exponent constants, a and b , are the orders of the reactions with respect to oxygen partial pressure (a) and fuel concentration (b). Data show that a ranges between 0.5 and 1.0, while b is close to 1.0. The reaction rate, K , is the Arrhenius constant, expressed as a function of temperature as follows:

$$K = A \exp(-E/RT), \dots\dots\dots (16.2)$$

where A = Arrhenius rate constant; E = activation energy, kJ/mol; T = absolute temperature, °K; and R = 0.00831 universal gas constant, kJ/mol °K.

When using literature values, be careful because the parameters in Eqs. 16.1 and 16.2 vary depending on the system of units used.

A variety of experimental techniques can be used to determine the kinetics of ISC reactions. Among those are differential thermal analysis, thermogravimetric analysis, accelerating rate calorimetry, and effluent analysis. The reference list contains several descriptions of various methods and results.

The effluent analysis method, also called the ramped temperature method in Canada, is quantitative and consists of heating a sample of oil and rock while flowing oxygen (for oxidation) or nitrogen (for pyrolysis) through the sample. The kinetic parameters can be calculated from effluent gas evolution with temperature and chemical analysis of post-test cores. Details of the analysis techniques can be found in Refs. 3, 6, and 9.

16.3.3 Combustion-Tube Studies. Although the kinetic studies can provide useful insight on ISC reactions, combustion-tube experiments are mandatory to determine the parameters needed to design and implement field projects. These data are used to make predictions of field test performance. As Sarathi¹ points out, “Combustion-tube studies are the necessary first step in the design of an ISC project.”

Combustion tubes aim at representing a small volume of the reservoir. They are usually packed with native reservoir cores or representative samples of matrix material and oil, placed in vertical position to minimize gravity effects and heated to reservoir temperature. Ignition is usually started at the top by electrical heaters, and the combustion front is propagated downward. This allows propagation of a combustion front and the associated chemical reactions at conditions close to those in a reservoir.

Temperature profiles, pressures, gas and liquid injection and production rates, and composition histories at the inlet and outlet are recorded. ISC tube runs are unscaled, and direct correlation of combustion-tube results to the field is not possible. However, as long as the runs

are performed with reservoir rock and fluids at reservoir conditions, the reactions of fuel deposition and combustion will be similar in both tube and reservoir.

Tube runs will not provide information on ISC sweep efficiency. They adequately model the chemistry of the process, but not the flow behavior in the reservoir, and only partially model the heat-transfer processes. Flow behavior in the reservoir is affected by gravity override, well spacing, and geometry and reservoir heterogeneities, and tube runs cannot reproduce these phenomena. Heat transfer from the tube to the surroundings can be much higher than reservoir heat losses.

Two different schools of thought exist on this heat-transfer problem. Many experimenters use strip heaters around the tube to lessen the temperature gradient between the tube and the surroundings. This practice can, however, lead to overestimation of water/oil ratios in wet combustion if the strip heaters provide too much energy to the system, as they often do. Information on front cooling by injected water may also be masked by the heaters. As a result, the extent of the steam plateau may not be correct. Most of these types of experiments are bulky and time consuming and require extensive instrumentation.

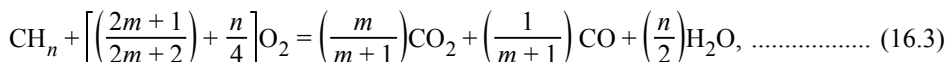
The other solution is to increase the air flux and minimize heat losses by insulation alone. This may slightly overestimate air requirements and fuel content but is much simpler and easier to operate. As a result, it is widely used. Descriptions of various setups for combustion-tube studies have been provided.^{5,6,10-12}

The information that can be acquired from tube runs includes:

- Fuel burned.
- Air required to burn a unit volume of reservoir.
- Atomic H/C ratio of burned fuel.
- Excess air and oxygen use.
- Air/fuel ratio.
- Oil recovery from the swept zone.
- Optimization of water/air ratio in wet combustion.
- Composition of produced fluids.
- Front temperature and stability.

This last piece of information is quite important in heavy oils to determine if the process is operating properly in the desired high-temperature regime. If high temperature cannot be achieved in ideal laboratory conditions, it is likely that field results would be worse.

Data Analysis. The following is a simple analysis of data from tube runs. It assumes that the combustion occurs at high temperature where the fuel exclusively combines with oxygen to produce water and carbon oxides. The stoichiometric equation¹³ is then



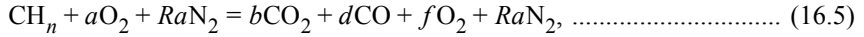
where n = hydrogen/carbon atomic ratio of fuel and m = CO₂/CO concentration ratio produced. The other symbols indicate the various components in the chemical-balance equation.

This equation is only an approximation of the process. It neglects LTO reactions, oxygen/mineral reactions, and water/organic fuel reactions. Alternate analysis when some of these reactions are important is detailed in Sarathi¹ based on work from Moore and Mehta.¹⁰ Assuming Eq. 16.3 to be valid, the apparent H/C ratio, n , can be estimated from the concentration of exhaust gases and the injected oxygen concentration.¹³

$$n = \frac{4[O_2 - CO_2 - CO/2 - (O_2)_{prod}]}{CO_2 + CO}, \dots\dots\dots (16.4)$$

where $(O_2)_{\text{prod}}$ = oxygen concentration produced.

It is prudent to normalize the concentrations by making a balance on the nitrogen, which in these conditions can be considered inert. The basic chemical equation is then



where R is the molar ratio of nitrogen to oxygen in the feed gas, and a , b , d , and f are stoichiometric coefficients similar to those in Eq. 16.3.

The range of the ratio, n , for high-temperature reactions should be from 0.5 to 2. Calculation of an unusually high value of n indicates that LTO is important. In the very early stages of field projects, large n values are often observed because of the solubility of the combustion gases (particularly CO_2) in the oil.

Once n and m are known, the amount of air required to burn one unit weight of fuel is found from Eq. 16.3. The heat generated by burning a unit weight of fuel can be calculated by simple addition of the heat generated by each reaction, as described in the stoichiometric equation (Eq. 16.3). The calculation of heat produced must take into account the production of carbon monoxide. The following formula¹³ can estimate heating values of fuels as a function of n and m .

$$H_c = \frac{m(174,000)}{(m + 1)(n + 12)} + \frac{52,500}{(m + 1)(n + 12)} + n \frac{61,500}{(n + 12)}, \dots\dots\dots (16.6)$$

where H_c = heating value, Btu/lbm fuel. To convert to J/kg, multiply by 2,326.

The air required to burn a given volume of reservoir is, of course, a very important design parameter and one of the keys to the economics of the combustion process. This is calculated directly from the experimental data by dividing the amount of oxygen consumed by the volume swept during the tube run. The mass of fuel burned in a unit volume of reservoir can be calculated from the oxygen consumed by a unit volume and by applying Eq. 16.3. All other relevant parameters can be estimated.^{13,14} It is prudent to perform multiple laboratory tube runs before field implementation.

16.4 Combining Material- and Heat-Balance Calculations

Many useful and reasonably accurate calculations can be made on ISC to predict the behavior of a proposed project. These ideas will be explained in the following diagrams and example calculations. They start with a very simple heat balance and are then extended to more closely represent what happens in the reservoir.

16.4.1 First Assumptions. Start by assuming that no combustion data are available to get an initial idea of the feasibility of a project. This preliminary work gives the engineer a sound basis to decide whether further work has economic promise.

Assume a sandstone formation with a porosity of 22%, a temperature of 100°F, a 24°API oil at a saturation of 65%, and an injection pressure of 300 psia. Also assume the CO_2/CO atomic ratio m to be

$$m = \frac{CO_2}{CO} = 20. \dots\dots\dots (16.7)$$

This is a reasonable ratio to assume, based on both laboratory and field experience.

H/C Ratio, <i>n</i>	Combustion Temperature (°F)
0.40	1,000
0.80	800
1.40	700
2.40	600

Because there are no tube run data, generalized correlation curves¹³ (Figs. 16.4 and 16.5) will be used to calculate expected results. From Fig. 16.4, the fuel availability, *W*, for 24°API crude is

$$W = 0.95 \text{ lbm } C / 100 \text{ lbm rock} \dots\dots\dots (16.8)$$

The apparent *H/C* atomic ratio (*n*) of the fuel is also needed. This is a function of the combustion-front temperature,¹³ as shown in Fig. 16.5. Selected data from the graph are listed in Table 16.1. These data for 21.8°API crude are close enough to 24°API crude for initial estimates.

16.4.2 Calculate Initial Heat Balances and Temperatures. Start by assuming that all heat generated is used to heat the rock formation through which the combustion front has moved. This assumption is not accurate, but it simplifies the understanding of the mathematics and concepts involved in heat-balance calculations. A sketch of the temperature profile generated is shown in Fig. 16.6. Corrections to this heat balance calculation will be discussed later.

Assuming 1.0 ft³ of rock formation burned and a front temperature of 1,000°F, from Eq. 16.8 and Table 16.1,

$$\begin{aligned} \frac{\text{lbm fuel}}{100 \text{ lbm rock}} &= \frac{\text{lbm carbon}}{100 \text{ lbm rock}} + \frac{\text{lbm hydrogen}}{100 \text{ lbm rock}} \\ &= 0.95 + \frac{0.95(0.40)}{12} = 0.9817 \dots\dots\dots (16.9) \end{aligned}$$

Quartz weighs approximately 164 lbm/ft³. The amount of fuel for a cubic foot of formation equals

$$\frac{(0.9817)(164)(1 - 0.22)}{100} = 1.256 \text{ lbm fuel} / \text{ft}^3 \text{ rock} \dots\dots\dots (16.10)$$

Using the heat of combustion, Eq. 16.6, with the appropriate parameters, becomes

$$\begin{aligned} H_c &= \frac{(20)(174,000)}{(21)(12.4)} + \frac{52,500}{(21)(12.4)} + \frac{(0.4)(61,500)}{12.4} \\ &= 15,550 \text{ Btu/lbm fuel} \dots\dots\dots (16.11) \end{aligned}$$

Thus, the total heat generated is

$$\frac{\text{Heat generated}}{\text{ft}^3 \text{ rock}} = (15,550)(1.256) = 19,530 \frac{\text{Btu}}{\text{ft}^3 \text{ rock}} \dots\dots\dots (16.12)$$

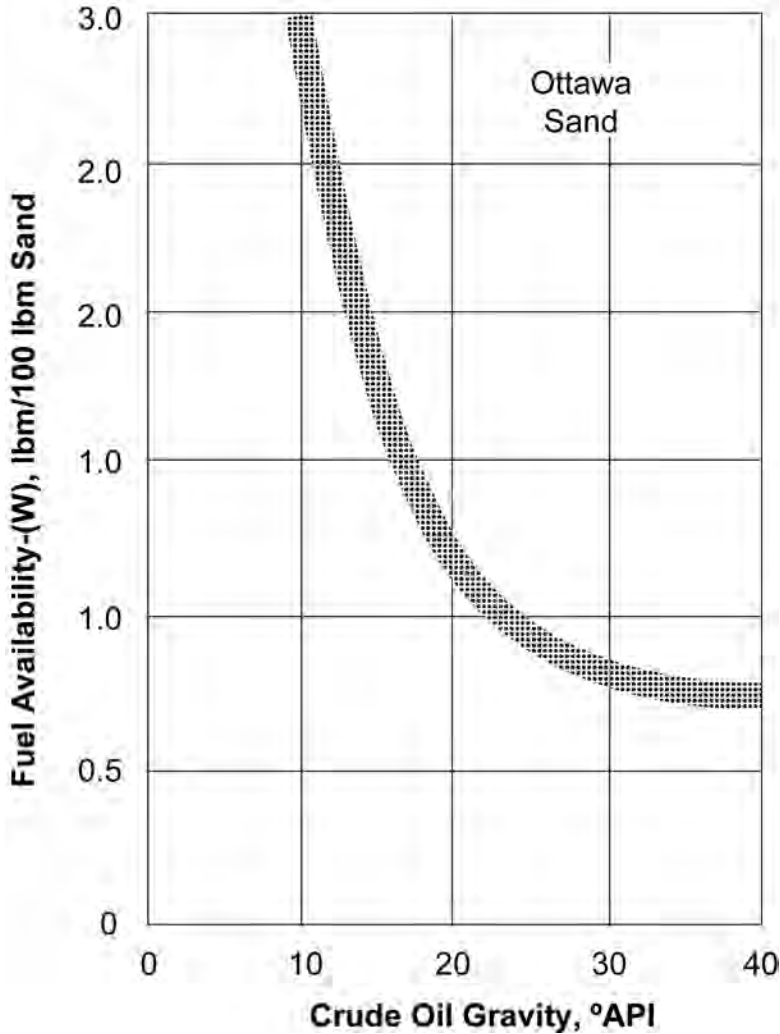


Fig. 16.4—Fuel availability vs. crude oil gravity.¹³

Next, calculate the temperature rise of the formation behind the front to see if it matches the temperature assumed by performing a heat balance behind the front. Because, for practical purposes, the only fluid in the formation behind the front is air (which has a very small volumetric heat capacity), we only need to calculate a heat balance on the sandstone itself. A good equation for average sandstone heat capacity is¹³

$$c_s = \frac{T_1 + 2,000}{10,000} + \frac{T_2 - T_1}{20,000} \dots\dots\dots (16.13a)$$

$$= 0.21 + \frac{1,000 - 100}{20,000} = 0.255 \text{ Btu/lbm-}^\circ\text{F}, \dots\dots\dots (16.13b)$$

where T_1 = initial reservoir temperature, °F and T_2 = final reservoir temperature, °F.

From a heat-balance calculation, the reservoir sand temperature is as follows:

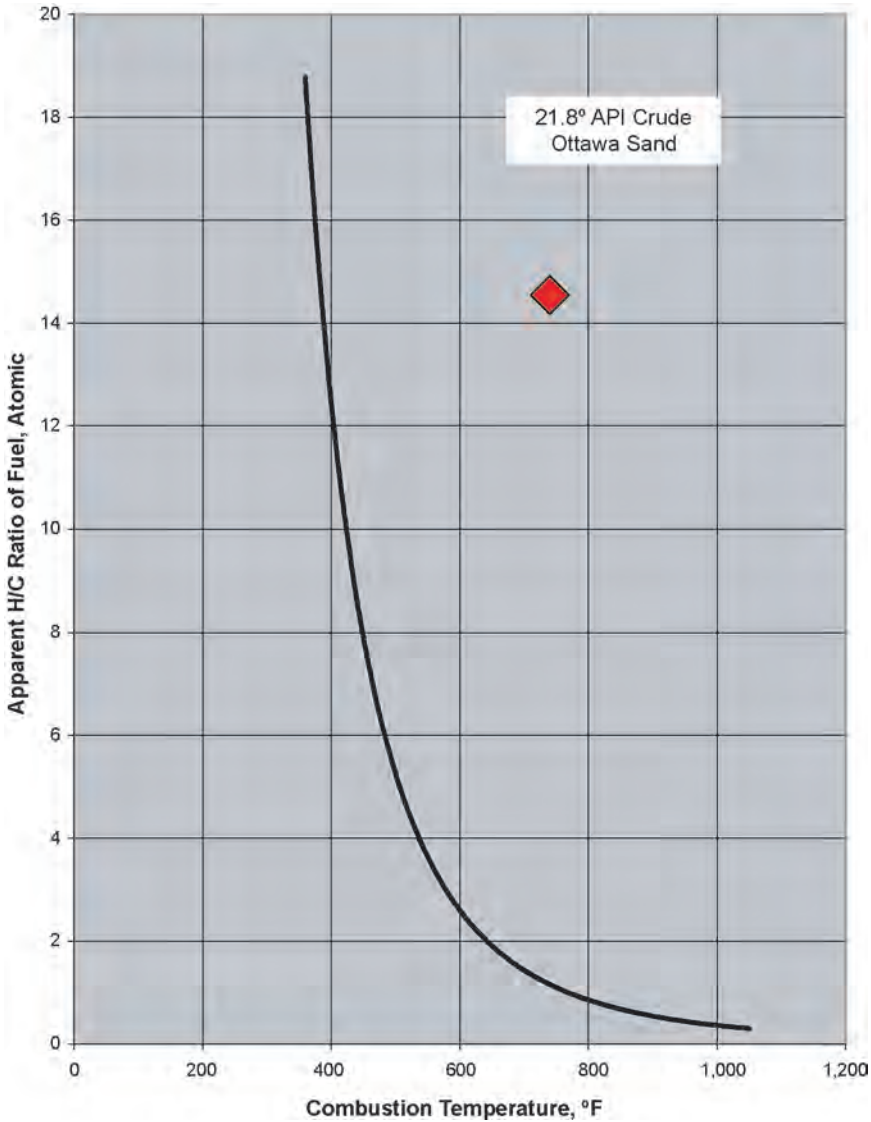


Fig. 16.5—H/C ratio vs. combustion temperature.¹³

$$T_2 - 100 = \frac{19,530}{(0.255)(164)(1 - 0.22)} = 598.7$$

or $T_2 = 699^\circ\text{F}$ (16.14)

The result from Eq. 16.14 does not agree with the assumed temperature of 1,000°F. Calculations with other assumed temperatures result in the calculated temperature values shown in Table 16.2.

The tabular data are graphed as circles in Fig. 16.7. The two temperatures match at 801°F. This is the calculated combustion-front temperature if all the heat generated is used to heat the formation behind the combustion front.

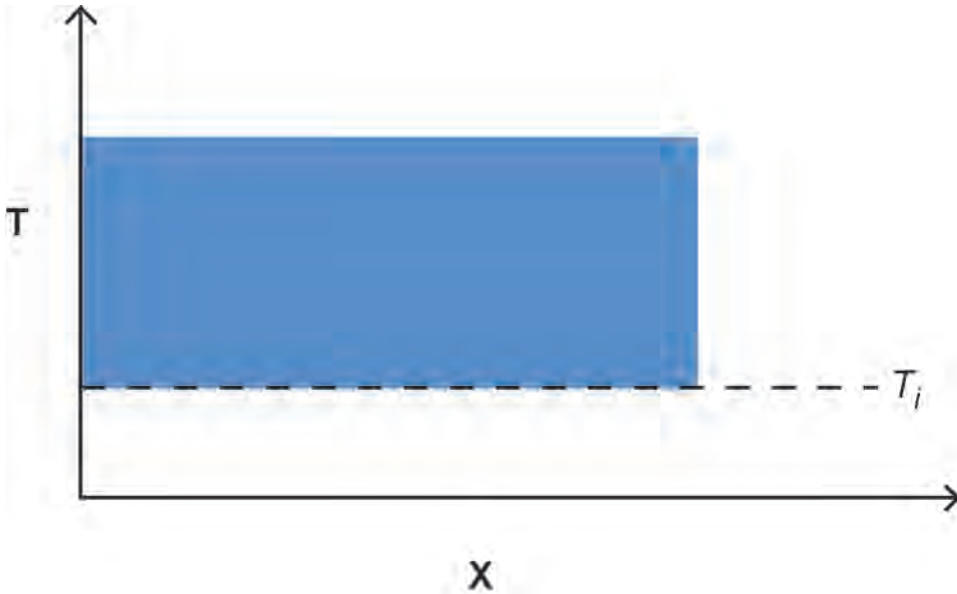


Fig. 16.6—Idealized temperature profile assuming all heat stays in the burned zone; x is the distance coordinate away from an injector at x = 0.

TABLE 16.2—ASSUMED AND CALCULATED TEMPERATURES AS A FUNCTION OF H/C RATIOS		
Assumed Temperature (°F)	H/C Ratio	Calculated Temperature (°F)
1,000	0.40	699
800	0.80	802
700	1.40	939

16.4.3 Correction for Water of Combustion. These results do not include all the processes occurring in the reservoir. First, the water formed by combustion will condense beyond the combustion front, absorb some heat of combustion, and reduce the heat of the formation behind the combustion front. This effect can be calculated as follows.

From Eq. 16.9, 0.0317 lbm of H₂ are burned per 100 lbm of rock at 1,000°F. Assuming that a pound of steam will release 1,000 Btu when cooling from combustion temperature and condensing (this number is only approximately correct but is adequate for estimation purposes), the amount of heat carried forward by the steam is calculated with concepts similar to Eqs. 16.10 and 16.12:

$$\begin{aligned}
 \text{Heat carried ahead by steam} &= 0.0317 \left(\frac{18}{2} \right) \frac{(1,000)(164)(1 - 0.22)}{100} \\
 &= 365 \text{ Btu/ft}^3 \text{ rock burned.} \dots\dots\dots (16.15)
 \end{aligned}$$

In this equation, 18/2 is the ratio of molecular weight of water and hydrogen. The heat given up by the steam is 1,000 Btu/lbm, and the other numbers are similar to those in Eq. 16.10. Thus, the calculated temperature is lower than it was in Eq. 16.14, as shown below:

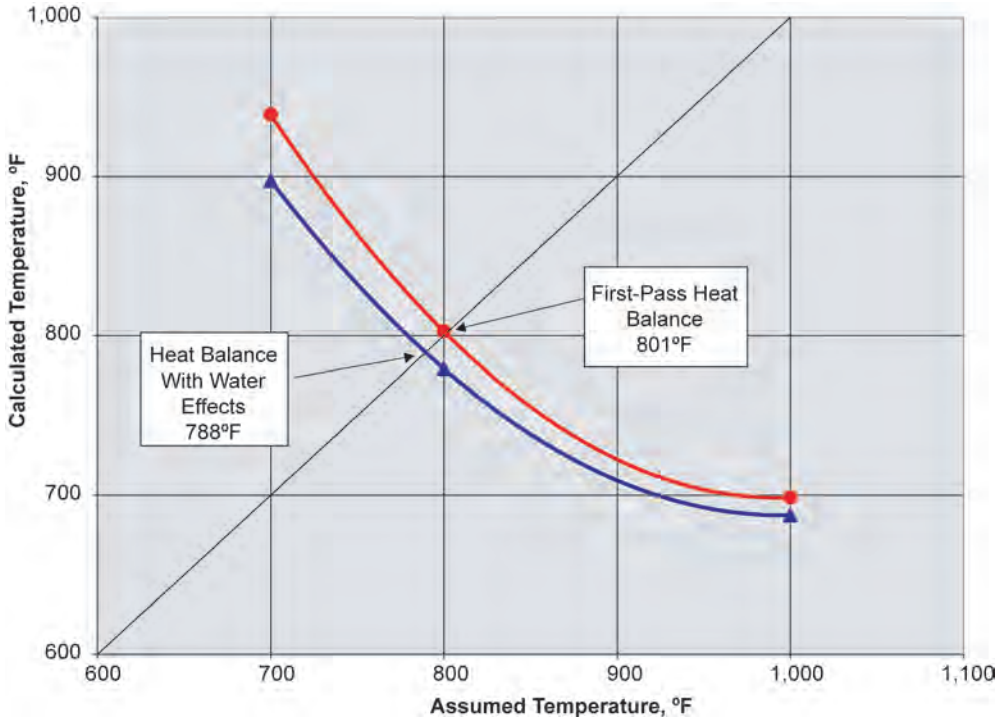


Fig. 16.7—Assumed and calculated combustion-zone temperatures.

$$T_2 - 100 = \frac{19,530 - 365}{(0.255)(164)(1 - 0.22)} = 587.5$$

or $T_2 = 688^\circ\text{F}$ (16.16)

Other temperatures were calculated in a similar way, and the results, graphed as triangles in Fig. 16.7, show a corrected combustion temperature of 788°F. At this temperature, the H/C ratio is 0.85, as indicated in Fig. 16.8.

16.4.4 Calculating the Volume and Temperature of the Steam Plateau. No calculations on the steam plateau were necessary in the above calculations. The steam-plateau temperature and volume directly affect the volume of oil moved as a result of the combustion process. To calculate these terms, use the H/C ratio of 0.85 and calculate the partial pressure of the water as follows.

The fuel composition is $\text{CH}_{0.85}$. From Eq. 16.3, the moles of oxygen used per mole of fuel are

$$\text{O}_2 = \frac{2m + 1}{2m + 2} + \frac{n}{4} = \frac{2(20) + 1}{2(20) + 2} + \frac{0.85}{4}$$

$= 1.189 \text{ mol O}_2$ (16.17)

Combustion products are calculated in a similar way:

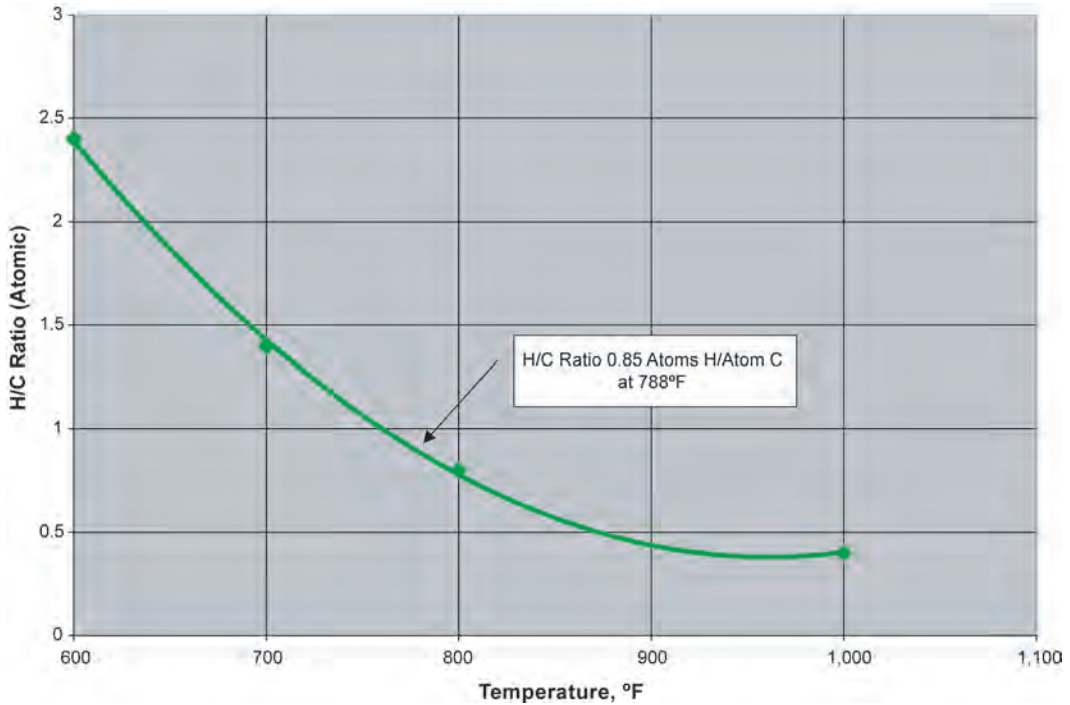


Fig. 16.8—H/C atomic ratio vs. combustion temperature.¹³

$$CO_2 = \frac{m}{m + 1} = \frac{20}{21} = 0.952 \text{ mol } CO_2 \dots\dots\dots (16.18)$$

$$CO = \frac{1}{m + 1} = \frac{1}{21} = 0.048 \text{ mol } CO \dots\dots\dots (16.19)$$

$$H_2O = \frac{n}{2} = \frac{0.85}{2} = 0.425 \text{ mol } H_2O \dots\dots\dots (16.20)$$

$$N_2 = \left(\frac{79}{21}\right)(O_2) = \frac{79}{21}(1.189) = 4.473 \text{ mol } N_2 \dots\dots\dots (16.21)$$

The operating pressure is 300 psia. The partial pressure of H₂O in the combustion gas is

$$p_{\text{water}} = \frac{0.425(300)}{0.952 + 0.048 + 0.425 + 4.473} = 21.6 \text{ psia.}$$

From steam tables, the saturation temperature for 21.6 psia is 232°F. This is the temperature of the steam plateau.

The volume of the steam plateau is a function of the amount of H₂O formed. Knowing that there are 0.95 lbm C/100 lbm rock burned, and knowing from Fig. 16.8 that the H/C ratio is 0.85, an equation similar to Eq. 16.10 yields the amount of water formed per cubic foot of rock burned.

$$\begin{aligned} \text{Water formed} &= 0.95 \left(\frac{0.85}{12} \right) \left(\frac{18}{2} \right) \frac{(164)(1 - 0.22)}{100} \\ &= 0.775 \frac{\text{lbm H}_2\text{O formed}}{\text{ft}^3 \text{rock burned}} \dots\dots\dots (16.22) \end{aligned}$$

Thus, the total heat carried forward by the water formed is

$$\begin{aligned} \text{Heat carried by steam} &= 0.775 (1,000) \\ &= 775 \text{ Btu/ft}^3 \text{ rock burned} \dots\dots\dots (16.23) \end{aligned}$$

Using Eq. 16.13a, the heat capacity of the formation is

$$c_s = 0.21 + \frac{232 - 100}{20,000} = 0.2166 \text{ Btu/lbm-}^\circ\text{F} \dots\dots\dots (16.13c)$$

The amount of heat required to raise the temperature of a cubic foot of sand from 100 to 305°F, from a heat balance, is

$$\begin{aligned} \Delta H &= \frac{0.2166 \text{ Btu}}{\text{lbm-}^\circ\text{F}} \left[\frac{164(1 - 0.22) \text{ lbm}}{\text{ft}^3} \right] (232 - 100)^\circ\text{F} \\ &= 3,701 \text{ Btu/ft}^3 \dots\dots\dots (16.24) \end{aligned}$$

Thus, the volume of rock heated by condensing steam is Eq. 16.23 divided by Eq. 16.24:

$$\text{Volume of steam heated rock} = \frac{775}{3,701} = \frac{0.209 \text{ ft}^3 \text{ steam zone}}{\text{ft}^3 \text{ rock burned}} \dots\dots\dots (16.25)$$

A sketch of the resulting temperature profile is shown in Fig. 16.9.

16.4.5 Calculating the Effects of Injected Air and Water. Further corrections are needed to increase the accuracy of the temperature profile in Fig. 16.9. Injected air will partially cool the burned zone, raise the temperature as it approaches the combustion front, and carry heat forward. This will have little effect on the combustion kinetics or the amount of heat generated by combustion, so, in essence, this amount of energy is merely carried forward to extend the size of the steam plateau.

A sketch of this idea is shown in Fig. 16.10. In this sketch, the area marked “1” is the temperature profile behind the burning front; Area 2 is the steam plateau, which is now larger than calculated before because of the heat carried forward by the combustion gases.

This temperature profile can be approximated as indicated in Fig. 16.11, where the profiles of the burned zone and steam plateau are treated as square waves that have been adjusted so that the total heat in Areas 1 and 2 is the same as in Fig. 16.10.

There are several reasons for using this square-wave concept. One is that it makes it easier to calculate heat losses to be expected from either a laboratory or field combustion operation using superposition calculations similar to those discussed by Ramey as seen in Prats.² The reference also indicate that the heat losses calculated with Fig. 16.11 are quite adequate.

When wet combustion is used, the temperature behind the front tends to change abruptly, as shown in Fig. 16.11. As a result, heat and material balances of the sort discussed next can be used to calculate the movement of the resulting cooling front, burn front, and steam plateau.

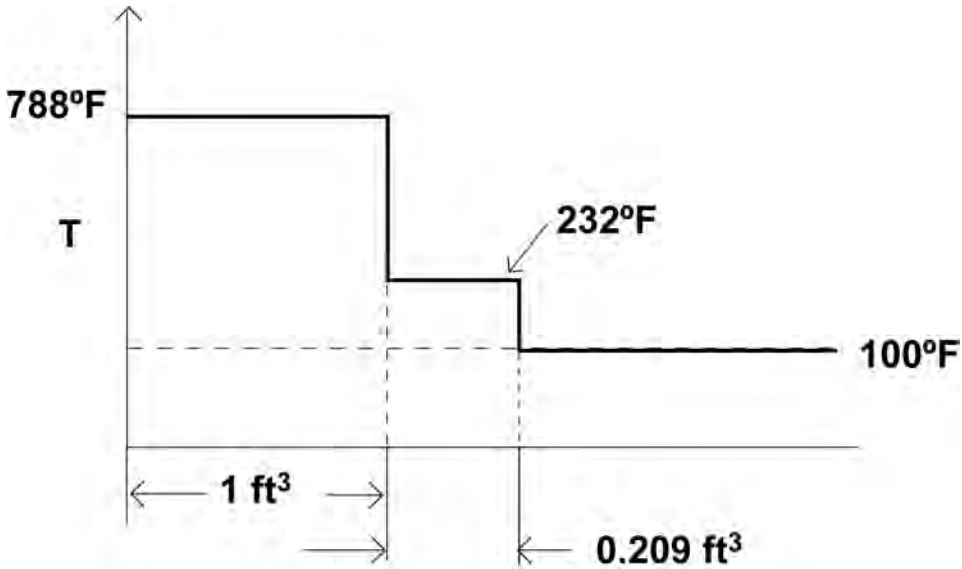


Fig. 16.9—Idealized temperature profile with steam plateau ahead of the combustion front.

The amount of air injected per cubic foot of rock burned and the heat capacity of air are needed to calculate this heat-transfer process for dry combustion. The volume of combustion gas should also theoretically be calculated, but normally this isn't necessary because its volume is nearly identical to the air volume. Further, its heat capacity is nearly the same—remember that most of the combustion gas is nitrogen (assuming that air is injected).

The moles of air injected are calculated by adding the O₂ from Eq. 16.17 to the N₂ from Eq. 16.21:

$$\text{Air injected} = 1.189 + 4.473 = \frac{5.662 \text{ mol air}}{\text{mol fuel}} \cdot \dots\dots\dots (16.26)$$

The heat capacity for air is 7.00 Btu/lbm mol-°F. With previously determined factors of 0.95 lbm of carbon burned for 100 lbm rock, 164(1 - 0.22) pounds of rock per cubic foot of rock, 12 lbm of carbon per mole, a combustion-zone temperature of 788°F (Fig. 16.7), and the results of Eq. 16.26, we obtain the amount of heat carried forward by the injected air as follows.

$$\begin{aligned} \frac{\text{Heat carried by air}}{\text{ft}^3 \text{ rock burned}} &= \left(\frac{0.95}{100} \right) \left[\frac{(164)(1 - 0.22)}{12} \right] (5.662)(7.00)(788 - 100) \\ &= \frac{2,761 \text{ Btu}}{\text{ft}^3 \text{ rock burned}} \cdot \dots\dots\dots (16.27) \end{aligned}$$

This heat extracted behind the burned zone is deposited into the steam plateau. The resulting size of the steam plateau can be calculated in a way similar to Eq. 16.25 by adding the heat carried by the combustion gas to that carried by the water as follows:

$$\text{Vol of steam heated rock} = \frac{775 + 2,761}{3,701} = 0.901 \text{ ft}^3 \cdot \dots\dots\dots (16.28)$$

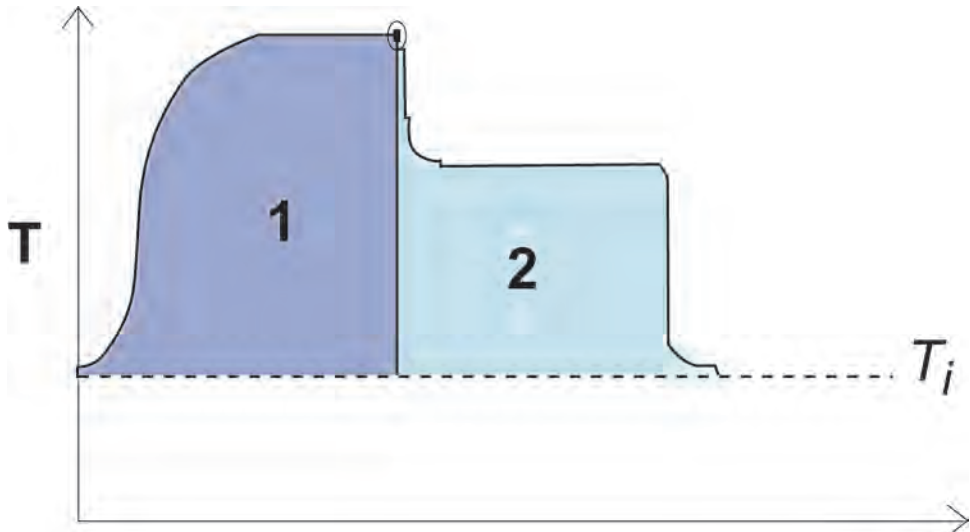


Fig. 16.10—Schematic of combustion temperature profile including cooling by injected air.

This calculation shows that the condensing steam front is far enough ahead of the combustion front to displace oil efficiently, and it is unnecessary to have the combustion front cover the entire reservoir to obtain good recovery. Recovery can be estimated by knowing the amount of fuel burned, by estimating the residual oil saturation in the steam plateau, and by estimating the volumetric sweep efficiency of the process.

16.4.6 Heat Losses. An estimate of heat losses using the superposition concepts seen in Prats,² based on Ramey's work, will make the calculations just presented more accurate. These estimates are particularly important if a laboratory heat balance indicates significant heat losses. The temperature profiles just calculated assuming no heat losses can be used to make a first estimate of heat losses and a recalculated steam-plateau size. This is a reasonable way to handle the heat balance. Because all heat transferred was assumed to be in the steam plateau, any reduction in that transferred heat because of losses will reduce the amount of heat in the plateau.

Because the size of the steam zone and the size of the calculated heat losses are interdependent, iterative calculations are necessary until the assumed and calculated heat balances match. This will usually require only two to three iterations to achieve this match.

Data used in the previous calculations were based on generalized predictions of combustion behavior (i.e., the amount of fuel per cubic feet of formation) and the H/C ratio of the fuel. If combustion tube runs are made in the laboratory, those parameters will be known and should be used in the calculations. In addition, accurate temperature and saturation profiles vs. time will allow reasonably accurate heat-balance calculations to determine the heat losses from the experiment. As an alternative, reasonable assumptions about the heat losses can be used to check the heat-balance calculations and indicate if there is significant experimental error.

Computer assisted tomography (CAT) scanner measurements produce the most accurate saturation histories. Accurate measurements of temperature profile and accurate oil, water, and gas production data also make it possible to estimate reasonable saturation histories. These are the major sources of error in the overall heat-balance calculations, but they are fairly small compared to the amount of heat stored in the hot matrix.

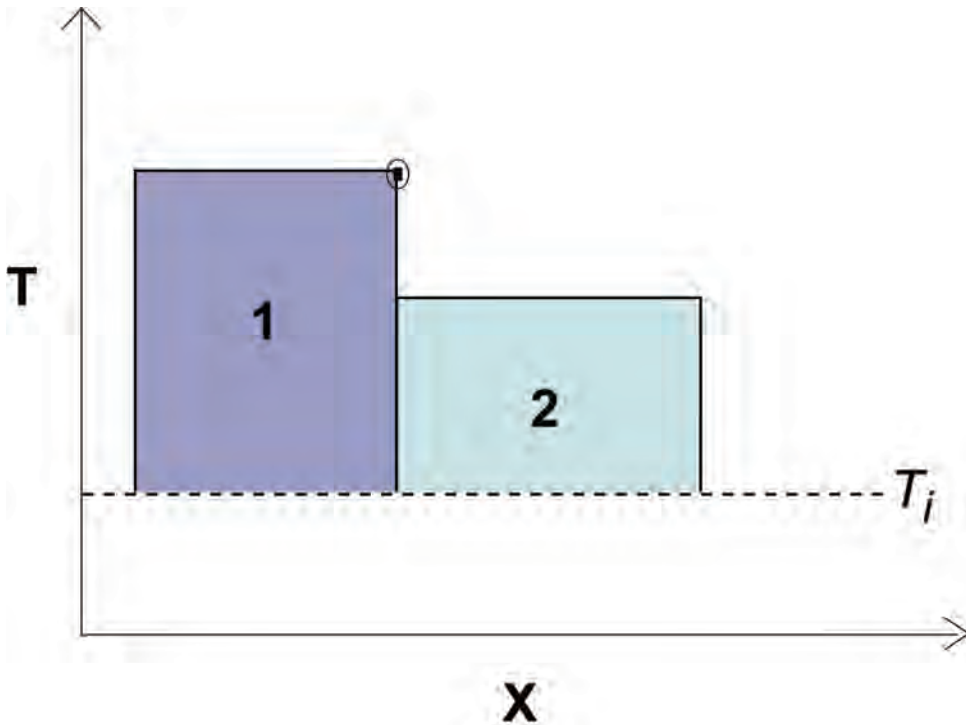


Fig. 16.11—Idealized temperature profile including injected-air cooling.

16.5 Design Considerations

Conditions favoring the use of ISC rather than steam include the following: (1) high reservoir pressure at which steam is inefficient, (2) potential for severe wellbore heat losses (i.e., depth, offshore, permafrost), (3) reservoir clay swelling in contact with fresh water, (4) limited water supply, and (5) environmental regulations prohibiting steam generation.

Like any other injection process, the design of ISC projects must consider injection-pressure limitations and reservoir flow resistance. These are especially important in heavy-oil reservoirs in which combustion must occur in the high-temperature regime to be successful. The minimum air flux needed to maintain high temperatures at the front is estimated to be 0.125 ft/D (0.04 m/d).¹⁴ Because the burn-zone growth is directly proportional to the injected air, the maximum air-injection rate determines the minimum lifetime of the project. Ways to increase the air-injection rate are often needed, especially in heavy-oil reservoirs. They may include reduced well spacing, cyclic steaming of injectors and producers, and an increase in injection pressure. These factors will determine the compressor pressure and volume output.

There has been some controversy over whether ISC projects should be developed using patterns or line drives. Many early projects were started as pilots with a single injector. Usually, this practice ultimately resulted in a five-spot pattern. These pilots behaved contrary to plan, with the combustion front moving in only one direction because of permeability variations, gravity effects, well spacing differences, or a combination of these factors.

Attempts to correct the unbalanced flow included stimulating unresponsive wells and limiting withdrawal rates of wells that producing excessive volumes of combustion gas. Generally, these efforts did not have the desired effect.

In retrospect, this reservoir behavior makes sense. Once a combustion front is even slightly asymmetric, the higher temperature and, thus, higher mobility will cause greater flow in that

direction. Thus, the flow will become more asymmetric, finally resulting in flow principally in only one direction.

Because it is often difficult to decide *a priori* which direction the major flow will take, operating plans should remain flexible until field performance indicates which injection scheme best uses the flow directions.

For the above reasons, many of the more successful ISC projects have been line-drive operations that start near the top of the reservoir and move down-dip. In such an operation, the direction of the fire front is known. The operating engineers can then plan the completion and operating history in a rational way that will mirror the front movement and breakthrough history. This operating practice can be seen in most of the successful ISC field projects to be discussed later.

16.6 Performance Prediction

Predicting the production response to ISC has been the topic of various studies. Complete numerical simulation of ISC is difficult because of the complex reactions and the thin burning front that requires small gridblocks for representation. Simulators range from tank models to complex 3D simulators. In addition to simulation, empirical models, hybrid models, and correlation methods have been developed. A discussion of some of these methods follows.

The easiest method is essentially a tank balance,¹⁴ adapted by Prats.² The oil and water produced are given by

$$N_p = \phi V_b (S_{oi} - S_f) + 0.4 S_{oi} (V_p - V_b) \dots \dots \dots (16.29)$$

and

$$W_p = V_b \phi (S_{wi} + S_{wf}), \dots \dots \dots (16.30)$$

where S_{oi} = initial oil saturation, fraction; S_f = oil saturation burned, fraction; V_b = volume burned, m³; N_p = oil produced, m³; W_p = water produced, m³; ϕ = porosity, fraction; V_p = volume of the pattern, m³; and S_{wf} = water saturation resulting from the combustion process, fraction.

If the volumes are in acre-ft and the production terms are in bbl, a multiplication factor of 7,758 must be used. The estimate of 40% of the oil produced coming from outside the burned volume is an empirical value based on experience. This is the 0.4 term in Eq. 16.29.

Fig. 16.12, presented by Gates and Ramey,¹⁵ combines laboratory results and field observations from the Belridge ISC projects. It shows the effect of initial gas saturation on the oil-recovery history. Oil production rates and instantaneous air/oil ratios can be estimated from the slopes of the curves. At late times, the above two techniques give similar results.

Satman and Brigham¹⁶ used data from dry combustion field tests to obtain two empirical correlations. Those are presented in **Figs. 16.13 and 16.14**. The terms in the ordinates are cumulative incremental oil produced (CIOP), original oil in place (OOIP), fuel burned (FB), and oil in place (OIP) at the start of the project.

In addition to original oil saturation S_o , thickness h , oil viscosity μ_o , and porosity ϕ , the abscissa includes cumulative air injected (CAI), and OIP at the start of the project, and fraction oxygen use. The second correlation, **Fig. 16.14**, is the most accurate except for oils with less than 10 cp original viscosity, where the first correlation must be used. These correlations were generated from pilot floods; thus, they would not be expected to be accurate for pattern flooding. However, the narrative in the previous section points out that pattern flooding is generally not the best way to operate an ISC project, and these correlations are expected to be reasonably accurate for line-drive projects.

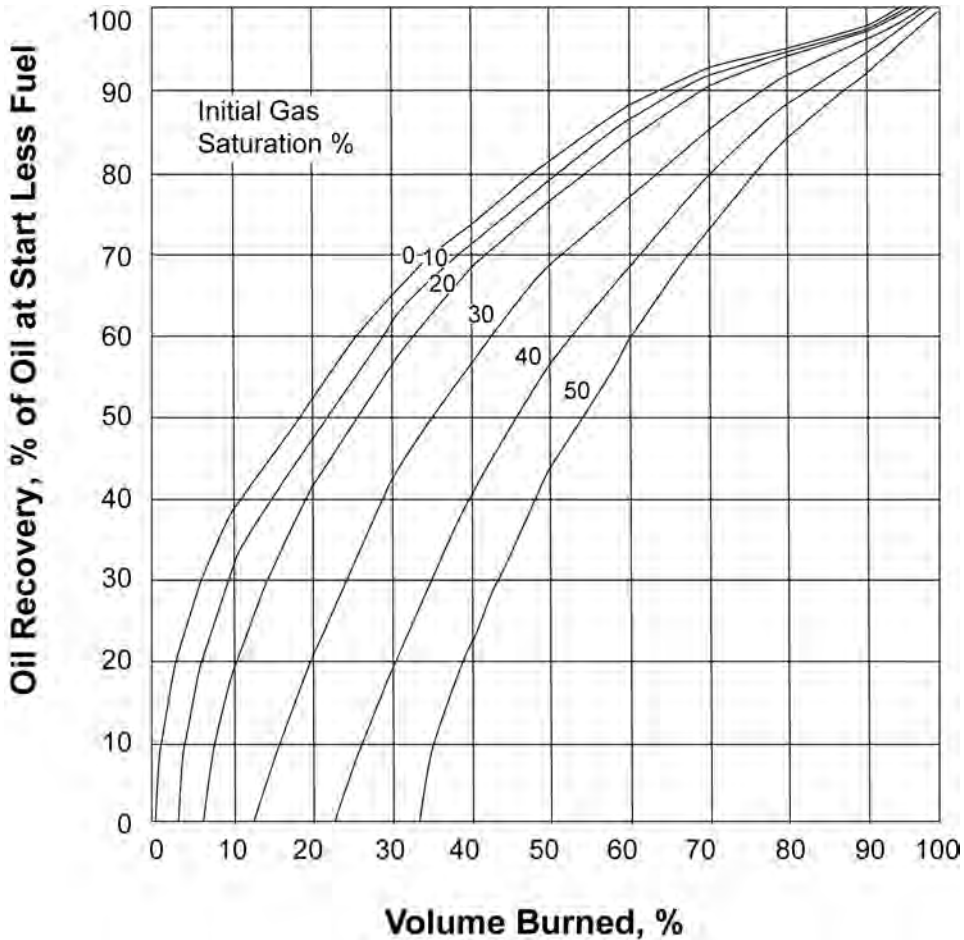


Fig. 16.12—Gates and Ramey method.¹⁵

16.7 Operating Practices

In addition to the standard field equipment for oil production, ISC requires particular attention to air compression, ignition, well design, completion, and production practices.

16.7.1 Compressors. Air-compression systems are critical to the success of any ISC field project. Past failures often can be traced to poor compressor design, faulty maintenance, or operating mistakes. A detailed discussion of compressors and sizing considerations appears in the Facilities and Construction Engineering volume of this *Handbook*. Other discussions are available in Sarathi.¹

The factors to be considered when selecting compressors include peak air requirements, injection pressure, capital cost, power requirements, operation and maintenance costs, and other relevant technical and economic parameters specific to the field considered. Compressor terminology varies among manufacturers. It is best to obtain a complete description including compressor, driver, interstage cooling system, and all ancillary equipment, including control and safety systems from each vendor being consulted.

Air compression causes high temperatures because of the large heat capacity (c_p/c_v ratio). Compressor design must consider these high temperatures to ensure continuous, sustained oper-

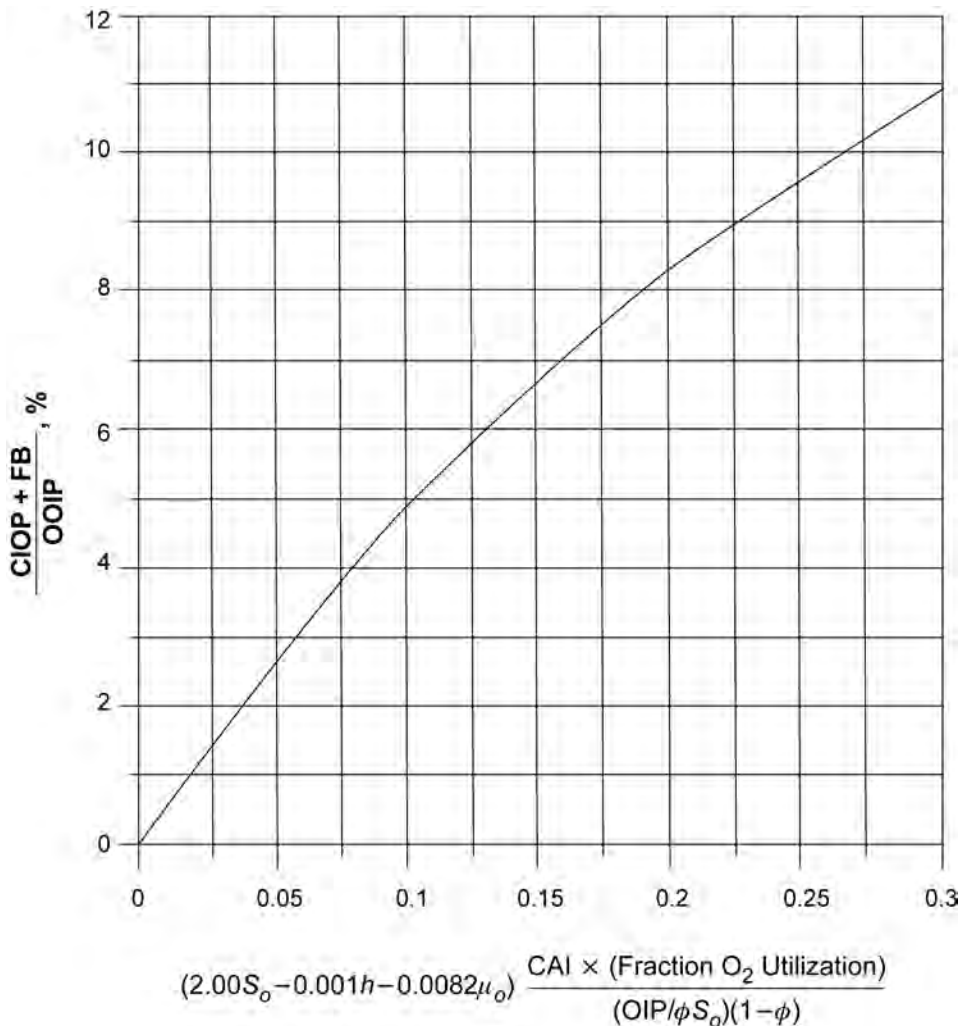


Fig. 16.13—First Satman correlation.¹⁶

ations free from the corrosive effects of air and the explosion hazards of some lubricating fluids. Mineral oils are not recommended. Synthetic lubricants withstand the higher temperatures and offer lower volatility and flammability than conventional lubricants.

16.7.2 Ignition. Ignition and maintenance of high combustion temperatures, especially in heavy-oil projects, are the most critical factors of an ISC project. Shallcross¹⁷ presented a complete review of ignition methods. The following is a summary of this study.

Ignition can occur spontaneously if the oil is reactive, the reservoir temperature is high enough, and the reservoir is reasonably thick. Various models have been proposed to determine the time for spontaneous ignition.^{18,19}

When spontaneous ignition does not occur or is not desired (i.e., in heavy oil reservoirs, where it is important to maintain high combustion temperatures), the most appropriate ignition method depends on the reservoir and the equipment available on site.

Downhole gas-fired burners allow good control of the temperature of injected gases and may be operated at a greater depth than other methods. The disadvantages include the need to

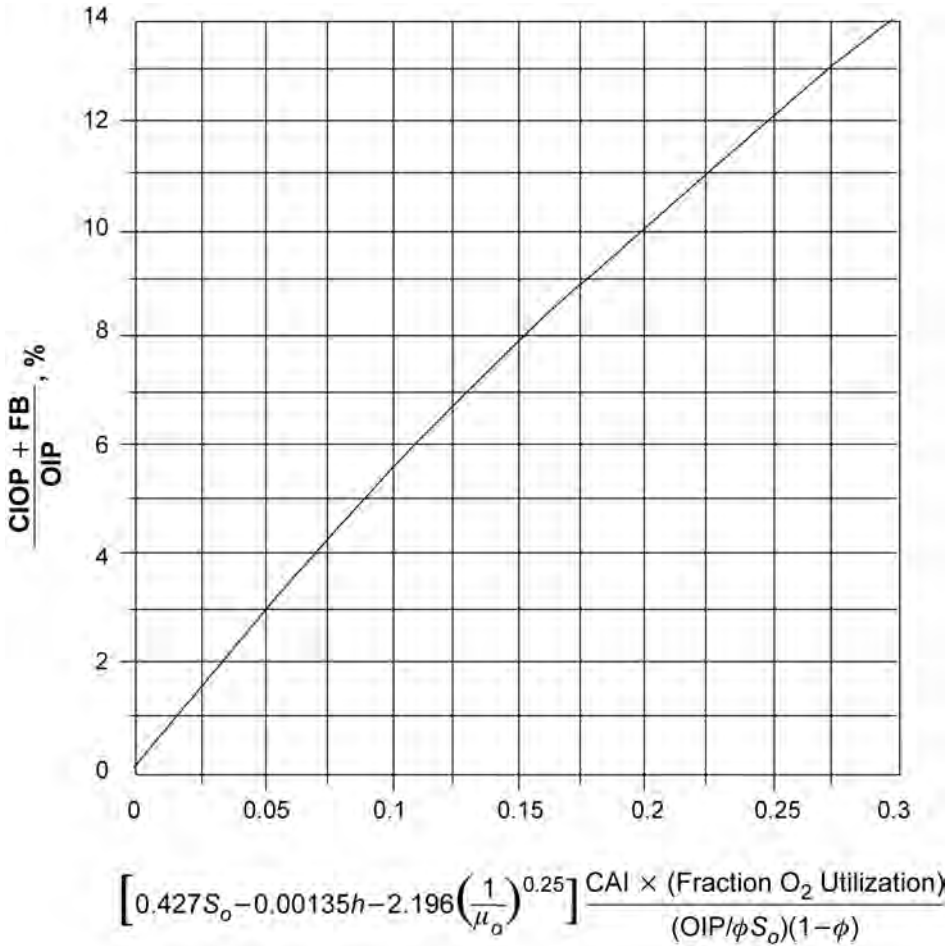


Fig. 16.14—Second Satman correlation.¹⁶

run multiple tubing strings in the injection wells. Some particulates such as soot may be carried into the formation if the gas does not burn cleanly.

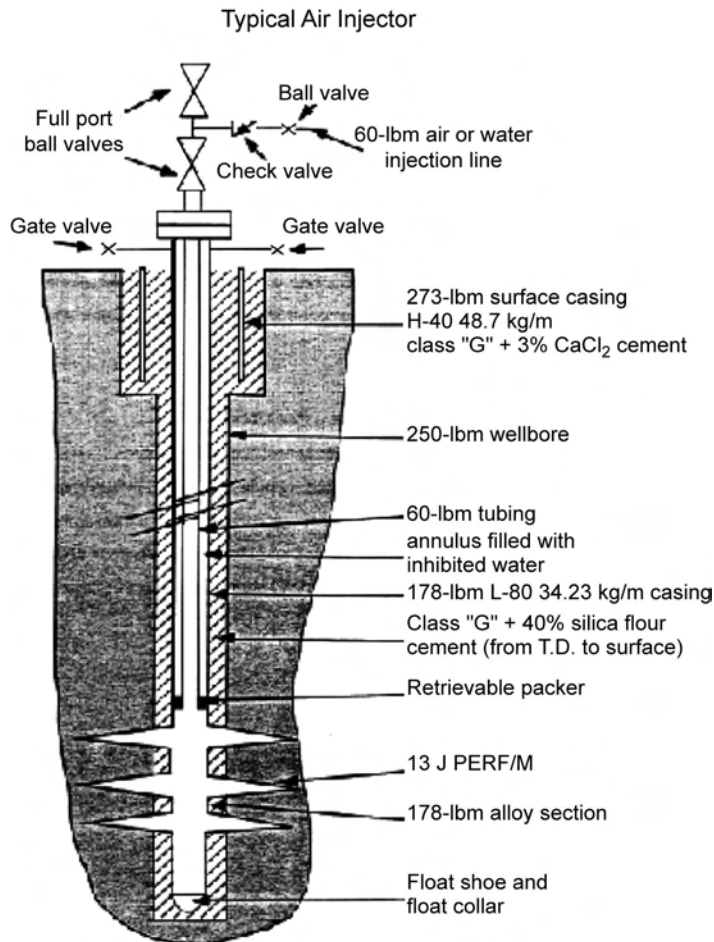
Catalytic heaters run at lower temperatures but are sometimes prohibitively expensive. Electrical heaters can be lowered with a single cable, can provide excellent temperature control, and can be reused repeatedly. There is, however, a depth limitation because of electrical power losses in the cable.

Chemically enhanced ignition does not have a depth limitation but may require handling and storage of dangerous materials. Fuel packs are not recommended because of poor temperature control and nonuniform ignition across the entire reservoir thickness. Well damage from elevated temperatures and plugging by particulate matter may occur.

Steam may be used to locally increase reservoir temperature and facilitate auto ignition. It suffers from depth limitation because of wellbore heat losses, but when the conditions are right, it can be a very simple and effective method for ignition.

The References section includes details of design and implementation of the above methods.

16.7.3 Well Design and Completions. ISC wells must be designed to account for several factors amplified by the combustion, namely high temperature, corrosive environment, and sand and clay control. Safe operations should be the primary concern.



Typical well designs for injection and production are shown in **Figs. 16.15 and 16.16**. Completion type and design depends on the reservoir being considered. Laboratory testing for sand control and completions can help to determine the best completion technique for a given field. Care must be taken to cement the wells properly. There are cement formulations that are stable at high temperatures.²⁰ Openhole completions may be used in conjunction with slotted liners, screens, gravel packs, or various other sand and clay control methods. To maximize productivity, producing wells should be completed toward the bottom of the zone of interest to take advantage of gravity drainage and avoid hot gases as long as possible. Rat holes have been used successfully in certain heavy-oil combustion projects to increase the effect of gravity drainage.²¹

16.7.4 Injection and Production Practices. Safe air injection requires that the surface injection equipment and the injection well are free of hydrocarbons. All lubricants used in compression and downhole operations should be synthetic or nonhydrocarbon types. All equipment, tools, lines, tubing, work strings, and injection strings must be clean and hydrocarbon free. Personnel at all levels should be aware of the importance of preventing hydrocarbons in the injection wells. As a safety measure to protect injection wells if the compressor is shut down, a system to prevent backflow of oil from the formation must be present at every injection well.

Typical Producing Well Completion

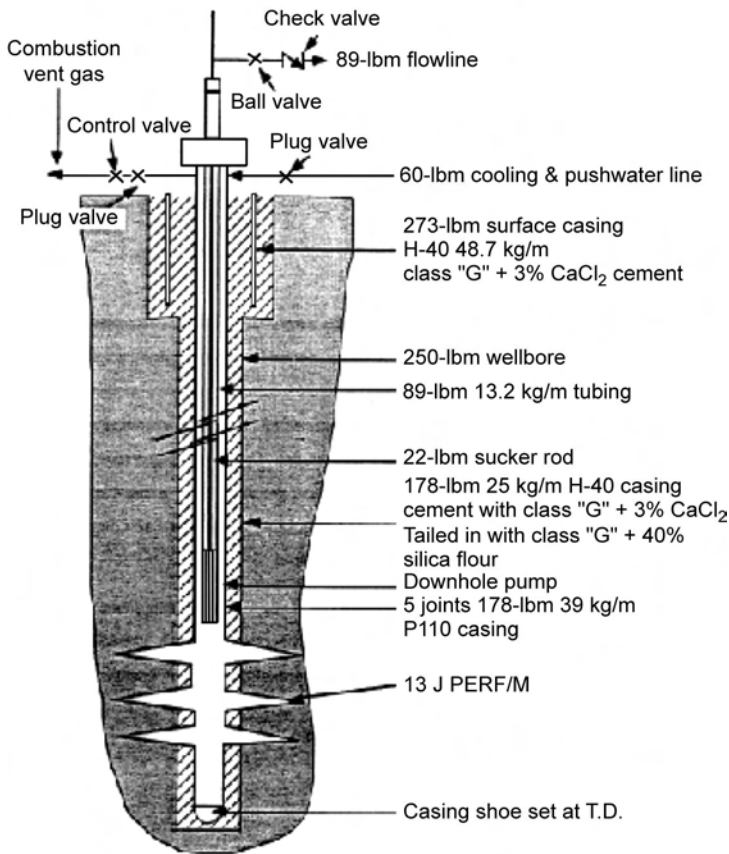


Fig. 16.16—Typical production-well design.¹

Downhole temperatures in producing wells increase as displaced oil, hot water, and steam fronts reach the well. Producers are preserved by downhole cooling and proper material selection. Fig. 16.17 provides an estimate of the water requirements to maintain bottomhole temperature no higher than 250°F as a function of oil and water production rate and formation flowing temperature. Significant additional oil recovery can be obtained from hot wells with downhole cooling, especially if the well is completed in the lower section of the producing zone to maximize gravity segregation in the reservoir. In many cases, after the combustion front has moved through the well, it is possible to convert the former producer to a new air injector, thus realizing significant cost reductions over the life of the project.

Monitoring is crucial for proper combustion operations. In addition to testing individual producers for oil and water rates, injected fluids must be measured. Also, produced gases must be measured and analyzed to determine the efficiency of the combustion operation. Downhole temperature measurements are essential to calculate the size and location of the burned zone. Flowline temperatures can indicate thermal stimulation or downhole problems.

Combustion projects generate waste water, flue gases, and pollutants from compression and oil-handling equipment. Local pollution disposal regulations must be consulted before designing any ISC operation.

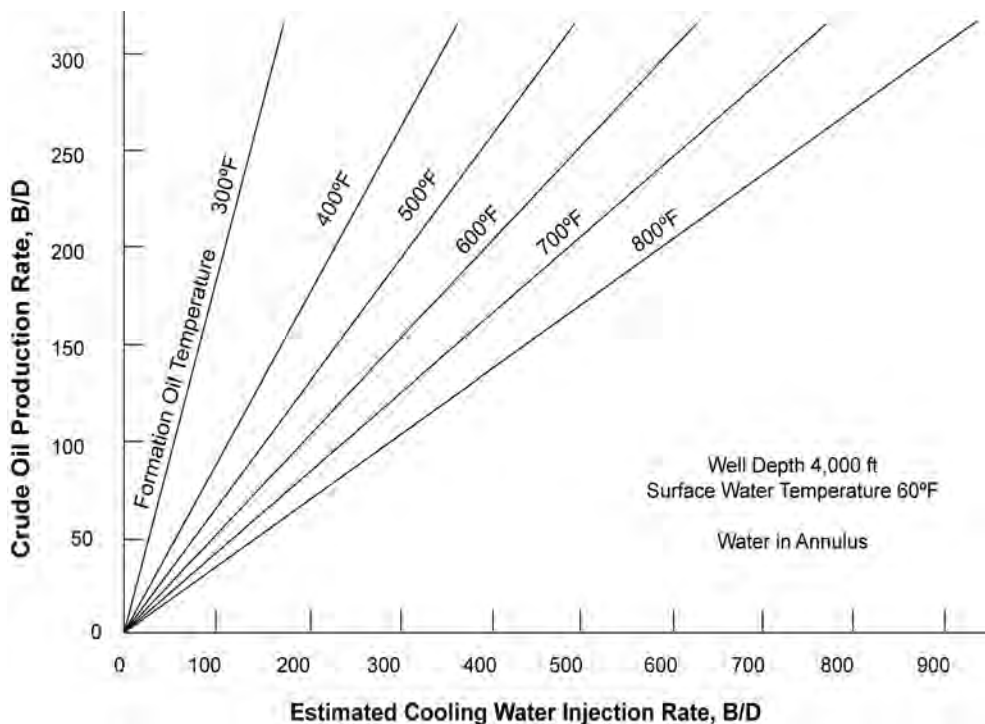


Fig. 16.17—Water needed to cool hot wells.¹

In general, environmental problems are similar to those posed by steam injection. The produced water may contain H₂S and/or CO₂, which may require special handling and anticorrosion equipment. Flue gases may contain hydrocarbons, H₂S, CO₂, CO, and other trace amounts of sulfur gases. **Table 16.3**¹ summarizes the various pollution-control systems suitable for combustion projects and their recommended applications. Sarathi¹ also provides detailed descriptions of the various types of systems and their uses. Other problems that can be encountered are sand production, corrosion, emulsions, well failures, and compressor failures.

16.8 Field Experience

ISC has been used in the field since 1920. In the U.S., more than 230 projects have been implemented. Many of those were technically and economically successful. Unfavorable reservoir and fluid characteristics, poor design, and engineering or operational problems caused failures. Most of the failed projects were small pilot projects implemented in unfavorable reservoirs. Worldwide, combustion accounts for approximately 10% of the oil produced by thermal methods; 29 projects were active as of 1998.¹ Most of the projects outside of the U.S. are large heavy-oil projects, while the current trend in the U.S. is to use ISC in deep, lighter-oil reservoirs in which waterflooding and steamflooding are not effective. Brief comments on these projects follow.

16.8.1 Heavy Oils. If we define heavy oil as under 20°API, 19 projects using ISC were active in 1998. Some general comments are applicable:

- Most of these projects last a long time; projects initiated in the 1960s are still active. Economics of successful projects are favorable even as compared to steamflooding and waterflooding.²²
- All the successful projects operate in the high-temperature mode.

**TABLE 16.3—APPLICATION OF POLLUTION-CONTROL SYSTEMS
TO A FIREFLOOD PROJECT¹**

Equipment	Gas Treated	Pollutant Removed	Method	Suggested Application
Flare stack	Flue gas	None	Vent to atmosphere	Flue gas meets air-quality regulations
Flare stack with flame burner	Flue gas	H/C ⁽¹⁾ , CO ⁽¹⁾ S-gases ^(1,2)	Burn	Flue gas with enough H/C to support combustion (>200 Btu/scf)
Thermal incinerator	Flue gas	H/C, CO, S-gases ^(1,2)	Burn	Flue gas not suitable for a flare with burner or a catalytic incinerator (heat value > 85 Btu/scf but < 200 Btu/scf)
Catalytic incinerator (excess air)	Flue gas	H/C, CO, S-gases ⁽²⁾	Burn	Flue gas with heat value <85 Btu/scf
H ₂ S scrubber	Flue gas	H ₂ S ⁽⁴⁾	Chemical reaction	Flue gas containing H ₂ S but acceptable amounts of other S gases
SO ₂ scrubber	Incinerator exhaust	SO ₂ ⁽⁴⁾	Chemical reaction	When H ₂ S removed from flue gas is inadequate or impractical

1. Removal efficiency may be poor.
2. S-gases are converted to SO₂.
3. May increase amount of CO for flue gas with heat values > Btu/Scf.
4. Typical removal efficiency is 90 to 95%.

- Gravity override and channeling do occur. Gravity drainage of the hot oil is an important mechanism and should be maximized. Frequently, improved production of oil continues after the air injection has been terminated.

- Line-drive projects, starting at the top of the reservoir and moving downward, exhibit superior performance compared to repeated pattern projects.

- Most of the projects failed when air injection was attempted in different layers of the reservoir at the same time. Air injectivity is a critical parameter, and injectivity contrast between layers is usually too difficult to overcome.

Because a detailed description of all or even a few of the projects is outside the scope of this narrative, the reader can find additional information on several current projects in the following references:

- Projects in Romania: Suplacu de Barcau is the world's largest combustion project; it started in 1964 and is operated in a line-drive mode from the top downward. Videle and Balaria are other ISC projects.^{23,24}

- In India, Balol, which started as a pilot in 1990, was expanded to the whole field. Designed as a wet combustion project, the water injection rate had to be cut in half because of too much cooling. This project also was changed from patterns to updip line drive because of premature breakthrough in the producers.^{25,26}

- Projects in Russia, Kazakhstan, and Azerbaijan are not very well described in Western literature.²⁷

- The Albanian project of Kasnice is described in Marko *et al.*²⁸

- Batrum in Canada is a successful project using horizontal wells as producers. The Eyehill field is another project with horizontal wells.^{26,29} Wabaska also uses the same concept of hori-

zontal wells as producers.³⁰ Horizontal wells in ISC operations have been successfully used in Canada since 1993.

Cyclic applications such as pressure-up and blowdown, have been described.^{30,31} This operational technique allows production from very low mobility oil fields or tar sands in which fracturing or cyclic steaming are needed before air injection. The Wabaska project is a cyclical combustion project with horizontal wells. This type of pressure-up, blowdown technique has also been successfully implemented at Wolf Lake.³¹ Air was injected until the front arrived at the producers. When the front reached a given producer, this well was shut down, and cooling water was circulated. When all the producers were shut down, injection was stopped, and the producers reopened to blow down the reservoir. This process was repeated for several cycles. Operating combustion in this fashion allows production from fields in which injectivity is low because of a high crude viscosity at reservoir conditions.

U.S. projects at Bellevue and Midway-Sunset have been described.²⁶ More details on the Midway-Sunset project can be found in Hoffmann.³² Ramey *et al.*²¹ describe the Belridge project as an economic success.

ISC in heavy-oil reservoirs has been successful in both the dry and wet modes. Dry combustion early in the life of the project is the preferred method to form the desired high-temperature regime. When the process is well established, moderate amounts of water can be added to improve efficiency. Quenched, or super-wet, combustion seems to have limited success except when used at the end of a field operation to scavenge the heat remaining in the rock.

Another operating variation includes the use of enriched air or pure oxygen. Oxygen-enriched combustion presents technical and economic advantages for reservoirs with high pressure or very low injectivity. It has been demonstrated successfully in the field.^{33,34} The additional literature covering the special handling methods and additional precautions needed for enriched air injection is listed in the References section. Commercial application of the oxygen technology has been limited because of oil-price variations.

16.8.2 Light Oils. ISC is used in light-oil reservoirs for two different purposes:

- To reduce the viscosity of unconventional light oils such as Demjen in Hungary³⁵ or Niemangu in China.¹ In these cases, thermal effects are important. In the case of Demjen, a catalyst had to be injected to promote combustion. Iron was used to increase the amount of fuel burned because the light oil by itself was not depositing enough fuel to sustain combustion. The oil is parafinic and almost solid at reservoir temperature despite an API gravity of 32°.
- To produce from light-oil reservoirs in which waterflooding or other enhanced oil recovery methods are not attractive. Combustion is used to generate flue gases for reservoir pressure maintenance and production by gravity drainage. Thermal effects are only minor for this process. An interesting case is the West Hackberry double displacement process,³⁶ in which the gas cap is expanded for gravity drainage to recover residual oil after waterflood.

Combustion is successful in tight carbonate reservoirs located in the Dakotas, such as Medicine Pole Hill, Buffalo, west and south Buffalo,³⁷ and Horse Creek. In those cases, combustion allows exploitation of thin reservoirs with large well spacing.

16.9 Screening Guidelines

ISC is a complex process; it combines the effects of steamdrive, hydrocarbon miscible and immiscible flooding, immiscible gas drive, and hot and cold waterflooding. Because of its complexity, there is a misconception that combustion has a low probability of success. The truth is that combustion is an economically attractive, proven recovery process, capable of economically recovering a large fraction of the oil in place.

ISC can be applied to many different reservoirs. Some suggested screening guidelines are:

- Nature of the formation: The rock type is not important provided that the matrix/oil system is reactive enough to sustain combustion. As in any drive process, high-permeability streaks are detrimental. Swelling clays may be a problem in the steam-plateau area.
- Depth: The reservoir must be deep enough to ensure containment of the injected air in the reservoir. There is no depth limit, except that this may affect the injection pressure.
- Pressure: This will affect the economics of the process but does not affect the technical aspects of combustion.
- Temperature: Temperature will affect the propensity for autoignition but is otherwise not critical.
- Reservoir thickness: Thickness must be greater than 4 m (15 ft) (Sarathi¹) to avoid excessive heat losses to surrounding formations. Thick formations may present sweep-efficiency problems because of gravity override.
- Permeability: This has to be sufficient to allow injection of air at the designed air flux. The air injectivity is especially important for heavy-oil reservoirs. Conditions are favorable when kh/μ is greater than 5md m/cp³.
- Porosity and oil saturation: These must be large enough to allow economic oil recovery. The product, ϕS_o , should be more than approximately 0.08 for combustion to be economically successful.
- Oil gravity: This parameter is not critical. In-situ viscosity has to be small enough to allow air injection and resulting oil production at the design rate.
- Oil nature: In heavy-oil projects, the oil should be readily oxidizable at reservoir and rock matrix conditions. This relationship must be determined by laboratory experiments. The same laboratory experiments can also determine the amount of air needed to burn a given reservoir volume. This is key to the economics of the process.

16.10 Conclusions

ISC is applicable to a wide array of reservoirs. In fact, it is the only thermal method that can presently be applied to deep reservoirs, though deep downhole steam generation is being tested. It can be used at any stage of reservoir depletion; it can be used in special situations such as offshore or in Arctic regions. Because of the lack of heat losses at the surface and in the injection wells, it is the most thermally efficient thermal-recovery method. The injectant (air) is readily available. Combustion allows wider well spacing than steam; economic results are comparable to those of steam injection.

Several aspects of operating ISC projects must be considered. First is the large compression ratio and associated costs required to inject air into the formation. Second is the planning and design requirements for a combustion project; these are more difficult than for steam injection. Third is extensive laboratory work to assess fuel availability, air requirements, and burning characteristics of the crude that are required before designing ISC projects. Fourth is the high degree of technical sophistication and the careful monitoring needed to ensure proper operation of a project. Fifth is the limitation of numerical simulation and other techniques that makes predictions of recovery more difficult than most other enhanced oil recovery methods.

Considerable improvements in the application of ISC have been made since the early projects. New developments, such as application to light-oil reservoirs, and the use of horizontal wells are reviving interest in ISC. This process deserves consideration for many reservoirs, including those in hostile environments or those not amenable to other recovery methods.

Nomenclature

- a, b, d, f = stoichiometric coefficients similar to those in Eq. 16.3
- A = Arrhenius rate constant
- c_p/c_v = heat capacity ratio
- C_f = concentration of fuel, kg/m³

- E = activation energy, kJ/mol
 H_c = heating value, Btu/lbm fuel
 K = reaction rate
 m = CO₂/CO atomic ratio
 m = CO₂/CO concentration ratio produced
 n = hydrogen/carbon atomic ratio of fuel
 N_p = oil produced, m³
(O₂)_{prod} = oxygen concentration produced
 p_{O_2} = oxygen partial pressure, Pa
 \bar{R} = 0.00831 universal gas constant, kJ/mol °K
 R_C = reaction rate of crude, kg/m³s
 S_f = oil saturation burned, fraction
 S_o = oil saturation, fraction
 S_{oi} = initial oil saturation, fraction
 S_{wf} = water saturation resulting from the combustion process, fraction
 T = absolute temperature, °K
 T_1 = initial reservoir temperature, °F
 T_2 = final reservoir temperature, °F
 V_b = volume burned, m³
 V_p = volume of the pattern, m³
 W = fuel availability
 W_p = water produced, m³
 ϕ = porosity, fraction
 μ = oil viscosity

References

1. Sarathi, P.: "In-Situ Combustion Handbook Principles And Practices," Report DOE/PC/91008-0374, OSTI ID 3175 (January 1999).
2. Prats, M. *Thermal Recovery*, Monograph Series, SPE, Richardson, Texas (1982) 7.
3. Burger, J., Sourieau, P., and Combarous, M.: *Thermal Methods Of Oil Recovery*, Editions Technip, Paris (1985; re-edited 1989).
4. Wu, C.H. and Fulton, F.P.: "Experimental Simulation of the Zones Preceding the Combustion Front of an In-Situ Combustion Process," *SPEJ* (March 1971) 38; *Trans.*, AIME, **251**.
5. Bousaid, S.: "Multiple-Quenched Fireflood Process Boosts Efficiency," *JPT* (November 1989) 1202.
6. Mamora, D. *et al.*: "Kinetics of in-situ combustion," Report No. DOE/BC/14600-51 (DE93000152) SUPRI TR 91, U.S. Dept. of Energy, Washington, DC (July 1993).
7. Burger, J.: "Chemical Aspects of In-Situ Combustion—Heat of Combustion and Kinetics," *SPEJ* (October 1972) 410; *Trans.*, AIME, **253**.
8. Moore, R.G.: "New Strategies for In-Situ Combustion," *J Cdn. Pet. Tech.* (December 1993) **32**, No. 10.
9. Fassihi, M.R., Brigham, W.E., and Ramey, H.J. Jr.: "Reaction Kinetics of In-Situ Combustion: Part 2—Modeling," *SPEJ* (August 1984) 408.
10. Moore, R.G. *et al.*: "A comparison of the laboratory in-situ combustion behaviour of Canadian oils," *Proc.*, 6th UNITAR Conference, Houston, February 1995.
11. Bardon, C. and Gabelle, C.: "Essais de laboratoire pour l'étude de la combustion in-situ," paper presented at the 1977 French Soviet Symposium on Enhanced Oil Recovery, Moscow, May.

12. Leaute, R.P. and Collyer, C.J.: "Laboratory studies of in situ combustion with cold lake crude," paper 5 presented at the 1984 Annual Conference on Upgrading Technology and Petroleum Recovery, Calgary.
13. Dew, J.N. and Martin, W.I.: "How to calculate air requirements for in-situ combustion," *Petroleum Engineer* (December 1964 and January 1965).
14. Nelson, T.W. and Mc Neil, J.S.: "How to engineer an in-situ combustion project," *Producer Monthly* (May 1961); *Oil & Gas J.* (5 June 1961).
15. Gates, C.J and Ramey H.J. Jr.: "A Method for Engineering In-Situ Combustion Oil Recovery Projects," *JPT* (February 1980) 285.
16. Brigham, W. and Satman, A.: "Recovery Correlations for In-Situ Combustion Field Projects and Application to Field Pilots," *JPT* (December 1980) 2132.
17. Shallcross, D.C.: "Devices and Methods for In-Situ Combustion Ignition," Report No. DOE/BC/14126-12 (DE 89000766), U.S. Dept. of Energy, Washington, DC (October 1989).
18. Burger, J.G.: "Spontaneous Ignition in Oil Reservoirs," *SPEJ* (April 1976) 73.
19. Tadema, H.J. and Weidjeima, J.: "Spontaneous ignition of oils," *Oil & Gas J.* **68**, No. 50.
20. Smith, D.K.: *Cementing*, Monograph Series, SPE, Richardson, Texas (1976) **4**.
21. Ramey, H.J. Jr. *et al.*: "Case History of South Belridge, California, In Situ Combustion Oil Recovery," paper SPE 24200 presented at the 1992 SPE/DOE Enhanced Oil Recovery Symposium, Tulsa, 22–24 April.
22. Ramage, W.E., Castanier, L.M., and Ramey, H.J. Jr.: "Economic Evaluation of Thermal Recovery Projects," paper SPE 16852 presented at the 1987 SPE Annual Technical Conference and Exhibition, Dallas, 27–30 September.
23. Machedon, V.: "Suplacu de Barcau field: 28 years of in situ combustion," *Proc.*, 7th European Symposium on Enhanced Oil Recovery, Moscow (1993).
24. Machedon, V.: "Romania: 30 years of experience in in-situ combustion," *Proc.*, NIPER/DOE Symposium on In-situ Combustion, Tulsa (21–22 April 1994); U.S. DOE Report NIPER/BDM-0086 (January 1995).
25. Roychoudhuri, S. *et al.*: "Experience with in-situ combustion pilot in presence of edge water," *Proc.*, 6th UNITAR Conference on Heavy Crudes and Tar Sands, Houston (12–17 February 1995).
26. Moritis, G. "EOR Oil Production Up Slightly," *Oil & Gas J.* (20 April 1998) 49.
27. Mamedov, Y.G. and Bocserman, A.A.: "Development of heavy oils and bitumen in the former Soviet Union and eastern and central Europe," *Proc.*, 6th UNITAR Conference on Heavy Crudes and Tar Sands, Houston (12–17 February 1995).
28. Marko, D.: "Oil production history in Albanian fields and their perspective," *Proc.*, 6th UNITAR Conference on Heavy Crudes and Tar Sands, Houston (12–17 February 1995).
29. Ames, B.G., Gramms, R.E., and Pabdani, F.N.: "Improved sweep efficiency through application of horizontal well technology in a mature combustion EOR," *Proc.*, NIPER/DOE Symposium on In-Situ Combustion, Tulsa (21–22 April 1994); U.S. DOE Report NIPER/BDM-0086 (January 1995).
30. Marjerrison, D.M. and Fassihi, M.R.: "Performance of Morgan Pressure Cycling In-Situ Combustion Project," paper SPE 27793 presented at the 1994 SPE/DOE Improved Oil Recovery Symposium, Tulsa, 17–20 April.
31. Hallam, R.J. and Donnelly, J.K.: "Pressure-Up Blow Down Combustion: A Channeled Reservoir Recovery Process," *SPE Advanced Technology Series* (April 1993) 153.
32. Hoffmann, S.J.: "Successful Application of In Situ Combustion to a Dipping Heavy Oil Reservoir Midway Sunset Field," paper 39639 presented at the 1998 SPE/DOE Symposium, Tulsa.
33. Hvizdos, L.J., Howard, J.V., and Roberts, G.W.: "Enhanced Oil Recovery Through Oxygen-Enriched In-Situ Combustion: Test Results From the Forest Hill Field in Texas," *JPT* (June 1983) 1061.
34. Moore, R.G. *et al.*: "New Insights Into Enriched-Air In-Situ Combustion," *JPT* (July 1990) 916; *Trans.*, AIME, **289**.
35. Racz, D. *et al.*: "Development of a thermocatalytic in situ combustion process in Hungary," *Proc.*, 1985 European Meeting on Improved Oil Recovery, Rome (April).
36. Gilham, T.H. *et al.*: "Keys To Increasing Production Via Air Injection in Gulf Coast Light Oil Reservoirs," paper SPE 38848 presented at the 1997 SPE Annual Technical Conference and Exhibition, San Antonio, Texas, 5–8 October.

37. Miller, R.J.: “Koch’s experience with deep in-situ combustion in Williston basin,” *Proc.*, NIPER/DOE Symposium on In-Situ Combustion, Tulsa (21–22 April 1994); U.S. DOE Report NIPER/BDM-0086 (January 1995).

General References

- Alexander, J.D., Martin W.L., and Dew, J.N.: “Factors Affecting Fuel Availability and Composition During In-Situ Combustion,” *JPT* (October 1962) 1154; *Trans.*, AIME, **225**.
- Bahtia, A.K.: “Reservoir management of heavy oil reservoirs of North Gujarat,” *Proc.*, 7th UNITAR Intl. Conference on Heavy Crude and Tar Sands, Beijing (1998).
- Basham, M.: “Planning an in situ combustion project: Cymric field, California,” *Proc.*, PTTC Meeting, Bakersfield, California (1999).
- Burger, J. and Sahuquet, B.: “Laboratory Research on Wet Combustion,” *JPT* (October 1973) 1137.
- Carcoana, A. *et al.*: “Balayage et recuperation d’un gisement d’huile lourde par combustion in situ,” *Proc.*, Colloque Int. sur l’exploitation des hydrocarbures, Paris (1975).
- Cato, R.W. and Franka, W.A.: “Getty Oil Reports Fireflood Pilot is Successful Project,” *Oil & Gas J.* (12 February 1968).
- Chu, C.: “State-of-the-Art Review of Fireflood Field Projects,” *JPT* (January 1982) 19.
- Coats, K.H.: “In-Situ Combustion Model,” *SPEJ* (December 1980) 533.
- Counihan, T.M.A.: “A Successful In-Situ Combustion Pilot in the Midway Sunset Field, California,” Paper SPE 6525 presented at the 1977 SPE California Regional Meeting, Bakersfield, California, 13–15 April.
- Craig, F.F. Jr. and Parrish, D.R.A.: “A Multipilot Evaluation of the COFCAW Process,” *JPT* (June 1974) 659.
- Dietz, D.N.: “Wet Underground Combustion, State of the Art,” *JPT* (May 1970) 605; *Trans.*, AIME, **249**.
- Dietz, D.N. and Wijema, J.: “Reverse combustion seldom feasible,” *Prod. Monthly* (May 1968).
- Ejiogu, J.G. *et al.*: “Wet combustion—A tertiary recovery process for the Pembina Cardium Reservoir,” *J. Cdn. Pet. Tech.* (July–September 1979).
- Farouq Ali, S.M.: “A Current Appraisal of In-Situ Combustion Field Tests,” *JPT* (April 1972) 477.
- Fassihi, M.R.: “Analysis of fuel oxidation on in-situ combustion oil recovery,” PhD thesis, Stanford U. (1981); U.S. DOE Report DOE/ET/12056-26, U.S. Dept. of Energy, Washington, DC (August 1982).
- Fattahi, B.: “Pyramids Hills Project, Mt. Poso Field, California,” Aera Energy, 1999 PTTC Meeting, Bakersfield, California.
- Gadelle, C. *et al.*: “Heavy Oil Recovery by In-Situ Combustion—Two Field Cases in Rumania,” *JPT* (November 1981) 2057.
- Galas, C.M.F. and Ejlogu, G.C.: “Enhancement of In-Situ Combustion by Steam Stimulation of Production Wells,” *SPEE* (November 1993) 270.
- Garon, A.M. and Wygal, R.J. Jr.: “A Laboratory Investigation of Fire-Water Flooding,” *SPEJ* (December 1974) 537.
- Gates, C.J. and Ramey, H.J. Jr.: “Field Results of South Belridge Thermal Recovery Experiment,” *Trans.*, AIME (1958) **213**, 236.
- Gates, C.F., Jung, K.D., and Surface, R.A.: “In-Situ Combustion in the Tulare Formation, South Belridge Field, Kern County, California,” *JPT* (May 1978) 799; *Trans.*, AIME, **265**.
- Gates, C.J. and Sklar, I.: “Combustion as a Primary Recovery Process – Midway Sunset Field,” *JPT* (August 1971) 981; *Trans.*, AIME, **251**.

- Joseph, C. and Pusch, W.H.: "A Field Comparison of Wet and Dry Combustion," *JPT* (September 1980) 1523.
- Koch, R.L.: "Practical use of combustion drive at West Newport field," *Pet. Eng.* (January 1965).
- Martin, W.L., Alexander, J.D., and Dew, J.N.: "Process Variables of In Situ Combustion," *Trans.*, AIME (1958) **213**, 28.
- Meldau, R.F., Shipley, R.G., and Coats, K.H.: "Cyclical Gas/Steam Stimulation of Heavy-Oil Wells," *JPT* (October 1981) 1990.
- Moss, J.T., White, P.D., and McNeil, J.S. Jr.: "In Situ Combustion Process—Results of a Five-Well Field Experiment in Southern Oklahoma," *Trans.*, AIME (1959) **216**, 55.
- Olsen, D. and Sarathi, P.: "Field application of in-situ combustion," Report No. NIPER/BDM 0086, U.S. Dept. of Energy, Washington, DC (1994).
- Showalter, W.E. and Maclean, A.M.: "Fireflood at Brea Olinda Field, Orange County, California," paper SPE 4763 presented at the 1974 SPE Improved Oil Recovery Symposium, Tulsa, 22–24 April.
- Showalter, W.E.: "Combustion-Drive Tests," *SPEJ* (March 1963) 53; *Trans.*, AIME, **228**.
- Terwilliger, P.L. *et al.*: "Fireflood of the P2-3 Sand Reservoir in the Miga Field of Eastern Venezuela," *JPT* (January 1975) 9.
- Widmeyer, R.H. *et al.*: "The Charco Redondo Thermal Recovery Pilot," *JPT* (December 1977) 1522.
- Williams, R.L., Jones, J.A., and Counihan, T.M.: "Expansion of a Successful In-Situ Combustion Pilot in Midway Sunset Field," paper SPE 16873 presented at the 1987 SPE Annual Technical Conference and Exhibition, Dallas, 27–30 September.

SI Metric Conversion Factors

°API	$141.5/(131.5 + \text{°API})$	= g/cm ³
bar ×	1.0*	E + 05 = Pa
bbbl ×	1.589 873	E - 01 = m ³
Btu ×	1.055 056	E + 00 = kJ
cp ×	1.0*	E - 03 = Pa·s
ft ×	3.048*	E - 01 = m
ft ³ ×	2.831 685	E - 02 = m ³
°F	$(\text{°F} - 32)/1.8$	= °C
°F	$(\text{°F} + 459.67)/1.8$	= K
kW-hr ×	3.6*	E + 00 = J
lbm ×	4.535 924	E - 01 = kg
psi ×	6.894 757	E + 00 = kPa

*Conversion factor is exact.

Chapter 17

Reservoir Simulation

Rod P. Batycky, **Marco R. Thiele**, StreamSim Technologies Inc.; **K.H. Coats**, Coats Engineering Inc.; **Alan Grindheim**, **Dave Ponting**, Roxar Software Solutions; **John E. Killough**, Landmark Graphics; **Tony Settari**, U. of Calgary and Taurus Reservoir Solutions Ltd.; **L. Kent Thomas**, ConocoPhillips; **John Wallis**, Wallis Consulting Inc.; **J.W. Watts**, Consultant; and **Curtis H. Whitson**, Norwegian U. of Science and Technology and Pera

17.1 Introduction—K.H. Coats

The Merriam-Webster Dictionary defines *simulate* as assuming the appearance of without the reality. Simulation of petroleum reservoir performance refers to the construction and operation of a model whose behavior assumes the appearance of actual reservoir behavior. The model itself is either physical (for example, a laboratory sandpack) or mathematical. A mathematical model is a set of equations that, subject to certain assumptions, describes the physical processes active in the reservoir. Although the model itself obviously lacks the reality of the reservoir, the behavior of a valid model simulates—assumes the appearance of—the actual reservoir.

The purpose of simulation is estimation of field performance (e.g., oil recovery) under one or more producing schemes. Whereas the field can be produced only once, at considerable expense, a model can be produced or run many times at low expense over a short period of time. Observation of model results that represent different producing conditions aids selection of an optimal set of producing conditions for the reservoir.

The tools of reservoir simulation range from the intuition and judgment of the engineer to complex mathematical models requiring use of digital computers. The question is not whether to simulate, but rather which tool or method to use. This chapter concerns the numerical mathematical model requiring a digital computer. The Reservoir Simulation chapter in the 1987 edition of the *Petroleum Engineering Handbook*¹ included a general description of reservoir simulation models, a discussion related to how and why they are used, choice of different types of models for different-reservoir problems, and reliability of simulation results in the face of model assumptions and uncertainty in reservoir-fluid and rock-description parameters. That material is largely omitted here. Instead, this chapter attempts to summarize current practices and trends related to development and application of reservoir simulation models.

TABLE 17.1—SPE COMPARATIVE SOLUTION PROJECT PROBLEMS

SPE1	Three-phase black oil 10×10×3 300-block grid 3,650-day depletion with gas injection
SPE2	Three-phase black oil 10×1×15 150-block <i>r-z</i> grid 900-day single-well coning depletion
SPE3	Nine-component retrograde gas 9×9×4 324-block grid 5,480-day cycling and blowdown
SPE4	Cyclic steam injection and steam displacement of heavy oils
SPE5	Six-component volatile oil 7×7×3 147-block grid 20-year WAG injection
SPE6	Three-phase black oil Single-block and cross-sectional dual porosity with drainage and gas and water injection cases
SPE7	Three-phase black oil 9×9×6 486-block grid with horizontal wells Eight 1,500-day injection-production cases
SPE8	Two-phase gas-oil black oil 10×10×4 400-block grid Comparison of 2,500-day 400-block grid results with 20-block unstructured and locally refined grid results
SPE9	Three-phase black oil 24×25×15 9,000-block 25-well grid with geostatistical description 900-day depletion
SPE10	Model 1: Two-phase gas-oil case with a 2,000-block 100×1×20 grid and gas injection to 2000 days Model 2: Two-phase water-oil case with a 1.12-million block 60×220×85 grid and water injection to 2,000 days Both models have geostatistical descriptions

Models have been referred to by *type*, such as *black-oil*, *compositional*, *thermal*, *generalized*, or *IMPES*, *Implicit*, *Sequential*, *Adaptive Implicit*, or *single-porosity*, *dual-porosity*, and more. These *types* provide a confusing basis for discussing models; some refer to the application (e.g., thermal), others to the model formulation (e.g., implicit), and yet others to an attribute of the reservoir formation (e.g., dual-porosity). The historical trend, though irregular, has been and is toward the *generalized* model, which incorporates all the previously mentioned types and more. The generalized model, which represents most models in use and under development today, will be discussed in this chapter. Current model capabilities, recent developments, and trends will then be discussed in relation to this generalized model.

The 10 SPE Comparative Solution Project problems, SPE1 through SPE10,²⁻¹¹ are used for some examples below. **Table 17.1** gives a brief description of those problems.

17.1.1 The Generalized Model. Any reservoir simulator consists of $n + m$ equations for each of N active gridblocks comprising the reservoir. These equations represent conservation of mass of each of n components in each gridblock over a timestep Δt from t^n to t^{n+1} . The first n (primary) equations simply express conservation of mass for each of n components such as oil, gas, methane, CO_2 , and water, denoted by subscript $I = 1, 2, \dots, n$. In the thermal case, one of the “components” is energy and its equation expresses conservation of energy. An additional m (secondary or constraint) equations express constraints such as equal fugacities of each component in all phases where it is present, and the volume balance $S_w + S_o + S_g + S_{\text{solid}} = 1.0$, where S_{solid} represents any immobile phase such as precipitated solid salt or coke.

There must be $n + m$ variables (unknowns) corresponding to these $n + m$ equations. For example, consider the isothermal, three-phase, compositional case with all components present in all three phases. There are $m = 2n + 1$ constraint equations consisting of the volume balance and the $2n$ equations expressing equal fugacities of each component in all three phases, for a total of $n + m = 3n + 1$ equations. There are $3n + 1$ unknowns: p , S_w , S_o , S_g , and the $3(n - 1)$ independent mol fractions x_{ij} , where $i = 1, 2, \dots, n - 1$; $j = 1, 2, 3$ denotes the three phases oil, gas, and water. For other cases, such as thermal, dual-porosity, and so on, the m constraint equations, the $n + m$ variables, and equal numbers of equations and unknowns can be defined for each gridblock.

Because the m constraint equations for a block involve unknowns only in the given block, they can be used to eliminate the m secondary variables from the block’s n primary or conservation equations. Thus, in each block, only n primary equations in n unknowns need be considered in discussions of model formulation and the linear solver. The n unknowns are denoted by $P_{i1}, P_{i2}, \dots, P_{in}$, where P_{in} is chosen as pressure p_i with no loss of generality. These primary variables may be chosen as any n independent variables from the many available variables: phase and overall mol fractions, mol numbers, saturations, p , and so on. Different authors choose different variables.¹²⁻¹⁵ Any sensible choice of variables and ordering of the primary equations gives for each gridblock a set of n equations in n unknowns which is susceptible to normal Gaussian elimination without pivoting. The (Newton-Raphson) convergence rate for the model’s timestep calculation is independent of the variable choice; the model speed (CPU time) is essentially independent of variable choice.

The l th primary or conservation equation for block i is

$$M_{iI}^{n+1} - M_{iI}^n = \Delta t \left(\sum_{j=1}^{j=N} q_{ijI} - q_{iI} \right) I = 1, 2, \dots, n, \dots \dots \dots (17.1)$$

where M_{iI} is mass of component I in gridblock i , q_{ijI} is the interblock flow rate of component I from neighbor block j to block i , and q_{iI} is a well term. With transposition, this equation is represented by $f_{iI} = 0$, the l th equation of gridblock i . All n equations $f_{iI} = 0$ for the block can be expressed as the vector equation $\mathbf{F}_i = 0$ where f_{iI} is the l th element of the vector \mathbf{F}_i . Finally, the vector equation

$$\mathbf{F}(\mathbf{P}_1, \mathbf{P}_2, \dots, \mathbf{P}_N) = 0 \dots \dots \dots (17.2)$$

represents the entire model, where the l th element of the vector \mathbf{F} is F_l . \mathbf{F} is a function of the N vector unknowns \mathbf{P}_i , where the l th scalar element of \mathbf{P}_i is P_{il} . Application of the Newton-Raphson method gives

$$\mathbf{F}^l + \delta \mathbf{F} = \mathbf{F}^l + A \delta \mathbf{P} = 0, \dots \dots \dots (17.3)$$

where $\delta\mathbf{P}$ is $\mathbf{P}^{l+1}-\mathbf{P}^l$ and the $N \times N$ matrix A represents the Jacobian $\partial\mathbf{F}/\partial\mathbf{P}$. The element A_{ij} of A is itself an $n \times n$ matrix $\partial\mathbf{F}_i/\partial\mathbf{P}_j$ with scalar elements $a_{rs} = \partial f_{ir}/\partial P_{js}$, r and s each = $1,2,\dots,n$. Eq. 17.3 is solved by the model's linear solver. The matrix A is very sparse because A_{ij} is 0 unless block j is a neighbor of block i .

The calculations for a timestep consist of a number of Newton (*nonlinear* or *outer*) iterations terminated by satisfaction of specified convergence criteria. Each Newton iteration requires:

- (a) Linearization of the constraint equations and conservation Eq. 17.1.
- (b) Linear algebra to generate the A matrix coefficients.
- (c) Iterative solution of Eq. 17.3 (*inner* or *linear* iterations).
- (d) Use of the new iterate \mathbf{P}^{l+1} to obtain from Eq. 17.1 the moles of each component in the gridblock.
- (e) A flash to give phase compositions, densities, and saturations which allow generation of the A matrix coefficients for the next Newton iteration.

17.1.2 Model Formulations. A major portion of the model's total CPU time is often spent in the linear solver solution of Eq. 17.3. This CPU time in turn reflects the many multiply operations required. The model formulation has a large effect on the nature and expense of those multiplies.

Implicit vs. Explicit. The interblock flow term in Eq. 17.1,

$$q_{ijI} = T_{ij} \sum_{J=1}^{J=3} \lambda_{j\rho} x_{IJ} (\Delta p_{J} - \gamma_J \Delta Z), \dots\dots\dots (17.4)$$

uses phase mobilities, densities, and mol fractions evaluated at the upstream blocks. A gridblock is *implicit* in, say, the variable S_g if the new time level value S_g^{n+1} is used to evaluate interblock flow terms dependent upon it. The block is *explicit* in S_g if the old time level value S_g^n is used.

The Implicit Formulation. The implicit formulation¹⁶ expresses interblock flow terms using implicit (new time level) values of all variables in all gridblocks. As a consequence, all nonzero A_{ij} elements of the A matrix of Eq. 17.3 are full $n \times n$ matrices. The resulting multiplies in the linear solver are then either matrix-matrix or matrix-vector multiplies, requiring work (number of scalar multiplies) of order n^3 or n^2 , respectively.

The IMPES Formulation. Early papers¹⁷⁻¹⁹ presented the basis of the IMPES (implicit pressure, explicit saturations) formulation for the black-oil case: take all variables in the interblock flow terms explicit, except for pressure, and eliminate all nonpressure variables from the linearized expressions for M_{ij}^{n+1} in Eq. 17.1. The obvious extension to any type model with any number of components was presented later,²⁰ and numerous IMPES-type compositional models have been published.^{13-15,21}

The model Eq. 17.3 can be written as:

$$A_{ii} \delta\mathbf{P}_i + \sum_{j \neq i} A_{ij} \delta\mathbf{P}_j = -\mathbf{F}_i^l \quad i = 1, 2, \dots, N \dots\dots\dots (17.5)$$

If all variables but pressure are explicit in the interblock flow terms, then all entries but those in the last column of the $n \times n$ A_{ij} ($j \neq i$) matrix are zero (recall, the n th variable in each gridblock, P_{in} , is pressure p_i). This allows elimination of all nonpressure variables and reduction of the vector Eq. 17.5 to the scalar equation in pressure only²²:

$$a_{ii}\delta p_i + \sum_{j \neq i} a_{ij}\delta p_j = -f_i^l, i = 1, 2, \dots, N \dots \dots \dots (17.6)$$

or

$$A\delta\mathbf{P} = -\mathbf{F}^l, \dots \dots \dots (17.7)$$

where A is now a scalar $N \times N$ matrix and the \mathbf{P} and \mathbf{F} vectors have N scalar elements p_i and f_i , respectively. The multiplications required in solution of the IMPES pressure Eq. 17.7 are scalar multiplications, requiring a small fraction of the work of the matrix-matrix and matrix-vector multiplications of the implicit formulation. Thus, the model CPU time per gridblock per Newton iteration for moderate or large n is much less for the IMPES formulation than for the implicit formulation.

The Sequential Formulation. The stability of the IMPES formulation for the two-phase water/oil case was improved by following the IMPES pressure equation solution with solution of a water saturation equation using implicit saturations (mobilities).²³ This concept was extended to the three-phase case and called the *sequential* formulation.²⁴ For each Newton iteration, this method requires solution of the IMPES pressure Eq. 17.7, followed by solution for two saturations from a similar equation where the A_{ij} elements of A are 2×2 matrices.

A sequential compositional model was described¹⁵ and mentioned the desirability of a sequential implicit treatment of mol fractions in addition to saturations.

The Adaptive Implicit Formulation. The Adaptive Implicit Method (AIM)²⁵ uses different levels of implicitness in different blocks. In each gridblock, each of the n variables may be chosen explicit or implicit, independent of the choices in other gridblocks. The choices may change from one timestep to the next. This results in the same equation $A\delta\mathbf{P} = -\mathbf{F}^l$ as the Implicit formulation except that the elements A_{ij} of the A matrix are rectangular matrices of variable size. The numbers of rows and columns in A_{ij} equal the numbers of implicit variables in blocks i and j , respectively; all A_{ii} are square matrices. The CPU expense per Newton iteration of an AIM model lies between those of IMPES and Implicit models, tending toward the former as more blocks are taken implicit in pressure only.

Choice of Formulation. For a given problem, the previous four formulations generally give widely different CPU times. Generalizations regarding the best formulation have many exceptions. Arguably, the trend is or should be toward sole use of the AIM formulation. This is discussed in the Stable Step and Switching Criteria sections to follow. Current simulation studies use all of these formulations. The Implicit formulation is generally faster than IMPES for single-well coning studies, and for thermal and naturally fractured reservoir problems. For other problems, IMPES is generally faster than Implicit for moderate or large n (say, $n > 4$). Most participants used IMPES for SPE Comparative Solution Project problems SPE1, SPE3, SPE5, and SPE10. All participants used the Implicit formulation for SPE2, SPE4, SPE6, and SPE9. No participants in SPE1 through SPE10 used a Sequential model, and, with few exceptions, none used AIM.

A frequently stated generalization is that numerical dispersion error is significantly larger for Implicit than for IMPES formulations. Truncation error analysis²⁶ shows this error to be proportional to $\Delta x + u\Delta t$ for Implicit and $\Delta x - u\Delta t$ for IMPES. Real problem nonlinearities and heterogeneity render the analysis approximate and the generalization of limited merit. For example, Figs. 17.1 through 17.3 show virtually identical Implicit and IMPES results for the black-oil 9,000-block SPE9 and 2,000-block gas/oil SPE10 problems. For SPE9 (SPE10), the average timestep was 67 (9.7) times larger for Implicit than for IMPES. The percentage of total CPU

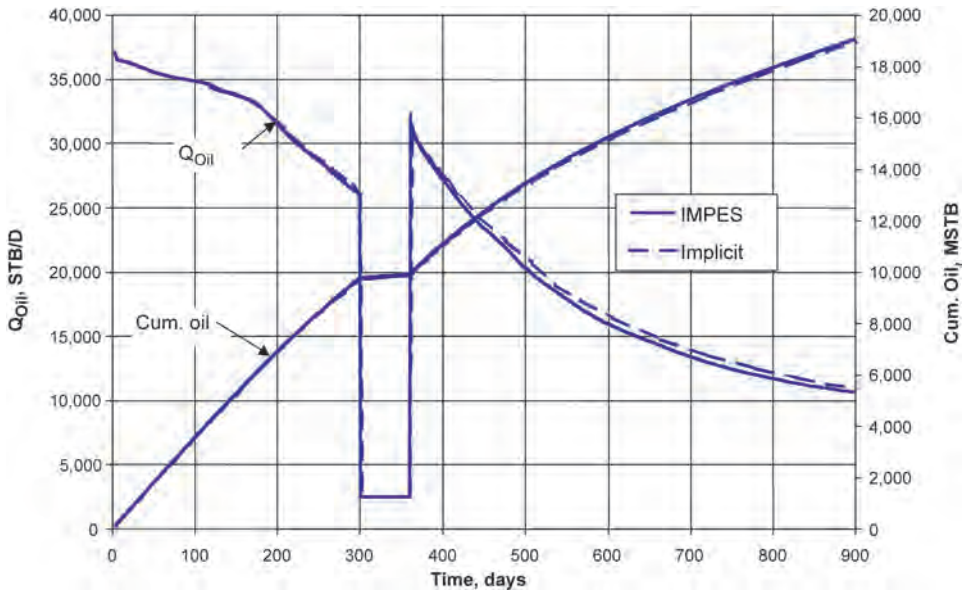


Fig. 17.1—IMPES vs. implicit oil rate and cumulative oil production, SPE9.

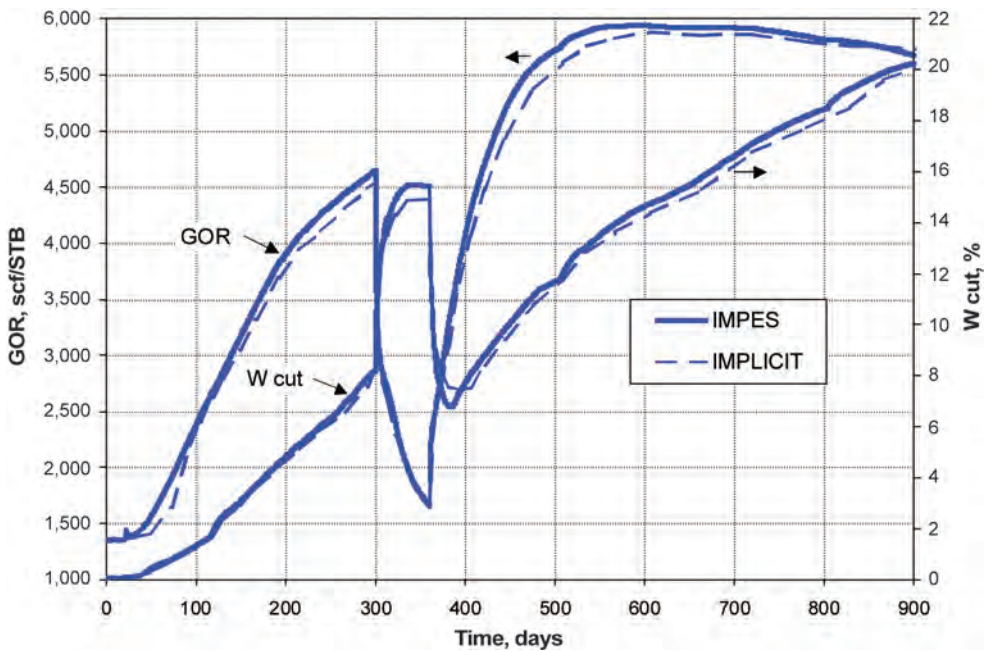


Fig. 17.2—IMPES vs. implicit GOR and water cut, SPE9.

time spent in the linear solver for IMPES (Implicit) was 23.7 (57.3) for SPE9 and 35.4 (73.4) for SPE10.

Implementation is an important factor in the relative efficiencies of different formulations. For a given problem, different models using the same formulation can give widely different

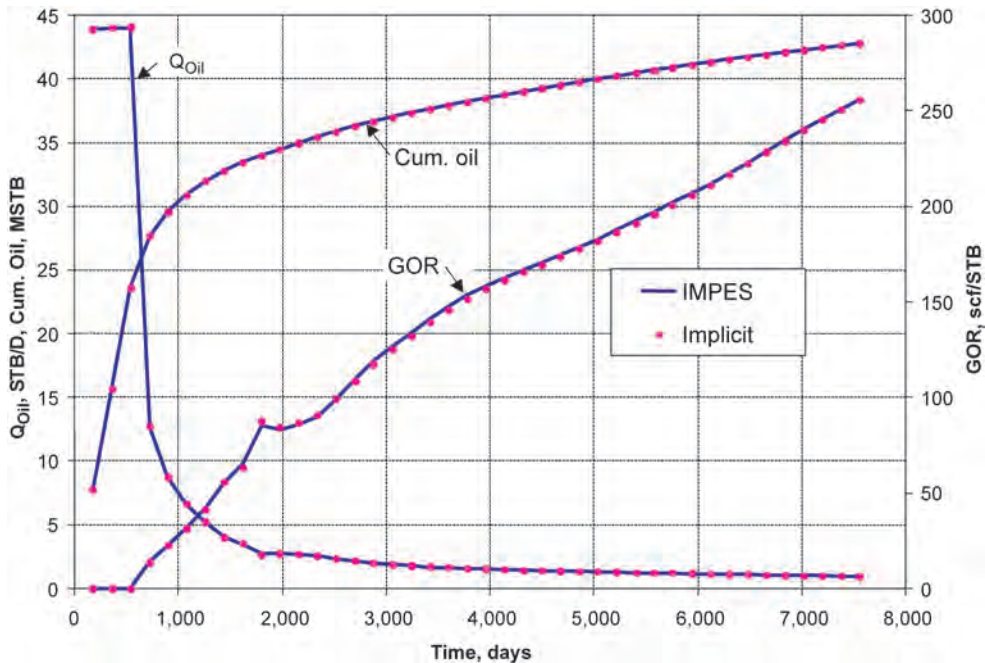


Fig. 17.3—IMPES vs. implicit oil rate, cumulative oil production, and GOR, SPE10 Model 1.

CPU times. For example, the IMPES CPU times reported by different participants in the six-component compositional SPE5 problem⁶ differed by a factor of over 50.

17.1.3 Advances in Model Formulations. The IMPES formulation was improved by concepts of relaxed volume,^{13–15} better choice of variables,¹³ and “adaptive” flash calculations.¹³

Relaxed Volume. The relaxed volume concept relates to the timestep calculation Steps (d) and (e) given previously. Step (d) gives the mass of each component in the gridblock, M_i^{l+1} , which in turn gives overall composition $\{z_i\}^{l+1}$. The Step (e) flash then gives phase amounts and densities which in turn give new iterate S_w , S_o , and S_g values. These saturations do not sum to 1.0 because of the nonlinear nature of the conservation Eq. 17.1. If the saturations are altered (e.g., divide each by their sum) to exactly satisfy the volume balance $\sum_j S_j = 1$, then an incremental (timestep) mass-balance error occurs. If the saturations are not altered, then mass is conserved but there is a volume-balance error $\sum_j S_j - 1$. The authors^{13–15} chose to preserve mass and *carry forward* the volume balance error from iterate to iterate and step to step. The volume balance going into iterate $l + 1$ is $\sum_j \delta S_j = 1 - \sum_j S_j^l$. This in effect conserves both mass and volume because there is no permanent or accumulating volume error—only that of the given timestep. Equally important, there is no need to iterate out the volume error to a “tight” tolerance, and Newton iterations and model CPU are reduced. In contrast, the previous or historical IMPES procedure reset saturations to preserve volume and iterated out the mass-balance error. Because the latter error was not carried forward, more Newton iteration (and CPU time) was required to keep the permanent, accumulating mass balance error tolerably low. This use of relaxed volume with carryover also reduces Newton iterations and CPU time in the Implicit formulation.²¹

This discussion implies some fundamental advantage of preserving mass and iterating out volume error as opposed to preserving volume and iterating out mass error. In the writer’s opinion, that is not true provided the error is carried forward in both cases. The Newton itera-

tion requirement and CPU time should be similar if “equivalent” mass and volume error tolerances are used as convergence criteria.

Variable Choice. The linear algebra required to reduce the gridblock’s n conservation equations to the IMPES pressure equation is influenced by the choice of variables. The influence is absent for black oil, moderate for “moderate” n and up to a factor of three for large n (say, > 15).²² The choices of p and mol fractions $\{z_j\}$ ¹³ or mol numbers^{14,15} are better than the choice of p , saturations, and phase mol fractions¹² for large n . The effect of this variable choice on total CPU time is often small because the affected work is often a small part of total CPU time. This IMPES reduction is absent in the Implicit formulation and the last of the above variable choices is arguably preferable.²²

Adaptive Flash Calculations.¹³ The work of EOS flash calculations, including the generation of fugacities and their derivatives, can significantly affect model efficiency when the linear solver does not dominate total CPU time. There may be little need to perform (most of) that work in a gridblock when p and composition are changing slowly. Use of internal, intelligent criteria dictating when that work is needed can significantly reduce the total-run flash calculation CPU time.¹³ This is similar in principle to the AIM selection of explicit variables for gridblocks which are quiescent in respect to throughput ratio.

17.1.4 Stable Timestep and Switching Criteria. This topic relates to the observation that lower run turnaround time can increase benefits from a reservoir study allotted a budgeted time period. As a corollary, time spent in repeated runs fighting model instabilities or time-stepping is counterproductive. While many factors affect this run time, it always equals the product (CPU time/step) \times (number of timesteps). The first factor is “large” and the second “small” for the Implicit formulation, and conversely for the IMPES formulation. IMPES is a conditionally stable formulation requiring that $\Delta t < \Delta t^*$ to prevent oscillations and error growth, where Δt^* is maximum stable timestep. The conditional stability stems from the explicit treatment of nonpressure variables in the interblock flow terms. Mathematicians performed stability analyses for constant-coefficient difference equations bearing some resemblance to IMPES. Authors in our industry extended and applied their results to derive expressions for Δt^* , in particular,²⁷

$$\Delta t^* = \frac{V_p}{f_g'(|q_x| + |q_y| + |q_z|) + 2P_{cgo}'\psi(T_x + T_y + T_z)} \dots\dots\dots (17.8)$$

for the black-oil 3D case of gas/oil flow. This shows that stable step Δt^* is dependent upon flow rates, phase mobility, and capillary pressure derivatives, which of course vary with time and from one gridblock to another. Thus, at a given timestep, there are block-dependent stable step values Δt^*_i , where $1 < i < N$, and the IMPES stable step is $\text{Min}(i) \Delta t^*_i$. An IMPES model using this internally determined stable step will run stably but may suffer from the weakest-link principle. As an extreme example, consider a 500,000-gridblock problem where, over a 100-day period, the Δt^*_i value is 0.01 day for one block and > 30 days for all other blocks. The IMPES model will require 10,000 timesteps over the 100-day period.

In the AIM formulation, the stable step Δt^*_i depends upon the number and identities of variables chosen explicit in block i ; theoretically, $\Delta t^*_i = \infty$ if all block i variables are chosen implicit. In the previous example, all nonpressure variables could be chosen implicit in the block where $\Delta t^*_i = 0.01$ and explicit in all other blocks. The AIM model would then require CPU time/step essentially no greater than the IMPES model but would require only three timesteps for the 100-day period.

Numerous papers²⁸⁻³³ address the problem of determining expressions for the Δt^*_i for use internally as switching criteria to select block variables as explicit or implicit in the AIM

model. The stability analyses involved are complex and may be impractically complex when allowing the implicit vs. explicit variable choice to include all permutations (in number and identity) of the n variables. The most reliable and efficient AIM models in the future will stem from continuing research leading to the following: (a) Δt^*_i estimates which are “accurate,” and (b) implicit vs. explicit variable choices, block by block, which are near-optimal³⁴ and minimize total CPU time, (CPU time/step) \times (number of steps).

17.1.5 The Linear Solver. Preconditioned Orthomin³⁵ is the most widely used method for iterative solution of Eqs. 17.3 or 17.7. Nested Factorization (NF)³⁶ and incomplete LU factorization [ILU(n)]³⁷ are the two most widely used preconditioners. The term “LU factorization” refers to the factoring of the matrix A into the product of a lower triangular matrix L and an upper triangular matrix U . That is an expensive operation but is straightforward, involving only Gaussian elimination. The term “ILU(n)” denotes incomplete LU factorization, where only limited fill-in is allowed and n is the “order of fill.”³⁷ NF performs exceptionally well when transmissibilities associated with a particular direction (in a structured grid) dominate those in other directions uniformly throughout the grid. In general, ILU(n) or red-black ILU(n)³⁸ [RBILU(n)] is less sensitive than NF to ordering of the blocks and spatial variation of the direction of dominant transmissibilities. In addition, RBILU(n) or ILU(n) have the parameter n (order of allowed infill) which can be increased as needed to solve problems of any difficulty.

A literature search and discussions with numerous developers and users have failed to establish consensus on whether NF or ILU preconditioning is better. Some are strong advocates of one method and others are just as adamantly supportive of the other. But many find, like this writer, that the better method is problem-dependent and it is difficult to find a reliable *a priori* indicator for making an up-front choice. In the writer’s experience, (a) when NF works well, it is faster than ILU methods, (b) RBILU(0) with no residual constraint is frequently the best of the ILU variants and a good default choice, and (c) in some cases, global residual constraint with the ILU or RBILU method is beneficial.

17.1.6 Cartesian Grids and Reservoir Definition. For many years, simulation used orthogonal Cartesian grids. In the past 15 years, numerous papers have described local grid refinement and various non-Cartesian grids, as discussed in the Gridding section. These papers show that non-Cartesian grids can reduce grid-orientation effects and provide definition and accuracy near wells, faults, highly heterogeneous areas, and so on more efficiently than Cartesian grids. The premise that Cartesian grids cannot provide required accuracy efficiently in these respects has come to be accepted as a fact. In addition, advances in geophysics have led to geostatistical description of permeability and porosity on a fine scale once unimaginable. Increasingly, our papers include examples using thousands of gridblocks for two- or few-well “patterns,” in part to reflect these geostatistical descriptions. The purpose of this section is to show, using a few examples, that Cartesian grids can provide adequate accuracy and reservoir and near-well definition efficiently in some cases, even without local grid refinement. No generalizations from the examples used are intended. For the most part, the examples are taken from the literature.

SPE7 is an x -direction horizontal well problem with a $9 \times 9 \times 6$ Cartesian grid representing a $2,700 \times 2,700 \times 160$ -ft reservoir section. The specified block Δy values decrease from 620 to 60 ft at the well, presumably to increase near-well definition and accuracy of results. The Δx are uniformly 300 ft. Fig. 17.4 compares Case 1A results for the SPE7 grid with results using uniform areal spacing $\Delta x = \Delta y = 300$ ft. The near-well y -direction refinement of the specified grid has no effect and is not necessary in this problem.

SPE8 is a gas/oil problem with one gas injector and two producers on the corners of a $5,000 \times 5,000 \times 325$ -ft square reservoir. A $10 \times 10 \times 4$ Cartesian grid with uniform $\Delta x = \Delta y = 500$ ft is specified. Five participants compared their results for that grid with results from their

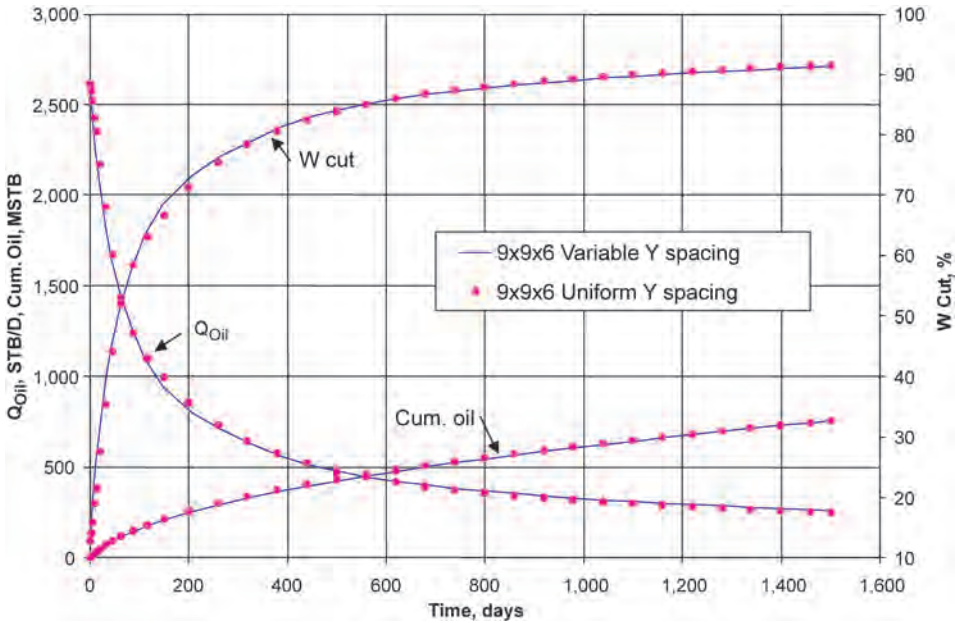


Fig. 17.4—Effect of near-well grid refinement, SPE7 Case 1A.

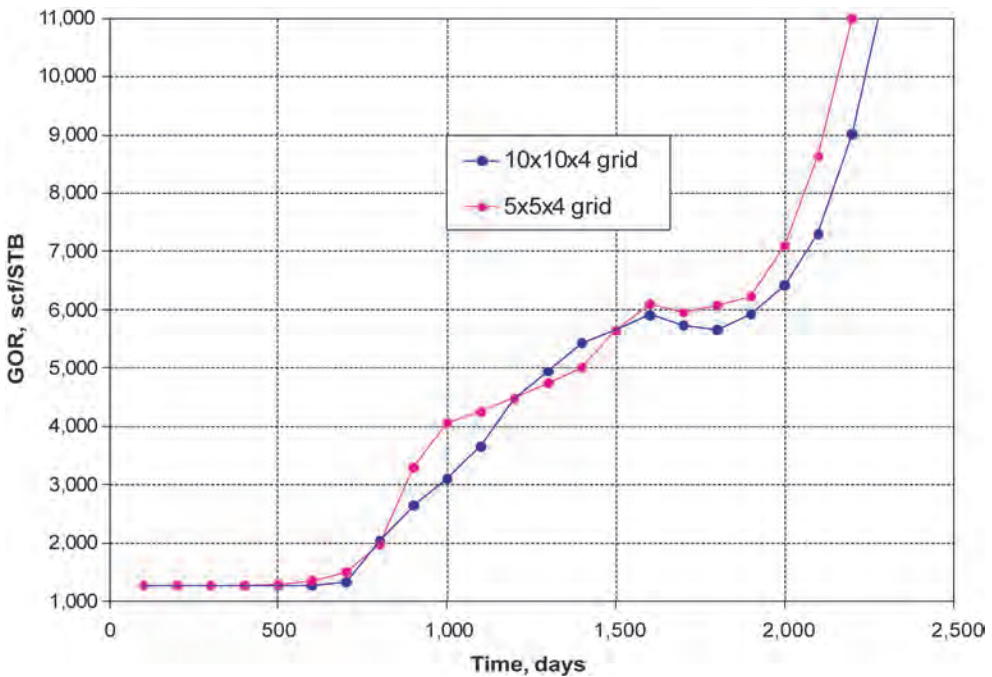


Fig. 17.5—Effects of coarser grids on producing GOR.

(areally) locally refined or unstructured grids. They showed good agreement for grids having approximately four times fewer blocks than the $10 \times 10 \times 4$ grid. Fig. 17.5 shows equally good agreement for a $5 \times 5 \times 4$ ($\Delta x = \Delta y = 1,000$ ft) Cartesian grid with no local refinement.

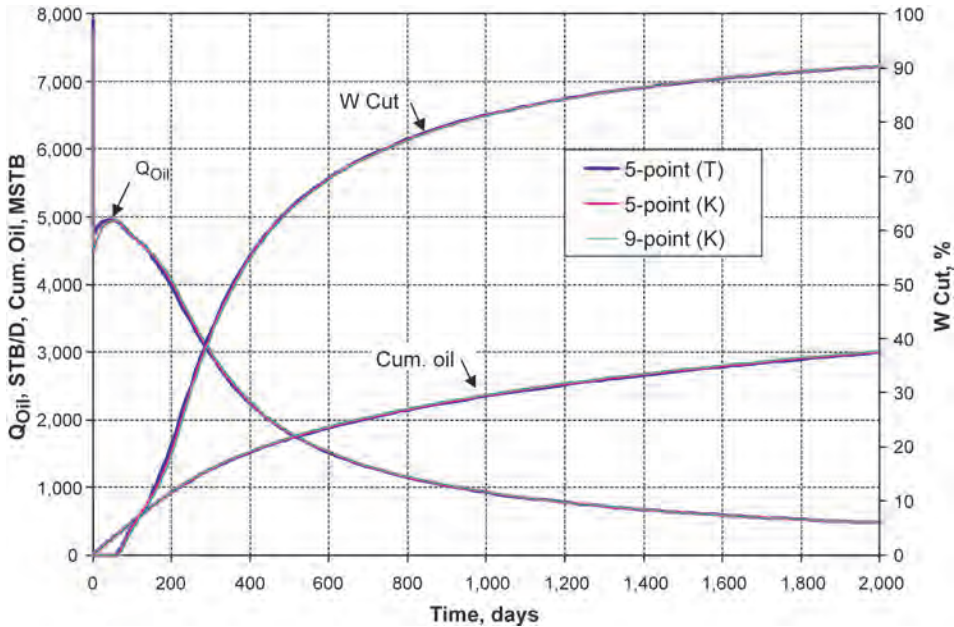


Fig. 17.6—9-point vs. 5-point, SPE10 Model 2.

SPE10 (Model 1) is a 2D cross-sectional gas/oil problem with a geostatistical permeability distribution given on a $100 \times 1 \times 20$ Cartesian fine grid. Coarse-grid submittals included results using upscaling and local grid refinement. A homogeneous $5 \times 1 \times 5$ Cartesian grid with no alteration of relative permeability matched the $100 \times 1 \times 20$ results nearly exactly.¹¹

SPE10 (Model 2) is a 3D water/oil problem with a 1.122 million-cell geostatistical grid. Some coarse grid submittals included sophisticated upscaling and gridding techniques with no pseudoization of relative permeability and grids from 4,810 to 70,224 blocks. Others used simple flow-based upscaling to 75- to 2,000-block Cartesian grids with moderate k_r changes. In general, the latter submittals showed the best agreement with the fine-grid solution.¹¹

Numerous papers show that non-Cartesian grids can significantly reduce the grid-orientation effects of Cartesian grids. However, most of the examples used to study those effects are highly adverse mobility ratio displacements in homogeneous, horizontal reservoirs. In reservoirs with more normal fluid mobilities, areal fluid movement is more strongly affected by heterogeneity and/or gravity forces associated with reservoir structure (variable dip), and grid-orientation effects tend toward a second-order effect. As an example, the SPE10 (Model 2) water/oil problem reservoir is highly heterogeneous. Fig. 17.6 compares five-point and nine-point field results for an upscaled $28 \times 55 \times 85$ Cartesian grid. The close agreement indicates an absence of grid-orientation effects even though the unfavorable oil/water viscosity ratio is 10 and there is no dip.

Example 17.1. Table 17.2 gives data for Example 17.1, a $\frac{1}{4}$ five-spot, vertical-well problem. Fig. 17.7 shows two block-centered grids (a) and (b) used for this type of problem. The four-fold smaller well blocks of grid (b) provide finer well definition and presumably increase the accuracy of results. Fig. 17.8 shows the identical results for 10×10 grid (a) and 11×11 grid (b). Results are nearly identical for the 5×5 grid (a) and 6×6 grid (b), and Fig 17.9 shows insignificant difference between 3×3 grid (a) and 4×4 grid (b) results. The grid (b) doubles the grid (a) IMPES run CPU time but contributes no greater accuracy. Well-index ef-

TABLE 17.2—EXAMPLE 1 DATA	
$\frac{1}{4}$ 40-acre five-spot with no dip and 180-ft pay thickness	
Incompressible oil and water properties:	
$\rho_o = 43 \text{ lbm/ft}^3$ $\mu_o = 3 \text{ cp}$ $R_s = 0$	
$\rho_w = 64 \text{ lbm/ft}^3$ $\mu_w = 0.3 \text{ cp}$	
Grid: $N_x = N_y$ $\Delta x = \Delta y$ $N_z = 15$ $\Delta z = 15 \text{ ft}$	
$\phi = 0.2$ $k_x = 1000 \text{ md}$ $k_z = 100 \text{ md}$	
$S_{wc} = S_{orw} = 0.2$ $k_{rwo} = 1.0$ $k_{rocw} = 1.0$	
$k_{rw} = k_{rwo}[(S_w - S_{wc}) / (1.0 - S_w - S_{orw}^2)]$, $k_{rw} < 1.0$	
$k_{ro} = k_{rocw}[(1.0 - S_w - S_{orw}) / (1.0 - S_{wc} - S_{orw}^2)]$	
Water injection well at $x = y = 0$ is completed in all 15 layers and injects 2,550.7 STB/D water	
Production well at $x = y = 660 \text{ ft}$ is completed in top 5 layers (upper $\frac{1}{3}$ of pay) and flows on pressure constraint against a bottomhole wellbore pressure of 4,000 psia	
Discussion of runs for this problem refers to various grids by their $N_x \times N_y$ dimensions because $N_z = 15$ in all cases	

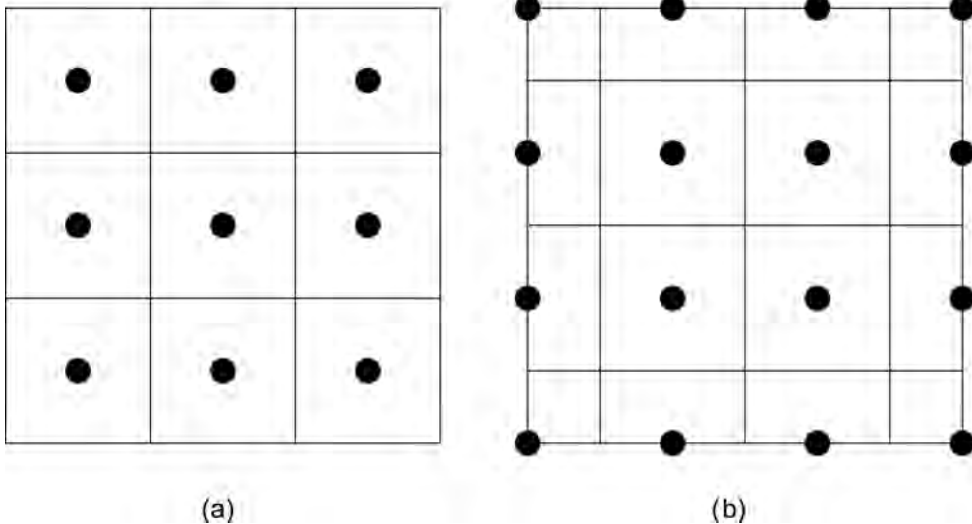


Fig. 17.7—Block-centered 3×3 and 4×4 Cartesian grids used in Example 17.1.

fects are not important here. When they are, a single one-layer single-phase run can be made to determine the index correction factor for grid (a) wells located in the corners of their gridblocks.

Fig. 17.10 shows a small effect of grid refinement on Example 17.1 results for grids from 20×20 to 3×3 . The results indicate little need to enhance near-well definition by unstructured grids or by grid refinement (global or local) for grids finer than 3×3 for this problem.

Example 17.2. Flexible non-Cartesian grids are shown to significantly reduce the required number of gridblocks.³⁹ An example provided⁴⁰ was water/oil coning in a horizontal well in a $600 \times 300 \times 230 \text{ m}$ homogeneous reservoir. Results were: (a) a 25,823-block 31×17

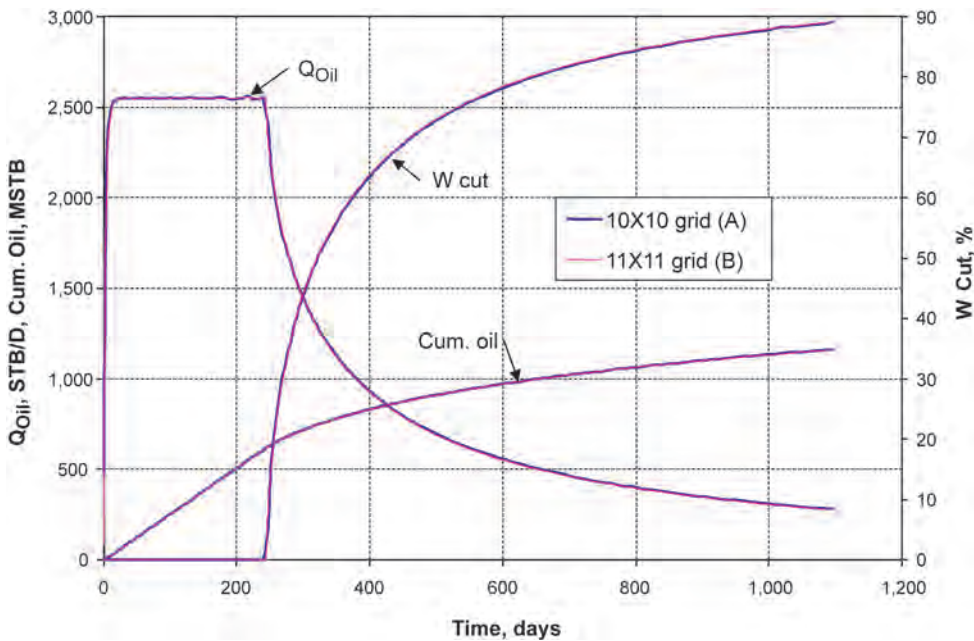


Fig. 17.8—Effect of (a) 10×10 vs. (b) 11×11 grid on Example 17.1 results.

$\times 49$ Cartesian grid was required to obtain a converged solution, and (b) a 3D 2,066-block CVFE unstructured grid gave correct results. Table 17.3 gives data for Example 17.2, a similar problem. Fig 17.11 compares Example 17.2 results for $60 \times 31 \times 48$ and $10 \times 7 \times 9$ Cartesian grids. The 630-block coarse Cartesian grid results here agree as well with the Cartesian $60 \times 31 \times 48$ fine-grid results as the reported 2,066-block CVFE results agree with the $31 \times 17 \times 49$ Cartesian fine-grid results.

Non-Cartesian grids are argued to define irregular reservoir boundaries more efficiently than Cartesian grids. This is not necessarily true. For over 30 years, many models have used active-block coding. While the Cartesian grid extends past boundaries to numerous inactive blocks, those inactive blocks are dropped by the model and require no computer storage or CPU. These numerous inactive blocks pose a problem only for models, if any, that do not use active-block coding.

17.2 Linear Solver—John Wallis and J.W. Watts

The linear equation solver is an important component in a reservoir simulator. It is used in the Newton step to solve the discretized nonlinear partial differential equations. These equations describe mass balances on the individual components treated in the model. For nonisothermal problems, an energy balance is added to the system. The matrix problem involves solving $Ax = b$, where A is typically a large sparse matrix, b is the right-side vector, and x is the vector of unknowns. In the IMPES formulation, there is a single unknown per cell pressure. In the fully implicit formulation, there is a fixed number n of unknowns per cell where $n \geq 2$. In the adaptive implicit formulation, there is a variable number of unknowns per cell. In most formulations, pressure is an unknown for each cell. The matrix A typically has associated well constraint equations and well variables and may be partitioned in block 2×2 form as

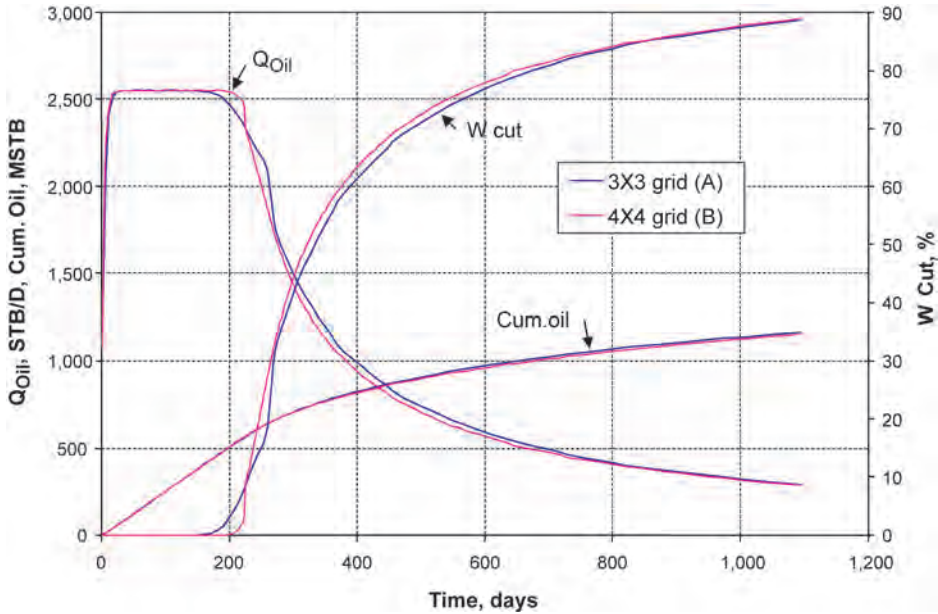


Fig. 17.9—Effect of (a) 3 × 3 vs. (b) 4 × 4 grid on Example 17.1 results.

$$\begin{bmatrix} A_{ww} & A_{wr} \\ A_{rw} & A_{rr} \end{bmatrix} \begin{bmatrix} x_w \\ x_R \end{bmatrix} = \begin{bmatrix} b_w \\ b_R \end{bmatrix}, \dots\dots\dots (17.9)$$

where x_w is the well variable-solution vector and x_R is the reservoir variable-solution vector. The matrix A_{ww} is often diagonal. In this case, the well variables may be directly eliminated, and the iterative solution is on the implicitly defined matrix system

$$(A_{RR} - A_{Rw}A_{ww}^{-1}A_{wR})x_R = \tilde{b}_R, \text{ where } \tilde{b}_R = b_R - A_{Rw}A_{ww}^{-1}b_w. \dots\dots\dots (17.10)$$

The well variables are then obtained by back substitution as

$$x_w = A_{ww}^{-1}(b_w - A_{wR}x_R). \dots\dots\dots (17.11)$$

If A is large, solution of the matrix equations is impractical using direct methods such as Gaussian elimination because of computer storage or CPU time requirements. Iterative solution based on projection onto Krylov subspaces is typically used. These Krylov subspaces are spaces spanned by vectors of the form $p(A)v$, where p is a polynomial. Basically, these techniques approximate $A^{-1}b$ by $p(A)b$. The commonly used methods for constructing $p(A)b$ are Orthomin³⁶ and GMRES.⁴¹ Both methods minimize the residual norm over all vectors in $span\{b, Ab, A^2b, \dots, A^{m-1}b\}$ at iteration m . They should yield identical results. From a practical standpoint, it does not matter which is used.

A technique known as preconditioning can improve both the efficiency (speed in a typical problem) and robustness (ability to solve a wide range of problems at least reasonably well) of Orthomin or GMRES. Preconditioning involves transforming the original matrix system into one with the same solution that is easier to solve. As a rule, the robustness of the iterative

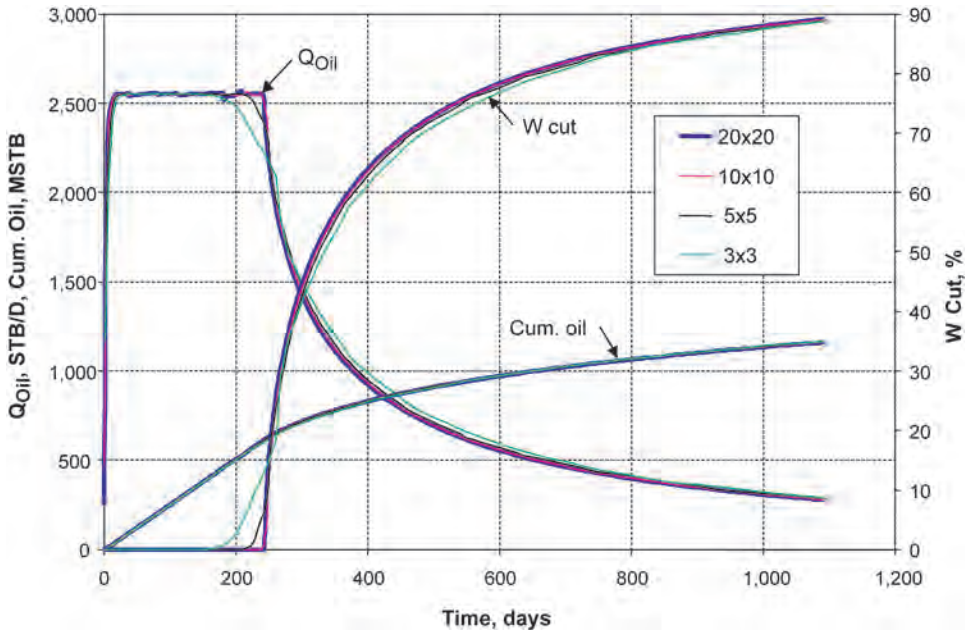


Fig. 17.10—Effects of Cartesian grid coarsening, Example 17.1 results.

TABLE 17.3—EXAMPLE 2 DATA
Water/oil coning problem with a 300-m x-direction horizontal well
Reservoir dimensions: 600×300×230 m
Pay zone thickness: 35 m
Aquifer thickness: 195 m
Producer: x = 150 m to 450 m, y = 150 m, z = 10 m, rate = 1,315 STB/D liquid
Water injector: x = 300 m, y = 150 m, z = 140 m, rate = 1,315 STB/D water
$k_x = k_y = 360$ md $k_z = 60$ md $\phi = 0.21$
Incompressible water and oil, $B_o = B_w = 1.0$ RB/STB, $R_s = 0$
$\rho_o = 53.04$ lbm/ft ³ $\mu_o = 1.2$ cp
$\rho_w = 64.27$ lbm/ft ³ $\mu_w = 0.52$ cp
$k_{rwo} = 0.22$ $k_{rogrw} = 1.0$ $S_{wc} = 0.296$ $S_{orw} = 0.31$
$k_{rw} = k_{rwo} S_{wi}^2$ ($k_{rw} < 1$) $k_{ro} = k_{rogrw} S_{oi}^2$
$P_{cwo} = 2.4 * [(1.0 - S_{wi}) / (1.0 - S_{wc}^2)]$ psi
Water/oil contact at z = 35 m ($P_{cwo} = 0$)

scheme is far more dependent on the preconditioning than on the specific Krylov subspace accelerator used. The preconditioner M is a matrix that approximates A, and has the property that the linear systems of the form $Mx = b$ are easily and inexpensively solved. For most linear solvers the following preconditioned system is solved:

$$AM^{-1}y = b, \text{ where } x = M^{-1}y .$$

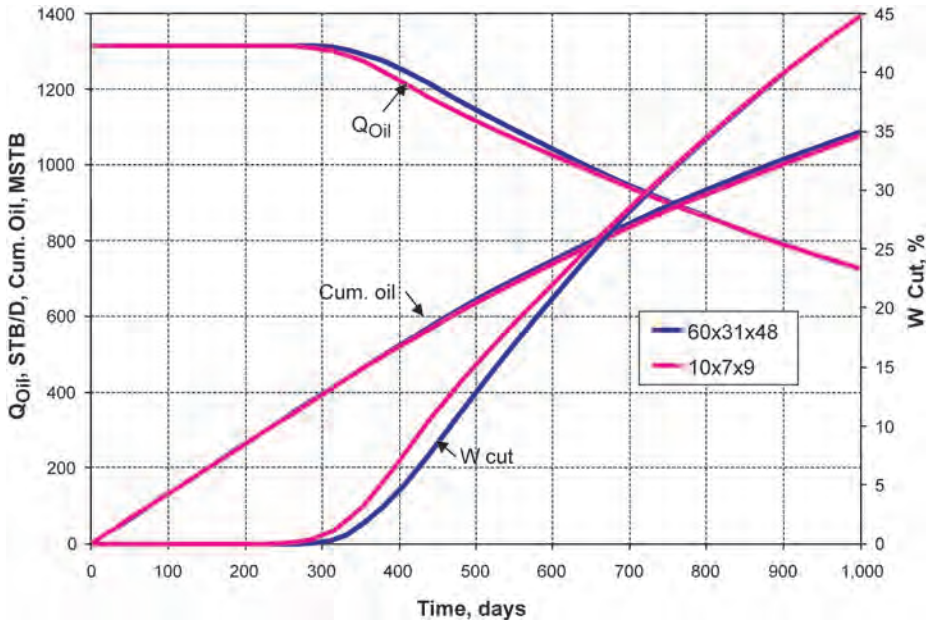


Fig. 17.11—Fine vs. coarse Cartesian grids, Example 17.2.

The preconditioned ORTHOMIN(k) algorithm, which retains the last k A -orthogonal direction vectors, is given by

1. Compute $r_0 = b - Ax_0$. Set $p_0 = M^{-1}r_0$.
2. For $j = 0, 1, 2, \dots$, until convergence Do :
3. $\alpha_j = \frac{(r_j, Ap_j)}{(Ap_j, Ap_j)}$
4. $x_{j+1} = x_j + \alpha_j p_j$
5. $r_{j+1} = r_j - \alpha_j Ap_j$
6. $\beta_{ij} = -\frac{(AM^{-1}r_{j+1}, Ap_i)}{(Ap_i, Ap_i)}$, for $i = j - k + 1, \dots, j$
7. $p_{j+1} = M^{-1}r_{j+1} + \sum_{i=j-k+1}^j \beta_{ij} p_i$
8. End Do

Because of the nature of the reservoir simulation equations, only certain preconditioners are effective in solving them. Reservoirs are typically shaped like pancakes, being much broader than they are thick. This geometry leads to strong vertical connectivity. Some preconditioners exploit this property. The most commonly used such preconditioner is NF.³⁷ The convergence of NF is sensitive to the cell ordering. Best results are usually obtained by ordering the cells first along the direction of highest transmissibility and then successively along directions of decreasing transmissibility. This nearly always means that NF should be ordered first in the vertical direction.

The other commonly used preconditioners are incomplete lower triangular/upper triangular factorizations of the matrix, or ILU(n), where n is the level of infill that is retained during the elimination process. Performance of these can be improved by using a red-black checkerboard ordering (also called D4 ordering) of the nodes.⁴² Red-black ordering on a five-point (in 2D) or seven-point (in 3D) grid leads to direct elimination of the unknowns at the red cells, leaving a

system containing only the unknowns at the black cells. The result is a halving of the number of unknowns. An ILU preconditioner using red-black ordering with zero infill on the reduced system is referred to as RBILU(0) and is the most frequently-used form of ILU.

In IMPES models with either no faults or vertical faults only, RBILU(0) or ILU(1) combined with z -line additive corrections,^{43,44} typically converges very rapidly. NF can also be used effectively in cases involving vertical faults and pinchouts because the matrix retains the structure required by NF. Nonvertical faults interrupt the matrix structure that makes red-black orderings attractive. In models containing them, ILU is the method of choice. Nine-point discretizations also cause problems for red-black orderings, but cause no difficulty for NF.

NF and RBILU(0) are commonly used in implicit models. Another very effective approach exploits the fact that pressure is the “stiff” variable. The Combinative⁴⁵ or CPR⁴⁴ method is a two-step preconditioning that extracts a pressure equation from the implicit matrix. It iteratively solves for a pressure correction at each iteration, uses the pressure correction to form a new residual, applies an inexpensive implicit preconditioning such as diagonal scaling or line Gauss-Seidel to the new residual, and then uses the sum of the two steps as the approximate solution. In compositional models, this two-step method can be much faster than one-step methods.

Many models include well-constraint equations that add well pressures to the set of unknowns. A simple but effective way of dealing with these equations is to order them first in the global matrix and then eliminate the well pressures from the set of unknowns.⁴⁶ In this approximate elimination, any infill terms are either column-summed or row-summed into the main diagonal of the reservoir matrix, which is then factored using NF. The reservoir matrix problem is then solved iteratively and the well variables are obtained by back substitution.

Parallel iterative solution typically uses a domain decomposition approach in which the grid is partitioned into domains that contain approximately the same number of cells. The partitioning should be done such that coupling is strongest between cells within a domain. As a result, domains normally are groups of columns of cells. One way to accelerate the iteration is to color the domains in red-black fashion and apply an NF-type procedure in which the outer level of nesting is the coupling between domains and either NF or an ILU variation is used to factor the individual domains.^{47,48}

The solution of matrices arising from unstructured grids typically involves some variant of ILU with cell orderings such as Reverse Cuthill-McKee (RCMK)⁴⁹ or Minimum Degree Fill (MDF).^{50,51}

17.3 Gridding in Reservoir Simulation—Dave Ponting

17.3.1 Introduction. The aim of gridding in reservoir simulation is to turn the geological model of the field into a discrete system on which the fluid-flow equations can be solved.

The basic structure of an oil reservoir is a set of geological horizons representing bedding planes. The reservoir may contain faults, at which the strata are displaced. It is usually possible to identify many more layers in the geological model than it is practical to include in reservoir flow simulation, so some upscaling of rock properties will normally be carried out. Even after this process, the geology to be represented is rarely homogeneous at the scale of the simulation grid.

Two related issues are involved in choosing a grid for reservoir simulation: the accuracy with which the geological description of the reservoir is matched, and the discretization of the flow equations. In a classical finite-difference scheme, the point values of pressures and saturations are used as solution variables, and the differential operators that appear in the fluid-flow equations may be expanded as difference expressions of these point values to some order. An alternative approach is to use an *integral finite-difference*⁵² or *finite-volume*⁵³ method in which the fluid-flow equations are integrated over a set of cell volumes. This yields a set of equations in which the mass conservation conditions for the fluid in the simulation cell volumes are relat-

ed to the flows through the interfaces between those cell volumes. Rock properties such as porosity are assumed constant over the cell or controlled volume. This yields a discretization scheme which is conservative (each outflow from one cell is an inflow to another) and for which the fluid in place may be obtained straightforwardly. The mass conservation equations for a timestep from T to $T + \Delta T$ then become:

$$V_{pa}^{T+\Delta T} \cdot m_{ca}^{T+\Delta T} - V_{pa}^T \cdot m_{ca}^T = \Delta T \cdot (Q_{ca} + \sum_b \sum_p F_{cpab}), \dots\dots\dots (17.12)$$

where V_{pa} is the pore volume of cell a , m_{ca} is the density of conserved component c in cell a , Q_{ca} is the injection or production rate of component c because of wells, and F_{cpab} is the flow rate of component c in phase p from cell a to its neighbor b . In general, the flows F_{cpab} may involve the solution values of a number of cells, the number of cells involved defining the *stencil* of the numerical scheme. The linear pressure dependence of flows given by Darcy’s law leads to an expression of the type:

$$F_{cpab} = \sum_x T_{ax} M_{cpax} \Delta\Phi_{pax} \cdot \dots\dots\dots (17.13)$$

M_{cpax} is the mobility of component c in phase p for the contribution to the flow between a and x , given by $x_{cp} \cdot K_{rp} / \mu_p$, where x_{cp} is the concentration of component c in phase p , K_{rp} is the relative permeability of phase p , and μ_p is the viscosity of phase p . This is often set to an *upstream* value of the mobility, depending upon the sign of the potential difference.

$\Delta\Phi_{pax}$ is the potential difference of phase p between cell a and cell x , which includes pressure, gravity and capillary pressure contributions:

$$\Delta\Phi_{pax} = P_a - P_x - g\rho_p \cdot (d_a - d_x) + P_{cpa} - P_{cpx} \cdot \dots\dots\dots (17.14)$$

The constant coefficients of mobility and potential difference products, T_{ax} , are commonly termed the *transmissibilities*.

When the flows between two cells a and b can be expressed as a function of the solution values in just those two cells, so that the summation over cells includes just $x = b$, the flow expression takes a *two-point* form. The flow expression then takes a simple form:

$$F_{cpab} = T_{ap} M_{cpab} \Delta\Phi_{pab} \cdot \dots\dots\dots (17.15)$$

When solution values from other cells are required, the flow takes a *multi-point* form.⁵⁴

Other options for discretization are available, such as Galerkin finite elements⁵⁵⁻⁵⁷ and mixed finite-element.⁵⁸ It is sometimes possible to cast a finite-element Galerkin discretization into the upstreamed transmissibility-based form.⁵⁷

17.3.2 Regular Cartesian Grids. A simple 3D grid is the regular *Cartesian* grid (**Fig. 17.12**). Cells in such a grid may be simply identified using their (i,j,k) index values.

Each of the grid elements will be assigned a single permeability or porosity value. In this case, it is possible to obtain the transmissibility value as a harmonic average:

$$T_{ap} = 1 / (1/T_a + 1/T_b), T_a = K_a \cdot A_a / (d_a/2), T_b = K_b \cdot A_b / (d_b/2), \dots\dots\dots (17.16)$$

where cell b is the neighbor to cell a in some direction and K is the cell permeability in that direction. A is the area of the cell orthogonal to the direction of flow, and d the dimension of

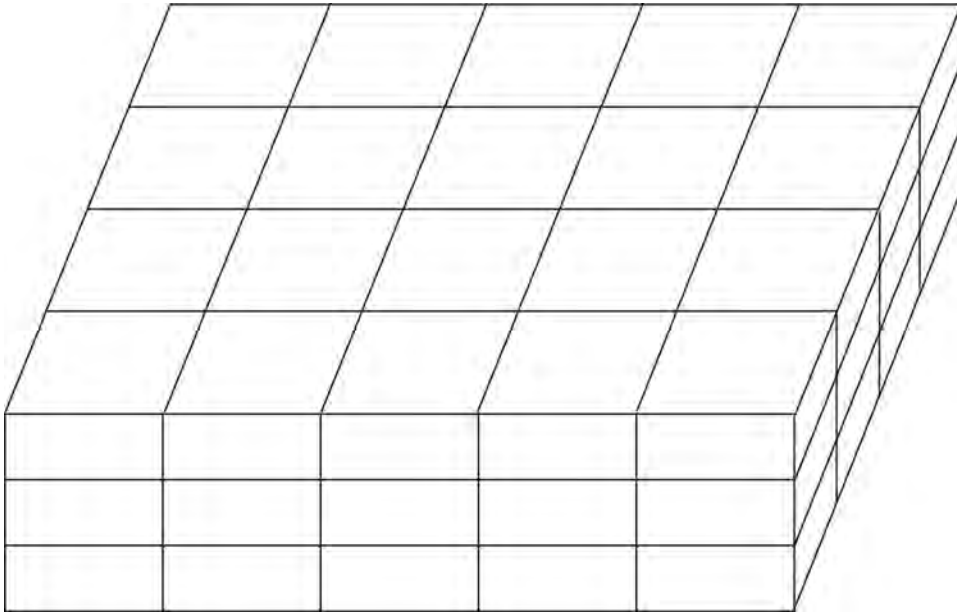


Fig. 17.12—Regular Cartesian grids.

the cell in that direction. Such a two-point transmissibility assumes a permeability tensor with primary axes aligned along the grid axes.

Although regular grids are normally defined in normal Cartesian coordinates, it is also possible to use an (r, ϕ, z) radial system.⁵² The resulting grid is *cylindrical* and is important for the special case of near-well studies dominated by radial inflow. For a 3D system, regular grids yield seven-point schemes, in which the flow equations for a cell involve solution values for just the cell and its six neighbors. Not all the elements in the grid need represent active solution variables in the simulation. Some cells may be inactive, representing volumes of the reservoir with zero porosity. Such inactive cells are usually compressed out of reservoir simulation solution arrays prior to the memory and time-intensive flow solution stage, and enable reservoirs with irregular boundaries to be represented within extended simulation grids.

The horizons that delimit rock strata are generally not horizontal, but are dipped, curved, or faulted. Unless extremely fine, a true regular grid that is orthogonal in all three axes will be unable to assign rock properties accurately to cell volumes. Such a layer-cake structure can be used, but will generally misalign property values (Fig. 17.13) in which the orthogonal grid provides a rather poor match to the dipping strata represented by the shaded layers. However, it is possible that improving computer power will bring such *rasterized* grids to a level of refinement at which a sufficiently good representation may be obtained.

Dip-Normal Geometry. A simple variation of a regular grid, in which the regular grid is rotated to bring the layers of cells into alignment with the bedding planes. Such a description would only suit a reservoir with a single, constant angle of dip. As geological descriptions have improved, fewer and fewer model reservoirs are found to fit this simple pattern, and something more flexible is required.

Block-Center Geometry. A simple model in which transmissibility between blocks is calculated on the basis of linear interpolation between the center values of the cells. This is a simple way of representing variable dip, but is difficult to represent graphically in a consistent way. Pore volumes are calculated on the basis of a series of flat regular cells with variable depths

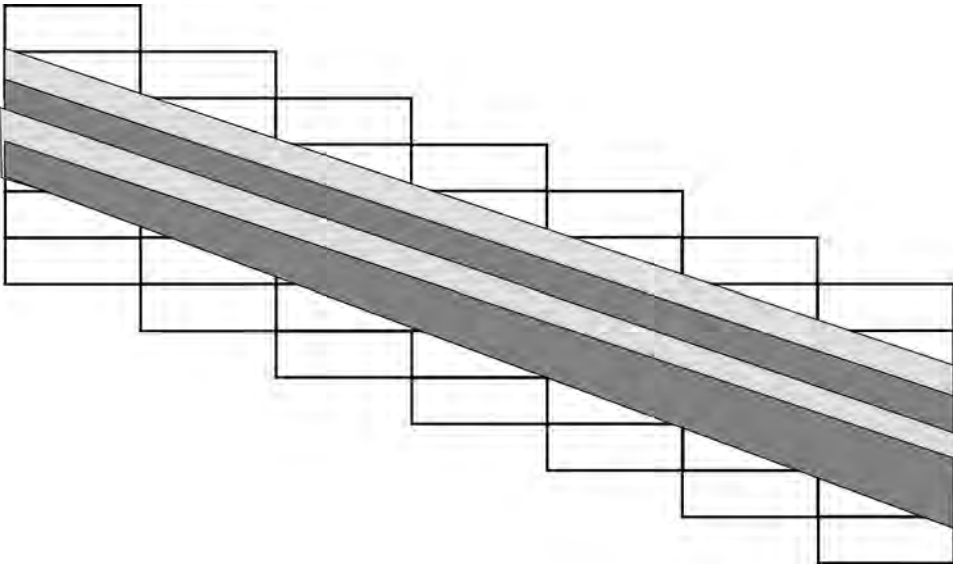


Fig. 17.13—Orthogonal grid used to represent dip.

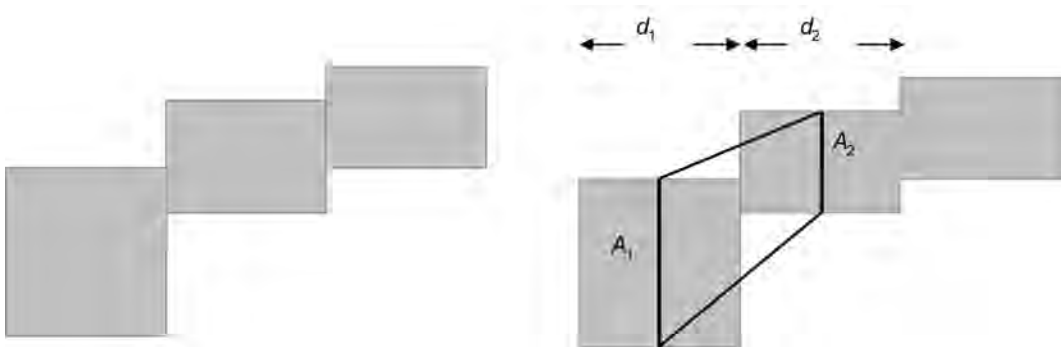


Fig. 17.14—(a) Obtaining pore volumes; (b) obtaining transmissibilities.

(Fig. 17.14a), but transmissibilities are calculated on the basis of interpolated values (Fig. 17.14b). The areal grid is rectangular.

Thus, for the pair of cells illustrated,

$$T = K \cdot A / d, \text{ where } K / d = 2 / (d_1 / K_1 + d_2 / K_2), \dots\dots\dots (17.17)$$

where A is the average area over which flow occurs and c is a dip correction given by $\cos^2\theta$, where θ is the angle of dip of a line joining the cell centers to the horizontal. Such a block-center option is suitable for unfaulted reservoirs and is commonly supplied as a simulator option.

17.3.3 Hexahedral Grids. Further improvements in geological modeling threw an emphasis on describing faults, and made it important to distinguish depth displacements due to dip and faulting. This is difficult in block centre geometry in which the cell is positioned by its centre depth and Δx , Δy , Δz dimensions. To define faulting more precisely it is useful to define the position of grid cell by its corner point locations. A hexahedral shape with eight corners and

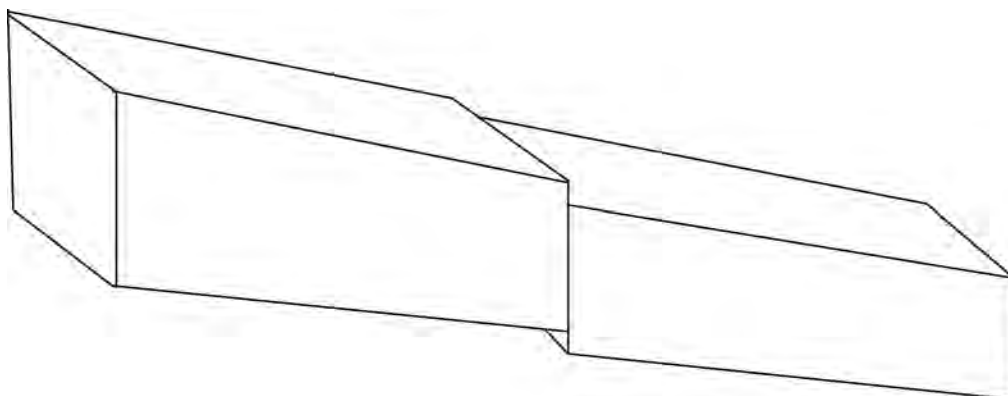


Fig. 17.15—Hexahedral grid system.

bilinear planes as surfaces then describes the cell geometry. Faults, both vertical and inclined, may be described precisely (Fig. 17.15). Such grids are often called *corner-point grids*.

In both the dipped and general hexahedral grids, the orthogonality of a completely rectangular grid no longer exists, and the result is that the two-point property of the flows between the cells is lost—the flow between cell *a* and cell *b* is not just a function of the solution values of cells and *a* and *b*.^{53,59–62} Typically, the result is a 27-point scheme in three dimensions. However, if the grid distortion is mild, it may be possible to ignore some additional couplings and use a low-order transmissibility scheme. This is normally done for extra couplings introduced by dip angles, which are often small.

Although this corner-point description handles the fault issue, the basic coordinate system remains a regular grid (i.e., the grid is structured). Fitting such a basically regular system to the irregular shapes of a reservoir remains a difficulty that may be solved in two basic ways—either by distorting the grid and fitting the cells into the geometry, or by truncating the grid to the reservoir position.

17.3.4 Multiple-Domain Hexahedral Grids. In some cases, a single structured grid system cannot match the overall structure of a reservoir, so a block grid or domain-based grid is used.⁶³ This consists of a number of subgrids, each with a local regular (*i,j,k*) structure, but linked together to model the entire reservoir. The block hexahedral system gives rise to multiple (*i,j,k*) indexing systems—(*i,j,k,l*), where the *l* index specifies the grid system. These comprise a series of regular grids. Such regular gridding systems have advantages for upscaling and downscaling—for example, a natural coarsening of a regular grid may be simply defined by grouping sets of coordinates in each direction.

17.3.5 Grid Refinement. A common requirement in reservoir simulation is an increased level of detail around an item of interest such as a well. This is frequently obtained in structured grids by *local grid refinement*, replacing a set of cells in the original grid by a finer grid (Fig. 17.16). The inserted grid may be Cartesian (center) or radial (upper left). Local refinement may be regarded as a form of multiple domain structured grid, in that it consists of a number of linked structured grids. Flows at the edges of local refinements generally take a multipoint form.⁵⁴

17.3.6 Unstructured Grids. The problems involved in using a regular structured grid to represent reservoir geometry can be avoided by using an *unstructured* grid. This is constructed around a set of solution points that need have no particular indexing scheme. These points may

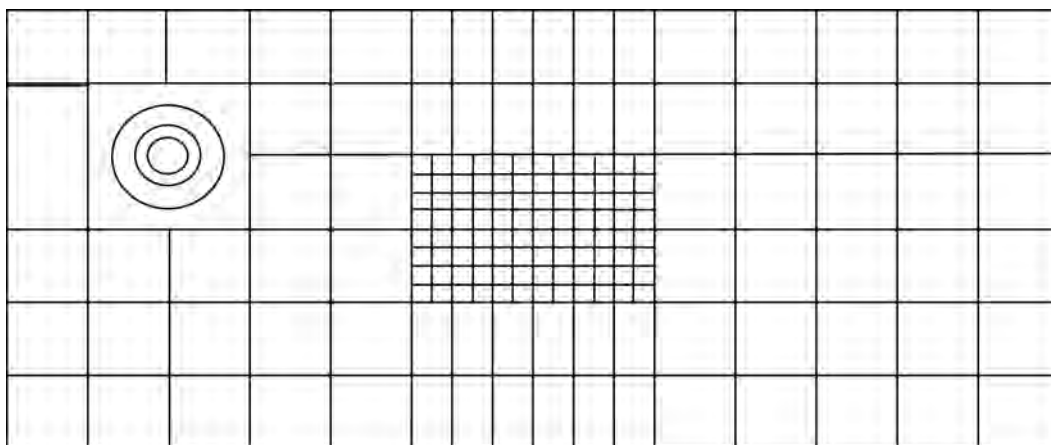


Fig. 17.16—Local grid refinement.

be triangulated into a mesh of triangles or tetrahedrons. A control volume is constructed around the nodes of the resulting mesh to define the simulator cell volumes. The perpendicular bisector (PEBI) method introduced into reservoir simulation by Heinemann^{64,65} used a technique also known as a *Voronoi* grid.^{58,66} Starting from any set of solution points, the PEBI cell volumes are defined by the perpendicular bisection planes between these points. The resulting control volume is defined by the perpendicular planes—it is the set of points closer to the node than any other. This is shown in Fig 17.17, in which the bisectors to the heavy lines joining the solution points enclose the control volume, represented by the shaded area. The grid is locally orthogonal, and the desirable property of two point flows is obtained. The actual cell volumes may have a variety of shapes, depending on the exact placement of the solution points, but are typically hexagonal in two dimensions. Grid refinement occurs naturally in areas where solution points are closely spaced.

The two-point property is not naturally preserved in anisotropic reservoirs, although it can be regained by transforming to a K -orthogonal grid in which the geometry is transformed so that \mathbf{K}_n is parallel to the vector joining the solution nodes, where \mathbf{K} is the permeability tensor and \mathbf{n} is the normal to the cell volume surface.⁶⁷ For nonisotropic cases in which the grid is not K -orthogonal, the flows will be functions of the solution values in more than two cells, as in the general hexahedral case.

An unstructured grid may be defined in two dimensions, and then applied to each layer of a reservoir model, so that a typical cell is a hexagonal prism. This is sometimes termed a 2½D unstructured grid.⁶⁸ Alternatively, a full 3D unstructured grid may be defined. The 3D approach is most effective when applied to model a local structure such as a branched well.

Unstructured grids yield an elegant and flexible grid description. However, the ability to identify cells by a simple set of indices is lost, and items such as wells need to be positioned in true space terms. The systems of linear equations generated by unstructured grids are also commonly regarded as more difficult to solve than those produced by structured grids. However, it may be more true to say that optimal solution schemes are simpler to find for structured grids, where the row and plane order provides a natural *ab initio* solution variable-ordering scheme.

17.3.7 Truncated Regular Grids.⁶⁹ The truncated approach fits in well with the rectangular grids used in geological modeling. A simple rectangular grid is always used in the areal direction, but faults may subdivide the rock volume in a given column. The areal grid is not

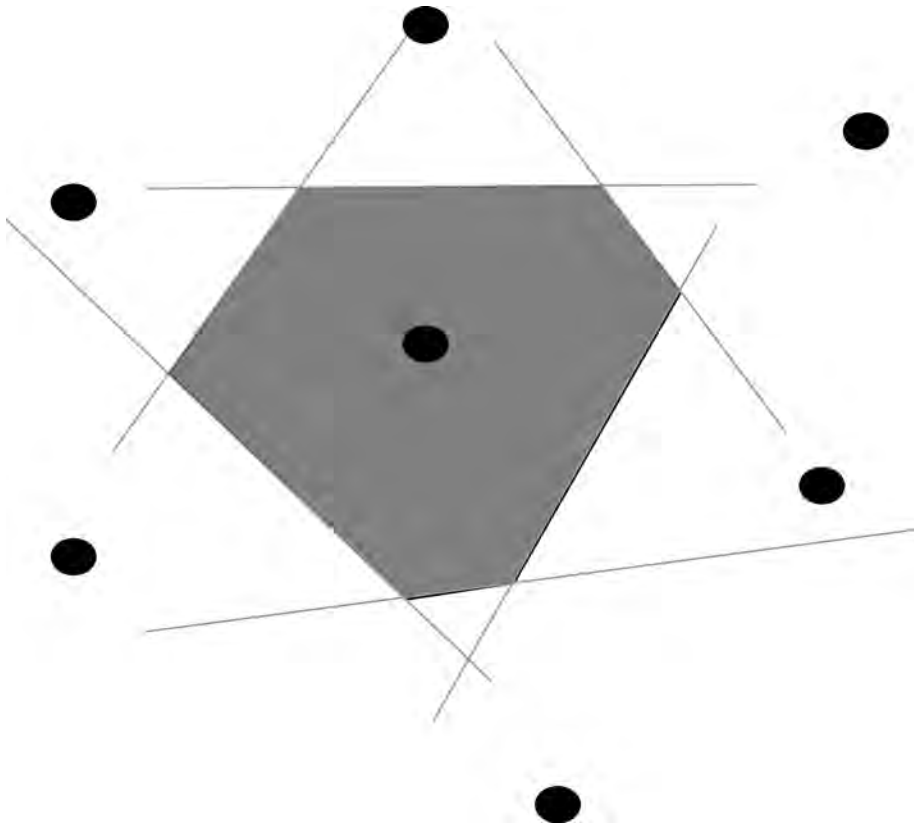


Fig. 17.17—Unstructured grids may result in hexagonal cells.

modified to match the faults. Thus the two marked volumes in Fig. 17.18 represent different cells, but may have the same i, j indices, so this creates a multiple-domain grid. A disadvantage is the more complex shape of cells at the edge of the grid. Transmissibilities for such cells may need to be calculated numerically. Apart from the truncated cells, all the grid cells are hexahedra that are rectangular in plan.

17.3.8 Other Gridding Systems. *Triangular or Tetrahedral Grids.* The underlying solution points of a PEBI mesh can be linked together into a Delaunay triangulation. In 2D, this creates triangles, and in 3D it creates tetrahedra. One option would clearly be to use triangular or tetrahedral cells directly and associate cell volumes with these. This technique is rather rarely used in reservoir simulation. Partly this may be historical, but the Delaunay triangulation is rather less stable under grid changes than a Voronoi grid, and triangulation can more often lead to “sliver” cells with a high surface area but a small volume.

Curvilinear Grid Systems. In some special cases, a transformed coordinate system may be used, based around an expected flow pattern. Such grids are not well adapted to represent geological data, and have been used less frequently as more detailed reservoir descriptions have become available.

17.3.9 Future Directions. Two themes emerge from current trends in reservoir simulation gridding. The increasing sophistication of data preparation and solver technology indicates a move towards unstructured grids as a general method of solving the flow equations for a given reser-

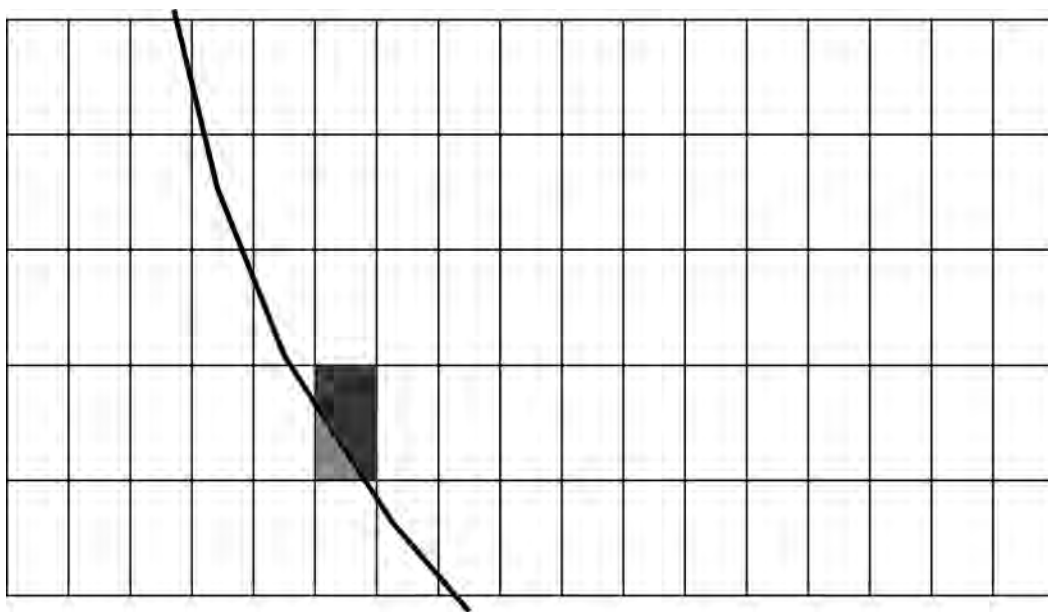


Fig. 17.18—A fault creating two cell volumes in a truncated grid.

voir simulation problem. On the other hand, reservoir simulation is increasingly seen as part of a decision-making process rather than an isolated activity, so the ability to map easily onto the generally regular data structures used in seismic and geological modeling becomes an important issue. In this role, structured grids may have advantages of simplicity and scalability.

An ideal is to separate the construction of the flow-simulation grid from the description of the reservoir geometry. This ties in with a further ideal, inherent in many discretization schemes, that the scale of the simulation grid should be below the scale of the problem structure.

For more complex shape-dominated problems, the unstructured approach looks general and flexible, providing that the data-handling and cell-identification methods can be moved to true x,y,z space preprocessing software.

17.4 Upscaling of Grid Properties—Alan Grindheim

17.4.1 Definition. Upscaling, or homogenization, is substituting a heterogeneous property region consisting of fine grid cells with an equivalent* homogeneous region made up of a single coarse-grid cell with an effective property value. It is performed for each of the cells in the coarse grid and for each of the grid properties needed in the flow-simulation model. Therefore, the upscaling process is essentially an averaging procedure in which the static and dynamic characteristics of a fine-scale model are to be approximated by that of a coarse-scale model. A conceptual illustration of the upscaling process is shown in [Fig. 17.19](#).

17.4.2 Can Upscaling Be Avoided? Typically, 3D geological models contain detailed descriptions of the reservoir that can be hard to capture properly with a significantly coarser model. Therefore, it would be preferable if upscaling could be avoided. Currently, an average-sized flow simulation model consists of approximately 100,000 active grid cells. This is to ensure that the CPU consumption of a simulation run will be reasonable (i.e., within practical limits).

* Either volume or flux vice, depending on the type of property that is to be upscaled.

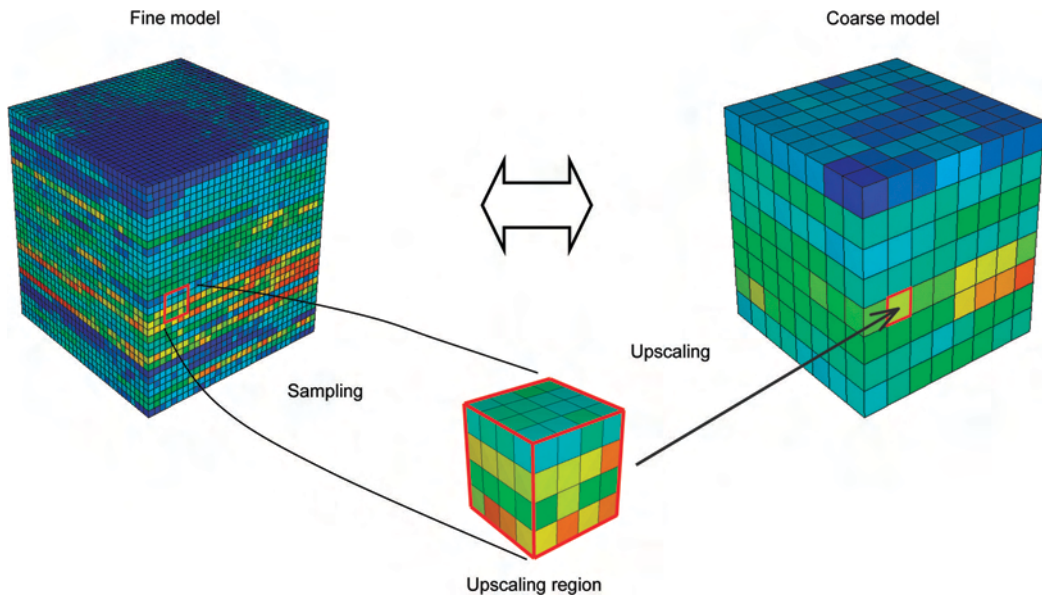


Fig. 17.19—Concept of upscaling.

Because a typical 3D geological model may consist of approximately 10 million active grid cells, it is obviously infeasible to run fluid-flow simulations directly on the geological model. Hence, upscaling is a required part of current reservoir modeling workflows.

Seen through the eyes of the geologist, the upscaling task may be a painful experience because all the geological details that were put into the model seem to be lost in the process. For a reservoir engineer, on the other hand, effective properties might be all that matter.

For volumetric (additive) properties such as porosity and saturation, the effective flow-cell value is simply given by the bulk and pore volume weighted arithmetic average, respectively, of the geo cells inside it. For the permeability, which is intrinsic (nonadditive) by nature, no such simple averaging method exists. The complexity one needs to take into account when upscaling permeability is considerable; therefore, all current techniques provide only an approximation of the true effective cell permeability. This approximation may range from very good to very poor, depending on the complexity of the fine-scale permeability distribution as well as the upscaling method used.

17.4.3 Upscaling Techniques for Absolute Permeability. Homogenization of absolute permeability does not have an exact analytical solution, except for in a few idealized cases. The challenge of computing an accurate effective permeability has resulted in a large number of upscaling techniques. These techniques range from simple statistical averages to advanced numerical methods.

Tensor methods are the most accurate techniques available for computing the effective cell permeability. These are based on solving a second-order elliptic differential equation describing single-phase, incompressible, steady-state fluid flow in a region without sources and sinks (i.e., wells). Some flow-based methods may provide a *full* permeability tensor. However, because most multiphase flow simulators can only handle a diagonal permeability tensor because of the use of a seven-point stencil in 3D, diagonal tensor methods are most frequently used whether directly or indirectly (through a diagonalization of a full tensor). For a diagonal tensor, only the effective permeability in the principal directions of flow (x , y , and z) will be nonzero.

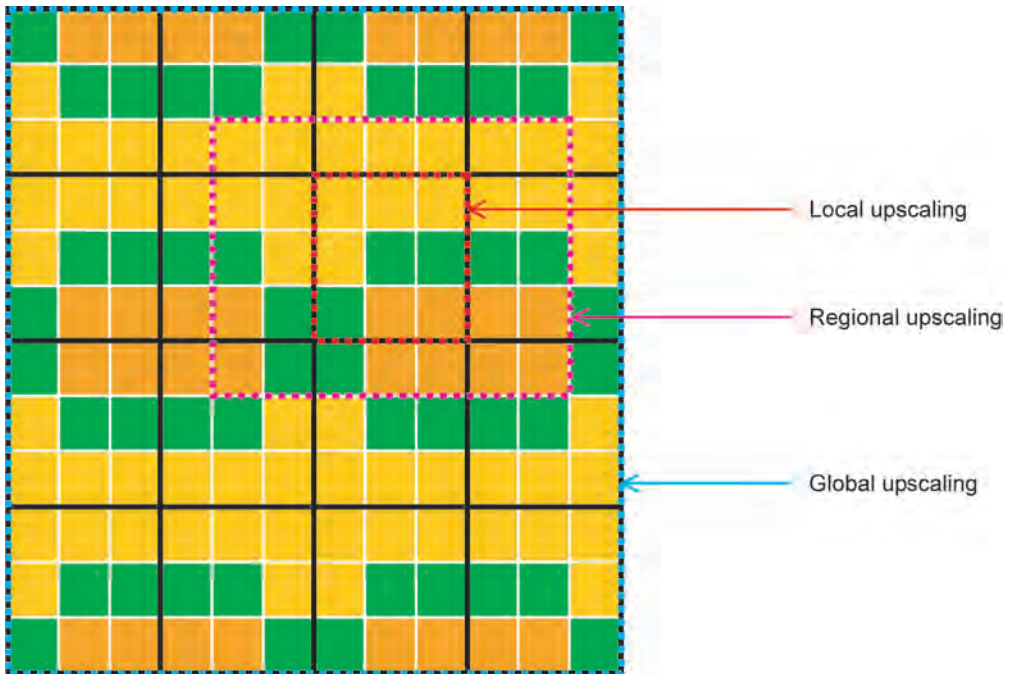


Fig. 17.20—Upscaling schemes and the size of the computational region (geo grid in white, flow grid in black).

The flow equation is usually discretized with a finite-difference scheme, although finite-element methods are also applied occasionally. To compute all the directional components of the permeability tensor, the discretization and solution of the flow equation must be performed for each of the principal flow directions (i.e., three separate single-phase simulations need to be performed). Each simulation involves the iterative solution of a linear equation system (typically, the linear solver is a conjugate gradient method, preconditioned by incomplete Cholesky or LU factorization). The unknowns in this equation system are the geo-cell pressures inside the flow cell, whereas known quantities are the geo-cell dimensions and permeabilities, as well as the pressure conditions along the faces of the flow cell. When the numerical solution of the fine-scale pressure distribution has converged, an effective permeability is computed by equating expressions for the flux through the heterogeneous geo cells with the flux through the equivalent homogeneous flow cell using some form of Darcy's law.

The pressure field is usually solved locally—that is, for one flow cell at a time. However, as discussed in the next subsection, the size of the *computational* region may not necessarily be limited to that of the upscaling region (i.e., the flow cell).

17.4.4 Upscaling Schemes for Absolute Permeability. Based on the size of the computational region, the single-phase upscaling process may either be described as local, regional, or global. With local upscaling techniques, the computational region is identical to the upscaling region (i.e., only geo cells inside the flow cell are considered in the upscaling computations). For regional upscaling, the computational region is expanded beyond that of the flow cell to include a buffer region of neighboring geo cells. In the case of global upscaling, the computational region is that of the entire geo model. Fig. 17.20 provides a schematic drawing of how the computational region varies with the different upscaling schemes. These are further discussed in the subsections that follow.

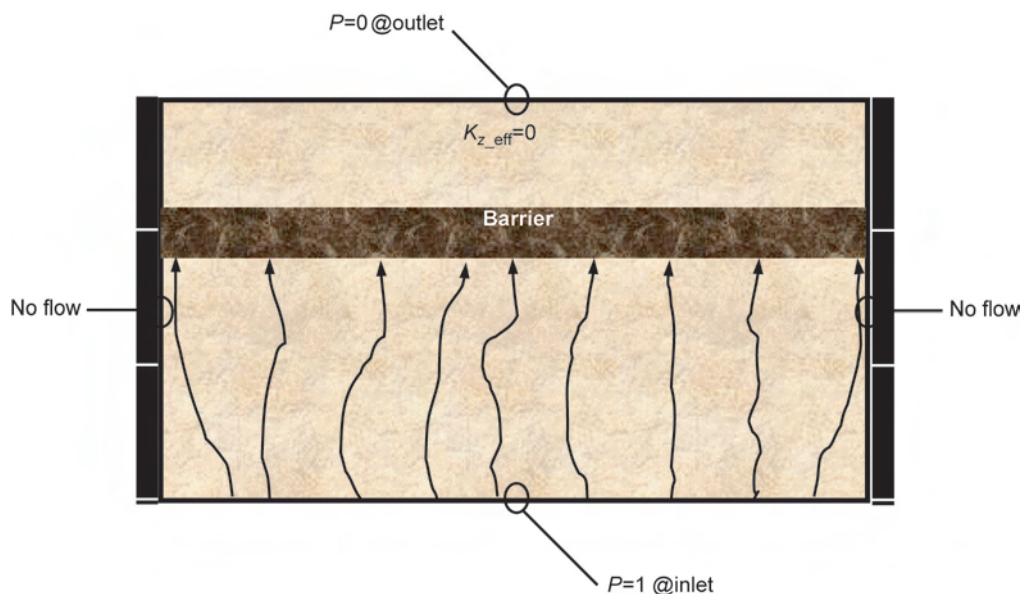


Fig. 17.21—The sealed sides boundary conditions (in z-direction).

It should be noted that the different upscaling schemes are only relevant when considering flow-based (tensor) methods. It is also important to realize that even though the computational region may vary according to the scheme used, the upscaling region remains unchanged and is of course defined by the flow cell, as in the case of the simple, analytical upscaling techniques.

17.4.5 Local Upscaling. Because it used to be too time-consuming to compute the fine-scale pressure field for the complete geo grid in a single operation, the flow-based methods have traditionally been restricted to solving the pressure field locally—that is, for a single flow cell at a time. Hence, the effective cell permeability is computed separately and independently of the other flow cells, which may or may not be correct depending on how representative the imposed pressure conditions along the faces of the flow cell are.

Different types of artificial boundary conditions for the flow cell have been suggested over the years, all with the objective of providing as good an approximation of the real boundary conditions as possible. An important design criterion for the artificial boundary conditions is the conservation of flux in and out of the flow cell.

The first type of boundary conditions proposed for the local solution of the pressure equation was published by Warren and Price in 1961.⁷⁰ Their approach is to impose a constant pressure gradient in a selected direction of flow by specifying a pressure of 1 on the inflow face and a pressure of 0 on the outflow face. By allowing no flow to pass through the sides of the cell, all fluxes are forced to go in the principal direction of flow. Therefore, this type of boundary conditions is often referred to as the no-flow or sealed-sides boundary conditions. The sealed-sides boundary conditions are graphically illustrated in Fig. 17.21 for flow in the vertical direction (here in the case of a flow cell containing a barrier).

The choice of boundary conditions emulates the way core permeability is measured in the lab. This is hardly a coincidence. As in the coreflood experiment, the local numerical flow simulation is in effect 1D because the cell faces parallel to the main flow direction are sealed. This implies that the estimated effective permeability will be scalar. Hence, the maximum number of directional permeability components that can be obtained with this type of boundary conditions is three, one for each of the principal directions of flow. In practice, the diagonal

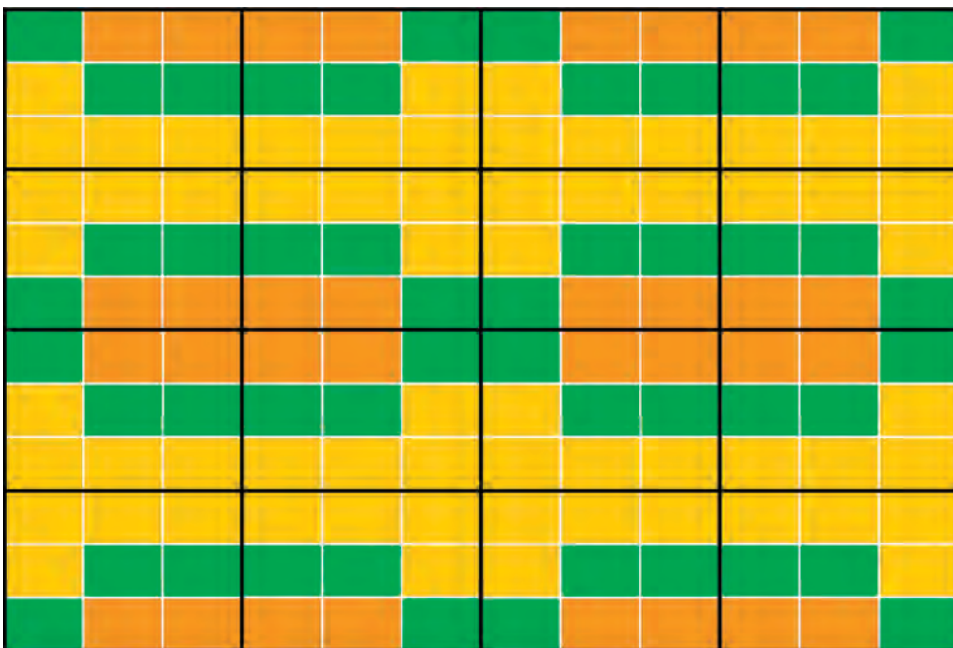


Fig. 17.22—The fine-scale permeabilities are symmetric on the scale of the flow cell (geo grid in white, flow grid in black).

permeability tensor is derived by setting up the boundary conditions for x , y , and z directions, respectively, in three independent single-phase simulations.

As documented in Refs. 71 and 72, a tensor technique based on the sealed-sides boundary conditions tends to bias the estimated effective permeability toward a low value. The physical implication of this is most clearly seen in the case of a bimodal permeability system of sand and shale. This is because the sealed-sides method consistently underestimates the reservoir flow characteristics by thickening shale barriers and narrowing sand channels. The latter effect also has a tendency of disconnecting stacked sand channels.

Take, for example, the flow illustrated by Fig. 17.21. Because the barrier extends across the entire length of the local upscaling region, the resulting effective permeability (in the z -direction) will be zero. For vertical flow, the result, therefore, is a thickening of the shale in the flow model equal to the thickness of the flow cell. Depending on which factors that affect fluid flow in the region of the cell, this may or may not be a representative value for that particular flow cell.

Strictly speaking, the sealed-sides boundary conditions are only valid if no wells are present and the flow cells are symmetric in each direction of the grid as illustrated in 2D by Fig. 17.22. Hence, the sealed-sides boundary conditions assume that the flow cell is surrounded by mirror images of itself.

By the end of the 1980s, 3D geological models had started to appear more regularly on the modeling scene. This resulted in a new demand for advanced upscaling. In this renewed effort, two alternative boundary conditions for solving the local pressure solution in a flow-based method were suggested more or less at the same time. One was based on linear boundary conditions, the other on periodic boundary conditions.

The use of linear boundary conditions in flow-based upscaling was suggested by Guerillot *et al.*⁷³ in 1989 and Samier⁷⁴ in 1990 to enable the computation of a full-permeability tensor. Instead of setting the flow through the sides of the cell to zero, the pressure along the sides is

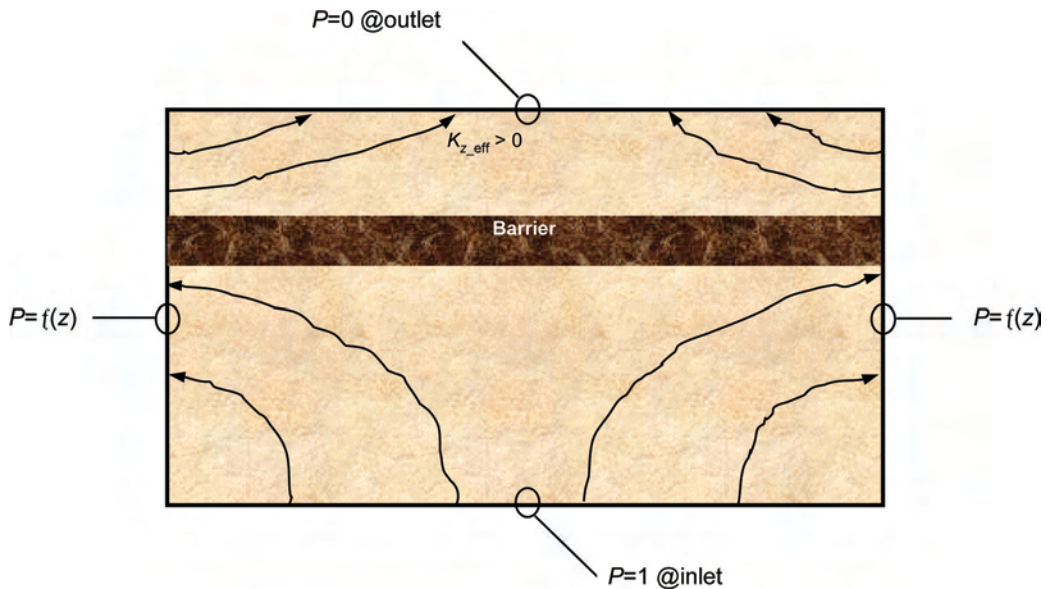


Fig. 17.23—The open sides boundary conditions (in z -direction).

allowed to vary in a linear fashion that matches the constant pressure on the two cell faces perpendicular to the flow. Hence, the imposed pressure gradient is still constant, but the flow is allowed to enter and leave the cell at any point along the sides parallel to the main flow direction. Therefore, this type of boundary conditions is also referred to as the open-sides boundary conditions. The situation is graphically illustrated in Fig. 17.23 for flow in the vertical direction (here in the case of a flow cell containing a barrier).

As with the sealed-sides boundary conditions, three independent single-phase simulations, with the main flow direction in x , y , and z , respectively, are needed to yield all of the components of the permeability tensor. With open-sides boundary conditions, however, also the off-diagonal components will generally be nonzero. Hence, unlike the sealed-sides boundary conditions where the effective permeability is limited to that of a diagonal tensor, the open-sides boundary conditions, as previously mentioned, give a full permeability tensor. The resulting full tensor may be either symmetric or nonsymmetric depending on the properties of the method under consideration.

As documented in Refs. 75 and 76, a tensor technique based on the open-sides boundary conditions tends to bias the estimated effective permeability toward a high value. The physical implication of this is most clearly seen in the case of a bimodal permeability system of sand and shale. This is because the open-sides method consistently overestimates the reservoir flow characteristics by narrowing shale barriers and thickening sand channels. The latter effect also has a tendency of connecting isolated sand channels.

Take, for example, the situation illustrated by Fig. 17.23. Even though the barrier extends across the entire length of the local upscaling region, the resulting effective permeability (in the z -direction) will be significantly larger than zero. For vertical flow, the result is therefore a narrowing of the shale in the flow model equal to the horizontal dimensions of the flow cell. Depending on which factors affect fluid flow in the region of the cell, this may or may not be a representative value for that particular flow cell.

The use of linear boundary conditions has its origin in the effective medium theory,⁷⁷ which states that any region of permeability behaves as if embedded within the average medi-

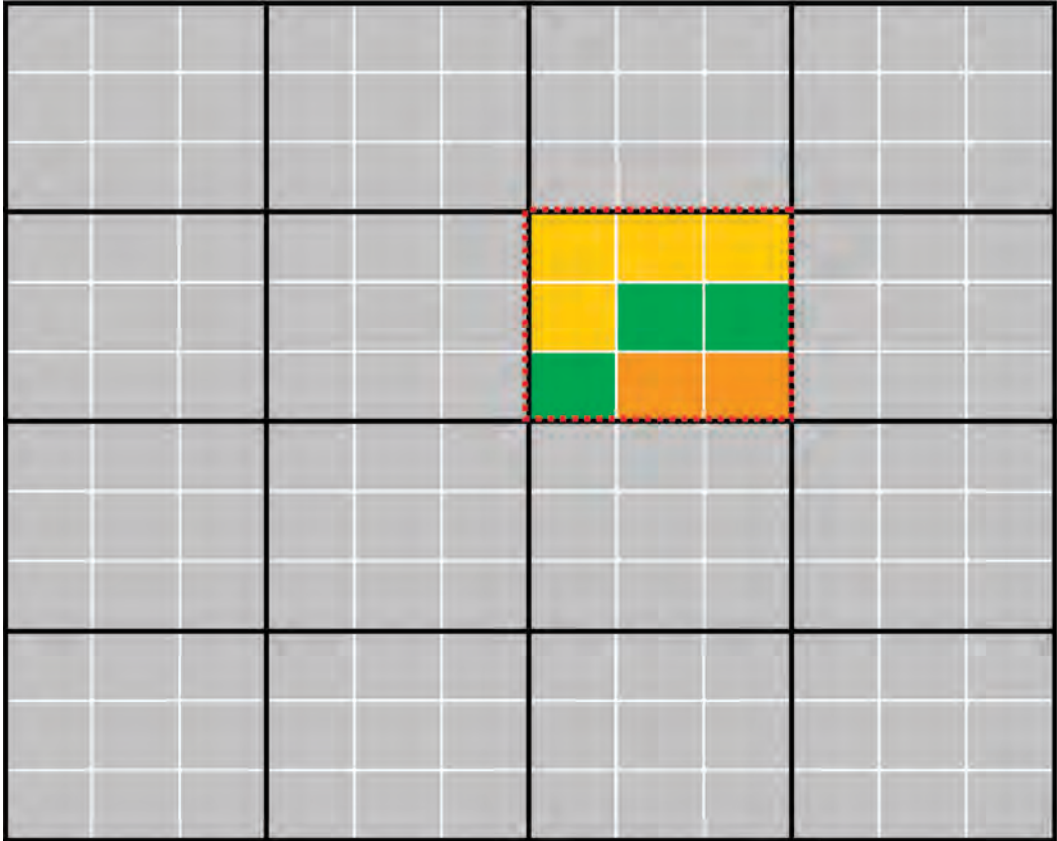


Fig. 17.24—The fine-scale properties are uniform and nonzero outside the upscaling region (the geo cells outside the upscaling region are drawn in gray to reflect that the average value need not be known).

um. Strictly speaking, these boundary conditions are therefore only valid if the neighboring flow cells are of a uniform, nonzero permeability. This is illustrated in 2D by [Fig. 17.24](#).

The use of periodic boundary conditions originates from the volume averaging theory, and its use in flow-based upscaling was first introduced by Durlofsky and Chung in 1990 and by Durlofsky in 1991.^{75,76} Durlofsky used periodic boundary conditions, together with Darcy's law and the classic requirement of flux conservation, to derive a full permeability tensor. A somewhat different approach, which also uses a periodic pressure field around the flow cell, was proposed by Øistein Bøe *et al.* in 1994.^{78,79} This uses a weak form of Darcy's law to prove that periodic boundary conditions result in a full permeability tensor that is both symmetric and positive definite. The Norsk Hydro tensor method is based on the conservation of dissipation (mechanical energy per unit weight of fluid), although it turns out that fluxes are conserved as well.

A simplistic illustration of the periodic boundary conditions is given in [Fig. 17.25](#) for flow in the vertical direction (here in the case of a flow cell containing a barrier).

Although the periodic boundary conditions generally result in an effective permeability that is higher than that computed with the sealed-sides boundary conditions, the effective vertical permeability for the upscaling region illustrated in [Fig. 17.25](#) will also be zero.

Strictly speaking, the periodic boundary conditions are only valid if no wells are present and the fine-scale medium is periodic on the scale of the flow cells (i.e., the fine-scale proper-

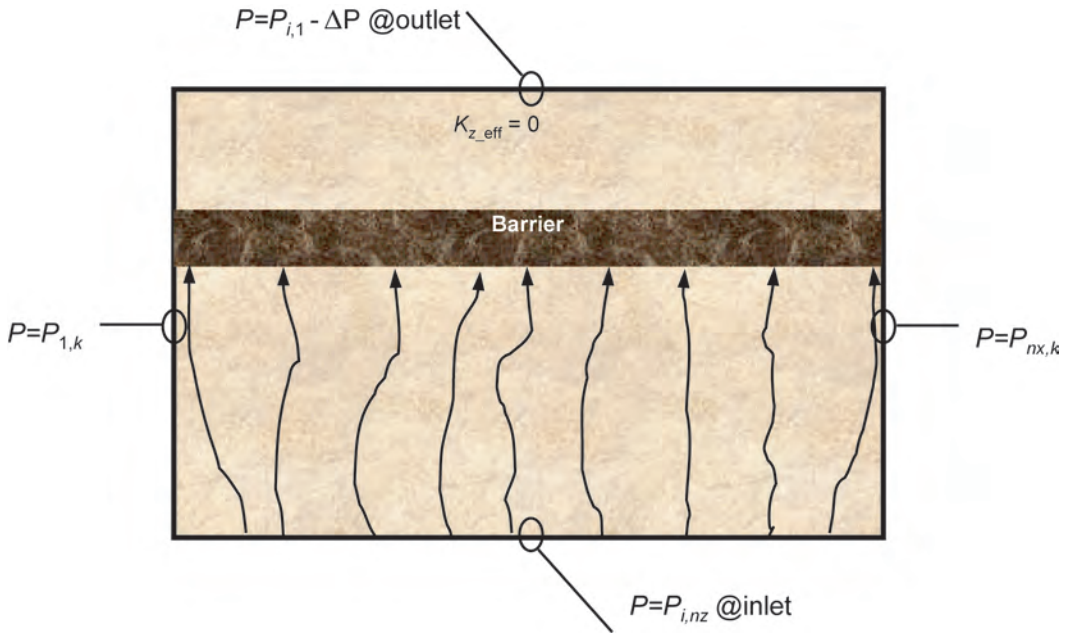


Fig. 17.25—The periodic boundary conditions in z-direction ($P_{1,k} = P_{nx,k}$, $P_{i,1} = P_{i,nz}$).

ty distribution inside each flow cell must be identical). This is illustrated in 2D by Fig. 17.26. Please note that if a medium is symmetric on the scale of ΔL , then it will be periodic on the scale of $2\Delta L$.

The relative performance of the tensor methods that is caused by the various boundary conditions has proven to be of considerable interest. As it happens, the sealed-sides method provides a lower bound and the open-sides method an upper bound of the effective permeability. The periodic-based method turns out to give an effective permeability estimate that generally lies in between the two previous methods.

With regard to the outer bounds of effective permeability, it is well known that the harmonic and arithmetic means provide the absolute lower and upper limit of the effective permeability, respectively. It is less known that the uncertainty range in the effective permeability may be narrowed using the composite averages. In fact, it may be mathematically proven that the harmonic-arithmetic average provides a closer lower limit than the pure harmonic mean, whereas the arithmetic-harmonic average provides a closer upper limit than the pure arithmetic mean (truly valid only for regular grids). In this context, it is important to realize that the two flow-based methods (sealed and open sides) provide an even narrower uncertainty band for the effective permeability, but at the expense of increased CPU time.

The relative performance of the most important local upscaling techniques is shown in Fig. 17.27. Fig. 17.27 also indicates the “inner” uncertainty range of the true effective permeability for the sake of comparison.

17.4.6 Regional Upscaling. Regional upscaling is applied to reduce the influence of the artificial boundary conditions on the effective permeability estimate by moving the boundary of the computational region away from the flow cell. This implies that the influence of neighboring geo cells is taken into account in addition to the geo cells inside the flow cell. In other words, regional upscaling represents an expansion of the local computational region outside the volume of the flow cell. The size of the so-called buffer or skin around each flow cell is usually

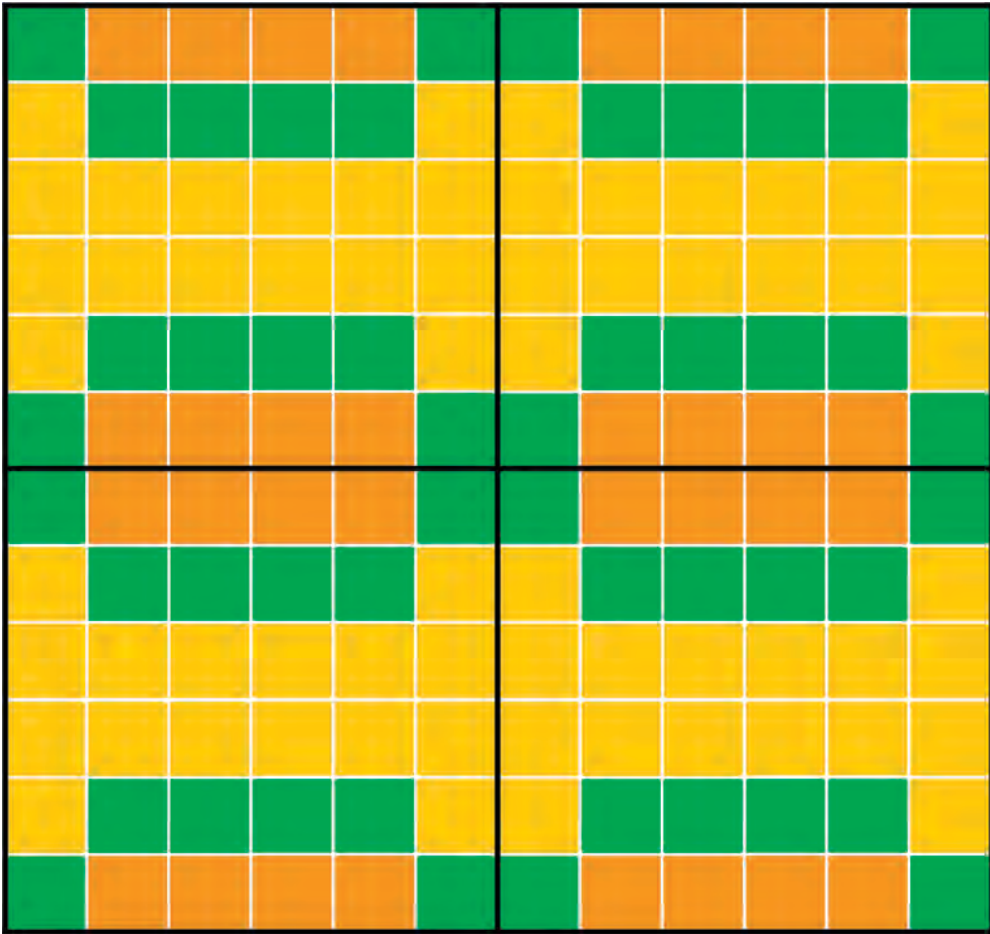


Fig. 17.26—The fine-scale properties are periodic on the scale of the flow cell (geo grid in white, flow grid in black).

given in number of neighboring geo cells to either side of the flow cell and must be specified by the modeler for each of the three coordinate directions.

The permeability estimate of a regional upscaling method will improve as the size of the buffer region increases, and it will ultimately be equal to the “true” effective permeability when the buffer size has reached the boundaries of the geo model for all three directions. The gain in accuracy is largest in the beginning (i.e., for small buffer values). This is illustrated by Fig. 17.28, showing the behavior of the lower- and upper-bound tensor techniques in the case of increasing buffer size. Please note that in Fig. 17.28, the outer bounds are shown to be symmetric around the “true” effective permeability. Generally, this is not the case.

17.4.7 Global Upscaling. Strictly, the fine-scale pressure field must be determined for the entire geo grid simultaneously to compute “exact” effective permeabilities for the flow cells. In the past, however, this has been too CPU-intensive to be performed in practice. With the introduction of new and promising solution algorithms such as the Output Least Squares (OSL) method, global upscaling schemes can now be realized. In the paper by Holden and Nielsen,⁸⁰ the OSL method is used to minimize the difference in pressure, as well as velocity, between the geo and flow grids in an iterative process. Because the CPU consumption of the applied

$$| \leftarrow K_{\text{true}} \rightarrow |$$

$$K_{\text{har}} \leq K_{h-a} \leq K_{\text{nbc}} \leq K_{\text{pbc}} \leq K_{\text{lbc}} \leq K_{\text{a-h}} \leq K_{\text{ari}}$$

Fig. 17.27—The relative performance of local upscaling techniques.

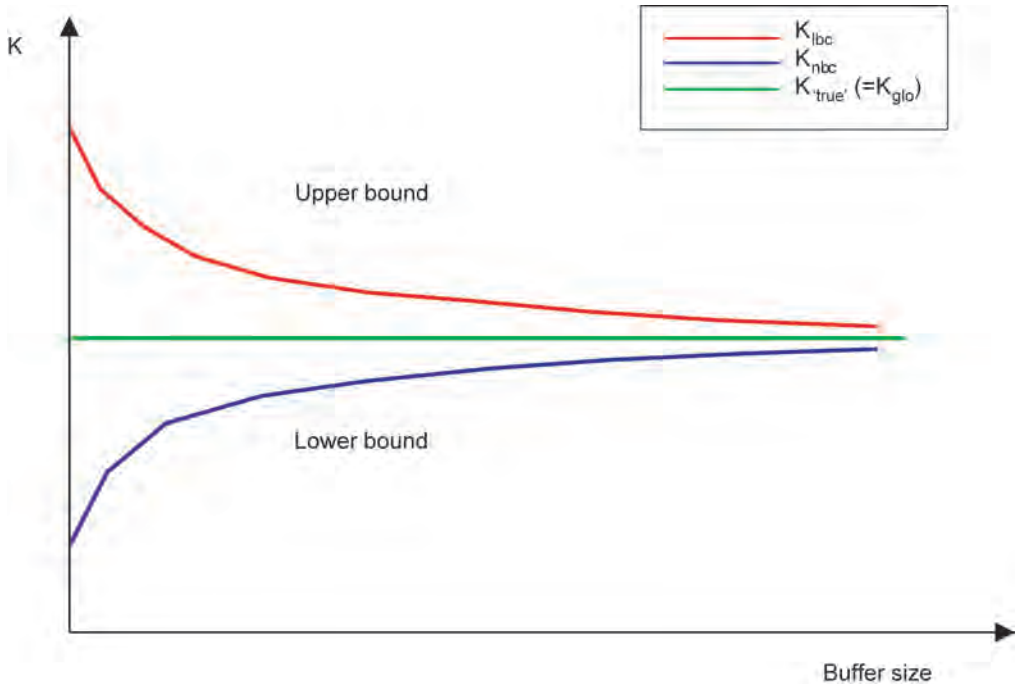


Fig. 17.28—The outer bounds of effective permeability and their behavior with increasing buffer size.

equation solver is proportional to the number of geo cells, a global solution will use approximately the same amount of computational time as the sum of all the local computations. Therefore, the new global upscaling scheme is just as fast as any local method.

An obvious advantage with the global upscaling approach is that one avoids using artificial boundary conditions around the upscaling region (i.e., instead of guessing what the boundary conditions for the flow cells might be, the pressure conditions surrounding the cells are explicitly known). Another important benefit is that a poor separation of scales in the upscaling will no longer occur because the size of the computational region is the same as the geo model.

Although still in its research stage, global upscaling has much potential for improving today’s permeability estimators, especially for models containing a complex facies architecture with large permeability contrasts between facies. In fact, according to Holden and Nielsen,⁸⁰ preliminary results show an improvement factor of 10 in some cases.

Still, as discussed by Holden and Nielsen,⁸⁰ the global upscaling approach is not enough to ensure maximum accuracy in the modeling of the effective permeability. Because the value of the effective permeability is influenced by changes in the pressure field, the flow-cell permeabilities should strictly be recomputed by the global method for every timestep taken by the multiphase flow simulator. In practice, though, it might be good enough to update the effective permeability field whenever a significant change occurs as a result of altering the well configuration or production/injection rates and so on. Hence, the ultimate upscaling scheme for the absolute permeability might be the one that is coupled with the multiphase flow simulator and automatically updates the absolute effective permeability field for each timestep. With the current computer power and the lack of proper integration between the geological model and the simulation model, this is hardly achievable yet.

17.4.8 Best Practice Guidelines. As may be understood from the previous sections, there exists no single upscaling method for absolute permeability that is superior to all other methods in all situations, at least not until it has been fully established that the global upscaling scheme represents the ultimate method of choice. Selecting the proper upscaling method from the many available choices can be quite a challenge. The choice of sophistication in the upscaling method generally depends on one or several of the following factors:

- The complexity of the fine-scale permeability distribution (i.e., the geo model).
- The degree of upscaling that needs to be performed (i.e., the coarsening factor).
- The number of permeability realizations that need to be upscaled.
- The time available to the project for performing upscaling.
- The intended use of the flow model.

Because an exact validation of the upscaling process cannot be performed unless a multiphase flow simulation is carried out on the geo model itself, two alternative upscaling approaches for identifying the proper homogenization method are presented here.

The Absolute Upscaling Approach. This approach assumes that there exists a way to properly validate the *absolute* performance of an upscaling method without resorting to an extremely time-consuming (if at all feasible) finite-volume simulation of the geo model. As documented in Ref. 81, streamline simulation offers a very efficient way of validating the performance of upscaling methods. The validation process is carried out by first running a streamline simulation on the geo model to compute the reference solution. Then a streamline simulation is run on the flow model for each of the upscaling methods that are to be evaluated. The simulated performance of the various upscaling methods is then compared to that of the geo model. The validation of upscaling methods is best done under single-phase flow conditions to avoid introducing other model parameters (e.g., relative permeabilities and associated rock types) that also need to be upscaled in one way or the other. A higher confidence may also be obtained for the validation process if the actual well pattern is used in the streamline simulations.

Using the previously described validation scheme, the modeler may choose to evaluate any upscaling method until one with a satisfactory performance is found. Still, a more systematic way of identifying the optimum upscaling method is desirable. With the absolute upscaling approach that is presented here, the modeler is offered a multistep procedure that is to be terminated as soon as a satisfactory upscaling method has been identified. The recommended procedure involves the following steps:

1. Compute the upper and lower bounds of the effective permeability using the arithmetic-harmonic (or pure arithmetic) and harmonic-arithmetic (or pure harmonic) average techniques, respectively. Being of the analytical type, these methods are very fast and will provide a first quantification of the upscaling uncertainty. Validate the performance of the two composite methods against that of the geo model using a single-phase streamline simulator with the actual well pattern.

2. If the performance of any of the two methods in Step 1 is within an acceptable range of the geo model, then terminate the procedure and choose the appropriate method. If, on the other hand, the performance of both methods is unsatisfactory because of the complexity of the geo model, then use the upper (open-sides) and lower (sealed-sides) bound diagonal tensor methods to narrow the uncertainty in the flow-model performance. Validate the performance of the two tensor methods against that of the reference solution.

3. If the performance of any of the methods in Step 2 is within an acceptable range of the reference solution, then terminate the procedure and choose the appropriate method. If, on the other hand, the performance of both methods is unsatisfactory, then the following alternatives may be worth considering:

a. If time allows, refine or coarsen the flow grid (whatever is best) to achieve a better separation of the length scales. Then repeat the upscaling of the outer bounds (in Step 2) and redo the validation to check if the performance of either method has improved.

b. Apply a tensor method with periodic or semi-open-boundary conditions [the semi-open boundary conditions alternative is available in some applications using a multiplier between 0 (sealed) and 1 (open) to the side faces of the computational region]. As previously mentioned, this should result in an intermediate estimate of the effective permeability tensor and therefore provide a flow model performance that lies somewhere in between the two methods in Step 2.

c. Select the best of the two tensor methods in Step 2 and convert the local method to a regional method using a buffer region of modest size. Validate its performance. If necessary, repeat this step using an increasingly larger buffer region until a satisfactory performance of the flow model is obtained.

d. If for some reason none of the previous alternatives are an option, then one needs to apply the method that best satisfies the wanted flow behavior of a given cell or cells in a given region. In other words, a combination of the outer bound techniques within one and the same model may be a fourth alternative.

As previously mentioned, the method using open-sides boundary conditions is a good estimator of sand continuity and quality, whereas the sealed-sides boundary conditions method is better at detecting the presence and effect of barriers.

Consider a long horizontal oil producer in the Troll West Gas Province that is protected against coning from the overlying gas cap by a calcite barrier just above the well. If the vertical grid resolution in the Troll full-field model was such that one could apply the open-sides boundary conditions technique on the cells containing the well, and the sealed-sides boundary conditions technique on the cells containing the barrier, then this would be the optimum local upscaling approach.

However, if both a segment of the well trajectory and a segment of the calcite are present inside the same flow cell, then the open-sides boundary conditions technique will give a good estimate of the well's PI but result in a much too early gas breakthrough, whereas the sealed-sides boundary conditions method will better capture the effect of the calcite but give a too low estimate of the well's PI. If this is the case, one needs to consider applying one of the alternatives A or C (alternative B will, in this particular example, give the same result as the sealed-sides method).

The multistep procedure of the absolute upscaling approach is graphically illustrated in [Fig. 17.29](#).

The Relative Upscaling Approach. This approach acknowledges the fact that an exact validation of the upscaling results cannot be achieved in practice. Therefore, instead of trying to validate the absolute performance of an upscaling method, the approach diagnoses the relative performance of outer bound methods using the actual multiphase finite-volume simulator. This implies that a full black-oil simulation is run on the flow model for each of the upscaling methods that are to be evaluated. The deviation in the simulated performance between outer bound

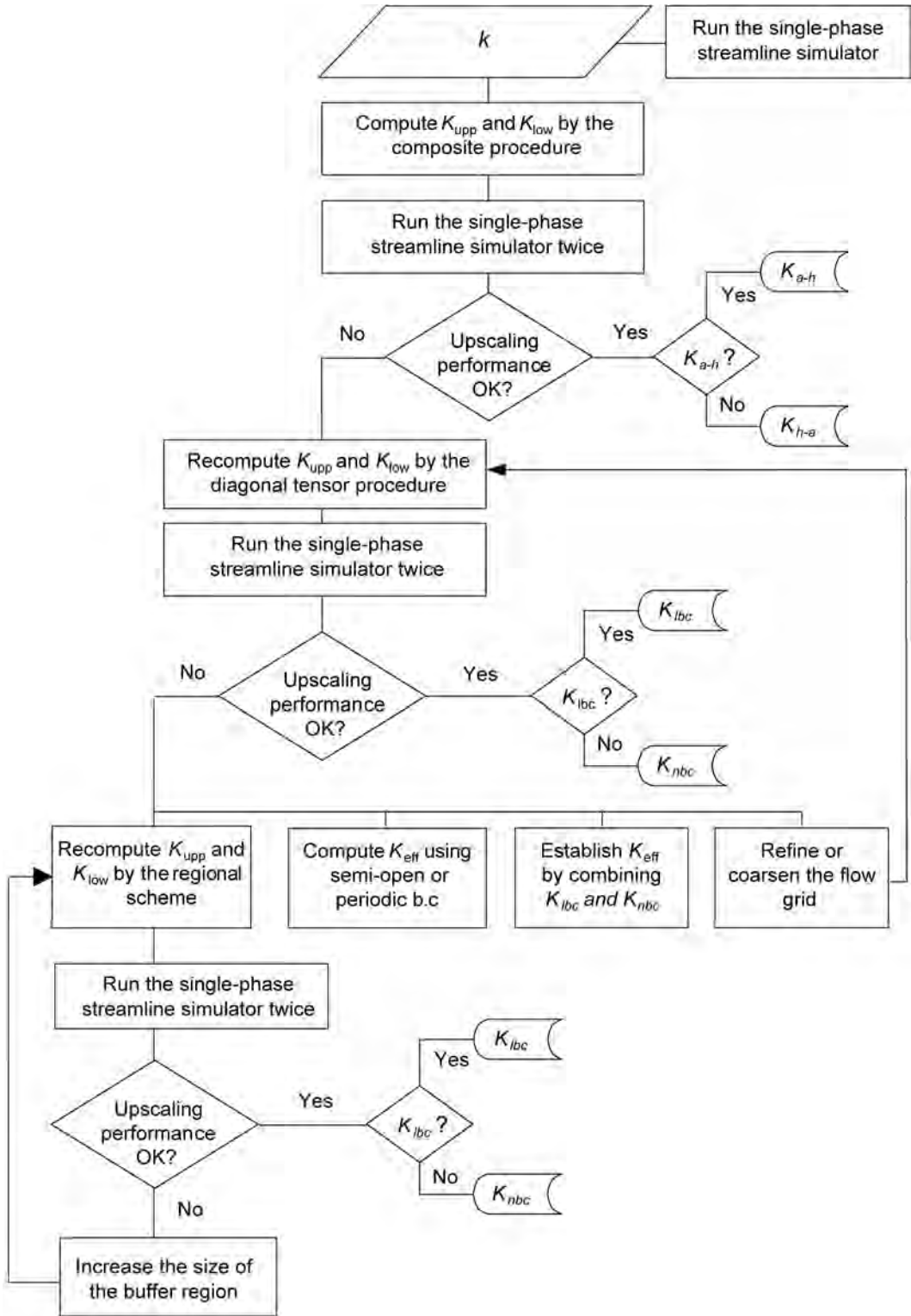


Fig. 17.29—Flow chart for the absolute upscaling approach.

methods will then reflect the part of the model uncertainty that originates from the upscaling process itself. To ensure a high degree of relevance in the diagnostics, it is important that the test simulations contain a representative description of the actual flow model.

If the project is pressed for time, the simulations may be skipped altogether in favor of a faster, although less robust, way of performing the diagnostics. Instead of analyzing simulation profiles, a normalized difference parameter may be computed on a cell by cell basis using the formula

$$\delta = (K_{\text{upp}} - K_{\text{low}}) / [(K_{\text{upp}} + K_{\text{low}}) / 2]. \dots\dots\dots (17.18)$$

The relative upscaling approach that is presented here utilizes a multistep procedure that applies outer bound methods of increasing accuracy until the best possible upscaling method can be identified. The recommended procedure involves the following steps:

1. Compute the upper and lower bounds of the effective permeability using the arithmetic-harmonic (or pure arithmetic) and harmonic-arithmetic (or pure harmonic) average techniques, respectively. Being of the analytical type, these methods are very fast and will provide a first quantification of the upscaling uncertainty. Run the finite-volume simulator for each of the two composite methods (or compute a grid-based difference parameter) and perform the diagnostics.

2. If the performance gap between the two methods in Step 1 is acceptable (small), then terminate the procedure and choose either of the two. If the deviation in performance is unsatisfactory because of the complexity of the geo model, then use the upper (open-sides) and lower (sealed-sides) bound diagonal tensor methods to narrow the uncertainty in the flow model performance. Run the finite-volume simulator for each of the two tensor methods (or compute a grid-based difference parameter) and perform the diagnostics.

3. If this reduces the upscaling uncertainty to within acceptable limits, then either of the two diagonal tensor methods may be used to provide the final permeability field for the flow model. If the deviation in the performance is unsatisfactory (large), then the following alternatives may be worth considering:

1. If time allows, refine or coarsen the flow grid (whatever is the best) to achieve a better separation of the length scales. Then repeat the upscaling of the outer bounds (in Step 2) and rerun the simulations (or recompute the difference parameter) to check if the performance gap (upscaling uncertainty) has narrowed.

2. Apply a tensor method with semi-open or periodic boundary conditions. As previously mentioned, this should result in an intermediate estimate of the effective permeability tensor and hence provide a flow model performance that lies somewhere in between the two methods in Step 2.

3. Convert the two local tensor methods in Step 2 into regional methods using a buffer region of modest size. Rerun the finite-volume simulator (or recompute the difference parameter) and check the performance gap. If necessary, repeat this step using an increasingly larger buffer region until the upscaling uncertainty reaches acceptable limits, at least as far as practically possible.

4. If for some reason none of the previous alternatives are an option, then one needs to apply the method that best satisfies the wanted flow behavior of a given cell or cells in a given region. In other words, a combination of the outer bound techniques within one and the same model may be a fourth alternative.

The multistep procedure of the relative upscaling approach is graphically illustrated in [Fig. 17.30](#).

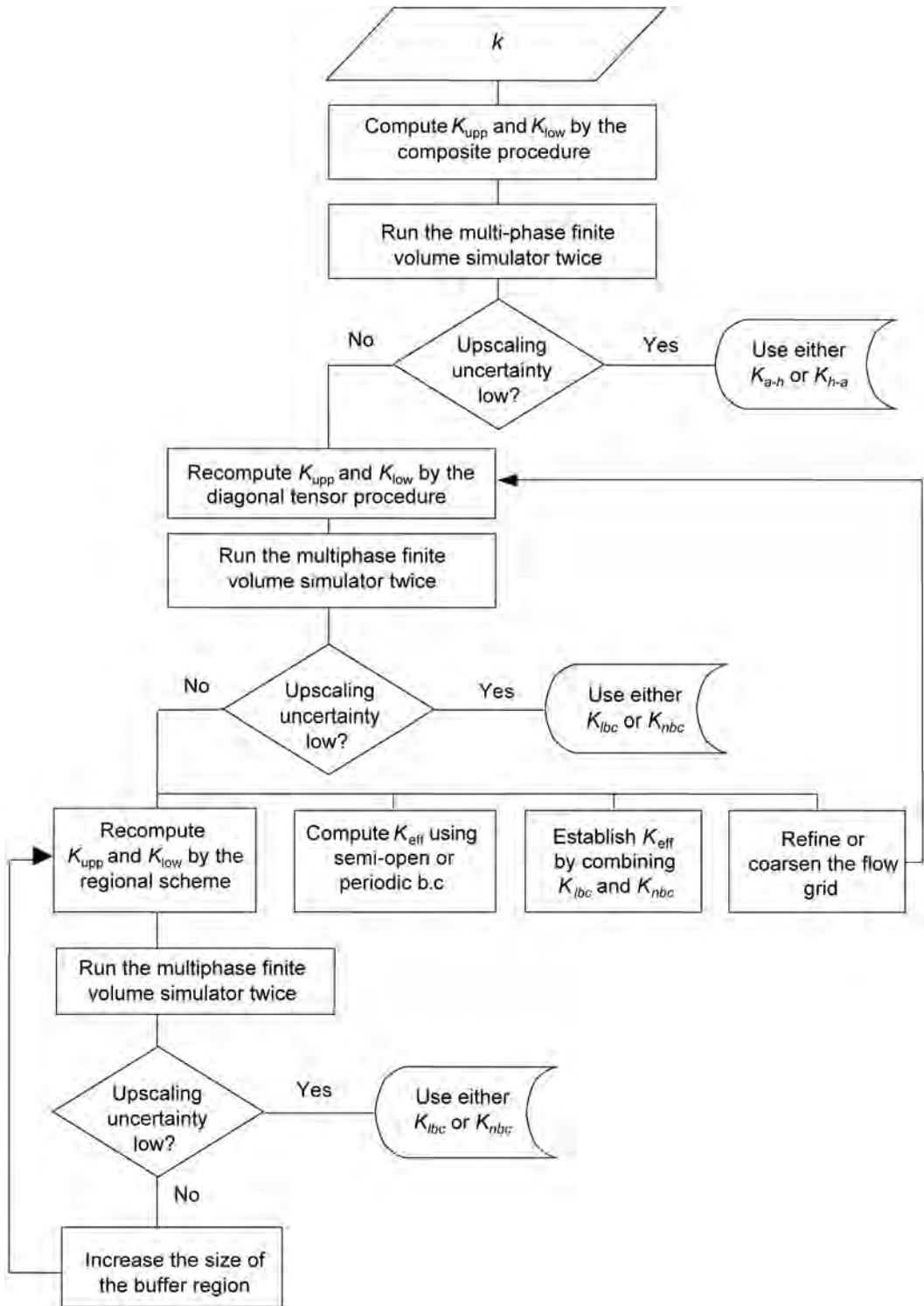


Fig. 17.30—Flow chart for the relative upscaling approach.

17.5 Streamline Simulation—Rod P. Batycky and Marco R. Thiele

17.5.1 Introduction. Streamline-based flow simulation differentiates itself from cell-based simulation techniques such as finite-differences and finite-elements in that phase saturations and components are transported along a flow-based grid defined by streamlines (or streamtubes) rather than moved from cell-to-cell. This difference allows streamlines to be extremely efficient in solving large, heterogeneous models if key assumptions in the formulation are met by the physical system being simulated (see below). Specifically, large relates to the number of active grid cells.

Streamlines represent a snapshot of the instantaneous flow field and thereby produce data such as drainage/irrigation regions associated with producing/injecting wells and flow rate allocation between injector/producer pairs that are not easily determined by other simulation techniques. The computational speed and novel solution data available have made streamlines an important, complementary approach to traditional simulation approaches to perform sensitivity runs, quantify the impact of upscaling algorithms used to move models from the geomodeling scale to the simulation scale, visualize the flow field, perform more reliable full-field simulations where sector models would normally be used, enable the ranking of predicted field behavior of given multiple production scenarios and input parameters, evaluate the efficiency of injectors and producers, reduce turnaround time in history matching, and perform other established reservoir engineering tasks. A comprehensive overview on streamline-based flow simulation has recently been presented by Thiele.⁸²

17.5.2 Applicability of Streamline Simulation. The power of streamline simulation lies in its simplicity. The main objective is to capture how injected reservoir volumes (usually water and/or gas) displace resident reservoir volumes given well locations, well rates, reservoir geometry, and geological description. One of the key underlying assumptions in streamline simulation is that the system be close to incompressibility. This decouples saturations from the underlying pressure field and allows each streamline to be treated as being independent from the streamlines next to it.

Many fields under waterflooding or other pressure maintenance schemes are excellent candidates for streamline modeling and have been successfully modeled in this way.^{83,84} Forecast simulations under the assumption of voidage replacement are another good example where streamlines can be very effective. Even miscible gas injection schemes have been successfully modeled.^{85,86} At high pressures, the displacement of resident oil by gas is primarily an issue of simulating local sweep efficiency and channeling, something streamlines are designed to model without incurring numerical difficulties associated with other formulations.⁸⁷ An early application to streamdrive projects was presented by Emanuel.⁸⁸ Crane and Blunt⁸⁹ used streamlines to model solute transport. More recently, streamlines have been shown to be very effective in modeling fractured reservoirs using a dual porosity formulation.⁹⁰

17.5.3 Historical. Streamlines have been in the petroleum literature as early as Muskat and Wyckoff's 1934 paper.⁹¹ In 1937, Muskat presented the governing analytical solutions for the stream function and the potential function for 2D domains using the assumption of incompressible flow.⁹² Since then, streamlines and streamtubes have received repeated attention as a way to numerically predict the movement of fluids, even after the advent of finite-difference methods in the early 1960s. Important early contributions were made by Fay and Pratts,⁹³ Higgins and Leighton,^{94,95} Bommer and Schechter,⁹⁶ Martin and Wegner,⁹⁷ Lake *et al.*,⁹⁸ and Emanuel *et al.*⁹⁹

In the early 1990s, streamlines were revived because advances in geological modeling techniques were producing models that were too large for finite differences to simulate in an acceptable time frame. For streamlines to be applicable to real field cases, important advances

were made that extended streamlines to 3D using a time-of-flight variable^{87,100–103} allowed for streamlines to be periodically updated^{87,104,105} and included gravity.¹⁰⁶

17.5.4 Mathematics of the Streamline Method. The streamline method and the underlying mathematics for incompressible multiphase flow are briefly outlined here. For a detailed discussion as well as additional references describing streamline methods, see Batycky *et al.*,⁸⁷ Batycky,¹⁰³ and Blunt *et al.*¹⁰⁷

Governing IMPES Equations. The streamline method is an IMPES-type formulation with the pressure field solved for implicitly and the oil/gas/water saturations solved for explicitly along streamlines. The governing equation for pressure, P , for multiphase incompressible flow without capillary or diffusion effects is given by

$$\nabla \cdot \sum_{j=1}^{n_p} \frac{\vec{k} k_{rj}}{\mu_j} (\nabla \cdot P + \rho_j \vec{g} D) = 0, \dots\dots\dots (17.19)$$

where D is the depth below datum, g is gravitational acceleration constant, k is the permeability tensor, k_{rj} is the relative permeability, μ_j is viscosity, and ρ_j is the phase density of phase j . The total velocity, \vec{u}_T , is derived from the 3D solution to the pressure equation and application of Darcy’s law. The explicit material-balance equation for each incompressible phase j is then given by

$$\phi \frac{\partial S_j}{\partial t} + \vec{u}_T \cdot \nabla f_j + \nabla \cdot \vec{G}_j = 0. \dots\dots\dots (17.20)$$

Each phase fractional flow, f_j , is given by

$$f_j = \frac{k_{rj}}{\mu_j} \frac{1}{\sum_{j=1}^{n_p} k_{rj} / \mu_j}, \dots\dots\dots (17.21)$$

and the phase velocity resulting from gravity effects because of phase density differences is given by

$$\vec{G}_j = \vec{k} \cdot g f_j \nabla D \sum_{i=1}^{n_p} k_{ri} (\rho_i - \rho_j) / \mu_i. \dots\dots\dots (17.22)$$

The difference between finite-difference simulation and streamline simulation is the way the explicit material balance equations (Eqs. 17.20 through 17.22) are solved. In finite difference, the material balance equations are solved between gridblocks, whereas in streamline simulation the material balance equations are solved along streamlines. How this is done is explained next.

Solution to the Transport Equation. In a standard finite-difference method, Eq. 17.20 is discretized and solved on the underlying grid on which the pressure field is computed. The solution to Eq. 17.20 is governed by the grid CFL condition, which can lead to prohibitively small timestep sizes, particularly for models with high permeability contrasts and/or high local flow velocities. With streamlines, this grid CFL limit is avoided completely by solving Eq. 17.20 along each streamline using a time-of-flight (TOF) coordinate transform.¹⁰⁶

Streamlines are traced from sources to sinks based on the underlying total velocity field. As each streamline is traced, compute the TOF along the streamline, which is defined as

$$\tau = \int_0^s \frac{\phi(\delta)}{|\vec{u}_t(\delta)|} d\delta \dots\dots\dots (17.23)$$

and leads to the definition

$$|\vec{u}_t| \frac{\partial}{\partial \delta} \equiv \vec{u}_t \cdot \nabla = \phi \frac{\partial}{\partial \tau} \dots\dots\dots (17.24)$$

Using Eq. 17.19, rewrite Eq. 17.20 as

$$\frac{\partial S_j}{\partial t} + \frac{\partial f_j}{\partial \tau} + \frac{1}{\phi} \nabla \cdot \vec{G}_j = 0 \dots\dots\dots (17.25)$$

Because the gravity term is not aligned along a streamline direction, Eq. 17.25 is split into two parts (operator splitting), giving two 1D equations. The convective portion of the material-balance equation along streamlines is given by

$$\frac{\partial S_j^c}{\partial t} + \frac{\partial f_j}{\partial \tau} = 0, \dots\dots\dots (17.26)$$

while the portion resulting from phase-density differences solved along gravity lines is given by

$$\frac{\partial S_j^g}{\partial t} + \frac{1}{\phi} \nabla \cdot \vec{G}_j = 0 \dots\dots\dots (17.27)$$

Both Eqs. 17.26 and 17.27 represent 1D equations that are solved using standard finite-difference numerical techniques. There are still CFL limits that restrict timestep sizes in these equations, but these are local to each streamline or gravity line, rather than at the 3D grid level.

Timestepping. In field-scale displacements, the streamline paths change with time because of the changing fluid distributions and the changing well conditions. As a result, the total velocity field is periodically updated, and new streamlines are recomputed to reflect the nonlinear nature of the displacement.

To move the 3D saturation distribution forward in time between successive streamline distributions from time T_i to $T_{i+1} = T_i + dT_i$, the algorithm pictured in Fig. 17.31 is used.

The basic algorithm for streamline-based flow simulation is as follows: (1) Given initial conditions (i.e., pressures and saturations for each active cell in the system) and well conditions, the pressure is solved implicitly for each cell, as is done in conventional finite-difference methods (Eq. 17.19). (2) With the pressures known, the total velocity for each cell interface can be determined using Darcy’s Law. The total velocity is then used to trace streamlines using Pollock’s algorithm.¹⁰⁰ (3) 1D mass conservation equations are then solved along each streamline, independently of each other (Eq. 17.26). The initial conditions for the streamlines are obtained by a mapping from the underlying 3D grid onto each streamline. The mass-transport problem is marched forward in time along each streamline for a pre-specified global timestep dT_i , and then the solution is mapped back onto the 3D grid. Gravity is included by

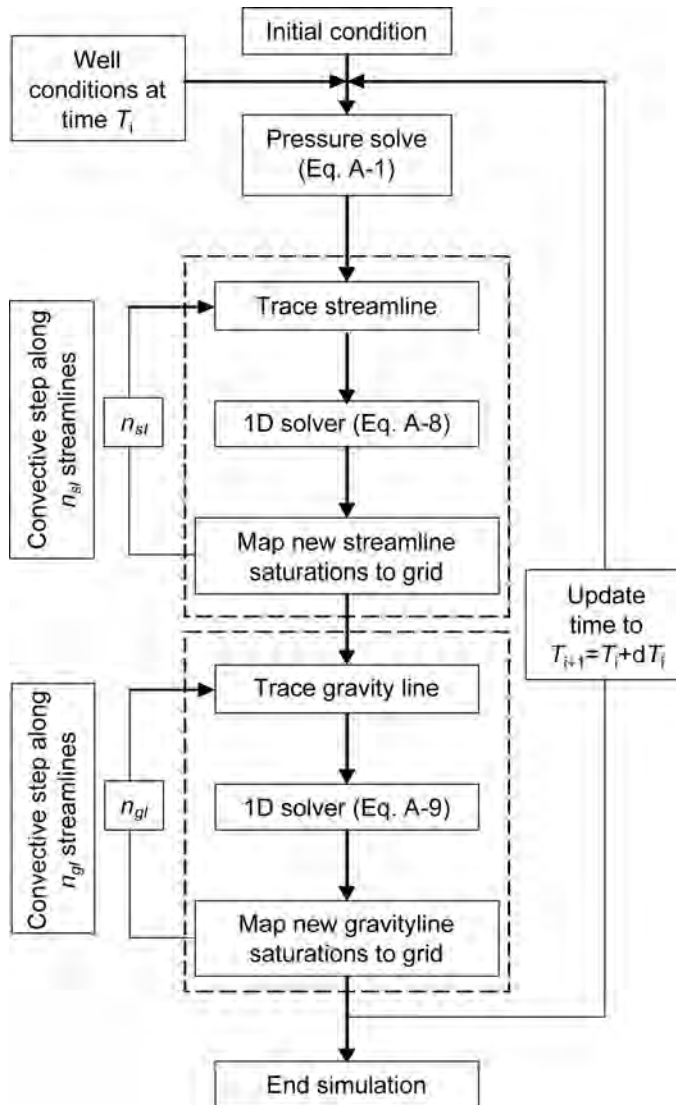


Fig. 17.31—Flow chart showing the basic algorithm for streamline-based flow simulation.

considering a vertical segregation step along gravity lines after movement along all streamlines (Eq. 17.27). While simple in its approach, important details must be considered. In particular:

1. The algorithm is similar to an IMPES approach, in that the pressure is solved implicitly for a new time level $n+1$ assuming saturations at level n . The saturations at time n are given by mapping back solutions from each streamline onto the 3D grid at the previous timestep. Because of the implicit nature of the pressure solution, there is no limitation on the timestep to reach $n+1$. However, for compressible systems numerical convergence problems might limit the actual size of the timestep. This is no different than in FD simulation.

2. The tracing of the streamlines using Pollock's algorithm assumes Cartesian cells. Nonorthogonal corner-point cells require an isoparametric transformation for tracing streamlines.¹⁰⁸

3. For incompressible systems, streamline will start at injection wells and end at production wells. For compressible systems, streamline can start/end anywhere in the system, because any

gridblock in the system might act as a source (volume expansion) or a sink (volume contraction). Multiphase gravity effects can give rise to circulation cells for both incompressible and compressible systems.

4. Initial launching of streamlines from wells can be proportional to the total flux at the wells, though this will in general leave many cells in the system without a streamline passing through them. For missed cells, tracing begins at the center of the missed cell and then traced backward until a source is encountered. If a cell does not have a streamline pass through it, then it is not possible to assign an updated saturation back to that cell.

5. In practice, it is not possible to have all streamlines carry the same flux and ensure at least one streamline per cell. Thus, streamlines do not carry the same flux. Furthermore, for incompressible problems the flux along each streamline is a constant, while for compressible systems it is not.

6. The tracing of streamlines using the TOF variable produces a highly irregular 1D grid along each streamline. To numerically solve the 1D problem efficiently, the 1D grid must be regularized, solved using an implicit approach, or regridded in some way to allow for a more efficient solution.

7. The tracing of the streamlines relies on an accurate solution of the velocity field. Excessive distortions of the grid (nonorthogonal) or a pressure solution that has not been solved to a small enough tolerance can cause problems in tracing streamline paths.

17.5.5 The Computational Efficiency of Streamlines. One advantage of streamline simulation over more traditional approaches is its inherent efficiency, both in terms of memory and computational speed. Specifically, streamline-based simulation can exhibit a near-linear scaling in run times as a function of active cells in the model. Memory efficiency is a result of two key aspects of the formula: streamline-based simulation is an IMPES-type method and therefore involves only the implicit solution of pressure, and tracing of streamlines and solution of the relevant transport problem along each streamline is done sequentially. Only one streamline needs to be kept in memory at any given time.

Computational speed, on the other hand, is achieved because the transport problem is decoupled from the 3D grid and instead solved along each streamline. Because transport along streamlines is 1D, they can be solved efficiently. Because the number of streamlines increases linearly with the number of active cells, and streamlines only need to be updated infrequently, the computational time exhibits a near-linear scaling with increasing number of gridblocks

The number of global timesteps is related to how often the flow field (streamlines) requires updating. Specifically, changing flow paths are a function of heterogeneity, mobility changes, gravity, and changing well conditions. For many practical problems, it is the changing well rates that introduced the greatest impact on a changing flow field and is therefore the limiting factor in deciding on global timestep sizes. Grouping well events into semiyearly or yearly intervals and assuming that the streamlines remain unchanged over each period is reasonable. This is why field simulations with 30- to 40-year histories are successfully and routinely simulated with 1-year timesteps.⁸⁴

A good example to demonstrate the efficiency of SL simulation is Model 2 of the 10th SPE comparative solution project.¹² The total run time, T , of any streamline simulation is approximately proportional to

$$T \propto \sum_1^{n_{ts}} \left(t^{\text{solver}} + \sum_1^{n_{sl}} t_j^{sl} \right), \text{ where}$$

n_{ts} number of timesteps (number of streamline updates)
 t^{solver} time required to solve for the global pressure field ($Ax = b$) at each timestep
 n_{sl} number of streamlines at each timestep
 t_j^{sl} time to solve transport equation for each streamline (17.28)

A near-linear scaling arises because:

1. The number of timesteps (streamline updates) is independent of the model size, heterogeneity, and any other geometrical description of the 3D model. It is mainly a function of the number of well events and the actual displacement physics. For the SPE10 problem in [Fig. 17.32](#), all cases were run with the exact same number of streamline updates—24.
2. An efficient pressure solver is expected to have a near-linear behavior as well.¹⁰⁹
3. The number of streamlines tends to increase linearly with the number of gridblocks, all else being equal. [Fig. 17.32](#) illustrates this behavior.
4. The time to solve the transport problem along each streamline can be made efficient by regularizing the underlying TOF grid and choosing the number of nodes to use along each streamline regardless of the size of the underlying 3D grid.

The linear behavior with model size is the main reason why streamline simulation is so useful in modeling large systems. In FDs, finer models not only cause smaller timesteps because of smaller gridblocks but usually face problems because of increased heterogeneity as finer models tend to have wider permeability and porosity distributions. The usual workaround is to use an implicit or adaptive-implicit formulation, but for large problems these solutions can become prohibitively expensive, both in terms of CPU time and memory.

17.5.6 Novel Data Produced by Streamlines. Streamlines produce new data not available with conventional simulators. Because streamlines start at a source and end in a sink, it is possible to determine which injectors are (or which part of an aquifer is) supporting a particular producer, and exactly by how much. A high water cut in a producing well can therefore be traced back to specific injection wells or boundaries with water influx. Conversely, it is possible to determine just how much volume from a particular injection well is contributing to the producers it is supporting—particularly valuable information when trying to balance patterns ([Fig. 17.33](#)) or optimize water injection over a field.

Streamlines can also identify the reservoir volume associated with any well in the system, because a block traversed by a streamline attached to a particular well will belong to that well's drainage volume. It is therefore possible to divide the reservoir into dynamically defined drainage zones attached to wells ([Fig. 17.33](#)). Properties normally associated with reservoir volumes can now be expressed on a per-well basis, such as oil in place, water in place, and average pressure, just to mention a few.

The most successful uses of new data produced by streamlines are in the area of waterflood management and reservoir surveillance,^{110,111} and in the area of history matching.^{112–115}

17.5.7 Applications of Streamlines. Streamlines are a powerful complementary tool to more traditional simulation techniques, and they are expected to play an important part in optimizing field production and management in the future. Specifically, streamlines can be used to:

1. Validate upscaling techniques by allowing to generate reference solutions of fine-scale models.⁸¹
2. Efficiently perform parametric studies.

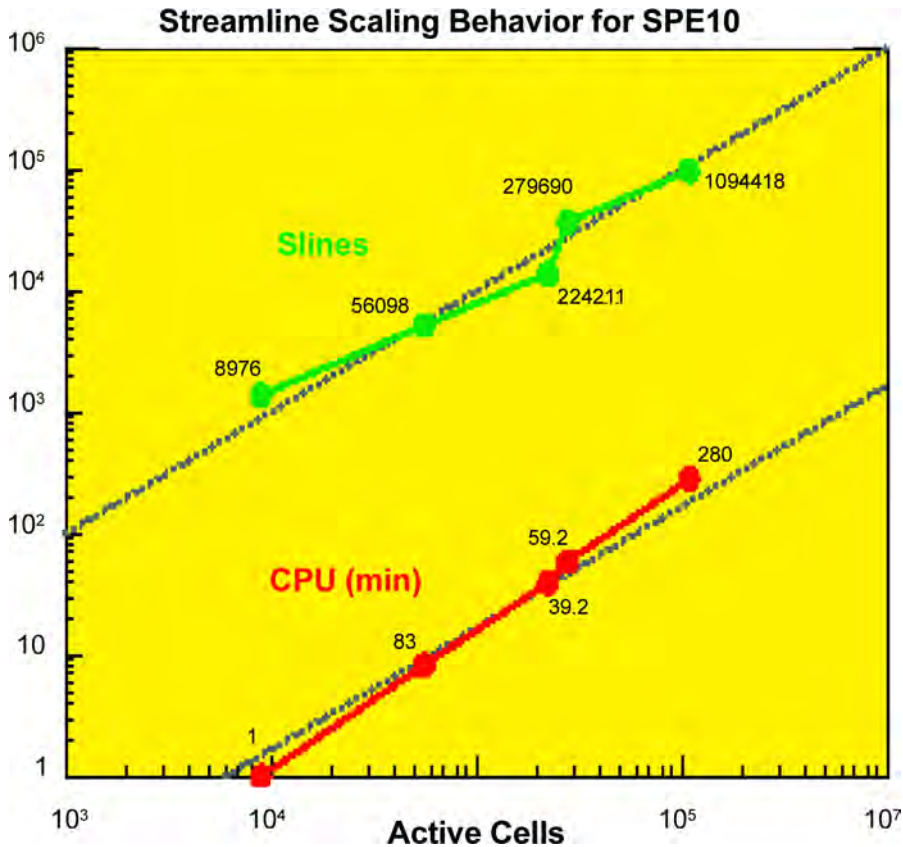


Fig. 17.32—Example of linear scaling of run time and number of streamlines as a function of active cells for SPE Comparative Solution Project 10 using 3DSL, a commercial streamline simulator, on a PIII 866MHz PC.

3. Visualize flow.
4. Balance patterns.
5. Determine efficiency of injectors and producers using data provided by streamlines.
6. Aid in history matching.
7. Enable ranking of production scenarios/geological models.
8. Optimize and manage field injection/production.
9. Conduct reservoir surveillance.

It is important to underline that the theory on which streamline simulation rests is firmly rooted in the incompressible formulation of exact voidage replacement. Thus, streamline simulation is particularly powerful for modeling systems that are not a strong function of absolute pressure, but are instead governed by a pressure gradient. In addition, the strong assumptions of independence between streamlines favors modeling displacements that are not a strong function of diffusive phenomena, such as capillary pressure, transverse diffusion, or compressibility. For example, streamline simulation offers little or no advantage over conventional simulation for modeling primary production. This is because the main feature of modeling primary production is to accurately capture the pressure decline over time, not the movement of a saturation front.

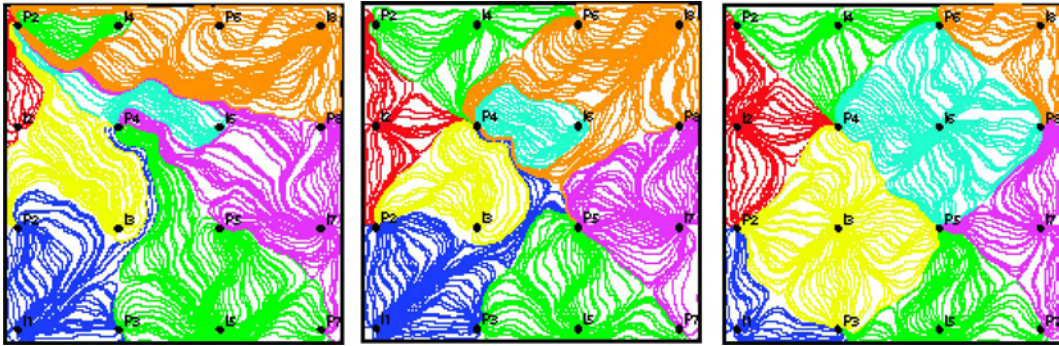


Fig. 17.33—Streamlines automatically allow the determination of the allocation of flow between wells by summing the flux of all streamlines associated with a particular well, well pair, or group of wells. Using this information and the visual display of streamlines allows patterns to be balanced correctly and efficiently. From left to right: rates are progressively changed to yield a balanced pattern.

17.5.8 The Future of Streamline Simulation. The next few years are expected to bring a further maturing and extended application of streamline-based flow-simulation technology. It is reasonable to expect that most companies using conventional simulation technology today will in one form or another use SL simulation in their future work. What remains uncertain is whether new user groups, such as geologists and geophysicists, will adopt the technology to bring a dynamic flow component to their analysis. Developments in the following areas are currently under way: the use of streamlines in conditioning static reservoir models to production data, extension of streamline simulation to compositional models, tracing of streamlines in structurally complex reservoirs, modeling of dual-porosity/dual-permeability models, and parallelization of streamline numerics for the solution of large models.

17.6 Simulation of Geomechanics—Tony Settari

Historically, much of the simulation has accounted for rock mechanics by simple use of a time-invariant rock compressibility c_R , spatially constant or variable. In reality, rock mechanics is intimately coupled with fluid flow in two aspects. First, the porosity changes are a direct result of the deformation of the skeleton, which is a complex function of both pressure and stress (effective stress state). Second, it is well known that the permeability of the media is also a function of effective stresses in the reservoir. Therefore, rigorous reservoir simulation should include simultaneous solution of multiphase flow and stresses as well as the appropriate dependencies between these processes. While these couplings physically exist to some extent in all reservoirs, they can be often ignored or approximated when the reservoir behaves elastically. However, the changes in porosity and permeability are more pronounced when rock failure occurs, such as in compacting reservoirs or in high-pressure injection operations, and these processes require use of more complex, coupled geomechanical modeling.

17.6.1 Types of Coupling. There are essentially two main types of coupling between reservoir flow and stress: pore-volume coupling and flow-properties coupling. In the past, the first led to the development of various simplified “compaction” modeling techniques, while the latter is reflected in the “pressure-dependent permeability” options available in many simulators. In a coupled geomechanical model, both can be treated more rigorously.

Pore-Volume Coupling. The porosity in the reservoir model is traditionally treated as a function of pressure via rock compressibility:

$$\phi = f(p) = \phi^0 [1 + c_R(p - p^0)], \dots\dots\dots (17.29)$$

and changes in block pore volume V_p are computed as $V_p = V_b^0 \phi$, where V_b^0 is the block (bulk) volume. In reality, pore volume changes are a result of complex interaction of fluid (pore) pressure, stresses acting on the element of the rock and temperature. The deformation of the rock solid (also called the skeleton) caused by combination of stress and pressure changes results in changes in the bulk volume of an element V_b , which is computed at any conditions as

$$V_b = V_b^0(1 - \varepsilon_v), \dots\dots\dots (17.30)$$

where ε_v is the volumetric strain at these conditions, and V_b^0 is the bulk volume at reference conditions at which the volumetric strain = 0. Then the true porosity is given by

$$\phi = V_p / V_b, \dots\dots\dots (17.31)$$

where V_p is the pore volume of the element. In Eq. 17.31, both pore volume and bulk volume are variable; therefore, true porosity and pore volumes are both functions of pressure, temperature and stress:

$$\phi = V_p / V_b = f(p, T, \sigma), V_p = g(p, T, \sigma), \dots\dots\dots (17.32)$$

which shows the coupling between fluid flow and geomechanics (stress modeling).

In stress modeling, the changes in volumetric strain and porosity are calculated from complex constitutive relations of the material, which define both the stress-strain and volumetric behavior.^{116,117} To compute pressure changes correctly in the reservoir simulator, it is necessary to force the changes in pore volume to be the same as computed by the stress model, which is the essence of the “volume coupling.” This can be achieved in two ways. The rigorous solution is for the reservoir model to recalculate the block sizes based on the stress solution, and use the true porosity. However, reservoir simulators do not allow for modifying the bulk volume. In this case, one can define a pseudoporosity $\phi^* = V_p / V_b^0$, which will give the correct pore volume.¹¹⁸ In either case, the usual treatment of porosity by rock compressibility must be replaced by the coupling with stress-strain solution. The porosity changes become more complex when failure of the skeleton is reached either in compression (rock compaction) or in shear.

Flow-Properties Coupling. The primary mechanism is the dependence of permeability on stress, usually of the form

$$k = f(\sigma_{\text{eff}}) = f(\sigma_{\text{avg}} - p), \sigma_{\text{avg}} = (\sigma_x + \sigma_y + \sigma_z) / 3. \dots\dots\dots (17.33)$$

This relationship is well established for many types of reservoirs¹¹⁹ and generally becomes stronger as permeability decreases. It is dominant (and more complex) in fractured reservoirs where stress-dependent fracture aperture and reopening/creating fractures under injection can cause large, anisotropic changes. The tensor character of permeability may be important in these applications. In soft formations and unconsolidated sands, deformations can lead to porosity dilation, which will also lead to permeability enhancement. On reloading, there is a hysteretic effect. Two to three orders of magnitude enhancements in permeability can occur because of injection at fracture pressure (e.g., in microfractured rock¹²⁰ or coal seams).

The permeability changes are a function of some measure of effective stress, but are often simplified (and laboratory data reported) as a function of pressure. The creation of new fractures can cause a transition from initially single-porosity media to dual-porosity, and in such a case will also have an effect on relative permeabilities.

17.6.2 Modeling of Reservoir Compaction and/or Dilation. Modeling reservoir deformation is of considerable importance in soft and/or thick reservoirs where the results of compaction may provide an important production mechanism, cause well failures, and/or cause ground subsidence or heave with environmental consequences. Review of the compaction mechanics and its consequences for field development is found in Ref. 121. Initial approach to modeling compaction was based on modifications of reservoir models.^{122–125} The common feature of such reservoir compaction models is that the compaction is treated as a 1D problem (uniaxial strain) by assuming that (a) only vertical deformations take place, and (b) each vertical column of blocks deforms independently. In such models, the porosity changes are calculated by modifying the conventional compressibility c_R as a function of pressure only, in the form of “compaction tables.” The tables are based on results of uniaxial strain laboratory experiments, and the stress problem is not solved. The compaction of the reservoir is then obtained analytically assuming uniaxial deformation. The relation between reservoir compaction and surface subsidence can be then obtained by an independent solution of a stress problem using the computed compaction as a boundary condition. Dilation (increase of porosity) is an important geomechanical mechanism occurring during steam injection into unconsolidated sands. This process has been also modeled by the “compaction-dilation” tables.¹²⁶ In chalk reservoirs, increased water saturation in waterflooding causes weakening of the rock and therefore S_w is an additional variable in Eq. 17.32.¹²⁷

The major drawback of the use of compaction tables is that the dependence on stress indicated in Eq. 17.32 must be either ignored, or the change of stress must be estimated in terms of change in pressure. A more accurate modeling approach is to couple in some fashion the reservoir simulator with stress-strain (geomechanics) solution. Such models typically combine the solution of the multiphase flow in the reservoir and elastoplastic solution of the deformations in a much larger domain including the reservoir, sideburden, underburden, and overburden. The majority of coupled models use the iterative coupling¹²⁸; the different variations and their shortcomings are discussed next.

Coupled models have much larger computing requirements compared with a reservoir model of the same reservoir, primarily for two reasons: first, the larger number of unknowns per gridblock, and second, the stress-solution grid must be usually much larger laterally than the reservoir grid to eliminate the effect of boundary conditions as well as extend up to surface to provide subsidence solution. Combination of these factors leads to computing times typically of one order of magnitude larger compared with conventional simulation, and even more if elastoplastic solution is required for the stresses.

17.6.3 Modeling of Stress-Dependent Flow Properties. The primary flow-dependent property is permeability, and the problems to model its dependency in Eq. 17.33 are similar to modeling the pore-volume coupling (Eq. 17.32). However, the problem is somewhat easier because stress-dependent permeability (or transmissibility) does not affect mass-balance formulation.

Again, the traditional approach is to use tables of k vs. pressure in an uncoupled model. However, the problem remains one of replacing the dependency on effective stress by one on pressure only. Even in a single-phase, single-porosity gas-flow case, different assumptions about the stress change during depletion can lead to large errors in well decline.¹²⁹ Different strategies for converting the stress-dependent data to pressure tables are based on local constraint assumptions.¹³⁰

In coupled models, the permeability dependency can be usually computed explicitly on a timestep basis, and “loose” coupling can be used. In fact, a “coupled” model that deals only with flow properties coupling and ignores the pore-volume coupling can be run successfully even if the stress solution is done in larger intervals of time compared to the reservoir. Such models have been used extensively to study permeability changes in waterfloods, particularly

in fractured or jointed media.^{131,132} Here, the advantage of coupled modeling is in its capability to predict the permeability changes from the geomechanics of reopening of fractures or failure (dilation) of joints.¹³³ The development of anisotropy is dictated by the orientation of fractures or faults, and requires a “full tensor” treatment of transmissibilities in the flow model. In the stress strain model, different methods of pseudoizing the fracture/joint networks into a continuum are used, which include predicting permeability as a function of effective stress and/or strain. While the need for the tensor transmissibilities in such models has been recognized,¹³⁴ in injection processes dual-porosity media can be created. Therefore, reservoir description may be changing in time because of geomechanics; this aspect has been ignored in coupled models to date.

The same principles can be also applied to model hydraulically induced fractures being represented by dynamically changing transmissibility multipliers in the potential fracture plane.¹³⁵ The effective stress dependency (as opposed to pressure in an uncoupled model) allows capturing the changes of the fracture propagation pressure with time, which can be large, in particular in steam injection. Another application is the prediction of production/injection-induced slippage on faults, which can induce communication between reservoir fault blocks and/or seismicity.

17.6.4 Types of Coupled Models. Coupled models can be either fully coupled (i.e., all unknowns solved simultaneously) or modular (reservoir simulator and stress code). In the latter case, different coupling strategies can be used, with consequences for running speed and accuracy. The majority of coupled models use a conventional finite-difference reservoir simulator coupled with a finite-element (FEM) stress simulator. However, attempts have been made to develop fully coupled FEM codes,¹³⁶ and a fully coupled geomechanics was implemented in a commercial model using a finite-difference stress solution.¹³⁷ Considering the proliferation and sophistication of the geomechanics codes available outside the petroleum engineering, the modular approach offers the best solution.^{119,127} Generally, the reservoir simulator is the “host” or “master.” Commercial stress simulators are, in principle, easy to couple to it (in particular if only permeability coupling is considered).

Because of the extreme complexity and large computing requirements of coupled models, different simplifications have been developed. The main types of models (in the order of increasing rigorosity, but also computing time) are as follows:

One-Way Coupling. Pressure and temperature changes are passed from the reservoir code to the geomechanics module, but no information is passed back on timestep basis. The geomechanics does not improve the flow solution, but the model can be useful for predictions of wellbore stability for infill drilling, fracturing pressures, and so on. Manual adjustment of “compaction tables” is possible manually through restarts. Such manually coupled solutions¹³⁸ of the stress problem (at intervals of time) or one-way coupling¹³⁹ were often used in early coupled modeling. The method can be satisfactory when the reservoir fluid system is highly compressible (i.e., in gas reservoirs), but can lead to errors when the porosity is strongly coupled to flow.

Loose Coupling. Reservoir and geomechanics modules are run sequentially on a timestep basis, passing converged solutions of flow and stress variables to each other. Pore volumes and permeabilities in the flow model are computed as a function of p , T , and σ_{avg} with stress variables lagged a timestep. However, the relationships are “distilled” into tables similar to the “compaction tables,” but now a function of effective stress. The advantages are functional similarity to the uncoupled reservoirs with “compaction tables,” no need for iteration during timestep, and the possibility of updating the stress solution less frequently than the reservoir solution. However, complex constitutive models of the solid (e.g., plasticity) may be difficult to represent.

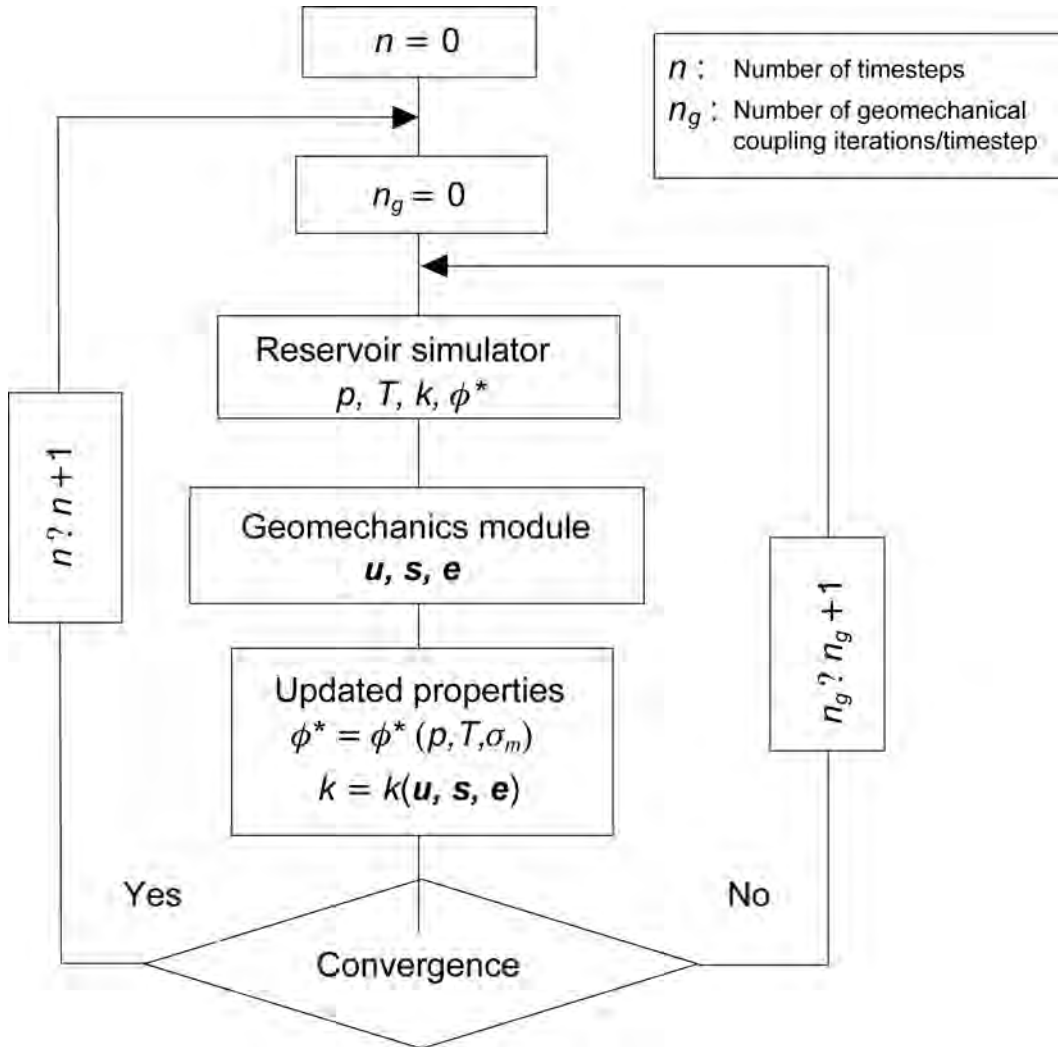


Fig. 17.34—Schematic of the iterative coupling algorithm.

Iterative Coupling. This method is shown schematically in Fig. 17.34. Iteration is carried out between the reservoir and stress solution at every timestep until the pore volumes and permeabilities calculated from the stress model and those used by the reservoir model agree. In each iteration, the previous guess of the V_p^{n+1} for the end of the timestep is used to converge the flow solution, and the changes of p and T over timestep are then used to solve for the new deformations and stresses, which in turn provide updated estimate of V_p^{n+1} . The changes of permeability are also iterated on. Therefore, each “geomechanical” iteration costs the equivalent of a timestep solution of the previous methods. The original formulation of the coupling iteration¹²⁸ is always convergent, and its efficiency has been recently improved.¹⁴⁰

The iterative coupling, when converged, is equivalent to a fully coupled code while it retains flexibility. In many problems, it is not necessary to fully converge the timestep, and if used with only one iteration per timestep, the method is similar to the loose coupling, except that the porosity is determined directly by the constitutive model of the solid rather than by a simplified relationship.

Full Coupling. This requires simultaneous formulation of the flow and stress variables and therefore results in larger matrices. The advantage is that consistent approach to discretization can be used, and the model is integrated from the point of view of code development. However, it is very costly to redevelop all the features of the physics and numerics now readily available in stress codes. Moreover, in published fully coupled models, the approach for solving the resulting matrix problem has been to partition the matrix in the same fashion as in the iterative coupling¹⁴¹ and to apply the geomechanical iteration at the matrix-solution level. Therefore, the fully coupled formulation, which results in larger, strongly nonlinear matrix equations, does not reduce the difficulty of the problem, and it may need to use geomechanical iteration in the solution process as the best strategy. These aspects need further study.

17.6.5 Future Trends and Needs. As a result of much larger computing requirements, coupled models lag behind conventional models in the size of the problems that can be currently handled. Therefore, they are a prime candidate for the use of massively parallel hardware and will require large future development effort in parallelization. Because of the increased understanding of the complexities of the geomechanics, the current trend is also toward more strongly coupled models with fewer simplifications. This further increases the computing requirements.

Given that not all problems require use of geomechanics, and the cost of the study may increase dramatically, it is important to be able to identify when coupled simulation is needed, and what approximations can be made without compromising the answers. There are no simple rules, but there is a growing need to conduct a “screening” process at an early stage of a reservoir study to determine if geomechanics is an issue. This process requires an integration of reservoir, production, and completion engineering data as well as field experience.

Finally, coupled geomechanical modeling is the future tool for truly integrated reservoir management. Conventional reservoir simulation studies ignore numerous constraints placed on the development scenarios from the point of view of drilling, completion, and operations. These constraints can be incorporated into coupled models, and additional modules can be integrated (e.g., long-term wellbore stability and sand production predictions, subsidence management, 4D seismic interpretation, and so on¹⁴²).

17.7 Pressure/Volume/Temperature (PVT) Treatment—Curtis H. Whitson

The PVT treatment of fluids in reservoir simulation describes the phase behavior of gas, oil, and water at reservoir and surface conditions. Phase behavior of a mixture with known composition consists of defining the number of phases, phase amounts, phase compositions, phase properties (molecular weight, density, and viscosity), and the interfacial tension between phases. In addition to defining the phase behavior of mixtures at a specific reservoir pressure, knowing the derivatives of all phase properties with respect to pressure and composition is important in reservoir simulation.

The calculation of phase behavior in a reservoir model can be made in one of two ways—using a “black-oil” approach^{22,143–146} based on simple interpolation of PVT properties as a function of pressure, or using a “compositional” approach based on a thermodynamically-consistent model such as a cubic EOS.^{14,15,22} With either approach, the PVT quantities required by a reservoir simulator are essentially the same. Modern reservoir simulators^{14,22} are usually written with a general compositional formulation, whereas black-oil PVT properties are converted internally to a two-component “compositional” model; the two components are surface gas and surface oil.

A reservoir simulator keeps track of overall composition in each computational grid cell as a function of time. A grid cell’s overall composition changes because of cell-to-cell fluxes and because of production or injection in wells. The phase fluxes and component movement within the reservoir are greatly affected by phase behavior (e.g., the mobility of each phase and which

components are carried in each phase). The surface products from wells are dependent on the phase behavior of produced wellstreams, but at conditions far removed from reservoir pressure and temperature.

In most reservoir simulators, the water phase and water component are treated in a simplified manner—namely, that the water component does not partition into the hydrocarbon phases, and the hydrocarbon components do not partition into the water phase; the term “hydrocarbon” also includes N_2 , CO_2 , and H_2S . Because of relatively high CO_2 solubility in water, and the potential importance of CO_2 “accounting” in CO_2 floods, some compositional models allow CO_2 partitioning in the water phase.¹⁴⁷

Conceptually and computationally, it is feasible to allow complete partitioning of all components in all phases in reservoir simulation. The partitioning related to the water phase and the water component could be treated with simple pressure-dependent tables, or even with an EOS model. The water-related K -values have simple composition dependence that would make EOS-based fugacity updates almost trivial. The main problem would be treating the impact of changing salinity on water-related K -values. From a practical point of view, however, modeling water-related component partitioning will have a marginal impact on reservoir performance. Hereafter, only phase behavior of nonaqueous phases will be discussed.

17.7.1 Number of Phases and Phase Type. The starting point for PVT calculations in a model grid cell is to determine if the overall composition is single-phase or two-phase at the current pressure estimate. If a cell is single-phase, the phase “type” (gas or oil) may also be needed to select the proper relative permeability and capillary pressure curves. For a black-oil PVT model (i.e., any model with simple pressure-dependent K -values), determining the number of phases and phase identification is trivial.

For EOS models, two methods can be used for establishing how many phases exist: the Michelsen¹⁴⁸ phase stability test or a saturation pressure calculation.¹⁴⁸ The stability test is relatively “slow” because good K -value estimates are not used to initiate the calculation, whereas a saturation pressure can be quite fast because good K -value estimates are often available. A stability test is more reliable in the sense of giving a conclusive result, whereas a near-critical saturation pressure test may not be found¹⁴⁹ or converge correctly to a nontrivial solution. Another advantage of using saturation pressure is that it gives a consistent method to define phase type for single-phase cells, something that is not provided by the stability test. The choice of which method to use depends on the tradeoff between speed and reliability. Both methods, if detecting two phases, give excellent starting K -values to initiate the two-phase flash calculation.

17.7.2 Two-Phase Flash. Having established that two phases exist in a cell, one must perform a flash calculation. The flash calculation uses the overall moles n and molar composition z_i to determine the molar amounts of each phase (n_g and n_o), and the phase compositions (y_i and x_i). For simple pressure-dependent K -value models, the Rachford-Rice^{150,151} (RR) procedure is used to find molar amounts and compositions,

$$\sum_{i=1}^N (y_i - x_i) = \sum_{i=1}^N \frac{z_i(K_i - 1)}{1 + \alpha_g(K_i - 1)} = 0, \dots\dots\dots (17.34)$$

solving for $\alpha_g = n_g / (n_g + n_o)$, with $x_i = z_i / [1 + \alpha_g(K_i - 1)]$ and $y_i = K_i x_i$.¹⁵²

For an EOS model, using the RR solution can be used, but an additional constraint must be satisfied; the fugacity of each component must be the same in each phase,¹⁵³ $f_{gi} = f_{oi}$. Using an initial set of K_i estimates, the RR equation is solved. Resulting compositions y and x are then used to calculate fugacities f_{gi} and f_{oi} . If the constraint $f_{gi} = f_{oi}$ is not satisfied for all compo-

nents, a new set of K -values is estimated using some form of a successive substitution (SS) update $K_{\text{new}} = K_{\text{old}}(f_{oi} / f_{gi})$.

For reservoir simulation, a Newton solution of the flash equation should be much faster than SS methods. Including the equal-fugacity constraint within the set of nonlinear equations used to solve for model pressures “automatically” provides the first Newton update of the flash equation.¹⁵³ Usually only one additional Newton iteration of the flash equation is needed to converge the fugacity constraints to required tolerance.

In summary, K -values alone determine the phase amounts and phase compositions (from the Rachford-Rice equation). The EOS model guarantees rigorous thermodynamic consistency through the equal-fugacity constraint, ensuring that K -values properly account for pressure and composition dependence of the phase split and component partitioning.

Having completed the flash calculation in a cell, the following information is known: phase moles, phase masses, phase densities, phase volumes (saturations), and phase compositions. The viscosity and gas/oil IFT can be calculated using compositional correlations,¹⁵² or interpolated from pressure-dependent tables for a black-oil model. The impact of PVT properties on reservoir performance will consider individual PVT properties and their impact on individual terms in the flow equations.

17.7.3 Density. Phase molar amounts, n_g and n_o , are converted to phase volumes using phase molecular weights and densities: $V_g = n_g M_g / \rho_g$ and $V_o = n_o M_o / \rho_o$, where $S_g = V_g / V_{\text{block}}$ and $S_o = V_o / V_{\text{block}}$. Saturations determine relative permeabilities, which can have a dramatic impact on phase fluxes. Typically, $k_r \sim S^n$, where $n \sim 2$ to 4. For $n = 3$, a 5% error in density results in a 15% error in k_r .

For reservoirs with sufficiently high vertical permeability, gravity will often play an important role in recovery. Gravity segregation is caused by vertical fluxes driven by the potential terms $\nabla \rho_g = d(p_g + \rho_g g z + P_{cgo}) / dz$, $\nabla \rho_o = d(p_o + \rho_o g z) / dz$, and $\nabla \rho_w = d(p_w + \rho_w g z + P_{cwo}) / dz$. Errors in densities have a direct impact on gravity segregation. It is actually the density difference between flowing phases that determines the magnitude of gravity segregation (i.e., $\Delta \rho_{wo} = \rho_w - \rho_o$, $\Delta \rho_{go} = \rho_o - \rho_g$, and $\Delta \rho_{wg} = \rho_w - \rho_g$). Likewise, the condition for equilibrium initialization $\nabla \rho_g = \nabla \rho_o = \nabla \rho_w = 0$ results in saturation-depth distributions, which must honor input $\Delta \rho_{go} g = P_{cgo}(S_g)$ and $\Delta \rho_{wo} g = P_{cwo}(S_w)$ relationships.

A +5% error in oil density (e.g., 630 instead of 600 kg/m³) and a -5% in gas density (e.g., 380 instead of 400 kg/m³) results in gravity segregation potential ($\Delta \rho_{go} = \rho_o - \rho_g$) in error by 25% (250 instead of 200 kg/m³). Similarly, in the initialization of a water/oil system, the inadvertent use of $\rho_w = 62.5$ lbm/ft³ instead of the correct value of 70.0 lbm/ft³ for a high-salinity brine could easily cause a 25% error in initial oil in place for a low-permeability (large capillary transition zone), low-API oil.

In black-oil models, it is particularly easy to model densities incorrectly because of the inadvertent use of “arbitrary” surface densities. The reservoir phase densities are not input directly in a black-oil model. Instead, they are calculated using the formation volume factors (FVF) B_o , B_g , and B_w , solution gas/oil and oil/gas ratios R_s and r_s , and surface densities ρ_{gs} , ρ_{os} , and ρ_{ws} , based on the relations $\rho_g = (\rho_{gs} + \rho_{os} r_s) / B_g$, $\rho_o = (\rho_{os} + R_s \rho_{gs}) / B_o$, and $\rho_w = \rho_{ws} / B_w$. Because reservoir densities are not usually tabulated as output by reservoir simulators, the user may not know how “wrong” the densities might be.

A well-tuned EOS using volume shift factors¹⁵⁴ should always predict reservoir and surface densities within 2 to 4%, and often within 1 to 2%. The author’s experience has found it generally unnecessary to use different volume shift factors for reservoir and surface calculations unless all densities are needed with accuracies of 1 to 2%. The use of either Peng-Robinson¹⁵⁵ or Soave-Redlich-Kwong¹⁵⁶ EOS with volume-shift factors provides densities as good or better than the more-complicated ZJRK¹⁵⁷ EOS model; in this author’s opinion, the ZJRK no longer

has a role in reservoir simulation, as supported by decreasing industrial use (almost to nonexistent) during the past 5 years.

17.7.4 Component Partitioning. The partitioning of components in gas and oil phases, as dictated by K -values, is important for properly describing vaporization and condensation. Vaporization is the process of “stock-tank oil” (STO) components (C_{6+}) moving from the oil phase to the gas phase, while condensation is the process of intermediate (C_3 – C_{10+}) components moving from the gas phase to the oil phase. Retrograde condensation is particularly important in the depletion of gas condensate reservoirs, where in-situ retrograde condensation results in decreasing surface liquid yields.^{22,152,158}

For most gas-injection projects, vaporization will play an important role. Proper modeling of vaporization usually requires a compositional model that uses a detailed description of the heavier (C_{7+}) components, typically three to five fractions.^{22,159,160} The lightest fractions (C_7 to C_{12}) will typically vaporize 80 to 100%, while intermediate heavies (C_{13} to C_{20}) may vaporize in varying amounts from 30 to 90%, and the heaviest components C_{20+} may vaporize from 0 to 50%. The degree of vaporization depends primarily on the local pressure and composition of displacing gas. Cook *et al.*¹⁴⁴ suggested a modification of the black-oil model that allows saturated properties to change as a function of how much injection gas has contacted a given cell, thereby allowing reasonable description of a vaporization-dominated process. Tang and Zick¹⁶¹ propose a limited three-component compositional model that allows accurate description of developed miscibility for use in models in which grid-related dispersion may result in underpredicted conditions of miscibility using an EOS-based simulator.

In some gas-injection processes, the injection gas may be enriched (1) during injection by adding NGLs (C_3 to C_5 components) and/or (2) within the reservoir by multiple contacts with reservoir oil, which gradually enriches the injection gas with intermediate components C_3 through C_{10} . For either type of enrichment, the vaporization process can become extremely efficient and result in a near-miscible or miscible displacement with near-100% recovery of the oil. When such a displacement results, it is often associated with the development of a complex process whereby the near-miscible front consists of upstream vaporization and downstream condensation—the “condensing/vaporizing” gas drive mechanism first described by Zick.¹⁶²

For an EOS model to properly describe complex phase behavior related to vaporization, condensation, and near-miscible mechanisms, special PVT experimental data should be measured and used to tune the EOS. For immiscible processes with significant vaporization, a single-cell multicontact PVT test is useful, quantifying the degree of vaporization in terms of oil volumetric stripping and gas compositional changes. For near-miscible or miscible processes, a swelling-type test which has the following features is strongly recommended: (1) five to seven mixtures of reservoir oil and injection gas are used, with two to three mixtures being bubble-points and two to three mixtures being dewpoints; (2) a constant composition expansion is conducted on each mixture, where saturation pressure and the oil relative volumes are measured and reported; and (3) a single equilibrium “flash” somewhat near the critical point is used for obtaining a set of equilibrium gas and oil compositions (K -values).

Proper EOS tuning of the complex phase behavior measured in such an experiment is difficult, and requires the ability to match near-critical volumetric and compositional changes. Such predictions are almost never available *a priori* with an EOS model that has been tuned only to simple depletion data. Small but important modifications of the heavy-end properties and binary interaction parameters are usually required to obtain a satisfactory match of near-critical PVT data provided by this special “swelling” test. A tuned EOS model that is able to match all PVT data, including near-critical phase behavior, has a good chance of properly predicting true multicontact near-miscible/miscible behavior.^{152,162}

17.7.5 Viscosity. Gas viscosities are typically estimated by correlation¹⁵² within 5 to 10%, and they are almost never measured experimentally. Such accuracy is adequate for most applications, and gas viscosities seldom vary beyond the range of 0.02 to 0.03 cp. For gas-injection processes at high pressure or near-miscible displacements, gas viscosities can range from 0.03 to 0.1 cp. Gas-viscosity correlations are not usually accurate for this higher range of viscosity, and errors up to 20 to 30% may be expected; compositional viscosity correlations also have the same level of accuracy.

Oil viscosities are notoriously inaccurate based on correlations,¹⁵² at best being within 10 to 30%, but often in error by 50% or more. Oil viscosities should always be measured and used to tune a viscosity model. A minimum requirement would be measurement of stock-tank oil viscosities, and normally live-oil viscosities are available from a differential liberation test.

For gas condensates, oil viscosities are almost never measured. This may be a serious problem if condensate blockage has a significant impact on well deliverability.¹⁶³ Condensate viscosities are difficult to measure because retrograde condensate volumes can be very small. The use of a separator condensate sample is recommended. Bring it to reservoir conditions (T and P) for density and viscosity measurements, then tune the viscosity model to these data. This approach is feasible for any gas condensate; it is not expensive, and it is better than relying on untuned compositional viscosity correlations.

Our experience has been that the compositional viscosity correlation by Lorenz, Bray, and Clark¹⁶⁴ (LBC) is not predictive, and it is highly dependent on accurate density predictions. Tuning the heavy-component critical volumes and, sometimes, careful modification of the higher-order constants in the LBC equation, provide the required accuracy for gas and oil viscosities in most reservoir processes. Unfortunately, modification of the LBC correlation to match a limited number of viscosities (in a narrow range of pressure and composition typical of depletion experiments) can lead to unphysical viscosity predictions at conditions developed during a gas injection process.

The Pedersen *et al.*¹⁶⁵ compositional viscosity correlation, though more complicated and CPU-intensive than the LBC correlation, has quite good predictive capabilities. The correlation is based on a corresponding states formulation in which methane viscosity is the reference compound.

17.7.6 Gas/Oil Interfacial Tension (IFT). Gas/oil IFTs may be used in a reservoir simulator¹³ to modify input capillary pressures P_{cgo} , relative permeabilities k_{rog} and k_{rg} , and residual oil saturation S_{org} . As IFT decreases, P_{cgo} decreases proportionately. Relative permeabilities and residual oil saturation change only marginally until IFT reaches a fairly low value (e.g., 1 mN/m), whereas at lower IFTs, the relative permeability-related properties change approximately as $\log(\text{IFT})$.

Practically, IFT impact on capillary pressure is limited to fractured reservoirs¹⁶⁶ in which displacement efficiencies may be strongly linked to the balance of gravity and capillary forces on a relatively small distance scale (e.g., block heights of 1 to 10 m).

IFT impact on relative permeabilities and residual saturations may have an impact on some gas-injection processes, though near-miscible and miscible processes have minimal IFT dependence because they are usually dominated by the strong compositional effects (vaporization and condensation) that result in near-100% recoveries. In fact, displacements that are miscible should, by definition, be independent of the relative permeabilities and residual oil saturation.

IFT impact on near-well relative permeabilities in gas condensate reservoirs can, together with high velocities, result in large capillary numbers, which have the tendency to “straighten” relative permeabilities and improve flow performance. It has been shown^{167,168} in a number of recent publications that this effect can have an important impact on gas-condensate well deliv-

erabilities. Neglecting IFT and velocity dependencies of relative permeability can lead to overly conservative prediction of well deliverability (i.e., overprediction of condensate blockage).

17.7.7 Black-Oil PVT Models. Black-oil PVT properties are generated in one of two ways. For low- to medium-GOR oils ($< 150 \text{ Sm}^3/\text{Sm}^3$), a traditional differential liberation experiment (DLE) is used, with corrections for separator flash to calculate oil FVF B_o and solution GOR R_s , as well as the gas FVF B_g .¹⁵² This approach assumes the reservoir gas contains unsubstantial amounts of condensate in solution, with solution oil/gas ratio $r_s \sim 0$.

The more common and general approach to generating black-oil PVT properties uses an EOS model to simulate a depletion-type PVT experiment (differential liberation, constant volume depletion, or constant composition expansion), with the equilibrium gas and equilibrium oil at each stage in the depletion being individually processed to surface conditions to provide the four black-oil properties B_o , R_s , B_g , and r_s .^{22,156} For highly volatile oils, the EOS method gives substantially different and improved black-oil properties compared with the traditional laboratory DLE/separator-corrected approach.

The conversion of black-oil PVT data (R_s , B_o , r_s , and B_g) to a compositional model¹⁴⁴ uses K -values of surface gas and oil pseudo “components” $K_{gs} = (R_s + C_{os}) / (1 + r_s C_{os}) / R_s$ and $K_{os} = r_s(R_s + C_{os}) / (1 + r_s C_{os})$, with $C_{os} = (RT_{sc} / p_{sc})(\rho_{os} / M_{os})$. The reservoir-phase densities are calculated from $\rho_g = (\rho_{gs} + \rho_{os} r_s) / B_g$ and $\rho_o = (\rho_{os} + R_s \rho_{gs}) / B_o$, while phase molecular weights are given by $M_g = (M_{gs} + r_s M_{os} C_{os}) / (1 + r_s C_{os})$ and $M_o = (R_s M_{gs} + M_{os} C_{os}) / (R_s + C_{os})$. Viscosities and gas/oil IFTs are interpolated directly from input tables.

Coats *et al.*,²² Coats *et al.*,¹⁴³ and Fevang *et al.*¹⁴⁵ have shown that black-oil models can be used for practically any type of reservoir produced by depletion or waterflooding, including reservoirs with large compositional gradients. Some issues require special treatment for complex fluids systems, including fluid initialization and the method for generating black-oil tables. In a nutshell, the recommended procedures¹⁴⁵ are to generate the black-oil tables with an EOS model using the fluids with the highest saturation pressure (e.g., at the gas/oil contact) and to initialize with solution GOR (R_s and r_s) vs. depth—not saturation pressure vs. depth.

A common problem with black-oil models is the calculation of “negative compressibility,”²³ meaning that a small pressure drop results in a reduction in total (gas + oil) volume. Another problem is physical extrapolation of saturated PVT properties to saturation pressures higher than given in the input table (e.g., caused by gas injection, gravity segregation in undersaturated reservoirs, or near-well behavior during rate reductions).

When can the black-oil PVT treatment not be used? Basically, for any gas-injection process with significant component partitioning that changes during the displacement.^{145,159} This would include processes with high-pressure vaporization using lean gas, condensation from enriched injection gas, and developed-miscibility processes such as the condensing/vaporizing mechanism. Surprisingly, a black-oil treatment is sometimes adequate even for complex gas injection problems, though it is not usually known *a priori*. To check the validity of a black-oil model in a gas injection project, the reservoir process should first be simulated with a compositional model, and preferably a relevant 3D model that captures all important flow characteristics.

17.7.8 Equation-of-State Models. The most common EOS used in reservoir simulation are the PR and the SRK models. Both models have two constants, a and b . Each constant must be calculated for each component based on component critical properties (T_c and p_c) and acentric factor (ω).

The PR EOS has two versions—the original 1976 version¹⁵⁵ and the modified 1979 version¹⁶⁹; the latter uses a third-degree polynomial expression for the correction term to constant a . For some systems, the difference in equilibrium calculations for the two PR EOS models is significant.

The Peneloux¹⁵⁴ volume shift factors should always be used with two-constant EOS models to ensure accurate oil and gas densities. The volume shift factors have no impact on calculated K -values or compositions, only densities. As mentioned earlier, the ZJRK¹⁵⁷ EOS is outdated and was used before the volume-shift method was introduced in 1980, with complex correction functions to constants a and b to improve liquid density predictions.

Binary interaction parameters (BIPs) k_{ij} are important for adjusting predictions of equilibrium properties (K -values and compositions).¹⁷⁰ These parameters represent a correction of the form $(1 - k_{ij})$ to the $a_i a_j$ term in the quadratic mixing rule for EOS constant a . BIPs can be positive or negative; they are symmetric ($k_{ij} = k_{ji}$); they are usually ~ 0 for most hydrocarbon-hydrocarbon pairs, except C_1 to C_{7+} pairs which may reach values as high as 0.25; and they are generally close to 0.1 for nonhydrocarbon (N_2 , CO_2 , H_2S)-hydrocarbon pairs.

17.7.9 Three-Phase PVT Behavior. Three-phase (L1-L2-V) behavior is an occasional but serious problem for EOS-based compositional models. The third phase (L2) is usually a light liquid and typically appears at low temperatures ($< 140^\circ F$) in gas-injection processes using CO_2 or NGL-enriched gas.¹⁷¹ Physically, three phases may actually exist, and the EOS model is correctly predicting the behavior. Sometimes a three-phase system is predicted without one physically existing; this may result for lower temperatures when the heaviest component properties are improperly modified to fit two-phase gas/oil PVT data.

For reservoir simulators, the three-phase problem is caused by the EOS formulation “allowing” only two phases. If three phases actually exist, the two-phase flash may find any of the three possible two-phase combinations: L1-V, L2-V, or L1-L2. These false two-phase solutions may indicate a single-phase condition, or they may actually appear as a valid solution (meeting the equal fugacity constraints). Unfortunately, the reservoir model, in a given cell during a given timestep, may flip-flop between two of the possible solutions, resulting in unstable behavior because the pressure solution is not continuous from one two-phase solution to the other. Models may have to simply give up because of repeated timestep reductions, which result from the inadequacy of the EOS two-phase model handling a three-phase condition.¹⁷²

17.7.10 Surface Phase Behavior. In compositional simulation, the surface calculations are usually made using multistage separation with an EOS model, with fixed K -values for each separator, or using so-called “gas plant” factors, which define the fraction of a wellstream component that is processed into the stock-tank oil.

For black-oil models, the surface separation is “built in” to the PVT tables. Consequently, if the surface process changes during a model run, all black-oil PVT tables must be reentered at the appropriate time. This also requires that vertical flow performance (VFP) tables be reentered because surface rate and volume ratio nodes change with the process change.

It is difficult to use traditional black-oil models for fields with various well groups that have significantly different processing facilities.¹⁴³

17.7.11 Thermal Model PVT Requirements. Additional PVT requirements for thermal processes such as steamflooding include quantifying the temperature dependence of K -values, densities, and viscosities. Water-phase behavior of liquid and steam must also be defined in terms of pressure and temperature. Water-hydrocarbon phase behavior is still assumed to be simple, without water/hydrocarbon component partitioning.

An EOS model can be tuned to distillation data for improving the predictive capabilities of K -value dependence; otherwise, a simple correlation of the form $K_i = a_i \exp(-b_i T) / p$ may be used for distillable components.¹⁷³ Using distillation data is an indirect approach to defining K -value behavior, and it is used in lieu of high-temperature gas/oil/water phase-behavior experiments, which are not usually available. Oil viscosities in thermal processes may be difficult to correlate with a compositional correlation, so empirical correlations may be used instead.

17.7.12 Fluid Initialization. As with rock and other petrophysical properties such as permeability and porosity, a reservoir simulator model must also initialize the spatial distribution of initial fluids. For an EOS-based model, the initial molar compositions are defined, $z_i(x,y,z)$. For a black-oil model, the initial solution gas-oil ratio R_s and solution oil-gas ratio r_s ratio are defined, $R_s(x,y,z)$ and $r_s(x,y,z)$; sometimes saturation pressures are used instead, $p_b(x,y,z)$ and $p_d(x,y,z)$, but this is not recommended.²⁶ Specifying a saturated gas-oil contact (GOC) is also a means to initialize fluids vertically in a reservoir simulator, where solution GOR R_s (and bubblepoint) are assumed constant below the GOC, while solution OGR r_s decreases upwards from the GOC to honor the model-imposed assumption that reservoir pressure equals dewpoint pressure, $p(z) = p_d(z)$.

Another fluid initialization data might include temperature $T(x,y,z)$. Some black-oil models allow spatial variation of stock-tank oil density, $\gamma_{API}(x,y,z)$, where black-oil properties are correlated in multidimensional tables as a function of pressure and γ_{API} . Across barriers such as faults and sealing shales, discrete PVT model data may be defined, such as EOS parameters or black-oil tables; such “discontinuous” fluid descriptions may cause physical and model incompatibilities if fluids mix in the reservoir or at the surface.

A typical problem with initialization is that the specified fluid distribution, initial pressure specifications, and fluid contacts lead to fluid movement when the model is turned on (without production or injection). Initial fluid movement may be unimportant without significantly changing the user-specified fluid system; serious inconsistencies may lead to time-zero flow that has an impact on model performance.

17.8 High-Performance Computing and Reservoir Simulation—John E. Killough

The motivation for high-performance computing in reservoir simulation has always existed. From the earliest simulation models, computing resources have been severely taxed simply because the level of complexity desired by the engineer almost always exceeded the speed and memory of the hardware. The high-speed vector processors such as the Cray of the late 1970s and early 1980s led to orders-of-magnitude improvement in speed of computation and led to production models of several hundred thousand cells. The relief brought by these models, unfortunately, was short-lived. The desire for increased physics of compositional modeling and the introduction of geostatistically/structurally based geological models led to increases in computational complexity even beyond the large-scale models of the vector processors. Tens of millions of cells with complete reservoir parameters now became available for use by the engineer. Although upscaling provided a tool to dramatically reduce model sizes, the inherent assumptions of the upscaling techniques left a strong desire by the engineer to incorporate all of the available data in studies. The only available solution to this problem became the subdivision of the model into small segments and the use of parallel computers for reservoir simulation. The recent introduction of fast, low-cost commodity hardware based on the INTEL architecture has led to a revolution in higher-performance computing based on clusters.

17.8.1 The Explosion of Data and the Chasm of Scale. From the earliest reservoir simulation models of the 1960s with only a few tens of finite-difference cells, reservoir simulation had progressed by several orders of magnitude in the early 1990s to hundreds of thousands of cells. Unfortunately, these fine-scale models still were far from the scale of the data. This chasm of scale was further exacerbated by the introduction of geocellular models with geostatistically derived attributes. With these geostatistically based models, it was possible to generate geological descriptions for the reservoir simulation with literally tens of millions of finite-difference cells. Although upscaling offered some relief to this problem, the resultant assumptions required often left the engineer wondering how far from reality the resultant solutions had been driven. If the additional degree of freedom of uncertainty of the reservoir data is added to this

problem, then the number and size of simulations becomes unlimited. This implies that the need for further improvements in high-performance computing will always exist for reservoir simulation. Parallel computing offers one approach to overcome the problem of the explosion of information through the use of fine-scale models with limited or no upscaling.

17.8.2 Characteristics of High-Performance Computing. The basis of high-performance computing is the use of specialized hardware to achieve computational speeds that are much faster than conventional computers. This idea of “speedup” is encapsulated in what is known as Amdahl’s Law:

$$\text{Speedup} = 1 / (\text{scalar} + \text{special} / n),$$

where “scalar” is the fraction of the program which is scalar and “special” is the fraction of computations performed on specialized hardware (one minus scalar). Simply stated, Amdahl’s law indicates that if there is a piece of specialized hardware that is n times faster than the scalar processor(s) in a computer or group of computers, it must be used a large fraction of the time to have a significant impact on overall performance. The earlier supercomputers primarily used specialized hardware known as vector processors for the speedup. More recently, parallel computers based on connecting tens to hundreds of processors have formed the basis of high-performance computers. The importance of the serial or single-processor computer cannot be overemphasized, however. The introduction of the reduced instruction set computer (RISC) with “superscalar” performance in 1990 spelled the end of the dominance of the Cray supercomputer in the high-performance reservoir-simulation market because of a rapid decrease in the price/performance of the new hardware. Similarly, the recent introduction of low-cost, commodity hardware based on the INTEL chipset has led to significant improvements in price/performance. The application of this hardware to reservoir simulation has been a natural evolution in the application of the lowest-cost, highest-performance computers to reservoir simulation.

17.8.3 The Parallel Reservoir Simulator. The earlier high-performance computing hardware such as the Cray Computer required that modifications be made to the reservoir simulator programs to efficiently use the hardware.^{174,175} The modifications known as vectorization led to different approaches in the data organization. One of the best examples of this is given in Refs. 176 and 177, in which a compositional model’s data structure is reorganized so that like phases in the finite-difference gridblocks of the reservoir are grouped. The notion behind parallel reservoir simulation is similar; however, in this case, the reservoir grid is subdivided into 3D blocks or domains. The computational work for each of the domains is then performed in parallel by a separate CPU of one of the computers in the parallel hardware. Profiles of computing workload for a typical reservoir simulation model often show tens, if not hundreds, of subroutines that are involved in a substantial portion of the calculations. Because of this, major reprogramming of reservoir simulation models is required to achieve high parallel efficiencies. As Ref. 178 points out, there are numerous obstacles to parallelization for reservoir simulation: recursive nature of the linear equation solver, load imbalance caused by reservoir heterogeneity and/or physics, and diverse data structure of well and facility management routines.

Several papers^{179–189} discuss techniques that have been used to bring about efficient parallel reservoir simulations. Each of these addresses the solutions to parallelization and, in particular, the obstacles mentioned previously in various ways. One of these simulators uses local grid refinement for parallelization.¹⁷⁹ The main concept of parallelization with local grid refinement (LGR) is that LGR is not necessarily used to add additional cells to the model but simply to facilitate the subdivision of the grid. With LGR, the same simulation program can be used to perform simulations either serially on a single processor or in parallel on multiple processors

The A_i blocks are ordered first and represent the red grids or domains, while the B_i blocks are the black grids and are ordered second. The diagonals of the B_i submatrices are modified from the original coefficients to maintain rowsum constraints (see Ref. 190). This approximate factorization leads to independent solutions on each processor for the first the red A_i and then followed by the black B_i grid matrices. For the block Jacobi approach, only a single color exists, and all grids at a given level are solved independently. As described in Ref. 179, parallelization of this preconditioning can be achieved in a manner almost identical to the technique used for the coefficient routines. Ref. 47 provides detail of a similar parallel solver developed independently, but almost simultaneously, by Burrows, Ponting, and Wood. As described previously, each grid is assigned to a processor. These may be the same or different processors. If all active grids lie on the same level, the composite grid solver performs all red or black preconditioning solutions independently [i.e., either block Jacobi (all red) or red-black orderings are used]. If grids are assigned to different levels, each grid of the same level and same color (Jacobi being all red) is solved simultaneously, with communication being performed after the entire solution of all grids on a level is completed. Factorization is performed so that rowsum constraints are also imposed. The flexibility of this solver allows the easy implementation of block red-black algorithms, or, as a special case, a red-black linear decomposition (“strip”) decomposition could be used.

17.8.5 Parallel Computers and Message-Passing Interface. With the rapid changes in technology for parallel computing, it is difficult to provide the state-of-the-art because this appears to change daily; however, current classification practice divides parallel computers into two distinct categories: shared and distributed memory. Shared-memory systems allow all of the memory associated with the parallel computer to be accessed by all of the processors. For UNIX systems, the memory sizes currently can range up to several tens of billion of bytes with hundreds of processors. For systems based on PC products, the shared-memory systems usually are limited to a few billion bytes of storage and fewer than 10 processors. (This may change with the recently introduced 64-bit processor Itanium.) The distributed memory systems allow access to local memory only by a small number of processors that reside on a “node” of the parallel system. Each of the “nodes” in the distributed memory parallel system often communicates with other nodes by a high-speed switch, although conventional ethernet communications are possible for some applications. Either of these parallel computers is capable of delivering several hundred million floating point operations per second (MFLOPS) for each node, or several billions of floating point operations per second (GFLOPS) for applications that can use the parallel hardware. Parallel PC hardware can be further subdivided into operating systems: Windows- and LINUX-based systems. Current trends indicated that it is likely that the Windows-based systems will dominate the engineer’s desktop because of the wide availability of engineering/business applications available for this operating system. LINUX-based systems will likely be limited to clusters of servers to perform computer-intensive work such as parallel simulations.

To perform calculations in parallel, data must be passed in the form of messages among processors of the parallel machine. Message-passing interface (MPI) has been primarily used for parallelization on all classifications of parallel machines because of the wide availability and portability of MPI. For shared-memory computers (Sun and SGI for example), other forms of message passing exist such as the recently popular OpenMP. There are generally three forms of message passing for a distributed memory system: synchronous, asynchronous, and global operations. Synchronous message passing requires that all messages be completed before computations can proceed. Asynchronous, on the other hand, allows some overlap of processing and communications. Global message-passing operations distribute data from single processors to one processor, or vice-versa. Often some form of arithmetic function, such as

summation, is performed as part of the global concatenation operation. These functions are particularly useful for evaluation of reduction functions such as dot products, or for distribution of data from a single node to all nodes in the parallel partition. Global communications are normally optimized for a particular architecture and are much more efficient than a simple set of send-receive operations for achieving the same results.

17.8.6 Application of Parallel Computing. The rationalization of parallel reservoir simulation is based on two concepts: the ability to run larger models, or simply the ability to improve turnaround time on existing models. A typical larger-size model would be considered to have more than 1 million gridblocks. Results for a 1-million-cell, black-oil, implicit model show scaling is almost perfect from 1 to 18 processors with only a small degradation up to 36 processors (speedup = 32) on an SGI shared-memory parallel computer. Although this is a somewhat idealized example, it does point out the excellent scaling possible because of low message-passing overhead for a parallel simulator using domain decomposition. Results for a real-world compositional example with 3.4 million cells have been obtained on an IBM SP parallel computer with 108 processors. For this case, with 12 to 27 processors, the problem scales extremely well with a speedup of a factor of 2 for slightly more than doubling the number of processors. The scaling falls off slightly from 27 to 54 processors with only a factor of 1.7, but from 54 to 108 processors, this scaling is maintained at a factor of 1.7. Overall, the speedup from 12 to 108 processors was a very good factor of 5.6. If perfect scaling on 12 processors is assumed, this indicates a factor of 68 overall for 107 processors for a parallel efficiency of approximately 64%. The total elapsed time for the 108 processor case was approximately 12 hours, indicating that overnight turnaround for this 3.4-million-cell model could be achieved. Another example application of parallel simulation with more than 1 million gridblocks was recently presented in a black-oil simulation study of complex water encroachment in a large carbonate reservoir in Saudi Arabia.¹⁸⁹

17.8.7 The Future of High-Performance Reservoir Simulation. It is clear that the uptake of parallel reservoir simulation has been limited by the hurdle of cost and the robustness of the technology. The recent advances in commodity hardware based on the INTEL architecture have provided a significant boost, however. Currently, the use of parallel INTEL-based clusters using inexpensive high-speed switches has lowered the entry point for significant parallel simulation by an order of magnitude. Just as the UNIX workstation caused a revolution in reservoir simulation, this new low-cost hardware will likely bring parallel computing to the engineer's desktop in the near future. The remaining hurdles for parallel simulation then are limited to enhancing parallel simulation technology. In particular, emphasis must be placed on load balancing and efficient linear equation solvers. Load balancing refers to the fact that all processors must perform the same amount of work to achieve high parallel efficiency. If only a few processors perform most of the work for a parallel simulation involving large numbers of processors, then poor parallel efficiency results—a case known as load imbalance. The allocation of optimization techniques to solve the load balancing problem offers some promise.¹⁹¹ An area of particular importance for load balancing is the coupled surface network/reservoir simulator. For this case, the network often dominates the simulation by almost an order of magnitude; therefore, to achieve reasonable parallel efficiency, the imbalance caused by the serial surface network calculations must be overcome. One approach to this is mentioned previously, the parallelization of the tubing hydraulics calculations; however, considerable additional parallelization effort will be required, especially if more than a few processors are to be used efficiently. Load imbalance is also brought about by complex geologies and complex locally refined grids. It is likely that the introduction of unstructured grids and associated load balancing using techniques such as “Hilbert space-filling curves”¹⁹² may well lead to the solution of this problem. Finally, the linear equation solver as the heart of the parallel simulator must be enhanced to

provide efficient and robust solutions. Solver degradation often results from the use of large numbers of domains (processors) or a poor choice of the decomposition geometry.¹⁷⁹ Although the previous examples show good parallel performance, future models with large, implicit systems must be routinely solved on large numbers of processors. Multigrid-like solvers may show the best promise for this improvement.^{183,193}

17.9 Reservoir Simulation Applications—L. Kent Thomas

Reservoir simulation is a widely used tool for making decisions on the development of new fields, the location of infill wells, and the implementation of enhanced recovery projects. It is the focal point of an integrated effort of geosciences, petrophysics, reservoir, production and facilities engineering, computer science, and economics. Geoscientists using seismic, well-log, outcrop analog data and mathematical models are able to develop geological models containing millions of cells. These models characterize complex geological features including faults, pinchouts, shales, and channels. Simulation of the reservoir at the fine geologic scale, however, is usually not undertaken except in limited cases. Generally, the fine-scaled geological model is partially integrated or “upscaled” to a coarse-grid model, which is computationally more tractable. The grid of the upscaled model is designed to capture the principal geological features of the geologic model to simulate the fluid flow. The grid may also be designed to capture the effects of complex wells. In the upscaling process, the laboratory relative-permeability and capillary-pressure functions may be upscaled to “pseudofunctions.” These pseudofunctions attempt to capture fluid-flow behavior that is lost because of the integration of fine-scale geologic features in the upscaling process. Phase-behavior treatment can range from simple black-oil PVT to compositional and thermal processes.

The reservoir simulation model may either be used directly to forecast the performance of a new reservoir or adjusted so that it reasonably models the historical behavior of an existing reservoir and wells. This adjustment process is called history matching. Programs called “pre-processors” and “post-processors” enable the engineer to prepare data, manipulate the model, and view results. Once a history-matched model is obtained, then forecasts are made under a variety of operating conditions. These results are combined together with economic models to enable the engineer to make decisions concerning the operation of the reservoir.

17.9.1 Development of the Geological Model. A sound understanding of the structural elements of the reservoir and the depositional environment under which the sediments were deposited is critical to the development of an accurate geologic model. Today, the geologic model is frequently constructed as a numerical representation of the reservoir and adjacent aquifer and is referred to as a static, or geocellular, model. This model provides the vehicle to capture and combine the seismic structural interpretation and well petrophysical data in a numerically consistent way with known depositional characteristics.^{194,195} Petrophysical properties such as porosity, permeability, and water saturation can be distributed throughout the interwell 3D volume using various techniques, many of which rely on geostatistics.¹⁹⁶ Efforts are also underway to condition these numerical, static models with production¹⁹⁷ and well-test¹⁹⁸ data to further reduce geologic uncertainty. The construction of a geocellular model represents a significant collaborative effort between geoscientists, petrophysicists, and reservoir engineers.

Geocellular models today may consist of over 25 to 50 million cells on large and/or geologically complex reservoirs. The ability to build static geologic models of this magnitude has outstripped the reservoir engineer’s ability to simulate an equal number of cells in a full physics reservoir simulator (and will continue to do so). Classical development geologic efforts have focused on defining and describing the reservoir geology using 2D maps, which depict the most likely interpretation of the depositional environment and the variability of the reservoir parameters between wells. These interpretations have historically been referred to as

“deterministic” reservoir descriptions. With the advent of geocellular models and the application of such technologies as geostatistics, it is now possible for geoscientists to generate multiple reservoir descriptions for the reservoir engineer to simulate. In some cases, one of these descriptions may be selected to represent the “deterministic” model. Regardless if one or several static models are handed over for reservoir simulation, it is generally necessary to reduce the cell count to run the problem with existing reservoir simulators. Significant effort is being spent improving techniques to reduce the number of reservoir cells in the areal and vertical dimension while maintaining the essential geologic character that impacts the recovery process under consideration. This approach is referred to as upscaling, and it will be discussed in greater detail in the following section. To date, the largest reservoir simulators consist of reservoir descriptions of 2 million grid cells and are run using massively parallel processing power.

17.9.2 Upscaling Geological Model to Reservoir Flow Model. Geological models, which contain the complex structural features of large oil and gas reservoirs, commonly have tens of millions of cells. These models, which contain pinchouts, faults, and other significant information including lithology and facies distributions, are upscaled in both the vertical and areal directions to tens or hundreds of thousands of cells for reservoir simulation.¹⁹⁹

Several upscaling methods have been developed over the last several years including analytical techniques, local flow-based methods, and global flow-based methods. Analytical methods use arithmetic, harmonic, power law, and geometric averaging to calculate effective properties for each reservoir model gridblock. Local flow-based methods calculate effective gridblock properties by performing single-phase flow simulations in each direction across the upscaled block.²⁰⁰ The diagonal permeability tensor is calculated by sealing the boundaries perpendicular to the applied pressure gradient. The full-permeability tensor can be calculated in a similar manner by leaving the boundaries normal to the imposed pressure gradient open and applying periodic boundary conditions. Global flow-based methods use pressure gradients across the entire field subject to a specific set of wells to calculate the permeability tensor. Local and global flow-based techniques can be used to compute upscaled transmissibilities directly.

17.9.3 Inclusion of Faults in Reservoir Flow Model. Faults and pinchouts of geological layers are incorporated in geological models to capture the complex geometry of many reservoirs. This information is then upscaled into the reservoir model, and it results in both neighbor and non-neighbor connections across the faults and non-neighbor connections across the pinchouts. In Cartesian coordinates, the trace of a fault may need to be represented by a “stair-stepped” line, while a somewhat better representation of faults can be made with corner-point grids. PEBI grids, which will be discussed subsequently, are best suited to accurately model fault geometry.

Models for calculating the transmissibility across the fault and parallel to the fault have been developed based on fault type, displacement, geochemical deposition, and whether open joints occur along the fault.²⁰¹ In general, transmissibilities across a fault can be at least an order of magnitude lower than those parallel to the fault. Inclusion of this information in a reservoir model is frequently a key parameter in reservoir description.

A recent paper describes the analysis that was performed to calculate fluid flow through conductive faults in the Khafji oil field in the Arabian Gulf.²⁰² Two sandstone reservoirs separated by a thick continuous shale are both connected to the same large aquifer and had the same initial WOC. The top reservoir has edgewater drive, while the deeper reservoir is bottomwater drive. Early water breakthrough in the upper sand was determined to be a function of supplemental water influx from the aquifer of the lower sand through conductive faults.

17.9.4 Development of Pseudofunctions for Multiphase Flow. Pseudorelative permeability curves are developed for upscaled reservoir models to match multiphase fluid flow at the fine-grid level. Several methods for performing these calculations have been presented in the literature.²⁰³ In the “10th SPE Comparative Solution Project: A Comparison of Upscaling Techniques,” the fine-scale geological model was chosen to be sufficiently detailed such that it would be difficult to run the fine grid and use classical pseudoization methods.¹² Several participants, however, used some level of fine-grid simulation to develop pseudorelative permeability curves, with two of the participants adjusting the exponents of the Corey equations to effect a reasonable match. This approach can be done manually or with an automated history-matching algorithm.

17.9.5 Gridding Techniques. The majority of reservoir simulation studies conducted today use Cartesian or corner-point structured grids with some application of local grid refinement to evaluate infill well locations or to more accurately calculate water and/or gas coning in a well. In a structured grid, cell locations are specified using a 3D, i, j, k , indexing system. This allows for ready access either numerically or visually, using pre- and post-processing software, to multilayer well information or data and calculated results at any physical location in the reservoir model.

A more flexible approach for modeling reservoirs with complex geometries that still relies on structured gridding was presented by Jenny *et al.*⁶³ Here, a hexahedral multiblock grid is used which is unstructured globally, but maintains an i, j, k structure on each subgrid.

PEBI grids⁵⁸ are now being used on a limited basis to simulate reservoirs with complex geological features that have been developed with nonconventional wells to maximize recovery.²⁰⁴ These grids are unstructured and are described internally in a simulator with a 1D index, i , that ranges from one to the number of nonzero pore volume cells in a model. Evaluation of simulator input and results relies heavily on pre- and post-processing software that allows the user to visually look at the model and make changes during the history-matching phase of a study.

17.9.6 Simulation of Nonconventional and Intelligent Wells. Nonconventional wells are routinely used to maximize production rates and ultimate recovery in oil and gas reservoirs. Wells in this category include deviated, horizontal, horizontal and vertical multilaterals, and multilateral fishbone designs. This latter well type is especially effective in low-permeability or heavy-oil reservoirs.

Simulation of nonconventional wells can be approached in several ways. First, the productivity of each perforation in a conventional model can be approximated by applying the appropriate skin and Peaceman's equation.²⁰⁵ Second, simulation grids can be constructed that closely follow the well path and allow a more accurate calculation of well rates.²⁰⁶ Another approach, which is quite appealing, is based on a semi-analytical method.²⁰⁷ It results in a good approximation for PIs in nonconventional wells and incorporates the near-wellbore skin because of heterogeneity in this region as well as mechanical skin. This method, which is very efficient, can also include wellbore hydraulic effects.

Nonconventional wells coupled with intelligent completions can be used to improve sweep efficiency and optimize recovery.²⁰⁸ One example of this technology is the use of surface-controlled, downhole-adjustable chokes, which can be used to apply different pressure drawdowns to separate zones along the well. This allows a more uniform inflow in the well and control of early water or gas breakthrough. Real-time measurements of wellbore pressures and temperatures are being made for use in conjunction with PLT tests for inflow performance analysis.

17.9.7 Integrated Reservoir and Surface Facilities Models. Integration of reservoir and surface facilities simulation can result in improved production forecasts and allows optimization of

the surface facilities structure and operating conditions. An integrated reservoir, well flow string, and surface network model of the Prudhoe Bay oil field was built and successfully applied to a facility optimization study.²⁰⁹ Production costs as a result of this effort were reduced by defining the optimum number of separator stages and their connections, and defining the optimum separator operating conditions and by using excess capacity in the Prudhoe Bay facilities to process production from satellite fields. Procedures for the simultaneous solution of the reservoir and surface pipeline network flow equations are described in Refs. 210 and 211.

In the Ekofisk field in the Norwegian sector of the North Sea, integrated reservoir and facilities simulations have been made to optimize throughput in existing surface facilities and to forecast production from planned expansion of current facilities.²¹² This optimization project has resulted in sustained high production of approximately 300,000 STB/D over the last several years. Another important aspect in the management of this field is the inclusion of compaction logic in the model based on both stress and water saturation changes during depletion and waterflooding.²¹³ Treatment of geomechanical effects in stress-sensitive reservoirs has received increased attention throughout the industry in recent years.

17.9.8 Simulation of Multiple Reservoirs. Simulation of multiple fields producing into a common production facility is routinely practiced today to capture the interplay between well deliverability, water and gas injection, operating constraints, and contract rates. In the J-Block area fields, in the U.K. sector of the North Sea, an integrated reservoir study was conducted that included a gas condensate reservoir with gas cycling that was simultaneously modeled with volatile oil reservoirs.²¹⁴ The fields were developed with a single platform and one subsea manifold completion and a combination of vertical and horizontal wells. Four separate PVT regions were used to describe the fluid behavior. The integrated model used in this study results in an efficient reservoir management tool for making development and operating decisions.

Another example of reservoir management of multiple fields with shared facilities is the Gannet cluster, located in the U.K. sector of the North Sea, which connects four fields.²¹⁵ Wells from one of the fields are directly linked to the production platform, and the other three fields are subsea tiebacks to the platform. Three of the four fields are oil fields and the fourth is a gas field. An integrated model was built to simulate the interaction of the subsurface and surface processes. The well-management objective on this project was to maximize hydrocarbon recovery while simultaneously meeting a long-term gas contract.

17.9.9 Use of Larger Models. The maximum practical model size has increased from tens of thousands to hundreds of thousands of cells at essentially a linear rate vs. time during the last decade. This trend has developed as a result of the dramatic increase in computer hardware speed accompanied with larger memory and cache. Both high-speed UNIX workstations and high-end PCs are used for reservoir simulation, with a close race developing between the two platforms in regard to run times. Additional advances in computing speed for megamodels have been achieved using parallel hardware along with the necessary developments in model software, discussed in a previous section. An example application of this technology was recently presented in a simulation study of complex water encroachment in a large carbonate reservoir in Saudi Arabia.¹⁸⁹

17.9.10 History Matching and Production Forecasting. Once a reservoir simulation model has been constructed, the validity of the model is examined by using it to simulate the performance of a field under past operating conditions. This is usually done by specifying historical controlling rates, such as oil rate in an oil reservoir vs. time, and then making a comparison of the nonspecified performance such as GOR, WOR, and reservoir pressure with measured data. If there are significant differences between the calculated performance and the known performance of the well/reservoir system, then adjustments to the reservoir simulation model are

made to reduce this difference. This process is called history matching. These adjustments should be made in a geologically consistent manner.¹⁹⁸ Modification of those parameters that have the highest degree of uncertainty will give the maximum reduction in the error. The history-matching process should be approached in a consistent manner to minimize the effort.²¹⁶ In addition to well rates and bottomhole pressures, and reservoir pressures measured at the time the well is drilled, production logs, long-term pressure gauges, and time-lapse seismic data enable the engineer to better constrain the model during the history-matching process. Time-lapse (4D) seismic^{217,218} is becoming an integral part of the field performance monitoring and history matching. Streamline models together with reservoir simulators^{219,197} can be used to improve the history-matching process, especially in waterflood operations. Tools to assist in the history-matching process consist of the use of parallel computers, sensitivity analysis, and gradient techniques.^{220,221}

Once a history match is obtained, then forecasts of future well/reservoir performance under various operating scenarios are made. Models of multiphase flow in the wellbore and production lines are used to constrain the production rate. These models may include subsea completions²²² with very long gathering lines or complex surface facilities with reinjection of produced fluids.²²³ Because of the uncertainty in the geological and reservoir simulation models for new fields, often multiple forecasts²²³ with different reservoir parameters are made to determine the uncertainty in the forecasts. Multiple history-matched models based on multiple geological models,²²⁴ and experimental design²²⁵ may also be used to characterize the uncertainty in production forecasts.

Nomenclature

- A = a matrix
- B = formation volume factor, reservoir volume/surface volume
- b = right-side vector
- C_{os} = equivalent surface gas volume for a unit volume of surface oil
- d = dimension in direction of flow
- D = depth below datum, ft
- D = future time, time units
- f = fractional flow
- f_i = fugacity of component i
- F = flow rate, volume/time unit
- F, F_i, f_{il} = see Eq. 17.2
- f_g = gas-phase fractional flow, $\lambda_g / (\lambda_g + \lambda_o)$
- $f_g' = \partial f_g / \partial S_g$
- g = acceleration constant (length/length/time) or gas phase, depending on use
- G = phase velocity
- k = permeability, md
- k_{ij} = binary interaction parameters
- k_r = relative permeability, fraction
- K = permeability, md
- K_i = equilibrium constant for component i
- K_r = relative permeability, fraction
- k_{rocw} = relative permeability of oil at S_{wc} , $S_g = 0$, fraction
- k_{rwo} = relative permeability of water at residual oil, fraction
- L = length, feet
- L1 = liquid type 1
- L2 = liquid type 2

- m = density, mass/unit volume
 M = mass, mobility, molecular weight, or preconditioner matrix depending on use
 n = number of components or number of moles
 n_{st} = number of streamlines
 n_{ts} = number of timesteps
 N = number of active gridblocks
 o = oil phase
 p = polynomial
 p_J = phase J pressure, psi
 P = pressure, psi
 P_c = capillary pressure, psi
 $P_{cgo}' = dP_{cgo} / dS_g$
 P_i = vector of primary unknowns for block i
 P_{ii} = i th scalar element of P_i
 q_{ii} = well production rate of component i from block i , volume/time
 q_{lji} = interblock flow rate of component I from block j to block i , volume/time
 q_x = total volumetric flow rate in the x direction, volume/time
 Q = production or injection volume
 r_s = solution gas-condensate ratio, volume/volume
 R_s = solution gas, scf/STB oil or nm^3/nm^3 oil
 S = saturation
 $S_{on} = (1.0 - S_w - S_{orw}) / (1.0 - S_{wc} - S_{orw})$, fraction
 S_{orw} = residual oil saturation after water displacement
 S_{wc} = connate water saturation, fraction
 $S_{wn} = (S_w - S_{wc}) / (1.0 - S_{wc} - S_{orw})$, fraction
 t^{solver} = time to solve for a global pressure field
 t^{st} = time to solve transport equation for each streamline
 T = time, time units or transmissibility, md-ft/cp
 T_{ij} = transmissibility connecting blocks i and j , md-ft/cp
 u = pore velocity, v/ϕ
 u_t = total velocity
 v = Darcy or superficial velocity
 V = vapor phase or volume
 V_p = pore volume, bbl
 w = water phase
 x = an unknown vector or concentration of a component in the liquid phase
 x, y, z = Cartesian coordinates
 x_i = concentration of component i in oil phase
 x_{iJ} = mol fraction of component i in phase J
 y = an unknown vector
 y_i = concentration of component i in the gas phase
 z = gas deviation factor
 z_i = overall mol fraction of component i in a gridblock
 Z = depth to gridblock center, measured positive downward, ft or m
 α = mole fraction vapor phase
 β = see Linear Solver section, Step 6
 γ = phase density expressed as psi/ft or bar/m

- $\delta = \delta X = X^{l+1} - X^l$, where l is the Newton iterate index and X is any quantity
 Δp = pressure difference, psi
 ΔQ = potential difference
 Δt = timestep
 Δt^* = maximum stable IMPES timestep
 $\Delta x, \Delta y, \Delta z$ = gridblock dimensions
 $\Delta Z = Z_j - Z_i$
 θ = dip angle of line joining cell centers, degrees
 λ = phase mobility, k_r / μ
 μ = viscosity, cp
 ρ = density, mass/volume or molar density, mols/volume unless noted otherwise
 Σ = sum
 τ = time-of-flight along a streamline
 ϕ = porosity, fraction
 $\psi = \lambda_o \lambda_g / (\lambda_o + \lambda_g)$
 ω' = acentric factor
 ∇ = potential term
 ∂ = normalized difference parameter

Subscripts

- a = cell designation
 $a-h$ = arithmetic-harmonic average
 ari = arithmetic average
 b = adjacent cell designation
 c = component designation
 eff = effective
 g = gas phase
 h = horizontal
 $h-a$ = harmonic-arithmetic average
 har = harmonic average
 i = component number, index counter, or initial condition
 j = index counter
 J = phase number
 k = index counter
 lbc = linear (open sides) boundary conditions
 low = lower bound
 $nlbc$ = no-flow (sealed sides) boundary conditions
 o = oil phase
 p = phase designation
 pb = periodic boundary conditions
 r = residual
 R = reservoir
 s = surface
 sc = standard conditions
 $true$ = true
 upp = upper bound
 v = vertical
 w = water phase or well
 x = cell designation
 x,y,z = Cartesian x,y,z directions

z_{eff} = effective in z direction

Superscripts

- 0 = reference (in compressibility equation)
- 1 = Newton iterate index
- n = timestep number

References

1. *The Merriam-Webster Dictionary*, New Revised Edition, Merriam-Webster, New York City (2004).
2. Coats, K.H.: "Reservoir Simulation," *Petroleum Engineering Handbook*, H.B. Bradley (ed.), SPE, Richardson, Texas (1987) Chap. 48.
3. Odeh, A.S.: "Comparison of Solutions to a Three-Dimensional Black-Oil Reservoir Simulation Problem," *JPT* (January 1981) 13.
4. Weinstein, H.G., Chappellear, J.E., and Nolen, J.S.: "Second Comparative Solution Project: A Three-Phase Coning Study," *JPT* (March 1986) 345.
5. Kenyon, D.E. and Behie, G.A.: "Third SPE Comparative Solution Project: Gas Cycling of Retrograde Condensate Reservoirs," *JPT* (August 1987) 981.
6. Aziz, K., Ramesh, A.B., and Woo, P.T.: "Fourth SPE Comparative Solution Project: Comparison of Steam Injection Simulators," *JPT* (December 1987) 1576.
7. Killough, J.E. and Kossack, C.A.: "Fifth Comparative Solution Project: Evaluation of Miscible Flood Simulators," paper SPE 16000 presented at the 1987 SPE Symposium on Reservoir Simulation, San Antonio, Texas, 1–4 February.
8. Firoozabadi, A. and Thomas, L.K.: "Sixth SPE Comparative Solution Project: Dual-Porosity Simulators," *JPT* (June 1990) 710.
9. Nghiem, L., Collins, D.A., and Sharma, R.: "Seventh SPE Comparative Solution Project: Modeling of Horizontal Wells in Reservoir Simulation," paper SPE 21221 presented at the 1991 SPE Symposium on Reservoir Simulation, Anaheim, California, 17–20 February.
10. Quandalle, P.: "Eighth SPE Comparative Solution Project: Gridding Techniques in Reservoir Simulation," paper SPE 25263 presented at the 1993 SPE Symposium on Reservoir Simulation, New Orleans, 28 February–3 March.
11. Killough, J.E.: "Ninth SPE Comparative Solution Project: A Reexamination of Black-Oil Simulation," paper SPE 29110 presented at the 1995 SPE Symposium on Reservoir Simulation, San Antonio, Texas, 12–15 February.
12. Christie, M.A. and Blunt, M.J.: "Tenth SPE Comparative Solution Project: A Comparison of Upscaling Techniques," *SPEE* (August 2001) 308.
13. Coats, K.H.: "An Equation of State Compositional Model," *SPEJ* (October 1980) 363.
14. Young, L.C. and Stephenson, R.E.: "A Generalized Compositional Approach for Reservoir Simulation," *SPEJ* (October 1983) 727.
15. Acs, G., Doleschall, S., and Farkas, E.: "General Purpose Compositional Model," *SPEJ* (August 1985) 543.
16. Watts, J.W.: "A Compositional Formulation of the Pressure and Saturation Equations," *SPEE* (May 1986) 243.
17. Blair, P.M. and Weinaug, C.F.: "Solution of Two-Phase Flow Problems Using Implicit Difference Equations," *SPEJ* (December 1969) 417; *Trans.*, AIME, **246**.
18. Stone, H.L. and Garder, A.O. Jr.: "Analysis of Gas-Cap or Dissolved-Gas Drive Reservoirs," *SPEJ* (1961) 92; *Trans.*, AIME, **222**.
19. Sheldon, J.W., Harris, C.D., and Bavyly, D.: "A Method for General Reservoir Behavior Simulation on a Digital Computer," paper SPE 1521-G presented at the 1960 SPE Annual Meeting, Denver, 2–5 October.
20. Fagin, R.G. and Stewart, C.H.: "A New Approach to the Two-Dimensional Multiphase Reservoir Simulator," *SPEJ* (June 1966) 175; *Trans.*, AIME, **237**.

21. Coats, K.H.: “Reservoir Simulation: A General Model Formulation and Associated Physical/Numerical Sources of Instability,” *Boundary and Interior Layers—Computational and Asymptotic Methods*, J.J.H. Miller (ed.), Boole Press, Dublin, Ireland (1980).
22. Coats, K.H., Thomas, L.K., and Pierson, R.G.: “Compositional and Black Oil Reservoir Simulation,” *SPEREE* (August 1998) 372.
23. Coats, K.H.: “A Note on IMPES and Some IMPES-Based Simulation Models,” *SPEJ* (September 2000) 245.
24. MacDonald, R.C. and Coats, K.H.: “Methods for Numerical Simulation of Water and Gas Coning,” *SPEJ* (December 1970) 425; *Trans.*, AIME, **249**.
25. Spillette, A.G., Hillestad, J.G., and Stone, H.L.: “A High-Stability Sequential Solution Approach to Reservoir Simulation,” paper SPE 4542 presented at the 1973 SPE Annual Meeting, Las Vegas, Nevada, 30 September–3 October.
26. Thomas, G.W. and Thurnau, D.H.: “Reservoir Simulation Using an Adaptive Implicit Method,” *SPEJ* (October 1983) 759.
27. Lantz, R.B.: “Quantitative Evaluation of Numerical Diffusion (Truncation Error),” *SPEJ* (September 1971) 315; *Trans.*, AIME, **251**.
28. Todd, M.R., O’Dell, P.M., and Hirasaki, G.J.: “Methods for Increased Accuracy in Numerical Reservoir Simulators,” *SPEJ* (December 1972) 515; *Trans.*, AIME, **253**.
29. Fung, L.S.-K., Collins, D.A., and Nghiem, L.X.: “An Adaptive-Implicit Switching Criterion Based on Numerical Stability Analysis,” *SPEE* (February 1989) 45.
30. Russell, T.F.: “Stability Analysis and Switching Criteria for Adaptive Implicit Methods Based on the CFL Condition,” paper SPE 18416 presented at the 1989 SPE Symposium on Reservoir Simulation, Houston, 6–8 February.
31. Grabenstetter, J. *et al.*: “Stability-Based Switching Criterion for Adaptive-Implicit Compositional Reservoir Simulation,” paper SPE 21225 presented at the 1991 SPE Symposium on Reservoir Simulation, Anaheim, California, 17–20 February.
32. Watts, J.W. and Rame, M.: “An Algebraic Approach to the Adaptive Implicit Method,” paper SPE 51900 presented at the 1999 SPE Reservoir Simulation Symposium, Houston, 14–17 February.
33. Coats, K.H.: “IMPES Stability: The CFL Limit,” paper SPE 66345 presented at the 2001 SPE Reservoir Simulation Symposium, Houston, 11–14 February.
34. Coats, K.H.: “IMPES Stability: The Stable Step,” paper SPE 69225 presented at the 2001 SPE Reservoir Simulation Symposium, Houston, 11–14 February.
35. Young, L.C. and Russell, T.F.: “Implementation of an Adaptive Implicit Method,” paper SPE 25245 presented at the 1993 SPE Symposium on Reservoir Simulation, New Orleans, 28 February–3 March.
36. Vinsome, P.K.W.: “Orthomin, an Iterative Method for Solving Sparse Sets of Simultaneous Linear Equations,” paper SPE 5729 presented at the 1976 SPE Symposium of Numerical Reservoir Simulation of Reservoir Performance, Los Angeles, 19–20 February.
37. Appleyard, J.R. and Cheshire, I.M.: “Nested Factorization,” paper SPE 12264 presented at the 1983 SPE Reservoir Simulation Symposium, San Francisco, 16–18 November.
38. Watts, J.W. III: “A Conjugate Gradient-Truncated Direct Method for the Iterative Solution of the Reservoir Simulation Pressure Equation,” *SPEJ* (June 1981) 345.
39. Forsyth, P.A. and Sammon, P.H.: “Local Mesh Refinement and Modeling of Faults and Pinchouts,” *SPEFE* (June 1986) 275.
40. Verma, S. and Aziz, K.: “A Control Volume Scheme for Flexible Grids in Reservoir Simulation,” paper SPE 37999 presented at the 1997 SPE Reservoir Simulation Symposium, Dallas, 8–11 June.
41. Saad, Y. and Schultz, M.H.: “GMRES: A Generalized Minimal Residual Algorithm for Solving Nonsymmetric Linear Systems,” *SIAM Journal on Scientific and Statistical Computing* (1986) 856.
42. Tan, T.B.S. and Letkeman, J.P.: “Application of D4 Ordering and Minimization in an Effective Partial Matrix Inverse Iterative Method,” paper SPE 10493 presented at the 1982 SPE Symposium on Reservoir Simulation, New Orleans, 31 January–3 February.
43. Watts, J.W.: “An Iterative Matrix Solution Method Suitable for Anisotropic Problems,” *SPEJ* (March 1971) 47; *Trans.*, AIME, **251**.

44. Wallis, J.R.: "Incomplete Gaussian Elimination as a Preconditioning for Generalized Conjugate Gradient Acceleration," paper SPE 12265 presented at the 1983 SPE Reservoir Simulation Symposium, San Francisco, 15–18 November.
45. Behie, A. and Vinsome, P.K.W.: "Block Iterative Methods for Fully Implicit Reservoir Simulation," *SPEJ* (October 1982) 658.
46. Holmes, J.A.: "Enhancements to the Strongly Coupled, Fully Implicit Well Model: Wellbore Crossflow Modeling and Collective Well Control," paper SPE 12259 presented at the 1983 SPE Reservoir Simulation Symposium, San Francisco, 15–18 November.
47. Burrows, R., Ponting, D., and Wood, L.: "Parallel Reservoir Simulation with Nested Factorization," presented at the 1996 European Conference on the Mathematics of Oil Recovery, Leoben, Austria, 3–6 September.
48. Killough, J.E. *et al.*: "Parallelization of a General-Purpose Reservoir Simulator," presented at the 1996 European Conference on the Mathematics of Oil Recovery, Leoben, Austria, 3–6 September.
49. Cuthill, E. and McKee, J.: "Reducing the Bandwidth of Sparse Symmetric Matrices," *Proc., 24th National Conference of the Assoc. for Computing Machinery*, Brandon Press, Princeton, New Jersey (1969) 157–172.
50. D'Azevedo, E.F., Forsyth, P.A., and Tang, W.-P.: "An Automatic Ordering Method for Incomplete Factorization Iterative Solvers," paper SPE 21226 presented at the 1991 Symposium on Reservoir Simulation, Anaheim, California, 17–20 February.
51. D'Azevedo, E.F., Forsyth, P.A., and Tang, W.-P.: "Ordering Methods for Preconditioned Conjugate Gradient Methods Applied to Unstructured Grid Problems," *SIAM Journal of Matrix Analysis and Applications* (July 1992) 944.
52. Aziz, K. and Settari, A.: *Petroleum Reservoir Simulation* (1979) ISBN 0–9730614–0–5, reprinted 2002, Blitzprint Ltd., Calgary.
53. Rozon, B.J.: "A Generalized Finite Volume Discretization Method for Reservoir Simulation," paper SPE 18414 presented at the 1989 SPE Symposium on Reservoir Simulation, Houston, 6–8 February.
54. Aavatsmark, I. *et al.*: "MPFA for Faults and Local Refinements With Application to Field Simulations," *Proc.*, 2000 European Conference on the Mathematics of Oil Recovery, Baveno, Italy, 5–8 September.
55. Forsyth, P.A.: "A Control-Volume Finite-Element Method for Local Mesh Refinement in Thermal Reservoir Simulation," *SPERE* (November 1990) 561.
56. Herge, T.M., Dalen, V., and Henriquez, A.: "Generalized Transmissibilities for Distorted Grids in Reservoir Simulation," paper SPE 15622 presented at the 1986 SPE Annual Technical Conference and Exhibition, New Orleans, 5–8 October.
57. Young, L.C.: "Rigorous Treatment of Distorted Grids in 3D," paper SPE 51899 presented at the 1999 SPE Reservoir Simulation Symposium, Houston, 14–17 February.
58. Aziz, K.: "Reservoir Simulation Grids: Opportunities and Problems," paper SPE 25233 presented at the 1993 SPE Symposium on Reservoir Simulation, New Orleans, 28 February–3 March.
59. Aavatsmark, I., Barkve, T., and Mannseth, T.: "Control Volume Discretization Methods for 3D Quadrilateral Grids in Inhomogeneous, Anisotropic Reservoirs," *SPEJ* (June 1998) 146.
60. Edwards, M.G. and Rogers, C.F.: "A Flux Continuous Scheme for the Full Tensor Pressure Equation," *Proc.*, 1994 European Conference on the Mathematics of Oil Recovery, Roros, Norway, 7–10 June.
61. Lee, S.H., Tchelepi, H., and DeChant, L.J.: "Implementation of a Flux-Continuous Finite Difference Method for Stratigraphic, Hexahedron Grids," paper SPE 51901 presented at the 1999 SPE Reservoir Simulation Symposium, Houston, 14–17 February 1999.
62. Ponting, D.K.: "Corner Point Geometry in Reservoir Simulation," *Proc.*, First European Conference on the Mathematics of Oil Recovery, 1989.
63. Jenny, P. *et al.*: "Modeling Flow in Geometrically Complex Reservoirs Using Hexahedral Multiblock Grids," *SPEJ* (June 2002) 149.
64. Heinemann, Z.E. and Brand, C.W.: "Gridding Techniques in Reservoir Simulation," *Proc.*, First Intl. Forum on Reservoir Simulation, Alpbach, Austria (1988) 339.
65. Heinemann, Z.E. *et al.*: "Modeling Reservoir Geometry With Irregular Grids," *SPERE* (May 1991) 225.

66. Palagi, C.L. and Aziz, K.: "Use of Voroni Grid in Reservoir Simulation," paper SPE 22889 presented at the 1991 SPE Annual Technical Conference and Exhibition, Dallas, 6–9 October.
67. Gunasekera, D.L., Cox, J., and Lindsey, P.: The Generation and Application of K-Orthogonal Grid Systems," paper SPE 37998 presented at the 1997 SPE Symposium on Reservoir Simulation, Dallas, 9–11 June.
68. Verma, S. and Aziz, K.: "Two- and Three-Dimensional Flexible Grids for Reservoir Simulation," *Proc.*, 1996 European Conference on the Mathematics of Oil Recovery, Leoben, Austria, 3–6 September.
69. Lasseter, T.J.: "A New Approach for the Efficient Construction of 3D Geological Models for Reservoir Applications," *Proc.*, Eighth European Conference on the Mathematics of Oil Recovery, Freiberg, Germany (2002).
70. Warren, J.E. and Price, H.S.: "Flow in Heterogeneous Porous Media," *SPEJ* (September 1961) 153; *Trans.*, AIME, **222**.
71. King, M.J. *et al.*: "Application of Novel Upscaling Approaches to the Magnus and Andrew Reservoirs," paper SPE 50643 presented at the 1998 SPE European Petroleum Conference, The Hague, 20–22 October.
72. King, M.J. and Mansfield, M.: "Flow Simulation of Geological Models," *SPEEE* (August 1999) 351.
73. Guerillot, D. *et al.*: "An Integrated Model for Computer Aided Reservoir Description: From Outcrop Study to Fluid Flow Simulations," paper presented at the 1989 IOR Symposium, Budapest, Hungary.
74. Samier, P.: "A Finite-Element Method for Calculating Transmissibilities," *Proc.*, 1990 European Conference on the Mathematics of Oil Recovery, Arles, France, 11–14 September.
75. Durlofsky, L.J. and Chung, E.Y.: "Effective Permeability of Heterogeneous Reservoir Regions," *Proc.*, 1990 European Conference on the Mathematics of Oil Recovery, Arles, France, 11–14 September.
76. Durlofsky, L.J.: "Numerical Calculation of Equivalent Grid Block Permeability Tensors for Heterogeneous Porous Media," *Water Resources Research* (1991) **27**, 699.
77. Kirkpatrick, S.: "Classical Transport in Disordered Media: Scaling and Effective-Medium Theories," *Phys. Rev. Lett.* (December 1971).
78. Tjølsen, C., Bøe, Ø., and Damsleth, E.: "Homogenisation of Absolute Permeability—Does it Affect the Final Results?" *Proc.*, Second Lerkendal Petroleum Engineering Workshop (1992).
79. Bøe, Ø.: "Analysis of an Upscaling Method Based on Conservation of Dissipation," *Transport in Porous Media* (1994) **77**, 17.
80. Holden, L. and Nielsen B.F.: *Global Upscaling of Permeability in Heterogeneous Reservoirs: The Output Least Squares (OLS) Method*, Norwegian Computing Centre, November 1998.
81. Samier, P. *et al.*: "Applications of Streamline Simulations to Reservoir Studies," *SPEEE* (August 2002) 324.
82. Thiele, M.R.: "Streamline Simulation," keynote address at the 2001 Intl. Forum on Reservoir Simulation, Schloss Fuschl, Austria, 3–7 September.
83. Lolomari, T. *et al.*: "The Use of Streamline Simulation in Reservoir Management: Methodology and Case Studies," paper SPE 63157 presented at the 2000 SPE Annual Technical Conference and Exhibition, Dallas, 1–4 October.
84. Baker, R.O. *et al.*: "Full-Field Modeling Using Streamline-Based Simulation: 4 Case Studies" paper SPE 66405 presented at the 2001 SPE Reservoir Simulation Symposium, Houston, 11–14 February.
85. Thiele, M.R., Batycky, R.P., and Blunt, M.J.: "A Streamline-Based 3D Field-Scale Compositional Reservoir Simulator," paper SPE 38889 presented at the 1997 SPE Annual Technical Conference and Exhibition, San Antonio, Texas, 5–8 October.
86. Thiele, M.R., Batycky, R.P., and Thomas, L.K.: "Miscible WAG Simulations Using Streamlines," paper presented at the 2002 European Conference on the Mathematics of Oil Recovery, Freiberg, Germany, 3–6 September.
87. Batycky, R.P., Blunt, M.J., and Thiele, M.R.: "A 3D Field Scale Streamline-Based Reservoir Simulator," *SPEEE* (November 1997) 246.

88. Emanuel, A.S.: "Development of an Analytical Streamtube Model for Estimating Stream-Drive Performance," paper SPE 21756 presented at the 1991 SPE Western Regional Meeting, Long Beach, California, 20–22 March.
89. Crane, M.J. and Blunt, M.J.: "Streamline-Based Simulation of Solute Transport," *Water Resources Research* (October 1999) **35**, No. 10, 3061.
90. Di Donato, G., Huang, W., and Blunt, M.J.: "Streamline-Based Dual-Porosity Simulation of Fractured Reservoirs," paper SPE 84036 presented at the 2003 SPE Annual Technical Conference and Exhibition, Denver, 5–8 October.
91. Muskat, M. and Wyckoff, R.: "Theoretical Analysis of Waterflooding Networks," *Trans., AIME* (1934) **107**.
92. Muskat, M.: *Flow of Homogeneous Fluids*, Intl. Human Resources Development Corp., Boston, Massachusetts (1937 and 1982).
93. Fay, C.H. and Prats, M.: "The Application of Numerical Methods to Cycling and Flooding Problems," *Proc., Third World Petroleum Congress, The Hague, 28 May–6 June* (1951).
94. Higgins, R.V. and Leighton, A.J.: "A Computer Method to Calculate Two-Phase Flow in Any Irregular Bounded Porous Medium," *JPT* (June 1962) 679.
95. Higgins, R.V. and Leighton, A.J.: "Computer Predictions of Water Drive of Oil and Gas Mixtures Through Irregularly Bounded Porous Media—Three Phase Flow," *JPT* (September 1962) 1048.
96. Bommer, M.P. and Schechter, R.S.: "Mathematical Modeling of In-Situ Uranium Leaching," *SPEJ* (December 1979) 393.
97. Martin, J.C. and Wegner, R.E.: "Numerical Solution of Multiphase, Two-Dimensional Incompressible Flow Using Streamtube Relationships," *SPEJ* (October 1979) 313.
98. Lake, L.W., Johnston, J.R., and Stegemeier, G.L.: "Simulation and Performance Prediction of Large-Scale Surfactant/Polymer Project," *SPEJ* (December 1981) 731.
99. Emanuel, A.S. *et al.*: "Reservoir Performance Prediction Methods Based on Fractal Geostatistics," *SPEJ* (August 1989) 311.
100. Pollock, D.W.: "Semianalytical Computation of Path Lines for Finite-Difference Models," *Ground Water* (November–December 1988) **26**, No. 6, 743.
101. King, M.J. *et al.*: "Rapid Evaluation of the Impact of Heterogeneity on Miscible Gas Injection," paper SPE 26079 presented at the 1993 SPE Western Regional Meeting, Anchorage, 26–28 May.
102. Datta-Gupta, A. and King, M.J.: "A Semi-Analytic Approach to Tracer Flow Modeling in Heterogeneous Permeable Media," *Advances in Water Resources* (1995) **18**, No. 1, 9.
103. Batycky, R.P.: "A Three-Dimensional Two-Phase Field Scale Streamline Simulator," PhD dissertation, Stanford U., Stanford, California (1997).
104. Renard, G.: "A 2D Reservoir Streamtube EOR Model with Periodic Automatic Regeneration of Streamlines," *In Situ* (1990) **14**, No. 2, 175.
105. Thiele, M.R. *et al.*: "Simulating Flow in Heterogeneous Systems Using Streamtubes and Streamlines," *SPEJ* (February 1996) 5.
106. Bratvedt, F., Gimse, T., and Tegnander, C.: "Streamline Computations for Porous Media Flow Including Gravity," *Transport in Porous Media* (October 1996) **25**, No. 1, 63.
107. Blunt, M.J., Liu, K., and Thiele, M.R.: "A Generalized Streamline Method to Predict Reservoir Flow," *Petroleum Geoscience* (1996) **2**, 256.
108. Prévost, M., Edwards, M.G., and Blunt, M.J.: "Streamline Tracing on Curvilinear Structured and Unstructured Grids," *SPEJ* (June 2002) 139.
109. Thiele, M. and Batycky, R.P.: "Water Injection Optimization Using a Streamline-Based Workflow," SPE paper 84080 presented at the 2003 SPE Annual Technical Conference and Exhibition, Denver, 5–8 October.
110. Batycky, R.P. *et al.*: "Revisiting Reservoir Flood Surveillance Methods Using Streamlines," SPE paper 95402 presented at the 2005 SPE Annual Technical Conference and Exhibition, Dallas, 9–12 October.
111. Wang, Y. and Kovscek, A.R.: "Streamline Approach for History Matching Production Data," *SPEJ* (December 2000) 353.
112. Agarwal, B. and Blunt, M.J.: "Streamline-Based Method With Full-Physics Forward Simulation for History-Matching Performance Data of a North Sea Field," *SPEJ* (June 2003) 171.
113. Caers, J. *et al.*: "A Geostatistical Approach to Streamline-Based History Matching," *SPEJ* (September 2002) 250.

114. Fenwick, D.H. *et al.*: “Reconciling Prior Geologic Information With Production Data Using Streamlines—Application to a Giant Middle-Eastern Oil Field,” SPE paper 95940 presented at the 2005 Annual Technical Conference and Exhibition, Dallas, 9–12 October.
115. Stüben, K.: “Algebraic Multigrid (AMG): An Introduction with Applications,” *Multigrid*, U. Trottenberg, C.W. Oosterlee and A. Schüller (eds.), Academic Press, New York City (2000) appendix.
116. Darve, F.: *Geomaterials: Constitutive Equations and Modeling*, Elsevier Applied Science, New York City (1990).
117. Coussy, O.: *Mechanics of Porous Continua*, John Wiley and Sons, Chichester, England (1995).
118. Settari, A. and Walters, D.A.: “Advances in Coupled Geomechanical and Reservoir Modeling With Applications to Reservoir Compaction,” *SPEJ* (September 2001) 334.
119. Lorenz, J.C.: “Stress Sensitive Reservoirs,” *JPT* (January 1999) 61.
120. Settari, A. *et al.*: “Brine Disposal Into a Tight Stress Sensitive Formation at Fracturing Conditions: Design and Field Experience,” *SPERE* (April 1999) 186.
121. Settari, A.: “Reservoir Compaction,” *JPT* (August 2002) 62.
122. Finol, A. and Farouq Ali, S.M.: “Numerical Simulation of Oil Production With Simultaneous Ground Subsidence,” *SPEJ* (October 1975) 411.
123. Merle, H.A. *et al.*: “The Bachaquero Study—A Composite Analysis of the Behavior of a Compaction Drive/Solution Gas Drive Reservoir,” *JPT* (September 1976) 1107.
124. Rattia, A.J. and Farouq Ali, S.M.: “Effect of Formation Compaction on Steam Injection Response,” paper SPE 10323 presented at the 1981 SPE Annual Technical Conference and Exhibition, San Antonio, Texas, 5–7 October.
125. Chase, C.A. and Dietrich, J.K.: “Compaction Within the South Belridge Diatomite,” *SPERE* (November 1989) 422.
126. Beattie, C.I., Boberg, T.C., and McNab, G.S.: “Reservoir Simulation of Cyclic Steam Stimulation in the Cold Lake Oil Sands,” *SPERE* (1991) 200.
127. Chin, L.Y. and Thomas, L.K.: “Fully Coupled Analysis of Improved Oil Recovery by Reservoir Compaction,” paper SPE 56753 presented at the 1999 SPE Annual Technical Conference and Exhibition, Houston, 3–6 October.
128. Settari, A. and Mourits, F.M.: “A Coupled Reservoir and Geomechanical Simulation System,” *SPEJ* (September 1998) 219.
129. Settari, A. and Price, H. S.: “Simulation of Hydraulic Fracturing in Low-Permeability Reservoirs,” *SPEJ* (April 1984) 141.
130. Settari, A.: “How To Approximate Effects of Geomechanics in Conventional Reservoir Simulation” paper SPE 97155 presented at the 2005 SPE Annual Technical Conference and Exhibition, Dallas, 9–12 October.
131. Heffer, K.J. *et al.*: “The Influence of Natural Fractures, Faults and Earth Stresses on Reservoir Performance—Geomechanical Analysis by Numerical Modelling,” *Proc.*, Third Intl. Conference on North Sea Oil and Gas Reservoirs, Trondheim, Norway (1992) 201–211.
132. Jin, M., Somerville, J., and Smart, B.G.D.: “Coupled Reservoir Simulation Applied to the Management of Production Induced Stress-Sensitivity,” paper SPE 64790 presented at the 2000 SPE International Oil and Gas Conference and Exhibition in China, Beijing, 7–10 November.
133. “Coupled Thermo-Hydro-Mechanical Processes of Fractured Media,” *Developments in Geotechnical Engineering*, O. Stephansson, L. Jing, and S.-F. Tsang (eds.), Elsevier, New York City (1996) 575.
134. Koutsabeloulis, N.C. and Hope, S.A.: “‘Coupled’ Stress/Fluid/Thermal Multiphase Reservoir Simulation Studies Incorporating Rock Mechanics,” paper SPE 47393 presented at the 1998 SPE/ISRM Eurock 98, Trondheim, Norway, 8–10 July.
135. Settari, A.: “Coupled Fracture and Reservoir Modeling,” *Proc.*, Advanced Hydraulic Fracturing Workshop, 2000 North American Rock Mechanics Conference, Seattle, Washington (2000).
136. Lewis, R.W. and Schrefler, B.A.: *The Finite Element Method in the Deformation and Consolidation of Porous Media*, John Wiley and Sons, New York City (1987) 344.
137. Stone, T. *et al.*: “Fully Coupled Geomechanics in a Commercial Reservoir Simulator,” paper SPE 65107 presented at the 2000 SPE European Petroleum Conference, Paris, 24–25 October.
138. Sulak, R.M., Thomas, L.K., and Boade, R.R.: “3D Reservoir Simulation of Ekofisk Compaction Drive,” *JPT* (October 1991) 1272.

139. Fredrich, J.T. *et al.*: "One-Way Coupled Reservoir-Geomechanical Modeling of the Lost Hills Oil Field, California," *Proc.*, 38th U.S. Rock Mechanics Symposium, Washington, DC (2001).
140. Tran, D., Settari, A., and Nghiem, L.: "New Iterative Coupling Between a Reservoir Simulator and a Geomechanics Module," paper SPE 78192 presented at the 2002 SPE/ISRM Rock Mechanics Conference, Irving, Texas, 20–23 October.
141. Dean, R.H.: "A Poroelastic Multicomponent Reservoir Simulator," paper SPE 62806 available from SPE, Richardson, Texas (2000).
142. Settari, A., Walters, D.A., and Behie, G.A.: "Use of Coupled Reservoir and Geomechanical Modeling for Integrated Reservoir Analysis and Management," *J. Cdn. Pet. Tech.* (2001) **40**, No. 12, 55.
143. Coats, B.K., Nolen, J.S., and Sherman, A.H.: "Application and Accuracy of Two Component Characterizations of Reservoir Oils for Numerical Modeling Purposes," paper SPE 17614 presented at the 1988 SPE International Meeting on Petroleum Engineering, Tianjin, China, 1–4 November.
144. Cook, R.E., Jacoby, R.H., and Ramesh, A.B.: "A Beta-Type Reservoir Simulator for Approximating Compositional Effects During Gas Injection," *SPEJ* (October 1974) 471; *Trans.*, AIME, **257**.
145. Fevang, Ø. and Whitson, C.H.: "Modeling Gas-Condensate Well Deliverability," *SPERE* (November 1996) 221.
146. Spivak, A. and Dixon, T.N.: "Simulation of Gas-Condensate Reservoirs," paper SPE 4271 presented at the 1973 SPE Annual Meeting, Houston, 10–12 January.
147. Chang, Y.-B., Coats, B.K., and Nolen, J.S.: "A Compositional Model for CO₂ Floods Including CO₂ Solubility in Water," paper SPE 35164 presented at the 1996 SPE Permian Basin Oil and Gas Recovery Conference, Midland, Texas, 27–29 March.
148. Michelsen, M.L.: "Saturation Point Calculations," *Fluid Phase Equilibria* (1985) **23**, 181.
149. Michelsen, M.L.: "The Isothermal Flash Problem. Part I. Stability," *Fluid Phase Equilibria* (1982) **9**, 1.
150. Muskat, M. and McDowell, J.M.: "An Electrical Computer for Solving Phase Equilibrium Problems," *Trans.*, AIME (1949) **186**, 291.
151. Rachford, H.H. and Rice, J.D.: "Procedure for Use of Electrical Digital Computers in Calculating Flash Vaporization Hydrocarbon Equilibrium," *JPT* (October 1952) 19; *Trans.*, AIME, **195**.
152. Whitson, C.H. and Brule, M.R.: *Phase Behavior*, Monograph Series, SPE, Richardson, Texas (2000) **20**.
153. Michelsen, M.L.: "The Isothermal Flash Problem. Part II. Phase-Split Calculation," *Fluid Phase Equilibria* (1982) **9**, 21.
154. Peneloux, A., Rauzy, E., and Freze, R.: "A Consistent Correction for Redlich-Kwong-Soave Volumes," *Fluid Phase Equilibria* (1982) **8**, 7.
155. Peng, D.Y. and Robinson, D.B.: "A New-Constant Equation of State," *Ind. Eng. Chem. Fund.* (1976) **15**, No. 1, 59.
156. Soave, G.: "Equilibrium Constants from a Modified Redlich-Kwong Equation of State," *Chem. Eng. Sci.* (1972) **27**, No. 6, 1197.
157. Zudkevitch, D. and Joffe, J.: "Correlation and Prediction of Vapor-Liquid Equilibrium with the Redlich-Kwong Equation of State," *AIChE J.* (1970) **16**, 112.
158. Whitson, C.H. and Torp, S.B.: "Evaluating Constant Volume Depletion Data," *JPT* (March 1983) 610; *Trans.*, AIME, **275**.
159. Cook, A.B. *et al.*: "The Role of Vaporization in High Percentage Oil Recovery by Pressure Maintenance," *JPT* (February 1967) 245.
160. Whitson, C.H.: "Characterizing Hydrocarbon Plus Fractions," *SPEJ* (August 1983) 683; *Trans.*, AIME, **275**.
161. Tang, D.E. and Zick, A.A.: "A New Limited-Compositional Reservoir Simulator," paper SPE 25255 presented at the 1993 SPE Symposium on Reservoir Simulation, New Orleans, 28 February–3 March.
162. Zick, A.A.: "A Combined Condensing/Vaporizing Mechanism in the Displacement of Oil by Enriched Gases," paper SPE 15493 presented at the 1986 SPE Annual Technical Conference and Exhibition, New Orleans, 5–8 October.

163. Fevang, Ø., Singh, K., and Whitson, C.H.: "Guidelines for Choosing Compositional and Black-Oil Models for Volatile Oil and Gas-Condensate Reservoirs," paper SPE 63087 presented at the 2000 SPE Annual Technical Conference and Exhibition, Dallas, 1–4 October.
164. Lohrenz, J., Bray, B.G., and Clark, C.R.: "Calculating Viscosities of Reservoir Fluids From Their Compositions," *JPT* (October 1964) 1171; *Trans.*, AIME, **231**.
165. Pedersen, K.S. and Fredenslund, A.: "An Improved Corresponding States Model for the Prediction of Oil and Gas Viscosities and Thermal Conductivities," *Chem. Eng. Sci.* (1987) **42**, 182.
166. Saidi, A.: "Twenty Years of Gas Injection History Into Well-Fractured Haft Kel Field (Iran)," paper SPE 35309 presented at the 1996 SPE International Petroleum Conference and Exhibition, Villahermosa, Mexico, 5–7 March.
167. Whitson, C.H., Fevang, Ø., and Saevareid, A.: "Gas Condensate Relative Permeability for Well Calculations," paper SPE 56476 presented at the 1999 SPE Annual Technical Conference and Exhibition, Houston, 3–6 October.
168. Mott, R.E., Cable, A.S., and Spearing, M.C.: "Measurements of Relative Permeabilities for Calculating Gas-Condensate Well Deliverability," *SPERE* (December 2000) 473.
169. Robinson, D.B. and Peng, D.Y.: "The Characterization of the Heptanes and Heavier Fractions," *Research Report 28*, Gas Producers Assn., Tulsa (1978).
170. Katz, D.L. and Firoozabadi, A.: "Predicting Phase Behavior of Condensate/Crude-Oil Systems Using Methane Interaction Coefficients," *JPT* (November 1978) 1649; *Trans.*, AIME, **265**.
171. Shelton, J.L. and Yarborough, L.: "Multiple-Phase Behavior in Porous Media During CO₂ or Rich-Gas Flooding," *JPT* (September 1977) 1171.
172. Nghiem, L.X. and Li, Y.K.: "Effect of Phase Behavior on CO₂ Displacement Efficiency at Low Temperatures: Model Studies With an Equation of State," *SPERE* (July 1986) 414.
173. Coats, K.H.: "Simulation of Steamflooding With Distillation and Solution Gas," *SPEJ* (October 1976) 235.
174. Killough, J.E.: "The Use of Vector Processors in Reservoir Simulation," paper SPE 7673 presented at the 1979 SPE Symposium on Reservoir Simulation, Denver, 1–2 February.
175. Nolen, J.S., Kuba, D.W., and Kascic, M.J. Jr.: "Application of Vector Processors to the Solution of Finite Difference Equations," paper SPE 7675 presented at the 1979 SPE Symposium on Reservoir Simulation, Denver, 1–2 February.
176. Killough, J.E. and Levesque, J.M.: "Reservoir Simulation and the In-house Vector Processor: Experience for the First Year," paper SPE 10521 presented at the 1982 SPE Symposium on Reservoir Simulation, New Orleans, 31 January–3 February.
177. Young, L.C.: "Equation of State Compositional Modeling on Vector Processors," paper SPE 16023 presented at the 1987 SPE Symposium on Reservoir Simulation, San Antonio, Texas, 1–4 February.
178. Killough, J.E.: "Is Parallel Computing Ready for Reservoir Simulation?" paper SPE 26634 presented at the 1993 SPE Annual Technical Conference and Exhibition, Houston, 3–6 October.
179. Killough, J.E. *et al.*: "A General-Purpose Parallel Reservoir Simulator," presented at the 1996 European Conference on the Mathematics of Oil Recovery, Leoben, Austria, 3–6 September.
180. van Daalen, D.T. *et al.*: "The Parallelization of BOSIM, Shell's Black/Volatile Oil Reservoir Simulator," *Proc. of the First IMA/SPE European Conference on the Mathematics of Oil Recovery*, Oxford U. (1990).
181. Killough, J.E. and Bhogeswara, R.: "Simulation of Compositional Reservoir Phenomena on a Distributed Memory Parallel Computer," *JPT* (November 1991) 1368.
182. Wheeler, J.A. and Smith, R.A.: "Reservoir Simulation on a Hypercube," *SPERE* (1990) 544.
183. Rutledge, J.M. *et al.*: "The Use of a Massively Parallel SIMD Computer for Reservoir Simulation," paper SPE 21213 presented at the 1991 SPE Symposium on Reservoir Simulation, Anaheim, California, 17–20 February.
184. Gautam S. *et al.*: "Parallel Computing Alters Approaches, Raises Integration Challenges in Reservoir Modeling," *Oil & Gas J.* (20 May 1996) 48.
185. Tchelepi, H.A.: "Practical Use of Scale Up and Parallel Reservoir Simulation Technologies in Field Studies," paper SPE 38886 presented at the 1997 SPE Annual Technical Conference and Exhibition, San Antonio, Texas, 5–8 October.
186. Chien, M.C.H. *et al.*: "A Scalable Parallel Multi-Purpose Reservoir Simulator," paper SPE 37976 presented at the 1997 SPE Reservoir Simulation Symposium, Dallas, 8–11 June.

187. Shiralkar, G.S. *et al.*: “Falcon: A Production-Quality Distributed-Memory Reservoir Simulator,” paper SPE 37975 presented at the 1997 SPE Reservoir Simulation Symposium, Dallas, 8–11 June.
188. Wang, P. *et al.*: “A New Generation EOS Compositional Reservoir Simulator: Part I—Formulation and Discretization,” paper SPE 37979 presented at the 1997 SPE Reservoir Simulation Symposium, Dallas, 8–11 June.
189. Pavlas, E.J. Jr.: “MPP Simulation of Complex Water Encroachment in a Large Carbonate Reservoir in Saudi Arabia,” paper SPE 71628 presented at the 2001 SPE Annual Technical Conference and Exhibition, New Orleans, 30 September–3 October.
190. Wallis, J.R. and Nolen, J.S.: “Efficient Linear Solution of Locally Refined Grids Using Algebraic Multilevel Approximate Factorizations,” paper SPE 25239 presented at the 1993 SPE Symposium on Reservoir Simulation, New Orleans, 28 February–3 March.
191. Song, T.: “A Load-Balancing Technique for Reservoir Simulation Based on Dantzig’s Transportation Model,” MS thesis, U. of Houston, Houston (1996).
192. *Reference Manual for Zoltan*, Los Alamos Natl. Laboratory, Los Alamos, New Mexico (1998).
193. Bogeswara, R. and Killough, J.E.: “Parallel Linear Solvers for Reservoir Simulation: A Generic Approach for Existing and Emerging Computer Architectures,” paper SPE 25240 presented at the 1993 SPE Symposium on Reservoir Simulation, New Orleans, 28 February–3 March.
194. Guerberoff, D. *et al.*: “Lateral Delineation of Sandstone Bodies Guided by Seismic and Petrophysical Data Using Geocellular Model: Canadon Seco Formation, San Jorge Basin, Argentina,” paper SPE 69487 presented at the 2001 SPE Latin American and Caribbean Petroleum Engineering Conference, Buenos Aires, 25–28 March.
195. Agarwal, B. *et al.*: “Reservoir Characterization of Ekofisk Field: A Giant, Fractured Chalk Reservoir in the Norwegian North Sea,” *SPEREE* (December 2000) 534.
196. Caers, J., Avseth, P., and Mukerji, T.: “Geostatistical Integration of Rock Physics, Seismic Amplitudes, and Geological Models in North Sea Turbidite Systems,” paper SPE 71321 presented at the 2001 SPE Annual Technical Conference and Exhibition, New Orleans, 30 September–3 October.
197. Al Qassab, H.M. *et al.*: “Conditioning Integrated Geological Models to Dynamic Flow Data of Giant Saudi Arabian Reservoir,” paper SPE 71319 presented at the 2001 SPE Annual Technical Conference and Exhibition, New Orleans, 30 September–3 October.
198. Raghavan, R. *et al.*: “Integration of Geology, Geophysics, and Numerical Simulation in the Interpretation of a Well Test in a Fluvial Reservoir,” paper SPE 62983 presented at the 2000 SPE Annual Technical Conference and Exhibition, Dallas, 1–4 October.
199. Durlofsky, L.J.: “Upscaling and gridding of fine-scale geological models for flow simulation,” *Proc.*, 2005 Intl. Forum on Reservoir Simulation, Stresa, Italy, 20–25 June.
200. Peaceman, D.W.: “Effective Transmissibilities of a Gridblock by Upscaling—Comparison of Direct Methods With Renormalization,” *SPEJ* (September 1997) 338.
201. Flodin, E.A. *et al.*: “Representation of Fault Zone Permeability in Reservoir Flow Models,” paper SPE 71617 presented at the 2001 SPE Annual Technical Conference and Exhibition, New Orleans, 30 September–3 October.
202. Nishikiori, N. and Hayashida, Y.: “Investigation of Fluid Conductive Faults and Modeling of Complex Water Influx in the Khadji Oil Field, Arabian Gulf,” *SPEREE* (October 2000) 401.
203. Barker, J.W. and Thikcan, S.: “A Critical Review of the Use of Pseudorelative Permeabilities for Upscaling,” *SPEE* (May 1997) 109.
204. Beckner, B.L. *et al.*: “EMpower: New Reservoir Simulation System,” paper SPE 68116 presented at the 2001 SPE Middle East Oil Show, Bahrain, 17–20 March.
205. Peaceman, D.W.: “Interpretation of Well-Block Pressures in Numerical Reservoir Simulation with Nonsquare Grid Blocks and Anisotropic Permeability,” *SPEJ* (June 1983) 531.
206. Mlacnik, M.J. and Heinemann, Z.E.: “Using Well Windows in Full Field Reservoir Simulation,” *SPEREE* (December 2003) 275.
207. Wolfsteiner, C., Durlofsky, L.J., and Aziz, K.: “Approximate Model for Productivity of Nonconventional Wells in Heterogeneous Reservoirs,” *SPEJ* (June 2000) 218.
208. Valvante, P.H., Durlofsky, L.J., and Aziz, K.: “Semi-Analytical Modeling of the Performance of Intelligent Well Completions,” paper SPE 66368 presented at the 2001 SPE Reservoir Simulation Symposium, Houston, 11–14 February.

209. Litvak, M.L. *et al.*: “Integration of Prudhoe Bay Surface Pipeline Network and Full Field Reservoir Models,” paper SPE 38885 presented at the 1997 SPE Annual Technical Conference and Exhibition, San Antonio, Texas, 5–8 October.
210. Fang, W.Y. and Lo, K.K.: “A Generalized Well-Management Scheme for Reservoir Simulation,” *SPE* (May 1996) 116.
211. Litvak, M.L. and Wang, C.H.: “Simplified Phase-Equilibrium Calculations in Integrated Reservoir and Surface-Pipeline-Network Models,” *SPEJ* (June 2000) 236.
212. Hermansen, H. *et al.*: “Twenty-Five Years of Ekofisk Reservoir Management,” paper SPE 38927 presented at the 1997 SPE Annual Technical Conference and Exhibition, San Antonio, Texas, 5–8 October.
213. Sylte, J.E. *et al.*: “Water Induced Compaction in the Ekofisk Field,” paper SPE 56426 presented at the 1999 SPE Annual Technical Conference and Exhibition, Houston, 3–6 October.
214. Ashton, K. *et al.*: “Judy/Joanne Field Development,” paper SPE 49128 presented at the 1998 SPE Annual Technical Conference and Exhibition, New Orleans, 27–30 September.
215. Pieters, J. and Por, G.J.A.: “Total System Modeling—A Tool for Effective Reservoir Management of Multiple Fields With Shared Facilities,” paper SPE 30442 presented at the 1995 SPE Offshore Europe Conference, Aberdeen, 5–8 September.
216. Williams, M.A. and Keating, J.F.: “The Stratigraphic Method: A Structured Approach to History Matching Complex Simulation Models,” paper SPE 38014 presented at the 1997 SPE Reservoir Simulation Symposium, Dallas, 8–11 June.
217. van Ditzhuijzen, R., Oldenziel, T., and van Kruijsdijk, C.P.J.W.: “Geological Parameterization of a Reservoir Model for History Matching Incorporating Time-Lapse Seismic Based on a Case Study of the Staffjord Field,” paper SPE 71318 presented at the 2001 SPE Annual Technical Conference and Exhibition, New Orleans, 30 September–3 October.
218. Bogan, C., Johnson, D., Litvak, M., and Stauber, D.: “Building Reservoir Models Based on 4D Seismic and Well Data in Gulf of Mexico Oil Fields,” paper SPE 84370 presented at the 2003 SPE Annual Technical Conference and Exhibition, Denver, 5–8 October.
219. Milliken, W.J., Emanuel, A.S., and Chakravarty, A.: “Applications of 3D Streamline Simulation to Assist History Matching,” paper SPE 63155 presented at the 2000 SPE Annual Technical Conference and Exhibition, Dallas, 1–4 October.
220. Schulze-Riegert, R.W. *et al.*: “Optimization Methods for History Matching of Complex Reservoir,” paper SPE 66393 presented at the 2001 SPE Reservoir Simulation Symposium, Houston, 11–14 February.
221. Grussaute, T. and Gouel, P.: “Computer Aided History Matching of a Real Field Case,” paper SPE 50642 presented at the 1998 SPE European Petroleum Conference, The Hague, 20–22 October.
222. Zapata, V.J. *et al.*: “Advances in Tightly Coupled Reservoir/Wellbore/Surface-Network Simulation,” *SPE* (April 2001) 114.
223. Gorell, S. and Bassett, R.: “Trends in Reservoir Simulation: Big Models, Scalable Models? Will You Please Make Up Your Mind?” paper SPE 71596 presented at the 2001 SPE Annual Technical Conference and Exhibition, New Orleans, 30 September–3 October.
224. Zabalza-Mezghani, I., Mezghani, M., and Blanc, G.: “Constraining Reservoir Facies Models to Dynamic Data-Impact of Spatial Distribution Uncertainty on Production Forecasts,” paper SPE 71335 presented at the 2001 SPE Annual Technical Conference and Exhibition, New Orleans, 30 September–3 October.
225. Manceau, E. *et al.*: “Combination of Experimental Design and Joint Modeling Methods for Quantifying the Risk Associated with Deterministic and Stochastic Uncertainties—An Integrated Test Study,” paper SPE 71620 presented at the 2001 SPE Annual Technical Conference and Exhibition, New Orleans, 30 September–3 October.

SI Metric Conversion Factors

bb1 × 1.589 873	E – 01 = m ³
cp × 1.0*	E – 03 = Pa·s
dyn × 1.0*	E – 02 = mN
ft × 3.048*	E – 01 = m

$$\begin{aligned} \text{ft}^3 &\times 2.831\,685 \\ \text{°F} & \quad (\text{°F} - 32)/1.8 \\ \text{lbm} &\times 4.535\,924 \end{aligned}$$

*Conversion factor is exact.

$$\begin{aligned} \text{E} - 02 &= \text{m}^3 \\ &= \text{°C} \\ \text{E} - 01 &= \text{kg} \end{aligned}$$

Chapter 18

Estimation of Primary Reserves of Crude Oil, Natural Gas, and Condensate

Ron Harrell, SPE, Ryder Scott Co. and Chap Cronquist, SPE, Consultant

18.1 Introduction

Most exploration and production companies' assets consist of the resources and reserves owned by that entity. Resources typically are classified as either contingent (discovered but presently uneconomic) or undiscovered, but their quantification is outside the scope of this work. This chapter discusses primary reserves, which are discovered quantities of hydrocarbons that can be produced at a profit and are classified by level of uncertainty. The discussion of estimated reserves in this chapter excludes limitations imposed by the terms of ownership.

Since publication of the first two petroleum handbooks,^{1,2} the international petroleum industry has increased its understanding of the need to develop more reliable estimates of petroleum reserves and to quantify the uncertainty associated with the classifications of reserves. Furthermore, the regulatory authorities of many countries, particularly of the U.S.A., have found it necessary to accommodate the increasing internationalization of the industry and to manage their increasing involvement and influence in the industry.

With this global expansion of the petroleum industry has come ongoing technological development that provides better tools and techniques for analyzing reservoirs and reservoir fluids as well as greater understanding of how reservoir geology affects reservoir performance. In developing mathematical models that replicate the geologic environment, the reservoir engineer must incorporate all available hard technical data and work closely with and use fully the experience of multidisciplinary teams of geophysicists, geologists, petrophysicists, and other specialists. The engineer must develop a working knowledge of the skills contributed by each member of the reserves assessment team and apply the professional judgment of each team member to the estimation and classification of reserves.

The estimation of reserves is more than just a periodic, statutory calculating and reporting of company assets (although those are important functions); it is an essential element of investment planning and resource management for every prudent operator. Estimating reserves begins with identifying a drillable prospect, and it continues while the prospect is developed and placed on production, and thereafter as warranted by well and/or reservoir performance, new geologic data, competitor (offset) operations, unitization, contract renegotiation, improved technology, and/or changing economic conditions.³

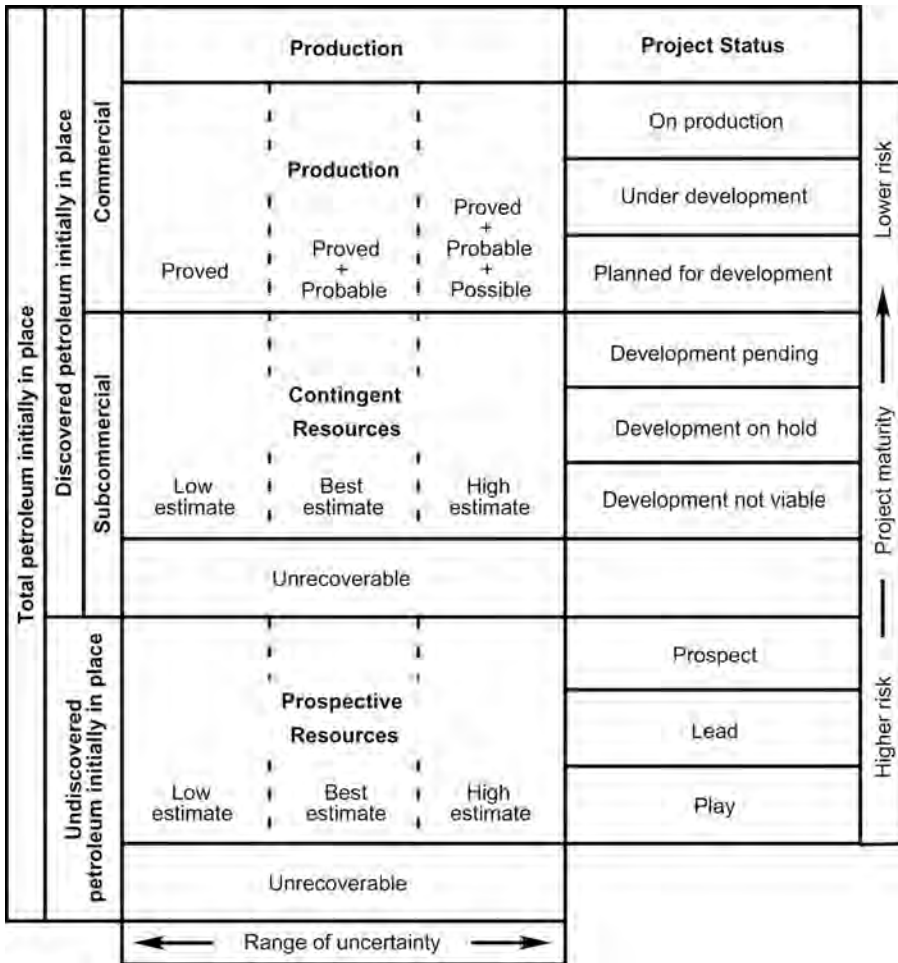


Fig. 18.1—Resource classification system, showing possible project status categories (after Ross⁴).

Fig. 18.1⁴ illustrates the entire spectrum of in-place and recoverable hydrocarbons, the total resource base that is contained within the subsurface of the Earth. The vertical scale represents the total resource base, including cumulative production, reserves, and the unrecoverable portions of the discovered and economic quantities, as well as the recoverable and unrecoverable portions of the two categories of resources.

The horizontal scale reflects the increasing degrees of uncertainty of reserves quantities, showing (left to right) reserves classifications of proved through possible and resource-estimates categories of low to high. A project status column on the far right contains terms typically used to describe the stage of exploration and development associated with the various degrees of uncertainty. The classifications of proved plus probable and proved plus probable plus possible reserves are consistent with those used with probabilistic methods of reserves estimation and classification.

Fig. 18.2 adapts the so-called McKelvey⁵ box to show the relationship between USGS reserves classifications and those of the 1997 Society of Petroleum Engineers/World Petroleum Congress (SPE/WPC),⁶ which are quoted in a subsequent section. USGS (McKelvey⁵) classifications of identified (discovered) reserves (measured, indicated, and inferred) are approximately equivalent to the 1997 SPE/WPC classifications of proved, probable, and possible, respectively.

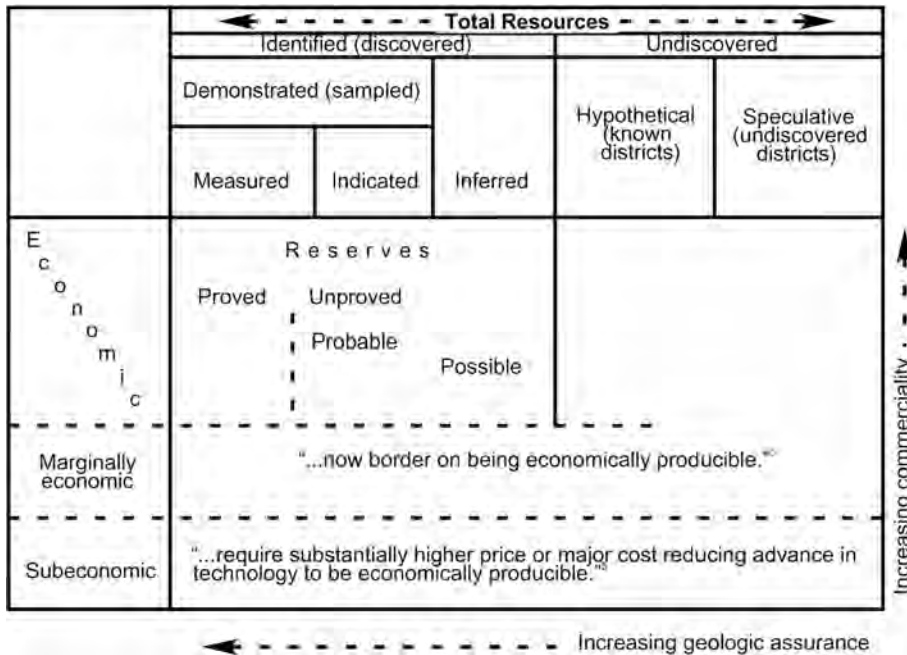


Fig. 18.2—The McKelvey box, illustrating the relationship between the U.S. Geological Survey (USGS) classification of resources and the 1997 SPE/WPC classifications of reserves. (After McKelvey.⁵)

The integration of this concept with the 2001 SPE/WPC/AAPG (American Assn. of Petroleum Geologists) resource definitions⁴ led to the development of Fig 18.1.

Reserves are the quantities that remain to be commercially produced as of a given date, under stated economic and operating conditions. Ultimate reserves are the sum of cumulative production and quantities (reserves) yet to be commercially produced. Terms such as “remaining reserves” and “recoverable reserves” are redundant. Terms such as “exploratory reserves,” “geologic reserves,” “potential reserves,” and “technical reserves” often are used in conversation, but are misleading. The use of such terms is discouraged.

For this chapter discussion, reserves are quantities that are available for sale following lease or platform separation. Oil and condensate quantities do not reflect any reduction for field losses or field use. Natural-gas reserves typically are reported net after field condensate removal, but no consideration is given herein to gas volume reduction resulting from the extraction of natural-gas liquids or for the removal of contaminants. (See McMichael and Spencer⁷ for a discussion of these issues.)

18.2 Reserves Definitions

18.2.1 1997 SPE/WPC Petroleum Reserves Definitions.*

Reserves are those quantities of petroleum which are anticipated to be commercially recovered from known accumulations from a given date forward. All reserves estimates involve some degree of uncertainty. The uncertainty depends chiefly on the amount of reliable geologic and engineering data available at the time of the estimate and the interpretation of these data. The relative degree of uncertainty may be conveyed by placing reserves into one of two principal classifications, either proved or unproved. Unproved reserves are

* Definitions here are quoted from Ref. 6. Cronquist³ has provided comments regarding interpretation of some of the terms used in these definitions. New definitions were approved in 2007.

less certain to be recovered than proved reserves and may be further subclassified as probable and possible reserves to denote progressively increasing uncertainty regarding their recoverability.

The intent of the SPE and WPC in approving additional classifications beyond proved reserves is to facilitate consistency among professionals using such terms. In presenting these definitions, neither organization is recommending public disclosure of reserves classified as unproved. Public disclosure of the quantities classified as unproved reserves is left to the discretion of the countries or companies involved.

Estimation of reserves is done under conditions of uncertainty. The method of estimation is called *deterministic* [our emphasis] if a single best estimate of reserves is made based on known geological, engineering, and economic data. The method of estimation is called *probabilistic* [our emphasis] when the known geological, engineering, and economic data are used to generate a range of estimates and their associated probabilities. Identifying reserves as proved, probable, and possible has been the most frequent classification method and gives an indication of the probability of recovery. Because of potential differences in uncertainty, caution should be exercised when aggregating reserves of different classifications.

Reserves estimates will generally be revised as additional geologic or engineering data become available or as economic conditions change. Reserves do not include quantities of petroleum being held in inventory, and they may be reduced for usage or processing losses if required for financial reporting.

Reserves may be attributed to either natural energy or improved recovery methods. Improved recovery methods include all methods for supplementing natural energy or altering natural forces in the reservoir to increase ultimate recovery. Examples of such methods are pressure maintenance, cycling, waterflooding, thermal methods, chemical flooding, and the use of miscible and immiscible displacement fluids. Other improved recovery methods may be developed in the future as petroleum technology continues to evolve.

Proved Reserves. Proved reserves are those quantities of petroleum which, by analysis of geological and engineering data, can be estimated with reasonable certainty to be commercially recoverable, from a given date forward, from known reservoirs and under current economic conditions, operating methods, and government regulations. Proved reserves can be categorized as developed or undeveloped.

If deterministic methods are used, the term reasonable certainty is intended to express a high degree of confidence that the quantities will be recovered. If probabilistic methods are used, there should be at least a 90% probability that the quantities actually recovered will equal or exceed the estimate.

Establishment of current economic conditions should include relevant historical petroleum prices and associated costs and may involve an averaging period that is consistent with the purpose of the reserves estimate, appropriate contract obligations, corporate procedures, and government regulations involved in reporting these reserves.

In general, reserves are considered proved if the commercial producibility of the reservoir is supported by actual production or formation tests. In this context, the term “proved” refers to the actual quantities of petroleum reserves and not just the productivity of the well or reservoir. In certain cases, proved reserves may be assigned on the basis of well logs and/or core analysis that indicate the subject reservoir is hydrocarbon-bearing and is analogous to reservoirs in the same area that are producing or have demonstrated the ability to produce on formation tests.

The area of the reservoir considered as proved includes (1) the area delineated by drilling and defined by fluid contacts, if any, and (2) the undrilled portions of the reservoir that can reasonably be judged as commercially productive on the basis of available geological and engineering data. In the absence of data on fluid

contacts, the lowest known occurrence of hydrocarbons controls the proved limit unless otherwise indicated by definitive geological, engineering, or performance data.

Reserves may be classified as proved if facilities to process and transport those reserves to market are operational at the time of the estimate or there is a reasonable expectation that such facilities will be installed. Reserves in undeveloped locations may be classified as proved undeveloped provided (1) the locations are direct offsets to wells that have indicated commercial production in the objective formation, (2) it is reasonably certain such locations are within the known proved productive limits of the objective formation, (3) the locations conform to existing well spacing regulations where applicable, and (4) it is reasonably certain the locations will be developed. Reserves from other locations are classified as proved undeveloped only where interpretations of geological and engineering data from wells indicate with reasonable certainty that the objective formation is laterally continuous and contains commercially recoverable petroleum at locations beyond direct offsets.

Reserves that are to be produced through the application of established improved recovery methods are included in the proved classification when (1) successful testing by a pilot project or favorable response of an installed program in the same or an analogous reservoir with similar rock and fluid properties provides support for the analysis on which the project was based, and (2) it is reasonably certain that the project will proceed. Reserves to be recovered by improved recovery methods that have yet to be established through commercially successful applications are included in the proved classification only (1) after a favorable production response from the subject reservoir from either (a) a representative pilot or (b) an installed program where the response provides support for the analysis on which the project is based and (2) it is reasonably certain the project will proceed.

Unproved Reserves. Unproved reserves are based on geologic and/or engineering data similar to those used in estimates of proved reserves; but technical, contractual, economic, or regulatory uncertainties preclude such reserves being classified as proved. Unproved reserves may be further classified as probable reserves and possible reserves.

Unproved reserves may be estimated assuming future economic conditions different from those prevailing at the time of the estimate. The effect of possible future improvements in economic conditions and technological developments can be expressed by allocating appropriate quantities of reserves to the probable and possible classifications.

Probable Reserves. Probable reserves are those unproved reserves which analysis of geological and engineering data suggests are more likely than not to be recoverable. In this context, when probabilistic methods are used, there should be at least a 50% probability that the quantities actually recovered will equal or exceed the sum of estimated proved plus probable reserves.

In general, probable reserves may include (1) reserves anticipated to be proved by normal step-out drilling where subsurface control is inadequate to classify these reserves as proved, (2) reserves in formations that appear to be productive based on well log characteristics but lack core data or definitive tests and which are not analogous to producing or proved reserves in the area, (3) incremental reserves attributable to infill drilling that could have been classified as proved if closer statutory spacing had been approved at the time of the estimate, (4) reserves attributable to improved recovery methods that have been established by repeated commercially successful applications when (a) a project or pilot is planned but not in operation and (b) rock, fluid, and reservoir characteristics appear favorable for commercial application, (5) reserves in an area of the formation that appears to be separated from the proved area by faulting and the geologic interpretation indicates the subject area is structurally higher than the proved area, (6) reserves attributable to a future workover, treatment, retreatment, change of equipment, or other mechanical procedures, where such proce-

ture has not been proved successful in wells which exhibit similar behavior in analogous reservoirs, and (7) incremental reserves in proved reservoirs where an alternative interpretation of performance or volumetric data indicates more reserves than can be classified as proved.

Possible Reserves. Possible reserves are those unproved reserves which analysis of geological and engineering data suggests are less likely to be recoverable than probable reserves. In this context, when probabilistic methods are used, there should be at least a 10% probability that the quantities actually recovered will equal or exceed the sum of estimated proved plus probable plus possible reserves.

In general, possible reserves may include (1) reserves which, based on geological interpretations, could possibly exist beyond areas classified as probable, (2) reserves in formations that appear to be petroleum-bearing based on log and core analysis but may not be productive at commercial rates, (3) incremental reserves attributed to infill drilling that are subject to technical uncertainty, (4) reserves attributed to improved recovery methods when (a) a project or pilot is planned but not in operation and (b) rock, fluid, and reservoir characteristics are such that a reasonable doubt exists that the project will be commercial, and (5) reserves in an area of the formation that appears to be separated from the proved area by faulting and geological interpretation indicates the subject area is structurally lower than the proved area.

Reserves Status Categories. Reserves status categories define the development and producing status of wells and reservoirs.

Developed Reserves. Developed reserves are expected to be recovered from existing wells including reserves behind pipe. Improved recovery reserves are considered developed only after the necessary equipment has been installed, or when the costs to do so are relatively minor. Developed reserves may be subcategorized as producing or nonproducing.

Producing. Reserves subcategorized as producing are expected to be recovered from completion intervals that are open and producing at the time of the estimate. Improved recovery reserves are considered producing only after the improved recovery project is in operation.

Nonproducing. Reserves subcategorized as nonproducing include shut-in and behind-pipe reserves. Shut-in reserves are expected to be recovered from (1) completion intervals that are open at the time of the estimate but that have not started producing, (2) wells which were shut in for market conditions or pipeline connections or (3) wells not capable of production for mechanical reasons. Behind-pipe reserves are expected to be recovered from zones in existing wells that will require additional completion work or future recompletion prior to the start of production.

Undeveloped Reserves. Undeveloped reserves are expected to be recovered (1) from new wells on undrilled acreage, (2) from deepening existing wells to a different reservoir, or (3) where a relatively large expenditure is required to (a) recomplete an existing well or (b) install production or transportation facilities for primary or improved recovery projects.

The 1997 SPE/WPC definitions⁶ quoted above evolved over many years through the efforts of several organizations. The Soc. of Petroleum Evaluation Engineers (SPEE) contributed significantly to the 1981 and 1987 SPE Petroleum Reserves definitions.^{8,9} The 1981 definitions refer only to proved reserves; the 1987 definitions introduce the concept of unproved reserves and the subclassifications of probable and possible reserves.

The 1997 SPE/WPC definitions recognize both the deterministic and probabilistic methods and establish relative standards for each. The SPE and the WPC continue to work together to improve these definitions in light of several unresolved ambiguities. Such ambiguities include reconciliation of the terms “reasonable certainty” and “at least a 90% probability” used to de-

scribe proved reserves. For deterministic estimates, quantities for each of the three reserves categories of proved, probable, and possible are estimated, and the evaluator is cautioned not to add these quantities together because of the differing degrees of uncertainty associated with each. Conversely, the probabilistic approach requires the addition of “proved plus probable” or “proved plus probable plus possible” categories to comply with the stated numerical levels of uncertainty. Further, definitions place certain specified limitations on the “lowest known occurrence of hydrocarbons,” average prices, and conformance to regulatory well spacing (where applicable), thus reducing the variables that are subject to classic probabilistic reserves assessment.

18.2.2 1978 U.S. Securities and Exchange Commission (SEC) Oil and Gas Reserves Definitions.¹ The U.S. SEC Regulation S X Rule 4 10 paragraph (a)¹⁰ defines proved reserves as follows:*

Proved Oil and Gas Reserves. Proved oil and gas reserves are the estimated quantities of crude oil, natural gas, and natural gas liquids which geological and engineering data demonstrate with reasonable certainty to be recoverable in future years from known reservoirs under existing economic and operating conditions; i.e., prices and costs as of the date the estimate is made. Prices include consideration of changes in existing prices provided only by contractual arrangements, but not on escalations based upon future conditions.

1. Reservoirs are considered proved if economic producibility is supported by either actual production or conclusive formation test. The area of a reservoir considered proved includes:

(A) that portion delineated by drilling and defined by gas/oil and/or oil/water contacts, if any; and

(B) the immediately adjoining portions not yet drilled, but which can be reasonably judged as economically productive on the basis of available geological and engineering data. In the absence of information on fluid contacts, the lowest known structural occurrence of hydrocarbons controls the lower proved limit of the reservoir.

2. Reserves which can be produced economically through application of improved recovery techniques (such as fluid injection) are included in the “proved” classification when successful testing by a pilot project, or the operation of an installed program in the reservoir, provides support for the engineering analysis on which the project or program was based.

3. Estimates of proved reserves do not include the following:

(A) oil that may become available from known reservoirs but is classified separately as “indicated additional reserves”;

(B) crude oil, natural gas, and natural gas liquids, the recovery of which is subject to reasonable doubt because of uncertainty as to geology, reservoir characteristics, or economic factors;

(C) crude oil, natural gas, and natural gas liquids, that may occur in undrilled prospects; and

(D) crude oil, natural gas, and natural gas liquids, that may be recovered from oil shales, coal,[†] gilsonite and other such sources.

Proved Developed Oil and Gas Reserves. Proved developed oil and gas reserves are reserves that can be expected to be recovered through existing wells with existing equipment and operating methods. Additional oil and gas expected to be obtained through the application of fluid injection or other improved recovery techniques for supplementing the natural forces and mechanisms of primary recovery should be included as “proved developed reserves” only after testing by a pilot project or after the operation of an installed program has confirmed through production response that increased recovery will be achieved.

Proved Undeveloped Oil and Gas Reserves. Proved undeveloped oil and gas reserves are reserves that are expected to be recovered from new wells on undrilled acreage, or from existing wells where a relatively

*Subsection formatting in this section follows that of the SEC.

[†]SAB12, following, modifies this ruling.

major expenditure is required for recompletion. Reserves on undrilled acreage shall be limited to those drilling units offsetting productive units that are reasonably certain of production when drilled. Proved reserves for other undrilled units can be claimed only where it can be demonstrated with certainty that there is continuity of production from the existing productive formation. Under no circumstances should estimates for proved undeveloped reserves be attributable to any acreage for which an application of fluid injection or other improved recovery technique is contemplated, unless such techniques have been proved effective by actual tests in the area and in the same reservoir.

18.2.3 U.S. SEC Staff Accounting Bulletins (SABs). Certain SABs published after Regulation S X¹⁰ concern the application of financial accounting and disclosure rules for oil and gas producing activities. In particular, the following interpretations extracted from a recent SEC compilation of SABs^{11,12,13} set forth the Commission staff's view on specific questions pertaining to proved oil and gas reserves:

Economic producibility of estimated proved reserves can be supported to the satisfaction of the Office of Engineering if geological and engineering data demonstrate with reasonable certainty that those reserves can be recovered in future years under existing economic and operating conditions. The relative importance of the many pieces of geological and engineering data which should be evaluated when classifying reserves cannot be identified in advance. In certain instances, proved reserves may be assigned to reservoirs on the basis of a combination of electrical and other type logs and core analyses which indicate the reservoirs are analogous to similar reservoirs in the same field which are producing or have demonstrated the ability to produce on a formation test.¹¹

In determining whether "proved undeveloped reserves" encompass acreage on which fluid injection (or other improved recovery technique) is contemplated, is it appropriate to distinguish between (i) fluid injection used for pressure maintenance during the early life of a field and (ii) fluid injection used to effect secondary recovery when a field is in the late stages of depletion? The Office of Engineering believes that the distinction identified in the above question may be appropriate in a few limited circumstances, such as in the case of certain fields in the North Sea. The staff will review estimates of proved reserves attributable to fluid injection in the light of the strength of the evidence presented by the registrant in support of a contention that enhanced recovery will be achieved.¹¹

Companies should report reserves of natural gas liquids which are net to their leasehold interest; i.e., that portion recovered in a processing plant and allocated to the leasehold interest. It may be appropriate in the case of natural gas liquids not clearly attributable to leasehold interests ownership to follow instruction (b) of Item 2(b)(3) of Regulation S K and report such reserves separately and describe the nature of the ownership.¹¹

The staff believes that since coalbed methane gas can be recovered from coal in its natural and original location, it should be included in proved reserves, provided that it complies in all other respects with the definition of proved oil and gas reserves as specified in Rule 4 10(a)(2) including the requirement that methane production be economical at current prices, costs, (net of the tax credit) and existing operating conditions.¹²

SAB statements are not rules or interpretations of the Commission, nor are they published as bearing the Commission's official approval. They represent interpretations and practices followed by the U.S. SEC's Div. of Corporation Finance and Office of the Chief Accountant in administering the disclosure requirements of the U.S. securities laws.

18.2.4 Unproved Oil and Gas Reserves. U.S. SEC Regulation S K¹³ prohibits the disclosure of estimated quantities of probable and possible reserves of oil and gas and any estimated value thereof in any documents publicly filed with the Commission.

18.2.5 Website Release. In a 21 February 2001 website release,¹⁴ the U.S. SEC addressed several topics relative to the reporting of proved reserves. No changes were made to the 1978 definitions, but the U.S. SEC engineering staff modified its application and interpretation of those definitions in light of the widespread technological advances in over the previous 20 years. The most significant of these application changes are discussed below.

18.2.6 Significance of the 1997 SPE/WPC and the 1978 U.S. SEC Reserves Definitions. The 1997 SPE/WPC definitions⁶ have been proposed as the technical standards for the international petroleum industry. Regulatory authorities worldwide have been encouraged to use these definitions as much they reasonably can for their specific purposes.

When the U.S. SEC definitions were approved (1978), virtually all regulated companies were in the U.S.A. and most reported reserves were located in North America, neither of which is now the case. Also, virtually all natural gas then was sold through long-term contracts with a defined pricing structure. Oil prices were less volatile then, compared with price swings seen over the past 10 to 15 years. Privatization of numerous national or state-owned oil and gas companies, with the sale of their securities within the U.S.A., has greatly enlarged the effective reach and importance of the U.S. SEC. The U.S. SEC's petroleum-engineering staff has been increased in recent years to enable the agency to monitor more effectively the reserves-reporting activities of an increasing number of oil and gas companies subject to the jurisdiction of the agency.

18.2.7 1997 SPE/WPC and 1978 U.S. SEC Definitions Comparison. *Reasonable Certainty.*

The SPE/WPC and the U.S. SEC definitions both use “reasonable certainty” to describe the controlling condition for proved reserves, but neither offers quantification of the term. Most engineers now accept that reasonable certainty indicates relatively high confidence. The 1997 SPE/WPC definitions require that for proved reserves estimated using probabilistic methods there be at least 90% probability (a “P90” estimate) that the quantity recovered will equal or exceed the estimated quantity. At least 50% probability (a “P50” estimate) is required for proved plus probable reserves estimated using probabilistic methods.

Proved reserves estimated using deterministic methods seldom, if ever, will meet a P90 requirement. Most volumetric estimates use *average* porosity, *average* water saturation, and recovery efficiencies (REs) that are consistent with expected reservoir drive mechanisms and operating conditions.

If an oil/water contact (OWC) or gas/water contact (GWC) is known, the resultant volumetric reserves estimate logically may be described as the “most likely” estimate, which might approach a P50 (probabilistic) estimate. For another example, when using a conservative RE because of an unknown drive mechanism and a lowest known limit of oil (LKO) or gas (LKG), the equivalent confidence level may be between P50 and P90.

For performance estimates using trend analysis, the engineer typically will extrapolate a “best fit” from the historical information, which essentially reflects a P50 estimate.³ Extrapolations could be prepared for P90, P50, and P10 estimates, but this seldom is done.

In summary, reasonable certainty for deterministic estimates will represent confidence levels approaching P50 in most instances, but will seldom approach the P90 level as defined in the 1997 SPE/WPC definitions.

Known Accumulations. The 1997 SPE/WPC definitions use the term *known accumulations*, which the U.S. SEC definitions refer to as *known reservoirs*. In the industry, a known accumulation is an underground collection of moveable petroleum—one or more reservoirs confirmed through the drilling and gathering of reservoir data from one or more wells. A known accumulation must be considered commercial before reserves of any classification may be assigned.

Economic Conditions. The U.S. SEC definitions¹⁰ specify that proved reserves are to be reported consistent with “existing economic and operating conditions; i.e., prices and costs as

of the date the estimate is made.” This is intended to be the contract price for the sale of oil and gas as of the report date, which typically is 31 December. For products sold in a spot market, the pricing available on the report date should be used. Operating costs typically are costs averaged over the preceding 12 months, unless a change material to the estimate has occurred during the preceding 6 months. In the estimation of proved reserves, the 1997 SPE/WPC definitions allow the use of a historical oil and gas price averaged over a time period that is “consistent with the purpose of the estimate.”

According to the 1997 SPE/WPC definitions, probable and possible reserves also must be considered commercial before they can be classified, but they may be based on more favorable economic conditions than those existing at the effective date of the estimate.

Development Status. The U.S. SEC continues to enforce the 1978 definitions regarding undeveloped well locations, requiring that the proved classification be given only to those locations beyond one offset from a productive well where “it can be demonstrated with *certainty* that there is continuity of production” [emphasis added] from the existing productive formation. A subsequent clarification released by the U.S. SEC in 2001¹⁴ stated that “there is no mitigating modifier for the word *certainty*.”

These provisions are troublesome in at least three regards. First, the term “offset” refers to regulatory-controlled well spacing in North America and to few areas, if any, elsewhere. Second, and more importantly, the term “certainty” is used here by the U.S. SEC to describe undeveloped reserves, whereas the controlling term in the first sentence of the U.S. SEC definitions is “reasonable certainty.” Third, the expression “continuity of production” is undefined, but is used in a context of a higher standard than reservoir continuity.

The 1997 SPE/WPC definitions leave the classification of reserves from undrilled locations to the discretion of the evaluator using good engineering practices.

Requirement for Flow Testing. Both the U.S. SEC definitions and the 1997 SPE/WPC definitions require evidence of producibility through actual production or conclusive formation tests. Both definitions also permit exceptions in certain cases. The U.S. SEC may grant an exception for a definitive flow test for a particular reservoir if core *and* log data indicate commercial productivity and the reservoir is analogous to one or more flow-tested or producing reservoir(s) in the same field. The 1997 SPE/WPC definitions have a similar but less restrictive flow-test exemption that requires favorable core *and/or* log data for the subject reservoir compared to an analogous reservoir(s) in the same area that has demonstrated commercial productivity.

There is increasing interest by evaluators using both the U.S. SEC and the 1997 SPE/WPC reserves definitions in certain instances, particularly for the deepwater areas of the U.S. Gulf of Mexico, where physical well testing is impractical because of costs and environmental concerns. Many of these discoveries are not close to other fields, but may be characterized by thick sections of highly permeable sandstones saturated with high-API-gravity, low-viscosity crudes and exhibiting reservoir pressures in excess of 8,000 psia. In such scenarios, flow calculations can confirm production rates that are considerably higher than the minimum commercial rates, and are adequate for producers to make commercial decisions about facility sizing and project sanctioning. The evaluator determines on a case-specific basis whether such indirect data are adequate to confirm commercial flow rates (without a physical flow test) in consideration of the applicable definitions.

Areal Extent of a Reservoir. The U.S. SEC definitions mandate the use of a recognized OWC, gas/oil contact (GOC), and GWC to define structural limits of proved reserves. In the absence of such contacts, limits are imposed by the LKO or LKG, which typically are defined as the subsea depth of the base of the (permeable) reservoir, as recorded on well logs. Only in recent years has the U.S. SEC begun to consider indirect measurements or calculations of controlling contacts. The U.S. SEC’s acceptance of indirect indicators such as pressure/depth

calculations, seismic information, pressure-gradient calculations, and capillary-pressure computations has been only in exceptional cases in which the quality of the data was excellent and the presentation of the interpretation was compelling. In their acceptance of a limiting contact below the base of the lowest logged interval, the U.S. SEC engineering staff may further consider the materiality of the quantity of reserves added through the use of pressure-gradient data. They provide no definition of materiality. Also, agreement between two or more indirect measurements would be required as the basis for establishing proved reserves. Such agreement also applies to 1997 SPE/WPC definitions.

Enhanced-Recovery Reserves. The U.S. SEC traditionally has required that the proved designation be limited to reservoirs where enhanced-recovery (improved-recovery) methods have been demonstrated through a successful pilot project or an installed program “in the reservoir.” This requirement was reinterpreted in 2001¹⁴ to allow successful, operating analog reservoirs in the same geologic area to be used as support for assigning proved enhanced-recovery reserves. The subject reservoir should have reservoir and fluid parameters that are equal to or more favorable than those of the analog reservoir(s). The 1997 SPE/WPC definitions also permit the use of successful analogs in the area as the basis for establishing proved enhanced-recovery reserves.

Other Differences. The 1997 SPE/WPC and 1978 U.S. SEC definitions contain many other wording differences regarding proved reserves, but those cited above are of major importance. For questions of interpretation or application, however, the U.S. SEC typically will respond to inquiries by interested parties.

18.2.8 Other Reserves Definitions. Other petroleum-producing countries and regulatory authorities have promulgated petroleum reserves definitions that are recognized and based on years of development and sound engineering judgment, but none—however important in their sphere of influence—with such far-reaching consequences as the 1978 U.S. SEC and the 1997 SPE/WPC definitions. (See Cronquist³ for a summary of many of these other definitions.)

18.3 Calculation Procedures

Although reserves estimates for known accumulations historically have used deterministic calculation procedures, the 1997 SPE/WPC definitions allow either deterministic or probabilistic procedures. Each of these is discussed briefly in the next two sections. Thereafter—except for another section on probabilistic procedures near the end—the chapter will focus on deterministic procedures because they still are more widely used. Both procedures need the same basic data and equations.

18.3.1 Deterministic Procedures. Deterministic calculations of oil and/or gas initially in place (O/GIP) and reserves are based on best estimates of the true values of pertinent parameters, although it is recognized that there may be considerable uncertainty in such values. Reserves calculated using such procedures are classified subjectively on the basis of professional judgments of the uncertainty in each reserve estimate and/or of pertinent regulatory and/or corporate guidelines.

18.3.2 Probabilistic Procedures. Probabilistic procedures recognize that uncertainties in input data and equations to calculate reserves may be significant. Accordingly, each input parameter uses a reasonable range of values, from which a set of reserves calculations is made. Reserves calculated using this procedure are classified on the basis of specified percentile rankings of reserves estimates within the calculated set and/or of pertinent regulatory and/or corporate guidelines.

18.4 Estimation Methods

Methods to estimate reserves may be categorized as either static or dynamic. Static methods typically are used before production is initiated in a subject reservoir, and include analogy methods and volumetric methods. Computer simulation that is used before production initiation is considered a static method. Dynamic methods might be used after sustained production has been initiated, and include production trend analysis, material-balance calculations, and computer simulation. Because dynamic methods typically consider well and/or reservoir performance, they generally are considered more reliable than static methods. A specific reserves estimate might involve one or more such methods. What method (or methods) are used depends on several factors, including production history of the area, if any; stage of development on the date of the estimate; geologic complexity; quality and quantity of data; maturity of production for the subject reservoir; and the purpose of the estimate. Each estimate should be corroborated using an alternate, preferably independent, method.

18.4.1 Analogy Methods. Analogy methods typically are used to estimate ultimate recovery—or unit recovery factors—of oil and/or gas for *undrilled locations* and to supplement volumetric methods of estimating reserves in the early stages of development and production. The analogy method assumes that the analogous reservoir or well is comparable to the subject reservoir or well in those aspects that control ultimate recovery of oil and/or gas. The method’s weakness is that this assumption’s validity cannot be determined until the subject reservoir or well has been produced long enough to estimate reserves using dynamic methods.

In some scenarios, analogy may be the *only* feasible method until there are sufficient pressure and/or production data for a reliable analysis of performance. Such scenarios include areas of widely spaced development, where subsurface information might be too sparse to facilitate reliable volumetric mapping, and reservoirs where log, core, and/or test data are insufficient for reliable characterization.

There are two broad categories of analogy methods: analytical and statistical. Regardless of the method used, however, analogous and subject reservoirs should be similar in their structural configuration; lithology and depositional environment of the reservoir rock; nature and degree of principal heterogeneity; average net thickness and ratio of net pay to gross pay; petrophysics of the rock/fluid system; initial pressure and temperature; reservoir-fluid properties and drive mechanism; spatial relationship between free gas (if any), oil, and aquifer at initial conditions (“stacked” vs. “en echelon”); well spacing; and economic scenario. Because all these reservoir aspects seldom, if ever, are similar, judicious compensating adjustments from analogous to subject reservoir usually are needed. Such adjustments require considerable local knowledge and reservoir engineering experience.

Analytical (analogy) methods include using recovery *factors* (e.g., STBO/acre-ft of reservoir) or recovery *efficiencies* (percent recovery) from analogous reservoirs to estimate oil and/or gas reserves for wells or reservoirs being studied. Basic rock and/or fluid parameters—porosity, water saturation, and formation volume factor (FVF)—may be used with, or as modifiers to, these recovery factors or recovery efficiencies. For example, the recovery factor observed in an analogous reservoir (F_{RA}) might be adjusted by:

$$F_{RS} = F_{RA}(\phi S_{hi})_S / (\phi S_{hi})_A \dots\dots\dots (18.1)$$

where the terms $(\phi S_{hi})_S$ and $(\phi S_{hi})_A$ refer to subject and analogous reservoirs, respectively.

Depending on circumstances, more complex relations might be appropriate, such as one or more of the factorial groups in Eqs. 18.14 and 18.15, which are discussed in the Recovery Efficiency section below.

TABLE 18.1—AGGREGATE RECOVERY EFFICIENCY FOR GROUPS OF OIL RESERVOIRS IN VARIOUS REGIONS OF THE U.S.A. (AFTER CRONQUIST³)

State or Region	Dominant Lithology	Main Drive Mechanism	Recovery Efficiency ^a
Northern Louisiana	Carbonate ^b	Pressure depletion	0.15
Southern Louisiana	Sandstone ^c	Waterdrive	0.51 ^d
Oklahoma	Sandstone ^e	Waterflood	0.34
Pennsylvania	Sandstone ^f	Waterflood	0.20
Permian Basin	Carbonate ^g	Waterflood	0.39 ^h
Texas Gulf Coast	Sandstone ⁱ	Waterflood	0.47 ^j
Texas Panhandle	Carbonates ^k	Pressure depletion	0.23
West Virginia	Sandstone ^l	Pressure depletion	0.21

^aCalculated from API data.¹⁵ Almost all fields included produced "light" oil. ^bMostly Lower Cretaceous/Jurassic, porosity = 5 to 20%, permeability = 1 to 500 md. ^cChiefly Miocene, porosity = 15 to 35%, permeability = 50 to 2,500 md. ^dEstimated ultimate recovery efficiency from a few high-quality giant fields = 56 to 66%. ^eMostly Pennsylvanian, porosity = 5 to 20%, permeability = 5 to 100 md. ^fMostly poor-quality Devonian graywackes. ^gChiefly Permian shelf carbonates, porosity = 5 to 20%, permeability = 1 to 100 md. ^hEstimated ultimate recovery efficiency from some of the better floods = 50 to 60%. ⁱChiefly lower Cenozoic, porosity = 15 to 35%, permeability = 50 to 2,500 md. ^jEstimated ultimate recovery efficiency from several high-quality giant fields = 52 to 61%, with a few approaching 70 to 74%. ^kMostly Upper Paleozoic, porosity = 5 to 15%, permeability = 1 to 100 md. ^lMiddle Paleozoic, porosity = 5 to 15%, permeability = 1 to 100 md.

In many areas, estimates of rock properties—porosity, initial water saturation, and net pay—made from wireline logs are subject to considerable uncertainty. Without core data or definitive formation tests, analogy may be the only method available initially to estimate reserves. Analogies can be drawn from mature reservoirs in comparable geologic and engineering settings. Several examples are provided for mature areas in the U.S.A.

Using American Petroleum Institute (API) data,¹⁵ aggregate REs were estimated³ for groups of oil reservoirs in various regions in the U.S.A. (Table 18.1). (Comparable data on natural gas reservoirs in the U.S.A. have not been published.) From Table 18.1, one might note (1) for northern and southern Louisiana, for example, the respective influence of lithology and drive mechanism on RE; (2) for Oklahoma and Pennsylvania, for example, the significant difference in waterflood (ultimate) RE, which probably results from the Pennsylvania waterfloods' significantly poorer rock quality; (3) for southern Louisiana and the Texas Gulf Coast, for example, the reasonable agreement in waterdrive RE. The slightly higher-quality sands in the Louisiana Gulf Coast probably cause small differences.

From a review of these (admittedly limited) data, it appears that variations in aggregate oil RE between regions are attributable principally to differences in reservoir rock/fluid systems and reservoir drive mechanisms. SPEE has published additional, useful summary discussions of regional variations in rock quality and reservoir drive mechanism for various areas in the U.S.A.¹⁶

In 1984, the API published estimates of oil initially in place (OIP) and primary RE for 533 reservoirs in the U.S.A. and estimates of primary and waterflood RE for 230 reservoirs in the U.S.A.¹⁷ (Table 18.2). Estimates such as these can be developed for other areas using detailed data published annually by most U.S.A. state oil and gas regulatory commissions, the Alberta Energy Resource Conservation Board (ERCB) [which since 1995 has been part of the Alberta Energy and Utilities Board (EUB)], the Saskatchewan Dept. of Energy and Mines, various regional geological societies, and other such agencies. This type of regional data might be useful

Lithology	State or Region	Number of Reservoirs	OIP, STB/NAF		Recovery, STB/NAF		Average RE
			Range	Average	Range	Average	
Solution Gas Drive							
Sandstone	California	51	328 to 2,146	1,148	55 to 644	273	0.24
	Louisiana	17	360 to 1,540	1,167	110 to 613	315	0.27
	Oklahoma	41	386 to 1,030	604	40 to 227	117	0.19
	NW Texas	24	Not reported	578	Not reported	86	0.15
	SE Texas	38	Not reported	827	Not reported	205	0.25
	West Virginia	13	546 to 882	678	100 to 250	143	0.21
	Wyoming	23	386 to 1,135	692	82 to 361	176	0.25
Carbonate	All	100	59 to 1,067	526	5 to 190	93	0.18
Natural Waterdrive							
Sandstone	California	9	508 to 1,770	1,020	169 to 568	367	0.36
	Louisiana	42	535 to 1,960	1,203	219 to 1,470	722	0.60
	Texas	101	547 to 1,801	1,167	125 to 1,094	633	0.54
	Wyoming	27	Not reported	860	Not reported	313	0.36
Carbonate	All	47	85 to 705	265	29 to 370	117	0.44

in making *preliminary* estimates of reserves, pending development of specific data for the well/reservoir in question.

Information presented in [Tables 18.1](#) and [18.2](#) is included only as reference information and should be considered only in the absence of definitive data available from specific wells or reservoirs.

Statistical (analogy) methods include using per-well recoveries of oil and/or gas from analogous wells in the same producing trend or in analogous geologic settings to estimate recoveries from wells being studied. Two types of statistical (analogy) methods are discussed here: isoultimate recovery maps and analysis of observed frequency distributions of ultimate recovery. Additional comments are provided in the Recovery Efficiency section below.

When analogy methods are used to estimate reserves for individual wells, the analogous and subject wells should be similar regarding well completion, including stimulation type (if any); production method; initial absolute open-flow potential for gas wells; initial potential and/or productivity index for oil wells; well spacing; and economic limit.

In some producing areas, ultimate recovery of oil or gas from individual wells may be controlled by geologic trends such as depositional environment, intensity of fracturing, or degree of diagenesis. In such cases, an isoultimate recovery map can be made by posting and contouring estimated ultimate recovery from individual wells in the area of interest. Such a map can be used to estimate reserves for undrilled tracts, *but one should use this technique cautiously!* Nongeologic factors might control ultimate recovery of oil or gas.

Different completion and stimulation procedures may yield different ultimate recoveries from individual wells. For example, for wells in several areas of the U.S.A., a correlation has been observed between size of fracture treatment and ultimate recovery.¹⁸ Thus, before relying on isoultimate recovery maps, one should determine whether there is a statistically valid relation between ultimate recovery and the completion or stimulation method or another parameter. Wells in the area of interest may be capable of draining more than a “spacing unit.” In this case, wells that are adjacent to undrilled tracts and those placed on production early in reservoir life may exhibit higher ultimate recoveries than wells in central locations and those placed on production late in reservoir life. One should investigate these possibilities before using an isoultimate recovery map to estimate reserves for undrilled tracts.

An alternative to isoultimate recovery maps is the use of “bubble maps,” in which the size of the circle drawn around a wellbore is proportional to the parameter or measurement being compared.

Factors such as well spacing, completion technique, operating cost, and operating procedure can affect ultimate recovery of oil and/or gas significantly. If there are significant differences in these factors from one property to the next, be careful in making comparisons or statistical analyses of wells between such properties.

If other factors are more or less the same, the RE of oil and/or gas generally will be greater in areas with low operating costs and closely spaced wells than in areas with high operating costs and widely spaced wells. Most statistical data on RE in the U.S.A. have come from operations with onshore properties, which historically have had relatively low operating costs and closely spaced wells. These are not typical conditions in other areas of the world, especially offshore areas; thus, one should exercise caution when using REs determined from U.S.A. reservoirs to estimate REs from otherwise analogous reservoirs elsewhere.

18.4.2 Volumetric Methods. Volumetric methods to estimate reserves generally are used early in the life of a reservoir, before there are sufficient production and/or pressure data to use the performance method, and for behind-pipe zones, which might not be placed on production until the current completion zone is abandoned. Although volumetric methods are the most widely used methods for estimating reserves, results from their use might be subject to considerable uncertainty, depending on the geologic setting and the amount and quality of geologic and engineering data. Thus, it is recommended that an evaluator *compare reserves estimated by volumetric methods against well and reservoir performance at the earliest practical stage of production and make adjustments as warranted.*

Volumetric methods for estimating reserves involve three steps:

1. Use volumetric mapping or another procedure to determine net volume of the reservoir.
2. Determine rock/fluid parameters to calculate unit volumes of oil, gas, and/or condensate initially in place (O/G/CIP).
3. Estimate REs for oil, gas, and/or condensate. Step 1 may involve the use of gross-rock-volume isopach maps and a net-to-gross net-pay ratio to obtain the net volume of the reservoir.

For oil reservoirs, initial reserves of oil and solution gas can be calculated using Eq. 18.2 and Eq. 18.4, respectively. (Remember, however, that all calculations of reserves must be considered *estimates*, and are accurate to no more than two significant figures.)

$$N_{Ri} = N_i E_{Ro} = [7,758 \phi_o (1 - S_{wo}) A_o h_{no} / B_{oi}] E_{Ro}, \dots\dots\dots (18.2)$$

where 7,758 = bbl/acre-ft (but if units in Eqs. 18.2 and 18.3 are ha and m, this constant becomes 1.0).

For analyses where $A_o h_{no}$ is determined from planimetry of isopach maps:

$$N_{Ri} = N_i E_{Ro} = [7,758 \phi_o (1 - S_{wo}) V_{to} R_{ngo} / B_{oi}] E_{Ro} \dots\dots\dots (18.3)$$

Eq. 18.3 assumes a *gross*-pay isopach and would be modified for a *net*-pay isopach by setting $R_{ngo} = 1$.

Initial reserves of solution gas can be calculated by:

$$G_{RSi} = G_{Si} E_{Rg} = N_i R_{si} E_{Rg} \dots\dots\dots (18.4)$$

For gas reservoirs—either gas caps or nonassociated gas—initial gas and condensate reserves can be calculated by:

$$G_{RFi} = G_{Fi} E_{Rg} = [43,560 \phi_g (1 - S_{wg}) A_g h_{ng} / B_{gi}] E_{Rg} \dots\dots\dots (18.5)$$

and

$$C_{Ri} = C_i E_{Rc} = G_{Fi} R_{ci} E_{Rc} \dots\dots\dots (18.6)$$

where 43,560 = ft³/acre-ft (but if units in Eq. 18.5 are ha and m, this constant becomes 1.0). Gas initially in place (GIP) may, alternatively, be calculated with an equation analogous to Eq. 18.3.

Reservoir Maps. Most volumetric methods begin with determining the bulk reservoir volume that contains hydrocarbons. This usually involves preparing structure maps of the top and base of the reservoir and an isopach map of the reservoir. The reliability of results derived from the construction of reservoir maps is directly related to the geologic complexity of the reservoir, the number of wells drilled, the quality and extent of seismic data, information gathered through the drilling and completion of wells, and the evaluator’s ability to accurately integrate all data into such maps.

Structure maps should be clearly marked to indicate reservoir limits related to faulting, fluid contacts, and/or facies changes, as well as to indicate all wellbores that penetrate the subject formation. The location of relevant seismic lines and shot points should be shown on all reservoir maps. Subsea depths (ft or m) typically are used to represent formation depths and fluid contacts. Structure maps prepared by explorationists often relate more to structural “markers” or log features that are recognizable over large areas. These lithological interval “tops” may be used to better define structural influences that may control hydrocarbon trapping forces and depositional trends; however, the reserves geologist should prepare reservoir structure maps that describe the top (and sometimes the base) of the reservoir interval in the mapped formation. Both logs and core data can be used in defining the mapped interval. Contouring may be hand drawn or accomplished using geologic mapping software.

The construction of isopach maps should incorporate the same level of detail as do structure maps, as described above. Net pay should be clearly marked for each well penetration. Failure to calculate gross reservoir volumes properly can lead to serious errors in the preparation of reservoir development plans, unwise expenditure of capital budget amounts, and seriously distorted estimates of reserves. Some of these concerns are discussed further in the Pitfalls section of this chapter.

Net Pay. Estimating net pay is one of the most important steps in volumetric mapping, but unfortunately, it also is one of its most subjective steps. Among the factors that influence it are the amount and quality of log, core, and test data; the nature of the rock/fluid system; and the anticipated drive/recovery mechanism.^{19–26} In the following discussion, the term “net pay” refers to “true vertical net pay”—logged net pay thickness that is corrected for borehole inclina-

tion and formation dip. [The correction procedure assumes that volumetric mapping is based on vertical projection of dipping formations onto a horizontal (mapping) plane. For steeply dipping formations, kh so derived must be corrected for calculations of fluid flow parallel to the formation bedding surface.]

Net pay in a given reservoir might be determined for different purposes,²⁵ for each of which the procedure and results might be different. For example:

- In an initial well-log evaluation to determine whether to run production casing and attempt a completion, net pay typically includes only intervals that are judged likely to contribute to well inflow at commercial rates. The log analyst might estimate net pay conservatively to minimize the monetary risk of a subcommercial completion.

- When evaluating a reservoir to determine total hydrocarbons in place (e.g., as an independent check on material-balance calculations), net pay usually includes all hydrocarbon-bearing intervals that are likely to contribute to the “energy balance.” Net pay for this purpose generally will be more than that estimated during initial completion.

- When considering a waterflood, net pay should include only intervals considered “floodable,” a criterion that implies interwell continuity. Also, the methods used to define floodable intervals are subjective and may exclude intervals that will contribute to recovery by imbibition. Net pay for waterflooding might be less than for initial well-log evaluation or for determining total hydrocarbons in place.

- If a reservoir is to be unitized and net pay is part of the unitization formula, the determination of net pay may be subject to arbitrary rules to ensure “uniformity,” which might require determination of net pay that is unrelated to the considerations above.

To facilitate visualization of pertinent data, prepare composite logs for all wells in the reservoir that is under study. Regional and individual variations are expected, but generally the two steps are:

1. Determine “gross interval” by establishing the top and bottom of the zone of interest. In sand/shale sequences, the inflection points of the spontaneous, or self, potential or the gamma ray curves usually are considered zone boundaries. For carbonates, establishing the zone boundaries might involve using one or more of the porosity curves to establish a minimum porosity (porosity cutoff) or using a combination of logs to determine lithologic top and bottom. (Choice of minimum porosity typically is quite subjective and is related to the minimum permeability that is considered productive in the area, which depends on petrophysics, reservoir fluid, and drive mechanism.)

2. Exclude nonpay intervals within the gross interval on the basis of maximum shaliness, minimum porosity, maximum water saturation, specified degree of reversal in either the spontaneous-potential or the gamma ray curve, or a combination of these.

The Petroleum Soc. of the Canadian Inst. of Mining²⁶ provides a list of “generally accepted (minimum) cutoffs” (Table 18.3). Local cutoff data for other regions are available in sources such as the Schlumberger* Well Evaluation Conference (WEC) publications for various regions (e.g., Ref. 27). Engineers should use published cutoff data only as general guidelines, however, and only when information for a specific reservoir or project is unavailable. There may be circumstances for which no minimum permeability, porosity, and/or saturation cutoffs are appropriate.

Historically, the objective of initially estimating net pay has been to determine which intervals in each well zone could be expected to contribute to fluid flow into the wellbore under the anticipated method of well and/or reservoir operation. (This is not a proposed definition of net pay; indeed, there is more than one recognized definition of net pay.). The criteria for determining net pay under primary drive should include fluid mobility (k_e/μ) and pressure

* This reference is not intended to be limiting and does not imply endorsement.

<u>Permeability^a</u>	
Medium- to high-gravity oil	1.0 md
Wet gas	0.5 md ^b
<u>Porosity^c</u>	
Carbonates	2 to 4%
Sandstones	7 to 10%
Heavy oil (sandstones)	26 to 28%
<u>Water saturation (maximum)</u>	50 to 60%
^a Unstressed, horizontal permeability from measurements on cores.	
^b As low as 0.1 md for dry gas under special circumstances.	
^c Unstressed, from cores.	

differential.²⁴ Permeability data, however, seldom are available on all wells in a reservoir. Typically, permeability is estimated using correlations between porosity and permeability measured in cores from the subject reservoir, empirical correlations based on global data, low-frequency acoustic log interpretation,^{**} and/or nuclear magnetic resonance (NMR) log response.

In some cases (e.g., shaly, laminated, sand reservoirs and many carbonate reservoirs), it may be difficult, at best, to determine net pay with an acceptable degree of confidence. [For examples of log response in shaly, laminated, sand reservoirs (known as low-resistivity, low-contrast), see publications of the Houston Geological Soc.,²⁸ the New Orleans Geological Soc.,²⁹ and the Rocky Mountain Assn. of Geologists.³⁰]

A net-pay isopach made with considerable interpretation uncertainty might have to be revised frequently when interpretive procedures are revised or when new data become available. In this situation, it might be desirable to map gross pay and apply an average net-to-gross ratio to account for nonproductive rock. The net-to-gross ratio can be revised as warranted, thereby avoiding the need to remap the entire reservoir; however, this procedure is not appropriate if there are significant spatial variations in the net-to-gross ratio.

Depending on circumstances, it might be appropriate to classify net pay as proved, probable, or possible to recognize the degree of uncertainty in such estimates and to provide a basis for classifying reserves associated with each estimate. Regardless of the method used to determine net pay, the porosity and water-saturation values used in the volumetric equations (Eqs. 18.2, 18.3, and 18.5) should be consistent with the cutoff values used to determine net pay.

Volumetric-Mapping Example. **Figs. 18.3 through 18.6** illustrate several mapping and reserves-classification principles. **Fig. 18.3** is a structure map of an oil reservoir along the upthrown side of a west/northwest dipping fault. A well log and core taken in Well 1 indicate that the sandstone section is oil-filled throughout the logged interval, thereby defining the highest known oil (HKO) at 10,500 ft subsea (ss) and LKO at 10,550 ft ss. A flow test indicated commercial rates of oil production. Pressure/volume/temperature (PVT) data indicate that the oil is gas-saturated. It is assumed that three wells (Well 1 and Locations A and B) are needed to effectively drain the oil reservoir, although B is contingent on the geologic interpretation after drilling A.

Although the production test in Well 1 does not indicate so, there is a possibility of a GOC just updip from the top of its logged interval, and of an OWC just below the base of the logged interval. Accordingly, *on the basis of available information at the conclusion of the logging and testing of Well 2*, only the reservoir volume between 10,500 and 10,550 ft ss can

^{**} Personal communication with E.C. Thomas, Bayou Petrophysics, 23 April 2002.

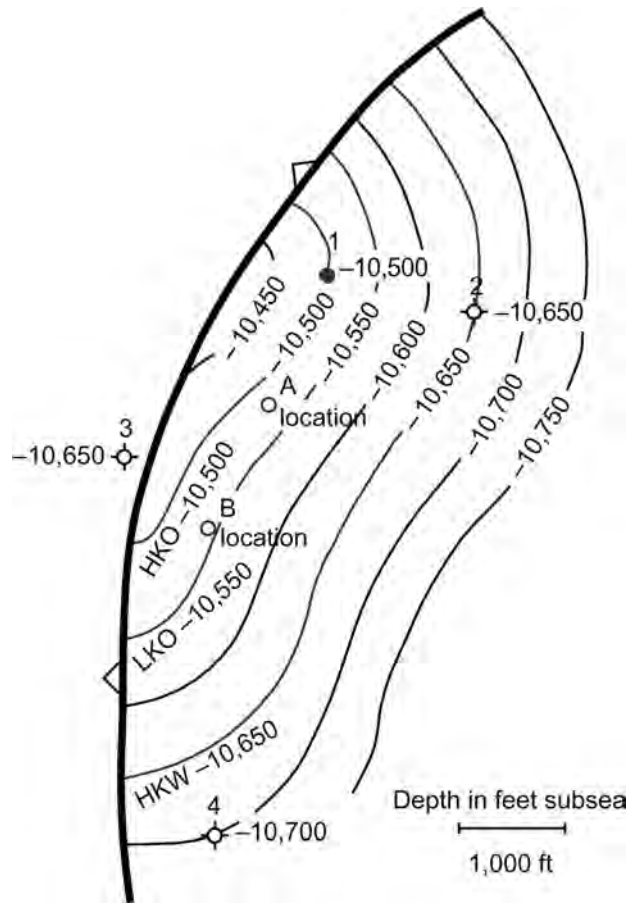


Fig. 18.3—Structure map on top of porosity.

be considered to contain proved reserves—by either the 1978 U.S. SEC or the 1997 SPE/WPC reserves definitions. Conversely, if the crude oil is undersaturated, the volume of the reservoir above the HKO may be considered to be oil-filled. (This proved volume might need to be reduced further because of lateral limitations imposed by optimum well spacing and geological uncertainty. See the later discussion in the Reserves Classifications section in this chapter.)

Fig. 18.4 is a “net sand” isopach of a channel sand, and it is based on an interpretation of the geologic and geophysical data available at the mapping date. This interpretation is supported by regional studies and the 2D seismic lines indicated on the net sand isopach. Note that using mechanically derived contours when contouring the net sand thickness in each of the wellbores would yield an entirely different interpretation, which illustrates the importance of using all available information, including subsurface data, geophysical interpretations, and experiential/analog data from the area.

Fig. 18.5 integrates Figs. 18.3 and 18.4 as a net oil isopach map of the reservoir volume between HKO and LKO, using the spatially correct “Wharton’s method”³¹ of contouring the “wedge edges.” “Wedging” of the net pay contours northwest of Well 1 and southeast of Well 3 reflects truncation of the net (oil) sand contours on Fig. 18.4 by the fault. Wedging in the crescent-shaped area on the northwest side reflects truncation of HKO by the fault. Wedging

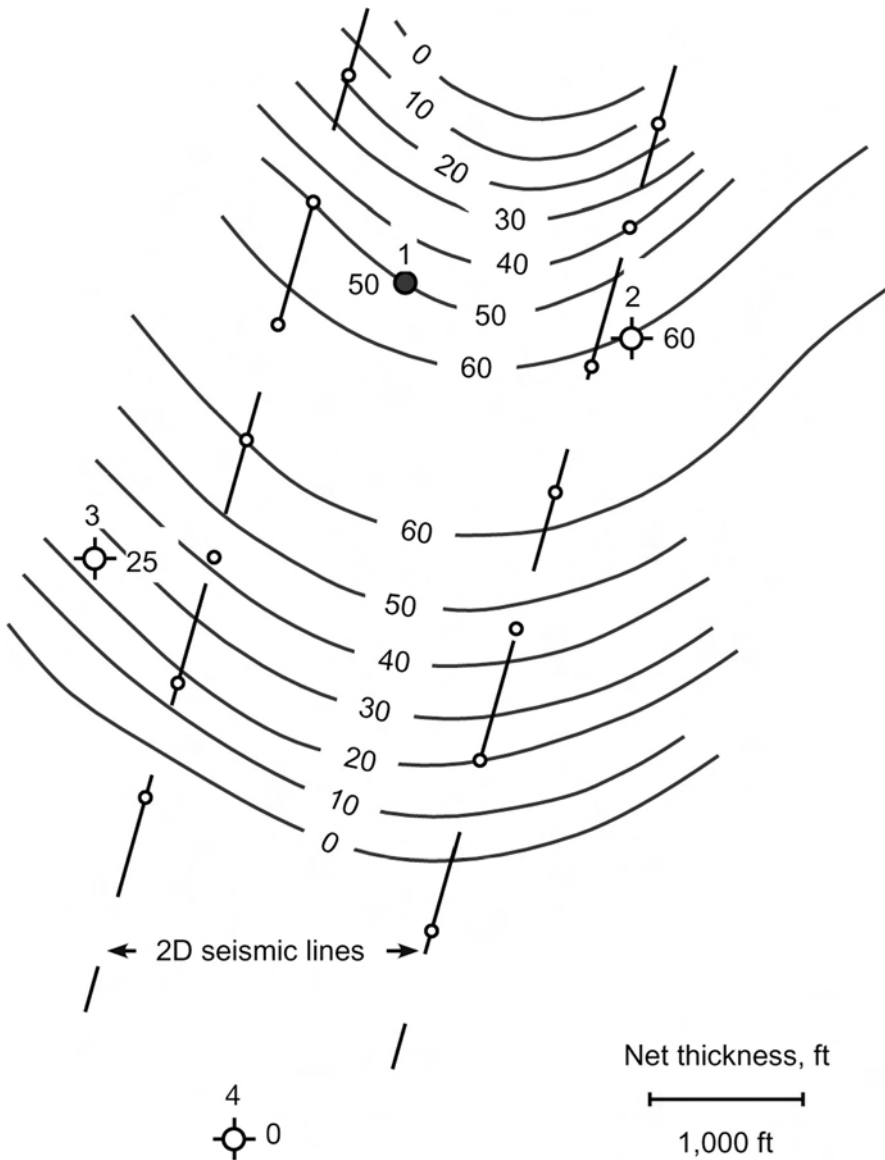


Fig. 18.4—Isopach map of total net sand.

on the southeast side reflects loss of structure between HKO and LKO, whereas thinning of the net oil contours to the northeast and southwest reflects thinning of the net (oil) sand.

Fig. 18.6 is an isopach map of the entire reservoir volume that is interpreted to exist above highest known water (HKW) at 10,650 ft ss, as seen in Well 2. By assuming the reservoir volume above HKO at 10,500 ft ss to be oil-filled, rather than (possibly) partially gas-filled, oil reserves in this volume might be considered to be proved plus probable plus possible (3P).

A map similar to Fig. 18.6 could be prepared for a proved-plus-probable (2P) interpretation, using an arbitrary downdip limit of 10,600 ft ss, which is the midpoint between LKO and HKW. If 3D seismic or other data are available to define or otherwise indicate an OWC, an alternate 2P interpretation based on this limit might be appropriate, as discussed on the section on reservoir limits.

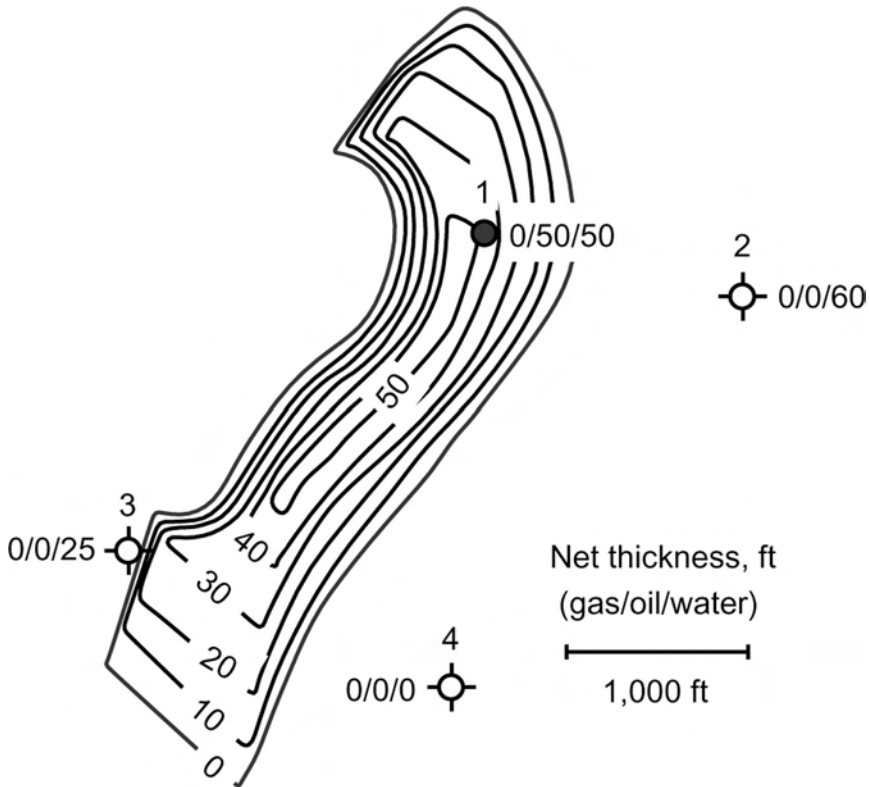


Fig. 18.5—Isopach map of total net (oil) sand.

Reservoir volumes for the proved case (P1) reserves usually are calculated directly by planimetry of the proved volume defined by an isopach map. Incremental probable (P2) reservoir volumes typically are the result of subtracting P1 volumes from the isopach of 2P volumes. Similarly, incremental possible (P3) reservoir volumes are the result of subtracting the 2P isopach volume from the 3P isopach volume.

It may be appropriate to clarify the terms P1, P2, and P3 at this point and to distinguish these from the seemingly similar terms 1P, 2P, and 3P as most often used in reservoir engineering vernacular. As stated previously, P1, P2, and P3 reflect reserves quantities for the classifications of proved, probable, and possible, respectively. The term 1P is synonymous with P1 as it applies to proved reserves only. The term 2P is a cumulative expression for the sum of proved and probable reserves; the term 3P embraces the sum of proved, probable, and possible reserves.

Seismic information, especially when “calibrated” through comparison to well log information, is especially important when well-control information is sparse and when faulting has not been defined through fault cuts recognized in wellbores. One should be alert to all circumstances in which reservoir extent may be limited by faulting, permeability changes, depositional discontinuities, or any other condition that might interrupt fluid flow. Individual reservoir compartments might be difficult to define without performance information, especially pressure information.

Typically, faults with a throw of less than the thickness of the productive formation are assumed to be nonsealing. Caution! One should not assume this without supporting evidence, which should be evaluated over time by a skilled, experienced engineer.

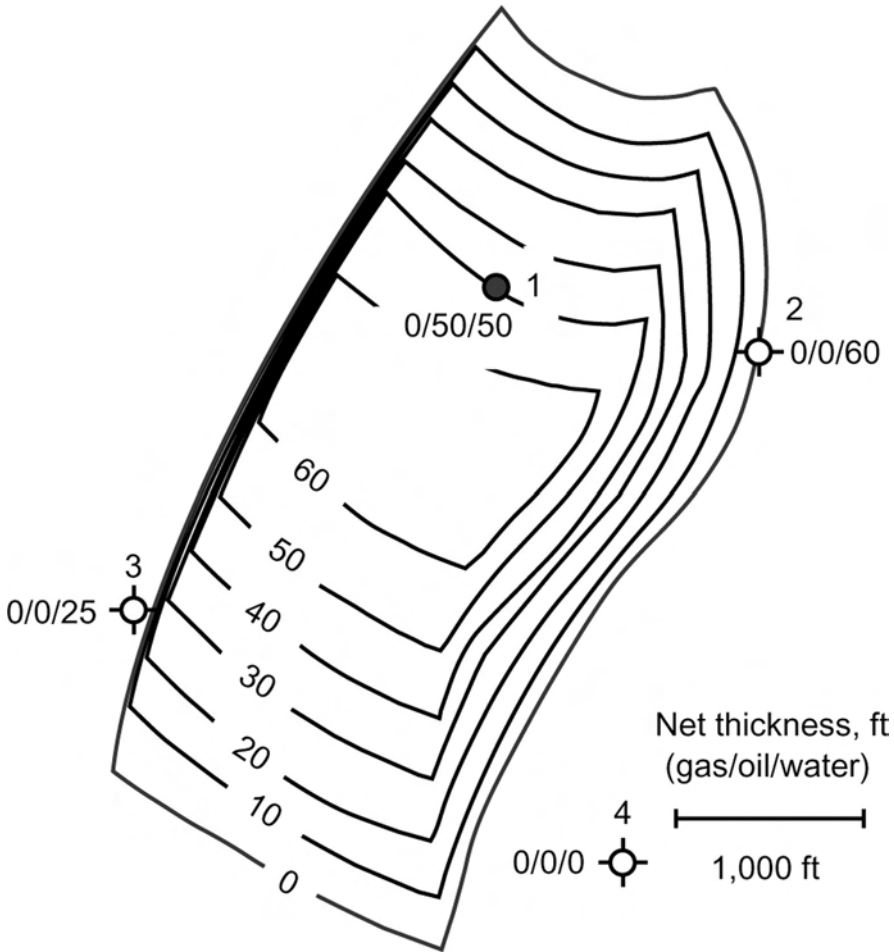


Fig. 18.6—Net oil isopach above HKW.

Isopach maps are designed to determine one or more measures of reservoir volume, and for a single-phase oil reservoir, they might include:

1. Bulk reservoir volume above an observed OWC or LKO. A net-to-gross pay ratio is applied to the bulk reservoir volume to yield net oil reservoir volume.
2. Net reservoir volume determined from the contouring of net oil pay thickness on the basis of log analysis and/or core analysis.
3. Isopore volume maps that reflect the product of net pay and wellbore weighted average porosity, $h_n \phi$.
4. Oil pore-volume (PV) maps that reflect the product of net pay, porosity, and oil saturation, $h_n \phi (1 - S_w)$.

For an oil reservoir with a gas cap, similar maps might be prepared, which include:

1. Bulk volume of the reservoir above the GOC, and that between the GOC and the OWC (or LKO), with net-to-gross pay ratios applied separately to the oil and gas portions of the reservoir.
2. Net reservoir volumes from the contouring of net oil and net gas pays on the basis of log and/or core analyses.
3. Isopore volume maps that reflect the product of net oil and net gas pays and wellbore weighted average porosity $h_n \phi$ for each of the oil- and gas-filled portions of the reservoir.

4. PV maps of the oil- and gas-saturated portions of the reservoir that reflect the products of net pay, porosity, and oil saturation and of net pay, porosity, and gas saturation, respectively.

In each set of isopach map design objectives, each subsequent objective requires more data and effort to complete. The amount and quality of the available data and the purpose of the reserves estimate are important in determining what type of maps to construct.

For hand-drawn isopach maps, reservoir volumes are calculated using manually operated planimeters. If computer software is used in map preparation, reservoir volumes are generated within that software. All reservoir maps, whether manually or computer-prepared, should be constructed without bias, should be consistent with the geology of the area, and should use sound mathematical and spatial fundamentals.

Computer-Aided Mapping. Many commercial software programs are available to help prepare reservoir maps and calculate ranges and distributions of reservoir parameters. Such programs range from relatively simple, 2D contouring utilities to fully integrated applications that help construct and visualize the complex distribution of various reservoir parameters and attributes in 3D geostatistical models. Few reservoir engineers are trained to use the more complex software to describe the structural and stratigraphic complexities of a reservoir. Similarly, not all geologists and geophysicists are aware of the reservoir engineer's concerns about the uncertainty of reservoir parameters in absolute terms and in the distribution of these parameters throughout the reservoir model.

For this and other reasons, the reservoir engineer must work closely with the geologists and/or geophysicists who have contributed data and interpretations to the models and have made critical decisions about the construction details. The quality, completeness, and unbiased use of the data are critical to the evaluation team's ability to make decisions about in-place hydrocarbons, compartmentalization, expected recovery mechanisms, and REs that are consistent with the development and production plan approved for the project. These considerations enable reliable quantification and classification of reserves.

The phrase "computer-aided mapping" firmly conveys that all such programs are useful tools, but cannot substitute for the judgment and experience of their users. All the basic reservoir-mapping principles and reserves definitions must be integrated in all reservoir maps, whether hand-drawn or computer-created.

Areal Assignments. Frequently, available geologic information is inadequate to prepare volumetric maps, especially with discovery wells. In such cases, an estimated productive area may need to be "assigned" to the completion interval and other productive intervals where reserves are attributed. Typically, such areal assignments are used only until adequate geologic or performance data become available.

Initial areal assignments should reflect the expected drainage area for the well and should use all available analogous, geologic, and test information. The product of the expected drainage area or spacing pattern and two-thirds to three-fourths of the apparent wellbore thickness often is used to account for possible reservoir thinning away from the wellbore.

Reservoir Limits. In general, there are two types of reservoir limits, external and internal. External limits define the zero-isopach contour for either oil or free gas. Internal limits may affect the flow of fluids in the reservoir. The following discussion is related to external limits, which usually are major faults and/or fluid/fluid contacts. Internal limits are discussed in a later section.

In the absence of observation through wellbores, several methods might be used to calculate an OWC/GWC, including pressure/depth, 3D seismic mapping, pressure gradients, and capillary pressure. These are listed in order of their commonly recognized degree of reliability, but their true reliability is a direct function of the extent and quality of the data from which the limits are calculated.

Well A, wet		Well B, discovery	
Depth ss, ft	BHP, psia	Depth ss, ft	BHP, psia
6,075	2,662	5,771	2,602
6,091	2,669	5,778	2,604
6,108	2,677	5,785	2,608
6,220	2,725	5,800	2,610
6,232	2,731	5,806	2,612
		5,813	2,614

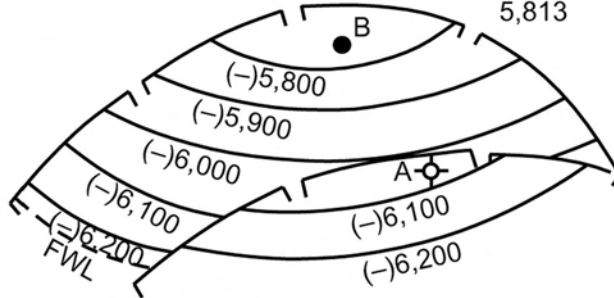


Fig. 18.7—Structure on top of productive sand (after Dake³²).

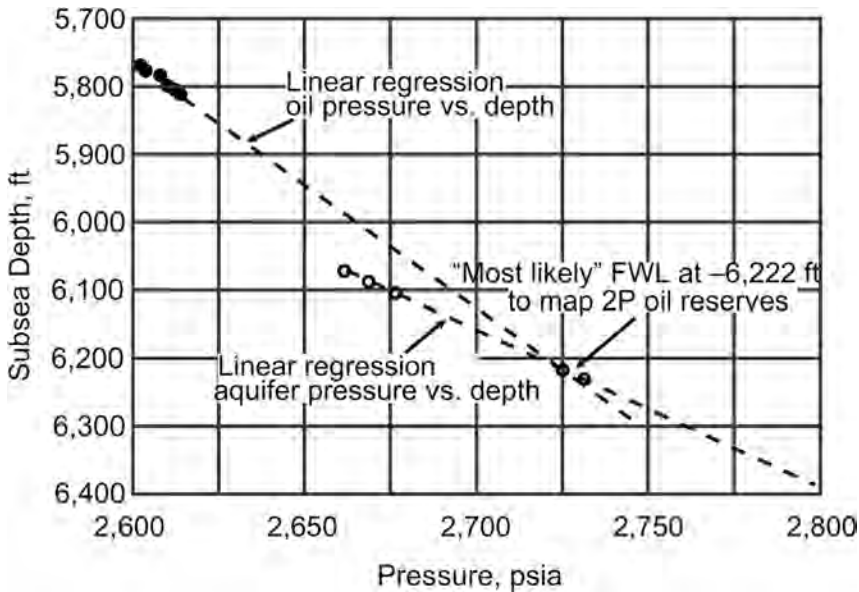


Fig. 18.8—BHP vs. depth, illustrating the pressure/depth method for estimating the FWL (after Cronquist³).

Pressure/Depth Method. If there are sufficient accurate subsurface pressure measurements at a series of depths within a given reservoir, such measurements can be used to calculate definitively the depth of a GOC, GWC, and/or an OWC. The principle is illustrated in [Figs. 18.7³² and 18.8.³](#)

[Fig. 18.7](#) is a structure map on the top of a productive sand, and it shows the locations of an oil completion (Well B) and a wet well (Well A). Well B encountered commercial oil throughout the logged interval. Well A apparently was in the aquifer. Static bottomhole pres-

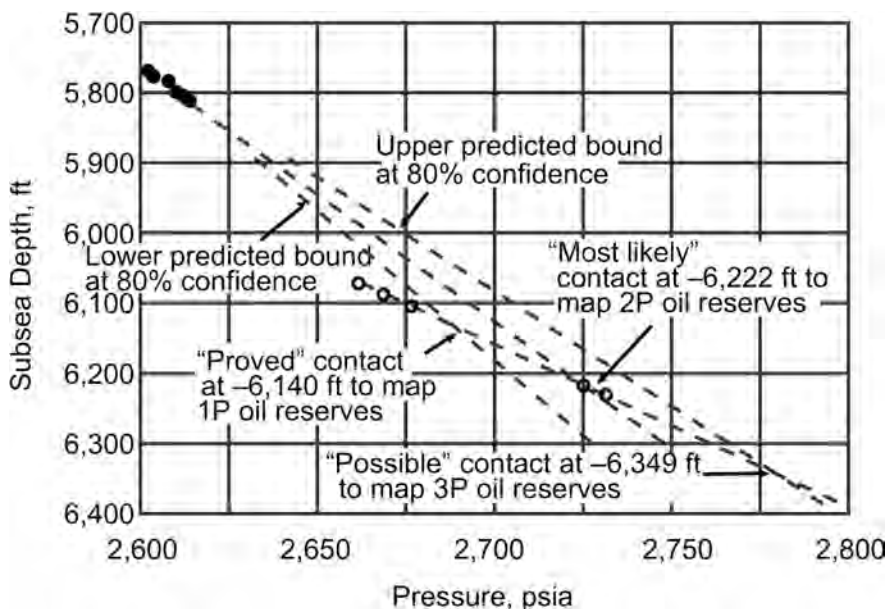


Fig. 18.9—BHP vs. depth, including the upper and lower bounds of predictions at 80% confidence and illustrating the pressure/depth method for estimating proved, most likely, and possible FWLs (after Cronquist³).

tures (BHP), measured in the fluid columns of each well using a wireline formation tester (WLFT), are tabulated in Fig. 18.7.

From linear regression through each data set, a “most likely” free-water level (FWL) is estimated at 6,222 ft ss, which may be used to map proved plus probable oil reserves.³ This interpretation is based on several considerations:

- The backflow periods during the WLFTs in the oil column were sufficient to reconnect the oil in the filtrate-invaded zone,³³ thereby ensuring valid BHP data.
- The oil gradient calculated from the regression is consistent with the reservoir oil density measured from PVT analysis.
- From available subsurface data, the fault separating the two wells at the eastern end of the structure appears to die out to the southwest, thereby supporting pressure communication between the two wells through the aquifer.
- Regional data support the assumption of constant oil density between LKO and the estimated FWL.

If appropriate, this analysis can be expanded through a probabilistic approach.³ From the regression results, the upper and lower bounds at 80% confidence can be used to estimate P10 and P90 projections of oil BHP vs. depth, respectively (Fig. 18.9). (At 80% confidence, oil gradients were calculated to range from 0.24 to 0.31 psi/ft, which is considered reasonable in light of other uncertainties in the data. Because the regression coefficient for the aquifer pressures is 0.9999, the projection of aquifer BHP vs. depth was considered error-free.) This analysis leads to a proved OWC at 6,140 ft ss, a most likely OWC at 6,222 ft ss, and a possible OWC at 6,349 ft ss. (Given the low density of the reservoir oil and the high quality of the reservoir rock in this example, the FWL is considered a reasonable approximation to the commercial OWC.) Note that the geologic interpretation (Fig. 18.7) would support an OWC at approximately 6,300 ft ss. Were there a significant disparity between the geologic and engineering interpretations, this analysis would have to be reviewed.

In more general applications of the pressure/depth method, be careful when estimating FWLs and commercial OWCs in cases where the density of the reservoir oil approaches that of the interstitial water in the aquifer, and/or the reservoir rock is of such low quality that there might be a significant vertical distance between the FWL and the 100% water level.³

3D Seismic Mapping. The widespread use of 3D seismic methods has increased confidence in the guiding of development drilling and defining of reservoir size and extent, especially in certain geographic locations. One should be cautious in assigning proved reserves to the entire area indicated to be productive, unless there is corroborating support from other measurements and unless such areas can be drained with the anticipated development plan. To classify gas as proved reserves on the basis of the analysis of seismic bright spots or flat spots in a faulted accumulation, Robertson³⁴ (quoted here) recommends that all the following conditions be met:

1. The flat spot and/or bright spot is clearly visible in the 3D seismic data.
2. The spatial mapping of the flat spot and/or downdip edge of the bright spot fits a structural contour, which usually will be the spill point of the reservoir.
3. A well penetrates the GWC in one fault block of the reservoir, so logs, pressure data, and test data provide a direct and unambiguous tie between the GWC in the well and the seismic flat spot and/or downdip edge of the bright spot; i.e., the borehole proves that there is producible gas, not residual gas, down to the seismic indicators of the GWC.
4. A well in another fault block penetrates the reservoir updip from the GWC.
5. This second well proves gas down to a lowest known depth, and pressure data show that this gas is in communication with the gas in the first fault block.
6. The seismic flat spot and/or downdip edge of the bright spot in the second fault block lies below the lowest known gas in the second well and is spatially continuous with and at the same depth as these seismic indicators in the first fault block.

Robertson further says that “[i]f all these conditions are met, the gas in the second fault block between the lowest known occurrence in the well and the seismic flat spot and/or downdip edge of the bright spot can reasonably be judged to be proved.”³⁴ Authors’ caution! This interpretation might not be accepted within all regulatory jurisdictions.

In exploration, good practice mandates the need for at least one well penetration into a seismic bright spot (amplitude anomaly) to demonstrate commercial producibility before the prospective resources in a pool defined by an amplitude anomaly can be classified as reserves.

There are recognized circumstances in which geophysical interpretations that are made using surveys designed for exploration can be considered reliable in determining reservoir thickness, certain petrophysical parameters, and fluid contacts, but these circumstances are few and currently apply minimally, if at all, to establishing proved reserves quantities. Using 3D surveys for reservoir evaluation increases opportunities for developing confidence in geophysical techniques to help quantify reservoir parameters and limits.

4D seismic analysis—a time sequence of 3D surveys—is an emerging technology that is beginning to be applied more widely to monitor the flow of hydrocarbons in a reservoir.^{35–38} 4D seismic interpretation analysis can benefit the understanding of reservoir compartmentalization and RE, but its greatest application might be in optimized reservoir management.

Pressure-Gradient Method. The pressure-gradient method for calculating a hydrocarbon/water contact is similar to that described in the *Pressure/Depth* section in this chapter, but it relies on the computation of fluid gradients from fluid analyses, rather than gradients calculated by repeat pressure measurements at different depths in a common reservoir. Extrapolation over a large depth interval will magnify slight errors in computing fluid gradients. Accordingly, one should not use the pressure gradient method to produce definitive results, but rather to provide approximations that will require confirmation by other sources.

The density of reservoir oil *at the bubblepoint* (lbm/bbl) can be calculated by³⁹:

Case	Updip Fluid	Downdip Fluid	GOC or FWL		
			1P	2P	3P
GOC	Gas	Oil	C	B	A
OWC (FWL)	Oil	Water	A	B	C
GWC (FWL)	Gas	Water	A	B	C

A, B, and C correspond to data points in Fig. 18.10.

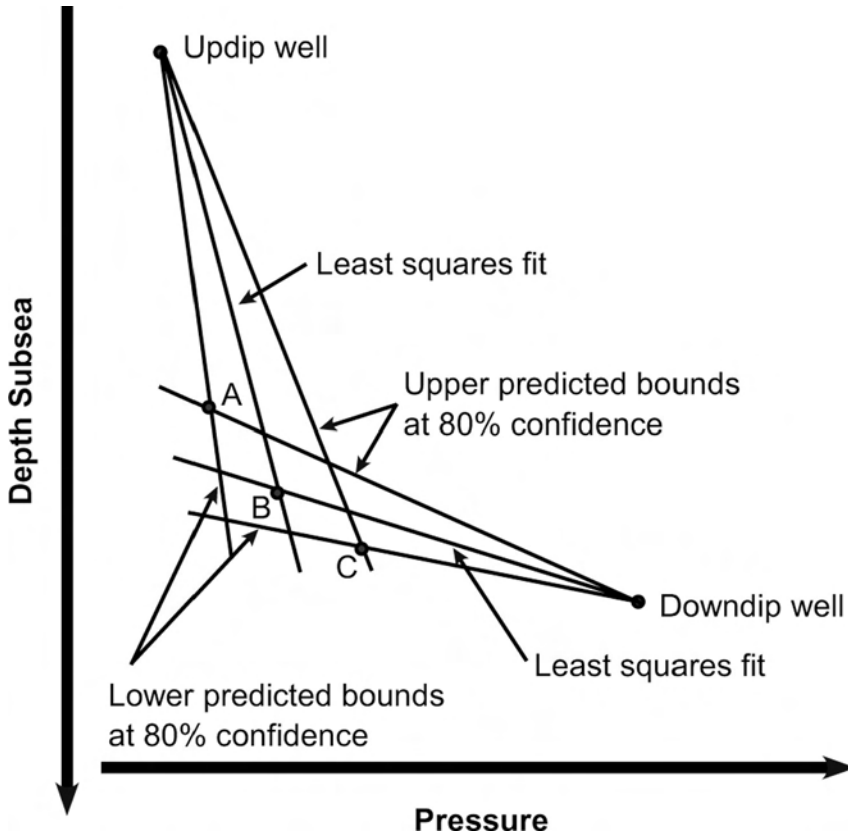


Fig. 18.10—Pressure-gradient method (after Cronquist³).

$$\rho_{or} = (350\gamma_{os} + 0.076R_{sb}\gamma_g) / B_{ob} \dots\dots\dots (18.7)$$

Oil density calculated from Eq. 18.7 can be converted to oil gradient (in psi/ft) by multiplying it by 0.00124. For calculations of density and gradient for undersaturated oil, see McCain.³⁹ Water gradients can be calculated from salinity or other compositional data.

The method discussed here and that in the Pressure Gradient section can be generalized to estimate the depths of 1P, 2P, and 3P GOCs and/or FWLs. The procedure is summarized in Table 18.4 and illustrated by Fig. 18.10.³

Capillary-Pressure Method. The capillary-pressure method to calculate the depth of an OWC or GWC is based on the principle that in a common reservoir the family of capillary-

pressure curves for various rock types in the reservoir has a common FWL. The capillary-pressure method involves several equations⁴⁰⁻⁴²:

$$F_g \approx \left[\ln \left(5.21 k_a^{0.1254} / \phi \right) \right]^2 / 2.303, \dots\dots\dots (18.8)$$

$$P_{dm} \approx 937.8 / \left(\phi k_a^{0.3406} \right), \dots\dots\dots (18.9)$$

$$\log \left(P_{cm} \right) \approx (-) F_g / \ln \left(1 - S_w \right) + \log \left(P_{dm} \right), \dots\dots\dots (18.10)$$

$$P_{cR} = P_{cL} \left(\sigma_R \cos \theta_R \right) / \left(\sigma_L \cos \theta_L \right), \dots\dots\dots (18.11)$$

and

$$Z_{fw} = P_{cR} / \left(\rho_w - \rho_o \right). \dots\dots\dots (18.12)$$

In Eqs. 18.8 through 18.12, the operator \approx denotes correlations, whereas = is reserved for analytical equations.

The capillary-pressure method has several limitations (discussed later) and involves four steps:

1. For each well log level for which porosity and permeability are known, calculate F_g using Eq. 18.8 and P_{dm} using Eq. 18.9. [The permeability value k_a in Eqs. 18.8 and 18.9 is absolute (air) permeability (md) and must be estimated independently from log-determined permeability, and typically is computed by logging-company interpretation programs, which assume that log-calculated water saturation is irreducible water saturation.]
2. Use the F_g and P_{dm} values and the log-determined value of S_w at the same level to calculate P_{cm} for that level, using Eq. 18.10.
3. Use Eq. 18.11 to convert from mercury/air capillary pressure—the basis for the Thomeer⁴³ curves—to the fluid system of interest.
4. Use Eq. 18.12 to calculate the vertical distance from the level investigated to the FWL, using the fluid densities in the reservoir being evaluated. To reduce statistical scatter, make such calculations for multiple points within the interval being evaluated.

Fig. 18.11 illustrates the basic principle of the capillary-pressure method, showing a good-quality sand layer underlain by a poor-quality sand layer in a hypothetical well that logged LKO to the base of the poor-quality sand. The presence of variable-quality sand layers enhances the method's reliability because more than one capillary-pressure curve must be fitted in the calculations.

There are several limitations to the capillary-pressure method:

1. The well-log interval of interest must be within the part of the hydrocarbon/water transition zone (HWTZ) that exhibits a significant water-saturation vs. depth gradient.
2. There must be a robust correlation between permeability and porosity.
3. The Archie equation, frequently used in logging programs to calculate S_w , may not be the "correct" model for the log interval of interest because the value for S_w that is computed from log analysis is a function of the saturation and cementation exponents, each of which is a function of lithology, which might vary over the logged interval.
4. Reservoir fluid densities should not vary significantly between the observation well(s) and the FWL.
5. Although the FWL may reasonably approximate the initial hydrocarbon/water contact in reservoirs with good-quality rocks containing free gas or light oil, in reservoirs with poor-quality

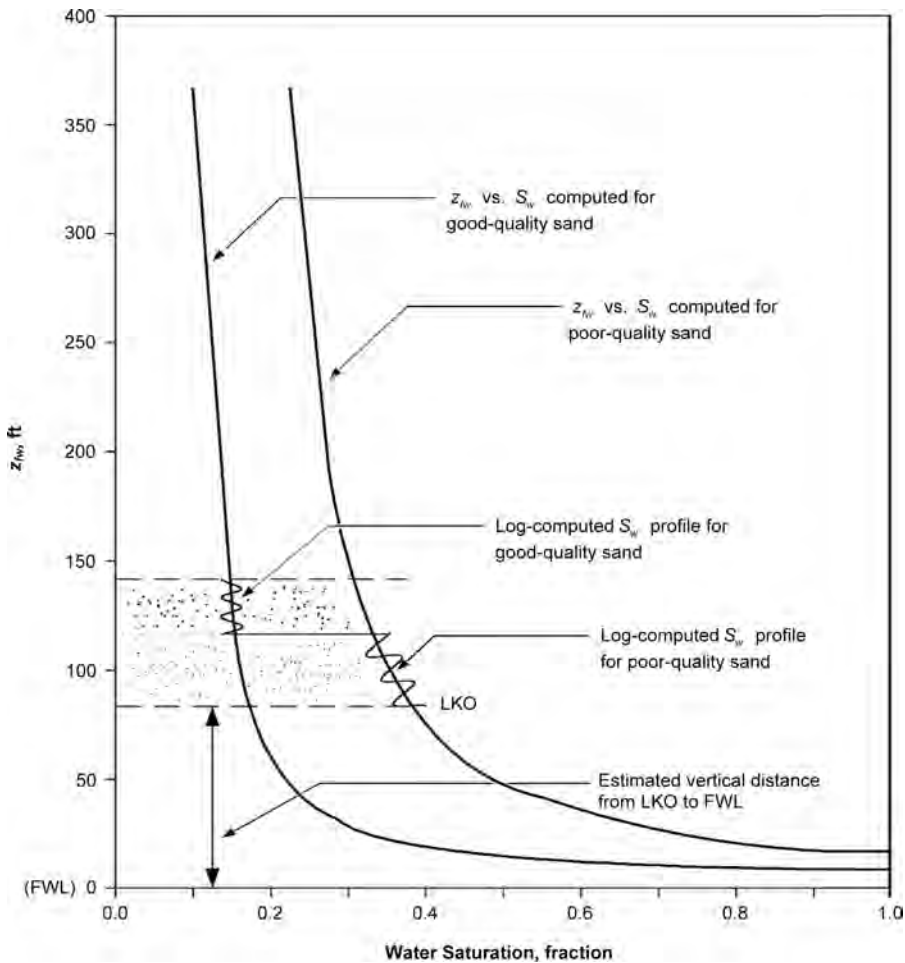


Fig. 18.11—Capillary pressure chart that illustrates the shift in capillary pressure across the boundary between good- and poor-quality sand (after Cronquist³).

ty rocks and/or those containing heavy oil, the commercial hydrocarbon/water contact may be significantly shallower than the FWL.

Internal Limits. In addition to external limits discussed in a previous section, there might be internal limits that could significantly affect RE. Two of these internal limits are internal faulting and depositional/diagenetic discontinuities.

Internal faults can be partial or complete barriers to fluid flow along all or part of their length. Under pressure gradients imposed by production, such barriers might respond differently from how they would under static conditions. Usually internal faults exhibit smaller vertical displacements than do bounding faults. In many cases, such faulting might be undetectable using existing well-control, or even seismic, data. Furthermore, internal faults might only become apparent after a period of sustained production, as happened in the Cormorant field in the North Sea⁴⁴ and in other fields in that area.

Depositional discontinuities internal to a reservoir might adversely affect RE. In the U.S.A. Gulf Coast, for example, in composite reservoirs that are producing by strong waterdrive, high-permeability (channel) sands typically flood out in preference to low-permeability (fringe) sands.⁴⁵ Such occurrences are common in comparable geologic and reservoir settings.

Several methods are used to detect internal limits, including repeat formation tester (RFT) depth/pressure traverses, differences in hydrocarbon isotopes, $^{87}\text{Sr}/^{86}\text{Sr}$ isotope ratios,⁴⁶ and differences in saturation pressure.

Volumetric Parameters. In addition to those determined from geologic mapping, volumetric parameters include petrophysical data (ϕ , S_w) and formation volume factors, all of which should be averaged over the reservoir; initial pressure and formation temperature, which are arguments for formation volume factors and other parameters; and REs, which are discussed in a subsequent section.

Petrophysical data used in Eqs. 18.2, 18.3, and 18.5 can be determined by several methods, including well logging, transient pressure testing, and routine and special core analysis, each of which is discussed in detail in separate chapters of the *Handbook*. Accordingly, only brief comments are provided here.

Porosity. Although reservoir porosity is estimable from well logs, it is good practice to calibrate log-determined porosity against core data, corrected for compressibility effects, if appropriate. As denoted in Eqs. 18.2, 18.3, and 18.5, porosity in the oil zone might differ from that in the gas zone. Depending on circumstances, procedures to estimate net pay (e.g., cutoff porosity and water saturation) might differ between the two zones. Accordingly, average porosity in each of the two zones should reflect such differences.

Water Saturation. In Eqs. 18.2, 18.3, and 18.5, the saturation terms S_{wo} and S_{wg} should reflect average initial water saturation—which might be greater than the irreducible saturation—in the oil zone and gas zone, respectively. Depending on the petrophysics and geometry of the reservoir, some of the accumulation might be in an oil/water or gas/water transition zone. This might reasonably be expected in reservoirs with low-relief, heavy oil, poor-quality rock, or a combination of these. In any event, the saturation terms in Eqs. 18.2, 18.3, and 18.5 should be consistent with the procedure(s) used to determine net pay and map the accumulation.

Compressibility Effects. For accumulations in geopressed reservoirs or friable, unconsolidated sands, it might be appropriate to correct properties measured at ambient conditions to those expected at reservoir conditions. For example, irreducible water saturation at reservoir conditions typically will be greater than that measured under ambient conditions in the same rock sample, and porosity and permeability will be less. Low-permeability rock, such as is seen in tight gas reservoirs, can have permeabilities of as much as two orders of magnitude less at reservoir conditions, compared to those measured at ambient conditions. (Geopressed reservoirs are discussed further in the Special Problems section of this chapter.)

Formation Volume Factor. In general, FVFs [expressed as reservoir volume/standard volume (RV/SV)] are a function of composition of the reservoir fluid, reservoir pressure and temperature, and surface separator(s) temperature(s) and pressure(s). As discussed in subsequent sections, such factors may be measured in a PVT cell; estimated from empirical correlations; or, for nonretrograde reservoir gases, calculated from the composition of the reservoir gas. The FVFs in Eqs. 18.2, 18.3, and 18.5 should reflect initial reservoir conditions and separator conditions that are anticipated over reservoir life.

Oil FVFs at a specified reservoir temperature and over a specified range of reservoir pressures and surface separator conditions can be measured in a PVT cell in a laboratory. Fluid samples used for these measurements are taken from the wellhead during carefully controlled flow and test conditions, or from bottomhole samples after careful conditioning of the sampled well. Such procedures are covered in detail by McCain³⁹ and elsewhere in the *Handbook*.

If PVT data are unavailable, oil FVFs at initial conditions can be estimated from empirical correlations. Since publication of Standing's correlation⁴⁷ in 1947—still considered industry standard—there have been at least 10 such correlations published. Each yields slightly different results, and it might not be apparent which correlation is best for a specific application.³

Gas reservoirs are either retrograde or nonretrograde. For retrograde gas reservoirs that are to be produced by pressure depletion below the dewpoint pressure, consider obtaining separator samples and running a PVT analysis at reservoir temperature and over an appropriate pressure range. For nonretrograde gas reservoirs, empirical correlations usually provide sufficient accuracy.

Gas Deviation Factor. The gas deviation factor—also called the supercompressibility factor or the z -factor—reflects the nonideal PVT behavior of real gases. Many engineers use this factor for the analysis of nonassociated gas reservoirs, as discussed later. The z -factor is a function of fluid composition, pressure, and temperature. Mathematically, it is the volume of a specific molar quantity of real gas, divided by the volume of the same molar quantity of an ideal gas, both measured at the same pressure and temperature:

$$z = V_R/V_I . \dots\dots\dots (18.13)$$

To ensure accuracy, the z -factor should be measured in a PVT laboratory, using a gas sample from the reservoir being analyzed; however, the z -factor estimated using empirical correlations is acceptably accurate for most engineering calculations.

For nonretrograde gases, the reservoir fluid composition does not change, regardless of reservoir pressure changes, and the initial z -factor can be used for calculations over the reservoir life. For retrograde gases, however, the composition of the reservoir fluid—and the z -factor—will change if reservoir pressure goes below the dewpoint pressure, under which scenario the two-phase z -factor must be used. Correlations are available to estimate the two-phase z -factor, but using PVT data might be preferable.

Initial Pressure. The initial reservoir pressure is needed to determine the initial FVFs, and it is the basis for material balance calculations of O/GIP. An accurate estimate of initial reservoir pressure is particularly important for geopressured reservoirs and undersaturated oil reservoirs, especially those for which material balance calculations might be necessary.

Reservoir Temperature. Reservoir temperature also is needed to determine the initial FVFs. Accurate determination of reservoir temperature is especially important for reservoir fluids anticipated to be close to critical conditions.

Recovery Efficiency. Estimation of RE is one of the most difficult aspects of volumetric estimation of reserves and—unless there is considerable local experience and/or good analogs—is fraught with uncertainty. In approximate order of importance, RE for developed oil/gas reservoirs depends on drive mechanism, formation quality, degree and type of reservoir heterogeneity, well spacing, fluid type, operating and completion methods, reservoir geometry and well locations, and economics. The interaction between these factors—some of which are discussed below—is complex enough to preclude quantitative analysis during the static phase of reserves estimation, and to allow only qualitative guidelines to be provided here.

Depending on geologic setting, drive mechanism, and reservoir geometry, RE might be strongly influenced by well spacing. Such scenarios include thin oil columns producing by bottom waterdrive; heavy oil, in general; low-permeability gas reservoirs; and reservoirs with discontinuities.

Oil Reservoirs. The viscosity of the reservoir oil strongly influences RE for oil reservoirs, and roughly correlates to the stock-tank oil gravity. Reservoir oils are broadly classified as either heavy (stock-tank gravity less than approximately 25°API) or light (stock-tank gravity greater than approximately 25°API).

For light oils that are producing by solution gas drive with insignificant gravity segregation, REs from reasonably homogeneous reservoirs generally range from 5 to 35% OIP, depending on formation quality, initial solution gas/oil ratio (GOR), and stock-tank gravity.

For heavy oils that are producing by solution gas drive, REs from reasonably homogeneous reservoirs generally range from < 5 to 20% OIP, depending on production mechanism, forma-

TABLE 18.5—RECOVERY EFFICIENCY OF OIL FROM SOLUTION GAS DRIVE RESERVOIRS FOR PRODUCTION FROM BUBBLEPOINT PRESSURE TO ABANDONMENT PRESSURE EQUAL TO 10% OF BUBBLEPOINT PRESSURE^{a,b}

Solution GOR	Stock-Tank Gravity, °API	Sandstones			Carbonates		
		Maximum ^c	Average ^d	Minimum ^e	Maximum ^f	Average ^g	Minimum ^h
60	15	0.128	0.086	0.026	0.280	0.040	0.006
	30	0.213	0.152	0.087	0.328	0.099	0.029
	50	0.342	0.248	0.169	0.390	0.186	0.080
200	15	0.133	0.088	0.033	0.275	0.045	0.009
	30	0.222	0.152	0.084	0.323	0.098	0.026
	50	0.374	0.264	0.176	0.398	0.193	0.074
600	15	0.180	0.113	0.060	0.266	0.069	0.019
	30	0.243	0.151	0.084	0.300	0.096	(0.025)
	50	0.356	0.230	0.138	0.361	0.151	(0.043)
1,000	15	n/a ⁱ	n/a	n/a	n/a	n/a	n/a
	30	0.344	0.212	0.126	0.326	0.132	(0.040)
	50	0.337	0.202	0.116	0.318	0.120	(0.031)
2,000	15	n/a	n/a	n/a	n/a	n/a	n/a
	30	n/a	n/a	n/a	n/a	n/a	n/a
	50	0.407	0.248	0.156	0.328	(0.145)	(0.050)

^aAfter Arps and Roberts.⁴⁸ ^bUse 0.75 as a preliminary estimate of RE of solution gas for reservoir pressure depleted to approximately 10% of bubblepoint pressure. ^cMaximum RE usually associated with unconsolidated or friable, well-sorted sands with porosity greater than approximately 25%. ^dAverage RE usually associated with moderately cemented sandstones with porosity between approximately 15 and 25%. ^eMinimum RE usually associated with highly cemented sandstones with porosity less than approximately 15%. ^fMaximum RE calculated using average k_r/k , data from 26 samples of Permian dolomite from west Texas. Because average primary RE from these reservoirs typically is less than that tabulated here, the results here should be used with caution. ^gAverage RE usually associated with intergranular, slightly vugular limestones and dolomites. ^hMinimum RE usually associated with highly vugular or fractured carbonates, or with fractured cherts. ⁱValues in parentheses are estimates made from calculations discontinued before reaching abandonment pressure. ^jAn unlikely combination of solution GOR and stock-tank gravity; therefore, calculations were not made.

tion quality, initial solution GOR, and stock-tank gravity. Additional comments about heavy oil are provided in the Special Problems section of this chapter.

Table 18.5 is based on analytical calculations for an assumed range of oil properties and gas/oil relative permeability characteristics.⁴⁸ The calculations assume pressure depletion from the bubblepoint pressure to 10% of that pressure. For reservoirs developed on wide well spacing, especially those in poor-quality formations, it is conjectural whether average reservoir pressure can be reduced to such levels at commercial production rates. The calculations for **Table 18.5** take no account of gravity segregation, which might increase RE; of possible heterogeneities, which might cause incomplete drainage; or of initially undersaturated reservoirs, where expansion of the rock/fluid system will contribute to overall RE when reservoir pressure is reduced from initial to bubblepoint pressure. Nevertheless, REs in **Table 18.5** reasonably agree with many REs observed in the field.

Eqs. 18.14 and **18.15**, published by the API in 1967, result from regression analyses of *observed* RE of oil vs. various rock/fluid properties.⁴⁹ **Eq. 18.14** was developed from 80 U.S.A. reservoirs that had produced by solution gas drive with no initial gas cap. **Eq. 18.15** was developed from 70 U.S.A. reservoirs that had produced by waterdrive.

$$(E_{Ro})_{sg} \approx 0.41815[\phi(1 - S_w)/B_{ob}]^{0.1611}(k/\mu_{ob})^{0.0979}S_w^{0.3722}(p_b/p_a)^{0.1741} \dots \dots \dots (18.14)$$

$$(E_{Ro})_{wd} \approx 0.54898[\phi(1 - S_w)/B_{oi}]^{0.0422}(k\mu_{wi}/\mu_{oi})^{0.077}S_w^{-0.1903}(p_i/p_a)^{-0.2159} \dots (18.15)$$

As with any correlation, these equations reflect the best fit through large data sets; there might be substantial errors when they are applied to a specific case. Accordingly, the user should seek independent corroboration.

Despite disclaimers⁵⁰ regarding the reliability of these correlations, their applicability has been corroborated in enough scenarios to warrant continued, but cautious, application. Estimates based on these correlations can be adjusted when more information becomes available. Early life performance data might be helpful in determining the drive mechanism (which correlation to use) or might lead to a better analysis of reservoir fluid properties (bubblepoints and/or formation volume factors).

The nature of water influx (bottomwater vs. edge water) apparently was not considered in the development of Eq. 18.15. In bottom waterdrive reservoirs, suboptimal well spacing might cause significantly lower RE than indicated by that correlation. (For additional comments regarding bottom waterdrive, see Cronquist.³)

Generalized application of these correlations to estimate REs outside onshore North America is limited by the absence of terms for well spacing and heterogeneity and by the economic scenario under which the reservoirs were operated. Data for these correlations were derived from onshore, U.S.A. reservoirs that generally were developed on relatively close spacing; thus, the reservoirs probably were produced under semisteady-state conditions, under which well spacing might not be a significant parameter. Also, with close well spacing, the effects of reservoir heterogeneity tend to be minimal. Operating costs and economic limits for onshore U.S.A. reservoirs tend to be significantly less than are typical elsewhere, such that REs tends to be greater.

Gravity Segregation. In nature, there always is some gravity segregation of free gas and oil during production of oil by solution gas drive. The relative importance of gravity segregation can be shown by a gravity number N_G :

$$N_G = k_o(\rho_o - \rho_g) \sin \alpha / \mu_o \dots (18.16)$$

The N_G and RE data in Table 18.6³ were compiled from published studies of actual reservoirs, and they may be useful for guidance in making a *preliminary* estimate of the relative importance of gravity segregation. These data do not show a correlation between N_G and oil RE; however, they do indicate that, in an oil reservoir with a N_G greater than approximately 15, significant gravity segregation is a reasonable expectation.³

Gas was injected into some of these reservoirs. The term m_i indicates the volume injected as a multiple of initial gas-cap volume. In the presence of gravity segregation, gas-cap injection reasonably is expected to have the same effect as a large initial gas cap.

Solution Gas. Industry literature rarely discusses RE of solution gas from oil reservoirs. This is because of the historically low economic value of solution gas and the expense of commercializing it (installation of multistage compressors). For oil reservoirs produced by strong waterdrive, such that abandonment pressure is not significantly less than initial bubblepoint pressure, RE of solution gas should be comparable to that for the oil in the same reservoir. For oil reservoirs produced by solution gas drive, such that abandonment pressure approaches atmospheric, as a *first approximation*, RE of solution gas reasonably can be estimated at approximately 75% solution gas initially in place (SGIP).

Volatile Oils. In composition and PVT behavior, volatile oils are transitional between black oil and retrograde gas, and their FVFs from differential liberation are greater than 2.0 RB/STB.

TABLE 18.6—COMPARISON OF N_G AND RE FOR SEVERAL OIL FIELDS PRODUCING UNDER GRAVITY DRIVE (AFTER CRONQUIST³⁾

Field (Pool), Location	Gravity Number	RE % OIP
Elk basin (Tensleep) ^a Wyoming, U.S.A.	15 ^b	61 ^c
Midway Sunset (Lakeview), California, U.S.A.	41	62 ^d
Mile Six, Peru	47	62 ^e
Oklahoma City, Oklahoma, U.S.A.	30 ^b	37
Shuler (Jones), Arkansas, U.S.A.	340 ^b	60 ^f

^aReportedly, reservoir is oil-wet. ^bEstimated from published data. ^c $m = 0$; $G_g = 110$ Bscf. ^d $m = 0$; $m_i = 0$. ^e $m = 0$; $m_i > 8.7$. ^f $m = 0.027$; $m_i = 14.8$. 1962 estimated ultimate recovery (70%) includes effects of water injection. *Eq. 18.16 is not dimensionless and hence is not meant as an absolute indicator of the importance of gravity drive. Values calculated from Eq. 18.16 and those in this table should be used in a relative sense only.

Their initial solution GOR ranges from approximately 1,750 to 3,200 scf/STB, and their stock-tank gravity ranges from approximately 40 to 60°API.

A significant volume of stock-tank liquids may be produced as condensate from the liberated solution gas. For a specific reservoir, the producing GOR and FVF strongly depend on separator conditions. Use the *flash* FVF that reflects anticipated separator conditions—not the differential liberation factor—to calculate OIP and reserves.

REs of volatile oils by primary drive mechanisms are comparable to those observed for light oils. Unless there are compelling data to the contrary, Eqs. 18.14 and/or 18.15 may be used for a preliminary estimate of RE. Depending on the anticipated drive mechanism, volatile-oil/primary-drive-mechanism reservoirs frequently are operated under high-pressure gas injection. Cronquist⁵¹ discusses several such projects.

Depending on circumstances, some or all of the wellhead production from accumulations of volatile oils might be processed through an off-site plant. One should take care to allocate products properly between lease and plant because ownership of each may differ.

Volatile oils sometimes are classified—erroneously—as retrograde gases. The reservoir temperature in such accumulations may be only slightly less than critical temperature, and a small error in measuring formation temperature can cause laboratory PVT analysis to be conducted at an incorrect temperature. Also, because producing GOR depends on separator conditions, recombination ratios might be incorrect, causing the laboratory fluid to be nonrepresentative.

Gas Reservoirs. RE of gas from nonassociated gas reservoirs is influenced by the ratio of abandonment to initial reservoir pressure and the degree to which the accumulation has been invaded by water from the aquifer, among other factors. In general, RE can be calculated by

$$(E_{Rg})_{pwa} = (1 - R_{pz}) + (R_{pz} E_V E_D), \dots\dots\dots (18.17)$$

where

$$E_D = (1 - S_{wi} - S_{gr}) / (1 - S_{wi}), \dots\dots\dots (18.18)$$

and where S_{gr} can be approximated by

$$S_{gr} \approx 0.62 - 1.3\phi \dots\dots\dots (18.19)$$

If there is no water influx, $E_V = 0$ and Eq. 18.17 becomes

$$(E_{Rg})_{pd} = (1 - R_{pz}) = 1 - p_a z_i / p_i z_a \quad \text{..... (18.20)}$$

For moderate- to high-permeability reservoirs that are producing by pressure depletion with no water influx, an RE of 85% GIP frequently is assumed, pending observation of well and/or reservoir performance. In many such reservoirs, multiple-stage compression may be warranted, and REs exceeding 95% can be achieved. Caution! Without actual installation of such equipment and/or operating data to demonstrate the commerciality of such an installation, such REs should not be assumed in booking proved reserves. For poor- to low-permeability reservoirs, however, RE might be substantially less than 85%.

If there is a strong waterdrive (where $R_{pz} \approx 1.0$), Eq. 18.17 reduces to

$$(E_{Rg})_{swd} \approx E_V E_D \quad \text{..... (18.21)}$$

and gas RE can be approximated by the product of the volumetric sweep efficiency, E_V , and the displacement efficiency, E_D .

RE of gas from partial waterdrive gas reservoirs is rate-sensitive.^{52,53} Some engineers advocate producing such reservoirs at high rates to minimize abandonment pressure, thereby maximizing RE of GIP.³² Depending on the nature of permeability distribution in a reservoir, well spacing and location, and the strength of the aquifer, however, high production rates might cause irregular water encroachment, which could cause lower ultimate recovery than if the reservoir were produced at a lower rate.^{3,54}

Volumetric sweep efficiency is influenced by reservoir geometry, spatial distribution of permeability, horizontal/vertical permeability ratio, well spacing, and well positioning, among other factors. For example, in thin gas accumulations underlain by water, the volumetric sweep efficiency will be significantly less than in thick gas accumulations underlain by water. Accordingly, closer well spacing—if commercially feasible—might be required for efficient drainage of such thin gas accumulations. Regardless of well spacing, a high horizontal/vertical permeability ratio generally will be conducive to effective sweep efficiency in bottom waterdrive gas reservoirs. Also, sweep efficiency by bottom waterdrive generally will be higher in reservoirs where permeability increases toward the top of the reservoir (as in offshore barrier bars) than in ones where permeability decreases toward the top (as in alluvial channels). Well positioning in the reservoir also is important. A long, narrow reservoir that is developed by a single well at one end might not drain effectively, requiring additional wells to achieve a reasonable RE.

Gas-Cap Gas. Estimating RE of gas from gas caps can be more complex than might be inferred from Eqs. 18.17 through 18.21. In addition to the factors discussed in the Gas Reservoirs section of this chapter, RE of gas from gas caps also depends on the thickness and spatial relation of the gas cap with respect to the oil column and on the completion and production practices for wells that are completed in the oil column. In general, estimation of RE of gas from gas caps using volumetric methods might be subject to considerable error, and such reserves should be checked against those estimated from well performance as soon as clearly defined, reliable production trends have been established.

In reservoirs with thin gas caps that are completely underlain by the oil column, making gas-well completions may be infeasible and, regardless of the drive mechanism, most of the gas-cap gas might be produced by downward coning into oil-well completions. In a strong-waterdrive reservoir, this scenario could lead to the presence of substantial volumes of unswept gas at crestal locations. In a depletion drive reservoir, if the oil-well completions can be operat-

ed to relatively low economic limits, RE of gas should be commensurate with that calculated from Eq. 18.20.

In reservoirs where the gas cap is en echelon to the oil column and where gas-well completions are feasible, RE of gas should be commensurate with that expected from a nonassociated free-gas accumulation.

Condensate. Condensate is defined here as a petroleum liquid consisting mostly of pentanes and heavier hydrocarbons that is in the gas (vapor) phase under initial reservoir conditions and that condenses to the liquid phase when the gas is produced through surface separation equipment operating under ambient conditions on a lease. (The definition of “condensate” has been controversial among OPEC countries. Less restrictive definitions that make it difficult to distinguish between condensate and light oil have been proposed.)

RE of condensate from gas reservoirs depends on composition of the reservoir gas, reservoir abandonment pressure relative to the dewpoint pressure, RE of gas from the same reservoir, and separation equipment used in the lease, among other factors. For nonretrograde reservoirs, RE of condensate should be comparable to that of the gas in the same reservoir, but either way, separator conditions might influence RE. For example, high-pressure gas wells—those with flowing tubing pressure (FTP) greater than approximately 1,000 psia—typically are produced through low-temperature separators (LTS). If FTP gradually decreases below approximately 1,000 psia because of pressure depletion, LTS equipment becomes progressively less efficient, which may lead to condensate carry-over.

For retrograde reservoirs, if PVT data are not available, the correlations in Eqs. 18.22 through 18.26⁵⁵ may be used to calculate condensate/gas ratio (CGR) as a function of reservoir pressure, dewpoint pressure, and initial CGR. Caution! These correlations are based on limited data.

$$R_c \approx R_{cd} [1 + nD(1 - p/p_d)]^{-1/n}, \dots\dots\dots (18.22)$$

where R_{cd} = the CGR at the dewpoint pressure, STB/MMscf, and n and D are defined as follows:

$$\text{If } R_{cd} \leq 15, \text{ then } n \approx 24.5 - 1.37R_{cd}. \dots\dots\dots (18.23)$$

$$\text{If } R_{cd} > 15, \text{ then } n \approx 3.91 [1 + 2.71(R_{cd} - 15)]^{-0.129}. \dots\dots\dots (18.24)$$

$$\text{If } R_{cd} \leq 150, \text{ then } D \approx 4.05 + 0.0099(R_{cd})^{1.48}. \dots\dots\dots (18.25)$$

$$\text{If } R_{cd} > 150, \text{ then } D \approx 24.3 \ln(R_{cd}) - 101. \dots\dots\dots (18.26)$$

If retrograde gas reservoirs are produced to reservoir pressures that are less than the dewpoint pressure, retrograde condensation might cause irreversible loss of condensate in the reservoir pore space. The loss will be proportionately greater for richer gases.

To illustrate this point, *producing* CGR vs. reservoir pressure (as calculated using Eqs. 18.22 through 18.26) is plotted on Fig. 18.12 as dimensionless CGR (R_c/R_{cd}) vs. dimensionless pressure (p/p_d). For example, if a reservoir with an initial CGR of 100 STB/MMscf is produced to a reservoir pressure that is 80% of dewpoint pressure, the producing CGR is estimated from Fig. 18.12 to be 40 STB/MMscf.

Eqs. 18.22 through 18.26 also are used here to calculate *ultimate* CGR for reservoirs produced to 10% of dewpoint pressure:

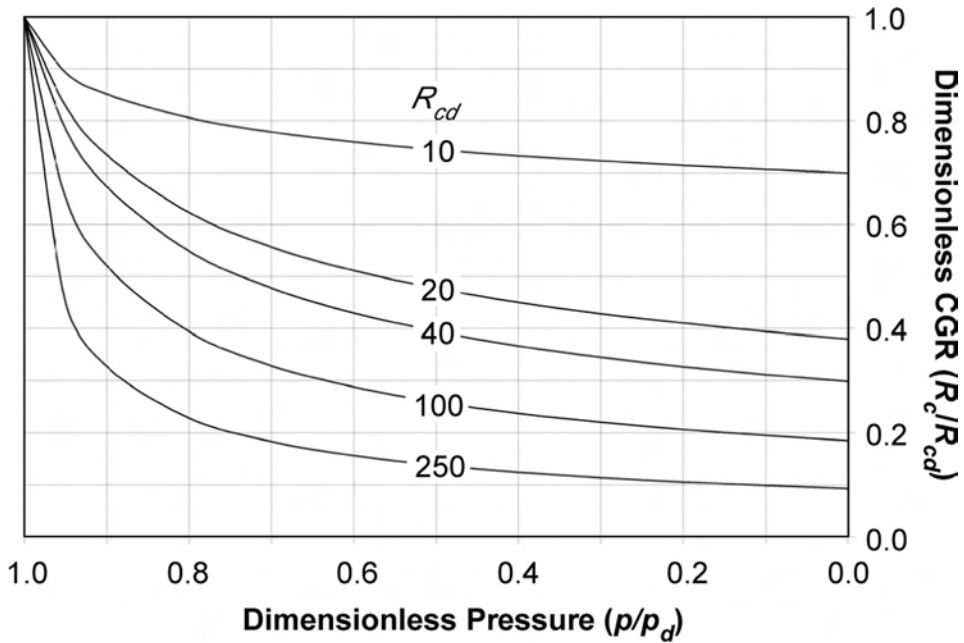


Fig. 18.12—Dimensionless CGR vs. dimensionless pressure (after Cronquist³).

$$R_{cuD} \approx 2.01 R_{cd}^{-0.412}, \dots\dots\dots (18.27)$$

where R_{cuD} = dimensionless ultimate condensate production ($C_{pu} / G_{pu} R_{ci}$). (In developing Eq. 18.27, it was necessary to assume $z = 1$, which may introduce intolerable errors.) For example, for a gas reservoir with an initial CGR of 100 STB/MMscf produced from dewpoint pressure to 10% of dewpoint pressure, from Eq. 18.27 the cumulative (ultimate) CGR is calculated to be 30 STB/MMscf.

These simple guidelines are adequate for retrograde gas reservoirs in good- formations; however, in poor-quality formations, estimating reserves from such reservoirs is a major problem. Producing such reservoirs by pressure depletion at reservoir pressures below the dewpoint pressure causes retrograde liquids to condense in the pore space. In the interwell areas of the reservoir, such condensation typically builds up to no more than a few percent of initial pore space, but around wellbores, it can build up to saturation levels that can substantially reduce the effective permeability to gas. Depending on circumstances, well productivity might be severely reduced, possibly causing premature abandonment.

A major difficulty continues to be reliable prediction of the depletion performance of such reservoirs, especially those with “rich gases” (high initial CGR) in low-permeability formations. Some of the problems are being overcome through advances in simulation technology, but as yet there are no simple guidelines in the open literature.

Classification of Volumetric Reserves. Classification of volumetric reserves may involve both updip/downdip limits and areal assignments.

Updip/Downdip Limits. The 1997 SPE/WPC⁶ and the 1978 U.S. SEC¹⁰ reserves definitions both limit proved reserves to a volume no deeper than GWC or OWC. The 1997 SPE/WPC definitions state: “In the absence of data on fluid contacts, the lowest known occurrence of hydrocarbons controls the proved limit unless otherwise indicated by definitive geological, engineering or performance data.” Their use of “geological” embraces all facets of geology, including geophysics. Similarly, the U.S. SEC definitions state: “In the absence of information

on fluid contacts, the lowest known structural occurrence of hydrocarbons controls the lower proved limit of the reservoir.”

Until areal and vertical reservoir limits are defined by the drilling of enough wells, the location or depth of an OWC or a GWC may be subject to much uncertainty. The extent of this uncertainty often can be narrowed to the vertical distance between the HKW in an off-structure dry hole and the LKO or LKG that is demonstrated by an upstructure well. Without other information to define the hydrocarbon/water contact, LKO/LKG depths typically are used to limit the downdip volume of proved oil and gas reserves.

A deterministic approach might arbitrarily assign incremental probable reserves to the portion of the reservoir between the LKO/LKG and the midpoint between that depth and the HKW, and it might assign incremental possible reserves to the interval between this midpoint and the HKW.

A probabilistic approach in one case might ascribe various confidence values to different levels between the LKO/LKG and the HKW, or in another case might consider that the LKO/LKG and the HKW define the endpoints of a probabilistic distribution and use Monte Carlo analysis to calculate appropriate probabilities for 2P and 3P reserves. In the first case, for instance, the reservoir volume above the LKO/LKG might be assigned a 90% (P90) value, and the maximum possible reservoir size down to the HKW might be given a 5 to 10% (P5, P10) value. An intermediate depth between the LKO/LKG and the HKW can be established to define the 50% (P50) confidence level.

The six simplified reservoir cross sections included in [Fig. 18.13](#) establish some basic guidelines in reserves classification, but do not include all potential variations. All examples in [Fig. 18.13](#) assume adequate geologic data to support the structural interpretation. See Cronquist³ for additional guidelines.

Part A of [Fig. 18.13](#) illustrates a one-well reservoir with the well interval fully saturated with oil or gas, but without direct evidence of a downdip GOC, GWC, OWC, or HKW. No other data are available. For gas or undersaturated crude, proved (P1) reserves are limited to the “lowest known occurrence” or the depth established by the base of the formation as seen in the well log. Some have assumed that one sand thickness below the LKG or LKO contains proved (P1) or probable (P2) reserves, even though little geologic data or logic typically supports this assumption. Possible (P3) reserves sometimes are assigned to the reservoir volume represented by one additional sand thickness below the assumed P2 limit, again often with little basis.

Part B of [Fig. 18.13](#) is similar to part A, but includes data from a downdip wet well located below the LKO/LKG contact. This wet well establishes the HKW, which is considered equivalent to the deepest (and largest) possible accumulation of gas or oil in the reservoir. As in part A of [Fig. 18.13](#), the volume of gas or oil above the LKG/LKO may be considered P1 reserves; the volume below the LKG/LGO, but above the HKW, often is split into P2 and P3 reserves.

Part C of [Fig. 18.13](#) is similar to part A, but the depth and location of a reservoir structural spill point (SP) can be mapped. The SP depth establishes a maximum size of a hydrocarbon accumulation in much the same way as does the dry hole shown in part B of [Fig. 18.13](#). The interval between the LKG/LKO and the SP may be subdivided into P2 and P3 intervals, assuming no other information to the contrary.

Part D of [Fig. 18.13](#) is identical to part C in structural attributes, but illustrates a further complication for a saturated oil reservoir that might have a gas cap with a GOC that potentially is as deep as the HKO shown at the top of the logged interval. The engineer judges what portion of the reservoir volume above the HKO should be allocated to oil and/or gas. In any event, only the reservoir portion limited by the LKO and HKO can be classified as P1 reserves

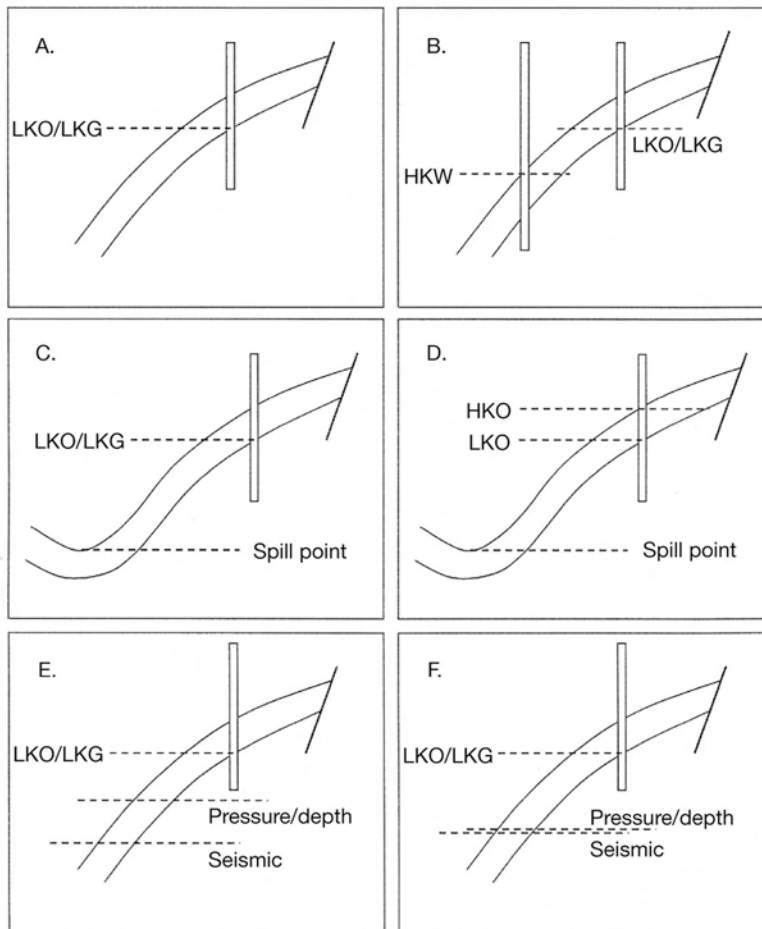


Fig. 18.13—Estimation of reservoir limits for classification of reserves.

in most circumstances. This limitation might have a significant impact on the value of the reservoir because oil usually has a higher value than natural gas.

Part E of Fig. 18.13 is a simplified example to guide where seismic interpretations lead to a downdip limit below that calculated through the use of pressure/depth data. Although using pressure and seismic data lead to different conclusions, they can be useful in defining P2 and P3 reserves allocations. In some cases, the quality of the pressure/depth data may warrant assigning P1 reserves to the calculated hydrocarbon/water contact, especially if the 3D seismic interpretation supports a larger reserves quantity.

Part F of Fig. 18.13 is an idealized case in which a reservoir limit below the LKG/LKO is corroborated by both pressure and seismic interpretations, perhaps enough to support the designation of P1 reserves to the lower depth. Such a conclusion would be a function of the amount and quality of the pressure and seismic data.

These six examples are useful, but they are only guidelines. The reserves engineer should consider fully the quantity and quality of all data used in reserves quantifications and classification and look beyond the specifics of any individual reserves determination for guidance obtainable from area analogs.

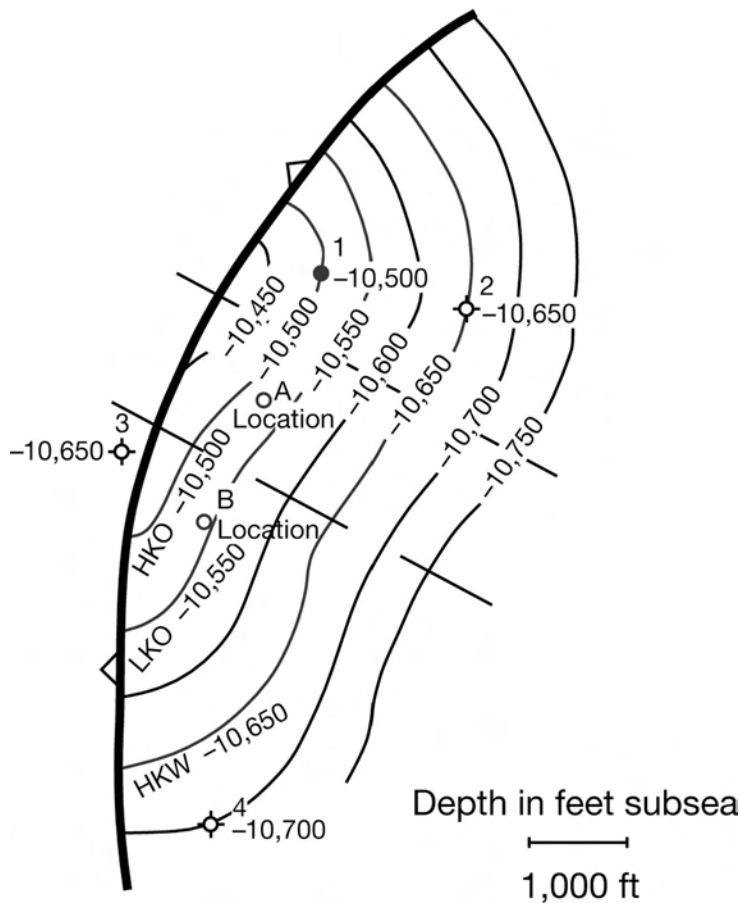


Fig. 18.14—Structure map on top of porosity.

Areal Assignments. Fig. 18.14 is identical to Fig. 18.3, except for the two dashed lines that suggest assignment of different classifications reserves from an areal perspective. Consistent with the Fig. 18.3 discussion, Locations A and B in Fig. 18.14 are required for effective drainage and depletion of the reservoir. Well 1 is classified as proved producing. Location A can be classified as proved (undeveloped) on the basis of *reasonable certainty* of the geologic interpretation and the adequacy of well control.

Location B cannot be classified as proved, given the uncertainty introduced by reservoir sand being absent in Well 4 and the structural uncertainty regarding the position of an LKO or an OWC. The southwest boundary of the interpreted channel sand is not defined and has been inferred through seismic interpretation (see Fig 18.4). Most would classify the reservoir volume southwest of the southern line and above 10,600 ft ss as probable undeveloped. Note that all or part of the reservoir volume above the HKO may be assumed to be oil-filled in the P2 or P3 cases.

18.4.3 Performance Methods. Performance methods are used after a field, reservoir, or well has been on sustained production long enough to develop a trend of pressure and/or production data that can be analyzed, usually mathematically, to estimate O/GIP and/or future production. The analysis may involve material-balance calculations, computer simulation, or “fitting” histor-

ical trends of production rates [water/oil ratio (WOR), gas/oil ratio, water/gas ratio (WGR), condensate/gas ratio, and/or pressure], or some combination of these.

Material Balance. Classic material balance (CMB) is a computational procedure by which the fluid properties and pressure/performance history of a *reservoir* are averaged, thereby treating the reservoir as though it were a tank. Computer simulation (discussed in a subsequent section) uses material-balance principles, but segments the reservoir into numerous cells or grid-blocks, rather than treating it as a tank. Also, simulation programs can be used to forecast production.

CMB equations are formulated to calculate volumes of O/GIP. These methods can be used when there are sufficient historical reservoir pressure and production data to perform reliable calculations. Computer simulation might seem to have rendered the CMB obsolete, but not so. For many scenarios, the CMB remains an essential adjunct to computer simulation.^{56,57} Indeed, the CMB sometimes is the *only practical approach* to reservoir analysis, such as in the following cases:

- In highly fractured reservoirs, which defy characterization needed for reliable computer simulation.
- In fractured/vugular carbonates where lost circulation problems preclude complete penetration and, accordingly, adequate characterization of the reservoir.
- In reservoirs (typically offshore-gas) that are developed from clusters of wells from widely spaced platforms, a scenario in which subsurface data may be inadequate to characterize the reservoir.

For reliable material-balance calculations, the reservoir must have reached semisteady-state conditions (pressure transients must have affected the entire hydrocarbon fluid system and contiguous aquifer, if any). Depending on reservoir fluid and formation properties and on reservoir drive mechanism, this could require cumulative production of as much as 5 to 10% of the O/GIP.

Reliable application of the material balance method requires accurate historical production data for *all* fluids (oil, gas, and water), accurate historical (static) bottomhole pressure data, and PVT data representative of *initial* reservoir conditions.

Limitations for CMB include reservoirs with strong waterdrives or large gas caps that maintain reservoir pressure close to initial pressure, a scenario in which reservoir-pressure errors cause erratic calculations of the expansion terms and, consequently, unstable solutions (discussed in the next section); thin, areally extensive, and/or low-permeability reservoirs that have wide areal variations in reservoir pressure and saturation conditions that cannot be averaged reliably; and volatile oils, in which the volumes of stock-tank liquids separated from the solution gas are unaccounted for. This last limitation might be overcome using procedures discussed by Walsh.⁵⁸

For gas reservoirs that are producing by pressure depletion, a graphical form of the material-balance equation (discussed in a subsequent section) can be used to estimate GIP *and* reserves. For oil reservoirs, the material-balance equation can be used to estimate O/GIP and likely drive mechanism. To estimate *reserves* from oil reservoirs, however, the material-balance equation must be used in a form that includes appropriate relative-permeability data and operating constraints in a predictive mode adapted for computer simulation. Otherwise, REs can be estimated by analogy.

Equations. In “expanded” form (including water influx), the material-balance equation may be stated as oil-and-gas production (plus water) equals expansion of oil and free gas initially in place plus water influx. Assuming an initial gas cap and, at this time, ignoring compressibility of PV and interstitial water, this relation may be written as:

$$\begin{array}{ccccccc}
 & & \text{PRODUCTION} & = & \text{EXPANSION} & + & \text{INFLUX} \\
 & \swarrow & \downarrow & & \swarrow & & \downarrow \\
 \text{GAS CAP} & + & \text{OIL COLUMN} & + & \text{AQUIFER} & = & \text{GAS CAP} & + & \text{OIL COLUMN} & + & \text{AQUIFER} \\
 \swarrow & & \downarrow & & \downarrow & & \downarrow & & \downarrow & & \downarrow \\
 \text{TOTAL GAS} & - & \text{SOLUTION GAS} & & & & & & & & \\
 \downarrow & & \downarrow & & \downarrow & & \downarrow & & \downarrow & & \downarrow \\
 N_p R_p B_g & - & N_p R_{si} B_g & + & N_p B_t & + & W_p B_w & = & \frac{N_i m B_{ti} (B_g - B_{gi})}{B_{gi}} & + & N_i (B_t - B_{ti}) & + & W_e
 \end{array}$$

..... (18.28)

and gathering terms,

$$N_p [B_t + B_g (R_p - R_{si})] + W_p B_w = N_i [(B_t - B_{ti}) + m B_{ti} (B_g - B_{gi}) / B_{gi}] + W_e \dots\dots\dots (18.29)$$

In Eqs. 18.28 and 18.29, units on both sides of the equal sign are RB. Also, units for B_g in these and subsequent equations in this section are RB/scf (whereas in Eq. 18.5, B_g is in Rcf/scf).

Depending on the magnitude of pore and water compressibility compared to overall system compressibility, it might be desirable to include compressibility terms for oil material balance calculations, both above and below the bubblepoint pressure. If compressibility terms were included for both the initial gas cap and the oil column, Eq. 18.29 would be written:

$$\begin{aligned}
 N_p [B_t + B_g (R_p - R_{si})] + W_p B_w = N_i [& (B_t - B_{ti}) + (1 + m)(c_p + c_w S_w) B_{ti} (p_i - p) / S_o \\
 & + m B_{ti} (B_g - B_{gi}) / B_{gi}] + W_e, \dots\dots\dots (18.30)
 \end{aligned}$$

where the pore compressibility c_p = the *integrated* value between p_i and p , and where p = the pressure at which Eq. 18.30 is evaluated.

There are three unknowns in Eqs. 18.29 and 18.30: OIP, N_i ; size of the initial gas cap, m ; and water influx, W_e . It is rarely possible to solve for all three with reasonable reliability,⁵⁹ but depending on circumstances, it might be possible to eliminate m or W_e , or both. For example, if PVT data indicate an undersaturated oil reservoir, m may be eliminated, and if geologic and/or well-performance data indicate no water influx, W_e may be eliminated. In general, however, the engineer might be faced with determining all three unknowns. In practice, after appropriate modifications, Eq. 18.29 or Eq. 18.30 is solved repeatedly and successively, using the cumulative production and pressure data corresponding to each time until stable solutions are achieved.

One approach to solving for all three unknowns is to group the terms in Eq. 18.30 to reflect the production and expansion⁶⁰:

$$F_{pR} = N_p [B_t + B_g (R_p - R_{si})] + W_p B_w \dots\dots\dots (18.31)$$

$$E_o = (B_o - B_{oi}) + (R_{si} - R_s)B_g - (B_t - B_{ti}) \dots (18.32)$$

$$E_c = (1 + m)(c_p + c_w S_w)B_{ti}(p_i - p) / S_o \dots (18.33)$$

$$E_g = B_g - B_{gi} \dots (18.34)$$

(E_c , which accounts for expansion of PV and interstitial water in the gas cap, in addition to that in the oil column, is taken from Dake.⁵⁶ Havlena and Odeh⁶⁰ neglected to include a compressibility term for reservoirs with an initial gas cap.) Substituting these new terms in Eq. 18.30 yields:

$$F_{pR} = N_i [E_o + (1 + m)E_c + mB_{ti}E_g / B_{gi}] + W_e \dots (18.35)$$

Depending on pressure/production history and subsurface data, it might not be apparent in the early stages of the analysis whether a reservoir being studied had an initial gas cap or whether there is water influx, or both. Eq. 18.35 can be used in various forms to estimate the amount of O/GIP and the most likely reservoir-drive mechanism.

For example, if there is no initial gas cap, $m = 0$, and if there is no water influx, $W_p B_w$ is dropped from Eq. 18.31. After dropping m and W_e , Eq. 18.35 reduces to

$$F_{pR} = N_i (E_o + E_c) \dots (18.36)$$

Without a gas cap and water influx, a plot of F_{pR} vs. $(E_o + E_c)$ should be a straight line passing through the origin, as shown in Fig. 18.15. (For consolidated formations in normally pressured reservoirs, the compressibility term E_c may be ignored, and the plot would be of F_{pR} vs. E_o .) The points represent successive solutions of the fluid production and expansion terms, up to the date of evaluation. The origin is a *must* point; thus, one has a fixed point to guide the straight-line plot. The first few points might be erratic and may be ignored in constructing the straight line. As implied by Eq. 18.36, the slope of the line is $F_{pR} / (E_o + E_c)$, dimensionally equal to RB/(RB/STB), which equals N_i (OIP, in STB).

There are three other possibilities: no gas cap and water influx, gas cap and no water influx, and gas cap and water influx. Each requires appropriate modifications to Eqs. 18.31 through 18.36 and the plotting of different groups. Havlena and Odeh,^{60,61} Dake,⁵⁶ Tehrani,⁵⁹ Sills,⁶² and Cronquist³ offer detailed discussion—and criticism—of these procedures.

p/z vs. Cumulative Wellhead Gas. For nonassociated gas reservoirs where there is no (or insignificant) aquifer influx, and where PV compressibility is negligible, the volume of the initial gas-bearing pore space typically is *assumed* to remain constant over life. For these *volumetric* gas reservoirs, the material-balance equation can be written as:

$$p/z = p_i/z_i - G_p p_i / G_{Fi} z_i \dots (18.37)$$

For such reservoirs, most engineers use a plot of p/z vs. G_p to monitor performance and estimate GIP and reserves, as shown by Fig. 18.16. In theory, such plots should be for a *reservoir*, which may involve averaging static BHPs for more than one well. Caution! G_p is cumulative *wellhead* gas, not just separator or pipeline gas, and should include the gaseous equivalent of stock-tank condensate (GEC).

Depending on the geologic setting and initial well spacing, however, it might not readily be apparent which wells are in a common reservoir, in which case it might be appropriate to plot

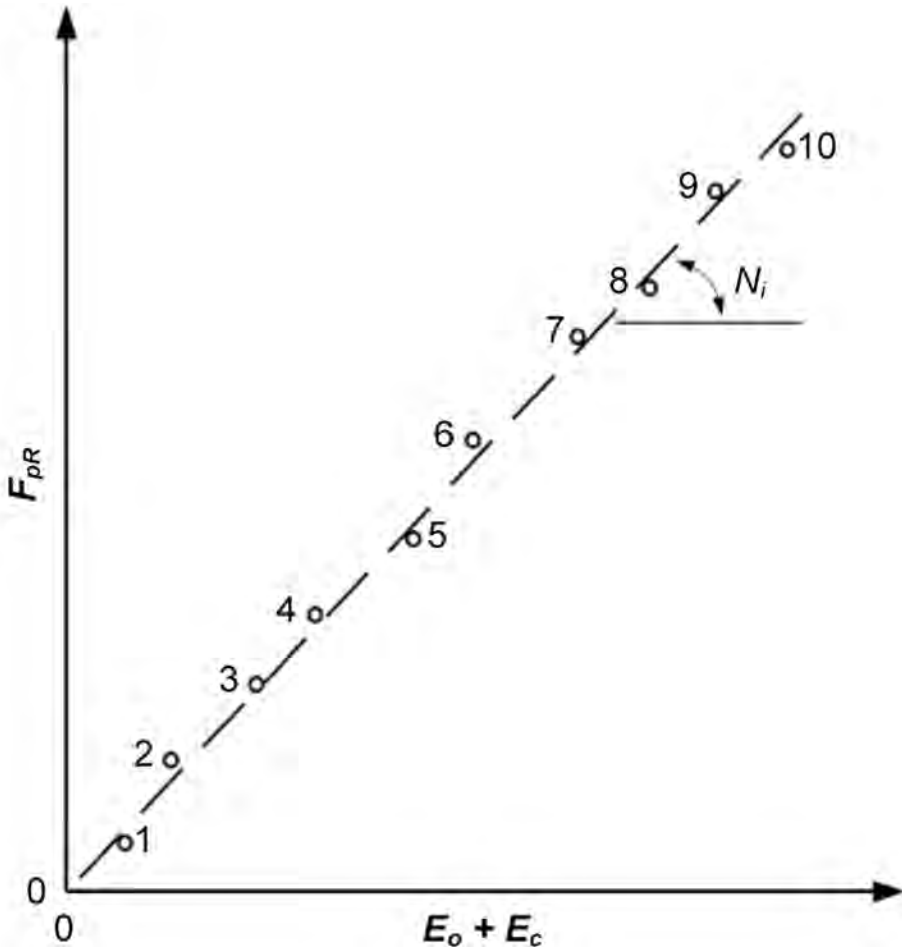


Fig. 18.15—Fluid production vs. compressibility (no gas cap and no water influx). (After Havlena and Odeh.⁶⁰)

initial static BHPs for the suspect wells vs. time on a common scale. It is good practice to maintain plots of p/z vs. G_p for each well until *performance* indicates which wells are in a common reservoir; however, even then it might be desirable to maintain a plot for each well because such plots might help to determine the drainage area of each well and to identify areas for infill drilling. In competitive reservoirs, well plots should be maintained over reservoir life.

Plots of p/z vs. G_p are among the most widely used reservoir engineering tools, as well as one of the most widely misused tools, as discussed in the Pitfalls section of this chapter.

Computer Simulation. Computer simulation is based, in part, on material balances, and can involve analysis of an entire reservoir, segments of a reservoir, or a single well. When such analysis includes a good-quality history match, future production forecasts might be considered proved reserves, depending on the constraints imposed on the forecast; however, if computer simulation is used to forecast production, considering such forecasts to be proved reserves is conjectural without a history match. More detailed comments regarding computer simulation are provided in a subsequent section.

Production/Decline Trend Analysis. Whereas material-balance methods focus on reservoirs, production/decline trend analysis (P/DTA) focuses on wells or aggregates of wells. In that

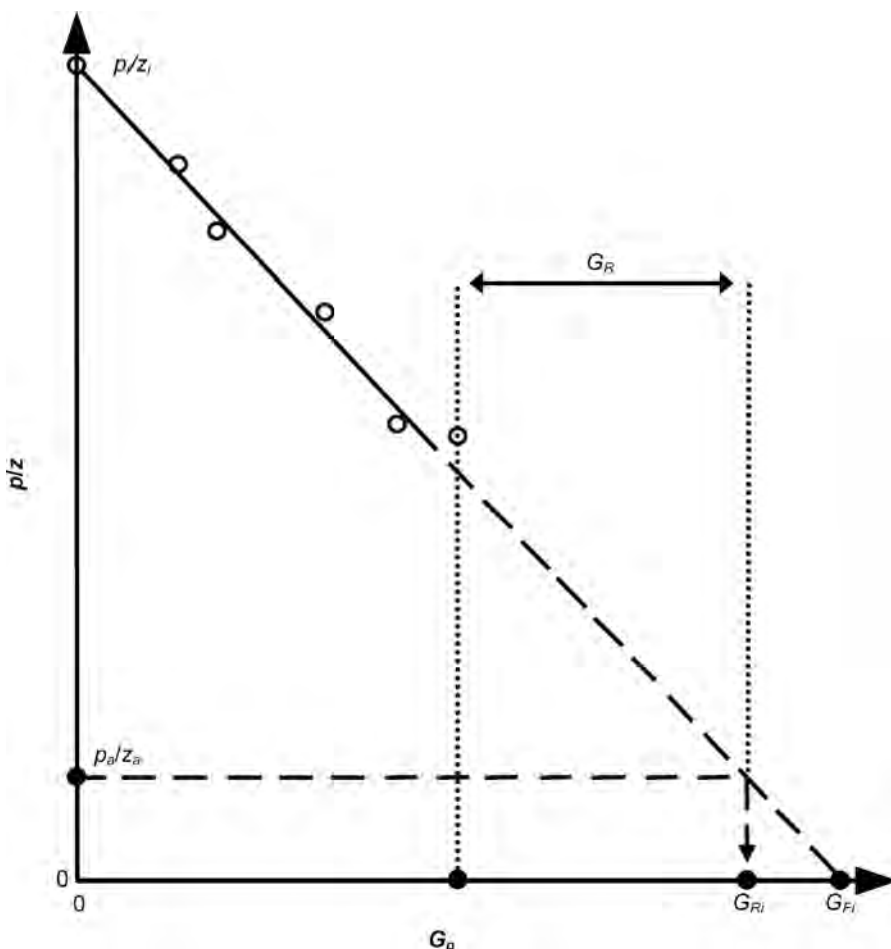


Fig. 18.16—Reservoir pressure vs. cumulative gas production for a volumetric reservoir.

sense, they are two fundamentally different, independent methods for estimating reserves. Depending on circumstances, their results might not agree, a situation that warrants further investigation. Pending resolution, the smaller of the reserves estimates might be classified as proved, and the larger one as proved plus probable or proved plus probable plus possible, depending on the degree of uncertainty.

Economic Limit. “Economic limit” generally refers to one or the other of the following:

- Producing characteristic(s) that typically are used locally to establish the practical limit of production—maximum WOR or maximum GOR—which are identified here as economic limit *conditions*.
- The minimum production rate at which income from such production is less than the cost of continued operation. This is known as the economic limit *production rate* or, simply, the economic limit.

The economic limit may refer to a single well; an aggregate of wells, a lease or unit, or other economic aggregation or financial grouping; or a production facility for an aggregate of wells with processing equipment that must be operated as a unit (e.g., offshore production platforms or fluid injection projects).

The economic limit generally is defined as the production *rate* at which the net revenue to the operator’s working interest that is attributable to production from a well, aggregate, or facil-

ity equals the “out-of-pocket” cost to operate the well, aggregate, or facility. Net revenue is gross revenue, less production and ad valorem taxes, royalties, transportation, and treating expense, if any. Out-of-pocket costs—sometimes called direct operating costs—are costs that would be saved if the well or facility were shut in (e.g., costs for power and materials). Accordingly, such costs include labor only if shutting in the well or facility would save that cost. State and federal income tax and corporate overhead usually are excluded from out-of-pocket costs.

The economic limit for an oil well can be calculated by

$$q_{oel} = \frac{C_D}{[(1 - F_{ro})p_o + R(1 - F_{rg})p_g] - (T_P + T_A + C_{TP})} \dots\dots\dots (18.38)$$

Application of production and ad valorem taxes varies from one jurisdiction to another, and Eq. 18.38 should be viewed only as an example.

Wellbore/Mechanical Problem vs. Reservoir Performance. A performance/decline trend in a well might, in some instances, be caused by a wellbore and/or mechanical problem, rather than by the performance of the well and/or reservoir. Extrapolation of such trends can lead to estimates that do not reflect production that might actually be recovered if the wellbore and/or mechanical problem were remedied.

Single Wells vs. Aggregates. Historical production data on single wells might not always be available, and reserves estimates might have to be made using production data aggregated to leases or to reservoir units that contain more than one well. Even if single-well data are available, such production might be volumes allocated from a common battery on the basis of periodic well tests.

In aggregates, various wells might be in different stages of decline and might have different GORs and/or different WORs. Remedial operations, infill drilling, and modifications to production equipment might have influenced the production history and may be expected to influence future trends. An evaluator should become familiar with past, current, and anticipated future operations before attempting to estimate reserves from production trends from multiwell aggregates. Routine lease operations that affect well performance might be reported only informally, if at all. Frequently, pumpers or lease foremen maintain records of well tests, pressures, and equipment changes in “daily gauge reports” that generally are not available elsewhere. Depending on circumstances, the engineer responsible for reserves estimates should consider making an on-site visit with field personnel to determine the nature of field operations and the possible influence of those operations on production rate.

The Pitfalls section of this chapter discusses some factors affecting production forecast reliability.

Production Curtailment. Production of oil and/or gas might be curtailed for many reasons, including capacity limitations on pipelines or plants, market restrictions, inability to handle all produced water or gas, limitations on treating facilities, contract arrangements, regulatory limits, and governmental interference. Here are several examples:

- If wellhead gas is being processed through a gasoline plant, total gas production might be limited by plant capacity. Wellhead gas may periodically bypass a processing plant if the relationship between oil and gas prices makes the sale of unprocessed gas more financially attractive.
- Production from low-pressure gas wells might have to be compressed before being sold, and such production might be constrained by available compressor capacity.
- Production from high-WOR oil wells might have to be limited because of limited capacity to separate, treat, and dispose of produced water.

Thus, before analyzing historical production trends, especially on multiwell aggregates, the engineer should determine whether there has been curtailment of production during the period

being analyzed and whether there are facilities constraints that might cause curtailment in the future.

Regarding possible future curtailments, the reserves engineer should ensure that extrapolations of historical trends to estimate reserves do not generate future fluid production forecasts that are inconsistent with existing or anticipated processing capacity. For example, tacit in a future oil and gas production forecast from a waterdrive reservoir is the idea that, after breakthrough, water production will gradually increase until wells reach the economic limit; however, such forecasts might not be realistic because of physical limitations to handling the produced water.

Performance Indicators. One or more of the performance indicators of a well might exhibit a trend before the production rate of the principal product begins to decline. Depending on reservoir type and drive mechanism, these performance indicators include fractional flow of oil (f_o), WOR, WGR, GOR, CGR, BHP, FTP, and shut-in tubing pressure (SITP).

Several performance methods have been used to estimate oil reserves from individual wells in waterdrive reservoirs. Two of the most widely used methods involve plotting either f_o vs. N_p or WOR vs. N_p . These and other methods are discussed briefly here.

In waterdrive reservoirs, after breakthrough of water in individual wells, semilog plots of f_o vs. N_p for each well might exhibit linear trends, as illustrated by Fig. 18.17. Usually, the trend can be extrapolated to f_o at economic limit conditions to estimate reserves. The f_o at the economic limit will be governed by the total liquid capacity (oil plus water) of the well and the completion equipment used to produce the well.

For such wells produced at an approximately constant oil rate after breakthrough of water, the logarithm of the rate of total liquid production (oil plus water) typically increases linearly with time, as illustrated by Fig. 18.18. This behavior has been observed for high-capacity oil wells in waterdrive reservoirs being produced by gas lift. Oil reserves can be estimated by extrapolating the total liquids rate (oil plus water) to the maximum capacity of the well. Plots such as Figs 18.17 and 18.18 should be prepared for each well that is producing significant water. In using plots such as Fig. 18.18 to estimate reserves, note that the production rate of oil will decrease after the production rate of total liquids increases to the maximum capacity of the well. As discussed in the Rate/Time Trends section, following, the nature of the decrease will depend on the trend of f_o vs. N_p .

In many cases, a linear trend of f_o vs. N_p might turn downward as f_o becomes small. The downturn reportedly occurs at smaller f_o values for heavy (viscous) oils than it does for light oils, as illustrated by Fig. 18.19.⁶³

In areas with high-permeability sands and a favorable water/oil-mobility ratio (e.g., offshore Nigeria), a Cartesian plot of f_o vs. N_p , rather than a semilog plot, might provide a more reliable basis for extrapolation.

Occasionally, the completion interval may extend across a shale break, as shown schematically by part A of Fig. 18.20. In many cases in bottom waterdrive reservoirs with such completions, discontinuities have been observed in the trend of f_o vs. N_p , as shown by part B of Fig. 18.20. After water breakthrough (point “a” on both figures), the trend of f_o vs. N_p decreases while the perforations below the shale break water out (point “b”). The trend stabilizes until the encroaching water rises above the shale break (point “c”). After water breakthrough into the perforations above the shale break, the trend again declines. The rate of decline of f_o after the stabilization period might be greater or less than the rate of decline before the stabilization period, as discussed below. During period b–c, f_o should be *approximately*:

$$f_o = \frac{k_o h_{n1}}{\mu_o (k_o h_{n1} / \mu_o + k_w h_{n2} / \mu_w)} \cdot \dots \dots \dots (18.39)$$

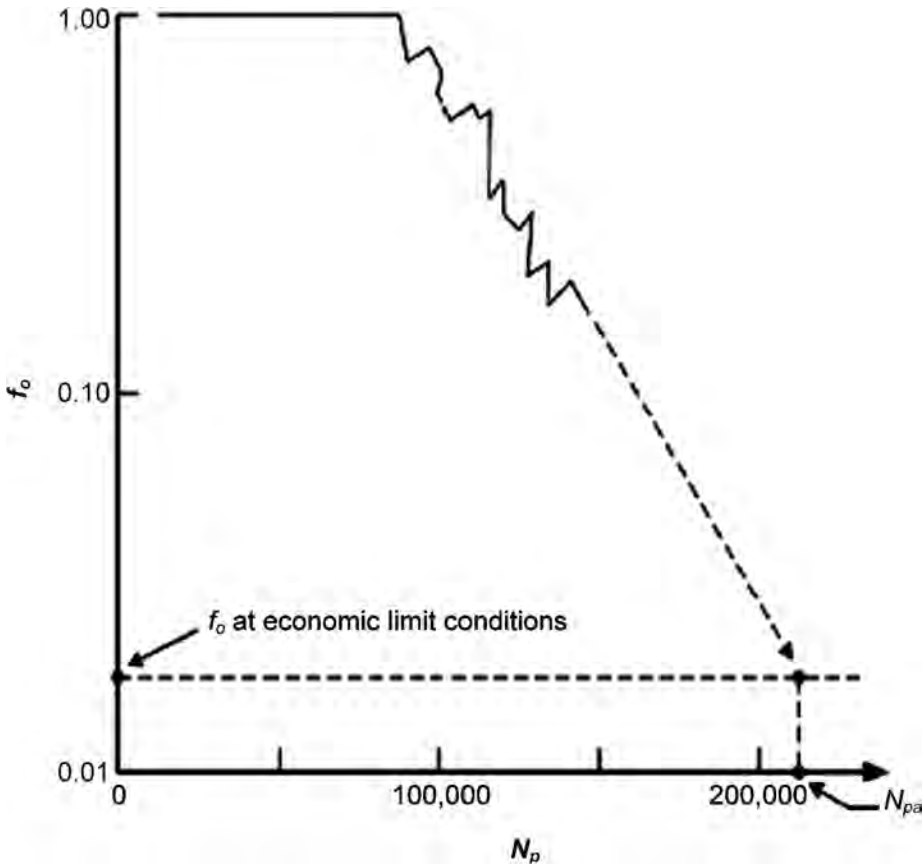


Fig. 18.17—Fraction of oil in total fluids vs. cumulative oil production for a typical well that is producing by waterdrive (after Cronquist³).

If such behavior is observed (trend a–b–c) and if well-completion geometry can be verified by Eq. 18.39, then, as a first approximation:

$$N_{pu} = N_{pc} \left(1 + h_{n1} / h_{n2} \right) \dots\dots\dots (18.40)$$

If $h_{n1} > h_{n2}$, the rate of decline in f_o after the stabilization period usually will be less than the rate of decline before the stabilization period. Conversely, if $h_{n1} < h_{n2}$, the rate of decline after stabilization will be more than before.

In a scenario like that shown by Fig. 18.20, extrapolation of trend a–b could lead to significant underestimation of reserves. Against such a possibility, one should check reserves from such an extrapolation against a reasonable volumetric estimate. In general, reserves estimated from any such extrapolation should be checked against those estimated from volumetric mapping and/or should be compared with reserves from analogous wells.

Trends of WOR vs. N_p also can be used to estimate reserves from waterdrive wells. In many scenarios, semilog plots of such data tend to become linear at WORs greater than approximately 1. In these cases, semilog plots of $(WOR + 1)$ vs. N_p tend to be linear at WORs of less than 1, which might help to define trends at low WOR values.⁶⁴ Be careful in using such plots, however, without first examining the nature of the fractional flow trend, as discussed in the Rate/Time Trends section, following.

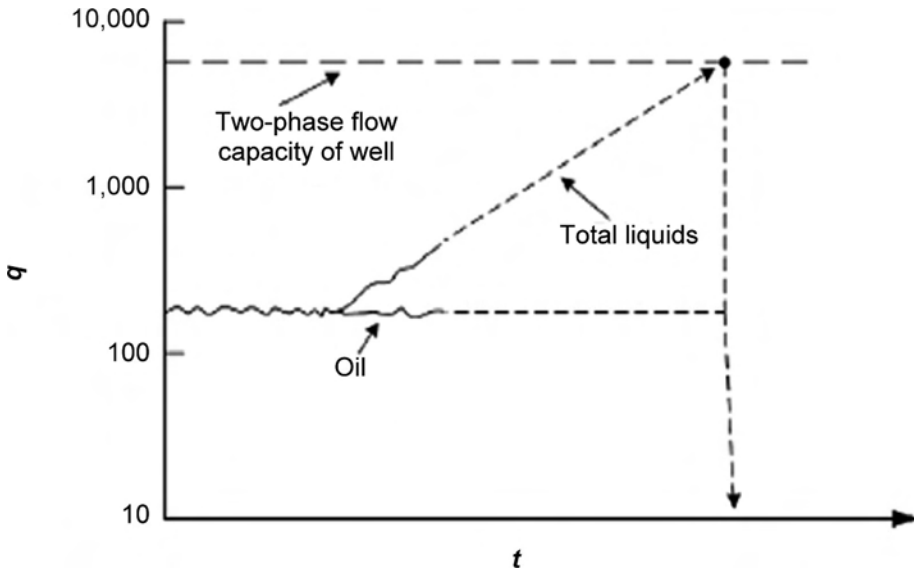


Fig. 18.18—Total liquids production vs. time for a typical waterdrive oil well (after Cronquist³).

Determining the correct performance plot to estimate reserves in waterdrive reservoirs is highly empirical. Many of the published procedures are based on the observation that a significant part of a semilog plot of (k_{rw}/k_{ro}) vs. S_w is linear. The floodout performance of wells and reservoirs, however, is governed not only by relative permeability, but also by formation heterogeneity and gravity/viscous forces, among other factors; thus, consider different types of plots, determining the best plot type by experience in analogous scenarios. Remember, however, that the best plot at low water cuts might not be the best plot at high water cuts.

Formation heterogeneity can have a significant and, typically, unpredictable influence on the WOR trend. For example, in naturally fractured reservoirs, the WOR trends in specific wells have varied sharply as a function of cumulative production and/or production rate.

Rate/Time Trends. Historically, engineers have used what have come to be known as “Arps equations” to analyze behavior and predict future production of wells. Three types of equations have been used: hyperbolic, harmonic, and exponential.⁶⁵ The rate/time equation for hyperbolic declines is:

$$q_2 = q_1(1 + ba_1t)^{-1/b} \dots\dots\dots (18.41)$$

Note that t , which should be written as Δt , is the *incremental* time $(t_2 - t_1)$ required for the production rate to decline from q_1 to q_2 .

After integrating with respect to time, Eq. 18.41 becomes the rate-cumulative equation for hyperbolic declines:

$$\Delta Q_p = q_1^b [q_1^{(1-b)} - q_2^{(1-b)}] / [a_1(1-b)], \dots\dots\dots (18.42)$$

where ΔQ_p = denotes incremental cumulative production, ΔG_p or ΔN_p , as the production rate declines from q_1 to q_2 . Eq. 18.42 may be solved to determine the *incremental* time for the production rate to decline from q_2 to the economic limit rate, q_{ej} :

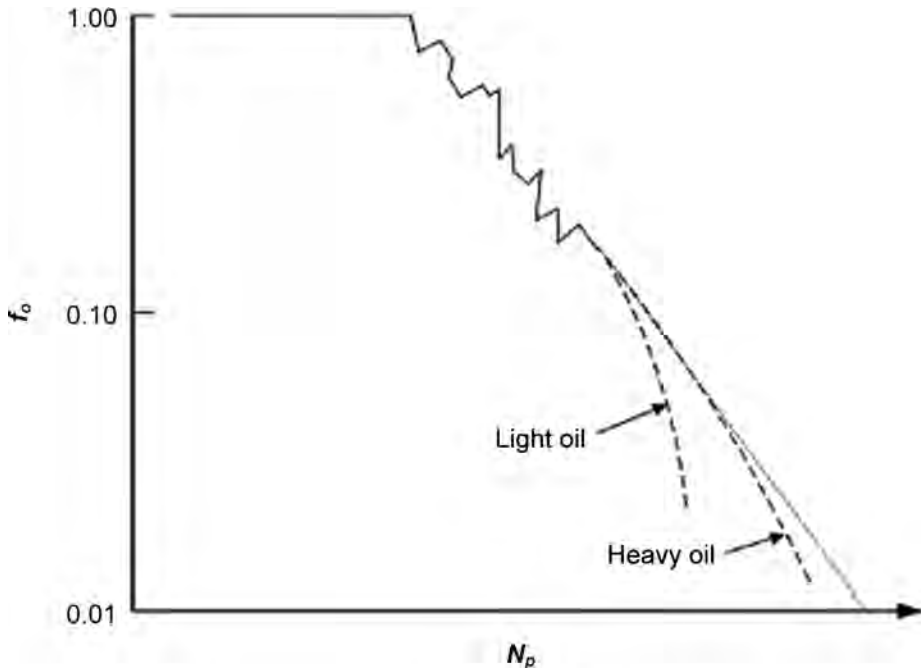


Fig. 18.19—Observed gas RE vs kh (after Brons⁶³).

$$t_{el} = [(q_2/q_{el})^b - 1] / a_1 b \dots\dots\dots (18.43)$$

The harmonic and exponential equations are special cases of a hyperbolic equation, where b is equal to 1 and 0, respectively. The three types of equations are compared graphically in Fig. 18.21,⁶⁵ which shows Cartesian and semilog plots of rate vs. time and rate vs. cumulative production for b values of 0, 0.5, and 1.0. This range of b values reflects semisteady-state, cylindrical flow of a single fluid with small, constant compressibility.⁶⁶ This is a reasonable approximation for many well/reservoir scenarios, but it is not universally applicable, and b values greater than 1 have been observed in many areas.⁶⁷

Historically, the Arps equations have been considered as empirical fits to observed trends of production rate vs. time (or vs. cumulative production). As discussed by numerous authors, such equations should, in theory, be used only to fit the constant terminal pressure period of production—the semisteady-state period during which flowing BHP is maintained at a constant value; however, in practice, this operating condition is seldom maintained over long periods of time, which contributes to uncertainties in reserves estimation based on decline trend analysis.

As implied by Fig. 18.19, if the production rate of total liquids is maintained at a constant rate (a common practice), then a linear, *semilog* trend of f_o vs. N_p reflects a harmonic decline. In this scenario, a linear trend of $\log(\text{WOR} + 1)$ vs. cumulative oil may be observed, which also may be extrapolated to estimate reserves. Linear, *Cartesian* trends of f_o vs. N_p , however, have sometimes been observed, as mentioned previously, and such trends reflect exponential declines. Apparently linear trends of $\log(\text{WOR} + 1)$ vs. cumulative oil might be observed at low WORs, but they typically depart from linearity at high WORs and should not be extrapolated to estimate reserves.

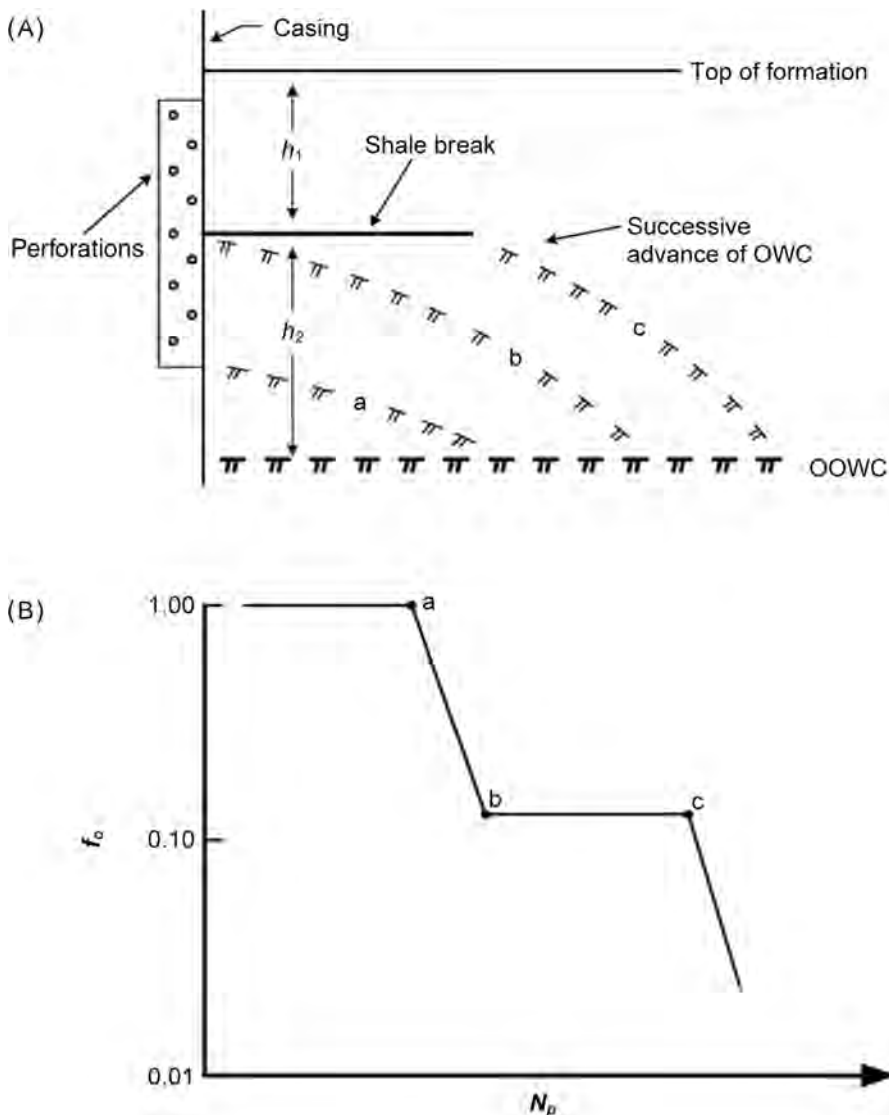


Fig. 18.20—Typical water encroachment and fractional flow behavior for a well in a bottom waterdrive oil reservoir with a shale break in the completion interval (after Cronquist³). OOWC = original oil/water contact.

Analysis and forward projection of rate/time trends (or rate/cumulative production or other trends) typically are handled with in-house or commercial software, as discussed in the next section.

Analysis, Forecasting, and Evaluation Software. In addition to in-house and other proprietary software, numerous commercial software products are available for analyzing historic trends and projecting future oil and gas production, or reserves. Typically, such products include a graphics module and an evaluation module. The graphics module is used to analyze historic trends and project future oil and gas production. These projections may be inserted into the evaluation module, together with prices, costs, taxes, ownership, and other pertinent data, to

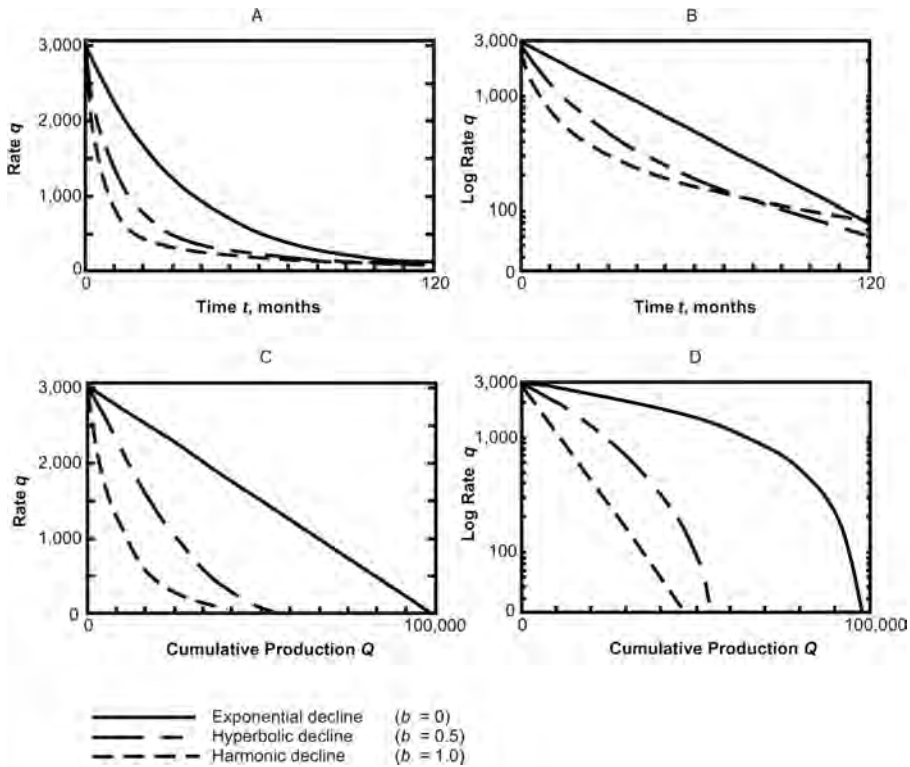


Fig. 18.21—Three types of production-decline curves (after Arps⁶⁵).

calculate the economic limit and the reserves of oil, gas, and condensate, and to generate a cash flow projection.

The graphics module can be used either to curve fit a historic trend of production and generate a production forecast of reserves on the basis of projection of the fitted trend, or to generate a production forecast of reserves that has been calculated by analogy and/or volumetric methods. Three curve-fitting/-projection parameters are most important: the initial decline rate D_i , the hyperbolic exponent b , and the terminal effective decline rate a .

Procedures for curve fitting depend on the production maturity of the well(s) being analyzed. For example, the production trend for an immature well might be so erratic as to require considerable local knowledge to ensure a curve fit that is consistent with analogous wells/reservoirs. If such a well is in the transient stage, apparent b factors from curve fitting might not represent of the semisteady-state stage.^{66,68,69} Projection of such curve fits might yield substantial overestimates of reserves. It might be appropriate to ignore the curve fit and impose a decline trend consistent with analogous wells in the area. The reasonableness of this procedure can be tested with volumetric and/or simulation analysis. In any event, the criterion of reasonable certainty should be observed in estimating proved reserves.

For wells in an advanced stage of production and in areas where there are good analogy wells, the appropriate b factors and terminal effective decline rates may be readily apparent.

For scenarios in which there is no production history, reserves can be estimated by analogy and/or volumetric methods, as discussed previously. The graphics module then can be used to compute a production forecast, given initial and final production rates, using any of the curve types (exponential, hyperbolic, or harmonic) that typically are programmed into the software. A constant rate period can be projected, followed by a prescribed decline period. Analogs are useful in selecting the decline curve parameters.

An evaluator should not automatically accept the best fit calculated by the software; rather, fully review and analyze the data it displays. Production histories can be affected by operational downtime, equipment modifications, market conditions, weather, and many other conditions that might distort the productive capacity of the property being reviewed. One should preview the pressure history, where relevant, to detect erroneous data. There might be a need to acquire missing data or to contact the operator for additional information.

The projection or forecast never should be made until the *engineering analysis* has been completed. Good engineering practice might require overriding the software-generated hyperbolic projection with an exponential projection.

Most graphics modules allow the user to exclude certain data points and to include all or a portion of the well history. One should use this feature cautiously and ensure that only erroneous or invalid data points are excluded.

Decline curves typically are used to forecast future production rates for properties that have some established performance history. In addition to monthly rates of oil and gas production, reservoir and surface pressure data and various fluid ratios can be analyzed and used in preparing reliable production forecasts. In most cases, the primary production stream volumes are forecast, and secondary products are estimated using constant or variable indices—primarily GOR or CGR. Gas and/or liquid handling constraints often are not considered in such projections. Iterative methods⁷⁰ are available to assist in forecasting oil production from a mature waterflood where there are surface or subsurface limitations on water handling, and in gas lift oil operations where gas-handling equipment imposes limitations.

Reconciliation of Estimates. For each well or reservoir, the reserves engineer should attempt to reconcile the estimates by comparing ultimate recovery estimated using P/DTA to ultimate recovery estimated using volumetric methods. (This reconciliation also should include results from computer simulation, as appropriate, but this is not specifically included in this discussion.) Consider the following possibilities:

1. If ultimate recovery estimated using volumetric methods is significantly greater than that from P/DTA, then

(a) The performance data might be representative only of the transient period (when the pressure sink around wells is still expanding) and not of semisteady-state conditions (when the drainage area has stabilized), which usually better represents well performance.

(b) The volumetric parameters might not be representative of the well or reservoir.

(c) Wells might need to be stimulated or equipped with higher-capacity equipment.

(d) Infill wells might be needed.

(e) Or, more than one of the foregoing factors may be relevant.

2. If ultimate recovery estimated using volumetric methods is significantly less than that from P/DTA, then

(a) The volumetric parameters might not be representative of the well or reservoir.

(b) The mapped area or volume might be too small and additional development might be warranted.

(c) Or, both factors may be relevant.

3. Pending determination of the reason for the difference in ultimate recovery estimated using the two methods, assign proved reserves only to those quantities demonstrated to be recoverable from performance methods.

As discussed earlier, reservoir heterogeneities often have an adverse effect on the recovery of oil and/or gas. A significant difference between ultimate recovery estimated using volumetric methods and that from P/DTA might indicate inefficient drainage caused by reservoir heterogeneities.

Computer Simulation. Computer simulation is a sophisticated method for analyzing well/reservoir performance and/or projecting future production (reserves). The widespread commer-

cial availability of simulation software and the greatly expanded capabilities of personal computers have increased use of this technology.

Engineers use models of varying complexity to guide reservoir development and production programs and to compare and evaluate well spacing, rate sensitivity, and improved recovery potential, as well as other scenarios. It is important to realize, however, that although computer simulation is widely used, these methods typically oversimplify representation of the spatial distribution of reservoir properties.^{71–73} Computer simulation results typically are sensitive to changes in reservoir characterization, and the degree of sensitivity may render moot an estimate of ultimate recovery that is based on this method.

Accordingly, check such estimates against simple models, as discussed by Richardson and Blackwell,⁷⁴ and against actual performance in analogous reservoirs. Saleri and Toronyi⁷¹ observe that “determination of ultimate recovery through simulation is an unattainable goal, particularly for heterogeneous reservoirs that are coarsely gridded.” Jacks⁷² notes that “an estimate of ultimate recovery from any single simulation is subject to considerable uncertainty, especially if it is developed early in the life of a reservoir.” Many forecasts of future performance have been significantly in error, despite the users’ best efforts at reservoir characterization and history matching.⁷⁵ In some cases, the reservoir characterization and history matching were sound, but the field development was not consistent with that modeled. Continuous monitoring of performance, then, is essential in reserve estimation by computer simulation—indeed, by any method!

Computer Simulation vs. Reserves Definitions. Despite its limitations, computer simulation may provide the only acceptable answer to analysis of complex reservoirs, but such use must be consistent with the purpose(s) for which a specific reserves estimate is made. For example, the presumed “most likely” case—consistent with proved plus probable reserves—is the case typically modeled by computer simulation.⁷³ Such a case might not be appropriate for reporting reserves under U.S. SEC guidelines.

To ensure that simulation results will comply with SEC reserves definitions, either configure the model using the observed hydrocarbon/water contact or imposing the lowest known occurrences of oil or gas, or, if the constructed model does not comply with proved reserves definitions, make necessary adjustments to the model results to estimate the recovery that would approximate recovery reached using a model that meets proved reserves requirements. Many model runs might be needed to accomplish this. Manually adjusting the output data causes some of the rigorous nature of the simulation process to not be realized fully.⁷³

One should not construct a reservoir model solely to comply with proved reserves definitions unless warranted by special, and perhaps limited, circumstances. Constructing a (3P) model may be best initially, with the ability to modify it to assist in estimating proved or proved plus probable reserves.

Reservoir models that do not comply with the limitations inherent in proved reserves definitions can help in understanding the hydrocarbon REs likely with each reserves category.⁷³ Sensitivities of various reservoir characteristics (e.g., relative permeability, drive mechanisms, and PV compressibilities) can be investigated to determine a range of recoveries that may comply with the “reasonable certainty” aspect of proved reserves.

In history matching, a fit typically is described as “poor,” “good,” or “excellent.” Such subjective terms mean little in establishing a confidence level in predictions of future production (reserves). However, if a history match can be obtained that replicates individual well producing rates and pressures with reasonable tolerance, without illogical adjustments, the model might be appropriate for the estimating proved reserves.

Palke and Rietz⁷³ observe (in part) that

- Although reservoir simulation is a sophisticated technique, it does not always produce reliable or applicable results suitable for reserves estimation.

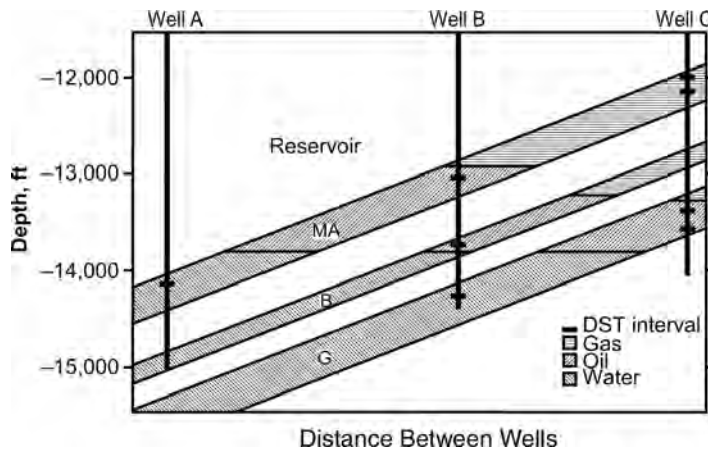


Fig. 18.22—Schematic cross section with fluid contacts and DSTs (after Rasor⁷⁶).

- Reservoir simulation should be used to improve the understanding of a reservoir, but should not be used to circumvent the intent of U.S. SEC reserves definitions.
- Although reservoir simulation increasingly is being used as a tool for reserves estimation, the results do not necessarily constitute U.S. SEC reserves estimates.
- Models that do not comply with U.S. SEC reserves definitions can be modified to comply, but this process may be difficult.
- Results from models that are not consistent with U.S. SEC reserves definitions can be used through the alteration of the simulation output itself, which requires a great deal of simulation output and might provide less rigorous solutions.
- For immature reservoirs, simulation is useful primarily for estimating the oil and/or gas RE, and for testing the limits in terms of uncertain parameters (permeability, aquifer support, O/GIP).
- Models of mature reservoirs should exhibit reasonable history matches before they are accepted for reserves purposes.
- The uniqueness and quality of the history match affect the confidence to be placed in a model's ability to predict future performance, and thus dictate the model's appropriate usage in the process of estimating reserves.

Example Study. Rasor⁷⁶ presents a field study comparing the results of a simulation study of a three-reservoir field with those of a classic reservoir-engineering approach. He uses a 3D compositional model and assumes gas processing to maximize liquid recovery. Laboratory PVT and special core analysis data are matched. The classic procedure is limited to a traditional volumetric study incorporating estimated REs based on the fluid and formation properties and the experience of the estimator. Fig. 18.22 is a schematic cross section of the three reservoirs, MA, B, and G, shallow to deep, respectively.

OWCs for reservoirs MA and G were calculated using the pressure/depth relationships illustrated in Figs. 18.23 and 18.24. The GOC in B is based on PVT analysis, Fig. 18.25. Table 18.7 compares the results from the classic and simulation methods. The REs of oil and gas from reservoirs B and G are in reasonably close agreement. The oil REs for MA range from 24 to 42%. Without other information or suitable analogies, an engineer might assign a proved (P1) recovery of 24% OIP and a proved plus probable (2P) recovery of 42% OIP.

The condensate REs are significantly different for all three reservoirs. In this situation, without reasonable explanation for the differences or compelling data to the contrary, the lower REs would be appropriate for booking proved reserves.

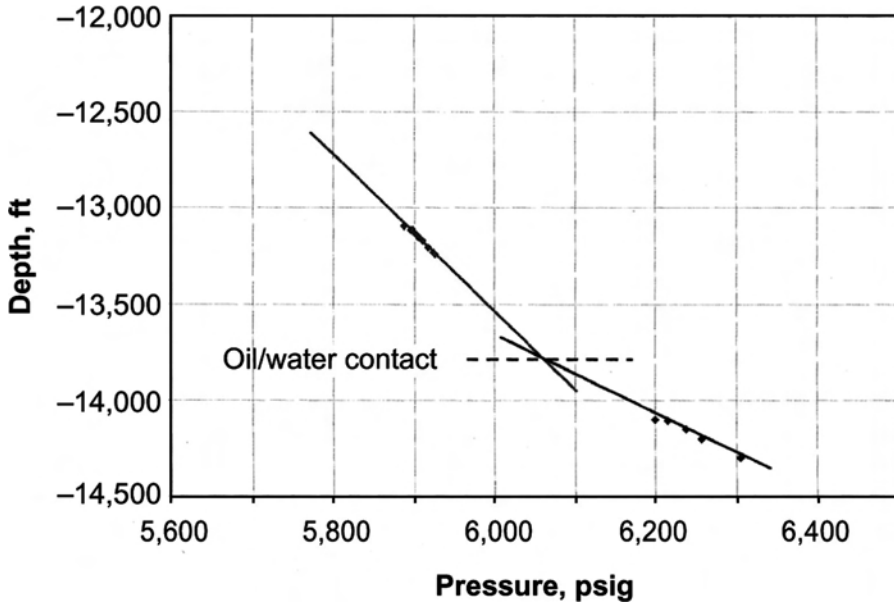


Fig. 18.23—Reservoir MA fluid gradients (after Rasor⁷⁶).

This study illustrates the range in results produced by the two methods—classic engineering and reservoir simulation—by a competent evaluator using a reasonable amount of data. It is a real-world example of the uncertainties of relying on computer simulation, without history matching, for the estimation of proved reserves.

18.5 Special Problems*

Some operating and/or reservoir scenarios are so complex as to defy conventional analysis and to require a high degree of skill and ingenuity. Because of the substantial degree of uncertainty, such scenarios may be better suited for probabilistic procedures than for conventional scenarios.

18.5.1 Coalbed Methane. Chap. 6 of the Emerging Technologies section of the *Handbook* discusses the development of coal deposits in the U.S.A. and around the world for recovery of natural gas. Such natural gas is predominantly methane, but it also may contain small amounts of ethane, carbon dioxide, and nitrogen.

Coalbed methane (CBM) is adsorbed onto the coal surfaces exposed through the matrix microporosity and the naturally occurring fracture or cleat system. This cleat system typically is water-filled, often with fresh or slightly saline water, but may also contain some free gas.

Calculation of gas in place for a unit volume of the coal layers being developed does not follow the “porous media” approach of determining effective porosity, saturations, pressures, temperatures, and gas quality. Instead, the gas in place is measured physically through the recovery of coal samples, the number and distribution of which are important to the estimation of total gas in place pertinent to the property being evaluated.

Cored samples are transferred carefully from the core barrel to canisters, which are sealed immediately and transported to an analysis laboratory. In analysis, two measurements are taken. First, free gas in the canister is measured, and then the coal sample is crushed and the

* Section sequence is not intended to convey authors' views of relative importance.

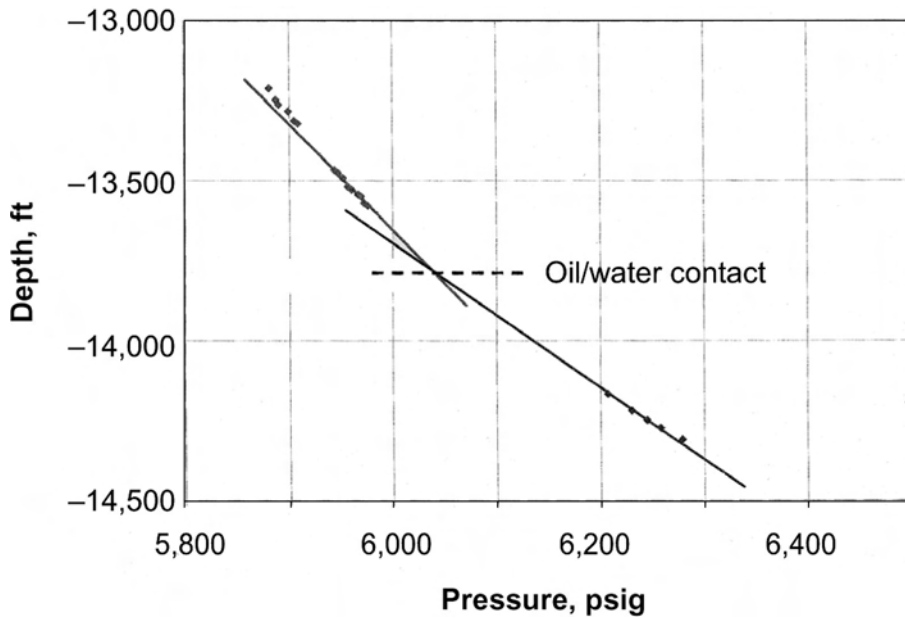


Fig. 18.24—Reservoir G fluid gradients (after Rasor⁷⁶).

liberated gas measured. These two measurements are combined with an estimate of gas lost during the core recovery operation. The lost gas volume is estimated as a function of the coal type and depth of burial and other factors. Total gas in place is calculated as the product of the unit gas in place—considering areal variations—and the mapped volume of the coal seams being developed.

A volumetric estimate of GIP (scf) in coalbed reservoirs can be calculated by⁷⁷

$$G_i = Ah \left[\frac{43,560 \phi_f (1 - S_{wfi})}{B_{gi}} + 1,359 C_{gi} \rho_c (1 - f_a - f_m) \right] \dots\dots\dots (18.44)$$

The first term in the square brackets of Eq. 18.44 is used to calculate the gas volume contained in the interconnected fracture or cleat system (if any) and is identical to the term used for porous media reservoirs. The second term in the square brackets is used to calculate the adsorbed gas in the coal matrix. The adsorbed gas quantity results from laboratory measurements of the adsorbed gas in a unit of dry, ash-free coal and other coal-quality factors.

In most cases, cleat porosity is water-filled, so that the free gas therein essentially is zero. Most engineers ignore the gas volume in solution in the water.

Most of the data on which the reservoir engineer must rely is gathered through core analysis, fluid analyses, and well tests. Table 18.8 presents certain pertinent data items and primary sources for each item.⁷⁷

Seismic data historically has not been used in CBM project analysis because most of these projects have been in areas that had an abundance of subsurface data obtained as a result of underground mining (e.g., the Black Warrior basin) or oil and gas wells drilled to deeper objectives (e.g., the San Juan basin). As the industry advances into areas with a dearth of existing subsurface information, seismic information is expected to become more important in determining reservoir extent and structure.

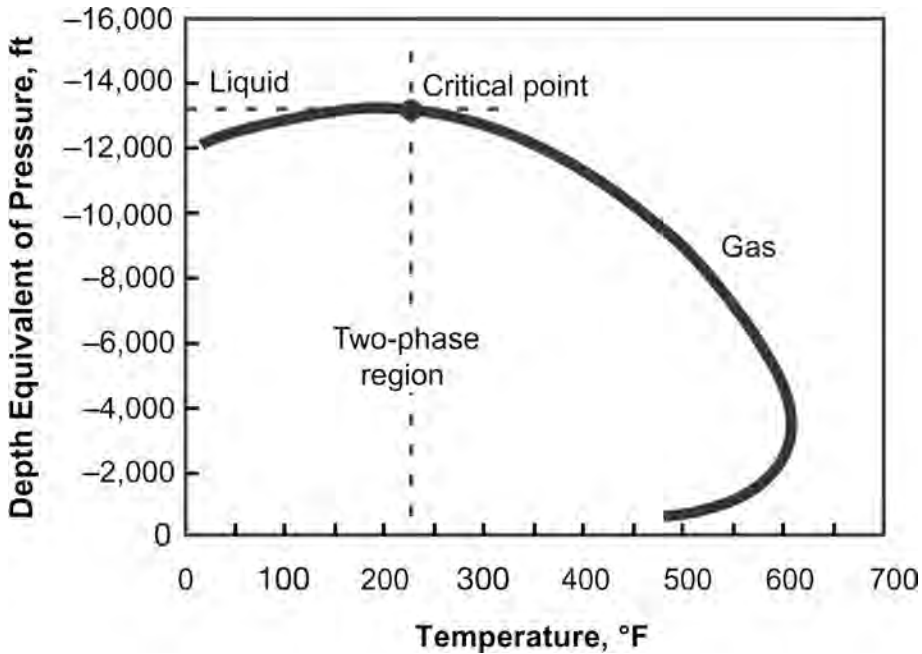


Fig. 18.25—Reservoir B PVT analysis (after Rasor⁷⁶).

TABLE 18.7—COMPARISON OF RECOVERY EFFICIENCIES—CLASSIC AND SIMULATION METHODS (AFTER RASOR ⁷⁶)				
Classic Reservoir-Engineering Case				
Reservoir	Oil	Solution Gas	Gas-Cap Gas	Condensate
MA	0.24	0.73	0.77	0.13
B	0.36	0.64	0.76	0.25
G	0.36	0.64	0.76	0.25
Simulation-Prediction Case				
Reservoir	Oil	Solution Gas	Gas-Cap Gas	Condensate
MA	0.42	0.62	0.73	0.88
B	0.38	0.68	0.76	0.42
G	0.38	0.68	0.76	0.42

REs, typically up to 75% GIP, are related to well density, the degree of naturally occurring fractures, the effectiveness of wellbore hydraulic fracturing programs, and the ability to “dewater” the reservoir to reduce the reservoir pressure to a level where desorption can be effective. Laboratory measurements can be used to develop composited desorption isotherms, which are useful in estimating the rate of gas liberation while reservoir pressure is reduced.

Proved reserves can be assigned to an area where wells have been drilled and have demonstrated that commercial gas rates can be maintained. Well spacing in the U.S.A. ranges from approximately 40 to 160 acres per well. For coalbed projects in areas remote from comparable analog operations, the time to confirm commerciality may be as long as several years. Some projects dewater quickly, allowing commercial gas rates to be attained early; other projects

TABLE 18.8—SOURCES OF DATA FOR ANALYZING AND ESTIMATING RESERVES FROM COALBED METHANE RESERVOIRS (AFTER ZUBER⁷⁷)

Data Item	Primary Source(s)
Permeability	Well test
Initial pressure	Well test
Initial water saturation	Well test
Gas desorption pressure	Well test
Pore compressibility	Well test
Desorption isotherm	Core test
Sorbed gas content	Core test
Desorption time	Core test
Relative permeability	Production data and core test
Porosity	Core test
Net pay thickness	Well logs and core test
Temperature	Well log
Gas PVT properties	Gas analysis
Water PVT properties	Water analysis
Completion effectiveness	Well test
Well drainage area (spacing)	Geologic description

might prove to be noncommercial because of dewatering failure. A cluster of wells might need to create a pressure sink large enough to overcome the influx of water from a large aquifer. High permeability, together with a large aquifer, might create enough water influx to cause project failure.

Fig. 18.26 illustrates a typical individual well decline curve exhibiting a 2-year period of dewatering that is characterized by increasing gas production rates. An exponential trend has been drawn through the approximate 1-year decline period.

Confidence in the forecast would increase if there were nearby analog wells with more production history supporting the exponential projection. Lacking such support, however, the projection should be confirmed through volumetric means before booking the forecast volumes as proved reserves. Many (perhaps most) coalbed wells producing from coal that has low to moderate permeability will exhibit a wide range of hyperbolic declines, underscoring the need for suitable analogs.

Type curves (production vs. time) from successful analog operations are the most useful tools for predicting the production profile and reserves for completed wells. As in traditional reserves estimation, volumetric reserves estimates should be checked against performance-driven reserves estimates.

Assigning of proved undeveloped reserves to coalbed projects usually should be restricted to the “one-offset” limitation imposed by the 1978 U.S. SEC definitions, unless the engineer can demonstrate “certainty of production” beyond the one-offset location. The 1997 SPE/WPC definitions may, in some circumstances, permit a larger area to be classified as proved, but one should be cautious until both the presence of coal of commercial thickness and adequate permeability are determined with reasonable certainty.

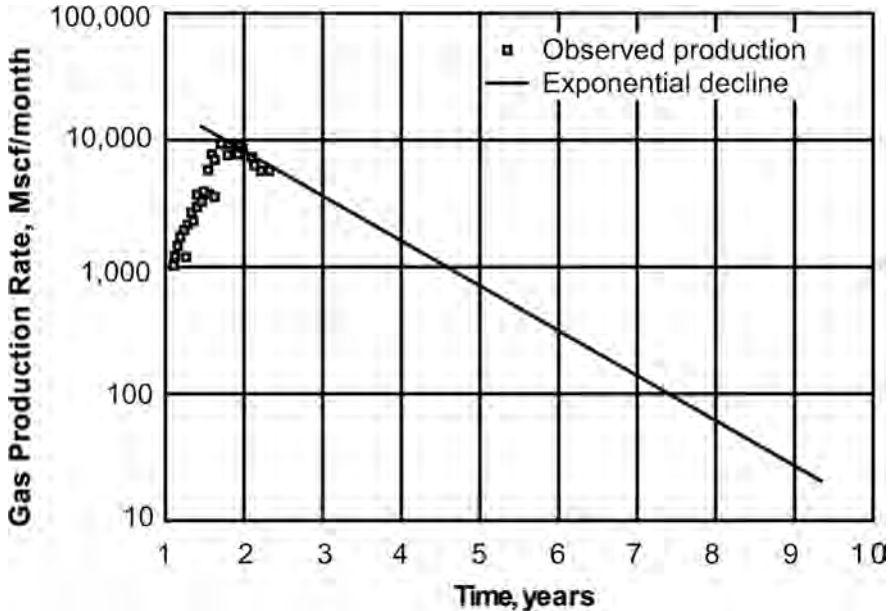


Fig. 18.26—Long-term forecast using exponential decline (after Zuber⁷⁷).

Probable and possible reserves typically are assigned to acreage at increasing distances from the commercially developed portion of the project.

18.5.2 Fractured Reservoirs. Fractured reservoirs have been observed in most producing areas of the world, in igneous/metamorphic rocks, sandstones, carbonates, shales, and cherts. The two broad categories of fractured reservoirs are those with a porous matrix and those with a nonporous matrix.⁷⁸ In the porous matrix type (the more common), most of the hydrocarbons are stored in the matrix porosity, and the fractures serve as the principal flow conduits. Such reservoirs typically are identified as “dual-porosity” systems. Examples include many of the Iranian fields, Ekofisk (North Sea), Palm Valley (Australia), and Spraberry (Texas, U.S.A.). Some cherts exhibit dual porosity and have significant storage capacity in the matrix but that contributes little to reserves. Fractured reservoirs with a nonporous matrix occur in fractured igneous and/or metamorphic rocks, fractured shales, and fractured cherts. Such reservoirs frequently are associated with basement rocks.⁷⁹ Examples include the Bach Ho field (offshore Vietnam), the Augila field (Libya), the Edison field (California, U.S.A.), the Big Sandy gas field (Kentucky, U.S.A.), and the Santa Maria basin fields (California).

When they occur in carbonates, fractures tend to facilitate extensive leaching and diagenesis, which may lead to the development of vugular, sometimes karstic, porosity. Examples include the Albion Scipio trend (Michigan, U.S.A.) and the Rospo Mare field (offshore Italy).

Fractured reservoirs pose formidable difficulties for estimating reserves. These difficulties are attributable to the heterogeneity of the reservoir formation, which causes substantial uncertainties in estimates of O/GIP and RE. Because of uncertainties in determining the flow characteristics of dual-porosity systems, estimates of reserves using volumetric methods are subject to substantial uncertainty. When feasible, compare such estimates with observed recovery in analogous reservoirs.

In general, the following scenarios cause problems:

- Boreholes frequently are severely washed out, making log interpretation difficult or impossible.

TABLE 18.9—RECOVERY FACTORS IN NATURALLY FRACTURED RESERVOIRS (AFTER AGUILERA⁸⁰)

Drive Mechanism	Recovery Efficiency, %					
	Oil Reservoirs Storage Ratio			Gas Reservoirs Storage Ratio		
	A ^a	B ^b	C ^c	A ^a	B ^b	C ^c
Solution gas (<i>depletion</i>)	10 to 20	20 to 30	30 to 35	70 to 80	80 to 90	>90
Solution gas plus gas-cap expansion plus water influx	35 to 45	45 ^d to 55	55 to 65			
Strong waterdrive				15 to 25	25 to 35	35 to 45

^aStorage mostly in matrix, with small amount in fractures. ^bStorage about 50/50 in matrix and fractures. ^cAll storage in fractures.
^dIn some areas, 25% might be a more appropriate lower limit (personal communication with Ed Holstein, 2 March 2002).

- Core recovery frequently is fragmental, at best.
- Even in good-quality boreholes, detection of fractures and measurement of fracture porosity using logging devices is highly empirical, although significant improvements have been made using formation imaging tools.
- In accumulations with a severe loss of circulation, operators typically stop drilling at the top of the reservoir section, a practice that, while necessary for safe operations, precludes characterization of the objective section.
- Well performance frequently is strongly influenced by proximity to major fractures, which can extend surprising distances. Because of this, be extremely cautious in assigning reserves to undrilled tracts that offset tracts at a mature stage of production.*
- Although transient pressure analysis provides useful data, applying modern interpretation techniques mandates using highly accurate quartz pressure transducers.
- The accuracy of type curve matching depends on the accuracy of the mathematical model used for the type curves. An invalid model cannot yield a valid interpretation. Even if the model is valid, analysis of results might not provide unique answers.
- In pressure-depletion reservoirs, the rate/time performance of wells typically is hyperbolic. The behavior of an average well might be used to estimate reserves, but one should expect wide variation in performance between wells.
- In reservoirs producing by pressure depletion, the early performance of wells typically is characterized by relatively rapid decline in the production rate, which usually is caused by transient pressure behavior. Reserves cannot be estimated with any degree of confidence using decline trend analysis until wells have passed through the transient pressure period and settled into semisteady-state conditions.

Aguilera⁸⁰ provides guidelines for estimating RE in fractured reservoirs, classifying fractured reservoirs by pore type and “storage ratio”—the relative amount of storage in matrix vs. fractures. **Table 18.9** is adapted from Aguilera’s Tables 2 and 3.

Aguilera does not state so, but “oil” presumably means light oil—stock-tank gravities greater than approximately 25°API. Also, Aguilera does not mention the influence of well spacing on RE, which could be a major factor, depending on the nature of the fracture system.

18.5.3 Natural Gas From Fractured Shale. As reported in mid-2000, natural gas produced from shale in the U.S.A. has grown to be⁸¹ approximately 1.6% (0.3 Tcf annually) of total gas production. The first commercial production of natural gas from shale was developed to supply

* Personal communication with Ed Holstein, retired, Exxon, 2 March 2002.

TABLE 18.10—U.S.A. SHALE GAS RESOURCES (AFTER REF. 82)

Basin	State(s)	Major Shale-Bearing Formation or Group	Basin Area	Total Organic Carbon (TOC)	Thermal Maturity	Shale Gas-in-Place		Estimated Recoverable Shale Gas	
				%	% R_o	Tcf	Resource	Tcf	Resource
Appalachian	Ohio Kentucky New York Pennsylvania West Virginia Virginia	Ohio shale	160,000	0 to 4.5	0.4 to 1.3	225.0 to 248.0 ^a	1980 NPC estimate ⁸⁴ 1992 NPC estimate ⁸⁵	14.5 to 27.5	1980 NPC estimate ⁸⁴ 1992 NPC estimate ⁸⁵
Michigan	Michigan Indiana Ohio	Antrim shale	122,000	1.0 to 20.0	0.4 to 0.6	35.0 to 76.0	1980 NPC estimate ⁸⁴ 1992 NPC estimate ⁸⁵	11.0 to 18.9	1992 NPC estimate ⁸⁵ 1995 USGS estimate ⁸⁶
Illinois	Illinois Indiana Kentucky	New Albany shale	53,000	1.0 to 25.0	0.4 to 1.0	86.0 to 160.0	1980 NPC estimate ⁸⁴ 1992 NPC estimate ⁸⁵	1.9 to 19.2	1992 NPC estimate ⁸⁵ 1995 USGS estimate ⁸⁶
Fort Worth	Texas	Barnett shale	4,200 ^b	4.5	1.0 to 1.3	NA		3.4	Schmoker ⁸⁷ Kuuskraa ⁸⁸
San Juan	Colorado New Mexico	Lewis shale	1,100 ^b	0.45 to 2.5	1.6 to 1.88	96.8	1999 Williams estimate ⁸⁹	NA	

^aBlack shales only. ^bPlay area only. NPC = National Petroleum Council.

gas to the town of Fredonia, New York, U.S.A., in the late 1820s, predating Col. Drake’s first oil well by almost 40 years.

By 1979, some 60 Bcf/year was being produced from wells in the Appalachian (Ohio) basin. Production from the Antrim shale (Michigan basin) began in the mid-1980s and by 1994 had surpassed production of the Appalachian basin. Three other U.S.A. basins—San Juan (Colorado, New Mexico), Fort Worth (Texas), and Illinois (Illinois, Indiana, Kentucky) currently are producing from shale. Total U.S.A. gas-bearing shale resources^{82–88} are shown in **Table 18.10**.

In a 1992 report,⁸⁹ the Gas Research Inst. (GRI) describes the Antrim shale as being organically rich and says that the majority of the in-place gas was sorbed into the organic constituent. Productivity is achieved by reducing reservoir pressure, and is maximized by hydraulic fracturing to access and connect the wellbore to the natural microfractures and other permeability pathways.

As in coalbed methane reservoirs, the naturally occurring fracture system usually is water-filled, requiring artificial lift equipment to dewater the wells to reduce the bottomhole pressure to a level consistent with maximum gas desorption and production.

Shale gas volumes initially in place (scf) can be calculated by:

$$G_i = 1,359 Ah_s \rho C_{gi}, \dots\dots\dots (18.45)$$

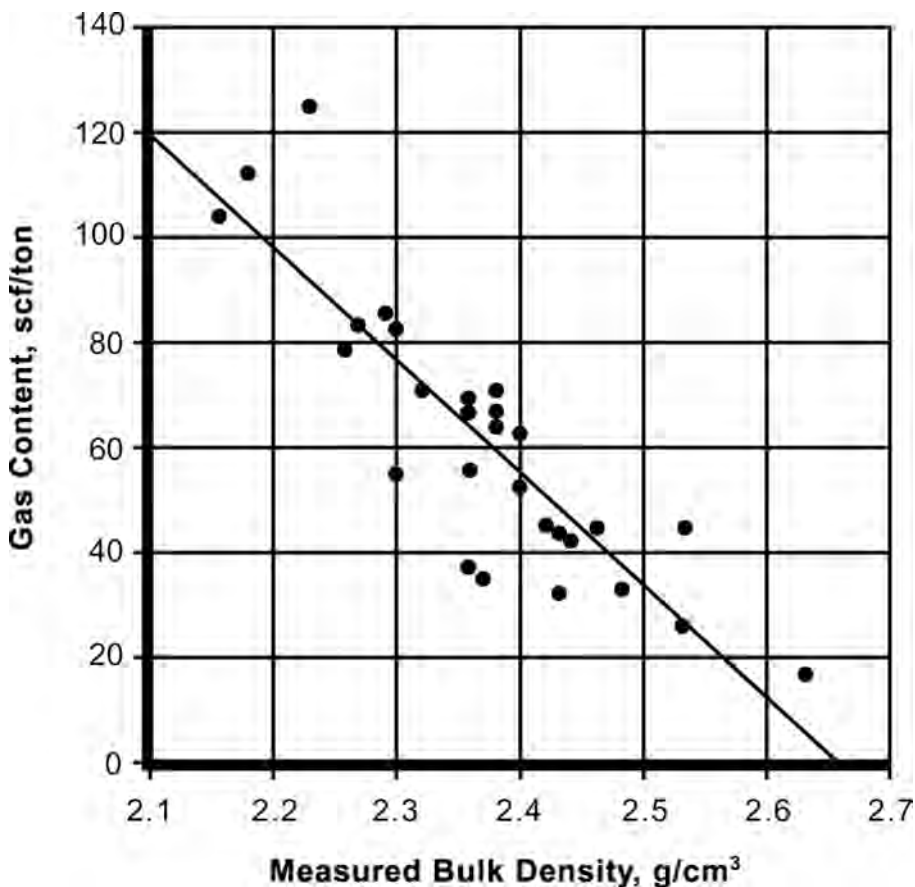


Fig. 18.27—Calculation of gas content from bulk density measurements from log, Antrim shale (after Ref. 82).

where 1,359 is a conversion factor to convert volume (acre-ft), shale density (g/cm^3), and gas content (scf/ton) to scf gas in place.

Shale density and gas content can be measured directly through core analysis or indirectly through well logs, using correlations established between gas content and shale bulk density. Core samples are taken and preserved to minimize the release of original gas in place. The free gas in the core sample canisters plus the gas that is released during core crushing is measured in the laboratory. This volume of gas may be adjusted to account for the volume estimated to have been lost during core retrieval. The analysis procedures are similar to those used for CBM.

Gas-content/shale-density correlations are an outgrowth of studies⁹⁰ in which the laboratory-measured shale densities and total organic content (TOC) of the samples were compared and related in a linear correlation. Similarly, gas content was found to have a linear relationship with TOC.

This research thus leads to the ability to measure bulk density from well logs and use this information to directly estimate gas content and log-derived gas in place.

Fig. 18.27⁸² is an example of the relationship between gas content and shale density for the Antrim shale in a defined area.

Gas REs vary widely and are related to many factors, including completion efficiency, reservoir pressure, water removal efficiency, and well spacing. The recoveries⁸² shown in Table

TABLE 18.11—KEY PROPERTIES FOR PRODUCTIVE GAS SHALES (AFTER REF. 82)

	Basin and Producing Shale				
	Fort Worth Barnett	Appalachian Ohio	Michigan Antrim	Illinois New Albany	San Juan Lewis
Depth, ft	6,500 to 8,500	2,000 to 5,000	600 to 2,200	500 to 2,000	3,000 to 6,000
Gross thickness, ft	200 to 300	300 to 1,000	160	180	500 to 1,900
Net thickness, ft	50 to 100	30 to 100	70 to 120	50 to 100	200 to 300
Bottomhole temperature, °F	200	100	75	80 to 105	130 to 170
TOC, %	4.50	0.00 to 4.70	1.00 to 20.00	1.00 to 25.00	0.45 to 2.50
Thermal maturity, % R_o	1.00 to 1.30	0.40 to 1.30	0.40 to 0.60	0.4 to 1.00	1.60 to 1.88
Total porosity, %	4.0 to 5.0	4.70	9.00	10.00 to 14.00	3.00 to 5.50
Gas-filled porosity, %	2.5	2.0	4.0	5.0	1.0 to 3.5
Water-filled porosity, %	1.9	2.5 to 3.0	4.0	4.0 to 8.0	1.0 to 2.0
kh , md-ft	0.01 to 2.00	0.15 to 50.00	1.00 to 5,000.00	NA	6.00 to 400.00
Gas content, scf/ton	300 to 350	60 to 100	40 to 100	40 to 80	15 to 45
Adsorbed gas, %	20	50	70	40 to 60	60 to 85
Reservoir pressure, psia	3,000 to 4,000	500 to 2,000	400	300 to 600	1,000 to 1,500
Pressure gradient, psi/ft	0.43 to 0.44	0.15 to 0.40	0.35	0.43	0.20 to 0.25
Well costs, U.S. \$1,000	450 to 600	200 to 300	180 to 250	125 to 150	250 to 300
Completion costs, U.S. \$1,000	100 to 150	25 to 50	25 to 50	25	100 to 300
Water production, BWPD	0	0	5 to 500	5 to 500	0
Gas production, Mcf/D per well	100 to 1,000	30 to 500	40 to 500	10 to 50	100 to 200
Well spacing, acre	80 to 160	40 to 160	40 to 160	80	80 to 320
Recovery factors, %	8 to 15	10 to 20	20 to 60	10 to 20	5 to 15
Gas-in-place, Bcf per section	30 to 40	5 to 10	6 to 15	7 to 10	8 to 50

18.11 range from 5 to 60% GIP, but probably average approximately 40% GIP in the Michigan basin (Antrim). A typical well production profile is shown in [Fig. 18.28](#).

The initial dewatering period of approximately 1 year is characterized by diminishing water production and increasing gas production. Following perhaps a year of relatively constant production, a decline rate of approximately 6% per year is typical for a Michigan-basin Antrim well. Most wells exhibit exponential decline during their economic life.

The booking of proved reserves must be delayed until the production rate reaches a commercial level and/or there is ample evidence from nearby analog wells. Undeveloped locations may be classified as proved if these locations are directly adjacent to commercial wells (1978 U.S. SEC definitions). Additional locations may be classified as proved under the 1997 SPE/WPC definitions⁶ if there is compelling evidence from nearby analogs and if the continuity of favorable reservoir conditions is reasonably certain.

18.5.4 “Tight” Gas Reservoirs. As defined by the U.S. Federal Energy Regulatory Commission (U.S. FERC), low-permeability (“tight”) gas reservoirs have an average in-situ permeability of 0.1 md or less. Others have placed the upper limit at 1 md. Such accumulations in the U.S.A. contain substantial resources. Estimates of ultimate recovery from these resources vary widely and depend chiefly on assumptions of wellhead gas price.

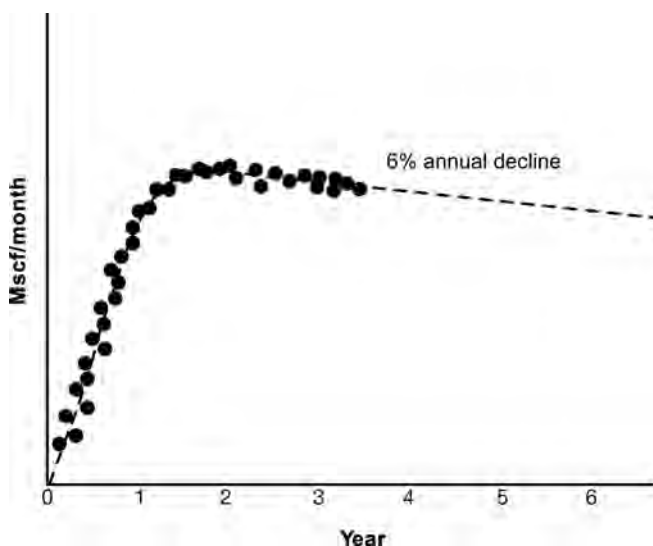


Fig. 18.28—Typical production graph for an Antrim shale well.

Methods for estimating gas reserves in moderate- to high-permeability reservoirs are unreliable in very-low-permeability reservoirs. The unreliability can be attributed to the geologic setting in which these reservoirs occur and the completion methods required to make them commercial. In general, their geologic setting is characterized by a high degree of permeability heterogeneity; lateral discontinuities in apparently blanket sands; stratigraphic, rather than structural, traps; and complex mineralogy, frequently with high-grain-density minerals randomly dispersed throughout the section as well as water-sensitive clays.

These attributes make it very difficult to determine porosity and interstitial water saturation by conventional log and core analysis.^{91–95} Petrophysical properties measured at ambient conditions (e.g., k and S_w) differ substantially from those at reservoir conditions, and corrections for formation compressibility are subject to considerable uncertainty. For example, permeabilities can be as much as two orders of magnitude greater at ambient conditions than at reservoir conditions. These problems and poor lateral continuity lead to substantial uncertainties in volumetric estimates of GIP. In many cases, it is impossible to distinguish between commercial and noncommercial intervals from log analysis alone. Drillstem tests rarely provide useful information because formations often are damaged during drilling.

Massive hydraulic fracturing usually is required to obtain commercial flow rates. Despite more than 35 years of experience with fracturing technology, however, the industry remains unable to design a treatment and predict the results with high confidence when relying solely on analytical methods.^{96,97} Typically, operators rely on analytical models coupled with analogy.

Along the U.S. Gulf Coast, tight-gas accumulations frequently occur in geopressured sections.^{98,99} In this environment, understanding the influence of reservoir stress on rock properties is important for differentiating between productive and nonproductive formations.

Over the life of a well completed in low-permeability gas reservoirs, the gas production rate typically exhibits a hyperbolic decline,^{100,101} with apparent b values generally >1 . In addition to decline curve analysis, empirical log-log rate/time models might provide useful short-term information for such wells—before the onset of significant pressure depletion. The following equations, developed in the 1980s for more than 2,500 then-new wells in the U.S. Rocky Mountains, have been used to estimate flow rates (Eqs. 18.46 and 18.47) and near-term reserves (Eqs. 18.48 and 18.49) for damaged fracture flow¹⁰²:

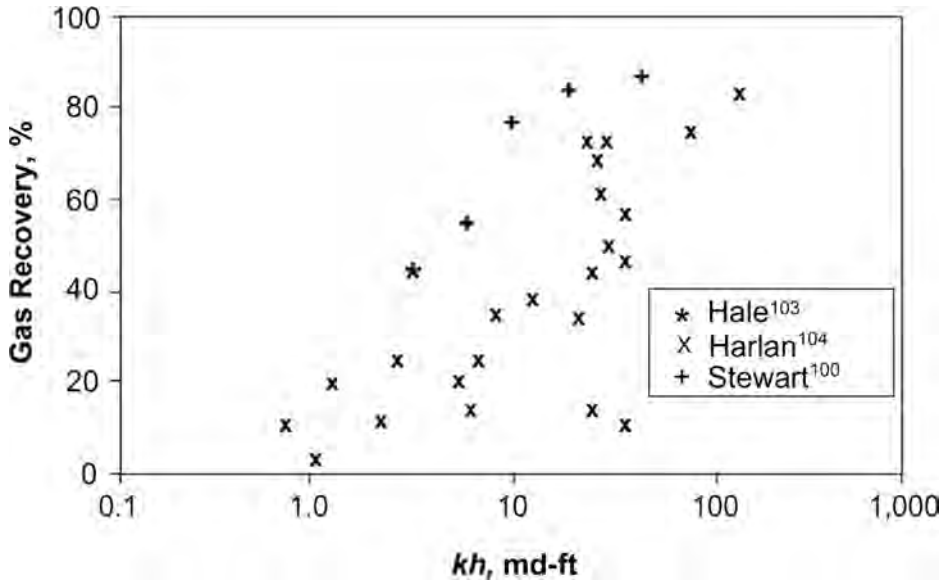


Fig. 18.29—Observed gas RE as related to kh . (After Cronquist.³)

$$q_g = K_A t^n, \dots\dots\dots (18.46)$$

$$q_g = K_A / (K_B + t^{0.5}), \dots\dots\dots (18.47)$$

$$G_p = K_A^{n+1} / (n + 1), \dots\dots\dots (18.48)$$

and

$$G_p = 2K_A K_B \ln [K_B / (K_B + t^{0.5})] + 2K_A t^{0.5}, \dots\dots\dots (18.49)$$

where K_A and K_B are coefficients calculated during fitting these equations.

For an undamaged, fractured well, initial values of n should equal approximately -0.5 . Because of damage, however, initial n values as small as -0.15 had been observed in the wells studied; the average was -0.34 . With the onset of depletion, n decreases to -1.0 or more.^{103,104}

Eqs. 18.46 and 18.48 can be used to account for the effects of a damaged fracture by using the field-observed value of n for each such well. Depending on circumstances, however, Eqs. 18.47 and 18.49 might provide a better fit to the observed data.

RE of gas from some of these reservoirs vs. $k_g h$ is shown in Fig. 18.29. Well spacing ranges from approximately 160 to 320 acres. For kh of less than approximately 50 md-ft, there is a decrease in RE, albeit erratically so.

Because of the high degree of permeability heterogeneity, drainage areas of individual wells vary widely. In the Green River basin (U.S.A.), for example, effective drainage areas reportedly have ranged from approximately 100 to 640 acres.¹⁰⁵ Depending on economics, such situations can offer opportunities for significant increase in reserves by infill drilling.

18.5.5 Heavy Oil. Discovered resources of heavy and extraheavy crude oil are estimated to be approximately 4,600 billion bbl, two-thirds of which are in Canada and Venezuela.¹⁰⁶ Bitumen

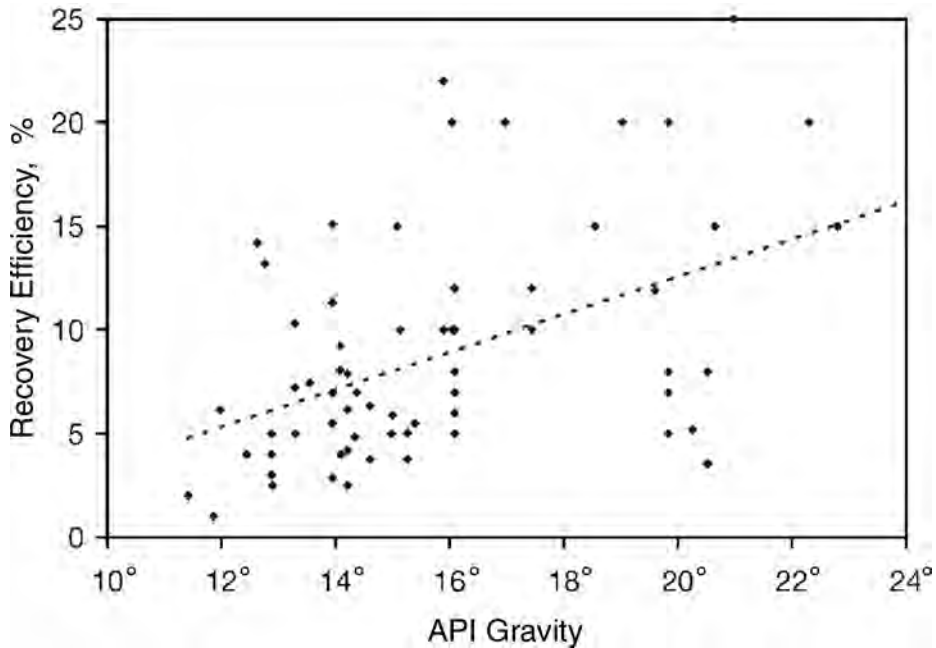


Fig. 18.30—Observed oil RE as related to oil gravity for 69 pools in Alberta and Saskatchewan (after Cronquist³).

and tar sands are excluded from this estimate. Published data on RE from this resource by primary drive mechanisms are sparse. Meyer and Mitchell¹⁰⁷ estimated worldwide ultimate recovery from heavy and extraheavy crude oils to be 476 billion bbl, which is 10% of the Briggs *et al.*¹⁰⁶ estimate of the discovered resource initially in place. Estimated primary RE ranges from 8 to 12% OIP for the Orinoco area of Venezuela, where stock-tank gravities range from 8 to 13°API.¹⁰⁸ Estimated primary RE ranges from 3 to 8% OIP¹⁰⁹ for the Lloydminster area of western Canada, where stock-tank gravities range from 13 to 17°API.

Primary RE vs. API gravity for heavy crude oil “pools” in Alberta and Saskatchewan* is plotted on Fig. 18.30. Data are from 69 “pools” with OIP > 10⁶ m³ (6.3 million STB). The trend line is not weighted by resource size and is shown only for reference; the regression coefficient, 0.21, is too small to infer a statistically significant correlation between RE and oil gravity. Of interest, however, is that the trend line is consistent with REs shown on Table 18.5 for “average” sandstone for 15°API and slightly-higher-gravity oils. Also interesting (lack of correlation notwithstanding) is the large number of heavy-oil reservoirs with significantly greater REs than would be predicted using “conventional” solution gas drive calculations. Reportedly, such REs are attributed to two mechanisms: the simultaneous production of oil and sand known as “cold production,”¹¹⁰ and “foamy oil.”¹¹¹

Although there are reports of REs that range from 5 to 20% OIP,^{110,112} no general correlations are available that relate specific rock/fluid properties and REs for heavy oil; thus, for volumetric methods, reserves engineers typically rely on analogy. The performance of wells in heavy oil reservoirs is erratic, however, and is influenced by varying production practices, varying volumes of sand production, and frequent downtime, among other factors, so that analogy estimates are subject to considerable uncertainty.

* Personal communication with Rajneesh Kumar, Ryder Scott Co., 2 April 2002.

Reserves estimates based on performance also are subject to considerable uncertainty. Production rates for single wells usually are erratic, thereby precluding meaningful trend analysis. Many engineers generate normalized production curves from groups of wells producing from zones comparable to those being analyzed.

In summary, the producing mechanisms for heavy oil are poorly understood; an optimum production strategy has yet to be developed; *a priori* prediction of the efficiency of the production mechanisms for heavy oil currently is impossible. Although progress is being made on computer modeling,¹¹³ it may be several years before sufficient data are compiled for reliable estimates of RE and/or reserves from heavy oil.

18.5.6 Thin Oil Columns. Thin oil columns overlain by free gas and underlain by water pose difficult problems in well spacing and completion method, production policy, and reserves estimation. In this context, “thin” is a relative term. Whether an oil column is considered thin depends on costs to drill and produce the accumulation. For example, in the Bream field (Australia Bass Strait, 230 ft water depth), 44 ft was considered thin,¹¹⁴ whereas in the Troll field (offshore Norway, 980 ft water depth), 79 ft was considered thin.¹¹⁵ Onshore U.S.A., 20 ft is considered thin. Irrgang¹¹⁶ takes a pragmatic approach, defining thin oil columns as those that “will cone both water and gas when produced at commercial rates.”

The overall RE of oil from such accumulations can be influenced by well spacing and completion method and by gas-cap management policy. Economics, though, tend to be controlled by individual well recoveries and production capacities, rather than by average RE from the reservoir; thus, development planning focuses on the economics of individual wells—the cost to drill, complete, and operate vs. the oil rate/time profile. Ultimate oil recovery from individual wells tends to be controlled by a number of factors, including the gross thickness of the oil column and the horizontal/vertical permeability ratio in the well’s drainage area. This ratio might vary significantly over the areal extent of the reservoir, depending on the depositional environment of the reservoir rock. Experience with such reservoirs indicates that this parameter typically is underestimated, causing underestimates of oil recovery. Localized shale breaks might contribute to suppressed coning of gas and/or water if wells can be completed to take advantage of these heterogeneities.

From limited data from conventional well completions in several such fields in Australia, Irrgang¹¹⁶ developed the relation

$$N_{paw} = \text{fn}[\phi(1 - S_w - S_{or})k_H h_t^{2.5} R_{ng}^{1.5} / \mu_o B_o], \dots\dots\dots (18.50)$$

where the bracketed term is a correlating parameter.

Irrgang does not provide details on estimation of k_H ; the median permeability probably is appropriate. Irrgang has observed, “a higher power may be appropriate for permeability—possibly even 2.”* The vertical/horizontal permeability ratio, k_V/k_H , influences volumetric sweep efficiency in bottom waterdrive reservoirs. The absence of this term in Irrgang’s correlation is puzzling, but might be because of measurement difficulties.

Depending on the water/oil mobility ratio and the horizontal/vertical permeability ratio, oil wells completed in this type of accumulation might exhibit coning of the overlying gas and/or coning of the underlying water early in life. These phenomena might cause rapidly increasing GOR or WOR and relatively short economic life; thus, how efficiently this type of accumulation can be exploited depends on the degree to which premature coning of gas and/or water can be avoided by appropriate completion methods and production practices. In one of the earliest published analyses of this problem, Van Lookeren¹¹⁷ advocated perforating below the

* Personal communication with H.H. Irrgang, Command Petroleum Holdings (December 1994).

TABLE 18.12—POTENTIAL FIELD ANALOGS FOR ESTIMATING OIL RECOVERY FROM THIN OIL COLUMNS (AFTER IRRGANG¹¹⁶)

Parameter	Field and Lithology			
	Bream ^a sandstone	South Pepper ^a sandstone	Chookoo ^b sandstone	Taylor ^b sandstone
Porosity, fraction	0.21	0.21	0.17	0.08 to 0.16
Net/gross ratio	0.65	0.96	0.90	0.40 to 1.00
Permeability, md	2,900	80 to 4,800	500	100 to 2,000
k_v/k_h	0.01	0.01 to 0.20	Not reported	Not reported
Oil viscosity, cp	0.24	0.48	0.21	0.26
Oil column, m	13.5	9.7	3.7	0 to 11.3
Gas column, m	105 ^c	18	19 ^c	33
Well spacing, m ^d	300 to 800	300 to 800	600 to 1,200	700 to 1,500
Oil recovery, 10 ⁶ bbl/well	2.00	1.50	0.26	0.09

^aOffshore. ^bOnshore. ^cProduced gas injected into gas cap. ^dAuthors' estimate.

initial OWC to minimize gas coning; however, the simple isotropic model used in his analysis essentially negates the practical application of this approach. In the last few years, horizontal drainholes have been used to develop these accumulations.¹¹⁸ Because this technology is still evolving, consider apparent successes in analogous reservoirs with caution.

Determination of optimum well spacing and estimation of oil reserves in such reservoirs is subject to substantial uncertainty, at least until a reasonably well-defined performance trend has been established for each well. Before performance trends are established, however, reserves typically are estimated using a combination of volumetric mapping and analogy or analytical methods. In this context, computer simulation can be extremely useful in establishing sensitivity of RE to various assumed scenarios, thereby helping to determine optimum well spacing and commerciality. Potential analogs are provided in [Table 18.12](#).¹¹⁶

A critical review of the more than 50 years of literature^{119–125} makes apparent that the industry has yet to develop a general treatment of coning that includes the influences of gas cap, aquifer influx, and other relevant parameters. For example, some authors investigate the problem of coning in the presence of an inactive aquifer, which is analogous to the classic coning problem first discussed by Muskat and Wyckoff,¹¹⁹ whereas others investigate it in the presence of an active aquifer. Clearly, the critical rate to avoid water coning would be less in the presence of an active aquifer than in the presence of an inactive aquifer, other factors being the same.

In addition to aquifer strength, another critical parameter to apply the correlations in [Refs. 119 through 125](#) is the horizontal/vertical permeability ratio over each well's drainage area. Laboratory measurements of vertical and horizontal permeability of small core samples are inadequate for estimating this parameter. In theory, vertical interference testing or vertical pulse testing can determine this parameter, as discussed by Earlougher,¹²⁶ but the test procedure involves two sets of perforations separated by a packer, an expense operators might be reluctant to incur. Another possible approach for wells exhibiting coning is computer simulation to establish the horizontal/vertical permeability ratio that yields an acceptable match to observed behavior. Whether results from a few such wells would apply to all wells in the reservoir depends on the depositional environment of the reservoir formation and the degree of lateral

heterogeneity; however, it is unlikely. It might be more practical to test wells at gradually increasing rates to determine a maximum rate at which each well can be produced without coning.

In the presence of a strong aquifer and a gas cap, the combination of water encroachment and gas-cap coning might cause displacement of part of the oil column into the gas cap. Depending on the size of the initial gas cap and the degree of gas-cap voidage, significant volumes of oil might be lost. In some cases, this loss might be minimized or avoided by injecting the produced free gas into the gas cap to maintain constant gas-cap volume.

18.5.7 Geopressured Oil/Gas. The term “geopressure,” introduced in the late 1950s by Charles Stuart of Shell Oil Co., refers to reservoir fluid pressure that significantly exceeds hydrostatic pressure (which is 0.4 to 0.5 psi/ft of depth), possibly approaching overburden pressure (approximately 1.0 psi/ft). Geopressured accumulations have been observed in many areas of the world.

Geologic Setting. In regressive tertiary basins (the geologic setting for most geopressured accumulations), such pressures in sand/shale sequences generally are attributed to undercompaction of thick sequences of marine shales. Reservoirs in this depositional sequence tend to be geologically complex and exhibit producing mechanisms that are not well understood. Both of these factors cause considerable uncertainty in reserves estimates at all stages of development/production and reservoir maturity. Geologic complexity contributes to uncertainty in estimates of O/GIP that are based on volumetric mapping. Poorly understood producing mechanisms contribute to uncertainty in estimates of reserves that are based on pressure/production performance. Each aspect is discussed below.

Geopressured reservoirs frequently are associated with substantial faulting and complex stratigraphy, which can make correlation, structural interpretation, and volumetric mapping subject to considerable uncertainty.

The resistivity of interstitial water in geopressured sections may approach that of fresh water, which may suppress the SP log. Under these conditions, it might be difficult to estimate net pay unless a gamma ray log also has been run. In addition, the relatively fresh waters frequently encountered in geopressured sections complicate interpretation of resistivity logs, especially in shaly sands. Cases have been reported in which reserves were booked on the basis of high resistivity observed in porous sands that later investigation proved bore fresh water.

Drive Mechanism(s). As discussed in the Material Balance section of this chapter, if gas production is attributed to gas expansion only, a plot of p/z vs. G_p should be a straight line. Because geologists considered them to be closed accumulations, during the early years of exploitation it was assumed that geopressured gas reservoirs would produce by pressure depletion and exhibit linear plots of p/z vs. G_p . Although this was observed to be true in many cases, it is not universally true. The p/z vs. G_p plots for many geopressured reservoirs initially appear to be linear, but curve downward as reservoir pressure approaches hydrostatic pressure. Extrapolation of the initial part of such a plot might yield an estimate of GIP that is approximately twice that estimated using volumetric methods. The anomalously low initial slope of the p/z vs. G_p plot has been attributed to several phenomena, including PV compression, expansion of interstitial water, and partial waterdrive. The downward curvature of the p/z vs. G_p plot has been attributed to other factors, including depletion of a limited protoshale water aquifer¹²⁷ and rock collapse.¹²⁸ [The American Geological Inst. (AGI) defines shale as an “indurated (hardened)...sedimentary rock formed by the consolidation...of clay.”¹²⁹ Because geopressures in tertiary basins generally are attributed to undercompaction, the term protoshale is adopted here to make that distinction.]

Producing mechanisms in a geopressured gas reservoir might include gas expansion; compressibility of the reservoir PV; expansion of the interstitial water; water influx because of water expansion from a contiguous aquifer; water influx because of dewatering of interbedded

protoshale; and/or evolution of natural gas dissolved in interstitial and aquifer water. Any or all of these mechanisms may be active at various stages in the life of a geopressed gas reservoir. Pressure/production data typically are insufficiently diagnostic to distinguish one mechanism from another, so that there may be considerable uncertainty in analysis of historical data and estimation of reserves.

There is disagreement regarding the relative importance of these mechanisms, especially compressibility of reservoir PV¹³⁰ and water influx from interbedded protoshale.¹³¹⁻¹³³ Because it is difficult to analyze geopressure mechanisms separately for a specific reservoir, many engineers use Eq. 18.51 to make an aggregate adjustment to the p/z vs. G_p plot¹³⁴:

$$p/z[\Delta p(c_w S_w + c_p)/(1 - S_w)] = p_i/z_i - G_p p_i / G_{Fi} z_i \dots\dots\dots (18.51)$$

Eq. 18.51 differs from Eq. 18.37 by inclusion of a p/z adjustment factor, which is the left-side square-bracketed term. Eq. 18.51 sometimes is simplified by adjusting the apparent gas in place (AGIP)—that estimated by extrapolation of the initial part of the p/z vs. G_p plot—by multiplying the AGIP by the gas-compressibility/effective-compressibility ratio.

Both methods assume that PV compressibility remains constant over the life of the reservoir being evaluated, which is contrary to the findings of numerous investigators. In addition, neither accounts for possible water encroachment.

Regardless of the method used to adjust the p/z vs. G_p plot, always check a reserves estimate so derived against analogies and/or a volumetric estimate for the same well.

Analytical Methods. Analytical methods outlined in the literature typically require more information than usually is available. As an alternative, a method was proposed³ that parallels that of Havlena and Odeh.⁶⁰ Under this method, Eq. 18.28 can be written for a gas reservoir as

$$G_p B_g + W_p B_w = G_{Fi}(B_g - B_{gi}) + G_{Fi} B_{gi} \Delta p(c_p + c_w S_w)/(1 - S_w) + W_e \dots\dots\dots (18.52)$$

Define

$$F_{pR} = G_p B_g + W_p B_w, \dots\dots\dots (18.53)$$

and

$$E_g = B_g - B_{gi} \dots\dots\dots (18.54)$$

Substituting Eqs. 18.53 and 18.54 into Eq. 18.52 leads to

$$\begin{aligned} F_{pR} &= G_{Fi} E_g + G_{Fi} B_{gi} \Delta p(c_p + c_w S_w)/(1 - S_w) + W_e \\ &= G_{Fi} [E_g + B_{gi} \Delta p(c_p + c_w S_w)/(1 - S_w)] + W_e \dots\dots\dots (18.55) \end{aligned}$$

Divide by the gas-expansion and rock/fluid-compression term in brackets:

$$\begin{aligned} &\frac{F_{pR}}{E_g + B_{gi} \Delta p(c_p + c_w S_w)/(1 - S_w)} \\ &= G_{Fi} + C \frac{W_e}{E_g + B_{gi} \Delta p(c_p + c_w S_w)/(1 - S_w)} \dots\dots\dots (18.56) \end{aligned}$$

If the water-influx term and the rock/fluid expansion/compression terms are estimated correctly, a plot of the left-side term vs. the fractional part of the second right-side term of Eq. 18.56 will be a straight line. The y intercept should be equal to G_{Fi} . The slope of the line should equal C , the water-influx constant. Note that c_p is a function of pressure and is $c_p(p)$ integrated over a change in net overburden pressure that corresponds to the value $p_i - p$.

The water-influx term probably will be the most difficult term to evaluate because water influx in a given reservoir could be attributable to expansion from a contiguous aquifer and/or to dewatering of interbedded protoshale. Favorable conditions for protoshale water influx include considerable interbedding of protoshale with the gas-bearing sand, a small contiguous aquifer, and a high initial fluid-pressure gradient. Opposite conditions would favor aquifer influx. Depending on the size and shape of the contiguous aquifer, W_e might be calculable using a limited linear aquifer model or a limited cylindrical aquifer model. If protoshale dewatering is suspected, a limited linear aquifer model might be more appropriate.

Geopressured gas reservoirs might exhibit retrograde behavior, a phenomenon discussed in the Condensate section of this chapter. Oil reservoirs are encountered less frequently than gas reservoirs in the geopressured section and rarely are discussed in the literature. Comments similar to those for geopressured gas reservoirs are appropriate regarding drive mechanism in geopressured oil reservoirs. Depending on circumstances, an approach analogous to that presented in Eqs. 18.52 through 18.56 might be appropriate for geopressured oil reservoirs.

PV Compressibility. On the basis of numerous studies of the influence of reservoir pressure on PV compressibility,¹³⁵⁻¹⁴⁴ it seems apparent that PV compressibility of porous rocks depends on the stress conditions in the reservoir, decreases as stress increases, decreases as rocks become more consolidated, and might increase as temperature increases.

There appears to be no correlation between compressibility and rock properties that is generally valid across a broad spectrum of lithologies and pressures. Hall's¹⁴⁵ correlation between compressibility and porosity—still widely cited—covers only a narrow range of stress conditions and apparently reflects only data from well-consolidated rocks.

Reportedly, some geopressured sands have compressibilities approaching those usually associated with consolidated rock¹⁴⁶; however, these data apparently were measured on rock samples taken from geopressured aquifers, rather than from hydrocarbon reservoirs. In the high temperatures usually associated with geopressured environments, sandstones undergo rapid diagenesis that can cause a geologically young rock to become tightly cemented. This is more likely to occur in aquifers (where the interstitial water is mobile) than in hydrocarbon reservoirs (where the interstitial water is immobile). Expect these tightly cemented sandstones to be less compressible than relatively uncemented sands; accordingly, measure compressibility on samples taken from the hydrocarbon-bearing zone, not from the aquifer. Take great care when using compressibility data from rocks that appear similar to the zone of interest or that have comparable porosity and permeability.

In the absence of laboratory data, the following correlation can be used to estimate PV compressibility¹⁴⁷:

$$c_p \approx A[K_1 p_{ob} - K_2 p_i + K_3(p_i - p) - B]^C + D, \dots\dots\dots (18.57)$$

where A , B , C , D , K_1 , K_2 , and K_3 depend on rock properties, as shown in **Table 18.13**.

During pressure reduction of reservoir fluids, the resultant stresses on reservoir rocks differ from those on core samples during hydrostatic testing in the laboratory. In the subsurface, when production reduces reservoir fluid pressure, the weight of the overburden compacts the reservoir rock, which uniaxially reduces the bulk volume of the rock and, consequently, reduces PV. This process can be replicated in the laboratory, but such tests require special

TABLE 18.13—CONSTANTS TO ESTIMATE PV COMPRESSIBILITY USING EQ. 18.57

Constant	Sandstones			Carbonates
	Unconsolidated	Friable	Consolidated	
A	-2.805 E-5	1.054 E-5	2.399 E-5	Not reported
B	300	500	300	Not reported
C	0.1395	-2.2250	0.0623	Not reported
D	1.183 E-4	-1.103 E-5	4.308 E-5	Not reported
K_1	0.95	0.90	0.85	0.85
K_2	0.95	0.90	0.80	0.85
K_3	0.75	0.60	0.45	0.55

equipment that is not used by most commercial laboratories. Most laboratory compressibility data are measured using hydrostatic stress, which can be related to reservoir stress by

$$p_n = K_1 p_{ob} - K_2 p_i + K_3 (p_i - p) \dots\dots\dots (18.58)$$

18.6 Probabilistic Procedures

18.6.1 Background. Experienced reservoir engineers know that uncertainty exists in geologic and engineering data and, consequently, in the results of calculations made with these data; however, the degree of uncertainty in most reservoir engineering calculations usually is not quantified.

Reserves estimates historically have been deterministic (“single-valued”), with the degree of uncertainty indicated by qualitative terms such as proved, probable, and possible. Additional information about the degree of uncertainty has been conveyed by describing producing category and development status (e.g., producing, behind-pipe, or not developed), as discussed in the Reserves Definitions section of this chapter.

Even now, deterministic estimates of reserves usually are considered appropriate in geologic settings and operating areas where there is substantial experience, and in fully developed, mature fields—situations having relatively little uncertainty; however, for new geologic settings (then, coalbed methane) and in new operating areas (then, the North Sea), the industry developed probabilistic procedures to estimate and classify reserves.^{148,149} These procedures have been used to quantify potential range of reserves attributed to risky ventures and their degree of uncertainty.

Probabilistic procedures have long been used to assess exploratory ventures, but have not been widely used to assess production ventures. There are, however, several considerations and potential application areas for probabilistic procedures discussed below.

18.6.2 Probabilistic Classification of Reserves. Probabilistic classifications of reserves for a specific entity usually are based on the cumulative density function of the quantities calculated for the entity. (Cronquist³ discusses basic principles of probabilistic methods.) As previously discussed, probabilistic classifications typically specify for proved reserves that

- There should be at least 90% probability that the quantities actually recovered will equal or exceed the estimate.
- There should be at least 50% probability that the quantities actually recovered will equal or exceed the sum of estimated proved plus probable reserves.

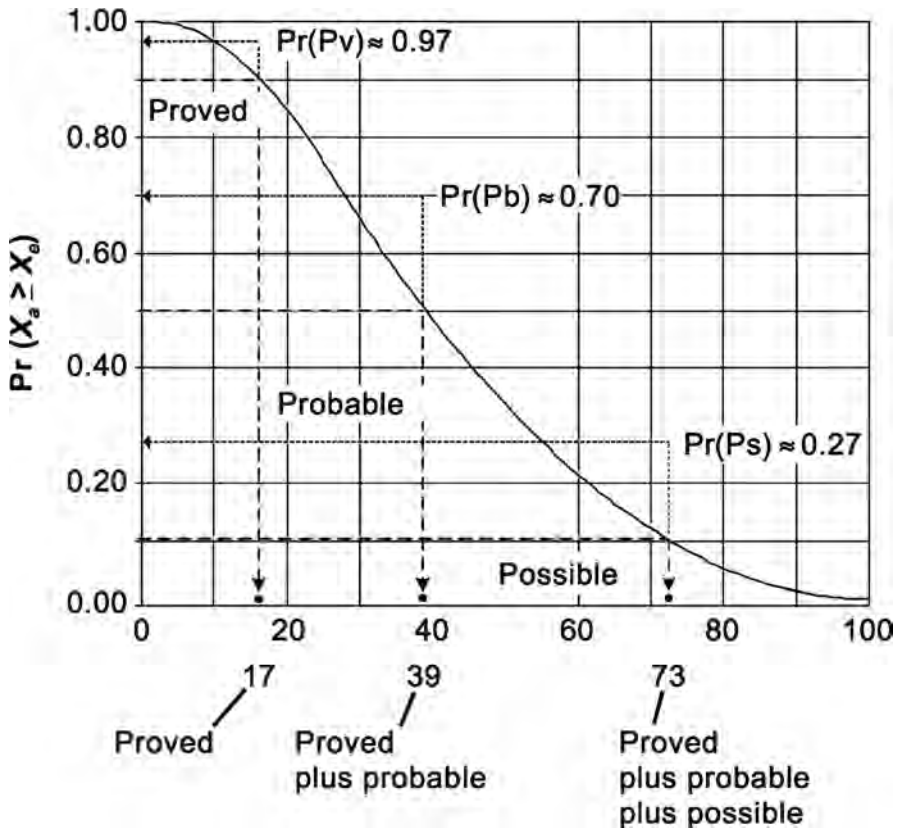


Fig. 18.31—Typical expectation curve for proved, proved plus probable, and proved plus probable plus possible reserves. X_a = the actual quantity of reserves and X_e = the estimated quantity of reserves.

- There should be at least 10% probability that the quantities actually recovered will equal or exceed the sum of estimated proved plus probable plus possible reserves.

Caution! Probabilistic notation and concepts discussed here should not be confused with those used by many exploration geologists [e.g., Rose,¹⁵⁰ in which probabilities refer to, among other considerations, *prospect reserves* distributions or *field size* distributions. In that context $P_{90\%}$ (Rose's notation) refers to *ultimate* reserves in a *yet to be discovered* accumulation. *After discovery*, reserves in such an accumulation might be estimated and classified using the procedures discussed here.]

For the expectation curve (EC) in Fig. 18.31, proved, proved plus probable, and proved plus probable plus possible quantities would be 17, 39, and 73, respectively.

The foregoing (probabilistic) definitions reflect a cumulative interpretation of the EC in Fig 18.31. An incremental interpretation is shown by the short dotted lines, which approximate the area under the EC having three rectangles with increments on the x -axis that are defined by the foregoing classifications; thus, for the EC in Fig. 18.31, it might be said that the probability of recovering proved reserves [Pr(Pv)] ≈ 0.97 , the probability of recovering *incremental* probable reserves [Pr(Pb)] ≈ 0.70 , and the probability of recovering *incremental* possible reserves [Pr (Ps)] ≈ 0.27 .

Despite the 1997 SPE/WPC definitions' emphasis on a cumulative approach to probabilistic estimation and classification, an incremental approach might be more appropriate in situations that involve undrilled and/or unproved reserves where incremental expenditures and/or regulatory approval are required to bring such reserves on production. Specific guidelines for these

situations are enumerated in separate paragraphs in the 1997 SPE/WPC reserves definitions for probable and possible reserves, respectively, and are preceded by the phrases “In general, probable reserves may include...” and “In general, possible reserves may include...”

18.6.3 Applications. Despite the (still) widespread use of deterministic methods for reserves estimation, there are several scenarios in which a probabilistic approach might be more appropriate.

Analogy/Statistical Methods. Historically, analogy/statistical methods have involved arithmetic averages of pertinent parameters, which have been considered “best estimates,” a procedure that assumes that such parameters are (approximately) normally distributed; however, there are scenarios in which arithmetic averages might lead to significant bias in reserves estimates, especially those intended to conform to a P90 standard. The statistical frequency distribution of ultimate recovery—initial reserves—for wells in a common reservoir or geologic trend typically can be *approximated* with a log-normal (frequency) distribution. Also, the frequency distribution of geologic and/or engineering parameters (e.g., net pay) typically can be *approximated* with log-normal distributions. Log-normal distributions generally exhibit positive (right) skew. Depending on the degree of skew, the arithmetic average of such a distribution might be significantly greater than the intended “best estimate,” which usually is considered the median of the distribution; thus, estimates based on arithmetic averages of pertinent parameters may (inadvertently) be biased on the high side. The more skewed the distribution, the greater the bias. With skewed distributions of pertinent parameters, consider using the median value for each such distribution, rather than the arithmetic average.³

These observations can be used to estimate reserves for new wells by analogy with data from older wells in the same trend. Before using this technique, however, determine whether per-well reserves are truly random, are not influenced by prior drainage, and are unrelated to a geologic or operating parameter. As drilling and production continue, update the analysis when reserves for existing and new wells are revised.

Random distributions of per-well reserves have been observed in many geologic/reservoir settings in the U.S.A. and elsewhere. In these areas, *at the time of the analysis*, there was no statistically valid correlation between ultimate production for individual wells and date of initial production, net pay, “frac” treatment, initial potential, or any other parameter for these same wells. In some of these areas, however, as infill drilling continued, correlations were observed between date of initial production and ultimate recovery; thus, in any mature area, one should be alert to similar possibilities.

Volumetric Methods. Depending on the geologic complexity, the stage of development, and the quality/quantity of subsurface and geophysical data, volumetric mapping might involve considerable uncertainty, including subsea depth of fluid/fluid contacts, location of bounding faults, position of sand pinchouts, and time/depth conversion(s) for seismic data, among other factors. Circumstances might make it appropriate to quantify one or more of these uncertainties using probabilistic procedures. There may be numerous perturbations and/or combinations, a subject that merits an entire chapter, but is only covered briefly here. (See Cronquist³ for a more in-depth discussion of this topic.)

As discussed in the *Reservoir Limits* section, the subsea depth(s) of fluid/fluid contacts in a specific reservoir—GOC, GWC, and/or OWC—might not have been penetrated by wells, and there might be considerable disparity between analyses based on pressure, seismic, and/or capillary pressure data. Given such a scenario, it might be appropriate to define the range of uncertainty in subsea depth using a triangular probability distribution, with the mode of the distribution determined by the analysis procedure considered the most robust.

Performance Methods. The analysis of performance data might involve, for example, regression analysis (a least squares fit) of a production trend vs. time or vs. cumulative produc-

tion. Historically, production projections based on such analyses have been classified as proved reserves. Regression analysis, however, yields a “fit” through the “means” of the analyzed trend. Probabilistically, such a fit is a P50, and reserves so calculated might, accordingly, be classified as proved plus probable. In a scenario where there is a long history of settled production and, consequently, a regression coefficient approaching unity, such a distinction is insignificant; however, where there is a relatively short, erratic production history and, consequently, a regression coefficient significantly less than unity, the distinction might be significant. Reserves engineers might consider a probabilistic analysis of the data.^{3,151,152}

18.7 Pitfalls*¹⁵³

A *pitfall* is a hidden or not easily recognized danger or difficulty that catches one unawares. In engineering, pitfalls are fallen into through mistakes from carelessness or ignorance. The potential petroleum engineering pitfalls below are described from the perspectives of an engineer preparing a reserves estimate and an engineer reviewing the work product of another.

Bias is not usually considered a pitfall, but rather is a conscious effort to “shape” a result for a specific purpose. An engineer must guard against all forms of external or internal bias and be careful to avoid the pitfalls that can affect the reliability of any reserves estimate. Some of the material presented here has been covered, in part, earlier in this chapter but is expanded here in light of the seriousness of these potential pitfalls.

18.7.1 Analogy/Statistical Methods. Assuming that reservoirs on trend and in the same geologic formation are analogous is a common pitfall. Depending on the geologic setting, depositional environment and, consequently, reservoir quality, might vary significantly over relatively short distances. For example, in a clastic deltaic environment both channel and fringe sands occur. Reservoirs in channel sands exhibit better quality than those in fringe sands and the two cannot be considered analogous; for the same drive mechanism, recovery factors in the former typically are significantly larger than those in the latter.

Statistical correlations—for recovery factor, for example—usually reflect the geologic, engineering, operational, and economic settings in which the correlated data were observed. Application of such correlations between disparate settings is a common pitfall and might lead to significant errors in reserves estimates.

Statistical correlations for PVT properties reflect the geologic setting from which the reservoir fluids originated.³ Failure to recognize this is a common pitfall. For example, such correlations developed for fluids from California reservoirs might be inappropriate for estimating PVT properties of fluids from North-Sea reservoirs. Use of inappropriate correlations might cause significant errors in estimates of reserves of both gas and oil. Cronquist has provided additional guidelines regarding application of PVT correlations.³

18.7.2 Volumetric Methods. Pitfalls in volumetric methods include failing to integrate subsurface (well) data with seismic data, incorrectly constructing net-pay isopachs, and applying global correlations without adjustments for local conditions. Some of these pitfalls are discussed in the following paragraphs.

Structural Mapping. Fig. 18.32 is a log section marked to indicate a structural top at 6,973 ft ss, top of first porosity at 7,018 ft ss, and an OWC at 7,133 ft ss. The three porosity intervals (at 7,018, 7,064, and 7,098 ft ss) might be part of a single pressure-connected reservoir, or they might be three separate reservoirs. Well log data alone usually are insufficient to resolve such uncertainties. If the single-reservoir scenario can be confirmed, a reservoir structure map incorporating the top of the first porosity (7,018 ft ss) and the OWC at 7,133 ft ss might be

* This section was inspired by a presentation by Harry Gaston Jr. at the 1992 Annual Convention of the SPEE on 13–16 June 1992 at Jackson Hole, Wyoming.

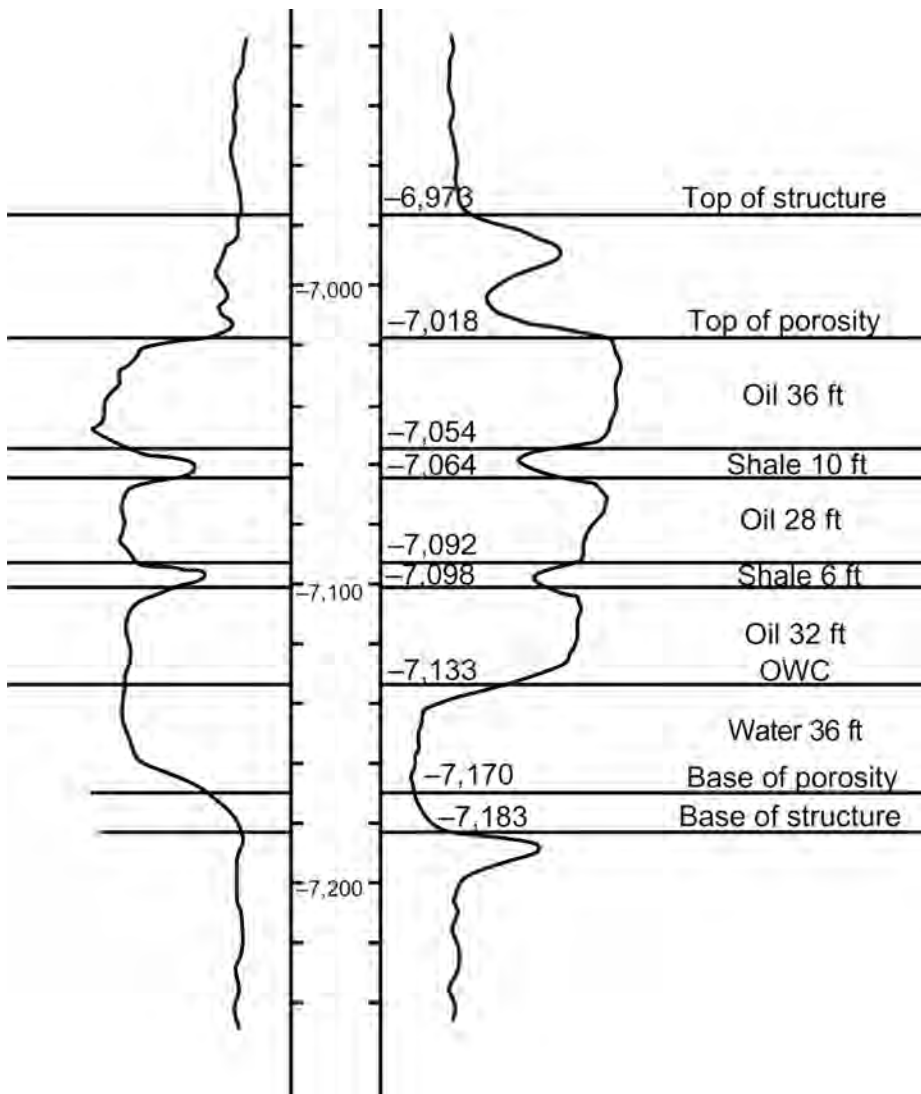


Fig. 18.32—Well log section (after Mistrot¹⁵⁴).

appropriate. Net-pay isopach maps of each pay interval could be constructed using a common OWC.

An alternate geologic interpretation might indicate the likelihood of the continuation of the two 10-ft shale breaks over the area of the accumulation. Should this situation exist, it would be appropriate to recognize three separate reservoirs. The upper two would have P1 reserves limited to the LKO depths of 7,054 and 7,092 ft ss, respectively.

Additional wells might be required to confirm or deny the effectiveness of the intervening shale members. Assuming a single reservoir in similar circumstances might cause P1 reserves to be overstated significantly, should subsequent information support the presence of more than one reservoir. A structure map using a structural top of 6,973 ft ss, without adjusting for the distance between this top and the top of porosity, would lead to overstatement of the productive area and reserves through exaggeration of the reservoir area. Fig. 18.33 illustrates the potential overstatement of reservoir extent, using lowest known hydrocarbons (LKH) limits for

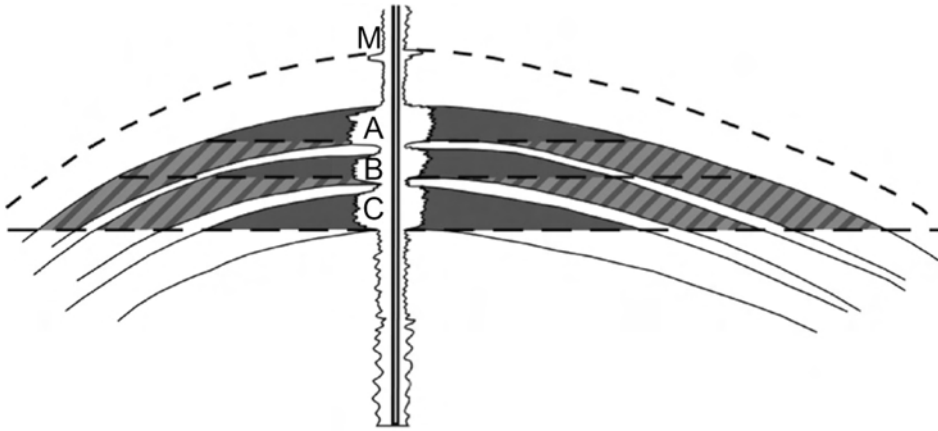


Fig. 18.33—Single-well cross section illustrating the possibility of three separate reservoirs.

three sand intervals, A, B, and C, that might be three individual reservoirs and the marker, M. Shaded areas above the individual LKH levels may be considered proved reserves. The crosshatched areas may be considered P2 or P3 reserves. Continued monitoring of performance history and/or development drilling would confirm the presence of a single accumulation or of two or three separate reservoirs.

Isopach Mapping. Isopach maps often are prepared improperly, which almost always leads to overstatement of O/GIP. Fig. 18.34 illustrates a common pitfall of assuming a net-pay buildup updip from well control. Given that the maximum net sand observed in the immediate area is only 45 ft, there is no justification to assume such a buildup. If the dry hole to the north had a total net sand thickness greater than 45 ft, then a buildup in net pay to the observed maximum net sand might be justified. Also, there is uncertainty regarding the position of the fault bounding the northwest side of the reservoir, and the geologist's interpretation might have been optimistic.

Fig. 18.35 is similar to Fig. 18.34, but the area updip from the highest productive wells is interpreted to be no more than 45 ft thick. Also, the fault has been shifted to the southeast as a result of an alternate fault interpretation, which results in significantly less reservoir volume than the original interpretation. Which is correct? Is the difference from a pitfall or bias? One should be vigilant in discerning the differences in reserves estimates resulting from either bias or a pitfall, and should make appropriate revisions as warranted.

18.7.3 Performance Methods. Many pitfalls await the unwary who use performance methods to estimate reserves. Several of the more common pitfalls are discussed here: analysis of production decline trends to estimate reserves for wells still in the transient stage; extrapolation of performance indicators to unrealistic economic limit conditions; misuse of composite decline curves; physical life limitations; failure to recognize the effect of interference between wells; failure to reconcile results of volumetric and performance analyses; and miscalculation/misuse of p/z vs. G_p plots.

Analysis of Production Decline Trends During Transient Flow. An expanding drainage radius and (initially) steep, hyperbolic declines in production rate characterize transient flow from wells. Reserves estimates during this stage of production usually will be too low if they are based solely on decline-trend analysis, without appropriate adjustments. The problem is especially severe in shallow, low-permeability gas reservoirs, where wells may exhibit transient flow over a substantial part of their productive life.

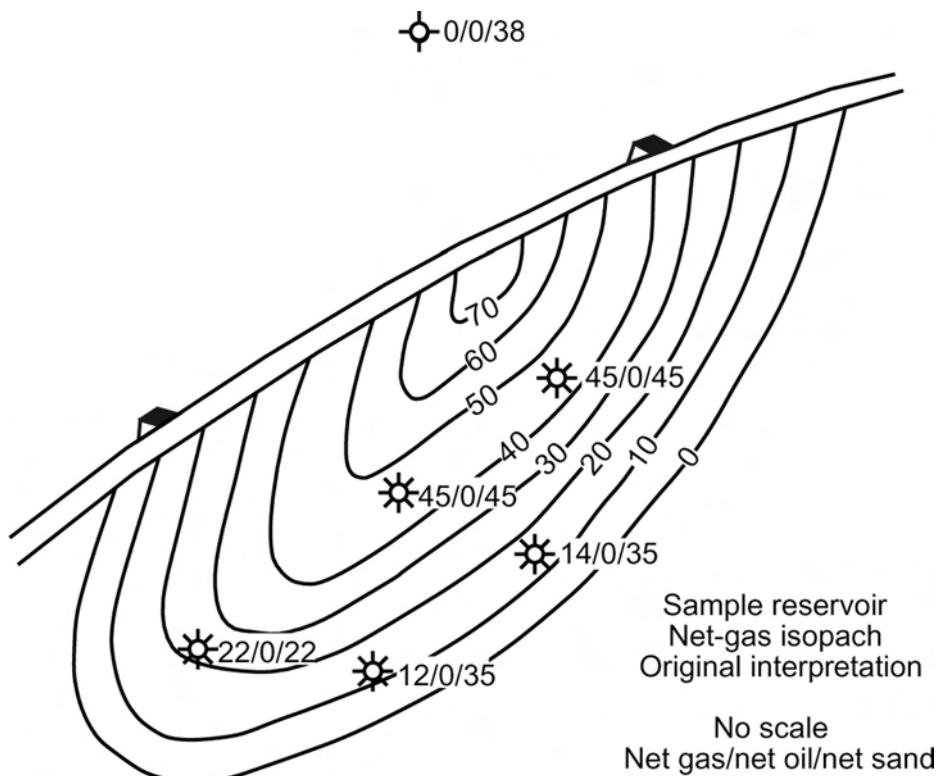


Fig. 18.34—Net gas isopach (after Gaston¹⁵³).

Unrealistic Economic-Limit Conditions. Semilog plots of f_o vs. N_p commonly are used to estimate reserves for oil wells in waterdrive reservoirs. Such plots frequently are used before there is a clearly defined decline in oil production rate, which can be a pitfall. Plots of f_o vs. N_p can be extrapolated to a local average “ f_o cutoff,” but this cutoff might be too low for wells with low productivity. For example, in many areas, the average f_o cutoff is 0.01; however, if a well is capable of producing only 250 B/D (oil plus water) and the economic limit is 5 BOPD, then the f_o cutoff for this well should be 0.02, not 0.01.

Misuse of Composite Decline Curves. Projecting decline trends of composited production from multiple wells to estimate proved reserves often leads to an overstatement of reserves. Failure to thoroughly analyze the effects of operator efforts to sustain production rates, as well as of marketing limitation or transportation restriction influences, is a common pitfall. Production declines of individual wells and the composite production stream might have been mitigated by workovers, recompletions, new wells, stimulation, and/or compression equipment upgrade or other equipment and facility upgrades, the benefits of which might not be available during the forecast period to sustain the demonstrated production trend. The engineer should always try to evaluate the performance of individual wells or completions, even if the production history has been computed using an allocation of the composite production quantities.

Physical Life Limitations. The extrapolation of monthly production rates of oil and/or gas from a well can extend for 40, 60, or maybe 100 years, depending on the economic assumptions that are used. When estimating such reserves, consider the cost of drilling a replacement well and the replacement of infrastructure facilities. Some engineers arbitrarily limit future projection lives to 30 to 50 years, depending on the specific circumstances of each production area.

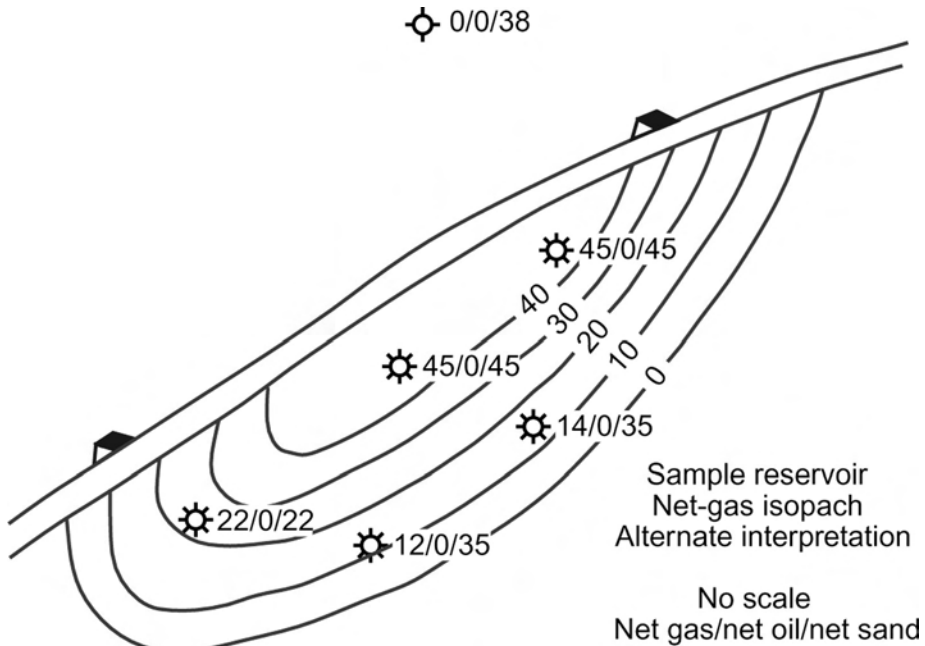


Fig. 18.35—Net gas isopach (after Gaston¹⁵³).

Failure To Recognize the Effect of Interference Between Wells. Analyzing each well in a common reservoir often is appropriate for estimating reserves, particularly for a fully developed reservoir being produced under the control of a single operator; however, when individual wells are not analyzed, be aware of the potential for interwell interference to affect individual well-drainage patterns. Examples are the drilling of infill wells, which might increase reserves or serve only to accelerate rate, and increased production, from competitor-operated wells.

Failure To Reconcile Results of Volumetric and Performance Analyses. During the early life of a reservoir, performance-data analysis might suggest more or less reserves than are indicated by volumetric methods. Depending on the degree of difference and the economic consequences thereof, it might be appropriate to review the performance and volumetric data, as well as the analysis methods, to resolve these discrepancies. Such a review might reveal one or more causes (e.g., inappropriate net-pay cutoffs, invalid drainage-volume estimates, poor assumptions regarding drive mechanism, and/or unrealistic decline-trend projections).

Misuse and/or Improper Calculation of p/z vs. G_p Plots. Plots of p/z vs. G_p are powerful tools for analyzing the performance of gas reservoirs; however, there are several reservoir scenarios in which these plots are misused or misinterpreted, including geopressured reservoirs, partial waterdrive, conjectural economics of multistage compression, and plot miscalculation.

Geopressured Reservoirs. In geopressured reservoirs, plots of p/z vs. G_p frequently exhibit an anomalously low initial slope, followed by a steeper slope. The initial low slope might be caused by water influx and/or PV compressibility. The steeper slope, which might not appear until later in reservoir life, might be because of depletion of a limited aquifer. As discussed in the Special Problems section of this chapter, depending on the stage of production maturity, it might not be possible to determine the dominant drive mechanism in such reservoirs. In such case, either adjust plots of p/z vs. G_p or use an alternate material-balance method.

Partial Waterdrive. In many cases, a plot of p/z vs. G_p is insufficient to determine whether there is water influx into a gas reservoir under study.^{3,139} Failure to recognize such influx may

lead to substantial overestimates of gas reserves. The uncertainty in such cases might be resolved by using a procedure, discussed in the Geopressured Oil/Gas section of this chapter, that is based on the Havlena and Odeh method.⁶⁰ Ignoring the rock-compressibility term and rearranging Eq. 18.52 yields:

$$G_p B_g / (B_g - B_{gi}) = G_{Fi} + (W_e - W_p B_w) / (B_g - B_{gi}) \quad (18.59)$$

If there is no water influx, the second right-side term equals zero and the left-side term vs. G_p should plot as a horizontal line, with the y -axis intercept equal to G_{Fi} . If there is water influx, however, the plot will be curved, with the degree and type of curvature dependent on the degree of water influx.

Conjectural Economics of Multistage Compression. In some operating and economic scenarios, RE of gas from volumetric reservoirs may exceed 95% GIP; however, such REs typically require multistage compression, the economics of which might be conjectural in the early stages of reservoir history. Be wary of assuming that installing such compression facilities can be justified economically, unless there is considerable experience in an analogous reservoir in a comparable operating and economic setting. On offshore platforms, for example, there may not be enough space to install such facilities, and major expansion may be infeasible, either structurally or economically.

Improper Calculations of p/z Values. Some of the more commonly seen problems associated with the determination of static reservoir pressures and related z -factor are:

- Nonrepresentative pressures obtained when some wells completed in the reservoir remain on production.
- Relying on shut-in wellhead pressures to calculate bottomhole pressures in the presence of water and hydrocarbon liquids.
- Shut-in time that is inadequate to achieve static pressure.
- Using inappropriate gas composition to compute z -factors.
- Not adjusting bottomhole pressures to a common subsea depth.

Each of these problems is discussed briefly in the following paragraphs.

Nonrepresentative pressures may occur when operators do not shut in certain wells because of high liquid ratios or other concerns. They allow these wells to continue to produce while other wells in the same reservoir are shut in for a pressure survey. Other operators might obtain static reservoir pressures in new wells being completed in a common reservoir at the same time when other reservoir wells continue to produce. Be cautious in relying on such pressure information in any circumstance wherein the reservoir is not allowed to approach an equilibrium pressure.

Shut-in wellhead pressures may be used to reliably calculate reservoir pressures only if the composition and relative volumes of the wellbore fluids are known. The range of error in the calculated values increases if there is a static liquid level (either condensate or water) in the wellbore at an unknown depth.

Inadequate shut-in time to achieve static reservoir pressure occurs commonly. Knowledge of actual shut-in time is important for assessing data reliability. Third-party engineers might not have full access to the operator's data. In many cases, such data may have been lost or misplaced because of transfers of interest. For example, a reserves engineer might have only publicly reported pressure data for use in reservoir analysis, and might not be aware of the length of the shut-in period before the pressure measurement or of the consequences of this lack of knowledge.

Using an inappropriate gas composition to calculate z -factors usually is the result of assuming a constant gas composition throughout the life of a gas reservoir. While this might be appropriate for a dry-gas reservoir, it could cause serious errors for a retrograde gas reservoir if

static reservoir pressure is reduced to less than the dewpoint pressure during production. Ignoring the resultant change in composition of the reservoir gas in retrograde accumulations can cause errors in calculation of the z -factor, in-place hydrocarbons, and reserves.

Not adjusting bottomhole pressures to a common depth in a given reservoir often is attributed to time constraints or carelessness. Although this might cause minor errors in low-pressure, low-relief, dry-gas reservoirs, it might be critical for high-relief oil reservoirs.

Nomenclature

- a = terminal effective decline rate
- a_1 = decline rate, initial, 1/t
- A = area of reservoir or accumulation, acre
- A = constant (in Eq. 18.57 and Table 18.13 only)
- A_g = area of gas cap or gas reservoir, acre or hectare
- A_o = area of the oil zone, acre or hectare
- b = hyperbolic decline exponent (same as n , used by earlier authors)
- B = constant
- B_g = formation volume factor, gas, Rcf/scf
- B_{gi} = initial formation volume factor, gas, Rcf/scf or RB/scf
- B_o = formation volume factor, oil, RB/STB
- B_{ob} = formation volume factor at the bubblepoint, oil, RB/STB
- B_{oi} = initial formation volume factor, oil, RB/STB
- B_t = formation volume factor, total, RB/STB
- B_{ti} = initial total formation volume factor, RB/STB
- B_w = formation volume factor, water, RB/STB
- c_p = compressibility, pore volume, vol/vol/psi
- c_w = compressibility, water, vol/vol/psi
- C = water-influx constant
- C = constant (in Eq. 18.57 and Table 18.13 only)
- C_D = direct operating cost, U.S. dollar/well
- C_{gi} = initial sorbed gas concentration, scf/ton, dry, ash-free coal or shale
- C_i = condensate (distillate) initially in place, STB
- C_{pu} = ultimate condensate production, STB
- C_{Ri} = initial condensate reserves, STB
- C_{ip} = transportation costs, U.S. dollar/bbl
- D = curve-fit coefficient
- D = curve-fit coefficient (in Eq. 18.57 and Table 18.13 only)
- D_i = initial decline rate
- E_c = “expansion” of initial reservoir pore volume caused by compression effects on pore volume and interstitial water, vol/vol/psi
- E_D = microscopic displacement efficiency, fraction
- E_g = expansion of the initial gas cap, if one is present, RB/scf
- E_o = expansion of a unit volume of oil and dissolved (solution) gas initially in place, RB/STB
- E_{Rc} = recovery efficiency of condensate, fraction
- E_{Rg} = recovery efficiency of gas, general, fraction
- $(E_{Rg})_{pd}$ = recovery efficiency of gas attributable to pressure depletion
- $(E_{Rg})_{pwd}$ = recovery efficiency of (free) gas attributable to partial waterdrive, fraction

- $(E_{Rg})_{swd}$ = recovery efficiency of (free) gas attributable to strong water drive, fraction
 E_{Ro} = recovery efficiency of oil, general, fraction
 $(E_{Ro})_{sg}$ = recovery efficiency of oil attributable to solution gas drive, fraction
 $(E_{Ro})_{wd}$ = recovery efficiency of oil attributable to waterdrive, fraction
 E_V = fraction of the initially gas bearing volume swept by the aquifer (volumetric sweep efficiency), fraction
 f_a = average weight fraction of ash, fraction
 f_m = average weight fraction of moisture, fraction
 f_o = fractional flow of oil
 F_g = Thomeer⁴³ parameter for capillary pressure curves
 F_{pR} = volume of cumulative oil, gas, and water production, RB
 F_{rg} = royalty on gas, fraction
 F_{ro} = royalty on oil, fraction
 F_{RA} = recovery factor, analogous reservoir
 F_{RS} = recovery factor, subject reservoir
 G_{Fi} = free gas initially in place, scf or m³
 G_i = gas-in-place at initial reservoir conditions, scf
 G_p = cumulative gas production, scf
 G_{pu} = ultimate cumulative gas production, scf
 G_R = (remaining) gas reserves, scf
 G_{RFi} = initial free gas reserves, scf
 G_{Ri} = initial gas reserves, scf
 G_{RSi} = initial solution gas reserves, scf
 G_{Si} = solution gas initially in place, scf
 h = thickness, ft
 h_n = net pay thickness
 h_{n1} = net thickness of upper (oil) zone, ft
 h_{n2} = net thickness of the lower (oil) zone, ft
 h_{ng} = average net thickness of gas cap or gas reservoir, ft or m
 h_{no} = average net oil pay, ft or m
 h_s = shale thickness, ft
 h_t = gross oil column thickness
 k = permeability, md
 k_a = air permeability, md
 k_e = effective permeability
 k_g = effective gas permeability, md
 k_H = horizontal permeability
 k_o = effective oil permeability, md
 k_{ro} = relative oil permeability, dimensionless
 k_{rw} = relative oil permeability, dimensionless
 k_V = vertical permeability, md
 k_w = effective water permeability, md
 K_A = coefficient
 K_B = coefficient

- K_1 = constant
 K_2 = constant
 K_3 = constant
 m = ratio of initial gas cap volume to initial oil column volume, dimensionless
 m_i = volume of gas injected, multiple of initial gas cap volume, dimensionless
 n = variable
 N_G = gravity number, dimensionless
 N_i = oil initially in place, STB or m³
 N_p = cumulative oil production, STB
 N_{pa} = cumulative oil production at abandonment, STB
 N_{paw} = cumulative oil production, well, at abandonment, STB
 N_{pc} = cumulative oil production at point "c," STB
 N_{pu} = ultimate oil production, STB
 N_{Ri} = initial oil reserves, STB
 p = pressure, static reservoir, general, psia
 p_a = abandonment pressure, psia
 p_b = bubblepoint pressure, psia
 p_d = dewpoint pressure, psia
 p_g = wellhead price of gas, U.S. dollar/STB
 p_i = initial reservoir pressure, psia
 p_n = laboratory net (hydrostatic) pressure (confining pressure minus pore pressure), psia
 p_o = wellhead price of oil, U.S. dollar/STB
 p_{ob} = overburden pressure, psia
 P_{cl} = capillary pressure at laboratory conditions, psia
 P_{cm} = mercury (air) capillary pressure, psia
 P_{cR} = capillary pressure at reservoir conditions, psia
 P_{dm} = mercury (air) displacement pressure, psia
 q = production rate, general, STB/month or scf/month
 q_1 = production rate at the beginning of a period
 q_2 = production rate at the end of a period
 q_{el} = production rate at the economic limit, general, scf/D or STB/D
 q_g = gas production rate, scf/month
 q_{oel} = oil production rate at economic limit, BOPD
 Q = cumulative production
 R = gas/oil ratio, general, scf/STB
 R_c = condensate/gas ratio, STB/MMscf
 R_{cd} = condensate/gas ratio at dewpoint pressure, STB/MMscf
 R_{ci} = initial condensate/gas ratio, STB/MMscf
 R_{cuD} = cumulative condensate/gas ratio at abandonment divided by initial condensate/gas ratio, dimensionless
 R_{ng} = net-to-gross pay ratio, dimensionless
 R_{ngo} = average net-to-gross pay ratio in initially oil-bearing zone
 R_o = vitrinite reflectance, %
 R_p = cumulative (producing) gas/oil ratio, scf/STB
 R_{pz} = ratio of abandonment p/z to initial p/z , or $p_a z_i / p_i z_a$

- R_s = gas/oil ratio, ft³/STB
 R_{sb} = gas/oil ratio at bubblepoint pressure, scf/STB
 R_{si} = initial solution gas/oil ratio, scf/STB
 S_{gr} = residual gas saturation, fraction
 S_{hi} = initial hydrocarbon saturation, fraction
 S_o = oil saturation, fraction
 S_{or} = residual oil saturation, fraction
 S_w = water saturation, fraction
 S_{wfi} = interconnected fracture water saturation, fraction
 S_{wg} = water saturation in the free-gas zone, fraction
 S_{wi} = initial water saturation, fraction
 S_{wo} = water saturation in the oil zone, fraction
 t = time, months or years
 t_{el} = (incremental) time for production to decline from current rate to economic limit rate, days, months, or years
 t_1 = time 1
 t_2 = time 2
 T_A = ad valorem tax, U.S. dollar/STB
 T_P = production tax, U.S. dollar/STB
 V_I = molar volume of ideal gas
 V_R = molar volume of real gas
 V_{io} = gross volume of initially oil-bearing rock, acre-ft
 W_e = cumulative water influx, RB
 W_p = cumulative water production, STB
 X_a = the actual quantity of reserves
 X_e = the estimated quantity of reserves
 z = gas compressibility factor, general, dimensionless
 z_a = gas compressibility factor at the economic limit, dimensionless
 Z_{fw} = vertical distance above free-water level, ft
 z_i = gas compressibility factor at initial conditions, dimensionless
 α = dip angle, degree
 γ_g = specific gravity of solution gas (air = 1.0), dimensionless
 γ_{os} = specific gravity of stock-tank oil, dimensionless
 ΔG_p = incremental cumulative gas production, scf
 ΔN_p = incremental cumulative oil production, STB
 Δp = pressure, incremental, psi
 ΔQ_p = incremental cumulative production, ΔG_p or ΔN_p , as the production rate declines from q_1 to q_2
 Δt = incremental time between t_1 and t_2
 θ_L = contact angle at laboratory conditions, degree
 θ_R = contact angle at reservoir conditions, degree
 μ = viscosity, general, cp
 μ_o = oil viscosity, general, cp
 μ_{ob} = oil viscosity at the bubblepoint, cp
 μ_{oi} = initial oil viscosity, cp
 μ_w = viscosity, water, general, cp

- μ_{wi} = initial water viscosity, cp
 ρ = density, general, g/cm³
 ρ_c = density, coal, g/cm³
 ρ_g = density, gas, g/cm³
 ρ_o = density, oil, psi/ft or g/cm³
 ρ_{or} = density of reservoir oil, lbm/bbl
 ρ_w = density, water, psi/ft
 σ_L = interfacial tension at laboratory conditions, dyne/cm
 σ_R = interfacial tension at reservoir conditions, dyne/cm
 ϕ = porosity, general, fraction
 ϕ_f = interconnected fracture (effective) porosity, fraction
 ϕ_g = porosity in gas zone, fraction
 ϕ_o = porosity in oil zone, fraction

References

1. *Petroleum Production Handbook*, T.C. Frick (ed.), McGraw-Hill Book Co. Inc., New York City (1962).
2. *Petroleum Engineering Handbook*, H.B. Bradley (ed.), SPE, Richardson, Texas (1987).
3. Cronquist, C.: *Estimation and Classification of Reserves of Crude Oil, Natural Gas, and Condensate*, SPE, Richardson, Texas (2001).
4. Ross, J.G.: "Petroleum Resources Classification and Definitions," *Guidelines for the Evaluation of Petroleum Reserves and Resources*, SPE, Richardson, Texas (2001) 25.
5. McKelvey, V.E.: "Mineral Resource Estimates and Public Policy," *American Scientist* (January–February 1972) **60**, 32.
6. *SPE/WPC Petroleum Reserves Definitions*, SPE, Richardson, Texas (1997).
7. McMichael, C. and Spencer, A.: "Operational Issues," *Guidelines for the Evaluation of Petroleum Reserves and Resources*, SPE, Richardson, Texas (2001) 25.
8. "Society Adopts Proved Reserves Definitions," *JPT* (November 1981) 2213.
9. "Reserves Definitions Approved," *JPT* (May 1987) 576.
10. "Regulation S-X, Rule 4-10," *Financial Accounting and Reporting for Oil and Gas Producing Activities Pursuant to the Federal Securities Laws and the Energy Policy and Conservation Act of 1975*, U.S. SEC, Washington, DC (1975).
11. *SEC Staff Accounting Bulletin: Codification of Staff Accounting Bulletins*, Topic 12 Oil and Gas Producing Activities, A.1. Estimates of Quantities of Proved Reserves, Questions 1–3 U.S. SEC, Washington, DC (19 May 2003).
12. *SEC Staff Accounting Bulletin: Codification of Staff Accounting Bulletins*, Topic 12 Oil and Gas Producing Activities, G. Inclusion of Methane Gas in Proved Reserves, U.S. SEC, Washington, DC (19 May 2003).
13. *SEC Staff Accounting Bulletin: Codification of Staff Accounting Bulletins*, Topic 12 Oil and Gas Producing Activities, A.3.b. Unproved Properties, U.S. SEC, Washington, DC (19 May 2003).
14. Website Release, www.sec.gov/divisions/corpfin/acctdisc.htm, U.S. SEC (21 February 2001).
15. *Reserves of Crude Oil, Natural Gas Liquids and Natural Gas in the United States and Canada as of December 31, 1979*, API, Washington, DC (1980) 34.
16. *Guidelines for Application of Petroleum Reserve Definitions*, second edition, Monograph Series, Soc. of Petroleum Evaluation Engineers, Houston (1998) 1.
17. *A Statistical Study of Recovery Efficiency*, API Bull. D14, second edition, API, Dallas (1984).
18. Fast, C.R., Holman, G.B., and Covlin, R.J.: "The Application of Massive Hydraulic Fracturing to the Tight Muddy 'J' Formation, Wattenberg Field, Colorado," *JPT* (January 1977) 10.
19. Havlena, D.: "Interpretation, Averaging, and Use of the Basic Geological-Engineering Data," *J. Cdn. Pet. Tech.* (October–December 1966) 236.

20. George, C.J. and Stiles, L.H.: "Improved Techniques for Evaluating Carbonate Waterfloods in West Texas," *JPT* (November 1978) 1547.
21. Sneider, R.M. *et al.*: "Predicting Reservoir Rock Geometry and Continuity in Pennsylvanian Reservoirs, Elk City Field, Oklahoma," *JPT* (July 1977) 851.
22. Wilhite, G.P.: *Waterflooding*, Textbook Series, SPE, Richardson, Texas (1986) 3.
23. Missman, R.A. and Jameson, J.: "An Evolving Description of a Fractured Carbonate Reservoir: The Lisburne Field, Prudhoe Bay, Alaska," *Proc.*, 1990 Archie Conference, Houston, 22–25 October, 204.
24. Cobb, W.M. and Marek, F.J.: "Net Pay Determination for Primary and Waterflood Depletion Mechanisms," paper SPE 48952 presented at the 1998 SPE Annual Technical Conference and Exhibition, New Orleans, 27–30 September.
25. Snyder, R.H.: "A Review of the Concepts and Methodology of Determining 'Net Pay,'" paper SPE 3609 presented at the 1971 SPE Annual Meeting, New Orleans, 3–6 October.
26. Determination of Oil and Gas Reserves, Petroleum Soc.-CIM, Calgary (1994).
27. *Venezuela Well Evaluation Conference*, Schlumberger Sorengo, C.A., Caracas (1997).
28. *Productive Low Resistivity Well Logs of the Offshore Gulf of Mexico*, Houston Geological Soc., Houston (1993).
29. *Productive Low Resistivity Well Logs of the Offshore Gulf of Mexico*, D. Moore (ed.), New Orleans Geological Soc., New Orleans (1993).
30. *Hydrocarbon Production from Low Contrast, Low Resistivity Reservoirs, Rocky Mountain and Mid-Continent Regions, Log Examples of Subtle Plays*, E.D. Dolly and J.C. Mullarky (eds.), Rocky Mountain Assn. of Geologists, Denver (1996).
31. Wharton, J.B.: "Isopachous Maps of Sand Reservoirs," *AAPG Bull.* (July 1948) **32**, 7.
32. Dake, L.P.: *The Practice of Reservoir Engineering*, Elsevier Science Publisher, Amsterdam (1994) **59**, 472
33. Elshahawi, H., Fathy, K., and Hiekali, S.: "Capillary Pressure and Rock Wettability Effects on Wireline Formation Tester Measurements," paper SPE 56712 presented at the 1999 SPE Annual Technical Conference and Exhibition, Houston, 3–6 October.
34. Robertson, J.D.: "Seismic Applications," *Guidelines for the Evaluation of Petroleum Reserves and Resources*, SPE/WPC/AAPG, SPE, Richardson, Texas (2001) 93.
35. King, G.: "4-D Seismic Improves Reservoir Management Decisions," *World Oil* (March 1996) 79.
36. Kristiansen, P. and Christie, P.: "Monitoring Foinaven Reservoir: Advances in 4-D Seismic," *World Oil* (November 1999) 71.
37. Hoover, A.R., Burkhart, T., and Flemings, P.B.: "Reservoir and Production Analysis of the K40 Sand, South Timbalier 295, Offshore Louisiana, With Comparison to Time-Lapse (4-D) Seismic Results," *AAPG Bull.* (October 1999) 1624.
38. Ashbaugh, J.P. and Flemings, P.B.: "Dynamic Reservoir Characterization of the ST295 Field (Offshore Louisiana): Reservoir Simulation, Acoustic Modeling, and Time-Lapse Seismic Refines Geologic Model and Illuminates Dynamic Behavior," SEG Workshop, Houston (1999) 5 November.
39. McCain, W.D. Jr.: *The Properties of Petroleum Fluids*, PennWell Publishing Co., Tulsa (1990).
40. Alger, R.P., Luffel, D.L., and Truman, R.B.: "New Unified Method of Integrating Core Capillary —Pressure Data With Well Logs," *SPEFE* (June 1989) 145.
41. Smith, D.: "Predicting a Downip Water Level Using Capillary Pressure Relations," paper presented at the 1990 SPWLA Annual Logging Symposium, Lafayette, Louisiana, 24–27 June.
42. Hawkins, J.M., Luffel, D.L., and Harris, T.G.: "Capillary Pressure Model Predicts Distance to Gas/Water, Oil/Water Contact," *Oil & Gas J.* (18 January 1993) 39.
43. Thomeer, J.H.M.: "Introduction of a Pore Geometrical Factor Defined by the Capillary Pressure Curve," *JPT* (March 1960) 354; *Trans.*, AIME, **219**.
44. Stiles, J.H. Jr. and Mc Kee, J.W.: "Cormorant: Development of a Complex Field," *SPEFE* (December 1991) 427; *Trans.*, AIME, **291**.
45. Hartman, J.A. and Paynter, D.D.: "Drainage Anomalies in Gulf Coast Tertiary Sandstones," *JPT* (October 1979) 1313.

46. Mearns, E. and McBride, J.J.: "Hydrocarbon Filling History and Reservoir Continuity of Oil Fields Evaluated Using $^{87}\text{Sr}/^{86}\text{Sr}$ Isotope Ratio Variations in Formation Water, With Examples From the North Sea," *Petroleum Geoscience* (February 1999) 17.
47. Standing, M.B.: "A Pressure-Volume-Temperature Correlation for Mixtures of California Oils and Gases," *Drill. & Prod. Prac.*, API, Washington, DC (1947) 275.
48. Arps, J.J. and Roberts, T.G.: "The Effect of the Relative Permeability Ratio, the Oil-Gravity and the Solution Gas-Oil Ratio on the Primary Recovery From a Depletion Type Reservoir," *Trans.*, AIME (1955) **204**, 120.
49. Arps, J.J. *et al.*: *Bull. D-14, A Statistical Study of Recovery Efficiency*, API, Washington, DC (1967).
50. Doscher, T.M.: "Statistical Analysis Shows Crude Oil Recovery," *Oil & Gas J.* (29 October 1984) 61.
51. Cronquist, C.: "Volatile Oils: Fluid Characteristics, Reservoir Behavior and Production Facilities," *World Oil* (April 1979) 159.
52. Agarwal, R.G., Al-Hussainy, R., and Ramey, H.J.: "The Importance of Water Influx in Gas Reservoirs," *JPT* (November 1965) 1336; *Trans.*, AIME, **234**.
53. Cronquist, C.: "Determining Recovery From Partial Water Drive Reservoirs," *World Oil* (September 1980) 107.
54. Cronquist, C.: "Turtle Bayou 1936–83: Case History of a Major Gas Field in South Louisiana," *JPT* (November 1984) 1941; *Trans.*, AIME, **277**.
55. Garb, F.A.: "Property Evaluation with Hand-Held Computers: Part 9—Liquid Yield for Depletion Drive Gas Reservoirs and Gas Recovery Factors for Depletion Directed Water Displacement Reservoirs," *Pet. Eng. Intl.* (October 1978) 72.
56. Dake, L.P.: *Fundamentals of Reservoir Engineering*, Elsevier Science Publisher, New York City (1978).
57. Pletcher, J.L.: "Improvements to Reservoir Material Balance Methods," *SPEE* (February 2002) 49.
58. Walsh, M.P.: "A Generalized Approach to Reservoir Material Balance Equations," *J. Cdn. Pet. Tech.* (January 1995) 55.
59. Tehrani, D.H.: "An Analysis of a Volumetric Balance Equation for Calculation of Oil in Place and Water Influx," *JPT* (September 1985) 1664.
60. Havlena, D. and Odeh, A.S.: "The Material Balance as an Equation of a Straight Line," *JPT* (August 1963) 896; *Trans.*, AIME, 228.
61. Havlena, D. and Odeh, A.S.: "The Material Balance as an Equation of a Straight Line—Part II, Field Cases," *JPT* (July 1964) 815; *Trans.*, AIME, **231**.
62. Sills, S.R.: "Improved Material-Balance Regression Analysis for Waterdrive Oil and Gas Reservoirs," *SPEE* (May 1996) 127.
63. Brons, F.: "On the Use and Misuse of Production Decline Curves," *API 801-39E*, API, Dallas (1963).
64. Purvis, R.A.: "Analysis of Production-Performance Graphs," *J. Cdn. Pet. Tech.* (July–August 1985) 44.
65. Arps, J.J.: "Analysis of Decline Curves," *Trans.*, AIME (1945) **160**, 228.
66. Fetkovich, M.J.: "Decline Curve Analysis Using Type Curves," *JPT* (June 1980) 1065; *Trans.*, AIME, **269**.
67. Long, D.R. and Davis, M.J.: "A New Approach to the Hyperbolic Curve," *JPT* (July 1988) 909.
68. Fetkovich, M.J. *et al.*: "Decline-Curve Analysis Using Type Curves—Case Histories," *SPEE* (December 1987) 637; *Trans.*, AIME, **283**.
69. Fetkovich, M.J., Fetkovich, E.J., and Fetkovich, M.D.: "Useful Concepts for Decline Curve Forecasting, Reserve Estimation and Analysis," paper SPE 28628 presented at the 1994 SPE Annual Technical Conference and Exhibition, New Orleans, 25–28 September.
70. Wilson, S.J., Miller, M.R., Frazer, L.C. and Digert, S.A.: "Multiple Trend Forecasting Accounts for Field Constraints," paper SPE 39939 presented at the 1998 SPE Rocky Mountain Regional/Low Permeability Reservoir Symposium and Exhibition, Denver, 5–8 April.
71. Saleri, N.G. and Toronyi, R.M.: "Engineering Control in Reservoir Simulation: Part I," paper SPE 18305 presented at the 1988 SPE Annual Technical Conference and Exhibition, Houston, 2–5 October.

72. Jacks, H.H.: "Forecasting Future Performance," *Reservoir Simulation*, C.C. Mattox and R.L. Dalton (eds.), Monograph Series, SPE, Richardson, Texas (1990) **13**, 99–110.
73. Palke, M.R. and Rietz, D.C.: "The Adaptation of Reservoir Simulation Models for Use in Reserves Forecasting," paper SPE 71430 presented at the 2001 SPE Annual Technical Conference and Exhibition, New Orleans, 30 September–3 October.
74. Richardson, J.G. and Blackwell, R.J.: "Use of Simple Mathematical Models for Predicting Reservoir Behavior," *JPT* (September 1971) 1145; *Trans.*, AIME, **251**.
75. Trewin, N. and Bramwell, M.G.: "The Auk Field, Block 30/16, UK North Sea," *United Kingdom Oil and Gas Fields, 25 Years Commemorative Vol.*, I.L. Abbotts (ed.), Geological Soc. of London, London (1991) 227.
76. Rasor, R.: "Presentation Case—Reservoir Simulation Prediction," SPEE Forum, Soc. of Petroleum Evaluation Engineers, Houston (2000) 31 October–1 November.
77. Zuber, M.D.: "A Guide to Coalbed Methane Reservoir Engineering," Gas Research Inst. (Gas Technology Inst.), Chicago, GRI-93/0293 (1996).
78. Reiss, L.H.: *The Reservoir Engineering Aspects of Fractured Formations*, Editions Technip, Paris (1980).
79. P'an, C.H.: "Petroleum in Basement Rocks," *AAPG Bull.* (October 1982) 1597.
80. Aguilera, R.: "Recovery Factors and Reserves in Naturally Fractured Reservoirs," *J. Cdn. Pet. Tech.* (July 1999) 15.
81. "Gas Production from Fractured Shales: An Overview and Update," *Gas Tips* (June 2000).
82. "United States Fractured Shales Gas Resource Map," Gas Research Inst. (Gas Technology Inst.) (2000) <http://griweb.gastechology.org/pub/content/Jul/200007/11130/resources.html>.
83. National Petroleum Council estimates, Volume III, Devonian Shales (1980).
84. National Petroleum Council Estimate, Volume II, Source and Supply (1992).
85. "1995 National Assessment of United States Oil and Gas Resources," USGS Survey Circular 1118, U.S. Government Printing Office, Washington, DC (1995).
86. Schmoker, J.W.: "Methodology for Assessing Continuous-type (Unconventional) Hydrocarbon Accumulations," *1995 National Assessment of United States Oil and Gas Resources—Results, Methodology, and Supporting Data*, D.L. Gautier, G.L. Dolton, K.I. Takahashi, and K.L. Varnes (eds.), USGS Digital Data Series DDS-30, release 2 (1996).
87. Kuuskraa, V.A. *et al.*: "Barnett Shale Rising Star in Fort Worth Basin," *Oil & Gas J.*, **96**, No. 21 (25 May 1998) 67–76.
88. Williams, P.: "San Juan Basin," *American Oil and Gas Investor* **19**, 6 (1999) 26–34.
89. Decker, D., Coates, J.-M.P., and Wicks, D.: "Stratigraphy, Gas Occurrence, Formation Evaluation and Fracture Characterization of the Antrim Shale, Michigan Basin," GRI, Chicago (December 1992).
90. Decker, A.H., Wicks, D.E., and Coates, J.-M.: "Gas Content Measurements and Log Based Correlations in the Antrim Shale," GRI-93/0293, GRI, Chicago (July 1993) 33–37.
91. Brown, C.A., Erbe, C.B., and Crafton, J.W.: "A Comprehensive Reservoir Model of the Low-Permeability Lewis Sands in the Hay Reservoir Area, Sweetwater County, Wyoming," paper SPE 10193 presented at the 1981 SPE Annual Technical Conference and Exhibition, San Antonio, 5–7 October.
92. Kukul, G.C. *et al.*: "Critical Problems Hindering Accurate Log Interpretation of Tight Gas Sand Reservoirs," paper SPE 11620 presented at the 1983 SPE/DOE Symposium on Low Permeability, Denver, 13–16 March.
93. Spencer, C.W.: "Geologic Aspects of Tight Gas Reservoirs in the Rocky Mountain Region," *JPT* (July 1985) 1308; *Trans.*, AIME, **279**.
94. Witherbee, L.J., Godfrey, R.D., and Dimelow, T.E.: "Predicting Turbidite-Contourite Reservoir Intervals in Tight Gas Sands: A Case Study From the Mancos B Sandstone," paper SPE 11609 presented at the 1983 SPE Symposium on Low Permeability, Denver, 13–16 March.
95. Lewis, D.J. and Perrin, J.D.: "Wilcox Formation Evaluation: Improved Procedures for Tight Gas-Sand Evaluation," *JPT* (June 1992) 724.
96. Kazemi, H.: "Low-Permeability Gas Sands," *JPT* (October 1982) 2229.
97. Veatch, R.W. Jr.: "Overview of Current Hydraulic Fracturing Design and Treatment Technology—Part 1," *JPT* (April 1983) 677.

98. Robinson, B.M., Holditch, S.A., and Lee, W.J.: "A Case Study of the Wilcox (Lobo) Trend in Webb and Zapata Counties, TX," *JPT* (December 1986) 1355; *Trans.*, AIME, **281**.
99. Lewis, D.J. and Perrin, J.D.: "Wilcox Formation Evaluation: Improved Procedures for Tight Gas-Sand Evaluation," *JPT* (June 1992) 724.
100. Stewart, P.R.: "Low-Permeability Gas Well Performance at Constant Pressure," *JPT* (September 1970) 1149.
101. Brown, C.A., Erbe, C.B., and Crafton, J.W.: "A Comprehensive Reservoir Model of the Low-Permeability Lewis Sands in the Hay Reservoir Area, Sweetwater County, Wyoming," paper SPE 10193 presented at the 1981 SPE Annual Technical Conference and Exhibition, San Antonio, Texas, 5–7 October.
102. Hale, B.W.: "Analysis of Tight Gas Well Production Histories in the Rocky Mountains," *SPE* (July 1986) 310; *Trans.*, AIME, **281**.
103. Hale, B.W.: "A Type Curve Approach to Reserves for the Big Piney Gas Field," paper SPE 9840 presented at the 1981 SPE/DOE Symposium, Denver, 27–29 May.
104. Harlan, L.E.: "A Method for Determining Recovery Factors in Low-Permeability Gas Reservoirs," paper SPE 1555 presented at the 1966 SPE Annual Meeting, Dallas, 25 October.
105. Cipolla, C.L. and Kyte, D.G.: "Infill Drilling in the Moxa Arch: A Case History of the Frontier Formation," paper SPE 24909 presented at the 1992 SPE Annual Technical Conference and Exhibition, Washington, DC, 4–7 October.
106. Briggs, P.J. *et al.*: "Development of Heavy Oil Reservoirs," *JPT* (February 1988) 206.
107. Meyer, R.F. and Mitchell, R.W.: "A Perspective on Heavy and Extra Heavy Oil, Natural Bitumen, and Shale Oil," paper presented at the 1987 Twelfth World Petroleum Congresses, Houston.
108. Martinez, A.R.: "The Orinoco Oil Belt, Venezuela," *J. of Petroleum Geology* (1987) **10**, 125.
109. Adams, D.M.: "Experiences With Waterflooding Lloydminster Heavy-Oil Reservoirs," *JPT* (August 1982) 1643; *Trans.*, AIME, **273**.
110. Dusseault, M.: "Cold Production and Enhanced Oil Recovery," *J. Cdn. Pet. Tech.* (November 1993) 16.
111. Maini, B.B., Sarma, H.K., and George, A.E.: "Significance of Foamy-Oil Behaviour in Primary Production of Heavy Oils," *J. Cdn. Pet. Tech.* (1993) **32**, 6.
112. Maini, B.: "Foamy-Oil Flow," *JPT* (October 2001) 54.
113. Kumar, R., and Pooladi-Darvish, M.: "Solution-gas Drive in Heavy Oil: Field Prediction and Sensitivity Studies with Low Gas Relative Permeability," *J. Cdn. Pet. Tech.* (March 2002) 26.
114. Sulaiman, S. and Bretherton, T.A.: "Thin Oil Development in the Bream Field," paper SPE 19493 presented at the 1989 SPE Asia-Pacific Conference, Sydney, 13–15 September.
115. Seines, K., Lien, S.C., and Haug, B.T.: "Troll Horizontal Well Tests Demonstrate Large Production Potential From Thin Oil Zones," *SPE* (May 1994) 133; *Trans.*, AIME, **297**.
116. Irrgang, H.H.: "Evaluation and Management of Thin Oil Column Reservoirs in Australia," *APEA J.* (1994) **1**, 64.
117. van Lookeren, J.: "Oil Production From Reservoirs With an Oil Layer Between Gas and Bottom Water in the Same Sand," *JPT* (March 1965) 354; *Trans.*, AIME (1965) **234**, 354.
118. Sognesand, S.: "Reservoir Management of the Oseberg Field During Eight Years' Production," paper SPE 38555 presented at the 1997 SPE Offshore Europe Conference, Aberdeen, 9–10 September.
119. Muskat, M. and Wyckoff, R.D.: "An Approximate Theory of Water-Coning in Oil Production," *Trans.*, AIME (1935) **114**, 144.
120. Chaney, P.E. *et al.*: "How To Perforate Your Well To Prevent Water and Gas Coning," *Oil & Gas J.* (7 May 1956) 108.
121. Chierici, G.L., Ciucci, G.M., and Pizzi, G.: "A Systematic Study of Gas and Water Coning by Potentiometric Models," *JPT* (August 1964) 923; *Trans.*, AIME, **231**.
122. Bournazel, C. and Jeanson, B.: "Fast Water-Coning Evaluation Method," paper SPE 3628 presented at the 1971 SPE Annual Meeting, New Orleans, 3–6 October.
123. Kuo, M.C.T. and DesBrisay, C.L.: "A Simplified Method for Water Coning Predictions," paper SPE 12067 presented at the 1983 SPE Annual Technical Conference and Exhibition, San Francisco, 5–8 October.
124. Kuo, M.C.T.: "Correlations Rapidly Analyze Water Coning," *Oil & Gas J.* (October 1989) 77.

125. Hoyland, L.A., Papatzacos, P., and Skjaeveland, S.M.: "Critical Rate for Water Coning: Correlation and Analytical Solution," *SPE* (November 1989) 495.
126. Earlougher, R.C. Jr.: *Advances in Well Test Analysis*, Monograph Series, SPE, Richardson, Texas (1977) 5.
127. Duggan, J.O.: "The Anderson 'L'—An Abnormally Pressured Gas Reservoir in South Texas," *JPT* (February 1972) 132.
128. Harville, D.W. and Hawkins, M.F.: "Rock Compressibility and Failure as Reservoir Mechanisms in Geopressured Gas Reservoirs," *JPT* (December 1969) 1528.
129. *Glossary of Geology*, Gary, M., McAfee, R. Jr., and Wolf, C. (eds.), American Geological Inst., Washington, DC (1972).
130. Bernard, W.J.: "Reserves Estimation and Performance Prediction for Geopressured Gas Reservoirs," *J. of Petroleum Science and Engineering* (1987) 15.
131. Wallace, W.E.: "Water Production from Abnormally Pressured Gas Reservoirs in South Louisiana," *JPT* (August 1969) 969.
132. Bourgoyne, A.T.: "Shale Water as a Pressure Support Mechanism in Gas Reservoirs Having Abnormal Formation Pressure," *J. of Petroleum Science and Engineering* (1990) 305.
133. Chierici, G.L. *et al.*: "Water Drive From Interbedded Shale Compaction in Superpressured Gas Reservoirs—A Model Study," *JPT* (June 1978) 93.
134. Ramagost, B.P. and Farshad, F.F.: "*P/Z* Abnormally Pressured Gas Reservoirs," paper SPE 10125 presented at the 1981 SPE Annual Technical Conference and Exhibition, San Antonio, Texas, 5–7 October.
135. Geertsma, J.: "The Effect of Fluid Pressure Decline on Volumetric Changes of Porous Rocks," *Trans., AIME* (1957) **210**, 331.
136. Fatt, I.: "Pore Volume Compressibilities of Sandstone Reservoir Rocks," *Trans., AIME* (1958) **213**, 362.
137. van der Knaap, W.: "Nonlinear Behavior of Elastic Porous Media," *Trans., AIME* (1959) **216**, 179.
138. Dobrynin, V.M.: "Effect of Overburden Pressure on Some Properties of Sandstone," *SPEJ* (December 1962) 360; *Trans., AIME*, **225**.
139. Chierici, G.L., Pizzi, G., and Ciucci, G.M.: "Water Drive Gas Reservoirs: Uncertainty in Reserves Evaluation From Past History," *JPT* (February 1967) 237; *Trans., AIME*, **240**.
140. von Gonten, W.D. and Choudhary, B.K.: "The Effect of Pressure and Temperature on Pore Volume Compressibility," paper SPE 2526 presented at the 1969 SPE Annual Meeting, Denver, 28 September–1 October.
141. Teeuw, D.: "Prediction of Formation Compaction From Laboratory Compressibility Data," *SPEJ* (1971) 263.
142. Newman, G.H.: "Pore-Volume Compressibility of Consolidated, Friable, and Unconsolidated Reservoir Rocks Under Hydrostatic Loading," *JPT* (February 1973) 129.
143. Jones, S.C.: "Two-Point Determinations of Permeability and PV vs. Net Confining Stress," *SPEFE* (March 1988) 235.
144. Yale, D.P. *et al.*: "Application of Variable Formation Compressibility for Improved Reservoir Analysis," paper SPE 26647 presented at the 1993 SPE Annual Technical Conference and Exhibition, Houston, 3–6 October.
145. Hall, H.N.: "Compressibility of Reservoir Rocks," *Trans., AIME* (1953) **204**, 309.
146. Bernard, W.J.: "Reserves Estimation and Performance Prediction for Geopressured Gas Reservoirs," *J. of Petroleum Science and Engineering* (1987) 15.
147. Yale, D.P. *et al.*: "Application of Variable Formation Compressibility for Improved Reservoir Analysis," paper SPE 26647 presented at the 1993 SPE Annual Technical Conference and Exhibition, Houston, 3–6 October.
148. Dhir, R., Dern, R.R., and Mavor, M.J.: "Economic and Reserves Evaluation of Coalbed Methane Reservoirs," paper SPE 22024 presented at the 1991 SPE Hydrocarbon and Evaluation Symposium, Dallas, 11–12 April.
149. Keith, D.R., Wilson, D.C., and Gorsuch, D.P.: "Reserves Definitions—An Attempt at Consistency," paper SPE 15865 presented at the 1986 SPE European Petroleum Conference, London, 20–22 October.

150. Rose, P.R.: *Risk Analysis and Management of Petroleum Exploration Ventures*, AAPG, Tulsa (2001).
151. Huffman, C.H. and Thompson, R.S.: "Probability Ranges for Reserves Estimates From Decline Curve Analysis," paper SPE 28333 presented at the 1994 SPE Annual Technical Conference and Exhibition, New Orleans, 25–28 September.
152. Jochen, V.A. and Spivey, J.P.: "Probabilistic Reserves Estimation Using Decline Curve Analysis With the Bootstrap Method," paper SPE 36633 presented at the 1996 SPE Annual Technical Conference and Exhibition, Denver, 6–9 October.
153. Gaston, H.: "Pitfalls in Oil and Gas Evaluations," presented at 1992 SPEE Annual Convention, Jackson Hole, Wyoming, 15 June 1992.
154. Mistrot, Gus A.: *Reserves Estimating—Common Errors and How To Avoid Them*, SPE Short Course, SPE, Richardson, Texas (1998).

SI Metric Conversion Factors

acre	×	4.046 856	E - 01	= ha
acre-ft	×	1.233 489	E + 03	= m ³
°API		141.5/(131.5 + °API)		= g/cm ³
bbl	×	1.589 873	E - 01	= m ³
°F		(°F - 32)/1.8		= °C
ft	×	3.048*	E - 01	= m
ft ³	×	2.831 685	E - 02	= m ³
lbm	×	4.535 924	E - 01	= kg
mile	×	1.609 344*	E + 00	= km
psi	×	6.894 757	E + 00	= kPa
psia	×	6.894 757	E + 00	= kPa
square mile	×	2.589 988	E + 06	= m ²
ton	×	9.071 847	E - 01	= Mg

*Conversion factor is exact.

Chapter 19

Valuation of Oil and Gas Reserves

D.R. Long, Long Consultants Inc.

19.1 Introduction

This chapter describes the use of a reserves estimate to prepare an economic evaluation and perhaps then place a value on the reserves. This chapter often refers to a document titled *Perspectives on the Fair Market Value of Oil and Gas Interests*¹ published by the Society of Petroleum Evaluation Engineers (SPEE) in the spring of 2002. In this chapter, that document is referred to as the SPEE FMV document. To value reserves, the nature of the ownership must be considered. Reserves ownership is usually derived from contractual agreements that specify the obligations of the parties to those agreements for the payment of costs and the sharing of revenues. These agreements often include specific commitment obligations such as the drilling of wells. A common arrangement for such contracts is the oil and gas lease. Another common contractual structure is the production-sharing arrangement. Appendix A, which describes common types of oil and gas property interests, is from the SPEE FMV document.¹

[Sec. 19.8](#) discusses fair market value (FMV). While an FMV estimate is often not the main reason an economic evaluation is prepared, it is useful to keep in mind that it may be used for such a purpose. Like the estimation of reserves, the preparation of an economic evaluation has subjective elements. If the evaluation, inclusive of the reserves estimates and production schedules, is prepared in a manner anticipating an FMV estimate as the goal, the objective evaluator will be inclined to use appropriate judgment. One must be cautious, however, and be mindful of the applicable reserves definition. For example, a reserves definition that might be used for property acquisition might not meet the reporting requirements of the U.S. Securities and Exchange Commission (SEC).

The use of the word “valuation” in the title of this chapter is a carryover from the first handbook.² J.J. Arps wrote the valuation chapter, and reference to his name in this chapter is generally the same as a reference to the chapter he authored in that handbook. Arps’ use of the term valuation seemed to have a relatively narrow scope. Valuation referred to the processes for the determination of FMV and embraced what he called an “analytical appraisal” method, which involved present worth discounting to address the time value of money. There are numerous references and comparative statements in this chapter about these methods because, despite a few variations that have occurred in the interim, enough is the same that presentation of the historical perspective is useful. Arps also included a section on “different concepts of valuation.” Those methods have been discarded.

The analytical valuation methods embraced by Arps² are still in use, but today's business environment is quite different. Arps' chapter was for use only in the U.S. domestic market, but the marketplace has expanded vastly. Interest and discount rates are considerably higher, and there have been significant changes in the U.S. federal tax code. U.S. federal tax rates are lower now than in 1962, but other aspects of the law also have changed.

In 1962, the primary buyers for oil and gas properties were major oil and gas companies. Sellers were successful wildcatters or small oil and gas companies called independents. Today, the independents are the buyers and the majors are the sellers. There are many more independents today, and the major oil companies are undergoing consolidation. The marketplace for oil and gas properties involves a much greater number of transactions and is more competitive.

The properties tend to be different from those familiar to Arps in 1962. Today, gas reserves are much more likely to be the major source of projected future income. Ownership is more fractionated. In addition, discussion is much more likely to be about the rate of decline than about how many more years the rate will remain constant. Production rates are much more likely to be governed by the capacity of wells to produce than by artificial restraint imposed by regulation. Constant price projections are unlikely because there are futures markets for both oil and gas. The value offered for properties is more likely to include a significant component for reserves involving higher degrees of uncertainty.

One of the most significant changes in the oil and gas reserves evaluations is the use of the computer. In 1962, most cash flow projections were tabulated by hand on large ledger sheets. After plotting historical production curves by hand, forecasting was done by field to reduce the computational load. Modern petroleum economic evaluation software has eased laborious procedures tremendously. Forecasts are often done on a well-by-well basis, and sensitivity studies are much easier. The most valuable attributes of petroleum economic software are the scheduling tools and the summarization capabilities.

Despite the changes since 1962, some things remain the same. The offering price of the buyer is still very sensitive to the cost of money. The buyer's intent is to derive some measure of profit. No matter what form that profit takes in the buyer's figuring of the offering price, it must be of a sufficient magnitude to cover risks inherent in the industry. Another factor that remains the same is that the U.S. still has a federal income tax.

To facilitate meaningful discussion, some basic definitions need to be understood.

- **Oil and Gas Reserves Study**—A study of geologic and other information for estimating oil and gas reserves within the scope of a specified set of definitions. The definitions will usually include reserves classed as proved and will often categorize unproved reserves. Unproved reserves classes include probable and possible reserves. If reserves are estimated to support an economic evaluation, the reserves estimator will generate or describe associated schedules of future production. For a description of the proved, probable, and possible reserves classification system, see the chapter on estimating oil and gas reserves in this section of the *Handbook*.

- **Oil and Gas Reserves Economic Evaluation**—A report, often inclusive of an oil and gas reserves study and usually prepared by or under the direction of a petroleum engineer, that presents schedules of future net cash flow and discounted net cash flow based on the reserves and production schedules from an oil and gas reserves study. The reserves classes of the reserves study can be expected to flow through to the summary levels of the economic evaluation because such classifications are a tool for the assessment of uncertainty.

- **Valuation**—The process of determining value, whether it be for estimating FMV or for another purpose and whether it be derived with discounted cash flow projection methods or with other methods.

In this chapter, the term "reserves report" refers, sometimes collectively and at other times individually, to both a reserves study and an economic evaluation of reserves. The meaning should be clear from the context of the discussion. Each of the processes has specific obliga-

tions for objectivity and disclosure regarding methods. SPEE, an organization sometimes referred to as a sister organization to SPE but with no official relation, recently developed a set of Recommended Evaluation Practices (REPs).³ These REPs and other information about SPEE, which is a strong promoter of ethical standards, are available at www.spee.org. SPEE also publishes *Guidelines for the Application of Petroleum Reserves Definitions*.⁴ Sec. 19.8 includes excerpts from the SPEE FMV document,¹ which similarly presumes the preparation of an oil and gas reserves economic evaluation as described here.

In the following sections, the term valuation is not limited to use with procedures purporting to represent, or necessarily closely tied to, FMV. For example, the U.S. SEC stipulates the use of a 10% discount rate for certain financial reporting purposes. This must be considered a valuation process, but the result is primarily for comparative purposes and is not represented as FMV. A calculation to determine the collateral value of a property or properties (the loan value) would be considered a valuation but would logically be less than FMV.

The term “appraisal” is not used beyond this introduction. Appraisal was a term used by Arps.² It is most commonly used today with real estate. It has specific connotations that may not be consistent with methods used in the valuation of oil and gas reserves. Real estate appraisals are commonly made with comparative sales principles. The principle valuation techniques described in this chapter are based on anticipations of future revenue and conceptually bear little resemblance to the common real estate appraisal processes. The term appraisal is avoided in connection with the valuation of oil and gas reserves. There is a place in oil and gas valuation work for the comparative sale method.

A common application of valuation methods is to determine value for taxation. Jurisdictions will usually specify procedures somewhat differently than those contained in this chapter. Those differences often involve the way the cash flow projections are prepared. For example, it is sometimes specified that the valuation procedure ignore anticipated taxes to be levied by the taxing authority requiring the valuation. The taxing authority might specify a discount rate or method for arriving at the discount rate to be used in determining value. The evaluator should be knowledgeable about local practices.

The valuation procedures discussed in this chapter are classed properly as methods for the valuation of underlying assets, as opposed to methods for the valuation of a company. The value of a company is some combination of a perception of how well the organization’s management will manage its assets for growth (or otherwise) and its debts and other liabilities. Individual property assets are, however, often more valuable when combined than when viewed separately.

In recognition of the international makeup of today’s SPE, it is appropriate to write from an exclusively international perspective. Oil and gas companies around the world with roots in capitalistic societies operate on the basis of an incentive for profit from operation and a share of either the volume of oil and gas sold or some benefit from that sale. In the U.S., fractional interests are usually of a nature described in Appendix A. In other parts of the world, it is more common for the operator of the property to receive revenue on the basis of a more complex sharing arrangement made with a country’s national government or other governmental faction. This chapter does not delve into the complexities of these sharing arrangements. The valuation circumstances described are generally specific to properties located in the U.S. An understanding of the principles should allow portability for universal application.

19.2 The Need for Economic Evaluations

Valuations of oil and gas properties are needed for many of the same reasons appraisals are needed for homes, cars, jewelry, or any other assets. Lenders require some type of valuation when assets are used as collateral for a loan. Taxes are often assessed on the basis of property value. Property values have a bearing on rates for insurance policies and settlements after loss, damage, or foreclosure. Economic evaluations are seldom made simply for curiosity. In most

cases, they are needed for some business reason. Here is a listing of reasons economic evaluations are needed in the oil and gas industry:

- **Project Evaluation**—Proposals to drill wells, set platforms, or otherwise provide for the facilities required to produce or enhance the production of oil and gas require economic justification before implementation.

- **Prioritize Opportunities**—When presented with a set of investment opportunities, all of which pass certain minimum criteria and assume some restraint on available capital, discussion and theorization are never exhausted during the selection process. Economic analysis is part of the process.

- **Acquisition and Divestiture**—Buyers and sellers of properties need valuations to prepare for acquisition and divestiture transactions. The buyer's need for an evaluation is obvious. Sellers with a compulsion to seek the highest compensation usually prepare an economic evaluation to gauge the adequacy of an offer.

- **Financing**—Loans by banks or other institutions are directly collateralized by a company's property portfolio or a specified group of properties.

- **Taxation**—Governmental entities from the Internal Revenue Service (IRS) to local taxing authorities such as school districts want money, and the taxes are often determined on the basis of the value of the reserves.

- **Securities Laws**—In the U.S., the SEC requires the reporting of reserves information, which mainly comes from oil and gas reserves and economic evaluations.

- **Legal Settlements**—Some of the most dramatic arguments over property values occur in settlement proceedings involving foreclosure. Foreclosure is often associated with a condemnation case wherein lands are rendered unusable for oil and gas development because of confiscation for a public use that covers a wide area, such as a new water reservoir or recreational lake. Alternatively, a company going through bankruptcy proceedings might convince the court that creditors would be better served under a plan in which the company retained the interest. At one time, there were many court cases involving take-or-pay provisions of contracts between producers and pipeline companies.

- **Allocation of Values**—Value allocation can be part of legal settlements when issues are fundamentally divisive, but allocation is often an element when parties are trying to work together to promote common interests. Unitization is the process in which groups of small properties are united into a larger unit with interest holders of the smaller properties trading their interests for a smaller fraction of the new unit. Sometimes the process is the reverse and involves the distribution of interests. Either way, economic valuation is usually part of the process.

19.3 Evaluation Methods

19.3.1 Deterministic Cash Flow. The primary method of evaluation discussed in this chapter is the deterministic cash flow method. Projected schedules of quantities of reserves from a deterministic reserves study projected in selected future time frames (usually calendar years) are displayed in the results, but computations are often made monthly. Schedules of future prices and costs are projected for the same time frames. Volumes are multiplied by prices, and costs are deducted to estimate future net revenue (FNR). Present worth calculations to factor in the time value of money are applied to the projected cash flow stream, and the results are reported. A table presenting a suite of present worth values over a range of discount rates is usually included. Individual projections are usually made by well or ownership entity. Each projection is classed in a reserves category (i.e., proved, probable, or possible) and more specific subclasses are common. The results are summarized at the reserves category level.

This valuation procedure is based on the methods used to estimate reserves in the chapter on the estimation of oil and gas reserves in this section of the *Handbook*. Within the limits of the reserves category definitions, the parameters used in the estimation of reserves are general-

ly average values. In the case of proved reserves, the results of the calculation are perceived to be best estimates. In the case of probable and possible reserves categories, the best estimate perception is inherently qualified with the perspective of “if they exist at all.” Probable and possible reserves quantities have not been adjusted for risk.

19.3.2 Decision Trees. Decision tree analysis is a very useful tool to value estimated reserves deterministically. The result is a calculation of expected value or a range of discrete values. [Sec. 19.6](#) illustrates this principle simply. The chapter on risk analysis and decision making in the Emerging and Peripheral Technologies section of this *Handbook* is a must-read chapter in connection with the application of the principles discussed here. Even if the methods are not physically used, the perspectives offered by both decision tree and Monte Carlo simulation must be considered. The chapter on general economics in the General Engineering section of this *Handbook* also presents a perspective on the use of decision trees for analysis.

19.3.3 Sensitivity Analysis. In this procedure, variables in a deterministic analysis are modified and results are recalculated to check the effect on the economic calculation. The results might be presented on a chart, or they might be expressed in a manner such as a one-dollar reduction in the projected gas prices reduces the FNR by 20%. The use of this type of procedure with decision trees has been a traditional evaluation tool with deterministic reserves valuation procedures.

19.3.4 Monte Carlo Simulation. Monte Carlo simulation is a method in which a frequency distribution representing what is perceived to be the full range of possible values for parameters is substituted for the single average values, instead of the use of single-value averages or estimates for parameters, as in a deterministic calculation. The frequency distribution for a parameter, such as porosity, might be shaped in a number of ways. Bell shapes, indicating a normal distribution, or triangular shapes are common. The value at the peak of the distribution’s shape is the most likely value (the mode), and the higher values to the right and lower values to the left are defined as less likely. See the chapter on risk analysis and decision making in the Emerging and Peripheral Technologies section and the chapter on general economics in the General Engineering section of this *Handbook*.

In the case of oil and gas reserves economic evaluation, all the parameters used in the estimation of reserves quantities (such as porosity and water saturation) and the additional variables introduced in the economics of the evaluation process (such as prices, costs, and sometimes timing) are often represented as probability distributions. If a parameter, such as oil price, is locked into a contract, there might be no reason to assign a distribution to that parameter unless the model is intended to consider the default of a contracting party. The simulator is then allowed to run through what are often thousands of iterations. At each iteration, the simulator selects a value for each parameter from the frequency descriptions and computes and stores results. Because of the way the distributions are defined and the way the simulator takes its samples, the values for the individual parameters from the distributions that are closer to the mode value are selected more often. Occasionally, but not often, the simulator will select values at the extremes of the distributions. The method of sampling the described distributions is a math problem of its own.

A Monte Carlo simulator is not a numerical reservoir simulator. It is not a model of the depletion process of a reservoir. In numerical reservoir simulators, the reservoir is characterized in discrete segments and those segments are assigned values of porosity, permeability, fluid saturation, and pressure. The rocks and fluid properties are characterized, and the model is run most often with the intent of mathematically replicating the physical behavior of pressure and fluid flow within the formation during reservoir depletion or enhanced-recovery process. Input to a Monte Carlo simulation will require distributions for expected production rates and recov-

ery factors. Those distributions might be determined with the aid of a reservoir simulator, but it is not expected (today) that the software be linked or integrated.

All the Monte Carlo generated results of reserves and cash flow projection would be incomprehensible; therefore, summary results, selected by the modeler, are reported. Output distributions often include only reserves quantities in total, FNR, and present worth values at a few discount rates. The results represent calculated distributions of expectations for reserves, FNR, and present worth (discounted FNR) at one or more discount rates. Depending on how the model is constructed, it may or may not be possible to distinguish between reserves and revenues derived from areas of the reservoir categorized (deterministically) as proved, probable, or possible.

Any (deterministic) model built in a spreadsheet can be converted to a Monte Carlo model by replacing some of the input values with probability distributions. Conversely, all the errors and pitfalls that might cause a deterministic model to lead to a false indication of value will similarly affect a Monte Carlo simulation. The construction of a Monte Carlo simulation model requires all the work and care that goes into a deterministic model and more.

19.3.5 Real Options. As applied to the evaluation of oil and gas reserves and associated opportunities, real options analysis is a new concept. In this *Handbook*, the use of option theory for the valuation of real options is mentioned in the chapter on risk analysis and decision making in the Emerging and Peripheral Technologies section and in the chapter on petroleum economics in the General Engineering section. Several SPE technical papers have addressed the subject in recent years.⁵⁻¹¹ Financial analysts use option-pricing models (OPMs) to value puts and calls on stocks. These stock options to sell or purchase at a specified price, at or before some specified time, always have some value of zero or greater. They are never negative because the option may be allowed to expire with no additional consequence to the holder. After the option is obtained, there is no further expectation of the possibility of financial loss. The value of the financial option stems from the opportunity to exercise the option immediately, plus the speculative potential that it can be held and exercised in the future for a greater financial gain. OPMs for valuing financial options consider the current stock price, the strike or exercise price associated with the particular option, the risk-free interest rate, the time to maturity of the option, and the variance in the stock price.

Real options represent investment opportunities outside the stock market that have some resemblance to stock options. The option to buy production from a lease in a future specified month at a specified price is essentially identical to a stock option. Most real options are not so ideal in nature and are often extremely complicated. Real options usually are not structured like the previous example, in which someone has contracted to purchase production. Real options are perhaps better thought of in oil and gas industry terms as anticipated opportunities and/or alternatives. Real options are more like the decisions we make in our everyday lives.

In most circumstances, real options will not have a specific exercise date, and many real options involve liability such that their value has the potential to be negative at a future date. The time frame associated with real options may be very long. Real option valuation (ROV) involves the application of the methods derived for the valuation of stock options to the valuation of real options. Real options that are perceived to be of value often revolve around management's perceived future opportunity to make an intelligent decision on the basis of the circumstances existing when the decision is made (i.e., an optional course in a future oil and gas property management decision).

In an attempt to acquire an oil and gas property, whether producing or not, many attach an additional value to being the operator. Sometimes that additional value has to do with cash flow projections and the opportunity to receive income from partners as overhead compensation [Council of Petroleum Accountants Soc. (COPAS) charges]. Perhaps more often, the

additional value attached to being operator has to do with a greater degree of control. The operator is able to exercise options, and that flexibility has value. The operator has more real options than the nonoperator does.

In attempting an acquisition in a competitive market, incremental value frequently is added in recognition that the acquirer will have specific opportunities, in the future, to deviate from and optimize the exploitation plan on the basis of anticipated future events and new information or technology that will become available. It is unlikely that either the deterministic reserves evaluator or the Monte Carlo modeler has made an exhaustive accounting for all possible opportunities. The details behind all possible future opportunities cannot be fully anticipated. ROV is a tool that might be useful for quantifying such potential incremental value.

When considering an acquisition, future potential opportunities sometimes will not be of any specific nature. A common incentive behind oil and gas properties acquisition is the experience that with ownership there is additional value often attributed to serendipity. Perhaps real option analysis could be of assistance in quantifying such value. The use of option theory to quantify oil and gas industry investment opportunities is not a widely accepted method at this time.

19.3.6 Rules of Thumb, Yardsticks, and Comparative Sales. A number of “unit value processes” have been referred to as evaluation methods, but they are more properly described as screening tools. As a comparative measure between transactions, the price paid per barrel of reserves is often computed. Because most transactions involve reserves of both oil and gas in inconsistent proportions, a value per equivalent barrel is often computed, which necessitates the application of a relationship of equivalency between a thousand cubic feet of gas and a barrel of oil. The value of a thousand cubic feet of gas can easily vary over a broad range (more than 20%, often much more) only on the basis of quality issues, exclusive of transportation costs related to location or cost of production or processing to make marketable. Oil has its own issues, of which quality is only one, but the equivalency issue is only the beginning of the problem with trying to use unit value methods as a means of valuation. Such methods make no allowance for the timing or cost of recovery, there is no provision for transportation or other cost to market the production, and there is no recognition of what capital might be required to accomplish the recovery.

There is nothing wrong with making these comparisons. They are of interest, and sometimes the questions raised expose errors or facts that have not been, but should be, disclosed. If there is a comparative method that helps you become comfortable with the result of a valuation, use it. If it exposes a weakness in the valuation, fix the valuation.

Sometimes there are attempts to value oil and gas interests on a multiple of current income with the current income rate expressed in dollars per month or dollars per year. The value approximation might be expressed as 3 years or 36 months at current. The number of potential flaws in this type of valuation are so numerous and varied that an attempt to initiate a list seems futile. There are circumstances that require a determination of value in which the time and effort required is not warranted for even a minimum effort to generate a cash flow projection. Given a general knowledge of the character of the reserves and knowledge of valuation results of other properties of somewhat similar character, the multiple of current income approach may be the best of bad alternatives. In such circumstances, the income rate multiple might be selected on the basis of analogy with the valuations of other properties thought to be similar in character but for which a more rigorous valuation procedure has been appropriate.

Another valuation method is the use of the comparative sale. This is often the only practical tool and is particularly useful. Unlike the real estate market, it is usually impossible to locate a suitable basis for the comparison. The comparative sale method relies on the use of analogy to infer value. It is easy for the technique to be flawed, unless the valuation is done with complete understanding and with great care. For instance, it is common for the purchaser

of an interest to attach an element of value that is not known to the observer. This attachment of added value occurs with the greatest frequency when small interests are traded but is not uncommon with transactions of any size. SPEE's FMV document labels these added values "strategic" values. An industrial user, for example, might purchase a fractional interest in a property near one of its facilities to provide an emergency fuel source in the event of a cutoff of its regular supply; therefore, it might pay a premium price for that interest. Given that the industrial user's needs are satisfied, someone valuing other interests in the same or nearby property could be mistaken in using that transaction as an analog. The SPEE FMV document suggests that the best use of comparative sale methods for oil and gas interests is in the valuation of nonproducing properties, but it points out that even then the process is more complicated than in the real estate business. It is not intended to imply that the use of the comparative sale method in the real estate market is easy, it is just much more difficult (perhaps less certain is a better perspective) when the value of minerals comes into play. Garb¹² discusses a variety of valuation methods, and his article is recommended reading.

19.4 The Nature of Reserves Reports and Discounted Cash Flow Schedules

While seldom listed as the preferred method by agencies requiring valuations (such as the U.S. IRS), the most practical valuation method for oil and gas properties is usually based on the expectations of future income. Reserves estimates and projections of future rates of production are used with expectations for oil and gas prices, items of burden, and costs to compute estimates, usually tabulated by calendar year, of future cash flow. [Table 19.1](#) presents the presentation form of the results of that calculation. Sometimes the form for the presentation is in greater detail, which results in the information being stacked on the page with the lines representing the calendar year period repeated two or three times. For valuation purposes, the projected cash flow stream is then analyzed in a variety of manners. [Table 19.1](#) represents a projection for a single producing property in which the only production stream is oil. In most cases, a valuation is based on a summary level cash flow in which projected economics are derived from the expectation for the sale of produced oil, gas, and other substances such as sulfur. [Table 19.1](#) illustrates certain elements to set the stage for later discussion.

[Table 19.1](#) contains the results of a reserves and cash flow projection. Col. 1 indicates the time intervals associated with the individual lines. The intervals sometimes are indicated by their ending month (with the beginning of each interval being the end of the previous one), but the times are indicated by calendar year in [Table 19.1](#). In [Table 19.1](#), the beginning of the first interval is as of 1 September 2001. Col. 2 presents the full well stream (commonly referred to as the gross or $\frac{\%}{8}$) production quantity schedule from the reserves report. (It is not production; it is a forecast of production. Terminology and proper expression in the economic evaluation business is a common problem.¹³) Col. 3 gives the production quantity schedules netted to the interest being evaluated by multiplying the gross quantities by the fractional revenue interest. The interest fractions will be displayed, unless the page is a summary. The revenue (income) interest is commonly less than the working (expense) interest because of royalty burdens or other sharing arrangements. Col. 4 presents the projected oil price schedules, which is projected to escalate in this example. Col. 5 is the product of the net oil quantity times the oil price. Col. 6 represents items of deduction for local taxes, and Col. 7 shows deductions for operation costs. Col. 8 presents capital cost (none is scheduled in this example), which is another deduction item. The values in Col. 9 represent the time interval's summary of revenue less items of deduction and the result of the net cash flow projection, which is computed by subtracting Cols. 6, 7, and 8 from Col. 5. Various items of identification and information are also presented. This identification information should include identification of the well or forecast entity and the reserves category. The present worth suite is also displayed. In [Table 19.1](#), it is in the bottom right corner and is presented with discount rates from zero to 100%. Cols. 11 through

TABLE 19.1—PRODUCTION FORECAST AND ECONOMIC CALCULATION DEMONSTRATING PRESENT WORTH DISCOUNTING AS OF 1 SEPTEMBER 2001

1	2	3	4	5	6	7	8	9	10	11	12	13	14
Year	Oil Gross (thousand bbl)	Oil Net (thousand bbl)	Price (\$/bbl)	Net Operating Revenue (U.S. \$ thousand)	Local Taxes (U.S. \$ thousand)	Lease Operating Expenses (U.S. \$ thousand)	Capital (U.S. \$ thousand)	Net Revenue (U.S. \$ thousand)	Cumulative Net Revenue (U.S. \$ thousand)	Time to Midpoint of Period (years)	12% Discount Factor	12% Discounted Present Worth (U.S. \$ thousand)	Cumulative 12% Discounted Present Worth (U.S. \$ thousand)
2001	165,000	14,025	24.00	336,600	24,235	132,000	0	180,365	180,365	0.167	0.9813	176,990	176,990
2002	222,024	18,872	24.72	466,517	33,589	190,000	0	242,928	423,292	0.833	0.9059	221,035	398,025
2003	196,000	16,660	25.46	424,190	30,542	184,000	0	209,649	632,941	1.833	0.8124	170,317	568,343
2004	173,000	14,705	26.23	385,645	27,766	180,000	0	177,879	810,820	2.833	0.7254	129,025	697,368
2005	153,000	13,005	27.01	351,294	25,293	176,000	0	150,001	960,820	3.833	0.6476	97,146	794,513
2006	136,000	11,560	27.82	321,629	23,157	172,000	0	126,472	1,087,292	4.833	0.5782	73,132	867,645
2007	121,000	10,285	28.66	294,740	21,221	170,000	0	103,519	1,190,811	5.833	0.5163	53,446	921,091
2008	107,000	9,095	29.52	268,457	19,329	168,000	0	81,128	1,271,939	6.833	0.4610	37,398	958,489
2009	86,000	7,310	30.40	222,242	16,001	167,000	0	39,241	1,311,179	7.833	0.4116	16,151	974,640
2010	77,000	6,545	31.31	204,954	14,757	166,000	0	24,197	1,335,376	8.833	0.3675	8,892	983,532
2011	69,000	5,865	32.25	189,170	13,620	166,000	0	9,549	1,344,926	9.833	0.3281	3,133	986,665

15	16
Working Interest Fraction	Present Worth Profile
Revenue Interest Fraction	Present Worth (U.S. \$ thousand)
0.1000	0
0.0850	8
	10
	12
	15
	20
	30
	40
	60
	100
	1,344,926
	1,082,096
	1,032,035
	986,665
	926,165
	841,722
	716,545
	629,006
	515,711
	398,536

Example oil well No. 1
Reserves category, Proved Developed Producing

13 are included to facilitate the following discussion of present worth discounting. They usually are not displayed in standard presentations.

Table 19.1 presents values and items that represent the projected cash flow for an existing well producing proved developed reserves. If the cost to drill and equip the well (\$800M) were included in the capital costs as an initial outlay before production started, the discount factor would be 1.0 and the cumulative net revenue and discounted values would be reduced by that amount. Further, the indicated rate of return (ROR) for such an investment can be determined from the present worth table to be between 20 and 30%.

Discounting is a widely used method for accounting for the time value of money. It is not a method for evaluating risk. Like the loan shark, cash outlays bearing substantial risk of recoupment require the potential of a high ROR. The high ROR should be the apparent result of an analysis of risk, not the method. The method of risk analysis should be based on the element of risk: production rate, reserves, prices, and cost. Elevating the discount rate reduces the value of income in proportion to its distance into the future. If the reserves are correct but the beginning production rate of a new well is off by 25%, sensitivity analysis should be used to assess the risk or lower the forecasted rate so that the projection represents an expected value. Arbitrary discount rate adjustments should not be made. Despite sharing this view, the SPEE FMV document presents some material involving one elevated discount rate risk analysis method. If you are contesting a valuation instead of establishing value, it might be worth review.

The discount rate may be thought of as an inverted interest rate. As the discount rate increases, the value of future income is reduced. At a given discount rate, the farther in the future a dollar of income is expected to be received, the less it is computed to be worth. The present worth profile of Table 19.1 shows that as the discount rate increases, the value of the projected cash flow stream decreases. At a discount rate of zero, the present worth is the same as the total of the projected cash flow.

Not all discounting methods are the same. Continuous discounting at a rate of 12% and annual midpoint discounting at a rate of 12% do not yield the same results. The standard discounting method historically used in the oil and gas industry is midpoint discounting with either annual or calendar year time frames, as Table 19.1 illustrates. Today, with software that is more sophisticated and with some change in logic, other discounting methods frequently are used. A logical means of discounting is a method that recognizes when the cash from the sale of oil or gas is received by the owner. From that view, middle-of-the-production-month discounting would be too optimistic and so would end-of-month discounting. A retarded discounting method that recognizes that income is often received a month or two after associated quantities are produced is a possibility but is not a method known to be supported by existing software.

A common method of discounting computes an annual discount rate factor with the following equation:

$$D_f = \frac{1}{(1+r)^t}, \dots\dots\dots (19.1)$$

where D_f = discount factor for the specific point in time, r = annual rate of discount expressed as a fraction, and t = time in years from the as of date to the point of reference for discounting. The value assigned to t determines if the discounting is midframe or end of frame and as suggested, could be set beyond the end of the frame. Table 19.1 illustrates calendar year midpoint discounting.

Example 19.1. Calculate the 12% discount factor for cash received at midyear in the fifth time interval of the projection in Col. 12 of [Table 19.1](#).

Solution. The effective date is 1 September of 2001; therefore, there are 4 months following the “as of” date remaining in 2001 at the effective date. Then there are 3 full years of 12 months each (2002, 2003, and 2004). You must go 6 months into 2005 to get to the middle.

$$t = 4 + 12 + 12 + 12 + 6 = 46 \text{ months} = 3.833 \text{ years.}$$

$$D_f = \frac{1}{(1 + 0.12)^{3.833}} = 0.647636. \dots\dots\dots (19.1)$$

The value of D_f is expressed in [Table 19.1](#) as 0.6476. Therefore, the discount FNR for the fifth year of the [Table 19.1](#) projection is $\$150,001 \times 0.647636 = \$97,146$. The sum of the discount factor net revenue for all years is referred to as the present worth of the income stream, but this amount should not be confused with the FMV. It is common to compute present worth values at multiple discount rates and to display the computed results as a set of numbers. The term present worth profile probably stems from the shape of the graph when the present worth values are plotted with the discount rates typically represented on the x -axis.

Other equations sometimes are used for discounting. Monthly discounting at the annual rate divided by 12 and envisioning monthly compounding is given by

$$D_f = \frac{1}{\left(1 + \frac{r}{12}\right)^{12t}} \dots\dots\dots (19.2)$$

If the example is recalculated with [Eq. 19.2](#), the discount factor is

$$D_f = \frac{1}{\left(1 + \frac{0.12}{12}\right)^{12 \times 3.833}} = 0.632727.$$

It is easy to see how the formula could be modified to discount daily or even hourly. Continuous discounting is accomplished with

$$D_f = \frac{1}{e^{rt}}, \dots\dots\dots (19.3)$$

where e is the base of the natural logarithm. Calculating the discount factor with [Eq. 19.3](#),

$$D_f = \frac{1}{e^{0.12 \times 3.833}} = 0.631284.$$

The size of the time intervals used for scheduling is independent of the compounding rate envisioned by the discount factor formula. The only logic behind the use of discount rate formulas other than the annual equation is that the factors are more conservative. There is some obvious logic behind end-of-period discounting or even a retarded discounting, but the logic behind compounded discounting with fractional portions of a year is not clear.

Whatever use is made of an economic evaluation of reserves, an assessment of uncertainty is usually required. Acceptable reserves reports always include definitions given partially to indicate the estimator's opinion of certainty. A guide to the level of certainty generally is expressed by the reserves category in which the reserves quantity falls. Even though the confidence in reserves quantity is theoretically the same between proved reserves classes of proved producing and proved undeveloped, there is unquestionably more uncertainty in the timing for recovery for classes of reserves that are not physically on production.

Within a reserves class such as proved, there are well-recognized subclasses like proved developed producing, proved developed nonproducing, and proved undeveloped. Many evaluators maintain additional reserves classes added by individual evaluators for distinction. Reserves categories like "proved developed nonproducing shut-in" and "proved developed nonproducing behind pipe" are common in that they give the user of the report additional insight as to the nature of the reserves. SPEE includes a suggested extended classification system in [Ref. 4](#). The list is potentially endless.

Regardless of the depth of the classification system, if the reserves estimate is made deterministically, which is still the most common method, the classification system cannot describe the uncertainty fully. An inspection of any of the common (deterministic) reserves definitions will reveal that the reserves class system is not based entirely on level of certainty. Even if certainty is the only criterion, the variations within a class may be significant. Probabilistic reserves estimating procedures, which yield values that quantify uncertainty, can be an important valuation tool. This discussion focuses on results from deterministic procedures. The nature of a reserves report is such that a true assessment of value (whether the report is prepared deterministically or probabilistically) can be made only with a thorough understanding of how the report was prepared and with an understanding of the nature of the properties. This assessment also must include judgment regarding the completeness, quality, and suitability of the availability of data, not only in the preparation of the reserves estimates but in the economic data as well. See [Sec. 19.6](#). Assuming that a suitable production schedule has been provided with the reserves report, the key elements in generating the cash flow projections are discussed in the order in which they are encountered in [Table 19.1](#).

19.4.1 Report Effective Date. The effective date is the time at which the elements that generate the cash flow projection start to be used. This is normally time zero for discounting purposes. The cumulative production (normally shown, although it is not included in the [Table 19.1](#) example) will include the cumulative actual production plus estimated production for a stub period if production up to the effective date was not complete. For example, if the effective date of the report is at the end of the year, but production was available only through October when the production projection was made, the cumulative production will include an estimate of production for the last two months of the year. In preparation of the economic projection, the estimated future production will be cropped at the front end and used only from the effective date forward. A distinction is sometimes made between "effective date" and "as of date." Effective date is the time zero for discounting and scheduling, and as of date is the date through which information was available. For example, given a report prepared for estate tax purposes with the date of death and a time zero of 1 January and with that report being published on 1 July of the same year with all the information available at the time of report preparation, the effective date might be considered 1 January but the as of date is 1 July. There is no standard terminology.

19.4.2 Interest Position. This is intertwined with the subject of Appendix A. Generally, the interest position is defined in terms of an entity's fractional responsibility for costs, with a separate fraction defining its share of the proceeds from sales. There are sometimes financial, accounting, security, and/or business issues relative to whether an entity owns its fractional

share of production or is merely the beneficiary of the revenue from sales. Such issues are ignored here, but [Ref. 4](#) discusses the subject. The displayed interest positions are generally the ones applicable on the effective date of the report, and subsequent changes that might occur may or may not be displayed. Reversionary interest positions, if they exist, are not likely to be clearly identified in the petroleum economics schedules that resemble [Table 19.1](#).

19.4.3 Prices. The prices used in generating the cash flows are often dictated by the report's intended user. The SEC sets forth its own requirements. Lending institutions generally have pricing guidelines as a part of their collateral valuation procedure. If the report is being prepared for the determination of FMV, the evaluation engineer will likely be the judge as to the view of the market place. For such purposes, it is not the evaluation engineer's place to be an economist and predict future prices of a global economy. The evaluator is attempting to reflect the view of the market. It is often convenient (and defensible) to rely on the indications by the New York Mercantile Exchange (NYMEX) futures market. One of the nice features of the NYMEX futures market is that it is available every business day. Other useful market indicators become available periodically, such as the State of Texas' annual budget. It is interesting to compare the numbers. Because of price volatility, the time over which any such comparison is valid might be very short or indeterminable.

NYMEX prices reflect benchmark prices for West Texas Intermediate Sweet crude and Henry Hub gas. While care must be used, it is usually possible to use historical prices over a brief period to arrive at suitable differentials to these NYMEX indexes and to then base future price projections appropriately. [Ref. 7](#) is a valuable source for an industry perspective. Like the State of Texas budget, it is sometimes difficult to pin down the time frame to which the perspective applies. It sometimes seems that the NYMEX futures market is out of sync with the mainstream of the industry and with what a property purchaser would use as a guide for a decision on an acquisition. Different segments of the industry are not always synchronized.

The evaluator must take care that the prices used in the economic projection reflect certain other sales features. If transportation charges apply, they usually should be reflected in a reduced price, unless care is taken to be sure those transportation fees are reflected in the cost column. Also, while oil production and sales volume difference usually balance out over time (assuming a lack of theft or errors), gas sales quantities are commonly less than produced quantities because of lease use and shrinkage. The reserves engineer commonly forecasts wellhead production by necessity. Net produced and reserves quantities are reported conventionally as the fraction of the wellhead volume indicated by the revenue interest fraction. To get the arithmetic correct, it is often necessary to account for lease use and shrinkage losses (commonly as high as 6% or greater), gas liquids recovered, and the net back of liquids recovered in an off-site gas processing plant in the gas price.

To ensure that input variables and/or the economic model will project future cash flow suitably, it is a good idea to determine if historical produced quantities and prices can be used to duplicate historical revenue. In a presentation before the SPEE annual meeting in Park City,¹⁴ Rick Riseden indicated the importance of being able to "follow the cash." His subject was the valuation of royalty interests where not all the operator's records might be available but the principle is the same. If you try to follow the cash and cannot, how can you predict future revenues with any accuracy?

19.4.4 Taxes. U.S. federal income taxes are not included in this item and the calculation of such taxes is not presented in this chapter, but [Sec. 19.7](#) discusses the characteristic impact on value. This tax element is what is often referred to as local property taxes. In reality, the taxes normally included are all taxes other than federal and state income taxes. The nature of the tax structure varies from state to state. SPEE maintains a document¹⁵ that presents a summary of the structure of these taxes by state. While the summary is quite helpful, caution is necessary.

Laws and rates change frequently, and some provisions of the laws might not be fully covered in the SPEE material. It is best to consult evaluators with local experience.

19.4.5 Operating Costs. It is common practice to use historical average costs for a preceding time period as the initial cost for projection purposes. Usually, the historical costs are calculated at a cost per well per month and projected forward in the same manner with future costs at the summary level declining as a direct function of the number of wells projected to be producing. Future costs typically are escalated at a rate commensurate with some perceived inflation rate thought to be consistent with the projection of oil and gas prices.

“Nonrecurring” costs are often removed from the historical averages before determining the parameters for projection of future costs. The costs projected in the economic evaluation are generally field-level expenses and exclude general and administrative (overhead) costs. To the extent a working interest owner is billed overhead charges by the operating company (COPAS charges are in that category), those charges are included in the operating costs of the nonoperating working interest owner.

There is much room for abuse, deception, and pitfalls concerning value on the operating cost side of the valuation process.¹⁶ In the case of an offshore platform, it is obvious that there is a substantial base level expense that is not proportional to the number of producing wells. On a property producing a lot of water, the operating cost is more likely to be related to the amount of water being produced than the number of wells or amount of oil. Whether or not onshore operating costs can be expected to vary directly with the number of wells is a matter of circumstances and judgment. It is usually a mistake to eliminate costs classed as nonrecurring. It might be appropriate to spread such costs over a number of wells or make a judgment as to expected frequency of occurrence.

Some costs of operation are classed as “make marketable” charges. The most common of these is the cost to compress gas to the pressure required to enter the sales line, to reduce the water content, or to extract impurities such as carbon dioxide, nitrogen, and/or hydrogen sulfide to meet pipeline specifications. These charges are not handled in proportion to expense interest but are usually charged to the property owner in proportion to the revenue interests; thus, it is not universally true that royalty owners do not bear any share of the costs of operations.

19.4.6 Capital Costs. These costs are listed separately from operation costs because of the difference in their nature and because, if any after income tax economic calculation projection is to be made, there is a difference in the structure of their deductibility in net income computations. The capital costs most commonly included in petroleum economic projections are for the drilling of new wells and the workover of existing wells. Other common costs are for the addition of compression; installation, expansion, or addition of production collection and separation systems; the addition of artificial lift; and the installation of offshore platforms. Planned improved-recovery projects require additional capital outlays for facilities.

There occasionally are repetitive needs for relatively small, but potentially significant, amounts of capital that go unnoticed by the evaluator during reviews of historical expenditures. Such capital items are often associated with large units with consolidated facilities and are not captured in the “operating cost” category of historical expenditures or budgets. Engineers are accustomed to including capital for new wells, recompletions, and workovers, but they are sometimes unaware that the operating costs they are provided include only expensed portions of repetitive historical costs.

Reserves reports sometimes include income from sources other than from the sale of produced oil and gas. When the income is from the sale of byproducts such as sulfur, the treatment is relatively straightforward because it is a third sales revenue stream. If the income results from the processing of gas for the recovery of liquids, the economic model is often adjusted to reflect the associated quantities, but at other times, it is considered sufficient to

make an adjustment of the gas price to reflect the elevated income level. A different approach might be required if reporting under U.S. SEC guidelines.

If the income results from providing a service such as disposing of produced saltwater for a fee paid by neighboring operators, the issue is less clear because the evaluation includes an income stream associated with a business other than the production of oil and gas. Evaluations have been observed that include, as a part of the petroleum economics, the operator's income (likely treated as a reduction or credit against other expenses) from COPAS payments received from others. The key to knowing the proper means of evaluation is to know the use of the report and any controlling regulations. Conspicuous disclosure of unusual circumstances is recommended.

Sometimes there are material exit costs such as well and offshore platform abandonments and site remediation. Future environmental liability also could be a significant cost. Economic evaluation of reserves should include such considerations; however, a report may present a fine perspective on specific underlying values but not be a complete expression of value. The preparers of reserves studies and evaluations usually have limited expertise in such matters. It is a good idea to read carefully the qualifications that are always contained in a thoughtfully prepared report or statement of opinion.

This section conveys the message that these projections of production and associated expense and income are constructed to be a model of the future and should include consideration of all parameters that bear on those expectations. A well-constructed model will include a specific value assignment to all the variables that might be included as a distribution should a Monte Carlo simulation be constructed later. As discussed in [Sec. 19.4.3](#), it is a very good idea to be sure you can “follow the cash.”

19.5 The Nature of Risk and Uncertainty

Forrest A. Garb is the author of the following text taken from the SPEE FMV document.¹

The petroleum industry has written extensively on the risk associated with exploration and development. Very little has been published, however, addressing the uncertainties associated with acquisition and operation of producing properties. The uncertainties associated with estimating the reserves and value of oil and gas producing properties are divided into three classifications. The technical uncertainty that the hydrocarbon volumes estimated do exist in the ground and that the recoverable amounts can be produced within the time frame projected, the economic uncertainty that product prices, operating costs, equipment costs, inflation, and market conditions will be in reasonable agreement with the assumptions used in the economic analysis, and the political uncertainty that world economics, international political stability, taxation, and regulations will not be significantly different than perceived at the time of the evaluation.

1. **Technical Uncertainty.** Technological uncertainty relates to whether or not the hydrocarbon volumes estimated actually exist in the ground and whether the reserves and recovery rates will be as projected. Technical uncertainty is strongly influenced by the length of time that the property has produced and the quantity and quality of the information available about that property. For example, porosity derived from well logs might truly measure the pore space of a rock, yet the logs may not identify how much of that pore space is interconnected. A Styrofoam™ cup is porous; however, the pores are not interconnected, otherwise the cup would leak. Because reservoirs depend on the pores to transmit oil or gas to the wellbore, pore space makes no contribution to reserves if, like the cup, it is not interconnected. In technical terms, the rock must have permeability. As the reservoir depletes during the production process, it is often possible to analyze its performance and, hopefully, confirm that its effective size is close to that indicated earlier through the use of logs, geological interpretations, and other data. Too often however, there are surprises. When prices for oil and gas are stable and/or expectations for future oil and gas prices fall within a narrow range, technical uncertainties (reservoir fluid content, productive area, porosity, net pay thickness, water saturation, producing mechanism, recovery factor, and producing rate) dominate the concerns. Somewhat stable industry costs and prices cause the estimation of reserves and producing rates to be the most significant inputs in the evaluation of a property.

2. **Economic Uncertainty.** Instability in oil and gas prices and questions about costs and taxation have, at times, caused economic uncertainty to take precedence over technical uncertainty. Prices at which oil and gas are expected to be sold are not the only variables that can affect the economic uncertainty. Capital, operating, and drilling costs react to increases and reductions in industry activity. Drilling costs during slow periods have been known to decline to as low as 50% of the costs prevalent during boom times. Operating costs do not necessarily follow changes in oil and gas prices as is frequently assumed in projections. Cost reductions, which may reflect the availability of equipment and services when the industry is operating below capacity (possibly due to low oil and gas prices), could disappear as quickly as they appeared and must be considered in the assessment of uncertainty. Inflation and interest rates on borrowed capital also add to uncertainty.

3. **Political Uncertainty.** Political uncertainty includes uncertainty regarding local and national taxes, environmental regulations, and global concerns. Oil prices have been significantly influenced by artificial supply restraints for almost all of the industry's life. There is the risk of nationalization, operational restrictions, and social unrest in foreign host countries. Exporting countries could restrict the exportation of crude produced within their boundaries or require the producer to sell that oil domestically at prices significantly below the world price. Revenues generated from local sales might not be easily repatriated by the producing company. In other circumstances, the terms of agreements and contracts might be subject to capricious interpretations or obligations.

A balance recognizing the element of romance and the possibility for better results than expected versus the uncertainty of predicted outcomes or the risk of loss is the target of an FMV analysis. The procedures for assessing risk and uncertainty include deterministic and probabilistic methodologies. Deterministic methods can be applied to yield one or a specific set of multiple results. Probabilistic methods target a description of all possible outcomes. The question, "What is the value of a property?" implies that there is a single answer. For most business transactions a single answer is required. The most frequently used procedure to assess the value of a property is deterministic.

If only a "most likely" case is developed, the fact that it is highly unlikely that this case will actually occur is ignored. The question, "What is the range of outcome possibilities for this property?" recognizes that there is no single answer and perhaps one should look to a probability theory as an aid in business decisions. Despite the limitations imposed, the thrust of this monograph is to address deterministic procedures. The consideration of alternate outcomes in the assessment of FMV is encouraged, whether it is through the use of multiple deterministic analyses or fully probabilistic procedures. Additional discussion of probabilistic procedures is included in the SPEE Monograph 1, second edition, dated October 1998.⁴

19.6 Methods to Adjust for Risk and Uncertainty

19.6.1 Application of Adjustment Factors for Risk and Uncertainty. For the economics presented in a reserves report to be useful in estimating value (loan value, exchange value, FMV, etc.), some method of adjustment may be needed so that the economics reflect an expected case. Garb¹² indicated "adjustment factors reflecting the uncertainties attributed to the different categories of reserves can be used to index or to equate their FNR stream of the equivalent of proved producing reserves." **Table 19.2** presents qualitative observed monetary value risk factors (MVRF). It replicates the table from **Ref. 4** that summarizes part of the results of the SPEE annual parameters surveys and includes a range of factors grouped by deterministic reserves category. **Table 19.2** presents value ranges generally greater than those presented by Garb,¹² but the intended application is similar and the ranges in **Table 19.2** are more current. The table uses the term uncertainty, but risk would have been a better term.

The footnotes state the factors "assume risk factors reported were those applied against monetary values," but it is not precisely clear what the values apply to because of the way the surveys were conducted. They undoubtedly apply to deterministic reserves categories. Consider

Deterministic Reserves Category	Adjustment Factors To Reflect Uncertainty** MVRF
Proved producing	0.85 to 1.00
Proved shut-in	0.65 to 1.00
Proved undeveloped	0.50 to 0.90
Proved behind-pipe	0.25 to 0.75
Probable behind-pipe	0.05 to 0.50
Probable undeveloped	0.00 to 0.40
Possible behind-pipe	0.00 to 0.25
Possible undeveloped	0.00 to 0.20

*The adjustment factors shown were derived from surveys of SPEE members and other presumed knowledgeable and informed persons in the industry over a period of years beginning in 1982. Comparison of the surveys shows little variation in the results over the period. These factors, which are included for reference and comparison, represent an approximated one standard deviation range, and assume risk factors reported were those applied against monetary values. The 1997 SPE/World Petroleum Congress definitions take a step toward the quantification of confidence levels associated with reserves estimates. The users of these data should be aware that, despite the noted consistency in the above adjustments factors over the years, reserves estimates that have been prepared with the "probabilistic option" provided in the new definitions may have a tendency to produce results at variance with the historical trend.

**These may also be considered chance of success (COS) factors expressed in decimal form.

Year	Revenue (\$ thousand)	Taxes (\$ thousand)	Expenses (\$ thousand)	Capital (\$ thousand)	Cash Flow (\$ thousand)	Discounted Cash Flow (\$ thousand)
1	5,000	320	1,350	8,000	(4,670)	(4,934)
2	4,300	430	850	0	3,020	2,356
3	3,500	350	700	0	2,450	1,620
4	3,000	311	620	0	2,069	1,159
5	2,500	250	500	0	1,750	831
6	2,000	200	400	0	1,400	563
7	1,500	150	350	0	1,000	341
Totals	21,800	2,011	4,770	8,000	7,019	1,936

the proved undeveloped reserves category and the simple cash flow schedule presented in [Table 19.3](#).

The discount rate for the present worth calculation in the right column is not shown. Assume that the discount rate used to calculate that column is the discount rate that would represent FMV, if this were a cash flow summary for proved developed producing reserves. [Table 19.2](#) shows a range of factors from 0.50 to 0.90 for the proved undeveloped reserves category. For this illustration, we used a factor of 0.70. Applying the 0.70 factor to the \$1,936,000 present worth value results in an adjusted value of \$1,355,000. Is this the correct application of the method? The answer depends significantly on precisely when the decision to spend the capital must be made.

Year	70% Revenue (\$ thousand)	Taxes (\$ thousand)	Expenses (\$ thousand)	Capital (\$ thousand)	Cash Flow (\$ thousand)	Cash Flow (\$ thousand)
1	3,500	224	1,350	8,000	(6,074)	(6,227)
2	3,010	301	850	0	1,859	1,450
3	2,450	245	700	0	1,505	995
4	2,100	218	620	0	1,262	707
5	1,750	175	500	0	1,075	510
6	1,400	140	400	0	860	346
7	1,050	105	350	0	595	203
Totals	15,260	1,408	4,770	8,000	1,082	(2,015)

Year	Revenue (\$ thousand)	Taxes (\$ thousand)	Expenses (\$ thousand)	Capital (\$ thousand)	Cash Flow (\$ thousand)	Discounted Cash Flow (\$ thousand)
1	0	0	0	8,000	(8,000)	(8,000)
2	5,000	320	1,350	0	3,330	2,598
3	4,300	430	850	0	3,020	1,997
4	3,500	350	700	0	2,450	1,373
5	3,000	311	620	0	2,069	982
6	2,500	250	500	0	1,750	704
7	2,000	200	400	0	1,400	477
8	1,500	150	350	0	1,000	289
Totals	21,800	2,011	4,770	8,000	7,019	420

What if the factor of 0.70 is applicable to reserves risk and all the capital must be committed up front? If the revenues were reduced to 70%, which could be expected to be the implication of a 0.70 factor applied to reserves, the values in Table 19.3 would appear as the values in Table 19.4 and would have no value at the discount rate used. This type of analysis is essentially a decision tree calculation of expected results, given the circumstances described.

Another possibility is that the need for adjustment may have nothing to do with uncertainty regarding the reserves quantity. Table 19.5 presents a cash flow example and present worth calculation that is the same as in Table 19.3, except that the receipt of revenues has been delayed by one year.

Again, the result is a value considerably less than the \$1,355,000 suggested in Table 19.3 after application of the 0.70 factor to the discounted value. There are other possibilities that could cause an evaluator to make value adjustments independent of concerns about the confidence associated with reserves quantities. Another crucial consideration relative to Table 19.5 would be the possibility of overexpenditure of capital cost. There are almost an infinite number of possibilities, which is why probabilistic analysis and Monte Carlo simulation can be useful decision-making tools.

There are many aspects of uncertainty other than those associated with reserves quantities. Risk and uncertainties of all aspects should be addressed. It is unlikely that subjectivity can be

eliminated from the evaluation. In making deterministic adjustments for risk, it is often helpful to think about how the distributions for variables might be described in a Monte Carlo simulation and to attempt to estimate what the most likely results would be. This will not help much in determining the breadth of the value range that might be revealed by Monte Carlo simulation, but it should help in coming up with values approximating the mode. If the deterministic method is the sole means of evaluation, it is hoped that the distribution of expected values will be narrow and the mode will be very meaningful.

19.7 The Effect of Federal Income Taxes on U.S. Acquisition Economics

This section shows how federal income taxes can affect the economic evaluation process and gives the reader some understanding of how after federal income tax (AFIT) and before federal income tax (BFIT) relate in the U.S. This section does not delve into the U.S. federal tax code and the mechanics of making after tax cash flow computations, which can be done with petroleum economic software packages. Any evaluator intending to make such an analysis should consult a tax professional.

The marketplace in which oil and gas interests are traded involves transactions in countries with income taxes at the federal and, sometimes, local levels. Cash flow calculations that have been described are BFIT. When a property is purchased, it is assumed that the buyer made the acquisition with the intent of making a profit. If one could determine precisely the nature of the bottom line economic return expectations of the buyer, it would help greatly in making estimates of FMV. If such expectations were known and universal, an FMV estimation formula could be devised that would be reasonably portable around the world. It is generally perceived by observers of the U.S. oil and gas property marketplace that the impact of income taxes is sufficiently small and the variations in other variables influencing perceived value are sufficiently large that it is not normally possible, from the data available on a specific transaction, to discern (back into) the AFIT (bottom line) economic parameters of the purchaser.

If BFIT rates of return that characterized market value are known and one is attempting to transport or compare the observations to another market, can the BFIT results be backed into an AFIT bottom line ROR? For example, when making computations relative to a company’s weighted average cost of capital (WACC), the results are usually first expressed in terms of an AFIT ROR. The following equations are suggested for calculating WACC:

$$C_{at} = C_{bt} \times (1 - T_R) \dots\dots\dots (19.4)$$

or

$$C_{bt} = \frac{C_{at}}{1 - T_R} \dots\dots\dots (19.5)$$

The relationships expressed in Eqs. 19.4 and 19.5 do not work in the evaluation of project economics because the purchase price of the property is, over time, a deductible item as a reduction of income on which tax is paid (i.e., the statutory tax rate is not the effective tax rate). Fig. 19.1 includes three computed present worth profiles that contain many assumptions but were constructed with the intent of illustrating theoretical differences in BFIT and AFIT (U.S.) rates of return. The federal income tax rate used to generate the AFIT profiles is 35%. In preparing the economics for one AFIT case, it was assumed that 70% of the purchase price was loaned to the buyer at an interest rate of 8% and that 90% of the revenue was dedicated to loan repayment. The other AFIT case was run with similar assumptions but without the loan. The economic life of the example is 19 years. The purchase price was deducted in the AFIT calculation with the units of depletion method.

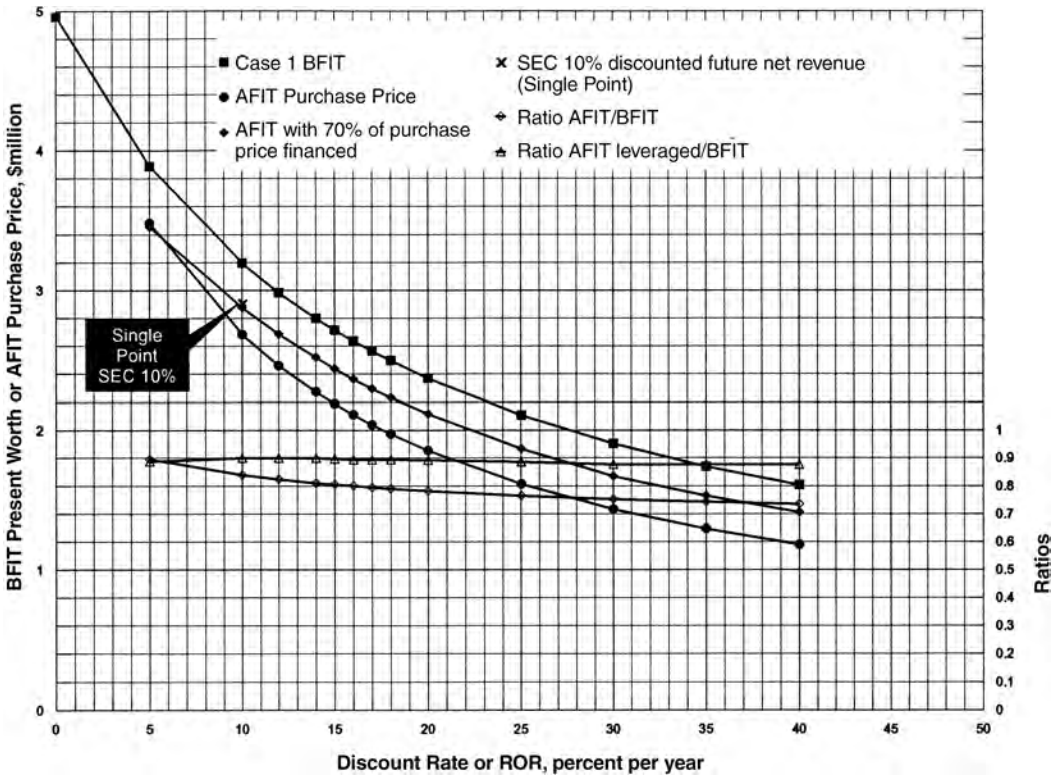


Fig. 19.1—Comparison of BFIT present worth and AFIT purchase price as functions of discount rates and ROR.

Discount Rate	BFIT Present Worth or AFIT Purchase Price (%)	Apparent Tax Burden Effect (%)
BFIT	15.4	
AFIT (leveraged)	12.0	3.4
AFIT (no leverage)	9.9	5.5

A specific purchase price can be represented by a horizontal line on Fig. 19.1 (ignore the posted lines on the graph that approach being horizontal for now and think about a horizontal line at a y-axis price of approximately \$2,700,000). From Fig. 19.1, it appears that such a purchase could be represented by three different discount rates as shown in Table 19.6.

The burden imposed by income taxes in terms of the discount rate is shown to vary more than 2 percentage points simply based on one financing option. In the U.S., it is generally perceived that income taxes cause the spread between the BFIT discount rate and the AFIT purchase price to be approximately 4 to 6%. There is a price to pay for leveraging up the purchase price through financing in the manner described. The payment of interest reduces the total future net revenue and absolute profit in terms of total dollars.

Another way to compare the BFIT and AFIT calculations is by looking at ratios rather than spreads in discount rates. Fig. 19.1 plots the ratios to show how the benefits of leveraging with a loan improve, from a discount rate point of view, as the ROR increases. In the example, a loan interest rate of 8% and a tax rate of 35% are used. The leveraging effect stems from the deductibility of the interest from otherwise taxable revenues and the fact that the after tax ROR is greater than the interest rate times one minus the tax rate. [$8 \times (1-0.35) = 5.2\%$.] From Fig. 19.1, it is clear that below a 5% discount rate, the ratio of AFIT (no leverage) purchase price to the BFIT present worth is greater than the corresponding ratio with leverage, which indicates an undesirable condition for financing. If the financing costs more than the desired after tax ROR times one minus the statutory tax rate, there is no leveraging benefit. The ratios plotted on Fig. 19.1 show that as the ROR increases beyond 5%, so do the benefits of leveraging with a loan.

In the example presented by Fig. 19.1, AFIT leveraged case purchase prices bear a relatively constant ratio to the BFIT present worth values at approximately 0.9 over a wide range of values. This flatness is a usual occurrence and if it were to hold true over a wide range of conditions, it would be easy to approximate the AFIT leveraged purchase price by “haircutting” the BFIT present worth by 10%. This is only an observation at this time.

Fig. 19.1 includes the 10% discounted present worth parameters that would result from flat future pricing, as set forth by the U.S. SEC filings. This “single point” on Fig. 19.1 is posted on the vertical 10% line approximately half way between the lines connecting the Case 1 BFIT present worth values and the lines connecting the AFIT indicated purchase prices. The SEC data point plots essentially on top of the AFIT ROR at 10% (loan-leveraged case) at a purchase price of \$2,900,000.

19.8 Fair Market Value

The FMV definition offered by SPEE¹ is “the price a willing buyer will pay and a willing seller will accept for a property, when the property is exposed to the market for a reasonable period and neither party has any compulsion to buy or to sell, and both have reasonable knowledge of relevant facts.” The market for oil and gas properties is not static. Because it can be expected to change in the future, it is helpful to reflect on how valuations or perceptions of value have changed from the past. Perhaps what is most surprising is what little change there has been.

Table 19.7 describes the valuation methods embraced by Arps.² Arps’ statements have been slightly modified to conform to today’s terminology. Additional perspective offered by Arps is added in *Italics*. Each of these methods presumes that ROR is the applicable criterion (or hurdle) for valuation but that is not always the case, as is discussed later. The reason for the reverse order is that it is helpful to present the method that Arps considered “the most sophisticated approach” first so that the latter methods can be related to it. Today it is more common to refer to “present worth” as discounted future cash flow or discounted future net revenue, but there is no difference.

Any adjustments for risk suggested or implied in the parameters of Table 19.7 are management’s judgment of general industry risk (perhaps inclusive of oil and gas price uncertainty) or experience and are not normally project specific unless the project is unusual in terms of a company’s normal business. The risk or uncertainty associated with specific projects must be assessed on the basis of the specific merits of the individual parameters of those projects. Adjustments for project risk are discussed in Sec. 19.6.

There is debate about how overhead or general and administrative (G&A) expenses enter the cash flow projections. Some suggest that all costs and capital expenditures should be inflated to account for G&A; others argue that G&A should be a scheduled expense; and still others conclude it should not be considered at all. Some perceive that the elevation of the AFIT ROR above the cost of capital includes a component to cover G&A in addition to components for

TABLE 19.7—HISTORICAL AND MODERN VALUATION METHODS

Arps' Method Number	Arps' Description of Method	Modern Description of the Most Similar Method
3	A value equal to the present worth of the net cash flow after federal income taxes computed at an intermediate (6 to 9%) rate of interest. Arps referred to this as "the most sophisticated approach to the fair-market-value problem."	A price that yields an AFIT ROR equal to the cost of capital plus an elevation of that interest rate to cover management's perceptions of the need for profit and to account for industry risk. The AFIT ROR target is commonly in the very low double-digit range when expressed as a percent.
2	A value equal to the present worth of the net cash flow before federal taxes computed at a speculative (13 to 21%) rate of interest. This was a "not recommended method" because discounting tends to overvalue short life properties and undervalue long life properties.	The price equal to the discounted future net revenue using a discount rate determined to be applicable to BFIT cash flow projections based on observations of the market, or alternately, a discount rate sufficiently elevated above the AFIT ROR target (from Method 3) to account for income taxes. This elevation of the discount rate above the AFIT ROR target is typically on the order of 4 to 6%.
1	A value equal to a fraction (typically 0.67 to 0.75) of the present worth of the net cash flow before federal taxes computed at a safe (4 to 6%) rate of interest that approximates the cost of money. This method was "simple, easy to understand, and therefore widely used" according to Arps.	A price calculated using the value of discounted future net revenue at a discount factor equivalent to an AFIT ROR target, then adjusting (haircutting) that value using a factor to account for income taxes. The factor is typically in the range of 0.75 to 0.90.

profit and industry risk. In practice, cash flow schedules in the majority of reserves reports do not include overhead expenses except for those billed to nonoperating working interest owners by the operator of the property. Such charges are frequently referred to as COPAS charges because of the manner in which the rates are established.

Method 3 is used today essentially unchanged except that the discount rates are higher because of differences in the cost of money and industry risk. Method 3 is used often internally by companies to arrive at a price they might offer to a potential seller, but it is seldom used by outside parties to estimate value. There likely will be several more columns of detail in the economics than shown by Table 19.1. There are many details, and people want to see that detail if it has been judged to be worth that much work. The basic calculations are handled easily by most petroleum economic software packages, but one must take care to model the company's internal cash flow mechanics. The need for detail is partly because the method is used to investigate the leveraging benefits of financing. The benefits of the use of loan leverage to increase the offering price while maintaining the ROR were illustrated previously. Such leveraging has the disadvantage of reducing the undiscounted projected cash flow because of the payment of interest. If Method 3 were to be used for a purpose other than internal use, it probably would be for estimating FMV while speculating as to complexion of the likely acquirer. Similarly, a third party could be investigating how a recent change in tax rates or structure might affect those in the acquisition market.

There is always interest in the components of the AFIT ROR target discount rate. Generally, the components are expected to include the cost to borrow money and/or acquire capital, a

margin to cover overhead and profit, and management's safety factor (referred to as industry risk component).

Method 2 uses an elevated discount rate to adjust for federal income tax effects. Arps classed this method as "not recommended."² The primary reason for Arps' criticism is that when the discount rate is elevated, the value of cash projected to flow at times more distant into the future is reduced more than warranted in comparison with Method 3. David and Hickman¹⁷ wrote about a market for long-life reserves in 1990; however, others suggest that there is greater uncertainty related to those more distant projections of cash flow and that such reduction is warranted. When Arps wrote the 1962 chapter from a U.S. perspective, production levels were often regulated and projections of production and future cash flow were more often expected to be constant at existing levels for a significant time.

Method 2 is the most popular method today. Its modern popularity seems to stem from at least two sources. In 1982, SPEE began an annual publication that is currently titled *Survey of Economic Parameters Used in Property Evaluation*.¹⁸ The questionnaire for that survey has inherently embraced Method 2 from inception. The publication has gained wide use and acclaim and is a source to those needing quantification of the discount factor required to apply Method 2. Another reason for Method 2's popularity is that it requires both a discount rate and a factor. Method 2 results in a simpler expression with a single parameter. Additionally, taxing authorities at state and county levels often require an expression of value in terms of the Method 2 discount rate, which might have had some bearing on the original construction of the SPEE questionnaire.

Method 1 uses discounted cash flow to estimate value, but a factor is applied to the discounted future net revenue to account for income taxes. In the Method 1 described by Arps, a "safe" discount rate was selected and value was determined by a factor that had a midrange of 0.71.² Arps' application of Method 1 used a discount rate lower than the rate used in Method 3. The modern application of Method 1 (although it is not used very much) uses the AFIT ROR target rate from Method 3 and a higher factor, the midrange of which is 0.825 from Table 19.1.

Because the modern application is to use a higher discount rate in comparison to the cost of money at the times being considered, a higher factor representing a smaller reduction in the discounted values is perhaps to be expected. Another factor that might bear on the difference in the factor is the U.S. federal income tax rate and structure. When Arps wrote the 1962 chapter, the income tax rate for corporations was 50% but there was a financial arrangement available known as an ABC transaction. Today the tax rate is lower and the ABC transaction was eliminated by Congress in the late 1960s. It is not clear how historical modification of tax rates and laws have affected market values.

FMV estimation has thus far focused on ROR considerations and the present worth of projected cash flow streams. That perspective is always important but is not necessarily the controlling factor. Other economic parameters that measure the nature of a contemplated investment also affect market value. The critical ones are payout, which is the length of time required for recovery of the investment (purchase price) from the projected cash flow stream, and return on investment (ROI), which is the projected future cash flow or FNR divided by the investment (in this case, the purchase price). Payout for oil and gas property acquisition is normally expected to be 5 years or less. Some suggest that this limitation is not a true evaluation parameter but the result of the application of other criteria

ROI is probably, or should be, a controlling parameter in many valuations. Arps,² in commenting on one of his own studies of 34 property transactions made during the postwar years in the Mid-Continent, Gulf Coast, and California, indicated "in none of these transactions did the total consideration exceed two-thirds of the undiscounted future net cash income before federal taxes." To be in line with this two-thirds observation by Arps, the ROI must be greater

than 1.5. Many¹² set higher limits, as high as 2 or 3, while others find 1.7 to be an acceptable minimum. Sometimes a correlation is perceived between ROI and acceptable minimum ROR. ROI is a good indicator of the susceptibility of an investment to risk. If reserves (or any other parameter factored into the cash flow calculation) are missed by 25% on a project evaluated with an ROI of 2, the economic result will probably be tolerable. If the originally projected ROI was 1.5, the results will be embarrassingly poor. Low ROI acquisition opportunities are usually of quite short life and often seem attractive because of short payout times. Investors willing to take such risks need to have cash because the value of the asset diminishes so rapidly that if any of the purchase is financed (with the properties being acquired put up for collateral), the loan value will be only a small fraction of the purchase price. When ROI is the parameter controlling the purchase price, the ROR will often seem to be abnormally high.

Estimates of FMV are probably best made with the insight derived by observing the characteristics of marketplace transactions. Rather than direct use of comparative sale methods, as might be done in real estate, it is better to use ROR, ROI, and payout as tools in the comparative process. Even then, adjustments must be made that account for differences in circumstances such as tax credits, tax structure, production-sharing contract terms, and risks. The parameter used as a basis for comparison most often is the ROR. Discussions over a property's value, if the risk components can be dealt with, often are reduced to what ROR represents value. The SPEE FMV document¹ suggests that the applicable BFIT ROR in the U.S. correlates with the 30-year Treasury bond rate according to the following formula:

$$i_R = 1.72 \times (R_{tb} + 2.87), \dots\dots\dots (19.6)$$

as a percent where R_{tb} = 30-year U.S. Treasury bond rate expressed as a percent.

This relationship was derived from a 20-year review of SPEE's annual *Survey of Economic Parameters Used in Property Evaluation*.¹⁸ The average BFIT ROR indicated by survey respondents in the summer of 2001 was 15.4%, and the mean was 15.0%. These survey results included participants outside SPEE. The membership was surveyed through an example problem to solicit opinions with a described set of circumstances to convey high levels of confidence. This survey resulted in a mode ROR of 19.2% in a narrow distribution. The results seem to be inconsistent, but the difference probably lies in perceptions of risk.

Nomenclature

- C_{at} = weighted average cost of capital after federal income tax
- C_{bt} = weighted average cost of capital before federal income tax
- D_f = discount factor for a specific point in time
- e = base of the natural logarithm
- i_R = ROR before federal income tax
- r = annual rate of discount expressed as a fraction or percent
- R_{tb} = 30-year U.S. Treasury bond rate, expressed as a percent
- t = time in years from the as of date to the point of reference for discounting
- T_R = tax rate

References

1. *Perspectives on the Fair Market Value of Oil and Gas Interests*, D.R. Long (ed.), SPEE, Houston (2002).
2. Arps, J.J.: "Valuation of Oil and Gas Reserves," *Petroleum Production Handbook*, T.C. Frick and R.W. Taylor (eds.), SPE, Richardson, Texas (1962) **2**, Chap. 38.
3. *SPEE Recommended Evaluation Practice Program*, SPEE, www.spee.org/rep-main.htm.

4. *Guidelines for the Application of Petroleum Reserves Definitions*, second edition, Monograph Series, SPEE, Houston (1998) 1.
5. Lohrenz, J. and Dickens, R.N.: “Option Theory for Evaluation of Oil and Gas Assets: The Upsides and Downsides,” paper SPE 25837 presented at the 1993 SPE Hydrocarbon Economics and Evaluation Symposium, Dallas, 29–30 March.
6. Walkup, G.W. Jr. and Chatwin, R.E.: “Case Studies of a Real Option Approach to Asset Valuation in the Petroleum Industry,” paper SPE 52952 presented at the 1999 SPE Hydrocarbon Economics and Evaluation Symposium, Dallas, 20–23 March.
7. Hooper, H.T. III and Rutherford, S.R.: “Real Options and Probabilistic Economics: Bridging the Gap,” paper SPE 71408 presented at the 2001 SPE Annual Technical Conference and Exhibition, New Orleans, 30 September–3 October.
8. Luehrman, T.A.: “Extending the Influence of Real Options: Problems and Opportunities,” paper SPE 71407 presented at the 2001 SPE Annual Technical Conference and Exhibition, New Orleans, 30 September–3 October.
9. Markland, J.T.: “Options Theory: A New Way Forward for Exploration and Engineering Economics?” paper SPE 24232 presented at the 1992 SPE Oil & Gas Economics, Finance, and Management Conference, London, 28–29 April.
10. Zettl, M.: “Extending the Option Pricing Theory for the Valuation of E&P Projects,” paper SPE 62968 presented at the 2000 SPE Annual Technical Conference and Exhibition, Dallas, 1–4 October.
11. Faiz, S.: “Real-Options Application: From Successes in Asset Valuation to Challenges for an Enterprisewide Approach,” *JPT* (January 2001) 42.
12. Garb, F.A.: “Which Fair-Market-Value Method Should You Use?” *JPT* (January 1990) 8.
13. Wright, J.D. and Thompson, R.S.: “A Comparative Analysis of 12 Economic Software Programs,” paper SPE 68588 presented at the 2001 SPE Hydrocarbon Economics and Evaluation Symposium, Dallas, 2–3 April.
14. Riseden, R.: “Valuation of Royalty Interests,” presented at the 2002 SPEE Annual Meeting, Park City, Utah, June.
15. “SPEE Oil & Gas Production Taxes, Section 29 and COPAS,” SPEE, www.spee.org/productiontaxes.htm.
16. Doering, M.A.: “Acquisition Pitfalls: Operating Cost Forecasts,” paper SPE 25841 presented at the 1993 SPE Hydrocarbon Economics and Evaluation Symposium, Dallas, 29–30 March.
17. David, A. and Hickman, T.S.: “What Is the Market Value of Long-Life Reserves?” paper SPE 20508 presented at the 1990 SPE Annual Technical Conference and Exhibition, New Orleans, 23–26 September.
18. “Survey of Economic Parameters Used in Property Evaluation,” presented at the 2001 SPEE Annual Meeting, San Diego, California, June.

Appendix A—Description of Asset

This appendix is a reproduction of Appendix A from [Ref. 1](#). It provides a general description of typical contractual arrangements for fractional ownership and/or beneficial rights.

A fundamental step in any property evaluation is a description of the asset. In the determination of FMV, the evaluator must be certain that the mineral interest is correctly described. The lease or production sharing agreement and any other significant issues relevant to ownership need to be reviewed and understood. If the asset is a piece of real estate, the physical dimensions and a complete description of the property are prepared along with a description of any structures that may be present. If the asset is the inventory of a retail business, then the stock must be counted and categorized. In these instances, the assets can be accurately described and quantified with little doubt as to their existence. In the oil and gas industry, however, the situation is somewhat different.

When evaluating oil and gas assets in the form of reserves, the process of describing the asset requires an estimate of the volume and quality of oil, gas, and by-product reserves that may be recovered in the future from subsurface reservoirs. These products are not available at the surface to be examined. One aspect of oil and gas property ownership is that ownership is

usually of a fractional nature. Even if the property ownership is in the U.S., taxing authorities will somehow share in the revenue stream.

Types of Oil and Gas Property Ownership. The most common types of oil and gas property interests or ownership are

- A. Working Interests
- B. Royalties (landowner's, overriding, and sliding scale)
- C. Net Profits Interests
- D. Production Payments
- E. Production Sharing Arrangements

The following discussion defines these types of contractual arrangements and, in addition, includes common variations of the basic oil and gas interest types.

In the United States and to a great degree in Canada, the minerals are deeded privately and, at least at the origin of the country's claim to lands, were transferred and/or deeded in tandem with ownership of the surface of the land. In almost all other parts of the world, the mineral ownership is the property of the government of the country and is separate from the private surface ownership, if any. All the indicated ownership types could be broadly classified as production sharing arrangements because all are strictly contractual in nature.

Today in the United States and Canada it is not uncommon to find that the surface and mineral interests have been severed through contractual agreement. Such severance occasionally (frequently) is the root of disputes when the mineral owners require access to the minerals through surface locations.

A. Working Interests. A working interest owner has an obligation to pay a share of costs. That share of costs is sometimes referred to as an expense interest. In some groups within the industry, the term working interest is synonymous with the term expense interest. Working interests receive a "revenue interest," also referred to as a net revenue interest (NRI) or division order interest. An NRI is a fractional interest in the gross revenue from the sales of oil, gas, and sometimes other products from a property. The NRI is normally less than expense interest due to royalty interest burdens.

Types of working interests are

1. Working Interest—This is the lessee's or operating interest (conventionally equal to the expense interest) under an oil and gas lease, which is also called a leasehold interest. A working interest is created by a lease agreement or a deed. Its primary characteristic is the right to enter the property to explore, drill, and conduct production operations. The working interest can be owned by one entity or partitioned between several entities as in a joint venture or unit operation. If there is more than one entity, one party is usually designated as the "operator." The other working interests, if any, are "nonoperating" working interests. The working interest fractions add up to 100%.

2. Carried Interest—A carried interest is a fraction of the total working interest in an oil and gas property that is not required to pay development and, in some cases, operating costs. The carried interest portion reflects the lack of participation in all or a portion of capital costs. The capital requirement normally attributable to the carried interest's working interest position is, through agreement, paid by others, normally by one or more of the other working interest owners putting up a disproportionate share. The classic reason for one of the working interest owners to carry the other is a means of buying one's way into participation. This type of buy-in is sometimes referred to as a "promote." In some provisions for carried interests, the owner of the carried interest does not receive any income until the other working interest owners that put up the disproportionate share receive the return of their capital investment or an otherwise agreed on sum of money, which might be considerably in excess of the disproportionate

amount put up to carry the carried interest. A carried interest may apply to one or more wells, the lease, or to the prospect.

3. Reversionary Interest—In some situations, a portion of the working interest (the expense part, the NRI part, or both) reverts to another party when a specified condition occurs. The carried interest described above is a form of a reversionary interest. The condition that triggers the reversion often is occasioned by a “payout” of an investment. There may be a change in the working interest, or an overriding royalty could become a working interest. Multiple reversionary interests with different triggers often apply to a single property.

4. Terminable Interest—A terminable interest is a working interest that terminates on the payment of specified charges from the production revenue. This is another description of a class of reversionary interest.

B. Royalty Interests.

1. Landowner’s Royalty Interest—This is the landowner’s share of production retained in the lease agreement. If the minerals have been severed from the surface, it is the interest retained by the mineral interest owner. This income is free from capital investment and from most operating expenses except for a pro rata share of production and severance taxes. Sometimes the lease requires the royalty to bear its share of power, substitute fuel, marketing costs, and other costs to make the produced oil and gas marketable substances. Other such costs include compression, dehydration, and the removal of impurities.

2. Overriding Royalty Interest (ORRI)—An overriding royalty interest is in addition to the landowner’s royalty interest, and its terms and conditions are similar to the “basic lease” unless otherwise specified. An ORRI is carved out of the working interest. It usually represents a payment to a middleman for services rendered. The ORRI holder’s benefit of ownership generally expires with the expiration of the lease to which it is associated.

3. Drillsite Royalty—A drillsite royalty is paid for the use of a parcel of land for drilling and production operations for directionally drilled wells when the completion interval is not under the drillsite tract.

4. Compensatory Royalty—This is also called an “offset” royalty. This is a payment from the lessee to the lessor in lieu of drilling an offset well. This usually occurs when the lease would require the drilling of an “offset” well, but the lessee does not consider the drilling of the required well to be economic.

5. Shut-in Royalty—A royalty is paid (usually in the form of a periodic fixed amount stipulated by the lease agreement) when a gas well, capable of economic production, is shut-in because of a lack of a market for the gas (e.g., pipeline is not yet installed).

6. Term Royalty—Any royalty on production from a lease that has a fixed duration in time (i.e., 20 years) is a term royalty. Most royalties are associated with leases that are evergreen (i.e., the lease continues as long as production is in paying quantities), and those royalties are not term royalties.

7. Minimum Royalty, Sliding Scale Royalty, Step-Scale Royalty—These royalties reflect minimum or varying royalty rates, which can depend on such variables as (1) total oil (or gas) rate, (2) average daily rate per producing well, and (3) the oil (or gas) price.

C. Net Profits Interests. A net profits interest is a share of the revenue from a well or property that bears a share of expenses and a share of the income, often very similar to a non-operated working interest. The holder of the net profits receives income when the operation to his position is profitable but has no (or a modified) cost burden when the income from the sale of production is insufficient to cover costs from operating a well or property. Net profits interests are carved out of the working interest. The net profits can be on an operating cost basis only or may also reflect the recovery of capital costs. The structure of net profits interests are often such that costs from periods of non-profitable or negative cash flow operations are paid

from later periods of operations when the operations are profitable or have positive cash flow. One of the working interest owners, frequently the one from which the net profits interest was carved, administers the funds of the net profits interest account and, on the occasion of negative cash flow, at least temporarily absorbs the loss. Net profits interests may have tax (U.S. federal income tax) consequences that are identical to a working interest with similar associated expense and revenue interest fractions.

D. Production Payment. A production payment describes a financial arrangement wherein the owner of the production payment is entitled to a specified portion of the oil or gas production for a limited period of time or, as in most cases, until a specified condition is satisfied [normally related to when an amount of money (plus interest) has been received]. This income is free of production costs. A production payment is often used in financing an acquisition or a portion of the sales price to the seller with a bank loan. It is sometimes a method of “nonrecourse” financing, wherein the production payment holder can look only to the property to satisfy the loan.

There are two basic types of production payments, the “reserved” and the “carved out” payment. It is “reserved” when the owner of an interest assigns all or part of his interest and obtains an oil payment for a specified sum of money or a specified volume of production (barrels or MCF). A “carved out” payment is one in which a party assigns only a payment of a specified sum of money (usually with interest) out of a certain share of the grantor’s production revenue. However, none of the grantor’s interest in the property has been assigned, only a certain sum of money. A production payment may be “deferred” and not begin until after the operator has realized a certain sum of money, or until a specified period of time has elapsed.

E. Production Sharing Arrangements. Production sharing agreements can have terms similar to production payments. However, production payments are normally structured to satisfy a previous monetary commitment, while a production sharing arrangement is normally structured to compensate and provide incentives for an operator to perform under a contract to produce a government’s minerals.

SI Metric Conversion Factors

$\text{bbl} \times 1.589\,873$ $\text{ft}^3 \times 2.831\,685$	$\text{E} - 01 = \text{m}^3$ $\text{E} - 02 = \text{m}^3$
---	--

Chapter 20

Reservoir Management Programs

E.D. Holstein, Consultant and E.G. Woods, Consultant

20.1 Introduction

Reservoir management has been in place in most producing organizations for several years. Several authors¹⁻⁸ have described how reservoir management is structured; however, the type, quality, and consistency of programs vary. This chapter defines reservoir management and suggests how to maintain an effective, ongoing program that can be sustained and continually updated to represent the changing needs of an organization or resource.

Reservoir management consists of processes that require the interaction of technical, operating, and management groups for success. The complexity of the problem and size of the asset dictate the type and number of personnel assigned to the task. Commitments can vary from part-time assignments for technical and operating staff members to the full-time use of multifunctional and, in some instances, multiorganizational teams. Personnel changes, altered priorities, insufficient surveillance data, and lack of documentation, however, can reduce the effectiveness of reservoir management programs.

Methods for assessing the effectiveness of reservoir management programs, including identifying strengths and areas for improvement, are needed to approach the topic from a quality perspective (i.e., benchmark to an ideal, best-practice standard). Making these assessments on a systematic, regular basis can be effective in developing a common terminology that improves communication and in ensuring a comprehensive review and a more complete listing of improvement opportunities. Reservoir management assessments are also effective in providing a comparison with ideal or best practices that result in a more innovative environment and in establishing a method of documentation and measurement to determine how well reservoir management is being sustained despite changes in personnel and priorities. This chapter includes a method for assessing the quality of a reservoir management program.

20.2 Reservoir Management Processes

Fig. 20.1 illustrates reservoir management processes. The processes are divided into those stewarded by the reservoir management team (RMT) and those guided by the supervisors and managers associated with reservoir management who comprise the reservoir management leadership team (RMLT). The arrows in the RMT box show work flow and how data and opportunities are captured.

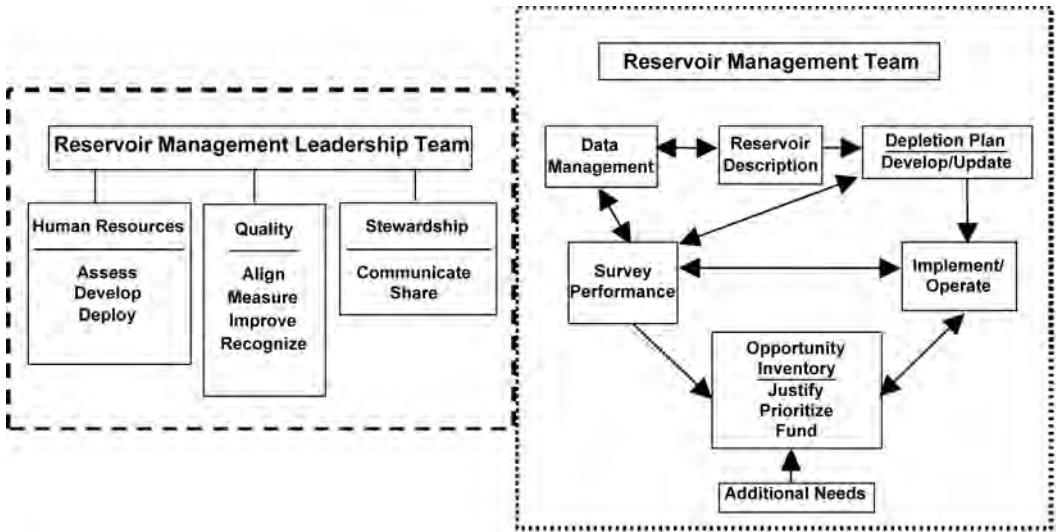


Fig. 20.1—Reservoir management processes.

20.2.1 Reservoir Management Team. The RMT members are the technical and operating personnel who perform reservoir management tasks. Fig. 20.2 shows the skills represented by the team members. The RMT is a multifunctional team, and organizational structure should not be inferred from this illustration. A team with all the skills shown could be a permanent part of an organization; however, it is more likely that the team would meet on a regular basis with individual members being assembled as needed from groups within an organization. In-house skills may need to be supplemented with outside personnel. The objective of the team is to bring together the skills needed to describe the reservoir, prepare depletion plans (including economic justification of projects), drill the wells, design and maintain wellbores, design and maintain production equipment, and conduct the day-to-day operations of producing the field according to the depletion plan. The team also meets to provide the information needed to upgrade and improve the depletion plan. A major focus of the team is to obtain reliable data on a timely basis to analyze production performance.

Data Management. This process represents the organizing of raw and interpreted data into a readily accessible form. It is not intended to imply what type or quantity of data is needed. Those issues are addressed in other processes.

Data Captured. This information includes raw data such as seismic records, well logs, conventional and special core analyses, fluid analyses, static pressures, pressure-transient tests, flowing pressures, periodic well production tests, and monthly produced volumes of oil, gas, and water. Interpreted data could include seismic time maps, seismic conversion of time-to-depth maps, seismic attribute maps, log analyses, formation tops, structure and isopach maps, cross sections, geologic models, and simulation models.

How much information and how to capture this information varies with the size of the database, size of the resource, and the remaining life of the resource. Hand-kept records and hard copies of information may be adequate for small resources. However, digital databases should be considered for all resources for the systematic acquisition of data, the growing usability of software for data interpretation, and the value of having data available to individuals in a distributed network.

Quality Assurance. Processes for the timely capture and quality maintenance of data also should be established. Personnel may be required for this specific purpose. While this assign-

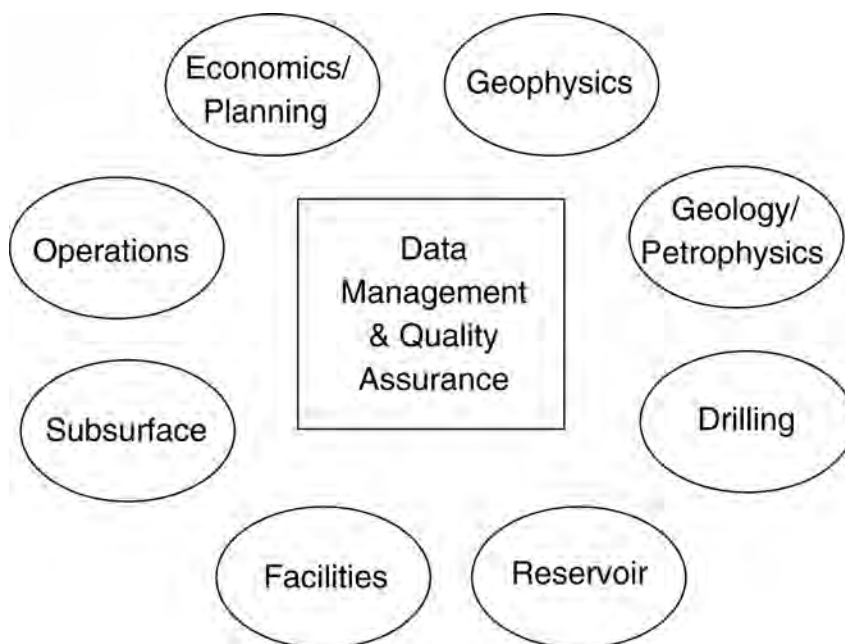


Fig. 20.2—Reservoir management team skills.

ment may be a drain on limited manpower, the benefits of readily available, high-quality data will save time spent in reorganizing, checking, and reinterpreting data each time a study is conducted. The time savings more than returns the cost of quality data capture. Studies of work output indicate that as much as 50% of the time spent on a project can be consumed by finding and organizing data that is not maintained in a readily accessible, high-quality format.

Reservoir Description. This process is the development of an up-to-date, detailed description of the reservoir that incorporates available data and technology into a fieldwide interpretation consistent with observed historical reservoir performance. Variations and risks in the description should be included. Again, the effort that goes into this description depends on the size of the remaining resource.

Geophysical, geological, and engineering interpretations are expected to produce information on the distribution of hydrocarbons in place and reserves. These interpretations include field and regional structure maps, including fluid-contact locations and the size of aquifers; isopach and porosity maps; the number of flow units or individual producing zones; the depositional environment including information on diagenetic changes and vertical and areal barriers to flow (or lack thereof); and variations in fluid saturations and permeabilities. The expected variability in these values should be included in these assessments. Descriptions from hand-drawn maps and correlations may suffice for small resources; however, in most cases, a geologic model is developed to capture these interpretations, with more complex models being needed for larger resources. The power of PCs and their software makes it more attractive to develop geologic models for all resources. (See the chapters on reservoir petroleum geology, geophysics fundamentals and outputs, and petrophysics in this section of the *Handbook* for information on geophysical, geological, and petrophysical interpretations and how they are used to develop a reservoir description. See the chapters on reservoir geophysics and geostatistics in the Emerging and Peripheral Technologies section of this *Handbook* for information on emerging technologies that can improve reservoir description.)

Original In-Place Volumes. Initially, the geologic model is used to estimate the amount and distribution of original in-place hydrocarbon volumes. These estimates include the range of uncertainties in rock properties, fluid saturations, and geologic interpretations and the resulting range in estimated in-place volumes.

Fluid-Flow Characteristics. The mapping of depositional environments, flow barriers, and flow test and core data aid in understanding the productivity and recovery trends in the reservoirs. This understanding is important in optimizing well placement and spacing and in recovery process selection.

Updating. Periodic collaboration between geoscientists and engineers is needed to include new seismic data and interpretations, well data, and performance characteristics into the geologic model. This work produces a better description of reservoir contents, reduces uncertainty, and establishes a basis for improved future development and reservoir operations.

Depletion Plan Development and Updating. Depletion plans define how to use primary drive mechanisms to deplete hydrocarbon resources and how, when, or if these mechanisms should be supplemented for additional recovery. The plan includes projected ultimate recoveries; producing rates of oil, gas, and water; and changes in reservoir pressure. As information is gained from field performance, the depletion plan is updated periodically to include any changes needed to better reflect how to optimize the depletion strategy. Specific parts of the plan include drilling schedules, well placement, individual well and total field offtake rates, total and well injection volumes, and wellbore utilization plans.

Determine the Primary Drive Mechanism. Determining the primary producing mechanism is the first step in selecting a depletion strategy. The chapters on oil reservoir primary drive mechanisms and gas reservoirs in this section of the *Handbook* describe primary drive mechanisms for oil and gas reservoirs, recovery potential, and methods to determine drive mechanism. This information can be used to project oil-, gas-, and water-producing rates, reservoir pressure trends, and ultimate recovery.

Well Placement and Well Density. The drilling and completion schedule and the number and placement of wells are a function of several factors:

- The total field offtake rate and individual well rates that can be sustained without ultimate loss of recovery.
- The number of wells and rates that are practical considering constraints such as the number of well slots on a drill pad or an offshore platform; the installed facility capacity; individual well capacities with the tubulars, completion techniques, and artificial lift used; and any regulatory limits on spacing and/or producing rates.
- The location of the wells for efficient drainage, that is, spaced evenly to contact all portions of the reservoir or targeted to specific areas because of reservoir geometry, quality variations, or invading water or gas. The amount of the reservoir that can be contacted is affected by limits on lateral drilling reach from existing platform or drill pads.

Infill drilling also should be considered at some point to sustain rates or contact portions of the reservoir inadequately drained with existing completions. The chapter on water injection in this section of the *Handbook* describes the benefits of infill drilling.

Horizontal/Multilateral Wells. Horizontal and multilateral wells increasingly are being used to contact more of the reservoir, to achieve higher rates with fewer wells, and to minimize coning of gas and/or water. Continuing technologic improvements are making horizontal wells an increasingly more cost-effective way to develop certain portions of a reservoir. The chapter on fluid flow through permeable media in this section of the *Handbook* covers performance characteristics of horizontal wells. It is now possible to simulate this performance with relatively simple models to determine the benefits of planning such wells for depletion of a reservoir. Horizontal wells are particularly effective in producing zones that have good vertical permeability, well-managed contact movements, and large drainage areas. These wells also have been

Process	Rock Type	Average k md	Depth ft	Oil Viscosity cp	T_R °F
Waterflood	Either	>5*	NR**	<100	NR**
Immiscible					
Hydrocarbon	Either	>1000	NR**	<20	NR**
CO ₂ , N ₂	Either	>1000	NR**	<20	NR**
Miscible					
High-pressure hydrocarbon	Either	All	>5,000	<5	NR**
Enriched hydrocarbon	Either	All	>3,000	<5	NR**
CO ₂	Either	All	>3,000	<10	NR**
N ₂	Either	All	>6,000	<5	NR**
Thermal					
Steam	Either	†	200 to 5,000	>20	NR**
Combustion	Sandstone	†	>1,000	NR**	NR**
Chemical					
Polymer	Either	>100	NR**	<40	<200
Alkaline	Sandstone	>100	NR**	<40 [‡]	<200

*Can be <1 md for carbonates. **NR = no restriction; † kh/μ >100. ‡acid number>0.2.

effective in fractured formations in which the horizontal well intersects more fractures than a vertical wellbore and, therefore, drains a greater volume of the reservoir. Horizontal wells are not as well suited to zones with low vertical permeability, rapidly moving contacts, and small remaining volumes to be drained. Where vertical permeability is low, high-angle wells may be more appropriate to contact the vertical interval and still provide a large drainage area.

The Need for Improved Recovery Projects. Improved recovery mechanisms refer to the injection of fluid (i.e., water, water with additives, hydrocarbon gas, nonhydrocarbon gas, steam, or air for in-situ combustion) to augment or replace the primary drive mechanism. **Table 20.1** presents screening criteria for selecting improved recovery processes.

The chapters on water injection; immiscible gas injection; foam, polymer, and resin injection; miscible processes; steam; and in-situ combustion in this section of the *Handbook* describe the characteristics and potential for several injection schemes in oil reservoirs. The chapter on gas reservoirs in this section of the *Handbook* explains the benefits of injection into gas caps and gas reservoirs. Historically, a field development progressed from primary production to fluid injection, such as water or immiscible gas, and then, in some instances, a second type of fluid injection, such as a miscible injection project, was needed. It is now important to determine the need for injection projects as early as possible to minimize depletion times, provide space for necessary equipment, avoid retrofitting facilities, and avoid other costly intermediate steps.

Wellbore Utilization Plan. This plan identifies the intermediate and final drainage points in each zone and outlines how each well will be used to deplete each producing zone and reservoir in a field. The plan includes guidelines on when to rework completions to sustain production by avoiding unwanted, excessive gas or water volumes. Where multiple producing zones exist, the plan should describe the zones to be completed in each well and provide guidelines on when to recomplete and the sequence of those recompletions to provide efficient recovery in each zone and minimize overall depletion time of the total resource.

Data Acquisition. The depletion plan should include the type of data to be acquired during the development stages of the reservoir and during the early, middle, and final production phases. Such data plans should include the type and number of open- and cased-hole logs; number, location, and frequency of static and transit pressure tests; number and location of fluid samples; number and location of cores and analyses to be made; type, location, and frequency of

production logs; frequency of individual well tests; and capture of monthly produced volumes of oil, gas, and water and monthly injected volumes. The chapters on petrophysics, production logs, single well chemical tracer testing, interwell tracer tests, and measurement of reservoir pressure in this section of the *Handbook* contain more information on these data.

Reservoir Models. Most depletion plans are based on some type of reservoir model.

Model Types. Reservoir models are basic tools for addressing reservoir management questions and issues. In selecting a model, it is normally desirable to select the simplest model that will give reliable results (i.e., selecting a model that will adequately discriminate among alternatives and lead to an optimal decision, although absolute results may not be precise). Several types of models of varying complexity are available that may be adequate for different uses. These models include analog, decline curve, analytical (material-balance, Darcy-law, Buckley-Leverett, pressure-transient), small numerical (well, cross-sectional, pattern-element, 3D-segment), and large-scale, full-field models. See the chapter on reservoir simulation in this section of the *Handbook* for details on building reservoir simulation models. Other chapters in this section also contain guidelines for models specific to the subject of the chapter.

Reservoir Issues. The first step in model selection is to identify the questions to be answered and their relative importance. The following issues must be addressed during this step.

- Exploration prospect forecast of oil, gas, and water production.
- Annual forecasts of oil, gas, and water production.
- Monthly tanker scheduling and storage requirements.
- Pressure maintenance requirements.
- Evaluation of alternative recovery processes: gas-cap expansion; natural waterdrive; and water, gas, or other fluid injection.
- Operational guidelines for pressure levels, injection volumes and distribution, and individual well and field total production targets.
- Well performance predictions: coning, artificial lift requirements.
- Stimulation evaluation.
- Gas- and water-handling requirements.
- The need for and timing of reservoir depressuring.

Model Description. A second consideration in model selection is deciding which primary forces will dominate reservoir performance. It must be determined whether viscous, gravity, or capillary forces, as reflected in coning, gas overrun, water underrun, or pressure drop, will dominate reservoir and well performance.

Model Data. Most models require at least some data describing fluid properties and reservoir description and may require multiphase flow (relative permeability and capillary pressure) and well performance [coning correlations, gas/oil ratio (GOR), water/oil ratio (WOR)] functions. Based on experience, certain simplifying assumptions may be acceptable. For example, if the reservoir description is dominated by a fining or coarsening upward depositional sequence, this may be more important than capturing the areal variation in reservoir description.

Case Design. Careful thought should be given to identifying cases to be run with the model to avoid running all combinations of the variables being studied, a number that can run in the several thousands for even modest-sized resources. In some cases, this may involve starting with a simple model to test the importance of some variables. For example, before building a full-field model, it can be helpful to build well, cross-sectional, 3D-segment, or pattern-element models.

Small Models. Coarse-grid 2D or 3D simulation models are useful for making a distributed volumetric balance in cases in which reservoir fluid migration and/or significant pressure gradients are issues. 3D models are useful for doing a multizone volumetric balance in which there is fluid migration between zones through commingled wellbores, along fault planes, or across fault planes by sand-on-sand contact. Also, these models are useful for regional aquifer model-

ing in which aquifers are irregular in shape, heterogeneous, or subject to pressure interference between fields.

Large Models. Large simulation models with more than 100,000 gridblocks are now constructed for many medium and large fields. The models usually are based on a detailed geologic model that may contain one million or more gridblocks. Methodologies are now in place to convert these geologic models into a more manageable reservoir model while retaining a good representation of the variation in reservoir characteristics. See the chapter on reservoir simulation in this section of the *Handbook* for more information on building and running reservoir models.

Implement and Operate. These are the specific activities required to implement and sustain the depletion plan.

Implementation Plan. This plan is developed with input from several engineering disciplines. The drilling engineers design drilling schedules, wellbore trajectories, and casing and cementing programs to locate wells at the required location for the lowest effective cost. The subsurface engineers design tubulars, completion techniques, stimulation processes, and artificial lift equipment required for target well rates. They also design workover procedures as needed. The facilities engineers design equipment needed initially to handle produced and injected fluids and provide plans for upgrades and additions when required. For offshore locations, the platform design engineers provide adequate sizing to accommodate wells and facilities within budget and physical restraints. The reservoir engineers assist in optimizing the drilling schedule to conform to available facility capacity and injection requirements, in providing well rate forecasts to aid well design, and in providing multiple production scenarios to aid facility design.

Need for Iteration. There is interdependence between depletion and implementation plans. Iteration normally is required to find the optimum combination of reservoir depletion objectives, equipment and completion constraints, and economic guidelines that result in optimum field development. For example, favorable mobility-ratio waterdrive reservoirs tend to have low sensitivity to rate of recovery; therefore, there is an economic tradeoff between the facility capacity and the time that the reservoir operates at a facility-constrained capacity (plateau rate).

Operating Plan. This plan guides operations personnel in implementing and accomplishing the depletion plan and can be strengthened by making operations part of the reservoir management team. Also, by establishing lines of direct communication between technical and operations staffs, early recognition of problem areas with individual well or facility performance will result in expedited solutions.

Survey of Performance. A periodic and systematic review of field performance, once the field has been placed on production, should be practiced. The types of activity vary with the type and size of resource and stage of depletion. At a minimum, frequent (daily to weekly) review of trends in individual well producing or injection rates, gas/oil ratios or gas/liquid ratios, water cut, wellhead pressure, and artificial lift performance should be required. Assuming the planned data are being captured, controlled for quality, and stored in a database, such reviews can be augmented by software packages that process data quickly, analyze performance trends, and generate exception reports.

Reservoir Performance Reviews. Surveillance includes periodic comparison (every 1 to 5 years) of performance (rates, pressures, recovery levels, injection volumes, contact movements, etc.) with the projections contained in the depletion plan. Significant deviations should trigger an update to the depletion plan to reflect the new information, to identify additional data needs, and to outline additional work programs needed to improve recovery and sustain rates. Reservoir reviews primarily should be an in-house assessment; however, the inclusion of experts not directly involved in day-to-day surveillance should be considered to provide another view and an independent source of ideas.

Rank, Justify, and Fund Opportunities. Opportunities that can increase the economic value of the reservoir will be an outgrowth of the initial development plan, the development and updating of the depletion plan, and surveillance activities. Assessing the economic benefits of each opportunity and obtaining the necessary management approvals is the next step.

Opportunities may involve investments in new wells, processing equipment, and improved recovery projects or changes to reservoir depletion strategies. Such assessments include recognition and evaluation of risks and benefits for programs to acquire data, improve recovery, increase production rates, or reduce operating costs. Outputs are a range of outcomes for each opportunity reflecting the associated risks for that opportunity and any alternative solutions. The natural outcome of such assessment is an up-to-date ranked list of opportunities. Outputs are recommendations to fund projects and/or implement changes to the depletion plan. The final phase is to obtain management approval for project funding consistent with budget and personnel resource constraints.

Additional Needs for Advancing Ideas. In the analysis of some opportunities, additional data, studies, or technology may be required to reduce the risks to an acceptable level. Additional data acquisition might include additional seismic, delineation drilling, or fluid analyses. Studies could include reinterpretation of seismic data or an in-depth reservoir study including complex geologic and reservoir simulation models. Acquiring technology could be by purchase or through liaison with a research organization in which the needs of the project are considered in planning research activities.

20.2.2 Reservoir Management Leadership Team. This group includes supervisors and managers responsible for allocating resources and creating an environment conducive to effective reservoir management.

Human Resources. The first objective of the RMLT is to assess and provide the personnel needed for successful reservoir management. This task involves the following procedures.

- **Assess.** Determine skills required to develop and manage a reservoir, and then judge the current staff's proficiency and need for improving such skills.
- **Develop.** Providing the training and work experiences needed to improve skills. Training includes in-house schools and seminars plus programs offered by third parties. Mentoring should be considered. This also includes the development of local training programs to meet specific needs not being met cost-effectively by more general programs.
- **Deploy.** Allocating supervisory, operations, and technical staff members consistent with established priorities and skill requirements to maximize the value of a resource. The process should consider the long-term benefits of skill development.

Achieving a Quality Program. The RMLT should have methods in place for determining the quality of the reservoir management program and how it can be improved to meet expectations. The quality model should be flexible to fit the needs of an organization. The needs most likely will vary from resource to resource depending on size, maturity, and perceived chance for developing additional investment opportunities.

- **Align.** There should be a process in place to ensure that all persons involved in reservoir management understand its importance, their role, and the quality objectives.
- **Measure.** Some process for systematically measuring the quality of a reservoir management program needs to be developed. Such a process would identify components of the program and the relative importance of each. A method of measuring how well each component is being accomplished needs to include the strengths in the current program that should be retained and areas that need improvement.
- **Improve.** Plans for improvements that lead to higher quality programs would include procedural issues, organizational structure changes, and the identification of skill needs. Such plans would also include goals for implementing the improvements.

- **Recognize.** A vital part of the quality program is the continuing recognition of both individual and team accomplishments. Whatever form of recognition is invoked, it offers an opportunity to reward good work and to reinforce the fact that management is dedicated to a good reservoir management program.

Stewardship. This process involves the periodic review and discussion of reservoir management activities and accomplishments with management and between groups.

- **Communicate.** These activities would involve various RMT and RMLT members and appropriate management. The primary purpose of these reviews is to describe reservoir management organization, future work plans, and historical performance of resources and to obtain management feedback on their expectations and support for continued reservoir management activities.

- **Share.** A corollary activity is the sharing of experiences between teams to identify best practices and company-wide improvement needs.

20.3 Measuring Reservoir Management Performance

Two questionnaires have been designed to survey and measure the quality of reservoir management performance. One is for RMT activities, and the second is for RMLT activities. **Tables 20.2 and 20.3** show suggested questions for the surveys.⁹ The questions are a guideline of what could be included in the surveys.

The surveys are self-assessment tools for the RMT and RMLT groups. The strengths of the surveys are the systematic consideration of all reservoir management activities, improved communication and understanding of the multifunctional issues by the team, identification of strengths to be sustained and areas for improvement, and a method for measuring improvement with subsequent surveys.

20.3.1 Conducting a Survey. Participants. As dictated by the specific situation, operating, supervisory, and technical persons would be included in the assessment. In some instances, it may be desirable to have outside experts participate in the assessment to obtain different views on specific areas in which weaknesses are suspected.

Frequency. The size and importance of a resource affects the timing and frequency of surveys. Considering the effort and personnel required for an effective survey, annual or less frequent timing may be appropriate.

Questionnaire Format and Scoring. **Fig. 20.3** shows the suggested format for capturing assessments as they are made. Only the section of RMT questions on database processes is included in this example. This form would be developed for each major process of the RMT and RMLT.

A performance rating for each question is to be judged on a four-point scale ranging from “seldom equals” to “essentially always equals” as compared with a best-practice standard that is determined by the group doing the assessment. Best-practice standards tend to be somewhat subjective, but experience has shown there is good agreement among knowledgeable persons participating in surveys. Best practice will depend on the field or fields involved. A prime asset that represents a significant resource with a long remaining life would be held to different standards than smaller resources or mature fields in an advanced stage of development.

The four-point scale should be adequate for differentiating the quality for various activities. Scales with five to ten increments were considered to be too fine and beyond the capability of this process, while fewer increments would not allow enough difference between poor and excellent.

Each participant rates each question, the scores are tabulated, and the team works to reach consensus on each question. While the scoring system could be viewed as a numerical result (1 to 4) to determine an overall outcome for each field or resource reviewed, the descriptions are intended to indicate qualitative results that are more appropriate for determining strengths that

TABLE 20.2—RMT QUESTIONNAIRE

Determining the Condition of a Database.*Do the databases (hardcopy/computer):*

1. Contain all existing geologic and geophysical data?
2. Contain all existing engineering and operational data?
3. Are these databases integrated?

Are the data:

4. Error free?
5. Easy to use? (Logically organized, clearly labeled with appropriate units?)

Are procedures/responsibilities effective for:

6. Inputting historical data?
7. Inputting newly acquired data?
8. Correcting errors in the data?

Describing the Reservoir.*Data Adequacy.*

1. Is the core coverage adequate to describe the reservoir?
2. Is the modern log density adequate to describe the reservoir?
3. Is the geophysical coverage adequate to describe the reservoir?
4. Has the potential in 3D, 2D, or time-lapse seismic to improve the reservoir description been adequately evaluated?

Interpretation Quality.

1. Are maps and interpretations field wide, up to date, and internally consistent?
2. Are log analyses up to date and performed with the latest techniques?
3. Are geological/geophysical and reservoir engineering interpretations integrated and consistent with observed field behavior?
4. Do the reservoir descriptions use current technical concepts?
5. Are technology experts (persons with a high degree of skill and knowledge in reservoir description and management) from within and outside the company regularly consulted?

Maintaining the Description.

1. Do systems exist to keep interpretations current?
2. Is reservoir description documentation complete?

Determining the In-Place Resource.

1. Is there a suite of core measurements to provide confidence in log-determined rock properties and fluid saturations?
2. Are there sufficient fluid samples to provide confidence in pressure-volume-temperature relationships?
3. Does an efficient system exist for converting reservoir description to volumes?
4. Are all potentially valuable resources included in the assessment (oil, gas, gas plant liquids, sulfur, helium, CO₂)?
5. Are the technical uncertainties quantified and their impact understood?
6. Is documentation of in-place volumes complete?

Depletion Plan Development and Updating.*Reservoir Performance.*

1. Is there a reservoir performance model that incorporates up-to-date reservoir description and establishes performance expectations including identification of the primary drive mechanism, the need for improved recovery projects, producing rates of all fluids and ultimate recovery?
2. Is the model appropriate for the size and complexity of the resource?
3. Are model predictions consistent with performance data?
4. Are alternative development and depletion schemes considered?
5. Is the reservoir performance model sufficiently documented to provide explanation and continuity when team members change?

Wellbore Management.

1. Have the planned number, type, and placement of wells been documented adequately?
2. Do well plans include the evaluation of horizontal wells and/or high angle wells?
3. Has a wellbore utilization plan been developed and documented?

Updating.

1. Is there a plan to collect the necessary data on which to base an updated analysis and projection of reservoir performance?
2. Is there a plan for systemic, periodic updates to the depletion plan?
3. Does a reservoir performance analysis compare actual to expectations from the theoretical modeling work?
4. Are recommended adjustments to operating and surveillance plans made systematically?
5. Are the revised plans reviewed periodically with technical experts?

TABLE 20.2—RMT QUESTIONNAIRE (continued)

Implement and Operate.

1. Are specific work plans, including schedules and data needs, developed for each project initiated?
2. Are the work plans integrated across technical and operating functions?
3. Are responsibilities and leadership clearly defined?
4. Have experts had the opportunity to offer comments and suggestions?
5. Is there sufficient access to experts?
6. Does a written plan exist for providing operating guidelines to field personnel?
7. Do operating plans recognize uncertainties and provide sufficient flexibility?
8. Do field personnel have sufficient information to know key issues?
9. Do depletion planners and field personnel communicate on implementation of the plan?
10. Are data collected as planned?
11. Are sufficient data collected to ensure that the operations plan is being followed?
12. Are ongoing data collection costs and value understood and endorsed by appropriate management?
13. Is there a process in place to compare progress against the depletion plan and make any appropriate changes to depletion or implementation plans?

Survey of Performance.

1. Is there a written surveillance plan?
2. Does the written surveillance plan provide for obtaining needed data?
3. Are the key reservoir performance indicators identified in the plan?
4. Is input from field personnel included in the plan?
5. Do surveillance plans recognize uncertainties and provide sufficient flexibility?
6. Are periodic reviews of reservoir performance planned?
7. Are reviews coordinated with technical and operations personnel to obtain the necessary input?
8. Is management's endorsement of reviews obtained?

Justify, Prioritize, and Fund Opportunities.**Identifying Opportunities.**

1. Does the process for identifying opportunities incorporate a field wide vs. wellbore analysis?
2. Does the process for identifying opportunities incorporate input from necessary technical and field functions?
3. Are ideas documented and maintained in an inventory system?
4. Is the inventory updated at appropriate intervals consistent with resource size and opportunity?
5. Are all possible opportunities captured in case improvements in technologies, economic, political, or risk factors occur?

Evaluating Opportunities.

1. Does an economic model exist that incorporates key issues such as costs, price forecasts, regulatory and legal boundaries, facility limitations, and/or royalty owner/host government issues?
2. Does the model forecast the economic drivers on the basis of specific field data?
3. Is the economic model sufficiently documented to provide explanation and continuity when team members change?
4. Are priorities evaluated on a timely basis with consistent criteria including long-term strategies?
5. Are the processes for obtaining expenditure authorization understood?
6. Are these processes documented?

Needs For Advancing Ideas.

1. Are plans formulated to acquire new information or analyses necessary to improve assessments of key opportunities and advance the idea?
2. Are these plans documented?
3. Are there plans to acquire new technology?
4. Are the costs of improving the assessments consistent with benefits?

are to be retained, barriers preventing execution of the process, and areas that require improvement. Also, some questions would have more importance than others and should be weighed accordingly.

Evaluation and Use of the Score. The initial assessment of a resource establishes a baseline and highlights areas of good practices and activities needing improvement. Subsequent reviews will show if targeted improvements are being accomplished while maintaining strengths. Over time, reviews also indicate where changes in emphasis are appropriate considering the changing maturity and needs of a resource. Another use of the results is the exchange of results

TABLE 20.3—RMLT QUESTIONNAIRE

Human Resources.*Assess.*

1. Are the skills needed to manage the company's reservoirs systematically assessed?
2. Is the staff's current proficiency in those needed skills systematically assessed?
3. Are the assessment processes and assessments documented?
4. Is information collected to measure and improve the effectiveness of determining skills and training needs?

Develop.

1. Are training programs implemented on the basis of an assessment of the staff's proficiencies?
2. Is this training supplemented with coaching and developmental work assignments in reservoir management?
3. Are these development and training plans documented?
4. Is the effectiveness of the skill development processes assessed periodically?

Deploy.

1. Do criteria and processes exist for ensuring that technical staffs are employed consistent with business priorities and skills requirements?
2. Are the criteria periodically re-examined?
3. Are the criteria and processes documented?
4. Is information collected to measure and improve the effectiveness of this process?
5. Are the needs for outside expert skills identified and supplied?

Quality.*Align.*

1. Are desired reservoir management goals and quality characteristics communicated to the organization?
2. Is multifunctional cooperation encouraged in forming reservoir management plans and goals?
3. Are the communication processes documented?
4. Is information collected to measure and improve the effectiveness of this process?

Measure.

1. Do processes exist for documenting reservoir management activities?
2. Are the critical components of reservoir management that need measuring periodically defined and documented?
3. Are the measures defined?
4. Are methods for collecting the data needed to measure the critical components established?
5. Are there efficient processes for analyzing the data?

Improve.

1. Do documented processes exist for identifying the needs (e.g., resources, skills, equipment, software) of people managing the reservoir?
2. Do documented processes exist that establish responsibilities for supplying the needs of people involved in managing the reservoir?
3. Are there established quality requirements?
4. Are near (1 to 2 years) and longer (> 5 years) term goals set for improving the reservoir management processes?
5. Are the strategies for achieving these goals established?
6. When setting goals, are business needs, current capabilities, and benchmarking data considered? (Benchmarking is a method of determining how your process compares with other company groups and/or competitors.)

Recognize.

1. Is there a process for recognizing individual and team accomplishments?
2. Is information collected to measure and improve the effectiveness of this process?

Stewardship.

1. Have all persons (customers) who will use the products of reservoir management been identified?
2. Have customer needs, quality characteristics, and use of product been identified?
3. Does a process exist for measuring and improving customer satisfaction?

Communicate.

1. Have the company's needs, including anticipated quality and use, been identified?
2. Does the RMLT take an active role in reviewing activities with management and gathering feedback?
3. Is the reporting process documented?
4. Is information collected to measure and improve the effectiveness of this process?

Share.

1. Are there processes for sharing approaches and lessons learned among various teams or groups that practice reservoir management?
2. Is this sharing process documented?
3. Does a process exist for identifying and communicating improvements in existing technology and new technology needed to achieve business goals?
4. Is information collected to measure and improve the effectiveness of this process?

	Seldom	Somewhat	Mostly	Essentially Always
Do the databases (hardcopy/computer)				
1. Contain all existing geologic and geophysical data?				
2. Contain all existing engineering and operational data?				
3. Are these databases integrated?				
Is the data				
4. Error free?				
5. Easy to use?				
Are procedures/responsibilities effective for				
6. Inputting historical data?				
7. Inputting newly acquired data?				
8. Correcting errors in the data?				
Strengths:				
Barriers:				
Areas for improvement:				

Fig. 20.3—Suggested format for capturing assessments.

between different RMT and RMLT groups with a focus on how strengths were accomplished and what has been implemented to improve the process.

20.4 Examples of Reservoir Management Benefits

In the following discussion of field histories, the reader should be aware that the small well spacing in some fields would not be optimal considering current technology and economic conditions. Some well spacings were driven by factors such as shallow reservoirs with low well costs, multioperator competitive operations, regulatory depth-acreage-based well allowables, oil price controls with two-tier pricing systems, and all vertical wells.

20.4.1 Sandstone Reservoir With Combination Drive Supplemented With Gas and Water Injection. Background and Geological Information. This field produces from a structure that lies above a deep-seated salt dome (salt has been penetrated at 9,000 ft) and has moderate fault density. A large north/south trending fault divides the field into east and west areas. There is hydraulic communication across the fault. Sands were deposited in aeolian, fluvial, and deltaic environments made up primarily of a meandering, distributary flood plain. Reservoirs are moderate to well sorted; grains are fine to very fine with some interbedded shales. There are 21 mapped producing zones separated by shales within the field but in pressure communication outside the productive limits of the field. The original oil column was 400 ft thick and had an associated gas cap one-third the size of the original oil column. Porosity averages 30%, and permeability varies from 10 to 1500 md.

Program Used. The primary recovery mechanism was a combination of a strong, directional waterdrive in the eastern part of the field, solution-gas drive in the western part of the field, and gas-cap expansion. Initial screened openhole completions resulted in uneven water advance caused by permeability differences between zones. A workover program converted all wells to selective, single-zone completions that allowed better control of aquifer advance. The directional waterdrive resulted in gas-cap tilting to the west despite return of all produced gas to the gas cap and extraneous water production on the east side. Water injection around the downdip periphery of the western part of the field was used to waterflood the western area, equalize pressure between east and west areas, and prevent gas-cap tilting. Because of low dip, recovery by gas-cap expansion was a less efficient recovery mechanism.

When field oil production declined to 4,500 B/D with 98% water cut and an average GOR of 30 Mcf/bbl, gas sales were necessary to maintain acceptable profitability. When gas-cap de-

pressuring was initiated, remaining oil production was thought to be coming from low permeability, thin intervals that would be affected minimally by accelerated water influx accompanying depressuring. Oil production is expected to continue well beyond the time the gas cap is depleted. Gas will be trapped behind advancing water, but reservoir-pressure decline will result in percolation of liberated dissolved gas from the residual oil in the water-invaded zone. This analysis came from a tank-type reservoir simulation model. To date, reservoir pressure has declined from 2,150 to 1,525 psi because the aquifer has been unable to offset the increased withdrawal rates.

Frac packing has provided sand control and near-wellbore stimulation. Conventional gravel packing also has been used when water proximity has been a concern. Plugback workovers and additional well conversions will be used to achieve maximum gas recovery. Original development was on 20-acre spacing. Selective infill drilling has been used to improve the sweep of injected water and to drain isolated parts of various zones.

Recovery Performance. The combined recovery factor for all the recovery mechanisms is 66% of OOIP. A contributing factor to this high recovery is a mixed wettability rock yielding waterdrive residual oil saturation of 12 to 13%, based on single-well chemical-tracer tests.

Field Surveillance and Management. There have been several major reservoir studies of the field during its history to determine and upgrade the depletion strategy. There also has been a sustained surveillance program to monitor reservoir performance. Surveillance has focused on maintaining liquid injection-production balance, monitoring area pressures, and the use of cased-hole logging to monitor gas/oil contacts (GOCs). Several segment and individual well simulation models have been used throughout the life of the field to better understand the waterfront movement, to adjust injection and offtake locations, and to mitigate bypassing of oil. Cased-hole logging programs (neutron or pulsed neutron) are now conducted at 3-month intervals to monitor the uneven water advance. Reservoir pressure is measured monthly. Pulsed-neutron logs are proving very valuable in locating bypassed oil in the shaley sand sections. Pressure maintenance by waterdrive and injection has permitted wells to produce by natural flow/artificial lift. This allowed cost-effective tubing logging and pressure surveillance.

20.4.2 Sandstone Reservoir With Strong Waterdrive and Crestal Gas Injection. Background and Geological Information. Production from this field is from several Upper Cretaceous sandstone formations. The producing zones are in pressure communication in the gas cap and aquifer but separate in the oil column. The structure is a complexly faulted anticline with a major fault separating the west and east flanks. There is minor communication across the fault. Gross thickness is 384 ft, and net-to-gross thickness is 0.7. Reservoir dip is 6° with somewhat higher dips upstructure. A tar layer exists at the original oil/water contact in the western flank of the field. The tar is 50 ft thick on the north flank and 100 ft thick on the south flank.

Porosity averages 27%, and zone permeability averages range from 1000 to 3000 md. The oil viscosity was 4 cp in the main oil column but grades higher near the tar and oil/water contact.

Program Used. The field was developed and produced competitively by several operators until unitization. The primary producing mechanism was a strong waterdrive that led to some gas-cap shrinkage despite an early gas return program. Performance analysis indicated a recovery efficiency of 65% by water displacement vs. 75% by gas displacement-gravity drainage. Formation of the unit allowed initiation of crestal gas injection. Water is being produced from down-structure wells to aid in moving the GOC downdip. Gas-cap pressure has been increased, water influx has been virtually eliminated, and the waterdrive recovery efficiency has been replaced with better gas-drive gravity-drainage efficiency.

A double displacement process (DDP) is under way to displace water-invaded portions of the original oil column with gas. The objective is to create a gravity-stable gas front that allows the ROS after waterdrive to be remobilized, drain to the base of each zone, and be captured in down-structure producing wells.

Down-structure oil production is from multiple zones. Wells are produced primarily from a single zone to maintain control of producing GOR and WOR. Recompletions to other sands are performed based on well performance, cased-hole logging results, and surveillance maps.

Recovery Performance. The recovery by waterdrive and gas injection is 63% OOIP. The DDP is expected to add another 6% of OOIP for a total of 69%.

Field Surveillance and Management. There have been several major reservoir studies of the field to determine and upgrade depletion strategies. The DDP was studied extensively with regional and detailed fault-block models before starting the field project. A recent sequence stratigraphy study located remaining oil and provided an improved basis for surveillance of the DDP. These studies have been used to guide infill drilling that has resulted in significant additional capture reserves. In addition, an aggressive well recompletion program has been essential in obtaining expected production and recovery performance.

A sustained surveillance program has been in place throughout the life of the field. Data on oil, gas, and water production are collected routinely each month, and annual cased-hole logging and pressure surveys are conducted. Fluid-contact mapping and material-balance models are used to monitor and balance gas-injection rates to offset fluid production and aquifer influx. The annual fieldwide cased-hole logging program to monitor fluid contacts is a very important surveillance tool in judging the effectiveness of the displacement process. Gas coning is one of the biggest operational challenges. Daily surveillance of GORs by field personnel and active involvement of the engineering staff combine to maintain maximum oil production rates. Water has swept heavier oil from deeper depths to shallower depths, reducing well productivity and slowing the gravity drainage process. Frequent measurements of oil gravities are used to understand and predict producing characteristics.

Heavy oil creates oil/water separation problems, which leads to injection of contaminants in saltwater disposal wells. This results in the need for frequent saltwater disposal well cleanout workovers. Keeping the surface-handling facilities clean minimizes these workovers. Techniques include regularly scheduled tank inspections and cleanouts, appropriate internal tank piping/oxygen exclusion, well-managed water chemistry surveillance and chemical programs, and the use and maintenance of appropriate transfer pumps. Periodic backflowing of gas-injection wells has had a significant positive impact in maintaining high levels of injectivity and minimizing gas-injection pressures.

20.4.3 Sandstone Reservoir With Strong Waterdrive and Selective Well Completion Strategy.

Background and Geological Information. This field produces from a series of stacked sandstone reservoirs situated in an angular unconformity trap consisting of an eroded 2 to 6° monocline and an oil/water contact common to all zones. The original oil column was 400 ft thick and contained a 43°API, highly undersaturated crude. Porosity averages 22%, and permeability averages 3 darcy.

Program Used. The primary recovery mechanism is strong waterdrive. All wells are now gas lifted, although this was not necessary in early field life. Wells have typically been drilled through multiple sands, which have been produced sequentially and, in some cases, comingled. Initial development was on 300-acre spacing. Two subsequent infill-drilling programs have been carried out to drain thin zones and areas in the extreme updip portions of the reservoir. The platform is currently constrained by water-handling capacity and, when wells reach high water cut, they are typically cycled on and off so that total production matches facilities limits.

Recovery Performance. The estimated recovery factor is approximately 75% of OOIP. Good rock and fluid properties plus good lateral continuity have contributed to this high recovery through gravity-stable displacement of oil by the invading water. Estimated S_{or} in invaded sections of the reservoir is 10% of pore volume (PV).

Field Surveillance and Management. Cross section and 3D computer models have been used to study reservoir behavior and upgrade the depletion strategy. A sustained surveillance program includes logging to monitor displacement and regular field performance reviews by the geoscience and engineering team members.

20.4.4 Sandstone Field With Waterflood, Gas Injection, and Miscible Projects. Background and Geological Information. The field is a structural stratigraphic trap that has been divided into several vertical zones. Complex, systematic depositional and diagenetic changes resulted in a dual pore system that was further impacted by structural and hydrocarbon histories, resulting in a highly variable vertical and areal distribution of net pay, porosity, and water saturation. Porosity values range from 10 to 30% with an average of 22%. Average well-zone permeabilities ranged from 100 to 1800 md with a field average of 500 md.

Program Used. The primary depletion mechanisms were gas-cap drive along with a very weak waterdrive (rock properties deteriorate rapidly off structure) and potential solution-gas drive. Waterflooding was planned as part of the initial field development to prevent significant pressure depletion.

Waterflooding was started in conjunction with an infill-drilling program that reduced spacing to 80 acres per well. Inverted seven- and nine-spot injection patterns were applied to areas of the oil column not overlain by the gas cap. A small enriched-hydrocarbon miscible injection project was later expanded to additional areas of the field.

Horizontal wells have been used extensively in areas close to the GOC to capture reserves from relatively thin oil columns that were previously uneconomic because of severe coning problems. A gas-cap cycling project has been expanded three times. A few 40-acre-spaced wells were drilled in areas of poor drainage, especially where locally large shale sections prevent good continuity. However, a more economical approach has been to drill 1,500- to 2,000-ft horizontal sidetracks, which can realize up to 85% of the 40-acre well recovery but at less than one-third the cost.

Recovery Performance. Estimated ultimate recovery is 60% OOIP with a miscible contribution of 10% OOIP in affected areas. The contribution of reservoir management to these high recovery levels is difficult to quantify. Initial estimates of recovery were in the range of 40 to 45% of OOIP. It is clear that a continuing effort to discover improved depletion techniques has added significantly to ultimate recovery.

Field Surveillance and Management. The unit collects surveillance data to manage the reservoir effectively. This includes day-to-day production tests, production/injection profiles for wells, and bottomhole-pressure surveys across the field. Additionally, repeat cased-hole neutron logs are taken to monitor gas movements across the reservoir. On new wells, a comprehensive suite of openhole logs is obtained to provide geologic information and to supplement production data and surveillance. The unit actively collected special reservoir surveillance data from pressure-pulse and pressure-transient well tests, repeat formation tests, and specially obtained cores. Both single-well chemical-tracer tests and log-inject-log tests have been conducted, and specialized core data have been obtained in the waterflood areas to measure and improve the effectiveness of the waterflood/miscible EOR project. Additionally, gas samples are collected routinely from flood area production wells to measure returned miscible injectant to further optimize and improve the miscible EOR project and from gravity-drainage area wells to monitor movement of injected cycle gas. Many different simulation models have been developed and updated over time.

There are frequent discussions, at both the technical and managerial levels, of surveillance techniques, operating strategies, reservoir and facility management programs, and future capital projects. Committees, forums, and teams continue to evolve to facilitate and improve these exchanges. In addition, corporate resources bring technical expertise and a worldwide perspective to the development decisions.

20.4.5 Steeply Dipping Sandstone Reservoir With Gravity Stable Miscible Project. *Background and Geological Information.* This field was formed by a piercement salt plug that breached a regional fault system. The reservoir is composed of unconsolidated sands that dip away from the salt dome at 65 to 85°. The reservoir is divided into several fault blocks. Within each block, the sand is relatively homogeneous. Porosity averages 26.5%, and permeability averages 1.3 darcy. Oil gravity is 38° API.

Program Used. This project is operated as a gravity-stable, hydrocarbon-miscible flood. The injection rate corresponds to a velocity of roughly one-half the critical velocity required for gravity-stable operations. A volume, corresponding to 17% PV, of enriched gas (natural gas liquids plus solution gas) was injected. This was followed by injection of solution gas alone. When injection is completed, blowdown of the gas cap is expected to recover approximately 90% of the enriched gas and a significant portion of the injected solution gas, thus reducing the effective cost of the solvent.

3D reservoir simulations were carried out to examine four depletion scenarios: primary depletion by gravity-stable gas-cap expansion, waterflooding at constant pressure, gravity-stable immiscible gas injection at constant pressure, and gravity-stable hydrocarbon miscible flood at constant pressure. Maintaining constant pressure improves recovery by eliminating shrinkage of oil over the course of displacement. Core flood experiments gave recoveries similar to those predicted by the simulations. Miscible residual oil saturation in core floods was 7% of PV. Slimtube experiments were also carried out to determine the level of enrichment required to achieve miscibility at a given pressure level. A minimum miscibility pressure (MMP) was selected that was consistent with the volume of enriching natural gas liquids available for the project.

Recovery Performance. Primary production occurred through gas-cap expansion. Approximately 6.2% of OOIP had been recovered when miscible gas injection began. Estimated ultimate recovery is 50% of OOIP for primary recovery in both sands, 74% for total recovery after miscible flood in one sand, and 86% for total recovery after miscible flood in a second sand. These recovery levels were determined by tracking gas fronts with pulsed-neutron capture logging and material-balance calculations. These recovery levels are consistent with simulations that were carried out during planning of the miscible project. To date, conformance has been excellent, with field recoveries similar to those seen in core floods.

Field Surveillance and Management. Routine pressure measurements, pulsed-neutron capture logs, and pressure-transient testing were used to monitor reservoir performance, contact movements, and identify areas of good and poor communication. Pressure initially was allowed to decline to slightly above the MMP and was then maintained by scheduling injection volumes equal to production. Pressure maintenance became a challenge because of increasing GOR, which resulted in watercut increases and reservoir pressures below the MMP in some areas. Pressures were then increased and maintained by curtailing production from high GOR wells.

Pressure communication between injectors and producers has been good in reservoir A. In reservoir B, pressure communication between injectors and producers has been somewhat hindered by faults and shale barriers that act as baffles.

20.4.6 Low Permeability Sandstone Waterflood. *Background and Geological Information.* The reservoir is a series of Cretaceous-age, prograding delta clastic sediments consisting of laminated fine-grained sands and shales that are trapped stratigraphically by overlying shales. Reservoir averages are approximately 50 ft of gross pay, 15% porosity, and 20 md permeability.

Program Used. The primary recovery mechanism was solution-gas drive. The field was converted to waterflood in 1961 with an inverted nine-spot injection pattern. Subsequently, a portion of the field was converted to line-drive water injection for improved sweep efficiency and increased water injection capacity.

Recovery Performance. Under primary recovery, the field produced 5% of OOIP. Incremental recovery to date under waterflood has been an additional 17% of OOIP. An ultimate recovery efficiency of 26% of OOIP is forecast.

Field Surveillance and Management. Exploitation of the reservoir is focused currently on reperfoming underperforming wells and infill drilling into portions of the reservoir that are shown to be poorly swept. Continuous rebalancing of water injection is proving effective in displacing oil from uncontacted layers.

20.4.7 Sandstone Reservoir With Solution-Gas Drive and Water- and Gas-Injection Projects.

Background and Geological Information. The highly faulted structure produces from six different productive horizons. The depositional settings range from deepwater marine turbidite fans through near shore and delta sand facies to fluvial deposits. Reservoir quality ranges from high permeability (350 md) in highly continuous tidal shoals to fair quality (100 md) in moderate continuity fluvial channels. The reservoir has been developed from two separate platforms and has an extensive subsea development of satellite fields. More than 140 wells have been drilled from two platforms since initial development in 1976 with well lengths varying from 9,800 to 19,000 ft. Six subsea fields have been developed with 28 subsea producing wells. There are 28 reservoirs that are managed separately.

Program Used. The primary recovery mechanism in the majority of these reservoirs was solution-gas drive with weak aquifer support, although some of the satellite fields have strong bottomwater drives. The main reservoir was developed from the two platforms: the Alpha platform began production in 1976, followed by the Bravo platform in 1984. Crestal gas injection and peripheral water injection were used in both areas in the main reservoir to maintain reservoir pressure and displace the oil zone. The secondary reservoir formations were developed with solution-gas drive mechanisms with water and gas injection applied where economically viable. The Alpha main reservoir achieved a 52% oil recovery factor. Gas-cap blowdown started in 1993. The pressure maintenance schemes continue to be used in the Bravo and Satellite fields.

Recovery Performance. The expected recovery in the main formation is expected to exceed 50% of the OOIP on both the Alpha and Bravo platforms, with the average recovery factor for all sands expected to reach 39% of the OOIP. The cumulative recovery to date of 33% of the OOIP compares with the 15 to 20% expected under primary depletion.

Field Surveillance and Management. Reservoir management in this complex field relied on a multidisciplinary team approach. The complex geological and structural natures of the fields are represented in detailed geological models. Improvements in the structural imaging of the fields through the use of ocean-bottom cable seismic and detailed sequence stratigraphic work has improved the understanding of the fields. Black oil reservoir simulation models have been built for all the major producing reservoirs. These models have sufficient detail to represent the geological and structural complexity properly. A surveillance program for each reservoir unit is defined so that cost effective and minimum production deferral interventions can be planned in advance. Asset development and depletion plans are defined for each field/reservoir unit that define the depletion plan and integrates study plans with surveillance and drilling activities. An opportunity list is developed that is reviewed routinely by the multidisciplinary asset team to ensure appropriate prioritization of resources. Reservoir surveillance data is combined with classical reservoir engineering techniques to create surveillance maps for each of the reservoir flow units. Surveillance techniques combined with simulation results are used to ensure quality forecasts and robust infill-drilling targets. Infill wells typically have a full suite of MWD logs and modular formation dynamics testers. More complex horizontal wells tend to have less comprehensive data gathering because of cost and the risk of losing the hole.

20.4.8 Sandstone Reservoir With a Polymer Injection Project. *Background and Geological Information.* Production is from three sandstone zones of a Cretaceous-age formation. Productive area of the polymer project was 3,560 acres. Gross thickness was 230 ft, and net-to-gross thickness averaged 0.3. Porosity averages 27%; permeability varies by zone and is less than 100 md in two of them and 170 md in the third, most extensive one. Oil gravity was 20°API, and viscosity varied from 18 to 24 cp. T_R was 150°F.

Program Used. The primary depletion mechanism was solution-gas drive. The field was developed competitively on 40-acre spacing. A unit was formed, and waterflooding began with a staggered line drive. Injection water with a salinity of only 3,500 ppm total dissolved solids (formation water 150,000 ppm) was used without any apparent damage caused by clay swelling or sloughing.

The adverse mobility ratio (see the chapter on foam, polymer, and resin injection in this section of the *Handbook* for a discussion on mobility ratios) was recognized early in the waterflood and polymer injection begun in 1976. Polymer concentrations were targeted to improve the mobility ratio by a factor of 16 (reduced to 0.5). The injection of polymer was targeted to reduce the cycling of water through previously water-swept oil sands and to divert injected-brine polymer into noncontacted zones to displace additional oil.

Recovery Performance. Waterflooding increased oil rates from 300 to 2,000 BOPD. The rate had declined to 1,600 BOPD when polymer injection began. The rate of oil production decline subsequently was reduced in several wells. Primary plus waterflooding recovery factor was 23% of OOIP. Subtle changes in production decline rates and WOR make it difficult to determine the incremental recovery from polymer injection. An incremental increase of 1 to 3% of OOIP has been estimated. Lower injectivity resulted when polymer was added.

Field Surveillance and Management. Surveillance activities focused on maintaining injectivity and pattern balancing. Well stimulations and cleanout were needed. 2D cross-section simulation was used to manage the injection volumes and distribution of polymer and to design the optimum concentrations of the final polymer injection. Rates were adjusted to inject an average of 20% PV of 600 ppm polyacrylamide polymer solution.

20.4.9 Carbonate Field With Waterflood and Miscible Projects. *Background and Geological Information.* This field produces primarily from a Jurassic-age limestone-dolomite section that has a simple plunging anticline structure. The updip trap is formed by a combination of facies change from dolomite to dense limestone and a bounding fault. The formation is layered and has been divided into 18 correlative zones.

Program Used. The field was developed competitively by several operators. When production began, the reservoir pressure declined rapidly under a fluid-expansion drive. The field was unitized, waterflooding began, and pressure decline was arrested. Miscible N₂ injection was started eight years later. N₂ was selected rather than methane or CO₂ because of cost and supply considerations.

The field was developed initially with 89 wells on 160-acre spacing. Selective infill drilling in poorer sections of the reservoir (both areally and vertically) improved the sweep of injected water. The need for fieldwide infill drilling to 80-acre spacing was tested with five wells and shown to be uneconomical because little extra recovery was achieved.

The waterflood was implemented with a 3-to-1 line-drive pattern with low salinity water from a water-source well. Produced water is also injected. Peak water-injection rates reached 250 kBOPD. Three air-separation units produced nitrogen, which was reinjected. Peak injection rate was 86 Mcf/D. A water-alternating-gas (WAG) process is used.

There is no downhole corrosion treatment and no internal treatment of flowlines and pipelines. Flowlines and pipelines are protected cathodically and require selective remediation.

Corrosion resistant alloy tubulars and flowlines are used to handle the 2% H₂S (originally 8% but reduced by N₂ contamination) sour gas produced from the field.

Recovery Performance. Primary recovery of 17% of OOIP was expected. Waterflooding increased this to 57%, and the miscible project added another 13% of OOIP.

Field Surveillance and Management. This field has had several periodic reservoir studies to update and refine the depletion strategy and a sustained surveillance program that includes acquisition of data needed to monitor reservoir behavior and injection efficiency. To obtain an accurate geologic description, the entire pay interval in virtually all the wells was cored. The reservoir surveillance program included the monitoring of production data, injection data, bottomhole pressures, flood balancing, WAG ratios, injection-to-withdrawal ratios, and profitability of each pattern. One of the tools used is a history-matched four-component compositional-simulation model that is based on a stochastic geologic model and advanced scale-up technology. The 3D model contains 100,000 gridblocks and 18 layers. Good matches of pressure and oil, water, and nitrogen production at the field and individual well levels were achieved with quality control of key input data and the use of extensive history-match experience.

20.4.10 Carbonate Field With Waterflood and Miscible Projects. Background/Geological Information. This field is a north/south trending anticline separated into north and south domes by a dense structural saddle running east and west near the center of the field. Deposition was in an intertidal-lagoon-bank sequence. Production comes from formations at depths ranging from 4,200 to 4,800 ft (subsurface). The formation is more than 1,400 ft thick. The upper 200 to 300 ft is productive, and the remaining is a water zone of relatively low permeability. The productive upper portion of the reservoir is divided further into the upper and lower reservoirs. The average porosity is 9%, and the average permeability is 20 md.

Programs Used. Primary/Waterflood Depletion. The field was developed initially on 40-acre spacing with 300 wells. The primary producing mechanism was a combination of fluid expansion with a weak waterdrive. In 1963, a unit was created and peripheral water injection began into 36 wells. Production from the unit began declining in 1967 because of insufficient pressure support. A detailed engineering and geologic study identified a flow barrier that was inhibiting pressure support between the upper and lower reservoirs. Implementation of a three-to-one line drive provided the needed pressure support, and production increased. When production began to decline again in 1972, a subsequent reservoir study resulted in a technique to correlate gamma-ray/neutron logs with core data, thus better defining porosity distribution and OOIP. The study resulted in an infill-drilling program to 20-acre spacing, conversion of the injection scheme to an 80-acre inverted nine-spot pattern, and a better reservoir surveillance program.

Infill Drilling/Miscible Process. An oil viscosity of 6 cp makes the waterflood mobility ratio relatively high. From pressure cores and laboratory core floods, waterflood residual oil saturation was estimated to be 34% of PV. Combined, these two factors provided incentive for further infill drilling and evaluation of other recovery methods. A CO₂ miscible project was evaluated with laboratory investigations, a field pilot, and reservoir simulations.

The proposed CO₂ project consisted of 167 patterns on approximately 6,700 acres that encompassed 60% of the productive acres and 82% of the OOIP of the unit. Every attempt was made to use the original 40-acre wells and the 20-acre infill wells. Infill drilling to 10-acre spacing was an integral part of project development. All the WAG injectors and central producers were new 10-acre wells as a part of 40-acre inverted nine-spot patterns.

Within 2 years of project implementation, 205 infill producers and 158 infill injectors had been drilled. Re-evaluation of the project during implementation resulted in changes to project scope. The CO₂ project now consists of 173 patterns on approximately 7,830 acres.

Recovery Performance. Projected recovery from primary and waterflooding methods is 30% of the OOIP. Incremental recovery because of the miscible CO₂ flood is 15% of the OOIP.

Field Surveillance and Management. Throughout the years, a number of reservoir description and engineering studies have been conducted with the goal of developing better reservoir management strategies. A detailed, integrated surveillance and reservoir management program was implemented to achieve areal-flood balancing, vertical-conformance monitoring, production monitoring, injection monitoring, data acquisition and management, pattern-performance monitoring, and optimization. The following are some key objectives of field surveillance and management.

- Integrate all knowledge and data, such as seismic, core, log, laboratory work, and outcrop and field observations, into a fieldwide geologic model and keep it up to date.
- Monitor and understand field performance.
- Increase WAG frequency to minimize problems associated with premature gas breakthrough.
- Maintain a system-operating pressure between the reservoir-parting pressure and the MMP. Falling outside this narrow range would compromise ultimate recovery by fracturing the reservoir or eliminating the miscibility component of the flood.
- Manage the GOR to fit compression limitations for recycled CO₂.
- Update assessments of facility capacity.
- Maintain automated injection, production, and artificial lift monitoring systems to capture data needed to develop programs for maintaining flood-front pressure by balancing the WAG schedule, ratios, and CO₂ slug sizes.
- Implement proactive corrosion- and scale-treatment programs.
- Use new infill wells for injection purposes to minimize downhole mechanical problems.
- Maintain a continuous injection-well profiling program for flood management purposes.

20.4.11 Carbonate Field With Waterflood, Polymer, and Miscible Projects. Background and Geological Information. The field is a carbonate reef-mound complex of Late Pennsylvanian to Early Permian age with a formation composed of limestone with minor amounts of shale. It reaches a maximum thickness of 918 ft and averages 315 ft. Skeletal and oolitic grainstone shoals form the most significant reservoir facies. More than 90% of the porosity is secondary because of freshwater dissolution of unstable framework grains. Cores indicate the presence of fracturing and enhanced dissolution along fractures. Channeling of water and/or CO₂ is evident between many injector/producer pairs.

Program Used. Primary development was followed by a centerline waterflood that was converted subsequently to a five-spot waterflood with two infill-drilling campaigns. A polymer-augmented waterflood was implemented on the basis of data from the new wells. The possibility of enhanced natural gas liquids production was identified with compositional reservoir simulation studies. A CO₂ miscible WAG injection process was then initiated.

Recovery Performance. CO₂-WAG injection is expected to result in an additional recovery of 12% of the OOIP, bringing the total estimated ultimate recovery to 64% of OOIP. The solvent extraction capability of CO₂ has resulted in an increase of up to 6,000 B/D in natural gas liquids production.

Field Surveillance and Management. Interdisciplinary teams composed of geoscientists; reservoir, production, and facilities engineers; and field operation staff conducted reservoir management. Cores from 30 of the wells were analyzed for stratigraphy and depositional sequences, and these interpretations provided the basis for a reservoir model that has been updated and enhanced throughout the life of the field. 3D geologic and simulation models are integrated into the surveillance process for flood optimization, workover and drill well planning, and WAG management.

20.4.12 Carbonate Waterflood With Strategic Well Placement. *Background and Geological Information.* The reservoirs in this field are part of a Devonian atoll reef and carbonate shoal complex consisting of limestone with traces of dolomite, pyrite, and anhydrite. The hydrocarbons are trapped stratigraphically by a calcareous shale seal. The reservoir averages approximately 200 ft of gross pay, 8% porosity, and 50 md permeability. Some stringers have permeabilities of 2000 to 3000 md, which result in high well productivities. Oil characteristics include a gravity of 44°API and a formation volume factor of 1.8 RB/STB. The reservoir depth averages 9,000 ft, and the initial water saturation was 14%.

Program Used. The primary recovery mechanism was solution-gas drive. In 1964, the field was converted to a downdip peripheral waterflood. Originally, the field was developed on 160-acre spacing. Selective infill drilling to 80- and 40-acre spacing has been used in updip portions of the field to develop areas of poor reservoir continuity that contain unswept oil.

Recovery Performance. Under primary recovery, the field produced 1% of OOIP. Recovery to date under waterflood has been an additional 45% of OOIP. An ultimate recovery efficiency of 49% of OOIP is forecast.

Field Surveillance and Management. The waterflood is being balanced in four discrete geologic regions or flow units to replace voidage and improve areal-sweep efficiency. The replacement ratio has averaged 100%.

20.5 Summary

Petroleum reservoir management is a dynamic process that recognizes the uncertainties in reservoir performance resulting from our inability to fully characterize reservoirs and flow processes. It seeks to mitigate the effects of these uncertainties by optimizing reservoir performance through a systematic application of integrated, multidisciplinary technologies. It approaches reservoir operation and control as a system, rather than as a set of disconnected functions. As such, it is a strategy for applying multiple technologies in an optimal way to achieve synergy, rather than being a technology in itself.

The reservoir management concepts in this chapter are keyed to RMT and RMLT teams. The RMT consists of experts in their field of technology who understand the impact of and are able to work with experts in other technologies. The RMLT is responsible for providing resources and determining customer needs. The effectiveness of the process depends on the timely acquisition, appropriate analysis, and use of high-quality data.

The reservoir management process must be tailored to individual fields depending on size, complexity, reservoir and fluid properties, depletion state, regulatory controls, and economics. The field cases discussed give some insight into how reservoir management has been applied and adapted to a variety of reservoir types and recovery processes.

Because reservoir management is a dynamic process tailored to individual fields and recovery processes, it is important to have timely assessments of how it is being applied. This helps ensure that best practices are being implemented, that the process is being improved continually and systematically, and that experience and technology is transferred among teams.

Nomenclature

h = thickness, L, ft

k = permeability, L², md

S_{or} = residual oil saturation, % PV

T_R = reservoir temperature, T, °F

μ = viscosity, m/Lt, cp

References

1. Eden, A.L. and Fox, M.L.: "Optimum Plan of Depletion," paper SPE 17458 presented at the 1988 SPE California Regional Meeting, Long Beach, California, 23–25 March.
2. Hickman, T.S.: "A Rationale For Reservoir Management Economics," paper SPE 26411 presented at the 1993 SPE Annual Technical Conference and Exhibition, Houston, 3–6 October.
3. Raza, S.H.: "Data Acquisition and Analysis for Efficient Reservoir Management," *JPT* (April 1992) 466.
4. Satter, A., Varnon, J.E., and Hoang, M.T.: "Reservoir Management: Technical Perspective," paper SPE 22350 presented at the 1992 SPE International Meeting on Petroleum Engineering, Beijing, 24–27 March.
5. Stiles, L.H. and Magruder, J.B.: "Reservoir Management in the Means San Andres Unit," *JPT* (April 1992) 469.
6. Thakur, G.C.: "Implementation of a Reservoir Management Program," paper SPE 20748 presented at the 1990 SPE Annual Technical Conference and Exhibition, New Orleans, 23–26 September.
7. Torvund, T.: "The Oseberg Reservoir Management Planning: A Case History From the Oseberg Field," paper OTC 6140 presented at the 1989 Offshore Technology Conference, Houston, 1–4 May.
8. Wiggins, M.L. and Startzman, R.A.: "An Approach to Reservoir Management," paper SPE 20747 presented at the 1990 SPE Annual Technical Conference and Exhibition, New Orleans, 23–26 September.
9. Holstein, E.D. and Berger, A.R.: "Measuring the Quality of a Reservoir Management Program," *JPT* (January 1997) 52.

General References

- "Bibliography," *Reservoir Management*, Reprint Series, SPE, Richardson, Texas (1998) **48**, 193–197.
- Abdullah, M.A.Y. and Olsen, B.S.: "Tapis—New Opportunities from a Maturing Field," paper SPE 54339 presented at the 1999 SPE Asia Pacific Oil and Gas Conference and Exhibition, Jakarta, 20–22 April.
- Chow, C.V. and Arnondin, M.C.: "Managing Risks Using Integrated Production Models: Process Description," *JPT* (March 2000) 54.
- Clayton, C.A.: "Ubit Field Rejuvenation: A Case History of Reservoir Management of a Giant Oilfield, Offshore Nigeria," paper SPE 49165 presented at the 1998 SPE Annual Technical Conference and Exhibition, New Orleans, 27–30 September.
- Day, S., Griffin, T., and Martins, P.: "Redevelopment and Management of the Magnus Field for Post-Plateau Production," paper SPE 49130 presented at the 1998 SPE Annual Technical Conference and Exhibition, New Orleans, 27–30 September.
- de Carvajal, G.: "Reservoir Management in the B-6/9, SVS-82, Lake Maracaibo, Venezuela—New Exploitation Policy for Maximizing Profit," paper SPE 39052 presented at the 1997 SPE Latin American and Caribbean Petroleum Engineering Conference and Exhibition, Rio de Janeiro, 30 August–3 September.
- Gallagher, J.J. *et al.*: "Brent Field Depressurization Management," paper SPE 56973 presented at the 1999 SPE Offshore Europe Conference, Aberdeen, 7–9 September.
- Gringarten, A.C.: "Evolution of Reservoir Management Techniques: From Independent Methods to an Integrated Methodology. Impact on Petroleum Engineering Curriculum, Graduate Teaching and Competitive Advantage of Oil Companies," paper SPE 39713 presented at the

- 1998 SPE Asia Pacific Conference on Integrated Modelling for Asset Management, Kuala Lumpur, 23–24 March.
- Hermansen, H.: “Twenty Five Years of Ekofisk Reservoir Management,” paper SPE 38927 presented at the 1997 SPE Annual Technical Conference and Exhibition, San Antonio, Texas, 5–8 October.
- Khataniar, S.K., Bora, A., and Borah, N.M.: “A Reservoir Management Case Study of the Nahorkatiya Oilfield,” paper SPE 39568 presented at the 1998 SPE India Oil and Gas Conference and Exhibition, New Delhi, India, 17–19 February.
- Langston, E.P., Shirer, J.A., and Nelson, D.E.: “Innovative Reservoir Management—Key to Highly Successful Jay/LEC Waterflood,” *JPT* (May 1981) 783.
- Satter, A. and Thakur, G.: *Integrated Petroleum Reservoir Management: A Team Approach*, PennWell, Tulsa (1994).
- Schaaf, R.P. and King, G.R.: “Numbi Field: Adapting a Reservoir Management Strategy to Changing Reservoir Conditions,” paper SPE 38925 presented at the 1997 SPE Annual Technical Conference and Exhibition, San Antonio, Texas, 5–8 October.
- Selemat, S., Goh, S.T., and Lee, K.S.: “Seligi Depletion Management,” paper SPE 57251 presented at the 1999 SPE Asia Pacific Improved Oil Recovery Conference, Kuala Lumpur, 25–26 October.
- Tewari, R.D. and Raju, A.V.: “Development Strategy and Reservoir Management of a Multilayered Giant Offshore Carbonate Field,” paper SPE 64461 presented at the 2000 SPE Asia Pacific Oil and Gas Conference and Exhibition, Brisbane, Australia, 16–18 October.
- Thakur, G.C. and Satter, A.: *Integrated Waterflood Asset Management*, PennWell, Tulsa (1998).

SI Metric Conversion Factors

acre	× 4.046 856	E + 03 = m ²
°API	141.5/(131.5 + °API)	= g/cm ³
bbbl	× 1.589 873	E – 01 = m ³
cp	× 1.0*	E – 03 = Pa·s
darcy	× 9.869 233	E – 01 = m ²
ft	× 3.048*	E – 01 = m
ft ³	× 2.831 685	E – 02 = m ³
°F	(°F – 32)/1.8	= °C
psi	× 6.894 757	E + 00 = kPa

*Conversion factor is exact.

AUTHOR INDEX

A

Agarwal, R.G., 746, 759
Aguilera, R., 23, 211, 1539
Ahmed, T., 994
Al-Hussainy, R., 846
Allard, D.R., 936
Alvarez, J.M., 1232
Ambastha, A.K., 1019
Anderson, B.I., 89–162
Archie, G., 455–456, 458–459, 461–462, 477, 488
Arps, J.J., 776, 783–784, 1530, 1571–1573, 1591, 1593
Attria, H.D., 1123
Auvenshine, W.L., 1025
Aziz, K., 864, 869–872, 875–876

B

Babu, D.K., 809, 814, 830–831, 834–835, 837, 839
Barber, A.H., 1062
Barber, T.D., 89–162
Barenblatt, G.E., 798
Beard, D.C., 16
Bennett, E.N., 1025
Berg, R.R., 1016, 1019
Bernard, W.J., 1019
Berry, V.J. Jr., 913, 1123
Bertram, G.T., 2
Bjørnstad, T., 654, 656, 661, 665
Blasingame, T.A., 1019
Boberg, T.C., 1333, 1335–1336
Boone, D.E., 371
Borchardt, J.K., 1236
Borling, D.C., 1215
Bourdet, D., 742, 744, 801–804
Bourgoyne, A.T., 373
Bourgoyne, A.T. Jr., 380
Bragg, J.R., 645
Brand, C.W., 830
Brar, G.S., 864, 869–872, 875–876
Brie, A., 89–162
Brinkley, T.W., 1031
Brons, F., 760, 776–779, 801, 882, 1016, 1528
Brule, M.R., 994
Buckley, S.E., 1024, 1053–1054, 1056, 1084, 1107–1110, 1123, 1125, 1604
Butler, R.M., 1353, 1355

C

Calhoun, T.G., 676
Campbell, J.M., 952
Campbell, R.A., 952
Carlisle, C., 615–647
Carlisle, C.T., 635, 638
Carter, R.D., 935–936
Caudle, B.H., 1107
Cawthon, G.J., 1337
Chaney, P.E., 963
Chang, H.L., 1265, 1350, 1353
Chang, S.-H., 1232
Chaperon, I., 875
Chastin, S., 220
Chauvel, Y., 683–716
Chen, S.M., 936
Chierici, G.L., 952, 963, 965, 971–973
Closmann, P.J., 1317

Coalson, E.B., 82
Cobb, W.M., 776, 781–782
Cole, F.W., 952, 1022–1024
Cordell, J.C., 913, 918
Craig, F.F., 677, 1037, 1069, 1250
Crampin, S., 220

D

Da Silva Araujo, R.G., 394
Dake, L.P., 952, 1071–1072, 1502, 1521
De Souza Padilha, S.T.C., 394
De Witte, L., 156
Deans, H., 615–647
Deans, H.A., 618, 635, 638
De Swaan, A., 798
Dietrich, J.K., 1351
Dietz, D.N., 781, 1004, 1032, 1070
Donaldson, A.B., 1319
Doscher, T.M., 1319
Dragoset, W.H., 29
Dria, D.E., 357–376
Dugstad, Ø, 651–680
Dunham, R.J., 10–11
Dunn, K.-J., 298
Dunning, H.N., 1025
Dyes, A.B., 1080
Dyes, A.G., 1107
Dykstra, H., 1066–1067, 1069, 1097, 1151

E

Eakin, J.L., 1025
Earlougher, R.C. Jr., 1008, 1547
Ebert, C.K., 913, 918
Economides, M.J., 830, 834–835, 837, 839
Edmundson, H.N., 281
El Sharkawy, A.M., 1019
Embry, A.J., 10–11
Enos, P., 10
Eoff, L., 1186, 1250
Ershaghi, I., 1084
Evans, E.M., 1239
Evers, J.F., 788

F

Farouq Ali, S.M., 1314, 1324, 1350, 1353
Fetkovich, M.J., 935–936, 1019
Firoozabadi, A., 1105, 1118
Fontaine, T.J.C., 1351, 1354
Forchheimer, P., 994
Frick, T.P., 830
Frisch, G.J., 392
Frost, E.M., 658

G

Galloway, E.W., 42
Galloway, W.E., 18
Gan, R.G., 1019
Gardner, J.S., 202
Gauglitz, P.A., 1225
Geffen, T.M., 1024
George, A.E., 439, 1350, 1353
George, C.J., 439
Ghassemi, F., 1319
Gogarty, W.B., 1176

Gold, D.K., 987
 Goldhammer, R.K., 9–10
 Gomaa, E.E., 1329
 Gonzalez, J.A., 1078
 Greaser, G.R., 1321
 Grigg, R.B., 1232
 Gringarten, A.C., 742–743
 Gruenenfelder, M.A., 1186

H

Hagoort, J., 1106
 Haldorsen, H.H., 1137
 Hale, B.W., 788
 Hall, H.N., 921
 Hammerlindl, D.J., 1019
 Hardage, B.A., 25–69
 Harrison, D., 683–716
 Havlena, D., 931, 951, 1521–1522, 1549, 1559
 Hawkins, M.F. Jr., 720
 Haworth, J.H., 369, 371
 Hazebroek, P., 760, 776–779, 801, 882, 1016
 Heintz, R.C., 1337
 Helbig, K., 220
 Higgins, R.V., 1059, 1437
 Hight, M.A., 1350
 Hild, G.P., 1216
 Hill, H.J., 460
 Hingle, A.T. Jr., 205
 Hirasaki, G.J., 1238
 Hobday, D.K., 18
 Hoefner, M.L., 1239
 Holstein, E.D., 981–1034, 1103–1145
 Horner, D.R., 734
 Houpeurt, A., 840–846, 848–855, 859–864
 Howard, J., 289–346
 Huang, W.S., 1350
 Hubbert, M.K.L., 5
 Hughes, B., 167–229
 Hundere, I.A., 665
 Hunt, E.R., 202
 Hurst, W., 935–936, 940
 Hwan, R.R., 952

I

Inglis, T., 381, 385

J

Jacoby, R.H., 913, 1123
 Jante, M.J. Jr., 1231–1232
 Jerauld, G.R., 1049, 1266–1267, 1293
 Jespersen, P.J., 1351
 Johnston, E.F., 1106
 Jones, J., 1309–1362
 Jorden, J.R., 373

K

Kaufman, A.A., 100
 Keelan, D.K., 458–459
 Kenyon, W.E., 298, 301
 Kerans, C., 8–9
 Kern, L.R., 1108, 1123
 Kimber, K.D., 1318
 Klein, G.E., 460
 Klinkenberg, L.J., 994–995
 Klins, M.A., 940
 Klován, R.E., 10–11
 Kohler, N., 1186
 Kozeny, J., 969–970
 Krause, R.E., 1234

Kuchuk, F.J., 814
 Kuo, C.H., 1337

L

Lake, L.W., 1180, 1437
 Langenheim, R.H., 1311, 1313, 1315, 1324
 Lantz, R.B., 1333, 1335
 Larsen, V.C., 782
 Lee, A.L., 985–986, 1033
 Lee, J., 719–885
 Leighton, A.J., 1059, 1437
 Lents, M.R., 1031
 Leverett, M.C., 460, 706, 1053–1054, 1056, 1084, 1107–1110, 1123, 1125, 1604
 Lo, H.Y., 1353
 Lucia, F.J., 1–23

M

Maerker, J.M., 1177
 Maggio, G.M., 654, 656
 Mandal, B., 392
 Mandl, G., 1314, 1324, 1326
 Mannhardt, K., 1236
 Manning, R.K., 1182
 Marsal, D., 939–941
 Martin, J.C., 762, 764
 Marx, J.W., 1311, 1313, 1315, 1324
 Matthews, C.S., 760, 776–779, 801, 882, 1016
 McAdams, W.H., 1341
 McBean, W.N., 1337
 McCain, W.D. Jr., 897, 904, 982–984, 994, 1505
 McCulloh, T.H., 408
 McEwen, C.R., 932, 943, 948–953
 McGinley, D.C., 458–459
 McMahan, J.J., 952
 McNab, G.S., 1353
 Miller, M.A., 981–1034
 Miller, M.G., 1031
 Milton, N.J., 2
 Moore, R.G., 1373
 Moses, P.L., 1025
 Murphy, D.P., 298
 Muskat, M., 776, 782–784, 895, 948, 963, 1125, 1133–1134, 1437, 1547
 Muskat, M.M., 948
 Myers, G.D., 243–286
 Myhill, N.A., 1314

N

Naegel, M., 375
 Neuman, C.H., 306, 1315, 1326, 1328, 1329, 1349
 Novosad, J.J., 1236

O

Odeh, A.S., 809, 814, 830–831, 834–835, 837–839, 931, 951–952, 1521–1522, 1549, 1559
 Osterloh, W.T., 1231–1232
 Owens, B.K., 1317, 1333
 Owens, W.D., 1317, 1333
 Ozkan, E., 839

P

Parsons, R.L., 1066–1067, 1069, 1097, 1151
 Patchett, J.G., 82, 250
 Patterson, D., 167–229
 Patzek, T.W., 1238
 Pedersen, K.S., 994, 1280, 1453
 Perkins, T.K., 1078
 Perrine, R.L., 762–764

Peterson, A.V., 1025
 Pickett, G.R., 205
 Pirson, S.J., 921
 Pixler, B.O., 369, 370
 Poston, S.W., 1016, 1019
 Prasad, R.K., 1019
 Prats, M., 787, 1309, 1314, 1332, 1367, 1381, 1383, 1385
 Prensky, S., 167–229, 289–346, 397

R

Ramey, H.J. Jr., 776, 781–782, 1314, 1345, 1381, 1383, 1385–1386, 1393
 Rathmell, J.J., 1049
 Rattia, A., 1324
 Rawlins, E.L., 840, 842–847, 849–850, 853–854, 858–859, 862, 864, 866–867, 869, 872, 1008
 Raymer, L.L., 197, 202, 281
 Richardson, J.G., 1116, 1532
 Rivero, R.T., 1337
 Roach, R.H., 1019
 Rogers, L.A., 1019
 Root, P.J., 797–799
 Rose, P.R., 1552
 Rose, S.C., 1037, 1073
 Rossen, W.R., 1238

S

Sagen, J., 675
 Saidi, A.M., 1139
 Salathiel, R.A., 1047, 1049
 Sandiford, B.B., 1158
 Sawatsky, L.H., 10
 Schellhardt, M.A., 840, 842–847, 844–847, 849–850, 853–854, 858–859, 862, 864, 866–867, 869, 872, 1008
 Schilthuis, R.J., 935
 Schols, R.S., 963–964, 971–972
 Seetharam, R.V., 635
 Senum, G.I., 658
 Seright, R.S., 1177
 Serra, K., 803–804
 Shallenberger, L.K., 618, 645
 Sharpe, H.N., 1318
 Sheriff, R.E., 37
 Shirley, O.J., 460
 Shreve, D.R., 1123
 Sills, S.R., 952, 1521
 Smith, A.E., 776, 783–784
 Smith, N.L., 408
 Sneider, R.M., 6
 Somaruga, C., 672
 Sorbie, K.S., 1180
 Southwell, G.P., 1214
 Spivey, J.P., 761
 Stegemeier, G.L., 1314
 Stephenson, D.J., 1239
 Stieber, S.J., 82–83
 Stiles, L.H., 439
 Stiles, W.E., 1068, 1124
 Strycker, A.R., 1236
 Suter, V.E., 1333
 Sydansk, R.D., 1149–1250

T

Taner, M.T., 37
 Tehrani, D.H., 931, 952, 1521
 Theys, P., 381
 Thomas, E.C., 77–87
 Thomsen, L., 220
 Timmerman, E.H., 952

Timur, A., 471
 Tinker, G.E., 676
 Tinker, S.W., 8–9
 Tipper, J.C., 42
 Tomich, J.F., 629
 Towson, D.E., 1335, 1336
 Tracy, G.W., 935–936

V

Vail, W.B., 100
 van der Knaap, W., 1326
 van Everdingen, A.F., 935–936, 940, 951–953
 van Lookeren, J., 1312, 1315
 Vilela, M.A., 676
 Vogel, J.V., 1328, 1329
 Volek, C.W., 1314, 1324, 1326

W

Wackowski, R.K., 1216
 Wagg, B., 289, 389
 Wagner, O.R., 651
 Walsh, M.P., 895–976
 Wang, B., 952
 Ward, R.C., 1318
 Warner, H.R. Jr., 421–489, 1037–1098, 1103–1145
 Warren, J.E., 797–799, 1425
 Welch, L.W. Jr., 1123
 Welge, H.J., 676, 1072, 1106, 1108, 1123, 1129
 Weyl, P.K., 16
 Wheatley, M.J., 963
 White, J.L., 1158
 Whitson, C.H., 994
 Wiley, R., 250, 547
 Willhite, G.P., 1037–1038, 1052, 1097–1098, 1101, 1213, 1250, 1343, 1345
 Wilson, K., 1025
 Woessner, D.E., 298
 Woodhouse, R., 421–489
 Worthington, P.F., 379–418
 Wyckoff, R.D., 963, 1547

Y

Yale, D.P., 1019
 Yuster, S.T., 1025

Z

Zaitoun, A., 1186
 Zemel, B., 653
 Ziegler, V.M., 1317, 1329, 1345–1346

SUBJECT INDEX

A

- Abo reef, 1117, 1138
- absolute open flow (AOF) potential, 840
- acid-generating chemical, 1191
- acoustic borehole imaging, 397–400
- acoustic caliper, 194
- acoustic coupling, 205
- acoustic-data processing, 214
- acoustic-energy propagation, 180
- acoustic-logging, 167, 169
 - measurements, 195, 203
 - tools, 172, 175–176, 206, 228
- acoustic receivers, 170
- acoustic-wave
 - attenuation of, 224
 - propagation of, 214
 - propagation theory, 167
 - train, 170
 - velocity of, 169
 - waveforms, 179, 195
- acrylamide-polymer, 1165, 1222–1223
- 2-acrylamido-2-methyl-propanesulfonic acid (AMPS)
 - monomers, 1164
- Adaptive Implicit Method (AIM). *See* model formulations
- adsorption/retention sacrificial agents, 1233
- after federal income tax (AFIT), 1589
- aggradational cycles, 8–9
- AGIP. *See* apparent gas in place
- air-gun wavelet, 29–31
- air/oil ratios, 1385
- AIT images, 138
- AIT logs, 102, 113–114, 116–117, 119–121, 126, 131
- Alani-Kennedy EOS method, 905
- alkaline-surfactant-polymer (ASP) flooding, 1240
- alluvial-fan system, 18
- alpha-olefin sulfonates, 1227, 1236
- alpha olefin-sulfonate-surfactant foam, 1231
- aluminum-citrate acrylamide-polymer gels, 1190
- aluminum-citrate colloidal dispersion gels, 1215
- aluminum crosslinked gels, 1190
- American Petroleum Institute (API), 79, 1079
 - data, 1491
 - gamma ray unit, 262, 269
 - gravity, 369
 - reports, 902
 - standards, 334, 426
 - units, 78, 258, 509
- americium-beryllium (Am^{241}Be) isotopic source, 269
- Amott tests, 1041
- amphoteric surfactants, 1227
- AMPS polymer, 1169
- anaerobic oil reservoirs, 1200
- analogous reservoir, 1490, 1559
- analytical valuation methods, 1572
- anionic surfactant, 1226
- anionic tracers, 654
- anisotropic reservoirs, 835, 878–879
- anisotropy-analysis methods, 211, 220, 335
- annual discount rate factor, 1580
- annular pressure, 563–566
- annular pressure source location, problems and tools, 611
- anticlinal reservoir, 1121
- anticline trap, 3
- API. *See* American Petroleum Institute
- API *RP* 40, 81–82, 86
- apparent gas in place, 1549
- apparent wellbore radius, 750–751
- appraisal, definition, 1573
- aqueous-based foams, 1225
- aqueous gel fluids, 1221
- aqueous polymer gels, 1203
- aquifer water, 1121
- Arbuckle formation, 1213
- Archie exponents, 454–457, 470
- Archie method, 84
- Archie parameters, 205
- Archie R_f -based S_w equation models, 469
- Archie water saturation equation, 145–146, 150–151, 155, 159–160
- ARC5 phase shift, 126–127
- areal conformance problems, 1152, 1153, 1155
- areal sweep efficiency, 1120, 1124, 1150, 1236
- ARI images, 137–138
- Arps equations, 1527–1528
- Arps-Smith method, 776, 783–785
- 6FF40 array, 107, 112
- array electrode tools, 97–99
- array-induction tools, 113–114
- array resistivity compensated tool (ARC5), 124–126
- Arrhenius expressions, 1372
- attenuation tomography, 65, 68
- autohydrolysis, 1164, 1177, 1189
- autoignition, 1368, 1388, 1394
- average primary oil recovery, 902
- average reservoir pressure, 699–700
- average sandstone heat capacity, 1376
- average steam zone thickness, 1315
- azimuthal anisotropy, 220
- azimuthal dual laterologs, 95–97
- azimuthal measurements, 181, 193
- Azimuthal Resistivity Imager (ARI), 95, 97, 128

B

- Babu-Odeh method, 830, 839
- bafflestone, 10–11
- Baker Atlas MREX devices, 308
- Baker Atlas Multi-Capacitance Flowmeter, 521–522
- balanced tangential method, principles of, 384
- barrels of oil per day (BOPD), 1309
- basin-floor sand lobe, 3
- basket (metal-petal) flowmeter, 523
- before federal income tax (BFIT), 1589
 - AFIT and, 1590–1591
- BHP. *See* bottomhole pressure
- BHP, and temperature data acquisition, 692–698
 - applications and interpretation, 699–701
 - bottomhole conveyance of gauges, 694
 - drillstem testing, 694–696
 - measurement while perforating (MWP), 695–697
 - openhole wireline pressure testing, 695
 - permanent pressure measurement installations, 697–698
 - production logging, 695
 - surface readout vs. downhole recording, 693
 - surface shut-in vs. downhole shut-in, 693
- BHP, and temperature gauges
 - accuracy, 686
 - dynamic response during pressure and temperature shock, 687
 - metrology of, 686–687
 - resolution, 686
 - sensitivity, 687
 - stability, 686–687

- bi-linear flow method, 767–768, 785, 790
 - billiard-ball-type collisions, 267, 269
 - bindstone, 10–11
 - biological stabilizers, 1177
 - biopolymer gels, 1191, 1222
 - biostratigraphy, 372
 - black-oil reservoir
 - numerical simulators, 1114
 - OOIP and, 913
 - simulation and fluid properties for, 912
 - blocking-agent conformance treatment, 1153
 - body waves and surface waves, 33–35
 - bonded wire transducers, 690
 - bond index (BI), 192
 - borehole acoustic array, 215
 - borehole-acoustic detection methods, 208
 - borehole acoustic logging, 168, 214
 - borehole-compensated (BHC) monopole devices, 167
 - borehole-corrected gamma ray log, 259
 - borehole flexural waves, 170
 - borehole fluids, 169
 - compressional velocity, 173
 - formation reflection, 183
 - ultrasonic attenuation, 183
 - velocity, 189
 - borehole-geophysical acoustic techniques, 167
 - borehole gravimetry, 408–412
 - borehole-guided modes, 182
 - borehole imaging
 - acoustic, 397–400
 - conjunctive acoustic and electrical, 406–408
 - electrical, 400–406
 - optical, 397
 - borehole televiewer (BHTV), 182
 - borehole-televiewer-type imaging devices, 210
 - Born response functions, 123
 - bottomhole conveyance, of gauges
 - coiled tubing, 694
 - electric line operations, 694
 - slickline operations, 694
 - wireless transmission, 694
 - bottomhole flowing pressures (BHFP), 840
 - bottomhole pressure, 724, 726, 759, 912
 - dynamic temperature correction and, 687
 - logging tools, 176
 - monopole-acoustic logs, 176
 - static metrological parameters, 686–687
 - and temperature data acquisition (*see* BHP, and temperature data acquisition)
 - and temperature gauges (*see* BHP, and temperature gauges)
 - transient response variation, 687
 - bottomwater-drive, 872, 900
 - boundary conditions
 - constant flow, 730
 - no-flow, 726
 - boundary-dominated flow, 726
 - boundary effects, 723, 805
 - bounded reservoir behavior, 770–776
 - boundstone, 10–11, 13
 - Boyles-law, sum-of-fluids porosity and, 476
 - Brar and Aziz method, 864, 869
 - brine-saturation distribution, 427
 - broadband transmitters, 171
 - BTU content, of gas, 360–362
 - bubblepoint pressure, 748, 1138
 - bubble size distribution, 1228, 1230
 - Buckley-Leverett equation/method, 1108, 1123, 1125
 - Buckley-Leverett solution, 1053–1054
 - saturation profile computed from, 1056
 - bulk magnetization, 292
 - bulk relaxation, 299
 - bulk tool response, 252
 - bulk-volume-irreducible (BVI) water, 298
 - Buna rubber, 1186
 - BVI determination, 316

C

- calcium-carbonate cementation, 15
 - calibration cycle, maximum hysteresis during, 688
 - calibration line-fitting, 444–447
 - Canadian Rapdan polymer flood, 1183
 - capacitance pressure transducer, 689
 - capillary absorption tube sampler (CATS) technology, 658–659, 669
 - capillary pressure, characteristics, 426, 1111
 - effects, 704–709
 - for intermediate wettability, 1047
 - method, depth of OWC/GWC calculation, 1505–1506
 - SCAL data, 459–460
 - of Tensleep Sandstone oil-wet rock, 1046
 - of water-wet rock, 1043
 - capillary processes control, 1225
 - capillary water, 432
 - carbonate(s)
 - buildup, 3
 - complex lithologies and, 335
 - diagenetic processes, 15
 - field, 1617–1619
 - formations, simulation of SWCT tests in, 638–639
 - layer thickness determination and, 79
 - platform, 13
 - porosity determination and, 83
 - reservoirs, 9–16, 431, 1062, 1067, 1088, 1117–1118
 - rock-fabric, facies, porosity, and permeability, 21–23
 - stratigraphy, 8
 - waterflood, with strategic well placement, 1620
 - carbonate sediments
 - classification of, 10–11
 - depositional environments, 13–14
 - diagenetic environments, 14–16
 - pore space classification, 12
 - porosity and permeability of, 10–12
 - ramp facies patterns, 13–14
 - sabkha and tidal-flat environment, 14
 - topography and ramp facies patterns, 13
 - vuggy pore space classification, 11–12
 - carbon-carbon bonds, 1160
 - carbon dioxide (CO₂)
 - flooding, 1236, 1241
 - foams, 1236
 - injection labeling, 677
 - projects, combustion project
 - Denver unit, 1296–1297
 - Means San Andres unit, 1293–1296
 - SACROC four-pattern flood, 1292–1293
 - sweep efficiency, 1236
 - carbon/oxygen (C/O) logs, 278
 - Carr-Meiboom-Purcell-Gill (CMPG) sequence, 295–297, 301, 303, 323
 - variations in, 326
 - Cartesian coordinates, 785, 863
 - Cartesian grid, 1407–1409, 1411
 - cased-hole
 - calipers, 388–389
 - logs, 175
 - neutron porosity, 204

- resistivity tools, 100–104
- saturation tool, 276
- wireline tools, 185
- cased-hole formation resistivity (CHFR) tool, 100, 102–103
- casing collapse part and split, problems and tools, 614
- casing-collar locator (CCL), 501
 - well-logging and, 411
- casing inspection logs, well-logging and
 - cased-hole calipers, 388–389
 - electromagnetic phase-shift tools, 391–392
 - flux-leakage tools, 389–391
 - ultrasonic tools, 392
- catalytic combustion detector (CCD), 362
- cation-exchange capacity (CEC), 18–19, 155, 457–458, 464
- cationic acrylamide polymers, 1165
- cationic polyacrylamides, 1165
- cationic surfactant, 1227
- cationic tracers, 655
- cavern collapse, 15
- CC/AP gel technology, 1205, 1214
- CDR logs, 130
- cementation sequence, 1118
- cement-bond devices, 187–188
- cement-bond logging, 185–186, 189
- cement-bond logs (CBLs), 185, 191, 392, 394–396
- cement-evaluation logs, 392–397
- Cement Evaluation Tool (CET™), 394
- cement-placement
 - evaluation of, 558–559
 - monitoring, 496
 - production logging and, 556–559
- cement-to-formation
 - bonding, 189
 - interface, 185
- cement tops detection, in temperature profiles, 714
- centrifuge technology, 1050
- Cesium-137, 263, 515, 518, 521
- CGR. *See* condensate/gas ratio
- chased slug approach, 571
- chemical condensation polymerization reaction, 1241
- chemical crosslinking reactions, 1162
- chemical-explosive energy sources, 26
- chemical fluid-flow shutoff material, 1153
- chemical gas tracers, 658–659
- chemical gel structure, 1198
- chemical-reaction (polymerization) rates, 1241
- chemical stabilizers, 1177
- chemical tracer, 1174
- chemical water tracers, 655–656
- chemostratigraphy, 372
- Chinese polymer floods, 1183
- choked-fracture
 - damage, 789
 - skin factor, 789
 - type curve, 794
- chromic triacetate (CrAc₃), 1194
- chromium (III)-carboxylate/acrylamide-polymer gels, 1189
- chromium (VI) redox gels, 1190
- chronostratigraphic approach, 7
- Cinco type curve, 793
- Circumferential Acoustic Scanning Tool (CAST™), 400
- Circumferential Acoustic Scanning Tool-Visualization version (CAST-V™), 397
- Circumferential Borehole Imaging Log (CBIL™), 400, 406
- classic material balance, 1519
- clay-bound fluids, 315
- clay-bound-water (CBW) components, 316–317, 336
- clay minerals, 21, 431–432
- clean-sand (Archie) model, 461–462
- CMB. *See* classic material balance
- CMPG acquisition, 341
- coalbed reservoirs, volumetric estimate of GIP (scf), 1535
- coarse-grid, 1408–1409
 - 2D and 3D simulation models, 1604–1605
- collapse brecciation, 15–16
- collar-locator log, 537, 549
- colloidal dispersion gels, 1215
- Combinable Magnetic Resonance (CMR) tool, 291, 316
- combustion
 - dry, 1368
 - in-situ combustion (ISC), 1367
 - kinetics, 1371–1372
 - projects, pollution-control systems for, 1392
 - reverse, 1367–1368
 - wet, 1369–1370
- commingled gas and water production profiling problems
 - back-scatter gamma-ray density surveys, 590, 592, 598, 604–605
 - continuous or fullbore spinner surveys, 593, 596, 599, 602, 608
 - differential-pressure density survey, 602
 - diverting-spinner flowmeter survey, 593
 - flowing spinner survey, 604–605
 - flowing survey with radioactive chemical tracer, 602
 - fluid-capacitance survey, 592, 595, 601, 605, 608
 - fluid density survey, 593
 - gradient-type density survey, 599, 604–605
 - gravel-pack surveys, 595, 598, 602, 604, 608
 - multiarm conductive and multiarm fluid capacitance surveys, 603
 - noise-logging survey, 590, 597, 599, 604–605
 - optical gas-detection surveys, 604
 - pulse-neutron surveys, 595, 599, 602, 608
 - temperature surveys, 592, 598, 601, 603, 605, 608
- commingled-gas production, profiling, 537–539
- commingled oil and water production profiling problems
 - gravel pack and continuous-spinner survey, 608–609
 - noise logging survey, 609
 - temperature and fluid capacitance survey, 608
- common interpretation method, 259
- compaction-drives, 956–961
 - material-balance analysis, 957–961
 - performance, 957
 - reservoir, 901
 - rock expansivity and compressibility, 958–961
- compensated dual resistivity (CDR) tool, 118–121, 123–126
- compensated neutron-porosity logging (CNL) tool, 267–268, 270
- compensated wave-resistivity (CWR) tool, 127
- complete-water drive reservoir, 900
- complex faulted structural trap, 3
- complex flow geometries, 756
- complex seismic trace, 37–39
- component analysis, mud logging and, 361–365
- composite decline curves, misuse of, 1557
- composite expansivities, 908, 917
- compressed gas/oil, 899
- compressional-slowness measurement, 181
- compressional velocity, 202
- compressional-wave(s), 169–170
 - acoustic logs, 210
 - velocity, 170
- compressive strength, 1222
- Compton scattering, 254–255
- computer-aided fluid-injection control, 1221
- computer simulation for well/reservoir performance, 1531–1532
- computer thermal-simulation work, 1208
- condensate/gas ratio, 1514
- condensate reservoirs, 982

1630 Subject Index

- condensate well fluid, volumetric behavior, 990
condensation polymerization, 1242
conformance-improvement treatment systems
 flooding operations, 1151
 fluid system, 1149
 foams, 1235
 gels, 1187
 gel treatments, 1218
 polymer technologies, benefits of applying, 1166
 systems for, 1149
coning, of well, 872–879
connate-brine, 1045
 resistivity (R_w), 453–454
connate-water, 908
 expansion, 917
 SWCT tests for, 644
connate water saturation (S_{wc}), 615, 1048
consolidated rock, 1550
constant-composition expansion (CCE), 988–989
constant-pressure boundary, 827
constant-rate drawdown test, 772
constant volume depletion (CVD), 904
continuous and fullbore spinner flowmeters, 526–535
continuous/fullbore spinner and temperature survey, profiling
 production problems, 600
cool hot wells, water for, 1391
cooling-fluid injection, 1244
core analysis, 78
core-flooding experimental testing, 1200
core/log calculation approaches, porosity determination and
 calibration line-fitting, 444–447
 density log, 447–449
core-plug Boyles-law porosity measurements, 442
core porosity (ϕ_c), 443
core sampling, 78
Corey theory, 1128
correlation coefficient, 444
corrosion detection problems
 magnetic flux-leakage surveys, 613–614
 multifeeler mechanical-caliper and Eddy current wall-
 thickness surveys, 612
 radial-type bond logging surveys, 614
corrosion-monitoring tools, 496
corrosive mixture, 1233
Council of Petroleum Accountants Socs. (COPAS) charges,
 1576–1577
counterclockwise rotation (CCW), 532
coupled models, in reservoir stimulation
 full coupling, 1449
 iterative coupling, 1448
 one-way coupling and loose coupling, 1447
coupling types, simulation of geomechanics
 flow-properties coupling, 1445
 pore-volume coupling, 1444–1445
crestal gas injection, 1119, 1135
critical spacing value, 172
crossed-dipole anisotropy analysis/logging, 211, 220, 224
crossflow behind casing, 563–566
crossflow detection behind casing, problems and tools, 611
crosslinked polymer gel, 1243
crosslinked styrene-butadiene block copolymers, 1243
crosslinker concentration, 1195
crosslinking agents, 1189
crosslinking chemistry, 1190–1191, 1206
crossplots, 280–283
cross-sectional gas/oil problem, 1409
crosswell seismic profiling, 26, 65–68
crude and matrix from ISC project, laboratory studies
 chemical reactions, 1370–1371
 combustion-tube studies, 1372–1374
 kinetics of combustion reactions, 1371–1372
crude oils, 1041, 1046
 properties, 1039
 temperature dependence of viscosity for, 1321
cryogenic nitrogen rejection plant, 1135, 1143
crystalline carbonate, 11
Crystal Quartz Gauge (CQG) design, 691
cumulative air injected (CAI), 1385
cumulative incremental oil produced (CIOP), 1385
cumulative oil recovery and steam zone size, design
 calculations for
 Jones model, 1325–1326
 Marx-Langenheim model and Mandl-Volek (M-V)
 models, 1324–1325
cumulative wellhead gas, 1521
cutoff-BVI (CBVI) model, 316–318
cutoff frequency, 512
cuttings analysis, mud logging and
 cuttings collection, 367
 sample examination and description, 367–368
 sample lagging, 365–366
cuttings board, mud logging and, 360
cuttings return, rate of, 375
cycle hierarchies, terminology of, 9–10
cyclic-steam injection, 1236, 1246
cyclic steam stimulation (CSS), 1324
cylindrical focusing technique (CFT), 103
- D**
dalmatian wetting, 1041, 1042. *See also* reservoir rocks
Darcy flow, 754, 841
Darcy's law, 276, 436, 719, 721, 756, 1108, 1127
 linear pressure dependence of flows for, 1416
data acquisition, 1080–1081
data fit—inversion, NMR and, 303–304
DataLatch system, 695
Dean-Stark water-extraction procedure, 426, 443–444, 452
decision tree analysis evaluation method, 1575
decline-trend analysis, 1556
deep laterolog tools, 453
Delaware basin, 1118
deliverability test
 analysis theory, 840, 845
 types and purposes of, 840
delta systems, 20
density and elevation survey, profiling production
 problem, 600
density log/tool, 387, 447–449
density/neutron log, 79, 428
density-porosity interpretation, 264–265
depositional facies model, 22
depth datum, of pressure, 699
depth-derived borehole compensation (DDBHC), 178
depth of investigation (DOI), 309, 335
derivative type curve, 743
deterministic cash flow evaluation method, 1574–1575
developed reservoirs, 704, 829, 841, 856
deviated well, 753
dewpoint pressure, 1560
diagenetic trap, 3–4
difference in gravity, Δg (mGal), 409
differential-spectrum (DSM) method, 326–327
differential-vaporization (DV), 904
diffusion analysis (DIFAN), 329
diffusion-weighted mechanism. *See* dual- T_w acquisition
dipole-acoustic sources, 221
dipole and multipole array devices, 180
dipole flexural shear mode, 221

- dipole-shear
 - acoustic measurements, 214
 - dispersion, 220
 - slowness processing, 218
 - wave, 215
 - wave splitting, 221
 - dipole transmission, 170, 180
 - directional flow trends, 652
 - direct-shear velocities, 180
 - discount rate risk analysis method, 1580
 - discretization, 937, 1415, 1416, 1449
 - dispersed clay model, 156–158
 - displacement efficiency, 437, 616, 901, 921, 1024
 - macroscopic, of linear waterflood, 1052–1055
 - displacement equations, 1123
 - disproportionate permeability reduction (DPR), 1157
 - dissolved-gas-drive reservoirs, 902
 - dissolved gas/water ratio, 918
 - divalent-ion concentrations, 1206
 - diverting-spinner flowmeter, 523–526
 - DLL tools, 99
 - dolomitic carbonate reservoir, 1239
 - dolomitization, 15–16, 431, 1118
 - dolostone reservoirs, 15–16
 - domal structures, 3
 - double displacement process (DDP), 1135
 - downhole acoustic measurements, 167
 - downhole data surface acquisition, 698
 - downhole gas-fired burners, 1387
 - downhole gel, 1222
 - downhole injection pressure, 1181
 - downhole magnetics, 412–414
 - downhole NMR spectrometer, 311
 - downhole shut-in benefits, in pressure transient testing, 709
 - drainage-area geometry, 725
 - drainage P_c/S_w curve, 1043
 - drawdown and buildup type curves, 745
 - drawdown test analysis, 870
 - drilling engineering and operations, 372
 - connection gas, 374
 - cuttings return, rate monitoring of, 375
 - lithology and mineralogy, 373
 - mud chloride content, 373
 - mud pit level, 373
 - normal geothermal gradient, 374
 - total gas, 374
 - weight on bit and rate of penetration, 373
 - drilling fluid, 358–359, 374
 - calcium carbide and, 366
 - flow path, 359
 - hydrocarbons and, 369
 - invasion, 748
 - properties, 369–371
 - drillpipe
 - induction tools on, 117–119
 - manipulation and constriction problems, 552
 - drillstem-test data, 485–486
 - drillstem-tool (DST) tests, 86, 454, 694–696
 - dry and wet-gas reservoirs, 901
 - dry gases, 896
 - dry-gas reservoirs, 983, 1559–1560
 - Dual Dipmeter tool, 137
 - dual induction tool (DIT), 107–108, 111
 - Dual Laterolog (DLL) Resistivity (R_{xo}), measurements, 93–95
 - dual-porosity, simulation model, 635
 - ethanol simulation, 641
 - ethyl formate simulation, 641
 - IPA cover tracer simulation, 635, 639–640
 - media, simulation of SWCT tests in, 636–638
 - reservoirs, 203, 785, 796, 802
 - systems, 801, 1538
 - Dual Propagation Resistivity (DPR) tool, 127
 - dual- T_E acquisition, 327–329
 - dual- T_W acquisition, 324–327
 - dual-water (DW) models, 158–161, 463
 - Dulang oil field, 478
 - dumpflooding, 1079
 - DV test, measurement volatilized oil, 918
 - Dykstra-Parsons coefficient, 1151
 - dynamic oscillatory viscometry, 1194
- E**
- early-radial flow, 809
 - Earth resistivity, 89–90
 - echo amplitude, 194
 - echo ratio method, 329–330
 - EDCON tools, 411
 - eddy-current device, 496
 - effective date, for oil and gas reserves, 1582
 - E_i -function, 720, 722, 735, 737, 739, 743, 756
 - Ekofisk oil field (North Sea), injection- and production-well locations, 1088, 1090
 - elastic-wave
 - propagation, 169
 - theory, 224
 - elastic wavefield
 - components, 33
 - imaging, 65–66
 - electrical borehole imaging, 400–406
 - Electrical Micro-Imaging tool (EMI™), 401, 407
 - electric double-layer repulsion, 1228
 - electric-line tools, advantages of, 550
 - electric log, 79
 - electrochemical component, SP logging and, 139–141
 - electrode resistivity devices
 - array electrode tools, 97–99
 - cased-hole resistivity tools, 100–104
 - laterologs, 93–97, 104
 - normal and lateral devices, 91–93
 - SFL device, 99–100
 - electrokinetic component, SP logging and, 141
 - Electromagnetic MicroImager (EMI) tool, 137
 - electromagnetic phase-shift tools, 391–392
 - electromagnetic wave resistivity (EWR) tool, 118
 - electromotive force (EMF). *See* membrane potential
 - El Furrial field, water and gas tracer injection in, 676
 - embar carbonate formation, 1212, 1216
 - Energy and Utilities Board, 1491
 - energy release, mechanisms of, 898
 - energy reservoir, types of, 898
 - Energy Resource Conservation Board, 1491
 - enhanced-diffusion method (EDM), 323, 329
 - enhanced oil recovery (EOR), 616
 - enriched-gas flooding, tracers for, 676
 - enriched-gas injection, tracers in, 676–677
 - enriched-hydrocarbon projects
 - Miscible Injectant Stimulation Treatment (MIST) concept, 1299–1300
 - Piercement Salt Dome field, 1300–1301
 - Prudhoe Bay field, 1297–1299
 - enthalpy, 1310, 1312
 - environmental capture sonde (ECS), 278
 - eolian system, 18
 - epoxy resins, 1240–1241
 - equation-of-state (EOS) method, 905, 983, 1114
 - equivalent drawdown time, 746
 - ERCB. *See* Energy Resource Conservation Board
 - ethylene diamine tetra-acetic acid (EDTA) complexes, 655

EUB. See Energy and Utilities Board

eustatic sea-level changes, 7–8

evaporite mineralization, 15

EWR-Phase 4 tool, 126

expansion-/compaction-drive reservoir, 900

expansion-drive reservoirs, 901

expansion of oil, rock, and water, 917

expectation curve (EC), 1552

Exxon model, 8

F

fair market value, 1571

fast-shear wave, 223

field application, design strategies for, 1238

field data interpretation, 670–675

analytical solutions, 674

levels of interpretation, 670

qualitative evaluation, 670–674

response curves, 672–675

sweep volume, 673–674

tracer-response curves with numerical simulation, 674–675

field-log, 114

field-test design, 667–668

filtration testing, 1199

finite-conductivity fractures, 785

fixed-gate systems, 189

Flagship, 522

flame ionization detector (FID), 361–362, 364

flexible-backbone polymer, 1163

flexural-mode propagation, 180

flexural waves, 215, 221

velocity, 171

floatstone, 10–11

flood basin deposits, 20

flood-front saturation, 1054–1055

flood plain deposits, 19

floodpot tests, 1049

flood sweep efficiency, 1151, 1157

flood volumetric sweep efficiency, 1247

Flory equation, 1168

flow-after-flow tests, 839, 845

flow barriers delineation, 652

flow coefficients, 842

flow efficiency, 751

flow geometries, 719

flowing tubing pressure, 1514

flow problems, origin of, 497–498

flow tests, 505

semilog methods for, 735–736

Flowview Plus, 522

flue gas, 1143

fluid-contacts identification

formation-pressure surveys, 451–452

log-based methods, 451

mud logs, 450–451

water-based-mud cores, 451

fluid-flow

bilinear flow, 767–768, 785

blocking, 1224

blocking agent, 1160

blocking treatments, 1238

boundary-dominated, 726

equations, mathematical derivation of, 1052

isothermal, 719

laminar, 721

linear, 730, 766–767

non-laminar, 761

pseudoradial flow, 785, 787

pseudosteady-state, 723–725

single-phase flow, 764

spherical flow, 769

steady-state, 726

two-state, 1110

unsteady-state linear, 730

fluid identification and characterization

oil-based drilling mud, 85

water-based drilling mud, 84–85

fluid(s)

capacitance-logging tool, 516–518, 540

crossflow, 1220

density log, 528

filled wellbore, 729

influx, 756

injection cycles, 652

injection extent determination, 568–569

movement/potential, 5

NMR properties of, 299–301

properties, 903–905

and rock interface, 171

sampling, 78

and saturated rocks, 169

type, mud logging and, 368–369

viscosities, 875, 895, 1110

fluid-shutoff

epoxy resins, 1242

gel, 1219

gel treatments, 1211

phenolic resins, 1241

plugging agent, 1243

resins, 1241

treatments, 1218, 1243

fluoro-surfactant foam, 1228, 1239

flushed-zone

device, 265

method, 150–151

fluvial system, 18–20

flux-leakage tools, 389–391, 496

FMV. See fair market value

foam(s)

advantages and disadvantages of, 1235

agents, 1226

ASP, 1240

blocking agents, 1221, 1237

chemicals, 1234

CO₂ flooding and, 1239

gas-blocking treatments, 1239

gas bubbles of, 1225, 1230

gels, 1221, 1238

general nature of, 1224

generation mechanisms, 1231

induced viscosity, 1229

injection mode, 1235

interactions of, 1234

lamellae films, 1229

for mobility control, 1235

mobility reduction of, 1229

in porous media, 1229

for reducing gas coning, 1237

steamflooding and, 1238

texture of, 1228

viscosity of, 1330

focused gamma-ray density-logging tool, 514–516

foot-by-foot log calculations, 437

formaldehyde, 1079, 1178

formation dip, 1111

Formation MicroImager (FMI™), 403–405, 407

formation permeability/porosity, mud logging and, 371

formation-pressure surveys, 451–452

- formation resistivity, 89–90, 135
 - formation volume factor (FVF), 896, 898, 1113, 1490
 - formation-water salinity, 139, 141
 - four-blade propeller-type spinner element, 527
 - four focused-resistivity measurements, 102
 - four-way-closure traps, 3
 - fractional-flow, 1074
 - curves, 1110–1111
 - equation, 1108
 - theory, 1125
 - viscosity ratio effect on, 1058
 - of water, 1054, 1070
 - fracture, 15–16
 - communication, 1155
 - damage, 789
 - face damage, 789
 - orientation, 1064–1065
 - plus-matrix flow, 804
 - porosity, 23
 - problem sweep-improvement treatments, 1212
 - fractured reservoir(s), 1216
 - porosity determination and, 83
 - water and gas tracer injection in, 675
 - framestone, 10–11
 - Free Fluid Index (FFI), 298, 306, 316–317, 340
 - free-fluid (Timur-Coates or Coates) model, 321
 - free-gas saturation, 748
 - free-induction decay (FID), 294, 298
 - free-pipe acoustic signal, 190
 - free-radical
 - chemical breaker, 1222
 - chemistries, 1241
 - crosslinking agent, 1243
 - free-water level, 450, 466, 1503
 - fluid contacts, 451
 - French polymer flood, 1183
 - Frio Sandstone reservoir, 629–630
 - FTP. *See* flowing tubing pressure
 - fuel availability vs. crude oil gravity, 1376
 - fuel burned (FB), 1385
 - fuel geometry, 1370
 - fuels heating values, estimation of, 1374
 - Fullbore Formation Microlmager (FMI) tool, 137–138
 - fullbore-spinner log, 528
 - Fullerton Clearfork reservoir, 1066
 - furan oligomers, 1242
 - furan resin polymerization, 1242
 - furfuryl alcohol, 1242
 - FWL. *See* free-water level
- G**
- Galerkin finite elements, 1416
 - gamma-gamma scattering density log/tools, 250, 263–264
 - gamma-ray
 - detector, 509, 515, 518
 - log cutoff, 441
 - log model, 475–476
 - tool, 118, 253, 278, 549
 - gas and oil, gravity segregation, 1511
 - gas-bearing zone, 228
 - gas-blocking agents, 1235, 1237
 - gas-blocking foam, 1234
 - gas blowout, after abandonment, 541–542
 - gas-cap drives, 920–922
 - characteristics, 921
 - dimensionless gas-cap volume, 929
 - effects on oil and gas recovery, west Texas black-oil reservoir and, 923, 925
 - material-balance analysis, 928–931
 - minimization algorithms speed solution, 630
 - OOIP and OGIP, solution procedure to estimate, 929–930
 - performance, nonsegregation-drive gas caps, 922–925
 - ratio of free-gas-phase and free-oil-phase volumes, 928–931
 - reservoir, conditions at economic limit, 925
 - segregation-drive gas caps, 925–928
 - segregation mechanisms, 921
 - solution method, 931
 - total expansivity (E), 929
 - Walsh's method, 930
 - water, oil, and gas in a nonsegregating-gas-cap reservoir, 922
 - gas caps, 901
 - characteristics, 921
 - cycling project, 1298, 1614 (*see also* enriched-hydrocarbon projects)
 - expansion-drive reservoir, 901
 - gas, 1513
 - injection, 1119
 - gas channeling and override reduction, 1235
 - gas chromatography (GC), 357–358, 361
 - analyses, 1132
 - catalytic combustion detector (CCD), 362
 - flame ionization detector (FID), 362
 - infrared absorption (IR) spectrometer, 364–365
 - mass spectrometer (MS) detector, 363–364
 - thermal conductivity detector (TCD), 362
 - gas-compressibility/effective-compressibility ratio, 1549
 - gas condensates, 896
 - gas coning, 1239
 - gas cycling, 902
 - gas deviation factor, 1509
 - gas-diffusivity equation, 846
 - gas-drive gravity drainage process, 1135
 - gas-drive reservoirs, 902
 - gaseous equivalent of stock-tank condensate, 1521
 - gas-expansion and rock/fluid-compression term, 1549
 - gas-expansion-drive reservoirs, 901
 - gas-filled porosity, 205
 - gas-filled reservoir, 1103
 - gas-flow equations, 740, 840
 - gas formation volume factor, 985
 - gas injection, 899
 - operations, types of, 1118–1119
 - tracers for, 676
 - gas kick, 535–537
 - gas law, 983
 - gas/oil and water profiling production problems
 - gradient-type density, continuous flowmeter surveys, 610
 - temperature and fluid capacitance surveys, 610
 - gas/oil capillary pressure, 1105, 1143
 - gas/oil compositional effects, 1113
 - gas/oil contact (GOC), 411–412, 450, 902, 1121, 1237
 - gas/oil displacement
 - efficiency, factors affecting, 1110
 - process, 1105, 1115, 1121
 - gas/oil gravity drainage, 1104
 - process, 1117
 - gas/oil linear displacement efficiency, 1107–1110
 - gas/oil problem, 1407
 - gas/oil ratio (GOR), 323, 873, 910, 912, 918, 1114, 1218, 1269, 1301
 - gas/oil relative permeability, 1107
 - gas-processing plants, 896, 1114–1115
 - gas reinjection, for improving oil recovery, 927–928
 - gas-reservoir performance and production
 - forecasting methods, 1028–1030
 - production rate-vs.-time curve for gas reservoir, decline graph, 1030
 - recycling of gas aids recovery, 1031

1634 Subject Index

- reservoir deliverability, 1027–1029
 - retrograde-condensate reservoirs, 1030–1032
 - system performance, 1026–1027
 - water influx, 1030
 - gas reservoirs, 437, 1512–1514
 - determining reservoir-fluid properties, 985–988
 - forecasting, 1025–1032
 - natural gas properties, 981–994
 - natural-gas reservoirs, phase behavior of, 982–983
 - performance, 1558
 - petrophysical properties, 994–995
 - volumes and recovery, 1014–1025
 - well performance, 981, 995–1014
 - gas sampling. *See* gas trap
 - gas saturation (S_g), 912
 - distributions, 1109
 - testing, SWCT tests for, 644–646
 - value, 1108
 - on waterflood oil recovery, 1050
 - gas-shutoff coning treatments, 1152, 1155, 1215
 - gas-shutoff gel squeeze treatments, 1215
 - gas trap, 359–361
 - gas/water contact (GWC), 439, 450, 466, 1487
 - gas wells, deliverability testing, 839–872
 - gas-zone porosity-correction technique, 202
 - Gates and Ramey method, oil recovery history, 1385–1386
 - GC-MS system, 363
 - GEC. *See* gaseous equivalent of stock-tank condensate
 - Geiger-Müller tube, 257
 - Geiger tubes, as gamma-ray detector, 515, 518
 - gelation rate
 - acceleration, 1196
 - retardation agent, 1197
 - gel(s)
 - bottle testing, 1200
 - breakers, 1222–1223
 - chemical-liner, 1210, 1216
 - conformance treatments, 1218
 - degradation process, 1222
 - dehydration, 1202
 - fluid injection, 1219
 - forming chemical system, 1188
 - onset time, 1199
 - placement in fractures, 1202
 - shear rehealing, 1204
 - strength, 1198
 - syneresis, 1196
 - technology selection, 1207
 - treated injection well, 1212
 - treated reservoir, 1222
 - geochemical logs, 278–279
 - Geological High-Resolution Magnetic Tool (GHMT™), 414–415
 - geomagnetic polarity time scale (GPTS), 413, 415–416
 - geomechanics simulation
 - coupled model types, 1447–1449
 - coupling types, 1444–1445
 - modeling of stress-dependent flow properties, 1446–1447
 - modeling reservoir, 1446
 - geometric skin, 751–756
 - geophone, 30–31, 35
 - geopressured oil/gas, 1548
 - geopressured reservoirs, 1550, 1558
 - geosteering, 379
 - Geovision Resistivity (GVR) tool, 102, 104, 138
 - Gold's correlation, condensate molecular weight estimation, 988
 - Gomaa model, project performance estimate for, 1329–1332
 - graben and horst block trap, 3
 - gradiomanometers, 516
 - grainstone, 11–14
 - gravel-packed wells, 1186
 - gravel-pack logs, 278
 - gravel-pack skin, 754
 - gravel placement, 568
 - gravitational energy, 898
 - gravitational forces, 875, 899
 - gravity drainage, 1120
 - gas caps, 901
 - immiscible gas/oil displacements, 1117
 - model, 1131
 - type projects, 1132
 - gravity-driven weight droppers, 26
 - gravity number, 927
 - gravity segregation, 899
 - gridding techniques, 1409
 - grid-orientation effects, 1409
 - grid properties, upscaling
 - absolute upscaling approach, 1432–1433
 - concept of, 1423
 - global, 1430–1432
 - local, 1425–1429
 - regional, 1429–1430
 - relative approach, 1433, 1435
 - schemes and techniques for absolute permeability, 1423–1425
 - grids, in simulation
 - block-center geometry, 1417–1418
 - curvilinear grid systems, 1421
 - dip-normal geometry, 1417
 - hexahedral grids, 1418–1419
 - multiple-domain hexahedral grids, 1419
 - refinement, 1419–1420
 - regular Cartesian grids, 1416–1418
 - triangular or tetrahedral grids, 1421
 - truncated regular grids, 1420–1421
 - unstructured grids, 1419–1420
 - Voronoi grid, 1420–1421
 - Gringarten type curve, 742
 - GR interactions, with formations
 - Compton scattering, 254–255
 - pair production, 255–256
 - PE absorption, 255
 - GR logs, 256, 261, 427, 433
 - API units on, 509
 - Groningen effect, 94–95, 97
 - gross bed thickness determination, 79
 - gross-count-rate gamma ray tool, 261
 - ground-force phase-locking technology, 27
 - GR spectroscopy tools, 81
 - guided waves, 168, 171, 173
 - gyroscope surveys, 381
- ## H
- Halliburton Gamma-Ray Backscatter Gas-Holdup Tool, 521
 - Halliburton tool (MRI-LWD), 310
 - Hall plots, 1204
 - Havlena and Odeh method, 1558–1559
 - hazardous waste injection, certification, 563–566
 - H/C atomic ratio, 1375, 1377–1380, 1383
 - health, safety, and environmental (HSE) considerations, 375
 - heat
 - balance, 1376, 1383
 - capacity, 1309–1310
 - conduction, complementary error function, 1312
 - losses, 1383
 - zone growth rate, 1313
 - heavy-oil, 1391–1393, 1544–1546
 - production, 1236
 - recovery operations, 1152

- reservoirs, 896, 1236
 - tar sands, and tar mats, 335
 - heavy-oil-tar (HOT) layer, 475
 - He-3 detectors, 268–269
 - Heft Kel field (Iran), 1138–1139
 - height-above-the-OWC (H_{owc}) basis, 429
 - hemiradial flow, 807, 811, 826
 - hem-packer, 523
 - Henry Hub gas prices, 1583
 - heptanes-plus content, 897
 - Hewlett-Packard (HP) design, for quartz pressure transducer, 690–691
 - high-angle wells, logging tools for fluid identification in, 521–523
 - high-conductivity fracture, 775
 - High-Definition Induction Log (HDIL) array, 114, 122–123
 - high-definition lateral log (HDLL) tool, 98
 - highest known water, 1498
 - high-frequency cycle (HFC), 8
 - highly resistive formations, SP and, 142–143
 - high-oil-saturation
 - flow, 1233
 - geological strata, 1221
 - matrix reservoir rock, 1188
 - high-permeability
 - anomaly, 1208
 - channels, 1157
 - geological strata, 1219
 - reservoirs, 843
 - high-pressure mercury injection (HPMI), 481–482
 - high-pressure N_2 miscible injection, 677
 - high-rate wells, 829
 - high-relief oil reservoirs, 1560
 - High-Resolution Array Induction (HRAI) tool, 116
 - High-Resolution Azimuthal Laterolog Sonde (HALS), 97–98, 102–103
 - High-Resolution Induction Tool (HRI), 111–112
 - high-resolution laterolog array (HRLA) tool, 97–99, 132
 - highstand system's tract (HST), 8–9
 - high-temperature oxidation (HTO), chemical reactions
 - associated with ISC, 1370
 - Hilbert transform, 37–38
 - Hill-Shirley-Klein method, 460
 - history matching water influx, 944
 - HKW. *See* highest known water
 - homogeneous reservoirs, 742, 1234
 - gravity effects of, 1069–1071
 - horizontal borehole, 829
 - horizontal exploration well, 825
 - horizontal wellbores, 1215
 - horizontal wells, 1064
 - analysis of, 805, 839, 1143
 - fractures intersecting, 1215
 - Horner analysis, 825
 - Horner equation, 763
 - Horner graph, 780
 - Horner plot, 763, 813
 - Horner time ratio (HTR), 738, 761
 - Houpeurt analysis technique, 846, 848
 - Houpeurt equations, 841–842, 844
 - Houpeurt flow coefficients, 867
 - HWTZ. *See* hydrocarbon/water transition zone
 - hydraulic seal, 191
 - hydrocarbon fluids, 899
 - spacer, 1244
 - suspensions/dispersions, 1181
 - hydrocarbon (fluid) typing, 322–324
 - dual- T_E acquisition method, 327–329
 - dual- T_W acquisition method, 324–327
 - echo ratio method, 329–330
 - multifluid methods, 330–331
 - hydrocarbon pore feet (F_{HCP}), 434, 440
 - vs. permeability, 441
 - hydrocarbon pore volumes (HCPV), 900, 1262
 - hydrocarbon(s)
 - expansion, 917
 - formation, 2
 - gas, 1103
 - indicators, 196
 - liquids, 1559
 - miscible flooding, 1234, 1236
 - miscible IOR in-situ evaluation, SWCT tests for, 642–643
 - reservoir maps, 1494–1501
 - reservoirs, 208, 899
 - resources and primary drive mechanisms, 1602–1604
 - traps, 1–3
 - volumes and technological uncertainty, 1585
 - wash preflush, 1245
 - hydrocarbon/water contact (H_{hwc}), 465
 - hydrocarbon/water transition zone, 1506
 - hydrodynamic retention, 1176
 - hydrogen index, 225
 - hydrogen-index linear mixing law, 249
 - hydrolyzed polyacrylamide (HPAM) polymer, 1162, 1173
 - hydrophones, 30, 35
 - hydrostatic gradient, 208
 - hypersaline reflux model, 15–16
- I**
- ideal-gas law, 991
 - ILD-ILM-SFL logs, 107
 - illite, 17
 - imaging reservoir targets, 45–52
 - imbibition process, 1043–1044
 - immiscible displacement
 - microscopic efficiency of, 1040
 - in two dimensions, 1057–1058
 - immiscible gas displacement, 1103, 1105
 - calculation methods for, 1122–1123
 - efficiencies of oil recovery by, 1120
 - immiscible gasflood monitoring, 1132–1133
 - immiscible gas injection, 1115, 1139
 - performance calculation, 1124
 - projects, use of horizontal wells in, 1143
 - immiscible gas/oil
 - displacement, 1118, 1124
 - gravity drainage process, applications of, 1137–1138
 - immiscible water-alternating-gas (IWAG), 1093
 - impermeable lithologies, 2
 - implicit pressure explicit saturations (IMPES), 1400, 1402–1403, 1406, 1411, 1438, 1440
 - improved oil recovery (IOR)
 - operations, 615–616
 - process, 639–643
 - impulsive sources, 26
 - inaccessible pore volume (IPV), 1174
 - incremental oil production, 1212
 - Indonesia model, 462–463
 - induction logging (*see also* resistivity logging)
 - array-induction tools, 113–117
 - dual-induction tools, 107–108
 - field-log examples, 114
 - induction response, 106
 - multicoil arrays, 106–107
 - phasor induction, 108–112
 - principles, 104–106
 - infill and observation wells, 1081
 - infinite-acting drainage, 735

infinite-acting radial flow, 743, 747, 790, 805
infinite-acting reservoir, 731, 733, 757–758, 762, 770–772
inflow performance relationship (IPR), 840
infrared absorption (IR) spectrometer, 364–365
initial free-gas cap volume, 910
injection fluids, 899
 relative velocities, 652
injection packer seal demonstration, 571
injection profile, 572–580
injection-water. *See* water-injection
injection wells, 1119, 1180
 density, 1120
 design, 1389
 fracturing, 1181
 spacing, 1120
inner zone mobility, 785
inorganic gels, 1186, 1191
in-place and recoverable hydrocarbons, resource classification system, 1480
in situ anisotropy analysis, 220
in situ combustion (ISC), 1367
 combining material- and heat-balance calculations, 1374–1384
 design considerations, 1384–1385
 field experience, 1391–1393
 laboratory studies, 1370–1374
 operating practices, 1386–1391
 predicting the performance, 1384–1385
 process description, 1367–1370
 production response prediction to, 1385
 screening guidelines for, 1393–1394
in situ polymerization, 1191, 1204
instantaneous phase and instantaneous frequency calculations, 39–41
intercommunicating fracture system, 1134
interconnected vugular porosity, 1154
interdistributary shales, 1115
interdune braided-stream deposits, 19
interfacial-tension (IFT), 427, 429, 465, 1040, 1105, 1281
intermediate-hydrocarbon components, 896
intermediate-wet reservoir rocks, 1041. *See also* reservoir rocks
intermediate wettability, water/oil capillary pressure and, 1047.
 See also wettability
Internal Revenue Service, 1574
interporosity flow coefficient, 797, 799–800
interwell interference, 1558
interwell permeabilities, 1118
intramolecular crosslinking, 1163
invaded-zone method, 151–152
invasion parameters, inversion for, 136–137
inversion-processing methods, 224, 228
IRS. *See* Internal Revenue Service
ISC, equipment for oil production
 air-compression systems, 1386–1387
 ignition, 1387–1388
 safe air injection, 1389–1391
 well design and completions, 1388–1389
isochronal tests, 839, 851
isopach maps, 1556
isothermal flow of fluids, 719
isotropic permeability, 826
isotropic reservoirs, 834
iterative methods, 1531

J

jet washing, 1245
J-function, 460
Joffre Viking miscible CO₂ flood, 1239
Jurassic-age limestone-dolomite section, 1617

K

kaolinite, 17
Kaufman-Vail principles, 100
Kirkuk oil field (Iraq), 1094–1095
 areal map of reservoir sands, 1093
 ultimate-recovery factors for, 1093–1094
Kozeny expression, to estimate the flow rate, 969
Kuparuk River oil field (Alaska North Slope), 1075,
 1092–1094, 1142
 conformance plot for, 1083–1084
 waterflood-analysis calculations for, 1086
K-U-Th logging, 263
K-values, water-related, 1450

L

LaCoste-Romberg borehole gravimeter, 411
laminated sand/shale model, 155–156, 462
Langmuir isotherm, 666
Larmor frequency, 293, 307
late-linear flow, 819
latent heat injection rate, on strategy economics, 1319
latent heat of evaporation, 1310
late-pseudoradial flow, 818
lateral and normal devices, resistivity measurement and, 91–93
laterolog and induction logging tools, 130–132
laterolog device (LLd), 90
 azimuthal dual laterologs, 95–97
 dual laterolog resistivity measurements, 93–95
 environmental effects on, 104
late-time region (LTR), 776
layered waterflood, surveillance-overview logic for, 1086
layer resistivities, 130
layer thickness, determination of, 78–80. *See also* petrophysics
leakoff current, 100
least-squares multivariate regression, 930
least-squares regression analysis, 848, 854, 863
Leduc miscible pilot, residual-oil saturation in, 677–678
light oil-recovery operations, 1149
light oils, 896, 1393
linear equation solver (*see also* reservoir simulation)
 combinative or CPR method, 1415
 IMPES models in, 1415
 Orthomin and GMRES method, 1412
 parallel iterative solution, 1415
 preconditioning technique, 1412–1415
linear flow, 730, 766–767
 method, 791–792
 pattern, 807
linear mixing law, 272, 280
linear no-flow boundary, 772–774
linear solver, Orthomin method and, 1407
linear waterflood, macroscopic displacement efficiency of,
 1052–1054
liquid hydrocarbon, 1104
liquid-junction potential, 140–141
Li-6 scintillator, 268
listric faulted structural trap, 3
lithology determination, 430
 clay-mineral properties, 431–432
 direct, 80
 evaluation of shale volume, 432–433
 indirect, 80–81
 reservoir zonation/layering, 433–434
lithology reservoirs, 203
LKG. *See* lowest known limit of gas
LKH. *See* lowest known hydrocarbons
LKO. *See* lowest known limit of gas and oil
LLd electrode array, 94
localized matrix reservoir rock, 1154

- logarithmic approximation, 735, 746
 - log-data
 - conditioning, 427
 - quality, evaluation of, 424–425
 - log-formation process, 113
 - logging documentation, 175
 - logging tools
 - downhole NMR spectrometer, 311
 - LWD tools, 310–311
 - NML tool, 305–306
 - pulse NMR, 306–308
 - wireline-tool designs, 308–309
 - logging while drilling (LWD), 78
 - acoustic services, 167
 - devices, 289, 292
 - gamma ray tools, 262–264
 - logs, 423
 - measurements, 258
 - resistivity images, 138–139
 - log-inject-log measurements, for residual oil saturation, 277
 - log-inject-log tests, 1614
 - log interpretation, nuclear logging and, 270
 - advanced processing, 274–275
 - fluid effects, 273
 - macroparameters, 275
 - Monte Carlo modeling, 275
 - log presentation, 311
 - longitudinal (spin-lattice) relaxation T_1 , 293–295, 298–299
 - Louisiana volatile oil
 - compositional analysis of, 909
 - material-balance calculations for, 920
 - PVT parameters for, 908
 - reservoir, pressure and producing GOR as function of OOIP recovered for, 917
 - reservoir, producing history of, 916
 - selected reservoir and fluid properties for, 915
 - Love waves, 34
 - low-energy gamma ray flux, 265
 - Lower San Andres (LSA), 1295
 - lowest known hydrocarbons, 1555
 - lowest known limit of gas and oil, 1487
 - low-permeability gas reservoirs, 1556
 - low-permeability shale, 825
 - low-permeability (tight) sandstones, 335
 - lowstand system's track (LST), 9
 - low-temperature oxidation (LTO), ISC and, 1370
 - low-temperature separators (LTS), 1514
 - LWD induction tools (*see also* induction logging)
 - on drillpipe, 117–119
 - multiarray propagation tools, 124–130
 - propagation measurement principles, 119–124
 - LWD-NMR services, 310
 - LWD tools, 310–311, 358
 - nuclear logging and, 268–270
- M**
- macroparameter methods, 275
 - magnetic resonance imaging (MRI), 298, 309, 1232
 - devices, 306
 - magnetic resonance imaging tool (MRIL), 308–309, 339
 - magnetic sector mass spectrometer, 365
 - magnetic survey, 380–381
 - MagTrak, LWD device, 311
 - Mandl-Volek (M-V) models, 1324–1325
 - Manning survey, 1182
 - marine air guns, 27–31
 - 4C marine seismic sensors, 31–32
 - marine seismic vessel with towed-cable technology, 27–28
 - Mark-Houwink equation, 1167–1168
 - Marx and Langenheim equations, 1313
 - Marx-Langenheim model, 1324–1325
 - mass conservation equations, for gridding, 1416
 - massive dissolution, 15–16
 - mass spectrometer (MS) detector, 363–364
 - mass-to-charge ratio, 363
 - mass-transfer effect, 1144
 - material- and heat-balance calculations
 - heat losses, 1383
 - initial heat balances and temperatures, 1375–1378
 - injected air and water, calculating effects of, 1381–1383
 - no combustion data available, 1374–1375
 - volume and temperature of steam plateau, 1379–1381
 - water of combustion, correction for, 1378–1379
 - material-balance, 905–910
 - analysis, 918
 - calculations, 903
 - equation, 906, 910
 - mass conservation, in reservoir, 903–910
 - method, 1519, 1558
 - object relationships, 1088
 - shell, RDBMS and, 1087
 - volatile-oil reservoir analysis, 918–920
 - matrix-block/fracture network carbonate reservoirs, 1118
 - matrix-blocks/fracture-system interaction, 1111
 - matrix-identification (MID) plot, 283
 - matrix rock, 1217
 - conformance, 1155, 1192
 - gelant, gel flow and placement in, 1201
 - oil reservoirs, 1153, 1155, 1192, 1195, 1211
 - strata, 1220
 - (unfractured) reservoirs, 1153
 - vertical conformance, 1221
 - Matthews-Brons-Hazebroek (MBH) method, 776, 778
 - maximum flooding surface (MFS), 9
 - maximum-length equation, 501
 - Maxwell's equations, 98
 - MCFL log, 134–135, 148
 - McKelvey box, 1480–1481
 - mean- T_2 model. *See* Schlumberger-Doll-Research (SDR) model
 - measurement while drilling (MWD)
 - devices, 78, 268
 - tools, 263, 358
 - mechanical and chemical compaction, 15
 - mechanical integrity, 277–278
 - mechanical pressure transducer, 689, 691
 - mechanical shear degradation, 1177, 1180
 - mechanical zone isolation, 1201, 1215, 1221
 - medium-temperature reactions, chemical reactions associated with ISC, 1370
 - membrane potential, 139–140
 - mercury-injection capillary pressure (MICP)
 - curves, 319
 - data, 460, 464–465
 - methods, 304, 430
 - metal-crosslinked synthetic-organic-polymer gels, 1222
 - metal crosslinking, 1190
 - metal debris, 343
 - microcylindrically focused log (MCFL) measurements, 97
 - microelectrical imaging tool, 137
 - microgas bubbles, 1225, 1229
 - microgel sweep-improvement treatments, 1215
 - Micro Laterolog (MLL), 99
 - microorganism fermentation processes, 1160
 - microresistivity imaging devices, 400
 - measurement principle of, 401, 403
 - microresistivity logs
 - MCFL device, 134–135
 - microlog, 133

- MSFL device, 134
 - tools, 137
 - microresistivity-vs.-porosity crossplots, 148–150
 - microscopic fossils, mud logging and, 372
 - microseismograms, 186
 - MicroSFL (MSFL) device, 134, 148
 - Middle East carbonate matrix/fracture-system reservoirs, 1118
 - middle-time region (MTR), 744, 776
 - mineral-identification-plot (MID) techniques, 204
 - minimum degree fill (MDF), 1415
 - minimum miscibility enrichment (MME), 1265
 - minimum miscibility pressure (MMP), 1265
 - miscible flood designing
 - CO₂-flood and enriched-gas-drive MMP, correlation for, 1268–1269
 - laboratory coreflooding studies, 1264
 - miscibility determination, 1264–1266
 - miscible project, economic viability of, 1268–1271
 - MMP and MME guidelines, 1266–1267
 - MMPs with solvents, guidelines, 1267
 - performance, factors affecting, 1263
 - in reservoir study, 1267
 - slimtube displacements, determining MMP or MME, 1265
 - miscible flood prediction, compositional reservoir simulator and equations of state, phase behavior with, 1277–1280
 - injection-fluid/crude-oil systems, phase behavior of, 1271–1277
 - miscible fluids, 1124
 - miscible gas flooding, 1235–1236
 - Miscible Injectant Stimulation Treatment (MIST) concept, 1299–1300
 - miscible injection, 1261
 - miscible processes
 - compositionally enhanced solvent flood behavior, prediction of, 1281–1292
 - compositional numerical simulation, 1271–1280
 - concepts of, 1261–1264
 - miscible flood designing, 1264–1271
 - projects using CO₂, hydrocarbon, and N₂ solvents, 1292–1302
 - miscible water-alternating-gas (MWAG), 1093
 - MIST injector 9-31C, 1300
 - mixed-wet and water-wet cores, waterflood behavior for, 1049
 - mobility-control
 - agent, 1236
 - flood, 1154
 - foams, 1224, 1234
 - mobility ratio, 1050–1052, 1062, 1068, 1107, 1151
 - on oil production for five-spot pattern, 1081–1082
 - model formulations (*see also* reservoir simulation)
 - choice of formulation, 1403–1405
 - IMPES vs. implicit GOR and water cut, 1404
 - IMPES vs. implicit oil rate and cumulative oil production, 1404–1405
 - implicit and IMPES formulations, 1402–1403
 - relaxed volume, advances in, 1405–1406
 - sequential and adaptive implicit formulation, 1402–1403
 - truncation and numerical dispersion error analysis, 1403
 - variable choice and adaptive flash calculations, model efficiency for, 1405–1406
 - modern and historical evaluation methods, comparison, 1591–1594
 - modified isochronal tests, 839–840
 - molecular weight (MW), 1167, 1194
 - monomer gels, 1186, 1191
 - monopole-array tool, 171, 179
 - monopole (axisymmetric) transducers, 172
 - monopole excitation, 173
 - monopole transmitters, 170, 178
 - Monte Carlo model, 249, 252, 275
 - Monte Carlo Nuclear Parameters (MCNP), 275
 - Monte Carlo simulation evaluation method, 1575–1576
 - montmorillonite, 17
 - moving-coil geophone, 30
 - MRI analysis (MRIAN), 336
 - MRIL-NMR data, 336
 - mudcake resistivity and thickness (h_{mc}), 133
 - mud chloride content, 373
 - mud contamination, sources, 359–360
 - mud filtrate, 748
 - mud-log gas and oil shows, 483–484
 - mud logging, 357, 450
 - component analysis, 361–365
 - cuttings analysis, 365–368
 - data acquisition, 358–360
 - data quality, maintaining, 368
 - drilling engineering and operations, 372–375
 - formation evaluation, 368–372
 - health, safety, and environmental considerations, 375
 - total gas analysis, 360–361
 - mud pit level, 373
 - mudstone, 11–14
 - multiarrray propagation tools
 - ARC5 tool, 124–126
 - geosteering with, 127–130
 - multicoil arrays, 106–107
 - multi-Darcy flow channels, 1240
 - multi-Darcy matrix rock, 1241–1242
 - multidimensional simulation models, 1127
 - multifingered caliper tool, 390
 - multifluid (forward modeling) methods, 330–331
 - multilateral wells, 1064
 - multilayer reservoir, 1215
 - multiphase flow, 1231
 - test analysis, 763
 - multiple-log interpretation
 - crossplot, visualization and, 280–283
 - multitrack log display, visualization and, 279–280
 - multiple propagation-resistivity (MPR) tool, 127, 129
 - multistage compression, conjectural economics of, 1559
 - multistage fracture placement, 568
 - multitrack log display, 279–280
 - Muskat method, 776, 783, 895
 - MWD gamma ray tools, 263
- N**
- nanoTesla (nT), 413
 - natural gamma ray spectroscopy, 278
 - natural gases properties
 - depletion studies, 991
 - EOSs, 993–994
 - gas density and formation volume factor, 984–985
 - phase diagrams, retrograde-condensate gas and wet gas, 982–983
 - pressure/volume/temperature (PVT) behavior, 983–984
 - retrograde behavior, 988–993
 - retrograde-liquid volume vs. pressure, 992
 - two-phase z factor, 991
 - viscosity, 985–986
 - visual-cell depletion, retrograde gas, 990–991
 - natural-gas foams, 1234
 - natural gas from shale, 1539–1542
 - natural-gas liquids (NGLs), 896, 1115, 1300
 - naturally occurring radioactive materials (NORMs), 1040
 - natural petroleum gases, 981
 - natural reservoir boundaries, 843
 - near-critical fluids, 896

- near-wellbore
 - conformance, 1222
 - polymer-gel treatments, 1153
 - pressure gradients, 1121
- near-well grid refinement, effect of, 1408
- near-well imaging, 213
- Nested Factorization (NF), 1407, 1415
- net/gross (N/G) ratio, 434, 436
- net oil sand isopach of channel sand, 1498–1500
- net-pay cutoff, 436–438
 - applications, 440–441
- net-pay determination, 434
 - calculations, conceptual bases for, 435–437
 - gas reservoirs and, 437
 - geologic considerations in, 438–440
 - isopach maps, 1554
 - netpay-cutoff, 438, 440–441
 - oil reservoirs and, 437–438
- neutron-density crossplot, 157, 282
- neutron logs, 448–449, 540
 - C/O logs, 278
 - gamma ray spectroscopy tools, 278
 - geochemical logs, 278–279
 - log-inject-log measurements, for residual oil saturation, 277
 - log interpretation, 270–275
 - LWD, 268–270
 - mechanical integrity, 277–278
 - neutron-scattering porosity tools, 267–268
 - PNL devices, 276–277
- neutron-porosity, 202, 273, 280
 - log, 253, 267, 269, 274
- neutron-scattering porosity tools, 267–268
- Newtonian fluid/viscosity, 1167
- Newton's law of motion, 170
- New York Mercantile Exchange, 1583
- nitrogen projects, Jay field, 1301–1302
- nitrogen rejection plant, 1120
- N₂ miscible injection, 677
- NML tool, 305–306, 314
- NMR applications, in petrophysics and formation evaluation, 289
 - anisotropy and geomechanics, 335
 - carbonates and complex lithologies, 335
 - combined, 336–338
 - heavy oil, tar sands, and tar mats, 335
 - historical development, 290–292
 - hydrocarbon (fluid) typing, 322–331
 - logging tools, 305–311
 - log presentation, 311
 - low-permeability (tight) sandstones, 335
 - NMR acoustic/density combination, 337–338
 - NMR-log job planning, 340–343
 - NMR-log quality control, 338–340
 - NMR petrophysics, 298–305
 - NMR physics, 292–298
 - NMR-resistivity combination, 336–337
 - permeability estimation, 319–322
 - porosity determination with, 311–319
 - producibility, 335–336
 - pseudocapillary-pressure curves, 335
 - residual oil (S_{xo}) calculation, 331–333
 - viscosity evaluation, 333–335
- NMR effective porosity (MPHI), 315, 322, 327
- NMR logging
 - measurements, 289
 - and reservoir, 86
 - tools, 294, 298, 304, 327
- NMR-log job planning, 340
 - borehole rugosity, 342
 - lithology, 341–342
 - logging speed and running average, 343
 - metal debris, 343
 - mud type, 342
 - wettability, 342
- NMR-log quality control, 338
 - post-logging quality check, 340
 - prejob calibration and quality checks, 339–340
- NMR petrophysics
 - data fit—inversion, 303–304
 - laboratory studies, 298
 - NMR properties of fluids, 299–301
 - properties, 298–299
 - T_2 decay, 301–303
 - T_2 distribution, 304–305
- NODAL analysis, 712–713
- no-flow boundary, 732
- noise log, 536
 - in relief well, 541–542
- noise-logging tool, 511–514
- noisy SP logs, 144–145
- non-Cartesian grids, 1407, 1411
- noncondensable gas, 1236
- non-Darcy flow, 754, 761, 796
 - coefficient, 842
 - effects, 722
- nonhydrocarbon components, 1143
- nonhydrocarbon gases, 1104
- nonideal SWCT tests simulation
 - fluid movement, 634
 - local equilibrium time length, 635
 - nonreversing flow, 635–636
- nonionic surfactant, 1227
- nonionic triple-stranded polysaccharide biopolymer, 1186
- non-laminar flow, 761. *See also* non-Darcy flow
- nonlinear partial-differential equation, 757
- nonlinear shale-volume models, 260
- non-Newtonian viscosity, 1166, 1168
- nonpolar hydrocarbon molecules, 1226
- nonradioactive water tracers, 655
- nonsegregation-drive gas caps, 901
- nonvolumetric reservoirs, 900
- nonzero skin, 751
- normal geothermal gradient, 374
- normal (pseudo-Rayleigh) waves, 168
- Norsk Hydro tensor method, conservation of dissipation, 1428
- North Burbank Unit Flood, 1182
- North-Sea reservoirs, 1554
- Mh-root stack processing, 218
- nuclear-log crossplot, 282–283
- nuclear logging, 243
 - gamma ray transport and, 254–256
 - multiple-log interpretation, 279–283
 - neutron logs, 267–279
 - nuclear radiation transport, 245–249
 - passive gamma ray tools, 256–267
 - physics of, 244–245
 - single-log interpretation, 249–253
- nuclear magnetic log (NML), 290, 307
- nuclear magnetic resonance (NMR), 245, 289
 - acoustic/density combination, 337–338
 - devices, 292–293
 - echo-decay, 318–319
 - logs, 79, 86
 - physics, 292–298
 - porosity model, 308
 - resistivity combination, 336–337
 - spectroscopy methods, porosity determination and, 82
- Nuclear Magnetic Resonance Tool (NMRT™), 309, 414

nuclear radial geometric functions, 251
 nuclear radiation transport, 245–249
 Numar's mandrel device (MRIL), 291
 numerical reservoir simulation model, 1121
 numerical reservoir simulators, 1144
 NYMEX. *See* New York Mercantile Exchange

O

- OBM-core-plug Dean-Stark water-volume determinations,
 S_w calculations with, 467
 OBM-core S_w data, 429, 460–461, 469–470, 476
 OBM-filtrate invasion, 330
 OBM routine-core-analysis data, 426
 ocean-bottom cable (OBC), 31–32, 34
 Ocean Drilling Program (ODP), 414, 416
 Odeh-Babu and Kuchuk equations, 814
 offending injectors, 651
 oil and gas prices, economic/political uncertainty, 1586
 oil and gas profiling production
 gravel pack density and fluid capacitance survey, 605
 multiarm fluid-conductivity and capacitance survey, 606
 temperature and back scatter gamma-ray density surveys, 605
 oil and gas property valuations, 1573–1574
 oil and gas property ownership
 net profits interest and production payment, 1597–1598
 royalty interest, 1597
 working interest, 1596
 oil and gas reserves
 adjustment factors for risk and uncertainty in, 1586–1589
 asset description, 1595–1598
 capital cost, 1584–1585
 classification system of, 1582
 economic evaluation, 1575
 interest positions and prices, 1582–1583
 reports and discounted cash flow schedules, 1578–1580
 risk and uncertainties in, 1585–1586
 study definition, 1572
 taxes and operating cost, 1583–1584
 oil and gas reservoir management
 benefits of, 1611–1620
 definition of
 description of, 1601–1602
 horizontal and multilateral wells for, 1602
 leadership team, 1599–1600
 models of, 1604–1605
 performance management, 1607
 performance survey, 1605
 process work flow of, 1600
 team skills of, 1600–1601
 wellbore utilization plan for, 1603
 oil and gas reservoirs and depletion plans, 1602–1605
 oil and gas zone, volumetric parameters, 1508–1509
 oil and wetting effects, 1233
 oil-based mud (OBM), 112–114, 199, 311, 342, 424, 426
 Oil-Base Microlmager (OBMI™), 406
 oil classes, 895
 oil-coated injection/film, 1244–1245
 oilfield foams, 1223
 oilfield furan resin treatments, 1242
 oilfield gels, 1192, 1221
 oil fields-Offshore Peninsular Malaysia, 478–480
 Block A-18, gas/condensate field, Malaysia-Thailand joint development area, 480–481
 oilfield surface separators, 1115
 oilfield tubulars, 1217
 oil fraction in, in total fluids and cumulative oil production for typical well, 1526
 oil, gas, and water saturation, 83–84
 oil/gas-expansion-drive reservoirs, 901
 oil gravity drainage, 1139
 oil in place (OIP), 1385
 oil-producing reservoir, 1151
 oil production
 mobility ratio effect on, 1081–1082
 under WAG recovery, profiling, 539–541
 water injection effect on, 1038
 oil recovery
 displacement fluid, 1151
 drive fluid, 1151–1152, 1247
 flood conformance, 1151
 fluid, 1149
 improvement, 902
 mechanisms, 1139
 production, 1241
 sweep efficiency, 1153
 oil-recovery flooding, 1224
 operations, 1149, 1166
 system, 1149
 oil reservoirs, 437–438, 895, 899, 1037
 geological aspects of, 1056
 gravity effects on, 1065
 structure, 1056, 1497
 oil/water
 fractional flow, 1155
 profile commingled, 587–589
 viscosity ratio, 1409
 oil/water contacts, 426, 439, 475, 1121, 1487
 oil-wet reservoirs, 1139, 1233
 pressure-depth plots and capillary pressure profiles, 706, 709
 oil-wet rocks, 1041, 1046
 oil-zone perforations, 1104
 oolitic limestone, 1132
 openhole caliper logs, well-logging and, 387–388
 openhole-imaging devices, 194
 openhole logging, 276
 openhole short-radius horizontal wellbores, 1210
 openhole wireline pressure testing, 695, 697
 OPMs. *See* option-pricing models
 optical borehole imaging, 397
 option-pricing models, 1576
 organic crosslinking agents, 1206
 organic-fluid-based gel, 1186
 organic-rich shales, 211
 original gas in place (OGIP), 421, 903, 910, 915
 original oil in place (OOIP), 421, 615–616, 897, 903, 910, 912, 916–917, 1038, 1063, 1120, 1179, 1261, 1385
 orthogonal Cartesian grids, 1407
 orthosilicate monomer, 1192
 Output Least Squares (OSL), 1430
 overdisplacement fluids, 1211
 OWC. *See* oil/water contacts
 oxygen free-radical degradation, 1176

P

- packer flowmeter, 524–525
 packer probe tests, 712
 packstone, 11–12, 14
 parallel resistivity relationship, 155–156
 Paroscientific design, for quartz pressure transducer, 691
 partial-penetration skin, 821
 passive gamma ray tools, 256–261
 density-porosity interpretation, 264–265
 environmental effects, 261–262
 gamma-gamma scattering density tools, 263–264
 LWD, 262–264
 PE, 265–266

- precision, 261
 - spectral gamma ray logs, 262
- pattern gas injection, 1119–1120
- P_c -derived S_w values, 470–471
- P_c/S_w data, 452–453, 460
 - laboratory-measured, S_w calculation and, 464–466
 - resistivity-log-derived S_w and, 467
 - routine OBM core S_w data with, 467–468
- PE factor (PEF), 255
- Peng-Robinson, EOS petroleum engineering applications, 993–994
- perfluorocarbon (PFC) gas tracers, 658, 669
- perfluorodimethylcyclobutane (PDMCB), 658
- 1,2-perfluorodimethylcyclohexane (1,2-PDMCH), 658
- 1,3-perfluorodimethylcyclohexane (1,3-PDMCH), 658
- perfluoromethylcyclopentane (PMCP), 658
- perforating depth control (PDC) log, 502
- performance-data analysis, 1558
- performance indicators extrapolation, 1556
- permanent pressure measurement installations, 697–698
- permeability
 - determination, 471–474
 - estimation, 319–322
 - matrix reservoir rock, 1235
 - reducing agents, 1188
 - reducing polymers, 1184
 - reduction, 1175
 - reduction ratio, 750
- perpendicular bisector (PEBI) method, reservoir simulation, 1420
- Perrine-Martin approximations, 764
- Perrine-Martin modification, 762
- petroleum fluids, 896–897
- petroleum production, types of energy available for, 898
- petroleum reserves, classification
 - proved, 1482–1483
 - unproved, 1483–1484
- petroleum reserves estimation
 - analogy methods, 1490–1493
 - volumetric methods, 1493–1494
- petroleum reserves status categories, 1484
- petroleum reservoirs, 899
 - commercially productive, 900
 - fluid flow, 719
 - fluids, major classes, 982
 - pressure drop, 725
- petroleum sulfonates, 1236
- petrophysical applications, 421
 - case studies, 474–483
 - data sources and databases, 422–430
 - fluid-contacts identification, 450–452
 - lithology determination, 430–434
 - net-pay determination, 434–441
 - permeability determination, 471–474
 - porosity determination, 441–450
 - water-saturation determination, 452–471
- petrophysical data sources and databases
 - acquisition of, 429–430
 - conditioning, for reservoir parameter calculations, 427–429
 - inventory of existing data, 422–423
 - quality evaluation of existing data, 423–427
- petrophysical properties, gas reservoir
 - Forchheimer equation, 994–995
 - Klinkenberg effect, 994
 - Klinkenberg permeability correction, 995
 - non-Darcy flow, 994–995
- petrophysics
 - absolute permeability determination, 85–86
 - definitions, 77–78
 - fluid identification and characterization, 84–85
 - and formation evaluation, NMR applications in, 289
 - fractional flow, 86–87
 - layer thickness, determining, 78–80
 - lithology and rock type, determining, 80–81
 - oil, gas, and water saturation, 83–84
 - porosity determination, 81–83
 - tools selection, 78
 - use of, 87
- phase-alternate pairs (PAP), 297
- phase redistribution, 796
- phase-shift, resistivity and, 121
- Phasor induction tool, 108–112, 115, 131
- phenolic resins, 1241
- photoelectric (PE) absorption, 255, 265–266
- piercement trap, 3
- piezoelectric crystals/transducers, 172, 511
- pilot waterflooding, 1078
- pipe dope, 368
- Pixler method, 369–370
- plastic-coated well tubulars, 1222
- Poisson distribution, 245–246
- Poisson's ratio, 169, 212
- polarization, 292–293
- polyacrylamide (PAM), 1162
- polyethyleneimine-crosslinked gel, 1190
- polyhedra liquid films, 1228
- polymer-gels, 1186, 1222
 - adsorption, 1165
 - bottle-test gel strength code, 1200
 - conformance, 1160, 1218
 - degelation, 1206
 - technologies, 1190
 - treatments, 1208, 1219, 1247
 - treatment technologies, 1155
 - water-shutoff, 1157
 - water-shutoff treatment, 1210, 1215
- polymer(s)
 - adsorption, 1163
 - concentration grading, 1179
 - degradation, 1176
 - degrading free radicals, 1178
 - dissolution, 1180
 - enhanced foams, 1237–1239, 1248
 - filtration, 1181
 - flood biopolymers, effects of salt and hardness on, 1172
 - flooding, 1168–1169, 1176–1177
 - macromolecules, 1221
 - microgels, 1154
 - precipitation, 1176
 - retention, 1175
 - self-induced gels, 1191
 - transport, 1174
 - waterflooding, 1150, 1153, 1160, 1166, 1171
- polymer-solution
 - injection wells, 1181
 - slug, 1179
 - viscosity, 1167, 1173
- polysaccharide biopolymers, 1177
- pore-fluid
 - composition and saturation, 169
 - mobility, 225
 - permeability, 224
- pore pressure, mud logging and, 372
- pore-to-pore interconnections, 1117
- pore volume (PV), 1179
 - contraction, 901, 915
 - porous rocks, 1550
- porosity determination, 441
 - calculations and uncertainty, consistency of, 449–450

1642 Subject Index

- core/log calculation approaches, 444–449
- core porosity data and, 442
- direct, 81–82
- indirect, 82–83
- total and effective porosity, 442–444
- porosity determination, with NMR, 311
 - BVI determination, 316
 - CBVI model, 316–318
 - measurement, tool version influence on, 314–315
 - porosity-logging modes, 315–316
 - SBVI model, 318–319
- porosity-logging modes, 315–316
- porosity transforms, 202
- Portland cement, 1157, 1198, 1217, 1243
- possible petroleum reserves, 1484
- possum belly, 358–359
- power-law, 1170
- prejob calibration and quality checks, logging and, 339–340
- pressure and temperature
 - calibration points, 687
 - nonlinearity in, 688
 - optical fiber measurement of, 692
 - subsea acquisition of, 698–699
- pressure-buildup (PBU)
 - permeability values, 473
 - test, semilog methods for, 736–739
- pressure/depth
 - method, 1502
 - plots, 701–704, 708–709
- pressure flow convolution and deconvolution, 708–709
- pressure gauges
 - calibration and standard evaluation tests for, 687–688
 - nonlinearity in pressures and temperatures, 688
 - pressure calibration function, 687–688
 - pressure-temperature calibration points, 687
 - scheduled time routine for pressure gauge calibration test, 688
 - temperature calibration function, 688
- pressure-gradient
 - density log, 516
 - instrument (see gradiomanometers)
 - method for hydrocarbon/water contact calculation, 1504–1505
- pressure maintenance, 899
 - by gas reinjection, 902
- pressure probes in duplex/triplex, 704
- pressure-squared and pressure approximations, 757–759
- pressure thermal sensitivity, 688
- pressure transducer technology, 689–691
 - bonded wire transducer, 690
 - capacitance pressure transducer, 689
 - mechanical pressure transducer, 689
 - quartz pressure transducer, 690–691
 - sapphire transducer, 690
 - strain pressure transducer, 690
 - thin-film transducer, 690
- pressure-transient analysis (PTA), 473
- pressure transient testing, 693, 707–715
 - analysis, 722–723, 839
 - to characterize reservoir fluids, 713–714
 - downhole shut-in benefits, 709
 - multilayer tests, 709–711
 - NODAL analysis, 712–713
 - pressure flow convolution and deconvolution, 708–709
 - temperature profiles in production and injection wells, 714–715
 - wireline pressure transient tests, 711–712
- pressure/volume/temperature (PVT), 1449
 - parameters, 903
 - properties, 1114
- primary gas caps, 901
- primary oil recovery, 895, 902–903
- probable petroleum reserves, 1483–1484
- producibility indexes, 202
- producing mechanisms
 - for oil, 899–903
 - petroleum reservoirs for, 899–902
 - recovery ranges, 902–903
- production/decline trend analysis (P/DTA), 1522–1523
- production-log flow survey, 829
- production logging
 - application tables (see production-logging application tables)
 - categories of, 495–496
 - depth control, 501–502
 - flow problems, origin of, 497–498
 - misconceptions about, 496–497
 - pricing and record keeping, 502–503
 - safety and environmental tips, 498–499
 - sinker bar weight, 499–501
 - suites of, 535–542
 - tools, operating principles and performance of, 503–535
- production-logging application tables, 549
 - classification tables, 550
 - tool-selection tables (see tool selection tables, production logging and)
- production-logging suite
 - commingled-gas production, profiling, 537–539
 - gas blowout after abandonment, 541–542
 - gas kick while drilling, 535–537
 - oil production under WAG recovery, profiling, 539–541
- production-logging tools, operating principles and performance
 - continuous and fullbore spinner flowmeters, 526–535
 - diverting-spinner flowmeter, 523–526
 - fluid-capacitance-logging tool, 516–518
 - fluid identification in high-angle wells, 521–523
 - focused gamma-ray density-logging tool, 514–516
 - noise-logging tool, 511–514
 - radioactive tracer-logging tool, 508–511
 - temperature-logging tool, 503–508
 - unfocused gamma ray (gravel-pack) density logger, 518–521
- production wells, 1078, 1083
 - and designs, 1390
- productivity index, 724, 751
 - horizontal well, Economides *et al.* method and, 834–839
- progradational cycles, 8–9
- propagation measurement principles, 119–124
- proved petroleum reserves, 1483
- Prudhoe Bay field, 433, 474–477
- Prudhoe Bay Sadlerochit reservoir, 1127
- pseudocapillary-pressure curves, 335
- pseudopressure, 756–757
 - equations, 842
 - transformation, 757–758
- pseudoradial flow, 785, 792–793, 822
- pseudo-shear measurement, 182
- pseudosteady-state
 - equations, 719, 841, 852
 - flow, 722, 778, 798, 831, 841–843
 - matrix flow, 801
 - matrix flow model, 798
 - solution, 841
- pseudotime transformation, 759
- pulsed caliper tools, 387
- pulsed neutron capture (PNC), 1301
- pulsed-neutron-lifetime (PNL) devices, 276–277
- pulse-echo tools, 307
- pulse-NMR
 - logging, 299, 306–308
 - spectrometers, 298

pure solution-gas-drive reservoirs, 910
 PVT treatment, of fluids in reservoir simulation
 black-oil PVT models, 1454
 component partitioning, 1452
 density, 1451
 equation-of-state models, 1454–1455
 fluid initialization, 1456
 gas/oil interfacial tension (IFT), 1454
 gas viscosities, 1453
 phases and phase type, 1450
 surface phase behavior, 1455
 thermal model PVT requirements, 1455
 three-phase PVT behavior, 1455
 two-phase flash, 1450–1451
 pyrolysis, 1368, 1370, 1372

Q

QGM™ process, 369
 quartz pressure transducer, 690–691
 Quartztronics design, for quartz pressure transducer, 691

R

RAB tool, 102
 Rachford-Rice (RR) procedure, 1450
 radial aquifer
 finite and infinite, 939
 model, 936
 OOIP, water-influx history and model parameters, 949
 reservoir partially surrounded by, 946
 radial-cement-evaluation devices, 193
 radial diffusivity equation, 719
 radial-flow, 826
 conformance, 1220
 diffusivity equation, 740, 840
 injection, 1177
 matrix-reservoir rock, 1158
 matrix-rock reservoir, 1219
 reservoirs, 771
 radioactive gas tracers, 656–658
 radioactive tracer-logging tool, 508–511
 radioactive water tracers, 652–655
 partition coefficients of, 653–654
 used in oil reservoirs, 653
 radio frequency (RF), 291, 309
 radius of investigation, 722, 739
 Ramey-Cobb method, 776, 781–782
 Raoult's law, 662
 rate-dependent skin, 721
 rate of penetration (ROP), 373–374
 rate of return, 1580
 Rawlins-Schellhardt analysis, 845, 853, 862, 864, 869
 Rawlins-Schellhardt deliverability plot, 869
 Rawlins-Schellhardt equation, 843, 871
 Rayleigh waves, 34
 Raymer-Hunt-Gardner equation, 199, 202
 real options analysis, 1576–1577
 Recommended Evaluation Practices, 1573
 recovery efficiencies (REs), 1487
 rectangular matrix-block geometry, 804
 reduced-major-axis (RMA) line-fit, 445, 447
 reef deposit, 1117
 reflection coefficients, 35–37
 regression analysis, 827
 relative permeability, 875, 1046–1048, 1050, 1076, 1110
 relative permeability modification (RPM), 1157
 repeat formation tester, 1508
 REPs. *See* Recommended Evaluation Practices
 reserves and cash flow projection, 1578

reserves classifications
 from areal perspective, 1518
 basic guidelines, 1516–1517
 reserves estimation, 1482, 1489
 reservoir heterogeneities
 forms of, 1055
 by permeability variation, 1068–1072
 Reservoir Management Leadership Team, 1606–1607
 reservoir management team (RMT), 77. *See also* petrophysics
 reservoir parameter calculations, data conditioning for
 density and neutron logs, 428
 gamma ray logs, 427
 log data, 427
 OBM S_w data, 429
 permeability data, 429
 porosity data, 428–429
 resistivity logs, 428
 routine-core-analysis and SCAL data, 428
 sonic logs, 428
 reservoir pressure, 683–685
 distribution, in reservoir during fluid flow, 684–685
 pseudosteady-state flow, 684–685
 steady-state flow, 684
 reservoir rocks, 1039
 biodegradation, and tracer flow in, 665–666
 pore geometry for, 1042
 pore system in, 1045
 shear failure and water-weakening of, 1089
 reservoir(s)
 absolute permeability determination, 85
 architecture, 1, 7–9
 base, 5–7
 boundary, 723
 carbonate reservoir, 9–16
 drive mechanism, 1521
 economic base of, 7
 efficiency, 1313
 energy, types of, 898–899
 evaluation, by material balance, 616–617
 external geometry of, 1–7
 fluid flow analysis software, 846
 fluids, 199, 206, 713–714, 839, 896, 985–988, 1175
 geology, 1–23
 heating, 1311–1314
 internal geometry, 1, 7–9
 lithology, 341–342
 matrix rock, 1242
 mineralogies, 1216
 models, 21–23, 719, 1532–1533
 oil, viscosity, 1509
 permeability impairment, 1074
 petrophysical properties, 1, 7–8
 producing mechanisms, classification of, 900
 quality, 1554
 rock lithologies, 1185
 sandstone layers, 1117
 saturation tool, 522
 sequence stratigraphy, 7–9
 siliciclastic reservoirs, 16–23
 simulations, 875
 stratigraphy, 1
 temperature, 685–686
 traps, 1–4
 zonation layering, 433–434
 reservoir simulation
 applications, 1461–1465
 gridding in, 1415–1422
 high-performance computing and, 1456–1461
 linear solver, 1407, 1411–1415

- models for application and development, 1399–1411
 - pressure/volume/temperature (PVT) treatment, 1449–1456
 - simulation of geomechanics, 1444–1449
 - streamline simulation, 1437–1444
 - upscaling of grid properties, 1422–1436
 - reservoir simulation applications
 - faults in reservoir flow model, inclusion of, 1462
 - geological model, 1461–1462
 - history matching and production forecasting, 1464–1465
 - integrated reservoir and surface facilities models, 1463–1464
 - larger model use, 1464
 - pseudofunctions for multiphase flow and gridding techniques, 1463
 - simulation of multiple reservoirs, 1464
 - simulation of nonconventional and intelligent wells, 1463
 - upscaling geological model, 1462
 - reservoir simulation high-performance computation
 - application of parallel computing, 1460
 - characteristics of, 1457
 - explosion of data and chasm of scale, 1456–1457
 - parallel computers and message-passing interface, 1459–1460
 - parallel linear-equation solver, 1458–1459
 - parallel reservoir simulator, 1457–1458
 - reservoir simulation models
 - advances in model formulations, 1405–1406
 - Cartesian grids and reservoir definition, 1407–1409
 - generalized model, 1401–1402
 - linear solver, 1407
 - model formulations, 1402–1405
 - Newton iteration method, 1043, 1402
 - Newton-Raphson method, 1401–1402
 - perpendicular bisector (PEBI) method, 1420
 - SPE Comparative Solution Project problems, 1400
 - stable timestep and switching criteria, 1406–1407
 - residual oil saturation (S_{or}), 615, 1048–1050, 1081
 - in Leduc miscible pilot, 677–678
 - residual oil (S_{xo}) calculation, 331–333
 - residue gas stream, 1132
 - resin(s), 1240
 - conformance fluid-shutoff treatments, 1247
 - fluid-shutoff treatments, 1244–1245
 - polymerization reaction, 1244
 - squeeze treatments, 1244
 - resistance temperature detectors (RTDs), 692
 - resistivity imaging
 - AIT images, 38
 - ARI images, 137–138
 - microresistivity images, 137
 - resistivity index (I_R), 427, 456–457
 - resistivity logging, 428, 453
 - Earth resistivity, 89–90
 - electrode resistivity devices, 91–104
 - environment, 90–91
 - formation-resistivity determination, 135
 - induction logging, 104–117
 - laterolog and induction logging tools, 130–132
 - LWD induction tools, 117–130
 - microresistivity logs, 132–135
 - S_w values, 470
 - traditional R_t methods, 135–139
 - resistivity-ratio methods, 150
 - resistivity-vs.-porosity crossplots, 146–148
 - resonant-frequency analysis/measurements, 194–195
 - retrogradational cycles, 8–9
 - retrograde-condensate reservoirs, 1030–1032
 - Reverse Cuthill-McKee (RCMK), 1415
 - reverse vertical seismic profiling (RVSP), 65–66
 - Reynolds number, 759
 - RFT. See repeat formation tester
 - RF-tipping pulse, correction for, 339–340
 - RMLT. See Reservoir Management Leadership Team
 - rock-cutting samples, mud-logging services and, 372
 - rock expansivity, 907–908
 - rock-fabric facies, 22–23
 - rock-fabric reservoir model, 23
 - rock/fluid expansion/compression terms, 1550
 - rock-pore distribution, 203
 - ROR. See rate of return
 - routine-core-analysis, 425–426, 477
 - permeability data, 429
 - porosity measurements, 428
 - routine OBM core S_w data
 - with P_c/S_w data, 467–468
 - with resistivity-log data, 468
 - R_f -based S_w calculations, strengths and weaknesses of, 464
 - R_t methods, traditional, 135
 - invasion parameters, inversion for, 136–137
 - LWD resistivity images, 138–139
 - resistivity imaging, 137–138
 - R_t/S_w models, 461
 - rudstone, 10–11
 - running horizontal well tests, 828. See also horizontal wells
 - R_{wa} comparison
 - flushed-zone method, 150–151
 - invaded-zone method, 151–152
 - resistivity-ratio methods, 150
 - R_{xo}/R_t quicklook method, 152–154
- S**
- SABS. See U.S. SEC Staff Accounting Bulletins
 - Sadlerochit reservoir, 433, 474–476
 - safety and environmental tips, production logging and, 498–499
 - SAGA. See surfactant-alternating-gas-ameliorated saline water, 1038
 - San Andres carbonate reservoirs, 1062, 1067
 - sands and shales, layer thickness determination and, 78–79
 - sandstone
 - deposits, 1115
 - formations, 1217, 1239
 - photomicrograph and water/oil relative permeability for, 1042–1044
 - waterflood with low permeability, 1615–1616
 - sandstone reservoirs, 1062, 1075, 1092, 1117, 1175
 - and gas and water injection, 1611–1612
 - polymer injection project, 1617
 - solution-gas drive and water- and gas-injection project, 1616
 - strong waterdrive and crestal gas injection, 1612–1613
 - sapphire transducers, 690
 - saturated oil reservoirs, 928
 - SCAL database, 441, 452, 454, 458
 - Schlumberger design, for quartz pressure transducer, 691
 - Schlumberger-Doll-Research (SDR) model, 321–322
 - Schlumberger Flowview, 522–523
 - Schlumberger NML tool, 290–291
 - Schlumberger's tool, 310–311
 - ultrasonic transducers and, 394
 - scintillation crystal detector, 521
 - scintillator crystal, 262
 - screen factor (SF) device, 1171
 - seals, 2, 4–5
 - and flow barriers, 6
 - lithologies, 5–6
 - SEC. See U.S. Securities and Exchange Commission
 - secondary gas caps, 901
 - sedimentology, 18

- Segmented Bond Tool (SBT™), 394
- segregating gas cap, 902, 921, 925
- seismic attributes, 37, 41–42
- seismic data
 - acquisition sources
 - attribute applications, 37, 41–42
 - body waves and surface waves, 33–35
 - calibrating seismic image time to depth, 62–65
 - complex seismic trace, 37–39
 - crosswell seismic profiling, 65–68
 - 3D seismic survey design, 52–59
 - imaging reservoir targets, 45–52
 - impedance, 35–36
 - impulsive sources, 26
 - instantaneous phase and frequency calculations, 39–41
 - interpretation, 42–43
 - marine air guns, 27–31
 - reflection coefficients, 35–37
 - sensors, 30–32
 - shear wave sources, 27
 - structural interpretation, 43–45
 - uses of, 25
 - vertical seismic profiling, 59–62
 - vibrators, 26–27
 - wave propagation, 32–33
- 3D-seismic data, 487
- seismic image time to depth calibration, 62–65
- seismic impedance, 35–36
- seismic interpretation, 42–43
- 3D seismic methods, 1504
- seismic-reflection exploration methods, 176
- seismic reflectivity parameters, 36
- seismic sensors, 30–32
- seismic surface-wave noise mode, particle motions
 - produced by, 34
- 3D-seismic surveys, 452
- 4D-seismic technique, 1081–1082
- seismic wave propagation, 32–33
- seismic-while-drilling techniques, 208
- selected field projects, expected incremental recovery in, 1302. *See also* miscible processes
- selective dissolution, 15
- semblance and *N*th-root stacking, 215
- semilog analysis techniques, 798, 804
- semilog coordinates, 811
- sensitivity analysis evaluation method, 1575
- SEOR project screening criteria, 1320
- sequence stratigraphy
 - model, 22
 - of reservoir, 7–9
- sequential-fluid injection mode, 1212
- SFL device, 99–100, 104, 108, 123, 153
- SGIP. *See* solution gas initially in place
- shale-baseline shifts, 143–144
- shale porosity, effects of pressure on, 210
- shale volume, evaluation of, 432–433
- shaly formations, 154
 - dispersed clay, 156–158
 - laminated sand/shale-simplified model, 155–156
 - total shale relationship, 158
- shaly-sand models, 462
- shear-non-rehealing gel, 1198
- shear-thinning fluids, 1210, 1235, 1237
- shear-thinning viscosity, 1169
- shear-wave, 170
 - amplitudes, 191, 210
 - birefringence, 220
 - parameters, 220
 - sources, 27
 - velocity, 173
 - vibrator, 27
- shelf systems, 20
- shifted-spectrum method (SSM), 328
- shore-zone systems, 20
- shoulder-bed effect, 97, 109
- shut-in and behind-pipe petroleum reserves, 1484
- shut-in injection well, 513
- shut-in logs, 540
- shut-in time, 1211
- shut-in tubing pressure, 1525
- shut-in wellhead pressures, 1560
- signal-to-noise ratio (S/N), 26–27, 180–181, 291, 296, 303, 307, 309, 327, 343
- siliciclastic reservoir, 16–23
 - classification of siliciclastic rocks in, 16–17
 - clay habit in, 17–18
 - depositional environments, 18–20
 - diagenetic environments, 20–21
 - porosity and permeability of, 16
 - reservoir models, 21–23
 - sandstone depositional systems, 18–19
 - texture, porosity, and permeability, 22
- siliciclastic rocks, petrophysical properties of, 23
- siliciclastic stratigraphy, 8
- simulation theory, 631–632, 634. *See also* SWCT test simulation
- Simultaneous Acoustic and Resistivity Imager (STAR™), 137, 406
- single-column gas chromatograph, 364
- single-fluid
 - aqueous gel, 1223
 - injection mode, 1211
- single-log interpretation, 249–253. *See also* nuclear logging
- single-phase fluid, 728
- single-phase sensitivity, 532
- single-point tests, 839
- single pressure-connected reservoir, 1554
- single-stage acid placement, 567
- single-stage fracture placement, 567–568
- single-well chemical tracer (SWCT) test. *See* SWCT test
- single-well data, 1524
- single-well (one-spot) IOR pilot, 639–642
- sinker bar weight, 499–501
- SITP. *See* shut-in tubing pressure
- skin equation, 818
- skin factor
 - altered zone and, 720
 - deviated well, 753
 - dimensionless, 742
 - two-region reservoir model, 750
- slickline operations, in bottomhole conveyance of gauges, 694
- slope and basin systems, 20
- slug tracking, 509
- small-scale drillstem testing, 712
- smectites, 17, 431–433, 442–444
- Snell's law, 168, 173
- SNUPAR program, 275
- Soave-Redlich-Kwong, EOS petroleum engineering
 - applications, 993
- 1997 Society of Petroleum Engineers/World Petroleum Congress, 1480
 - classifications of reserves, 1481
 - definition of reserves, 1481–1485
 - deterministic calculation procedures of, 1489
 - significance of, 1487
- Society of Petroleum Evaluation Engineers, 1571
- solid-earth seismology, 220
- solid fillers, 1240, 1243
- solution-gas-drive reservoir, 902, 914–915

- solution-gas drives, 910–920
 - field examples, 913–915
 - key characteristics of each stage production, 910–911
 - material-balance analysis, 915–918
 - performance, 911–913
 - production, stages of, 910–911
- solution gas initially in place, 1511
- solvent flood behavior prediction
 - fine-grid reference models, 1285–1287
 - full-field behavior, 1287
 - permeability relations and pseudoproperties, 1287–1288
 - segment models, 1288–1290
 - solvent trapping and solvent relative permeability hysteresis, 1282–1285
 - streamtube and streamline models, 1290–1292
- sonic logs, 428
- sonic vibration, 172
- SP anomalies
 - highly resistive formations, 142–143
 - invasion-related, 144
 - noisy SP logs, 144–145
 - shale-baseline shifts, 143–144
- SP curve, shape of, 142
- special core analysis (SCAL), 423, 426–429, 433, 441, 472, 477
- spectral BVI (SBVI) model, 318–319
- spectral gamma ray log, 261–262
- spectral natural gamma ray systems, 263
- SPEE. *See* Society of Petroleum Evaluation Engineers
- SPEE FMV document, 1571
- 1997 SPE/WPC. *See* 1997 Society of Petroleum Engineers/World Petroleum Congress
- 1997 SPE/WPC and 1978 U.S. SEC definitions comparison
 - economic conditions and development status, 1487–1488
 - enhanced-recovery reserves, 1489
 - flow testing requirement and reservoir areal extent of, 1488–1489
 - reasonable certainty and known accumulations, 1487
- spherical flow, 730, 769
- spherically focused log (SFL), 90
- spill point, 2–3
- spin-echo technique, 295
- SP log (*see also* resistivity logging)
 - origin of, 139–141
 - and permeability, 141
 - static, 141–145
- spontaneous ignition, 1387
- spontaneous-potential (SP) log, 79, 453
- Squirrel-sandstone, oil and water relative permeabilities for, 1048
- stabilized C method, 866, 869
- stacking bins, in 3D seismic survey design, 52–54
- stacking fold, in 3D seismic survey design, 55–59
- standard PVT parameters
 - methods to calculate, 904–905
 - of volatile and black oil determination, 904
- standard PVT properties
 - as a function of pressure for Louisiana volatile oil, 909
 - as a function of pressure for a west Texas black oil, 905
- Standing's correlation, 1508
- static bulk foam, 1231
- static nonflowing foam, 1225
- static pressure measurements, 699–701
 - from buildup tests, 699
 - from productivity index, 700–701
- static SP (SSP)
 - determination of, 141–142
 - SP anomalies, 142–145
 - SP curve, shape of, 142
- station spacings, in 3D seismic survey design, 54–55
- statistical correlations, 1554
- steady-shear viscometers, 1171
- steady-state foam flow, 1232
- steady-state radial flow equation, 720
- steam
 - flooding, 1227, 1236
 - foams, 1236
 - plateau, 1368–1369, 1373, 1379–1383, 1394
 - saturated, properties of, 1309–1311
 - steam specific volume vs. saturation pressure, 1311
 - stimulated injection wells, 1246
 - zone shape/thickness, equation, 1315
- steam enhanced oil recovery (SEOR), 1309
- steamflood design, 1319–1324
 - analogy, 1321–1322
 - recovery mechanisms, 1322–1324
 - screening criteria for steamflood candidates, 1319–1321
- steamflood injection wells, 1246
- steam injection rates, calculations, gravity drainage models
 - Neuman method, 1326–1328
 - Vogel method, 1328–1329
- steam zone growth
 - bypass, 1315–1317
 - combination, 1317–1319
 - viscous displacement, 1314–1315
- steeply dipping sandstone reservoir with gravity stable miscible project, 1615
- Stoneley wave(s), 168, 171, 173
 - amplitude, 196, 224
 - attenuation, 210
 - data, 180
 - reflection, 228
 - velocity, 224
 - velocity dispersion, 171
- storativity ratio, 797, 800
- strain pressure transducer, 690
- strandplain sand, 20
- stratal-bounded analysis window, 51–52
- stratal-surface concept, 51–52
- stratified systems
 - with communicating layers and assumed vertical equilibrium, 1071–1072
 - with noncommunicating layers, 1067
- stratigraphic traps, 2–3
- streamline-based flow simulation
 - applicability of, 1437
 - applications of streamlines, 1442–1443
 - computational efficiency of, 1441–1442
 - governing IMPES equations, 1438
 - novel data produced by, 1442
 - solution to transport equation, 1438–1441
 - timestepping, 1439
- streamtube waterflood calculations, 1059–1060, 1063–1064
- stress-induced anisotropy, 220
- stripping compositional effects, 1114
- structural interpretation, 43–45
- structural traps, 2–3
- styrene-butadiene block copolymer resin, 1246
- subsea acquisition, of pressure and temperature, 698–699
- successive substitution (SS), 1451
- sulfate-reducing bacteria, 1079
- sum-of-fluids porosity measurements, 442
- supercritical gas, 1225
- superposition, principle of, 731
- surface acquisition
 - of downhole data, 698
 - system, 172
- surface and volume ratio (S/V), 300–303, 319
- surface-data-acquisition system, 179
- surface gas injection, 910

- surface-injection equipment, 1177
 - surface mapping, 3
 - surface readout vs. downhole recording, 693
 - surface relaxation, 299–302
 - surface seismic maps, 176
 - surface seismic methods, 168
 - surface shut-in vs. downhole shut-in, 693
 - surface water injection, 910
 - surfactant adsorption/retention, 1233
 - surfactant-alternating-gas-ameliorated, 1234
 - surfactant-alternating-gas foam, 1236
 - surfactant molecule, 1226–1227
 - surfactant slug, 1236
 - Susceptibility Measurement Tool (SUMT™), 414–415
 - Swanson River Field (Alaska), 1139
 - SWCT S_{or} tests, 618–643
 - for connate water, 644
 - data interpretation, 629–632
 - design, 625–628
 - ester distribution, between oil and water in pore in, 623
 - features, 620–621
 - field procedures, 628–629
 - gas-saturation testing, 644–646
 - injection of ester tracer and push volume, 619
 - nonideal simulation, 634–635
 - parameters using simulator, 632–634
 - procedure, 624–625
 - production period, 620–621
 - quantitative working, 621–624
 - shut-in (reaction) period, 619–620
 - single-well IOR pilot project, 639–642
 - tracer-concentration profiles, 620, 622
 - working of, 618–620
 - SWCT S_{or} test design, 625–628
 - formation-water salinity, 628
 - oil cut of test well, 626
 - production rate, 627–628
 - reservoir lithology, 626–627
 - reservoir temperature, 626
 - test-interval size and average porosity, 628
 - SWCT S_{or} test field measurements, 643–646
 - connate water saturation testing, 643–644
 - gas saturation testing, 644–646
 - SWCT test (see also SWCT S_{or} tests)
 - candidate, 618
 - features, 620–621
 - field setup for production step, 629
 - history, 615
 - injection step field setup, 629
 - for in-situ evaluation of hydrocarbon-miscible IOR, 642–643
 - pressure difference effects on, 635
 - S_{or} measurement, 615–617
 - S_{wc} measurement, 617–618
 - SWCT S_{or} tests, 618–643
 - SWCT test simulation
 - in carbonate formation, 638–639
 - in dual-porosity media, 636–638
 - in layered formation, 635–636
 - nonideal, 634–635
 - parameters for, 632–634
 - S_w data, integration of
 - adjustments to, 468–469
 - core, total, and effective systems compatibility, 469
 - P_c/S_w data, resistivity-log data with, 467
 - routine OBM core S_w data, 467–468
 - sweep efficiency
 - methods for evaluating, 1124
 - in uniform linear systems, 1070, 1073
 - sweep-improvement treatment evaluations, 652
 - swelling compositional effects, 1113
 - swelling effect, 1114
 - S_w physical-model equations, 453
 - S_w techniques, applications of, 461–467
 - S_w values
 - P_c -derived, 470–471
 - resistivity logs, 470
 - synthetic oil-based mud (SOBM), 311, 342
 - synthetic seismograms, 61–62, 207
 - system geometry, 797
 - system noise (ringing), 339
- T**
- tank balance, performance prediction to ISC, 1385
 - taxation value, 1573
 - T_2 decay, 301–303
 - T_2 distribution, 304–305
 - tectonic fracture development, 825
 - tectonic processes/stresses, 220
 - televviewer-type devices, 183
 - temperature and noise-logging survey, 607
 - temperature gauges, metrology of, 688–689
 - temperature log, 535–536
 - temperature-logging tool, 503–508
 - temperature profiles
 - detecting cement tops, 714
 - in production and injection wells, 714–715
 - recommendations for, 714
 - vertical extent of fracturing and detecting lost circulation, 715
 - temperature sensors, 691–692
 - mechanical transducers, 691
 - resistance temperature detectors, 692
 - thermistors, 692
 - Tensleep Sandstone oil-wet rock, 1046
 - tensor methods, cell permeability and, 1423, 1429
 - tertiary flooding oil-recovery drive fluids, 1151
 - tertiary-mode flooding, 1150
 - Texas San Andres oil reservoir, 477
 - thermal conductivity, 1313
 - gas detector, 365
 - thermal conductivity detector (TCD), 362
 - thermal cracking, 1368, 1370
 - thermal diffusivity, 1314
 - thermal enhanced oil recovery (TEOR), 1309
 - thermal stabilizers, 1177
 - thermistors, 692
 - thermosetting resins, 1244
 - thin-bed target, 49–52
 - thin-film liquid lamellae, 1248
 - thin-film transducer, 690
 - thin liquid films, 1225
 - thin oil columns, operating procedures for, 1143
 - Thomas-Stieber method, 82–83
 - three-axis magnetometer, 382
 - three-dimensional seismic survey design, 52–59
 - stacking bins, 52–54
 - stacking fold, 55–59
 - station spacings, 54–55
 - three-layer multirate test, 710–711
 - through-casing acoustic measurements, 179–180
 - Through-Casing Resistivity (TCR) tool, 102
 - thrust-fault structural trap, 3
 - tidal-dominated delta system, 20
 - tight gas reservoirs, 1542–1544
 - time-domain analysis (TDA), 323, 326
 - time-of-flight (TOF), 1438
 - time-stratigraphic unit, 8
 - Timur equation, 471

- tool selection tables, production logging and, 550–551
 - acid, fracture-proppant and, 567–568
 - annular pressure, crossflow behind casing and, 563–566
 - casing inspection, 560–562
 - cement placement, 556–559
 - confinement demonstration, 569–571, 576, 578
 - corrosion detection, 612–614
 - crossflow detection behind pipe, 611
 - detection of holes or parting, 614
 - drillpipe manipulation and construction problems, 552
 - injection profile determination, 572–575, 577, 579–580
 - injection well, 569–575
 - with screen or slotted linear, 576–577
 - with tubing across perforations, 578–580
 - location of annular pressure source, 611
 - lost returns, 553
 - newly cased, unperforated well, 556–566
 - production wells and, 581–611
 - tracking single-phase production, 581–585, 594, 600, 607
 - tracking three-phase production, 592–593, 598–599, 605–606, 610
 - tracking two-phase production, 586–591, 595–597, 601–604, 608–609
 - underground flow, 554–555
 - well being stimulated, fractured, or gravel-packed, 567–568
 - well down for tubing or casing inspection, 612–614
 - well still being drilled, 552–555
 - tornado-chart calculations, 251
 - total and effective porosity
 - core analysis, 442–444
 - log analysis, 444
 - total-fluid-shutoff gel treatments, 1192
 - total gas analyzer (TGA), 360–361
 - total hydrocarbon analyzer (THA), 360
 - total methane equivalents (TME), 360
 - total shale relationship, 158
 - tough logging conditions (TLC) logging, 97
 - toxic heavy-metal ions, 1151
 - tracer flow, in porous reservoir rock, 659–666
 - biodegradation, 665–666
 - flow equations, 663–664
 - ion exchange, 666
 - partition coefficient, 662–663
 - residual-oil measurements, 664–665
 - retention, by partitioning between phases, 659–665
 - tracers
 - active, 651
 - analysis, sample collection for, 668–670
 - application in well-to-well test, 651–659
 - assumptions regarding, 632
 - chemical gas tracers, 658–659
 - chemical water, 655–656
 - in enriched-gas injection, 676–677
 - flow in porous reservoir rock, 659–666
 - for gas injection, 676
 - health, safety, and environment constraints, 659
 - passive, 651–653
 - program timing, 666–667
 - radioactive gas tracers, 656–658
 - radioactive water tracers, 652–655
 - types of, 651–659
 - tracer tests
 - field data interpretation, 670–675
 - field experience, 675–678
 - planning and design of, 666–670
 - tracer test planning and design, 666–670
 - field-test, 667–668
 - sample collection, 668–670
 - timing for, 666–667
 - transgression, 8–9
 - transgressive system's track (TST), 8–9
 - transient flow equation, 841
 - transient matrix flow model, 802
 - transit-time measurements, 218
 - transmissibility value, 1416, 1418
 - transmitter-to-receiver spacing (TR), 172, 176
 - traps, 1–4. *See also* specific traps
 - travel-time (TT) measurements, 189
 - triangular probability distribution, 1553
 - triaxial coordinate system, 223
 - tritiated water (HTO), 653–655
 - tritium, 85, 653, 657, 659
 - true vertical depth (TVD), for geological mapping, 385
 - tube (Stoneley) waves, 168
 - turbulent flow effects, 722, 841
 - T_1 -weighted mechanism. *See* dual- T_w acquisition
 - two-coil induction array, 106
 - two-phase flow, 1110
 - two-phase gas FVF, 907
 - two-phase reservoir simulation, 1131
 - type curves, 739
 - analysis technique, 801
 - matching, 747
- U**
- ultradeep perforation techniques, 1221
 - ultra low hydrolysis, 1163, 1197
 - Ultrasonic Borehole Imager (UBI™), 400–401
 - Ultrasonic Corrosion Imager (UCI™), 392
 - Ultrasonic Imager (USI™), 394
 - ultrasonic pressure pulses, 183
 - ultrasonic radial-cement-evaluation devices, 194
 - ultrasonic reflection (pulse/echo) acoustic devices, 182
 - ultrasonic tools, 392, 394
 - interpretation, 194
 - unbalanced-formation-stress components, 223
 - unconformity and buried-hill trap, 3
 - undersaturated oil reservoirs, 748, 909
 - undip sedimentary trap, 3–4
 - unfocused gamma ray (gravel-pack) density logger, 518–521
 - uniaxial compressive stress, 212
 - uniform linear systems, sweep efficiency in, 1070, 1073
 - unitization, 1574
 - Universal Transverse Mercator (UTM) geographic coordinate system, 379
 - unproved petroleum reserves
 - possible, 1484
 - probable, 1483
 - unsteady-state flow, 723
 - unsteady-state linear flow, in unbounded reservoir, 730
 - U.S. Acquisition Economics and federal income taxes, 1589–1591
 - U.S. Bureau of Mines (USBM) Amott wettability index, 1047
 - U.S. federal tax code, 1572
 - U.S. Polymer-Flood Project Production Survey, 1183
 - U.S. SEC Staff Accounting Bulletins, 1486
 - U.S. Securities and Exchange Commission, 1571
 - 1978 U.S. Securities and Exchange Commission (SEC) Oil and Gas Reserves Definitions, 1485–1486
 - UV-fluorescence technique, 371
- V**
- valuation, definition of, 1572
 - value allocation, 1574
 - van der Waals' equation, 993
 - van Everdingen-Hurst (VEH) model, water drive calculations, 942
 - cumulative water influx, 938
 - discretization, 937

- geometries, radial- and linear-flow systems of, 936
 - infinite and finite, radial aquifer, 939–940
 - linear aquifer, 941–942
 - superposition theorem application, 936
 - variable density (VDL), 186, 311, 336.
 - See also microseismograms
 - VDL transmitter, 194
 - velocity approach, 571
 - velocity/porosity logging, 176
 - velocity-porosity predictive model, 203
 - velocity-shot survey, 509–511
 - velocity tomography, 65–67
 - vertical boundary, 813
 - vertical fluid communication, 1153
 - vertical gravity drainage, 1143
 - gas displacement, 1120–1122
 - vertical interference testing, packer and multiple-probe tests for, 712–713
 - vertical permeability, 879, 1117
 - variation, 1067–1069
 - vertical resolution, of NMR-logging tools, 343
 - vertical seismic profiling (VSP), 25, 59–66, 207
 - based calibration of thin-bed stratigraphy, 63–64
 - depth-to-time calibration, 62–63
 - source-receiver geometry used in, 59–60
 - synthetic seismograms, 61–62
 - vertical sweep efficiency, 1124
 - vertical-to-horizontal-permeability ratio, 753
 - vibrators, 26–27
 - Vibroseis™ energy sources, 26
 - virgin reservoirs, 703–704
 - pressure gradients in well drilled in, 683–684
 - viscosity, of fluid phase, 1050–1051, 1054, 1058–1059
 - enhancing agents, 1162, 1168
 - enhancing polymers, 1247
 - evaluation, 333–335
 - voidage replacement, 1037, 1061, 1080, 1083
 - volatile- and black-oil fluid, characteristics of, 896–898
 - volatile-oil reservoirs, 897
 - material-balance analysis of, 897, 918–920
 - producing GORs, 913
 - volatile oils, 896, 1511
 - volatilized-oil/gas ratio, 896, 904, 918
 - voltage-frequency circuit, 387
 - volumes and recovery
 - determining average reservoir pressure, 1015–1017
 - gas in place, 1014–1015
 - highly compressive reservoirs, 1018–1020
 - pressure maintenance and cycling operations, 1024–1025
 - retrograde-condensate reservoirs, 1024
 - volumetric reservoirs, 1017–1018
 - waterdrive reservoirs, 1020–1024
 - volumetric heat capacity, 1313
 - volumetric reserves classification, 1515
 - volumetric sweep, 651
 - VTI anisotropy, 220
 - vugular-porosity conformance, 1155
- W**
- WACC. See weighted average cost of capital
 - wackestone, 11–14
 - WAG. See water alternating gas
 - wait time (T_w), 296
 - wall-exclusion effect, 1174
 - Walsh-Towler algorithm, characterization of volatile oil, 905
 - Warren and Root's model, 798
 - water/air ratio, 1369
 - water alternating gas, 1107, 1215, 1262
 - flooding operation, 1239
 - injection, 1142, 1236
 - injection program, 670, 675
 - injector 939, 1300
 - process, 1617
 - ratio, 1292, 1297–1298
 - water and gas coning, 961–973
 - additional measures to control, 970
 - Chierici correlation, 965–968
 - computing critical rate and optimum perforation length, 971–972
 - critical coning rate (q_c), 964
 - Kozeny expression, 969
 - partially penetrating wells, 968–970
 - prevent coning in bottom-water, gas-cap reservoir, 972–973
 - producing well, 961–962
 - Schols' correlation, 964–965
 - variables affecting coning, 970
 - water and gas tracer
 - in El Furrial field, 676
 - injection in fractured reservoir, 675
 - water-based mud (WBM), 113, 333, 424, 426, 451
 - water-bearing reservoirs, 899–900
 - geological strata, 1212
 - zones, 185
 - water channeling, problem and tools, 604, 610
 - waterdrive petroleum reservoirs, 762, 900
 - alternative material-balance methods, 951–952
 - and aquifer classification, 931–932
 - aquifer performance, 945–947
 - diagnosis of, 932
 - and fluid properties, 945
 - GOR, gas saturation, oil recovery and pressure histories, 933
 - material-balance analysis, 932, 947–952
 - performance, 932–935
 - performance data, 944
 - phases of assessment, 931
 - van Everdingen-Hurst (VEH) model, 935–942
 - water-influx mechanism, 931, 933
 - water-influx effect on pressure vs. percent OOIP recovered, 933
 - water-influx histories, comparison of, 949–950
 - water-influx models, 935–936, 942–944
 - water-encroachment treatments, 1246
 - water expansivity calculation, 917
 - waterflood
 - displacement, in five-spot pattern (see waterflood pattern)
 - miscible EOR project, 1614
 - mobility ratio, 1166
 - oil recovery, 1039, 1050, 1060
 - performance, viscous and capillary forces, 1050
 - and sandstone field, 1614
 - waterflood design considerations, 1072–1074
 - injection-water-sensitivity studies, 1074–1076
 - injection wells, injectivity and allocation approaches, 1076
 - pilot waterflooding, 1078
 - produced fluids, surface facilities for, 1079–1080
 - production wells, 1078
 - water-injection surface facilities, 1079
 - waterflood field case studies, 1087
 - Ekofisk (North Sea), 1088
 - Kirkuk oil field (Iraq), 1094–1095
 - Kuparuk River oil field (Alaska North Slope), 1092–1094
 - West Texas carbonate waterfloods, 1094
 - Wilmington oil field (California), 1089–1092
 - waterflood monitoring techniques
 - data acquisition–routine-data gathering, 1080
 - infill and observation wells and 4D-seismic data, 1081
 - log(WOR) vs. cumulative-oil-production plots, and decline curves, 1082–1084

1650 Subject Index

- numerical reservoir simulator, 1085
- X-plot, 1082–1084
- waterflood pattern, 1059–1061, 1077
 - and well-spacing considerations, 1061–1063
- waterflood technology
 - 2D-areal calculation of, 1058
 - injector/producer-pattern layout of, 1061, 1073
 - limitations of, 1040
 - production response of, 1085
 - reservoir-geology considerations in, 1055–1057
 - saturation profile during, 1040, 1052
 - in U.S., 1038
 - X-ray shadowgraphs of, 1061
- water flow detection, underground, 555
- water influx, 910 (see also waterdrive petroleum reservoirs)
 - constant, 1550
 - history matching for, 944
 - material balance, estimation with, 952–953
 - predicting history for, 957, 960
 - water-influx parameters and OOIP determination, 952–956
- water-injection
 - cooling effect of, 1077
 - in oil production, 1038
 - sensitivity studies, 1074
 - sources, 1078
 - surface facilities for, 1079
 - well fracturing, 1076
 - well bubble map, 1082–1083
- water-intolerant epoxy resin, 1244
- water/oil
 - mobility ratio, 1546
 - problem, 1409
 - saturation distribution, 1045–1046
- water/oil contact (WOC) in waterdrive reservoir, 901
- water/oil displacement process, 1040
 - gravity in, role of, 1069
 - for homogeneous linear systems, 1052
 - vertical displacement characteristics of, 1066, 1071
- water/oil ratio (WOR), 1157, 1269
- water production (W_p), 910
- water-reactive diverting agents, 1221
- water saturation (S_w) determination (see also S_w data, integration of; S_w values; S_w techniques, applications of)
 - approaches for, 461–467
 - calculation techniques for, 452–453
 - clean formations, 145–146
 - data availability and data quality, 453–461
 - methods, 467–469
 - microresistivity-vs.-porosity crossplots, 148–150
 - resistivity-vs.-porosity crossplots, 146–148
 - uncertainties, 469–471
- water-shutoff gels, 1157
 - treatment, 1211–1212
- water-soluble polymer, 1237
- water source location behind casing, problems
 - activated-oxygen survey, 594
 - density and gravel-pack and temperature survey, 594
 - flowing fluid-capacitance survey for oil detection, 591–592
- water-swelling polymer, 1242
- water-wet reservoir matrix rock, 1330
- water-wet reservoirs, 342, 706, 708
- water-wet rock, 1041, 1051
 - capillary pressure characteristics of, 1043, 1045
- wave-delta system, 20
- wave-separation processing, 224
- Waxman-Smits relationship, 158–159
- Waxman-Smits shaly-sand model, 481
- Waxman-Smits-Thomas (WST) model, 454, 457–458, 463
- WBM routine-core-analysis data, 426
- WEC. See Well Evaluation Conference
- weighted average cost of capital, 1589
- Welge equation, 1108
- Welge technique, 1106
- well(s)
 - casing wear bend/collapse, 561–562
 - category, 549–550 (see also production-logging application tables)
 - circulation lost returns, 553
 - damage, altered zone and skin effect, 748–750
 - drainage patterns, 1558
 - hydraulic fracture, 747, 755–756, 766, 785
 - hydraulic fracture conductivity, 721, 767
 - placement and density, 1602
 - production, economic limit, 1523–1524
 - profile production, 581–586
- wellbore
 - geological/petrophysical information and, 372
 - hydraulics, 983
 - hydrostatic pressure, 1240
 - unloading, 728, 735
- wellbore, geometry and integrity, 379
 - balanced tangential method and, 384
 - casing-collar locators, 388
 - casing inspection logs, 388–392
 - cement-evaluation logs, 392–397
 - gyroscope surveys, 381
 - magnetic survey, 380–381
 - minimum curvature method, 385
 - openhole caliper logs, 387–388
 - simultaneous casing inspection and cement evaluation, 397
- wellbore storage (WBS), 727, 744, 773
 - coefficient, 742, 794
 - distortion, 759, 771
 - effects, 785, 840
- Well Evaluation Conference, 1495
- wellhead environments, 698–699
 - subsea acquisition of pressure and temperature, 698–699
 - surface acquisition of downhole data, 698
- wellhead injection pressure, 1079
- well in virgin reservoir, pressure gradients in, 683–684
- well logging, specialized
 - borehole gravimetry, 408–412
 - borehole imaging, 397–408
 - downhole magnetics, 412–414
 - wellbore, geometry and integrity of, 379–397
- well logs uses and interpretation
 - R_{wa} comparison, 150–152
 - R_{xo}/R , quicklook, 152–154
 - saturation determination, 145–150
- well magnetic stratigraphy (WMS), 414–415
- well performance
 - deliverability testing, 1008–1012
 - drainage shapes, estimation, 1007
 - effects of skin, 1014
 - gas-well deliverability relationships and, 1012–1014
 - ideal gas, steady-state radial-flow equation for, 997
 - near-wellbore phenomena, 1000
 - non-Darcy flow, 1001
 - pressure-transient testing of gas wells, 1008
 - radius of investigation, 1007–1008
 - real-gas potential, 996–998
 - skin, 1000–1001
 - steady-state radial and horizontal liquid and gas flow, basic equations, 996–999
 - transient flow, 1001–1007
- well-test analysis
 - methods of, 792, 839
 - software, 759, 770

well-to-well tracer tests, 624
 tracer application in, 651–659
 value and importance, 651
 West Howard-Glasscock unit oil field, 477–478
 West Texas black oil
 compositional analysis of, 906
 oil and gas viscosities as pressure function, 907
 PVT parameters for, 904–905
 West Texas carbonate waterfloods, 1094
 West Texas Clearfork, 1062
 West Texas intermediate sweet crude prices, 1583
 wet-gas reservoir, 982
 wetness method, 369, 371
 wettability
 mineralogy to, 1042
 of oil/water/solid system, 1040–1042
 wetting-phase saturation, 1231
 Wharton's method, 1497
 Wheatstone Bridge circuit, 362
 Whitney Canyon-Carter Creek Gas Field, 481–483
 Whitson-Torp method, characterization of volatile oil, 905
 whole-core Boyles-law porosity measurements, 442
 Wilcox formation black oil, reservoir and aquifer properties, 955
 Wilmington oil field (California), 1089–1092
 injection and production wells, 1091
 ultimate-recovery factors for, 1092
 wireless transmission, 694
 wireline formation testers, 86, 1503
 wireline logging correlations, 78, 86
 wireline pressure testing, 695, 697
 wireline pressure transient tests, 711–713
 packer and multiple-probe tests for vertical interference testing, 712
 packer probe tests, 712
 wireline-tool designs, 308–309
 WLFT. *See* wireline formation testers
 world incremental oil production, by gas injection, 1303
 worldwide polymer flood review, 1183
 WST exponents, cation-exchange capacity and, 457–459
 Wyllie equation, 196, 199
 Wyllie time-average formula, 199
 Wyoming polymer floods, 1182
 Wyoming's Big Horn basin, 1213

X

xanthan biopolymer, 1161, 1177
 xanthan gum polymer, 1160
 X-ray diffraction (XRD), 423, 430, 432

Y

y-on-x method, 445

Z

zero-offset VSP, 65
 z-factor, PVT behavior of real gases, 1509
 zones types, starting from injector, 1368